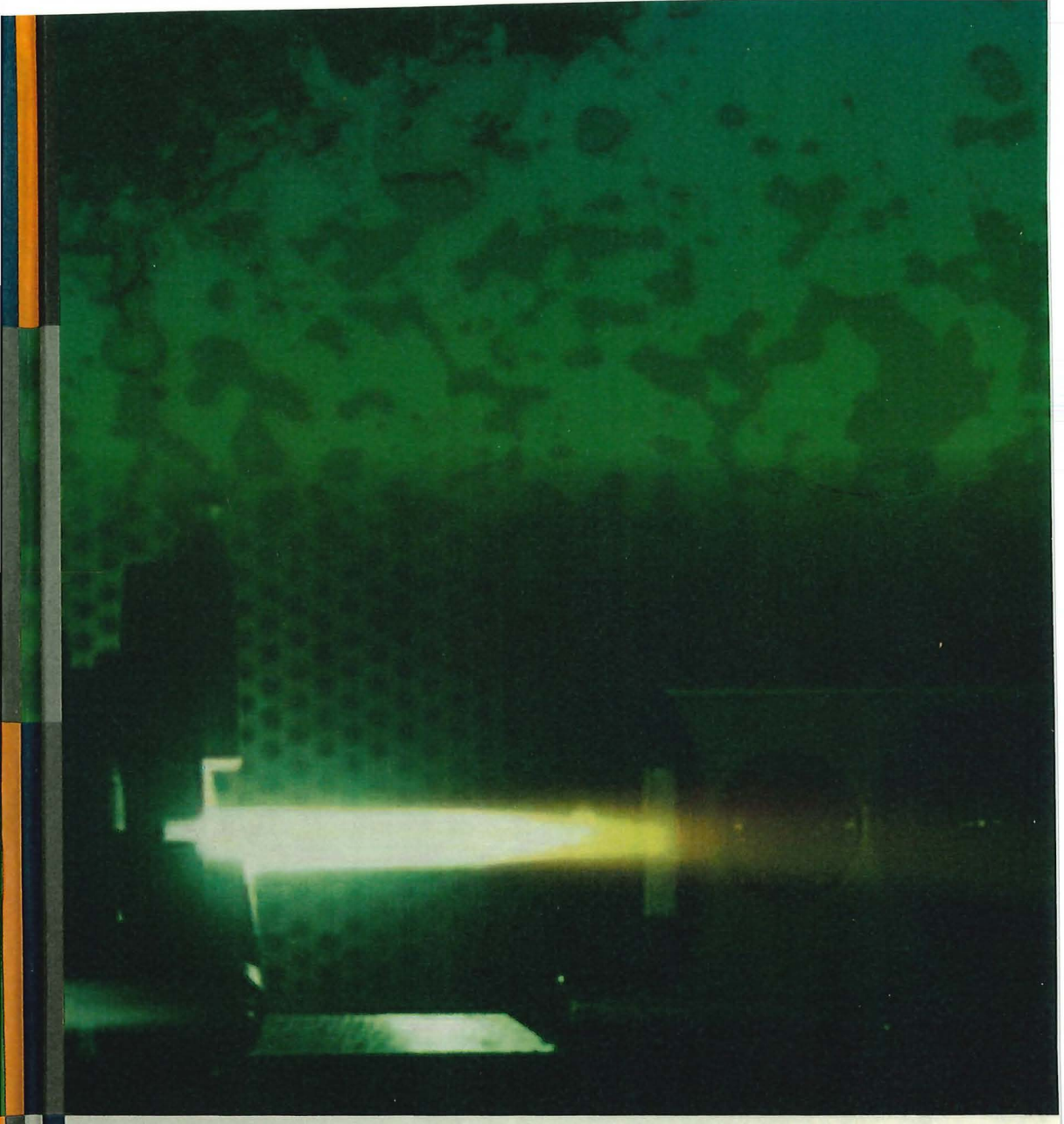

Materials for Advanced Power Engineering 2010

Jacqueline Lecomte-Beckers, Quentin Contrepois, Tilmann Beck und Bernd Kuhn (Hrsg.)

JÜLICH
FORSCHUNGSZENTRUM

Mitglied der Helmholtz-Gemeinschaft

Schriften des Forschungszentrums Jülich
Reihe Energie & Umwelt / Energy & Environment Band / Volume 94

Forschungszentrum Jülich GmbH
Institute of Energy and Climate Research (IEK)
Microstructure and Properties of Material (IEK-2)

Materials for Advanced Power Engineering 2010

Jacqueline Lecomte-Beckers, Quentin Contrepois, Tilmann Beck und Bernd Kuhn (Hrsg.)

Schriften des Forschungszentrums Jülich
Reihe Energie & Umwelt / Energy & Environment Band / Volume 94

ISSN 1866-1793 ISBN 978-3-89336-685-9

Bibliographic information published by the Deutsche Nationalbibliothek.
The Deutsche Nationalbibliothek lists this publication in the Deutsche Nationalbibliografie; detailed bibliographic data are available in the Internet at http://dnb.d-nb.de.

Publisher and Distributor:	Forschungszentrum Jülich GmbH Zentralbibliothek 52425 Jülich Phone +49 (0) 24 61 61-53 68 · Fax +49 (0) 24 61 61-61 03 e-mail: zb-publikation@fz-juelich.de Internet: http://www.fz-juelich.de/zb
Cover Design:	Grafische Medien, Forschungszentrum Jülich GmbH
	Cover photographies courtesy of Forschungszentrum Juelich, IEK-1
Printer:	Druckerei Gehler, Düren-Birkesdorf
Copyright:	Forschungszentrum Jülich 2010

Schriften des Forschungszentrums Jülich
Reihe Energie & Umwelt / Energy & Environment Band / Volume 94

ISSN 1866-1793
ISBN 9978-3-89336-685-9

The complete volume ist freely available on the Internet on the Jülicher Open Access Server (JUWEL) at http://www.fz-juelich.de/zb/juwel

Neither this book nor any part of it may be reproduced or transmitted in any form or by any means, electronic or mechanical, including photocopying, microfilming, and recording, or by any information storage and retrieval system, without permission in writing from the publisher.

Proceedings :

9^{th} Liege Conference : Materials for Advanced Power Engineering 2010

Jacqueline Lecomte-Beckers, Quentin Contrepois,
Tilmann Beck, Bernd Kuhn (Editors)

2010, the 27, 28, 29^{th} of September

Foreword

The 9^{th} Liège Conference on Materials for Advanced Power Engineering presents the results of the materials related COST Actions 536 "Alloy Development for Critical Components of Environmentally Friendly Power Plants" and 538 "High Temperature Plant Lifetime Extension". In addition, the broad field of current materials research perspectives for high efficiency, low- and zero- emission power plants and new energy technologies for the next decades are reported.

Amongst several premises reliable energy supply is one of the key factors the societies of modern industrialized and furthermore ambitious emerging nations are based on. Consequently, future scenarios forecast an increase in the energy demand of the world for the upcoming decades. Along with the predicted moderate economical growth of the OECD countries particularly the strongly growing economies of the non OECD - countries will account for a nearly doubling energy demand until year 2030. Having in mind the environmental impact of energy production and the need to preserve valuable primary resources for future generations, international R&D efforts target more and more towards sustainable energy conversion technologies. Although emerging renewable technologies along with nuclear energy are of great interest, fossil fuels will continue to play a considerable role for future energy security. With the availability of fossil fuels being predicted to shorten and their mining becoming more cost-intensive, and due to the fact that vast amounts of CO_2 are generated in fossil fuel combustion, the efficiency of plant will play a leading role in resource conservation, cost saving and environmental protection.
Improved power plant efficiency implies rising process temperature and pressure resulting in the general requirement for improved materials, manufacturing technologies, components, design codes and service and maintenance rules and standards.

The series of Liège Conferences on Materials for Advanced Power Engineering reflects the requirement for joint material research and component development for critical components of power generation equipment by bringing together material scientists, design engineers, alloy producers and component manufacturers.
To put European efforts into an international framework there are several invited research and review papers covering materials, component and process development in the USA, Japan and India. In addition there are more than 110 contributed papers from 20 countries that are presented as posters at the conference.

The Conference Proceedings are organised as follows:

- Materials for Advanced Steam Power Plants;
- Gas Turbine Materials;
- Materials for Nuclear Fission and Fusion;
- Solid Oxide Fuel Cells;
- Corrosion, Thermomechanical Fatigue and Modelling;
- Zero Emission Power Plants.

The Technical and Editorial Board members would like to express their gratitude to all the members of the COST 536 and COST 538 Management Committees, for their supervision and support to the considerable research and development efforts. Those who were involved in the reviewing of the submitted papers are sincerely thanked for their important contribution to the production of the proceedings.

Forschungszentrum Jülich GmbH

"Forschungszentrum Jülich pursues cutting-edge interdisciplinary research on solving the grand challenges facing society in the fields of health, energy and the environment, and also information technologies. In combination with its two key competencies - physics and supercomputing - work at Jülich focuses on both long-term, fundamental and multidisciplinary contributions to science and technology as well as on specific technological applications. With a staff of about 4400, Jülich - a member of the Helmholtz Association - is one of the largest research centres in Europe. More and more people are living longer and longer. Jülich health research aims to improve the diagnosis and treatment of age-related diseases of the brain using biophysical methods and imaging techniques. Reliably supplying future generations with environmentally friendly, affordable and secure energy is another research priority at Jülich. Photovoltaics, fuel cells, improved power plant technology and nuclear fusion - these are the fields of work for Jülich's energy researchers. Conversely, environmental researchers at Jülich are working on the impacts that technological processes have on the environment and the climate. They are investigating how plants react to changing environmental conditions and how food can be provided for a steadily growing global population. Nanoelectronic engineers investigate and develop new materials and manufacturing processes for the computer generation after next. In doing so they pursue three concepts: exploiting the electron spin as a unit of information, developing innovative architectures using proven semiconductor technology, and linking electronic and biological systems. Of major significance in Jülich is simulation research on one of the largest supercomputers in the world."

University of Liège (ULg)

The University of Liège devotes more than half of its annual budget to high-level research, recognized throughout the world. Its activities extend from fundamental to applied research. More than 2000 people- lecturer/researchers, scientists and technicians- are involved in its research programmes. The moderate size of the University encourages inter-disciplinary research and, more generally, contacts between scientists from various disciplines. There exist numerous partnerships with the industrial sector and the University plays an active role in enhancing the creation of spin-off companies and guiding their development.
In terms of research, the University of Liège offers several possibilities for

- companies or organisations from both the public and private sectors who wish to set up partnerships or subcontract research tasks;
- master's graduates wishing to engage in research while pursuing a doctorate;
- post-doctoral researchers seeking to broaden the scope of their activities as part of one of our reputed research teams;
- experienced researchers interested in an academic position enabling them to combine teaching activities with top range research activities.

The ULg has chosen inter-disciplinarity and partnership of the research units in order to develop a quality collaborative research, rich in diversity and differences, by also favouring the critical size through forming research centres to have access to international partnerships of high quality. It encourages researchers in particular to create spin-offs on the basis of their research findings and to guide their development.

The ULg has been resolute in its desire to become involved in a Free Access policy, by putting PhD theses of its students online on the Internet (BICTEL/e Project), by inviting members of the ULg to deposit their scientific publications in order to enable the free circulation of them over the Internet (Digitheque Project ORBI) and by creating a publication portal of scientific periodicals of the ULg. Furthermore, it wishes to make science available to the general public through the scientific popularisation website Reflections.

International Advisory Board

Abe, F.	NIMS	Japan
Aguero, A.	INTA	Spain
Allen, D.	Alstom Power	UK
Barnard, P.	Doosan Babcock	UK
Beck, T. (chairman)	FZ Juelich	Germany
Berger, C.	TU Darmstadt	Germany
Bordenet, B.	Alstom Power	Switzerland
Charcaluk, E.	Univ. Lille	France
Czyrska-Filemonowicz, A.	AGH Krakow	Poland
Delannay, F.	UCL	Belgium
Fry, T.	NPL	UK
Gandy, D.	EPRI	USA
Hald, J.	TU Denmark	Denmark
Hernderson, P.	Vattenfall	Sweden
Herzog, R.	MAN-Turbo	Germany
Holdsworth, S.	EMPA	Switzerland
Jochum, K.	Boehler Schweißtechnik	Germany
Kern, T.	Siemens	Germany
Kuhn, B.	FZ Juelich	Germany
Lupinc, V.	CNR-IENI	Italy
Massaut, V.	SCK-CEN	Belgium
Mathieu, P.	Université de Liège	Belgium
Mogensen, M.	Risoe DTU	Denmark
Nazmy, M.	Alstom Power	Switzerland
Oakey, J.	Cranfield U	UK
Osgerby, S.	NPL	UK
Quadakkers, W.	FZ Juelich	Germany
Raj, B.	IGCAR	India
Remy, L.	EDM	France
Scarlin, B.	Alstom Power	Switzerland
Scholz, A.	TU Darmstadt	Germany
Xie, X.	USTB	China

Technical and Editorial Board

Allen, D.	Alstom Power	UK
Barnard, P.	Doosan Babcock	UK
Beck, T. (chairman)	FZ Juelich	Germany
Berger, C.	TU Darmstadt	Germany
Bordenet, B.	Alstom Power	Switzerland
Contrepois, Q.	Université de Liège	Belgium
Czyrska-Filemonowicz, A.	AGH Krakow	Poland
Fry, T.	NPL	UK
Hald, J.	TU Denmark	Denmark
Herzog, R.	MAN-Turbo	Germany
Holdsworth, S.	EMPA	Switzerland
Jochum, K.	Boehler Schweißtechnik	Germany
Kern, T.	Siemens	Germany
Kuhn, B.	FZ Juelich	Germany
Lecomte-Beckers, J. (chief editor, vice-chairman)	Université de Liège	Belgium
Lupinc, V.	CNR-IENI	Italy
Nazmy, M.	Alstom Power	Switzerland
Oakey, J.	Cranfield U	UK
Osgerby, S.	NPL	UK
Quadakkers, W.	FZ Juelich	Germany
Scarlin, B.	Alstom Power	Switzerland
Scholz, A.	TU Darmstadt	Germany

Organisation of Sessions

Materials for Advanced Steam Power Plants	Hald, J.
Gas Turbine Materials	Oakey, J.
Materials for Nuclear Fusion and Fission	Beck, T. (chairman)
Solid Oxide Fuel Cells	Kuhn, B.
Corrosion, Thermomechanical Fatigue and Modelling	Lecomte-Beckers, J. (chief editor, vice-chairman)
Zero-Emission Power Plants	Oakey, J., Singheiser, L.

Local Organisation Committee

Beck, T. (chairman)	FZ Juelich
Lecomte-Beckers, J. (chief editor, vice-chairman)	Université de Liège
Kuhn, B.	FZ Juelich
Contrepois, Q.	Université de Liège

Conference Secretaries

Wittig, E., Abdel-Fattah, Y., Fix, U., Kuhn-Stassar, S.	FZ Juelich
Pirson, R.	Université de Liège

Contents

Table of Contents ix

A Materials for Advanced Steam Power Plants 1

Invited Papers 3

ADVANCED USC TECHNOLOGY DEVELOPMENT IN JAPAN
Fukuda M
. 3

700°C POWER PLANT TECHNOLOGY - STATUS AND CHALLENGE
Tschaffon H
. 18

THE EUROPEAN EFFORTS IN DEVELOPMENT OF NEW HIGH TEMPERATURE ROTOR MATERIALS COST536
Kern T-U, Mayer K H, Donth B, Zeiler G, DiGianfrancesco A
. 27

MATERIAL DEVELOPMENTS FOR SUPERCRITICAL BOILERS PIPEWORKS - BRIDGING THE GAP ?
Barnard P M, Buchanan L W, Barrie M
. 37

DEVELOPMENT STATUS AND FUTURE POSSIBILITIES FOR MARTENSITIC CREEP RESISTANT STEELS
Hald J
. 53

Contributed Papers 65

BENEFICIAL EFFECT OF Re ON THE LONG-TERM CREEP STRENGTH OF HIGH Cr FERRITIC HEAT RESISTANT STEELS
Hashizume R, Tamura O, Miki K, Azuma T, Ishiguro T, Murata Y, Morinaga M
. 65

INFLUENCE OF DELTA FERRITE ON MECHANICAL AND CREEP PROPERTIES OF STEEL P92
Mohyla P
. 75

THE EFFECT OF MICROSTRUCTURAL STABILITY ON LONG-TERM CREEP BEHAVIOUR OF 11%CR STEELS FOR STEAM POWER PLANTS WITH OPERATING STEAM TEMPERATURES UP TO 650°C
Wang W, Kauffmann F, Mayer K-H, Scholz A, Berger C, Maile K
. 84

LONG TERM PROPERTIES AND MICROSTRUCTURAL EVOLUTION OF 18Cr-10Ni-3Cu-Ti-Nb AUSTENITIC STAINLESS STEEL FOR BOILER TUBE APPLICATION
Minami Y, Fukui T, Ono T
. 95

INITIAL STUDY ON Z-PHASE STRENGTHENED 9-12% Cr STEELS BY ATOM PROBE TOMOGRAPHY
Liu F, Andrn H-O
. 105

EFFECTS OF ALLOYING ELEMENTS AND CONSTITUENT PHASES ON LONG-TERM CREEP STRENGTH OF MODIFIED 9Cr1Mo STEEL
Tokunaga T, Yoshida K, Sakanaba M, Masuyama F
. 115

EFFECTS OF NICKEL AND COBALT ADDITION ON CREEP STRENGTH AND MICROSTRUCTURE OF THE PRECIPITATION-STRENGTHENED 15Cr FERRITIC STEELS
Shibuya M, Toda Y, Sawada K, Kushima H and Kimura K
. 123

CREEP STRENGTH AND RUPTURE DUCTILITY OF CREEP STRENGTH ENHANCED FERRITIC STEELS
Kushima H, Sawada K, Kimura K
. 131

CREEP OF EX-SERVICE AISI-316H STEEL AT VERY LOW STRAIN RATES
Kloc L, Spindler M, Sklenička
. 142

SERVICE-CYCLE COMPONENT-FEATURE SPECIMEN TMF TESTING OF STEAM TURBINE ROTOR STEELS
Radosavljevic M, Mazza E, Grossmann P, Ripamonti L and Holdsworth R
. 150

ASSESSMENT OF LONG-TERM CREEP STRENGTH OF GRADE 91 STEEL
Kimura K, Sawada K, Kushima H
. 160

MICROSTRUCTURAL CHANGES OF T91 STEEL DURING CREEP UNDER LOW STRESS
Sawada K, Kushima H, Tabuchi M and Kimura K
. 170

BORON EFFECTS ON CREEP RUPTURE STRENGTH OF W CONTAINING ADVANCED FERRITIC CREEP RESISTANT STEELS
Mito N, Hasegawa Y
. 176

GRAIN BOUNDARY PRECIPITATION STRENGTHENING MECHANISM IN W CONTAINING ADVANCED CREEP RESISTANT FERRITIC STEELS
Shibata T, Hasegawa Y
. 186

PREDICTION OF LONG-TERM PRECIPITATE EVOLUTION IN AUSTENITIC HEAR-RESISTANT STEELS
Shim J-H, Kozeschnik E, Jung W-S, Cho Y W
. 196

FUNDAMENTAL MODELLING OF PARTICLE STRENGTHENED 9-12% Cr STEELS
Magnusson H, Sandstrom R
. 206

CREEP PERFORMANCE OF WELDED PIPE MATERIAL MADE OF 7CrMoVTiB10-10 (T/P24) STEEL
Rantala J, Auerkari P, Salonen J, Holmström S, Nevasmaa P
. 221

REHEAT CRACKING SUSCEPTIBILITY OF P23 (7CrWVMoNb9-6) STEEL WELDS MADE USING MATCHING AND MIS-MATCHING FILLER METALS
Nevasmaa P, Salonen J, Auerkari P, Rantala J, Holmström S
. 229

LONG-TERM AGING EFFECT ON THE CREEP STRENGTH OF THE T92 STEEL
Panait C, Gourgues-Lorenzon A F, Besson J, Fuchsmann A, Bendick W, Gabrel J, Piette M
. 239

MICROSTRUCTURAL EVOLUTION DURING CREEP DEFORMATION OF AN 11CrMoVNb FERRITIC HEAT RESISTANT STEEL
Lee K-H, Park D-B, Kwon S-I, Suh J-Y, Jung W-S
. 249

CREEP STRENGTH AND MICROSTRUCTURAL EVOLUTION OF 9-12% CR HEAT RESISTANT STEELS DURING CREEP EXPOSURE AT 600°C AND 650°C
Mendez Martin F, Panait C G, Bendick W, Albu M, Sonderegger B, Kothleitner G, Sommitsch C, Gourgues-Lorenzon A-M, Besson J, Fuchsmann A
. 259

MICROSTRUCTURAL EVOLUTION OF ASTM P91 AFTER 100,000 HOURS EXPOSURE AT 550°C AND 600°C
Cipolla L, Caminada S, Venditti D, Danielsen H K, Gianfrancesco A
. 270

HEAVY STEEL CASTING COMPONENTS FOR ADVANCED POWER PLANTS "MEGA-COMPONENTS" MADE OF HIGH Cr-STEELS
Hanus R
. 284

TRANSFORMATION OF MX INTO Z-PHASE IN 9-12%Cr MODEL ALLOYS
Danielsen H K, Cipolla L, Venditti D, Hald J
. 294

INFLUENCE OF Z-PHASE ON LONG-TERM CREEP STABILITY OF MARTENSITIC 9-12%Cr STEELS
Danielsen H K, Hald J
. 308

CALCULATION OF PHASE BOUNDARY ENERGIES AND APPLICATION IN MULTICOMPONENT STEELS
Sonderegger B, Hacksteiner M, Mendez-Martin F, Holzer I, Kozeschnik E
. 318

BOUNDARY AND SUB-BOINDARY HARDENING IN TEMPERED MARTENSITIC 9Cr STEEL DURING LONG-TERM CREEP AT 650°C
Abe F
. 328

HIGH-TEMPERATURE PERFORMANCE OF A NEW NICKEL-BASED FILLER METAL FOR POWER GENERATION APPLICATIONS
Shingledecker J, Coleman K, Siefert J, Tanzosh J, Newell W
. 338

IMPROVED CREEP AND OXIDATION BEHAVIOR OF A MARTENSITIC 9CR STEEL BY THE CONTROLLED ADDITION OF BORON AND NITROGEN
Mayr P, Holzer I, Mendez-Martin F, Albu M, Mitsche S, Gonzalez V, Agüero A
. 348

DEVELOPMENT OF Fe-Ni AND Ni-BASE ALLOYS WITHOUT γ' STRENTHENING FOR ADVANCED USC BOILERS
Semba H, Okada H, Igarashi M, Hirata H and Yoshizawa M
. 360

MICROSTRUCTURE DEVELOPMENT OF WELDING JOINTS IN HIGH Cr FERRITIC STEELS
Kubushiro K, Takahashi S, Morishima K
. 370

CREEP PROPERTIES AND MICROSTRUCTURE OF THE NEW WROUGHT AUSTENITIC STEEL
Vlasák T, Hakl J, Navák P, Výrostková A
. 380

EVALUATION OF BASE MATERIAL AND WELDED JOINTS DESIGNATED FOR MEMBRANE WALL COMPONENTS MADE FROM LOW-ALLOY STEELS IN LARGE BOILERMAKER CONDITIONS
Dobrzański J, Pasternak J, Zieliński A
. 390

WELDED REPAIR JOINTS OF BOILER STEELS FOLLOWING OPERATION IN CREEP CONDITIONS EXCEEDING THE DESIGN TIME OF OPERATION
Dobrzański J, Paszkowska H, Zieliński A
. 400

PROPERTIES OF THICK WELDED JOINTS ON SUPERHEATER COLLECTORS MADE FROM NEW GENERATION HIGH ALLOY MARTENSITIC CREEP-RESISTING STEELS FOR SUPERCRITICAL PARAMETERS
Dobrzański J, Pasternak J, Zieliński A
. 412

HIGH TEMPERATURE CREEP PROPERTIES AND MICROSTRUCTURAL EXAMINATIONS OF P92 WELDS
Kalck C, Fournier B, Barcelo F, Forest L, Dalle F, Giroux P-F, Tourni I, Gourgues-Lorenzon A-F
. 424

ASSESSMENT OF THE INTEGRITY OF FERRITIC-AUSTENIC DISSIMILAR WELD JOINTS OF DIFFERENT GRADES OF Cr-Mo FERRITIC STEELS
Laha K, Chandravathi K S, Parameswaran P, Goyal S and Mathew M D
. 435

EXPERIENCES WITH THE CHARACTERIZATION OF NEW AND EX-SERVICE GRADE 91 MATERIAL
De Bruycker E, Huysmans S
. 445

CREEP PROPERTIES AND MICROSTRUCTURE EVALUATION OF WELD JOINT OF THE PIPE MADE OF P92 STEEL
Kasl J, Jandová D, Chvostová E, Folková E
. 455

MICROSTRUCTURE ANALYSIS OF E911 STEEL AFTER MORE THAN 100,000 HRS OF CREEP EXPOSURE
Jandová D, Kasl J, Chvostová E
. 465

COMPUTATIONAL THERMODYNAMIC INVESTIGATIONS OF GROWTH AND COARSENING OF LAVES PHASE PRECIPITATES IN 12%Cr CREEP RESISTANT STEELS
Prat O, Garcia J, Rojas D, Kaysser-Pyzalla A R
. 475

TEM CHARACTERIZATION OF MICROSTRUCTURE EVOLUTION OF 12%Cr HEAT RESISTANT STEELS
Rojas D, Prat O, Garcia J, Sauthoff G, Kaysser-Pyzalla A R
. 485

LONG-TERM CREEP RUPTURE STRENGTH OF WELDMENT OF Fe-Ni BASED ALLOY AS CANDIDATE TUBE AND PIPE FOR ADVANCED USC BOILERS
Bao G, Sato T, Marumoto Y
. 494
INFLUENCE OF WELD STRUCTURE ON CROSS-WELD CREEP BEHAVIOR IN P23 STEEL
Allen D J, Degnan C C, Brett S J and Buchanan L W
. 500
DEVELOPMENT OF MATCHING FILLER METALS FOR WELDING CB2 AND FIRST EXPERIENCE
Heuser H, Jochum C, Kreuzer-Zagar D
. 514
Z PHASE STABILITY IN AISI 316LN + Nb AUSTENITIC STEELS DURING CREEP AT 650°C
Vodárek V
. 522
APPLICATION OF NEW GMAW WELDING METHODS USED IN PREFABRICATION OF P92 (X10CrWMoVNb9-2) PIPE BUTT WELDS
Urzynicok M, Kwieciński K, Szubryt M, Słania J
. 532
PRACTICAL EXPERIENCE WITH WELDING NEW GENERATION STEEL PB2 ASSIGNED FOR POWER INDUSTRY
Kwieciński K, Urzynicok M, Łomozik M
. 542
DEGRADATION OF SUPERHEATER TUBES MADE OF AUSTENITIC T321H STEEL AFTER LONG TERM SERVICE
Hernas A, Augustyniak B, Chmielewski M, Sablik M J
. 552
DESIGN OF HEAT TREATMENTS FOR 9-12%Cr STEELS TO OPTIMISE CREEP RESISTANCE FOR POWER PLANT APPLICATIONS
Morris P F, Sachadel U, Clarke P D
. 562

B Gas Turbine Materials **573**

Invited Papers **575**
MODELLING OF MICROSTRUCTURE AND MECHANICAL PROPERTY CHANGES IN GAS TURBINE ALLOYS
Scholz A, Nazmy M, Fedelich B, Tinga T, Huls R
. 575
RECENT TRENDS IN SUPERALLOYS RESEARCH FOR CRITICAL AERO-ENGINE COMPONENTS
Rémy L, Guédou J Y
. 596

DEVELOPMENT OF SUPERALLOYS FOR A 1700°C ULTRA-EFFICIENT GAS TURBINE
Harada H
. 612

Contributed Papers **623**

DEGRADATION OF Ni-BASE SUPERALLOYS UNDER HIGH TEMPERATURE CREEP CONDITIONS
Epishin A, Link T, Klingelhoffer H, Fedelich B, Namzy M, Staubli M
. 623

NEW CONCEPT OF COMPOSITE STRENGTHENING IN Co-Re-BASED ALLOYS FOR HIGH TEMPERATURE APPLICATIONS IN GAS TURBINES
Mukherji D, Rosler J, Fricke T, Piegert S, Schmitz F
. 633

ANALYSIS OF HAYNES 230 CREEP BEHAVIOUR
Maldini M, Angella G, and Lupinc V
. 643

DESIGNING OF INTERMETALLIC Ni3Al-BASED SUPERALLOY
Kablov E N, Petrushin N V, Nazarkin R M
. 654

ANISOTROPY OF MECHANICAL PROPERTIES OF SINGLE CRYSTALS IN FOURTH GENERATION NI-BASED SUPERALLOY
Svetlov I L, Petrushin N V, Shchegolev D V, Khvatskiy K K
. 660

MULTILAYER STACKS OBTAINED BY ION ASSISTED EB PVD AIMED AT THERMAL BARRIER COATING
Roos E, Maile K, Lyutovich A
. 668

ASSESSMENT OF A RESIDUAL LIFE EVALUATION TOOL FOR GAS TURBINE BLADES AND VANES BASED ON MICROSTRUCTURAL EVOLUTION OF A NiCoCrAlY+Re COATING
Barbareschi E, Bonadei A, Costa A, Guarnone P, Vacchierri E
. 676

LIFE ASSESSMENT OF GAS TURINE BLADES AFTER LONG TERM SERVICE
Auerkari P, Salonen J, Mäkinen S, Karvonen I, Tanttari H, Kangas P, Scholz A, Vacchieri E
. 685

EFFECTS OF LONG -TERM HIGH TEMPERATURE EXPOSURE ON THE MICROSTRUCTURE OF HAYNES ALLOY 230
Veverkova J, Strang A, Marchant G R, Atkinson H V
. 695

DEGRADATION OF LCF PROPERTIES OF CMSX-4 SINGLE CRYSTAL SUPERALLOY, AFTER CREEP EXPOSURE AT 850°C AND 950°C
Cammi A, Concari S, Rinaldi C
. 705

APPLICATION OF COATING AND BASE MATERIAL LIFING MODELS TO EVALUATE DEGRADATION AND ESTIMATE THE MEAN LOCAL OPERATING TEMPERATURE OF TWO EX-SERVICE 1ST STAGE BLADES
Mandelli M, Rinaldi C, Vacchierri E
. 715

EFFECT OF COHERENCE FAILURE ON γ'-PHASE PARTICLE GROWTH IN NICKEL SUPERALLOYS
Zaitsev D V, Alekseev A A
. 725

BEHAVIOR OF RESIDUAL STRESSES AND LATTICE SPACING IN γ-AND γ'-PHASES AT CREEP-RUPTURE TESTS OF SINGLE-CRYSTAL NICKEL SUPERALLOY
Treninkov I A, Alekseev A A
. 731

PRECIPITATION IN SOLID SOLUTION AND STRUCTURAL TRANSFORMATIONS IN SINGLE CRYSTALS OF HIGH RHENIUM RUTHENIUM-CONTAINING NICKEL SUPERALLOYS AT HIGH-TEMPERATURE CREEP
Alekseev A A, Petrushin N V, Zaitsev D V, Treninkov I A, Filonova E V
. 741

INFLUENCE OF CHEMICAL COMPOSITION ON MICROSTRUCTURE AND STRENGTH OF ALLOY 718
Fedorova T, Rösler J, Gehrmann B, Klöwer J
. 749

PHASE-FIELD SIMULATION OF MICROSTRUCTURE EVOLUTION IN NI-BASED SUPERALLOYS
Tsukada Y, Murata Y, Koyama T and Morinaga M
. 759

DEVELOPMENT OF CORROSION-RESISTANT Ni-BASE SINGLE CRYSTAL SUPERALLOY
Kawagishi K, Yokokawa T, Koizumi Y, Kobayashi T, Sakamoto M and Harada H
. 769

MICROSTRUCTURAL CHANGE AROUND GRAIN BOUNDARY IN POLYCRYSTALLINE IN100 DURING CREEP DEFORMATION
Takahashi S, Kubushiro K, Morishima K, Miura N, Kondo Y
. 775

MONITORING THERMALLY GROWN OXIDES UNDER THERMAL BARRIER COATINGS USING PHOTOLUMINESCENCE PIEZOSPECTROSCOPY (PLPS)
del Corno A, De Maria L, Rinaldi C, Nalin L, Simms N J
. 784

OXIDATION RESISTANCE OF HIGH Re AND Ru CONTAINING Ni-BASE SINGLE CRYSTAL SUPERALLOYS
Suzuki A, Kawagishi T, Yokokawa T, Kobayashi T and Harada H
. 794

SEM AND TEM ANALYSES OF MICROSTRUCTURAL CHANGES IN CREEP DEGRADED AND TENSILE TESTED CMSX-4 SUPERALLOY
Dubiel B, Nazmy M, Lapin J, Czyrska-Filemonowicz A
. 802

MORPHOLOGY OF γ' PRECIPITATES OF NICKEL-BASED SUPERALLOY SERVICED AS FIRST STAGE HIGH PRESSURE TURBINE NOZZELE GUIDE VANE
Miura N, Nakada K, Kondo Y
. 812

PRECIPITATION OF TCP PHASES IN Ni-BASE ALLOYS WITH A HIGH CHROMIUM CONTENT
Pigrova G D
. 822

STUDY ON THE HOT CORROSION BEHAVIOR OF A CAST Ni-BASE SUPERALLOY
Wang W, Guo J T, Zhang J, Yuan C, Zhou L Z, Hu Z Q
. 826

CREEP CURVE MODELLING OF A CONVENTIONALLY CAST NICKEL BASE SUPERALLOY
Lupinc V, Maldini M, Poggio E, Vacchieri E
. 834

LCF- AND LCF/HCF-BEHAVIOR OF THE SUPERALLOY MAR-M247LC
Gelmedin D, Lang K-H
. 844

HIGH TEMPERATURE CORROSION OF THERMALLY SPRAYED NiCr- AND AMORPHOUS Fe-BASED COATINGS COVERED WITH A KCl-K_2SO_4 SALT MIXTURE
Varis T, Bankiewiczv D, Yrjas P, Suhonen T, Tuurna S, Ruusuvuori K, Holmström S and Salonen J
. 854

EFFECTS OF WITHDRAWAL RATE ON THE MICROSTRUCTURE AND MECHANICAL PROPERTIES OF A DS NI-BASE SUPERALLOY
Qin X Z, Xu C, Zhou L Z and Guo J T
. 866

INFLUENCE ON TIME, TEMPERATURE AND ENVIRONNEMENT ON CYCLIC BEHAVIOUR OF A GAS TURBINE BLADE COATING SYSTEMS
Bordenet B, Bachegowda S, Bossmann H P
. 874

C Materials for Nuclear Fusion and Fission 885

Invited Papers 887

DEVELOPMENT AND EVALUATION OF PLASMA FACING MATERIALS FOR FUTURE THERMONUCLEAR FUSION REACTOR
Linke J, Pintsuk G, Rödig M, Schmidt A, Thomser C
. 887

DEVELOPMENT OF MATERIALS AND MANUFACTURING TECHNOLOGIES FOR INDIAN FAST REACTOR PROGRAMME
Raj B, Jayakumar T, Bhaduri A K, Sumantra M
. 890

MATERIALS CHALLENGES FOR THE NEXT GENERATION OF FISSION REACTOR SYSTEMS
Buckthorpe D
. 906

D Solid Oxide Fuel Cells 923

Invited Papers 925

RECENT DEVELOPMENTS IN SOLID OXIDE FUEL CELLS AT FORSCHUNGSZENTRUM JUELICH AND IN EUROPE
Steinberger-Wilckens R, Blum L, Buchkremer H P, de Haart L J G, Malzbender J, Pap M, Gross S M
. 925

RECENT ACTIVITIES OF SOLID OXIDE FUEL CELL RESEARCH AND DEVELOPMENT IN JAPAN
Yokokawa H
. 938

Contributed Papers 949

$MnCo_2O_4$ SPINEL CHROMIUM BARRIER COATINGS FOR SOFC INTERCONNECTS BY HVOF
Lagerbom J, Varis T, Puranen J, Pihlatie M, Himanen O, Saarinen V, Kiviaho J, Turunen E
. 949

E Corrosion, Thermomechanical Fatigue and Modelling 957

Invited Papers 959

STEAM OXIDATION AND THE EVALUATION OF COATINGS AND MATERIAL PERFORMANCE THROUGH COLLABORATIVE RESEARCH
Fry A T, Aguero A
. 959

ADVANCES IN THE ASSESSMENT OF CREEP DATA
Holdsworth S R
. 970

COMBATING CORROSION IN BIOMASS AND WASTE FIRED PLANT
Henderson P, Hjörnhede A
. 986

Contributed Papers 1000

FIRESIDE CORROSION OF SUPERHEATERS-REHEATERS IN ADVANCED POWER PLANTS
Syed A U, Simms N J, Oakey J E
. 1000

MODELLING OF DEGRADATION PROCESSES IN CREEP RESISTANT STEELS THROUGH ACCELERATED CREEP TESTS AFTER LONG-TERM ISOTHERMAL AGEING
Sklenicka V, Kucharova K, Svoboda M, Kroupa A, Kloc L, Cmakal J
. 1010

IMPROVEMENT OF STEAM OXIDATION RESISTANCE OF MARTENSITIC AND AUSTENITIC ALLOYS BY ALUMINIUM CONTAINING COATINGS
Knödler R, Straub S
. 1020

STEAM OXIDATION SCALE GROWTH AND THERMAL INSULATION EFFECT ON CREEP LIFE OF CREEP STRENGTH ENHANCED FERRITIC STEELS
Masuyama F, Tokunaga T, Takao M, Arakawa K
. 1028

PROTECTIVE COATING OF INNER SURFACE OF STEEL TUBES VIA VACUUM ARC DEPOSITION
Maile K, Roos E, Lyutovich A, Böse J, Itskov M, Ashurov Kh, Mirkarimov A, Kazantsev S, Kadirov Kh
. 1040

STEAM OXIDATION OF TP 347H FG: LABORATORY EXPOSURES VERSUS SERVICE CONDITIONS AT THE POWER PLANT
Hansson A N, Montgomery M
. 1046

9% Cr STEEL HIGH TEMPERATURE OXIDATION SOLUTIONS INVESTIGATED FOR IMPROVING CORROSION RESISTANCE OF THE STEEL
Evin H N, Heintz O, Fojer C, Jakani S, Dhont A, Claessens S, Chevalier S
. 1056

OXIDATION PERFORMANCE OF HIGH TEMPERATURE STEELS AND COATINGS FOR FUTURE SUPERCRITICAL POWER PLANTS
Auerkari P, Salonen J, Toivonen A, Penttilä S, Häkkilä J, Aguero A, Fry T
. 1068

OXIDATION PERFORMANCE OF HIGH TEMPERATURE MATERIALS UNDER OXYFUEL CONDITIONS
Tuurna S, Pohjanne P, Yli-Olli S, Kinnunen T
. 1076

SOLID PARTICLE EROSION OF STEELS AND NICKEL BASED ALLOYS CANDIDATES FOR USC STEAM TURBINE BLADING
Cernuschi F, Guardamagna C, Lorenzoni L, Robba D
. 1085

MODELLING OF DIFFUSIONAL CREEP IN POLYCRYSTALS
Pein C, Sommitsch C
. 1095

A NUMERICAL APPROACH TO PREDICT THE LONG-TERM CREEP BEHAVIOUR AND PRECIPITATE BACK-STRESS EVOLUTION OF 9-12% CHROMIUM STEELS
Holzer I, Kozeschnik E, Cerjak H
. 1101

FATIGUE LIFE PREDICTION OF Ni-BASE THERMAL SOLAR RECEIVER TUBES
Von Hartrott P, Schlesinger M, Uhlig R, Jedamski J
. 1112

HIGH TEMPERATURE CORROSION TESTING AT MARIBO SAKSKBING BIOMASS FIRING POWER PLANT
Montgomery M, Jesen S A, Hansson A, Biede O, Vilhelmsen T
. 1120

FALLING SAND TESTS ON VARIOUS COATINGS
Manetti M, Zonfrillo G, Pratesi F
. 1130

A STEAM LOOP FOR MATERIALS TESTING AT 600°C IN A BIOMASS AND WASTE FIRED BOILER RESULTS OF CORROSION TESTING
Henderson P and Lundberg M
. 1140

A COMPUTATIONAL APPROACH FOR THERMOMECHANICAL FATIGUE LIFE PREDICTION OF DISSIMILARLY WELDED SUPERHEATER TUBES
Kumar-Krishnasamy R, Seifert T, Siegele D
. 1150

CREEP BEHAVIOUR AND MICROSTRUCTURAL EVOLUTION IN P23/P91 DISSIMILAR WELDS
Vodárek V, Kuboň Z, Střílková L and Hainsworth S V
. 1160
RECIPROCATING WEAR IN A STEAM ENVIRONMENT
Brown L J and Gee M G
. 1170
STEAM OXIDATION OF 9-12%Cr STEELS: CRITICAL EVALUATION AND IMPLICATIONS FOR PRACTICAL APPLICATION
Zurek J, De Bruycker E, Huysmans S, Quadakkers W J
. 1182
MODELLING FIRESIDE CORROSION OF HEAT EXCHANGERS IN CO-FIRED PULVERISED FUEL POWER SYSTEMS
Simms N J and Fry A T
. 1192
RESISTANCE OF VARIOUS COATINGS TO HIGH TEMPERATURE CORROSION IN HCl AND SO_2 CONTAINING ENVIRONMENTS
Cizner J, Mlnarik J, Hruska J
. 1202
INTERFACIAL, MECHANICAL PROPERTIES OF Al_2O_3-NiAl COMPOSITES RESPECTIVE TO LONG TERM THERMAL STABILITY
Song J, Hu W, Gottstein G
. 1210
SEWADGE SLUDGE AS ADDITIVE TO REDUCE THE INITIAL FIRESIDE CORROSION CAUSED BY COMBUSTION OF SHREDDER RESIDUES IN A WASTE-FIRED BFB BOILER
Jonsson T, Pettersson J, Davidsson K, Johansson L-G and Svensson J-E
. 1218

F Zero Emission Power Plants 1229

Invited Papers 1231
OXYCOAL-AC : INNOVATIVE COMPONENTS AND CONCEPTS FOR THE POWER PLANTS OF THE FUTURE
Kneer R, Toporov D, Föster M
. 1231
PRELIMINARY EXPERIENCES WITH MATERIAL TESTING AT THE OXY-FUEL PILOT PLANT AT SCHWARZEPUMPE
Hjörnhede A, Montgomery M, Bjurman M, Henderson P, Gerhardt A
. 1244
CERAMIC MEMBRANES FOR GAS SEPARATION IN ADVANCED FOSSIL POWER PLANTS
Meulenberg W A, Baumann S, Ivanova M, van Gestel T, Bram M, Stöver D
. 1260

Contributed Papers **1278**

CORROSION STUDIES OF OXYGEN PERMEATING MEMBRANE MATERIALS
Waindich A, Müller M
. 1278

METALLIC SUBSTRATE MATERIALS FOR THIN FILM OXYGEN TRANSPORT MEMBRANES FOR APPLICATION IN A FOSSIL POWER PLANT
Xing Y, Baumann S, Sebold D, Meulenberg W A, Stöver D
. 1287

AUTHORS Index **i**

KEYWORDS Index **iv**

Part A

Materials for Advanced Steam Power Plants

9th Liege Conference : Materials for Advanced Power Engineering 2010
edited by J. Lecomte-Beckers, Q. Contrepois, T. Beck and B. Kuhn.

Advanced USC Technology Development in Japan

Masafumi Fukuda

National Institute for Materials Science
High Temperature Materials Center
1-2-1 Sengen, Tsukuba, Ibaraki, 305-0047
Japan

Abstract

The 600deg-C class Ultra Super-Critical(USC) steam condition technology was mainly developed through projects led by J-Power in the '80s and '90s. In 2001, the project was successfully finished with newly developed 9-12% chromium steels. These materials were selected for the major parts of the USC power plants in Japan and almost half of the coal power plants have the USC steam condition today.
However, aged plants, which were built in the '70s and early '80s, will reach the point where they will need to be rebuilt or refurbished in the near future. The steam temperatures of the older plants are 538deg-C or 566deg-C. We did a case study, retrofitting these plants with the USC and an advanced USC technology that takes a 700deg-C class steam temperature to increase thermal efficiency and to reduce CO_2 emissions. The study showed that the advanced USC Technology(A-USC) is suitable for the retrofitting of aged plants and can reduce CO_2 emissions by about 15%.
The Japanese government launched the "Cool Earth-Innovative Energy Technology Program" in 2008 March to promote international cooperation and actively contribute to substantial global greenhouse gas emissions reductions. 21 technologies that will contribute to substantial reductions in CO_2 emissions by efficiency improvement and low carbonization were selected. The A-USC that aims at 46% (net, HHV) thermal efficiency of coal power generation is included in the technologies.
We started a large-scale development project of the A-USC technology in 2008 August. 700deg-C class boiler, turbine and valve technologies, which include high temperature material technology, will be developed. Some candidate materials for boilers are being tested. Turbine rotor and casing materials are being developed and tested, as well. Two years from the beginning of the project, we have obtained some useful test results regarding the candidate materials.

Keywords: power plant, steam condition, heat resistant alloy, creep failure, greenhouse gas

1. Introduction

Almost all primary energy resources used in Japan are imported from abroad. The 'Oil shock' in the '70s awakened us to the harsh facts before us. Since then, coal fired power plants have been steadily replacing oil fired power plants. Today, one-quarter of the electricity in Japan is produced by coal. Because of the relatively high cost of imported coal and the dense population in Japan, highly efficient and clean technology has been preferred historically to reduce fuel consumption and environmental stress. The improvement in the efficiency of the coal fired power plants has been mainly achieved by raising steam conditions as shown in Figure 1. The steam temperature was raised from 538deg-C to 566deg-C at the end of the 50's, and remained at this temperature until 1993. Steam power plants that have been built recently

usually have a steam temperature of around 600deg-C and a steam pressure of 25MPa. We usually call such a steam condition USC (Ultra Super Critical steam condition).

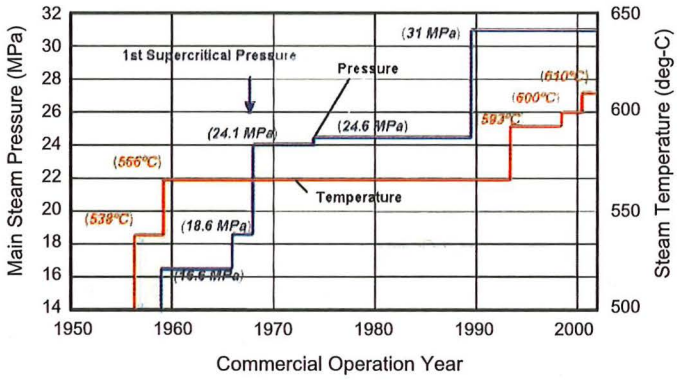

Figure 1 Trend of steam conditions in Japan

Figure 2 shows the history of the capacity of coal power plants. The capacity has risen to 35GW today and about half of the capacity is produced using USC technology.

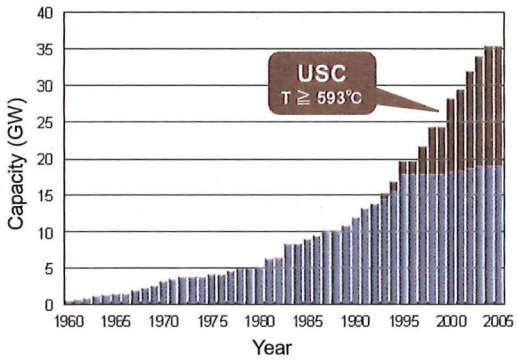

Figure 2 Capacity of coal power plant in Japan

Electric Power Development Company (J-Power) started a comprehensive development program of USC technology in 1981, subsidized by the Japanese government. Materials to be used for 600 to 650deg-C systems were developed through the year 2000 (Figure 3) [1]. The materials which contain 9 to 12 Cr steels and were developed at that time are being used for the USC plants in Japan today.

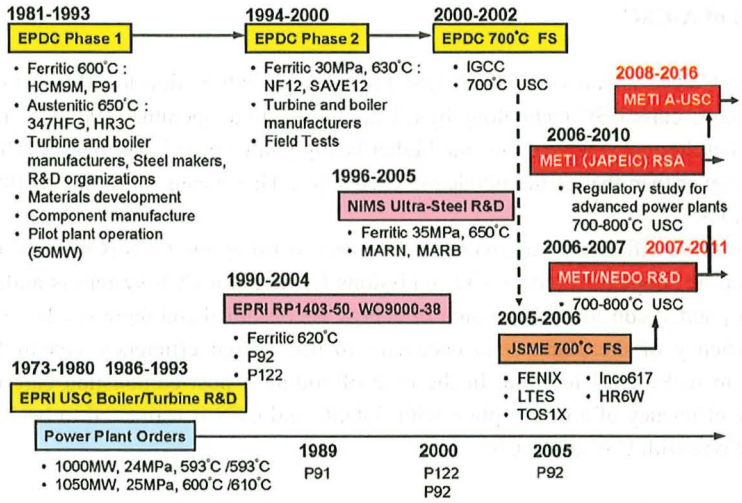

Figure 3 USC technology development (Courtesy of Prof. Masuyama) [1]

Figure 4 shows J-Power's Isogo power station which is located in the Tokyo metropolitan area [2]. Isogo #2, the newest power plant in Japan, was built last year. The temperatures of the main steam and reheat steam are 600 and 620deg-C.

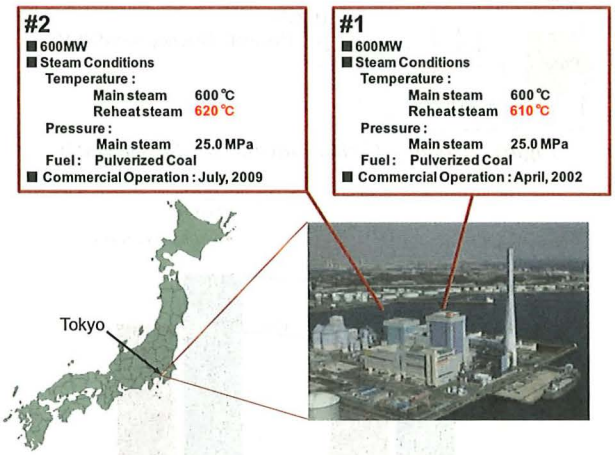

Figure 4 Isogo Power Station [2]

Following these programs, from 2000 to 2006, we studied the feasibility of a system which has a 700deg-C class steam temperature. Encouraged by the results of this study, which will be shown in the next section, we began the advanced USC technology (A-USC) development project in 2008, which features a 700deg-C steam temperature.

2. Concept of A-USC

The 700deg-C class advanced USC (A-USC) technology will be developed based on today's latest 600deg-C class USC technology by raising the steam temperature 100deg-C (Figure 5). The target net thermal efficiency for the higher heating value base is 46 to 48%. This is more than 10% higher than that of the 600deg-C class USC. That means more than a 10% drop in CO_2 emissions.

In addition to the efficiency improvement, biomass co-firing and CCS (Carbon Capture and Storage) can be coupled to reduce CO_2 emissions further. If a CCS system is added on to a coal power plant, a considerable amount of energy is consumed and there is a large reduction in the efficiency of the plant. It is necessary to use a high efficiency system for power generation to make CCS feasible. In the case of adding a post combustion carbon capture system, the efficiency of a power plant with A-USC and CCS is estimated to be 13% higher than that of one with USC and CCS.

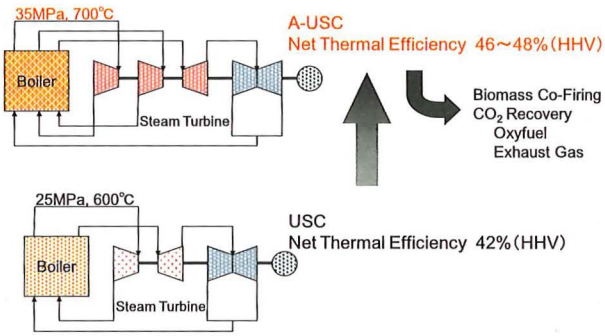

Figure 5 700deg-C class advanced USC (A-USC)

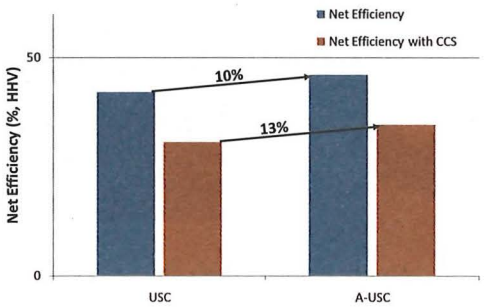

Figure 6 Efficiency of power plant with CCS (Post combustion capture)

A-USC was selected as one of technologies which are expected to contribute to substantial reductions in CO2 emissions through efficiency improvement by the Japanese government's 'Cool Earth-Innovative Energy Technology Program' in March 2008 [3]. The net thermal

efficiencies which are targeted by the Cool Earth Program are shown in Figure 7[4]. In the near future, A-USC and IGCC both aim at 46 to 48% efficiency.
We think that the A-USC technology is more suitable for the retrofitting of old coal power plants because the basic system configuration of A-USC is similar to that of the old plants. It will be possible to reuse many parts of the old plants such as their environmental equipment and water system.

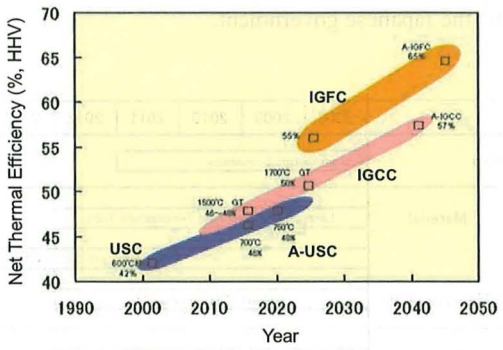

Figure 7 Net thermal effciencies of coal power plants (HHV) [4]

A typical example of material selection for A-USC is shown in Figure 8. The blue color represents conventional materials, green means gas turbine materials, pink means materials under development. And solid dark pink means Ni-based alloys under development. Ni-based alloys, which have not been used for USC, were chosen for a part of the super heaters and reheaters, the large steam pipes and the valves going from the boiler to the turbines, and a part of the turbine rotors and casings. The turbine nozzles and blades for the high temperature stages use Ni-based materials that are being used for gas turbines.

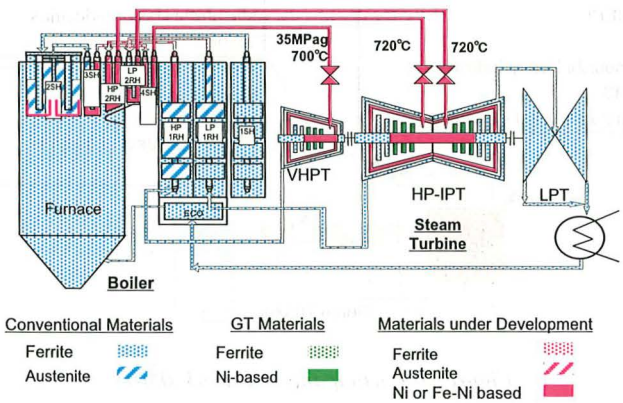

Figure 8 Selected materials for double reheat system

3. A-USC technology development project

A long term A-USC technology development project began in 2008. In the first half of the project, boiler, turbine and valve materials are being developed and verified. In the second half, boiler components and small turbine tests will be done to verify the reliability of each component (Figure 9). Throughout the project, long term creep rupture tests will be done on each candidate material and welded joint. The total budget for this project is 13 billion yen and 2/3 is subsidized by the Japanese government.

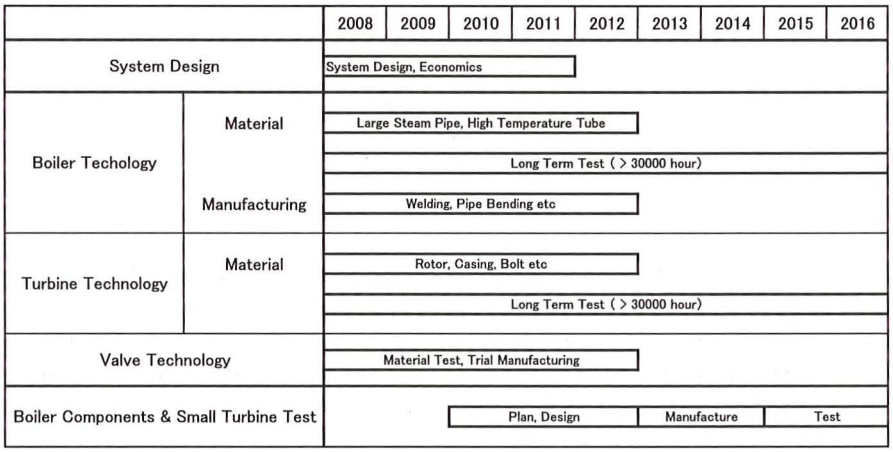

Figure 9 Master Schedule

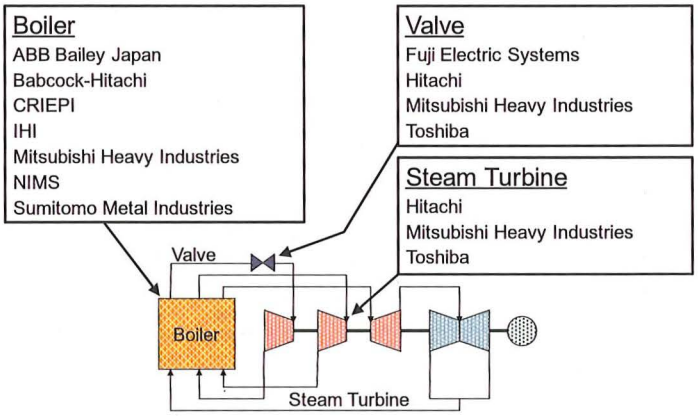

Figure 10 Participants and work share

10 companies and institutes, NIMS, ABB Bailey Japan, IHI, Sumitomo, Toshiba, Babcock-Hitachi, Hitachi, Fuji, MHI and Central Research Institute of Electric Power Industry (CRIEPI) are participating in this project (Figure10). ABB Bailey Japan, Babcock-Hitachi, CRIEPI, IHI, Mitsubishi, NIMS, Sumitomo are working together on the boiler technology development. ABB Bailey Japan is developing the valve technology for boiler valves. The boiler materials for testing are provided mainly by Sumitomo. Fuji is in charge of the valve technology for steam turbines. Hitachi, Mitsubishi and Toshiba are supporting Fuji's research. The steam turbine technology is being developed by Hitachi, Mitsubishi and Toshiba.

Once we decide to develop and use a new material, we need to thoroughly develop related technologies such as maintenance, fabrication, component, and system design technology (Figure 11). Long term reliability, high temperature corrosion resistance, steam oxidation resistance, and fatigue resistance are crucial characteristics for the material. Life assessment and welding technology for aged materials are necessary to repair used components. Welding, bending, and NDT technologies must be developed to fabricate components. Valves, desuperheaters, and headers are essential to build a boiler system. In addition to the hardware technologies, system design technologies, such as piping design, structural design, and thermal analysis are the key to the successful construction and operation of the boiler system. The companies participating in the project are working together to develop each technology.

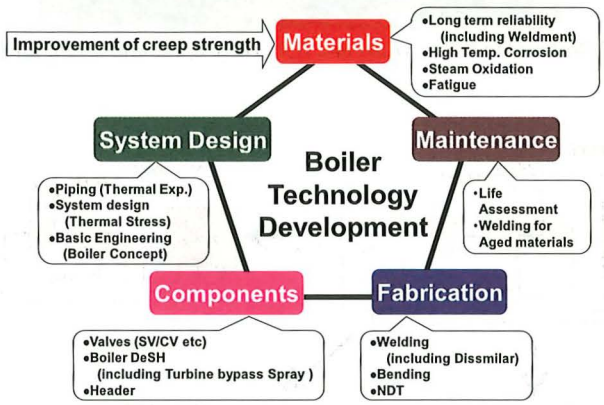

Figure 11 Boiler development tasks

Figure 12 shows the candidate materials for boilers which were prepared by Sumitomo Metals. HR6W is a Ni-Fe based alloy and HR35, Alloy 617, Alloy263, Alloy740, and Alloy141 are Ni based alloys for use at temperatures higher than 650deg-C. High boron 9Cr steel, low carbon 9Cr steel and SAVE 12AD are ferritic steels for use at temperatures lower than 650deg-C. These materials are being tested to verify the characteristics regarding creep rupture, fatigue, oxidation and corrosion. Welding and bending tests have been conducted to check the manufacturability of the materials.

A 100,000hr creep rupture strength higher than 90MPa at 750deg-C is the target for super heater tube materials. HR35, Alloy617, Alloy263, Alloy740, Alloy141 are the candidates for these. A 100,000hr creep rupture strength higher than 90MPa at 700deg-C is the target for large steam pipe materials. HR6W, HR35, Alloy617 are the candidates because they have favorable characteristics for making large pipes. The advanced 9Cr steels, B-9Cr, LC-9Cr, SAVE12AD are targeting 80MPa at 650deg-C. If these targets are successfully achieved, we will have a material list to build the system shown on Figure 8. In addition, as Figure 13 shows, we can select other system configurations to satisfy various customer needs.

Figure 12 Boiler Candidate Materials (Courtesy of Sumitomo Metal Industries)

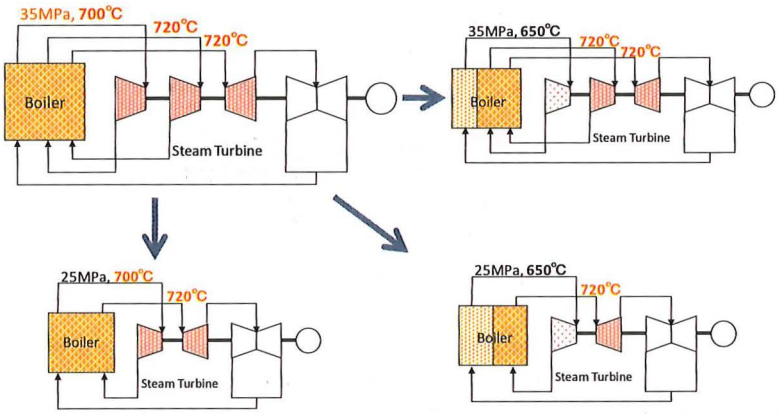

Figure 13 Variety of system configurations

Figure 14 shows an example of creep rupture strength which was derived from HR6W creep rupture tests. HR6W is being developed by Sumitomo Metals for pipes and tubes in the A-USC system, and designed to have good corrosion resistance to combustion gas in the boiler and good creep strength for pressurized pipes and tubes at 700deg-C. 100,000hr creep rupture

stress at 700deg-C is expected to be about 90MPa which is the target for large steam pipe materials

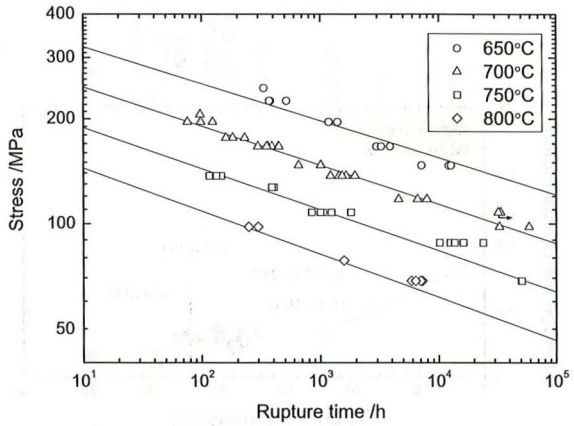

Figure 14 HR6W creep rupture strength (Courtesy of Sumitomo Metal Industries)

The creep rupture strength of HR6W weld joint is shown in Figure 15. Creep tensile specimens which contain welded portions were cut out from welded HR6W plates. Weld material was Alloy617. When tested, all specimens broke at base material. We can see that the strength of the welded material is equivalent to or higher than that of HR6W without weld joint.

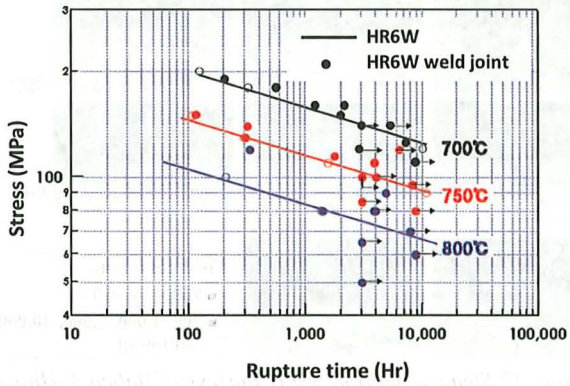

Figure 15 Creep rupture strength of HR6W weld
(Courtesy of Babcock-Hitachi, IHI, Mitsubishi Heavy Industries)

We have carried out the hot corrosion test on all candidate materials. Figure 16 shows the average metal loss after the 100 hr exposure test. All candidate materials were coated with compound ash, and then exposed to a gas containing sulfur dioxide, 0.2% by volume. The average metal loss decreases with the higher chromium content in the alloys. We confirmed

that the candidate materials and austenitic steels have good hot corrosion resistance because of their high chromium content.

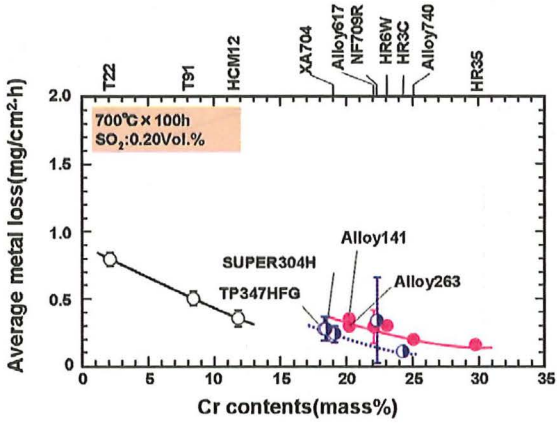

Figure 16 Hot corrosion test (Courtesy of Mitsubishi Heavy Industries)

Figure 17 shows the sections of the materials which have been exposed to 750deg-C steam for 3,000 hours. The thickness of the scale on the Ni based alloys is considerably smaller than the scale on the 25Cr steel, Ka-SUS310J1TB(HR3C). The test will be conducted for a total of 10,000 hours.

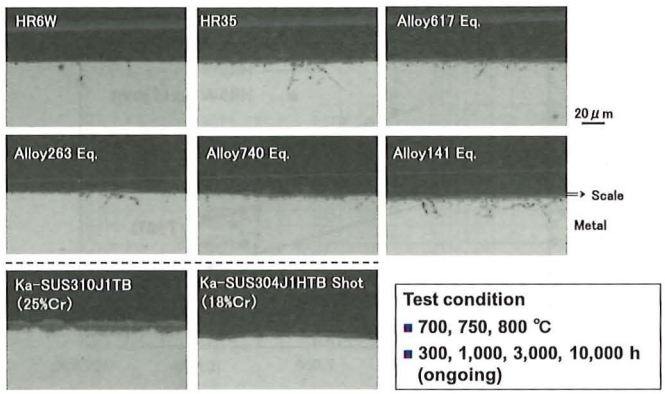

Figure 17 Steam oxidation test (Courtesy of Babcock-Hitachi)

Last year, we made pipes of HR6W, HR35 and Alloy617 using the Ehrhardt push bench method (Figure 18). These pipes were prepared in order to conduct material tests, such as welding, bending and the long term creep test.

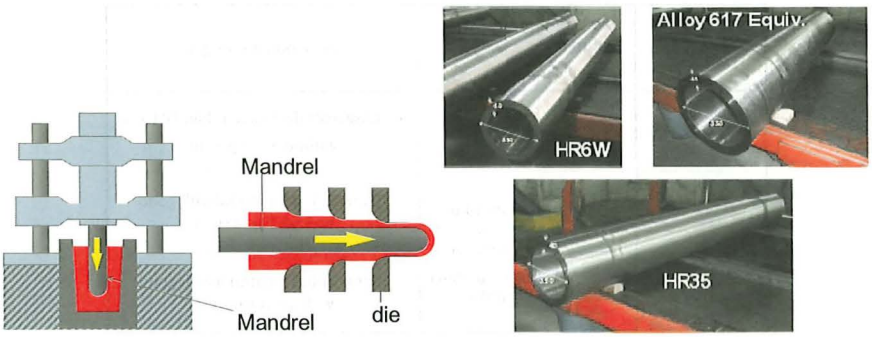

Figure 18 Pipes prepared for material test (Courtesy of Sumitomo Metal Industries)

Figure 19 shows bended pipes which are made of Alloy617 and HR6W. These pipes were cut into pieces to check the shape of the cross section and to make test specimens. Pipe welding tests are being carried out now. A sample of welded pipes is shown on Figure 20.

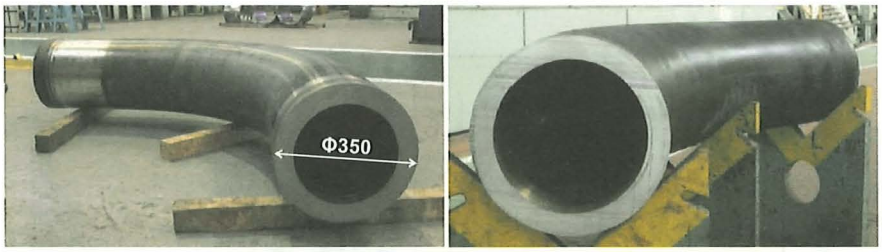

Figure 19 Pipe trial bending (Courtesy of Babcock-Hitachi and Mitsubishi Heavy Industries)

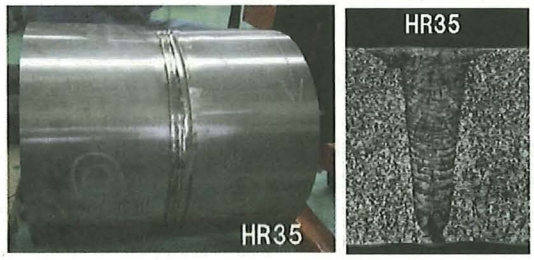

Figure 20 Pipe welding test (Courtesy of IHI)

There are three candidate materials for steam turbine rotors (Figure 21). Ni based alloys, *FENIX-700*, *LTES* and *TOS1X*, are being developed and tested for use at temperatures higher than 700deg-C. The aim of the development of *FENIX-700* is to build a rotor heavier than 10tons without segregation in the material. The purpose of *LTES* and *TOS1X* is to target a weight of around 10tons which will be welded to steel parts to make a 30 to 40-ton rotor.

Materials	Temper-ature Level	Weight	Development Target
FENIX-700	700°C	>10ton	Ni-base material heavier than 10 tons without segregation
LTES700R	>700°C	30～40ton ↑ Ni:10ton + Steel:20~30ton Welding	10 ton Ni-base material with good weldability to steel
TOS1X	>720°C		10 ton Ni-base material with good weldability to steel

Figure 21 Steam turbine rotor materials

FENIX-700 which has superior long-term stability at 700deg-C was developed from Alloy706 by reducing Nb content and increasing Ti and Al content [5]. More than 40,000 hours of creep testing have been done, so far (Figure 22). The 100,000 hour creep rupture strength at 700deg-C is expected to be higher than 100MPa.

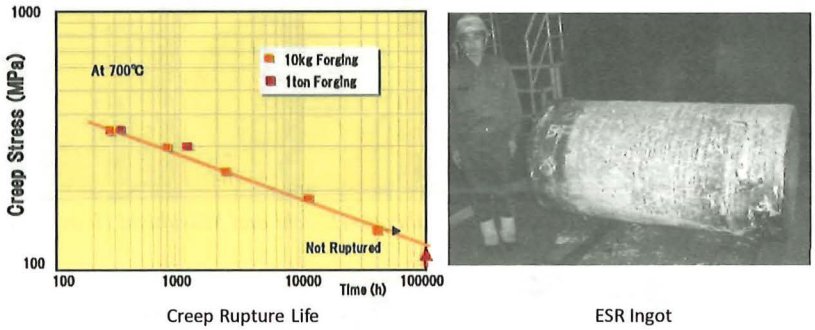

Figure 22 FENIX-700 (Courtesy of Hitachi) [5]

LTES700R is a Ni-based alloy that has been developed by Mitsubishi Heavy Industries. This alloy was developed to have a thermal expansion coefficient similar to 12Cr steel, so it conforms well to conventional steels (Figure 23). Originally, *LTES700* was developed for small parts, such as casing bolts. *LTES700R* was developed from *LTES700* for large steam turbine rotors. Welding technology is crucial for this material. Welding tests including the welding of dissimilar materials is being carried out. Figure 24 shows a disc made of 12Cr steel prepared to be welded to *LTES700R*.

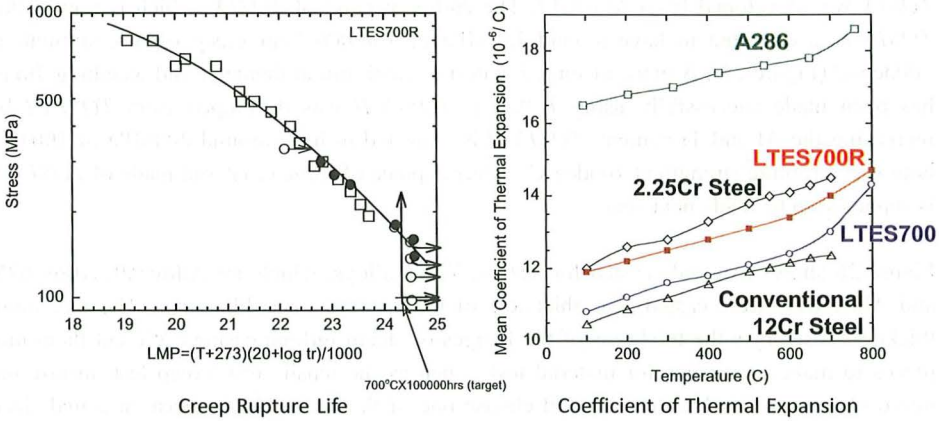

Figure 23 LTES700R (Courtesy of Mitsubishi Heavy Industries)

Figure 24 12Cr steel disc for welding test with LTES700R (Courtesy of Mitsubishi Heavy Industries)

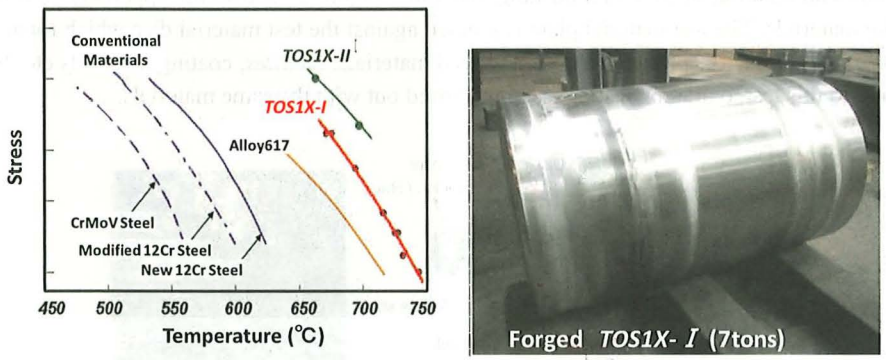

Figure 25 TOS1X (Courtesy of Toshiba)

TOS1X was developed from Alloy617. The earlier version of *TOS1X*, which is now called *TOS1X-I*, is expected to have around 150MPa of 100,000 hour creep rupture strength at 700deg-C (Figure 25). A piece of forged material, 1000 mm in diameter and weighing 7tons, has been made successfully using *TOS1X-I*. *TOS1X-II* was developed from *TOS1X-I* by increasing the Al and Ti content. *TOS1X-II* is expected to have around 200MPa of 100,000 hour creep rupture strength at 700deg-C. A larger piece of forged material made of *TOS1X-II* is supposed to be made next year.

Figure 26 shows materials casted for testing. Three alloys, which are Alloy740, Alloy 625, and Alloy 617, were casted. The thickness of the casting varies like steps. The maximum thickness resembles the thickness of the flanges of steam turbine casings. We cut them into pieces to make specimens for material tests, such as the tensile test, creep test, macro and micro observation and so on. We will choose one of these materials to cast an actual sized casing of a steam turbine valve.

Figure 26 Casted materials (Courtesy of Toshiba and Mitsubishi Heavy Industries)

We are testing valve materials, which rub against each other in 700deg-C steam, to find the optimum combination of stem and bushing materials. Figure 27 shows the apparatus used to test the materials. The test material plate is pressed against the test material disc which rotates at 300rpm. The materials tested here are Ni based materials, *Stellites*, coating materials etc. In addition to this test, oxidation testing is being carried out with the same materials.

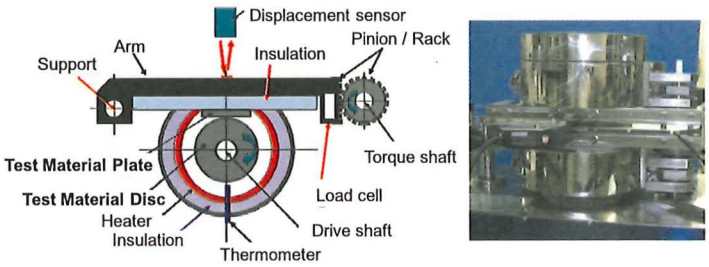

Figure 27 Valve material friction test (Courtesy of Fuji Electric Systems)

4. Conclusion

The development of the USC technology began in Japan in the '80's, aiming at a cleaner and more economical use of coal.
Today, almost half of the coal power plants have a 600deg-C class USC steam condition.
A-USC is one of the remarkable technologies being developed to reduce CO2 emissions from fossil fuel power plants and one which was chosen by Japan's 'Cool Earth-Innovative Energy Technology Program' which was launched in 2008 to contribute to substantial CO2 emissions reductions.
A large scale 9-year project began in 2008 to develop A-USC technology thoroughly. Major Japanese manufacturers of boilers and steam turbines and some institutes are cooperating in the project to develop the technology efficiently and quickly.
Almost two years from the beginning of the project, we have made some boiler materials and begun some fundamental tests, such as tensile, creep, welding, bending etc. Turbine rotor and casing materials have been forged and casted and are being tested as well. We are testing valve materials to find the optimum combination of stem and bushing materials.

References

[1] Fujimitsu Masuyama, Introduction to Advanced material Project for A-USC Plants, *8th International NIMS-MPA-IfW-Workshop on Advances in High Temperature Materials for High Efficiency Power Plants*, March, 2010.
[2] J-Power, Commencement of Commercial Operation of New No. 2 Unit at Isogo Thermal Power Station, available at http://www.jpower.co.jp/news_release/news090716.html.
[3] Ministry of Economy, Trade and Industry, "Cool Earth-Innovative Energy Technology Program", available at
http://www.meti.go.jp/english/newtopics/data/pdf/CoolEarth_E_revised.pdf.
[4] Ministry of Economy, Trade and Industry, available at
http://www.meti.go.jp/report/downloadfiles/g90630a01j.pdf, pp. 43.
[5] Shinya Imano, Jun sato, Koji kajikawa and Tatsuya Takahashi,
'Mechanical Properties and Manufacturability of Ni-Fe base Superalloy
(FENIX-700) for A-USC Steam Turbine Rotor Large Forgings'
5th international conference on advances in materials technology for fossil
power plants, EPRI, 2007

Product names mentioned herein may be trademarks of their respective companies.

9th Liege Conference : Materials for Advanced Power Engineering 2010
edited by J. Lecomte-Beckers, Q. Contrepois, T. Beck and B. Kuhn.

700°C POWER PLANT TECHNOLOGY – STATUS AND CHALLENGE

Helmut Tschaffon E.ON Energie

D-80333 München, Brienner Straße 40

Coal will remain an indispensable major source of energy for power generation in the world in the coming decades, because there are resources for hundreds of years. Coal fired power plants can be operated very flexible which gets increasing importance due to the stochastic input from regenerative energies like wind and solar energy. Sustainable technologies for coal-fired power plants have to be developed to optimise environmental protection and to save valuable resources and reduce CO_2 -emissions. Future coal fired steam power plants aim an elevated steam temperature of about 700 °C to reach a net efficiency of about 50%. This paper will give an overview over the status of the development of the 700°C technology and will highlight the challenges to be overcome before their commercial use.

The European way to a 700°C Power Plant started with the project AD700 in the year 1998. In this project the basic design of a 400 MW demo plant was done and some material tests and component qualifications for nickel-based alloys and new austenitic steels were started and terminated. AD700 delivered the basis of the design of the Component Test Facility COMTES700 (RFCS funded project with European manufacturers and utilities, see Figure 1). COMTES700 was operated between 2005 and 2009. It was integrated into the E.ON power plant Scholven in Germany to test mainly nickel based materials and power plant components. In the project NRWPP700 (2006-2010, funded by NRW and financed by European utilities) the detail design of the steam generator, piping system and turbine of a 500 MW power plant was done. In 7 material projects the qualification of components and materials was supported. At the same time a lot of national and international R&D projects (e.g. MARCKO and COORETEC) were performed. Due to the high amount of these projects they cannot be mentioned here in a detailed way. In 2007 the E.ON project 50plus was started. The aim was to plan and build a 700°C demo plant in Wilhelmshaven. The project was accompanied by a lot of additional material projects with the aim to qualify production procedures and manufacturers. Due to the later on described open challenges the project had to be stopped in 2010.

Figure 1: Parties involved in the COMTES700 project

Public funding:	European Commission (RFCS)
Host Plant:	PP Scholven from E.ON Kraftwerke
Coordinator:	VGB
Suppliers:	Alstom, BWE, Hitachi, Siemens
Utilities:	DONG Energy, EDF, Electrabel, EnBW, Enel, E.ON Energie, EVN, PPC, RWE, Evonik, Vattenfall

In the following chapters the results of some main projects are shown.

1. COMTES700

COMTES700 was operated between July 2005 and August 2009. Until 2011 the project will be evaluated. In Figure 2 the flow chart, the used materials and components and some characteristic photos were shown. The objective of the COMTES700 project was to design, manufacture, erect and operate high temperature materials needed to realise a coal fired 700°C power plant.

Figure 2: COMTES700 evaporator and superheater

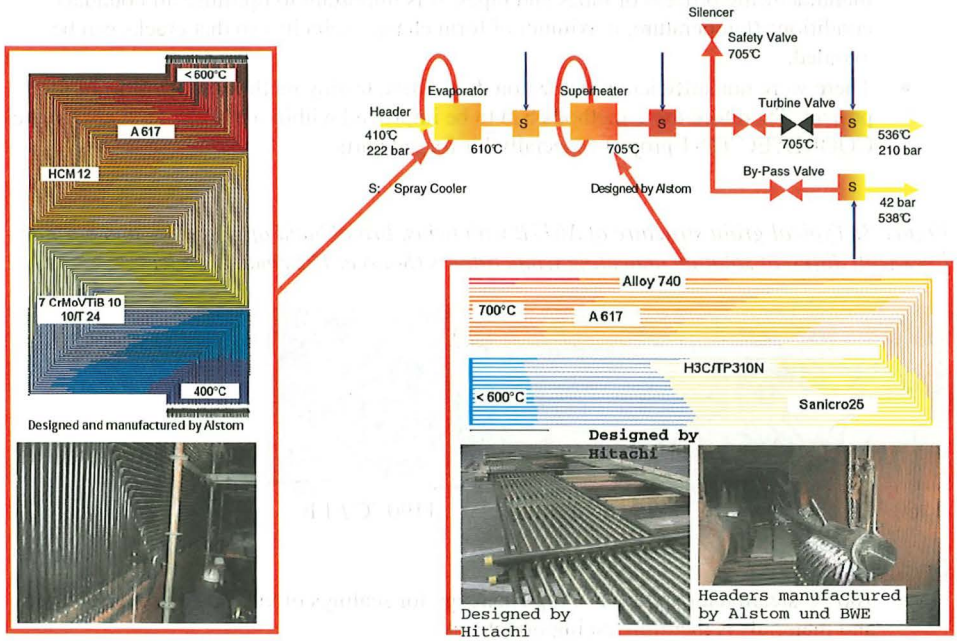

So in COMTES700 the following components were tested:

- Evaporator panel operated as superheater
- A number of superheater banks including a steam header
- Injection of water to control temperature
- A long steam line
- Different valves (forged and casted)

During the manufacturing phase and the four years of operation with more than 20,000 hours a lot of information was gained. After the ongoing evaluation phase the report will be ready in the year 2012. The following important knowledge can be pointed out:

Manufacturing of parts:

- Manufacturing of components of nickel-based alloys needs a lot of experience, special machines and allowances. With COMTES700 and other projects we succeeded to qualify a lot of companies and production procedures in Europe.
- Forging thick walled components brings the risk of increasing grains, which can have a negative influence on material properties. Solution annealing temperature or time, design of the component, forging and cooling conditions can have a big influence. With increasing solution annealing temperature the grain size increases as shown in Figure 3. A lot of experience is needed to get the right conditions for optimised forgings.
- The high strength of Alloy materials can lead to cracks on the surface during the manufacturing process of tubes and pipes. It is important to optimise all boundary conditions (temperature, maximum of form change velocity) so that cracks can be avoided.
- There were not sufficient reliable non destructive testing methods at the start of the project. Therefore these methods had to be improved within the project but also in the COORETEC TD-1 project especially for forged parts.

Figure 3: Typical grain structure of A617B with twins, broad band of grain size and carbide lines with different solution annealing temperatures (Source: Husemann, Bader)

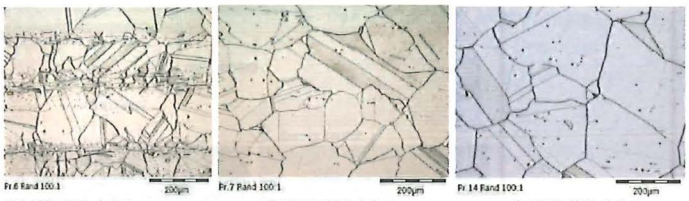

1160 °C / 1 h 1175 °C / 1 h 1190 °C / 1 h

Operation:

- 700 °C steam temperature is a big challenge for sealings of valves. Improving design and materials is therefore an important task.
- Some thick walled A617B pipes (wall thickness 50mm) cracked (see Figure 4). In any case we registered first a leakage of the pipes, so the material is ductile enough. All cracks appeared in the welds or in the heat affected zone and were circumferential Additional forces caused by the welding procedure, very high temperature differences from the water injection in the attemperator and restraint of the expansion are supposed to be the reasons for the cracks.
- With the start of operation there was no repair concept for aged A617B pipes. The usual way to repair pipes (with and without heat treatment) led to many indications in the welds. The time consumption to get a sufficient weld was therefore very high, because they had to be grinded, examined with PT and than rewelded.
- Different non destructive examinations (PT and UT) were tested in the test rig. In the end enough methods were developed for safe detection of defects at the surface and in the volume of the pipes with a wall thickness up to 50mm.

Figure 4: Crack in a COMTES700 pipe

In May 2010 the COMTES700 team decided to enhance the tasks of the project due to the experiences which were made in the test rig.

An "Additional Investigation" program was launched with the following tasks:

- Find the cause of PT indications at repaired weld seams after 500h of operation
- Development and verification of a repair concept on service exposed A617B material including creep tests
- Tests on piping with circumferential welds for service exposed material
- Attemperator failure assessment
- Crack growth rates under thermo mechanical loading conditions
- Valve investigation
- Consumed lifetime

Combined with the knowledge out of the original planned evaluation program a broad knowledge base for manufacturing and operation of components out of nickel-based alloys up to 50mm wall thickness for forged A617B parts and up to 80mm for casted A625 parts will be available end of 2011.

2. Design of a 550 MW_{gr} Demonstration Plant (NRWPP700 and 50plus)

In the pre-engineering study NRWPP700 (duration: 2006 until 2010, see Figure 5) the design of a coal fired 550 MW_{gr} demonstration plant was fixed. The focus was on the 700°C components steam generator, piping system and turbines. In the first phase the basic engineering for three designs for the tower boiler was done. Burmeister&Wain, Babcock Hitachi and Alstom Power worked out the variants. The detail engineering was done by Alstom for the chosen boiler design (single reheat, hp-conditions: 350 bar, 705°C). Siemens planned the turbine island. E.ON Engineering was responsible for the piping system. The costs for the power plant were calculated. In addition the basic design for commercial 1000 MW power plants with tower boiler fired with lignite and coal was done.

Figure 5: Parties involved in the NRWPP700 project

Funding:	State of NRW and European Commission
Coordination:	VGB
Project partners:	DONG Energy, EDF, Electrabel, EnBW, E.ON Energie, Evonik, EVN, RWE, Vattenfall
Supporter:	Enel
Contractors:	Alstom, BWE, E.ON Engineering, Hitachi, Siemens

Beside the design the manufacturing resources were examined. It was shown, for which components enough suppliers are qualified and where there is a necessity to find additional providers. Mainly for thick walled components (forged, casted, welds, NDE) we have to qualify additional suppliers.

An important work within NRWPP700 was the execution of 7 material projects:
a) Steam generator projects:

- Manufacturing, bending and welding of a A617B superheater tube with 10mm wall thickness
- Qualification of a A740 superheater weld
- Formability of A740 and A617B under cyclic conditions

b) Piping system projects:

- Manufacturing and examination of a A617B hp pipe. (da=350mm, s=72,5mm)
- Manufacturing and examination of a A617B bypass valve (da=600mm)
- Manufacturing, bending and welding of a A617B ip pipe (centrifugal casted, da=488mm, s=30mm)

c) Steam turbine project:

- Manufacturing and examination of a dissimilar shaft weld (A617B to 10% and 2%Cr-steel)

These material projects deliver some basics for the construction of a 700 °C power plant. The detailed results will be published by VGB.

Parallel to this study E.ON started end of 2006 with their plans for a 700 °C power plant in Wilhelmshaven (50plus) which should have the same power output of 550 MW_{gr} and an efficiency of about 50%. In connection with 50plus a lot of additional R&D work was done to qualify manufacturers and production processes. The aim was to get more than one supplier for every 700 °C component. For some important parts (e.g. pipes) E.ON tried to develop together with the suppliers different production processes. In the end we have now the possibility to manufacture thick walled pipes as a drilled and forged shaft, as extruded pipe and as a pilgered one. For ip pipes we can also use the Erhardt procedure. This gives us the opportunity to choose between different offers.

The 50plus R&D program covered different Nickel-based materials (A617B, A625, A740). We worked together with manufacturers for steam generator, piping system and turbine as well as companies or institutes for tasks like examinations, approvals and production of welds. Especially for the turbine projects we have the duty to keep confidentiality.

To mention one example E.ON worked together with TNO to reduce the forces caused by the welding procedures in thick walled components. We compared the crack behaviour of new A617B welds (see Figure 6) with and without a heat treatment with 980°C and 3 hours. TNO used a 3 point bending test for their examinations. The result was that without heat treatment the material does not withstand the high forces of the test and cracks interdendritic. With heat treatment the internal forces were reduced and the bending test led only to very small cracks. The ductility of the material increased. This test can also be made with base and/or aged material. In any case the improvement with heat treatment is evident, but we also recognise that the sensitivity of new base material without heat treatment is very low.

For verification that the heat treatment does not reduce creep values additional creep tests were started in 2009. Up to now all registered values are within the scatter band of A617B. If this intermediate result will be confirmed an important procedure was found to handle thick walled A617B parts.

Figure 6: TNO-test: Crack behaviour with and without heat treatment with 980°C, 3h

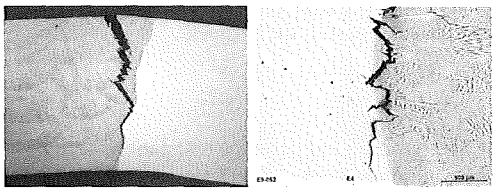

Without heat treatment: Interdendritic macro crack in the weld metal next to the fusion line propagating towards the HAZ

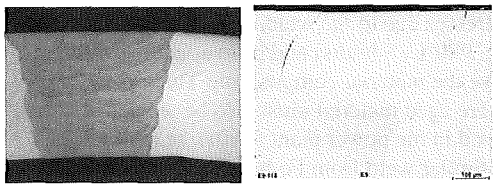

Nearly no cracks with heat treatment (high ductility of the material)

During the operation of COMTES700 and the execution of the other R&D projects we learned that it is advisable to adjust the time schedule for the erection of a 700 °C power plant. We have to get first more experience.

3. Residual R&D for a 700 °C power plant

Before the erection of a 700 °C power plant it is necessary to reduce the risk of operation, to enlarge the amount of suppliers in some cases and to reduce the costs. The operational risk must be in the height of normal coal fired power plants. The additional investment costs have to be in the right proportion, regarding at the cost reduction due to a higher efficiency.

Therefore manager of the suppliers and the utilities worked out a task list for additional R&D. This list led in the end to the following R&D program:

3.1 Verification of technical challenges in additional test rigs

The main remaining challenges of the 700 °C technology should be solved in additional test rigs. They should have the task to reduce the operational risk and the production costs. The primary task of the projects should be to test

- very thick walled components,
- repaired COMTES700 pipes,
- components which are produced by an innovative procedure which can reduce the producton costs effectively,
- an improved composition of A617B for a better weldability,
- a procedure to calculate life time consumption during operation and
- the dynamic behaviour of components.

Potential partners for such projects should be utilities and manufacturers which were involved in 700°C projects in the last years. Due to the increasing importance to save resources it should be possible to convince additional partners to take part in the projects.

3.2 Alloy617 membrane wall

For a 700 °C power plant with a hp pressure of 350 bar high temperature resistant materials are necessary for the membrane wall. One of the candidates is the Nickel-based alloy 617B. Within the project Marcko700 a cyclic membrane test was done (see Figure 7), but it did not lead to a sufficient result. Cracks appeared even with a very low load. The reason(s) for the failure have to be evaluated and a new project has to be started with adapted conditions. One of the causes of cracks may be high residual stresses due to the welding procedure. Therefore it may be necessary to do a heat treatment (e.g. 980°C, 3 hours) and/or to adapt the welding procedure to reduce these stresses or to improve the material composition. The repair concept is also an important part of the project. Therefore aged material must also be welded and then examined. To reduce costs of the membrane wall in the power plant ferrites or martensites will be used where possible. Therefore the dissimilar weld from Fe-based to Nickel-based material must also be part of the examination.

At the moment the project proposal will be worked out and is foreseen to be discussed and applied within the COORETEC program in this year. MPA Stuttgart wants to do the scientific work. FDBR is coordinating the work. The application is foreseen to be sent out end of 2010. The project is at the moment scheduled to last 4 years.

Figure 7: Stress/time diagram from Marcko700 (Source: MPA Stuttgart)

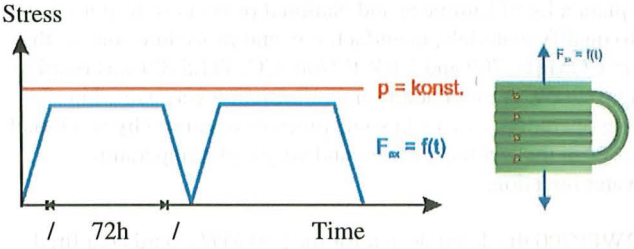

3.3 NDE for casted Alloy625 (COORETEC TD-2)

In COORETEC TD-1 the boundaries for NDE of forged Nickel-based alloys were determined. Different methods especially for ultrasonic testing were examined. In the next phase it is necessary to do the same work with casted Nickel-based materials (e.g. Alloy625). The wall thickness of casted materials in a 700°C power plant can be more than 200mm. Therefore beside PT and UT we have to use a linear accelerator for NDE. Therefore German utilities and manufacturers intend to bring this project forward. VGB is working out the project content and is looking for partners. The application is foreseen to be sent out end of 2010. The project is at the moment scheduled to last 3 years.

3.4 Other open R&D tasks

There are a lot of other activities which should be initiated to bring the 700 °C technology forward. It is not possible to describe them all in this paper. So I will only mention some.

In the future optimisation of materials by simulation will get an increasing importance, because it should be cheaper to model the properties of materials or components in a computer program than to do the work by vary the hardware. To reach this aim it is first necessary to develop these programs for the base and welding materials and to have enough data for validation. In a planned DFG project some German institutes are on the way.

Gamma prime hardening alloys (A263, A740) have a higher strength at 700 °C than A617B, but they may have some disadvantages for example in welding. Therefore it is necessary to examine their relaxation behaviour more deeply and to develop an optimised welding procedure for new material with/without heat treatment and a repair concept for aged material.

T24 is used in the membrane walls of modern coal fired power plants. As we now know under certain circumstances cracks can appear especially in the welds. The optimisation of production procedures but also the composition of the (weld) material can be subject of further examinations.

4. Summary

On the way to the 700 C power plant a lot of European and National projects were started and realised. Beside many projects to qualify materials, manufacturers and procedures one of the main projects of the last years are COMTES700 and NRWPP700. COMTES700 was running for about 22.000 hours until August 2009. A lot of additional information was gained in the production process but also during operation. Cracks in some pipes were caused by additional forces, which may have their causes in the welding process and very high temperature differences in the pipes due to water injection.

In the pre-engineering study NRWPP700 the detail design for the 550 MW_{gr} hard coal fired 700 °C power plant was developed. A lot of additional material projects deepened the knowledge of the Nickel-based alloys.

There are some important challenges remaining out of the past projects. The repair concept of aged Nickel-based alloys has to be developed and tested. Very thick walled forged and casted alloy components have to be manufactured, welded, examined and tested. Production costs have to be reduced by innovative procedures. The sensibility of alloys against relaxation cracking should be examined more deeply and decreased by optimisation of material composition, welding procedures and heat treatment.

If all the planned projects can start soon and lead to a satisfying result it is possible to start with the project phase of a 700 °C power plant after the year 2016, start of operation can be about 5 years later.

9th Liege Conference : Materials for Advanced Power Engineering 2010
edited by J. Lecomte-Beckers, Q. Contrepois, T. Beck and B. Kuhn.

THE EUROPEAN EFFORTS IN DEVELOPMENT OF NEW HIGH TEMPERATURE ROTOR MATERIALS – COST536

T.-U. Kern [1], K.H. Mayer [2], B. Donth [3], G. Zeiler [4], A. DiGianfrancesco [5]

[1] Siemens Energy, Muelheim, Germany
[2] Alstom Power, Nuremberg, Germany, [3] Saarschmiede, Voelklingen, Germany
[4] Boehler Schmiedetechnik, Kapfenberg, Austria
[5] CSM, Roma, Italy

Abstract

Despite the ongoing efforts to increase the amount of available alternative energy sources, fossil fuels such as lignite and hard coal will remain important for the energy mix and sustainability of energy supply. Fossil-fuelled Steam Power Plants (SSP's) or Combined Cycle Power Plants (CCPP's) will also continue to supply a significant portion of our energy needs.
Within the frame of European COST536, a new project was installed with the aim of Alloy development for Critical Components of Environmentally friendly Power planTs (ACCEPT) aiming for material solutions for steam conditions up to 650°C.
Martensitic materials should be used for thick-walled components to maintain high operational flexibility of such large plants. Rotors, casings, bolts, tubes, pipes, and water walls, are the critical components under current investigation. The class of the 9-12%Cr steels offers the highest potential to meet the required property levels for critical components such as rotor forgings. Therefore a significant effort to increase the application temperature of these steels was and is the focus of studies within Europe. Although there are 600°C materials already being successfully utilised in a number of advanced European power plants, further improvement in creep strength is being achieved by the addition of Boron and a well balanced Co content. Full-size prototype components are now being tested.
New ideas to improve the behaviour and increase the application temperatures are under investigation. Results are reported here.

Keywords: COST536, 10Cr steels, high-temperature application, creep strength, material development

1. Introduction

Energy is the source of general well-being and the standard of living in each country. In the coming decades, there will continue to be heavy reliance on fossil fuels, such as coal, oil and natural gas. Power plant utilities are forced to increase the efficiency of their plants for environmental and economic reasons.
This improvement in efficiency of modern steam power plants is related to raising the temperature as well as the pressure of the steam generated in the boiler. New materials are required with improved high-temperature capability. At the same time the material solution has to be cost effective and reliable. Here the steels of the 9 to 12%Cr class have shown highest potential in long-term creep strength and oxidation resistance in steam, along with ease of fabrication for large forgings, castings and pipe sections.
In Europe, the efforts to further improve the available 9-12%CrMoV steels have been concentrated in the COST programmes, COST501 (1986-1997), COST522 (1998-2003) and COST536 (2004-2009) [1-3]. The resulting improved steels are in commercial operation in advanced European power stations and have made it possible to increase the operating steam temperatures from a range of 530-565°C to 580-620°C with a corresponding increase in thermal efficiency. This article describes the work performed in Europe within COST536 to improve the basic knowledge and to develop improved steels for large rotor forgings.

2. Rotor Materials Requirements

For power ranges up to 1,000MW, several basic steam turbine types with the following thermodynamic characteristics are possible:
- High pressure (HP) turbines with high temperature and pressure (≥530°C/ ≥180bar)
- Intermediate pressure (IP) with high temperature and reduced pressure (≥530°C/ ≥30bar)
- Low pressure (LP) turbines (≤ 350°C/10bar)

Combined HP-IP and IP-LP turbines for the smaller power range for Combined Cycle Power Plants (CCPP) complete the solutions for power generation with steam turbines.
Specific design requirements for the single components have to be met by the materials in order to offer a certain flexibility in fulfilling the various customer needs for the power plant.
The property profile of rotors for temperature application T>450°C and the appropriate material properties are given in *Table 1*.

Table 1: Requirements and material properties for steam turbine high-temperature rotors

Requirement in design and service	Material property
Static strength	Tensile strength (UTS) 0.2 Yield Strength (0.2YS)
Long-term strength	Creep Rupture Strength (CRS) Creep elongation limits (CEL)
Toughness - short-term - long-term	 Fracture toughness (K_{IC}) Creep rupture elongation Toughness values after long-term aging
Fatigue strength	Low Cycle Fatigue (LCF) High Cycle Fatigue (HCF) Creep Fatigue Interaction (CFI)
Crack tolerance	Static: Creep Crack Growth behaviour (CCG) Alternating: Fatigue Crack Growth (FCG)
Oxidation resistance	Steam oxidation behaviour
Erosion resistance	Erosion behaviour

As shown, the HP and IP rotor forgings, which can reach diameters of up to 1,200mm, need to be made in carefully selected material in order to meet all property requirements. Creep behaviour plays an important role for areas such as the rotor centre and the blade attachment, whereas the fatigue resistance is mainly considered in the surface regions.
The material class of the 9-12%CrMoV steels meets well all boundary conditions relevant for a flexible design:
- A good through-hardenability up to larger diameters >1,000mm
- Balance between strength and toughness (short and long term)
- Physical property profile
- Weldability
- Potential for high oxidation resistance
- Lower cost than Austenites and Ni-base alloys and ease of fabrication

The development aim for new high class materials in Europe was defined as follows:

- 100,000 h creep rupture strength at target temperature (≤650°C) of about 100 MPa
- Good creep rupture ductility (>10% elongation), and no notch sensitivity
- Through-hardening up to at least 1,200 mm diameter
- Minimum 0.2-yield strength of 700 MPa
- Other properties such as toughness and susceptibility to embrittlement should not be worse than with conventional 12%CrMoV and 1%CrMoV rotor steels

Details about the achievements in COST536 are described in the following chapters.

3. Materials Development in Europe

3.1. Rotor Material Qualification for 620°C

The outcome of the previous round, COST522, was the demonstration of the manufacturability of large rotor forgings in the alloy with the highest potential for 620°C application which is a 9Cr-1Mo-1Co-100ppm Boron type material named FB2.
Three trial rotor forgings have been manufactured in Europe. The forgemasters Boehler Kapfenberg/Austria, Saarschmiede/Germany and Societa delle Fucine, Terni/Italy, started with the same material specification but have followed different steelmaking routes [3, 4]. Boehler/Austria has used a 29to ingot made by Boehler-BEST process, a pouring process with special measures to improve the homogeneity of the ingot.
SdF Terni/Italy has applied the steelmaking process VCD with an ingot weight of 53to.
Saarschmiede/Germany has used their wide experience in ESR melting by making an ingot of 56to weight.
A summary of the main prototype rotor dimensions are given in *Figure 1*.
The largest diameter D2 with 1,100mm to 1,200mm is comparable for all three rotor forgings. Heat treatment parameters have been chosen to fulfil strength requirements of 0.2YS(RT) >700MPa. The heat treatment conditions used for final quality heat treatment are given below. The double-tempering applied previously for the 600°C alloys of the COST material family was again chosen to ensure a fully tempered martensitic microstructure, *Table 2*.

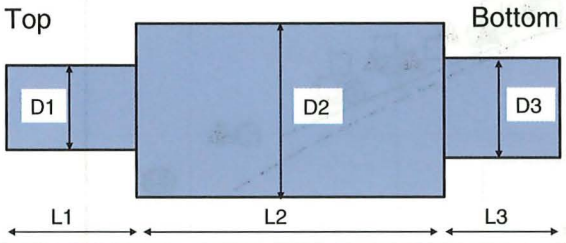

Forge-master	Process	D1 mm	D2 mm	D3 mm	L1 mm	L2 mm	L3 mm
Boehler/A	BEST	770	1180	865	1350	930	1110
Terni/I	EAF+ ASEA	925	1110	790	800	2750	830
Saarschm/ D	ESR	800	1215	1050	1085	2130	800

Fig. 1: Dimensions of the COST trial rotor forgings in FB2 composition made in Europe

Table 2: Quality heat treatment conditions for COST FB2 trial rotor forgings

	Austenitizing 1,100°C	**1st tempering 570-590°C**	**2nd tempering 700°C**
Boehler / Austria	10h/ water-air spraying	22h/ air	22h/ air
SdF Terni / Italy	17h/ oil	24h/ air	24h/ air
Saarschmiede / D	16h/ water spraying	22h/ air	22h/ air

The NDT results show a minimum detectable flaw size of 1.5-2.0mm for the rotor body location. The quality of the rotor forgings was inspected by determining the basic strength and toughness values at different positions showing the homogeneity in different former ingot locations (top, middle, bottom of ingot) and from surface to centre [4].
The long-term creep strength determination of the trial rotor forgings is ongoing. Maximum testing times achieved so far are 55,000 h. The results show that all three rotor forgings confirm the behaviour of the 500kg trial melt, as in *Figure 2*.
For comparison, reference lines are given for the 600°C materials COST Rotor-E (10Cr-1Mo-1W) and COST Rotor-F (10Cr-1.5Mo) together with the line of material B2. Alloy B2 of COST501 containing 0.18C-1.5Mo-100ppm Boron was the benchmark for further improvements of European 9-10%Cr steels. The results show that the FB2 rotor forging data are well above the reference lines offering therefore improved creep rupture strength values for the high temperature design. The rupture ductility is maintained on a high level which means that notch weakening effects can be excluded. The homogeneity of the long-term properties resulting from the different steelmaking processes is still under investigation.

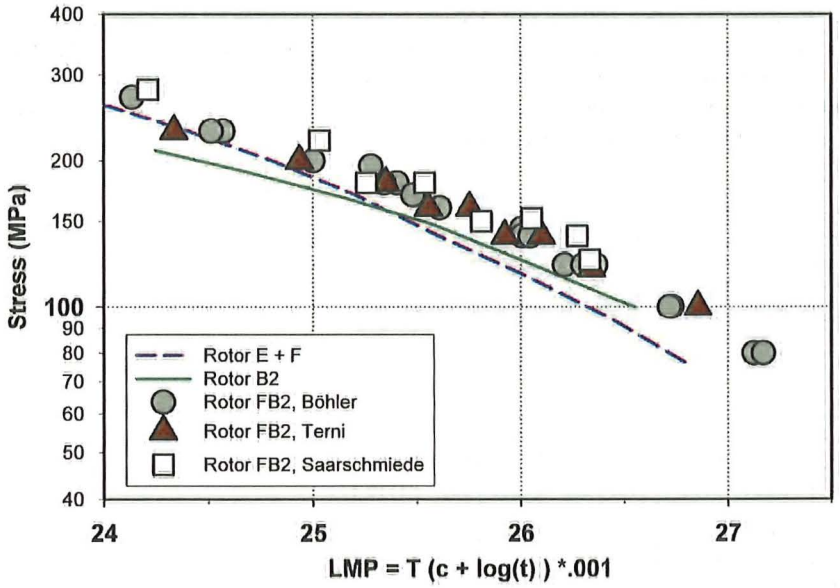

Fig. 2: COST trial rotor forgings FB2, lon- term creep strength in Larson-Miller plot, position middle of ingot, surface

Other properties like high temperature strength, toughness, low cycle fatigue strength, and fracture toughness, are not so different from the known range of 9-12%Cr steels. Furthermore the weldability of FB2 is improved compared to rotor B2. No changes in design rules have to be made by applying this material.
To summarize, it can be stated that with the chosen balance in chemical composition and the applied manufacturing processes the requirements for high-temperature rotor forgings up to 620°C application are well fulfilled.
Currently there are new USC Steam Power Plants under construction in Europe which apply the FB2 rotor material in the high-temperature area.

3.2. Material Development for Application Temperatures above 620°C

Additional improvement of the ferritic-martensitic grades is necessary with respect to creep strength. Experience has shown that steels with higher microstructure stability also show higher long-term creep strength. The development work so far was based on the knowledge acquired under the COST501 and COST522 programmes, especially the intensive microstructure investigations, the commercially available computing tools such as ThermoCalc and Dictra, the newly developed calculation methods of the equilibrium transformation temperature, and the diffusion parameters of potential candidate test materials.
On the basis of the promising composition FB2, different strategies have been developed to follow in the further work packages.
The first block is dealing with experiments to replace Niobium by Tantalum.

3.2.1. Replacement of Niobium by Tantalum

The idea was to investigate the role of Niobium and Tantalum in the long-term creep stability. It originated in a German basic research project (DFG) in which around 80 different model steels were investigated with Cr contents of 11% to 13% and additional variations of the alloying elements W, Mo, Cu, V, Nb, Ta, N and B [5, 6]. Based on this, three different 50kg melts have been produced.
The Cr-content was fixed for two alloys FN6-Ta and FN7-Ta at about 11% to ensure sufficient oxidation resistance. In order to generate a ferritic-martensitic microstructure with precipitates of M23(C,B)6, MX and Laves phase, the different choices of alloying elements were made as in *Table 3*.

Table 3: Chemical composition and heat treatment of the Ta trial melts

Melt	C	Cr	Mo	Co	W	V	Nb	B	N	Ta	B/N	QHT °C	0.2YS at RT MPa
FB2	0.13	9.4	1.50	1.0	-	0.21	0.070	0.010	0.020	-	0.50	1100 710	714
FB2-3 Ta	0.12	8.9	1.49	1.0	-	0.20	0.003	0.013	0.009	0.08	1.44	1150 700	680
FN6-Ta*)	0.19	10.9	0.53	1.0	2.0	0.28	0.006	0.023	0.014	0.08	1.64	1150 765	636
FN7-Ta*)	0.19	11.0	0.48	1.0	2.0	0.27	0.006	0.012	0.009	0.08	1.33	1150 765	597

*) FN6-Ta: 0.71%Cu, FN7-Ta: 0.73%Cu

The rationale can be summarized as follows:

- balanced amounts of Co, Mn, C and Cu to obtain a ferritic-martensitic matrix
- Cr, W, B and C for strengthening by M23C6 precipitates
- W for strengthening by Laves phase
- Cu to promote a fine distribution of Laves phase by nucleation at Cu-precipitates
- V and Nb or Ta for strengthening by MX precipitates

Trial melt FB2-3Ta is based on FB2 composition with higher Si content for steam oxidation resistance, a changed B/N ratio, lowest Ni content, and replacement of Nb by Ta.

On the basis of calculations with the software ThermoCalc the heat treatment was specified as Austenitizing at 1,150°C and tempering at 700°C or 765°C to dissolute Boron and carbides of different type and to stabilize the microstructure. The results are shown in *Figure 3.*
The results for the trial melt FB2-3Ta suggest that Tantalum in the chosen alloy composition at 650°C creep rupture testing would not be more effective than Niobium for a replacement ratio Ta/Nb = 1.14 compared to FB2. At the same time, the effect of lower creep strength is also affected by a lower Nitrogen content (only 50% of FB2) causing possibly a deficit in strengthening MX particles.
Compared to FB2 the melts FN6-Ta and FN7-Ta contain a higher percentage of C, Cr of about 11%, less Mo, 2%W, and different amounts of Boron and Nitrogen. But even FN6-Ta with the highest Boron content of 230ppm does not exceed the reference line for COST rotor B2 with 100ppm Boron meaning that there is no advantage observed. Therefore the tests will be interrupted. The reason for the low creep strength is not fully understood yet. Different aspects can play a role if the chemistry is compared to FB2, such as a possible effect of missing MX (lower N content), higher Cr content (11%), replacement of Mo by W, replacement of Nb by Ta. The COST group will deal with these aspects in the near future.

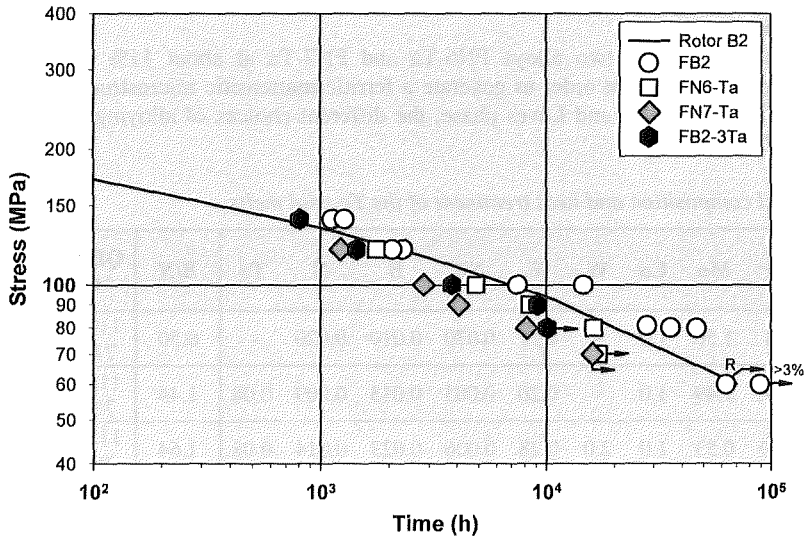

Fig. 3: Creep rupture strength of the COST trial melts with Tantalum at 650°C

3.2.2. The Role of Niobium, Boron, Nitrogen and Heat Treatment

A second work package deals with modifications made in the C-, Cr-, B-, N- and Nb-contents, and by the addition of W in one case.

The melts FB2-3, FB2-5 und FB2-6 are based on FB2 but reflect different ideas: the Nb is reduced, the B/N ration is increased up to B/N=3.5, the QHT was changed once in Austenitising temperature to 1150°C, and the first tempering temperature was increased to T1=700°C with the aim of improving the microstructure stability, *Table 4*.

The test data up to 10,000h show that the alloy FB2-6 with the highest B-content is not clearly improved compared to FB2-3. The B/N ratio is twice that of FB2-3 but a large effect has not been observed yet, as in *Figure 4*.

Melt FB2-5 with the lowest N content but about the same B/N ratio as FB2-6 seems to behave better. It is note worthy that FB2-5 had a modified Austenitizing temperature of 1,150°C. Further tests have to clarify which effect this change will have in the long term.

The melt FB3-1 was made by replacing the 1.50% Mo of FB2 by W and reducing the N content to 1/3 of FB2. At the same B content like FB2, the B/N ratio is therefore increased to B/N=1.14 compared to 0.5 for FB2. The first annealing temperature was also increased to T1=700°C for microstructure reasons. There are no disadvantages in creep observed up to 10,000h.

Further tests have to show which concept can offer further advantages compared to FB2.

Table 4: Chemical composition and heat treatment of the trial melts with different B/N ratios

Melt	C	Mn	Cr	Mo	Co	W	Nb	B	N	B/N	QHT °C	0.2YS at RT MPa
B2	0.16	0.06	9.3	1.60	-	-	0.060	0.010	0.015	0.67	1100 570/700	650
FB2	0.13	0.90	9.0	1.50	0.96	-	0.065	0.010	0.020	0.50	1100 570/710	714
FB2-3	0.15	0.35	9.4	1.60	1.10	-	0.035	0.017	0.010	1.70	1100 700/700	660
FB2-5	0.13	0.15	9.0	1.54	1.00	-	0.034	0.021	0.006	3.50	1150 700/700	665
FB2-6	0.15	0.35	9.4	1.60	1.10	-	0.035	0.032	0.010	3.20	1100 700/700	691
FB3-1	0.14	0.79	9.2	0.20	1.00	2.47	0.051	0.008	0.007	1.14	1100/ 700/700	691

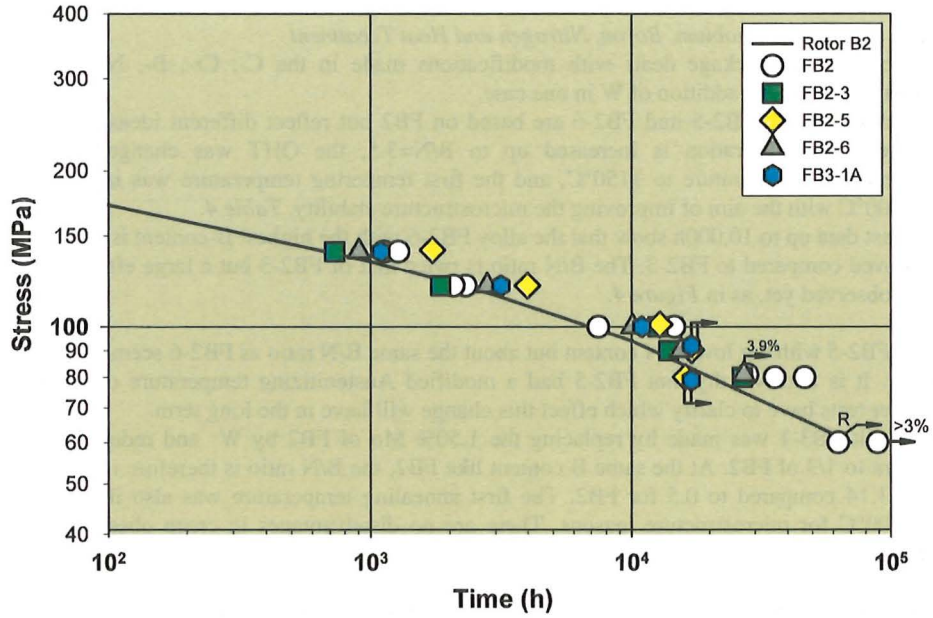

Fig. 4: Creep rupture strength of the COST trial melts with different B/N ratios at 650°C

3.2.3. The Role of B-N Ratio and Heat Treatment

Further work has been started to investigate the role of the Boron to Nitrogen ratio in FB2 basic chemistry and to further understand the influence of heat treatment.

For this the content of C and B has been increased, and the N level reduced to 110ppm. Two heat treatment versions have been applied for the same mother melt to enable a direct quantification in creep, *Table 5.*

Table 5: Chemical composition and heat treatment of the trial melts with low Nitrogen

Melt	C	Mn	Cr	Mo	Co	Nb	B	N	B/N	QHT °C	0.2YS at RT MPa
B2	0.16	0.06	9.3	1.60	-	0.060	0.010	0.015	0.67	1100 570/700	650
FB2	0.13	0.90	9.0	1.50	0.96	0.065	0.010	0.020	0.50	1100 570/710	714
FB2-2 LNP-A	0.16	0.31	8.8	1.41	0.97	0.045	0.015	0.011	1.36	1100 700/700	696
FB2-2 LNP-M3										1100 570/700	710

It is too early to draw any conclusions. Up to now no negative influence is observed for testing times of 10,000h, *Figure 5.* The results are still comparable to the FB2 trial melt. Longer testing is required and will become a part of the next COST action.

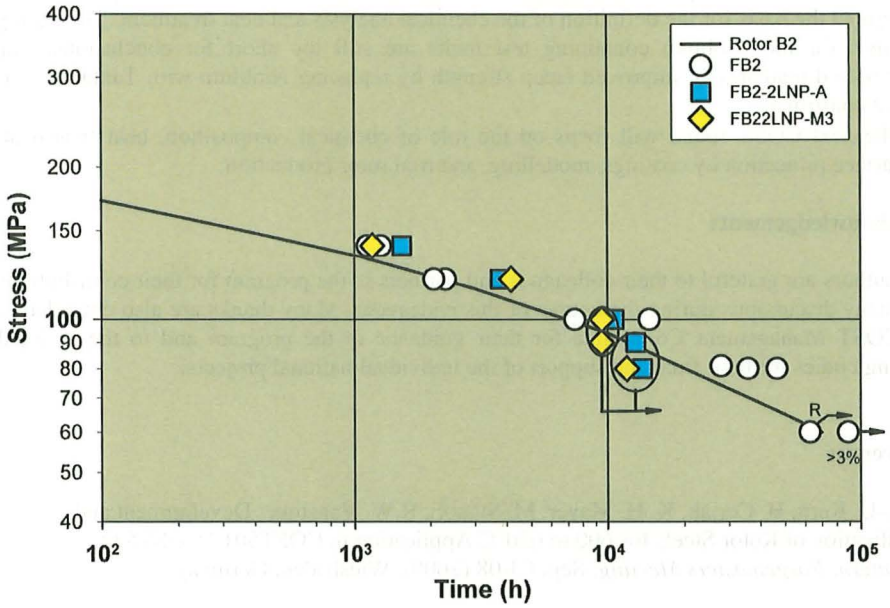

Fig. 5: Creep rupture strength of the COST trial melts with low Nitrogen at 650°C

The knowledge and experience gained with the new alloy types underlines the findings that the further increase of the application temperature above 620°C for ferritic-martensitic steels has become problematic, thus making it clear that the limit could be near.

4. Future work

The next COST round is already under preparation. It has been agreed that the described work packages will be continued up to the start of the next round.
Intensive microstructure investigations are planned to accompany the ongoing tests to further sharpen the modeling tools. The influence of heat treatment parameters is included in the work packages and will remain in focus.
The manufacturing of full size 20to rotor forgings is under preparation. The influence of preliminary heat treatment on the results of NDT, such as detectable flaw size and sound attenuation, and the influence on creep behavior are going to be investigated.

5. Summary and Conclusions

- After identifying a potential alloy composition for 620°C application, three full-size prototype rotor forgings with different steelmaking routes have been manufactured in Europe. The creep results with currently 55,000h show that the transformation from the

trial melt to the rotor forgings was performed successfully. The material is currently being manufactured commercially for new power plant projects in Europe and USA.

- A series of new trial melt compositions was designed with different directions of the development strategy. Microstructure investigations and modern modelling tools have formed the basis for the definition of the chemical analysis and heat treatment. The testing times for the Niobium containing test melts are still too short for conclusions. The expected tendency of improved creep strength by replacing Niobium with Tantalum was not confirmed.
- The next COST round will focus on the role of chemical composition, heat treatment, surface protection by coatings, modelling, and trial rotor production.

6. Acknowledgements

The authors are grateful to their colleagues and partners in the program for their contributions and many discussions during the course of this endeavour. Many thanks are also extended to the COST Management Committee for their guidance in the program and to the national funding bodies for their financial support of the individual national projects.

References

[1] T.-U. Kern, H. Cerjak, K. H. Mayer, M. Staubli, R.W. Vanstone: Development and Qualification of Rotor Steels for 600 to 650°C Application in COST501 / COST522.
14th Intern. Forgemasters Meeting, Sept 03-08 (2000), Wiesbaden, Germany.

[2] T.-U. Kern, M. Staubli, K. H. Mayer, K. Escher, G. Zeiler: The European Efforts in Development of New High Temperature Rotor Materials up to 650°C - COST522.
7th COST Conference, Sept 30–Oct 02 (2002), Liège, Belgium.

[3] T.-U. Kern, M. Staubli, K. H. Mayer, B. Donth, G. Zeiler: The European Effort in Development of New High Temperature Rotor Materials – COST536.
8th COST Conference, Sept 18-20 (2006), Liége, Belgium.

[4] T.-U. Kern, B. Scarlin, B. Donth, G. Zeiler, A. DiGianfrancesco: The European COST536 Project for the Development of New High Temperature Rotor Materials.
17th Intern. Forgemasters Meeting, Nov 03-07 (2008), Santander, Spain.

[5] K. H. Mayer, C. Berger, A. Scholz, Y. Wang: Improvement of Creep Strength of 650°C Ferritic/Martensitic Super Heat Resistant 11-12%Cr Steels.
8th COST Conference, Sept 18-20 (2006), Liége, Belgium.

[6] Y. Wang, F. Kauffmann, K. H. Mayer, A. Scholz, C. Berger, K. Maile: The Effect of Microstructure Stability on Long-Term Creep Behaviour of 11%Cr Steels for Steam Power Plants with Operating Temperatures up to 650°C.
9th COST Conference, Sept 27-29 (2010), Liége, Belgium.

9th Liege Conference : Materials for Advanced Power Engineering 2010
edited by J. Lecomte-Beckers, Q. Contrepois, T. Beck and B. Kuhn.

MATERIAL DEVELOPMENTS FOR SUPERCRITICAL BOILERS AND PIPEWORK – BRIDGING THE GAP ?

P.M. Barnard, L.W. Buchanan and M. Barrie
Doosan Power Systems, Technology & Engineering, Porterfield Rd, Renfrew, PA4 8DJ, UK

Abstract

This paper briefly reviews the current state of developments for ferritic, austenitic and nickel alloys for supercritical steam raising power plant applications. Some of the challenges are touched upon as well as various activities ongoing to meet these challenges. It is likely that, although the technical challenges are significant, developments in ferritic alloys will allow a more incremental increase in plant efficiency than the step change required to justify the cost of nickel alloys. This conclusion may change as the cost of fuel increases such that the economic and commercial risks of using nickel are compensated by the saving in fuel costs.
Key Words: Boilers, Ferritics, Austenitics, Nickel Alloys.

1 INTRODUCTION

The drive for ever-increasing efficiency of power plant has always been present but in recent years it has been given greater impetus by the concerns over global warming, particularly in relation to the emission of the greenhouse gas carbon dioxide. Apart from simple economics demanding lower electrical energy unit costs, there is the need to reduce the amount of emissions per megawatt generated, summarised in figure 1. This also suggests that the main contributor to emissions reduction will be plant efficiency [1]. The maximum available thermal efficiency of power plant is that of a reversible device absorbing thermal energy by heat transfer at the source temperature and rejecting thermal energy at the sink temperature, in which case

$$\text{Efficiency} = 1 - (\text{T sink}/\text{T source})$$

The sink temperature is normally fixed depending on geographical location leaving the source temperature as the major variable in the quest for higher efficiency. No real cycle is truly reversible, and when this is taken into consideration efficiency is also a function of pressure. In particular, when the pressure is above the critical pressure i.e. supercritical, efficiency improvement is gained by avoiding the latent heat of evaporation.

For example, an increase in conditions from 305bar at 585/602°C to 320bar at 620/640°C will result in an overall increase in efficiency estimated at about 6% [2]. The gradual increase in temperature and pressure is shown diagrammatically in figure 2, which also indicates the target for 2020 [3]. The step change in the target for 2020 results from the move from thick section ferritic headers and pipework to nickel alloys and their higher capabilities as determined through the AD700 European initiative. Because of the resultant significant increase in material costs, it would be necessary to maximise the efficiency by operating at as high a temperature and pressure as practicable.

This step change is more radical than the usual incremental improvements traditionally seen in the boiler industry and would inevitably be technically challenging. Nevertheless a project known as EON50+ was started in 2008 with the objective of achieving in excess of 50% net

plant efficiency (%LHV basis) at final steam conditions around 700°C and 350 bar. Several boiler makers developed outline designs with a view to plant operation around 2015 but due to the economic downturn the project is currently shelved. However, the need for efficiency improvements is driven, in part, by the energy penalty for CCS (Carbon Capture and Storage), see figure 3, with estimates ranging from 5 to 8% efficiency loss for the implementation of CCS [1].

Increasing the temperature and pressure increases the demand for higher creep strength and steam oxidation resistant materials. In addition to these attributes the most suitable material types can vary depending on the application and fabrication or performance requirements. These can be divided into three areas –

- Waterwalls should preferably be fabricated without the requirement for post weld heat treatment.
- Other heat transfer tubing experiences a range of temperatures up to the highest metal temperatures in the final superheater section.
- Headers and manifolds are the thickest components and require good fatigue and creep/fatigue performance to accommodate thermal stresses during heating/cooling. This is related to the thermal conductivity and coefficient of expansion of the material.

On this basis for the thick section piping components the current best in class Creep Strength Enhanced Ferritic (CSEF) steel, P92, has an upper limit in non-heat transfer applications of ~610°C primarily due to the steam oxidation consideration. For the same reason it is limited to even lower temperatures when heat flux is relevant as in superheater elements or waterwalls. For thin section applications it is possible to move to the higher chromium alloys such as austenitic stainless steels but in thick section, due to poorer thermal conductivity and high thermal expansion of this class of material this is currently not considered practicable. The simplest technical solution for temperatures in excess of ~610°C is the use of nickel based superalloys, see figure 4, which have physical properties closer to the ferritic/martensitic alloys than the austenitic alloys. Unfortunately the cost of the nickel materials is very high and the increased demand in the market would place a strain on the supply chain. Furthermore the effects of fabrication and welding on long term properties require more comprehensive evaluation and there is limited field experience. Consequently the commercial cost and risks involved makes the use of nickel based alloys somewhat less attractive.

One of the fundamental questions that need to be addressed is: can higher efficiency plant be achieved without the need or the limited use of nickel based alloys. Figure 3 suggests that efficiency losses can be reduced by improvements in the CCS process. Similarly plant improvements can assist in contributing to overall plant efficiency [4]. The real questions for the materials community are can ferritic materials be used above 610°C, or can the application range of austenitic stainless steel alloys be extended and thereby limit the need for the expensive nickel alloys?

In essence, can the gap between the best available CSEF alloy grade 92 and the very expensive nickel based alloys be bridged and thus enable a more incremental and hence lower

risk approach to improving power plant efficiency? In this review some of the issues are considered for each class of metal that will affect the answer to this question.

2 FERRITIC/MARTENSITIC ALLOYS

Fleming et al [5] and Viswanathan & Bakker [6] provide a good review of developments for ferritic alloys up to the year 2000 for thick section components. At the time P91 was the industry standard for thick section components. Since then the nominally 2% tungsten alloyed variant P92 has become more popular due to its higher creep strength. The 1% tungsten alloy (E911) developed in a European Programme (COST 522) has not proved so popular with its creep strength intermediate between grade 91 and grade 92. All of these alloys suffer from in service issues relating to type IV cracking, and other critical factors such as low N:Al ratios and inferior martensitic structure due to criticality of the thermal processing parameters [7][8]. Both grade 92 and E911 with W additions have been approved in European and ASME codes, but their allowable stresses have been progressively reduced due to the continuing accumulation of long term data. It has been considered that this has been contributed to by the weakening effect of Laves phase $(Fe,Cr)_2(Mo,W)$ formation [9] which reduced the solid solution strengthening contribution of tungsten. Another potential issue with the 9%Cr alloys is their lack of steam oxidation resistance as the operating temperature exceeds 610°C in pipework applications, as indicated in figure 5 [10].

For many years higher Cr alloys have been evaluated without success primarily due to the formation of a coarse Z-Phase, where the chromium combines with the strengthening MX precipitates containing niobium, vanadium and nitrogen, [11] thereby removing them from the microstructure. This generally occurs at extended time and hence the effect is not noted till a considerable proportion of the creep life is exhausted after which a sudden drop in properties is experienced. Current developments in creep enhancing this class of alloy are centred on the MarBN philosophy developed by F.Abe or using controlled precipitation of Z-phase as the strengthening mechanism as proposed by J.Hald.

MarBN uses controlled additions of Boron and Nitrogen to the Martensitic matrix but care must be taken with the latter to avoid formation of boron nitride which is detrimental to the creep properties [12]. This can result in an improvement in creep life for a 9% Cr alloy of up to 50% in stress compared with grade 92. It has also been reported that the boron prevents grain refinement within the heat affected zone and should thus reduce or eliminate the type IV problem prevalent in this type of alloy [13]. However obtaining a matching weld metal, with the required close control of the chemistry especially nitrogen and boron, may prove problematic with one possible option being to use overmatched nickel filler materials. It is also perhaps not surprising that weld metals, essentially a series of small castings and only subjected to post weld tempering, fail to demonstrate matching creep strength for these types of alloys, bearing in mind the critical thermal cycles applied to the CSEF base metals to fully develop their long term properties.

Danielsen and Hald have studied the deleterious effect of Z-phase [14] in some detail and support the mechanism of the precipitation of non strengthening coarse Z-phase at the expense of strengthening MX particles and consider this to be the main reason for the inability to

develop higher strength 11 – 12% Cr steels. An experimental steel has been produced based on the concept of accelerating the Z-phase formation by chemical composition control in order to suppress deleterious growth [15], shown schematically in figure 6. This 12Cr-0.2N-0.2(V+Nb)-balance Fe material has been demonstrated to cause each MN particle to turn in to one Z phase particle, and be immune to the dissolution of strengthening nitrides. Creep tests on the alloy are currently underway.

These two main avenues of research are focussed upon creep strength enhancement potentially resulting in adequate creep strength (100MPa – 100khrs) up to 650°C, but there is still the question regarding steam oxidation resistance particularly for the 9% Cr MarBN type. The main routes to enhance steam oxidation other than chromium additions have been to enhance the chromium diffusion and surface coating. For austenitic superheater and reheater tubes fine grain structures and cold working the surfaces have been used to enhance chromium diffusion and hence the rapid development of the protective magnetite layer. This is discussed in more detail in the "Austenitic Alloys" section. The current ferritic materials e.g. grade 91 are already considered to be fine grained, typically ASTM 6 or finer. The effect of cold work, e.g. peening and the resultant grain refinement, has been shown to enhance chromium diffusion [16] and could be further explored.

Coatings have the potential to give long term benefits in terms of protection from steam oxidation, [17] [18] see figure 7. Many coating compositions have been trialled using chemical vapour deposition (CVD), slurry and pack cementation techniques. The primary aim of the coating process is to form a sufficiently thick Fe_2Al_5 so that the stable oxide formed is Al_2O_3 and a sufficient reservoir of aluminium for the expected service duration, see figure 8 [19] [20]. The long term microstructural stability and mechanical integrity of slurry deposited coatings on P91 and P92 have been evaluated in SUPERCOAT; an EU funded 5th Frame Work Project. The main conclusions from this work are "*Slurry aluminide diffusion coatings are protective for at least 41,000 h but degrade by coating-substrate interdiffusion leading to a decrease on the Al concentration at the surface, at the deposition of AlN precipitates within the substrate and to the development of Kirkendall porosity at the coating-substrate interface. However, based on long term steam oxidation experimental data, the life of the coating can be estimated to surpass 78,000 h.*" [17]

3 AUSTENITIC ALLOYS

Figures 4 and 5 summarise the advantage the austenitic alloys have over the ferritic alloys, namely improved creep strength and with typically 18%Cr a greater resistance to steam oxidation. The super austenitic alloys have even greater oxidation resistance with HR3C containing 25%Cr and Sanicro 25 containing with 22.5%Cr. Even though there is a cost penalty for using the austenitic alloys relative to the ferritic alloys the main issue is that of $\alpha\Delta T$, i.e. thermal fatigue. This family of alloys have a low thermal conductivity, typically 16W/m°C vs. 50W/m°C, and high thermal expansion, typically $18x10^{-6}$ vs. $11x10^{-6}$, relative to the ferritic alloys. For these reasons austenitic alloys are currently restricted to the superheater and reheater tubing and seldom for thick section components, a notable exception being the stub headers at Drax Power Station, UK which employed 15%Cr10%Ni6%Mn alloy (1.4982) the most creep strong austenitic alloy at that time circa 1975.

A recent review of service experience has been conducted by Shingledecker and can be found in reference 21. Of particular note in this review were the tests conducted at Eddystone Unit 1 where 6 different tubes were run for 13 years (75,075 hrs) nominally at 615°C and 35 MPa where the higher chromium containing alloys showing little sign of either steam or fireside corrosion, with the fine grained 18%Cr 347HFG performing as well as the 21%Cr Tempalloy A3. Post service samples of 304H from Callide C3 and C4 units tested in stress rupture showed minimal reduction in life expectancy relative to virgin material even after 80,000 hours service, see figure 9.

The improved creep strength of the current super austenitic alloys would mean that, for the same steam conditions thinner sections would be possible compared with the conventional austenitic alloys e.g. 304H and 316H making pipe sized components feasible. In particular the recently developed Sandvik alloy Sanicro 25, which exhibits 100khrs average rupture life at 700°C and almost 100MPa, would seem like a good candidate. It has also been reported that ORNL together with Caterpillar are currently assessing the creep-fatigue performance of a cast alloy CF8C-plus in high temperature thick section applications [22]. If such materials could be used safely this would help to bridge the gap between the current best available ferritic alloys and the very expensive nickel alloys and permit incremental improvements in steam conditions and efficiencies.

The development of the advanced austenitic alloys has come about partly by specialised thermo-mechanical treatment but mainly by the addition and optimisation of alloying elements in particular niobium [23]. This forms fine NbX precipitates both with carbon and nitrogen and also contributes to Z-phase all of which greatly increase the creep strength [21]. However there is evidence that this also has the greatest influence on Strain Induced Precipitation Hardening. This results from cold working the material for example during bending and subsequent thermal exposure in the temperature range 540°C to 750°C. This can result in reduced creep ductility and premature failure. This carbide precipitation can also lead to reduced impact toughness [21] which becomes more significant for the higher chromium containing alloys [24]. For the HR3C type alloy Peng et al.[24] show that at 700°C both grain boundary and intra grain $M_{23}C_6$ precipitate out within 1000 hrs with a huge reduction in toughness, see figure 10.

Steam oxidation of 18/8 type austenitic tubes has proven to be of concern in many recently commissioned boilers with excessive growth of the bore oxide leading to tube blockage and failure and /or turbine erosion.
Steam oxidation problems can be reduced by four main methods:

- Employing a higher Cr content alloy.
- Chemical alteration of the surface by, for example chromising.
- Employing fine grained materials.
- Shot peening of the surface.

The first two options are obviously expensive, and from that point of view the latter two options would appear more attractive. The logic behind the fine grained structure of an alloy such TP347HFG is based on increasing the diffusion of chromium in the alloy by considerably increasing the number of grain boundaries. Grain boundaries are regions of high disorder and vacancies which allow the substitutional chromium atoms low energy sites and also "corridors" to the surface where they can lower the energy of the system even more by

forming oxide. So TP347HFG has enhanced oxidation resistance in comparison to TP 347H by virtue of having a higher chromium level in its scale. Cold working, by introducing slip lines and point defects, also promotes Cr diffusion [25] giving rise to the same protective mechanism as fine grained material. Both methods of enhancing Cr transportation make a considerable difference to scale growth as can be noted in figure 11.

Welding of the austenitic stainless alloys is fairly straightforward with the same welding processes being generally available as for the ferritic steels. However these alloys are austenitic at room temperature and do not go through the phase transformation on cooling which the ferritic/martensitic alloys do hence cooling rate from welding is not critical. Consequently preheating is neither required nor desired but on the other hand heat input and interpass temperature should normally be more controlled to avoid solidification cracking issues particularly for the fully austenitic grades [26]. As mentioned previously the alloys have a low thermal conductivity and high coefficient of thermal expansion which combine to make them more susceptible to distortion. Inspectability by the ultrasonic technique, which is often carried out both pre-service and in-service, can prove difficult due to the epitaxial grain structure causing high attenuation and beam deflection. For this reason on thick section components many fabricators favour narrow gap reduced weld volume welding techniques. This also brings obvious economic benefits after the purchase of the equipment and helps to de-skill the operation resulting in more consistent, defect free welds with minimum distortion.

It may be concluded that up to circa 650°C for tube applications austenitic alloys could perform satisfactorily, but above this temperature or for thick sections much work needs to be performed. One active area of research is the alumina forming austenitic alloys where at temperatures above 600°C the alumina scale is more adherent and protective than the chromia scale formed with low aluminium containing austenitic alloys [27] [28]. These alloys are strengthened by MC, primarily NbC, and NiAl intermetallics that are very stable at elevated temperatures. Laves phase, $Fe_2(Mo,Nb)$, formation is controlled by careful control of the Mo and Nb content [28]. The use of the alumina forming austenitic alloys may allow their use up to 700°C, although for thick section there still remains the thermal expansion issue. This was touched on by Perrin and Fishburn where they recommended the need to review the ASME Boiler and Pressure Vessel Code and the Water Tube Boiler Code, EN12952 to account for thermal cycles [29].

4 NICKEL ALLOYS

High creep strength nickel alloys were originally developed for the aeroengine industry leading to significant improvements in performance [30]. These alloys are often highly alloyed with exacting thermal cycles required to develop the optimum properties for the relatively short lived components. For the power generation industry a few of these aeroengine alloys are being evaluated along with a new generation of alloys that have been developed where fabrication and long term creep are the primary considerations [31]. The current use of nickel alloys in pressure parts of power plant is limited but the advantages in terms of creep, see fig 4, and oxidation resistance [32] over the austenitic alloys are driving the interest in these alloys. There are factors other than creep and oxidation resistance, however, which have to be taken into consideration.

The nickel alloys being FCC materials can suffer the same propensity to ductility dip cracking (DDC) as the ferrous based austenitic alloys [33] [34]. DDC is a grain boundary sliding creep-like phenomenon principally affecting welds and heat affected zones. DDC is linked to grain size, impurity segregation, grain boundary tortuosity, and intergranular precipitation. If welded under high constraint conditions the available ductility may be exceeded by the welding induced strain, i.e. contraction, leading to DDC. With a higher coefficient of expansion relative to iron, nickel alloys need careful handling during welding. Ramirez et al [33] advocate the controlled additions of Nb and Ti, strong carbide and nitride formers, to the welding consumable to promote grain boundary tortuosity via grain boundary precipitation.

A similar mechanism variously called relaxation cracking; stress induced cracking; strain age cracking etc., again a grain boundary creep-like phenomenon, involves the re-precipitation of phases dissolved during welding [35]. At critical temperatures very fine intergranular carbides rapidly precipitate acting as dislocation pins in the intergranular regions, whilst grain boundary carbide growth absorbs any local fine carbides leading to channels of weak material along the grain boundaries. Standard tests have been developed to assess the susceptibility of nickel alloys to relaxation cracking e.g. the controlled heating rate tensile test (CHRT) [36] see figure 12. This shows that the high γ' forming alloys, i.e. high Al and Ti, are more prone to relaxation cracking than the low γ' forming alloys making these attractive for power plant applications.

Woodford's review on Gas Phase Embrittlement in aeroengine nickel alloys [37] suggests that consideration to environmental grain boundary attack needs to be considered for power plant nickel alloys. It is suggested that time dependent intergranular crack propagation in air under either sustained or cyclic stress is a result principally of oxygen attack ahead of the crack tip and that any separate effect of time dependent deformation (creep) is very small relative to the environmental effect. The ability to form a stable oxide scale can reduce or eliminate oxygen damage and time dependent cracking. The interaction of environment and applied loading in service is a further complication, see figure 13. Although the test conditions are severe for power plant applications, the data provide indications for plant operation. Figure 13 shows that life expectancy is reduced when oxygen is present, but of more interest is the observation that the life expectancy for a dwell of 18 and 1800 seconds are the same, i.e. there may be no creep fatigue interaction [38]. This observation is also confirmed by Hu and Wang with their work on super Waspaloy at 600°C [39].

For applications where high creep strength is required the γ' forming materials are necessary where control and stability of this phase is critical i.e. the greater the volume fraction and number of particles the greater the creep strength [40]. Coarsening of the γ' phase, and hence reduction in creep strength, is controlled by diffusion of Al and Ti through the Ni matrix [41] and very dependent upon temperature, see figure 14. Consideration of the coarsening rate and dissolution temperature of the γ' phase is a major consideration in deciding the upper operating temperature of an alloy. For thick section components, the reduced cooling rate from the solution treatment temperature can prevent ideal conditions for γ' precipitation. Mitchel et al [42] working on aeroengine alloys found that reducing the cooling rate produced a bimodal γ' distribution with increased precipitate size. It was also noted that slow cooling rates generate low γ-γ' mismatch which in turn may promote γ' instability during subsequent ageing heat treatments or during prolonged in-service exposure.

5 CONCLUSIONS

Some of the factors driving the need for higher efficiency in power plant cycles have been reviewed and the role of materials developments and the nature of these developments in relation to steam raising plant components have been considered.

In summary:

- There is a simple economic driver to increase cycle efficiency and this will become greater with the incorporation of carbon capture technologies into plant designs.
- The highest thermal efficiency in presently operating plant is achieved with final steam temperatures around 610°C and this limit is dictated by the strongest available CSEF alloy P92 employed in thick section components such as headers, manifolds and main steam pipework.
- Designs of plant with final steam temperatures of 700°C have been developed (AD700 programme). Construction of such plant would result in an historically unprecedented increment in cycle efficiency only made possible by the use of nickel alloys.
- Nickel alloys bring with them a different catalogue of potential integrity threatening mechanisms without any significant plant experience and introduce a level of risk. For these reasons, smaller increments in efficiency brought about by moderate improvements in ferrous alloys, may be preferred.

It is considered that the following areas of development can help bridge the gap between the current steel based alloys and the nickel superalloys.

- Mechanisms to increase the creep strength of the 9-12%Cr steels are currently under active investigation; these include boron containing steels and steels incorporating chemical composition restrictions to alter the precipitation mechanism of the normally deleterious Z-phase.
- Enhanced creep strength of 9-12%Cr steels could elevate the permissible operating temperature to a level in excess of their steam oxidation or corrosion capabilities creating the need to develop suitable internal and external coating technologies.
- Creep stronger and more oxidation resistant austenitic alloys have been developed for thin section components where the intrinsic low thermal conductivity and high thermal expansion are of little consequence. It may be possible, by design, to extend the application of these to thicker components.
- Thick section austenitic stainless steels however, may require controlled start up and shut down cycles restricting them to base load duties. With the advent of significant renewable energy production it is likely that the need for a more flexible grid will become paramount.

Hence these developments may allow a more incremental increase in plant efficiency than the step change required to justify the high cost of nickel alloys. This conclusion may change as the cost of fuel increases such that the economic and commercial risks of using nickel are compensated by the saving in fuel costs.

REFERENCES

[1] M. Pontremoli; "Materials and Technologies for Energy Efficiency", Materials and Technologies for Energy Efficiency Workshop, CSM, Rome, March 2010

[2] Anon; "Steam its Generation and Use Edition 41", Eds J.B. Kitto and S.C. Stultz, The Babcock & Wilcox Company, Baberton, Ohio, USA, 2005

[3] S. Pasini, "ENEL Initiatives in the Field of Energy Efficiency", Materials and Technologies for Energy Efficiency Workshop, CSM, Rome, March 2010

[4] R. Blum et al; "Development of a PF Fired High Efficiency Power Plant (AD700)", Symposium on Heat resistant Steels and Alloys for USC Power Plant 2007, Seoul, Korea, July 2007

[5] A. Fleming et al; "Material Developments for Supercritical Boilers and Pipework", Conference Proceedings of Materials Congress, UK, 1998

[6] R. Viswanathan & W. T. Bakker; "Materials for Boilers in Ultra Supercritical Power Plants", Proceedings of 2000 International Joint Power Generation Conference, Miami Beach, Florida, July 23-26, 2000

[7] S. J. Brett & J. Sanchez-Hanton; "UK Plant Experience with Grade 91", Materials and Technologies for Energy Efficiency Workshop, CSM, Rome, March 2010

[8] J.F. Henry; "Cracking Problems with Grade 91 and Other Creep Strength Enhanced Ferritic (CSEF) Steels", Weld Cracking VII: The Heat-Affected Zone Conference, Chicago, USA, Nov 2009

[9] P.J. Ennis &A. Czyrska-Filemonowicz; "Recent Advances in Creep Resistant Steels for Power Plant Applications", OMMI, Vol. 1, No. 1, April 2002

[10] K.Zabelt, B.Melzer & A.Reuter; "Results from Long Term Field Trials: Variants for the use of Materials and the Maintenance Strategy for Highly Stressed Components in Coal Fired Power Plant", Corrosion in Power Plant, Wurzburg 29/30 Sept 2009.

[12] J. Hald; "The Experience of DONG Energy with Efficiency Improvement of Power Generation Plants", Materials and Technologies for Energy Efficiency Workshop, CSM, Rome, March 2010

[13] F.Abe ; "Additive Strengthening Due to Boron and MX Carbonitrides", Symposium on Heat Resistant Steels and Alloys for USC Power Plant 2007.

[14] F.Abe, M.Tabuchi & S.Tsukamoto; "Metallurgy of Type IV Fracture in Advanced Ferritic Power Plant Steels", Fundamental Studies on Technologies for Steel Materials with Enhanced Strength and Functions – Consortium of JRCM.

[15] H.K.Danielsen and J.Hald; "Behaviour of Z-Phase in 9-12%Cr Steels", Energy Materials 2006, pp49-57.

[16] J.Hald; "Z-Phase in 9-12%Cr Steels", VGB Materials Seminar – Copenhagen, 13-15 May 2009.

[17] X.Ren,K.Sridharan,T.R.Allen; "Effect of Shot Peening on the Oxidation of Ferritic-Martensitic Steels in Supercritical Water", CORROSION 2008, New Orleans LA. Mar 16-20, 2008

[18] B.A. Pint et al; "Long-Term Performance of Aluminide Coatings on Fe-base Alloys", Intermetallics 17, 2009, pp387–393

[19] L. Sánchez et al; "Temperature Dependence of the Oxide Growth on Aluminized 9–12%Cr Ferritic-martensitic Steels Exposed to Water Vapour Oxidation", Thin Solid Films 517, 2009, pp3292–3298

[20] Z.D. Xiang & P.K. Data; "Relationship Between Pack Chemistry and Aluminide Coating Formation for Low-temperature Aluminisation of Alloy Steels", Acta Materialia 54, 2006, pp4453–4463

[21] A. Agüero et al; "Cyclic Oxidation and Mechanical Behaviour of Slurry Aluminide Coatings for Steam Turbine Components", Surface & Coatings Technology 201, 2007, pp6253–6260.

[22] J. Shingledecker; "State of Knowledge for Advanced Austenitics: Final Report", EPRI Report 1020241, Dec 2009.

[22] J.Shingledecker, "Fossil Materials & Repair EPRI Program 87 – General Advisory Meeting: Introduction and 2009 Review", Orlando FL 2010.

[23] A.I.Z. Farahat & T.A. El-Bitar; "Effect of Nb, Ti and Cold Deformation on Microstructure and Mechanical Properties of Austenitic Stainless Steels", Materials Science & Engineering A, 2008

[24] B. Peng et al; "Effect of aging on the impact toughness of 25Cr-20Ni-Nb-N steel", Materials Science & Engineering A, 2008

[25] Y. Minami & S. Caminada; "Effect of Internal Shot-blasting on Steam Side Oxidation of Austenitic Stainless Steel Tubes", VGB Workshop "Material and Quality assurance", Copenhagen, May 2009

[26] G.Mather "Job Knowledge for Welders -20 Weldability of Stainless Steels" TWI Connect 1996.

[27] R.L. Plaut et al; "A Short Review on Wrought Austenitic Stainless Steels at High Temperatures: Processing, Microstructure, Properties and Performance", Materials Research, Vol. 10, No. 4, 453-460, 2007

[28] H. Bei et al; "Aging effects on the mechanical properties of alumina-forming austenitic stainless steels", Materials Science & Engineering A, 2008

[29] I.J. Perrin & J.D. Fishburn; "A Perspective on the Design of High-Temperature Boiler Components", International Journal of Pressure Vessels and Piping, 85, 2008, pp14–21

[30] W. Betteridge & J. Heslop; "The Nimonic Alloys", 2nd Edition, Edward Arnold (Publishers) Ltd, 1974

[31] J. deBarbadillo et al; "Nickel Alloy Development and Use in USC Boilers", 2010 to be published.

[32] R. B. Dooley; "Program on Technology Innovation: Oxide Growth and Exfoliation on Alloys Exposed to Steam", Final Report, 1013666, EPRI, June 2007.

[33] A. J. Ramirez et al; "Improving the ductility-dip cracking resistance of Ni-base alloys", Journal of Materials Processing Technology, 179, 2006, pp212–218.

[34] G. A. Young et al; "The Mechanism of Ductility Dip Cracking in Nickel-Chromium Alloys", Welding Journal, February, Vol. 87, 2008

[35] J.C. van Wortel; "Prevention of Relaxation Cracking by Material Selection and/or Heat Treatment: Final Report", RC00-42A, TNO, November 2000.

[36] M. D. Rowe; "Ranking the Resistance of Wrought Superalloys to Strain-age Cracking", Private Communication.

[37] D. A. Woodford; "Gas Phase Embrittlement and Time Dependent Cracking of Nickel Based Superalloys", Energy Materials, Vol. 1, No 1, 2006.

[38] T. C. Totemeier & H. Tian; "Creep-Fatigue–Environment Interactions in INCONEL 617", Materials Science and Engineering A, 468–470, 2007, pp81–87.

[39] D. Hu & R. Wang; "Experimental Study on Creep-Fatigue Interaction Behavior of GH4133B Superalloy", Materials Science and Engineering A, 515, 2009, pp183-189.

[40] R. Reed; "The Superalloys: Fundamentals and Applications", Cambridge University Press, 2006

[41] S. Zhao et al; "Gamma prime coarsening and age-hardening behaviors in a new nickel base superalloy", Materials Letters 58, 2004, pp1784– 1787.

[42] R.J. Mitchell et al; "The influence of cooling rate from temperatures above the γ' solvus on morphology, mismatch and hardness in advanced polycrystalline nickel-base Superalloys", Materials Science and Engineering A, 473, 2008, pp158–165.

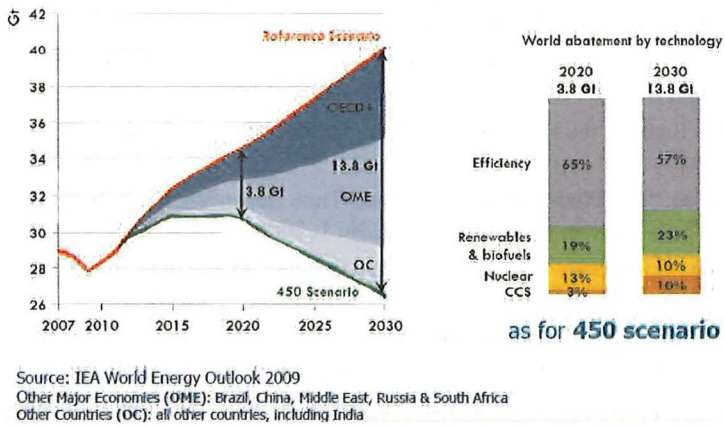

Fig. 1:- The Driver for Higher efficiency Power Plant (1)

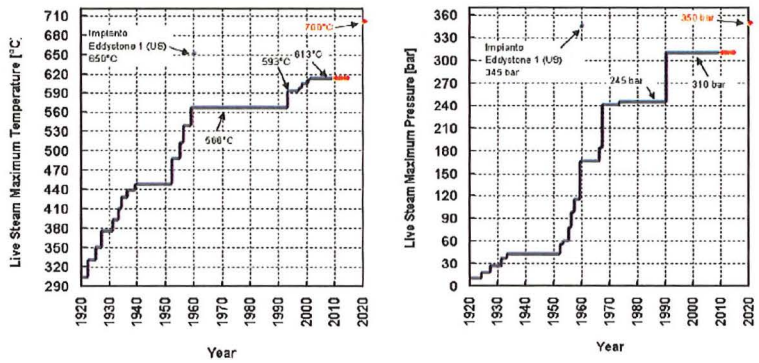

Fig. 2:- Change in steam temperature and pressure required for HSC plant (3)

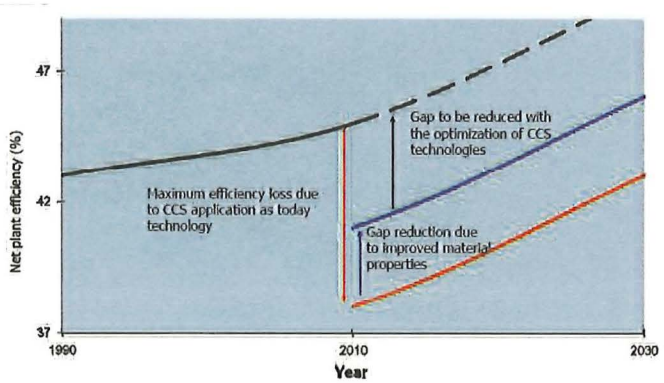

Fig. 3:- The Energy Penalty for CCS (1)

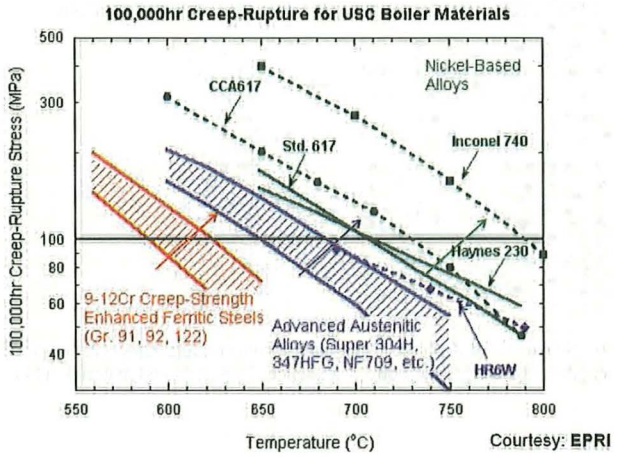

Fig. 4:- Comparison of creep strength for different classes of metals.

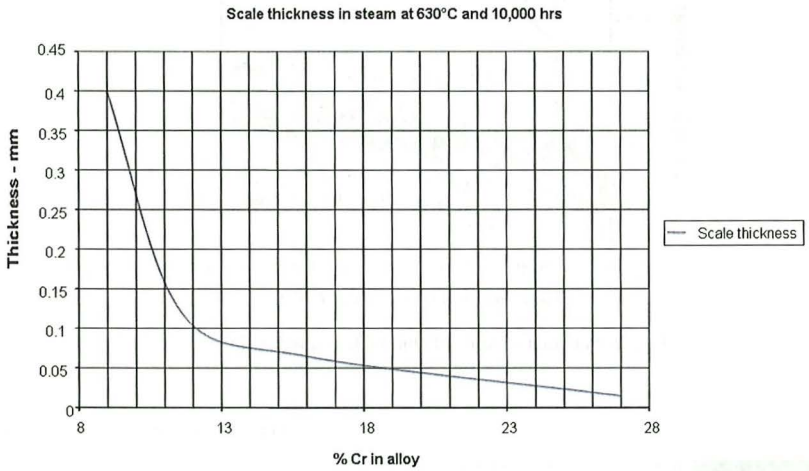

Fig. 5:- Effect of Cr content on steam oxidation resistance (10).

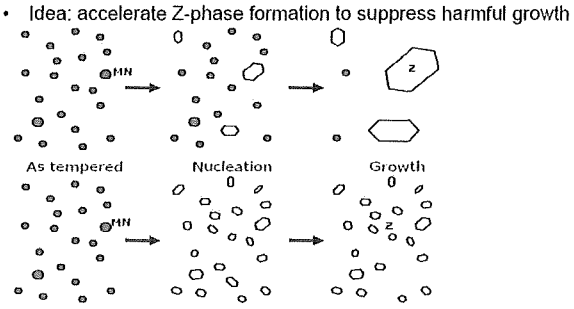

Fig. 6:- Schematic of Z-phase strengthening concept, top sequence shows MN strengthened material and bottom sequence Z strengthened material (11).

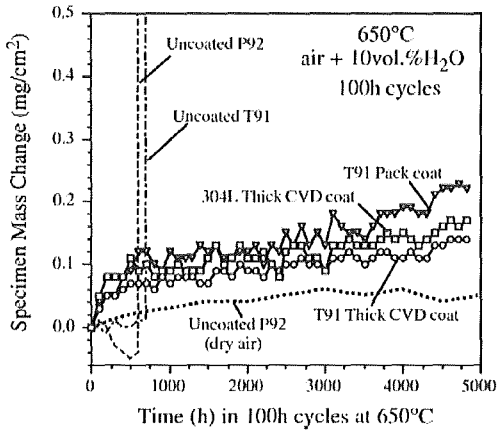

Fig. 7:- Potential benefits of aluminide coatings (17).

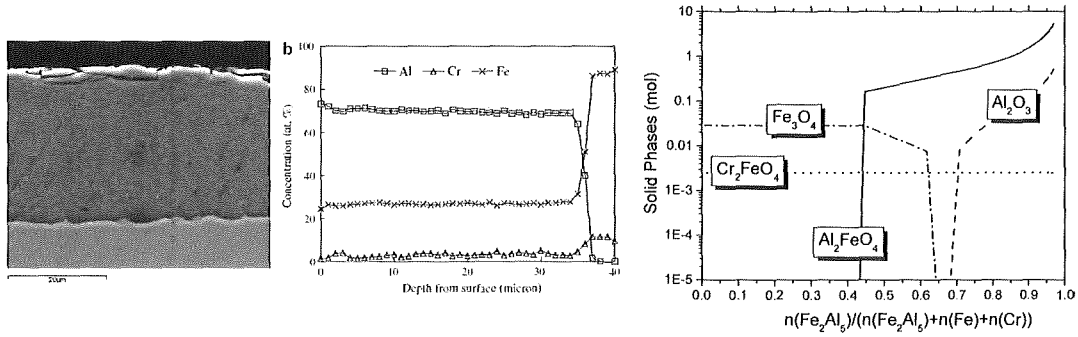

Fig. 8:- Micrograph of pack coating deposited on P92, left, with composition profile, middle (19). Thermodynamic calculation, showing the stable oxide phases formed under steam oxidation conditions (18).

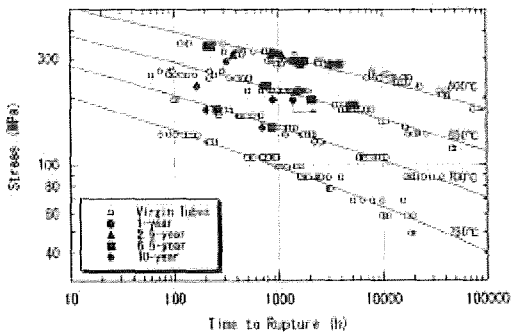

Fig. 9:- Stress-rupture properties of Super 304H tubes removed at various times from an industrial boiler (closed symbols) compared to virgin material (open symbols) for times up to ~80,000 hours (10 years) (21)

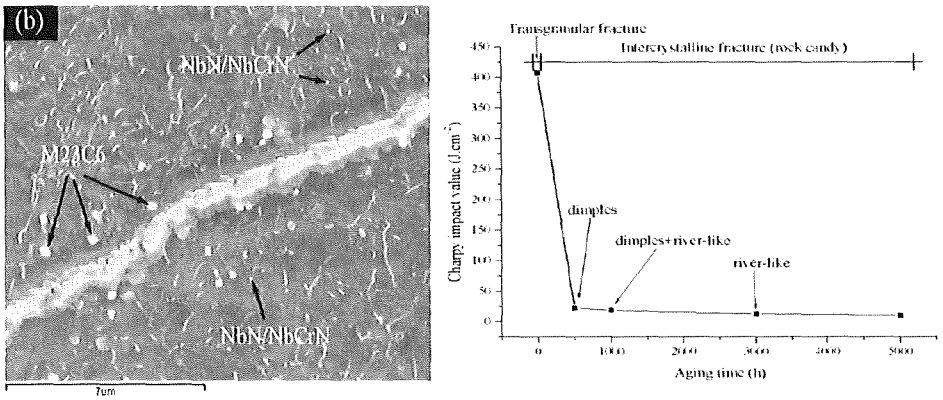

Fig. 10:- HR3C type alloy aged at 700°C. Precipitation of carbides and nitrides after 500hrs, left, and associated reduction in impact energy, right (24)

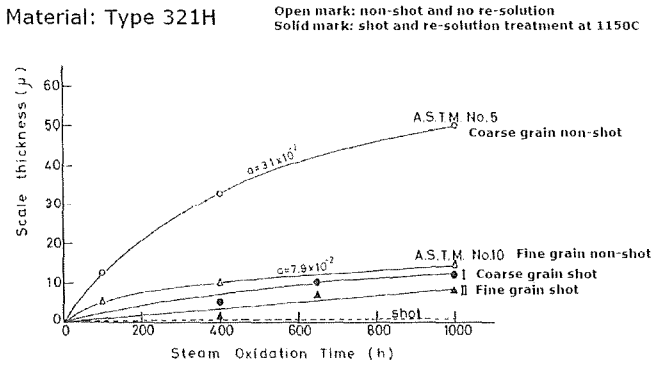

Fig. 11:- Effect of grain size and shot blasting on steam oxidation of 321H at 600°C (25)

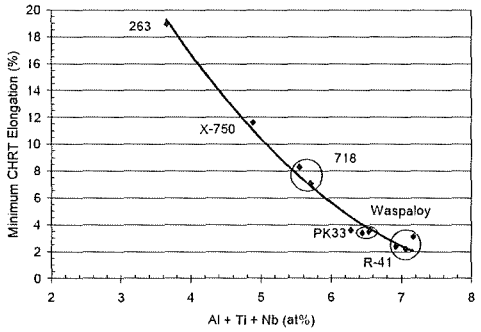

Fig. 12:- CHRT minimum elongation as a function of the total atomic percentage of precipitation-strengthening elements in a set of commercial alloys (36).

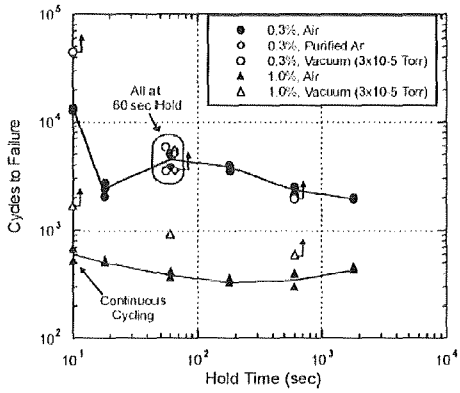

Fig. 13:- Alloy 617 creep-fatigue life at 1000°C as a function of hold time (38).

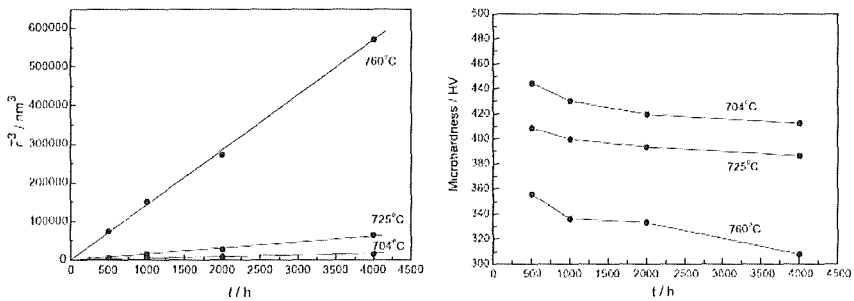

Fig. 14:- Coarsening of γ' precipitates in a 740 type alloy, left, and the corresponding effect on hardness, right (41).

9th Liege Conference : Materials for Advanced Power Engineering 2010
edited by J. Lecomte-Beckers, Q. Contrepois, T. Beck and B. Kuhn.

DEVELOPMENT STATUS AND FUTURE POSSIBILITIES FOR MARTENSITIC CREEP RESISTANT STEELS

J. Hald, DONG Energy/Vattenfall/DTU

DTU Mechanical Engineering, Technical University of Denmark, Kemitorvet b. 204,

DK-2800 Kgs. Lyngby, Denmark

e-mail: joh@mek.dtu.dk

Abstract

In the last four decades new stronger modified 9%Cr martensitic creep resistant steels have been introduced in power plants, which has enabled increases in maximum achievable steam conditions from the previous 250 bar and 540-560 °C up to the values of 300 bar and 600-620 °C currently being introduced all over the world.

In order to further increase the steam parameters of steel based power plants up to a target value of 650°C/325 bar it is necessary to double the creep strength of the martensitic steels. At the same time the resistance against steam oxidation must be improved by an increase of the chromium content in the steels from 9% to 12%. However, so far all attempts to make stronger 12%Cr steels have led to breakdowns in long-term creep strength.

Significant progress has been achieved in the understanding of microstructure stability of the martensitic 9-12%Cr steels: Observed microstructure instabilities in 11-12%Cr steels are explained by Z-phase precipitation, which dissolves fine MN nitrides.

Improved understanding of effects of B and N on long-term creep properties has formed the basis of a series of new stronger 9%Cr test alloys with improved creep strength. In parallel 9%Cr test steels with low C content show very promising behavior in long-term tests. However, the 9%Cr steels must be surface coated to protect against steam oxidation at high temperature applications above 620°C.

A possibility to use fine Z-phases for strengthening of the martensitic steels has been identified, and this opens a new pathway for development of stable strong 12%Cr steels.

There are still good prospects for the realization of a 325 bar / 650°C steam power plant all based on steel.

Key-words: 9-12%Cr steels, Microstructure and modelling, Z-phase, Boron, Alloy design

1. Introduction

Martensitic creep resistant 9-12%Cr steels are vital materials for further increases in steam parameters of fossil fired steam power plants. They provide a unique combination of high creep strength, high resistance against thermal fatigue, high steam oxidation resistance, low cost and good manufacturability. Over the past 50 years they have found increasing application in thick section components of steam power plants, i.e. steam piping and large forgings and castings. Beginning with the 12CrMoV steel introduced in power plant in the mid 1960s alloy development over the past 40 years has led to a number of new stronger steels such as the 9Cr steam pipe steels P91 and the tungsten-modified 9CrW grade P92. In the COST Actions 501, 522 and 536 new 9-10CrMo(W)B forged and cast alloys for steam turbines were developed and validated. Long-term creep testing has been undertaken in the COST Actions [1] as well as in

joint projects under the European Creep Collaborative Committee - ECCC [2] and the German association of large boiler operators - VGB [3]. Consequently, it is now well-documented that all of the 9-10Cr steels show stable long-term creep behaviour up to 100,000 hours and more at application temperatures. Currently, the best available alloys are the P92 for steam pipes and the FB2 for forgings and CB2 for castings. They have creep rupture strength at 600°C twice as high as the 12CrMoV steel, see table 1.

	Steam pipe steels			Turbine steels		
Mass %	**12CrMoV**	**P91**	**P92**	**Steel E/F**	**Steel FB2**	**Steel CB2**
C	0.2	0.1	0.1	0.1	0.13	0.12
Mn	0.5	0.5	0.5	0.5	0.8	0.9
Cr	11	9	9	10	9	9
Mo	0.9	0.9	0.5	1/1.5	1.5	1.5
W	-	-	1.8	1/0	-	-
Ni	0.5	0.1	0.05	0.6	0.15	0.15
Co	-	-	-	-	1	1
V	0.3	0.2	0.2	0.2	0.2	0.2
Nb	-	0.05	0.06	0.05	0.05	0.06
N	-	0.06	0.06	0.05	0.02	0.02
B	-	-	0.001	-	0.0085	0.011
Austenitisation	1050°C	1050°C	1065°C	1070°C	1100°C	1100°C
Pre tempering	-	-	-	570°C	570°C	-
Tempering	750°C	750°C	770°C	690°C	710°C	730°C
$\sigma_{B/10^5h/600°C}$	59 MPa	90 MPa	113 MPa	≈95 MPa	≈125 MPa	≈125 MPa

Table 1. *Chemical composition and heat treatment of a number of 9-12% Cr steels. The quoted creep rupture strength values for the pipe steels P91 and P92 are from the most recent evaluations by the ECCC [2,4].*

The improved creep rupture strength of the martensitic 9-12% Cr steels has enabled the construction new advanced fossil fired steam power plants. Increases in steam parameters from previous subcritical 180 bar/530-540°C up to ultra supercritical values of 300 bar and 600-620°C are now being realized in new coal or lignite fired steam power plants. Unit sizes of the new plants are up to 1100 MW and all have extensive use of the newly developed materials to their full potential.

The mentioned increase in steam parameters has led to increases of the thermal efficiency from the previous 30-35% to current 42-47%, equivalent to approximately 30% reduction in specific CO_2 emissions [5].

On top of this very impressive development there is still a strong need for further improvements of power plant efficiency for economical and environmental reasons. Table 2

shows the best available steels for critical components in the steam cycle of a power plant. It is clear that improved steels are needed for furnace panels, steam pipes and turbine forgings and casings in order to further increase of the steam parameters above the current 300 bar and 600-620°C.

Component/ Material	Composition	Max. metal temperature	Max. live steam temperature (400MW/325 bar)
Furnace panel			
T23	0.06C-2.25Cr-0.3Mo-1.6W-V-Nb-N-B	525 °C	625 °C
T24	0.7C-2.4Cr-1Mo-V-Ti-N-B	525 °C	625 °C
Superheater			
TP347HFG	18Cr-10Ni-1Nb	655 °C	≈ 620 °C
Super 304	18Cr-9Ni-0.4Nb-Cu-N	655 °C	≈ 620 °C
Sanicro 25	23Cr-25Ni-3.5W-3Cu-1.5Co-Nb-N	685 °C	≈ 650 °C
Steam pipe			
P92	0.1C-9Cr-0.5Mo-1.8W-V-Nb-N-B	600 °C	600 °C
Turbine			
FB2/CB2	0.13C-9Cr-1.5Mo-1Co-V-Nb-N-B	≈ 620 °C	≈ 620 °C

Table 2. *Best available steels for critical components in steam power plant. The maximum metal temperature in the component is shown together with the limitations this puts on the live steam temperature of a 400MW plant with 325 bar steam pressure.*

It is also clear from Table 2 that an improvement of the temperature capability of the martensitic creep resistant steels up to 650°C, which could allow the use of such materials for furnace panels, steam pipe and turbine, would enable the construction of power plants with steam parameters of 325 bar and 650°C. In order to reach such values it is necessary to double the creep strength compared with the currently best 9Cr steels P92/FB2/CB2 to reach a strength value of 100 MPa for rupture after 10^5h at 650°C. At the same time the resistance against steam oxidation must be improved, and if the oxidation protection is to be achieved through alloy additions instead of surface coatings, it is necessary to increase the chromium content in the steels from 9% to 12% [6].

Unfortunately, all attempts to make stronger 12%Cr steels in the recent 20 years have been unsuccessful because the high chromium content introduced severe microstructure instabilities in the tested steels, which led to breakdowns in long-term creep strength [7]. Consequently, recent developments like the European AD700 project [8,9] have focused on a leap in steam temperature up to 700°C based on the use of very expensive Nickel based alloys like the 617, 625 and 263 for steam lines, boiler components and turbines.

However, due to challenges facing the 700°C power plant based on Nickel based alloys, a steel based 650°C power plant would be a very strong competitor both from an economical and a technical point of view. Furthermore, stronger 12% Cr steels would also help the 700°C power plant, since part of the expensive of nickel base alloys can be replaced by cheaper steel.

The present paper summarises current understanding of essential strengthening mechanisms and microstructure instability of the 9-12%Cr steels, and outlines possibilities to reach the ambitious goal of a martensitic 12% Cr steel with double creep strength compared with P92/FB2/CB2.

2. Microstructure and creep strengthening mechanisms of 9-12%Cr steels

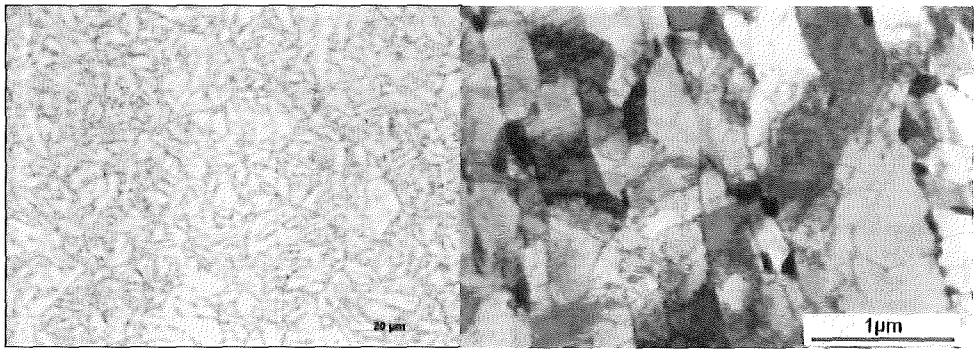

Figure 1. Tempered martensite in steel P92. Light optical (left) and transmission electron micrograph (right)

2.1 Creep and strengthening mechanisms

The 9-12%Cr steels have mainly tempered martensite microstructures formed during a final normalising and tempering heat treatment, although for some compositions considerable amounts of δ-ferrite may form in the microstructure. The tempered martensite consists of prior austenite grains separated by high angle grain boundaries. These grains are subdivided by high angle boundaries into blocks of martensite laths [10]. After tempering the blocks consist of subgrains with an average width of 0.3-0.5 µm separated by low angle boundaries. The dislocation density of the tempered martensite is high (in the order of 10^{14} m^{-2}), Fig. 1.

The technically interesting stress and temperature ranges for creep testing and service exposure of the 9-12%Cr steels are 250MPa-20MPa at 500°C-700°C. In these ranges the main creep mechanism in the steels is dislocation creep. This leads to glide of free dislocations and migration of subgrain boundaries during creep, resulting in a reduction of the dislocation density and growth of subgrains [11,12]. These deformation processes can be delayed by precipitate particles, which pin dislocations and subgrain boundaries.

A number of different precipitates can be found in the 9-12% Cr steels. Depending on their particle hardening effect and stability against coarsening or dissolution during long-term exposure the precipitates determine the microstructure stability of the steels. Precipitate hardening should be regarded as the most significant creep strengthening mechanism to obtain high long-term creep strength in the 9-12%Cr steels [2,13]. The most useful precipitates are the Cr carbides $M_{23}C_6$, the intermetallic Laves phases $Fe_2(Mo,W)$ and the MN nitrides (V,Nb)N. Boron addition to the steels may stabilise the $M_{23}C_6$ carbides, especially near the prior austenite grain boundaries. [14,15]. The MN nitrides precipitate in high number densities as very fine particles, which are much more stable against coarsening than the other precipitates [16]. As such they contribute significantly to long-term precipitation hardening in the steels.

2.1.1. Effect of MN and Z-phase on long-term creep strength

The long-term creep strength of the new generation of martensitic creep resistant steels since the well-known steel Grade 91 relies strongly on particle strengthening by fine MN nitrides

based on V and Nb. Additions of 0.15-0.25%V, 0.04-0.08%Nb and 0.02-0.07%N are common to all of the new steels, due to results obtained by Fujita in the late 1970s [17]. However, recent research has demonstrated that the MN nitrides, (V,Nb)N, may be replaced by the thermodynamically more stable Z-phases, Cr(V,Nb)N, which precipitate as coarse particles and dissolve the fine nitrides [18,19]. This phase transformation has been found to play a major role in observed long-term microstructure instabilities of the new martensitic creep resistant steels.

Studies of Z-phase precipitation in a number of 9-12%Cr steels, which rely on MN strengthening, show a clear correlation with the Cr content of the steels. For Cr contents above 10.5% Z-phase precipitation is strongly accelerated and leads to a breakdown in long-term creep strength steels. In steels with Cr contents below 9% Z-phase precipitation is so slow that they are largely unaffected up to very long testing times at 600-650°C [18].

Mass %	9Cr3W3Co	9Cr3W3CoB	P92	P122
C	0.078	0.077	0.11	0.12
Si	0.31	0.29	0.10	0.24
Mn	0.50	0.51	0.45	0.63
Cr	8.94	8.95	8.82	10.73
Mo	-	-	0.47	0.38
W	2.94	2.93	1.87	1.97
Ni	-	-	0.17	0.36
Co	3.03	3.03	-	-
Cu	-	-	-	0.97
V	0.19	0.19	0.19	0.22
Nb	0.050	0.050	0.06	0.056
N	0.002	0.001	0.047	0.072
B	-	0.0048	0.0020	0.0039
Norm	1050°C	1050°C	1070°C	1050°C
Temp	790°C	790°C	780°C	770°C

Table 3. *Chemical composition and heat treatment of steels discussed.*

The quantitative effect of MN precipitates on long-term creep strength of modern 9-12%Cr steels can be demonstrated by comparisons of selected steels, which all have fully tempered martensite microstructures free of δ-ferrite. The chemical composition and heat treatment of the discussed steels are shown in table 3 and results of creep rupture tests at 650°C are shown in Fig. 3. The 9Cr3W3CoVNb and 9Cr3W3CoVNbB steels have very low Nitrogen content and consequently they contain only $M_{23}C_6$ carbides and intermetallic Fe_2W Laves phase, but no MN nitrides. The 9Cr3W3CoVNbB steel is stabilised by Boron addition. As such these two steels represent baseline strength levels of the modern 9% Cr steels without nitrides. The P92 steel contains fine (V,Nb)N MN nitrides in addition to $M_{23}C_6$ carbides, Fe_2W Laves phases and Boron stabilisation. Because of the low Cr content the nitrides in steel P92 are stable against Z-phase precipitation up to long-term creep exposures. In short-term tests up to 2,000 hours the three steels have similar rupture strength. Above 2,000 hours the Boron addition in steels 9Cr3W3CoVNbB and P92 is effective, and above 10,000 hours the MN nitrides in steel P92 are effective to stabilise the microstructure and increase the strength. All three steels have similar heat treatment.

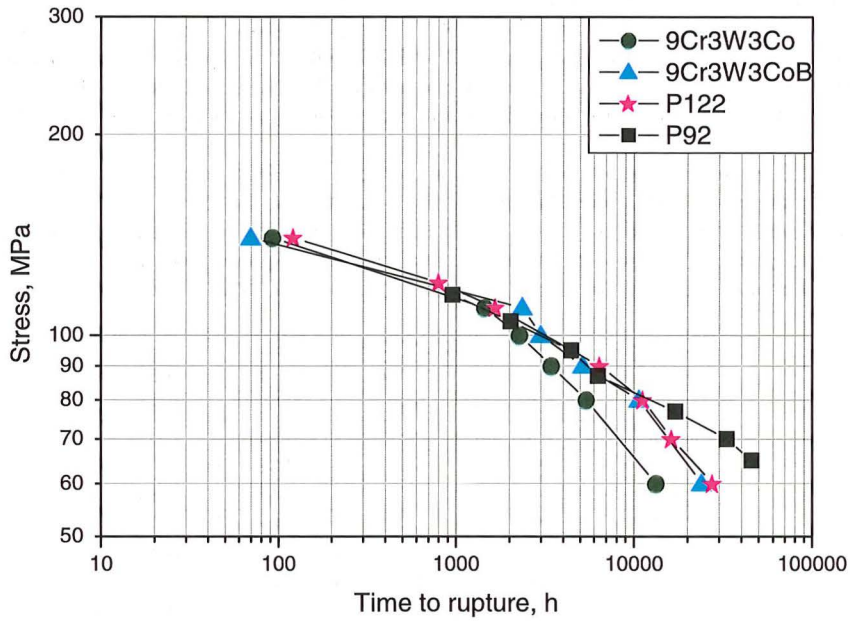

Fig. 3. Creep rupture tests at 650°C of the 9-12% Cr steels discussed [20,21].

If the MN nitrides disappear from the microstructure during creep it has a clear negative effect on the strength. The P122 steel contains MN nitrides, $M_{23}C_6$ carbides, Fe_2W Laves phases and Boron similar to the P92 steel, but due to the high Cr-content of 10.7%, strong precipitation of Cr(V,Nb)N Z-phase occurs above 10,000 hours and this dissolves the MN nitrides [18]. Consequently, the strength of the P122 steel stays at the level of the 9Cr3W3CoVNbB steel, which is without nitrogen, but has a similar Boron content as P122, see Fig. 3.

It is clear from above that the MN nitrides play a crucial role in the long-term microstructure stability of the 9-12%Cr steels, and that the removal of MN nitrides by Z-phase precipitation leads to a clear drop in strength. The Cr content in the steels controls the Z-phase precipitation rate, which explains the lack of success for all attempts to develop martensitic creep resistant steels with Cr content higher than 10.5% combined with high long-term strength based on MN nitrides.

3. Possibilities for improvement of the creep strength of the martensitic steels

3.1 Best test alloys

The creep rupture strength of the martensitic steels can be increased significantly above the level of steel P92 by optimisation of chemical composition and heat treatment. Table 4 and Fig. 4 show the current status of test alloys resulting from recent developments.

Mass %	P92	NF12	TAF	MARBN	MARN	BH Steel
C	0.11	0.085	0.18	0.078	0.002	0.03
Si	0.10	0.25	0.5	0.31	0.29	0.36
Mn	0.45	0.44	1.0	0.49	0.51	0.49
Cr	8.82	11.60	10.5	8.88	9.19	9.12
Mo	0.47	0.14	1.5	-	-	0.15
W	1.87	2.68	-	2.85	2.96	2.40
Ni	0.17	0.17	0.1	-	-	0.01
Co	-	2.48	-	3.00	3.09	1.8
V	0.19	0.20	0.2	0.20	0.2	0.20
Nb	0.06	0.08	0.15	0.051	0.06	0.05
N	0.047	0.045	0.020	0.0079	0.049	0.050
B	0.0020	0.0026	0.0400	0.0135	0.0070	0.0060
Norm.	1070°C	1100°C	1150°C	1150°C	1070°C	1050°C
Temp.	780°C	760°C	700°C	770°C	800°C	780°C

Table 4. *Chemical composition and heat treatment of best available test alloys of 9-12%Cr steels.*

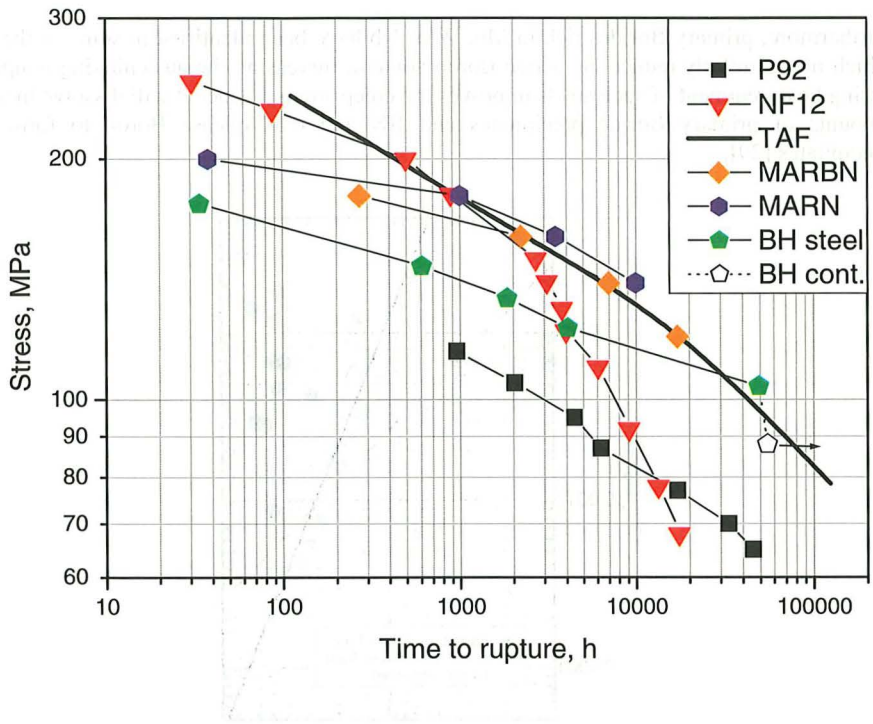

Figure 4. *Creep rupture strength at 650°C of the currently best available test alloys of 9-12%Cr steels [21,23,24].*

3.1.1. Optimised Boron and Nitrogen

Additions of 100 ppm or more of Boron to the 9-10%Cr steels has proven to be a very effective way to achieve high long-term creep strength. The TAF steel developed by Fujita in the 1950s is actually the strongest martensitic 10%Cr steel ever produced [23]. It contains 300ppm Boron, 0.2%C and 0.02%N. However, due to limited weldability this steel has limited practical applicability.

Detailed investigations including TEM and APFIM of creep specimens from a number of high Boron containing steels with very long exposure times [25-27] have indicated that Boron increases the microstructure stability by a reduction of the coarsening rate of $M_{23}C_6$ carbides. Even though detailed studies of the Boron distribution have demonstrated that most of the Boron is dissolved in these carbides it is still unclear how this can affect the coarsening rate.

Studies of BN precipitates in 9-12%Cr steels by NIMS in Japan have shown that not all of the Boron added to the steels will be active in the $M_{23}(C,B)_6$ carbides, since part of it can be tied up in large BN precipitates [28]. The studies at NIMS led to optimization of the Boron and Nitrogen levels in the steels in order to stay below the solubility line of BN, Figure 5. This is implemented in the MARBN and similar steels, which have low Nitrogen and high Boron contents, see Figure 4.

Furthermore, primary Borides rich in Mo, W or Nb have been identified in some of the steels, which may similarly reduce the active Boron content. Increasing the austenitizing temperature during heat treatment of such steels improves the creep strength since it will dissolve increasing amounts of primary Boride precipitates and BN and thus release Boron to form useful precipitates [29].

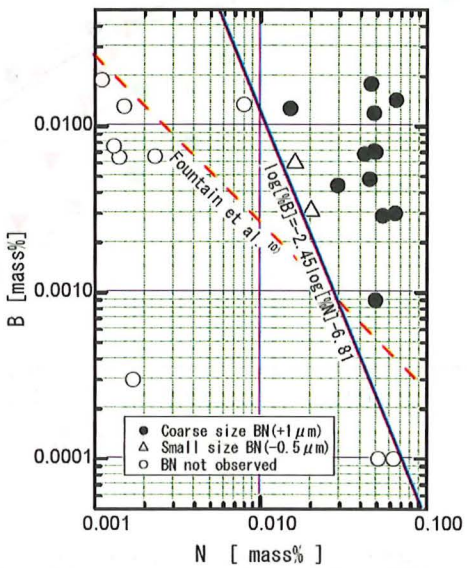

Figure 5. *BN Solubility at 1150°C according to NIMS [28].*

3.1.2 Low C steels

9%Cr steels with low C (steels BH and MARN) also seem to be able to increase the long-term strength close to the target level of 100 MPa for rupture after 10^5 hours at 650°C, see Fig. 3. The very good long-term stability based on the low C 9%Cr steels is based on fine MN nitrides, and medium level Boron. The very high long-term stability of the low C steels is obtained even though their chemical compositions should not suppress coarse BN formation according to Figure 5; and even though their austenitizing temperature is not considered high enough to dissolve Boride precipitates in steels. The high microstructure stability could possibly be due to the absence of $M_{23}C_6$ carbides in the low C steels, which provide more available nucleation site for the MN nitrides. However the exact reasons for the high stability still needs to be investigated.

3.1.3. Effect of high Cr

As mentioned, so far only test steels with Cr contents lower than 10.5% indicate stable long-term strength at the required level. The NF12 steel demonstrates the behaviour of test steels with high Cr content. It has 11.6%Cr and it shows high short-term strength, but in long-term tests the MN nitrides are dissolved by Z-phase precipitation [18], and the strength drops below the level of steel P92. In no case has it been possible to combine high Cr-content with stable long-term strength. Both the steels with optimised Boron and Nitrogen contents and the steels with low C rely on fine MN nitrides for high creep strength, and if the Cr content is increased the MN nitrides will inevitably be dissolved by Z-phase formation.

If the strong 9-10%Cr steels are to be used at service temperatures significantly higher than 600°C it is necessary to apply some sort of surface coating for oxidation protection. This will lead to increased production cost and open a wealth of new possibilities for component failure and risks for unexpected plant outages. It is thus very desirable to develop a stable strong martensitic 12%Cr steel.

3.1.4. Z-phase strengthened 12%Cr steels

MN strengthening based on (V,Nb)N has been very useful for the microstructure stability of all new 9Cr martensitic steels since Grade 91. However, it is clear from above that MN strengthening is not a way forward to develop stable 12Cr steels. This is through irrespective of Boron additions or low C content, and it means that other strengthening phases than MN nitrides need to be introduced in order to combine high Cr content and high microstructure stability.

One possible way currently being investigated is to use the Z-phase itself as a strengthening phase. If the Z-phase could be provoked to precipitate very quickly in a fine distribution, which could provide particle strengthening, then the steel could be expected to be immune to dissolution of its strengthening nitrides [29].

The necessary steps to accelerate Z-phase precipitation involve an increase of the Cr-content to the highest possible level. Further, in order to accelerate Z-phase formation the Carbon content should be low and Cobalt should be added. The latter also limits delta ferrite formation. The high Cr content would then be turned from being the main cause of instability into being a necessary beneficial element to secure the long-term microstructure stability of the steels. And at the same time the necessary oxidation resistance would be obtained, which would again make it possible to combine strength and oxidation resistance in the same alloy.

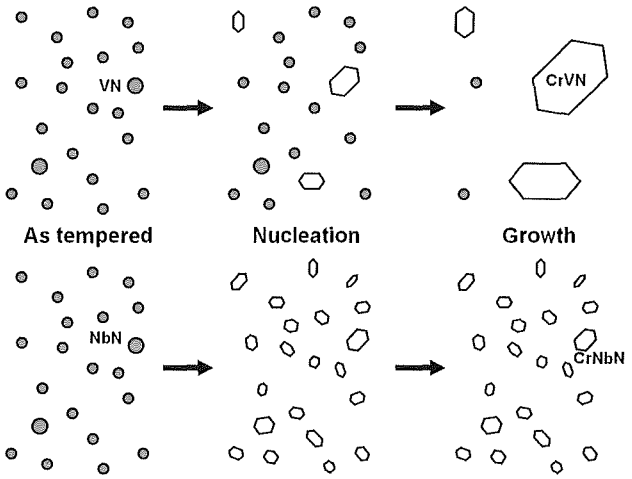

Figure 6. Z-phase transformation in a traditional 12CrMoVNbN steel (top) and in a Z-phase strengthened 12CrNbN steel (bottom)

Investigations of 12%Cr test alloys have shown that fine NbN or TaN nitrides, which are precipitated during tempering, transform to a fine distribution of Z-phase after short time at 650°C. The strong acceleration of the Z-phase transformation means that each individual MN nitride transforms quickly into one Z-phase. Thereby the detrimental Z-phase growth process involving MN dissolution is effectively suppressed. The result is a fine distribution of Z-phase particles; see Fig. 6, which has a similar stability against coarsening as the MN nitrides.

Ongoing work aims to optimise the composition and heat treatment of Z-phase strengthened 12%Cr steels to obtain the desired strength level [30].

5. Summary

In the last four decades new stronger modified 9Cr steels such as P91 and P92 for steam pipes and FB2 and CB2 for steam turbine forged rotors and cast valves and casings have been introduced in new power plants. This has enabled increases in maximum achievable steam conditions from the previous 250 bar and 540-560°C up to the values of 300 bar and 600-620°C currently being introduced all over the world.

In order to further increase the steam parameters of steel based power plants up to a target value of 650°C/325 bar it is necessary to double the creep strength of the martensitic steels. At the same time the resistance against steam oxidation must be improved by an increase of the chromium content in the steels from 9% to 12%. However, so far all attempts to make stronger 12%Cr steels have led to breakdowns in long-term creep strength.

Significant progress has been achieved in the understanding of microstructure stability of the martensitic 9-12%Cr steels: Observed microstructure instabilities in 11-12%Cr steels are explained by Z-phase precipitation, which dissolves fine MN nitrides.

Improved understanding of effects of B and N on long-term creep properties has formed the basis of a series of new stronger 9%Cr test alloys with improved creep strength close to the target values at 650°C. In parallel 9%Cr test steels with low C content show very promising behavior in long-term tests.

However, the 9%Cr steels must be surface coated to protect against steam oxidation at high temperature applications above 620°C. Due to challenges with coatings it is very desirable to develop stable strong steels with 12%Cr.

A possibility to use fine Z-phases for strengthening of the martensitic steels has been identified, and this opens a new possibility for development of stable strong steels with 12%Cr. This means that there are good prospects for the realization of a 325 bar / 650°C steam power plant all based on steel in the coming decades.

6. References

[1] T.-U. Kern, M. Staubli, K. H. Mayer, B. Donth, G. Zeiler and A. DiGianfrancesco: Proc. Conf. *Materials for Advanced Power Engineering 2006*, (ed. J. Lecompte-Beckers et. al.), Part II, 843-854, Forschungszentrum Jülich (2006)
[2] J. Hald: Proc. 1st Int. Conf. *Super-high strength steels*", AIM and CSM, Paper 3.4, Rome (2005)
[3] K-H. Mayer, T. -U. Kern, M. Staubli, E. Tolksdorf in proc. Fifth International Charles Parsons Turbine Conference, Cambridge, 3-7 July 2000. A. Strang et. al. (Eds.), 372-385, IOM, London (2000).
[4] W. Bendick, L. Cipolla, J. Gabrel and J. Hald, *International Journal of Pressure Vessels and Piping* 87, 304-309 (2010)
[5] C. Henderson: *Case studies on recently constructed fossil-fired plants and summary of status of gasification combined cycle technology*, Paris, IEA/OECD (2007)
[6] G. Scheffknecht, Q. Chen and G. Weissinger: Proc. Conf: *Parsons 2003, Engineering Issues in Turbine Machinery, Power Plant and Renewables* (ed. A. Strang et. al.), 112-128, IOM3, , London (2003)
[7] J. Hald, *VGB PowerTech 12*, 74 (2004)
[8] R. Blum and R. W. Vanstone: Proc. Conf. *Materials for Advanced Power Engineering 2006*, (ed. J. Lecompte-Beckers et. al.), Part I, 41-60, Forschungszentrum Jülich (2006)
[9] H. Tschaffon: Proc. Conf. *Materials for Advanced Power Engineering 2006*, (ed. J. Lecompte-Beckers et. al.), Part I, 61-68, Forschungszentrum Jülich (2006)
[10] F. Abe, *Current Opinion in Solid State and Materials Science* 8, 305 (2004).
[11] S. Straub, *Verformungsverhalten und Mikrostruktur warmfester martensitischer 12%-Chromstähle*, 405, VDI Forschungsberichte 5, VDI Verlag, Düsseldorf (1995)
[12] P. Polcik, *Modellierung des Verformungsverhalten der warmfesten 9-12% Chromstähle in Temperaturbereich von 550-650°C*, 92, Shaker Verlag, Aachen (1999)
[13] F. Abe, *Sci. Technol. Adv. Mater.* 9, 1 (2008)
[14] F. Abe, *Int. J. Mat. Res.* 99, 387 (2008)
[15] M. Hättestrand and H.-O. Andrén, *Mater. Sci. Eng. A*, 270, 33 (1999)
[16] J. Hald and L. Korcakova, *ISIJ Int.* 43-3, 420 (2003)
[17] T. Fujita, *Metal. Trans. A* 12, 1071 (1981)
[18] H. K. Danielsen and J. Hald, *Energy Mater.* 1, 49 (2006).
[19] A. Strang and V. Vodarek: Materi. Sci. Tech 12, 552, (1996)
[20] F. Abe: Proc. *Int. Conf. on New Developments on Metallurgy and Applications of High Strength Steels,* Buenos Aires (2008)
[21] NIMS Creep Data Sheet, No 51, National Institute For Materials Science, Japan (2006)
[22] H. Naoi, M. Oghami, Y. Hasegawa and T. Fujita: Proc. Conf *Materials for Advanced Power Engineering 1994* (ed. D. Coutsoradis et. al.), Part I, 425-434, Kluwer, Dordrecht (1994)
[23] T. Fujita, N. Takahashi, *Trans. ISIJ*, 18, 702-711 (1978)
[24] T. Fujita, Personal Communication (2010)
[25] F. Kaufmann, G. Zies, D. Willer, C. Scheu, K. Maile, S. Straub, *31. MPA-Seminar*, Stuttgart, 13. And 14. October 2005, lecture 27, (2005)

[26] P. Nowakowski, PhD Thesis, TU WIEN (2000)
[27] A. Golpayegani, M. Hättestrand, H.-O. Andrén, in proc. *Sixt International Charles Parsons Turbine Conference*, Dublin 16-18 September 2003. A. Strang et. al. (Eds.), 365-377, IOM, London (2003)
[28] K. Sakuraya, H. Okada, F. Abe, in Proc. Conf: *Advances in Materials Technology for Fossil Power Plants*, R. Viswanathan, et. al. (Eds.), Hilton Head Island, USA, October 2004, 1270-1279, ASM International (2005)
[29] H. K. Danielsen, J. Hald, *VGB PowerTech* 5, 68-73 (2009)
[30] H. K. Danielsen and J. Hald, *This conference*

9th Liege Conference : Materials for Advanced Power Engineering 2010
edited by J. Lecomte-Beckers, Q. Contrepois, T. Beck and B. Kuhn.

BENEFICIAL EFFECT OF Re ON THE LONG -TERM CREEP STRENGTH OF HIGH Cr FERRITIC HEAT RESISTANT STEELS

Ryokichi Hashizume [1], Osam Tamura [1], Kazuhiro Miki [2],Tsukasa Azuma [2]
Tohru Ishiguro [3], Yoshinori Murata [4] and Masahiko Morinaga [4]

1) The Kansai Electric Power Company Inc., Amagasaki , JAPAN
e-mail: hashizume.ryokichi@c4.kepco.co.jp
2) Muroran Research Laboratory, The Japan Steel Works, Ltd., Muroran, JAPAN
3) Muroran Plant , The Japan Steel Works Ltd., Muroran, JAPAN
(Present address: Institute of Multidisciplinary Research for Advanced Materials, Tohoku University, Sendai, JAPAN)
4) Department of Materials Science and Engineering, Nagoya University, Nagoya, JAPAN

Abstract

9-12%Cr ferritic steels were designed by using the d-electrons concept for the use of steam turbine rotors operated in the USC power plants at the steam temperature of 620°C to 650 °C. The crucial issue for the design is to suppress the deterioration of the long-term creep strength by alloying. First, the Re addition was found to give a beneficial effect on the creep strength of a 10%Cr-4%W steel. Then, the creep tests were performed with the six Re-free and 3.5%W ferritic steels to get an optimum Cr content in the range of 8.5% to 11.5%. As a result, it was found that an excess amount of Cr yielded a detrimental effect on the creep properties, and 9% Cr steel was the best in view of the very long-term creep strength tested in the condition of 650 °C, 98 MPa. Subsequently, a series of creep tests was conducted with the steels by fixing at 9%Cr, but by varying the W content from 2% to 4% and the Re content from 0% to 0.5%. From the prolonged creep tests and creep rate tests for more than 30,000-40,000 hours, it was shown that the 9Cr-4W without Re steel had the long creep rupture life for more than 32,000 hours at 650 °C 0,98MPa and the 9Cr-4W-0.5Re steel had the longer one for more than 43,000 hours. It was the longest creep rupture life among all the tested steels.

Keywords: ferritic steel, heat resistant steel, creep strength, Re , turbine rotor, martensite , microstructure

1. Introduction

There is a growing need to reduce CO_2 emissions from fossil fuel power plants. In Europe and Japan, 700°C class A-USC power plant is now being developed to meet these demands.[1,2] For the use of the steam turbine rotors in the power plants operated in the USC conditions above 600 °C, high Cr heat resistant steels with high temperature creep strength have been developed [3-6]. For these ferritic heat resistant steels used at above 600 °C, improvement in the long-term creep strength is the most important issue. However, it is known that the creep rupture life under the lower applied stress at 650 °C is often much shorter than the one extrapolated from the short-term creep test [7-10]. This premature failure has been discussed in terms of collapse of the lath structure , coarsening of carbides and nitrides, formation of the Z phase, *etc.*[11-14] On the other hand, we have found for the first time that Re improves the short term creep strength of high Cr ferritic heat resistant steels on the basis of Dv-Xα cluster method [15] and also that 9%Cr is desirable content in the 9-12%Cr ferritic steel for suppressing the premature failure at the condition of 98MPa and 650 °C[16-19]. The purpose of this study is to examine the effect of Re with the optimum content

of 9%Cr heat resistant steels for the A-USC high-temperature rotor shafts in the long term condition at 98MPa and 650 °C.

2. Experimental Procedure

The steels tested in this study are 9-10%Cr-Mo-V-Re-W-Co-B steels . Table 1 shows the chemical compositions of the laboratory heats. Hereafter, the compositions are expressed in mass% unless otherwise noticed. Cr varied in two levels of 9% and 10% in the steels. Also, W varied from 2% to 4%, and Re varied from 0% to 0.9% in the steels. Alloy A, B alone contain 0.07%Mn and 0.20%Ni, originally these elements are contained considering the steel making process from the scrap, but after many studies, these element levels are suppressed to be lower level, because it became clear Mn and Ni have no creep strengthening effect. Every steel contain V and Nb to form MX and 100ppm B which is known effective to keeping high creep strength. 3%Co is contained in order to avoid remaining of the δferrite after forging and heat treatment. In the table, Cr-equivalent supplied by Newhouse and the two electronic parameters average Md and Bo values are also listed.

Table1 Chemical compositions of tested steels (mass%)

steel	C	Si	Mn	Ni	Cr	Mo	V	Nb	W	Co	B	Re	N	Cr-eq.	$\overline{Md}$	$\overline{Bo}$
A	0.09	0.03	0.07	0.20	10.14	0.01	0.19	0.06	3.99	2.98	0.007	0.01	0.026	7.41	0.852	1.804
B	0.09	0.03	0.07	0.21	10.20	0.01	0.19	0.06	3.97	3.00	0.007	0.23	0.025	7.37	0.855	1.811
C	0.12	0.02	0.01	<.01	10.09	0.40	0.20	0.08	1.89	3.01	0.008	<.01	0.016	5.83	0.853	1.803
D	0.12	0.03	0.01	0.02	10.00	0.41	0.21	0.08	1.89	3.02	0.009	0.18	0.017	5.92	0.852	1.805
E	0.12	0.02	0.01	0.02	10.04	0.39	0.20	0.08	1.91	3.00	0.009	0.90	0.018	5.75	0.856	1.808
F	0.10	0.02	0.01	0.02	8.97	0.01	0.21	0.07	3.97	3.04	0.009	<0.01	0.019	6.99	0.854	1.805
G	0.11	0.03	0.01	0.01	9.04	0.01	0.21	0.06	3.97	3.01	0.009	0.19	0.021	6.71	0.855	1.805
H	0.11	0.02	0.01	0.01	9.04	0.01	0.21	0.07	3.97	3.01	0.009	0.48	0.022	6.69	0.855	1.805
I	0.10	0.02	0.01	0.02	8.97	0.01	0.21	0.06	2.94	3.03	0.009	<0.01	0.019	5.43	0.851	1.802
J	0.11	0.03	0.01	0.02	9.01	0.01	0.21	0.07	2.98	3.02	0.008	0.18	0.019	5.26	0.852	1.802
K	0.10	0.02	0.01	0.02	9.01	0.01	0.20	0.06	2.98	2.99	0.008	0.45	0.019	5.51	0.852	1.803
L	0.12	0.03	0.01	0.02	9.02	0.41	0.21	0.06	1.87	3.04	0.009	<0.01	0.016	4.81	0.849	1.800
M	0.12	0.03	0.01	0.02	8.98	0.41	0.21	0.08	1.87	3.01	0.007	0.18	0.016	4.90	0.849	1.800

Cr-eq.=[Cr%]+6[Si%]+4[Mo%]+1.5[W%]+11[V%]+5[Nb%]-40[C%]-2[Mn%]-4[Ni%]-30[N%]-2[Co%]

The 50kg ingots of the tested materials were cast by vacuum induction melting and forged into plates of 35mm thickness. They were normalized at 1100 °C for 5h followed by tempering at 720 °C for 20h. The quality heat treatment was performed on austenitizing at 1070°C for 5h and controlled cooling at 100 °C/h corresponding to the cooling rate on oil quenching on the center of turbine rotor shaft forging, followed by 1st tempering at 570 °C for 20h and 2nd tempering at 680 °C for 20h. Phase transformation temperatures (Ac_1,Ac_3,M_s,M_f) were measured by a dilatometer and controlled cooling rate of M_s, M_f measuring is 100°C/h same above. After quality heat treatment, tensile tests at room temperature (RT) and 600 °C,

creep test at 650 °C and aging at 650 °C were performed. The micro-structural observation was carried out for aged or crept materials with transmission electron microscopy (TEM). Precipitates are identified based on their chemical compositions obtained by EDX analysis.

3. Experimental Results

3.1 Microstructure and Transformation temperatures

Every tested steel had a uniform martensitic structure and no δferrite was seen in the optical microstructure observation after quality heat treatment. It was confirmed that every steel was capable to be produced with a uniform martensitic structure in oil quenching process of large turbine rotor with a diameter of 1200mm. Fig.1 shows the transformation temperatures Ac_1, Ac_3, M_s and M_f of the 13 tested A-M steels which varied mainly in Cr,W and Re contents . In the figure, it was plotted in the groups of similar chemical composition, namely 10Cr4Wsteels A, B, 10Cr2Wsteels C, D, E , 9Cr4Wsteels F, G, H , 9Cr3Wsteels I, J, K and 9Cr2Wsteels L, M. Ac_1 temperatures are about 813 °C, and they scarcely varied irrespective of their chemical compositions. This means that tested steels have appropriate starting temperature of austenite forming or Ac_1 points considering the tempering temperature of 760-780 °C, when they are applied to the boiler pipes. On the contrary, Ac_3, M_s and M_f temperatures changes with Re content, but they do not exhibit systematical change depending on Re content.

3.2 Tensile strength and toughness

Figure 2 shows the results of tensile tests conducted at room temperature and high temperature of 600°C and the Fracture Appearance Transition Temperature ; FATT, estimated from the results of Charpy impact tests of various temperatures. At room temperature, tensile strength increased with increasing W content, but did not change with Re content. In both kinds of 9Cr and 10Cr steels, the increases of tensile strength with W content become small compared to that at room temperature, but it becomes high with a small amount of Re addition. FATT increased with increasing W content, but did not change with Re content. It can be said that Re has a lowering effect of FATT in spite of similar atomic weight of W.

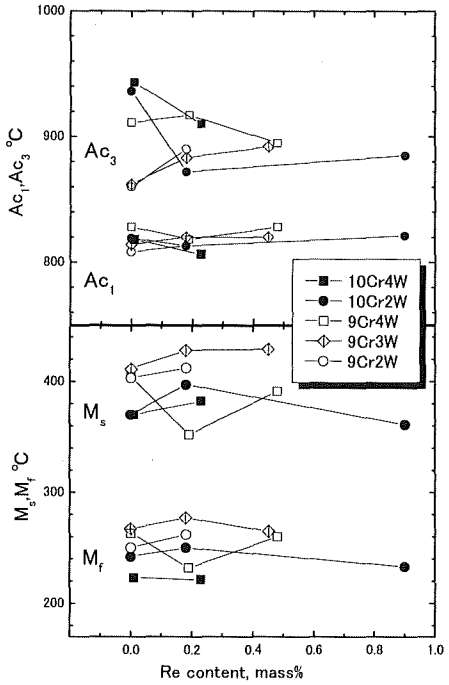

Fig.1 Effect of Re content on tranformation temperatures

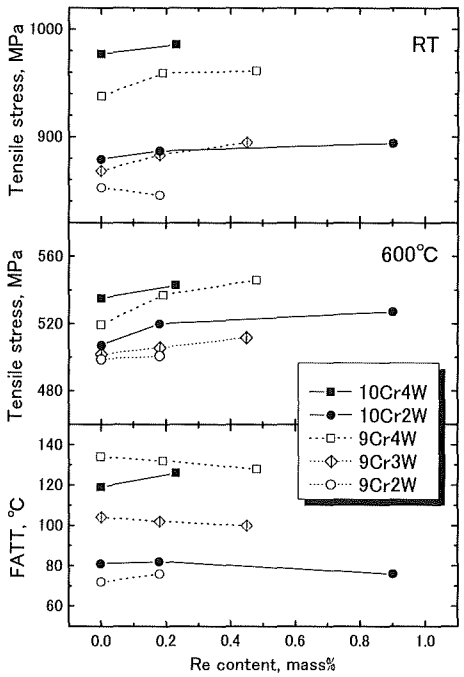

Fig.2 Effect of Re content on strength and toughness

3.3 Creep Strength

3.3.1 Creep strength of 10%Cr steels (A-E steels)

The results of the creep rupture tests of A and B steels are given in Fig. 3. Although both steels show the deterioration of creep strength in the stress condition of less than 157MPa, steel B shows longer creep rupture life than steel A. For example, the creep rupture life of B is 22,700 hours and that of A steel is 14,700 hours at 98MPa. This result shows clearly the beneficial effect of Re on the creep rupture life of 4W10Cr steels. On the other hand, the results of the creep rupture tests of 10Cr2W steels, C, D and E, are given in Fig. 4. Every steel also shows the premature failure in the condition of less than 157MPa. In this case, the Re effect is not observed. It can be said that at least more than 2%W is needed to obtain the beneficial effect of Re on the creep strength.

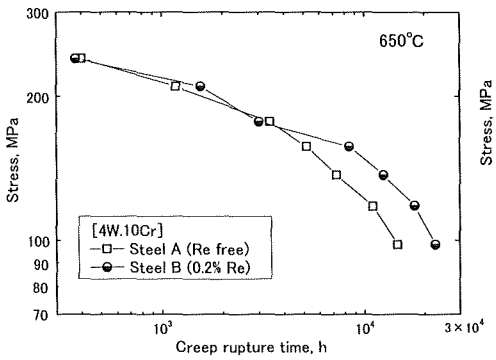

Fig.3 Results of creep rupture tests of steels, A and B

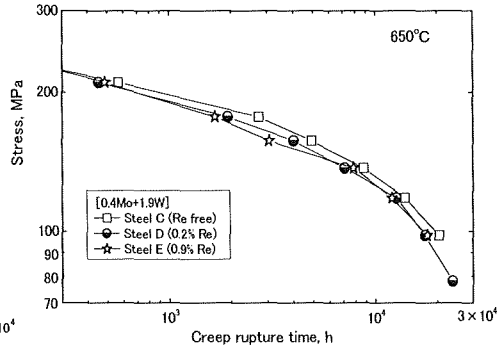

Fig.4 Results of creep rupture tests of steels, C, D and E

3.3.2 Creep strength of 9%Cr steels (F-K steels)

The results of the creep rupture tests of 9Cr4W steels, F,G and H, are given in Fig. 5. It is clearly seen that the creep rupture life become longer with increasing Re content and the premature failure is not observed at the lower stress condition. The rupture life of steel H at the condition of 650 °C,118MPa is 23,000h. Also,the rupture lives of steel F,G and H at the condition of 650°C 0,98MPa are 32,700h, 34,685h and 43,800h respectively. these are very long rupture lives as for high temperature rotor steels The results of creep rupture tests of 9Cr3W steels, I, J and K, are given in Fig.6. The curves have a similar feature to those of 9Cr4W steels, F, G and H. 9Cr3W0.5Re steel, K, shows the longest creep rupture life among these steels at 118MPa condition, but these three steels exhibit a similar life to each other at 98MPa condition, i.e., 28,830h of I, 27,690h of J and 29,291h of K. The results of creep rupture tests of 9Cr2W steels, L and M, are given in Fig.7. Creep rupture lives of steel L and steel M, are 21,847 and 21,882 hours, respectively. The beneficial Re effect on creep strength is not observed in these two steels as also indicated in 10Cr2W steels. Based on the results of Fig.3-Fig.7, the effect of Re on the creep rupture life is summarized in Fig.8. It is found that the Re effect is remarkable in 4W steels compared with 2 or 3W steels.

Creep curves of 10%Cr A and B steel and the strain rate-creep time curves at the condition of 157MPa are shown in Fig. 9 and in Fig.10 respectively. And also Creep curves of 9%Cr F and H steel and the strain rate-creep time curves at the condition of 137MPa are shown in Fig. 11 and in Fig.12 respectively. The initial creep strain rates of both 9Cr and 10Cr steels are almost the same regardless of Re content, but after about several hundreds hours, the creep strain rate of Re containing steel becomes low and its minimum strain rate is smaller than that of Re free steels. And the onset of accelerating creep is delayed to the later side. As a result, the creep rupture lives of Re containing steels are extended.

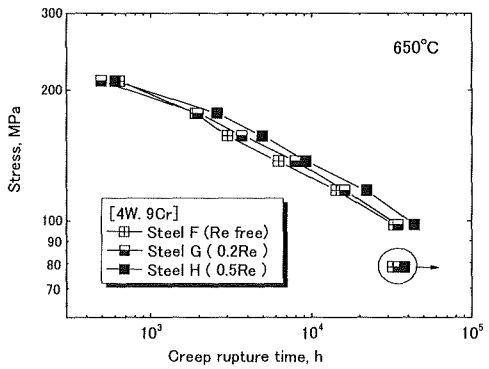

Fig.5 Results of creep rupture tests of steels, F,G and H

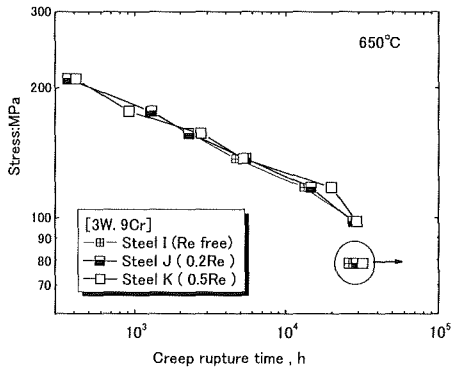

Fig.6 Results of creep rupture tests of steels, I, J and K

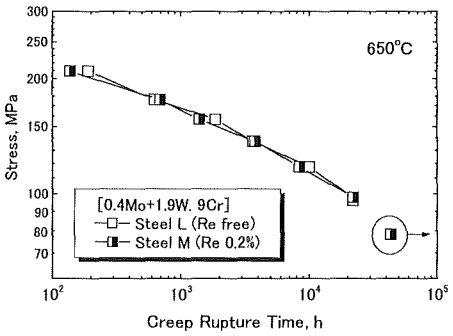

Fig.7 Results of creep rupture tests of steels, L and M

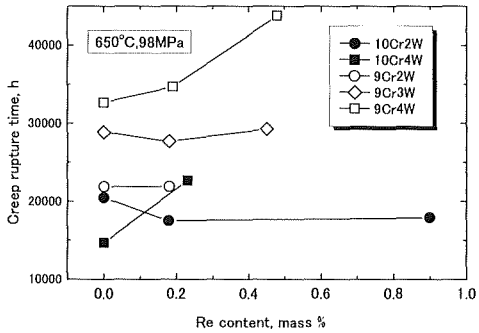

Fig.8 Effect of Re content on creep rupture time of 9Cr,10CR steels measured in the condition of 650°C, 98MPa

4. Discussion

The experimental results observed in Fig.9-12 suggest that the change of microstructure is suppressed by Re content. It is considered that creep strength directly related to the microstructural evolution in high Cr ferritic steels. So, the microstructures of the steels were investigated with TEM and the extracted residues were analyzed about 9Cr4W steels, F and H, which exhibit longer creep rupture life among tested steels. Figure 13(a)-(f) show TEM microstructures of carbon extraction replica taken from steels, F and H, after quality heat treatment and aged specimens. In both steels, lump shaped precipitates are observed in lath and block boundaries, and fine precipitates are observed within lath. After 10000h aging at 650 °C, all precipitates coarsen in both steels, but a number of fine precipitates still remain in steel H containing Re. After 30000h aging, the fine precipitates are not observed in steel F,

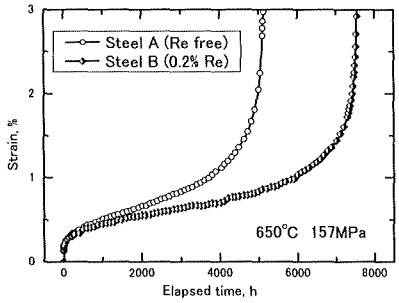

Fig.9 Creep curves of steel A and B at 650℃ and 157MPa

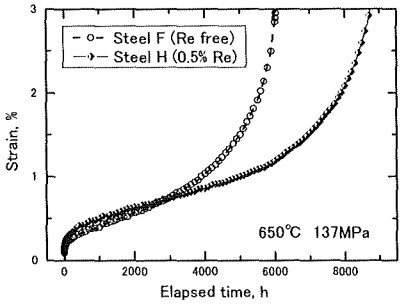

Fig.11 Creep curves of steel F and H at 650℃ and 137MPa

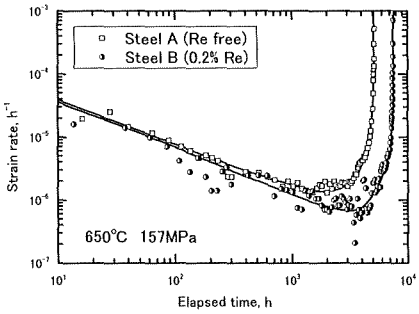

Fig.10 Strain rate-time curve of steel A and B at 650℃ and 157MPa

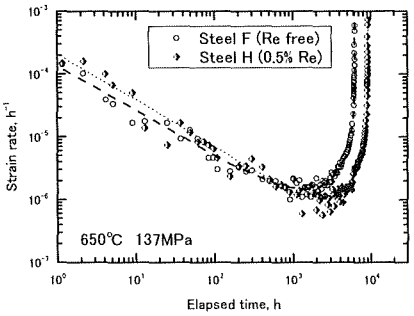

Fig.12 Strain rate-time curve of steel F and H at 650℃ and 137MPa

but they are still observed in steel H after 30000h at 650 °C, as shown in Fig.13(f) and Fig.15. Fig.14 shows precipitates in steel F aged at 650°C for 30000h. These precipitates are identified based on their chemical compositions obtained by EDX analysis. In the lath boundaries, a large amount of both $M_{23}C_6$ carbide and the Laves phase are observed in-line, and a small amount of MX carbonitride is also present. These kind of precipitates are also observed in steel H. Fig.15 shows the fine precipitates within the lath in steel H both after quality heat treatment and aging at 650°C for 30000h, and they are the Laves phases precipitated semi-coherently within the lath as identified by white arrows in the figure [20]. Comparing Fig.14 and Fig15, the main difference of microstructural evolution between steel F and steel H is the state of existence of the fine semi-coherent precipitates. This kind of fine precipitates is known to be Fe_2W type Laves phase, which is observed in high W heat resistant ferritic steels, as semi coherent precipitates [20]. Therefore, it can be concluded that the Re addition makes stable the fine Laves phase precipitate within lath semi-coherently, resulting in strengthening the steel even in a long term of creep. In fact, it has been reported that Re retards W diffusion in a Fe-Cr alloy [21,22]. In other words, it can be said that the existence of Re suppress W diffusion, resulting in suppressing the coarsening of precipitates

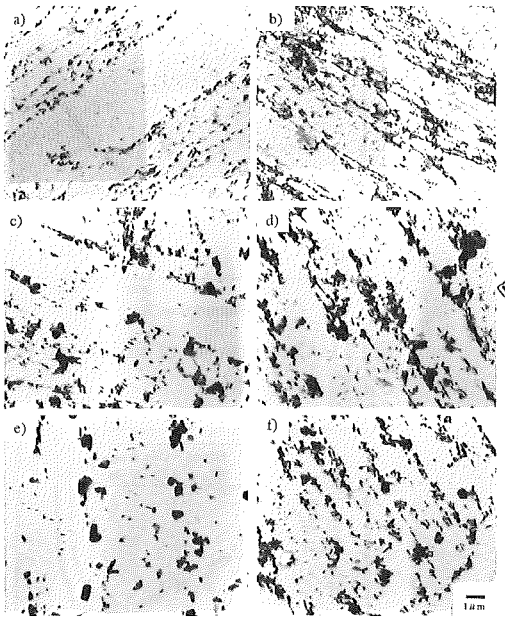

Fig.13 Transmission electron micrographs of steel F and H after the heat treatment and aged specimens.

	Steel F	Steel H
as quality heat treatment	a)	b)
aged for 10000h	c)	d)
aged for 30000h	e)	f)

containing W. This is probably the main reason why steel H exhibits higher creep strength in long term than steel F.

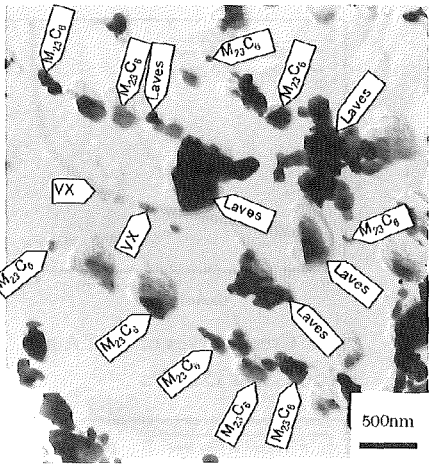

Fig.14 Transmission electron micrograph of material aged at 650℃ for 30000h in Steel F

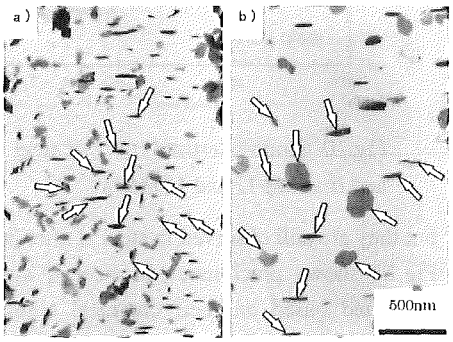

Fig.15 Transmission electron micrographs of Laves phase within lath in Steel H before and after aging at 650℃. a) as quality heat treatment, b) aged for 30000h

5 Summary

Investigations were carried out on the effect of Cr, Re and W on creep strength and heat resistant characteristics of high Cr ferritic steels to be used for the USC turbine rotor shafts. The results are summarized as follows.

1. It is proved that the premature failure in creep strength at 650 °C can be prevented by lowering Cr content to 9% in high Cr ferritic steels.

2. It is found that the creep strength is improved remarkably by increasing W content up to 3- 4% W in 9%Cr steels, Furthermore, it is also greatly improved by the addition of 0.2-

0.5%Re to the steels. The longest creep rupture life among the tested steels is obtained in 9Cr4W0.5Re, steel H, at 650 °C,98MPa and it is 43,800h.

3. The minimum creep rate in both kinds of 9%Cr and 10%Cr steels is decreased and the onset of accelerating creep is delayed by the addition of Re when present together with a 3-4%W, resulting in extending the rupture life of the steel.

4. Fine plate shape (semi-coherent) Laves phases are precipitated within the lath of 4%W steels. These fine Laves phases existed stably in 4%W0.5%Re steel for the long time. It can be concluded that excellent long term creep rupture strength of Re containing steel is attributable to the existence of the fine precipitates.

6. References

[1] R.Blum : Materials Development for Boilers and Steam Turbines operating at 700℃, *Proccedings of the 8th Liege Conference on Materials for Advanced Power Engineering 2006*, September 17-20,(2006), P41-67

[2] M Fukuda : A-USC Technology Development, a challenge to the Global Warming, *CAMP-ISIJ*, Vol.21(2008)-1018

[3] T. Fujita : "Development of High Chromium Ferritic Heat Resistant Steels for Power Plants", *Thermal and Nuclear Power*, 42 (1991), p.1485.

[4] Y. Tsuda, M. Yamada, R. Ishii, Y. Tanaka, T. Azuma and Y. Ikeda : "Development of High Strengthening 12%Cr Ferritic Steel for Turbine Rotor Operating Above 600oC", *13th International Forgemasters Meeting*, Oct. 12-16 (1997), Pusan, Korea, p.417

[5] R. Kaneko, S. Nakamura, Y. Watanabe and Y.Tanaka : "Development of Steam Turbine Materials at Target Temperature 650oC", *Thermal and Nuclear Power*, 46(1995), p.968.

[6] C. Berger, E. Potthast, R. Bauer and G. A.Honeyman : "Development of High Strength 9-12% CrMoV Steels for High Temperature Rotor Forging", *11th International Forgemasters Meeting*, June 11-14(1991), Terni/Spoleto, Italy, IX.5

[7] Y. Hasegawa, T. Muraki, M. Ohgami and H.Mimura : "Optimum Tungsten Content in High Strength 9 to 12% Chromium Containing Creep Resistant Steels ", *Proceedings of 8th International Conference on Creep and Fracture of Engineering Materials and Structures*, November 1-5 (1999), p.427

[8] J. Hald : "Microstructure Stability of Steels P92 and P122 ", *Proceedings of 3rd* conference on Advances in material technology for fossil power plants, April 5-6 (2001), p.115

[9] F. Abe : "Contribution of Tungsten to Microstructure Stabilization and Improvement of Creep resistance in Simple 9Cr-W Steels", *Proceedings of 8th International Conference on Creep and Fracture of Engineering Materials and Structures*, Tsukuba, Japan, (1999), p.395

[10] H. Kushima, K. Kimura and F. Abe : "Degradation of Mod. 9Cr-1Mo Steel during long-term Creep Deformation", *Tetsu-to-Hagane*, 85 (1999), p.841

[11] F. Abe : "Contribution of Tungsten to Microstructure Stabilization and Improvement of Creep resistance in Simple 9Cr-W Steels", *Proceedings of 8th International Conference on Creep and Fracture of Engineering Materials and Structures*, Tsukuba, Japan, (1999), p.395
[12] K. Kimura, K. Suzuki, Y. Toda, H. Kushima and F.Abe : "Precipitation of Z-phase and degradation behavior of mod.9Cr-1Mo steel", *7th Liege Conference Materials for Advanced Power Engineering 2002*, Liege, Belgium, (2002), 1171
[13] M. Igarashi, M. Yoshizawa, A. Iseda, H. Matsuo and T. Kan :Long Term Creep Strength Degradation in T122/P122 Steels for USC Power Plants", *Proc. of 8th Liege Conference on Materials for Advanced Power Engineering 2006*, Liege, Belgium, (2006), 1095
[14] K. Kimura, K. Sawada, H. Kushima and Y. Toda : "Degradation Behaviour and Long-Term Creep Strength of 12cr Ferritic Creep Resistant Steels", *Proc. of 8th Liege Conference on Materials for Advanced Power Engineering 2006*, Liege, Belgium, (2006), 1105
[15] M.Morinaga, R.Hashizume and Y.Murata : An electronic approach to the design of ferritic steels for power plants *Proceedings of the 5th Liege Conference on Materials for Advanced Power Engineering October 1994*, Liege Belgium, 319
[16] R.Hashizume, K.Miki, T.Azuma,T.Ishiguro, Y.Murata, M.Morinaga , Optimization of Cr content in high Cr heat resistant steels on the basis of long term creep strength, *Tetsu-to-Hagane*, 88 (2002), 91
[17] K. Miki, T. Azuma, T. Ishiguro, R. Hashizume, Y.Murata and M. Morinaga : "Effect of Cr Content on the Creep Strength and Microstructural Change in High Cr Heat Resistant Steel", *7th Liege Conference Materials for Advanced Power Engineering, Liege, Belgium*, (2002) p.1497
[18] K.Miki, T.Azuma, T.Ishiguro, R.Hashizume, Y.Murata, M.Morinaga,; Improvement of long term creep strength in high Cr heat resistant steel, *Proc.15th Int. Forgemasters Meeting* (2003) JSCFA
[19] K.Miki , T.Azuma, T.Ishiguro, R.Hashizume, Y.Murata, M.Morinaga,; Optimization of Cr content for long-term creep strength in high Cr heat resistant steel, *Proc.4th Int. Conf. on Advances in Materials Technology for Fossil Power Plants* (2004)ASM International
[20] Y.Murata, K. Takami, M. Kamiya, M. Morinaga, R. Hashizume, K. Miki, T. Azuma and T. Ishiguro : Coherent Laves Phase Finely Precipitated in Heat Resisting High-W and 10%Cr Ferritic Steels, *Tetsu-to-Hagane*, 88 (2002), 46
[21] T.Kunieda,K.Yamashita,Y.Murata,M.Morinaga, T.Koyama, K.Miki, T.Azuma, and R.Hashizume : Dependence of microstructural evolution and creep strength of heat resistant steels on W diffusivity affected by the existence of Rhenium in Iron, *ISIJ the forlum of the stability of structure and estimationof life about heat resisting steels.*(2006)12
[22]. T.Kunieda, K.Yamashita, Y.Murata, T.Koyama, and M.Morinaga, : Effect of Rhenium Addition on Tungsten Diffusivity in Iron-Chromium Alloys, *Material Transactions* Vol.47,No8(2006).2106

9th Liege Conference : Materials for Advanced Power Engineering 2010
edited by J. Lecomte-Beckers, Q. Contrepois, T. Beck and B. Kuhn.

INFLUENCE OF DELTA FERRITE ON MECHANICAL AND CREEP PROPERTIES OF STEEL P92

Petr Mohyla, Zdeněk Kuboň*
VŠB - Technical University of Ostrava, Faculty of Mechanical Engineering, Ostrava, Czech Republic
* Material and Metallurgical Research Ltd., Ostrava, Czech Republic

Abstract

This article presents some new results obtained during research of chromium modified steel P92. This steel is considered the best modified 9-12% Cr steel for the construction of modern power plants with ultra-super-critical steam parameters. High creep rupture strength of steel P92 is characterized by its chemical composition and by microstructure as well. Optimal microstructure of steel P92 is ideally composed of homogeneous martensite and fine dispersion of secondary particles.

During the research program one P92 heat with an occurrence of about 20% delta ferrite was produced. The article describes the microstructure of the heat in various modes of heat treatment, as well as the results of mechanical properties tests at room temperature and also creep test results. The results are confronted with properties of other heats that have no delta ferrite. The relevance is on the significant difference while comparing of creep test results. The comparison of results brings conclusions, defining influence of delta ferrite on mechanical and creep properties of P92 steel.

Keywords: Delta ferrite, mechanical properties, creep, steel P92

1. Introduction

With increasing demands on the efficiency of advanced power plants and environmental protection, worldwide attention is paid to the development of modified 9-12% Cr steels with creep resistant strength (CRS) higher than 100 MPa at 600°C and 100.000 hours.

In Europe, steel X20CrMoV12-1 has been used for thick-walled steel components. This steel is suitable for temperatures up to 560°C [1]. Increasing steam parameters required the development of steels with higher creep properties. Firstly, was developed a modified 9% Cr, designated P91. Further development brings alloying of steels by tungsten. Typical representatives of modified chrome steel with tungsten are steels E911, P122 and P92 in particular.

High creep resistance of modified chromium steels is done by precipitation of vanadium nitrides. These very finely dispersed and stable particles effectively prevent the movement of dislocations and thereby slow down the creep. Vanadium nitrides precipitate not only during tempering but also during creep exposure, especially on dislocations within subgrains. Higher creep resistance can be thus expected in steels with high density of dislocations. It follows that the desired microstructure for the steel structure is martensitic.

Currently considered one of the best modified chromium steel in terms of achieved values of creep rupture strength is steel P92. Initial estimates of creep rupture strength of this steel, based on short-term creep tests, were about 190 MPa at 600 ° C for 100.000 hours. Recent research based on long-term creep tests resulted in settlement of CRS between 110 and 120 MPa [2, 3], which are far less, but compared to other steels it still has high value.

In addition to dispersion hardening, which is caused by vanadium nitrides and $M_{23}C_6$ particles, a solid solution strengthening is involved in high creep resistance of steel P92. This is due to substitution elements Mo and W dissolved in the solid solution. The maximum value of creep rupture strength according to the Japanese authors is reached with 1.8% W and 0.5% Mo [3].

The latest research shows that to achieve high values of creep rupture strength of steel P92 nitrogen and especially boron is essential. It has been shown that P92 steel without boron has low values of creep rupture strength, even lower than steel P91 (containing 9% Cr, 1% Mo, 0.2% V, 0.05% Nb and about 0.005% N) [3]. According to our opinion, it is not only the lower coarsening rate of $M_{23}C_6$ carbides that can explain the beneficial effect of boron on CRS of chromium modified steels.

The product of martensitic transformation in steel P92 is lath martensite, which is formed in a wide range of cooling rate. Inside the original austenitic grains creates several parallel martensitic laths that may be separated by films of residual austenite. Establishment of ferritic-carbidic components in the microstructure at very slow cooling rate is accompanied by a sharp drop in hardness of the material. The decrease in hardness of martensite at the medium cooling rates is associated with the occurrence of ε-carbide or cementite in martensite [4]. Cementite in the steel is not stable minor phase and during tempering it is rapidly dissolved [5]. Depending on the chemical composition of steel a small amount of δ-ferrite can be also presented in the microstructure [4].

Delta ferrite can be stable even after forging or after austenitization. The delta ferrite in steel P92 has very adverse effects, its presence reduces the hardenability and toughness of steel, significantly degrades creep properties. Stability of delta ferrite depends on the balance between austenite-forming elements Ni, Mn, Cu, C, N and ferrite-forming elements Cr, Si, Mo, W, V and Nb. Influence of chemical composition can be expressed e.g. by specific chromium equivalent Cr_{ekv}, [6].

$$Cr_{ekv} = Cr+6Si+4Mo+1,5W+11V+5Nb+8Ti+12Al-40C-30N-4Ni-2Mn-2Co-Cu \quad (1)$$

The work [6] shows that when the value of the Cr equivalent is less than 10, no delta-ferrite can be expected in microstructure. If the value of the Cr-equivalent is in the range between 10 and 12 smaller quantities δ-ferrite may occur. Higher values of Cr-equivalent mean high content of δ -ferrite in the structure of steel P92.

2. Experimental material

Three heats of steel P92 were analyzed during this project. Chemical composition of investigated heats is shown in Table 1.

Tab. 1: Comparison of the chemical composition of cast steel P92

Heat	C	Mn	Si	Cr	Mo	V	W	Ni	Nb	Al	N	Cr_{ekv}
A	0.090	0.51	0.33	8.50	0.52	0.21	1.70	0.20	0.060	0.020	0.0345	10.322
B	0.090	0.50	0.34	8.85	0.50	0.21	1.90	0.31	0.084	0.008	0.0595	9.752
C	0.110	0.53	0.33	9.20	0.44	0.20	1.60	0.30	0.050	0.005	0.0460	9.750

The heat A revealed a large amount of delta ferrite, approx. 21%. The calculated value of Cr equivalent of the heat is 10.322. Such value admits the presence of small quantities of delta ferrite in the structure, but not 21%. The reason of such high amount of delta ferrite cannot only be the chemical composition of the heat. A technological mistake during the casting has probably been made. The result was a substantial inhomogeneity of chemical composition with sharp increase in local content of ferrite-forming elements, which resulted in the emergence of delta ferrite islands. Figure 1 shows the microstructure of the sample annealed at 1050 °C for 2 hours and then cooled in oil. White islets are particles of delta ferrite. Figure 2 shows microstructure of the same heat cooled in water, resp. in oil and then tempered.

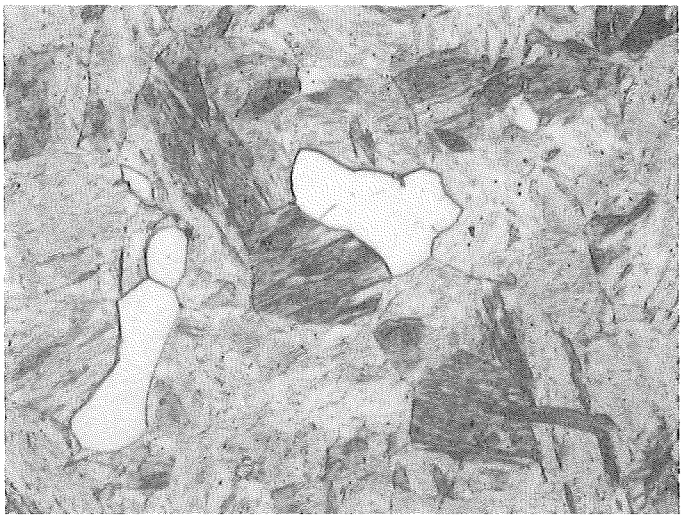

Fig. 1: Microstructure of sample of heat A, austenitization at 1050 °C/ 120 min., cooling in oil, magnified 500x

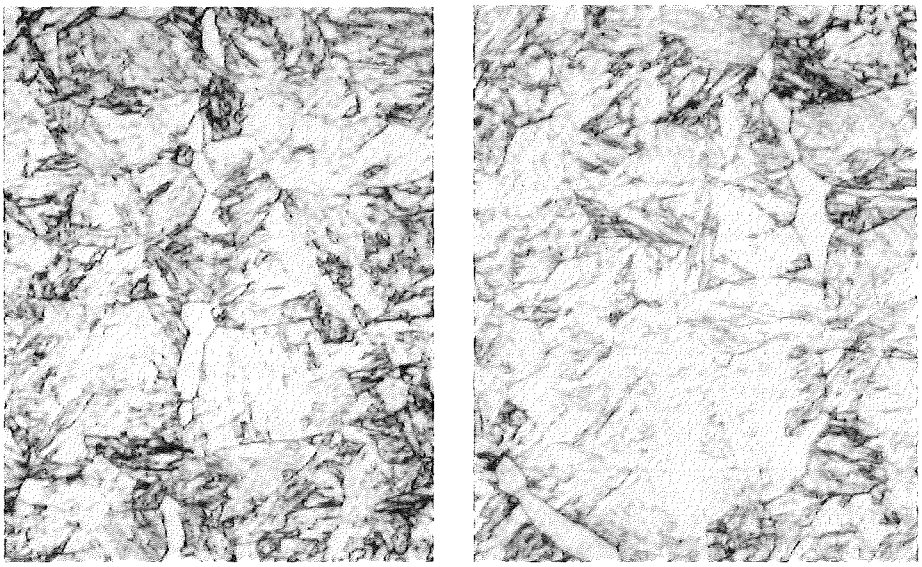

a *b*

Fig. 2: Microstructure of heat A, magnified 500x
a – austenitization 1065°C/330 min. / water + tempering 770°C/330 min./ air
b - austenitization 1065°C/330 min. / oil + tempering 770°C/330 min./ air

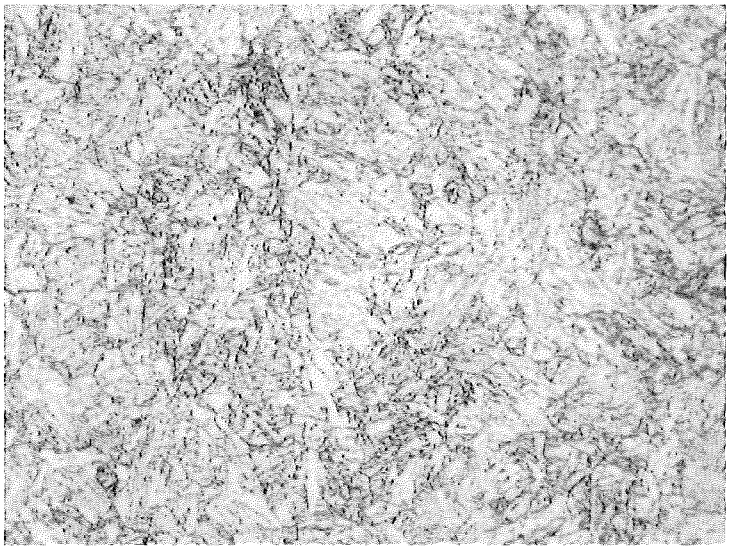

Fig. 3: Microstructure of sample of heat B, austenitization at 1060 °C/ 180 min., cooling in water +tempering at 770°C/ 240 min., magnified 500x

Heat B shows no delta ferrite in microstructure (Cr_{ekv} = 9.752). After complete heat treatment the microstructure is homogenous, consisting of tempered martensite, see Figure 3. Heat C shows no delta ferrite in microstructure, too (Cr_{ekv} = 9.750). The microstructure consists of tempered martensite, see Figure 4.

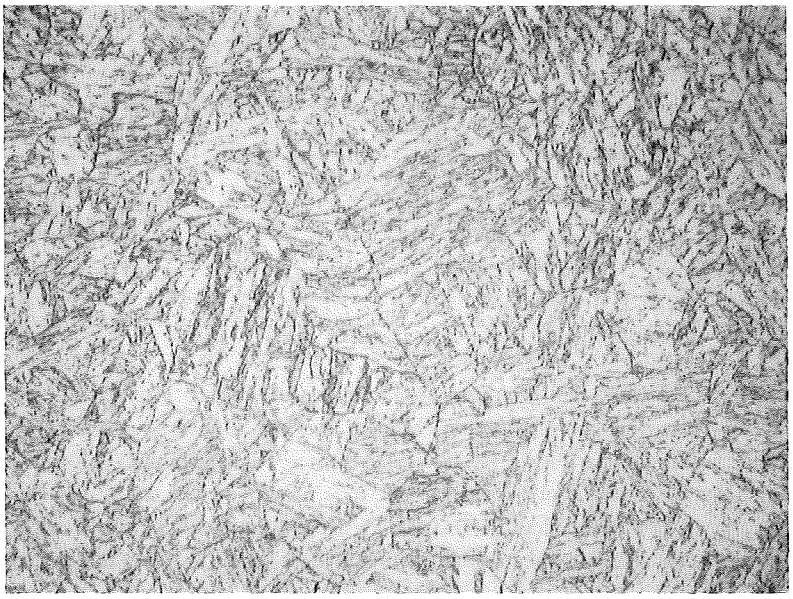

Fig. 4: Microstructure of sample of heat C, austenitization at 1060 °C/ 330 min., cooling in oil + tempering 770°C/330 min., magnified 500x

3. Results

Samples from all heats were subjected to several regimes of heat treatment, i.e. normalizing and tempering, and as a cooling medium was used water or oil. Subsequently, mechanical testing was carried out altogether with creep tests of heat A and B. The results of mechanical properties are presented in tables 2 to 4.

Tab. 2: Mechanical properties of heat A, Samples after heat treatment 1065°C/330 min. + 770°C/330 min., A-W cooling in water, A-O cooling in oil

	$R_{p0,2}$ at 20°C	R_m at 20°C	A_5 at 20°C longitudinal	RoA at 20°C	KV at 20°C longitudinal	KV at 20°C transverse	$R_{P0,2}$ at 600°C
	(MPa)	(MPa)	(%)	(%)	(J)	(J)	(MPa)
A-O	481	649	21	69.8	117	89	298
A-W	499	668	23.4	68.6	153	92	295

Tab. 3 Mechanical properties of heat B, Samples after heat treatment 1060 °C/ 180 min. + 770°C/ 240 min., B-W cooling in water

	$R_{p0,2}$ at 20°C	Rm at 20°C	A at 20°C longitudinal	RoA at 20°C	KV at 20°C longitudinal	KV at 20°C transverse	$R_{p0,2}$ at 600°C
	(MPa)	(MPa)	(%)	(%)	(J)	(J)	(MPa)
B-W	554	726	18.4	61.6	137	63	358

Tab. 4: Mechanical properties of heat C, Samples after heat treatment 1060 °C/ 330 min. + 770°C/330 min, C-W cooling in water, C-O cooling in oil, C-F after forging

	$R_{p0,2}$ at 20°C	R_m ati 20°C	A at 20°C longitudinal	RoA at 20°C	KV at 20°C longitudinal	KV at 20°C transverse	$R_{p0,2}$ at 600°C
	(MPa)	(MPa)	(%)	(%)	(J)	(J)	(MPa)
C-O	554	719	23.8	66.4	158	66	345
C-W	528	707	21.6	66.4	148	74	332
C-F	331	547	26.2	53.8	12	8	173

The obtained results show that optimum properties were achieved in case of heat C in the state after oil quenching and tempering. Heat A reached higher strength and toughness properties after quenching in water (A-W). Heat B after water quenching showed relatively high strength characteristics, but the elongation value was low, even lower than the required minimum value of 19% stated in EN 10216-2 [7]. Heat C in the state after forging reported unsatisfactory results. It was expected and therefore these results are presented here only for comparison.

Tables 5 and 6 and figures 5 and 6 are showing the current results of creep tests for heats A and B. Larson–Miller parametric equation was used for construction of these diagrams:

$$P_{LM} = T(25 + \log(t))$$

where T is the absolute temperature [K], t is the time to rupture [h] and L-M constant C=25 represents value usually used in chromium modified steels [8, 9].

Diagrams 5 and 6 show a dramatic difference in the level of creep properties of these two heats. Results of heat B lie between standardized mean curve and the allowed -20% range. Values of heat A however lie below the allowed -20% range. Such a result means that this heat has no potential to meet the requirement of creep resistance of grade P92.

Tab. 5: Results of creep tests, heat A

T	σ	t	A_5	RoA
(°C)	(MPa)	(hour)	(%)	(%)
600	190	32	35.7	86.0
600	165	250	37.5	91.2
600	145	(283)	-	-
625	135	312	31.9	89.2
625	115	(362)	-	-
650	120	51	36.9	87.6
650	100	427	40.0	91.7
650	80	(837)	-	-
650	65	(837)	-	-

Tab. 6: Results of creep tests, heat B

T	σ	t	A_5	RoA
(°C)	(MPa)	(hour)	(%)	(%)
600	230	7	34.5	90.0
600	210	30	29.8	86.8
600	190	128	27.0	83.0
600	165	726	31.6	86.4
600	145	6944	19.2	78.7
600	130	12910	24.4	71.9
625	195	17	31.2	86.8
625	175	135	30.4	84.1
625	155	413	34.5	86.9
625	135	1864	35.8	84.8
625	115	7934	38.0	83.1
625	95	(14500)	-	-
650	160	9	34.4	85.7
650	145	66	29.0	81.8
650	120	301	41.2	86.7
650	100	1007	32.2	82.4
650	80	9512	34.4	82.2
650	65	(12700)	-	-

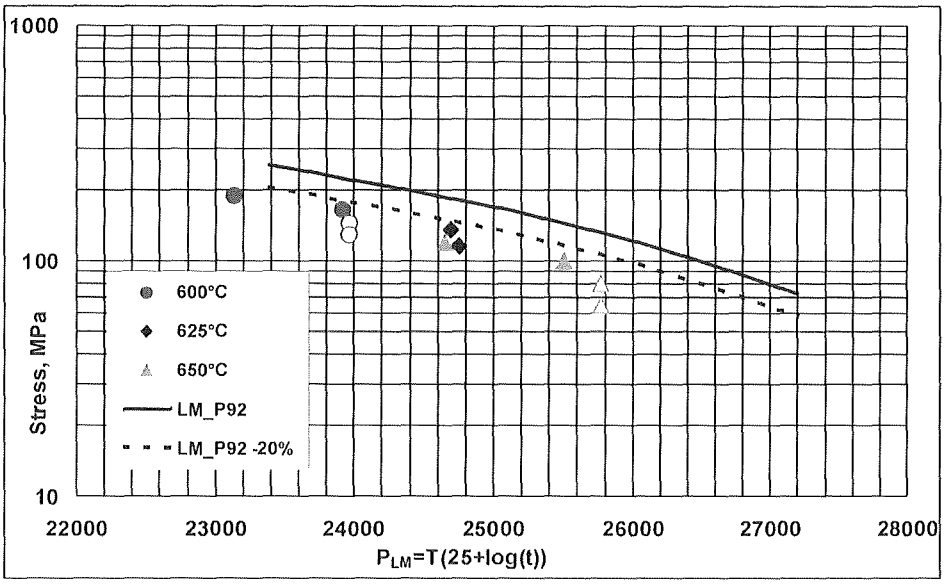

Fig. 5: Dependence of stress on the Larson-Miller parameter for the heat A in comparison to the standardized mean values for steel P92, C = 25

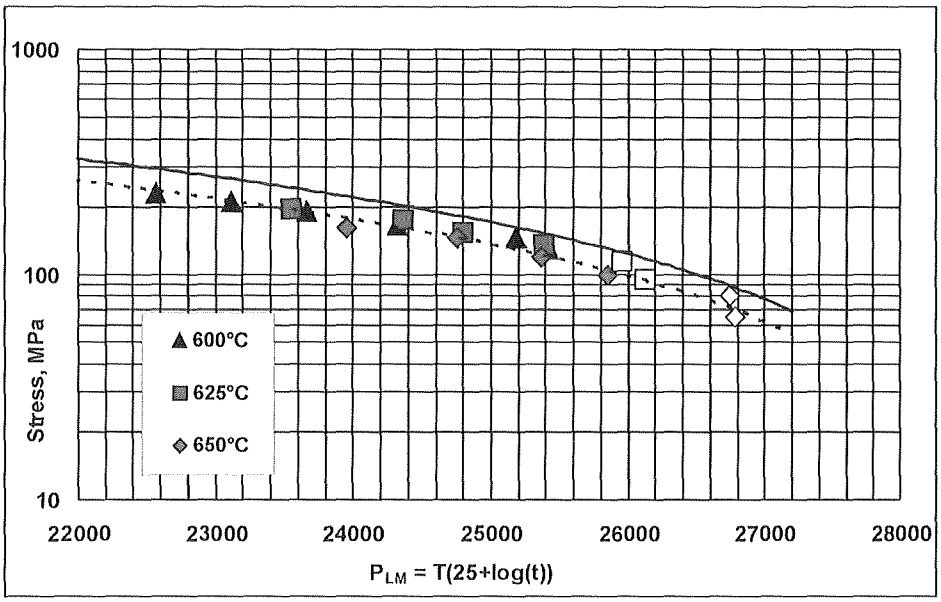

Fig. 6: Dependence of stress on the Larson-Miller parameter for the heat B in comparison to the standardized mean values for steel P92, C = 25

4. Conclusions

Delta ferrite contained in steel P92 adversely affects the properties of the steel. The danger lies in the fact, that influence of delta ferrite is largely absent when evaluating short-term strength properties. The presented creep test results show, that the delta ferrite radically degrade creep resistance of steel P92.

In our opinion, drop of creep properties of P92 steel is caused by excessive amount of delta ferrite. Heat A shows higher values of creep elongation and reduction of area than heat B without delta-ferrite. It is supposed, that delta ferrite leads to higher creep plasticity, even if it significantly decreases times to rupture. Influence of delta ferrite on creep resistance of steel P92 and other modern advanced chromium steels will be subject to further research.

References:

[1] CHEN Q., SCHEFFKNECHT G. Boiler design and materials aspects for advanced steam power plants. In: *Proceedings of COST Programe part II: Materials for Advanced Power Engineering* 2002, Vol. 21, p.1019-1033. ISBN: 3-89336-312-2
[2] ECCC DATA SHEETS 2005, September 2005
[3] FOLDYNA, V. a kol Development of Advanced Creep Resistant Ferritic Steels and their Weldability. In: *Proceedings of conference Progresívne kovové materiály a ich spájanie, 25.-27.10. 2004*, Bratislava
[4] BRÜHL, F., CERJAK, H., SCHWAAB, P., WEBER, H.:*Steel Research*, 62, 1991, p. 75
[5] THOMPSON, R.C., BHADESIA, H.K.D.H.: *Metallurgical Transactions*, 23A, 1992, p.1171
[6] HALD, J., STRAUB, S.: Microstructural stability of 9-12% CrMo(W)VNbN-steels, *In: Proc. Konf. "Materials for Advanced Power Engineering 1998"*, Liege, Oct. 1998, J. Lecomte-Beckers et al. (Eds) Jülich 1998, Part I, p. 155-169
[7] EN10216-2:2002 Seamless steel tubes for pressure purposes. Technical delivery conditions. Non-alloy and alloy steel tubes with specified elevated temperature, CEN, 2002, p 42
[8] Y. TSUDA, et all.: in Proc. of the 6th Liege Conference on Materials for Advanced Power Engineering, Proc. ed. by J. Lecomte-Beckers, F. Schubert and P. J. Ennis, Liege, Belgium, October 1998, p. 331
[9] T.-U. KERN, et all.: in Proc. of the 6th Liege Conference on Materials for Advanced Power Engineering 2002, Ed. by J. Lecomte-Beckers, M. Carton, F. Schubert and P. J. Ennis, Liege, Belgium, October 2002, Part II, p. 1049

Acknowledgement:

This work was supported by the Ministry of Industry and Trade of Czech Republic in the project FT-TA4/021.

9th Liege Conference : Materials for Advanced Power Engineering 2010
edited by J. Lecomte-Beckers, Q. Contrepois, T. Beck and B. Kuhn.

THE EFFECT OF MICROSTRUCTURAL STABILITY ON LONG-TERM CREEP BEHAVIOUR OF 11%CR STEELS FOR STEAM POWER PLANTS WITH OPERATING STEAM TEMPERATURES UP TO 650 °C

Y. Wang [a)], F. Kauffmann [b)], K.-H. Mayer [c)] A. Scholz [a)], C. Berger [a)], K. Maile [b)]

[a] Institut fuer Werkstoffkunde, Technical University Darmstadt,
[b] MPA University of Stuttgart, Germany
[c] ALSTOM Power, Nürnberg

Abstract

The investigations of advanced ferritic/martensitic steels for 650 °C power plant components focus on the improvement of high-temperature creep properties with respect to chemical composition. This study deals with the development of new heat resistant 11–12%Cr ferritic-martensitic steels with sufficient creep and oxidation resistance up to 650°C application by using basic principles and concepts of physical metallurgy. The highest creep strength could be achieved with a 0.04% Nb alloyed 11%CrWCoMoVB melt, which is in addition alloyed with a higher C and B content as well as with lower W and Co portions. The microstructure evolution during creep of this newly developed steel was investigated in comparison to a sister alloy which comprises 0.06% Ta instead of the Nb.

Current creep tests have exceeded 40 000 h at 650°C. The Ta alloyed steel exhibits a creep strength which is in accordance with the 9%Cr piping steel P92. The Nb alloyed steel shows a significant higher creep strength. EDX analysis was carried out on extraction replicas in STEM and supplement by dark field TEM to identify the individual types of precipitate phases. The evolution of sizes and volume fractions of the precipitates during creep was quantified. Both steels containing Nb and Ta show quantitative differences in their microstructural development which helps to understand the observed differences in creep behaviour.

Keywords: Creep behaviour, 11%CrWCo(Cu)B(V, Nb,Ta) steels

1. Introduction

In order to establish fossil power plants with ultra high efficiency, the development of new steels for steam turbine components is in the focus of the COST framework. Improved creep properties and corresponding ductility properties in the long term regime are the main goal for turbine components such as rotors, castings and valves. Further, sufficient oxidation resistance is needed. Within COST 501/522 type 9-12% Cr forging steels and cast steels for applications at up to 620°C steam temperatures have been developed and characterised [1]. Based on these experiences investigations on new optimised steels for applications up to 650°C inlet steam temperatures have been started within COST 536. The present paper reports about long term creep behaviour and microstructure investigations of two similar 11%CrWCoMoVB candidate steels which are additionally alloyed with 0,04%Nb respectively with 0,06%Ta. Both steels exhibited the highest creep rupture strength in a German basis research project (DFG) in which around 80 different model steels have been

investigated with Cr contents of 11% to 13% and additional variations of the alloying elements W, Mo, Cu,V, Nb, Ta, N and B [2].

2. Alloying concept

Tables 1 and 2 give the chemical compositions, the mechanical properties and the grain sizes for two key melts called 59As and 62As. The Cr-content was fixed at about 11% to ensure an oxidation resistance of sufficient level. In order to generate a ferritic-martensitic microstructure with precipitates of $M_{23}(C, B)_6$, MX and Laves phase, the following choices of alloying elements were made (see *Table 1*):

- balanced amounts of Co, Mn, C and Cu to obtain a ferritic-martensitic matrix;
- Cr, W, B and C for strengthening by $M_{23}C_6$ precipitates;
- W for strengthening by Laves phase;
- Cu to promote a fine distribution of Laves phase by nucleation at Cu-precipitates;
- V and Nb or Ta for strengthening by MX precipitates;
- Si in addition to Cr for improved oxidation resistance.

The 25kg test melts were prepared in a high frequency furnace. The dimension of the forged bars was a cross section of 40mm x 20 mm. On the basis of calculations with the software ThermoCalc the heat treatment was specified as 0.5 h at 1150°C + 2 h at 765°C + air cooling [2].

Table 1: Chemical composition of test melts 59As and 62As as measured by OES[1] (weight-%)

Steel	C[2]	Si	Mn	Cr	Mo	W	Co	Cu	V	Nb	Ta	Al[2]	N[2]	B[2]
59As	.20	.31	.31	10.9	.51	2.2	1.1	.71	.26	.04	-	.001	.030	.020
62As	.19	.42	.30	11.1	.49	2.2	1.0	.67	.25	-	.06	.001	.030	.022

1) new determined values at the creep specimens which are different to earlier published results [2 and 6],
2) melt analysis

Table 2: Mechanical properties and grain size at RT of test steels 59As and 62As

Steel	0.2-Limit MPa	Tensile strength MPa	Elongation %	Reduction of Area %	Hardness HV30	ASTM grain size
59As	675	880	17,4	51	270	2-3
62As	636	844	18,4	55	262	2-3

3. Creep Rupture Behaviour

The creep tests achieved test durations of max. 41000 h at 650°C and max. 18000 h at 625°C and 600°C (*Figure 1 to Figure 3.*) The test melt 11%Cr-Nb (59As) shows a higher creep strength than the sister alloy 11%Cr-Ta at all three investigated temperatures. This superiority of the Nb content melt is in accordance with the findings of other researchers, for example [4 and 5].

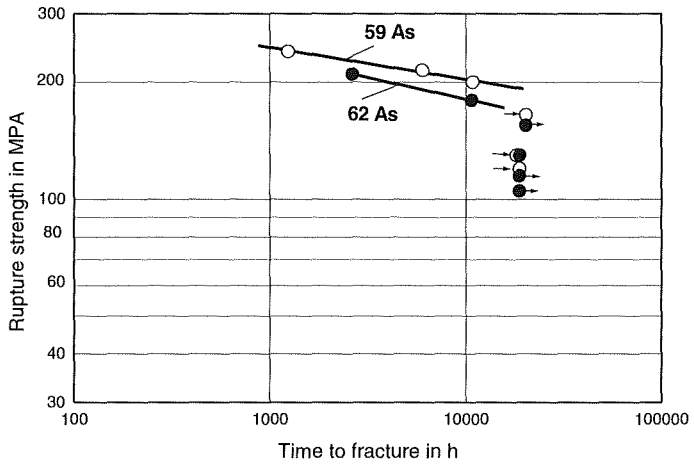

Figure 1: Creep rupture strength of test melts 59As and 62As at 600°C

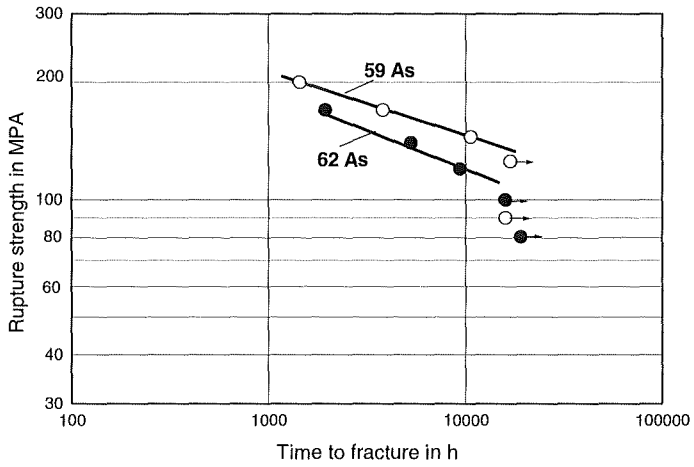

Figure 2: Creep rupture strength of test melts 59As and 62As at 625°C

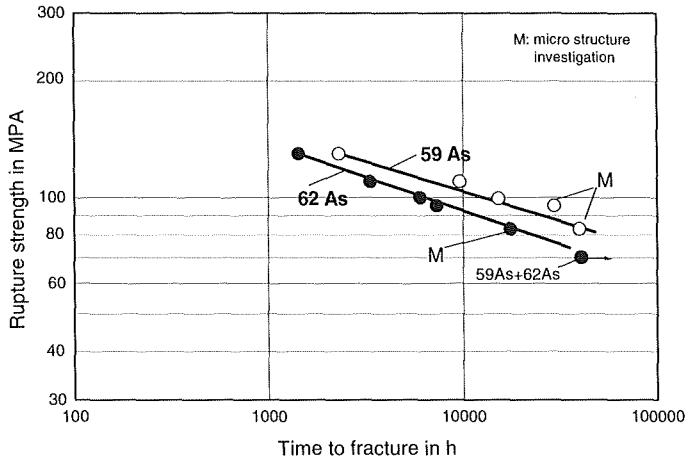

Figure 3: Creep rupture strength of test melts 59As and 62 As at 650°C

An estimation of the creep rupture strength of both test melts at the temperature of 650°C up to 100 000 h shows *Figure 4* by using the extrapolation methods of Wilshire-Scharning (mod.) and of Abe (mod.) [6 to 8]. The extrapolated curves indicate a further stable long term behaviour of both melts.

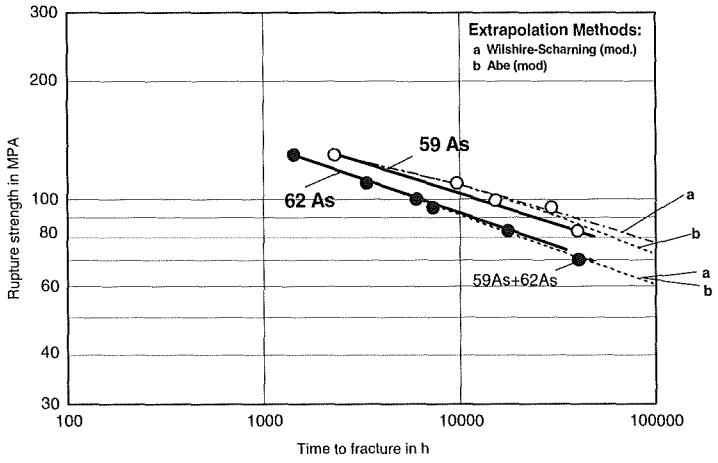

Figure 4: Creep rupture strength of test melts 59As and 62As at 650°C compared with long term extrapolated curves

Figure 5 demonstrates a comparison of the test results of 59As and 62As at 650°C with the creep rupture strength of the high strength ferritic-martensitic TAF steel [9] and of the 9%Cr piping steel P92 (ECCC mean values).The results of the melt 59As tend to a similar high strength level as the TAF steel at 100 000 h and the results of the melt 62As are well in accordance with the creep rupture strength of the steel P92. The results indicates in general that inspite of the relativ high Cr content of 59As and 62As an improvement of the creep strength is achievable by a moderate content of Boron of about 0,020%. Further improvements of the 59As typ can be probably realized by a finer tuning of the chemical composition.

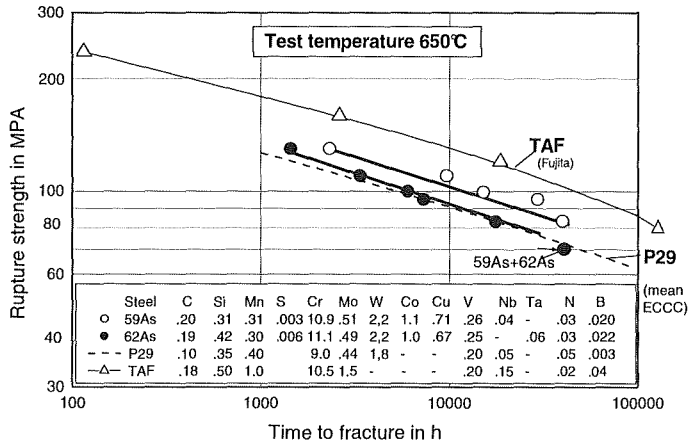

Figure 5: Creep rupture strength of test melts 59A and 62 As at 650°C compared with creep rupture strength of TAF steel and piping steel P92

4. Microstructural Characterization

The optical microscopy (OM) analysis was done using a Leitz Aristomet. The specimens were prepared by standard metallographic methods such as cutting, grinding and polishing. To develop the microstructure the specimen were etched by 3% HNO_3.

Conventional transmission electron microscopy (TEM) investigations were performed using a JEOL JEM 2000 FX operated at 200 kV to determine the subgrain size and dislocation density. For analytical measurements the TEM is equipped with an EDX detector (Kevex Sigma 1 from NORAN, capable for detection of elements with an atomic number ≥ 11) and with a GATAN energy filter. The latter was used for acquiring elemental maps. A detailed description of energy filtered TEM (EFTEM) measurements can be found for example in [9, 10]. For the quantitative evaluation of the precipitate state (type, size, shape and distribution)

a digital image processing system was used to analyze the EFTEM images and/or TEM bright field micrographs. For each specimen an area of about 40 μm^2 was quantitatively analyzed.

The analytical TEM investigations of the specimens (creep condition of the specimens see *Figure 3*) were performed on formvar extraction replica [11]. Each precipitation type was characterised by electron diffraction to determine the crystallographic structure and by EDX measurements to determine the chemical composition. A detailed description of the applied methods can be found in [12].

The initial state of the 59As steel as observed by OM is shown along with the creep tested conditions in *Figure 6*. This steel has a ferritic-martensitic microstructure. Prior austenite grain boundaries and martensite laths can be observed. The martensitic lath structure and the grain size did not change visibly during creep. For the creep tested specimens a slightly enlarged grain size was observed along with several creep pores. The pore density was especially high for the 62As alloy. For analyzing the changes in microstructure, electron microscopy methods are needed.

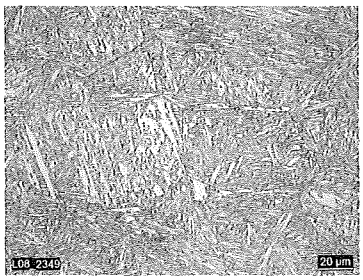

59As initial

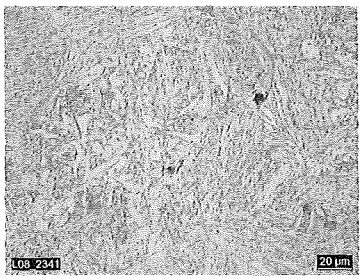

59As, after creep test at 29293h

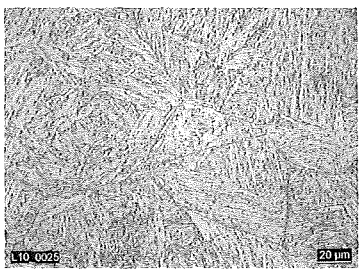

59As, after creep test at 39766h

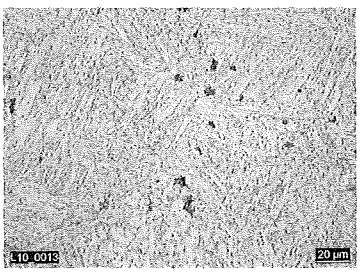

62As, after creep test at 17461h

Figure 6: Optical Microscopy images of the investigated alloys

The TEM observations of the subgrain sizes revealed a slow growth rate in the 59As steel. The initial subgrain size of 328 nm reached 474 nm after 29293h and 503 nm after 39766 h. This microstructure was efficiently stabilized at a low level. For comparison, the subgrain size of the 62As alloy was 532 nm after 17461 h. *Figure 7*.

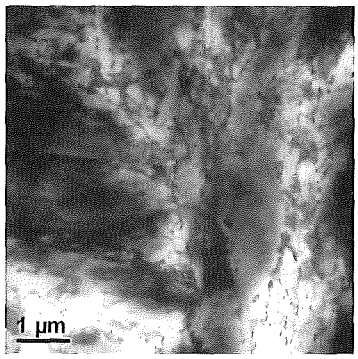

59As initial

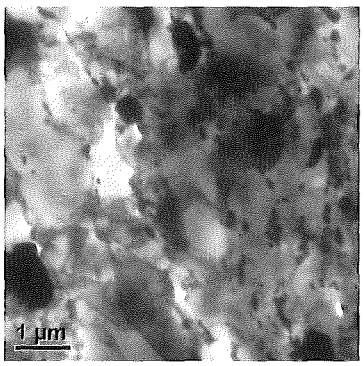

59As, after creep test at 29293h

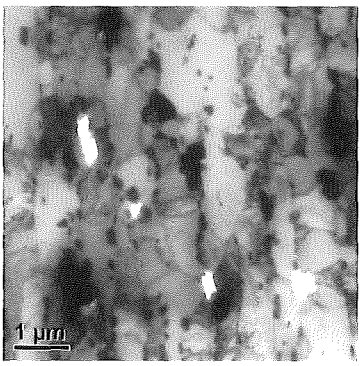

59As, after creep test at 39766h

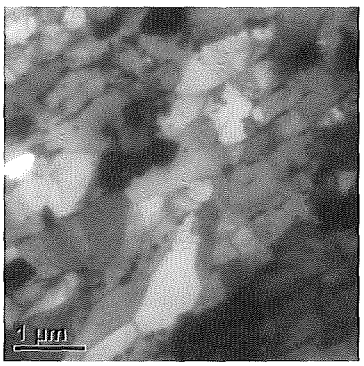

62As, after creep test at 17461h

Figure 7: Bright field TEM images depicting the subgrain structure

The results of the precipitate analysis is summarized in *Figure 8*. The $M_{23}C_6$ precipitates exhibit a slow growth rate from 95 nm in the initial state to 121 nm after 39766 h. After 29293 h a size of 153 nm was measured, which indicate inhomogenities in the initial size distribution of the test alloy. On the other hand a comparison of the size evolution with other alloys tested at 650°C exhibits clearly a very slow coarsening of the precipitates. The growth rate is comparable to that of the TAF alloy, see *Figure 9*. The size of these precipitates in the 62As alloy after 17461 h is also low with only 117 nm, but as data for the initial state is lacking, a growth rate could not be projected.

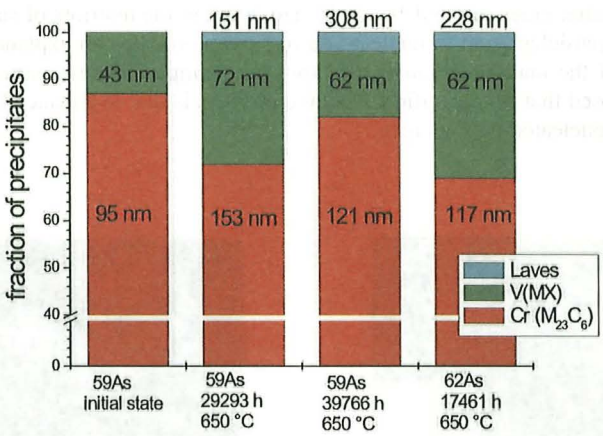

Figure 8: Fraction of precipitates and the equivalent diameters of the analysed specimens.

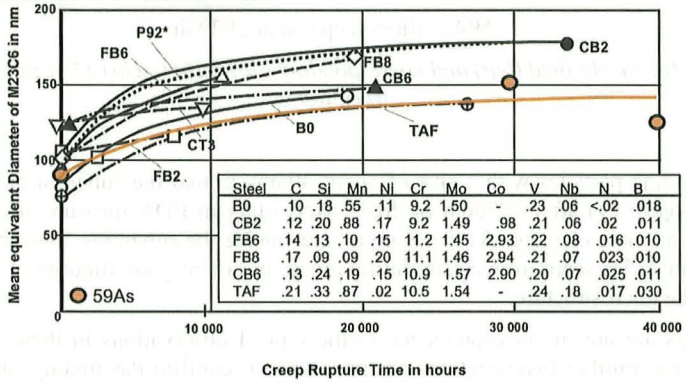

Figure 9: Development of the precipitate sizes of $M_{23}C_6$ during creep at 650 °C of 59As in comparison to other alloys.

The investigated alloys also show a constant amount of very stable fine V-rich MX particles. The alloying elements Nb or respectively Ta are partially embedded in these particles. No Z-phase has been found, which could consume these particles and negate their strengthening effect. Also a significant amount of Laves phase was observed in all cases after creep, as expected for tungsten alloyed steels. No carbonitrides with Ta or Nb as the main element were observed in all investigated specimens.

Besides the slow growth rate of the $M_{23}C_6$ particles, two special features of the 59As alloy were observed, which were not present in comparable alloys and may help to understand the

excellent creep properties. TEM observations of steel foils on 59As revealed the existence of fine precipitates after creep, around 10 nm in size, lying in the interiors of subgrains. The fact that these small particles seem to nucleate during creep provides an explanation for the high creep strength of the material. *Figure 10* shows an example of these particles in dark field TEM. It is proposed that one specific advantage of 59As is due to enhanced strengthening by fine precipitates nucleated during creep.

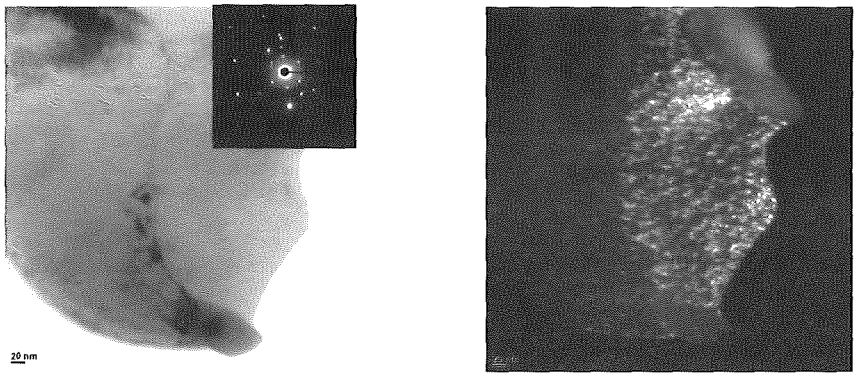

59As, after creep test at 29293h

Figure 10: Bright field (left) and corresponding dark field (right) TEM image of fine precipitates.

Additionally fine particles with a size of about 30 nm around the subgrain boundaries were observed (*Figure 11*) after 39766 h of creep. According to EDX measurements, these have tungsten as the main element. As the fine particles inside the subgrains, these particles at the subgrain boundaries seem to nucleate during creep, prolonging the lifetime of this alloy and stabilizing the microstructure.

Both findings are not in correspondence to the typical observations in these kind of creep resistant alloys. Further investigations are necessary to confirm the findings and to identify the type of the particles.

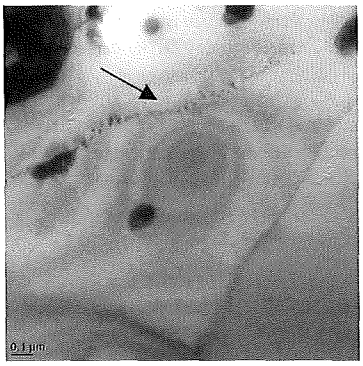

59As, after creep test at 39766h

Figure 11: TEM Bright field of fine particles at subgrain boundaries

5. Summary

The test melt 59As with 11 wt.% Cr, relatively high contents of C and B, low contents of W and Co, 0.04 wt.% Nb and 0.01 wt.% Ta yields promising results. The results confirm the finding derived from the literature that the effectivity of strengthening by fine precipitates is enhanced, when the Cr content is somewhat reduced relative to the value of 12 wt.% recommended for oxidation stability. The creep strength of 59As markedly exceeds that of the piping steel P92 at 650°C in tests extending over 41000 h. TEM observations indicate that the extraordinary creep resistance of 59As is due to the slow coarsening of the $M_{23}C_6$ particles, the fine and stable MX precipitates and likely to fine precipitates inside the subgrains as well as on the subgrain boundaries, which nucleate during creep and thereby significantly stablilize the microstructure. These fine precipitates need further study and verification to understand the special creep resistance of this alloy.

The results of the creep test indicate that the creep strength with respect to the P92 alloy could be significantly improved by the increased amount of Cr and B. The comparison of 59As and 62As shows that Nb seems to be better suited to improve the creep resistance than Ta.

Acknowledgement

Financial support by the Deutsche Forschungsgemeinschaft is gratefully acknowledged. We thank the members of the working group for providing the test materials and performing ThermoCalc calculations. We also acknowledge the financial support for continuation of creep tests of 59As and 62As samples beyond 25 000 h within framework of the COST 536 Action from German Industry and the Bundesministerium für Wirtschaft und Technologie.

References

[1] Kern, T.-U., K.H., Mayer, C. Berger, G. Ziess, M. Schwienheer, Stand der Entwicklungsarbeiten in COST 522 für Hochtemperatur-Dampfturbinen, *27. Vortragsveranstaltung "Langzeitverhalten warmfester Stähle und Hochtemperaturwerkstoffe" der Arbeits-gemeinschaft für warmfeste Stähle und der*

Arbeitsgemeinschaft für Hochtemperaturwerkstoffe am 26. November 2004 im Stahl-Zentrum Düsseldorf. Hrsg.: Stahlinstitut VDEh, Tagungsband 2004, S.5/19 (in German)

[2] Mayer, K.-H., C. Berger, A. Scholz, Y. Wang, Improvement of Creep Strength of 650°C Ferritic/Martensitic Super Heat Resistant 11-12%Cr Steels, *Proceedings of the 8th COST Conference "Materials for Advanced Power Engineering 2006"*, Part II, Lecomte-Beckers, Carton, Schubert, Ennis (Ed), 2006, Liège, Belgium, page 1053/1064

[3] Abe, F., R & D of advanced ferritic steels for 650°C USC boilers, *Ultra Steel 2000*, Tsukuba, Japan, 12. -13. January 2000, page 119/129

[4] Abe, F., Strengthening mechanisms in steel for creep and creep rupture, *Book Creep-resistant steel*, WOODHEAD PUBLISHING Ltd, Cambridge England,pages 279-304, 2008

[5] Schwienheer, M., A. Scholz, Y. Wang, S. Linn, K.-H. Mayer, Extrapolationsmethoden der Zeitstandfestigkeit - Bericht aus der Projektgruppe W13, 31. Vortragsveranstaltung "Langzeitverhalten warmfester Stähle und Hochtemperaturwerkstoffe" der Arbeits-gemeinschaft für warmfeste Stähle und der Arbeitsgemeinschaft für Hochtemperaturwerkstoffe am 28. November 2008 im Stahl-Zentrum Düsseldorf. Hrsg.: Stahlinstitut VDEh, *Tagungsband 2008*, S. 77/84 (in German)

[6] Wilshire, B., P.J.Scharning, Prediction of long term creep data for forged 1Cr-1Mo-0.25V steel, *Materials Science and technology*, Vo.24, No 1, 2008

[7] Abe, F., Effect of boron on creep deformation behavior and microstructure evolution in 9%Cr steel at 650°C, *Int. J. Mat.* Res.99, 4, (2008)

[8] T. Fujita, Twenty-first century electricity generation plants and materials, *International workshop on development of advanced heat resisting steels*, Yokahama, Japan, 8. November 1999

[9] F. Hofer, P. Warbichler, W. Grogger, Ultramicroscopy, 59 (1995) 15-31

[10] F. Hofer, W. Grogger, G. Kothleitner, P. Warbichler, Ultramicroscopy, 67, 83-103, (1997)

[11] J.S. Brammer, M.A.P. Dewey, Specimen Preparation for Electron Metallography, *Blackwell Scientific Publications*, Oxford, (1966)

[12] C. Scheu, F. Kauffmann, G. Zies, K. Maile, S. Straub, K.H. Mayer. *Metallkunde*, 06, 653-659, (2005)

9th Liege Conference : Materials for Advanced Power Engineering 2010
edited by J. Lecomte-Beckers, Q. Contrepois, T. Beck and B. Kuhn.

LONG TERM PROPERTIES AND MICROSTRUCTURAL EVOLUTION OF 18Cr-10Ni-3Cu-Ti-Nb AUSTENITIC STAINLESS STEEL FOR BOILER TUBE APPLICATION

Y. Minami[1], S. Caminada[2]
T. Fukui[1], T. Ono[1]

[1] TenarisNKKTubes, 1-10 Minamiwatarida, Kawasaki, 210-0855 Kanagawa, Japan
[2] TenarisDalmine, Piazza Caduti 6 Luglio 1944 1, 24044 Dalmine (BG), Italy

Abstract
The allowable tensile stress of 0.1C-18Cr-10Ni-3Cu-Ti-Nb steel (TEMPALOY AA-1; ASME C.C. 2512) is more than 30% higher compared with that of ASME SA-213 Grade TP347H in the temperature range 600-700°C. This high creep rupture strength is obtained by the precipitation of MC and $M_{23}C_6$ carbides, and Cu-rich phase. Long term creep rupture tests over 10^5h enabled to verify the superior creep rupture strength of this steel. The investigation of microstructural evolution on the creep ruptured and aged specimens has shown the high structural stability of this material. Hardness and impact properties after high temperature aging reveal similar performance as conventional 18-8 stainless steels. Excellent steam oxidation resistance can be achieved by a shot-blasting method. The scale thickness of shot-blasted tube after 1000h at 750°C is below a few micron meters. These results have revealed that the mechanical properties and environmental resistance of this steel enable the use of TEMPALOY AA-1 in the latest generation of advanced USC boiler.

Keywords
TEMPALOY AA-1, 18%Cr steels, Copper, Creep, Microstructural Evolution, Shot-blasting, Coal-ash corrosion

1. Introduction

The increased service temperature in the new generation of advanced Ultra Super Critical (A-USC) power plants demands materials with excellent mechanical and creep strength, steam oxidation and corrosion resistance as well as long term stability during service.
Since super-heater and re-heater tubes of A-USC power plants are exposed to temperatures exceeding 650°C, the choice of materials for this application falls on stainless steels due to their superior steam oxidation, hot corrosion and creep resistance.
The long experience of TenarisNKKTubes in the production of austenitic grades has driven to the development of TEMPALOY AA-1 [1-8], an improved version of 18Cr10NiNbTi with addition of 3%Cu, which shows high creep strength and corrosion resistance.
The good steam oxidation resistance of 18%Cr steels is significantly improved through a tailored shot-blasting process on the internal surface.
The main microstructural and mechanical properties of this austenitic grade, the assessment of its creep resistance, the effect of shot blasting on high temperature steam oxidation resistance and its resistance to hot coal-ash corrosion are presented and discussed in this paper.

2. Chemical Composition and production route

The chemical compositions of TEMPALOY AA-1 steel is shown in Table 1. The chemical analysis is based on that of TP304H with the additions of Ti and Nb to promote the precipitation of fine carbides and of Cu, which forms coherent precipitates.

TEMPALOY AA-1 is registered as ASME code Case N° 2512 and in ASTM A213 as UNS S30434. It is also registered as KA-SUS321J2HTB in METI Standards of Japan. TÜV approval is also available (VdTÜV Werkstoffblatt 564/2).

TEMPALOY AA-1 tubes are supplied after solution heat treatment at a temperature above 1160°C in order to bring the most part of carbides into solution.

Table 1 – Chemical composition of TEMPALOY AA-1 according to ASTM A213 standard

mass%		C	Si	Mn	P	S	Cu	Ni	Cr	Ti	Nb	B	N	(Ti+Nb/2)C
TEMPALOY	min	0.07	-	-	-	-	2.5	9.0	17.5	0.10	0.1	0.001	-	2.0
AA-1	max	0.14	1.00	2.00	0.04	0.01	3.5	12.0	19.5	0.25	0.4	0.004	-	4.0

3. Mechanical properties and long term microstructural evolution

3.1 Mechanical Strength and Creep Properties

Table 2 summarizes the minimum required mechanical properties for TEMPALOY AA-1 according to the ASTM A213 standard. Figure 1 shows the effect of temperature on yield strength (YS) and ultimate tensile strength (UTS): TEMPALOY AA-1 steel shows a high stability of mechanical strength over a wide range of temperatures, even above the target service temperature.

Table 2 – Minimum required mechanical properties of TEMPALOY AA-1 according to the ASTM A213 Standard

Steel Grade	YS [MPa]	UTS [MPa]	Elongation [%]	Hardness [HRB]
TEMPALOY AA-1	>205	>500	>35	<90

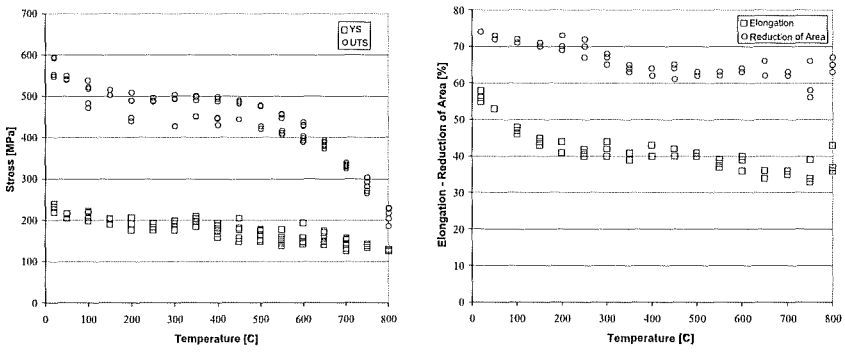

Figure 1 – Mechanical tensile properties (YS, UTS, El and RoA) at high temperature.

The creep-rupture strength has been extensively characterized in a wide temperature range (600°C-800°C) in order to obtain a reliable database. More than 1.6 million hours of creep tests have been accumulated and some tests with durations over $1.3*10^5$h are still running on TEMPALOY AA-1 tubes.
Creep data have been assessed by Mendelson-Robertson-Manson (MRM) method, following the European Creep Collaborative Committee (ECCC) guidelines [9-11]: the average creep rupture stresses are shown in Table 3. The calculated isotherms have been validated by Post Assessments Tests (PATs): the PATs cover extrapolations within 150kh.
Figures 2-a and 2-b show respectively the average creep-rupture isothermal curves of TEMPALOY AA-1 as well as its PAT 2.1.

Table 3 – Average creep rupture stresses for TEMPALOY AA-1

CREEP RUPTURE STRESS (MPa)		Stress (MPa) at Duration (h)				
		TEMPALOY AA-1				
		10000	30000	100000	150000	*200000
Temperature (C°)	550	321	294	266	256	250
	560	303	277	249	240	234
	570	287	261	234	225	219
	580	271	245	218	209	204
	590	255	230	204	195	189
	600	240	215	189	181	175
	610	225	201	175	167	162
	620	211	187	162	155	149
	630	197	174	150	142	137
	640	184	161	137	130	125
	650	171	149	126	119	114
	660	158	137	115	108	104
	670	146	126	105	98	94
	680	135	115	95	89	84
	690	124	105	86	80	76
	700	114	95	77	72	68

* extrapolation not covered by PATs

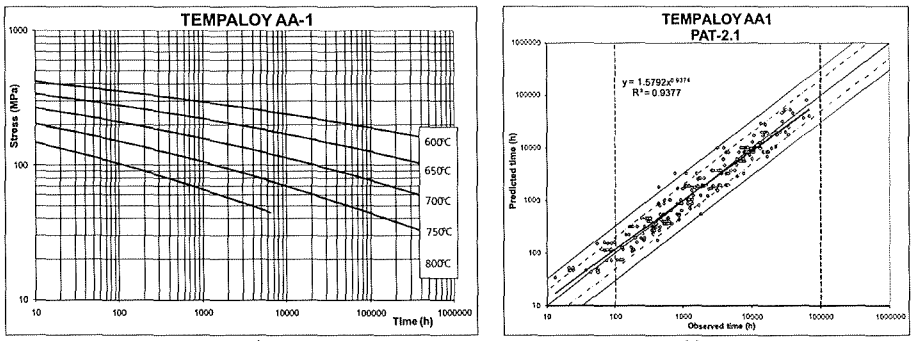

a) b)

Figure 2 – a) Creep-rupture assessment of TEMPALOY AA-1 by MRM method; b) PAT 2.1

Creep tests on similar butt welded joints of TEMPALOY AA-1 were conducted to study the effect of the welding process on cross-weld creep properties. Figure 3 shows the creep resistance of butt welded joints obtained by GTAW and GTAW+SMAW processes, using specific similar welding consumables produced by Kobelco. Creep resistance of welded joints is very close to that of base material in the temperature range 600°C-800°C.

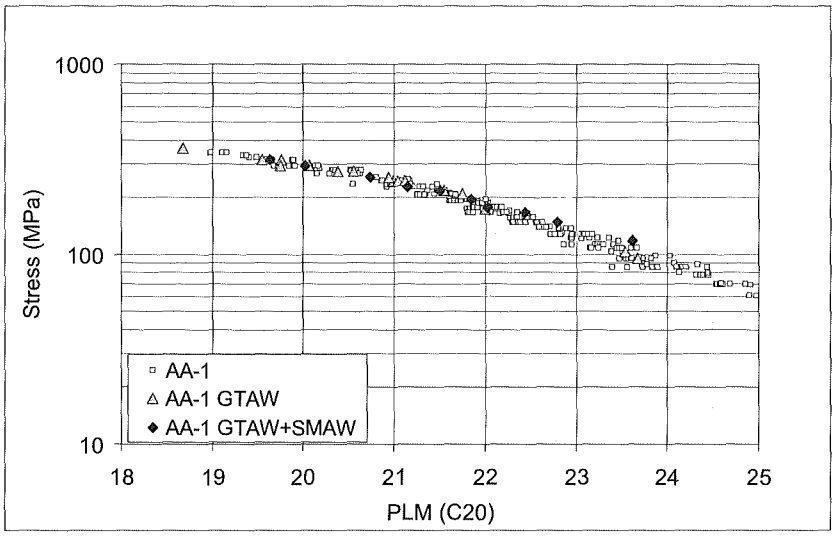

Figure 3 - TEMPALOY AA-1: comparison of creep strength of base metal and cross weld joints (CLM=20).

3.2 Long Term Microstructural Evolution

TEMPALOY AA-1 microstructure is fully austenitic, free from δ-ferrite, thanks to the balanced additions of Cr and Ni; Figures 4-a and 4-b show its microstructure in the as-treated state by Light Microscope (LM) and Scanning Electron Microscope (SEM). After the solubilisation heat treatment the precipitation of TEMPALOY AA-1 consists of primary Nb- and Ti-carbides (• 1μm average), located along grain boundaries as well as inside the grain.

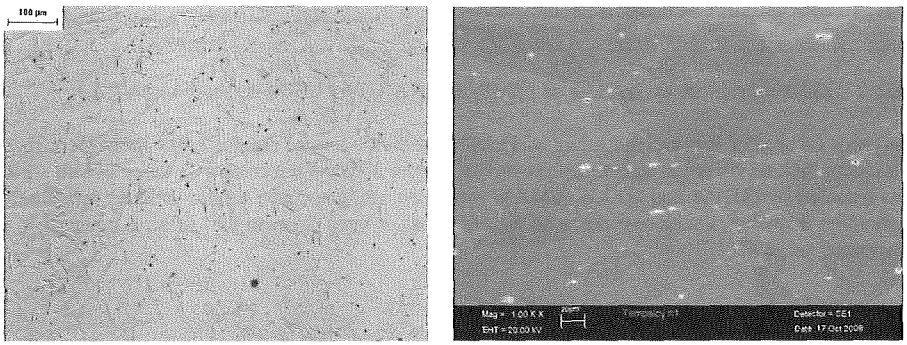

Figure 4 – TEMPALOY AA-1 microstructure in as treated condition a) by LM and b) by SEM.

The exposure at service temperatures in the range 600°C-750°C promotes the precipitation of fine and evenly distributed Ti- and Nb-carbides (MC) inside the grain as well as $M_{23}C_6$ carbides along grain boundaries; the presence of these precipitates determine an effective creep strengthening of the steel [12-13].
Besides, the addition of Cu determines the precipitation of fine and diffuse Cu-rich coherent precipitates, which further increases the creep resistance of the steel. Figure 5 shows the results of

creep tests conducted on 16Cr-14Ni steel samples at 700°C with different Cu content: a Cu addition up to 3% increases the creep rupture stress to achieve rupture within 1000h, while further addition of Cu over 3% has no incremental strengthening effect [14].

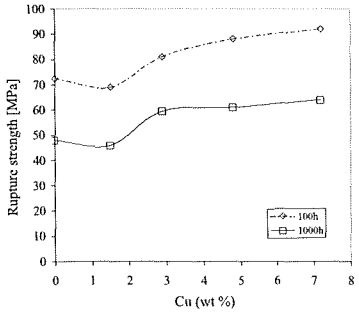

Figure 5 – Effect of Cu addition on creep strength at 700°C in a 16Cr-14Ni steel

The microstructure of TEMPALOY AA-1 steel after two years of service in a power plant is shown in Figure 6: the presence of MC and $M_{23}C_6$ precipitates as well as Cu phase, not present in the solution annealed material, is evident.

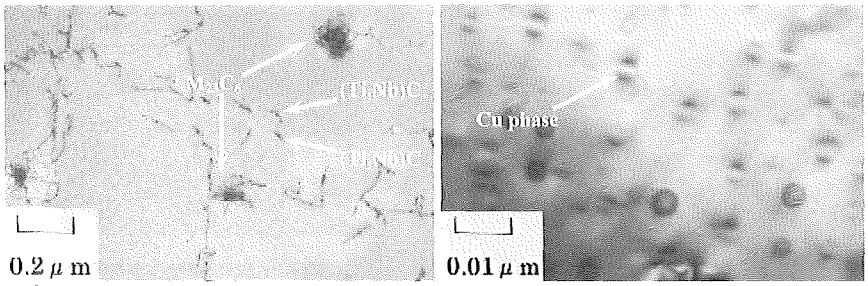

Figure 6 – TEMPALOY AA-1 after 2 years operation in a power plant; TEM microstructures show $M_{23}C_6$, MC and Cu phase.

TEM and SEM investigations were performed on broken creep samples after long exposure at different temperatures.
Figure 7, 8 and 9 show the TEM microstructures obtained on thin foils extracted from creep samples exposed 33kh at 600°C, 63kh at 700°C and 68kh at 750°C respectively.

Fine and dispersed Nb and Ti carbides were found in all the analyzed samples; their size remains very small: the average diameter is lower than 10nm after 63kh at 700°C and lower than 40nm after 68kh at 750°C.
$M_{23}C_6$ particles were identified in all the samples investigated: these precipitates are mainly located along grain and twin boundaries.
Few particles of sigma phase were identified on the samples. According to the literature, its presence could cause a reduction of the toughness [13, 16]; however its low quantity (below 1%) does not have any detrimental effect, as confirmed by the ageing tests which show that after 10^4 h of ageing at 650°C, 700°C and 750°C the residual impact energy is always above 100J/cm^2.

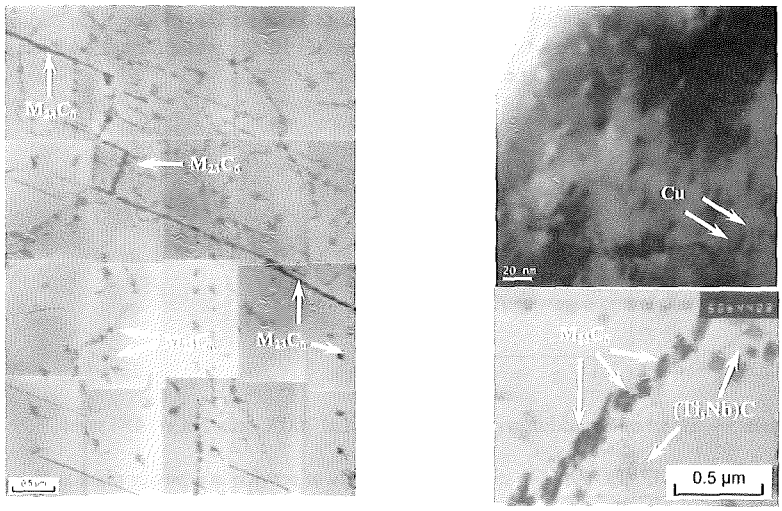

Figure 7 – Microstructure of TEMPALOY AA-1 aged sample after 33kh at 600°C by TEM thin foil

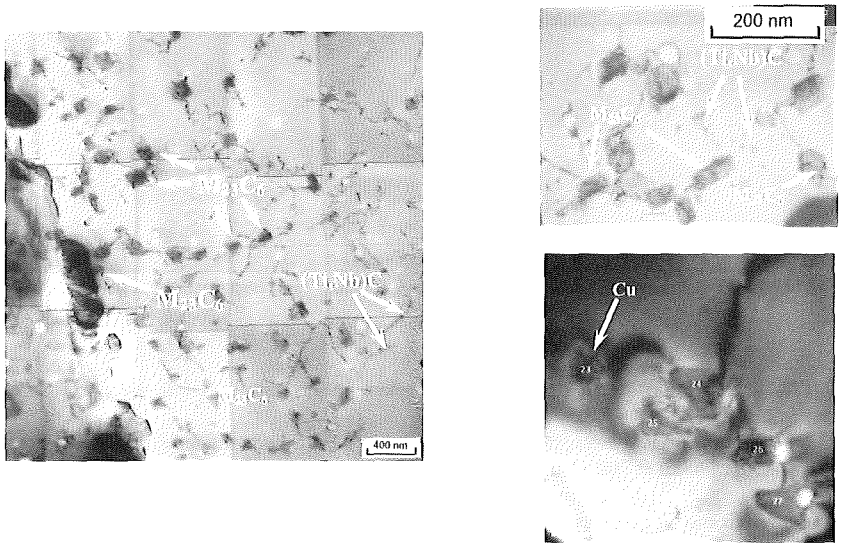

Figure 8 – Microstructure of TEMPALOY AA-1 aged sample after 63kh at 700°C by TEM thin foil

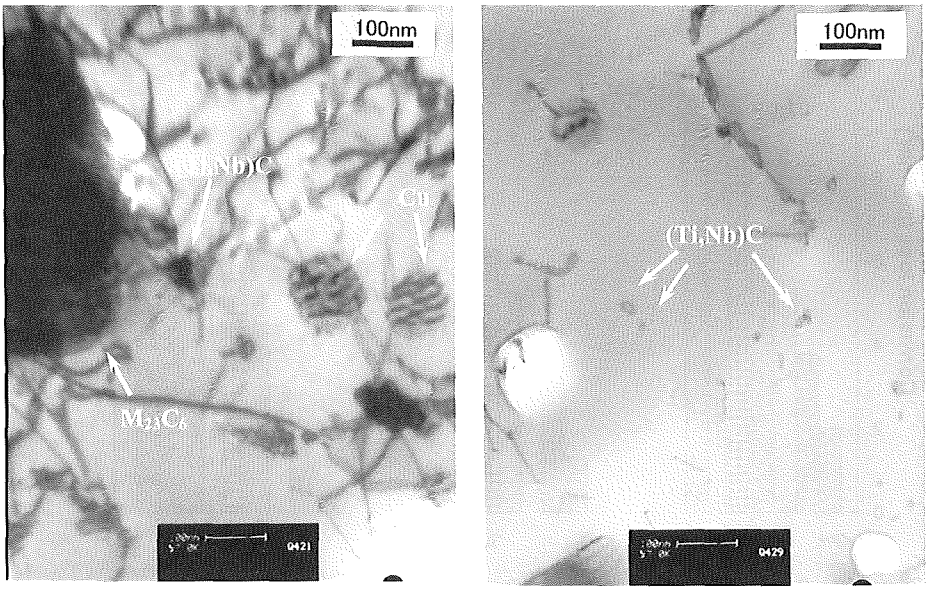

Figure 9 – Microstructure of TEMPALOY AA-1 after 68kh at 750°C

7.3 Hot corrosion and steam oxidation resistance

Long term (up to 5000h) high-temperature corrosion tests were performed in a simulated coal-fired boiler atmosphere.
TP321H and TP304H steels were selected as benchmark materials. Tests were performed in an environment simulating coal ash combustion: a synthetic ash composed by 5% Na_2SO_4 + 5% K_2SO_4 +30% Fe_2O_3 +30% Al_2O_3 +30% SiO_2 was applied on the samples which were surrounded by a mixture of 0.25% SO_2 + 3.5%O_2 +15%CO_2 and N_2 balance. The testing temperature was 700°C being this the most critical temperature in such environment. The mass change has been measured at intervals of 500h.
Test results are graphically summarized in Figure 10. TP321H samples have been completed corroded before reaching 4000h, so corrosion loss at 4000h and 4500h could not be measured for this steel. Grain boundary corrosion was observed on none of the test specimens subjected to the high-temperature corrosion test. The metal loss of TEMPALOY AA-1 is nearly equivalent to that of TP304H steel and around 25% lower than that of TP321H. This behaviour is explained by the differences of Cr content, within the limits set by international standards, found in the three steels: 17.15%, 18.40% and 17.85% respectively for steel 321H, 304H and TEMPALOY AA-1. Steel 321H exhibits the lowest Cr content and shows the highest corrosion rate. TEMPALOY AA-1 and steel 304H have higher Cr content and offer higher resistance against coal ash corrosion.

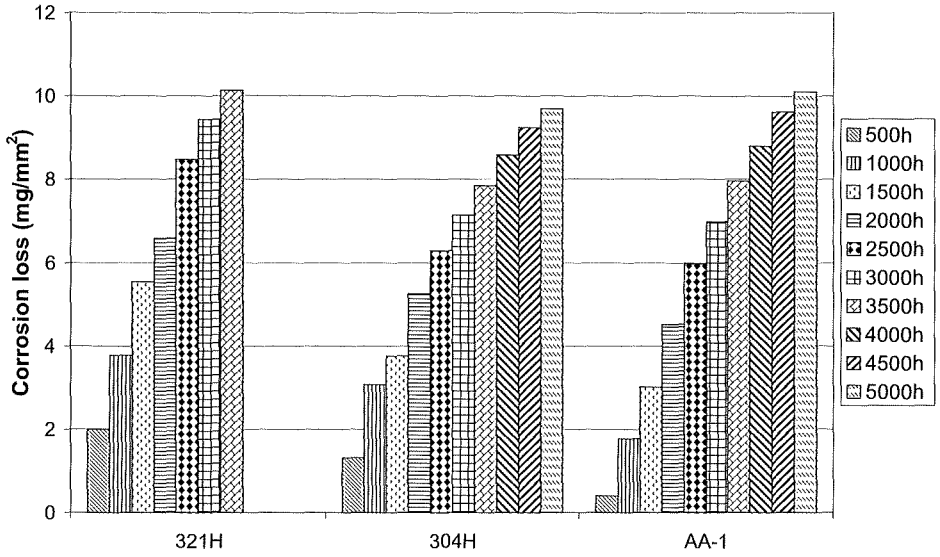

Figure 10 – Results of corrosion tests simulating coal ash combustion after different exposure times.

Steam oxidization properties were also evaluated using the inner surface of the tube as the test surface. The testing temperatures were 600°C, 650°C, 700°C and 750°C. For TEMPALOY AA-1 the oxidation test was performed also with and without shot-blasting; TP321H tube has been adopted as a benchmark material. Test duration was 1000h. The results of the steam oxidization tests are shown in Figure 11 and 12. The base metal exhibited steam oxidation resistance nearly equivalent to that of the TP321H tube. Presumably, this is because both materials have same levels of Cr content. Shot blasting is proved to be extremely effective for suppressing the generation of steam-oxidation scale. The localized cold-working induced by this process promotes the fast Cr diffusion along slip-lines towards the inner surface during the first stage of material service life; a thin and stable Cr-rich layer is formed reducing significantly the oxidation rate.

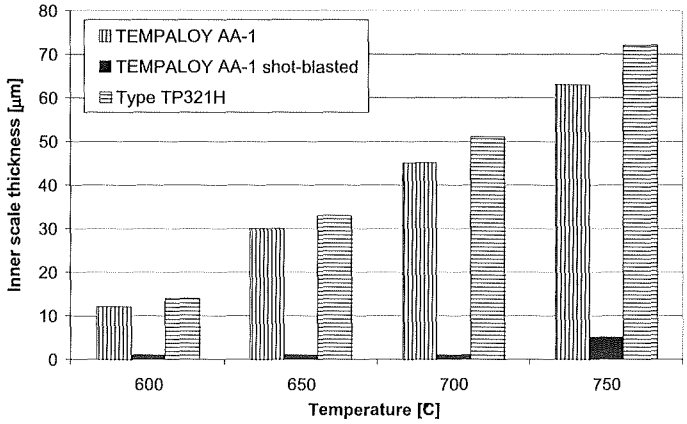

Figure 11 – Results of steam oxidation tests

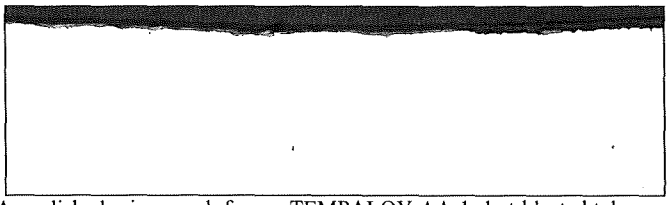

Figure 12a – As-polished micrograph from a TEMPALOY AA-1 shot-blasted tube exposed to steam at 750°C for 1000h

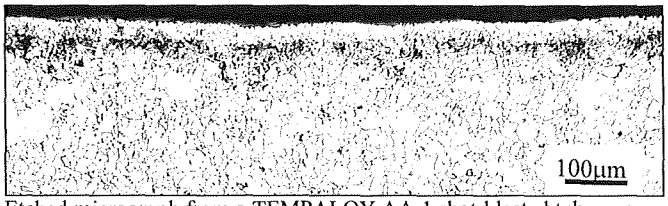

Figure 12b – Etched micrograph from a TEMPALOY AA-1 shot-blasted tube exposed to steam at 750°C for 1000h

7.4 Exposure tests in Power Plant

TEMPALOY AA-1 seamless tubes have been installed and exposed to actual service conditions in the following power plants:

- Ogishima Thermal Power Plant Unit 1, Japan, in 1997
- Esbjerg Power Station, Unit No.3, Denmark, in 1997
- Fyn Power Station, Unit No.8, Denmark, in 2009

8. Conclusions

The production route, the main microstructural features and properties of the austenitic stainless steel TEMPALOY AA-1 have been described.

The average creep rupture strength of TEMPALOY AA-1 was assessed by means of MRM method. Its high creep rupture strength is promoted by the precipitation of $M_{23}C_6$ and MC carbides, and Cu-rich phase. TEM analyses on exposed material showed that these precipitates are stable even after very long term exposure at service conditions. The hot corrosion resistance and long term aging properties of this steel are at the same level of 18Cr-8Ni stainless steels; steam oxidation resistance on inner tube surface can be significantly improved with the internal shot-blasting method.

Laboratory and field tests on Tenaris' TEMPALOY AA-1 advanced stainless steels have shown that this grade fulfils all the severe requirements for the use in the last generation of advanced Ultra Super Critical Boiler.

9. Acknowledgements

The authors wish to thank Leonardo Cipolla and Dario Venditti from Centro Sviluppo Materiali (Rome, Italy) for their hard work on TEM analyses.
Long term coal ash corrosion tests have been carried at Oak Ridge National Laboratory, TN, USA, with the precious supervision of James Keiser.

9. References

1. Minami Y, Tohyama A., Hayakawa H.: Properties And Experience With A New Austenitic Stainless Steel (TEMPALOY AA-1) For Boiler Tube Application; 8th Liege Conference, 18-20 September 2006
2. Minami Y., Tohyama A.: High Temperature Characteristics of High Cr Austenitic Stainless Steel Boiler Tubes for Ultra Super Critical Pressure Thermal Power Plants; First Int. Conf. on Heat Resistant Materials, 23-26 Sept. 1993, p. 533, Fontana, Wisconsin USA
3. Minami Y., Tohyama A.: Development of the High Temperature Materials for Ultra Super Critical Boilers (NKK TEMPALOY Series), Int. Conf. Advanced Heat Resistant Steels for Power Generation, April 1998, San Sebastian, Spain
4. Y. Minami, M. Yuzuki: TEMPALOY A-3 Tubes with High Corrosion Resistance for High Temperature Use; NKK Technical review N° 61 (1991)
5. S. Caminada, G. Cumino, T. Ono, Y. Minami, L. Cipolla, A. Di Gianfrancesco, D. Venditti: Microstructure and long term creep behaviour of the advanced austenitic stainless steel TEMPALOY AA-1; 11th International Conference on Creep and Fracture of Engineering Materials and Structures - Creep 2008, May 2008, Bayreuth, Germany
6. S. Caminada, G. Cumino, T. Ono, Y. Minami, L. Cipolla, A. Di Gianfrancesco, D. Venditti: Ferritic and austenitic grades for new generation of Steam Power Plants; New developments on Metallurgy and Applications of high strength steels, May 2008, Buenos Aires, Argentina
7. Y. Minami, T. Fukui: Properties and experience of high Cr austenitic stainless steel for boiler tubes; Eighth International Conference on Creep and Fatigue at Elevated Temperatures, July 22-26, 2007, San Antonio, Texas
8. S. Caminada, G. Cumino, L. Cipolla, D. Venditti, A. Di Gianfrancesco, Y. Minami, T. Ono Creep properties and microstructural evolution of austenitic TEMPALOY steels, 2nd International ECCC Creep Conference, April 21-23, Dübendorf, Switzerland
9. Creep data validation and assessment procedures, ECCC Recommendations Volumes (2005). Published by European Technology Development.
10. ECCC Data Sheets 2005. Published by European Technology Development
11. S.R. Holdsworth, C.K. Bullough and J. Orr, BS PD6605 creep rupture data assessment procedure. ECCC Recommendations 2005, Volume 5, Appendix D3
12. Metallografic Atlas of long term crept materials No. M-5
13. T. Sourmail, Precipitation in creep resistant austenitic stainless steels; Materials science and technology, Vol. 17 (2001)
14. H. Kimura, Y. Minami et al.: International Conference on Creep, April 1986, Tokyo, pp. 221-226
15. N. Komai, M. Igarashi, Y. Minami, H. Mimura, F. Masuyama, M. Prager, P.R. Boyles: Field test results of newly developed austenitic steels in the Eddystone unit no.1 boiler; Eighth International Conference on Creep and Fatigue at Elevated Temperatures, July 22-26, 2007, San Antonio, Texas
16. Y.Minami, H.Kimura, Y.Ihara: Microstructural change in austenitic stainless steels during long-term aging, Material Science and Technology, 1986, Vol.2

9th Liege Conference : Materials for Advanced Power Engineering 2010
edited by J. Lecomte-Beckers, Q. Contrepois, T. Beck and B. Kuhn.

INITIAL STUDY ON Z-PHASE STRENGTHENED 9-12% Cr STEELS BY ATOM PROBE TOMOGRAPHY

Fang Liu, Hans-Olof Andrén

Department of Applied Physics, Chalmers University of Technology, Sweden

Abstract

The microstructure of two different types of Z-phase strengthened experimental steels, CrNbN-based or CrTaN-based, was investigated. Both steels underwent aging at 650°C for relatively short period of time, 24 hours or 1005 hours. Atom probe tomography was used to study the chemical composition of the matrix and precipitates, and the size and number density of the small precipitates. Both steels contain Laves phase at prior austenite grain boundaries and martensitic lath boundaries. The CrTaN-based steel was found more promising due to its finer and more densely distributed precipitates after 1005 hour aging.

Keywords: 9-12% Cr steels, Z-phase strengthening, microstructure, atom probe tomography

1. Introduction

In steam power plants, higher steam temperature and pressure means a higher thermal efficiency, and thus lower CO_2 emission. It also means higher requirements on the materials in the power plant. The nearest goal for the steam temperature and pressure is 650°C/350 bar [1]. Martensitic 9-12% Cr steels have been playing an important role in these plants, applied e. g. in steam pipes and turbines. However, the present 9-12% Cr steels have an upper limit of 600-620°C. At this high temperature range, both creep and corrosion can cause material failure. It is well established that fine, densely distributed and stable precipitates of type $M_{23}C_6$ (M = Fe, Cr, Mo, W) and MX (M = V, Nb; X = C, N) are crucial for a good creep resistance [2, 3], while a high Cr content is necessary for a good corrosion resistance [4].

There have been several recent trials to improve both creep and corrosion properties by adding e.g. Co, W and B to the steels, in combination with a higher Cr content than the most widely used commercial steam pipe steel, P92 (11-12% vs. 9%). Nevertheless, all of them turned out to be failures. Although they showed better creep resistance at 650°C than older steels until ~10 000 hours, they then suffered a dramatic loss of creep strength [5]. It has been shown that this is mainly attributed to precipitation of a complex nitride known as Z-phase (Cr (Nb,V) N) during creep, since many small MX precipitates are dissolved to form large Z-phase particles, which are thermodynamically more stable at this temperature but give very little contribution to creep strength [6, 7].

However, Hald and Danielsen et al. from the Technical University of Demark are trying to make use of Z-phase as a strengthening dispersion, instead of MX. They proposed a new alloy design concept within the European COST 536 action. The new steels are supposed to be strengthened by fine Z-phase precipitates, which are formed during heat treatment or at the early stage of application. It is expected that the alloys have both good creep and corrosion resistance, which is attributed to a dense distribution of stable Z-phase precipitates and a high Cr content (up to 13 at.%). In order to examine this concept, several experimental steels have been developed, and two of them: one contains Nb, forming CrNbN; the other contains Ta,

forming CrTaN, were selected for further investigation in the present study. Creep tests on these two steels have been carried out by CSM in Italy.

The biggest challenge of the present study is to deal with very small precipitates formed after a short aging time. To tackle this problem, atom probe tomography (APT) was used. In an APT instrument, the investigated sample with a sharp needle shape (radius ~50 nm) is kept at a cryogenic temperature. During analysis a very high electric field is applied to the apex of the sample. In addition, high frequency (typically >100 kHz) voltage or laser pulses are superimposed to the base electric field to ionize atoms, ideally one by one, from the surface of the sample and finally the ions hit a position-sensitive detector. The chemical species is determined by the charge-to-mass ratio, which is measured based on the flight time. All the data is recorded in time sequence, and can be used to reconstruct the atoms in 3-Dimensional images afterwards. ATP provides chemical analysis with atomic resolution [8]. Furthermore, it is capable of detecting small amount of light element (e.g. C and B), and giving quantitative results. The present study used APT to measure the chemical composition of the matrix and precipitates, and the size and number density of the small precipitates.

2. Experimental

2.1. Materials

Two experimental Z-phase strengthened steels were received from the Technical University of Denmark. The Nb-containing Z-phase strengthened steel is referred to as "ZNb", and the Ta-containing Z-phase strengthened steel is referred to as "ZTa". The chemical compositions of the two steels are given in Table 1. Both materials were solution treated at 1150°C for 1 hour, and then aged at 650°C. For the ZNb steel, only one sample aged for 1005 hours was investigated. For the ZTa steel, two samples were investigated, one aged for 24 and the other for 1005 hours.

*Table 1. Nominal composition of the experimental ZNb and ZTa steels (in **atomic** percent).*

Steel	Fe	Ni	Co	Cr	W	Nb	Ta	C	B	N	Si	Mn
ZNb	bal	1.41	5.17	12.64	0.87	0.16	-	0.02	0.02	0.15	0.6	0.5
ZTa	bal	0.48	7.01	12.84	0.89	-	0.12	0.02	0.02	0.13	0.6	0.49

2.2. Sample preparation for atom probe tomography

The steels were cut into small rods (~ 8 × 0.25 × 0.25 mm^3) by a low speed saw. The rods underwent a two-step electropolishing procedure in order to obtain APT samples with a final radius of less than 50 nm. First a thin neck was produced in 10% perchloric acid in methanol by using an ElectroPointer™ equipment that uses an electrolyte drop suspended by a platinum wire loop. Then fine polishing was made in a bath of 2% perchloric acid in 2-butoxyethanol until the lower part of the rod dropped off.

2.3. SEM

All the APT samples were examined in a Leo Ultra 55 Field Emission Gun Scanning Electron Microscope (FEG-SEM) before being investigated in the atom probe. Besides the apex, a large area at the shank of the AP needle is also fine polished, revealing some general microstructure of the steels. Therefore, these samples were also analyzed by the Oxford Inca Energy Dispersive X-ray Spectrometry (EDX) system fitted to the SEM. The operation voltage was at 20 kV.

2.4. Atom probe tomography

In order to analyze the chemical composition of the matrix as well as the small precipitates of the aged steels an Imago LEAP 3000X HR local electrode atom probe instrument was used. The sample temperature during analysis was in the range of 55-65K. For the Nb-containing steel, the pulsed voltage mode was used with a pulse fraction of 20%. To avoid premature specimen failure for Ta-containing steel pulsed laser mode was used, with a laser energy of 0.3 nJ. The acquired data were further analyzed by using the IVAS^{TM} 3.4.1 software developed by Imago.

3. Results

3.1. General microstructure

To obtain an overview of the microstructure of the aged steels, SEM was used to investigate the electropolished areas on the shank of the AP samples. The secondary electron images shown in Figure 1 a, b and c are from the ZNb steel after 1005 hour aging, the ZTa steel after 24 hour and 1005 hour aging, respectively. Precipitates decorating the prior austenite and lath boundaries are nicely displayed after electropolishing. SEM/EDX analyses showed high concentration of W in almost all precipitates, indicating that they are Laves phase (Fe_2W). The size evolution of these precipitates can be seen in the the ZTa steel steel (Figure 1. b and c). From 24 hours to 1005 hours, the size increases from ~50 nm to ~200 nm. However, no Nb- or Ta-rich precipitates were observed by SEM, which suggests that the Z-phase precipitates might have very small size.

3.2. Atom probe tomography of the matrix

The results from APT analyses of the matrix are given in Table 2. It shows that in both the ZNb and ZTa steels, Cr and W concentration decrease after aging. For the ZTa steel, W concentration continues to drop off from 24 hours to 1005 hours. The Z-phase building elements: Ta/Nb and N, together with B and C, are totally consumed out of the matrix. It is noticeable that at least for the ZTa steel the depletion occurred during a rather short period of time, i.e 24 hours.

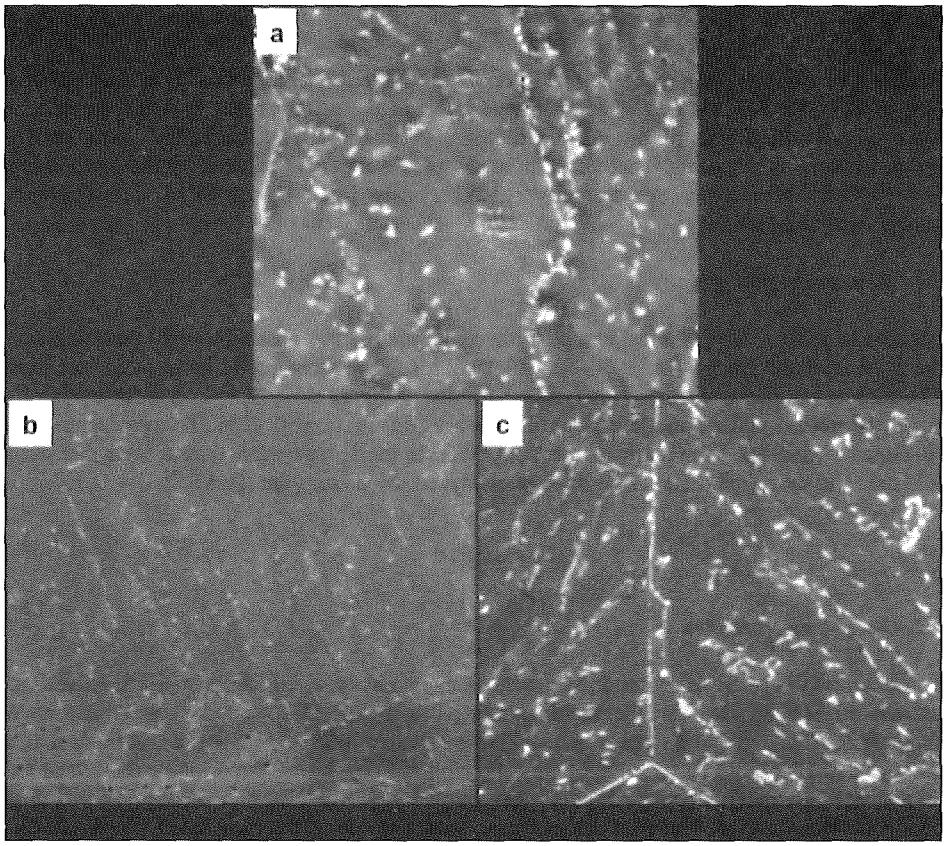

Figure 1. Typical microstructure of the experimental steels (SEM secondary electron images). a) The ZNb steel aged for 1005 hours. b) The ZTa steel aged for 24 hours. c) The ZTa steel aged for 1005 hours. The bright Laves phase particles decorate the prior austenite and martensitic lath boundaries. Comparing b) and c), Laves phase particles grow in size.

3.3. APT of the precipitates

3.3.1. The ZNb steel

A couple of AP samples, with a total volume of around 10^6 nm^3, were analyzed for each material with different aging times. For the ZNb steel after 1005 hour aging, only a part of a big Nb-containing Z-phase precipitate together with two small ones in the immediate vicinity to it was observed. The part of the precipitate detected has a size of ~ 60 x 20 x 10 nm^3. No small Z-phase precipitate was found elsewhere. The chemical composition of the big precipitate is given in Table 2. Considering experimental errors, the ratio of Cr:Nb(+Ta+V):N is reasonably close to 1:1:1. Although not given in the nominal composition, small amounts of V and Ta were detected, which are believed to be incorporated impurity from material preparation. Some Fe, Ni, Co, W, Mn, together with B and C, were found in the precipitate as well.

*Table 2. AP analysis (in **atomic** percent) of the matrix of the ZNb and ZTa steels for different times of aging, as well as of Z-phase precipitates after 1005 hour aging.*

	Fe	Ni	Co	Cr	W	Nb	Ta	V	C	B	N	Si	Mn
matrix													
ZNb 1005 h	Bal.	1.23	5.59	12.07	0.25	0	-	0	0	0	0	0.59	0.41
ZTa 24 h	Bal.	0.67	7.40	12.65	0.63	-	0	0	0	0	0	0.59	0.51
ZTa 1005 h	Bal.	0.57	7.47	12.54	0.24	-	0	0	0	0	0	0.61	0.49
Z-phase													
ZNb 1005 h	5.75	0.20	0.24	29.03	1.03	29.91	0.13	1.28	0.60	0.34	31.26	-	0.23
ZTa 1005 h	3.08	0.09	0.13	36.20	1.26	1.35	23.76	1.15	0.32	0.14	32.32	-	0.20

Although the C and B concentrations were elaborately controlled to a low level (50 wt. ppm and 40 wt. ppm, respectively, corresponding to approximately 0.02 at.%) in these experimental steels, much higher C and B levels (0.6 at.% and 0.34 at.%, respectively, in average) were found in this precipitate. The quantitative concentration profiles across the precipitate/matrix interface are shown in Figure 2. Obviously, carbon is distributed rather evenly in the entire precipitate, while B is enriched only at the interface. The B concentration peak lies at about 1.1 at.%, compared to the value of 0.34 at.% given in Table 2 which averages over the entire particle.

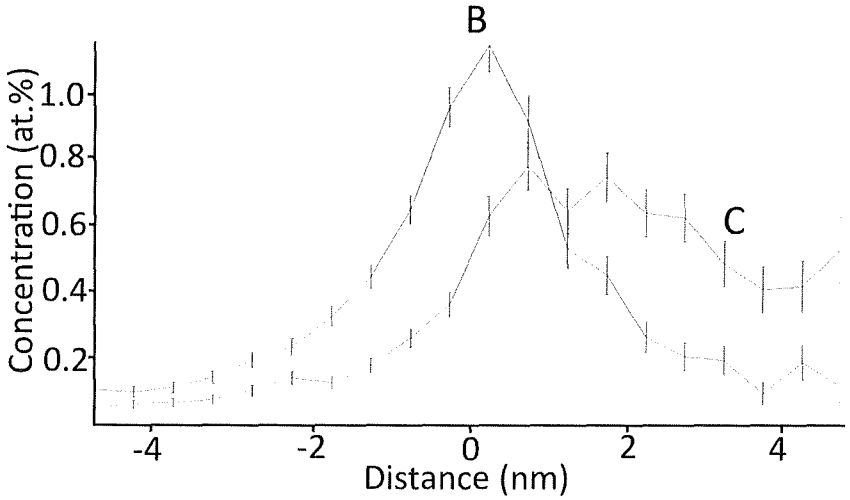

Figure 2. Proxigram analysis showing quantitative B and C concentration profiles across a big-particle/matrix interface in the ZNb steel.

3.3.2. The ZTa steel

For the ZTa steel after 24 hour aging, only small precipitates rich in Cr, Fe, Ta, Co, N and W were observed. The precipitates can be visualized by the atom reconstruction (box size: 85 × 85 × 60) in Figure 3, where Ta atoms are displayed as dots. Ta-atom enriched areas show the location of the precipitates. These precipitates are blade-like, with typical thickness ~1 nm, and length 5-15 nm. In this figure, the arrowed precipitate aligns so that its thinnest plane is roughly parallel to the projection plane, and it gives the reader an idea of the thickness. The precipitates are in a large number; their number density is $\sim 10^{23}$ m^{-3}. The chemical composition varies for individual precipitates depending on the size.

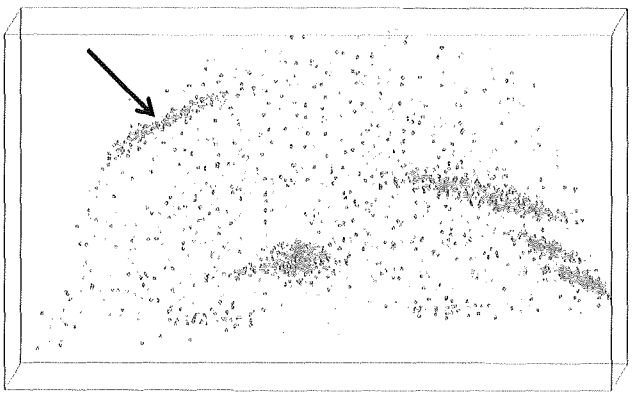

Figure 3. The ZTa steel after 24 hour aging. The dots are Ta atoms for visualizing the precipitates (box size: 85 × 85 ×60 nm^3). Note the precipitates have a blade-like shape.

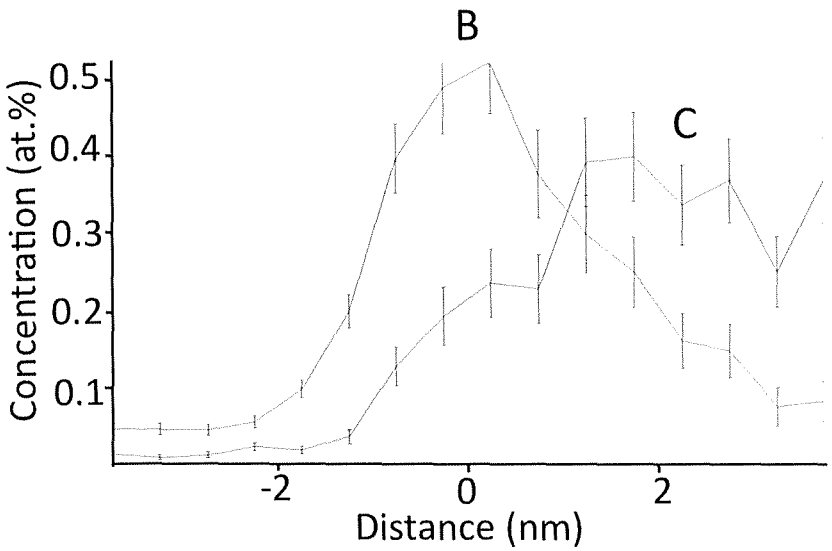

Figure 4. Proxigram analysis showing quantitative B and C concentration profiles across a big-particle/matrix interface in the ZTa steel.

For the ZTa steel after 1005 hour aging, one big and some small Z-phase precipitates were observed. The chemical composition of the big Ta-containing Z-phase particles is listed in Table 2. It is noticeable that the Ta concentration is remarkably less than 33%; even after counting in Nb and V, the concentration only makes up to 27%. On the other hand, Cr concentration is more than 33%, reaching 36%. The concentration of W, Mn and V are close to those in the ZNb steel, while Fe, Ni, Co, C and B concentration are somewhat lower compared to the ZNb steel.

Again, it was found that C was distributed rather evenly in the entire particle. On the other hand, B was enriched at the interface between the precipitate and the matrix (Figure 4).

After 1005 hour aging, the Z-phase precipitates have coarsened to some extent, compared to after 24 hour aging. The precipitates becomes spherical or rod in shape. The typical size is 5-15 nm. In Figure 5 iso-concentration surfaces of Ta were drawn to guide the eyes to several such precipitates. The number density of the precipitates are $\sim 2 \times 10^{22}$ m^{-3}, based on the APT results.

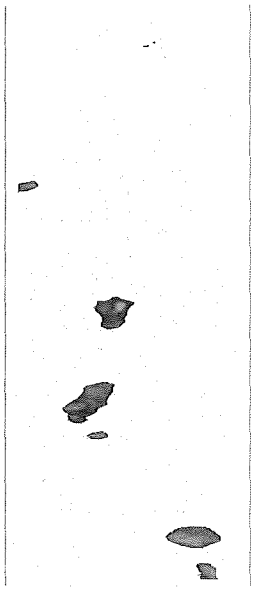

Figure 5. Small Z-phase precipitates visualized by Ta 10% iso-concentration surface in the ZTa steel after 1005 hours aging. The small dots are Ni atoms for visualizing the shape of the apex. Box size: 58 × 58 ×150 nm³.

4. Discussion

4.1. Ta-containing vs. Nb-containing Z-phase strengthened steel

Comparing the Ta-containing Z-phase (CrTaN) strengthened steel to the Nb-containing Z-phase (CrNbN) strengthened steel, after prolonged aging, rather densely distributed fine Z-phase precipitates were found in the Ta-containing the ZTa steel, while this is not the case for the ZNb steel. The densely distributed Z-phase precipitates can hinder the movement of boundaries and dislocations, and thus giving a better creep resistance. Creep tests carried out by CSM in Italy, confirm that the ZTa steel is more promising [9] in terms of creep. That Ta tends to form finer precipitates compared to Nb was also reported by Wang and her coworkers, who aimed to use Ta and Nb to form MX precipitates in their experimental 9-12% Cr steels. They found that Ta-containing MX precipitates in one test steel are finer compared to the Nb-containing MX precipitates in another steel [10].

4.2. Precipitation reactions

The matrix chemical composition gives a valuable clue to the precipitation reactions. First of all, the decrease in W concentration, combined with SEM/EDX analyses on the visible precipitates, show evidently the formation of Laves phase. The Laves phase starts to precipitate already at the very early stage of aging. However, this process is not completed immediately, it continues with time as can be seen in the ZTa steel. It has been reported that

Laves phase usually has a long growth period at this temperature [11]. For the nitride precipitation, at least for the ZTa steel, the full volume fraction of nitrides and/or carbides has precipitated during 24 hours.

For CrNbN the ratio between Cr, Nb+V+Ta and N falls rather nicely to ~1:1:1. However, for CrTaN the Cr and Ta ratio is rather high: Cr:Ta ≈1.2:0.8. This ratio matches very well with what was reported by Ettmayer, who managed to prepare tantalum Z-phase [12]. Both CrNbN and $Cr_{1+x}Ta_{1-x}N$ contain significant amount of Fe and W, which are believed to be incorporated into the precipitates due to their relatively high content in the matrix.

The C and B levels in the Z-phase precipitates are also remarkably high, considering their extremely low amount in steels (0.3-0.6 at.% and 0.1-0.3 at.% in precipitates vs. 0.02 at.% in the steel). There is some interesting observation on the distribution of C and B in the Z-phase precipitates. C is distributed rather evenly in the CrNbN and $Cr_{1+x}Ta_{1-x}N$ Z-phase, which means that C might have a certain solubility in both types of Z-phase. In contrast, B was only found at the interface between the Z-phase and the matrix, which means that the solubility of B in the Z-phase is limited. The B at the interfaces is believed to be beneficial, since they may decrease the interfacial energy of the precipitates, and thus retard the coarsening of the precipitates.

One issue of great concern is whether the Ta and N rich precipitates in the ZTa steel after 24 hour aging is already Z-phase. Unfortunately, in this case one cannot tell directly from the atom probe results, despite the atomic resolution of the instrument. This is because the precipitate atoms are smeared by the matrix atoms due to the different evaporation fields for different phases, the so-called local magnification effect [13]. We tried to get rid off the influence from the matrix and to compare the composition of the precipitates in 24 hours to that in 1005 hours, where only Z-phase is expected. The preliminary results indicate the formation of Z-phase after 24 hours. However, to confirm this and to have a more comprehensive understanding of the material TEM work is planed for the future.

5. Conclusions

- Compared to the Nb-containing Z-phase strengthened steel ZNb, the Ta-containing steel ZTa contains finer and more densely distributed Z-phase particles.
- For the ZNb steel aged for 1005 hours, and the ZTa steel aged for 24 hours, their matrices are depleted of Nb/Ta and N, while Cr and W concentrations decreases, due to the formation of Z-phase and Laves phase.
- The APT results indicate that for the ZTa steel, Z-phase has already formed after 24 hours. After 24 hours, the Z-phase particles, rich in Ta, N, Cr, Fe, are blade-like, with a high number density (10^{23} m^{-3}). After 1005 hours, most Z-phase particles become spherical or rod like (~5-15 nm), with a lower number density of 2×10^{22} m^{-3}. Some bigger Z-phase particles are also formed.

Acknowledgement

Financial support by KME, the Consortium for Materials Technology in Thermal Energy Processes as well as the Research Foundation of VGB in Germany and the Swedish

Foundation for Strategic Research (SSF) is gratefully acknowledged. This work is part of the European COST 536 action and collaboration of all members is acknowledged.

References

[1] Staubli M, Scarlin B, Mayer KH, Kern TU, Bendick W, Morris PF, Digianfrancesco A, Cerjak H. Materials for advanced power plants: The European COST 522 Action. In: A.Strang, R.D.Conroy, W.M.Banks, M.Blacker, J.Legget, G.M.McColvin, S.Simpson, M.Smith, F.Starr, R.W.Vanstone, editors. Parsons 2003 Engineering issues in turbine machinery, power plant and renewables. Dublin, Ireland: The Institute of Materials, London, 2003, 2003. p.305.
[2] Hald J. Long-term stability of 9-12%Cr steels - Current understanding and future perspectives. VGB W6Q. Dortmund, 2004.
[3] Hald J, Straub S. Microstructural stability of 9-12% CrMo(W)VNbN-steels. In: Lecomte-Beckers J, Schubert F, Ennis PJ, editors. Materials for advanced power engineering. Liege: Forschungszentrum Jülich GmbH, 1998. p.155.
[4] Sedriks AJ. Chapter 10: Corrosion by hot gases and molten compounds. Corrosion of stainless steels. A Wiley-Interscience publication John Wiley & Sons, Inc., 1996.
[5] Uehara T, Toji A, Komatsubara S, Fujita T. Improvement of creep rupture strength of high strength 12Cr ferritic heat-resistant steel. In: Lecomte-Beckers J, Carton M, Schubert F, Ennis PJ, editors. Materials for advanced power engineering, vol. Part 3. Liege, Belgium: Forschungszentrum Jülich GmbH, 2002. p.1311.
[6] Strang A, Vodarek V. Z phase formation in martensitic 12CrMoVNb steel. Materials Science and Technology 1996;12:552.
[7] Svobda M, Bursik J, Podstranska I, Krouppa A, Sklenicka V, Mayer KH. In: Lecomte-Beckers J, Carton M, Schubert F, Ennis PJ, editors. Materials for advanced power engineering, vol. 3. Liege, Belgium: Forschungszentrum Jülich GmbH, 2002. p.1521.
[8] Cerezo A, Clifton PH, Galtrey MJ. Atom probe tomography today. Materials today 2007;10:36.
[9] Danielsen H. personal communication.
[10] Wang Y, Mayer K-H, Scholz A, Berger C, Chilukuru H, Durst K, Blum W. Development of new 11%Cr heat resistant ferritic steels with enhanced creep resistance for steam power plants with operating steam temperatures up to 650°C. Materials Science and Engineering A 2009;510-511:180.
[11] Korcakova L. Ph.D. Dissertation: Microstructure evolution in high strength steel for power plant application: microscopy and modelling. Department of manufacturing engineering and management: Technical University of Denmark, 2002.
[12] Ettmayer P. Die Struktur der Komplexnitride NbCrN und Ta1−xCr1+xN Monatshefte für Chemie / Chemical Monthly 1971;102:858.
[13] Miller MK. Atom probe tomography - analysis at the atomic level. Kluwer Academic/Plenum Publishers, 2000. p.151.

9th Liege Conference : Materials for Advanced Power Engineering 2010
edited by J. Lecomte-Beckers, Q. Contrepois, T. Beck and B. Kuhn.

EFFECTS OF ALLOYING ELEMENTS AND CONSTITUENT PHASES ON LONG-TERM CREEP STRENGTH OF MODIFIED 9Cr–1Mo STEEL

Tatsuya Tokunaga[1,2], Kohei Yoshida[3], Masaki Sakanaba[4], Fujimitsu Masuyama[1,2]

[1] Department of Applied Science for Integrated System Engineering
Kyushu Institute of Technology, 1-1, Sensui-cho, Tobata-ku, Kitakyushu 804-8550, Japan
[2] "Fundamental Studies on Technologies for Steel Materials with Enhanced Strength and Function", Consortium of JRCM (The Japan Research and Development Center for Metals)
[3] Graduate student of Kyushu Institute of Technology, now with Mitsui High-tec Inc.
[4] Graduate student of Kyushu Institute of Technology
now with Mitsubishi Heavy Industries, Ltd.

Abstract

The effect of the alloying elements and constituent phases on the long-term creep strength of modified 9Cr–1Mo steel has been investigated using creep data from 34 heats of this steel. The creep rupture strength for 10^5 h at 600 °C was evaluated using the Larson–Miller parametric method, and the constituent phases and their composition at 600 °C were obtained from thermodynamic equilibrium calculations. From various alloying elements, the long-term creep rupture strength was found to depend on the Cr, Mo, V, and N content. Regarding the effect of the constituent phases, the long-term creep rupture strength increased with increasing amount of NaCl-type carbonitride, MX (NbX + VX), and in particular, materials with higher VX/NbX ratios tended to exhibit higher creep strength. Furthermore, the enrichment of Mo in the $M_{23}C_6$ carbide rather than in the bcc matrix may be effective in maintaining a higher creep strength.

Keywords: modified 9Cr–1Mo steel, creep rupture strength, alloying elements, constituent phases, thermodynamic calculations.

1. Introduction

Creep-strength enhanced ferritic steels are used in the high-temperature components of power plants. Their composition range and heat treatment conditions are tightly controlled to maintain the appropriate mechanical properties, including hardness, tensile strength, impact test, creep, and fatigue properties. On the other hand, it is well known that the creep strength of this type of steel is affected by its chemical composition, thermal history, and amount and/or composition of the constituent phases. The creep strength varies from heat to heat, although the chemical composition range may be within the given specification. Thus, it would be useful to obtain knowledge on the effect of chemical composition and constituent phases on the long-term creep rupture strength to establish a design concept for advanced creep-resistant ferritic steels. The role of the alloying elements in the development of high Cr ferritic steels has been extensively studied by a number of investigators in the past, and has already been reviewed [1]. Recently, long-term creep data has been made available of many heats of commercial 9Cr–1Mo–VNb steel. In this study, we used these creep data to study the

effect of the alloying elements and constituent phases on the long-term creep strength of this steel using the Larson–Miller parametric method and thermodynamic equilibrium calculations.

2. Analytical procedures

The creep data from 34 heats of 9Cr–1Mo–VNb steel were taken from the data book compiled by the Iron and Steel Institute of Japan (ISIJ) [2], variation of the chemical composition is shown in Table 1. The creep strength of each heat for 10^5 h at 600 °C was evaluated using the Larson–Miller (LM) parametric method with optimized values of the constant C in the LM parameter. In addition, the creep rupture strength was also evaluated for $C = 20$ using all the creep data and with optimized values of a constant C using the data obtained from creep tests at relatively low stress levels. In this analysis, the LM parameter was treated as a dependent variable, and was described by the second-order polynomial function of the logarithm of the stress. The constituent phases and their composition for each heat at 600 °C were obtained from thermodynamic equilibrium calculations using the SGTE solution database [3]. Additional thermodynamic parameters for the NaCl-type carbonitride, MX, phase were taken from the literature [4] to take into account the phase separation of the MX phase into the Nb-rich, NbX, and V-rich, VX, phases. The constituent phases and their composition in the as-normalized and tempered materials were not in the thermodynamic equilibrium state. However, a previous study has shown that the amount of precipitated W in the residue of 9Cr–0.5Mo–1.8W–VNb steel did not change for an ageing time >30,000 h at 600 °C [5]. Thus, an evaluation of the constituent phases and their composition after treatment for a period of 10^5 h at 600 °C for 9Cr–1Mo–VNb steel using thermodynamic calculations was assumed to be reasonable.

Table 1. Variation in the chemical composition of the 9Cr–1Mo–VNb steel heats (mass%).

C	Si	Mn	P	S	Ni	Cr	Mo	V	Nb	N	Al
0.09 – 0.12	0.24 – 0.43	0.32 – 0.45	0.004 – 0.018	0.001 – 0.005	< 0.29	8.25 – 9.15	0.89 – 1.03	0.19 – 0.24	0.07 – 0.1	0.034 – 0.064	< 0.018

3. Results and discussion

The effect of various alloying elements on the creep rupture strength estimated for 10^5 h at 600 °C is summarized in Figs. 1(a)–1(h), together with the effect of the Cr equivalent (Cr-eq.) on the creep rupture strength. It should be noted that the value of the creep rupture strength shown in Fig. 1 and other figures shown later are those values obtained using optimized values of the constant C in the LM parameter using all the creep data. The value of Cr-eq. was calculated using the following equation [6]:

$$\text{Cr-eq.}=[\text{Cr\%}]+6[\text{Si\%}]+4[\text{Mo\%}]+1.5[\text{W\%}]+11[\text{V\%}]+5[\text{Nb\%}]-40[\text{C\%}]-2[\text{Mn\%}]-4[\text{Ni\%}]-30[\text{N\%}]-2[\text{Co\%}] \quad (1).$$

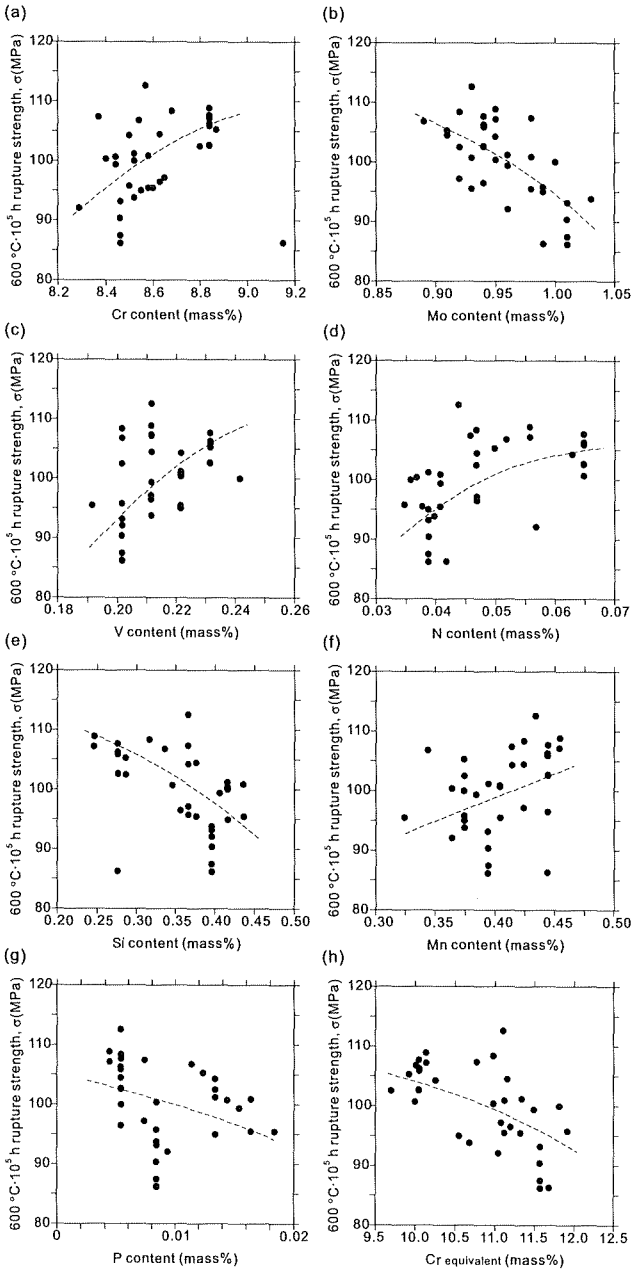

Fig. 1. The relationship between various alloying elements and the creep rupture strength for 10^5 h at 600 °C estimated from the best fit in the Larson-Miller parameter (LMP) method of all the data: (a) Cr, (b) Mo, (c) V, (d) N, (e) Si, (f) Mn, (g) P, and (h) Cr equivalent.

From these data, in the composition range studied, it was found that the creep rupture strength increased with increasing Cr, V, Mn, and N content, whereas the creep rupture strength decreased with increasing Mo, Si, and P content and Cr equivalent. Regarding the effect of the Cr content of 9%–12% Cr–Mo–V–Nb–W–Co–B steels, a previous investigation has shown that the creep rupture time at 650 °C and 98 MPa increased with increasing Cr content, reaching a maximum value at a Cr content of 9%, and then decreased for higher Cr contents up to 11.5% [7], and this trend is consistent with our results for a Cr content below 9%. Concerning the effect of Mo content, although Mo is known to be an effective solid solution strengthener for ferritic steels, the present trend was opposite to what is generally expected. In addition, it has been reported that the creep rupture strength is not affected by Mo content in the range of 1%–2% Mo for 9Cr–1Mo–VNb steels [8]. This point will be further discussed later. The trend for V and N may be related to the amount of MX formed, which acts as a precipitation strengthener, but a previous study has indicated that an increase in V addition causes a decrease in creep rupture strength because of the sparse precipitation of VN [9]. Regarding the effect of other alloying elements that are not shown in Fig. 1, there was no clear relationship with creep rupture strength found.

Figure 2 shows the relationship between the amount of MX and $M_{23}C_6$ and the creep rupture strength for 10^5 h at 600 °C. According to these results, an increase in the creep rupture strength with increasing MX (NbX + VX) amount was observed, and this is presumably because the precipitation hardening effect increased with increasing amounts of MX. On the other hand, no clear relationship was observed for the amount of $M_{23}C_6$. However, the creep rupture strength decreased slightly with increasing ratio of $M_{23}C_6$/MX, as shown in Fig. 3(a). The effect of the ratio of VX/NbX on the creep rupture strength is shown in Fig. 3(b). It was found that materials with a higher VX/NbX ratio exhibited a higher creep rupture strength. It has been reported that the microstructural morphology of the phase separation of MX into NbX and VX is such that VX precipitates adhere to the spherical NbX, resulting in a composite precipitate called a V-wing [10]. Since the probability of dislocation trapping occurring at a V-wing site is higher than that at a spherical NbX site, an increase in the VX/NbX ratio may be effective in increasing the creep rupture strength.

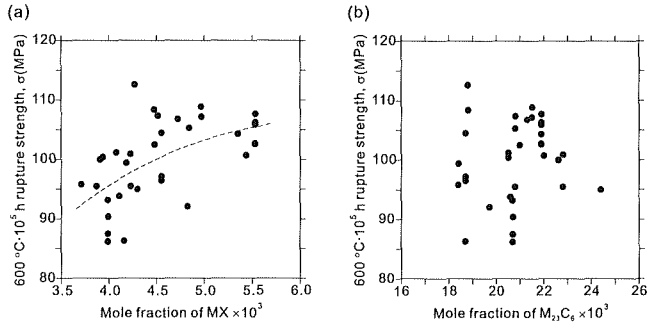

Fig. 2. The relationship between the amount of: (a) MX, and (b) $M_{23}C_6$, and the creep rupture strength for 10^5 h at 600 °C estimated from the best fit in the LMP method of all the data.

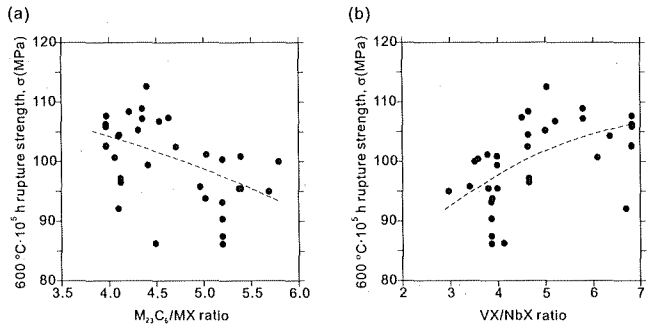

Fig. 3. The relationship between the ratio of: (a) $M_{23}C_6$/MX, and (b) VX/NbX, and the creep rupture strength for 10^5 h at 600 °C estimated from the best fit in the LMP method of all the data.

The estimated value of the creep rupture strength is plotted against the partitioning ratio of Mo between $M_{23}C_6$ and the bcc matrix in Fig. 4. It should be noted that the rate of diffusion of Mo in steels is generally low. The plot shown in Fig. 4 indicates that materials with a higher partitioning of Mo in $M_{23}C_6$ may exhibit a higher creep rupture strength. It is well known that fine $M_{23}C_6$ particles at sub-boundaries act as obstacles to dislocation climb motion. However, the coarsening of these particles during creep induces a recovery of the lath or subgrain structure along the sub-boundaries, resulting in a loss of rupture strength [11]. Our results imply that a coarsening of the $M_{23}C_6$ is effectively suppressed by the high partition value of Mo in $M_{23}C_6$, resulting in a higher creep rupture strength because of the retardation of the recovery of the lath or subgrain structure.

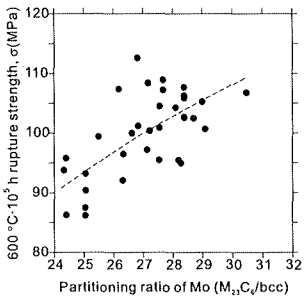

Fig. 4. The relationship between the partitioning ratio of Mo between $M_{23}C_6$ and the bcc matrix and the creep rupture strength for 10^5 h at 600 °C estimated from the best fit in the LMP method of all the data.

The relationship between the Mo content in the bcc matrix and the creep rupture strength is shown in Fig. 5. This plot shows that the creep rupture strength decreases with increasing Mo

content in the bcc matrix. This result is not consistent with the finding that Mo is an effective strengthener in α-Fe [12]. On the other hand, it has been reported that the dominant factor for the observed creep strength of 9Cr–1Mo–VNb steel is precipitation hardening rather than solid solution strengthening [13]. Figure 6 shows the relationship between the Mo content in the bcc matrix and the amount of MX. It was found that the increase in Mo content in the bcc matrix reduced the amount of MX, which is the dominant strengthening factor controlling the creep strength. Therefore, it is likely that an increase in the Mo content of the material, as well as in the bcc matrix, has little effect on the solid solution strengthening, but instead, has a decreasing effect on the amount of MX formed. Regarding the Nb, V, C, and N content of the MX phase (NbX and VX), no clear relationship with creep rupture strength was found. It should be noted that the Fe_2Mo Laves phase is known to form during creep in 9Cr–1Mo–VNb steel, but the Laves phase was not taken into account in our thermodynamic calculations because of discrepancies in the phase stability. Calculations using the SGTE database [3] gave a solution temperature of about 500 °C. The incorporation of a Laves phase in the constituent phases at 600 °C is important, and further study on the modification of the thermodynamic parameters for the Laves phase is in progress, taking into account the solubility of the third element.

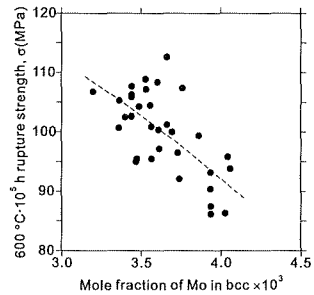

Fig. 5. The relationship between the Mo content in the bcc matrix and the creep rupture strength for 10^5 h at 600 °C estimated from the best fit in the LMP method of all the data.

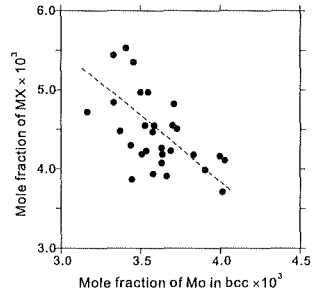

Fig. 6. The relationship between the Mo content in the bcc matrix and the amount of MX.

The estimated creep rupture strength for 10^5 h at 600 °C shown in this section was based on the results obtained from an analysis using optimized values of the constant C in the LM parameter using all the creep data. Although no results are shown here, the findings obtained for two other analyses: (1) a method with $C = 20$ using all the creep data, and (2) a method using optimized values of the constant C using the data obtained under low stress conditions, were almost the same as those discussed in this section.

4. Conclusions

The effect of the alloying elements and the constituent phases on the long-term creep rupture strength of 34 heats of commercial 9Cr–1Mo–VNb steel has been investigated using the Larson–Miller parametric method and thermodynamic equilibrium calculations. Some useful relationships were obtained, and the thermodynamic equilibrium calculations will serve as a guide in the design of this type of steel.

Acknowledgements

This work was partially carried out as a part of the research activities of the "Fundamental Studies on Technologies for Steel Materials with Enhanced Strength and Functions" by the Consortium of JRCM (The Japan Research and Development Center of Metals). Financial support from NEDO (New Energy and Industrial Technology Development Organization) is also gratefully acknowledged.

References

[1] S. Ohta, *Ferritic Heat-Resisting Steels, Unrelaxing Research and Development for the World Highest Performance*, Chijin Shokan Co., Ltd., Japan, (1998), (in Japanese).

[2] *Atlas of Stress-Strain Curves and Rupture data at High Temperatures*, The Iron and Steel Institute of Japan (ISIJ), (1994), (in Japanese).

[3] *SGTE (Scientific Group Thermodata Europe) Solution Database*, ed. by B. Sundman, Royal Institute of Technology, Stockholm, Sweden, (1994).

[4] K. Inoue, N. Ishikawa, I. Ohnuma, H. Ohtani, K. Ishida, Calculation of phase equilibria between austenite and (Nb, Ti, V)(C, N) in microalloyed steels, *ISIJ Int.*, 41, 175–182, (2001).

[5] J. Hald, Metallurgy and creep properties of new 9-12%Cr steels, *Steel Research*, 67, 369–374, (1996).

[6] D. L. Newhouse, C. J. Boyle, R. M. Curran, 68th ASTM Annual Meeting, Lafayette, Indiana, (1965).

[7] R. Hashizume, K. Miki, T. Azuma, T. Ishiguro, Y. Murata, M. Morinaga, Optimization of Cr content in high Cr heat resistant steels on the basis of long term creep strength, *Tetsu-to-Hagane*, 88, 793–800, (2002), (in Japanese).

[8] K. Asakura, T. Fujita, H. Watanabe, Effects of molybdenum content on creep-rupture strength and toughness of 9% chromium ferritic heat resisting steels containing V and Nb, *Tetsu-to-Hagane*, 74, 2001–2008, (1988), (in Japanese).

[9] Y. Tsuchida, K. Okamoto, Y. Tokunaga, Role of vanadium in creep rupture strength of 9Cr–1Mo–V–Nb–N steel, *Tetsu-to-Hagane*, 81, 571–576, (1995), (in Japanese).

[10] K. Hamada, K. Tokuno, Y. Tomita, H. Mabuchi, K. Okamoto, Effects of precipitate shape on high temperature strength of modified 9Cr–1Mo steels, *ISIJ Int.*, 35, 86–91, (1995).

[11] J. Hald, S. Straub, *Materials for Advanced Power Engineering, Proc. 6th Liege Conference*, ed. by J. Lecomte-Beckers, F. Schubert, P.J. Ennis, Forschungszentrum Jülich GmbH, Jülich, Germany, 155–169, (1988).

[12] S. Takeuchi, Solid-solution strengthening in single crystals of iron alloys, *J. Phys. Soc. Jpn.*, 27, 929–940, (1969).

[13] Y. Kadoya, E. Shimizu, Effects of solute Mo, W and dispersoid carbonitride on high temperature creep of ferritic steels, *Tetsu-to-Hagane*, 85, 827–834, (1999), (in Japanese).

9th Liege Conference : Materials for Advanced Power Engineering 2010
edited by J. Lecomte-Beckers, Q. Contrepois, T. Beck and B. Kuhn.

EFFECTS OF NICKEL AND COBALT ADDITION ON CREEP STRENGTH AND MICROSTRUCTURE OF THE PRECIPITATION-STRENGTHENED 15Cr FERRITIC STEELS

Masachika Shibuya*, Yoshiaki Toda, Kota Sawada, Hideaki Kushima and Kazuhiro Kimura

National Institute for Materials Science,
1-2-1, Sengen, Tsukuba, Ibaraki 305-0047, Japan

Abstruct

Creep strength of 15Cr ferritic steel with ferrite matrix was increased by precipitation strengthening of intermetallic compounds. It was higher than those of 9-12Cr ferritic steels with a tempered martensitic microstructure strengthened by carbide and carbonitride. Addition of nickel was confirmed to improve Charpy impact toughness of the 15Cr steels, however, creep strength was slightly reduced by the addition of nickel. Microstructure of the 15Cr steel changes from ferrite single phase to dual phases of ferrite and martensite with the addition of nickel which is an austenite stabilizing element. The 15Cr steels investigated in the previous study, contain 3mass% of cobalt which is also an austenite stabilizing element, therefore, the influence of nickel and cobalt combination on mechanical properties and microstructure of the 15Cr-1Mo-6W-V-Nb steel is investigated in this study. Creep strength, Charpy impact toughness and microstructure of the steel were strongly influenced by the composition of nickel and cobalt. Design guideline of the 15Cr steel is discussed with respect to a role of microstructure and combination of nickel and cobalt addition.

Keywords: 15Cr ferritic steel, creep strength, Charpy impact toughness, microstructure, nickel

1. Introduction

Heat-resistant and high strength steels have been investigated to improve the energy efficiency of power plants in order to save fossil fuel resources and reduce the carbon dioxide emissions [1]. Ferritic heat-resistant steel is suitable for large and thick structural components which are exposed to high temperatures and high pressure. It is in wide used in headers and main steam pipes of the power plants. The conventional ferritic heat-resistant steels such as 9-12Cr ferritic steels have the microstructure of tempered martensite strengthened by numerous precipitates of carbide and MX-type carbonitride [2]. However, microstructural degradation owing to preferential recovery at the vicinity of prior austenite grain boundaries results in decreased creep strength, especially in the long-term [3]. Chromium is the most effective alloying element for improving oxidation resistance under high temperature and high pressure. However, maximum Cr composition in the conventional high strength ferritic heat-resistant steel is restricted to less than about 11 mass% in order to avoid the formation of δ-ferrite, which a phase that is detrimental to creep strength and fracture toughness. Improvements in both the long-term creep strength and the oxidation resistance are important for the development of high strength ferritic heat-resistant steel. Recently, 15Cr ferritic steel (15Cr-1Mo-6W-V-Nb) with annealed ferrite

matrix has been investigated on a possibility of improvement in long-term creep strength [4-9]. Kimura et al. reported that the creep strength of the 15Cr ferritic steels could be improved by additions of tungsten and cobalt through precipitation-strengthening effects of intermetallic compounds and carbide [4-6]. Moreover, carbon and nitrogen concentrations affected on stability of the microstructures in the 15Cr ferritic steels, and the long-term creep strength was increased through small coarsening rates of fine particles and homogeneous distribution in the precipitations [7]. Impact toughness of the precipitation-strengthened 15Cr ferritic steels with 3mass% of cobalt was improved by an addition of nickel and an increase in cooling rate from annealing temperature, although it has been pointed out that the 15Cr steels have the drawback of poor toughness due to the presence of the ferrite matrix [8]. However, the creep strength was slightly reduced by an addition of nickel [9]. Thus, the mechanical properties of the steel were strongly influenced by the composition of the metals. In the present study, the effect of combination of nickel and cobalt addition in the 15Cr steels was investigated on the mechanical properties and the microstructure.

2. Experimental procedure

The base material was 0.05C-15Cr-1Mo-0.2V-0.05Nb-6W-0.04N-0.003B (mass%) steel, and the test steels contain several composition of cobalt and nickel as shown in Table 1. These steels were prepared in a vacuum induction furnace. Ingots with a weight of 10 kg were hot forged and solution-treated for 30 min at 1473 K followed by water-quenching. The dimensions of the creep test specimen were 6 mm in gauge diameter and 30 mm in gauge length according to Type 14A of the Japanese Industrial Standard (JIS) Z 2201 [10]. Creep tests were conducted at 923 K and a range of stresses from 120 to 300 MPa in air. Creep deformation was measured using an extensometer attached to the gauge portion of the specimen. The microstructure of the steels was examined by an optical microscope (OM). The microstructure of the creep ruptured specimen was observed by a scanning electron microscope (SEM), and the compositions of the matrix and the precipitates were measured using an energy-dispersive X-ray fluorescence spectrometry (EDX). The precipitates in the creep ruptured specimen were identified by X-ray diffraction analysis of electrolytically extracted residues obtained from the steels.

Table 1 Typical chemical compositions of the steels used in the present study (mass%).

	C	Cr	Ni	Co	Mo	W	V	Nb	N	B
2Co-0.8Ni	0.051	15.16	0.86	1.96	1.03	6.03	0.21	0.06	0.037	0.0031
2Co-1.4Ni	0.048	15.13	1.41	1.99	1.03	6.02	0.21	0.058	0.037	0.0031
2Co-2.1Ni	0.051	15.07	2.15	2.04	0.98	6.03	0.21	0.054	0.036	0.0031
3Co	0.046	15.00	<0.01	2.96	1.00	6.07	0.19	0.043	0.033	0.0030
3Co-0.8 Ni	0.048	15.00	0.78	2.96	1.00	6.05	0.20	0.050	0.042	0.0029
3Co-1.2 Ni	0.049	15.02	1.21	2.96	1.00	6.04	0.20	0.051	0.042	0.0028
3Co-1.6 Ni	0.048	15.00	1.60	2.95	1.00	6.03	0.20	0.050	0.044	0.0026
3Co-2.0 Ni	0.048	14.96	2.00	2.98	1.00	6.07	0.20	0.050	0.036	0.0029

3. Results and discussion

Figure 1 shows optical micrographs of the 15Cr steels containing (a) 2Co-0.8Ni, (b) 2Co-1.4Ni, (c) 2Co-2.1Ni, (d) 3Co, (e) 3Co-1.2Ni and (f) 3Co-2.0Ni (mass%) after solution-treated at 1473 K for 30 min followed by water-quenching. V_f inserted on each micrograph indicates the volume fraction of the martensite phase with block and packet boundaries. Volume fraction of the martensite phase increased with increasing nickel content, which is an austenite stabilizing element. The grain size of the ferritic phase was reduced as a result of increase in marrtensite phase. It is clear that volume fraction of the martensite phase in the15Cr steels containing 3mass%Co is larger than that in the 2mass%Co addition.

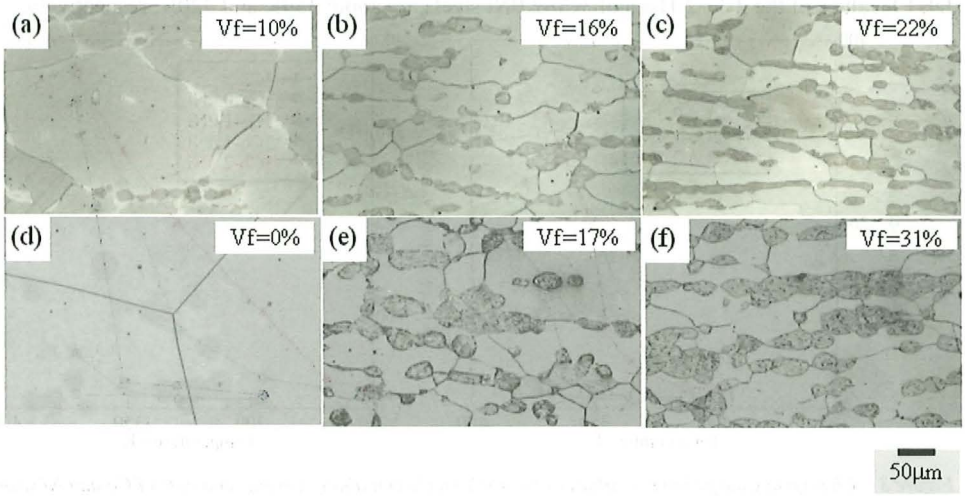

Figure 1 Optical micrographs of the 15Cr steels containing (a) 2Co-0.8Ni, (b) 2Co-1.4Ni, (c) 2Co-2.1Ni, (d) 3Co, (e) 3Co-1.2Ni and (f) 3Co-2.0Ni (mass%) after solution treatment at 1473K for 30min.

Tensile strength and 0.2% offset yield stress of the 15Cr steels were plotted against temperature as shown in Figure 2. The tensile strength at room temperature increases with nickel

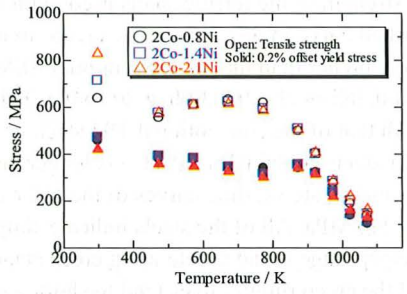

Figure 2 Tensile strength and 0.2% offset yield stress of the15Cr steels containing 2mass%Co and various Ni additions with test temperature.

addition. It can be thought that the marrtensite phase in the steel increases tensile strength. However, the tensile strength is almost the same over a range of temperatures from 473K to 800K. The tensile strength and the 0.2% offset yield stress decreases drastically with increase in temperature in excess of 850K.

Figure 3 shows change in Charpy impact values of the 15Cr steels containing various contents of cobalt and nickel with temperature. It is obvious that the impact toughness is improved by an increase in nickel contents, and the impact toughness of the steels containing 3mass%Co [8] is higher than that of the steels containing 2mass%Co. The ductile-brittle transition temperature (DBTT) was defined as temperature which corresponds with the average energy level of the both values in this study. The DBTT decreases with an increase in nickel and cobalt contents. The DBTT values of the 2Co-2.1Ni and 3Co-2.0Ni steels are about 350K and 320K, respectively.

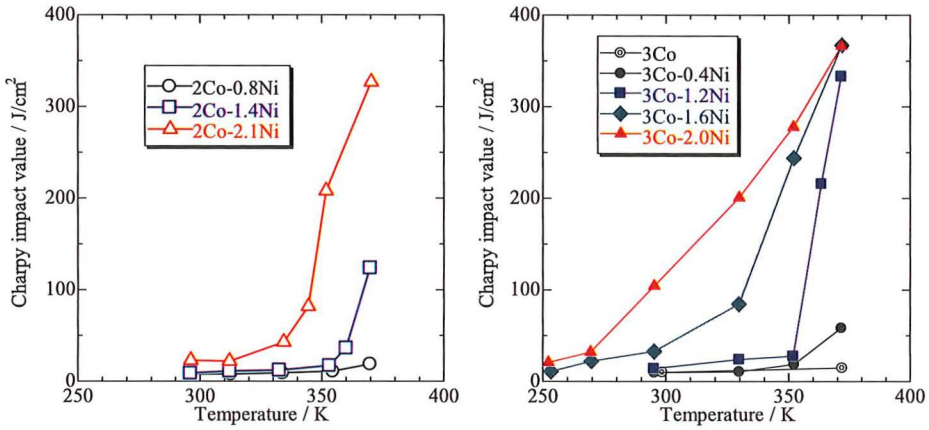

Figure 3 Change in Charpy impact values of the 15Cr steels containing various contents of Co and Ni with test temperature.

Figure 4 shows stress vs. time to rupture curves at 923K of the 15Cr steels with various nickel and cobalt contents. The curve of 9Cr-0.5Mo-1.8W-V-Nb steel (ASME T92), which is conventional ferritic heat-resistant steel with a tempered martensitic microstructure, and which possesses the highest creep strength of the ferritic steels used in the modern thermal power plant [11], was inserted by the dashed curve in this figure. The creep strength of the 15Cr steels containing cobalt is extremely higher than that of conventional ASME T92. For example, the creep rupture life of the 3Co-0.4Ni steel is 9203.6h at 200 MPa. This result indicates an increase of 1000 times, compared with that of the conventional T92 steel. At 923K and 240 MPa, the creep rupture life of the 15Cr steels contain 3mass% Co is longer than those of the steels with 2mass% Co. Figure 5 shows creep rate vs. time curves of the 15Cr steels with various cobalt and nickel contents at 923K and 240 MPa. All of the steels indicate simple creep behaviors, which change from the transition creep stage to the accelerating creep stage. The onset time of the accelerating creep stage and the creep rupture lives tend to shorten with an increase in cobalt content. Effect of nickel addition on the creep strength is complex due to the microstructure with different size, quantity and distribution of the precipitations at the elevated temperature.

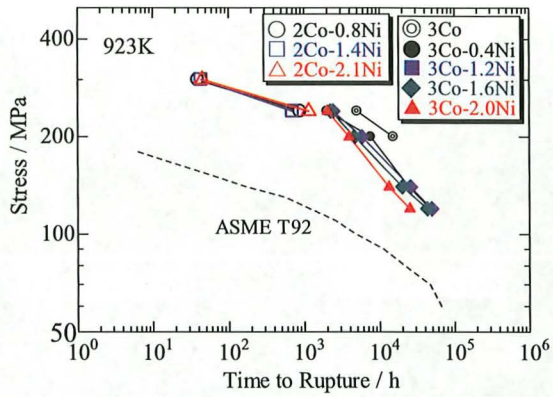

Figure 4 Stress vs. time to rupture curves of the15Cr steels with the various Co and Ni contents at 923K, and the conventional heat resistant steel at 923K.

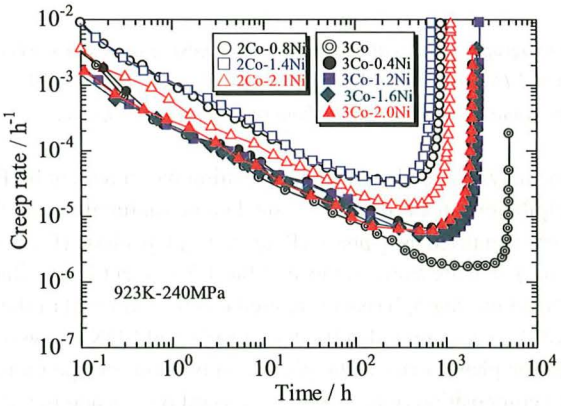

Figure 5 Creep rate vs. time curves of the 15Cr steels tested with the various Co and Ni contents at 923K and 240 MPa.

Figure 6 shows SEM micrographs (backscattered electron images) of the 15Cr steels containing (a) 2Co-0.8Ni, (b) 2Co-1.4Ni, (c) 2Co-2.1Ni, (d) 3Co-0.8Ni, (e) 3Co-1.6Ni and (f) 3Co-2.0Ni (mass%) creep ruptured at 923K-240MPa. The value (t_r) inserted in each image indicates time to rupture. Many particles smaller than 1 μm were precipitated in the ferritic matrix except for martensitic phase. The particles precipitated in the ferritic matrix of the steels containing 3mass% Co are more fine and homogeneous distribution, compared with those of the steels containing 2mass% Co. Moreover, another precipitation with gray color aggregated in the grain boundaries between ferritic and martensitic phases.

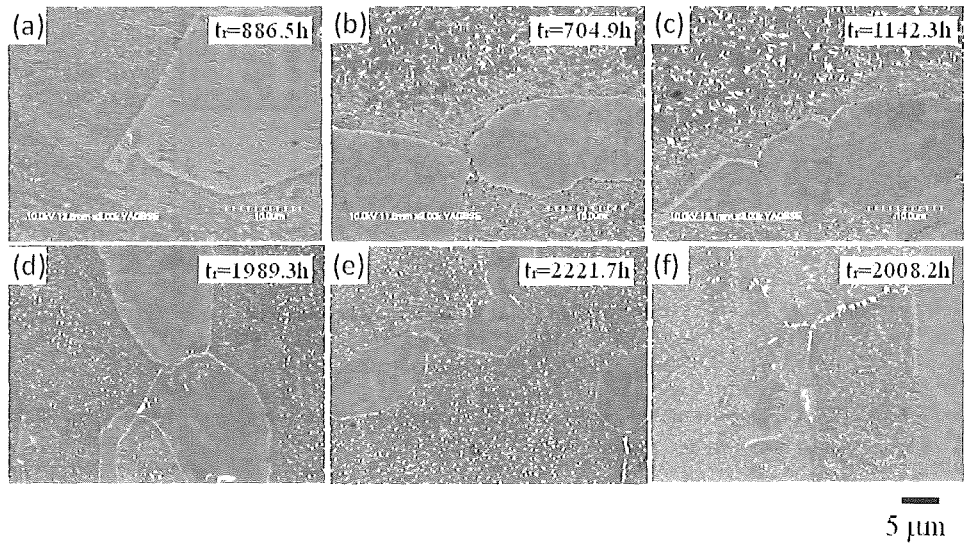

Figure 6 SEM micrographs (backscattered electron images) of the 15Cr steels containing (a) 2Co-0.8Ni, (b) 2Co-1.4Ni, (c) 2Co-2.1Ni, (d) 3Co-0.8Ni, (e) 3Co-1.6Ni and (f) 3Co-2.0Ni (mass%) creep ruptured at 923K-240MPa. The value of tr inserted each photo refers to time to rapture.

X-ray diffraction analysis and elemental composition measurement by EDX were conduced to identify the precipitations in a typical 15Cr steel creep ruptured. From XRD analysis, the precipitations were identified as χ-phase ($Fe_{36}Cr_{12}W_{10}$), μ-phase (Fe_7W_6), Laves phase (Fe_2W) and carbide ($M_{23}C_6$), and are same as those of the 15Cr steel (3Co) without nickel addition [9]. Figure 7 shows SEM micrograph (backscattered electron images) of the 15Cr steel containing of 2Co-2.1Ni (mass%) creep ruptured at 923K-240MPa and EDX analysis points. EDX analysis conducted for ferritic phase, martensitic phase and two kinds of precipitations. Table 2 shows average chemical composition (mass%) of the several phases and the precipitations. It is clear that, P1 and P2 are the ferritic and the martensitic phases, respectively. The precipitations with gray color in grain boundary (P3) could be identified as the carbide. It can be derived that the carbide is acting as obstacles for the movement of grain boundaries. The fine and cohered precipitations with white color (P4) could be assumed as the Laves phase and the χ-phase. The typical Laves phase particles appear normally on the grain boundary or in the centre of the grains, and the additions of W and Mo promote clearly the Laves phase precipitation on high Cr content steels such as 9Cr steels [2]. The elemental compositions of these precipitations (P3 and P4) are almost same as those of the precipitations of the 15Cr steel (3Co) without Ni addition [9].

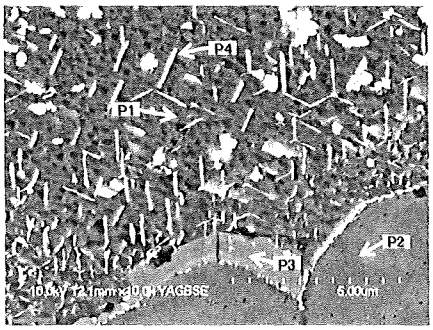

Figure 7 SEM micrograph (backscattered electron images) of the 15Cr steel containing of 2Co-2.1Ni (mass%) creep ruptured at 923K-240MPa. P1, P2, P3 and P4 show the typical EDX analysis points.

Table 2 Average chemical composition (mass%) of several points in the 15Cr steel containing of 2Co-2.1Ni (mass%) creep ruptured at 923K and 240MPa.

Element	P1	P2	P3	P4
Fe	70.5	71.9	44.9	46.1
Cr	14.8	14.6	36.4	11.9
Co	2.6	2.7	1.7	1.9
Ni	1.8	2.4	1.4	1.7
Mo	1.2	0.9	2.2	4.4
W	7.9	6.3	11.2	32.6

Consequently, it was found that mechanical properties and microstructure of the 15Cr steels are strongly influenced by nickel and cobalt additions. A nickel addition caused decrease in grain size of ferritic phase as a result of increase in marrtensite phase. In the creep ruptured specimen, the precipitates of intermetallic compounds in the ferritic phase and carbide on the grain boundary between ferritic and marrtensite phases increased with nickel addition. On the other hand, an increase in cobalt addition led to fine particles and homogeneous distribution of the precipitations in the ferritic phase. The mechanical properties, therefore, were improved by precipitation strengthening of the intermetallic compounds and the carbide in the15Cr steels. Charpy impact toughness of the 3Co-2.0Ni steel has maximum value, and creep strength of the 3Co steel is highest at 923K and 240 MPa. Thus, addition of cobalt and nickel in the 15Cr steels need to consider relation of tradeoff between the impact toughness and the creep strength.

4. Conclusions

The effect of Ni and Co addition in the 15Cr ferritic steels with ferrite matrix was investigated on the mechanical properties and the microstructure. Addition of Ni and Co was improved the Charpy impact toughness and the creep strength of the 15Cr steels. The creep strength is higher

than that of the conventional 9Cr ferritic steels (T92). The mechanical properties particularly depend on the microstructure of the steels. Decreasing grain size of the ferritic matrix and increasing martensite phase were enhanced by Ni and Co addition. On the 15Cr steels creep ruptured, fine particles of the intermetallic compounds, which have size of sub-micron, precipitated in the ferritic matrix, and the carbide precipitated on the grain boundaries. An increase in Co addition led to precipitation of the fine particles and homogeneous distribution in the ferritic matrix. Thus, precipitation strengthening of the intermetallic compounds and the carbide was advanced the mechanical properties of the15Cr steels.

Acknowledgements

A part of this work was financially supported by Grant-in-Aid for Scientific Research (KAKENHI) (B) 20360323.

References

[1] F. Masuyama, 'History of Power Plants and Progress in Heat Resistant Steels',*ISIJ Int.*, **41**, 612-625, (2001).

[2] H. Cerjak, P. Hofer and B. Schaffernak, 'The Influence of Microstructural Aspects on the Service Behaviour of Advanced Power Plant Steels', *ISIJ Int.*, **39,** 874-888, (1999).

[3]K. Kimura, H. Kushima and F. Abe, 'Heterogeneous Changes in Microstructure and Degradation Behaviour of 9Cr-1Mo-V-Nb Steel During Long Term Creep', *Key Eng. Mater.*, **171-174**, 483-490, (2000).

[4]K. Kimura, K. Seki, Y. Toda and F. Abe, 'Development of High Strength 15Cr Ferritic Creep Resistant Steel with Addition of Tungsten and Cobalt', *ISIJ Int.*, **41**, S121-S125, (2001).

[5]Y. Toda, K. Seki, K. Kimura and F. Abe, 'Effects of W and Co on the Microstructure and Creep Strength of the Precipitation Strengthend 15Cr Ferritic Steels', *JSME Int. J.*, **A45**, 25-29, (2002).

[6]Y. Toda, K. Seki, K. Kimura and F. Abe, 'Effects of W and Co on Long-term Creep Strength of Precipitation Strengthend 15Cr Ferritic Heat Resistant Steels', *ISIJ Int.*, **43**, 112-118, (2003).

[7] Y. Toda, H. Tohyama, H. Kushima, K. Kimura and F. Abe, 'Improvement in Creep Strength of Precipitation Strengthend 15Cr Ferritic Steel by Controlling Carbon and Nitrogen Contents', *JSME Int. J.*, **A48**, 35-40, (2005).

[8] Y. Toda, H. Tohyama, H. Kushima, K. Kimura and F. Abe, 'Influence of Chemical Composition and Heat Treatment Condition of Impact Toughness of 15Cr Ferritic Creep Resistant Steel', *JSME Int. J.*, **A48**, 125-131, (2005).

[9] Y. Toda, M. Iijima, H. Kushima, K. Kimura and F. Abe, 'Effects of Ni and Heat Temperature on Long-term Creep Strength of Precipitation Strengthend 15Cr Ferritic Heat Resistant Steels', *JSME Int. J.*, **45**, 1747-1753, (2005).

[10] Japanese Industrial Standard, "Test Pieces for Tensile Test for Metallic Materials: JIS Z 2201," Japanese Standard Association, Tokyo, (1998).

[11] Data Package for NF616 Ferritic Steel (9Cr-0.5Mo-1.8W-Nb-V), Second Edition, Nippon Steel Corporation, Tokyo, (1994).

9th Liege Conference : Materials for Advanced Power Engineering 2010
edited by J. Lecomte-Beckers, Q. Contrepois, T. Beck and B. Kuhn.

CREEP STRENGTH AND RUPTURE DUCTILITY OF CREEP STRENGTH ENHANCED FERRITIC STEELS

Hideaki Kushima, Kota Sawada and Kazuhiro Kimura

National Institute for Materials Science
1-2-1, Sengen, Tsukuba, Ibaraki 305-0047, Japan

Abstract

Creep strength and rupture ductility of Creep Strength Enhanced Ferritic (CSEF) steels were investigated from a viewpoint of stress dependence in comparison with conventional low alloy ferritic creep resistant steels. Inflection of stress vs. time to rupture curve was observed at 50% of 0.2% offset yield stress for both CSEF and conventional ferritic steels. Creep rupture ductility tends to decrease with increase in creep exposure time, however, those of conventional low alloy steels indicate increase in the long-term. Creep rupture ductility of the ASME Grades 92 and 122 steels indicates drastic decrease with decrease in stress at 50% of 0.2% offset yield stress. Stress dependence of creep rupture ductility of the ASME Grades 92 and 122 steels is well described by stress ratio to 0.2% offset yield stress, regardless of temperature. Drop of creep rupture ductility is caused by inhomogeneous recovery at the vicinity of prior austenite grain boundary, and remarkable drop of creep rupture ductility of CSEF steels should be derived from those stabilized microstructure.

Keywords: creep, rupture ductility, ferritic steel, 0.2% offset yield stress, recovery

1. Introduction

Creep strength enhanced ferritic (CSEF) steels have been widely used in Ultra Supercritical (USC) thermal power plant as high temperature structural components such as header and main/reheat steam pipe because of its improved creep strength. Energy efficiency of thermal power plant has been increased by increasing steam temperature and pressure from Supercritical to USC conditions, and it has been contributing to reduce CO_2 emission and to save energy resources. However, unexpected drop in creep rupture strength [1-3] and remarkable drop in creep rupture ductility in the long-term [4] have been reported. Many investigations have been conducted on microstructural change of CSEF steels during creep exposure in order to understand a mechanism of creep rupture strength drop. Precipitation and coarsening of Z-phase have been pointed out as an important cause of degradation, since it is a complex nitride of chromium, niobium and vanadium, therefore, it results in disappearance of fine MX carbonitride particles [2, 5-10]. On the other hand, Kimura et al. pointed out an influence of stress on creep strength property and proposed a region splitting analysis method for creep rupture life assessment [11, 12]. According to a region splitting analysis, creep rupture data is divided into two regimes with a boundary condition of 50% of 0.2% offset yield stress (hereinafter referred to as a half yield) and creep rupture life in each regime is evaluated independently. Since a half yield is considered to be a proportional limit stress [12-14], creep strength property seems to be different in two regimes. In the present study, not

only creep rupture strength, but also creep rupture ductility of CSEF steels and conventional low chromium steels have been investigated from a viewpoint of stress dependence.

2. Experimental procedure

Three groups of creep strength enhanced ferritic (CSEF) steels of ASME Grades 91 [15], 92 [16] and 122 [17] and two conventional low alloy of 2.25Cr-1Mo steel [18] and 1Cr-1Mo-0.25V steel [19] were used. 2.25Cr-1Mo steels were quenched and tempered plate with a tempered martensite microstructure and 1Cr-1Mo-0.25V steels were taken from turbine rotor with a bainite microstructure. Chemical composition and heat treatment condition of the steels are described in the NRIM/NIMS Creep Data Sheets [15-19]. Creep test data over a range of temperatures from 500 to 650°C were used for low alloy steels and the creep data up to 700°C were investigated on CSEF steels. Tensile test was conducted under a constant nominal strain rate of 5×10^{-5} s^{-1} up to about 2% of total strain and 0.2% offset yield stress was evaluated, then it was increased to 1.25×10^{-3} s^{-1} in order to evaluate tensile strength. Vickers hardness was measured under a load of 98N on CSEF steels in the as tempered condition and head portion of the creep ruptured specimens.

3. Results and Discussion

3.1. Creep rupture strength

Stress vs. time to rupture curves of (a) 2.25Cr-1Mo steels, (b) 1Cr-1Mo-0.25V steels, (c) Grade 91, (d) Grade 92 and (e) Grade 122 steels are shown in Figure 1. Slope of the stress vs. time to rupture curve of 2.25Cr-1Mo steel (a) becomes steeper at about 10,000h and 1,000h at 500 and 550°C, respectively, and that in the low stress long-term regime is almost the same over a range of temperatures from 500 to 650°C. That of 1Cr-1Mo-0.25V steel (b) also changes from gentle to steep at about 10,000h at 550°C. Linear relationship of stress and time to rupture is observed on Grade 91 steels (c) at 500°C, however, slope of the curves becomes steeper in the long-term at 550°C and above. Similar trend is also observed on Grades 92 (d) and 122 steels (e). An overall aspect of stress dependence of the time to rupture, that is change from large stress dependence to small one with decrease in stress and increase in temperature, is a common feature for all the steels qualitatively.

Creep rupture life of the steels shown in Fig. 1 are plotted against a yield ratio, and shown in Figure 2. Relation between yield ratio and time to rupture indicates inflection and slope of the curve changes from gentle in the high yield ratio regime to steeper in the low yield ratio regime. An inflection of that is observed at about 0.5 of yield ratio for not only CSEF steels [14, 20], but also conventional low alloy ferritic steels [12]. Since the half yield corresponds empirically a proportional limit stress, that is a macroscopic elastic limit stress, inflection should be caused by difference in creep deformation mechanism in the high- and low-yield ratio regimes divided by a half yield. It should be considered, therefore, that correspondence

between the half yield and a macroscopic elastic limit stress is a mutual character for ferritic steel with bainitic and/or martensitic microstructures. Region splitting analysis of creep rupture strength, in which creep rupture strength is evaluated separately for high- and low-yield ration regimes with a boundary condition of half yield, should be applied for not only CSEF steels, but also conventional low alloy ferritic steels.

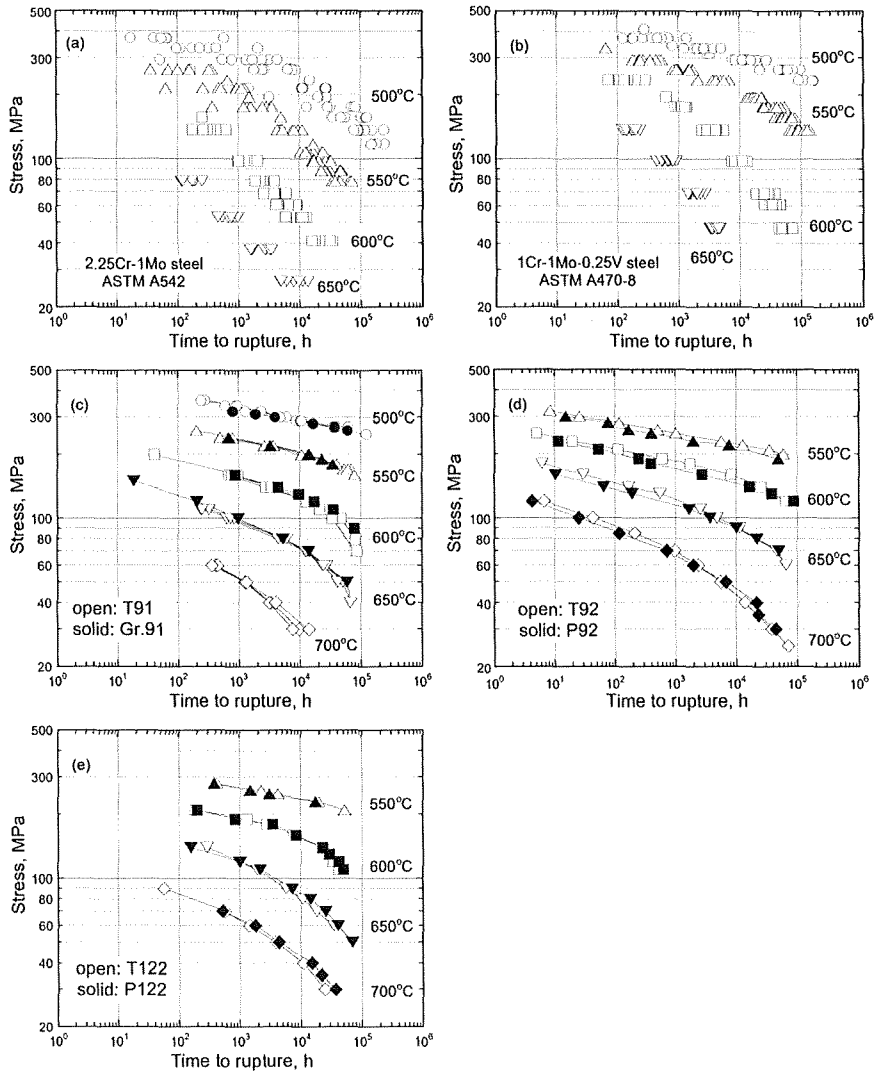

Figure 1 Stress vs. time to rupture curves of the steels studied.

3.2. Creep rupture ductility

Appearance of creep ruptured specimens of Grades T91, T92 and T122 steels crept for about 1,000 hours and 22,000 to 34,000 hours at 600°C are shown in Figure 3. Good rupture ductility with necking is observed for the specimens creep ruptured after about 1,000 hours of all the grades. On the other hand, similar good rupture ductility is observed only on T91 steel

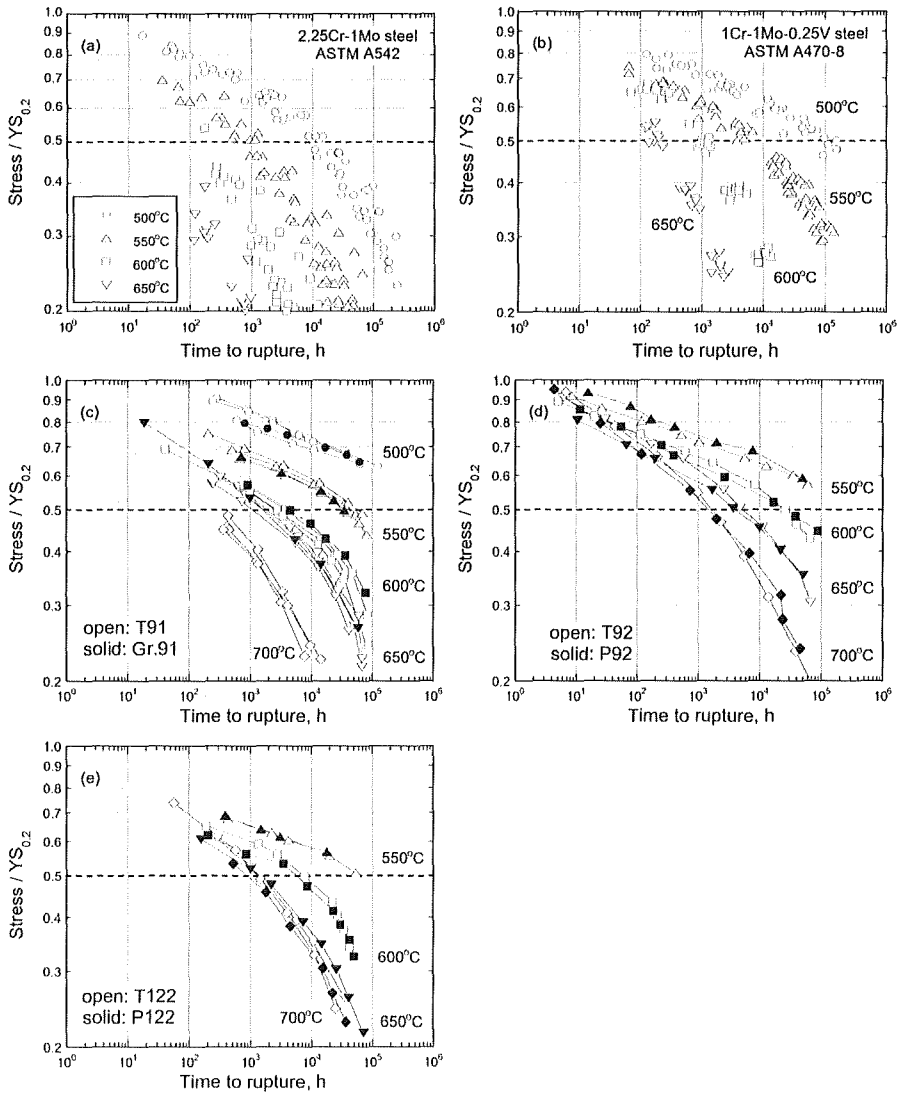

Figure 2 Creep rupture life vs. yield ratio of the steels studied.

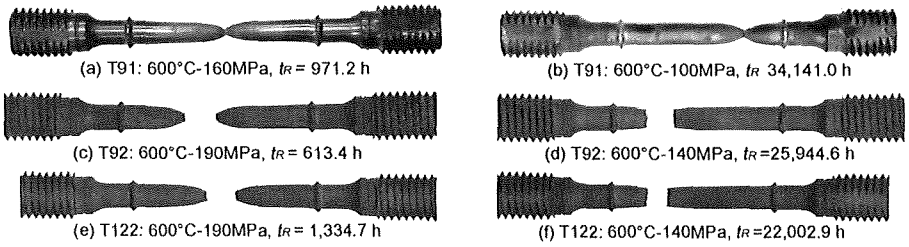

Figure 3 Appearance of creep ruptured specimen of Grades (a, b) 91, (c, d) 92 and (e, f) 122.

and the other two grades of T92 and T122 steels indicates poor rupture ductility. Grade T92 steel shows remarkable drop in creep rupture ductility with increase in creep exposure time and this is important issue of the CSEF steels [4].

Reduction of area of (a) 2.25Cr-1Mo steels, (b) 1Cr-1Mo-0.25V steels, (c) Grade 91, (d) Grade 92 and (e) Grade 122 steels are plotted against time to rupture and shown in Figure 4. Widely scattered creep rupture ductility is observed from short-term to long-term for (a) 2.25Cr-1Mo steels. On the other hand, reduction of area of the other steels is large in the short-term and it decreases with increase in creep exposure time. As a result of remarkable drop in reduction of area, it is widely distributed from very low value to high value in the long-term for all the steels.

In order to investigate the influence of stress and yield ratio on creep rupture ductility, reduction of area shown in Fig.4 are plotted against a yield ratio and shown in Figure 5. It is clearly recognized that creep rupture ductility depends on yield ratio rather than time to rupture, and yield ratio dependence of that is not the same for all the steels. Reduction of area of 2.25Cr-1Mo steel decreases with decrease in yield ratio and then turns to increase after indication of minimum value in the range of yield ratio from 0.3 to 0.6, with some exceptions. That of 1Cr-1Mo-0.25V steel is larger than 60% in the range of yield ratio higher than 0.6, however, it is widely scattered from 10 to 90% in the range of yield ratio from 0.4 to 0.3 and the minimum value of it increases with further decrease in yield ratio.

A remarkable drop in reduction of area is observed on T91 steels in the yield ratio of 0.4 and below. On the other hand, abrupt decrease in reduction of area is observed at half yield for Grades 92 and 122 steels independent of temperatures. Since reduction of area decreases to almost 0%, a sharp decline of reduction of area is appeared prominently in Grade 92 steels rather than the other steels. Not only an effect of microstructural evolution during long-term creep exposure, but also an influence of stress on creep rupture ductility should be considered, since a half yield is considered to be a proportional/elastic limit.

3.3. Influence of recovery

It has been found that creep rupture ductility is strongly influenced by not only creep exposure time, but also stress condition as a yield ratio, and its yield ratio dependence is different for every type of steels. In this section, large drop in creep rupture ductility in the long-term is discussed from a viewpoint of microstructural change during creep exposure.

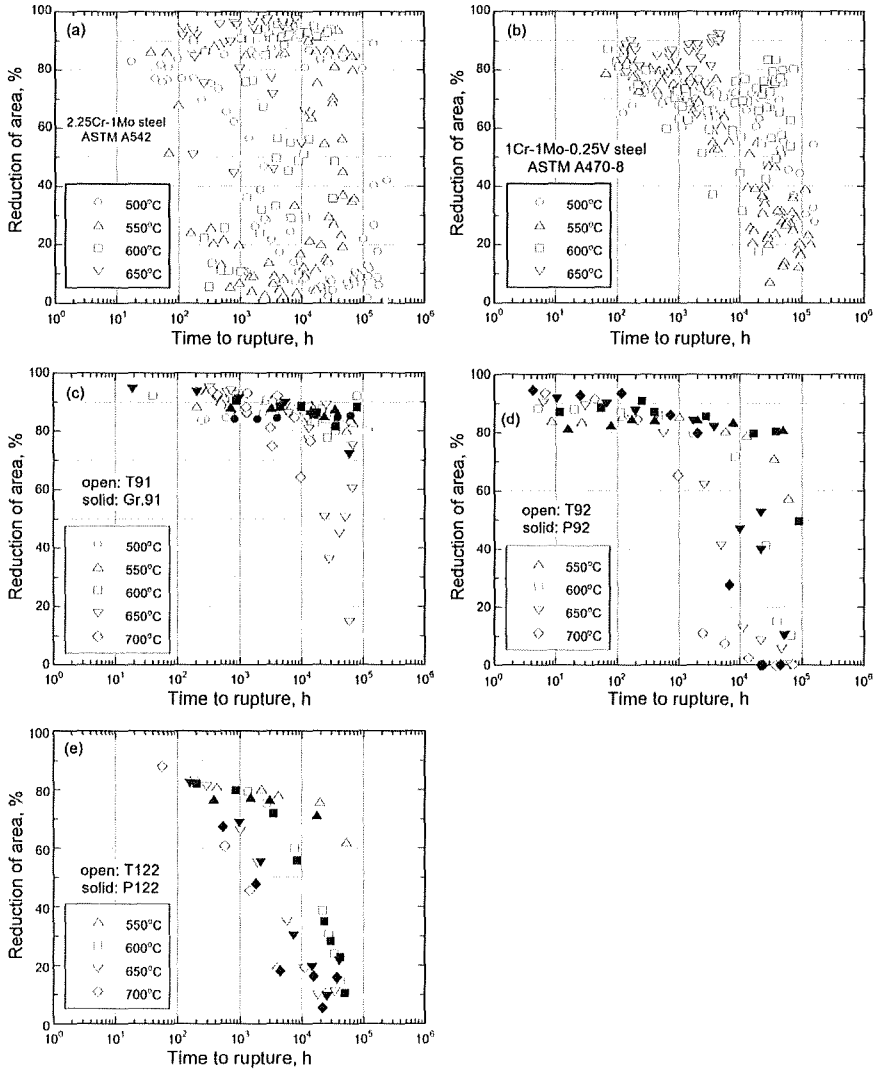

Figure 4 Reduction of area of (a) 2.25Cr-1Mo steels, (b) 1Cr-1Mo-0.25V steels, (c) Grade T91/Gr.91, (d) Grade T92/P92 and (e) Grade T122/P122.

Bright field TEM image of the T91 steel creep ruptured after 34,141.0h at 600°C and 100MPa is shown in Figure 6 [3]. Significantly recovered area is observed along the prior austenite grain boundary (PAGB), however, the microstructure in the grain interior is still fine in comparison with that in the vicinity of PAGB. Similar phenomenon of preferential recovery in the vicinity of PAGBs has been also reported on 1Cr-1Mo-0.25V turbine rotor steel with a bainitic microstructure as a degradation mechanism during long-term creep exposure [21].

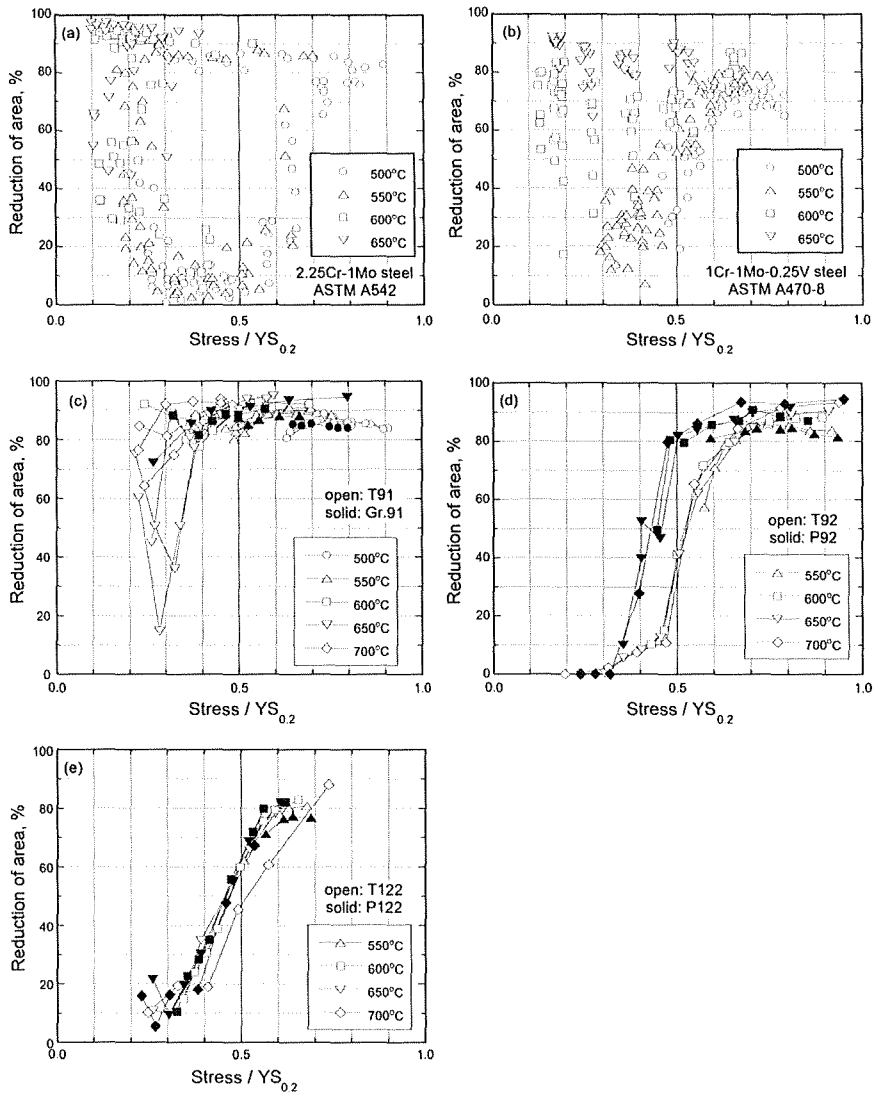

Figure 5 Reduction of area vs. yield ratio of (a) 2.25Cr-1Mo steels, (b) 1Cr-1Mo-0.25V steels, (c) Grade T91/Gr.91, (d) Grade T92/P92 and (e) Grade T122/P122.

Reduction of area of the 2.25Cr-1Mo and 1Cr-1Mo-0.25V steels plotted against a Larson-Miller parameter (LMP, C=20) is shown in Figure 7. Reduction of area of the steels decreases with increase in LMP and turns to increase after showing a minimum value. In the high-stress plastic regime, creep deformation easily takes place homogeneously within grain interior with the assistance of external stress higher than the elastic limit, however, dislocation motion is restricted by many boundaries of lath, block, packet and prior austenite grain in the low-stress elastic regime. Remarkable drop in creep rupture ductility is considered to be caused by an inhomogeneous recovery, since creep deformation is concentrated in the tiny area. It turns to increase after long-term creep exposure as a result of recovery of overall microstructure.

Changes in Vickers hardness in the specimen head portion of T91 and T92 steels with increase in time to rupture at 600°C are shown in Figure 8. A slight decrease in hardness is observed on T92 steel in the short-term, however, it is almost constant independent of creep exposure time up to about 65,000h. On the other hand, hardness drop of T91 steel is larger than that of T92 steel in the long-term. It indicates that microstructural stability at the elevated

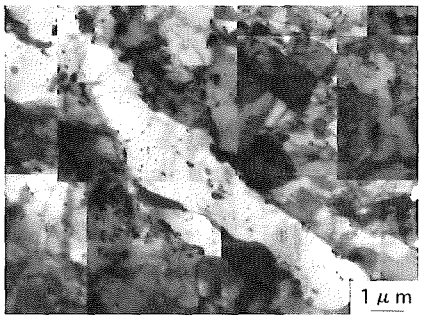

Figure 6 Bright field TEM image of MGC heat of Grade T91creep ruptured after 34,141.0h at 600°C and 100MPa [3].

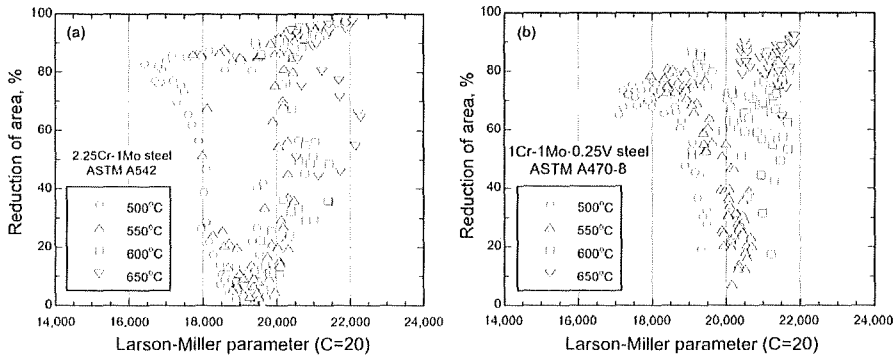

Figure 7 Reduction of area plotted against a Larson-Miller parameter (C=20) for (a) 2.25Cr-1Mo steels and (b) 1Cr-1Mo-0.25V steels.

temperature of T92 steel is higher than that of T91 steel and recovery of the former steel is slower than that of the latter one. It should be a cause of significant drop in rupture ductility of Grade 92 steels in the long-term, since concentration of creep deformation in a preferentially recovered tiny area is more pronounced.

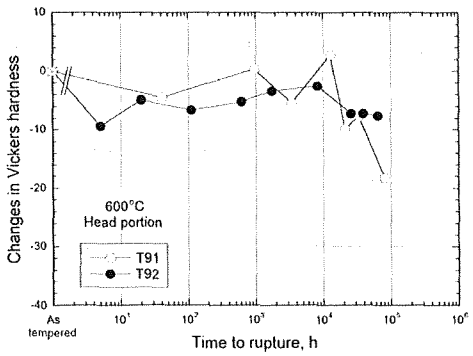

Figure 8 Comparison of changes in Vickers hardness of T91 and T92 in the specimen head portion with increase in time to rupture at 600°C [21].

4. Conclusions

Creep rupture strength and ductility of the creep strength enhanced ferritic steels and low alloy conventional one were investigated. Inflection of stress vs. time to rupture curves was observed at half yield for all the steels investigated. Decrease in creep rupture ductility in the long-term was observed on all the steels except for 2.25Cr-1Mo steel which indicates widely scattered rupture ductility in the wide range of time to rupture. Creep rupture ductility of low alloy steels decreased with increase in LMP and it changed to increase after showing minimum value. Significant drop in creep rupture ductility of Grades 92 and 122 steels was observed with decrease in yield ratio at half yield independent of temperature. It has been concluded that remarkable drop in creep rupture ductility at half yield of Grades 92 and 122 steels could be caused by a concentration of creep deformation in the inhomogeneously recovered tiny area.

Acknowledgement

A part of this study was financially supported by the Budget for Nuclear Research of the Ministry of Education, Culture, Sports, Science and Technology, based on the screening and counseling by the Atomic Energy Commission.

References

[1] V. Foldyna, Z. Kubon, M. Filip, K.H. Mayer, C. Berger, Evaluation of structural stability and creep resistance of 9-12% Cr steels, *Steel Res.*, 67, pp.375-381, (1996).
[2] A. Strang, V. Foldyna, A. Jakobova, Z. Kubon, V. Vodarek and J. Lenert, Factors Affecting the Prediction of the Long Term Creep Rupture Properties of Microstructurally Unstable 9-12% Cr Power Plant Steels, *Advances in Turbine Materials, Design and Manufacturing*, The Institute of Materials, London, pp.603-612, (1997).
[3] K. Kimura, H. Kushima and F. Abe, Heterogeneous Changes in Microstructure and Degradation Behaviour of 9Cr-1Mo-V-Nb Steel during Long Term Creep, *Key Engineering Materials*, 171-174, pp.483-490, (2000).
[4] J. Hald, Creep strength and ductility of 9 to 12% chromium steels, *Materials at High Temperatures*, 21, pp.41-46, (2004).
[5] J. Bursik and N. Merk, Quantitative Microstructural Assessment of P91 Ferritic Steel after Long Term Creep at High Temperature, *Proc. Mechanical Behaviour of Materials at High Temperature*, Kluwer Academic Publisher, Netherlands, pp.299-307, (1996).
[6] A. Strang and V. Vodarek, Z phase formation in martensitic 12CrMoVNb steel, *Mat. Sci. Tech.*, 12, pp.552-556, (1996).
[7] P. Hofer, H. Cerjak and P. Warbichler, Quantification of precipitates in a 10%Cr steel using TEM and EFTEM, *Mat. Sci. Tech.*, 16, pp.1221-1225, (2000).
[8] K. Kimura, H. Kushima, F. Abe, K. Suzuki, S. Kumai and A. Satoh, Microstructural Change and degradation behaviour of 9Cr-1Mo-V-Nb steel in the long term region, *Advanced Materials for 21st Century Turbines and Power Plant*, The Institute of Materials, London, pp.590-602, (2000).
[9] H.K. Danielsen and J. Hald, Behaviour of Z phase in 9-12%Cr steels, *Energy Mat.*, 1, pp.49-57, (2006).
[10] K. Sawada, H. Kushima, K. Kimura and M. Tabuchi, TTP Diagrams of Z Phase in 9-12% Cr Heat-Resistant Steels, *ISIJ Int.*, 47, pp.733-739, (2007).
[11] K. Kimura, H. Kushima and F. Abe, Degradation and Assessment of Long-term Creep Strength of High Cr Ferritic Creep Resistant Steels, *Proc. Int. Conf. Advances in Life Assessment and Optimization of Fossil Power Plants*, Orlando, Florida, (2002).
[12] K. Kimura, K. Sawada, K. Kubo and H. Kushima, Influence of Stress on Degradation and Life Prediction of High Strength Ferritic Steels, *Proc. 2004 ASME/JSME PVP Conf.*, San Diego, California, pp.11-18, (2004).
[13] K. Kimura, K. Sawada, H. Kushima and Y. Toda, Stress Dependence of Degradation and Creep Rupture Life of Creep Strength Enhanced Ferritic Steels, *Proc. Fifth Int. Conf. Advanced in Materials Technology for Fossil Power Plants*, Marco Island, Florida, (2007).
[14] K. Kimura, K. Sawada, H. Kushima and K. Kubo, Effect of Stress on the Creep Deformation of ASME Grade P92/T92 steels, *Int. J. Mat. Res.*, 99, pp.395-401, (2008).
[15] NRIM Creep Data Sheet, National Research Institute for Metals, No.43, (1996).
[16] NIMS Creep Data Sheet, National Institute for Materials Science, No.48, (2002).
[17] NIMS Creep Data Sheet, National Institute for Materials Science, No.51, (2006).
[18] NIMS Creep Data Sheet, National Institute for Materials Science, No.36B, (2003).
[19] NRIM Creep Data Sheet, National Research Institute for Metals, No.9B, (1990).

[20] K. Kimura, K. Sawada, H. Kushima and Y. Toda, Degradation Behaviour and Long-term Creep Strength of 12Cr Ferritic Creep Resistant Steels, *Proc. 8th Liege Conf., Materials for Advanced Power Engineering 2006*, pp.1105-1116, (2006).
[21] T, Matsuo, K. Kimura, R. Tanaka and M. Kikuchi, Degradation of 1Cr-1Mo-1/4V Steel at High Temperatures, *Proc. Fourth Int. Conf. Creep and Fracture of Engineering Materials and Structures*, Swansea, UK, pp.477-486, (1990).

9th Liege Conference : Materials for Advanced Power Engineering 2010
edited by J. Lecomte-Beckers, Q. Contrepois, T. Beck and B. Kuhn.

CREEP OF EX-SERVICE AISI-316H STEEL AT VERY LOW STRAIN RATES

Luboš Kloc[1], Michael Spindler[2] and Václav Sklenička[1]

[1]Institute of Physics of Materials v.v.i, Academy of Sciences of the Czech Republic
Žižkova 22, CZ-61662 Brno, Czech Republic
[2]British Energy Generation, Barnett Way, Barnwood, Gloucester, GL4 3RS, UK

Abstract

The creep response of ex-service Type 316H austenitic steel was investigated at temperatures from 470 to 550 °C and stresses from 80 to 120 MPa. These conditions lead to very low strain rates. Both helicoid spring specimen tests and conventional uniaxial creep tests were used to measure these very low creep strains. An internal stress model was used to analyse the creep curves and the results were compared to creep curves obtained on a Type 316H in the as-received condition, which for austenitic steels is after solution heat treatment. The creep behaviour of the ex-service steel was very similar to that of the as-received steel. Thus, no creep damage or significant change of microstructure was detected during the service period of 65,000 hours at ~520 °C . It was found that the helicoid spring specimen technique provides results compatible with that of conventional creep tests, but with superior accuracy with very low creep strains.

Keywords: low stress creep; primary creep; stress exponent; creep resistant steel;

1. Introduction

The process of creep deformation under conditions corresponding to the industrial use of steels is much slower than that found in normal laboratory testing. Laboratory experiments are usually accelerated by the application of higher temperature and/or stress. Such data are inevitably subject to extrapolation to give data for design and life assessment however, these extrapolations may be a source of error that could lead to non-conservative engineering assessments.

Extrapolation can particularly provide false results if the creep deformation mechanism changes. Examples of such changes at very low creep rates are given in [1-5]. Which show that in most cases, both the stress and temperature dependencies of the creep rate become weaker at low stresses. Furthermore, it is well known that the stable cavities, which can grow to cause creep failure, are nucleated mostly during primary creep [6]. Thereby, the primary stage may be an important indicator of overall creep properties. Thus, any models of creep deformation should be able to describe the primary creep stage correctly. Unfortunately, many current approaches tend to ignore the primary stage completely which makes their reliability questionable.

In order to measure primary creep at conditions close to real plant application, where the creep strains are very low, it is necessary to use high sensitivity creep techniques.

The aim of this work is to collect low strain rate creep data of the AISI-316H creep resistant steel after long-term service and to compare them to the similar results obtained on the same type of steel in the as-received (solution heat treated) condition.

2. Experimental material and procedure

Three different samples of the AISI-316H steel were used for creep tests; the majority of the experiments were carried out on the ex-service steel (Material A).

A) (Material A) Specimens from a thick section forging produced in the UK, cast number 69431. Solution treatment at 1050 °C for 3 hours followed by water quench. Service at between 490 and 530 °C for 65,000 hours with a hoop stress of approximately 45 MPa

B) (Material B) Specimens from new tubes produced by Sandvik A.B., heat no. 509885. Solution treatment at 1100 °C for 3 minutes and quickly cooled with water.

C) (Material C) Specimens from new tubes produced by Vítkovice Steel a.s., heat number and heat treatment details are not available.

Chemical composition of the steels is summarized in the table 1.

Material	Cr	Ni	Mo	Co	C	Si	Mn	P	S
A	17.2	11.6	2.3	0.07	0.07	0.39	0.98	0.024	0.017
B	16.9	11.25	2.04	0.089	0.05	0.53	1.55	0.029	0.0054
C	16.9	12.5	2.45		0.07	0.45	1.21	0.028	0.014

Table I: *Chemical composition of the steel in mass %, Fe is balance*

A helicoid spring specimen test technique [7] was employed for creep testing at 80 MPa. Purified argon was used for protective atmosphere to prevent oxidation since the technique is sensitive to surface quality. Helicoid spring specimens with square cross section of the "wire" were manufactured by careful machining from the tubes to preserve the original microstructure of the steel. Creep tests were conducted at temperatures from 470 to 550 °C . Since the state of stress in this testing technique is essentially shear the stresses and strains were converted to the equivalent tensile quantities using the von Mises criterion, that is $\sigma = \sqrt{3}\tau$ and $\varepsilon = \gamma/\sqrt{3}$.

Conventional uniaxial creep tests with extensometer gauge lengths of about 100 mm were used for testing at 120 MPa and temperatures from 470 to 525 °C .

3. Results

3.1. Helicoid spring specimens tests

Examples of creep curves recorded in the helicoid spring specimens experiments are shown in Figure 1. The curves were fitted by the elasto-plastic model of pre-primary creep [8]:

$$\varepsilon = a \log\left(\frac{\exp(bt) - c}{\exp(bt) + c} \cdot \frac{1+c}{1-c}\right) + dt$$

where ε is creep strain, t is time and a, b, c and d are parameters.

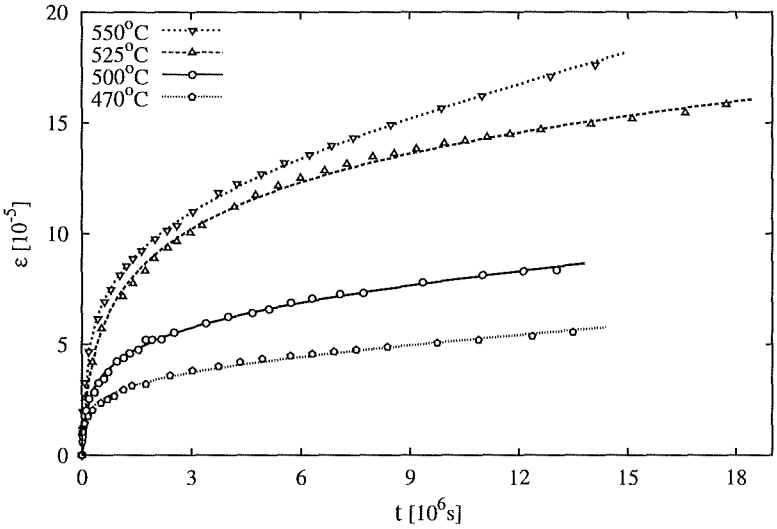

Fig. 1: *Creep curves of ex-service steel (A) at* 80 MPa. *Helicoid spring tests.*

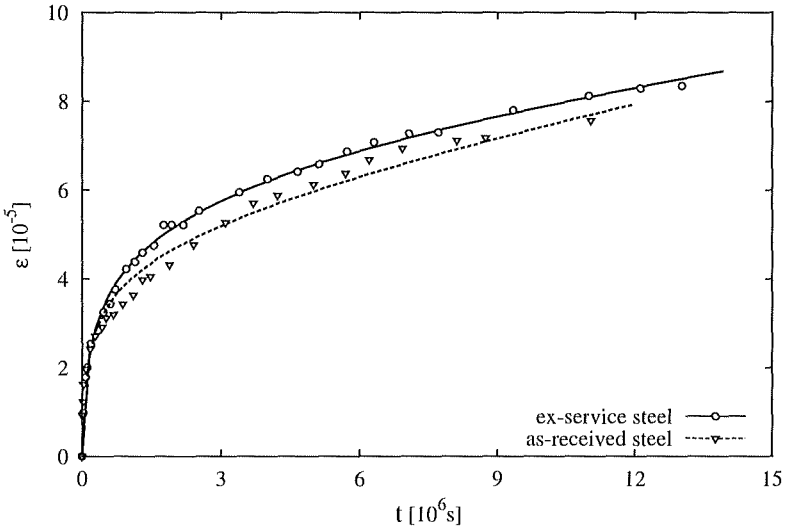

Fig. 2: *Creep curves of ex-service steel (A) and as-received steel (C) at* 500 °C *and* 80 MPa. *Helicoid spring tests.*

The model provides a good fit to the measured creep curves, as can be seen from Figures 1 to 4.

The creep curve of the ex-service steel (A) at 500 °C and 80 MPa is compared to that of the as-received steel (C) under the same conditions in Figure 2. It is clear that the creep behaviour of the two materials is practically identical.

3.2. Conventional uniaxial creep tests

Creep curves from conventional uniaxial creep tests on the ex-service steel are shown in Figure 3, and a comparison of the ex-service steel with the as-received steel is shown in Figure 4. The curves were fitted by the previous equation, though it is clear that the measurement errors due to extensometer instability and limited resolution do not allow for deeper analysis of creep behaviour. In this case, the as-received steel (B) creeps notably faster than the ex-service steel (A), but the transient strain is approximately equal.

4. Discussion

4.1. Creep curves

Creep curves of the AISI-316H steel at low temperatures and low stresses show typical pre-primary shape [9]. No considerable differences were found between the as-received and ex-service material. Thus the microstructure was stable during the service period of 65,000 hours at approximately 510 °C and 45 MPa. The creep behaviour is mostly affected by the initial composition and microstructure.

4.2. Creep rate

The creep rates were derived from the creep curves obtained from the helicoid spring testing technique using a moving parabola method. Results are shown in Figures 5 and 6. On the other hand, it is not possible to derive creep rate values from the uniaxial creep test curves due to large scatter of measured strains.

It is clear from the figures, that the creep strain is too small for the secondary stage to be reached. Nevertheless, the parameter d of the model equation can be taken as a rough estimate of "stabilized" creep rate. The value of d ranges from $1 \times 10^{-12}\,\mathrm{s}^{-1}$ to $6 \times 10^{-12}\,\mathrm{s}^{-1}$ for all creep curves. Since the stress ranges from 80 to 120 MPa, this yields the stress exponent to be $n \leq 4$.

The temperature dependencies of the creep rate at constant time or constant stress are given in Figure 7. The dependencies are relatively weak giving apparent activation energies of $Q_t = 87\,\mathrm{kJ/mol}$ and $Q_\varepsilon = 290\,\mathrm{kJ/mol}$. These values are considerably lower than that derived for common accelerated creep tests of the AISI-316H steel, where values of $Q \approx 400\,\mathrm{kJ/mol}$ and $n \approx 7$ are usually reported [4]. Thus the creep behaviour under the low stress and low temperature conditions used in this paper give weaker stress and temperature dependencies than those derived from normal laboratory creep test condition [4,5]. Thereby it is clear that the extrapolation of normal laboratory creep data to the conditions relevant to plant operation might give unrealistic engineering assessments.

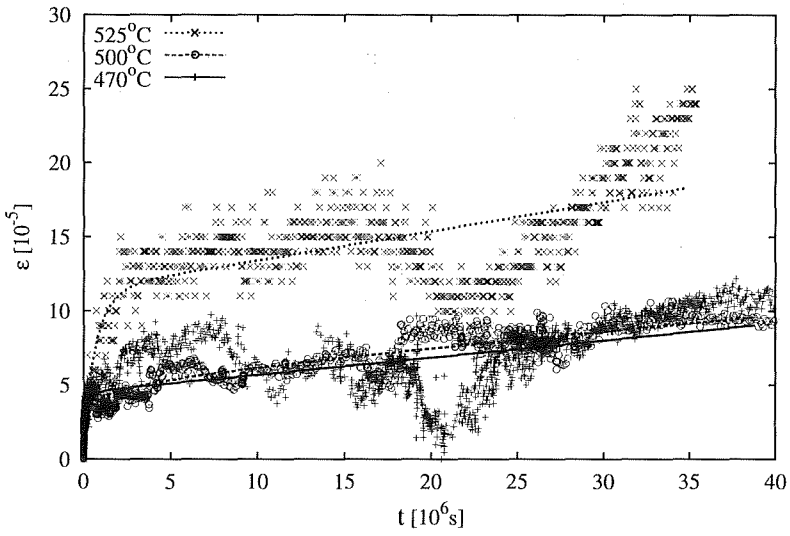

Fig. 3: *Creep curves of ex-service steel (A) at* 120 MPa. *Uniaxial tensile creep tests.*

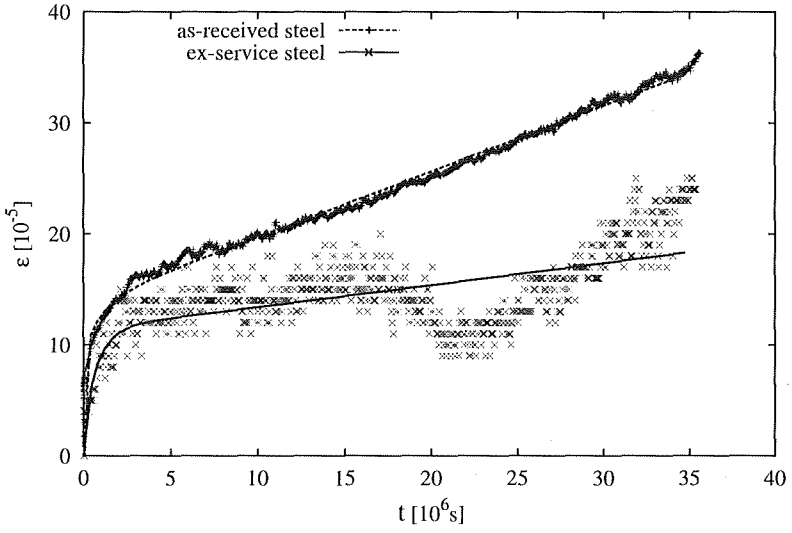

Fig. 4: *Creep curves of ex-service steel (A) and as-received steel (B) at* 525 °C *and* 120 MPa. *Uniaxial tensile creep tests.*

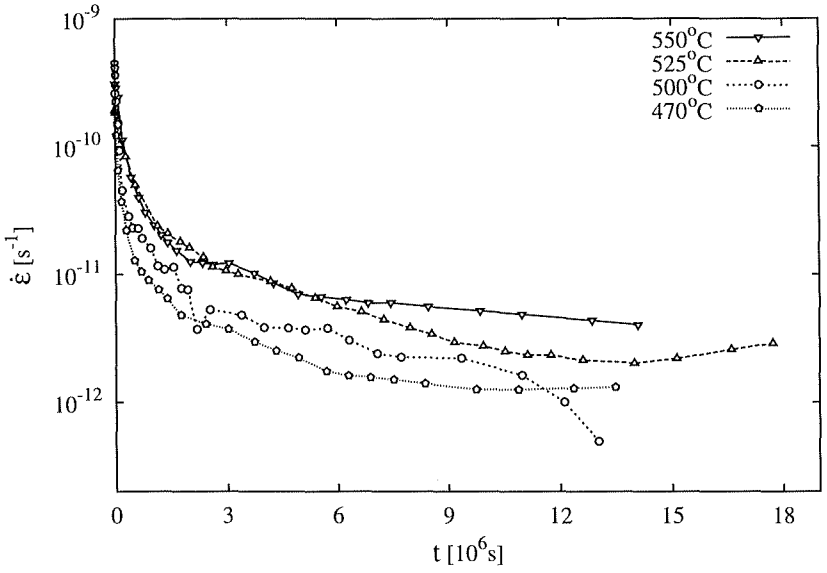

Fig. 5: Creep rates of the ex-service steel (A) at 80 MPa *evolving in time. Data for helicoid spring tests.*

5. Conclusion

Primary creep of ex-service AISI-316H steel was investigated at stresses from 80 to 120 MPa and temperatures between 470 and 550 °C . Some similar experiments were carried out on as-received steels of the same type for comparison. Results can be summarized as follows:

- No significant differences were found between creep curves of as-received and ex-service steels under the same conditions. Creep behaviour is dependent rather on initial constitution and microstructure; the microstructure is stable during service.
- No exhaustion of the transient creep mechanisms during service was observed.
- The dependency of the creep rate to the applied stress and temperature are weaker than those reported for conventional accelerated creep tests at higher stress and/or temperature. Thereby it is suggested that "low stress" creep deformation mechanisms should be taken into account. This means that simple extrapolation procedures may yield unrealistic estimations of creep properties when extrapolated to low stress and low temperature conditions.
- Conventional uniaxial creep tests results show high amounts of scatter due to the instability and limited resolution of extensometers, even when gauge lengths as long as 100mm are used. Thus, uniaxial tests are not reliable to measure very low creep strains. On the other hand, the helicoid spring specimen test technique provides smooth creep curves even with very low creep rates.

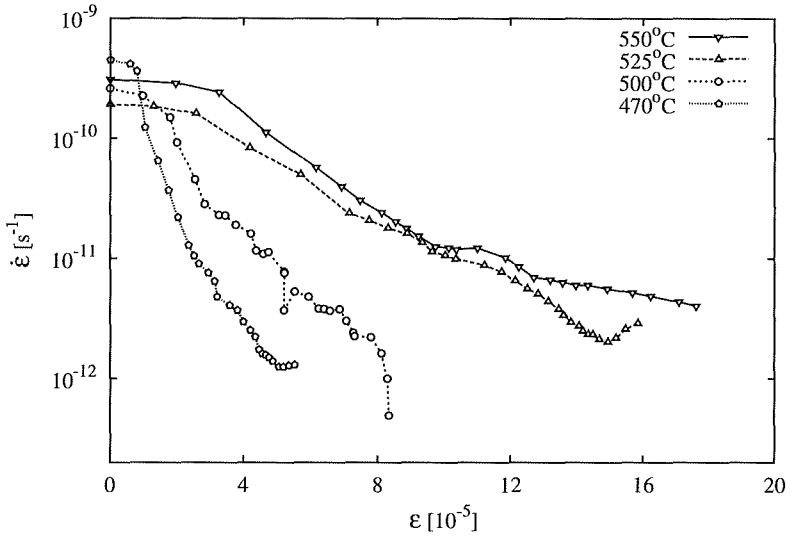

Fig. 6: *Creep rates of the ex-service steel (A) at* 80 MPa *plotted against creep strain. Data for helicoid spring tests.*

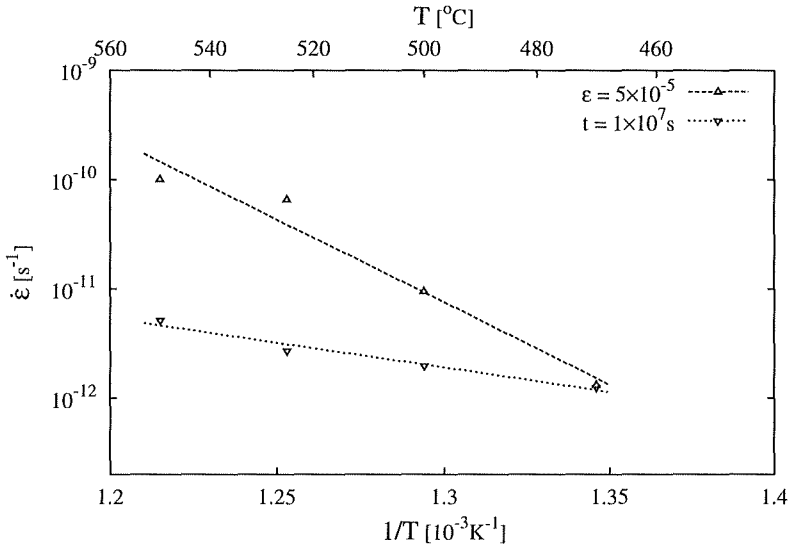

Fig. 7: *Temperature dependencies of creep rates at given time* $t = 10^7$ s *and given strain* $\varepsilon = 5 \times 10^{-5}$.

6. Acknowledgment

This paper is published by permission of British Energy Generation Ltd. Financial support by the Grant Agency of the Academy of Sciences of the Czech Republic under contract no. IAA200410701 is gratefully acknowledged.

References

[1] T. Sritharan and H. Jones, The creep of type 304 stainless steel at low stresses, *Acta Metall.* 28, 1633-1639, (1980).
[2] T. Sritharan and H. Jones, Creep of type 316 stainless steel at low stresses, *Metal Sci.* 15, 365, (1981).
[3] J. Fiala, L. Kloc and J. Čadek, Creep in Metals at Intermediate Temperatures and Low Stresses - A Review, *Mater. Sci. Eng. A* 137, 163-172, (1991).
[4] L.Kloc, V. Sklenička and J. Ventruba, Comparison of low stress creep properties of ferritic and austenitic creep resistant steels, *Mater. Sci. Eng. A* 319-321, 774-778, (2001).
[5] L. Kloc and V. Sklenička, Confirmation of low stress creep regime in 9% chromium steel by stress change experiments, *Mater. Sci Eng. A* 387-389, 633-638, (2004).
[6] A. S. Argon, Intergranular cavitation in creeping alloys, *Scripta Metall.* 17, 5-12, (1983).
[7] L. Kloc and P. Mareček, Measurement of very low creep strains, *J. Test. Eval.* 37, 53-57, (2009).
[8] L. Kloc, Internal stress model for pre-primary stage of low-stress creep, presented at ICSMA-15, Dresden 2009, to be published in *Journal of Physics: Conference Series.*
[9] L. Kloc and V. Sklenička, Pre-primary stage of low strain rate creep in metals, *Mater. Sci. Forum* 604-605, 351-356, (2009).

9th Liege Conference : Materials for Advanced Power Engineering 2010
edited by J. Lecomte-Beckers, Q. Contrepois, T. Beck and B. Kuhn.

Service-Cycle Component-Feature Specimen TMF Testing of Steam Turbine Rotor Steels

M Radosavljevic[1], E Mazza[1,2], P Grossmann[3], L Ripamonti[3] & S R Holdsworth[1]

[1] *EMPA: Swiss Federal Laboratories for Materials Testing & Research, Dübendorf*
[2] *ETH: Swiss Federal Institute of Technology, Zurich (Switzerland)*
[3] *ALSTOM Power (Ltd) Switzerland*

Abstract

This paper reviews the methodology adopted in a Swiss Research Collaboration to devise a component-feature representative specimen geometry and the TMF cycle parameters necessary to closely simulate arduous steam turbine operating duty. Implementation of these service-like experimental conditions provides a practical indication of the effectiveness of deformation and crack initiation endurance predictions. Comprehensive post test inspection provides evidence to demonstrate the physical realism of the laboratory simulations in terms of the creep-fatigue damage generated during the benchmark tests. Mechanical response results and physical damage observations are presented and their practical implications discussed for the example of a 2%CrMoNiWV rotor service cycle.

Keywords: Notched specimen, service-cycle TMF, 2%CrMoNiWV

1 Introduction

The adoption of advanced steels for the manufacture of newer high temperature steam turbine rotors has created a requirement to benchmark the latest analytical procedures developed to exploit the possible early introduction of such materials and to eliminate excessive conservatism in the design of locations prone to the accumulation of creep-fatigue. One solution is to perform service-cycle component-feature specimen thermo-mechanical fatigue (TMF) tests in the laboratory to represent the conditions experienced by such locations during operation.

A simplified representation of the common steps in a number of published creep-fatigue defect-free assessment procedures (e.g. [1-4]) is shown in Fig. 1. The component is fully assessed in terms of the external thermo-mechanical boundary conditions imposed during the operating lifetime, and these are used in conjunction with material constitutive equations to define the distribution of stress and strain throughout the structure. Having established the stress/strain state history at life limiting locations, cyclic and creep damage fractions (D_F and D_C) are determined by reference to the appropriate material endurance property data. The D_F and D_C fractions are finally compared with the crack initiation locus in a creep-fatigue damage assessment diagram and the risk of failure evaluated.

The locus in the creep-fatigue damage summation diagram is typically based on the results of cyclic/hold and/or low strain rate creep-fatigue test results (e.g. [5]). Verification of the effectiveness of complete creep-fatigue assessment procedures is typically based on the results of service experience and/or service-cycle component-feature specimen TMF tests.

The following paper describes the results of a Swiss Research Collaboration with the objective of devising the conditions for a service-cycle component-feature specimen TMF test

to provide experimental evidence to verify the effectiveness of creep-fatigue assessment procedures when applied to new steam turbine rotor applications.

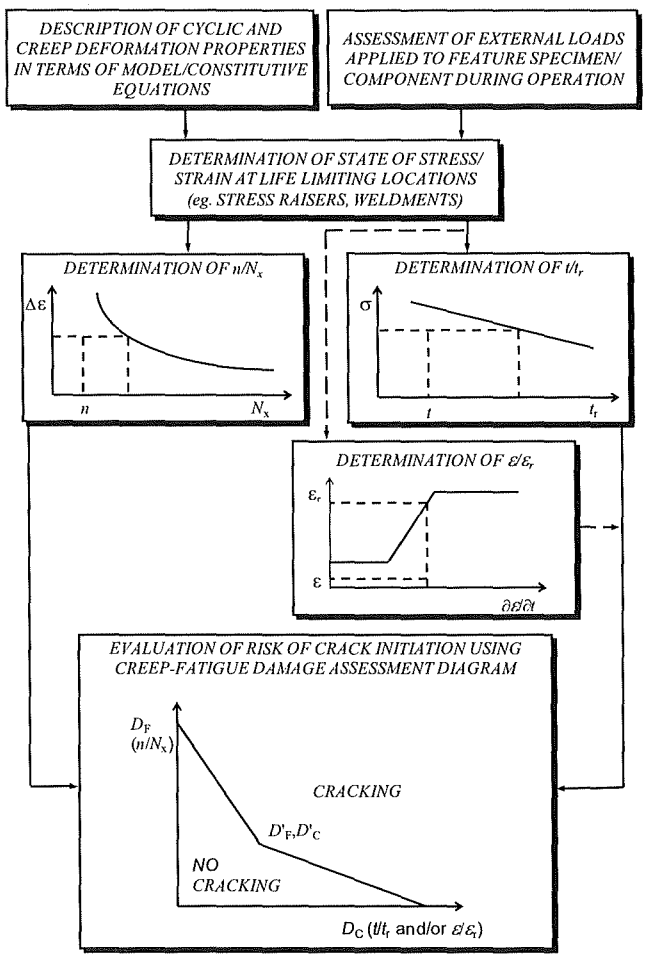

Fig. 1 Common steps in creep-fatigue assessment procedure

2 Benchmark Test Design

2.1 Concept

In this Research Collaboration, service-cycle component-feature specimen TMF test design involved the following steps:

i) Thermo-mechanical rotor analyses to identify the creep-fatigue life limiting (feature) location and operating cycle,

ii) Determination of the cyclic stress-strain hysteresis behaviour at the life limiting surface location, and the associated stress/strain states (at, and below the surface) in terms of:
- Mechanical strain range

– $\sigma_1/\bar{\sigma}_{VM}$ triaxiality factor, and
– Creep strain accumulated in tension per cycle

iii) Design of a laboratory cycle to replicate, as closely as possible, the rotor-feature in-service stress-strain hysteresis behaviour,

iv) Design of a laboratory specimen with a geometrical feature having the stress/strain characteristics (at, and below the groove root surface) to be as close as possible to those defined in *ii)*

Stress strain states were determined by FE analysis using Abaqus (re. [6] for laboratory specimen), and material property input parameters for the constitutive model equations described in the following sections.

2.2 State of Stress/Strain

2.2.1 Cyclic Plasticity

Time-independent and time dependent plastic strain accumulation were treated separately in the adopted model. Material parameters were dependent on loading history, and in particular the accumulated plastic strain. For this purpose, accumulated plastic strain was defined by:

$$\varepsilon_p = \int_0^t \sqrt{\frac{2}{3}\sum_i\sum_j \dot{\varepsilon}_{ij}^p.\dot{\varepsilon}_{ij}^p}\,.\mathrm{d}t \tag{1}$$

In Eqn. 1, $\dot{\varepsilon}_{ij}^p$ is the time-independent plastic strain rate tensor. Time-independent plasticity was modelled by Eqns. 2 and 3, where Eqn. 2 determines the yield stress criterion, with $\bar{\sigma}$ denoting the stress tensor and J_2 the second deviatoric invariant of the difference between the stress tensor and the back stress tensor, $\bar{\alpha}$.

$$f = J_2\left(\bar{\sigma} - \bar{\alpha}\right) = \sigma_o \tag{2}$$

$$\dot{\alpha}_{ij} = C.\dot{\varepsilon}_{pl}.\left(\frac{\sigma_{ij} - \alpha_{ij}}{\sigma_o}\right) - \gamma.\alpha_{ij}.\dot{\varepsilon}_{pl} + \frac{\alpha_{ij}}{C}.\dot{C} \tag{3}$$

Eqn. 3 represents the development during a single cycle of the back-stress tensor as a function of the strain hardening parameters, C and γ. This formulation is based on the nonlinear isotropic kinematic strain hardening deformation model of Lemaitre and Chaboche [7]. The parameters σ_o, C and γ are all temperature dependent, evolving internally with respect to accumulated plastic strain [8].

2.2.2 Creep Deformation

The time dependent component of the model was based on the characteristic strain formulation [9], i.e.

$$\varepsilon_C = \frac{\varepsilon_\chi}{\left(R_{w/t}/(Z_C.\sigma) - 1\right)} \tag{4a}$$

where ε_χ is a constant characteristic strain determined from datum values of rupture strength $R_{w/t1}$ and strength $R_{D/t1}$ to produce datum creep strain ε_D in datum time t_1, i.e.

$$\varepsilon_\chi = \varepsilon_D\left(R_{w/t1}/R_{D/t1} - 1\right) \tag{4b}$$

and Z_C is a plastic strain dependent evolutionary creep softening factor [8]. $R_{w/t}$ is the rupture strength at the current time t, given by:

$$R_{w/t} = R_{w/t1}(t_1/t)^{1/m} \quad (4c)$$

where $m = \log(t_2/t_1)/\log(R_{w/t1}/R_{w/t2})$ and $R_{w/t2}$ is a second datum rupture strength at time t_2.

2.3 Component-Feature Specimen Development

2.3.1 Hysteresis Behaviour at Life Limiting Surface Location

Target rotor analyses were first performed to establish the most demanding turbine operating conditions, and the stress/strain state existing at the life limiting (feature) location during this transient. Predictably, this assessment revealed a critical location surface strain range which in a service-cycle test with representative start-up (loading) and shut-down (un-loading) times and a hold time at peak temperature of ~1h would result in an impractically long laboratory test time. In order to increase the surface mechanical strain range to a magnitude of ~1% to result in a test time to crack initiation of ~≤1,000h, start-up and shut-down times were reduced in rotor simulations with the objective of generating enhanced service representative stress/strain state distributions to form the basis of component-feature specimen design. The stabilised stress-strain loop associated with the enhanced start-up conditions is shown as the dotted hysteresis loop in Fig. 2. The TMF test conditions required to generate the Type-E_r and Type-E_g experimental service cycles are given in Fig. 3. The consequent enhanced life limiting location stress/strain state distributions (according to the criteria defined in Sect. 2.1) are shown as thick solid lines in Fig. 4.

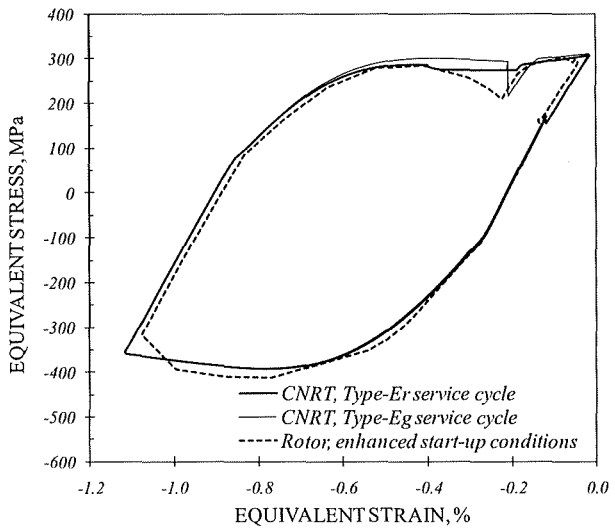

Fig. 2 Comparison of stress-strain responses at groove roots of CNRT($R5$) testpieces subject to Type-E_r and Type-E_g service-type TMF cycles with that at rotor life limiting feature during enhanced start-up conditions

The fundamental problem with the development of a laboratory cycle to represent even the enhanced service representative rotor cycle was that following the attainment of peak stress at peak temperature at the life limiting location, it was experimentally impossible to get from the maximum stress to the same minimum stress during a 1h laboratory hold period at maximum temperature by adopting the same elastic follow-up characteristics existing during service operation (during which creep relaxation occurred over a much longer period). The adopted solution was to consider two laboratory service-cycles to bound the situation existing during operation; one in which loading during the hold period was close to pure stress control (i.e. the Type-E_r cycle in Fig. 2) and one in which the loading during the hold period was close to pure strain control (i.e. the Type-E_g cycle in Fig. 2).

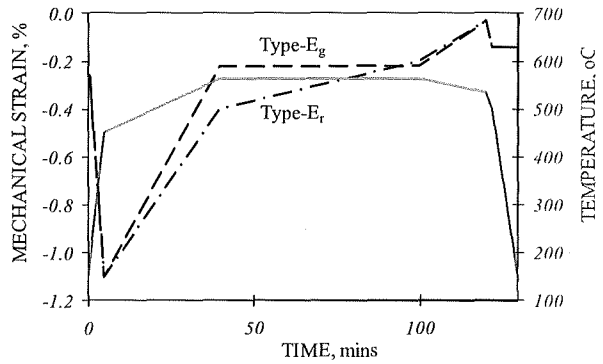

Fig. 3 Details of Type-E_r and Type-E_g enhanced service type TMF cycle (the solid line indicates the temperature transient for both cycle variants)

2.3.2 Stress/Strain States at and below Surface

A preliminary analysis of the suitability of several candidate laboratory feature-specimens indicated that, according to the stress/strain distribution criteria defined in Sect. 2.1, the most representative geometry was the circumferentially notched round tensile (CNRT) specimen with a 5mm notch root radius (Fig. 5a). This was confirmed by comparing FEA determined CNRT(*R5*) groove root stress/strain distributions arising from Type-E_r and Type-E_g service-type TMF cycles with that at the rotor life limiting feature during enhanced start-up conditions (Fig. 4). In this case, equivalent strain range and stress triaxiality factor distributions to a depth of ~8mm below groove roots were well matched for actual and experimental rotor features (Fig. 4a,b), but this was not so for the creep strain accumulated per cycle distributions (Fig. 4c). Only within 1mm of the CNRT(*R5*) groove root was the creep strain accumulated per cycle due to the Type-E_r cycle directly comparable with that ahead of the rotor feature subject to enhanced start-up conditions.

3 Experimental Details

3.1 Material

Enhanced service-cycle component-feature specimen TMF tests were performed on material taken from close to the periphery of a 2%CrMoNiWV turbine rotor forging. The chemical composition and mechanical properties are summarised in Table 1. Following an extensive preliminary heat treatment procedure, the forging had been oil quenched from 950°C and

tempered for 30h at 665°C [10]. The test material exhibited a mid-to-upper bainitic microstructure typical of large production forgings manufactured in this class of creep resistant low alloy ferritic steel.

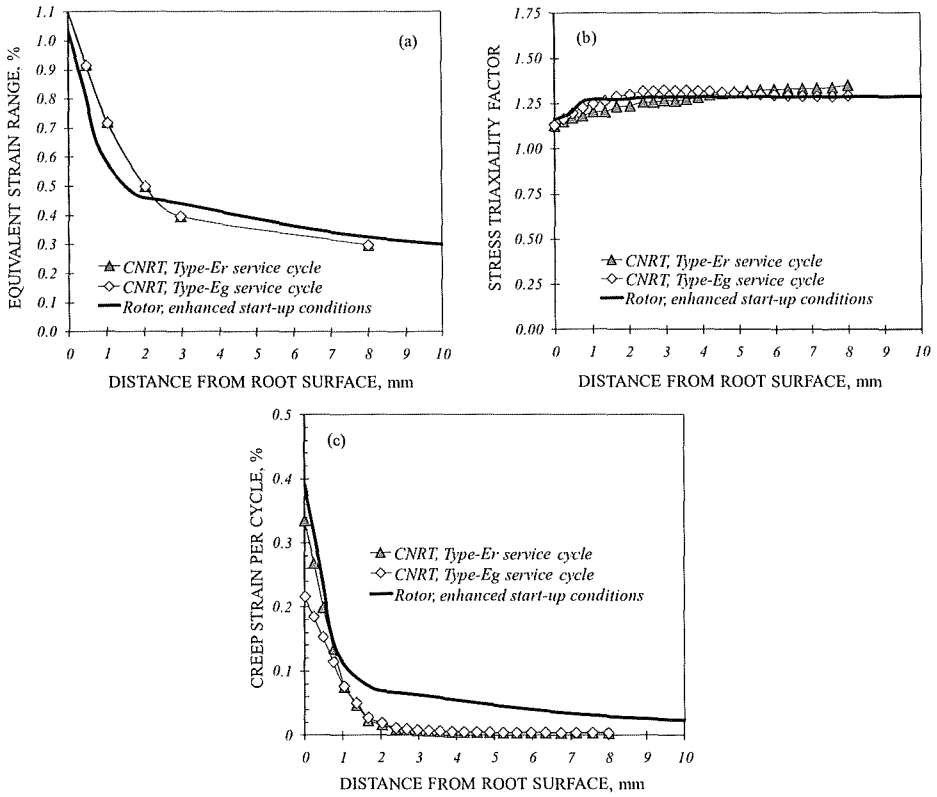

Fig. 4 Comparison of stress/strain distribution criteria at groove roots of CNRT(*R5*) testpieces subject to Type-E_r and Type-E_g service-type TMF cycles with that at the rotor life limiting feature during enhanced start-up conditions: Variation with distance from groove root of (a) axial mechanical strain, (b) stress triaxiality factor, and (c) creep strain accumulated per cycle

Table 1: Chemical Composition and RT Tensile Properties of 2%CrMoNiWV Steel

C wt.%	S wt.%	Mn wt.%	P wt.%	S wt.%	Cr wt.%	Mo wt.%	Ni wt.%	W wt.%	V wt.%	$Rp_{0.2}$ MPa	Rm MPa
0.23	0.08	0.68	0.006	0.004	2.08	0.83	0.74	0.65	0.30	625	740

The 2%CrMoNiWV steel had been developed during the 1980s within the COST 505 activity as a candidate combined HP/IP-LP turbine rotor material with the same creep resistance as that of 1%CrMoV, but with superior fracture toughness properties [10]. Subsequent

experience indicated that 2%CrMoNiWV was significantly more creep ductile than the more widely adopted 1%CrMoV HP/IP turbine steel and consequently more resistant to creep-fatigue.

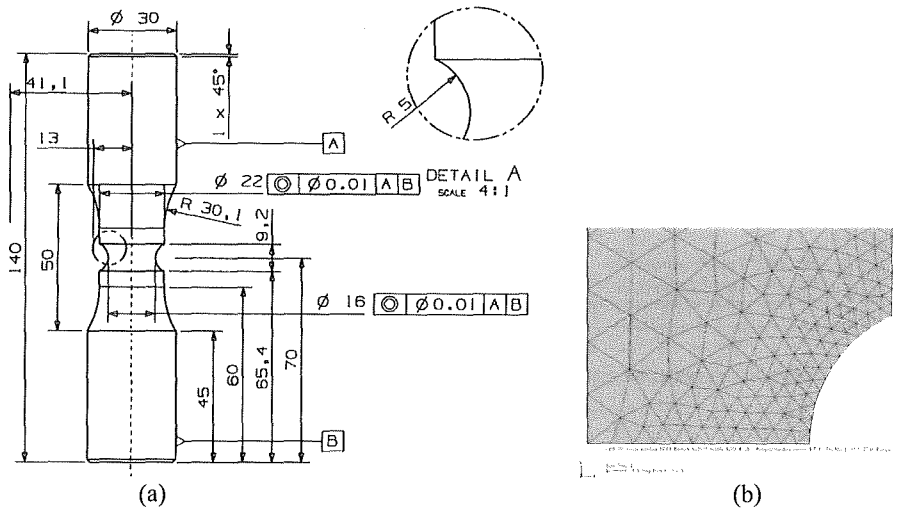

Fig. 5 Circumferentially notched round tensile CNRT(*R*5) specimen: (a) geometrical details, and (b) FEA mesh details at groove root

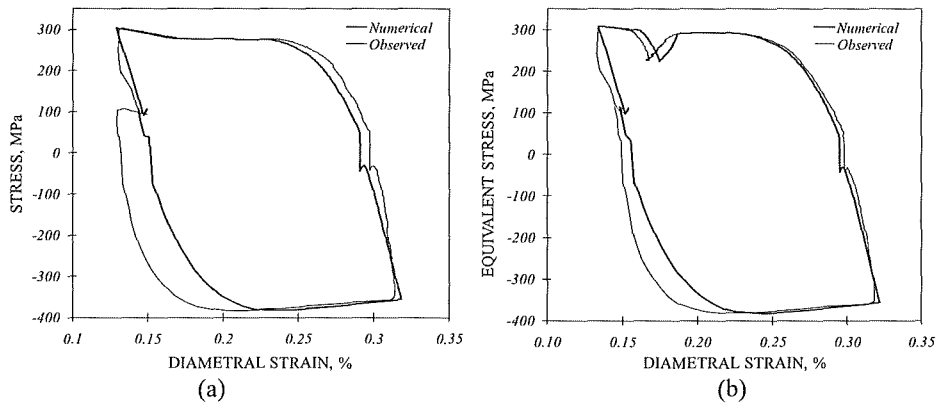

Fig. 6 Comparison of experimentally observed and FEA predicted stress-strain responses at groove roots of CNRT(*R*5) testpieces subject to (a) Type-E_r and (b) Type-E_g enhanced service-type TMF cycles

3.2 TMF Testing

Tests were performed on CNRT(*R*5) specimens (Fig. 5a) in accordance with the requirements of [11], but with tighter limits on steady and transient temperature control and permissible temperature gradients in the testpiece gauge section.

Enhanced TMF service cycle details are shown in Fig. 3. In this example for a 2%CrMoNiWV rotor feature, the temperature varied between 145 and 565°C. Groove root strain range transients were indirectly controlled using an axial side entry extensometer and an FEA based algorithm determined using the constitutive model formulations outlined in Sect. 2.2. Groove root strain was monitored by means of a diametral extensometer.

A comparison of experimentally observed and FEA predicted groove root stress-strain histories is given in Fig. 6.

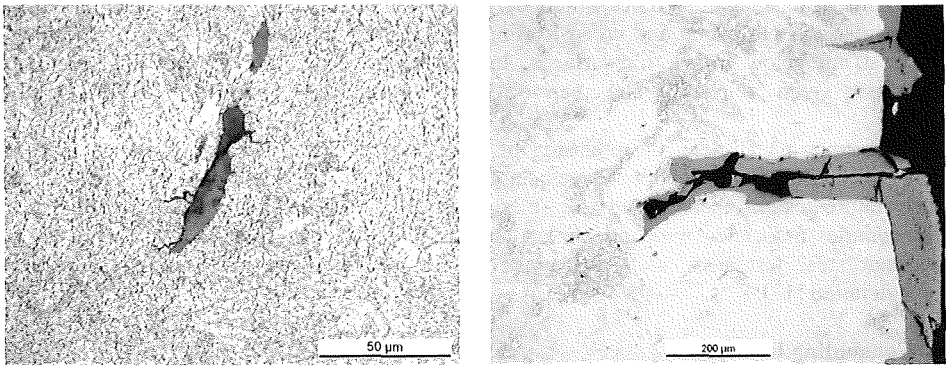

(a) (b)

Fig. 7 Creep-fatigue crack development: (a) at the groove root of a CNRT(*R*5) specimen, and (b) in a uniaxial testpiece, both subject to service-cycle TMF loading

4 Post Test Inspection

An important part of this benchmark testing strategy was characterisation of the damage generated at the groove root during testing to ensure that the mechanism was consistent with anticipated service behaviour. Post test inspection revealed that creep damage formed predominantly as a consequence of particle matrix decohesion (Fig. 7a) and that crack development was due to the interaction of groove root surface initiated fatigue cracks with accompanying creep damage (Fig. 7b). Creep damage formation appeared to be mainly associated with the development of dominant cracking rather than stress redistribution within the net section ahead of CNRT(*R*5) specimen grooves. This consequential creep-fatigue interaction mechanism (as defined in [6]) was very different to the simultaneous creep-fatigue interaction mechanism experienced with 1%CrMoV steel in similar service cycle TMF tests [6,12].

Creep void formation as a consequence of particle/matrix decohesion is usually associated with high stress and high creep ductility in low alloy creep resistant steels, and the observed creep damage characteristics are consistent with the known high creep ductility of the 2%CrMoNiWV steel [10].

5 Sources of Uncertainty

Enhanced service-type TMF cycle conditions and a representative component-feature specimen geometry have been developed, and their potential to demonstrate the effectiveness of deformation response at a high temperature turbine rotor feature evaluated (Fig. 6). The FEA predicted stress-strain response is not a perfect match with the experimentally observed response at the groove roots of CNRT(*R*5) testpieces using a diametral extensometer, although it is reasonably close. There are a number of sources of uncertainty which are the subject of ongoing investigation.

The numerical simulation relies on model assumptions about the way in which inelastic strains due to both cyclic and creep loading accumulate with the magnitudes of stress and strain at, and below groove root surfaces. In particular, it depends on the material sensitivity of primary creep strain and cyclic creep softening response to these quantities.

On the experimental side, the precision of the diametral strain measurement must also be considered. Standard procedures have been followed to calibrate the ISO 9513 Class 0.5 high temperature extensometer used for these tests. Nevertheless, there are recognised uncertainties associated with indentation and oxidation in the grooves of low alloy creep resistant steel testpieces with this type of displacement sensor which require further consideration [13].

6 Concluding Remarks

The authors have reviewed the methodology adopted in a Swiss Research Collaboration to devise and implement enhanced service-cycle component-feature specimen TMF test conditions to provide representative deformation and crack development observations to underpin the effectiveness of creep-fatigue deformation and crack initiation endurance predictions for new high temperature steam turbine rotor steel applications. The approach relies on observations from enhanced service-cycle component-feature specimen TMF tests with:

- thermo-mechanical cycle detail and testpiece geometry design based on the results of material constitutive modelling and advanced numerical simulation, and
- confirmatory physical damage mechanism checks by comprehensive post test inspection.

7 Acknowledgements

The authors gratefully acknowledge ALSTOM Power for supporting the work and giving permission to publish.

8 References

[1] ASME Boiler and Pressure Vessel Code, Section III, Division 1: Sub-section NH, Class 1 Components in Elevated Temperature Service, ASME, New York, 2001.

[2] TRD 301, Annex I – Design: Calculation for Cyclic Loading due to Pulsating Internal Pressure or Combined Changes of Internal Pressure and Temperature, Technical Rules for Steam Boilers, 1978.

[3] RCC-MR: Design and Construction Rules for Mechanical Components of FBR Nuclear Islands, AFCEN, Paris, 1985.

[4] R5: Assessment Procedures for the High Temperature Response of Structures, Procedure R5, Issue 3, British Energy, Gloucester, 2003.

[5] Holdsworth, S.R., 'Creep-fatigue properties of high temperature turbine steels', *Materials at High Temperatures*, 18(4), 261-265 (2001).

[6] Holdsworth, S.R., Mazza, E., Binda, L. & Ripamonti, L., ' Development of thermal fatigue damage in 1CrMoV rotor steel, *Nucl. Engng. & Design*, 237(24), 2292-2301, (2007).

[7] Lemaitre, J. & Chaboche, J.L., *Mechanics of Solid Materials*, Cambridge University Press (1994)

[8] Mazza, E., Hollenstein, M., Holdsworth, S.R. & Skelton, R.P., 'Notched specimen thermo-mechanical fatigue of a 1CrMoV turbine steel', *Nucl. Engng. & Design*, 234, 11-24 (2004).

[9] Bolton, J.L., 'A "characteristic strain" model for creep', *Proc. ECCC Conf. on Creep & Fracture in High Temperature Components – Design & Life Assessment Issues*, I.Mech.E, London, 12-14/9/05, eds. Shibli, I.A., Holdsworth, S.R. & Merckling, G., DEStech Publ., 465-477 (2005).

[10] Wiemann, W., 'The development of an improved 2%CrMoNiWV HP/IP rotor material', *COST Status Review, EUR-13452EN* (1991).

[11] GRD2-2000-30014, 'Code of practice for strain-controlled thermo-mechanical fatigue testing', TMF-STANDARD Project, EC Competitive and Sustainable Growth Programme (2005).

[12] Holdsworth, S.R., Mazza, E. & Jung, A., 'The response of 1CrMoV rotor steel to service-cycle thermo-mechanical fatigue testing, *ASTM J. Test & Evaluation*, July, 255-261 (2004).

[13] Skelton, R.P. & Webster, G.A., 'Extensometer probe indentation during low-cycle fatigue of plain and circumferentially notched cylindrical bars at 550°C, *Intern. J. Fatigue*, 31, 1505-1516 (2009).

9th Liege Conference : Materials for Advanced Power Engineering 2010
edited by J. Lecomte-Beckers, Q. Contrepois, T. Beck and B. Kuhn.

ASSESSMENT OF LONG-TERM CREEP STRENGTH OF GRADE 91 STEEL

Kazuhiro Kimura, Kota Sawada and Hideaki Kushima

National Institute for Materials Science
1-2-1 Sengen, Tsukuba, Ibaraki 305-0047, Japan
kimura.kazuhiro@nims.go.jp

Abstract

In 2004 and 2005, long-term creep rupture strength of ASME Grade 91 type steels of plate, pipe, forging and tube materials was evaluated in Japan by means of region splitting analysis method in consideration of 50% of 0.2% offset yield stress. According to the evaluated 100,000h creep rupture strength of 94MPa for plate, pipe and forging steels and 92MPa for tube steel at 600°C, allowable tensile stress of the steels regulated in the Interpretation for the Technical Standard for Thermal Power Plant was slightly reduced. New creep rupture data of the steels obtained in the long-term indicate further reduction of long-term creep rupture strength. Not only creep rupture strength, but also creep deformation property of the ASME Grade 91 steel was investigated and need of reevaluation of long-term creep strength of Grade 91 steel was indicated. A refinement of region splitting analysis method for creep rupture life prediction was discussed.

Keywords: creep, grade 91, allowable tensile stress, 0.2% offset yield stress

1. Introduction

Development and popularization of renewable energy has been investigated energetically in order to harmonize an increasing demand of energy with global environment. However, thermal power plant is useful measures to meet increasing energy demand and it will be a dominant power source for some time in the future. It is important, therefore, to improve energy efficiency of thermal power plant, since it can reduce CO_2 emission and save limited natural energy resources. Creep strength enhanced ferritic (CSEF) steels are widely used as one of the key materials as header and main/reheat steam pipes in Ultra Supercritical (USC) power plant and heat recovery steam generator (HRSG) in combined cycle power plant. Creep strength of CSEF steels is increased by precipitation strengthening of fine MX carbonitrides, solid solution strengthening of molybdenum and/or tungsten with a tempered martensitic microstructure, however, degradation of it in the long-term has been reported [1]. Since difference in microstructural changes as a degradation behaviour during creep exposure was observed in the high- and low-stress regimes, a region splitting analysis method was proposed [2]. In 2004 and 2005, reevaluation of long-term creep rupture strength was conducted by Committee on Establishing Allowable Stress Value etc. of High Chromium Ferritic Steel (SHC) on both base material and welded joints of several CSEF steels [3-6], and a region splitting analysis method was employed for the above assessment of creep rupture strength. According to the above reevaluation, allowable tensile stress of several CSEF steels

regulated in the Interpretation for the Technical Standard for Thermal Power Plant in Japan was revised [7]. Experimental data on long-term creep, however, was not exactly sufficient to evaluate precisely the creep rupture strength at 100,000 hours, therefore, a review of the results was suggested to be continued based on additional new long-term creep data. Reevaluation of long-term creep strength of Grade 91 has been also reported by Cipolla and Gabrel [8], and Bendick et al. [9] as a new assessment by European Creep Collaborative Committee (ECCC) in 2009. In this study, long-term creep strength of Grade 91 steel was investigated with a special attention to long-term creep rupture data recently obtained in NIMS.

2. Experimental Procedure

Creep data of three heats (MGA, MGB and MGC) of ASME SA-213 T91 tube material and single heat (MgC) of ASME SA-387 Grade 91 plate steel [10] were investigated in this study. Chemical composition and heat treatment condition of the steels are shown in Table 1. Creep tests were conducted in air under a constant load condition using specimens with 6 mm diameter and 30 mm gauge length for T91 and 10 mm diameter and 50 mm gauge length for Grade 91 plate steel. Creep data over a range of temperatures from 500 to 700°C were investigated.

Table 1 Chemical composition (mass%) and heat treatment condition of the steels studied.

Code	Form	C	Si	Mn	P	S	Ni	Cr	Mo	Cu	V	Nb
MGA	tube	0.10	0.38	0.40	0.015	0.001	0.12	8.53	0.96	0.022	0.21	0.076
MGB	tube	0.09	0.34	0.45	0.015	0.001	0.20	8.51	0.90	0.026	0.205	0.076
MGC	tube	0.09	0.29	0.35	0.009	0.002	0.28	8.70	0.90	0.032	0.22	0.072
MgC	plate	0.10	0.24	0.44	0.005	0.001	0.04	8.74	0.94	0.012	0.21	0.076

Code	Al	N	Normalizing	Tempering	SR
MGA	0.010	0.050	1045°C, 10min. A.C.	780°C, 60min. A.C.	-
MGB	0.02	0.042	1050°C, 60min. A.C.	760°C, 60min. A.C.	-
MGC	0.001	0.044	1050°C, 10min. A.C.	765°C, 30min. A.C.	-
MgC	0.014	0.0582	1060°C, 90min. A.C.	760°C, 60min. A.C.	730°C, 504min. F.C.

A.C.: air cooling, F.C.: furnace cooling

3. Results and Discussion

3.1. Revision of allowable stress in 2007 in Japan

Result of creep rupture strength evaluation on base material of Grade 91 steel conducted by SHC committee in Japan [11] is shown in Figure 1 with that of new assessment conducted by ECCC in 2009 [9]. Creep rupture strength evaluated by SHC is slightly lower than that of ECCC at 500 and 550°C, on the other hand it is reverse at 600 and 650°C. Evaluated creep rupture strength at 100,000 hours and 600°C is 94MPa and 90MPa for SHC and ECCC, respectively. According to the creep rupture strength evaluated by SHC committee, allowable

tensile stress values of Japanese regulation [7] for Grade 91 were revised in 2007 as summarized in Table 2. Since creep rupture strength of tube material of Grade 91 (T91) was evaluated separately from the other product form of plate, pipe and forgings in SHC [3], revised allowable tensile stress value of Grade T91 steel is slightly different from that of the other product form.

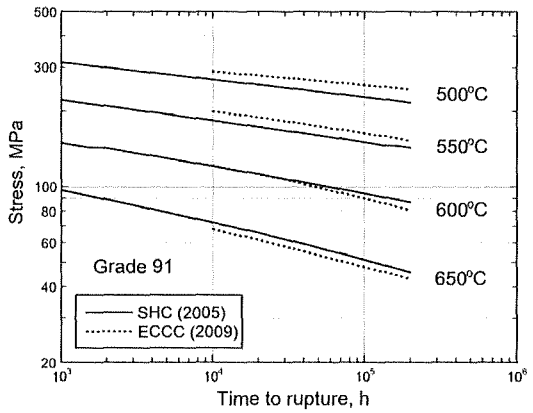

Figure 1 Comparison of evaluated creep rupture strength of SHC committee [11] and ECCC [9] for Grade 91.

Table 2 Revision of allowable tensile stress of Grade 91 type steels in 2007 [7].

Material		Allowable tensile stress (MPa)							
		previous				revised in 2007			
		575°C	600°C	625°C	650°C	575°C	600°C	625°C	650°C
plate pipe forging	$t \leq 76$mm	83	66	45	29	**81**	**63**	45	29
	$t > 76$mm	82	62	45	29	**81**	62	45	29
tube		83	66	45	29	83	**62**	**44**	29

t : thickness, Bold indicates revised stress value

3.2. Creep strength of Grade 91 steels

Creep rupture strength of the Grade 91 steels are shown in Figure 2. Linear relationship in double logarithm plots of stress and time to rupture is observed at 500°C, however, slope of the stress vs. time to rupture relation becomes steeper in the long-term at 550°C and above. Creep rupture strength of tube and plate materials are almost the same each other, except in the long-term at 600 and 650°C, where tube material indicates remarkable drop in creep rupture strength.

Rupture elongation (a) and reduction of area (b) of the Grade 91 steels are shown in Figure 3. High value of creep rupture ductility is observed in the short-term less than 10,000 hours, and decrease in creep rupture ductility is recognized over 10,000 hours especially at 650°C. However, creep rupture ductility of Grade 91 steels is higher than those of Grade 92 and Grade 122 steels [12].

Stress vs. minimum creep rate curves of the Grade 91 steels over a range of temperatures from 550 to 650°C are shown in Figure 4. Those of tube and plate materials are essentially the same each other. A large stress dependence with a stress exponent n value of about 20 in the high-stress regime at 550°C decreases with not only increase in temperature to about 10 at 650°C, but also decrease in stress to about 3 in the low-stress regime. This change in stress dependence of minimum creep rate is considered to be caused by different degradation mechanism in high- and low-stress regimes [1, 2].

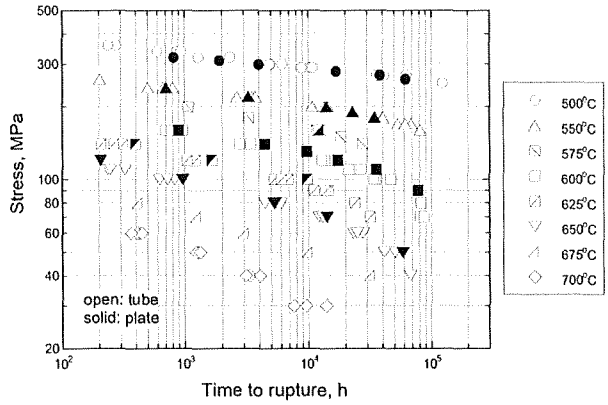

Figure 2 Creep rupture strength of the Grade 91 steels.

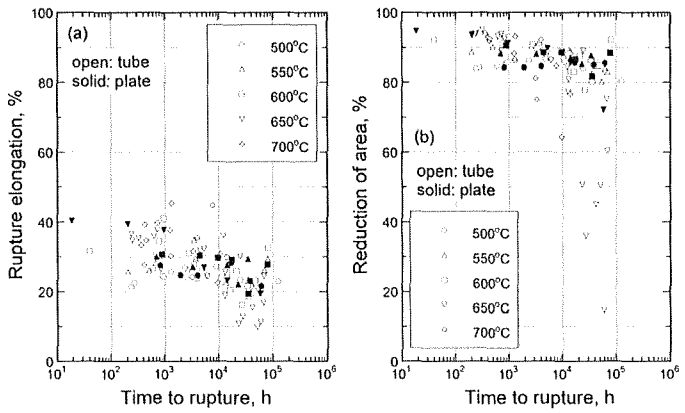

Figure 3 Rupture elongation (a) and reduction of area (b) of the Grade 91 steels.

Creep rate vs. time curves of the MGC heat at 600°C over a range of stresses from 200 to 70MPa are shown in Figure 5. Only a creep test under stress of 80MPa is still in progress and it is unbroken data. Creep deformation of the steel consists of transient and tertiary creep stages and a steady state creep stage is not observed. In the transient creep stage, creep rate decreases linearly with increase in time in a double logarithmic plot. Although shape of creep rate vs. time curve is almost the same regardless of stress level, minimum creep rate is observed at almost the same time of about 10,000 hours in the low-stress regime of 100MPa and below. This indicates that tertiary creep stage initiates at the relatively small life fraction in the low stress condition of 80 and 70MPa, since onset time of tertiary creep stage is almost the same regardless of difference in creep rupture life.

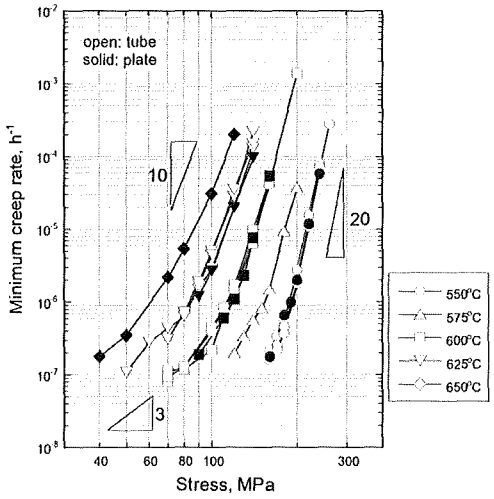

Figure 4 Stress vs. minimum creep rate curves of the steels.

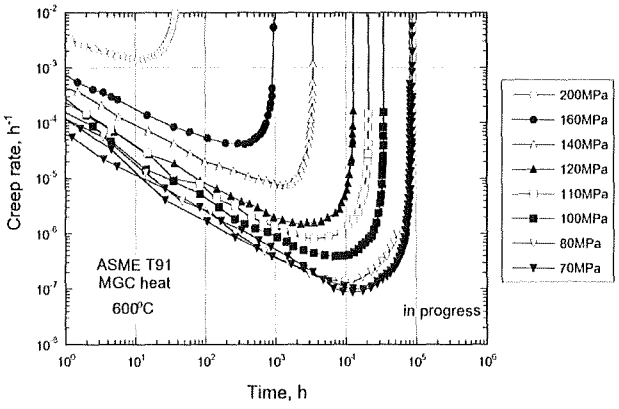

Figure 5 Creep rate vs. time curves of MGC heat at 600°C.

The creep rate data described in Fig.5 is plotted against strain instead of time and shown in Figure 6. Stress dependence of creep deformation behaviour is not clearly observed in creep rate vs. time curves shown in Fig.5, however, that is clearly recognized in creep rate vs. strain curves. In the high-stress regime of 140MPa and above, creep rate indicates minimum value at a relatively large strain of 0.02 to 0.03. On the other hand, minimum creep rate is observed at small strain which is less than 0.01 in the low-stress regime of 120MPa and below, especially at 80 and 70MPa where the initiation of tertiary creep stage occurs at very small strain of about 0.004. Decrease in onset strain of tertiary creep stage with decrease in stress is regarded to be a cause of early initiation of tertiary creep stage in the lower stress condition. It should be taken into consideration, since design of high temperature structural components is controlled by not only creep rupture strength, but also creep deformation property [13].

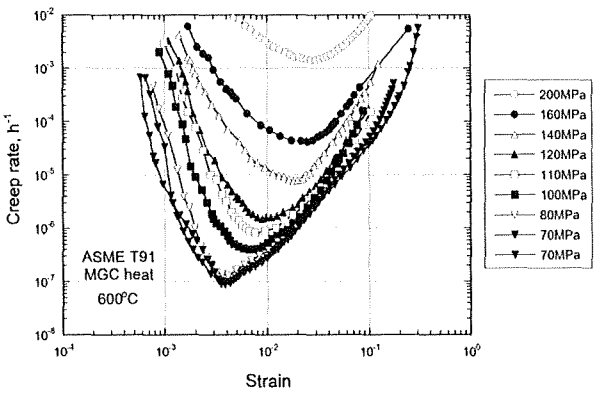

Figure 6 Creep rate vs. strain curves of MGC heat at 600°C.

3.3. Degradation and long-term creep strength of Grade 91 steels

Creep rupture strength of the Grade 91 steels are shown in Figure 7 together with the evaluation of SHC committee [11]. At 500 and 550°C, creep rupture strength of the present Grade 91 steels is slightly higher than the evaluation of SHC committee. Although creep rupture strength at 600 and 650°C is equivalent to the evaluation of SHC committee in the short-term less than about 30,000 hours, however, deviation from the evaluation of SHC committee is observed in the long-term due to remarkable drop in creep rupture strength, especially for Grade T91 tube materials. Creep rupture strength of the present Grade 91 steels at 100,000 hours is estimated to be below 80MPa and 40MPa at 600 and 650°C, respectively.

Vickers hardness in the gauge and head portions of the specimens creep ruptured at 600°C are plotted against time to rupture and shown in Figure 8. Vickers hardness is in a range of HV220 to HV235 in the as tempered condition, and it decreases to HV200 and below after creep rupture in the gauge portion, even after short-term creep exposure. On the other hand, decrease in hardness in the head portion is very small up to about 10,000 hours, and it

indicates decrease clearly in the long-term after about 10,000 hours. It suggests a progress in recovery and softening of tempered martensite microstructure during thermal ageing for longer than 10,000 hours. It should be considered that recovery and softening of microstructure is markedly promoted during creep exposure for 10,000 hours and longer [14].

Bright field TEM images of the MGC heat of T91 steel creep ruptured after (a) 34,141.0h and (b) 80,736.8h at 600°C under stress of 100MPa and 70MPa, respectively, are shown in Figure 9. In the specimen creep ruptured after 34,141.0h at 600°C and 100MPa, inhomogeneously recovered area is observed along the prior austenite grain boundary. On the other hand, grain interior of the specimen creep ruptured after 80,736.8h at 600°C and 70MPa is fully covered by equiaxed subgrains and recovery has already extended overall microstructure. Since a lot of Z-phase and only a few MX particles are observed in the specimen creep ruptured after 80,736.8h [14], creep strength is remarkably reduced during creep exposure for about 80,000 hours.

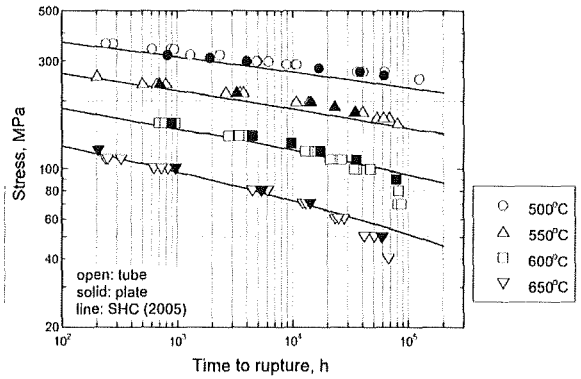

Figure 7 Comparison of creep rupture strength with the evaluation of SHC committee [11].

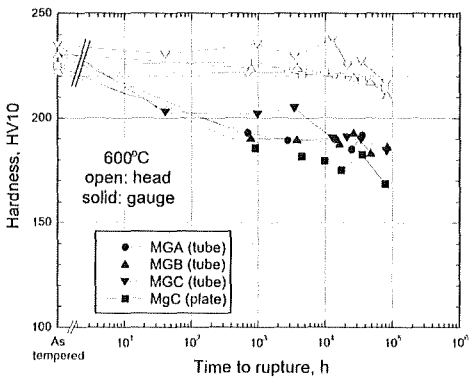

Figure 8 Changes in hardness in the gauge and head portions of the creep ruptured specimen with increase in time to rupture at 600°C.

Stress vs. time to rupture curves of the Grades T91, T92 [15] and T122 [16] steels are shown in Figure 10. Creep rupture strength of T92 and T122 steels are higher than that of T91 steels in the short-term and high-stress regime. However, T122 steel indicates remarkable drop in creep rupture strength with decrease in stress and it gets close to that of T91 steel after several tens of thousands hours of creep exposure at 600°C and above. Although long-term creep rupture strength of T92 steel is higher than those of the others, similar tendency of drop in long-term creep rupture strength is observed. Remarkable drop in the long-term creep rupture strength of T91 steels at 600°C is similar to that of T122 steel, and three grades steels exhibit equivalent trend of strength drop in the long-term at 650°C. Consequently, significant drop in long-term creep rupture strength of Grade 91 steels in comparison to the evaluation of SHC committee is considered to be an essential creep strength property. Since boundary condition of region splitting analysis, that is 50% of 0.2% offset yield stress, corresponds to macroscopic elastic limit [2], decrease in yield stress during long-term creep exposure due to recovery and softening of tempered martensitic microstructure should be also taken into account for assessment of long-term creep strength.

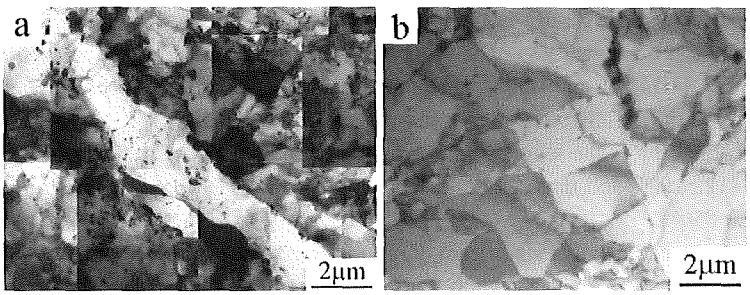

Figure 9 Bright field TEM images of the MGC heat of T91 steel creep ruptured after (a) 34,141.0h and (b) 80,736.8h at 600°C under stress of 100MPa and 70MPa, respectively.

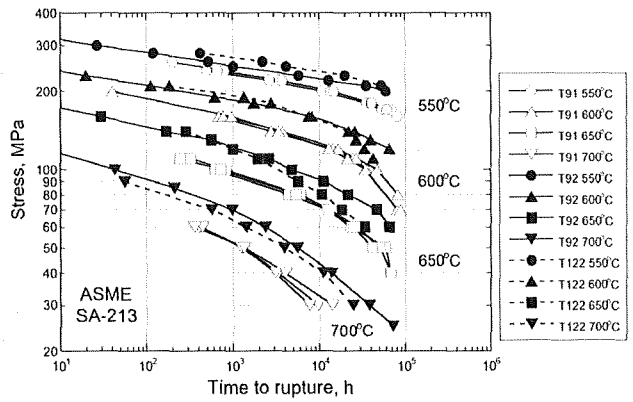

Figure 10 Comparison of creep rupture strength of Grades T91, T92 [15] and T122 [16].

4. Conclusions

Long-term creep strength of ASME Grade 91 steel was investigated in consideration of current allowable tensile stress. The following results are obtained.
(1) Creep rupture strength evaluated by SHC is slightly lower than that of ECCC at 500 and 550°C, on the other hand it is reverse at 600 and 650°C. According to the creep rupture strength evaluated by SHC committee, allowable tensile stress values of Japanese regulation for Grade 91 were revised in 2007.
(2) Creep rupture strength of tube and plate materials are almost the same each other, except in the long-term at 600 and 650°C, where tube material indicates remarkable drop in creep rupture strength.
(3) In the high-stress regime, creep rate indicates minimum value at a relatively large strain of 0.02 to 0.03. On the other hand, minimum creep rate is observed at small strain which is less than 0.01 in the low-stress regime, especially at 80 and 70MPa where the initiation of tertiary creep stage occurs at very small strain of about 0.004.
(4) Decrease in hardness in the head portion is very small up to about 10,000 hours at 600°C, and it indicates decrease clearly in the long-term after about 10,000 hours. Inhomogeneously recovered area is observed along the prior austenite grain boundary in the specimen creep ruptured after 34,141.0h at 600°C, and grain interior of the specimen creep ruptured after 80,736.8h at 600°C is fully covered by equiaxed subgrains.
(5) Remarkable drop in the long-term creep rupture strength of T91 steels at 600°C is similar to that of T122 steel, and three grades steels exhibit equivalent trend of strength drop in the long-term at 650°C.
(6) It has been concluded that significant drop in long-term creep rupture strength of Grade 91 steels in comparison to the evaluation of SHC committee is considered to be an essential creep strength property. Decrease in yield stress during long-term creep exposure due to recovery and softening of tempered martensitic microstructure should be also taken into account for assessment of long-term creep strength.

Acknowledgement

The creep tests were performed as a part of NRIM/NIMS Creep Data Sheet project. The authors are grateful to all the members participated in the NRIM/NIMS Creep Data Sheet project for their sincere efforts.

References

[1] K. Kimura, H. Kushima and F. Abe, Heterogeneous Changes in Microstructure and Degradation Behaviour of 9Cr-1Mo-V-Nb Steel during Long Term Creep, *Key Engineering Materials*, 171-174, pp.483-490, (2000).

[2] K. Kimura, K. Sawada, K. Kubo and H. Kushima, Influence of Stress on Degradation and Life Prediction of High Strength Ferritic Steels, *Proc. 2004 ASME/JSME PVP Conf.*, San Diego, California, pp.11-18, (2004).
[3] K. Kimura, Assessment of Long-term Creep Strength and Review of Allowable Stress of High Cr Ferritic Creep Resistant Steels, *Proc. PVP2005*, Denver, USA, PVP2005-71039, (2005).
[4] K. Kimura, Creep Strength Assessment and Review of Allowable Tensile Stress of Creep Strength Enhanced Ferritic Steels in Japan, *Proc. PVP2006-ICPVT-11*, Vancouver, Canada, PVP2006-ICPVT-11-93294, (2006).
[5] Y. Takahashi and M. Tabuchi, Evaluation of Creep Strength Reduction Factors for Welded Joints of HCM12A (P122), *Proc. PVP2006-ICPVT-11*, Vancouver, Canada, PVP2006-ICPVT-11-93488, (2006).
[6] K. Yoshida, H. Nakai, S. Inui and N. Yuki, Regulatory Review Results on Allowable Tensile Stress Values of Creep Strength Enhanced Ferritic Steels, *Proc. PVP2007/CREEP8*, San Antonio, USA, CREEP2007-26512, (2007).
[7] *The Interpretation for the Technical Standard for Thermal Power Plant*, Nuclear and Industrial Safety Agency (NISA), The Ministry of Economy, Trade and Industry (METI), (2007).
[8] L. Cipolla and J. Gabrel, New Creep Rupture Assessment of Grade 91, *Proc. 1st Int. Conf. Super High Strength Steels*, Rome, Italy, (2005).
[9] W. Bendick, L. Cipolla, J. Gabrel and J. Hald, New ECCC Assessment of Creep Rupture Strength for Steel Grade X10CrMoVNb9-1 (Grade 91), *Proc. 2nd ECCC Creep Conf.*, Zurich, Switzerland, pp.56-67, (2009).
[10] Creep Deformation Properties of 9Cr-1Mo-V-Nb Steel Tubes for Boilers and Heat Exchangers (ASME SA-213/SA-213M Grade T91) and 9Cr-1Mo-V-Nb Steel Plate for Boilers and Pressure Vessels (ASME SA-387/SA-387M Grade 91), Atlas of Creep Deformation Property, NIMS Creep Data Sheet, NIMS, Tsukuba, No.D-1, (2007).
[11] M. Tabuchi and Y. Takahashi, Evaluation of Creep Strength Reduction Factor for Welded Joints of Modified 9Cr-1Mo Steel (P91), *Proc. PVP2006-ICPVT-11*, Vancouver, Canada, PVP2006-ICPVT-11-93350, (2006).
[12] H. Kushima, K. Sawada and K. Kimura, Creep Strength and Rupture Ductility of Creep Strength Enhanced Ferritic Steels, *Proc. 9th Liege Conf., Materials for Advanced Power Engineering 2010*, (2010).
[13] ASME Boiler and Pressure Vessel Code, Section III, Division 1, Subsection NH, (2007).
[14] K. Sawada, H. Kushima, M. Tabuchi and K. Kimura, Microstructural Changes of T91 Steel during Creep under Low Stress, *Proc. 9th Liege Conf., Materials for Advanced Power Engineering 2010*, (2010).
[15] NIMS Creep Data Sheet, NIMS, Tsukuba, No.48, (2002).
[16] NIMS Creep Data Sheet, NIMS, Tsukuba, No.51, (2006).

9th Liege Conference : Materials for Advanced Power Engineering 2010
edited by J. Lecomte-Beckers, Q. Contrepois, T. Beck and B. Kuhn.

MICROSTRUCTURAL CHANGES OF T91 STEEL DURING CREEP UNDER LOW STRESS

K. Sawada, H. Kushima, M. Tabuchi and K. Kimura

National Institute for Materials Science
1-2-1, Sengen, Tsukuba, 305-0047, Japan
sawada.kota@nims.go.jp

Abstract

Microstructural changes in ASME T91 steel were investigated under low stress at 600°C, focusing on martensitic lath, dislocation density, coarsening of $M_{23}C_6$ and MX, and precipitation of Z-phase. Creep tests were interrupted at 10,000 h, 20,000 h, 30,000 h, 50,000 h and 70,000 h under 70 MPa. (tr = 80,736.8 h) to evaluate the process of microstructural changes. The hardness decreased during aging and creep at 600°C. The process of the change in hardness in the gauge portion was almost the same as that in the grip portion up to 30,000 h. However, the hardness markedly dropped during creep after 30,000 h, compared with that during aging. The occurrence of the drastic change in hardness roughly corresponds to the beginning (20,000 h) of the tertiary creep stage. The change in martensitic lath structure was very small up to 30,000 h, although the lath structure gradually recovered during creep. The lath structure suddenly recovered after 30,000 h, contributing to the drastic drop in hardness. Preferential recovery was observed around prior austenite grain boundaries (PAGBs) after 30,000 h, compared with inside prior austenite grains. Z phase particles were confirmed around PAGBs after 30,000 h during creep. The disappearance of MX carbonitrides was clear after 30,000 h due to the formation of Z-phase particles. The preferential recovery of the lath structure around PAGBs and the disappearance of MX carbonitrides contribute to a decrease in creep resistance, leading to the occurrence of tertiary creep.

Keywords: long-term creep, interrupted test, martensitic lath structure, Z-phase formation

1. Introduction

In order to further reduce CO_2 emissions in steam power plants, it is important to maintain a high thermal efficiency, based upon the safe operation of power plants. High Cr ferritic steels are widely used for power plants components because of their higher creep strength. However, degradation of creep strength in the long term is a problem in high Cr ferritic steels [1]. Kimura [2] has proposed region splitting analysis for stress versus time to rupture curve, as the deformation mechanism of high Cr ferritic steel is different in high-stress regions and low-stress regions. For safety of components, we need to know the degradation and damage mechanisms under a low-stress condition corresponding to actual service conditions in power plants. In high Cr ferritic steels, preferential recovery around PAGB [3], intergranular fracture [4], and Z phase formation [5] contribute to the degradation of creep strength. Many of the aforementioned studies are based on investigations into ruptured samples. It is necessary to know when the harmful microstructural changes mentioned above occur in the creep process under low stress in order to clarify the degradation mechanism. Some of researchers have

reported on the process of microstructural changes during creep on interrupted samples [6,7]. In the case of low-stress (long-term) conditions, it takes a great deal of time to obtain interrupted samples. Therefore, existing information on the process in microstructural changes under low-stress conditions is not adequate.

Japan's next fast breeder reactor will have a design life of 60 years [8]. In this case, it is difficult to obtain directly 60 years creep rupture strength and creep deformation property by means of a creep test. A prediction of creep life based on degradation and damage mechanisms is important. In order to understand the actual degradation mechanism under long-term conditions, we have to obtain experimental data for microstructural changes under a stress condition that is as low as possible, and then predict the process of microstructural changes.

This paper clarifies the processes of microstructural changes under low stress using interrupted samples of ASME T91 steel, focusing on recovery of martensitic lath structure, decrease in dislocation density, and formation of Z-phase. In addition, the relation between the processes of microstructural changes and the creep process are discussed to clarify the degradation mechanism.

2. Experimental procedure

The steel examined was ASME-T91 [9]. The chemical composition and heat treatment condition of the steel is given in Table 1. Creep rupture tests were performed under a constant load in air using specimens 6 mm in gauge diameter and 30 mm in gauge length. Creep tests were interrupted at 10,000 h, 20,000 h, 30,000 h, 50,000 h and 70,000 h under 70 MPa at 600°C. The stress under 70MPa was lower than the proportional limit (150 MPa) that was obtained by a tensile test with a strain rate of 5×10^{-5} s^{-1} at 600°C [10]. The microstructures were observed using a conventional TEM and a STEM-EDX at 200 kV. Extracted carbon replicas and thin foils were prepared from the gauge portions of the crept samples for TEM observation.

Table1 : Chemical composition(in mass%) and heat treatment condition of the steel studied.

	C	Si	Mn	P	S	Ni	Cr	Mo	Cu
ASME-T91	0.09	0.29	0.35	0.009	0.002	0.28	8.70	0.90	0.032

V	Nb	Al	N	Normalizing	Tempering
0.22	0.072	0.001	0.044	1050°C, 10min A.C.	765°C, 30min A.C.

3. Results and Discussion

3.1 Creep property and hardness change during creep

Figure 1 shows an applied stress and time to rupture diagram of the steel. The creep strength at a temperature below 550°C does not drop in the long term. Conversely, at 600°C to 700°C, the creep strength in the long term is lower than that predicted by the trend for short-term

creep strength. The deformation mechanism under lower stresses is different from that under higher stresses. The proportional limit is the boundary between the high-stress region and the low-stress region [2]. We focused on the degradation mechanism under 70 MPa, which is below the proportional limit. Creep rate versus time curve under 70 MPa at 600°C is plotted in Fig. 2. The interrupted times are also shown in the figure. The interrupted time of 20,000 h corresponds to the beginning of tertiary creep stage. The interrupted times of 30,000 h, 50,000 h and 70,000 h are in the range of the tertiary creep stage.

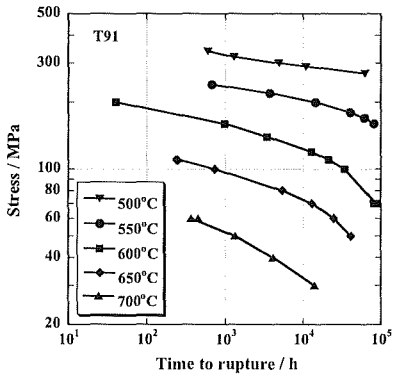

Figure 1 : Creep rupture strength of the steel studied.

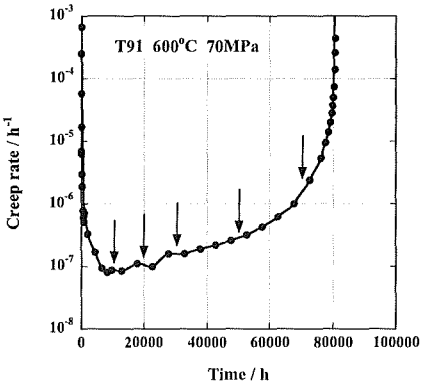

Figure 2 : Creep rate vs. time curve. Arrows indicate interrupted time.

Figure 3 demonstrates the change in hardness in the grip and gauge portions of crept samples at 600°C. The hardness in the grip portion of ruptured samples gradually decreases with an increase in time, however, the drop in hardness is very small. This means that hardness is relatively stable during aging. The hardness in the gauge portion of the interrupted specimen is almost the same as that in the grip potion of ruptured specimen up to 30,000 h. The hardness in the gauge portion drastically dropped after 30,000 h, compared with the hardness change in the grip portion. The marked drop in hardness is clear in the tertiary creep stage, as the tertiary stage starts around 20,000 h, as shown in Fig. 2. The martensitic lath structure, dislocations, and precipitates contribute to the hardness [11], indicating that the occurrence of microstructural changes is drastic in the tertiary stage.

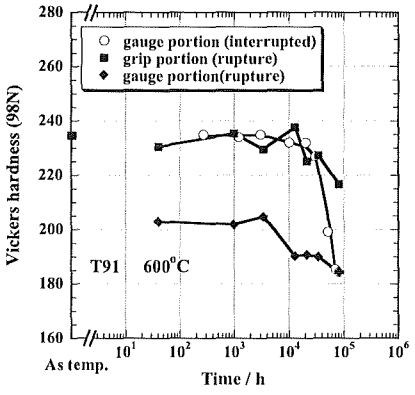

Figure 3 : Hardness change in grip(ruptured specimens) and gauge portions (ruptured and interrupted specimens.

3.2 Change in martensitic lath structure during creep

Figure 4 shows the change in the martensitic lath structure (gauge portions) during creep. No large change in lath structure was observed up to 30,000 h. The lath structure locally recovered during creep after 30,000 h. Many of the laths recovered and changed to equiaxed subgrains after 70,000 h. The dislocation density was high up to 30,000 h, and gradually decreased after this time. The stable lath structure up to 30,000 h contributes to the lack of a large change in hardness, as shown in Fig. 3. Kushima et al. reported that preferential recovery around PAGB occurred after a creep rupture under low stress [1]. The microstructures around PAGB are shown in Fig. 5. The dashed lines in the figure are PAGB. The lath structure was not different between PAGB and inside prior austenite grains up to 30,000 h. However, at 50,000 h and 70,000 h, the lath structure clearly recovered around PAGB, compared with inside prior austenite grains. The preferential recovery around PAGB contributes to the occurrence of tertiary creep.

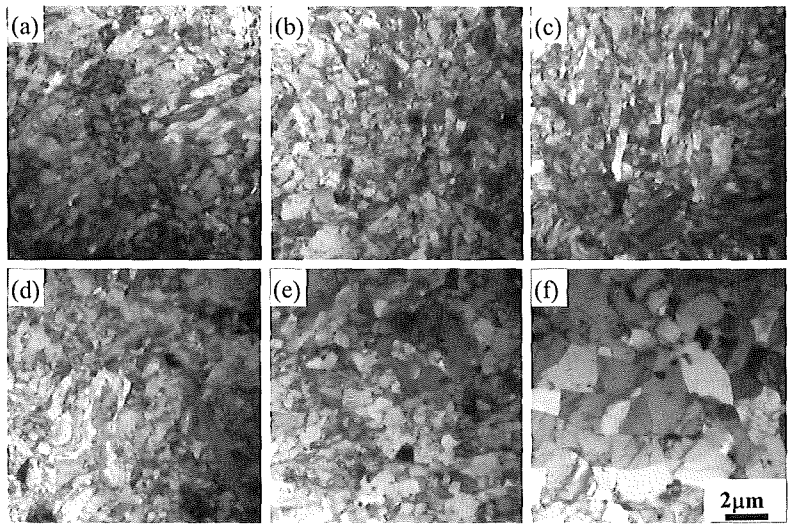

Figure 4 : Change in lath structure of gauge portion during creep. (a) before creep,(b)10000h,(c)30000h, (d)50000h, (e)70000h, (f)80736.8h 600°C / 70MPa

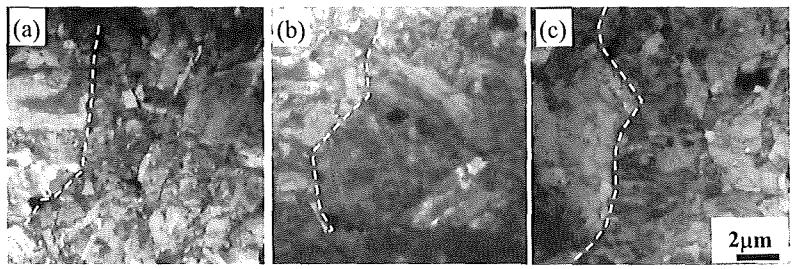

Figure 5 : Change in lath structure of gauge portions around PAGB. (a) 30000h, (b) 50000h, (c)70000h 600°C / 70MPa Dashed lines are PAGBs.

3.3 Change in precipitates during creep

A change in precipitates distributions during creep is shown in Fig. 6. It was confirmed by STEM-EDX mapping that fine $M_{23}C_6$ and MX particles were located before creep. It appears that $M_{23}C_6$ and MX particles gradually coarsen during creep. According to elemental mapping, the smaller and larger particles are basically MX and $M_{23}C_6$, respectively. A large number of MX particles are distributed up to 10,000 h. However, the number of MX particles clearly decreases after 30,000 h, and then only a few MX particles are observed in the ruptured specimen after 80,736.8 h. Arrows indicate Z-phase particles confirmed by EDX analysis [12]. No Z-phase particles were observed up to 10,000 h. The Z-phase particles were formed around PAGBs after 30,000 h. The dashed lines are PAGBs predicted by particle distributions. The apparent decrease in number of MX particles after 30,000 h is due to the disappearance of MX particles caused by nucleation and coarsening of Z-phase particles [13]. The decrease in the number of MX particles was clearly seen in the tertiary creep stage (30,000 h), indicating a decrease in creep resistance caused by the disappearance of MX particles. MX particles around PAGBs may disappear during creep, compared with inside prior austenite grains as many of the Z-phase particles are located around PAGBs. This means that creep resistance around PAGB will decrease during creep, promoting the occurrence of preferential recovery of the lath structure around PAGB shown in Fig. 5.

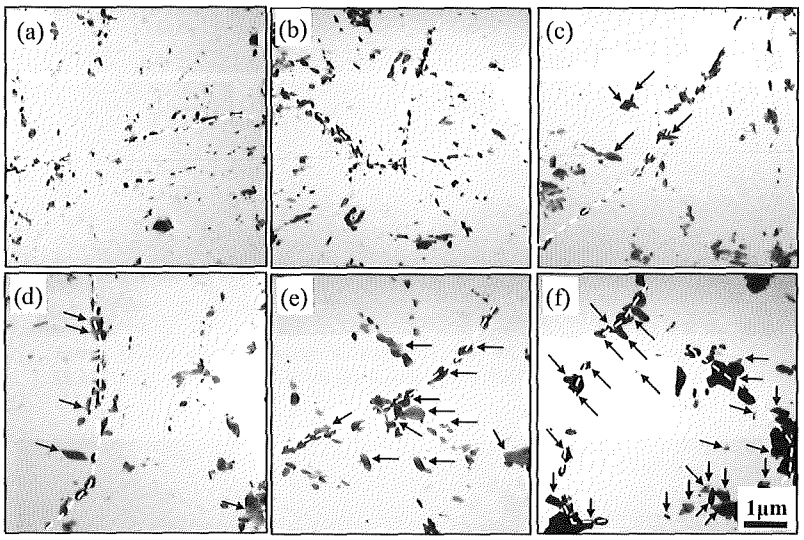

Figure 6 : Change in precipitates distributios during creep.
(a) before creep, (b) 10000h, (c)30000h, (d)50000h, (e)70000h, (f)80736.8h
Dashed lines are PAGBs predicted by precipitates distributions. Arrows indicate Z-phase particles.

4. Conclusions

The process of microstructural changes was investigated in ASME T91 steels crept for 10,000

h, 20,000 h, 30,000 h, 50,000 h and 70,000 h under 70 MPa at 600°C, focusing on martensitic lath structure, dislocation density, and precipitates distributions. The results are summarized as follows.

(1) The creep rupture strength of T91 steel dropped under low stress (long term) at 600°C to 700°C. The hardness (grip portion) decreased a little during aging at 600°C. Conversely, the hardness (gauge portion) abruptly decreased during creep deformation after 30,000 h under 70 MPa at 600°C, although the hardness of the gauge portion was almost the same as that of the grip portion up to 30,000 h.

(2) No large recovery in the martensitic lath structure was observed during creep up to 30,000 h. After 30,000 h, the martensitic lath structure started to recover. The lath structure around PAGBs clearly recovered during creep for 50,000 h, compared with inside laths. Many of the laths changed to equiaxed subgrains during creep for 70,000 h.

(3) A large number of fine $M_{23}C_6$ and MX particles were distributed before creep. After 30,000 h, the number of MX particles decreased due to Z-phase formation. A few MX particles were confirmed after rupture (80,736.8 h).

(4) The recovery of the lath structure and disappearance of MX particles occurred in the tertiary creep stage, indicating these microstructural changes causes the tertiary creep.

References

[1] H. Kushima, K. Kimura and F. Abe : Tetsu-to-Hagane, 85 (1999), 841.
[2] K. Kimura : Proc. Creep and Fracture in High Temperature Components – Design and Life Assessment Isuues, ed. by I. A. Shibli et al., DE*Stech* Publications, Inc., (2005), 1009.
[3] K. Kimura, H. Kushima and F. Abe : Key Eng. Mater., 171-174 (2000), 483.
[4] J. S. Lee, H. G. Armaki, K. Maruyama, T. Muraki and H. Asahi : Mater. Sci. Eng. A, A428 (2006), 270.
[5] J. Hald : 8th Liege Conf. on 'Materials for Advanced Power Engineering, ed. by J. Lecomte-Beckers et al., Forshungs-zentrum, Jülich GmbH, Jülich, (2006), II.917.
[6] J. Hald and L. Korcakova : ISIJ Int., 43 (2003), 420.
[7] A. Aghajani, Ch. Somsen and G. Eggeler : Acta Mater., 57 (2009), 5093.
[8] T. Onizawa, T. Wakai, M. Ando and K. Aoto: Proc. Creep and Fracture in High Temperature Components – Design and Life Assessment Issues, ed. by I.A. Shibli et al., DE*Stech* Publications, inc., (2005), p.130
[9] NRIM Creep Data Sheet, No.43, National Research Institute for Metals, Tsukuba, Japan, 1996.
[10] K. Kimura, K. Sawada, K. Kubo and H. Kushima : Proc. of 2004 ASME/JSME Pressure Vessel and Piping Conference, 2004, PVP2004-2566.
[11] K. Sawada, K. Miyahara, H. Kushima, K. Kimura and S. Matsuoka : ISIJ Int., 45 (2005), 1934.
[12] K. Sawada, H. Kushima and K. Kimura : ISIJ Int., 46 (2006), 769.
[13] L. Cipolla, H. K. Danielsen, D. Venditti, P. Emilio, D. Nunzio, J. Hald, M. A.J. Somers : Acta Mater., 58 (2010), 669.

9th Liege Conference : Materials for Advanced Power Engineering 2010
edited by J. Lecomte-Beckers, Q. Contrepois, T. Beck and B. Kuhn.

BORON EFFECTS ON CREEP RUPTURE STRENGTH OF W CONTAINING ADVANCED FERRITIC CREEP RESISTANT STEELS

N. Mito and Y. Hasegawa

Tohoku University, Japan
Aoba 6-6-20 Aramaki Aoba-ku Sendai 980-8579, JAPAN

abstract

The creep strength in ferritic creep resistant steels is increased by boron addition. However, the strengthening mechanisms have not yet been studied. This study clarifies the strengthening mechanism of 9% chromium steels with 10~100ppm boron and 0.5~2.0mass% tungsten in the laboratory. The strengthening effect of simultaneous addition of boron and tungsten was analyzed by hardenability, room-temperature strength and creep tests at 650°C. Changes in the microstructure as a result of the addition of boron and tungsten were also examined by optical microscope and transmission electron microscope (TEM). In addition, Alpha-ray Track Etching (ATE) method was used to detect the boron distribution and analyze the mechanisms change in the mechanical properties. Boron addition did not affect room-temperature strength, however, simultaneous addition of boron and tungsten increased room-temperature and high-temperature strength. According to ATE analysis, boron exists at the grain boundary. Therefore, synergistic effects of boron and tungsten on the creep strength suggest the tungsten precipitates stabilization by boron at the grain boundary.

Keywords: ferritic creep resistant steels, ATE, TEM, boron, tungsten

1. Introduction

Ferritic creep resistant steels are widely used in fossil fuel power plants. It is suggested that dislocation microstructure, carbides and inter-metallic compound precipitates and solid solution dragging enhance the creep resistance [1]. Some studies have reported that the addition of a little boron dramatically increases the creep strength [2]. Many studies have investigated the strengthening mechanism by the dislocation microstructure of ferritic steels through direct observation by transmission electron microscope (TEM) of the dislocation microstructure [3]. However, it is not still clear how their microstructure including the martensitic pagket structure, and the block and lath structure affect creep behavior. Additionally, ordinary TEM can detect neither boron atoms nor their morphology. Therefore, the mechanism by which boron addition increases the creep strength is not clear.

Therefore, this study examined the strengthening mechanism of boron in the recently

developed 9% chromium ferritic creep resistant steels. In particular, the relationship between microstructure and mechanical properties, especially creep strength was examined in model alloys with various amounts of tungsten and boron. In addition, TEM images of microstructures in ruptured specimens were compared to analyze the effect of alloy elements on their microstructure during heat treatments and long-term high-temperature creep. Furthermore, detection of boron distribution and its morphology assumption by alpha-ray track etching (ATE) and TEM suggested three strengthening mechanisms of initial microstructure enhancement through increasing hardenability, precipitate stabilization and grain boundary segregation of solute boron by boron addition. In conclusion, the precipitate stabilization by boron is probably the decisive factor in the model steels studied.

2. Experimental procedure and samples

2.1 Samples

Six 100 kg ingots were made in a vacuum induction furnace in the laboratory. Table 1 indicates the chemical compositions. In all steels, 0.05 % titanium decreased solute nitrogen to restrict the boron precipitation as nitride. In order to evaluate the boron effect on the microstructure steels WB1, WB2 and WB3 boron content was changed 10, 50 and 100 ppm. The synergistic effect of boron and tungsten addition was analyzed in steels WB4, WB5 and WB6 varying the tungsten content from 0.5 to 2.0 mass % through Fe_2W precipitation behavior. Ingots were pre-heated at 1,150 °C, hot rolled to 30 mm thick steel plates, and cooled in air. Plate specimens were normalized at 1,070 °C for 1 hour, and tempered at 760 °C for 1 hour in order of there microstructure. The amount of precipitated element was determined by extracted residue analysis.

Table 1. Composition of the six investigated steels (mass %)

Name	C	Si	Mn	Cr	W	Co	Ti	N	B(ppm)
WB1	0.097	0.056	0.49	9.16	2.02	3.03	0.052	0.0192	10
WB2	0.096	0.057	0.49	9.15	2.02	3.02	0.052	0.0196	51
WB3	0.095	0.057	0.49	9.17	2.03	3.02	0.051	0.0196	103
WB4	0.095	0.065	0.49	9.15	0.47	3.03	0.050	0.0190	49
WB5	0.094	0.063	0.49	9.13	0.86	3.04	0.050	0.0193	49
WB6	0.090	0.066	0.49	9.20	1.90	3.05	0.050	0.0196	48

2.2 Hardenability evaluation and mechanical properties

Dilatometry determined the transformation temperatures and quantified hardenability for boron and tungsten addition. Charpy impact tests, hardness tests and tensile tests were used to evaluate mechanical properties with different hardenabilities.

2.3 Creep tests

Specimens with a cylindrical cross section and a diameter of 6 mm and gauge length of 30 mm were used to evaluate the creep properties. The creep tests were conducted at temperatures from 550 to 650 °C.

2.4 Microstructural observations

Each sample was observed by transmission electron microscope (TEM) to identify the morphology of precipitates and the dislocation microstructures after creep tests. The comparison of precipitates was determined by quantification of the extracted residue and TEM-EDX analysis. Alpha-ray track etching (ATE) was used to detect the boron distribution. Figure 1 shows the method of ATE. ATE activates boron by neutrons, and films catch the alpha-rays emitted by boron, then, the boron distribution is identified. The following formula shows the alpha-ray emitting reaction [4].

$$^{10}B+^{1}n\rightarrow{}^{7}Li+4\alpha+2.4MeV$$

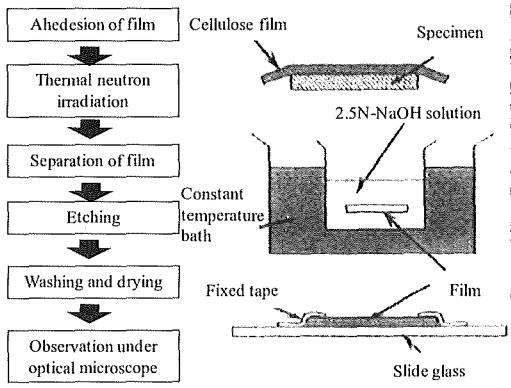

Fig. 1. Procedure of ATE method [4].

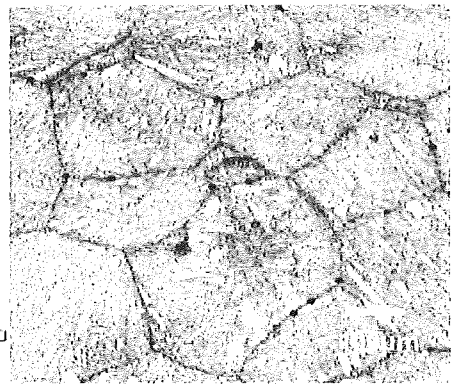

Fig. 2. Grain boundary segregation and precipitation of boron detected by ATE

Figure 2 is a boron distribution map in tempered martensite detected by ATE. It is clear that boron tends to segregate at the high angle boundary. Further study is required to obtain a

precise identification of the boron distribution and clarify the strengthening mechanism of the model steels.

3. Experimental results

3.1 Comparison of the micrographs and the hardenability of the specimen

Figure 3 indicates the optical micrographs showing the microstructures before creep tests. No significant microstructural change can be observed among the steels WB1, WB2 and WB3, specimens with varied boron content, among those of WB4, WB5 and WB6, specimens with varied tungsten content.

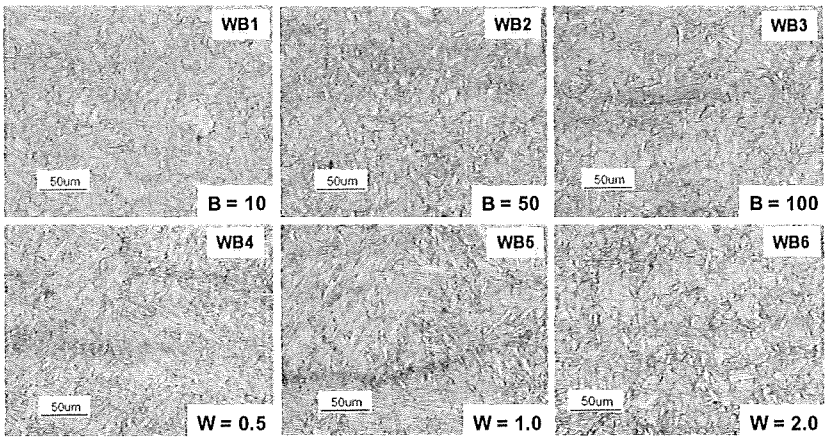

Fig. 3. Optical micrographs of WB1, WB2 and WB3 (upper column) and WB4, WB5 and WB6 (under column) Boron content is indicated in mass ppm. W content is indicated in mass %. All the microstructures are typical tempered martensite.

Figure 4 indicates the strength of the steels WB1, WB2 and WB3 at room temperature. Tensile and yield strength are independent of the significant boron content increase. The results agree with the micrographs in Fig. 3. On the other hand, Fig. 5 shows the tensile strength increases with tungsten contents in the steels WB4, WB5 and WB6. This result does not agree with microstructural observations.

Table 2 shows the transformation temperatures of the specimens by dilatometry. All steels show little difference of Ms-temperatures. Boron and tungsten addition does not seem to affect the hardenability. Table 2 also indicates the hardness (98 MPa of load) after the

dilatometry tests. No change in hardness was observed. This suggests that the boron addition does not affect the hardenability or optical microstructure except the room temperature tensile properties in the specimens with varied tungsten content, WB4, WB5 and WB6.

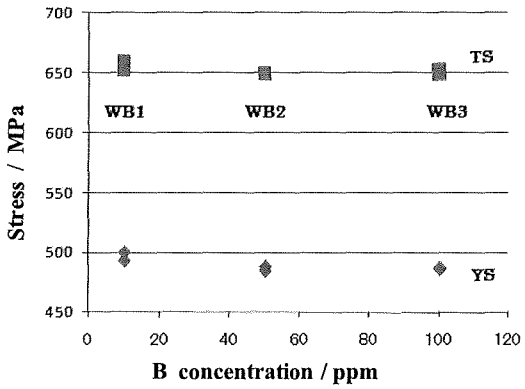

Fig. 4. Room temperature strengths of specimens with varied boron content

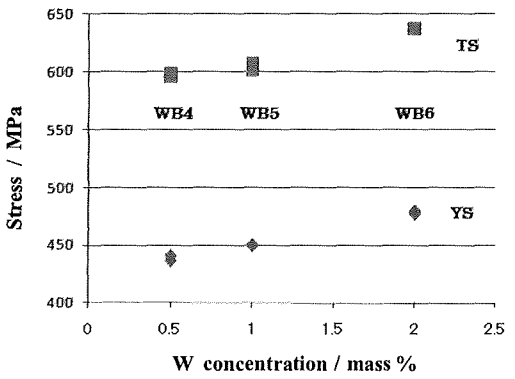

Fig. 5. Room temperature strengths of specimens with varied W content

Table 2. Transformation temperatures and hardness of the model steels

Steels	Ac1 (°C)	Ac3 (°C)	Ms (°C)	Mf (°C)	Hardness HV
WB1	780	815	380	275	407
WB2	780	825	405	270	411
WB3	800	825	390	270	407
WB4	780	800	400	275	402
WB5	780	810	400	280	404
WB6	780	820	380	280	413

3.2 TEM observation of the microstructure before creep tests

Figure 6 shows the TEM micrographs of each specimen before creep tests. Precipitates at grain boundary seem to increase with W contain increasing. EDX analyses suggested little Laves Phase precipitation. Some precipitates, $M_{23}C_6$ type carbide according to EDX analyses extracted replica, contain a little amount of tungsten in precipitates of WB4 and WB5. The number density of $M_{23}C_6$ type carbide in the WB6 specimen was relatively increased also by replica observation through TEM. Therefore, the tungsten content increase in the steels supposedly increased the $M_{23}C_6$ precipitation density at the grain boundary. As a result, boron does not seem to affect the microstructure of 9% chromium containing ferritic steels.

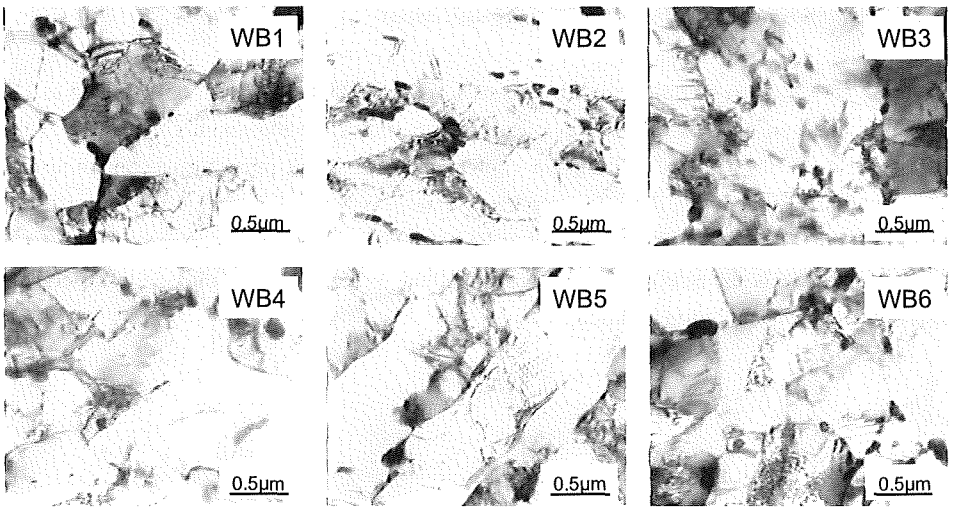

Fig. 6. TEM micrographs of all specimens

3.3 Extracted residue analyses of the heat treated specimens

The results of extracted residue analyses are shown in Table 3. Most of the boron precipitated in $M_{23}C_6$ according to the results in Table 3 except the steel WB3. In steel WB3, two-thirds of the boron, 60 ppm, solved in matrix. Most of the tungsten precipitate as a part of $M_{23}C_6$ type carbide as suggested by EDX analyses.

Table 3. The results of extracted residue analyses (mass % except B)

	Cr	W	Fe	Ti	N	B (ppm)
WB1	1.12	0.29	0.46	0.051	0.017	9
WB2	1.06	0.28	0.47	0.048	0.018	45
WB3	1.14	0.31	0.55	0.054	0.017	39
WB4	0.88	0.085	0.39	0.39	0.018	47
WB5	1.03	0.17	0.44	0.46	0.018	50
WB6	0.96	0.25	0.43	0.44	0.018	48

3.4 Creep deformation of W content varying specimens

Figure 7 shows creep strain curves of the steels WB4, WB5 and WB6 at 650 °C and at 110 MPa. W addition increases the creep life. Figure 8 shows the minimum creep rates of the steels WB4, WB5 and WB6. Tungsten content increase in 50 ppm boron containing 9% chromium steels decreases the minimum creep rate to 2.7×10^{-6} for steel WB4, 1.5×10^{-6} for steel WB5 and 0.59×10^{-6} (s^{-1}) for steel WB6. Minimum creep rate decrease with tungsten content increase is expected to show creep resistant increase as a result of the synergistic effect of tungsten and boron addition.

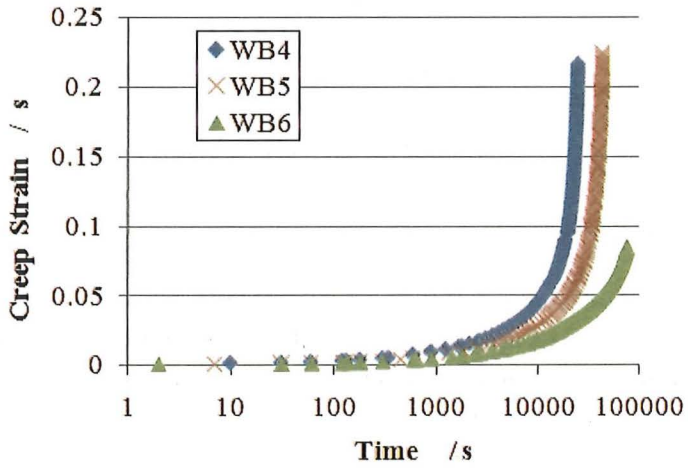

Fig. 7. Creep strain curves of steels WB4, WB5 and WB6

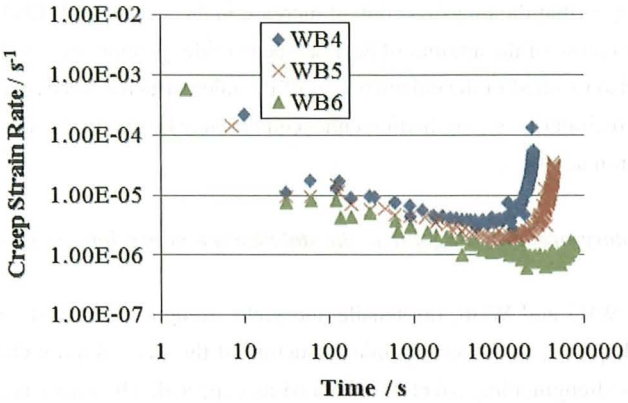

Fig. 8. Creep strain rate of the steels WB4, WB5 and WB6

4 Discussion

4.1 Initial microstructure strengthening by hardenability enhancement

No significant difference of the optical micrographs before creep tests and the static transformation temperatures by dilatometry show that the boron content change, from 10 to 100 ppm, does not enhance their hardenability. No increase of room-temperature strength among the steels WB1, WB2 and WB3 also agrees with the above results. On the other hand, room-temperature strength of steels WB4, WB5 and WB6 increased with the tungsten content in 50 ppm boron containing steels. Almost no report can be found concerning the hardenability increase by tungsten. Despite the possible confirmation of the synergistic effect of boron and tungsten addition on the hardenability, the transformation temperature, a hardenability index, did not change. However, the comparison of tungsten in precipitates obviously increase with tungsten content in the steels WB4, WB5 and WB6 as listed in Table 4.

Table 4. Constituents of precipitates in steels WB4, WB5 and WB6 by EDX analyses

	Mass %			Atomic %		
Steels	Cr	Fe	W	Cr	Fe	W
WB4	66.01579	25.88947	8.094737	71.43158	26.06842	2.515789
WB5	64.53889	24.20556	11.26111	71.27222	25.11111	3.805556
WB6	57.24615	23.81538	18.96154	67.28462	26.48462	6.230769

Such results suggest that the tungsten content increase in the steels WB4, EB5 and WB6 resulted in the increase of the amount of $M_{23}C_6$ type carbide, precipitating at the grain boundary, and also resulted in the enhancement of the microstructure recovery resistance. Therefore, the precipitation strengthening enhancement may be due to the synergistic effect of tungsten and boron addition.

4.2 Grain boundary strengthening due to the stabilization of precipitates by boron

In Steels WB4, WB5 and WB6, the tensile and yield strengths increased simultaneously as mentioned in Chapter 3. However, the microstructure of the steels did not change. Therefore, the precipitation strengthening effect is enhanced as expected. The effect is also expected to decrease the creep deformation. In addition, some studies reported that precipitates such as $M_{23}C_6$ type carbide and Fe_2W type inter-metallic compound, Laves phase at the high angle boundary affect the creep strength, and their coarsening and disappearance at the grain boundary might decrease the creep deformation resistance [5]. Therefore, boron possibly solves in the precipitates and restricts the coarsening. Indeed, most precipitates were identified $M_{23}C_6$ by TEM analyses. Extracted residue analyses suggest the boron precipitation to be a part of $M_{23}C_6$. If the decisive strengthening factor is $M_{23}C_6$ type carbide in high-chromium containing ferritic creep resistant steels, boron possibly contributes to the carbide precipitation strengthening. Stabilization of carbides by boron can be explained as following hypothesis.

Grain boundary migration resulted in the creep deformation at the precipitation free boundary due to the inter-particle space increase by precipitation coarsening driven by diffusion. Boron increases the thermal stability of the precipitates by solution in the carbide, and restricting the growth of precipitates. This hypothesis, at the same time, suggests the same effects on Laves phase, inter-metallic compounds. As a result, this study suggests that boron restricts precipitation coarsening for a long time and results in dislocation of microstructure stabilization and long creep life.

4.3 Possibility of solute boron segregation and dragging effects on the grain boundary

Solute boron segregation at the grain boundary and possible enhancement of the creep rupture strength have been reported [6]. On the other hand, some reports also state the solute boron amount to be at most 10 ppm and it is does not significantly increase the creep strength [7]. Extracted residue analyses show that steel WB3 contains about 60 ppm of solute boron, contrary to the usual report even though the effect on creep strength is not clear. Confirming

whether the solute boron is a decisive factor for creep deformation, precise analyses of state of the boron at the grain boundaries through TEM and ATE are necessary for each creep tests' condition in order to determine the possibility of the solution dragging effect of boron. Boron cannot stay in solid solution for long time creep. Therefore, the effect of solution dragging of boron seems to be restricted independent of the boron content in the steels. Further research is necessary to quantify the boron solution dragging effect on the grain boundary even though it seems not significant.

5 Conclusion

In order to clarify the strengthening mechanism as a result of the addition of boron and tungsten in ferritic creep resistant steels, 9 % chromium ferritic steels with various amounts of tungsten or boron were manufactured in the laboratory and the relation between the microstructure and mechanical properties including creep strength were investigated. Three hypotheses were verified experimentally: initial microstructure strengthening by hardenability increasing, grain boundary strengthening through precipitate stabilization and solution dragging effect of boron at the grain boundary.

1) Boron does not strengthen the microstructure in a single addition.
2) Neither boron nor tungsten has a large effect on hardenability. On the other hand, the amount of tungsten change in boron containing steels affects the number density of precipitates and enhances the resistance of microstructure recovery.
3) The synergistic effect of simultaneous addition of boron and tungsten possibly stabilizes precipitates, $M_{23}C_6$ and Fe_2W, and increases the creep deformation resistance.
4) Most boron precipitates as a part of $M_{23}C_6$ type carbide. Therefore, solid solution dragging effect by boron at the grain boundary can't be observed. Precise analyses of the boron distribution by ATE and TEM are necessary.

6 Reference

[1] M.Sato, Y.Hasegawa, T.Muraki and K.Maruyama : *J.J apan Inst. Metals*, 64, 371-374, (2000)

[2] B.Kim, H.Yun, D.Lee and B.Lim : *Journal of Physics*, 144, 1-4, (2009)

[3] K.Sawata, M.Takeda, K.Maruyama, R.Komine and Y.Nagae : *Tetsu-to-Hagane*, 84, 580-585, (1998)

[4] K.Asakura, T.Koseki, M.Kawate, M.Ishimoto : *Tetsu-to-Hagane*, 93, 634-641, (2007)

[5] Y.Hasegawa, M.Ogami and T.Muraki : *J.Soc.,Japan*, 52, 124-131, (2003)

[6] Y.Kamada, H.Kurayasu, S.Watanabe : *Tetsu-to-Hagane*,74, 2153-2160, (1988)

[7] M.Yamada, Y.Tokunaga and M.Yamamoto : *Tetsu-to-Hagane*, 73, 1049-1056, (1987)

9th Liege Conference : Materials for Advanced Power Engineering 2010
edited by J. Lecomte-Beckers, Q. Contrepois, T. Beck and B. Kuhn.

GRAIN BOUNDARY PRECIPITATION STRENGTHENING MECHANISM IN W CONTAINING ADVANCED CREEP RESISTANT FERRITIC STEELS

T. Shibata and Y. Hasegawa
TOHOKU University, Japan
Aoba 6-6-20 Aramaki Aoba-ku Sendai 980-8579, JAPAN

Abstract

Grain boundary precipitation strengthening is expected to be a decisive factor in developing ferritic creep resistant steels. This study examined the grain boundary precipitation strengthening mechanism extracting the effect of the tempered martensitic microstructure and precipitates on the high angle grain boundary in $M_{23}C_6$ type carbide and the Fe_2W type Laves phase effect of the creep deformation fixing the grain boundary according to transmission electron microscope (TEM) observation. A creep test was carried out at high temperature in order to evaluate the high angle boundary strengthening effect simulating the long-term creep deformation microstructure by the lath structure disappearance. The correlation of the creep rupture time and the grain boundary shielding ratio were found to be independent of precipitate type. The creep deformation model represents block boundary shielding by precipitates as the decisive factor for W containing ferritic creep resistant steels.

Keywords: Grain boundary precipitation strengthening, $M_{23}C_6$ type carbide, Laves phase, Ferritic steel, Creep strength

1. Introduction

The efficiency of thermal power generation plants should be improved to reduce the consumption of fossil fuels and lessen global warming. As increased steam temperature and pressure improve the efficiency of steam power generation, it is important to increase the creep resistance of materials for thermal power plants. In Japan, the steam temperature of fossil power plants reaches 610°C and a steam temperature of 650°C is the development target for next generation power plants [1].

Ferritic steels are used for boiler materials of the main steam piping and headers due to their small coefficient of thermal expansion and large thermal conductivity compared to those of austenitic steels. However ferritic steels have relatively lower creep strength.

Therefore various creep strengthening mechanisms have been researched to obtain the optimal alloy design. For example, solid solution dragging [2], intragranular precipitation

strengthening [3] and dislocation microstructure strengthening [4] have been considered as effective strengthening mechanisms, and more recently, grain boundary precipitation strengthening has been discussed.

Grain boundary precipitation strengthening is the hypothesis that precipitates on the high angle grain boundary, especially the block boundary, enhance the creep strength [5]. The processes of mobile dislocation at the grain boundary and grain boundary bulge by absorbing the dislocation at a precipitation free grain boundary induce local deformation. In the hypothesis, precipitates fix the grain boundary, resist the bulge and restrict creep deformation. In advanced ferritic creep resistant steels, fine precipitates and dislocation cause resistance to the dislocation gliding. The microstructure of such steels recovers from the zone adjacent to the high angle boundary [6]. On the other hand, deformation initiates at the precipitation free grain boundary, and not from the boundary with precipitates.

Precipitates on a high angle grain boundary of tungsten containing 9%Cr steel are mainly Laves phase (Fe_2W) inter-metallic compounds and $M_{23}C_6$ type carbide. It has been considered that tungsten enhances high temperature strength by solid solution dragging and tungsten containing precipitates (Laves phase) do not contribute to enhancing the creep strength due to the Laves phase that easily coagulates and coarsens. However, Hasegawa et al. suggested that tungsten does not contribute to solid solution dragging at high temperature, and enhances the creep strength by Laves phase precipitation [7]. Takeyama et al. suggested that grain boundary precipitation strengthening occurs in austenitic steels [8]. Hasegawa revealed the correlation of the creep rupture time and the grain boundary shielding ratio on the high angle grain boundary [5]. Varying the chromium, the main constituent of $M_{23}C_6$ type carbide, which commonly precipitates on the grain boundary, this research analyzed the grain boundary strengthening mechanism by precipitation through creep rupture tests and the grain boundary shielding ratio definition by TEM observation.

2. Experimental procedure

2.1 Specimens

Table 1 shows the chemical compositions of steels with various chromium contents. The 50 kg ingots of these steels were manufactured in a laboratory-scale high frequency induction furnace. These steels may reveal the effect of the grain boundary precipitation strengthening factor due to the absence of intragranular precipitates. In this study, the chromium content was varied from 5 to 11.5% because chromium is the main component of $M_{23}C_6$ type carbide, which precipitates on the grain boundary. Ingot specimens were warmed to 1,150°C and hot rolled to 20 mm thick plate specimens. These specimens were normalized at 1,070°C for 1

hour and tempered at 770°C for 1 hour and fundamental properties such as the Vickers hardness and tensile strength were investigated.

Table 1 Chemical compositions of prepared steels (mass%)

Name	C	Si	Mn	Cr	Mo	W	Co	N
A	0.100	0.052	0.051	5.28	0.49	2.00	3.07	0.0462
B	0.099	0.054	0.051	7.33	0.49	2.00	3.05	0.0481
C	0.098	0.055	0.050	8.34	0.49	2.00	3.05	0.0509
D	0.097	0.057	0.050	9.33	0.49	2.00	3.03	0.0549
E	0.096	0.059	0.050	10.42	0.49	2.01	3.05	0.0612
F	0.093	0.057	0.050	11.46	0.49	1.99	3.02	0.0752

2.2 Creep rupture test

The creep rupture test specimen was a round bar smooth specimen with a diameter of 6 mm and a gauge length of 30 mm. The rupture life was measured by single spindle type constant load creep rupture test. The test temperatures were from 650°C to 700°C. A creep rupture test and creep strain test were carried out.

2.3 Precipitates observation through TEM

In order to investigate the precipitation behavior, thin foil samples obtained from the gauge portion of ruptured specimens were observed through TEM. TEM-EDX analyses of the carbon extraction replica samples were used to determine the morphology of precipitates compared to those in steels under heat treated conditions.

3. Results

3.1 Initial microstructure

All steels had a tempered martensitic microstructure. Figure 1 shows the optical micrographs of Steels A and F. Figure 2 shows the TEM micrographs of Steels A, D and F. Increase of chromium contents resulted in a decrease of the block width and lath width. Precipitates were observed mainly at high angle grain boundaries. Table 2 shows the room temperature strength and hardness. Increase of the chromium content tended to increase the tensile strength. On the other hand, the yield strength stayed constant. Precipitation strengthening and the increase of mobile dislocation density possibly explain the constant yield strength in spite of the tensile

strength increase. Tempering treatment precipitates carbides. Carbides improve the uniform elongation and resulted in the increase of tensile strength and yield strength simultaneously. On the other hand, increase of mobile dislocation by matensite transformation decrease the yield strength and increase the tensile strength. Therefore, carbide precipitation increases the yield strength and mobile dislocation decreases the yield strength. Consequently, yield strength was maintained about 460MPa. Hardness was also enhanced by an increase in the chromium content. This result represents the improvement of the tensile strength and the hardenability of the specimens depending on the chromium contents.

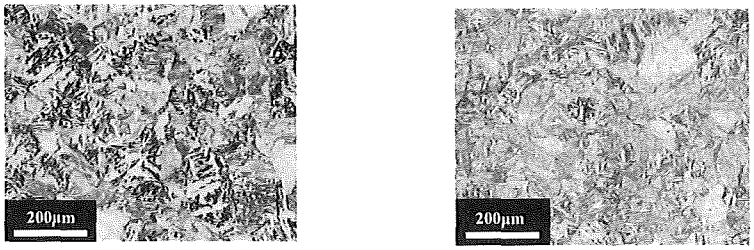

(a) Steel A *(b) Steel F*

Fig. 1 Optical micrograph of initial microstructure

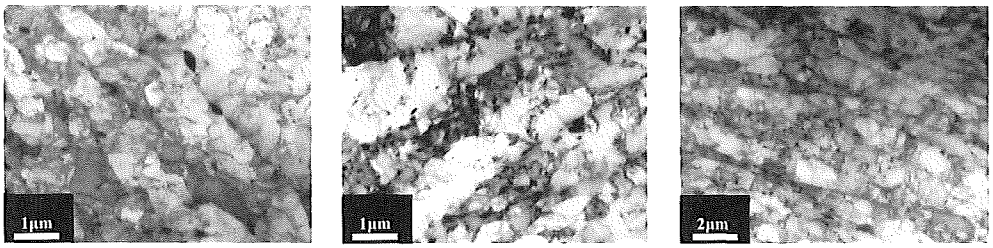

(a) Steel A *(b) Steel D* *(c) Steel F*

Fig. 2 TEM micrographs of initial microstructure

Table 2 Basic property of samples

Sample	Vickers hardness	Proof stress (N/mm^2)	Tensile strength (N/mm^2)
A	193	463.4	636.0
B	196	447.8	630.6
C	198	458.0	646.1
D	202	450.8	648.3
E	208	459.0	665.2
F	214	472.9	683.0

3.2 Creep rupture life

Figure 3 shows the results of the creep rupture test at 700°C and at 60 MPa, and at 650°C and at 170 MPa. The relation of the chromium contents and the creep rupture life is plotted. Room temperature strength increased with the chromium content, however, the creep rupture life did not indicate a similar tendency, that is, the chromium content and creep strength did not correlate. Figure 3(a) shows that 8 and 9 mass % chromium containing steels achieved the longest creep life. Figure 3(b) shows that from 7 to 9 % chromium containing steels achieved the longest creep life. Both results indicate the optimum chromium content for the creep rupture life at 650°C and at 700 °C.

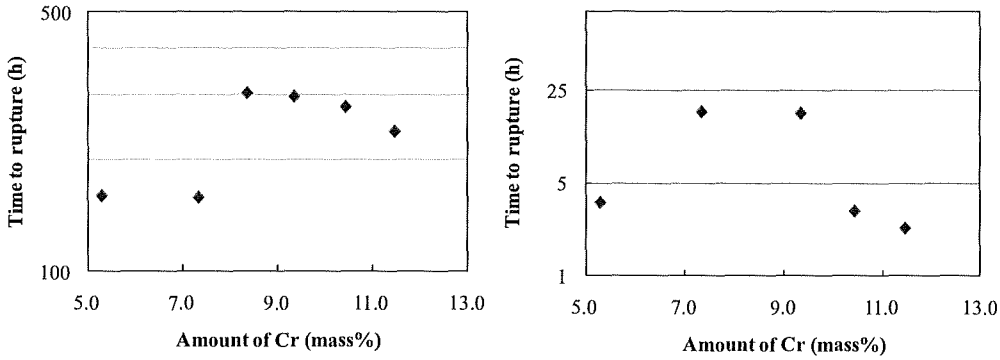

(a) Creep rupture life at 700°C, and at 60MPa *(b) Creep rupture life at 650°C, and at 170MPa*

Fig. 3 Rupture time dependence on the chromium content in the steels

3.3 TEM analysis of Precipitates

Figure 4 shows the micrographs of the thin foil samples showing the microstructure and precipitates at the grain boundary of a creep ruptured specimen at 700°C and at 60 MPa. Precipitates occupied the prior austenitic grain boundary in most cases, therefore no significant migration of the grain boundary was observed as shown in Photograph (d). However, the block boundary, which contained several laths grew wide compared with that of the initial microstructure and the relative straight block boundary was deformed and migrated. Photograph (a) shows precipitates restricting the deformation of the block boundary. The precipitation occupancy ratio seems to be high for the specimens with a relatively long creep life as shown in photographs (b) and (c).

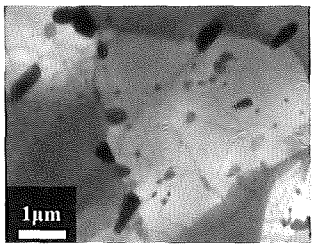

(a) 157.6 hours rupture life for Steel B

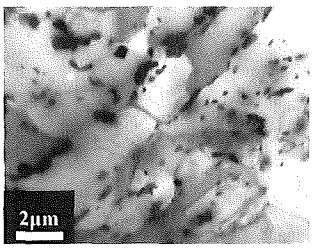

(b) 301.7 hours rupture life for Steel C

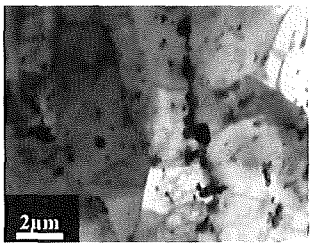

(c) 295.0 hours rupture life for Steel D

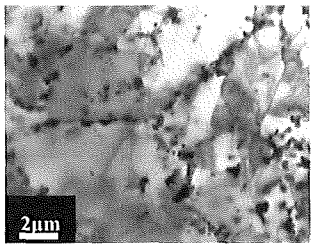

(d) 237.8 hours rupture life for Steel F

Fig. 4 TEM micrographs of the creep ruptured specimen.

Figure 5 shows TEM micrographs of the replica samples, and Figure 6 shows EDX analyses of the precipitates indicated in Figure 5(b) by arrows in Steel D. EDX analysis identified the precipitates as Fe_2W type inter-metallic compound, Laves phase, and $M_{23}C_6$ type carbide. Increase of chromium contents induced the $M_{23}C_6$ precipitation depending on the chromium content. Observation of an extracted replica revealed no change in precipitation morphology of any of the steels.

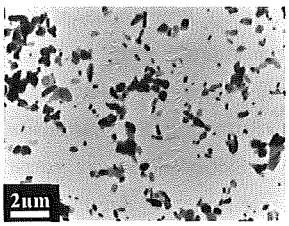

(a) Steel A ruptured after 159.3 hours creep test

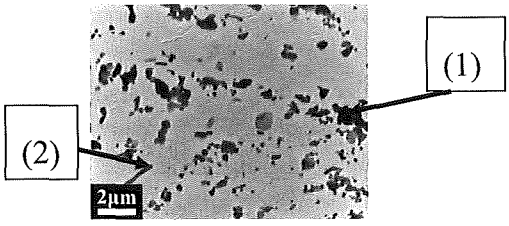

(b) Steel D ruptured after 295.0 hours creep test

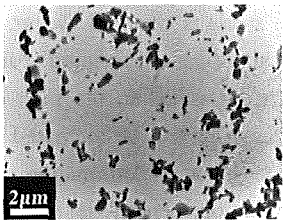

(c) Steel F ruptured after 237.8 hours creep test

Fig. 5 TEM micrographs of replica of creep rupture samples

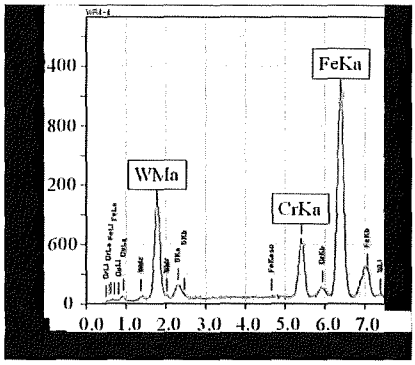

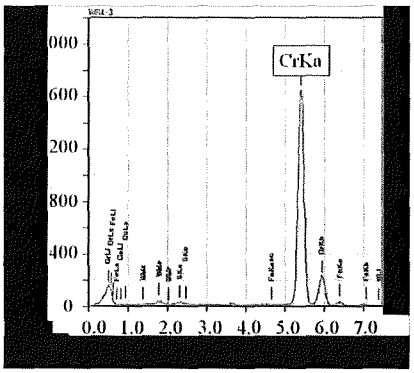

(1) Fe_2W Laves phase *(2) $M_{23}C_6$ type carbide*

Fig. 6 TEM-EDX analyses of precipitates in ruptured specimen of steel D indicated in Fig. 5(b)

4. Discussion

4.1 Decisive microstructure of creep deformation mechanism

The lath structures in Figure 2 almost disappeared in Figure 4. The martensite lath seemed to grow and the lath boundary changed to an ambiguous dislocation substructure boundary. Precipitates can be observed mainly at the high angle grain boundaries and almost no precipitates were observed at the lath boundary in steels before creep. Precipitates at the high angle grain boundary did not disappear even after the creep rupture tests and possibly suppress the bulge of the grain boundary. The coarsening of precipitates was always observed by creep test. In case of high temperature or long-term creep deformation, the martensite lath structure, the minimum component of the microstructure, possibly does not resist the deformation, on the other hand, the block boundary resists the deformation due to the fixing by precipitates. TEM micrographs also indicated the deformation and migration of the block boundary in the creep ruptured specimen. When the migration of the block boundary is not significant, the creep deformation of steels is small. However, creep deformation progresses when block boundary migration is significant. Precipitates fixed the block boundary and suppressed the creep deformation, and resulted in the high creep deformation resistance. Therefore, the creep deformation resistance will be increased when precipitates occupy the high angle grain boundary densely, and the creep deformation resistance will deteriorate when precipitates coarsen and the precipitation density is decreased at the grain boundary. Hypotheses of previous reports on industrial application steels do not estimate the effect of intragranular precipitates such as NbC and VN. The present study was able to relate the creep

rupture strength with the microstructure change because of no addition of an intragranular precipitation strengthening element, for example Nb and V, in the model steels. $M_{23}C_6$ type carbide precipitated at the lath boundary in previous reports. However, TEM observation confirmed little amount of precipitation at the lath boundary in the present study. Especially in the microstructure in which the lath structure disappeared, ignoring the lath boundary precipitation strengthening effect, these research results suggest the possibility of a strengthening mechanism by block boundary precipitation shielding.

4.2 *Relation between grain boundary shielding ratio and creep strength*

Thin foil samples observation by TEM indicated that block boundary shielding by precipitates possibly related to creep strength. Therefore TEM micrographs were used to mesure the block boundary shielding ratio by precipitates. "Shielding ratio" is the occupied length by precipitates on an estimated block boundary observed by TEM, and the measurement method is illustrated in Figure 7. Here, "f" is the grain boundary shielding area ratio obtained from the square of the precipitation occupancy length of the block boundary. Table 3 and Figure 8 show the grain boundary shielding ratio and the correlation with rupture lives. The calculated results indicate a definite correlation between the creep rupture life and the grain boundary shielding ratio.

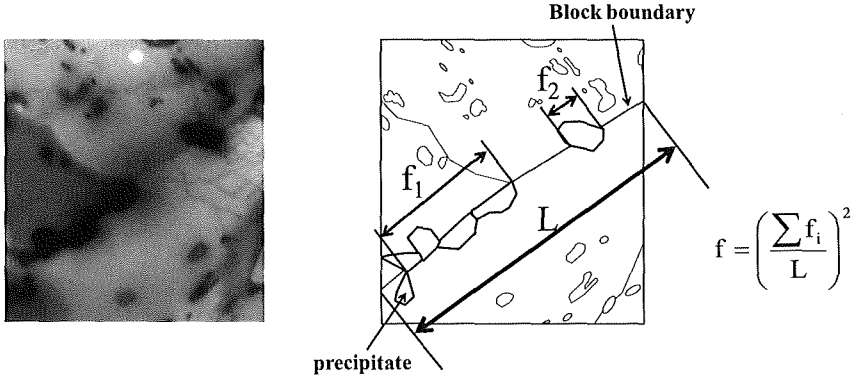

Fig. 7 Measurement and definition of grain boundary shielding ratio

Table 3 Grain boundary shielding ratio by precipitates after creep rupture test (%)

Steel	A	B	C	D	F
Shielding ratio (%)	10.4	7.5	14.0	12.0	11.82
Creep life (h)	159.3	157.6	301.7	295.0	237.8

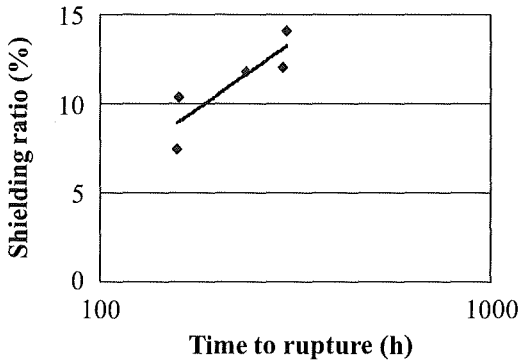

Fig. 8 Relation between creep rupture lives and grain boundary shielding ratio by precipitates

Figure 8 supports the hypothesis that the block structure determines the microstructural deformation resistance, and also the precipitation free boundary bulge with creep deformation as shown in Figure 9. Such grain boundary migration possibly determines the creep deformation. However, the hypothesis can only apply for a microstructure consisting of a block structure, and for a creep condition in which the lath structure migrates easily. The hypothesis cannot yet be applied to a creep condition with high stress and an early creep deformation stage. The optimum chromium content for the creep life shown in Figure 3 and 4 possibly explain the optimum precipitation shielding and alloy design concept.

Further observation and analyses of the microstructure will advance additional possible application of the hypothesis.

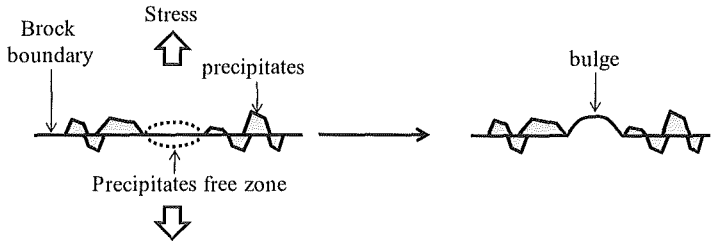

Fig. 9 Schematic image of grain boundary bulge

5. Conclusion

A grain boundary precipitation strengthening hypothesis was suggested based on TEM analyses of precipitates at the high angle grain boundary of creep ruptured specimens of laboratory manufactured model steels with 5 % to 11.5 % chromium content. The following results were also obtained.

(1) Increase of chromium content of the model steels resulted in the increase of hardenability.

(2) Initial microstructure strength and creep life did not correlate

(3) Optimum chromium content is expected for the creep life among the model steels.

(4) TEM observation clarified that precipitates possibly suppress the migration of the block boundary.

(5) Bulge and migration of the block boundary possibly determines the creep deformation.

(6)A definite correlation between the creep rupture life and the block boundary shielding ratio was confirmed experimentally.

6. References

[1] F.Abe, high temperature of steels for power generation, *Materials research outlook 2006*, 11, 334

[2] Y.Kadoya, E.Shimizu, Effect of solute Mo and W on Transient Creep Deformation of High-Cr-Ferritic Steels, *Tetsu-to-Hagane*, 86, 617-624, (2000)

[3] N.Nishimura, M.Ozaki, F.Masuyama, Effect of Dislocations Substructure on Creep Behavior of Steels Strengthened by Fine Carbides, *Key Engineering Materials*, 171-174, 297-303, (2000)

[4] M.Shiga, Y.Fukui, S.Kirihara, S.Kirihara, R.Kaneko, F.Ito, S.Sugai, Improved 12Cr Rotor Forging for Ultra-Super-Critical Steam Turbine, *Tetsu-to-Hagane*, 76, 1092-1099, (1990)

[5] Y.Hasegawa, M.Ohgami, T.Muraki, Grain Boundary Strengthening Mechanism on Tungsten Containing 9 to 12% Chromium Ferritic Heat Resistant Steels at 650℃, *zairyo*, 52, 843-850, (2003)

[6] M.Kimura, K.Yamaguchi, M.Hayakawa, K.Kobayashi, Microstructure and Grain Boundary Precipitates in 9~12% Cr Ferritic Heat-resisting Steels. *Tetsu-to-Hagane*, 90, 27-32, (2004)

[7] Y.Hasegawa, T.Muraki, Discussion of Main Strengthening Factor in W Containing Ferritic Heat Resistant Steels, 71,(2005)

[8] M.Takeyama, K.Kawasaki, T.Matsuo, R.Tanaka, Effect of Grain Boundary Precipitates on High Temperature Creep Properties of Ni-20Cr-Nb-W Alloy, *Tetsu-to-Hagane*, 72, 1605-1612, (2008)

9th Liege Conference : Materials for Advanced Power Engineering 2010
edited by J. Lecomte-Beckers, Q. Contrepois, T. Beck and B. Kuhn.

PREDICTION OF LONG-TERM PRECIPITATE EVOLUTION IN AUSTENITIC HEAR-RESISTANT STEELS

Jae-Hyeok Shim[1], Ernst Kozeschnik[2], Woo-Sang Jung[1], Young Whan Cho[1]

[1]Materials/Devices Division, Korea Institute of Science and Technology, Seoul 136-791, Republic of Korea
[2]Institute of Materials Science and Technology, Vienna University of Technology, A-1040 Vienna, Austria

Abstract

Numerical prediction of the long-term precipitate evolution in five different austenitic heat-resistant stainless steels, NF709, Super304H, Sanicro25, CF8C-PLUS and HTUPS has been carried out. MX and $M_{23}C_6$ are predicted to remain as major precipitates during long-term aging in these steels. The addition of 3 wt% Cu produces very fine Cu-rich precipitates during aging in Super304H and Sanicro25. It is found that the amount of Z phase start to increase remarkably between 1,000 and 10,000 hours of aging at the expense of MX precipitates in the steels containing a high nitrogen content. However, the growth rate of Z phase is relatively slow and its average size reaches at most a few tens of nanometers after 100,000 hours of aging at 700 °C, compared with 9-12 % Cr ferritic/martensitic heat-resistant steels. The predicted precipitation sequence and precipitate size during aging are in general agreement with experimental observations.

Keywords: Heat-resistant steel; Precipitate; Aging; Creep strength; Numerical simulation

1. Introduction

There is urgent need to improve the thermal efficiency of fossil fuel power plants by raising the operation temperature and pressure in order to reduce CO_2 emission as well as the cost of fuel. Plant operation at higher temperatures inevitably requires the development of heat-resistant alloys with a higher creep strength at an acceptable level of creep ductility [1]. 9-12 % Cr ferritic heat-resistant steels have so far been widely used in fossil fuel power plants, owing to their high thermal conductivity, low thermal expansion coefficient and low susceptibility to thermal fatigue. Nevertheless, there has recently been increasing interest in applying austenitic heat-resistant steel to fossil fuel power plants in order to raise their operation temperature, because austenitic heat-resistant steels have a higher creep strength than ferritic ones. It is generally accepted that ferritic and austenitic steels are useful up to about 620 and 675 °C, respectively, purely from the creep strength point of view at a steam pressure of 35 MPa [1].

The important role of precipitation in the achievement of good creep properties of heat-resistant steels has long been recognized. One of the most effective ways for improving the creep properties is to uniformly distribute fine precipitates with a good long-term stability at elevated temperatures. Conventional austenitic heat-resistant steels are known to exhibit quite complicated precipitation behavior together with various precipitates such as carbides,

nitrides and intermetallic phases, as Sourmail [2] gave a detailed review. However, the experimental investigation of the precipitate evolution behavior in austenitic heat-resistant steels, which have recently been developed for applications around 700 °C, have not often been performed, although it is important in understanding the creep properties.

The purpose of this study is to simulate the long-term precipitate evolution in various austenitic heat-resistant steels for applications around 700 °C using a numerical model based on the classical nucleation theory and evolution equations derived from the thermodynamic extremum principle [3,4] that maximizes the dissipation rate of the total Gibbs energy of the system [5,6]. The simulation results, such as the precipitation sequence and the precipitate size, will be compared with experimental observations in the literature.

2. Materials and simulation method

Five different austenitic heat-resistant steels, NF709, Super304H, Sanicro25, CF8C-PLUS and HTUPS have been chosen for the simulation of the precipitate evolution. The chemical compositions of these steels are given in Table 1.

Table 1. Chemical compositions of the austenitic heat-resistant steels (wt%).

Steel	Fe	C	Cr	Ni	Mn	Si	Mo	W	Nb	Ti	V	Cu	N
NF709	bal.	0.15	20.0	25.0	1.0	0.5	1.5	-	0.2	0.1	-	-	0.167
Super304H	bal.	0.1	18.0	9.0	0.8	0.2	-	-	0.4	-	-	3.0	0.1
Sanicro25	bal.	0.08	22.0	25.0	1.0	0.1	-	3.5	0.5	-	-	3.0	0.2
CF8C-PLUS	bal.	0.07	19.0	12.5	4.0	0.5	0.3	-	0.8	-	-	-	0.25
HTUPS	bal.	0.08	14.0	16.0	2.0	0.15	2.5	-	0.15	0.3	0.5	-	0.021

The simulation of the precipitate evolution in the steels has been performed with the thermo-kinetic software package MatCalc (version 5.30) developed by Kozeschnik et al. [7-9], which deals with the kinetics of microstructural processes based on the classical nucleation theory and evolution equations for the radius and composition of each precipitate derived from the thermodynamic extremum principle. The details of the basic principles composing MatCalc are given in the appendix. During the simulation, the thermodynamic and kinetic data are calculated from the MatCalc database 'mc_steel', version 1.18, and the MatCalc mobility database 'mc_sample_fe', version 1.10.

MX, M_3C_2, M_6C, M_7C_3, $M_{23}C_6$, Laves phase, Z phase, σ phase and Cu were included in the simulation as possible precipitates. For the crystal structure and chemical composition of these precipitates, see Sourmail's review [2]. The nucleation sites of MX, $M_{23}C_6$, Laves phase,

Z phase, σ phase and Cu were set to be dislocations, grain boundaries and subgrain boundaries, according to Sourmail's review [2]. It was assumed that M_3C_2, M_6C and M_7C_3 nucleate at grain and subgrain boundaries, as no sufficient information on their nucleation sites is revealed in the literature.

The heat treatment started with the solution treatment at 1200 °C for one hour. It was initially assumed that all elements were homogeneously distributed in the matrix and no precipitates existed. After the solution treatment, the steels were cooled linearly down to room temperature within one hour and then heated up to 700 °C, which corresponds to aging (service) temperature, in 30 minutes. The aging was simulated at 700 °C for 100,000 hours.

3. Results and discussion

Fig. 1(a) shows the variation of the simulated phase fraction of precipitates during the heat treatment in NF709. Three kinds of precipitate, MX, $M_{23}C_6$ and Z phase appear during the heat treatment. The precipitation of MX starts as soon as the solution treatment starts and is almost complete in a very short time. $M_{23}C_6$ and M_7C_3 start to precipitate during the cooling after the solution treatment. While $M_{23}C_6$ stays stable during the long-time aging at 700 °C, M_7C_3 completely disappears after 3,000 hours of aging. The amount of Z phase starts to increase significantly after 10,000 hours of aging and continues to increase until the service terminates, which is in contrast with MX and $M_{23}C_6$ exhibiting the saturation of precipitation in a short time. As the amount of Z phase increases, that of MX starts to decrease slowly. It has been well known that Z phase grows at the expense of MX in 9-12 % Cr ferritic heat-resistant steels containing Nb or V and a high content of nitrogen in a long-term service ..
This growth behavior of Z phase seems to be common in both ferritic and austenitic heat-resistant steels. Sourmail and Bhadeshia [10] investigated the precipitation behavior of NF709 during long-term aging for up to 10,000 hours at 750 °C using TEM and X-ray diffraction (XRD) analyses. The XRD measurements of extracted residues of NF709 revealed that $M_{23}C_6$ remains as a major precipitate together with MX type precipitates such as TiN, NbN and (Ti,Nb)C through the long-term aging, which is in good agreement with the simulated results. Z phase started to precipitate after 200 hours of aging and its fraction consistently increased up to 10,000 hours at the expense mainly of NbN. Although the consistent increase in the fraction of Z phase with increasing aging time agrees with the present simulation, Z phase started to form quite earlier than the simulation. This difference might result from the difference in aging temperature. Since they performed aging at higher temperature than the present simulation by 50 °C, the transformation from MX to Z phase was probably accelerated. They also observed Cr_3Ni_2SiN after 2,500 hours of aging. However, Cr_3Ni_2SiN was unfortunately not included in the present simulation due to the lack of the thermodynamic data .. The precipitation sequence in NF709 proposed by Sourmail and Bhadeshia [10] is MX → MX + $M_{23}C_6$ → MX + $M_{23}C_6$ + Z phase → MX + $M_{23}C_6$ + Z phase + Cr_3Ni_2SiN, which is in agreement with the simulated results. Although they did not present the quantitative information on the phase fraction of precipitates, which can be compared with the

simulation results, the relative fraction ratio of $M_{23}C_6$ to MX can be estimated in the XRD patterns after 2,500 and 5,000 hours of aging. The estimated ratios after 2,500 and 5,000 hours of aging are approximately 5 and 7, respectively, which agrees with the simulated value (~6.4).

The variation of the simulated average precipitate size during the heat treatment in NF709 is given in Fig. 1(b). The size of $M_{23}C_6$ precipitates is generally in the order of hundred nanometers. The size of MX stays around 10 nm during the aging. On the other hand, Z phase continually grows up to about 60 nm during the aging. Sourmail and Bhadeshia [10] summarized the precipitate size after 200 hours of aging at 750 °C in NF709 using TEM. The observed size range of $M_{23}C_6$ was 200 to 500 nm, which is similar to the simulated value in order of magnitude, as shown in Fig. 1(b). The observed size range of Z phase was 20 to 50 nm. There is a significant difference in MX size between the experimental observation and the present simulation. The observed size range of MX was 1 to 5 μm, a few hundred times larger than the simulated one. As Sourmail and Bhadeshia [10] mentioned, these very coarse MX particles were likely to form during solidification and remain undissolved during solution treatment. This simulation considered only the precipitation of MX in austenite, assuming that all the precipitates were not present before the solution treatment. Unfortunately, they did not mention the presence of fine MX precipitates, which form in austenite after the solution treatment.

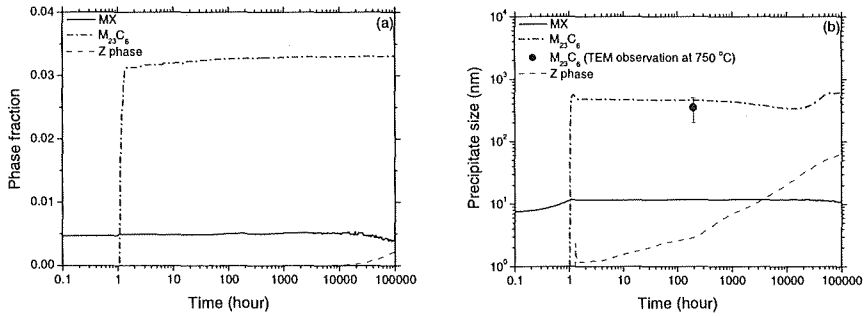

Fig. 1. Variation of the simulated (a) phase fraction and (b) average size of precipitates during heat treatment in in NF709.

Fig. 2(a) shows the variation of the simulated phase fraction of precipitates during the heat treatment in Super304H. Cu develops as a major precipitate during the service in addition to $M_{23}C_6$ and MX. The fraction of $M_{23}C_6$ slowly increases until about 1,000 hours of aging, after the considerable amount of $M_{23}C_6$ forms instantaneously at the initial stage of the aging. Compared with NF709, the precipitation of $M_{23}C_6$ tends to be quite slowly saturated. This might be attributed to a lower driving force for the precipitation of $M_{23}C_6$ in Super304H due to a lower content of Cr and C than in NF709. It is found that the precipitation of Cu is saturated in about 50 hours of aging. Although Z phase starts to form after about 10 hours of

aging, its fraction remarkably increases after about 1,000 hours of aging. The fraction of MX slowly decreases with increasing Z phase fraction after about 1,000 hours of aging. M_7C_3 exists for a short time at the initial stage of the aging. Wu [11] investigated the precipitation behavior in Super304H that had been aged at 700 °C for up to 10,000 hours using TEM analysis. He confirmed that the presence of MX, $M_{23}C_6$ and Cu-rich precipitates, as predicted by the present simulation. However, he did not mention the presence of Z phase, although NbCrN type precipitates were observed without confirming their crystal structure. The variation of the simulated average precipitate size during the heat treatment in Super304H is presented in Fig. 2(b). The size of $M_{23}C_6$ stays around 100 nm until 10,000 hours of aging and it grows relatively fast after 10,000 hours of aging. The size of Cu precipitates stays around 20 nm until 5,000 hours and grows to about 70 nm after 100,000 hours. While MX maintains its size at about 50 nm through the aging, Z phase continually grows up to about 20 nm. Wu [11] measured the sizes of $M_{23}C_6$ and Cu-rich precipitates using TEM between 100 and 3,000 hours of aging. The measured sizes are compared with the simulated ones in Fig. 2(b). The comparison exhibits the accordance in the order of magnitude, although the growth rate of Cu-rich precipitates observed by TEM is faster.

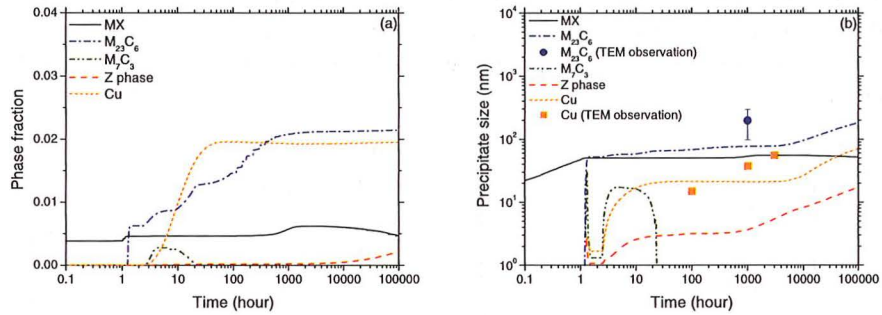

Fig. 2. Variation of the simulated (a) phase fraction and (b) average size of precipitates during heat treatment in in Super304H.

As shown in Fig. 3(a), the simulated precipitate evolution in Sanicro25 is similar to that in Super304H, except that M_7C_3 does not form and the precipitation of $M_{23}C_6$ and Cu exhibits faster saturation behavior. Rautio and Bruce [12] performed microstructural examination of Sanicro25 aged at 700 °C for up to 3,000 hours using scanning electron microscopy (SEM) and TEM. They observed $M_{23}C_6$ and Nb-rich precipitates that were enriched with Cr. The observed Nb-rich precipitates can be Z phase and/or MX enriched with Cr, since Cr continues to be enriched in MX during the aging. The enrichment of Cr in MX during aging is common in the simulated austenitic heat-resistant steels. However, they did not mention whether Cu precipitates existed or not in aged samples. The simulated average size of MX and Z phase in Sanicro25 is very similar to that in Super304H, as shown in Fig. 3(b). On the other hand, the sizes of $M_{23}C_6$ and Cu in Sanicro25 are quite larger than those in Super304H. Unfortunately,

Rautio and Bruce [12] did not give the information on the precipitate size comparable with the simulation results.

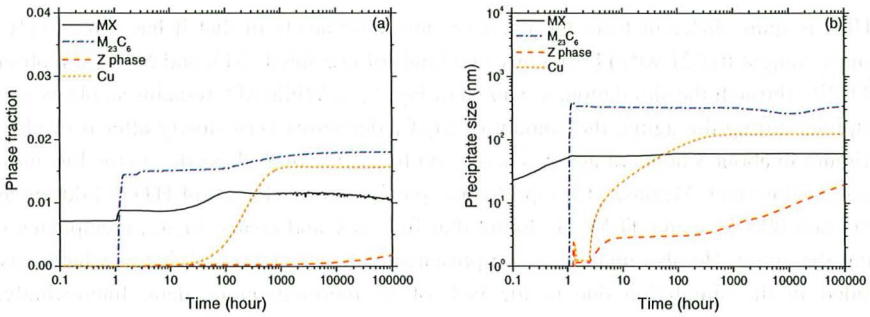

Fig. 3 .. Variation of the simulated (a) phase fraction and (b) average size of precipitates during heat treatment in in Sanicro25.

The simulated precipitation evolution in CF8C-PLUS is also similar to that in Super304H, except that Cu precipitates do not form and the fraction of MX is larger (Fig. 4(a)). Actually, CF8C-PLUS exhibits the largest amount of MX among the simulated steels, which might be attributed to the largest content of Nb in CF8C-PLUS. Shingledecker et al. [13] observed $M_{23}C_6$ and MX precipitates consisting mainly of NbC in CF8C-PLUS aged at 850 °C for 24,100 hours. They did not mention the presence of other precipitates, although it is predicted that a small fraction of M_7C_3 appears and disappears at the initial stage of aging and the fraction of Z phase starts to increase remarkably after about 7,000 hours at the expense of MX. The variation of the simulated average precipitate size during the heat treatment in Super304H is presented in Fig. 4(b). The simulated average precipitate size of MX and Z phase in CF8C-PLUS is very similar to that in Super304H and Sanicro25. The size of $M_{23}C_6$ shows a tendency to increase continually during aging and exceeds that of MX after about 1,000 hours .. The size of MX precipitates that form in austenite Shingledecker et al. [13] observed using TEM at 850 °C ranges from 30 to100 nm, which is in good agreement with the simulated one, as shown in Fig. 4(b).

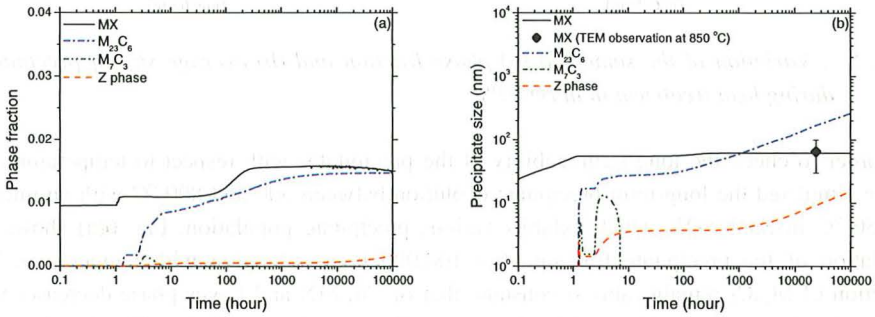

Fig. 4. Variation of the simulated (a) phase fraction and (b) average size of precipitates during heat treatment in in CF8C-PLUS.

HTUPS is quite different from the previous austenitic steels in that it has a relatively low nitrogen content (0.021 wt%) [14]. Only two kinds of precipitate MX and $M_{23}C_6$ are observed in HTUPS through the simulation, as shown in Fig. 5(a). While MX remains stable as a major precipitate during the aging, the amount of $M_{23}C_6$ decreases very slowly after it reaches the maximum in about 3 hours of aging. There is no formation of Z phase due to the low nitrogen content in this steel. Maziasz [15] reported the precipitation behavior of HTUPS during aging at 700 and 800 °C using TEM. He found that fine MX and coarse $M_{23}C_6$ precipitates form during the aging. He also mentioned the presence of fine FeTiP precipitates, which was not included in the simulation due to the lack of its thermodynamic data. Interestingly, he observed that Laves phase (Fe_2Mo) precipitates form occasionally adjacent to the austenite grain boundary, which is not predicted in the simulation. Actually, Laves phase was not experimentally observed in the previous austenitic steels. The reason for the formation of Laves phase adjacent to the grain boundary is presumably because HTUPS has a relatively high content of Mo (2.5 wt%) and Mo tends to segregate to austenite grain boundaries so that the local concentration of Mo can be enough to form Laves phase [16]. The average size of MX precipitates is maintained at about 80 nm during the aging in the simulation, which agrees with the size (30-100 nm) after 168 hours of aging at 800 °C measured by Maziasz [15] and the average size of $M_{23}C_6$ precipitates continues to increase and exceeds that of MX precipitates after about 2,000 hours of aging (Fig. 5(b)).

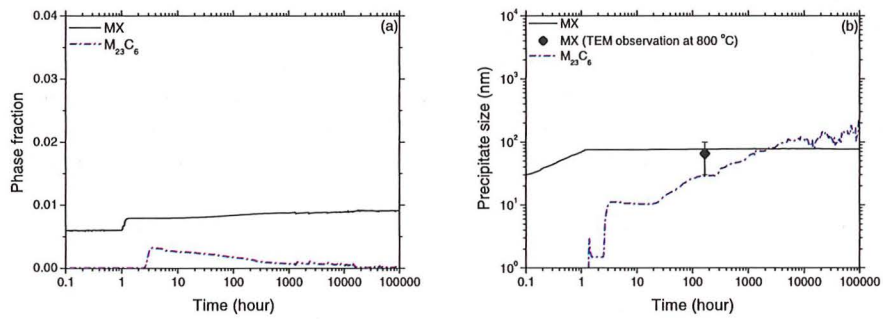

Fig. 5 .. Variation of the simulated (a) phase fraction and (b) average size of precipitates during heat treatment in in HTUPS.

In order to check the long term stability of the precipitates with respect to temperature, we have simulated the long-term precipitate evolution between 500 and 800 °C with an interval of 50 °C in Sanicro25, which exhibits various precipitate population. Fig. 6(a) shows the variation of the precipitate fraction after 100,000 hours of aging with temperature. The fraction of $M_{23}C_6$ remains almost constant, that of Cu, MX and Laves phase decreases with increasing temperature. MX and Z phase show the opposite correlation. The fraction of Z

phase increases as much as that of MX decreases and exceeds that of MX at 750 °C. The formation of Laves phase is predicted below 650 °C, whereas the formation of Laves phase is not predicted even below 650 °C in the other steels. For comparison, the equilibrium phase fraction of the precipitates calculated by MatCalc is presented in Fig. 7. It is found that the precipitation behavior of $M_{23}C_6$ and Cu after 100,000 hours of aging approaches the equilibrium irrespective of temperature. The fraction of Z phase is much less than its equilibrium value below 750 °C and instead MX takes the place of Z phase. This is presumably because the precipitation kinetics of Z phase is particularly slow. The precipitation start temperature of Laves phase is quite lower than its equilibrium value, which implies that Laves phase needs a relatively large driving force for precipitation. The corresponding variation of the average precipitate size is plotted in Fig. 6(b). As expected, the size of all the precipitates exhibits increases with increasing temperature. Especially, the growth tendency of $M_{23}C_6$ is very large. On the other hand, the size of MX does not vary much with respect to temperature. The size of Z phase becomes similar to that of MX at 800 °C ..

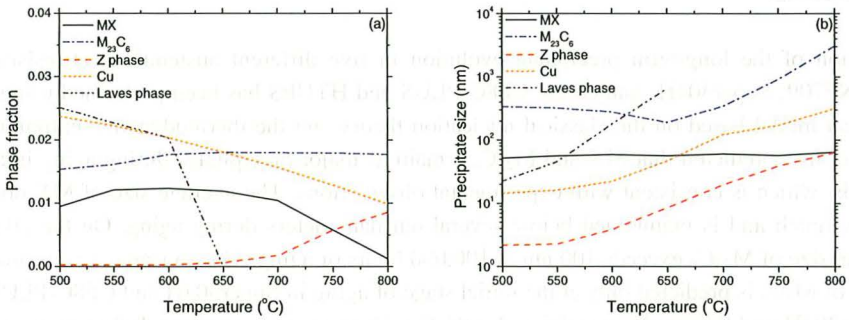

Fig. 6 .. Variation of the simulated (a) phase fraction and (b) average size of precipitates after 100,000 hours of aging with aging temperature in Sanicro25.

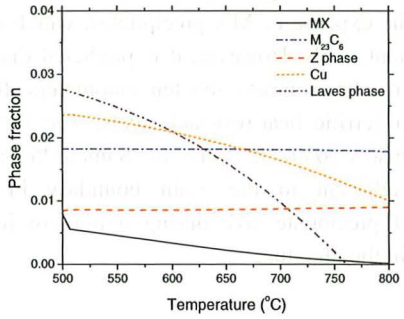

Fig. 7. Variation of the equilibrium phase fraction of precipitates with temperature.

The formation of Z phase has been regarded as a main cause of a drastic loss of the creep strength in 9-12 % Cr ferritic heat-resistant steels, because Z phase dissolve fine MX precipitates that are major contributors to creep strength over long periods of time [17]. However, it has not been well known if the formation of Z phase is also detrimental to the creep strength in austenitic heat-resistant steels. In 9-12 % Cr ferritic heat-resistant steels, the amount of Z phase tends to increase remarkably at the expense of MX precipitates after 10,000-30,000 hours of aging and it grows very fast up to several hundred nanometers [17]. On the other hand, our simulation results show that Z phase grows relatively slowly and its average size reaches at most a few ten nanometers after 100,000 hours of aging in austenitic heat-resistant steels, although the amount of Z phase starts to increase significantly between 1,000 and 10,000 hours of aging, which is quite early compared with 9-12 % Cr ferritic heat-resistant steels. Therefore, it seems that the formation of Z phase is not so detrimental to the creep strength in austenitic heat-resistant steels as 9-12 % Cr ferritic heat-resistant steels, although it is difficult to judge if the formation of Z phase is rather beneficial.

4. Conclusions

Simulation of the long-term precipitate evolution in five different austenitic heat-resistant steels, NF709, Super304H, Sanicro25, CF8C-PLUS and HTUPS has been performed using a numerical model based on the classical nucleation theory and the thermodynamic extremum principle. It is predicted that MX and $M_{23}C_6$ remain as major precipitates during aging in all the steels, which is consistent with experimental observations. The average size of MX does not vary much and is maintained below several ten nanometers during aging. On the other hand, the size of $M_{23}C_6$ exceeds 100 nm at 100,000 hours of aging. The appearance of a small amount of M_7C_3 is predicted only at the initial stage of aging in Super304H and CF8C-PLUS. In Super304H and Sanicro25 containing 3 wt% Cu, Cu starts to precipitate during aging and the precipitation of Cu is saturated before 1,000 hours of aging. Although the size of Cu precipitates is very fine like MX precipitates, they tend to grows continually during aging. The formation of Z phase is predicted in all the steels except HTUPS, which has a relatively low nitrogen content. The fraction of Z phase starts to increase remarkably between 1,000 and 10,000 hours of aging at the expense of MX precipitates, which is similar to the case in 9-12 % Cr ferritic heat-resistant steels. However, it is predicted that Z phase grows relatively slowly and its average size reaches at most a few ten nanometers after 100,000 hours of aging, compared with 9-12 % Cr ferritic heat-resistant steels. The formation of Laves phase is predicted during aging below 650 °C only in Sanicro25, although Laves phase is experimentally observed adjacent to the grain boundary in HTUPS. The simulated precipitation sequence and precipitate size during aging are in general agreement with experimental observations in the literature.

References

[1] R. Viswanathan, J.F. Henry, J. Tanzosh, G. Stanko, J. Shingledecker, B. Vitalis, R. Purgert, J. Mater. Eng. Perform. 14, 281-292 (2005) ..

[2] T. Sourmail, Mater. Sci. Tech. 17, 1-14 (2001).
[3] L. Onsager, Phys. Rev. 37, 405-426 (1931).
[4] L. Onsager, Phys. Rev. 38, 2265-2279 (1931).
[5] J. Svoboda, I. Turek, F.D. Fischer, Philos. Mag. 85, 3699-3707 (2005).
[6] J. Svoboda, F.D. Fischer, P. Fratzl, E. Kozeschnik, Mater. Sci. Eng. A 385, 166-174 (2004).
[7] E. Kozeschnik, J. Svoboda, P. Fratzl, F.D. Fischer, Mater. Sci. Eng. A 385, 157-165 (2004).
[8] E. Kozeschnik, J. Svoboda, F. D. Fischer, CALPHAD 28, 379-382 (2004).
[9] http://www.matcalc.com.
[10] T. Sourmail, H.K.D.H. Bhadeshia, Metall. Mater. Trans. A 36A, 23-34 (2005).
[11] Q. Wu, Ph.D. Dissertation, University of Cincinnati, 2006.
[12] R. Rautio, S. Bruce, Sandvik Sanicro 25: A new material for ultrasupercritical coal fired boilers, Technical article, Sandvik Materials Technology, 2004.
[13] J.P. Shingledecker, P.J. Maziasz, N.D. Evans, M.J. Pollard, Int. J. Press. Vessels Piping 84, 21-28 (2007).
[14] T ..S. Byun, K. Farrell, E.H. Lee, J.D. Hunn, L.K. Mansur, J. Nuclear Mater. 298, 269-279 (2001) ..
[15] P.J. Maziasz, JOM 41(7), 14-20 (1989).
[16] S.-H. Song, R.G. Faulkner, P.E.J. Flewitt, Mater. Sci. Eng. A 281. 23-37 (2000).
[17] J. Hald, Int. J. Press. Vessels Piping 85, 30-37 (2008).

9th Liege Conference : Materials for Advanced Power Engineering 2010
edited by J. Lecomte-Beckers, Q. Contrepois, T. Beck and B. Kuhn.

FUNDAMENTAL MODELLING OF PARTICLE STRENGTHENED 9-12% CR STEELS

Hans Magnusson and Rolf Sandström

Materials Science and Engineering and Brinell Centre,
KTH, 100 44 Stockholm, Sweden, hansm@mse.kth.se

Abstract

Creep strength of particle strengthened 9-12% Cr steels can be predicted by fundamental modelling. The creep strength is evaluated from the state of the microstructure during creep. Particle hardening at high temperatures can be predicted by taking dislocation climb across particles into account. Work hardening is calculated from immobile dislocations in subgrain interiors and at boundaries using the composite theory. Subgrain coarsening will lower the influence of the mechanically hard boundaries. Recovery in dislocation density is predicted through static recovery by climb and dynamic recovery by locking and dipole formation. Solid solution hardening is needed in order to explain the difference in creep strength between different 9-12% Cr steels. The accumulation of large atoms such as Mo and W will slow down the dislocation climb velocity, and thereby the microstructure recovery rate. 100000h rupture strength is predicted for X20, P91, P92 steels without any use of fitting parameters. The creep strength of P91 steel with different microstructure due to Al additions, Z-phase transformation and heat affected material is presented.

Keywords: Creep rate modelling; heat affected zone; Z-phase; AlN; fundamental modelling;

1 Introduction

The nature of creep, with a continuous high temperature deformation taking place over long times makes it understandable that a fundamental model for creep requires a careful description of how the microstructure develops in these conditions. The combination of high temperature, deformation and long-term exposure can activate several different metallurgical processes in the material. It therefore becomes a rather comprehensive task to produce a general model for creep based on this physical understanding. As a consequence, practically all descriptions for primary creep, secondary, and tertiary creep such as the Φ-model, the Norton-model, and the Ω-model have been established in an empirical way by analysis of experimental data. With such approaches, the evaluated creep data for an evaluated material can be well reproduced by the creep model, although it will probably fail when applied to other materials, temperatures, or stress levels.

Fundamentally based classical models, such as the model by Weertman for secondary creep [1] involve a number of constants that are difficult or impossible to give a value with good precision. As a consequence, it will become difficult to estimate how these constants will vary for different conditions. This lack of precision makes it impossible to use these kinds of models for example in alloy development. In addition, there is a serious limitation in using these models for extrapolation of creep data or in the residual life time assessment of service exposed material. In order to develop an applicable model for creep, the underlying mechanisms that are used as input in creep curve modelling must also have a physical basis.

9-12% Cr steels are cost efficient materials used in high temperature applications where creep is of importance. The oxidation resistance requires the high Cr content, although the mechanical strength relies on minor additions of alloying elements. These elements will

precipitate into carbides and nitrides which are more or less stable during creep. In the tempered state of 9-12% Cr steel MX and $M_{23}C_6$ particles are present. During creep, Laves phase and the modified Z-phase will precipitate [2, 3]. Laves phase is typically fully precipitated for 9% Cr steels within 10000h, whereas Z-phase requires more than 50000h for any significant precipitation.

Alloying influences creep strength by the precipitation of stable particles. In addition, those elements that do not precipitate can produce solid solution hardening. The existence of solid solution hardening for particle strengthened steels is not fully clarified [4]. On the other hand, when analysing nearly pure metals there are clear indications of the presence of solid solution hardening at creep. Some examples of solid solution hardening are Al-Mg, Au-Ni, Cu-P and Fe-Mo systems [5, 6, 7, 8]. For particle strengthened steels there are several possible strengthening mechanisms that have to be taken into consideration, and it is not straightforward to separate the solid solution contribution from the other strengthening mechanisms. However, by simulating creep strength for a range of alloys it will become clear that solid solution hardening is an important mechanism.

The creep strength of 9-12% steels as well as of other commercial alloys is related to the state of the microstructure. Microstructure evolution can be predicted by combining tools for thermodynamic modelling with modern dislocation theory. As the microstructure evolution is described the strength can be predicted throughout creep. Based on this approach, a fundamentally derived model for creep can be developed, thus the creep curve can be predicted. The outline of this paper is to summarise the main assumptions of the creep model for particle strengthened materials. Simulated creep strength will be presented for different 9-12% Cr steels without any use of fitting parameters. The influence on creep strength by Al additions, growth of modified Z-phase, and heat affected material will be discussed.

2 Basic assumptions in creep modelling

The work hardening is based on Orowan's equation but expanded with the help of the model of Roters et al. [9]. Different types of dislocations are involved, such as free dislocations and immobile dislocations at subgrain interiors and boundaries. This enables the description of transient creep also in the cases of 9 and 12% Cr steels [10]. The model for dynamic recovery is taken from [9]. This model has a form similar to the empirical approach by Bergström and Hallen [11], but where the constants have a fundamental meaning and their values can be derived. Static recovery is derived using Hirth and Lothe's expression for climb rate [12]. In recovery creep a balance is assumed between work hardening and static recovery. Taking this balance into account the Norton equation can be derived. For pure copper it is shown that realistic values can be obtained for the constants in the Norton equation over a wide temperature range [13]. The evolution in dislocation density for free dislocations ρ_f and immobile dislocations ρ_{im} are summarised as [10]:

$$\begin{cases} \dfrac{d\rho_f}{dt} = \dfrac{1}{L_{eff}}\dfrac{\dot{\varepsilon}m}{b} - 2\rho_f \dfrac{\dot{\varepsilon}m}{b}\left[\dfrac{d_{dip}}{n_{slip}} + \dfrac{2d_{lock}(n_{slip}-1)}{n_{slip}}\right] \\ \dfrac{d\rho_{im}}{dt} = \dfrac{\dot{\varepsilon}m}{b} 4d_{lock}\dfrac{n_{slip}-1}{n_{slip}}\rho_f - 2M_{cl}T_L\rho_{im}^2 \end{cases} \quad (1)$$

$\dot{\varepsilon}$ is the creep rate, L_{eff} the mean free path, m Schmidt factor, b Burgers vector, M_{cl} the climb mobility, T_L the dislocation line tension. Expressions and values for d_{dip} the dipole distance, d_{lock} the locking distance, and n_{slip} the number of active slip systems are given by Roters et al [9].

The 9-12% Cr steels have a dense dislocation structure, as a consequence of the martensitic transformation when cooling from the austenite regime. The subgrain size is assumed to be primarily controlled by coarser particles that are situated at the subgrain boundaries. The coarsening of the substructure during creep takes place by the exchange of dislocations with the subgrain interiors, coarsening of particles, and the intrinsic coarsening of the substructure [14]. The subgrain growth is given by:

$$\frac{dw}{dt} = \frac{3M_{cl}T_L}{2w} \cdot \left[1 - \left(\frac{w}{w_{\inf}}\right)^2\right]^2 \tag{2}$$

where the long-term subgrain size is given from the particles that hold back the growth as $w_{\inf} = 2r_p\sqrt{3\pi/2f_{p,h}(r_{crit})}$, where r_p is the particle size, $f_{p,h}(r_{crit})$ the phase fraction particle at boundary which are not climbed, as will be explained later by Eqn. (5) and (6).

In 9 and 12% Cr steels particle growth and coarsening are frequently occurring. Both these processes are controlled by the diffusion of alloying elements. Fundamental models and data for diffusion controlled growth and coarsening are well established. How to estimate the multi-component coarsening coefficients to be used in Ostwald ripening expressions are given by Ågren et al [15]. The growth or dissolution rate can be estimated by assuming a local equilibrium at the particle and matrix interface. The movement of the interface is then calculated by solving the diffusion equations for a given multi-component system. These equations can be solved by using the DICTRA software [16]. The coarsening, growth and dissolution processes will determine the number density of particles. The individual particle spacing is given by [18, 21]:

$$L_{p,j,i} = 1.23r_{p,j}\sqrt{\frac{2\pi}{3f_{p,j,i}(r_{crit})}} \tag{3}$$

where i denotes the region subgrain interiors of walls, and j the precipitate kind. For $M_{23}C_6$ and Laves it is assumed that these particles are mostly located at boundaries, using the long term distribution given by Straub et al [17]. The MX particles are assumed to be homogeneously distributed. The summarised particle spacing using a Pythagorean addition is [18]:

$$\frac{1}{L^2_{p,tot,i}} = \frac{1}{L^2_{p,MX,i}} + \frac{1}{L^2_{p,M23,i}} + \frac{1}{L^2_{p,Laves,i}} \tag{4}$$

Fundamental modelling of particle strengthened steels requires a detailed understanding on how the particles will influence the creep strength. In the past, two main approaches have been used to estimate the amount precipitation hardening during creep. The first one is based on the Orowan mechanism, which itself is a temperature independent mechanism. The second

kind of approach is related to the amount of energy that is required to climb across particles. This latter approach gives a hardening of only a few percent of the creep stress [19]. It is clear that none of these mechanisms alone can reproduce the temperature dependence of experimental creep data. A more reasonable situation would be to analyse the amount of dislocation climb as function of climb and glide parameters [20]. This gives the possibility to simulate creep strength at high temperatures and low stresses even though there is a relatively stable particle structure that would suggest a high strength according to Orowan. The largest particle size that can be climbed is given by [21]:

$$r_{crit} = L_{p,tot} \cdot M_{cl} b \sigma_{eff} \cdot \frac{b\rho_f}{\dot{\varepsilon} m} \tag{5}$$

σ_{eff} is the effective stress. The second factor on the right hand side is the climb velocity of a dislocation, and the third term is the inverse of the glide velocity. For instance, a high temperature will promote dislocation climb through the climb mobility factor, while a high creep rate will give little time for climb. By using a size distribution, the remaining phase fraction that is not climbed can be determined. The precipitates can be represented by a cumulative size distribution. The area fraction of particles $f_{p,j}(r)$ that are larger than a given particle size r can be expressed as [20]:

$$f_{p,j}(r_{crit}) = F_{p,j} \exp\left(-\beta_j (r - r_{res,j})\right) \tag{6}$$

$F_{p,j}$ is the equilibrium area fraction of particle kind j, $r_{res,j}$ the smallest accurately recorded particle size, and β_j a constant.

Some alloying elements form Cottrell atmospheres around the dislocations that slow down their speed. Following Takeuchi and Argon the effect of solid solution by dragging Cottrell atmosphere can be estimated. The climb mobility for pure metals M_s and the solute drag mobility M_d [12, 22, 23]

$$\begin{cases} M_s = \dfrac{2\pi D_s v_{atom}}{b^2 kT \ln(r_2/r_1)} \\ M_d = \dfrac{v_{atom} D_i kT}{c_{0,i} \beta_{m,i}^2 \ln(r_2/r_1)} \end{cases} \tag{7}$$

where D_s is the self diffusion coefficient, D_i the diffusion coefficient of solutes in ferrite matrix, $c_{0,i}$ the concentration of solutes, $\beta_{m,i}$ the size interaction parameter of solutes [22, 23], v_{atom} the atomic volume, $\ln(r_2/r_1)$ the ratio between outer and inner cut-off. Diffusion coefficient and concentrations can be evaluated by DICTRA software using mob2 database [16]. The resulting climb mobility M_{cl} is determined from $1/M_{cl} = 1/M_s + 1/M_d$ [22], which implies that the lowest mobility will dominate.

The strengthening from dislocations, substructure, and particles but not from solid solution hardening is taken into account by introducing a back stress. The back stress $\sigma_{back,i}$ is calculated from the separate contribution of subgrain interiors and walls, according to the

composite model [24, 25]. The stress in each region i is the contribution from immobile dislocations $\sigma_{def,i}$ and particle strengthening $\sigma_{part,i}$:

$$\sigma_{back,i} = \sigma_{def,i} + \sigma_{part,i} = \alpha m G b \sqrt{\rho_{im,i}} + \frac{2mT_L}{bL_{p,tot,i}} \quad (8)$$

where αm is a constant that is approximately unity, and $\rho_{im,i}$ the immobile dislocation density. The total back-stress is summarised according to the composite theory $\sigma_{back,tot} = f_s \sigma_{back,s} + f_h \sigma_{back,h}$, where f_s and f_h are the area fractions of subgrain interiors and boundaries.

The creep curve is modelled by using the modified Norton equation. This expression summarises the temperature and stress dependence of creep. By using effective stresses, which is the applied stress minus the obstructing back stress, the role of microstructure can be included in the equation:

$$\dot{\varepsilon} = A_N \exp\left(-Q_C/RT\right)\left(\sigma_{app} - \sigma_{back,tot}\right)^n \quad (9)$$

where A_N is the Norton constant. Q_C is the activation energy for self diffusion, and n the Norton exponent with value $n = 5$. The Norton exponent has been derived on a fundamental basis, and is a typical value for pure Fe [10, 26]. The activation energy is evaluated for a P91 composition giving $Q_C = 293$ kJ/mol [16]. The temperature and stress dependent backstress will cause higher effective values of the stress exponent and the activation energy, which is in agreement with experimental observation. This will be shown in the following section.

3 Results

Figure 1 presents the results from creep modelling of P91 at 450-650°C and rupture times at 1000-50000h. Predictions are compared to the ECCC mastercurve [27]. The predictions show a rather good correspondence to the observations at high temperatures, although there is some disagreement at 450°C and shorter times to rupture.

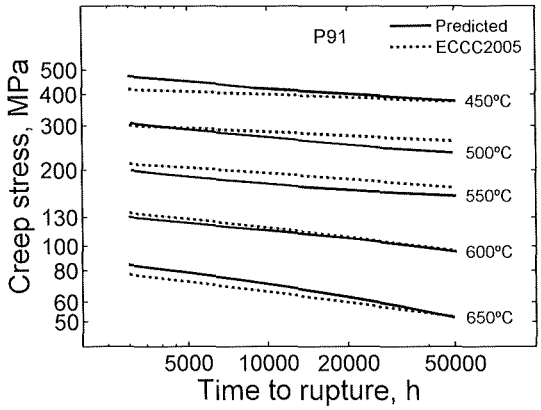

Figure 1. Predicted rupture stress for P91 at 450-650°C and 1000-50000h rupture times. Predictions are compared to the ECCC2005 mastercurve [27].

Figure 2 shows the predicted 100000h rupture stress as function of temperature for P91, P92 and X20 material. A comparison is made with values from the ECCC assessment of P91 [27].

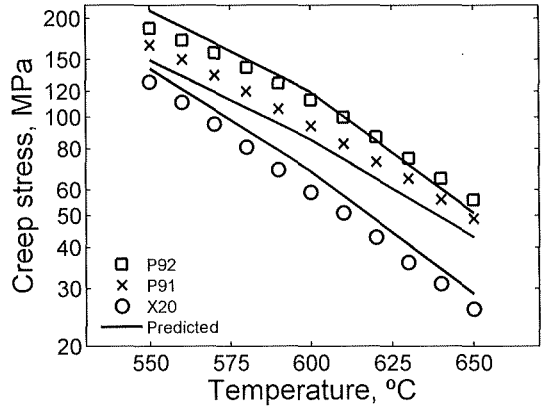

Figure 2. Predicted 100000h rupture stress of steels X20, P91 and P92. Predictions are compared to values from ECCC assessment [27].

Figure 3 presents the influence of solid solution hardening by giving the climb mobility with solutes divided with the climb mobility for pure metals, according Eqn. (7). The solid solution hardening is calculated from W, Mo, V, and Cr, where the first element is the most important one. Equilibrium concentrations are used. P92 has a high amount of Mo and W in solid solution, even after Laves phase precipitation. P91 and X20 rely mainly on a rather high Mo concentration in solid solution. The high phase fraction of $M_{23}C_6$ in steel X20 consumes a greater part of the Mo additions, thereby producing less solute hardening compared to P91. At 550°C the solid solution hardening lowers the climb mobility 15 times for P92, 7 times for P91, and 5 times for X20 compared to the climb mobility for pure Fe.

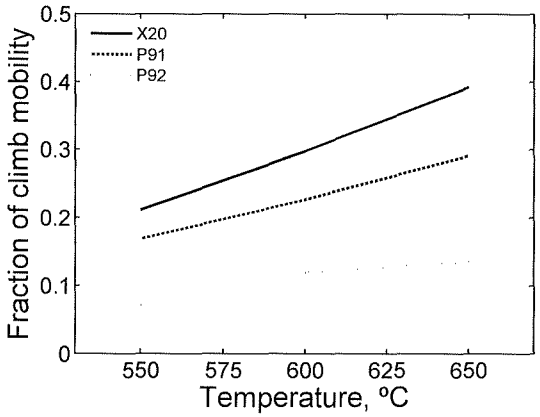

Figure 3. Decrease in climb mobility due to solute hardening compared to the climb mobility for pure metals.

The long-term subgrain size after 100000h simulation at 550-650°C is presented in Figure 4. The rupture stresses for the different materials are from Figure 2. The subgrain growth follows Eqn. (2). The climb parameter in this expression is predicted throughout creep by Eqns. (5) and (6), and its square root increases approximately linearly with the applied stress. The predictions are compared to a well proven empirical relation, with subgrain size inversely proportional to the stress.

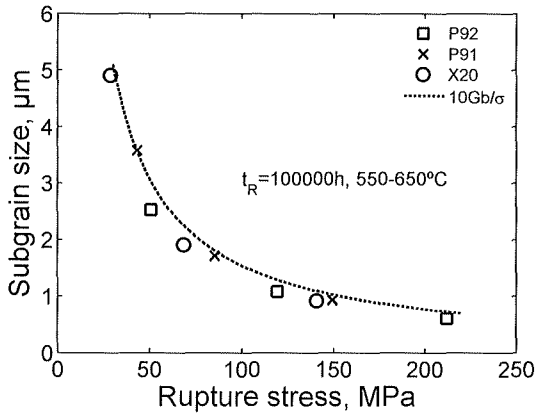

Figure 4. Subgrain size as function of 100000h rupture stress at 550-650°C. Predictions are compared to an empirical relation for subgrain size.

The interparticle spacing in subgrain interiors after 100000h at 550-650°C is presented in Figure 5 for X20, P91 and P92 material. It is shown how the X20 material has a rather dense distribution of $M_{23}C_6$ particles that are quite stable at 550°C, although they cannot withstand the coarsening at higher temperatures. The coarsening rate of $M_{23}C_6$ particles is more than 100 times higher compared to MX particles. Following experimental data from [3, 28], interfacial energies for $M_{23}C_6$ coarsening in P92 are 0.1 J/m^2, in P91 1J/m^2, and for X20 5J/m^2. The high interfacial energies for both P91 and X20 might suggest that the growth is not

fully completed after tempering, or that the initial coarsening depends on the solubilities given by the equilibrium at tempering temperatures rather than at creep temperatures [3]. However, the main difference in particle spacing is found between X20 compared to P91 and P92, where the latter materials relies on the more stable MX particles.

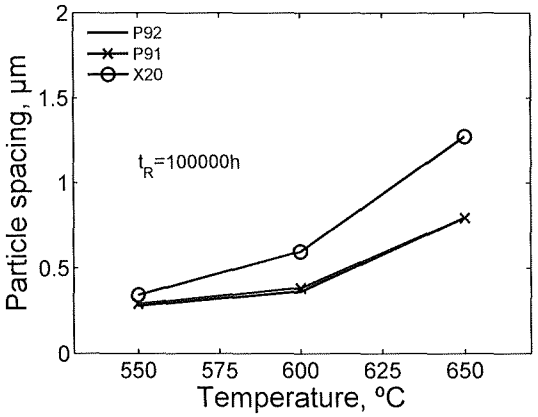

Figure 5. Predicted particle spacing after 100000h at 550-650°C

The growth of modified Z-phase due to the dissolution of MX particles has been simulated. Diffusion of V from the dissolving VN particles to the growing Z particle is the rate controlling step. At higher temperatures the nucleation of Z particles will probably be rate controlling [2]. The simulations are performed at 550-650°C for a Fe-9Cr-0.2V-0.05N composition. The calculations are performed for a two-cell calculation. In the first cell there is a single Z-phase particle that will grow on the expense of the MX particles in the other cells. In order to have a more significant dissolution and loss in number density of particles, the MX cell is multiplied by 100. This means that every Z particle replaces 100 VN particles. Dissolution of a 20nm VN radius results in a 175nm Z radius. The size of the simulation cell is chosen so that a correct mass balance of elements is achieved. For a spherical geometry the following expression can be used $f_{p,MX} = (r_{MX}/r_{cell})^3$, where $f_{p,MX}$ is the equilibrium phase fraction of MX particles, r_{MX} the size of MX particle and r_{cell} the size of the simulation cell. Figure 6 presents the dissolution rate of MX particles, and thereby the growth rate of Z phase. The results show how the transformation rate increases with temperature due to a quicker diffusion of mainly V in matrix. The timescale suggests that Z-phase transformation will only be of practical importance at 650°C for 9% Cr steels.

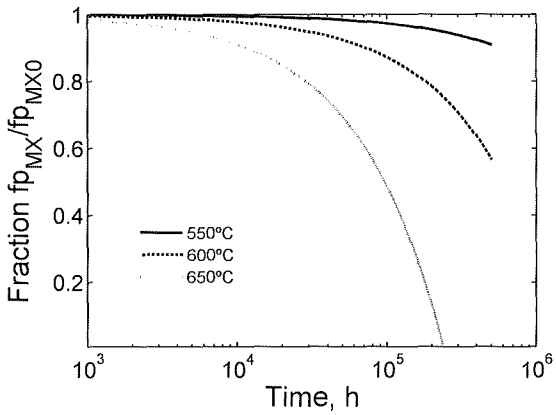

Figure 6. Predicted dissolution rate of MX particles due to Z phase growth at 550-650°C.

Figure 7 shows the influence of Z-phase transformation at 650°C on rupture strength. The predictions are made for steel P91 with and without Z-phase according to Figure 6. At 40MPa the difference in rupture time is approximately a factor 2.

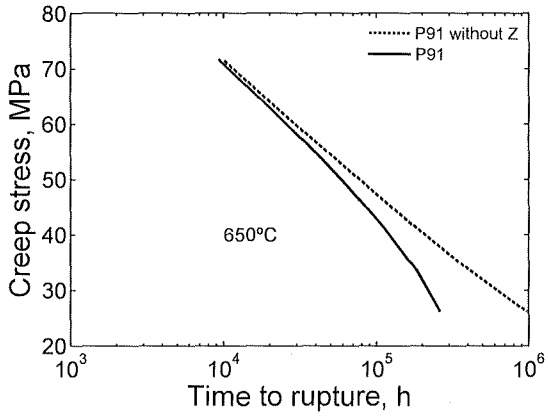

Figure 7. Influence of Z phase transformation on 650°C ruptures stress.

The influence of Al on creep strength has been analysed [29]. In this work another geometric distribution for $M_{23}C_6$ particles is used, compared to the previous work [29]. The simulations follow the suggestions by Straub et al [17], although the long-term distribution of particles is used in this work rather than the initial distribution that was used in previous work. These values indicate a less homogeneous distribution of $M_{23}C_6$, which suggests that these particles are mostly located at subgrain and grain boundaries. This will increase the relative importance of MX particles which are more homogeneously distributed. As a consequence, any change in the MX population will have a more severe effect. The equilibrium phase fractions of MX and AlN phases are shown in Figure 8 as function of Al concentration for a P91 steel at 600°C. It is clearly shown how the AlN particles are formed at the expense of the MX particles. A

special composition Bar257 is shown as well, which has been simulated with a composition identical to P91 except a lower N content at 0.03wt% and Al at 0.028wt%.

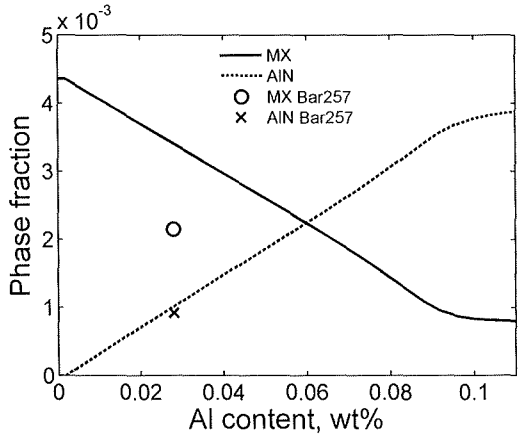

Figure 8. Phase fraction of MX and AlN as function of Al content for P91 steel. Point values are for a specific composition with lower N content at 0.03wt%. and Al at 0.028wt%.

The rupture stress of P91, and steel Bar257 is shown in Figure 9. The simulations are performed at 600°C. The phase fraction of MX in Bar257 is nearly half the original phase fraction, as shown in Figure 8. This is the reason for the low creep strength of Bar257. Experimental data is from [27, 29].

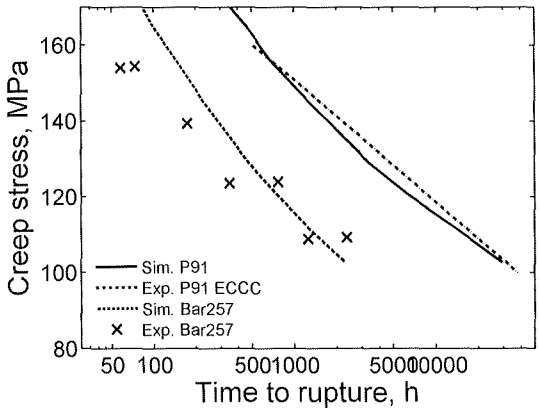

Figure 9. Rupture stress of P91 and P91 steel with 0.03wt% N and 0.028wt% Al.

The influence of heat affected material has been analysed in detail in [30]. In order to simulate the microstructure of heat affected material, Figure 10 presents the average particle size of $M_{23}C_6$ and MX due to a 6 minutes heat treatment at various temperatures [30]. The increase in average size is mainly due to the dissolution of small particles with a following reprecipitation on the remaining ones during post weld heat treatment. Particle coarsening is of importance, especially for $M_{23}C_6$ in BCC matrix which is below 850°C.

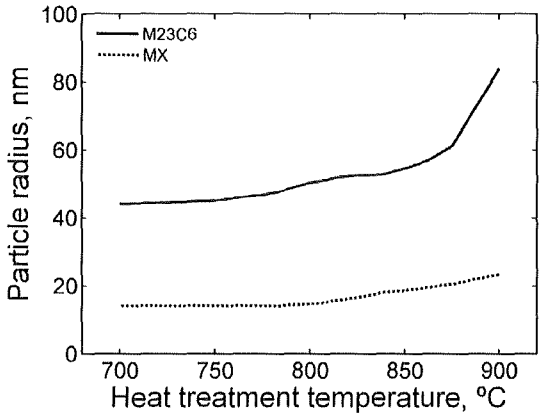

Figure 10. Particle size due to a 6 minutes heat treatment in order to simulate the microstructure of heat affected material [30].

The 100000h rupture stress of weld simulated heat affected material is shown in Figure 11. The simulations are performed for P91 steel and P91 steel with a simulated heat treatment at 900°C for 6 minutes, according to Figure 10. It is clearly shown how this heat treatment lowers the creep strength. The experimental data suggests up to 36% decrease in creep stress of crossweld material at 650°C, 28-35% at 600°C, and 11-15% at 550°C [31, 32]. The values from Jandová et al [31] are an estimation of the weld reduction factor at 100000h based on creep data of crosswelded P91 with a maximum rupture time at 43000h. The values from Watanabe et al [32] are evaluated as a weld reduction factor from crossweld P91 at around 10000h.

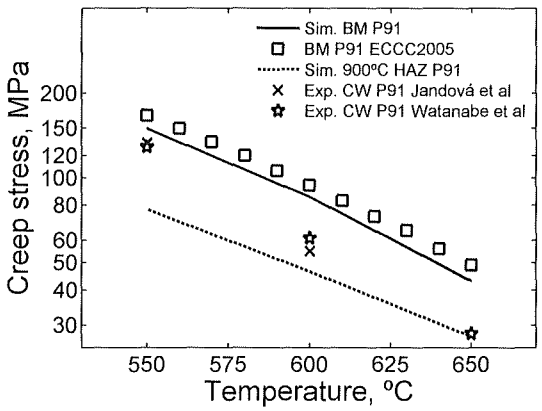

Figure 11. 100000h rupture stress of P91 simulated for both base material and heat affected material simulated for 6 minutes at 900°C. Experimental data is evaluated from [27, 31, 32].

4 Discussion

An approach to fundamentally model creep of particle strengthened materials has been presented. Predictions are made for different 9-12% Cr steels without the use of fitting parameters. By carefully describing the microstructure evolution during creep and evaluating the corresponding strengthening, the creep rate can be predicted. Work hardening and particle hardening are considered. For dislocation rich material a distinction between different types of dislocations is needed in order to explain the transient creep. The substructure can be taken into account by considering the composite model. Static recovery by climb of immobile dislocations, and dynamic recovery and locking of free dislocations are treated. Subgrain growth occurs by the migration of the dislocation network, which is held back by the particles located at the boundaries. Particle hardening is calculated when allowing the dislocations to climb past the smallest particles. With this approach it is possible to predict the particle hardening at high temperatures and long rupture times.

The activation energy for the secondary creep rate is close to that of self diffusion for pure metals [33]. However, for particle strengthened steels, as well as other alloys, the activation energy is often considerably higher. In a similar manner, the stress exponent can be related to fundamental mechanisms for pure metals [26], although it will continuously increase with decreasing temperature. The activation energy for self diffusion was used as input to Norton's equation in Eqn. (9). Due to a temperature dependent backstress, the effective activation energy is higher and in better agreement with experimental data. Evaluating the creep data at 100MPa and 550-650°C gives an effective activation energy of 421kJ/mol. Similarly, a Norton exponent of 5 was used in Eqn. (9) but resulted in an effective exponent of 12 at 550°C and decreasing to 5.6 at 650°C. The different stress exponents are due to the gradual change to a more climb controlled creep at higher temperatures and longer times to rupture.

The main difference between X20, P91 and P92 is that X20 relies on a dense distribution of carbides, which show a more significant coarsening at high temperature creep. The $M_{23}C_6$ particles are also less homogeneously distributed compared to MX, and thereby give a less effective obstructing to the moving dislocation. The main difference between P92 and P91 is the addition of W which provides more solid solution hardening. The solute atoms will accumulate around the dislocation which requires an extra force to push it forward. The W atom has a large lattice misfit parameter and the slowest mobility in the matrix and will consequently be the most important solute element. The climb mobility is an important parameter in this creep model, as it influences both the dislocation recovery rate and the amount of climb across particles.

Three different changes in the microstructure of P91 have been analysed in this work. These are the influence of Al, Z-phase, and heat affected material. The influence of Z-phase transformation is difficult to verify for 9% Cr steels since it takes such a long time for any significant effect to appear. The stability of the Z-phase increases with Cr content which will result in faster transformation rates for 12% Cr steels. A rough estimation of the influence of the Z-phase transformation has been made by considering the dissolution of 100 VN particles due to Z growth. This will clearly lower the number density and strongly influence the creep strength when fully precipitated. However, the slow transformation rate for this 9% Cr steel indicates that the Z transformation is of limited concern at practical applications at 600°C or

lower. However, for 12% Cr steels aimed for service above 600°C the Z transformation will most likely determine the long-term strength. Simulations for P91 show that the rupture time decreases a factor of 2 at 40MPa and 650°C service due to Z transformations.

In similarity with the Z transformation, the AlN are formed at the expense of MX particles. In contrast, these particles are quickly formed at tempering and it is possible to evaluate the effect on creep strength. Figure 9 shows how a high ratio of Al to N lowers the creep strength. In this case, a P91 composition but with 0.03wt% N and 0.028wt% Al lowered the strength by nearly 30% due to fewer MX like particles. The phase fraction of MX in the high Al steel is nearly half the standard phase fraction for these steels.

Finally, the influence of heat affected material has been evaluated as well. The studies show how the smallest particles can be dissolved already at 800°C where the stability of MX slowly decreases up to around 1250°C where it is fully dissolved. The smallest particles get dissolved even though the total population will act rather stable. Furthermore, many small particles can be dissolved before any significant volume loss of MX has been reached. The $M_{23}C_6$ particles will dissolve as well, and at a higher rate compared to the MX particles. However, their higher dissolution rates will be limited below 850°C by their much larger volumes. The 900°C heat treatment with corresponding creep strength shown in Figure 11 is a combination of a loss in number density due to dissolution of both MX and $M_{23}C_6$. This will also lead to a coarsening of substructure due to fewer particles pinning down the subgrain networks.

5 Conclusions

Creep strength of particle strengthened 9-12% Cr steels can be predicted by fundamental modelling. The state of the microstructure throughout creep can be used as input to creep rate modelling. The most important strengthening mechanism is particle hardening with dislocation climb across particles taken into consideration. This gives the possibility to explain the high temperature creep strength. In addition, work hardening for substructure forming materials can be simulated by the composite theory. Dislocation evolution and transient creep can be predicted by making a distinction between different types of dislocations. Solid solution hardening is needed in order to explain the difference in creep strength between different 9-12% Cr steels. The accumulation of Mo and W will slow down the dislocation climb velocity, and thereby the rate of recovery in microstructure.

6 Acknowledgements

This work was supported by the Swedish foundation for strategic research (SSF) programmes CROX, "Mechanisms of creep and oxidation of high performance alloys" and MATOP, "Development of tools for integrated optimisation of materials".

7 References

[1] J. Weertman, Steady state creep through dislocation climb, *J. Appl. Phys.*, vol. 28, pp. 362-364 (1957).

[2] A. Golpayegani, H-O. Andrén, H. Danielsen, J. Hald, A study on Z-phase nucleation in martensitic chromium steels, *Mater. Sci. Eng.*, vol. A20, pp. 310-318 (2008).

[3] L. Korcakova, Microstructure evolution in high strength steel for power plant application: microscopy and modelling, Doctoral Thesis, Technical University of Denmark, (2002).
[4] J. Hald, Metallugry and creep properties of new 9-12%Cr steels, *Steel research*, vol. 67, pp. 369-374 (1996).
[5] H. Oikawa, K. Honda, S. Ito, Experimental study on the stress range of class I behavior in the creep of Al-Mg alloys, *Mater. Sci. Eng.*, vol. 64, pp. 237-245 (1984).
[6] F. Mohamed, Y. K. Kim, Creep behaviour of Au-Ni solid solutions, *Scripta Met.*, vol. 11, pp. 879-882 (1977).
[7] R. Sandström, H. C. M. Andersson-Östling, The effect of phosphorus on creep in copper, *J. Nucl. Mater.*, vol. 372, pp. 66-75 (2008).
[8] H. Oikawa, M. Maeda, S. Karashima, Variation in type of transient creep curve with applied stress in iron-molybdenum solid solutions, *Scripta, Met.*, vol. 6, pp. 339-334 (1972).
[9] F. Roters, D. Raabe, G. Gottstein, Work hardening in heterogeneous alloys - A microstructural approach based on three internal state variables, *Acta Mater.*, vol. 48, pp. 4181-4189 (2000).
[10] H. Magnusson, R. Sandström, Creep strain modeling of 9 to 12 pct Cr steels based on microstructure evolution, *Metall. Mater. Trans. A*, vol. 38, pp. 2033-2039 (2007).
[11] Y. Bergström, H. Hallén, An improved dislocation model for the stress-strain behaviour of polycrystalline alpha-Fe, *Mater. Sci. Eng.*, vol. 55, pp. 49–61 (1982).
[12] J. P. Hirth, J. Lothe, Theory of dislocations, 2nd ed., Wiley, New-York, NY, USA, 1982.
[13] R. Sandström, H. C. M. Andersson-Östling, Creep in phosphorus alloyed copper during power-law breakdown, *J. Nucl. Mater.*, vol. 372, pp. 76-88 (2008).
[14] R. Sandström, Subgrain growth occurring by boundary migration, *Acta Mater.*, vol. 25, pp. 905-911 (1977).
[15] J. Ågren, M. T. Clavaguera-Mora, J. Golcheski, G. Inden, H. Kumar, C. Sigli, Application of computational thermodynamics to phase transformations, nucleation and coarsening, *CALPHAD*, vol. 24, pp. 41-54 (2000).
[16] A Borgenstam, A. Engström, L. Höglund, J. Ågren, DICTRA, a tool for simulation of diffusional transformations in alloys, *Phase Equilib.*, vol. 21, pp. 269-280 (2000).
[17] S. Straub, T. Hennige, P. Polcik, W. Blum, Microstructure and deformation rate during long-term cyclic creep of the martensitic steel X22CrMoV12-1, *Steel Res.*, vol. 66, pp. 394-401 (1995).
[18] J. W. Martin: Precipitation hardening, 2 nd ed., Butterworth-Heinemann, Oxford, UK (1998).
[19] W. Blum, B. Reppich, Creep Behaviour of Crystalline Solids, Pineridge Press, Swansea, UK, pp. 83-135 (1985).
[20] J. Eliasson, Å. Gustafson, R. Sandström, Kinetic modelling of the influence of particles on creep strength, *Key Eng. Mat.*, vol. 171-174, pp. 277-284 (2000).
[21] H. Magnusson, R. Sandström, The role of dislocation climb across particles at creep conditions in 9 to 12 pct Cr steels, *Metall. Mater. Trans. A*, vol. 38, pp. 2428-34 (2007).
[22] S. Takeuchi, A. S. Argon, Steady-state creep of single-phase crystalline matter at high-temperature, *Acta Metall.*, vol. 24, pp. 883-889 (1976).
[23] J. P. Hirth, J. Lothe, Theory of dislocations, 2nd ed., Wiley, New-York, NY, USA, 1982.

[24] R. Sedláček, W. Blum, Microstructure-based constitutive law of plastic deformation, Comput. *Mater. Sci.*, vol. 25, pp. 200-206 (2002).
[25] H. Mughrabi, Dislocation wall and cell structures and long-range internal stresses in deformed metal crystals *Acta Metall.*, vol. 31, pp. 1367-1379 (1983).
[26] M. E. Kassner, M. T. Pérez-Prado, Five-power-law creep in single phase metals and alloys, *Prog. Mater Sci.*, vol. 45, pp. 1-102 (2000).
[27] ECCC Data sheets 2005, Ed. D. G. Robertson and S. R. Holdsworth, ETD Ltd, Ashstead, UK, www.ommi.co.uk/etd/eccc/advancedcreep/DSheets05ax.pdf.
[28] P. Polcik, Doctoral Thesis, Erlangen, Germany, (1998).
[29] H. Magnusson, R. Sandström, Influence of aluminium on creep strength of 9-12% Cr steels, *Mater. Sci. Eng. A*, vol. 527, pp. 118-125 (2009).
[30] H. Magnusson, R. Sandström, Modelling creep strength of welded 9-12% Cr steels, Submitted to Metall. Mater. Trans.
[31] D. Jandová, J. Kasl and V. Kanta: Creep & Fracture in High Temperature Components – Design & Life Assessment, 2nd International ECCC Conference, Empa, Dübendorf, Switzerland, 21-23 April, 2009.
[32] T. Watanabe, M. Tabuchi, M. Yamazaki, H. Hongo and T. Tanabe: Int. J. Press. Vessels Pip., 2006, vol. 83, pp. 61-71.
[33] O. D. Sherby, J. Weertman, Acta Metall., 1979, vol. 27, pp. 387-400.

9th Liege Conference : Materials for Advanced Power Engineering 2010
edited by J. Lecomte-Beckers, Q. Contrepois, T. Beck and B. Kuhn.

CREEP PERFORMANCE OF WELDED PIPE MATERIAL MADE OF 7CrMoVTiB10-10 (T/P24) STEEL

Juhani Rantala, Pertti Auerkari, Jorma Salonen, Stefan Holmström, Pekka Nevasmaa
VTT, Espoo, Finland

Juha Häkkilä
Foster Wheeler Energia, Varkaus, Finland

Abstract

The creep strength of welded low-alloy ferritic steels is typically somewhat lower than that for parent metal, but this is generally due to an inherent weakness of the heat affected zone and accounted for in the common design codes. However, the parent material strength is much higher in certain modern low alloy steels such as 7CrMoVTiB10-10 (P24), and then it can be a significant challenge to develop weld metals (welding consumables) to match this strength. Acceptable weld performance has been previously demonstrated for thin-wall tubes where sufficient mixing with the base material can occur. The objective of this work was to achieve satisfactory properties for a thick-wall welded pipe by using an Nb-modified consumable to avoid weld metal weakening due to arc losses of Ti of a consumable composition approximately matching the base material. A considerable improvement was indeed noted in comparison with earlier experience using matching electrode composition. All short term test results for weld qualification showed acceptable properties, the cross-weld creep strength remain very close to the -20% band from the parent metal creep strength. However, creep testing at lowest stress levels approaching those expected in service resulted in weld metal failure. Although a clear improvement is evident from the previous generation of weld metals, there appears to be some further scope of development of the welding consumables, to improve the long term creep ductility of the welded joints particularly when applying production-like welding parameters.

Keywords: steam header, 7CrMoVTiB10-10, steel, weld, creep

1. Introduction

The basic 10CrMo9-10 steel, a normalized and tempered ferritic-bainitic steel, was introduced in the 1940's and is still one of the most widely used steels in boiler components of conventional power plants, with modest strength properties, but no other obvious weak points. Improvements of this work horse steel in the sense of high temperature creep properties have been introduced by micro alloying by small amounts of V, Ti, Nb, (W), B, N, contributing mainly to precipitate strengthening, but also in lesser extent to solid solution strengthening with Mo and /or W. In 7CrMoVTiB10-10 (T/P24) the addition of V, Ti and N contribute to the precipitation hardening and B is added for improving the hardenability and to maintain the bainitic-martensitic microstructure. The maximum recommended design temperature of for T/P 24 is 580°C [1][2]. In this work a thick walled 7CrMoVTiB10-10 (P24) component is welded with an Nb-alloyed consumable, originally developed for an earlier steel variant 7CrWVMoNb9-6 (T/P23). The properties of the weld metal have been a major challenge for the quality and expected life welded joints in thick walled components made in these steels.

2. Materials and methods

A circumferential welded joint was made in a ∅ 400 x 30 mm pipe of 7CrMoVTiB10-10 steel by Foster Wheeler Energia (Finland), using SMAW and Thermanit 24 consumables and welding procedure provided by Böhler Welding as a part of the COST 536 Welding Group program. A rotating fixture was used to provide the same welding position for the entire welded joint, with as constant properties as possible. The welded component is shown in Fig. 1A together with a cross-section of the weld (Fig. 1B). The parent material composition, corresponding EN 10216-2 specification [3], and the composition of the mid-weld position of the weld metal are shown in Table 1. The welded joint with thick-wall dimensions met the specifications.

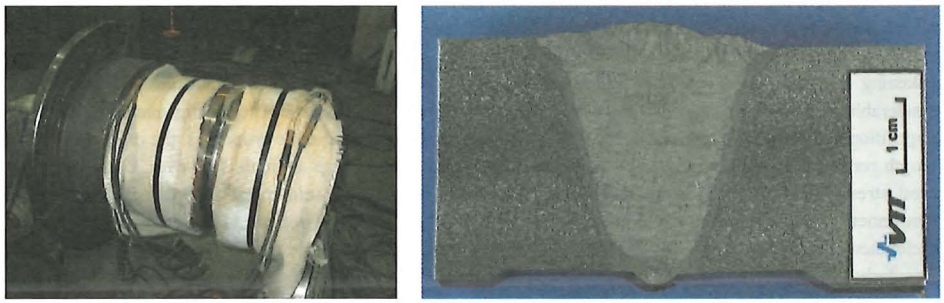

A) *B)*

Fig. 1. A) 7CrMoVTiB10-10 pipe welded at Foster Wheeler Energia (Finland), B) cross-section of the weld.

Table 1. Composition of the parent 7CrMoVTiB10-10 (P24), its requirements in EN 10216-2 [3] and the composition of the mid-weld position

Mat'l	C	Si	Mn	P	S	Cr	Mo	V	Ti	Nb	Al	N[2)]
P24	0.05	0.24	0.43	0.013	0.001	2.30	0.90	0.24	0.064	0.01	0.012	nd
EN [1)]	0.05	0.15	0.30	-	-	2.20	0.90	0.20	0.05	-	-	-
	0.10	0.45	0.70	0.02	0.01	2.60	1.10	0.30	0.10	-	0.20	0.01
Weld	0.09	0.22	0.56	0.011	0.003	2.54	0.89	0.26	0.003	0.05	<0.003	nd

1) also 0.0015-0.0070% B; 2) nd = not detected

It should be noted that the root pass was GTAW (TIG)-welded using an older, Ti-alloyed consumable Union I P24. For the most part of the results this is of no consequence as the subsequent testing specimens were machined outside the root region. However, no root

cracking was observed in the quality assurance (QA) of fabrication, and there were no indications to suggest clearly inferior material at the weld root.

Peviously, relatively thin wall welded boiler tubes have been successfully applied using the low alloy steel 7CrMoVTiB10-10 (or T24) and welding consumables either roughly matching composition with the parent metal (with some Ti) or corresponding to the conventional steel 10CrMo9-10 [4]. In the latter case, sufficient alloying of the weld metal has been possible by mixing with the parent metal. However, during the initial attempts when trying to join thick-wall pipes made of steel 7CrMoVTiB10-10 (P24) with Ti-alloyed consumable, the joint has tended to show low ductility or even weld metal cracking already after welding and post-weld heat treatment, and low creep strength when using a 10CrMo9-10 consumable due to negligible mixing with the parent material in multipass welds. Nb-alloyed consumables have been originally developed for the steel variant 7CrWVMoNb9-6 (T/P23), and are applied here in an attempt to produce satisfactory welds thick-wall components made of 7CrMoVTiB10-10.

This work aimed to produce a representative arc welded joint in a relatively thick-wall pipe of the steel 7CrMoVTiB10-10. The main purpose was to evaluate the joint and its creep properties applicability and performance in power plant service.

3. Results

With on-shop quality assurance of fabrication passed, the weld was subjected to a testing program as shown in Table 2. All the tests showed satisfactory results for the whole joint and particularly for the weld metal that is thought to be the critical part of the joint. The creep testing program targeting 5000 h tests included cross-welded, longitudinal pure weld metal, and parent metal samples. The testing conditions and results are shown in Table 3. The calculated weld strength factor (WSF) are related to the corresponding parent material.

The weld strength factor is defined as:

$$WSF = \frac{R_{u(W)/t/T}}{R_{u/t/T}},$$

where $R_{u(W)/t/T}$ is the predicted strength of the weld at specified time and temperature and the $R_{u/t/T}$ is the corresponding strength of the parent material.

The microstructures of the as-new parent and weld metal are shown in Fig. 2.

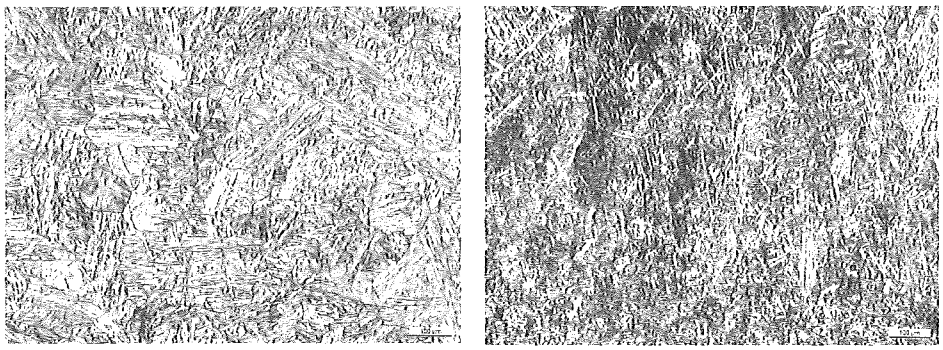

A *B*

Fig. 2. The as-new microstructure of the A) parent material and B) the weld metal

Table 2. The testing program for the welded joint.

Testing	Test types	Results	Notes
Initial NDT (QA)	Surface, UT	Passed	-
Bending tests	Top and root side	Passed	No visible cracks
Impact tests	Charpy-V, WM	Passed	-
Metallography	As-new weld	Passed	No cracking
Reheat cracking tests	Gleeble simulation	Passed	-

Table 3. Creep testing conditions and results for parent material (PM), weld metal (WM) and cross weld (CW) creep tests for 7CrMoVTiB10-10 (P24).

Specimen	Temperature,°C	Stress, MPa	Time to rupture, h	WSF[1] (SRF)[1]	Z_u, %	Failure location
PM-1	600	130	5555	(0.96)	78	(PM)
PM-2	600	140	5994	(1.05)	64	(PM)
CW-1	600	140	1235	0.80	9	WM
CW-2	600	120	1965	0.74	5	WM
CW-3	600	105	4373	0.74	11	WM
CW-4	600	95	9540	0.78	5	WM
WM-1	600	130	4723	0.93	15	(WM)
WM-2	600	160	714	0.85	4	(WM)

1) in relation to the actual parent material (stress correction to fit PM data to a model based on EN10216-2 and data extracted from [5]).

Clearly, parent metal and (longitudinal) pure weld metal specimens seem to show higher creep strength at 600°C than cross-weld specimens. Parent metal was also much more ductile

in creep than the weld metal specimens, including pure weld metal (longitudinal specimens) as shown in Fig. 3A.

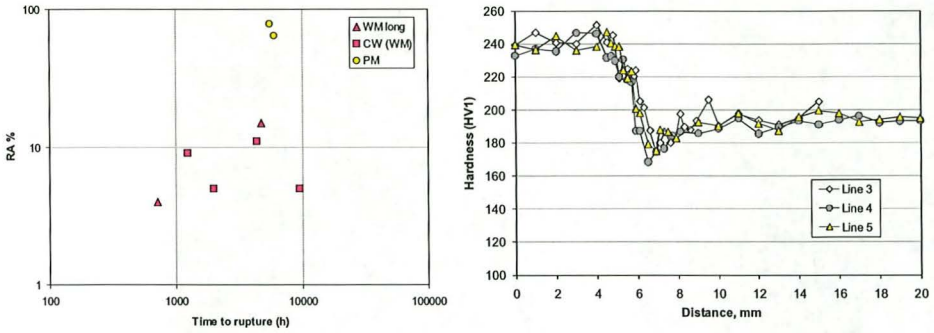

A B

Fig. 3. A) Ductility in the creep tests, B) hardness profiles of the weld (see Fig. 1 B).

The failed specimens were inspected in longitudinal mid-section metallography for indications of damage. The appearance of the weld metal is shown in Fig. 4 and Fig. 5.

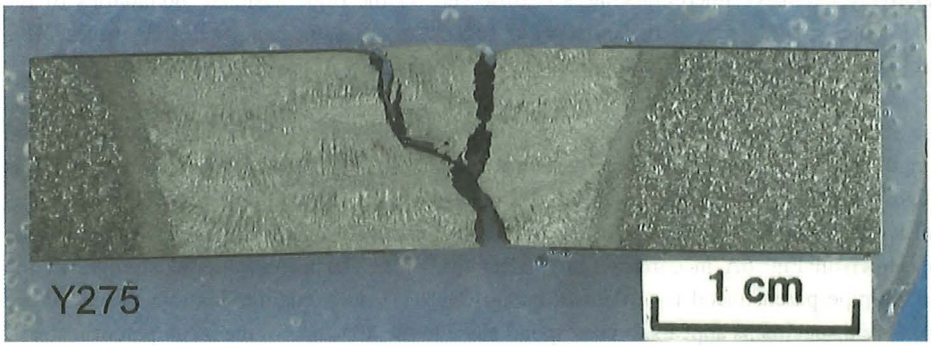

Fig. 4. Longitudinal midsection of the creep specimen CW-3 (4373 h / 600°C / 105 MPa).

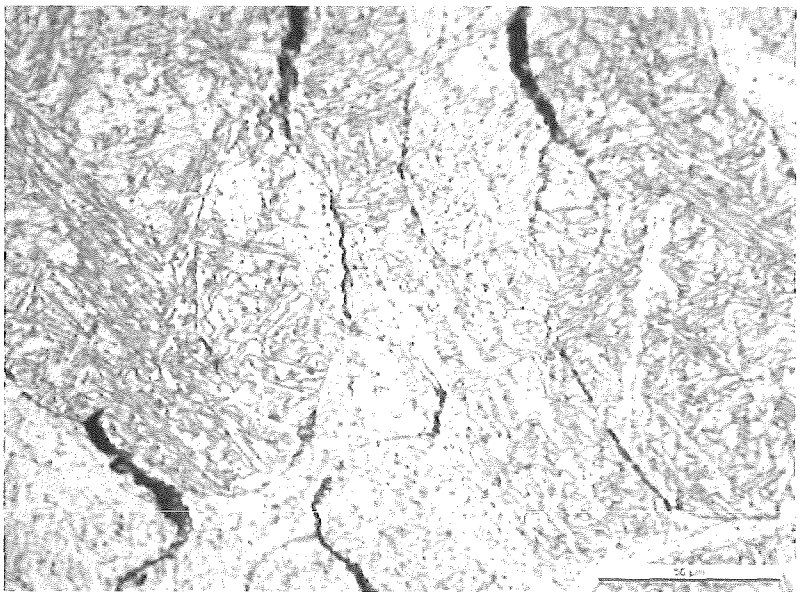

Fig. 5. Detail of the WM microstructure from specimen CW-3 of Fig. 4.

Relatively extensive microcracking was observed on the prior austenite boundaries of the weld metal, particularly in the cross-weld specimens after the longest testing times. This cracking is taken to explain the relatively low creep ductility of the cross-weld specimens.

The results show a relatively large difference in the creep life of the cross-weld and (longitudinal) pure weld metal specimens. The observed creep ductility (reduction in area was roughly similar for both types of weld specimens (see Fig. 3 A). Some relative weakness is still apparent in the creep strength and ductility of the weld metal. The creep testing results are shown in Fig. 6A in comparison to data from [5]. The mean material strength of the welded pipe parent metal is presented, using EN-10216 for trending. Time to failure of the cross-weld specimens appears to correspond close to the 80% line of the mean parent material strength. However, as the creep strength of the actual tested parent material appears to be somewhat higher than from EN-10216 (see Fig. 6B), the cross-weld creep strength falls slightly below a WSF of 0.8. More importantly, all cross-weld specimens failed in weld metal and none in the heat affected zone. The longest test durations close 10000 h should have shifted the failure to heat affected zone if this had been the weakest constituent. Together with the observed weld metal cracking and low ductility this suggests that further development of the welding consumable may be necessary for the thick walled components made of 7CrMovTiB10-10.

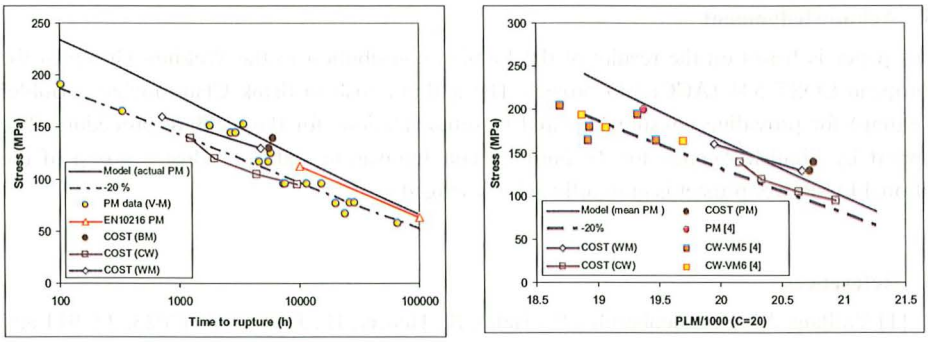

A B

Fig. 6. A) Time to rupture plot for the creep tests at 600°C (BM, WM and CW) as in Table 3. The PM (V-M) data for comparison is from [5]. B) Larson-Miller presentation of the creep tests (600°C) and for comparison CW data (575°C) from [4].

4. Discussion and conclusions

The quality tests of the ∅400 x 30 mm pipe of 7CrMoVTiB10-10 (P24) including NDT, impact and reheat cracking testing showed satisfactory results for the weld metal that appears to be the critical part of the joint. In particular, no weld metal cracking was observed in the as-new and post-weld heat treated condition when using the newer Nb-alloyed consumable, even after extensive bending, and the impact properties were also satisfactory. Comparison to other experimental weld metals for P23 and P24 suggest that the tested P24 weld with a Nb-alloyed consumable is satisfactory in terms of resistance to e.g. reheat cracking. Also, the weld showed acceptable as-fabricated properties, with no obvious initial defects after welding and PWHT.

The creep testing program including cross-weld, longitudinal pure weld metal, and parent metal creep rupture tests showed systematic failure in weld metal, suggesting that further development of the consumable would be preferable. Time to rupture for the cross-weld specimens corresponded close to the 80% strength level of the mean parent material strength, but fell slightly below it when compared to the actual parent material strength.

Weld metal microcracking is associated with the relatively low ductility creep failures of the pure weld metal and cross-weld specimens. Pure weld metal specimens extracted in the direction of the weld beads were not significantly more ductile than the cross-weld specimens in creep, although the pure weld metal specimens showed a longer creep life in uniaxial testing. Some improvement could be expected by welding with even lower heat input than was done here (and recommended by the consumable provider), but this would change the requirements of reasonable productivity in fabrication.

5. Acknowledgement

This paper is based on the results of the Finnish contribution to the Welding Group of the European COST 536 (ACCEPT) project. The authors wish to thank Claus Jochum (Böhler Welding) for providing consumables and recommendations for the welding procedure. The support by Finnish Agency for Technology and Innovation and the industry group of the national LC-Power project is gratefully acknowledged.

6. References

[1] Vaillant, J.C., Vandenberghe, B., Hahn, B., Heuser, H., Jochum C. T/P23, 24, 911 and 92: New grades for advanced coal-fired power plants - Properties and experience, International Journal of Pressure Vessels and Piping Vol. 85 (2008), pp. 38–46

[2] Auerkari P., Salonen J., Nevasmaa P. 2%CrMo(W)V steels for welded high temperature applications. VTT Research Report TUO74055258, 2005.

[3] EN 10216-2:2002+A2:2007. Seamless steel tubes for pressure purposes. Technical delivery conditions. Part 2: Non-alloy and alloy steels steel tubes with specified elevated temperature properties. 1+78 p.

[4] Dhooge A., Vekeman J. New generation 21/4 Cr steels T/P23 and T/P24 weldability and high temperature properties. Welding in the World 49 (2005), 75-93

[5] Bendick, W., Gabrel, J., Hahn, B., Vandenberghe, B. New low alloy heat resistant ferritic steels T/P23 and T/P24 for power plant application. International Journal of Pressure Vessels and Piping, Vol. 84, pp. 13-20

9th Liege Conference : Materials for Advanced Power Engineering 2010
edited by J. Lecomte-Beckers, Q. Contrepois, T. Beck and B. Kuhn.

REHEAT CRACKING SUSCEPTIBILITY OF P23 (7CrWVMoNb9-6) STEEL WELDS MADE USING MATCHING AND MIS-MATCHING FILLER METALS

Pekka Nevasmaa, Jorma Salonen, Pertti Auerkari, Juhani Rantala, Stefan Holmström

VTT Technical Research Centre of Finland, Espoo, Finland

Abstract

Reheat cracking sensitivity of 7CrWVMoNb9-6 (P23) thick-section multipass welds has been investigated by Gleeble simulation, mechanical testing, fractography and metallography. The results demonstrate that the experimental weld metal made using a *high-Nb–W–Ti–B* type filler metal was sensitive to reheat cracking, with a reduction of area no more than 2–3 % in the BWI reheat cracking (RC) test. Welds made using a *high-W –low-Ti* type filler metal with Nb content similar to the parent steel, as well as welds made using a *Ni–Nb–Ti-free–(W-free)* type filler metal with the chemical composition closer to P24 grade material, were more ductile and crack-resistant, though with reduced cross-weld creep strength. Fractography of RC test specimens showed evidence of pronounced localisation of damage at the prior austenite grain boundaries of the thermally reheated, experimental P23 weld metal. The reheat cracking susceptibility of the less ductile weld metal was apparently related both to the chemical composition (higher B, Nb and Ti content) and sub-structural features of the coarse-grained reheated weld metal microstructure. Appropriate single- and multi-cycle thermal Gleeble simulations to produce representative HAZ and reheated weld metal microstructures (as function of peak temperature), in conjunction with the BWI RC test were successfully applied to characterise the reheat cracking sensitivity of the candidate weld metals and parent steel HAZ.

Keywords: weld, reheat cracking, creep resisting steel, 7CrWVMoNb9-6 (P23)

1. Introduction

Weldability of low alloy creep-resisting steels is mainly governed by their reheat cracking and hydrogen cracking tendency. Welding procedures intended for practical boiler service conditions must therefore contain the necessary safeguards against cracking. This calls for appropriate preheating, the use of optimised filler metals and, sometimes, also post-weld heat treatment (PWHT). For power generation applications, the maximum allowable weld hardness is generally limited to below 350 HV, whereas hydrogen containing environments tend to permit hardness of no more than 248 HV [1].

The T/P23 steel [1,2] has been developed from the conventional 10CrMo9-10 (T/P22); it contains about 2.25 % Cr, but the C content has been lowered to 0.1 % max to improve weldability. The T/P23 steel was developed by Sumitomo Metal Industries, Japan, and originally marketed by the trade name HCM 2S (7CrWVMoNb9-6). In the steel, Mo is for the most part substituted by W (0.2 % Mo, 1.6 % W) to keep the Mo equivalent (%Mo + 0.5 × %W) at the level of about 1 %. For MX-precipitates, the steel contains about 0.25 % V, some (0.02–0.085 %) Nb and N (0.03 % max). A small amount of B (0.0005–0.006 %) is added to increase hardenability by promoting formation of the bainitic-martensitic microstructure and stabilise the $M_{23}C_6$ carbides [1,2].

New 2 % Cr grades were developed especially for tubes in water-walls of modern boilers. They provide enhanced creep properties at 550 °C, as well as low hardness in the as-welded condition and hence lesser risk to HAZ cracking. In comparison to conventional grade T/P22, the modified steel T/P23 (and T/P24) show approximately twice the creep strength at typical service temperatures of about 520–570 °C. Since the oxidation properties of T23 (and T24) seem comparable to those of T22, the modified steels are attractive for super-heaters and waterwalls. Using grade T/P23, thin-wall components can be welded without preheating or PWHT, yet ensuring sufficient mechanical properties; consequently, T23 and T24 grades have been introduced to practical boiler service [1].

Further application of P23 steel in thick-wall components, such as super-heater headers and steam pipes, appears accordingly attractive in principle. However, weldability of thick-wall sections is usually limited by tendency to hydrogen cold cracking and reheat cracking in the HAZ and/or the weld metal. Susceptibility to cracking increases with the wall-thickness and structural rigidity of the component. The balance of suppressed cracking sensitivity and sufficient creep strength cannot be considered fully solved particularly for thick-wall components, which curtails practical application of the P23 (and P24) materials. Thick section welds generally require the use of PWHT and, sometimes, preheating as well. For thick-wall applications and multipass welds, welding consumables still require further development to improve creep strength and ductility of weld metal [1].

This paper is concerned with reheat cracking behaviour of the P23 grade (ASTM A335) pipe steel, with emphasis on thick-section multipass welds made using closely matching and mis-matching filler metals.

2. Materials and experiments

The P23 pipe steel (219.1×31.75mm) was produced as seamless hot rolled pipe according to ASTM A355; the actual chemical composition is given in Table 1.

Table 1 – Chemical composition of P23 grade pipe steel [6].

Base material	Chemical composition (w-%)							
	C	Si	Mn	S	P	Cr	Ni	Mo
P23	0.07	0.29	0.45	0.002	0.013	2.33	0.09	0.21

Base material	Chemical composition (w-%)							
	Cu	Nb	Al	W	V	Ti	Co	B
P23	0.10	0.043	0.022	1.52	0.22	0.03	n.a	0.003

The multipass weldments were made [3] at ISQ, Portugal, using Metrode *B323(experimental)* filler metal with closely matching chemical composition to P23 steel. Two electrode sizes: ∅ 3.2 and ∅ 4 mm were used. Circumferential butt weld joints were produced onto the 219 x 31.75 mm pipe, with horizontal axis (1G), using shielded-metal arc welding (SMAW) and U-groove preparation with 10° groove angle, 2 mm root gap and 2 mm root face. The applied preheat temperature was 200 °C, while the interpass temperature was kept below 250 °C [3]. A PWHT at 760 °C for 2h was carried out, except for the present weldment c.f. Figure 1 that was consciously delivered without PWHT to allow for characterisation of weld properties in

the as-welded condition. The welding parameters [3] are given in Table 2. The macrograph of the original P23 pipe weldment [3] is shown in Figure 1.

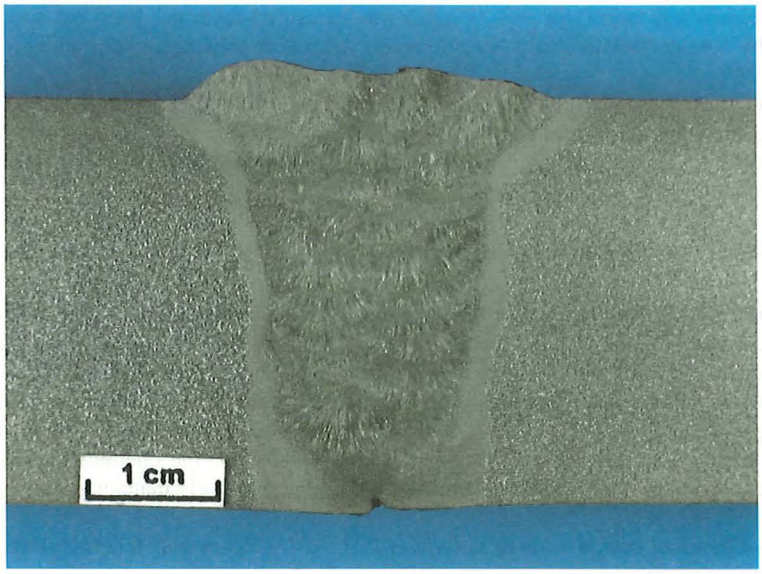

Figure 1 – Macrograph of the P23 pipe weldment; filler metal: B323(experimental).

Table 2 – Welding process parameters for the SMAW butt weld joints applied at ISQ for the P23 pipe steel – filler metal: Metrode B323(experimental) [3].

Run	Process	Electrode diameter (mm)	Current (A ± 10)	Voltage (V ± 10)	Type of current / Polarity
1	SMAW	3.2	115	22	DC/+
Others	SMAW	4	125	25	DC/+

The Gleeble 1500 simulator was applied to thermally simulate different HAZ microstructures using single-cycle and multi-cycle simulations with various peak temperatures (T_p) and weld $t_{8/5}$ cooling times. The original P23 weld was subjected to similar Gleeble simulations in order to produce a set of thermally reheated multipass weld metal microstructures. To ensure compatibility between thermal cycles experienced in real welding and simulation, authentic welding parameters were analysed from a typical *WPQT* certificate [4] for a thick-wall P23 pipe and applied further to derive the corresponding thermal cycles for Gleeble simulations.

Reheat cracking tests for the Gleeble-simulated HAZs and thermally re-heated weld metals were carried out using the isothermal slow strain rate tensile test denoted as 'Belgian Welding Institute (BWI) type RC test' [5]. In the test, cylindrical round-bar specimens (L = 110 mm, L_m = 10 mm, ϕ = 7 mm) are firstly exposed to the thermal cycle with the peak temperature T_p resulting in the desired microstructure, then let to cool down following the relevant weld $t_{8/5}$

[4] and subsequently re-heated (100 °C/sec) to the temperature of 760 °C (that corresponds to the actual PWHT temperature for the present P23 steel). Immediately after reaching this temperature, the specimen is strained to fracture at a low tensile displacement rate of 0.5 mm/ min. Specimen's reduction of area (RA-%) was measured from the fractured specimen and the thereby obtained relative value used to assess the reheat cracking susceptibility [4,5].

Microstructural investigation of the simulated HAZs and re-heated welds was performed by preparing metallographic sections that were then investigated with an optical microscope. Hardness testing as Vickers hardness numbers was performed on the metallographic sections using the load of 49.1 N (5 kp).

3. Results of experimental tests and investigations

Results of the *chemical analysis* for the weld metals made using the *B323(experimental)* filler metal are given in Table 3. The chemical compositions of the filling layers (surface beads) and the weldment mid-thickness areas (centre bead) appeared nearly identical. Thus, dilution from parent steel had been practically negligible. The weld Nb and B contents were found rather high, i.e., 0.09 % and 0.005 %, respectively; this obviously being a consequence of the ultimate intention to maximise the creep strength. Otherwise, the chemical composition is considered typical to a weld made using P23 consumable of closely matching alloying.

Table 3 – Chemical composition of multipass P23 weld; filler metal: B323(experimental).

Sample	Chemical composition (w-%)							
	C	Si	Mn	S	P	Cr	Ni	Mo
Surface bead	0.06	0.35	0.57	0.007	0.011	2.15	0.06	0.11
Centre bead	0.07	0.35	0.57	0.007	0.010	2.13	0.06	0.11

Sample	Chemical composition (w-%)							
	Cu	**Nb**	Al	W	V	Ti	Co	**B**
Surface bead	0.04	0.09	0.007	1.54	0.27	0.02	0.02	0.005
Centre bead	0.05	0.09	0.006	1.60	0.26	0.02	0.01	0.005

Table 4 – Chemical composition of multipass weld made using 'P24 filler metal'.

Sample	Chemical composition (w-%)							
	C	Si	Mn	S	P	**Cr**	**Ni**	**Mo**
Weld surface	0.09	0.22	0.56	0.003	0.011	2.54	0.16	0.89
Weld root	0.10	0.24	0.56	0.003	0.011	2.54	0.18	0.89

Sample	Chemical composition (w-%)							
	Cu	Nb	Al	W	V	Ti	Co	B
Weld surface	0.02	0.05	<0.003	<0.01	0.26	0.003	0.003	0.005
Weld root	0.05	0.05	<0.003	<0.01	0.22	0.064	0.004	0.006

Table 4 shows the chemical composition of another multipass weld made using Nb-alloyed, 'Ti-free' consumable intended for P24 grade steel (denoted as 'P24' weld). In comparison to the *B323(experimental)* weld metal, the 'P24' weld metal contained slightly higher C, Cr, Ni

and Mo, as well as Nb instead of Ti, whereas W is obviously non-existent. The other alloying elements, including B, were more or less similar to the P23 weld metal.

Results of the *Vickers hardness measurements* (HV5) on the P23 pipe multipass weldment and Gleeble simulated HAZs are given in Table 5. Comparatively high hardness in the range of 353–384 HV was recorded from the original weld metal in the re-heated weld metal areas.

Table 5 – Hardness of original P23 weldment and simulated HAZs & re-heated welds.

Weld/simulated microstructure	Condition	Hardness (HV5)
actual weld metal	as-welded (final bead)	313 ; 328
actual weld metal	as-welded	315 – 353
actual weld metal	re-heated (softened) (*	288 – 312
actual weld metal	reheated (coarse-grained) (*	**353 – 384**
actual CGHAZ	close to fusion boundary	**341 – 368**
actual FGHAZ	≈ 1.5 mm from fusion boundary	324
actual ICHAZ	≈ 2.0 mm from fusion boundary	285
Gleeble-reheated weld metal	FG(R)-CG(R)-WM (**	**358 – 371**
Gleeble-reheated weld metal	SC(R)-CG(R)-WM (**	**374 – 385**
Gleeble_CGHAZ	as-simulated	**356**
Gleeble_CGHAZ	PWHT	216
Gleeble_FGHAZ	as-simulated	311
Gleeble_FGHAZ	PWHT	190
Gleeble_IC(R)-CGHAZ	as-simulated	291
P23 grade steel	as-delivered	194 – 203

(* Note: reheated by repetitive thermal cycles caused by multiple-pass welding.
(** Note: reheated by multiple thermal Gleeble simulation cycles c.f. Table 6.

Table 6 summarises the results of the *BWI reheat cracking tests* for the P23 and 'P24' grade multipass weld metals; the applied test temperatures being 760 °C and 740 °C, respectively. Specimens in the transverse direction were extracted from an authentic circumferential pipe weld, whereas the longitudinal ones were taken form multiple-pass welded pads.

The results show a remarkable difference in reheat cracking susceptibility between the two Gleeble re-heated *B323(experimental)* weld metal microstructures. Whereas the CG(R)-WM (T_{p1} = 1340 °C) exhibited extremely low RA values of no more than 1.5–3 %, introduction of the second re-heating thermal cycle (T_{p2} = 1020 °C) led into a modest elevation of the RA values for the FG(R)-CG(R)-WM up to the range of 15–17 %. Overall, the RA values for the *B323(experimental)* weld metal were significantly lower than in the case of the simulated P23 steel HAZs, although the applied Gleeble cycles were identical. Above all, there appeared a considerable difference in reheat cracking susceptibility between the P23 and 'P24' grade weld metals. When exposed to equivalent reheating thermal cycles, the 'P24' weld displayed the RA values in the range of 15 to 40 %, that is, about 2 to 5 times greater than those for the P23 weld. The difference in favour of the 'P24' weld was particularly evident in the case of the CG(R)-WM, i.e., the region with the highest sensitivity to reheat cracking. Irrespective of the specimen orientation, the CG(R)-WM of the 'P24' weld made using a consumable

intended for P24 grade steel exhibited RA-% values 5 to 7 times greater than those for the CG(R)-WM of the P23 weld made using the *B323(experimental)* filler metal.

Table 6 – Reheat cracking test results for the thermally simulated P23 steel HAZs and thermally re-heated microstructures of P23 (high-Nb-Ti-B) and P24 (Ni-Nb-Ti-free) grade multipass weld metals.

Weld metal specimen / Case	Weld configuration	Specimen orientation	Reduction of area RA (%)
P23 parent steel HAZs			
CGHAZ_10	simulated HAZ	-	15 ; 16
CGHAZ_15	simulated HAZ	-	19 ; 16
CGHAZ_25	simulated HAZ	-	16 ; 16
FG(R)-CGHAZ_10	simulated HAZ	-	59 ; 59
FG(R)-CGHAZ_25	simulated HAZ	-	74 ; 57 ; 70
P23 weldment; high-Nb –W–Ti–B type filler metal B323(experimental)			
CG(R)-WM_10	circumferential pipe butt-weld	transverse	**3.0** **3.0**
	welded pad	longitudinal	**1.7** **1.4**
FG(R)-CG(R)-WM_10	circumferential pipe butt-weld	transverse	15 15
	welded pad	longitudinal	16 17
'P24' weldment; Ni–Nb–Ti-free type filler metal intended for P24 steel grade			
CG(R)-WM_10	circumferential pipe butt-weld	transverse	18 15
	welded pad	longitudinal	19 19
FG(R)-CG(R)-WM_10	circumferential pipe butt-weld	transverse	28 28
	welded pad	longitudinal	33 32
IC(R)-CG(R)-WM_10	welded pad	longitudinal	43 42
SC(R)-CG(R)-WM_10	welded pad	longitudinal	19 16

Note: CG(R)-WM: Tp1 = 1340°C ; FG(R)-CG(R)-WM: Tp1 = 1340°C & Tp2 = 1020°C ; IC(R)-CG(R)-WM: Tp1 = 1340°C & Tp2 = 900°C ; SC(R)-CG(R)-WM: Tp1 = 1340°C & Tp2 = 675°C ; t8/5 = 10 sec.; PWHT = 760°C / 2h (P23 weldment) and 740°C / 2h ('P24' weldment).

Metallographic investigation of the actual P23 pipe weld revealed [6] that reheating due to subsequent weld layers had resulted in the formation of new grains into the originally as-welded (as-cast) microstructure. In case of the weld metal reheated into *high peak*

temperatures, the inherent solidification grain size had coarsened substantially and newly formed, 'prior-austenite' grain boundaries were clearly visible. There existed only minor, if any, traces of the original weld solidification structure. Contrary to this, weld regions reheated into *lower peak temperatures* retained the original columnar grain solidification structure in the FG(R)-WM and the IC(R)-WM with newly formed small-grained martensitic-bainitic structures co-existing at the prior-austenite grain boundaries.

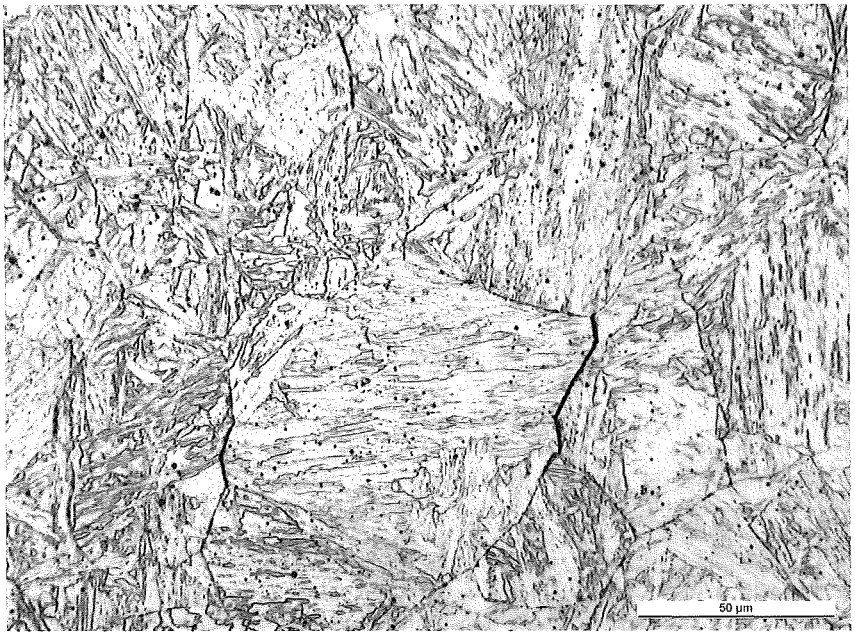

Figure 2 – Reheat cracking in original P23 weld metal subsequently reheated into the coarse-grained temperature region (T_p = 1340 °C): CG(R)-WM [6].

Comparison of microstructures between simulated HAZs and thermally re-heated weld metals proved [6] that the overall microstructural features of the CG(R)-WM (T_p = 1340 °C) were practically identical to that of the respectively simulated CGHAZ. Both microstructures consisted essentially of martensite and bainite. In accordance with the CGHAZ, the prior-austenite grain boundaries in the CG(R)-WM microstructure were clearly discernible, see Figure 2. Fractography of the reheat cracking test specimens showed clear evidence of pronounced localisation of damage at the prior-austenite grain boundaries, c.f., Figure 2.

4. Discussion

The results for the thick-wall P23 pipe multipass weldments demonstrated that the weld metal made using the *B323(experimental)* filler metal closely matching to parent steel was, itself, far more critical than the parent steel HAZ, both in terms of reheat cracking sensitivity and ductility. In the as-welded condition, the weld metal exhibited excessive hardness of ≈380 HV hence exceeding the 350 HV level specified for power generation applications. The high weld

metal maximum hardness can be explained by the fact that the present P23 pipe weldment was delivered without the PWHT. Besides, the weld had rather high contents of B and Nb, which is known [1,5] to contribute to hardness elevation. The highest and the lowest hardness were both found to associate with re-heated microstructures close to boundaries between successive weld layers. Formation of local, hardened and softened microstructures within re-heated multipass weld metal is obviously a result of complex precipitation reactions causing re-precipitation, over-ageing and tempering.

Normally, PWHT would be carried out for any P23 steam pipe weldment with a 31 mm wall thickness. Adoption of the PWHT (760 °C / 2h) did reduce the weldment hardness sufficiently; however, it also inevitably raised risk to reheat cracking in the P23 grade *B323(experimental)* weld metal that exhibited reduction of area (RA) of no more than 2–3 % in the BWI reheat cracking tests. It is evident that the reheat cracking susceptibility of the present P23 pipe weld made using the *B323(experimental)* filler metal is classified as "extremely susceptible" [6]. A startling observation was that the recorded RA values for the thermally reheated weld metals, particularly in the case of the coarse-grained temperature region (T_p = 1340 °C), were significantly lower than those for the correspondingly simulated HAZ microstructures, even though the applied Gleeble thermal cycles were identical. Introduction of the second 'normalising' re-heating thermal cycle ($T_{p2} \approx$ 900–1020 °C) was found to result in modest elevation of the weld metal RA values from those recorded for the single-cycle CG(R)-WM, see Table 6. This suggests that the P23 grade steel will benefit from multipass welding techniques that maximise the microstructural refining/normalising effect.

Fractography of cracked specimens revealed pronounced localisation of damage characteristic to the *B323(experimental)* weld metal, see Figure 2. Once initiated, extension and propagation of reheat cracking did not follow any original weld solidification cell boundaries, but the new prior-austenite grain boundaries that had formed as a result of subsequent Gleeble reheating of the original weld metal into the coarse-grained temperature region (T_p = 1340 °C), followed by the solid-state γ-α phase transformation during successive cooling stage. The underlying causes of deficient RA and hence high susceptibility to reheat cracking cannot therefore be attributed to the original weld solidification structure, but to the chemical composition and sub-structure. The overall features of the bainitic-martensitic microstructure, namely, appeared more or less similar between the CG(R)-WM and the simulated CGHAZ associated with identical thermal cycles (T_p = 1340 °C). Thus, differences in reheat cracking sensitivity between the weld metal and the HAZ must originate from sub-structural features such as carbide precipitation structure and/or martensite lath morphology, further contributed by the weld's high B, Nb and Ti content. Detailed characterisation of sub-structures would, however, require TEM microscopy, which was out of the scope of the present work.

Further evidence demonstrating high reheat cracking sensitivity of the *B323(experimental)* weld metal were obtained [6] from another P23 weldment otherwise similar to that in Figure 1, except that it was in the PWHT condition. Microstructural examination revealed significant number of small reheat cracks close to weld in the case of a relatively small laboratory-scale sample, which can be considered as undisputable evidence of the high cracking sensitivity. This implies that the high cracking susceptibility of the weld metal discovered in the BWI reheat cracking tests c.f. Table 6, is likely not to be an overestimation of cracking sensitivity associated with the thermal Gleeble simulation and BWI test itself, but instead a realistic demonstration of weld metal's inherently high sensitivity to reheat cracking. Consequently,

the present methodology [5,6] comprising thermal (Gleeble) reheating of the actual weld metal in conjunction with the BWI tensile reheat cracking test was successfully applied in characterising the material' s sensitivity to reheat cracking.

The PWHT appeared mandatory to guarantee weldment hardness not exceeding 350 HV, as well as to ensure adequate toughness for the multipass P23 pipe weld made using matching *B323* type consumable [6]. Welding techniques accentuating the normalising effect of multipass welding should be beneficial in terms of reheat cracking, ductility and toughness.

The results showed that thick-section multipass welds made using consumables with the chemical composition intended for P24 grade steel are much less susceptible to reheat cracking than matching P23 welds made using the *B323(experimental)* consumable, see Table 6. With improvements for welding procedures and tailoring of filler metal chemistries, P23 (and P24) grades can be economical materials for waterwall headers and super-heater headers, as well as hot steam lines operating under temperature range within power plants. For thick-wall P23 steel welds, the use of filler metals with mis-matching chemical compositions is expected to reduce weld metal reheat cracking sensitivity.

5. Summary and Conclusions

The present paper discusses the cracking sensitivity of 7CrWVMoNb9-6 (P23) pipe steel thick-section multipass welds made using different SMAW consumable variants. Full scale circumferential butt welded joints were made onto a 219x31.75mm pipe in the as-welded and PWHT conditions. Reheat cracking susceptibility was evaluated applying thermal (Gleeble) simulation of parent steel and reheating of the actual weld metals to produce representative HAZ and weld metal microstructures, respectively. These were then subjected to Belgian Welding Institute (BWI) slow strain rate tensile reheat cracking (RC) tests.

The results demonstrated that the *B323(experimental)* weld metal made using a *high-Nb–W–Ti–B* type filler metal closely matching to parent steel was far more sensitive to reheat cracking than the P23 steel HAZ, with a reduction of area (RA) no more than 2–3 % in the BWI RC test. In the as-welded condition, the weld metal exhibited excessive hardness of ≈ 380 HV. Formation of local, hardened and softened microstructures within reheated multipass weld metal is presumably a result of complex precipitation reactions causing re-precipitation, over-ageing and tempering. Adoption of a PWHT (760 °C / 2h) reduced weldment hardness sufficiently; however, it also inevitably raised the risk to reheat cracking. Nevertheless, PWHT appears mandatory for thick-wall sections in order to achieve an adequately low hardness in conjunction with sufficient toughness. Fractography of RC test specimens revealed pronounced localisation of damage at the prior-austenite grain boundaries of Gleeble reheated P23 weld metal. Once initiated, propagation of cracking did not follow any original weld solidification cell boundaries, but the new prior-austenite grain boundaries that had formed as a result of subsequent Gleeble reheating of the original weld metal into the coarse-grained temperature region (1340 °C). This implies that the underlying causes of deficient RA values cannot be attributed to the original, retained as-cast weld solidification macrostructure. The pronounced reheat cracking susceptibility of the experimental P23 weld metal with only moderate ductility was apparently related both to the chemical composition (i.e., high Nb, B and Ti contents) and sub-structural features of the coarse-grained reheated weld metal.

Welds made using a *high-W –low-Ti* filler metal with a Nb content similar to the P23 steel were found more ductile, though at the expense of cross-weld creep strength. Similarly, welds made using a *Ni–Nb–Ti-free–(W-free)* type filler metal with the chemical composition closer to P24 grade material appeared much less susceptible to reheat cracking than experimental P23 grade welds. Exposed to equivalent re-heating thermal cycles, the coarse-grained-reheated 'P24' weld metal exhibited RA values in the range of 15–19 %, i.e., about 5 to 7 times greater than those for the P23 weld metal.

Appropriate single- and multi-cycle thermal Gleeble simulations to produce representative HAZ and reheated weld metal microstructures (as function of peak temperature), in conjunction with the BWI reheat cracking test, were successfully applied to characterise the reheat cracking sensitivity of the candidate weld metals and parent steel HAZs.

Acknowledgements

The present work formed part of the EU/RFCS project 'ALoAS' co-ordinated by CSM, Italy. Technical contributions by E.ON, U.K., TenarisDalmine, Italy, and ISQ, Portugal, are highly appreciated. The financial support of the European Commission and VTT is gratefully acknowledged.

References

[1] Auerkari, P., Salonen, J. and Nevasmaa, P.: 'Modified 2%CrMo(W)V steels for welded high temperature applications'. *VTT Research Report No TUO74-055258.* Finland (2005).

[2] ASTM designation A 213/A 213M–03c. Standard specification for seamless ferritic alloy-steel boiler, superheater and heat exchanger tubes. ASTM International, West Conshohocken, PA, USA.

[3] Caminada, S., Nevasmaa, P., Holmström, S., Di Gianfrancsco, A., Pillot, S., Rodrigues, M.M., Allen, D. and Siegele, D.: 'Development of weldments of Grade 23 steel for new generation power plants'."*The 11th International Conference on Creep and Fracture of Engineering Materials and Structures (Creep 2008)*". Germany: Bayreuth, 4-9 May (2008).

[4] Nevasmaa, P., Salonen, J., Holmström, S. and Caminada, S.: 'Reheat cracking susceptibility and ductility & toughness behaviour of modified 2%CrMo(W)V P23 steel simulated HAZs and multipass welds made using matching and mis-matching filler metals' *IIW-Doc. IX-L-1003-07 / IX-2237-07. VTT Research Report No VTT-R-02973-07.* Finland (2007).

[5] Dhooge, A. & Vekeman, J.: 'New Generation 2 1/4 Cr Steels T/P 23 and T/P 24 Weldability and High Temperature Properties' *Welding in the World* **49**, pp. 75-93 (2005).

[6] Nevasmaa, P. & Salonen, J.: 'Reheat Cracking Susceptibility and Toughness of 2%CrMoWVNb P23 Steel Welds'. *Welding in the World* **52**, pp. 68-78 (2008).

9th Liege Conference : Materials for Advanced Power Engineering 2010
edited by J. Lecomte-Beckers, Q. Contrepois, T. Beck and B. Kuhn.

LONG-TERM AGING EFFECT ON THE CREEP STRENGTH OF THE T92 STEEL

C. Panait[1,2], A.-F. Gourgues-Lorenzon[1], J. Besson[1], A. Fuchsmann[2], W. Bendick[3], J. Gabrel[2], M. Piette[2]

[1]Centre des Matériaux, MINES ParisTech, UMR CNRS 7633, B.P. 87, 91003 Evry Cedex, France
[2] V&M France CEV, Route de Leval, B.P. 20149, 59620 Aulnoye-Aymeries, France
[3]SZMF, Salzgitter Mannesmann Forschung GmbH, Ehinger Straβe 200, D-47259 Duisburg, Germany

Abstract

Creep strength loss of T92 steel after long-term creep exposure at 600°C and 650°C is partially due to a thermal aging of the steel during the first part of the test. In order to quantify the effect of long-term aging on the creep strength loss, creep tests were conducted at 600 and 650°C on T92 steel thermally aged for 10,000h at the same temperature and on as-received T92 steel.

Laves phases precipitates were found after thermal aging at 600°C and 650°C with an average equivalent diameter of about 200nm and of about 350nm, respectively. No significant change in hardness and in the matrix substructure as revealed by electron backscatter diffraction occurred during aging.

For stresses higher than 170MPa at 600°C and higher than 110MPa at 650°C the time to rupture is four times lower in the aged steels compared to the as-received steel, this is correlated to a secondary creep rate four times higher for the aged specimens compared to that of the as-received steel. Creep tests conducted at 650°C under lower stresses revealed a creep lifetime only twice lower after aging.

Keywords: creep, thermal aging, Grade 92 steel, Laves phases

1. Introduction

High temperature exposition causes a microstructural evolution, which could degrade the good mechanical proprieties of heat-resistant steels, such as creep strength. The effect of thermal aging on the creep strength degradation is most significant at high temperature (e.g. 600°C and 650°C) and during long-term creep exposure (times higher than 10^4h).

During long-term creep exposure or aging at 600°C and 650°C of 9-12%Cr heat resistant steels the following microstructural mechanisms were reported: precipitation of new secondary phases (Laves phases, Z-phase), growth of precipitates and recovery of the matrix (decrease in dislocation density inside subgrains, growth of subgrains) [1, 2]. Precipitation of Z-phase is much less intense in 9%Cr steels compared to 12%Cr steels [3], for which it is sometimes associated with premature loss of creep strength [4]. The main microstructural degradation mechanisms of 9%Cr heat resistant steels during long-term creep and/or aging are Laves phase precipitation and recovery of the matrix rather than precipitation of Z-phase [5].

After stress-free thermal aging at 600°C and 650°C for 10^4h some subgrain growth was reported in a 9% Cr tempered martensite steel [6] but the dominant microstructural evolution is precipitation of Laves phases. Nevertheless, the effect of microstructural evolution on the creep strength loss is not fully understood and there are still few quantitative data on the microstructure of 9-12%Cr heat resistant steels after long-term creep exposure.

The purpose of this study was to investigate the effect of prior thermal aging on the creep strength of the T92 steel. The steel was thermally aged at 600°C and 650°C for 10^4h in order to precipitate large Laves phases. Then creep tests were conducted at the same temperature as the aging heat treatments to study the effect of Laves phase precipitation on the loss of the creep strength and on creep damage development.

2. Experimental procedure

2.1 Materials and creep testing

The T92 steel investigated in this study was delivered by V&M Tubes France as a tube having 48.3mm outside diameter and 11.2 mm wall thickness. Its chemical composition and heat treatment are given in Table 1.

Table 1. *Chemical composition and heat treatment of the investigated T92 steel*

	Chemical Composition, wt. %													
	C	**Si**	**Mn**	**P**	**S**	**Al**	**Cr**	**Ni**	**Mo**	**V**	**Nb**	**W**	**N**	**B**
T92 steel	0.12	0.20	0.50	0.015	0.002	0.001	8.79	0.15	0.38	0.20	0.056	1.67	0.047	0.0026
Heat treatment : 1060°C for 20 min +780°C for 60 min														

During creep or thermal exposure at 600°C and 650°C of the 9-12%Cr heat resistant steels, there is a precipitation of Laves phases. A significant growth of Laves phases is observed during the first 10^4h of exposure followed by a slight increase for longer times [7]. Thus the duration of the aging heat treatments was chosen to be 10^4h in order to precipitate large Laves phases.

To this aim, full-thickness specimen blanks were cut parallel to the tube axis. Some of them were aged in induction furnaces at 600±2°C and 650°±2°C for 10^4h. The temperature during aging heat treatments was controlled with thermocouples welded on the samples.

Creep specimens with a gauge diameter of 5mm and a gauge length of 27mm were cut at mid-thickness from both as-received and aged materials and tested at 600°C and 650°C under levels of stress in the ranges 170-210MPa and 95-150MPa respectively. The purpose of creep tests on the as-received material was i) to compare the creep strength of the investigated T92 steel with available published creep rupture data for the Grade 92 steel and ii) to get reference samples for microstructural investigations to be further compared with aged T92 steel creep tested under the same conditions.

The secondary creep rate was estimated using simplified data processing of creep curves by assuming a heuristic decomposition of the creep strain as follows:

$$\varepsilon(t) = E_0 + Q\left(1 - \exp\left(\frac{t}{\tau}\right)\right) + \dot{\varepsilon}_{ss} t \qquad (1)$$

where t is time in hours; E_0 is the instantaneous elastic/plastic strain due to loading; Q and τ are fitting parameters characterizing the primary creep stage and $\dot{\varepsilon}_{ss}$ is taken as the secondary creep rate. The value of $\dot{\varepsilon}_{ss}$ was determined by fitting equation 1 up to half the creep lifetime of each specimen.

2.2 Microstructural characterization

Microstructural characterization was realized using Scanning Electron Microscopy (SEM), Electron Backscatter Diffraction (EBSD) techniques and hardness measurements. All investigations were conducted on mid-thickness longitudinal cross-sections.

Because Laves phase are relatively large particles, average equivalent diameter larger than 150 nm, SEM techniques are best suitable to study growth and coarsening of these

phases during creep exposure compared to transmission electron microscopy techniques [8]. Due to their chemical composition, Laves phases can be easily revealed as bright precipitates in a dark matrix using backscatter electron (BSE) imaging, whereas $M_{23}C_6$ carbides have lower average atomic number compared to that of the matrix. Thus all bright precipitates in such images are Laves phases. The size distribution of Laves phases was thus determined in aged samples by analysis of SEM-BSE images acquired after a final mechanical-chemical polishing with colloidal silica. For each sample almost forty images with a magnification of 2000 were analyzed and thousands of particles were quantified.

To investigate matrix recovery, EBSD investigations of the steel microtexture were conducted on the aged T92 samples after a final polishing with colloidal silica. EBSD maps were acquired with a step size of 0.15 μm, high voltage 20kV, working distance 19 mm, aperture 120 μm, probe current between 0.1 and 1nA using a Zeiss DSM 982 Gemini field emission gun (FEG) SEM equipped with a Shottky filament together with a Hjelen-type camera and TSL OIM facilities.

Creep damage was investigated using SEM on longitudinal cross-sections of the crept specimens in the gauge length after final mechanical-chemical polishing with colloidal silica.

3. Microstructural characterization of the thermally aged material

3.1 Hardness

No significant change in hardness was observed after aging at 600°C and 650°C for 10^4h: 231 ±3 $HV_{0.5}$ for the as-received material, 236 ±4 $HV_{0.5}$ and 232±4 $HV_{0.5}$ for the material aged at 600°C and 650°C, respectively.

3.2 Size of Laves phases

The size distribution of Laves phases follow a lognormal distribution with an average equivalent diameter of ~250nm and of ~350nm in specimens thermally aged at 600°C and 650°C, respectively (Figure 1). This is consistent with literature data [8]. Typical images used for the quantification of Laves phases are shown in Figure 2.

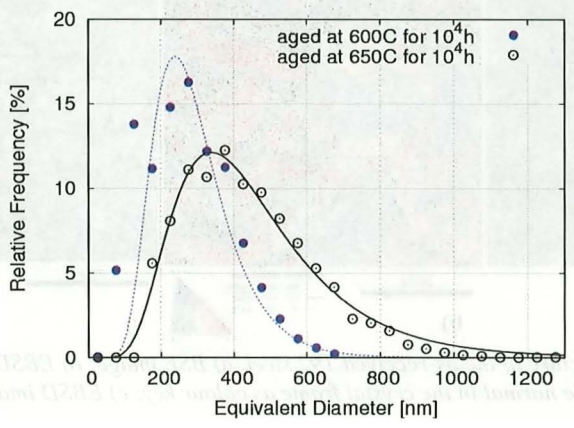

Figure 1 *Size distribution of Laves phases in the T92 aged steels determined by image analysis of SEM-BSE images (symbols) compared with a lognormal fit (lines)*

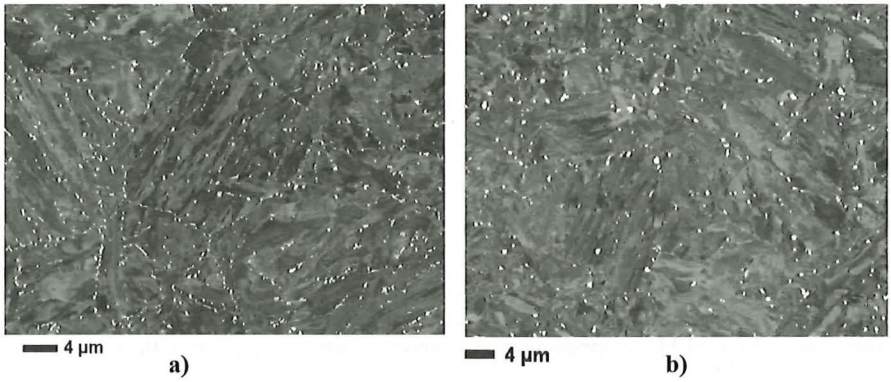

Figure 2 *Typical SEM-BSE images used for quantification of Laves phases a) T92 steel aged at 600°C for 10^4h; b) T92 steel aged at 650°C for 10^4h*

3.3 Microtexture

EBSD maps revealed no significant change in the microtexture after aging at 600°C and 650°C (Figures 3-5). All inverse pole figure (IPF) and image quality maps showed typical tempered martensite with blocks and packets. This is confirmed by the histograms of boundary misorientation angles (Figure 6) showing a typical distribution of boundaries between martensite variants formed from the same parent austenite grain [9, 10]. Only a slight decrease in the amount of low angle boundaries is observed after aging both at 600°C and 650°C.

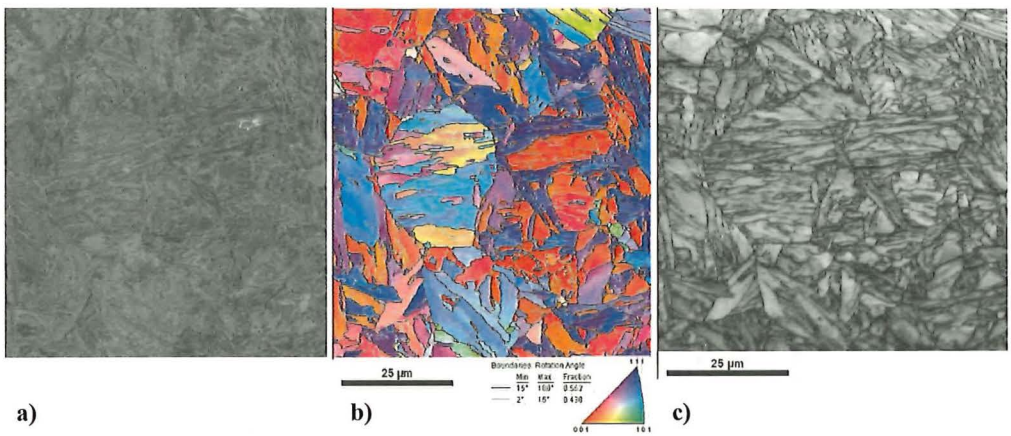

Figure 3 *Microstructure of the as-received T92 steel. a) BSE image; b) EBSD IPF map with orientation of sample normal in the crystal frame as colour key; c) EBSD image quality map*

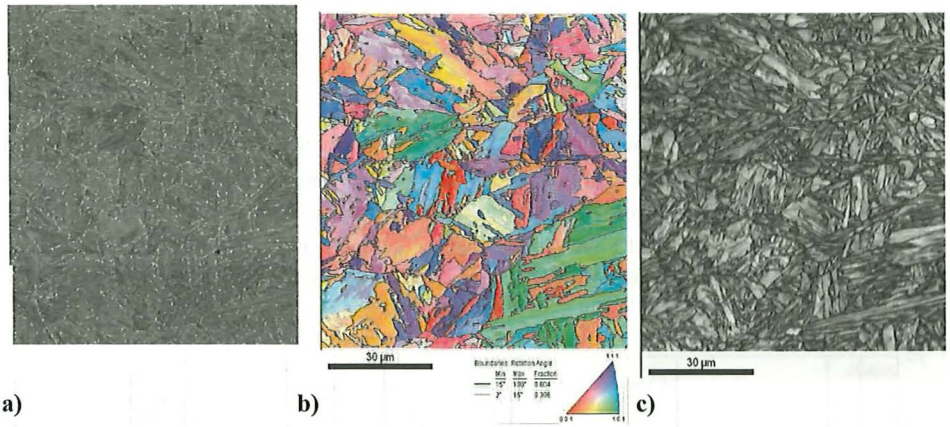

Figure 4 *Microstructure of the T92 steel aged at 600°C for 10^4h. a) BSE image; b) EBSD IPF map (same colour key as in Figure 3b); c) EBSD image quality map*

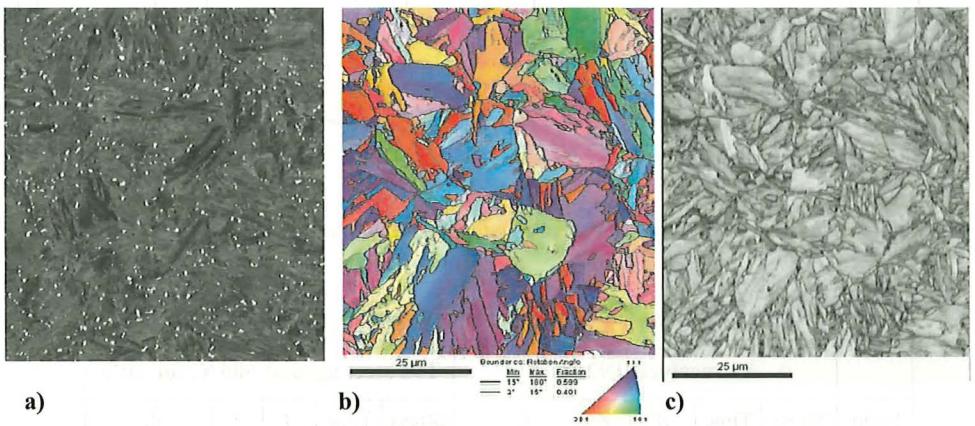

Figure 5 *Microstructure of the T92 steel aged at 650°C for 10^4h. a) BSE image; b) EBSD IPF map (same colour key as in Figure 3b); c) EBSD image quality map*

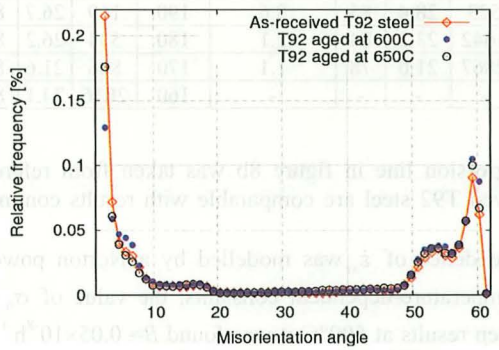

Figure 6 *Boundary misorientation angle distributions from EBSD maps shown in figures 3-5*

4. Results of creep tests

4.1 Effect of thermal aging at 600°C for 10^4h

After aging at 600°C for 10^4h the T92 steel shows a higher secondary creep rate ($\dot{\varepsilon}_{ss}$) and a lower time to rupture (divided by about 3) compared to the as-received T92 steel for the same testing conditions (Figures 7-8 and Table 2). The increase in $\dot{\varepsilon}_{ss}$ after aging might be attributed to the precipitation of Laves phases, which depletes the matrix of W and Mo atoms in solid solution. Thermal aging at 600°C for 10^4h does not seem to significantly influence the creep ductility of the T92 steel in the investigated conditions.

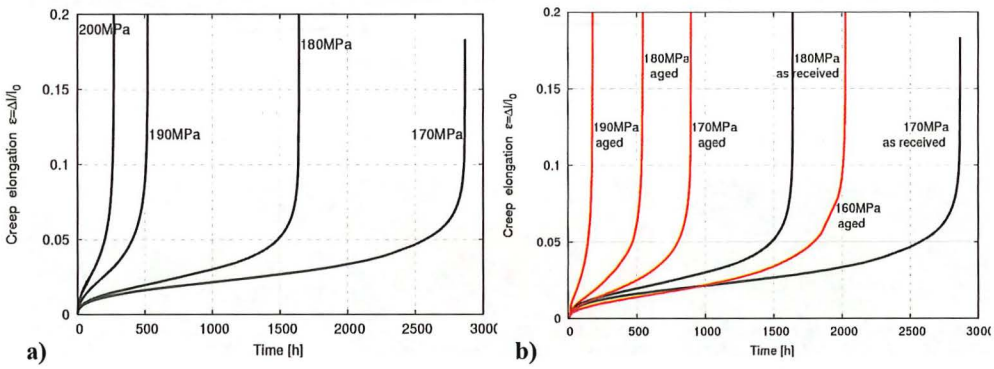

Figure 7 *Creep curves at 600°C. a) As-received material, b) material aged at 600°C for 10^4h*

Table 2 *Creep results at 600°C (A: fracture elongation; Z: reduction in area)*

	As-received T92 steel					T92 steel aged at 600°C for 10^4h				
Temp. [°C]	Stress [MPa]	Time [h]	A [%]	Z [%]	$\dot{\varepsilon}_{ss}$ [10^{-5} h^{-1}]	Stress [MPa]	Time [h]	A [%]	Z [%]	$\dot{\varepsilon}_{ss}$ [10^{-5} h^{-1}]
600	210	112	28.7	89	43.8	-	-	-	-	-
	200	270	29.8	90	17.4	-	-	-	-	-
	190	523	28.4	85	8.6	190	169	26.7	87	25.3
	180	1642	23.2	84	2.1	180	534	26.2	87	7.3
	170	2867	21.0	78	1.1	170	886	21.6	82	3.9
	-	-	-	-	-	160	2016	24.1	82	1.6

The ECCC regression line in figure 8b was taken from reference [11]. The creep results of the as-received T92 steel are comparable with results commonly reported for the Grade 92 steel.

The stress dependence of $\dot{\varepsilon}_{ss}$ was modelled by a Norton power law, (equation 2), where B and n are temperature-dependent constants; the value of σ_0 was arbitrarily set to 100MPa. From the creep results at 600°C it was found $B = 0.05\times10^{-8}$h^{-1} and n=18 for the as-received T92 steel and $B = 0.21\times10^{-8}$h^{-1} and n=18 for the thermally aged T92 steel.

$$\dot{\varepsilon}_{ss} = B\left(\frac{\sigma}{\sigma_0}\right)^n \qquad (2)$$

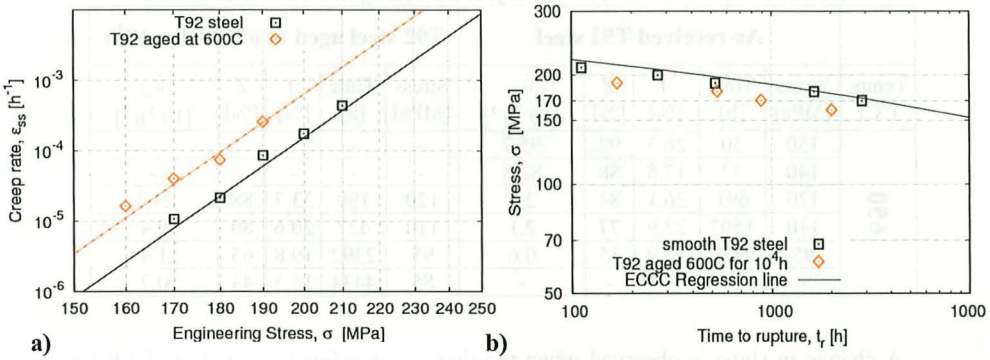

Figure 8 *Secondary creep rate (a) and time to rupture (b) as a function of engineering stress at 600°C. Symbols: experimental results; lines in (a): fit using a Norton flow rule*

4.2 Effect of thermal aging at 650°C for 10^4h

The results of creep at 650°C are summarized in Table 3 and Figure 9. Relatively high values of reduction of area (Z) and fracture elongation (A) are observed for creep lifetime lower than 1000h, indicating failure by viscoplastic instability (necking). For longer lifetimes, another damage mechanism is expected to occur.

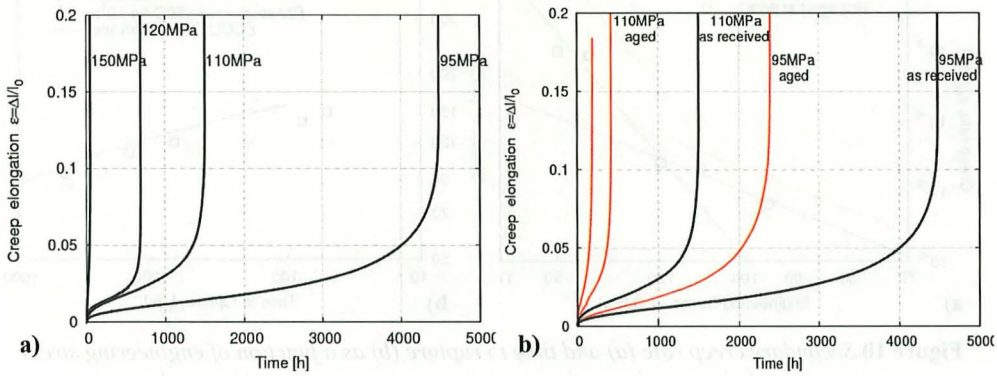

Figure 9 *Creep curves at 650°C. a) As-received material, b) material aged at 650°C for 10^4h*

Creep tests conducted on the T92 steel thermally aged 650°C for 10^4h revealed a lower time to rupture and a higher $\dot{\varepsilon}_{ss}$ compared to the as-received T92 steel for the same testing conditions. The difference between the values of $\dot{\varepsilon}_{ss}$ of the as-received T92 steel and those of

aged T92 steel depends on the level of applied stress. Compared to the as received T92 steel for same testing conditions the $\dot{\varepsilon}_{ss}$ of the aged T92 steel is four times higher for levels of stress higher than 110MPa and only twice higher for levels of stress lower than 110MPa.

Table 3 *Creep results at 650°C (A: fracture elongation; Z: reduction in area)*

	As-received T92 steel					T92 steel aged at 650°C for 10^4h				
Temp. [°C]	Stress [MPa]	Time [h]	A [%]	Z [%]	$\dot{\varepsilon}_{ss}$ [10^{-5} h^{-1}]	Stress [MPa]	Time [h]	A [%]	Z [%]	$\dot{\varepsilon}_{ss}$ [10^{-5} h^{-1}]
650	150	50	26.3	92	95.7	-	-	-	-	-
	140	77	17.8	88	82.8	-	-	-	-	-
	120	691	26.1	84	2.5	120	199	33.7	88	21.1
	110	1502	22.9	77	2.1	110	427	20.6	80	9.4
	95	4480	14.9	35	0.6	95	2392	19.8	65	1.4
	-	-	-	-	-	85	4434	15.3	43	0.7

A change in slope is observed when plotting $\dot{\varepsilon}_{ss}$ as a function of stress both for as-received and aged materials (Figure 10). Two regions can be distinguished: high stresses (σ>110MPa) and low stresses (σ<110MPa). For each region the dependence of $\dot{\varepsilon}_{ss}$ upon applied stress can be described by a Norton power-law equation (equation 2). In equation 2 σ_0 was also set to 100MPa. For high stresses it was found B=1.07×10^{-6}h^{-1} and n=18 and for low stresses it was found B= 9.78×10^{-6}h^{-1} and n=6. A Norton law with B=4.06×10^{-6}h^{-1} and n=18 for high stresses and B=19.6×10^{-6}h^{-1} and n=6 for low stresses well represents the results of creep tests conducted on the T92 steel aged at 650°C for 10^4h.

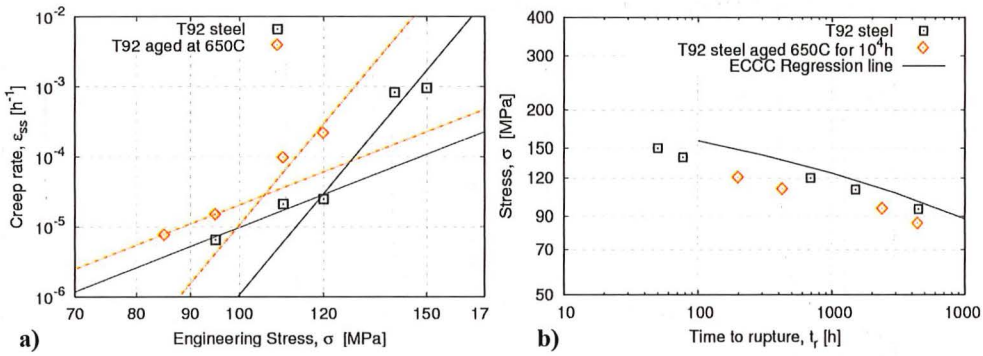

Figure 10 *Secondary creep rate (a) and time to rupture (b) as a function of engineering stress at 650°C. Symbols: experimental results; lines in (a): fit using a Norton flow rule*

The adjusted values of the Norton exponent are very high compared to the well-known theoretical values but they correspond to the values reported in literature for the creep flow of the Grade 92 steel [1, 12]. This is probably mainly due to the absence of a threshold stress in equation 2. Thus, the apparent change in Norton exponent could be due to a change in internal stresses during long-term creep testing rather than to a change in the dominant creep

mechanism. Moreover, the low number of tests conducted here at low stresses does not allow accurate estimation of the Norton law exponent in the low stress region. No evidence of diffusional creep has so far been reported in the Grade 92 steel, in contrast with Grade 91 steel [13, 14].

5. Investigations of the crept specimens

Creep damage investigations conducted on longitudinal cross sections of the crept specimens tested at 600°C revealed cavities only on the necking area. Stress triaxiality due to necking at the end of specimen lifetime could have caused nucleation and growth of these cavities. No creep damage was observed on the part of the specimens homogeneously deformed during the creep test.

In specimens of both as-received and aged T92 steel tested at 650°C for times lower than 1000h, cavities were observed only in the necking area. Scarcely distributed creep damage cavities (typically a few μm in size) were observed in all the gauge part of the crept specimens tested for times higher than 4000h (Figure 11).

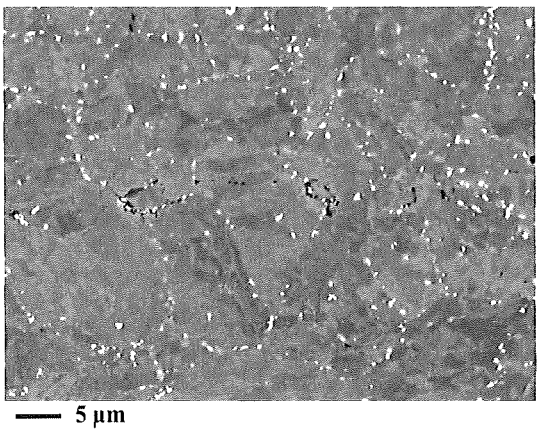

Figure 11 *Creep damage cavities (in black) observed with SEM-BSE in the homogeneously deformed part of the specimen of as-received steel crept at 650°C for 95 MPa*

6. Summary and conclusions

The most obvious change in the microstructure of the T92 steel after aging was the significant precipitation of Laves phases. In this study no significant evolution of the matrix during aging heat treatments was observed using EBSD. Complementary transmission electron microscopy observation could be made to clarify this point. This is beyond the scope of the present study, which focuses on Laves phases.

After aging an increase in secondary creep rate ($\dot{\varepsilon}_{ss}$) is observed. At 650°C this increase depends on the level of applied stresses. Creep tests conducted at 600°C on both as-received T92 steel and T92 steel aged at 600°C revealed a $\dot{\varepsilon}_{ss}$ four times higher in the aged T92 steel. Anyway the levels of stress investigated at 600°C were in the range 170-210MPa, which is relatively high and corresponds to the high stress region of the Grade 92 steel at

600°C [1, 13]. The difference between the $\dot{\varepsilon}_{ss}$ of the as-received T92 steel and T92 steel aged at 600°C might also decrease with decreasing the applied stress, as is the case at 650°C. This is also suggested by literature results on P92 steel aged at 650°C for 10^4h and then creep tested at 600°C [12].

Aging does not seem to significantly influence on creep damage development in the investigated conditions. Low amounts of creep damage was observed in crept specimens in as-received T92 steel and T92 steel aged at 650°C tested for times higher than 4000h.

References

1. Ennis P.J., Zielińska-Lipiec A., Wachter O., Czyrska-Filemonowicz A., Microstructure stability and creep rupture strength of the martensitic steel P92 for advanced power plant, *Acta Mater.* 45 (1997) 4901-4907

2. Seung Lee J., Armaki H. Gh., Maruyama K., Muraki T., Asahi H., Causes of breakdown of creep strength in 9Cr-1.8W -0.5Mo-VNb steel, *Mater. Sci. Eng. A* 428 (2006) 270-275

3. Danielsen H., Hald J., Behaviour of Z phase in 9-12%Cr steels, *Energy Materials* 1 (2006), 49-57

4. Danielsen H., Hald J., A thermodynamic model of the Z-phase Cr(V,Nb)N, *Computer coupling of phase diagrams and thermochemistry* 31 (2007) 505-514

5. Panait C., Bendick W., Fuchsmann A., Gourgues-Lorenzon A.-F., Besson J., Study of the microstructure of the Grade 91 steel after more than 100,000h of creep exposure at 600°C, *Proc. "Creep & Fracture in high temperature components: Design & life assessment issues (ECCC Creep Conference);* 877-888, London, UK. Lancaster, PA: DEStech Publications. ISBN 978-1-60595-005-1

6. Ghassemi-Armaki H., Chen R.P., Maruyama K., Yoshizawa M., Igarashi M., Static recovery of tempered lath martensite microstructures during long-term aging in 9–12% Cr heat resistant steels, *Materials Letters* 63 (2009) 2423-2425

7. Dimmler G., Weinert P., Kozeschnik E., Cerjak H., Quantification of Laves phase in advanced 9-12%Cr steels using a standard SEM, *Mater. Charact.* 51 (2003) 341- 352

8. Korcakova L., Hald J., Somers A. J., Quantification of Laves phase particle size in 9CrW steel, *Mater. Charact.*, 47 (2001), 111-117

9. Morito S., Huang X., Furuhara T., Maki T., Hansen N., The morphology and crystallography of lath martensite in alloy steels, *Acta Mater.* 54 (2006) 5323-5331

10. Gourgues, A.-F., Flower H. M. and Lindley T.C., Electron backscattering diffraction study of acicular ferrite, bainite and martensite microstructure, *Mater. Sci. Technol.* 16 (2000) 26-40

11. Yoshizawa M., Igarashi M., Moriguchi K., Iseda A., Armaki H. G., Maruyama K., Effect of precipitates on long-term creep deformation properties of the P92 and P122 type advanced ferritic steels for USC power plant, *Mater. Sci. Eng. A* 510-511 (2009) 162-169

12. Sklenička V., Kuchařová K., Svoboda M., Kloc L., Buršík J., Kroupa A., Long-term creep behavior of 9–12%Cr power plant steels, *Mater. Charact* .51 (2003) 35-48

13. Kloc L., Sklenička V., Confirmation of low stress creep regime in 9% chromium steel by stress change creep experiments, *Mater. Sci. Eng. A,* 387-389 (2004) 633-638

14. Kloc L., Sklenička V., Transition from power-law to viscous creep behaviour of p-91 type heat-resistant steel, *Mater. Sci. Eng. A* 234-236, (1997) 962-965

9th Liege Conference : Materials for Advanced Power Engineering 2010
edited by J. Lecomte-Beckers, Q. Contrepois, T. Beck and B. Kuhn.

Microstructural Evolution during Creep Deformation of an 11CrMoVNb Ferritic Heat Resistant Steel

Kyu-Ho Lee[1,2], Dae-Bum Park[1,2], S.I. Kwun[2], Jin-Yoo Suh[1], Woo-Sang Jung[1*]

[1]Materials & Devices Division, Korea Institute of Science and Technology, 39-1 Hawolgok-dong, Seongbuk-gu, Seoul 136-791, Korea
[2]Department of Materials Science, Korea University, Anam, Seoul 136-701, Korea
*Corresponding author: +82-2-958-5429, wsjung@kist.re.kr

Abstract

The effect of creep deformation on the microstructural development of an 11CrMoVNb ferritic heat resistant steel during high temperature creep test is investigated. Coarsening behavior of the precipitates, $M_{23}C_6$ and MX, and growth behavior of martensite laths of crept specimens are carefully observed from both gage and grip parts of the specimens in order to discuss the effect of deformation. Particle coarsening and martensite lath widening are pronounced in the gage part due to the creep deformation.

Keywords: 11Cr ferritic steel, creep, precipitate, growth, coarsening

1. Introduction

Because it is generally accepted that power generation industry will continue to depend on coal-fired boilers for a significant fraction of its production for upcoming 20-30 years, achieving higher efficiencies is crucial in reducing CO_2 emission. The power generation efficiency can be improved by adopting Ultra-Supercritical (USC) power generation, and development of heat resistant materials that can resist creep deformation at temperature higher than 600°C is necessary.

9-12Cr ferritic steels(ferritic stainless steels containing 9-12% of Chromium) have superior oxidation, corrosion and creep properties. Moreover, lower coefficient of thermal expansion(CTE), and higher thermal fatigue resistance than those of austenitic stainless steels make the ferritic heat resistant steel constitute major components of coal-fired power plants [1-3]. Therefore, many research is ongoing in order to develop new ferritic heat resistant steels. Studies on the effect of alloying elements on creep and oxidation properties as well as studies for process optimization are reported [3-5].

Tempered martensite and precipitates, metal-carbonitrides, MX(M=V, Nb/X=C, N), and $M_{23}C_6$ (M=Fe, Cr), constitute major microstructural components of 9-12Cr ferritic steels. Therefore, the decomposition rate of the martensite laths and the growth rate of the precipitates during service determine the high temperature creep property. $M_{23}C_6$ forms at the beginning stage of tempering treatment mainly on grain boundaries and martensite lath

boundaries. Thus, $M_{23}C_6$ contributes to increase the strength during early tempering stage. MX forms inside grains as well as on grain boundaries with a size of nanometer scale, less than 100nm, to effectively suppress the dislocation movement during creep deformation [5,6]. The precipitates formed during tempering treatment are likely to grow during creep deformation leading to degradation of the creep strength. Therefore, optimization of alloy design and heat treatment condition is required to control the growth rate of the precipitates.

Not only the high temperature, but the combination of applied stress and corresponding strain during creep deformation is known to accelerate the growth of the precipitates. As an underlying mechanism of higher growth rate of precipitates under stress-strain condition, high concentration of dislocation accumulates during creep deformation around particles resulting in accelerated diffusion of solute elements heading to the particles [1,7]. However, reports on evaluation of such an effect in a quantified way are rare. There are not many studies on quantifying the effect of stress and strain on the growth rate of precipitates during creep deformation to separate the mechanical contribution out from the overall contributing factors. The mechanical contribution can be addressed by comparing the microstructural degradation of gage part and grip part of creep specimens after creep deformation, because at least the effect of deformation can be excluded during the microstructural change of the grip part. In this study, the effect of creep deformation on the microstructural change of 11CrMoVNb ferritic steel including the growth of precipitates and the decomposition of martensite laths is investigated by comparing the gage and grip parts of creep specimens.

Table 1. *Chemical composition of 11CrMoVNb ferritic steel used in this study. (wt. %)*

Element	Fe	C	Si	Mn	Ni	Cr	Mo	V	W	Cu	Nb	N
Content	Bal.	0.18	0.23	0.69	0.52	10.9	0.98	0.20	0.16	0.03	0.06	0.072

2. Experimental procedure

The chemical composition of 11CrMoVNb ferritic steel is shown in Table 1. The rolled ingot was provided by Doosan heavy industry company. The specimens were normalized at 1052°C and, subsequently, tempered at 677°C for 8 hours. Creep specimens were machined to have gage length of 32mm and diameter of 6.35mm, which is close to the size requirement of ASTM E139 standard. The creep specimens were machined along the rolling direction of the provided ingot. Creep tests were performed by a constant load with 200, 250, and 300MPa at 593°C and 130, 160, and 200MPa at 621°C. The creep rupture time varied up to 7,300 hours. The temperature difference inside a creep specimen, between gage center and grip, was carefully controlled to be less than ±1°C.

Growth kinetics of precipitates was analyzed by transmission electron microscopy (TEM) on carbon extraction replica of gage and grip part of the specimens. In order to observe the development of martensite laths, thin foil specimen was prepared by twin jet polishing at the condition of -20°C, 7V with 25% perchloric acid + 75% methanol solution using Struers Tenupol 5 jet polisher. Size of over 1,000 precipitates per a specimen was measured using image analyzer software from TEM images on carbon replica. And, over 300 martensite laths per each specimen were used to calculate average lath width from TEM images on thin foils.

Also, thermodynamic-kinetic simulation using MatCalc software was performed in order to compare the experimentally collected data on the growth behavior of precipitates with the numerical estimation.

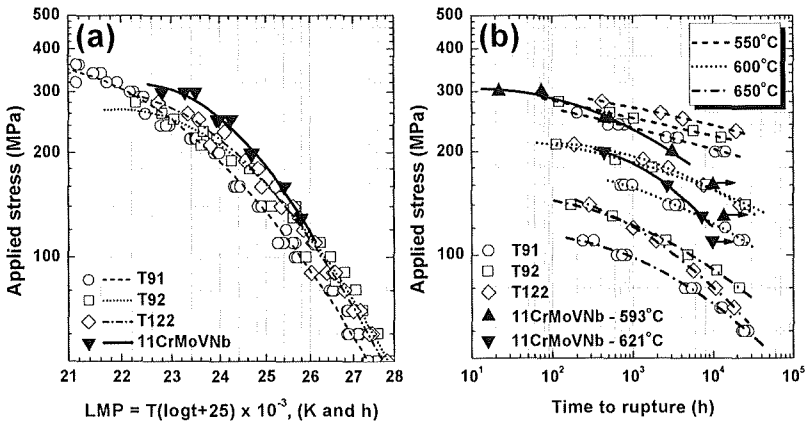

Figure 1. *Creep rupture properties of T91, T92, T122 and 11CrMoVNb steel. (a) LMP, (b) applied stress vs. time to rupture.*

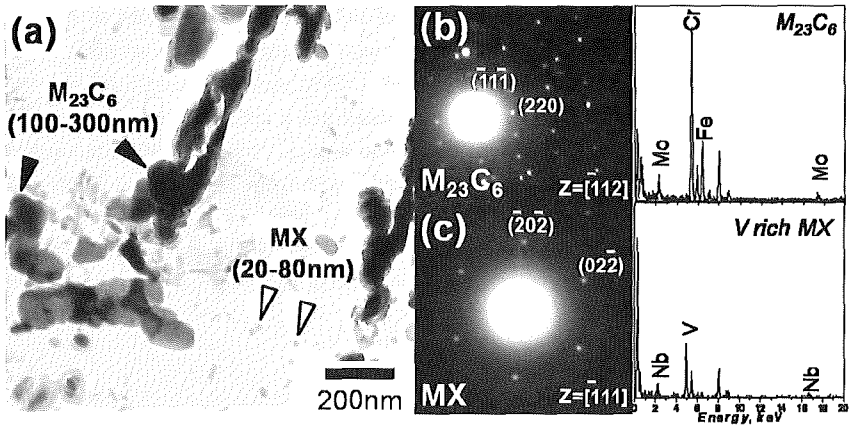

Figure 2. *(a) Carbon extraction replica images of crept specimen in gage part at 593 ℃ under 200 MPa (t_r=3,117h), SADP and its EDS results obtained from (b) $M_{23}C_6$ and (c) MX, respectively.*

3. Results and Discussion

3.1. Creep properties

Creep strength is closely related to the microstructural features such as dislocation density, types of precipitates, distribution of precipitates, and lath width [6-7]. Therefore, the microstructure has to contain components that are stable at high temperature for creep resistance. Figure 1 shows results of creep-rupture test performed at 593 and 621°C also with reported data of other 9-12Cr ferritic steels, T91, T92, and T122 [8-10]. These steels are known to have over 100,000 hours of time to rupture at 600°C and 100-130MPa [11]. It is noted that the ferritic steel used in this study has better or comparative creep properties up to 10,000hours. The higher content of Cr, C and N appears to contribute to the enhanced creep properties by solid solution strengthening and distribution of fine precipitates.

3.2. Development of microstructure and precipitates

It is reported that the δ-ferrite inside 9-12Cr ferritic steel would significantly deteriorate creep strength [12-13]. According to Ryu [13], δ-ferrite forms when Cr-equivalence is higher than 10. The Cr-equivalence of the steel used in this study is 7.75, which is lower than the critical value reported. As expected by this criterion, no δ-ferrite is observed from optical microscopy (OM) and scanning electron microscopy (SEM). Prior austenite grain (PAG) is observed to have the size of 50-60μm. Martensite laths fill in the PAG and significant amount of precipitates is formed along the grain boundaries and martensite lath boundaries.

Figure 2 shows carbon replica image of gage part which is ruptured at 593°C and 3,117 hours. Particles with 100-300nm size are identified as $M_{23}C_6$, and finer precipitates which are less than 80nm are mostly V-rich MX. No other type of precipitate is found at 593°C.

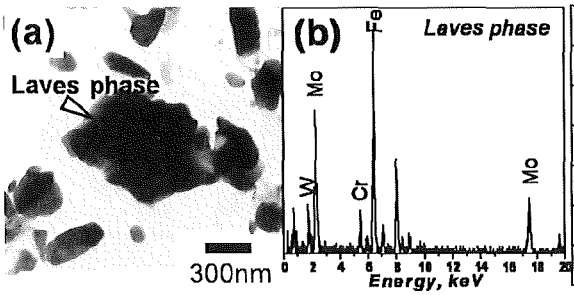

Element	wt. %	at. %
Si (K)	2.425	6.009
Cr (K)	6.791	9.087
Fe (K)	38.652	48.156
Mo (K)	49.070	35.587
W (L)	3.060	1.158
Total	100	100

Figure 3. *(a) TEM micrographs of extraction replica of Laves phase. Gage part of specimens ruptured at 621 ℃ under 130MPa (t_r=7,313h), (b) EDS of Laves phase.*

On the other hand, at 621°C, laves phase is observed. Figure 3 shows the image of laves phase formed in the specimen ruptured at 621°C and 7,313 hours. This particle turns out to be Fe_2Mo laves phase with substituting elements like Cr, Si and W to have chemical composition of $(Fe_{0.761}Cr_{0.144}Si_{0.095})_2(Mo_{0.968}W_{0.032})$. Laves phase is also reported to form after long exposure at creep temperature in the 9-12Cr ferritic steels [14]. The reason why laves phase forms only after long-term exposure is its low driving force to nucleate. The larger size of critical nucleus due to the low thermodynamic driving force leads to longer incubation time for nucleation than the other precipitates such as $M_{23}C_6$ and MX. Also, laves phase is known to have fast growth rate [14]. That is, laves phase has long incubation time, but, once it starts to form, it grows fast. Therefore, after long-term exposure, the solid solution strengthening effect is expected to diminish as the solute elements like Mo and W disappear by the formation and growth of laves phase.

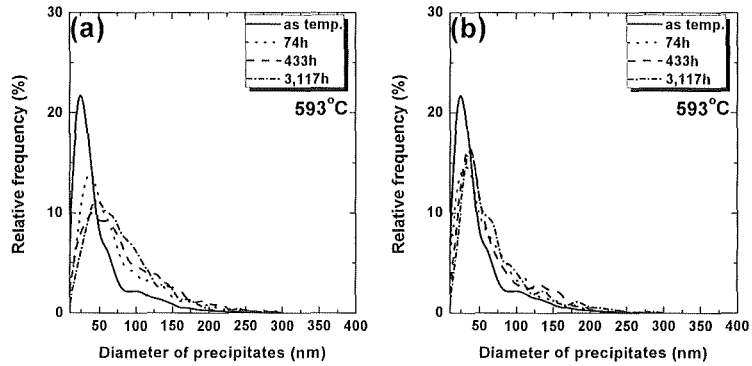

Figure 4. *Precipitates size distribution during creep deformation in (a) gage and (b) grip part.*

3.3. Microstructural change by creep deformation

Figure 4 shows size distribution of precipitates measured from TEM images taken from carbon replica of gage and grip parts of each specimen ruptured at 593°C. At gage part, average precipitate size as well as width of size distribution increases as a function of creep rupture time. On the other hand, at grip part, size distribution of the precipitates does not appear to change as much as the change in gage part. From this, it is conceivable that the stress and strain during creep deformation accelerate the growth rate of precipitates. Deformation causes accumulation of dislocations around particles and martensite lath boundaries [14, 15], and resultant increase in diffusion through the dislocations is thought to be dominantly causing the accelerated growth of the precipitates.

High density of dislocation accumulates on martensite lath boundaries as creep deformation proceeds. By the recovery and coalescence of the lath boundaries, the lath width increases during creep process. Figure 5 shows TEM micrograph of martensite laths around gage and grip parts of the creep specimens ruptured at 593°C. Distribution of fine precipitates is observed along the grain boundaries and laths boundaries. The lath width is also observed to increase as a function of creep rupture time. This is because the accumulated dislocations drive the lath boundaries to move. The comparison of mean lath width between gage and grip parts is given in Figure 6. Gage part has faster growth rate of lath width than that of grip part. As can be seen from Figure 6, there is a clear difference in growth rate of lath width between gage and grip parts, which is caused by the combination of stress and strain.

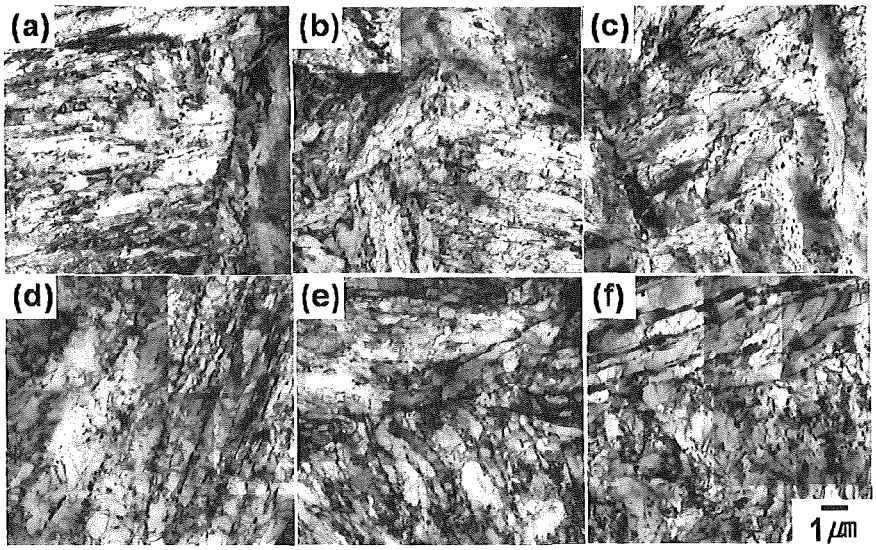

Figure 5. *TEM micrographs of creep ruptured specimens at 593 ℃ under (a) 300 MPa, (b) 250 MPa, (c) 200 MPa in grip part and (d) 300 MPa, (e) 250 MPa, (f) 200 MPa in gage part.*

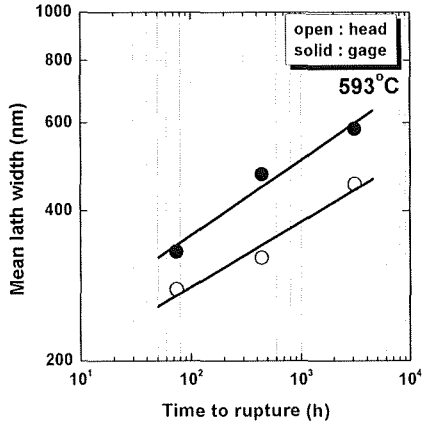

Figure 6. *Change of mean lath width as a function of creep rupture time.*

3.4. Kinetics simulation of precipitate growth

Figure 7 shows radius of MX precipitates measured from gage and grip parts of all specimens creep-ruptured in this study. The mean size of MX precipitates increases as a function of creep-rupture time. The initial mean radius of MX, before creep test, is 12nm. According to Miyata [16], coherency strain plays a major role in creep strengthening with precipitates under 15nm. Since initial precipitates of 12nm turns out to grow to more than 20nm during initial 100 hours at both temperature levels, 593 and 621°C, it is conceivable that the precipitation strengthening effect gradually decreases during creep deformation. Therefore, the growth behavior of precipitates during creep is crucial factor determining creep property.

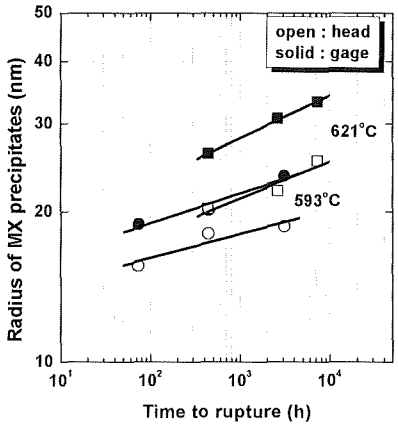

Figure 7. *Change of mean radius of MX particle as a function of creep rupture time.*

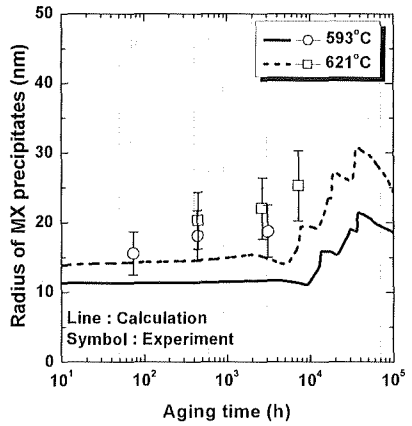

Figure 8. *Comparison of calculated size of MX precipitates during aging with experimental results from grip part of specimens.*

In this context, estimation of precipitate growth behavior based on thermodynamics and kinetics provides crucial information for designing alloys. A thermodynamics-kinetics simulation software MatCalc is used to estimate the growth behavior of 11Cr ferritic steel used in this study. Since MatCalc currently does not consider the effect of deformation, the calculation result is compared with the experimental data acquired from grip part of specimens in Figure 8. Simulation shows almost linear growth up to 4,000-9,000 hours and then a change of growth rate. Because the creep experiment is still on the way to get specimens ruptured at longer time, there is no experimental data available to compare with the simulation result at the time range where the change of growth rate occurs. However, the overall experimental growth behavior agrees well with the simulation result.

As the precipitates grow, the concentration of solute elements approaches equilibrium. After equilibrium, the precipitates still grow, but at the expense of other precipitates. This Ostwald ripening [17] can be described by the following equation,

$$r^m - r_0^m = k \cdot t \quad (1)$$

where r, r_0, k and t are mean particle radius as a function of time t, initial mean radius, rate constant and time, respectively. The exponent, m, is a constant determined by diffusion path; m=2 (coarsening controlled by interface diffusion), 3 (volume diffusion), 4 (grain boundary diffusion), and 5 (pipe diffusion) [14]. 12Cr ferritic steels is reported to have m=3 [18] and m=5 [19].

However, the exponent, m, fitted to the experimental data in this study is 16 for 593°C and 11.6 for 621°C for gage part. The exponent, m, fitted to the data from grip part is even higher, m=18 and 12.2 for 593 and 621°C, respectively. According to Sawada et al. [1], the high m value indicates high thermal stability of the precipitates. On the other hand, there is a report on additional precipitation of small MX particles during service [20] suggesting another factor that could possibly cause high m values. However, in this study, such a secondary MX precipitation has not been observed. Therefore, the unusually high m values appear to be originated from high stability of the precipitates against growth up to 10,000hours.

4. Conclusion

11CrMoVNb ferritic steel turns out to have higher creep strength for short-term creep deformation (<10,000 hours) than creep properties of T91, T92 and T122 ferritic steels, and further creep testing is ongoing to evaluate creep properties of the steel for longer duration time. The major precipitates are $M_{23}C_6$ and MX after tempering, and coarse laves phase forms after long-term creep test. The mean size of precipitates increases along with the creep duration time. In addition, the combination of applied stress and corresponding strain causes faster growth kinetics. Growth rate of martensite lath width also increases by the combination of stress and strain. The exponent term, m, of Ostwald ripening equation is fitted to have values ranging from 11 to 18, which indicates the growth rate of the precipitates is significantly slow.

5. References

[1] K. Sawada, K. Kudo and F. Abe, Creep behavior and stability of MX precipitates at high temperature in 9Cr-0.5Mo-1.8W-VNb steel, *Mater. Sci. Eng.*, A319, 784, (2001).

[2] L. Helis, Y. Toda, T. Hara, H. Miyazaki and F. Abe, Effect of cobalt on the microstructure of tempered martensitic 9Cr steel for ultra-supercritical power plants, *Mater. Sci. Eng.*, A510, 88, (2009).

[3] S.M. Song, S.W. Hong, D.S. Bae, W.S. Jung, S.H. Jung and S.I. Kwun, The effect of thermo mechanical treatment on thermal degradation characteristic in 11Cr ferritic steel, *J. Kor. Inst. Met. & Mater.*, 45(1), 1, (2007).

[4] J. Hald, Microstructure and long-term creep properties of 9-12% Cr steels, *Int. J. Pressure Vessels and Piping*, 85, 30, (2008).

[5] T. Onizawa, T. Wakai, M. Ando and K. Aoto, Effect of V and Nb on precipitation behavior and mechanical properties of high Cr steel, *Nucl. Eng. Des.*, 238, 408, (2008).

[6] M. Taneike, F. Abe and K. Sawada, Creep-strengthening of steel at high temperatures using nano-sized carbonitride dispersions, *Nature*, 424, 294, (2003).

[7] G. Eggeler, The effect of long-term creep on particle coarsening in tempered martensite ferritic steels, *Acta Mater.*, 37, 3225, (1989).

[8] NRIM Creep Data Sheet, No. 43, NRIM, Tsukuba, Japan, (1996).

[9] NIMS Creep Data Sheet, No. 48, NIMS, Tsukuba, Japan, (2002).

[10] NIMS Creep Data Sheet, No. 51, NIMS, Tsukuba, Japan, (2006).

[11] M. Yoshizawa, M. Igarashi, K. Moriguchi, A. Iseda, H.G. Armaki and K. Maruyama, Effect of precipitates on long-term creep deformation properties of P92 and P122 type advanced ferritic steels for USC power plants, *Mater. Sci. Eng.*, A510, 162, (2009).

[12] M. Yoshizawa and M. Igarashi, Long-term creep deformation characteristics of advanced ferritic steels for USC power plants, *Int. J. of Pressure Vessels and Piping.*, 84, 37, (2007).

[13] S.H. Ryu and J. Yu, A new equation for the Cr equivalent in 9 to 12 Pct Cr steels, *Metall. Mat. Trans.*, 29A, 1573, (1998).

[14] K. Maruyama, K. Sawada and J. Koike, Strengthening mechanisms of creep resistant tempered martensitic steel, *ISIJ Int.*, 41, 641, (2001).

[15] F. Abe, Mater. Analysis of creep rates of tempered martensitic 9%Cr steel based on microstructure evolution, *Mater. Sci. Eng.*, A510, 64, (2009).

[16] K. Miyata, Y. Sawaragi, H. Okada, F. Masuyama, T. Yokoyama and N. Komai, Microstructural evolution of a 12Cr-2W-Cu-V-Nb steel during three-year service exposure, *ISIJ Int.*, 40, 1156, (2000).

[17] W. Ostwald, *Analyticsche Chemie, 3rd edn*, Engelman, Leipzig, 23, (1901).

[18] M. Taneike, M. Konde and T. Morimoto, Accelerated coarsening of MX carbonitrides in 12%Cr steels during creep deformation, *ISIJ Int.*, 41, Supplement, S111, (2001).

[19] Y. Kadoya, B.F. Dyson and M. McLean, Microstructural stability during creep of Mo-or W-Bearing 12Cr steels, *Metall. Mater. Trans. A*, 33A, 2549, (2002).

[20] S. Straub, P. Polcik, W. Blum, H. König and K.H. Mayer, Microstructural evolution of the martensitic cast steel GX12CrMoVNbN9-1 during long-term annealing and creep, *Steel Res.* 66, 402, (1995).

9th Liege Conference : Materials for Advanced Power Engineering 2010
edited by J. Lecomte-Beckers, Q. Contrepois, T. Beck and B. Kuhn.

CREEP STRENGTH AND MICROSTRUCTURAL EVOLUTION OF 9-12% CR HEAT RESISTANT STEELS DURING CREEP EXPOSURE AT 600°C AND 650°C

Francisca Mendez Martin[1], Clara Gabriela Panait[2,5], Walter Bendick[3], Mihaela Albu[4], Bernhard Sonderegger[1], Gerald Kothleitner[4], Christof Sommitsch[1], Anne-Françoise Gourgues-Lorenzon[4], Jacques Besson[4], Arno Fuchsmann[5]

[1] Institute for Materials Science and Welding, Graz University of Technology, Graz, Austria.
[2] Centre des Matériaux, MINES ParisTech, UMR CNRS 7633, B.P. 87, 91003 Evry Cedex, France.
[3] SZMF, Salzgitter Mannesmann Forschung GmbH, Ehinger Straβe 200, D-47259 Duisburg, Germany.
[4] Institute for Electron Microscopy, Graz University of Technology, Graz, Austria.
[5] V&M France CEV, Route de Leval, B.P. 20149, 59620 Aulnoye-Aymeries, France.

Abstract

9-12 %Cr heat resistant steels are used for applications at high temperatures and pressures in steam power plants. 12 %Cr steels show higher creep strength and higher corrosion resistance compared to 9 %Cr steels for short term creep exposure. However, the higher creep strength of 12 %Cr steels drops increasingly after 10,000-20,000 h of creep. This is probably due to a microstructural instability such as the precipitation of new phases (e.g. Laves phases and Z-phases), the growth of the precipitates and the recovery of the matrix.

9 %Cr and 12 %Cr tempered martensitic steels that have been creep tested for times up to 50,000 h at 600°C and 650°C were investigated using Transmission Electron Microscopy (TEM) on extractive replicas and thin foils together with Backscatter Scanning Electron Microscopy (BSE-SEM) to better understand the different creep behaviour of the two different steels.

A significant precipitation of Laves phase and low amounts of Z-phase was observed in the 9 %Cr steels after long-term creep exposure. The size distribution of Laves phases was measured by image analysis of SEM-BSE images. In the 12 %Cr steel two new phases were identified, Laves phase and Z-phase after almost 30,000 h of creep test. The quantification of the different precipitated phases was studied.

Keywords: Laves phases, Z-phases, 9 %Cr tempered martensitic steels, 12 %Cr tempered martensitic steels, creep strength.

1. Introduction

9-12 %Cr tempered martensitic steels are used for applications at high temperature in Ultra Super Critical (USC) power plants. They are considered as excellent candidates due to their lower thermal expansion and higher thermal conductivity compared to austenitic steels [1]. During service, a microstructure evolution can impair their mechanical properties, such as creep strength. Thus, the microstructure stability of these steels during exposure at 600°C-650°C is of a great importance, a better understanding of relationships between the microstructure state and loss of creep strength is needed.

The microstructure of 9-12 %Cr tempered martensitic steels consists of various types of precipitate phases distributed in a tempered martensitic matrix, namely, carbides of $M_{23}C_6$-type located mainly at boundaries and carbonitrides of MX-type finely dispersed inside

martensite laths. The creep strength of these steel grades combines coupled precipitation/subgrain strengthening given by $M_{23}C_6$-type and MX-type precipitates and solid solution strengthening provided by W and Mo atoms in solid solution.

During service, at high temperatures and high pressures, the microstructure of 9-12 %Cr steels evolves. Coarsening of different precipitate populations (such as $M_{23}C_6$ or Cr_2N), dissolution of vanadium carbonitrides, precipitation of new phases (mod. Z phase [2] or Laves phase) and recovery of the matrix [3] are the possible microstructural evolution mechanisms in these steels.

The purpose of the present study is to report new quantitative data on the microstructure of two 9 %Cr steels and of a 12 %Cr steel after long term creep exposure at 600°C and 650°C to better understand their different creep behaviour. In *Figure 1* is presented the creep results for the studied materials at different temperatures.

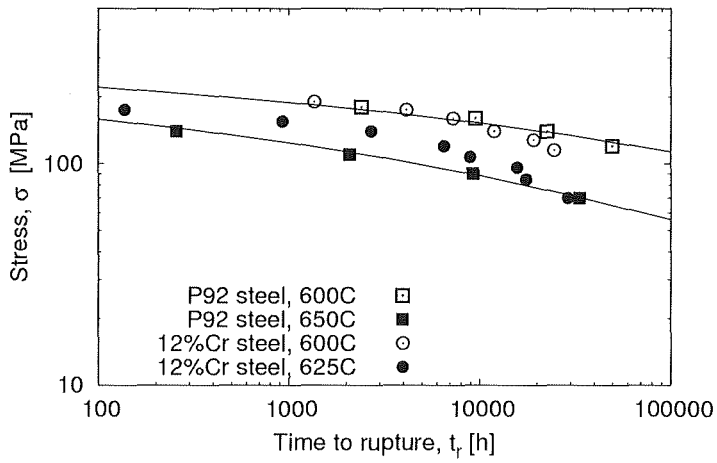

Figure 1 Creep data of P91 and 12 %Cr steel tested at 600 °C, 650°C and 625°C in comparison to base material mean lines of the well established Grade 92 steel at 600°C and 650°C taken from the reference [4]

2. Materials and experimental procedure

2.1 Materials and creep specimens

Three different 9-12 %Cr tempered martensitic steels have been investigated. Two different 9 %Cr steels (ASME Grades P91 and P92 respectively), and a 12 %Cr martensitic steel alloyed with relatively low concentration of Mo and high W, compared with the other two.

The chemical composition and the heat treatment of the investigated steels are presented in *table 1* and *table 2* respectively. In *table 3* is summarized the investigated creep specimens and the applied testing techniques for each material.

Table 1 Chemical composition of the investigated tempered martensitic steels.

	Chemical Composition, wt.%							
Material	*C*	*Cr*	*Mo*	*V*	*Nb*	*W*	*N*	*B*
P92 steel	0.12	9.32	0.49	0.20	0.055	1.75	0.049	0.0012
P91 steel	0.1	8.43	0.92	0.20	0.068	-	0.059	-
12Cr steel	0.115	11.50	0.290	0.260	0.050	1.500	0.066	0.0049

Table 2 Heat treatments of the investigated tempered martensitic steels.

Material	***Heat treatment***
P92 steel	1060°C 1 h + 770°C 2 h a.c.
P91 steel	1050°C 1 h + 730°C 1h + 750°C 1 h a.c.
12Cr steel	1060°C 30 min a.c. + 780°C 2 h a.c.

Table 3 Creep testing conditions and the different investigations techniques used for the characterization of the studied martensitic steels.

Material	***Creep testing conditions (Temperature, stress and time to rupture)***	***Feature of the microstructure and Investigation techniques***
P92 steel	600°C, 160 MPa, 9,497 h	Laves phases (image analysis of SEM-BSE images)
	600°C, 140 MPa, 22547 h	
	600°C, 120 MPa, 49,721 h	
	600°C, 120 MPa, 49,721 h	Z-phases (TEM on extraction replica)
	650°C, 110 MPa, 2,092 h	Laves phases (image analysis of SEM-BSE images)
	650°C, 90 MPa, 9,211 h	
	650°C, 70 MPa, 33,308 h	
P91 steel	600°C, 80 MPa, 113,431 h	Z-phase, size of $M_{23}C_6$ and Laves phase (TEM on extraction replica, image analysis of SEM-BSE images)
12Cr steel	600°C, 115 MPa, 24,639 h	MX, M_2X, $M_{23}C_6$ (TEM on ion milled and extraction replica samples
	625°C, 70 MPa, 28,983 h	$M_{23}C_6$ and MX (TEM on ion milled sample)

2.2 Transmission Electron Microscopy (TEM) investigations

For the characterization of the 12% Cr steel, mainly transmission electron microscopy (TEM) has been used. The specimens were prepared from the head of the specimen at only thermally aged conditions by two different techniques. First, extraction replicas were prepared, see experimental procedure in [5]. Second, ion milled specimens were prepared by grinding and polishing with different suspensions to get a thickness of 10-15 μm in the central position. Afterwards, the final thinning was done using argon ions until a hole was produced in the middle of the specimen.

The accomplished investigations were carried out on a Philips CM20/Scanning TEM (STEM) equipped with a Gatan imaging filter (GIF), see operation conditions in [5].

The different phases were identified using the energy filtered transmission electron microscopy (EFTEM) technique and their elemental composition was established via electron energy loss spectroscopy (EELS) and energy dispersive X-ray spectroscopy (EDX). For more details on the chemical quantification procedure, see [5].

The real mean diameter and the size distribution of the $M_{23}C_6$ and MX precipitates were calculated out of the elemental distributions of chromium and vanadium micrographs. The precipitate parameters were evaluated by improved stereological methods, described by Sonderegger [6]. The measurements were done in the ion milled specimens and the thickness was calculated from thickness maps produced by dividing an unfiltered and a zero-loss image, recorded in the same dynamical conditions.

2.3 Scanning Electron Microscopy (SEM) investigations

Because Laves phase are relatively large particles, average equivalent diameter larger than 150 nm, SEM techniques are better suitable to study growth and coarsening of these phases during creep exposure. SEM techniques are recommended [7] because it allows sampling larger areas, obtaining more particles per image and better statistics compared to TEM techniques.

Due to their chemical composition, enriched in heavy metals such as W and Mo, Laves phases have a much higher average atomic number compared to that of the matrix. Because of that, they can be easily revealed as bright precipitates in a dark matrix using SEM in Backscatter electron mode (BSE). In 9-12% Cr tempered martensitic steels discrimination of Laves phases from $M_{23}C_6$ carbides is possible using SEM-BSE observations because $M_{23}C_6$ carbides are enriched in Cr and have lower average atomic number compared to that of the matrix. Thus, all bright precipitates in SEM-BSE images are Laves phases.

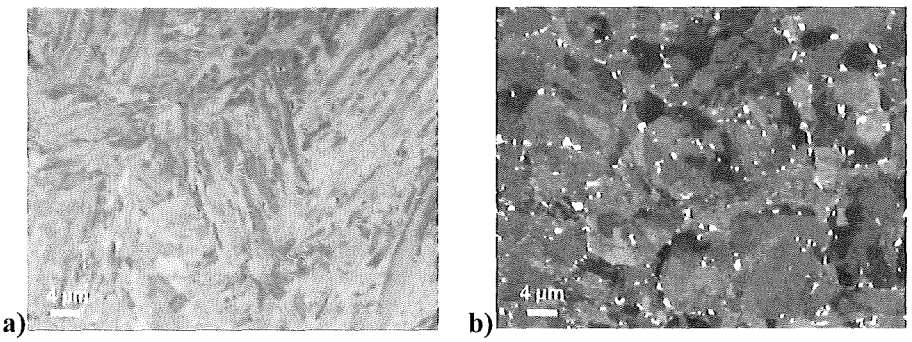

Figure 2 SEM-BSE images after final colloidal silica polishing: a) microstructure of the as-received P92 steel; b) microstructure of the P92 steel after 33,308 h of creep at 650°C showing Laves phases as bright precipitates.

The size distribution of Laves phases was measured for P92 crept specimens by the analysis of approximately forty SEM-BSE images per sample with a magnification of 2000. *Figure 2b* shows a typical SEM-BSE image used for the quantification of Laves phase. SEM-BSE images were acquired on longitudinal cross-sections of the crept specimens in the gauge length after a final mechanical-chemical polishing with colloidal silica.

Together with SEM-BSE investigations, TEM investigations were conducted on single extractive replicas for the characterization of the mod. Z-phase and $M_{23}C_6$-type precipitates after long-term creep exposure. TEM investigations were performed with a FEI Tecnai F20 ST microscope operating at 200kV equipped with an energy dispersive X-ray spectrometry (EDX). The chemical composition of each precipitate was determined by EDX analysis and identified as follows: $M_{23}C_6$ (enriched in Cr), Laves phase (enriched in Mo in the P91 steel and enriched in W in the P92 steel), modified Z phase (50 at.% (Cr + Fe) and 50 at.% (V+Nb), N not quantified) and MX (enriched in V and Nb).

3. Results

3.1. Microstructural evolution of P91 and P92 steels during creep at 600°C and 650°C

The following features of microstructure were investigated in the crept specimens in 9% Cr tempered martensitic steels: Laves phase, $M_{23}C_6$ precipitates and Z-phase.

The P91 steel creep tested for 113431 h at 600°C had been investigated previously and results on precipitation ($M_{23}C_6$-type, Laves phase, mod. Z-phase precipitation) and creep damage were reported in reference [8].

3.1.1 Laves phases
Figure 2 shows the size distribution of Laves phases in the P92 steel after creep exposure at 600°C (a) and 650°C (b) determined by image analysis of SEM-BSE images. The equivalent diameter of these particles follows a lognormal distribution.

An average diameter of about 200 nm is found after almost 10,000 h of creep exposure at 600°C. The average equivalent diameter increases slightly during longer exposure time at 600°C while the frequency of large Laves phases increases, see *figure 3a*.

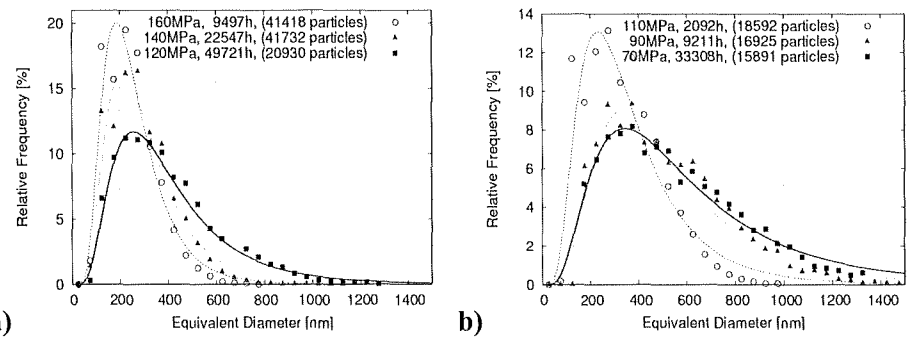

Figure 3 Size distribution of Laves phases in the P92 steel after long-term creep exposure at 600°C (a) and 650°C (b).

The average size of Laves phases increases with increasing temperature. An average diameter of about 250 nm is found after only 2,000 h of creep exposure at 650°C. The average equivalent diameter increases up to 350 nm during almost 10,000 h creep exposure at 650°C.

No significant change is observed in the size of Laves phases between 10,000 h and 33,308 h of exposure at 650°C.

Thus, significant precipitation and growth of Laves phases are observed in the first 10,000 h of exposure both at 600°C and 650°C, followed by a slight growth for longer exposure times both at 600°C and 650°C. This is confirmed by previous studies [9, 10].

An average equivalent diameter of about 400nm was found for Laves phases in the P91 creep specimen tested for 113,431h at 600°C [8].

3.1.1 Z-phase and $M_{23}C_6$ carbides

The main purpose of the TEM investigations, conducted on carbon extractive replicas, was to study the precipitation of Z-phase during long-term creep exposure in 9% Cr tempered martensitic steels. Previous studies reported that the precipitation of Z-phase is lower in the 9 %Cr steel compared to that in 12 %Cr steels [11]. Nevertheless the precipitation of this phase in 9% Cr steel was only investigated for testing times lower than 50,000 h [12, 13], with only few quantitative data. Thus TEM investigations were focused on the 9 %Cr steel creep specimens with the longest testing times, namely, P91 steel, 113,431 h and P92 steel, 49,721 h both creep tested at 600°C. Low amounts of Z-phase were observed in these specimens with respect to the total number of the investigated precipitates or to the size of the investigated area. Only 41 precipitates out of 640 identified precipitates were found to be Z-phases in the P91 crept specimen. Amongst almost 600 investigated precipitates in the P92 creep specimen tested for 49,721 h only 6 particles were identified to be Z –phase.

On both investigated crept specimens, the observed Z-phases are widely spaced particles; thus, a density number i.e. a ratio between number of Z-phases reported to the size of the investigated area could not be relevant. The observed Z-phases have an average equivalent diameter of about 400 nm.

A change in average chemical composition of the $M_{23}C_6$-type precipitates after 49,721 h of creep at 600°C was observed compared to the as received state. For metal elements, an increase in Cr content from about 60 at.% to 70 at.% and a decrease in Fe content from about 30 at.% to 20 at.% are observed in the crept specimen. A similar change in the average chemical composition of $M_{23}C_6$-type precipitates was also observed in the P91 steel after 113,431h of creep at 600°C.

The size of $M_{23}C_6$-type carbides in P92 steel crept specimens was not investigated in detail as there are already published data on this issue [14, 15]. Ennis et al. [15] reported an increase in average diameter of $M_{23}C_6$ carbides from ~90nm (in as received conditions) up to ~130nm after 33000h of creep exposure at 600°C.

Growth of the $M_{23}C_6$-type carbides was reported in the P91 steel specimen creep tested for 113,431 h at 600°C [8]. The equivalent diameter increases from about 150 nm (in the as received state) to about 300 nm after creep exposure.

3.2. Microstructural evolution of the 12% Cr steel thermally aged at 600°C and 625°C

The microstructure of the 12% Cr martensitic steel was characterized in as-received condition (after heat treatment), after thermal aging at 600°C for 24,639 h and after thermal aging at 625°C for 28,983 h.

The material; in as-received condition; feature a martensite lath structure where no delta ferrite was observed. Different precipitates populations at the prior austenite grain boundaries, subgrain boundaries and martensite laths boundaries could be identified. The precipitates were identified as $M_{23}C_6$, MX (NbC and VN) and M_2X (Cr_2N). The material thermally aged at 600°C and 625°C shows the same tempered martensitic structure besides two new precipitates populations, Laves phase and Z-phase. The chemical composition of the different phases was analyzed via EDX and EELS in extraction replica specimens. The EDX values for each analysed particle have been scaled to the nitrogen content. The results for the chemical composition of the different analysed nitrides (MX (NbC and VN), M_2X (Cr_2N) and Z-phase) is already published in [5]. *Figure 4* depicts the chemical composition for the different material conditions and particles.

$M_{23}C_6$ shows an increase in the chromium content with increasing exposure temperature and time. The chemical composition of MX phase is similar in the as-received condition and in the thermally aged condition at 600°C specimen. M_2X phase shows reduced variations in chromium content.

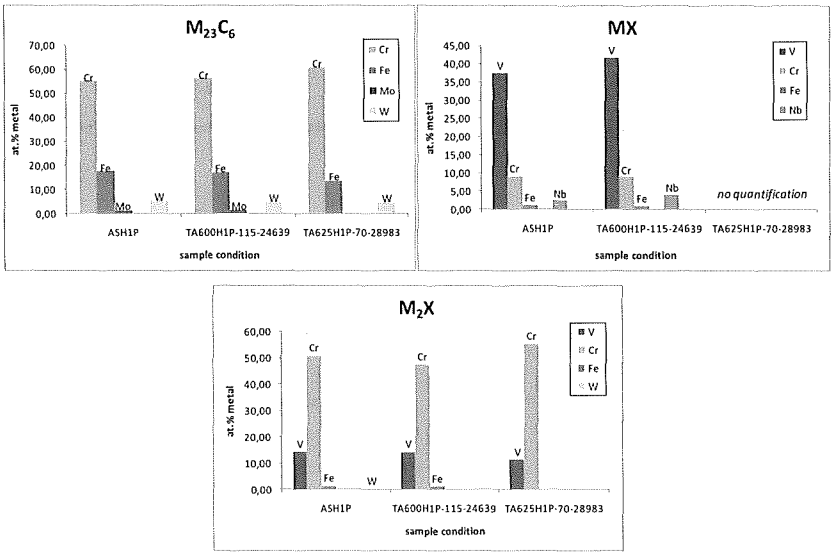

Figure 4 Chemical composition of $M_{23}C_6$, MX and M_2X for all for the 12 %Cr steel. The acronyms of the different studied specimens are defined as: *ASH1P*= as-received material (after heat treatment), *TA600-115-24639*= thermally aged at 600°C for 24,639 h and *TA625-70-28983*= thermally aged at 625°C for 28,983 h.

The precipitates $M_{23}C_6$, MX and M_2X were present in the as-received and the thermally aged material. During ageing and creep the diameter of these particles increases. Coarsening of the different precipitation populations (e.g. $M_{23}C_6$, MX and M_2X) is an important degradation

mechanism that causes softening of the materials. Because of that, the mean diameter of $M_{23}C_6$, MX and M_2X precipitates in as-received condition and after aging were calculated.

The $M_{23}C_6$ phase shows an increase of the mean diameter from 80-100 nm in the as-received condition to 100-140 nm in the aged specimen at the highest temperature (625°C). Moreover, a significant number of precipitates with a mean diameter between 200-300 nm was observed after thermal ageing.

For the MX phase, a mean diameter of 40 - 60 nm was found in the as-received condition. After thermal ageing at 600°C, there is an increase up to 80 nm.

The results of the size distribution of $M_{23}C_6$ and MX particles for all the sample conditions are presented in *figure 5*. For the M_2X, Laves phase and Z-phase, no particle size distribution is yet available.

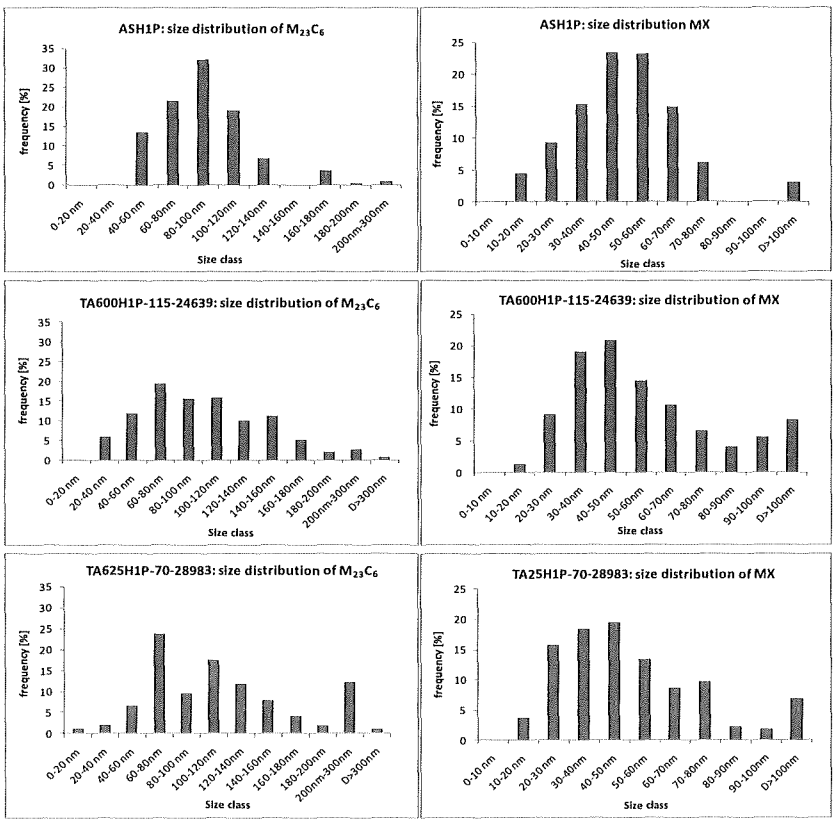

Figure 5 Size distribution of $M_{23}C_6$ and MX precipitates. The acronyms are defined in figure 4.

4. Summary and discussion

During long-term creep exposure of the 9% Cr tempered martensitic steels, such as P92 and P91 steel significant precipitation of Laves phase, growth of $M_{23}C_6$ carbides and low amounts of Z-phases was observed. Precipitation of Laves phases leads to a depletion of W and Mo in solid solution in the matrix and might thus reduce solid solution strengthening in these steels.

The precipitation of Z-phase could not be considered as a major microstructural degradation mechanism since only few particles of Z-phase were observed after long-term exposure to creep at 600°C both in P91 steel and P92 steel. Moreover, no significant change was observed on the number density of the MX-type precipitates in these steels.

Creep damage development and recovery of the matrix such as growth of subgrains, are also believed to have a significant influence on the loss of the creep strength of the 9% Cr steels during long term creep exposure. Observations about these two mechanisms were not presented in this study, details can be found in references [8, 16].

The microstructure of the investigated 12 %Cr tempered martensitic steel changes (evolves) during creep exposure i.e. precipitation of Laves phases and Z-phase. The chemical composition of the different precipitates populations, $M_{23}C_6$, MX and M_2X, show smoothly changes that can be related with the precipitation of the new phases: Laves phase and modified Z-phase. The mean size of the $M_{23}C_6$ phase increased from 80 nm to 120 nm during thermal ageing at the highest temperature whereas MX phase coarsened from 50 to 80 nm. However, a high number of MX particles were identified with values from 30 to 50 nm.

In reference [9] the size distribution of the $M_{23}C_6$ phase in the P91 steel showed a shift of the highest frequency from 150-180 nm to 300 nm after creep exposure at 600°C for 113,431 h. The results presented for the 12% Cr steel, revealed only a slight shift of the highest (80 nm) peak frequency to larger values however the testing time in reference [8] is much higher then that of the investigated 12%Cr steel (i.e. 625°C for 28,983h).

5. Conclusions

The microstructural investigations of the P92 steel and P91 steel specimens creep tested for long term at 600°C and 650°C revealed that precipitation and significant growth of Laves phases is the dominant degradation mechanism of the microstructure of these steels during creep exposure.

Low amounts of mod. Z-phase and a change in the average chemical composition of the $M_{23}C_6$-type precipitates were also observed. Precipitation of Z-phase could not be considered as a major degradation mechanism of the microstructure of the 9%Cr steel during creep exposure at 600°C and 650°C.

Recovery of the matrix, such as growth of subgrains and creep damage development should be also considered in understanding loss of the creep strength after long term exposure of 9-12% Cr tempered martensitic steels. These issues are not discussed in this study.

A drop in the creep strength is observed for the 12%Cr steel after almost 20,000h of creep testing at 600°C. No significant changes in the chemical composition of the different studied

precipitates populations could be observed. As reported in the literature [2] the drop in the creep strength at this 12 %Cr steel could be due to the dissolution/transformation of the MX phases to Z-phases. Only values of the mean radius of MX could be presented at this point of time. However, a quantification of the number density and phase fraction of this phase is in progress to corroborate this hypothesis.

6. References

[1] F. Abe,T. Kern, R. Viswanathan, Physical and elastic behavior of creep-resistant steels, *Creep-resistant steels*, 225-234, (2008).
[2] J. Hald, in: J. Lecomte-Beckers, M. Carton, F. Schubert, P.J. Ennis, Metallography and alloy design in the COST 536 action, *Proceedings of the Conference Materials for Advanced Power Engineering*, 2, 917- 930, (2006).
[3] J.S. Lee, H.G. Armaki, K. Maruyama, T. Muraki, H. Asahi, Causes of breakdown of creep strength in 9Cr-1.8W-0.5Mo-VNb steel, *Materials science and engineering A*, 428, 270-275, (2006).
[4] M. Yoshizawa, M. Igarashi, K. Moriguchi, A. Iseda, Hassan Ghassemi Armaki, K. Maruyama Effect of precipitates on long-term creep deformation properties of P92 and P122 type advanced ferritic steels for USC power plants *Materials Science and Engineering: A*, 510-511, 15, 162-168, (2009).
[5] M. Albu, F. Méndez Martín, G. Kothleitner, B. Sonderegger, Compositional characterisation and thermodynamic modelling of nitride precipitates in a 12 % Cr steel, *International Journal of Materials Research*, 99, 422-427, (2008).
[6] B. Sonderegger, Modifications of stereological correction methods for precipitate parameters using transmission microscopy, *Ultramicroscopy*, 106 10, 941-950, (2006).
[7] L. Korcakova, J. Hald, A. J. Somers, Quantification of Laves phase particle size in 9CrW steel, *Materials Characterization*, 47, 111-117, (2001).
[8]. C. Panait, W. Bendick, A. Fuchsmann, A.-F. Gourgues-Lorenzon, J. Besson, Microstructure of the Grade 91 steel after more than 10^5h of creep at 600°C, in *"Creep & fracture in high temperature components-Design & life assessment; Proceddings of ECCC Creep Conference", DEStech Publications, Lancaster, U.S.A, ISBN 978-1-60595-005-1*
[9] G. Dimmler, P. Weinert, E. Kozeschnik, H. Cerjak, Quantification of the Laves phase in advanced 9–12% Cr steels using a standard SEM, *Materials Characterization*, 51, 341-352, (2003).
[10] L. Korcakova, J. Hald, Marcel A. J. Somers, Quantification of Laves phase particle size in 9CrW steel, *Materials Characterization*, 47, 111-117 (2001)
[11] H. Kj. Danielsen, J. Hald, A thermodynamic model of the Z-phase Cr(V, Nb)N, *Calphad*, 31, 505-514, (2007).
[12] K. Sawada, M. Tabuchi, Hongo H., T. Watanabe, K. Kimura, Z-Phase formation in welded joints of high chromium ferritic steels after long-term creep, *Materials Characterization*, 59, 1161-1167, (2008).
[13] K. Sawada, H. Kushima, K. Kimura, M. Tabuchi, TTP diagrams of Z phase in 9-12% Cr heat-resistant steels, *ISIJ International*, 47, 733-739, (2007).
[14] A. Zielinska-Lipiec, A. Czyrska-Filemonowicz, P.J. Ennis, O. Wachter, Microstructural investigations on the 9% chromium steel P92 after long-term creep deformation, *Proceedings of the Conference Materials for Advanced Power Engineering*, 559-566, (1998).

[15] PJ Ennis, A. Zielinska-Lipiec, A. Czyrska-Filemonowicz, Influence of heat treatments on microstructural parameters and mechanical properties of P92 steel, *Materials Science and Technology 16*, 1226-1232 (2000)
[16] C. Panait, Ph.D. thesis, MINES ParisTech, Paris, France, 2010

9th Liege Conference : Materials for Advanced Power Engineering 2010
edited by J. Lecomte-Beckers, Q. Contrepois, T. Beck and B. Kuhn.

MICROSTRUCTURAL EVOLUTION OF ASTM P91 AFTER 100,000 HOURS EXPOSURE AT 550°C AND 600°C

L. Cipolla[1),*], S. Caminada[2),#], D. Venditti[1)], H. K. Danielsen[3)], A. Di Gianfrancesco[1)]

1) Centro Sviluppo Materiali SpA, Rome, Italy
2) TenarisDalmine, Dalmine, Italy
3) Technical University of Denmark, Lyngby, DTU, Denmark
* also Ph.D Student at Technical University of Denmark, DTU, Lyngby, Denmark
# also Ph.D Student at Politecnico di Milano, Mechanical Department, Milan, Italy

Abstract

ASTM A335 P91 samples were investigated after creep testing at 550°C and 600°C for over 10^5 h.
X-Ray Diffraction, Scanning and Transmission Electron Microscopy were adopted to assess the microstructural evolution of the material in terms of precipitation changes during high temperature exposure. Mean equivalent diameters and average chemical compositions of MX and $M_{23}C_6$ precipitates and Laves phases were assessed through the analysis of a large number of particles. Their growth and coarsening kinetics were determined at 600°C on many samples with increasing exposure times up to 100,000 hours. Also the presence of modified Z-phase, Cr(V,Nb)N, was investigated.
The high microstructural stability of Grade 91 is related to the presence of fine and distributed MX carbonitrides, always present even after very long term temperature exposure. The mean size of MX carbonitrides remains almost constant and stays below 45 nm after 10^5 h at 600°C.
Although MX particles exhibit a Cr enrichment with increasing ageing times, indicating that they are absorbing Cr atoms from the surrounding matrix, their transformation into Z-phase is still at a very preliminary stage: only a few hybrid MX/Z particles and a few Z-phase precipitates were identified in the most aged sample after 10^5 h at 600°C.
Coarsening of $M_{23}C_6$ occurs during thermal exposure, but their average equivalent diameter, initially of 140 nm in the as-treated material, remains below 200 nm after 10^5 h at 600°C.
Laves particles form at grain boundaries after a relatively short time and soon become the largest precipitates.

Keywords: 9%Cr steels, long-term creep, microstructure evolution, Z-phase.

1. Introduction

In the last two decades several advanced 9%Cr ferritic steels were developed and some of them, such as ASTM Grades 91 and 92, are currently used in modern power plants [1, 2]. This has allowed the service pressure and temperature of components for advanced power plants to be increased significantly and more severe requirements on strength, oxidation resistance and creep properties to be imposed on high temperature steels.
Long term creep tests, even longer than 100,000 hours, are available today and reliable long term creep strength values have been established, based on comprehensive creep databases [3, 4]. The average 100,000 hours creep rupture strength values at 600°C of ASTM Grades 91 and 92 were recently assessed by the European Creep Collaborative Committee (ECCC) as 90 MPa [3] and 113 MPa, respectively [4].
A key element for the creep strengthening of the advanced 9%Cr steels is the formation of a fine dispersion of small MX carbonitrides, (V,Nb)(C,N), which are very stable against coarsening and thus provide a fundamental contribution to the creep resistance by means of precipitation hardening [5]. It has been well established that the main microstructural evolution mechanisms during high temperature exposure of 9%Cr steels are the coarsening of

carbides, $Cr_{23}C_6$, and the precipitation, growth and coarsening of Laves phase particles, $Fe_2(Mo,W)$ [5, 6, 7].
It has been found that the modified Z-phase, a complex nitride Cr(V,Nb)N, develops in 9-12%Cr steels during thermal exposure in the temperature range 600°C-700°C [8, 9, 10]. The formation of Z-phase has been associated with a dissolution of the fine dispersion of small MX nitrides, (V,Nb)N. Unfortunately, Z-phase particles grow much larger than MX precipitates and, thus the Z-phase formation results in a quick and severe loss of creep strength [6, 9], especially for 12%Cr steels.
A thermodynamic model of the Z-phase has recently been developed [11]. It predicts that in the 9-12%Cr steels Z-phase is the most stable nitride in the temperature range 600°C-700°C and, accordingly, at equilibrium it fully replaces the finely dispersed MX nitrides which precipitate during normalising and tempering heat treatment. It has been found that in advanced 12%Cr steels, such as P122, Z-phase formation occurs much faster than in 9%Cr steels and large colonies of Z-phase are observed in 12%Cr samples exposed for few thousand hours at 650°C [10]. It was concluded by model studies that the chromium content has a major influence on the driving force for Z-phase formation and on its growth rate, which explains why 12%Cr steels suffer from rapid and abundant formation of Z-phase, while this occurs much more slowly in 9%Cr steels [11].
Recently, it was explained that the formation of Z-phase occurs by Cr diffusion from the matrix into the original V- and Nb-nitrides, through the formation of metastable hybrid MX/Z particles [12, 13, 14].
The aim of this paper is to investigate the microstructural evolution of an industrial P91 by analysing several aged samples up to 100,000 hours at 550°C and 600°C.
In particular, the precipitate evolution at increasing times and temperatures are described and discussed in the paper, in order to demonstrate the high microstructural stability of Grade 91 even after long-term thermal exposures.
This work also investigates the presence of Z-phase in aged samples and the mechanism of its formation by means of hybrid MX/Z particles.

2. Material

An industrial ASTM A335 P91 seamless pipe produced by TenarisDalmine (heat 28145), with an outside diameter (OD) of 355 mm and a wall thickness (WT) of 35 mm, was extensively characterised in terms of microstructural, mechanical and creep properties after long-term thermal exposure. The chemical composition of the investigated pipe is reported in Table 1, compared with the requirements of ASTM A335-06. This pipe was normalised at 1040°C and tempered at 760°C.
Samples from a second industrial pipe from TenarisDalmine (heat 801141), 343mm OD and 74mm WT, were investigated after 7,000h and 58,000h at 600°C. This pipe was also normalised at 1040°C and tempered at 760°C. Its chemical composition is also shown in Table 1.
Both as-treated pipes fulfil the ASTM mechanical requirements.
The microstructure of the 355mm OD as-treated pipe consists of fully tempered martensite, with an average hardness of 230 HV_{10}.
The creep resistance of the 355mm OD pipe was extensively tested in the range of 550°C-650°C; in particular three creep specimens from this batch broke after 110,301h at 550°C and 150 MPa, 104,076h at 600°C and 90 MPa and 115,808h at 650°C and 50 MPa; the first two

specimens were selected for the extensive microstructural characterization reported in this work.
Figure 1 shows the comparison among all the creep rupture data from the 355mm OD pipe and the average creep-rupture strength of ASTM A335 P91, assessed by ECCC in 2009 [3]. This confirms that the creep strength of the industrial pipe selected in this work is in line with the ECCC creep rupture assessment for Grade 91.
The samples broken at longest times show the typical low values of elongation to rupture observed in 9-12%Cr steels [15]: 20%, 4% and 5%, respectively after 110,301h at 550°C, 104,076h at 600°C and 115,808h at 650°C.

3. Experimental

All the microstructural investigations were conducted on the heads of the broken creep specimens, since it was demonstrated that no differences in the precipitation occur between gauge and grip portion of the same crept specimen for 9%Cr steels [16, 17].
In addition to Light Microscopy (LM), Scanning Electron Microscope (SEM) investigations were carried out using a JEOL 5900, with a tungsten filament. As Laves phase is a Mo-based particle, this was easily identified by Back Scattered Electron (BSE) images. BSE images were processed adopting an Automatic Image Analysis (AIA) procedure, coupling particle size with chemical composition. During each SEM session, several hundred random particles from 50 random frames at 3000X magnification were identified, for a total scattered area of 3150 μm^2. A cut-off of particles with mean diameter less than 200 nm and a Mo content less than 5 wt% was imposed.
The morphology and the composition of finest precipitates were investigated with a Field Emission Gun Transmission Electron Microscope (FEG-TEM), JEOL 3000F, operating at 300kV and equipped with an Oxford Instruments Inca Link ISIS Energy Dispersive Spectroscopy (EDS) unit and a Gatan Imaging Filtered (GIF) Electron Energy Loss Spectroscopy (EELS).
A 200kV Scanning/Transmission Electron Microscope (STEM), JEOL 200CX, equipped with an EDS Noran Instruments was also used.
Occasionally, a FEG-TEM, FEI TITAN 80-300, operating at 300kV, has been used.
TEM observations were carried out on carbon extraction replicas as well as on thin foils. The replicas were prepared by a chemical etching with Vilella's reagent (1% picric acid and 5% hydrochloric acid in ethanol).
Several particles from each extraction replica were analysed in order to determine their equivalent diameter and, through EDS, their average chemical composition; only the particles above 10 nm and sufficiently far from each other to avoid overlapping were analysed.
This methodology was applied also to identify the presence of Z-phase precipitates; the following compositional criterion was adopted to discriminate Z-phase: Fe(at%)+Cr(at%)≈V(at%)+Nb(at%), with $40 \leq Cr(at\%)+Fe(at\%) \leq 60$.
A Selected Area Diffraction (SAD) analysis was performed on a limited number of particles, in order to couple lattice parameters with the chemical composition obtained through EDS.
The average dislocation density and the average sub-grain size were measured with a standard procedure based on the intercept method applied on thin foils [18].
For the determination of the different phases, X-Ray powder Diffraction (XRD) was also applied, using a Siemens D500 X-Ray Diffractometer equipped with Co-radiation source. The step size was 0.2° in 2θ and the counting time was 34s per step. In order to avoid interference from matrix reflections, the precipitates were extracted from the bulk by electrolysis in an

acidic solution of 5% HCl in 95% ethanol to dissolve the matrix. The solution thus obtained was filtered through a 20 nm Millipore filter to capture the extracted powders. The dissolution of samples for XRD investigation involved at least 10g of material from each sample.

4. Results

4.1 Microstructure evolution

The microstructure of both crept samples after 100,000h at 550°C and 600°C consists of tempered martensite with average hardness values of 225 HV_{10} and 224 HV_{10}, respectively. The microstructure by LM of the sample after 104,076 hours at 600°C is shown in Figure 2-a. Figure 2-b shows the same sample by SEM: grain boundaries and tempered martensite laths are decorated by precipitates.

TEM investigations by thin foils allowed to get information on the substructure evolution after long term exposure, without straining (specimens were taken from the heads of creep specimens). The thin foil images of as-treated, 550°C/110kh and 600°C/104kh samples are presented in Figure 3.

The as-treated material exhibits a well recovered matrix with polygonized structures. Precipitates at grain boundaries and laths were identified as $M_{23}C_6$ carbides (see section 4.2).

After long exposure at 550°C and 600°C, the substructure does not exhibit significant changes, being the tempered martensite lath still recognized in many regions.

The mean subgrain size of 600°C/104kh aged sample was found to be close to that of the as-treated material. Also the dislocation density values of the as-treated and 600°C/104kh samples are similar.

4.2 Precipitation evolution

The evolution of precipitates of the aged samples with increasing exposure times at high temperature is a diffusion controlled mechanism. The microstructural changes, in terms of progressive variation of precipitate morphology and their chemical composition, are described and quantified, as a function of temperature and time, adopting the Larson Miller Parameter (LMP) using a constant equal to 20.

The mean equivalent diameters and average chemical compositions (at%) of MX, $M_{23}C_6$ and Laves particles in the aged samples are reported in Table 2, where crept samples are sorted by Larson-Miller Parameter (LMP) values. Two samples, 600°C/7kh and 600°C/58kh, belong to heat 801141; they have been included in Table 2 to offer a complete view of the microstructural evolution of P91 over time.

TEM investigations enabled to detect very fine MX particles (mean size of 36 nm) in the as-treated material. TEM analyses on exposed samples showed that many fine particles, smaller than 40 nm, are still present in the matrix even after 100,000h at 550°C and 600°C.

EDS and Energy Filtered (EF) TEM investigations demonstrated that these fine precipitates, distributed within laths, are V- and Nb- rich carbo-nitrides. Figure 4 shows the precipitates extracted by carbon replica in the 600°C/104kh sample at higher magnification: in particular MX carbonitrides are indicated. Table 3 reports the EDS analyses (at%) of the main chemical elements found in some particles shown in Figure 4. MX carbo-nitrides contain mainly V (57-75 at%), Cr (14-30 at%) and Nb (3-29 at%). The presence of V, Nb and N as constitutional elements of MX is shown also in Figure 5, together with the zero loss image and the jump ratio images of Cr, N and V of the frame, which enabled to identify several small (V,Nb)N particles, together with a larger Cr carbide ($M_{23}C_6$ type).

Although hundreds of particles were analyzed on each sample, no traces of Z-phase were identified in the 550°C/113kh and 600°C/58kh samples. Only seven modified Z-phase particles, Cr(V,Nb)N, were detected in the 600°C/104kh sample (Figure 6) over several hundred investigated particles. Table 4 reports the EDS chemical compositions (at%) of some particles visible in Figure 6. An average equivalent diameter of 140 nm and the following average chemical composition (at%): 50%Cr, 33%V, 12%Nb, 4%Fe, 1%Mo were measured. Modified Z-phase is not included in Table 2, since the number of identified particles is too small for a reliable data assessment.

In addition to the well known MX and Cr(V,Nb)N phases, particles with a "hybrid" (V,Nb)N and Cr(V,Nb)N composition were also identified in the 600°C/104kh crept sample. A small hybrid particle with a V-rich core and a Cr-rich rim is shown in Figure 7. In addition to the High Annular Angular Dark Field (HAADF) image of the particle (Figure 7-a), the EF-TEM thickness map and the vanadium map of the hybrid particle are shown in Figures 7-b and 7-c, respectively. The variation in composition within the particle was also investigated using an EDS linescan with 50 measurements (Figure 8). The chemical composition gradually varies within the precipitate: there is an area with a MX-like composition in the middle, (V:~50 at%; Cr:~30 at%), while the "wings" of the particle have a Z-phase like composition (V:~35 at%; Cr:~55 at%). Between the core and the outer particle surface a relatively smooth Cr and V gradient was measured.
No such hybrid particles were found in the samples aged at 550°C for 110kh and at 600°C for 58kh.

$M_{23}C_6$ carbides are Cr-rich (72-80 at%) and contain also Fe (13-18 at%) and Mo (5-6 at%).
TEM investigations on the as-treated sample showed small $M_{23}C_6$ carbides distributed along grain boundaries and martensite laths (Figure 3-a).
Slightly coarser $M_{23}C_6$ carbides were observed in both 550°C/110kh and 600°C/104kh aged samples, mainly along grain boundaries and tempered martensite laths (Figures 3-b, 3-c and Figure 4).

No Laves phases are present in the as-treated material, confirming that it nucleates and precipitates during the exposure at service temperature, well below the tempering temperature at which it is not a stable phase.
Figures 3-b, 3-c and 4 show that large Laves phase particles are found in aged specimens. Figure 9 shows a SEM image of Laves particles at high magnification and their typical EDS spectrum. Size distribution of Laves particles from 600°C/104kh sample, measured by SEM-AIA, is shown in Figure 10: the highest frequency corresponds to an equivalent diameter of 450 nm (the standard deviation of the distribution is 290 nm). This value is in agreement with literature results from the investigation of an industrial P91 exposed 113,431h at 600°C (where the highest frequency corresponds to an equivalent diameter of 400 nm) [16].

Results from X-Ray powder Diffraction for 600°C/104kh sample are in line with the TEM results: $Cr_{23}C_6$, MX and Fe_2Mo phases were identified by means of their crystallographic reflections in the 2θ range (40°-60°), see Figure 11. The main Z-phase peak at $2\theta \approx 46.5$ is visible albeit quite small, and the MX peaks are still relatively large. The presence of Cr-nitrides in the sample, Cr_2N type, was also revealed by the diffractogram of Figure 11, although this could be not verified by electron microscopy.

5. Discussion

At the present time the samples investigated in this paper are among the most aged P91 crept specimens described in literature and represent an important opportunity to assess the microstructural evolution of this material up to 100,000 hours at 550°C and 600°C, especially because all the samples come from the same production batch.
The evolution of the average size of the detected precipitates (MX, $M_{23}C_6$ and Laves phases) at different exposure times at 600°C is shown in Figure 12-a and 12-b (average equivalent diameters are taken from Table 2). Fitting curves in Figure 12-a and 12-b have been traced adopting the calculated values of coarsening rate coefficient, Kd, according to the equation of Ostwald ripening kinetics [19, 20]

$$d^3 - d_0^3 = K_d \cdot t \qquad (1)$$

where d [m] is the average diameter of the particles at time t [s] and d_0 [m] is the initial average diameter of the particle before the coarsening process starts; Kd [m3/s] is the coarsening rate coefficient.
It can be noticed that the average dimension of MX carbonitrides, which precipitate during the tempering treatment, remains almost constant during exposure and stays below 45 nm; the average diameter of M23C6 carbides, which are also formed during the tempering, remains below 200 nm. On the contrary Laves particles, which are not present in the normalized and tempered pipe, but precipitate during the exposure at service temperature, reach an average diameter of about 450 nm after 100,000 hours.
Literature results show that VN and NbN are not thermodynamically stable in 9-12%Cr steels and tend to transform at equilibrium into Cr(V,Nb)N, modified Z-phase [11]. From the analysis of the data reported in Table 2, it can be noticed that the average Cr content in MX particles increases progressively with increasing exposure at temperature. The average Cr content of MX particles passes from 11-at% in the as-treated sample to 13/17-at% in the samples exposed between 7kh and 58kh at 600°C up to 25-at% in the 600°C/104kh sample. The increased average Cr content in MX particles indicates that the nitrides in the 600°C/104kh sample are absorbing Cr atoms from the surrounding matrix. This can be interpreted as the start of a slow conversion process into Z-phase through hybrid particles. Such effect is also seen for 12%Cr steel at shorter exposures [21]. The authors believe therefore that hybrid particles represent the nucleation stage of Cr(V,Nb)N particles, formed by Cr diffusion from the matrix into the original MX particle, as described also in [12, 13, 14].
However, it can not be predicted how long the transformation of all MX nitrides into Z-phase will take, because the available kinetic models do not account for a MX/Z conversion.
The experimental results show that Z-phase formation at the expense of V- and Nb-nitrides cannot be listed among the degradation mechanisms of the microstructure after 100,000 hours at 600°C, since just few particles of this phase were found (less than 1% of total investigated particles) and even fewer hybrid particles were identified in the 600°C/104kh sample, while many fine and distributed MX particles are still present.
Surely it can be stated that, due to their small size, MX precipitates found after exposure for 104kh at 600°C are still effective for strengthening the matrix against creep deformation.

Literature results indicate two main microstructural evolution mechanisms for 9%Cr grades after long exposure times [5, 6]: 1) coarsening of $M_{23}C_6$ carbides; 2) precipitation, growth and coarsening of Laves phases.
Coarsening of $M_{23}C_6$, is listed among the degradation processes, because Cr concentration will be depleted in the matrix around the particles and the pinning force for the boundary migration will be also reduced. However, the experimental results on long term exposed samples show that coarsening of $M_{23}C_6$ is relatively limited: the average equivalent diameter, initially of 140 nm in the as-treated material, remains below 200 nm after 100 kh at 600°C, thus still contributing to hinder the boundaries movement and giving some creep strengthening in any case.
On the other hand, the nucleation, growth and coarsening of Laves phases (Fe_2Mo) produce large particles at grain boundaries after a relatively short time which reach an average diameter of about 450 nm after 100,000 hours. Laves phase coarsens faster than all the other phases present and some of the particles reach a size of few micrometers after 100,000 hours at 600°C. The precipitation, growth and coarsening of Laves phase can be definitely accounted as a degradation mechanism of the microstructure.

However, the experimental observations of the limited coarsening of $M_{23}C_6$ and the high stability of MX allow to state that Grade 91 steel, even after more than 100kh of exposure at 600°C, shows a precipitation state still very effective for creep strengthening, due to the presence of many and diffuse fine precipitates.

6. Conclusions

Crept samples taken from a TenarisDalmine ASTM P91, 355mm OD pipe, exposed for over 100,000 hours at 550°C and 600°C, were extensively investigated in terms of microstructural evolution by Electron Microscopy and X-Ray Powder Diffraction.
The creep resistance of the pipe is in line with the average creep resistance of Grade 91, as recently assessed by the ECCC in 2009.

The high microstructural stability of Grade 91 is attributed to the presence of fine and uniformly distributed MX carbonitrides even after long term exposure. The mean size of MX carbonitrides remains almost constant and stays below 45 nm after 100 kh at 600°C.
Although MX particles exhibited a Cr enrichment with increasing ageing times, indicating that they are absorbing Cr atoms from the surrounding matrix, their transformation into Z-phase, is still at a very preliminary stage since only a limited number of hybrid MX/Z particles and Z-phase precipitates were detected in the most aged sample after 104kh at 600°C.

Coarsening of $M_{23}C_6$ occurs, but does not play a primary role since the average equivalent diameter, initially of 140 nm in the as-treated material, remains below 200 nm after 100 kh at 600°C.
The formation of Laves phase at grain boundaries and its coarsening is the main microstructure evolution mechanism. Laves particles form after a relatively short time and soon become the largest precipitates.
However, it is the presence of many and diffuse fine MX precipitates, even after more than 100kh of exposure at 600°C that determines a precipitation state still very effective for creep strengthening.

7. Acknowledgement

The authors wish to acknowledge their colleagues M. Ballone (CSM) and F. B. Grumsen (DTU) for excellent support during TEM analyses, as well as J. Hald (DONG/DTU) and M. A. J. Somers (DTU) for their supervision of the research activity.
Silvia Tiberi Vipraio (CSM) and Paolo Emilio di Nunzio (CSM) are thanked for their technical help during the research activities. We thank also E. Anelli (TenarisDalmine) for his precious suggestions during the research activities.
A. Carlsson (FEI Company) is kindly acknowledged for her precious support during TEM sessions.
This paper is published under authorization of Tenaris Dalmine R&D, directed by M.A. Rossi.

8. References

[1] J. Hald, Steel Research Journal 67 (1996) 369-374.
[2] L. Cipolla, A. Di Gianfrancesco, D. Venditti, G. Cumino, S. Caminada, Microstructural Evolution during Long Term Creep Tests of 9%Cr Steel Grades, Proceedings of the ASME Pressure Vessels and Piping Conference - 8th International Conference on Creep and Fatigue at Elevated Temperatures - CREEP8, July 22-26, 2007, San Antonio, Texas, USA.
[3] W. Bendick, L. Cipolla, J. Gabrel, J. Hald, New ECCC Assessment of Creep Rupture Strength for Steel Grade X10CrMoVNb9-1 (Grade 91), Proceedings of the Creep & Fracture in High Temperature Components – Design & Life Assessment Issues, April 21-23, 2009, Zurich, CH.
[4] W. Bendick, J. Gabrel, Assessment of Creep Rupture Strength for the New Martensitic 9%Cr Steels E911 and T/P92, Proceedings of the Creep & Fracture in High Temperature Components – Design & Life Assessment Issues, September 12-14, 2005, London, UK.
[5] V. Foldina, Microstructural Stability of Ferritic 9-12% Chromium Steels, COST Report No. COST-94-0076-CZ (DG 12CSMC).
[6] F. Abe, Strengthening Mechanisms in Steel for Creep and Creep Ruptures, Creep-Resistant Steels, F. Abe, T-U. Kern, R. Viswanathan editors, 279-304, ISBN-10: 1845691784.
[7] J. Hald, International Journal of Pressure Vessels and Piping 85 (2008) 30-37.
[8] E. Schnabel, P. Schwaab and H. Weber: Stahl Eisen 107 691 (1987).
[9] A. Strang and V. Vodarek: Material Science and Technology 12 (1996) 552.
[10] H. K. Danielsen, J. Hald, Energy Materials 1 (2006) 49-57.
[11] H. K. Danielsen, J. Hald, Computer Coupling of Phase Diagrams and Thermochemistry 31 (2007) 505-514.
[12] H. K. Danielsen, J.Hald, Materials Science and Engineering A 205 (2009) 169-177.
[13] H. K. Danielsen, J. Hald, F. B. Grumsen, M. A. J. Somers. Metallurgical and Materials Transactiona A 37A (2006), 2633-2640.
[14] L. Cipolla, H. K. Danielsen, D. Venditti, P. E. Di Nunzio, J. Hald, M. A.J. Somers, Acta Materialia 58 (2010) 669-679.
[15] J. Hald, Creep Strength and Ductility of 9 to 12% Chromium Steels, ECCC Seminar: Advanced Creep Data, 26 September 2003, SVUM, Prague, Czech Republic.
[16] C. Panait, W. Bendick, A. Fuchsmann, A.F. Gourgues-Lorenzon, J. Besson, Study of the Microstructure of the Grade 91 Steel after more than 100,000h of Creep Exposure at 600°C, Proceedings of the Creep & Fracture in High Temperature Components – Design & Life Assessment Issues, April 21-23, 2009, Zurich, CH.

[17] Ennis P. Creep Strengthening mechanisms in 9-12% Chromium Steels. EPRI 4th International Conference on Advances in Materials Technology for Fossil Power Plants 2004;1120-1133. USA: Hilton Head Island.
[18] P. Hirsch, A. Howie, R. Nicholson, W. Pashley, M.J. Whelan, Electron Microscopy of Thin Crystals, second edition, Krieger Publishing Company, Malabar, Florida, 1977.
[19] C. Wagner, Z. Elektrochem 65 (1961) 581.
[20] J. M. Lifshiz, V. V. Sloyzov, J. Phys. Chem. Solids 14 (1961) 35.
[21] M. Yoshizawa; M. Igarashi; K. Moriguchi; A. Iseda, H.G. Armaki; K. Maruyama: *Effect of Precipitates on Long Term Creep Deformation Properties of P92 and P122 Type Advanced Ferritic Steels for USC Power Plan*, Materials Science and Engineering A 510–511 (2009) 162–168 doi:10.1016/j.msea.2008.05.055.

Table 1 – Chemical composition of the investigated materials, compared with ASTM A335-06 P91 compositional range (wt%).

		C	Mn	P	S	Si	Cr	Mo	V	N	Ni	Al	Nb	Ti	Zr
ASTM A335-06	Min	0.08	0.3	-	-	0.2	8.0	0.85	0.18	0.03	-	-	0.06	-	-
	Max	0.12	0.6	0.02	0.01	0.5	9.5	1.05	0.25	0.07	0.4	0.02	0.10	0.01	0.01
Heat 28145		0.12	0.52	0.01	0.003	0.27	8.52	0.98	0.21	0.051	0.12	0.007	0.08	0.005	0.002
Heat 801141		0.093	0.46	0.02	0.002	0.40	9.12	0.94	0.19	0.038	0.07	0.004	0.05	-	-

Table 2 – Mean diameters and average chemical compositions (at%) of MX, $M_{23}C_6$ and Laves particles in long-term aged P91 samples.

Particle Type	LMP (C=20)	Sample	Number of particles	Mean diameter (nm)	Cr at-%	Mo at-%	Fe at-%	V at-%	Nb at-%
MX	-	As-treated♦	16	36	11	4	3	61	21
	20.6	550°C/110kh♦	39	44	13	2	1	59	25
	20.8	600°C/7kh♣	46	40	15	3	1	65	16
	21.2	600°C/20kh♦	20	36	17	3	1	59	20
	21.5	600°C/41kh♦	Not available (n.a.)	n.a.	15	4	2	60	19
	21.6	600°C/58kh♣	29	41	17	3	2	62	16
	21.8	600°C/104kh♦	21	39	25	5	4	45	21
$M_{23}C_6$	-	As-treated♦	34	139	73	6	18	2	1
	20.6	550°C/110kh♦	42	151	73	7	17	1	2
	20.8	600°C/7kh♣	30	145	78	4	16	1	1
	21.2	600°C/20kh♦	15	154	75	7	17	1	0
	21.5	600°C/41kh♦	21	160	78	7	15	0	0
	21.6	600°C/58kh♣	48	189	75	5	18	1	1
	21.8	600°C/104kh♦	40	200	75	7	14	3	1
Fe_2Mo	-	As-treated♦	0	not present	/	/	/	/	/
	20.6	550°C/110kh♦	15	325	16	39	43	1	1
	20.8	600°C/7kh♣	8	130	14	41	45	0	0
	21.2	600°C/20kh♦	n.a.	n.a.	n.a.	n.a.	n.a.	n.a.	n.a.
	21.5	600°C/41kh♦	15	375	10	46	43	1	0
	21.6	600°C/58kh♣	20	421	15	47	38	0	0
	21.8	600°C/104kh♦	15	464	11	50	37	1	1

♦: the sample belongs to heat number 28145. ♣: the sample belongs to heat number 801141.

Table 3 – Chemical composition (at%) of particles in Figure 4.

	Cr at%	V at%	Nb at%	Fe at%	Mo at%	Precipitate type
Site 1	72	6	1	16	5	$M_{23}C_6$
Site 2	80	1	1	13	5	$M_{23}C_6$
Site 3	77	0	0	17	6	$M_{23}C_6$
Site 4	16	68	11	4	1	MX
Site 5	16	75	7	1	1	MX
Site 6	30	56	8	5	1	MX
Site 7	77	0	0	18	5	$M_{23}C_6$
Site 8	17	72	7	3	1	MX
Site 9	20	63	14	2	1	MX
Site 10	25	57	12	4	2	MX
Site 11	30	31	29	7	3	MX
Site 12	14	62	22	2	0	MX
Site 13	26	53	14	4	3	MX
Site 14	15	65	16	4	0	MX
Site 15	29	55	7	5	4	MX
Site 16	76	0	0	19	5	$M_{23}C_6$
Site 17	24	69	3	3	1	MX
Site 18	21	74	4	0	1	MX

Table 4 – Chemical composition (at%) of particles in Figure 6.

	Cr at%	V at%	Nb at%	Fe at%	Mo at%	Precipitate type
Site 1	50	35	9	4	1	Cr(V,Nb)N
Site 2	51	30	13	6	1	Cr(V,Nb)N
Site 3	49	28	17	4	2	Cr(V,Nb)N
Site 4	50	32	13	5	0	Cr(V,Nb)N
Site 5	77	0	0	17	4	$M_{23}C_6$
Site 6	80	0	0	17	3	$M_{23}C_6$
Site 7	23	71	2	4	0	MX
Site 8	77	1	1	17	4	$M_{23}C_6$

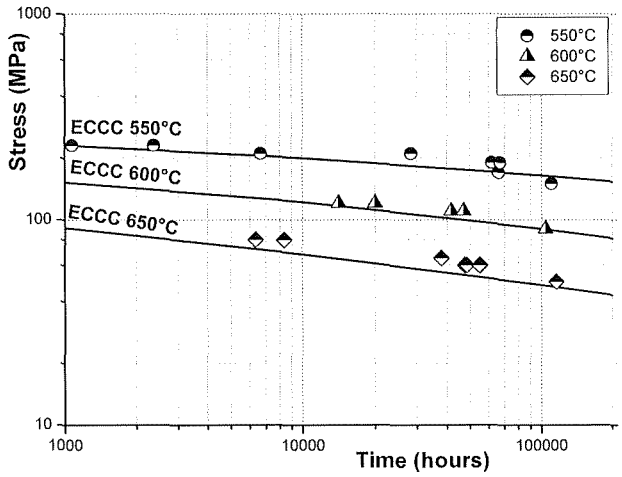

Figure 1 – Creep rupture tests from the 355mm OD pipe. Solid lines are the ECCC isotherms (year 2009) [3].

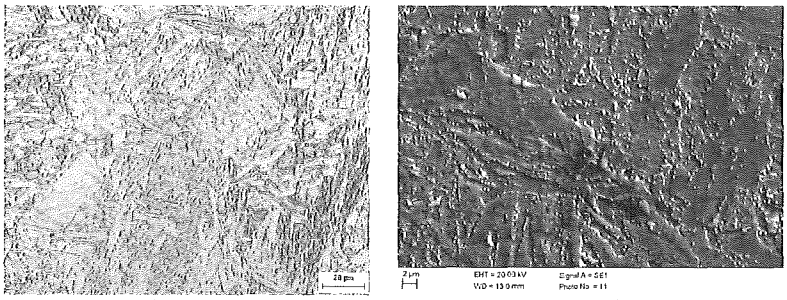

a) *b)*

Figure 2 – Microstructure of 600°C/104kh sample at (a) LM and (b) SEM.

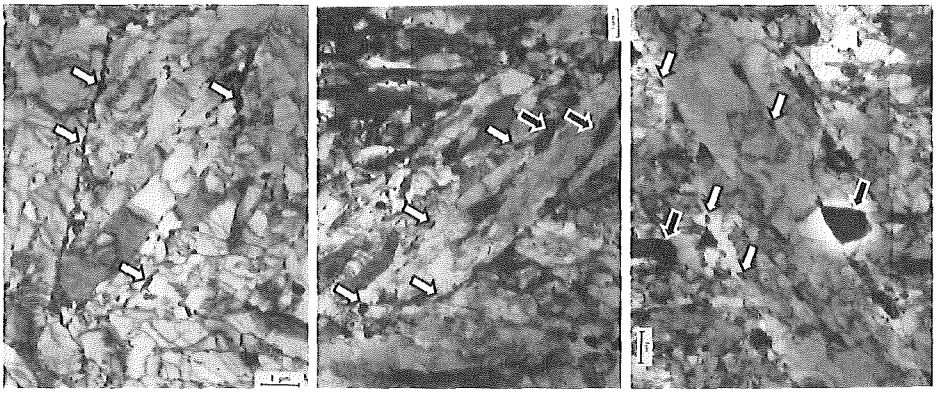

a) As-treated *b) 550°C – 110kh* *c) 600°C – 104kh*

Figure 3 – Evolution of substructure: thin foils taken from the heads of crept specimen. Also precipitates are indicated: black arrows: Laves phase; white arrows: $M_{23}C_6$.

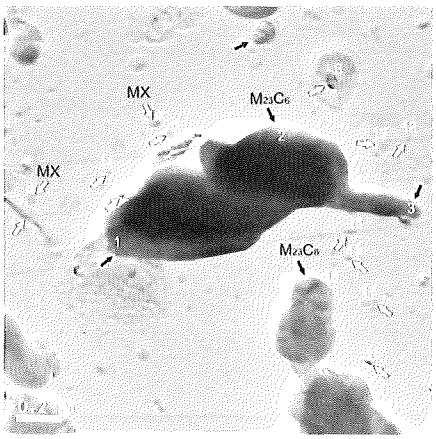

Figure 4 – Precipitates in the 600°C/104kh sample; white arrows: MX; black arrows: $M_{23}C_6$.

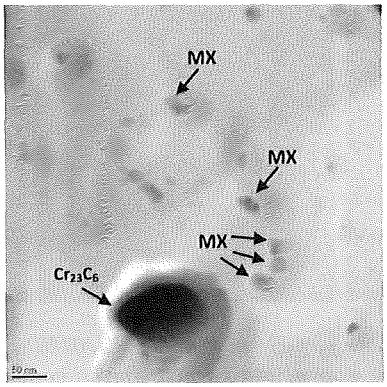

a) Zero-loss image

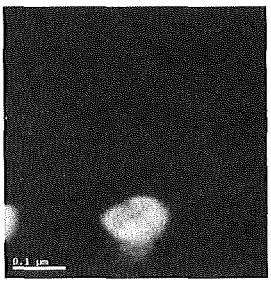

b) Cr-map

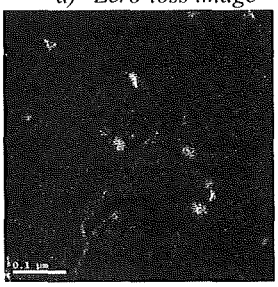

c) N-map

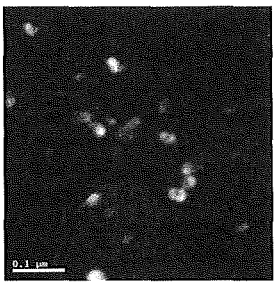

d) V-map

Figure 5 – a) Zero loss Image and jump ratio images of b) chromium, c) nitrogen, d) vanadium map on a frame of 600°C/104kh aged sample (investigation carried out on extraction replica).

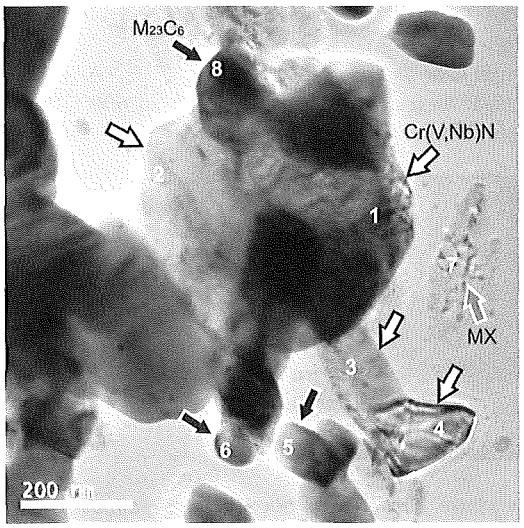

Figure 6 – Z-phase particles in 600°C/104k sample. Grey arrow: MX; black arrows: $M_{23}C_6$; white arrows: Cr(V,Nb)N.

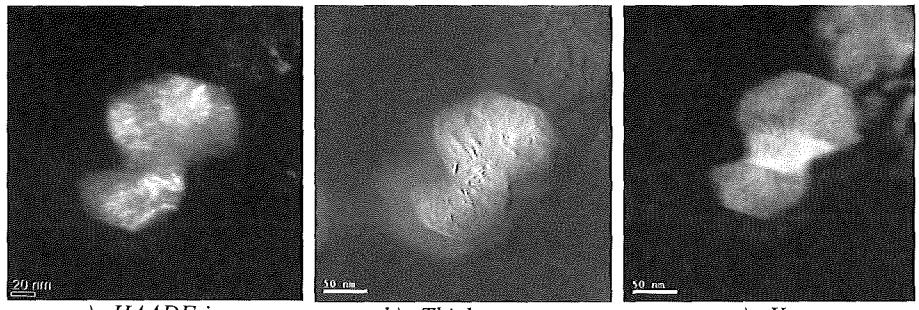

a) HAADF-image *b) Thickness-map* *c) V-map*

Figure 7 – Hybrid MX/Z-phase particle in P91 600°C/104kh sample: a) HAADF image, b) thickness map, c) vanadium map of the particle (investigation carried out on extraction replica).

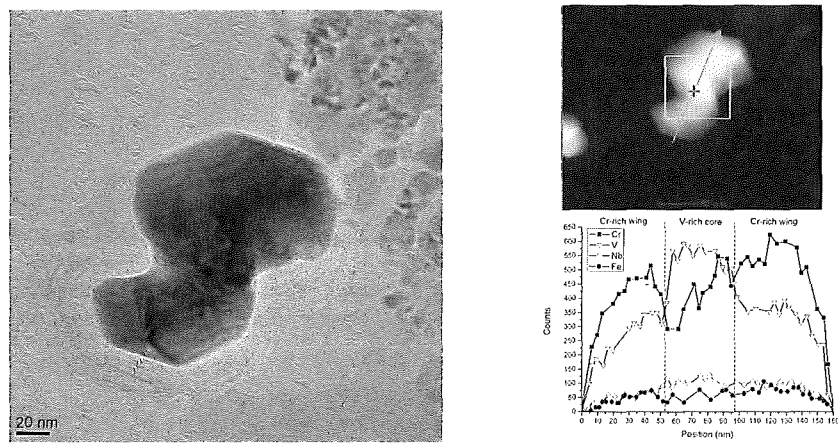

a) Bright field image. *b) EDS linescan.*

Figure 8 – a) Bright Field image of the hybrid particle in 600°C/104kh sample; b) linescan along main particle axis: Nb, Fe, Cr and V EDS counts.

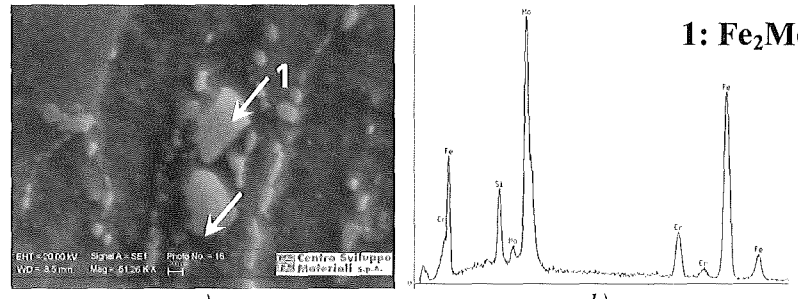

a) *b)*

Figure 9 – (a) Laves phase particles of 600°C/104kh sample and (b) their typical EDS spectrum by SEM.

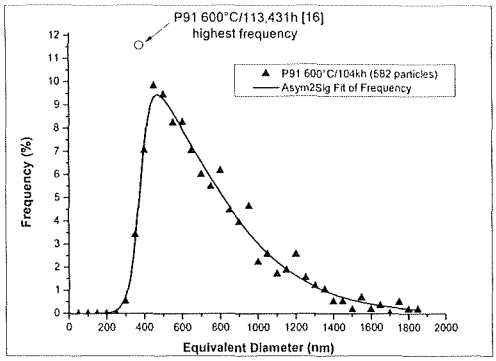

Figure 10 – Size distribution of Laves phase particles in the P91 600°C/104kh sample by SEM Automatic Image Analysis. Particles below 200nm were not detected. Comparison with data from literature [16].

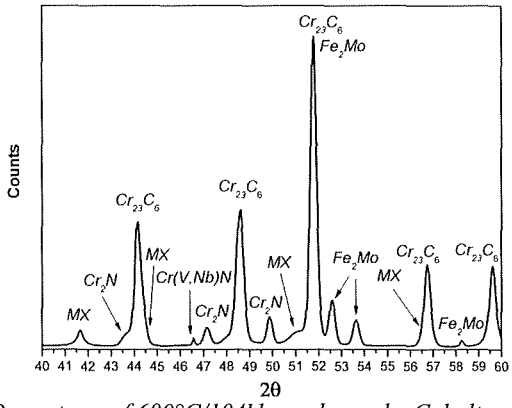

Figure 11 – XRD spectrum of 600°C/104kh aged sample. Cobalt radiation was used.

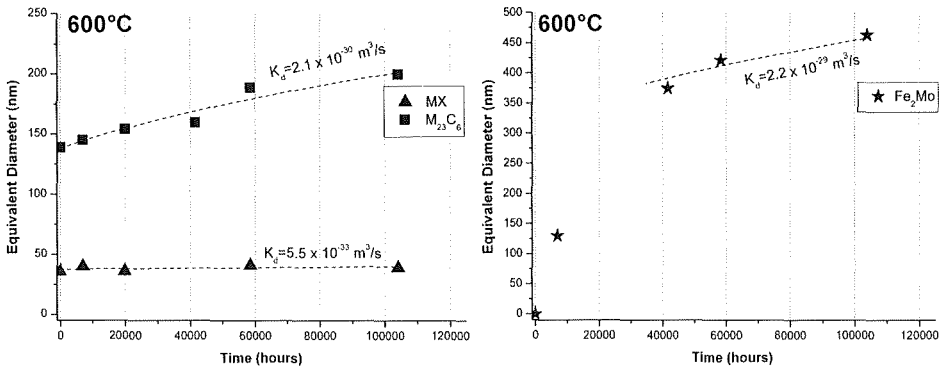

a) *b)*

Figure 12 – Evolution of equivalent diameter of a) MX, $M_{23}C_6$ and b) Fe_2Mo precipitates of Grade P91 at 600°C (data from Table 2).

9th Liege Conference : Materials for Advanced Power Engineering 2010
edited by J. Lecomte-Beckers, Q. Contrepois, T. Beck and B. Kuhn.

HEAVY STEEL CASTING COMPONENTS FOR POWER PLANTS "MEGA-COMPONENTS" MADE OF HIGH CR-STEELS

Reinhold Hanus

voestalpine Giesserei Linz

Abstract

Steel castings of creep resistant steels play a key role in fossil fuel fired power plants for highly loaded components in the high and intermediate pressure section of the turbines. Inner and outer casings, valve casings, inlet connections and elbows are examples of such critical components.

The most important characteristic in a power plant is the efficiency, which mainly drives the CO2-emission. As a consequence of steadily improving power plant efficiencies and ever stricter emission standards, steam parameters become more critical and the creep resistance of the cast materials must also be constantly improved.

The foundries voestalpine Giesserei Linz and voestalpine Giesserei Traisen participated in the development of the new 9-10% Cr-steels for application up to 625°C/650°C and in the THERMIE project where Ni-base alloys for 700°C-power plants were developed. Beside the material development in the European research projects the commercial production had to be established for industrial processes and the newly developed materials have to be transferred from research into the commercial production of heavy cast components

After selecting the most promising alloy from the laboratory melts, welding tests were performed - mostly with matching electrodes also produced within COST/THERMIE. Base material and welds were investigated in respect of microstructure, creep resistance, mechanical properties and weldability. Heat treatment investigations were also necessary for optimization of the mechanical properties.

Based on the results of these studies, pilot components and plates for testing welding processes were cast in order to verify the castability and weldability of larger parts and to make any necessary adjustments to chemical composition, heat treatment or welding parameters.

Parallel to the ongoing creep tests within COST/THERMIE-program, the newly developed steel grades were introduced into the commercial production of large components. This involved finding solutions to process related problems such as deoxidation, solidification behavior, heat treatment with long hold times, welding on the casting, stresses, etc.

Cast components for power plants, made of high Cr-steels and Ni-base alloys are becoming bigger. Development work and investments in new processes and technologies are necessary, process-modelling is an indispensable tool for the ability to to produce also these "mega-components".

Keywords: steel castings, mega components, high-Cr cast steel

1. Introduction

The foundry group of voestalpine with the Austrian locations in Linz and Traisen produces heavy steel castings for steam and gas turbines, compressors for the oil and gas production, as well as for the chemical industry, mechanical engineering and for the offshore technology. In the group a weight range between 1 and 200 tons can be covered. Each of these markets has its special challenges. Here we want to focus on characteristics, which a large steel foundry within the range of the steam power plants has to master. In the special we want to describe this on the basis of produced steam turbines for power stations in the highest power segment, up to 1700 MW.

2. Cast steel for the energy industry

Components from cast steel play a key role in all thermal power stations. These are particularly the static parts of the turbines: outer and inner casings, blade carriers, valve casings, elbows within the weight range between 1 to 100 tons per individual part. The components are subjected with internal pressure and thermally highly stressed. The Designs are very complex with highest requirements on casting technology engineering, material treatment, process planning and execution. Particularly the thermal treatments are very extensive and due to the large wall thicknesses long persisting. The orders are usually special orders, which practically do not permit a series effect, each cast part is individual.

2.1. Materials and developments in the steam turbine process

As well known the yield point at elevated temperatures of cast steel drops with increasing temperature. Up to an application temperature of 400-450°C the yield point at elevated temperatures is one of the most substantial material parameters. If construction units are suspended still higher temperatures over a longer time, the material begins to creep. Creep resistant are considered unalloyed and alloyed cast steel grades, which keep their characteristic material properties within the high temperature range under long-term loading. The cast steel materials mainly used in the power station range for turbine components are the Mo, CrMo, and/or CrMoV alloyed types G20Mo5, G17CrMo5-5, G17CrMo9-10, G17CrMoV5-10. These low alloyed, heat resistant materials are used within the creep range up to an application temperature of 550°C. Due to the efforts toward the decrease of pollution and CO2-emissions, turbine designers endeavor to achieve ever higher efficiencies in the power generation processes. Beside the constant improvement of the turbine design, or the combination of gas and steam process in thermal power stations, this can be achieved with an increase of the process temperatures and - presses (live steam, overheated steam). Particularly in the intermediate pressure range of steam turbines, temperatures up to 625°C are in demand, the appropriate materials are developed in the framework of large-scale, international research projects. Apart from increased contents of Cr, the elements V, Nb, W, CO, N, B are to supply a substantial contribution for the increase of creep strength. Wc gencrally speak of the group

of the 9-10% Cr steel. In order to realize even higher temperatures (up to 700°C) and further improve the efficiency, large-scale research projects in Europe (COST, THERMIE, Marcko, Cooretec, 50 plus,...) ever continue to develop the materials. By means of Ni-base materials and complex 9-10% Cr steel-alloys, a thermal pilot power station with an efficiency over 50% shall be established. An overview of the limitations of use of high-temperature turbine materials picture is given in *figure 1.*

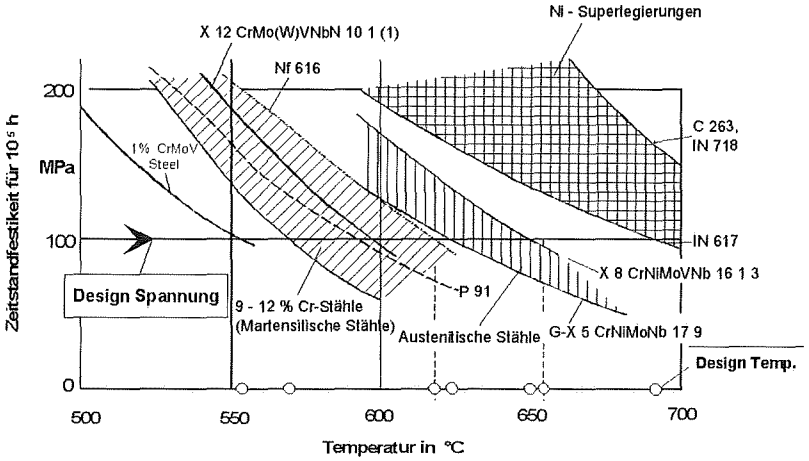

Figure 1: limitations of use for high temperature - turbine materials

2.2 Cast steel components for thermal power stations

Together with the materials, also the processes are improved by the turbine manufacturers to gain higher efficiencies. On the one hand new process routes like simple and double superheating of steam after the first compression phases. On the other hand also the designs of steam carrying components are arranged more efficiently and thus more complex. Steam power plants, built for generation of electrical basic load, increase apart from their efficiency also their power. This causes, that the key components, such as turbine casings, continue to increase in size and weight. On these challenges the processes of the foundry must be aligned. Some of the necessary large investments are described in the following. Examples of the different cast steel components are to be seen in *figures 2 and 3.*

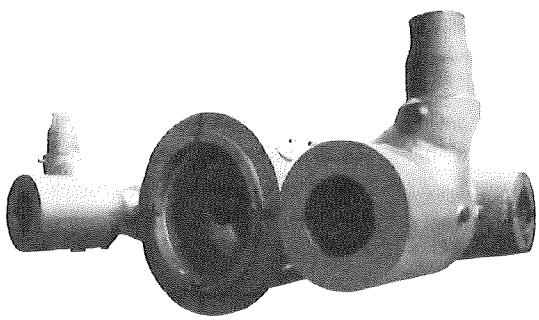

Figure 2: high pressure outer casing with welded on valves (31 t + 2x19 t = 69 t)

Figure 3: gas turbine casing (27 t), finish machined

3 Manufacturing process in the steel foundry

3.1 Standard processes

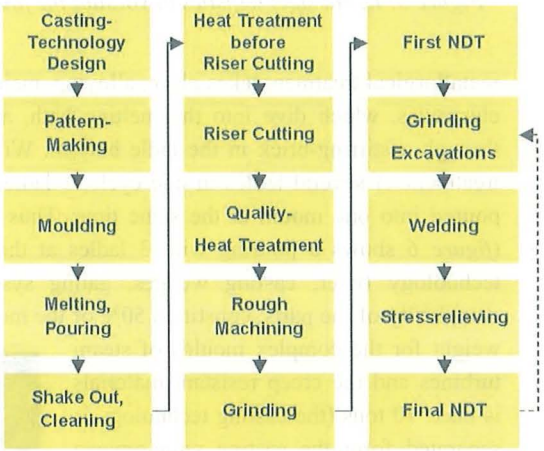

Figure 4: typical production sequence for heavy steel castings

Figure 4 shows the main steps in the manufacturing process of heavy steel castings for the power plant construction. After the creation of the casting technology, the building of the wooden pattern and the molding, the existence of the casting begins with the melting and pouring process. After the solidification time (2 to 6 weeks, depending upon wall thickness, complexity and material) the solid casting is removed from the sand mold. The quality heat treatment is apart from the chemical composition the most important step for adjustment the desired microstructure and the required mechanical properties, as a basis for the creep resistance at high temperatures. After rough machining, the casting is subjected to non destructive testing (magnetic particle and ultrasonic examination). All detected indications not conforming to the acceptance standard must be excavated. After a repeat magnetic particle inspection of the excavations, these are welded (manufacturing welding), followed by stress-relief heat treatment. Dimension checks are performed repeatedly between the individual production cycles in order to determine whether particularly specified dimensions, could become critical for finish machining or for final use. A final non destructive testing is the last production step in the foundry, before the casting is sent for finish machining.

3.2 Melting aggregates

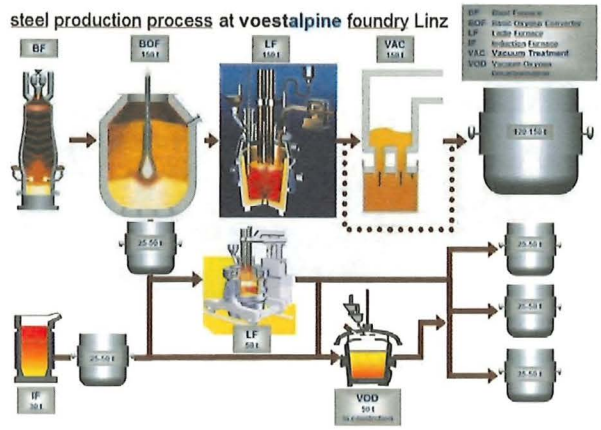

Figure 5: liquid steel logistics at voestalpine foundry Linz

The main process line for steel melting of the voestalpine foundry starts in the LD-steel plant of the parent company, in a LD-converter with approx. 150 tons capacity. Here unalloyed steel is manufactured and tapped into the ladles of the foundry in a partial tap. The capacity of the foundry ladles amounts in between 20 and 50 tons. These ladles, containing the unalloyed molten steel, are transported into the ladle furnace of the foundry. Over there the secondary metallurgical treatment takes place: alloying, mainly with ferro-alloys, heating with 3 graphite electrodes, which dive into the melting bath, as well as bubbling with argon or nitrogen through a stirring-brick in the ladle bottom. With a particularly developed logistics for the treatment of several ladles in one cycle, 3 ladles can be treated in such a way they can be poured into one mould at the same time. Thus max.150 tons of molten steel are pourable (*figure 6* shows a pouring with 3 ladles at the same time). Considering that the casting technology (riser, casting wedges, gating system, etc.), depending upon material and complexity of the parts, constitute 50% of the molten steel quantity, the resulting raw casting weight for the complex moulds of steam turbines and the creep resistant materials is max. 70 tons (the casting technology is separated form the casting with oxygen lances after shake out). The demand of the turbine manufacturers for the thermal base-load power stations, for ever larger units of power and thus larger casting components causes for the foundry the necessity to make more molten steel available. Turbine casings with 100 tons raw weight must be manufactured. Therefore the foundry developed a new process line for molten steel in a large investment. This will be described in the next chapter.

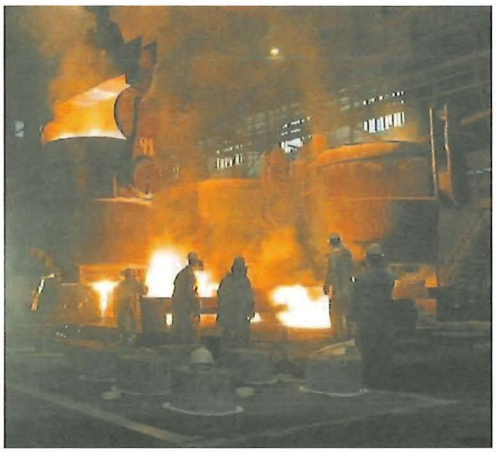

Figure 6: pouring-standard process with max. 3 ladles, a' 50 tonns

4 Example project course in the steel foundry for a turbine casing with 100 tons per half „a giant takes shape“

The market of steam turbines is a market of the large projects, which are adapted individually to the customer needs. Here location, climatic conditions and existing infrastructure play a special role. Custom-made projects need a steel foundry, which can covert those customer needs flexibly and rapidly. Even if the basic design of the turbine casing remains the same, in co-operation with us the casting technology design is adapted.

4.1 Characteristics within the foundry processes, for „mega components“

The enormous size of the parts require special measures, investments and sophisticated logistics at almost all foundry processes for transport, heat control, testing execution, welding, etc. Steam turbine casings are usually divided into halves (upper part + lower part) and the casing halves are screwed together with bolts during assembling of the turbine, after the runner with the blades is installed. Such large external casings, often paired with high alloyed materials (12% Cr steel grades) and complex designs, are a challenge for engineers and foundry skilled workers.

4.1.1 Engineering - quality specification

Here we speak about highly stressed turbines, where, beside the technological planning, the quality assurance has a large value. Beginning of the first technical negotiations with the customer up to the final inspection always several parties (customer=turbine manufacturer, final customer=power plant owner, 3rd-Party=inspection authority) are involved. In a manufacturing and a testing sequence plan for each part, all individual process steps with activities and responsibilities, basis lying specifications and the necessary inspection-, information, hold- and witness- points are fixed. *Figure 7* shows exemplarily the first 7 of approx. 50 process steps of a manufacturing and testing plan. All examinations must be witnessed by a 3rd-Party, authorized for the project. This causes an enormous effort of quality work and engineering in the preparatory phases. All quality relevant procedures for heat treatment, construction, manufacturing and built up welds, welding procedure qualifications, non destructive examinations, etc., mentioned in the manufacturing and testing plan, must be approved by all parties involved on customer side.

Schr. Nr. Steps no.	Tätigkeiten Activities	Vorschriften Specification	Prüfungen/Inspections M	C	X	H	Bemerkungen Remarks
1	Modellfertigung und Kontrolle Pattern making and inspection	Modellzeichnung/ Pattern Drawing	RI				
2	Form- und Kernherstellung mit anschließender Kontrolle Moulding and core making with follow up inspection	Modellzeichnung Pattern Drawing Interne Vorschrift/ Supplier Procedure	RI				Probenlagen sind zu beachten Observe location of test coupons FLK M-3673 Rev. 0
3	Stahlherstellung und Gießen; Schmelzenfreigabe Melting and pouring, heat analysis release	TLV 9166 01, TLV 0100, QS Ves 111105 Interne Vorschrift Supplier Procedure	RE	ct			Attest - chem. Zusammensetzung Certificate - chemical composition Acc. QS Ves. 111105 steps 8.1.3 Review of chemical composition melt analysis
4	Überprüfung der eingegossenen Oberstückkennzeichnung Review of cast on identification on the castings	TLV 9166 01, TLV 0100,	RI				
5	Anwärmen zum Seigerbrennen Preheating for riser cutting	Interne Vorschrift Supplier Procedure WHI 40 FOM 9-10	RI				Interner Protokoll Internal Record
6	Seigerbrennen, Cutting of riser and gates	Interne Vorschrift Supplier Procedure	RI				
7	Sichtprüfung auf außergewöhnlich große Fehlerstellen Visual inspection for uncommon large defects		RI				Information an Kunden im Falle von außergewöhnlich großen Fehlerstellen Notify to customer in case of uncommon large defects

Figure 7: excerpt of the manufacturing and testing plan of an outer casing

4.1.2 Pattern making and moulding

Figure 8: wooden pattern for an outer casing, upper half with a steam exhaust pipes

Due to the size of each outer casing half (here approx. 6.5 x 6 x 3 m), the stability of the wooden pattern (see *figure 8*) was one of the problems to be solved in the pattern shop. Further challenge was the support and stabilization of the exhaust pipes, rising from the main part on both sides, each having a diameter of 2 m, first with the pattern in production and second when fixing of the sand-core in the mould.

4.1.3 Melting and pouring process

The pouring of a "mega-part" with 100 t is done with the new process line with an entire molten steel weight of approx. 200 tons. The ladle with 150 tons molten steel, treated in the LD-converter (basic oxygen process), is finished alloyed in the ladle furnace of the steel plant according the chemical composition, required by the foundry, further treated in a vacuum aggregate and then transported with special vehicles into the foundry. There parallel to it two „small "20-45 ton ladles can be posed, so that at the same time 3 ladles (1 large ladle with approx. 150 tons and 2 small ladles with each up to 45 tons liquid steel) with same temperatures, are ready for pouring. Considering a 2 km - distance between LD-steel plant and foundry, one can imagine the technically high achievement for planning and execution is performed here. An indispensable condition is the good coordination between LD-steel plant and foundry.

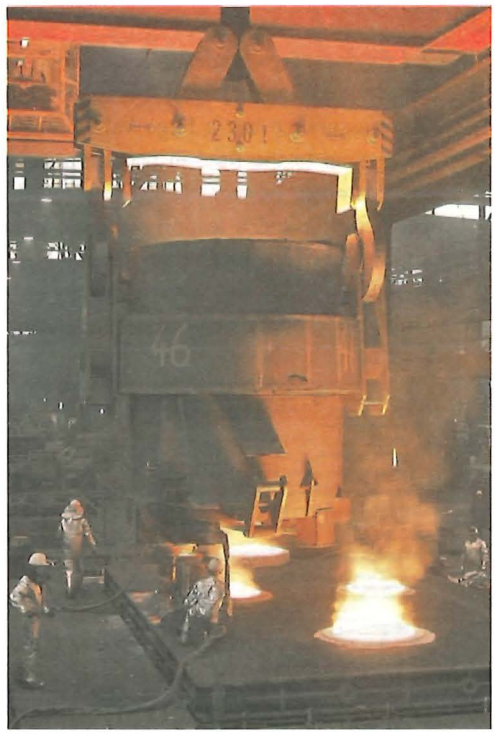

Figure 9: Pouring with a heavy ladle (150 t liquid steel), finish alloyed in the LD-steel plant

4.1.4 Heat treatment - shot blasting - upgrading

Upgrading activities (arc air burning, grinding, shot blasting and heat treatment) take a substantial part in the manufacturing of cast steel components. For parts of this magnitude, large aggregates were invested in the voestalpine foundry Linz. The characteristic of this project was, that the construction of the new heat treatment furnace and the new shot blasting equipment in „super size" had to be co-ordinated exactly with the process flow. Each day too late would have caused waiting period and would have delayed delivery. *Figure 10* shows above the two new plants (centrifugal wheel radiation house right open and heat-treatment furnace left, with a special construction for the opening of the high furnace gate).

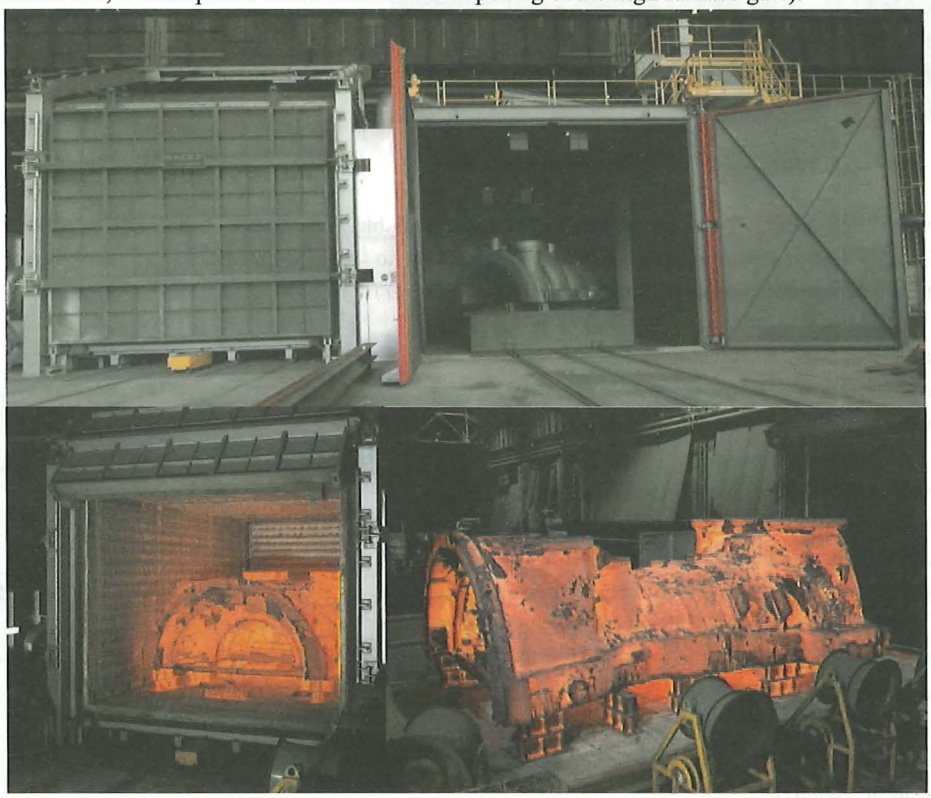

Figure 10: new heat treatment furnace und new shot blasting chamber „super size"
Quality heat treatment of an outer casing half
(furnace exit after austenitisation-950°C and forced air cooling with vans)

4.1.5 Rough machining

Figure 11: outer casing half at rough machining

The castings are transported to the machine shop after quality heat treatment, over there the machining with a stock of 5-6 mm from the finished surface takes place. Transport is simply said, however, for the large parts it means special activities for vehicles, transport with the cranes into the workshops and safety precautions for entire logistics planning. The finish machining takes place later on, following the entire foundry process. For parts of this magnitude there are few machining workshops, which have appropriate machines available. The good co-ordination between foundry and machine shop is substantial condition to avoid dimensional problems, which have catastrophic impact on those large parts (*figure 11*).

4.1.6 Welding

Welding represents a substantial manufacturing step with the production of cast steel components. Manufacturing welds, fabrication welds (welding on of rolled, forged or poured pipes, connecting pieces, elbows, nipples, etc.) and build-up welds for special surface requirements (hardness or corrosion) are accomplished in the welding shop of the foundry. For the large outer casings special precautions were necessary concerning preliminary heating, welding parameter, welding position (see *figure 12*).

Figure 12: positioning for fabrication welding

4.1.7 Non destructive examination, and witness inspection

Figure 13: outer casing-upper half at witness inspection by customer and third party

Both from technical, and logistic view non destructive examination needs special attention. All cast parts for the energy industry are tested 100% with magnetic particle and ultrasonic examination with normal and angle probes, weld edges for preparatory tubing welding are examined with radiographic isotopes. That means an enormous effort to test personnel with high experience. The testing sequence must be planned exactly, since the part is to be turned several times and certain areas are attainable only in one positions of the casting. Apart from the internal examinations (initial inspection and examination after the heat treatment cycles), very often a triple witness inspection (internal, customer and final customer representative) takes place, these many inspection sequences cause high effort for the NDT department. The witness inspection for non destructive examination, mechanical characteristics and the documentation extended over some weeks for both casing halves. Meanwhile several sets could be made, witnessed and delivered successfully with individual weights from approx. 100 t of low alloyed and highly alloyed 12% Cr cast steel. This is a milestone for the voestalpine foundry Linz and shows the competence, to produce difficult cast steel components in highest material grades and weight ranges.

Since excellent engineering and skilled work, as well as highest personal commitment of each particular foundry man are the basis for such successes, we would like to express pride and gratitude to our employees on this occasion.

9th Liege Conference : Materials for Advanced Power Engineering 2010
edited by J. Lecomte-Beckers, Q. Contrepois, T. Beck and B. Kuhn.

TRANSFORMATION OF MX INTO Z-PHASE IN 9-12%CR MODEL ALLOYS

H.K. Danielsen[1], L. Cipolla[1,2], D. Venditti[2], J. Hald[1,3]

1: Technical University of Denmark (DTU), Mechanical Engineering, Denmark
2: Centro Sviluppo Materiali (CSM), Italy
3: DONG Energy/Vattenfall, Denmark

Abstract

Three 9-12%Cr model alloys were designed with the purpose of studying the nucleation and precipitation kinetics of modified Z-phase, Cr(V,Nb)N. The alloys were similar except for changes in the Cr and Nb contents, which allowed easy comparisons to estimate the effect these elements. The interferences from the presence of carbides and Laves phases were avoided by keeping the C, W and Mo contents as low as possible.
Transmission Electron Microscopy of extraction replicas and quantitative X-Ray Diffraction analysis of extracted particles were used to follow the evolutions of phase composition, phase morphology and phase fraction of Z-phase during ageing at 650°C up to 10,000h. The Z-phase appears to nucleate by diffusion of Cr atoms into (V,Nb)N particles which subsequently convert into cubic or tetragonal Z-phase. Studies at various temperatures indicate that Z-phase development proceeds fastest at 650°C and comparison of the alloys indicate that Z-phase precipitation is greatly enhanced by elements such as Cr and Nb.

Keywords: Z-phase, 9-12%Cr steels

1. Background

In the last couple of decades the pressure and temperature service conditions of components for advanced power plants have increased, imposing more severe requirements on strength, corrosion resistance and creep properties of high temperature steels. To comply with these requirements, advanced 9-12% Cr martensitic steels were developed and are now extensively applied in new high efficiency Ultra Super Critical (USC) power plants. These steels are generally furnished after a normalising and a tempering heat treatment, with the final microstructure consisting of fully tempered martensite.
During high temperature service, 9-12%Cr steels show a gradual degradation of their properties due to the evolution of the microstructure. In order to improve the creep resistance, the microstructural evolution should be delayed. Attempts to stabilise the microstructure involve the precipitation of finely dispersed MX nitride particles, (V,Nb)N [1]. Recently, it was found that the modified Z-phase, a complex nitride Cr(V,Nb)N, develops in 9-12%Cr steels during long term exposure in the temperature range 600°C-700°C [2]. The development of Z-phase has been accredited a detrimental effect on the creep strength, since it is associated with the consumption of the finely dispersed small nitrides, which are considered to provide the most important contribution to the creep resistance [3]. Unfortunately, Z-phase develops as large particles and thus cannot compensate for the loss in creep strength as a consequence of the dissolution of MX. A thermodynamic model for Z-phase has recently been proposed based on literature and complementary experimental data [4]. The model predicts that Z-phase is the most stable nitride in 9-12%Cr steels in the creep service temperature range 600°C-700°C and, accordingly, it will attempt to fully replace the finely dispersed MX nitrides, which precipitate during normalising and tempering heat treatment. It was concluded that the chromium content has a major influence on the driving force for Z-phase formation, which explains why advanced 12%Cr steels suffer from abundant formation of Z-phase, while 9%Cr steels do not [2]. One exception is Grade X20, which contains a high Cr content, but still has

a very low Z-phase precipitation rate. Since the X20 does not contain Nb, it has been speculated that the presence of Nb accelerates Z-phase formation [2].

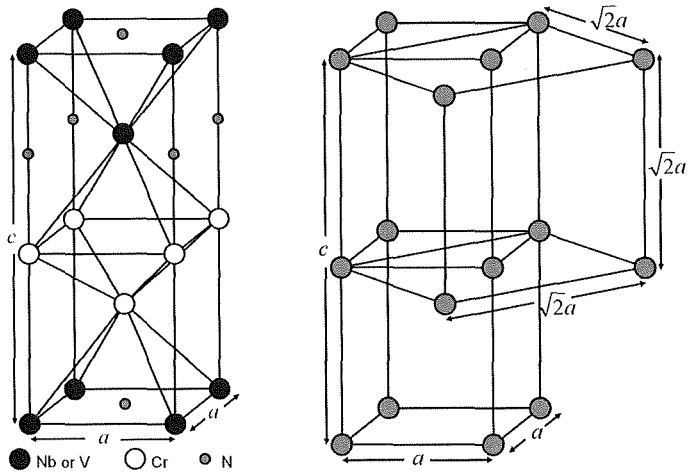

Figure 1: The tetragonal crystal structure of Z-phase and its relation with the cubic crystal structure of Z-phase. [5]

The Z-phase which forms in 9-12%Cr martensitic steels is primarily a CrV-based nitride, but also contains limited quantities of Nb and Fe, and is usually addressed as modified Z-phase. The crystal structure of the modified Z-phase has generally been described as tetragonal, with a=0.286nm and c=0.739nm [3], as shown in Figure 1a. Extensive electron diffraction on various exposed 9-12%Cr steels has recently revealed a more complex crystal structure of modified Z-phase. NaCl type cubic diffraction patterns, similar to those found in MX precipitates, albeit with a slightly lower lattice parameter of a=0.405nm (very favourable according to baker-nutting in BCC iron matrix) were identified [5]. This cubic structure was found to coexist with the tetragonal structure in the Z-phase. The proposed hybrid crystal structure is shown in Figure 1b. Furthermore, investigations showed that the cubic structure was predominant in 9-12%Cr samples which had been aged for relatively short times (in the order of 10,000 hours at 600°C), while the tetragonal diffraction patterns become more pronounced upon prolonged ageing [6]. The cubic Z-phase structure is regarded as an intermediate meta-stable crystal structure and is expected to be completely replaced by the tetragonal structure, although this process may well take hundreds of thousands of hours.
Recent work on commercial 12%Cr steels has revealed the nucleation mechanism of Z-phase to be closely related to the MX particles themselves. In fact hybrid particles consisting of areas with both MX and Z-phase composition could be observed. Thus the nucleation could be described as a chromium diffusion controlled transformation of MX into Z-phase [7]. This would explain the presence of the hybrid crystal structure in Z-phase particles, as shown in Figure 1b.
In the present work, three model alloys have been produced, with the sole objective to study Z-phase precipitation. Particular emphasis has been put on investigating the nucleation mechanism, and the precipitation kinetics as a function of temperature and composition.
The first model alloy, 12CrVNbN, hereby named M1, was specifically designed to rapidly precipitate the modified Z-phase, Cr(V,Nb)N, during high temperature exposure. Its chemical

composition was tailored on the basis of the thermodynamic model proposed in [4]: 12 wt% Cr to promote fast Z-phase formation; high Ni to guarantee the martensitic microstructure after normalising; Nb, V and N in amounts similar to industrial 9-12%Cr creep steels. A very low carbon content was chosen as to avoid carbide formation of $Cr_{23}C_6$ or NbC; tungsten and molybdenum were excluded to avoid the formation of Laves phase, $Fe_2(Mo,W)$, during ageing. With no overlapping signals, the evolution of nitrides could be followed by XRD measurements. As such this model alloy was perfectly suited for studying the decomposition of the MX nitrides and the development of Z-phase [8].
The second alloy, 12CrVN hereby named M2, was made similar to the M1, except that the Nb content was omitted and replaced by a similar amount of V (in at%). The purpose of M2 was to compare it with M1, and thus verify the influence of Nb on Z-phase precipitation rate. By accident the N content obtained was higher in M2.
The third alloy, 9CrVNbN hereby named M3, is again similar to M1, but this time except for the Cr content. Together with M1, it should provide input data on the effect of Cr for kinetic modelling of the Z-phase in 9-12%Cr steels.
The specific goals of investigation of the model alloys were: verifying the cubic crystal structure of Z-phase with XRD, verifying the nucleation mechanism of Z-phase by TEM, investigating the composition dependence of Nb and Cr on Z-phase kinetics, investigating the temperature dependence on Z-phase kinetics on 9%Cr and 12%Cr steels and using all data obtained for a kinetic model of Z-phase in commercial 9-12%Cr steels.

	Cr	V	Nb	N	C	Ni	Mn	Si
M1	11.85	0.183	0.076	0.061	0.0048	1.29	0.32	0.40
M2	11.57	0.23	-	0.088	0.0017	1.27	0.31	0.35
M3	9.11	0.207	0.080	0.059	0.0040	1.27	0.34	0.41

Table 1: Composition of the three model alloys in wt%. The higher N content in M2 was not intentional.

2. Experimental

Three 80kg ingot model alloys were produced by Vacuum Induction Melting (VIM); the chemical compositions as determined by X-ray fluorescence spectroscopy are given in Table 1. The ingots were hot rolled into 20 mm thick plates, and subsequently normalised at 1050°C for 1h, followed by air cooling. Thereafter they were tempered at 750°C for 2h, followed by air cooling to obtain a tempered martensite morphology. The microstructure of the normalised and tempered materials consisted entirely of tempered martensite, with an average hardness of around $235HV_{10}$. After normalising and tempering, samples of dimensions 100mm x 20mm x 15mm were aged at 600°C, 650°C and 700°C for up to 10,000h in laboratory furnaces flushed with air.
For determination of the precipitated phases present X-Ray powder Diffraction (XRD) was applied, using a Bruker D8 Advance powder diffractometer equipped with Cu-radiation. In order to avoid interference from matrix reflections, the precipitates were extracted from the bulk by electrolysis in an acidic solution of 5% HCl in 95% ethanol, dissolving the matrix

while gathering the precipitates by sedimentation. Some of the very small VN precipitates may not have been fully recovered by the sedimentation process.
The morphology and composition of the precipitates in the as-treated and aged samples were investigated with a Field Emission Gun Transmission Electron Microscope (FEG-TEM), JEOL 3000F, operated at 300 kV and equipped with Oxford Instruments Inca Link ISIS Energy Dispersive Spectroscopy (EDS) unit. For statistical measurements a 200 kV Scanning/Transmission Electron Microscope (STEM), JEOL 200CX, equipped with an EDS Noran Instruments was applied.
All TEM observations were carried out on carbon extraction replicas. The replicas were prepared by a chemical etch with Vilella's reagent (1% picric acid and 5% hydrochloric acid in ethanol).

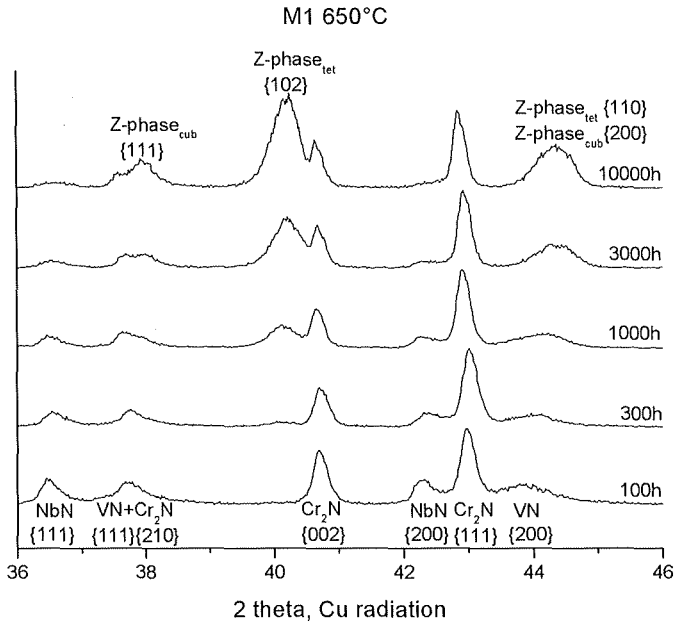

Figure 2: XRD spectra of M1. Notice Z-phase peaks have two different crystal structures, cubic and tetragonal.

3. XRD results

After normalising and tempering, the precipitates in the model alloys consisted only of the nitrides M_2X and MX. Two populations of MX nitrides were identified in the Nb alloyed steels: V-rich and Nb-rich. Both VN and NbN have a NaCl type crystal structure (fcc lattice of metal atoms), with lattice parameters of 0.413 nm and 0.439 nm, respectively. Since a significant dissolution may occur of Nb in VN and of V in NbN, the actual compositions of the nitrides are rather (V,Nb)N and (Nb,V)N. Accordingly, the lattice parameter of (V,Nb)N will be higher than 0.413nm and that of (Nb,V)N will be lower than 0.439nm. The Cr_2N particles have a hexagonal crystal structure, with lattice parameters a=0.481nm and c=0.448nm. Although significant amounts of V can be dissolved into the Cr_2N, this will not

affect the lattice parameter to a large extent, as V and Cr atoms have almost the same atomic size. All diffractograms were normalised with respect to the highest intensity peak of Cr_2N, {111}, for graphical representation, as the Cr_2N quantity only changes slightly with time. Note there is a peak overlap with (Nb,V)N in M3.

3.1. M1

Comparison among powder diffractograms of aged samples at 650°C is shown in Figure 2. Qualitatively, the XRD results show a gradual reduction of the NbN and VN peak intensities with increasing ageing times and after 10,000h at 650°C only small NbN peaks remain. The intensity reduction of (Nb,V)N and (V,Nb)N peaks corresponded to the appearance of three new peaks, which were identified to belong to modified Z-phase, Cr(V,Nb)N. As the main Z-phase peak is clearly visible after only 300h, this alloy manifested a very fast rate of Z-precipitation as compared to other 9-12%Cr steels, where high Z-phase quantities are usually first observed after several thousands of hours at 650°C [2]. The XRD spectra also confirm the presence of a cubic Z-phase peak, otherwise the cubic Z-phase has only been observed with electron diffraction [5].

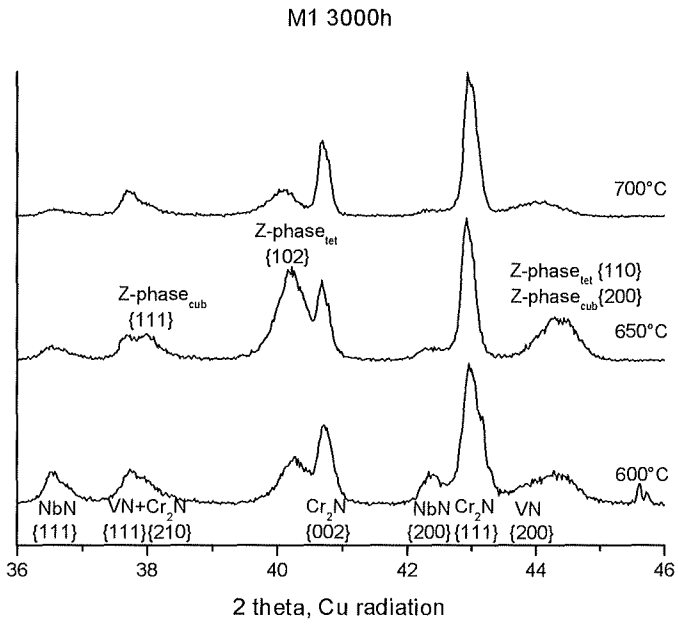

Figure 3: XRD spectra of M1 after 3000h at different temperatures.

Figure 3 shows diffractograms from samples aged for 3,000h at 600°C, 650°C and 700°C. The largest Z-phase peak was determined in the sample aged at 650°C. This suggests that the fastest Z-phase formation in M1 occurs at 650°C. These results are consistent with Time-Temperature-Precipitation (TTP) maps for Z-phase formation in 9-12%Cr commercial steels, which show fastest Z-phase precipitation at 650°C [9].

3.2. M2

After normalising and tempering, the precipitates in the M2 alloy consisted of nitrides M_2X, $(Cr,V)_2N$, and MX, (V,Cr)N. The diffractograms of extracted precipitates from the aged samples show no indication of any emerging Z-phase peak, only MX and M_2X peaks are visible. The VN have a NaCl type crystal structure (fcc lattice of metal atoms), with lattice parameter which is lower than the theoretically expected 4.13 nm, although it is difficult to determine as peaks are very small and broad. This would however be in accordance with a baker-nutting orientation relationship with the iron matrix, which requires a lattice parameter of 0.405nm.

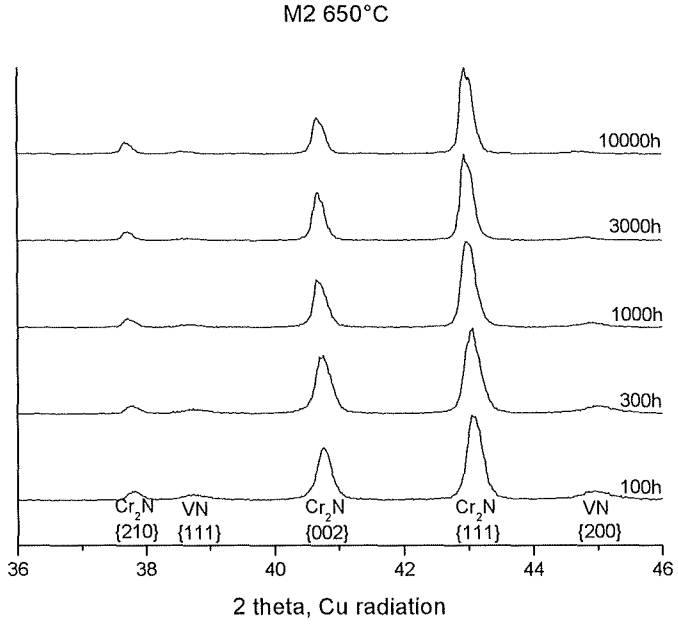

Figure 4: XRD spectra of M2. VN peaks are very small compared to Cr_2N because of the high N content.

Qualitatively, the XRD results show a very high M_2X amount, most likely because of the very high N content and no Nb content to stabilise VN. There is a gradual reduction of the MX peak intensities with respect to M_2X peak intensities up to about 1000 hours at 650°C. The reduction of the MX peaks is not associated with an appearance of new peaks in the diffractograms, even after 10,000 hours. The relative reduction of the MX peaks is probably due to a rise in M_2X volume fraction, as it is not very stable at the tempering temperature (750°C), but more stable at annealing temperature (650°C).

3.3. M3

Generally there are few Cr-nitrides in M3 compared to the other model alloys because of the lower Cr content. This makes it easier to study the MX behaviour and dissolution. The MX

peaks also have a slightly different position compared to M1. There does not seem to be much dissolution of V-rich MX after exposure of 10,000h at 650°C, indeed the VN peaks seem to grow compared to the Nb-rich MX and M_2X, as opposed to what happens in M2. The Z-phase precipitation was expected to be slow in a 9%Cr steel, so no investigations were performed before 1000h of annealing. After 10,000h the spectra show the first signs of an emerging Z-phase peak, while it took only 300h for M1 to develop a discernable peak. More ageing time is needed in order to make a better comparison between M1 and M3.

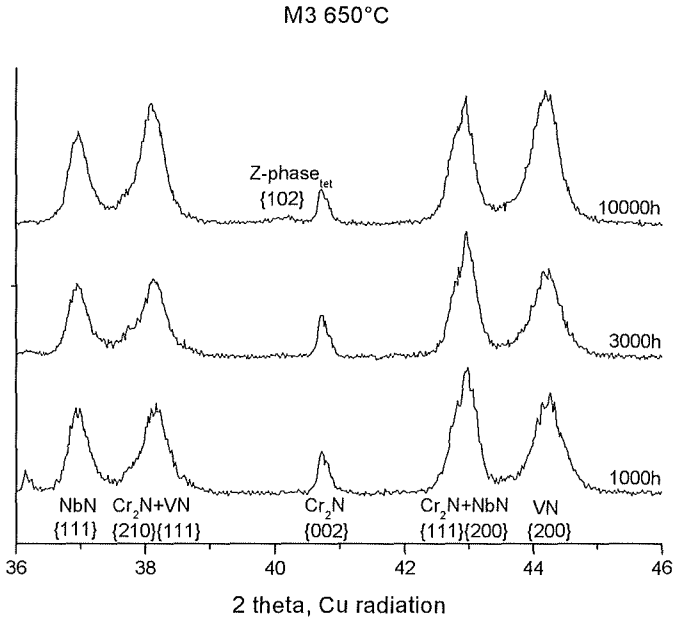

Figure 5: XRD spectra of M3. At 10.000h there are indications of an emerging peak at the primary peak position of Z-phase.

4. TEM results

In addition to XRD, the model alloys were also investigated with TEM (carbon extraction replica) using EDS for further identification of the particles found in XRD. On the basis of the EDS composition analysis the evolution in particle precipitation could be followed. The MX nitrides could be recognised by their high V and/or Nb contents; particles with [V]+[Nb]≥70 at.% were identified as MX. In Nb containing steels the overall composition of the MX could vary from Nb rich to V rich, and particles with Nb rich cores and V rims were not uncommon. Cr_2N nitrides were characterised by the following compositional criterion: [Cr]≥70 at.%, with the rest being V. Z-phases are characterised in aged samples by the following compositional criterion: [Fe]+[Cr]≈[V]+[Nb], were 45<[Fe]+[Cr]≤65 at.%. In some samples, niobium- and vanadium-rich nitrides with an average [Fe]+[Cr] of 30-45 at% were observed. These particles could neither be classified as complex (V,Nb)N nor as proper Cr(V,Nb)N, and are hereby referred to as hybrid MX/Z-phase particles.

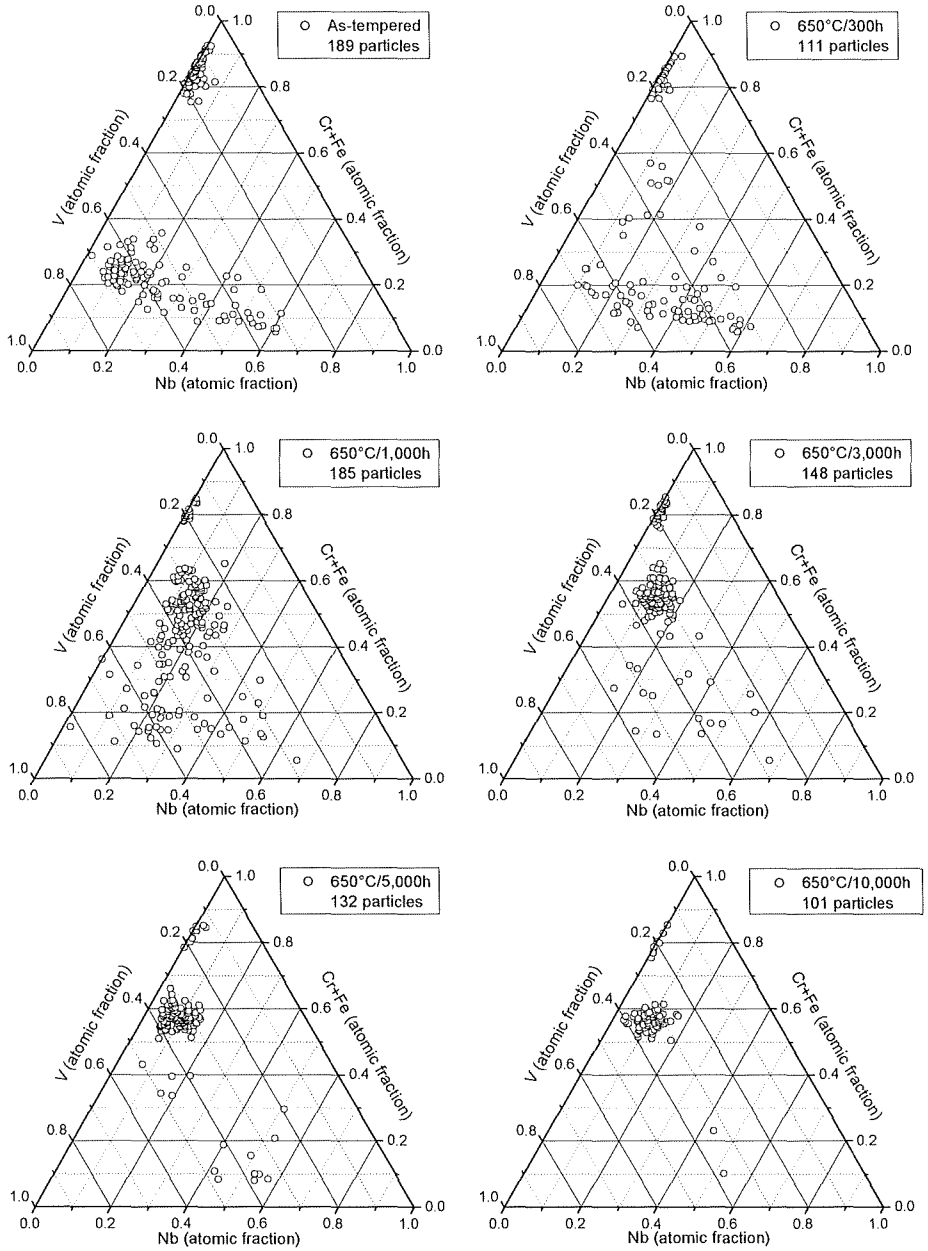

Figure 6: Ternaries showing the composition change of the precipitates in M1 at 650°C. [8]

4.1. M1

The chemical evolution of the analysed particles in as-treated and annealed samples is depicted in the quasi-ternary (Cr+Fe)-V-Nb diagrams in Figure 6. The average chemical compositions of (V,Nb)N and (Nb,V)N particles changed gradually during temperature exposure. Clearly, the Cr content increases in the MX particles and an overall shift towards a Z-phase composition appears on prolonged ageing. The chemical compositions of the observed Z-phase are similar to those reported for Z-phase particles that have developed in commercial 9-12%Cr steels [7,10].
Fully developed Z-phases can be found after only 100h of exposure at 650°C. For the longer ageing times no (V,Nb)N particles were detected (Figures 6e-f), while a few (Nb,V)N particles were still present. This observation is consistent with Figure 2, where it is observed that (Nb,V)N is present up to longer ageing times than (V,Nb)N.

Sample	Particle type	Number of analysed particles	Average Equivalent Diameter (nm)	Av. chemical composition (at%)		
				Cr	V	Fe
As-Treated (78 particles)	VN	46	60	30	69	1
	Cr_2N	32	124	81	18	1
650°C / 1,000h (85 particles)	VN	40	70	27	72	1
	Cr_2N	45	155	80	19	1
650°C / 5,000h (115 particles)	VN	55	75	22	77	1
	Cr_2N	60	250	78	21	1
650°C / 10,000h (127 particles)	VN	54	80	18	81	1
	Cr_2N	73	377	77	22	1

Table 2: Composition and size of precipitates found in M2 at different ageing times.

4.2. M2

TEM investigations confirmed results from XRD measurements: M_2X and MX nitrides were identified in all aged samples. The mean chemical compositions (in metallic at%) of M_2X and MX nitrides of as-treated and aged samples are given in Table 2, together with their average equivalent diameter. It can be seen there is a change of composition in both M_2X and MX, as the Cr content decreases with time for both precipitate types.
Z-phase was not found up to 10,000 hours at 650°C, while very few hybrid VN/CrVN particles could be identified, but only in the 10,000h sample. Hybrids are not included in the Table 2 since there were too few for reliable statistical analysis.

4.3. M3

The M3 samples have not yet been investigated as thoroughly as M1 and M2 in TEM, so there are no statistical data available. However the presence of a few Z-phases in aged samples can be confirmed, some have reached micrometer sizes after 10,000h.

5. Discussion

5.1. Hybrid MX/Z-phase particles

Niobium- and vanadium-rich nitrides where 30<[Fe]+[Cr]<45 at.% were observed in both M1 and M2. These particles can neither be classified as complex MX nor as proper Z-phases. The occurrence of such Cr-rich MX particles has been reported for commercial steel grades such as P122 [7,10]. These Cr-rich MX particles were investigated further and were found to contain both MX and Z-phase regions (according to the composition analysis). Therefore, these particles are referred to as *hybrid* particles. The spatial variation of the chemical composition within the hybrid particles was investigated using EDS microprobe.

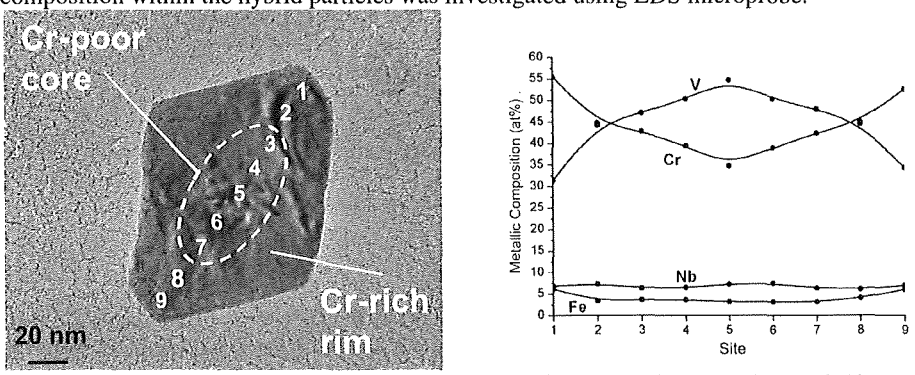

Figure 7: A symmetrical hybrid MX/Z-phase particle found in M1 after 1000h at 650°C. [8]

Generally, composition profiles of hybrid particles showed a smooth transition from Cr-rich regions, with chemical composition close to Z-phase, towards Cr-poor regions, with compositions close to V-rich MX. Usually the Z-phase composition was observed at the rim of the particle, while the core consisted of MX. An example is given in Figure 7, which shows a symmetric hybrid particle found in the M1 650°C/1,000h sample; the entire rim has a composition similar to Z-phase, while the core has a considerably lower chromium content. The concentration profile shows a smooth transition from core to rim without any observable phase boundary. These observations would be consistent with a straightforward chemical transformation of MX into Z-phase by the incorporation of Cr from the surroundings which has previously been reported for commercial steels [7].

More complex concentration profiles and morphologies of particles were also found, especially in relatively large particles. Such particles frequently had a Nb-rich core, usually encased in V-rich composition, and with several separate Z-phase areas. Figure 8 shows two examples of large MX particle where Z-phase has formed on opposite sides of the particles. This could indicate that Z-phase reduces the interfacial energy in certain orientation relationships with the matrix. For such relatively large particles it is unlikely that Cr diffuses from the surroundings into the centre (i.e. the straightforward conversion of V-rich MX particles to Z-phase above).

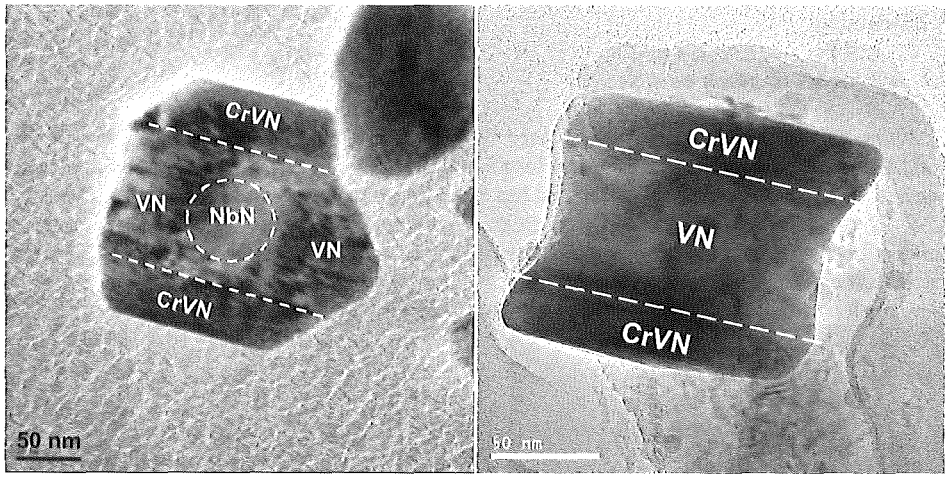

Figure 8: A MX particle with a Nb core encased in VN and flanked by Z-phase from M1 650°C/3000h [8] and a VN flanked by Z-phase from M2 650°C/10000h.

5.2. Mechanisms of Z-phase formation

Investigation of the hybrid particles suggests that a possible path for the formation of Z-phase is a transformation of V-rich MX into Z-phase through Cr diffusion from the matrix into the nitride [7]. This mechanism is illustrated in Figure 9. The transformation of (V,Nb)N into Cr(V,Nb)N by Cr diffusion would explain the hybrid crystal structure observed in several Z-phase particles [5,6]. The (V,Nb)N precipitates have a cubic crystal structure, with lattice parameter of about 0.420 nm. Upon incorporation of Cr into the particles, the composition gradually changes to Cr(V,Nb)N, while the metal-to-nitrogen ratio changes from 1:1 to 2:1. The lattice remains cubic and the lattice parameter is reduced to 0.405 nm, as only half the interstitial sites are now occupied by N. It is speculated that on continued ageing the atoms in this meta-stable cubic Z-phase rearrange themselves into the ordered tetragonal lattice of the modified Z-phase, see Figure 1.
A less straightforward mechanism initiates at (Nb,V)N particles and is illustrated in Figure 10. Here, several Cr-rich areas form separately on larger MX particles with Nb-rich centres. The Z-phase tends to form on the opposite sides of the particle by incorporation of Cr from the matrix. After the development of Cr-rich regions of a certain size, the Z-phase grows by consumption of the V, Nb and N from the host precipitate, probably assisted by diffusion through the ferrite matrix rather than through the particle (see arrows in Figure 10) and consequently leading to dissolution of the "core", leaving several Z-phase particles, most often observed as parallel particles.

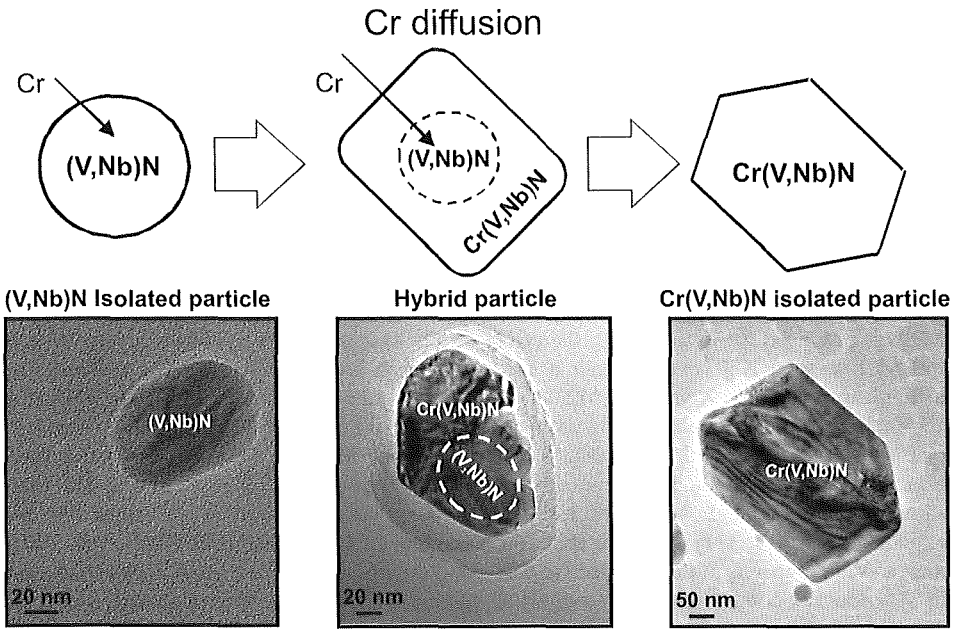

Figure 9: Transformation of MX into Z-phase by Cr diffusion from the matrix as seen in M1. [8]

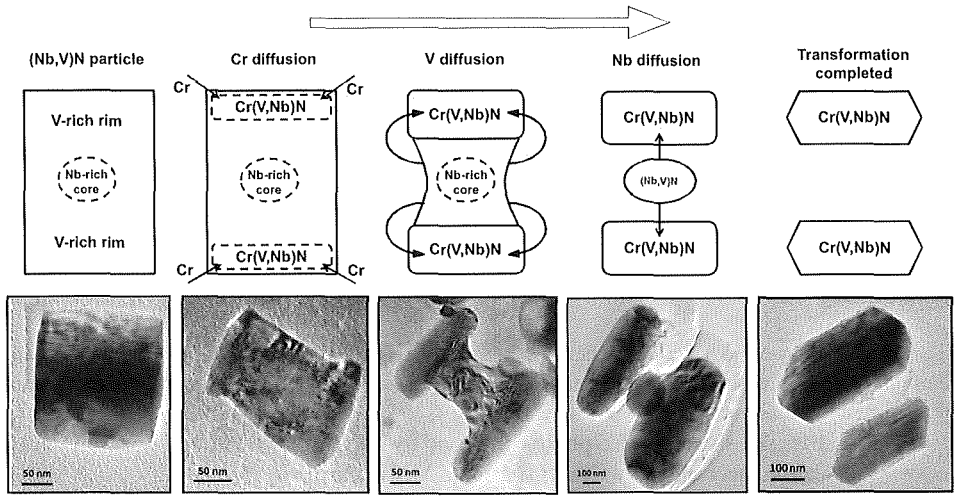

Figure 10: Formation of separate Z-phases with same orientation relationship as seen in M1. [8]

5.3. Z-phase precipitation kinetics

It was sought to make the three model alloys identical except for variations in Cr and Nb in order to investigate the effect of these element on the precipitation kinetics of Z-phase. A

large effect of Cr was to be expected based upon observations from industrial steels [2]. Thermodynamical calculations also show Cr to be the most important element regarding the driving force for Z-phase precipitation, as the difference between Cr(V,Nb)N and (V,Nb)N is Cr [4]. As expected the Cr-rich M1 clearly shows the fastest Z-phase precipitation, at least 30 times faster than the Cr-poor M3 at 650°C when comparing 10.000h M3 and 300h M1. Further ageing of M3 is needed to show exactly how large the effect of increasing the Cr content from 9 to 12% is. It is also shown in M1 that the fastest precipitation takes place at 650°C, also in accordance with 12%Cr industrial steels [9]. Again further ageing is needed for M3 to investigate the temperature dependence of 9%Cr steels. One also has to note that there is a large difference in the amount of M_2X between M1 and M3, even though the N content is the same, but this will probably not have much influence on the Z-phase precipitation rate.
M2 was produced for investigating the effect of Nb, as Z-phase precipitation is very slow in the Nb-free steel X20, even though it contains a high level of Cr. Indeed it seemed very difficult to precipitate Z-phase in M2, as only hybrid stage Z-phases could be observed after 10,000h. Thus the precipitation rate seems to be about 100 times slower than in M1, where Z-phase could be identified after 100h. Further ageing of M2 may be needed to get a more accurate estimate. Although M2 contains more N and thus more M_2X compared to M1, there should still be enough MX particles present acting as nucleation sites. There are two explanations for the very slow precipitation behaviour of CrVN. First CrNbN is more stable than CrVN compared to their respective MX counterparts. Even if modified Z-phase, as seen in M1, does not contain much Nb (roughly 10 atomic % of the metallic component) it may act as a catalyst for the nucleation itself. A second explanation may be offered by looking at the lattice parameters of MX. When niobium is present the MX lattice parameter is around 0.420nm, but when transforming into Z-phase, the cubic unit cell is reduced to 0.405nm because of fewer N atoms in the interstitial sites. As 0.405nm is very favourable for a baker-nutting relationship with BCC ferrite ($0.286nm*\sqrt{2}=0.405nm$) the interfacial energy will be reduced. It is known that the interfacial energy has a very large effect on nucleation, so this could be very important for the relatively slow nucleation of Z-phase. Furthermore there does seem to be a preference for nucleation of Z-phase in certain orientation relationships, see figure 8. For Nb-free VN the lattice parameter seems to be much closer to the ideal 0.405nm, thus the effect of lowering the interfacial energy is not as high, resulting in a slower nucleation rate.

6. Summary

This model alloy project was launched in order to systematically study the Z-phase behaviour, and although investigations are not finished yet, it has already been successful in accomplishing most of the goals set for it:

- Cubic crystal structure of Z-phase confirmed by XRD
- Nucleation mechanism by Cr diffusion into MX confirmed
- Z-phase precipitates fastest at 650°C in 12%Cr steels
- Increase of Cr content from 9% to 12% enhances Z-phase precipitation (estimated as at least 30 times at 650°C)
- Confirmed that the presence of Nb enhances Z-phase precipitation (100 times, estimated)

Acknowledgements
MAJ Somers (DTU) and PE Di Nunzio (CSM) are thanked for valuable discussion.

References
[1] Hald J: *VGB PowerTech*, **12**, p74 (2004)
[2] Danielsen HK, Hald J, *Energy Mater*, **1**, p49 (2006)
[3] Strang A, Vodarek V, *Mater Sci Tec*, **12**, p552 (1996)
[4] Danielsen HK, Hald J, *Calphad*, **31**, p505 (2007)
[5] Danielsen HK, Hald J, Grumsen FB, Somers MAJ, *Metall Mater Trans A*, **37A**, p2633 (2006)
[6] Vodarek V, Danielsen HK, Grumsen FB, Hald J, Strang A, *8th Liege Conference Proceedings*, **3**, p1251 (2006)
[7] Danielsen HK, Hald J, *Mater Sci Eng A*, **505**, p169 (2009)
[8] Cipolla L, Danielsen HK, Venditti D, Di Nunzio PE, Hald J, Somers MAJ, *Acta Mater*, **58**, p669 (2010)
[9] Sawada K, Kushima H, Kimura K, Tabuchi M, *ISIJ Int*, **47**, p733 (2007)
[10] Yoshizawa M, Igarashi M, Moriguchi K, Iseda A, Armaki HG, Maruyama K, *Mater Sci Eng A*, **510-511**, p162 (2009)

9th Liege Conference : Materials for Advanced Power Engineering 2010
edited by J. Lecomte-Beckers, Q. Contrepois, T. Beck and B. Kuhn.

INFLUENCE OF Z-PHASE ON LONG-TERM CREEP STABILITY OF MARTENSITIC 9-12%Cr STEELS

Hilmar K. Danielsen[1], John Hald[1,2]

1: Technical University of Denmark (DTU), Mechanical Engineering, Denmark
2: DONG Energy/Vattenfall, Denmark

Abstract

The long-term creep strength of the new generation of martensitic creep resistant 9-12%Cr steels since the well-known steel Grade 91 relies strongly on particle strengthening by fine MN nitrides based on V and Nb. During long-term high-temperature exposures the MN nitrides may be replaced by the thermodynamically more stable Z-phases (Cr(V,Nb)N) causing a breakdown in creep strength. Cr contents above 10.5% strongly accelerate Z-phase precipitation, which explains the lack of success for all attempts to develop martensitic creep resistant steels with high Cr content for oxidation protection. However 9%Cr steels do not seem to be affected by the Z-phase.

Careful control of the Z-phase precipitation process has led to the design of experimental 12%Cr martensitic steels strengthened by fine Z-phase nitrides based on Nb or Ta. Such steels may again enable the combination of high strength and oxidation resistance in the same alloy. This opens a new pathway for further alloy development of the heat resistant martensitic steels.

Keywords: Z-phase, 9-12%Cr steels

1. Background

Because of their combination of high creep strength and moderate cost the martensitic 9%Cr steels are vital materials in fossil-fired power plants. Over the last decades, focus has been on improving the efficiency of such power plants by increasing steam parameters. Current state of the art amongst these steels is grade P92 which allows power plants to operate with supercritical live steam parameters up to 600°C/300bar [1-2]. In order to further increase the steam parameters of steel based power plants up to a target value of 650°C/325 bar it is necessary to double the creep strength compared with Grade 92, and at the same time the resistance against steam oxidation must be improved. If the oxidation protection is to be achieved through alloy additions instead of surface coatings, it is necessary to increase the Chromium content in the steels from 9% to 12% [3]. However, so far all such attempts to make stronger 12%Cr steels have been unsuccessful because the high chromium content introduced severe microstructure instabilities in the tested steels, which led to breakdowns in long-term creep strength [4].

1.1. Precipitates

Precipitate hardening should be regarded as the most significant creep strengthening mechanism to obtain high long-term creep strength in the 9-12%Cr martensitic steels [5-6]. A number of different precipitates can be found in these steels. Depending on their particle hardening effect and stability against coarsening or dissolution during long-term exposure, the precipitates determine the microstructure stability of the steels.

The most useful precipitates are the Cr carbides $M_{23}C_6$, the fine intermetallic Laves phases $Fe_2(Mo,W)$ and especially the MN nitrides (V,Nb)N. The long-term creep strength of the new generation of martensitic creep resistant steels since the well-known steel Grade 91 relies strongly on particle strengthening by fine MN nitrides based on V and Nb. Additions of ca. 0.15-0.25%V, 0.04-0.08%Nb and 0.02-0.07%N are common to all of the new steels, due to results obtained by Fujita in the late 1970s [7]. The MN nitrides precipitate in high number densities as very fine particles, which are much more stable against coarsening than the other precipitates [8]. As such they contribute significantly to long-term precipitation hardening in the steels. More recently, boron is being added to these steels as it stabilises the $M_{23}C_6$ carbides, especially near the prior austenite grain boundaries. [9-10].

1.2. Z-phase

Z-phase Cr(V,Nb)N was first found in a martensitic 11%Cr steel by Schnabel et.al. in 1987 [11]. In 1996 Vodarek and Strang realised that Z-phase precipitation could explain observed sigmoidal creep behaviour in older 12CrMoVNb steels, since the Z-phase precipitates as coarse particles and dissolves fine MN nitride particles [12].
Recently, the authors made systematic studies of Z-phase content in a number of 9-12%Cr steels, which rely on MN strengthening [13]. Both commercial and experimental grades were investigated after exposure to creep, and a clear correlation between the Cr content of the steels and the observed Z-phase quantity was found. Comparisons with creep testing on a number the investigated steels show that for Cr contents above 10.5% the strongly accelerated Z-phase precipitation leads to a breakdown in long-term creep strength. In steels with Cr contents below 9% Z-phase precipitation is so slow that they are largely unaffected up to very long testing times at 600-650°C [13].

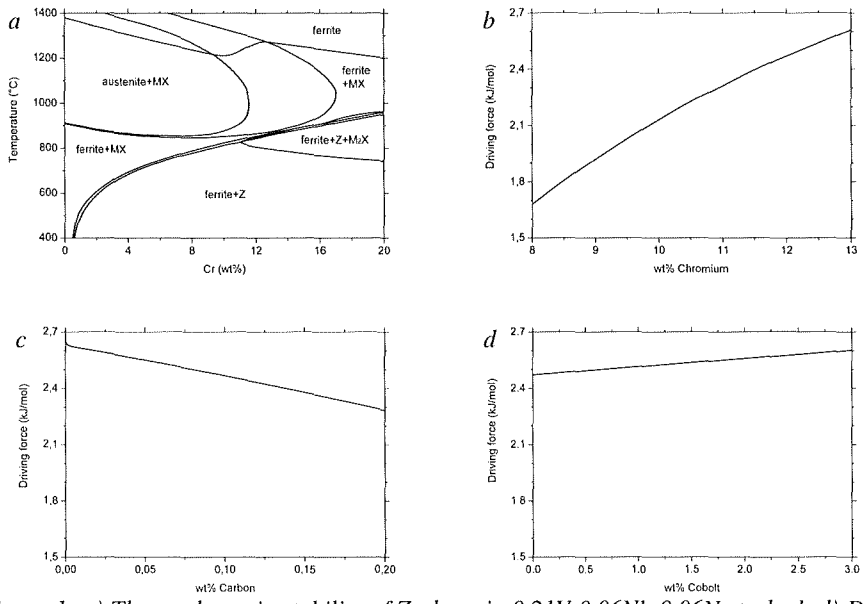

Figure 1: a) Thermodynamic stability of Z-phase in 0.21V-0.06Nb-0.06N steels. b-d) Driving force for Z-phase precipitation in 0.10C-0.21V-0.06Nb-0.06N steel at 650°C (wt%, bal Fe).

Results from detailed studies of the mentioned steels were used to develop a thermodynamic equilibrium model of the Z-phase [14]. This model has demonstrated that Z-phase Cr(V,Nb)N is thermodynamically the most stable nitride in all 9-12%Cr steels containing V, Nb and N, see figure 1. This means that Z-phase should eventually form in all of the new generation 9-12%Cr steels with potentially detrimental effects on their creep strength. However, large differences in Z-phase precipitation rate has been found, which seem to correlate well with similarly observed large differences in the rate of breakdown in creep strength.

The thermodynamic equilibrium model can be used to estimate Z-phase precipitation rates by calculations of the thermodynamic driving force for the Z-phase precipitation. This driving force is the difference in free energy between the steel with all MN nitrides present and the steel with only Z-phase present, and it can give indications of the influence of chemical composition on the Z-phase precipitation rate. Such calculations clearly demonstrate that Cr is the most influential element for the Z-phase driving force, see figure 1b. Further it is found that elements like C or Co, which are not included in the Z-phase, also affect its driving force. C forms as $M_{23}C_6$, which ties up Cr and thus effectively lowers its content, while Co may reduce the Cr affinity in the matrix, thus encouraging it to form as Z-phase. Results by Strang and Vodarek indicated a strong accelerating effect of Ni content on Z-phase precipitation [12]. However, the model studies provide no support to any effect of Ni content on the precipitation rate of the Z-phase [14].

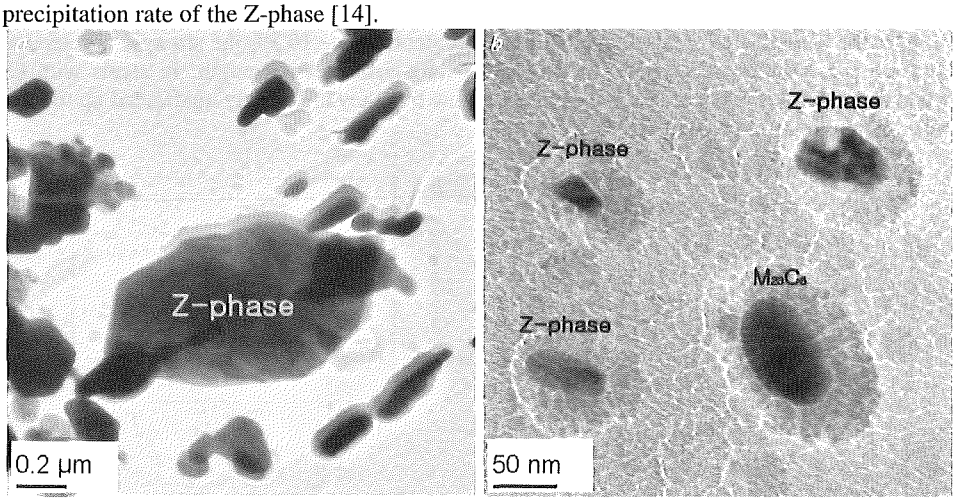

Figure 2: a) Large and b) small Z-phase particles co-existing in a 10.5%Cr steel after 43,000h exposure at 600°C.

Even though the Cr(V,Nb)N Z-phase is thermodynamically the most stable nitride in 9-12%Cr steels alloyed with V, Nb and N it seems quite difficult for it to nucleate. Z-phase has never been observed in any of the steels directly after tempering in the normal range 650-800°C. Even in the high Cr steels, where Z-phase forms most rapidly, widespread Z-phase formation has only been observed after quite long exposure times of 1000 hours or more at 650°C. Experimental studies of Z-phase TTP diagrams indicate that the fastest precipitation happens at 650°C [15-16].

Once a Z-phase has nucleated it can grow fast, and large Z-phase particles can be observed after relatively short exposures. The Cr(V,Nb)N Z-phase grows by dissolution of the MN precipitates, which provide V, Nb and N, and by picking up Cr from the steel matrix. In spite of the fast growth, observations of long-term exposed specimens always reveal both large and small Z-phase particles, figure 2. This indicates that the nucleation of Z-phase is slow and continuous, and thus the nucleation process should be regarded as rate controlling for the Z-phase transformation [17-18]. The fact that Z-phase grows fast means that even in early stages of the transformation large Z-phase particles can be observed in the microstructure even though only a very limited part of the MN population has been dissolved. Thus, an observation of a few large Z-phase particles in the steel microstructure is not necessarily alarming for the creep stability. Instead, attention should be focused on the rate of removal of the MN nitrides by measurements of their number density.

	9Cr3W 3Co	9Cr3W 3CoB	P92	P122	BH Steel	NF12	MARBN	MARN
C	0.078	0.077	0.11	0.12	0.03	0.085	0.078	0.002
Si	0.31	0.29	0.10	0.24	0.36	0.25	0.31	0.29
Mn	0.50	0.51	0.45	0.63	0.49	0.44	0.49	0.51
Cr	8.94	8.95	8.82	10.73	9.12	11.60	8.88	9.19
Mo	-	-	0.47	0.38	0.15	0.14	-	-
W	2.94	2.93	1.87	1.97	2.40	2.68	2.85	2.96
Ni	-	-	0.17	0.36	0.01	0.17	-	-
Co	3.03	3.03	-	-	1.8	2.48	3.00	3.09
Cu	-	-	-	0.97	-	-	-	-
V	0.19	0.19	0.19	0.22	0.20	0.20	0.20	0.20
Nb	0.050	0.050	0.06	0.056	0.05	0.08	0.051	0.060
N	0.002	0.001	0.047	0.072	0.050	0.045	0.0079	0.049
B	-	0.0048	0.0020	0.0039	0.0060	0.0026	0.0135	0.0070
Norm	1050℃	1050℃	1070℃	1050℃	1050℃	1100℃	1150℃	1100℃
Temp	790℃	790℃	780℃	770℃	780℃	760℃	770℃	800℃

Table 1: Chemical composition and heat treatment of 9 to 12%Cr steels discussed. [19-23]

2. MN strengthening

The quantitative effect of MN precipitates on long-term creep strength of modern 9-12%Cr steels can be demonstrated by comparisons of selected steels, which all have fully tempered martensite microstructures free of δ-ferrite. The chemical composition and heat treatment of the discussed steels are shown in table 1 and results of creep rupture tests at 650°C are shown in figure 3. The 9Cr3W3CoVNb and 9Cr3W3CoVNbB steels have very low Nitrogen content and consequently they contain only $M_{23}C_6$ carbides and intermetallic Fe_2W Laves phase, but no MN nitrides. The 9Cr3W3CoVNbB steel is stabilised by Boron addition. As such these two steels represent baseline strength levels of the modern 9% Cr steels without nitrides. The P92 steel contains fine (V,Nb)N nitrides in addition to $M_{23}C_6$ carbides, Fe_2W Laves phases and Boron stabilisation. Because of the low Cr content the nitrides in steel P92 are stable against Z-phase precipitation up to long-term creep exposures. In short-term tests up to 2,000 hours the three steels have similar rupture strength. Above 2,000 hours the Boron addition in steels 9Cr3W3CoVNbB and P92 is effective, and above 10,000 hours the MN nitrides in steel

P92 are effective to stabilise the microstructure and increase the strength. All three steels have similar heat treatment.

If the MN nitrides disappear from the microstructure during creep it has a clear negative effect on the strength. The P122 steel contains MN nitrides, $M_{23}C_6$ carbides, Fe_2W Laves phases and Boron similar to the P92 steel, but due to the high Cr-content of 10.7%, strong precipitation of Cr(V,Nb)N Z-phase occurs above 10,000 hours and this dissolves the MN nitrides [13]. Consequently, the strength of the P122 steel stays at the level of the 9Cr3W3CoVNbB steel, which is without nitrogen, but has a similar Boron content as P122, see figure 3.

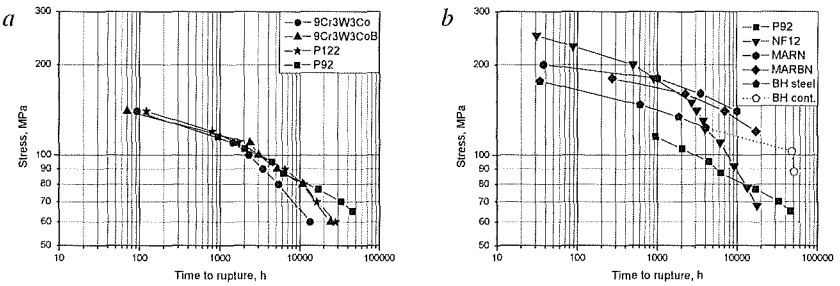

Figure 3: Creep rupture tests at 650°C of the 9 to 12%Cr steels discussed. [19-23]

The creep rupture strength of the 9-12%Cr steels can be increased above the level of steel P92 by optimisation of chemical composition and heat treatment. Figure 3 shows the effect on high W steels of a) lowering the carbon content (BH and MARN); b) increasing the normalising temperature (NF12) and c) increasing normalising temperature together with an optimisation of the Boron and Nitrogen contents (MARBN). Here, the effects on strength are clear also in the short-term tests, but they only remain in the long-term tests if the nitrides are maintained in the steels. The BH, MARN and MARBN steels have low Cr content and good long-term stability based on MN nitrides. In the NF12 steel with 11.6%Cr the MN nitrides are dissolved by Z-phase precipitation [13], and consequently the strength drops below the level of steel P92.

It is clear from above that the MN nitrides play a crucial role in the long-term microstructure stability of the 9-12%Cr steels, and that the removal of MN nitrides by Z-phase precipitation leads to a clear drop in strength. The Cr content in the steels controls the Z-phase precipitation, which explains the lack of success for all attempts to develop martensitic creep resistant steels with Cr content higher than 10.5% combined with high long-term strength based on MN nitrides.

3. Z-phase strengthening

Since it has not been possible to combine 12%Cr steels with MN strengthening, other alternatives are considered, such as Nickel-based superalloys or coating of 9%Cr steels. However such solutions would be very costly and/or introduce new possibilities for technical problems. Another alternative would be to replace the MN precipitates with another type of precipitates which could be finely distributed in the matrix and be resistant to coarsening

during long term exposure. This would combine 12%Cr oxidation resistance and creep strength from precipitate hardening.

As mentioned, calculations of the driving force for Z-phase precipitation allows estimations of the precipitation rate of the Z-phase. The obvious strategy is then to minimise the driving force in order to delay the harmful Z-phase precipitation to very long times (beyond 300,000 hours), where it would have no influence on the long-term stability of the steel in practical use. Unfortunately, as shown this leads to limitations on the Cr content, which prevent attaining the necessary oxidation resistance of the steels.
However, if the Z-phase itself could be provoked to precipitate very quickly in a fine distribution, which could provide particle strengthening, then the steel could be expected to be immune to dissolution of its strengthening nitrides. Inspections of the thermodynamic model show that the necessary steps to accelerate Z-phase precipitation involve an increase of the Cr-content to the highest possible level. Results from MARN and BH show that it is possible to combine a low Carbon content with high creep strength, see fig 3b. According to the thermodynamic model, using the low Carbon concept could accelerate the Z-phase formation further, together with additions of Cobalt which would also limit the amount of delta ferrite. The high Cr content would then be turned from being the main cause of instability into being a necessary beneficial element to secure the long-term microstructure stability of the steels. And at the same time the necessary oxidation resistance would be obtained, which would again make it possible to combine strength and oxidation resistance in the same alloy.
Scrutinising of the thermodynamic model suggests that Z-phases based on CrNbN could possibly serve as strengthening agents, as the driving force for their formation are significantly higher compared to that of CrVN or Cr(V,Nb)N, see figure 4. Finally, calculations of coarsening rates based on thermodynamic data made as described in [8], indicate coarsening stabilities of the Z-phases similar to or better than the MN nitrides.

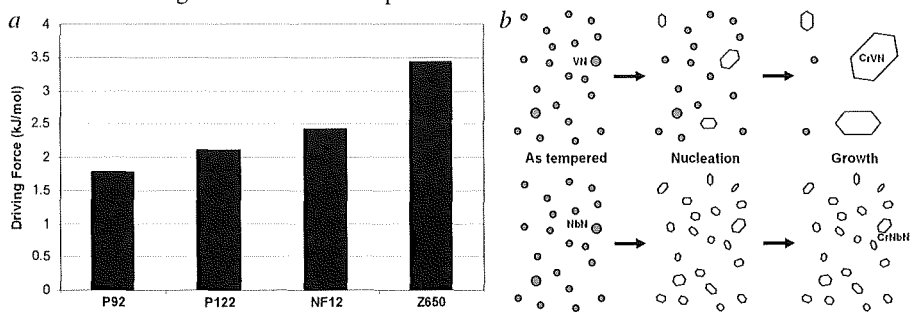

Figure 4: a) Driving force for Z-phase precipitation in 9 to 12%Cr steels. Z650 is an Nb-based alloy. b) The concept of Z650 is to avoid growth of Z-phase by accelerating the transformation rate, thus obtaining a fine distribution of nitrides for precipitate hardening.

3.1. Z650

Ongoing work at TU Denmark to study possibilities to use the Z-phase as a strengthening agent has included design and production of experimental high Cr martensitic steels. The alloying concept used, named Z650, is to produce a fully martensitic 12%Cr alloy with the fastest possible rate of Z-phase precipitation. The key of the concept is to avoid Vanadium, as VN is relatively stable compared to CrVN. Instead focus has been turned to Nb or Ta, which

can form very stable Z-phase (compared to their MN counterparts). In addition the alloys contain very low C, and very high Co as to maximise the driving force for Z-phase, but also to avoid MC precipitation and delta ferrite respectively. So far these experimental steels have demonstrated that it is indeed possible to produce a stable distribution of fine Z-phase particles in 12%Cr martensitic steels.

Fine NbN or TaN nitrides, which are precipitated during tempering, transform to a fine distribution of Z-phase in relatively short time at 650°C. Ideally, a strong acceleration of the Z-phase transformation would mean that each individual MN nitride transforms quickly into one Z-phase. Thereby the detrimental Z-phase growth process involving MN dissolution is effectively suppressed. The result should be a fine distribution of Z-phase particles, see figure 4b, which should be very stable against coarsening.

	Cr	C	Nb	Ta	N	W	Ni	Co	Si	Mn	B
Nb-based	11.64	0.005	0.26	-	0.036	2.82	1.47	5.40	0.30	0.49	0.004
Ta-based	11.79	0.005	-	0.39	0.033	2.90	0.50	7.30	0.30	0.48	0.004

Table 2: Composition of two experimental alloys used to investigate the possibility of obtaining small Z-phases in 12%Cr steels.

The two experimental steels, one Nb-based and one Ta-based, were produced to investigate the behaviour of Nb Z-phase and Ta Z-phase, see table 2. In both cases a fully martensitic microstructure is achieved after normalising, see figure 5. In both steels Laves phase have precipitated along grain boundaries and subgrain boundaries, thus effectively occupying the sites where $M_{23}C_6$ carbides would usually be found, see figure 6. Some Laves phase nucleate during tempering, but most Laves phase precipitates during the first 100h hours of exposure. A very fine distribution of NbN/TaN particles is achieved, which then turns into Z-phases relatively quickly. For the Nb-based a complete transformation happens after a few hundred hours at 650°C. For Ta-based the transformation process is somewhat faster and can take place already during tempering. As a whole, the Ta variant seems to be more promising, having a finer distribution of Z-phases after thousands of hours of annealing. Preliminary creep tests also show the Ta variant to be stronger compared to the Nb variant.

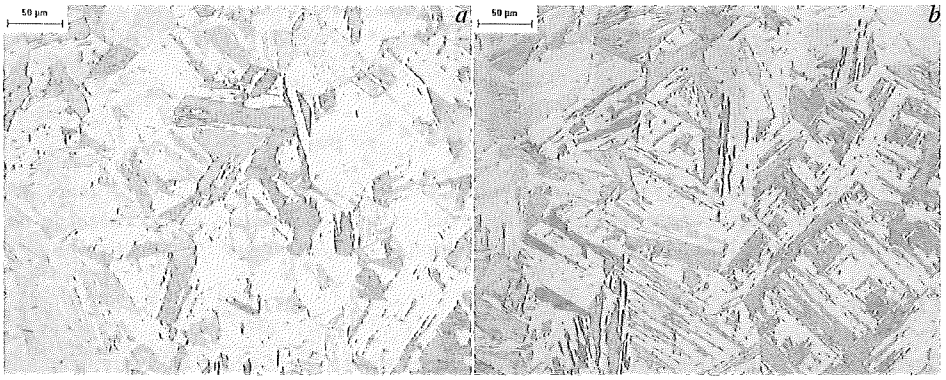

Figure 5: a) Fully martensitic microstructure obtained after normalising in a) Nb-based and b) Ta-based.

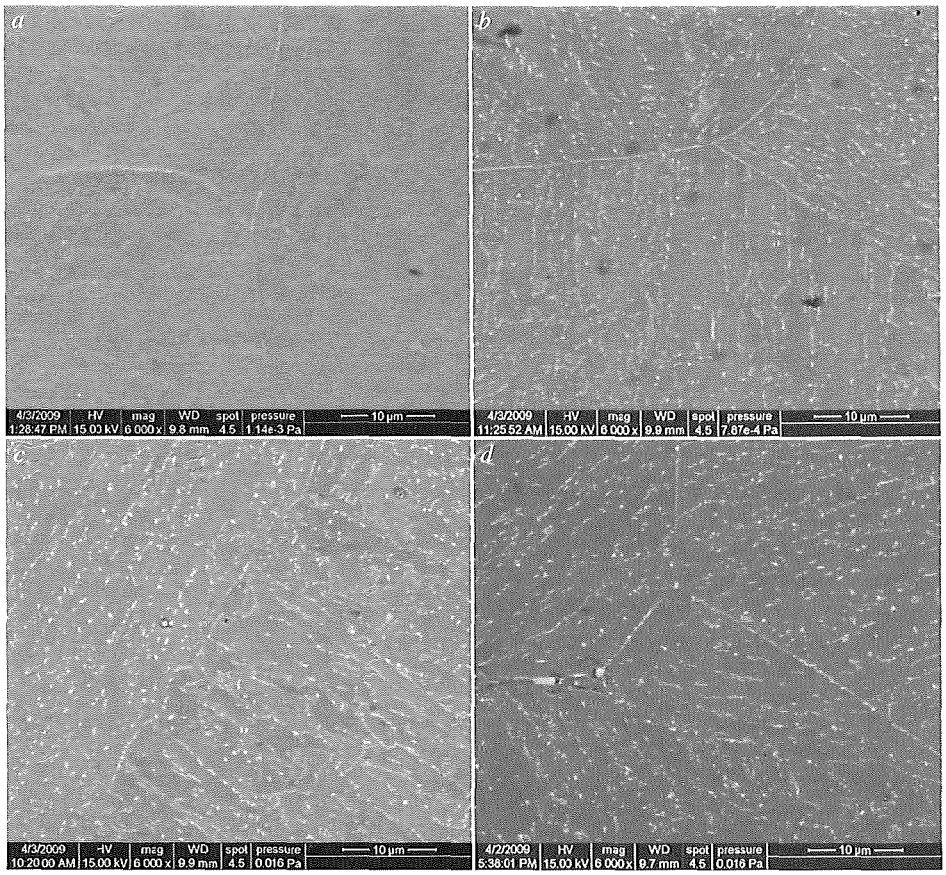

Figure 6: Backscatter SEM image of Laves phase distribution Ta-based, a) as tempered b) 100h/650°C c) 300h/650°C d) 1000h/650°C. Some large primary TaN and porosities are present on the grain boundary in image d.

Figure 7 shows precipitate sizes after 10.000h hours of annealing at 650°C. Figure 7a shows a former austenite grain, where laves phase is present along grain boundaries but also inside the grain, figure 7b-c. After 10.000h of exposure, Laves phases are generally large, figure 7b, rarely being below 100nm. As a general rule darker particles in figure 7c are Laves phase while brighter (presumably plate-like) particles are Z-phase. Most Z-phases are still below 50nm in diameter, as seen in figure 7c-d, but Z-phases with a diameter over 100nm can also be found. Very small Z-phases with diameters below 10nm are still present after 10.000h of exposure, figure 7d.

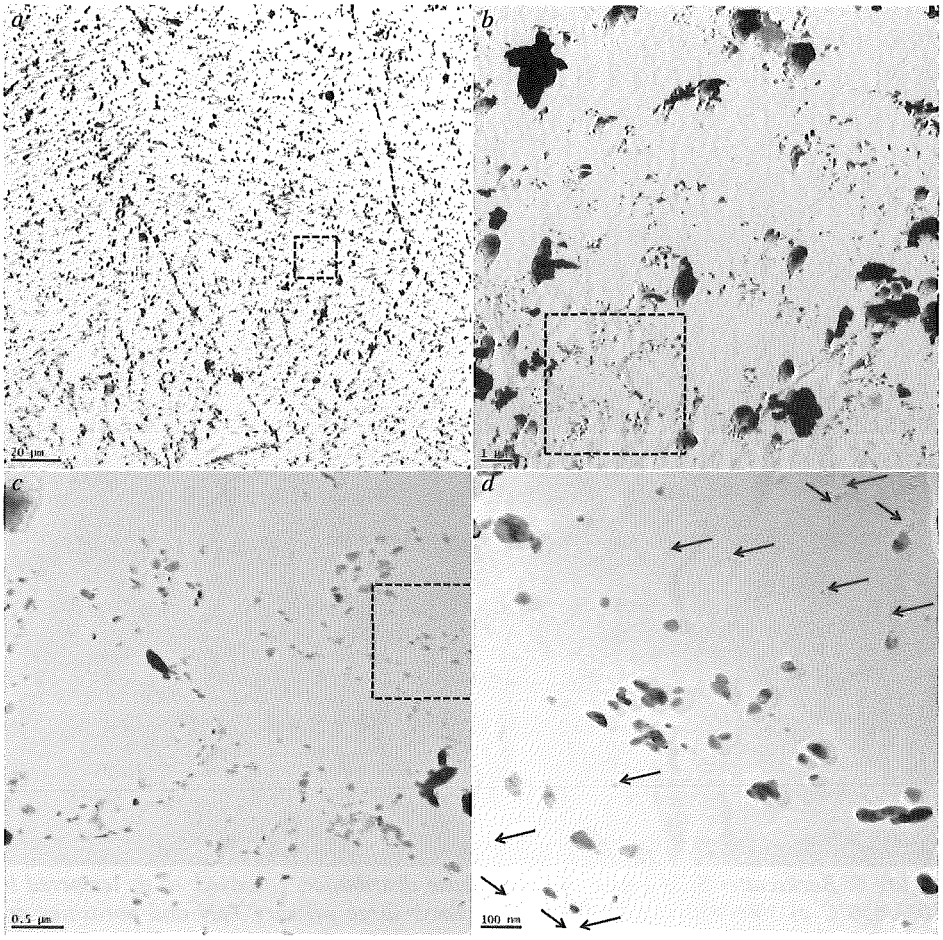

Figure 7: TEM replica of Ta-based after 10.000h of exposure at 650°C. Square indicates were the next image was taken; notice rotation of 180° from b) to c). Arrows point out Z-phases smaller than 10nm.

4. Summary

The long-term creep strength of the new generation of martensitic creep resistant 9-12%Cr steels since the well-known steel Grade 91 relies strongly on particle strengthening by fine MN nitrides based on V and Nb. The MN nitrides may be replaced by the thermodynamically more stable Z-phases, Cr(V,Nb)N causing a breakdown in long-term creep strength.

Thermodynamic modelling show that Cr contents above 10.5% strongly accelerates Z-phase precipitation and the breakdown in creep strength. This explains the lack of success for all attempts to develop martensitic creep resistant steels with high Cr content for oxidation protection.

Careful control of the Z-phase precipitation process has led to the design of experimental 12%Cr martensitic steels strengthened by Z-phase. Such steels may again enable the

combination of high creep strength and oxidation resistance in the same alloy. This opens a new pathway for further alloy development of heat resistant martensitic steels.
If successful, the 12%Cr martensitic steels strengthened by Z-phase could enable the construction of low cost USC power plants with steam parameters approaching 325bar/650°C entirely based on steels.

Acknowledgments
Thanks to Dario Venditti (CSM) for help with sample preparations.

References
[1] Masuyama F: Proc. Conf. *Materials for Advanced Power Engineering 2006*, (ed. J. Lecompte-Beckers et. al.), Part I, p175, Forschungszentrum Jülich (2006)
[2] Kern TU, Staubli M, Mayer KH, Donth B, Zeiler G, DiGianfrancesco A: Proc. Conf. *Materials for Advanced Power Engineering 2006*, (ed. J. Lecompte-Beckers et. al.), Part II, p843, Forschungszentrum Jülich (2006)
[3] Scheffknecht G, Chen Q, Weissinger G: Proc. Conf: *Parsons 2003, Engineering Issues in Turbine Machinery, Power Plant and Renewables* (ed. A. Strang et. al.), 112-128, IOM3, London (2003)
[4] Hald J: *VGB PowerTech*, **12**, p74 (2004)
[5] Hald J: Proc. 1st Int. Conf. *Super-high strength steels*, AIM and CSM, Paper 3.4, Rome (2005)
[6] Abe F: *Sci Tech Adv Mater*, **9**, p1 (2008)
[7] Fujita T: *Metall Trans A*, **12**, p1071 (1981)
[8] Hald J, Korcakova L: *ISIJ Int*, **43**, p420 (2003)
[9] Abe F: *Int J Mat Res*, **99**, p387 (2008)
[10] Hättestrand M, Andrén HO: *Mater Sci Eng A*, **270**, p33 (1999)
[11] Schnabel E, Schwaab P, Weber H: *Stahl Eisen*, **107**, p691 (1987)
[12] Strang A, Vodarek V: Materi. *Sci Tech*, **12**, p552 (1996)
[13] Danielsen HK, Hald J: *Energy Mater*, **1**, p49 (2006)
[14] Danielsen HK, Hald J: *Calphad*, **31**, p505 (2007)
[15] Sawada K, Kushima H, Kimura K, Tabuchi M: *ISIJ Int*, **47**, p733 (2007)
[16] Cipolla L, Danielsen HK, Venditti D, Di Nunzio PE, Hald J, Somers MAJ: *Acta Mater*, **58**, p669 (2010)
[17] Danielsen HK: *Z-phase in 9-12%Cr steels*, PhD Thesis, Technical University of Denmark (2007)
[18] Danielsen HK, Hald J: *Mater Sci Eng A*, **505**, p169 (2009)
[19] Abe F: *Proc. Int. Conf. on New Developments on Metallurgy and Applications of High Strength Steels*, Buenos Aires (2008)
[20] *NIMS Creep Data Sheet*, **51**, National Institute for Materials Science, Japan (2006)
[21] Naoi H, Oghami M, Hasegawa Y, Fujita T: Proc. Conf: *Materials for Advanced Power Engineering 1994* (ed. D. Coutsoradis et. al.), Part I, p425, Kluwer, Dordrecht (1994)
[22] Fujita T: *Personal Communication*, (2008)
[23] Sawada K, Taneike M, Kimura K, Abe F: *ISIJ Int*, **44**, p1243 (2004)

9th Liege Conference : Materials for Advanced Power Engineering 2010
edited by J. Lecomte-Beckers, Q. Contrepois, T. Beck and B. Kuhn.

CALCULATION OF PHASE BOUNDARY ENERGIES AND APPLICATION IN MULTICOMPONENT STEELS

B. Sonderegger[1,2], M. Hacksteiner[1], F. Mendez-Martin[1], I. Holzer[1], E. Kozeschnik[2,3]

[1]Institute for Materials Science and Welding, Graz University of Technology, Kopernikusgasse 24, A-8010 Graz, Austria
[2]Materials Center Leoben Forschung GmbH, Roseggerstraße 12, A-8700 Leoben, Austria
[3]Christian Doppler Laboratory "Early Stages of Precipitation", Institute of Materials Science and Technology, Vienna University of Technology, Favoritenstraße 9-11, A-1040 Vienna, Austria

Abstract

In precipitation kinetics simulation, phase boundary energies play a key role for predicting nucleation, growth and coarsening rates of precipitates. Recently, a new concept has been proposed for the calculation of phase boundary energies, being applicable to multicomponent systems and requiring only minimal computational effort. This approach, based on the nearest-neighbor broken-bond concept, is particularly useful for the application in complex multi-component- multi-phase alloys, where calculation time can become costly. In this work, predictions and limitations of the concept are discussed, and the application is displayed on the example of the precipitate evolution during heat treatment of a complex 9-12% Cr steel.

Keywords: Interfacial energy, nucleation, precipitation kinetics, 9-12% Cr steel

1. Introduction

Precipitation of a fine dispersion of second phases can tremendously influence the mechanical and technological properties of a material. In many alloying systems such as nickel-base, aluminum or steel, high strength or good creep resistance is achieved by controlled precipitation during specific heat treatments. Also, in 9-12% Cr steels, a high number of evenly distributed particles are essential to achieve good creep resistance. This microstructural feature has to be achieved after the heat treatment and it must be conserved during long-term creep exposure, within a typical reference time of 10^5 hours or 12 years. A sufficiently accurate prediction of the precipitation process can significantly accelerate alloy design and development. This is, however, not a simple task.

Since materials are becoming increasingly complex, a computational model for precipitation kinetics has to be capable of handling this complexity while at the same time remaining numerically inexpensive enough to ensure practicable calculation times. A model applicable to 9-12% Cr steels should be able to cover compositions with up to 10 components, carbides, nitrides and intermetallic phases, and include arbitrary time-temperature histories for heat treatments and thermal ageing. Over the years a number of models have been proposed to handle different aspects of precipitation processes, each of them with specific limits and capabilities. The next section briefly outlines a number of models dedicated to the task.

Back in the 1930ies, the fundaments of Classical Nucleation Theory (CNT) have been laid by Volmer and Weber [1] and Becker and Döring [2]. In essence, CNT is a continuums-mechanical approach, and it describes the probability of formation of a supercritical nucleus. The latter is a nucleus, which is stable against decomposition due to its overcritical size. CNT is founded in Boltzmann statistics of microscopic fluctuations and the concept of a critical nucleation energy or nucleation barrier. The energy of the nucleus is formulated in terms of a bulk energy contribution from, originally, only the chemical driving force and a surface energy contribution from the precipitate / matrix interfacial region.

Once the nucleus is overcritical, it is usually assumed to grow by diffusional transport of atoms to the existing precipitate. This process is commonly described by deterministic models. The earliest analytical solutions for diffusion controlled precipitate growth date back to the late 1940ies, when, for instance, Zener has published his famous parabolic growth rate model for advancing planar interfaces [3]. However, it should be realized that most of the early growth laws for precipitate growth, and still many of the more recent ones, consider a single rate-controlling diffusing species. These models can therefore not be considered as a rigorous approach for multi-component systems.

The first general multi-component treatment of the diffusion-controlled movement of interfaces goes back to the early 1980ies, where corresponding models have been developed and implemented in the commercial software DICTRA [4]. Though its numerical difficulties in higher-order multi-component systems, this software represents a standard tool for a rigorous solution of the multi-component moving-interface problem in solid materials.
Several years later, in 2004, an alternative approach to modeling growth kinetics of precipitates in multi-component alloys has been developed within an ambitious and multi-disciplinary research project [5, 6]. Based on a mean-field description of the precipitation problem, evolution equations have been formulated for the growth of spherical precipitates. The theoretical foundation of this approach is laid in the thermodynamic extremal principle of Onsager [7]. After implementing this novel approach into the software MatCalc [8], it became possible to simulate the evolution and interaction of several different types of precipitates throughout entire industrial thermal and thermo-mechanical heat treatment cycles [9].

Despite this recent success, a major drawback of all simulation approaches for precipitation kinetics is the dependence on numerous simulation input parameters. Some of these are the thermodynamic properties of the alloy system, volume misfit and coherency effects, interfacial energies or the number of potential nucleation sites. Among these parameters, the interfacial energy is certainly the most critical. On one hand, it is not accessible to direct experimental measurement. On the other hand, it is the most widely used quantity for fitting precipitation simulation and experiment.

In order to overcome these difficulties with unknown or uncertain input quantities, intensive work has been carried out recently to develop theoretical approaches that allow for determination of the value of the interfacial energy from independent thermodynamic information, i.e. the thermodynamic databases that are also basis for calculation of chemical potentials or chemical driving forces for phase transformation. Subsequently, the present status of this work is reviewed.

2. Precipitation Kinetics

The first stage in precipitate life is determined by the stochastic process of nucleation. Nucleation occurs by the formation of supercritical clusters of atoms driven by random thermal, structural and compositional fluctuations. These are caused by random, vacancy-assisted atomic migration processes. Following the treatment of CNT in multi-component environments, as summarized in Ref. [10], the steady state nucleation rate J_{SS} can be expressed as

$$J_{SS} = Z\beta^* N_C \exp\left(-\frac{\Delta G^*}{kT}\right). \quad (1)$$

where Z is the Zeldovich factor, β^* is the atomic attachment rate, N_C is the number of potential nucleation sites, ΔG^* is the critical nucleation energy, k is the Boltzmann constant and T is temperature. A major ingredient of classical nucleation theory is the interfacial energy γ, which appears in the critical nucleation energy ΔG^* in the exponent of the nucleation rate (1), with

$$\Delta G^* = \frac{16\pi}{3}\frac{\gamma^3}{F^2}. \quad (2)$$

F is the total driving force. Since F and Z can be calculated from independent thermodynamic databases, N_C is given by the materials microstructure and β^* is determined mainly by the atomic mobilities, the most important unknown parameter left in Eq. (1) is the interfacial energy γ. As can be seen in Eq. 1 and 2, J_{SS} is extremely sensitive to changes in the value of the interfacial energy, where small deviations in γ can cause tremendous changes in the nucleation rate. It is thus of utmost significance that the interfacial energy is predicted as precise as possible in the nucleation regime.

Once a precipitate has reached super-critical size, the evolution of its radius and composition can be calculated according to the following rule: Consider an n-component system with an arbitrary number m of spherical precipitates of different size, composition and phase type. The total Gibbs Free energy G of this system can be written as

$$G = \sum_{i=1}^{n} N_{0i}\mu_{0i} + \sum_{k=1}^{m} \frac{4\pi\rho_k^3}{3}\left(\lambda_k + \sum_{i=1}^{n} c_{ki}\mu_{ki}\right) + \sum_{k=1}^{m} 4\pi\rho_k^2\gamma_k \quad (3)$$

with N_{0i} being the number of moles of component i in the matrix phase, μ_{0i} the corresponding chemical potentials, λ_k the elastic strain energy due to volumetric misfit, ρ_k the radius of precipitate k, c_{ki} the concentration of component i in the precipitate k, μ_{ki} the corresponding chemical potential and γ_k the interfacial energy. The processes dissipating energy can then be identified: the migration of interfaces, diffusion in the matrix and diffusion in the precipitates. The evolution equations obtained by application of the thermodynamic extremal principle are described in refs. [5, 6].

3. Interfacial Energies

3.1. Planar, sharp interfaces

The basis of the following treatment have been laid by in the late 1930ies by Becker [11] with introduction of the nearest-neighbor broken-bonds concept. Becker suggested a thought experiment involving two homogeneous blocks of material of phases α and β. The total energy (enthalpy) of this system can be calculated by adding up all bond energies between neighboring atoms. Then, half of the blocks α and β are interchanged (see Fig. 1), and the energy of the system is calculated again. The difference between the initial and the final system is identified as the interfacial energy.

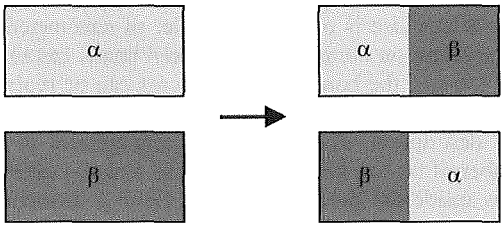

Fig. 1: Thought experiment for determination of interfacial energies.

In the original treatment of Becker, the interaction energies between neighboring atoms act as input parameter. Later, Turnbull [12] linked the interaction energies to the enthalpy of solution ΔE_{sol}. His expression for γ reads

$$\gamma = \frac{n_S \cdot z_S}{N \cdot z_L} \cdot \Delta E_{sol} \quad . \quad (4)$$

where n_S is the number of atoms per unit interface area, z_S the number of bonds per interface atom across the interface and z_L is the coordination number of one atom.

This treatment of the interfacial has originally been derived for 2-component systems. Very recently [13] it has been shown that Eq. (4) is also valid for multi-component systems without any change in the formalism. Nevertheless, modifications have been introduced for z_S and z_L. The original treatment has only considered interactions between first nearest neighbors. In order to incorporate longer distance interactions, these quantities have to be replaced by $z_{S,eff}$ and $z_{L,eff}$. In Ref. [13], the structural factor $z_{S,eff}/z_{L,eff}$ is derived for up to 100 nearest neighbor shells in fcc and bcc systems. The results show a small anisotropy of 18% stemming from the orientation of the interface, with a mean value of the structural factor of 0.3280 for bcc and 0.3291 for fcc systems. Therefore, the mean interfacial energy can be considered as only weakly dependent on the actual crystallographic system. After determining values for the

structural factor, the major unknown for determining the interfacial energy γ is the enthalpy of solution ΔE_{sol}. However, this quantity can straightforwardly be calculated from the thermodynamic data used to evaluate chemical potentials and chemical driving forces. In this sense, one can assume that it is possible to evaluate all input quantities for the precipitation simulation from these relations. However, when using the numerical values for γ in precipitation simulations, it turns out that the value obtained from the classical model for sharp and planar interfaces is systematically too large and experimentally observed nucleation rates are underestimated. In numerical studies in the NbC system [14] and other systems, reasonable agreement between experiment and simulation could be obtained with values of 70% - 80% of the value from Eq. 4. This is further investigated in the following section.

3.2. Non-planar interfaces and impact of high temperatures

The generally observed trend for overestimation of the value of the interfacial energy needs a closer look at geometric effects on the precipitate / matrix interface. In precipitation processes in metals, the critical nucleus size is often in the order of nanometers and less. This means that the influence of curvature on the number of broken bonds has to be taken into account, too. For mathematical reasons, the bonds between atoms can be replaced by bonds between volume elements. Thus treatment of the bond energies is transferred from a discrete, atomistic view to a continuums description. The geometrical arrangement in a spherical precipitate leads to a smaller number of broken bonds compared to a planar interface. This is due to the finite number of atoms inside the precipitate phase. From a theoretical point of view, this means that the interfacial energy of spherical bodies is always smaller than the one of planar phase boundaries. Recently, this case has been treated quantitatively [15], yielding a correction function for the interfacial energy which is only dependent on the precipitate radius:

$$\alpha(\rho) = 1 - \frac{6}{11}\cdot\frac{r_1}{\rho} + 0.08921\cdot\frac{r_1^2}{\rho^2} + 0.045\cdot\ln\left(\frac{10}{3}\frac{\rho}{r_1}\right)\cdot\frac{r_1^2}{\rho^2} \qquad (5)$$

α is the correction factor and r_1 is the nearest neighbor distance. If compared to surface tensions traditionally derived via the Kelvin relation by Tolman [16], Kashchiev [17], Rasmussen [18] and Vogelsberger [19], our results lie well in between the upper and lower estimates of the values given by these authors (Fig. 2).
When applied to the analysis of NbC precipitation in microalloyed steels [14], excellent agreement between prediction and experimental values could be found: For the nucleation stage, the model predicts values of about 75% of the interfacial energy for planar interfaces, which has been identified in previous analyses [14] as the value necessary for prediction of NbC precipitation kinetics.

Finally it should be mentioned that another effect can also contribute significantly to the effective interfacial energy: Entropic effects [20] in the vicinity of the phase boundary cause a dilution of the otherwise sharp precipitate / matrix interface. This effect introduces a finite thickness of the interfacial area. These entropic effects lead to a reduction of the interfacial energy, thereby enhancing the effect of geometry and further decreasing γ. The quantitative analysis of this effect is currently ongoing.

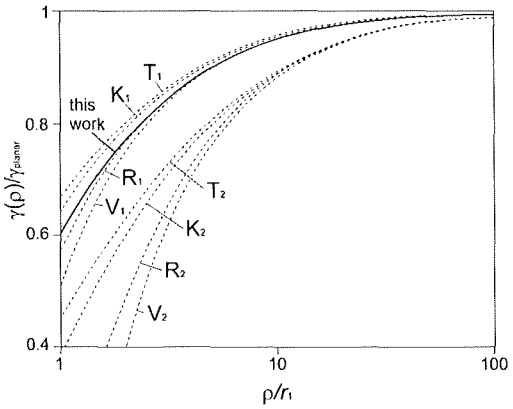

Fig. 2: Upper and lower estimates for surface tensions by Tolman (T), Kashchiev (K), Rasmussen (R) and Vogelsberger (V), compared to the actual results for interfacial energies.

4. Experiment and Numerical Simulation

In the following the numerical model for interfacial energy determination outlined in section 3 is applied on the heat treatment of a 9% Cr steel. The chemical composition of the investigated alloy is shown in Table 2.

Table 2: Chemical composition of the investigated 9% Cr steel in wt.%.

C	Si	Mn	Cr	Ni	W	V	Nb	Co	N	B
0.074	0.29	0.44	9.26	0.06	2.84	0.21	0.056	2.95	0.013	0.012

The samples were solution treated at 1150°C for 1h and tempered at 770°C for up to 50h (Fig. 3, top image). Since no pronounced precipitation has been observed until the end of austenitizing, detailed microscopical investigations were carried out only in the heat treated material (see experimental data in Figure 3).
The microstructural investigations were carried out at the Institute for Materials Science and Welding and the Institute for Electron Microscopy of Graz University of Technology. The investigations were carried out with a Philips CM20/Scanning TEM (STEM) equipped with a Gatan imaging filter (GIF). 35 micrographs were investigated in which a total number of 671 precipitates were analyzed. The quantitative evaluation of particle size, number densities and volume fractions were carried out by recently proposed stereological methods [21]. Due to the high number of particles and the careful analysis, the experimental data give a solid reference to the outcomes of the simulated precipitation kinetics.

The numerical simulations were carried out with the software MatCalc (version 5.31.1033) and the corresponding thermodynamic and diffusion databases mc_steel.tdb [22] and mc_sample_fe.ddb [23]. In the present simulations, the precipitate phases $M_{23}C_6$, M_7C_3, VN and NbC are taken into account in accordance with experimental findings in this steel. The

energy of the precipitate/matrix interface γ is calculated from the generalized broken-bond (GBB) approach outlined in section 3 and the precipitate size effect is taken into account by the radius-dependent correction factor stated in eq. (5).

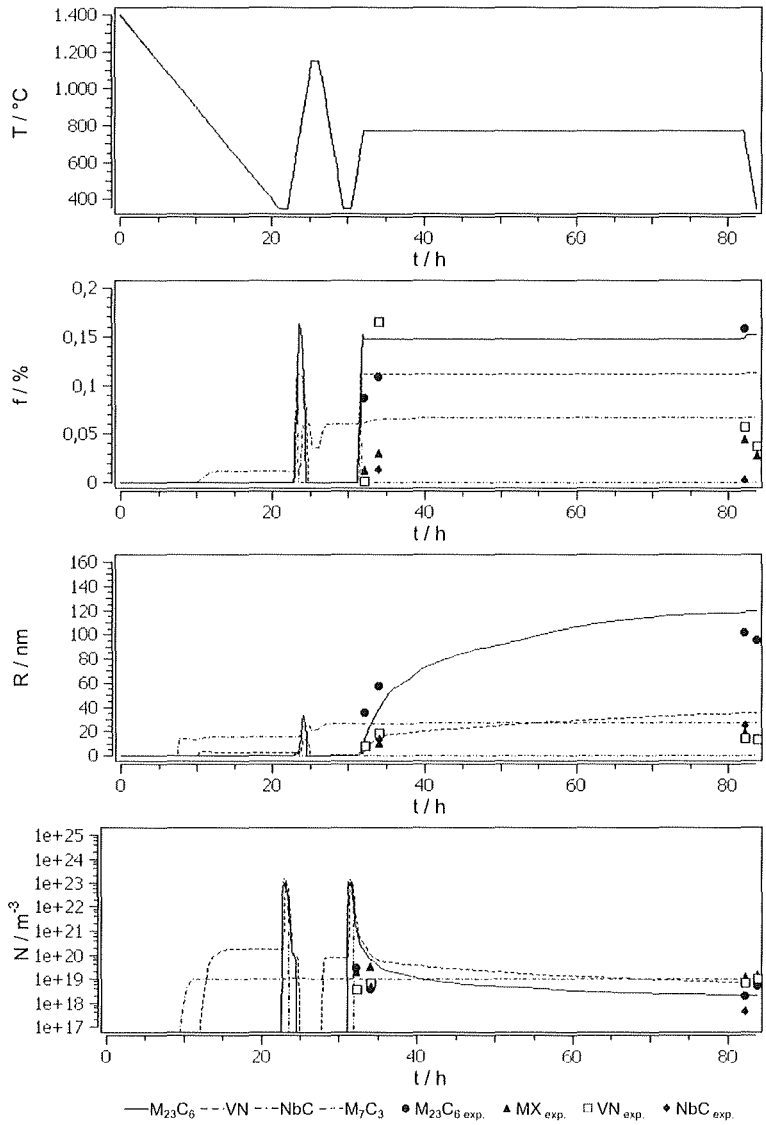

Fig. 3: Result of the numerical simulation of the evolution of phase fraction f, particle radius R and number density N during austenitization and tempering compared with experimental findings. For a better representation of the results the phase fraction of the $M_{23}C_6$ precipitates is multiplied by a value of 1/10.

The numerical simulation starts with a cooling segment in an austenitic matrix starting at 1400°C. Cooling down slowly to the calculated MS temperature of 350°C is carried out within 21h. At this temperature, the austenite matrix (thermodynamic phase FCC_A1) is assumed to fully transform into martensite. It is further assumed that no precipitation reactions occur below this temperature due to sluggish diffusion. In the next simulation step, the temperature is increased again. The simulation is then performed in a ferritic matrix (thermodynamic phase BCC_A2) up to the calculated A1 temperature of 855°C. Then, the matrix is switched to austenite again. Austenitization is simulated at 1150°C for 1h with subsequent cooling to MS at 350°C. The following tempering at 770 °C takes place in ferrite again.

Figure 3 shows the results of the numerical simulation for the evolution of the phase fraction f, particle radius R and number density N of the considered phases, respectively. For a better representation of the results in Fig. 3, the phase fraction of the $M_{23}C_6$ precipitates is multiplied by a value of 1/10. Considering the particle radii, the simulation agrees well with the experimental data. Since growth and coarsening rates of precipitates are moderately dependent on interfacial energies, this result confirms a good estimation of this parameter. The prediction of number densities and nucleation rates agrees satisfactorily with the experiments. The extreme sensitivity of the nucleation rate demands a very precise estimation of γ; otherwise number densities would be incorrect by several orders of magnitude. The agreement again testifies the accuracy of the predicted interfacial energy calculations. It should be emphasized that the results were obtained without using any fit parameter.

5. Summary and Conclusion

In this work, the energy of matrix/precipitate interfaces has been calculated by a novel concept based on the nearest-neighbor broken-bond approach. The model has been implemented in the MatCalc framework for the calculation of precipitation kinetics in multi-component multi-phase materials. The new concept considers planar interfaces of large precipitates as well as the interfacial curvature of small particles and nuclei.

This new approach for planar and non-planar interfaces has then been applied in a numerical simulation of the precipitation kinetics of a 9% Cr steel. The results were compared to experimentally obtained precipitate parameters. The agreement in particle radii was found to be encouraging, phase fractions and number densities were predicted with satisfying accuracy.

Because growth, coarsening and particularly nucleation rates are sensitive to the interfacial energy, the agreement indicates the accurate estimation of γ. Since γ generally had to be fitted to experimental findings in the past, this result is significantly improving the predictive capabilities of kinetic calculations.

6. Acknowledgment

Financial support by the Austrian Federal Government (in particular from the Bundesministerium für Verkehr, Innovation und Technologie and the Bundesministerium für Wirtschaft und Arbeit) and the Styrian Provincial Government, represented by Österreichische Forschungsförderungsgesellschaft mbH, within the research activities of the K2 Competence Centre on „Integrated Research in Materials, Processing and Product Engineering", operated by the Materials Center Leoben Forschung GmbH in the framework of the Austrian COMET Competence Centre Programme, is gratefully acknowledged.

References

[1] M. Volmer and A. Weber: "Keimbildung in übersättigten Gebilden", Z. Phys. Chem. Vol. 119 (1926), p. 277-282
[2] R. Becker and W. Döring: "Kinetische Behandlung der Keimbildung in übersättigten Dämpfen", Ann. Phys.-Berlin Vol. 24 (1935), p. 719-752
[3] C. Zener: "Theory of growth of spherical precipitates from solid solution", J. Appl. Phys. Vol. 20 (1949), p. 950-953.
[4] J. O. Andersson, T. Helander, L. Höglund, P. Shi and B. Sundman: "THERMO-CALC & DICTRA, Computational tools for materials science", CALPHAD Vol. 26 (2002), p. 273-312
[5] J. Svoboda, F. D. Fischer, P. Fratzl and E. Kozeschnik: „Modelling of kinetics in multi-component multi-phase systems with spherical precipitates: I: Theory", Mat. Sci. Eng. A Vol. 385 (2004), p. 166-174
[6] E. Kozeschnik, J. Svoboda, P. Fratzl and F. D. Fischer: „ Modelling of kinetics in multi-component multi-phase systems with spherical precipitates: II: Numerical solution and application", Mat. Sci. Eng. A Vol. 385 (2004), p. 157-165
[7] L. Onsager: "Reciprocal relations in irreversible processes. II", Phys. Rev. Vol. 38 (1931), p. 405; Vol. 38 (1931), p. 2265-2279
[8] E. Kozeschnik and B. Buchmayr: "MatCalc-a simulation tool for multicomponent thermodynamics, diffusion and phase transformation kinetics", in: Mathematical Modelling of Weld Phenomena 5, Institute of Materials, London, book 738 (2001), p. 349-361
[9] E. Kozeschnik, B. Sonderegger, I. Holzer, J. Rajek and H. Cerjak: „Computer simulation of the precipitate evolution during industrial heat treatment of complex alloys", Mat. Sci. Forum Vols. 539-543 (2007), p. 2431-2434
[10] E. Kozeschnik, J. Svoboda and F. D. Fischer: „On the role of chemical composition in multi-component nucleation", in: Proc. Int. Conference Solid-Solid Phase Transformations in Inorganic Materials, Phoenix, AZ, USA, 29.5.-3.6.2005 (2005), p. 301-310
[11] R. Becker: „Die Keimbildung bei der Ausscheidung in metallischen Mischkristallen", Ann. Phys. Vol. 32 (1938), p. 128-140
[12] D. Turnbull: "Role of structural impurities in phase transformations", Impur. and Imperf., American Society of Metals, Metals Park, OH (1955), p. 121-144
[13] B. Sonderegger and E. Kozeschnik: „Generalized nearest-neighbor broken-bond analysis of randomly oriented coherent interfaces in multicomponent fcc and bcc structures", Metal. Mater. Trans. A Vol. 40 (2009), p. 499-510

[14] M. Pudar, E. Kozeschnik, A. Sorman and E. Parteder: „Numerical analysis of the Nb(C,N) precipitation kinetics in microalloyed steels“, Steel Res. Vol. 79 (2008), p. 660-664
[15] B. Sonderegger and E. Kozeschnik: „Size dependence of the interfacial energy in the generalized nearest-neighbor broken-bond approach“, Scripta Mater. Vol. 60 (2009), p. 635-638
[16] R. C. Tolman: "The effect of droplet size on surface tension", J. Chem. Phys. Vol. 17 (1949), p. 333-337
[17] D. Kashchiev, in: Nucleation: Basic Theory with Applications (Butterworth-Heinemann, Burlington MA 2000), p. 79
[18] D. H. Rasmussen: „Thermodynamics and nucleation phenomena – a set of experimental observations“, J. Cryst. Growth Vol. 56 (1982), p. 45-55
[19] W. Vogelsberger and G. Marx: "Curvature dependence of surface-tension of small drops", Z. Phys. Chem. Vol. 257 (1976), p. 580-586
[20] Y.W. Lee and H.I. Aaronson: "Anisotropy of coherent interphase boundary energy", Acta Metall. Vol. 28 (1980) 539-548.
[21] B. Sonderegger: "Modifications of stereological evaluation methods for precipitate parameters using transmission microscopy", Ultramicr. Vol. 106 (2006), p. 941-950
[22] Thermodynamic Database 'mc_steel', version 1.50, Institute of Materials Science and Technology, Vienna University of Technology.
[23] Mobility Database 'mc_sample_fe, version 1.03, Institute of Materials Science and Technology, Vienna University of Technology.

9th Liege Conference : Materials for Advanced Power Engineering 2010
edited by J. Lecomte-Beckers, Q. Contrepois, T. Beck and B. Kuhn.

BOUNDARY AND SUB-BOINDARY HARDENING IN TEMPERED MARTENSITIC 9CR STEEL DURING LONG-TERM CREEP AT 650 °C

Fujio Abe
National Institute for Materials Science, 1-2-1 Sengen, Tsukuba 305-0047, Japan

Abstract

The boundary and sub-boundary hardening is shown to be the most important strengthening mechanism in creep of the 9% Cr steel base metal and welded joints. The addition of boron reduces the coarsening rate of $M_{23}C_6$ carbides along boundaries near prior austenite grain boundaries during creep, enhancing the boundary and sub-boundary hardening. This improves long-term creep strength of base metal. The enhancement of boundary and sub-boundary hardening is significantly reduced in fine-grained region of Ac_3 HAZ simulated specimens of conventional steel P92. In NIMS 9Cr boron steel welded joints, the grain size and distribution of carbonitrides are substantially the same between the HAZ and base metal, where fine carbonitrides are distributed along the lath and block boundaries as well as along prior austenite grain boundaries. This is essential for the suppression of Type IV fracture in NIMS 9% Cr boron steel welded joints. Newly alloy-designed 9Cr steel with 160 ppm boron and 85 ppm nitrogen exhibits much higher creep rupture strength of base metal than P92 and also no Type IV fracture in welded joints at 650 °C.

Keywords: 9Cr steel, boron, creep strength, boundary, sub-boundary, Type IV fracture

1. Introduction

The basic methods by which creep-resistant steels can be strengthened are solute hardening, precipitation or dispersion hardening, dislocation hardening, and boundary or sub-boundary hardening. 9 to 12Cr steels subjected to normalizing and tempering heat treatment are usually observed to have a tempered martensitic microstructure, which consists of laths and blocks with a high density of dislocations and fine carbonitrides dispersed along the lath and block boundaries and in the matrix, Fig.1 [1]. The laths and blocks can be regarded as elongated subgrains. Precipitation or dispersion strengthening is inversely proportional to the mean inter-particle distance, while sub-boundary hardening is inversely proportional to the mean width of sub-boundaries.

In welded joints, we have revealed that the multi-axial stress condition in fine-grained heat-affected-zone (HAZ) with lower creep strength, resulting from mechanical constrain effect by the surrounding weld metal and base metal with higher creep strength, is essential for the formation of creep voids and brittle Type IV fracture in HAZ [2]. We have also revealed that the addition of about 100 ppm boron to 9Cr steel effectively suppresses the formation of fine-grained HAZ and hence suppresses the Type IV fracture, which causes no degradation in creep rupture strength of welded joints compared with the base metal [3]. At present, however, detailed mechanisms responsible for the lower creep strength of fine-grained HAZ than the base metal are not fully understood.

The purpose of the present research is to make clear the strengthening mechanisms for 9Cr steel base metal and welded joints during creep at 650°C and also to make clear the controlling factors for the creep rates in primary or transient creep region, by taking the distributions of $M_{23}C_6$ carbides and MX carbonitrides in the matrix and along boundaries into account.

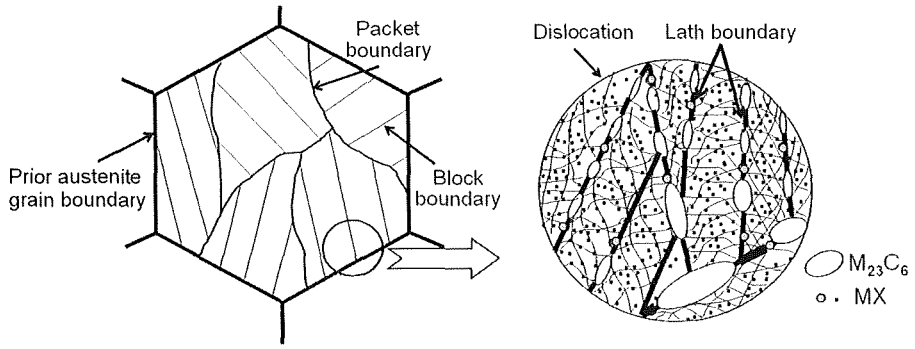

Strengthening mechanisms :

1. Solute hardening
2. Precipitation or dispersion hardening
   $\sigma_{or} = 0.8MGb / \lambda_p$ λ_p : mean inter-particle distance
3. Dislocation hardening
   $\sigma_\rho = 0.5\ MGb\ (\rho_f)^{1/2}$
4. Sub-boundary hardening
   $\sigma_{sg} = 10Gb / \lambda_{sg}$ λ_{sg} : short width of elongated subgrain

Fig.1 Schematic illustration of tempered martensitic microstructure of 9 to 12% Cr steels and strengthening mechanisms

2. Experimental procedure

The steels examined were 9Cr-3W-3Co-0.2V-0.05Nb (mass %) steel with different carbon and boron concentrations [4-6]. Creep testing was carried out at 650 °C up to about 7 x 10^4 h under constant load condition, using specimens of 10 mm in gauge diameter and 50 mm in gauge length.

The simulated-HAZ specimens of 9Cr-3W-3Co-0.2V-0.05Nb steel with 90 and 130 ppm boron and P92 were kept for 180 s at various peak temperatures between 850 and 1100°C and then cooled in air [7, 8]. Finally, the post weld heat treatment (PWHT) was carried out for each specimen including the base metal at 740°C for 4.7 h.

3. Results and discussion

3.1 Boundary and sub-boundary hardening in base metal

3.1.1 Effect of dispersion of fine MX carbonitrides along boundaries

Fig.2 shows the creep rate versus time curves of the 9Cr-3W-3Co-0.2V-0.05Nb steel with different carbon concentrations at 650 °C and 140 MPa [4]. The creep and creep rate curves consist of the primary or transient creep region, where the creep rate decreases with time, and of the tertiary or acceleration creep region, where the creep rate increases with time after reaching a minimum creep rate. There is substantially no steady-state region, where the creep rate is constant. The observed longer creep life by reducing carbon concentration results from a decrease in minimum creep rate. For example, the minimum creep rate of the 0.002C steel

is about 1/10 of that of the 0.078C steel, while the time to rupture of the 0.002C steel is about 10 times of the 0.078C steel. The decrease in minimum creep rate by reducing carbon concentration results from both the decrease in initial creep rate in the transient region and the retardation of onset of acceleration creep.

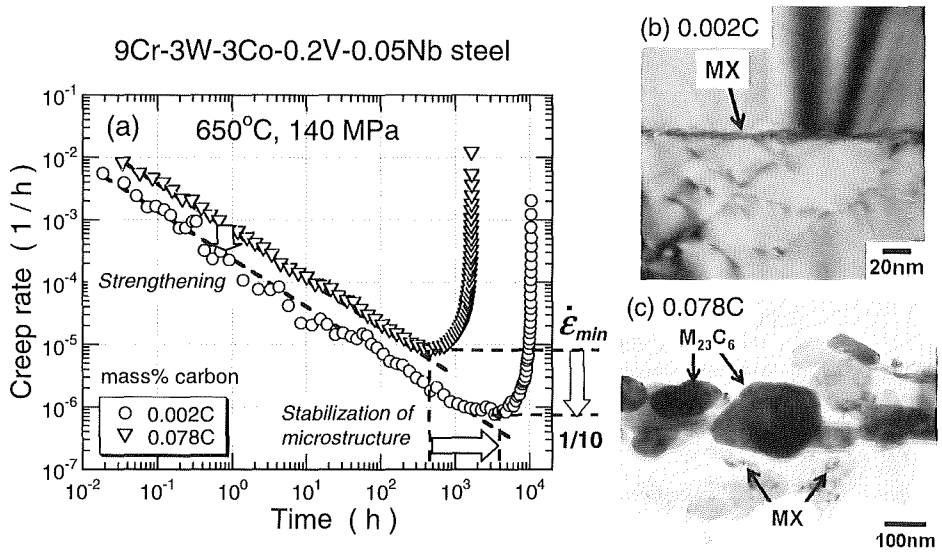

Fig.2 Creep rate versus time curves of the steel with 0.002 and 0.078% at 650°C and 140MPa and microstructure near prior austenite grain boundaries

The present author has revealed for tempered martensitic 9Cr steel that the transient creep is basically a consequence of the movement and annihilation of a high density of dislocations produced by martensitic transformation during cooling after normalizing and that the acceleration creep is a consequence of gradual loss of creep strength due to the microstructure evolution [9]. He has also suggested that the onset of migration of lath or block boundaries, causing the coarsening of the lath or block by dynamic recovery and the gradual loss of creep strength, is closely correlated with the onset of acceleration creep.

The decrease in initial creep rate in the transient region by reducing carbon concentration is much smaller than the decrease in minimum creep rate, Fig.2. The creep rate of the 0.002C steel at 1 h is 1/3 of that of the 0.078C steel, which is much smaller than the decrease in minimum creep rate of one order of magnitude. The retardation of onset of acceleration creep further decreases the creep rate in the transient region, resulting in a significant decrease in minimum creep rate. According to the creep deformation mechanism proposed by the present author, the retardation of onset of acceleration creep correlates with the retardation of onset of migration of lath or block boundaries, suggesting the stabilization of microstructure.

The precipitates were identified as MX carbonitrides consisting of mainly vanadium nitrides and of small amount of niobium carbides in the 0.002C steel after tempering, while those were mainly $M_{23}C_6$ carbides and small amount of MX carbonitrides in the 0.078C steel. The

MX carbonitrides having a size of less than 10 nm are distributed along boundaries as well as in the matrix within lath in the 0.002C steel after tempering. It should be noted that the density of precipitates along boundaries is much higher in the 0.002C steel than in the 0.078C steel but that the density of MX carbonitrides in the matrix is lower in the 0.002C steel than in the 0.078C steel; 5.5 x 10^{13} and 7.5 x 10^{13}/m^2 for the 0.002C and 0.078C steels, respectively. This is owing to a fact that the total amount of MX carbonitrides is the same between the two steels but that the amount of MX carbonitrides along boundaries is much larger in the 0.002C steel than in the 0.078C steel, because of no $M_{23}C_6$ carbide in the 0.002C steel. On the other hand, the dislocation density in the matrix is roughly the same between the two steels after tempering; 4 x 10^{14} and 3 x 10^{14}/m^2 for the 0.002C and 0.078C steels, respectively. During creep at 650 °C, the decrease in dislocation density and the increase in lath width with time during creep are less significant in the 0.002C steel than in the 0.078C steel.

Schematic illustrations of dislocation movement during transient creep are shown in Fig.3. The lower creep rates in the transient region and the lower density of MX carbonitrides in the matrix of 0.002C steel than those of 0.078C steel suggest that the movement and annihilation process of excess dislocations in the transient region is controlled by not only the movement of dislocations in the matrix but also the annihilation of dislocations at lath and block boundaries, because the lower density of MX in the matrix results in higher movement of dislocations in the matrix causing higher creep rates. At lath and block boundaries, climbing and re-distribution of dislocations in the boundary wall, causing an increase in dislocation spacing and a decrease in subgrain misorientation, are prohibited when dense distributions of MX and $M_{23}C_6$ in the boundary wall act as obstacles. This decreases the efficiency of dislocation absorption or annihilation at boundaries, which decreases the creep rate. The higher density of precipitates along boundaries in the 0.002C steel than in the 0.078C steel suggests lower efficiency of dislocation absorption or annihilation at boundaries in the 0.002C steel. The observed lower creep rates of the 0.002C steel in the transient region than the0.078C steel suggest that the lower efficiency of dislocation absorption or annihilation at boundaries for the 0.002C steel is a main factor for determining the creep rate rather than the movement of dislocations in the matrix strengthened by fine MX.

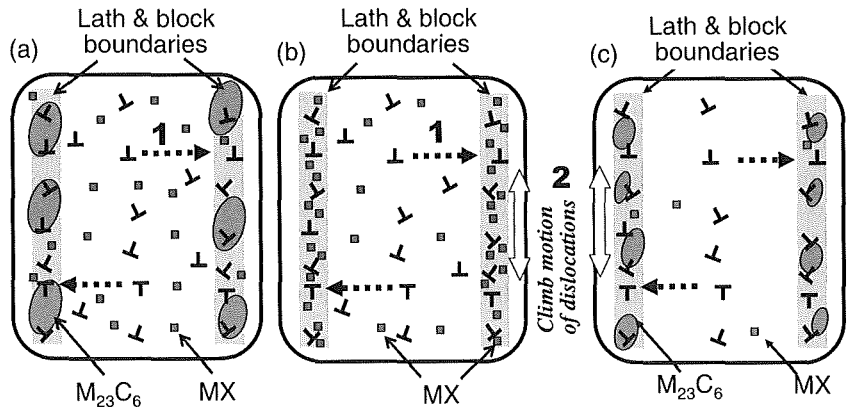

Fig.3 Schematics of dislocation movement in lath and block microstructure of 9Cr steel. (a) 0.078%C-0.05%N, (b) 0.002%C-0.05%N and (c) 0.078%C-0N-(0-0.014)%boron

The present results suggest that the subgrain boundaries act as obstacles and also absorption sites for dislocation movement in the matrix during creep. The lower efficiency of dislocation absorption at boundaries corresponds to obstacle nature of sub-boundaries similar as the hard sub-boundary regions in the composite model proposed by Blum and co-workers [10], while the higher efficiency of dislocation absorption at boundaries characterizes sink nature.

3.1.2 Effect of stabilization of $M_{23}C_6$ carbides along boundaries by boron

The creep rupture data and creep rate versus time curves of the 9Cr-3W-3Co-0.2V-0.05Nb steel with different boron concentrations at 650°C and 80 MPa are shown in Fig.4 [5, 6]. The addition of boron does not decrease the creep rate in the transient region, which is quite different from the effect of a dispersion of nano-size MX carbonitrides described in the previous section, but it significantly decreases the minimum creep rate by retarding the onset of acceleration creep. As nitrogen was not added in the steel, only $M_{23}C_6$ carbides are distributed along lath, block and packet boundaries and also along prior austenite grain boundaries (PAGBs) after tempering but there are substantially no MX carbonitride in the matrix.

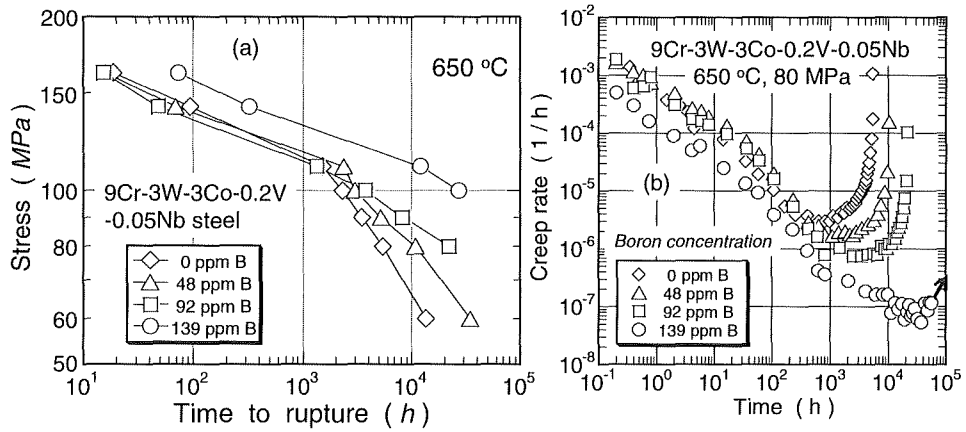

Fig.4 Effect of boron addition on creep rupture strength of 9Cr-3W-3Co-0.2V-0.05Nb-0.08C steel at 650°C

The fine distribution of $M_{23}C_6$ carbides in the vicinity of PAGBs is still maintained in the steel with 139 ppm boron during exposure at elevated temperature as shown in Fig.5. In the base steel without boron, the fine distribution of $M_{23}C_6$ carbides is observed after tempering but extensive coarsening takes place in the vicinity of PAGBs during exposure at elevated temperature. This indicates that the addition of boron reduces the rate of Ostwald ripening of $M_{23}C_6$ carbides in the vicinity of PAGBs during exposure at elevated temperature.

Based on the movement and annihilation process of excess dislocations in the transient region shown in Fig.3, the velocity of free dislocations in the matrix and the efficiency of dislocation absorption at boundaries are considered to be the same for the steels containing different boron concentrations in the initial stage of creep, because the distribution of $M_{23}C_6$ carbides along boundaries is substantially the same for the investigated steels as described above. This

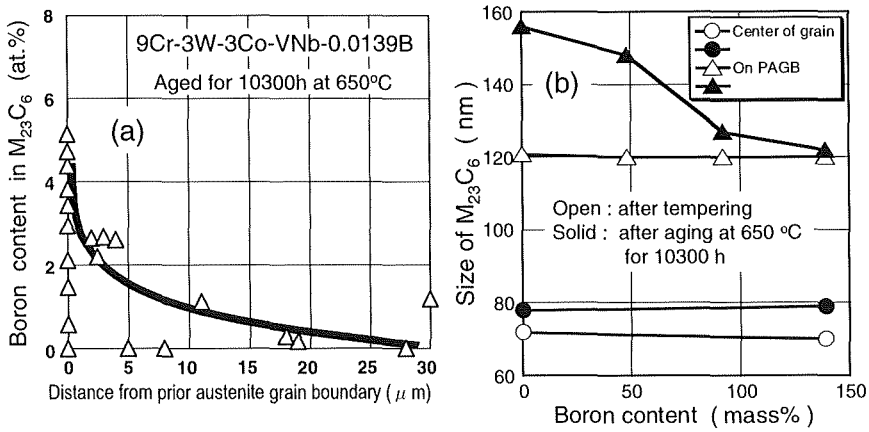

Fig.5 (a) Enrichment of boron in $M_{23}C_6$ carbides near PAGBs in 9Cr-3W-3Co-0.2V-0.05Nb-0.08C steel with 139ppm boron and (b) size of $M23C_6$ particles

causes the same creep rates for the steels with boron in the transient region. However, the fact that boron reduces the coarsening rate of $M_{23}C_6$ carbides near PAGBs suggests that the onset of acceleration creep is retarded, which results in lower minimum creep rate and longer time to rupture. The subboundary hardening enhanced by $M_{23}C_6$ carbides along lath and block boundaries is a main strengthening mechanism in the present steel and the addition of boron enhances the subboundary hardening in the vicinity of PAGBs at long times through stabilization of fine distributions of $M_{23}C_6$ carbides.

Excess addition of nitrogen to the 9Cr-3W-3Co-0.2V-0.05Nb steel, for example, higher than 100 ppm nitrogen at 140 ppm boron promotes the formation of large boron nitrides during normalizing heat treatment, which significantly reduces soluble boron available for enhancing the boundary and subboundary hardening in the vicinity of PAGBs [11].

3.2 Effect of grain size and boundary hardening on creep strength of simulated-HAZ specimens of Gr.92 and 9Cr-boron steel

Figure 6 shows the time to rupture of the simulated-HAZ specimens of Gr.92, Gr.92N, Gr.92NN and the 9Cr-90 ppm B steel at 650 °C and 110 MPa, as a function of peak temperature in the thermal cycle [7, 8]. Gr.92 was subjected to normalizing and tempering heat treatment, while Gr.92N was subjected to only normalizing but no tempering before the thermal cycle, Table 1. Gr.92NN was subjected to sub-zero treatment at liquid nitrogen temperature after normalizing but no tempering before the thermal cycle. In Fig.6, Gr.92 exhibits a significant decrease in time to rupture after the thermal cycle to a peak temperature near A_{C3}. On the other hand, the time to rupture of Gr.92N, Gr.92NN and the 9Cr-boron steel is substantially the same as that of their base metals, independent of peak temperature.

Gr.92 is observed to be the fine-grained microstructure having a prior austenite grain size of smaller than 10 μm after the A_{C3} heating, while Gr.92N exhibits the coarse-grained microstructure even after the A_{C3} heating, substantially the same prior austenite grain size as

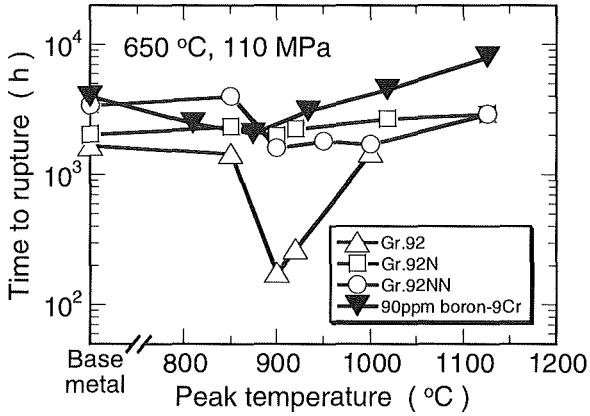

Fig.6 Time to rupture of simulated-HAZ specimens at 650 °C and 110 MPa

Table 1 Heat treatment conditions for simulated HAZ specimens of Gr.92, Gr.92N and Gr.92NN and microstructure after PWHT

	Heat treatment	Grain size after PWHT	GB $M_{23}C_6$ after PWHT
Gr.92	Normalizing → Tempering → Thermal cycle	fine grain	poor
Gr.92N	Normalizing → Thermal cycle	coarse grain	enough
Gr.92NN	Normalizing → Sub-zero → Thermal cycle	fine grain	enough

Normalizing : 1070 °C x 0.5 h, Tempering : 780 °C x 1 h, Sub-zero : immersed in liquid nitrogen, Thermal cycle : Peak Temp. 950 °C → PWHT (740 °C x 4.7 h)

the base metal. The average prior austenite grain size of the base metals of Gr.92 and Gr.92N is roughly 50 μm. Gr.92NN exhibits the fine-grained microstructure after the A_{C3} heating, similar as Gr.92. Fig.7 shows the scanning electron micrographs in the vicinity of PAGBs of Gr.92, Gr.92N and Gr.92NN after the thermal cycle to a peak temperature of 950 °C, just above the A_{C3} temperature [7, 8]. The row of large precipitates, from the upper left to the lower right direction, identified as $M_{23}C_6$ carbides in Gr.92 suggests a trace of PAGBs in the original microstructure before the thermal cycle. It should be noted that very few precipitates are formed along PAGBs in the fine-grained microstructure of Gr.92 and that the lath-block subgrain structure is not clearly seen inside the grain. The present results suggest that the boundary and subboundary hardening is significantly reduced in the fine-grained microstructure of Gr.92 after the thermal cycle to a peak temperature of A_{C3}, compared with that in the base metal. In the base metal, PAGBs and lath and block boundaries are covered by enough $M_{23}C_6$ carbides, because of preferential precipitation of $M_{23}C_6$ carbides along PAGBs and also along lath and block boundaries during tempering.

In the Gr.92N, not only PAGBs but also lath and block boundaries are covered by enough $M_{23}C_6$ carbides after the thermal cycle to a peak temperature of 950 °C, similar as the base

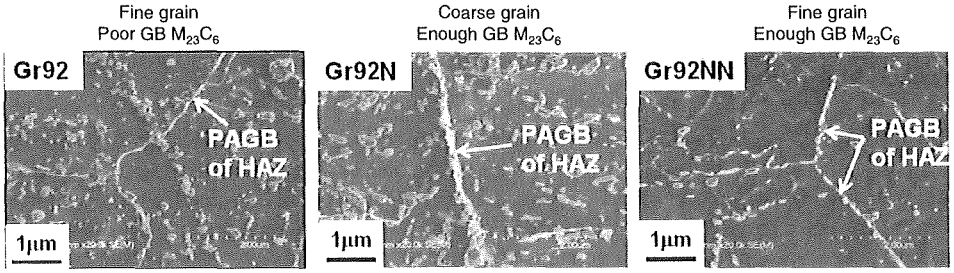

Fig.7 SEM micrographs of Gr.92, Gr.92N and Gr.92NN after thermal cycle to a peak temperature of 950 °C

metal. The reconstitution of original prior austenite grain structure is observed in Gr.92N after the thermal cycle to a peak temperature of 950 °C. This is due to an austenite memory effect. Shirane et al. [8] observed 3 vol% retained austenite in Gr.92N after normalizing. The austenite memory effect has been shown to be a consequence of the growth of thin films of retained austenite in starting bainitic or martensitic microstructure during subsequent heating [12, 13]. The growing thin films of retained austenite coalesce on impingement, which leads to the reconstitution of original prior austenite grain structure and reproduces the same crystal orientation and the same grain size as the original austenite. It should be noted in Fig.6 that the time to rupture of Gr.92NN is substantially the same as that of base metal, in spite of fine grains. The present results on Gr.92, Gr.92N and Gr.92NN suggest that whether the microstructure is fine grains or coarse grains is not important for the time to rupture but that the reduction of boundary and sub-boundary hardening in the fine-grained microstructure of Gr.92 after the thermal cycle to a peak temperature of 950 °C, near

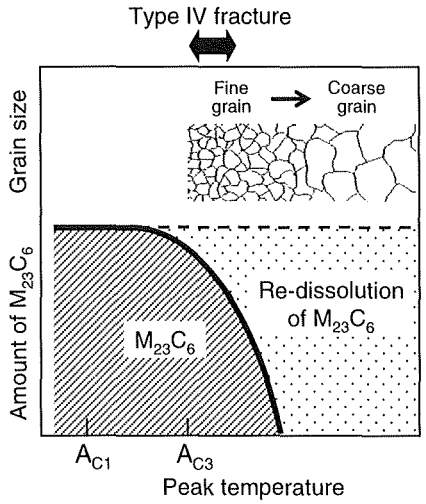

Fig.8 Schematics of grain size and amount of $M_{23}C_6$ carbides in Gr.92 during simulation heating

the A_{C3} temperature, is the most important for the significant decrease in time to rupture. The temperature range for appearrance of the fine-grained microstructure is overlapped with that of the very few precipitates along grain boundaries as shown in Fig.8, where the Type IV fracture takes place [14].

The 9Cr-boron steel consists of coarse grains of roughly 200 to 300 μm after A_{C3} heating, which is substantially the same as that of base metal, and of fine grains of 10 to 50 μm along grain boundaries of coarse grains as shown in Fig.9(b). The fine-grained region develops toward the inner parts of the coarse grains with increasing peak temperature. After heating to a peak temperature of 1100 °C, a greater part of the 9Cr-boron steel consists of fine grains of 10 to 50 μm as shown in Fig.9(c), while the time to rupture of the 9Cr-boron steel is substantially the same as that of the base metal as shown in Fig.6, in spite of fine grains. This indicates that the grain refinement due to simulated heating does not cause a significant decrease in time to rupture.

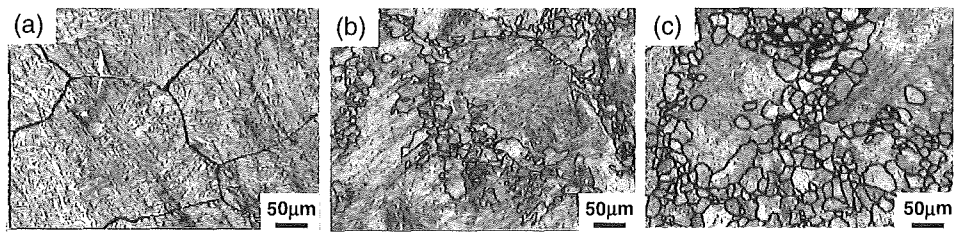

Fig.9 Optical micrographs of 9Cr-130 ppm B steel.
(a) Base metal, (b) after thermal cycle to peak temperatures of 950 °C, and (c) 1100 °C

The PAGBs and lath and block boundaries in the 9Cr-boron steel after the thermal cycle to a peak temperature of A_{C3} were observed to be covered by enough $M_{23}C_6$ carbides, which was substantially the same as those in the base metal.

Newly alloy-designed 9Cr steel with 160 ppm boron and 85 ppm nitrogen exhibits much higher creep rupture strength of base metal than P92 and also no Type IV fracture in welded joints at 650 °C [15].

4. Summary

(1) The creep rates in the transient region of the present 9Cr steel base metal is controlled by not only the movement of dislocations in the matrix but also the annihilation of dislocations at lath and block boundaries. The sub-boundary hardening is the most important strengthening mechanism in creep of the present steel and is enhanced by fine dispersions of precipitates along boundaries.
(2) The simulated-HAZ specimens of Gr.92 exhibit the fine-grained microstructure after the A_{C3} thermal cycle, where very few precipitates are formed along PAGBs and the lath-block subgrain structure is not clearly seen inside the grain. The degradation in creep life in Gr.92 after the A_{C3} thermal cycle is not caused by the grain refinement but that the reduction of boundary and sub-boundary hardening is the most important.

(3) The simulated-HAZ specimens of 9Cr-boron steels exhibit substantially the same microstructure as the base metal even after the A_{C3} thermal cycle and hence substantially the same time to rupture as the base metal, independent of peak temperature,
(4) For the improvement of long term creep strength of high-Cr ferritic steels, alloy design for enhancing fine dispersions of coarsening-resistant precipitates along various boundaries in the vicinity of PAGBs is essential for both the base metal and welded joints.

References

[1] F. Abe, 'Precipitate design for creep strengthening of 9%Cr tempered martensitic steel for USC power plant', Science and Technology of Advanced Materials, 9 (2008) 013002.
[2] F. Abe and M. Tabuchi, 'Microstructural and Creep Strength of Welds in Advanced Ferritic Power Plant Steels', Materials Science and Technology of Welding and Joining, 9 (2004) 22-30.
[3] M. Tabuchi, M. Kondo, T. Watanabe, H. Hongo, F. Yin and F. Abe, 'Improvement of Type IV Cracking Resistance of 9Cr Heat Resisting Steel Weldment by Boron Addition', Acta Metallurgica Sinica, 17 (2004) 331-337.
[4] M. Taneike, F. Abe and K. Sawada, 'Creep-strengthening of steel at high temperatures using nano-sized carbonitride dispersions', Nature, 424 (2003) 294-296.
[5] T. Horiuchi, M. Igarashi, F. Abe, 'Improved Utilization of Added B in 9Cr Heat-Resistant Steels Containing W', ISIJ International, 42 (2002) S67-S71.
[6] F. Abe, 'Effect of boron on creep deformation behavior and microstructure evolution in 9%Cr steel at 650°C', International J. Materials Research (formerly: Zeitschrift fuer Metallkunde), 99 (2008) 387-394.
[7] S. Tsukamoto, M. Tabuch, T. Shirane and F. Abe, 'Suppression of Type IV fracture in high-Cr heat resistant steel welded joint', Proc. of 60th Annual Assembly and International Conference of IIW, July 1, USA, (2007) CD-ROM.
[8] T. Shirane, S. Tsukamoto, K. Tsuzaki, Y. Adachi, T. Hanamura, M. Shimizu and F. Abe, 'Ferrite to austenite reverse transformation process in B containing 9%Cr heat resistant steel HAZ', Sci. Technol. of Welding and Joining, 14 (2009) 698-707.
[9] F. Abe, S. Nakazawa, H. Araki and T. Noda, 'The Role of Microstructural Instability of a Low Radioactivation Martensitic 9Cr-2W Steel', Metall. Trans., 23A (1992) 469-477.
[10] M. Meier and W. Blum, 'Modeling high temperature creep of academic and industrial materials using the composite model', Mat. Sci. Eng., A164 (1993) 290-294.
[11] H. Semba and F. Abe, 'Alloy design and creep strength of advanced 9%Cr USC boiler steels containing high concentration of boron', Energy Materials, 1 (2006) 238-244.
[12] S.T. Kimmins and D.J. Gooch, 'Austenite memory effect in 1Cr-1Mo-0.75V(Ti,B) steel', Metal Science 17 (1983) 519-32.
[13] R.K. Shiue, K.C. Lan and C. Chen, 'Toughness and austenite stability of modified 9Cr-1Mo welds after Tempering', Mater Sci Eng A287 (2000) 10-16.
[14] F. Abe, M. Tabuchi and S. Tsukamoto, 'Metallurgy of Type IV Fracture in Advanced Ferritic Power Plant Steels', Proc. Intern. Conf. on High-Temperature Defect Assessment (HIDA-5), 23-25 June, 2010,University of Surrey, Guildford, UK
[15] F. Abe, M. Tabuchi, H. Semba, M. Igarashi, M. Yoshizawa, N. Komai, A. Fujita, 'Feasibility of MARBN Steel for Application to Thick Section Boiler Component in USC Power Plant at 650 °C', Proc. Intern. Conf. on Advances in Materials Technology for Fossil Power Plants, October 3-5, 2007 (2007) CD-ROM.

9th Liege Conference : Materials for Advanced Power Engineering 2010
edited by J. Lecomte-Beckers, Q. Contrepois, T. Beck and B. Kuhn.

HIGH-TEMPERATURE PERFORMANCE OF A NEW NICKEL-BASED FILLER METAL FOR POWER GENERATION APPLICATIONS

J. Shingledecker[1], K. Coleman[1], J. Siefert[2], J. Tanzosh[2], W. Newell[3]

1. Electric Power Research Institute, Charlotte, NC USA
2. Babcock & Wilcox Research Center, Barberton, OH USA
3. Euroweld, Mooresville, NC USA

Abstract

A new nickel-based weld filler metal, EPRI P87, has been developed as a superior alternative to ERNiCr-3 for use in dissimilar metal welds (DMW) between ferritic and austenitic materials. EPRI P87 has a low coefficient of thermal expansion more closely matching alloys such as Grade 91 and 92 than other available filler metals. Additionally, the size of the carbon denuded region adjacent to the weld in the heat-affected-zone is minimized/eliminated by proper control of weld metal composition. In this work, the high-temperature mechanical behavior of DMWs utilizing EPRI P87 (GTAW and GMAW processes) was characterized through tensile and long-term creep-rupture testing. Microstructure analysis was also conducted on tested specimens to evaluate the HAZ regions and failure modes. Performance of the weld metal and welded joints is discussed and compared with ERNiCr-3 and typical 9%CrMoV filler metals.

Keywords: Dissimilar metal welds, DMW, nickel-based filler metal, Inco 82, ERNiCr-3, EPRI P87

1. Introduction

The metallurgical sources of failure in dissimilar metal welds (DMW) between ferritic and austenitic materials, specifically in high-temperature boiler tubing, include: the mismatch in coefficient of thermal expansion (CTE) between the weldment constituents, and the formation of a 'weak' carbon-free interface or carbon-denuded zone between the stainless or nickel-based filler metal and the ferritic steel during high-temperature exposure [1,2]. ERNiCr-3 (N06082), also referred to as Inco 82 or Inconel 82, is generally the preferred filler metal for DMWs today, but it is not immune to these metallurgical phenomenon. EPRI P87 filler metal was developed to address these issues as an alternative to ERNiCr-3 [3, 4]. Figure 1 compares the mean CTE as a function of temperature for EPRI P87 and ERNiCr-3 to various alloys. Over a broad range of temperatures, EPRI P87 has a CTE below that of ERNiCr-3 and closer to Grade 91 making it an attractive choice for DMWs involving creep strength enhanced ferritic (CSEF) steels. Figure 2 shows the carbon denuded region of a CrMo steel weldment interface after normalization for 2 hours at 1038°C (1900°F). The samples welded with nickel-base and stainless filler metals both show large carbide free regions, greater than 100μm in thickness, whereas the interface of the weldment produced with EPRI P87 is clean with no indication of carbon migration.

All research, development, and initial stress-rupture testing on EPRI P87 was conducted using shielded-metal-arc welding (SMAW). A heat of EPRI P87 wire has been produced and subjected to extensive weldability trials as reported in [5]. In this work, the behavior of EPRI P87 filler metal and DMWs from gas-tungsten arc and gas-metal arc welding (GTAW and GMAW) are presented and discussed.

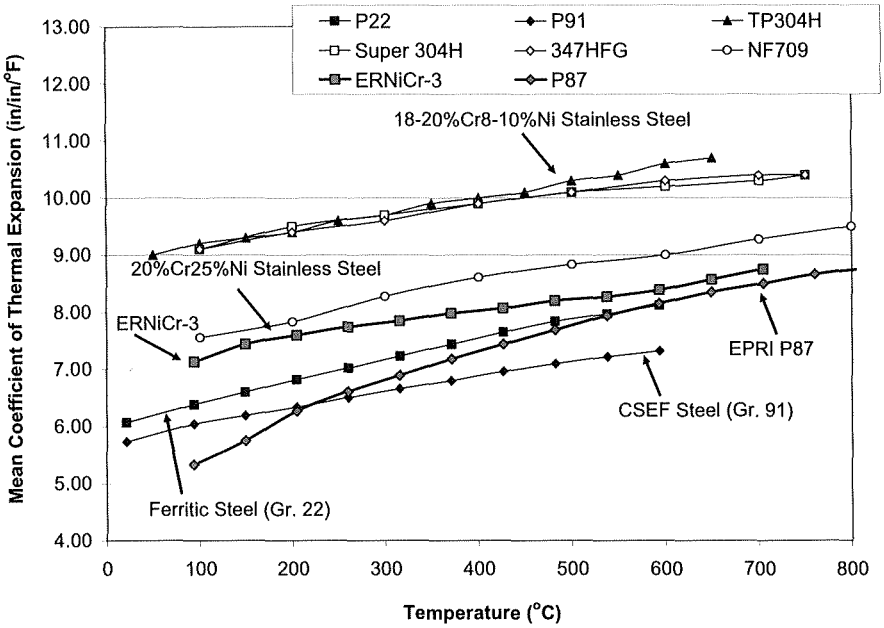

Figure 1. Mean Coefficient of Thermal Expansion for EPRI P87 compared to other filler metals and alloys, data from ref. [5]

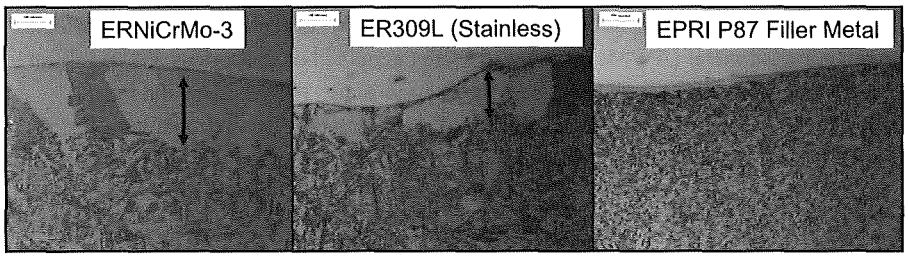

Figure 2. Micrographs of the weldment interface of a CrMo steel using a nickel-based (ERNiCrMo-3), stainless (ER309L) and EPRI P87 filler metals after normalizing and tempering (scale bar = 100μm) showing EPRI P87 has virtually no carbon-denuded zone [3]

2. Experimental Procedure

Two weldment configurations were used to produce the material for this study. The composition of the EPRI P87 filler metal and the 347H and Grade 91 plates are provided in Table 1. Chemical composition of the EPRI P87 wire conformed to the SMAW consumable target composition. 50.4 mm (2") thick plates of 347H and grade 91, approximately 915mm (36") in length, were welded with approximately 6.4mm (0.25") of cold-wire GTAW in the root, and the remaining ~44.5 mm (1.75") of the joint was filled using hot-wire GTAW. 25.4mm (1") plates of 347H and grade 91, approximately 361mm (15") in length, were welded using the GMAW process. Figures 3 and 4 show the joint designs for these thick section welds. Following welding, all plates were given a post-weld heat-treatment (PWHT) at 746°C (1375°F) for 4 hours.

Table 1. Chemical Composition (wt%) for Filler Metal and Alloys Used in this Study (EPRI P87 composition target based on ref. [6])

	C	Mn	Si	S	P	Cr	Ni	Mo	Nb	Fe	Al	N	Ti	Co	Cu	V	Zr	Nb+Ta
EPRI P87 Wire	0.11	1.45	0.14	0.001	<0.005	8.92	44.8	2.05	1.26	40.98	0.16	0.003	0.11	0.002	0.008	0.002	<0.001	
SMAW ERPI P87 Target	0.1	1.5	0.3	0.008	0.008	9	bal	2	1	38								
347H	0.054	1.3	0.51	0.0003	0.029	17.41	9.88	0.51	0.73	Bal.		0.065		0.25	0.4			0.74
Gr. 91	0.12	0.415	0.24	0.0026	0.011	8.901	0.222	0.856	0.07	Bal.	0.02	0.045	0.003		0.031	0.194	0.006	

After PWHT, the weldments were subjected to destructive metallurgical analysis. No microfissuring or cracking was observed in any weldment except in the cold-wire GTAW root passes. These cracks were found in the weld metal and did not extend into the hot-wire GTAW passes. Extensive testing did not indicate impaired weld metal ductility or a high residual condition, thus the source of cracking appears to be joint geometry/backing bar material related [5]. All mechanical test specimens for the GTAW welds were taken from the hot-wire region to avoid any cracks which could influence test results.

Creep testing and elevated temperature tensile testing was performed in accordance with ASTM E21 and E139. Cross-weld (CW) tensile and stress-rupture tests were conducted on specimens , with a gauge length (GL) = 57.2mm (2.25") and a diameter (dia.) of 12.8mm (0.505"), from both the GTAW and GMAW plates with the weld centerline in the middle of the gauge. All weld metal (AWM) tensile tests were conducted on specimens, GL=31.8mm (1.25") and diameter of 6.4mm (0.25"), from the GTAW plate. AWM creep and creep-rupture tests were also conducted on specimens, GL=35.6mm (1.4") and dia=8.9mm (0.35"), from both the GTAW and GMAW plates.

3. Results

Cross-weld (CW) tensile tests were conducted on both weld joints from 427 to 760°C (800 to 1400°F) and on all-weld-metal (AWM) GTAW specimens from 482 to 704°C (900 to 1300°F). The weld metal elevated temperature yield strength was ~300 MPa (43.5ksi) in this temperature range. The tensile strength for the weld metal and weldments is plotted in figure

5 and compared to other EPRI P87 GTAW room temperature tensile tests which failed in the EPRI P87 filler metal [5,7]. The current tensile strength for 347H plate and grade 91 in Figure 5 is taken from the ASME Boiler and Pressure Vessel Code, Section II Table U [8]; these data are based on a trend curve tied to the minimum room temperature strength of the alloy. Failure location is also indicated in the figure.

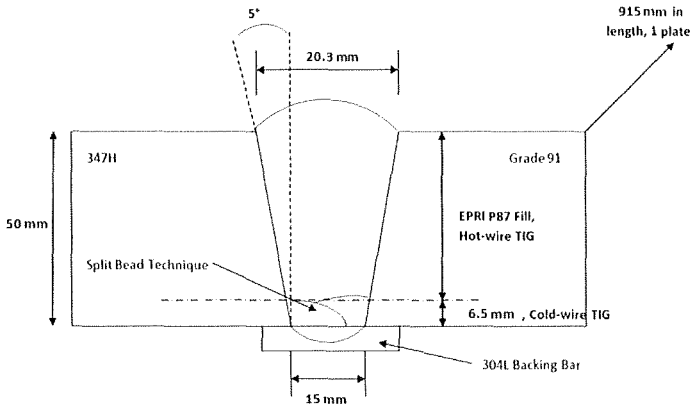

Figure 3. Joint Design for the 50mm (2") Thick GTAW Joint

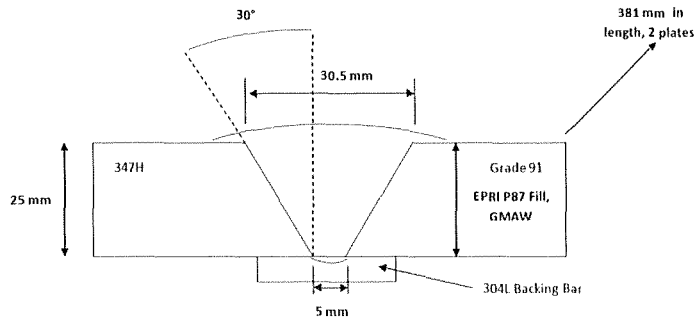

Figure 4. Joint Design for the 25mm (1") Thick GMAW Joint

Examination of the plot shows the room temperature EPRI P87 filler metal tensile strength is above the room temperature minimum strength of Grade 91 (586MPa – 85ksi), and above ~538°C (1000°F) EPRI P87 exceeds the strength of Grade 91. The cross-weld failure locations confirm this trend with tests at 427-482°C (800-900°F) failing in the 347H. At temperatures above 900°F, all CW failures were in the grade 91.

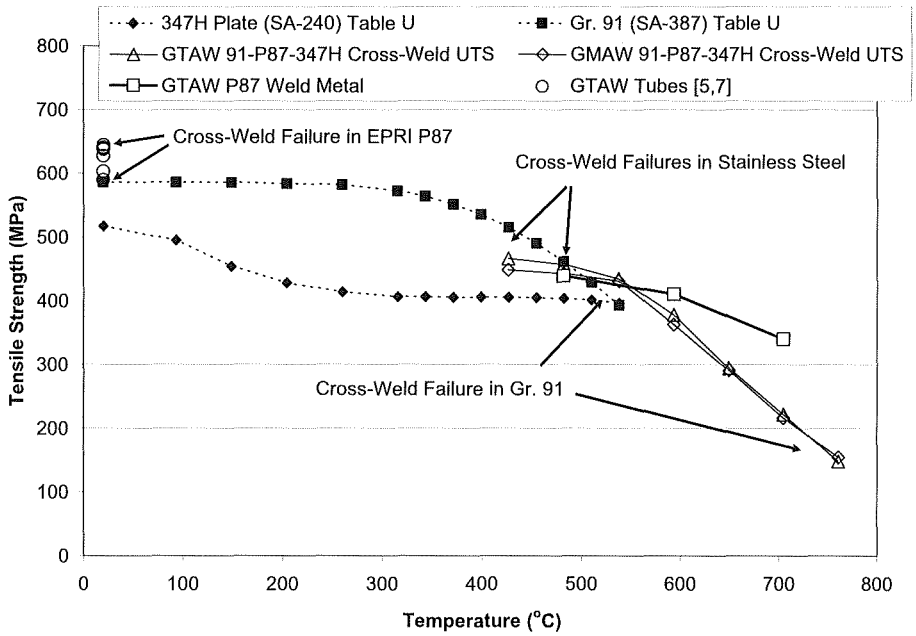

Figure 5. Tensile Strength as a function of temperature for GTAW and GMAW CW, GTAW AWM, and GTAW CW Tubes (from ref [5,7]) compared to Gr. 91 and 347H minimum specified properties [8]

The test conditions and results for CW testing of the GTAW and GMAW joints is provided in Table 2. These data are plotted as a function of Larson-Miller-Parameter (LMP) with a constant of C=28 against the Grade 91 average and minimum (-20% on stress) rupture behavior in Figure 6. Cross-weld rupture data from subcritically PWHT'ed grade 91 joints made with EPRI P87 by SMAW process [3] and using nominally matching 9%CrMoV filler metals [9] are plotted for comparison. High-stress ruptures were within the grade 91 scatterband and failures were in the base metal (BM). In the lowest stress tests, failures were at or below the minimum scatterband for Grade 91 and failures were confirmed, by optical microscopy, to be in the heat-affected-zone (HAZ) of the weldment which is consistent with subcritically heat-treated Gr. 91 and other CSEF steels.

Table 2. Cross-Weld Stress-Rupture Test Conditions and Results

Conditions		Time to Rupture (hrs)		Failure Location	
Temperature C (F)	Stress MPa (ksi)	GTAW	GMAW	GTAW	GMAW
593 (1100)	172.4 (25.0)	326.1	208.2	91 BM	91 BM
593 (1100)	151.7 (22.0)	507.0	674.0	91 BM	91 BM
625 (1157)	100 (14.5)	899.2	551.5	91 HAZ	91 HAZ

Creep-rupture tests were conducted on AWM samples from 593 to 760°C (1100 to 1400°F) between 77 and 172 MPa (11.2 to 25ksi). Test times ranged from a few hours to a few thousand hours with some tests continuing beyond 8800 hours. Minimum creep rate ($\dot{\varepsilon}_{min}$) data were evaluated using a simple Norton-Bailey approach with a standard Arrhenius equation [10] where n is the stress exponent, A is a constant, Q is the activation energy, R is the gas constant, and T is the temperature in Kelvin as follows:

$$\dot{\varepsilon}_{min} = A\sigma^{n}e^{-Q/RT} \qquad \text{Equation 1}$$

where A=1.1398668x10^4/hr, n=8, and Q=452.84916 KJ/mol. The test data for both the GTAW and GMAW weld metal and the Equation 1 fits are shown in Figure 7. No significant differences were observed between GTAW and GMAW test results.

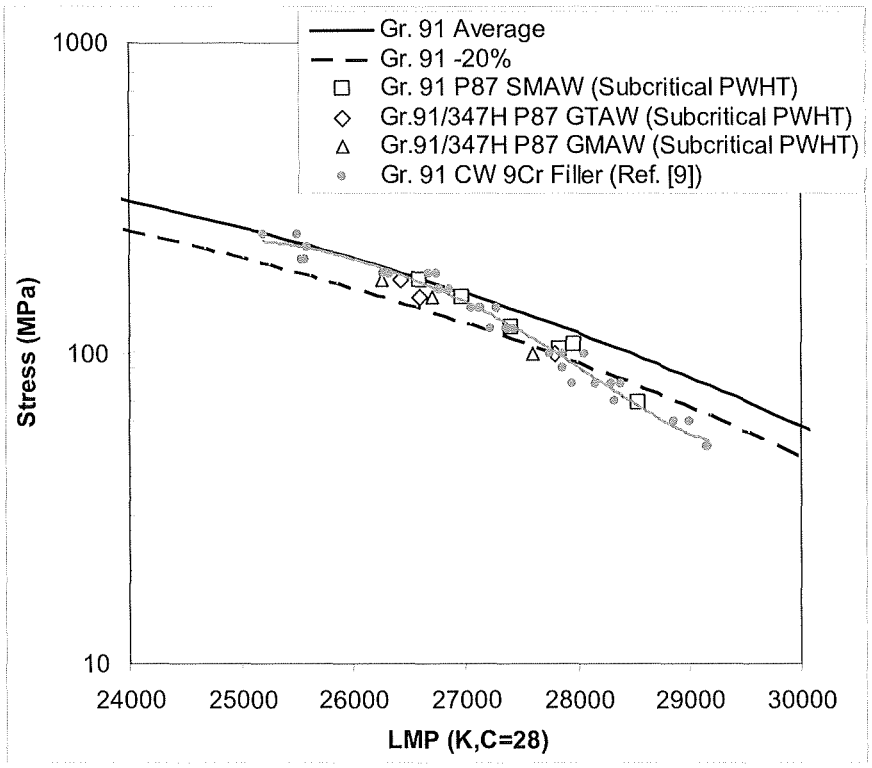

Figure 6. Stress-rupture results for the GTAW and GMAW CWs plotted using the Larson-Miller Parameter (LMP, constant C=28) and compared to EPRI P87 CW SMAW process [3] and typical grade 91 cross-weld data using matching 9%CrMoV filler metals from [9]

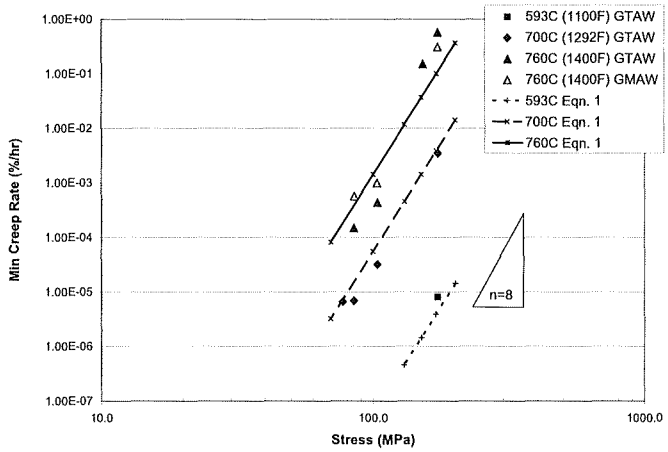

Figure 7. Minimum creep-rate as a function of temperature and stress for EPRI P87

Rupture results for the EPRI P87 GTAW and GMAW weld metal are shown in Figures 8, 9, and 10. Figure 8 shows the rupture ductility for the completed tests. In all cases, rupture elongation exceeded 20% and reduction of area exceeded 50%. Figure 9 is a comparison of the GTAW and GMAW weld metal and reported behavior of ERNiCr-3 [11] at 760°C (1400°F). For tests greater than 100 hours, both the GTAW and GMAW EPRI P87 exceed the average reported time to rupture for ERNiCr-3 and the slope of the time to rupture curve fit to the EPRI P87 GTAW suggests this will persist at longer test times. GMAW rupture strength appears to be slightly less than the GTAW. Figure 10 is a LMP plot of all the rupture data compared to the EPRI SMAW development work [3] and the reported 100, 1000, and 10,000 hour data for ERNiCr-3. A dashed line is fit through the ERNiCr-3 data for comparison. At high stresses, all of the EPRI P87 product forms appear equivalent in terms of rupture strength. The lower-stress GTAW data appears to exceed the strength of the ERNiCr-3.

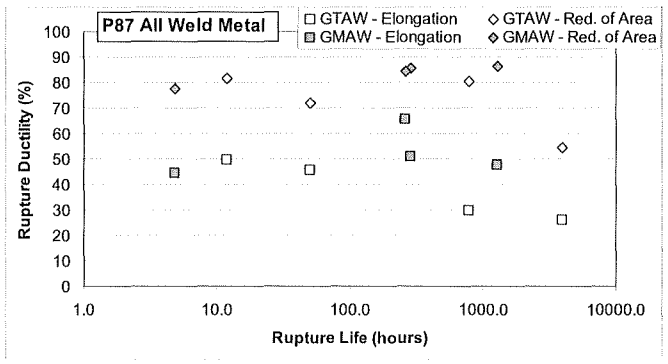

Figure 8.Post-test creep-rupture ductility for EPRI P87 GTAW and GMAW weld metal

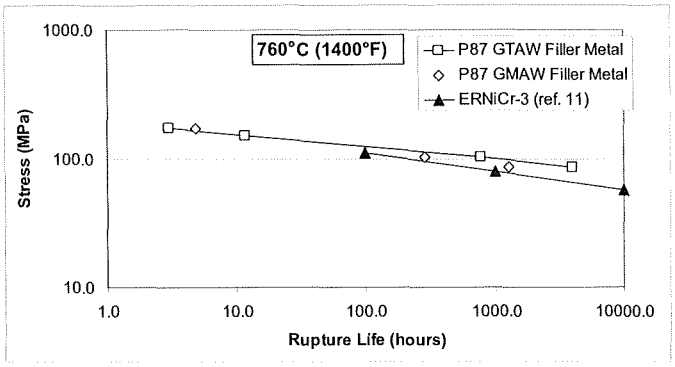

Figure 9. Time to rupture for EPRI P87 GTAW and GMAW weld metal at 760°C (1400°F) compared to reported ERNiCr-3 rupture strength [11]

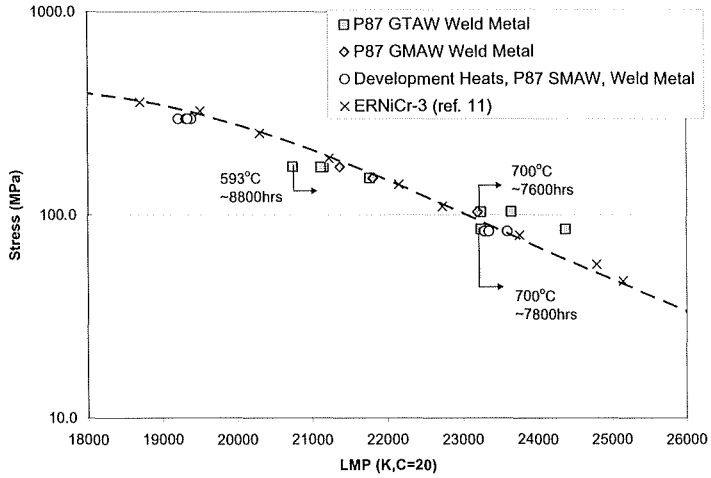

Figure 10. LMP plot of EPRI P87 GTAW and GMAW rupture data (arrows indicate ongoing tests) compared to EPRI P87 SMAW [3] and reported ERNiCr-3 data [11]

4. Discussion

Tensile tests on EPRI P87 DMWs show the filler metal exceeds the minimum strength of both Grade 91 and 347H stainless steel at room temperature. At elevated temperature, cross-weld tensile tests failed in either the 347H (lower temperatures) or in the grade 91 (higher temperatures). However, at room temperature, the strength of the EPRI P87, although above the grade 91 minimum, was inferior to the base metals and failure occurred in the weld metal. For higher strength alloys such as CSEF steel P92 or advanced stainless steels such as HR3C (310HCbN), the low ambient temperature strength of EPRI P87 may result in failure of a qualification test. However, as demonstrated by the elevated temperature data in Figure 5, the filler metal will have more than adequate strength at service temperatures, even for higher

tensile strength materials. Thus for EPRI P87 to be used in higher-strength joints, relief from current welding qualification rules by supplemental elevated temperature testing requirements may be needed.

Cross-weld creep-rupture results show that the behavior of subcritically heat-treated grade 91 joints made with EPRI P87 filler metal (GTAW, GMAW, and SMAW) are similar to cross-weld tests of joints made with typical 9%CrMoV filler metals. At high-stresses, creep failure is observed in the base metal but with decreasing stress failure occurs in the fine-grained HAZ region of the grade 91. The data in Figure 6 suggest little difference between the various filler metals. However, the creep strength of the EPRI P87 far exceeds that of grade 91. In the case of a normalized and tempered (N&T) grade 91 weld made with EPRI P87, the large mismatch in creep strength could affect rupture results. Creep-rupture testing on N&T grade 91-EPRI P87 joint produced by SMAW exhibited fusion line failures almost independent of test condition [3]. Therefore, more cross-weld rupture testing is advisable prior to utilizing EPRI P87 in N&T CSEF steels.

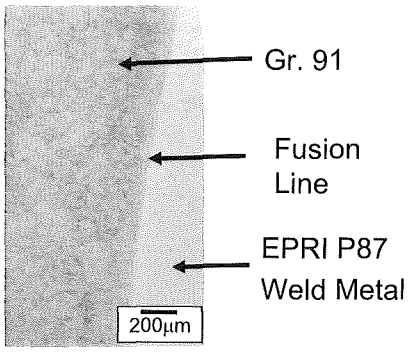

Figure 11. Micrograph of Grade 91-EPRI P87 FM Fusion Line region after completed stress-rupture testing at 625°C-100MPa (rupture life 899.2 hours)

All weld metal tests on EPRI P87 GTAW and GMAW show excellent rupture ductility and consistent creep rates irrespective of welding process. A power-law creep exponent of n=8, which is in the typical range of many engineering alloys, appears to fit the data over the range of stresses and temperatures in this study. Creep-strength was as good or better compared to ERNiCr-3 with longer-term tests suggesting a small creep strength advantage for the EPRI P87 GTAW welds. Additionally, unlike the high Cr content in ERNiCr-3 which contributes to the formation of a carbon denuded region during service, the EPRI P87's low Cr content, essentially matching that of Grade 91, results in a uniform structure near the weld fusion line. Figure 11 is a post stress-rupture test micrograph of the Gr. 91 and EPRI P87 (GTAW) weld after almost 900 hours at 625°C and 100MPa. Clearly, if carbon migration has occurred, it is not at a level distinguishable in this optical micrograph (as opposed to the carbon free regions in the micrographs in Figure 2).

5. Conclusions

GTAW and GMAW cross-weld and weld metal tensile and creep-rupture tests were conducted on dissimilar metal welds between grade 91 and 347H using EPRI P87 filler metal. Evaluation of the test results show the elevated tensile strength of the weld metal exceeds that of either base metal at service conditions. For joining higher-strength alloys, welding qualification modifications may be necessary due to the low room temperature strength of the EPRI P87 filler metal, but the elevated temperature strength is adequate. Creep-rupture results show EPRI P87 has excellent creep ductility. The test data from this study were used to provide a simple representation of minimum creep-rate behavior over the range of temperatures and stresses tested. Rupture life was compared to ERNiCr-3 on both an isothermal and a time-temperature parameter basis. At high-stress, the EPRI P87 had equivalent rupture strength to ERNiCr-3. At lower-stresses, the data suggest the EPRI P87 produced by GTAW is slightly stronger than ERNiCr-3. Microstructural analysis confirmed little to no carbon denuded region was present in the grade 91 after stress-rupture testing. Overall, the tensile strength, creep behavior, rupture strength, lack of carbon migration, and physical properties show EPRI P87 filler metal is an excellent alternative to ERNiCr-3 for dissimilar metal welds.

Acknowledgements

Special thanks to D. Glanton and M.K. Havens for their assistance with the metallography.

References

[1] *Dissimilar-Weld Failure Analysis and Development Program.* EPRI, Palo Alto, CA: 1985-1989. CS-4252.
[2] D.I. Roberts, R.H. Ryder, R. Viswanathan, "Performance of Dissimilar Metal Welds in Service," *Journal of Pressure Vessel Technology*, Vol. 107 August 1985.
[3] *Development of a New Nickel Filler for Dissimilar Metal Welds and Repair.* EPRI, Palo Alto, CA: 2009. 1018991.
[4] D. Gandy and K. Coleman. "Alternative Filler Materials for DMWs Involving P91 Materials," *Proceedings to the EPRI Fifth International Conference on Advances in Materials Technology for Fossil Power Plants (Marco Island, FL, Oct. 3-5, 2007)*
[5] J.A. Siefert, J.M. Sanders, J.M. Tanzosh, W.F. Newell, J.P. Shingledecker. "Development of EPRI P87 Solid Wire." *Proceedings to WELDS2009 (Fort Meyers, FL, June 24-26, 2009).*
[6] "EPRI P87 Product Data Sheet," *Metrode Data Sheet D87*, 2006
[7] *"Welding Qualifications for Advanced Alloys."* Unpublished EPRI research, 2009.
[8] 2007 ASME Boiler and Pressure Vessel Code. Section II – Materials © 2007 The American Society of Mechanical Engineers.
[9] D. Jandova, J. Kasl, V. Kanta. "Influence of Substructure on Creep Failure of P91 Steel Weld Joints." *Proceedings: Creep & Fracture in High Temperature Components, 2nd ECCC Creep Conference, April 21-23, 2009, Zurich, Switzerland.* © 2009 DEStech Publication, Inc.177-188.
[10] T.H. Courtney. Mechanical Behavior of Materials. © 2000, McGraw-Hill Companies, Inc.
[11] Incoloy® alloy 800H & 800HT®, SMC-047 © Special Metals Corporations, 2004 (Sept 04).

9th Liege Conference : Materials for Advanced Power Engineering 2010
edited by J. Lecomte-Beckers, Q. Contrepois, T. Beck and B. Kuhn.

IMPROVED CREEP AND OXIDATION BEHAVIOR OF A MARTENSITIC 9CR STEEL BY THE CONTROLLED ADDITION OF BORON AND NITROGEN

Peter Mayr[1,2], Ivan Holzer[2], Francisca Mendez-Martin[2], Mihaela Albu[3], Stefan Mitsche[3], Vanessa González[4], Alina Agüero[4]

[1] Department of Materials Science and Engineering, Massachusetts Institute of Technology, 77 Massachusetts Av, MA 02139, USA

[2] Institute of Materials Science and Welding, Graz University of Technology, Kopernikusgasse 24, 8010 Graz, Austria

[3] Institute for Electron Microscopy, Graz University of Technology, Steyrergasse 17, A-8010 Graz, Austria

[4] Instituto Nacional de Técnica Aeroespacial, Ctra. de Ajalvir Km 4, 28850 Torrejón de Ardoz, Spain

Abstract

This manuscript gives an overview on recent developments of a martensitic steel grade based on 9Cr3W3CoVNb with controlled additions of boron and nitrogen. Alloy design by thermodynamic equilibrium calculations and calculation of boron-nitrogen solubility is discussed. Out of this alloy design process, two melts of a 9Cr3W3CoVNbBN steel were produced. The investigation focused on microstructural evolution during high temperature exposure, creep properties and oxidation resistance in steam at 650°C.
Microstructural characterization of "as-received" and creep exposed material was carried out using conventional optical as well as advanced electron microscopic methods. Creep data at 650°C was obtained at various stress levels. Longest-running specimens have reached more than 20,000 hours of testing time. In parallel, long-term oxidation resistance has been studied at 650°C in steam atmosphere up to 5,000 hours.
Preliminary results of the extensive testing program on a 9Cr3W3CoVNbBN steel show significant improvement in respect to creep strength and oxidation resistance compared to the state-of-the-art 9 wt. % Cr martensitic steel grades. Up to current testing times, the creep strength is significantly beyond the +20% scatterband of standard grade P92 material. Despite the chromium content of 9 wt. % the material exhibits excellent oxidation resistance. Steam exposed plain base material shows comparable oxidation behavior to coated material, and the corrosion rate of the boron-nitrogen controlled steel is much lower compared to standard 9 wt.% Cr steel grades, P91 and P92.

Keywords: 9-12% chromium steels, microstructural evolution, creep testing, oxidation testing

1. Introduction

In Japan and Europe, research and development works in the field of advanced martensitic creep resistant steels has a long history [1-3]. The applications for such materials are in particular large diameter and thick section boiler components, such as main steam pipes and headers of ultra-supercritically (USC) operated power plants. The current target of ferritic steel development is set to a creep rupture strength of 100 MPa after 100,000 hours at 650°C and oxidation rates lower than for grade P91 steel.

Within the last years, the alloy design philosophy for martensitic steels strongly targets the enhancement of long-term microstructural stability [4]. Migration of lath and block boundaries, causing the coarsening of martensite laths and blocks by annihilation of excess dislocations, closely correlates with the onset of accelerated creep. A fine dispersion of $M_{23}C_6$ and MX particles, which exert a pinning force on migrating boundaries and dislocations, has been identified as main contributor in suppressing recovery of the martensitic microstructure.
The work presented in this manuscript is following an extensive research program published by the National Institute for Materials Science (NIMS), Japan [4]. In detail, the NIMS alloy design concept follows stabilization of $M_{23}C_6$ carbides and grain boundaries by the addition of boron in combination with finely dispersed MX particles as a possible solution to stabilize the martensitic substructure. As basis for the systematically study of the influence of boron and nitrogen on long-term creep behavior, a Fe-0.08C-9Cr-3W-3Co-0.2V-0.05Nb (wt. %) steel with different concentrations of boron and nitrogen was investigated [5,6].

The influence of boron on 9Cr3W3CoVNb steel was studied in the range of 0 to 140 ppm (parts per million) while nitrogen level was kept constant at a minimum between 10 to 30 ppm [5]. The influence of boron additions on creep properties was studied by uniaxial-creep testing at 650°C at different stress levels. At stress levels higher than 100 MPa, no big difference in creep strength between 0B, 0.0048B and 0.0092B steel was found. Only 0.0139B steel showed improved creep strength. While at lower stress levels, creep strength of the lower boron steels decreased significantly, 0.0139B steel showed a stable creep behavior. It was concluded that controlled addition of boron can delay the drop of creep strength in 9Cr3W3CoVNb steel. As a result of the boron series creep tests, a boron content of 140 ppm was identified as optimum for improved creep behavior.
The combined effect of boron plus additional MX precipitation was studied by 9Cr3W3CoVNb test melts with a fixed boron content of 140 ppm and varying nitrogen levels of 15, 79 and 650 ppm [6]. Increasing the nitrogen level to 79 ppm resulted in further improvement of the creep strength of the base 9Cr3W3CoVNb-0.0140B steel. However, further increase of nitrogen to 650 ppm showed no beneficial effects and in turn reduced creep strength of the alloy.
The main idea behind the NIMS alloying concept is to combine boron-strengthening with nitride-strengthening. However, excess addition of nitrogen in combination with boron causes the formation of boron nitrides (BN) during processing and heat treatments at elevated temperatures. Precipitation of boron nitrides offsets the beneficial effect of boron and nitrogen addition. Sakuraya et. al [7] showed in their work on BN formation in high Cr heat resistant steels that, a particular relationship between boron and nitrogen has to be kept to avoid

formation of coarse BN particles. From their experimental observations the authors derived a mathematic formulation of the solubility product of BN.

Within the present work, the NIMS alloy design strategy is expanded by thermodynamic studies of the boron nitride solubility product. Slightly modified alloy chemistry is proposed and first results of creep and oxidation tests as well as the microstructural evolution during creep are presented.

1. Experimental

1.1. Alloy Design

Thermodynamic equilibrium calculations were performed using the software Matcalc [8-11] utilizing the thermodynamic database Fe-data6 [12]. The description of BN in the database was slightly modified, based on the work of Fountain et al. [13]. Alloy design was supported through a calculated equilibrium phase diagram for the 9Cr3W3CoVNbBN steel and a boron nitride and boride solubility diagram.

1.2. Materials

A 20 kg heat (Heat 1) of 9Cr3W3CoVNb steel with controlled additions of 120 ppm boron and 130 ppm nitrogen was produced by vacuum induction melting. The addition of boron and nitrogen was set to avoid the formation of large boron nitrides but still allow the precipitation of strengthening MX particles. For homogenization of Heat 1, the ingot (110 mm square) was forged to final dimensions of 50 mm square. A second heat (Heat 2) of a 9Cr3W3CoVNb steel with slightly reduced boron (110 ppm) and nitrogen (100 ppm) content was cast (100 kg) and rolled to 20 mm thick plates. The exact chemical composition in weight % (wt. %) for Heat 1 and Heat 2 is given in Table 1. The final quality heat treatment for both heats consisted of normalizing at 1150 °C for 1 hour followed by tempering at 770 °C for 4 hours.

Table 1: Chemical composition of 9Cr3W3CoVNbBN test melts in wt. % (balanced Fe).

Analysis	C	Si	Mn	Cr	W	Co	V	Nb	B	N
Heat 1	0.074	0.29	0.44	9.26	2.84	2.95	0.21	0.056	0.012	0.013
Heat 2	0.090	0.30	0.51	9.26	2.92	2.88	0.20	0.050	0.011	0.010

In both heats, precipitation of BN particles was investigated. Material of Heat 1 was used for microstructural characterization and creep testing. Fractured creep samples were investigated by means of optical and electron microscopy to determine the microstructural evolution during creep. Heat 1 material was also used for oxidation testing in steam atmosphere.
Heat 2 material was used for basic metallographic investigations and for additional creep tests.

1.3. Steam Oxidation Laboratory Testing

The schematic of the closed loop laboratory rig employed at INTA is shown in *Figure 1.* Prior to testing, laboratory air is displaced from the chamber by means of N_2 which is kept flowing while heating up to the test temperature (approximately 600°C/h). Once the test

temperature is reached, the N_2 flow is closed and pure steam is introduced at a linear velocity of 8 cm/s. To carry out weight measurements or to remove samples, the furnace is cooled to about 300°C under N_2 atmosphere and the specimens are subsequently removed. The reheat cycle is also carried out under N_2 atmosphere.

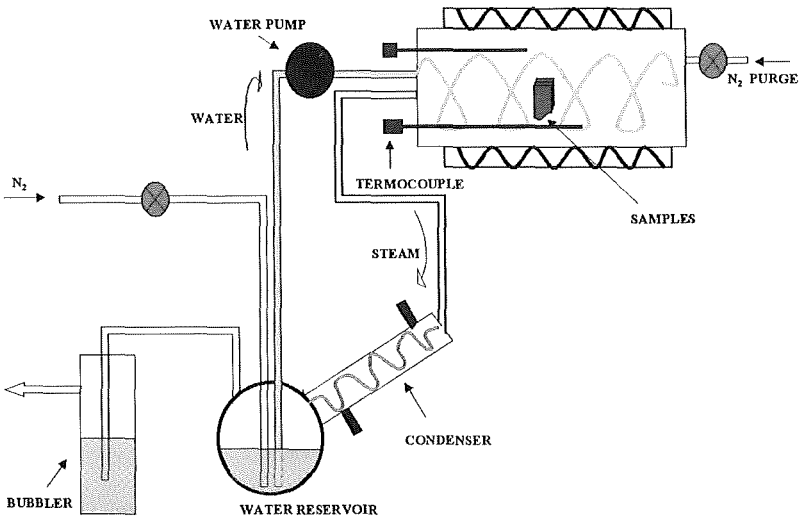

Figure 1: Sketch of the closed loop laboratory test rig for the oxidation testing of samples in steam atmosphere at 650°C.

1.4. Microstructure Characterization

Base material microstructure was characterized by light optical microscopy, scanning electron microscopy (SEM) and analytical transmission electron microscopy (TEM). Precipitation of BN was studied by SEM and energy dispersive X-ray spectroscopy (EDS) on fracture surfaces of base material specimens. The smallest BN particle size being able to identify is about 0.3 μm. Details are reported in [14]. The oxidized specimens were characterized by optical and field emission scanning electron microscopy (FESEM) using a JEOL JSM 840 system equipped with an energy dispersive X-ray spectrometer (EDS) KEVEX MICROANALYST 8000 with a RÖNTEC signal processor.

2. Modified Alloy Design Concept

The investigated alloys are based on a 9Cr3W3CoVNbBN steel. The calculated equilibrium phase diagram for the chemical composition equal to that of Heat 1 (see Table 1) indicates that the steel should be free of delta ferrite at room temperature. The nominal chromium content of 9 wt.% enables a complete austenitization on cooling in the temperature range from 1183°C to 881°C. Normalizing at 1150°C will therefore dissolve most of the precipitates

formed during solidification and allow a homogenization of the elemental distribution through diffusion. On cooling, a uniform martensitic microstructure will form which then is tempered at 770°C.

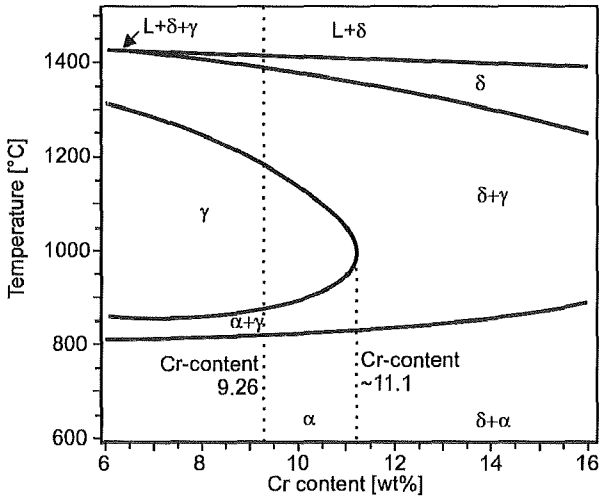

Figure 2: Calculated equilibrium phase diagram with varying chromium content for a 9Cr3W3CoVNbBN steel with a chemical composition equal to that of Heat 1.

To take advantage of boron and nitrogen addition, the formation of large boron nitrides (BN) and borides (M_2B) has to be avoided. Therefore, in the present work the allowable boron and nitrogen limits for high chromium martensitic steels were determined by thermodynamic equilibrium calculations. The BN solubility product for a 9Cr3W3CoVNbBN steel, based on the chemical composition of Heat 1, was calculated for various B/N ratios and different normalizing temperatures, including also possible formation of borides (M_2B). Similar to boron nitrides, boride particles would also reduce the amount of boron dissolved in the metal matrix or incorporated in chromium carbides ($M_{23}C_6$) and therefore diminish the beneficial effect of boron addition.

Results of the BN solubility calculation are shown in *Figure 3*. The solubility products (solid lines) are shown for different normalizing temperatures ranging from 900°C to 1250°C. The dashed grey lines represent the solubility product for the M_2B phase. For reason of comparison, the BN solubility lines reported by Fountain et al. [13] at 1150°C and Sakuraya et al. [15] are included in the figure.

The grey shaded area in *Figure 3* indicates critical B/N ratios e.g. at 1250°C where BN formation is to be expected. No formation of BN is expected below the respective BN solubility line.

Figure 3 clearly shows that the experimental findings reported by Sakuraya et al. [15] are well described by the thermodynamic equilibrium considerations in the temperature range between 900°C and 1250°C. Sakuraya et al. [7] reported no BN formation for temperatures higher than 1250°C.

Due to the temperature dependence of the BN solubility product it can be assumed that coarse BN (>1μm) exist for high boron and nitrogen contents and low normalizing temperatures.

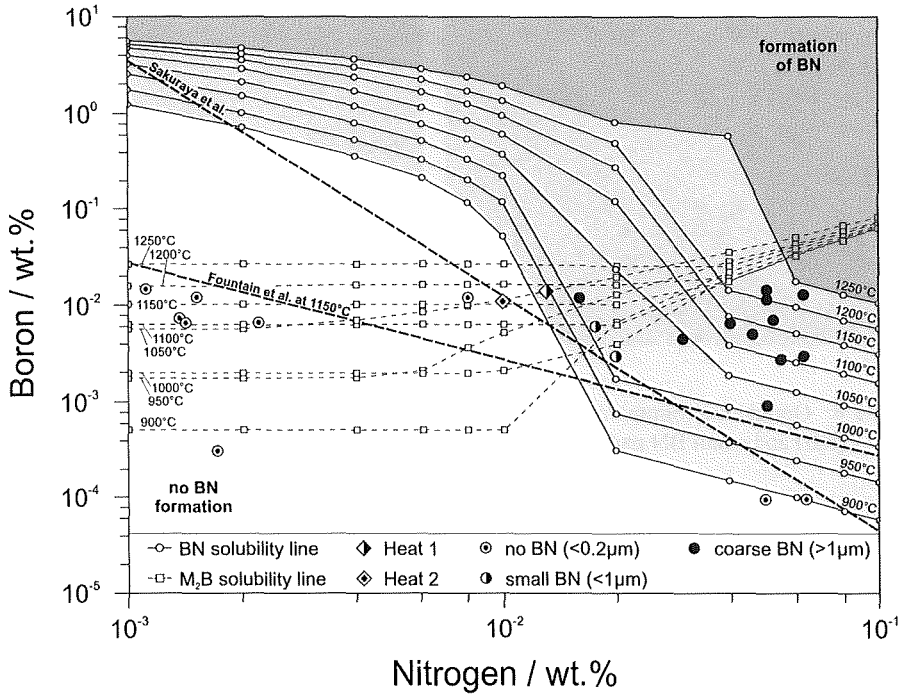

Figure 3: BN solubility product for a 9Cr3W3CoVNbBN steel as a function of normalizing temperature in the range of 900°C to 1250°C. The grey shaded areas indicate BN formation. The calculation is compared to the solubility products reported by Sakuraya et al. [15], and Fountain et al. [13], and the two heats investigated within this work.

3. Microstructure of 9Cr3W3CoVNbBN steel

Optical micrographs of 9Cr3W3CoVNbBN base material (Heat 1) show a tempered martensitic microstructure (see *Figure 4*). The average prior austenite grain size is 250 µm in diameter, and precipitates are finely distributed mainly along prior austenite grain and martensite lath boundaries.

Via electron microscopy, MX (V,Nb)(N,C) carbonitrides and $M_{23}C_6$ $(Cr,Fe,Mo,W)_{23}C_6$ carbides have been identified at grain and lath boundaries and/or in the matrix of the base material. MX (V,Nb)(N,C) particles have a representative diameter smaller than 100 nm, and Cr-rich carbides have a diameter between 150 and 250 nm. By SEM and EDS only very few and small (<1µm) BN particles for Heat 1 and no BN particles for Heat 2 have been detected. A detailed description of the method of detecting BN particles is given in [15]. These experimental findings support the results of the thermodynamic equilibrium calculations in the alloy design stage.

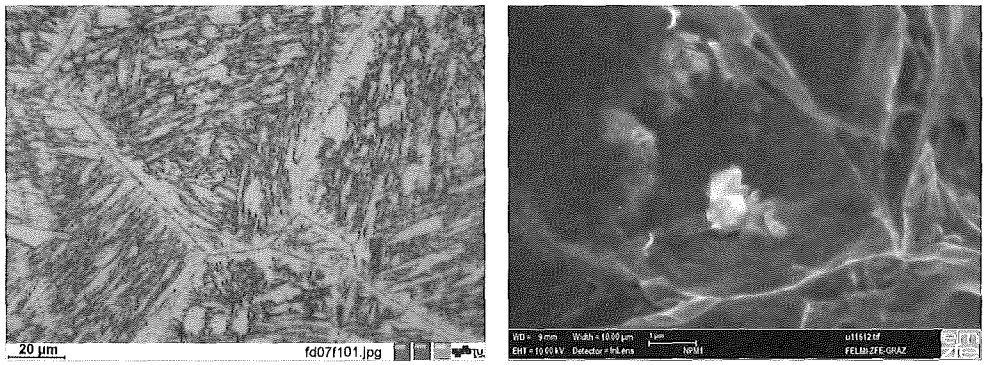

Figure 4: Optical micrograph of normalized and tempered 9Cr3W3CoVNbBN base material (left) and small BN particle (right) identified by EDS - both images for Heat 1.

After creep exposure for 8,971 hours at 650 °C and 130 MPa, light-optical and electron-microscopic investigations have been performed to study the microstructural evolution during creep exposure. The prior austenite grain and martensite lath structure, after almost 10,000 h of creep, show no significant changes. The precipitate size and number density of carbonitrides and carbides remain almost the same as in the base material. The electron microscopy investigation reveals the precipitation of two new phases: laves phase (intermetallic phase A_2B, $(Fe,Cr)_2(W,Mo)$ with approximately 38 atom % of tungsten and more than 45 atom % of iron, distributed mainly at the grain boundaries, and modified Z-phase (complex nitride [(Cr,V,Nb)N]) with a very low phase fraction. Details on the microstructural evolution of 9Cr3W3CoVNbBN steel during creep exposure can be found in [16]. Based on this study, an enhanced microstructural stability can be attributed to 9Cr3W3CoVNbBN steel.

4. Oxidation behavior

Specimens of 9Cr3W3CoVNbBN (Heat 1) were exposed to pure, flowing steam at 650°C for 4,908 h. *Figure 5* shows the mass variation of the new steel as function of time as well as that of 9 wt.% ferritic steels P91 and P92 for comparison purposes. 9Cr3W3CoVNbBN exhibits a mass gain considerably lower than that of the other two 9 wt. % Cr steels. This behavior is surprising, as work done by several research groups have indicated the steam oxidation resistance of steels strongly correlates with the Cr contents, and results so far have indicated that 9 wt. % Cr steels oxidized very fast when exposed to steam at T > 600°C [17-20]. For instance, Quadakkers and collaborators have concluded that a chromium content of 11 wt. % or more is required to form a protective scale [17].

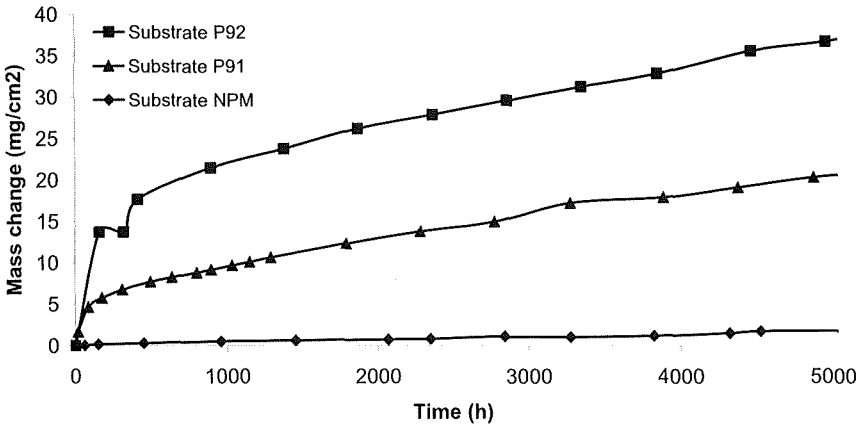

Figure 5: Mass gain of conventional (P91, P92) 9 wt. % steel and 9Cr3W3CoVNbBN (NPM1) substrates exposed to flowing steam (1 bar) at 650° C

Figure 6 shows an image of a specimen exposed to 650°C hot steam for 4,908 h. Several nodular features can be observed, especially at the samples edges but most of the surface still appears to be smooth. On the cross section of the exposed surface, a very thin (< 100 nm) Cr and O rich layer, most likely Cr_2O_3 can be observed with difficulty. This type of oxide is typical of steels containing 11 wt. % of Cr or more. Quadakkers found that Co tends to increase the oxidation resistance of 9-12 Cr wt. % ferritic steels [17], but not to the extent observed for 9Cr3W3CoVNbBN. On the other hand, other groups have observed that the higher the W content, the lower the oxidation resistance of these types of steels [18,21,22]. It is therefore not clear yet why this 9 wt. % steel forms a protective oxide layer and exhibits such high steam oxidation resistance. Further studies are required.

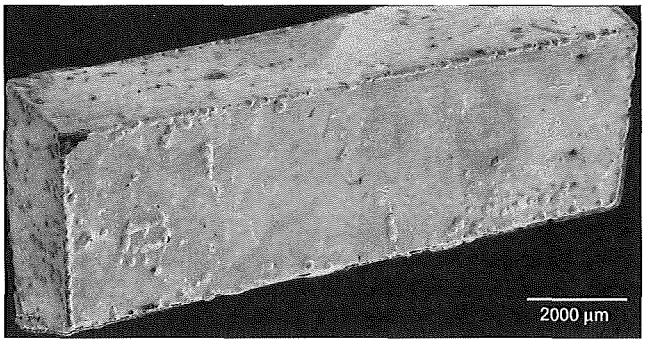

Figure 6: SEM image of a 9Cr3W3CoVNbBN specimen exposed to steam at 650°C for 4,908 h

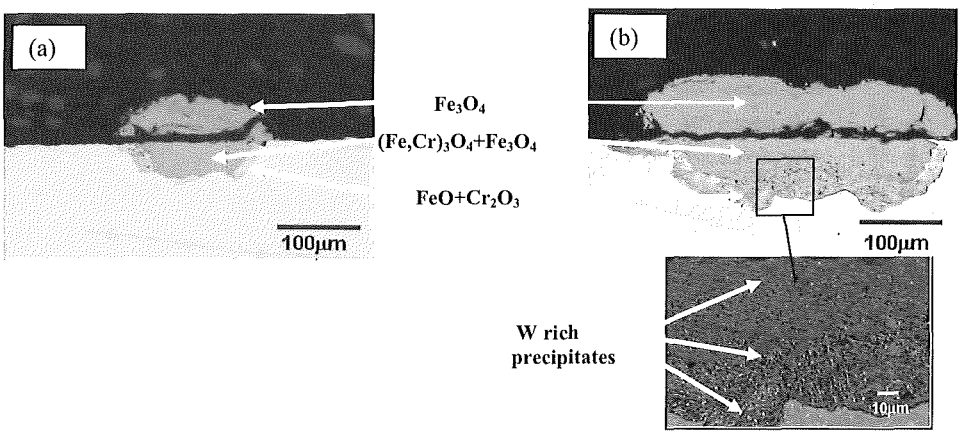

Figure 7: FESEM image of the cross section of 9Cr3W3CoVNbBN exposed to steam at 650°C at a nodule site: (a) for 1,260 h, (b) for 4,908 h

The cross section of representative nodules formed after 1,260 and 4,908 h are shown in *Figure 7a* and *b* respectively. The microstructure corresponds to a dual oxide layer similar to that observed on ferritic steels containing 9 wt.% in Cr, with a top outwards growth of a Fe_3O_4 layer and an inside growing mixed oxide layer containing $(Fe, Cr)_3O_4$, FeO and Cr_2O_3 [23] which also contains W, Co and V. Interestingly, W rich nanoscale precipitates which are also present in the substrate can be observed in this inner oxide layer. The nodules in the 1,260 h specimen exhibit lower thickness and width than those observed in the specimen exposed for 4,908 h, indicating that these oxides are growing and therefore are not protective. Moreover, the number of nodules on the 4,908 h specimen is higher than that observed on the 1,260 h specimen.

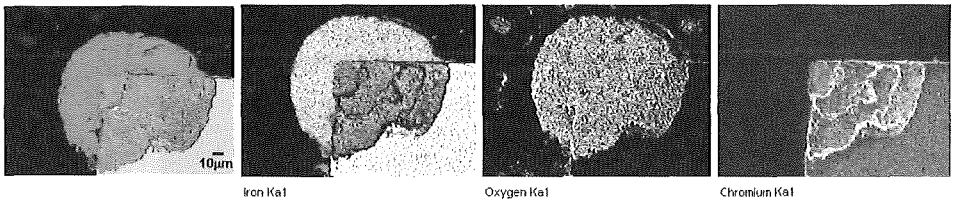

Figure 8: Cross section of the edge of a 9Cr3W3CoVNbBN specimen exposed to steam at 650° C for 4,908 h

At one specimen's edge (*Figure 8*), the corresponding EDS composition map reveals Cr-rich layers within the inner oxide and the original specimen surfaces. The average Cr content (19 wt. %) in this inner oxide zone is significantly higher than that of the substrate, but because it is not uniformly distributed it is not of a protective nature. According to Quaddakers and coworkers, this pattern results from the repetition of cycles in which Cr rich spinels form due to rapid Cr diffusion from the bulk alloy until the spinel cannot be sustained due to continuous

Cr depletion, resulting in the formation of Fe rich oxides [17]. Formation of oxidation nodules has been observed on oxidation resistant 12 wt. % steels and has been attributed to compositional inhomogeneity [17,24]. For this 9Cr steel the presence of nodules can be rather attributed to local cracks, imperfections and/or rupture of the protective scale on a Cr depleted substrate. The fact that the samples edges are fully covered with nodules support this hypothesis as due the higher triaxiality of stresses, corners and edges are more prone to develop cracks.

5. Creep Strength

Uniaxial creep tests of 9Cr3W3CoVNbBN base material specimens have been carried out at 650°C. Both Heat 1 specimens tested at 130 MPa and 100 MPa have already fractured, as shown in *Figure 9*. The base material specimen tested at a higher stress level of 130 MPa fractured after 8,971 h. This corresponds to an improvement of rupture stress at approximately 9,000 hours of +60 MPa and +40 MPa compared to grades P91 and P92 respectively. After 23,997 hours of creep exposure, creep rupture strength of 9Cr3W3CoVNbBN steel is still beyond the +20% average creep strength of grade 92 material. Heat 2 material tests are still running but up to almost 10,000 hours of testing, creep strength is superior to that of standard grade 92 material by more than +20%.

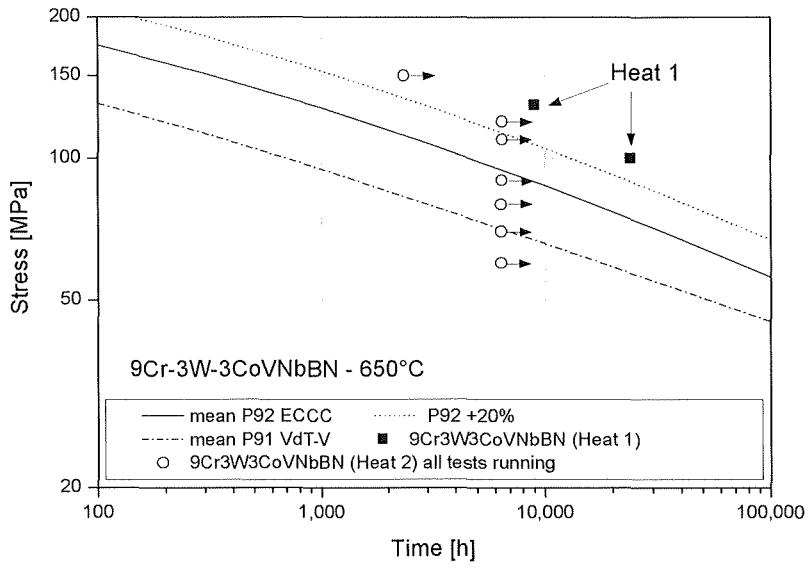

Figure 9: Creep testing data of 9Cr3W3CoVNbBN base material of Heat 1 and Heat 2 at 650°C compared to creep rupture data of well-established grades P91 and P92.

6. Summary and Conclusions

Alloy design for a 9 wt. % Cr steel has been successfully improved by thermodynamic studies of the boron-nitrogen solubility product. The boron and nitrogen content of a 9Cr3W3CoVNbBN steel was adjusted to have either only very small boron nitrides (Heat 1) or no precipitation of BN (Heat 2). This confirms that in these two heats most of the boron stays either in solution or is incorporated in $M_{23}C_6$ carbides. Therefore, the added boron can develop its maximum strengthening contribution.

The boron strengthened 9Cr3W3CoVNbBN steels exhibits an unexpected high resistance to steam oxidation at 650°C. Despite its low Cr content it develops a thin Cr rich protective oxide scale. However, several oxidation nodules form, very likely due to imperfections in the protective oxide layer. These nodules grow in thickness, width and number as a function of steam exposure time. Nevertheless, the increased oxidation resistance of the new steels shows high potential and is currently studied in detail.

The creep behavior up to testing times of almost 25,000 hours at 650°C is very promising. The 9Cr3W3CoVNbBN steel shows an improved creep rupture strength more than +20% beyond the average creep strength of standard grade 92 steel. This higher creep rupture strength is attributed to an enhanced microstructural stability due to the controlled addition of boron and nitrogen. Soluble boron stabilizes the martensitic microstructure and delays recovery whereas boron incorporated in $M_{23}(C,B)_6$ carbides reduces their tendency to coarsening.

Acknowledgements

PM would like to thank the Austrian Academy of Sciences and the Max Kade Foundation for granting a one-year research fellowship. The authors would like to acknowledge the support by the European Cooperation in Science and Technology (COST) through Action 536 "Alloy development for Critical Components of Environmental friendly Power planT (ACCEPT)" and the Austrian Research Promotion Agency - FFG (#818512). AA and VG wish to acknowledge the Spanish Ministry of Science and Innovation for the financial support (ENE2008-06755-C02-01).

References

[1] Kern T U, Wieghardt K and Kirchner H, in 4th int conf Advances in Materials Technology for Fossil Power Plants, Hilton Head Island, ASM International, 2005.
[2] Masuyama F, in 4th int conf Advances in Materials Technology for Fossil Power Plants, Hilton Head Island, ASM International, 2005.
[3] Cerjak, H.-H.; Dimmler, G.; Holzer, I.; Kozeschnik, E.; Mayr, P.; Pein, C.; Sonderegger, B.: Materials science forum 539-543 (2007) , S. 2954 - 2959
[4] Abe F, in 4th int conf Advances in Materials Technology for Fossil Power Plants, Hilton Head Island, SC, EPRI, 2004.
[5] Abe F, Horiuchi T and Sawada K, Materials Science Forum, 2003, 426-432, 1393-1398.
[6] Semba H and Abe F, "in 4th int conf Advances in Materials Technology for Fossil Power Plants, Hilton Head Island, SC, EPRI, 2004.

[7]Sakuraya K., Okada H., Abe F., ISIJ Int., vol. 46 (2006), 1712.
[8]Kozeschnik E., Buchmayr B., Mathematical Modelling of Weld Phenomena 5, Institute of Materials, London, 2001, 349.
[9]Svoboda J., Fischer F. D., Fratzl P., Kozeschnik E., Mater. Sci. Eng. A, vol 385 (2004) 166.
[10]Kozeschnik E., Svoboda J., Fratzl P., Fischer F. D., Mater. Sci. Eng. A, vol 385 (2004) 157.
[11]Kozeschnik E., Svoboda J., Fischer F. D., CALPHAD, vol 28 (2005) 379.
[12]Saunders M., Fe-data6.tdb.
[13] R.W. Fountain, Chipman J., Transactions of the Metallurgical Society of AIME, vol. 224 (1962) 599.
[14]Mayr P., PhD-Thesis, Graz University of Technology, 2007
[15]Sakuraya K., Okada H., Abe F., in: Advances in Materials Technology for Fossil Power Plants: Proceedings of the Fourth International Conference, (2004) 1270.
[16] Mayr, P.; Mendez Martin, F.; Albu, M.; Cerjak, H.-H.: in: Creep and Fracture in High Temperature Components - Design & Life Assessment Issues (2009), S. 1029 - 1037
[17]Quadakkers W.J. and Ennis P.J., Materials for Advanced Power Engineering 1998, Part I (1998) p. 123
[18]Nava-Paz J.C. and Knödler R., Materials for Advanced Power Engineering 1998, Part I (1998) p. 451
[19]Fukuda Y., Tamura K. and Sato T., Materials for Advanced Power Engineering 1998, Part I (1998) p. 461
[20]Ennis P.J. and Quadakkers W.J., Materials for Advanced Power Engineering 2002, Part II (2002) p. 1131
[21]Knödler R. and Scarlin B., Materials for Advanced Power Engineering 2002, Part III (2002) p. 1601
[22]Agüero A. and Muelas R., Materials Science Forum, 461-464 (2004) p. 957
[23]Zurek J., Nieto-Hierro L., Piron-Abellan J., Niewolak L., Singheiser L. and Quadakkers W.J., Materials Sceince Forum, 461-464 (2004) p. 791
[24]Lepingle V., Louis G., Petelot D., Lefevre B. and Vandenberghe B., Materials Science Forum, 461-464 (2004) p. 1039

9th Liege Conference : Materials for Advanced Power Engineering 2010
edited by J. Lecomte-Beckers, Q. Contrepois, T. Beck and B. Kuhn.

DEVELOPMENT OF Fe-Ni AND Ni-BASE ALLOYS WITHOUT γ' STRENGTHENING FOR ADVANCED USC BOILERS

Hiroyuki Semba, Hirokazu Okada, Masaaki Igarashi, Hiroyuki Hirata
and Mitsuru Yoshizawa*)

Corporate Research and Development Laboratories,
Sumitomo Metal Industries, Ltd.
1-8 Fuso-cho, Amagasaki, Hyogo 660-0891, Japan

*) Steel Tube Works, Sumitomo Metal Industries, Ltd.
1 Higashi-Mukojima Nishino-cho, Amagasaki, Hyogo 660-0856, Japan

Abstract

An Fe-Ni base alloy, 23Cr-45Ni-7W alloy (HR6W) strengthened by Fe_2W-type Laves phase is one of the candidate materials for the piping application. Stability of long-term creep strength and superior creep rupture ductility have been proved by creep rupture tests up to 60000h at 650-800°C. The 10^5h extrapolated creep rupture strength at 700°C approved by TUV is 85MPa. It has also been confirmed that HR6W has excellent microstructural stability by means of microstructural observations after long term creep tests and aging. A thick wall pipe of HR6W, which is 457mm in diameter and 60mm in wall thickness, has successfully been manufactured by the Erhart Push Bench press method. This trial production has shown that hot workability of HR6W is sufficient for manufacturing thick wall piping for A-USC plants. A new Ni-base alloy, 30r-50Ni-4W alloy (HR35) has been proposed for piping application having comparable creep rupture strength with Alloy 617 at 700°C. This alloy is not strengthened by γ' phase but mainly by α-Cr phase. The 10^5h extrapolated creep rupture strength is estimated to be 114MPa at 700°C. It has sufficient creep rupture ductility compared with Alloy 617. A thick wall pipe of HR35 has also been successfully manufactured. Capability of HR6W and HR35 as structural materials for A-USC plants has been examined in detail. They have high resistance to relaxation cracking after welding. It is, therefore, concluded that both the alloys are promising candidates especially for thick wall piping in A-USC power plants.

Keywords: Laves, α-Cr phase, creep, microstructural stability

1. Introduction

Advanced ultra super critical (A-USC) power plants operated at steam temperatures of 700-760°C are the most promising technology to improve the efficiency of fossil power plants for reducing their CO_2 emission. R&D projects on A-USC plants and relevant materials technologies have been launched in Europe and the US [1][2]. In Japan, development of advanced heat resistant steels and alloys for USC plants with steam temperatures of 600-650°C has successfully progressed [3] and a new project on A-USC plants and further innovations in materials technology has been initiated based on the established alloy design and application technologies so far [4]-[7]. High strength 9-12%Cr ferritic steels are favourable and widely used for thick sections such as main steam pipes in 'conventional' USC boilers with steam temperatures at around 600°C. However, it is difficult to apply these ferritic steels to the components exposed above 650°C in A-USC plants in terms of creep strength and steam oxidation resistance. 18-25%Cr austenitic steels also have limitations on use as thick wall pipes from the standpoints of thermal fatigue resistance due to higher thermal expansion coefficient. Therefore, Alloy 617 and other Ni-base superalloys having

superior creep strength at around 700°C due to precipitation of γ′ and lower thermal expansion coefficient than austenitic steels, are candidate materials for thick section components as well as tubing in A-USC plants. However, it seems that these γ′-hardened Ni-base superalloys have poor ductility, toughness, fatigue resistance and workability. Furthermore, it has been reported that failures at heat affected zone of welded joints in γ′-hardened Ni-base alloys, which is due to stress relaxation cracking [8]. It may be enhanced by fine precipitation of γ′.

23Cr-45Ni-7W alloy (HR6W) has originally been developed for a tubing alloy of near future USC plants with steam temperatures above 650°C in order to overcome the above disadvantages of conventional heat resistant steels and alloys [9][10][11]. It is strengthened by Laves phase without γ′. 30Cr-50Ni-4W (HR35) has also developed for tubing and thick wall piping materials for A-USC boilers having comparable creep rupture strength with Alloy 617 at 700°C. It is mainly strengthened by Cr-rich bcc phase without γ′. Both alloys are evaluated in the A-USC project in Japan [6] as candidate materials for tubing and piping. This paper describes alloy design, creep properties, microstructure and strengthening mechanisms of HR6W and HR35, and then capability of these alloys as a material applied to A-USC plants is discussed.

2. Alloy design of HR6W and HR35

HR6W with a nominal composition of 0.08C-23Cr-45Ni-7W-0.1Ti-0.2Nb-B has been developed, considering with creep strength, corrosion resistance and microstructural stability at around 700-800°C [9][10][11]. A combination of Nb and N in austenitic steels, employing precipitation strengthening of NbCrN and solid-solution strengthening of N is capable for increasing creep strength as shown in HR3C (25Cr-20Ni-0.45Nb-0.25N) steel. It was, however, found that addition of Mo or W to high nitrogen bearing austenitic steels aiming for further improvement of creep strength causes precipitation of blocky nitrides, leading to degradation of long-term creep strength and toughness [12]. Therefore, a chemical composition of HR6W has been optimized without N in austenitic alloys containing more than 20%Cr from the viewpoint of corrosion resistance. Although addition of Mo is effective for improving high temperature strength of austenitic steels and alloys, calculation of phase diagram followed by experiment revealed that precipitation of σ phase is inevitable in a Cr-Ni-Fe-Mo system with more than 20%Cr. On the other hand, addition of W to a Cr-Ni-Fe system containing more than 20%Cr stabilizes Laves phase and does not cause precipitation of σ phase with appropriate amount of Ni as shown in Fig. 1. It is also found that the two-phase region of γ+Laves is extended in the Cr-Ni-Fe-7W system compared with the Cr-Ni-Fe-3W system. These calculations indicate that the addition of adequate amount of W to austenitic alloys can enhance precipitation strengthening of Laves phase without instability of austenite matrix. Indeed, Laves phase has been observed in addition to $M_{23}C_6$ carbides in 0.08C-23Cr-45Ni-7W alloys aged at 750°C for 3000h without σ phase precipitation as shown in Fig. 2. Fig.3 shows calculated phase fractions of HR6W. It is seen that Laves phase still precipitates above 800°C. This suggests that strengthening of Laves phase sufficiently contributes to creep resistance at 700-800°C.

It is found that further addition of Cr with appropriate amount of Ni to HR6W stabilize the Cr-rich bcc phase with Laves phase as shown in Fig.1 (b). This Cr-rich phase, that is α-Cr phase, is the primary strengthening phase in HR35. Fig. 4 shows TEM micrographs of the extraction replicas for grip portion of HR35 crept for 2527h at 750°C. It is seen that the α-Cr phase is uniformly precipitated inside grain (rod shaped precipitates in the figure) and other intermetallic phases such as Laves phase are observed. A typical composition of HR35 is 0.06C-30Cr-50Ni-4W-0.8Ti-B.

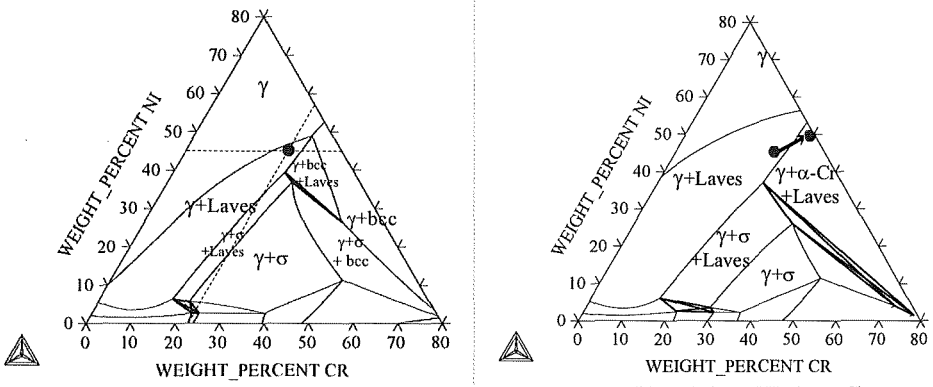

(a) Cr-Ni-Fe-3W (750°C) (b) Cr-Ni-Fe-7W (750°C)

Fig. 1 Phase diagrams of Cr-Ni-Fe-W quaternary system computed by Thermo-Calc.

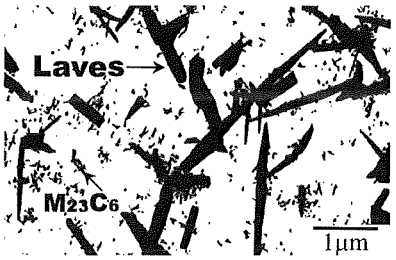

Fig. 2 TEM image of extraction replica of HR6W aged at 750°C for 3000h

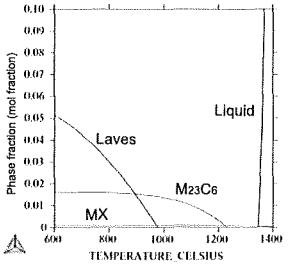

Fig.3 Phase fractions of HR6W computed by Thermo-Calc.

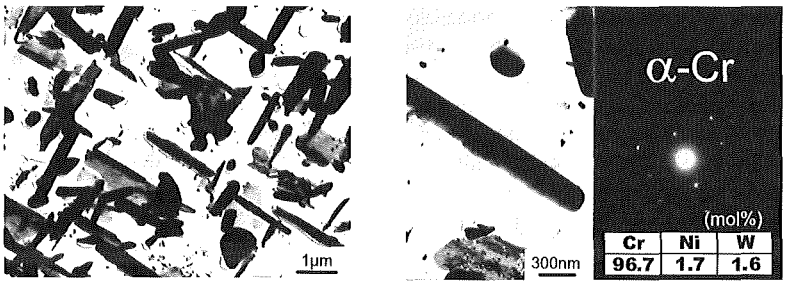

Fig. 4 TEM images of extraction replicas showing the α-Cr phase observed for HR35 crept for 2527h at 750°C with 127MPa

3. Creep properties and microstructure of HR6W and HR35

3.1. Creep properties

Creep rupture strength of the developed HR6W plates, tubes and pipes are shown in Fig. 5. Long-term creep rupture tests have been performed and progressed up to 60000h at 650-800°C. It has been proved that the average creep strength curves at 650-800°C are stable by long-term creep tests over 10000h. The 10^5h extrapolated creep rupture strengths of HR6W approved by TUV are 118MPa at 650°C, 85MPa at 700°C and 62MPa at 750°C, respectively. The creep rupture strength of HR6W at 800°C is comparable with that of Alloy 617 [13]. Fig. 6 shows creep rupture elongations of HR6W. It is noted that HR6W demonstrates superior rupture ductility, compared with Alloy 617 and other Ni-base superalloys strengthened by γ' phase even in the long-term tests. Fig. 7 shows a creep curve of HR6W at 750°C with 108MPa and ruptured for 1047h. Creep rate decreases about one

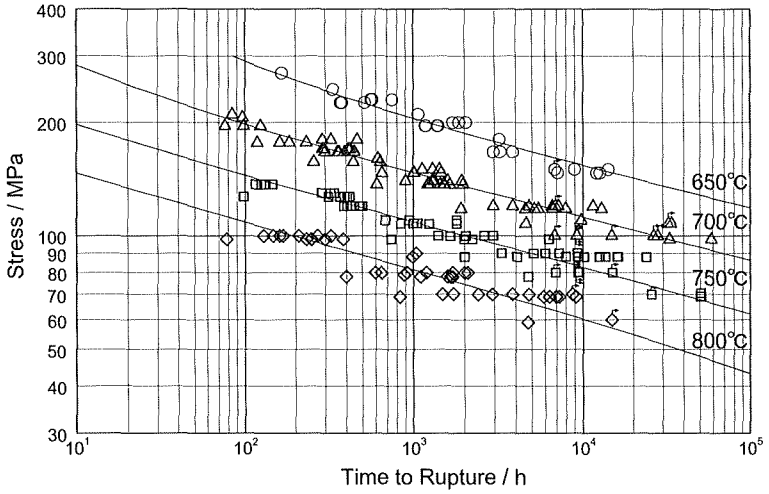

Fig. 5 Creep rupture strength of HR6W.

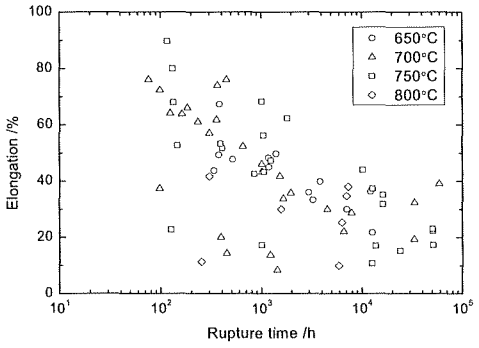

Fig. 6 Creep rupture ductility of HR6W

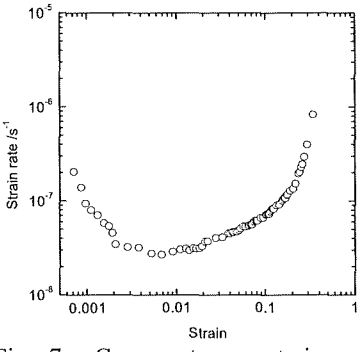

Fig. 7 Creep rate vs. strain curve of HR6W at 750°C, 108MPa.

order of magnitude in the primary region, then gently increases, leading to tertiary creep. While the onset strain of tertiary creep is around 0.01, the tertiary stage is relatively long, resulting in sufficient creep strain of 0.4. Good creep rupture ductility of HR6W should result from this deformation behaviour.

Fig. 8 shows creep rupture strength of HR35 at 700-800°C. It is obvious that creep strength of HR35 is comparable with that of Alloy 617. The 10^5h extrapolated creep rupture strengths of HR35 by Larson-Miller method are estimated to be 114MPa at 700°C, 78MPa at 750°C and 54MPa at 800°C, respectively. Creep rupture ductility, reduction of area, is shown in Fig. 9. HR35 demonstrates good rupture ductility compared with Alloy 617 and hence does not exhibit the long-term grain boundary embitterment which leads to relaxation cracking and low ductility failure at high temperatures. Fig. 10 shows the creep curve of HR35 at 750°C with 150MPa and ruptured for 174h. Creep rate decreases about one order of magnitude in the primary region and reaches to the minimum creep rate with a large onset strain of about 0.03 and then gently increases, leading to tertiary creep. This behaviour indicates that creep deformation is very homogeneous in contrast with Alloy 617 [14] and the resultant creep rupture strain is very large, about 0.3. This may be attributed by the gradual precipitation and the relatively large size of the α-Cr phase.

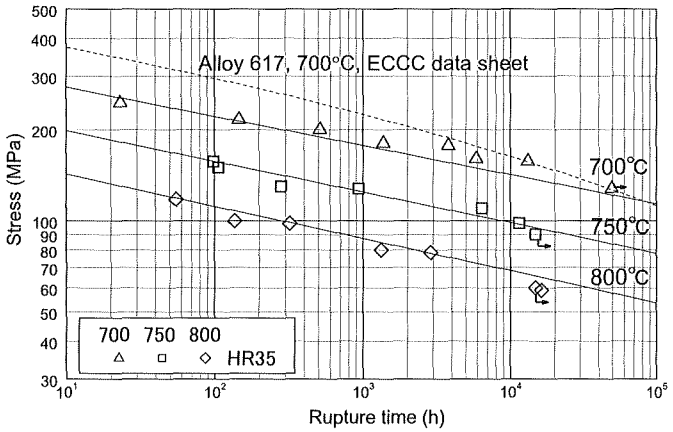

Fig. 8 Creep rupture strength of HR35.

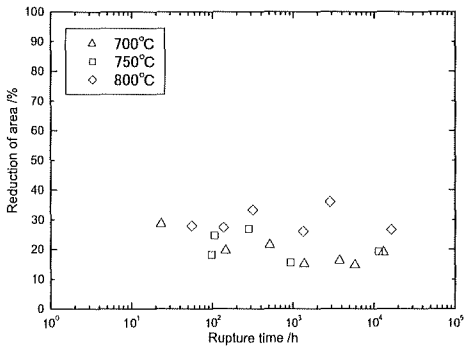

Fig. 9 Creep rupture ductility of HR35

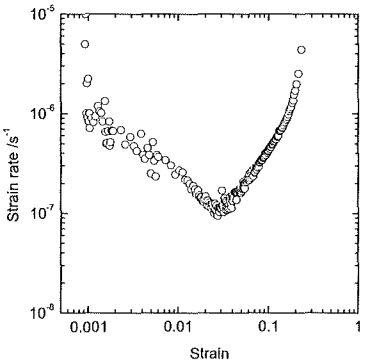

Fig. 10 Creep rate vs. strain curve of HR35 at 750°C, 150MPa.

3.2. Microstructure

TEM observations of the crept specimen have revealed that fine dispersion of Laves phase in HR6W has been kept even after long-term creep deformation for 58798h at 700°C (Fig. 11 (a)). Laves phase slightly coarsens at higher temperatures as shown in Figs. 11 (b) and (c). It is, however, noted that the amount of Laves phase does not decrease rapidly, as indicated by computed results [14]. Furthermore, coarse and brittle intermetallic phases, such as σ, have not been identified in the long-term creep ruptured samples (Fig. 12). Those may lead to relatively stable long-term creep rupture strength as shown in Fig. 5.

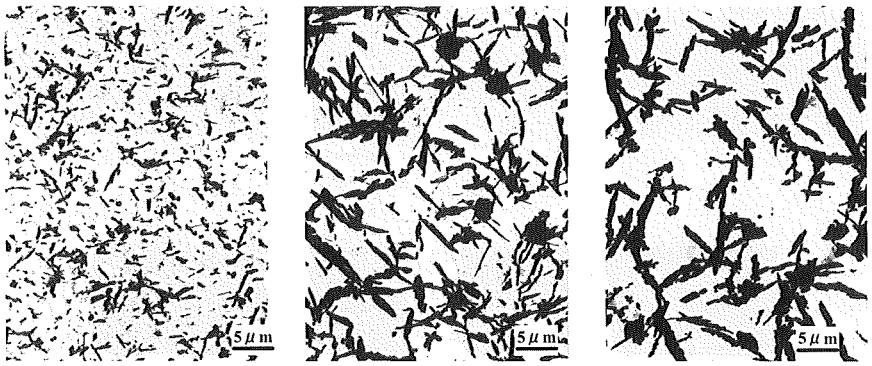

(a) 700°C, 98MPa, 58798h (b) 750°C, 88MPa, 16039h (c) 800°C, 69MPa, 7306h

Fig. 11 TEM images of extracted replica for HR6W crept at 700, 750 and 800°C.

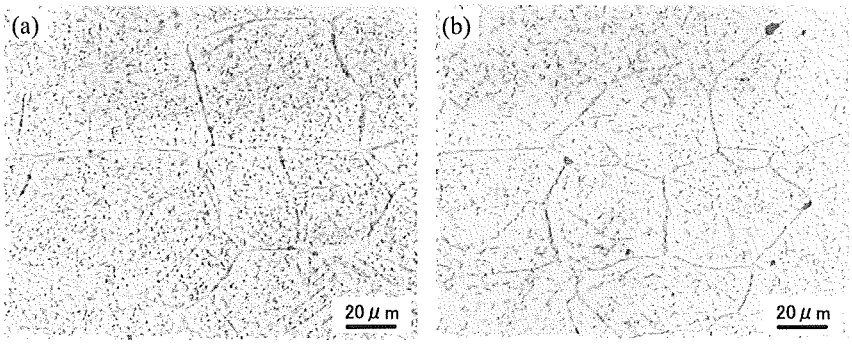

(a) 700°C, 98MPa, 58798h (b) 750°C, 88MPa, 16039h

Fig. 12 Optical micrographs of HR6W after creep rupture.

Fig. 13 shows optical micrographs of HR35 crept for 13110h at 700°C with 157MPa and for 16259h at 800°C with 59MPa. σ phase and other coarse, brittle intermetallic phases have not been identified. Results of EPMA analysis of the grain boundary in HR35 crept at 700°C are shown in Fig. 14. It is seen that Cr carbides precipitate and cover the grain boundary of HR35. These are $M_{23}C_6$ and may contribute to grain boundary strengthening. Fig. 15 shows a TEM image of the same crept samples at 700°C for 13110h. It is noted that the α-Cr phase is relatively small even after long-term creep deformation. These

microstructural stability and strengthening of α-Cr phase results in excellent creep strength and ductility.

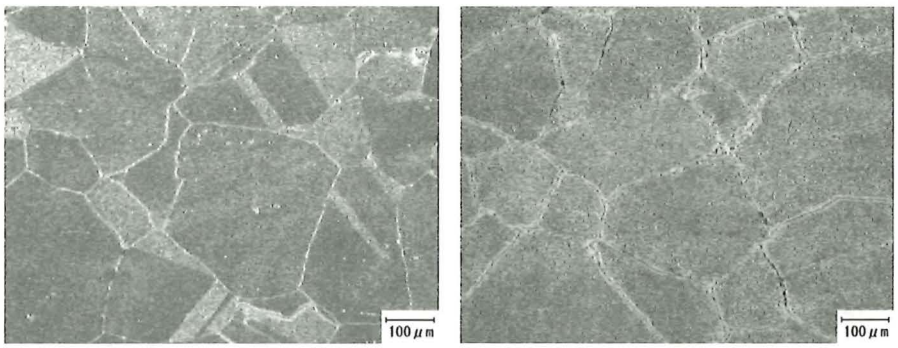

(a) 700°C, 157MPa, 13110h (b) 800°C, 59MPa, 16259h

Fig. 13 Optical micrographs of HR35 after creep rupture.

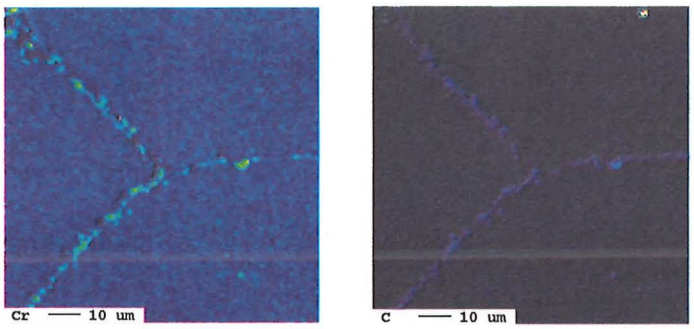

(a) Cr (b) C

Fig. 14 Results of EPMA analysis for HR35 crept for 13110h at 700°C with 157MPa .

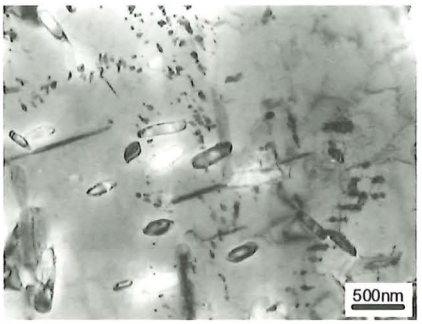

Fig. 15 TEM image of HR35 crept for 13110h at 700°C with 157MPa .

4. Capability of HR6W and HR35 as A-USC boiler alloys

Creep-fatigue tests for HR6W and Alloy 617 have been carried out at 700°C [15] as shown in Fig. 16. It has been revealed that creep-fatigue life of HR6W under the CP (slow-fast) type strain waveform is much longer than that of Alloy 617, resulting from its higher creep ductility compared with Alloy 617 (see the reference [15]). Slow strain-rate tensile tests have been carried out in order to reveal the resistance to relaxation cracking [16]. The observed tensile ductility at the strain-rate of 10^{-6}/s is shown in Fig. 17. It is found that HR6W and HR35 have excellent ductility compared with Alloy 617 at around 700°C. These results indicate that HR6W and HR35 have high resistance to relaxation cracking after welding. Weldability of both the developed alloys has also been confirmed. Fig. 18 shows the appearance of welded joints consisting of HR6W, HR35 and Alloy 617 tubes with the Alloy 617 filler. It has been shown that they can be welded without defect.

Gleeble testing has revealed that hot workability of HR6W and HR35 is much better than Alloy 617. Indeed, thick wall pipes, which are 350mm in diameter and 40mm in wall thickness, have been successfully manufactured by Erhart Push Bench press method (Fig. 19). It has been confirmed that other size of pipes, such as 457mm in diameter and 60mm in wall thickness can be manufactured for HR6W [17]. Considering these results in addition to excellent creep properties and microstructural stability mentioned before, it is concluded that HR6W and HR35 are promising candidates for A-USC components, especially for thick wall piping.

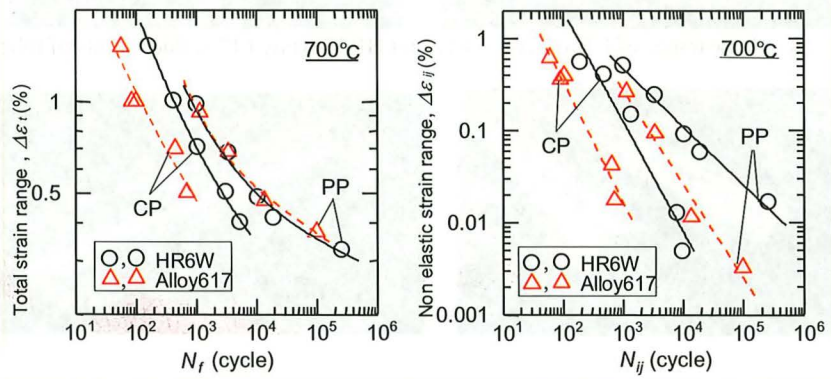

Fig. 16 High temperature creep-fatigue properties of HR6W and Alloy 617 [15]. Strain PP (fast 0.8%/s-fast 0.8%/s), CP (slow 0.01%/s-fast 0.8%/s)

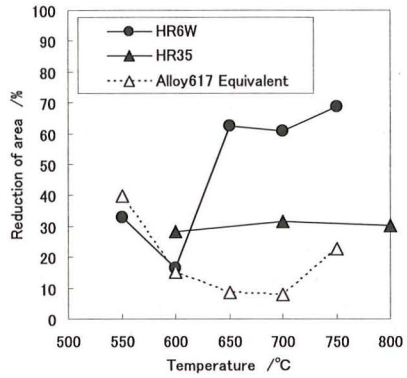

Fig. 17 Tensile ductility of HR6W and HR35 at the strain-rate of 10^{-6}/s.

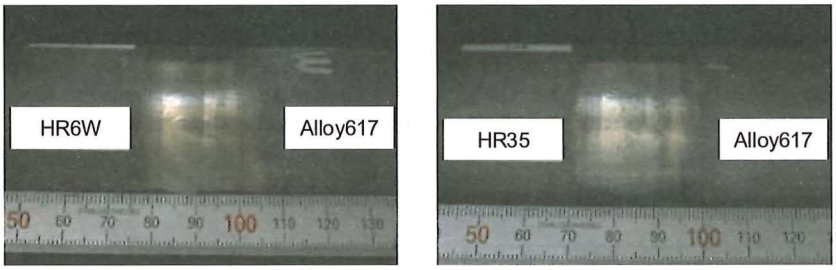

Fig. 18 Appearance of HR6W/Alloy 617 and HR35/Alloy 617 welded joints of tubes.

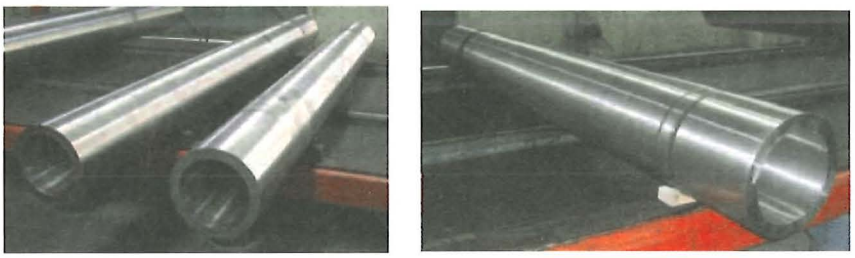

HR6W HR35

Fig. 19 Appearance of thick wall pipes of HR6W and HR35 (350 ϕ ×40t).

5. Conclusions

An Fe-Ni base alloy, HR6W strengthened by Fe_2W type Laves phase is a marginal strength level material with good ductility for large diameter thick wall piping such as main steam pipes and hot reheat pipes. A new Ni-base alloy, HR35 has been proposed for piping in A-USC plants, which is strengthened by α-Cr phase and other intermetallic phases without γ′ strengthening. This alloy is specially designed for good resistance to relaxation cracking as well as high strength and good corrosion resistance at higher temperature over 700°C. It is,

therefore, concluded that both the alloys are promising candidates especially for thick wall piping in A-USC power plants.

References

[1] R. Blum and R. W. Vanstone, Materials for Advanced Power Engineering 2006, Proceedings of the 8th Liege Conference (2006), pp.41-60.
[2] R. Viswanathan and R. Purgert, Proceedings of 8th International Conference on Creep and Fatigue at Elevated Temperatures, July 22-26, 2007, CREEP2007-26826.
[3] F. Masuyama, Materials for Advanced Power Engineering 2006, Proceedings of the 8th Liege Conference (2006), pp.175-187.
[4] J. Iwasaki, A. Shiibashi, S. Takano. T. Sato, H. Okada and F. Abe, The Thermal and Nuclear Power, 58(2007), pp.649-655.
[5] T. Fujikawa, M. Fukuda, E. Saito, T. Takahashi and S. Izumi, The Thermal and Nuclear Power, 58(2007), pp.656-662.
[6] M. Fukuda, Proceedings of 3rd Symposium on Heat Resistant Steels and Alloys for High Efficiency USC Power Plants, 2009.
[7] http://www.enecho.meti.go.jp/info/tender/tenddata/0806/080626a/1.pdf
[8] M. Speicher, A. Klenk, K. Maile and E. Roos, Proceedings of 3rd Symposium on Heat Resistant Steels and Alloys for High Efficiency USC Power Plants, 2009.
[9] Y. Sawaragi, Y.Hayase and Y. Yoshikawa, Proceedings of International Conference on Stainless Steels, Chiba, ISIJ (1991), p.633
[10] H. Semba, M. Igarashi, Y. Yamadera, A. Iseda and Y. Sawaragi, Report of the 123rd Committee on Heat-Resisting Materials and Alloys, JSPS, 44 (2003), pp. 119-127.
[11] M. Igarashi, H. Semba and H. Okada, Proceedings of 8th Workshop on the Innovative Structural Materials for Infrastructure in 21st Century, NIMS, Tsukuba, Japan (2004), pp.194-199.
[12] Y. Sawaragi, H. Teranishi, K. Yoshikawa and N. Otsuka, *Tetsu-to-Hagané*, 70 (1984). p.s1409.
[13] ECCC Creep Datasheets 2005
[14] H. Semba, H. Okada, M. Yonemura and M. Igarashi: Proceeding of 34th MPA-Seminar, 2008, Stuttgart, Germany, Paper No. 14.1.
[15] Y. Noguchi, M. Miyahara, H. Okada, M. Igarashi and K. Ogawa, Proceedings of 8th International Conference on Creep and Fatigue at Elevated Temperatures, July 22-26, 2007, CREEP2007-26471.
[16] H. Okada, H. Hirata, H, Semba and M. Igarashi, Proceedings of 8th NIMS-MPA-IfW Workshop on Advances in High Temperature Materials for High Efficiency Power Plants, March 24-26, 2010, NIMS, Tsukuba, Japan
[17] A. Iseda, H. Okada, H. Semba, M. Igarashi and Y. Sawaragi, Proceedings of Symposium on Heat Resistant Steels and Alloys for USC power Plants 2007, July 2-6, 2007, Seoul, Korea, pp.229-237.

9th Liege Conference : Materials for Advanced Power Engineering 2010
edited by J. Lecomte-Beckers, Q. Contrepois, T. Beck and B. Kuhn.

Microstructure Development of Welding Joints in High Cr Ferritic Steels

Keiji KUBUSHIRO, Satoshi TAKAHASHI, Keiko MORISHIMA

Research Laboratory IHI corporation

Abstract

Creep failure in high Cr ferritic steels welding joints are Type IV failure. Type IV failure was ruptured in fine grained region of heat affected zone, microstructure and phase transformation process at welding in fine grained region were very important to clarify.Microstructure difference of heat affected zone was investgated in Gr.91, Gr.92, Gr. 122 welding joint. The fraction of 60degree block boundary, packet boundary, random boundary (including prior gamma boundary) length was compared in three ferritic steels by EBSP(Electron Backscatter Diffraction Pattern) analysis. HAZ was almost fully martensite phase in Gr.122 weld joint. On the other hand, HAZ in Gr.91 welding joint were some equiaxial grain and martensite strucutre.

Keywords: High Cr ferritic steel, Heat affected zone, Martensite, Weld joint, EBSP(Electron Backscatter Diffraction Pattern)

1. Introduction

High Cr ferritic heat resistant steels, which in the 1990s were put into actual use for applications such as large-diameter thick-walled tubes in 600°C-class thermal power plants in Japan[1], are now being utilized in many plants. Particularly, applications of ferritic heat resistant steels aiming for higher strength, such as Gr.91, Gr.92, and Gr.122, have recently been advancing in many areas. These three types of steel all have a tempered martensitic lath structure, achieving high creep strength by dislocation strengthening through the introduction of dislocation at the quenching stage and by precipitation dispersion strengthening through the fine precipitation of carbides both on grain boundaries and within grains at the temper heat treatment stage. In addition, the creep rupture strength of welded joints of high Cr ferritic heat resistant steels is lower than that of the base material, causing Type-IV cracking that occurs at the HAZ fine-grained region of the heat affected zone[2]-[7]. Research on the occurrence of Type-IV cracking and creep voids has been reported in many types of steel. For example, it has been reported for the creep deterioration of Gr.91 welded joints where creep voids occur from the first half of its life, develop to combine together, and eventually cause a fracture. On the other hand, the creep deterioration of Gr.122 joints occurs after the middle stage of its life. Thus the generation mechanism of creep voids can be expected to differ depending on the types of individual steels. The present research examines the differences in structure by focusing on the material structure of Gr.91 and Gr.122 welded joints.

2. Experimental Method

Test specimens were made of either Gr.91 or Gr.122. They underwent annealing and tempering. Table 1 shows the welding procedures and PWHT conditions. In order to observe the changes dependent on post-weld heat-treatment time, heat treatment was applied to Gr.91 under four different conditions. The EBSP method was used for measuring the crystal orientation. Test specimens were polished with emery paper up to grade #1500 and then chemically polished in OPA (opaque: alumina suspension) for 30 minutes before observed by the EBSP method. The measurement pitch was 0.2 μm, the measurement range of KA-SUS410J3TP was 30 μm × 50 μm, and the measurement range of KA-SCMV28 was 40 μm × 80 μm. The measurement was carried out at eight points between the weld line and the HAZ region/base material at a 0.5-μm pitch.

Table 1 Welding condition and PWHT condition

Steel	Welding method	PWHTcondition
Gr.91	SAW	1013K x 0,2,12,24,48h
Gr.122	SMAW	1013K x 8h

3. Experimental Results

3.1 Structure analysis method

We carried out a martensite structure analysis by using the EBSP method as our structure analysis method. The EBSP method uses crystal orientation data to allow us to identify grain boundaries with the same orientation relationship as block boundaries and packet boundaries. The K-S (Kurdjumov-Sacks) relationship holds and 24 variants exist on block boundaries and packet boundaries[8],[9]. In this measurement, however, 4 combinations of rotation axes and rotation angles for block boundaries and 12 combinations of them for packet boundaries were adopted because the martensite structure was dealt with as a BCC structure and the rotation axes and rotation angles were calculated only from the orientation relationship between two measurement points. Tables 2 shows the relationship between the rotation angles and the rotation axes used for the calculation. We calculated the length of each grain boundary from the data in these tables with the allowance of 5° for the rotation angles. The rotation axes are set for the error from the real value to be within 3°. Figure 1 shows the analytical results for Gr.91. The gray lines represent grain boundaries with the same orientation as block boundaries, the black lines represent grain boundaries with the same orientation as packet boundaries and the other grain boundaries. In Figure 1, both block and packet boundaries in the martensite structure are clearly identified. Particularly in the present research, we analyzed the structure by focusing on block boundaries.

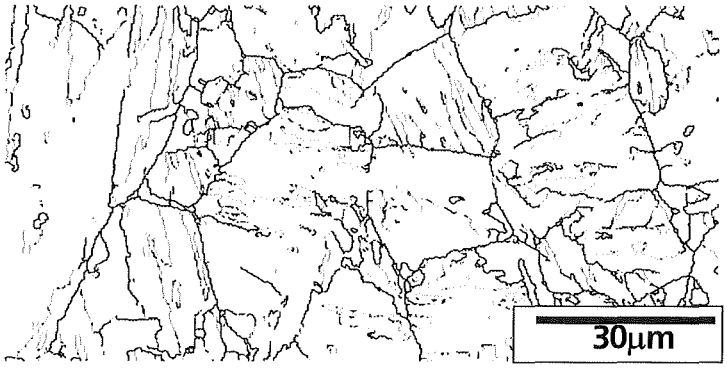

Fig.1 EBSP image of base metal in Gr.91

Table 2 K-S relationship of boundary

Packet boundary					Block boundary				
No	angle	Rotation Axis			No	Angle	Rotation Axis		
	°	h	k	l		°	h	k	l
1	10	-1	1	1	1	11	0	-1	1
2	15	-14	5	-1	2	49	0	1	-1
3	21	-2	-2	1	3	60	0	-1	1
4	21	-3	0	1	4	60	-1	1	1
5	21	-2	-1	0					
6	47	7	-3	-6					
7	49	1	-1	-1					
8	50	-1	4	-3					
9	51	5	5	8					
10	52	2	1	2					
11	57	7	-2	-6					
12	57	-4	7	6					

3.2 EBSP images of welded joints

Figure 2 shows the analytical results for the structure in the Gr.91 weld-heat affected zone through the method described in 3.1. The coarse grain area shown in (a) is a tempered martensitic structure, where gray-colored block boundaries are clearly observed. In the region 2.0 mm from the weld line shown in (b), only few block boundaries are identified, whereas many equiaxed grains are observed. Figure 3 shows the results of the structural observation of Gr.122. In the region 0.5 mm from the weld line shown in (a) (corresponding to the HAZ coarse grain area), many linear block boundaries are identified. This trend is also found in Gr.91. In the region 2.0 mm from the weld line (corresponding to the HAZ fine grain area), clear block boundaries are also observed, whereas almost none of the equiaxed grains identified in Gr.91 are observed. Similarly, in the region 3.5 mm from the weld line shown in (c) (corresponding to the base material), equiaxed grains are also not identified.

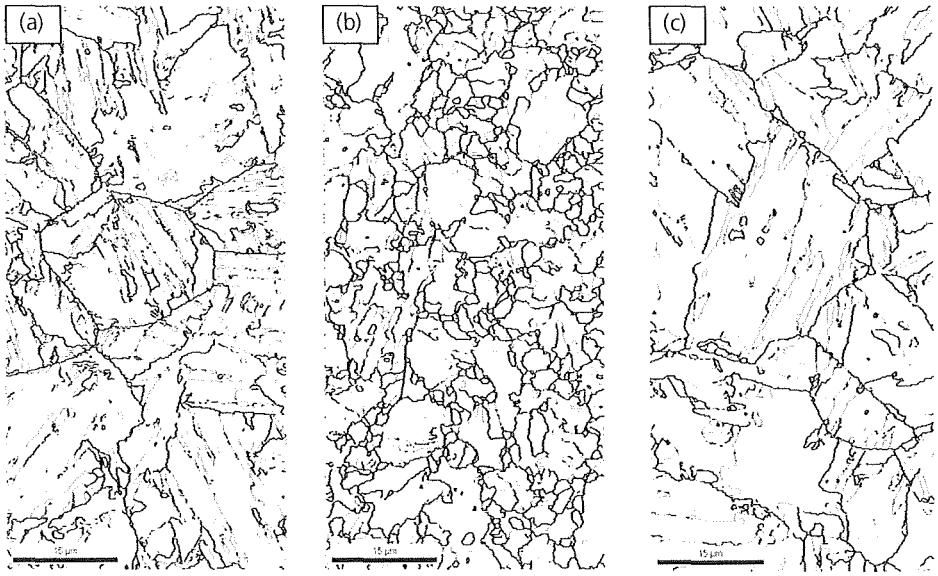

Fig.2 Grain boundary maps of Gr.91 (a) HAZ region in 0.5mm distance from bond line

(b) HAZ region in 2mm distance from bond line, (c) HAZ region in 3.5mm distance from bond line

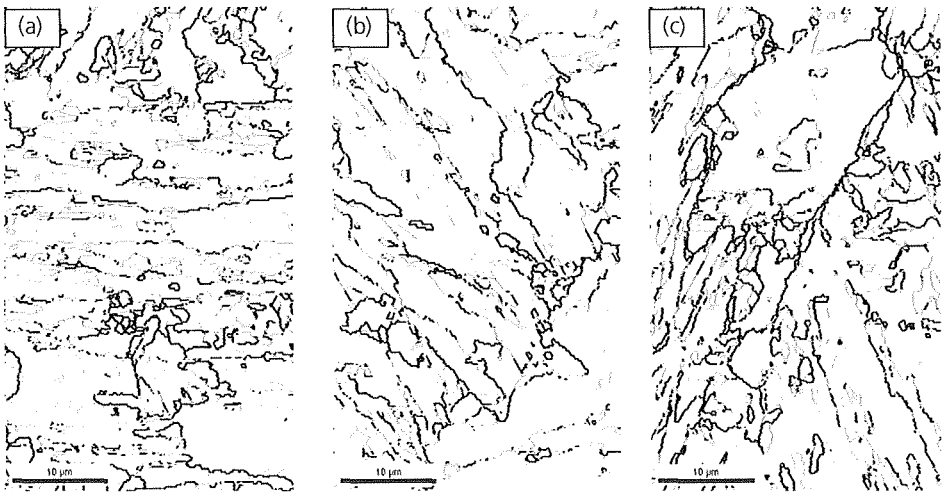

Fig.3 Boundary maps in Gr.122 (a) HAZ region in 0.5mm distance from bond line

(b) HAZ region in 2.0mm distance from bond line(c) HAZ region in 3.5mm distance from bond line

3.3 Comparison of grain boundary distributions

In order to quantify the proportion of grain boundaries, we examined the distribution of rotation angles. Figure 4 shows the distribution of rotation angles in the grain boundaries of Gr.91 welded joints. The distribution of the rotation angles shown here represents the proportion of all the grain boundaries, because the rotation axes are not taken into account. There is a sharp peak of block boundaries in the vicinity of 60°, so that the distribution is divided into two regions of 5° to 50° and 50° to 64° to be shown. The symbol ▼ indicates the same rotation angle as that of the block boundary, and the symbol ▽ indicates the same rotation angle as that of the packet boundary. The measurement was carried out at a 0.5-mm pitch from the weld line. The region 3.5 mm from the weld line is little affected by heat. In the region 0.5 mm from the weld line and the base material region 3.5 mm from the weld line, peaks are identified in part of the rotation angles of block and packet boundaries; particularly, the peak is highest at 60°, corresponding to the block boundary. In addition, almost no grain boundaries between 22° and 46°, which do not exist in the K-S relationship, are identified. On the other hand, in the region 1.5 mm to 2.5 mm from the weld line, which is assumed to be in the HAZ fine grain area, the grain boundary proportion at 60° decreases, whereas the grain boundaries between 22° and 46° occupy large proportion. With the results of the structural observation shown in Figure 4 taken into account, the grain boundaries in the region of angles between 22° and 46° presumably consist of the grain boundaries of fine grains. This dissipation of the orientation relationship allows us to presume that equiaxed fine grains were heated and then cooled from the α' (martensite) single-phase region to the $\alpha + \gamma$ (ferrite and austenite) 2-phase region at welding, undergoing transformation from α' to γ and then to α' or transformation from α' to α over the entire process including the subsequent post-weld heat treatment.Figure 5 shows the analytical results for Gr.122 welded joints. Unlike the welded joints of Gr.91 heat resistant steels, Gr.122 welded joints have a substantially low proportion of boundaries other than block and packet boundaries between 22° and 46° in all the regions. Thus, even if affected by welding heat, Gr.122 presumably maintains the tempered martensitic structure on almost the entire surface, unlike the two other steels. It is supposed that, with the γ transformation caused by crystal nucleation reduced, the γ transformation caused by shear is increased during the rapid heating of welding in Gr.122 compared with Gr.91 and Gr.92. The behavior of Gr.122 differs from the other steels presumably because it contains more Cr than 9Cr steel and also contains Cu in its composition.

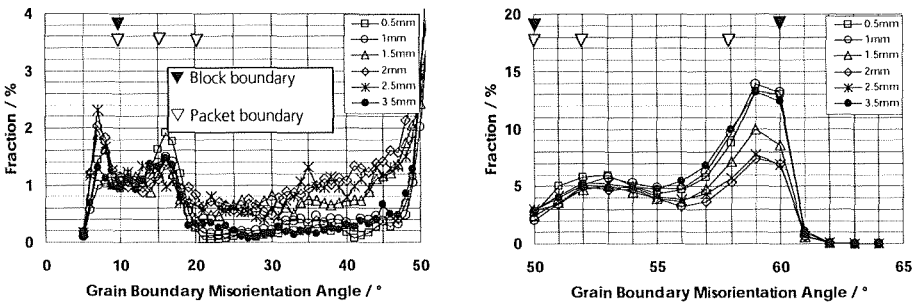

Fig.4 Relationship between grain boundary misorientation and fraction in Gr.91

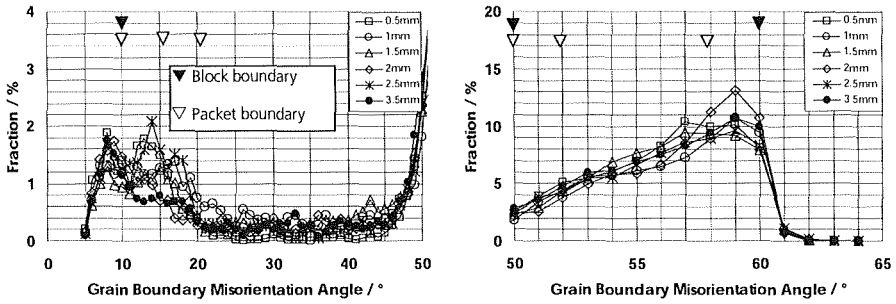

Fig.5 Relationship between grain boundary misorientation and fraction in Gr.122

3.4 Structural change of Gr.91 weld-heat affected zone in PWHT treatment

Only Gr.91 welded joints developed numerous equiaxed grains in the HAZ fine grain area. In order to examine the formation mechanism of the equiaxed grains, we observed the as-welded structure. Figure 6 shows the results for the as-welded EBSP structure observation. The region 0.5 mm from the weld line shown in (a) (corresponding to the HAZ coarse grain area) is characterized by linear block boundaries, which is a characteristic of lath martensite. In the region 2.0 mm from the weld line shown in (b) (corresponding to the HAZ fine grain area), many extremely fine grains with a diameter of about 1 μm are identified. In the region 3.5 mm from the weld line shown in (c) (corresponding to the base material), block and packet boundaries, the characteristics of tempered martensite, are clearly identified. In addition, many grain boundaries that have the same orientation relationship as the block boundaries are observed in (b). However, it has been clarified that, unlike the boundaries shown in (a) and (c), the grain boundaries shown in (b) are non-linear and very short, being found in the grain boundaries of fine grains. Moreover, a few block boundaries with a length

of more than 10 μm are present. These grain boundaries are about as long as the block boundaries of the base material.

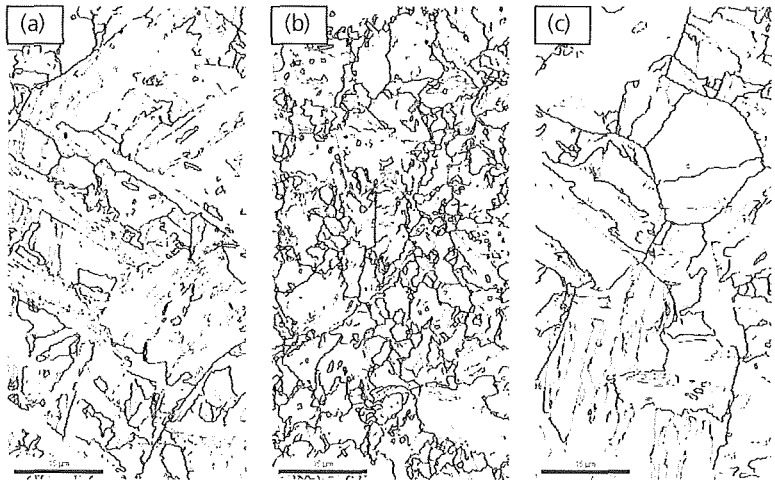

Fig.6 Grain boundary maps of Gr.91 (a) HAZ region in 0.5mm distance from bond line

(b) HAZ region in 2mm distance from bond line, (c) HAZ region in 3.5mm distance from bond line

This fact allows us to presume that they had been present before welding. Figure 7 shows the examination results for the structural change of the region 2.0 mm from the weld line. The comparison of the as-welded structure shown in (a) with the structure after heated at 740°C for two hours shown in (b) reveals that fine grains surrounded by fine block boundaries have been dissipated due to tempered heat treatment. In addition, the number of linear crystal grain boundaries has been decreased with spheroidization progressing. In the structure after 48-hour tempering shown in (c), fine grains and coarse grains have formed a duplex grain structure with equiaxed crystal grains developing. Moreover, this structure shows that linear block boundaries exist among coarse grains even after 48-hour tempering. It is thought that these block boundaries are martensitic grain boundaries remaining even at heating by welding. Figure 3-8 shows the relationship between the length of grain boundaries between 57° and 62° in the region 2.0 mm from the weld line and the heat-treatment time. This relationship is used for quantifying the length of block boundaries. This length of grain boundaries is that of the grain boundaries contained in the measurement area of 40 μm × 80 μm. For comparison, the results for the region 3.5 mm from the weld line (corresponding to the base material that has not been affected by welding heat) are also shown. In the region 2.0 mm from the weld line, brief tempering caused the length of the block boundaries between 57° and 62° to decrease by about one-half from 1600 μm to 900 μm. This decrease is due to the dissipation of fine grains surrounded by fine block boundaries as described in the results of the structural observation. As tempering time increases, the length of block boundaries decreases to reach 600 μm after

48 hours. In the region of the base material, on the other hand, the length of block boundaries during tempering ranged from 1000 μm to 1100 μm and deceased only to about 900 μm even during prolonged tempering lasting 48 hours. Therefore, almost all of the martensitic structure formed in welding dissipates in tempering, and only the region of martensitic structure that had been formed before welding presumably remains without undergoing virtually any changes in structure during tempering. Thus, it is thought that in Gr.91, unlike in Gr.122, the equiaxed structure developed in post-weld heat treatment.

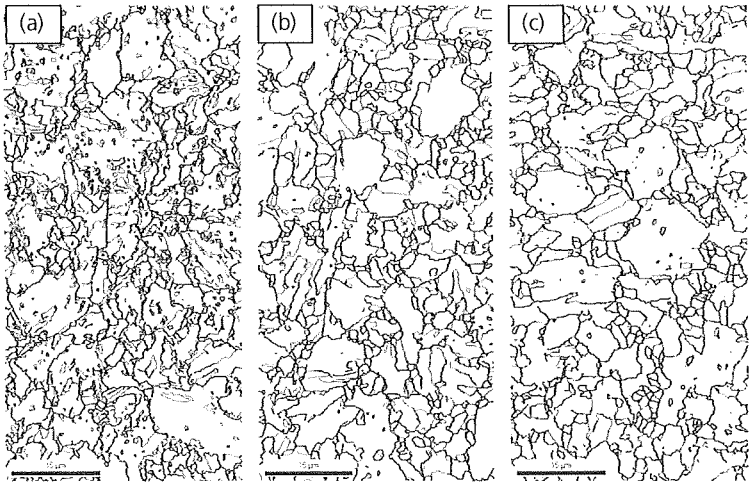

Fig.7 Boundary map at the HAZ region on distance from 2.0mm in as-welded Gr.91

(a) is as welded, (b) is 740C x 2hr, (c) is 740C x 48hr

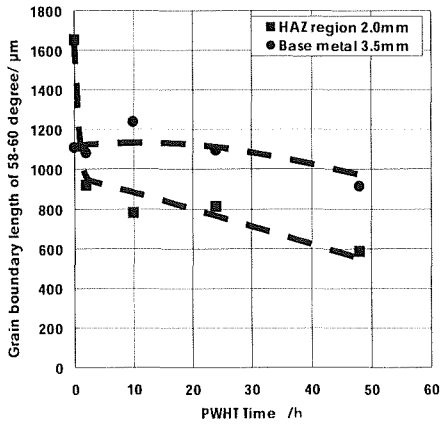

Fig.8 The Changing of Block boundary length with PWHT time

4. Conclusions

We observed the structure of Gr.91 and Gr.122 welded joints by using the EBSP method. We also examined the effects of PWHT treatment on the Gr.91 structure. The following information has been obtained.

1) In part of the Gr.91 weld-heat affected zone, many grain boundaries between 22° and 46° have been observed that are not block or packet boundaries. The grain boundaries are observed most at 60°. In the HAZ fine grain area, block grains with the same size as grains in the base material and fine martensite formed a duplex structure. This fact allows us to presume that transformation occurred from α' to $\alpha' + \gamma$ and then to α'.

2) In the Gr.122 weld-heat affected zone, almost no grain boundaries were found other than block and packet boundaries. The proportion of block boundaries was almost constant regardless of the distance from the weld line.

3) Temper heat treatment dissipated fine martensite in the structure of the Gr.91 HAZ fine grain area, allowing us to observe an equiaxed structure. This phenomenon is presumably because the recovery progression in tempering induced recrystallization.

Reference list

[1] H. Umaki, I. Kajigaya, T. Kunihiro, T. Totsuka, M. Nakashiro and R. Kume "Application of Large Diameter Steam Welded and Header of Super 9Cr Steel for 700MW Coal-Fired Boiler with 593C Reheat Steam Temperature" Ishikawajima-Harima Engineering Review, Vol.31, No.5, pp.339-345(1991).

[2] N. Komai and F. Masuyama "Microstructural Degradation of the HAZ in 11Cr-0.4Mo-2W-V-Nb-Cu Steel(P122) during Creep", ISIJ international, Vol.42, No12, pp.1364-1370 (2002)

[3]M. Tabuchi, H. Hongo and Y. Takahashi " Effect of Boron on Microstructures and Creep Properties of Welded Joint for High Cr Heat Resisting Steels" Journal of the Society of Materials Scinence, Japan, Vol.58, No.2, pp108-113 (2009).

[4] T. Ogata, T. Sakai and M Yaguchi "Uniaxial Creep Rupture Property of Mod.9Cr-1Mo steel Weld Joint and Proposal of Creep Damage Evaluation Method", Journal of the Society of Materials Scinence, Japan, Vol.58, No.2, pp.94-100 (2009).

[5] H. Hongo, M. Tabuchi, Y. Li and Y. Takahashi " Creep Damage Behavior of Mod.9Cr-1Mo Steel Welded Joint" Journal of the Society of Materials Scinence, Japan, Vol.58, No.2, pp101-107 (2009).

[6] Y. Hasegawa, T. Muraki and M. Ohgami "Identification and Formation Mechanism of a Deformation Process Determining Microstructure of Type IV Creep Damage of the Advanced High Cr Containing Ferritic Heat Resistant Steel" Tetsu-to-Hagane, Vol.90, No.10, pp.609-617 (2004).

[7] H. Hongo, Masaaki Tabuchi, T. Watanbe and Y. Takahashi "Type-IV Damage Behavior in P122 Steel Weld" Proceedings of the 58th JSMS Annual Meetings pp.371-372 (2009) JSMS.

[8] S. Morito , H. Tanaka, R. Konishi, T. Furuhara, T. Maki "The Morphology and Crystallography of Lath Martensite in Fe-C Alloys" Acta Materialia Vol.51, pp.1789–1799 (2003)

[9] H.Kitahara, R.Ueji, N. Tsuji, Y.Minamino "Crystallographic Features of Lath Martensite in Low-Carbon Steel" Acta Materialia., Vol.54, pp.1279-1288 (2006).

9th Liege Conference : Materials for Advanced Power Engineering 2010
edited by J. Lecomte-Beckers, Q. Contrepois, T. Beck and B. Kuhn.

CREEP PROPERTIES AND MICROSTRUCTURE OF THE NEW WROUGHT AUSTENITIC STEEL

T.Vlasák[1]-J.Hakl[1]-P.Novák[1]-A.Výrostková[2]

[1]SVÚM a.s., Prague, Czech Republic
[2] Slovak Academy of Sciences, Institute of Materials Research, Košice, Slovakia

Abstract

The contribution is oriented on the new wrought austenitic steel BGA4 developed by the British Corus Company. Our main aim is to present creep properties studied in SVUM a.s. Prague during COST 536 programme. The dependencies of the creep strength, strength for specific creep strain and minimum creep strain rate were evaluated on the basis of long term creep tests carried out at temperature interval (625; 725)°C. Important part of a paper is metallographic analysis.

Key words: austenitic steel, creep, long term exposure, delta ferrite, metallography.

1. Introduction

Austenitic steels are used in temperatures within 620 up 680°C in area against creep and corrosion is required. These steels can be devided into four categories: 18Cr-8Ni, 15Cr-15Ni, 20Cr-25Ni and higher content of Cr and Ni. Survey of this material, which is convenient in energy industry, is shown in Tab.I [1].

Tab.I. Nominal chemical composition of austenitic steels for boiler (wt %).

Type of material	Steel	C	Si	Mn	Ni	Cr	Mo	W	V	Nb	Ti	B	Other
18Cr-8Ni	ASME TP304H	0,08	0,6	1,6	8,0	18,0	-	-	-	-	-	-	-
	Super 304H	0,10	0,2	0,8	9,0	18,0	-	-	-	0,40	-	-	3,0Cu 0,10N
	ASME TP321H	0,08	0,6	1,6	10,0	18,0	-	-	-	-	0,5	-	-
	Tempaloy A-1	0,12	0,6	1,6	10,0	18,0	-	-		0,10	0,08	-	-
	ASME TP316H	0,08	0,6	1,6	12,0	16,0	2,5	-	-	-	-	-	-
	ASME TP347H	0,08	0,6	1,6	10,0	18,0	-	-	-	0,8	-	-	-
15Cr-15Ni	17-14CuMo	0,12	0,5	0,7	14,0	16,0	2,0	-	-	0,4	0,3	0,006	3,0Cu
	Esshete 1250	0,12	0,5	6,0	10,0	15,0	1,0	-	0,2	1,0	0,06	-	-
20-25Cr 15-32Ni	ASME TP310	0,08	0,6	1,6	20,0	25,0	-	-	-	-	-	-	-
	HR3C	0,06	0,4	1,2	20,0	25,0	-	-	-	0,45	-	-	0,2N
	Alloy 800H	0,08	0,5	1,2	32,0	21,0	-	-	-	-	0,5	-	0,4Al
	Tempaloy A-3	0,05	0,4	1,5	15,0	22,0	-	-	-	0,7	-	0,002	0,15N
	NF 709	0,15	0,5	1,0	25,0	20,0	1,5	-	-	0,2	0,1	-	-
	SAVE25	0,10	0,1	1,0	18,0	23,0	-	1,5	-	0,45	-	-	3,0Cu 0,2N
high Cr	CR30A	0,06	0,3	0,2	50,0	30,0	2,0	-	-	-	0,2	-	0,03Zr
high Ni	HR6W	0,08	0,4	1,2	43,0	23,0	-	6,0	-	0,18	0,08	0,003	-

In British company CORUS four austenitic steels have been investigated – see Tab.II. Content of Cr is higher for better resistance against corrosion. They contain also higher quantity of austenite-stabilizing element Mn, austenitic element Mn and alloying additions are more complex [2].

In SVÚM was studied creep resistance of one of these steels – BGA4. The aim of this contribution is to present results of creep testing. Our description is concerned in creep rupture strength, strength for specific creep strain and creep rate. Detailed description of microstructure is important part of the contribution.

Tab.II. Nominal chemical composition of CORUS steel (wt %).

Type of material	Chemical composition											
	C	Si	Mn	Ni	Cr	Mo	W	V	Nb	B	N	Cu
BGA1	0,11	0,64	6,3	15,2	23,1	1,0	-	0,29	0,19	0,005	0,095	-
BGA2	0,11	0,54	9,7	13,0	23,2	1,0	-	0,30	0,57	0,005	0,18	-
BGA3	0,11	0,55	6,2	15,0	23,1	1,0	-	0,30	0,57	0,006	0,18	3 Cu
BGA4	0,10	0,54	6,1	14,9	22,8	0,2	1,4	0,29	0,57	0,006	0,19	3 Cu

2. Experimental material

The CORUS company supplied to SVUM the best material BGA4 material (containing W) – identified as CORUS CODE H4F53 – with chemical composition stated in Table III. The supply included rods with length of 160-300 mm with diameter of approximately 20 mm that had been rolled from original material with cross section with diameter of 183 mm. The rods were subjected to an ultrasound test the aim of which was to identify internal defects. This test did not reveal any defects that could be affecting consequent results. The experimental material was heat treated using the 1 200°C/20 min/water procedure at the manufacturer. Test specimens with specific dimensions of ∅ 5x25 mm were made and creep tests carried out in SVÚM.

Tab. III – Chemical composition of BGA4 steel (wt.%)

C	Si	Mn	P	S	Cr	Mo	Ni	B	Nb	V	N	Cu	W
0,11	0,49	6,10	0,02	0,024	22,9	0,14	15,4	0,007	0,61	0,31	0,185	2,70	1,49

The creep tests were performed at temperatures 625-725°C and stress values 90-330MPa. The creep tests have been carried out on air at a constant load. Deformation time changes were measured. The SVÚM a.s. laboratory is accredited in accordance with EN ISO/IEC 17025.

3. Results of the creep tests

The dependence of stress on the Larson-Miller parameter (P_{LM}) was assessed at first. A following regression model was used for assessment [3]

$$\log\sigma = A_1 + A_2 P_{LM} + A_3 P_{LM}^2, \qquad (1)$$

where

$P_{LM}=T.(\log t_r+A_4)$,

σ is stress (MPa), T is temperature (K),

t_r is time to rupture (h), A_1-A_4 are material constants listed in Tab.IV.

Fig. 1 illustrates the results of creep tests. There is assessed the dependence of time to rupture on stress and temperatures.

Tab. IV – Material constants of regression models (1), (2) and (3).

Model					
(1)		(2)		(3)	
A_1	-2,29537364E+00	B_1	8,66864452E+00	C_1	-1,42822301E+01
A_2	5,46339300E-04	B_2	-4,48340085E-04	C_2	-2,55821347E+00
A_3	-1,49047411E-08	B_3	5,55963130E-09	C_3	-3,94226416E+00
A_4	2,16018327E+01	B_4	1,65163609E+01	C_4	-1,32610010E+01
				C_5	1,03641552E+03
				C_6	7,30214009E-06

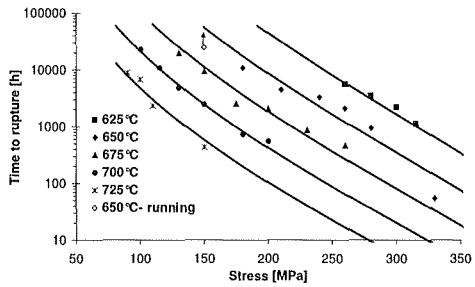

Fig. 1 Time to rupture dependence on temperature and stress of BGA4 steel

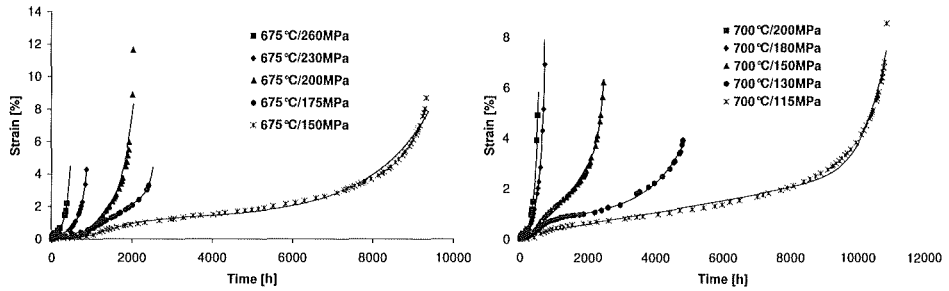

a) Curves at 675°C *b) Curves at 700°C*

Fig. 2 Creep curves of BGA4 steel

Some creep curves which were evaluated using model [4] are shown on Fig.2. The curves allowed specifying temperature and stress dependencies of the creep limit. The identical equation (1) in the form

$$\log \sigma_1 = B_1 + B_2 {}^1P_{LM} + B_3 {}^1P_{LM}^2 , \qquad (2)$$

where

$^{1}P_{LM} = T_1 \cdot (\log t_1 + B_4)$,

σ_1 is stress (MPa), T_1 is temperature (K),
t_1 is time to creep strain 1% (h), B_1-B_4 material constants given in v Tab.IV.,

was used. The result of assessment of 1% creep limit is illustrated in Fig. 3.

The model according to [5] was used to assess the creep rate.

$$\log \dot{\varepsilon} = C_1 + C_2 \cdot \log\left|\frac{1}{T} - \frac{1}{C_5}\right| + C_3 \cdot \log[\sinh(C_6 \cdot \sigma \cdot T)] + C_4 \cdot \log\left|\frac{1}{T} - \frac{1}{C_5}\right| \cdot \log[\sinh(C_6 \cdot \sigma \cdot T)], \quad (3)$$

where

$\dot{\varepsilon}$ is minimum creep rate (%/h), σ is stress (MPa),
T is temperature (K), $C_{1\text{-}6}$ are material constants shown in Tab.IV.

The assessed creep rate is illustrated in Fig. 4.

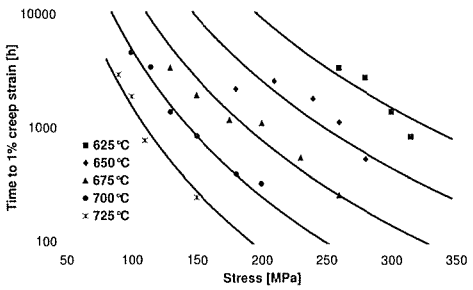

Fig. 3 Comparison rupture strength and strength for 1% creep strain of BGA4 steel

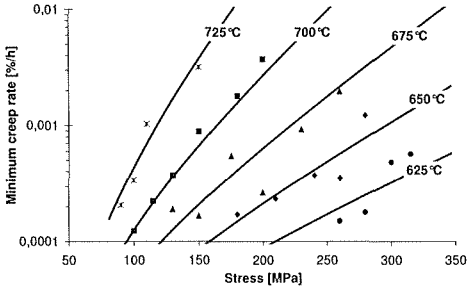

Fig. 4 Minimum creep rate of BGA4 steel

4. Occurrence of delta ferrite in structure

Delta ferrite should not be present in the BGA4 steel structure. This structural component could be transformed relatively soon to a sigma phase during exposure at higher temperatures, which would result in steel embrittlemet. Occurrence of delta ferrite can be predicted using the Schaeffler's diagram [6] which is shown in Fig. 5. The values of Cr and Ni equivalents can be calculated from the equations below [7,8]

C_{eq}= Cr+2Si+1.5Mo+5V+5.5Al+1.75Nb+1.5Ti+0.75W,

Ni_{eq}=Ni+Co+0.5Mn+0.3Cu+25N+30C,

where contents of individual elements are in weight percentage.

For BGA4 steel the values Cr_{eq}=27.83%, Ni_{eq}=27.19% were calculated. It is apparent from Fig. 5 that delta ferrite should not be present in the BGA4 steel. This structural component has not been detected during our metallographic investigation.

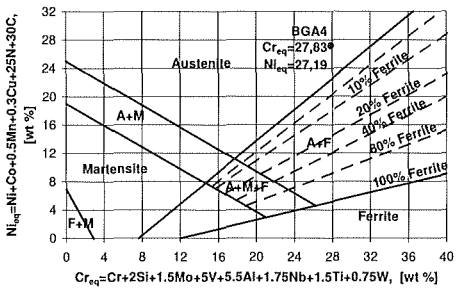

Fig.5 Shaeffler's diagram of microstructure state of BGA4 steel

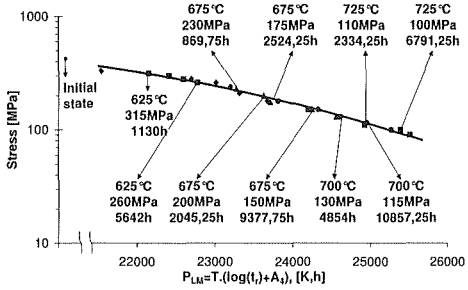

Fig. 6 Specimens chosen for metallographic study

5. Optical microscopy

Metallographic study was carried with 11 samples identified in Fig.6. The samples were prepared for examination using usual methods of grinding and polishing. An agent consisting of 10 ml of HNO3+10 ml of acetic acid + 15 ml of HCl +5 drops of glycerine was used for sample surface etching characterizing the initial condition. All the other samples were etched using an agent consisting of 2 g of CuCl2 + 40 ml of HCl + 60 ml of ethanol.

The samples had an austenitic structure. The size of grain was assessed using a comparison method with 100x magnification and it was found out to be 4.5 according to ASTM E112. The dimension of 75 μm corresponds to this value. The effect of the parameters of thermal exposure on grain coarsening was not apparent; the size of grains of the investigated samples was constant.

The structure does not contain any precipitates in the initial condition; the boundaries of grains and twins are sharp (see Fig. 7.). This figure also shows the changes that occur at exposure to a creep temperature. The structures are arranged with the time to fracture increase. However, these values are re-calculated for maximum temperature of austenitic steels application (680°C). It can be seen that precipitates create inside the grains already after a short exposure when compared with the initial condition. The precipitates coarsen with the time of temperature exposure. Growth of the particles layer connected to the carbon depleted zone thickness along the grain boundaries is another phenomenon found out. This was assessed using photographs of the individual states (from 10 to 15 states). As can be seen in Fig.8, the change of the layer thickness at grain boundaries has the opposite character than creep resistance of BGA4 steel. The size of the precipitated particles layer seems to be used to estimate the creep lifetime of real parts.

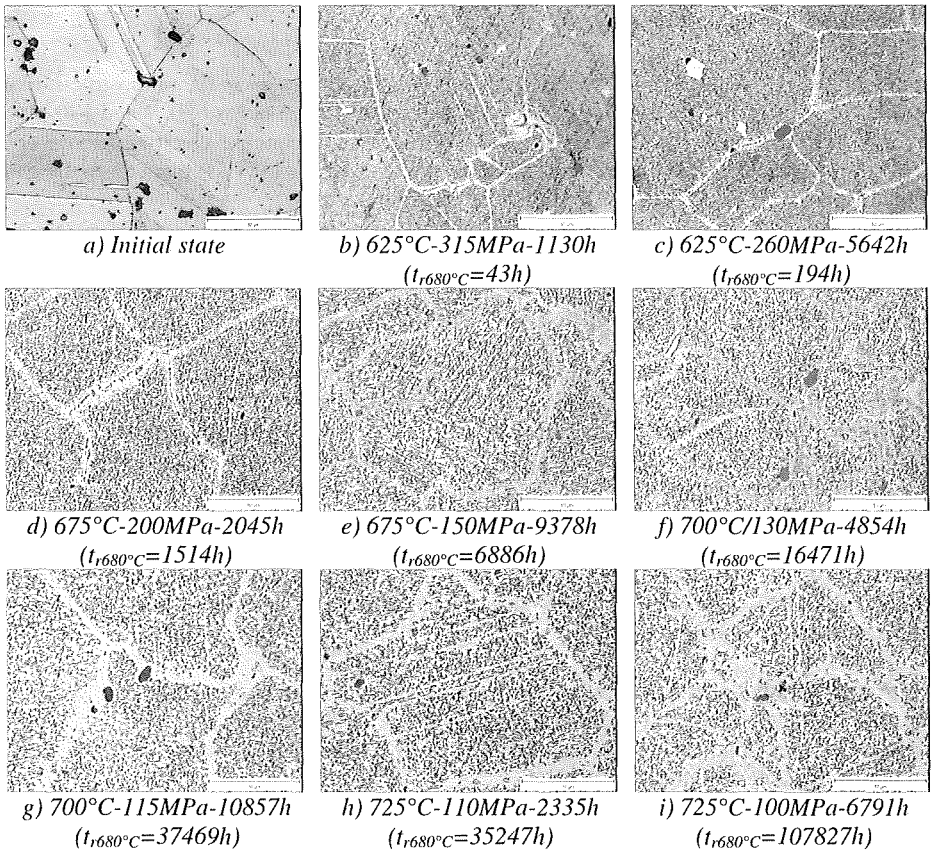

a) Initial state | b) 625°C-315MPa-1130h ($t_{r680°C}$=43h) | c) 625°C-260MPa-5642h ($t_{r680°C}$=194h)

d) 675°C-200MPa-2045h ($t_{r680°C}$=1514h) | e) 675°C-150MPa-9378h ($t_{r680°C}$=6886h) | f) 700°C/130MPa-4854h ($t_{r680°C}$=16471h)

g) 700°C-115MPa-10857h ($t_{r680°C}$=37469h) | h) 725°C-110MPa-2335h ($t_{r680°C}$=35247h) | i) 725°C-100MPa-6791h ($t_{r680°C}$=107827h)

Fig. 7 Changes of BGA4 steel microstructure caused by temperature exposure

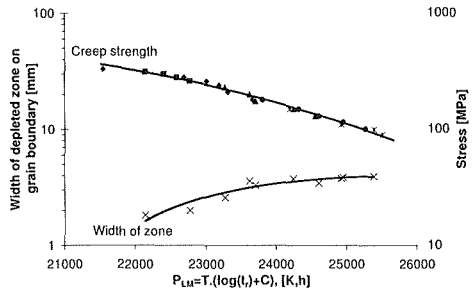

Fig. 8 Changes of particle layer at grain boundaries in relation to creep strength of BGA4 steel

6. Microstructure and phase analysis

Detailed study was performed to find out what phases are present in the microstructure of the steel. For this purpose the specimen after the creep test carried out at 650°C and 170 MPa for 2318 h was chosen. Results are described by means of scanning electron microscope (SEM) metallography, scanning transmission electron microscope (STEM) metallography and energy dispersive X-ray spectrometry (EDX) of thin foils.

The sample for metallographic analyses were prepared by common way of grinding, polishing and etching, thin foils were polished electrolytically in solution consisted of acetic acid (95%) and hydrochloric acid (5%) at 10 °C and 90 V.

The boundaries of austenitic grains are decorated with thick layer of particles as illustrated in Fig. 9a,b. Detailed view at the grain boundary in Fig.10 reveals almost continuous chain of oval particles (10a) at the boundaries and a carbon depleted zone (CDZ) (10b) followed by the layer of particles. The particles in the layer have cuboidal shape. Both mentioned kinds of particles have been analysed as Cr-rich $M_{23}C_6$ carbides as documented by selected area diffraction (SAD) in Fig.11. Further into the grain interior, there are fine particles mainly, and arrays of more or less ordered dislocations often pinned by fine particles and/or the rows of cuboidal particles, Fig.12a,b. These fine particles have been analysed as Fe-Cr-rich $M_{23}C_6$ carbides. After the creep tests the chain of particles, CDZ, and layer of particles have been found also at twin boundaries, Fig.13.

At proper conditions (magnification, foil thickness) a population of Cu-based particles can be seen in the microstructure, Fig.14. The distribution of the dispersion particles is very dense and most of them demonstrate a well-known "coffee bean"-like contrast, which can be attributed to the coherent dispersoids [9].

Taking into account the chemical composition of the alloy, Nb-V-rich particles should be awaited in the microstructure. However, no such particles have been found. Large, rounded Nb-rich particles of various shapes are embedded in the microstructure instead, Fig.15. The SADs on different particles give ambiguous results, Nb element and $Nb_{15}Ni_2$ phase.

The white small "stains" in the pictures are most probably thinned parts in the foil originated by the fine particles falling out during polishing of the foils.

According to the thermodynamic calculation the phases in equilibrium at the test temperature should be Cr-rich $M_{23}C_6$ carbide, MX nitrides, Cu particles, and austenitic matrix.

Semi-quantitative composition (EDXS) of metallic part of particles in the investigated microstructure [in at.%] is approximately as follows:

- Cr- rich oval and cuboidal particles mostly at GB-$M_{23}C_6$: 72Cr-18Fe-1Nb-3Ni-0.5Cu-1.8V-1Nb (+ Si ..).
- Fine (up to 30 nm) and longer narrow particles in the matrix are Fe-Cr-rich $M_{23}C_6$ carbides: 50Fe-24 Cr-18Ni-2,5Cu + (~1V~1Nb-Si..).
- Cu-rich coherent particles.
- Nb-rich (88-92 %), large particles

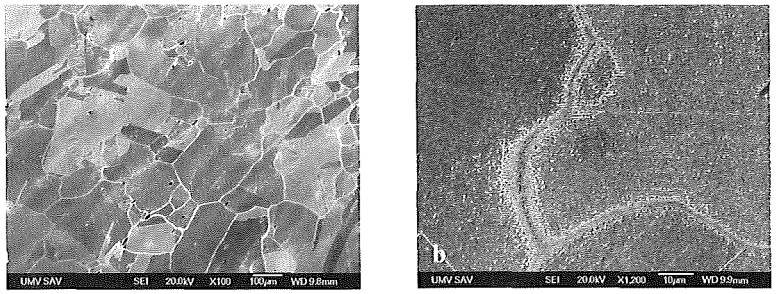

Fig.9 -Microstructure of the sample (a), detail view of particles at grain boundaries (b), SEM.

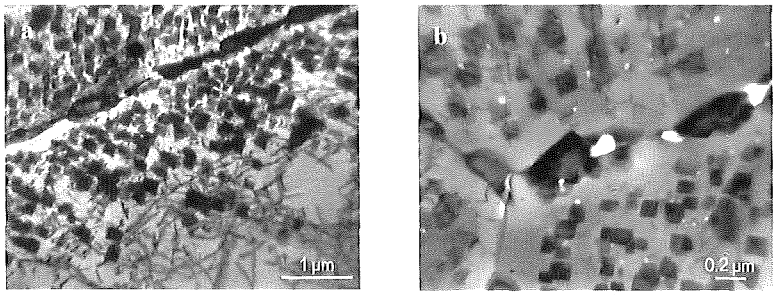

Fig. 10 Layer of particles (a) and carbon depleted zone (b) at boundaries, thin foil.

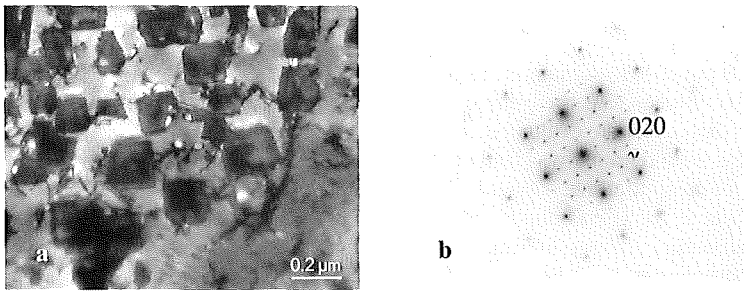

Fig. 11 Cuboidal $M_{23}C_6$ particles (a) and SAD from this area (b), thin foil.

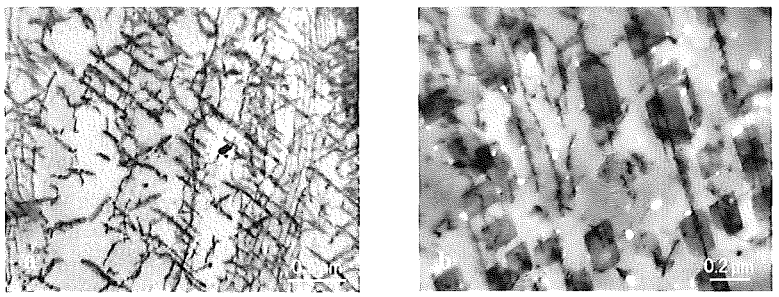

Fig. 12 Interior of grains. Dislocations pinned by rows of fine particles (a), cuboidal particles (b), thin foil.

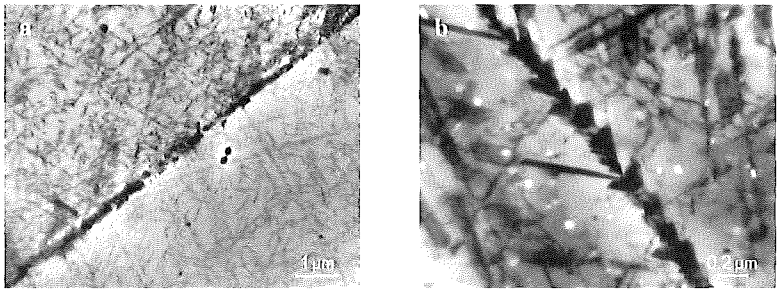

Fig. 13 Twin boundary (a), detail (b), thin foil.

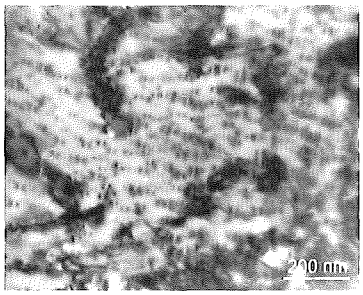

Fig. 14 Cu-rich coherent particles, thin foil.

Fig. 15 Nb-rich large particles

7. Conclusions

The investigation is possible to summarise as follows:

1) From results of creep tests the rupture strength, strength for 1% creep strain and minimum creep rate were evaluated.
2) From optical metalography was find out that depleted zone could be used for estimation of creep lifetime. – zmenila by som to na: The width of the precipitated particles layer at the grain boundaries connected to the carbon depleted zone may be used for estimation of creep lifetime.
3) The microstructure of BGA4 steel was found to consist of austenite and particles of Fe and Cr-rich $M_{23}C_6$ carbide, Cu –rich coherent dispersoid, and large Nb-rich particles.

Refrences

[1] VISWANATHAN,R.-PURGERT,R.-RAO,U.: Materials for ultra-supercritical coal-fired power plant boilers. Materials for Advanced Power Engineering 2002. Proc. 7th Liege Conference, p.1109-1129, Part II, Ed. J.Lecomte-Beckers, M.Carton, F.Schubert, P.J.Ennis. Forschungszentrum Juelich 2002.

[2] SCARLIN,B.-STAMATELOPOULOS,G.N.: New boiler materials for advance steam conditions. Materials for Advanced Power Engineering 2002. Proc. 7th Liege Conference, p.1091-1108, Part II, Ed. J.Lecomte-Beckers and all. Forschungszentrum Juelich 2002.

[3] SEIFERT,W.-MELZER,B.: Rechnerische Auswertung von Zeitstandversuchen am Beispiel des Stahles 13CrMo4-4.15. Vortragveranstaltung „Langezeitverhalten warmfester Stähle und Hochtemperaturwerkstoffe“, Düsseldorf, 06.11.1992.

[4] BÍNA,V.-HAKL,J.: Relation between creep strength and strength for specific creep strain at temperatures up to 1200°C. Materials Science and Engineering A234-236(1997), pp.583-586.
[5] PECH,R.-KOUCKÝ,J.-BÍNA,V.: Matematizace hodnot pevnosti při tečení československých ocelí pro výrobu trub. Strojírenství 29(1979), č.7, s.389.
[6] KOTECKI,D.J.: Welding of Stainless Steels. ASM Handbook, Vol.6, Welding, Brazing and Soldering, p.678-709. ASM International, December 1993.
[7] SHINGLEDECKER,J.P-MAZIASZ,P.J.-EVANS,N.D.-POLLARD,M.J.: Creep Behaviour of a New Cast Austenitic Alloy. Creep and Fracture in High Temperature Components – Design and Life Assessment Issues. Proc. ECCC Creep Conference, Ed. I.A.Shibli, S.R.Holdsworth, G.Merckling, p.99-101, Sept. 12-14,2005, London.
[8] GABREL,J.-BENDICK,W.-VANDENBERGHE,B.-LEFEBVRE,B.: Status of development of the VM12 steel for tubular application in advanced power plants. Material for Advanced Power Engineering 2006, ed. J.Lecomte-Beckers, M.Carton , F.Schubert, P.J.Ennis. Proceedings of the 8th Liege Conference, part II., p.1065-1075.
[9] Williams DB, Carter CB, editors. Transmission electron microscopy. New York: Plenum Press; 1996. p. 289.

Acknowledgements

This work was supported by Ministry of Education, Youth and Sports of Czech Republic – COST 536 (OC09067). Technical support of our colleagues from Corus in carrying out this work is gratefully acknowledged.

9th Liege Conference : Materials for Advanced Power Engineering 2010
edited by J. Lecomte-Beckers, Q. Contrepois, T. Beck and B. Kuhn.

EVALUATION OF BASE MATERIAL AND WELDED JOINTS DESIGNATED FOR MEMBRANE WALL COMPONENTS MADE FROM LOW-ALLOY STEELS IN LARGE BOILERMAKER CONDITIONS

Janusz Dobrzański[1], Jerzy Pasternak[2], Adam Zieliński[1]
[1] Institute for Ferrous Metallurgy,44-100 Gliwice, Poland
[2] Boiler Engineering Company RAFAKO S.A., 47-400 Raciborz, Poland

jerzy.pasternak@rafako.com.pl

Abstract

Supercritical operating parameters of lower emission power units require novel creep resisting steels. Therefore, this paper contains selected information, results of collectors made from the new low-alloy bainitic creep-resistant steels as 7CrWVNb9-6 (P23) and 7CrMoVTiB10-10 (P24) performed in large boilermaker conditions. The research and implementation process includes:
- evaluation, comparison of requested properties of base material and welded joints as tensile strength, impact strength and technological properties,
- destructive examinations with evaluation of welded joints and HAZ structure and hardness distribution,
- evaluation of creep resistance properties and structure stability after heat treatments and again process of base material, HAZ and welded joints,
- influence of manufacturing process in large boilermaker conditions and after simulated operation.
A new creep-resistant steels to be used, in order to comply with the operational requirements, as to assure the appropriate reliability and safety of the boiler equipment in operation process.

Keywords: technological and mechanical properties, steel structure stability, corrosion and creep resistance.

1. Introduction

The boilers of supercritical working parameters and the requested low emission level of harmful substances into the atmosphere, require higher and higher outlet steam parameters. Any increase of those parameters necessitates a search for and application of new materials, having higher strength parameters and more complex technological manufacturing process for boiler pressure part components, made of such materials [1-6]. Among the critical boiler pressure part components, membrane walls play a vital role. Their materials, as used in supercritical parameters installations, can be capable of being operated at temperatures reaching approx. 550°C, including new bainitic steels applied for membrane wall components. New generation low-alloy steels, type 2.25%Cr-1%Mo with micro-additions, i.e. steel grades 7CrWVNb9-6 (P23) and 7CrMoVTiB10-10 (P24), have been developed and applied for manufacture of such components. They have been elaborated as the result of vast scale research works, mainly within the European programmes COST 511, 522 and COST 536, where welding materials and manufacturing technologies have been worked out with the objective to make boiler components of them [8-11]. The materials of the fabricated boiler components have their material and welded joints characteristics created, so as to obtain knowledge on their behaviour in operating conditions. Owing to the specific nature of these materials' operation, the creation of their characteristics and revealing the processes of degradation and destruction is extremely time-consuming, i.e. it takes approximately 15 to 20 years.

Below we have presented a brief analysis of the requirements, which precede the implementation of the new steel grades, as well as some selected examination results of base materials and homogeneous welded joints on the manufactured components, fabricated at a large boiler producer's. Strength properties and long-term annealing influence on material and welded joint properties and structure have been compared. Suitability of the examined

materials for production purposes of boiler pressure part membrane walls, installed on boilers operated at supercritical parameters, has been assessed in relation to the prevailing requirements.

2. Basic requirements of the European safety system with regard to pressure equipment manufacturers.

The functional principles of the product compliance assessment system with the requirements regarding life protection, safeguarding of health, property and environment protection in Poland, have been comprised in the Act, dated 30 August, 2002 (Law Journal No. 166, e.g. item 166), as well as a number of executive regulations, which specify the most important requirements pertaining to the pressure equipment and installations. Production of pressure equipment is included in the "regulated area", defined by the European Union's safety policy with regard to the equipments being introduced into goods traffic for the first time in the territory of a given country. Therefore, EU Directive No. 97/23/WE defines the processes of designing, fabrication and the compliance assessment for pressure installations and their assemblies, to be supplied to the EU market, the highest admissible PS pressure of which exceeds 0.5 bar. Directive - PED 97/23/WE – restrains the government's intervention policy into the process of manufacture of goods and imposes particular obligations onto the manufacturer. It is equivalent with assuring the implementation of all the Directives' requirements by the manufacturer, which are applicable to the product in question. The Directive defines the types of products, which undergo its requirements, however, it specifies only the main technical requirements with regard to a product. If there are a few directives, which are applicable to a product, the manufacturer is obligated to satisfy the requirements of all of them. The detailed technical requirements are included in harmonised European standards, such as:

- EN 12952 – Water-tube boilers and auxiliary installations,
- EN 12953 – Fire-tube boilers,
- EN 13445 – Unheated pressure vessels,
- EN 13480 – Metal industrial pipelines.

The compliance evaluation process, divided into "modules" by means of which manufacturers can prove and confirm the product conformity with the requirements, constitutes the foundation of the adopted PED Directive "philosophy". The conformity assessment, which can be carried out in many various ways, is based on 4 fundamental "modes", namely:

- A product undergoes examinations performed by the manufacturer or an authorised representative,
- A product undergoes examinations carried out by a notified laboratory – independently of the supplier and the purchaser,
- A product undergoes conformity assessment by a controlling Notified Body,
- A product undergoes certification by a Notified Body. If the product is compliant with the main requirements, the Certified Body issues the conformity certificate.

The manufacturer may choose the technical solutions, i.e. he can select a module to be applied for confirmation of meeting the Directive requirements. Thus, the pressure installation manufacturer is obligated to adjust the product quality to the requirements of the European Union's legislation, among other things, by the following:

- Determining the category, from I to IV, depending on the equipment working parameters,
- Selection of the appropriate module of conformity assessment; from A to H1,
- Performance of the product conformity assessment on the basis of the selected module,

- Marking the product with the CE mark,
- Issuance of Declaration of Conformity for the product, as well as the Instruction and Operating Manuals, as required by the Directive.

Drawing No. 1 presents the detailed design and qualitative requirements concerning fabrication of membrane wall components, as included in harmonised standard No. PN EN 12952-5.

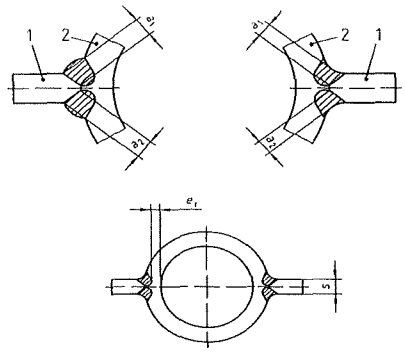

Drawing 1. Exemplary specification of the executive requirements for welded joints between a tube and fin of a membrane wall component.

Obviously, application of the harmonised standards is voluntary, nevertheless, there is an accepted supposition principle that the product is compliant with the basic safety requirements if it is fabricated in accordance with the harmonised EN standards.

The directive requirements regarding the materials applied for pressure equipment and installations have also been determined. The design documentation for pressure equipment shall meet the requirements included in Appendix No. 1 to the Directive, when selecting appropriate materials for pressure equipment – in accordance to one of the following principles:

- The materials to be issued in the design are mentioned in the harmonised standards, e.g. EN 12952-2, in relation to the installations to applied as water-tube boiler components and auxiliary equipment,
- The materials to be used are included in the European material "approvals", i.e. so-called EMDS – in accordance with Article 11 of the Directive,
- The materials have a single-use approval for application – so-called PMA.

Additionally, Appendix No. 1 to the Directive specifies the minimum requirements for the materials, which may be applied for manufacture of pressure equipment, among other things determining the following:

- The minimum elongation of ferritic materials, which are applied for pressure equipment at the level of $A_5 > 14\%$,
- The minimum impact strength KV > 27[J] at temperature 20°C or at the lowest foreseeable working temperature of the equipment.

The pressure installations and equipment, which belong to categories II, III and IV, their materials ought to have conformity certificates issued by the material producer. The certificates shall be issued in form of a material certificate, according to PN EN 10205, i.e. type 3.1., 3.2 or 2.1, respectively. In compliance with the requirements of Directive PED 97/23/WE, the pressure equipment manufacturer is obligated to verify the technology, which is to be applied for fabrication of the pressure part components, including the check of the welding technology, cold and hot working, with the objective to satisfy the requirement of

meeting the expected reliability and service life of the welded joints. The assessment of the welded joint quality, describing the required level of properties and its quality of fabrication, so as to assure the reliable operation of the pressure equipment and installations, has been described in standard EN ISO 15614-1. The quality of welded joints – in view of the boiler operational safety – constitutes an integral part of the designing process, as well as the production of the welded joints. In order to achieve the assumed goals, various quality evaluation methods for welded joints are applicable. One of them is the evaluation system, as presented in standard EN ISO 5817.
The definition of the pressure equipment reliability/ infallibility criterion and operational safety is understood by the authors of this paper to also cover the requirement to assess the wear degree, service life evaluation, residual life and changes due to the influence of temperature, loads and operation time of the materials and boiler pressure components, taking into account the operational conditions, such as: the actual working parameters, number of start-ups and shutdowns from various boiler operating conditions, number, type and characteristics of damages, temperature shocks and aggressiveness of the environment [1].

3. Materials to be tested.

Thick-walled tube test pieces, following the necessary normalising and tempering processes, have been taken for examinations of low-alloy chromium steels with molybdenum micro-additions, in grades 7CrWVNb9-6 and 7CrMoVTiB10-10. They have been collected from industrial heat tubes, delivered by the company of V&M, within the scope of the international co-operation in programmes COST536 [2,3]. Collector components have been fabricated from these tubes in the premises of RAFAKO S.A. The collector circumferential welded joints have been made using the technology and welding materials previously agreed with the company of Thyssen Welding, within the scope of the aforementioned co-operation.

The scheduled scope of the examinations has been carried out on the steam collector test pieces, having the dimensions ϕ216x28mm, made of steel 7CrWVNb9-6 (P23) and the steam collector ϕ406x32mm, made of steel 7CrMoVTiB10-10 (P24). Complex non-destructive examinations and controlled analyses of the chemical compositions of the examined collector test pieces, which are compliant with the requirements assigned for steels 7CrWVNb9-6 and 7CrMoVTiB10-10, have been performed on the material of the collectors and homogeneous circumferential welded joints, which were fabricated at RAFAKO S.A. With such preparation of test pieces, tests and examinations are being carried out at the Institute for Ferrous Metallurgy, with the objective to evaluate their properties and structure, as well as the behaviour of the materials and welded joints in the operational conditions. In particular, we are focusing on the findings regarding the influence of temperature, loads and time on the usable properties characteristics.

4. Strength properties at elevated temperatures.

Comparison of strength properties test results, i.e. tensile strength and yield point at room temperature and at temperature risen to 550°C, of collector material ϕ216x28mm, made of steel 7CrWVNb9-6 (P23) and ø406x32mm, made of steel 7CrMoVTiB10-10 (P24) and similar circumferential welded joints, is shown in Table 2. Table 2b presents changes to elongation A_5 and reduction Z, as achieved in tensile strength test at room temperature and at the temperature elevated to 550°C of the examined materials and welded joints.

Table 2a. Comparison of strength properties with regard to parent material and welded joints, made of steels 7CrWVNb9-6 (P23) and 7CrMoVTiB10-10 (P24) [3].

Grade		Tensile strength TS [MPa]						Yield point YP [MPa]					
		Test temperature [°C]						Test temperature[°C]					
		20	200	300	400	500	550	20	200	300	400	500	550
7CrWVNb9-6 (P23)	Base material	575	495	475	457	387	350	452	400	383	368	330	300
	Welded joint	564	468	447	440	365	301	423	372	355	343	315	280
Test temperature [°C]		20	200	300	400	450	500	20	200	300	400	450	500
7CrMoVTiB 10-10 (P24)	Base material	604	522	513	506	482	455	516	458	446	439	422	399
	Welded joint	580	518	505	500	481	433	505	468	428	427	408	368

Table 2b. Comparison of plastic properties of parent material and welded joints made of steel 7CrWVNb9-6 (P23) and 7CrMoVTiB10-10 (P24) [3].

Grade		Elongation A_5 [%]						Reduction Z [%]					
		Test temperature [°C]						Test temperature[°C]					
		20	200	300	400	500	550	20	200	300	400	500	550
7CrWVNb9-6 (P23)	Base material	19	14	12	12	15	17	75	75	70	74	79	80
	Welded joint	13	10	10	11	11	9	75	78	75	68	76	81
Test temperature [°C]		20	200	300	400	450	500	20	200	300	400	450	500
7CrMoVTiB 10-10 (P24)	Base material	21	10	12	10	10	12	79	78	78	72	70	66
	Welded joint	11	8	10	8	6	9	75	75	80	66	65	66

5. Temperature influence on impact energy.

The obtained impact energy results, as measured on a V-notch specimens of the collector base material, in the heat-affected zone and similar circumferential welded joint, made of steel 7CrWVNb9-6 (P23), are shown in Drawing 2a. Additionally, Drawings 2b and 2c present a comparison of the impact energy, measured on test pieces with a V-notch, of the collector base material and similar circumferential welded joint, as obtained at test temperature range from "-"60 to 100°C.

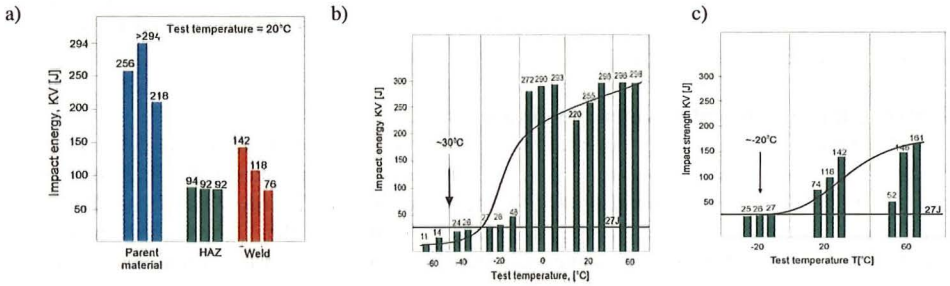

Drawing 2. Comparison of impact transition temperature, on test pieces with a V-notch:
a) Parent material, HAZ and welded joint, at temperature T_b = 20°C,
b) Parent material depending on the test temperature range from "-"60°C to 60°C,
c) Welded joint depending on the test temperature range from "-"20°C to 60°C, of collector base material and similar welded joint made of steel 7CrWVNb9-6 (P23).

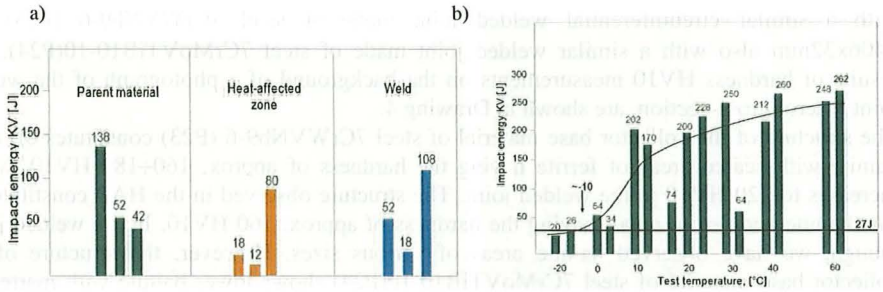

Drawing 3. Comparison of impact transition temperature, on test pieces with a V-notch:
a) Parent material, HAZ and welded joint at temperature T_b = 20°C,
b) Depending on the test temperature range from "-"20 °C to 60 °C, of collector base material and similar welded joint made of steel 7CrMoVTiB10-10 (P24).

They also show the temperature of transition into brittle state, which is approx. "-"30°C for the base material, whereas, for the examined welded joint material it is approx. "-"20°C.
The obtained test results have been compared with those of the collector test specimen, made of steel 7CrMoVTiB10-10 (P24), especially with the impact energy measured on test pieces with a V-notch of the collector base material, as well as in the HAZ and welded joint, as shown in Drawing 3a. They have also been compared with the impact energy measured on test pieces with a V-notch of the collector base material, in relation to the test temperature range from "-"20 to 60°C and the level of transition temperature into brittle state, which is approx. "-"10°C for the tested material, as shown in Drawing 3b [11].

6. Hardness and structure of similar circumferential welded joint material.

The hardness and structure examinations of the similar circumferential joint of the tested collectors, have been carried out by means of a transmission electron microscope and a scanning electron microscope, at magnifications up to 800 and 5,000x respectively. Observations have been conducted on the test piece material of the collectors: ϕ216x28mm

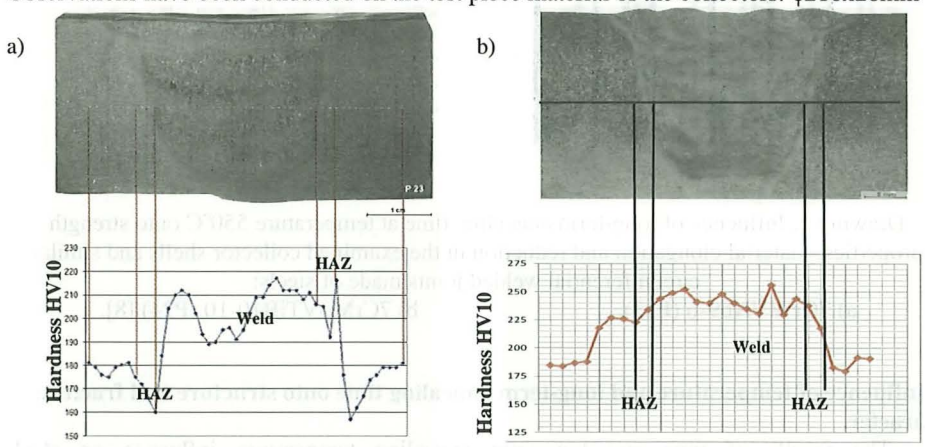

Drawing 4. Comparison of hardness test results on similar circumferential welded joints of collector components, following normalising, tempering and stress relief annealing, made of low-alloy steels:
a) 7CrWVNb9-6 (P23), b) 7CrMoVTiB10-10 (P24)

with a similar circumferential welded joint made of steel 7CrWVNb9-6 (P23) and ϕ406x32mm also with a similar welded joint made of steel 7CrMoVTiB10-10(P24). The results of hardness HV10 measurements on the background of a photograph of the welded joint macro- cross-section, are shown in Drawing 4.
The structure of the collector base material of steel 7CrWVNb9-6 (P23) constitutes of lower bainite with scarce areas of ferrite having the hardness of approx. 160÷180 HV10, which increases to 220 HV10 in the welded joint. The structure observed in the HAZ constitutes of fine bainite and ferrite areas, having the hardness of approx. 160 HV10. In the welded joint, though, we have observed bainite areas of various sizes. However, the structure of the collector base material of steel 7CrMoVTiB10-10(P24) shows lower bainite with martensite and scarce ferrite areas, having the hardness of approx. 180÷192 HV10.
The hardness in the welded joint increases to 245 HV10. The structure detected in the welded joint heat-affected zone constitutes of the areas of bainite and martensite with presence of ferrite, having the hardness from 180 to 220 HV10. In the welded joint we have observed a mixture of martensite and bainite. In such fabricated welded joints we have not observed any rapid changes in hardness and structure [3,7-11].

7. Mechanical properties following long-term annealing.

The comparison of the obtained strength properties results, elongation and reduction of the base material and similar circumferential welded joints of the examined collector test pieces, in the original condition and following long-term annealing lasting 3,000 and 10,000 hours, on the basis of the results obtained at the temperature of 550°C, is shown in Drawing No. 5.

a) b)

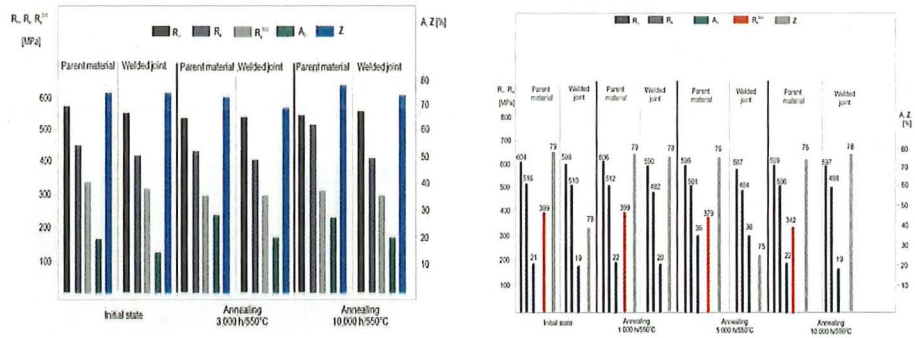

Drawing 5. Influence of long-term annealing time at temperature 550°C onto strength properties, material elongation and reduction in the examined collector shells and similar circumferential welded joints made of steels:
a) 7CrWVNb9-6 (P23), b) 7CrMoVTiB10-10 (P24) [8].

8. Influence of temperature and long-term annealing time onto structure and fracture character.

The results of time and long-term annealing temperature influence on steels 7CrWVNb9-6 (P23) and 7CrMoVTiB10-10 (P24), i.e. on the structure and character of fractographic pictures of the fractures obtained on impact strength test pieces, observed in a scanning electron microscope, following 67,000 hours of annealing at the temperatures of T_b

= 550°C and T_b = 600°C, in comparison with the structure and fracture picture of the original state, are shown in Drawings No. 6 and 7.
Long-term annealing of steel 7CrWVNb9-6 (P23), i.e. up to 67,000 hours, to steel P23 working temperature (550 and 600°C), has not resulted in a considerable lowering of impact energy or HV10 hardness. The impact strength remains at the level of approx. 144 to 172[J], and the corresponding hardness ranges from 166 to187 HV10. The impact test piece fractures, following 67,000 hours of annealing, are mixed fractures, however, with a considerable predominance of ductile areas over brittle ones, which are characteristic for brittle fractures. The structure after 67,000 hours is different from the structure picture in the original state. An increase of the carbide release size inside grains is visible and also on the grain boundaries, which locally form release chains. The performed long-term annealing of steel 7CrMoVTiB10-10 (P24), i.e. up to 67,000 hours at the temperature similar to the working temperature (i.e. 550 and 600°C), similarly as for steel P23, has not resulted in any considerable decrease of impact strength KV or hardness HV10.

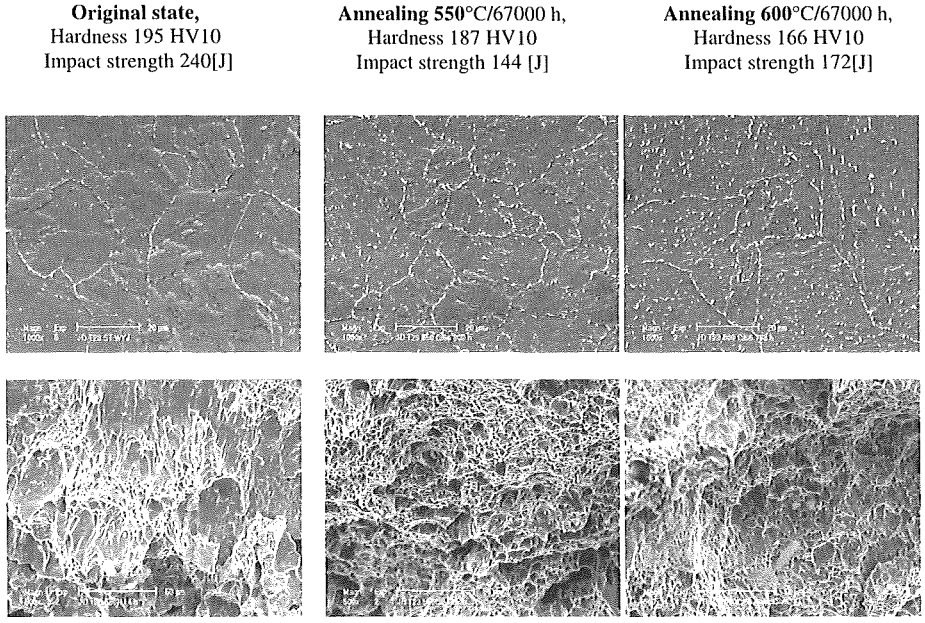

Drawing 6. Test temperature and long-term annealing influence on hardness, structure and impact strength of steel P23 (7CrWVNb9-6) [11].

Long-term influence of elevated temperature has revealed partial decay of bainitic areas at the annealing temperature of 550°C. However, in the picture of the examined steel structure, having been annealed at the temperature of 600°C, we have discovered some considerable decay of bainitic areas. This structure can be characterised by considerably degraded bainite areas, with releases of carbides of substantial sizes on the boundaries of and inside the grains. The impact strength is high, ranging at the level from approx. 122 to 138[J], whereas the corresponding hardness amounts to approx. from 162 to181 HV10. The test pieces impact strength fractures, following 67,000 hours of annealing, are mixed fractures. Nevertheless, they contain considerably more brittle areas than the areas with cleavage plane, which are the most common for ductile fractures.

When compared to the structure at the original state, following 67,000 hours of annealing the structure has undergone change, i.e. it is now ferrite with bainite and releases on the ferrite grain boundaries. The increase of the carbide release size inside grains is visible and also on the grain boundaries, which form the release chains.

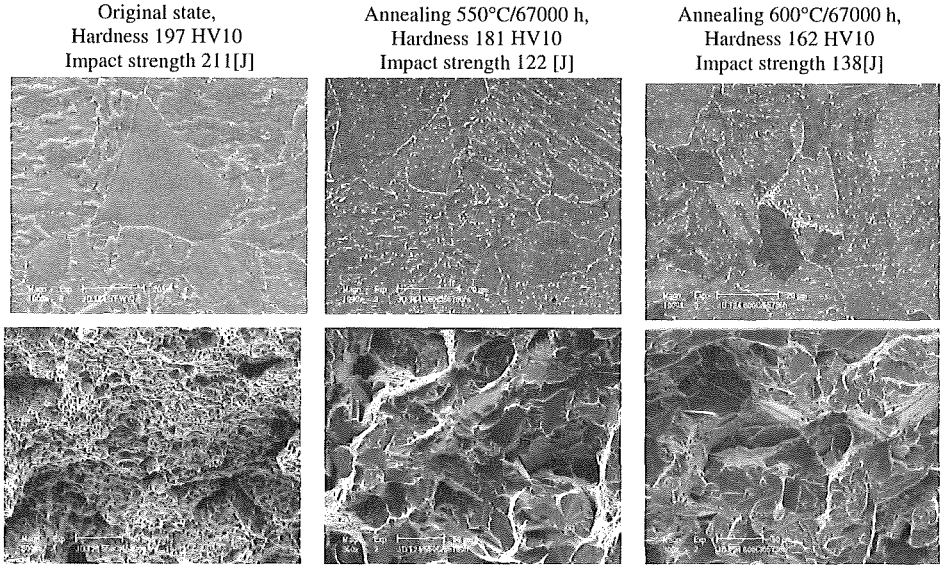

Drawing 7. Test temperature and long-term annealing influence on hardness, structure and impact strength of steel P24 7CrMoVTiB10-10[11].

The long-term influence of the elevated temperature has exposed the partial decay of the bainite areas at the annealing temperature of 550°C. However, in the picture of the examined steel structure, having been annealed at the temperature of 600°C, we have discovered a substantial decay of bainitic areas. Such a structure can be characterised by considerably degraded bainite areas, with releases of carbides of substantial sizes on the boundaries of the former austenitic grains, as well as inside the grains.

9. Conclusions

1. The strength properties of steel 7CrWVNb9-6 (P23), at elevated temperature, have revealed a considerable deterioration, starting already at temperature 400 ^{0}C (R_e^{500}=330 MPa, R_e^{550}=300MPa) in comparison with the strength properties achieved at room temperature (R_e=450 MPa).
2. Steel 7CrMoVTiB10-10 (P24) maintains the high level of those strength properties up to the temperature of approx 500^{0}C, i.e. about 100^{0}C higher than with steel 7CrWVNb9-6 (P23). Nevertheless, in both cases, those steel grades are capable of keeping the requirements and expectations made for metallurgical steel products.
3. The long-term annealing at temperatures 550 and 600^{0}C, having the duration up to 10,000 hours, does not cause any significant changes to the strength properties at room temperature or at the elevated temperature, which is similar to the operating one.
4. Some decrease of rupture labour with V-notch test pieces has been observed following 10,000 hours for the welded joint material of steel 7CrWVNb9-6 (P23), i.e. it is approx. from 40 to 70[J], whereas for those of steel 7CrMoVTiB10-10 (P24), it ranged from approx. 40 to

100[J]. Anyway, the achieved values are considerably higher than the required minimum ones.

5. The annealing lasting 67,000 hours, in case of both T23 and T24 steels, has resulted in a visible increase of carbide releases inside the grains and on the grain boundaries, which locally form release chains. The long-term impact of the elevated temperature has revealed partial decay of bainitic areas at the annealing temperature of 550°C. In the picture of the examined steel, annealed at the temperature of 600°C, we have observed a decay of the bainitic areas.

6. The continuation of the long-term annealing examinations is also indispensable. The ongoing tests of creep resistance and long-term annealing enable to trace the changes in the structure and development of the carbides release processes, which are indispensable for assessment of the examined steels, in the conditions similar to the actual operating ones [9].

Acknowledgements

The authors wish to thank the Science and Higher Education Ministry for financial support of SPB/COST/96/2005 project, the selected test results of which are presented above. Special thanks are due to the company of Valourec & Mannesmann for supplying the tube segments, as well as Thyssen Welding for providing the necessary welding materials and consultations on welding technologies, which have been very useful for this project.

10 References.

[1] Hernas A., Dobrzański J.: Trwałość i niszczenie elementów kotłów i turbin parowych. Wyd. Politechniki Śl., Gliwice, 2003 (in polish only).

[2] Maciosowski A., Dobrzański J., Zieliński A.: Mechanical and creep testing of new steel and welds for critical elements of friendly Power Plant. Report No2 SPB/COST/96/2006. Cost 536, Gliwice 2006, Poland.

[3] MaciosowskiA., Dobrzański J., Zieliński A.: Mechanical and creep testing of new steel and welds for critical elements of friendly Power Plant. Report No3 SPB/COST/96/2006. Cost 536, Gliwice 2007, Poland.

[4] MasuyamaF.: Steam Plant Material Developments in Japan. 6th Int. Conf. on Materials for Advanced Power Engineering 1998, Liege, Belgium. ISBN 389336, Forschungszentrum Jülich 1998, p.1087.

[5] Vaillant J. C., Vandenberghe B.,Zakine Z., Gabrel J., Bendick W., Deshayes F.: The T23/P23 Book, Vallourec&Mannesmann Tubes 2006.

[6] Hernas A., Wala T.: Rozdział pt. Dobór materiałów na przegrzewacze o podwyższonych parametrach pracy; Materiały i Technologie Stosowane w Budowie Kotłów Nadkrytycznych i Spalarni Odpadów. Wydawnictwo SITPH, Katowice, marzec 2009, s.154-171 (in polish only).

[7] Dobrzański J., Hernas A., Zieliński A.: Rozdział pt. Struktura i własności nowych stali żarowytrzymałych o osnowie ferrytycznej Materiały i technologie stosowane w budowie kotłów nadkrytycznych i spalarni odpadów, ,Wydawnictwo SITPH, Katowice, marzec 2009, s.47-101.

[8] Dobrzański J., Zieliński A., Sroka M.: Structure, properties and method of the state evaluation of low-alloyed steel T23 (HCM2S) worked in creep conditions. Journal of Mat. Proc. Tech. W druku.

[9] Dobrzański J., Zieliński A., Sroka M.: Structure, properties and method of the state evaluation of low-alloyed steel T23 (HCM2S) worked in creep conditions" 11 International Scientific Conference CAM3S, Gliwice – Zakopane, 4-7 December 2005.

[10] Dobrzański J., Pasternak J.: Properties and application of welded joints in heat resisting bainitic and martensitic steels. 25 International Conference "Welding 2008", 406, str. 137.Subotica, Serbia, 4-6 Jul 2008.

[11] Dobrzański J., Zieliński A., Sroka M., Microstructure, properties investigation and methodology of the state evaluations of T23(2,25Cr-0,3Mo-1,6W-V-Nb) steel in boilers application, Journal of Achievements in Materials and Manufacturing Engineering. Vol. 32, Issue 2, p. 142-153, February 2009.

9th Liege Conference : Materials for Advanced Power Engineering 2010
edited by J. Lecomte-Beckers, Q. Contrepois, T. Beck and B. Kuhn.

WELDED REPAIR JOINTS OF BOILER STEELS FOLLOWING OPERATION IN CREEP CONDITIONS EXCEEDING THE DESIGN TIME OF OPERATION

Dobrzański J[1]. Paszkowska H[1]. Zieliński A[1]
[1] Institute for Ferrous Metallurgy, 44-100 Gliwice, Poland

jdobrzanski@imz.pl

Abstract

The assessment of suitability for further operation for materials and welded repair joints of thick-walled main steam pipeline components, made of steel 14MoV63, as well as steam superheater outlet headers made of steel X20CrMoV121 following operation in creep conditions in time periods considerably longer than the specified calculated time of operation. Strength properties, impact strength and transition temperature into brittle condition, as well as structure condition have been evaluated. On the basis of shortened creep tests, the residual life and disposable residual life of materials and welded joints have been determined. Material properties following operation and those of fabricated circumferential welded repair joints have been compared. The condition of examined components and suitability of the fabricated welded repair joints for further operation have been assessed.

Keywords: welded repair joints, mechanical properties, creep resistance, residual life.

1. Introduction

There have not been many new units, which have been erected in the Polish power sector recently. Therefore, the producers of electric energy make their best endeavours to maintain the availability of the existing power plants, simultaneously assuring the safety of their operation. Inspections and repairs of the currently operated power installations, whose calculated operational time has, most frequently, expired or been exceeded to a considerable extent, accompanied by the performed rational diagnostics, seem to be the reliable way to achieve those objectives. However, in order to maintain the power energy and heat production in Poland at the required level, it is not sufficient to carry out periodical inspections or repairs. It is also indispensable to modernise the power units in operation. It has been evaluated that modernisation of units, having the total capacity of at least 2000MW [1,2] is absolutely necessary in order to preserve the current production level.

The small number of new power units, which have been commissioned and put into operation for the last dozen of years, have caused the situation, where modernisation of the existing power units plays an important part. Therefore, the main problem to be solved is the evaluation of the boiler pressure part condition and prediction of its further safe operation, with simultaneous modernisation of the construction, selecting and applying new materials, which are to be used for retrofitting and fabrication of new components [2-5].

Another important objective is to increase the efficiency and extend the operation time of the existing units considerably beyond the calculated design operation time, i.e. up to the expected minimum 300,000 hours, at the same time fulfilling the valid requirements concerning the limited emissions of harmful substances into the atmosphere. This goal is being achieved by modernisation of those power units. Such modernisation has to take into account not only repairs but also replacements of some components, to be frequently manufactured of the new generation steels. These activities require, first of all, performance of the assessment of the materials and components condition, which are in operation, as well as a forecast of their further safe operation at the working parameters of such further operation. Following that, it is required to manufacture welded joints of the materials being operated and the materials being operated or new ones with those being operated [6-9]. The

assessment of the operational suitability of such welded joints in creep conditions constitutes the subject of this paper.

2. Materials to be examined.

The materials do be examined in form of manufactured circumferential welded repair joints: of tubes ø273x32mm made of steel 14MoV63 in the original condition and following 105,000 and 193,000 hours of operation in creep conditions in the live steam main pipelines, of tubes ø324x46 mm made of steel X210CrMoV12.1 in the initial condition and following 108,649 hours of operation in creep conditions in the III^0 primary steam superheater outlet header, have been presented in Table 1. The results of the inspection analysis of the chemical composition of the individual examined welded joint components, in comparison with the requirements of the examined steels, are shown in Table 2. The test results of the parent material structure of the examined welded joints, as observed on transverse micro-sections using a scanning electron microscope, at magnification up to 5,000x, in form of description, assessment in accordance with the Institute of Ferrous Metallurgy's own classification, with the evaluation of the depletion degree, have been presented in Table 3. Additionally, making use of such prepared transverse micro-sections, macro-photographs have been taken for deeply etched welded joints and HV10 hardness measurements from the parent material through the heat-affected zone, welded joint, heat-affected zone to the parent material.

Table 2. Control analysis of examined steels parent material chemical composition in their original condition, after long-term operation in creep conditions and welded joint material of the fabricated circumferential welded repair joints.

Material	Content of elements, mass %								
	C	Cr	Mn	Mo	Ni	P	S	Si	V
14MoV63 (13HMF) steel									
Parent material14MoV63 initial state	0.17	0.48	0.51	0.63	0.086	0.022	0.010	0.32	0.32
Parent material 14MoV63 after 105 000 h service	0.13	0.46	0.54	0.65	0.090	0.021	0.023	0.25	0.31
Welded joint	0.083	0.42	1.28	1.01	0.057	0.014	0.007	0.043	0.55
Parent material 14MoV63 after 193 000 h service	0.11	0.48	0.44	0.62	0.10	0.022	0.022	0.25	0.25
Weld metal	0.083	0.42	1.28	1.01	0.057	0.014	0.007	0.043	0.55
14MoV63 according to PN-85/H84024	0.10 0.18	0.30 0.60	0.40 0.70	0.500 0.65	max. 0.30	max. 0.040	max. 0.040	0.15 0.35	0.22 0.35
X20CrMoV12 1 (20H12M1F) steel									
Parent material X20CrMoV12.1 initial state	0.21	10.7	0.49	0.88	0.65	0.013	<0.005	0.26	0.26
Parent material X20CrMoV12.1 after 108 649 h long term service	0.21	11.9	0.56	1.03	0.51	0.019	<0.005	0.37	0.30
Weld metal	0.21	11.1	0.68	0.83	0.54	0.019	<0.005	0.31	0.27
X20CrMoV12.1 according to PN-85/H84024	0.17 0.23	11.01 2.5	0.30 0.80	0.8 1.2	-	max. 0.035	max. 0.035	0.10 0.50	0.25 0.35

Table 1. Material for examinations in the form of repair circumferential welded joints

<table>
<tr><td colspan="4">14MoV63 (13HMF) steel</td></tr>
<tr><td rowspan="4">1E</td><td colspan="3">The primary steam pipeline circumferential welded joint</td></tr>
<tr><td>Grade of steel: 14MoV63 initial state /14MoV63 after 105 000 hrs service</td><td colspan="2">Dimensions: ϕ273x32mm (D_n/g_n)</td></tr>
<tr><td rowspan="2">Operating time of material t_e = 105,000 hrs
Operating time of welded joint: new welded joint</td><td colspan="2">Work condition</td></tr>
<tr><td>Calculation</td><td>Working</td></tr>
<tr><td></td><td>t_o = 540°C; p_o = 16.5 MPa</td><td>t_r =540 °C; p_o14.00 = MPa</td></tr>
<tr><td colspan="2"> </td><td colspan="2"> 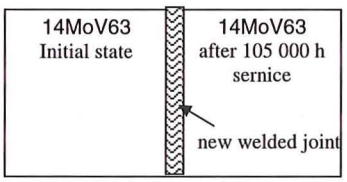
</td></tr>
<tr><td rowspan="4">8E</td><td colspan="3">The primary steam pipeline circumferential welded joint</td></tr>
<tr><td>Grade of steel: 14MoV63 after 193,000 hrs service/14MoV63 initial state</td><td colspan="2">Dimensions: ϕ273x32mm (D_n/g_n)</td></tr>
<tr><td rowspan="2">Operating time of material t_e = 193,000 hrs
Operating time of welded joint: new welded joint</td><td colspan="2">Work condition</td></tr>
<tr><td>Calculation</td><td>Working</td></tr>
<tr><td></td><td>t_o = 540°C; p_o = 16.5 MPa</td><td>t_r =540 °C; p_o14.00 = MPa</td></tr>
<tr><td colspan="2"> </td><td colspan="2"> 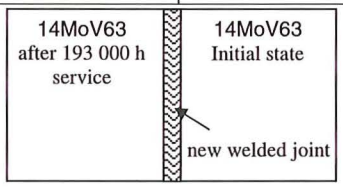
</td></tr>
<tr><td colspan="4">X20CrMoV12.1 (20H12M1F) steel</td></tr>
<tr><td rowspan="4">3s</td><td colspan="3">The chamber outlet of primary steam superheater III°
the repair circumferential welded joint</td></tr>
<tr><td>Grade of steel: X20CrMoV12.1 initial state / X20CrMoV121 after 108,649 hrs service</td><td colspan="2">Dimensions: ϕ 327x42mm (D_n/g_n)</td></tr>
<tr><td rowspan="2">Operating time of material t_e = 108,649 hrs
Operating time of welded joint: new welded joint</td><td colspan="2">Work condition</td></tr>
<tr><td>Calculation</td><td>Working</td></tr>
<tr><td></td><td>t_o =550°C; p_o =21.0 MPa</td><td>t_r =540 °C; p_o =19.6 MPa</td></tr>
<tr><td colspan="2"> 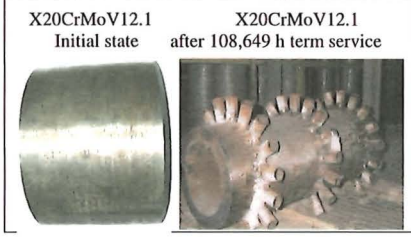
</td><td colspan="2">
</td></tr>
</table>

Table 3. Microstructure assessment of materials of repair circumferential welded joints of 14MoV63 and X20CrMoV12.1steels in initial state with steels after service.

14MoV63 (13HMF) steel			
Operating time, hrs	Description of microstructure material condition – life exhaustion extent	Hardness HV10	Phase composition
Initial State	Bainitic-ferritic structure. Numerous bainitic areas of diverse size. At ferrite grain boundaries fine precipitations in places. *Bainitic areas: class 0, precipitations: class 0* *Damage processes: class 0* **Class 0, Life Exhaustion Extent: 0**	208	$Fe_3C_{m.ph}$, $MC(V)_m$ $MC(Mo)_s$ M_2C_s
After 105,000 hr service	Ferrite structure with coagulated bainite areas. At ferrite grain boundaries precipitations of diverse size, some of them rather significant, forming chains. Numerous, very fine precipitations inside ferrite grains, distributed rather evenly. Initiation of damage process has not been observed. Discretions or micro-cracks have not been found in the structure. *Bainitic areas: class I, precipitations: class a/b, damage processes: class 0* **Class 2/3; Life Exhaustion Extent: 0.3÷0.4**	138	MC(CV), M_2C, $M_{23}C_6$
After 193,000 hr service	Ferrite structure with partially coagulated bainite areas. Fine precipitations at ferrite grain boundaries. Very fine precipitations inside ferrite grains, distributed evenly within the structure. Initiation of damage process has not been observed. Discretions or micro-cracks have not been found in the structure. *Bainitic areas: class I; precipitations: class a* *Damage processes: class 0* **Class 2; Life Exhaustion Extent:~0.3**	142	$MC(V)_{m.ph}$, M_2C $M_{23}C_{6,m}$ Fe_3C_s.
X20CrMoV12 1 (20H12M1F) steel			
Initial state	Tempered martensite structure. Strap-like structure with distinctly marked fine releases of carbides type $M_{23}C_6$, mainly on the strap boundaries and grain boundaries of former austenite. *Martensite straps: class 0, releases: class 0* *Damage processes: class 0* **Class 0, Life Exhaustion Degrees: 0**	248	$M_{23}C_{6\ m.ph}$ $MC(V)_m$
After 108,649 hr service	Tempered martensite structure. The martensite shows some slight increase in release quantity and size on the boundaries of former austenite grains and partial decay of martensite straps and considerable increase in release quantity on strap boundaries and in the areas of their former boundaries. Initiation of damage process has not been observed. Discretions or micro-cracks have not been found in the structure. *Martensite straps: class I, releases: class a* *Damage processes: class 0* **Class 1, Life Exhaustion Degree: 0.3**	216	$M_{23}C_{6\ m.ph}$, $MC(V)_s$
m. ph – main phase; m – medium; s – small			

3. Comparison of mechanical properties for circumferential welded repair joints and materials in original condition and following long-term operation, making the joints.

3.1.Steel 14MoV63

Strength properties

Mechanical properties tests have been performed on the examined materials in the initial condition and following 105,000 and 193,000 hours of operation, as well as on the fabricated welded joints. Drawing 1 presents the achieved test results, in particular tensile

strength and yield point at room temperature and at elevated temperature of the examined materials following long-term operation for the periods of 105,000 and 193,000 hours, which are not compliant with the requirements for the examined steel in the condition as delivered from the steel mill in accordance with the standards. However, the test results obtained for the material of the fabricated welded joints, made of those materials, following operation, with the material at the initial condition are higher than the minimum required ones for parent material in the condition as delivered from the steel mill in accordance with the standards. Drawing 2 shows the test results of yield point at room temperature and at elevated temperature for the examined materials.

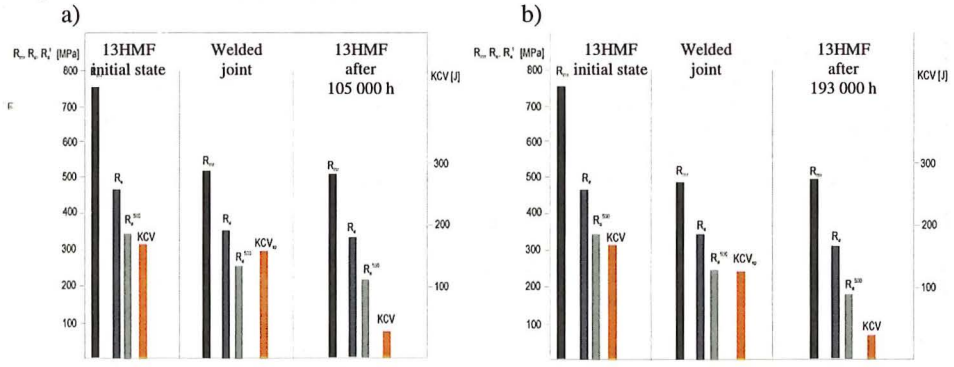

Drawing 1. Comparison of mechanical properties test results for parent material with test results of welded joint made of steel 13HMF in the condition as delivered from the steel mill with steel 13HMF following operation:
a) throughout 105,000 hours, b) throughout 193,000 hours.

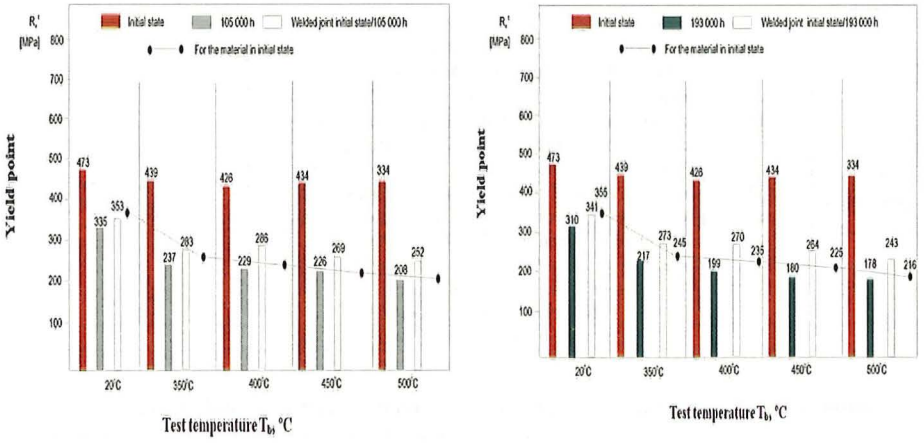

Drawing 2. Comparison of test results for yield point at elevated temperature of parent material and the material of circumferential welded joints of steel 13HMF in the condition as delivered from the steel mill with steel 13HMF following long-term operation in creep conditions:
a) throughout 105,000 hours, b) throughout 193,000 hours.

The welded joints of the examined steel in the initial condition with this steel following 105,000 and 193,000 hours of operation are compliant with the minimum requirements for yield point at elevated temperature, which is close to the actual working temperature. Although, the parent material of steel 14MoV63 following 105,000 and 193,000 hours of operation does not meet the requirements for material in the original condition.

Impact strength

The impact strength tests, performed with the objective to determine the impact transition temperature for the examined steel, following 105,000 and 193,000 hours of operation in creep conditions, have shown that the impact strength measured on test specimens with a V-notch is not compliant with the minimum requirements of the rupture labour 27[J] at room temperature. The impact transition temperature is above zero and amounts to +20 and +25°C respectively in comparison to the maximum temperature of "-" 20°C for the initial condition. However, the impact energy at room temperature measured on test specimens with a V-notch of circumferential welded repair joints of materials following operation with the material in the initial condition: for the heat-affected zone on the side of the material following operation, welded joint and HAZ on the side of the material in the initial condition exceeds considerably the required minimum value of 27[J].

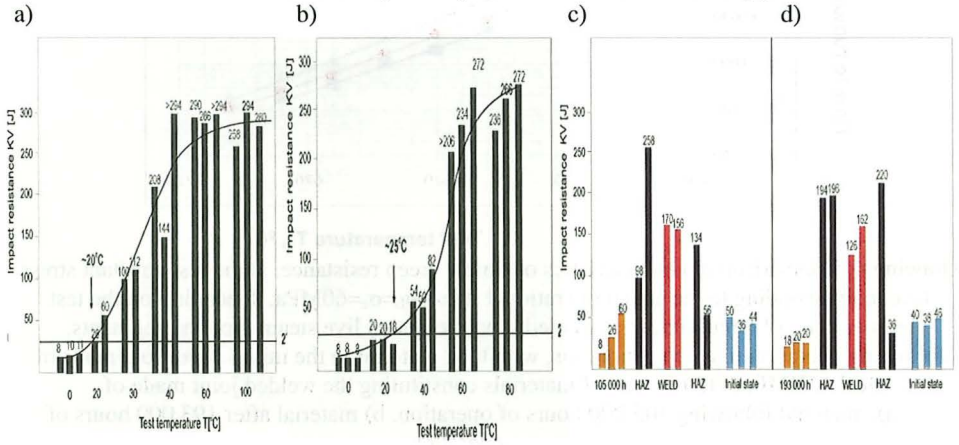

Drawing 3. Comparison of rupture labour results on test specimens with a V-notch:
a), b) depending on test temperature with a specified transition temperature into brittle state of live steam pipeline material, made of steel 13HMF, following long-term operation in creep conditions for 105,000 and 193,000 hours respectively,
c), d) heat-affected zone and the welded joint of the circumferential welded repair joints of steel 13HMF, in the condition as delivered from the steel mill, with steel 13HMF, following long-term operation in creep conditions throughout 105,000 and 193,000 hours respectively, to the test results of parent material.

Creep resistance

Taking the examined materials, following 105,000 and 193,000 hours of operation, as well as the fabricated welded repair joints, shortened creep tests have been carried out with the objective to determine the time of further safe operation in the existing working conditions. These tests have been performed at constant stress level of σ_b = 60MPa and at various test temperature levels, i.e. T_b = 600, 620, 640, 660, 680 ^{0}C. They have proven that the creep resistance of the examined circumferential welded joints is comprised within the lower material dispersion range of -20% following the operation.

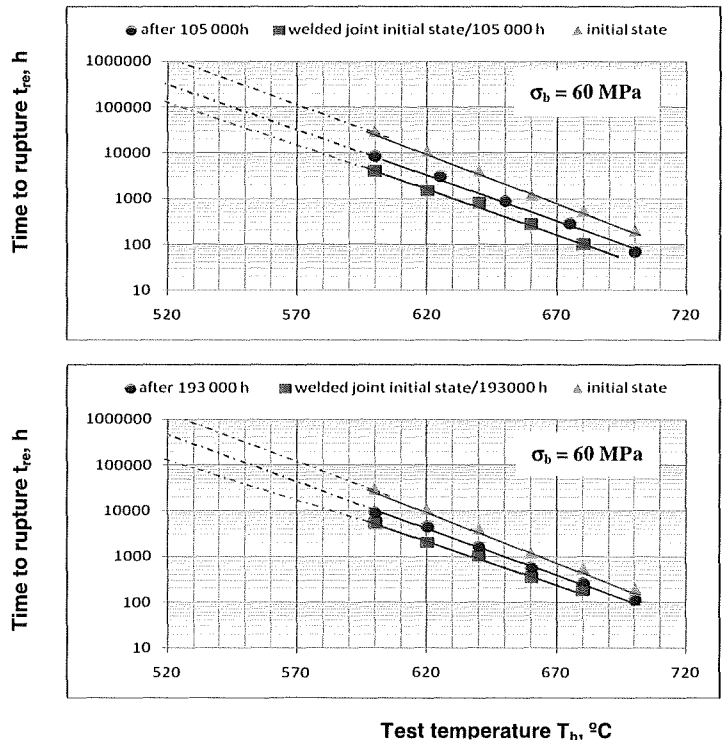

Drawing 4. Comparison of characteristics of timely creep resistance, at the test constant stress level corresponding to the actual operational stress $\sigma_b=\sigma_e=60$MPa, depending on the test temperature, of circumferential welded repair joints on live steam pipeline segments, following operation in creep conditions, with tube material in the initial condition, made of steel 13HMF, to test results of materials constituting the welded joint made of:
a) material following 105,000 hours of operation, b) material after 193,000 hours of operation.

3.1. Steel X20CrMoV12 1

Strength properties and impact energy

Mechanical properties testing at room temperature has been carried out on the fabricated circumferential welded joint of steel X20CrMoV12, in the initial conditions, to this steel following 108, 649 hours of operation, as presented in Drawing 5. The obtained test results of yield point, at room temperature and at elevated temperature, of the similar welded repair joint and the materials constituting the welded joint are compared in Drawing 6a, whereas the impact test results are compared in Drawing 6b. On the basis of the performed examinations of mechanical properties at room temperature and yield point at elevated temperature of the material following 108,649 hours of operation, as well as the examined welded joint made of this steel, following long-term operation, to this steel in the initial condition, it can be stated that, in accordance with the valid standards, the achieved figures are higher than the required minimum ones for the parent material in the condition as delivered from the steel mill. However, the impact strength of the examined welded joint of this steel, following 108,649 hours of operation, to this steel in the initial condition, as measured at room temperature, both in the welded joint and the heat-affected zone, does not meet the requirements for the parent

material in the condition as delivered from the steel mill, as provided in the standards. It is higher, although insignificantly, than the value specified for the brittleness threshold (i.e. 27J). This enables the proper behaviour of the welded joint during the operation. Nevertheless, it requires strict compliance with the currently valid procedures of boiler start-ups and shutdowns.

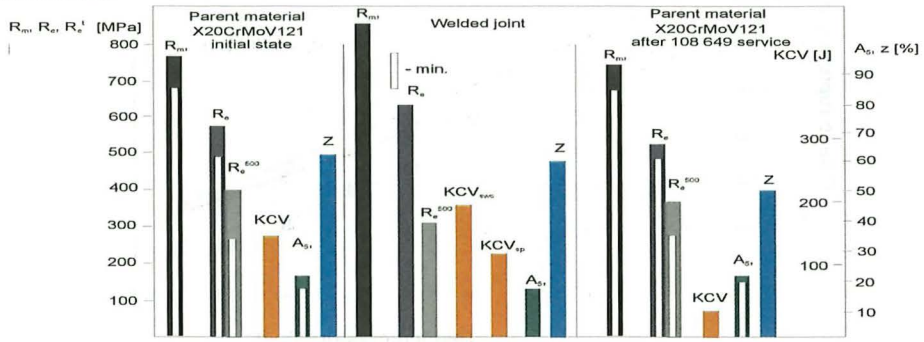

Drawing 5. Comparison of examination results of mechanical properties of welded joint made of X20CrMoV12.1 steel in steelwork delivery state with X20CrMoV12.1 steel after 108,649 hours of service with the examination results for parent material.

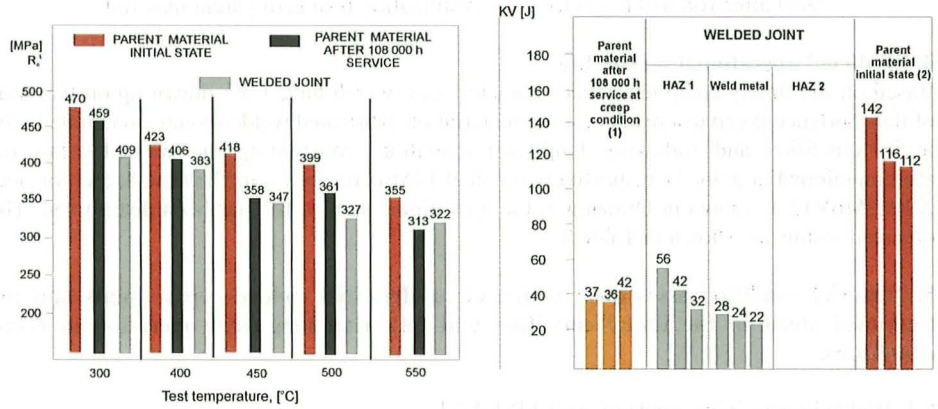

Drawing 6. Comparison of examination results of mechanical properties of welded joint of X20CrMoV121 steel in steelwork delivery state with X20CrMoV12.1 steel after 108 649 h service with examination results of parent material:
a) yield strength at elevated temperature, b) impact strength at room temperature.

Creep resistance

Shortened creep tests have been carried out on the examined materials and welded joints made thereof. Those tests have been carried out at the constant level of test stress, i.e. σ_b=100 MPa, and various test temperature levels, i.e. T_b= 600, 620, 640, 660 and 680^{0}C, being considerably higher than the specified operational temperatures. The results obtained have been shown in form of function log t_r =.f (T_b), at σ_b = const. Drawing 7 presents the comparison of the obtained shortened creep resistance test results of the circumferential welded joint for the steel, examined in the condition as delivered from the steel mill, with the steel following 108,649 hours of operation, with the test results of the material in initial condition and following 108,649 hours of operation. The results obtained show that the creep resistance of the examined circumferential welded joint is place in the lower dispersion range -20% of the material following operation. However, the specified available residual service

life, i.e. the time of further safe operation in the existing operational conditions, is but a half shorter for the welded repair joint than the time for the material following 108,000 hours of operation in creep conditions.

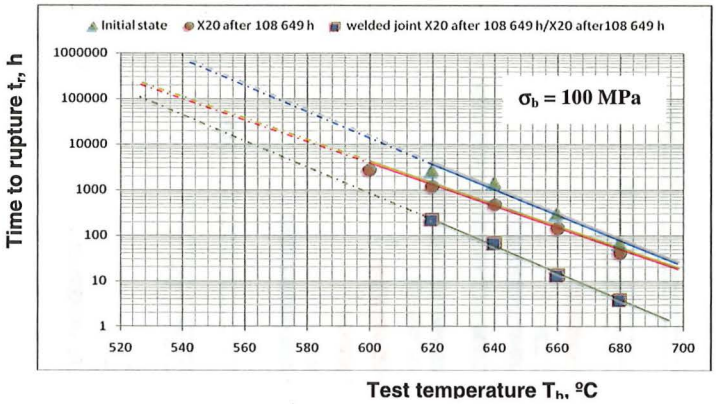

Drawing 7. Comparison of results of abridged creep tests of circumferential welded joint of X20CrMoV121 steel in the condition as delivered from the steel mill with X20CrMoV121 steel after 108 649 h service with examination results of parent material.

4. Predicted operational service life.

Based on the timely creep resistance characteristics, which have been drawn up on the basis of the shortened creep test results for the material of: fabricated welded joints, materials in the initial condition and following long-term operation, constituting the welded joints (as aforementioned in point 3), respectively for steel 14MoV63 shown in Drawing 4, and for steel X20CrMoV12 1, shown in Drawing 7, the operational service life has been determined. The obtained results are shown in Table 8.

5. Material condition assessment of the circumferential welded repair joints and the examined steels in the initial condition and following long-term operation in creep conditions.

5.1. Welded repair joints made of steel 14MoV63.

1. The assessed depletion degree of the examined live steam main pipeline segments following long-term operation in creep conditions, based on the evaluation of the structure pattern, amounts to:
   - Approx. 0.3÷0.4 for the material following 105,000 hours, which corresponds to structure class 2/3, in accordance with the Institute for Ferrous Metallurgy's own classification,
   - Approx. 0.3 for the material following 193,000 hours, which corresponds to structure class 2, in accordance with the Institute for Ferrous Metallurgy's own classification.
   Neither initiation of internal damage processes nor discontinuities have been observed in the materials examined.
2. The obtained tests results of strength properties, in particular the tensile strength or yield point, at room temperature and at elevated temperature, of the examined materials following long-term operation throughout 105,000 and 193,000 hours, in accordance with

Table 4. Service life, residual life, available life and available residual service life of circumferential welded repair joints for boiler pressure part components following operation in creep conditions, with material in initial condition, in comparison with test results for materials constituting the welded joints.

Assumed parameters for further operation		Designation	Predicted operational service life	
Stress σ_e, MPa	Temperature T_e, ^{0}C		Residual service life t_{re}, hr (service life t_r, hr)	Available residual service life t_{be}, hr (available service life t_b, hr)
1	2	3	4	5
60	540	Item 1	(500,000)	(275,000)
		Item 2	130,000	72,000
		Item 3	55,000	30,000
Item	Material for examinations			
1	Tube ø273x32 mm; steel 14MoV63 in the initial condition			
2	Live steam pipeline segment; steel 14MoV63 following 105,000 hrs of operation			
3	Circumferential welded joints of materials Item 1 to Item 2			
1	2	3	4	5
60	540	Item 1	(500,000)	(275,000)
		Item 2	180,000	99,000
		Item 3	60,000	33,000
Item	Material for examinations			
1	Tube ø273x32 mm; steel 14MoV63 in the initial condition			
2	Live steam pipeline segment; steel 14MoV63 following 193,000 hrs of operation			
3	Circumferential welded joints of materials Item 1 to Item 2			
1	2	3	4	5
100	540	Item 1	(800,000)	(440,000)
		Item 2	100,000	55,000
		Item 3	35,000	19,000
Item	Material for examinations			
1	Tube ø324x46 mm; steel X20CrMoV12 1in the initial condition			
2	Live steam superheater outlet header segment; steel X20CrMoV12 1 following 108,649 hours of operation			
3	Circumferential welded joints of materials Item 1 to Item 2			

the standards are not in compliance with the requirements for the examined steel in the condition as delivered from the steel mill. However, the test results as obtained for the material of the fabricated circumferential welded joints, made of those materials, following operation, with the material in the initial condition, are higher than the minimum required ones for the parent material in the condition as delivered from the steel mill, in accordance with the standards.

2. The impact strength measured on test specimens with a V-notch does not meet the minimum requirements for the rupture labour of 27J, at room temperature, with regard to the materials following 105,000 and 193,000 operational hours. The transition temperature into brittle condition is positive and amounts to +20 and +25°C respectively in relation to the maximum of -20°C for the initial condition. Nevertheless, the rupture labour at room temperature, as measured on the test specimens with a V-notch, of the circumferential welded repair joints of the materials following operation to the material in the initial condition: with regard to the heat-affected zone of materials following operation, the welded joint and the heat-affected zone of material in the initial condition, exceeds to a large extent the required minimum figure of 27J.
3. The hardness of the examined areas of the welded repair joints made of the steel, following long-term operation in creep conditions, to the steel in the initial condition, is ranged

within the limits from approx. 150 to approx. 280 HV10, i.e. it does not exceed the maximum admissible figure of 350HV10, whereas, the course of its modifications, on the transition through the welded joint individual zones, is relatively smooth.

4. The material creep resistance tests and examinations, following 105,000 and 193,000 hours of operation, as well as those of the circumferential welded joints, performed on creep tests at the constant stress level of σ_b = 60MPa and at various test temperature levels, i.e. T_b=600, 620, 640, 660 and 680 ^{0}C, have proven that the creep resistance of the examined circumferential welded joints is included within the lower dispersion range of -20% for the material following operation.
5. The available residual service live t_{be}, being the safe time for further operation, at the working temperature of T_r=540 °C at the assumed level of the working stress amounting to σ_r = 60MPa, has been assessed, respectively, for:
   - The material following 105,000 hours of operation: 72,000 hours,
   - The material of the welded repair joint material, following 105,000 hours of operation, to the material in the initial condition: approximately 30,000 operational hours,
   - The material following 193,000 hours of operation: 99,000 hours,
   - The material of the welded repair joint material, following 193,000 hours of operation, to the material in the initial condition: approximately 33,000 operational hours.

5.2. Welded repair joints made of steel X20CrMoV12.1.

1. The long-term operation in creep conditions, i.e. throughout 108,649 hours, has resulted in a change to the structure image of tempered martensite, preserving the martensite straps. The quantitative and dimensional increase in carbides has been observed, both on the straps as well as on the former austenite grain boundaries. Neither discontinuities nor initiation of the internal damage processes in the structure have been detected. The assessed material depletion degree, at structure class 2 in accordance with the Institute for Ferrous Metallurgy's own classification, is approximately 0.3 – 0.4.
2. The main strength properties at room temperature, as well as the yield point at elevated temperature for the material, following 108,649 hours of operation, including those of the examined welded joint, made of steel 20H12M1F, following long-term operations, are obligatory for the parent materials, in the condition as delivered from the steel mill.
3. The impact strength of the examined welded joint of steel X20CrMoV12.1.following 108,649 operational hours, to this steel in the initial condition, as measured at room temperature, both in the welded joint and the heat-affected zone, does not comply with the requirements, included in the standards, however, it is higher, insignificantly though, from the value specified for the brittleness threshold (i.e. 27[J]).
4. The examinations of the material following operation and circumferential welded joint creep resistance, which have been carried out on creep test specimens at constant stress level, i.e. σ_b= 100 MPa, as well as at various test temperature levels, i.e. T_b=600, 620, 640, 660, 680 and 700 °C, have proven that the creep resistance of the examined circumferential welded joint is not considerably different from the creep resistance obtained for material following operation. The residual service life, as specified in creep tests for working temperature T_r = 540 °C and working stress σ_r = 100 MPa, amounts to respectively:
   - Approx. 100 000 hours for parent material, following 108,649 hours of operation,
   - Approx. 35,000 hours for welded repair joint material of steel 20H12M1F, following long-term operation, to the same steel in the initial condition.

6. Final conclusions

1. The elaboration of the characteristics for the examined steels 14MoV63 and X20CrMoV12.1, following long-term operation in creep conditions, the material

characteristics of the circumferential welded repair joints and critical thick-walled components of power boilers operated above the limit temperature, with regard to changes in structure, changes to mechanical properties and creep resistance, are the most crucial elements for the behaviour of these materials, as well as of the components made thereof.

2. The test and examinations performed have allowed to assess the operational suitability of the applied materials, technologies and the ways of making welded joints thereof, which are applied in the industrial practice, i.e. welded repair joints of materials following long-term operation in creep conditions and materials in the initial condition, manufactured of one and the same steel grade. Such assessment has allowed us to determine the time of safe operation for the applied materials and the fabricated welded joints at the predicted working parameters of their further operation.

Acknowledgements

The authors wish to thank the Ministry of Science and Higher Education for their financial contribution to project SPB/COST/95/2005, performed within the scope of COST 538 programme, the selected results of which are presented above. Special thanks are due to the companies of ZRE Lublin and BOT Belchatow for their co-operation with regard to preparation of the welding and fabrication technologies for welded joints in the industrial environment.

Literature

[1] Hernas A., Materiały i Technologie do budowy kotłów nadkrytycznych i spalarni odpadów, Praca zbiorowa pod redakcją A. Hernasa, Katowice 2009 – in polish only.

[2] Dobrzański J., Zieliński A., Hernas A., Struktura i własności nowych stali żarowytrzymałych o osnowie ferrytycznej, Materiały i Technologie do budowy kotłów nadkrytycznych i spalarni odpadów, Praca zbiorowa pod redakcją A. Hernasa, Katowice 2009, 48-49 – in polish only.

[3] Dobrzański J., The classification method and the technical condition evaluation of the critical elements' material of power boilers in creep service made from the 12Cr-1Mo-V, J. of Mat. Proc. Tech. Vol.164-165, pp. 785-794, 2005.

[4] Dobrzański J., Kowalski B., Wodzyński J., Diagnostyka techniczna elementów krytycznych części ciśnieniowej kotłów energetycznych pracujących w warunkach pełzania po przekroczeniu obliczeniowego czasu pracy, Aktualne Problemy Budowy i Eksploatacji Kotłów; Politechnika Śląska ,Prace IMiUE, Zeszyt 23 T1, s. 85-126., Październik 2009 – in polish only.

[5] Dobrzański J., Zieliński A., Krztoń H., Mechanical properties and structure of the Cr-Mo-V low-alloyed steel after long-term service in creep condition, Journal of Achievements in Materials and Manufacturing Engineering. Vol. 23, Issue 1, pp. 39-42. July 2007,

[6] Dobrzański J., Zieliński A., Ocena przydatności do dalszej pracy materiału elementów rurociągu pary świeżej ze stali 14MoV63 (13HMF) po 200 000 godzin eksploatacji w warunkach pełzania, Energetyka; Zeszyt tematyczny nr XVIII, p. 32-36. Listopad 2008.

[7] Dobrzański J., Zieliński A., Paszkowska H., Wyznaczanie trwałości resztkowej i czasu dalszej bezpiecznej pracy na przykładzie materiału rodzimego i złącza spawanego, Prace IMŻ, T 61, nr 1, 2009, s.9-25 – in polish only.

[8] Dobrzański J., Ocena przydatności do eksploatacji stali 14MoV63 (13HMF) i naprawczych złącz spawanych grubościennych elementów rurociągów parowych pracujących w warunkach pełzania przez 100 000 i 200 000 godzin, Energetyka, Zeszyt tematyczny nr XVIII, s. 23 – 28, Listopad 2008 – in polish only.

[9] Dobrzański J., Pasternak J., Zieliński A.: Properties of Welded Joints of Martensitic Creep Resistance Steels Applied in Polish Power Plants, 3rd Int. Conf. on Integrity of High Temperature Welds, April 2007, London, United Kingdom.

9th Liege Conference : Materials for Advanced Power Engineering 2010
edited by J. Lecomte-Beckers, Q. Contrepois, T. Beck and B. Kuhn.

PROPERTIES OF THICK WELDED JOINTS ON SUPERHEATER COLLECTORS MADE FROM NEW GENERATION HIGH ALLOY MARTENSITIC CREEP-RESISTING STEELS FOR SUPERCRITICAL PARAMETERS

Janusz Dobrzański[1], Jerzy Pasternak[2] Adam Zieliński[1]

[1] Institute for Ferrous Metallurgy, Gliwice, Poland
[2] Boiler Engineering Company RAFAKO S.A., Raciborz, Poland

jerzy.pasternak@rafako.com.pl

Summary
The continuously developing power generation sector, including boilers with supercritical parameters, requires applications of new creep-resistant steel grades for construction of boilers steam superheater components. This paper presents selected information, experience within the field of research and implementation of a new group of creep-resistant as X10CrMoVNb9-1(P91), X10CrWMoVNb9-2(P92) and X12CrCoWVNb12-2-2(VM12) grades, containing 9-12%Cr. During welding and examination process the results of mechanical properties, requested level for base material and welded joints, as well as: tensile strength, impact strength and technological properties have been evaluated. Additional destructive examinations, with evaluation of structure stability, hardness distribution, for base material and welded joints after welding, heat treatment, again process have been determined. Recommendations due to the implementation influence of operating parameters of the main boiler components are part of this paper.

Keywords: boiler operating parameters, mechanical properties of welded joints, creep resisting steels,

1. Introduction

In order to keep up with the constantly growing demand for energy and to assure the safety for functioning of the Polish power system, it is absolutely required to increase the installed power from 3,000 do 5,000MW [1]. Therefore, a fast-pacing development of the power sector is indispensable. Such a quick growth in the power sector ought to take into account erection of the most efficient units, having high availability and minimum negative impact onto the environment. Boilers with supercritical parameters are the most suitable for this purpose.

The creep-resisting steels, which are used for superheater components in the "typical" power units, having supercritical parameters, steam temperature of approx. 580^0C (600^0C) and steam pressure of approx. 27MPa, with steam reheat in the reheat part up to 610^0C, have to assure adequate creep resistance and heat resistance at the temperature, which reaches:

- 610^0C – for boiler thick-walled components located outside the flue gas zone,
- 640 $(650)^0$C – for steam superheater components located in the flue gas zone.

This paper presents a review of the currently manufactured martensitic creep-resisting steels, containing 9-12%Cr, which are recommended for use in the European and domestic power sector. The evaluation of the new creep-resisting steels' properties has been carried out, the material test results have been presented for the base material and homogeneous welded joints made of X10CrMoVNb9-1(P91), X10CrWMoVNb9-2(P92) and X12CrCoWVNb12-2-2(VM12). In particular, this paper presents the evaluation of strength properties, rupture labour, hardness, structure, time resistance to creep and technological properties of the base materials and circumferential welded joints of steam superheater outlet collector segments, as fabricated at a large boiler manufacturer's, following welding and heat treatment, as well as

after the long-term annealing, with the objective to meet the design requirements, which has been illustrated with some selected test results.

2. Analysis of martensitic steels development, to be used for steam superheater components.

The expected configuration of the usage properties for steels in group 9-12%Cr has been obtained by modification of the chemical composition, including the adequate quantities of alloy additions V, W, Ni, Cu, Co, micro-additions N, B and Nb, at considerable decrease of carbon and Mo contents [5-16].

This group can be characterised by two trends of development:

- Modification of steel containing approx. 9%Cr with addition of Mo. As the results of introduction of additions V, W and micro-additions N, B and Nb, new steels P/T91, P/T92, NF616 and E911 have been obtained,
- Modification of steel containing 12%Cr with addition of Mo and V. Implementation of additions W, Ni, Cu or Co, as well as micro-additions N, B and Nb has resulted in formation of new steels NF12, TB12M, HCM12, HCM12A and VM12.

The development of this group has assured high strength and resistance properties, tensile properties and weldability of the steel, as well as considerably high resistance to creep conditions and heat-resistance at temperatures up to 610(620)^{0}C. The presentation of chemical composition for the new high-chromium steels of tempered martensite structure, which are recommended for use in the Polish power sector for supercritical boiler superheaters, is shown in Table 1.

Table 1.
The required chemical compositions of the new high-chromium creep-resisting steels, having the structure of tempered martensite, which are to be used in the Polish power sector for boilers having supercritical parameters.

Steel grade	Chemical composition, in %									
	C	Si	Mn	Cr	Ni	Mo	V	W	Nb	Others
X10CrMoVNb9-1 (T/P91); W-1.4903	0.08-0.12	0.20-0.50	0.30-0.60	8.0-9.5	< 0.40	0.85-1.05	0.18-0.25	-	0.06-0.10	N 0.03-0.07
X10CrWMoVNb9-2 (T/P92)	0.07-0.13	< 0.5	0.30-0.60	8.5-9.5	< 0.40	0.30-0.60	0.15-0.25	1.5-2.0	0.04-0.09	N 0.03-0.07 B 0.001-0.006
X12CrCoWVNb12-2-2 (VM12)	0.11-0.14	0.40-0.60	0.15-0.45	11.0-12.0	0.20-0.40	0.20-0.40	0.20-0.30	1.30-1.70	0.03-0.08	Co: 1.40-1.60 N:0.030-0.070 B:0.0030-0.006

3. Welding and heat treatment processes of the welded joints.

Steels 9-12%Cr, in "as delivered" condition, undergo normalisation (hardening) in air and high-temperature tempering afterwards. The recommended austenitising temperature for those steels has been determined at the level of approx. 1050°C, whereas the tempering temperature has been established at the range of 740 – 780°C. The main structure of 9-12%Cr steel is tempered martensite with separated carbides on the grain boundaries of the former austenite and martensite strips, frequently with little presence of ferrite δ. In case of lower cooling rates after austenitising, one can expect a structure being the mixture of tempered martensite with lower bainite and also with smaller amounts of ferrite δ.

In the welding process for those steels, it has been assumed that the chemical composition of the welding materials shall be similar to those of the base materials. With the purpose to weld the root bead on the collectors, RAFAKO S.A. have implemented GTAW method, using SMAW technique for welding the other welded joint filling passes. Martensitic steels containing 9%Cr are welded in the temperature range of martensite occurrence, i.e. between 200 and 350°C. Steels containing 9%Cr, such as P91, P92, are characterised by relatively high temperature at the beginning of the martensitic process M_s, which is approx. 400°C. As the result of welding, a strapped martensite structure is formed, with effects of self-tempering. The cooling rate $t_{8/5}$, as well as the cooling temperature after welding of those steels should be selected in such a way so as to assure full martensitic transformation, i.e. it shall be finished at a temperature below M_f. However, martensitic steels containing 12%Cr produce considerably more difficulties in order to master the welding technology. This concerns, in particular, X12CrCoWVNb12-2-2 (VM12) steel, which contains tungsten and cobalt additions. Following welding, all welded joints undergo stress relief annealing at the temperature range from 740 to 780°C. Additionally, the welded joints on the collector components have undergone the required non-destructive examinations and the evaluation of the mechanical properties, technological properties and examinations of the base material and welded joints' structure, in compliance with the requirements of EN 15614-1.

4. Material to be tested.

The authors of this paper have evaluated the material and similar circumferential welded joints made on the steam superheater outlet collectors. Steam collectors, originating from industrial heats – after normalisation and tempering in the "as delivered" condition – having the dimensions of: ϕ355.6x50mm, made of steels X10CrMoVNb9-1 (P91), ϕ160x40mm, made of steels X10CrWMoVNb9-2 (P92) and ϕ355.6x35mm made of steels X12CrCoWVNb12-2-2 (VM12), have been provided by V&M, as the contribution within the European international co-operation programme COST 536. The chemical composition of the collector material to be tested is in compliance with standard EN 10216-2, which has been confirmed on the basis of the testing analyses.

The scope of examinations included the correctness/ accuracy of welding and heat treatment processes by the analysis of: the steel immediate strength properties, technological properties of the welded joints, creep test results, structure stability and properties assessment as the result of the timely influence of the temperature, the level of which corresponds to the operating temperature of a boiler in operation (i.e. the assessment of resistance to ageing process).

5. Test results.

The testing programme included the checking of: strength properties at room and elevated temperature, assessment of the concurrent influence of temperature and time and temperature, the impact of time and load on the properties and structure changes, as well as the examinations which verify creep resistance of materials and similar circumferential welded joints of the superheater outlet header segments. On the basis of the obtained results and analyses thereof, the base materials have been evaluated, as well as the welded joints of the steam superheater outlet headers, which were fabricated according to the worked out technology, in the conditions relevant to a large boiler manufacturer.

5.1. Microstructure of steel and welded joints following welding and stress relief annealing.

Drawing 2 shows the assessment of material micro-structure of the examined steam superheater header shell segments, as revealed by a transmission electron microscope and scanning electron microscope, at magnifications 500 and 1,000x respectively. The typical header material structure is tempered martensite, with separated carbides on the grain boundaries of the former austenite and martensite strips. In case of lower cooling rates after austenitising, one can expect a structure being the mixture of tempered martensite with lower bainite and also with smaller amounts of ferrite δ [5]. The typical separations of carbides in steel X10CrMoVNb9-1 (P91) are $M_{23}C_6$, rich in vanadium and niobium, as well as fine carbide-nitrides, mainly those of vanadium.

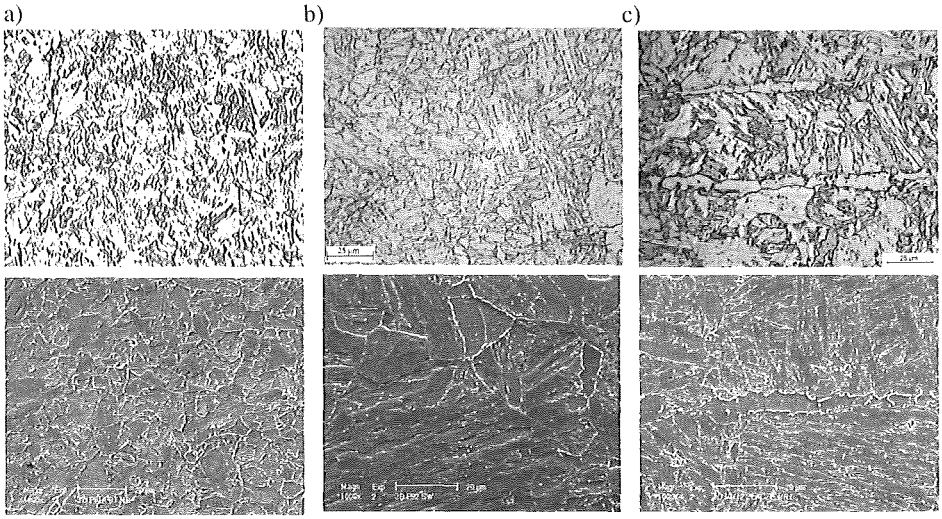

Drawing 2. Comparison of the assessment of material micro-structure of the examined steam superheater header's segments, made of martensitic steel 9-12%Cr, as observed on a transmission electron microscope and scanning electron microscope, at magnifications 300, 500 and 1,000x respectively, made of steels:
a) X10CrMoVNb9-1 (P91) [23,25], b) X10CrWMoVNb9-2 (P92), c) X12CrCoWVNb12-2-2.

In order to improve weldability of steel 9-12%Cr, the carbon content has been limited therein to approx. 0.10%. The reinforcement effect in those steels has been achieved mainly by reinforcing them with nitrides, carbon-nitrides, carbon-borides or inter-metallic phases (e.g. Fe_2W), which appear both on the boundaries and inside the ferrite grain, in dispersion form. Release hardening is the result of presence of numerous fine carbon-nitride separations, which also considerably influence the creep resistance. Additionally, carbides $M_{23}C_6$ stabilise mainly the martensite strap structure.

In steel X10CrWMoVNb9-2 (P92), carbides $M_{23}C_6$, containing mainly ferrum, chromium and molybdenum, strengthening the solid solution, whereas niobium and vanadium carbon-nitrides contribute to a considerable increase of the timely creep resistance. Taking steel X12CrCoWVNb12-2-2 (VM12), the main carbides phase is formed by $M_{23}C_6$ carbides, which are particularly rich in chromium, but also contain ferrum and molybdenum. Apart from them, there are fine releases of carbon-nitrides M(C, N), which are rich in vanadium and niobium.

Hardness of the materials having such a structure, depending on the steel grade, its chemical composition and heat treatment parameters, amounts to approx. 210 up to approx. 250HV. The level of hardness and other properties depends mostly from the applied temperature and tempering time. In case of lower cooling rates after austenitising, one can expect a structure being a mixture of tempered marteniste with lower bainite and some amounts of ferrite δ [3,5].

The assessment of the structural properties of the examined steels, has been supplemented with the analysis of the formed CTP_c diagrams. The examples of the obtained CTP_c diagrams for steels X10CrMoVNb9-1 (P91) and X12CrCoWVNb12-2-2 (VM12) are presented in Drawing 3.

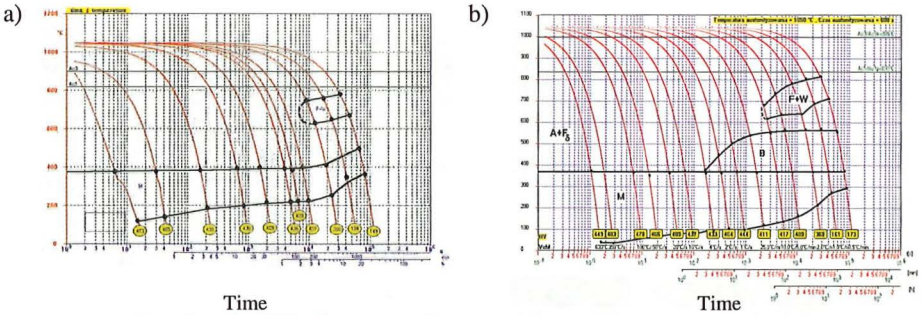

Drawing 3. CTP_c diagrams of martensitic steels containing 9-12%Cr
a) steel X10CrMoVNb9-1 (P91) [23,25] b) steel X12CrCoWVNb12-2-2(VM12)

5.2. Temperature influence on modification of mechanical properties

Comparison of strength properties test results.

The comparison of the tensile strength test results and yield point at room temperature and at elevated temperature of 600°C, on the basis of the base material and circumferential welded joint on steam superheater outlet header made of steel X10CrMoVNb9-1 (P91), has been shown in Drawing 4. Drawing 5 shows a comparison of tensile strength test results and yield point at room temperature and elevated temperature up to 600°C of steam superheater outlet collector's materials, made of steels X10CrWMoVNb9-2(P92) and X12CrCoWVNb12-2-2(VM12).

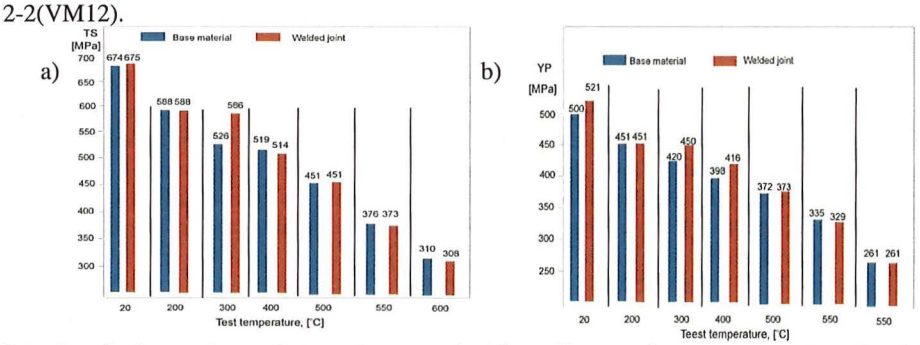

Drawing 4. Comparison of strength properties depending on the test temperature T_b of the base material and similar welded joint on the steam superheater outlet collector, made of steel X10CrMoVNb9-1 (P91):
a) Tensile strength R_m (R_m^t), b) Yield point R_e (R_e^t)

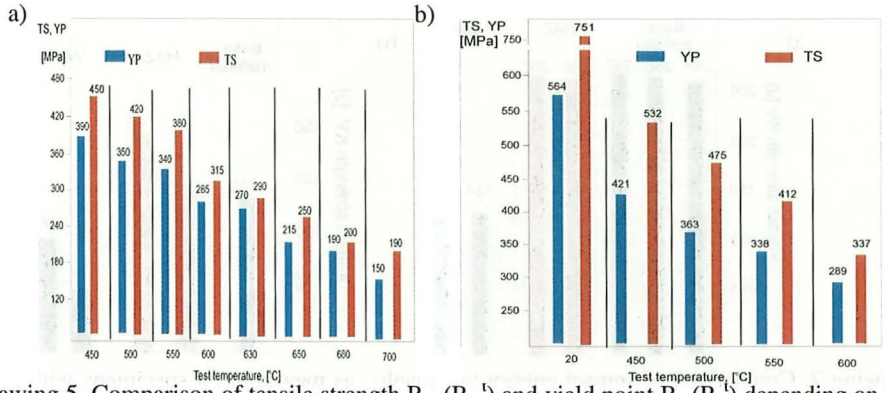

Drawing 5. Comparison of tensile strength R_m (R_m^t) and yield point R_e (R_e^t) depending on the test temperature T_b of the base material of steam superheater outlet header specimens made of steel:

a) X10CrWMoVNb9-2 (P92), b) X12CrCoWVNb12-2-2(VM12)

Comparison of impact energy test results:

A comparison of impact energy, measured on specimens with a V-notch, has been made for base material of steam superheater headers within the temperature range from "-"100 to 60°C. The impact transition temperature level, into brittle condition has been presented, i.e. approx. "-"100°C for steel X10CrWMoVNb9-2 (P92) and only approx. "-"20°C for steel X12CrCoWVNb12-2-2(VM12).

Some selected test results of steels X10CrWMoVNb9-2 (P92) and X12CrCoWVNb12-2-2(VM12) are shown in Drawing 6.

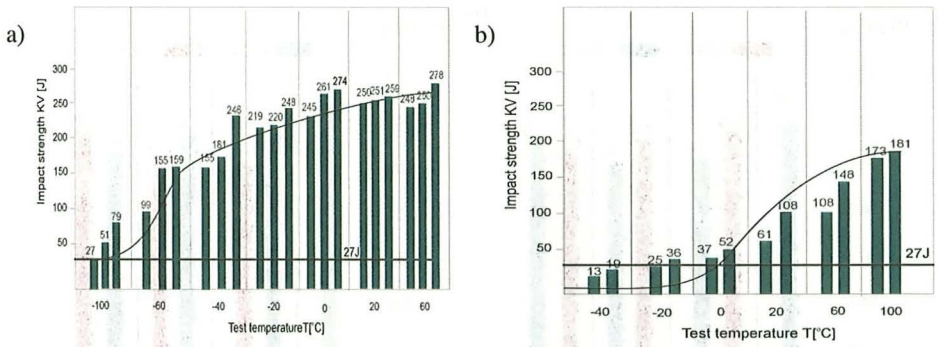

Drawing 6. Comparison of impact transition temperature, as measured on specimens with a V-notch, depending on test temperature, within the range from "-"100°C to 100°C, on base material of steam superheater outlet header specimens, made of steel:

a) X10CrWMoVNb9-2 (P92), b) X12CrCoWVNb12-2-2(VM12)

In Drawing 7 one can see a comparison of impact energy test results, measured on specimens with a V-notch, at room temperature, for the base material, HAZ and similar circumferential welded joints of steam superheater headers, made of steels X10CrMoVNb9-1(P91) and X10CrWMoVNb9-2(P92). The results, as obtained in both cases, are satisfactory and do not raise any reservations.

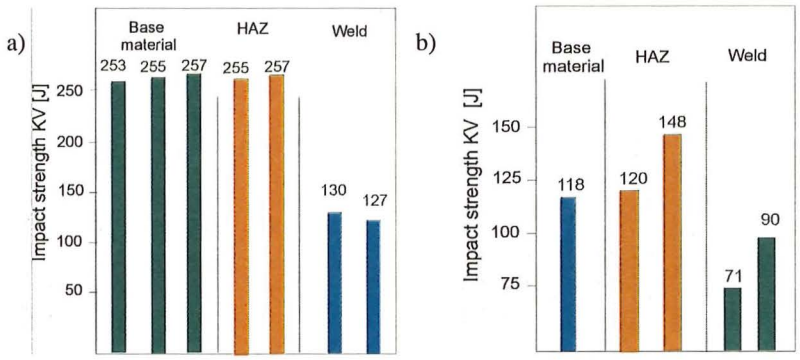

Drawing 7. Comparison of impact energy test results, as measured on specimens with a V-notch, at room temperature, for the base material, HAZ and a similar circumferential welded joint of steam superheater header segments, made of steels:
a) X10CrMoVNb9-1 (P91), b) X10CrWMoVNb9-2 (P92)

5.3. Influence of temperature and annealing time on mechanical properties and carbides phase composition.

Simultaneous influence of temperature and annealing time on the mechanical properties was compared. The duration of the long-term annealing tests was from several hundreds to several dozen thousands of hours. Drawing 8 presents some exemplary test results of long-term annealing temperature and time (up to 10,000 hours) influence onto tensile strength R_m and yield point R_e in relation to the base material of the tested steam superheater outlet header specimen, made of steel X12CrCoWVNb12-2-2(VM12). Whereas, the influence of the long-term annealing time onto the rupture energy of the steam superheater header material,

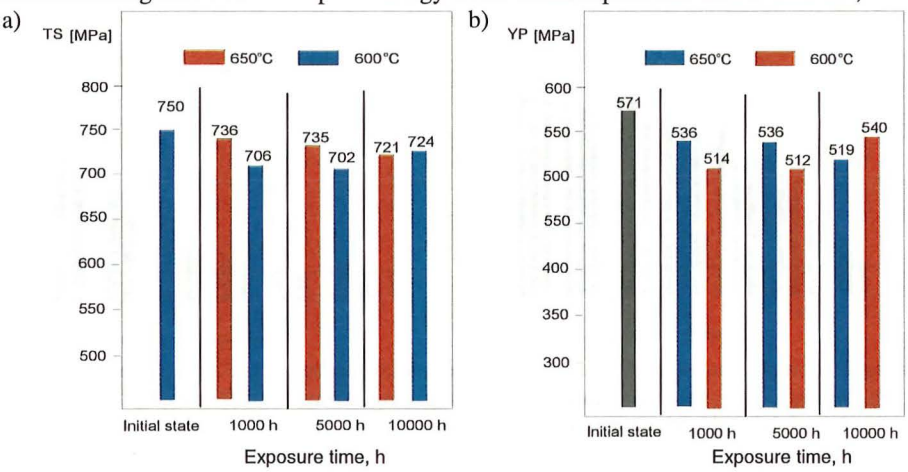

Drawing 8. Long-term annealing time and temperature influence on material properties of steam superheater outlet header, made of steel X12CrCoWVNb12-2-2 (VM12):
a) Tensile strength R_m, b) Yield point R_e

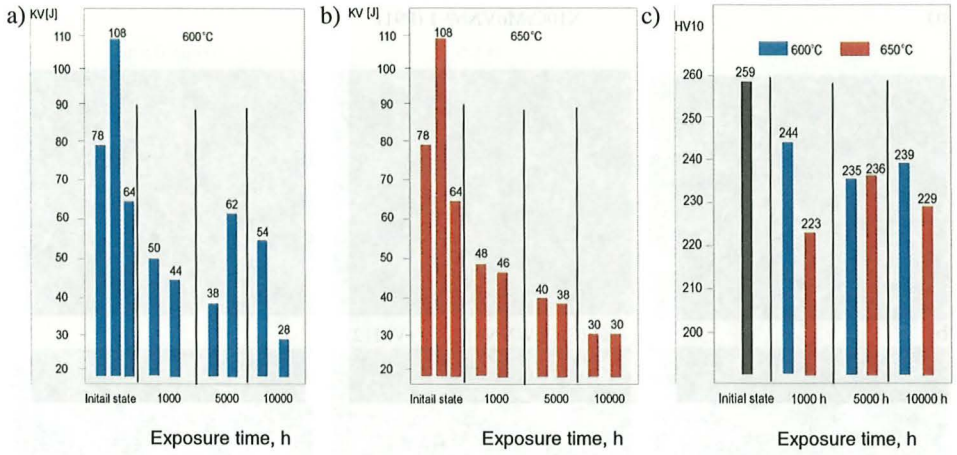

Drawing 9. Influence of long-term annealing time and temperature on steam superheater outlet header material, made of steel X12CrCoWVNb12-2-2 (VM12):
a) onto impact energy, as measured on test pieces with a V-notch at temperature T_b = 600°C,
b) onto impact energy, as measured on test pieces with a V-notch at temperature T_b = 650°C,
c) onto hardness HV10 at temperature 600 and 650°C.

as measured on test pieces with a V-notch at the temperature of 600°C, has been presented in Drawing 9a, whereas, at the temperature of 600°C in Drawing 9b. The HV10 hardness changes owing to long-term annealing (up to 10,000 hours) at the temperature of 600 and 650°C in Drawing 9c.
Additionally, following the long-term annealing, the materials undergo examinations of development of carbides release processes, with the application of radiographic phase analysis of carbide isolates, as well as observations of changes in the microstructure and identification of releases by means of transmission and scanning electron microscopy. The obtained results of the release processes development analyses will be presented in another publication.

5.4. Comparison of base material and welded joints' hardness and structure

The structure examinations have been performed with a transmission electron microscope and scanning electron microscope, at magnifications up to 800 and to 5,000x, respectively. Observations have been carried out on transverse metallographic micro-sections of the material and circumferential welded joint of the fabricated steam superheater headers. Some obtained exemplary results of testing the structure of circumferential welded joints material, as observed in a scanning electron microscope at magnifications 2,000x, are shown in Drawing 10. The base material structure, depending on the examined steel grade, is mainly tempered martensite, however, the steel containing 9%Cr, frequently with lower bainite and few ferrite areas (the hardness of the examined materials has ranged from approx. 200 to 240 HV10).

The hardness measurements of the header circumferential welded joints have been taken on transverse metallographic micro-sections. The measurements have been taken at close-to-surface zones, on the side of the weld face and root, as well as in the centre of the component thickness.

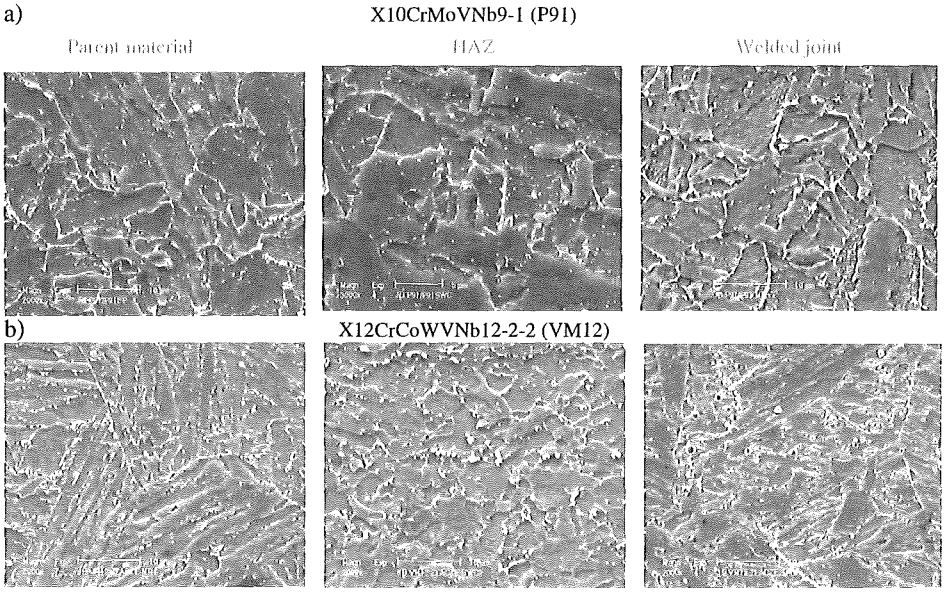

Drawing 10. Comparison of microstructure of circumferential welded joints elements: parent material, HAZ and welded joint, steam superheater outlet header shell, as detected by means of SEM and made of steels:
a) X10CrMoVNb9-1 (P91), b) X12CrCoWVNb12-2-2 (VM12)

The structure, which is most frequently observed in the heat-affected zone, constitutes of martensite with some share of bainite, having the hardness from approx. 220 to 260 HV10. In the welded joint, one can observe the mixture of martensite with a small quantity of bainite, where its hardness increases to approx. 300 HV10 in case of steel X10CrWMoVNb9-2 (P92).

Hardness, parent material/ HAZ/ welded joint/ HAZ/ parent material, following welding and heat treatment, has not exceeded 300 HV10, with the maximum difference being not higher than 50 HV10.

5.5. Comparison of the timely creep resistance.

With regard to the creep resistance examinations, creep test have been carried out having the duration of approx. 10,000 hours. For the shell material of each examined superheater header specimen, time creep resistance curves have been built for various levels of testing temperature, within the temperature range of that of the foreseen operation. The obtained results of the time creep resistance, in the form of dependence $\log\sigma_b = f(\log t_r)$, at T_b = const, at four levels of testing temperature, i.e. T_b=500, 550, 650 and 700°C, of shell material of the examined header specimen, made of steel X10CrWMoVNb9-2 (P92), have been presented in Drawing 11. The test results, as obtained for the header made of this steel, are included within the admissible dispersion range in comparison with the requirements for the medium values, pertaining to this steel. Similar results have been obtained with specimens of the shell material test pieces, made of the other examined two steel grades.

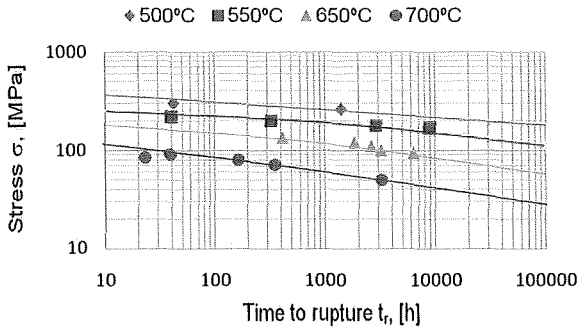

Drawing 11. Creep resistance test results in form of function log σ_b=f(log t_r), at T_b= 600 and 650°C, of steam superheater outlet header base material, made of steel grade X10CrWMoVNb9-2 (P92), against the background of the medium creep resistance curve, in accordance with the requirements.

Drawing 12 presents the comparison of the creep test results on the basis of the shell and similar circumferential welded joint material, as on superheater header test pieces, which have been made of steel grades X10CrMoVNb9-1 (P91) and X12CrCoWVNb12-2-2(VM12), in form of dependence log σ_b = f(logt_r), at T_b = 600 and 650°C. The comparison between the base material and welded joint shows that the time creep resistance of the welded joint is comprised in the lower dispersion range of the results obtained for the base material.

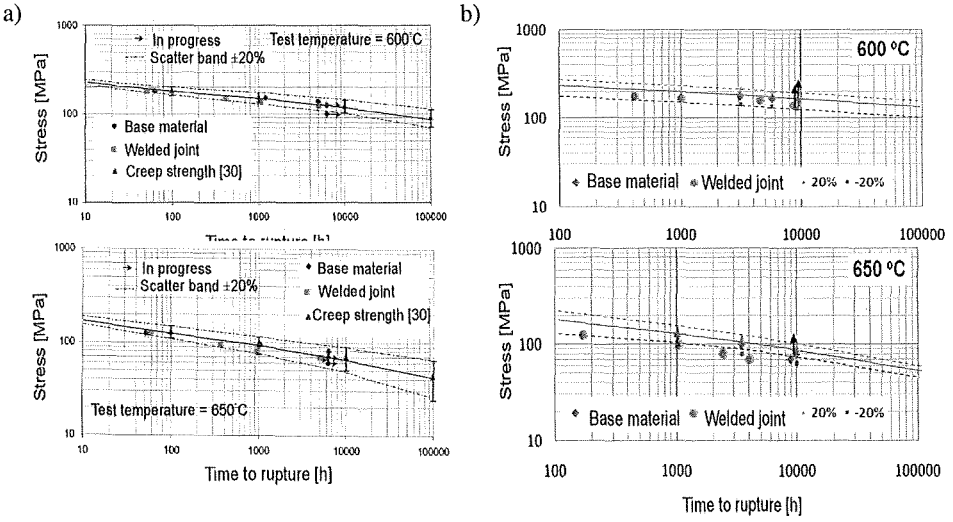

Drawing 12. Creep resistance test results in form of function log σ_b=f(log t_r), at T_b= 600 and 650°C, of steam superheater outlet header material and similar circumferential welded joint, shown against the background of creep resistance medium curve, in accordance with the requirements for steel grades:

a) X10CrMoVNb9-1 (P91), b) X12CrCoWVNb12-2-2 (VM12)

5.6. Resistance to oxidation.

The tests on oxidation in air, within the temperature range from 600 to 700°C, have been carried out in electric furnaces, which have been specially adapted for this purpose. Steel susceptibility to oxidation in air has been assessed by means of the gravimetric method. Drawing 13 shows the obtained test results, in form of the dependence of mass increase, in relation to the surface in proportion to the exposure time, at constant testing temperature, for steels grades X10CrMoVNb9-1 (P91) and HCM12A (P122). On the basis of the achieved test results within the temperature range from 600 to 700°C for steel X10CrMoVNb9-1 (P91), it can be concluded that the steel is useful for applications in the power sector, i.e. for components which are operated at temperatures which do not exceed 650°C, at which the mass increase for a surface unit, following 9,000 hours of operation, does not exceed 25g/m^2, as shown in Drawing 13a. Steel HCM12A (P122) is even more advantageous, with regard to the oxidising conditions in air, than steel X10CrMoVNb9-1 (P91). For the former steel, within the temperature range from 600 to 700°C, the mass increase per surface unit following 7,000 hours does not exceed 3g/m^2, as shown in Drawing 13b. Similar behaviour as that from steel X10CrMoVNb9-1 (P91) can be expected from steel X10CrWMoVNb9-2 (P92), whereas steel X12CrCoWVNb12-2-2 (VM12) should behave similar to steel HCM12A(P122).

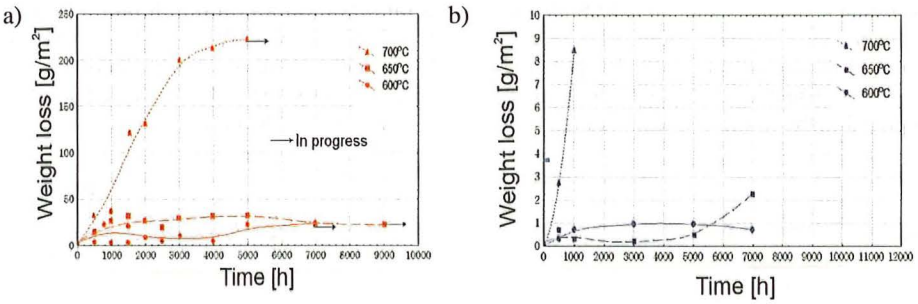

Drawing 14. Resistance to temperature influence in air, in the temperature range from 550 to 650°C, depending on the exposure time, of martensitic steels 9-12%Cr:
a)X10CrMoVNb9-1 (P91), b) HCM12A(P122)

6. Conclusions.

1. The impact energy of the steam superheater header base material at room temperature exceeds considerably the required minimum value of 27[J]. The impact transition temperature into brittle condition for the header material, i.e. steel X10CrMoVNb9-1 (P91), is "-"100^{0}C, whereas, for that made of steel X12CrCoWVNb12-2-2 (VM12), the transition temperature is "-"20^{0}C. As regards the header material of steel X10CrWMoVNb9-2 (P92), this temperature is an intermediate one in comparison with those made of the other steel grades.
2. The impact energy for the similar circumferential welded joint material, at room temperature, with regard to the parent material, heat-affected zone, as well as the welded joint, is comparable to the base material results, however, in the welded joint it is the lowest.
3. Impact energy resulted in a considerable decrease to the level of rupture labour of test samples with a V-notch, i.e. from approx. 70 to 90[J] in the "as delivered" condition, down

to approx. 30[J] following 10,000 hours. The values obtained are slightly higher than the required minimum ones for the initial condition.

4. A considerable decrease in hardness, i.e. by approx. 50HV, has also been observed. The long-term annealing tests are continued and will be continued up to at least several dozen thousands hours, with the objective to confirm the described tendencies.
5. Long-term annealing at temperatures 600 and 650^{0}C (which is similar to the operating temperature), having the duration up to 10,000 hours, has not produced considerable changes to the strength properties at room temperature or at elevated temperature.
6. The changes in the microstructure, resulting from the influence of temperature 600 and 650^{0}C, as well as time up to 10,000 hours, have to be described as substantial. We have observed a slow disintegration of martensite by means of the initiated process of decay of martensite straps, with the simultaneous formation of sub-grains. A similar assessment can be applicable to the release processes.
7. The timely creep resistance of the steam superheater header base material, as assessed on the basis of a creep test, which lasted up to approx. 10,000 hours, is in compliance with the requirements as set for the examined steels X10CrMoVNb9-1 (P91), X10CrWMoVNb9-2 (P92) and X12CrCoWVNb12-2-2(VM12). As concerns the creep resistance of the material of the fabricated circumferential welded joints on those headers, it is included in the admissible lower dispersion range, as achieved for the parent material. It has been confirmed that steel X10CrWMoVNb9-2 (P92) has a higher creep resistance than steel X10CrMoVNb9-1 (P91), whereas steel X12CrCoWVNb12-2-2 (VM12) has a similar creep resistance to steel X10CrWMoVNb9-2 (P92).

Acknowledgements

The authors wish to thank the Science and Higher Education Ministry for financial support of SPB/COST/96/2005 project, the selected test results of which are presented above. Special thanks are due to the company of V&M for supplying the tube segments, as well as Thyssen Welding for providing the necessary welding materials and consultations on welding technologies, which have been very useful for this project.

9. References.

1. Gabrel J., Bendick W., Vanderberghe B., Lefabrre B: "Status of development of the VM12 steel for tubular applications in advanced power plants". 8th Int. Conf. on Materials for Advanced Power Engineering 2006, Liege, Belgium. ISBN 389336-436-6, Forschungszentrum Jülich 2006, p.1065.
2. Kouichi Maruyama, Kota Sawada, Junichi Koike: Strengthening Mechanisms of Creep Resistant Tempered Martensitic Steel. ISIJ International, Vol. 41 (2001), No. 6, p. 641–653.
3. Deshayes F, Bendick W, Haarmann K, Vaillant J.C, Vallourec Research Center, Mannesmann Research Institute, Vallourec-Mannesmann Tubes – New 2÷3%Cr Steel Grades for Waterwall Panels and Superheaters, Raport COST 501 –Liege, Oct. 1998.
4. Masuyama F.: Steam Plant Material Developments in Japan. 6th Int. Conf. on Materials for Advanced Power Engineering 1998, Liege, Belgium. ISBN 389336, Forschungszentrum Jülich 1998, p.1087.
5. Zielińska-Lipiec A.: The Analysis of Microstructural Stability of Modified Martensitic Deformation. AGH 2005 Kraków ISSN 0867-8631, Poland.

HIGH TEMPERATURE CREEP PROPERTIES AND MICROSTRUCTURAL EXAMINATIONS OF P92 WELDS

Kalck Charlotte[1, 3*], Fournier Benjamin[1], Barcelo Françoise[1], Forest Laurent[2], Dalle France[1], Giroux Pierre-François[1, 3], Tournié Ivan[1], Gourgues-Lorenzon Anne-Françoise[3]

1 : CEA Saclay, DEN/DANS/DMN/SRMA, 91191 Gif sur Yvette Cedex, France
2 : CEA Saclay, DEN/DANS/DM2S/LTA, 91191 Gif sur Yvette Cedex, France
3 : MINES ParisTech, Centre des Matériaux, UMR CNRS 7633, BP 87, 91003 Evry, France
**corresponding author: charlotte.kalck@cea.fr*

Abstract

The present study deals with the creep properties of welded joints made of P92 steels. The purpose is to determine the weakest zone at 550°C under various load levels (160-240 MPa) and to investigate the evolution of the microstructure during creep.

The study of the fracture surfaces and the microstructural examination of welded joints prior to and after creep tests allow to investigate damage development. Ductile fracture occurs in the heat affected zone, more precisely, in the intecritical area, together with pronounced necking. Observation of the necking area shows many cavities and cracks.

Keywords: P92, welded joint, creep rupture strength, EBSD

1 Introduction

In the framework of the development of generation IV nuclear reactors, 9% chromium martensitic steels present both a high strength and high creep resistance. They also have a better thermal conductivity, lower thermal expansion and are cheaper than austenitic steels. Among them, P92 (ASME Grade 92) steel seems to be an appropriate candidate for high temperature components and especially for welded components. Its main targeted applications are heat exchangers and hot fluid pipes, which are exposed to long-term creep between 550 and 650°C. However, it has been demonstrated that welding has a significant effect on the creep strength of those steels [1, 2], so that long term mechanical properties of P92 welded joints at 550°C still need further investigation. The objective of this paper is to describe the microstructure of a P92 welded joint and to provide new experimental data on the creep behaviour of welded joints at 550°C.

2 Materials and experimental procedures

The study focuses on a P92 butt welded joint. The base metal was provided as a pipe of 219 mm in outer diameter and 19 mm in thickness. The chemical composition of the base metal and filler metal are given in Table 1. We can see that the filler metal does not contain any boron, whereas boron is known to have good influence on creep properties. The as-received base material had been austenitized at 1060°C for 30 minutes, quenched and then tempered at 770°C for 60 minutes.

The joint concerns the assembly of 2 tubes in butt welding configuration with the manual GTAW (Gas Tungsten Arc Welding) process. The welding position is flat. A preheating and an interpass temperature have applied (~220°C).

A post weld heat treatment (PWHT) was applied to the weld in order to relieve residual stresses induced by welding and also to temper the newly formed martensite. The PWHT is a tempering at 760° C during 4h30 hours with heating and cooling rates.

	C	Mn	P	S	Si	Cr	W	Mo	V	Nb	N	B	Al	Ni
Base Metal	0.12	0.54	0.014	0.004	0.23	8.68	1.59	0.37	0.19	0.06	0.046	0.002	0.020	0.26
Filler rod	0.109	0.46	0.008	0.001	0.38	8.76	1.55	0.40	0.201	0.06	0.044	-	-	0.53

Table 1: Chemical composition (wt %) of the base and weld metal.

2.1 Metallographic investigations of the welded joint and of crept samples

2.1.1 Microstructural observations

The microstructure of the welded joint was observed with an optical microscope after mechanical polishing down to 1 µm with diamond paste followed by vibrating colloidal silicon suspension (OPS) polishing. Finally, a Villela (1g of acid picric acid + 5mL of HCl + 100mL of ethyl alcohol) etching was performed.

Thin foils were also prepared from the base metal and observed with transmission electron microscopy.

Electron backscatter diffraction (EBSD) examinations were conducted with a scanning electron microscope (SEM) with a working distance of 25mm, an accelerating voltage of 25kV and a beam current of 6 nA. The maps were obtained with a beam step size of 0.5 µm, using a JEOL JSM 6400 SEM with a LaB_6 cathode and an EBSD HKL system with Channel 5 software [2].

2.1.2 Microhardness measurements

Vickers Microhardness tests were carried out along the transversal axis of the welded joint sample, before and after creep tests. Measurements were performed using a LEITZ WETZLAR GERMANY machine. Indents were made with a weight of 500g and a holding time of 10 seconds.

2.2 Creep tests

Smooth cross-weld specimens were extracted from the weldment, along the longitudinal axis of the pipe. Their geometry is presented in figure 1.

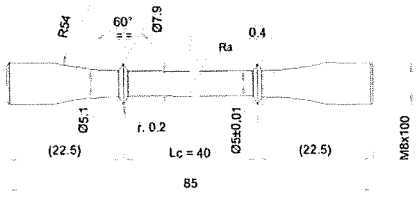

Figure 1: Scheme of creep specimen geometry.

Creep tests were conducted in air under uniaxial tensile load control using ADAMEL creep machines. The temperature gradient between both ends was kept lower than 3°C. These

tests were performed at 550°C from 160 to 240 MPa (See table 2). Specimen elongation was continuously measured and recorded using extensometers with a sensitivity of 1µm.

After creep, macrostructure and microstructure were revealed using Villela etching of longitudinal cross-sections in order to locate fracture with respect to the various zones of the welded joint. In order to investigate damage developed during creep, fracture surfaces and longitudinal cross-sections of the creep specimens were observed by SEM.

3 Results and discussion

3.1 Metallographic characterization of the as-received material

The various zones in the welded joint are schematically represented in Figure 2.

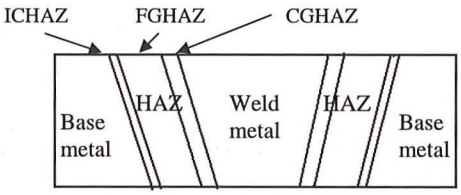

Figure 2: Scheme of the welded joint.

The welded joint is composed of a range of different microstructures which constitute the base metal, the welded joint and the heat affected zone (HAZ). The microstructure is related to the thermal history experienced during the welding.

The microstructure of HAZ varies along the distance from the fusion line.

The area close to the weld metal shows coarse parent austenite grains and is called the coarse-grained zone (CGHAZ). Then, next to the CGHAZ, the HAZ presents an area with very fine parent austenite grains (FGHAZ). A last zone, located between the base metal and the FGHAZ, presents a particular microstructure, made of martensite laths and prior austenite grains denoted the intercritical zone (ICHAZ).

A microhardness profile performed at mid-thickness is symbolized by the dash-dot line in Figure 3. The combination of microhardness profiles and observations of the welded joint allows highlighting the location and the width of the different areas of the HAZ (Figure 4).

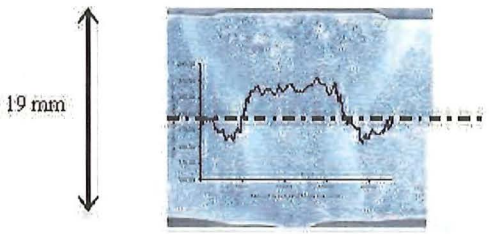

Figure3: Cross-weld microhardness profile combined with observations of the welded joint.

The weld metal is the harder part of the joint (the average value is 265 HV). The hardness in the HAZ is varying. A softened zone (200 HV) is observed in the HAZ next to the base metal. It probably corresponds to the ICHAZ. Then, the hardness strongly increases in the HAZ towards the weld metal. The area which is harder than the other zones and located close to the weld metal corresponds to the CGHAZ.

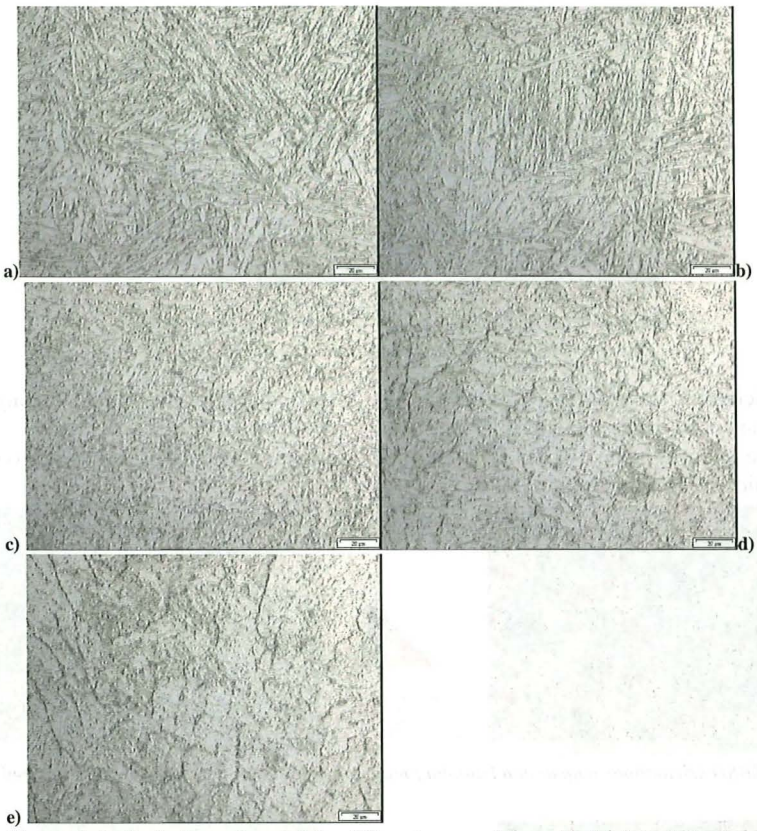

Figure 4: Optical observations of the different areas of the welded joint: a) the base metal, b) the intercritical area, c) the FGHAZ, d) the CGHAZ and e) the weld metal.

EBSD maps display the microstructure of different zones of the welded joint (figures 5, 7 and 8).

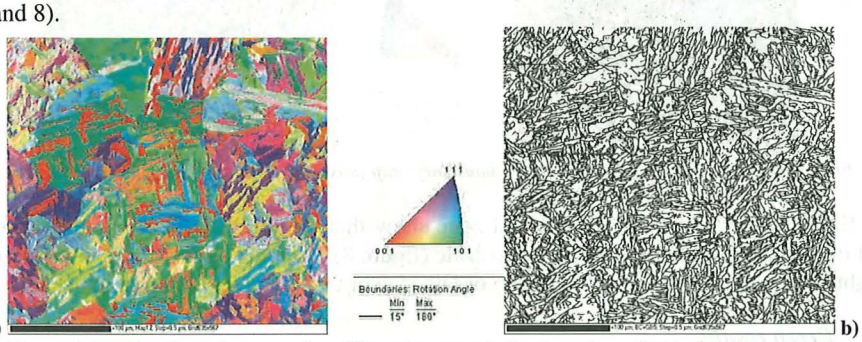

Figure 5: EBSD orientation map a) and boundary map (misorientation >5°) b) of the base metal.

The microstructure of the base metal is a usual martensitic microstructure made of laths, arranged in blocks and packets (Figures 5 and 6) [4, 5].

The average size of a block is about 4 µm (Detection criterion: misorientation > 5°). Giroux [6] estimated the subgrain size of the same base metal to be 0.37 µm. He estimated the average dislocation density of the material at about 2.10^{14} m^{-2}.

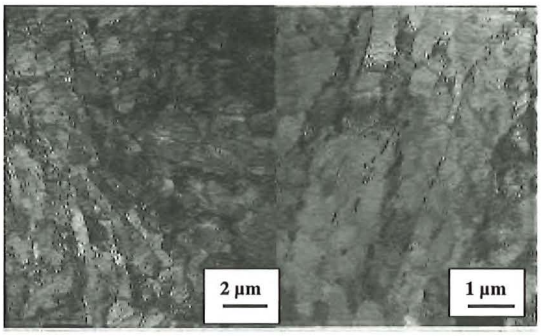

Figure 6: Bright Field TEM observations of the Base metal.

The microstructure of the base metal also displays many precipitates along grain boundaries and also inside the grains [4, 5].

The fine–grained zone (FGHAZ) (figure 7) presents a microstructure with very fine crystals, which mean size is about 2.9 µm.

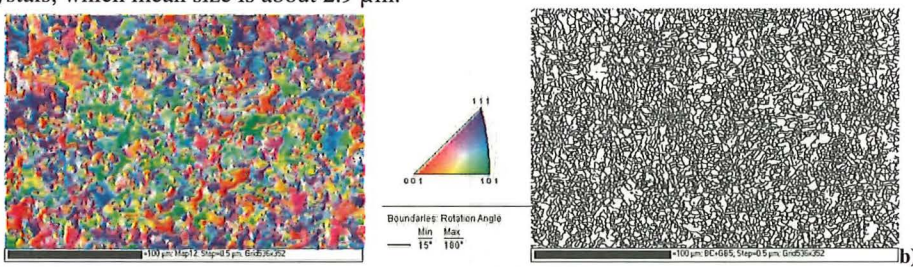

Figure 7: EBSD orientations map a) and boundary map (misorientation >5°) b) of the fine-grained zone.

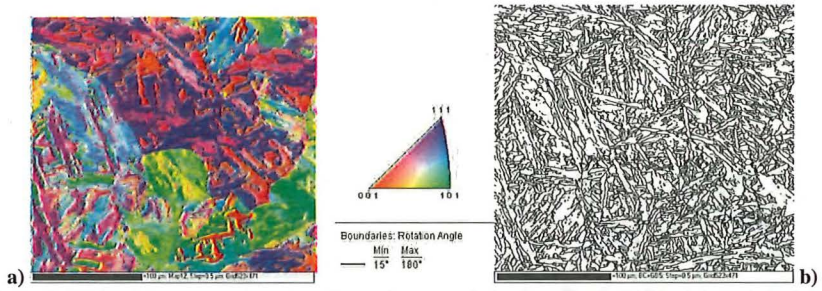

Figure 8: EBSD orientations map a) and boundary map (misorientation >5°) b) of the softened zone.

EBSD observations of the softened zone show that the microstructure is very similar to that of the base metal at the investigated scale (figure 8). This suggests that the lower hardness might be due to a difference of subgrain or lath size or to a different precipitation state.

3.2 Creep results

3.2.1 Creep curves

Creep tests results are summarized in Table 2 and Figure 9. Specimens subjected to applied stresses of 229.6 MPa and 240 MPa both broke in the HAZ, very close to the base metal, namely, in the ICHAZ. The specimen crept at 205 MPa has not been observed yet.

Applied stress (MPa)	Test duration (h)	Current state
160	7700	Non Fractured
174.6	7300	Non Fractured
205	6187	Fractured
205	8700	Non Fractured
229.6	2837	Fractured
240	1127	Fractured

Table 2: Creep results. "Non Fractured" means that the creep test is still in progress.

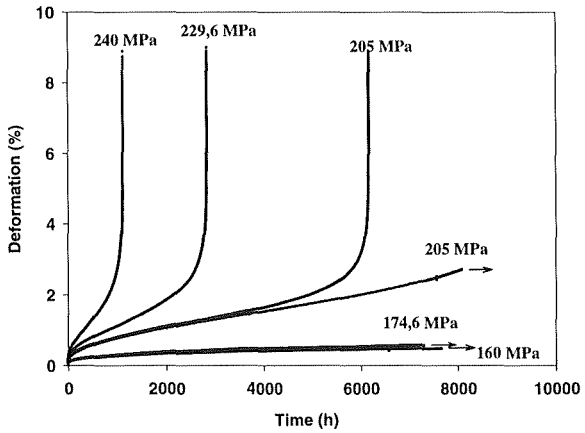

Figure 9: Creep curves at 550°C.

The fracture elongation is rather high (several percents). The three typical creep stages are clearly visible in Figure 9. The values of strain at the end of the first two stages are indicated in Table 3. The two creep curves at 205 MPa are superimposed for the first two creep stages but differ in the third stage. However, the ratio between both lifetimes will probably not exceed 2 or 3 as the third stage already started for the ongoing test.

Applied stress (MPa)	Deformation at the end of the first stage (%)	Time at the end of the first stage (h)	Deformation at the end of the second stage (%)	Time at the end of the second stage (h)
160	-	-	-	-
174.6	0.552	6556	-	-
205-broken	0.983	1480	1.942	4780
205	0.885	1400	2.06	6400
229.6	0.703	300	1.725	1800
240	0.593	140	1.558	680

Table 3: Amount of strain and time at the end of the primary and the secondary creep stages.

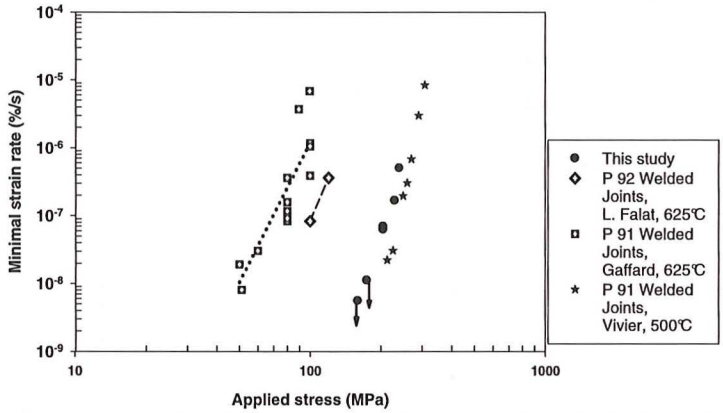

Figure 10: Minimal strain rate versus applied stress for welded joints [3, 6 and 7].

The minimum creep rates of the crept samples can be modelled by a typical Norton power-law curve defined by equation 1:

$$\dot{\varepsilon} = A\sigma^n \qquad (equation1)$$

Where $\dot{\varepsilon}$ is the minimum creep rate, σ the applied stress, A and n are parameters depending on material and temperature. For this study, the model gives n=11.57. This relatively high value suggests that the creep deformation mechanism is controlled by dislocations motion, possibly together with an effect of internal stresses. This result can be compared with the values found at 500°C by Vivier [1] and at 625°C by Gaffard [7] for welded joints of P91 (Figure 10).

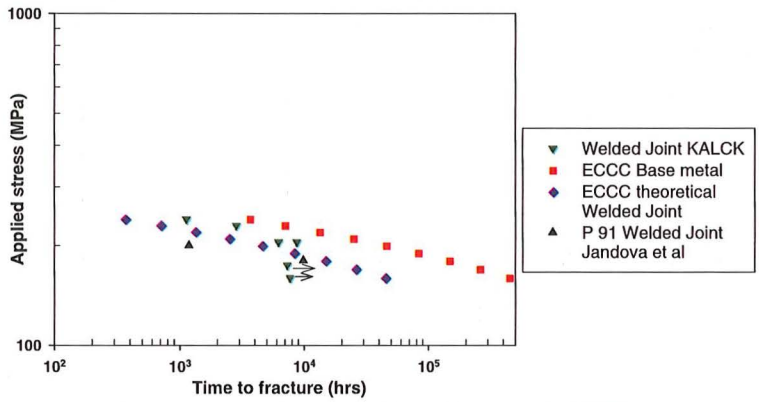

Figure 11: Applied stress versus time to fracture, at 550°C [1, 8].

In Figure 11, ECCC "theoretical" values correspond to times to fracture of welded joint calculated from ECCC base metal values and reduced by a factor of 10 compared to time to fracture of base material [8].

As expected, the creep strength of the welded joint is lower than the creep resistance of the base metal. The ratio between the values of the base metal and the actual welded joint is about 3.3 i.e. three times lower than that expected from "theoretical" ECCC values.

Moreover, creep lifetime is larger for P92 welded joints than for P91 welded joints [9] at the same temperature. The Monkman-Grant constant (Figure 12) is also higher than that of P91.

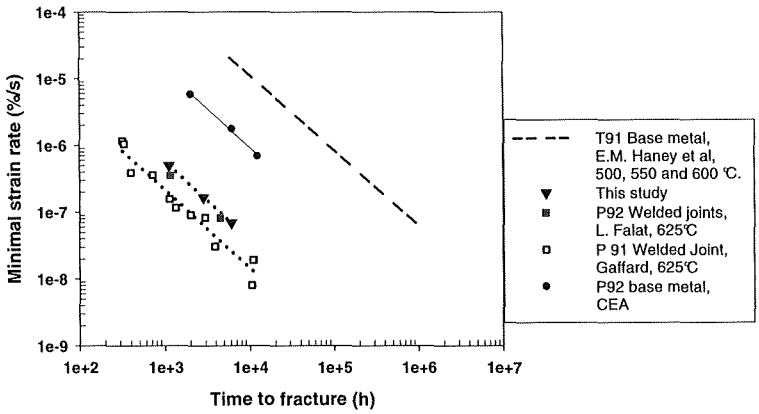

Figure 12: Monkman-Grant curve for crept specimens [8, 9 and 10].

The dashed line in Figure 12 corresponds to a linear approximation of a set of data about T91 at temperatures ranging from 500 to 625°C, studied by E.M. Haney et al [10]. Data about P92 welded joints coming both from this study and from L. Falat experiments [4] are spread homogeneously along the same line.

Besides, we can see that the diminution of P92 properties due to the welding is less significant than for P91. The difference between the Monkman-Grant properties (figure 12) of the welds compared to the base metal is much more pronounced for P91 than P92. This is consistent with the 3.3 ratio observed on the lifetime in figure 11.

3.2.2 Fracture surface examination

Fracture surfaces of broken samples present a circular shape. The facture mode is transgranular ductile. The facture surfaces in figure 13 exhibit many dimples, which is typical of a ductile fracture in the dislocation creep regime.

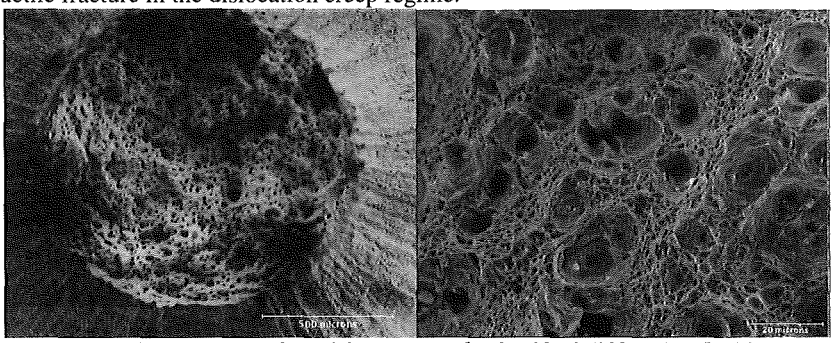

Figure 13: Fracture surface of the crept sample after 2837h (229.6 MPa, 550°C).

3.2.3 Damage mechanisms

The samples (figure 14) display a pronounced reduction of area at the fracture surface, which highlights significant plastic deformation before fracture.

Applied Stress (MPa)	Necking (%)
205	72
229,6	81
240	79

Table 4: Necking of the broken sample

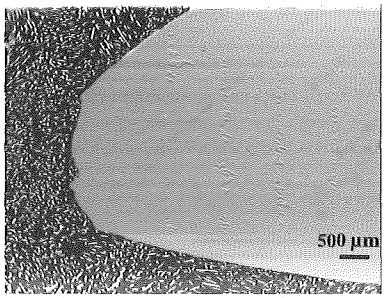

Figure 14: Necking area of a crept sample (240 MPa, 550°C).

A lot of cavities and short cracks can be observed in the necking area of the broken specimen (Figure 15). Cavities are elongated along the loading direction.

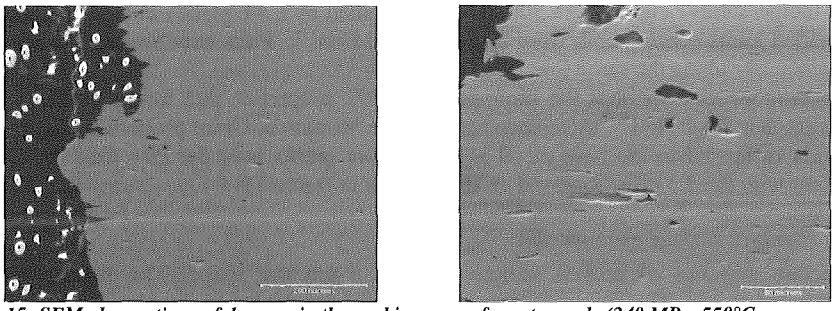

Figure15: SEM observations of damage in the necking area of crept sample (240 MPa, 550°C, cross-section).

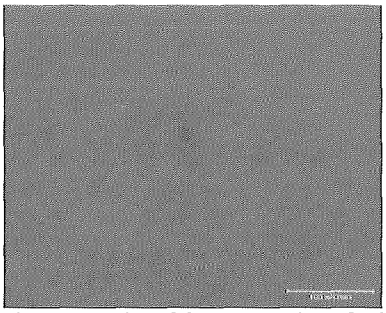

Figure 16: SEM observations of the cross-section of the crept specimen far from the necking area (240 MPa, 550°C).

Far from the necking area (figure 16), much lower cavities are concentrated in the necking zone. Therefore, the damage mechanism does not seem to be controlled by vacancy diffusion at 550°C in the tested conditions. This assumption is in agreement with the significant reduction of area and the Norton parameters.

3.2.4 *Hardness measurements after creep*

Microhardness profiles were measured on longitudinal cross sections of two creep fractured samples (figure 17), showing a significant increase in hardness in the necking area. This fact is linked to the strain hardening occurring during deformation. Moreover, in the weld metal, hardness values are more scattered than before creep.

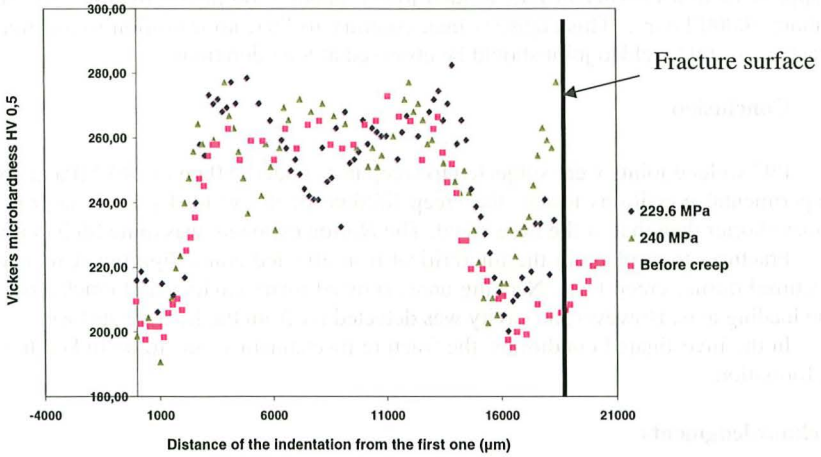

Figure 17: Cross-weld microhardness profiles of two crept specimens

The microhardness profiles allowed determining the location of fracture in two specimens. Fracture occurred in the intercritical area for both samples. Table 5 presents the fracture location of samples having experienced creep tests under different conditions.

	P 91			P 92		
Temperature / Stress(MPa)	500 (°C)	550(°C)	625(°C)	550(°C)	600(°C)	625(°C)
50			ICHAZ			
60			ICHAZ			
70						
80			ICHAZ			ICHAZ
100			ICHAZ			ICHAZ
120						ICHAZ
140						
160	WM	WM			ICHAZ	
180	WM	WM				
200		WM				
210	WM					
220	WM	WM				
230	WM	WM		**ICHAZ**		
240	WM			**ICHAZ**		
250	WM					
260	WM					
280	WM					
300	WM					

Table 5: Comparison of fracture location in welded joint for various values of stress and test temperature [1, 2, 9 and 11]. The results of the present study are in bold.

Concerning P91 welded joints we can observe that for high stresses, fracture occurs in the weld metal, whereas for lower stresses, it takes place in the ICHAZ. The experiments of this study, performed on P92 welded joints, show that type IV fracture occurs even at high stresses. For a given stress and temperature the creep lifetime of P92 welded joint is much longer than that of P91 welded joint. However at 550°C, we notice that the type IV fracture happens 19 times earlier in P92 welded joints (about 1000 hours) than in P91 welded joints (about 20000 hours). This suggests that, contrary to P91, no transition to a different type of fracture for P92 welded joint should be observed at long durations.

4 Conclusion

P92 welded joints were subjected to creep tests under 160 up to 240 MPa at 550°C. In the experimental conditions tested, the creep lifetime of the welded joint is approximately 3.3 times shorter than that of the base metal. The Norton exponent was quite high (11.5).

Fractures took place in the intercritical heat-affected zone. Significant reduction of area occurred during creep tests. Necking areas showed many cavities and cracks, oriented along the loading axis. However, no cavity was detected far from the fracture surface.

In the investigated conditions, the fracture mechanism seems to be linked to viscoplastic deformation.

Acknowledgments

The direction of the Nuclear Energy Department of the CEA is acknowledged for financial support through the DISN/TEMAS project. The authors are grateful to E. Cini from Vallourec for fruitful discussions.

References

[1] Vivier F., Fluage à 500°C d'un joint soudé d'un acier 9Cr-1Mo modifié. Evolution de la microstructure & Comportement mécanique, PhD thesis, Ecole des Mines de Paris, 2009.
[2] Gaffard V., Experimental study and modelling of high temperature creep flow and damage behaviour of 9Cr1Mo-NbV steel weldments, PhD thesis, Ecole des Mines de Paris, 2005.
[3] HKL Technology, Channel 5, 2001
[4] Falat L., Vyrostková A., Homolová V., Svoboda M., Creep deformation and failure of E911/E911 and P92/P92 similar weld-joints, *Engineering Failure Analysis* 16 (2009) 2114–2120
[5] Fournier B., Fatigue –fluage des aciers martensitiques à 9-12 % de chrome: comportement et endommagement, PhD thesis, Ecole des Mines de Paris, 2007.
[6] Giroux P.F., Mechanical and microstructural stability of P92 steel under uniaxial tension at high temperature.
[7] Gaffard V., Gourgues-Lorenzon A.F., Besson J., High temperature creep flow and damage properties of9Cr1MoNbV steels: Base metal and weldment.
[8] ECCC datasheets 2005, Steel ASTM Grade 92
[9] Jandova D., Kasl J., Kanta V., Influence of Substructure on Creep Failure of P91 Steel Weld Joints, *ECCC Creep conference*, April 2009.
[10] Haney E. M., Dalle F., Sauzay M., Vincent L., Tournié I., Allais L., Fournier B., Macroscopic results of long-term creep on a modified 9Cr–1Mo steel (T91).
[11] Wanatabe T., Tabuchi M., Yamazaki M., Hongo H., Tanabe T., Creep damage evaluation of 9Cr-1Mo-V-Nb steel welded joints showing type IV fracture, *International Journal of Pressure Vessels and Piping* 83 (2006) 63–71

9th Liege Conference : Materials for Advanced Power Engineering 2010
edited by J. Lecomte-Beckers, Q. Contrepois, T. Beck and B. Kuhn.

ASSESSMENT OF THE INTEGRITY OF FERRITIC-AUSTENITIC DISSIMILAR WELD JOINTS OF DIFFERENT GRADES OF Cr-Mo FERRITIC STEELS

K. Laha, K. S. Chandravathi, P. Parameswaran, Sunil Goyal and M. D. Mathew

Metallurgy and Materials Group
Indira Gandhi Centre for Atomic Research
Kalpakkam – %03 (0), India

Abstract

Integrity of the).)5Cr-(Mo , Alloy 800, . Cr-(Mo , Alloy 800 and . Cr-(Mo-/ 0 1 , Alloy 800 ferritic-austenitic dissimilar 2oints, fusion welded employing Inconel (8) electrode, has 1een assessed under creep conditions at 8)3 K. 3he dissimilar weld 2oints displayed lower creep rupture strength than their respective ferritic steel 1ase metals. 3he strength reduction was more for).)5Cr-(Mo steel 2oint and least for . Cr-(Mo steel 2oint. 3he failure location in the 2oints was found to shift from the ferritic steel 1ase metal to the intercritical region of heat-affected 4one 56 A78 in ferritic steel 5ype I/ cracking8 with decrease in stress. At still lower stresses the failure occurred at the ferritic,austenitic weld interface. Locali4ed creep deformation and cavitation in the soft intercritical 6 A7 induced type I/ failure whereas creep cavitation at the weld interface particles induced ferritic , austenitic interface cracking due to high creep strength mismatch across it. Micromechanisms of type I/ failure and interface cracking in the ferritic,austenitic 2oints and different susceptil1ility to failure for different grades of ferritic steels are discussed 1ased on microstructural investigation, mechanical testing and 9: M analysis.

Keywords; Cr-Mo ferritic steel, 9erritic , austenitic dissimilar weld 2oint, Creep rupture strength, 3 ype I/ cracking, Interface failure.

1. Introduction

Dissimilar weld 2oints 1etween Cr-Mo ferritic steels and austenitic stainless steels are used extensively in conventional as well as in nuclear power generating plants and petrochemical industries. In fossil fuel fired power generating plants, austenitic stainless steel tu1es are used in the high temperature sections, such as the final stages of the superheaters and reheaters, where higher creep rupture strength and oxidation resistance are required. In the primary 1oiler and heat exchanger where the temperatures are lower, Cr-Mo steels such as).)5Cr-(Mo and . Cr-(Mo steels are used. In the steam generator circuit of sodium cooled fast 1reeder reactor 5S9R8, 3(%L50 8 austenitic stainless steel pipes from the intermediate heat exchangers are required to 1e welded with the modified . Cr-(Mo steel pipes of steam generators. In such 2oints, a transition weld 1ond is formed in which the distri1ution of microstructure, chemical composition, stress, physical properties such as thermal expansion coefficient and thermal conductivity and mechanical properties are very inhomogeneous. 3he mismatch in thermal expansion coefficient across the 2oint is reduced with the insertion of an Alloy 800 piece and adapting Inconel (8) welding electrode having thermal expansion coefficient intermediate 1etween austenitic and ferritic steels. 6 owever, premature creep failure is encountered in such dissimilar weld 2oints [(,)]. An understanding of the microstructural changes across the weld 1ond and their effects on high temperature creep deformation and fracture 1ehaviour are of primary concern for a realistic life prediction of the dissimilar weld 2oints. 3his study is conducted to understand the creep rupture 1ehaviour of the).)5Cr-(Mo , Alloy 800, . Cr-(Mo , Alloy 800 and . Cr-(Mo-/ 0 1 , Alloy 800 dissimilar

2oints welded with Inconel (8) electrode. 3he microstructures developed across the ferritic , austenitic weld interface and creep strength heterogeneity across it are expected to differ for different grades of Cr-Mo steel to influence the creep rupture life of dissimilar weld 2oints. 3he creep properties are compared in order to arrive at a comprehensive understanding of the premature creep failure of the ferritic-austenitic dissimilar weld 2oints of the different grades of ferritic steels.

2. Experimenta(Detai(s

Dissimilar weld 2oints of the).)5Cr-(Mo, . Cr-(Mo and . Cr-(Mo-/ 0 1 ferritic steels with Alloy 800 were fa1ricated 1y the shielded metal arc welding process 5SMA8 using Inconel (8) electrodes. Chemical compositions of the 1ase metals and weld metal are shown in 3a1le.(. 3he).)5Cr-(Mo, . Cr-(Mo and . Cr-(Mo/ 0 1 steel 2oints were su12ected to one hour post weld heat treatment 5PW6 3 8 at . 73 K, (0)3 K and (033 K respectively. Optical and S: M metallographic examinations and microhardness testing across the 2oints were carried out. 3: M studies were performed on some critical regions of the weld 2oints 1efore and after creep. : DAX associated with S: M was used to analy4e the elemental distri1ution across the ferritic-austenitic weld interface of the 2oints. Creep rupture tests were conducted on the ferritic steel 1ase metals and on the cross-weld 2oints at 8)3 K over a stress range (00 -)50 MPa. Creep specimens were of 50 mm gauge length and 5 mm gauge diameter. Creep deformation inhomogeneity across the weld 2oints was monitored 1y interrupting creep tests at periodic intervals and measuring the distance 1etween the hardness-indentation marks made across the 2oint specimens 1efore creep tests. 9inite element 59: M8 analysis was performed to estimate the stress distri1ution across the ferritic , austenitic weld interface. Creep deformation rates of the different constituents 5ferritic 1ase metal, inconel weld metal and simulated heat affected 4ones 56 A78 in ferritic steel8 required as the input for 9: M analysis were determined 1y carrying out stress change creep tests at 8)3 K.

Table.1 Chemical composition (wt %) of the materials used

: lements , Materials	C	Si	Mn	P	S	Cr	Mo	0 i	Al	Co	0 1	/	0	3 i	9e
).)5Cr-(Mo	0.0%	0.(8	0.45	0.008	0.008	).(8	0..3	-	-	-	-	-	-	-	1al
. Cr-(Mo	0.(	0.4.	0.4%	0.008	0.00)	8.38	0..3	-	-	-	-			-	1al
. Cr-(Mo-/ 0 1	0.0. %	0.3)	0.4%	0.0(	0.008	8.7)	0..0	0.(0	-	-	0.08	0.))	0.05		
Alloy 800	0.03	0.)7	0.8%	0.00.	0.00.	(..5	0.(0	30.8	0.(4	0.)	0.0(7	-	-	0.3.	1al
Inconel (8)	0.05	0.5%	7.84	0.0(	0.004	(3.8	-	%)	-	-	(.84	-	-	0.40	1al

). Resu(ts and Discussion

3.1 Microstructural variation across dissimilar weld joints

3he as-received normali4ed and tempered condition).)5Cr-(Mo ferritic 1ase metal had a tempered 1ainitic structure 59ig.(5a88, whereas 1oth the . Cr-steels had tempered martensitic structures 59ig.(5188. 3he Cr-Mo ferritic steels derive their high temperature strength from the solid solution strengthening, phase transformation induced dislocation su1-structure and intra- and inter-granular car1onitride precipitates [3-5]. 3he most effective creep strengthening in).)5Cr-(Mo steel results from the fine dispersion of semicoherent acicular Mo_2C particles. 6owever, the Mo_2C precipitates are relatively less sta1le against thermal and creep exposures and are eventually replaced 1y M_6C precipitates through the intermediate precipitation of M_7C_3 and $M_{23}C_6$ particles [4,5]. 3he relatively coarser chromium rich $M_{23}C_6$

precipitates olserved in . Cr-(Mo steel on grain and sulgrain loundaries help to stalili4e the sulgrain structures against coarsening on thermal and creep exposures, thus indirectly contriluting to strengthening. In . Cr-(Mo-/ 0 1 steel, intragranular precipitation of 5/ ,0 185C,0 8 particles impart high creep strength. 3 he undissolved primary 0 15C,0 8 particles act as nucleating centres for $M_{)3}C_{\%}$ precipitates to increase density of $M_{)3}C_{\%}$ and also the dissolved vanadium in the $M_{)3}C_{\%}$ increases its coarsening resistance against thermal and creep exposures. 3 he $M_{)3}C_{\%}$ precipitates stalili4e the martensitic sul-structures to a greater extent in . Cr-(Mo-/ 0 1 steel than in . Cr-(Mo steel [3].

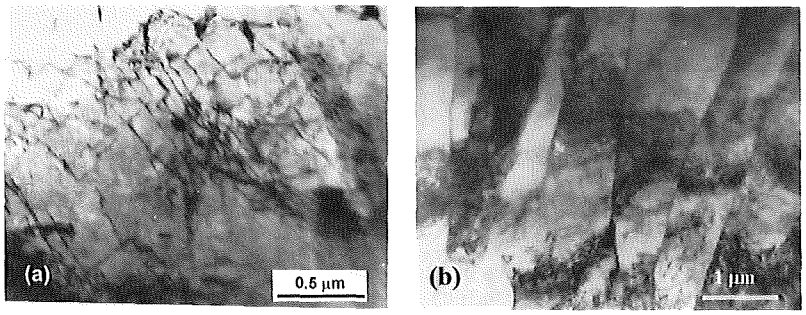

Fig.1. TEM micrographs (a) 2.25Cr-1Mo base metal; and (b) 9Cr-1Mo-V%b base metal

3 he deposited austenitic Inconel (8) weld metal had a columnar structure and the Alloy 800 1ase metal had austenitic structure with equiaxed grains 59ig.) 8 3 he weld metal grew epitaxially from the alloy 800 1ase metal. 3 he 6 A7 microstructure in ferritic of the) .) 5Cr-(Mo steel 2bint consisted of coarse prior austenite grain 1ainite, fine prior austenitic grain 1ainite and intercritical structure in an order away from the weld fusion 1oundary to the 1ase metal [%]. 3 he 6 A7 of 1oth the . Cr-steels 2bints consisted of coarse prior austenitic grain martensiticstructure, fine prior austenitic grain martensitic structure and intercritical region [7]. A hardness trough developed at the intercritical 6 A7 at outer edge of 6 A7 next to the unaffected ferritic steel in all the dissimilar weld 2bints 59ig.38 Partial dissolution of $Mo_{)}C$ precipitates with higher order less effective carlides on intercritical heating during weld

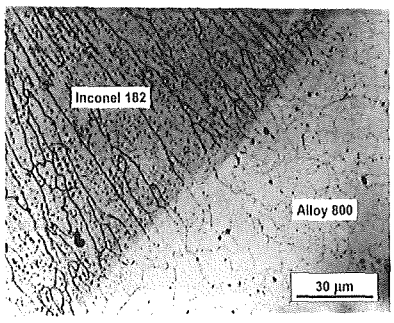

Fig.2. Optical microstructure of Allo( ) 00 / ,nconel 1) 2 weld interface.

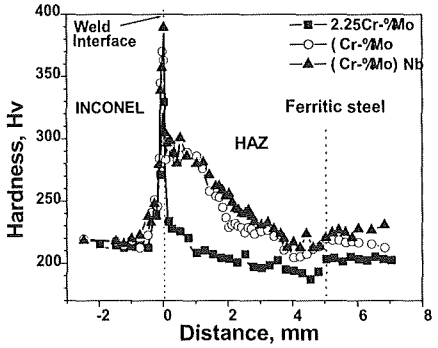

Fig.3. . ardness profile across the ferritic-austenitic weld interface of the /oints.

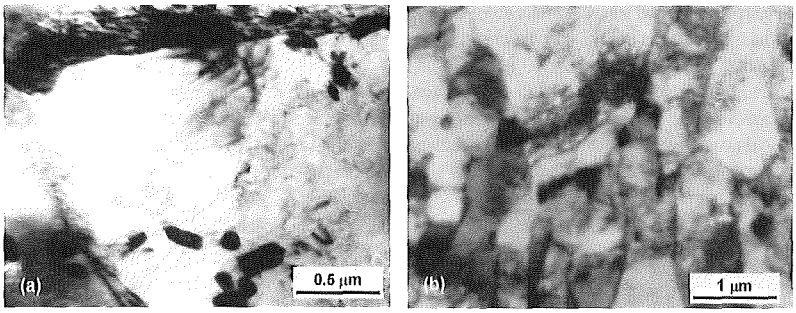

Fig.0 TEM micrographs of intercritical . A1 of weld /oint (a) 2.25Cr-1Mo and (b) 9Cr-1MoV%b steel .

thermal cycle 59ig.45a88 is considered to 1e responsi1le for lower hardness of the intercritical 6 A7 in the) .) 5Cr-(Mo dissimilar weld 2bint [8]; whereas coarsening of $M_{)3}C_{\%}$ precipitates which triggers instal1ility in martensitic structure with the replacement of lath structure having high dislocation density 1y equiaxed su1-grain structure with low dislocation density 59ig.4518 8 is considered responsi1le for the lower hardness of intercritical 6 A7 in the . Cr-dissimilar weld 2bints [8]. 3he weld interface 1etween ferritic steel 1ase metal and Inconel (8) weld metal of the dissimilar weld 2bints displayed as a light-etched 1and in the as-welded condition 59ig.55a88. 3he width of the 1and varied along the weld interface and was much larger at the weld-1ead over lapping region that occurred during su1sequent weld passes [(]. 3he 1and was found to grow epitaxially from the ferritic 1ase metal. 3he solidification of Inconel weld metal proceeded in the dendritic mode from this 1and. Part of the light-etched 1and in the ferritic steel side had 1een converted into dark-etched 1and on PW6 3. 6igher magnification S: M images revealed that the weld interface had a line of discrete particles of approximately elliptical shape with long axis in the plane of the interface 59ig.5518 8 [)]. 3he particles were at a distance less than (μm away from the weld interface in the ferritic steel. X-ray dispersive analysis of the particles extracted from the weld interface 1y car1on replica technique revealed that the particles were chromium rich $M_{)3}C_{\%}$type of car1ides. 3he particles appear finer in the . Cr-steel dissimilar weld 2bints than

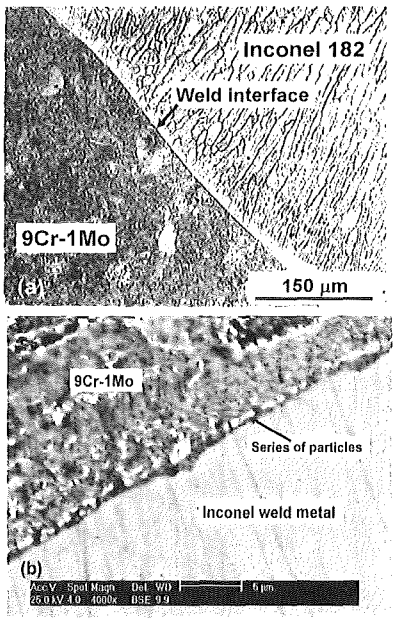

Fig.5 Ferritic/austenitic microstructure of 9Cr-1Mo steel weld /oint; (a) optical and (b) 2EM.

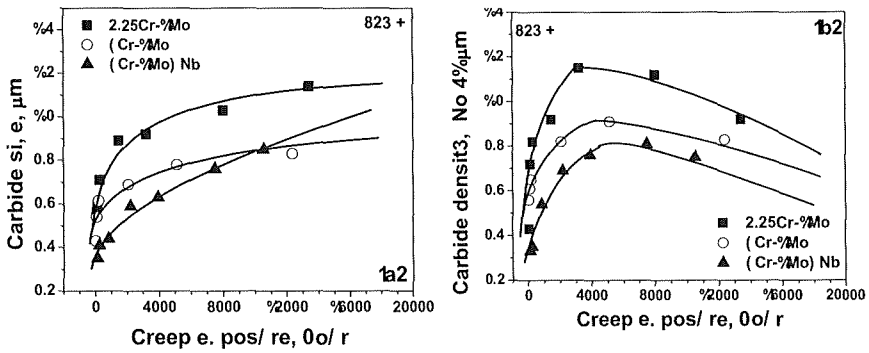

Fig.3 Variations of particle (a) si4e and (b) densit(along the ferritic/austenitic weld interface with creep e5posure at) 23 6 .

in the).)5Cr-(Mo steel weld 2oint 59ig.%8a88 and precipitate density was less in . Cr-(Mo/ 0 1 2oint 59ig.%5l88 3he weld interface lond displayed very high hardness even after PW6 3 59ig.388 3he microstructure at weld interface of dissimilar 2oint has 1een investigated 1y several researchers [. -(( ]. : aton and Glossop [.] have suggested that it is consisted of lamellar intermetallic precipitates. 0 ath [(0]; and Klueh and King [(( ] have reported the presence of martensite at the weld interface. During welding nickel, manganese, chromium and nio1ium from the austenitic Inconel weld metal diffuse into the ferritic steel while iron diffuses into Inconel from ferritic steel. 3he interface region had high contents of nickel, manganese, chromium, and iron 59ig.788 3he interface region might have transformed into martensite on cooling after welding 1ecause of the increase in hardena1ility due to the presence of high nickel and chromium contents. 6 igh content of chromium at the weld lond makes this region resistant to etching 59ig.55a88 Upon PW6 3 at . 73-(033 K, a part of the light-etched 1and in the ferritic side turned into 1lack etched 4one with high concentration of second phase particles 59ig.5518& Pro1a1ly re-austeni4ation of the part of interface 1and on Inconel side would have occurred during PW6 3 and su1sequently on cooling transformed into martensite 59ig.888 3he freshly formed martensite imparted high hardness to the interface even after PW6 3 59ig.388 0 io1ium rich intermetallic phase was also o1served on the weld interface 59ig.888

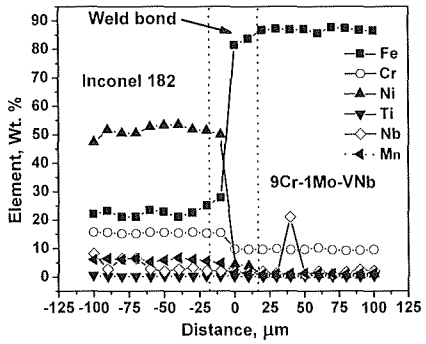

Fig.7 Elemental profile across the ferritic /austenitic weld interface of 9Cr-1Mo /oint.

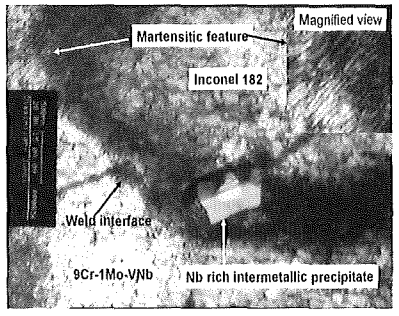

Fig.) TEM microstructure of ferritic/austenitic weld interface of 9Cr-1Mo-V%b /oint.

3.2 Creep Behaviour

/ ariations of creep rupture life with applied stress at 8)3 K for the ferritic steel 1ase metals and the dissimilar weld 2oints are shown in 9ig.. 5a8 3he . Cr-(Mo-/ 0 1 steel possessed higher creep rupture strength than 1oth the).)5Cr-(Mo and . Cr-(Mo steels. 6 ighly sta1le fine intragranular 5' ,0 185C,0 8 car1onitride particles imparted higher creep rupture strength to the tempered martensitic . Cr-(Mo-/ 0 1 steel than in the tempered 1ainitic).)5Cr-(Mo steel and tempered martensitic . Cr-(Mo steel having no intragranular MX type of particles. 3he).)5Cr-(Mo and . Cr-(Mo steels had compara1le creep rupture strength. 3he dissimilar weld 2oints of the ferritic steels had lower creep rupture strength than their respective ferritic steel 1ase metals. 3he . Cr-(Mo-/ 0 1 steel dissimilar weld 2oint had creep rupture strength higher than 1oth the).)5Cr-(Mo and . Cr-(Mo 1ase steels. 3he stress-rupture life variation of the dissimilar weld 2oints showed a two-slope 1ehaviour and the slope change occurred at around the same creep exposure. 3he variations of reduction in area with creep rupture life of the ferritic steels and their dissimilar weld 2oints are shown in 9ig.. 518 3he dissimilar weld 2oints of the ferritic steels possessed very low creep rupture ductility especially after relatively long-term creep exposures.

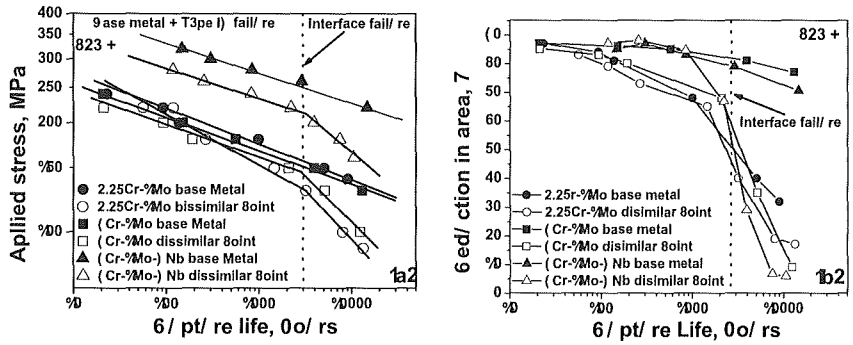

Fig.9 Comparison of (a) creep rupture life (b) rupture ductilit(of different ferritic-austenitic dissimilar weld /oint with ferritic steel base metals.

3he variations of steady state creep rate of the different constituents of the . Cr-(Mo-/ 0 1 dissimilar weld 2oint are shown in 9ig.(0. 3he different 6 A7 microstructures in ferritic steels were simulated on the 1ase steels 1y appropriate heat treatments cycles [7,( )]. 3he creep deformation resistance of the different constituents of the dissimilar weld 2oint varied considera1ly. 3he intercritical 6 A7 had the highest creep deformation rate whereas the Inconel weld metal had the lowest. Similar results were o1tained for).)5Cr-(Mo dissimilar weld 2oint. 3he progress of creep deformation along the gage length of . Cr-(Mo-/ 0 1 , Alloy 800 dissimilar weld 2oint at))0 MPa, 8)3 K is shown in 9ig.((. As expected, the creep deformation accumulation in the different constituents of the 2oint was not uniform. 3he creep deformation 1ecame progressively locali4ed in the intercritical 6 A7 in ferritic steel, resulting in the failure of the 2oint in this 4one at))0 MPa at 8)3 K. 3he failure resem1led type I/ failure o1served in ferritic steel similar weld 2oint [8]. 3he failure was characteri4ed 1y the preferential accumulation of creep strain coupled with creep cavitation in the intercritical 6 A7 59igs.((and ( )8 Similar creep strain distri1utions across the).)5Cr-(Mo

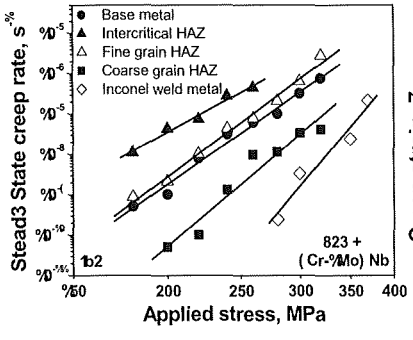

Fig.10. Variation of creep rate of the differen constituents across ferritic/austenitic interfac of 9Cr-1MoV%b /oint with stress at) 23 6.

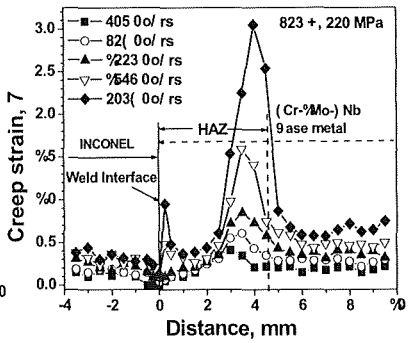

Fig.11. Variation of creep strain accumulation across the ferritic / austenitic interface of 9Cr-1MoV%b /oint with time (220 M8a9) 23 6).

and . Cr-(Mo ferritic , austenitic).) 5Cr-(Mo and . Cr-(Mo ferritic- austenitic dissimilar weld 2oints were olserved. Softening in the intercritical region of 6 A7 occurred during weld thermal cycle and PW6 3 59ig.38 3he softening resulted from the 518 dissolution of precipitate particles 5Mo)C in).) 5Cr-(Mo steel8 59igs. (5a88 and 45a88 5ii8 coarsening of $M_{)3}C_{\%}$ type of carlides 5iii8 recovery of martensitic-lath structure 59igs. (518 and 4518 8 and 5iv8 formation of fine prior-austenite grain structure [8]. : ven though failure occurred in the intercritical 6 A7, crack developed at the ferritic-austenitic weld interface at))0 MPa, 8)3 K 59ig.(35a88 3he olserved creep strain accumulation close to the weld interface 59ig.((8 is apparent and this caused 1y the initiation and propagation of creep cracks along the weld interface. Creep failure in the . Cr-(Mo-/ 0 1 dissimilar weld 2oint occurred at the weld interface at stresses lower than))0 MPa 59ig.(3518 8 At relatively higher applied stress, the failure in the dissimilar weld 2oint occurred in the ferritic steel 1ase metal away from the weld 4one. At lower stresses the failure location shifted to the intercritical region of 6 A7 in the ferritic steel 59ig.(35a88 At still lower stresses, failure in dissimilar weld 2oint occurred at the weld interface with very low creep ductility 59ig.(3518 8 3he interface cracking coincided with the change in slope in the variation of rupture life with applied stress 59ig.. 5a88 [(3]. Similar changes in creep failure location with applied stress were olserved in the).) 5Cr-(Mo and . Cr-(Mo steels dissimilar weld 2oints. Creep cavity was found to nucleate at the weld interface 59ig.(45a88 and the cavitation was associated with coarse particles at the weld interface 59ig.(4518 8 6igh creep strength heterogeneity across the ferritic , austenitic weld interface 59ig.(08 of the 2oints as estimated 1y) D 9: M analysis yielded a complex stress distrilution across it 59ig.(58 9our nodded quadrilateral elements with appropriate 1oundary condition were used for the analysis. 3he 0 orton's creep law relating steady state creep rate

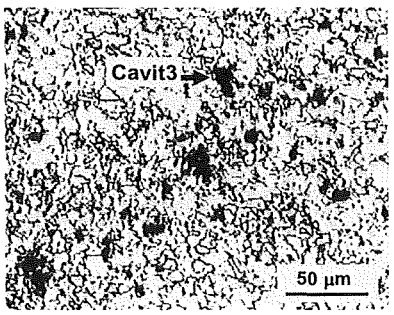

Fig.12. Creep ca:itation in the intercritical . A1 of 9Cr-1MoV%b steel /oint creep tested at 220 M8a9) 23 6 (t_r ; 2203 hours)

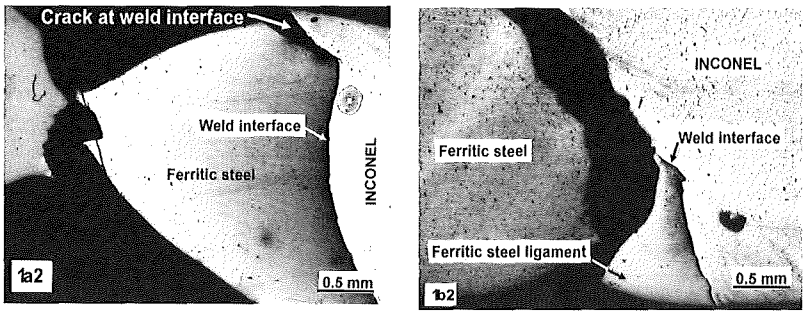

Fig.13. Creep failure location in 9Cr-1Mo-V%b dissimilar weld /oint: (a) 200 M8a and (b) 1) 0 M8a.

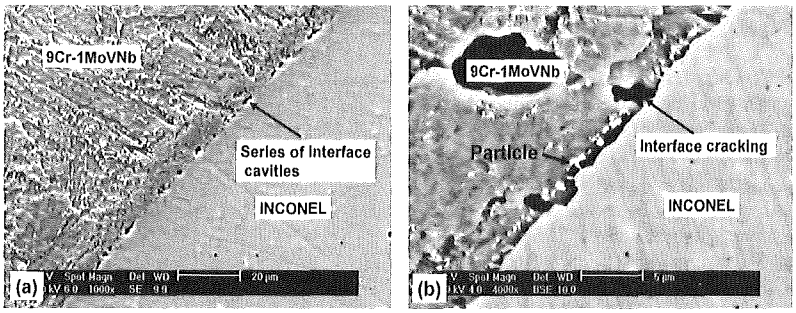

Fig.10. (a) series of creep ca: ities at the weld interface; (b) Ca: ities are associated with interface particles of in 9Cr-1Mo-V%b dissimilar weld /oint creep tested at 1) 0 M8a.

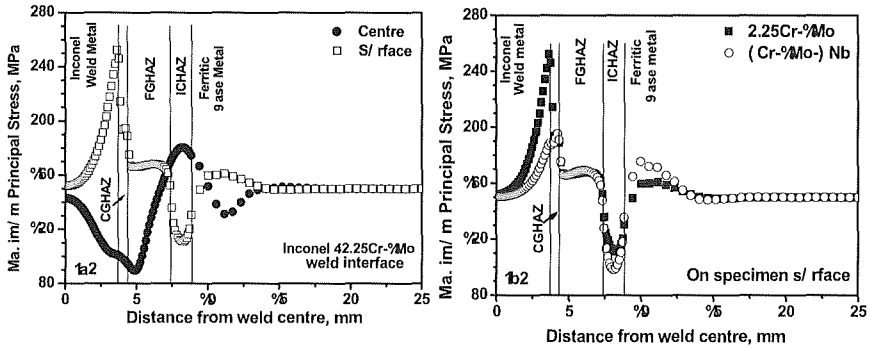

Fig.15 Variation of principal stress across the ferritic-austenitic interface of dissimilar weld /oint: (a) 2.25Cr-1Mo /oint9 at specimen central and surface locations and (b) on specimen surface of 2.25Cr-1Mo and 9Cr-1Mo-V%b /oints.

with stress was employed as material model in the analysis. 6 igher principal stress at the ferritic , austenitic weld interface on specimen surface location promotes creep cavitation at interface precipitates 59ig.(4518 8 to produce interface cracking 59ig.(3518 8 Susceptilility of dissimilar weld 2oint cracking of the different ferritic steels is compared in 9ig.(% 3he cracking susceptilility is defined as the reduction in creep rupture strength of weld 2oint compared to its ferritic 1ase metal for a given rupture life. Comparison is also made of the cracking susceptilility of the dissimilar weld 2oints with the similar weld 2oints of the ferritic steels [8]. 3he).)5Cr-(Mo steel dissimilar weld 2oint was found to 1e more susceptille to failure than the . Cr-steel dissimilar weld 2oints. 6 igher creep strength gradient across the ferritic,austenitic weld interface of).)5Cr-(Mo dissimilar weld 2oint than that in . Cr-(Mo-/ -0 1 dissimilar weld 2oint 59ig.(78 produced high stress concentration across the).)5Cr-(Mo 2oint 59ig.(5 518 8 to promote more extensive interface cracking to reduce the rupture life. 3his is expected to produce more weld interface cavitation in).)5Cr-(Mo dissimilar weld 2oint to increase its cracking susceptilility than that in the . Cr-(Mo-/ 0 1 dissimilar weld 2oint 59ig.(%8 3he dissimilar weld 2oints were more susceptille to creep failure than the similar weld 2oints of the ferritic steels. 6 igher creep strength gradient across the weld interface of ferritic-austenitic dissimilar weld 2oint than that across the soft intercritical 6 A7 in similar weld 2oint produced higher stress concentration across the ferritic-austenitic weld interface region than across the soft intercritical region 59ig.(45a88 3he high stress concentration yielded more cavitation at the weld interface to reduce the creep rupture strength of dissimilar weld 2oint than the similar weld 2oint 59ig.(%8

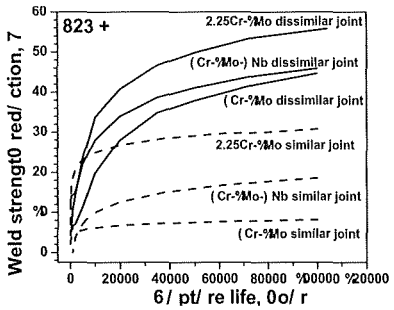

Fig.13 = eld strength reduction of dissimilar weld /oints of different ferritic steels as compared with similar weld /oints.

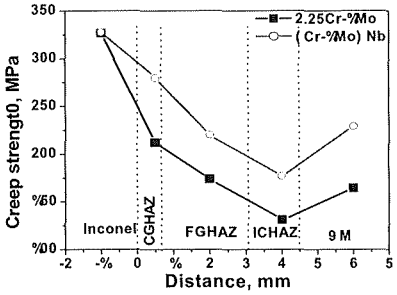

Fig.17 Creep strength of different constituents of the /oints for the creep rate of 1510^{-} s^{-1} at) 23 6

4. Conclusions

(. Dissimilar weld 2oints of ferritic and austenitic steels possessed lower creep rupture strength than the ferritic steel 1ase metals.

). 3he failure location in the dissimilar weld 2oints shifted from ferritic 1ase metal to intercritical 6 A7 in ferritic 53ype I/ 8with the decrease in stress. At still lower stress the failure in dissimilar weld 2oint occurred in the ferritic-austenitic weld interface.

3. 3ype I/ failure was associated with creep strain and cavitation locali4ation in the soft intercritical 6 A7; whereas weld interface failure was associated with the creep cavitation at the interface particles under high stress concentration raised due to high creep strength gradient across the interface.

4. 3he).) 5Cr-(Mo dissimilar weld 2oint was more susceptil le to creep failure than the . Cr-steel dissimilar weld 2oints. 6 igher stress concentration at weld interface resulting from stiffer creep strength gradient across it in).) 5Cr-(Mo 2oint than that in . Cr-steel 2oints, produced higher creep strength reduction.

Acknowledgment

3he authors express their deep sense of gratitude to Dr. Baldev Ra2 Director, Indira Gandhi Centre for Atomic Research 5IGCAR8 Kalpakkam and Dr. 3. Jayakumar, Director, Metallurgy and Materials Group, IGCAR for their keen interest in this work.

References

(. K. Laha, K.S.Chandravathi, K. Bhanu Sankara Rao, S.L.Mannan, "An Assessment of Creep Deformation and 9racture 1ehaviour of).) 5Cr-(Mo similar and Dissimilar Weld 2oints", Met. and Mats. 3rans. A, 3) A, ((5-( ) 4, 5) 00(8
). J.D. Parker and G. C. Stratford, "Characterisation of microstructures in nickel 1ased transition 2oints", J. Mats Sci. 35, 40. . -4(07, 5) 0008
3. J.M. / itek and R.L. Klueh, "Precipitation reactions during the heat treatment of ferritic steels", *Metall. Trans* (4A, (047–(055, 5(. 838
4. R. G. Backer and J. 0 utting, "3he tempering of) ¼% Cr-(%Mo steel after quenching and normali4ing", JISI, (.),) 57-) %8, 5(. 5. 8
5. P.Parameswaran, M./ i2ayalakshmi, P.Shankar and / S Raghunatahan "Influence of carlon content on microstructure and tempering 1ehaviour on).) 5Cr-(Mo steel", J Mater Sci.,) 7, 54) %5) 34, 5(. .) 8
% K. Laha, K. Bhanu Sankara Rao and S.L.Mannan, "Creep 1ehaviour of post weld heat treated).) 5Cr-(Mo ferritic steel 1ase, weld metal and weldments", Mat. Sci. : ngg. A ( ) . , (83-(. 5, 5(. . 08
7. K. S. Chandravathi, K. Laha, K. Bhanu Sankara Rao and S. L. Mannan, "Microstructures and 3ensile Properties of Modified . Cr-(Mo Steel Grade . (", Materials Science and 3echnology, / ol. (7, 55. – 5%5, 5) 00(8
8. K. Laha, K. S. Chandravathi, P. Parameswaran and K. Bhanu Sankara Rao, "3ype I/ Cracking Suscepti1ility in Weld Joints of Different Grades of Cr-Mo 9erritic Steels", Met. and Mat 3rans. A, 40 5) 8 38%3. 7, 5) 00. 8
. . 0 . 9. : aton and B. A. Glossop, "3he welding of dissimilar creep resisting ferritic steels, Conf. on Welding Dissimilar Metals", Met. Const. Br. Weld. J., Paper . , %(0, 5(. % 8
(0. B. 0 ath, in Proc. Int. Conf. on "Creep 9racture of : ngineering Materials and structures, Part II", edited 1y B. Wilshire and D.R.J.Owen, Pineridge Press, Swansea, U.K., 8) 7-38, 5(. 848
((. R.L. Klueh and J. 9. King, "Austenitic-ferritic weld-2oint failures" =*elding Journal* %(5. 8 30) -s to 3((-s, 5(. 8) 8
( ) . K. Laha, K. S. Chandravathi, K. Bhanu sankara Rao and S. L. Mannan, "3emperature dependence of tensile properties of).) 5Cr-(Mo sreel 1ase, welments simulated heat-affected 4one structures", 3rans Ind. Met. 3echnol., 4% 77-87, 5(. . 38
(3. M.Yama4aki, 3. Watana1e, 6 . 6 ongo and M. 3a luchi, "Creep Rupture Properties of Welded Joints of 6 eat Resistant Steels", *Journal of 8ower and Energ(2(stems*,) 548 ((40-((4. , 5) 0088

9th Liege Conference : Materials for Advanced Power Engineering 2010
edited by J. Lecomte-Beckers, Q. Contrepois, T. Beck and B. Kuhn.

EXPERIENCES WITH THE CHARACTERIZATION OF NEW AND EX-SERVICE GRADE 91 MATERIAL

Evy De Bruycker, Staf Huysmans

Laborelec, Rodestraat 125, B-1630 Linkebeek, Belgium

Abstract

Martensitic Grade 91 steel is intensively used for tubes and pipes as a replacement for Grade 22 and in the new ultra super critical power plants for components subject to temperatures up to 600°C. This relatively new material is more complex than its predecessors, as its high temperature strength depends on the precise distribution of fine precipitates. Hence small deviations in composition or heat treatment can have a significant influence on, for example, the creep strength. As the amount of available data on ex-service components in Grade 91 is still limited, a characterization of two ex-service materials and a comparison with new material was carried out. The chemical composition, microstructure, creep strength, mechanical properties and hardness of two new tubes, one new pipe, one ex-service tube and one ex-service pipe in Grade 91 were determined. For the determination of the creep strength the stress relaxation testing technique was used and compared with conventional creep tests on the same material. Stress relaxation testing proved to be an adequate technique to determine the current creep strength of Grade 91 material. A strong dependency of small deviations in composition on the creep strength was noted. A low carbon content seemed to decrease the creep strength significantly. The distribution of the precipitates was investigated with TEM for one new and one ex-service tube. The ex-service tube did show a slight coarsening of the $M_{23}C_6$ compared to the new tube. However, the overall amount of precipitates (fine MX and $M_{23}C_6$) was larger for the ex-service tube, which had a higher amount of carbon. This could explain the higher creep strength of this tube.

Keywords: Grade 91, creep strength, stress relaxation testing, microstructure

1. Introduction

To improve the efficiency and reduce the CO_2 emission of coal power plants, there is a tendency towards higher steam temperatures and pressures. This resulted in a demand for ferritic steels with higher creep strength and lead to the development of the 9-12%Cr martensitic steels. Although the 9%Cr Grade 91 steel has been in use for about 20 years in a few plants in Europe and Japan, its use has become widespread only more recently (over the past 10 years), not only in these new high efficiency plants, but also as a replacement of Grade 22 in older power plants. So the availability of ex-service data of the long-term performance of Grade 91 is still somewhat limited [1].

Meanwhile, several incidents of premature failure of Grade 91 material have already been reported. Deficient material has been found in both weldments and base material. Part of the problem is that the excellent properties of Grade 91 recorded under laboratory conditions are only achieved with strict control of composition and heat treatment [2]. The more fabrication steps involved, the greater the risk of inappropriate procedures. This means that even new Grade 91 material can have inferior properties and quality assurance during and after

fabrication is very important. Another concern is that, at present, insufficient information is available to accurately characterize the deficient material when it is found.

In this context several new and ex-service Grade 91 components were characterized. Chemical composition, mechanical properties and microstructures were checked. Special emphasis was laid on the characterization of creep properties and the suitability of the stress relaxation technique to determine the creep strength of Grade 91 material was tested.

2. Investigated material

Two new tubes, one new pipe, an ex-service tube and an ex-service pipe in Grade 91 material were characterized. Their chemical compositions are listed in Table 1.

Table 1: Chemical composition in wt% of the characterized materials measured with ICP/OES and LECO CS.

Material and ref. number		**Composition (wt %)**						
New tube T91		**C**	**Mn**	**Si**	**S**	**P**	**Cr**	**Ni**
06-11-022	measured	0.061	0.51	0.43	0.007	0.022	8.3	0.15
	certificate	0.1	0.53	0.35	0.002	0.016	8.27	0.14
		Mo	**Cu**	**V**	**Nb**	**Al**	**Ti**	**N**
	measured	0.96	0.16	0.20	0.092	0.007	0.003	0.05
	certificate	0.94	n.s.	0.23	0.077	0.01	n.s.	0.04
New tube T91		**C**	**Mn**	**Si**	**S**	**P**	**Cr**	**Ni**
07-04-019	measured	0.071	0.4	0.37	0.008	0.020	8.63	0.07
		Mo	**Cu**	**V**	**Nb**	**Al**	**Ti**	**N**
	measured	0.92	0.02	0.20	0.074	0.005	0.004	0.05
Ex-service tube		**C**	**Mn**	**Si**	**S**	**P**	**Cr**	**Ni**
T91	measured	0.115	0.35	0.44	0.006	0.024	8.77	0.10
06-10-062		**Mo**	**Cu**	**V**	**Nb**	**Al**	**Ti**	**N**
(56kh, 553°C)	measured	0.99	0.02	0.19	0.088	0.008	0.004	0.04
New pipe P91		**C**	**Mn**	**Si**	**S**	**P**	**Cr**	**Ni**
08-02-066	measured	0.09	0.56	0.27	0.004	0.013	8.30	0.18
	certificate	0.09	0.52	0.29	0.005	0.017	8.21	0.17
		Mo	**Cu**	**V**	**Nb**	**Al**	**Ti**	**N**
	measured	0.91	0.11	0.18	0.090	0.004	n.s.	0.06
	certificate	0.88	n.s.	0.20	0.08	0.004	n.s.	0.05
Ex-service pipe		**C**	**Mn**	**Si**	**S**	**P**	**Cr**	**Ni**
P91	measured	0.10	0.36	0.34	0.004	0.015	8.7	0.16
07-08-034		**Mo**	**Cu**	**V**	**Nb**	**Al**	**Ti**	**N**
(39.5kh)	measured	0.98	0.14	0.20	0.090	0.010	n.s.	0.04
standard EN10216-2 for Grade 91		**C**	**Mn**	**Si**	**S**	**P**	**Cr**	**Ni**
		0.08-0.12	0.3-0.6	0.2-0.5	≤0.01	≤0.02	8-9.5	≤0.4
		Mo	**Cu**	**V**	**Nb**	**Al**	**Ti**	**N**
		0.85-1.05	n.s.	0.18-0.25	0.06-0.1	≤0.04	n.s.	n.s.

n.s.: not specified

Compositions were determined by Inductively Coupled Plasma/Optical Emission Spectroscopy (ICP/OES) and LECO CS carbon sulfur analyzer. Values at the edge of or even outside the composition interval specified by the European standard are highlighted. The most striking irregularities were too low C content and a too high amount of P. Also noticable is the rather high amount of Cu in some of the alloys.

3. Mechanical characterization

3.1. Mechanical properties and hardness

Yield strength, tensile strength, elongation and fracture toughness of the materials at room temperature were determined according to the ASTM A370 standard (Table 2). All values were well within the specifications of the European standard.

Table 2: Mechanical properties of the Grade 91 materials at room temperature.

Material	Yield strength (MPa)	Tensile strength (MPa)	Elongation (%)	Impact energy (J)	Microhardness (HV0.5)
New tube T91 **06-11-022**	594	715	25	92	227
New tube T91 **07-04-019**	579	707	25	94	238
Ex-service tube T91 **06-10-062**	480	681	25	77	218
New pipe P91 **08-02-066**	508	684	46	223	232
Ex-service pipe P91 **07-08-034**	631	760	46	106	213
standard EN10216-2	>415	>585	>20	>40	

In addition, microVicker hardness measurements were carried out on cross sections of the material. The average values are also listed in Table 2. The ex-service materials have slightly lower hardnesses, as is expected [3].

For the tubes, measurements were done at different positions along the perimeter in the middle of the tube thickness and similar values were found, independent of the position.

For the pipes, measurements over the wall thickness were carried out, in order to see if there was a difference in hardness close to the inner or outer surface of the pipe compared to the bulk of the material. For the new pipe (08-02-066) a slightly higher hardness close to the outside surface (235Hv) and lower hardness close to the inside surface (227Hv) was observed, while for the ex-service pipe both inside and outside surface had a slightly lower hardness level (209Hv).

3.2. Creep strength

3.2.1. Conventional creep testing

Conventional creep tests were carried out on four materials at 100MPa at 630 and 650°C. The results are listed in Table 3.

Table 3: Results of the conventional creep tests on Grade91 material.

Material	Temperature (°C)	Stress (MPa)	Minimal creep rate $\dot{\varepsilon}_P$ (%/s)	Time to 1% (h)	Rupture time (h)	Elongation (%)
New tube T91 **06-11-022**	630	100	3.47E-7	344	3577	17.5
	650	100	4.33E-6	30	331	27.1
Ex-service tube T91 **06-10-062**	630	100	1.55E-7	994	7827	17.8
	650	100	1.22E-6	111	772	19.3
New pipe P91 **08-02-066**	650	100	4.61E-6	39	225	23.0
Ex-service pipe P91 **07-08-034**	650	100	1.66E-6	123	599	20.8

3.2.2. Stress relaxation testing

Stress relaxation tests are mechanical tests that provide information on the creep behaviour of the tested material. By keeping the strain constant and letting the stress relax over time at a certain temperature, the secondary creep rate can be determined.

The first step of a stress relaxation test consists of applying a certain strain to the specimen at the test temperature. This strain is usually small, but should, however, be large enough so the specimen has reached strains of the secondary creep zone. During the subsequent stress relaxation test, both strain and temperature are kept constant and the stress is allowed to relax over time. This leads to a stress vs. time curve. Out of this stress vs. time curve, the secondary creep strain rate can be determined as a function of stress [4].

Stress relaxation tests were carried out at 650°C on three materials. The results are shown in Figure 1. For comparison, the creep rates determined with conventional creep tests are also depicted. In general, there was a rather good correlation between the stress relaxation and conventional creep test results. The same trend can be seen for the stress relaxation test results, as for the conventional creep test results.

The Monkman-Grant equation correlates creep rate and rupture time as follows:

$$\dot{\varepsilon_p} x {t_r}^m = C$$

with $\dot{\varepsilon_p}$ creep rate, t_r rupture time and m and C material specific constants. Bose et al. (2004) [5] determined m and C for Grade 91 material leading to the specific equation:

$$\dot{\varepsilon_p} x t_r = 0.02$$

By making use of this Monkman-Grant equation for Grade 91, the rupture time can be calculated from the creep rate $\dot{\varepsilon}_p$. This was done for the stress relaxation curves and the corresponding stress vs. rupture time graph is shown in Figure 2. The ECCC data for Grade 91 and for X20 are also depicted for comparison. It can be seen that the stress relaxation test results are more conservative than the conventional creep test results.

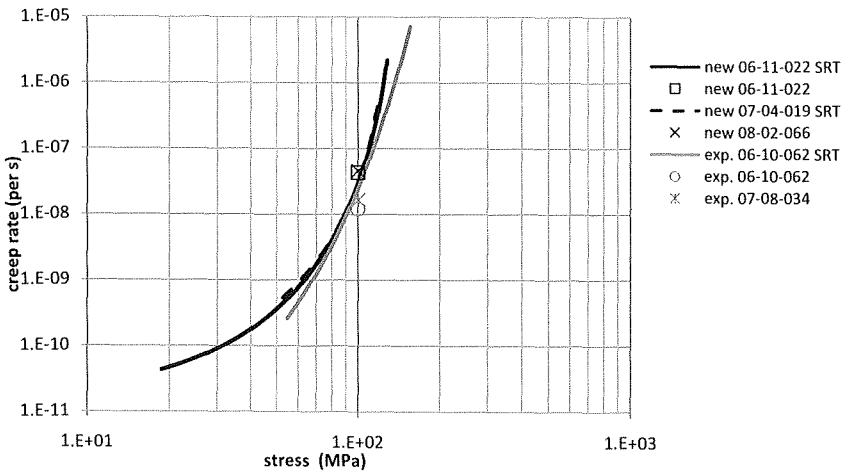

Figure 1: Creep rate results of the stress relaxation test (SRT) on Grade 91 material at 650°C and comparison with conventional creep test results.

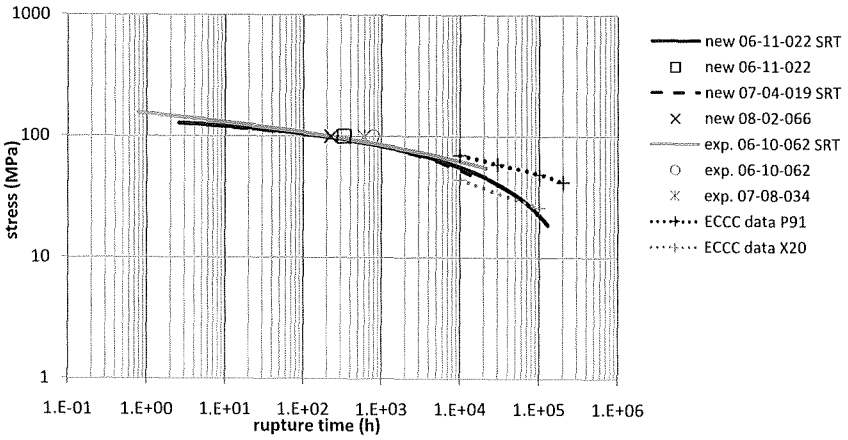

Figure 2: Stress vs. rupture time for different Grade 91 materials determined by conventional creep tests and stress relaxation tests (SRT) at 650°C and compared with the ECCC curves for Grade 91 and X20.

4. Microstructural characterization

4.1. General microstructure

The general microstructure of the materials was investigated with Light Optical Microscopy (LOM) after polishing and etching with Villella's reagent (Figure 3 to Figure 6). For all materials a martensitic structure was observed.

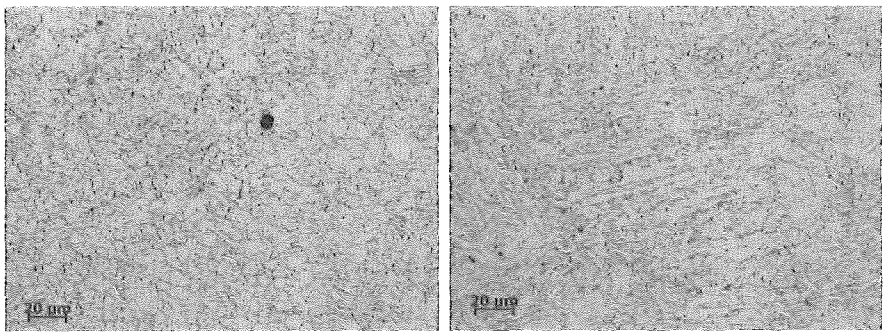

(a) (b)

Figure 3: LOM image after etching with Villella of new T91 material. a) 06-11-022; b) 07-04-019.

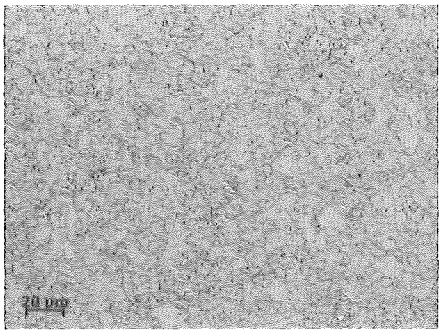

Figure 4: LOM image after etching with Villella of ex-service T91 material (06-10-062, 56000h).

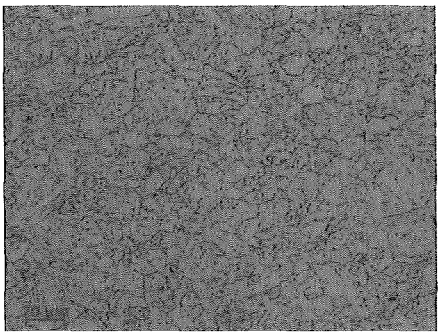

Figure 5: LOM image after etching with Villella of new P91 material (08-02-066).

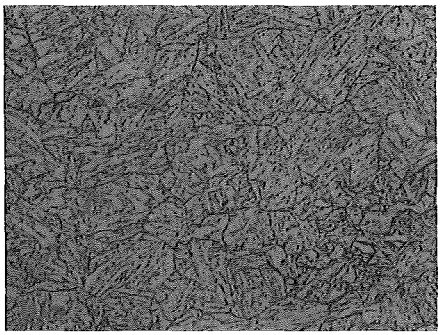

Figure 6: LOM image after etching with Villella of ex-service P91 material (07-08-034, 39500h).

4.2. Precipitates

Since the high temperature strength of Grade 91 material depends largely on the distribution of fine precipitates, Transmission Electron Microscopy (TEM) was used to study these precipitates for one new T91 material and one ex-service T91 material.

Carbon extraction replicas were made by deposition of a carbon film (20nm) onto the polished and etched samples. Then the carbon film with the precipitates was stripped with Villella and caught on a small Cu-grid. An overview of the precipitate distribution is shown in Figure 7.

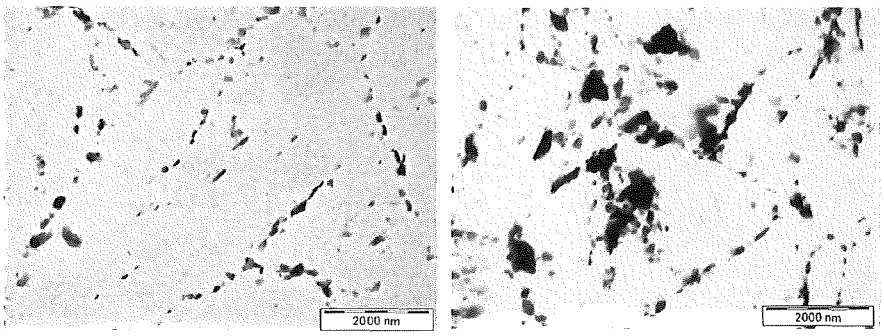

(a) (b)

Figure 7: Overview of the precipitates in T91 material. a) New material (06-11-022); b) ex-service material (06-10-062, 56000h).

In the new T91 material most of the precipitates were situated along the prior austenite grain boundaries. Most of the precipitates were the larger (100-400nm) $M_{23}C_6$ (with M=Cr, Fe, Mo)

(Figure 8a). In addition small (10-100nm) MX precipitates (with M=V, Nb and X=C,N) were present along the grain boundaries as well as inside the grains (Figure 8b).

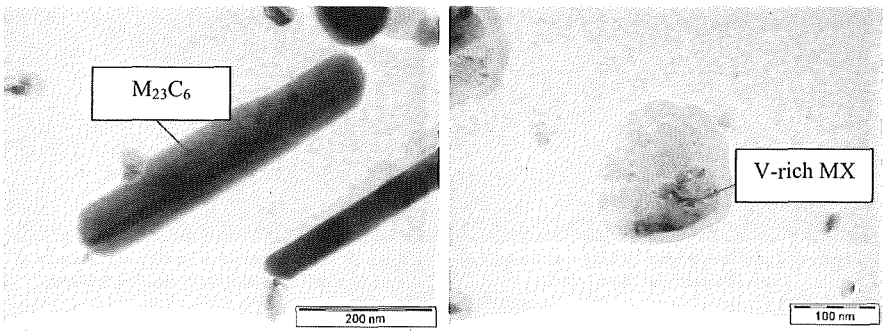

(a) (b)

Figure 8: Details of the precipitates present in the new T91 material (06-11-022).

In the ex-service T91 material the precipitates were situated along the grain boundaries as well as inside the grains and there was a larger number of precipitates compared to the new T91 material. The material contained both small and larger precipitates. The $M_{23}C_6$ precipitates were present along the grain boundaries and inside the grains and were larger (65-850nm) than in the new T91 material (Figure 9a). The smaller MX precipitates (15-50nm) were found in the bulk and along the grain boundaries (Figure 9b).

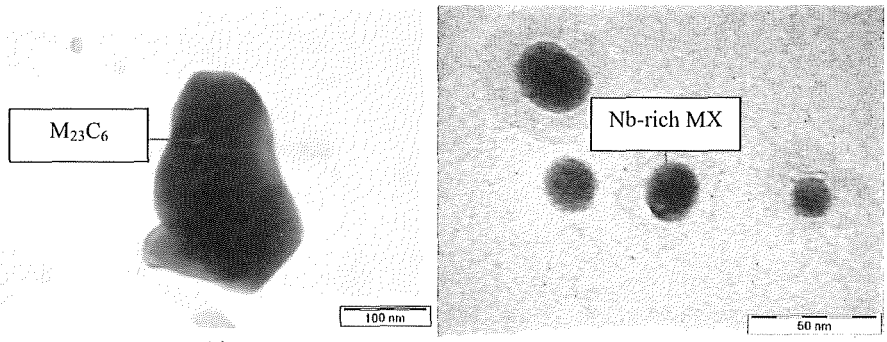

(a) (b)

Figure 9: Details of the precipitates present in the ex-service T91 material (06-10-062, 56000h).

5. Discussion

A remarkable observation is that for the three new grade 91 materials that were creep tested the creep strength was on the low side and leaned more towards the reference creep for X20,

while the two tested ex-service materials showed creep behaviour that was as good as for new grade 91 material (Figure 2).

For the new tube materials 06-11-022 and 07-04-019 the reason for this can be found in the C content which is below minimum limit for both steels (Table 1). This was confirmed by the TEM investigation of material 06-11-022 which revealed a lower amount of $M_{23}C_6$ and MX precipitates compared to the ex-service 06-10-062 material (Figure 7).

Both ex-service materials contained a high amount of C (Table 1). Although the ex-service material 06-10-062 showed some typical coarsening of $M_{23}C_6$ precipitates compared to the new grade 91 material (Figure 7), this coarsening was not large enough to have a detrimental effect on the strengthening. This can be explained by the fact that the material has been used at an average temperature of 553°C, which is well below 600°C, which is the maximum allowable application temperature for grade 91.

The chemical composition of the new pipe material 08-02-066 is within the limits (Table 1). However, the amount of V and C are on the low end side of the tolerated range, which could have a significant influence on the precipitate distribution. Further investigation using TEM analysis of the precipitates could help in finding the cause of the lower creep strength for this material.

6. Conclusion

The main conclusions that can be drawn from this work are the following:

- The chemical composition of new Grade 91material is not always in accordance to the standard and can deviate from what is mentioned on the certificate.
- A too low amount of C can lead to a significant decrease in creep strength.
- Short term stress relaxation tests can be used to determine the current creep strength of Grade 91 material.
- TEM investigation is a useful tool to study the precipitation structure of the material, where optical microscopy is insufficient.

Acknowledgement

This work was made possible through financial support from GDF Suez.

References

[1] A. Shibli, Development of NDE techniques for early stage creep damage detection in P91 steel, *Proceedings of the ECCC Creep Conference, 21-23 April 2009, Zurich*, p.402-413, (2009).

[2] J. Parker, K. Coleman, Life management issues for creep-strength enhanced ferritic steels, *Proceedings of the ECCC Creep Conference, 21-23 April 2009, Zurich*, p.68-78 (2009).
[3] F. Masuyama, T. Tokunaga, N. Shimohata, T. Yamamoto, M. Hirano, Comprehensive approach to creep life assessment of martensitic heat resistant steels, *Proceedings of the ECCC Creep Conference, 21-23 April 2009, Zurich*, p.19-30, (2009).
[4] E. De Bruycker, J.-P. Keustermans, S. Huysmans, Stress relaxation testing as an alternative to conventional creep rupture testing, *Proceedings of the ECCC Creep Conference, 21-23 April 2009, Zurich*, p.1138-1145, (2009).
[5] S.C. Bose, K. Singh, J. Swaminathan, D.S. Sarma, Prediction of creep life of X10CrMoVNbN-91 (P-91) steel through short term stress relaxation test methodology, *Materials Science and Technology*, Vol.20, p.1290-1296, (2004).

while the two tested ex-service materials showed creep behaviour that was as good as for new grade 91 material (Figure 2).

For the new tube materials 06-11-022 and 07-04-019 the reason for this can be found in the C content which is below minimum limit for both steels (Table 1). This was confirmed by the TEM investigation of material 06-11-022 which revealed a lower amount of $M_{23}C_6$ and MX precipitates compared to the ex-service 06-10-062 material (Figure 7).

Both ex-service materials contained a high amount of C (Table 1). Although the ex-service material 06-10-062 showed some typical coarsening of $M_{23}C_6$ precipitates compared to the new grade 91 material (Figure 7), this coarsening was not large enough to have a detrimental effect on the strengthening. This can be explained by the fact that the material has been used at an average temperature of 553°C, which is well below 600°C, which is the maximum allowable application temperature for grade 91.

The chemical composition of the new pipe material 08-02-066 is within the limits (Table 1). However, the amount of V and C are on the low end side of the tolerated range, which could have a significant influence on the precipitate distribution. Further investigation using TEM analysis of the precipitates could help in finding the cause of the lower creep strength for this material.

6. Conclusion

The main conclusions that can be drawn from this work are the following:

- The chemical composition of new Grade 91material is not always in accordance to the standard and can deviate from what is mentioned on the certificate.
- A too low amount of C can lead to a significant decrease in creep strength.
- Short term stress relaxation tests can be used to determine the current creep strength of Grade 91 material.
- TEM investigation is a useful tool to study the precipitation structure of the material, where optical microscopy is insufficient.

Acknowledgement

This work was made possible through financial support from GDF Suez.

References

[1] A. Shibli, Development of NDE techniques for early stage creep damage detection in P91 steel, *Proceedings of the ECCC Creep Conference, 21-23 April 2009, Zurich*, p.402-413, (2009).

[2] J. Parker, K. Coleman, Life management issues for creep-strength enhanced ferritic steels, *Proceedings of the ECCC Creep Conference, 21-23 April 2009, Zurich*, p.68-78 (2009).
[3] F. Masuyama, T. Tokunaga, N. Shimohata, T. Yamamoto, M. Hirano, Comprehensive approach to creep life assessment of martensitic heat resistant steels, *Proceedings of the ECCC Creep Conference, 21-23 April 2009, Zurich*, p.19-30, (2009).
[4] E. De Bruycker, J.-P. Keustermans, S. Huysmans, Stress relaxation testing as an alternative to conventional creep rupture testing, *Proceedings of the ECCC Creep Conference, 21-23 April 2009, Zurich*, p.1138-1145, (2009).
[5] S.C. Bose, K. Singh, J. Swaminathan, D.S. Sarma, Prediction of creep life of X10CrMoVNbN-91 (P-91) steel through short term stress relaxation test methodology, *Materials Science and Technology*, Vol.20, p.1290-1296, (2004).

9th Liege Conference : Materials for Advanced Power Engineering 2010
edited by J. Lecomte-Beckers, Q. Contrepois, T. Beck and B. Kuhn.

CREEP PROPERTIES AND MICROSTRUCTURE EVALUATION OF WELD JOINT OF THE PIPE MADE OF P92 STEEL

Josef Kasl[1] - Dagmar Jandová[1] – Eva Chvostová[1] - Eva Folková[2]
[1] ŠKODA VÝZKUM s.r.o., Tylova 1/57, 316 00 Plzeň, the Czech Republic
[2] ŠKODA POWER a.s., Tylova 1/57, 316 00 Plzeň, the Czech Republic

Abstract

One-side weld joint of W type was prepared from P92 type steel using GTAW & SMAW method. Creep test to the rupture of smooth cross-weld samples has been carried out at temperatures ranging from 575 to 650 °C and at stresses from 70 to 240 MPa. Fractographic analysis, hardness measurement and detailed study of submicrostructure have been performed using light, scanning and transmission electron microscopy. Changes of microstructure were correlated with the creep strength. Increase in size of secondary phases and cavities formation were evident after creep tests at temperatures above 575°C. Voids were concentrated in the fine prior austenite grain heat affected zones, where fracture occurred. In addition, a sporadic occurrence of individual cavities was found out in the base material and the weld metal after tests at 625 and 650 °C. During creep exposures at temperatures above 600 °C Laves phase precipitated.

Keywords: steel P 92, weldments, creep test, microstructure, TEM

1. Introduction

Turbines, boilers and steam piping belong to the most exposed parts of steam power plants. They have been operating under severe service conditions for several decades. Therefore high mechanical strength, good corrosion/oxidation resistance and high structural stability of materials used for their production are desired. Several new grades (P91, P92, P911) were developed in the last decades and they are currently used for producing various parts of high efficiency power plants.

Grade P92 (X10CrWMoVNb9-2, ASME SA 335-P92) is ferritic 9Cr - 1.75W - 0.5Mo steel alloyed with vanadium and niobium and with controlled boron and nitrogen contents. Due to excellent creep properties and high corrosion/oxidation resistance, which is equal to other high chromium ferritic steels, it is used for production of headers, boiler superheater and reheater tubes and main steam pipes for of advanced power plants. This steel is now being used in different countries, and at the moment it is regarded as the benchmark ferritic steel for power plants operating at extremely severe steam conditions (temperatures exceeding 600 °C and pressures of over 25 MPa) [1]. Steel P92 reaches creep strength from 110 to 120 MPa at the temperature of 600 °C for 10^5 hours. This steel contains only a small amount of nitrogen to reduce formation of boron nitrides. Low speed of coarsening of $M_{23}C_6$ particles positively influences microstructure stability. During tempering and/or creep exposure an intensive precipitation of Laves phase occurs, which leads to tungsten and molybdenum depletion of

solid solution. However, it does not tend to more prominent decrease of creep strength. In spite of the fact that the amount of MX particles is rather low, only a moderate recovery as well as slow growth of subgrain generally occurred.

It is well known that notwithstanding design for plant is based on creep strength of the base materials, operating experience shows that welds are the most critical parts of high temperature operating plants. Welded joints are commonly susceptible to fracture. Rupture is usually initiated in a specific region as a result of structural heterogeneity of the weldment formed either during fabrication or during service [2]. Since cyclic thermal and stress loading after each weld pass affects the steel structure, great attention has to be paid to welding technologies and selection of convenient filler materials. This paper deals with a study of microstructure evaluation in the similar weld joints of P92 steel fabricated in industrial condition. Microstructure after creep testing is compared with as received on.

2. Experimental procedure

2.1. Experimental material

Trial weld joints were prepared from segments of tubes of wrought ASME SA 335 Gr. P92 steel. Their outer diameter and wall thickness were 219 mm and 40 mm respectively. Normalising of the base material was done at 1,060 °C and after cooling to room temperature tempering at 770 °C for 2 hours was applied. Tubes were joined in both PC and PF positions.

One-side welds of W type were carried out using manual welding; the root pass was done in internal protection by argon and filling passes using covered electrode (method 141 + 111 according to EN ISO 4063, GTAW & SMAW according to ASME). Inductive heating with thermal insulation ensured a preheating temperature ranging from 200 to 250 °C. The welding interpass temperature was kept below 300 °C. The post weld heat treatment (PWHT) temperature of 760 °C for 4 hours was applied. Thermanit 616 was used for root pass as well as for filler material. The chemical composition of the base metal and the filler material used is given in Table 1.

Table 1: Chemical composition of base and filler materials (in wt. %)

	C	Mn	Si	P	S	Cr	Mo	V	W	Ni	Nb	N	B	Al
P92 - tube	0.12	0.41	0.25	0.015	0.003	8.6	0.47	0.17	1.75	0.11	0.06	0.045	0.002	0.029
Thermanit 616	0.13	0.61	0.24	0.007	0.002	8.93	0.99	0.18	1.55	0.67	0.07	0.041	0.005	0.005

2.2. Experimental procedures

Mechanical properties of weldments were measured.

Smooth cross-weld specimens with the length of 92 mm and the diameter of 8 mm were fabricated from the middle part (outside of the weld root) of the weld joint made in PC position. Creep tests to the rupture of these specimens were carried out at temperatures ranging from 575 °C to 650 °C and stresses from 70 MPa to 240 MPa.

Fracture surfaces of ruptured samples were observed using scanning electron microscope (SEM). Then specimens were cut along their longitudinal axis. Macrostructure was revealed using Villela-Bain's reagent and location of fracture in the weldment was specified. Hardness measurement along the specimen axis was performed. Microstructure was observed on longitudinal sections using light microscopy (LM) and scanning electron microscopy. The substructure was evaluated using transmission electron microscope (TEM). Both thin foils and extraction replicas were prepared from the selected most important parts of weld joint. The foils were thinned by a jet polishing in 6 percent solution of perchloric acid in methanol at the temperature of -40 °C. Energy dispersive X-ray microanalysis (EDX) and electron diffraction were used for the identification of secondary phases.

3. Results

3.1. Mechanical testing

Integrity and mechanical properties of weld joints have been evaluated according to the welding standards EN 288-2,3. All results were satisfactory. Selected mechanical properties of the base material as well as of the weld joints after PWHT are summarized in Table 2.

Table 2: Mechanical properties of weld joints

Weld position	$R_{p0,2}$ [MPa]	R_m [MPa]	A [%]	Z [%]	Fracture location	KV [J]			
						HAZ	WM	HAZ	WM - root
PC	540	698	16.4	66.4	BM	185,193,172	49,42,36	137,96,44	32,37,29
PF	527	689	15.6	68.6	BM	94,185,179	19,16,22	200,182,181	33,33,37

3.2. Creep testing

The creep testing was carried out. Summary of samples, conditions of tests as well as obtained results are given in Table 3. Time to the rupture of already broken samples ranged from 100 to 7,700 hours. One sample is still running. Creep rupture strength was evaluated using Larson-Miller parametric equation

$$P = T * [C + \log \tau] \quad (1)$$

where T represents temperature given in degree Kelvin, C is a specific constant for the given material (C = 36 for P92 steel) and τ means time to fracture in hours. Results of creep tests are graphically represented in Fig. 1. Creep rupture strength of weld joint is compared with the standardized creep rupture strength data of P92 steel [3].

Table 3: Creep data and fracture location

	Temp. [°C]	Stress [MPa]	Duration [h]	A [%]	Z [%]	(σ_{BM}-σ_{WM})/σ_{BM} [%]	Fracture Location	Average hardness HV 10			Notice
								B M	HAZ	WM	
1	-	-	-	-	-	-	-	226	248	262	not tested
3	575	200	9,674	6.0	25.6	8	BM/HAZ IC	224	231	251	
4	575	240	100	15.5	82.9	-4	BM	222	232	242	
6	600	120	16,927			(-16)					test continues
7	600	140	15,904	1.4	4.9	-2	HAZ FG/IC	219	233	242	
5	600	160	7,715	5.5	14.4	5	HAZ FG	226	232	249	
8	600	160	4,796	2.6	9.3	1	HAZ FG/IC	207	215	236	
15	600	180	2,160	13.3	59.4	6	BM	216	218	241	
2	600	210	262	16.7	76.2	6	BM	216	221	235	
11	625	80	16,493	1.7	4.9	-27	HAZ FG	213	215	235	
12	625	90	12,306	4.0	2.0	-20	HAZ FG	212	219	235	
9	625	100	6,732	-	12.1	-17	HAZ FG	217	229	240	
10	625	120	5,380	6.0	7.4	-3	HAZ FG	216	217	229	
16	625	140	2,116	2.9	12.1	3	HAZ IC	214	228	234	
14	650	70	5,960	5.6	12.1	-23	HAZ FG	215	215	234	
13	650	80	3,228	6.0	7.4	-19	HAZ FG	219	226	242	
18	650	100	2,052	3.8	12.1	-4	HAZ FG	205	209	220	

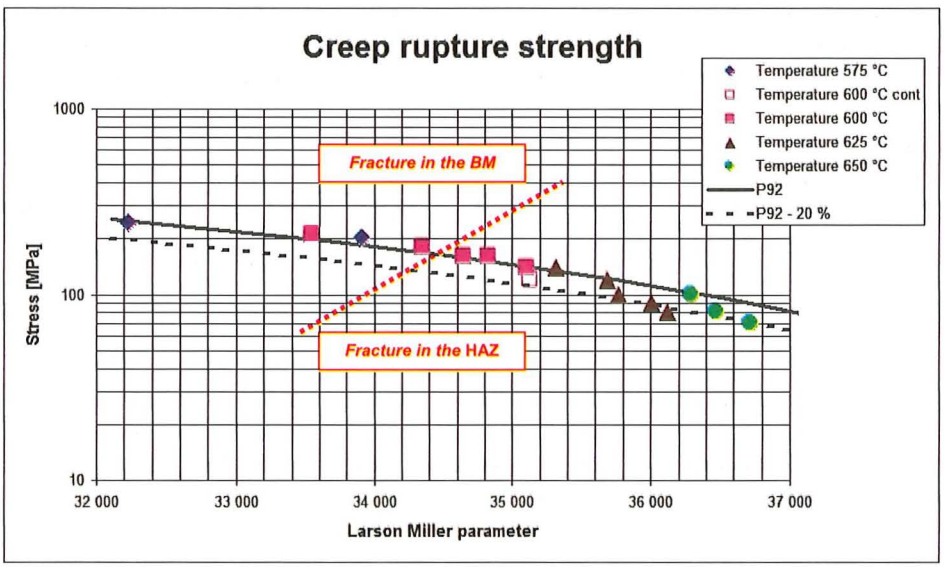

Figure 1: Creep rupture strength in dependency on Larson-Miller parameter (creep test results labeled with open symbol are still running, full line represents creep strength for base material, dashed line represents creep strength of base material minus 20 percent).

Up to 600°C the creep strength of the weld joint falls into the usually permitted scatter band ± 20 percent of the creep strength of the base material used for production of piping. For the testing temperature of 625°C the creep strength of the weld joint decreases below the scatter band for sample tested at stress below 80 MPa and lies on the boundary of the scatter band for sample tested at stress 90 MPa while for higher stresses falls into the scatter band. For the testing temperature of 650°C the creep strength of the weld joint decreases below the scatter band only for sample tested at the lowest stress 70 MPa. Comparatively differences between he creep strength of the weld joint and the creep strength of the base material are shown in Table 3.

3.3. Fractographic analysis

Fractographic analysis and observation of longitudinal sections of the ruptured cross-weld specimens show that samples tested at lower temperatures and higher stresses failed in the base material (BM) unaffected by welding while those ones tested at higher temperatures and lower stresses ruptured in the heat-affected zone (HAZ) of the base material (in the grain refined part or in the intercritically reheated part of the zone). Fracture locations of samples are given in Table 3 and suggested in Fig. 1. In the first above mentioned group ductile fracture occurred after very short durations of creep tests (up to two thousands hours). The fractures are transcrystalline ductile with considerable macroplastic deformation (elongation about 15%) and with the dimple morphology of the fracture surface. The second one includes samples ruptured by transgranular creep fracture. Longitudinal elongations of these specimens were usually a few percent. Individual small cracks formed of growing cavities joined and spread step by step across the sample. Finally the shear lips were formed on the sides of the test bar. Intercrystalline facets were not observed. Fracture surfaces of samples tested at temperatures above 625 °C are covered with an oxide layer, so in some cases it is rather difficult to determine real fracture micro-mechanism.

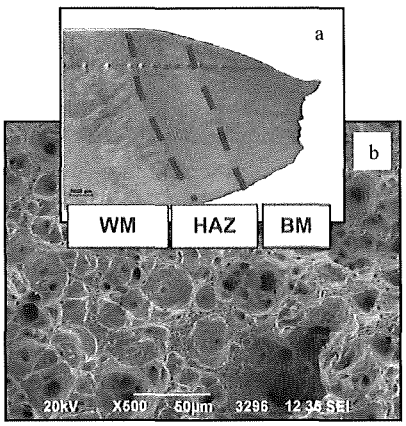

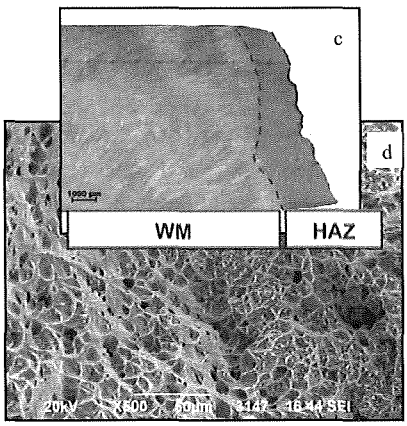

Figure 2: Macrostructure and fracture surface of sample tested at 600°C and 210 MPa (a,b); Macrostructure and fracture surface of sample tested at 600°C and 160 MPa(c d).
Particles of BN and fine (Al,Ca)-oxides with diameter about one micrometer were found on the fracture surfaces using ED microanalysis.

3.4. Hardness profile measurement

Hardness profiles across the longitudinal sections of specimens were determined before and after creep testing. Average values of hardness HV10 of the different parts of samples are summarised in Table 3 and shown in Fig. 3. Before creep testing hardness HV10 of the base material and the weld metal were 226 and 262 respectively. Local hardness maximum in the coarse grained HAZ (CG HAZ) near the fusion line and local minimum in the fine grained HAZ (FG HAZ) or in the overheated part of HAZ were detected. During creep tests hardness decreased in all regions of samples already after short durations and hardness differences among regions become smaller. The biggest drop was found for sample tested at 650 °C/100 MPa in both the weld material (220 HV10) and in the base material (205). Some examples of hardness profile of weld joint after creep test at 650 °C/100 MPa compared with hardness profile before creep testing is shown in Fig. 4.

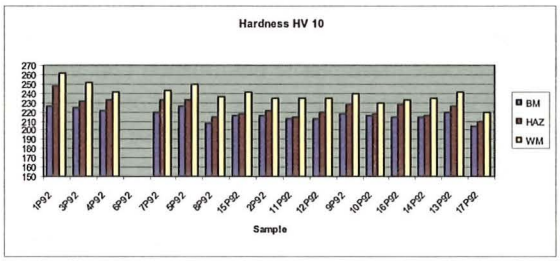

Figure 3: Average values of hardness HV10.

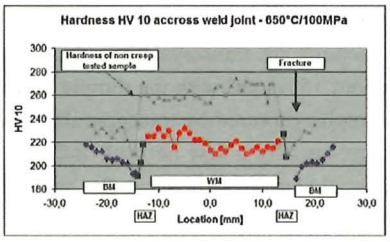

Fig. 4: Hardness profile of sample tested at 650°C and 100 MPa.

3.5. Microstructure

Microstructure of the base material, which was used for production of trial weld joint, corresponds to tempered martensite with a small amount of δ-ferrite. Single particles of δ-ferrite occurred only rarely in central parts of metallographic sample in the cross section of the ring segments while rows of δ-ferrite particles were observed in the surface layers of rings (the region of top pass and root). Both weld joints examined were of the W type, the width of the heat affected zone (HAZ) was 2 mm. Severely tempered martensitic structures were observed in all parts of weld joints – the lath like structures in the base material (BM), the weld metal (WM) and coarse austenite grain heat affected zone (CG HAZ), and the fine featureless structure in the fine prior austenite grain heat affected zone (FG HAZ). In the base material and also in the weld metal some particles of boron nitride were observed in size of a

few micrometers. They usually originated on the surface of oxides – aluminium oxides in the base material and silicon oxides in the weld metal (Fig. 5).
Substructure of samples was investigated using TEM. The microstructure of tempered martensite consisted of ferrite laths divided into subgrains, coarse particles at grain and subgrain boundaries and fine intragranular precipitate. Some differences in dislocation density and distribution of precipitates were observed in individual zones. In the WM dislocation density was higher than that in the BM, while density of coarse particles was relatively low. Size of subgrains in the WM was similar to that in the BM. In the CG HAZ minimum density of coarse particles was observed, dislocation density was relatively high, intragranular fine precipitate was detected and subgrains were coarser than those in BM and WM. Microstructure in the FG HAZ exhibited a subgrain structure often of polygonal shape instead of typical martensitic lath-like structure. Size of subgrains was significantly higher and number of coarse particles was higher in comparison to other parts of the weld joint. Post-weld heat treatment at 760 °C resulted in precipitation of $M_{23}C_6$ carbides and vanadium/niobium carbonitride. Coarse particles of $M_{23}C_6$ carbide were present especially at boundaries of prior austenite grains and ferrite laths, while fine vanadium carbonitrides were spread at boundaries and also within laths.

An increase in size of $M_{23}C_6$ particles, Laves phase particles precipitation and cavities formation were observed after creep tests at 575 °C and lower stresses and at temperatures above 600 °C. Growth occurred especially in the weld metal. Laves phase formed the largest observed particles. No important changes of fine precipitates were found out among samples after PWHT and after creep testing. A lot of cavities were indicated in FG HAZ, where fracture occurred. Some cavities were also present in the base material and the weld metal. Quantity and size of cavities increased with increasing temperature of creep testing.

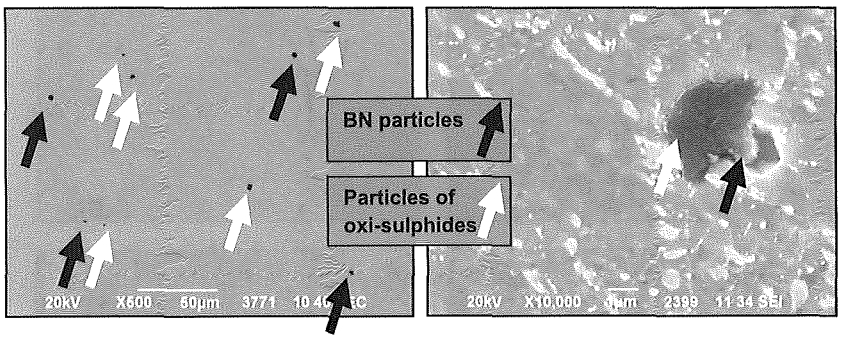

Figure 5: Particles of BN and oxi-sulphides, SEM.

A development of precipitates - coarsening of particles, changes in distribution of particles and formation of new particles of Laves phase - is shown in Fig 6. Changes in the substructure during creep test in the individual part of the weld joint are shown in Fig. 7.

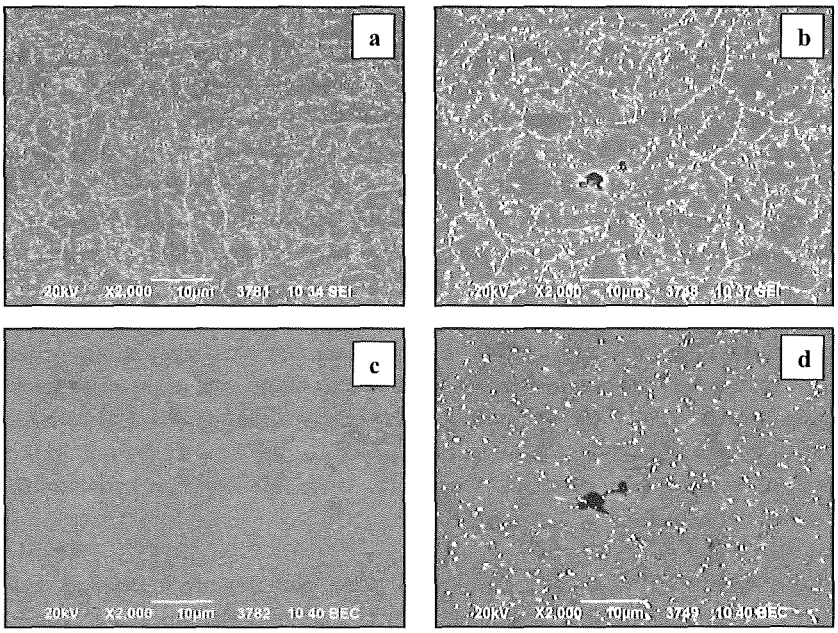

Figure 6: SEM micrographs of FG HAZ: sample after PWHT (a) - secondary el. image, (b) – back-scattered image; sample tested at 625 °C, 80 MPa (c) - secondary el. image, (d) – back-scattered image; new particles of Laves phase are visible in Fig (d).

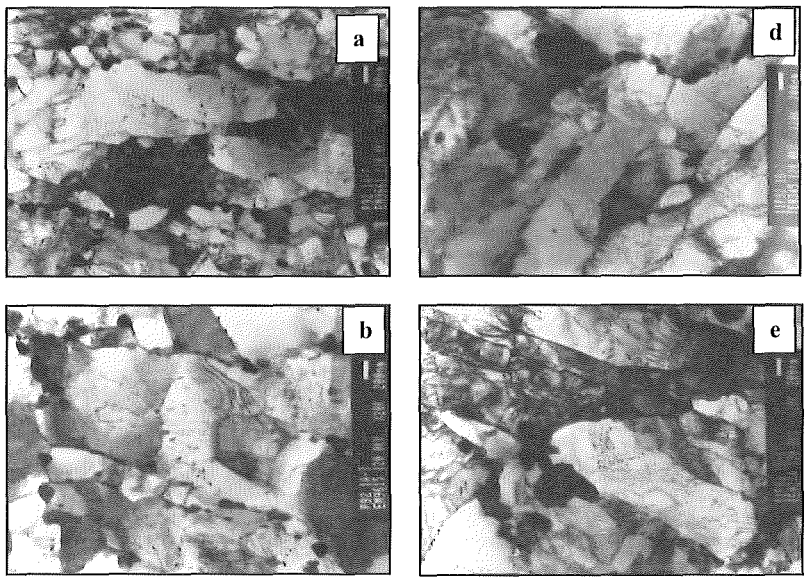

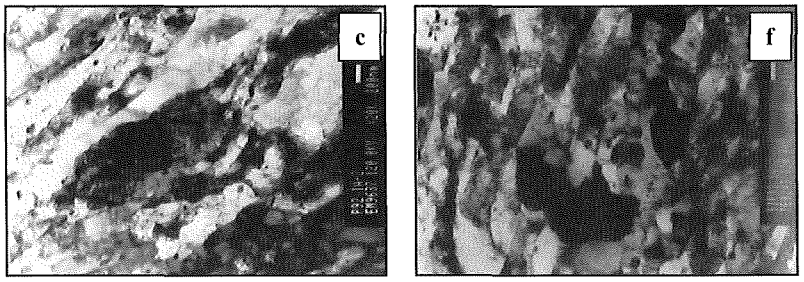

Figure 7: TEM micrographs of sample after PWHT - (a) BM, (b) FG HAZ, (c) WM and of sample tested at 625 °C, 80 MPa - (d) BM, (e) FG HAZ, (f) WM.

Quantitative evaluation of secondary phase particles in both the WM and the BM was performed for weld joint after PWHT and selected crept specimens using carbon extraction replicas. All particles observed were assigned to fine intragranular particles of a diameter from up to 40 nm or to coarse particles with a diameter higher than 40 nm, which were usually located at grain or subgrain boundaries. Coarse and fine particles were evaluated separately and type of phase was not taken into account. For each of assessed zones equivalent diameter was calculated for about 1,000 and 2,000 fine and coarse particles, respectively using image analysis software. Results are shown in table 4. After creep test at 575°C/240MPa/100hrs any changes in size and distribution of secondary phases were observed. After test at 600°C/160MPa/7,715hrs slight growth of coarse particles was found out. Significant increase was evident after test at 625°C/100MPa/6,732hrs.

Table 4: Secondary phase particle dimensions

Sample		Number of particles	Equivalent diameter	Number of particles	Equivalent diameter
Temperature/ stress	Position	Particles 10-40 nm		Particles > 40 nm	
after PWHT	WM	543	20	2444	121
	BM	782	24	2593	120
575/240	WM	479	23	3152	102
	BM	731	23	1046	113
600/160	WM	866	22	3096	126
	BM	914	24	2365	149
625/100	WM	363	22	2375	144
	BM	1057	22	2502	153
650/80	WM	776	20	2515	118
	BM	1125	23	3153	128

4. Conclusions

This paper deals with creep properties of the weld joint of pipelines fabricated from P92 steel using welding technology developed for industry praxis.

Up to 600 °C the creep strength of the weld joint falls into usually permitted scatter range ± 20 percent of the creep strength of the base material used for production of piping. At higher temperatures it decreases below this scatter range.

Critical zone from the point of view of the creep failure is located in the fine prior austenite grain heat affected zone and in the overheated zone of the base material where cavitation failure was evident.

Chemical composition of used steel and filler material lead to a formation of coarser particles of boron nitrides causing a decrease of ability of boron to inhibit coarsening of $M_{23}C_6$ carbides. Coarsening of these particles together with precipitation and coarsening of new particles of Laves phase were observed after relatively short duration of creep tests at temperatures above 600°C.

One sample is still in progress.

Two samples, namely 5P92 and 8P92 were performed at the same conditions. Time to ruptures differ: 7,715 hours and 4,796 hours respectively. This shows a certain scatter of results and exhorts to a caution in interpretation of results.

[1] "The T92/P92 Book". Vallourec & Mannesmann Tubes, edition 2000.
[2] Mythili, R. - Thomas, P. V. – Saroja, S. – Vijayalakshmi, M. – Raughunathan, V. S.: Microstructural modification due to reheating in multipass manual arc welds of 9Cr-1Mo steel. J. Nucl. Mater., 312, 199 – 206 (2003).
[3] Creep strength of steel X10CrWMoVNb 9-2 according the ECC data sheet.

Acknowledgements

This work was supported by Grant projects MSM 4771868401 and OC09041 from the Ministry of Education, Youth and Sports of the Czech Republic

9th Liege Conference : Materials for Advanced Power Engineering 2010
edited by J. Lecomte-Beckers, Q. Contrepois, T. Beck and B. Kuhn.

MICROSTRUCTURE ANALYSIS OF ROTOR STEEL E AFTER MORE THAN 100,000 HOURS OF CREEP EXPOSURE

Dagmar Jandová, Josef Kasl, Eva Chvostová

ŠKODA VÝZKUM s.r.o., Tylova 1/57, Plzeň, Czech Republic
dagmar.jandova@skodavyzkum.cz, josef.kasl@skodavyzkum.cz,
eva.chvostova@skodavyzkum.cz

Abstract

The material of trial rotor E made of X12CrMoWVNbN 10-1-1steel underwent creep testing at temperatures from 500°C to 650°C. Three specimens crept at different conditions were selected for TEM investigation. Quantitative analyses of substructure and particles of secondary phases were performed. Microstructure corresponded to tempered martensite with ferritic laths subdivided into subgrains. Coarse $M_{23}C_6$ carbides occurred at grain and subgrain boundaries and fine vanadium nitride was present within grains. Precipitation of new particles and recovery taking place during creep test at 500°C/250MPa/107,514h resulted in decrease in dislocation density and subgrain formation and increase in precipitation and substructural strengthening. Size of coarse precipitates only slightly increased in comparison to the creep test at 500°C/335MPa/587h. Important changes occurred after test at 575°C/155MPa/34,707h, which caused a significant decrease in creep strength. The mean size of coarse particles remarkable increased thanks precipitation and growth of Laves phase, dislocation density decreased and size of subgrains increased.

Keywords: ferritic creep resistant steel, creep, microstructure, electron microscopy

1. Introduction

The steel investigated belongs to modified (9-12)% Cr steels, which are used for production of components for fossil fuel power plants operating at creep conditions at temperatures above 550°C. These components have to operate at severe conditions for years. Therefore a high structural stability is the essential material feature, which is required.

Rotor steel E has been developed in the frame of the European programme COST 501. Subsequent trial melts with modified compositions signed A, B, ..., F were carried out and tested with the aim to obtain material with the following properties [1]:
- 100,000 hours creep rupture strength at 600°C of about 100 MPa,
- good creep rupture ductility (elongation above 10%) and no notch sensitivity,
- through-hardening up to least 1,200 mm diameter,
- minimum yield strength of 600 MPa or 700 MPa,
- oxidation resistance, toughness and susceptibility to embritlement should not be worse than those of conventional 12% CrMoV and 1% CrMoV rotor steels.

Two the most promising steel compositions were selected for the production of full-scale rotor forgings (E steel with 1% W and 1% Mo and steel F with 1.5% Mo). Samples from

these trial rotors underwent a huge testing programme. A short-term creep testing showed an excellent combination of creep rupture strength in the temperature range from 550°C to 650°C, iso-stress rupture times at σ = 100 MPa and toughness that exceeded mechanical properties of conventional 12% CrMoV steel [2]. However next long-term creep testing revealed that addition of 1% W did not lead to expected improvement of creep strength in low stress region [3].

Long-term creep testing of samples made of trial rotor steel E was performed in seven European laboratories. Testing at 500°C and 575°C was assigned to Laboratory of Mechanical testing in ŠKODA VÝZKUM s.r.o. Times to rupture of specimens tested at 500°C exceeded 100,000 hours although expected times were about 60,000 hours. Results of these long-term creep tests are of a great importance as they allow improving and making accurate an estimation of creep resistant properties yielded from short-term creep tests.

2. Experimental procedures

Rotor E of a maximum diameter of 1,200 mm was fabricated from ingot of X12CrMoWVNbN 10-1-1steel of a total weight of 42 tons produced by Saarstahl Völklingen (Germany). Chemical composition of the forging is given in the Table 1. Heat treatment was carried out in two variants that should have led to material with low yield strength (630 MPa) and high yield strength (750 MPa). In the first case the heat treatment consisted of 1070°C/17h/oil + 570°C/25h + 690/24h + 715°C/22h/furnace, while in the second one of 1070°C/17h/oil + 570°C/25h + 690°C/24h. A final structure was tempered martensite with a large amount of particles of secondary phases, which contribute to strengthening of the steel and retard recovery during creep exposures.

Table 1. Chemical composition in weight %.

C	Si	Mn	Cr	Mo	Ni	V	W	Nb	N	Al	B
0.12	0.10	0.45	10.4	1.06	0.74	0.18	0.81	0.045	0.052	0.008	0.002

Standard creep samples with a diameter of 8 mm and a gauge length of 40 mm were machined out of a surface part of the rotor. Creep tests to the rupture at 500°C and 575°C with measuring of strain were conducted in ŠKODA VÝZKUM s.r.o. The ruptured creep test bars were used for fractographic analyses using scanning electron microscopy (SEM), microstructure assessment using transmission electron microscopy (TEM) and image analysis software NIS-Elements 3.0. The foils for TEM observation were thinned by a jet electropolishing in 6% solution of perchloric acid in methanol at a temperature of -40 °C. Energy-dispersive X-ray microanalysis (EDX) and selected area electron diffraction were used for the identification of secondary phases.

3.Results

3.1. Creep testing

Complete results of creep testing for both variants of heat treatment obtained in ŠKODA VÝZKUM s.r.o. up to February 2002 are graphically represented in Fig. 1 [4]. The full line represents mean values of creep strength of X12CrMoWVNbN 10-1-1 steel according the standard SEW 555 [5]. One sample was removed (R) and the last test (500°C/250MPa/107,514h) was finished only in January 2009. Results of long-term creep tests of samples of rotor heat treated on the low yield stress level are summarized in the Table 2. From crept samples, which were still available, three samples termed E61, E65 and E69 were selected for microstructural investigation.

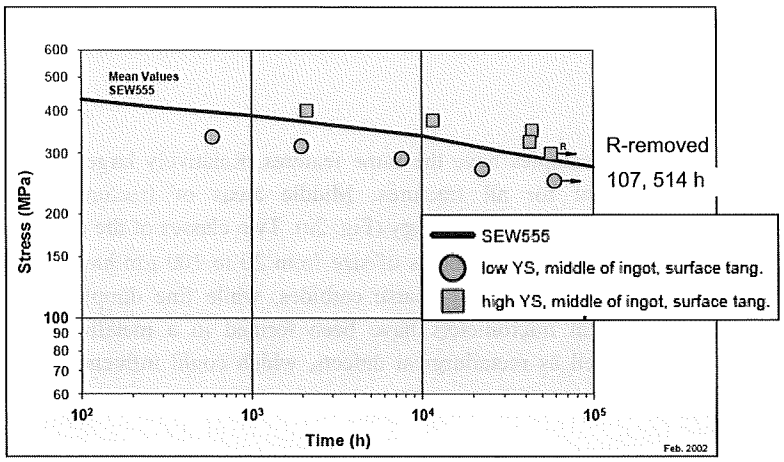

a

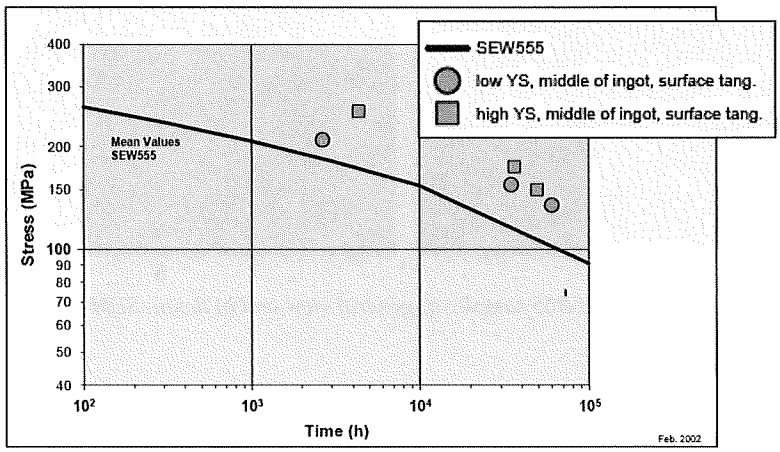

b

Figure 1. Dependence of stress on time to rupture: a) at 500°C, b) at 575°C [4].

Table 2. Conditions and results of creep tests.

Temperature [°C]	Stress [MPa]	Sample	Time to rupture [h]	Elongation [%]	Area reduction [%]	Notice
500	335	E61	587	25.3	81.9	TEM
	315	E62	1,968	26.0	81.9	
	290	E63	7,363	24.0	79.7	
	270	E64	22,511	19.9	80.8	
	250	E65	107,514	23.1	80.8	TEM
575	210	E66	2,653	-	-	
	155	E69	34,707	21.9	84.0	TEM
	135	E70	60,292	19.1	85.0	

3.2. Fractography

Fracture surfaces of tested samples have the same features. Relatively large area reduction and contraction are typical for all fractures. Middle areas of fracture surfaces are transcrystalline ductile with dimple morphology (Fig. 2a). Two classes of the dimple size can be distinguished (Fig. 2b). The large dimples of size from 20 to 100 μm have been formed around either non-metallic inclusions or coarse carbides, while fine dimples of diameter ranging from one to several micrometers have been formed in a metallic matrix. Any intercrystalline facets as well as metallurgical defects, which could influence the fracture, were not found.

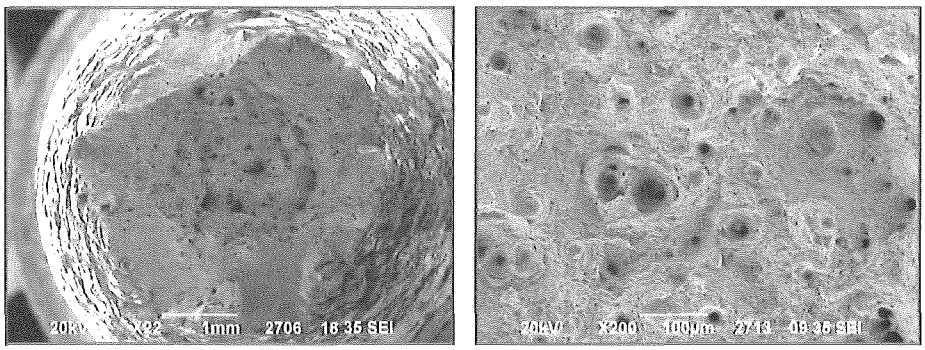

a *b*

Figure 2. Fracture surface of E65 sample: a) general view and b) detail. SEM micrographs.

3.3 Microstructure analysis

Microstructural analysis of three samples of the steel treated on the low yield stress level was carried out. The virgin material used for creep test bars production was not available. Sample E 61 (500°C/ 335 MPa/ 587 h) represented material in condition only slightly influenced by

creep testing and therefore could serve as a reference sample. Samples E65 and E69 underwent substantially longer creep exposures. Sample E65 was tested at 500°C and a stress of 250 MPa for 107,514 hours and sample E69 at 575°C and a stress of 155 MPa for 34,707 hours. Microstructures of all samples can be described as tempered martensite consisting of less plate-like than lath-like ferritic matrix and particles of secondary phases (Fig. 3). Coarse particles occur at the boundaries of prior austenitic grains, ferritic laths and subgrains while fine precipitates are spread within laths and subgrains. Non-uniform dislocation density is a typical feature of such material. Dislocation form non-arranged dislocation network or cellular structure or arranged dislocation walls in dependency on conditions of the creep test. Higher density is usually related to occurrence of fine intragranular precipitate.

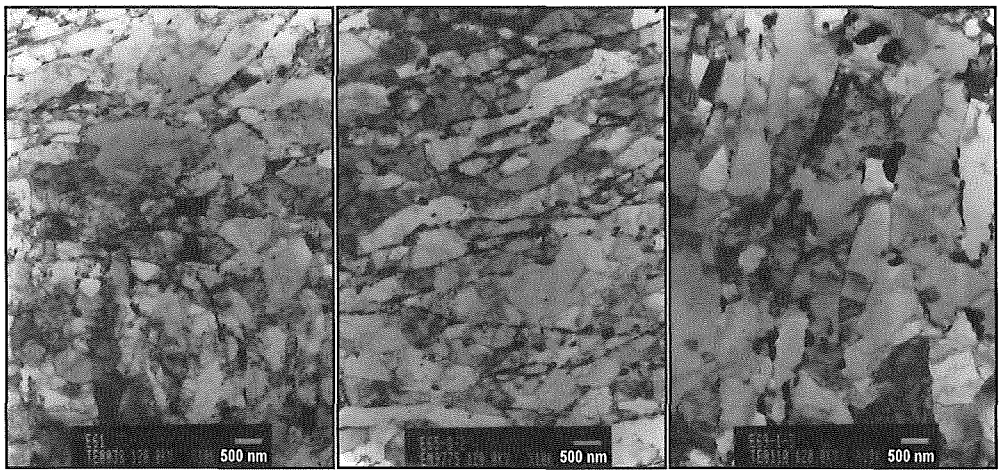

a *b* *c*

Figure 3. Substructure of the crept specimens: a) E61, b) E65 and c) E69. TEM micrographs.

Quantitative evaluation included measurement of size of coarse particles (diameter above 20 nm), size of subgrains and the dislocation density. A binary image was created for each TEM micrograph using editor of manual processing and the following features have been determined: equivalent diameters, MaxFerets and MinFerets (maximum and minimum values of a length of particles and subgrains measured in various directions). Ferets were measured at slope of testing line of 10, 20, 30, ..., 180°. The average values of measured quantities including tested areas and numbers of tested objects are given in the Tables 3 and 4.

The density of dislocation has been calculated using intercept method according equation

$$\rho = (\frac{n_1}{L_1} + \frac{n_2}{L_2})\frac{x}{t},$$

where n_1 and n_2 are numbers of intersections of dislocations with perpendicular lines of length L_1 and L_2 respectively, x is an correction factor of visibility of dislocations, which is equal 2

and 1 for two beam approximation in $(110)_\alpha$ reflection and in $(200)_\alpha$ reflection, respectively, t is a thickness of sample calculated as an product of number of fringes in a grain boundary and extinction depth (28.89 nm and 42.27 nm for imaging in a reflection $(110)_\alpha$ and $(200)_\alpha$, respectively). Results are summarised in the Table 5.

Table 3. The size of subgrains.

Sample	Evaluated area	Number of subgrains	Equivalent diameter	MaxFeret	MinFeret
	[μm^2]		[nm]	[nm]	[nm]
E61	48	724	516	846	415
E65	54	1,239	473	740	393
E69	47	710	525	862	416

Table 4. The size of particles of secondary phases.

Sample	Evaluated area	Numer of particles	Equivalent diameter	Max equivalent diameter	Max Feret	Min Feret
	[μm^2]		[nm]	[nm]	[nm]	[nm]
E61	6.6	241	83	232	117	65
E65	7.9	1,134	90	328	124	71
E69	7.2	437	125	723	178	99

Table 5. The dislocation density.

Sample	Average dislocation density	Maximum dislocation density	Minimum dislocation density
	[10^{13} m^{-2}]	[10^{13} m^{-2}]	[10^{13} m^{-2}]
E 61	7.7	12.5	2.0
E 65	2.1	3.4	0.9
E 69	1.4	3.0	0.5

Dislocation substructure of E61 sample (500°C/335MPa/587h) consisted of non-arranged dislocation net in some of laths, while a cellular structure or subgrains were present in the others. It was rather difficult to apply quantitative evaluation of such heterogeneous dislocation substructure in order to get representative results. Within the frame of measurement of subgrains, not only well developed subgrains bounded with arranged dislocation walls were taken into account, but also the whole laths with tangle of dislocations and dislocation cells. Size of "subgrains" of 516 nm was determined as an average value of the equivalent diameter. Measurement was carried out only for laths in two-beam conditions, when substructure is legible. Width of subgrains, which is considered to be a controlling parameter of substructure strengthening, was determined as an average value of MinFerets

(415 nm). The density of slip dislocations was relatively high; it ranged from $2.0 \cdot 10^{13}$ m^{-2} to $12.5 \cdot 10^{13}$ m^{-2} and average value was $7.7 \cdot 10^{13}$ m^{-2} (Fig. 4a).

Sample E65 (500°C/250 MPa/107,514 h) showed better developed subgrains. Their size was smaller in comparison to sample E61. The average subgrain size was 473 nm, the average width was 393 nm. Dislocations were mostly concentrated in dislocation walls and density of slip dislocations within subgrains was very low. In such subgrains density of fine precipitate was also relatively low (Fig. 4b). The dislocation density ranged from $0.9 \cdot 10^{13}$ m^{-2} to $3.4 \cdot 10^{13}$ m^{-2} and average value was $2.1 \cdot 10^{13}$ m^{-2}.

Substructure of E69 sample (575°C/155 MPa/34,707h) is shown on Fig. 4c. Nearly all laths were subdivided into subgrains. The average size of subgrains of 525 nm is larger that of E61 sample. However, the average width of subgrains of both samples is nearly the same. The density of free dislocations is very low on the level of $(0.5 - 3.0) \cdot 10^{13}$ m^{-2}.

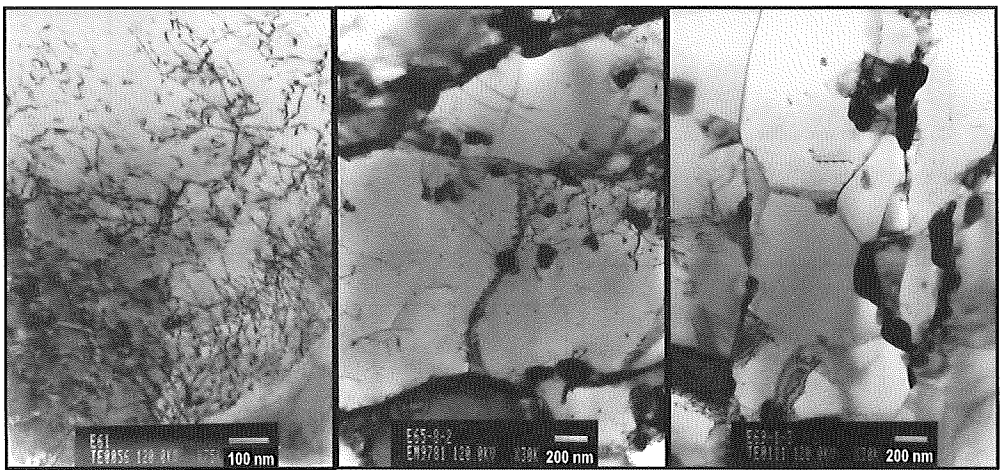

a *b* *c*

Figure 4. Particles of secondary phases in the crept specimens: a) E61, b) E65 and c) E69. TEM micrographs.

Concerning to secondary phases a fine vanadium nitride VN was observed in most of ferrite laths in E61 sample (Fig. 4a). At boundaries of prior austenite grains and ferrite laths coarse chromium rich $M_{23}C_6$ particles were identified with an average diameter of 83 nm. The largest observed particle was of 232 nm in diameter. The same phases were present in E65 sample; however a density of coarse carbides was much higher (Table 4). Subgrains were well developed in most of laths and new particles nucleated at grain and subgrain boundaries. Some of them revealed a contrast, which arises in stacking faults and which is characteristic of Laves phase. Therefore it was concluded that both phases, namely Laves phase and $M_{23}C_6$ carbide precipitated during very long creep exposure. They often formed strings along previous austenite or ferrite laths boundaries and many particles were observed also at

subgrain boundaries (Fig. 4b). Fine particles of vanadium nitrides inhibit a motion of slip dislocations, while coarse precipitates stabilize dislocation walls. Only gentle coarsening of particles occurred in comparison with E61 sample. The average diameter of coarse particles was 90 nm and diameter of the largest particle was 328 nm.

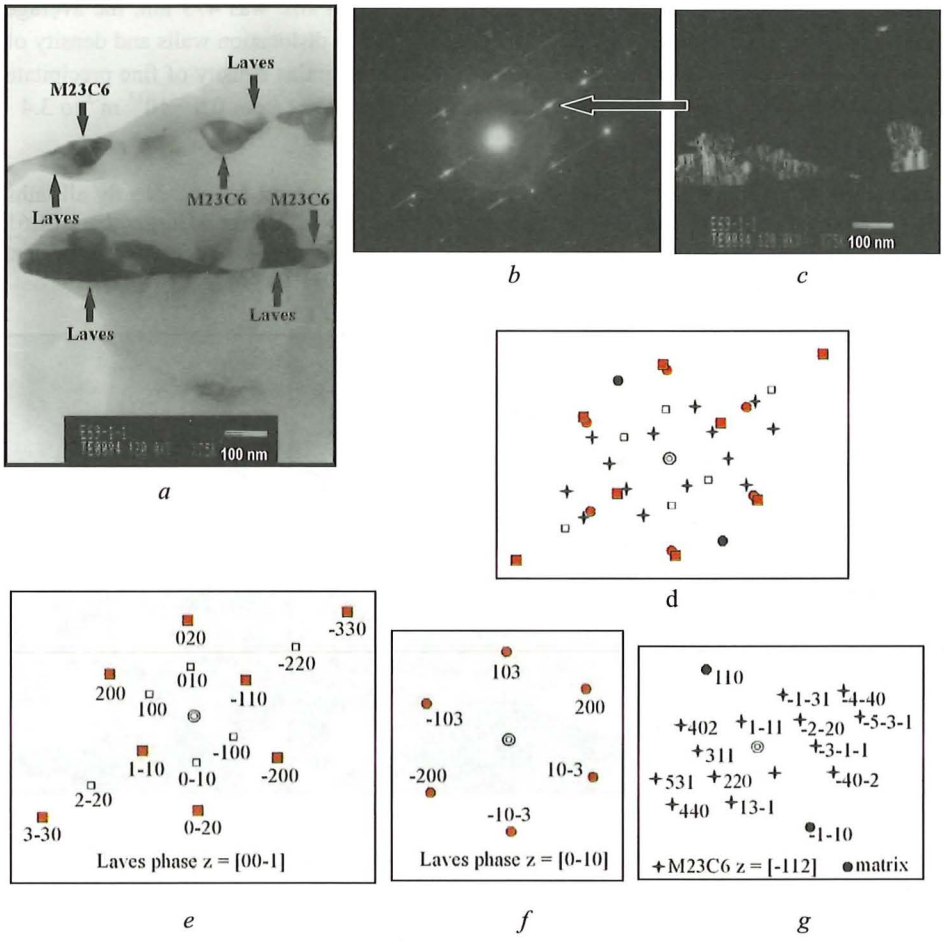

Figure 5. TEM micrographs of particles of secondary phases in E69 sample and corresponding diffraction pattern: a) bright field image, b) diffraction pattern, c) dark field image of Laves phase, d) scheme of complete diffraction pattern, e), f), g) scheme of diffraction pattern originated in individual particles.

In E69 sample nearly all laths were subdivided by dislocation walls into subgrains, at grain and subgrain boundaries coarse particles occur more frequently in comparison with E61 sample, but their density was lower in comparison with E65 sample (Fig. 4c). Particles were significantly coarser then those in E61 and E65 samples. The average equivalent diameter

increased to 125 nm and the largest particle was of 723 nm in diameter. Coarse precipitates corresponded to $M_{23}C_6$ carbides and Laves phase. Density of the fine vanadium nitride seamed to be lower in comparison to two previous samples; this precipitate was observed only exceptionally in compliance with a low dislocation density. Laves phase often nucleated at the interface between chromium carbide and matrix and formed clusters of several individual particles. Several particles of Laves phase and $M_{23}C_6$ carbides at grain boundaries near the edge of foil are shown in Fig. 5a. Corresponding selected area diffraction pattern is shown in Fig. 5b. Laves phase contains generally a lot of stacking faults, which were clearly evident on micrographs taken in dark imaging conditions (Fig. 5c). Diffraction spots in complete diffraction pattern (Fig. 5d) were originated in several particles of Laves phase in $[0\bar{1}0]$ and $[00\bar{1}]$ orientation and $M_{23}C_6$ carbide in $[\bar{1}12]$ orientation (Fig. 5e, f and d). Empty symbols correspond to faint diffraction spots.

3. Discussion

The Laves phase is considered to be harmful for long term creep strength at 550°C and higher temperatures, however during short creep exposures precipitation of Laves phase results in increase of total volume fraction of the secondary phases and consequently in increase in precipitation strengthening. At longer creep duration fast growing Laves phase remove Mo and W atoms from solid solution and strengthening of matrix falls [6]. Laves phase precipitated during the creep exposure at 500°C for more than 100,000 hours and it had positive effect on creep strength in the steel investigated. At this temperature Laves phase particles grew slowly and their size did not exceed that of $M_{23}C_6$ carbides, while at 575°C significant growth of Laves phase occurred that caused an important decrease in creep strength. Nevertheless long-term creep tests of the rotor steel E exceeded expectations and the results of detailed microstructure analysis of three samples crept at various conditions at temperatures 500°C and 575°C can be summarized as follows:

1) Chromium rich $M_{23}C_6$ carbides and Laves phase particles precipitated during long creep exposure at the temperature of 500°C. They stabilized dislocation substructure and consequently any growth of subgrains was not observed even after 100,000 hours of the creep exposure.
2) Fine intragranular precipitates of MX particles were stable at temperature of 500°C. They persisted in subgrains even after 100,000 hours of the creep exposure.
3) At 575°C Laves phase precipitated, which formed large particles and caused depletion of matrix about molybdenum and tungsten and decrease in substitution strengthening. In addition, the coarse particles served as origins for cavities formation.
4) Decrease in density MX precipitate was evident after creep exposure of nearly 35,000 hours at 575°C that caused decrease in precipitation strengthening.

A detrimental effect of Laves phase on drop in creep strength of steel E911, which was developed on the base of the rotor steel E and had similar composition to the steel investigated, was also demonstrated in a temperature range from 600°C to 650°C [7].

5. Conclusions

Long-term creep tests and microstructure evaluation of rotor steel E after heat treatment 1070°C/17h/oil + 570°C/25h + 690/24h + 715°C/22h/furnace proved both high creep resistance and microstructure stability at 500°C. At this temperature microstructure of the steel investigated consisted of tempered martensite structure with a high density of relatively coarse precipitates at grain and subgrain boundaries, which cause substructural strengthening. A high density of fine intragranular precipitate contributes significantly to precipitation strengthening of subgrains. At 575°C growth of Laves phase particles and also decrease in fine intragranular precipitate occurred. Both these effects are responsible for drop in the creep strength.

The results obtained in this study correspond to earlier published fact that alloying of 9Cr-1Mo steel with one percent of tungsten does not lead to significant improvement of creep resistance at high temperatures and relatively low stresses. However at 500°C tungsten supports precipitation of Laves phase, which increased at such relatively low temperature creep strength of the steel.

Acknowledgements
This work was supported by Grant projects MSM 4771868401 and OC09041 from the Ministry of Education, Youth and Sports of the Czech Republic.

References

[1] Scarlin, R. B. et al.: COST 501-III Advanced Materials for Power Engineering Components. *WP 11: Advanced Power Plant*, Final Report, GEC Alsthom, Baden, March (1998).

[2] Kern, T.-U. et al.: High Temperature Forged Components for Advanced Steam Power Plants. *Proc. Materials for Advanced Power Engineering 1998.* J. Lecomte-Beckers, et. al., eds, Forsungszentrum Julich, Liege, Part I - pp. 53 -70 (1998).

[3] Mayer, K. H. et al.: Development Steps of New Steels for Advanced Steam Power Plant., *Proc. Materials for Advanced Power Engineering 2002.* J. Lecomte-Beckers, et. al., eds, Forsungszentrum Julich, Liege, Part II – p. 1385 (2002).

[4] Kern, T.-U.: General minutes of COST 501/Rotor - Forgings, Siemens PG. COST 536 meeting - Tatranská Lomnica, Czech Republic, March (2006).

[5] SEW 555: Steels for larger Forgings for Components in Turbine and Generator Instalations, Stahl-Eisen-Werkstoffblätter (SEW) des Vereins Deutscher Eisenhüttenleute, Januar 2001.

[6] Korcakova, L., Hald, J., Somers, M. A. J.: Quantification of Laves Phase Particles in 9CrW Steel. *Material Characterization*, Vol. 47, p.111 (2001).

[7] Qin, G. et al.: TEM Studies of Microstructural Evolution in Creep Exposed E911. *Proc.2nd Creep Conference – Creep & Fracture in High Temperature Components.* Eds. I. A. Shibli, S. R. Holdsworth, DEStech Publications, Inc., Lancaster, U.S.A., p. 889 (2009).

9th Liege Conference : Materials for Advanced Power Engineering 2010
edited by J. Lecomte-Beckers, Q. Contrepois, T. Beck and B. Kuhn.

COMPUTATIONAL THERMODYNAMIC INVESTIGATIONS OF GROWTH AND COARSENING OF LAVES PHASE PRECIPITATES IN 12%Cr CREEP RESISTANT STEELS

O. Prat [1], J. Garcia [2,3], D. Rojas[1], A.R. Kaysser-Pyzalla [2,3]

[1] Max-Planck-Institut für Eisenforschung GmbH, Max Planck Str. 1, D-40237 Düsseldorf
[2] Helmholtz-Zentrum Berlin für Materialien und Energie GmbH, Hahn-Meitner-Platz 1 D-14109 Berlin
[3] Ruhr Universität Bochum, Universitätsstr. 150, D-44780 Bochum

Abstract

Precipitation phenomena in 12%Cr high alloyed steels have been investigated at creep conditions of 650°C and 150 MPa up to 6.500 hours in two different alloys. Growth and coarsening of Laves phase was determined experimentally by measuring the size of Laves phase on crept samples using scanning transmission electron microscopy (STEM). The simulations were performed using the software DICTRA based on the assumption the local equilibrium at the moving phase interface. For equilibrium calculations, the Thermo-Calc software was used. The experimental results were compared with DICTRA simulations, showing good agreement. Both the quantitative metallographic measurements as well as the simulations indicate very low coarsening for Laves Phase. The influence of different elements such as Co, Si and Cu on coarsening of Laves phase was simulated.

Keywords: Creep resistant steel, STEM, Dictra simulation, Laves Phase, Coarsening, Growth.

1. Introduction

9-12% Cr steels are mainly used as components in power plants due to their good corrosion and oxidation resistance, as well as good creep properties at high temperatures. The development of creep resistant steels is of relevance in order to increase the thermal efficiency of the steam cycle in power plants, so that fuel consumption, costs and emission of CO_2 can be reduced [1,2].
In creep steels, different types of carbides have been identified and examined regarding their crystal structure, such as $M_{23}C_6$, carbonitrides of the type MX, Laves phase and Z-phase [3]. The microstructure governs the creep strength during isothermal aging or creep exposure; therefore, it is important to understand the microstructure evolution (like growth and coarsening of precipitates) under creep conditions.
The aim of the present research is to simulate the growth and coarsening of Laves phase in two different 12%Cr alloys recently investigated in [4] and to compare the results of the Dictra simulation with the experimental values obtained by quantitative microscopy.

2. Experimental

2.1 Materials

The investigated alloys were produced by vacuum induction melting with masses of about 1 Kg. The composition of the alloys (see Tab.1) was designed to produce a master alloy with mainly Ta(C,N) precipitates and Laves phase (alloy A1, high Ta content) and a similar master alloy with formation of V(C,N) precipitates, $M_{23}C_6$ carbides as well as Laves phase (alloy A2, low Ta, relative high V content) [4]. The samples were hot-forged at 1150°C (total area reduction of 70%) and cooled in air. Standard heat treatments, with austenitisation at 1070°C for 0.5 hours, subsequent air-cooling and annealing for 2 hours at 780°C with air-cooling, were carried out to produce the initial microstructure of the novel alloys. The samples investigated in this work were crept at 650°C, 150 MPa for 1200 h, 2000 h, 3650 h and 6150 h.

Tab.1 *Chemical compositions of alloys investigated (wt %).*

Alloy	Fe	Cr	Mn	Ta	W	Cu	C	B	N	Si	Co	V
A1	Bal.	12.9	0.6	0.85	3.8	1.0	0.06	0.01	0.05	0.5	4.2	-
A2	Bal.	12.6	0.7	0.16	3.6	1.0	0.15	0.033	0.06	0.5	2.5	0.24

2.2 Transmission Electron Microscopy (STEM)

The microstructures of the investigated alloys in the initial state and after creep were analyzed using transmission electron microscopy (FEI Tecnai F20 G² operating at 200kV equipped with an energy dispersive chemical analysis system (EDS)). This technique, which is capable of separating different types of precipitates if they differ in composition, has been applied previously to 9–12% Cr steel [5]. TEM specimens were prepared from 3 mm discs which were ground and polished down to a thickness below 0.1 mm to reduce the magnetic mass of the specimens. These discs were electropolished using a standard double jet procedure (TenuPol-5 Struers) with a solution of 95% acetic acid and 5% perchloric acid as electrolyte. The electropolishing was performed at 15°C and a voltage of 43 V. Observations were carried out in the bright field (BF) and scanning (STEM) mode. Precipitates were identified by a combination of electron diffraction and EDS analysis.

2.3 Quantitative determination of precipitate size

Identified precipitates were measured with an image editor to measure the equivalent circle diameters of the particles. For the case that the precipitates present a non spherical form, a mean particle diameter d was measured by determining the minimum d_{min} (see particle 2 in Fig.1) and maximum d_{max} (see particle 3 in Fig. 1) projected diameters of all particles. The mean value d and the corresponding mean deviation d_{corr} of this mean value was obtained by:

$$d = \frac{1}{n}\sum_{i=1}^{n}\left[(d_{\min,i} + d_{\max,i})/2\right] = \frac{1}{n}\sum_{i=1}^{n} d_i \quad (1)$$

$$\Delta d_{corr} = \frac{1}{n}\sum_{i=1}^{n}\left|d_i - d_{corr}\right| \quad (2)$$

The volume fraction f_A was obtained by dividing the sum of the projected areas A_i of the particles (see particle 4 in Fig.1) by the area of the sampling field s^2 [6,7]:

$$f_A = \left(\sum_{i=1}^{n} A_i\right) : s^2 \quad (3)$$

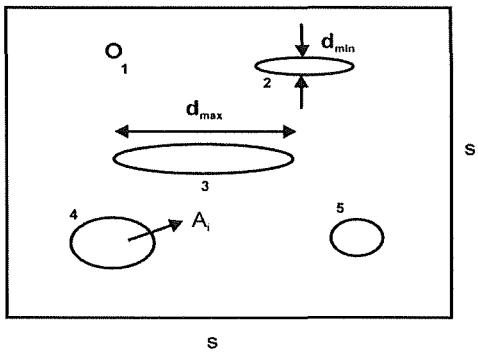

Fig.1 *Schematic figure illustrating the parameters which were retrieved from TEM micrographs: particle size and volume fraction of phases.*

Tab. 2 *Measured size of particles for alloy A1 and A2 at 650°C and different creep times.*

A1	**0h**	**1200h**	**3650h**
Ta(C,N)	30 ± 1.5	31 ± 1.5	32 ± 1.5
TaC	137 ± 14.6	-	142 ± 8.0
Laves	196 ± 34.6	268 ± 33.6	302 ± 48.5
A2	**0h**	**2000h**	**6150h**
(V,Ta)(C,N)	20 ± 1.5	36±1.8	38 ± 2.2
M23C6	140 ± 10.1	180 ± 8.4	185 ± 8.5
Laves	-	285 ± 41.6	307 ± 41.3
Z-Phase	-	-	273 ± 47.2

3. Simulation Method

3.1 Conditions for simulations

The microstructure evolution of the different phases was modeled with the DICTRA software package [8]. For the simulations, the mobility database MOB2 [9] and the thermodynamic database SSOL2 [10] were used. The composition of the different precipitates in alloys A1 and A2 were calculated with the Thermocalc database TCFE6 [11]. The elements Fe, Cr, W, C and Co were used in the simulation for growth and coarsening of the Laves phase at 650°C (see Tab.3 and Tab.4). For the simulations, a closed spherical particle in the center surrounded by a ferritic matrix was considered (see Fig.2). The particle is supposed to maintain its spherical shape throughout the whole process.

Tab.3 *Equilibrium phases and corresponding composition for alloy A1 at 650°C calculated with Thermocalc (in wt%).*

Elements	Ferrite	Laves
Fe	81.74	28.39
Cr	13.11	8.97
C	0.063	0.00
W	0.66	62.51
Co	4.42	0.12

Tab.4 *Equilibrium phases and corresponding composition for alloy A2 at 650°C calculated with Thermocalc (in wt%).*

Elements	Ferrite	M23C6	Laves
Fe	85.37	15.5	29.10
Cr	11.17	61.00	8.31
C	0.00	4.86	0.00
W	0.78	18.5	62.51
Co	2.67	0.058	0.065

For alloy A1, the initial radius of the Laves phase particle, R_1, is 98 nm (see Tab.2, initial diameter, time 0). The particle growths until a radius R_2 of 151 nm (see Tab.2, time 3650 h). The relationship between the volume fraction of the carbide and the radius of the matrix is given by the following equation:

$$V_f^{carb} = \frac{V_2}{V_3} = \frac{R_2^3}{R_3^3} \tag{4}$$

where V_f^{carb} is the volume fraction of Laves phase, V_2 the volume of the Laves phase, V_3 the volume of the cell; R_2 the final radius of the Laves phase and R_3 the radius of the cell.

For Dictra simulations, the size of the cell was then calculated as:

$$R_3 = \sqrt[3]{\frac{R_2^3}{V_f^{carb}}} \tag{5}$$

No Laves phase is actually present in the initial microstructure of the alloy A2. Nevertheless, previous observations showed the precipitation of Laves phase after 2000h for alloy A2 [4]. So in order to calculate the initial radius of the Laves phase in alloy A2 following equation was used:

$$\Delta G_m = \frac{2\sigma V_m}{r^*} \tag{6}$$

where σ is the interfacial energy in J/m^2, r the particle radius in meters, and V_m the molar volume in m^3 per mole of substitutional atoms.
For the case of the A2 alloy, the calculated initial radius of the particle, R_1, is 4 nm.

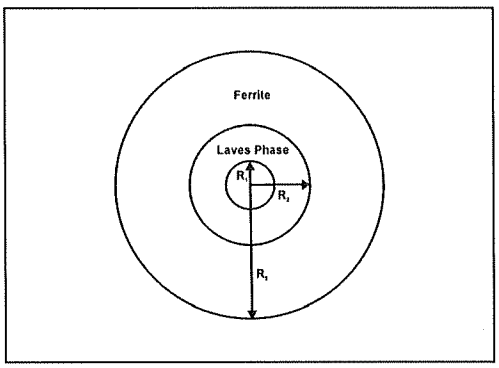

***Fig.2** Schematic description of the coarsening model in DICTRA for the Laves phase. A closed spherical system is chosen. A Laves phase particle with a radius R_1 growth until a radius R_2 in a ferritic matrix.*

4. Results and discussion

4.1. Microstructure characterization (STEM)

The microstructure of alloys A1 and A2 after creep of 1200 h and 2000 h respectively are shown in Fig.3. In Fig.3a, MX nano-precipitates corresponding to Ta(C,N) (white arrows) and Laves phase (dark arrows) are found in the microstructure. As expected for

alloy A1, no $M_{23}C_6$ is observed, due to the higher stability of TaC carbides, which consume the total carbon content of the alloys.
In alloy A2, $M_{23}C_6$ (dark arrows) and Laves phase (white arrows) are observed in Fig.3b. The Laves phase was observed in the initial microstructure of alloy A1 and after creep of 2000 h in alloy A2.

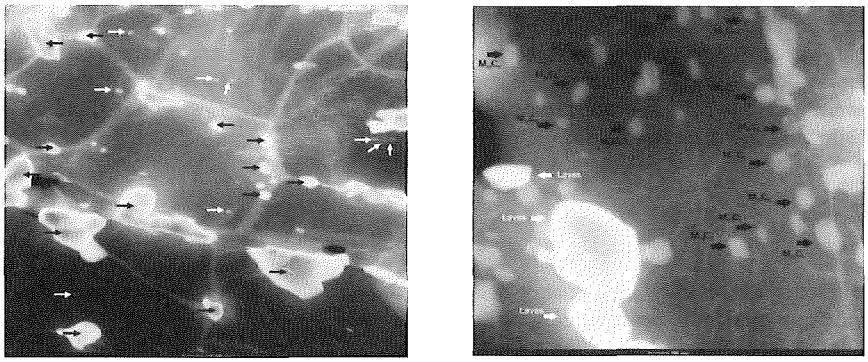

a) *b)*

Fig.3 *a) STEM micrograph of alloy A1 at 1200 h; b) STEM micrograph of alloy A2 at 2000 h.*

A detailed description of the microstructure evolution of these alloys is described in paper 110 of this proceeding.

4.2 Simulation

4.2.1Growth and Coarsening of Laves Phase
The simulation of coarsening and growth for Laves phase in alloy A1 is shown in Fig.4a. This figure shows the calculated average diameter as a function of time in h. The process begins with pure growth until 3000 h and changes gradually into coarsening. The symbols indicate the measured diameters in TEM images. The agreement between simulation and experiments is satisfactory.
For alloy A2 a cell size of 0.54 μm was chosen because it yields a final radius of 307 nm. The process starts with pure growth and changes gradually to coarsening between 3000 h and 4000 h ending with pure coarsening. The agreement between the DICTRA simulation and the experimental results (TEM measurements, Fig.4b) is very good.

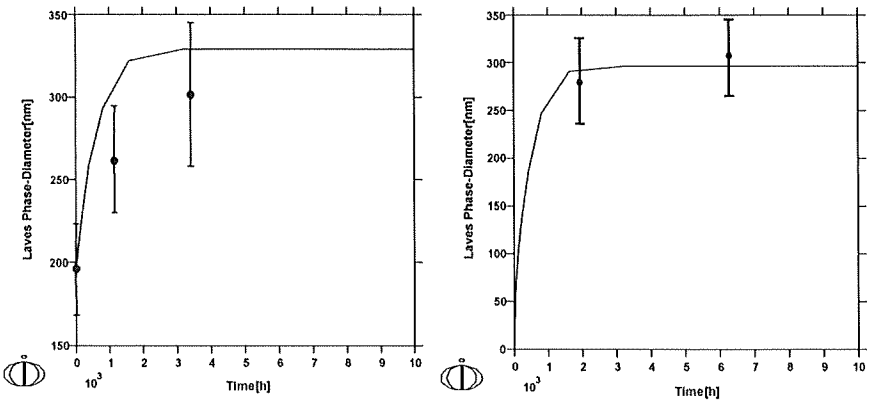

a) *b)*

Fig.4 *Dictra simulation of growth and coarsening of Laves phase and experimental values obtained by quantitative metallography a) alloy A1; b) alloy A2*

Figure 5a and 5b shows the volume fraction of Laves phase as a function of time for alloys A1 and A2, respectively. DICTRA simulations and experimental results show good agreement.

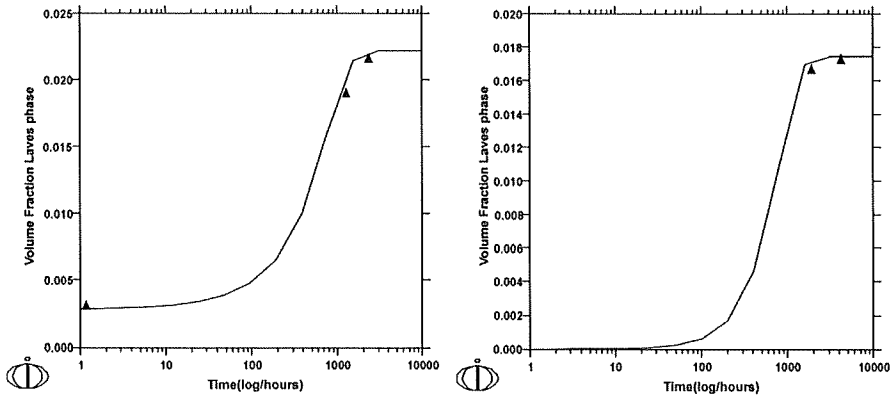

a) *b)*

Fig.5 *Dictra simulation and experimental values (dark triangles) of volume fraction of Laves phase as function of the time at 650°C a) alloy A1; b) alloy A2*

In alloy A2 the growth of $M_{23}C_6$ and Laves phase was simulated for a two step heat treatment (see Fig.6). The simulation was performed with two spherical cell of radius 5

μm. In Fig.6, the calculated fractions of phases are plotted as function of time. The 2h treatment leads to the formation of $M_{23}C_6$, while the amount of Laves phase is negligibly small at this stage. The reduction in temperature of 780°C to 650°C after 2 hours leads to a clear reduction in growth rate. This is due to the smaller mobilities. The driving forces for diffusion from the ferritic matrix to the precipitates are increased by the change of temperature. $M_{23}C_6$ has reached its equilibrium volume fraction after 11 days approximately.

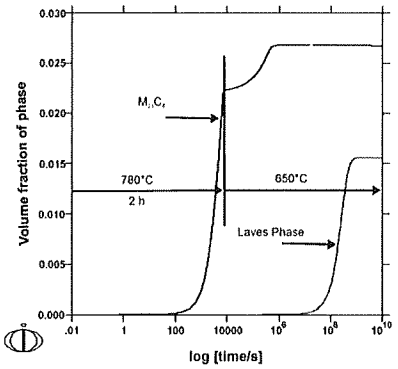

Fig. 6 *Dictra simulation of simultaneous growth of $M_{23}C_6$ and Laves phase in A2 alloy*

4.2.2 Effect of additions of Co, Cu, Si, on the growth kinetics of Laves phase in Fe-Cr-W-C.

Cobalt is a well known austenite forming element. The addition of this element is important in order to suppress the formation of δ-ferrite during high temperature normalizing of martensitic-ferritic steels [5]. The simulations of the addition of Co to alloys A1 and A2 show an increase in the volume fraction of Laves phase for both alloys (see Fig.7a and Fig.7b).

Copper has been added to alloys A1 and A2 with the purpose of avoiding the formation of δ-ferrite during austenisation and to act as possible nucleation sites for Laves precipitation [4]. Cu precipitates were found in alloy A2 with an average size of about 20 nm. No Cu precipitates were found in alloy A1. Hättestrand et al. [12] showed that Cu particles may work as suitable nucleation sites for Laves phase particles, and that the precipitation of Laves phase is much faster in alloys with Cu addition. Dictra simulations show that the addition of Cu (1wt%) increase the volume fraction of the Laves phase (Fig.7a and Fig.7b.) compared to the base alloy without Cu.

DICTRA simulations of the influence of Si in the Laves phase formation show no influence of this element in the precipitation of Laves phase (see Fig. 7a and 7b). It was demonstrated that the elimination of Si in steels reduce the precipitation of Laves phase in ferrite grains [13], so that Si may play a key role in the formation and growth of Laves phases. The contradictory result of the simulations (no effect) may be due to a lack in the definition of the solubility of Si in the Laves phase in the thermodynamic database used.

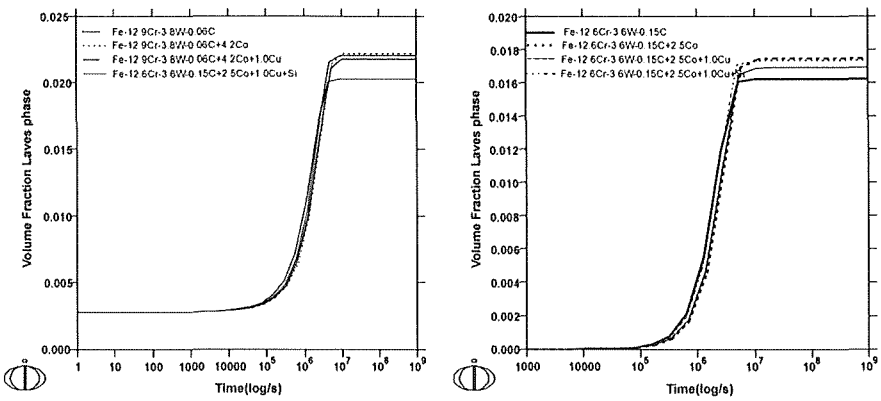

a) *b)*

***Fig. 7** Dictra simulation of the effect of Co, Cu, Si on Laves phase formation a) alloy A1 b) alloy A2.*

5. Conclusions

- Coarsening and growth of Laves phase was simulated in two 12%Cr alloys. DICTRA simulations indicate very low coarsening rates for Laves phase precipitates. The results were compared with experimental results and the agreement is satisfactory.
- The growth of $M_{23}C_6$ and Laves phase was simulated for a two step heat treatment. The 2h treatment leads to the formation of $M_{23}C_6$, while the amount of Laves phase is negligibly small at this stage. After 11 days $M_{23}C_6$ has reached its equilibrium volume fraction. On the other hand, the Laves phase reaches equilibrium after several years.
- The effect of additions of Co, Cu, Si, on the growth kinetics of Laves phase was simulated on a Fe-12.9Cr-3.8W-0.06C and Fe-12.6Cr-3.6W-0.15C. The simulations show that Co and Cu promote the formation of Laves phase. The modeling with the addition of Si is less reliable due to limitations of the database used.

6. Acknowledgements

The authors thank Prof. G. Inden (Max-Planck-Institut für Eisenforschug GmbH) for valuable discussions on Dictra simulations.

7. References

[1] *Chapter 2: The development of creep-resistant steels* in: Creep Resistant Steels, F. Abe, T.-U. Kern, R. Viswanathan (Eds.), Woodhead Publishing in Materials, Cambridge (2008) England.
[2] L. Korcakova, J. Hald, M.A.J. Somers, *Quantification of Laves phase particle size in 9CrW steel*, Mat. Charact. 47 (2001) 111-117.
[3] R. Agamennone, W. Blum, C. Gupta, J. K. Chakravartty, *Evolution of microstructure and deformation resistance in creep of tempered martensitic 9-12%Cr-2%W-5%Co steels*, Acta Mat. 54 (2006) 3003-3014.
[4] D. Rojas, O. Prat, J. Garcia, G. Sauthoff, A.R. Kaysser-Pyzalla, *Design and characterization of microstructure evolution during creep of 12%Cr heat resistant steels*, Mat Sci Eng A (2010) in press.
[5] L. Helis, Y. Toda, T. Hara, H. Miyazaki, F. Abe, *Effect of cobalt on microstructure deformation behavior of tempered martensitic 9% Cr Steel for USC Power plants*, Proc. 34th MPA-Seminar (2008) Stuttgart.
[6] A. Aghajani, C. Somsen, G. Eggeler, *On the effect of long- term creep on the microstructure of a 12% chromium tempered martensite ferritic steel*, Acta Mat. 57 17 (2009) 5093-5106.
[7] G. Dimmler, P. Weinert, E. Kozeschnik, H. Cerjak, *Quantification of the Laves phase in advanced 9-12% Cr steels using a standard SEM*, Mat. Char. 51 (2003) 341-352.
[8] A. Borgenstam, A. Engström, L. Höglund, J. Ågren, *DICTRA a tool for simulation of diffusional transformation in alloys*. J. Phase Equil. (2000) 269-280.
[9] A. Engström, MOB2 mobility database, Thermo-Calc AB, Royal Institute of Technology, Stockholm (1998).
[10] Solution Database SSOL, SGTE (Scientific Group Thermodata Europe).
[11] Thermo-Calc AB, http://www.thermocalc.com/index.html
[12] M. Hättestrand, Hans-Olof Andrén, *Microstructural development during ageing of an 11% chromium steel alloyed with copper*, Mat. Sci. Eng. A318 (2001) 94-101.
[13] Y. Hosoi, N. Wade, T. Urita, M. Tanino and H. Komatsu, *Change in microstructure and toughness of ferritic-martensitic stainless steels during long-term aging*, J. Nucl Mater 1984; 337-342.

9th Liege Conference : Materials for Advanced Power Engineering 2010
edited by J. Lecomte-Beckers, Q. Contrepois, T. Beck and B. Kuhn.

TEM CHARACTERIZATION OF MICROSTRUCTURE EVOLUTION OF 12%Cr HEAT RESISTANT STEELS

D. Rojas [1], J. Garcia [2,*], O. Prat [1], G. Sauthoff [1], A.R. Kaysser-Pyzalla [2,3]

[1] Max-Planck-Institut für Eisenforschung GmbH, Max Planck Str. 1, D-40237 Düsseldorf
[2] Helmholtz-Zentrum Berlin für Materialien und Energie GmbH, Hahn-Meitner-Platz 1 D-14109 Berlin
[3] Ruhr Universität Bochum, Universitätsstr. 150, D-44780 Bochum

Abstract

A detailed characterization of the microstructure evolution of 12%Cr heat resistant steels at different creep times (100 MPa / 650°C / 8000 h) were carried out by scanning transmission electron microscopy (STEM). The results of the microstructure analysis are correlated with the mechanical properties in order to investigate the influence of different precipitates (especially $M_{23}C_6$) on the creep strength of the alloys. Precipitation of Laves phase and Z-phase was observed after several hours creep time. Very few Z-phase of the type Cr(V,Ta)N nucleating from existing (V,Ta)(C,N) was observed. Both alloys show growth and coarsening of Laves phase, meanwhile the MX carbonitrides present a very slow growth and coarsening rate. Alloys containing Laves phase, MX and $M_{23}C_6$ precipitates show best creep properties.

Keywords: Creep resistant steel, Microstructure evolution, TEM, Laves, $M_{23}C_6$

1. Introduction

Ferritic/martensitic 9-12%Cr steels are used as structural materials for power plant components such as main steam pipes or high temperature boilers. The continuous development of creep resistant steels is reflected on the improvement of the efficiency of power plants. In the last decade, the steam parameters were raised from 530 °C / 18 MPa to 600 °C / 30 MPa, meaning an increment of the efficiency from 30-35 % into 42-47 %, with an equivalent reduction of the CO_2 emission of 30% [1]. Due to environmental regulations and energy saving requirements there is still a strong demand for more efficient power plants, and a general goal is to reach creep rupture lives of 100.000 h under a stress of 100MPa at temperatures of 650°C or above.
Increasing the working temperature reduces the long-term creep and mechanical properties, especially due to coarsening of carbonitrides and carbides (i.e. MX, $M_{23}C_6$) and precipitation of undesirable phases (i.e. Z-phase). In a recent work by Sauthoff et al. [2], 12%Cr martensitic/ferritic heat resistant steels aiming at applications at 650°C were designed based on a combination of physical metallurgy principles and thermodynamic modeling. The main objective of this work was to investigate the microstructure evolution and to compare the mechanical properties of two set of ferritic/martensitic 12%Cr alloys.

* Corresponding author: jose.garcia@helmholtz-berlin.de (J. Garcia)

The first group (alloy A1) was designed in order to have a microstructure consisting of MX and Laves phase in the temperature range of interest (650°C), whereas the second group (alloy A2) was designed to have a microstructure with Laves phase, MX and $M_{23}C_6$ precipitates in the investigated range of temperatures.
A detailed characterization of the microstructure of the alloys at the different creep stages was carried out by TEM.
The results of the microstructure analysis are compared with the macro-mechanical properties (creep tests) in order to investigate the influence of the different precipitates on creep strength of 12%Cr heat resistant steels, especially the influence of the $M_{23}C_6$ carbide.

2. Experimental procedure

2.1. Alloy production

Alloys were prepared by vacuum induction melting with masses of about 1 kg (see Tab.1). Samples were hot forged at 1150°C (resulting in 70% final area reduction) with posterior air cooling. Heat treatments were carried out based on the standard heat treatments for 12%Cr heat resistant steels for power plant parts [1]: austenitization at 1070°C for 0.5 h followed by air-cooling (lead to martensite transformation); and annealing for 2 h at 780°C with subsequent air-cooling (lead to recovery of ductility, annihilation of dislocations and precipitation of carbonitride particles, $M_{23}C_6$ or Laves phase).

Tab. 1 *Chemical composition of the alloys investigated (in wt%).*
Alloy A1

Cr	Mn	Ta	W	V	Cu	C	B	N	Si	Co
12.9	0.6	0.85	3.8	-	1	0.06	0.001	0.05	0.5	4.2

Alloy A2

Cr	Mn	Ta	W	V	Cu	C	B	N	Si	Co
12.6	0.7	0.16	3.6	0.24	1	0.15	0.033	0.06	0.5	2.5

2.2. Microstructure investigations

The microstructure evolution after different creep times was analyzed by transmission electron microscopy (TEM TECNAI F20 G^2 operating at 200kV). To prepare the TEM specimens mechanical polishing was followed by twin-jet-polishing (TenuPol-5 of Struers) with a solution of acetic acid and perchloric acid as electrolyte (95 vol% acetic acid, 5 vol% perchloric acid) at 15°C and 43 V. Observations in TEM were carried out in the bright field (BF) and scanning (STEM) mode. Precipitates were identified by a combination of electron diffraction and electron dispersive spectroscopy (EDS) analysis. Equivalent circle diameters of the particles were calculated with an image editor in order to carry out a quantitative analysis of precipitates. In the case that the carbides present a non spherical form, two perpendicular axes were measured (a and

b) and an average diameter (a+b)/2 was calculated. It was assumed that the selected area is representative for the whole material at the creep stage investigated.

2.3. Creep tests

Tensile creep tests in air at constant temperature of 650°C (± 5 K) with constant load between 80 and 250 MPa were used to determine the creep rupture times. Standard cylindrical samples according to DIN50125 B 4x20 were used.

3. Results

3.1. Microstructure evolution during creep

SEM investigations of the final microstructure after heat treatment of the produced alloys show a ferritic/martensitic matrix and precipitates. TEM and STEM investigations are carried out to quantify the microstructure of the alloys in the initial stage and after different creep times.

3.1.1. Alloy A1

Initial microstructure: a STEM micrograph of alloy A1 in the initial condition after annealing at 780°C for 2 h is shown in Fig.1A. Two precipitates are identified by EDS analysis: Laves phase and MX carbonitrides. A detailed TEM investigation of the MX particles actually shows two types of MX, relative large TaC precipitates with an average size of 137 ± 14.6 nm, which are not dissolved in the austenisation treatment and nitrogen-rich Ta(C,N) particles with an average size of 30 ± 1.6 nm. The Laves phase has an average size of 196 ± 34.6 nm in the initial stage (see Table 2).

Crept microstructure: After 1200 h and 3650 h creep at 650°C (Fig.1C), alloy A1 presents the same precipitates as in the initial stage. The evolution of the precipitates in the microstructure can be observed. Especially the distribution of the Laves phase is not homogeneous, showing small Laves phase particles of 70 ± 34.6 nm throughout the microstructure. The relatively small size of the Laves phase compared to the size of the Laves phase observed in 12%Cr-Mo steels under similar creep conditions [3] may be related to the high W-content in this alloy (3.8%), which produces a large number of finely dispersed nuclei for Laves phase formation [2]. The average size of the Laves phase is 302 ± 48.5 nm. Occasionally, Laves phase particles with a very large size of up to 787 ± 48.5 nm are observed. Slow coarsening of TaC is observed, with an average final size of 142 ± 8.0 nm (137 ± 14.6 nm in the initial state, see Tab. 2). The size of the Ta(C,N) remains almost constant with an average size of 30 ± 1.5 nm. The TaC and the Laves phase usually precipitate on the grain boundaries, whereas the Ta(C,N) forms inside the grains and sub-grains. Z-phase was not observed, probably due to short creep times. Danielsen and Hald [4] demonstrated that Ta(C,N) acts as nucleation sites for Z-Phase formation at long creep times. So we can conclude that the N-rich MX observed in the initial microstructure will be transformed into Z-Phase after several thousand hours. No BN was observed in any microstructure of alloy A1.

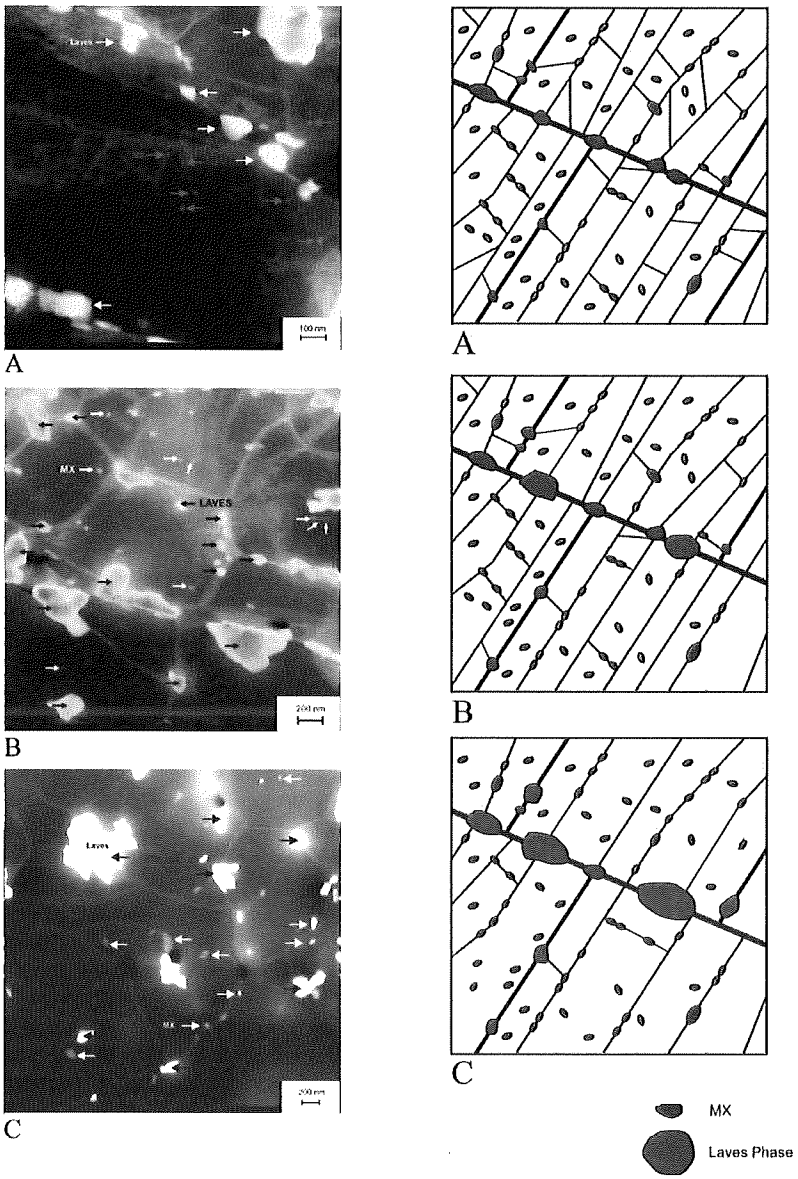

Fig. 1: *TEM images of alloy A1 showing the microstructure evolution after 0 h (A), 1200 h (B), 3650h (C) and corresponding schematic description (adapted from [5]).*

3.2.2. Alloy A2

Initial microstructure: TEM investigations of alloy A2 after heat treatment reveal $M_{23}C_6$, MX precipitates and nano-sized Cu precipitates, as well as few W-Cu inclusions in the initial microstructure (Fig.2A). EDS analysis show that the main elements of the MX precipitates are V, Ta, C and N. These MX carbonitrides have an average size of 20 ± 1.5 nm in the initial stage (Tab. 2 / A2). $M_{23}C_6$ precipitates are of the type $(Cr,Fe,W,V)_{23}C_6$ and form principally at the grain boundaries with an average size of 140 ± 10.1 nm. As expected, no Laves phase was present in the microstructure of alloy A2 after annealing. Laves phase precipitates during creep condition (tensile creep test with constant load at 650°C) on grain and sub-grain boundaries [6] as well as on existing Cu-precipitates [7]. No Z-phase is observed in the initial microstructure, due to the nucleation kinetics of the Z-phase, which precipitates on existing MX carbonitrides during creep after several thousand hours.

Crept microstructure: Fig.2B and Fig.2C show the microstructure of alloy A2 after 6150h creep. $M_{23}C_6$ precipitates of an average grain size of 185 ± 8.5 nm and MX of the type (V,Ta)(C,N) with an average size of 38 ± 2.2 nm are observed. After 2000 h under creep conditions Laves phase is observed. At 6150h the average particle size is 307 ± 41.3 nm (Tab.2 / A2). Both, Laves phase and $M_{23}C_6$ precipitate on the grain boundaries.

After 6150 h the Z-phase was first observed in the microstructure of alloy A2 (Fig.3). EDS analysis reveals that Cr, Ta, V and N are the main elements in this phase. This is in accordance with previous observations of Danielsen and Hald in Ta-rich heat resistant steels, where a Z-phase of the type Cr(V,Ta)N formed [4]. The volume fraction of the Z-phase is very low, and only a very small amount of Z-phase was identified. The MX carbonitride is still present in the microstructure after 6150 h. It can be expected that by reaching the equilibrium conditions almost all MX carbonitrides should have transformed into Z-phase following the mechanism explained by Danielsen in [8]. BN was not observed in any microstructure of alloy A2.

3.2. Mechanical properties

Results of the creep tests are shown in Fig. 4. Creep tests at 650°C show an increment of the creep strength for alloy A2 compared to alloy A1. The increased creep strength of alloy A2 may be related to the observed and calculated formation of numerous dispersed nano-sized MX carbonitrides, which are mainly responsible for the pinning of dislocations and sub-grains during creep. In alloy A1 two types of MX were observed, relatively large TaC (formed in the melt) as well as nano-sized Ta(C,N). The presence of large TaC could be a reason for a reduced pinning of dislocation in alloy A1, but this fact is very difficult to be proved, because a combination of several strengthening mechanisms is often present during creep [9].

The increased creep strength of alloy A2 can be explained by the presence of the $M_{23}C_6$ carbide. $M_{23}C_6$ carbides may improve the creep strengthening due to the relative high volume fraction of this phase, which provides a higher mechanical stability to the alloy. A similar observation was recently reported by Aghajani et al. [3] in 12%Cr tempered martensitic/ferritic steels under long-term creep of 139.971 h. Moreover, the effect of B should also be taken into consideration, especially in the presence of $M_{23}C_6$ carbides as reported by Abe [10]. In our investigations the quantification of this light element was not possible due to limitations of the equipment used.

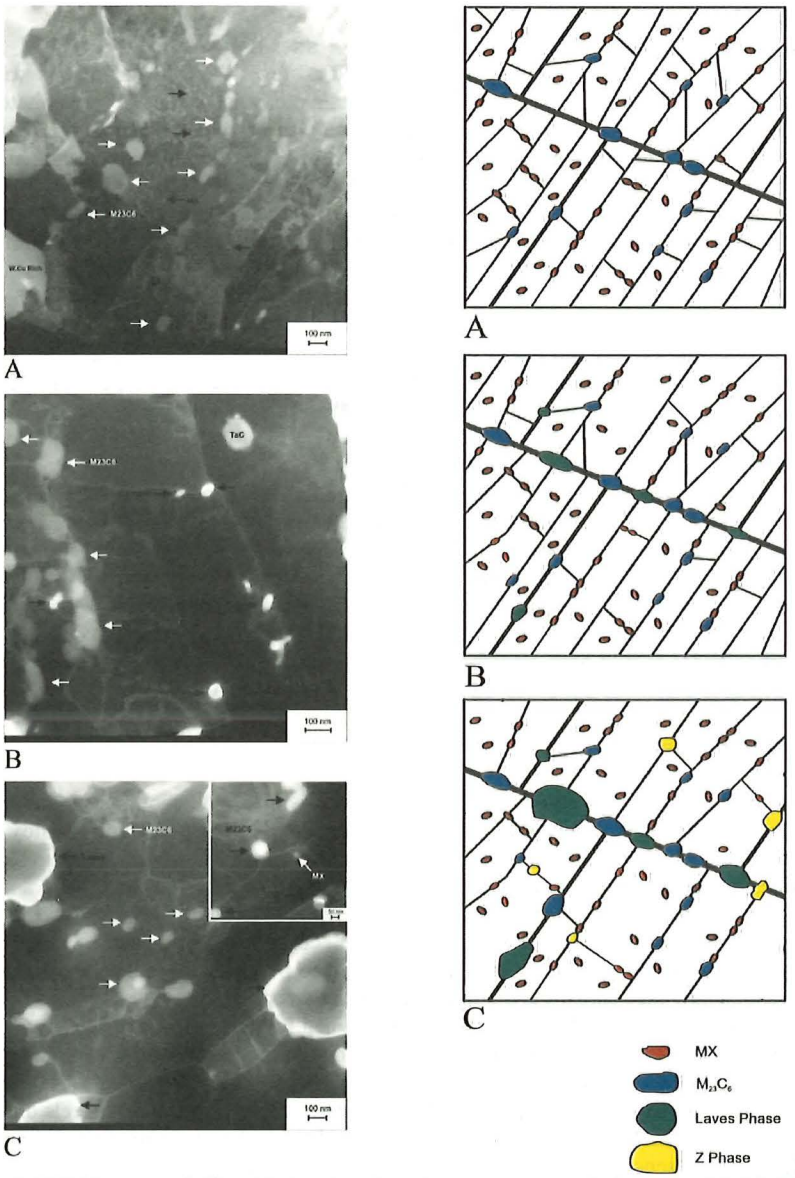

Fig. 2: *TEM images of alloy A2 showing the microstructure evolution after 0 h (A) 2000 h (B) 6150h (C) and corresponding schematic description (adapted from [5]).*

Tab. 2 *Mean average size of precipitates (size in nm) and calculated volume fraction of phases at 650°C at equilibrium conditions with ThermoCalc (*) For more details see Ref. [12].*

A1	**0h**	**1200h**	**3650h**	**Vol. Fraction of phase (*)**
Ta(C,N)	30 ± 1.5	31 ± 1.5	32 ± 1.5	0.28
TaC	137 ± 14.6	-	142 ± 8.0	0.75
Laves	196 ± 34.6	268 ± 33.6	302 ± 48.5	2.42
A2	**0h**	**2000h**	**6150h**	**Vol. Fraction of phase (*)**
(V,Ta)(C,N)	20 ± 1.5	36±1.8	38 ± 2.2	-
$M_{23}C_6$	140 ± 10.1	180 ± 8.4	185 ± 8.5	3.03
Laves	-	285 ± 41.6	307 ± 41.3	2.27
Z-Phase	-	-	273 ± 47.2	0.74

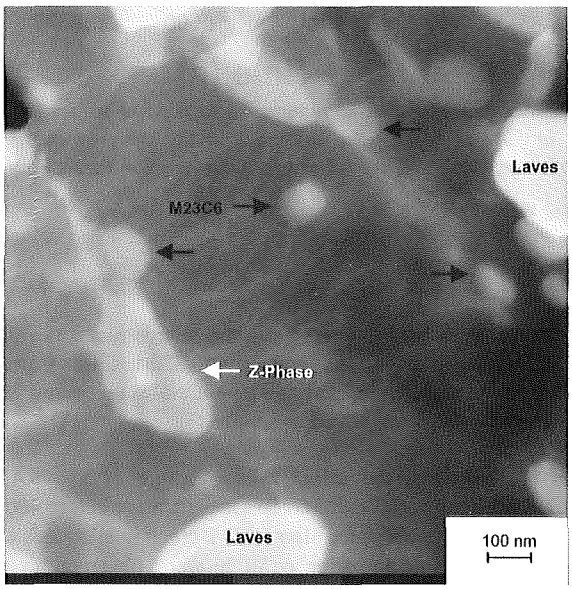

Fig. 3: *TEM image of microstructure of alloy A2 after 6150 h creep showing Laves phase, $M_{23}C_6$ (dark arrows) and Z-Phase (white arrow).*

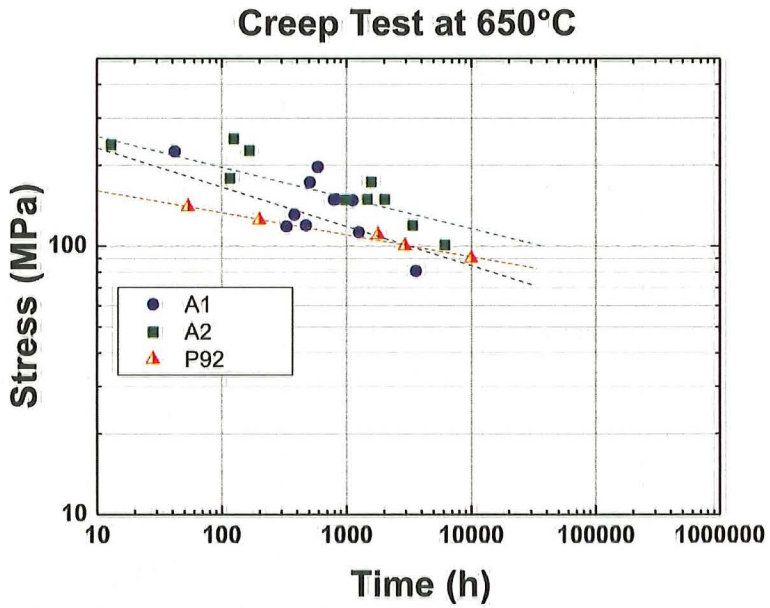

Fig. 4: *Results of the tensile creep tests showing time to rupture values as a function of applied stress for alloys A1 and A2 at 650°C. An increment of the creep strength for alloy A2 can be observed. Results of creep tests of a P92 steel under similar conditions [11] are shown as reference.*

4. Conclusions

The main objective of this work was to investigate the microstructure evolution of two 12%Cr heat resistant steels during creep at various loads at 650°C by TEM. Correlations between the microstructure evolution and the creep properties in the initial stages (until 8000 h) of creep were investigated. The conclusions are summarized as follows:

- Laves phases are found in the initial microstructure of alloy A1. No Z-phase was observed, probably due to insufficient creep times (rupture before 4000 h).
- The Laves phase already precipitates after 2000 h creep in alloy A2.
- Very few Z-phase precipitates after 6150 h were observed in alloy A2, probably nucleating at existing (V,Ta)(C,N) to form a Cr(V,Ta)N precipitate.
- Both alloys show growth and coarsening of Laves Phase, whereas the MX carbonitrides present very slow growth and coarsening rates.
- Alloy A2 presents better creep properties than alloy A1. This difference in performance may be attributed to the high volume fraction of the $M_{23}C_6$ in alloy A2 in combination with the presence of boron, providing further strengthening to the alloy.

Thermodynamic modelling of the microstructure evolution in the alloys investigated was presented by the authors in [12]. Investigations of the microstructure at different creep conditions show good agreement with the thermodynamic modelling, except for the Z-phase and Laves phase which precipitate after several thousand hours creep.

Acknowledgements

The authors thank Mr. G. Bialkowski (Max-Planck-Institut für Eisenforschung) for carrying out creep tests.

References

[1] J. Hald, *Microstructure and long-term creep properties of 9-12% Cr steels*, Int. J. Pressure Vessel Pip. 85 (2008) 30-37.
[2] V. Knezevic, J. Balun, G. Sauthoff, G. Inden, A. Schneider, *Design of martensitic/ferritic heat-resistant steel for application at 650°C with supporting thermodynamic modeling*, Mat. Sci. Eng. A 477 (2008) 334-343.
[3] A. Aghajani, C. Somsen, G. Eggeler, *On the effect of long- term creep on the microstructure of a 12% chromium tempered martensite ferritic steel*, Acta Mat. 57 17 (2009) 5093-5106.
[4] H. K. Danielsen, J. Hald, Tantalum-containing Z-phase in 12%Cr martensitic steels, Scripta Mat. 60 (2009) 811-813.
[5] H. Cerjak, I. Holzer, P. Mayr, C. Pein, B. Sonderegger, E. Kozeschnik, *The relation between microstructure and creep properties of martensitic 9-12%Cr steels,* New Developments on Metallurgy and Applications of High Strength Steels, Buenos Aires, Argentina, 26th - 28th May (2008).
[6] J. Hald, *Precipitate Stability in Creep Resistant Ferritic Steels-Experimental Investigation and Modeling*, ISIJ International Vol. 43 (2003) 3, 420-427.
[7] B. S. Ku, J. Yu, *Effects of Cu addition on the creep rupture properties of a 12% Cr steel*, Scripta Mat. 45 (2001) 205-211.
[8] H.K. Danielsen, J. Hald, *On the nucleation and dissolution process of Z-phase Cr(V,Nb)N in martensitic 12% Cr steels*, Mat. Sci. Eng. A 505 (2009) 169-177.
[9] M. Meier and W. Blum, *Modelling high temperature creep if academic and industrial materials using the composite model*, Mater Sci Eng (1993) A164, 290–294.
[10] F. Abe, *Analysis of creep rates of tempered martensitic 9%Cr steels based on microstructure evolution*, Mat. Sci. Eng. A510-511 (2009) 64-69.
[11] F. Abe, M. Taneike, K. Sawada, *Alloy design of creep 9Cr steel using a dispersion of nano-sized carbonitrides*, Int. J. Pressure Vessel Pip. 84 (2007) 3-12.
[12] D. Rojas, O. Prat, J. Garcia, G. Sauthoff, A.R. Kaysser-Pyzalla, *Design and Characterization of microstructure evolution during creep of 12%Cr heat resistant steels*, Mat Sci Eng A (2010) doi:10.1016/j.msea.2010.02.056.

9th Liege Conference : Materials for Advanced Power Engineering 2010
edited by J. Lecomte-Beckers, Q. Contrepois, T. Beck and B. Kuhn.

LONG-TERM CREEP RUPTURE STRENGTH OF WELDMENT OF Fe-Ni BASED ALLOY AS CANDIDATE TUBE AND PIPE FOR ADVANCED USC BOILERS

Gang Bao[1], Takashi Sato[1], Yoshihide Marumoto[2]

[1] Kure Research Laboratory, Babcock-Hitachi K.K. 5-3 Takaramachi, Kure, Hiroshima, Japan
[2] Kure Division, Babcock-Hitachi K.K. 6-9 Takaramachi, Kure, Hiroshima, Japan

Abstract

A lot of works have been going to develop 700C USC power plant in Europe and Japan. High strength Ni based alloys such as Alloy617, Alloy740 and Alloy263 were the candidates for boiler tube and pipe in Europe, and Fe-Ni based alloy HR6W (45Ni-24Fe-23Cr-7W-Ti) is also a candidate for tube and pipe in Japan. One of the Key issues to achieve 700C boilers is the welding process of these alloys. Authors investigated the weldability and the long-term creep rupture strength of HR6W tube. The weldments were investigated metallurgically to find proper welding procedure and creep rupture tests are ongoing exceed 38,000 hours. The long-term creep rupture strengths of the HST weld joints are similar to those of parent metals and integrity of the weldments was confirmed based on with other mechanical testing results.

Keywords: Fe-Ni based alloy, creep rupture strength, advanced USC, weld

1. Introduction

Recently the environmental restrictions on CO_2 emission require the application of advanced power plants with higher efficiency than the existing plants. These restrictions have prompted to adopt the fossil fired power plants with higher steam temperature and pressure conditions. The research and development on advanced USC (Ultra Super Critical) power plants with the steam conditions of 700°C or higher are ongoing in Europe, USA and Japan [1-4]. In Europe, the demonstration plant is also being planned in 2010s [3]. To achieve such advanced steam conditions, the application of Ni based or Fe-Ni based alloys becomes essential, the most critical issues to be settled is the development of materials for boiler tube and thick-walled pipe as well as the establishment of the responding fabrication procedures.

Fe-Ni based alloy HR6W (45Ni-23Cr-7W-Ti-Nb) has been developed as a tube and pipe material used for the USC plant with steam temperature higher than 650°C [5]. Different from the γ' phase strengthened Ni based alloy, it is strengthened by the Laves phase precipitation. Besides of the good corrosion resistance, HR6W also shows lower thermal expansion coefficient [5] in the temperature range from 600 to 800°C comparing with the conventional austenitic steel (Figure 1). Recently it was reported that HR6W also showed lower relaxation cracking susceptibility than Ni based Alloy617 [6]. Although the creep rupture strength of HR6W is lower than that of Ni based Alloy617 [5], it is now under investigation in Japan as one of the tube and pipe candidate materials for advanced USC boilers with the consideration of cost and workability [4].

In present work, to investigate the possibility of boiler application of HR6W welding trial on tube was conducted. Its weldability and long-term creep rupture strength of weld joint were experimentally examined.

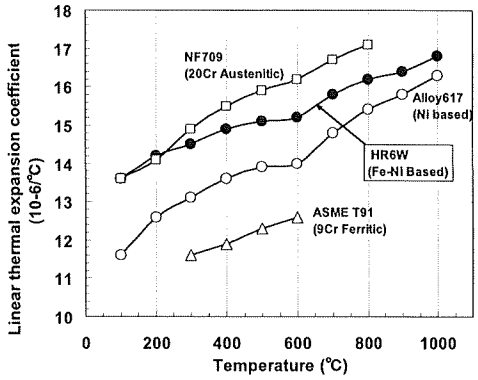

Figure 1 Comparison of thermal expansion

2. Experimental procedure

The material used for weld test and creep test is HR6W tube with the outside diameter of 38.0mm and the thickness of 6.3mm. The other tube with the outside diameter of 50.8mm and the thickness of 8.8mm was used for the creep rupture strength evaluation of the parent metal. The final heat treatment for both tubes mentioned above is the solution treatment.

Preliminary studies [1,7-9] have indicated that Shield Metal Arc Welding (SMAW) procedure, was probably not feasible for Ni based welding material due to the problems such as slag control, oxidation loss of the alloy elements (Al, Ti) for strengthening, hot cracking sensivity, ductility reduction of weld metal, and so on. Thus, Hot wire Switching TIG (HST) welding procedure [10] originally developed by Babcock-Hitachi K.K was adopted in present study.

Table 1 shows the chemical compositions of the tested materials and filler wire. Since the similar welding material for HR6W was still under development, the matching filler wire of Alloy617 was used for the test to assure enough weld metal strength. The interpass temperature was controlled to reduce the high temperature cracking susceptibility. The post weld heat treatment was not performed. After welding, the weldability and high temperature strength properties were evaluated.

Table 1 Chemical compositions of tested HR6W tubes and weld consumable

(Wt%)

	C	Si	Mn	P	S	Ni	Cr	W	Ti	Nb	Fe	Co	Al	Mo	Cu
HR6W tube (OD38.0, WT6.3)	0.08	0.22	1.04	0.009	<0.001	45.05	23.65	7.00	0.09	0.25	Bal.	-	-	-	-
HR6W tube (OD50.8, WT8.8)	0.08	0.11	1.12	0.01	0.002	44.92	23.55	7.18	0.01	0.18	Bal.	-	-	-	-
Filler wire (Wel AutoTIG 617, φ1.0)	0.08	0.10	<0.01	0.001	0.001	Bal.	21.70	-	0.40	-	0.27	12.50	1.10	9.50	0.01

3. Results and Discussion

3.1. Weldability and Integrity of Weldment

All butt welds were done in the flat position while the workpiece was turned and the torch was fixed. HST welding procedure was conducted successfully. The non-destructive tests following the welding process were done using both the radiographic inspection and the liquid penetrant examination, which showed sound results without defects like cracks, porosity or lack of fusion.

Figure 2 shows the macrostructure and the hardness profiles on the cross section of the weld joint. Hardness measurement was carried out along the mid-wall of the butt weld joint. The weld joint showed a gradual slight increase in hardness from the parent metal towards the HAZ (Heat Affected Zone) near the weld metal. There was no extremely hardening or softening zone in the weld joint. The higher hardness in the HAZ was assumed to be the result of precipitation process induced by the heat input of the welding thermal cycle.

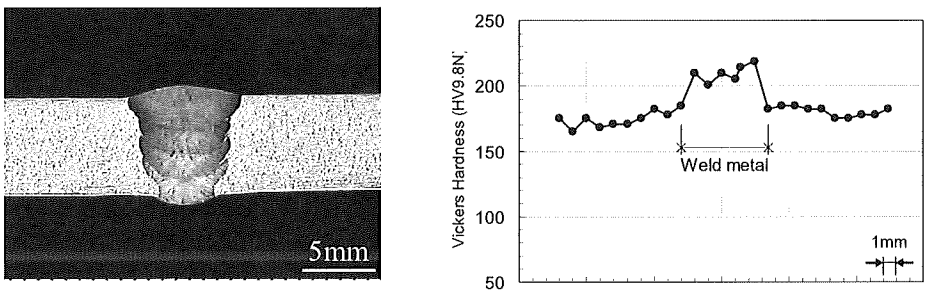

(a) Macrostructure *(b) Hardness profiles*

Figure 2 Macrostructure and Hardness profiles of cross section of HR6W weldment

As shown in Figure 3, the microstructure observation of the weld metal demonstrates a typical solidification microstructure of Ni-based alloy. There is also no defect such as porosity or micro-crack detected in both of the weld metal and heat-affected zone by the optical microscope inspection. There is no extremely coarsening microstructure observed in the HAZ near the fusion boundary. As shown in Figure 4, the results of side and root bend tests also demonstrated defect-free and good ductility of the weld joint.

According to the results of non-destructive tests, microstructure observation, and bend test, the HST welding procedure was confirmed to be suitable for HR6W tube welding and the metallurgical integrity of the weld joint was proved.

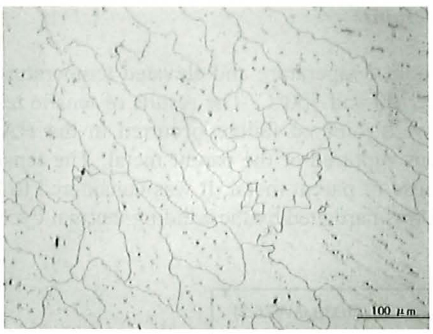

(a) Weld metal

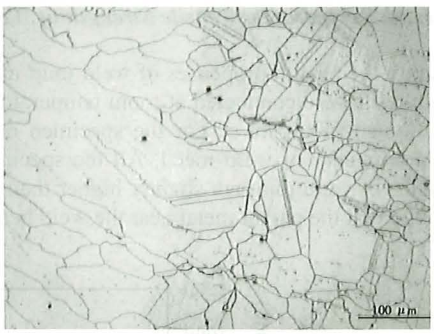

(b) Fusion boundary

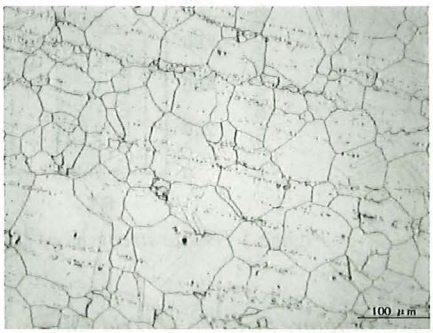

(c) Parent metal

Figure 3 Microstructures of HR6W weldment

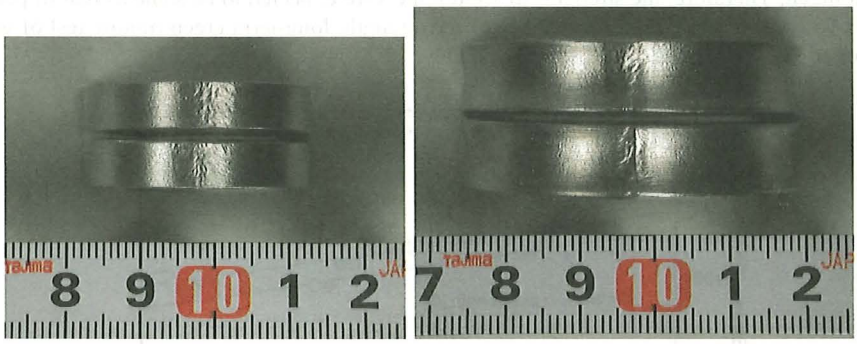

(a) Side bend *(b) Root bend*

Figure 4 HR6W weldment after bend test

3.2. High Temperature Tensile Strength of Weld Joint

To study the tensile properties of weld joint at room temperature and elevated temperatures, tensile tests were conducted at room temperature, 700 and 750°C. The results of tensile tests were shown in Figure 5. For the specimen of weld joint no failure occurred in the HAZ, fusion boundary or weld metal. All the specimens ruptured at the parent metal. The tensile strengths of weld joint are slightly higher than those of parent metal. It was considered to be owing to that the parent metal near the weld bead was hardened by the welding thermal cycle.

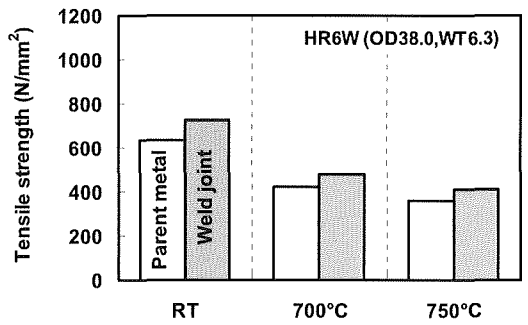

Figure 5 Tensile strengths of HR6W parent metal and weld joint

3.3. Creep Rupture Strength of Weld Joint

Creep rupture test of the weld joint was conducted at 700 and 750°C. Figure 6 shows a plot of the creep rupture test results. The solid line is the average strength of parent metal [5] for reference. Similar to the tensile test, all the creep specimens of weld joint also ruptured in the parent metal. Therefore, the strengths of weld joint were expected to be same as that of parent metal. To confirm the long-term stability of the strength, long-term creep rupture test of weld joint over 38,000 hours at 700°C is still ongoing.

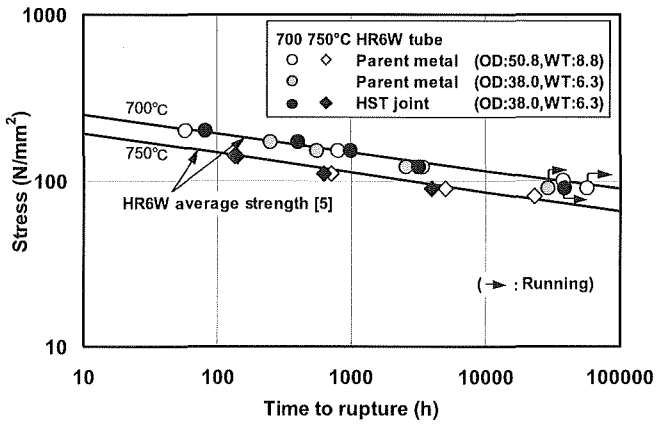

Figure 6 Creep rupture strength of HR6W tube

4. Conclusions

The weldability and the long-term creep rupture strength of Fe-Ni-based alloy HR6W were experimentally investigated.

The HST welding trial of HR6W tube was conducted successfully. Defect-free weld joint was obtained. The metallurgical and mechanical integrity of the weld joint was proved by the non-destructive testing, microstructure observation and long-term creep rupture test. The HST weld joint showed comparable strength with the parent metal.

Based on results achieved above, it is considered that Fe-Ni based alloy HR6W has a promising potential as candidate material for boiler tube and pipe of the advanced USC power plant.

References

[1] R.Viswanathan et al.: U.S. Program on Materials Technology for Ultrasupercritical Coal-Fired Steam Power Plants, *Proceedings of CREEP8*, Creep2007-26826, San Antonio, (2007).

[2] R. Blum: USC Power Plant-State of the Art, *8th International NIMS-MPA-IfW-Workshop on Advances in High Temperature Materials for High Efficiency Power Plants*, pp.5-45, Tsukuba, (2010).

[3] H. Tschaffon: On the Way to the Coal Fired Power Plant with 50% Efficiency, *34th MPA-Seminar*, pp. 2.1- 2.30, Stuttgart, (2008).

[4] M. Fukuda: A-USC Development Project in Japan, *8th International NIMS-MPA-IfW-Workshop on Advances in High Temperature Materials for High Efficiency Power Plants*, pp.46-78, Tsukuba, (2010).

[5] H. Semba et al.: Creep Strength and Microstructure in 23Cr-45Ni-7W Alloy (HR6W) and Ni-base Superalloys for Advanced USC Boilers, *34th MPA-Seminar*, pp. 14.1- 14.18, Stuttgart, (2008).

[6] H. Okada et al.: Strengthening Mechanism and Relaxation Cracking Resistance of HR6W and Ni-base Alloys, *8th International NIMS-MPA-IfW-Workshop on Advances in High Temperature Materials for High Efficiency Power Plants*, pp.143-166, Tsukuba, (2010).

[7] A. Klenk et al.: Qualification of Ni-based Material for Tubes and Piping of 700°C Power Plant, *Proceedings of the 8th Liege Conference*, pp.1597-1608, Liege, (2006).

[8] Q. R. Chen et al.: Materials Qualification for 700°C Power Plants, *Fifth International Conference on Advances in Materials Technology for Fossil Power Plants*, 3A-07, Marco Island, (2007).

[9] G. Bao et al.: Narrow Gap HST Welding Process and Its Application to Candidate Pipe Material for 700°C USC Boiler Component, *34th MPA-Seminar*, pp. 45.1- 45.11, Stuttgart, (2008).

[10] K. Mitsuhata et al.: Application of Narrow Gap Oscillating GTA Welding Process with Hot Wire for Fixed Heavy Wall Pipes, *Japan Welding Society, Welding Guide Book IV*, pp. II -213, (2007).

9th Liege Conference : Materials for Advanced Power Engineering 2010
edited by J. Lecomte-Beckers, Q. Contrepois, T. Beck and B. Kuhn.

INFLUENCE OF WELD STRUCTURE ON CROSS-WELD CREEP BEHAVIOR IN P23 STEEL

D. J. Allen and C. C. Degnan (E.ON Engineering),
S. J. Brett (RWE npower), and L.W. Buchanan (Doosan Babcock)

Abstract

A thick section pipe weld in low alloy steel P23 has been characterised by cross-weld creep rupture testing at a range of stresses, together with all-weld-metal and parent material testing, under the auspices of the UK High Temperature Power Plant Forum. The results generally show that the weld metal can be weak when tested in the transverse (cross-weld) orientation, and can fail with limited overall ductility by cracking in the zone of refined weld metal beneath the fusion boundary of the superposed weld bead. However, one specimen showed a much superior performance, which could be understood in terms of its locally more creep resistant weld macrostructure. The implications for P23 performance and weld manufacture are discussed.

Keywords: creep, weld, P23, cracking, microstructure

1. Introduction

The advanced low alloy steels T/P23 and T/P24 offer improved creep properties and weldability compared with the older steel T/P22. To date, these steels have primarily gained acceptance as tubing materials, where their lower carbon contents and hence moderate as-welded hardness values are claimed to make them suitable for welding without post-weld heat treatment (PWHT).

Pipe sizes must in any case normally be PWHTd in component manufacture, to minimise residual stresses and the risks of in-service reheat cracking. Nevertheless, there could still be substantial economic advantages in the wider use of P23 and P24 for steam pipework. Their increased creep strength could lead to cost savings due to wall thickness reductions, and/or reduced long term cracking risks, when compared with P22 and CrMoV steels. Whilst their high temperature strength levels do not reach those of the higher alloy steels P91 and P92, and their oxidation performance is inferior, they do benefit from a much lower content of expensive alloying elements. P23 and P24 may also have advantages if, as seems likely, these steels are less prone to the two major problems which currently plague the industry with the present leading pipe steels P91 and P92 – their very high sensitivity to errors in steelmaking and welding heat treatment, and their high weld creep strength reduction factors associated with premature cracking in the "Type IV" region of the weld heat affected zone [1].

The prospects for promoting P23 and P24 as pipe steels have recently been explored in a European Research Fund for Coal and Steel (ERFSC) project "ALoAS" on **A**dvanced **Lo**w **A**lloy **S**teels. This included high temperature testing, microstructural assessment, component testing and service performance modelling [2]. One ongoing concern is that the creep rupture data at realistic plant stresses appear to be poor. Whilst this may be to some extent an artefact due to the oxidation and decarburisation of creep specimens, reliable design data are lacking [3]. Another concern is the potential risk of reheat cracking at welds [4, 5], associated with the poor creep ductility of the HAZ and weld metal. ALoAS carried out a substantial programme of welding consumable development, and identified compositional features which

may be adapted to improve weld metal creep ductility without undue loss of creep strength [6]. As yet, however, it has not been possible to match the creep ductility of parent P23.

The work described here pre-dated ALoAS, and began as part of a collaboration between the predecessor companies of Doosan Babcock and RWE npower, funded by the UK DTI Cleaner Coal Programme. The manual metal-arc (MMA) welding consumable employed, Metrode Chromet 23L, was a low-carbon variant selected for its particularly high suitability for "cold" welding without PWHT due to its low as-welded hardness. Hence, the chosen weld metal was not optimised for creep performance or ductility, though initial all-weld-metal creep test results indicated reasonable performance. In the ALoAS programme, Chromet 23L showed mediocre but not exceptionally low creep ductility when compared with alternative weld metals [6].

The specific results presented here came from a continuation test programme based on welded material from the DTI project. To obtain data relevant to pipe manufacture, the welds were PWHTd and supplied to the UK High Temperature Power Plant Forum (HTPPF), an industrial consortium which undertakes collaborative long term creep testing and thereby coordinates UK input into ECCC (European Creep Collaborative Committee) test programmes. The expectation was that cross-weld creep testing should provide data on failure by weld HAZ "Type IV" cracking. As will be seen, the tests instead primarily provided some very useful information on the behaviour of the weld metal.

2. Experimental

A fully circumferential pipe butt weld was made by Doosan Babcock in a thick HCM2S (P23) pipe supplied by Sumitomo, matching typical UK main steam pipework dimensions, Table 1.

Table 1. Steel and weld metal compositions (wt. %)

	C	Si	Mn	P	S	Cr	Mo	Ni
Parent	0.06	0.22	0.29	0.009	0.002	2.51	0.29	0.05
Weld	0.062	0.3	0.71	0.01	0.007	2.26	0.18	0.03
	Al	**B**	**O**	**N**	**Nb**	**Ti**	**V**	**W**
Parent	0.021	0.0045	0.0026	0.0063	0.046	0.014	0.22	1.65
Weld	<0.005	<0.0005	0.049	0.011	0.005	0.005	0.21	0.65

The tungsten inert-gas (TIG) root / MMA fill-up weld was deposited in a single-sided, double angle V welding preparation in pipe of original thickness 60mm, machined down to 40mm for welding. The preparation sidewall angles were 45° in the vicinity of the weld root, reducing to 15° for the majority of the weld preparation. Following root welding, a two-layer refinement procedure was employed to "butter" the sidewall with a layer of 2.5mm electrodes, followed by a second layer of 3.25mm electrodes. A 50% bead overlap was employed, with a heat input ratio between layers of approximately 2. The aim of two layer buttering was to refine and temper the HAZ and thereby avoid high hardness in a weld which was originally manufactured without PWHT. For the current programme, however, a block section was conventionally PWHTd at 715°C for 3 hours prior to creep testing.

The parent pipe material was creep rupture tested at 575°C, showing substantially below mean properties, perhaps linked to the high pipe thickness. Short-term rupture tests were also carried out by Doosan Babcock on all-weld-metal specimens oriented longitudinally with respect to the welding direction. These data indicated that the weld metal was substantially stronger than the parent material, Figure 1, thus encouraging an expectation that cross-weld tests would fail in the parent or HAZ.

Cross-weld creep testing was carried out at 575°C, initially using five specimens (here denoted 1A to 1E, the letter labels showing the order of decreasing applied stress) taken from the outer half of the weld, with one fusion boundary placed at the centre of the gauge length. To obtain additional data, three further cross-weld specimens (similarly labelled 2C, 2E and 2F to denote the decreasing stress sequence) were later taken from the inner half of the weld. In these cases, a long specimen design was used to include the whole of the (relatively narrow) weld zone, plus a length of parent material equating to three times the specimen diameter on each side. All specimens had a 10mm gauge diameter, large enough to include multiple weld beads and hence designed to avoid undue variations in macrostructure between the different test specimens.

3. Results

3.1. Creep Testing

The creep test results are shown in Figure 1.

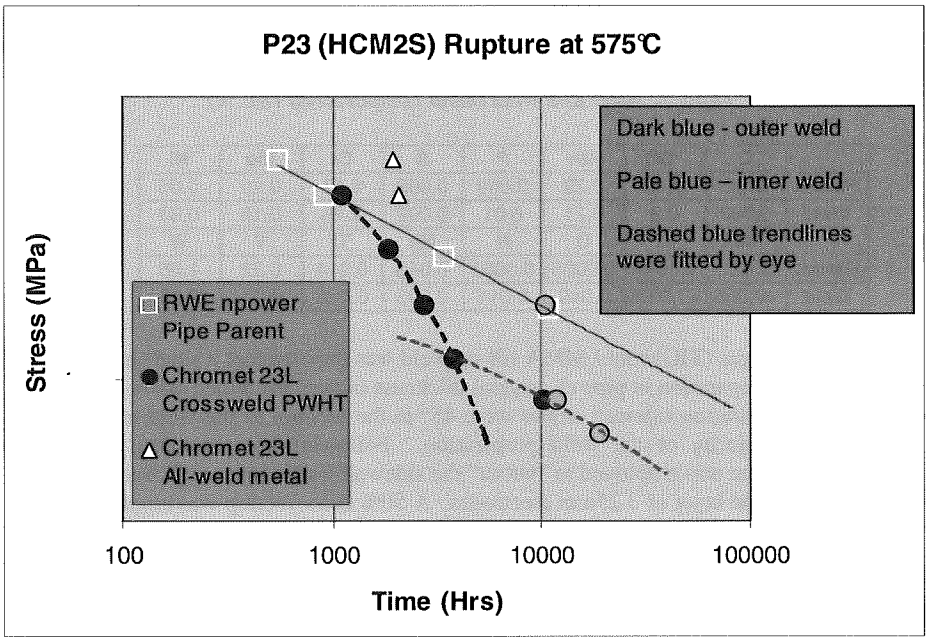

Figure 1. Creep test results.

The first series of tests (outer weld) are shown in dark blue. All five tests failed wholly within the weld metal. Their creep lives fell below the parent data line, the shortfall in life increasing sharply as the test stress was reduced from about 150MPa toward 100MPa.

The final 1E data point, at below 100MPa and close to a 10,000 hour life, showed somewhat better performance. This last result was suggestive of sigmoidal behaviour, with the weld strength reduction factor in the lower stress tests apparently "bottoming out" at a relatively constant value, of the order of 25% with respect to the (weak) parent P23 material used in this work. However, it was obviously unreasonable to draw firm conclusions on the basis of this single data point.

It was therefore decided to carry out three further tests, using the additional "inner half" material. Two of these tests, at stresses corresponding to the C and E values of the previous series, were included partly as a check on whether the outer and inner half regions of the weld would give comparable results, while the final and lowest stress test 2F extended the series out toward 20,000 hours. These results are shown in pale blue, Figure 1.

The 2E and 2F tests from this series, at below 100MPa, again produced failures in the weld metal. They also showed good agreement with the results from the outer half of the weld. The combined set of three data points below 100MPa clearly confirm the change in trendline slope at about 100MPa, with the lower stress data trendline turning approximately parallel to and 25% below the parent data line.

The single 2C test at close to 120MPa, however, produced an apparently quite anomalous result. Its data point, again shown in pale blue on Figure 1, lies virtually on the parent material trendline. This test, which lasted more than three times longer than its equivalent from the "outer weld" series, failed in the HAZ.

The recorded elongation values varied from 3% in lower stress tests to 7% in the two highest stress tests. Corresponding reduction in area values typically fell within a range of 10-25%, again tending to increase with stress. The HAZ failed test 2C showed a comparable overall ductility to the other tests, and there was no evidence of systematic differences in ductility between the outer and inner weld samples.

The questions arising were therefore:

- Why was the weld metal so weak when tested in the cross-weld orientation?
- Why does the stress rupture curve for failure in the weld metal change its slope at about 100MPa, and "bottom out" at an approximate 25% weld strength reduction factor?
- What light does the single test 2C result throw on the HAZ failure mechanism?
- Why did the weld metal in test 2C perform abnormally well, surviving over three times longer than expected, and thereby enabling a different, longer term failure mechanism to operate?

3.2. Metallographic Investigation

3.2.1. Weld metal failures

Macroscopic sections through failed specimens are shown in Figure 2. Test 1A shows cracking at an angle to the specimen axis, running along one side of an angled light-etching refined zone within the weld metal. Test 1C similarly shows cracking within an angled refined zone, with a planar morphology suggestive of failure within a shear band, but with occasional local excursions around microstructural regions. In Test 1D, it is evident that two separate cracks, which ran along opposite sides of the same refined band, grew and met. Turning to the inner weld series, Test 2E similarly shows cracking along the edge of the outermost refined zone in the weld metal. In slight contrast, Test 1B shows a more mixed form of cracking, including some crack propagation along columnar grain boundaries within unrefined regions of the weld metal. Thus, most though not all of the cracking ran within refined zones, often toward one edge of such a zone, and commonly within the buttering layer dilution beads adjacent to the HAZ and parent material. Chemical composition variations, and/or regularity of weld bead alignment, may tend to favour cracking in this part of the weld.

The refined zone itself may be somewhat heterogeneous. Figure 2 test 1A, for example, suggests that there is a fully retransformed equiaxed zone just below the weld bead fusion boundary, with a lower temperature reheated zone outside it, in which traces of the as-deposited columnar weld structure remain visible.

Test 1E also showed a mixture of columnar and refined zone cracking, Figure 3a. The refined zone structure is detailed in Figure 3b, while Figure 3c shows a linking crack through a columnar region, with associated microcracking on columnar grain boundaries.

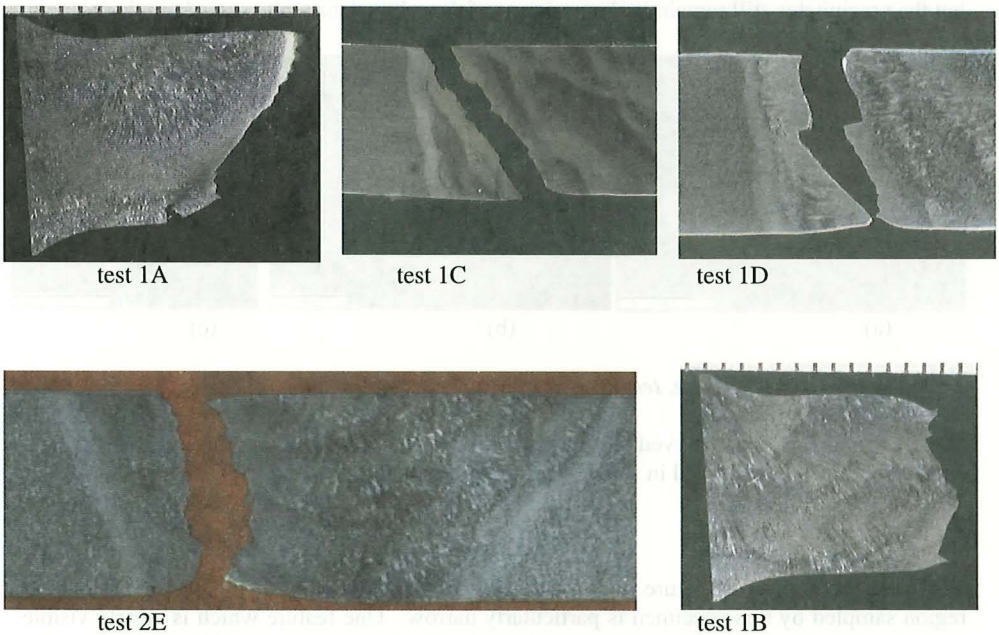

Figure 2. Specimens failed in weld metal.

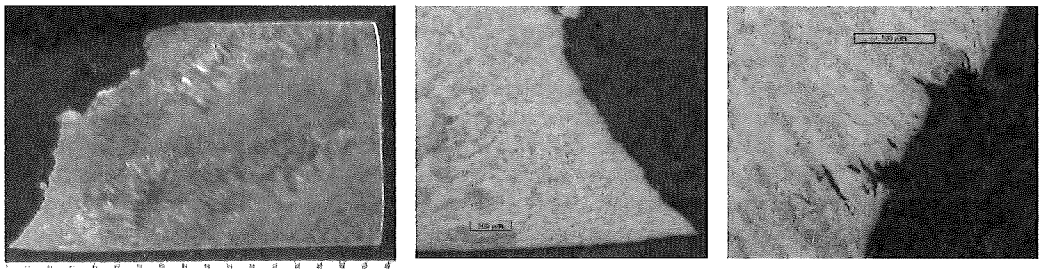

(a) (b) (c)

Figure 3. Failure in weld metal, test 1E: (a) general, (b) refined zone, (c) columnar zone

3.2.2. HAZ failure

The test 2C HAZ failure is shown in Figure 4. The crack is located at about 0.25mm into the HAZ from its outer edge, i.e. from the Ac_1 position at which the prior austenite grain structure of the parent material first shows evidence of partial retransformation. Associated creep cavitation in this material is located primarily within the intercritical outer part of the HAZ, where a mixture of the coarse untransformed parent material grain structure is interspersed with a finer-scale retransformed structure. It is less easy to identify the Ac_3 position where the structure becomes wholly retransformed. Even at the centre of the HAZ, chains of inclusions indicative of the original coarse-grained prior austenite grain boundary position are still observable, Figure 4 (c). It seems likely that the matrix material has fully retransformed, but the precipitates still remain in the positions of the original austenite grain boundaries.

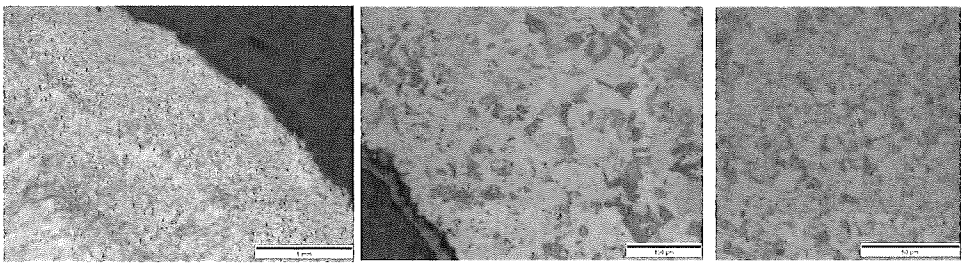

(a) (b) (c)

Figure 4. HAZ failure, test 2C: (a) weld side, (b) parent side, (c) HAZ above Ac_3

No HAZ cracking was observed in any other specimen. However, some light HAZ Type IV zone cavitation was observed in some of the lower stress tests.

3.2.3. Unfailed weld metal

The weld metal macrostructure within creep specimen 2C, Figure 5, is notable. The weld region sampled by this specimen is particularly narrow. One feature which is clearly visible at the bottom of the picture is a large single weld bead (probably an MMA bead, rather than

the small TIG root bead beneath it) which spans the entire weld width, and which has a clear columnar structure. Above this single weld bead, a multiple bead structure is evident, with two or three weld beads spanning the preparation, and with refined zones at their boundaries.

Figure 5. Test 2C – Wide weld root region bead and HAZ failure

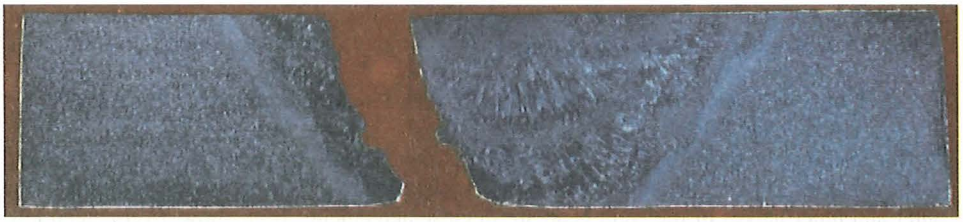

Figure 6. Test 2F – Weld root region beads not sampled, weld metal failure

However, no refined zone extends into the lowest 2-3mm of the creep specimen. There is, therefore, no continuous weak shear zone that extends all the way across this particular specimen. By contrast, specimen 2F shows no such prominent single weld bead toward its innermost edge, Figure 6. It thus appears that a weak refined zone shear band does extend across virtually the full width of the specimen in this case, and that as with all other specimens except 2C, this has enabled early weld metal creep cracking and failure. The presence of the root bead in specimen 2C, and its apparent absence from specimens 2E and 2F, is probably just the accidental consequence of a slight variation in the through-wall location of the different creep specimens.

4. Discussion

4.1. Multipass weld anisotropy – Why is the weld metal weaker in transverse orientation?

Excluding test 2C, the cross-weld specimens showed markedly poorer performance than the all-weld-metal specimens, Figure 1. The cross-weld specimens were of course oriented transversely with respect to the welding direction, whereas the all-weld-metal specimens were oriented longitudinally.

A multipass weld can be simply modelled as akin to a sheaf of pencils held together by glue. The "pencils" are the strong, albeit brittle, as-deposited columnar regions of each weld bead. The "glue" regions are the weaker, albeit probably more ductile, refined zones beneath the fusion boundaries of superposed weld beads.

When this composite structure is tested in the longitudinal welding direction, the tensile load is required to deform the "pencils" and the "glue" together. Hence, the strong "pencils" prevent rapid strain accumulation in the weak "glue". Cracking takes place only when the most brittle material – probably the as-deposited "pencils" – reaches its limit of ductility.

When the same structure is tested transversely, however, it is possible for the sheaf of pencils to fall apart merely by means of rapid failure within the weak "glue", since this forms a continuous path around and between the array of pencils. In a multipass weld metal, therefore, such a path of weakness normally extends across the full width of the creep specimen. In this orientation, therefore, it is the weak and ductile material which fails.

It can be seen from Figure 2 that this model of failure is broadly appropriate. There are some indications that continuous refined zones extending across the specimen may act as rapid shear zones. There are also indications that, whilst it is the refined zone that deforms, the crack location within this zone may tend to be close to the interface with columnar material. In this location, the local mismatch in creep behaviour may also act to promote cracking.

4.2. Multipass weld behaviour – Why is the weld metal stress rupture curve sigmoidal?

For the six cross-weld specimens showing failure in the refined zones within a multipass weld deposit, Figure 1 shows a clearly "sigmoidal" stress rupture curve. The data points from the outer and inner halves of the weld bead are in close agreement. Both show a very steep fall-off in creep strength in the short term, but a much gentler decline in the longer term.

Sigmoidal behaviour of this type is often associated with creep failure within thin weak zones. Thus, the behaviour of a thin refined weld metal zone may be comparable with that of the thin HAZ Type IV zone in a material such as P91. In the latter case, cross-weld specimen failure in high stress tests commonly takes place in the parent material, apparently because constraint effects prevent the thin weak zone from deforming more rapidly and hence failing earlier. By contrast, at low stresses, the thin weak Type IV zone shows behaviour comparable to that of bulk thermally simulated "Type IV" material. It thus appears that at low stresses, the thin Type IV zone is able to deform without constraint from the adjacent strong parent material. The intermediate range of stresses, in which the constraint effect changes from overriding at high stress toward negligible at low stress, therefore shows a transition in creep performance. Since high stress failure is governed by the properties of the strong parent material, while low stress failure is governed by the properties of the much weaker HAZ Type IV material, the fall-off in rupture strength within the transition range of stresses is exceptionally steep.

A similar general model, therefore, appears to explain the sigmoidal stress rupture curve of P23 weld metal tested in transverse orientation, where the relevant thin weak zone is the refined weld metal. As with HAZ Type IV cracking, a very steeply declining stress rupture plot can be obtained by testing in the transition region, but if this is simply extrapolated to lower stresses, the results are over-pessimistic. Actual longer term test data, out to 10,000 hours and beyond in this case, are necessary to gain a true picture.

The long term weld strength reduction factor, of the order of 25%, is of course still of some concern. However, this is not an exceptionally high figure compared with many other materials, for example the high alloy steels, where strength reduction factors of the order of

30-50% have been identified in respect of Type IV cracking. It must also be borne in mind that Chromet 23L is a low carbon weld variant not optimised for creep strength. It can therefore be argued that these results are not especially unfavourable in terms of their implications for the long term service performance of P23 welds. Nevertheless, they do imply that where system (bending) stresses are significant, P23 pipe butt welds could still fail in long term service by longitudinal weld metal cracking. A creep crack with this orientation typically propagates around part of the pipe circumference and, if not correctly detected and repaired during periodic plant inspection, may eventually propagate through the pipe wall thickness and cause failure.

4.3. HAZ performance – What can be deduced from these results?

The single HAZ Type IV failure recorded, specimen 2C, showed almost no weld strength reduction factor, compared to the thick Sumitomo parent pipe data. It was, however, obtained at a fairly high stress level, close to 120MPa. This might be toward the upper end of the "transition" region of stresses discussed earlier, where high stress failure in parent material is transitioning to lower stress failure in a weak (HAZ Type IV or refined weld metal) weld zone. If so, the very low weld strength reduction factor observed in this single test may not necessarily imply that the Type IV strength reduction factor will always be low.

Indeed, the HAZ performance in the lower stress tests may be more important. In all those tests, the HAZ proved itself stronger than the weld metal, since it was not the location of failure, although some HAZ cavitation was found. Thus, the longer term HAZ creep strength reduction factor corresponding to the lower stress tests will have been, at worst, substantially less than 25% with respect to the Sumitomo parent. This is a reasonably favourable finding, though further test data are obviously needed to obtain a clearer picture.

5. Implications – Can weld structure be controlled to optimise creep performance?

5.1. Conventional multipass welding

Figure 7 shows a typical schematic MMA weld macrostructure. The root bead and one or more "hot pass" beads commonly bridge the narrow gap between sidewalls at the base of the weld preparation. However, two or more weld beads per layer are generally required to span the weld preparation within the bulk fill-up region of a thick section weld. The Figure also shows the location of the weak refined zone material just below each weld bead boundary. It also indicates how two cross-weld specimens might be cut from the test block: an upper specimen (solid lines) within the multiple-bead region, and a lower specimen (dotted lines) extending into the one-bead-per-layer region.

The upper specimen has a continuous path of weakness extending across its full cross-section. It can therefore fail by crack growth wholly within the weak refined zone. However, the lower specimen as sketched has no such continuous weak path. Instead, the weak zone between two weld layers is supported by stronger columnar-grained material above and below. As indicated by this work, any such specimen is therefore likely to show much improved performance.

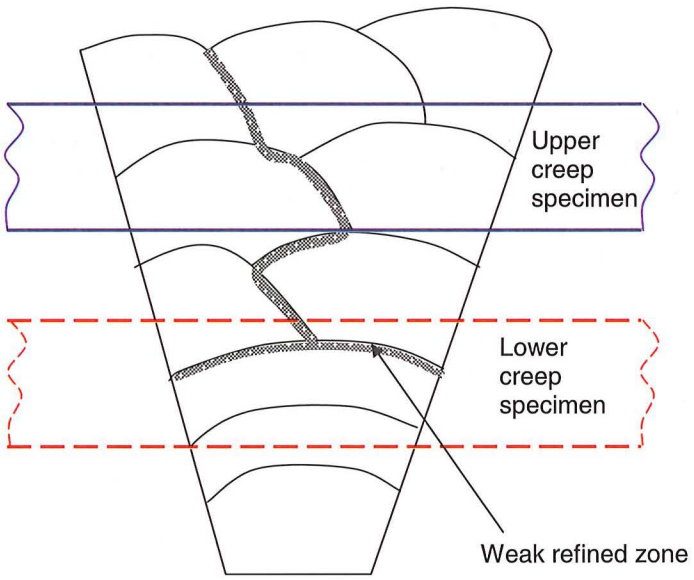

Figure 7. Weld macrostructure - Schematic

In thick section P23 pipe welded with conventional multipass processes such as MMA, TIG, or submerged arc (SA), the upper specimen macrostructure will be representative of the majority of the weldment. Hence, the locally more crack-resistant macrostructure near the weld root probably has little influence on the initiation and growth of longitudinal weld metal creep cracking in the bulk of the pipe butt weld.

By contrast, tube welds are often made wholly or substantially by depositing successive single weld beads spanning the narrow weld preparation. This weld geometry could evidently have a significantly beneficial effect on T23 tube butt weld performance. It could therefore be worthwhile to reassess T23 tube welding procedures and, where possible, eliminate two-beads-per-layer welding.

5.2. Narrow gap welding

An exciting possibility suggested by this work is that advanced narrow gap welding processes could offer real advantages in control of macrostructure and optimisation of creep performance, in addition to the productivity benefits for which they have been developed. Narrow gap processes, which commonly use techniques such as arc oscillation or twisted wire feed to produce wide flat weld beads with good sidewall fusion characteristics, can produce thick section welds with a consistent single-bead-per-layer macrostructure. This weld structure exhibits no continuous plane of weakness other than the refined zone beneath each layer. Unless there is substantial through-thickness loading, such a weak zone parallel to the component surface should not cause any practical concern.

It is likely, therefore, that the transverse creep test performance of a Grade 23 all-weld-metal single-bead-per-layer deposit will be consistently superior, and broadly similar to that of a creep test in longitudinal orientation. In either case, creep deformation behaviour will be largely controlled by the strong columnar zone material. Hence, whilst a cross-weld test on a conventional multiple-beads-per-layer weld shows a substantial weld strength reduction factor, no similar strength reduction is likely to apply to the single-bead-per-layer narrow gap weld, Figure 1. Thus, changing the macrostructure of a P23 pipe weld from conventional multiple-beads-per-layer to narrow gap single-bead-per-layer is likely to eliminate the potential premature creep failure mechanism by longitudinal weld metal cracking in weak refined zones. Confirmation of these predictions will of course require actual all-weld-metal transverse creep testing on single-bead-per-layer weld deposits.

5.3. Applications to alternative high temperature materials

Narrow gap welding offers potential advantages with P23 because this particular type of weld metal is at risk of premature creep failure in a narrow weak zone, with very low macroscopic ductility. By contrast, steels such as P91 almost invariably show HAZ failures in cross-weld tests, suggesting that the weld metal is not the weak link, and that a modified P91 weld metal macrostructure may therefore offer no real advantages.

Experience with the older UK coal-fired plant pipework system, where CrMoV steel is welded with 2CrMo (P22) weld metal, also demonstrates the significance of creep ductility. Plain bar cross-weld creep tests on this material generally fail with high ductility in the 2CrMo weld metal, but the actual problem which occurs on plant is low ductility creep cracking in the CrMoV steel HAZ Type IV zone. This can be understood on the premise that plant cracking driven by bending loads is to a large extent displacement controlled, and that the weak and ductile weld metal simply deforms and off-loads stresses during plant operation, without incurring cracking.

The potential problem with T/P23 weld metal may therefore be linked to the presence of a specific narrow zone of weakness, such that even if creep failure may be locally ductile, the macroscopic strain level is very low. Hence, reheat cracking on conversion of elastic strain (at around the 1% level) to macroscopic creep strain is a possibility. Premature weld metal failure during creep testing [6] or in service, due to ductility exhaustion by a combination of residual welding stress relaxation followed by limited additional creep under pressure loading, is also a possibility with this material. T24 weld metals exhibit similarly low creep ductilities, which may be suggestive of similar risks [6].

Turning to the high alloy steels, the indications are that as P91 is gradually superseded by newer and stronger materials such as P92, improvements in parent and HAZ creep strength are not entirely matched by corresponding improvements in weld metal performance [7]. This may indicate that there are potential metallurgical advantages in applying narrow gap welding technology to the newer steels, especially if features such as cracking at "white band" carbon-depleted zones beneath fusion boundaries act to promote low ductility failure [8]. Finally, the novel MARBN steels [9] promise major improvements in parent and HAZ creep performance, and it is not yet clear whether weld metals of adequately matching creep strength can be developed. Again, therefore, there may well be scope to optimise weld performance through control of a single-bead-per-layer macrostructure.

Conclusions

1. In cross-weld creep testing, multipass P23 steel weld metal is liable to cracking in weak refined zones between superposed weld beads. The creep strength curve shows a steep fall in the short term, bottoming out at about 25% below the parent material strength in the longer term.
2. One test specimen from near the root region demonstrated much better performance. This may be attributed to its single-bead-per-layer structure, which eliminated the weak refined zone perpendicular to the test stress direction.
3. A single-bead-per-layer structure may thus have real advantages in reducing the risk of longitudinal weld metal cracking in circumferential tube butt welds.
4. For thick section pipe applications, a narrow gap welding procedure could potentially achieve similar benefits.
5. These potential benefits may also be applicable to materials such as P24 and to those higher alloyed steels which have comparatively weak and creep brittle weld metals.

Acknowledgements

Acknowledgement for permission to publish the creep test results is given to the members of the UK High Temperature Power Plant Forum. The authors thank HTPPF for sponsorship of the test programme, Philip Clarke of Corus for creep testing and chemical analysis, and the DTI Cleaner Coal Programme for supporting the original project on P23. This paper is published by permission of E.ON Engineering, RWE npower, and Doosan Babcock.

References

[1]. S J Brett, D J Allen and L W Buchanan, "The Type IV Creep Strength of Grade 91 Materials", *2nd Int'l Conf. "Integrity of High Temperature Welds"*, London, IOM Communications, pp.409-419, (2007).

[2]. S. Caminada, P. Nevasmaa, S. Holmstrom, A. Di Gianfrancesco, S. Pillot, M. Mendes Rodrigues, D. J. Allen and D. Siegele, "Development of Weldments of Grade 23 Steel for New Generation Power Plants", *Creep 2008, 11th. Int. Conf. on Creep and Fracture of Engineering Materials and Structures*, Bayreuth, Germany, Paper CP-009, (2008).

[3]. K. Sawada, M. Fujitsuka, M. Tabuchi and K. Kimura, "Effects of Microstructural Change and Oxidation on Creep behaviour of P23/T23 Steels", *ECCC Conference "Creep and Fracture in High Temperature Components"*, Dubendorf, Switzerland, pp. 79-90, (2009).

[4]. J. G. Nawrocki, J. N. Dupont, C. V. Robino, and A. R. Marder, "The Stress-Relief Cracking Susceptibility of a New Ferritic Steel", *Welding Journal* 79(12), p355-s, (2000); and 80(1), pp.18s-24s, (2001).

[5]. P. Nevasmaa, J. Salonen, and S. Holmström, "Reheat Cracking Susceptibility of New Generation 2%CrMo(W)V P23 Steel Multipass Welds made using Matching and Mis-Matching Filler Metals", *7th International Conference on Life Management and Maintenance for Power Plants (Baltica VII)*, Symposium 246, VTT Technical Research Centre of Finland, Vol. 1. pp. 128-142, (2007).

[6]. Allen, D J, Holloway, G, Marshall, A W, and Rodrigues, M M, (2008), "Development of High Temperature Weld Metals for Advanced Low Alloy Steels", *Proc. Conf.*

"Safety and Reliability of Welded Components in Energy and Processing Industry", IIW, Graz, pp. 437-442, (2008).

[7]. Allen, D J, Harvey, B, and Brett, S J, (2005) "FOURCRACK – An Investigation of the Creep Performance of Advanced High Alloy Steel Welds", *Proc. ECCC Creep Conf.*, London, UK, pp. 772-781, (2005).

[8]. Zhang Y., Shipway P.H., Hyde T.H. and Sun W., "Anisotropy Creep Behaviour of P91 Weld Metal - a Microstructural Study", *2nd Int. Conf. on Integrity of High Temp. Welds*, London, pp. 373-388, (2007).

[9] F. Abe, "Precipitate design for creep strengthening of 9% Cr tempered martensitic steel for ultra-supercritical power plants", *Science and Technology of Advanced Materials* 9(1), 013002, (2008).

9th Liege Conference : Materials for Advanced Power Engineering 2010
edited by J. Lecomte-Beckers, Q. Contrepois, T. Beck and B. Kuhn.

DEVELOPMENT OF MATCHING FILLER METALS FOR WELDING CB2 AND FIRST EXPERIENCE

Dr. Herbert Heuser, Dr. Claus Jochum, Dr. Dorothea Kreuzer-Zagar

Böhler Schweisstechnik Deutschland GmbH, Unionstraße 1, 59067 Hamm, Germany

Abstract

This paper gives an overview about the properties of a new martensitic welding consumable which is matching to CB2, FB2, PB2. This material has been developed in the frame of COST 536 research program. Thermanit MTS 5 Co1 shows high strength properties with moderate toughness in the range about 40 J. The mechanical properties have been tested after different PWHT, the influence of Boron was evaluated with respect to weldability, creep strength and toughness. Creep tests are still running, up to now, the filler metal behaves as expected.

Keywords:
filler metals matching to COST CB2/PB2; mechanical properties; Thermanit MTS 5 Co1

Introduction

It is the endeavour of operators of fossil fuel fired power stations to increase the efficiency of their installations through an increase of steam pressure and temperature in order to assure supply of electricity on a low cost level and with reduced CO_2 emission. Increase of service parameter requires adequate materials with sufficient creep strength. This is true for both base materials and welding consumables, as well. The focus of this contribution is to present the status of filler metal development which is an important part of the COST 536 welding group's work. Here, the most important material of interest was CB2 material.

Development of new martensitic creep resistant base material

The demand for higher efficiency in fossil fired power plants lead to the development of new creep resistant materials during the last decades. They made it possible to increase the steam temperature up to the range of 625°C for permanent service, using ferritic and martensitic materials. Further increase up to 650°C for steam inlet temperature demands martensitic material with better oxidation and creep behaviour. This development is based on the knowledge of former COST research, especially on intensive micro structural investigation of commercially available and well known martensitic base materials [1]. As a result of many different test melts, the cast alloy CB2 has been developed with best properties. During the last Conference in Liège in 2006, this grade was subject of several presentations [2, 3].

Development of a new creep resistant martensitic filler metal: Thermanit MTS 5 Co1

During the development of new base materials it is of great importance, that corresponding filler metals with matching creep strength and corrosion properties will be developed simultaneously. The chemical composition of the welding consumable is more or less identical to the base material. Additional micro alloying elements and specialities concerning improvement of weldability and handling are the detailed knowledgement of the individual development departments. In the framework of the different COST 536 subgroups different cast materials have been produced and tested. So far, CB2 materials proved to be the best. For this material matching filler metals have been developed [4]. Chemical composition and mechanical properties of CB2 are listed in table 1. The all weld metal can be characterized as high strength material with YS in the range of about 630 MPa and with TS about 780 MPa. Toughness property of the welding consumable at room temperature is – even with the addition of Ni and after PWHT - on a level of above 35-45 J (average values). This level is the result of a long and intensive development and improvement process, and now, these values are corresponding to the base material. With such a toughness level it is most important to take outmost care during welding (limitation of heat input, correct choice of electrode Ø, welding thin layers with gentle weaving technique, etc. [5]). Table 1 show the chemical composition and mechanical properties of the weld metal. The chemical composition of the filler metal is matching the base material except Boron and Nickel. Boron is known to influence properties like creep strength, toughness and hot crack susceptibility. A Boron content of max. 0,004 % seems to be of best compromise concerning the before mentioned properties. Ni is added in order to increase toughness. After welding a PWHT has to be carried out. As different heat treatments can be applied due to different application, several PWHT conditions have been tested (s. table 1). Finally, high temperature strength at 550 and 600°C has been determined.

Table 1. Chemical composition of CB2 base material (pilot cast component) and of all weld metal of matching filler metal (SMAW), Thermanit MTS 5 Co1, mechanical properties of all weld material

Chemical composition (weight %)											
	C	**Si**	**Mn**	**Cr**	**Ni**	**Mo**	**V**	**Co**	**Nb**	**B**	**N**
Base metal											
CB2 range	0,11-0,14	0,20-0,30	0,80-1,0	9,0-9,6	0,10-0,20	1,40-1,60	0,18-0,22	0,9-1,1	0,05-0,07	0,008-0,015	0,015-0,030
CB2 base material, pilot component	0,13	0,30	0,85	9,14	0,22	1,44	0,19	0,96	0,062	0,011	0,021
Filler metal											
Thermanit MTS 5 Co1	0,14	0,23	0,55	9,30	0,75	1,50	0,22	1,00	0,06	0,003	0,028

Mechanical properties of all weld, Thermanit MTS 5 Co1 (Heat Input 15 – 18 kJ/cm)						
El-Ø mm	**Test temp. °C**	**PWHT °C, h**	**YS MPa**	**TS MPa**	**Elong. %**	**CVN (ISO-V) J**
3,2	+20	2 x 730/12	628	779	17,2	28 60 68
4,0	+20	2 x 730/12	688	825	17,0	34 40 33
5,0	+20	2 x 730/12	637	777	17,8	52 46 48
4,0	550	2 x 730/12	474	548	17,0	
4,0	600	2 x 730/12	403	476	19,2	
4,0	+20	740/10	629	773	17,6	37 40 46
4,0	+20	760/4	602	759	18,5	61 52 50
4,0	550	760/4	357	503	15,4	
4,0	600	760/4	366	423	19,0	

Table 2 shows the mechanical properties of the base material CB2 and of a cross weld, welded with Thermanit MTS 5 Co1. For both cases, a heat treatment at 730°C/ 24 h has been performed. The heat treatment was required for cast materials. Under these conditions, the filler metal is of higher strength than the base material and the fracture of the cross weld is located in the base material. Toughness of weld and parent metal is comparable and on a level of 35 J each.

As for other martensitic grades it is known, that the toughness will decrease during service life due to formation of precipitations. This question is of more importance, the lower the starting level of toughness is. For that reason, exposure tests of the all weld metal have been carried out at two different temperatures and after different PWHT conditions. Figure 1 shows the exposure at 550°C after a PWHT at 730°C/24 h and after 760°C/4 h. The first PWHT corresponds more to the procedures of castings, while the second is often used for welding martensitic pipes like P91 or P92. It can bee seen in fig. 1, that there is only a small difference between the two PWHT conditions with better values after 760°C/4h. Nevertheless in both cases there is a gentle drop with time, and after 1000 h a level of about 30 J is reached. This behaviour is known from other martensitic grades like X20, P91, P92.

Table 2. Mechanical properties of base metal CB2 and of cross welds, welded with matching filler metal, Thermanit MTS 5 Co1

Test temp. °C	PWHT °C, h	YS MPa	TS MPa	Elong. %	CVN (ISO-V) J	Fracture location
Base metal properties						
+20	730/24	550	698	19,4	30 – 34	
Cross weld properties with Thermanit MTS 5 Co 1						
+20	730/24		737		31 33 37	BM

Figure 1. Thermanit MTS 5 Co1, influence of exposure at 550°C on toughness properties of the all weld metal, different PWHT: 730°C/24h and 760°C/4h. Each column shows the mean of three values.

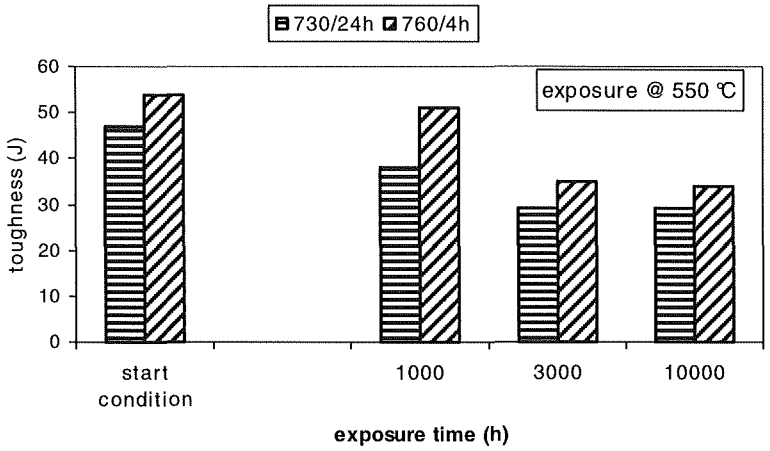

Figure 2 shows the aging effect at 600°C after a PWHT at 730°C/24 h. In general, toughness seems to be on a slightly higher level that in figure 1, but that can be related to scatter band variations between two different welds of the same heat. Nevertheless here also the resulting toughness level after long exposure is less than 30 J after 30.000 h.

Figure 2. Thermanit MTS 5 Co1, influence of exposure at 600°C on toughness properties of the all weld metal, PWHT: 730°C/2x12h

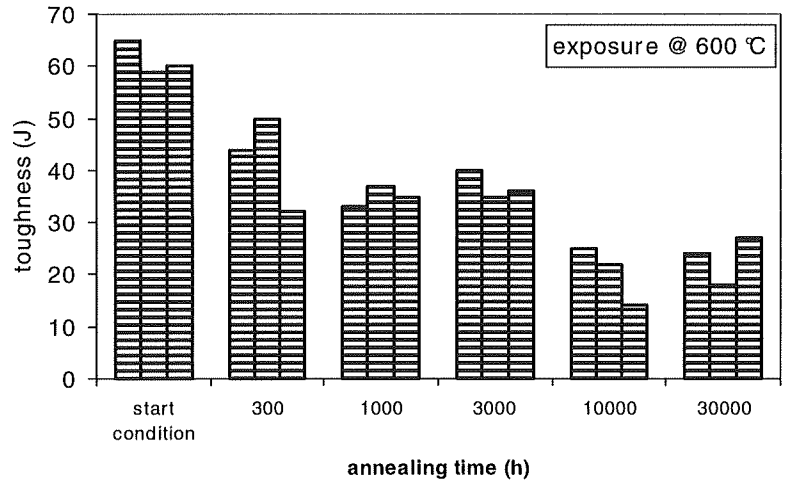

Table 3. Mechanical properties of a pipe PB2 and of a joint welded with Thermanit MTS 5 Co1

Chemical composition (weight %)											
	C	**Si**	**Mn**	**Cr**	**Ni**	**Mo**	**V**	**Co**	**Nb**	**B**	**N**
Base metal											
PB 2 pipe	0,14	0,11	0,34	9,31	0,13	1,59	0,19	1,31	0,06	0,007	0,026
Joint											
MTS 5 Co1	0,124	0,17	0,52	9,39	0,83	1,59	0,25	1,18	0,04	0,004	0,039

Test temp. °C	**PWHT °C, h**	**YS MPa**	**TS MPa**	**Elong. %**	**CVN (ISO-V) J**	**Fracture location**	**Bending angle 180°**
Base metal properties							
+20		610	763	21,5	128 (mean of 3)		
550		424	463	27			
Cross weld properties with the MTS 5 Co 1							
+20	760/4		723		41 44 46	BM	ok
550	760/4		478			BM	
600	760/4		427			BM	

In the frame to the COST 536 Program a pipe of PB2 (composition identical to that of CB2) has been welded with Thermanit MTS 5 Co1. The pipe dimension was ODxWT 219mm x 31.75mm. Table 3 shows the chemical composition and the mechanical properties of both the pipe and the joint, as well. The location of the fracture of the cross weld was in the base material. The heat treatment was carried out at 760°C/4 h, which is a typical PWHT condition for martensitic pipes.

Figure 3 shows the result of bending tests from this cross weld. All bending tests with root- , side- and cap-bending show no defects at a bending angle of 180°. Out of this joint, specimens for creep tests have been machined. These tests are ongoing.

Figure 4 shows a macro section of the pipe joint and figure 5 shows the hardness distribution across the cross weld in the cap and in the root area. After a PWHT at 760°C/4h the max. hardness was 274 HV10 in the HAZ and 264 HV10 in the weld.

Figure 3: Bending tests of PB2 pipe cross welds with Thermanit MTS 5 Co1; side-, root- and cap- bending show not defects at a bending angle of 180°.

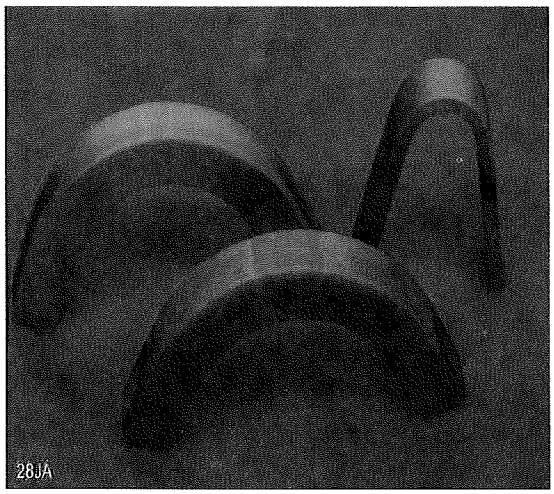

Figure 4: Macro section of the joint PB2 welded with Thermanit MTS 5 Co1 and corresponding hardness at cap and root side.

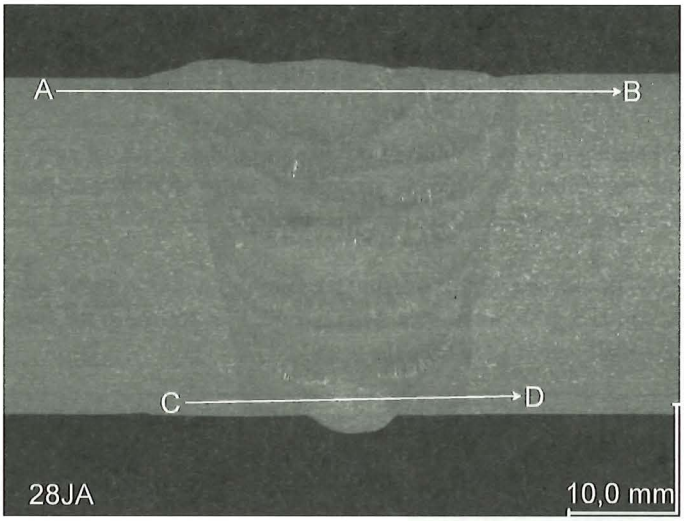

Figure 5: Hardness distribution in a joint PB2 welded with Thermanit MTS 5 Co1

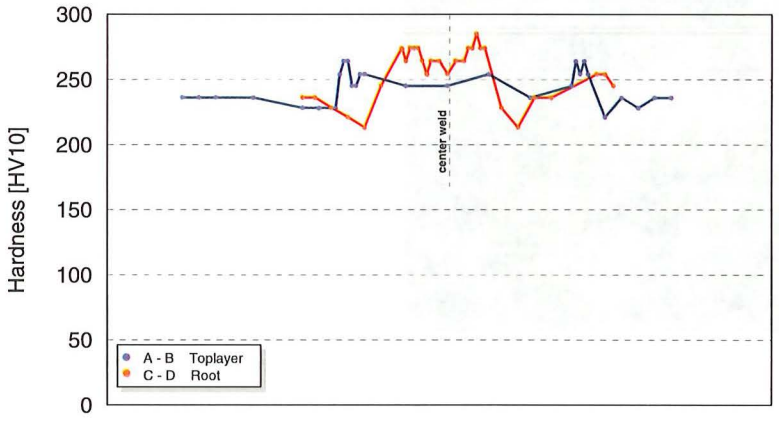

Conclusion

Within the COST 536 Research Program Böhler Schweisstechnik Deutschland GmbH has developed a new martensitic filler metal, matching CB2 material and its variants. The weld metal of Thermanit MTS 5 Co1 meets the same requirements as the base material concerning the mechanical properties, even when not welded under laboratory conditions. Creep tests are still running, fractures observed so far occur within the scatter band limits of the base material. Due to high strength properties and the alloy concept, it requires a more careful welding, respecting all rules such as: choice of proper diameter and adequate heat input. A matching cored wire is also under development within the Böhler Welding Group.

References

[1] Hald, J; Metallography and alloy design in the COST 536 action, Proceedings of the 8th Liège Conference. European Commission, Université de Liège, Vol. 53. p. 917-930 (Part II). Liège 2006

[2] Staubli, M; Hanus, R; Weber, T; Mayer, K.-H; Kern, T; The European efforts in development of new high temperature casting materials, COST 536, Proceedings of the 8th Liège Conference. European Commission, Université de Liège, Vol. 53. p. 855-870 (Part II). Liège 2006

[3] Cerjak, H; Letowsky, E; Jochum, C; Nies, H; Weldability and weld properties for advanced power plant materials. Proceedings of the 7th Liège Conference. European Commission, Université de Liège, Vol. 21. p. 1081-1090 (Part II). Liège 2003

[4] Bauné, E; Cerjak, H; Caminida, S; Jochum, C; Mayr, P; Pasternak, J; Weldability and properties of new creep resistant materials for Use in ultra supercritical coal fired power plants, Proceedings of the 8th Liège Conference. European Commission, Université de Liège, Vol. 53. p. 871-893 (Part II). Liège 2006

[5] Blume, R.; Heuser, H.; Leich, K.E.; Meyer., F.: Verbesserungen der mechanisch-technologischen Eigenschaften von Schweißverbindungen an CrMoVNb-Stählen mit 9 % Cr durch Optimierung von Schweißzusätzen und Schweißparametern, DVS Bericht 162, S. 206-210.

9th Liege Conference : Materials for Advanced Power Engineering 2010
edited by J. Lecomte-Beckers, Q. Contrepois, T. Beck and B. Kuhn.

Z PHASE STABILITY IN AISI 316LN + Nb AUSTENITIC STEELS DURING CREEP AT 650°C

Vlastimil Vodárek

Technical University of Ostrava, Ostrava, Czech Republic

E mail: vlastimil.vodarek@vsb.cz

Abstract

The creep resistance of austenitic CrNi(Mo) steels strongly depends on microstructural stability during creep exposure. Nitrogen additions to CrNi(Mo) austenitic steels can significantly improve the creep strength. One of the most successful methods of improving the long-term creep resistance of austenitic steels is based on increasing the extent of precipitation strengthening during creep exposure. The role of precipitates in the achievements of good creep properties has been extensively studied for a long time. Although many minor phases are now well documented there are still contradictions and missing thermodynamic data about some minor phases.

This contribution deals with results of microstructural studies on the minor phase evolution in wrought AISI 316LN niobium stabilised steels during long – term creep exposure at 650°C. Microstructural investigations were carried out on specimens taken from both heads and gauge lengths of ruptured test-pieces by means of optical metallography, transmission and scanning electron microscopy. The attention has been paid to evaluation of thermodynamic and dimensional stability of Z phase and other nitrogen bearing minor phases. Only two nitrogen-bearing minor phases formed in the casts investigated: Z phase and M_6X. The dimensional stability of Z phase particles was very high.

Keywords: AISI 316LN niobium stabilised steels, creep behaviour, microstructural stability, Z phase, M_6X.

1. Introduction

Austenitic stainless steels have been used in power plant applications in severe environments and temperatures up to 650°C [1]. They are expected to provide reliable service for 20 years and even more. Creep properties of austenitic stainless steels are dependent on the stability of the microstructure, particularly the formation, dissolution and coarsening of precipitates [2]. Since many factors can influence the microstructure, it is not surprising that dramatic differences in creep rupture properties of austenitic stainless steels have been reported. The most important factors are chemical composition, thermomechanical pretreatments, temperature, stress and environment of creep tests [1]. A better understanding of the causes of scatter in creep properties of austenitic stainless steels requires controlled creep experiments involving casts with intentional additions followed by detailed microstructural investigations and surveys of the failure mechanisms of creep test-pieces. It is very important to evaluate the creep properties of austenitic steels by long-term laboratory testing because empirical methods based on extrapolations of relatively short-term data are likely to cross creep mechanism boundaries and tend to prediction of unreliable values of creep strength. The objectives are to develop a balance of creep strength with adequate creep rupture and room temperature ductilities. The matrix solid solution and a high number density of the stable intragranular precipitates provide resistance to dislocation creep. The presence of grain boundary precipitates and the nature of precipitates determine grain boundary diffusion and sliding contributions to the creep rate.

Nitrogen additions to CrNi(Mo) austenitic steels can significantly improve the creep strength [1]. Nitrogen suppresses the formation of δ-ferrite, delays the precipitation of intermetallic phases and destabilises $M_{23}C_6$ carbides. One of the most successful methods of improving the long-term creep resistance of austenitic steels is based on increasing the extent of precipitation strengthening during creep exposure. This can be achieved by alloying of these steels with small amounts of strongly carbide or nitride forming elements, such as niobium or titanium. Keown and Pickering [3] showed that in the case of niobium stabilised steels optimum creep lives were obtained for the Nb/C ratio matching the stoichiometry Nb_4C_3, other studies [4] showed the optimum results for a Nb/C atomic ratio of 1:1. However in nitrogen-bearing steels NbX particles can also dissolve nitrogen which makes the problem more complex [2].

The role of precipitates in the achievements of good creep properties has been extensively studied for a long time. The precipitation reactions in the usual 300 grades of austenitic steels are well understood [1], however it is not true for the new generations of nitrogen-bearing stabilised austenitic steels, such as 347LN, Tempaloy A-3, SAVE25 or NF709. A limited amount of information is available about phases such as Z phase which is a nitride with an ideal composition of NbCrN [5]. Raghavan et al. [6] suggest that Z phase can also dissolve some carbon. Conditions of the Z phase formation are not very clear and even less clear is its relative stability when compared with other carbonitrides [2]. Knowles [7] reported that Z phase formed from MX precipitates, while Robinson and Jack [8] suggested its formation from solid solution. The conclusions of such a comparison must be examined carefully as the steel compositions were different. It is difficult as yet to build a coherent view of the various kinetics observed [9]. Another important minor phase in nitrogen-bearing austenitic stainless steels is M_6X [10]. This phase has a diamond cubic structure (η phase, Fd3m) with a wide composition range from $M_3M'_3X$ to $M_3M'_2SiX$, where M and M′ indicate substitutional elements while X indicates an interstitial element, such as N or C [1].

The evolution of microstructure during creep exposure is of considerable interest, to ensure that no phase forms that is very detrimental to mechanical or other properties. This paper deals with studies on the precipitation reactions in the wrought AISI316LN niobium stabilised steels during long-term creep/thermal exposure at 650°C.

2. Experimental Procedures and Materials

The evaluation of creep properties was carried out on two casts of the AISI 316LN steel with additions of 0.1 and 0.3wt.%Nb, respectively. As a reference material the niobium free AISI 316LN steel was used. Chemical composition of all casts is given in Table 1. Long-term creep rupture tests with a constant tensile load were carried out in air at temperatures 600 and 650°C. The stress temperature dependences of the time to rupture were described by the Seifert parametric equation [11]. The creep ductility evaluation of individual casts was carried out using isothermal dependencies of creep rupture elongation versus the time to rupture.

Detailed microstructural studies were conducted on ruptured test-pieces of the Casts B and C in order to understand the factors and processes responsible for the observed differences in creep behaviour. Investigations were carried out by means of optical metallography,

transmission and scanning electron microscopy. Specimens were taken from both heads and gauge lengths of ruptured specimens.

Table 1 Chemical compositions of the casts investigated, wt.%

Cast	C	N	Mn	Si	P	S	Cr	Ni	Mo	B	Nb
A	0.023	0.145	2.50	0.27	0.015	0.017	17.8	14.6	2.68	0.0037	<0.003
B	0.023	0.161	1.34	0.48	0.014	0.013	18.1	12.5	2.82	0.0012	0.106
C	0.021	0.158	1.11	0.42	0.025	0.009	17.8	12.6	2.64	0.0020	0.300

3. Experimental Results

3.1 Microstructure in the As-Received State

Table 2 shows temperatures of solution annealing, austenitic grain sizes and the yield points at 20°C for each material in the as-received state. As can be seen, small niobium additions resulted in a significant strengthening of steels. Grain sizes in niobium stabilised casts were markedly reduced. It suggested that some inhibiting particles were present in the austenitic matrix of niobium stabilised casts during solution annealing.

Table 2 Temperatures of solution annealing, austenitic grain sizes and $R_p0.2$ at 20°C

Cast	T [°C]	d [mm]	$R_p0.2$ [MPa]
A	1100	0.120	285
B	1050	0.020	392
C	1120	0.029	349

In order to verify this hyphotesis the following laboratory heat treatment was carried out on a specimen of the Cast C:

1300°C/0.5h./water + 1100°C/1.5h./water.

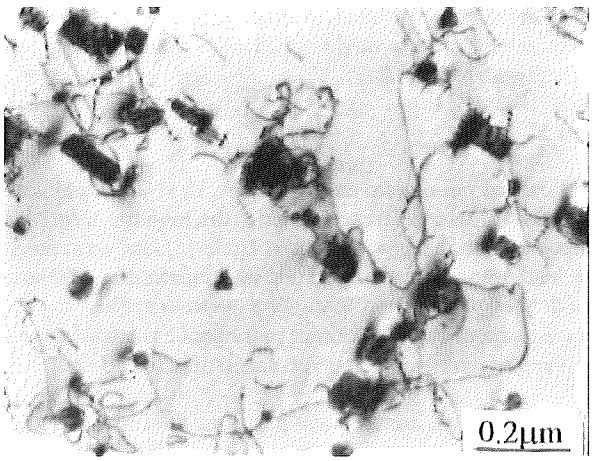

Fig. 1 Prim. Z phase particles in the specimen of the Cast C after laboratory heat treatment

Solution treatment at 1300°C was intended to dissolve particles of minor phases which had been present in the austenitic matrix. Microstructural studies confirmed only a very small number density of NbX particles in the austenite. Subsequent annealing at 1100°C resulted in heavy precipitation. Grain boundaries were decorated by a network of particles, many fine particles were also present inside austenitic grains, Fig. 1. Both intergranular as well as intragranular precipitates were identified as Z phase, Fig. 2. Only a few NbX particles were found. The average size of intragranular rod-like Z phase particles was

about 110nm. Chemical composition of Z phase particles, as determined by EDX, is shown in Table 3. As evident some molybdenum and iron are dissolved in NbCrN particles.

Table 3 Chemical composition of Z phase particles, wt.%

Cr	Fe	Nb	Mo
26.2 ±0.6	7.8±0.4	60.9±0.7	5.1±0.5

The results of the above experiment are consistent with the published data. The solvus temperature of the NbCrN phase in austenitic stainless steels was reported to be between 1300 and 1350°C, depending on the steel composition [2,9,12]. It can be concluded that in the as-received state the Casts B and C contained a high number density of primary Z phase particles in the austenitic matrix.

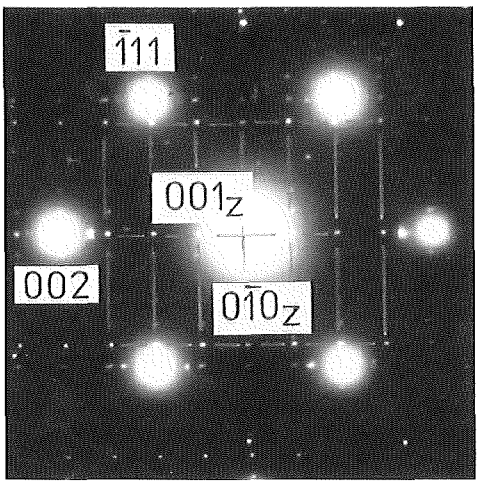

Fig. 2 The composed spot diffraction pattern $[100]_Z$ and $[110]_\gamma$

3.2. Creep Rupture Properties

The results of creep rupture tests are summarised in Fig. 3. At short times to rupture all casts investigated revealed approximately the same level of creep rupture strength, in spite of significantly smaller austenitic grain size in the niobium-bearing casts. At times to rupture exceeding 10^4 hours the creep rupture strength of casts with niobium additions was slightly inferior to the niobium free Cast A, see Table 4.

Table 4 Long-term creep strength of steels investigated

Cast	$R_{mT/10}^4$ [MPa]		$R_{mT/10}^5$ [MPa]	
	600°C	650°C	600°C	650°C
A	212	147	157	86
B	225	130	151	71
C	221	144	140	77

The growing niobium content strongly reduced the minimum creep rate and prolonged the time to the onset of the tertiary stage of creep [13]. However, the enhanced creep resistance of the niobium-bearing casts in the primary and secondary stages is not accompanied by the longer creep lives that might have been expected [10]. The observed differences in creep ductility are decisively affected by failure mechanisms which depend on the temperature, applied stress and microstructural evolution during creep exposure [14]. The creep rupture elongation plot for the Cast A shows a marked rise of elongation values at times to rupture in excess of 10^4 hours, see Fig. 3.

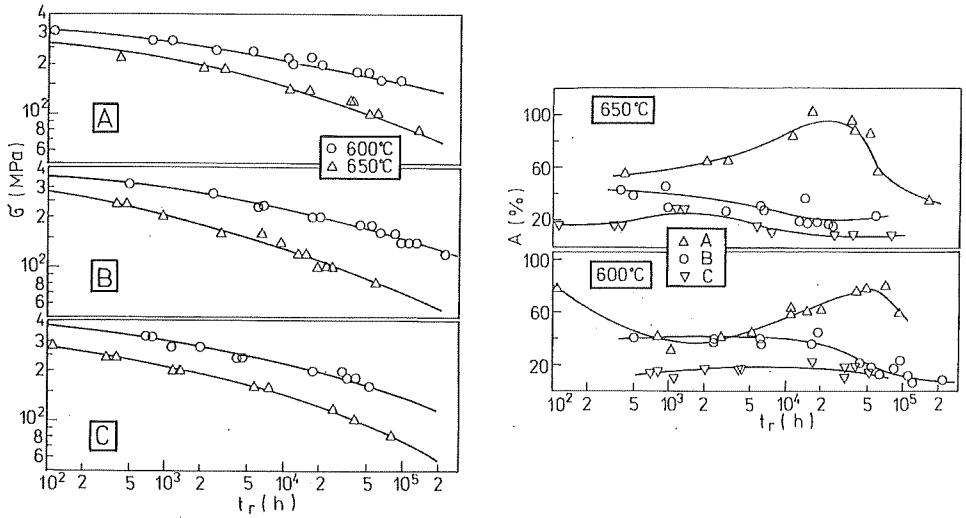

Fig. 3 Creep rupture strengths and rupture ductility of the Casts A, B and C at 600 and 650 °C

It can be speculated that the excellent combination of long-term creep strength and rupture ductility in the Cast A is positively affected by boron [1]. The niobium-bearing Casts B and C display no well-defined trend at times to rupture shorter than 10^4 hours and a pronounced decline of creep ductility at the longer durations to rupture. The coarse intergranular particles of σ phase on grain boundaries facilitated the formation of cavities, their growth and interlinking which resulted in intergranular fracture, see Fig. 9.

3.3. Microstructural Evolution in the Cast B during Creep at 650°C

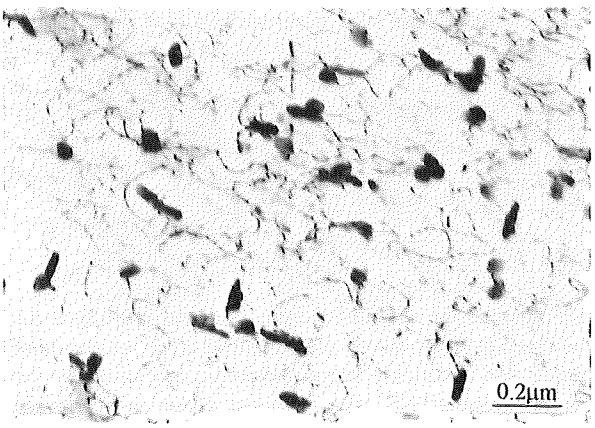

Fig. 4 η Laves and prim. Z phase particles, fine sec. Z phase particles on dislocations, 650°C/483h.

The same precipitation sequence was found in both heads and gauge lengths of creep ruptured specimens. Results of studies on minor phase evolution during long-term creep/thermal exposure are summarised in Table 5. Intragranular primary Z phase, η Laves and very fine secondary Z phase particles (on dislocations) in the specimen after exposure for 483hours are shown in Fig. 4. In this specimen a small number density of chromium rich $M_{23}C_6$ carbides was identified on grain boundaries. This minor phase was gradually replaced by M_6X phase (Cr_3Ni_2SiX type) at longer creep

exposures. During long-term creep exposure secondary Z phase particles continued to precipitate on dislocations and grain boundaries. Particles of Z phase were very dimensionally stable, even after 58936 hours the average size of secondary Z phase particles reached only several tens of nanometres. Intragranular η Laves (Fe_2Mo) particles in the form of rods continued to form with the prolonging time of exposure. Intensive intragranular precipitation of η Laves needles, primary and secondary Z phase particles in the specimen after 14864 hours is shown in Fig. 5. In this specimen the precipitation of σ phase was firstly detected. Particles of this phase formed preferentially on grain boundaries. The rate of σ phase coarsening was very high. Coarse σ phase particles were surrounded by denuded zones which facilitated grain-boundary sliding. After long-term creep/thermal exposure two dominant minor phases on grain boundaries were σ phase and M_6X. No Cr_2N and/or NbX particles were found to precipitate during creep exposure.

Table 5 Summary of minor phases identified in the Cast B

Time to Rupture [h.]	Minor Phases
483	prim. Z phase, sec. Z phase, $M_{23}C_6$, very small amounts of η Laves and M_6X
936	prim. Z phase, sec. Z phase(↑), η Laves(↑), $M_{23}C_6$(↓), a small amount of M_6X
6195	prim. Z phase, sec. Z phase(↑), η Laves(↑), $M_{23}C_6$(↓),M_6X (↑)
14864	prim. Z phase, sec. Z phase(↑), σ phase, η Laves(↑),$M_{23}C_6$(↓),M_6X (↑)
58936	σ phase(↑), prim. Z phase, sec. Z phase(↑), η Laves(↑), M_6X (↑)

Note: (↑) indicates a phase forming during the creep exposure and (↓) a phase dissolving.

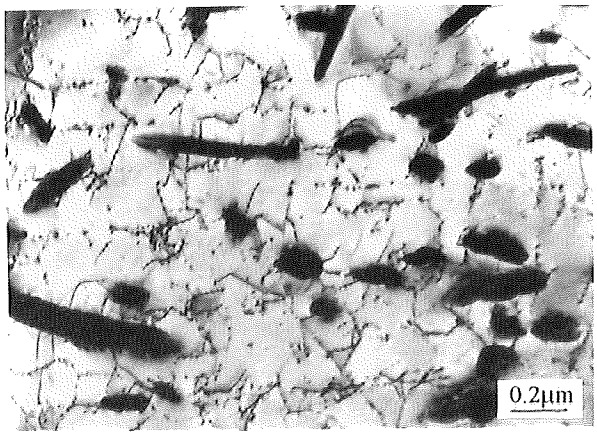

Fig. 5 η Laves and prim. Z phase particles, fine sec. Z phase particles on dislocations, 650°C/14864h.

3.4 Microstructural Evolution in the Cast C during Creep at 650°C

The precipitation reactions in the Cast C are summed up in Table 6. In the course of the long-term creep/thermal exposure the same minor phases have formed as in the Cast B. Secondary Z phase particles precipitated on grain boundaries and on dislocations, Fig. 6. The dimensional stability of Z phase particles during long-term creep exposure was very high. $M_{23}C_6$ carbides on grain boundaries were gradually replaced by M_6X phase. The kinetics of the both σ phase and η Laves formation was faster than that in the Cast B. Particles of σ phase preferentially formed on grain boundaries, Fig. 7. Only a small fraction of σ phase particles formed inside austenitic grains. The coarsening rate of this phase was very high. After long-term exposure at 650°C

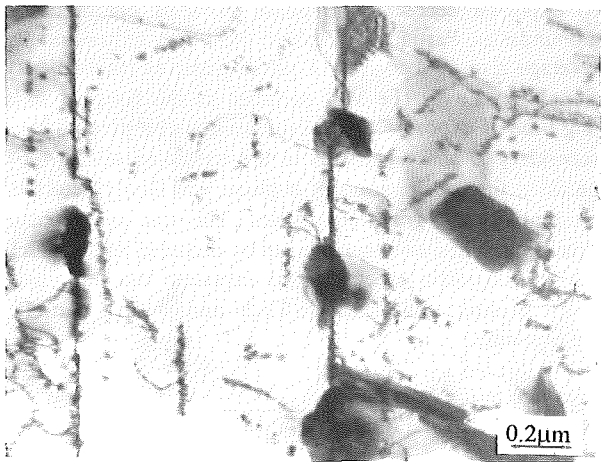

Fig. 6 Sec. Z phase particles on dislocations, η Laves and prim. Z phase particles on twin boundaries and in the austenitic matrix, 650°C/ 7849h.

grain boundaries were mainly decorated by M_6X and σ phase particles, while intensive precipitation of η Laves and Z phase was observed inside austenitic grains. Coarse σ phase particles (up to 10μm) on grain boundaries were surrounded by the denuded zones. These coarse σ phase particles facilitated the formation of intergranular creep cavities, Fig. 9. No Cr_2N and/or NbX particles were found to precipitate during long-term creep exposure.

3. Discussion

The results of microstructural investigations prove that the precipitation sequence in the Casts B and C during creep at 650°C was identical: fine secondary Z phase particles, chromium rich $M_{23}C_6$ particles which are gradually replaced by M_6X, η Laves and σ phase.

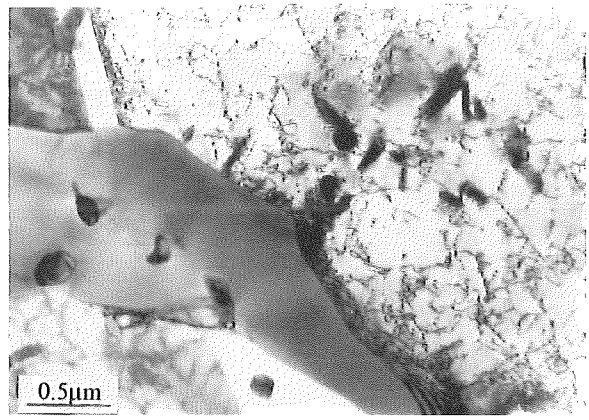

Fig. 7 Coarse σ phase particle, intragranular η Laves, secondary Z phase particles on dislocations, 650°C/26505h.

Table 7 shows Nb/C and Nb/(C+6/7N) ratios for the casts investigated. The Nb/C ratio is in the Cast B below and in the Cast C over the MX stoichimetric ratio (the weight ratio for NbC is about 8:1). When we take into account nitrogen then Nb/(C+6/7N) ratios for both casts are low and competition for niobium between NbX and NbCrN is to be expected. The results of microstructural investigations proved that Z phase was fast enough to form first. Dimensional stability of secondary Z phase particles forming during creep exposure at 650°C was excellent. No NbX particles were found to precipitate during long-term creep exposure at 650°C. This demonstrates that in steels investigated Z phase is more stable than NbX. Precipitation reactions in the niobium free Cast A started with the formation of a small amount of Cr_2N phase and $M_{23}C_6$ particles, preferentially on grain boundaries [10]. However no Cr_2N particles were detected in the niobium-bearing Casts B and C.

Table 6 Summary of minor phases identified in the Cast C

Time to Rupture [h.]	Minor Phases
81	prim. Z phase, sec. Z phase, $M_{23}C_6$, small amounts of η Laves and M_6X
1350	prim. Z phase, sec. Z phase(↑), η Laves(↑), $M_{23}C_6$(↓), M_6X (↑), a small amount of σ phase
7849	prim. Z phase, sec. Z phase(↑),σ phase(↑), η Laves(↑), $M_{23}C_6$(↓),M_6X (↑)
26505	prim. Z phase, sec. Z phase(↑), σ phase(↑), η Laves(↑),$M_{23}C_6$(↓),M_6X (↑)
37890	σ phase(↑), prim. Z phase, sec. Z phase(↑), η Laves(↑), M_6X (↑), a very small amount of $M_{23}C_6$

Note: (↑) indicates a phase forming during the creep exposure and (↓) a phase dissolving.

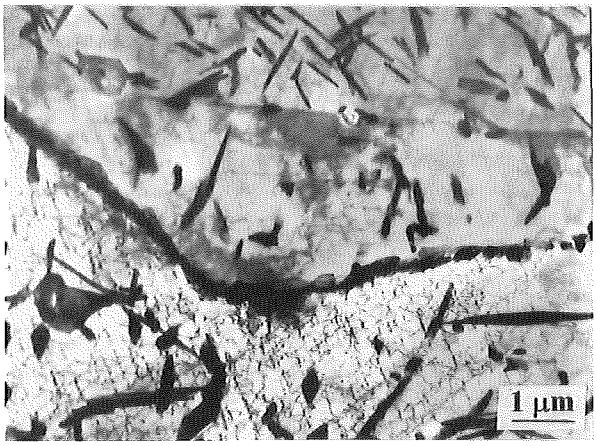

Fig. 8 A network of M_6X, prim. Z phase and σ phase particles on grain boundary, intragranular η Laves rods, prim. Z phase and sec. Z phase on dislocations, 650°C/37890hours

In these casts some nitrogen was bound in primary Z phase and the nitrogen content available in the solid solution probably dropped below a critical value needed for precipitation of Cr_2N. A small amount of $M_{23}C_6$ particles formed in the Casts B and C on grain boundaries and incoherent twin boundaries at short times of creep exposure. This phase was gradually replaced by M_6X (Cr_3Ni_2SiX) phase at longer exposures. In nitrogen-bearing austenitic steels M_6X phase is rich in nitrogen [9]. Typical contents of substitutional elements in this phase, as determined by EDX,

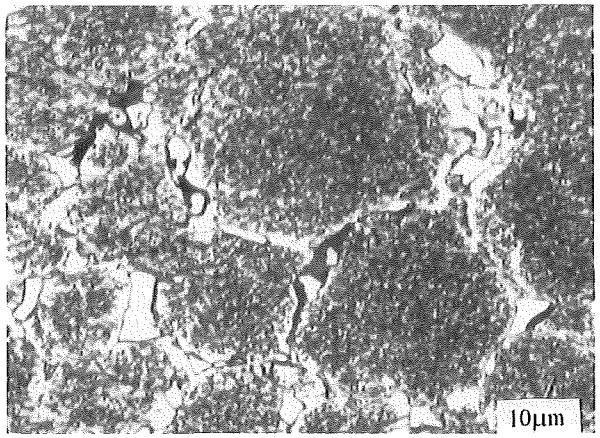

Fig. 9 Creep cavities formed on coarse σ phase particles in the Cast C, 650°C/33624h.

were as follows, in wt.%: Si-2, Cr-41, Mn-1, Fe-4, Ni-28, Nb-2, Mo-22. The niobium content in this phase is low.

Table 7 The weight ratios Nb/C and Nb/(C+6/7N) in the Casts B and C

Cast	Nb/C	Nb/(C+6/7N)
B	4.6	0.7
C	14.2	1.9

Elements like Cr, Nb, Ti and Mo are known to promote the formation of σ phase and therefore its formation is faster in stabilised austenitic grades [15]. Also Si promotes and accelerates its formation [2]. It has been reported that σ phase forms when the carbon content in the matrix falls below a critical value when the chromium equivalent is higher than 18wt.% [2]. The kinetics of the σ phase formation and coarsening in the niobium free Cast A was much slower than that in the niobium-bearing casts [10]. The σ phase coarsening was the most pronounced in the Cast C containing 0.3wt.%Nb. The typical composition of σ phase was as follows, in wt.%: Si-1 , Cr-35 , Mn-1 , Fe-51 , Ni-3 , Nb-1 and Mo-8 .

The coarse σ particles on grain boundaries facilitated the formation and interlinking of creep cavities and contributed to relatively poor creep ductility. Niobium in the Casts B and C also accelerated η Laves precipitation. This phase started to form on grain and twin boundaries. At longer times of exposure an intensive precipitation of η Laves in the form of needles was observed inside austenitic grains. In niobium stabilised steels, Fe_2Nb is frequently reported after long aging times. It is a transient phase which disappears when Fe_3Nb_3C forms [2]. However η Laves in the Casts B and C was a Fe_2Mo phase. Typical contents of elements in this phase were as follows, in wt.%: Si-1, Cr-16, Mn-1, Fe-39, Ni-4, Nb-1 and Mo-32. The niobium content in both η Laves and σ phase was low.

Based on the typical size the precipitates in the Casts B and C after long-term creep/thermal exposure at 650°C can be classified as follows:

- less than 50nm: secondary Z phase particles,
- 100 to 1000nm: M_6X, η Laves, primary Z phase particles,
- 1 to 10μm: σ phase.

Only two nitrogen rich minor phases were identified in the niobium-bearing Casts B and C: Z phase and M_6X. The kinetics of the Z phase formation was much faster than that of M_6X. It can be expected that these two minor phases will compete for nitrogen. However creep specimens with time to rupture about 50000 hours at 650°C are not long enough to assess the relative stability of these minor phases.

4. Conclusions

1. The following minor phases were identified in the niobium-bearing Casts B and C after long-term creep/thermal exposure at 650°C: primary Z phase, secondary Z phase, η Laves, M_6X and σ phase.
2. Only two nitrogen rich minor phases were found: Z phase and M_6X. The kinetics of the Z phase formation was faster than that of M_6X. Creep specimens with time to

rupture about 50000 hours at 650°C are not long enough to assess the relative stability of these phases.

3. The dimensional stability of secondary Z phase particles forming during creep/thermal exposure was excellent. M_6X particles grew/coarsened much faster.
4. The enhanced creep resistance of the niobium-bearing casts in the primary and secondary stages is not accompanied by the longer creep lives that might have been expected. The development of creep damage was facilitated by the fast formation and coarsening of σ phase particles. The coarse σ particles on grain boundaries contributed significantly to relatively poor creep ductility.

Acknowledgement

The author wishes to acknowledge the financial support from the Grant Agency of the Czech Republic under the project No. 106/09/1868.

References

[1] Marshall P.: Austenitic Stainless Steels, Elsevier, London – New York, (1984).
[2] Sourmail T.: Precipitation in Creep Resistant Austenitic Stainless Steels. Mat. Sci. Techn., Vol. 17, pp.1-14, (2001).
[3] Keown S. R., Pickering F. B.: In Proc. Creep Strength in Steels and High Temperature Alloys, London, The Metals Society, p. 134, (1974).
[4] Adamson J. M., Martin J.W.: JISI, Vol. 210, p. 271, (1972).
[5] Jack D. H. and Jack K. H.: Structure of Z phase, NbCrN, JISI, Vol. 209, pp. 790-792, (1972).
[6] Raghavan A., Klein C. F., Marzinski C. N.: Instabilities in Stabilized Austenitic Stainless Steels, Met. and Mat. Trans. A, Vol. 23A, pp. 2455-2462, (1992).
[7] Knowles G.: Metal Science, Vol. 11, p. 117, (1977).
[8] Robinson P.W., Jack D. H.: In Proc. New Developments in Stainless Steel Technology, Metals Park, OH, ASM, , p. 71, (1985).
[9] Sourmail T., Bhadeshia H.K.D.H.: Microstructural Evolution in Two Variants of NF709 at 1023 and 1073K, Met. and Mat. Trans. A, Vol. 36A, pp. 23-34, (2005).
[10] Vodárek, V., Sobotková M., Sobotka, J.: The Effects of Microstructural Evolution on the Creep Rupture Behaviour of of CrNi(Mo)N Austenitic Steels, In Proc. Microstructural Stability of Creep Resistant Alloys for High Temperature Plant Applications, The Institute of Materials, London, pp. 69-88, (1998).
[11] Sobotka, J., Vodárek V., Sobotková M.: Hodnocení vlivu molybdenum na dlouhodobou žárupevnost vybraných typů austenitických ocelí, Metallurgical Journal, Vol. 47, pp. 31-36, (in Czech), (1992).
[12] Hughes H.: Complex Nitride in Cr-Ni-Nb Steels, JISI, Vol. 205, pp. 775-778, (1967).
[13] Vodárek V., Sobotka J., Sobotková M., Sojka J.: Effect of Niobium on the Microstructure and Creep Properties of AISI 316LN Type Steels, In Proc. Applications of Stainless Steel 92, Stockholm, pp. 123-132, (1992).
[14] Vodárek V., Liška M., Sobotka J.: Creep Behaviour and Microstructural Evolution in AISI 316LN Steels with Niobium Additions. In Proc. 10th Int. Conference on High Nitrogen Steels, Moscow, MISIS, pp. 83-89, (2009).
[15] Minami Y., Kimura H., Ihara Z.: Microstructural Changes in Austenitic Stainless Steels during Long-Term Aging, Mat. Sci. Techn., Vol. 2, pp. 795-806, (1986).

9th Liege Conference : Materials for Advanced Power Engineering 2010
edited by J. Lecomte-Beckers, Q. Contrepois, T. Beck and B. Kuhn.

APPLICATION OF NEW GMAW WELDING METHODS USED IN PREFABRICATION OF P92 (X10CrWMoVNb9-2) PIPE BUTT WELDS

Michał Urzynicok[1)], Krzysztof Kwieciński[2)], Marian Szubryt[3)], Jacek Słania[2)]
[1)] Boiler Elements Factory „ZELKOT", 42-286 Koszęcin, Poland, ul. Nowy Dwór 8
[2)] Instytut Spawalnictwa, 44-100 Gliwice, Poland, ul. Bł. Czesława 16-18
[3)] TÜV Nord, 40-085 Katowice, Poland, ul. Mickiewicza 29

Abstract

Welding of collector pipes, flat heads, dished ends and connector pipes performed with high temperature and creep-resistant steels most often has been performed using TIG process combined with MMA processes. Progress in MAG process and availability of high quality filler materials (solid wires) enables welding of the above connections also using this method. In order to prove its efficiency, this article presents the results of related tests. The range of tests was similar to that applied during the qualification of welding technology. The investigation also involved microscopic and fractographic examinations. The results reveal that welding with new methods such as GMAW is by no means inferior to a currently applied MMA method yet the time of the process is shorter by 50%. The article present the world's first known positive results in welding of P92 grade steel using GMAW welding method.

Keywords: P92, MAG, TIG, pipe butt welds, welding.

1. Introduction

The production of critical structures of power boiler pressure elements requires special attention to be attached to the quality of welded joints. In order to accomplish this objective the manufacturer of power engineering equipment must be supported by advanced technological solutions as steel grades intended for operation at higher temperature are characterised by limited weldability and thus demand complete supervision and monitoring at pre-weld, welding and post-weld stages. Most steel grades used in operation at high temperature and, in particular, martensitic molybdenum-chromium steels require pre-heating, maintaining proper inter-run temperature and post-weld heat treatment of the joint usually through stress relief annealing. The whole process of production of butt joints, especially in case of collector pipes of diameters exceeding 114.3 mm and wall thickness over 10 mm, using standard technologies applied today proves time-consuming and costly. Therefore it remains desirable to further improve the welding process, reduce joint production time, significantly decrease labour costs without compromising high mechanical and plastic properties of welded joints, process purity and low noxiousness to the welder [1, 2].

Until today collector pipes of water-tube steam boilers are TIG-welded (fusion layer) with covered electrode (filling layers). The combination of both methods guarantees high quality of joints but, unfortunately, increases their production time. The major factors prolonging the welding process time are additional operations such as removal of slag or post-weld spatters. In addition, welding with covered electrodes is connected with significant emission of welding fumes and gases known to be detrimental to welder's health [2].

The availability of welding consumables in the form of solid wires as well as access to modern welding equipment enabled the MAG-, and in particular, pulse current-based investigation focused on welding of materials exploited at higher temperature [2, 4].

2. General characteristic of P92 steel

Martensitic steel 9Cr-1Mo-0.25V designated as P/T91 was developed in the USA in order to meet the needs of nuclear and conventional power engineering. In Europe the steel is designated as X10CrMoVNb9-1.

The modifications of the chemical composition of P91 steel consisting in the reduction of molybdenum content by approx. 0.5% and addition of 1.7% tungsten resulted in the development of steel whose creep resistance is by approx. 30% higher than that of P91 grade. The steel obtained through the aforesaid modifications was designated as P92 or NF616 or, otherwise as, X10CrWMoVNb9-2. Tungsten, similarly to molybdenum, is an element enhancing solid solutions as it increases recrystallisation temperature thus improving long-term stability of matrix at higher temperature. Through stabilising carbides a microaddition of boron used in P92 steel increases its creep resistance and limits excessive liberation of carbides on grain boundaries [5].

The chemical composition of steels with 9% Cr content is presented in Table 1; the comparison of mechanical properties of such steels is presented in Table 2.

Table 1. Comparison of chemical composition of 9%Cr steels according to EN 10216-2 [6]

Grade	Chemical composition, %									
	C	Si	Mn	Cr	Mo	Nb	Co	V	W	Others
P91	0.08-0.12	0.2-0.5	0.3-0.6	8-9.5	0.85-1.05	0.06-0.1	-	0.18-0.25	-	N=0.03-0.07
P92	0.07-0.13	<0.5	0.3-0.6	8.5-9.5	0.3-0.6	0.04-0.09	-	0.15-0.25	1.5-2	N=0.03-0.07 B=0.0005-0.005
E911	0.09-0.13	0.1-0.5	0.3-0.6	8.5-9.5	0.9-1.1	0.06-0.1	-	0.18-0.25	0.9-1.1	N=0.05-0.09 B=0.0005-0.005
PB2*	0.135	0.076	0.31	9.28	1.51	0.053	1.33	0.19	-	N=0.026 B=0.0091

* test melt data

Table 2. Comparison of mechanical properties of 12%Cr steels according to steel-makers

Grade	Mechanical properties		
	R_e, MPa	R_m, MPa	A min., %
P91	450	630	19
P92	440	620	19
E911	450	620	19
PB2*	601	754	19

* test melt data

3. Subject of investigation

The subject of investigation included butt-welded joints of pipes (ø219.1 x 31.75mm) made of X10CrWMoVNb9-2 (P92) steel. The chemical composition of the steel as delivered is presented in Table 3, whereas its mechanical properties are detailed in Table 4.

Table 3. Chemical composition of tested P92 steel grade [5]

Grade	Chemical composition, %									
	C	Si	Mn	Cr	Mo	V	W	Co	Others	
P92	0.103	0.223	0.484	8.986	0.456	0.164	1.900	0.027	B-0.002 N-0.047 Ti-0.002	Nb-0.053 Ni-0.116 Cu-0.111

Table 4. Mechanical properties of tested P92 steel grade [5]

Grade	Mechanical properties				
	Re, MPa	Rm, MPa	A min., %	HV	KV, J
P92	666	805	23	228	255

4. Welding consumables

Properly selected welding consumables are decisive for obtaining required joint properties. Their role is to ensure that the chemical composition of the weld and its mechanical properties will be as close to those of the parent metal as possible. Table 5 presents welding consumables while welding test joints [5, 7].

Table 5. Welding consumables used for P92 steel grade

Method	Filler metal	Diameter	Manufacturer, designation
Welding consumables used with P92 steel (X10CrWMoVNb9-2)			
111	E ZCrMoWVNb 9 0.5 2 B 4 2 H5	3.2; 4	Böhler Thyssen Thermanit MTS 616
135 (TP)	G ZCrMoWVNb 9 0.5 1.5	1.2	Böhler Thyssen Thermanit MTS 616
141	W ZCrMoWVNb 9 0.5 1.5	2.4	Böhler Thyssen Thermanit MTS 616

5. Welding process

Today the most widespread method of producing butt-welded joints of collector pipes is TIG-welding of the root combined with filling performed with a covered electrode. TIG-welding was applied in the research for comparison-related purposes; the other method being MAG-welding with double pulse current.

Prior to welding the joints were prepared as shown in Figure 1a. The welding process involved the production of a root run and filling runs as shown in Figure 1b. The shielding gas applied to safeguard the root was 4.8 grade argon. The test joints were produced in PA position [8-10].

a) b)

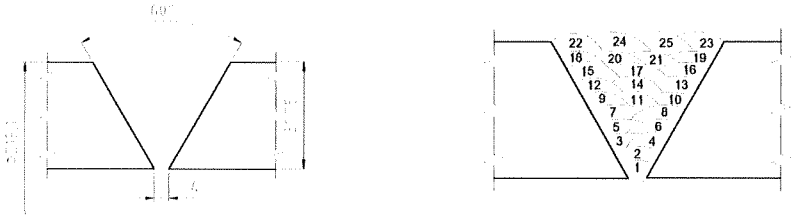

Figure 1. Joint preparation diagram: weld groove geometry (a), weld run sequence (b)

6. Welding thermal cycle and post-weld heat treatment

Prior to welding the pipe was heated up to 200°C. During welding the inter-pass temperature was subject to continuous monitoring and did not exceed 280°C. Temperature was measured In the weld area as well as about 15 mm from the weld grove on pipe surface. After the completion of welding the joints were cooled down to ambient temperature. The welding thermal cycle and the diagram of post-weld heat treatment are presented in Figure 2 [5].

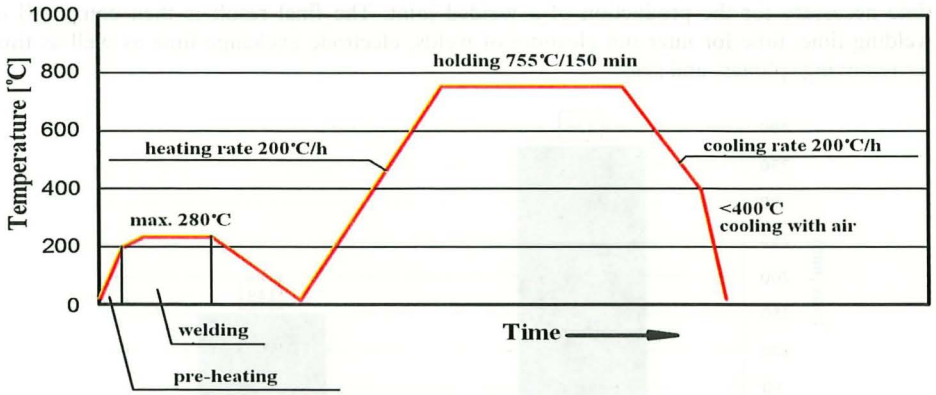

Figure 2. Welding and PWHT cycle

7. Investigation plan

The production of welded joints was followed by non-destructive tests i.e. VT, PT and RT in 100% scope. The tests were performed taking into consideration quality level B pursuant to standard PN-EN ISO 5817 [11]. After obtaining positive NDT results, the joints were sampled for specimens for destructive tests (see the diagram in Figure 3).

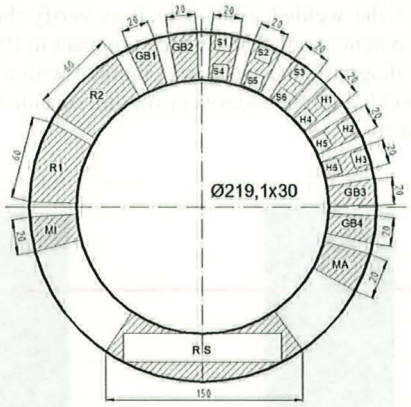

Figure 3. Manner of cutting specimens out of butt-welded joints of tubes

The scope of mechanical tests included the static tensile test of the welded joint (samples R1 and R2), bend test (samples GB1÷GB4 – side bend tests), impact tests (samples S1÷S6 – notch cut in the weld; samples H1÷H6 – notch cut in HAZ), macroscopic examination (sample MA), microscopic examination (sample MA), hardness measurements (sample MA) and fractographic examination from break tests.

8. Welding time measurement

During the production of all joints related welding times were measured for comparative purposes. The measurements were performed so that it would be possible to assess the total

time necessary for the production of a welded joint. The final result is then composed of welding time, time for inter-run cleaning of welds, electrode exchange time as well as time for removing splinters and slag.

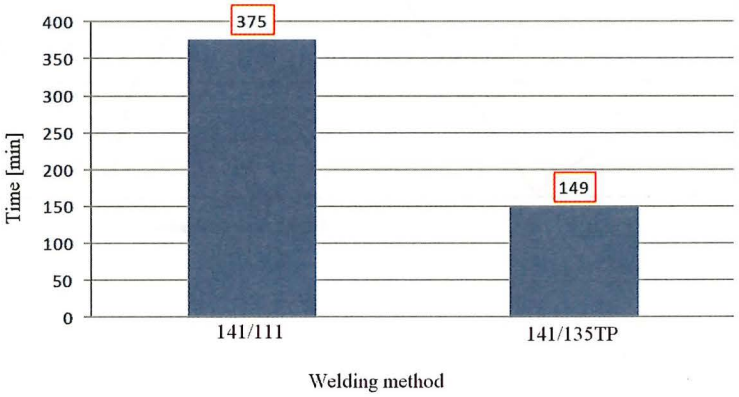

Figure 4. Total time measured for butt welding of P92 pipe

9. Results of joint static tensile tests

The tests were performed pursuant to standard PN-EN 895 [12] and aimed to determine the tensile strength (R_m) of the welded joint as well as verify the results in relation to the minimum R_m value for the parent metal (PM), which pursuant to PN-EN 10216-2 [6] standard stands at 620 MPa. In the diagrams the value was marked with a thick line (Figure 5). The tests revealed that all the welded joints underwent rupture outside the weld and met strength- and quality related requirements.

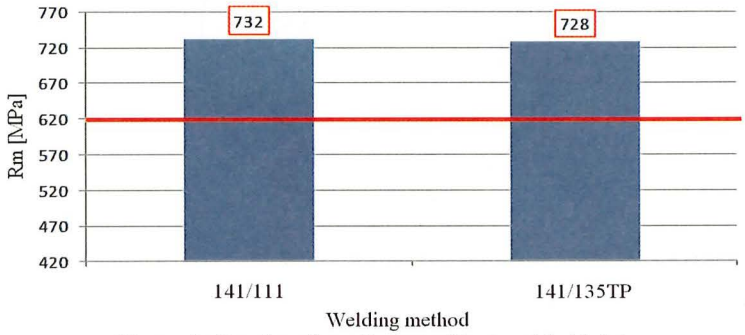

Figure 5. Results of tensile test of butt welded joints

10. Results of weld and HAZ impact tests

The tests in question were performed in order to determine the impact energy of weld and that of HAZ. Standard PN-EN 12952-6 [13] sets the minimum value of impact energy in HAZ at 24J and that in the weld at 27J; both values being provided for ambient temperature conditions. In the diagrams the said values were marked with thick lines (Figure 6).

The impact energy results concerning the weld and HAZ are higher than the values specified in the cited standard and the minimum values declared by the manufacturer.

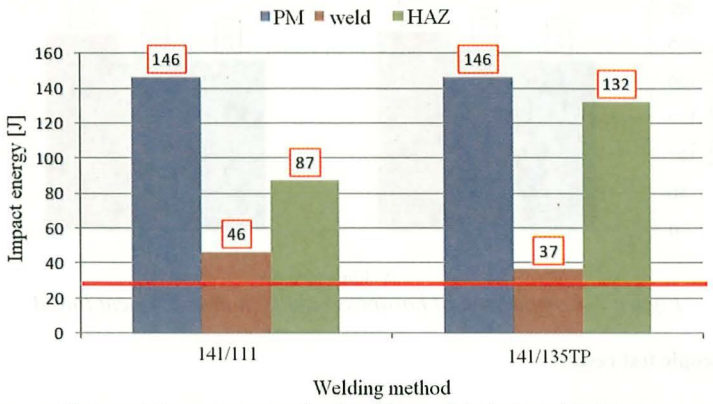

Figure 6. Impact strength of weld metal in butt welded joints

11. Hardness measurements results of weld

The hardness tests were conducted pursuant to standards PN-EN 15614-1 [14] and PN-EN 12952-6 [13]. In the aforementioned standards the maximum value specified for joints subject to heat treatment stands at 350 HV10. Figure 7 presents the arrangement of hardness measurement points, whereas Figures 8-9 present the results of corresponding measurements. All the results are considerably lower than the allowed values and thus confirm the proper selection and performance of welding process and heat treatment.

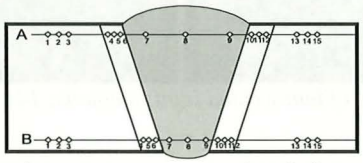

Figure 7. Hardness measurement points in butt welded joints

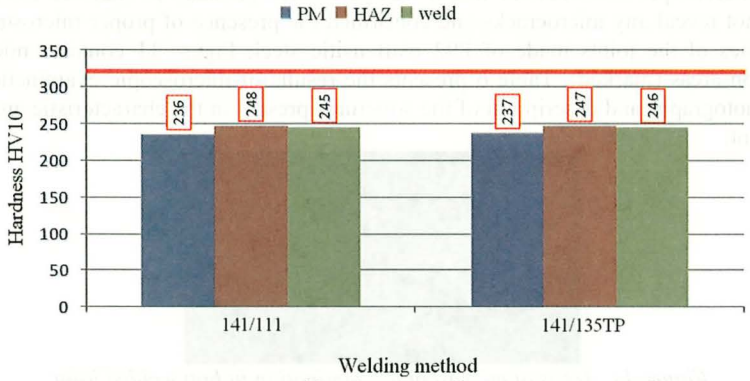

Figure 8. Comparison of hardness results in measurement line A

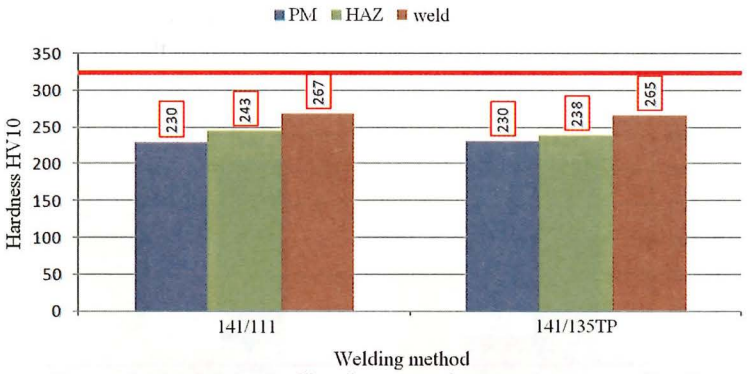

Figure 9. Comparison of hardness results in measurement line B

12. Macroscopic test results

The examination was performed pursuant to standard PN-EN 1321 [15]. The criterion applied for assessment-related purposes was quality level B pursuant to standard PN-EN ISO 5817 [9]. The aforesaid quality requirement was met in case of all of the joints. Figure 10 presents the results of macroscopic examination of the joint welded with 141/111 method (left) and those related to the joint produced with 141/135 method (right).

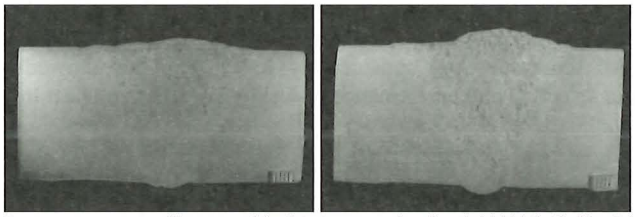

Figure 10. Macrostructure of butt welded joint; methods: 141/111 (left), 141/135 (right)

13. Microscopic test results

The microscopic examination, which was performed pursuant to standard PN-EN 1321 [15], did not reveal any microcracks and confirmed the presence of proper microstructure in all the zones of the joints made of P92 martensitic steel. Figure 11 contains microscopic examination areas (marked). Table 6 presents the results of microscopic examination in the form of photographs and description of the structures present in the characteristic areas of the welded joint.

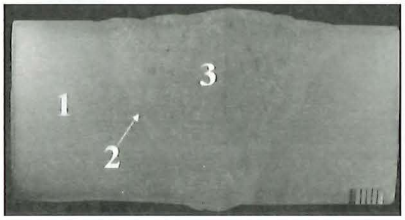

Figure 11. Areas of microscopic examination in butt welded joint

Table 6. Examples of result of microscopic examination of butt welded joint

	141/111	141/135
parent metal **area 1**, mag. 500x, etch. $FeCl_3$	tempered martensite	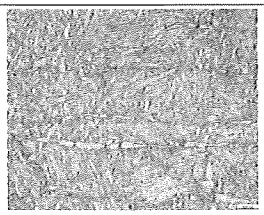 tempered martensite
HAZ **area 2**, mag. 500x, etch. $FeCl_3$	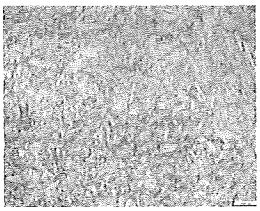 tempered martensite	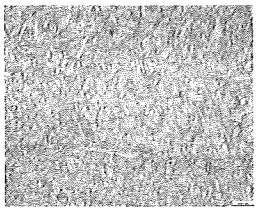 tempered martensite
weld **area 3**, mag. 500x, etch. $FeCl_3$	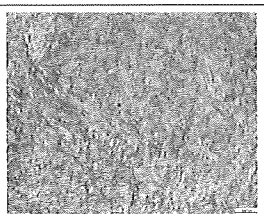 tempered martensite	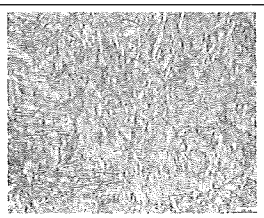 tempered martensite

14. Fractographic examination results

The fractographic examination was conducted on the fractures following the impact test and involved the samples welded with method 135 (sample series 1) and joints welded with method 111 (sample series 2).

The topography of fractures of welds welded with method 135 following the impact test are presented in figure 12a), whereas the HAZ fractures are presented in figure 12b). Figures 13a) and 13b) present the fractures of the weld and HAZ welded with method 111 respectively.

The fractographic analysis and microanalysis of the chemical composition of precipitates in the weld welded with the covered electrode reveals that the joint was produced properly and should meet the requirements of operation at higher temperature. The aforesaid fact is confirmed by impact energy values, which for the weld and HAZ amounted to 49J and 87 J respectively. Also the hardness of the joint, which did not exceed 280 HV, confirms the correctness of the applied technology.

During fractographic examination both MC carbides and MX carbonitridies were found. Both precipitates were analyzed with chemical microanalysis and it was found that chromium carbides and tungsten carbides were present in weld and HAZ.

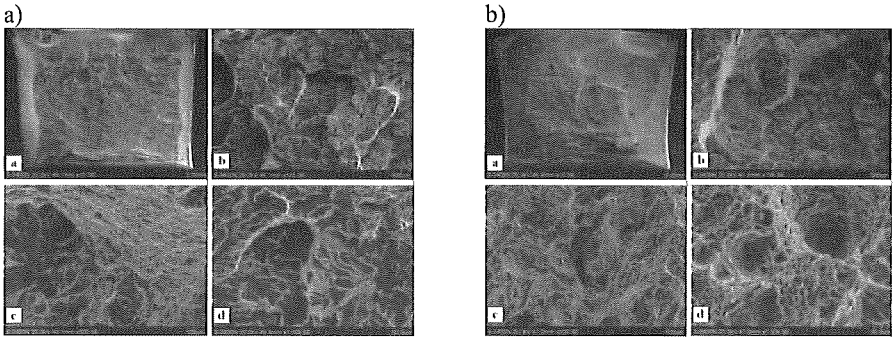

Figure 12. Weld topography for 135 welding method

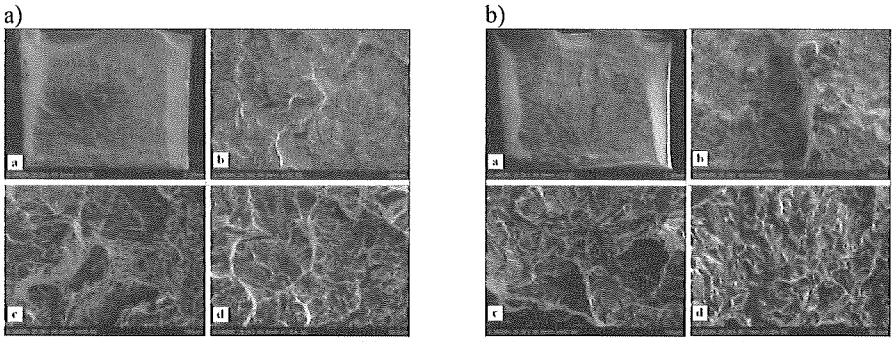

Figure 13. Weld topography for 111 welding method

In all cases it was possible to observe mixed plastic-brittle fracture with rare scrap cracks. Such morphology is characteristic of tempered martensite structures. As opposed to conventional method 141/111 no anomalies were diagnosed for the samples welded with method 141/135TP.

15. Conclusions

On grounds of the tests it was possible to formulate the following conclusions:

1. Both NDT and DT confirmed high quality pf that butt-welded joints made of P92 steel in workshop conditions.
2. In all cases it was possible to observe mixed plastic-brittle fracture with rare scrap cracks. Such morphology is characteristic of tempered martensite structures. As opposed to conventional method 141/111 no anomalies were diagnosed for the samples welded with method 141/135TP.
3. The application of MAG method reduces impurities and increases the comfort of welder's work.
4. The mechanisation of method 135 may lead to a further increase in the effectiveness of production of butt-welded joints and at the same time decrease their manufacturing costs.
5. Base on the performed examinations it can be concluded that weld properties in service temperature will meet the standard requirements

Acknowledgments

The authors of the article wish to express their thanks to TenarisDalmine for providing the pipes used for the investigations and to BÖHLER Schweißtechnik Deutschland for providing the covered electrodes used for welding P92 steel

Reference list:

[1] Shankar V., Bhaduri A., Raj B., Welding Technology for Engineers. *Alpha Science International*, (2006).
[2] Urzynicok M., Kwiecinski K., Słania J., Properties of welded joints in 7CrMoVTiB10-10 (T24) bainitic steel used in power stations operated at supercritical parameters, Gliwice, *Welding Institute Bulletin*, no 6 p. 59-62, (2009).
[3] Dobrzański L. A., *Metalowe materiały inżynierskie. WNT*, Gliwice-Warszawa, (2004).
[4] Urzynicok M., Kwieciński K., Szubryt M., Experience in the welding of martensitic steel VM12-SHC, *Materials Investigation for Power Industry, XVI. scientific and technical seminar,* Zakopane, (2009).
[5] Urzynicok M., Kwieciński K., Szubryt M., Application of new GMAW welding methods used in prefabrication of P92 (X10CrWMoVNb9-2) pipe butt welds, *Energetyka, no XIX*, SIMP, p. 168-170, 11.2009.
[6] PN-EN 10216-2+A2. Seamless steel tubes for pressure purposes. Technical delivery conditions. Part 2: Non-alloy and alloy steel tubes with specified elevated temperature properties.
[7] Heuser H., Jochum C., Alloy design for similar and dissimilar welding and their behaviors. *I^st International Conference Super-High Strength Steels. Rome*, (2-4.11.2005).
[8] Urzynicok M., Szubryt M., Time optimalization of welding 16Mo3 pipe butt welds for power industry. *XVI International Conference „Welding in Power Industry"*, Jarnołtówek, (23-25.04.2008).
[9] Urzynicok M., Szubryt M., Zastosowanie nowoczesnych odmian metody MAG do spawania rur kolektorowych w energetyce zawodowej, *XV, scientific and technical seminar,* Zakopane, (18-20.06.2008).
[10] Urzynicok M., Kwieciński K., Szubryt M., Experience in the welding of martensitic steel VM12-SHC, *Materials Investigation for Power Industry, XVI. scientific and technical seminar,* Zakopane, (2009).
[11] PN-EN ISO 5817. Welding. Fusion-welded joints in steel, nickel, titanium and their alloys (beam welding excluded). Quality levels for imperfections
[12] PN-EN 895. Destructive tests on welds in metallic materials. Transverse tensile test.
[13] PN-EN 12952-6. Water-tube boilers and auxiliary installations. Part 6: Inspection during construction. Documentation and marking of pressure parts of the boiler.
[14] PN-EN ISO 15614-1. Specification and qualification of welding procedures for metallic materials. Welding procedure test. Part 1: Arc and gas welding of steels and arc welding of nickel and nickel alloys.
[15] PN-EN 1321. Destructive tests of welds in metallic materials. Macroscopic and microscopic examination of welds.

9th Liege Conference : Materials for Advanced Power Engineering 2010
edited by J. Lecomte-Beckers, Q. Contrepois, T. Beck and B. Kuhn.

PRACTICAL EXPERIENCE WITH WELDING NEW GENERATION STEEL PB2 ASSIGNED FOR POWER INDUSTRY

Krzysztof KWIECIŃSKI[1)], Michał URZYNICOK[2)], Mirosław ŁOMOZIK[1)]

[1)] Instytut Spawalnictwa, 44-100 Gliwice, Poland, ul. Bł. Czesława 16-18
[2)] Boiler Elements Factory „ZELKOT", 42-286 Koszęcin, Poland, ul. Nowy Dwór 8

Abstract

This paper presents a new generation steel PB2 assigned for the power industry. In this article the authors present the results of non-destructive (VT, PT, RT) and destructive (tensile test, bending test, hardness measurements, impact strength, macro- and micrograph, fractography) tests. The major objective of the examinations was to verify properties of welded joints made of PB2 steel. Investigation of welded joints made of PB2 steel was performed in Instytut Spawalnictwa in Gliwice and it brings one of the first positive results for this type of steel in the world.

Keywords: PB2, pipe butt welds, new steel grades, welding,

1. Introduction

A continuous trend aimed to reduce pollutant emissions to atmosphere and lower power generation costs is directly related to increasing efficiency of power units in conventional power stations. An increase in efficiency is obtained through boosting key working parameters i.e. steam pressure and temperature. Currently applied martensitic steels such as P92 make it possible to design power stations in which the temperature of superheated steam may reach as much as 625°C. Obtaining higher parameters can be possible only through continual search for modern materials used in fabrication of boiler and pipeline elements. This necessity has provided a stimulus to start studies of new steel grades, whose mechanical properties and creep resistance can be high enough for use in boiler elements operating under even higher parameters [1].

Many years of research has brought in many new steel grades with PB2 steel as one of them. This modern martensitic steel was developed within the framework of the European Research Programme COST 536. Due to the fact that the material is still under investigation, parallel efforts are being made to work out optimum parameters related to joint preparation, welding process and post-weld heat treatment. The parameters for the production of the joint described in the article were selected by the authors on grounds of available publications [2] as well as their own experience [3, 4, 5]. The welded joint was produced in Zakłady Elementów Kotłowych (Boiler Elements Factory) "ZELKOT" in Koszęcin, Poland.

2. Subject of investigation

The subject of the study was a pipe (ø 219.1 x 31 mm) made of PB2 steel, manufactured by Italy's Tenaris Dalmine. The chemical composition of the steel is detailed in Table 1. The mechanical properties of PB2 steel as delivered are presented in Table 2.

Table 1. Chemical composition of PB2 steel as provided by manufacturer

Steel designation	Element content [%]									
	C	Cu	Al.	N	Mn	Sn	Ti	B	Si	Ni
PB2	0.135	0.031	0.07	0.026	0.310	0.004	0.001	0.0091	0.076	0.150
	Nb	As	P	Cr	V	Sb	S	Mo	Co	-
	0.053	0.002	0.0058	9.28	0.190	0.005	0.001	1.51	1.33	

Table 2. Mechanical properties of PB2 steel as provided by manufacturer

Steel grade	R_e [MPa]	R_m [MPa]	A min. [%]
PB2	610	763	21.5

3. Filler metal

The research welding involved the application of Metrode-manufactured covered low-hydrogen electrodes (3.25 mm and 4 mm in diameter); the electrodes were developed for pipes and forgings made of B2 steel/cast steel. As PB2 steel has not been classified in standards yet, the aforementioned electrodes are not provided with designations pursuant to currently valid European Standards either. Electrodes Metrode Chromet WB2 were manufactured under specification AWS A5.5-96/ASME SFA 5.5 E9015-G [6]. The chemical composition of the filler metal is presented in Table 3.

Table 3. Chemical composition of filler metal as provided by manufacturer

Element content [%]													
C	Mn	Si	S	P	Cr	Ni	Mo	Nb	Cu	V	N	B	Co
0.110	0.590	0.190	0.008	0.011	9.220	0.660	1.460	0.040	0.030	0.22	0.023	0.006	1.020

4. Test joint production

The test joint was prepared for welding in accordance with Figure 1a. The root run was TIG-welded (141) using a solid rod for welding P92 steel. Today's market offer does not include solid rods for welding PB2 steels. The filling runs and face were welded manually with covered electrodes (111). The weld run sequence is presented in Figure 1b; the forming gas being argon. The welding was performed in the vertical up position (PF). Prior to welding the test elements were pre-heated up to approx. 200°C; during welding the inter-run temperature was constantly monitored. After welding the joint was cooled down to ambient temperature and next subject to stress relief annealing. The course of the whole welding thermal cycle and diagram of the post-weld heat treatment are presented in Figure 2.

a) b)

Figure 1. Joint preparation diagram: geometry of weld groove (a), weld run sequence (b)

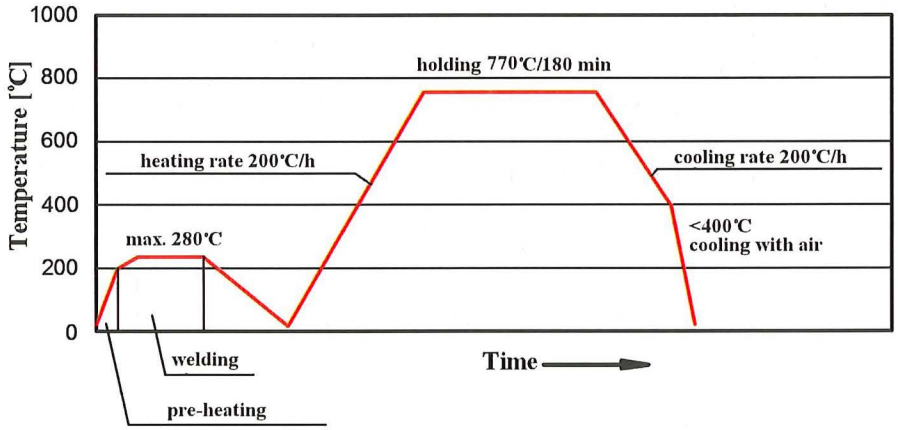

Figure 2. Course of welding thermal cycle and diagram of heat treatment following welding of PB2 steel

5. Testing procedure

The test weld was subject to non-destructive testing (visual VT, penetrant PT and radiographic RT). The quality level obtained according to standard PN-EN ISO 5817 [7] was that of B. Afterwards the joint was sampled for destructive testing. The scope of destructive testing included a static tensile test of welded joint, side bend test, impact test (notch cut in the weld, HAZ and parent metal), micro- and macroscopic metallographic examination and hardness measurements.

6. Welded joint tensile tests

The tensile strength of the welded joint (R_m) was determined using a testing machine INSTRON 4210 pursuant to standard PN-EN 895 [8]. The test results are presented in Figure 3; both specimens rupture outside the weld.

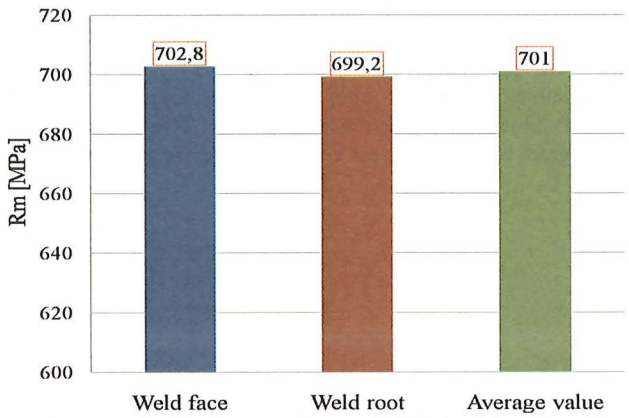

Figure 3. Tensile strength of butt joint of pipes (ϕ 219.1 x 31 mm) made of PB2 steel

7. Impact tests of individual welded joint areas

The impact energy of the weld metal, HAZ and parent metal was tested using Charpy V samples pursuant to the requirements of standard PN-EN 12952-6 [9]. The standard specifies the minimum value of impact energy of HAZ using samples of normal cross-section (10 x 10 mm) as 24J at ambient temperature, whereas standard PN-EN 10216-2 [10] specifies the minimum value for parent metal (PM) as 27J for samples positioned crosswise in relation to pipe rolling. The results obtained in the test are presented in Figure 4.

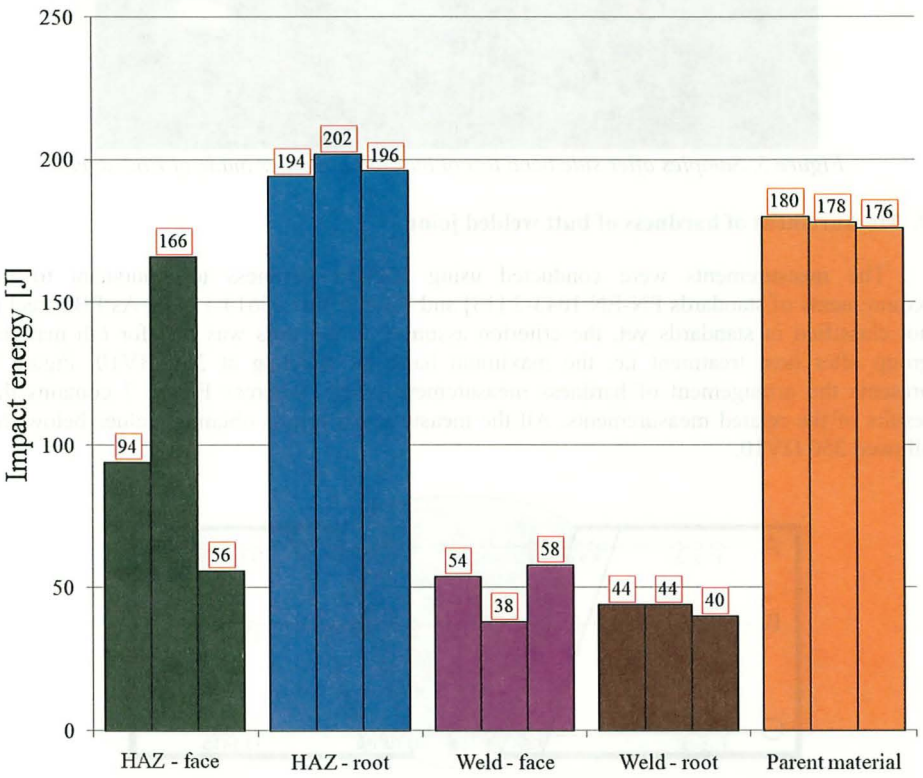

Figure 4. Impact energy of weld, HAZ and parent metal of butt joint of pipes (ϕ 219.1 x 31 mm) made of PB2 steel

8. Side bend test of welded joint

A side bend test of the weld was performed pursuant to the regulations of standards PN-EN ISO 15614-1 [11] and PN-EN 910 [12] using a bending mandrel of 60 mm - diameter. According to the standard [10] the positive criterion of a bending test is obtaining a bending angle of 180° without scratches or cracks on the stretched surface of the sample. The results obtained in the test (Fig. 5) meet the requirements of the aforesaid standard.

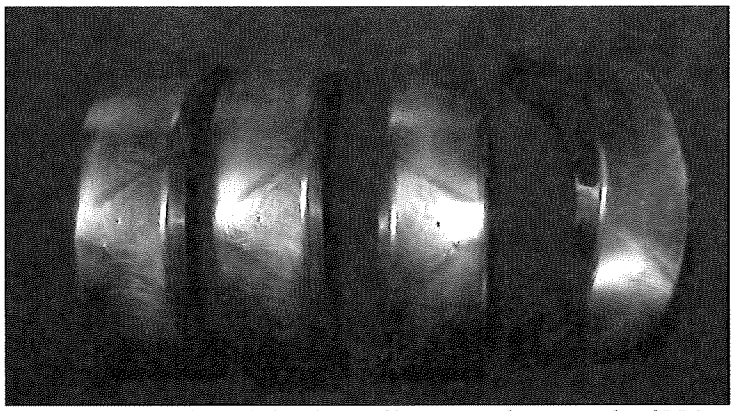

Figure 5. Samples after side bend test of butt joint of pipes made of PB2 steel

9. Measurement of hardness of butt welded joint

The measurements were conducted using Vickers hardness test pursuant to the requirements of standards PN-EN 1043-2 [13] and PN-EN ISO 15614-1 [11]. As PB2 steel is not classified in standards yet, the criterion assumed in the tests was that for 6th material group after heat treatment i.e. the maximum hardness standing at 350 HV10. Figure 6 presents the arrangement of hardness measurement points, whereas Figure 7 contains the results of the related measurements. All the measurement results obtained values below the allowed 350 HV10.

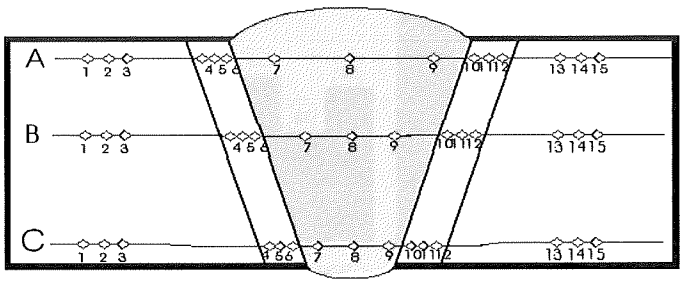

Figure 6. Arrangement of hardness measurement points in welded joint

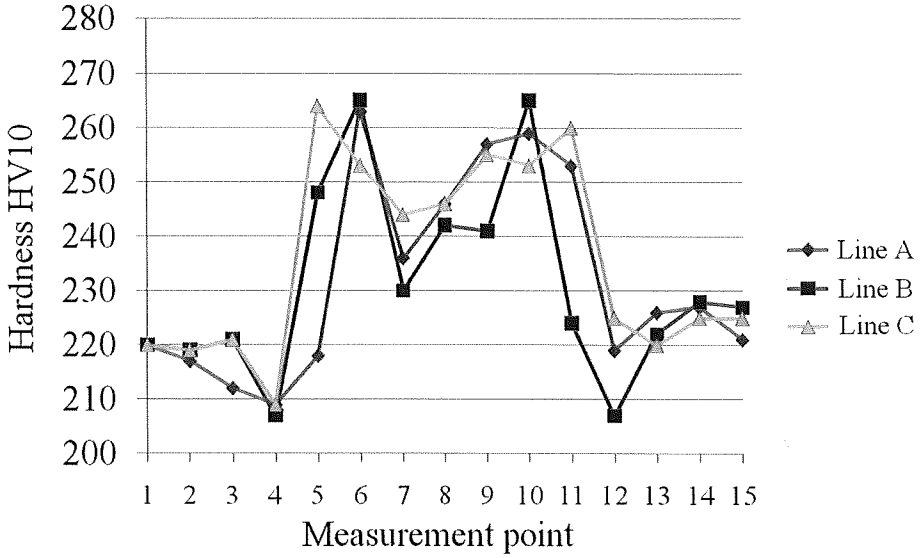

Figure 7. Distribution of hardness in cross-section of welded joint of pipes (ϕ 219.1 x 31 mm) made of PB2 steel

10. Metallographic macro- and microscopic examination of welded joint

The examination was conducted pursuant to standard PN-EN 1321 [14]. The assessment criterion assumed for the test was quality level B according to the standard [11]; the test joint met the assumed requirement. The macrostructure of the test welded joint is presented in Figure 8.

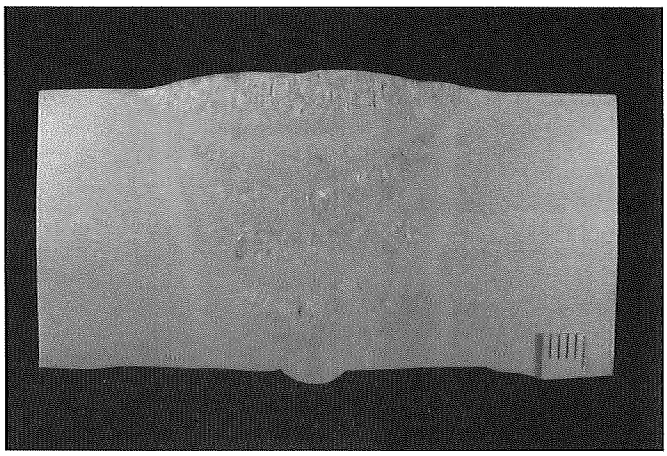

Figure 8. Macrostructure of butt joint made of PB2 steel; quality level B (etch. Adler)

The microscopic examination, conducted pursuant to the standard [14] revealed proper microstructure in individual areas of the butt joint made of PB2 steel. Table 4 contains the areas (marked) which were subjected to the microscopic examination as well as the results presented in the form of photographs and descriptions of the structures present in the characteristic areas of the welded joint.

Table 4. Results of microscopic examination of butt joint of pipes made of PB2 steel

<table>
<tr><td colspan="4"> 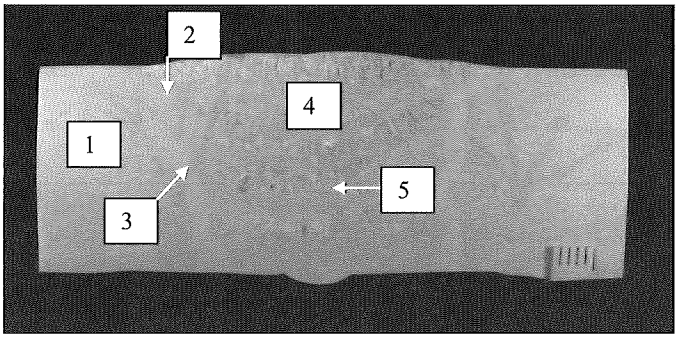

Microscopic examination areas</td></tr>
<tr><td colspan="2">Area 1

Parent metal of PB2 steel
Tempered martensite</td><td colspan="2"> 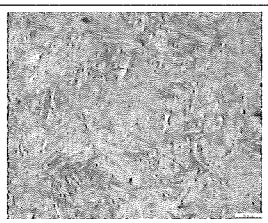
etch. $FeCl_3$ mag. 200x</td></tr>
<tr><td>Area 2

HAZ
Martensite</td><td> 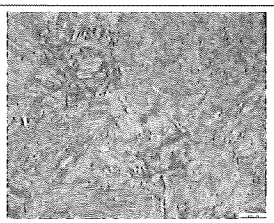
etch. $FeCl_3$ mag. 200x</td><td>Area 3

HAZ
Martensite</td><td>
etch. $FeCl_3$ mag. 200x</td></tr>
<tr><td>Area 4

Weld
Martensite</td><td>
etch. $FeCl_3$ mag. 200x</td><td>Area 5

Weld
Martensite + traces of delta ferrite</td><td> 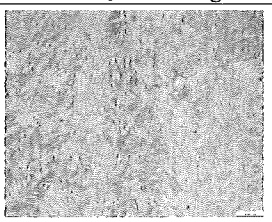
etch. $FeCl_3$ mag. 200x</td></tr>
</table>

11. Fractographic examination of welded joint

The fractographic examination was performed by means of a scanning electron microscope (SEM) with variable vacuum SEM VP S-3600N HITACHI combined with a THERMO NORAN-manufactured EDS X-ray spectrometer equipped with a System Six analyser. The observation focused on the surface of fractures following the hardness test. The examination incorporated secondary electron imaging (SEI) as well as backscattered electron imaging (BSE). Examples of weld fracture topography are presented in Figure 9.

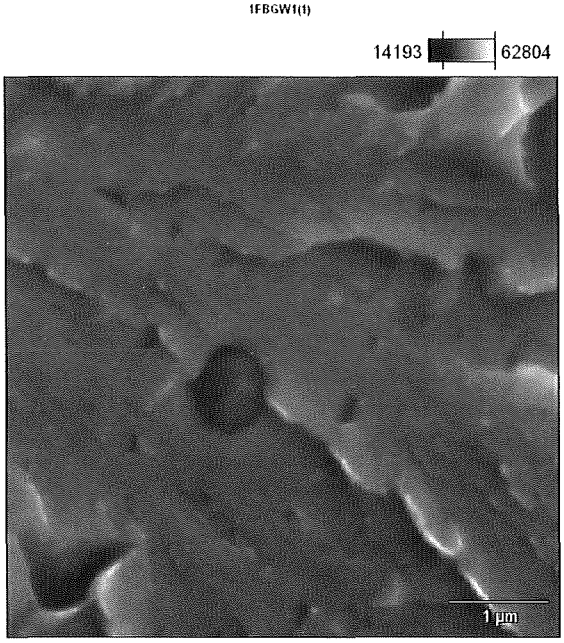

Figure 9. Topography of fracture of weld made of PB2 steel

The investigation also involved the analysis of the chemical composition of the weld made of PB2 steel and was performed with a Niton 898xlt spectrometer using X-ray fluorescence (XRF) technique. The results of the microanalysis of the chemical composition are presented in Figure 10, whereas the results obtained are detailed in Table 6.

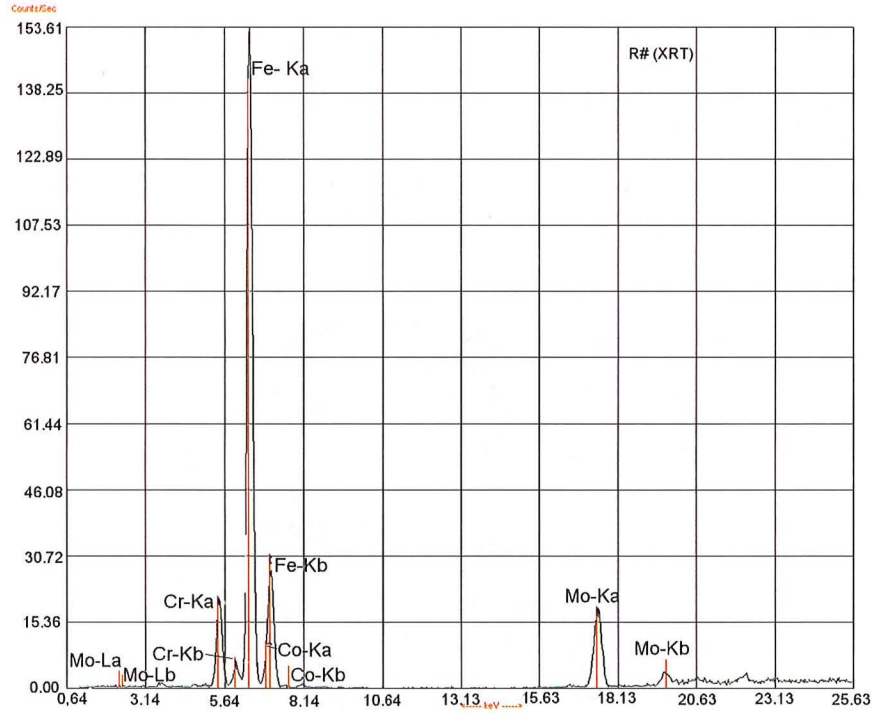

Figure 10. X-ray radiation spectrum of PB2 weld

Table 6. Chemical composition of weld made of PB2 steel

Chemical composition of test welded joint										
Sb	**Sn**	**Pd**	**Ag**	**Al**	**Mo**	**Nb**	**Zr**	**Bi**	**Pb**	**Se**
0.00	0.06	0.00	0.07	0.00	1.50	0.03	0.00	0.00	0.00	0.00
W	**Zn**	**Cu**	**Ni**	**Co**	**Fe**	**Mn**	**Cr**	**V**	**Ti**	
0.00	0.12	0.01	0.29	1.02	86.89	0.60	9.08	0.32	0.00	

During fractographic examination both MC carbides and MX carbonitrides were found. Both precipitates were analyzed with chemical microanalysis and it was found that chromium carbides and cobalt carbides were present in weld and HAZ. According to known literature those precipitates positively affect creep resistance of martensitic steels and welded joints made out of steels like P92.

12. Conclusions

On grounds of the tests it was possible to formulate the following conclusions:

1. The butt joint of pipes ϕ 219.1 x 31 mm made of PB2 steel welded in a fixed position (PF) is characterised by high quality which was confirmed by destructive and non-destructive testing results.

2. The process of welding with a covered electrode is intense in character and the liquid metal of the weld pool spreads well on the walls of joined elements. The production of

successive weld layers proves difficult as the fusion into previously made runs is problematic. The fabrication of similar joints made of P91 and P92 steels led to a conclusion that the aforesaid phenomenon is natural and does not impede the achievement of desired joint quality.

3. The fractographic analysis and the microanalysis of the chemical composition of precipitates in the weld reveals that the joint was produced properly and should meet the requirements of operation at increased temperature.

4. The positive findings of the mechanical tests justify optimistic expectations related to the application of the test steel in the power sector. However, the creep resistance of PB2 steel requires further research.

Acknowledgments

The authors of the article wish to express their thanks to TenarisDalmine for providing the pipes used for the investigations and to Metrode UK and Lincoln Electric Poland for providing the covered electrodes used for welding of PB2 steel.

Reference list:

[1] Hernas A., High-temperature creep resistance of steels and alloys, *Publishers of the Silesian University of Technology*, Gliwice, (1999).
[2] Collective work under the leadership of prof. dr hab. inż. J. Pilarczyk, Engineer Guide - Welding, Part 1, Warsaw, *WNT*, (2003).
[3] Urzynicok M., Kwieciński K., Szubryt M., Experience in the welding of martensitic steel VM12-SHC, *Materials Investigation for Power Industry, XVI. scientific and technical seminar,* Zakopane, (2009).
[4] Urzynicok M., Kwiecinski K., Słania J., Properties of welded joints in 7CrMoVTiB10-10 (T24) bainitic steel used in power stations operated at supercritical parameters, Gliwice, *Welding Institute Bulletin*, no 6 p. 59-62, (2009).
[5] Urzynicok M., Kwieciński K., Szubryt M., Application of new GMAW welding methods used in prefabrication of P92 (X10CrWMoVNb9-2) pipe butt welds, *Energetyka, no XIX*, SIMP, p. 168-170, 11.2009.
[6] Kwieciński K., Urzynicok M., Łomozik M., Practical experience with welding New generation steel PB2 assigned for the power. *Energetyka, no XIX*, SIMP, p. 84-87, 11.2009.
[7] PN-EN 12952-6. Water-tube boilers and auxiliary installations. Part 6: Inspection during construction. Documentation and marking of pressure parts of the boiler.
[8] PN-EN 10216-2+A2. Seamless steel tubes for pressure purposes. Technical delivery conditions. Part 2: Non-alloy and alloy steel tubes with specified elevated temperature properties.
[9] PN-EN ISO 15614-1. Specification and qualification of welding procedures for metallic materials. Welding procedure test. Part 1: Arc and gas welding of steels and arc welding of nickel and nickel alloys.
[10] PN-EN 910. Destructive test on welds in metallic materials. Bend tests.
[11] PN-EN 1043-2. Destructive test on welds in metallic materials. Hardness test. Part 2: Micro hardness testing on welded joints.
[12] PN-EN 1321. Destructive tests of welds in metallic materials. Macroscopic and microscopic examination of welds.

9th Liege Conference : Materials for Advanced Power Engineering 2010
edited by J. Lecomte-Beckers, Q. Contrepois, T. Beck and B. Kuhn.

DEGRADATION OF SUPERHEATER TUBES MADE OF AUSTENITIC T321H STEEL AFTER LONG TERM SERVICE

Adam HERNAS[1], Bolesław AUGUSTYNIAK[2], Marek CHMIELEWSKI[2], M. J. SABLIK[3]

[1)]Silesian Technical University, Faculty of Material Science, 40-019 Katowice,
ul. Krasińskiego 8, Poland

[2)]Gdansk University of Technology, Mechanical Department, 80-223 Gdansk,
ul. Narutowicza 11/12, Poland

[3)]Applied Magnetic and Physical Modeling, LLC, San Antonio, TX 78240-2307, USA

Abstract

There are presented results of complementary tests performed for the evaluation of creep damage in austenitic steel grade T321H exploited over 200,000 hours in the secondary superheater part of a power plant boiler. The following techniques have been applied: SEM microscopy, X-ray diffraction, tensile tests, hardness measurements and novel eddy current inspection. The novel eddy current inspection is proposed as a non-destructive method of estimating the creep damage stage of austenite steel boiler tubes after long-term service in power plants. We compare the results provided by the different techniques and discuss the correlations and also point out the problems which need to be addressed in order to elaborate the remaining life assessment of austenitic boiler tubes.

Keywords: austenitic steel, creep damage, nondestructive testing

1. Introduction

Further development of energy power technology is possible due to the construction of boilers with higher energy efficiency and with lower emission of harmful oxides damaging the environment. This can be achieved by an increase of steam pressure and temperature. An energy efficiency of order 40-50% can be obtained using boilers working under supercritical conditions: with steam pressure above 28 MPa and temperature between 560 °C and 620 °C [1]. In order to produce steam of such high parameters, the superheater and reheater tubes of the boiler should be made of steel with appropriate mechanical properties--mainly high resistance to (1) creep damage, (2) high temperature corrosion of the outer tube wall surface, and (3) steam oxidation of the inner wall surface of the tube. The first supercritical boilers were built in the 1950s and 1960s in the USA, Japan and Russia (Ukraine) using austenitic steels type 18/10 and 18/13. The steam pressure in those boilers was higher than 25 MPa with temperature of order 560-570 °C. However, due to technological problems with welding as well as with relatively large numbers of breakdowns, the idea of supercritical boiler construction was not further developed for about 40 years. Most power plants over the world worked at this time under conventional parameters (steam pressure of order 19 MPa and temperature not greater than 540 °C) with an energy efficiency of order 33 % [1-3]. In spite of these difficulties, in the USA before 1990, there were constructed 121 supercritical blocks (coal heated) with energy efficiency about 36 %. These boilers were made of austenitic steels grades T321H , T316H and T347H. The 304 and 347 steels are most commonly used in the US (each in about 40% of the plants). The 321 steels are used in about 20% of the plants.

The 321 and 316 austenitic steels are used in the UK. Transition to a supercritical power plant block started in the late 1990s, with new grades of austenitic steels such as ultra small grain steel TP347HFG, Super 304 and HR3C, characterized by high quality properties [4-7].

Long-term creep ends by creation of micro-cracks which develop to macro-cracks. This leads to final failure of superheater and reheater tubes. This is valid for all types of materials (ferritic steels as well as austenitic).

To facilitate cost-effective replacement, it is necessary to know how much creep damage is present in the tubes at various places so that the remaining safe life of the tubes can be properly estimated. The best method (from an economical point of view) is the method which can be applied for *in situ* estimations. In recent years, in-service failures of austenitic stainless steel superheater and reheater tubes have started to become a significant cause of lost plant availability. Steamside oxide-scale based remaining life methods developed for ferritic tubing are commonly used by utilities to estimate austenitic tube life. Unfortunately, this approach does not provide a direct method for estimating the life of austenitic stainless steel tubing. In the case of ferritic steels, creep damage is 'detected' by means of measurement with ultrasonic waves of the thickness of inner wall oxide scale. This technique is not applicable for austenitic tubes because of the relatively lower thickness of this scale and because of higher attenuation of ultrasonic waves in comparison to ferritic steels. The next NDT method, potentially very useful for creep damage evaluation of ferritic steels, utilizes magnetoacoustic emission [8]. This technique is also not valid for austenite tubes because of their practically zero level of magnetisation.

We now elaborate a novel technique of austenite creep damage assessment based on the eddy current effect [9]. The intensity of eddy current induced in the tested material depends on the electrical conductivity and magnetic permeability of the material. Austenite has low conductivity and very low magnetic permeability. It means that eddy current techniques reveal mainly electric properties of austenite tube. However, the high temperature service causes a hard scale oxide with detectable magnetic properties to be formed on the outside of the austenite tube. The eddy current measurement can provide information about the amount of magnetisation of the oxide and this appears to correlate to the amount of creep damage. The relationship between magnetisation of the oxide and the amount of creep damage should be calibrated in order to 'calibrate' this novel technique. Our paper reports the results of various complementary laboratory tests performed for evaluation of the creep damage stage of austenitic steel grade T321H exploited over 200,000 hours in the secondary superheater part of a power plant boiler.

2. Tested material and experimental

There were tested parts of 10 superheater tubes made of 321H grade steel cut from different parts of a secondary superheater in the same boiler, exploited about 200,000 h. The specimens were provided by the Electric Power Research Institute (EPRI) in the USA. These samples are very important for our purpose due to their very long exploitation time and thus expected high level of creep damage. It should be stressed that the test was a 'blind' test because we had no information about exact positions of the samples as taken from the superheater tubes nor any information about the creep damage state of these tubes, which was nominally known by the provider (based on its own metallurgical tests and procedures).

These tubes had outer diameter Do = 57 mm and wall thickness h = 6 mm. There was also tested an unexploited tube of the same dimensions. Table 1 provides information about the chemical composition of 321H austenite.

Table 1. Chemical composition of tested steel

Grade	Chemical components [% wt]						
	C	Si	Mn	Cr	Ni	Other	N
T321	0.08	0.60	1.60	18.0	10.0	Ti :0.5	-

There were used the following complementary techniques of sample properties evaluation:

- measurement of sample geometry
- optical metallographic tests (with σ phase detection)
- SEM microscopy with EDS analysis of precipitates and oxides
- X-ray analysis of isolates
- mechanical tensile test at room temperature
- eddy current technique.

The first five techniques are all well known standard techniques. The last technique – applying the 'eddy current effect' - was described in detail in [9]. We give here a brief description of this technique.

The method of eddy current (EC) measurement of the austenite tube state uses a probe consisting of a primary coil surrounded by two secondary coils, one a measuring coil close to the specimen and the other a reference coil inside the top of the primary coil away from the specimen. The current driving primary coil is sinusoidal in form and with frequency of order of 10 kHz. Two voltage signals induced in the primary coil (*Ua*) and in a reference coil (*Ub*) are transformed electronically to the output voltage signal *Ur*, which is the time average of the product of the *Ua* signal with the difference signal $U = Ua\text{-}Ub$, divided by square of amplitude of signal *Ub* from the reference coil. The *Ur* depends in a specific way on electric conductivity (the higher the conductivity, the more negative is *Ur*) and on magnetic permeability (the higher the permeability, the less negative is *Ur*). With this probe, the tube properties can be scanned quickly in the hoop direction or in the axial direction. In the case of an exploited tube, the signal *Ur* is always less negative than the signal detected for an unexploited tube. This occurs because of oxide magnetic properties (due to the magnetite component) and also due to an increase of magnetic properties of the bulk material.

3. Results of investigations

3.1. Microstructural analysis

In the initial state, an investigated steel (sample no. 10) has a typical austenite uniform microstructure with a standard grain diameter (class 8-9 ASTM) with twins and TiC primary precipitates, regular in shape. Microstructure inspection of all samples, using light microscopy (LM) and SEM microscopy, revealed essentially different stages of degradation of the exploited samples. Some examples of this investigation are given in Fig. 1 and 2. There are well shown σ phase particles and TiC and $M_{23}C_6$ carbides.

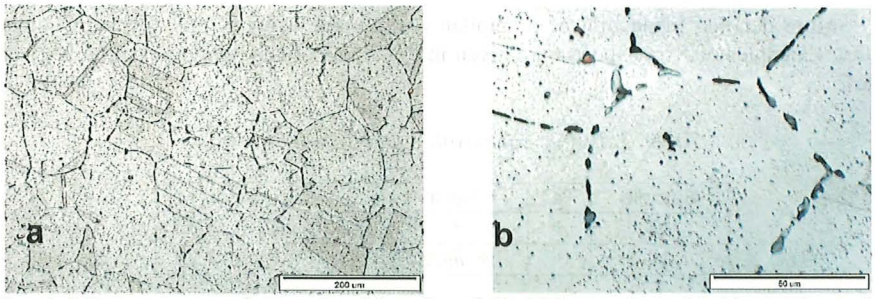

*Fig. 1. Microstructure after service (class **B** and **C**), LM; sample no 17, b) sample no. 16*

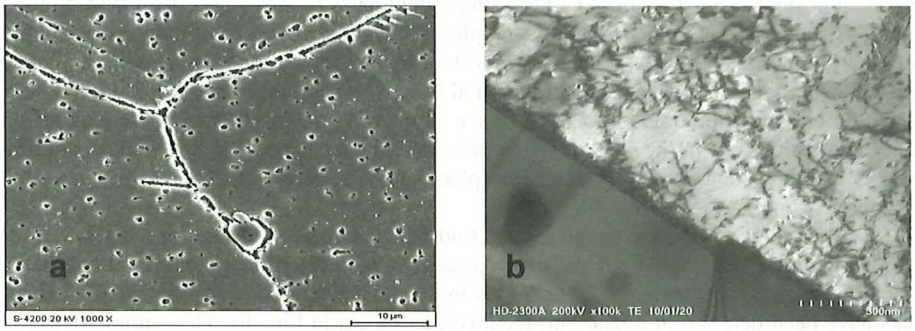

Fig. 2. Microstructure of material after service: a) no. 17, LM and b) no. 20,TEM

We state that long-time exploitation leads to the following specific modifications of the austenite microstructure with different degrees between the samples:

- evolution of precipitates type TiC, $M_{23}C_6$ and σ phase;
- evolution of thickness and morphology of the scales on inner and on outer surface of the tube;
- evolution of creep cavities.

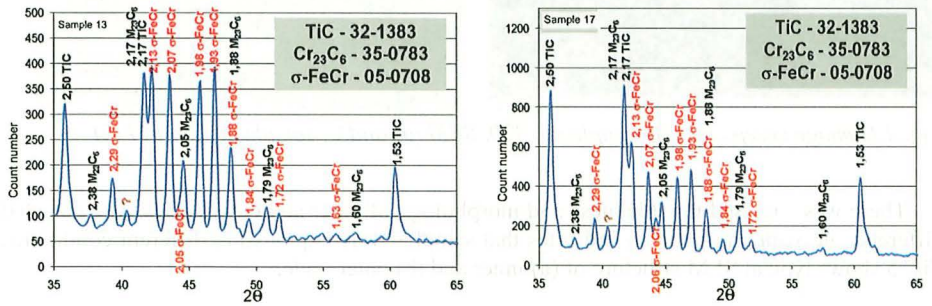

Fig. 3. X-Ray diffraction spectra of isolates taken from the samples: a) no.13 and b) no. 17

More detailed inspection of precipitates was made using X-ray diffraction plots of isolates. Examples of X-ray spectra are given in Fig. 3, and qualitative description is given in Table 2.

Table. 2. Isolate composition and its mass fraction

Sample	TiC	FeCr	$M_{23}C_6$	% wt.
13	+	+	+ *very little*	3,92
17	+	+ *little*	+	2,29

The X-ray diffraction spectra peaks denote concentration of a given component of the isolate. From Fig. 3 one can find that concentration of carbide $M_{23}C_6$ in sample no. 13 is much lower than in sample no. 17 while σ - FeCr phase dominates in sample no. 13. Concentration of the TiC phase is quite equal for both samples. Table 2 gives also estimations of weight fraction of the isolates. Higher level of isolate concentration indicates a more exploited sample. We argue that σ phase concentration and its spatial distribution are the quantities very suitable for classification of exploitation lifetime. The TiC is important for steel strengthening but does not participate in the creep damage process. Concentration of $M_{23}C_6$ carbides at first increases and after long exploitation, when σ phase appears, decreases. This is quite revealed using thin foil on TEM (Fig.2b).

Metallographic inspection enabled us to find creep damage voids and micro-cracks [12] attributed to classes A, B and C of structure damage, D- not found. An example of high level of damage (stage C) is sample no. 20 as shown in Fig. 4a. In the case of sample no. 23, micro-cracks have been detected at a near surface layer, as shown in Fig. 4b. This sample does not reveal a very late stage of precipitate evolution, and thus we attribute the micro-cracks to be introduced by mechanical load and not by thermal diffusion process.

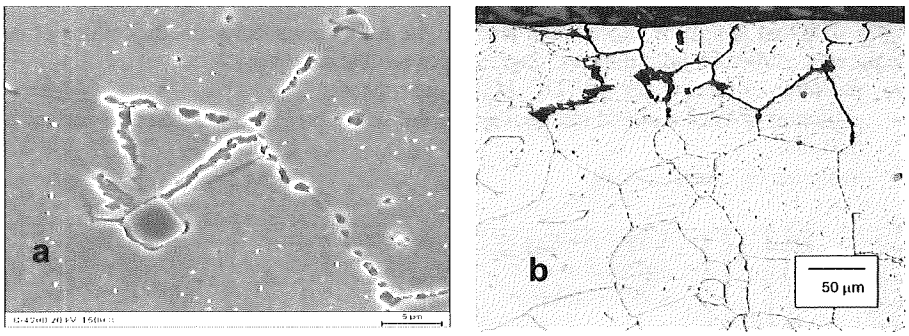

Fig. 4 Damage creep class B, sample no. 320, SEM (a) and C, sample no. 23, LM (b)

There was analysed the thickness and morphology of inner and outer scales. The detected difference in oxide morphology indicates that samples were exploited at different conditions. Fig. 5 shows typical SEM structure of (a) inner and (b) outer scale.

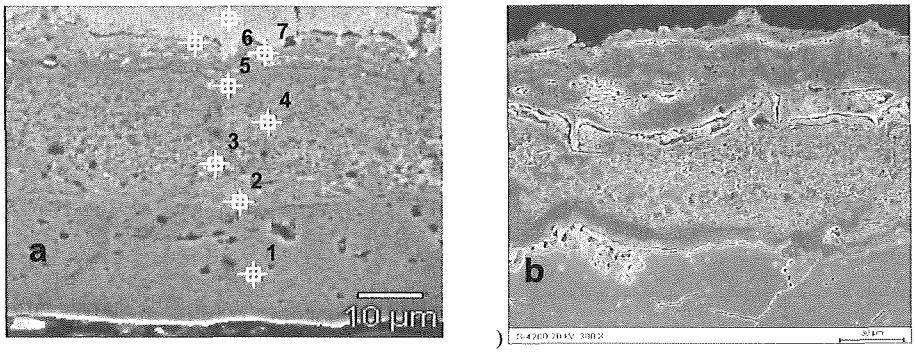

Fig. 5. The SEM microstructures: a) inner scale sample no. 23; b) outer scale sample no. 16.

The 'points' in Fig. 5 indicate areas where chemical composition has been analysed with the EDX technique of SEM microscopy (1 – outside, 7 – near base material). Table 3 contains information about chemical composition of the tested areas in Fig. 5a. The last column of this table gives an expression defining the structure of the area.

Table 3. Chemical composition of inner scale of sample no. 23 at points indicated in Fig. 5a

	Component concentration [% wt]						suggested
point	Si	Ti	Cr	Mn	Fe	Ni	oxides
1				2.45	94.31	3.24	Fe_3O_4
2		1.21	86.22		12.57		Cr_2O_3
3			5.79		23.30	70.91	
4	2.58	0.60	35.70		38.74	22.37	Cr_2O_3 - Fe_3O_4
5	2.21		64.96		32.83		
6	1.20		20.21		68.14	10.45	Fe_3O_4 -
7	2.10		20.70		38.21	38.99	Cr_2O_3

Mean values of scale thickness for the inner and outer surface of the indicated sample are given in Table 4. We worry that the outer scale of tested samples might sometimes be damaged and thus its thickness level should be treated as a quantity with not a high level of certitude. It should be also mentioned that scale thickness varies along the tube in the hoop direction and there should be given not only a 'mean' level but also the distribution of this scale around the tube surface. Table 4 shows very scattered values of outer scale thickness. Readings for inner scale are less scattered and often seem to be bigger than the outer thickness of outer scale.

Table 4. Thickness of the outer and inner scales of the given samples

Sample	13	16	17	20	21	23
Outer scale [µm]	57.68	140.34	56.53	39.36	97.41	31.21
Inner scale [µm]	101.57	107.59	150.42	140.43	53.34	94.74

3.2. Mechanical tests

Some results of mechanical tests are presented in Table 5. The samples have been cut along tube axis. It should be stated that back surfaces of the sample were not polished and thus mechanical test results reflect real properties of the material due to the microstructure of outer and inner subsurface layers.

Table 5. Mechanical properties of 321H samples

Sample	HV10	A_5 [%]	RoA [%]	0.2 YS [MPa]	UTS [MPa]
10 not exploited	138	57	64	268	567
13	167	36	34	245	630
17	156	36	34	187	487
20	152	40	37	250	578

These results reveal very good mechanical stability of the exploited material in comparison to unexploited material. One finds also that exploited steel reveals a high level of plasticity.

3.3. Eddy current test

The results of eddy current measurement are shown in Fig 6. The measurements have been performed in the hoop direction along several 'lines' and *Urm* represents the mean value at a given angle.

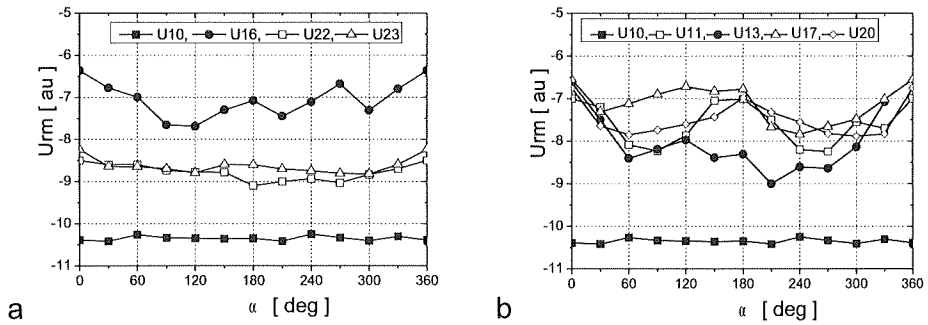

Fig. 6. Angular distribution of eddy current Ur output signal

The plot 'U10' exhibits properties of the unexploited sample. These plots reveal that *Urm* plots for all exploited samples are higher than for the unexploited sample. There is also evident different level of the *Urm* level (Fig.6a) and an angular distribution of *Urm* level in the hoop direction, as shown in Fig.6b. We argue that areas of higher *Urm* signal are those which are more affected by exploitation and thus are more creep damaged. We like to establish for each sample the correlation between eddy current readings and creep damage stage assessment for different microstructure states.

Such correlation will be a base for further development of the eddy current technique used for assessment of austenite material creep damage.

4. Estimation of state of material after service by means of metallographic inspection

There are used various procedures of estimation of creep damage stage of exploited ferritic materials in power plants. The Institute of Ferrous Materials in Poland has proposed 9 stages of scale for microstructure description [10]. In the case of austentic steels there are proposed procedures elaborated by EPRI for long-term overheat creep damage remaining life assessment [11]. For austenitic steels, we propose to use microstructural-based creep damage estimators which correspond to the scale proposed in Poland for ferritic steels. This procedure applies the models of microstructure stages and the 4-stage scale of creep damage as proposed by Neubauer [12].

More detailed inspection of precipitates was made using X-ray diffraction plots of isolates. Examples of X-ray spectra are given in Fig. 3, and qualitative description is given in Table 2.

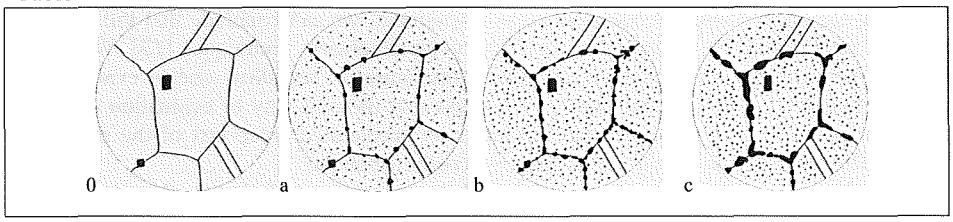

Fig. 7. Models of the degradation microstructure during long-term service

We propose to use the following description of microstructure stages related to the so-called exhaustion parameter f. This parameter value varies from $f = 0$ (initial stage) to $f = 1$ (final stage, failure). Below are described four main stages of microstructure modifications attributed to the increased values of the parameter f.

1. f **= 0.2 – 0.4:** material is without creep voids, TiC and $M_{23}C_6$ carbides are uniformly distributed, very low concentration of σ phase.
2. f **= 0.4 – 0.6**: appearance of isolated and oriented voids (class A); carbides start to be spheroidal inside the grain and TiC and $M_{23}C_6$ carbides form also at grain boundaries (Fig.2a, 7a).
3. f **= 0.6 – 0.8**: advanced stage of damage due to high concentration of voids and linear micro-cracks (classes A and B); TiC and $M_{23}C_6$ carbides and σ phase form discontinuous 'lines' along grain boundaries (Fig.1a, 2a, 4a, 7b).
4. f **= 0.8 – 1.0**: very advanced stage of damage – appearance of micro- and macro-cracks (classes C and D) and net of large σ phase precipitates along grain boundaries (Fig.1b, 4b, 7c).

It should be stressed that the critical stage of microstructure is the stage with microstructure damage (which starts by voids creation) without regard to morphology of precipitates. This classification allows an estimation of further safety exploitation time : $f = 0.2 - 0.4$; max. 60,000 hours, $f = 0.4$-0.6; max. 45,000 hours., $f = 0.6$-0.8; max. 30,000 hours and $f = 0.8$ -

1.0 max.15,000 hours. Of course, f =1 corresponds to zero remaining life. It should be stressed that these estimations are valid under the condition that the wall thickness of tested exploited tube is larger or equal to the 'calculated' thickness.

It is also possible to evaluate the remaining lifetime (RCL) of austenitic steel by means of voids surface analysis [11]. This is given by the following formula:

$$RCL = t\,[(0.2/f_a^{0.6}) - 1]\,,$$

where t is exploitation time and f_a is ratio of grain boundary length with voids.

5. Summary

Our last tests of exploited 321H steel samples by various laboratory inspections and by novel eddy current technique have been made in order to elaborate an effective method of assessment of the actual stage of austenite elements of power plant boiler components (namely steam heater and superheater tubes). Information about the material stage is necessary for evaluation of remaining lifetime of the element in question. From our many-years-long experience with ferritic steel stage assessment, we can conclude that the stage of exploited steel should be evaluated by different complementary techniques [13]. We know also that mechanical tests performed at room temperature do not allow one to evaluate the damage stage level with good reliability. We stress that the best way of evaluation of creep damage stage as well as of remaining lifetime is an accelerated creep test of the exploited material. However, this is a time-consuming and costly technique.

Microstructure of the exploited material (with precipitates morphology and creep damage voids and micro-cracks structure) is one aspect of the degradation process, related with bulk properties. The second aspect of degradation process is the state of near surface layer and scale morphology. In the case of austenite tubes, these quantities can be evaluated by means of eddy current techniques. Such a conclusion is supported by the results of our performed tests. Estimations provided by eddy current inspection correlate very well with thickness and morphology of outer scale. The direct correlation of eddy current inspection indications with bulk material microstructure is not so obvious. It is because the eddy current technique is sensitive to averages (over volume) of electric conductivity and magnetic permeability of bulk material. These quantities do not differ very much across varying amounts of exploitation. In fact, the eddy current readings obtained for cleaned exploited tubes differ very little from readings for unexploited. However, we find good correlation for angular distributions of *Ur* values measured over cleaned surface and over uncleaned tube [9]. This is explained by an increase of magnetic properties of bulk material which is correlated with an increase of thickness of outer scale. The outer scale reveals magnetic properties because of its magnetite component. This technique can be used for quick inspection of large tube lengths, thus providing reasonable information about scale thickness and thus about 'creep damage' stage of bulk material. This means that the as-elaborated eddy current technique can be applied for effective checking of austenite steam heater and superheater tubes.

Our last test has been made with samples with relatively long time of exploitation (200,000 hours). Some of them reveal relatively high level of creep damage (close to final damage). It is thus a very important experiment because it enables one to establish some extreme points on the dependence between eddy current technique *Ur* signal and creep damage stage of 321H steel.

It should be pointed out here that the creep damage reported here has been accomplished under stress because at the high temperatures of the boiler, the tube metal has a tendency to expand, but because the tubes are locked in a network, at least some of the expansion results in creation of stress in the tubel.

Acknowledgments

This work was partially supported by project PBZ-MEiN-4/2/2006. Eddy current experiments were supported by Southwest Research Institute (SWRI) in San Antonio in cooperation with EPRI. The authors thank the EPRI for the samples.

Literature

[1] HERNAS A; *Materials and technology for supercritical boilers and ... Ed.* SITPH, Katowice, 2009 [in Polish]
[2] PAWLIK M., IV in Proc. of Conference . N-T Power plants, Bełchatów, 1996 [in Polish]
[3] INGO P., *A technology successfully developed in developing countries*, http://www.worldbank.org/html/fpd/em/supercritical/supercritical.htm.
[4] SMITH J.W., *Supercritical (once through) boiler technology*, Babcock & Wilcox Company nr BR-1658, 1998.
[5] HERNAS A., WALA T., STASZEWSKI M., Inżynieria Materiałowa, nr 3, 2009 [in Polish]
[6] HUSEMANN R., Babcock-Hitachi Europe, *Advanced Material for AD700 Boilers*, CESI Audytorium, Milano, Italy, 2005.
[7] ISEDA A., OKADA H., *Creep Properties and Microstructuren of Super 304, TP347HFG, HR3C*, 5th Int. Conf.on Advances in Mater. Technol. for Fosil Power Plants, EPRI, Floryda, USA 2007.
[8] AUGUSTYNIAK B. CHMIELEWSKI M., PIOTROWSKI L. , SABLIK M.J.; *Designing a Magnetoacoustic Emission Measurement Configuration for Measurement of Creep Damage in Power Plant Boiler Tubes*; J. Appl. Phys. 91, (2002) 8897-8899.
[9] AUGUSTYNIAK B., CHMIELEWSKI M., SABLIK M. J., AUGUSTYNIAK M., WALKER S., *A new eddy current method for nondestructive testing of creep damage austenitic boiler tubing*, Nondestructive Testing and Evaluation, 24, Nos. 1-2 (2009) 212-241.
[10] DOBRZANSKI J. *The classification method and the technical condition evaluation of the critical elements' material of power boilers in creep service made from the 12Cr–1Mo–V*; Journal of Materials Processing Technology 164–165 (2005) 785–794.
[11] Remaining Life Assessment of Austenitic Stainless Steel Superheater and Reheater Tubes; EPRI, Palo Alto, CA: 2002 Technical report no. 1004517.
[12] NEUBAUER B.; Proc. Int. Symp. on Creep and Fracture of Eng. Mat. and Structures, Swansea, 1984
[13] HERNAS A., DOBRZANSKI J., *Life-time and damage of power plant components*, Ed. Silesian University of Technology, Gliwice, 2003. [in Polish]

9th Liege Conference : Materials for Advanced Power Engineering 2010
edited by J. Lecomte-Beckers, Q. Contrepois, T. Beck and B. Kuhn.

DESIGN OF HEAT TREATMENTS FOR 9-12%Cr STEELS TO OPTIMISE CREEP RESISTANCE FOR POWER PLANT APPLICATIONS

P.F. Morris, U.A. Sachadel, P.D. Clarke

Tata Steel Europe, Swinden Technology Centre, Rotherham, England & CRD&T, IJmuiden, the Netherlands

Abstract

Optimisation of the creep rupture properties of Steel 92 (9%Cr, 0.5%Mo, 2%W) by modification of heat treatment and C:N ratio has been studied. It was shown that a higher austenitization temperature and double tempering at lower temperature can significantly extend creep life of the standard composition. The increase in austenitization temperature from 1060°C to 1150°C and double tempering at 660°C/3h instead of single tempering at 780°C/2h resulted in the increase of stress rupture life from 1,734 to 6,179h at 650°C/110MPa. Even greater improvement in creep life was achieved by the combination of the modified heat treatment and decreased C:N ratio. In this case the creep life was extended to 10,255 h at 650°C/110MPa. A further increase in austenitization temperature to 1200°C for the decreased C:N ratio variant extended the rupture life to 17,118h. Initial results indicate that this modified heat treatment schedule does not result in notch brittle behaviour and most of the improvement in creep strength remains after a simulated post weld heat treatment at 740°C. The stress rupture programme is continuing and at 600°C test durations are approaching 60,000h.

To explain the effect on rupture life thermodynamic calculations, microscopic investigations and a literature study were performed. Electron metallography investigations revealed that the lower tempering temperature resulted in a finer distribution of nano-size particles. Calculations show that increasing the austenitization temperature gave more dissolved B, N, C, Nb and V. The lower C:N ratio resulted in a higher atomic fraction of N in nano-size particles on subsequent tempering. Dissolved B should stabilize $M_{23}C_6$ and dissolved N, C, Nb and V should allow precipitation of a higher volume fraction of nano-size carbo-nitrides during tempering. Literature data suggest that lower tempering temperatures could also change their type from MX to M_2X.

Keywords: Steel 92, heat treatment, creep properties, microstructure, precipitates

1. Introduction

Global requirements for energy are forecast to double by 2030 with a projected build of 40 nuclear power stations alone in the EU. In addition to this significant increase in fossil fuelled stations will be required to meet the predicted demand. In order to minimise emissions of greenhouse gases improved generating efficiency, through increased steam temperatures and pressures, and carbon capture technology will be required.

Currently martensitic steels used for turbine blades and casings, bolting and boiler tubes are limited to service temperatures of about 620°C and the best commercially available alloy is Steel 92 – 9%Cr, 0.5%Mo, 2%W. Over the last 15 years significant effort has been invested by international consortia, such as COST 522 and 536, in Europe to improve the operating

temperatures of these martensitic alloys. Attempts at alloy modifications have not thus far yielded any solutions backed up by long term creep data.

Little effort has been put into enhancing the properties by optimising the heat treatment despite this providing significant opportunities to modify the starting microstructure. This paper presents an update on work carried out within Tata Steel - Corus R,D&T to examine this approach. The use of increased solution treatment temperatures and lower tempering temperatures have yielded significant improvements in creep performance compared with conventional heat treatments with creep data approaching 60,000 hours now available.

Possible objections to this approach are that the material will be notch brittle and that any benefits in creep performance will be removed by any post weld heat treatments (PWHT) as required in tubing applications. To address these issues test programmes to generate data on notched samples and materials with simulated post weld heat treatments have been started and early results are presented.

2. Background

Martensitic 9-12%Cr steels given conventional tempering treatments close to the A_1 temperature derive their creep strength from four principal sources:

- Solid solution strengthening
- Dislocation substructure
- $M_{23}C_6$ precipitation at lath boundaries
- MX precipitation at both inter- and intra-granular locations

During exposure at elevated temperature the dislocation density is reduced and precipitate coarsening occurs both of which reduce the resistance to creep deformation. Coarsening of $M_{23}C_6$ is more rapid than MX, but the rate can be reduced by boron additions. However the long term creep strength of these alloys is strongly dependent on the volume fraction and stability of the MX precipitate dispersion. It is generally accepted that in martensitic steels stability of precipitates is enhanced by tempering well above the service temperature and the volume fraction is controlled by the solution treatment temperature and cooling rate prior to tempering. The use of lower tempering temperatures will produce a high density of fine precipitates and may also alter the composition and precipitate type.

High solution treatment temperatures increase the alloy in solution prior to tempering, but in practice solution temperatures are restricted in order to ensure a fully martensitic microstructure and to prevent excessive grain growth which might lower creep ductility.

In the present work these assumptions are tested in Steel 92 type material 9%Cr, 0.5%Mo, 2%W by studying the effect on creep strength of increased solution treatment temperatures and the use of tempering temperatures close to the intended service temperature. In addition compositional modifications intended to increase the nitrogen content of MX precipitates have also been explored.

3. Experimental Procedure

A 50kg air induction melt of Steel 92 material was produced. A second 60kg cast with higher nitrogen and lower carbon contents was produced by vacuum induction melting. The chemical analyses are shown in Table 1. The ingots were forged to 50mm square bar then rolled to 19mm diameter round bar for the production of test specimens.

Table 1: Chemical Analyses of Experimental Casts

Source	Composition, wt%													
	C	Si	Mn	P	S	Cr	Mo	Ni	Al	B	N	Nb	V	W
ECCC	0.07	0.00	0.30	0.000	0.000	8.50	0.30	0.00	0.00	0.001	0.03	0.04	0.15	1.50
(spec.)	0.13	0.50	0.60	0.020	0.010	9.50	0.60	0.40	0.04	0.006	0.07	0.09	0.25	2.00
Steel A	0.11	0.33	0.48	0.012	0.005	9.05	0.46	0.22	0.007	0.0056	0.053	0.065	0.22	1.85
Steel B	**0.073**	0.22	0.48	0.010	0.009	9.01	0.46	0.21	0.005	0.005	**0.065**	0.068	0.20	1.73

Samples from Steel A were given a standard heat treatment or a treatment involving a higher solution treatment temperature at 1150°C and lower tempering temperature of 660°C as outlined in Table 2. In order to study the effect of PWHT samples with the standard and non-standard treatments were given a simulated PWHT of 1 hour at 740°C followed by air cooling.

For steel B samples were prepared with the low temperature temper. However for this alloy two solution treatment temperatures were used, 1150 and 1200°C, to allow for the lower solubility of nitrogen-rich precipitates. Additional samples with both standard and non-standard treatments were also given the simulated PWHT.

Table 2: Heat Treatment Schedule

Treatment	Purpose	Austenitization	Tempering
Standard	Typical (commercial)	1060°C/1 h/AC	780°C/2 h/AC
Non-standard	High austenitization temperatures and double tempering	1150°C/1 h/AC 1200°C/1 h/AC	660°C/3 h/AC & 660°C/3 h/AC

Plain and notched stress rupture tests in the temperature range 600-675°C were carried out according to BS EN 10291:2000. Full details of the tests on each alloy are given in the results section.

In order to explain the effect of heat treatment and the influence of C:N ratio on microstructure and resulting creep performance, thermodynamic calculations were performed using JMatPro 4.1 software. Phase fractions and phase compositions vs. temperature were estimated.

4. Results

4.1. Stress Rupture Properties

Stress rupture results for the conventional Steel 92 composition, Alloy A, are shown in Table 3 (here and after *b* stands for broken and *ub* for unbroken samples). Tests were carried out at 600-675°C at stresses designed to give aim lives between 1,000 and 30,000 hours based on the ECCC mean line for this alloy [1]. In most cases for the standard heat treatment the alloy failed close to the aim lives. However at longer aim durations and higher temperatures the

actual lives were shorter than intended indicating that the mean line may be non-conservative under these conditions.

The non-standard heat treatment gave dramatic improvements in creep life compared with material given the standard treatment. Aim lives were generally exceeded by significant margins, although the improvement decreased with increasing temperature.

Table 3: Plain Stress Rupture Properties for Steel A

Temp. (°C)	Stress (MPa)	Aim (h)	Non-standard HT (h)	Standard HT (h)
600	187	1000	-	856 b
	172	3000	50,584 b	2722 b
	156	10,000	58,832 ub	8222 b
	140	30,000	-	11,992 b
625	140	3000	16,967 b	-
	122	10,000	26,280 b	-
	107	30,000	41,808 b	-
650	122	1000	-	807 b
	110	3000	6179 b	1734 b
	92	10,000	12,089 b	6109 b
	78	30,000	-	14,729 b
675	81	3000	4192 b	2456 b
	66	10,000	10,625 b	-

The stress rupture data for the high nitrogen Steel B at 600 and 650°C are shown in Table 4 for material given the low temperature temper and at two solution treatment temperatures of 1150 and 1200°C. The performance is compared with the conventional composition given the low temperature temper.

Table 4: Plain Stress Rupture Properties for Steel B

Temp. (°C)	Stress (MPa)	Aim life (h)	Steel B with non-standard HT (h)		Steel A with non-standard HT (h)
			1150°C	1200°C	1150°C
600	187	1000	18,648 ub	28,098 ub	-
	172	3000	23,905 ub	28,298 ub	50,584 b
	156	10,000	18,048 ub	28,298 ub	58,832 ub
650	122	1000	7544 b	7973 b	-
	110	3000	10,255 b	17,118 b	6179 b
	92	10,000	16,920 b	24,213 ub	12089 b

The test programme is not as far advanced as that for the conventional Steel 92 (Steel A), but tests in progress approaching 30,000 hours duration are available. The only failures so far for steel B are at 650°C. However, the high nitrogen alloy is outperforming the conventional composition, where failures have occurred. The best properties are obtained using the higher solution treatment temperature of 1200°C. At 650°C and 92MPa Steel A with the non-standard heat treatment failed after 12,089 hours for a 10,000 hour aim. The high nitrogen Steel B given a 1200°C solution treatment has already exceeded 24,000 hours and remains unbroken.

The results of a small test programme for Steel A to assess notched properties are given in Table 5. Samples given the non-standard heat treatment were tested at 600 and 650°C with aim lives for plain samples of 3,000 and 10,000 hours.

Table 5: Notched Stress Rupture Properties for Steel A

Temp. (°C)	Stress (MPa)	Aim (h)	Plain (h)	Notched (h)
600	172	3000	50,584 b	23,905 ub
	156	10,000	58,832 ub	18,048 ub
650	110	3000	6179 b	6305 b
	92	10,000	12,089 b	16,133 b

The only failures so far have occurred at 650°C. For these the notched properties have been similar to, or in excess of, the plain properties. At 600°C the notched tests are still in progress, but the durations at the time of writing were well in excess of the original aim values.

In Table 6 the tests looking at the effect of PWHT are given. Tests were carried out at 600 and 650°C for Steel A with the standard and the non-standard heat treatment. For the high nitrogen Steel B tests were carried out for samples given the non-standard low temperature temper and solution treatment at 1150 or 1200°C.

Table 6: Effect of PWHT on Stress Rupture Properties

Material	Heat treatment	600°C / 172MPa		650°C / 110MPa	
		+ PWHT	- PWHT	+ PWHT	- PWHT
Steel A	1060/780°C	3059 b	**2722 b**	1714 b	**1734 b**
Steel A	1150/660/660°C	7688 ub	50,584 b	4688 b	6179 b
Steel B	1150/660/660°C	7729 ub	23,905 ub	6521 ub	10,255 b
Steel B	1200/660/660°C	7729 ub	28,298 ub	6462 ub	17,118 b

Steel A with the standard heat treatment provides the basis against which the other tests should be compared and these tests are shown in bold in the table. As would be expected PWHT has little effect on the conventionally heat treated material as the tempering and PWHT temperatures are similar. For both steels the non-standard heat treated material has exceeded the base values for normally heat treated materials.

Currently for the PWHT material failures have been observed at 650°C. Only in Steel A sufficient failures have occurred to allow direct comparison to be made between samples with and without PWHT. At 600°C and 110MPa the non-standard heat treatment with no PWHT gave a life of 6179 hours compared with 1734 hours for the standard heat treatment. However despite the 660°C tempering temperature the 740°C PWHT only reduced the creep life to 4688 hours, 76% of the non-PWHT value and an increase of 170% compared with the standard heat treatment.

4.2. Thermodynamic calculations and literature data

Calculated phase fractions versus temperature in the equilibrium state for Steel A (standard C:N ratio) and Steel B (lower C:N ratio) are shown in Figures 1 and 2. The results of the calculations are used to explain the effect of austenitization temperature, tempering temperature and C:N ratio on microstructure and resulting creep life

During austenitization it is important to avoid the formation of δ-ferrite to ensure a fully martensitic (α') matrix on cooling which is more beneficial for creep resistance than dual phase (α' + δ) [2]. The calculations suggest a maximum austenitization temperature of 1200°C for Steel A and 1180°C for steel B. Steel A was austenitized at 1060°C and at 1150°C

and no delta-ferrite was observed [3]. In the case of Steel B, austenitized at 1150 and 1200°C, a low fraction of delta-ferrite can be expected to form at 1200°C, due mainly to the lower level of carbon which is a strong austenite stabiliser. However, the presence of delta-ferrite has not yet been confirmed by the microscopic investigations.

The solution treatment temperature should be high enough to dissolve completely the BN, MX and $M_{23}C_6$ particles. Calculated temperatures of complete dissolution of BN are 1405°C for Steel A and 1420°C for Steel B. In Steel A the MX particles should dissolve at 1290°C and in Steel B at 1310°C. Therefore, not all BN and MX particles will dissolve at the austenitization temperatures used (Figure 2). Higher dissolution temperatures of nitrides in Steel B are mainly related to the higher nitrogen content. In both steels the volume fraction of undissolved precipitates decreases with increasing temperature and is much lower in austenite (at 1060°C and above) than in ferrite (Table 7). In the case of $M_{23}C_6$ particles all austenitization temperatures used in this work allow their complete dissolution.

On tempering, alloys dissolved during austenitization are precipitated. According to the calculations lowering the tempering temperature from 780°C to 660°C increased the volume fraction of MX and $M_{23}C_6$ (Figure 2 and Table 7). Lowering C level (Steel B) significantly decreased the volume fraction of $M_{23}C_6$ in the ferrite region (below about 800°C). In the case of MX particles lowering the C:N ratio resulted in a further increase in their volume fraction. The volume fraction of MX particles in Steel B after tempering was estimated at the temperature prior to the Z-phase precipitation to see the trend. This is because despite Z-phase being predicted to form in Steel B at 670°C which is above the tempering temperature it is not generally observed in these 9%Cr steels. For the present analysis the Laves phase is not taken into consideration either as this phase is not present after tempering. All the calculations are for the equilibrium condition and take no account of precipitation kinetics.

The calculations indicate that the MX particles are of the form (V,Nb,Cr)(N,C) with increased nitrogen content for lower C:N ratio in Steel B (Figure 3). For both steels at temperatures below about 1150°C the (V,Nb,Cr)(N,C) particles are gradually richer in V than Nb and for the temperatures below around 800° they are also richer in N. Hence lower tempering temperatures will result in particles richer in V and N.

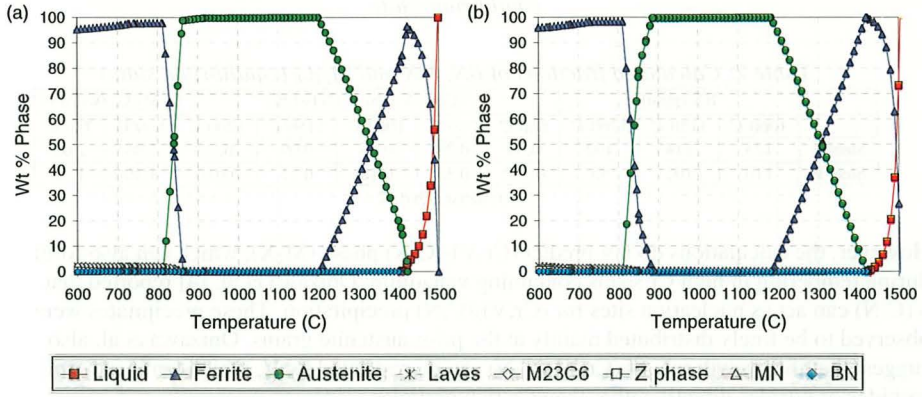

Figure 1: Calculations of phase fractions vs. temperature for (a) Steel A and (b) Steel B – equilibrium state

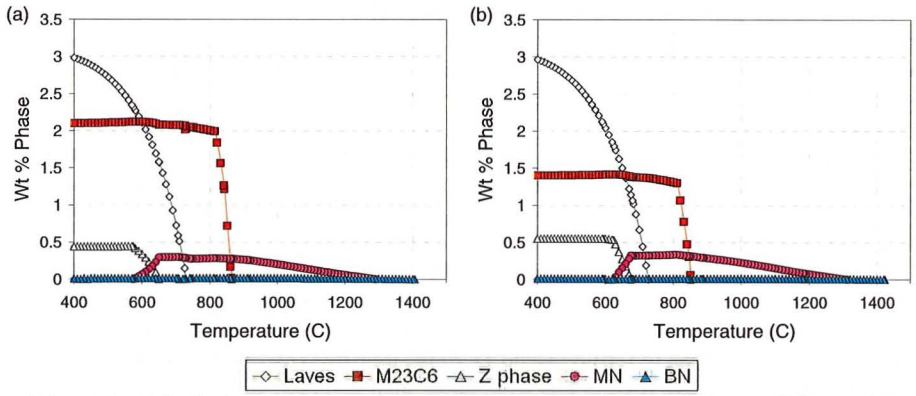

Figure 2: Calculations of minor phases vs. temperature for (a) Steel A and (b) Steel B – equilibrium state

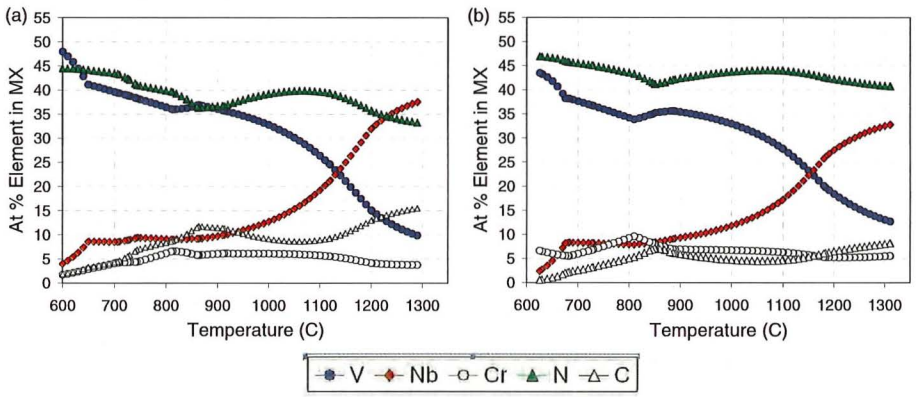

Figure 3: Calculations of MX composition vs. temperature for (a) Steel A and (b) Steel B – equilibrium state

Table 7: Calculated fractions of BN, MX and $M_{23}C_6$ (equilibrium state)

	BN (ppm)			MX – (V,Nb)(N,C) (wt.%)					$M_{23}C_6$ (wt. %)	
	1060°C	1150°C	1200°C	660°C	780°C	1060°C	1150°C	1200°C	660°C	780°C
Steel A	123	114	102	0.30	0.28	0.16	0.09	0.06	2.08	2.02
Steel B	110	102	93	0.33*	0.33	0.18	0.11	0.07	1.40	1.33

* Estimated at 670°C

However, the calculations do not predict $(Cr,V)_2(C,N)$ phase (M_2X), which can also form during tempering in high Cr steels containing vanadium. Onizawa et al. [4] reported that V(C,N) can act as nucleation sites for $(Cr,V)_2(C,N)$ precipitation. These precipitates were observed to be finely distributed mainly at the prior austenite grains. Onizawa et al. also suggest that the growth rate of $(Cr,V)_2(C,N)$ can be restricted by V, which tends to form carbides or nitrides directly rather than Cr-rich particles.

5. Discussion

The use of higher solution treatment and lower tempering temperatures in the standard Steel 92 composition (Steel A) results in a dramatic improvement in creep rupture life. This is particularly marked at 600°C, but even at 650°C a doubling of the creep life is obtained at a stress of 92MPa with a failure duration in excess of 12,000 hours despite the use of a tempering temperature only 10° higher. Further significant improvements are obtained by using a lower C:N ratio, Steel B, particularly when solution treated at 1200°C. The test programmes on both these steels are continuing but some unfailed samples are approaching durations of 60,000 hours.

A Larson-Miller Parameter analysis shows the improvement compared with conventionally heat treated Steel 92, Figure 4. A simple linear extrapolation of the failed samples for the high nitrogen Steel B solution treated at 1200°C suggests a 100MPa, 10^5 hour temperature of 637°C compared 614°C with the standard heat treatment and composition.

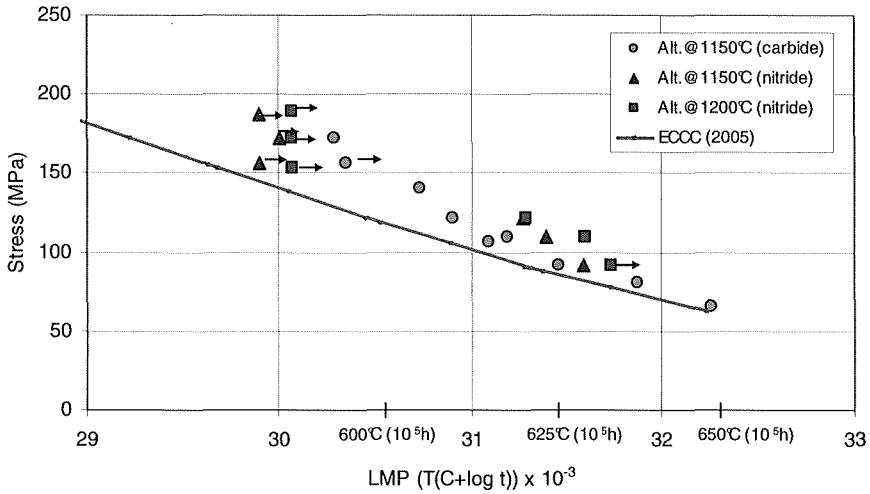

Figure 4: Larson Miller Analysis (C=30) for Plain Creep Rupture Data - carbide stands for Steel A, nitride for Steel B

Two possible objections have been raised to this approach of modifying the heat treatment. Firstly that the material will behave in a notch brittle manner and secondly, if a post weld heat treatment is required at a temperature well in excess of the tempering temperature, the improved creep performance will be lost. Test programmes are in progress to examine these aspects.

Notched tests at 650°C for the standard composition with the low temperature temper show notched strengthening behaviour, particularly for longer durations in excess of 10,000 hours. Tests at 600°C have not yet produced any failures.

Tests are in progress for materials given a simulated PWHT at 740°C. For the conventional composition (Steel A) tested at 650°C, there was no significant difference in rupture lives with or without the PWHT, which might be expected because of the small difference between the PWHT temperature and the tempering temperature of 740°C. However, for material given a 660°C tempering treatment, at a stress of 92MPa, failure occurred after 6,179 hours with no PWHT. After the PWHT this was reduced only to 4,688 hours, a reduction of only 25% and an improvement of 170% compared with the conventionally heat treated samples. Again further tests are in progress at 600°C but insufficient failures have occurred to characterise the effect of PWHT. Thus, it seems that the use of a lower temperature temper gives a precipitate distribution which provides greater long term creep resistance than material given a higher temperature temper. This may well be related to the higher number density of nano-scale precipitates for the former.

Good, long term creep resistance requires a high density of small precipitates which are resistant to coarsening during long term exposure under stress at elevated temperatures. The purpose is to stabilise the dislocation substructure and to inhibit dislocation mobility. The former is controlled mainly by $M_{23}C_6$ precipitates at lath boundaries and the latter by the nano-scale precipitation at boundaries and within laths.

The use of high solution treatment and low tempering temperatures is designed to maximise the alloy in solution prior to transformation to martensite and to produce the greatest number of fine precipitates on tempering. The thermodynamic calculations show that for the solution treatment temperatures used δ-ferrite should be largely avoided in the compositions studied resulting in a fully martensitic microstructure and maximising the dislocation density in the transformed microstructure. The low tempering temperature will increase the driving force for precipitate nucleation from the supersaturated bcc microstructure and minimise coarsening on tempering. It will also increase the dislocation density in the microstructure prior to service.

The thermodynamic calculations focused on $M_{23}C_6$, MX and BN particles important for the analysis of heat treatments. At the solution treatment temperatures used, 1050°C and above, only MX and BN will remain out of solution. The volume fraction of BN is low because only 0.005-0.006% B is present in the steels, but it is significant as boron in solution influences the coarsening kinetics of $M_{23}C_6$. For MX there is a significant decrease in the volume fraction which remains out of solution on raising the solution temperature from 1060 to 1150 or 1200°C. Thus, higher solution temperatures will give more alloy in solution for precipitation on tempering. It will also result in a coarser austenite grain prior to transformation which will reduce creep rates, but may also reduce ductility. The results of calculations support the development of an increased volume fraction of V and N-rich MX particles with lower tempering temperature.

However, some researchers [7] indicate that formation of M_2X type V-rich precipitates instead of MX can occur with lower tempering temperatures (Table 8). Furthermore, Sawada et al. [7] indicate that lowering tempering temperatures is beneficial for creep life due to the effect of nano-size M_2X particles.

Table 8: Reported experimental data on vanadium containing precipitates in high Cr steels

Steel & Reference	Low temperature: 570-700°C		Intermediate temperature: 730°C		High temperature: 760-765°C	Mixed
	Short time	Long time	Short time	Long time	Short time	
9.5-10.7%Cr Götz & Blum [5]		**M_2X** 10.7%Cr: 570°C/10.25h + 690°C/10h		**VN** 9.5%Cr: 730°C/12h + 730°C/10h		**VN + M_2X** 9.5%Cr: 730°C/12h + 730°C/10h + 570°C/10.25h + 690°C/10h
8.7-12%Cr Agamennone et al. [6]		**M_2X** 12%Cr: 570°C/10h + 700°C/8h			**VX** 8.7-12%Cr: 760°C/2h	
8.7-8.9%Cr Sawada et al. [7]	**M_2X** 680°C/0.5h		**M_2X + VX** 730°C/0.5h		**VX** 765°C/0.5h	

The correlation between improved creep rupture life and a higher number of finer V-rich precipitates due to the high austenitization and low tempering temperature is confirmed by the initial microscopic investigations for Steel A [3]. However, based on the overview presented in Table 8, the improvement in creep life may not only be due to the higher number of fine precipitates but also to a shift in precipitate type from MX to M_2X for lower tempering temperatures, but this remains to be confirmed.

6. Conclusions

The use of higher solution treatment and lower tempering temperatures produces a marked improvement in stress rupture lives for Steel 92 type material. This is especially marked at 600°C but is still present at 650°C.

For 600°C tests are still in progress, but durations are approaching 60,000 hours for an aim life of 10,000 hours for a conventional heat treatment.

Further improvements in stress rupture lives are produced by modifying the composition to lower the C:N ratio.

In limited test programmes there is no evidence that this modified heat treatment results in notch brittle behaviour and even after a simulated PWHT at 740°C the majority of this improvement in stress rupture performance is maintained.

In the compositions studied in order to maximise alloy in solution for precipitation on subsequent tempering solution treatment temperatures up to 1200°C can be used without the formation of δ-ferrite.

The lower tempering temperature results in a higher number of fine MX particles on tempering which become richer in V and N as the tempering temperature is reduced. There is evidence in the literature that low tempering temperatures may also change the precipitate type from MX to M_2X.

7. Acknowledgements

The authors are deeply thanking Prof. S. van der Zwaag and Dr S. Neelakantan, for the arrangement of the usage of JMatPro software at Delft University of Technology.

8. References

[1] European Creep Collaborative Committee, ECCC data sheets, 1999 and 2005.
[2] Yoshizawa M., Igarashi M., Long-term creep deformation characteristics of advanced ferritic steels for USC power plants, *Proc. ECCC Creep Conference*, 12-14 September 2005, London, 110-118 (2005).
[3] Yescas M.A., Morris P.F., Improved creep resistance of Steel 92 by the use of modified heat treatments, *Proc. ECCC Creep Conference*, 12-14 September 2005, London, 143-152 (2005).
[4] Onizawa T., Wakai T., Ando M., Aoto K., Effect of V and Nb contents on mechanical properties of high Cr steels, *Proc. ECCC Creep Conference*, 12-14 September 2005, London, 130-142 (2005).
[5] Götz G., Blum W., Influence of thermal history on precipitation of hardening phases in tempered martensite 19%Cr-steel X12CrMoWVNbN 10-1-1, *Materials Science and Engineering* A 348, 2001-2007 (2003).
[6] Agamennone R., Blum W., Gupta C., Chakravatty J.K., Evolution of microstructure and deformation resistance in creep of tempered martensitic 9-12%Cr-2%W-5%Co steels, *Acta Materialia* 54, 3003-3014 (2006).
[7] Sawada K., Suzuki K., Kushima H., Tabuchi M., Kimura K., Effect of tempering temperature on Z-phase formation and creep strengthening in 9Cr-1Mo-V-Nb-N steel, *Materials Science and Engineering* A 480, 558-563 (2008).

9th Liege Conference : Materials for Advanced Power Engineering 2010
edited by J. Lecomte-Beckers, Q. Contrepois, T. Beck and B. Kuhn.

Part B

Gas Turbine Materials

9th Liege Conference : Materials for Advanced Power Engineering 2010
edited by J. Lecomte-Beckers, Q. Contrepois, T. Beck and B. Kuhn.

Modelling of Microstructure and Mechanical Property Changes in Gas Turbine Alloys

Alfred Scholz *, Mohamed Nazmy **, Bernard Fedelich [x], Tiedo Tinga [+], Rob Huls [#)]
* Institut fuer Werkstoffkunde, Technische Universitaet Darmstadt, Germany
** ALSTOM Power, Baden, Switzerland, [x] BAM, Berlin, Germany
[+] Netherlands Defence Academy, Den Helder, The Netherlands
[#)] National Aerospace Laboratory, Emmeloord, The Netherlands

Abstract

High efficiency in gas turbines requires increased gas temperatures. Gas temperatures above 1100°C can only be handled using air cooled structures to keep the metal temperatures below 1000°C. Nickel-base single crystal (SX) superalloys have higher elevated temperature strength than conventionally or directionally cast superalloys. SX superalloys are therefore very attractive for use in aero engines and gas turbines as blade material since they allow higher operating temperatures.

Within the Work Packages 3 & 4 of the COST 538 Action "Plant life extension" deformation and lifetime of SX alloy CMSX-4 using different material simulation concepts were in the focus. Of special interest are the efforts to incorporate degradation effects into the models. At first, two multi-scale models were developed for the purpose of connecting the macroscopic material behaviour to the microstructural composition of the material. The matrix and precipitate phase constitutive behaviour was considered. Formulations are based on the physical mechanisms acting on the microscopic level. The developed damage model combines creep-fatigue damage accumulation. Furthermore, the capability of the model to predict the effect of microstructural degradation on mechanical response was demonstrated by the simulation of experiments on degraded material.

Moreover, a constitutive model demonstrates the potentiality to predict rafting in superalloys with large volume fraction of the γ' phase and its influence on the alloy strength. Hence it can be regarded as a candidate for use in structural analysis of blades in service conditions. Finally, the developed micro-structural based models have been successfully applied to an ex-service un-cooled blade i.e. a case study.

Keywords: Nickel base superalloys, Degradation, Modelling, Microstructure, Mechanical properties

1 Background

Gas turbines are extensively used for the propulsion of aircrafts and in power generation. Their most severely loaded parts, the turbine rotor blades, are manufactured from single crystal nickel-base superalloys. The superior high temperature behaviour of these materials is attributed to the two-phase composite microstructure of a γ-matrix consists of solid solution of Ni,Cr,W,Mo etc and a large volume fraction of the second phase precipitates of γ'- Ni_3 (Al,Ta). During service, the initially cuboidal precipitates evolve to elongated plates through a diffusion-based process called rafting. In order to include this deterioration process in the life assessment of gas turbine components, models must be

available to handle the specific microstructural changes and the corresponding mechanical behaviour.

The main objectives of the COST538 activities are the extension of the reliable lifetime of the critical components in the high temperature power plants. The corresponding components require detailed investigations of the degradation processes on the microstructure and the mechanical properties (**Figure 1**).

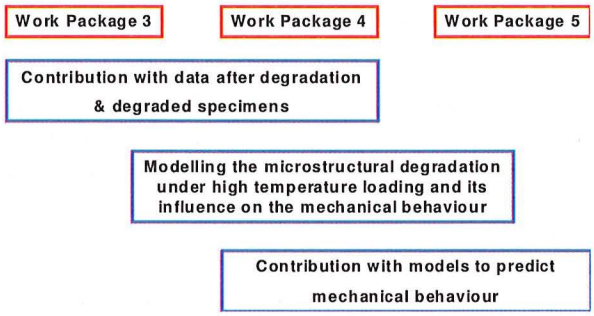

Figure 1: Illustration of interaction with Work Package 3 (material degradation), Work Package 4 (Modelling) and Work Package 5 (Case Studies)

In Work Package 4 of the COST 538 Action two models have been developed that incorporate the effect of microstructure degradation on the mechanical response (Work Package 3). In this paper the models developed by the Bundesanstalt für Material-forschung (BAM) and the National Aerospace Laboratory in cooperation with the Netherlands Defence Academy (NLR/NLDA) are introduced briefly with reference to extensive papers being available from the corresponding authors. Moreover, both models have been applied to predict the degradation and fatigue life of test specimens and real gas turbine components.

In order to establish the relationship between parameters relevant to application i.e. temperature, time & stresses and the mechanical properties experiments have been conducted. Microstructural investigations were performed to identify material model parameters.

Investigations reported here are focused on the crystallographic orientation <001>, which is the most relevant case. In addition the case <111> has also been investigated on the base of a limited amount of experiments.

2. Experimental

Test bars (20mm diameter, 160mm length) of alloy CMSX-4, orientation <001> were received from HOWMET, Exeter (Master heat: GE148, Cast 704P6253/9556). Chemical composition is given in **Table 1** [1].

Table 1: Chemical composition and heat treatment

Main alloying elements

	Cr	Ni	Co	Mo	W	Ta	Nb	Al	Ti	Re
Bar stock	6.4	bal	9.5	0.58	6.4	6.5	<0.01	5.7	1.06	2.8
Cast sample	6.3	bal	9.5	0.59	6.3	6.45	0.01	5.73	1.06	2.8

Residal elements

	C	B	Zr	Fe	Cu	Si	Mn	P	S	Hf	Pt	V
Bar stock	0.0043	<0.0020	0.0034	0.08	<0.005	<0.02	<0.01	<0.001	<0.0005	0.09	<0.05	<0.01
Cast sample	0.005	<0.002	0.0031	0.09	<0.005	0.02	<0.01	<0.001	<0.0005	0.1	<0.05	<0.01

Trace elements

(in ppm)	Bi	Tl	Ag	Pb	Te	Se	Sn	Ga	Mg	O2	N2
Bar stock	<0.1	<0.2	<0.5	<0.5	<0.2	<0.5	<10	<10	20	6	3
Cast sample	<0.1	<0.2	<0.5	<0.5	<0.5	<1	<10	<10	13	6	3

Heat treatment

SV6365	Proprietary cycle of three stages to give eutectic <3% maximum and <1% avarage of ten frames measured on Micro WF67

Chemical composition as well as the short term properties were in accordance with data from earlier batch of the same material [2]. The metallographic investigations showed typical microstructure in the as delivered condition as shown in (**Figure 2**).

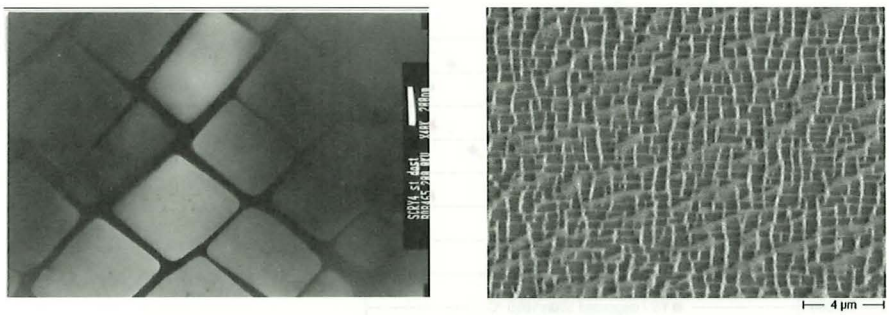

Figure 2: SEM dark field image of CMSX-4 microstructure (taken from γ' reflection), (left) & SEM image (right)

In order to investigate degradation effects, the underlying conditions were chosen as follows: 1050°C/115MPa/300h and 1050°C/68 MPa/2500 h. Tensile tests were conducted on samples which have been degraded. The degradation led to a significant drop in the 0.5% yield stress as given in (**Figure 3**). The results reported here have been partly published in earlier works [3] & [4].

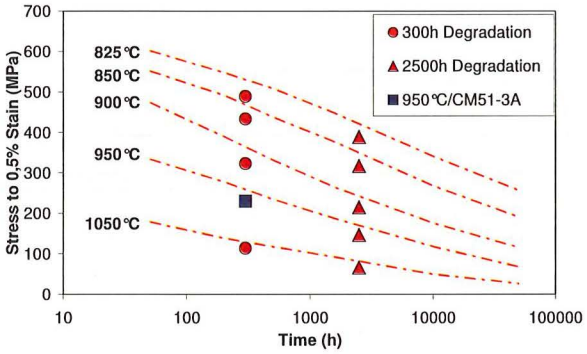

Figure 3: Reduction of tensile stresses to achieve 0.5% plastic strain at tensile testing (CMSX-4) with increase of degradation time

In order to achieve a temperature dependant overview of degradation, a series of tensile tests were performed at room temperatures to 950°C. A significant reduction in yield stress is observed throughout the investigated temperature range as shown in **Figure 4**. A remarkable influence of the effect of degradation on yield stress was observed at room temperature [3]. The results on ultimate strength also show a clear influence of the effect of degradation (**Figure 5**). Rupture elongation at room temperature is increased after degradation, while at elevated temperatures ductility is somewhat reduced (**Figure 6**).

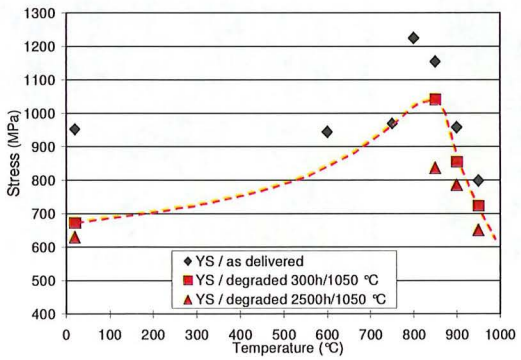

Figure 4: Yield stress vs. temperature at tensile testing and influence of degradation, CMSX-4, <001>

In summary, the degradation has a strong effect on yield stress at low temperatures. Figures **7-a, b & c** show fracture surface after testing at RT, microstructure of degraded specimen and a corresponding TEM micrograph of the dislocation structure of the tested

specimen. The γ' morphology also changed sligtly in comparison to the as delivered condition i.e. as in **Figure 2**.

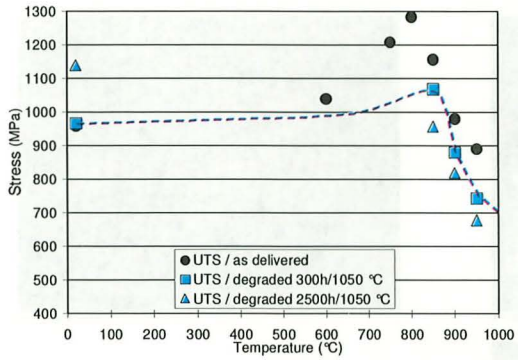

Figure 5: Ultimate strength vs. temperature at tensile testing and influence of degradation, CMSX-4 <001>

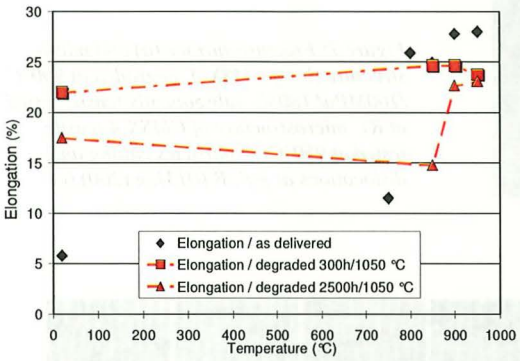

Figure 6: Rupture elongation vs. temperature at tensile testing and influence of degradation, CMSX-4 <001>

Figure 8 shows the shape of the specific creep specimen used to generate results on degradaded microstructures, at different stresses, required for the development of the degradation model presented in reference [6].

The changes in γ'-morphology were identified and illustrated in **Figure 9**. The rafting time, the corresponding stress, and temperature were plotted as shown in **Figure 8**. The γ'-morphological changes after degradation were used to develop the quantitative model for CMSX-4 [5].

Besides static loading, the degradation followed by cyclic loading is also of design relevance. A limited amount of fatigue experiments were performed at 950°C. **Figure 10** shows the results of a limited number of fatigue tests, performed at 950°C and a strain ratio R_ε = -1, illustrating the effect of degradation on low cycle fatigue (LCF). A

significant reduction of fatigue life, after degradation with the conditions 1050°C/ 68MPa/2500h, was observed in **Figure 10**. At a lower fatigue testing temperature e.g. 750°C, the fatigue life was also affected by degradation [1].

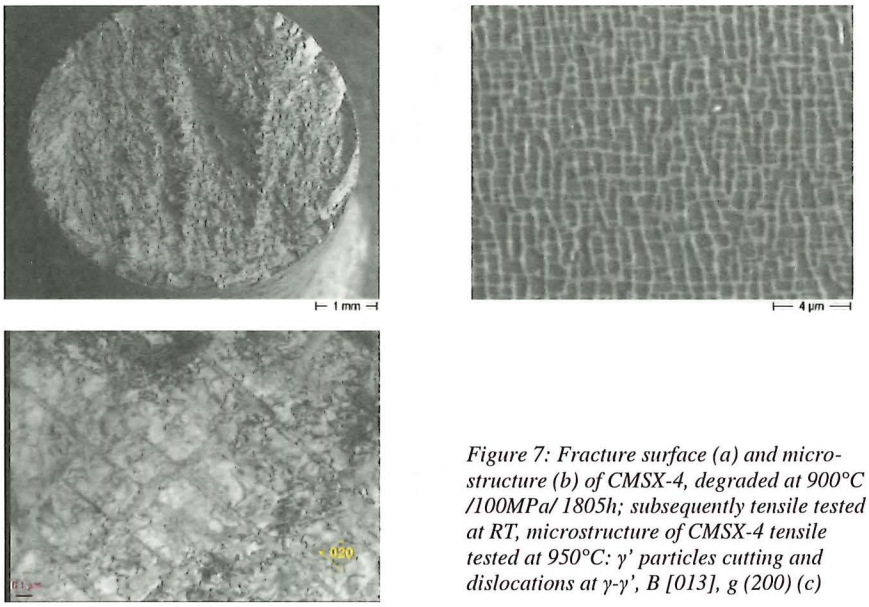

Figure 7: Fracture surface (a) and microstructure (b) of CMSX-4, degraded at 900°C /100MPa/ 1805h; subsequently tensile tested at RT, microstructure of CMSX-4 tensile tested at 950°C: γ' particles cutting and dislocations at γ-γ', B [013], g (200) (c)

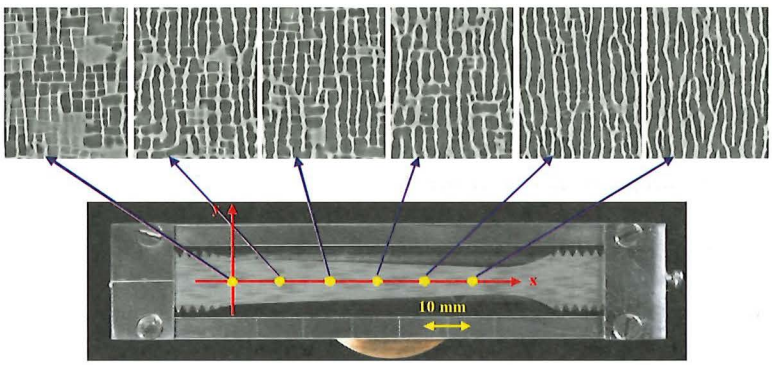

Figure 8: SEM holder with conical specimen degraded at 1050°C/175 h. Areas of analysis and SEM images correspond to the stress range 59 to 94 MPa [6]

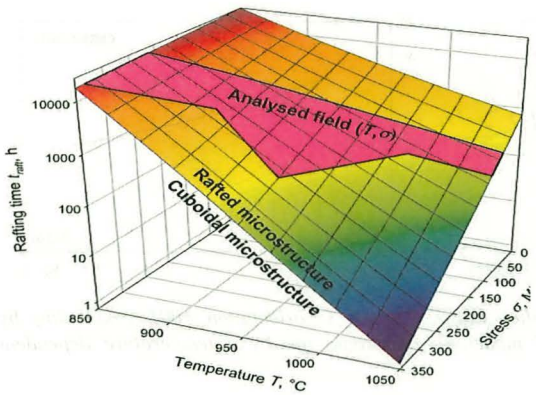

Figure 9: Time for complete raft formation as a function of temperature and stress. The field of degredation experiments is marked with the solid line [6]

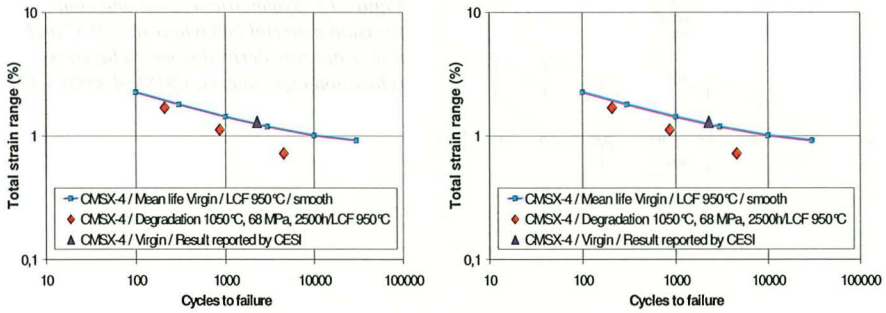

Figure 10: Reduction of fatigue life at 950°C (left) and 750°C (right) after degradation

In the following sections the two material models are presented. BAM has developed a model for microstructural degradation under high temperature loading and its influence on the mechanical behaviour while NLR / NLDA developed a "Multi-Scale Model" to connect macroscopic material behaviour to the microstructural changes of material.

In terms of material parameter identification, significant experimental results were made available by the partners of references [1], [2], [5] and [7] as shown for example in **Figure 11**. Creep data were contributed to identify the static recovery in the material model. The fatigue life behaviour of CMSX-4 has been described with a new temperature dependent approach. In addition, specific strain controlled cyclic relaxation experiments were performed. These experimental results were needed to model the kinematic hardening effects as shown in **Figure 12**.

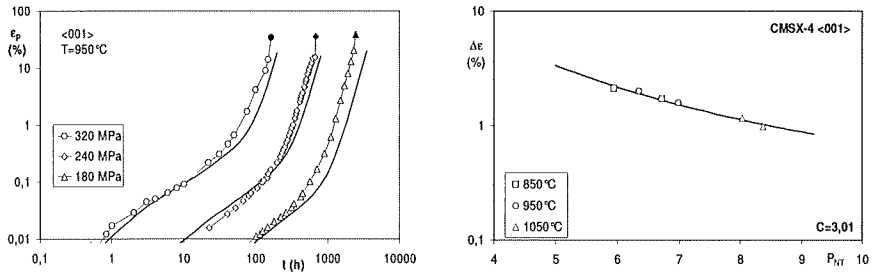

Figure 11: Creep behaviour of SX alloy CMSX-4 at 950°C, orientation <001>, modelling by Garofalo creep equation (left) and modelling of fatigue life by a temperature dependent approach, [2] (right)

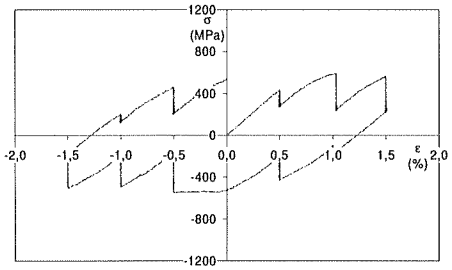

Figure 12: Symmetric tension and compression material behaviour at 950°C and low strain rate derived from cyclic stress relaxation experiments, CMSX-4 <001> [7]

3. BAM Constitutive Material Model

A constitutive material model with capacity to predict rafting in components has been developed and calibrated for the SX alloy CMSX-4. Herein, the microstructure influence is assumed to mostly depend on the channel width $w(t)$, which increases during creep due to two phenomena:

- the homothetic growth of γ'-precipitates, called isotropic coarsening,
- the coalescence of adjacent precipitates, called rafting.

In accordance, $w(t)$ varies between two time-dependent limits, which correspond to either the ideal cube or the infinite plate microstructure under isotropic coarsening. This evolution is shown in **Figure 13**.

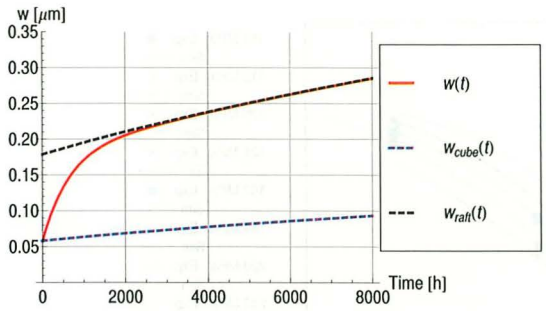

Figure. 13: Schematic evolution of the channel width between its two limits

The degree of rafting progress, as opposed to isotropic coarsening is defined by the variable

$$\xi = \frac{w - w_{cube}}{w_{raft} - w_{cube}}, \quad 0 \le \xi \le 1 \tag{1}$$

where w_{cube} and w_{raft} are the previously mentioned limiting cases of the microstructure. The microstructure dependent constitutive model has been presented in details in [5] [8]. It is based on crystal viscoplasticity for octahedral and cubic slip systems and on the assumption of thermally activated deformation mechanisms. In particular, the shear rate of the octahedral systems crucially depends on the Orowan stress τ^{Orowan}, which acts as a smooth threshold for yielding

$$\dot{\gamma}_g^o = \rho_g^o \sinh\left[\frac{V_f^o}{kT}\left|\tau_g^o - x_g^o\right|\left\{1-\left[1+\left(\frac{\left|\tau_g^o - x_g^o\right|}{\tau^{Orowan}}\right)^s\right]^{-1/s}\right\}\right] \operatorname{sign}\left(\tau_g^o - x_g^o\right), \tag{2}$$

$$\tau^{Orowan} = \alpha \frac{K\, b}{\sqrt{3/2}\, w},$$

where the parameter s controls the degree of smoothness of the elastic-plastic transition, g is the (octahedral) slip system, ρ_g^o is the mobile dislocation density and x_g^o the kinematic hardening variable.

Rafting is assumed to be controlled by the difference of the dislocation densities between the vertical and the horizontal channels and the resulting distribution of internal stresses. In the frame of a macroscopic model, a detailed description of the dislocation distribution is not possible. Alternatively, the driving force for rafting X is assumed to be a measure of the kinematic hardening (see [5] [8] for details) and rafting progress is described by a phenomenological law with saturation

$$\dot{\xi} = (1-\xi)\, f^{raft}\, X^n. \tag{3}$$

Rafting completion, i.e. $\xi = 1$ and $w = w_{raft}$, corresponds to the ideal case of infinite plates (see equ. (1)). The model parameters f^{raft} and n have been estimated from direct measurements of the channel widths in crept specimens under several loadings. **Figure 14** shows an example of calculated and measured channel widths.

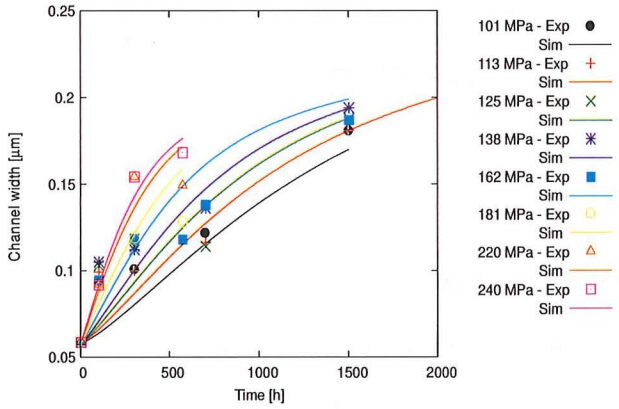

Figure 14: Evolution of the channel width during creep at 950°C for several load levels.

The remaining model parameters have been estimated from a large number of test results including monotonic tensile, cyclic, relaxation and creep tests in <001> and <111> specimens. As an example, **Figure 15** shows the comparison between model simulations and experiments for creep tests at 950°C with <001> specimens.

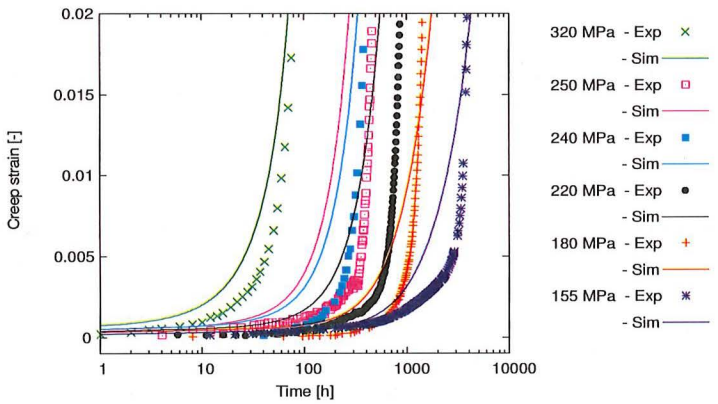

Figure 15: Simulation of creep tests at 950°C

The present model has been implemented in a UMAT subroutine for use with the FE program ABAQUS. An example of analysis of a complex loading condition is presented in section 5.

Finally, the ability of the model to describe the post-rafting mechanical behaviour has been assessed with mechanical tests on pre-crept, i.e. degraded specimens, under several conditions. In the case of a subsequent tension loading, the results are presented in **Figure 16** for several degradation conditions resulting in several final channel widths. The measured channel widths are indicated. It is clear that the tensile strength decreases as function of the channel width, a feature which is correctly captured by the model.

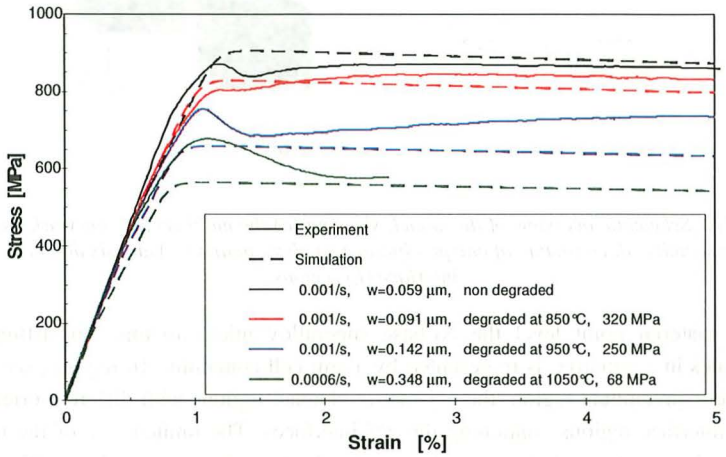

Figure 16: Influence of degradation on tensile strength.

4. NLR / NLDA Constitutive Material Model

In the NLR / NLDA approach, a multi-scale framework has been developed in which the different aspects of the Ni base superalloy behaviour are modelled [9] to [13]. The developed multi-scale model [10] for the prediction of the superalloy mechanical behaviour covers several length scales, as is shown schematically in **Figure 17a**. The macroscopic length scale characterises the engineering level on which a finite element (FE) model is commonly used to solve the governing equilibrium problem. The mesoscopic length scale represents the level of the microstructure within a macroscopic material point. At this length scale the material is considered as a compound of two different phases: γ'-precipitates embedded in a γ-matrix. Finally, the microscopic length scale reflects the crystallographic response of the individual material phases. The constitutive behaviour is defined on this level using a strain gradient crystal plasticity framework.

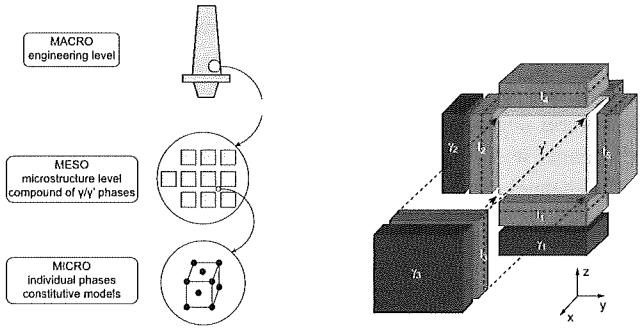

a) b)

Figure 17: Schematic overview of the model, showing (a) the multi-scale framework and (b) the multi-phase unit cell, consisting of one precipitate (γ'), three matrix (γ_i) and six double interface (I_i) regions.

On the material point level the Ni-base superalloy microstructure, consisting of γ'-precipitates in a γ-matrix, is represented by a unit cell containing 16 regions, see **Figure 17b**: one γ'-precipitate region, three γ-matrix channel regions with different orientations and 12 interface regions containing the γ/γ'-interfaces. The limited size of the unit cell and the micromechanical simplifications make the framework particularly efficient in a multiscale approach and is computationally much more efficient than a detailed FE based unit cell discretization.

The matrix phase constitutive behaviour is simulated by using a non-local strain gradient crystal plasticity model. In this model, non-uniform distributions of geometrically necessary dislocations (GNDs), induced by strain gradients in the interface regions, affect the hardening behaviour. The basic ingredient of the model is the relation between the slip rates $\dot{\gamma}$ and the resolved shear stresses τ^{α} for all the slip systems α. The following formulation is used:

$$\dot{\gamma} = \dot{\gamma}_0 F(\Omega^{\alpha}) \left\{ \frac{|\tau^{\alpha}_{eff}|}{s^{\alpha}} \right\}^{m} \left\{ 1 - \exp\left(- \frac{|\tau^{\alpha}_{eff}|}{\tau^{or}} \right) \right\}^{n} sign(\tau^{\alpha}_{eff}) \tag{4}$$

where τ^{or} denotes the Orowan stress, s^{α} the actual slip resistance and τ^{α}_{eff} the effective shear stress on slip system α, obtained from the effective stress tensor $\boldsymbol{\sigma}_{eff}$ using the symmetric Schmid tensor. The factor F is a cross slip factor that will be discussed below, while $\dot{\gamma}_0$, m and n are material constants.

The majority of the superalloy constitutive models available in literature contain, in addition to the octahedral systems, a set of cube slip systems to correctly simulate the material behaviour at orientations other than <001>, whereas experiments show that the

occurrence of macroscopic cube slip is quite exceptional. In the present model, the octahedral cross slip processes, that are physically responsible for the major part of the cube slip, are modelled and their effect is incorporated [11]. A parameter Ω^α is introduced to quantify the amount of cross slip. A higher value of Ω^α indicates a more favourable condition for cross slip. Therefore, a cross slip factor F based on the value of Ω^α is incorporated to enhance the slip rate of the slip systems:

$$F\left(\Omega^\alpha\right)=\left(C_{cs}\frac{\tau}{s^\alpha}\right)^{\varphi\left(\Omega^\alpha\right)} \quad \text{with} \quad \tau=\max\left(\tau_{eff}^\alpha,\tau_{cs}\right) \tag{5}$$

where $\varphi\left(\Omega^\alpha\right)$ quantifies the stress dependence of the cross slip, whereas C_{cs} and τ_{cs} are material constants.

The major part of plastic deformation is accommodated by the matrix phase, where dislocations are moving through relatively narrow channels. When encountering a precipitate, a loop is created around the particle, enabling the dislocation to continue its motion on the slip plane behind the precipitate. The dislocation loop around the precipitate may disappear by two different mechanisms, precipitate shearing or recovery climb, both involving inelastic deformation of the precipitate. These mechanisms are incorporated in the model [11], yielding the following slip law:

$$\dot{\gamma}^\alpha=\frac{SbS_{\text{int}}}{V}\rho_{GND,\min}^\alpha\left[f_{diss}\left\{1-\exp\left(-\frac{\left|\tau_{eff}^\alpha\right|}{s_0^\alpha}\right)\right\}^p+\frac{4v_{c\lim b}^\alpha}{H_\gamma}\left\{1-\exp\left(-\frac{\left|\tau_{eff}^\alpha\right|}{\tau_{cr}^\alpha}\right)\right\}\right]sign\left(\tau_{eff}^\alpha\right) \tag{6}$$

where S, S_{int}, V and H_γ are geometrical constants related to the dimensions of the microstructure. $\rho_{GND,\min}^\alpha$ represents the number of dislocations available for climb or shearing, v_{climb} is the climb velocity and f_{diss}, p and τ_{cr} are model parameters.

In addition to the model describing the material deformation, a damage model has been developed [12] that integrates time-dependent and cyclic damage into a generally applicable time incremental damage rule. The time dependent part of the damage rule is based on the model proposed by Levkovitch et al. [14], whereas the fatigue damage is attributed to irreversibility in the slip mechanism [15, 16]. This is incorporated in the model by introducing a criterion based on the Orowan stress to detect slip reversal on the microscopic level. The cyclic damage accumulation is quantified using the maximum values of resolved shear stress and slip rate during the "cycle". Also, the interaction between cyclic and time-dependent damage accumulation is incorporated in the model.

Finally, the rafting and coarsening processes are modelled by defining evolution equations for several of the microstructural dimensions [13] that are defined in **Figure 18**.

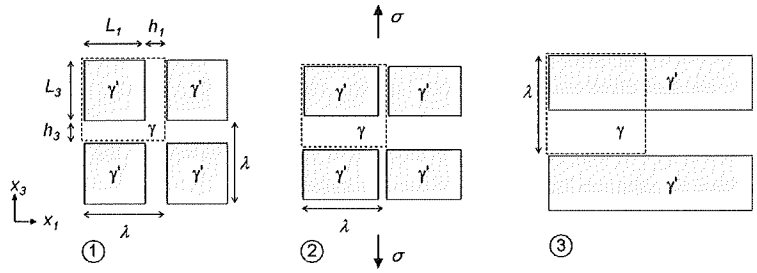

Figure 18: Schematic representation of the changes in microstructural dimensions at three different stages of the degradation process: 1) initial state; 2) microstructure in a rafted state; 3) fully rafted microstructure after a certain amount of coarsening.

The phenomenological relation for the horizontal channel widening rate $\dot{h}_i$ during vertical tensile loading as derived by Epishin et al. [4] was taken as the point of departure for the present model. However, the relation was extended to be applicable for a general multiaxial stress state. The evolution rate of the precipitate size ($\dot{L}_i$) is then given by:

$$\dot{L}_i(T,\sigma) = -\frac{3}{2} L_i \left[\frac{\sigma_{ii}^d}{\sigma_{VM} + \varepsilon} \right] \frac{A^*}{L} \exp\left[-\frac{Q - \sigma_{VM} U(T)}{RT} \right] \tag{7}$$

where σ_{ii} and σ_{VM} are the deviatoric and von Mises stress, respectively. The function $U(T)$ defines the temperature dependence, whereas ε, A^* and Q are model parameters. In addition to the rafting, a formulation for the coarsening process is derived, quantifying the evolution of the microstructure periodicity λ, see **Figure 18**. Since the microstructural dimension are already part of the model, the effect of the microstructure degradation on the mechanical response of the material is almost automatically obtained.

The framework capabilities are demonstrated by applying the model to smooth CMSX-4 specimens that have been tested within the COST 538 Action. The predicted tensile response is compared to the experimental results in **Figure 19** for specimens with different degrees of degradation (characterized by the increasing channel width h). The model simulates these test quite well.

Finally, the fatigue lives of several test bars, both virgin and degraded, have been predicted. In **Figure 20** these values are compared to the experimentally obtained numbers of cycles to failure. The figure shows that only a few tests at 750°C are outside the factor-2 band, while the other tests could be simulated quite accurately.

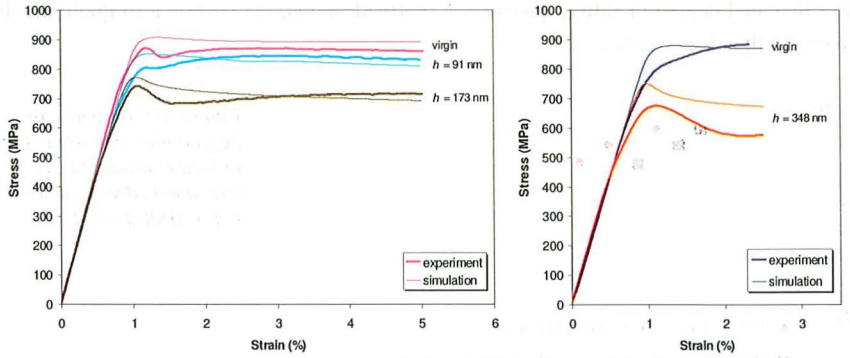

Figure 19: Simulated tensile tests at 950 °C and strain rates 10^{-3} s^{-1} (left) and $0.6 \cdot 10^{-3}$ s^{-1} (right) compared to experimental results for virgin material and different degrees of degradation [9].

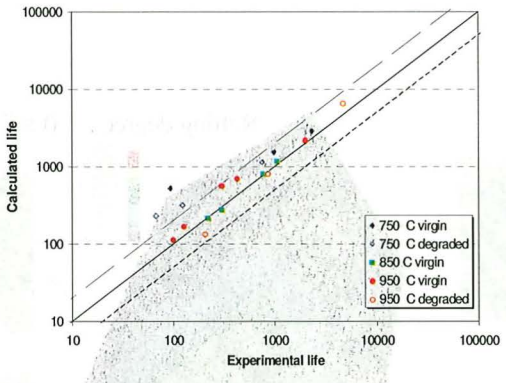

Figure 20: Calculated versus experimental life times using the damage model including the degradation mechanism [9].

5. Validation

For validation purposes, a limited number of notched specimens with K_t=1.41 in both as delivered and degraded conditions, were fatigue tested using stress control mode [1]. The results of this investigations are shown in **Figure 21**.

As an important validation step, the material models have been applied to Finite Element calculations in order to recalculate the stress strain distribution at notches under different loading situations. Details of calculation are available in the report [8]. In **Figure 22** the results of the simulation of rafting with the BAM constitutive model in a notched specimen at 950°C is presented and compared with SEM morphology observations after 1000h creep loading.

The calculated degree of rafting progress ξ defined in equ. (1) is shown to qualitatively agree with the observations.

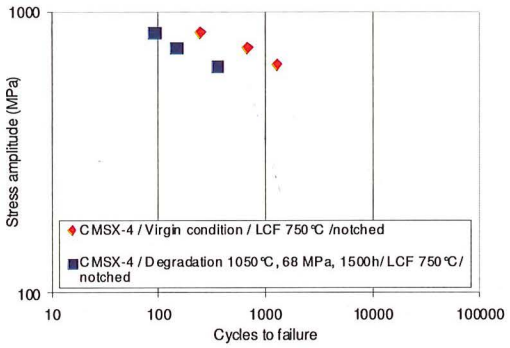

Figure 21: Influence of degradation on fatigue life at load controlled tests with notched specimens [1], CMSX-4 <001>

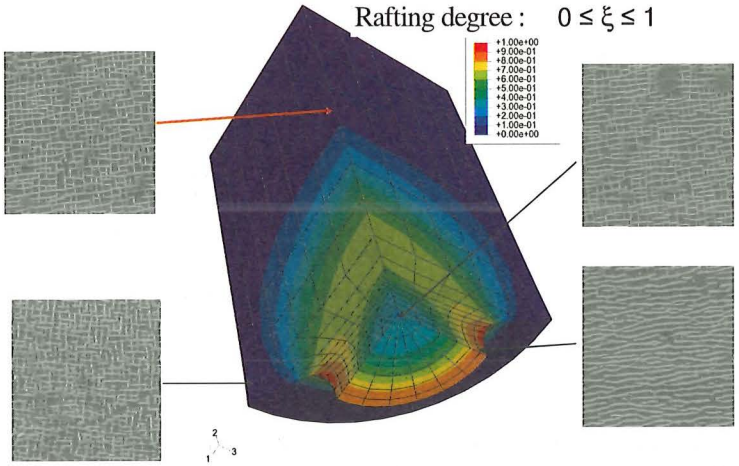

Figure 22: Simulation of rafting in a notched specimen crept at 950°C and comparison with the SEM observations after 1000h

6. Case Studies

Five ex-service blades of SX-CMSX-4 were supplied by SIEMENS Industrial Turbo-machinery Ltd, Lincoln, for mechanical and metallographic investigations. The following service conditions were reported for these blades:

Operation hours: 12,700
Number of starts: 200
Coating: Sermaloy 1515
Length of airfoil: 40mm
Temperature distribution in airfoil: Section 1: 807°C; Section 2: 927°C; Section 3: 997°C
Stress distribution : Section 1: 189MPa, Section 2: 111MPa, Section 3: 30MPa

The ex-service blade, the machined specimens, the distribution of temperatures and stresses along the airfoil (acc. to SIEMENS) are shown in **Figure 23**.

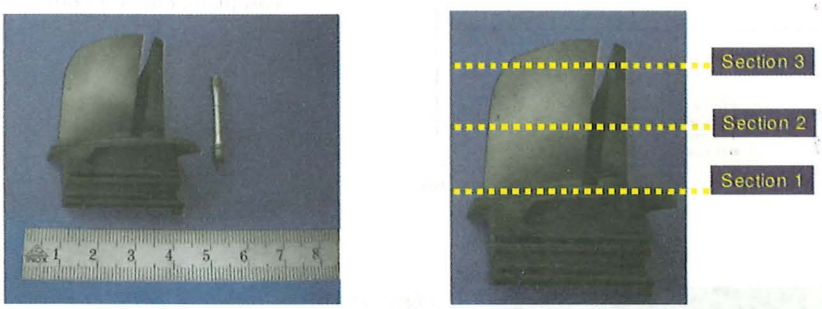

Figure 23: Ex-service blade and distribution of temperatures and stresses along the airfoil (reported by Siemens) [1]

From each blade a specimen was taken from the airfoil in order to perform tensile tests. Service loading led to a reduction in yield stress at room temperature as compared with that of the as-delivered conditions (**Figure 24**). At 800 and 850°C service loading also leads to a reduction in yield stress and corresponding rupture elongation (**Figure 25**). The microstructure of the ex-service blade as shown in **Figure 26**, illustrates the effect of long term high temperature exposure in inducing the changes in the morphology of γ/γ` phases.

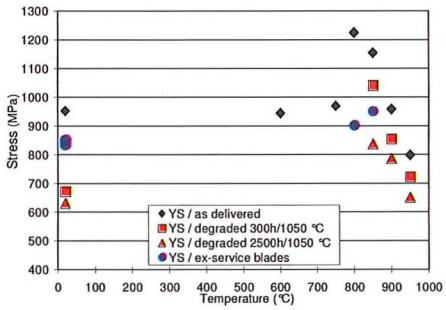

Figure 24: Influence of service loading on yield stress in comparison to as-delivered and degraded conditions, CMSX-4 <001>

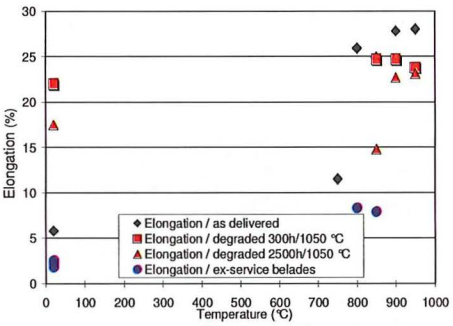

Figure 25: Influence of service loading on rupture elongation in comparison to as-delivered and degraded conditions, CMSX-4 <001>

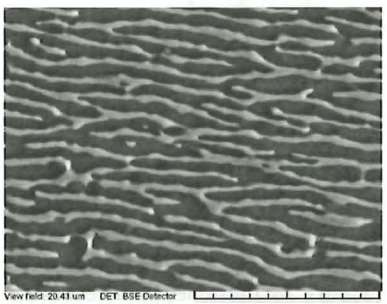

Figure 26: Microstructure of airfoil, ex-service blades CMSX-4

Simulation of microstructural evolution by NLR /NLDA model [9] on an internally and film cooled turbine blade can be compared with the results presented in [4]. The experimentally examined microstructure (**Figure 26**) at three different locations in an ex-service CMSX-4 (uncooled) turbine blade correspond to the results shown in the simulation (**Figure 27**). Here the almost virgin microstructure at the blade platform (Section 1) and the varying orientation of the rafts at the tip region (Section 3) nicely correspond to the results shown in **Figure 27**.

The fully rafted microstructure at the blade centre was not observed here for two reasons: the simulated duration of 1,000hrs is much shorter than the 12,700 hrs in [4], and the internal blade cooling yields much lower temperatures in the centre region of the blade, which reduces the degradation rate there. These results clearly demonstrate that the typical case of a material loaded uniaxially in radial direction, which is mostly studied in literature, is not representative for most of the locations in this real component. That is especially due to the fact that the present blade is internally cooled, resulting in thermal stresses that cause the stress state to be multiaxial.

Concurrent with the microstructure degradation, the creep deformation of the blade is calculated. The results indicate that the high creep strain regions at the suction side of the blade are hardly affected by the degradation. Moreover, the maximum value of the creep strain, located at the inner surface of the blade in one of the cooling channels, has decreased slightly from $1.30 \cdot 10^{-3}$ m/m in the virgin blade to $1.27 \cdot 10^{-3}$ m/m in the degraded blade. However, the equivalent creep strain near the tip at the pressure side is much higher in the degraded blade than in the virgin blade. The evolution of the creep strain at this location is plotted in **Figure 28** for both the virgin and the degraded blade, showing a significant increase in the creep rate.

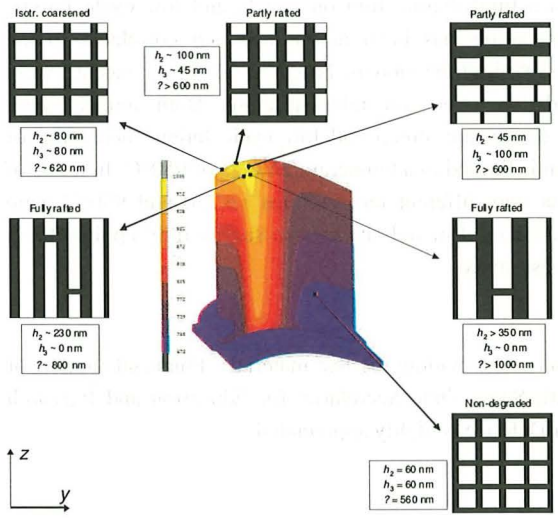

Figure 27: Overview of degraded microstructures observed after a simulation of degradation in a cooled turbine blade under service conditions for 1000 hours. The contours indicate the blade temperature distribution

These results demonstrate that the effect of degradation on the overall creep deformation is rather limited for this specific component, so the blade elongation is hardly affected by the degradation. However, local creep strain rates, especially in the hot regions of the blade, considerably increase after degradation. Neglecting the effects of rafting and

coarsening in the numerical analysis would thus lead to non-conservative life predictions. This clearly demonstrates the benefit of a model that includes the effects of degradation.

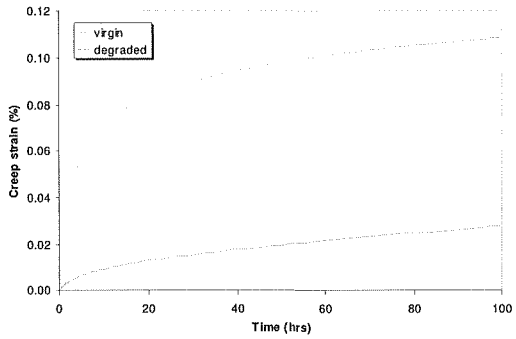

Figure 28: Comparison of the equivalent creep strain evolution in a virgin and a degraded blade for a specific location at the blade tip [9]

7. Conclusions

Different models on the effect of microstructural changes due to degradation have been developed. The effect of microstructural degradation on tensile and low cycle fatigue properties and at different temperatures has been determined and correlated to the microstructure based models. The two lifetime models, based on different concepts, were developed including the degradation effect on microstructure. Both models were successfully applied to simulate the tensile, creep and low cycle fatigue behaviour of degraded material. The application is limited to a temperature range of 950°C. In terms of validation notched fatigue data at two different temperatures i.e.750 and 950°C were considered. The developed microstructural models have been successfully applied to an ex-service un-cooled blade i.e. a case study.

8. Acknowledgement

The authors thank Howmet, Exeter for providing the test materials. Financial support of Deutsche Forschungsgemeinschaft, Swiss State Secretariat for Education and Research SER and Netherlands Ministry of Defence is highly appreciated.

9. References

[1] Nazmy, M., M. Staubli and A. Künzler, Evaluation of Microstructural & Property Changes of Ni-Base Superalloys after High Temperature Creep Loading and its Rejuvenation, *COST 538, Final Report* (2004-2008).

[2] Scholz, A., Y. Wang, S. Linn, C. Berger and R. Znajda, Modelling of Mechanical Properties of Alloy CMSX-4, *Materials Science and Engineering*, A 510-511 (2009), 278-283

[3] Nazmy, M., A. Epishin, T. Link, M. Staubli: Degradation In Single Crystal Nickel-Superalloys – A Review, in "Materials For Advanced Power Engineering 2006", Eds. J. Lecomte-Beckers, et. al., *Proc. of the COST Conf.*, Liège 18 – 20 Sept. (2006), 205-216.

[4] Epishin, A., T. Link, M. Nazmy, M. Staubli, H. Klingelhoeffer and G. Nolze: Microstructural Degradation of CMSX-4: Kinetics and Effect on Mechanical Properties, Superalloys 2008", Eds. R.C. Reed et. al., *The Minerals, Metals & Materials Society*, 725-731, 20.

[5] Fedelich, B., G. Künecke: Modelling the Microstructural Degradation of the alloy CMSX-4 under High Temperature Loading and its Influence on the Mechanical Behaviour, *COST 538 Final Report*, BAM (2008).

[6] Epishin, A., T. Link, H. Klingelhoffer, B. Fedelich, U. Bruckner, P. D. Portella: New technique for characterization of microstructural degradation under creep: Application to the nickel-base superalloy CMSX-4, *Materials Science and Engineering* A 510–511 (2009), 262–265.

[7] Scholz, A.: Modelling of Microstructural and Mechanical Property Changes in Gas Turbine Alloys, COST 538 Final Task Leader Report, TU Darmstadt (2008)

[8] Fedelich, B., G. Künecke, A. Epishin, T. Link and P. D. Portella: Constitutive modelling of creep degradation due to rafting in single-crystalline Ni-base superalloys, *Materials Science and Engineering* A 510-511 (2009), 273/277.

[9] R. Huls, T. Tinga: Multi-scale Modelling of SX superalloys, *COST 538 Final Report* (NLR) 2008

[10] Tinga, T., W. A. M. Brekelmans, and M. G. D. Geers, Incorporating strain-gradient effects in a multi-scale constitutive framework for nickel-base superalloys, *Philosophical Magazine* 88, 30-32 (2008), 3793-3825.

[11] Tinga, T., W. A. M. Brekelmans, and M. G. D. Geers, Cube slip and non-Schmid effects in single crystal nickel-base superalloys, Modelling and Simulation in Materials Science and Engineering 18(015005) (2010), 1-31.

[12] Tinga, T., W. A. M. Brekelmans, and M. G. D. Geers, Time-incremental creep-fatigue damage rule for single crystal Ni-base superalloys, *Materials Science and Engineering* A 508 (2009), 200-208.

[13] Tinga, T., W. A. M. Brekelmans, and M. G. D. Geers, Directional coarsening in nickel-base superalloys and its effect on mechanical properties, *Computational Materials Science* 47 (2009), 471-481.

[14] Levkovitch, V., R. Sievert, and B. Svendsen, Simulation of deformation and lifetime behavior of a fcc single crystal superalloy at high temperature under low-cycle fatigue loading, *International Journal of Fatigue*, 28 (2006), 1791-1802.

[15] Shyam, A. and W. W. Milligan, A model for slip irreversibility, and its effect on the fatigue crack propagation threshold in a nickel-base superalloy, *Acta Materialia*, 53 (2005), 835-844.

[16] Fedelich, B., A microstructural model for the monotonic and the cyclic mechanical behavior of single crystals of superalloys at high temperatures, *International Journal of Plasticity* 18 (2002), 1-49.

9th Liege Conference : Materials for Advanced Power Engineering 2010
edited by J. Lecomte-Beckers, Q. Contrepois, T. Beck and B. Kuhn.

RECENT TRENDS IN SUPERALLOYS RESEARCH FOR CRITICAL AERO-ENGINE COMPONENTS

Luc Rémy*, Jean-Yves Guédou**

*Centre des Matériaux, Mines ParisTech, CNRS UMR 7633, B.P. 87, 91003 Evry Cedex, France
** Materials and Processes Department, Snecma, Safran Group, 77550 Moissy-Cramayel, France

Abstract

This paper is a brief survey of common research activity on superalloys for aero-engines between Snecma and Mines ParisTech Centre des Matériaux during recent years. First in disks applications, the development of new powder metallurgy superalloys is shown. Then grain boundary engineering is investigated in a wrought superalloy. Secondly, design oriented research on single crystals blades is shown: a damage model for low cycle fatigue is used for life prediction when cracks initiated at casting pores. The methodology developed for assessing coating life is illustrated for thermal barrier coating deposited on AM1 single crystal superalloy.

Keywords: Nickel base superalloys, microstructure, low cycle fatigue, thermal barrier coatings, damage model

1. Introduction

Turboengines for aircrafts represent a major challenge for mechanics and materials (Fig. 1). Major requirements are resistance to long duration operation under severe environmental and thermal – mechanical loading, lightness and reliability. Aero-engine manufacturers have therefore to develop high tech engineering methods, materials and lifing techniques. There is a continued improvement of aircraft engine performance with an increase of turbine entry temperature and pressure ratio. During the last three decades, the increase of Turbine Entry Temperature has been was approximately 15°C per year. This increase in performance is heavily relying on disks and blades in the high pressure turbine that are the most critical parts (Fig. 1). These components are made of nickel base superalloy and the increase in performance has been achieved first through material improvement. These alloys are strengthened by a high volume fraction of γ' Ni_3 (Ti, Al) precipitates and the continuous trend has been to increase the volume fraction of strengthening precipitates. The content can reach about 0.50-0.55 in powder metallurgy alloys for discs and about 0.7 in cast directionally solidified single crystals for blades. A long cooperation has been developed between SNECMA and Centre des Matériaux, in particular in superalloy research for disks and blades. This has involved alloy development with powder metallurgy alloys for disks, and single crystals for blades, investigation of damage mechanisms in creep, low cycle fatigue (LCF) and thermal-mechanical fatigue (TMF), assessment of constitutive models and damage models over 30 years. This has involved interactions with mechanical engineering groups at SNECMA, ONERA and Mines ParisTech and the materials science group at ONERA.

Figure 1: Aero-engines and a rotor with disk and blades made of superalloys.

The present paper gives a brief survey of common research activity along these lines during recent years. Alloy development and optimization of microstructures will be first shown with the development of improved PM superalloys and the investigation of grain boundary engineering in alloys for disks. Design-oriented research will be then illustrated with the development and assessment of life prediction models for single crystals blades: low cycle fatigue life prediction for the substrate with cracks initiating at casting pores and prediction of spalling of thermal barrier coatings that are now deposited on blades in advanced high pressure stages.

2. Alloy development and optimisation of microstructures.

2.1. Powder Metallurgy superalloy for disks.

The decrease of NO_x and CO_2 emissions and noise reductions on the short term, and increasing fuel saving levels for optimized acquisition and life cycle costs on the long term are major targets in modern gas turbine engines. These challenges are a major drift for higher overall pressure ratios and turbine entry temperatures. This results in higher temperatures and loadings for long durations for disks in high pressure compressors and turbines.

Today such parts are made of a powder metallurgy (PM) superalloy N18 [1]. This alloy has a high volume fraction of γ' precipitates (55%) and hence it has a high γ' solvus temperature (ST) and a very narrow solution heat treatment window. In addition it is sensitive to quench cracking and prone to TCP (topologically close-packed) phase precipitation during long time exposure at 650°C.

Therefore a collaborative program was undertaken between Snecma, ONERA and Centre des Matériaux to develop a new PM superalloy with the following specifications: capability of supersolvus solutioning which implies a reduced γ' content, higher creep and fatigue resistance with respect to N18 up to 700°C, increased strain hardening, density lower than 8.35 $Kg.dm^{-3}$ [2]. The γ' content decrease has therefore to be counterbalanced by the improvement of strengthening of both matrix and precipitate. A careful balance between Cr, Mo and W was optimized to achieve matrix strengthening and avoiding TCP phases, using the new PHACOMP method; the Co content was used mainly to decrease the solvus temperature. Then in order to strengthen the γ' phase, the ratio (Ti+Nb+Ta)/Al (in at%) was increased from 0.57 in alloy N18 to about 1. The content of minor elements was kept in the

range 150-320 wt ppm for C, 150-200 wt ppm for C, 0.3 wt% for Hf and 600 wt ppm for Zr when added [2].

A total of 22 experimental heats were processed with alloys N18 and René 88. Electrodes of each grade were machined from vacuum induction melted ingots of 3.2 kg. Pre-alloyed powders were produced by the rotating electrode process (REP). The phase transformation temperature (solvus, incipient melting) were measured through differential thermal analysis (DTA) analysis. Powders were extruded in subsolvus conditions (ST-25°C). Screening tests consisted in metallography, tensile tests and creep tests. From 22 alloys, 5 remain after these tests and two of these were chosen for more detailed analysis [2].

Alloy	Ni	Co	Cr	Mo	W	Al	Ti	Nb	Hf	B	C	Zr
N18REP	Bal.	14.9	12.4	3.8	-	9.1	5.1	-	0.13	0.09	0.07	0.02
SMO48	Bal.	14.9	12.3	3.6	4.0	3.2	4.4	0.8	0.3	0.01	0.03	-
SMO43	Bal.	12.2	13.3	4.6	3.0	2.9	3.6	1.5	0.25	0.01	0.015	0.05

Table 1. Chemical composition of alloys (wt%)

Two alloys were selected SMO43 and SMO48, and provided by Aubert & Duval (composition is given in Table 1). Powders were produced using an argon atomization industrial facility (Aubert & Duval). They were then processed using the industrial route as for N18 PM alloy: sieving (<53 µm), container filling and hot isostatic pressing (1150°C). Two bars were extruded at Snecma quite below the solvus temperature. The amount of γ' phase was computed as 43% and 48% in alloys SMO43 and SMO48 respectively. Alloy density was 8.34 and 8.31 $Kg.dm^{-3}$ respectively (instead of 8.00 for N18). Complete solutioning was possible due to the decrease in solvus temperature.

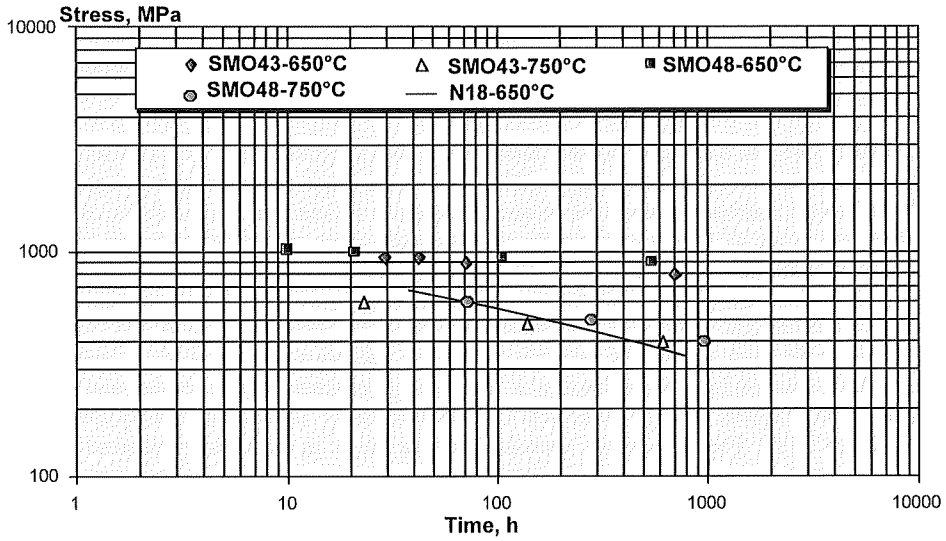

Figure 2: Creep times to 0.2% strain for new PM superalloys compared with alloy N18.

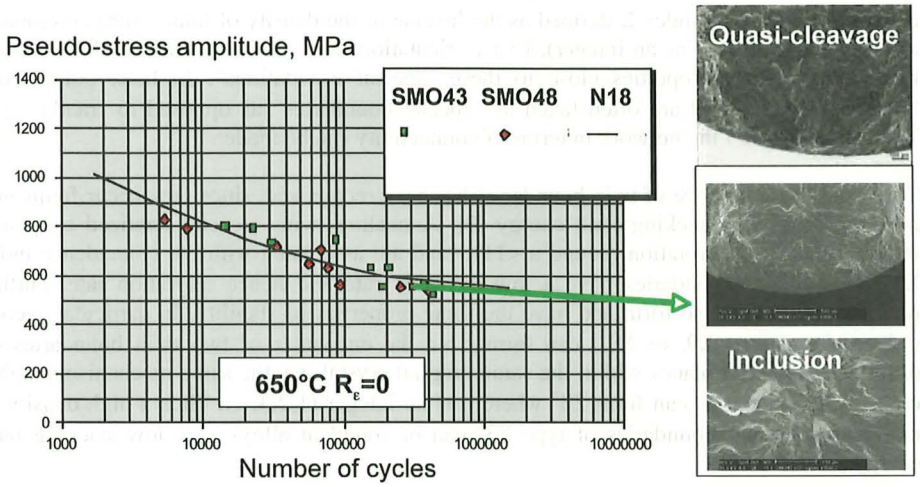

Figure 3: Low cycle fatigue at 650°C of new PM superalloys compared with alloy N18. Initiation sites by quasi-cleavage or at ceramic inclusions (SMO43).

SMO alloys with a medium grain size (45-60 µm) exhibit similar tensile properties with fine grain size N18. However tailored chemistries for matrix strengthening, and medium grain size result in a major improvement in the creep times to rupture and even more in creep times to 0.2% creep strain (Fig.2). This yields a 100°C increase in temperature capability.
Fatigue properties are of major importance for disks, but PM superalloys are known to be very sensitive to inclusions [3, 4] which requires good fatigue crack growth resistance [5] for damage tolerance and to increase inspections intervals. Only a limited number of LCF tests have been completed on smooth specimens under strain controlled conditions (zero to maximum strain, at 0.5Hz). At 650°C SMO43 exhibits a higher life than N18 (average): crack initiation often occurs in grains along quasi-cleavage facets and less often on ceramic inclusions (Fig.3). These alloys seem to have a reduced sensitivity to inclusions as compared to alloy N18 but this has to be confirmed on a large number of specimens. Fatigue crack propagation remains fairly good, nearly as good as for alloy N18 [2, 6].

The LCF resistance is the major criterion for disk life. Therefore the alloy SMO43 was selected as the new superalloy for disks. An extensive study in underway to optimize the microstructures and fatigue properties, both LCF and fatigue crack propagation of this alloy.

2.2. Evaluation of Grain boundary engineering in alloys for disks.

2.2.1. Basics of grain boundary engineering

As illustrated in the previous paragraph, the conventional way to improve alloy properties is mostly through the optimization of alloy chemistry, and then that of microstructure parameters such as grain size, or precipitation. This is mostly achieved through the choice of appropriate heat treatments. In recent years grains boundary engineering (GBE) has been proposed as an alternative way to improve alloy properties by optimizing the strength of the grain boundary network taking advantage of the crystallography of grain boundaries [7].

Grain boundaries are classified using the coincidence site lattice (CSL) model [8]. Each boundary is given an index Σ defined as the inverse of the density of lattice sites common to adjacent grains (taken as an integer). Exact orientations are rare but within small deviations boundaries exhibit properties close to these "special orientations". In f.c.c. polycrystals boundaries with $\Sigma<29$ are often taken as "special boundaries" as opposed to random [7]. Then an analysis of the network in terms of connectivity can be made.

The peculiar importance of twin boundaries has been recognized, since they occur frequently in alloys with low stacking fault energy [9]. Annealing twins are characterized by planar interfaces and a 60° rotation around a <111> and are associated with the coincidence index Σ3. Their planar boundaries have a low diffusion rate and hence migration rate. Further multiple twins can also form and have the same properties of stability. In particular second order twins (noted Σ9. or $\Sigma3^2$) can form from the encounter of two twin boundaries on different octahedral planes within the same original crystal. By the same mechanisms higher order twin boundaries can form $\Sigma3^n$ where n is an integer (1,2,3...). Thus a high density of non-coherent grain boundaries of type $\Sigma3^n$ can be found in alloys with low stacking fault energy.

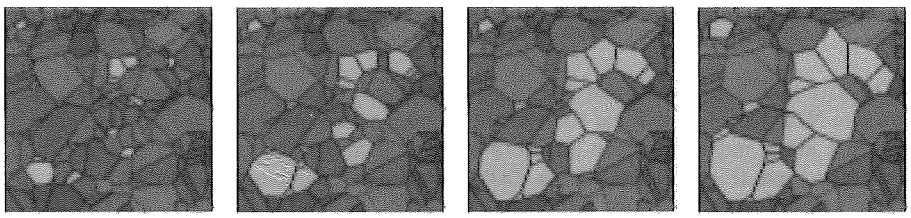

Figure 4: Recrystallisation sequence computed using the vertex theory (after [11]).

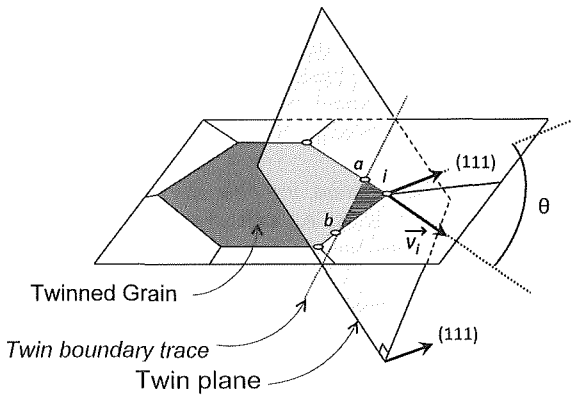

Figure 5: Sketch showing the incorporation of annealing boundary in the recrystallisation scheme (after [12]).

The influence of twinning can be simulated on the evolution of the grain boundary network. The GBE process typically consists in straining followed by subsequent annealing. The

energy stored in the deformation stage is the driving force for the nucleation and growth of new grain during the re-crystallization phase. The kinetics of grain boundary network evolution depends on the stored energy, temperature and duration of the annealing treatment. The migration of grain boundary assumes a minimisation of the global energy, stored energy in each grain, interfacial energy as a function of crystallographic misorientation between grains. Vertex models are used for re-crystallisation [10] (Fig.4). An adaptation has been proposed recently [11, 12] to include the description of annealing twins (Fig.5).

At high temperature creep as well as low cycle fatigue crack propagation are known to favor inter-granular fracture, especially in superalloys [13]. Therefore if one reduces the number of random grain boundaries and increase the proportion of special boundaries such as $\Sigma 3^n$, increased mechanical resistance at high temperature should follow. Some recent experiments under hold time creep fatigue crack growth have shown that the crack was growing preferentially along random boundaries [14].

2.2.2. Application to nickel base superalloys

The application of such a concept to Ni alloys is attractive since they have often a strong tendency to form annealing twins due to their moderate stacking fault energy. This is the aim of the ongoing project so-called ORGANDI and supported the french National Research Agency involving Snecma-Safran, CEA, Turbomeca-Safran, Aubert & Duval, ONERA, CEMEF and Centre des Matériaux (Mines-ParisTech).

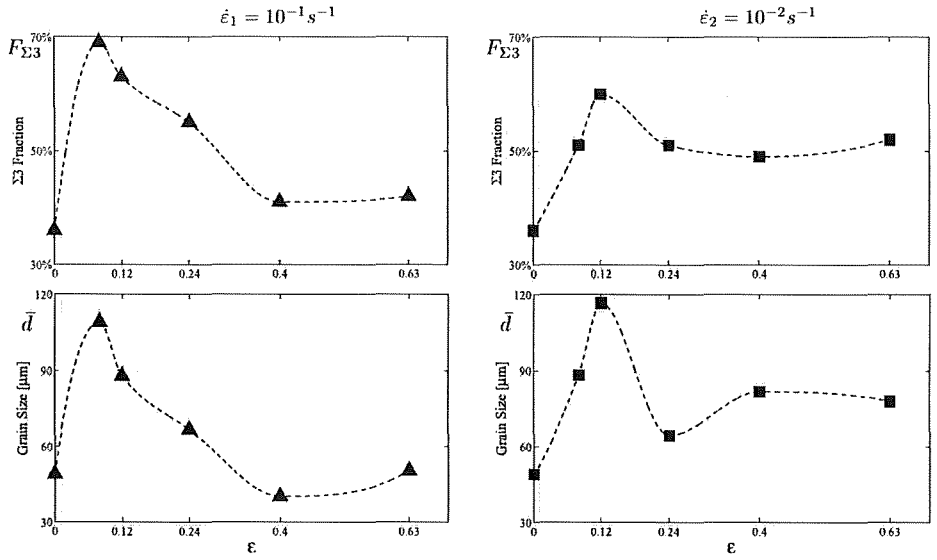

Figure 6: Evolution of the fraction of twin boundaries/to grain boundaries and of the grain size of U720 LI with torsion strain (after [15]).

However superalloys with a high volume fraction of γ' precipitates can only be hot-worked whereas most literature investigations used room temperature deformation. The applicability of GBE is investigated using a french grade of U720 LI. A thermo-mechanical route has been chosen in accordance with industrial needs i.e. to achieve a determined final shape from an initial billet; Compression and torsion were used to finish with a strain of 0.8 [15, 16]. A prestrain of 0.5 was used to cancel billet thermo-mechanical history. The remaining strain was applied in several steps at a temperature below the solvus of secondary precipitates (coherent with matrix, 20-100nm in size); therefore boundary migration is largely inhibited by the distribution of primary precipitates 1-5 μm in size, incoherent with matrix and located at grain boundaries. Two strain rates (10^{-1} s^{-1} and 10^{-2} s^{-1}) were investigated and 30 min final heat treatment was carried above the solvus temperature. The proportion of twin boundaries increases rapidly up to a maximum after 0.12 strain and then decreases to a saturation level, as does the grain size when dynamic re-crystallisation occurs (Fig.6). A very large proportion of Σ3 boundaries can thus be achieved, much higher than in the standard processing route (as received condition): more special boundaries are created during the super-solvus annealing treatment in the microstructures retaining high dislocations density after straining, i.e. those do not show dynamic re-crystallisation and especially those deformed at high strain rates.

Therefore this work shows that grain boundary engineering is clearly a way to improve the mechanical properties of superalloys for disks. Creep and fatigue testing is currently under way to compare the properties of GB engineered alloy with standard processing route.

3. Design oriented research for blades: life assessment for increased durability.

3.1. Introduction.

There is a continued improvement of aircraft engine performance with an increase of turbine entry temperature and pressure ratio. During the last three decades, the increase of blade maximum temperature has been approximately 15°C per year (Fig. 7).

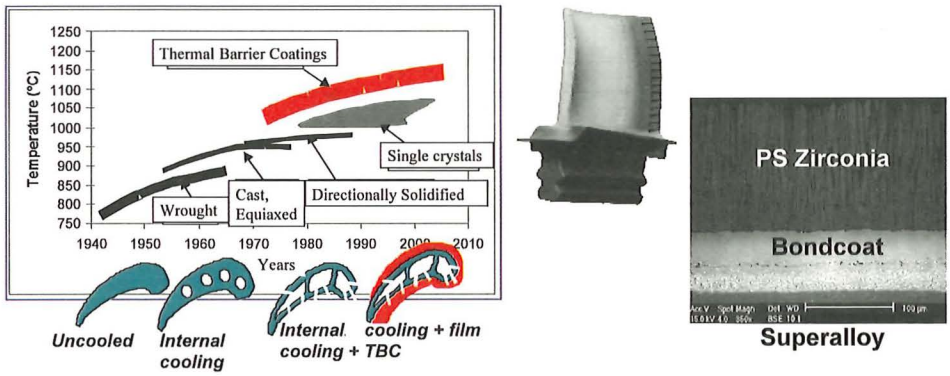

Figure 7: Variation of maximum blade temperature with years and evolution of materials and cooling technologies (left); Turbine blade coated by TBC and scanning electron microscope observation of various layers in the TBC (right).

A limit to alloy development for blades is now achieved with incipient melting temperature around 1350°C and volume fraction of 0.7 of γ' Ni_3 (Ti, Al) precipitates in nickel based alloy single crystals. Recent improvements were achieved combining alloy development and cooling technologies, using hollow components [17]. Thermal – Barrier coating are now introduced to keep average component temperature to a suitable level.

2.2. Low cycle fatigue life in single crystals based on micro-crack growth from pores.

A predominant source of failure in nickel based single crystal superalloys remains, however, the internal pores resulting from the solidification process [18, 19]. A damage model based on the propagation of micro-cracks originating at casting defects has been developed for single crystal (SX) turbine blades, operating under thermo-mechanical creep-fatigue conditions [20-23]. The model basically used a process zone concept, using a characteristic microstructure element modeled as a cube of side L. The volume L^3 corresponds to that of a secondary dendrite of SX superalloy. A probabilistic analysis is carried out in order to determine the number and size of casting pores present in a given volume of material. Another peculiarity of Ni-based SX superalloys is their constitutive and damage anisotropy. The anisotropy of these face-centered cubic materials is therefore considered in this model in the following way: stresses applied to a given volume of material are resolved onto all octahedral ({111} <011>) and cubic ({001}<011>) slip systems.

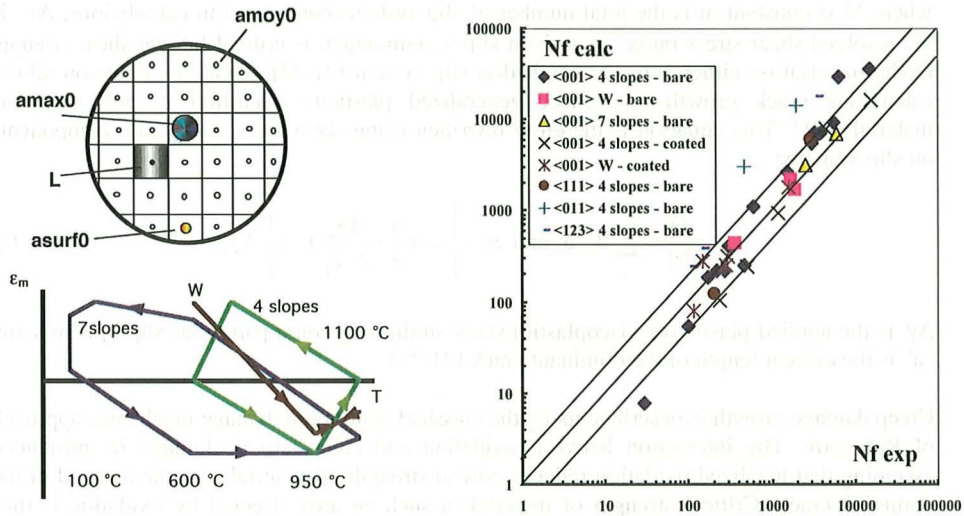

Figure 8: Sketch showing the competition between initiation at sub-surface and initiation at internal pores for low cycle fatigue of single crystals. Comparison between model predictions and experiments for various TMF cycles and specimen orientations.

Finite element analyses of blades are made using a crystallographic viscoplastic model [24, 25] where constitutive equations are written at the level of these slip systems. The damage equations are then applied on slip systems themselves using resolved shear and normal

stresses on every slip system. Material parameters chosen in the model are obtained from uni-axial material data generated on <001> and <111> specimens. Material properties thus obtained are considered to be intrinsic properties of octahedral and cubic slip systems respectively. Any other combination of loading and crystal orientation can then be reduced to shear and normal stresses applied on active slip systems.

In reality, the pores are of random irregular shapes but for the sake of simplicity the encircling diameter of pores was measured. The distribution of material pores is modeled on the basis of three types of pores (Fig. 8) i.e. mean size pores uniformly distributed over the entire volume, the largest pore within a given volume and the largest pore in the sub-surface zone. This latter is responsible for a single surface crack initiation. Depending upon the applied stress range, the growth of the dominant crack nucleating from the largest surface pore or the largest internal pore can take place in globally elastic or plastic material behaviour. Therefore two different crack propagation regimes are used in parallel. One is denoted here as Basquin's crack propagation regime and the other one as Tomkins' crack propagation regime. Basquin's relation caters for stress controlled crack propagation regime under globally elastic material behaviour. In terms of resolved shear stresses, it can be written as in eqn (1):

$$\frac{da}{dN} = \frac{L}{n} \cdot \sum_{s} \left[\frac{\Delta \tilde{\tau}_s}{2 \cdot \tau_f} \right]^M \tag{1}$$

where M is constant, n is the total number of slip systems considered in calculations, $\Delta\tau_s$ is the resolved shear stress range on a given slip system and τ_f is critical fatigue shear strength of the material on either cubic or octahedral slip system [21-23]. Tomkins' equation allows calculating crack growth rate under generalized plasticity condition in polycrystalline materials [21]. This equation is therefore rewritten using shear stress and strain components on slip systems:

$$\frac{da}{dN} = \sum_{s} B_s \cdot a, \text{ and } B_s = \left[\sec\left(\frac{\pi}{2} \cdot \frac{\Delta \tilde{\tau}_s}{2 \cdot \tau_f}\right) - 1 \right] \cdot \Delta \gamma_s \tag{2}$$

$\Delta\gamma_s$ is the applied plastic (or viscoplastic) shear strain range on a particular slip system s and "a" is the current length of the dominant crack [21-23].

Creep damage growth is described using the classical continuum damage mechanics approach of Rabotnov. The interaction between oxidation and creep-fatigue damage is introduced assuming that localized oxidation reduces critical strength of material in an area ahead of the dominant crack. Critical strength of material in such an area affected by oxidation is thus lower than in non-oxidized material. This procedure has already been described in some detail for polycrystalline superalloys in cast and wrought forms [see e.g. 21]. One can estimate the size of the area embrittled by simple oxidation performing crack growth tests on non-oxidized compact tension specimens as well as tests on pre-oxidized specimens. The crack length, over which crack growth rates for pre-oxidized or non-oxidized specimens are different, gives direct access to the embrittled zone size. The depth of the embrittled zone l_f is supposed to be proportional to the oxidized depth l_{ox} (with a constant ratio). The kinetics of oxidation in the

interdendritic zone of single crystal superalloys, as in polycrystalline material [13] follows a power relation with time and is triggered by plastic strain [22, 23].

Tests lifetime under various cycle shapes, loading conditions and material orientations have been calculated using the same set of equations and model parameters. Different examples of model applications can be found elsewhere for LCF lifetimes under a wide range of test frequencies, temperatures, dwell times, load orientation effects as well as TMF on volume elements tests [21, 23]. This has been applied to simple structures [20, 21] and components with good success. Fig. 8 shows the TMF lifetime prediction capabilities of the model, for different TMF test cycles applied to AM1 single crystals specimens of various orientations. These cycles have different shapes and lead to different lifetime values under the same applied strain range. The graph shows the comparison of experimental and calculated values. A good correlation is achieved. This work is nonetheless completed currently by an investigation of LCF at sharp notches to investigate the situation in the immediate vicinity of pores, and anomalous regimes of short crack growth can occur under some conditions, depending upon local plasticity and oxidation [26].

2.3. Coated single crystals : Thermal Barrier Coatings.

Blades and vanes in aero-engines are protected against oxidation and corrosion using aluminide coatings. HPT (High Pressure Turbine) blades of SNECMA aircraft engines were first made of AM1 single crystal superalloy with C1A coating. This coating is elaborated by, at first, a chromium deposition and then a nickel aluminide (NiAl) deposition on the substrate surface, through Chemical Vapor Deposition (CVD) process. The presence of these coatings is often ignored in component design. Coating resistance is usually assessed using oxidation or cyclic oxidation tests on different kinds of specimens. Under service conditions however, coatings are experiencing cyclic oxidation under stress (due to centrifugal load) as well as thermal transients. Thermo-mechanical creep – fatigue using hold times under load is especially appropriate to assess damage of coated systems under realistic conditions [27]. The industrial need is to know at what time the NiAl tank, which provides the resistance to oxidation in the turbine aggressive environment, will be completely destroyed.

Advanced blades are now coated with a thermal barrier. Fig.7 shows cooled blades used by SNECMA with a TBC that is manufactured by electron beam physical vapour deposition (EBPVD) of yttria partly stabilized zirconia on a platinum modified nickel aluminide bondcoat. EBPVD confers a well-known columnar structure to the partly stabilized zirconia that improves its resistance to transverse cracking. A small layer of alumina is present from the initial condition at the interface between partly stabilized zirconia and bondcoat. The bond coat (BC) inserted between the blade and the ceramic protects the substrate against oxidation by the growth of an alumina layer, the thermally grown oxide (TGO), on its surface. The bond coat also accommodates the substrate strain to prevent ceramic rupture [27-30]. The purpose of Thermal Barrier Coating is to insulate the blade from outside environment and particularly to reduce heat transfer between hot gas flow and the blade alloy. Thermal barrier coatings (TBC) are used in advanced turbines to increase the turbine entry temperature when the temperature capability of the alloy comes to a limit. A strong thermal gradient occurs in the thin outer layer of ceramic, which reduces metal temperature particularly during thermal transients and during steady operation too. This results in a significant increase in component life. The TBC coated blade is actually a multi-material component. In this case coating

integrity is a key issue in the life of component: coating spallation results in a large temperature increase in alloy substrate, which is detrimental for the overall component integrity.

Many publications investigated the mechanisms leading to spalling of TBC systems. The most important factor is the growth of thermally grown oxide (TGO) at the interface between the ceramic layer (zirconia partly stabilised with yttria) and the bondcoat. Detailed damage mechanisms are dependent on the nature of the bondcoat and alloy substrate, NiAl and AM1 in the present study. The mechanisms of oxidation as well as the influence of segregating species like sulfur were investigated in our group, as well their influence of TBC adherence to substrate [29-33]. More information on the present system can be found elsewhere [27-30]. Damage of the TBC-substrate interface is a delamination process viewed as a sequence of nucleation, growth and coalescence events of interfacial cracks. Macroscopic buckling near room temperature can result and then lead to catastrophic failure and spalling off the TBC.

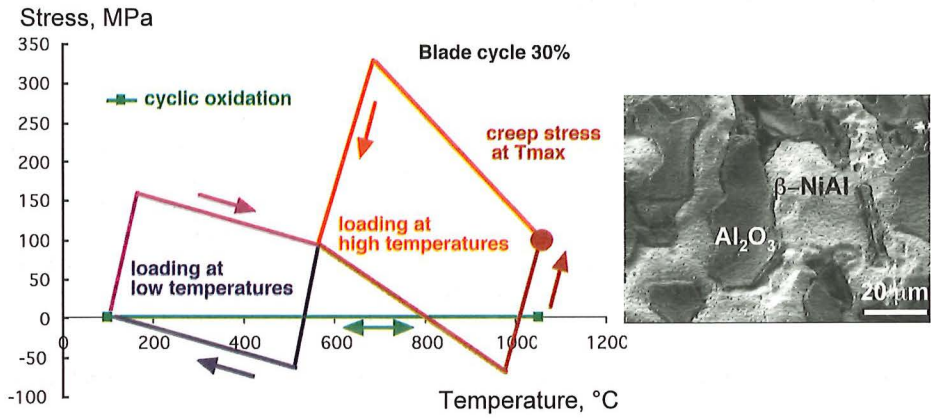

Figure 9: Thermal-mechanical fatigue cycle used to simulate service loading for a CVD nickel aluminide coating deposited on AM1 single crystals, using a 5 min hold time at maximum temperature; micro-spalling of alumina scale on specimen surface after 800 cycles.

Therefore a general methodology has been proposed to develop damage models that applicable to coatings. The need for such an approach is triggered by the search for longer lives in civil applications, where oxidation and aging problems become a major issue. Basically there is a need to develop an extensive data basis using cyclic oxidation tests that are commonly in industrial practice. Relevant thermal-mechanical fatigue tests [27, 34] are added to identify interactions between loading and oxidation effects, which might occur in service. Figure 9 shows a thermal-mechanical fatigue cycle, with a 5 min hold time at maximum temperature, used to simulate service loading at critical areas on single crystal blades that are protected by an aluminide layer. More severe damage is generated during the TMF cycles than during conventional cyclic oxidation tests, that results in surface rumpling and micro-spalling of alumina layers; this favours re-oxidation events and accelerates aluminium depletion of the NiAl coating [27]. Micromechanical models [36, 37] can be of special use as well as detailed observations at fine scales to identify major mechanisms of

damage accumulation. However it is essential to use interrupted oxidation tests on specimens and to estimate damage evolution using observations or mechanical tests. This methodology has been used for alumina-former coating as well as for TBC.

Cyclic oxidation tests that combine oxidation during high temperature exposure and thermal fatigue during thermal transients are used first. Figure 10 is an example of the effect of maximum temperature and of cycle period on the life to TBC spalling off. Compressive tests were used after different exposure times to static (or cyclic) oxidation [29, 30] to investigate the reduction of the resistance of TBC to spalling off induce by increased exposure times (Fig.11). Observations using scanning electron microscope shows that delamination occurs first before buckling and catastrophic spalling as usually admitted [39]. On a local scale rumpling of the TGO is observed which is triggered by thermal cycling as reported for aluminide, and thermal-mechanical fatigue [27]. While small pores nucleate preferentially at the TGO-boncoat interface, this rumpling favours the nucleation of cracks at the TGO-zirconia interface [40].

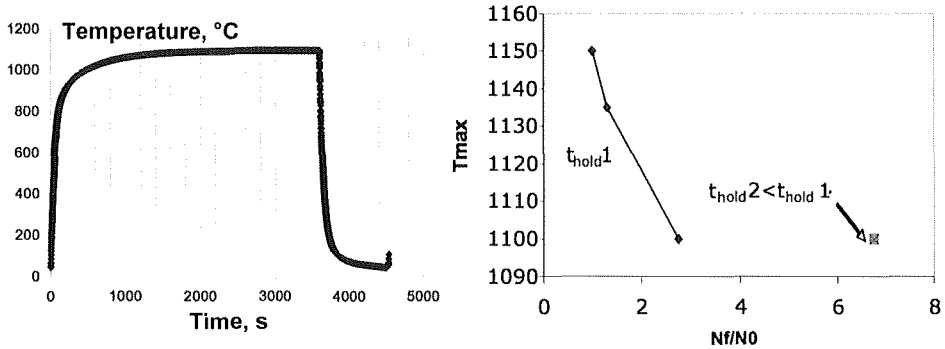

Figure 10: Thermal cycle and influence of maximum temperature (and hold time) on the lifetime to TBC spalling off on AM1 superalloy during cyclic oxidation.

A life prediction model for TBC systems has been developed, taking into account a local scale where damage takes place at interfaces and a macroscopic scale where buckling leads to the TBC spallation. A post-processor is built assuming that in plane strain of the substrate is imposed to the multi-layer system composed of bondcoat, TGO and zirconia topcoat. Zirconia is described using as transversely isotropic elasticity, TGO was assumed elastic and bondcoat obeys a Norton type viscoplastic behaviour, with hardening. The total thickness of the TGO layer was described though a parabolic equation, identified from thickness measurements. The damage model is then identified assuming two major contributions: one due to oxide growth D_{ox}, and the other due to the development of rumpling and thermal cycling $D_{rumpling}$. Rumpling is observed for cyclic loading involving viscosity of the bondcoat at high temperature. Therefore an engineering description of this effect was made using viscous strain of bondcoat ε_v^{cum} and oxide thickness to simulate the damage induced by thermal transient:

$$dD_{OX} = f(h_{OX}) \quad (4)$$

$$dD_{rumpling} = g(h_{ox}, \varepsilon_v^{cum}, N_{th}) \quad (5)$$

where N_{th} represents the number of thermal cycles experienced.
The final spallation of the system was identified from buckling of the delaminated area, considered as a circular blister. The critical strain with clamped boundary conditions, ε_{crit}, is thus predicted by the classical buckling theory for elastic analysis [39]:

$$\varepsilon_{crit} = 1.223\left(\frac{h_{TBC}}{R_0}\right)^2 (1-D) \quad (6),$$

D is total damage, R_0 is determined from a spalling test applied in the initial condition (when D is equal to 0). This critical condition is applied to the strain tensor experienced by the TBC.
The model is tested for different thermal cycles used in the experimental database. Compression tests conducted to spalling are used to identify damage parameters of the model after different thermal-mechanical conditions giving rise to different oxidation conditions and oxide thicknesses. Figure 11 (left) shows for instance the evolution of macroscopic compression strain to spalling with isothermal oxidation times. A good fit is actually achieved between model and experiment. Predictions are finally shown for cyclic oxidation tests (Fig.11 right) where the number of oxidation cycles predicted is in good agreement with experimental data. The developed model is able to represent oxidation effect for long time exposure at high temperature as well as thermal fatigue life.

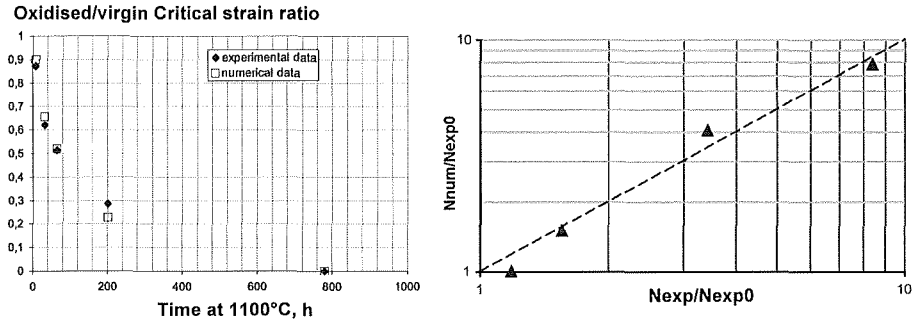

Figure 11: Thermal cycle and influence of maximum temperature (and hold time) on the lifetime to TBC spalling off on AM1 superalloy during cyclic oxidation.

4. Conclusions

For disk application, several ways seem promising. A new PM superalloy has been developed with improved creep and fatigue resistance. Grain boundary engineering seems to be applicable to wrought alloys but still needs proper assessment.
For blades made of single crystal superalloys, a lifetime model has been identified using micro-crack growth from casting pores. A methodology proposed for the degradation of coating seems promising for thermal barrier coating spalling.

Acknowledgements
The financial support of Snecma, French Defence Agency, European Community and French National Research Agency is gratefully acknowledged. The authors are indebted to many collaborators who have contributed to various aspects of this work within Snecma, Mines ParisTech and at ONERA.

References

[1] J.Y. Guédou, J.-C. Lautridou, Y. Honnorat, N18 PM superalloy for disks: development and applications, *Superalloys 1992*, ed. S.D.Antolovich et al., Warrendale, PA, USA, TMS, 267-276, (1993).
[2] J.Y. Guédou, I. Augustins-Lecailler, L. Nazé, P. Caron, D. Locq, Development of a new fatigue and creep resistant PM nickel-base superalloy for disk applications, *Superalloys 2008*, ed. R. Reed et al., Warrendale, PA, USA, TMS, 9p, (2008).
[3] J.C. Lautridou, J.Y. Guédou, Y. Honnorat, Effect of inclusions on LCF life of PM superalloys for turboengine discs, *High Temperature materials for Power Engineering 1990*, E. Bachelet et al. eds., Liège, Kluwer, Dordrecht, 1163-1172, (1990).
[4] J. Grison, L. Rémy, "Fatigue failure probability in a powder metallurgy Ni-base superalloy", *Engineering Fracture Mechanics*, 57, 41-55, (1997).
[5] P. Bernède, L. Rémy, "Fatigue crack growth of small defects in a superalloy at high temperature in air and in vacuum", *Short Fatigue Cracks*, ESIS 13, K.J. Miller and E.R. de los Rios, Eds, Mechanical Engineering Publications, London, 251-262, (1992).
[6] I. Augustins-Lecailler, P. Caron, J.Y. Guédou, D. Locq, L. Nazé, European Patent EP 1 840 323 A1, 29/03/07; US Patent US 2007/0227630 A1, 30/03/07 , (2007).
[7] V. Randle, G. Owen, Mechanisms of grain boundary engineering, *Acta Materialia*, 54, 1777-1783, (2006).
[8] D. Brandon, The structure of high-angle grain boundaries, *Acta Metallurgica*, 14, 1479-1484, (1966).
[9] V. Randle, Twinning-related grain boundary engineering, *Acta Materialia*, 52, 4067-4081, (2004).
[10] K. Piekos, J. Tarasiuk, K. Wierzbanowski, B. Bacroix, Generalized vertex model of recrystallization-Application to polycrystalline copper, *Computational Materials Science*, 42, 584-594, (2008).
[11] H. Tézenas du Montcel, L. Nazé, V. Maurel, N. Souai, R. Logé, J.Y. Guédou, Ingénierie des joints de grains dans les alliages à base de nickel (in French), *19th french Congrès de Mécanique*, Marseille, 2009, 24-24 August.
[12] H. Tézenas du Montcel, L. Nazé, V. Maurel, *Euromat 2009*, Glasgow; 1- A method to analyse grain boundary network by vertex discretisation; 2- A new model of multiple twinning during recrystallisation, papers in preparation, (2010).
[13] E. Chateau, L. Rémy, Oxidation-assisted creep damage in a wrought nickel based superalloy : Experiments and modelling, *Materials Science and Engineering A*, 527, 1655-1664, (2010), doi : 10.1016/j.msea.2009.10.054.
[14] V. Lebreton, unpublished results, Centre des Matériaux, (2008).
[15] N. Souai, R. Logé, Y. Chastel, N. Bozzolo, V. Maurel, L. Nazé, Effect of thermomechanical processes on Σ3 grain boundary distribution in a nickel base superalloy, *Materials Science Forum*, 638-642, 2333-2338 (2010).
[16] N. Souai, N. Bozzolo, L. Nazé, Y. Chastel, R. Logé, About the possibility of grain boundary engineering via hot-working in a nickel-base superalloy, *Scripta Mat* doi:10.1016:j.scriptamat.2010.02.19, (2010).
[17] L. Rémy, J-Y. Guédou , Thermal-mechanical fatigue problems in aeroengine components, *Fatigue 2002*, A. F. Blom, Ed., EMAS, Cradley Heath, UK, 3, 1045-1062 (2002).

[18] E. Fleury, L. Rémy, Low cycle fatigue damage in nickel-base superalloy single crystals at elevated temperature, *Materials Science and Engineering A*, 167, 23-30, (1993).
[19] E. Fleury, L. Rémy, Behaviour of nickel-base superalloy single crystals under thermal-mechanical fatigue, *Metallurgical and Materials Transactions A*, 25, 99-109, (1994).
[20] A. Koster, A. Alam, L. Rémy, A physical-base model for life prediction of single crystal turbine blades under creep-fatigue loading and thermal transient conditions, in: *Temperature –Fatigue Interaction*, L. Rémy and J. Petit Eds., *ESIS Publication 29*, Elsevier, 203-212, (2002).
[21] L. Rémy, Thermal-Mechanical Fatigue (Including Thermal Shock), in: *Comprehensive Structural Integrity*, I. Milne, R. O. Ritchie and B. Karihaloo, Eds., *Creep and High-Temperature Failure* (vol. ed. A. Saxena), Elsevier, Amsterdam, 5, 113-200, (2003).
[22] A. M. Alam, L. Rémy, A lifetime prediction model for single crystal superalloys subjected to thermomechanical creep-fatigue-oxidation damage, *11th international Conference on Fracture*, Turin, 21-25 march 2005, CD-Rom, A. Carpinteri et al. Ed., 6p, (2005).
[23] L. Rémy, N. Haddar, A. Alam, A. Koster, N. Marchal, Growth of small cracks and prediction of lifetime in high temperature alloys, *Materials Science and Engineering A*, 468-470, 40-50, (2007).
[24] L. Méric, P. Poubanne, G. Cailletaud, Single crystal modelling for structural applications, *ASME J. of Eng. Materials and Technology* 113, 165-170, (1991).
[25] F. Hanriot, G.Cailletaud, L. Rémy, Mechanical behaviour of a nickel base superalloy single crystal, in *High temperature constitutive modeling. Theory and application*, A.D. Freed and K.P. Walker Eds., the American Society of Mechanical Engineers, New-York, USA, MD-vol.26/AMD-vol.121, 139-150, (1991).
[26] M. Geuffrard, L. Rémy, A. Köster, Lifetime modelling of fatigue crack initiation from casting defects, ICF12, *12th International Conference on Fracture*, July 12-17, 2009, Ottawa, Canada, CD-Rom, 10 p. (2009).
[27] L. Rémy, A. Alam, A. Bickard, Thermo-mechanical Creep-Fatigue of Coated Systems, *Thermomechanical Fatigue Behavior of Materials, 4th volume, ASTM STP 1428*, M. A. Mc Gaw, S. Kalluri, J. Bressers and S. D. Peteves, Eds., American Society for Testing and Materials, West Conshohocken, PA, 98-111, (2003).
[28] C. Guerre, L. Rémy, R. Molins, Alumina scale growth and degradation modes of a TBC system, *Materials at high Temperature*, 20, 481-485, (2003).
[29] M. Harvey, M. Rambaudon, V. Maurel, L. Rémy, Oxide spallation in beta-NiAl coated systems under mechanical loading, *Materials Science Forum, High temperature corrosion and protection of materials 7*, 595-598, 101-106, (2008).
[30] M. Harvey, C. Courcier, V. Maurel, L. Rémy, Oxide and TBC spallation in beta-NiAl coated systems under mechanical loading, *Surface and Coating Technology*, 203, 432-436, (2008).
[31] I. Rouzou, R. Molins, L. Rémy, F. Jomard, Study of the sulfur segregation for a TBC system, *Materials science forum, High temperature corrosion and protection of materials 6*, 461-464, 101-108, (2004).
[32] R. Molins, I. Rouzou, L. Rémy, K. Le Biavant-Guerrier, F. Jomard, Study of sulfur distribution in a NiPtAl bondcoat, *Materials at High Temperatures*, 22, 359-366, (2005).
[33] M. Chieux, R. Molins, L.Rémy, C. Duhamel, M. Sennour, Y. Cadoret, Effect of material and environmental parameters on the microstructure evolution and oxidation behavior of a Ni-based Superalloy covered by a Pt modified Ni aluminide, *Materials Science Forum, High temperature corrosion and protection of materials 7*, 595-598, 33-41, (2008).

[34] A.Peichl, T. Beck, O. Vöhringer, Behaviour of an EB-PVD thermal barrier coating system under thermal-mechanical fatigue loading, *Surface and Coating Technology*, 162, 113-118, (2003).
[35] T. Beck, R. Herzog, O. Trunova, M. Offerman, R.W. Steinbrech, L. Singheiser, Damage mechanisms and lifetime behavior of plasma-sprayed thermal barrier coating systems for gas turbines- PartII: Modeling, *Surface and Coatings Technology*, 202, 5901-5908, (2008).
[36] M. Caliez, F. Feyel, S. Kruch, J-L. Chaboche, Oxidation induced stress fields in an EBPVD thermal barrier coating, *Surface and Coatings Technology*, 157, 103 – 110 (2002).
[37] D.S. Balint, J.W. Hutchinson, An analytical model of rumpling in thermal barrier system, *Journal of the Mechanics and Physics of Solids,* 53, 949 – 973, (2005).
[38] V.K. Tolpygo, D.R. Clarke, Temperature and cycle-time dependence of rumpling in platinum-modified diffusion aluminide coating, *Scripta Materialia,* 57, 563 – 566, (2007).
[39] J.W. Hutchinson, M.D. Thouless, E.G. Liniger, Growth and configurational stability of circular buckling-driven film delaminations, *Acta Materialia*, 40, 295 – 308, (1992.)
[40] C. Courcier, V. Maurel, L. Rémy, A. Phelippeau, Damage based life prediction model for EBPVD thermal barrier coatings , LCF6, *Sixth International Conference on Low Cycle Fatigue*, September 8-12, 2008, Berlin, DVM, 155-160, (2008).

9th Liege Conference : Materials for Advanced Power Engineering 2010
edited by J. Lecomte-Beckers, Q. Contrepois, T. Beck and B. Kuhn.

Development of Superalloys for 1700°C Ultra-Efficient Gas Turbines

Hiroshi Harada

National Institute for Materials Science
High Temperature Materials Center
1-2-1 Sengen, Tsukuba, Ibaraki, 305-0047
Japan

Abstract

Mitigation of global warming is one of the most outstanding issues for the humankind. The Japanese government announced that it will reduce its greenhouse gas emissions by 25% from the 1990 level by 2020 as a medium-term goal. One of the promising approaches to achieving this is to improve the efficiency of thermal power plants emitting one-third of total CO_2 gas in Japan. The key to improving the thermal efficiency is high temperature materials with excellent temperature capabilities allowing higher inlet gas temperatures. In this context, new single crystal superalloys for turbine blades and vanes, new coatings and turbine disk superalloys have been successfully developed for various gas turbine applications, typically 1700°C ultra-efficient gas turbines for next generation combine cycle power plants.

Keywords: CO_2, gas turbine, superalloys, blade, single crystal, disk, cast-and-wrought, EQ coating.

1. Introduction

A significant amount of CO_2 gas has been emitted from thermal power stations in all over the world. For example, in Japan, one-third of the national total CO_2 gas is emitted by the thermal power generation. Thermal power generation is classified into coal fired power generation, oil fired power generation, and natural gas combined cycle power generation, depending on the fuel used. However, there is a great difference in the amount of CO_2 emission per unit of power among these three systems; 1.00, 0.76, and 0.53, respectively (Fig. 1). That is, CO_2 can be significantly reduced if the conventional coal fired power generation is replaced with natural gas combined cycle power generation [1].

If the inlet gas temperature of turbines currently used in combined cycle power generation - popular type: 1,100 to 1,300°C, thermal efficiency: 43 to 48% (HHV standard); latest type: 1,500°C, thermal efficiency: 52% - is raised to 1,700°C, thermal efficiency can increase to 56 to 60% (Fig. 2), resulting in a greater economic efficiency as well as a further reduction in CO_2 emissions as a consequence of less fuel being consumed. If an existing 1,250 to 1,350MW class coal fired power plant is substituted by such an ultra-high efficiency natural gas combined power generation, the CO_2 emission from a single power plant can be reduced by about 0.4% of the total emissions in Japan. This means there will be a 4 to 8%

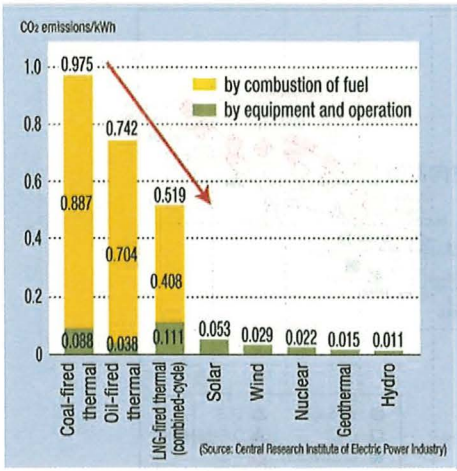

Fig. 1 CO_2 emissions by electric power source.

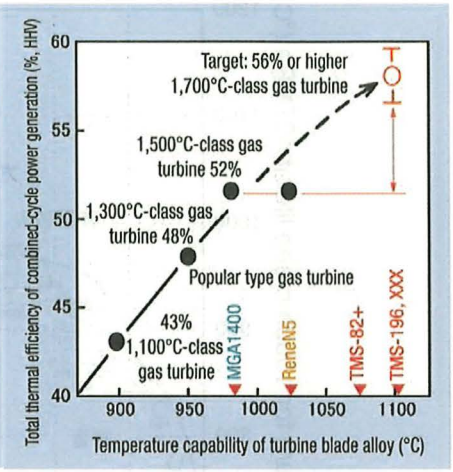

Fig. 2 Relationship between the temperature capability of turbine blade superalloys and power generation efficiency.

reduction if 10 to 20 conventional coal fired power plants are switched. If this technology can be disseminated in overseas countries, where the efficiency of thermal power generation may be comparatively lower, greater emissions reduction can be obtained effectively. One of the most important keys to realize this is the high temperature material.

In this context, High Temperature Materials Center at NIMS initiated High Temperature Materials 21 Project (Phase1 and 2, 1999-2010) and developed single crystal (SC) superalloys with world's highest temperature capability of 1100°C, new coating materials, and Ni-Co base new cast-and-wrought superalloys for turbine disks. NIMS has also been working with private companies to promote practical use of the materials, e.g., for 1,700°C ultra-efficient gas turbine under collaboration with Mitsubishi Heavy Industries Ltd.

2. Single crystal superalloys

Due to the progress on manufacturing process from conventional casting to directional solidification in which the grain boundary is parallel to the tensile axis, and to single crystal solidification without grain boundaries, superalloys have improved the temperature capability (Fig. 3). The temperature capability of SC superalloys further increases with more addition of refractory elements such as W, Ta, and Re. For example, a typical SC superalloy CMSX-4 has temperature capability of about 1,040°C, where the temperature capability is defined as a temperature at which an alloy creep rupture life becomes 1,000 hours under a stress of 137 MPa. Typical chemical compositions of SC superalloys are presented in Table 1.

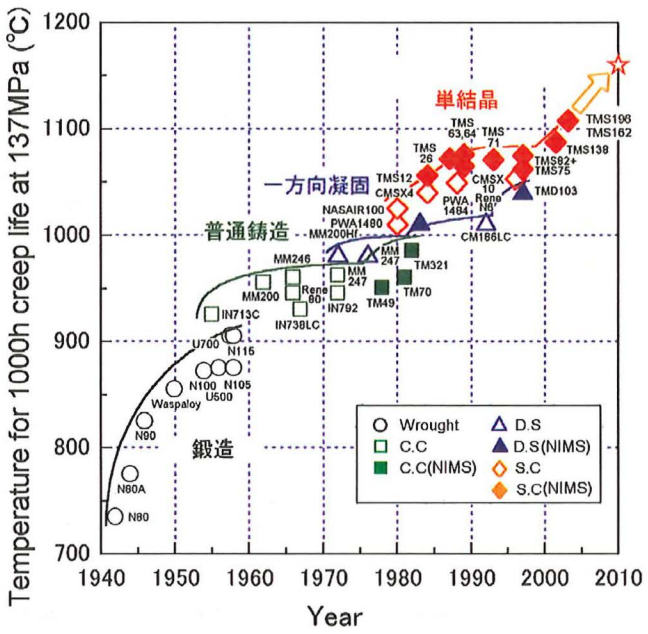

Fig. 3 Improvement of temperature capability in Ni-base superalloys [2].

Table.1 Nominal chemical composition of single crystal superalloys

Alloy	Alloy Composition														Genera tion	Organisation
	Co	Cr	Mo	W	Al	Ti	Nb	Ta	Hf	Re	C	B	Zr	Others		
PWA1480	5	10	–	4	5	1.5	–	12	–	–	–	–	–	–	1st	Pratt&Whitney
Rene'N4	8	9	2	6	3.7	4.2	0.5	4	–	–	–	–	–	–	1st	GE
CMSX-2	4.6	8	0.6	8	5.6	1	–	6	–	–	–	–	–	–	1st	Cannon Muskegon
TMS-6	–	9.2	–	8.7	5.3	–	–	10.4	–	–	–	–	–	–	1st	NIMS
PWA1484	10	5	2	6	5.6	–	–	9	–	3	–	–	–	–	2nd	Pratt&Whitney
Rene'N5	8	7	2	5	6.2	–	–	7	0.2	3	–	–	–	–	2nd	GE
CMSX-4	9	6.5	0.6	6	5.6	1	–	6.5	0.1	3	–	–	–	–	2nd	Cannon Muskegon
TMS-82+	7.8	4.9	1.9	8.7	5.3	0.5	–	6	0.1	2.4	–	–	–	–	2nd	NIMS and Toshiba
YH 61	1	7.1	0.8	8.8	5.1	–	0.8	8.9	0.25	1.4	0.07	0.02	–	–	2nd	Hitachi
Rene'N6	12.5	4.2	1.4	6	5.75	–	–	7.2	0.15	5.4	0.05	0.004	–	0.01Y	3rd	GE
CMSX-10	3	2	0.4	5	5.7	0.2	0.1	8	0.03	6	–	–	–	–	3rd	Cannon Muskegon
TMS-75	12	3	2	6	6	–	–	6	0.1	5	–	–	–	–	3rd	NIMS
MX-4/PW A1497	16.5	2	2.8	5.9	5.9	–	–	8.25	0.15	5.95	0.03	0.004	–	3Ru	4th	GE/P&W/NASA
MC-NG	<0.2	4	1	5	6	0.5	–	5	0.1	4	–	–	–	4Ru	4th	ONERA
TMS-138	5.8	3.2	2.8	5.9	5.9	–	–	5.6	0.1	5.0	–	–	–	2Ru	4th	NIMS and IHI
TMS-162	5.8	2.9	3.9	5.8	5.8	–	–	5.6	0.09	4.9	–	–	–	6Ru	5th	NIMS and IHI
TMS-196	5.6	4.6	2.4	5.0	5.6	–	–	5.6	0.1	6.4	–	–	–	5Ru	5th	NIMS

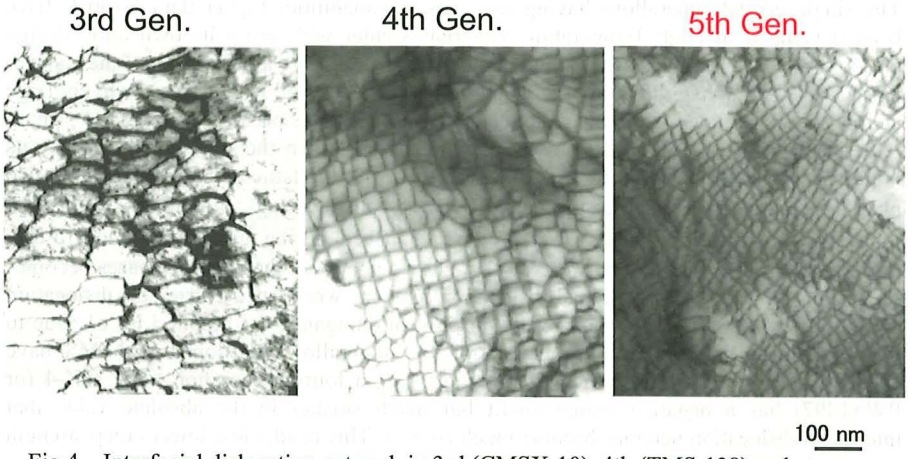

Fig.4 Interfacial dislocation network in 3rd (CMSX-10), 4th (TMS-138) and 5th (TMS 162) generation single crystal superalloys [2].

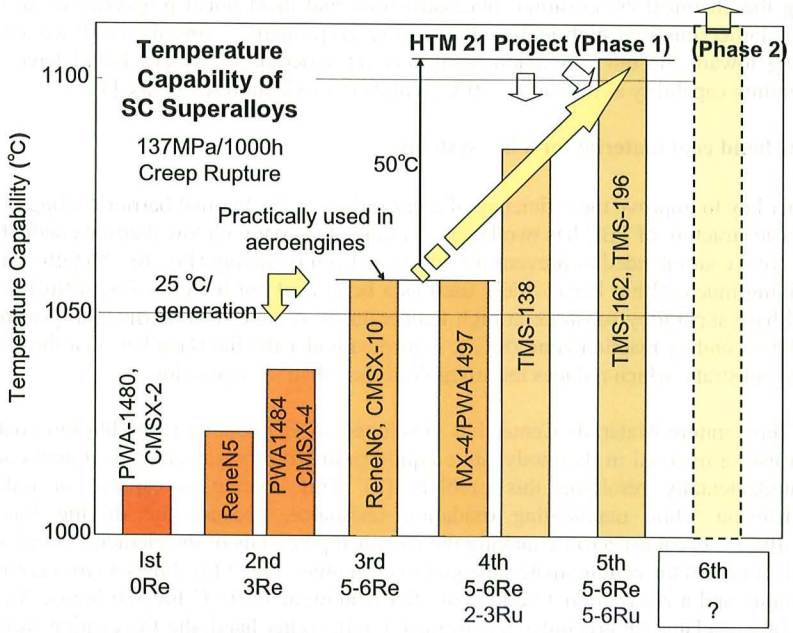

Fig. 5 Temperature capability of generations of single crystal superalloys [3].

The single crystal superalloys having temperature capabilities higher than 1,100°C have been developed in High Temperature Materials Center with using its own alloy design program(ADP). The alloys are designed to have larger negative lattice misfit of the γ and γ' phases (aγ'<aγ). When refractory elements such as Mo, Re, and Ru, having relatively large atomic sizes, are added to a Ni-base superalloy, these elements partition more to the γ phase rather than γ' phase [4]. Consequently, they substitute Ni in the γ phase to increase its lattice parameter compared with that of the γ' phase. As the lattice misfit between the two phases increases toward larger in negative, the so-called rafting the cubic γ precipitate transforms into a plate-shaped structure is enhanced during high temperature creep. Furthermore, the dislocation network on the interface between the γ and γ' phases becomes finer (Fig. 4). The finer interfacial dislocation network works as a barrier for dislocation cutting through the interface, and results in prevention against deformation [5, 6]. Due to this mechanism, fourth and fifth generation SC superalloys developed in NIMS have excellent creep strength at higher temperatures, i.e., a fourth generation alloy MX-4 (or PWA1497) has a negative lattice misfit but much smaller in the absolute value that interfacial dislocation network became much coarser. This results in a lower creep strength at beyond 1,000°C, almost equivalent to the third generation alloys (Fig. 5).

The ADP used in above alloy development work is capable of predicting the relationship among the chemical composition, microstructural and mechanical properties of an alloy, such as lattice misfit at high temperature and creep property. Using the ADP we are now working toward the 6th generation single crystal superalloys, which should have creep temperature capability as high as 1,150°C, with better oxidation resistance [7].

3. New bond coat material for TBC systems

Another key to improve the efficiency of a gas turbine is the thermal barrier coating (TBC). The basic structure of TBC has two layers - ceramic top coat with low thermal conductivity, and a bond coat intended to prevent the substrate from oxidizing (Fig. 6). Metallic coating containing much Al has been widely used as a bond coat but it causes interdiffusion with the Ni-base superalloy substrate at high temperatures. A zone with detrimental precipitate, called a secondary reaction zone (SRZ), is formed under the interface between the coating and the substrate, which reduces the strength of the substrate superalloy.

High Temperature Materials Center has developed an EQ coating (EQuilibrium coating), which uses a material in thermodynamic equilibrium with the substrate, as a new concept for fundamentally resolving this problem [8]. This coating is capable of reducing interdiffusion while maintaining oxidation resistance, because the driving force of interdiffusion becomes zero by making the chemical potentials of the elements contained in the substrate and the coating material equal to each other. Fig. 7 (a) shows a cross section of a substrate and a conventional bond coat after heating at 1,100°C for 300 hours. An SRZ consisting of plate-like precipitates is formed. On the other hand, the EQ coating shown in Fig. 7 (b) forms very thin diffusion layer even under the same conditions and does not form

any precipitates under the interface, so that the substrate does not lose its mechanical strength. We are also committed to research into a top coating process using electron beam - physical vapor deposition (EB-PVD). We are looking for optimum materials that have lower thermal conductivity, higher thermal expansion coefficient, and higher spalling resistance.

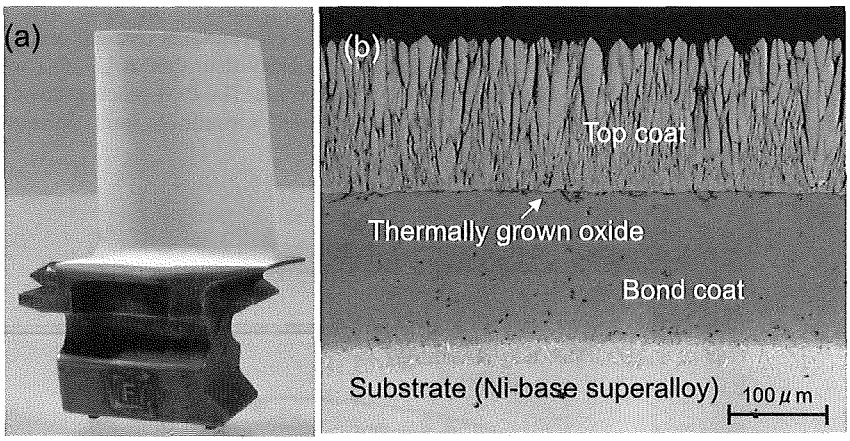

Fig.6 (a) Turbine blade with thermal barrier coating, (b) cross section of coating layer.

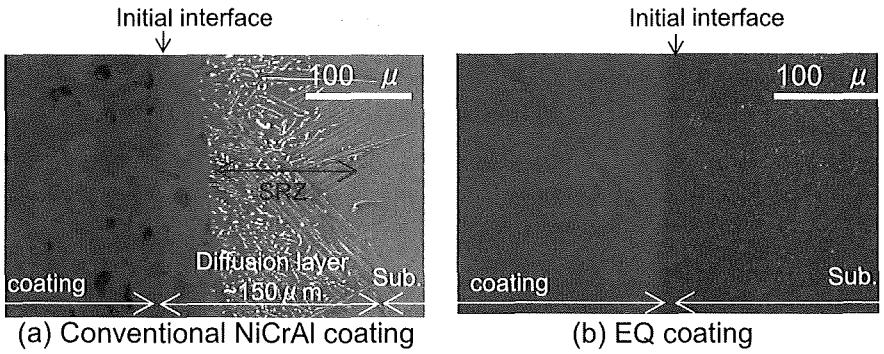

Fig. 7 Cross section of bond coat/substrate interface after 1,100°C for 300hours exposure [8].

4. New turbine disk superalloys

The temperature capability of turbine disk superalloys must be increased. The materials for turbine disks are normally made through wrought process because of high requirements for mechanical properties including creep, fatigue, and fracture toughness. Fig. 8 shows the history of the creep temperature capability development of turbine disk superalloys. The temperature capability has been improved by adding alloying elements for solid solution strengthening or by increasing the volume fraction of γ'. U720Li is the alloy with the highest temperature capability as well as processability by conventional cast-and-wrought (C&W) process. The alloys with higher temperature capability than that of U720Li were thought to be processed only by powder metallurgy (P/M) route. The P/M process, however, is expensive because of high requirement for powder cleanliness and following consolidation processes.

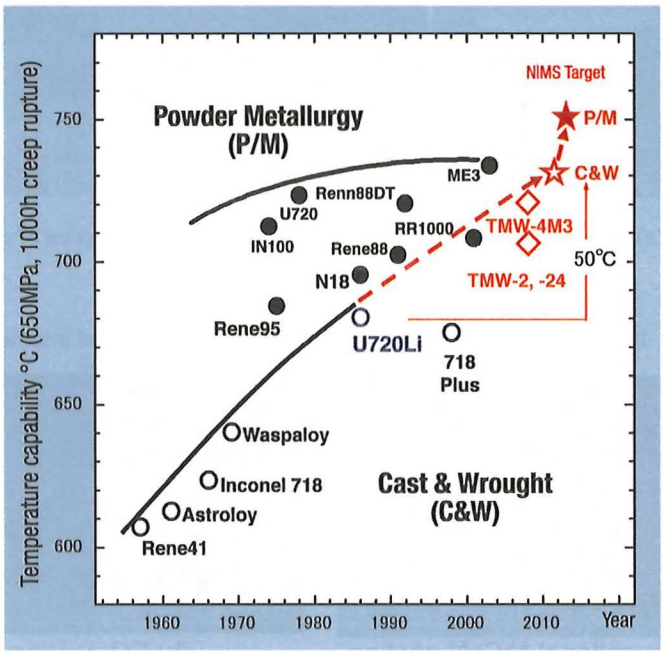

Fig. 8 Improvement in temperature capability of disk superalloys [9].

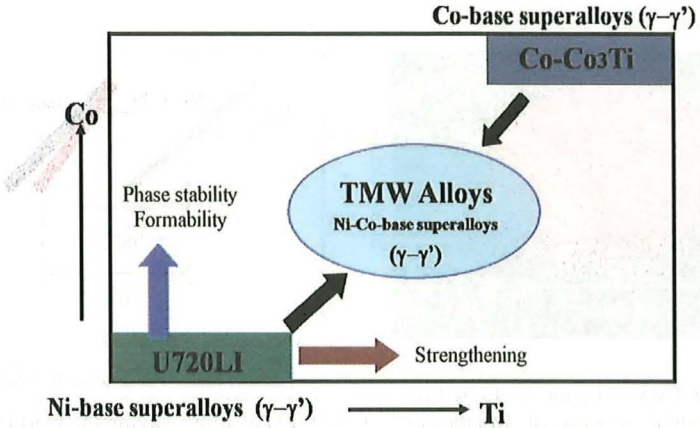

Fig.9 Design concept of Ni-Co base superalloys [9, 10].

Table.2 Nominal chemical composition of C&W superalloys [9,10].

Alloy	Cr	Co	Mo	W	Ti	Al	C	B	Zr	γ' vf
U720Li	16.0	15.0	3.0	1.25	5.0	2.5	0.025	0.018	0.03	45
TMW-2	14.4	21.8	2.7	1.10	6.2	2.25	0.023	0.015	0.033	48.7
TMW-24	13.8	25.0	2.6	1.1	5.6	2.2	0.015	0.015	0.03	45
TMW-3	16.5	23.3	3.1	1.2	5.1	1.9	0.026	0.018	0.022	40
TMW-4	14.9	26.2	2.8	1.1	6.1	1.9	0.014	0.017	0.019	45
TMW-4M3	13.5	25.0	2.8	1.2	6.2	2.3	0.015	0.015	0.03	49.5

γ' vf : Volume fraction of γ' at 760°C

Recently, NIMS developed a new C&W Ni-Co-base superalloy with the innovative concept of combining the characters of two kinds of γ–γ′ two-phase alloys, Ni-base and Co-base alloys (Fig. 9). The results from 50kg ingots indicated that the alloys show excellent high temperature strength and forge-ability, and provided 50°C temperature advantage in 0.2% strain creep performance over alloy U720Li, which may match with the materials processed by P/M route. The chemical compositions of the developed alloys are presented in Table 2.

To put these alloys into real practical applications, we try to manufacture the full-size pancakes with the alloys. By cooperating with Mitsubishi Materials Corporation in a NEDO project, we succeeded in making practical-scale pancakes with diameter of 440 mm and grain size of 10 μm by selecting suitable parameters for melting and forging (Fig.10). The evaluations of mechanical property of the pancakes indicate that the developed alloys, designated as TMW alloys, provide 58 to 76°C temperature advantage in 0.2%-strain creep performance over alloy U720Li (Fig.11) [9,10], which is higher than all the existing C&W disk superalloys, and as high as P/M processed advanced disk superalloys.

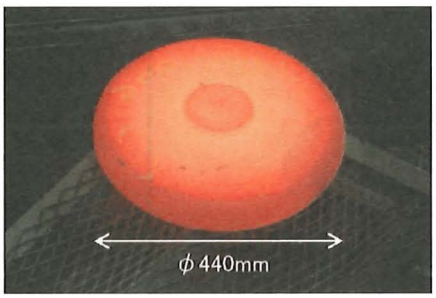

Fig.10 Alloy TMW-24 pancake forged by cast-and-wrought process at Mitsubishi Material Co. Ltd.

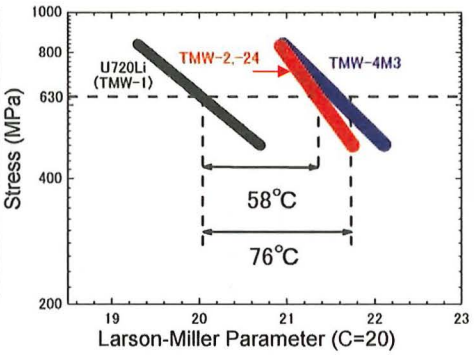

Fig.11 TMW alloys having the world highest temperature capability in C&W superalloys [9, 10].

5. Researches for practical use of the developed materials

The materials that High Temperature Material Center has developed in High Temperature Materials 21 Project to date include Ni-base single crystal superalloys, EQ coatings, and Ni-Co-base wrought alloys which have the highest temperature capabilities in the world. We are working with private companies to promote the practical use of these achievements to gas turbines and jet engines to improve the thermal efficiencies by increasing their operating temperatures, and make a contribution to reducing CO_2 emissions and fuel consumption.

At present, the highest turbine inlet temperature of a natural gas driven combined cycle power plant is 1,500°C, and its thermal efficiency is 52% (HHV standard). If the temperature is raised to 1,700°C, the thermal efficiency will increase to 56 to 60%. It is estimated that the total CO_2 emissions in Japan will decrease by about 4% if 10 existing coal fired power plants are replaced with such natural gas combined cycle power plants. The key to realizing a 1,700°C ultra-high temperature gas turbine is the turbine blades (Fig.2). The High Temperature Materials Center and Mitsubishi Heavy Industries Ltd. jointly modify the single crystal superalloys to have excellent creep strength and thermal fatigue strength, achievable at a lower cost than the currently available alloys, and making prototypes of blades for actual turbines (Fig.12). We are continuing research and development to put this superalloy into practical use around 2015.

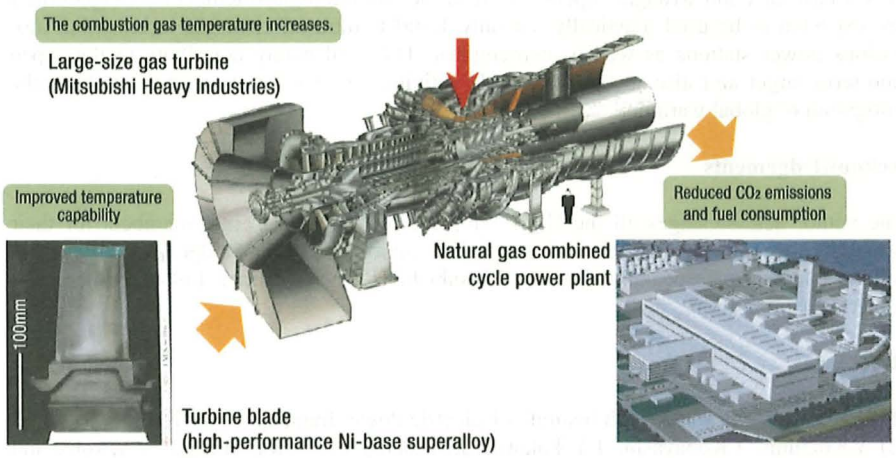

Fig.12 Research into practical use of high-performance Ni-base single crystal superalloy for large-size ultra-efficient gas turbine for natural gas combined cycle power generation [11].

On the other hand, the CO_2 emission from airplanes, which is estimated to amount to 1 to 2% of world total emissions, may rise to 5% or so depending on the future increase in demand. It is, therefore, important to reduce CO_2 emissions by increasing the thermal efficiency of jet engines, and expectations for high temperature material technology capable of fulfilling these requirements are growing accordingly. The Rolls-Royce Centre of Excellence for Aerospace Materials at NIMS, established in June 2006, is promoting a joint research with Rolls-Royce. Jet engine technology was a field in which Japanese industries were, and still are, lagging behind overseas original engineering manufacturers (OEMs) in the postwar era. From the viewpoint of recovering the status of the domestic aeroengine industry, high temperature materials, which put Japan ahead of the rest of the world, are attracting great attention.

6. Conclusions

The Japanese government announced that it will reduce its greenhouse gas emissions by 25% from the 1990 level by 2020 as a mid-term target. One of the promising approaches to achieving this is to improve the efficiency of thermal power generation. Also for aeroengines, reducing fuel consumption is an important issue. The key to improving thermal efficiency as a solution to these issues is high temperature materials with excellent temperature capabilities. The single crystal superalloys, EQ (EQuilibrium) coatings, and

Ni-Co base cast-and-wrought superalloys with the world's highest temperature capabilities are expected to be used practically not only 1,700°C ultra-efficient gas turbines but also various power stations as well as aeroengines. This will surely contribute to the Japan mid-term target and also to the worldwide activities for the CO_2 reduction towards the mitigation of global warming.

Acknowledgements

The author acknowledges all the High Temperature Materials Center members for their providing the results presented in this paper. The author also acknowledges collaborators in private companies, especially those in Mitsubishi Heavy Industries Ltd and Mitsubishi Materials Corporation.

References

[1] H.Hondo, Central Research Institute of Electric Power Industry News, No.338(2000).
[2] Y.Koizumi, T.Kobayashi, T.Yokokawa, J.X.Zhang, M.Osawa, H.Harada, Y.Aoki, and M.Arai, *Superalloys 2004*, p.35.
[3] H.Harada, K.Kawagishi, Y.Gu, T.Yokokawa, J.Fujioka, *Journal of the Gas Turbine Society of Japan*, 39(2010), p.71.
[4] T.Yokokawa, M.Osawa, K.Nishida, Y.Koizumi, H.Harada, *Scripta Mat*, 49(2003), p.1041.
[5] J.X.Zhang, T.Murakumo, Y.Koizumi, T.Kobayashi, H.Harada, S.Masaki,JR: *Mat. and Mat. Trans.A*, Vol.33A(2002), p.3741.
[6] J.X.Zhang, J.C.Wang, H.Harada, Y.Koizumi: *Acta Mater*, Vol.53(2005), p.4623.
[7] K.Kawagishi, A.Sato, H.Harada, AC.Yeh, Y.Koizumi, T.Kobayashi, *Mat. Sci. Tech*, 25(2009), p.271.
[8] K.Kawagishi, A.Sato, H.Harada, JOM, July(2008), p.31.
[9] Y.Gu, H.Harada, C.Cui, D.Ping, A.Sato, and J.Fujioka, *Scripta Mat.* 55(2006), p.815.
[10] YF.Gu, T.Fukuda, C.Cui, H.Harada, A.Mitsuhashi, T.Yokokawa, J.Fujioka, Y.Koizumi, T.Kobayashi, *Met.Mat.Trans.A*, 40A, 13(2009), P.3047.
[11] I..Okada, I.Nagano, S.Shimohata, M.Taneike, H.Oguma, E.Ito, K.Tsukagoshi, T.Yokokawa, H.Harada, Proceedings of the International Gas Turbine Congress 2007 Tokyo, TS-077.

9th Liege Conference : Materials for Advanced Power Engineering 2010
edited by J. Lecomte-Beckers, Q. Contrepois, T. Beck and B. Kuhn.

DEGRADATION OF NI-BASE SUPERALLOYS UNDER HIGH TEMPERATURE CREEP CONDITIONS

A. Epishin[1], T. Link[1], H. Klingelhöffer[2], B. Fedelich[2], M. Nazmy[3], M. Staubli[3]

[1]Technical University of Berlin, Germany
[2]Federal Institute for Materials Research and Testing (BAM), Berlin, Germany
[3]Alstom Ltd., Baden, Switzerland

Abstract

The kinetics of microstructural degradation of the single-crystal nickel-base superalloy CMSX-4, widely used as blade material, was investigated under creep conditions in the temperature range 850-1050°C. To cover a wide range of stress levels a new experimental technique was applied, namely repeated load annealing of flat wedge shaped specimens. A mathematical model developed on the base of the metallographic results predicts the kinetics of microstructure coarsening and the time for complete rafting. Mechanical tests of degraded specimens performed at different temperatures showed that the microstructural degradation decreases yield stress at room temperature as well as causes a significant reduction of the LCF life.

Keywords: nickel-base superalloys, creep, microstructure

1. Introduction

During service in gas turbines the blade material microstructurally degrades under the influence of high temperatures and applied stresses [see e.g. 1, 2]. Therefore for reliable prediction of the blade lifetime this microstructural damage has to be considered. Improvement of lifetime prediction in turbine engineering was a target of European Action COST538 "High Temperature Plant Lifetime Extension" run in 2004-2008. The kinetics of microstructural degradation of the single-crystal nickel-base superalloy CMSX-4, widely used as blade material, was investigated under creep conditions in the temperature range 850-1050°C. To cover a wide range of stress levels a new experimental technique was applied, namely repeated load annealing of flat wedge shaped specimens. The flat geometry allows non-destructive SEM investigations of the γ/γ'-microstructure after each load annealing test, the wedge geometry to investigate the influence of stress in a single specimen. Degradation of the γ/γ'-microstructure was analysed qualitatively by observation of the change of γ'-morphology (cuboidal→rafted) and quantitatively by the increase of the γ-channel width w and the increase of the microstructure period $\lambda^{[001]}$ (raft thickness plus channel width) measured along the loading axis [001]. A mathematical model for the microstructural degradation was developed on the base of the obtained results. The model predicts the kinetics of microstructure coarsening as well as the time for complete rafting. Metallographic investigation of microstructural degradation was accompanied by mechanical tests of degraded material. Tensile tests of degraded specimens performed at different temperatures showed that the microstructural degradation causes a significant reduction of yield stress at room temperature, which has importance for thermal fatigue. The LCF tests of specimens load annealed for different times showed that the lifetime of CMSX-4 drops after rafting. The results obtained were introduced into the mechanical models developed by participants of the COST538 consortium (BAM, Berlin, Germany [3] and NLR, Emmeloord, Netherlands [4]), which consider the effect of microstructural degradation on the material properties of CMSX-4.

2. Experimental

The characterisation of the microstructural degradation in a wide parameter field (temperature T, stress σ, time t) typical for the service conditions of turbine blades is extremely material and time consuming. Therefore a new experimental technique was introduced: repeated load annealing of Flat Wedge shaped (FW) specimens. The geometry of the specimen differs from the conventional rod shaped specimens under two aspects. Firstly, the flat surfaces allow to observe the microstructure non-destructively after removing the surface layer and thus to continue the mechanical test after the metallographic investigation. This procedure saves not only specimens but also testing time because the starting time of test number n is the total time of the proceeding (n-1) tests. Secondly, it has a wedge shape, thus the stress changes linearly along the specimen axis. The specimen gage length is 50 mm within which the specimen width changes from 6 mm up to 10 mm, i.e. the cross-section area S changes by the shape factor $SF=S_{max}/S_{min}=10/6=1.67$. Hence, one specimen is sufficient to cover a whole range of times and stresses. The initial thickness of the FW specimen is 10 mm. After each load annealing (called degradation) the specimen was grinded and polished for SEM investigation, which reduces it thickness by 1 mm. The test series was terminated when the specimen thickness was reduced down to 5 mm, i.e. the applied procedure allowed to perform up to 5 successive degradation experiments accompanied by metallographic analysis of the evolving microstructure. Experimental details of this technique are presented in [5].
The FW specimens of CMSX-4 were annealed under constant load at different temperatures in the range of 850-1050°C. The load at each temperature was chosen in such a way, that the stress in the thinnest cross-section $\sigma_{max}(T)$ corresponds to rupture after 10000 h. The lifetime of 10000 h is close to what is required for gas turbine aeroengines in civil aircrafts. The stress $\sigma_{min}(T)$ in the thickest cross-section is given by $\sigma_{min}(T)=\sigma_{max}(T)/SF$. The total testing time was up to several thousand hours. The degradation conditions of FW specimens are listed in *Table 1*. Additionally three cylindrical specimens were degraded at: 1050°C/68 MPa/1500 h, 950°C/110 MPa/8760 h and 850°C/230 MPa/11175 h.

Table 1. Degradation conditions of FW specimens.

Spec. No.	T, °C	σ_{min} - σ_{max}, MPa	Accumulated time t, h				
1	1050	56 – 94	25	75	175	375	775
2	1000	72 – 120	50	150	350	750	1550
3	950	97 – 162	100	300	700	1500	3100
4	950	155 – 259	100	300	572 rupture	-	-
5	900	137 – 228	200	600	1400	3000	6200
6	850	200 – 334	500	1500	3500	7500	-

The investigation of the γ/γ'-microstructure was performed in a SEM with a computer controlled stage, which allows to position easily the SEM frame within the specimen gage at defined locations corresponding to certain stress levels. The kinetics of the microstructural degradation was characterized qualitatively by observing the transition of the γ'-morphology from cuboidal to rafted shape. In addition, the increase of the γ-channel width w and of the microstructure period $\lambda^{[001]}$=(γ-width + γ'-width), along the load axis [001] were measured. The main parameter is the channel width w, because it provides a measure of the degree of

rafting (see below) and the Orowan back stress. The Orowan stress is important for the plastic deformation of the γ-matrix. The microstructure period $\lambda^{[001]}$ is relevant, because it characterizes the global coarsening of γ/γ'-microstructure. The images were processed by the line section method using the software a4i, Olympus. In order to minimize the scatter of the results due to the dendritic inhomogeneity, all images were taken in the same area of the dendrite, namely the secondary dendrite arms representing most of the material.
The second type of mechanical tests were sequential experiments: first degradation, then either tensile or low cycle fatigue (LCF) testing. The degradation was performed at different temperatures between 850°C and 1100°C. After degradation the specimen surface was grinded to remove the oxide layer, which could influence the results of the second test. The tensile tests were performed at temperatures within the interval 20-950°C with a strain rate of about 5%/min. The LCF tests were carried out under completely reversed strain controlled cyclic loading at the temperatures 700, 750 and 950°C.
Small, un-cooled ex-service blades of CMSX-4, which passed 12700 h of operation in a small industrial gas turbine, were used as case study. The investigation included the metallographic inspection of different parts of the blades as well as room temperature tensile tests of mini specimens excised from these blades.

2. Results

2.1. Kinetics of rafting

The large scatter of the results did not allow an unambiguous identification of a specific growth function $w = f_w(t)$. Therefore as a first approximation a linear function was used. However, from the data obtained it follows that a single straight line could not fit the whole time range, which is not surprising, since two successive processes govern degradation. At the beginning the dominant process is rafting [e.g. 6, 7]. Here the γ-channels parallel to the load direction become narrow and disappear, the perpendicular channels widen. This results in the formation of rafted γ/γ'-microstructure where the γ'-rafts are separated by γ-channels much wider than the initial channel width w_0. The kinetics of rafting of the cuboidal γ/γ'-microstructure was characterized by the widening rate $\dot{w}_{cub}$ of the perpendicular channels. After rafting has completed the second process becomes dominant, namely coarsening of the rafted microstructure controlled by the migration of γ'-terminations according to the Graham-Kraft model [8]. The kinetics of coarsening of the rafted γ/γ'-microstructure was characterized by the channel widening rate $\dot{w}_{raft}$. *Figure 1a* shows the increase of channel width in CMSX-4 during load annealing at 950°C and 110 MPa. The dependence $w = f_w(t)$ is fitted by two straight lines with the slopes $\dot{w}_{cub}$ and $\dot{w}_{raft}$. It is seen that the widening rate slows down after rafting is completed ($\dot{w}_{raft} < \dot{w}_{cub}$), which in agreement with the well-known fact that the plate-like microstructure is more stable than the cuboidal one [e.g. 9].
The transition from rafting to coarsening has been determined by defining a fixed ordinate $w = w_{raft}$, where rafting is completed and then fitting the time of rafting t_{raft} and the slopes of the lines. w_{raft} was calculated according to geometrical considerations [10]:

$$w_{raft} = c \cdot w_0 \tag{1}$$

with

$$c = \frac{\lambda_{raft}^{[001]}}{\lambda_0^{[001]}} \frac{1 - V'_{raft}}{1 - \sqrt[3]{V'_{raft}}} \tag{2}$$

where, $\lambda_0^{[001]} = \lambda^{[001]}(t=0)$ and $\lambda_{raft}^{[001]} = \lambda^{[001]}(t_{raft})$ are the microstructure periods at start and end of rafting, $V_0' = V'(t=0)$ and $V_{raft}' = V'(t_{raft})$ the corresponding γ'-volume fractions. From our measurements it follows that $\lambda^{[001]}$, characterizing the global coarsening of the microstructure according to LSW-mechanism, did not change remarkably during rafting. Under the degradation conditions used here (*Table 1*) the ratio $\lambda_{raft}^{[001]}/\lambda_0^{[001]}$ was in the range 1-1.2. The volume fraction remained constant too $V_0' \approx V_{raft}' \approx 0.73$. In this case formula (2) gives $c \approx 3$, which allows to formulate a simple criterion for the end of the rafting process: rafting ends when the channel width w achieves $3w_0$. This "$3\,w_0$-criterion" is in agreement with our metallographic observations.

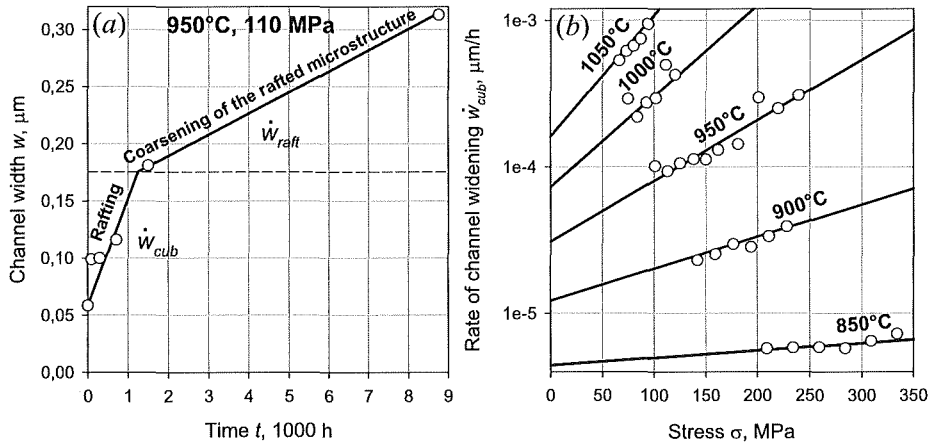

Figure 1. The kinetics of widening of γ-channels in [001] single-crystals of CMSX-4.
(a) – Increase of the channel width w during load annealing at 950°C, 110 MPa.
(b) – Widening rate during rafting $\dot{w}_{cub}$ as a function of temperature and stress.

The dependence of the widening rate $\dot{w}_{cub}$ on T and σ is shown in *Figure 1b*. These results were fitted by the Arrhenius formula for processes activated by temperature and stress:

$$\dot{w}_{cub}(T,\sigma) = A \cdot \exp\left[-\frac{Q - U(T)\cdot\sigma}{RT}\right] \tag{3}$$

where A is a pre-exponential factor, Q the activation energy, R the universal gas constant and $U(T)$ the temperature dependent activation volume described by a power function $U(T) = U_T(T - T_0)^n$ for $T > T_0$. The fitted parameters A=9.31·10^4 µm/h, Q=221780 J/mol, U_T=0.19 J/(mol·MPa·K^n), T_0=1100.7K (827.7°C), n=1.294 are temperature and stress independent. Comparison of the experimental points for $\dot{w}_{cub}$ with the fitting curves (*Figure 1b*) shows good agreement.
From the "$3\,w_0$-criterion" follows:

$$t_{raft} \approx 2w_0/\dot{w}_{cub} \tag{4}$$

which allows to predict the rafting time t_{raft} as:

$$t_{raft}(T,\sigma) \approx \frac{2w_0}{A} \cdot \exp\left[\frac{Q - U(T)\cdot\sigma}{RT}\right] \tag{5}$$

The shape of the function $t_{raft} = f_t(T,\sigma)$ with the obtained fit parameters A, Q, U_T, T_0, n is shown in *Figure 2*.

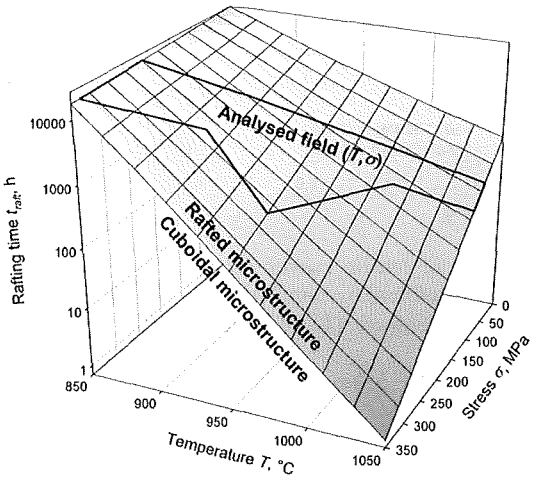

Figure 2. Time for complete raft formation as a function of temperature and stress. Solid line shows analyzed field of degradation parameters (T,σ).

2.2 Effect of degradation on tensile properties

It was found that, at all investigated temperatures (20-950°C) the degradation generally deteriorates the tensile properties, i.e. decreases the yield stress (YS) and the ultimate tensile stress (UTS). *Figures 3a* and *b* show the effect of degradation on the shape of the tensile stress-strain diagrams at room temperature and 950°C respectively. It is seen that in both cases the degradation changes the stress-strain curves and these changes are stronger for higher degradation temperatures. The first important change is a decrease in YS, which is especially pronounced at room temperature. After 1050°C/68 MPa/2500 h degradation YS at 20°C decreases from 952 MPa down to 630 MPa, so 34%. The effect of this degradation on YS at 950°C, as shown in *Figure 3b*, is essentially smaller, about 18%. It is remarkable that at room temperature the degraded material shows work hardening, i.e. an ascending stress-strain curve in the region of plastic flow (*Figure 3a*), while at 950°C degradation has the opposite effect (*Figure 3b*). The consequence of this work softening at 950°C is a reduction in UTS, e.g. after 1050°C/68 MPa/2500h degradation from 891 MPa[1] down to 678 MPa, so 24%. Thus degradation reduces UTS at high temperatures, whereas the deteriorative effect on YS is stronger at lower temperatures.

[1] Maximum on the stress-strain curve for virgin material is out of the 2%-strain range presented in *Figure 3b*.

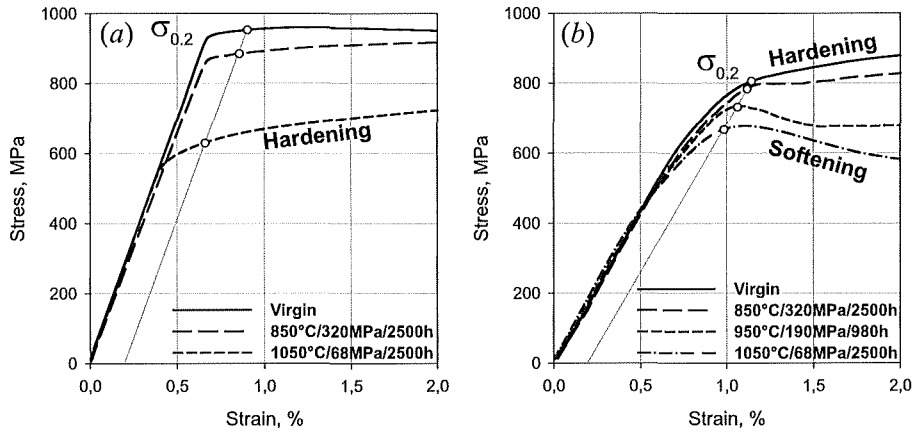

Figure 3. The initial parts of tensile curves (up to 2% strain) for virgin and degraded material. The degradation conditions are marked in the graphics.
(a)– Tensile tests at room temperature. (b) - Tensile tests at 950°C.

2.3 Effect of degradation on LCF behaviour

CMSX-4 degraded at 1100°C/90 MPa showed in strain controlled LCF tests at 700°C with a strain amplitude $\Delta\varepsilon/2$=0.625% that even after a short degradation time of about 100 h the number N of cycles to failure decreased by a factor of about 8. From the creep curves recorded during the degradation tests follows that 100 h correspond to the end of primary creep.

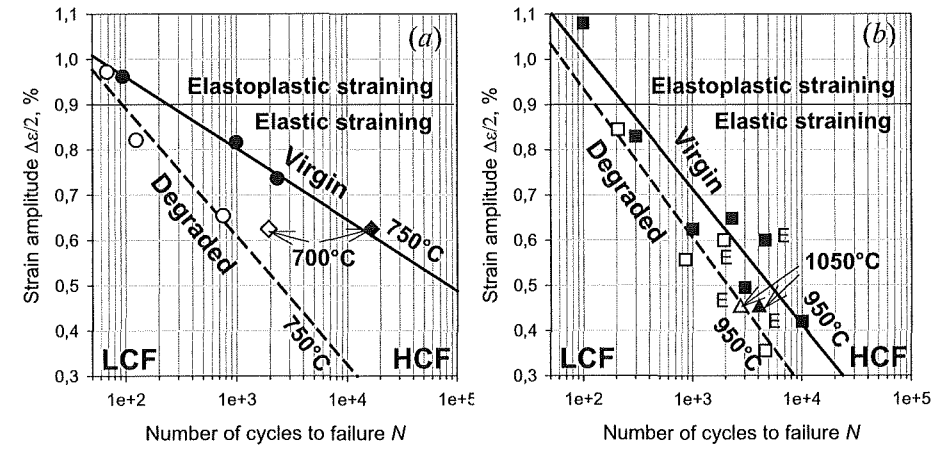

Figure 4. Effect of degradation on the number of cycles to failure N under cyclic strain controlled loading (R_ε =–1) at 700, 750°C (a) and 950, 1050°C (b). Black symbols and solid lines correspond to virgin material, white symbols and dashed lines to degraded one. Points for 700 and 1050°C are marked by arrows, data from University Erlangen-Nürnberg [11] by letter E.

Metallographic inspection of the degraded specimens shows that at this time the γ'-raft formation is completed. After the rafted structure has formed N retains almost constantly at this low level until the end of secondary creep, which corresponds to 1800 h for these degradation conditions. *Figure 4* shows the effect of degradation at 1050 or 1100°C on the LCF lifetime, with LCF tests performed at 700-1050°C and strain amplitudes 0.3-1.1%. The presented data were mostly obtained in this work and partially taken from literature. It follows that the effect of degradation on LCF is much stronger at the lower LCF test temperatures 700 and 750°C (*Figure 4a*) and weaker at the higher temperatures 950°C and 1050°C (*Figure 4b*). At these low temperatures the degradation effect becomes pronounced when the strain amplitude $\Delta\varepsilon/2$ is smaller than the elasticity limit for virgin CMSX-4, about 0.9% in the temperature range 700-1050°C (horizontal lines in *Figures 4a, b*). Fitting the black symbols (virgin material) with straight lines shows, that the virgin material has higher fatigue strength at 750°C than at 950°C and this difference is expected to be stronger for high cycle fatigue (HCF). The degraded material has almost the same fatigue behavior for both temperatures.

2.4. Ex-service blade

As a case study, small un-cooled solid blades of CMSX-4 were investigated after 12700 h service in a small industrial gas turbine. The γ/γ'-microstructure of the blade was investigated in different longitudinal sections and some results are presented in *Figure 5*.

The γ/γ'-microstructure near the blade platform (position 1 in *Figure 5*) retained the initial condition, i.e. it remains cuboidal with the same period, $\lambda^{[001]}/\lambda_0^{[001]} \approx 1$, as one could expect from the local operation parameters 800°C/190 MPa. In the blade middle (position 2, 920°C/110 MPa) the microstructure is completely rafted and somewhat coarsened, $\lambda^{[001]}/\lambda_0^{[001]} \approx 1.3$. The γ'-rafts are long and always oriented perpendicular to the blade axis. In the blade tip (position 3, 980°C/30 MPa) the microstructure is also rafted but the γ'-rafts are thicker and shorter than in the blade middle. Most of the γ'-rafts are perpendicular to the blade axis but in some areas they are oriented along the blade axis. In the blade tip the microstructure is obviously coarsened. The measurement gives an increase of the microstructure period by the factor of about 2.3. The observed morphological changes generally fit with formula (5), which predicts for the considered service conditions no rafting near the blade platform and complete rafting in the blade middle and top. Cylindrical mini specimens (2 mm in diameter) were cut from the central part of blade, where temperature and stress were about 920°C/110 MPa, and tested for tension at room temperature. The tests gave yield stress of about 840 MPa, which is about 13% lower than that for virgin material (952 MPa).

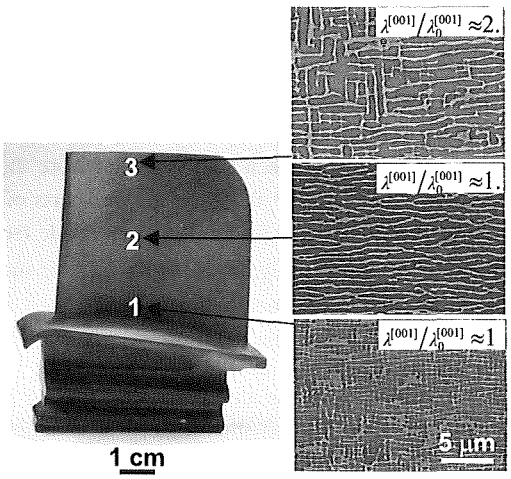

Figure 5. A blade of CMSX-4 and γ/γ'-microstructure of blade material after service.

3. Discussion

The kinetics of the microstructural degradation of CMSX-4 was characterized by the widening of the γ-channels similar to the approach used in [12]. The analytical description of the results obtained in a wide parameter field (T, σ, t) made it possible to derive a formula for the evaluation of the rafting time t_{raft} (5) based on the "$3w_0$-criterion" for the end of rafting. The function $t_{raft} = f_t(T,\sigma)$ has similarity with the well-known Larson-Miller dependence $p(\sigma) = T(C + \log t)$, allowing to calculate creep rupture lifetime t as a function of temperature T and stress σ. This is not surprising, because creep and microstructure evolution are closely connected. Both dependencies $t_{raft} = f_t(T,\sigma)$ and $p(\sigma) = T(C + \log t)$ follow from the generalized Arrhenius formula describing the kinetics of temperature activated processes under stress.

The "$3w_0$-criterion", used to calculate t_{raft}, assumes that the microstructure period $\lambda^{[001]}$ does not change significantly during rafting, which is valid for the analyzed parameter field (T, σ, t). This hypothesis works satisfyingly for stresses above a certain level as in the case of the lower and middle parts of the investigated blades, where $\lambda^{[001]}/\lambda_0^{[001]} \leq 1.3$. The fact, that e.g. in the blade middle the microstructure period $\lambda^{[001]}$ increased by the factor 1.3 does not necessarily mean, that here the "$3w_0$-criterion" can not be applied, because the time for rafting, t_{raft}~100 h (see *Figure 1a*), is much shorter than 12700 h and therefore the microstructure period $\lambda_{raft}^{[001]}(t_{raft})$ is smaller than $\lambda^{[001]}$(12700 h). For very low stresses however rafting process is very slow and therefore there is time enough for the cuboidal microstructure to coarsen significantly before the cuboids coalesce, which results in a clear increase of $\lambda^{[001]}$. This is typical for the parts of the blade where temperatures are high but stresses very low, e.g. for the tip of the blade (see *Figure 5* left-top), where $\lambda^{[001]}/\lambda_0^{[001]}$ was found to be significantly larger, about 2.3. For such a special degradation condition the "$3w_0$-criterion" and consequently formula (5) have to be modified by taking into account the change of $\lambda^{[001]}$ but this requires additional investigations at very low stress levels. The γ'-coarsening during rafting is considered in [13].

The explanation of the observed reduction of YS, especially at room temperature, is not simple, because several microstructural changes taking place, namely γ-channel widening, loss of interfacial coherency, coalescence of the γ'-cubes and a topological inversion[2]. To identify the relevant mechanism, comparison with degradation caused by load free annealing [e.g. 14, 15] could be helpful. Here a very similar reduction in YS was found but of course without rafting and topological inversion. So it can be concluded that the global coarsening of microstructure, characterized by the increase of $\lambda^{[001]}$, and the loss of coherency, measured e.g. by the increase of the γ/γ'-misfit δ, are the decisive factors. However a physical explanation of the reduction of YS observed at low temperatures as well as the material softening at high temperatures is not possible without detailed investigations of the deformation mechanisms, which are temperature and stress dependent.

The decisive factor for LCF strength however is rafting. It is well known that the fatigue strength of plate-like structures is lower under cyclic loading including tension perpendicular

[2] γ'-phase forms junctions and becomes the matrix.

to the plate plane. The reason for this effect is the fast growth of fatigue cracks along the interface between the plates, which is generally weaker than the bulk material. Such a material behavior is reported for the superalloy CMSX-2 [16], where the growth rate of fatigue cracks was found to increase by several times when the material becomes rafted. The preferable crack growth along the extended γ/γ'-interfaces was confirmed metallographically [11, 16, 17]. So from general considerations about plate-like structures and the results above [11, 16, 17] it is reasonable to assume that for the LCF properties of superalloys the relevant point is the γ'-morphology, cuboidal or rafted. This is confirmed by our finding that after primary creep at 1100°C, so when rafting is completed, the number of cycles to failure has strongly decreased, but then remains nearly constant until the end of secondary creep.
Two questions regarding the results presented in *Figure 4* are not quite clear:
1. Why is the rafting effect on LCF pronounced only at the low temperatures 700°C and 750°C and diminishes at the high temperatures 950°C and 1050°C?
2. Why does the difference between virgin and degraded material strongly increase for low strain amplitudes, i.e. in the field of macroscopically elastic straining?
The first question is difficult, because several material parameters as well as deformation mechanisms remarkably change in the considered temperature range 700-1050°C. For example, when temperature rises from 700°C up to 1050°C the superalloy ductility increases by a factor of about 10, while the YS and UTS significantly decrease. At lower temperatures the main mechanism of plastic deformation is gliding, at high temperatures climbing controlled creep is involved. For the second question an answer could be, that rafting has an even stronger effect on crack nucleation than on crack propagation. At small strain amplitudes $\Delta\varepsilon/2$ when most of the material deforms elastically without damage the decisive factor for the fatigue lifetime becomes the local damage at structural inhomogeneities acting as stress concentrators. In single-crystal superalloys these critical defects are micropores, as could be shown by HIP (hot isostatical pressure) experiments. Fatigue tests performed under the conditions of macroscopically elastic straining (700°C, $\Delta\varepsilon/2$=0.625%, R_ε= −1) gave for the UNHIPPed specimen $16{\cdot}10^3$ cycles to failure, whereas the test of the HIPPed specimen was interrupted after $180{\cdot}10^3$ cycles (no rupture). It is reasonable to expect that in rafted material the extended incoherent raft interfaces which crop out the pore surface facilitate crack initiation and hereby reduce fatigue lifetime.

5. Conclusions

The following conclusions can be drawn from this work:
1. For the first time the kinetics of the microstructural degradation of CMSX-4 was characterized in a wide field of (T, σ, t) and described analytically. This was possible due to a new technique, namely repeated load annealing of flat wedge shaped (FW) specimens. On the base of the obtained results a "$3w_0$-criterion" for rafting was proposed and a formula for the rafting time derived.
2. The microstructural degradation of CMSX-4 results in a deterioration of the tensile properties: reduction of YS, pronounced at low temperatures, and material softening, pronounced at high temperatures. The effect on the tensile properties is stronger for higher degradation temperatures.
3. The deteriorative effect of degradation on the LCF lifetime was found to be pronounced at the low temperatures 700 and 750°C. The effect increases when lowering the strain amplitude $\Delta\varepsilon/2$ down to the field of macroscopically elastic straining. Therefore it should be expected

that this deterioration effect is stronger for HCF. For the fatigue lifetime mostly the change of the γ'-morphology (cuboidal→rafted) is important.

References

[1] M. Nazmy, A. Epishin, T. Link and M. Staubli, A Review of degradation in single crystal nickel based superalloys, *Energy Materials*, Vol. 1, pp. 263-268 (2006).
[2] N. Miura, N. Harada, Y. Kondo and T. Matsuo, Morphological changes in γ' phase in different portions of first stage high pressure turbine blade of PWA 1480, *Materials for Advanced Power Engineering,* Part 1, pp. 217-254 (2002).
[3] B. Fedelich, G. Künecke, A Epishin, T. Link and P. Portella, Constitutive modelling of creep degradation due to rafting in single crystal Ni-base superalloys, *Materials Science and Engineering A*, Vols 510-511, pp. 273-277 (2009).
[4] T. Tinga, Multiscale modelling of single crystal superalloys for gas turbine blades, PhD theses, Eindhoven University of Technology (2009).
[5] A. Epishin, T. Link, H. Klingelhöffer, B. Fedelich, U. Brückner and P. D. Portella, New technique for characterization of microstructural degradation under creep: Application to the nickel-base superalloy CMSX-4, *Materials Science and Engineering A*, Vols 510-511, pp. 262-265 (2009).
[6] F. R. N. Nabarro, Rafting in superalloys, *Metall. Trans.*, Vol. 27A, pp. 513-529 (1996).
[7] N. Matan, D. C. Cox, C. M. Rae and R. C. Reed, On the kinetics of rafting in CMSX-4 superalloy single crystals, *Acta mater*, Vol. 47, pp. 2031-2045 (1999).
[8] L. D. Graham and R. W. Kraft, Coarsening of Eutectic Microstructures at Elevated Temperatures, *Trans. Metall. Soc. A.I.M.E.*, Vol. 236, pp. 94-101 (1966).
[9] M. V. Nathal and R. A. MacKay, The Stability of Lamellar γ-γ' Structures, *Mater. Eng.*, Vol. 85, pp. 127-138 (1987).
[10] DFG report PO 405/10-1, LI 494/4-1 "Microstructural degradation of the single-crystal superalloy CMSX-4 during annealing under load: Implementation of rafting kinetics in mechanical modelling". BAM – TU Berlin (2007).
[11] M. Ott and H. Mughrabi, Dependence of the high-temperature low-cycle fatigue behaviour of the monocrystalline nickel-base superalloys CMSX-4 and CMSX-6 on the γ/γ'-morphology, *Mater. Sci. and Engineering A*, Vol. 272, pp. 24-30 (1999).
[12] K. Serin, G. Göbenli and G. Eggeler, On the influence of stress state, stress level and temperature on γ-channel widening in the single crystal superalloy CMSX-4, *Mater. Sci. Eng.*, Vols A387-390, pp. 133-137 (2004).
[13] W. Chen and J-P. Immarigeon, Thickening Behaviour of γ' Precipitates in Nickel Base Superalloys during Rafting, *Scripta Mater.*, Vol. 39, pp. 167-174 (1998).
[14] R.G. Davies and N.S. Stoloff, On the yield stress of aged Ni–Al alloy, *Trans. AIME*, Vol. 233, pp. 714–719 (1965).
[15] R.A. Stevens and P.E.J. Flewitt, The effect of the γ′ precipitate coarsening during isothermal aging and creep of the Ni-base superalloy IN-738LC, *Mater. Sci. Eng.*, Vol. 37, pp. 237–247 (1979).
[16] S. H. Ai, V. Lupinc and G. Onofrio, Influence of precipitate morphology on high temperature fatigue crack growth of a single crystal nickel base superalloy, *Scripta Metall. Mater.*, Vol. 29, pp. 1385-1390 (1993).
[17] A. Epishin, T. Link, U. Brückner, H. Klingelhöffer and P. D. Portella, The effect of high temperature creep damage on low cycle fatigue of CMSX-4, *Materials for Advanced Power Engineering*, Part 1, pp. 317-325 (2006).

9th Liege Conference : Materials for Advanced Power Engineering 2010
edited by J. Lecomte-Beckers, Q. Contrepois, T. Beck and B. Kuhn.

NEW CONCEPT OF COMPOSITE STRENGTHENING IN CO-RE BASED ALLOYS FOR HIGH TEMPERATURE APPLICATIONS IN GAS TURBINES

D. Mukherji[1], J. Rösler[1], T. Fricke[1], S. Piegert[2], F. Schmitz[1],

[1] TU Braunschweig, IfW, Langer Kamp 8, 38106 Braunschweig, Germany
[2] Siemens AG, Energy F PR GT EN, Huttenstraße 12, 10553 Berlin, Germany

Abstract

High temperature material development is mainly driven by gas turbine needs. Today, Ni-based superalloys are the dominant material class in the hot section of turbines. Material development will continue to push the maximum service temperature of Ni-superalloys upwards. However, this approach has a fundamental limit and can not be sustained indefinitely, as the Ni-superalloys are already used very close to their melting point. Within the frame work of a DFG Forschergruppe program (FOR 727) – "Beyond Ni-base Superalloys" - Co-Re based alloys are being developed as a new generation of high temperature materials that can be used at +100°C above single crystal Ni-superalloys. Along with other strengthening concepts, hardening by second phase is explored to develop a two phase composite alloy. With quaternary Co-Re-Cr-Ni alloys we demonstrate this development concept, where Co_2Re_3-type σ phase is used in a novel way as the hardening phase. Thermodynamic calculation was used for designing model alloy compositions.

Keywords: Co-Re alloys, Superalloy, Thermo-Calc, SEM, XRD

1. Introduction

Today, Ni-base superalloys are the dominant material class in the hot section of gas turbines. It is very likely that in the near future, material development will continue to push the maximum service temperature of Ni-superalloys upwards. However, improving the temperature capability of superalloys, which are already used very close to their melting point (which is in the range of 1300° – 1400°C and > 0.8 T_M of Ni), is limited by the possibility to raise further their melting point. A desire to increase the turbine inlet gas temperature and the compression ratio to obtain a higher efficiency in the gas turbines and lower CO_2 emission demands materials for applications at much higher temperatures. This is presently met partly through component cooling and application of thermal barrier coatings (TBC). However, for a significant increase in turbine gas temperature, the base metal temperatures must increase in the long term future. Hence, there is an urgent need today, for the development of new alloy systems to supplement Ni-base superalloys in the future. Many efforts are being pursued world-wide in this direction [1]. Development of Co-Re-based alloys is being pursued at the Technische Universität of Braunschweig with this aim. The goal is set to develop alloys for applications aimed at +100°C metal temperature above present day Ni-base superalloys [2].

The refractory metal Re has the third highest melting point (3182°C) amongst the elements in the periodic table, which is more than double the melting point of Co (1495°C). Moreover, it dissolves readily in Co and a complete miscibility exists in the Co-Re system. Therefore, it is possible to continuously increase the melting temperature of Co alloys with the addition of Re, opening up a unique possibility to steadily elevate the melting range in the Co-Re system, changing the character of the material from that of a contemporary Co-based alloy to that of a high melting point material. Further, the "tuneability" in the Co-Re system gives a good

chance to find a proper balance between the need for toughness and ductility on the one hand and strength at temperatures beyond the capability of Ni-based superalloys on the other hand. Yet it is clear that further alloying additions are required to impart sufficient strength and oxidation resistance. Ternary and quaternary alloying is therefore necessary. A judicious choice of alloying addition gives a good chance to tune the microstructure in Co-Re-base alloys and explore new concepts in strengthening.

Higher application temperatures also impose severe demand on the high temperature oxidation behaviour of the alloy, which is generally met in Ni-superalloys through Cr and Al additions. Oxidation resistance along with high temperature strength is an important consideration in any high temperature alloy development program. Cr along with small amount of Si was explored in Co-Re alloys with good success [3]. Cr in combination with Re however, stabilizes Cr_2Re_3 type σ phase. We will present results on how with the addition of Ni to the Co-Re-Cr ternary base the seemingly unwanted topologically close packed (tcp) σ phase is exploited to produce a ductile alloy. This opens up a new possibility to use the σ phase as a strengthening phase in high temperature Co-alloys. In this contribution we briefly present the general development strategy and design considerations we adapted for the Co-Re alloy development. Amongst other strengthening mechanisms that are being pursued, one strategy is to develop a new concept of composite strengthening using the σ phase.

2. Alloy Development Strategy

Co-based alloys are not new and are presently used in gas turbines for static parts up to 1000°C. In these conventional cast Co-base alloys, the matrix phase has a face centred cubic (fcc) γ structure. There is even a new development trend in Co-Al-W alloys [4] to produce a γ / γ' structure similar to that in Ni-superalloys, however, this does not promise application temperatures beyond Ni-superalloys. In contrast, Re addition stabilizes the hexagonal close packed (hcp) ε Co phase as the matrix in the new Co-Re alloys. In actual, very few studies exist on the Co-Re system, except for some studies on structural investigations and phase diagrams [e.g. 5]. This demanded a new strategy in the Co-Re alloy development. It was necessary, first to explore the different possibilities of strengthening of the Co-Re alloys from a more fundamental basis, using simple model alloy compositions. Strengthening mechanisms like precipitation hardening by carbide precipitates ($M_{23}C_6$ and MC types) or solid-solution hardening by large atoms e.g. Re were explored. Initial development of the cast polycrystalline Co-Re alloys showed that grain boundary embrittlement is a critical issue in this system, which limit both the strength and ductility of the alloys at room and high temperatures. Following clues from polycrystalline Ni superalloy development of the past, addition of B (and Zr) was considered in experimental Co-Re alloys. A small amount of B (and Zr) addition in ppm level (from 200 to 2000 ppm by weight) could strengthen the grain boundaries and mitigate the environmental embrittleness effect [6].

It is mentioned above that along with high temperature strength, oxidation resistance is an important aspect in high temperature alloy development. The Co-Re alloys were never investigated for oxidation behaviour. Since the Co-Re system is rather new for high temperature applications, there was a need to isolate the two main aspects of alloy development, namely – i) strength and ii) oxidation, and study them separately for understanding the physical basis. One set of model alloy compositions were therefore designed for studying the strengthening mechanisms and another set of compositions for the

oxidation behaviour. Even for strengthening, each mechanism was explored separately with tailored compositions. The knowledge gained from these studies provided the basis for the design and development of a technical alloy. Cr which promotes the formation of a protective Cr_2O_3 oxide layer in conventional iron, nickel and cobalt alloys was a logical choice as alloying addition for intermediate temperature oxidation resistance. It is however clear that chromium alone will not suffice for oxidation protection at higher temperatures. An addition of a small amount of Si in conjunction with Cr, to the Co-Re system, provided good oxidation resistance to 1100°C [3].

However, addition of Cr to Co-Re alloys stabilizes a significant amount of the Cr-Re-rich (Cr_2Re_3 type) σ phase. The tcp σ phase has a very high strength, but unfortunately, it is also a very brittle phase and therefore is generally undesirable in Ni and Fe base alloys. A novel development strategy is adapted for the Co-Re alloy development in which a new concept of composite strengthening using the σ phase is explored; thereby the very strong σ phase is used for high temperature strengthening of the alloy. It will be shown that σ phase is very stable at high temperatures up to 1300°C.

Extensive thermodynamic calculations guided the choice of alloy compositions. Thermo-Calc [7] was used to determine the stability of phases in the different temperature regions in the multi-component Co-Re-base alloys containing Ni addition and design model alloy compositions and heat treatments.

3. Experimental

3.1. Material and heat treatment

Two alloys with nominal compositions Co-17Re-23Cr-15Ni and Co-17Re-23Cr-25Ni (*all compositions are expressed in at. %*) and designated CoRe-5 and CoRe-6 were melted in a vacuum arc furnace and cast into 10mm x 10mm square bars about 70 mm long. The bars were homogenised between 1350° and 1450°C for a total of 15 h and then hipped at 1400°C under an Argon pressure of 200 MPa for 3 h. Heating and cooling rates for the HIP cycle were 15K/min. Hipping did not alter the microstructure significantly and it was followed by a solution heat treatment (ST). Alloys were heat treated at different ageing temperatures to control the size and dispersion of σ phase in the microstructure. The choice of heat treatment temperatures were based on the thermodynamic calculations of phase stability as a function of temperature and composition. The various ageing cycles adopted in this study for CoRe-5 and CoRe-6 alloys are listed in Table-1.

Tabel-1: Heat treatment details

Ageing heat treatment*	Sample Designation	
	CoRe-5	**CoRe-6**
980°C / 4h / WQ	-	STA1
1050°C / 4h / WQ	STA1	STA2
1100°C / 4h / WQ	STA2	-
1225°C / 3h / WQ	STA3	STA3
1325°C / 6h / WQ	-	STA4

* all samples were solution treated at 1350°C/5h + 1400°C/5h + 1450°C/5h and WQ prior to ageing

Further, to study the effect of cooling rate on the microstructure, samples from CoRe-5ST and CoRe-6ST were aged either at 1000°C or at 1200°C for 3h and then cooled in 3 different ways, namely water quench (WQ), air cool (AC) and furnace cool (FC).

3.2. Thermo-Calc

A comprehensive combination of thermodynamic and kinetic models makes it possible to predict composition, structure and properties in alloys. This takes even more significance when one studies little explored material systems like the Co-Re alloys. Thermodynamics of the multi-component Co-Re systems, particularly, the quaternary Co-Re-Cr-Ni system was numerically modelled by means of the software package Thermo-Calc Version S using the TTNi7 database established by Thermotech Ltd. [7]. The software package has been extensively utilised to describe material states and processes in Ni-superalloys and other systems and is a versatile tool for calculation of phase diagrams according to the CALPHAD (CALculation of PHAse Diagrams) method [8]. In the present study it was used to calculate isothermal sections of ternary Co-Re-Ni phase diagrams and isoplethal sections of the quaternary Co-Re-Cr-Ni system. As the elements Co, Re and Cr are included in the TTNi7 database, it gave reasonable success in the prediction of the phase equilibrium in Co-Re system, even when essentially a Ni database is used. This is confirmed by microstructural observations and diffraction measurements.

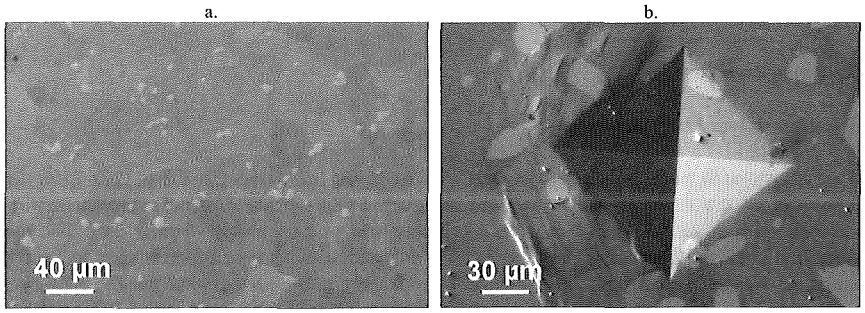

Fig. 1: a) High strength (~ 1500 HV) σ phase (bright) present in solution heat treated Co-17Re-23Cr alloy. b) Hardness impression in Co-17Re-23Cr alloy showing cracks in σ particles and slip bands in matrix.

4. Results

4.1. Reference alloy (Co-17Re-23Cr)

The microstructure of the ST heat treated Co-17Re-23Cr reference alloy is presented in Fig. 1a. The ternary addition of Cr to the Co-Re alloy stabilizes the Cr_2Re_3-type σ phase in the alloy. A small volume of σ phase islands, which has very high hardness (~ 1500 HV) is present at the grain boundaries and also within the grains. It was found that the σ volume fraction increases with increasing Re addition. As can be seen in Fig. 1b, the σ phase particles are brittle and develop cracks due to deformation caused by hardness indentation. It is however, interesting to note that the alloy as such is not inherently brittle. There is large plastic deformation in the matrix, indicated by slip band formation near the hardness

indentation. Moreover, as σ particles are isolated, they do not provide an easy crack path and the alloy can be plastically deformed at room temperature (RT).

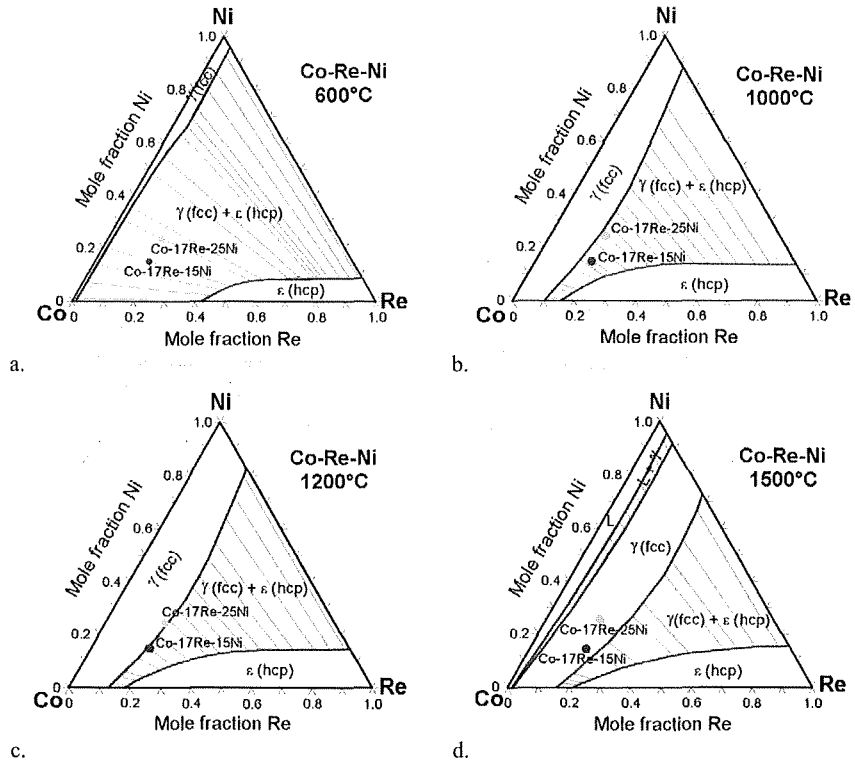

Fig. 2: Isothermal sections of Co-Re-Ni ternary system calculated by Thermo-Calc: a) 600°C, b) 1000°C, c) 1200°C and d) 1500°C. The compositions Co-17Re-15Ni: and Co-17Re-25Ni: i.e. the Cr-free version of alloys corresponding to CoRe-5 and Core-6 are marked in the diagrams.

4.2. CoRe-5 and CoRe-6 alloys (Co-17Re-23Cr + Ni)

The isothermal section of the Co-Re-Ni phase diagram at different temperatures (between 600° - 1500°C) was calculated by Thermo-Calc, and some selected ones are shown in Fig. 2. The ternary compositions Co-17Re-15Ni: and Co-17Re-25Ni: corresponding to the Cr-free versions of the quaternary alloys CoRe-5 and CoRe-6, selected for this study, are marked in these diagrams. Different databases (e.g. ssol2 and TTNi7) were tested for the simulation studies first, and only the TTNi7 database which includes the element Re, gave feasible results and therefore was used for all other calculations (quaternary and multi-component systems). The calculation suggests that both the alloy compositions lie in the two phase (hcp + fcc) field at lower temperatures. With increasing temperature, the fcc phase field expands, such that the matrix in both CoRe-5 and CoRe-6 alloys has the γ fcc structure above 1200°C.

The thermodynamic calculation clearly shows that the ternary Co-Re-Ni alloys are solid solutions of Co and no intermetallics or tcp phases occur. However, when a quaternary addition of Cr is made, the Cr_2Re_3 σ phase becomes thermodynamically stable. In Fig 3 two isoplethal sections from the quaternary Co-Re-Cr-Ni are presented with Co-23Cr-15Ni and Co-23Cr-25Ni and varying Re content. The alloys CoRe-5 and CoRe-6 are marked in Figs 3a and 3b respectively. The calculations show that the 3 phase field containing γ (fcc) and ε (hcp) Co + σ phase extends over a wide temperature range in these compositions. Due to the varying Ni content the proportion of the fcc and the hcp phases are however different in the two compositions, and more fcc phase is stabilized by a higher Ni content.

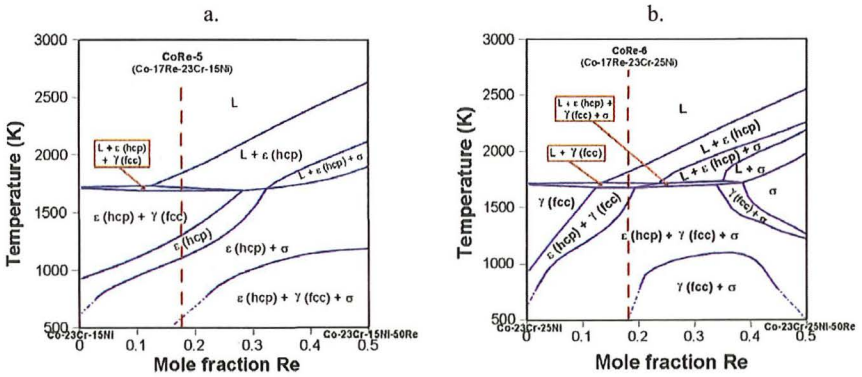

Fig. 3: Isoplethal sections of Co-Re-Cr-Ni quaternary system calculated by Thermo-Calc: a) Co-23Cr-15Ni + Re and b) Co-23Cr-25Ni + Re. The alloy CoRe-5 and Core-6 are marked in the diagrams.

A SEM image from the alloy CoRe-5 in STA1 heat treated condition is presented in Fig. 4a. It represents a typical microstructure of the Co-Re-Cr-Ni alloys in the heat treated condition. It is interesting to observe that fine σ phase is dispersed very homogenously in alloys containing Ni, which is in stark contrast to the ternary Co-17Re-23Cr alloy without Ni (Fig. 1a). More interestingly, the σ phase present in such a fine dispersion, is no more brittle. This is clearly seen in Fig. 4b which shows that no cracks form in the σ particles around the hardness indentation.

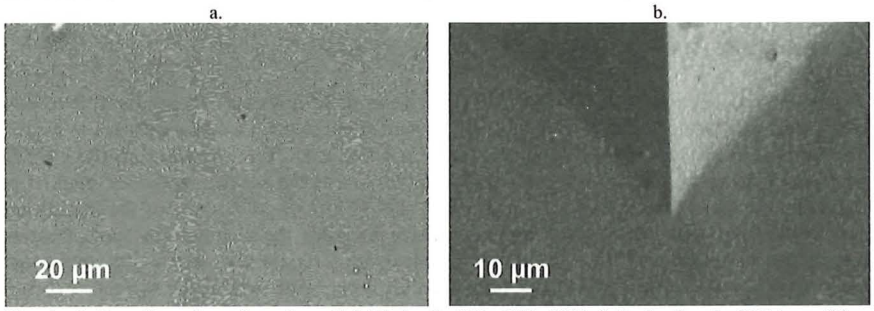

Fig. 4: a) Fine dispersion of σ phase (bright) in Co-17Re-23Cr-15Ni CoRe-5 alloy in STA1 condition. b) Hardness impression in CoRe-5 alloy showing no cracks in σ particles.

4.2.1. Effect of Ni content and heat treatments on σ phase morphology

A careful look at Fig. 4a shows that the σ phase is present in two different forms, i.e. as lamellae and as fine globular particles. CoRe-6 (25 at.% Ni) in general has a larger fraction of σ in the lamellar form than CoRe-5 (15 at.% Ni), see Fig. 5. The σ morphology is affected by the heat treatment temperature, but not by the cooling rate after the ageing. A quantitative measurement of the proportion of the two σ morphologies in different heat treatment conditions was done using the image analysis software – ImageJ [9], to optimize the heat treatments in CoRe5 and CoRe-6. The original SEM image was converted to a binary B & W image by thresholding and the two different morphologies were separated using the "Circularity" function of the particle shape, for measurement (Fig. 6). The evolution of the σ phase morphologies in the two alloys after different heat treatments (ageing and cooling rates) and after long exposure at high temperatures (100-1000 h at 1000°C and 1200°C) were measured (e.g. see below – figures 8 and 9).

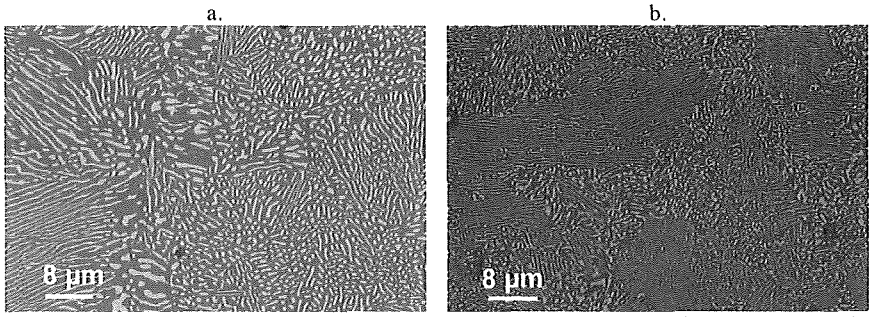

Fig. 5: σ phase present in two different morphologies in a) CoRe-5 STA1 and b) CoRe-6 STA1. The morphology of σ phase is influenced by the Ni content and ageing temperature but not the cooling rate after ageing.

4.2.2. X-ray diffraction

The room temperature X-ray diffraction pattern from alloys CoRe-5 and CoRe-6 in STA conditions are shown in Fig. 7. The measured data was analysed by Rietveld method using the FullProf program [10]. Presence of three phases, namely the γ (fcc) and ε (hcp) Co-Re-Cr solid solution and the Cr_2Re_3 σ phase was necessary to fit the diffraction patterns from both the alloys (Fig. 7). This agrees well with the thermodynamic calculations.

4.2.2. Stability of σ phase at high temperatures

In-situ measurements at high temperatures up to 1300°C by synchrotron and neutron diffractions at the Hasylab and FRMII has shown that σ phase is stable at high temperatures. Further, microstructures after exposures at 1000 and 1200°C for 100h, 300h and 1000h were quantitatively measured in order to monitor the evolution of the σ phase morphology on high temperature exposures. Results shown in Fig. 8 and 9 indicate that the fine σ phase structure is generally stable. There is a coarsening of the globular σ after long exposures at 1200°C.

5. Discussion

Although σ phase is very brittle and is generally a taboo in conventional superalloys, it is seen that their presence in Co-Re based alloys do not render the alloys inherently brittle. In ternary Co-Re-Cr alloys, however, the σ phase is distributed as large (~ 5 to 10 μm) second phase islands at grain boundaries and within the grains. The σ phase is extremely hard and when present in large sizes, cracks occurred in the σ particles during deformation at RT. The cracks however, remained confined within the σ particles and did not propagate through the matrix, which is ductile. Therefore, it is worthwhile as an alloy development strategy to explore the possibility of developing a composite two phase alloy with the very hard σ phase and a ductile Co solid solution matrix. Thermodynamic calculations showed that a quaternary addition of Ni to the Co-Re-Cr system produces stable σ phase over a wide temperature range and also stabilizes some amount of the high temperature γ Co phase in the microstructure.

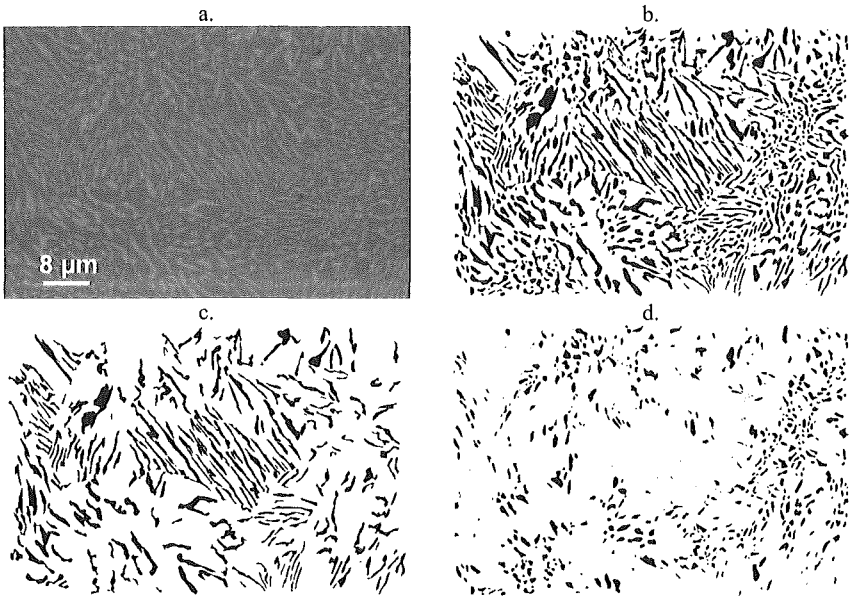

Fig. 6: Measurement of the two σ phase morphologies by image analysis. a) Typical SEM image, b) the binary thresholded image, c) and d) the lamellae and globular σ particles separated using the "Circularity" function.

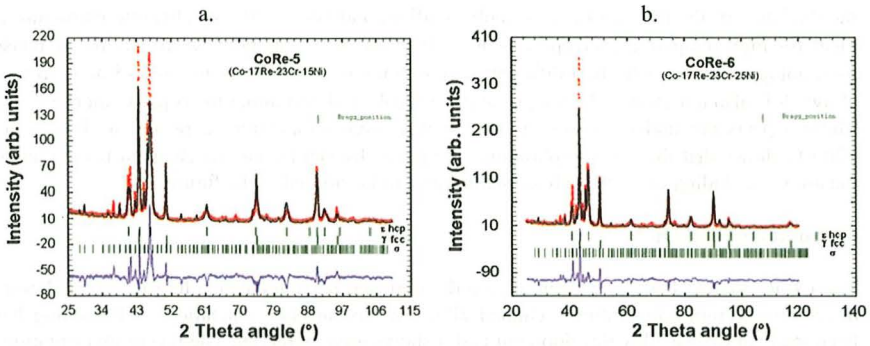

Fig. 7: X-ray diffraction patterns at room temperature: a) CoRe-5 STA1 and b) CoRe-6 STA3, fitted by Reitveld analysis in FullProf programme. 3 phases γ, ε and σ where needed to fit the data completely.

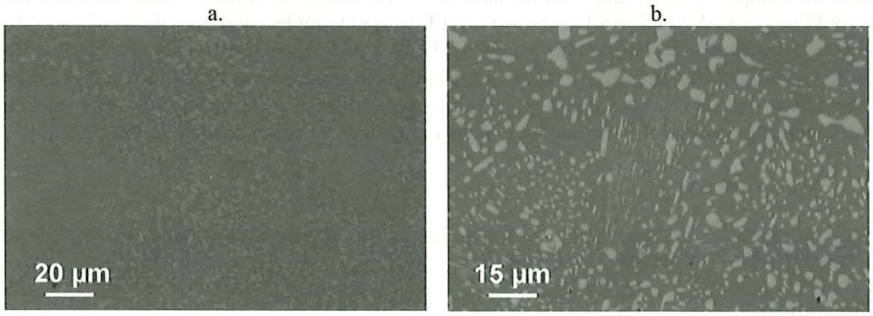

Fig. 8: σ phase morphology after long exposure (300h) at: a) 1000°C and b) 1200°C on CoRe-5 STA1 samples.

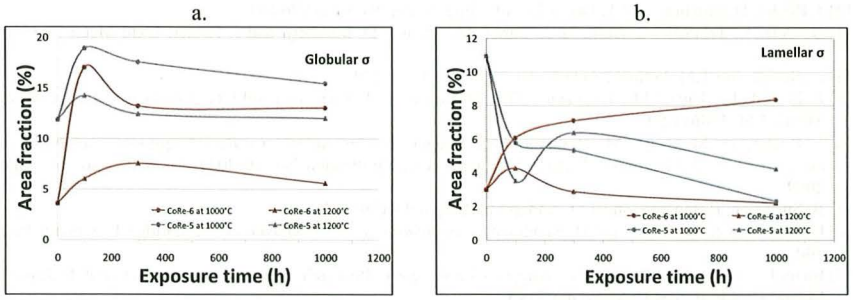

Fig. 9: Stability of σ phase morphologies in CoRe-5 and CoRe-6 on exposure a) 1000°C b) 1200°C; up to 1000h.

Surprisingly, the σ phase in Co-Re-Cr-Ni alloys can be obtained in a fine dispersion with suitable heat treatments. Further, in CoRe-5 and CoRe-6 alloys it is observed that the σ phase has two distinct morphologies (lamellar and globular). The σ particle size (in case of lamellae,

the thickness of the platelets) is extremely small around 100 - 200 nm. This microstructure is ideal for high temperature creep resistance. It is not yet clear how Ni affects the σ phase morphology, or even why two different σ morphologies are present in CoRe-5 and CoRe-6 alloys. It is also not clear if the fcc phase plays a role in determining the σ phase morphology. These aspects are under investigation. However, high temperature exposure to 1000° and 1200°C shows that these σ morphologies are generally stable. The mechanical behaviour of the alloys, including creep at high temperatures will be studied in the future.

6. Summary and Outlook

The Co-Re system has never been explored so far and basic understanding is needed before developing a high temperature technical alloy for gas turbine application. A beginning has been made in Co-Re alloy development and it shows great potential. The recent investigations have identified potential strengthening mechanisms and showed us how the oxidation and the environment embrittlement problems can be addressed. Stage is now set for starting the development of a first generation technical alloy. The results presented here clearly suggest that the composite hardening with σ phase in Co-Re alloys containing Ni has potential and should be pursued. Much work, is however, still needed to understand the role Ni plays in the system. Systematic microstructural study by TEM is also needed to characterise the fcc Co phase and see if it is responsible for the presence of the lamellar σ morphology. Lattice misfit between σ and the fcc and the hcp Co-matrix may have an important role in this respect. Mechanical properties at room and high temperatures will be determined in the future.

7. Acknowledgements

Financial support by the Deutsche Forschungsgemeinschaft in the frame of the research project "Beyond Nickelbase Superalloys" is gratefully acknowledged.

References

[1] M. Heilmaier, M. Krüger, H. Saage, J. Rösler, D. Mukherji, U. Glatzel, R. Völkl, R. Hüttner, G. Eggeler, Ch. Somsen, T. Depka, H.-J. Christ, B. Gorr, and S. Burk, JOM 61 (2009) 61- 67.
[2] J. Rösler, D. Mukherji and T. Baranski, Adv. Eng. Mater. 9 (2007) 876-881.
[3] B. Gorr, V. Trindade, S. Burk, H.-J. Christ, M. Klauke, D. Mukherji and J. Rösler, Oxid Metal 71 (2009) 157-172.
[4] A. Suzuki and T.M. Pollock, Acta Mater 56 (2008) 1288–1297.
[5] E. M. Sokolovskaya, M.L. Tuganbaev, G. I. Stepanova, E. F. Kazakova and I. G. Sokolova, J. Less-Common Metals 124 (1986) L5-L7.
[6] J. Rösler, D. Mukherji, M. Heilmaier, M. Krüger, *Hochwarmfeste Co-Re-B-Legierung: Legierung für mechanisch höchst belastete Bauteile*, German Patent Application No. 10 2009 037 622.4 dtd. 14 August 2009.
[7] B. Sundman, B. Jansson, and J-O. Andersson, Calphad 9 (1985) 153-199.
[8] H. L. Lukas S. G., Fries and B. Sundman, *Computational Thermodynamics*, Cambridge University Press, 2007.
[9] ImageJ – by Wayne Rasband (wayne@codon.nih.gov), Research Services Branch, National Institute of Mental Health, Bethesda, Maryland, USA.
[10] J. Rodriguez-Carvajal, Physica B 192(1993) 55-69.

9th Liege Conference : Materials for Advanced Power Engineering 2010
edited by J. Lecomte-Beckers, Q. Contrepois, T. Beck and B. Kuhn.

ANALYSIS OF HAYNES 230 CREEP BEHAVIOUR

M. Maldini, G. Angella, and V. Lupinc

CNR – IENI, Via Cozzi 53, 20125 Milano, Italy

Abstract

The creep behaviour of Haynes 230, a solid solution and carbide strengthened nickel-based superalloy, has been investigated in the temperature range 750-1000°C under constant and variable load. The creep tests have been performed on as received alloy, after the conventional solution treatment. A few creep tests have been run on overaged specimens in order to evaluate the effect of the carbide evolution, on the creep curve shape.
The experimental results have shown a very strong dependence of the creep curve shape with the testing stress/temperature conditions. In general, in the tests performed at high stresses/low temperatures, the primary/decelerating stage takes an important portion of the creep curves and the accelerating creep is mainly caused by the increase of the applied stress with the strain as it happens in constant load creep tests. In the tests performed at low stresses/high temperatures, the primary decelerating stage is very small, often negligible and the accelerating creep dominates the creep curve. The analysis of the creep curves on the as received and overaged alloy has shown that a great portion of the accelerating creep at low stresses/high temperatures is caused by microstructural instability. Detailed studies of the microstructural changes taking place in the alloy have been made using Scanning Electron Microscopy (SEM) with Energy Dispersion Spectroscopy (EDS) and Transmission Electron Microscopy (TEM).

Keywords: Haynes 230, creep, microstructure evolution.

1. Introduction

Not only the time to rupture, but also the shape of the creep curves can dramatically depend on testing conditions. A change in the creep curve shape reflects a change in the relative importance of the factors influencing the strain rate at different applied stresses/temperatures: for example a microstructure instability, like precipitation/evolution of reinforcing particles, strongly depending on the testing temperature, or the activation of different stress/temperature depending creep and damage mechanisms. This paper reports the creep behaviour, in the temperature range 750-1000°C, of Haynes 230, a solid solution and carbide strengthened nickel base superalloy with excellent high temperature strength and resistance to oxidation [1]. The initial microstructure of the alloy, characterized by the presence of primary Cr rich carbides that stabilize the grain size and big W rich carbides in the γ matrix, can change during high temperature service. In particular further carbides precipitation happens and they evolve both in composition and type [2, 3], influencing mechanical properties. The present paper is focused on the microstructure evolution assessment and on the shape of the creep curves, more than on the creep strength, in order to understand the creep mechanisms and the contribution of the microstructural evolution on the creep behaviour.

2. Experimental procedures

The creep tests have been carried out on cylindrical specimens having 5.6 mm gauge diameter and 27 mm gauge length supplied by Siemens. The specimens were machined off from a 38 mm thick sheet that has been solution annealed.

Creep strain was continuously monitored using capacitive transducers connected to extensometers clamped to the ridges delimiting the specimen gauge length. Three thermocouples were placed on the gauge length in order to control the presence of any temperature gradient along the specimen gauge. The furnace was controlled by the central thermocouple. All creep tests were performed in air at constant load. All strains in this report are true strains.

Material microstructure investigation was obtained through scanning electron microscopy (SEM) with Energy Dispersion Spectroscopy (EDS) on the as-received condition and crept specimen sections parallel to the loading direction. The surfaces were mechanically polished and electrolytically etched with 60% H_2O + 40% HNO_3 at T_{Room}. Transmission Electron Microscopy (TEM) investigations were performed on as-received and crept Haynes 230 in order to investigate the fine microstructure evolution in the alloy after creep. The thin foils for TEM observations were obtained electrolytically through using the electrolyte 10% percloric, 35% butyoxyethanol and 55% methanol at -50°C and an applied voltage in order to have a current of about 1 mA.

3. Microstructure stability investigations

The Haynes 230 microstructure in as-received conditions is reported in Fig. 1. The alloy is a nickel based superalloy with the average grain size of 5.5 ASTM. The chemical composition of the studied heat is reported in Table 1 and compared to Inconel 617 alloy. Scanning electron microscopy (SEM) observations has shown that fine precipitates at the grain boundaries and big precipitates in the γ matrix that are elongated reminding the rolling direction. EDS analysis found that the fine precipitations at the grain boundaries were carbides rich in Cr, whilst in the γ matrix the carbides were rich in W.

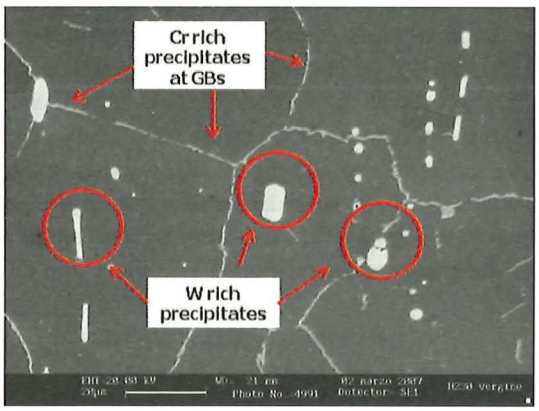

Fig. 1 – Haynes 230 microstructure: small carbides rich Cr at the grain boundaries and big primary carbides rich in W in the γ matrix. SEM micrograph in secondary electron imaging (SEI) mode.

*Table. 1 – Chemical composition of the here studied Haynes 230 superalloy and the nominal composition of IN617 (weight %, * maximum) for comparison.*

	Ni	Cr	W	Mo	Fe	Co	Mn	Si	Al	Ti
HA230	Balan.	22.33	14.32	1.3	1.37	0.24	0.52	0.40	0.33	<0.01
IN617	Balan.	20-24		8-10	3*	10-15	1*	1*	0.5-0.8	0.6*

	C	La	B	Cu	S	P
HA230	0.10	0.015	<0.003	0.01	<0.002	<0.005
IN617	0.05-0.15		0.006*		0.015*	

The microstructure evolution was investigated through SEM in the material of Haynes 230 after different creep testing conditions. In Fig. 2a the microstructure of the alloy after 2507 h (rupture time) at 800°C with a nominal initial stress of 85 MPa is reported, whilst in Fig. 2b the microstructure of the alloy after 377 h (rupture time) at 1000°C with a nominal initial stress of 23 MPa. The precipitation appeared to be quite evolved at 800°C and dramatically changed at 1000°C with respect to the as-received conditions. At 800°C the Cr precipitation at the grain boundaries is less continuous in distribution and the primary W rich precipitation fraction in the matrix is not changed appearing quite stable. At 1000°C the precipitation is very significant and Cr rich and W rich carbides are both found at the grain boundaries, whilst the primary W rich carbides are still visible in the γ matrix. The temperature seems to have dramatic effects on the microstructure stability.

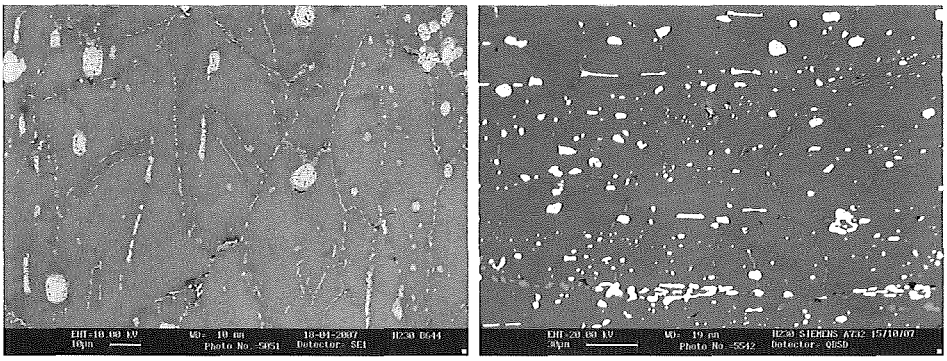

(a) (b)

Fig. 2 – Haynes 230 microstructure (a) after 2507 h (rupture time) at 800°C with a nominal initial stress of 85 MPa is reported; (b) after 377 h (rupture time) at 1000°C with a nominal initial stress of 23 MPa.

TEM observations on the as-received alloy revealed that no fine precipitation was present in the matrix. Focussed investigations at the grain boundaries, reported in Fig. 3a, resulted that the fine precipitation at the grain boundaries was $M_{23}C_6$, in accordance with the rich in Cr carbides observed in SEM. As reported in Fig. 3b the diffraction pattern revealed a cube-cube relationship, i.e. {001}γ // {001}precipitate, between precipitates at the grain boundaries and matrix, which is typical of Cr rich $M_{23}C_6$ carbides.

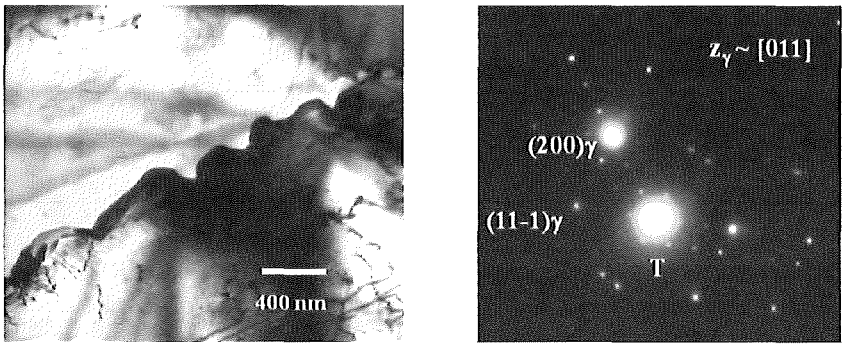

(a) (b)

Fig. 3 – TEM micrographs from (a) as-received Haynes 230 at the grain boundaries revealing fine precipitation; (b) selected area diffraction pattern from carbide at the grain boundary: γ matrix zone axis z_γ = [011].

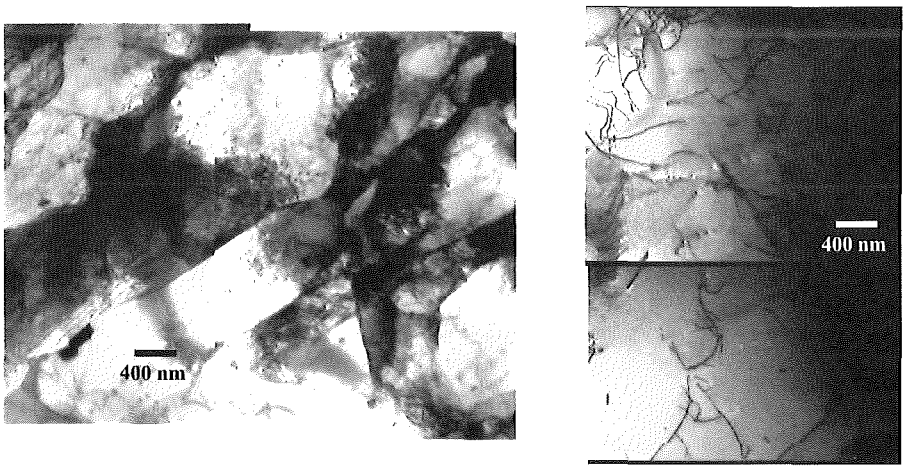

(a) (b)

Fig. 4 - TEM micrographs of Haynes 230 from (a) crept at 800°C with an initial stress of 85 MPa and time to rupture 2507 h; (b) crept at 1000°C with an initial stress of 23 MPa and time to rupture 377 h.

Microstructure micrographs obtained through TEM from selected creep conditions are reported in Fig. 4. In Fig. 4a the structure of the alloy after 2507 h (rupture time) at 800°C with a nominal initial stress of 85 MPa is reported. In the matrix, no fine precipitation was observable in the resolution limit of the microscope whilst dislocation cells were found. In Fig. 4(b), the microstructure of the alloy after 377 h (rupture time) at 1000°C with a nominal initial stress of 23 MPa is shown. Also at higher temperature there was no presence of fine microstructure in the matrix and there were dislocation cells.

In both cases big precipitates were observed at the grain boundaries, quite often not transparent to the electrons. However, when it was possible to index them through diffraction pattern analysis, they were found to be $M_{23}C_6$ carbides.

4. Constant load/temperature creep tests: results and discussion

The temperature explored were 750, 800, 900 and 1000°C (Fig. 5) and the stresses were selected in the range 14-200 MPa in order to produce times to rupture up to 3000 h.

The experimental results exhibited a very strong dependence of the creep curve shape with the tests conditions, as evident in the log $\dot{\varepsilon}$ vs. ε plots of Fig. 5. In the tests performed at 750 and 800°C the primary/decelerating stage tends to become more important with the decreasing of the applied stress: at the lowest stresses, it can end at creep strains around 10%, corresponding to 30-40% of the creep life.

A quite large and long primary/decelerating creep is also exhibited by the creep curves performed at 900°C and applied stresses of 60 and 55MPa. At lower stress, 50MPa/900°C and in all the tests at 1000°C, the shape of the decelerating stage drastically changes: a large strain rate decrement happens in the first few percent of the creep life and after having accumulated a creep strain that can be as small as 0.1% which can be hardly detected in a plot strain vs. time. For these test conditions, the accelerating stage resulted to dominate the creep curves.

At all the explored temperatures, the decelerating stage is not followed by a steady state, as generally reported on the textbooks, but rather by an accelerating stage. In the tests performed at 750 and 800°C, when the decelerating stage takes an important portion of the creep curves, the accelerating stage continuously goes on preserving a positive curvature in a plot log $\dot{\varepsilon}$ vs. ε up to the rupture. In the tests at 1000°C and at 900°C/50MPa, the tertiary creep is characterized by different accelerating creep stages: a strongly accelerating stage appears after the minimum creep rate, followed by a stage with lower slope, then the strain rate continuously increases up to the specimen fracture as it happens in the tertiary stage of the tests performed at 750-800°C.

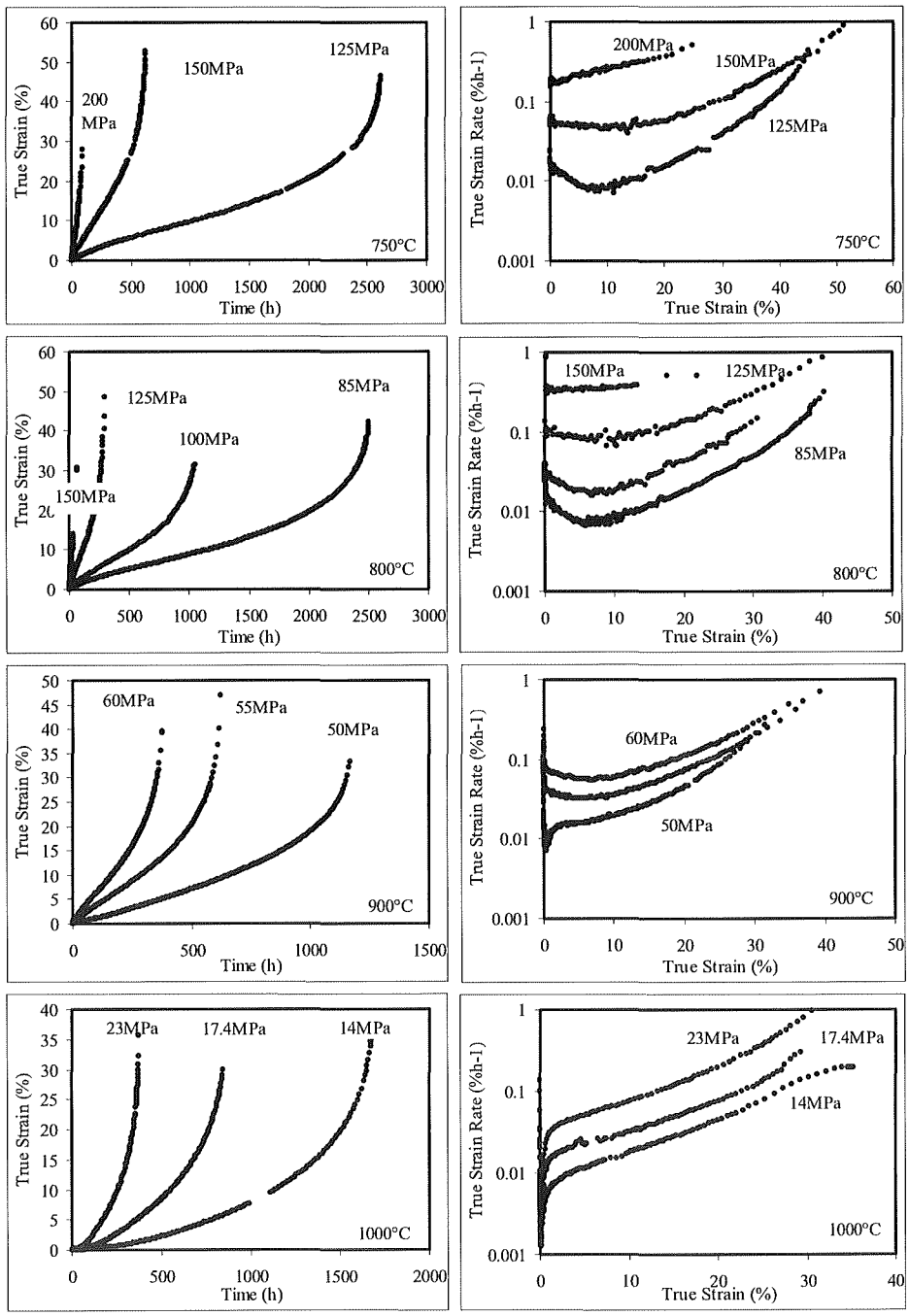

Fig. 5 – Creep curves : true strain vs. time and log (true strain rate) vs. true strain.

4.1 Tertiary/accelerating creep

Among the damage mechanisms producing strain acceleration, grain boundary cavitation cannot explain the convex shape of the accelerating stage exhibited in the log (strain rate) vs. strain plots in Fig. 5 appearing in the tests run at 1000°C. Specifically they cannot be responsible of the rapid increment of strain rate after having accumulated only a small creep strain. The cavitation, with the localised necking, seems to play an important role in a more advanced stage, producing marked creep acceleration close to the final fracture.

In order to understand if the growth/dissolution of carbides is the main responsible of the experimental strong acceleration, creep tests at 17MPa/1000°C and 50MPa/900°C have been performed on overaged material. The overaging consisted in furnace heat treatment, without applied load, of 500h/1000°C for the specimen tested at 17MPa/1000°C and 2000h/900°C for the specimen tested at 50MPa/900°C.

In Fig. 6 are compared the creep curves obtained on as received and overaged material. It is evident the rapid acceleration following the minimum creep rate disappears in the overaged material that indicates, unlike the behaviour of as-received material, a more stable microstructure behaviour during the creep test.

The creep tests have been performed at constant load, and then some creep acceleration, not associated to a real damage in the material, is due to the increment of the applied stress with the strain. In fact, during creep tests, the true applied stress, σ, increases in a uniformly deforming specimen, with the true strain as: $\sigma = \sigma^{\circ} \exp(\varepsilon)$ where σ° is the engineering/initial applied stress.

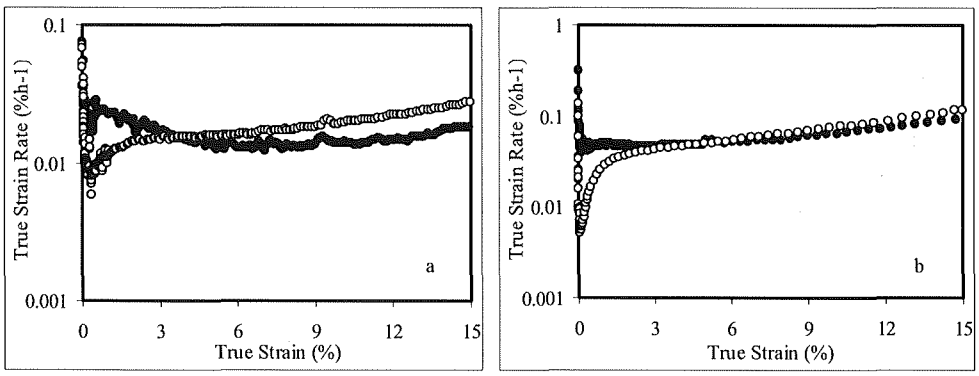

Fig. 6 – Comparison of the creep curves performed at 50MPa/900°C (a) and 23MPa/1000°C (b), on virgin (◦) and overaged material(•) (Overaging: 2000h at 900°C(a), 500h at 1000°C (b)).

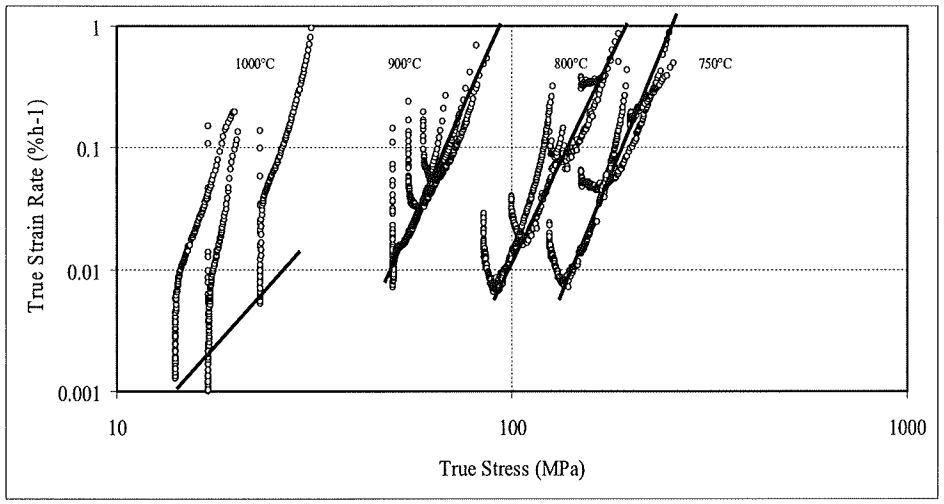

Fig. 7 – True strain rate vs. true stress at different temperatures. The straight lines represent the linear interpolation of the minimum creep rate at the four explored temperatures.

The contribution of the increasing applied stress with strain in accelerating the creep can be estimated in the plot of Fig. 7 where the creep curves are reported in terms of true strain rate vs. true stress.

A clear difference in the character of the accelerating creep appears between tests performed at 1000°C and tests performed at lower temperatures: for the tests performed in the temperature range 750-900°C, the accelerating portion of the creep curves, after the minimum creep rate, tend to overlap. This result suggests that, during the accelerating stage, the strain rate is mainly a function of the *true* applied stress and then, in these stress/temperature ranges, the accelerating strain is mainly due to the increment of the stress with the strain. No other damage mechanisms, depending on strain or time, seem to strongly influence the strain rate.

For the tests performed at 1000°C and at 900°C at the lowest stress, it is evident that the contribution of applied stress increment with strain to the creep acceleration is low, indicating that one or more material damage mechanisms, mainly the microstructure instability at such high temperatures, produce most of the strain rate increment.

4.2 Primary/decelerating creep

In the tests run at the lowest temperatures, mainly at 750 and 800°C, the initial portion of the creep curves is generally associated to a strong hardening of the alloy, overcompensating the effect of the stress increment with the strain. The resulting creep curves are characterized by a decelerating creep stage up to a minimum creep rate, reached after having accumulated a large creep strain, when the hardening mechanisms are close to be saturated.

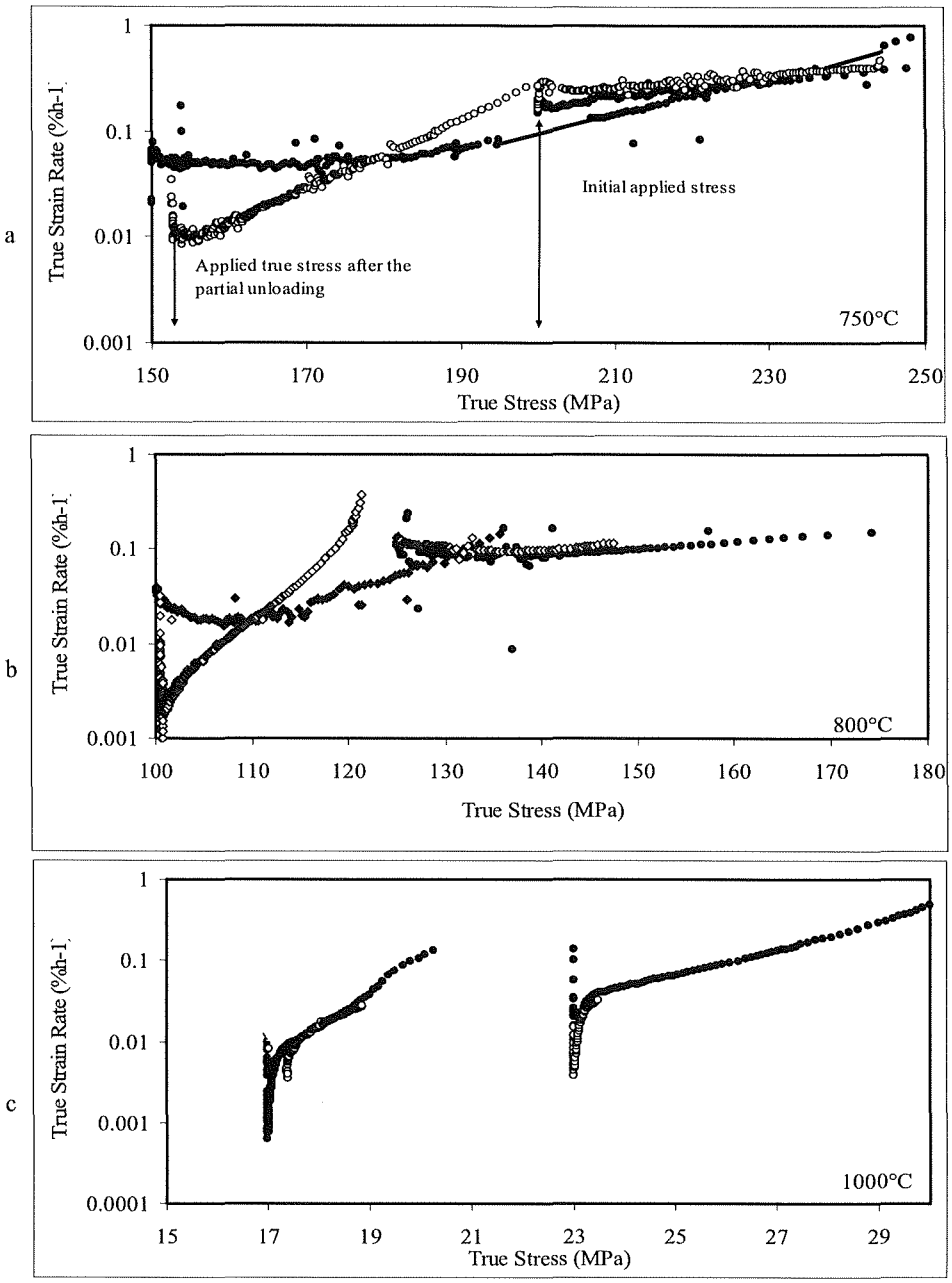

Fig. 8 Comparison of experimental step-like decreasing creep curves (open points) with reference constant load creep tests (see text).

In the tests performed at the highest stress at 750 and 800°C, the creep curves do not exhibit any primary/decelerating stage; they consist instead of a tertiary stage characterized by an acceleration (750°C/200MPa) or of a steady state like stage (800°C/150MPa). The analysis of the results suggests, for these two tests, that the hardening processes are overcome, since the first creep, by the increment of the true stress with the strain. In fact the slopes of these two curves in Fig. 7 are ***lower*** then expected by the increment of the stress with strain. All the tests should indeed exhibit a long decelerating stage if performed at constant stress.

To confirm the hardening of the material during the initial portion of the creep tests at the highest stresses, a few creep tests at step-like decreasing load have been performed: after spending about half of the creep life at high stresses at 750, 800 and 1000°C, the load was step decreased. The experimental results are plotted as true strain rate vs. true strain in Fig. 8, where reference constant load creep tests are also reported.

For the tests performed at 750 and 800°C, after the step like load decrement, the strain transient is characterised by a very short and small strain rate decreasing stage, down to a minimum value, followed by a strain acceleration. After the initial transient decelerating stage, the minimum creep rate (MCR) lies below the MCR of the reference constant load creep test performed at the final stress. This result suggests the strain accumulated at high stress has hardened the material.

A different result has been obtained for the test run at 1000°C (Fig. 8c): the strain accumulated at high stress does not significantly harden the material: in fact, after the step decreased load, the creep curve seems to overlap the reference constant load creep test. This result suggests the dislocations produced during the strain accumulated at high stress are free to move and do not obstruct the strain accumulation after the stress decrement.

Conclusions

The creep curve shape of the Haynes 230 superalloy strongly depends on the applied stress and temperature.

At low temperatures, the creep curves are characterized by an important decelerating/primary stage. It can end at creep strains around 10%. In these tests, with a large primary stage, the main reason of the tertiary creep seems to be the increment of the stress with strain that always happens in constant load creep tests.

In the creep tests performed at 1000°C, primary creep ends after having accumulated small strain: around 0.1%. The whole creep curve is dominated by a long accelerating creep. The evolution of the microstructure seems to play an important role to describe the accelerating creep at the highest temperatures.

Acknowledgements: The authors would like to thank the Siemens Industrial Turbomachinery LtD., Lincoln, UK to have supplied the Haynes 230 specimens. The authors are grateful to E. Signorelli for his valuable help in experimental work.

References

[1] Haynes International, Haynes 230 Alloy Product Brochure. www.haynesintl.com.

[2] J. Veverkova, A. Strang, G.R. Marchant, G.M. McColvin and H.V. Atkinson, in: Superalloy 2008, edited by R.C.Reed et al., The Minerals, Metals and Materials Society, Seven Springs, Pennsylvania, USA (2008).

[3] G. Angella, V. Lupinc, M. Maldini, M. Pojaghi, E. Signorelli and A. Stefanuto, in COST 538 High Temperature Plant Lifetime Extension, WP3 Superalloy degradation, "Microstructural evolution and creep behaviour of alloys for gas turbines, Commission of European Communities, Brussels, Belgium.

9th Liege Conference : Materials for Advanced Power Engineering 2010
edited by J. Lecomte-Beckers, Q. Contrepois, T. Beck and B. Kuhn.

DESIGNING OF INTERMETALLIC Ni_3Al-BASED SUPERALLOY

E.N. Kablov, N.V. Petrushin, R.M. Nazarkin

All-Russian Scientific-Research Institute of Aviation Materials (VIAM), Moscow, Russia

Abstract

The influence of alloying elements, including tantalum, tungsten and molybdenum on the physicochemical parameters and mechanical properties of Ni_3Al-base superalloys has been analyzed. A regression model for calculation of characteristics of alloys has been obtained. Results are used at computer designing of the single crystal alloy containing 90-95 vol.% of γ′-phase. <001> single crystals of the designed intermetallic superalloy were produced by the LMC method and investigated in as-cast condition. The investigations included: characterization of the superalloy microstructure, the γ′-lattice spacing, solidus, liquidus, strength and ductility in the temperature interval of 20–1200 °C.

Keywords: Intermatallic Superalloys, γ′-phase, Computer Designing

1. Introduction

Now in many research centers works on creation of constructional materials on the base of intermetallics are developed. Nickel and titanium aluminides, niobium intermetalics are the most perspective materials for high-temperature application. Ni-base superalloys VKNA-4Y, VKNA-1V (VIAM, Russia) intended for manufacturing gas turbine engine single crystal blades and vanes by DS method with cooling in aluminum melt (LMC method) relates to intermatallic materials on the base of Ni_3Al [1]. These alloys have high content of aluminum (up to 8.5 wt.%) and due to this fact the volume fraction of γ′-phase increases up to 85-90 vol.% that provides thermal stability of structure up to 1250 °C and good oxidation resistance. The present paper explains the physicochemical principles used by the authors in the development of Ni_3Al-base superalloys for manufacturing single-crystal blades for aviation gas turbine engines. To increase the efficiency of a new alloy development a method of computer design was used. The basis of this method are regressive models of "composition-property" type to for calculate the phase composition and material properties (for example, γ′-phase volume fraction, chemical composition of γ- and γ′-phases, γ′-lattice spacing, phase transformation temperatures etc) [2].

2. Results and discussion of experiments

2.1. Influence of alloying elements on physicochemical parameters and strength of intermetallic alloys

Corresponding experimental research was carried out for the intermetallic Ni_3Al-base superalloys γ′+γ system of Ni–Al–Cr–Ta–W–Mo. In the given alloying system the concentration of alloying elements Ta, W, Mo was broken into two levels: minimum and maximum for Ta – 1.0 and 8.0 wt.%, for W – 1.0 and 8.0 wt.%, for Mo – 1.0 and 5.0 wt.% respectively. Further, the complete factorial experiment (CFE) was described by a design matrix of 2^n+2n+1 type, where n = 3 number of the variable alloying elements without aluminum, chromium and nickel. In all compositions the nominal content of aluminum and chromium has been 8 and 3 wt.% respectively.

Compositions of all 2^n+2n+1 (n = 3) alloys were melted in the vacuum furnace. After remelting of these alloys bars of the specimens with conventionally grains has been obtained from the alloys. Thermal treatment of bars, including homogenization at 1200 °C for 4 hours was performed for microstructure optimization.
Solidus T_S and liquidus T_L temperatures of alloys were measured by DTA method (heating rate of specimens 5 K/min).
Mechanical tensile properties of alloys (ultimate strength, yield strength, relative elongation) were measured using MTS-810 machine at a strain rate of 1 mm/min in the temperature range of 20–1200 °C by standard method.
The phase precipitation were analyzed using SEM/EDX for all the alloys. X-ray structure analysis of alloys was carried out with X-ray diffractometer at monochromatic Fe-Kα radiation. For precision definition of γ′-lattice spacing and γ-lattice spacing the reflex (222) has been chosen. Diffraction pattern record has been executed using computer program EXPRESS, division of reflexes γ/γ' was executed using computer program OUTSET.
As a result of statistical processing of experimental data of all experiments the regression equations (models) for designing of characteristics and properties of intermetallic γ'+γ alloys for system Ni–Al–Cr–Ta–W–Mo have been obtained:

$$T_S = 1401-4.4\cdot C_{Ta}-1.1\cdot(C_{Mo})^2-0.2\cdot(C_W)^2,\ °C \quad (1)$$

$$T_L = 1425+2.9\cdot C_W-5.3\cdot C_{Mo}-0.2\cdot C_{Ta}\cdot(C_{Ta}+2\cdot C_W),\ °C \quad (2)$$

$$\sigma_{0.2}^{20} = 492.6-C_{Ta}\,(103.6\cdot-5.4\cdot C_W-5.9\cdot C_{Mo}-8.5\cdot C_{Ta})-C_W\cdot(19.7-4.1\cdot C_{Mo}),\ MPa \quad (3)$$

$$\sigma_B^{1200} = 34.1+C_{Mo}\,(9.4+1.2\cdot C_W)+0.8\cdot(C_{Ta})^2,\ MPa \quad (4)$$

$$a_{\gamma'} = 0.3561+0.00012\cdot C_{Mo}+0{,}00002\cdot C_W+0{,}00017\cdot C_{Ta},\ нм \quad (5)$$

Where T_S is the solidus temperature, T_L the liquidus temperature, $\sigma_{0.2}^{20}$ the yeld strength at 20 °C, σ_B^{1200} the ultimate strength at 1200 °C, $a_{\gamma'}$ the γ′-lattice spacing at 20 °C. The element concentrations C_i (i = Ta, W, Mo) in (1–5) are taken in wt.%.
The analysis of models (1–5) shows that alloying elements Ta, W, Mo have ambiguous effect on characteristics of intermetallic alloys. So additives of Ta, W, Mo decrease solidus temperature of the alloys, however tantalum and molybdenum has defining influence on this characteristic.
Tantalum and tungsten has stronger positive effect on yield strength (20 °C), molybdenum has weaker effect on this characteristic. At the same time molybdenum and tantalum content has stronger effect on ultimate strength at 1200 °C (4) and tungsten has weaker effect on this characteristic.
It is established that there is a good correlation between strength of studied alloys and γ′-lattice spacing: yield strength and ultimate strength of Ni_3Al-base superalloys increases at increasing of the lattice spacing of the phase (Fig. 1) that, in turn, correlates with the content of alloying elements Ta, W, Mo (see Eq. 5).

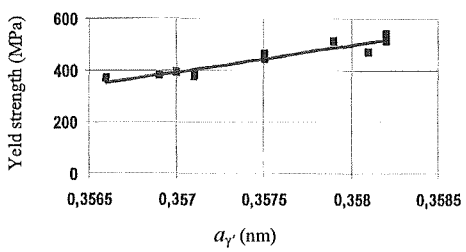

Figure 1a. The effect of γ'-lattice spacing on the yield strength at 20 °C of Ni_3Al-base superalloys

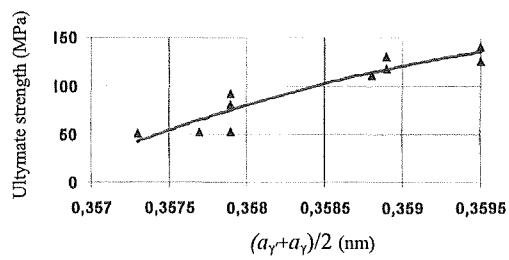

Figure 1b. The effect of γ'-lattice spacing and γ-lattice spacing on the ultimate strength at 1200 °C of Ni_3Al-base superalloys

2.2. Alloy design

Optimization of the intermetallic superalloy γ'+γ composition was carried out for nickel-base system Ni–Al–Cr–Ta–W–Mo by the method of computer design described in [2]. For the given alloying system initial conditions of designing have been formulated: a volume fraction of γ'-phase 90-95 vol.%, density of the alloy less than 8.5 $g \cdot cm^{-3}$, solidus temperature more than 1350 °C, liquidus temperature less than 1400 °C, the γ'-lattice spacing more than 0.358 nm, acceptable phase stability, etc. The algorithm of this method consists in following. In the chosen alloying system the concentration of each alloying element was broken into two levels: minimum and maximum. The CFE was described by a design matrix of 2^n type, where $n = 5$ are number of the main alloying elements without nickel.
The compositions of all 2^n alloys were evaluated by parameter ΔE [3]:

$$\Delta E = E_{alloy} - E_0 \text{ with } E_0 = 6.28 + 0.036 A_{alloy} \qquad (6)$$

where $A_{alloy} = \sum_{i=1}^{n} A_i C_i$ is the average atomic mass of alloying element in mole, $E_{alloy} = \sum_{i=1}^{n} E_i C_i$ the average number of valence electrons, A_i, E_i and C_i respectively the atomic mass, number of valence electrons and atomic concentration of i-element.
The equation for parameter E_0 in (6) is obtained by regression of the experimental data on phase composition for a large group of different nickel-base superalloys.
In coordinates $E_0 - A_{alloy}$ the parameter E_0 determines the boundary of phase stability of the γ/γ'-microstructure of a nickel-base superalloy. For commercial nickel-base superalloys the value of E_{alloy} usually differs slightly from E_0 by $\pm\Delta E$, called the "alloying imbalance". The sign and value of ΔE determines the probability of formation of different undesirable phases. For example, in alloys with a large negative alloying imbalance ($\Delta E < 0$) the probability of formation of carbides such as M_6C or TCP phases is high. Alloys with $\Delta E > 0$ are disposed to form such phases as Ni_3Ti and Ni_3Nb or eutectic (peritectic) phases on the base of Ni_3Al. If $\Delta E = 0$ the alloy is accepted as a balanced one.
In this work the intermetallic alloy γ'+γ composition was accepted as a balanced (i.e. the alloy has only γ'- and γ- phases) if the condition $\Delta E = \pm 0.04$ was fulfilled. The physicochemical and mechanical characteristics of the alloy were calculated by equations (1–5). Some

equations obtained in [2] were used in work for calculated of phase structure, γ'-lattice spacing, density etc parameters of the alloy:

$$a_{\gamma'} = 0.35691+0.000014\cdot C_{Cr}+0.000097\cdot C_{Mo}+0.000151\cdot C_{W}+0.000398\cdot C_{Ta}-0.000002\cdot C_{Co}+ 0.000275\cdot C_{Nb}+0.000149\cdot C_{Ti}-0.000189\cdot C_{V}-0.000504\cdot C_{Re}+0.000083\cdot C_{Ru}+ 0.001339\cdot C_{Hf}, \text{ nm} \quad (7)$$

$$F_0 = 14.7+0.54\cdot C_{Al}+1.07\cdot C_{Cr}-1.27\cdot C_{Mo}+0.23\cdot C_{W}+4.96\cdot C_{Ta}+0.31\cdot C_{Co}+2.54\cdot C_{Nb}+ 3.81\cdot C_{Ti}-0.75\cdot C_{Re}-3.11\cdot C_{V}+1.87\cdot C_{Hf}-1.91\cdot C_{C}+0.17\cdot (C_{Al})^2-0.08\cdot (C_{Cr})^2, \text{ vol.\%} \quad (8)$$

$$\rho = 0.144\cdot A_{alloy}, \text{ g}\cdot\text{cm}^{-3}. \quad (9)$$

Where F_0 is the γ'-volume fraction at 850 °C, ρ the alloy density. The element concentrations in (7, 8) are taken in at.%.
The chemical composition of γ'-phase of the chosen alloy $\gamma'+\gamma$ is presented in Table 1. Table2 gives some physicochemical characteristics predicted for this alloy in comparison with the experimental data.

Ni	Al	Cr	Mo	W	Ta
Base	18.3	0.9	0.4	1.5	3.7

Table 1. Chemical composition of γ'-phase for designed alloy $\gamma'+\gamma$ (at.%)

	Designed	Experimental
Physicochemical characteristics:		
ρ (g·cm^{-3})	8.469	8.5
T_S (°C)	1352	1365
T_L (°C)	1391	1392
Structural characteristics:		
F_0 (vol.% at 850 °C)	96	-
$a_{\gamma'}$ (nm at 20°C)	0.358	0.3573
Phase stability parameter:		
ΔE	0.038	-
Mechanical properties:		
$\sigma_{0.2}^{20}$ (MPa)	531	369
σ_{B}^{1200} (MPa)	129	256
Note: designed values of characteristics and properties are given for the alloy with conventionally grains structure, experimental values – for the <001> single crystals.		

Table 2. Parameters of structure and properties of designed alloy $\gamma'+\gamma$

2.3. Solidification of single-crystals

Single-crystal bars (∅ 16 mm and length 185 mm) with crystallographic direction <001> (deviation within 10 degrees) of the designed superalloy $\gamma'+\gamma$ were produced by the LMC method (liquid metal cooling) in full-scale plant. The <001> growth was initiated by a seed of a high temperature Ni-W alloy placed in a special cavity of the ceramic mould.

2.4. Microstructure

After the directed solidification the single-crystal bars of the alloy have a cellular macrostructure (Fig. 2a).

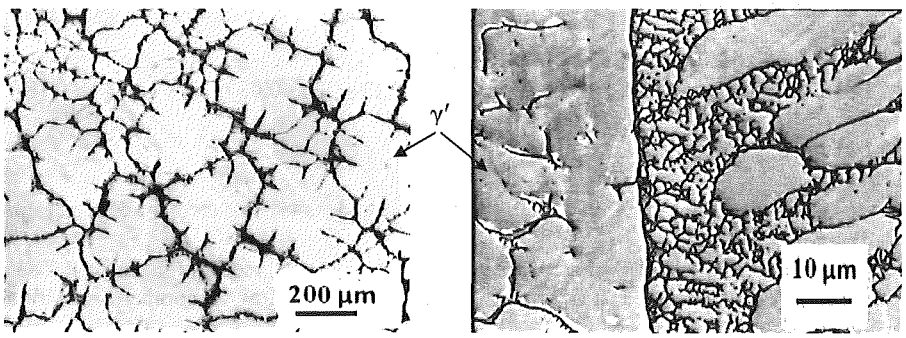

a) *b)*

Figure 2. Structure of intermetallic alloy γ'+γ after the directed solidification (cross-section of the <001> single crystal):
a – crystallites of γ'-phase; b – heterophase layers γ+γ'

The microstructure of single crystals consists of columnar crystallites of γ'-phase with preferred orientation <001> (linear size in cross-section is 300-400 μm). Crystallites of γ'-phase have parameter of a crystal lattice of 0.3573 nm, they are surrounded by heterophase layers of alloy γ+γ' (Fig. 2b). In layers γ+γ' particles of a phase γ' have globular shape; the size of particles makes 1–10 μm. According to DTA data solidus temperature of the alloy makes 1365 °C, liquidus temperature makes 1391 °C. The chemical composition of γ'-phase crystallites is given in Table 1.

2.5. Strength and tensile ductility

The temperature dependences of ultimate and yield strengths and relative tensile elongation of <001> single crystals of intermetallic alloy are shown on Fig. 3. It is obvious that single crystals of intermetallic alloy γ'+γ as well as Ni_3Al, have abnormal dependence of ultimate strength and yield strength on temperature. With increase in temperature ultimate strength and yield strength increases from 770 and 369 MPa accordingly at 20 °C up to 903 and 840 MPa at peak temperature 700800 ° C and decreases up to 256 and 231 MPa at temperature 1200 °C.
Ductility of <001> single crystals of intermetallic alloy γ'+γ goes down to 5–6 % at increase in temperature up to 600 °C and remains constant at increase in temperature up to 1200 °C.

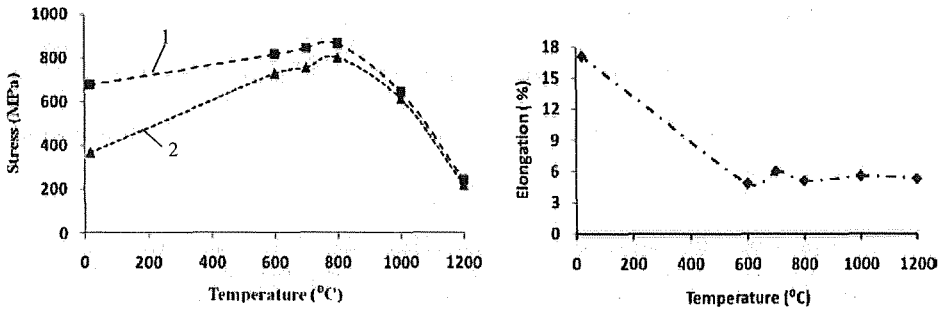

a) *b)*

Figure. 3. Dependence of tensile strength of characteristics of <001> single crystals of intermetallic alloy γ'+γ on temperature:
a –ultimate strength σ_B (1), yield strength $\sigma_{0.2}$ (2);
b- relative elongation

3. Conclusions

1. New single crystal intermetallic superalloy γ'+γ containing approximately 95 vol.% γ'-phase has been designed using calculations of phase structure, physicochemical and structure-phase characteristics of alloys on the Ni_3Al-base for system Ni–Al–Cr–Ta–W–Mo. To improve phase stability and increase mechanical properties the total content of refractory (Ta, W, Mo) and γ'-forming (Al, Ta) elements in an alloy has been balanced.
2. Single crystals <001> of the alloy after the directed solidification have the cellular macrostructure, their microstructure is formed by columnar crystallites γ'-phase. Layers between crystallites γ'-phase are filled with heterophase γ+γ' alloy.
3. Single crystal intermetallic superalloy with density 8.5 g·cm-3 and solidus temperature 1365 °C have a good relation of strength and ductility within the interval of 20–1200 °C.

References

[1] Buntushkin V.P., Kablov E.N., Bazyleva O.A., Mechanical and operating properties of a casting superalloy on the base of intermetallic Ni_3Al, *Metals*, 3, (1995), 70–73.
[2] Kablov E.N., Petrushin N.V., Computer method of designing casting nickel-base superalloys, in *Casting Superalloys: Kishkin's Effect,* E.N. Kablov (ed.), Nauka, (Moscow, Russia), 2006, 56–78.
[3] Morozova G.I., Formation of the chemical composition of the γ'/γ matrix of multicomponent nickel alloys, *Dokl. Akad. Nauk SSSR*, V. 320, 6, (1991), 1413–1416.

9th Liege Conference : Materials for Advanced Power Engineering 2010
edited by J. Lecomte-Beckers, Q. Contrepois, T. Beck and B. Kuhn.

ANISOTROPY OF MECHANICAL PROPERTIES OF SINGLE CRYSTALS IN FOURTH GENERATION NI-BASED SUPERALLOY

I.L. Svetlov, N.V. Petrushin, D.V. Shchegolev, K.K. Khvatskiy

All-Russian Scientific-Research Institute of Aviation Materials (VIAM), Moscow, Russia

Abstract

Single crystals of Ni-based superalloys have significant anisotropy of mechanical properties.. Data about anisotropy of Young modulus, ultimate strength and yield strength, deformation diagrams and rupture strength of Russian single crystal Ni-based superalloys of fourth generation with <001>, <011>, <111> crystallographic orientation are presented in this article.

Keywords: anisotropy of mechanical properties, Ni-based superalloys, single crystal.

1. Introduction

In contrast to polycrystalline isotropic materials mechanical properties of single crystals of Ni-based superalloys with face-centered cubic structure are significantly anisotropic and depend on crystallographic directions, along which these properties are defined [1]. For structural strength analysis of single crystal blades and life-time projecting of GTE it's necessary to have data about temperature and orientation dependence of physical-mechanical properties in superalloys.

Vital information, mentioned in this article, shows fundamental mechanisms of temperature and orientation dependence of Young modulus and characteristics of short-time strength (ultimate strength and yield strength, elongation and reduction area), strength rupture of Russian single crystal Ni-based superalloys of fourth generation with <001>, <011>, <111> crystallographic orientations.

2. Materials and data processing technique

The chemical composition of the investigated single crystal superalloy is given in table 1 [2].

Table 1. Chemical composition single crystal superalloy, wt.%

Al	Cr	Mo	W	Ta	Co	Re	Ru	Ni
6.0	3.3	4.0	4.0	5.0	7.0	6.5	4.0	basic

Specimens for mechanical tests (gage length – 25 mm, diameter – 5 mm) were manufactured from round single crystal bars, which axes coincide within 10 degrees of the crystallographic directions <001>, <011> or <111>. Single crystal bars were produced by DS method with cooling in aluminum melt (LMC method) in full-scale plant. Thermal treatment, including step-by-step homogenization in 1285–1320 °C temperature range for 26 hours and two-step aging at 1130 and 870 °C was performed in order to form optimal microstructure.

Characteristics of short-time strength, elasticity and Young modulus were measured using MTS-810 machine at a strain rate of 1 mm/min at temperature range of 20–1150 °C.

Long-term strength tests were conducted at 950–1150 °C temperature range and rupture times > 1000 hours in air without protective coats.

Experimental data treatment was made using equation of temperature – strength dependence of creep-rupture lifetime τ [3]:

$$\tau = \xi T^{m} \sigma^{-n} \exp\left(\frac{U_0 - \eta\sigma}{RT}\right) \qquad (1)$$

where T – temperature; σ – stress; ξ, m, n, U_0, η are coefficients, defined by test results; R – universal gas constant.

3. Experimental results and discussion

3.1 Young modulus anisotropy

Fig. 1 shows diagrams of Young modulus vs temperature in single crystals with <001>, <011> and <111> crystallographic orientations. While increasing test temperature from 20 up to 1150 °C, Young modulus monotonically decreases. The single crystals with <111> crystallographic orientation have maximum value of Young modulus and <001> the single crystals – the minimum value. Intermediate values of Young modulus are typical for <011> single crystals. It should be mentioned, that the significant anisotropy of Young modulus remains in all investigated temperature interval.

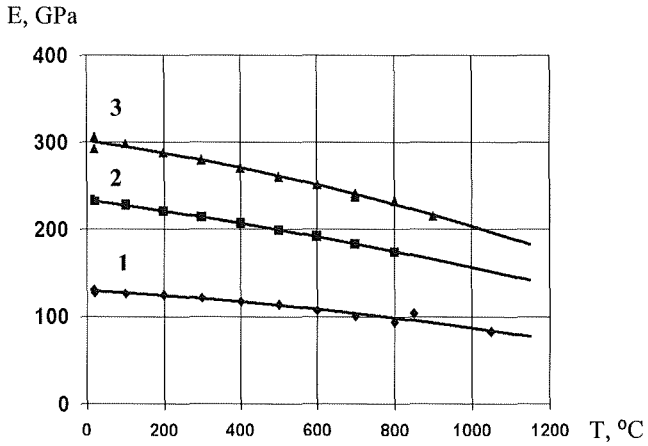

Fig. 1 Temperature dependence of Young modulus in single crystals of 1 - <001>, 2 - <011>, 3 - <111> orientations

3.2 Anisotropy of short-time strength properties

The anisotropy of short-time strength properties in single crystals is defined by the specific slip systems in the existing experimental conditions. Since plastic deformation behavior is defined as interaction of slip systems, tensile test diagrams will be different for different orientation of the single crystals [4-6].

3.2.1 *Stress- Strain diagrams*

Fig. 2 shows stress-strain diagrams at 20, 700 and 1000 °C of single crystals with <001>, <011> and <111> crystallographic orientations. Generally, stress-strain diagrams of specimens with <001> and <111> crystallographic orientations at 20 °C are characterized by linear stage, then by yield line and hardening stage. Diagrams with sharp yield point with the next stage of easy glide at constant mean stress are typical for <011> single crystals. At test temperature of 700 °C (fig. 2b) there is no hardening stage on stress-strain diagrams and plastic deformation is achieved at permanent stress until rupture. Besides this, serrated yielding stage is presented on stress-strain diagrams of single crystals with <001> and <011> orientations. Stress-strain diagrams of single crystals with <001> and <111> orientations at 1000 °C are defined by a stage of intensive softening, yield drop is typically observed in <011> crystallographic orientation (fig. 2c).

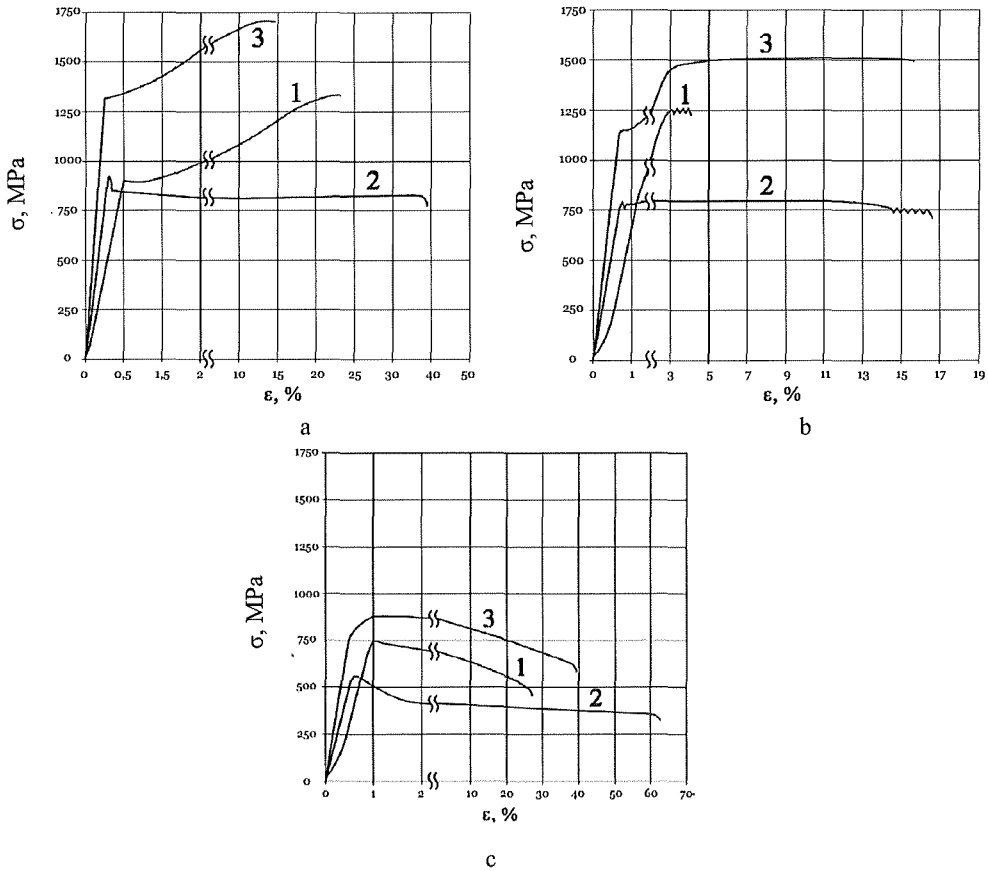

Fig. 2 Deformation diagrams of the investigated alloy with crystallographic orientations, close to <001>,<011> and <111> at temperatures: 20 °C (a), 700 °C(b) and 1000 °C (c)

3.2.2 *Strength and plasticity*

The temperature dependences of ultimate and yield strengths of single crystals with the three tested crystallographic orientations are shown on fig. 3. In 20–700 °C temperature range, the single crystals with <001> and <011> orientations, have a small temperature dependence of σ_B and $\sigma_{0.2}$. On further increasing of temperature one can see increasing of these parameters up to maximum at peak temperature of 800 °C, then alloy softening is proceeded at more elevated temperatures. Such changing of σ_B and $\sigma_{0.2}$ in two-phase single crystal Ni-based superalloys at elevated temperatures can be explained using the abnormal temperature dependence of yield stress in particles of intermetallic γ'-phase [1]. With respect to single crystals with <111> crystallographic orientation, monotonic decrease of the ultimate and yield strengths in all analyzed temperature range is typical.

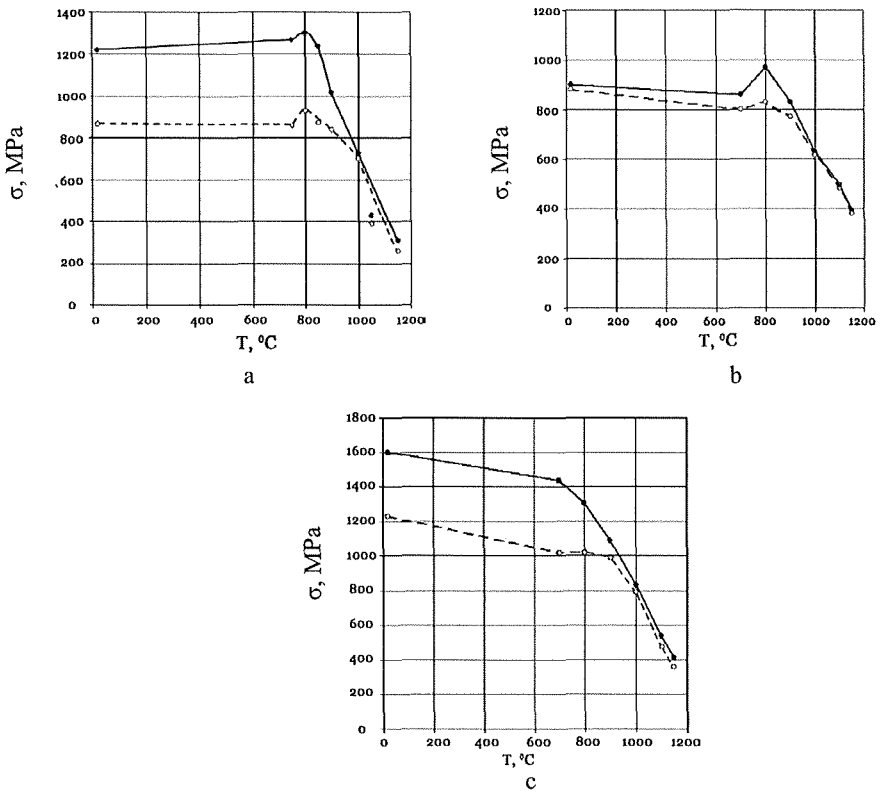

Fig. 3. Temperature and orientation dependence of yield and tensile strengths in the single crystals of investigated alloy. a - <001> orientation, b - <011> orientation, c - <111> orientation

It should be mentioned, that yield strength of the Re-Ru containing single crystals superalloys IV generation has lower values, than the Re-containing single crystals superalloys III generation. Similar ratio of ultimate strength and yield strength is observed for single crystals of Re-containing superalloy PWA 1484 and Ru-containing superalloy EPM 102 [7]

The reduced yield strength is typical characteristic of single crystals in Re-Ru-containing superalloys. It can be associated with the influence of Ru on the dislocation mechanism of plastic deformation.

The temperature dependence of the elongation and reduction area in the single crystals with the three crystallographic orientations are shown on fig. 4. On increasing the temperature, both of these properties decrease to a minimum at peak temperature. At temperatures, higher than the peak, significant increasing of elongation and reduction of area was observed.

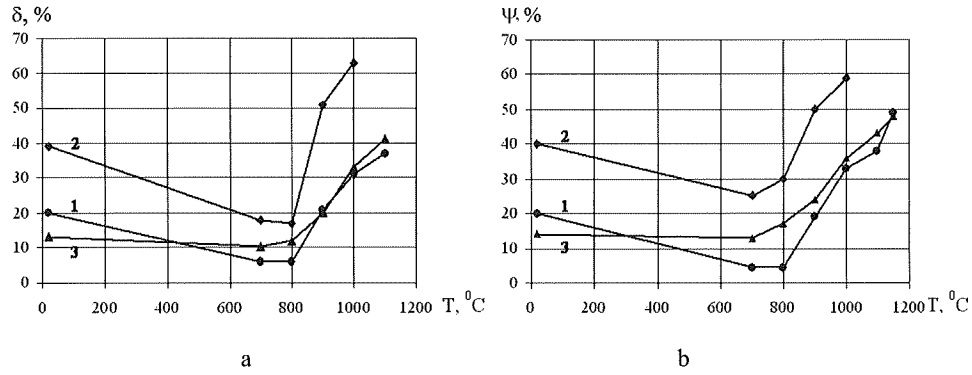

Fig 4 Temperature-oriented dependence of elongation δ (a) and reduction area ψ (b) of <001> (1), <011> (2) and <111> (3) single crystals

3.2.3 Creep rupture strength

Table 2 shows rupture strength for 100 and 1000 hours, calculated using experimental data, for three crystallographic orientations in 750–1150 °C temperature range. For estimation of anisotropy of stress rupture it's suitable to use coefficient [8]:

$$K_{\tau}^{hkl} = \frac{\sigma_{\tau}^{hkl}}{\sigma_{\tau}^{001}},$$

where σ_{τ}^{hkl} – stress rupture of single crystal with <hkl> crystallographic orientations for τ hours, σ_{τ}^{001} – stress rupture of single crystal with <001> crystallographic orientations for τ hours.

As it can be seen from the table, coefficient K_{100}^{011} is less than 1 in 750–1150 °C temperature range, i.e. stress rupture for 100 hours for <011> single crystals is less, than for <001> single crystals. Stress rupture of <111> in 850–950 °C temperature range is more, than for <001> single crystals, as K_{100}^{111} is more than 1. But at temperature of 1150 °C coefficient of anisotropy K_{100}^{111} is less than 1, i.e. <111> single crystals are softening more intensive and their heat resistance is less, than for <001> single crystals. Similar dependence is observed while long-run tests for 1000 hours.

Table 2. Stress rupture for 100 and 1000 hours of <001>, <011> and <111> single crystals

Temperature, T°C	Rupture strength for 100 hours, σ_{100}, MPa, and K_{100}					Rupture strength for 1000 hours, σ_{1000}, MPa, and K_{1000}				
	<001>	<011>	K_{100}^{011}	<111>	K_{100}^{111}	<001>	<011>	K_{1000}^{011}	<111>	K_{1000}^{111}
750	1015	690	0.67	-	-	835	616	0.73	-	-
850	725	485	0.67	800	1.1	565	395	0.78	640	1.13
950	405	340	0.83	540	1.33	265	240	0.90	360	1.35
1150	125	102	0.82	115	0.92	74	77	1.04	65	0.87

Irreversible changes of alloy phase structure and morphology of strengthening γ′ phase particles is proceeded while high-temperature creep in the structure of single crystals. Such changes are visually illustrated by the evolution of voluentary unit microstructure, enclosured with <001> planes, in single crystal specimen <001> of initial state and after high – temperature creep at temperatures of 1000 and 1100 °C (fig. 5).

a b c

Fig. 5. Voluentary unit microstructure of <001> single crystal after heat treatment (a), creep tests at 1000 °C, σ=200 MPa test period – 1274 h (b) and 1100 °C, σ=120 MPa test period – 1303 h (c)

As it can be seen from fig. 5a, alloy voluentary unit microstructure in initial conditions consists of γ-solid solution matrix, where cuboidal particles of γ′ phase have tendency to ordered arrangement, forming quasiperiodic three-dimensional macro lattice. Such microstructure is morphologically unstable at high temperature creep tests. In transition phase of high temperature creep initial cuboidal particles of γ′-phase are specifically coagulated at the expense of plate splicing. Broad facets of plates are perpendicular to load axis (raft-structure) (fig.5b).

Regular raft-structure of single crystals make active reaction on to plastic creep deformation at high temperatures, blocking γ'-phase plates intersection. Dislocations migrate in interlayers of γ-solid solution. In this connection any disturbance of raft-structure promotes softening and decreasing of stress rupture.

Phase instability in single crystals of analyzed alloy is discovered in creep process in 1000–1100 °C temperature range. Phase instability is visualized in initiation of lamellate particles, Re inreached (TCP phases). TCP phases are isolated in first order dendrite axes in <111> plates. These plates transverse with voluentary unit cube face in <110> crystallographic direction (fig. 5c). Volume concentration and geometry (thickness and length) of TCP phase plates increase while increasing test period at 1100 °C. Lamellate

isolations in single crystal structure are not visualized after creep tests at 1150 °C during 3000 hours test period.

3.3 Deformation porosity

One of mechanisms of Ni-based superalloys stationary creep at elevated temperatures and low tension provides for nonconservative motion of dislocations along interface of γ'/γ plates in raft-structure. Supernumerary vacancies, condensed in pores of deformation origin, were generated [9] These pores were visualized in single crystals at 1000, 1100 and 1150 °C and low tension, i.e. at 1000 hours test period. Pores are located in interaxial areas at lineages of blocks (fig. 6a). Unique feature of such pores is contained in cuboidal morphology and enclosing <110> plates. Such enclosure is stipulated because of significant anisotropy of surface tension at 1000–1100 °C test temperatures.

Pores in the single crystals are stress raisers, and micro cracks are initiated while tertiary creep. Micro crack initiation originates either on coarse homogenized spherical form pores, or fine deformation pores, generated while high temperature creep in wide test period. It depends on temperature and test period.

At temperatures, more than 1000 °C and low stress i.e. long rupture time micro crack initiation take place by deformation pores (fig. 6b).

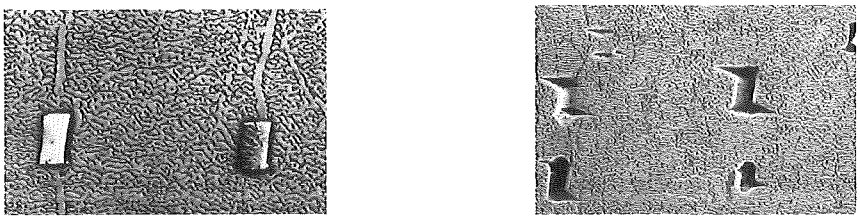

а *б*

Fig. 6. Morphology of deformation pores at lineages of blocks in specimen volume (a); micro crack nucleation on deformation pores (b)

Micro cracks initiate in interdendritic areas. Microcrack coalescence in most damaged area reduces to a main crack propagation and final specimen destruction.

4 Conclusions

1. The Youngs modulus anisotropy remains in all temperature range 20–1150 °C, <111> single crystals have the maximum value of Young modulus, <001> single crystals – minimum.
2. Significant anisotropy of ultimate strength and yield strength is observed only down to 800 °C. The anisotropy almost degenerates up to this temperature, i.e. crystals begin to soften with the same speed. At 800 °C strength properties of <001> and <011> single crystals are at peak values, plasticity properties – minimum. Monotonic decreasing of strength is typical for <111> single crystals when increasing test temperature in 20–1150 °C range.

3. Significant stress rupture anisotropy for single crystal of three orientations is observed, <111> single crystals have maximum value of heat resistance, <011> single crystals – minimum. Stress rupture anisotropy is almost degenerated at 1150 °C.

5 References

1. Shalin R.E., Svetlov I.L. Kachanov E.B.,Toloraia V.N., Gavrilin O.S. Single-crystals of nickel-base superalloys. Mashinostroenie (Moscow) 1997, 336 p. (in Russian).

2. Svetlov I.L., Petrushin N.V., Golubovskiy E.R. ., Khvatskiy K.K., Shchegolev D.V. Mechanical properties of single crystals from high temperature alloy containing the rhenium and ruthenium //Deformation and Fracture of Materials, 2008, №11, pp.26-35.

3. Kablov E. N, Golubovskiy E.R, High temperature strength of nickel alloys, Mashinostroenie (Moscow, Russia) 1998, 464 p. (in Russia).

4. Koji Kakehi. Influence of precipitate size and crystallographic orientation on strength of a single crystal Ni-base superalloy //Materials Transactions, JIM, 1999, v.40, №2, pp.159-167.

5. Miner R.V., Voigt R.C., Gayda J., Cabb T.P. Orientation and temperature dependence of some mechanical properties of the single crystal nickel-base superalloy Rene N4: Pt.1. Tensile behavior //Metallurgical Transaction, 1986, v.17A, №3, pp.491-496.

6. Kear B.H., Piearcy B.J. Tensile and creep properties of single crystals of the nickel-base superalloy Mar-M200 //Transaction Met. Sos. AIME, 1967, v.239, pp.1209-1215.

7. Walston S., Cetel A., MacKay, Hara K.O., Duhl D. Dreshfield R. Joint development of a fourth generation single crystal superalloy //In: Superalloys 2004, TMS, 2004, pp.15-24.

8 Golubovskiy E.R., Nozhnitsky Y.A., Svetlov I.L., Relationship of Stress Rupture and Crystallographic Orientation for Ni-base Superalloys Single Crystal //Proc. of the European Conference for Aerospace Sciences (EUCASS), 2005, Moscow, Russia, N. 4.

9. Epishin A., Link T. Mechanisms of high temperature creep of nickel-base superalloys under low applied stresses //Philosophical Magazine, 2004, v.84, №19, p.p.1979-2000.

MULTILAYER STACKS OBTAINED BY ION ASSISTED EB PVD AIMED AT THERMAL BARRIER COATING

E. Roos, K. Maile, A. Lyutovich*
MPA, University of Stuttgart, Germany
*corresponding author <lyutovich@mpa.uni-stuttgart.de>

Abstract

Thermal Barrier Coating (TBC) using Electron Beam Physical Vapour Deposition (EB PVD) is widely implemented, especially for aero-engine turbine blades. Generally, multilayer stacks are used for these aims.
For the additional improvement of intermediate layers with graded transitions to the initial Ni-based alloy, the use of accelerated ions in the EBPVD-process is advantageous. The effect of the substrate bias potential, ion current density and deposition temperature on the structure and properties of Ti and Zr intermediate layers are investigated.
The morphology of the films is studied using optical microscopy, scanning electron microscopy (SEM) and atomic force microscopy (AFM). It is found that the surface morphology becomes smoother with rising bias potential and decreasing ion current density.
Measurements of Vicker`s micro-hardness performed on these coatings have shown its increase with higher values of the bias and its reduction with the growing temperature. This effect is caused by the observed decrease in grain size and higher porosity of the films.
A multilayer coating system Ni (based substrate)-Si-Si_xAl_y-Al with graded transitions between the layers is obtained using ion assisted EBPVD. Architecture of a multilayer stack for TBC with graded transitions is proposed.

Keywords:
Ion assisted EB PVD, Ti, Zr, SEM, AFM, micro-hardness

1. Introduction

The microstructure and composition of the coatings by EB PVD can be altered by controlling the process parameters and source composition. The assistance of accelerated ions within the film growth process offers additional benefits such as formation of porous or dense, textured or columnar coatings with improved adhesion. In this method, the bombardment of growing layers with accelerated ions affects the migration of atoms, nuclei coalescence, ion "mixing" and activation of chemical reactions on the surface. These phenomena have an influence on the morphology and mechanical properties of the films. The employment of ion assistance enables the coating at a relatively lower vacuum of 10^{-5} mbar and does not require complicated and expensive installations.
Ion bombardment-induced changes in film properties, including stress, resistivity, and hardness of metal films is described in [1]. The effect of the substrate bias potential on crystalline grain size, intrinsic stress and hardness of vacuum evaporated TiN/c-Si coatings was investigated in [2]. The hardness of the coatings was analyzed in correlation with the grain size distributions. Influence of porosity on hardness and Young`s modulus of nanoporous EB PVD TBCs was studied by nanoindentation in [3]. The authors have shown a significant dependence of the hardness on the porosity. The improvement of the mechanical properties of coatings manufactured by ion assisted EB PVD is demonstrated in [4]. Microhardness, scratch and friction tests were carried out on Cr coatings deposited on Ni-based alloys. EB PVD coated specimen manufactured with bias potential show more uniformity and toughness. Accordingly, the Young's modulus and hardness was higher.

In this work, an investigation of the contribution of ion bombardment to the growth, microstructure formation and specific mechanical properties of Ti, Zr, Si, Al coatings on Ni-based substrates which are promising components for the development of TBC have been done.
To get unambiguous results about the effect of processing parameters on ion assisted EB PVD coatings, also the influence of the bias potential applied to the substrate at constant ion current and the effect of ion current density under fixed bias was studied.

2. Experimental work

Ti-, Zr, Si and Al-coatings were deposited by ion assisted electron beam evaporation system on nickel based alloy 617 substrates, Fig. 1.

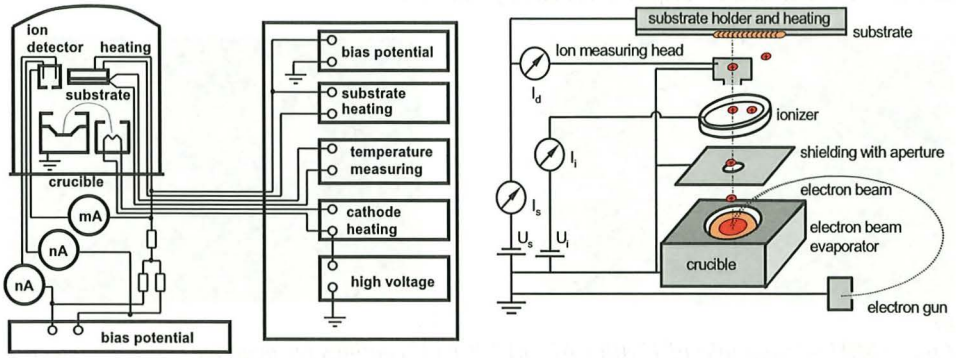

Fig. 1: Schematic representation of IA EBPVD

A 6 kW electron beam evaporator with a 270° beam deflection by a permanent magnet and 10 kV acceleration voltage were used for the deposition of metal films.
To measure the density of the ionic and electronic current a special ion detector was installed at the position of the substrate [5]. The vacuum in the chamber was $5x10^{-6}$ mbar. The coating process was carried out at temperatures 300°C, 500°C, 600°C and 700°C. The emission current of the e-gun varied from 40 mA to 350 mA depending on the evaporated metal. The film growth assisting ion current density ranged from 1.5 $\mu A/cm^2$ to 10 $\mu A/cm^2$. The bias potential was varied from 0 V to 1000 V. The distance between the evaporation point of the substrate was 150 mm. Details of the deposition experiments are described in [4]. The thicknesses of the deposited films were measured with a microprofilometer Dectac 3030ST and with direct SEM examinations of cross-sections.
The morphology of the films was studied using optical microscopy, scanning electron microscopy (SEM), and atomic force microscopy (AFM). The distribution of the elements in the system coatings/interface/substrate was measured using line-scan electron probe on the cross-sections of the samples.

3. Results and Discussion

3.1 Morphology and Microstructure of the coatings

3.1.1. Effect of substrate bias potential

It was observed by optical microscopy that as the negative substrate bias increases the microstructure becomes finer. To get the clear understanding, scanning electron microscopy of specific samples was performed. As shown in Fig. 2 it is obvious that the grain size decreased from 0.892 μm to 0.454 μm as the negative substrate bias increases from 0 V to 1000 V. The evolution of such topography could be explained by increased energy of the bombarding ions during deposition with increase of the substrate bias leading to the rising number of nuclei and, consequently, smaller grain sizes.

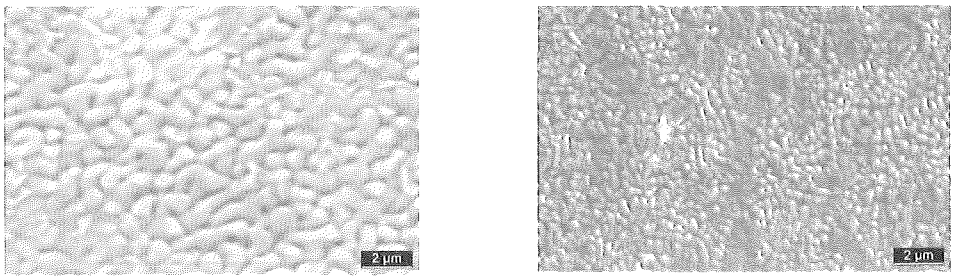

a) b)

Fig. 2: SEM micrographs of Ti/Alloy 617 IA EB-PVD coatings for negative substrate bias (a) 0 V (b) 1000 V

The SEM micrographs shown in Fig. 3 also demonstrate that the grain size of Zr-films decrease from 0.30 at 0 V to 0.18 μm at 1000 V – comparable to the findings in Fig. 2.

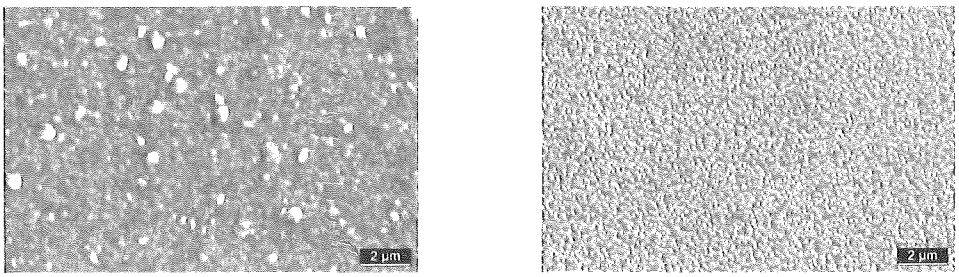

a) b)

Fig. 3: SEM micrographs of surfaces of Zr/Alloy 617 IA EB-PVD coatings with substrate temperature 300 °C and for negative substrate bias a) 0 V, b) 1000 V

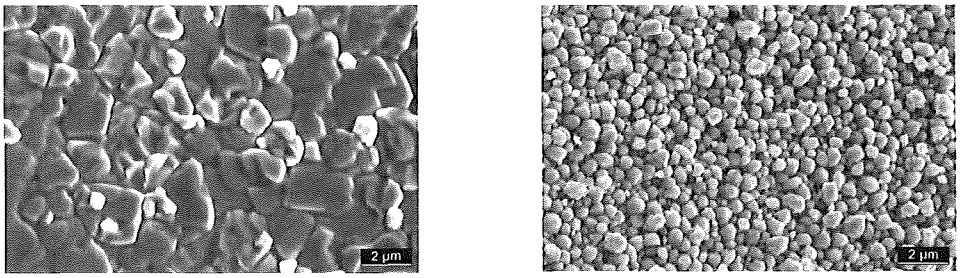

a) b)

Fig.4: SEM micrographs of surfaces of Zr/Alloy 617 IA EB-PVD coatings with substrate temperature 700 °C for negative substrate bias a) 0 V, b) 1000 V

The grain size decreased from 1.99 to 0.592 µm as the negative substrate bias increased from 0 V to 1000 V.

3.1.2. Effect of ion current density

These series of experiments were performed by different ion current densities: 0 $\mu A/cm^2$ - sample A; 6.3 $\mu A/cm^2$ - sample B, and 10 $\mu A/cm^2$ - sample C.

As one can see from the AFM images in Fig. 5, the grain sizes revealed by linescans, are larger with increasing ion current density (J_i).

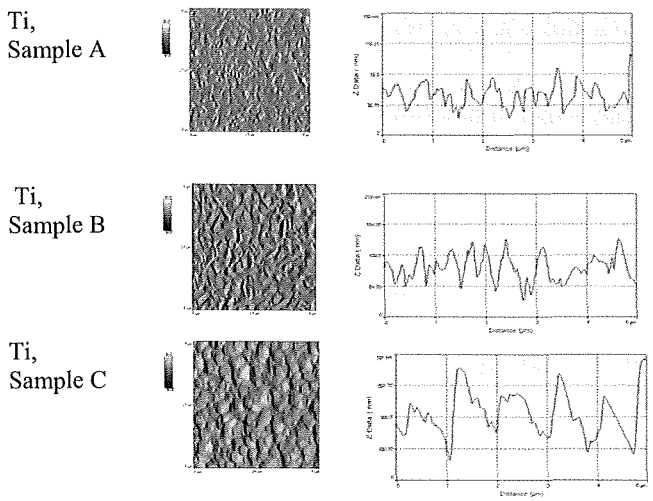

U_S = 0 V
J_i = 0 $\mu A/cm^2$
t = 20 min
H ~ 50 nm
ϕ ~ 250 nm

U_S = -800 V
J_i = 6.3 $\mu A/cm^2$
t = 20 min
H ~ 70 nm
ϕ ~ 400 nm

U_S = -800 V
J_i = 10 $\mu A/cm^2$
t = 20 min
H ~ 400 nm
ϕ ~ 600 nm

Us – Bias; Ji – ion current density; t – time; H – thickness; ϕ - roughness

Fig. 5. AFM – surface morphology (5x5µm²) and linescans on Ti films.

On Zr and Ti coatings on Ni based substrates it could be stated that an increased ion density leads to increased roughness (ϕ) of the Zr and Ti films. The ion current density (I_s) to the substrate defines the kinetic energy of the particles impacting and forming the coating. The

increasing ion current activates the surface mobility of the atoms, leading to better accommodation of the atoms in crystalline lattice sites, and as a consequence, formation of larger crystalline grains. With larger grain sizes, the three-dimensional interspace between them is larger and the resulting porosity if of a higher amount which is important for the lower thermal conductivity.

3.2. Effect of substrate bias on microhardness of Zr and Ti/Alloy 617 IA EB-PVD coatings

Fig. 6 shows the microhardness values for Ti /Alloy 617 IA EB-PVD coatings for different values of the substrate bias.

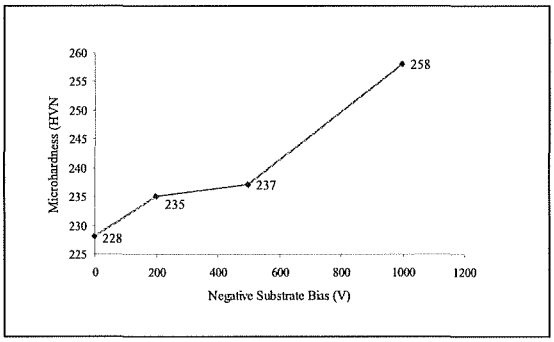

Fig.6: Microhardness vs negative substrate bias for Ti /Alloy 617 IA EB-PVD coatings.

It can be observed, from Fig. 6, that the microhardness of the sample shows a clear dependency of the negative substrate bias: it increases from 228 HVN without bias to 258 HVN at 1000 V.

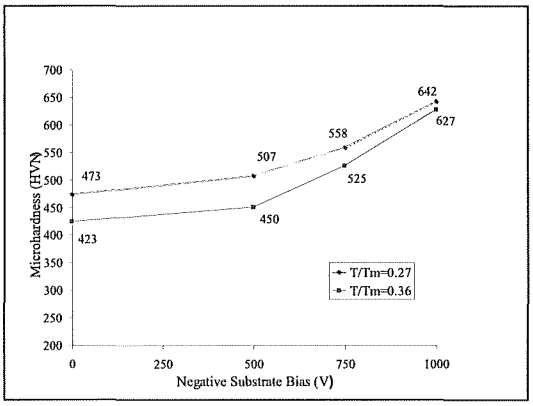

Fig. 7: Microhardness vs negative substrate bias for Zr /Alloy 617 IA EB-PVD coatings grown at substrate temperature of 300 °C (upper curve) and 500 °C (lower curve).

The microhardness was also measured for Zr/Alloy 617 IA EB-PVD coatings, Fig. 7. The character of the curves was found to be similar to that of Ti coatings depicted in Fig. 6. The

microhardness gradually increases for lower values of negative substrate potential and then rapidly for higher values.

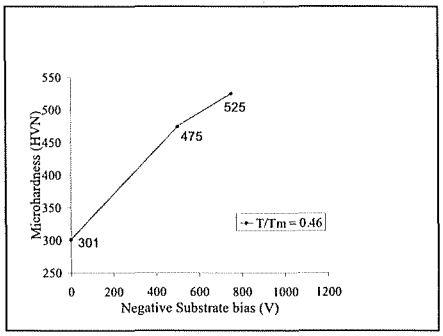

Fig. 8: Microhardness vs negative substrate bias for Zr /Alloy 617 IA EB-PVD coatings at 700 °C substrate temperature.

Fig. 8 shows the effect of negative substrate bias on microhardness of Zr/Alloy 617 IA EB-PVD coatings at a substrate temperature of 700 °C. The microhardness increases from 300 HVN at 0 V to 525 HVN at 750 V. The tendency of the curve is similar to the afore mentioned other coatings up to 750 V.
These results demonstrating the influence of the applied bias potential within the layer deposition on the microhardness are in a good agreement with the observations of changes in the surface morphology by SEM.

3.3 Effect of substrate temperature on microhardness

The substrate temperature is important parameter considering adhesion and the relevant structure. In order to obtain optimal adhered layers the PVD method requires temperatures of several hundred degrees.

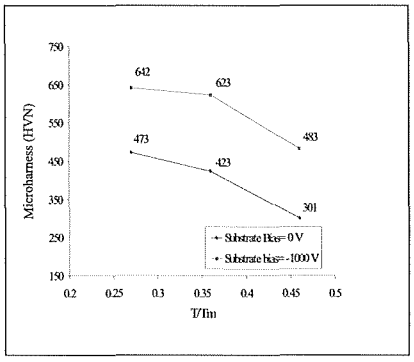

Fig. 9: Effect of substrate temperature on microhardness of Zr/Alloy 617 IA EB-PVD coatings deposited without bias (lower curve) and under -1000V (upper curve).

The microhardness is observed to be decreasing with increase in substrate temperature as shown in Fig. 9. At higher T/Tm ratios a steeper decline takes place. For both values of the negative substrate bias 0 V as well as 1000 V, the slope of the graphs is comparable. The grain size was observed to be decreased with increase in substrate temperature.
The decrease in grain size is one of the contributing factors to the observed increase in microhardness.

4. Proposed TBC design

The microhardness is an indicator of porosity, which itself is an important parameter for the control of thermal conductivity of the TBC. Porosity in the coatings strongly influences the thermal conductivity. Taking in consideration this aspect and after experimental realizing graded transitions between the multi-layers, Fig.10, the following design for TBC as shown in Fig.11 is proposed.

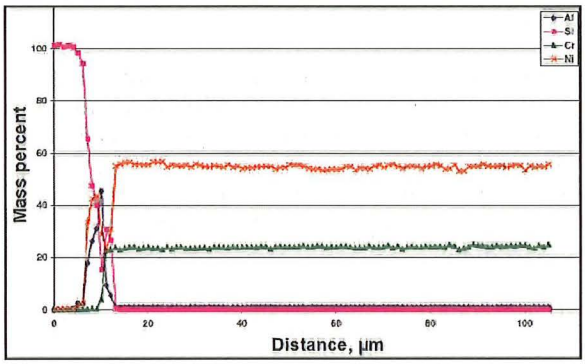

Fig. 10: Line-scan profiles of the elements, measures by electron probe microanalyses on cross-sections of the multilayer coatings.

Ceramic top layers of the thermal barrier coatings needs as a virtual substrate an intermediate layers stack for the compatibility with the basic substrate and for corrosion resistance.
The basic ideas of the multilayer stack architecture are:

- each layer consists of a chemical element as in previous layer. This ensures the chemical compatibility
- the graded compositional transition between the layers ensures mechanical compatibility
- the use of accelerated ions for activating of the films growth leads to formation of necessary morphology and better adhesion.

In detail the proposed architecture of the multilayer stack for the protection of the base metal shown could be described as follows:

- Layer L1 Base material (substrate)
- L2: Ni-based substrate will be siliconized for better corrosion resistance and for the compatibility to the next layer which contains Si, too
- L3: bonding layer consisting of AlSi which will replace conventionally used expensive PtAl. The graded composition provides a good adjustment of thermal expansion coefficients

- L4: serves as an oxidation barrier
- L5: functional layer with low thermal conductivity

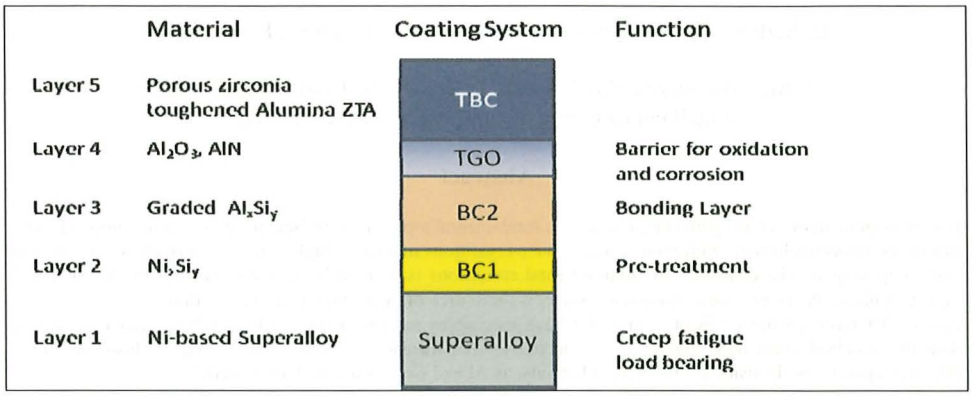

Fig. 11: Design of Thermal Barrier Coatings: Proposed Concept

5. Conclusion

Ion assisted EBPVD method with different bias potential and different ion current density influences the morphology and the microstructure of the Zr and Ti coatings. This leads to differences in microhardness of the coatings.
It can be summarised that the control of bias and ion current density in such processes is an important key for the deposition of coatings with pre-designed porosity and mechanical properties. Taking in consideration the role of porosity of the thermal conductivity of the coatings and experimentally realized graded transitions between the multilayers Ni-Si-Si_xAl_y-Al by IA EBPVD, an innovative design of TBC is proposed.

References

[1] R. Roy: Low Energy ion-assisted deposition of metal films, *Surf. and Coat. Technol.*, 51, 1-3, 203-211, 2002
[2] F.J. Espinoza-Beltran, O. Che-Soberanis, L. Garcia-Gonzalez, J. Morales-Hernandez: Effect of the substrate bias potential on crystalline grain size, intrinsic stress and hardness of vacuum arc evaporated TiN/c-Si coatings, *Thin Solid Films* 437, 170-175, 2003
[3] B. K. Jang, H. Matsubara: Influence of porosity on hardness and Young`s modulus of nanoporous EB-PVD TBC by nanoindentation, *Materials Letters* 59 3462 – 3466 2005
[4] K. Maile, A. Udoh, A. Lyutovich, K. Berreth, E. Pflüger: Mechanische Eigenschaften von dünnen Metallschichten mittels ionenunterstütztem EB PVD hergestellten Schichten auf Nickel-Basis Legierungen, *MP Mechanische Werkstoffprüfung*, Jahrgang 45, 7-8, 2003
[5] A. Lyutovich, K. Maile, A. Gusko, Kh. Ashurov, S. Morosov: Characterisation of the generation of ions in electron beam evaporator for the control of metal deposition processes, *Surf. and Coat. Technol.*, 2002

9th Liege Conference : Materials for Advanced Power Engineering 2010
edited by J. Leconte-Beckers, Q. Contrepois, T. Beck and B. Kuhn.

ASSESSMENT OF A RESIDUAL LIFE EVALUATION TOOL FOR GAS TURBINE BLADES AND VANES BASED ON MICROSTRUCTURAL EVOLUTION OF A NiCoCrAlY+RE COATING

E. Barbareschi*, A Bonadei*, A.Costa*, P.Guarnone*, E.Vacchieri*

* Ansaldo Energia S.p.A. Corso Perrone 118, 16161 Genoa, Italy
e-mail contact: emma.barbareschi@aen.ansaldo.it

Abstract

Life management of hot gas path components is a fundamental topic in gas turbine for power generation. The gas turbine components have to withstand severe service conditions in term of high temperature oxidation, corrosion and creep-fatigue. The resistance to environmental conditions is assured by metallic coatings of the MCrAlY family. β phase, NiAl, present as secondary phase, is the source of protection against oxidation.
Among MCrAlY coatings, NiCoCrAlY + Re have a complex microstructure with a higher number of phases than the standard ones; these phases are subjected to transformations during service. The addition of Re is effective against the diffusion of protective elements, as Al and Cr, toward the base material.
For the estimation of residual life a first approach has been developed using the decrease of β phase amount after static oxidation test at high temperature and for long time. This type of prediction tool is not complete for the assessment of the hot gas path components life management and a deep study focused on the transformation of the other phases is necessary.
Experimental tests have been performed to identify the phase stability range by annealing at different temperatures and durations. Moreover after static oxidation tests a systematic data collection of phase evolution has been carried out through EDS, XRD and EBSD techniques in order to define the kinetic laws that rule the phase transformations. The tuning of thermodynamic and kinetic results allows to build up another residual life tool that, even if it is more complex, is more reliable in temperature evaluation in GT components.
Both models have been applied to a component after service and a comparison between the different models evaluation has been conducted.

Keywords: NiCoCrAlY+Re coating, Microstructure Evolution, Isothermal Oxidation, Phase Transformation, Temperature Evaluation.

ABBREVIATIONS:
GT: Gas Turbine
TGO: Thermally Grown Oxide
TBC: Thermal Barrier Coating
APS: Air Plasma Spray
BC: Bond Coat
BM: Base Material
ODZ: Outer Depletion Zone
IDZ: Inner Depletion Zone

1. Introduction

The increasing demand of gas turbines efficiency and power output improvement has led to a rise of the turbine inlet temperature that has a great impact on materials performances. The evaluation of the service conditions, and in particular the estimation of the service temperature, is an important tool to predict materials lifetime. In case of MCrAlY coatings, applied on gas turbines blades and vanes to withstand oxidation and corrosion, the evaluation of the service temperature is generally based on the depletion of the dispersed β phase or on the evolution of the interdiffusion layers [1, 2, 3].

New metallic coatings are characterised by the addition of small amount of other elements like Re. Re is effective in reducing interdiffusion and improving the high temperature mechanical properties. Moreover, it has been found that Re additions can decrease the extension of the β-depleted zone beneath the surface oxide scale [4].
MCrAlY-Re coatings have a more complex microstructure with a higher number of phases, which are subjected to evolutions during high temperature exposure. The evaluation of the service temperatures based only on the β phase depletion can become inadequate due to the influence of the other phases on the total behaviour of the coating.

This paper, starting from a tool based on β phase depletion, is focused on a case in which this method shows its limits. The analysis of the evolution of other secondary phases in the coating demonstrates that only taking into account all coating phases and transformations a correct temperature estimation is possible, especially for the lower service temperatures.

2. Experimental procedures

The microstructural degradation of a NiCoCrAlY-Re coating, SiCoat2453, has been studied through laboratory test samples exposed at high temperature and examination of an ex-service blade.
The composition of the studied coating is reported in table 1.

Composition (wt%)	Ni	Co	Cr	Al	Y	Re	Mo	W	Ti	Hf	C	B	Zr
SiCoat2453	54	12	21	11	0.4	2.0	-	-	-	-	-	-	-

Table 1: Chemical composition of SiCoat 2453.

Long term oxidation tests have been performed at temperature between 800°C to 1000°C from 300 hours to 15000 hours in chamber furnaces; then some short heat treatments have been performed to explore the phases' stability ranges. Finally an ex-service component, a blade from an Ansaldo GT, has been chosen to check the ongoing developed tools.

The samples have been observed in section by standard and advanced metallographic techniques. In particular optical microscopy has been used for quantitative metallography by Image Analysis Software, and for the color metallography on the samples etched with a modified Grosbeck etching. Phase identification has been performed using a Tescan VEGA/LSU SEM equipped with an EDAX Genesis EDS system and an EDAX-TSL OIM 5 EBSD system. Also XRD has been carried out on the surface of the samples to confirm the EDS/EBSD results.

3. Results and discussion.

The decrease of the β phase amount during high temperature oxidation tests has been used as significant parameter to construct a tool for the residual life evaluation of serviced blades and vanes in gas turbines. In fact the Al_2O_3 oxide scale protects coating from oxidation during service, and the β phase is the Aluminum reservoir that permits the formation of a continuous protective external oxide. In order to follow the degradation of the material, the area fraction occupied by this phase has been measured on exposed samples.

In figure 1 the optical micrographs show the modifications of the β phase layer in the metallic coating after different exposure times at two different tests temperature. During the isothermal oxidation the coating changes its aspect:

- a continuous growth of the TGO at the TBC-BC interface, with a classical parabolic trend;
- the formation of two β phase depleted layers (ODZ and IDZ, Figure 2) respectively under the TBC-BC interface due to oxidation phenomena and near the BC-BM interface due to interdiffusion phenomena; the two layers increase their thickness with test duration;
- the ripening of the β phase fine grains, that grow and coalesce together in bigger grains.

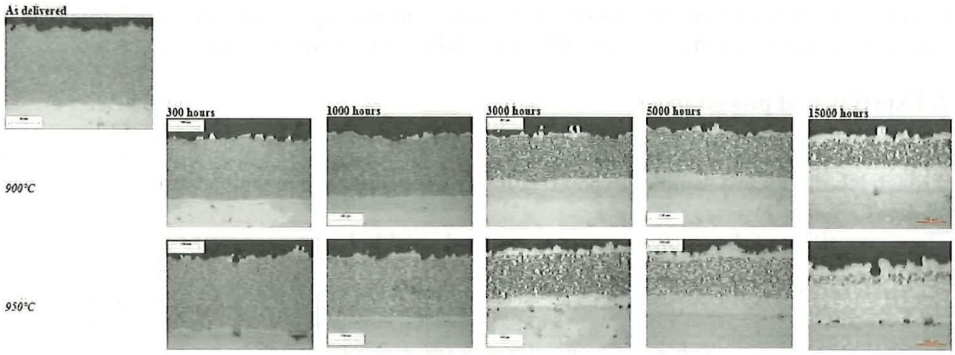

Figure 1: Microstructural evolution of the whole metallic coating after high temperature exposure.

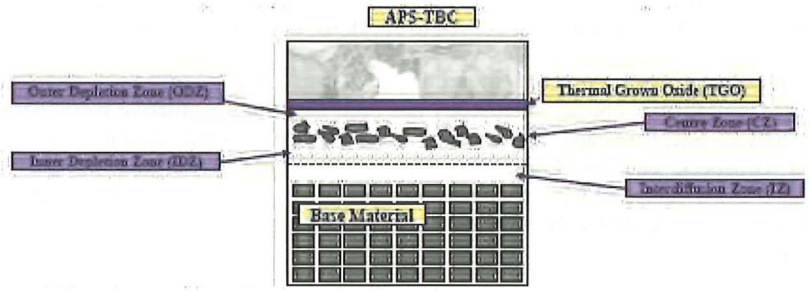

Figure 2: schematic representation of the coating layers.

The β phase amount measured on the exposed samples has been related to an empirical parameter considering both time and temperature dependence. In Figure 3 the graph reports the relationship between the β phase amount and the empirical parameter; the data show a quite linear trend (as depicted by the black line in Figure 3). This simple relationship could be used for the estimation of the service temperature in ex-service components by measuring the β phase amount in different location of the blades' airfoils.

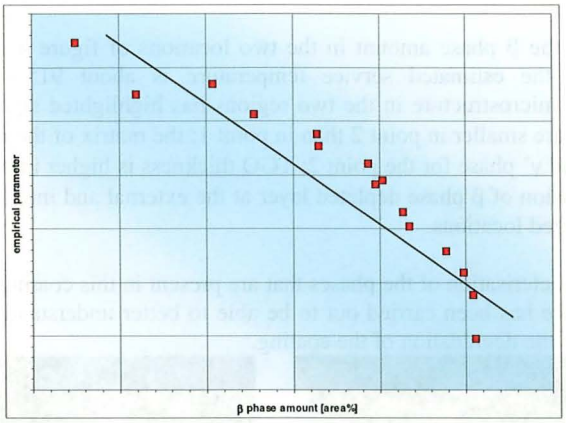

Figure 3: Elaboration of the experimental data throughout the empirical parameter.

This instrument is a quick and easy way to determine service temperature but has some limits in its application because the microstructure of the coating is not simply described by a dispersion of β phase in a γ matrix.
A typical illustration of the technique limits is reported below. A blade from an Ansaldo GT has some overheating problems during service due to the detachment of the top coat. Along the airfoil profile different aspects of the microstructure have been observed as reported in figure 4.

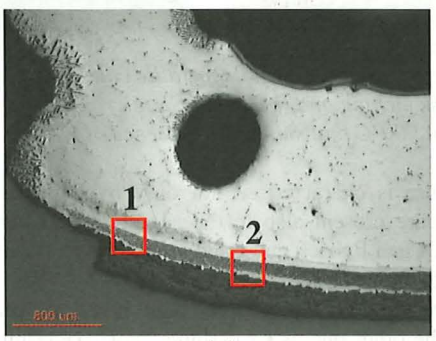

(a)

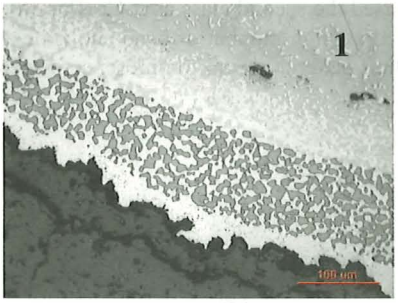

(b)

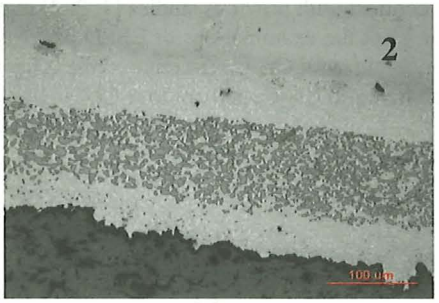

(c)

Figure 4: LOM micrographs (a) from the leading edge of an ex-service component and particulars (b and c) of the microstructure in two different locations in the airfoil profile.

The evaluation of the β phase amount in the two locations of figure 4 gave similar results around 29% and the estimated service temperature is about 915°C. Nonetheless the observation of the microstructure in the two regions has highlighted significant differences: the β phase grains are smaller in point 2 than in point 1; the matrix of the metallic coating is γ phase in point 1 and γ' phase for the point 2; TGO thickness is higher in point 1 than in point 2; finally the extension of β phase depleted layer at the external and internal zone is different for the two considered locations.

So a complete characterisation of the phases that are present in this coating after the oxidation test and after service has been carried out to be able to better understand the effects of time and temperature on the degradation of the coating.

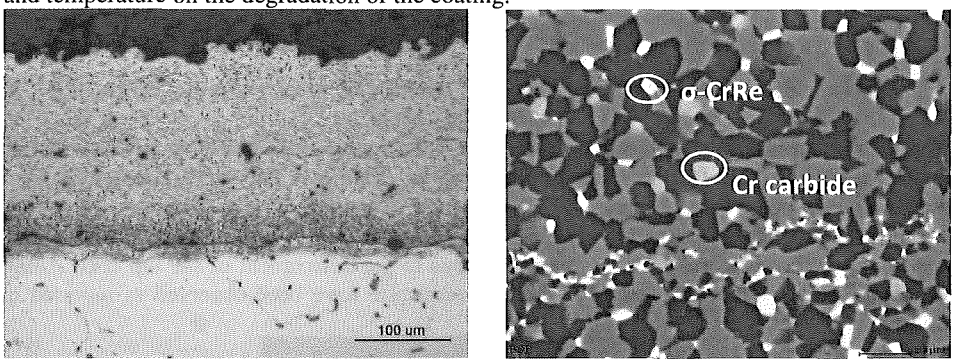

(a) *(b)*

Figure 5: (a) LOM micrograph of the whole metallic coating in the as delivered condition after modified Groesbeck etching and (b) SEM/BSE micrograph of the centre of the coating after oxidation test at 900°C that shows the presence of the two intermetallic classes.

The coating microstructure is characterised not only by β phase but also by some other intermetallic phases that are present also in the as delivered condition (Figure 5-a). These intermetallic phases are Cr and Re rich and are divided in two classes with different chemical composition and crystallographic structure (Figure 5-b).
EBSD and XRD measurements on our samples have identified one class of particles as σ-Cr_2Re_3 (P42/mnm) and the other one as Cr carbide-$Cr_{23}C_6$ (P42/mnm). This identification is in contrast with previous studies [1, 2, 3] that recognised the second class as α-Cr (Pm-3n). In our work the examinations of EBSD patterns revealed an high number of band and zone axis consistent with $Cr_{23}C_6$ structure while Xray diffraction patterns reveal the presence of peaks belonging to $Cr_{23}C_6$ and not to α-Cr.

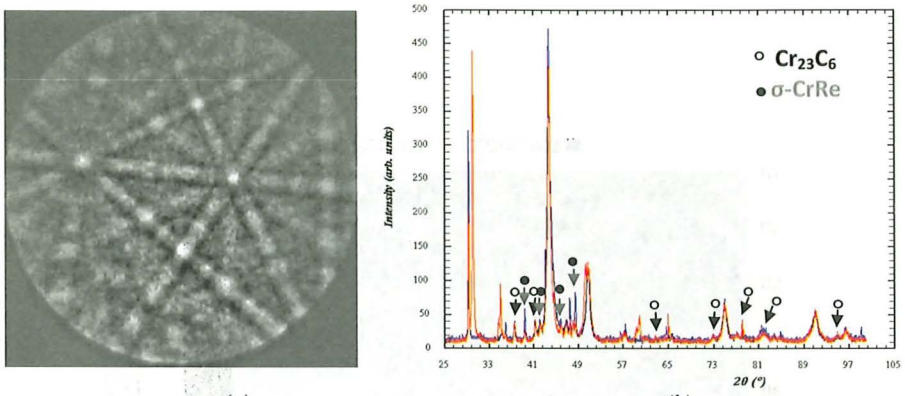

(a) (b)

Figure 6: (a) EBSD pattern of a Cr carbide particles and (b) XRD pattern of surface sample after high temperature exposure at 800°C.

After high temperature oxidation the coating phases show different behaviours regarding changes in compositions, morphology and size with temperature and exposure times:

- the observation of the exposed samples has shown that σ phase completely disappears after long exposure at the higher temperatures (900°C and 950°C). At lower temperatures (800°C and 850°C) the phase is stable but its composition is different from that observed after test at the higher temperature. In particular the chemical composition of σ-CrRe phase is about 45wt% of Cr and 15wt% of Re at 900 and 950°C while about 53wt% of Cr and 9wt% of Re at 800° and 850°C with the inversion of the content of Co and Ni as reported in Figure 7.

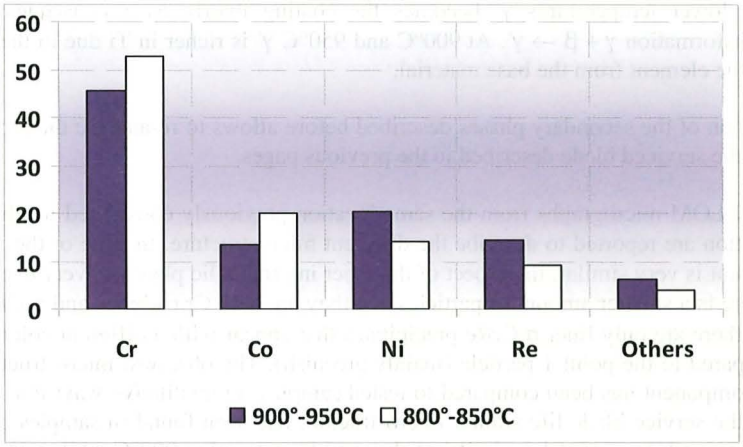

Figure 7: Mean composition of σ-CrRe phase in the two explored temperature ranges.

- The amount of α phase is higher in the samples exposed at 900°C and 950°C, the composition of this phase is constant in the whole temperature range investigated.
- The evolution of β phase is mainly evident in the increased dimensions of phase grains and in the thickness reduction of the layer in which the phase is present. The phase composition is constant in the whole temperature range investigated (figure 8).

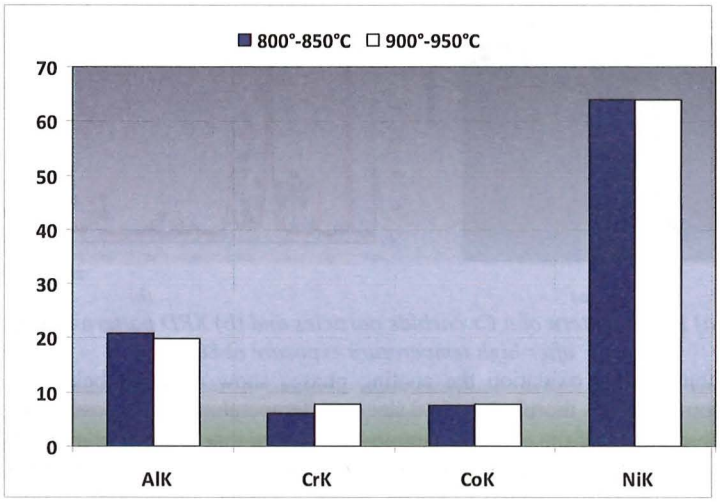

Figure 8: evolution of the β phase composition after different durations of 950°C exposure

- γ' phase has been observed in the IDZ at the higher temperatures probably due the transformation $\beta \rightarrow \gamma'$, induced by the diffusion of Al towards the base material. At the lower temperatures γ' becomes the coating matrix as a consequence of the transformation $\gamma + \beta \rightarrow \gamma'$. At 900°C and 950°C γ' is richer in Ti due to the diffusion of the element from the base material.

The evolution of the secondary phases described before allows to re-analyse the aspect of the coating in the serviced blade described in the previous pages.

In Figure 9 LOM micrographs from the same location previously considered for the residual life evaluation are reported to describe the different microstructure. In spite of the fact that β phase amount is very similar, the aspect of the other intermetallic phases is very dissimilar: In point 1 there is a smaller amount of particles and they are both Cr carbides and σ-CrRe, while in point 2 there are only finer σ-CrRe precipitates that appear with a different colour (mainly pink) compared to the point 1 particle (mainly greenish). The observed microstructure in the operated component has been compared to tested samples' in qualitative way: For a duration similar to the service blade life similar microstructure has been found in samples exposed at different temperatures: point 1 is similar to the sample exposed at 900°C while point 2 shows a similar microstructure to the sample tested at 850°C, as reported in Figure 10.

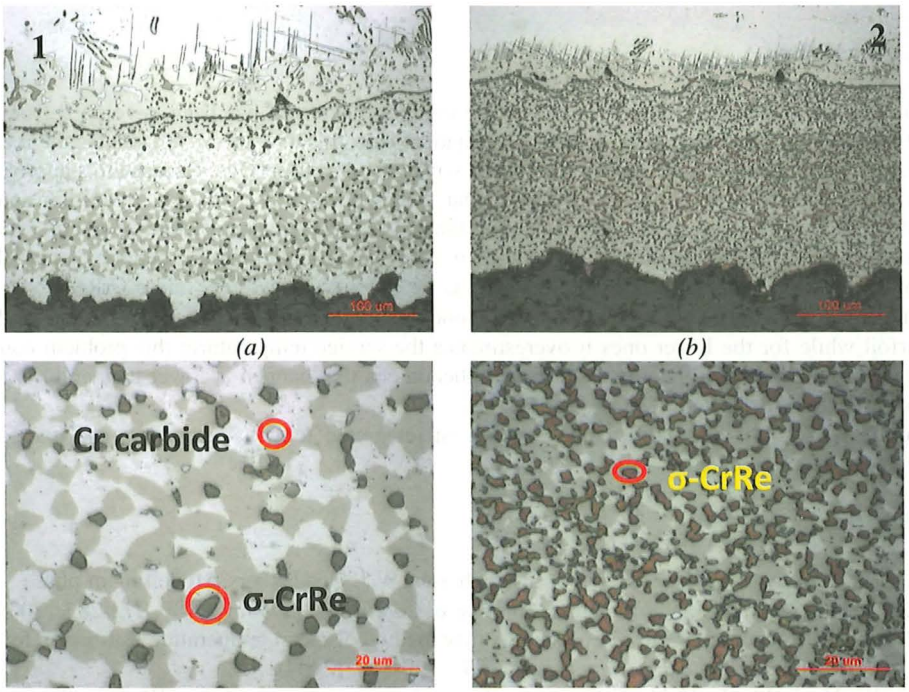

Figure 7: LOM micrographs, microstructure of the whole metallic coating and in particular of its centre in (a and c) point 1 and (b and d) point 2, after the modified Groesbeck etching.

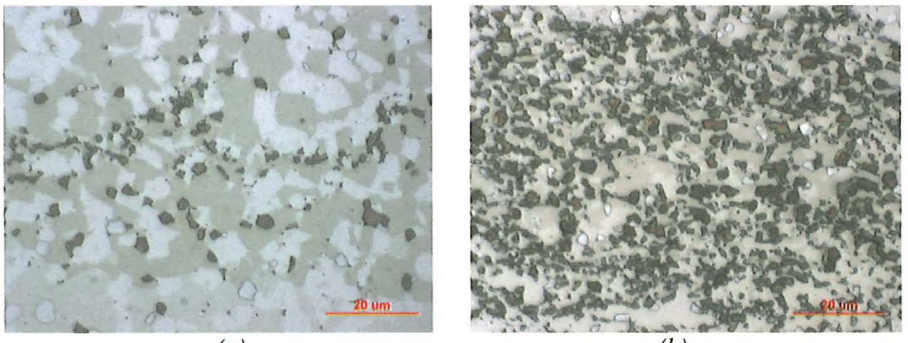

Figure 8: LOM micrographs, microstructure of the metallic coating centre (a) in the sample exposed at 900°C and (b) in the sample exposed at 850°C.

4. Conclusions

For the residual life evaluation of ex-service components a tool has been developed from β phase amount decrease during isothermal oxidation tests; this tool allows to estimate the mean temperature that the blades and vanes airfoils withstand during service. Because this approach greatly simplifies the degradation phenomena that happen in the coating, it fails in some cases. A deep analysis on the evolution of all the coating phases has been carried out on tested samples. The results of this study allow to discern among dubious situations upon the microstructural features of secondary phases, as for example Cr carbides and σ-CrRe.
The developed tool based on β phase gives good results for high temperature locations in the airfoil while for the lower ones it overestimates the service temperature; this problem could arise because this tool ignores the different phenomena that happen at lower temperature, for example the σ-CrRe and γ' phase features.
Future works will be conducted to develop an integrated tool that considers also the low temperature phenomena.

Reference

[1] D.R.G. Achar, R. Munoz-Arroyo, L. Singheiser, W.J. Quadakkers, Modelling of phase equilibria in MCrAlY coating systems, *Surface & Coatings Technology*; 187, 272-283, (2004).
[2] K.A. Ellison, J.A. Daleo, K. Hussain, A new method of metal temperature estimation for service-run blades and vanes; *Superalloys 2004*, 759-768, (2004).
[3] K. V. Dahl, J. Hald, Estimation of metal temperature of McrAlY coated IN738 components based on interdiffusion behaviour; *Energy Materials*, 1, 106-115, (2006)
[4] N. Czech, F. Schmitz, W. Stamm, Improvement of McrAlY coatings by addition of Rhenium; *Surface and Coatings Technology*, 68/69, 17-21, (1994).

9th Liege Conference : Materials for Advanced Power Engineering 2010
edited by J. Lecomte-Beckers, Q. Contrepois, T. Beck and B. Kuhn.

LIFE ASSESSMENT OF GAS TURBINE BLADES AFTER LONG TERM SERVICE

Pertti Auerkari, Jorma Salonen
VTT, Espoo, Finland

Sari Mäkinen
Helsingin Energia, Helsinki, Finland

Ilkka Karvonen & Heikki Tanttari
Lappeenrannan Lämpövoima, Lappeenranta, Finland

Pekka Kangas
Neste Oil, Kilpilahti, Finland

Alfred Scholz
TU Darmstadt, Germany

Erica Vacchieri
Ansaldo Richerche, Italy

Abstract

Turbine blade samples from three land based gas turbines have been subjected to systematic condition and life assessment after long term service (88 000 - 109 000 equivalent operating hours, eoh), when approaching the nominal or suggested life limits. The blades represent different machine types, materials and design generations, and uncooled blading outside the hottest front end of the turbine, i.e. blades with relatively large size and considerable expected life. For a reasonable assessment, a range of damage mechanisms need to be addressed and evaluated for the impact in the residual life.

The results suggested significant additional safe life for all three blade sets. In some cases this could warrant yet another life cycle comparable to that of new blades, even after approaching the nominal end of life in terms of recommended equivalent operating hours. This is thought to be partly because of base load combined cycle operation and natural gas fuel, or modest operational loading if the design also accounted for more intensive cycling operation and more corrosive oil firing. In any case, long term life extension is only appropriate if not intervened by events of overloading, overheating or other sudden events such as foreign object damage (FOD), and if supported by the regular inspection and maintenance program to control in-service damage. Condition based assessment therefore remains an important part of the blade life management after the decision of accepted life extension.

Keywords: gas turbine, blade, life

1. Introduction

The designers and suppliers of gas turbines will initially rely on the available information of the future service conditions. As these are not really accurately known and as the design must accommodate a range of possible service histories, the machine and at least some of its major components can have considerable life extension potential when used under relatively conditions than assumed. On the other hand, new turbines tend to be "prototypes" in the sense of including new features even when compared to nominally similar "sister" machines. Also, during long term service some changes can be expected because of the opportunities created by the technical evolution. Therefore, the actual remaining life of a particular component is not necessarily well established when approaching the recommended life (replacement) limits.

The first rows of turbine blades have the shortest cycles of reconditioning and renewal, and are targets for most life assessment and maintenance effort. The last blade rows require less frequent attention but will also have a finite life. Although less intricate in detail than in the first rows, these blades are large and contain much more of the expensive nickel superalloys. There may be limited information on design, material and service history, and multiple damage mechanisms can affect the blade life. However, at this stage there is accumulated information on the service history, and also the blade condition can be evaluated in detail.

This work aims to review selected example cases on life assessment of uncooled gas turbine blades after long term service, particularly when approaching the nominal or suggested life limits. The examples cover different machine types, materials and design traditions for blades outside the hot front end of the turbine, to explore the potential for their life extension.

2. Ex-service turbine blades

Principal features of the three example blade types are shown in Table 1 and in Fig 1. Two blades from each turbine were sacrificed for detailed assessment, except only one blade for the case 1. The case 1 blade from a vintage turbine was also the only one not to come from the last row of the turbine. The case 2 blades included in the same row two geometries with differences in the tip section. To avoid potentially non-conservative conclusions, the selection aimed to target blades that were dimensionally typical but otherwise by visual and other non-destructive inspection among the worst blades within the each blade set.

Table 1. Features of the blades; all in base load operation and natural gas firing

Case/feature	1: 2nd row blade	2: 4th row blade	3: 3rd row blade
Turbine type	W251	V64.3	F6A
Operation/process	CHP*, district heat	CHP*, district heat	CHP*, industrial
Time in service	88 000 eoh	109 000 eoh	90 000 eoh
Row / no. of rows	2/3	4/4	3/3
Blade material	Udimet 500	IN738 [1)]	GTD 111
Coatings	None	None	Chromizing
Cooling	No	No	No [2)]

1) according to OEM documentation; for actual composition see results below
2) air cooling in blade root only
* CHP = combined heat and power

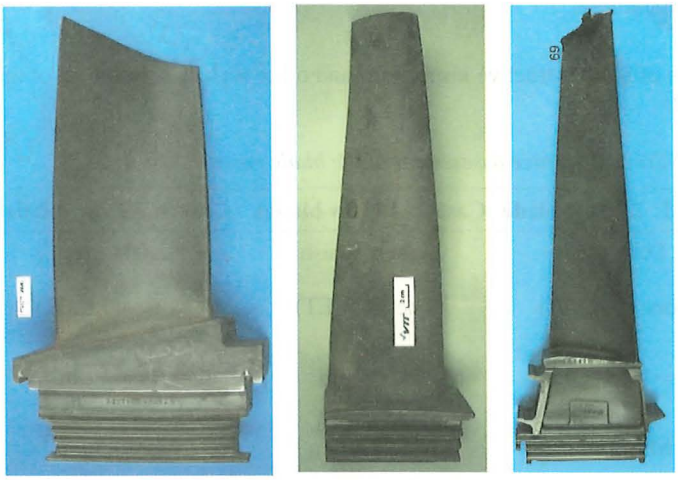

Fig 1. Uncooled turbine blades: from left, blade cases 1 to 3 (cf. Table 1)

3. Methods of assessment

In addition to on-site inspections for initial sampling, the sample blades were subjected to non-destructive testing (NDT) including surface inspections by visual inspection, stereo microscopy, fluorescent penetrant inspection (FPI) and eddy current (ET) methods, to detect any macroscopic surface/near-surface cracks or comparable defects in the blades. Surface roughness measurements were performed using contacting line profiling. Dimensional comparison to as-new reference blades was not possible for the example blades of cases 1 and 3. However, five as-new and five ex-service case 2 blades were compared using 3D coordinate measuring equipment. Optical 3D modelling was used for ex-service case 3 blades to characterise the blade geometry. The sample blades were then sectioned for assessment of microstructures and possible internal defects, typically at the blade root, at 55-60% of the aerofoil length position (close to the hottest region estimated from external colouring), and close to the tip of the blade. The sections were inspected by light optical and scanning electron microscopy (SEM). X-ray spectrum analysis and EDS were used for chemical analysis of the blade materials.

The materials properties, such as mean expected creep strength at the operating temperatures, were obtained from mostly public sources available for the exercise. For the case 1 blade, Udimet 500 creep properties were available from the NIMS materials database [3], and for case 2 blade, the required properties were obtained from the materials databases of TU Darmstadt. For the case 3 blades, GTD 111 properties were assumed to comply with those included in [1]. The blade and material condition was assumed to be sufficiently described by the expected properties, expired service history, the findings in the non-destructive and microstructural assessment, and other experience on gas turbine life assessment regarding the potential damage mechanisms.

4. Results

An overview of the results of non-destructive inspections and other surface assessment of the blades is shown in Table 2.

Table 2. Observations in NDT and surface assessment of the blade cases

Feature/case	Case 1: 2nd row blade	Case 2: 4th row blades	Case 3: 3rd row blades
Surface colour	Dark grey	Light greenish	Light grey
Crack indications	None (FPI, ET)	None (FPI, ET)	None (FPI, ET)
Surface roughness[1)]	Ra = 4.8 ± 0.9 µm	Ra < 5 µm	Ra < 4 µm
Impacted particle size	Max 1 mm	Max 0.5 mm	Max 0.5 mm
Tip condition	Scratches < 0.2 mm	Small dent [2)]	Some wear

1) at leading edge; 2) in one blade only

In the case 2 blades, the 3D coordinate measurements of five ex-service and five as-new blades showed that the original dimensional differences between the individual blades were sufficiently large to mask any possible systematic change in the blade dimensions during service. Nevertheless, no obvious and significant strain or distortion was observed in any of the blades. The chemical composition of the blade materials is shown in Tables 3 and 4.

Table 3. Chemical composition (wt%) of the case 1 and case 2 blades in comparison with typical compositions of alloys Udimet 500, Udimet 720 and IN738LC [1,2].

%	Ni	Cr	Co	Mo	Al	Ti
Udimet 500 [1)]	bal. (~ 53)	16-20	16-20	3.0-5.0	2.5-3.25	2.5-3.25
Udimet 720 [2)]	bal. (~ 55)	18	15	3.0	2.5	5.0
IN738LC	bal (~62.5)	16	8.5	1.7	3.4	3.4
Case 1 blade	52	20	19	3.6	2	2
Case 2 blade	55	20	15	3.2	2.7	4.3

1) in addition C ≤ 0.1% and B 0.003-0.010%; 2) in addition W 1.25%, also C, Zr, B ~0.035

Table 4. Chemical composition (wt%) of two case 3 blade samples in comparison with typical composition of alloy GTD 111 [2]

%	Ni	Cr	Co	Mo	Ta	Al	Ti	W	B	C
GTD 111 [1)]	bal.	14.0	9.5	1.5	3.15	3.0	5.0	3.8	0.014	0.10
Sample 1	bal	14.8	9.8	1.7	3.0	3.3	4.2	3.6	0.01	0.07
Sample 2	bal	14.7	9.9	1.7	3.2	3.3	4.1	3.6	0.01	0.07

1) in addition Zr ~0.007%

The results are taken to confirm that the materials of the case 1 and case 3 blades are Udimet 500 and GTD 111, as expected. However, the case 2 blade material appears to conform to the composition of Udimet 720, instead of IN738LC quoted in the OEM documentation.

In general, most extensive service-related changes in the aerofoil cross-sections appear at or close to the leading and trailing edges. The observed features are likely to reflect the influence of the flue gas temperature, and in cool regions possibly also of the heat treatments. Where more than one blade was sectioned (cases 2 and 3), there was very little difference between the sample blades in the surface cross-sections. No clearly defective features related to e.g. fabrication were observed from the inspected sections. An example of the microstructure at the hot section of the case 1 blade aerofoil is shown in Fig 2; and the assessments of all inspected blades are summarised in Table 5.

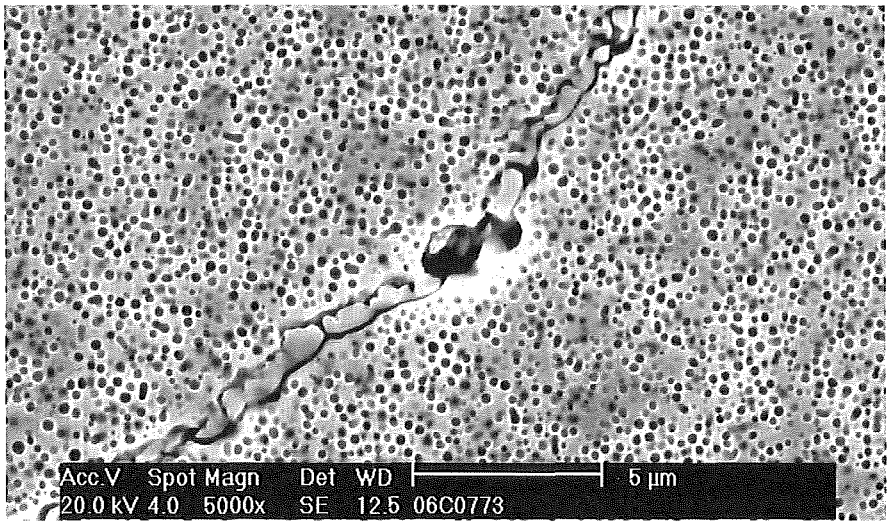

Fig 2. Blade microstructure at 60% cross-section of the aerofoil (case 1 blade)

Table 5. Features observed from the aerofoil and root sections

Feature	Case 1 blade	Case 2 blades	Case 3 blades
Material	U500	U720	GTD 111
Hot section	60 %	60 %	55 %
Surface layer [1)]	≤ 0.1 / 0.3 mm	≤ 0.1 / 0.2 mm	≤ 0.1 / 0.2 mm
Size of γ', hot [2)]	0.25 µm	0.3-0.4 µm [4)]	Double peaked [4)]
Size of γ', root [3)]	0.20 µm	0.3-0.4 µm [4)]	Double peaked [4)]

1) Oxidised + transformed material on leading/trailing edge, hot sections
2) Mean size, aerofoil hot section below the transformed surface
3) Mean size, fir tree attachment (root section)
4) As in the root section or otherwise in practically as-new state

Using the classical model for thermally activated coarsening of second phase particles (gamma') with a radius growing from r_0 to r:

$$r^3 - r_0^3 = \frac{B \cdot t}{T} \cdot \exp(-\frac{Q}{RT}) \qquad (1)$$

where t is time, T absolute temperature, Q the apparent activation energy of coarsening, R the gas constant and B a material-dependent constant [1]. From known time of exposure t, characteristic (mean) particle radius r and material specific constants Q and A, the effective temperature T can be solved. This approach has mostly been applied for the hot end materials, where sufficient change will occur.

In the blade of case 1, comparison of the microstructures at 60% aerofoil cross-section (Fig 2) and at the blade root suggests that some thermal coarsening has taken place in the aerofoil (Table 5). Applying the equation (1) on the gamma' particles with the mean size from the aerofoil section as r and that from the root section as r_0, the resulting estimate of the effective material temperature at the hot section is obtained and shown in Table 6. For the blades of case 2, the microstructure at the 60% cross-section of the aerofoil showed no significant change between the aerofoil and root section materials, indicating that the low service temperature has rendered the approach based on particle coarsening inapplicable. Therefore, the estimate of the blade material temperature was based on the measured flue gas inlet and outlet temperatures that must limit the temperatures of uncooled blades. For the blades of case 3, the microstructure of the aerofoil cross-section showed only small differences between blade samples at equivalent sections, and in all aerofoil sections the original two-peak size distribution and other as-new features of the gamma' particles were still clearly observable. Again, the differences in particle coarsening were judged inadequate for assessing the effective material temperatures, the estimates of the blade material temperatures were based on the flue gas inlet and outlet temperatures.

Table 6. Estimated maximum temperatures at the blade hot sections

Feature	Case 1 blade	Case 2 blades	Case 3 blades
Location/section	60%, leading edge	60%, leading edge	55%, leading edge
Max temperature	765°C	≤ 600°C	≤ 700°C
Estimate from	Gamma' coarsening	Flue gas temp.	Flue gas temp.

Assuming that under base load service the static tensile stress from the centrifugal mass loads of the blade will dominate, this stress at a blade radius r [2,4]

$$\sigma_z = \frac{\rho \cdot \omega^2}{A} \cdot \int_r^{ra} A \cdot r \cdot dr \qquad (2)$$

where *ra* is the tip radius of the blade, A the blade cross-section area at radius r, ω the angular velocity and ρ the blade metal density. As the level of this stress increases towards the root of

the aerofoil, and material becomes weaker towards the location of the maximum temperature, it is the combined influence of mechanical loading and temperature-dependent material strength that determines the location of critical position along the aerofoil. To account for the impact of the additional stress components and other uncertainties, a safe side approach could use a stress assessed for a cross-section towards the root of the aerofoil and a temperature assessed for a location closer to the observed maximum. The estimates of the static stress levels are summarised in Table 7.

Table 7. Estimated stress levels at the blade cross-sections of interest

Feature	Case 1: 2nd row blade	Case 2: 4th row blades	Case 3: 3rd row blades
Rpm	4918	5400	5150
Location/section	60% / aerofoil root	60% / aerofoil root	55% / aerofoil root
Stress [1)]	137.6 / 184.3 MPa	- / 321 MPa	216.2 / 357.4 MPa
Notes	One sample blade	Two sample blades	Two sample blades

1) static, at the selected hot section / root of the aerofoil

4. Discussion

An overview of the blade condition as indicated by the measurements for the example cases is shown in Table 8, considering the most common damage mechanisms of gas turbine blades.

Table 8. Summary of the impact by potential damage mechanisms on the example blades

Mechanism	Case 1	Case 2	Case 3	Notes
Overheating	No indications	No indications	No indications	From microstructure
Overloading	No indications	No indications	No indications	No distortion, no cracks
Wear/erosion	Minor influence	Minor influence	Minor influence	LE roughness Ra ≤ 5μm
FOD	Minor influence	Minor influence	Minor influence	Depth < 0.1 mm
Corrosion	No indications	No indications	No indications	Natural gas firing
Oxidation	Modest	Minor influence	Modest	Depth ≤ 0.1 mm
Embrittlement	No indications	No indications	No indications	From microstructure
Fatigue [1)]	Minor influence	Minor influence[1)]	Minor influence[1)]	No cracks, Ra ≤ 5 μm
Creep [2)]	Life limiting	No indications	Minimal [2)]	Max temp in case 1
Combined	Minor influence	Minor influence	Modest/minimal	See Fig. 3

1) As demonstrated; however possibly life-limiting, for case 3 also in combination with creep
2) At high temperatures only

In general, only few indications of degradation were observed, mainly some modest oxidation, wear and impact traces on the blade surfaces, and some coarsening of the gamma' microstructure at the hot section, particularly in case 1 blade. Based on the evidence, it was judged likely that creep could be the life limiting damage mechanism for case 1 blades, and

fatigue for case 2 and case 3 blades, although there was as yet no evidence of progressing fatigue damage or cracking. This conclusion would only apply provided that short term mechanisms, e.g. FOD, overheating or overloading, do not intervene. For the blades of case 2, it is also possible that attachment clearances and fretting can require mitigating action. The outcome of the resulting life assessment is summarised in Table 9 and in Fig 3.

Table 9. Comparison of the blade cases including the predicted residual life

Issue	Case 1	Case 2	Case 3
Operational hours	88 000 eoh	109 000 eoh	90 000 eoh
Effective temperature	765°C	≤ 600°C	≤ 700°C
Effective stress	138 / 184 MPa	- / 321 MPa	216 / 357 MPa
Location/section	60% / aerofoil root	60% / aerofoil root	55% / aerofoil root
Critical mechanism	Creep	Fatigue	Fatigue
Additional life	25 000 h [1)]	> 100 000 h	90 000 h

1) also expected benefit from coating

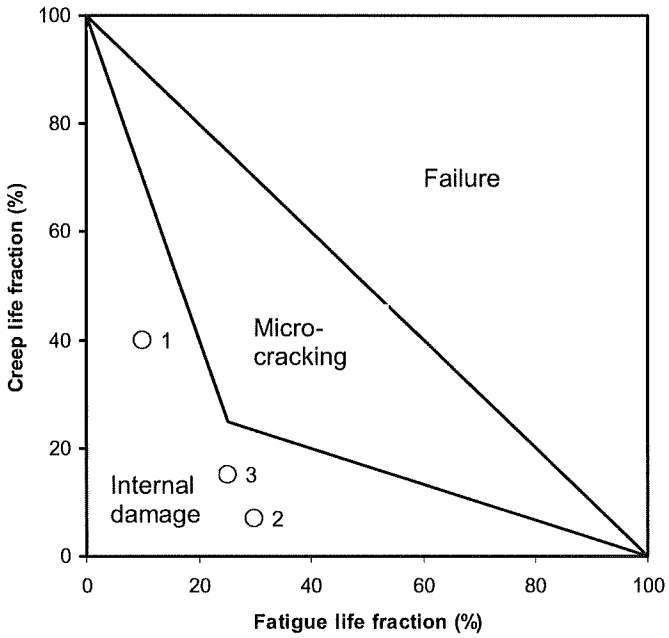

Fig 3. Estimated position of the blade cases on a creep-fatigue life fraction map

The predicted residual life appears considerable in all cases, suggesting that the example blades can allow further operation while replacement had been recommended by OEM or the

maintenance service provider. Particularly in cases where the operating temperature is low, the impact from most potential damage mechanisms seems to be modest or minimal after reaching the nominal (recommended) service life. Inversely, increasing temperatures will boost the rate of life consumption through several damage mechanisms. It is also to be remembered that the operator, control system and the maintenance procedures must remain alert to short term events and mechanisms that could intervene and in the worst case terminate the blade life abruptly. For example, overheating, overloading, foreign or internal objects, or control failure could result in dramatic loss of the residual life.

Nevertheless, the results from the example cases suggest that considerable life extension and related savings can be expected for the last blade rows, when the service environment is not aggressive. The benefits from base load operation, good quality natural gas fuel, and proper maintenance are likely to magnify the life extension potential towards the end blade rows of the turbines.

5. Summary

Three example cases on land based gas turbines have been reviewed for life assessment of uncooled turbine blades after 88000-109000 eoh of service, i.e. at or close to the nominal or suggested life limit. The examples cover different machine types, materials and designs for blades outside the hottest front end of the turbine, where a relatively long blade life may be possible.

The results suggest that the life of the example blades could be considerably extended from the nominal limits in all cases, up to a similar life as for new blades in terms of recommended equivalent operating hours. Likely reasons for the positive outcome are thought to include base load operation with natural gas fuel, modest operating temperatures, and conservative design to allow for more severe than actual in-service loads and environments. Nevertheless, blade life cannot be extended beyond the acceptable levels of any intervening significant damage, which must therefore be controlled in the condition monitoring, inspection and maintenance programs. Several mechanisms and their combinations can threaten the blade life, and some vigilance is needed to follow the progress of the most important ones. For example, local or temporary thermal (heating/cooling) excursions and increasing cyclic service will consume the remaining blade life much faster than the usual steady-state operation of a base load plant. For a reasonable assessment, a range of damage mechanisms need to be addressed for the impact in the residual life, using the results from recurring evaluation of the blade condition.

Acknowledgement

This work was a part of the European COST 538 project, and the national project LC-Power/LifePower. The authors wish to acknowledge the financial and technical support by the Finnish Funding Agency for Technology and Innovation (Tekes), the national industry group of the projects, and VTT. For providing the baseline cases and background information, appreciation is particularly due to Helsinki Energy, Lappeenrannan Lämpövoima, and Neste Oil, Finland.

References

1. Viswanathan R, 1989. Damage mechanisms and life assessment of high-temperature components. ASM International, 497 p.
2. Reed RC. Superalloys - fundamentals and applications. Cambridge University Press 2006, 372 p.
3. Bohl W. Strömungsmaschinen 2 – Berechnung und Kalkulation. Vogel Buchverlag 2005, Würzburg. 286 S.
4. NRIM Creep Data Sheet 34B, 1993. NRIM, Tokyo. 62 p.
5. Auerkari P, Salonen J, Gustafsson TE, Karvonen I, Tanttari H, Mäkinen S. Evaluation of the operating conditions of gas turbine blades and vanes after long term service. Baltica VII – Life Management and Maintenance for Power Plants, Helsinki-Stockholm 12-14 June, 2007. VTT Symposium 247, vol 2, p. 25-34.
6. Auerkari P, Salonen J. Life assessment of a gas turbine blade (in Finnish). VTT Research Report VTT-R-06443-06. VTT, Espoo 2006. 18 p.
7. Auerkari P, Salonen J, Gustafsson TE. Condition and life assessment of the blades of a gas turbine. VTT Research Report VTT-R-08049-06. VTT, Espoo 2007. 27 p.
8. Jauhiainen P, Salonen J, Auerkari P. Rotating blades of a gas turbine – part 1: microstructural evolution (in Finnish). VTT Research Report VTT-R-02847-08. VTT, Espoo 2008. 47 p.
9. Auerkari P, Salonen J. Rotating blades of a gas turbine – part 2: condition and life (in Finnish). VTT Research Report VTT-R-08980-07. VTT, Espoo 2008. 17 p.

9th Liege Conference : Materials for Advanced Power Engineering 2010
edited by J. Lecomte-Beckers, Q. Contrepois, T. Beck and B. Kuhn.

EFFECTS OF LONG -TERM HIGH TEMPERATURE EXPOSURE ON THE MICROSTRUCTURE OF HAYNES ALLOY 230

J. Veverková[1], A. Strang[1], G.R. Marchant[2] and H.V. Atkinson[1]

1- Department of Engineering, University of Leicester, University Rd., Leicester, LE1 7RH, UK (hva2@le.ac.uk)

2- Siemens Industrial Turbomachinery Ltd, Lincoln, UK (geoff.marchant@siemens.com)

Abstract

Haynes Alloy 230 was specifically designed to have excellent long-term thermal stability and resistance to the precipitation of damaging phases.

This paper describes in detail studies on the effects of long-term high temperature exposure on the hardness, microstructural changes and tensile properties of thermally exposed samples of Haynes Alloy 230. The samples from the 2mm thick sheet material have been investigated using X-Ray diffraction and advanced electron microscopy techniques (FEGSEM, TEM etc.). The evolution of the precipitating phases was monitored across a wide range of temperatures (from 500°C to 1170°C) and durations (from 24 hours up to 30000 hours) and several key phases have been identified. In addition to the primary W-rich carbide and the precipitation of Cr-rich $M_{23}C_6$, a new brittle phase/carbide was observed within the microstructure at the highest exposure temperatures (above 930°C).

The microstructurally based model assists in the assessment of in-service operating temperatures as a means of evaluating the remaining operational life of the components.

Keywords - HA230, microstructural evolution, thermal ageing, hardness, tensile testing

1. Introduction

Haynes Alloy 230™ (HA230) is a solid solution strengthened nickel-based alloy used for combustion components in industrial gas turbines. These components must demonstrate an extended operational life-time at high temperature exposures (with and without mechanical loading) without structural failures. High temperatures together with cyclic mechanical and thermal stresses during long periods of operating service lead to degradation of the microstructure of the alloy and consequently to its mechanical properties. It is important to develop understanding of these processes in order to optimise performance.

Haynes Alloy 230™ has a combination of high temperature strength, long-term thermal stability and outstanding corrosion resistance in oxidising and nitriding environments at service temperatures up to 1150°C. These properties, together with its good formability and weldability characteristics, have made HA230 an ideal material for many aerospace and power industry applications [1].

The alloy was originally developed from the Ni-Cr-Mo-W system with the high nickel content providing a stable austenitic matrix, tungsten effective solid solution strengthening and carbon promoting the formation of chromium rich $M_{23}C_6$ carbide. A range of studies are available in the literature [2-8].

2. Experimental procedure

HA230 for testing was provided by Siemens Industrial Turbomachinery Ltd (SIT) in the form of 2mm thick sheet. All the specimens were taken from this single heat of HA230 (No 8305-5-7170) supplied in the solution treated and quenched condition by Haynes International Ltd to the specification AMS 5838. The chemical composition of the material is shown in *Table 1*.

Table 1 Test certificate: Chemical analysis (wt%) of as-supplied material provided by Haynes Intl..

Heat	Ni	Cr	W	Mo	Fe	Co	Mn	Si	Al	C	La	B
8305-5-7170	Bal	21.75	13.96	1.32	1.40	0.37	0.49	0.36	0.29	0.12	0.013	0.004
AMS 5878	Bal	20.0 to 24.0	13.00 to 15.00	1.00 to 3.00	3.00 max	5.00 max	0.30 to 1.00	0.25 to 0.75	0.20 to 0.50	0.05 to 0.15	0.005 to 0.05	0.015 max

The coupons were thermally exposed in still air at temperatures in the range of 500-1170°C and for duration from 24 hours up to 30000 hours. The microsections were mounted and firstly ground to 600 grit finish for hardness tests and then prepared for metallurgical review by polishing to a 1μm finish and etching in hydrofluoric acid. The microsections were examined using optical microscopy and FEGSEM.

Tensile testing was performed at room temperature on the 3000, 10000, and 20000 hours thermally exposed specimens. The specimens were exposed at six different temperatures (750°C, 810°C, 870°C, 930°C, 990°C, and 1050°C) for all three durations of exposure. The heat treated specimens were cut into the form shown in *Figure 1*, using a milling machine. The summary of all the tests performed is presented in *Figure 2*.

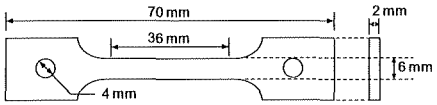

Figure 1 Design of the tensile specimen.

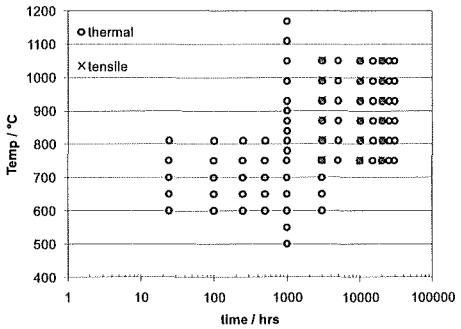

Figure 2 Overview of the tests performed.

3. Result and discussion

3.1. Hardness studies

Vickers hardness tests have been carried out at a load of 20kg along the length of the microsection of unstressed coupons of HA230. The average hardness value of as-received unexposed material was 218 ± 2 Vickers.

The hardness testing provided useful information about the behaviour of the alloy with increasing exposure time and temperature. *Figure 3a* shows hardness variation with time. The specimens exposed at 750°C demonstrate a stable behaviour with only a small fall observed over 30000 hours. For the rest of the exposure temperatures, the primary drop in hardness happens after 1000 hours and then for longer exposures the hardness stays quite stable. The lowest values were obtained for 990°C. In the case of 1050°C the hardness is slowly increasing with exposure time.

One of the aims of this project was to create a Master Curve of Hardness vs. Larson-Miller Parameter (LMP) as a first step in evaluation (i.e. the estimation of the average operating temperature) of ex-service components.

The hardness values are shown in the form of a parametric Larson–Miller plot (see *Figure 3b*), using a C-value of 20 for the Larson-Miller constant. The results indicate that systematic changes in the hardness of the HA230 occur with increasing temperature and exposure duration.

It is evident from the data curve that the material initially hardens from the original solution annealed value of 218 Vickers to a peak value of the curve of about 246 Vickers and LMP=22. Then re-softening of the alloy occurs reaching its original hardness value at LMP equal to 27.5 approximately. All the curves reach a minimum at a temperature of about 990°C. The minimum value was about 208 Vickers and LMP=30. With additional increase of temperature the material hardens again. The maximum hardness value was obtained for the specimen thermally exposed for 1000 hours at 650°C and the minimum value after exposure of 3000 hours at 990°C.

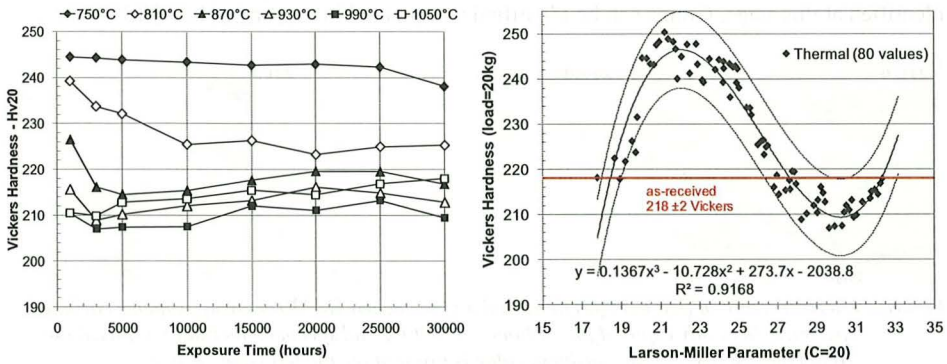

Figure 3 a) Variation of hardness with exposure time for temperatures in the range 750° C-1050° C. b) Hardness data for HA230 thermally exposed coupons plotted versus Larson-Miller parameter. Dotted lines represent the 95% prediction interval.

To analyse the hardness data a least squares regression analysis was used. A good fit for the data set plotted in *Figure 3b* is obtained using a cubic polynomial of the form $Hv = aP^3 + bP^2 + cP + d$, where a, b, c, and d are constants, Hv is a hardness value and P is the Larson-Miller parameter defined as $P = (273 + T)(20 + \log t)/1000$. The regression constants and R^2 value for hardness data obtained in the project are in *Figure 3b*.

3.1.1. Statistical analysis

The set for the statistical analysis contained 80 hardness values of thermally exposed samples. The sample thermally exposed for 1000 hrs at 1170 °C (203 Vickers) has been excluded from the calculation. Using 80 observations the 95% confidence interval (CI) and prediction interval (PI) (*Figure 3b*) were calculated. Only two low temperature observations (LMP=19.48 and 21.76) have untypical behaviour. The maximal width of the confidence interval is 3.7 and the maximal width of the prediction interval is equal to 17. The method of maximum likelihood was used for the determination of the optimum value for the LMP constant C. For thermally exposed samples (80 observations) 95% confidence interval for C is 15.1 to 25.5 with the optimum value equal to 19.3. The new optimum value of C (LMP constant) was used to replot the hardness values. The R^2 values change little. Any differences can only be observed in the fourth decimal place. The LMP constant equal to 19.3 made the R^2 value of the 'thermal' set increase from 0.9168 to 0.9169.

3.2. Microstructural studies

Metallographic studies of the microstructure of HA230 are based on an evaluation of images obtained by light optical microscopy and scanning electron microscopy.

3.2.1. As-received HA230

Figure 4 shows the microstructure of the as-received solution treated and quenched HA230 taken from the same batch as for all the coupons for thermal exposure. It contains primary carbides which were identified by X-Ray Diffraction as $M_{12}C$, in the literature usually presented as M_6C type carbides, *e.g.* [2-4, 6-8]. Primary carbides are tungsten rich (see below), equiaxed in shape, sometimes associated with grain boundaries, also dispersed throughout the microstructure in the form of stringers. Any other precipitation has not been identified at this stage. Grains can be identified as equiaxed in the range of ASTM 4-6.

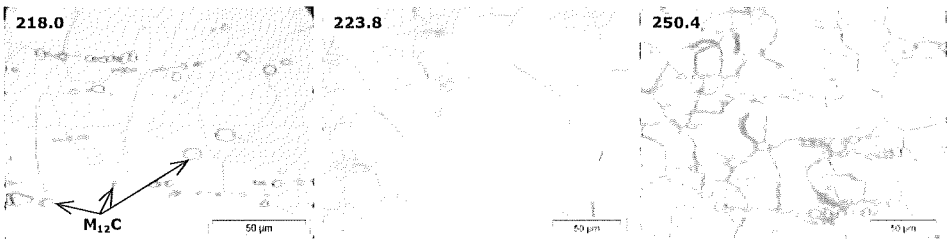

Figure 4 Microstructure of (left to right) annealed and quenched HA230 showing primary carbides; specimen thermally exposed for 24 hours at 650°C; and specimen thermally exposed for 1000 hours at 650°C. The hardness value is given in the top left hand corner.

3.2.2. Thermally Exposed HA230

The microstructural examination was conducted on the thermally exposed HA230 coupons at various conditions as identified in *Figure 2*.

The effect of exposure temperature is prevailing. Heating of the specimens above 500°C initialises the precipitation on the grain boundaries after 1000 hours, but the microstructure in general looks very similar to the as-received material (*Figure 4*). Temperatures above 600°C are causing wider precipitation, mainly on the grain boundaries. After 24 hours, the boundaries are finely decorated but after 1000 hours the precipitation of

the fine carbides can be seen as a cluster on some of the boundaries (see *Figure 4*). Temperatures between 650°C and 750°C create the peak in hardness which is caused by the fine precipitation not only on the grain and annealing twin boundaries but also within the grains.

Typical optical micrographs documenting the microstructural changes in HA230 in the temperature range 750°C and 1050°C for duration of 1000 hours to 30000 hours are shown in *Figure 5*.

The microstructure of the specimens exposed at 750°C contains some primary carbides randomly distributed within the matrix and the fine secondary precipitation on the boundaries and within the grains. At this temperature, the big primary carbides are 'breaking down' (*i.e.* particles which were previously showing no substructure now appear to be no longer homogenous), see *Figure 6*. With increase of the temperature (810°C and 870°C) more and more precipitates are concentrating on the grain boundaries. At 930°C the grain boundary precipitates start to coarsen and primary carbides become more uniform in shape. The lowest hardness of the material at 990°C can be associated with the grain boundary phase coarsening. Rather the phase starts to create 'pools' after long exposures and at 1050°C this 'pool-like' phase creates isolated clusters within the microstructure, see *Figure 5* bottom right.

Figure 6 outlines in detail the transformation of the primary, W-rich, carbide. The 'breaking down' initiates at the edge of the uniform and rounded particles. The Cr-rich phase starts to precipitate in these areas and the two phases can be observed coexisting. As the temperature increases the W-rich carbide is transforming right through to its centre and then again, around 850°C, depending on the duration of exposure, regains its original shape with some cracks in the middle. At the same temperature the Cr-rich phase starts to coarsen. The composition of this phase is complex and varies (transition phase Cr-rich, *Figure 6*). The 'pool-like' phase (*Figure 5*, samples exposed for 20000 and 30000 hours at 1050°C) is very hard and brittle and its composition is mostly the same as that for Cr-rich secondary carbide.

3.3. X-Ray Diffraction

X-Ray diffraction was used to illustrate the phase transformation during the thermal exposure. Initially, analysis was carried out on the bulk material, taking advantage of the non destructive technique, but the necessity to map the phase evolution led to the use of phase extraction in 10% bromine-ethanol solution. The chemical extraction was conducted on as-received material and on the specimens thermally exposed for 3000 hours and 20000 hours at 750°C, 810°C, 870°C, 930°C, 990°C and 1050°C.

The X-Ray radiation is that emitted by copper, with characteristic wavelength (λ) 1.5418Å (Cu). The step size was set to the lowest possible of 0.016° and the speed to 0.15°/min.

The lattice parameter for Haynes Alloy 230 was calculated from the diffractogram and is equal to 3.573Å. Lattice parameter plays an important role in subsequent phase precipitation (*e.g.* influencing distribution and size) [9]. The lattice parameter of pure fcc nickel is 3.523 Å (JCPDS 4-850). Elements in this alloy, such as W, Mo, with atomic radii 1.41 Å, 1.39 Å respectively, distort the lattice and hence shift the lattice parameter.

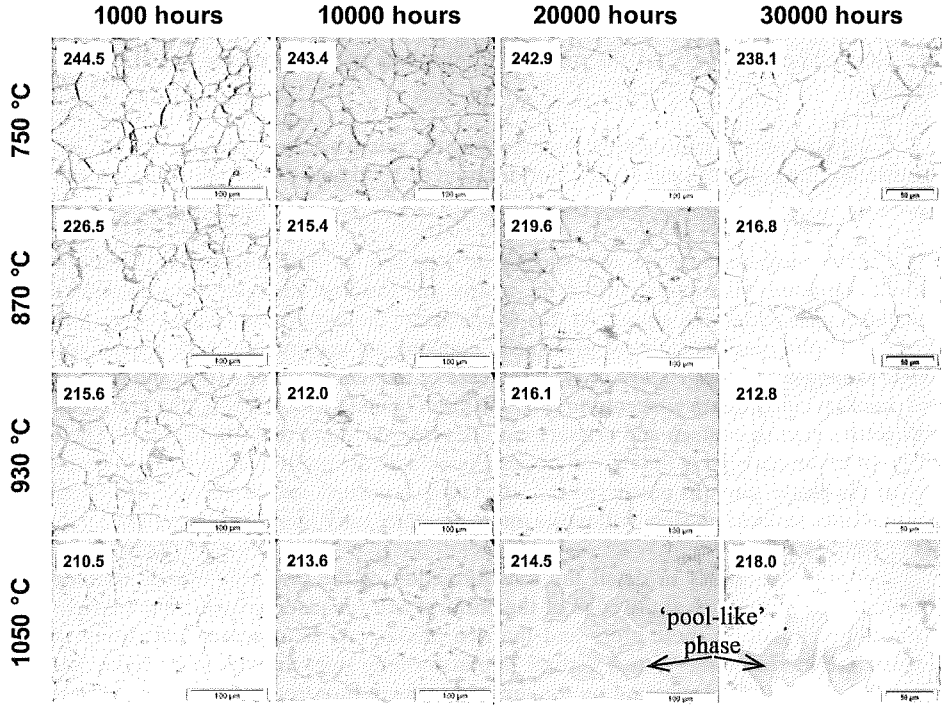

Figure 5 Effects of exposure at temperatures in the range 750℃ to 1050℃ on the microstructure of HA230 showing average Vickers hardness of each specimen (Hv20).

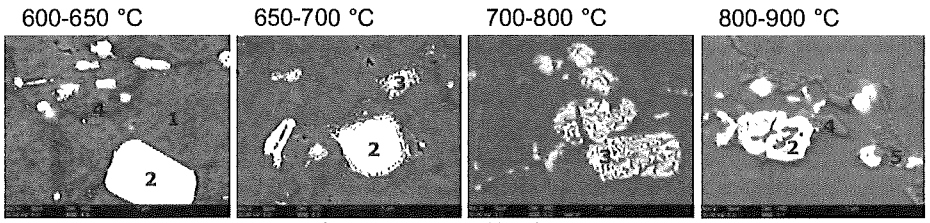

	1 matrix	2 primary C (W-rich)	3 transition phase (W-rich)	4 secondary (Cr-rich)	5 transition phase (Cr-rich)
Ni	58	16	20	9	32
Cr	23	13	33	58	35
W	16	69	43	29	27
Mo	2	6	4	3	5

Figure 6 Transformation of the primary carbide with increase of the temperature and EDX analysis of the phases present in HA230 (average over the set, composition in wt%). For lower temperatures, a longer time is required for transformation to take place.

The peak assignment determined the second phase in the as-received material as the primary carbide, which has the lattice parameter equal to 10.96Å. This value is very close to the carbide, generally identified as $M_{12}C$ with a lattice parameter equal to 10.95Å and composition Fe_6W_6C (JCPDS 23-1127). The finding contradicts the literature, where this

carbide is usually presented as M_6C type, *e.g.* [2-4, 6-8]. The $M_{12}C$ carbide was found, for example by Tawancy in Hastelloy X at 870°C [10].

The overlay of the XRD spectra for specimens thermally exposed for 20000 hours, *Figure 7*, documents the phase evolution within the temperature range from 750°C to 1050°C.

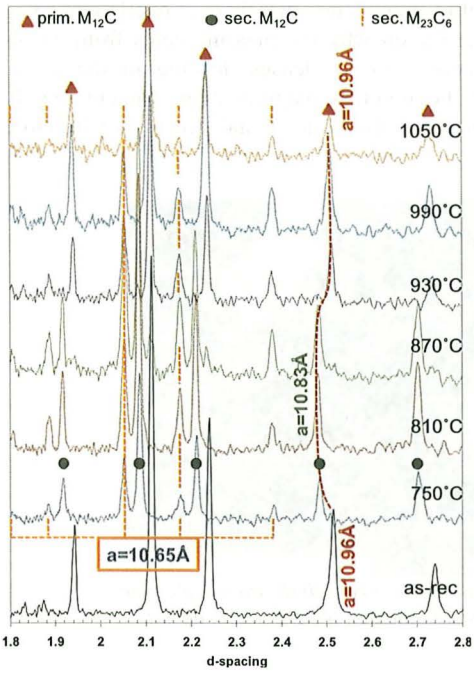

Figure 7 Overlay of XRD spectra acquired on specimens thermally exposed for 20000 hours and the as-received material.

As was mentioned above, the as-received material contains carbide with the lattice parameter equal to 10.96Å, identified as $M_{12}C$. This phase was not detected at 750°C and 810°C. The weak peak appears again at 870°C and the increase of its intensity can be observed with increase of the temperature. The peaks of two secondary phases appear at 750°C. One is the carbide with lattice parameter equal to 10.65Å which corresponds to $M_{23}C_6$ type carbide ($Cr_{23}C_6$ JCPDS 35-783, a=10.66Å), chromium rich. Other peaks correspond to the lattice parameter a=10.83Å and here are called secondary $M_{12}C$ (Co_6W_6C JCPDS 23-939, a=10.89Å), the transition phase tungsten rich. All these carbides are complex and M stands for Cr, W, Ni, Fe, Co. The composition of the carbides is presented in *Figure 6*. Considering the overall intensities of the diffractograms, the $M_{23}C_6$ has the lowest intensity at 750°C but for other temperatures the intensity does not change. Cr-rich phases are sharing the same lattice parameter and the only process occurring is the substitution of the Cr atoms by Ni. The evolution of the secondary $M_{12}C$ is well connected with exposure time.

3.4. Transmission Electron Microscopy

TEM studies have been focused on the identification of phases formed as a result of a long term thermal exposure. The results given here illustrate some of the difficulties. *Figure 8* shows the microstructure of the as-received material with the systems of dislocations on the slip planes, as well as associated with annealing twins within the matrix. There are no precipitates along the dislocations. Some very fine precipitates can be observed along some grain boundaries. These were rich in chromium and are therefore likely to be $M_{23}C_6$ type carbide based on the associated evidence presented earlier.

The exposed specimens were thinned using the Focused Ion Beam technique. This was the most successful approach of those experimented with. Some diffraction patterns have been obtained and evaluated, all of them are from the cubic structures. The lattice parameter of the nickel matrix in HA230 from all the reflections varies reasonably between 3.52 - 3.60 Å.

The estimation of the lattice parameters from other electron diffraction patterns has not provided uniform results. The lattice parameter of the W-rich phase according to the calculation lies between 10.71- 12.45Å and the lattice parameter of the Cr-rich phase lies between 10.27-12.90Å. The results obtained from the electron diffraction patterns for these two phases have such a wide spread of their lattice parameters that there is overlap meaning that a unique identity cannot be achieved. The reason why the measurements from TEMs have the scatter could be, for example hysteresis in the lenses, leading to the actual magnification/ camera length differing from the nominal magnification/ camera length. Consequently it is not possible to distinguish between the same crystal structures with close lattice parameters.

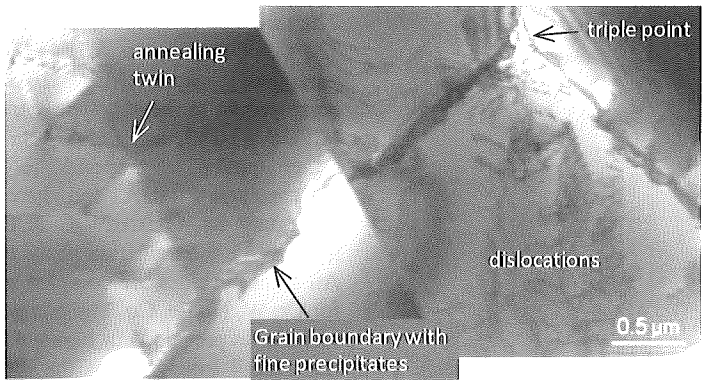

Figure 8 TEM images of the microstructure of the as-received HA230 showing triple point, dislocations, annealing twins and fine precipitation on the grain boundaries.

3.5. Tensile Testing

The effects of high temperature exposure on the mechanical properties of HA230 have been investigated by carrying out room temperature tensile tests on HA230 material exposed for durations of 3000, 10,000 and 20,000 hours at temperatures in the range from 750°C to 1050°C. A plot showing the effects of increasing exposure duration and test temperature on the UTS and 0.2% proof strengths of HA230 is presented in *Figure 9*. The results indicate that following an initial increase in tensile strength both the 0.2% PS and UTS decrease linearly with increasing exposure temperature for all three of the exposure durations investigated.

The 0.2%PS and UTS tensile data are shown plotted against the corresponding hardness values for the thermally exposed HA230 material in *Figure 10*. This indicates that although there is some scatter in the results there is a clear correlation between hardness and tensile strength with increases in hardness corresponding to increases in both the 0.2% PS and UTS in the alloy.

The failure mechanism of the tensile fractured specimen was analyzed using scanning electron microscopy. *Figure 11* compares the fractographs of the tensile specimens exposed for 3000 hours in the temperature range from 750°C to 1050°C. The failure mechanism in all the samples was intergranular fracture. Triple point wedge cracking is shown in the

micrograph. At low temperatures the faceting can be observed. With increase of the temperature carbide cleavage appears. At the highest temperatures ductile rupture takes place.

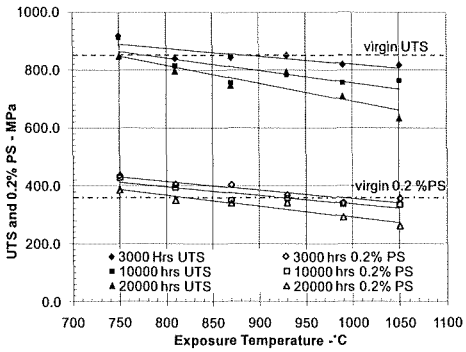

Figure 9 Plot of 0.2% PS and UTS tensile data for HA230 material as a function of temperature for exposure durations of 3K, 10K and 20K hours.

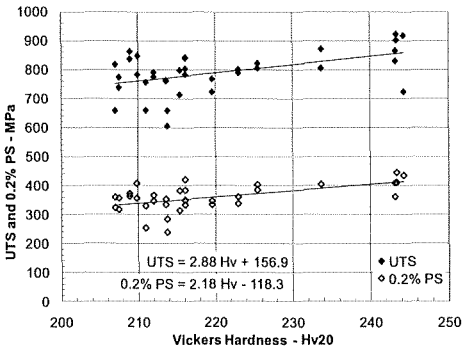

Figure 10 Variation of 0.2% PS and UTS with hardness for thermally exposed HA230.

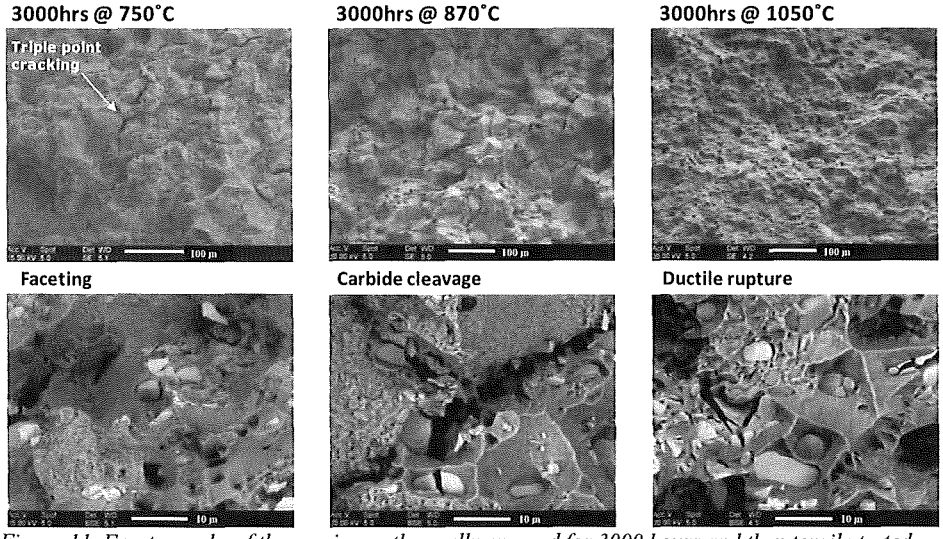

Figure 11 Fractographs of the specimens thermally exposed for 3000 hours and then tensile tested.

Conclusions

The results have demonstrated that a master Hardness v Larson-Miller parametric plot can be generated from the hardness data. A least squares regression analysis has shown that a cubic polynomial gives a good fit to these data with an R^2 value of 0.917. The optimum LMP constant for this set of data was 19.3 but a conventional value of 20 gives almost the same R^2 value. Optical microscopy and FEGSEM studies on thermally exposed HA230 have revealed microstructural factors which can be directly correlated with the observed changes in hardness

due to thermal exposure over the range of temperatures and durations investigated [11]. XRD studies revealed the presence of three precipitating phases in HA230 viz. primary $M_{12}C$ type carbide (~70wt% W), secondary $M_{12}C$ type carbide (~45wt% W) and secondary $M_{23}C_6$ type carbide, with a complex composition over the range of exposures.

Acknowledgements
The authors would like to thank Dr M. Phillips for help with statistical analysis. The authors are also grateful to the COST consortium (Action 538) for facilitating the programme that this study formed part of. Funding from EPSRC and from Siemens is gratefully acknowledged. The EPSRC is thanked for funding the access to the TEM instruments in Oxford Materials under the Materials Equipment Access scheme.

References

1. Haynes International. *HAYNES 230 Alloy Product Brochure, H-3000.* www.haynesintl.com
2. Klarstrom, D.L., The Development of Haynes 230 Alloy, *Corrosion*, p. 407/1-407/12, (1994).
3. Klarstrom, D.L., Heat treatment/Property Relationships for Solid-Solution Strengthened Heat Resisting Alloys, in *1st International Conference on Heat Resistant Materials,* Lake Geneva, (1991).
4. Klarstrom, D.L., The Thermal Stability of a Ni-Cr-W-Mo Alloy, in *NACE Corrosion 94*, (1994).
5. Matthews, S.J., Thermal Stability of Solid Solution Strengthened High Performance Alloys, *Superalloys: Metallurgy and Manufacture*, p. 215-226, (1976).
6. Jordan, C.E., Raserfske, R.K., Castagna, A., Thermal Stability of High Temperature Structural Alloys, Long Term Stability of High Temperature Materials, *Proceedings of TMS Annual Meeting*, p. 55-67, (1999).
7. Whittenberger, J.D., 77 to 1200K Tensile Properties of Several Wrought Superalloys after Long-term 1093K Heat Treatment in Air and Vacuum, *Journal of Materials Engineering and Performance*, **3**(1), p. 91-103, (1994).
8. Vecchio, K.S., Fitzpatrick, M.D., and Klarstrom, D., Influence of Subsolvus Thermomechanical Processing on the Low-Cycle Fatigue Properties of Haynes-230 Alloy, *Metallurgical and Materials Transactions A: Physical Metallurgy and Materials Science*, **26**(3), p. 673-689, (1995).
9. Wang, T., Chen, L.Q., and Liu, Z.K., Lattice parameters and local lattice distortions in fcc-Ni solutions, *Metallurgical and Materials Transactions A: Physical Metallurgy and Materials Science*, **38**(3), p. 562-569, (2007).
10. Tawancy, H.M., Long-term ageing characteristics of Hastelloy alloy X, *Journal of Materials Science*, **18**(10), p. 2976-2986, (1983).
11. Veverkova, J., Strang, A., Marchant, G. R., McColvin, G. M., Atkinson, H. V., High temperature microstructural degradation of Haynes Alloy 230, in *Proceedings of the International Symposium on Superalloys*, p. 479-488 (2008).

9th Liege Conference : Materials for Advanced Power Engineering 2010
edited by J. Lecomte-Beckers, Q. Contrepois, T. Beck and B. Kuhn.

DEGRADATION OF LCF PROPERTIES OF CMSX-4 SINGLE CRYSTAL SUPERALLOY, AFTER CREEP EXPOSURE AT 850°C AND 950°C

A. Cammi, S. Concari, C. Rinaldi
ERSE, via Rubattino 54; Milan (Italy)

Abstract

In the frame of the COST 538 programme one important aspect of the activity was the collection of quantitative information about the influence of service degradation on mechanical properties of Ni-based alloys, used in the hot parts of gas turbines. To reach such goal material degradation was obtained by preliminary creep exposure to conditions similar to those experienced by blades during service. Preaged specimens were tested to determine the tensile and LCF behaviour of the degraded material at high temperature.
The experiments were performed with CMSX-4 single crystal superalloy. Specimens with double heads for creep and LCF were machined from as delivered bars. In this paper the influence of creep ageing in the two following conditions is described: 2500h both at 850°C and at 950°C with applied stress of 320 and 150 MPa respectively, which let to obtain deformation levels in the range 0.3 to 0.5%. On the superalloy degraded in the two conditions LCF tests were performed at the same temperatures of the pre-ageing. In both cases a reduction in LCF resistance close to a 2 factor was observed on respect that of the virgin alloy. This can be explained by the results of fractographic and metallographic observations performed in the three material conditions (virgin, aged at 850°C and at 950°C) . At the lower temperature only an initial microstructural degradation level (mainly increase of the gamma channels width and some coarsening) was observed, as expected; rafting was observed on the material degraded at the higher temperature, in agreement with predictions of published models of microstructural degradation of CMSX-4 due to creep aging.

Keywords: LCF, creep, degradation, single-crystal, microstructure

1. Introduction

The general aim of the COST 538 was to prepare a "tool box" containing techniques, algorithms, models and data to be used as a basis in the evaluation of the residual life of plant components. In this frame the WP3 was particularly devoted to the collection of quantitative information about the influence of service degradation on mechanical properties of Ni-based alloys, used in the hot parts of gas turbines. In particular both tensile and LCF resistance at high temperature of the degraded alloy are necessary to calculate the residual life of ex-service components. Several creep ageing conditions were examined by the different laboratories involved in the COST 538 programme – WP3, to obtain a wide data base relative to different levels of material degradation, as is actually found in the various regions focused on the influence of rafting happening at the higher temperature (950°C), but also to the less evident microstructural evolution observed at lower temperatures (850-700°C), more typical of the regions near the root of single crystal blades [1].

The present paper describes ERSE's (former CESIRICERCA) activity on CMSX-4 (single crystal) performed as contribution to the whole project matrix for determining the LCF properties of degraded material.
ERSE's activity included the following phases:

- Strain controlled fatigue tests on as delivered CMSX-4 materials;
- Creep ageing of CMSX-4 bars (at 850°C and 950°C);
- Strain controlled fatigue tests on creep aged CMSX-4
- Fractography and metallography of the tested specimens
- Comparison with results and models of other partners [1,2]

2. Experimental activity

2.1. *Strain controlled fatigue tests on CMSX-4*

Strain controlled fatigue tests were performed on bars with nominal 001 orientation. As stated in the agreed test matrix of COST 538 Work Programme, tests were performed in the as received condition, both at 850 °C and at 950°C. The results of the tests performed following the ASTM E-606 are shown in Table 2.
A first analysis of these data shows that in terms of Cycles to Failure vs. Strain Range all the data lie inside the scatter band previously estimated on the CMSX-4 alloy.
The different behaviour between the two temperatures can be noticed comparing the maximum stress of the half life cycle with that of the first cycle: at 850°C a slight increase is present indicating a tendency to hardening (except test with total strain range 1.6 % where the increase is very limited). On the opposite at 950°C the maximum stress is lower at half life than at the beginning of the test, indicating that the superalloy is softening during fatigue cycling.

Table 2 – LCF tests on virgin CMSX4

Test Temperature (°C)	Total Strain Range [%]	Young's Modulus Cycle 1 [GPa]	Young's Modulus HL Cycle [GPa]	Plastic Strain Range Cycle 1 [%]	Plastic Strain Range HL Cycle [%]	σ max Cycle 1 [MPa]	σ max HL Cycle [MPa]	Δσ Cycle 1 [MPa]	Δσ HL Cycle [MPa]	Cycles to Failure
850	1.0(I)	92	91	0.0023(I)	0.0038(I)	465(I)	467(I)	909(I)	918(I)	46874(I)
850	1.3	97	98	0.0050	0.0151	644	694	1269	1262	4060
850	1.4	91	91	0.0024	0.0250	646	717	1259	1263	2600
850	1.6	96	97	0.0154	0.0408	763	766	1503	1500	894
950	1.2	86	85	0.0125	0.0552	498	478	1004	980	2619
950	1.3	88	88	0.0023	0.0560	569	559	1109	1097	2280
950	1.6	89	89	0.0219	0.1131	710	652	1372	1327	442

(I) Interrupted test, not considered as proper LCF regime

2.2. *Creep and Strain controlled fatigue on CMSX-4*

Other bars in nominal 001 orientation from the same supplier were received later to perform ageing in creep conditions and Strain controlled fatigue tests of degraded material in creep conditions.

The specimens were machined with double heads, as shown in figure 1 (upper), to perform:
- the interrupted creep test (exposure at high temperature under load);
- the cut away of the creep threaded heads;
- the remachining of the gauge to eliminate the surface layer affected by oxidation in the furnace during the interrupted creep test;
- the Strain controlled fatigue test

The two conditions for the ageing of CMSX-4 under load were the following:

1. T= 850 °C, σ = 320 MPa, t = 2500 h

2. T= 950 °C, σ = 150 MPa, t = 2500 h

At the end of the creep ageing the specimens were remachined as shown in figure 1 (bottom) It must be noticed that the specimen surfaces were machined with the finishing level required by the ASTM standard, to eliminate the surface alteration due to oxide formation during creep tests.
The specimens were tested at the same temperature of their preliminary creep ageing with strain ranges similar to those used to characterise the behaviour of the virgin material.
Results of Strain controlled fatigue tests on creep aged specimens at 850°C are summarised in Table 3.

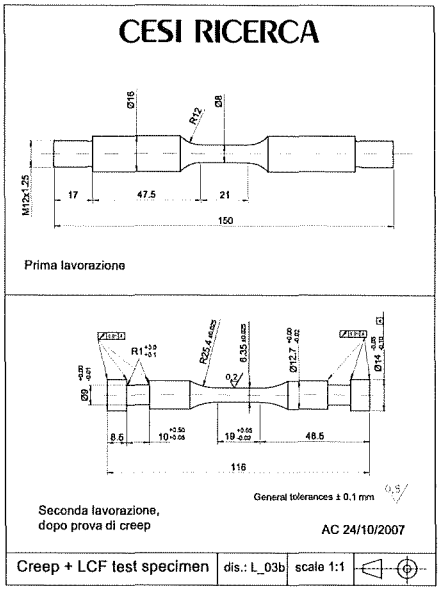

Figure 1 - Specimen for preageing of CMSX-4 material in interrupted creep tests (top). The bottom drawing indicates the final dimensions of LCF specimens after ageing and remachining to eliminate the oxide layer.

Table 3 LCF result on CMSX-4 creep aged at 850°C

Test Temperature (°C)	Total Strain Range [%]	Young's Modulus Cycle 1 [GPa]	Young's Modulus HL Cycle [GPa]	Plastic Strain Range Cycle 1 [%]	Plastic Strain Range HL Cycle [%]	σ max Cycle 1 [MPa]	σ max HL Cycle [MPa]	Δσ Cycle 1 [MPa]	Δσ HL Cycle [MPa]	Cycles to Failure
850	1.3	97	97	0.0082	0.0387	628	618	1235	1236	2950
850	1.4	91	92	0.0027	0.0388	625	612	1242	1255	1151
850	1.6	94	95	0.1332	0.1223	744	755	1410	1424	388

Comparing results at 850°C of Tab. 1 (virgin) and Tab. 2 an increase of the plastic range can be observed, particularly large for the 1.6% strain range; in his condition a small hardening of the pre-aged alloy during fatigue can be noticed while in the tests at the lower strain ranges the degraded material begins to soften (this behaviour is opposite to that of the virgin alloy).
These findings are in agreement with the tensile behaviour of virgin and degraded CMSX-4 reported in Fig. 3 of ref. [1]

The comparison between the LCF behaviours at 850°C of the creep aged CMSX-4 and the as received material is shown in figure 2, where also a reference scatterband for CMSX-4 virgin at the same temperature is included. A 2 factor reduction of fatigue resistance in term of life (number of cycles) at the same applied strain range is visible mainly at the higher strain ranges.

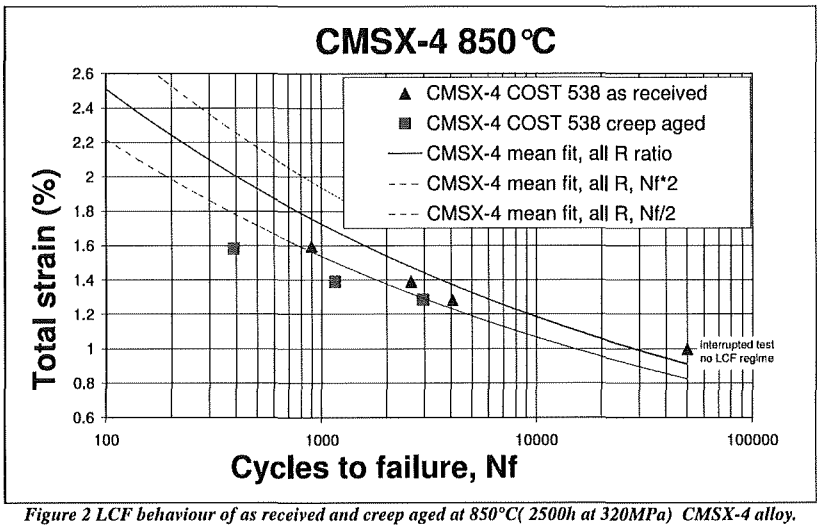

Figure 2 LCF behaviour of as received and creep aged at 850°C(2500h at 320MPa) CMSX-4 alloy.

At the end of the creep ageing at 950 °C a similar work of remachining and testing was done. Results of strain controlled fatigue tests on creep aged specimens at 950°C are summarised in Table 4.

Table 4 - LCF result of creep aged CMSX-4 at 950°C

Test Temperature (°C)	Total Strain Range [%]	Young's Modulus Cycle 1 [GPa]	Young's Modulus HL Cycle [GPa]	Plastic Strain Range Cycle 1 [%]	Plastic Strain Range HL Cycle [%]	σ max Cycle 1 [MPa]	σ max HL Cycle [MPa]	Δσ Cycle 1 [MPa]	Δσ HL Cycle [MPa]	Cycles to Failure (§)
950	1.2	89	90	0.0514	0.0817	538	514	1041	1040	1500
950	1.3	96	94	0.1551	0.1756	544	512	1062	1065	499
950	1.4	89	88	0.1604	0.1886	561	547	1068	1083	520
950	1.6	88	86	0.2226	0.2520	612	588	1184	1174	362

Comparing the plastic range of the virgin material with the degraded one (Tab. 1 and 3) at the first and at the half life cycles, a much higher value can be observed on the degraded alloy, in good agreement with the softening observed during tensile testing (fig. 3 of ref. [1])

The comparison between the LCF behaviours at 950°C of the creep aged CMSX-4 and the as received material is shown in figure 3, where also the reference scatterband at the same temperature for CMSX-4 virgin is included. A reduction in LCF life on respect the virgin alloy can be clearly seen..
The comparison of the stress vs. strain loop at the initial and half life cycles shown in figure 4 for the 1.6% deformation tests at 950°C indicates that both the as received and the degraded at 950°C alloys soften during fatigue cycling; this effect is higher for the creep aged condition.

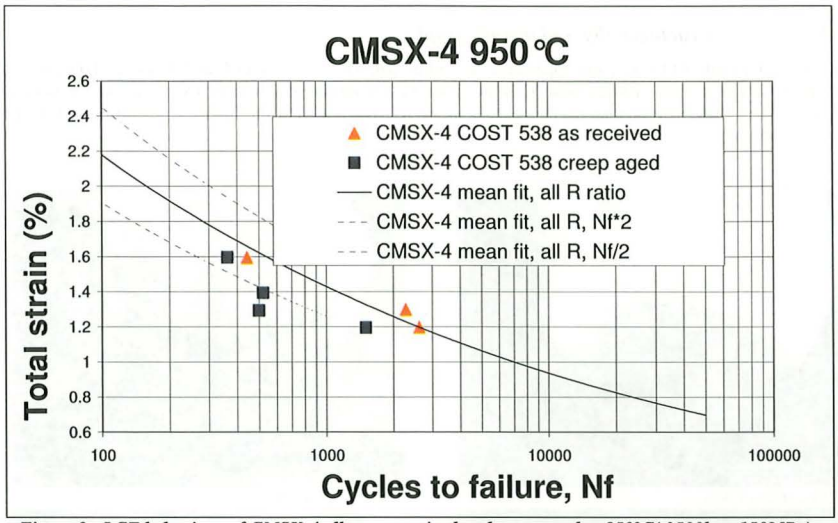

Figure 3 - LCF behaviour of CMSX-4 alloy: as received and creep aged at 950°C(2500h at 150MPa) .

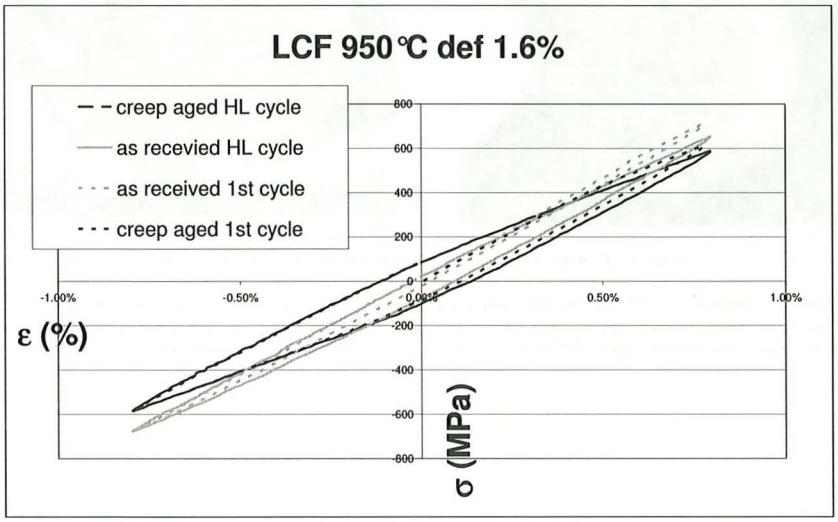

Figure 4 - Stress-strain loops at the initial and half life cycles for LCF test at 950°C and 1.6% total strain: both the virgin and the degraded material soften during the test; the creep aged more than the virgin.

2.3. *Fractography and metallography*

The general aspect of LCF fracture appearance for virgin material tested at 850°C and 950°C is shown in figure 5, where the fatigue crack propagation (in some cases progressing on double front from separated initiation) is limited to less than 50% of total surface except in the test performed at the higher temperature and with the higher strain range.

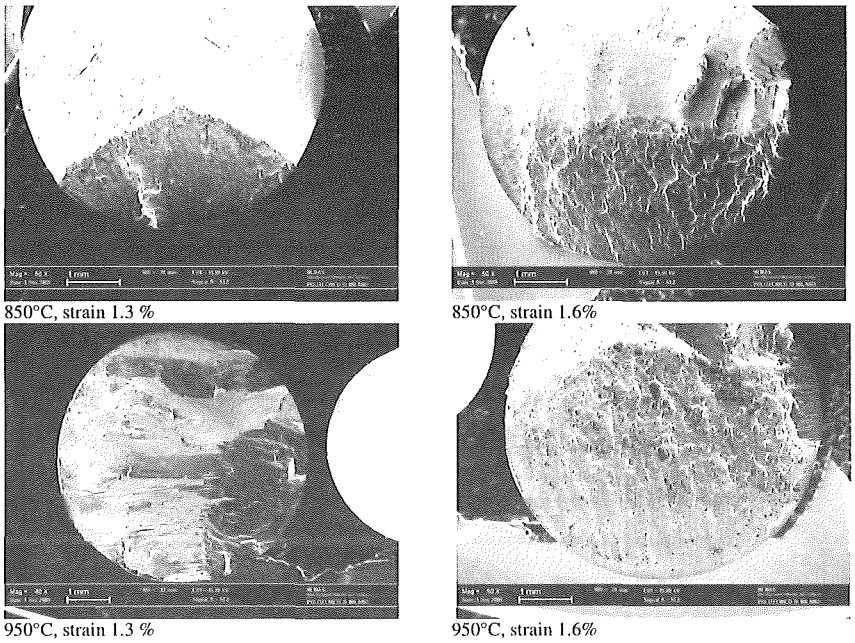

Figure 5 – Fracture appearance of virgin material CMSX-4 LCF tested.

Equivalent overview of LCF fracture appearance for the degraded material is presented in figure 6 where the fatigue crack propagation is approaching 80% of the total surface except in the case of the higher temperature and the higher strain range where the fatigue area is reduced on the respect virgin material.

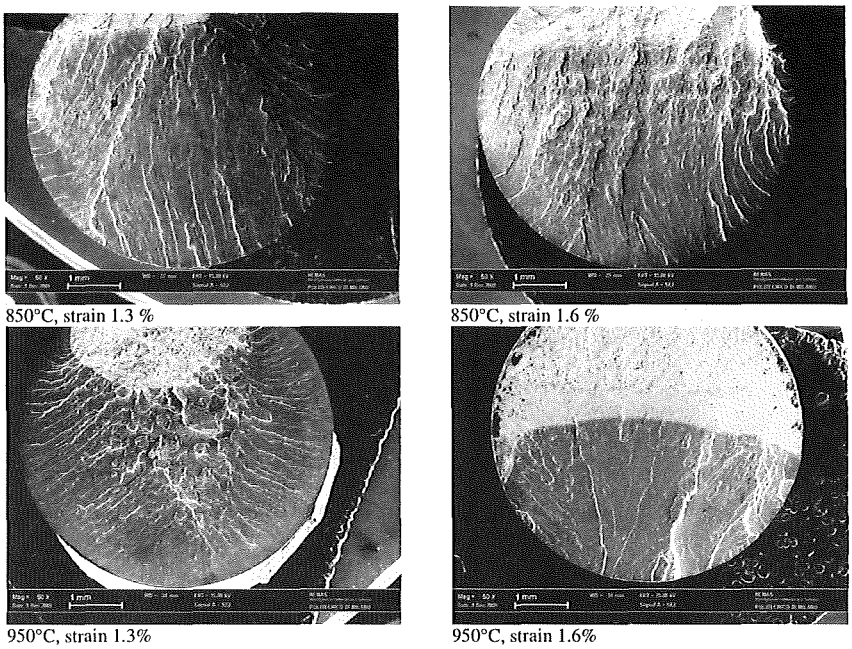

850°C, strain 1.3 %

850°C, strain 1.6 %

950°C, strain 1.3%

950°C, strain 1.6%

Figure 6 – Fracture appearance of creep aged material (LCF test and ageing at the same temperature)

The microstructure observed in the area close to the fatigue crack initiation is shown in figure 7 for the two specimens of the virgin material tested at different temperatures with the same strain 1.3%. A regular cuboidal γ' structure is observed with a limited tendency to an increase of the γ channels' width in the specimen tested at the higher temperature. A similar microstructure is observed close to the final fracture surface and in the area far from the fracture surface in both specimens.

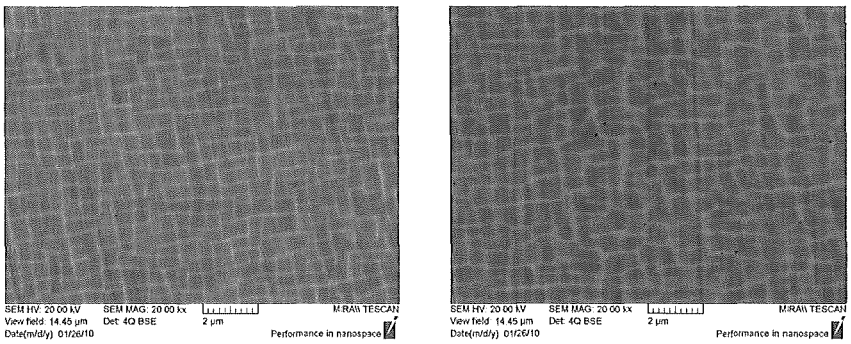

850°C

950°C

Figure 7 – Microstructure observed close to fatigue crack surface of virgin CMSX-4 alloy after LCF tests. Notice the coarsening of the microstructure and the wider γ' channel width in the test at 950°C.

The microstructure observed for the creep aged specimens after LCF test is presented in figure 8 with reference to the tests with $\Delta\varepsilon$= 1.3%. The specimen creep aged at lower temperature with higher stress (850°C and 320

MPa) shows a coarsening of γ channels' width and a partial aggregation of some γ' cuboids with phase coarsening. In the specimen creep aged at the higher temperature with reduced stress (950°C and 150 MPa) the original microstructure with cuboidal γ' disappeared and rafting perpendicular to the applied load direction is present. The well known presence of TCP precipitates in the 950°C creep aged specimens is shown in Fig. 9.

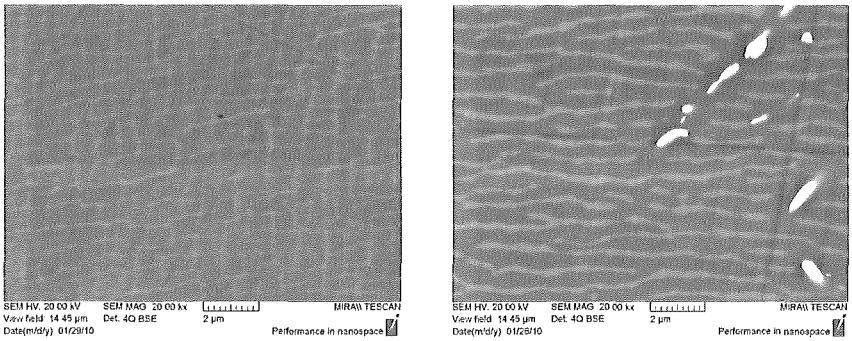

850°C **950°C**

Figure 8 – Microstructure observed close to fatigue crack surface of creep aged (at the same temperature of LCF tests) CMSX-4 LCF tested.

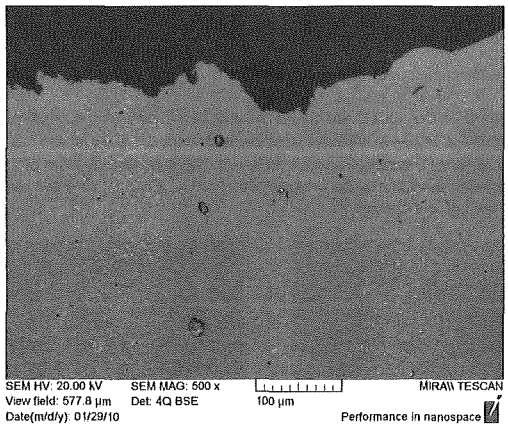

Figure 9 Section of the CMSX-4 specimen aged at 950°C for 2500h at 150MPa and then tested at 950°C and 1.6% strain: TCP phases precipitation

Some aspects of the crack propagation and of the microstructure in the specimen creep aged at 850°C and LCF tested at the same temperature are shown in figure 10; the growth of the fatigue crack is along the γ channel between γ' cuboids at the interface between γ and γ' phases which lost coherence during the previous creep ageing (figure 10a); the cutting of γ' cuboids is limited to the final fracture (right side of figures 10b and 10c) and the blunting of a secondary crack (figure 10d).

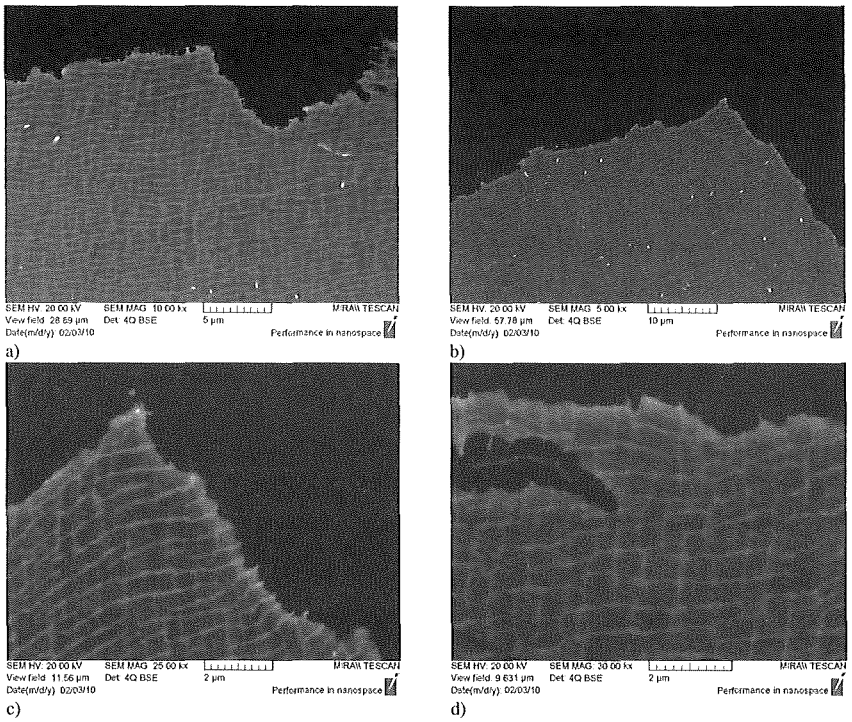

Figure 10 Correlation of microstructure and crack propagation: a) fatigue propagation, b) and c) fatigue propagation on the left and final brittle cut on the right, d) blunting of a secondary crack

3. Discussion of experimental results

The initial assumption for creep ageing conditions was based on an estimated equivalent macro strain in the range 0.3 - 0.5 % at the two different temperatures 850 and 950°C.

A quite different evolution of γ/γ' microstructure was observed in the 1.3% strain controlled fatigue tested specimens of figure 8: rafting at 950°C after a preageing for 2500h at 150MPa, but no rafting at 850°C, after 2500h at 320MPa. This is in agreement with the results of a microstructural transformation study for CMSX-4 in creep ageing [1,2] performed in the frame of the same Action COST 538 .

The LCF life reduction observed for equivalent tests of virgin and creep aged material shows an averaged value of 2 for both temperatures. A similar value has been estimated also in another work [3] performed on the same material with a higher temperature creep preageing (1050-1100 °C and 110-120 MPa).

A comparison of LCF life reduction trend vs. controlled strain, based on best fitting curves of experimental data, is presented in figure 11. The tendency of increased LCF life reduction at lower strain observed by Epishin & [1] is confirmed for tests at 950°C while an opposite trend appears at 850°C. For comparison of these data with the above mentioned authors [1,2] it should be considered that in that work a wide range of creep ageing conditions were considered, while presented results of strain controlled tests also at lower temperature (750°C) referred to creep ageing transformation of microstructure with rafting appearance.

Better understanding of the behaviour observed now, can be expected from the completing of the microstructural characterisation of every tested specimens and through a further analysis focused on the γ/γ' interface forces acting in virgin material (regular cuboidal), aged material without rafting (850°C creep ageing) and totally transformed with rafting (950°C creep ageing).

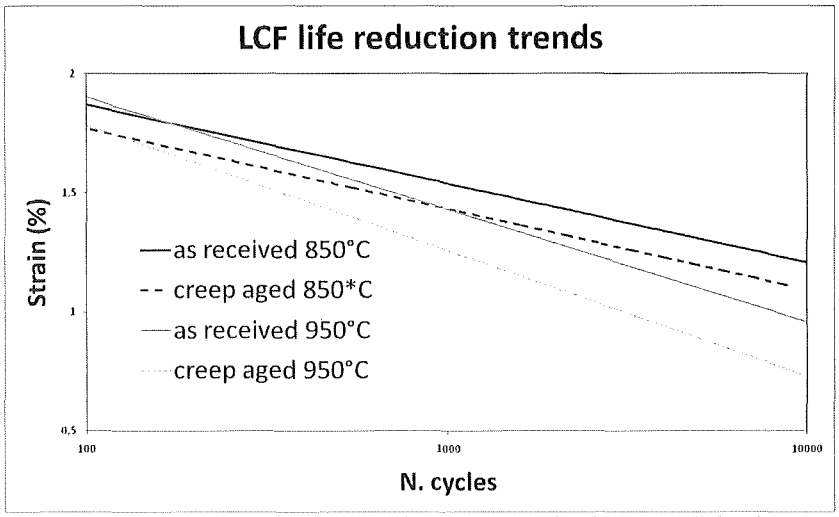

Figure 11 Trend of life reduction induced by creep ageing as function of controlled strain

4. Conclusions

The activity performed shows the different levels of LCF degradation properties of CMSX-4 induced by two different creep ageing conditions, giving a contribution to the target of COST 538, aimed at collecting elements useful in the residual life evaluation of a single crystal alloy applied in high temperatures components. The metallographic analyses performed after tests give also indications about the correlation of mechanical properties degradation with the microstructural evolution of CMSX-4. The results obtained at 950°C are in agreement with other experimental data obtained in the past for the virgin condition and also for the creep aged alloy at 950°C. The rafted morphology of these specimens is also a confirmation of the model developed in the same Action [1,2], describing the dependence of the microstructural degradation by t, T, stress. Moreover a significant reduction of LCF life is found also in the specimens creep aged at 850°C, even if no rafting is present in the microstructure produced by the pre-ageing done at this temperature.

Acknowledgements

This work has been financed by the Research Fund for the Italian Electrical System under the Contract Agreement between the Ministry of Economic Development - General Directorate for Energy and Mining Resources and ERSE S.p.A. (formerly CESI RICERCA). The authors are also grateful for the fruitful collaborations with partners of the Cost 538 programme.

Reference list

[1] A. Epishin, T.Link, M. Nazmy, M. Staubli, H. Klingelhoffer, G. Nolzo; Microstructural degradation of CMSX-4: kinetics and effect on mechanical properties, *Superalloy 2008* ed. by Reed et al., TMS 2008

[2] A. Epishin, T. Link, H. Klingelhoffer, B. Fedelich, P.D. Portella; Creep damage mechanisms of single-crystal nickel base superalloys, *ECCC Creep conference 2009* ed. by Shibli I.A., Holdsworth S., ECCC 2009

[3] M. Ott, H. Mughrabi; Dependence of the high-temperature low-cycle fatigue behaviour of the Ni-based single crystal superalloy CMSX.4 and CMSX-6 on the γ- γ' morphology, *Material Science and Engineering* A272, 1999

9th Liege Conference : Materials for Advanced Power Engineering 2010
edited by J. Lecomte-Beckers, Q. Contrepois, T. Beck and B. Kuhn.

APPLICATION OF COATING AND BASE MATERIAL LIFING MODELS TO EVALUATE DEGRADATION AND ESTIMATE THE MEAN LOCAL OPERATING TEMPERATURE OF TWO EX-SERVICE 1ST STAGE BLADES

M. Mandelli*, C. Rinaldi** E. Vacchieri***

* Proing Italia, Torbole sul Garda, Trento, Italy
** ERSE (ex. CESI RICERCA),Milan, Italy
*** Ansaldo Energia; Genova, Italy

Abstract

In the frame of the collaborative program COST 538 a coating life prediction code was implemented by Proing and ERSE with an inverse problem solution routine able to calculate the local mean operating temperature from the operating conditions and the extension of the coating depleted regions. Moreover base material degradation models were developed by Ansaldo Energia on both equiaxed and single crystal superalloys. This paper describes the application of such methodologies to two ex-service 1st stage gas turbine blades delivered to COST 538 by AEN after operation in two different plants with different operating conditions. The objective of the study was the application and validation of an innovative NDT and the estimate of the mean operating temperature at different positions of the components. The destructive metallographic analysis of the blades let to validate the non destructive frequency scanning eddy current technique (F-SECT). Coating life modelling results are compared with those of the base material degradation models. An interesting correlation was found between the estimated temperatures with the two methods and also with the NDT findings at the most significant component positions.

Keywords: lifing models, temperature evaluation, NDT, F-SECT, blades

1. Introduction

To minimize the operating costs of gas turbine operation, the possibility to increase the maintenance intervals is a very important goal as hot parts refurbishment and replacement is one of the most expensive factors. This goal can be reached studying degradation mechanisms on specimens exposed in the laboratory to conditions representative of operation (e.g. cyclic oxidation and creep) to develop lifing models and codes, see for example [1]. Such reference degradation models can be used to evaluate the degradation of operated components, to evaluate the spent life fraction of the part. Both coating beta phase depletion and base material microstructural degradation are elements to be taken into account in such evaluations. In such activities NDTs can play a fundamental role because high cost savings could be obtained from the possibility to measure degradation parameters reliably without cutting the component [2,3].

A very important element is the mean operating temperature of the hottest regions of the component. Even if this datum can be known from finite element calculations (FEM) performed to design the gas turbine, in several cases the plant operation is actually performed in conditions different from those of the original design (different fuels, cyclic operation...). Moreover the real behaviour of the component (e.g. local cooling) could be not precisely predicted by calculations. As a consequence the analysis of components dismounted from a gas turbine after operation is very useful because the true local degradation can be

determined. Information about actual local temperatures can be obtained if lifing models were previously developed exposing representative specimens at high temperatures in laboratory furnaces.

In the frame of the European Collaborative Project COST 538 (Life Extension of high Temperature Components) [4] both lifing models and NDTs were developed and applied to some case studies. The case histories here described were analysed to exemplify the capability of a NDT technique (F-SECT [2,3,5]) and of the coating and base material lifing models developed respectively by ERSE and Ansaldo Energia. After a short description of the two models and of the F-SECT technique, their application is presented to two ex-service 1st stage blades, with the aim to evaluate the degradation level and mean operating temperatures at different positions of the examined components.

2. Models and NDT

Ni based superalloys and metallic coatings used to protect them from oxidation/corrosion have the best performance if the microstructure contains intermetallic phases (gamma prime, γ', in the base alloy and beta phase, β, in the coating) optimised in shape and size by suitable heat treatments. The high temperature exposure during service causes microstructure evolution and consequently mechanical property degradation, due to diffusion phenomena nowadays well known and widely studied [6]. Moreover the presence of stress accelerates such degradation processes [6, 7].
The quantification of the behaviour of the single superalloy and coating requires extensive laboratory testing and quantitative metallography and X-ray microanalysis to determine oxidation rates and diffusion coefficients, strongly depending on the chemical composition in so complex alloys. Both in the COST programme and in national R&D project such studies were performed on IN738LC equiaxed alloy and CMSX-4 single crystal superalloys. Also coating degradation was studied by cyclic oxidation testing. Quantitative metallography performed on exposed specimens let to determine the coefficients of the equations of the models chosen to describe the material/coating degradation as described in the following.

2.1. Base material degradation model (ANSALDO)

In the frame of COST 538 Ansaldo Energia carried out a deep microstructural characterisation on IN738LC equiaxed alloy. This superalloy is reinforced by a bimodal distribution of γ' phase precipitates as reported for the as delivered condition in Figure 1 top left. The microstructural characterisation was performed after isothermal exposures in the temperature range that a real component could probably withstand during service: from 800°C to 1000°C. Moreover the ageing times were selected from 300 to 15,000 hours, compatibly with project duration, to follow in detail the microstructural evolution from the starting condition to long term exposure. In Figure 1 some micrographs from the exposed samples are reported to show the evolution of γ' precipitates: at higher temperatures, primary γ' phase particles coarsen much more at the expense of secondary γ' phase particles, which were dissolved completely before 3000 hours; primary γ' phase shape changes from cuboidal to spheroidal or roundish with increasing ageing time. Microstructural data of γ' phase from exposed specimens were obtained using a semi-automatic routine of an image analysis software on several high magnification micrographs per sample captured by SEM. The collected γ' phase features, in

particular mean size of primary γ' phase, were elaborated to construct a model to evaluate operating temperature in ex-service components. Experimental data were worked out with two different methods [8]: a chemical physical approach based on Ostwald ripening kinetics, called Lifshitz-Slyozov-Wanger model [9], an empirical approach based on a parameter time and temperature dependent, well correlated to microstructural measurements (Figure 2).
After the validation of both approaches the empirical method was chosen to be applied to the case studies here reported because it is very easy to use.

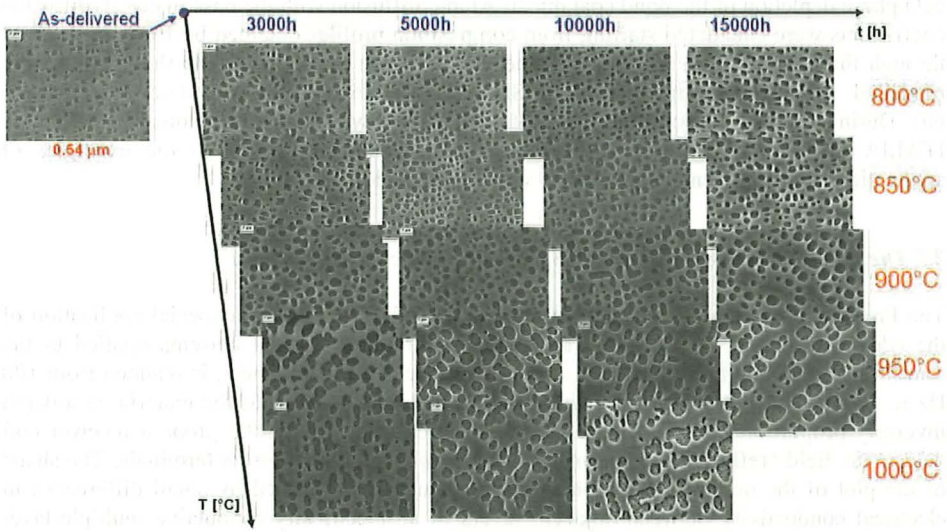

Figure 1: Microstructure evolution of primary γ' phase in IN738LC superalloys after isothermal exposure.

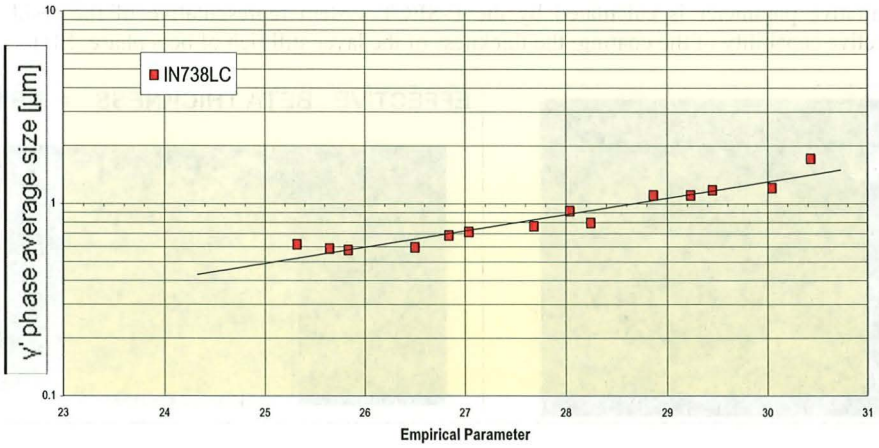

Figure 2: Relationship between primary γ' phase size in IN738LC superalloy after long term isothermal exposure and empirical parameter P(t,T).

2.2 Coating degradation model (ERSE) and IPS routine

The model used in the coating life evaluation code was developed by CESI RICERCA on the basis of extensive cyclic oxidation tests perfomed in the frame of a National R&D programme since 2000 and prosecuted in the frame of COST 538. Initially the code was based on the oxide growth laws for the Amdry 995 coating and for NiCoCrAlYRe bond coats under an EB-PVD TBC, as determined interpolating experimental data. Oxide thickenss and depleted regions of the coating were measured on SEM micrographs. Moreover to model the beta phase depletion of the bond coat due to Al interdiffusion with the base material, diffusion coefficients were calculated starting from composition profiles obtained by EDS in the SEM through the base material/coating interface; the diffusion processes inside the coating were modelled using the principles of the COSIM code (main elements considered were Al, Cr, Ni). During COST 538 activities the coating life code was further developed by PROING ITALIA in collaboration with ERSE, as widely described in [10]. Some examples of applications to components were used to validate the code [10,11].

2.3 The non destructive technique F-SECT for bond coat degradation

The Frequency Scanning Eddy Current method (F-SECT) [2,3,5] is a special application of the eddy current (EC) technique. The frequency of the sinusoidal currents applied to the transmitter coil of an EC probe, held near the surface of the component, is scanned from 100 Hz to 100kHz. At each frequency the magnetic field penetrates into the material at a depth inversely proportional to the square root of the frequency. Inside the probe a receiver coil detects the field "reflected" by the material as an induced voltage at its terminals. The shape of the plot of the probe output voltage vs. frequency is influenced by small differences in electrical conductivity between adjacent layers of an electrically conductive multiple-layer material, such as the metallic coating-substrate system of gas turbine hot parts. From the measured raw data a physical parameter is obtained by a computerised system and named "normalised impedance". Different shapes of the impedance vs frequency plot (Figure 3 left) result to be associated to different damage levels of an MCrAlY coating [5]. Moreover a quantitative parameter is calculated by the F-SECT system representative of the residual protective capability of the coating: the thickness of the layer still rich of beta phase, EBT.

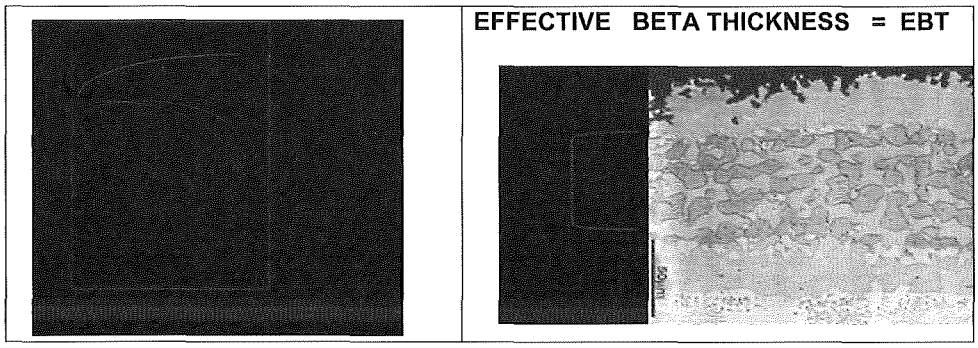

Figure 3: Schematic of typical curves obtained with F-SECT system (left) and definition of the quantitative coating degradation parameter, EBT (right).

3. Case histories

In this section the component's histories are presented, together with material/coating information and NDTs results obtained from F-SECT technique applied to evaluate the degradation of the metallic coating. For each component also the results of the metallographic analysis and of temperature estimation with the two degradation models are reported.

3.1 Blade with metallic coating

3.1.1 Material and coating of the blade

The first examined blade is a first stage from an Ansaldo GT, that has been dismounted after 20,000 EOH (equivalent operating hours) of service. The base material of this component was in its second life after the refurbishment process and worked totally for 40,000 EOH, mainly in base load regime. In Table 1 the chemical compositions of the base material and of the metallic coating applied on the component, SiCoat 2231, are reported. In Figure 4 some pictures of the blade are shown.

Table 1: Chemical composition of the base material and metallic coating of the blade 1.

Element [wt%]	Ni	Cr	Co	Al	Ti	Mo	W	Ta	Nb	B	C	Y	Si
IN738LC	bal	16	8.5	3.5	3.5	1.8	2.6	1.8	0.85	0.01	0.11	-	-
SiCoat 2231	30	28	bal	7.5	-	-	-	-	-	-	-	0.6	0.5

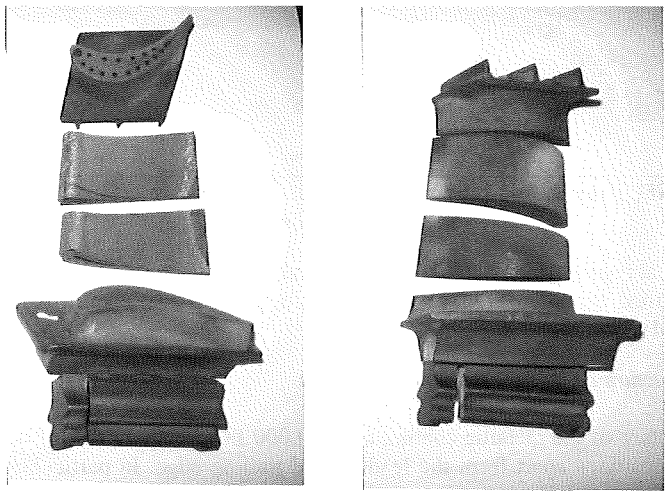

Figure 4: Pictures of the suction and pressure side of the blade 1, after the cut off of the three airfoil horizontal sections where the microstructural investigation was performed.

3.1.2. F-SECT results

The blade was inspected by the F-SECT technique, to evaluate the residual protective capability of the bond coat through the parameter EBT (equivalent effective beta thickness). The measured values are shown in Figure 5 and indicate local variations, both between suction and pressure sides and near leading and trailing edges at the central part of the blade. The measurements of F-SECT were compared with the regions still rich of beta phase on the corresponding metallographic sections. On these latter the presence of a double layer of coating was found; the two layers are separated by an oxide rich boundary. If only the thickness of the upper BC layer are considered a better agreement with the F-SECT measurements can be found. Some pictures of the metallographic sections are reported in Figure 5.

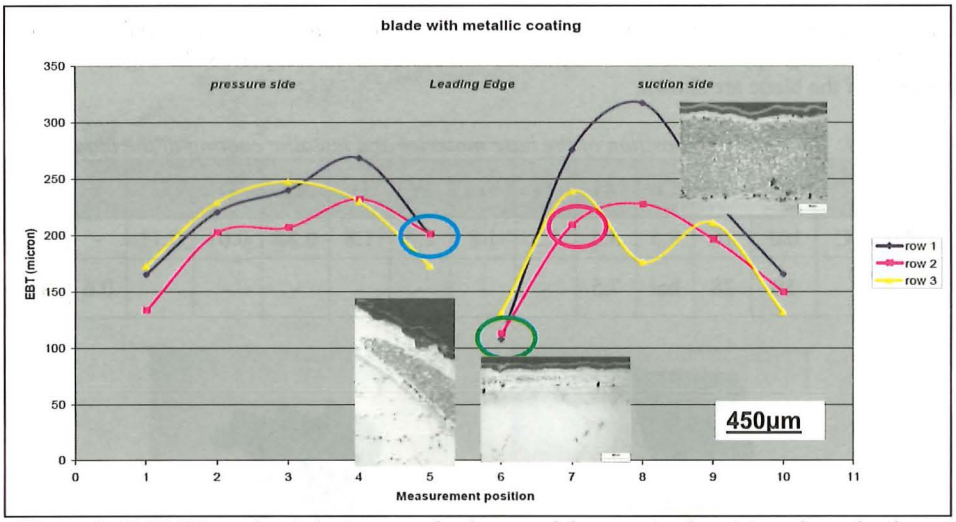

Figure 5: F-SECT results and micrograph of some of the examined position along the three blade sections.

The most critical region of the blade was the leading edge, where the Sicoat2231 coating was completely burned during operation; at that position the oxidation/nitridation of the base metal happened (micrograph in Figure 5).

3.1.3 Microstructure degradation and T estimation

The microstructure of the metallic coating after 20,000 EOH is quite rich of beta phase in all the examined positions apart from the leading and trailing edge. In particular at the leading edge the metallic coating thickness is low, possibly due to a not proper deposition process, but also to higher temperatures during operation, as the beta phase depleted regions are wide and beta phase particles have larger size here than in other regions of the blade (Figure 6).
The base material microstructure was examined at the central section of the blade. The biggest γ' phase grains were found in the leading and trailing edge, while the pressure side positions

show slightly smaller γ' phase particles than suction side. This behaviour is in agreement with the metallic coating degradation level.

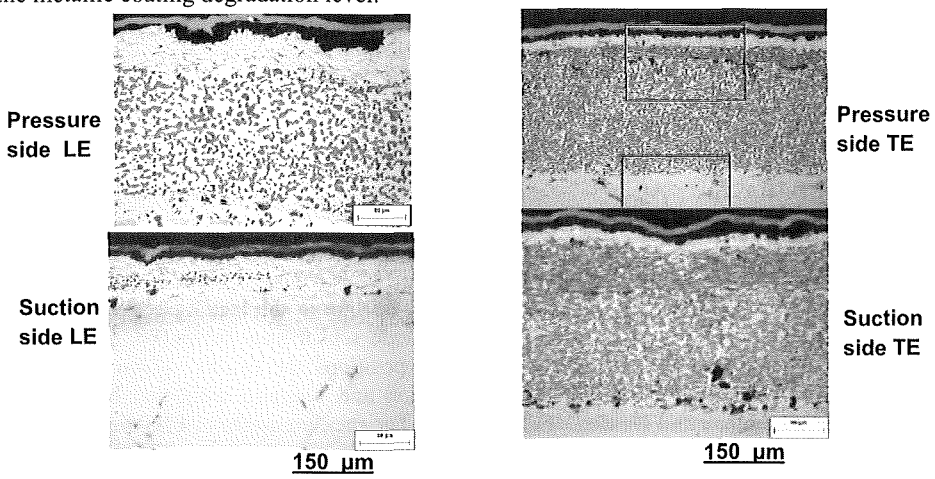

(a) (b)

Figure 6: OM x200 micrograph of the metallic coating on the pressure side and suction side in the (a) position near the leading edge and (b) positions near the trailing edge.

The mean operating temperatures were estimated from both the coating and base alloy degradation models on the analysed positions of the central section. Results are shown together with values coming from the calculated thermal maps in Table 2; there is a good agreement among them. As expected the coating is exposed to higher temperatures than the base material, internally cooled.

Table 2: Temperature values at midheight of blade 1, estimated from coating degradation model (CO-M), base material model (BM-M) and calculated by finite element methods(maps).

	Position	*Leading edge*	*Near leading edge from the suction side*	*Trailing edge*	*Centre of the Pressure side*	*Centre of the Suction side*
T [°C]	Calculated Thermal Maps	900	840	890	800	790
	Coating Model	952	885	863	820	750
	Base Material Model	810	810	860	800	780

3.2 Blade with TBC

3.2.1 Material and coating of the blade

The first examined blade is a first stage from an Ansaldo GT, that has been dismounted for problems only after 3,000 EOH of service. This blade is similar to the previous case, but the applied coating is different: the metallic coating is a SiCoat 2453 and it was coated by an

APS-TBC, PSZ. In Table 3 chemical compositions of base alloy and metallic bond coat are reported.

Table 3: Chemical composition of the base material and metallic coating of the blade 2.

Element [wt%]	Ni	Cr	Co	Al	Ti	Mo	W	Ta	Nb	B	C	Y	Re
IN738LC	bal	16	8.5	3.5	3.5	1.8	2.6	1.8	0.85	0.01	0.11	-	-
SiCoat2453	54	21	12	11	-	-	-	-	-	-	-	0.4	2

3.2.2. F-SECT results

The blade was inspected by the F-SECT technique, but not at the leading edge, the hottest position where the TBC detached, due to the too wide sensor size (nowadays new smaller probes are under development). At the measured positions the results shown in Figure7 indicate some local variations, both between suction and pressure sides and between the central part of the blade and leading/ trailing edges. The measurements of EBT performed by F-SECT are in reasonable agreement with those done later on metallographic sections; two examples are reported in Figure 8 (a) and (b). It must be noticed that the probe face is about 10mm in diameter, while the metallographic picture is relative to only half mm in length.

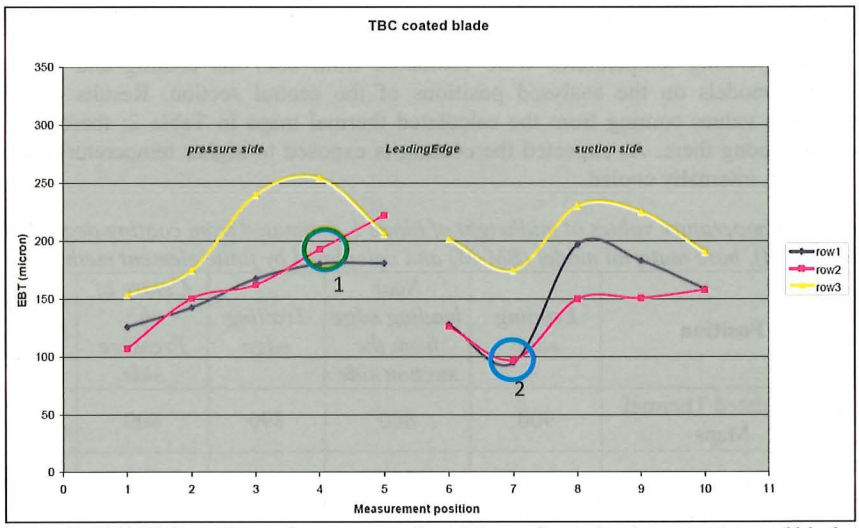

Figure 7: F-SECT results at the examined positions along the three sections of blade 2.

3.2.2 Microstructural degradation and temperature estimation

The metallic coating is not greatly affected by the service probably because of the short duration. Only at the leading edge some consumption of the β phase is observed; in this area the TBC detached from the metallic coating (Figure 8-c) so that the bond coat reached the high temperatures of gases. In the base material the γ' phase is generally regular and similar to an as delivered material; only at the leading edge in correspondence with the TBC detachment the morphology of the γ' phase indicates high temperature exposure. This is shown by the

micrographs reported in Figure 9 relative to the leading edge from the hot region just under the bond coat to the cooling channel. The temperature of the blade was estimated at each examined position of the three horizontal sections by the base material model, starting from the γ' size and three examples were reported in Table 4.

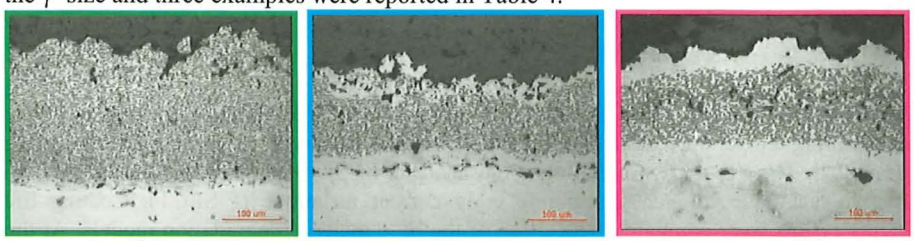

(a) (b) (c)

Figure 8: OM x200 micrograph of the metallic coating in (a) point 1 and (b) point 2 highlighted in Figure 9, and (c) from the leading edge where TBC spalled.

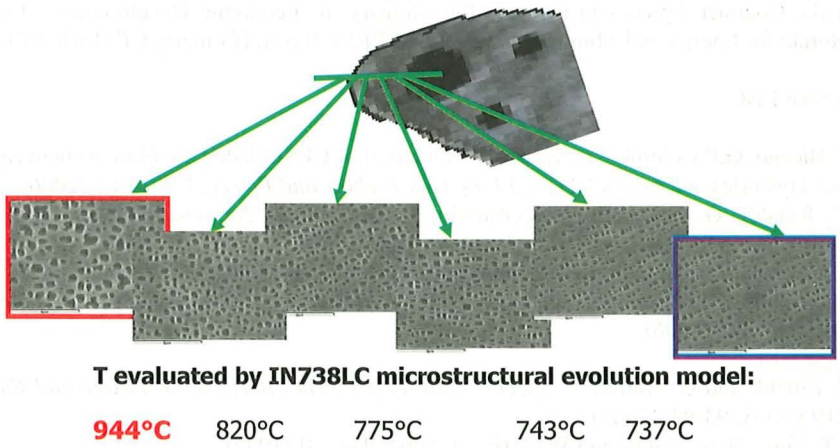

Figure 9: SEM/SE x7500 micrograph of the primary γ' phase in the leading edge from the hot side under the metallic coating to the cooling channel.

Table 4: Estimated temperatures in the central section of the blade with TBC.

	Position	*c*	*b*	*a*
T [°C]	Calc.Thermal Maps	700	670	630
	Coating Model	>950	880	820
	Base Material Model	942	725	725

Table 4 reports estimated temperatures in the most significant positions on the central section. It can be noticed the good agreement between T estimated by the two models in the hottest position; here the calculated thermal maps predict a much lower value due to the hypothesis of TBC presence, while TBC actually spalled. At all the other positions the different values of

T estimated by the two models confirm the fact that these models are not very precise for low degradation conditions, such as those caused by only 3000hours as in this blade, as these models are obtained from accelerated exposures in laboratory at high T and/or very long times.

6. Conclusive Remarks

Both the NDT evaluation of the bond coat degradation by F-SECT and the estimate of the mean operating temperature at different positions of two ex-service 1st stage blades by lifing are described. The destructive metallographic analysis of the blades let to validate the non destructive technique frequency scanning eddy current technique (F-SECT). Coating life modelling results were compared with those of the base material degradation models. At the hottest component positions a good correlation was found between the estimated temperatures with the two methodologies and also with the NDT findings.

Acknowledgments
This work was financially supported by the Research Fund for the Italian Electrical System under the Contract Agreement between the Ministry of Economic Development - General Directorate for Energy and Mining Resources and ERSE S.p.A. (formerly CESI RICERCA).

Reference List

[1] V. Bicego, G.P.Colombo, C. Rinaldi "Validation of CESI blade Life Management System by Case Hystories and in situ NDT", *J.Eng. Gas Turbine and Power,* 128,73-80 (2006)
[2] C. Rinaldi, G. Antonelli, F. Cernuschi, L. De Maria, 'An integrated approach with innovative NDTs for TBC assessment', *paper ASME ESDA2006-95555,* (2006).
[3] S. Osgerby, C. Rinaldi, L. De Maria, 'Recent Advances In NDT Techniques For Gas Turbine Coatings', *Materials for Advanced Power Engineering 2006, Eds J Lecomte-Beckers et al,* pp. 217-232 (2006)
[4] www.cost
[5] C. Rinaldi and G. Antonelli, *Special Issue Paper Proc. Imech E, J. Power and Energy*, vol. 219 Part A, 93-99, (2005).
[6] C.T. Sims, N. S. Stoloff and W.C. Hagel, Superalloys II (1987).
[7] M. Nazmy, A. Epishin, T. Link, M Staubli, 'Degradation in single crystal nickel-base superalloys - A review', *Materials for Advanced Power Engineering 2006, Eds J Lecomte-Beckers et al,* pp.205-216 (2006)
[8] E. Vacchieri, A. Bonadei, G. Delogu, E. Cordano, S. Corcoruto, E. Poggio, "Operating temperature estimation based on microstructure evolution of Ni-base superalloys for GT blades/vanes", *Proc. The Future of Gas Turbine Technology, 4th International Conference,* 15-16 October 2008, Brussels, Belgium (2008).
[9] A.Baldan, "Review: Progress in Ostwald ripening theories and their applications to gamma prime precipitates in nickel-*base superalloy: Part II – Ni-base superalloys", J. of Materials Science* 37, 2379-2405, (2002).
[10] C.Rinaldi and M. Mandelli, "The Role of Oxidation and Diffusion Kinetics in a Coating Life Prediction Code - Application to Components" *Proc. ASME TURBO 2009, Orlando, Florida* ASME Paper GT2009-60063.
[11] C. Rinaldi, L. de Maria, M. Mandelli 'Assessment of the Spent Life Fraction of Gas Turbine Blades by Coating Life Modelling and Photostimulated Luminescence Piezospectroscopy', *J. Eng. Gas Tubines and Power*, April 2010, vol.132 (2010).

9th Liege Conference : Materials for Advanced Power Engineering 2010
edited by J. Lecomte-Beckers, Q. Contrepois, T. Beck and B. Kuhn.

EFFECT OF COHERENCE FAILURE ON γ′-PHASE PARTICLE GROWTH IN NICKEL SUPERALLOYS

Zaitsev D.V., Alekseev A.A.

All-Russian Scientific Research Institute of Aviation Materials "VIAM"
Moscow, Radio st. 17, 105005, admin@viam.ru

Abstract

A comparative analysis of the structure of samples of a Re- and Ru-containing heat-resistant Ni alloy after the full heat treatment (FHT) and in the heads of the samples after creep tests was carried out in this work. It was shown that after the FHT during long-term holds at temperatures up to 900°C and time interval up to 1500 hrs, the γ′-phase particle size practically remains unchanged. An average size of the γ′-phase particles was 380-430 nm. An analysis of the impact of the γ- and γ′-phase coherent contingency disarrangement process on the growth of the γ′-phase particles was made. It was shown that after the disarrangement of coherence, the average energy of a γ′-phase cubic particle, depending on its size (cube side value ℓ), varies in a non-monotone way. During the growth of the particles with simultaneous disarrangement of coherence, a particle in the discussed alloy is caught in an energy trap. Thus, under the FHT in the single crystals of Re- and Ru-containing heat-resistant Ni alloys, the coherent contingency of the γ- and γ′-phases is disturbed and the γ′-phase particle size becomes stable.

1. Introduction

At present, it is persistently believed that the γ′-phase particles in heat resistant nickel alloys after the FHT remain coherent [1]. According to the Lifshits-Slesov theory about the kinetics of the formation and growth of particles during diffusion decomposition of oversaturated solid solutions, an average size of an equaxial-shape coherent particles increases during annealing [2].

In this work, a comparative analysis of the structure of samples of Re- and Ru-containing heat-resistant Ni alloys after the full heat treatment (FHT) and in the heads of the creep-tested samples was performed. It was shown that after the FHT during long-term holds at temperatures up to 900°C and time interval up to 1500 hrs, the size of the γ′-phase particles did not change significantly. The effect of the disarrangement of coherence on the growth of the γ′-phase particles in heat-resistant nickel alloys was studied.

2. Materials and procedures

In this work, the study on the structure of a heat-resistant nickel alloy, containing 6.8% Re and 5% Ru, after the FHT and creep tests was carried out.

The study was performed using the scanning electron microscope JSM 6490-LV, transmission electron microscope JEOL JEM200CX and X-ray diffractometer D/MAX-2500.

3. Results of electron-microscopic investigation

For the alloy containing 6,8% of Re and 5% of Ru, an average size of the γ′-phase particles is 380-430 nm (Fig.1)

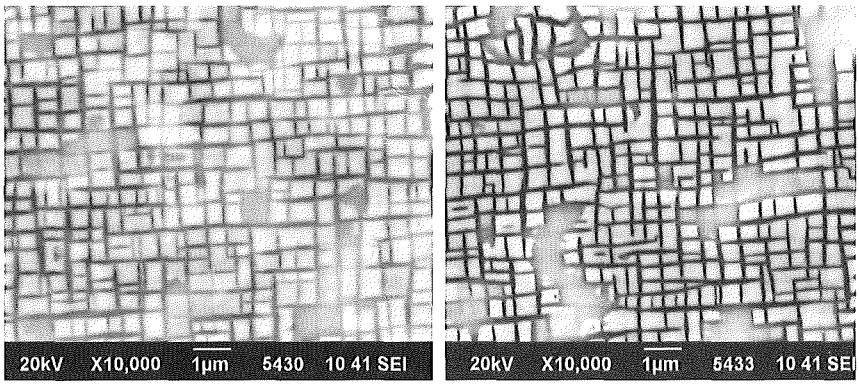

a b

Fig. 1 Structure of the samples of heat-resistant Ni-alloy with 5% Ru: a) after FHT; b) the head of a sample after creep test (900°C, 1210 hrs.)

The analysis of the nature of contingency of the γ′-phase particles with the γ-matrix after the FHT was performed. The results of the investigation by dark field techniques of transmission electron microscopy are shown in Figure 2.

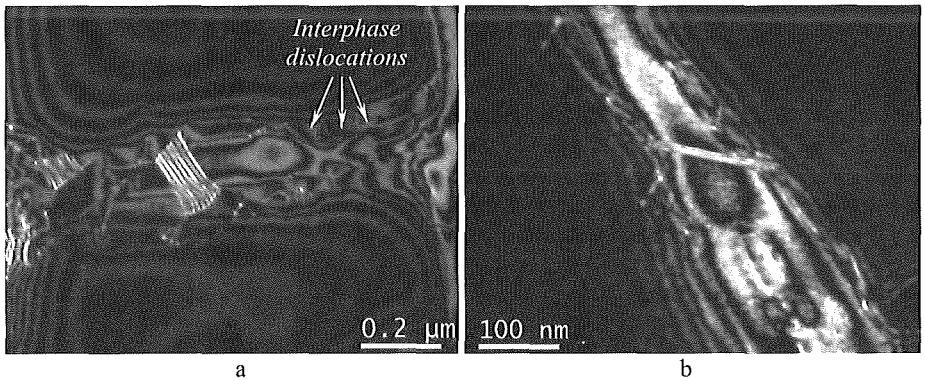

a b

Fig. 2 Interphase dislocations on γ/γ′ boundaries and packing defects in γ-interlayers: a) axis of zone (100); b) axis of zone (110).

It was shown by a TEM analysis that the dislocations of a/2 <110>-type are formed on the interphase boundaries. The splitting of the dislocations with the formation of packing defects is also observed. The splitting of the dislocation takes place as a result of the dissociation of interphase dislocations with the Burgers vector a/2[110] into two partial dislocations: a negative Frank dislocation with the Burgers vector a/3[111] and a Shockley dislocation with the Burgers's vector a/6[112] (Fig.3). This allows us to suggest that the addition of Ru

decreases the energy of the packing defect, which is favorable to the dislocation reaction of dislocation splitting owing to an interaction with another interphase dislocation on the opposite interphase boundary (Fig.3):

$$a/2[110] = a/3[111] + a/6[11\bar{2}]_{(111)}$$

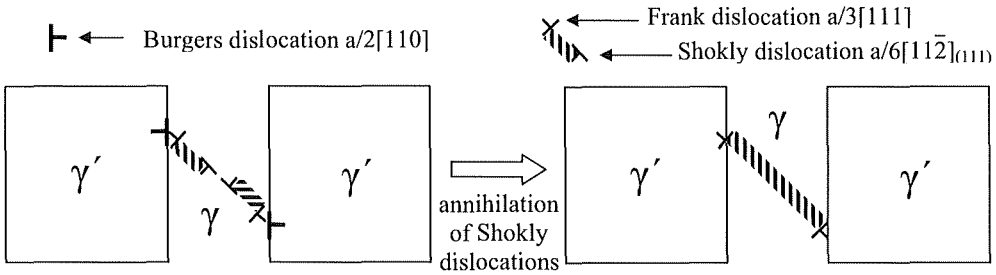

Fig.3 Diagram of dislocation reactions with the formation of a deduction-type packing defect in γ-phase

4. Theory

A theoretical analysis of the effect of the γ- and γ′-phase coherent contigency disturbance process on the growth of the γ′-phase particles was performed. In heat resistant nickel alloys, nonconformity in the lattice constants of the γ′-phase and matrix e_o^T is of positive value, i.e.:

$$e_o^T = \frac{\left|a^{\gamma} - a^{\gamma'}\right|}{a} \quad \text{at } a^{\gamma} > a^{\gamma'},\ a = \frac{a^{\gamma} + a^{\gamma'}}{2}$$

where a^{γ} and $a^{\gamma'}$ are the lattice constants of the γ-matrix and γ′-phase in the stress-free states. Consequently, the interphase prismatic dislocation loops of an interstitial type with the Burgers vector: $\bar{b} = \frac{a^{\gamma}}{2} < 110 >$ where $b = \frac{a^{\gamma}\sqrt{2}}{2}$, formed at the disarrangement of coherence, compensate a difference between the volumes of a cubic-shape γ′-particle and the matrix. To compensate the difference between the volumes, six prismatic loops are necessary in this case. The balance is given below:

$$\Delta V = 6\frac{a^{\gamma}\sqrt{2}}{2}\ell^2\sqrt{2} = 6b\ell^2\sqrt{2} = 3e_o^T\ell^3,$$

where ℓ is the cube side. Then the minimal ℓ, at which the particle remains coherent, is equal to:

$$\ell_0 = \frac{2a^{\gamma}}{e_o^T}.$$

The disarrangement of coherence of the γ′-phase with the γ-matrix changes the e^T discrepancy. When $\ell < \ell_0$, the particle remains coherent, and $e^T = e_o^T$; when $\ell = \ell_0$, $e^T = 0$. Thus, with increasing ℓ, e^T changes discontinuously. In the general case:

$$\frac{e^T_{(x)}}{e^T_0} = 1 - \frac{n}{x} \quad \text{for} \quad n < x < n+1 \quad \text{at} \quad n = 0,\ 1,\ 2,\ 3,\ldots, \text{ where } x = \frac{\ell}{\ell_0}.$$

The plot of $\frac{e^T_{(x)}}{e^T_0}$ against x is shown in Figure 4a.

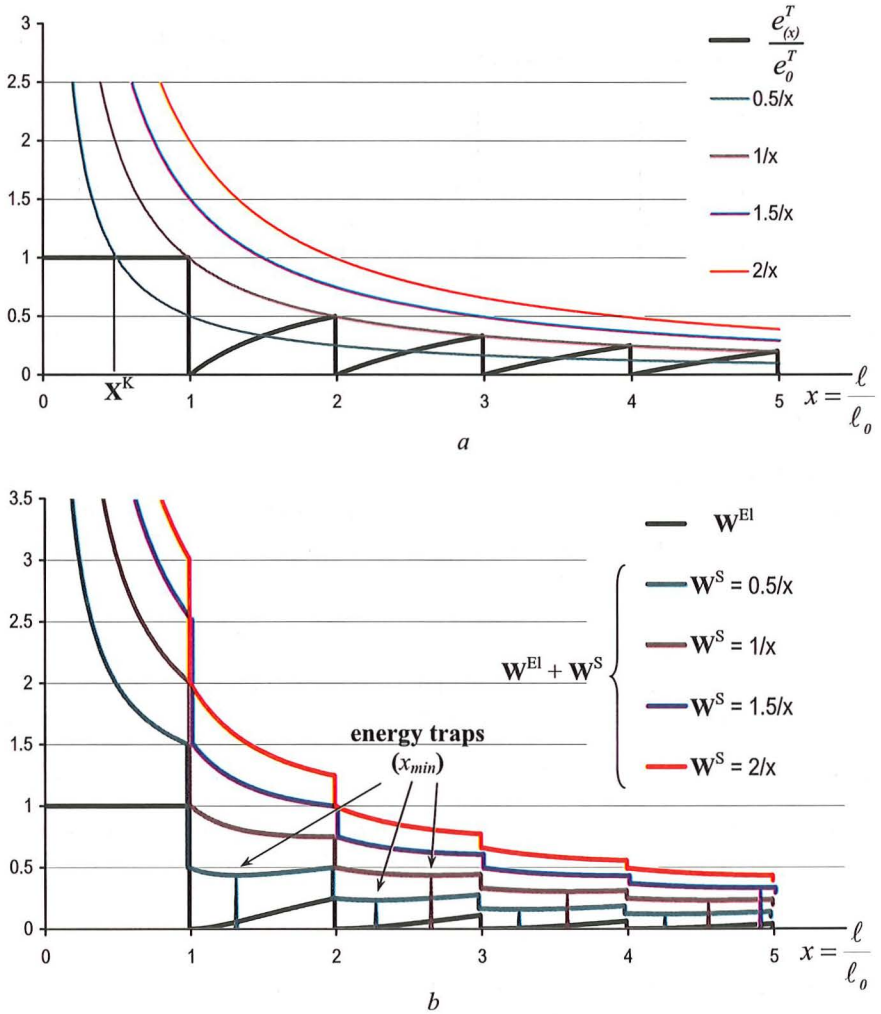

Fig.4 The γ'- particle properties vs. x-size: a) misfit $\frac{e^T_{(x)}}{e^T_0}$ and *surface energy* W^S*; b) strain energy* W^{El} *and total energy* $(W^{El} + W^S)$

If a γ′-phase cubic particle has a discrepancy of $e^T(x)$, the energy of elastic distortions in the material is defined by the formula:

$$E^y = 2G\frac{1}{9}\frac{(1+\nu)}{(1-\nu)}e^{T^2}\ell^3,$$

where G is the shear modulus, ν is the Poisson's ratio.

The energy of the interphase boundary of such a particle is $E^S = 6\ell^2 T$, where T is the specific boundary energy.

Since the T value is the square energy of the interphase surface, it is convenient to present it in the nondimensional form: $T=\alpha G b$, where α is the numerical factor.

For the analysis of the effect of the coherence process on the growth of the particles, it is necessary to analyze a change in the total energy $E^y + E^S$ with increasing ℓ. It is convenient to consider nondimensional values.

$$W^{El} = \frac{E^y}{\ell^3 (e_0^T)^2 G\frac{2}{9}\frac{(1+\nu)}{(1-\nu)}} = \left(\frac{e_{(x)}^T}{e_0^T}\right)^2$$

$$W^S = \frac{E^S}{\ell^3 (e_0^T)^2 G\frac{2}{9}\frac{(1+\nu)}{(1-\nu)}} = A\frac{1}{x},$$

where $A = \frac{3\sqrt{2}}{2}10^{-4}\frac{\alpha}{\frac{2}{9}\frac{(1+\nu)}{(1-\nu)}e_0^T}$

The plots of W^S against x, calculated for A=0.5; 1; 1.5; 2, are given in Fig. 4a. The size of the particles $\ell^\kappa = x^\kappa \ell_0$ shown in Fig. 4a has a definite physical meaning. At $\ell < \ell^\kappa$, the γ′-phase particles remain spherical, but at $\ell > \ell^\kappa$ they acquire a cubic shape. Thus, having knowledge of e_o^T, from the value of the γ′-phase particle size, at which the transformation from a spherical to cubic shape occurs, it is possible to determine the T-specific energy of the γ/ γ′ interface.

5. Discussion

In Fig. 4b the plots of W^{El} and $(W^{El} + W^S)$ against the x value and A are given. As it is shown, the sum of the energy $W^{El} + W^S$ during the growth of the γ′-phase may have local minima. These local minima are realized for the sizes:

$$x_{min} = \frac{2n^2}{2n - A}, \quad n = 1, 2, 3, \ldots$$

If the γ′-phase particles in the alloy have the size coinciding with one of the x_{min}, the structure will be stable under heat treatment. Since the A value depends on e_o^T, it is of interest to analyze the sizes of the stable γ-phase particles from the discrepancy between the γ and γ′-

phases. At A>2, there are no stable particles (low e_o^T values). When e_o^T increases at A<2, A decreases. The condition for the formation of a particle with the size corresponding to a particle within the $n<x_{min}<n+1$ interval, is $A<\frac{2n}{n+1}$, n=1,2,3,..... At A<1, the x_{min} is present in each interval of the sizes. At A>1, the x_{min} is absent even in the interval 1<x<2, etc., for the 1<A<2 region. With increasing e_o^T, A decreases, and the sizes of energetically stabilized particles tend to the condition x_{min}=n, n=1,2,3,...

In the considered example, the X-ray structural investigation of the alloys with 5% of Ru showed that $e^T = 0.17*10^{-2}$, $a_\gamma = 0.356$ нм. In this case ℓ_0 = 420 нм. Thus, during the growth of the particles with simultaneous disarrangement of coherence, the particle in the alloy in question is caught in a first energy trap ($\ell = \ell_0$).

6. Conclusion

1. In single crystals of Re-, Ru-containing heat-resistant nickel alloys, partially coherent particles of the γ′-phase are formed after the FHT.
2. The process of disarrangement of the γ′-phase coherence can lead to the formation of energetically stable γ′-phase particles, which do not increase their size during further heat treatment. In this case, the coherent stresses in the alloy disappear.

7. Literature

1. Lifshitz I.M., Slezov V.V. The kinetic of precipitation from supersaturated solid solution.- J.Phys. Chem.Sol., 1961, 19, № 1/2, p.35-50.
2. Chester T.Sims, Norman S.Stoloff, William C.Hagel. Superalloys II, New York, 1987.
3. Alekseev A.A., Pavlenko S.G. Influence of coherency disarrangement on growing of precipitations, FMM,1984, V57, issue 1, p. 108-113.
4. Eshelby J.D., Solid State Physics, New York, 1956, p.79. In J. Eshelby book "Continuous theory of dislocations", 1963, 240 p.

9th Liege Conference : Materials for Advanced Power Engineering 2010
edited by J. Lecomte-Beckers, Q. Contrepois, T. Beck and B. Kuhn.

BEHAVIOUR OF RESIDUAL STRESSES AND LATTICE SPACINGS IN γ- AND γ'-PHASES DURING CREEP-RUPTURE TESTS OF SINGLE-CRYSTAL NICKEL SUPERALLOY

I.A. Treninkov, A.A. Alekseev

FGUP «VIAM» GNC RF, tria@mail333.com 105005, Moscow, ul.Radio, 17

Abstract

A method for the determination of residual stresses separately in the phases of a multiphase single-crystal material, including the determination of true lattice spacings of these phases, by a non-destructive X-ray technique has been developed. In this study, the residual stresses generated in single-crystal samples of a nickel-based superalloy at different stages of creep (200 h, 300 h, 400 h and 500 h) at a load of 210 MPa and at a temperature of 1000°C have been measured. The stresses were measured by the non-destructive X-ray technique separately in the γ- and γ'-phases; in the process, the lattice spacings of these phases, undistorted by the stresses, were measured independently. The measured stresses vary in the range from +186 (tensile stresses) to -307 (compression stresses) MPa. It has been revealed that the γ- and γ'-phase lattice spacings vary during creep. The respective curves are plotted.

Keywords: Single-crystal; Stresses; X-ray diffraction; Creep

1. Introduction

Multiphase single-crystal blades of nickel-based superalloys in advanced gas-turbine engines are the most thermally stressed parts of a hot channel: they should be capable of operating for tens of thousands of hours in a wide range of temperatures and stresses. A multiphase single crystal can be regarded as a specimen, in which the single crystal is formed by one phase (the matrix), while the remaining phases are formed as particles whose lattices are oriented in the matrix crystal lattice according to certain orientation patterns. To prevent the destruction of the blades during operation and design the blades with optimum geometry, it is necessary to know the values of residual stresses in different sections of a blade. Considering a wide range of temperature variations, these residual stresses, added to the applied external stresses, can cause blade rupture during operation. It is currently believed that the level of residual stresses is one of key parameters determining the high-temperature strength level [1], [2].

The specific feature of the alloys operating at high-temperatures is the presence of thermal stresses. The formation of a two-phase nickel-based superalloy takes place in the 1200 ÷ 900°C temperature range, while the measurements are taken at room temperature. Thermal stresses appear during the cooling of the alloy because of the difference in the linear expansion coefficients of the γ - and γ'-phases, and the level of these stresses varies from 100 to 600 MPa [3]. The high level of thermal stresses is due to the fact that the volume fractions of the γ - and γ'-phases are comparable. Besides, during creep, the residual stresses of the deformation origin (the Brown back stresses) are generated in the alloy [4]. In creep-rapture tests, the deformation stresses are superimposed on the thermal stresses and the sum of these stresses is calculated in the experiment.

Measuring residual stresses in coarse-grained materials, especially in single crystals, is a difficult problem. Presently, the value of the residual stresses in the single-crystal blades is estimated by computations using various models [4]. Experimentally, the residual stresses are

measured using destructive methods [5]. Conventional techniques of measuring residual stresses in single crystals by the non-destructive method [6] do not allow the determination of the true lattice spacings in the phases without the distortions caused by the residual stresses. Moreover, the above techniques do not permit the separate determination of the stresses in the phases of multiphase alloys, for example, in the γ and γ' phases of nickel-based superalloys.

The present work is aimed at developing a technique for the determination of residual stresses separately in the phases of a multiphase single-crystal material by the non-destructive X-ray method, including the determination of the true lattice spacings of these phases without the distortions caused by residual stresses. This technique can be used for measuring the residual stresses in almost all single-crystal materials, for example, the single-crystal blades of gas turbines, epitaxial films, single-crystal silicon plates, printed circuit boards, etc. This work is also aimed at studying the behaviour of residual stresses and lattice spacings in the γ- and γ'-phases in creep-rupture tests of the single-crystal nickel-based superalloy.

2. Material and methods

The structure of the modern cast nickel-based superalloys is a two-phase system, consisting of a nickel-based γ-solid solution and precipitates of the γ' phase (intermetallic Ni_3Al) [4]. The samples of the single-crystal nickel-based superalloy VZHM4 (6 % Re, 4 % Ru) with the orientation of [010] were examined. The cast samples were subjected to a complete heat treatment cycle (homogenization and ageing). The creep tests were carried out at the same temperature of 1000°C and load of 210 MPa. The samples were not tested to failure but were removed from the bench in turn over a specified period of time: 200 h, 300 h, 400 h, and 500 h. The similar samples under the same test conditions failed after 640-650 h. The microstructure of the samples represents a raft-structure (Fig. 1). After 200 h, the raft-structure in the sample was not completely formed.

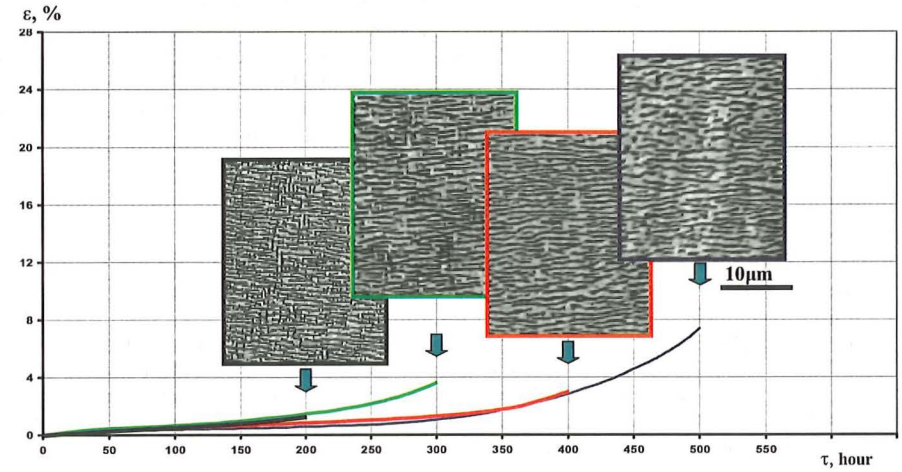

Fig. 1. Creep curves (σ = 210 MPa; T = 1000 °C) of the samples of VZHM4 alloy [010] and their microstructure(E.V. Filonova)

During creep, no neck was formed in the examined samples. After the creep tests, the working section of the samples represents a cylinder-shaped rod. The strain is directed along the cylinder axis [010]. It is convenient when the surface of the sample coincides with one of the symmetrical crystal planes. The measurements were made on the longitudinal section [001] of said cylindrical sample cut out so that the axis of tension lies in the plane of cutting. The cutting-out of a sample in the above manner naturally changes the stress pattern, which is taken into consideration in the developed technique. Metrological assurance of any measurement involves the setting up of the indicator systems in which measurements are taken. In this case there are three such systems: a sample, an instrument, and a crystallographic orientation. Cutting the sample out along a certain crystal plane links the sample to its crystal lattice. For fixing the sample coordinate systems to the instrument coordinate system, it is necessary to secure the sample in the X-ray diffractometer sample holder so that the plane of the sample is parallel to the sample holder surface (alignment plane), while the cylinder axis is set to a zero position by azimuth.

The experiment was carried out using the D/MAX-2500 X-ray diffractometer based on a powerful (18 kW) X-ray source with a twirled copper anode and fitted with the multipurpose MPA-2000 attachment. The γ and γ' phases have a face-centered cubic lattice with similar unit cell parameters; as a result, the main reflexes of the γ and γ' phases are superimposed (Fig. 2a). This superposition of the reflexes complicates the determination of the unit cell parameters, the lattice misfit value, and the value of residual stresses. For a better separation between the γ and γ' phase reflexes, the diffraction patterns were taken in the characteristic K_β-radiation (Fig. 2b). In spite of the fact that the intensity of the K_β line is lower than that of the K_α lines, the intensity loss is compensated by the use of the powerful X-ray source with the twirled anode. The pole figures were measured in K_α-radiation.

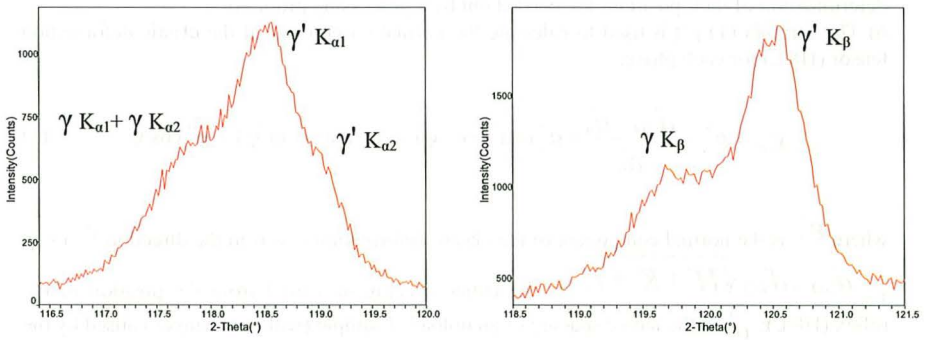

a b

Fig. 2. Radial section of the reflexes of the γ and γ' phases: a) (004) Cu K_α-radiation; b) (024) Cu K_β-radiation

3. Calculation procedure

When refining the calculation procedure, the assumptions were made that the concentration inhomogeneity, causing stresses and affecting the lattice parameter value, is absent.

Description of the procedure. 1) The unit vector of the normal line $\vec{t}$ to the crystal plane (HKL) is introduced into the crystallographic coordinate system:

$$\vec{t} = \frac{[H,K,L]}{\sqrt{H^2+K^2+L^2}}$$

The unified laboratory coordinate system (x, y, z) is set, where z is the normal line to the surface of the sample; y is the direction along the axis of tension. The vector $\vec{t}$ in the spherical coordinate system assumes the form:

$$\vec{t} = \{\sin\psi\cos\varphi;\ -\sin\psi\sin\varphi;\ \cos\psi\}$$

where $\psi = \psi_{HKL}$ is the polar angle $\vec{t}$, $\varphi = \varphi_{HKL}$ is the azimuth angle $\vec{t}$.

2) The combined pole figure is plotted; from the direction in which reflexes are drawn, the deformation direction is refined and corrected.
3) The planes with a large angle of 2θ, in which the stresses will be determined, are selected and orientated.
4) The diffractions from each of the selected planes are recorded.
5) The splitting of the reflexes from the γ and γ' phases by a singlet selection method and the determination of their positions are carried out by a processing program.
6) The formula (1) [7] is used to calculate the normal component of the elastic deformation tensor (HKL) for each phase.

$$\varepsilon^i_u = \varepsilon^i_u = \frac{a^i_{HKL} - a^i_0}{a^i_0} = \varepsilon^i_x(\sin^2\psi\cos^2\varphi) + \varepsilon^i_y(\sin^2\psi\sin^2\varphi) + \varepsilon^i_z\cos^2\psi \qquad (1)$$

where ε^i_u is the normal component of the elastic deformation tensor in the direction $\vec{t}$; i = γ, γ'; $a^i_{HKL} = d^i_{HKL}\sqrt{H^2+K^2+L^2}$ is the lattice spacing measured from the position of the reflex (HKL); a^i_0 is the lattice spacing of an unloaded sample (without changes caused by the stresses); ε^i_x, ε^i_y, ε^i_z are the normal components of the elastic deformation tensor along the axes X, Y, Z; $\psi = \psi_{HKL}$ is the polar angle between the normal line of the plane parallel to the surface of the sample (in this case [001]) and the normal line of the plane (HKL); $\varphi = \varphi_{HKL}$ is the azimuth angle between the deformation direction and the normal line of the plane (HKL).

7) From (1) and Hooke's law [7] after transformations we obtain:

$$\varepsilon_{\varphi}^{i}=\frac{a_{HKL}^{i}-a_{0}^{i}}{a_{0}^{i}}=\frac{\sigma_{z}^{i}-\nu\sigma_{y}^{i}}{E}-\frac{\sigma_{z}^{i}}{E}(1+\nu)\sin^{2}\psi+\frac{\sigma_{y}^{i}}{E}(1+\nu)\sin^{2}\psi\sin^{2}\varphi \qquad (2)$$

where σ_{z}^{i} is the stress in the i-phase along the Z-axis; σ_{y}^{i} is the stress in the i-phase along the Y-axis; E is the non-isotropic modulus of elasticity (used the value of the Young modulus for nickel, 137500 MPa, which is the most typical value for the given class of materials in the direction [010]), $E=\frac{1}{S_{11}}$, where S_{11} is the compliance module; ν is the non-isotropic Poisson's constant (0.38 is the most typical value for the given class of materials in the direction [010]) $\nu=-\frac{1}{S_{12}}$, S_{12} is the compliance module.

Eq. (2) is convenient to be given in the form:

$$a_{HKL}=a_{\exp}+k_{1}\cdot\sin^{2}\psi+k_{2}\cdot\sin^{2}\varphi\cdot\sin^{2}\psi,$$

where $a_{\exp}$, k_1 and k_2 are the coefficients calculated from the experimental data using the method of least squares.

$$\sigma_{y}=\frac{(k_{1}+k_{2})E}{(1+\nu)a_{0}}$$

$$\sigma_{x}=\frac{k_{1}E}{(1+\nu)a_{0}}$$

$$a_{0}=a_{\exp}-\frac{\nu k_{2}}{1+\nu}$$

The purpose of the procedure is the definition of six unknown values:

(a) the stresses in the γ phase along the Z- and Y-axes: σ_{y}^{γ} and σ_{x}^{γ}, respectively;

(b) the stresses in the γ′ phase along the Z- and Y-axes: $\sigma_{y}^{\gamma'}$ and $\sigma_{x}^{\gamma'}$, respectively;

(c) the lattice spacings of the γ and γ′ phases (a^{γ} and $a^{\gamma'}$, respectively) without the distortions caused by the residual stresses.

4. Experimental

The stresses were calculated separately in the γ and γ' phases in the tensile direction (the Y-axis) and perpendicular direction (the X-axis lies in the metallographic section plane). It was assumed that residual stresses in the direction Z (perpendicular to the metallographic section

surface) are absent. In the process, the lattice spacings of the γ and γ′ phases were determined independently without the distortions caused by residual stresses.

In the calculations of stresses, the following assumptions were used: the dendritic segregation in the sample is absent; the lattice spacings of the γ and γ' phases do not vary in the axes of the firstf, secondf, etc.forder dendrites, in the interdendritic space.

The residual stresses were calculated from c reflexes: ()4), ()$\bar{2}$4), ()24), ()$\bar{4}$2), ()42),($\bar{2}$)4), (2)4), ($\bar{4}$)2), (4)2). The profile processing, doublet splitting, and the determination of the reflex position were performed using nade software. The example of the profile processing is given in t ig. 3.

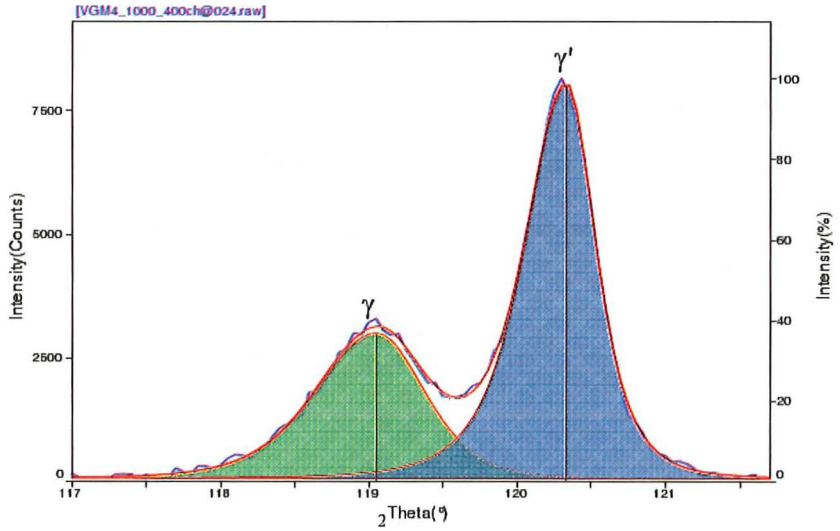

Fig. 3. The example of the doublet splitting of the γ and γ' phases (024) in Jade software

The Iualitative evaluation of measurement error in determining the lattice spacing of the phases (h) was given by formula:

$$\Delta = \frac{R}{\sqrt{N}} \quad ,$$

where R is the Rffactor (the meanfsI uare interpolation error of selection of singlets), o is the number of pulses.

The average value of R , 1,l 3c i , the average value of h , gγl)[fd].

The results of the calculations of the residual stresses and lattice spacings of the γ and γ' phases without the distortions caused by the residual stresses are presented in the Table.

Table. Results of the calculations of the residual stresses and lattice spacings of the samples after creep tests at T = 1000°C, σ = 210 MPa; y - the extension direction

Time, h	Base (no creep)		200		300		400		500	
Phase	γ	γ'	γ	γ'	Γ	γ'	γ	γ'	γ	γ'
σ_y, MPa	-91	3	86	186	-52	56	-47	56	-102	28
σ_x, MPa	-307	-240	80	53	19	0	30	19	17	6
Lattice spacing, Å	3.6161	3.5905	3.6081	3.5819	3.6123	3.5852	3.6109	3.5850	3.6119	3.5855
Misfit, %	0.708		0.725		0.751		0.715		0.732	

For refining the deformation direction, the direct pole figures were taken. Fig. 4 presents the three-dimensional combined pole figure (001)+{011}+{111} taken from the sample of the VZHM4 superalloy after creep tests for 200 h. Fig. 5 presents the combined pole figure (001)+{011}+{111}+{113}.

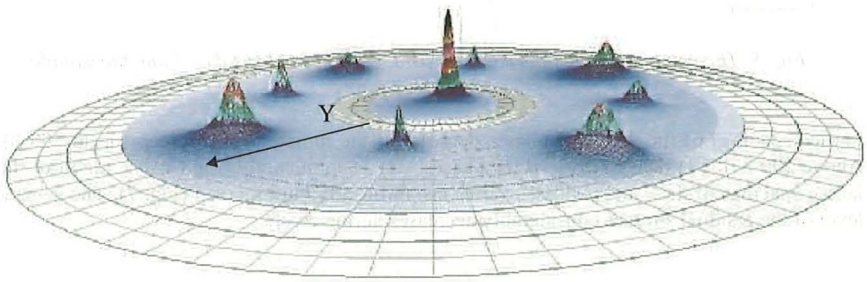

Fig. 4 – The combined pole figure (001)+{011}+{111} in a three-dimensional form of the sample of the VZHM4 superalloy after creep tests for 200 h

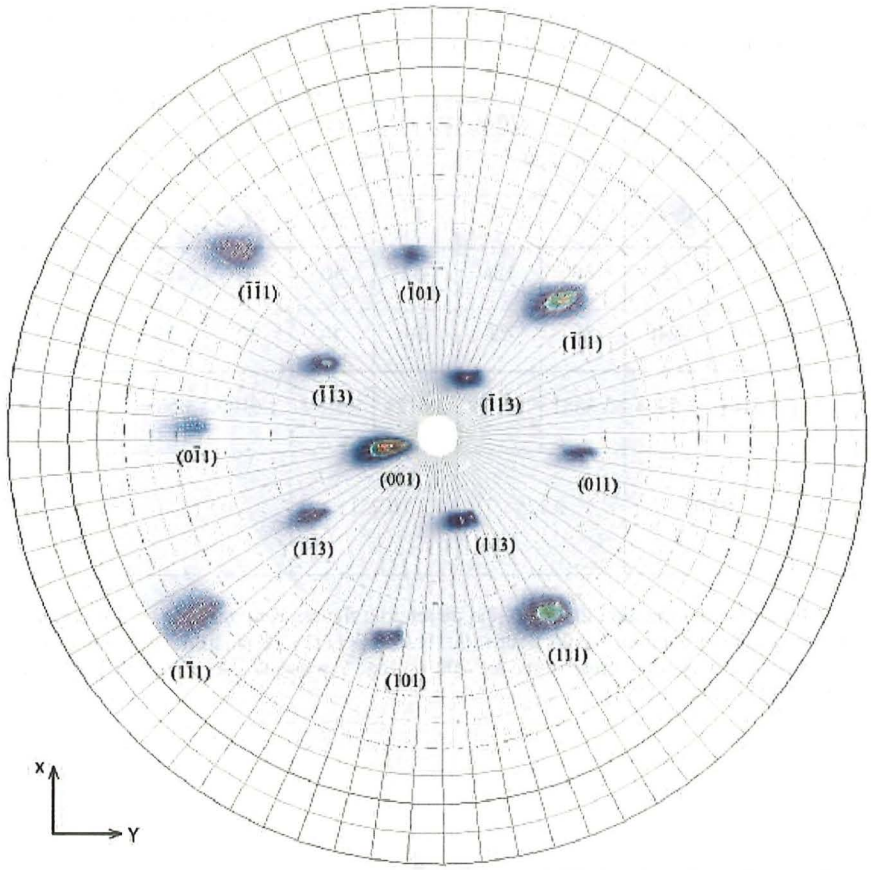

Fig. 5. The combined pole figure (001)+{011}+{111}+{113} taken from the sample after creep tests

Lattice spacings of the γ and γ ' phases decrease at the initial stage of creep (up to 200 h). Above 200 h, the lattice spacings of the phases vary insignificantly (Fig 6). The misfit of the lattice spacings of the γ and γ' phases varies insignificantly during creep (Fig. 7). The general level of the residual stresses considerably decreases during creep.

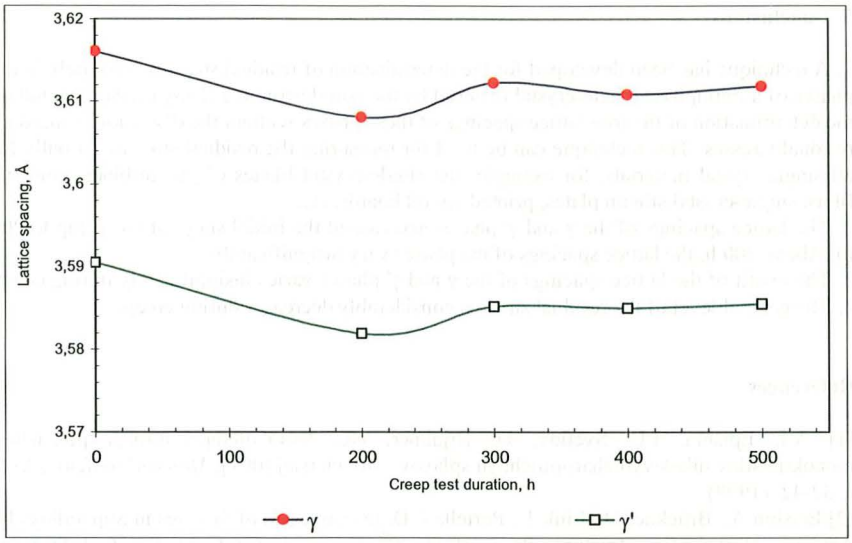

Fig. 6. Variation of stress-free lattice spacings of the γ and γ' phases depending on creep test duration

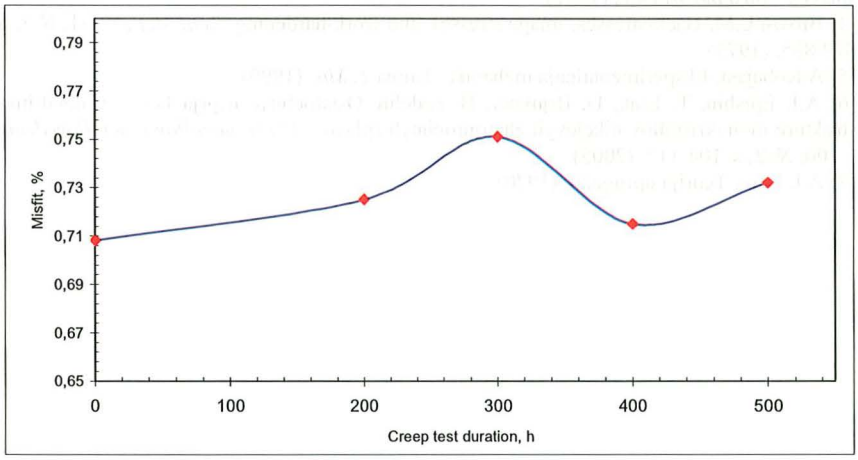

Fig. 7. Variation of stress-free misfit of lattice spacings of the γ and γ' phases depending on the creep test duration

5. Conclusions

1. A technique has been developed for the determination of residual stresses separately in the phases of a multiphase single-crystal material by the non-destructive X-ray method, including the determination of the true lattice spacings of these phases without the distortions caused by residual stresses. This technique can be used for measuring the residual stresses virtually for all single-crystal materials, for example, the single-crystal blades of gas turbines, epitaxial films, single-crystal silicon plates, printed circuit boards, etc.
2. The lattice spacings of the γ and γ' phases decrease at the initial stage of creep (up to 200 h). Above 200 h, the lattice spacings of the phases vary insignificantly.
3. The misfit of the lattice spacings of the γ and γ' phases varies insignificantly during creep.
4. The general level of the residual stresses considerably decreases during creep.

References

[1] A.I. Epishin, I.L. Svetlov, U. Brjukner, etc. Vysokotemperaturnaja polzuchest monokristallov nikelevyh zharoprochnyh splavov s orientatsiej [001]. *Materialovedenie,* № 5, c. 32-42. (1999)
[2] Epishin A., Brückner U., Link T., Portella P.D. Investigation of Stresses in Superalloys by Analysis of γ/γ'-Microstructure, Proc. of the *6th European Conf. on Residual Stresses,* Portugal. Trans Tech Publications, p. 287-292. (2002)
[3] R.E. Shalin, I.L. Svetlov, E.B. Kachanov, etc. Monokristally nikelevyh zharoprochnyh splavov. *Mashinostroenie.* (1997)
[4] Brown L.M. Back-stresses, image stresses, and work-hardening. *Acta Met.*, V. 21, N 7, p. 879-885. (1973)
[5] A.Kobajasi. Eksperimentalnaja mehanika: Kniga 2. *Mir.* (1990)
[6] A.I. Epishin, T. Link, U. Brjukner, B. Fedelih. Ostatochnye naprjazhenija v dendritnoj strukture monokristallov nikelevyh zharoprochnyh splavov. *Fizika metallov i metallovedenie,* t. 100, № 2, s. 104-112. (2005)
[7] A.I. Lure. Teorija uprugosti. (1970)

9th Liege Conference : Materials for Advanced Power Engineering 2010
edited by J. Lecomte-Beckers, Q. Contrepois, T. Beck and B. Kuhn.

PRECIPITATION IN SOLID SOLUTION AND STRUCTURAL TRANSFORMATIONS IN SINGLE CRYSTALS OF HIGH RHENIUM RUTHENIUM-CONTAINING NICKEL SUPERALLOYS AT HIGH-TEMPERATURE CREEP

A.A. Alekseev, N.V. Petrushin, D.V. Zaitsev, I.A. Treninkov, E.V. Filonova
All-Russian Scientific Research Institute of Aviation Materials "VIAM"
Moscow, Radio st. 17, 105005, admin@viam.ru

Abstract

The phase composition and structure of single crystals of two superalloys (alloy 1 and alloy 2) were investigated in this work. For alloy 1 (Re - 9 wt %) the kinetics of precipitation in solid solution at heat treatment (HT) was investigated. TEM and X-Ray examinations have revealed that during HT rhombic phase (R-phase) precipitation (Immm class (BCR) occurs. The TTT diagram is plotted, it contains the time-temperature area of the existence of R-phase particles. The element content of R-phase is identified (at. %): Re- 51.5; Co- 23.5; Cr- 14.8; Mo- 4.2; W- 3.3; Ta- 2.7. For alloy 2 (Re - 6.5 wt %, Ru - 4 wt %) structural transformations at high-temperature creep are investigated. By dark-field TEM methods it is established, that in alloy 2 the additional phase with a rhombic lattice is formed during creep. Particles of this phase precipitate in γ-phase and their quantity increases during high-temperature creep. It is revealed that during creep 3-D dislocation network is formed in γ-phase. At the third stage of creep the process of inversion structure formation is observed in the alloy, i.e. γ′-phase becomes a matrix. Thus during modeling creep the volume fraction of γ′-phase in the samples increases from 30 % (at creep duration of 200 hrs) up to 55 % (at 500 hrs). The processes of structure formation in Re and Ru-containing nickel superalloys are strongly affected by decomposition of solid solution during high-temperature creep that includes precipitation of additional TCP-phases.

1. Introduction

Rhenium-containing single-crystal nickel-based superalloys are promising materials for gas turbine blades. Extra phases can often be formed in these alloys during heat treatment. These phases have a strong effect on material characteristics.
The present investigation is aimed at:
- Working out the methods for research into structure and phase composition of single-crystal nickel-based superalloys;
- Researching into structure and phase analysis of Re+Ru containing single-crystal Ni_3Al-based superalloys.

2. Materials and the equipment

Single-crystal alloys with the orientation of [001] shaped cylindrically are investigated in the present work. Re and Ru contents of the alloys are presented in Table 1.
The cast samples were heat treated under the complete cycle conditions of: homogenization at 1340°C during 20 hours and two-level ageing: 1130°C, 6 hours + 870°C, 48 hours.

Table 1. Re and Ru contents of alloy 1 and alloy 2 (wt %).

Alloy	Re	Ru	Ni
1	9.3	–	bal.
2	6.5	4	bal.

Metallographic specimens for examination were prepared using a complex of the equipment of "Struers". Studies by methods of scanning electron microscopy (SEM) are carried out using JEOL's JSM-6490 LV microscope. X-ray analysis is carried out using Rigaku's D/MAX-2500 X-ray diffractometer. Study by methods of transmission electron microscopy (TEM) are carried out using JEOL's JEM - 200CX electron microscope. The local micro X-ray spectral analysis is carried out using INCA TEM 250 attachment to the scanning electron microscope. Foils for transmission electron microscopy were prepared using automated Tenupol-5 unit that ensures preparation of thin foils by a method of two-sided jet polishing.

3. Phase structure of single crystals of alloy 1

Samples were examined after the complete cycle of heat treatment and additional annealing. Besides γ - and γ′-phases an additional phase (R-phase) was detected by using the methods of scanning electron microscopy (Fig. 1).

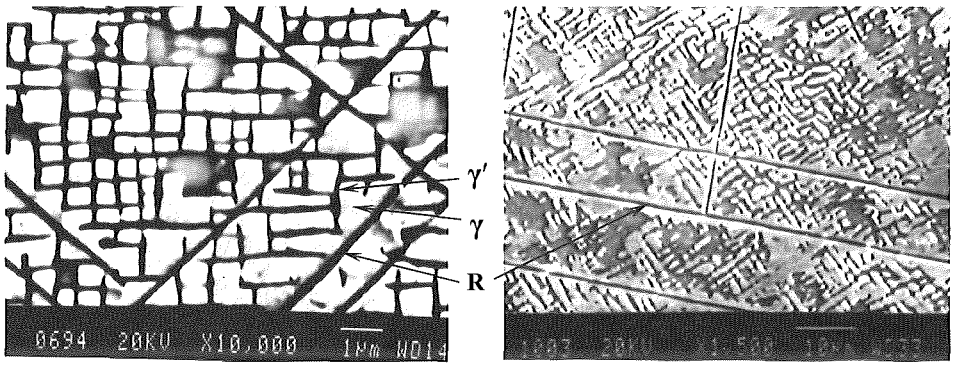

a *b*

Fig. 1 Sequence of R-phase formation: a) the intermediate condition of 1100 °C, 71hrs.; b) the condition after long-term treatment of 1100°C, 1027hrs.

Figure 2 shows the temperature-time field of existence of this phase (R-phase). Crystallographic analysis of R-phase has revealed that the particles are shaped as the plates with habitus of {110}, drawn along the direction of <110>. γ′-phase starts forming around R-phase particles at the late stage of decomposition of the solid solution. The chemical composition of R-phase is identified using micro X-ray spectral analysis methods (at %): Re - 51.5; Co-23.5; Cr-14.8; Mo - 4.2; W - 3.3; Ta - 2.7.

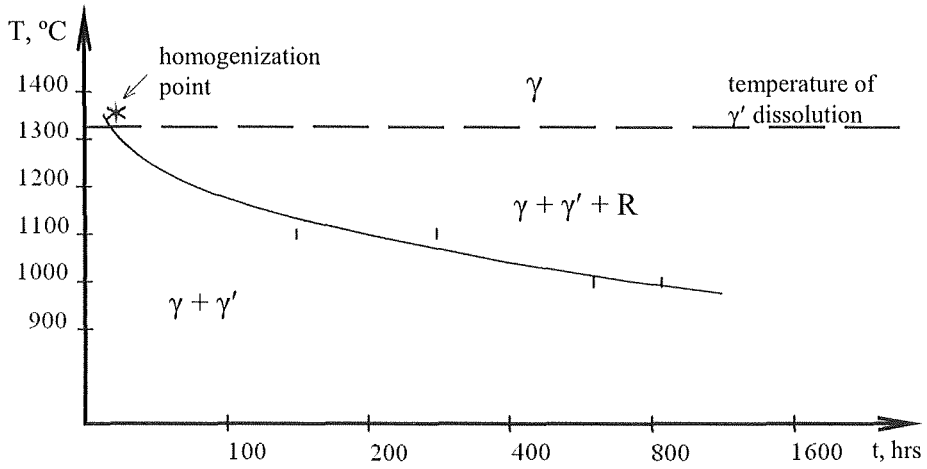

Fig. 2 The temperature-time field of existence of γ - γ′ - and R - phases in alloy 1

Crystallographic structure of R-phase and its certain orientation patterns within the matrix are identified using transmission electron microscopy (Fig. 3) and X-ray analysis of single crystals (Fig. 4). The extra system of reflexes of hexagonal δ-phase is detected in diffraction patterns and also in X-ray pattern of single crystals.

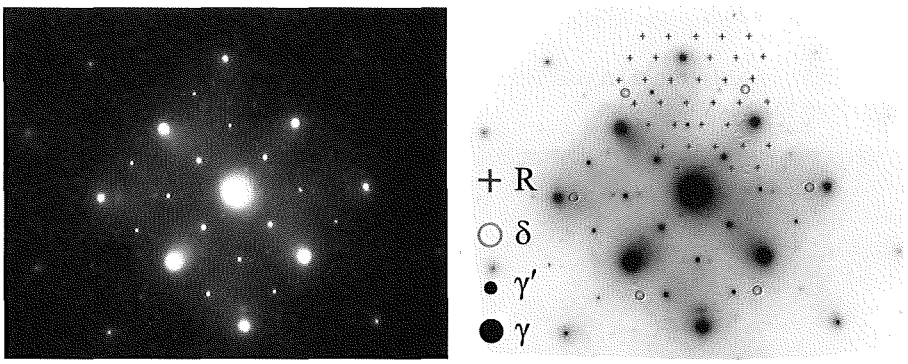

a *b*

Fig. 3 Diffraction (a) and reflexes scheme (b) for <100> foil orientation

Rhombic phase (R-phase) of Immm class (BCR) precipitated lattice parameters were as follows:

$$\vec{a}_R = \frac{5a_\gamma}{2}[110]_\gamma;\ \vec{b}_R = \frac{3a_\gamma}{2}[1\bar{1}0]_\gamma;\ \vec{c}_R = a_\gamma[001]_\gamma,$$

where a_γ - γ-phase lattice period.

The δ-phase of P63/mmc class (HCP) precipitated lattice parameters were as follows:

$$\vec{a}_\delta = a_\delta \frac{\sqrt{2}}{2}[110]_\gamma ; \quad \vec{c}_\delta = a_\delta [001]_\gamma ,$$

where $a_\delta = 2.80Å \pm 0{,}05$ Å; $c_\delta = 4.15Å \pm 0{,}02$ Å.
The X-Ray investigation of alloy shown at Figure 4.

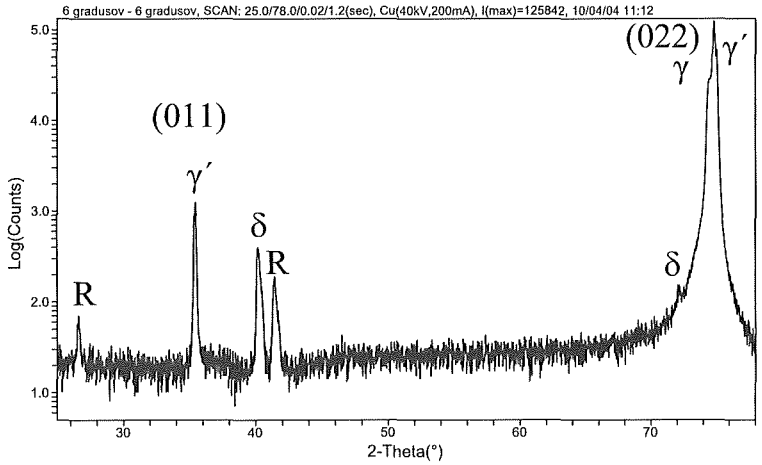

Fig. 4 Diffraction of alloy 1 single crystal for <011> scanning direction

Data of TEM analysis (Fig. 5) reveal that R-phase plates have complex structure. δ-phase morphology may vary (Fig. 6).

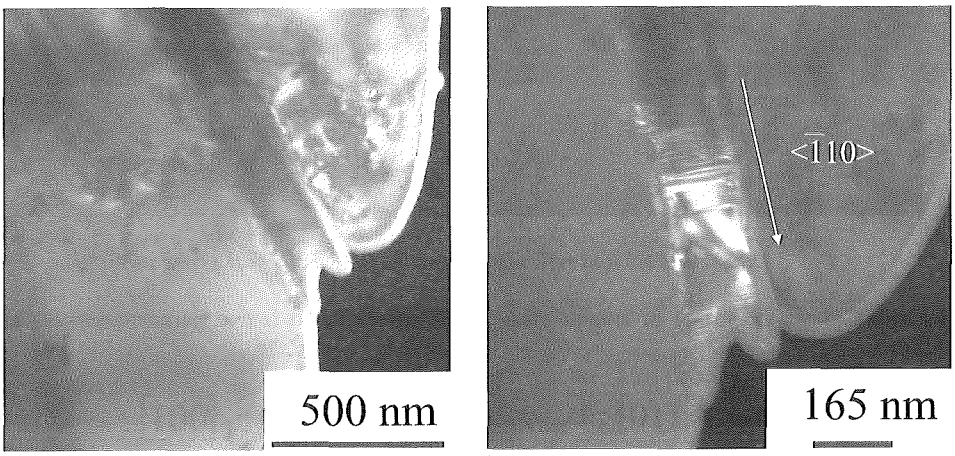

Fig. 5 Dark field images of R-phase for <100> foil orientation

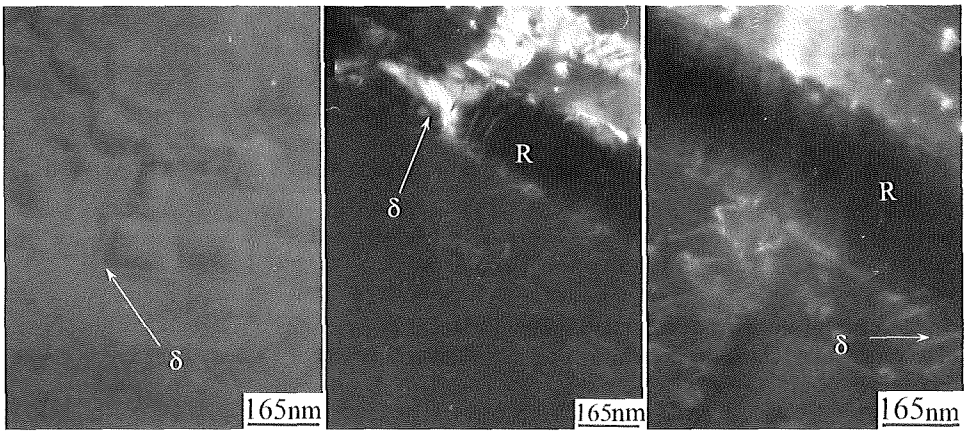

a *b* *c*

Fig. 6 δ-phase dark field images for <100> foil orientation:
a) at γ/γ′-phase interface; b) inside R-phase particles; c) around R-phase

Three types of δ-phase particles are detected. In the bulk of the sample the particles are at γ/γ′-phase interface. Many of α-phase particles are observed inside R-phase particles. It is noteworthy that inside each particle of R-phase δ-phase particles possess all the possible crystallographically equivalent orientations. It indicates the sequence of their forming. At first R-phase particles appear and then δ-phase particles with all possible crystallographicly equivalent orientations are formed inside them. Besides that, the plates of δ-phase with a habitus of {100} are observed in an envelope of γ′-phase formed around R-phase. Proceeding from the facts that δ-phase crystalline structure is hexagonal and it is at γ / γ′-phase interface the assumption can be made that δ-phase is δ-Re-based solid solution. In this case forming δ-phase on γ / γ′-phase interface can be explained by forced diffusion of Re into γ-solid solution during γ′-particle growth as γ′-phase does not contain Re.

4. γ′-phase structure features in alloy 1

Regular X-Ray researches into Re and Re, Ru containing single crystals presented in this work have shown that superstructural γ′-phase reflexes intensity is abnormally low in comparison with structural reflexes (Fig. 4). It is known that W in Re-containing nickel-based alloy diffuses almost completely from γ into γ′-phase. Besides that, γ′-phase contains Ta. It is possible to assume, that intensity of superstructural lines falls dramatically because of distribution of heavy elements X (W, Ta) in γ′-phase in Al nodal points. In fact

$$F_{ss} \sim (\bar{f}_{Al} - \bar{f}_{Ni}); \qquad F_s \sim (\bar{f}_{Al} + 3\bar{f}_{Ni}),$$

where F_{ss} and F_s– structural factors of superstructural and structural reflexes; $\bar{f}_{Al}$ and $\bar{f}_{Ni}$ - average nuclear factors of Al and Ni nodal dispersion respectively, in view of alloying elements distribution in these nodal points.

For example, for $Ni_3(Al, X)$:

$$(\bar{f}_{Al} - \bar{f}_{Ni}) \sim (1-C)f_{Al} + Cf_X - f_{Ni},$$

where C – conditional partial concentration of X in Al nodal points,
f_{Al}, f_X, f_{Ni} – nuclear factors of Al, X and Ni nodal dispersion respectively.

Alloying γ′-phase with X results in dramatic fall in the case when X atoms are in Al nodal points

$$\text{if} \quad (\bar{f}_{Al} - \bar{f}_{Ni}) = 0 \quad \text{then} \quad C = \frac{f_{Ni} - f_{Al}}{f_X - f_{Al}}.$$

In this case the intensity of all superstructural lines is close to zero.
The calculations show the possibility of the qualitative analysis of γ′-phase structure in single crystals by X-ray methods.

5. Research into phase and structural changes during high-temperature creep in alloy 2

Four single-crystal samples of alloy 2 with [001] axial orientation were tested for creep at 1000 °C, 210 MPa and different holding periods. Each sample corresponds to the certain stage of creep:

200 hrs - the steady stage of creep;
300 hrs - the beginning of the 3rd stage of creep;
400 hrs - the middle of the 3rd stage of creep;
500 hrs - the end of the 3rd stage of creep, transition to sample failure (after 640-650 hrs).

The kinetics of structural transformations was investigated at various stages of creep together with alloy microstructure examination by SEM and TEM methods.

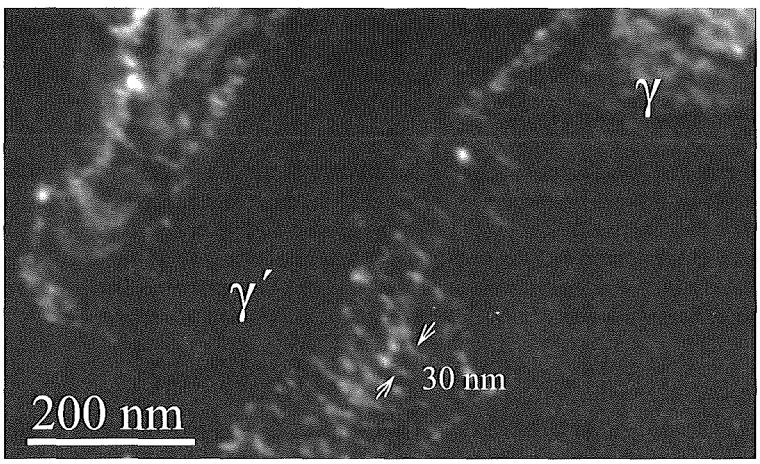

Fig. 8. 3-D dislocation network (dark field image). Creep for 400 hrs.

Such network develops through the bulk of γ-phase during creep. The change of a γ′-phase volume fraction during creep was detected by SEM (Fig. 9).

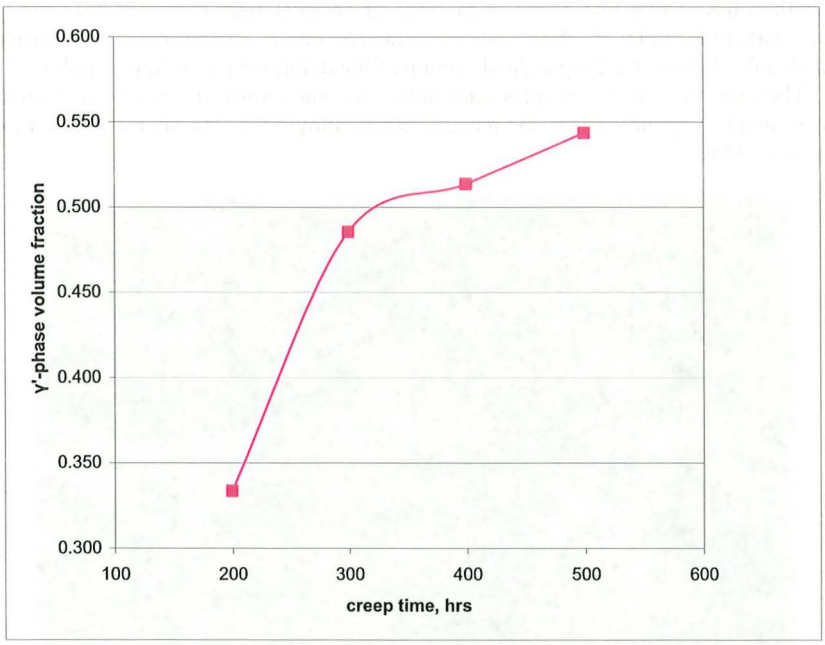

Fig. 9 γ'-phase volume fraction changes during creep

The volume fraction was measured from SEM images of microstructural samples with the surface orientation of [010] perpendicular to the axis of tension. γ-phase structure and phase transformations during creep were investigated by TEM.

Darkfield methods of TEM have allowed us to reveal that additional precipitation of disperse phases formed in γ-phase at initial stage of creep. The precipitation has different morphology and demonstrates both equiaxial and lamellar particles. This additional decomposition enhases during ageing (Fig. 10).

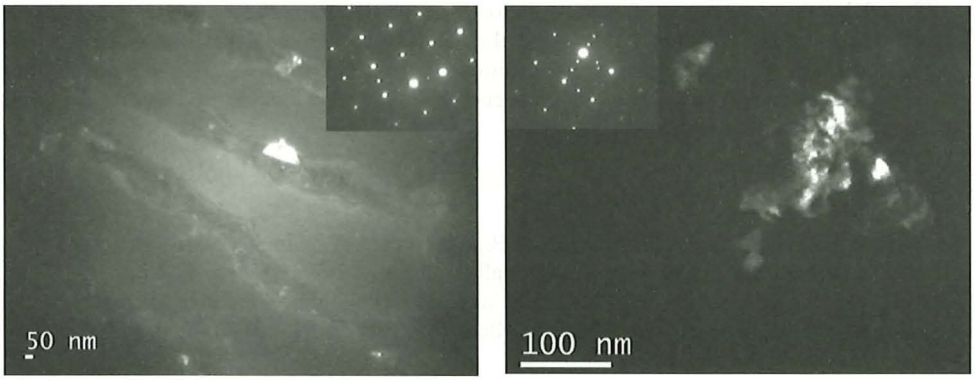

a *b*

Fig. 10 Darkfield images of additional decomposition during creep: a) 200 hrs. b) 400 hrs.

SEM method has shown that at the third stage of creep (longer than 200 hrs.) the inverse structure starts to form, i.e. γ′-phase becomes a matrix. Figure 10 presents inverse structure of the sample after failure (the longitudinal section of the deformed part of the sample).

The research into the samples after failure has shown that the cracks nucleate at γ/γ'-interphase that is perpendicular to the tensile axis. In alloy 2 the area of crack nucleation is in γ'-phase (Fig. 11).

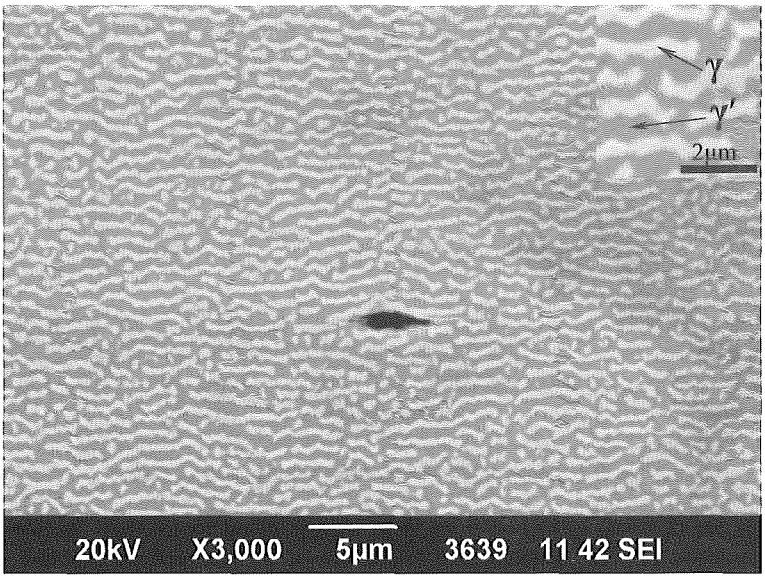

Fig. 11 Cracknucleation in γ'-phase (inverse structure)

6. Conclusions

The processes of structure formation in Re and Ru-containing nickel superalloys are strongly affected by decomposition of solid solution during high-temperature creep that includes precipitation of additional TCP-phases. At the third stage of creep dislocation network forms in γ-phase simultaneously with decomposition of the solid solution. The γ-phase volume fraction decreases and the alloy structure becomes inverse. Crack nucleation that results in the sample failure starts in γ′-phase.

Literature

1. Kablov E.N., Petrushin N.V., Bronfin M.B., Alekseev A.A. "Single crystals structural features on Re containing Ni-based superallos" Metally, 2006, №5, pp. 47-57.
2. Kablov E.N., Petrushin N.V. "Physicochemical and technological features of creating metal-based high-superalloys", Pure Applied Chemistry, 2004, v. 76, №9, p. 1679-1689.

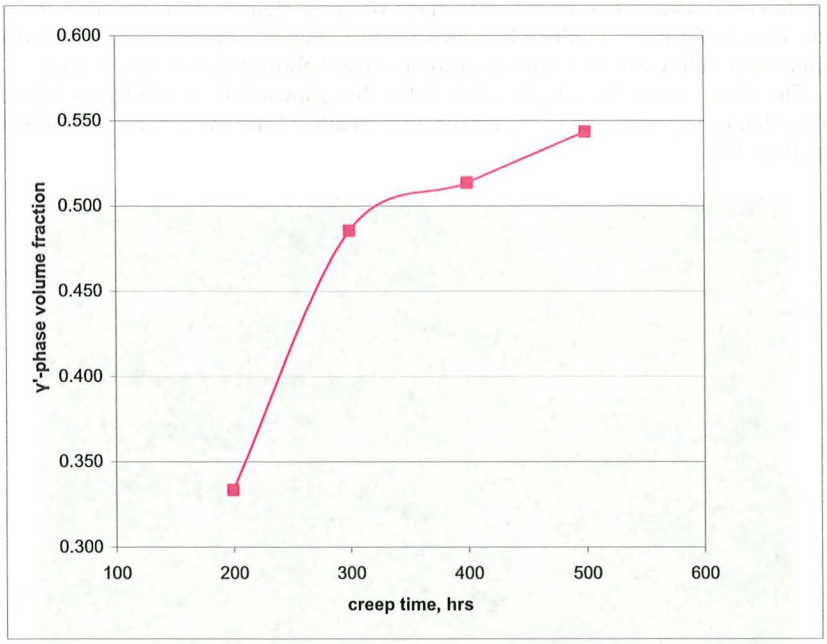

Fig. 9 γ'-phase volume fraction changes during creep

The volume fraction was measured from SEM images of microstructural samples with the surface orientation of [010] perpendicular to the axis of tension. γ-phase structure and phase transformations during creep were investigated by TEM.

Darkfield methods of TEM have allowed us to reveal that additional precipitation of disperse phases formed in γ-phase at initial stage of creep. The precipitation has different morphology and demonstrates both equiaxial and lamellar particles. This additional decomposition enhases during ageing (Fig. 10).

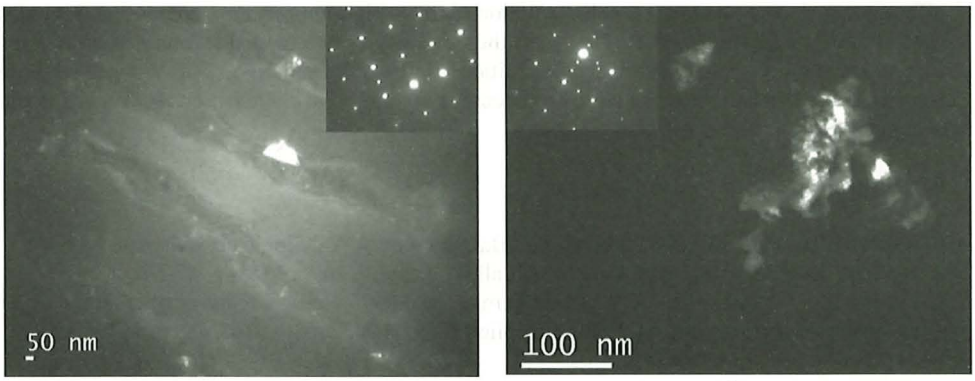

a *b*

Fig. 10 Darkfield images of additional decomposition during creep: a) 200 hrs. b) 400 hrs.

SEM method has shown that at the third stage of creep (longer than 200 hrs.) the inverse structure starts to form, i.e. γ′-phase becomes a matrix. Figure 10 presents inverse structure of the sample after failure (the longitudinal section of the deformed part of the sample).

The research into the samples after failure has shown that the cracks nucleate at γ/γ'-interphase that is perpendicular to the tensile axis. In alloy 2 the area of crack nucleation is in γ'-phase (Fig. 11).

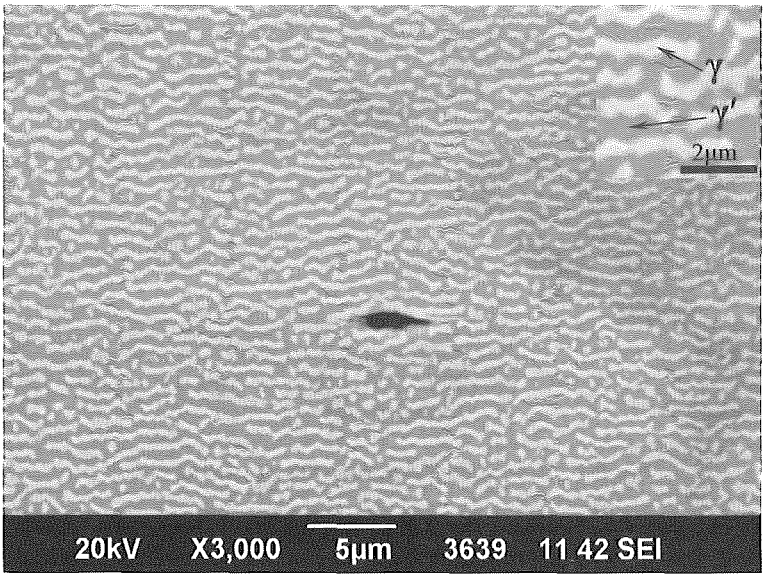

Fig. 11 Cracknucleation in γ'-phase (inverse structure)

6. Conclusions

The processes of structure formation in Re and Ru-containing nickel superalloys are strongly affected by decomposition of solid solution during high-temperature creep that includes precipitation of additional TCP-phases. At the third stage of creep dislocation network forms in γ-phase simultaneously with decomposition of the solid solution. The γ-phase volume fraction decreases and the alloy structure becomes inverse. Crack nucleation that results in the sample failure starts in γ′-phase.

Literature

1. Kablov E.N., Petrushin N.V., Bronfin M.B., Alekseev A.A. "Single crystals structural features on Re containing Ni-based superallos" Metally, 2006, №5, pp. 47-57.
2. Kablov E.N., Petrushin N.V. "Physicochemical and technological features of creating metal-based high-superalloys", Pure Applied Chemistry, 2004, v. 76, №9, p. 1679-1689.

9th Liege Conference : Materials for Advanced Power Engineering 2010
edited by J. Lecomte-Beckers, Q. Contrepois, T. Beck and B. Kuhn.

INFLUENCE OF CHEMICAL COMPOSITION ON MICROSTRUCTURE AND STRENGTH OF ALLOY 718

T. Fedorova, J. Rösler, B.Gehrmann* and J. Klöwer *

Technical University Braunschweig, D-38106 Braunschweig
*ThyssenKrupp VDM GmbH, D-58791 Werdohl

Abstract

Alloy 718 has been used for many years due to its unique mechanical properties and good processing characteristics. However, the temperature limit for Alloy 718 is about 650°C because of the thermal instability of the main strengthening phase γ′′ - Ni_3(Nb, Ti, Al) . At high temperatures meta-stable γ′′ changes into stable δ-Ni_3Nb with large size and plate-like morphology. As a consequence of this the alloy looses its microstructural stability and strength.

The basic intent of this paper is to examine the role of major and minor elements within typical specification limits for Alloy 718 with respect to (i) microstructure evolution, (ii) strengthening effects and (iii) thermal stability of γ′ and γ′′. For this purpose, thermodynamic calculations using the software THERMOCALC were performed, varying the content of Nb, Ti, Al as well as B and Zr. In addition, alloys with precisely controlled chemical composition were prepared by drop casting in a vacuum arc furnace and hot forged, so that it was possible to compare the theoretical predictions with experimental results. The microstructure evolution was studied in detail by means of scanning electron microscopy and x-ray diffraction. Furthermore, mechanical properties including tensile and creep behaviour were examined. Based on these results, dependencies between chemical composition and microstructural stability will be elucidated.

Keywords: Alloy 718, microstructure, phases, Nb, B, Zr

1. Introduction

The strength of Fe-Ni-based superalloys is dependent on several factors, such as solid solution strengthening, volume fraction and size of the precipitation. Since these factors are controlled by the composition of each phase, numerous studies have been carried out on the partition behavior of alloying elements between the γ, γ′ and γ′′ phases [1].

The niobium-containing Alloy 718 is strengthened by a combination of DO_{22} –ordered Ni_3(Nb,Ti) γ′′ and Ni_3(Al,Ti,Nb) γ′ phases in a face centered cubic γ matrix [2]. This alloy has been widely used in gas turbine and related applications due to its good mechanical properties up to 650°C and excellent manufacturability. The employment of Alloy 718 at higher temperatures is not expedient because of the instability of the main strengthening phase γ′′ and formation of stable δ-Ni_3Nb with large size and plate-like morphology. The major element modifications as Al, Ti, Nb were analyzed in recent twenty years [3]. Many studies have been made to improve the elevated temperature properties of alloy 718 by chemical composition modification, including changes in both major and minor elements [4-8]. For example, Xie, Dong, Wang and You raised the ratio of (Al+Ti)/Nb and the sum (Al+Ti+Nb) and developed a compact morphology of γ′′+ γ′ by appropriate heat treatment [9]. It was shown that 718 type alloys were very difficult to forge and even break down during hot working process when the sum of (Al+Ti+Nb)%at was higher than 7.5%. The characteristic of this major elements modification was to enhance the microstructure and mechanical property stability.

The influence of minor elements, especially B, on the mechanical properties of Alloy 718 and its derivatives was also studied extensively in the last years [10-15, 16]. It was realized that small additions of B and Zr were extremely beneficial to the creep-rupture properties of nickel-base superalloys. In the late 1950s, it was reported that B (up to 0.01 pct)

and Zr (up to 0.1 pct) improved high-temperature strength, ductility, and notch sensitivity of several alloys. In the study of Floreen and Davidson the influence of B and Zr on the creep and fatigue crack growth behaviour of Ni-base superalloys was shown. They realized that additions of B and Zr markedly improved the smooth specimen creep properties and the threshold stress intensity values for creep crack growth [17].

In another study it was shown that B and C strongly influenced the formation of grain boundary precipitates, and B causes the formation of an intergranular M_3B_2 boride. Both, B and Zr, were observed to be critical for improvement of the mechanical properties of the superalloys [18]. Recently, Cao and Kennedy have proposed to add B and P and showed that B and P increased the resistance to creep deformation [19]. The effect on creep strength of Alloy 718 due to addition of both elements was more visible than the effect due to their separate addition.

However, it has not been investigated in many studies how the addition of B and Zr influences the microstructure of Alloy 718 (grain coarsening and morphology of δ-Ni_3Nb phase). This paper seeks to define the role of B and Zr in forming the microstructure of Alloy 718 with the aim to improve its microstructural stability and strength. Furthermore, the influence of the Nb concentration on the microstructure is investigated within the specification limit for Alloy 718.

2. Experimental procedures

The alloys studied in this paper were made by induction melting under Ar atmosphere (alloys 1-3) and by plasma arc melting, followed by casting the material into a water-cooled copper crucible (alloys 4-10). Their nominal chemical compositions are given in Table I. The Nb concentrations of alloys 1-3 were taken in the limits of the ASTM specification and SAE AMS for Alloy 718. The B concentration is limited to 60ppm. The Zr concentration is not indicated. All alloys were homogenized at 1140 °C/6 h + 1175 °C/20 h in vacuum.

Table. 1. Nominal chemical compositions of the alloys

Alloy	C	Ni	Cr	Fe	Mo	Nb	Ti	Al	B	Zr
ASTM Spec.	Max 0.08	50-55	17-21	balance	2.80-3.30	4.75-5.50	0.65-1.15	0.20-0.80	Max 60ppm	-
Alloy 1	0.025	balance	18.7	17	2.96	5.07	0.96	0.48	-	-
Alloy 2	0.025	balance	18.7	17	2.96	5.23	0.96	0.48	-	-
Alloy 3	0.025	balance	18.7	17	2.96	5.37	0.96	0.48	-	-
Alloy 4	0.025	balance	18.7	17	2.96	5.4	0.96	0.48	60ppm	-
Alloy 5	0.025	balance	18.7	17	2.96	5.38	0.96	0.48	150ppm	-
Alloy 6	0.025	balance	18.7	17	2.96	5.41	0.96	0.48	200ppm	-
Alloy 7	0.025	balance	18.7	17	2.96	5.39	0.96	0.48	60ppm	200ppm
Alloy 8	0.025	balance	18.7	17	2.96	5.37	0.96	0.48	80ppm	200ppm

The alloys 4-8 with additions of B and B plus Zr were deformed from 13 mm to 9 mm by rotary swaging at 1075 °C. The resulting rods were solution annealed at 980 °C/ 1.5 h, followed by water cooling to room temperature (RT). The material was then double aged at 721 °C/ 8 h + furnace cooled at 50 °C/h + 620 °C/8 h air cooled to RT.

In order to predict the phases in the alloys, ThermoCalc software version S and a commercial TTNi7 database were used to calculate the phases and their precipitation temperatures. The phases considered in the calculations were face centered cubic γ, $L1_2$-ordered γ', DO_{22}-ordered γ'', σ, Laves, MC, M_6C, M_3B_2, MB_2 and liquid. It was necessary to

suppress the orthorhombic δ-Ni_3Nb phase from the calculations due to the interference with the γ′′ phase and vice versa.

The V2A etching reagent was used during the microstructure preparation. It was possible to identify the morphology of γ′, γ′′, δ, σ, Laves and carbides because the matrix was selectively etched on contrast to the precipitates named above. With help of this etching reagent, the grain boundaries and respectively grain sizes could also be identified. The chemical composition of V2A-stain is 200 ml H_2O, 200 ml HCl, 20 ml HNO_3 and 0,6 ml "Vogels Sparbeize".

Then SEM was used to observe the morphology and the distribution of all the phases. The chemical composition of the precipitates was identified by means of EDX.

3. Experimental results

The thermodynamic prediction of the phase's solvus temperature in case of the solid phases and the solidus temperature in case of the liquid phase for alloys 1-3 with continuous changing of Nb concentration is shown in Fig. 1a and Fig. 1b.

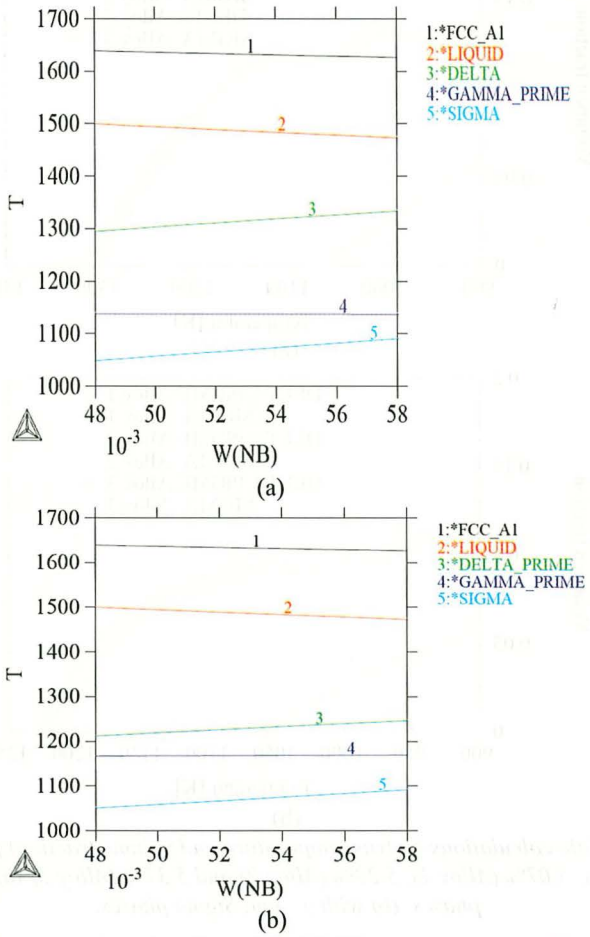

Fig.I . ThermoCalc calculations for alloys 1-3 with Nb concentration 4.8% to 5.8%. (a) with δ phase, (b) with γ′′ phase

The Nb concentration was varied from 4.8 % to 5.8 %. The Ni concentration was balanced; the other elements stayed constant. These calculations show the observable difference between solvus temperature of δ (DELTA) and γ′′ (DELTA_PRIME) phases. On the one hand, the solvus temperature and stability of δ-Ni_3Nb and γ′′ phases rise with increasing Nb concentration. On the other hand, the solvus temperature and volume fraction of Sigma phase rise with increasing Nb concentration. This effect is not wanted because Sigma phase leads to the embrittlement of the Alloy 718.

Fig. 2 shows the solvus temperatures and the volume fractions of δ (DELTA) and Sigma phases (a) and γ′′ (DELTA_PRIME) and Sigma phases. ThermoCalc calculations do not illustrate significant differences, but the upward tendency for the increase of solvus temperatures and volume fractions of δ and γ′′ phases with increasing Nb concentration can be identified.

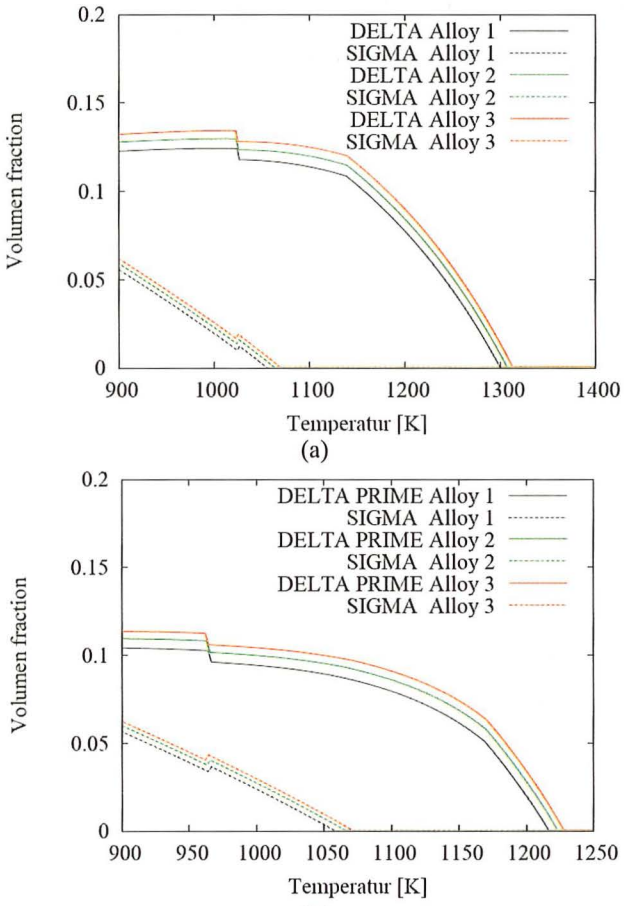

Fig.2 . ThermoCalc calculations (solvus temperature and volume fraction) for alloys 1-3 with Nb concentration: 5.07% (Alloy 1), 5.23% (Alloy 2) and 5.37% (Alloy 3) (a) with δ and Sigma phases, (b) with γ′′ and Sigma phases.

Grain boundary precipitations of δ-Ni_3Nb (in short rods and globular morphology) and grain boundary precipitations of carbides are typical for the microstructure of Alloy 718. The

main fine precipitates of disk-like γ'' and precipitations of fine globular γ' can not usually be detected in the SEM. There is an observable difference between alloys 1, 2 and 3 in amount and morphology of δ-Ni_3Nb phase with increasing Nb content (see Fig. 3).

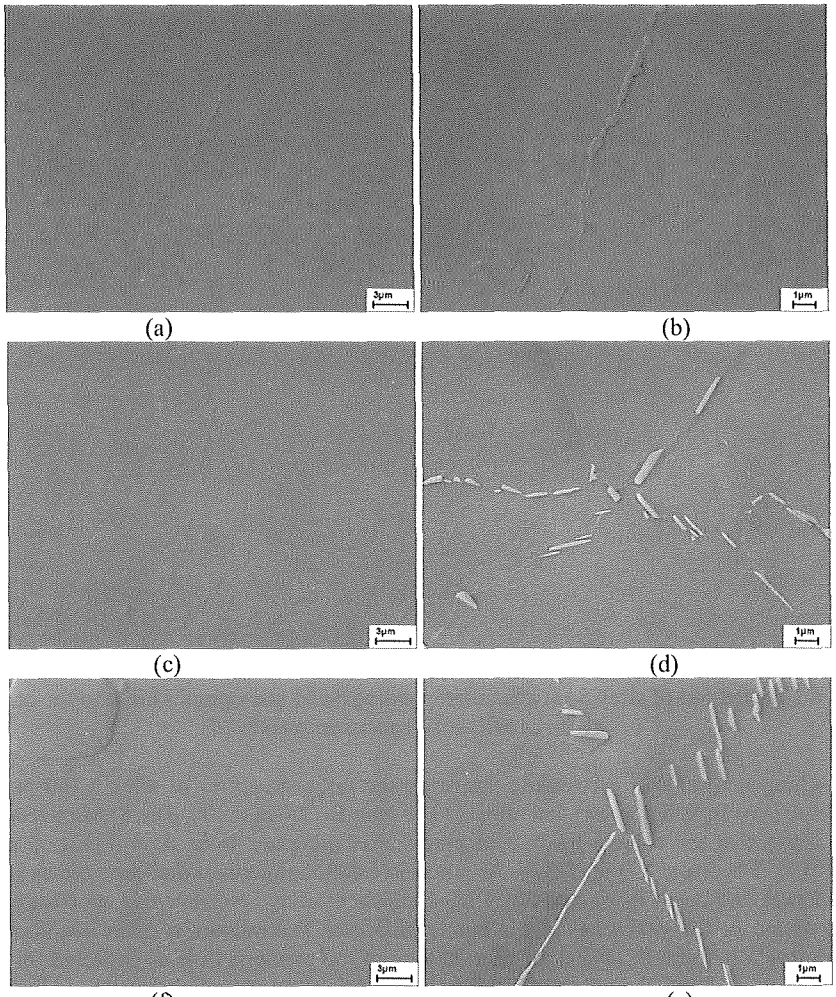

Fig.3. Microstructures of alloy 1 (5.07% Nb) (a, b), alloy 2 (5.23% Nb) (c, d) and alloy 3 (5.37% Nb) (f, e)

The microstructure of alloy 1 with 5.07% Nb is shown in Fig. 3a and 3b. The δ-Ni_3Nb phase is visible, but the volume fraction is smaller than in alloy 2 (Fig. 3 c-d) and alloy 3 (Fig. 3 f-e). The increase of the alloy hardness from 430 HB in alloy 1 to 444 HB in alloy 2 and to 450 HB in alloy 3 shows that even the little additions of Nb change microstructure and hardness of the alloys at RT.

Investigation of alloys 4-8 demonstrated that boron and zirconium have a large influence on castability. All solidification rods of alloys 5 and 6 with 150ppm B and 200ppm B respectively showed cracks in their middle part after melting and casting into a water-cooled copper mould (Fig. 4a) and could not be deformed. Obviously, these alloys are sensitive to

hot cracking due to high concentration of B (Fig. 4b). The fracture morphology is shown in Fig. 4 (b-d) at higher magnification. It is typical for hot tearing, often exposing dendrite arms.

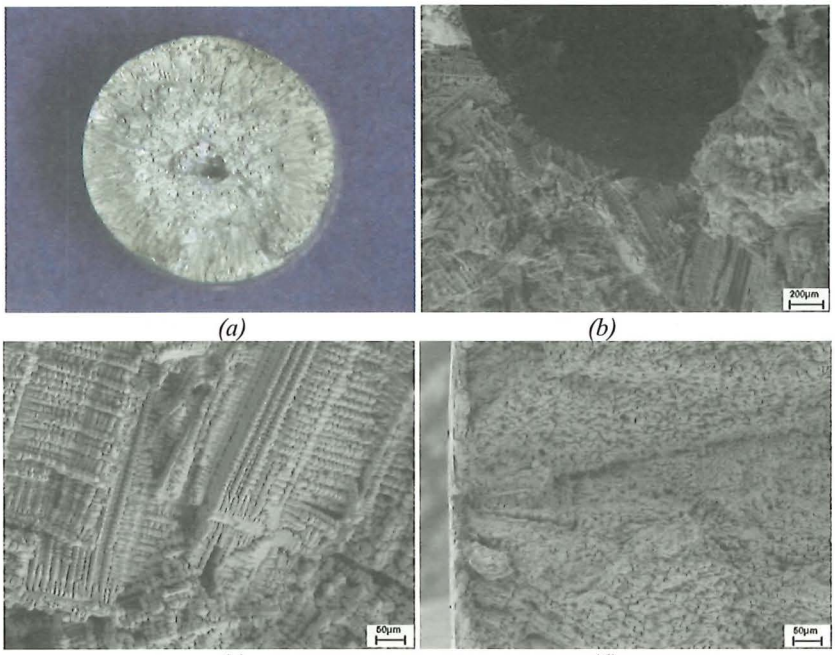

(a) *(b)* *(c)* *(d)*

Fig. 4. Cracked rod of alloy 5 (a) and corresponding SEM micrographs close to the central cavity (b, c) and to the specimen surface (d)

V2A etching reagent was used while preparing the microstructures of alloy 4 (60 ppm B), alloy 7 (60 ppm B, 200 ppm Zr) and alloy 8 (100 ppm B, 200 ppm Zr). The SEM micrographs show clearly that the volume fraction of precipitates increases from alloy 4 (Fig. 5 a-b) to alloy 7 (Fig. 5 b-c) and 8 (Fig. 5 d-e). As a boride creator, zirconium increases the amount of $(Nb,Ti,Zr)_xB_y$ borides (Fig. 5a and 5c). EDS analysis of alloy 7 verifies this conclusion (Fig. 6). Zirconium in Alloy 718 has also a big influence on precipitates at grain boundaries. In case of alloy 4 (60ppm B, no Zr) the morphology of the precipitates is as expected for Alloy 718 (Fig. 5 a, b). Thus, the effect of small boron additions on the microstructure is limited to the formation of isolated borides as discussed above. However, when zirconium is added the result is vastly different. Alloys 7 and 8, containing 200ppm zirconium at essentially unaltered boron content, exhibit agglomerates of the δ-Ni_3Nb phase and its volume fraction increases significantly (Fig. 6 c-f). EDS analysis (Fig. 7) confirms the critical role of zirconium, which strongly partitions to the δ-Ni_3Nb phase.

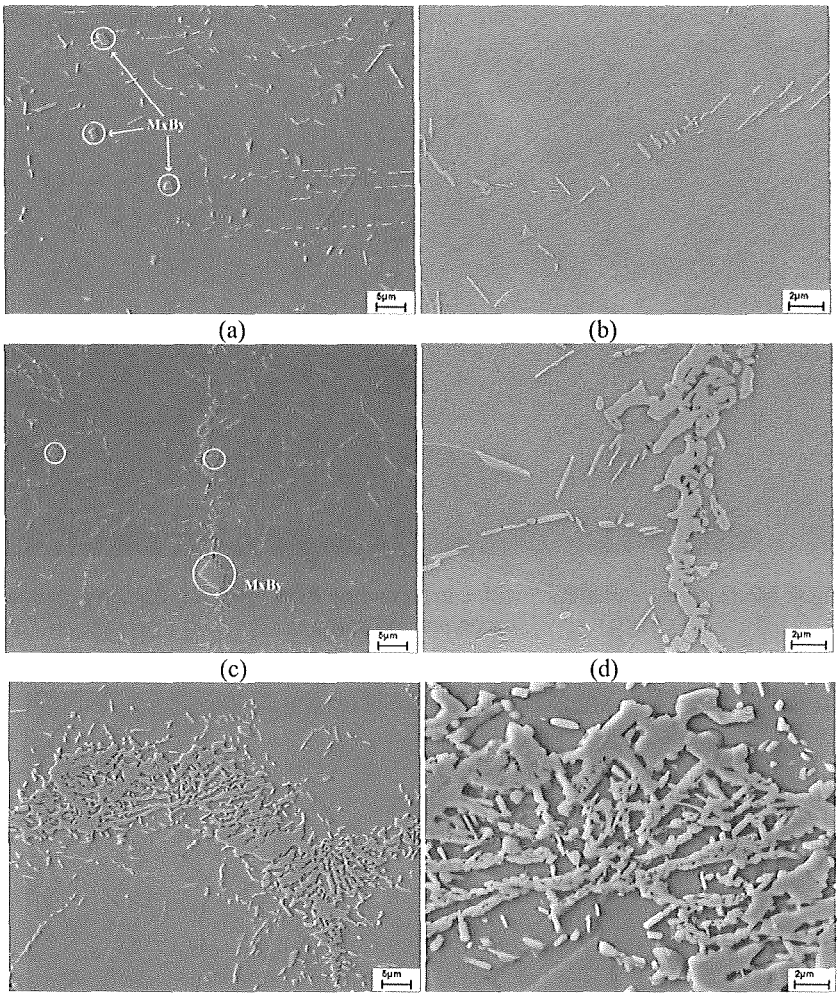

Fig.5. Microstructure of alloy 4 (a-b) with borides M_xB_y ($(Nb,Ti,Zr)_xB_y$), alloy 7 (c-d) with borides M_xB_y ($(Nb,Ti,Zr)_xB_y$) and alloy 8 (f-e)

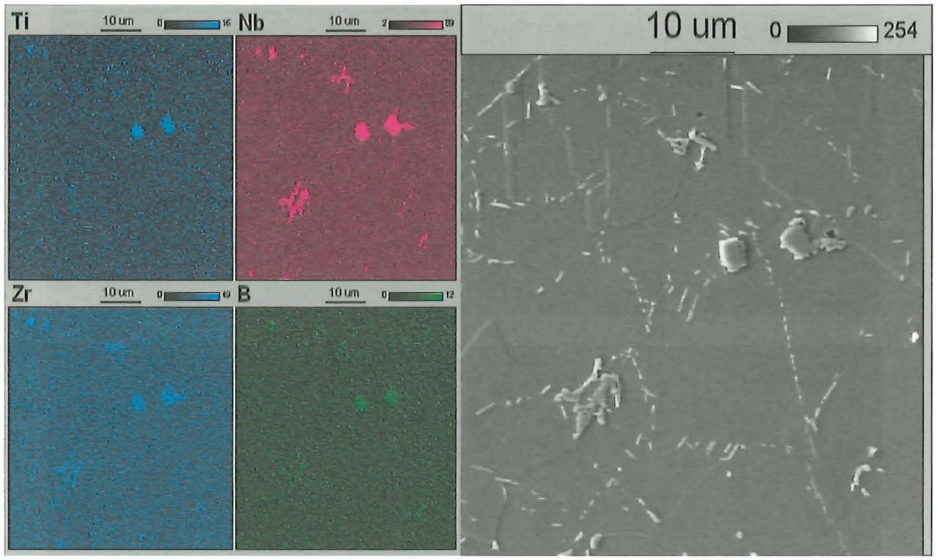

Fig.6. Microstructure of alloy 5 with corresponding EDS maps for niobium, titanium, zirconium and boron

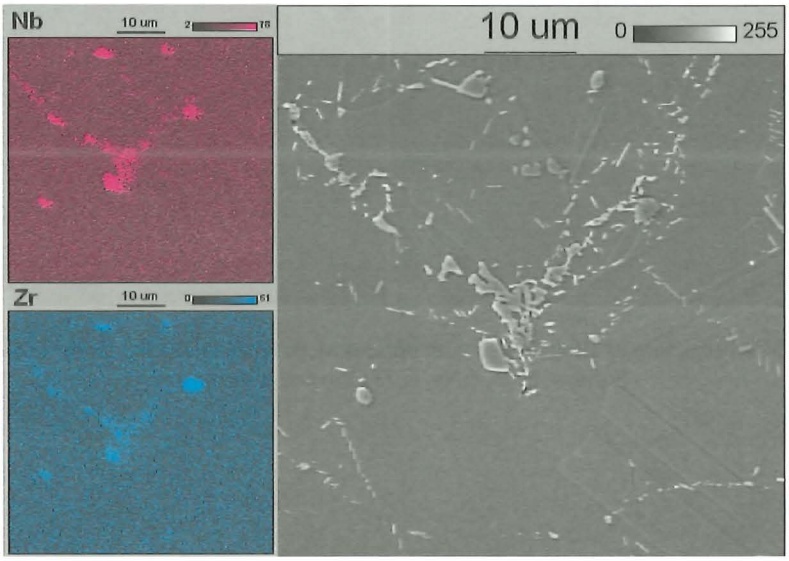

Fig.7. Microstructure of alloy 5 with corresponding EDS maps for niobium and zirconium

Summary:

The results of this work show that even small changes in the concentration of the element Nb and also B and Zr in the Alloy 718 have large influence on its microstructure:

- Addition of niobium in the limits of ASTM specification leads to the increase of δ-Ni_3Nb phase and accordingly to changed mechanical properties of the Alloy 718.
- Boron addition leads to the formation of borides in the microstructure while the morphology of all other phases remains unchanged.
- Boron concentrations beyond about 100ppm strongly increase the tendency to hot cracking of alloy 718 and are therefore not advisable.
- The addition of zirconium strongly changes the morphology and volume fraction of borides and δ-Ni_3Nb phase, leading to large agglomerates, which are expected to adversely affect mechanical properties. Hence, the zirconium content should be kept below 200ppm.

References:

[1] C.C. Jia, K. Ishida, and T. Nishizawa, Partition of Alloying Elements between γ (A1), γ′ (L12), and β (B2) Phases in Ni-Al Base Systems, *Metallurgical and Materials Transactions*, Volume 25A, 473-482, (1994).
[2] M.K. Miller, S.S. Babu, M.G. Burke, Comparison of the Phase Compositions in Alloy 718 Measured by Atom Probe Tomography and Predicted by Thermodynamic Calculations, *Materials Science and Engineering*, A327, 84-88, (2002).
[3] X. Xio, G. Wang, J. Dong, C. Xu, W.-D. Cao, R. Kennedy, Structure Stability Study on a Newly Developed Nickel-base Superalloy – ALLVAC 718Plus, *Superalloys 718, 625, 706 and Derivatives 2005*, 179-191, (2005).
[4] S. Benhadad, N.L. Richards, and M.C. Chaturvedi, The Influence of Minor Elements on the Weldability of an INCONEL 718-Type Superalloy, *Metallurgical and Materials Transactions*, Volume 33A, 2005-2012, (2002).
[5] W.R. Sun, H.R. Guan, M. Wang, Z.G. Wang, L.F. Huang, Z.Q. Hu, Influence of Prosphorus on Deformation Mechanism and Mechanical Properties of IN 718, *Superalloys 718, 625, 706 and Derivatives 2005*, 399-407, (2005).
[6] G.D. Smith and S.J. Patel, The Role of Niobium in Wrought Precipitation-Hardened Nickel-base Alloys, *Superalloys 718, 625, 706 and Derivatives 2005*, 135-154, (2005).
[7] R.L. Kennedy, ALLVAC 718PLUS, Superalloy for the Next Forty Years, Superalloys 718, 625, 706 and Derivatives 2005, 1-14, (2005).
[8] R. Cozar and A. Pineau, Morphology of γ′ and γ′′ Precipitates and Thermal Stability of Inconel 718 Type Alloys, *Metall. Trans.*, 47-59, (1973).
[9] X. Xie, J.Dong, G. Wang, W. You, The Effect of Nb, Ti, Al on Precipitation and Strengthening Behavior of 718 Type Superalloys, *Superalloys 718, 625, 706 and Derivatives 2005*, 287-298, (2005).
[10] S. Benhadad, N.L. Richards, and M.C. Chaturvedi, The Influence of Minor Elements on the Weldability of an INCONEL 718-Type Superalloy, *Metallurgical and Materials Transactions*, Volume 33A, 2005-2012, (2002).
[11] W. Chen, M.C. Chaturvedi, N.L. Richards, and G. McMahon, Grain Boundary Segregation of Boron in INCONEL 718, *Metallurgical and Materials Transactions*, Volume 29A, 1947-1954, (1998).
[12] S.J. Sijbrandij, M.K. Miller, J.A. Horton, W.D. Cao, Atom Probe Analysis of Nickel-Based Superalloy IN-718 With Boron and Phosphorus Additions, *Materials Science and Engineering*, A250, 115-119, (1998).
[13] W.R. Sun, S.R. Guo, J.H. Lee, N.K. Park, Y.S. Yoo, S.J. Choe, Z.Q. Hu, Effects of Phosphorus on the δ-Ni_3Nb Phase Precipitation and the Stress Rupture Properties in Alloy 718, *Materials Science and Engineering*, A247, 173-179, (1998).

[14] L. Xiao, D.L. Chen, M.C. Chaturvedi, Effect of Boron and Carbon on Thermomechanical Fatigue of IN 718 Superalloy Part I. Deformation Behavior, *Materials Science and Engineering*, A437, 157-171, (2006).
[15] L. Xiao, D.L. Chen, M.C. Chaturvedi, Effect of Boron and Carbon on Thermomechanical Fatigue of IN 718 Superalloy Part II. Deformation Microstructures, *Materials Science and Engineering*, A437, 172-182, (2006).
[16] S. Floreen and J.M. Davidson, The Effects of B and Zr on the Creep and Fatique Crack Growth Behavior of a Ni-Base Superalloy, *Metallurgical Transactions*, Volume 14A, 895-901, (1983).
[17] T.J. Garosshen, T.D. Tillman, and G.P. McCarthy, Effects of B, C, and Zr on the Structure and Properties of P/M Nickel Base Superalloy, *Metallurgical Transactions,* Volume 18A, 69-77, (1987).
[18] X. Xio, G. Wang, J. Dong, C. Xu, W.-D. Cao, R. Kennedy, Structure Stability Study on a Newly Developed Nickel-base Superalloy – ALLVAC 718Plus, *Superalloys 718, 625, 706 and Derivatives 2005*, 179-191, (2005).
[19] J. Rösler, S. Müller, Protection of Ni-Base Superalloys Against Stress Accelerated Grain Boundary Oxidation (SAGBO) by Grain Boundary Chemistry Modification, *Scripta Materialia*, Volume 40, 257-263, (1999)

9th Liege Conference : Materials for Advanced Power Engineering 2010
edited by J. Lecomte-Beckers, Q. Contrepois, T. Beck and B. Kuhn.

PHASE-FIELD SIMULATION OF MICROSTRUCTURE EVOLUTION IN NI-BASED SUPERALLOYS

Yuhki Tsukada[1], Yoshinori Murata[1], Toshiyuki Koyama[2] and Masahiko Morinaga[1]

[1]Department of Materials, Physics and Energy Engineering, Graduate School of Engineering, Nagoya University, Nagoya 464–8603, Japan
[2]National Institute for Materials Science, Tsukuba 305–0047, Japan

Abstract

The morphological evolution of the ($\gamma + \gamma'$) microstructure in Ni-based superalloys is investigated by a series of phase-field simulations. In the simulation for simple aging heat treatment, the effect of elastic constant inhomogeneity between the γ and γ' phases is investigated. The elastic anisotropy or the shear modulus is changed independently in the simulation. The variation of the anisotropy affects the morphology, particle size distribution and coarsening kinetics of the γ' phase, whereas the variation of the shear modulus does not affect them. In the simulation for high temperature creep, formation and collapse of the rafted structure are reproduced under the assumption that the creep strain in the γ matrix increases with creep time. This morphological evolution is related to the change in the energetically stable morphology of the γ' phase with increasing the creep strain.

Keywords: phase-field model, nickel-based alloy, elastic inhomogeneity, creep, rafting

1. Introduction

Ni-based superalloys have excellent creep strength at high temperatures and are applied to gas turbine materials. The superior mechanical property of the alloy originates from the γ' strengthening phase precipitating in the γ phase, and depends on the γ' volume fraction, morphology and size distribution of the ($\gamma + \gamma'$) two-phase microstructure. In aging heat treatment without external stress, the cuboidal γ' phase precipitates and arranges along the <100> crystallographic directions in the γ phase. During creep tests, on the other hand, the cuboidal γ' phase evolves into the rafted structure, in which plate like γ and γ' phases are stacked alternately. The rafted structure collapses especially in the late stage of long term creep, and the creep strength of the superalloys is related to the stability of the rafted structure [1]. It is useful to reveal contributing factors in the morphological evolution during both aging heat treatment and high temperature creep for stabilizing the ($\gamma + \gamma'$) microstructure.

In recent years, the phase-field method has been applied for simulating microstructural evolution in materials [2–6]. The phase-field approach describes a microstructure using a set of conserved and non-conserved field variables which change continuously across the interface regions. By solving a set of equations governing the evolution of the fields, the microstructural evolution can be simulated under the condition of reducing the total free energy of the system, which includes chemical free energy, interfacial energy and elastic strain energy. The purpose of this study is to investigate the contributing

factors in microstructural evolution in Ni-based superalloys using a series of phase-field simulations. In the simulation for aging heat treatment, the effect of elastic constant inhomogeneity between the γ and γ' phases on microstructural evolution is examined. On the other hand, in the simulation for high temperature creep, the formation and collapse of the rafted structure are reproduced and the microstructural stability is discussed on the basis of the simulation results.

2. Calculation method

We consider the (γ + γ') two-phase model, and the volume fraction of the γ' phase, $f(\mathbf{r}, t)$, and four artificial order parameters, $\phi_i(\mathbf{r}, t)$ ($i = 1, 2, 3, 4$), which describe the four types of ordered domains of the γ' phase [2], are employed as field variables. These field variables vary spatially ($\mathbf{r}$) and temporally (t). The temporal evolution of the field variables is given by solving the Cahn-Hilliard and Ginzburg-Landau equations,

$$\frac{\partial f(\mathbf{r},t)}{\partial t} = M\nabla^2 \frac{\delta G_{\text{sys}}}{\delta f(\mathbf{r},t)}, \tag{1}$$

$$\frac{\partial \phi_i(\mathbf{r},t)}{\partial t} = -L\frac{\delta G_{\text{sys}}}{\delta \phi_i(\mathbf{r},t)} \quad (i = 1, 2, 3, 4), \tag{2}$$

where G_{sys} is the total free energy of the system, M is the diffusion mobility and L is the structural relaxation coefficient. The total free energy is given by

$$G_{\text{sys}} = \int_{\mathbf{r}} \left[G_{\text{chem}}(f, \phi_i) + E_{\text{grad}}(\phi_i) + E_{\text{str}}(\phi_i) \right] d\mathbf{r}, \tag{3}$$

where G_{chem} is the chemical free energy density, E_{grad} is the gradient energy density and E_{str} is the elastic strain energy density. The chemical free energy density is expressed as

$$G_{\text{chem}} = \{1 - h(\phi_i)\} G^{\text{m}}_{\text{chem}}(f^{\text{m}}) + h(\phi_i) G^{\text{p}}_{\text{chem}}(f^{\text{p}}) + wg(\phi_i), \tag{4}$$

where w is the double-well potential height [5,6]. In Eq. (4), $G^{\text{m}}_{\text{chem}}$ and $G^{\text{p}}_{\text{chem}}$ are the chemical free energy density of the γ matrix and the γ' precipitate, respectively, and are approximated using parabolic functions

$$G^{\text{m}}_{\text{chem}} = \frac{1}{2} W_1 f^2, \tag{5}$$

$$G^{\text{p}}_{\text{chem}} = \frac{1}{2} W_2 (1 - f)^2, \tag{6}$$

where W_1 and W_2 are the coefficients determined by the Gibbs energy calculation based on the sub-lattice model using the thermodynamic database. The functions $h(\phi_i)$ and $g(\phi_i)$ are selected as [6]

$$h(\phi_i) = \sum_{i=1}^{4} [\phi_i^3 (10 - 15\phi_i + 6\phi_i^2)], \tag{7}$$

$$g(\phi_i) = \sum_{i=1}^{4} [\phi_i^2 (1 - \phi_i)^2] + \alpha \sum_{i=1}^{4} \sum_{j \neq i}^{4} \phi_i^2 \phi_j^2. \tag{8}$$

Employing the description by Kim et al. [7], the interface region is regarded as a mixture of the γ and γ' phases with different volume fractions of the γ' phase but with equal chemical potentials:

$$f = \{1 - h(\phi_i)\} f^{\mathrm{m}} + h(\phi_i) f^{\mathrm{p}}, \tag{9}$$

$$\left(\frac{\partial G^{\mathrm{m}}_{\mathrm{chem}}}{\partial f} \right)_{f=f^{\mathrm{m}}} = \left(\frac{\partial G^{\mathrm{p}}_{\mathrm{chem}}}{\partial f} \right)_{f=f^{\mathrm{p}}}. \tag{10}$$

The gradient energy density is estimated from the artificial order parameters as

$$E_{\mathrm{grad}} = \frac{1}{2} \kappa_\phi \sum_{i=1}^{4} (\nabla \phi_i)^2, \tag{11}$$

where κ_ϕ is the gradient energy coefficient of the order parameter [8]. The gradient energy in the phase-field model is correlated with the interfacial energy, and the parameter, w, in Eq. (4) and κ_ϕ in Eq. (11) are related to both the interfacial energy density, γ_{s}, and the interface width, 2λ, as [7]

$$\gamma_{\mathrm{s}} = \frac{\sqrt{w \kappa_\phi}}{3\sqrt{2}}, \tag{12}$$

$$2\lambda = \alpha \sqrt{\frac{2\kappa_\phi}{w}}. \tag{13}$$

The elastic strain energy density, E_{str}, arising from the lattice misfit between the γ and γ' phases is calculated on the basis of micromechanics: [9,10]

$$E_{\mathrm{str}} = \frac{1}{2} C_{ijkl} \varepsilon^{\mathrm{el}}_{ij}(\mathbf{r},t) \varepsilon^{\mathrm{el}}_{kl}(\mathbf{r},t) - \sigma^{\mathrm{appl}}_{ij} \bar{\varepsilon}_{ij}, \tag{14}$$

where ${\sigma^{\mathrm{appl}}}_{ij}$ and $\bar{\varepsilon}_{ij}$ represent the external stress and the macroscopic strain, respectively. The elastic strain ${\varepsilon^{\mathrm{el}}}_{kl}$ is expressed as

$$\varepsilon^{\mathrm{el}}_{kl}(\mathbf{r},t) = \varepsilon_{kl}(\mathbf{r},t) - \varepsilon^{0}_{kl}(\mathbf{r},t), \tag{15}$$

where ε_{kl} and ${\varepsilon^{0}}_{kl}$ represent the total strain and eigenstrain, respectively. The eigenstrain is expressed as

$$\varepsilon^{0}_{kl}(\mathbf{r},t) = \varepsilon_0 \delta_{kl} h(\phi_i), \tag{16}$$

and

$$\varepsilon_0 = \frac{a_{\mathrm{m}} - a_{\mathrm{p}}}{a_{\mathrm{m}}}, \tag{17}$$

where ε_0 represents the lattice misfit and δ_{kl} is the Kronecher delta function. In Eq. (17), a_{m} and a_{p} are the lattice parameters of the γ matrix and the γ' precipitate, respectively. The total strain ε_{kl} is represented as the sum of the homogeneous strain ($\bar{\varepsilon}_{kl}$) and heterogeneous strain ($\delta\varepsilon_{kl}(\mathbf{r})$):

$$\varepsilon_{kl}(\mathbf{r}) = \bar{\varepsilon}_{kl} + \delta\varepsilon_{kl}(\mathbf{r}), \tag{18}$$

and heterogeneous strain can be expressed as

$$\delta\varepsilon_{kl}(\mathbf{r}) = \frac{1}{2}\left\{\frac{\partial u_k(\mathbf{r})}{\partial r_l} + \frac{\partial u_l(\mathbf{r})}{\partial r_k}\right\}, \tag{19}$$

where u_i (**r**) represents the ith displacement component. The Hooke's law gives the local elastic stress as σ^{el}_{ij} (**r**) = $C_{ijkl}\varepsilon^{el}_{kl}$ (**r**), where C_{ijkl} denotes the elastic constants. Assuming homogeneous elasticity (C_{ijkl} = constant), the local displacement field is evaluated by solving the local mechanical equilibrium equation ($\partial\sigma^{el}_{ij}/\partial r_j = 0$) in Fourier space, and then the elastic strain energy density is calculated from Eq. (14). When inhomogeneity in the elastic constant is incorporated into the calculation, an iterative approach is used for solving the inhomogeneous elasticity equation [3].

3. Results and Discussion

3.1. Elastic inhomogenetiy and microstructural evolution during aging heat treatment

2D phase-field simulation at 1373 K was performed by solving Eqs. (1) and (2) numerically using the conventional difference method under the periodic boundary conditions. The system size is 1280×1280 nm^2. The coefficients in the chemical free energy density given by Eqs. (5) and (6) are determined as $W_1 = 1.20\times10^3$ and $W_2 = 1.45\times10^3$ J·mol^{-1} on the basis of the Gibbs energy calculation using the thermodynamic database [11]. By fitting to the interfacial energy density, γ_s = 14.2 mJ·m^{-2}, in Ni-Al binary alloys [12], the double-well potential height and the gradient energy coefficient are set to be $w = 1.7\times10^7$ J·m^{-3} and $\kappa_\phi = 2.1\times10^{-10}$ J·m, respectively. Elastic constants of the TMS-26 alloy at 1373 K (C^m_{11} = 184, C^m_{12} = 135, C^m_{44} = 88.1, C^p_{11} = 209, C^p_{12} = 142 and C^p_{44} = 90.4 GPa; the superscripts m and p represent the elastic constants of the γ and γ' phases, respectively) [13] are employed in this simulation, and the volume fraction of the γ' phase in the equilibrium state is set to be 55 %. The lattice misfit is $\varepsilon_0 = -0.003$, which is close to the value for TMS-26 alloy [13]. This simulation is started from the supersaturated solid solution with a random noise of the filed variables (f, ϕ_i). Figure 1 shows 2D morphological evolution of the γ' phase in the late stage of coarsening at 1373 K. The γ' phase is expressed as white area in Fig. 1. It is found that the cuboidal γ' phase arranges along the <10> crystallographic direction of the γ matrix due to the anisotropic elastic interaction.

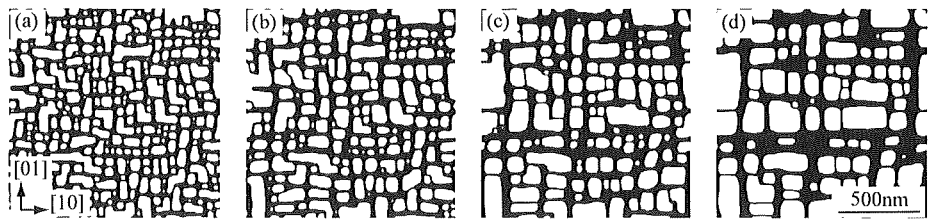

Fig. 1 Morphological evolution of the γ' phase calculated from 2D phase-field simulation at 1373K using the elastic constants of a practical Ni-based superalloy. (a) t = 10000, (b) t = 20000, (c) t = 40000 and (d) t = 80000. All time expressed here are dimensionless time steps.

In order to examine the effect of elastic inhomogeneity, we focused on three independent elastic quantities in cubic system, i.e., the bulk modulus ($B = C_{11} + C_{12}$), the shear modulus ($G = 2C_{44}$) and the elastic anisotropy ($\delta = 2C_{44} / (C_{11} - C_{12})$), and only the anisotropy or the shear modulus was changed independently while keeping the other two quantities constant in the simulation. On the basis of the elastic constants of the TMS-26 alloy ((B^m, B^p) = (319, 351), (G^m, G^p) = (176, 180) and (δ^m, δ^p) = (3.59, 2.69)), each quantity was changed under the limitation that the Young's modulus of the γ' phase was larger than that of the γ phase ($E^m < E^p$) along all the crystallographic directions.

Figure 2 shows the results of the phase-field simulation obtained in the late stage of

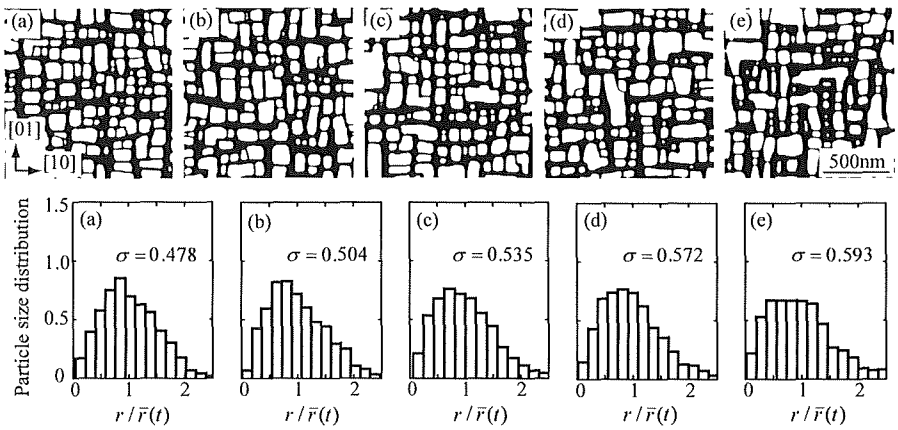

Fig. 2 Dependence of the γ' phase morphology and particle size distribution on elastic anisotropy in the γ matrix and γ' precipitate. (δ^m, δ^p): (a) (6.07, 2.17), (b) (4.51, 2.40), (c) (3.59, 2.69), (d) (2.98, 3.07) and (e) (2.55, 3.57). δ is $2C_{44} / (C_{11} - C_{12})$.

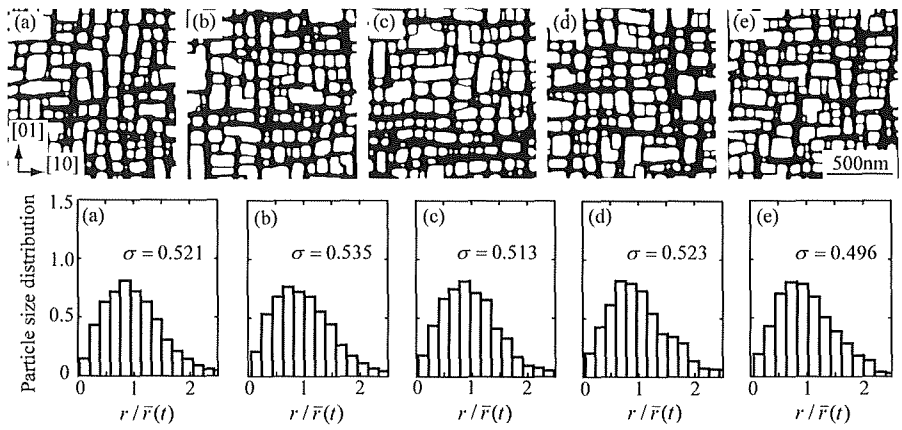

Fig. 3 Dependence of the γ' phase morphology and particle size distribution on shear modulus in the γ matrix and γ' precipitate. (a) κ = 0.90, (b) κ = 1.02, (c) κ = 1.16, (d) κ = 1.32 and (e) κ = 1.74. κ is C^p_{44} / C^m_{44}.

coarsening of the γ' phase, indicating the γ' morphological dependence on the anisotropy in the γ and γ' phases. The anisotropy is varied in five sets as (δ^m, δ^p) = (6.07, 2.17), (4.51, 2.40), (3.59, 2.69), (2.98, 3.07) and (2.55, 3.57). It is found that the cuboidal γ' phase shows irregularity when the ratio of δ^p to δ^m becomes large (see Fig. 2 (e)). In the previous work by Hu and Chen [3], it was shown that a harder phase tended to consist of isolated particles wrapped by a softer phase. The simulation condition of Fig. 2 (e) is the case that the γ' phase exhibits slightly larger Young's modulus than the γ phase. This condition seems to lead to the destabilization of the cuboidal γ' phase.

In Fig. 2, scaled particle size distribution of the γ' phase is also shown for each simulation condition. In this study, according to a similar way reported by Vaithyanathan and Chen [4], averaged particle size distribution was constructed from the simulation results for four different time steps corresponding to Fig. 1. It is obvious that the spectrum becomes broad with increasing the ratio of δ^p to δ^m, whereas the normalized radius at the maximum size distribution (hereinafter referred to as the peak radius) of about $r/\bar{r} = 0.75$ does not change. This result is consistent with the previous report that the peak radius is $r/\bar{r} = 0.7 \sim 0.8$ when the volume fraction of the precipitate is about 55 % [4]. It is found that the variation of the anisotropy affects only the width of the distribution spectrum without changing the peak radius.

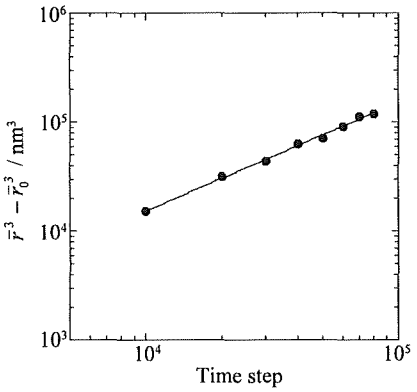

Fig. 4 Growth of the γ' particle plotted as cube of average radius vs. simulation time step.

Figure 3 shows the simulation results obtained in the late stage of coarsening of the γ' phase, indicating the dependence of the γ' morphology and particle size distribution on the shear modulus in the γ and γ' phases. The shear modulus is varied in five sets as $\kappa = C^p_{44} / C^m_{44}$ = 0.90, 1.02, 1.16, 1.32 and 1.74. It is found that the elastic inhomogeneity with respect to the shear modulus affects scarcely the morphology of the γ' phase. Furthermore, from the particle size distribution shown in Fig. 3, it is shown that the peak radius and the spectrum shape are not affected by the variation of the shear modulus.

Using a series of simulation results, coarsening kinetics of the γ' particles is investigated by the following growth law

$$\bar{r}^3 = \bar{r}_0^3 + kt, \qquad (20)$$

where $\bar{r}$ is the average precipitate radius, $\bar{r}_0$ is

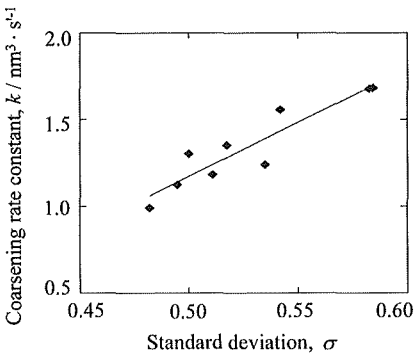

Fig. 5 Correlation between the standard deviation of the particle size distribution and the coarsening rate constant of the γ' phase.

the average precipitate radius at the start of coarsening, k is the coarsening rate constant, and t is time. As shown in Eq. (20), the growth exponent is fixed as 3 in this study, and the coarsening rate constant is evaluated. Figure 4 shows the plots of $\bar{r}^3 - \bar{r}_0^3$ vs. simulation time step on a logarithmic scale obtained from the simulation results shown in Fig. 1. The coarsening rate constant is estimated from the slope of the linear regression line using the data holding the linear relationship shown in Eq. (20). Similar analysis is carried out for a series of simulation results shown in Figs. 2 and 3. Figure 5 shows the summarized results on the relationship between the standard deviation of the particle size distribution and the coarsening rate constant. The results in Fig. 5 are obtained from the average of two simulation runs for each condition. It is shown that the coarsening rate constant of the cubic growth law depends on the standard deviation of the γ' particle size distribution. This indicates that the elastic inhomogeneity affects the coarsening kinetics of the γ' particles. It should be emphasized that the difference of about 20 % in elastic constants between the γ and γ' phases affects the evolution of the (γ + γ') two-phase microstructure.

3.2. Formation and collapse of the rafted structure during high temperature creep

We perform the simulation of microstructural evolution of the γ' phase during creep under a tensile stress along [001] crystallographic direction. Under the assumption that only the γ phase is uniformly deformed, the total transformation strain is calculated as

$$\varepsilon_0^{\text{total}} = \begin{pmatrix} \varepsilon_0 & 0 & 0 \\ 0 & \varepsilon_0 & 0 \\ 0 & 0 & \varepsilon_0 \end{pmatrix} + \begin{pmatrix} \varepsilon_p/2 & 0 & 0 \\ 0 & \varepsilon_p/2 & 0 \\ 0 & 0 & -\varepsilon_p \end{pmatrix}, \tag{21}$$

where ε_p represents the plastic strain of the matrix along the [001] tensile axis. Then, the eignstrain is expressed as

$$\varepsilon_{kl}^0(\mathbf{r},t) = \varepsilon_0^{\text{total}} h(\phi_i). \tag{22}$$

3D phase-field simulation at 1193 K was carried out under the periodic boundary conditions. The system size is 384×384×384 nm^3. The coefficients of the chemical free energy density in Eqs. (5) and (6) are $W_1 = 2.25\times10^3$ and $W_2 = 2.90\times10^3$ J·mol^{-1} [11]. The double-well potential height and the gradient energy coefficient are set to be $w = 3.6\times10^7$ J·m^{-3} and $\kappa_\phi = 1.0\times10^{-10}$ J·m, respectively. Elastic inhomogeneity is ignored for efficient computation, and the elastic constants of pure Ni (C_{11} = 250, C_{12} = 150 and C_{44} = 123 GPa) [14] are employed for the entire system. The volume fraction of the γ' phase in the equilibrium state is set to be 60 % and the lattice misfit is assumed to be $\varepsilon_0 = -0.004$ [1]. The external tensile stress along [001] direction is set to be 130 MPa.

Figure 6 shows the morphological evolution of the γ' phase during high temperature creep obtained from the 3D phase-field simulation. Figure 6 (a) shows initial configuration of the (γ + γ') microstructure, which was prepared using the phase-field simulation without incorporating external stress and plastic strain. The cuboidal γ' precipitates aligned along the <100> direction of the γ matrix is observed. In Fig. 6, the plastic strain (creep strain) is

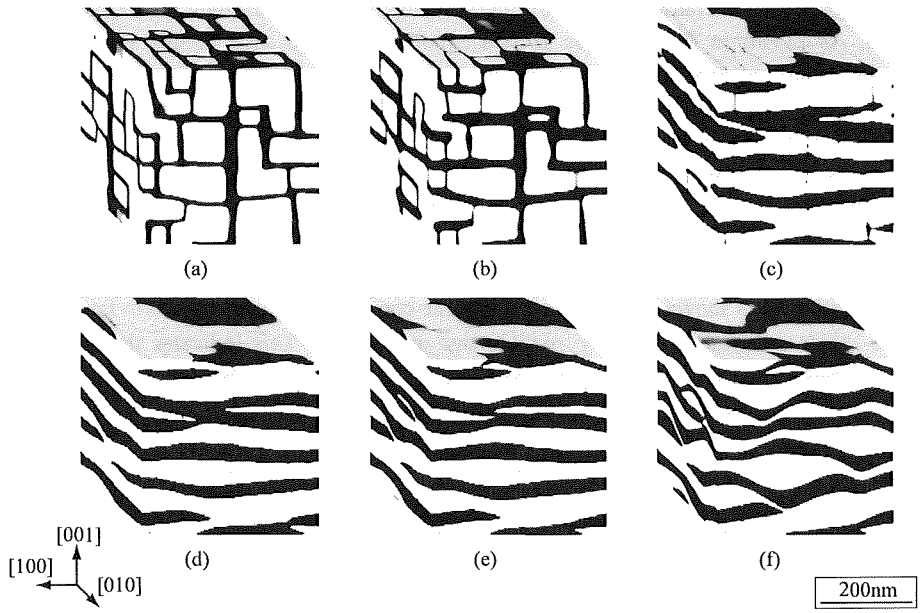

Fig. 6 Morphological evolution of the γ' phase during creep at 1193 K under 130 MPa tension along [001] calculated from 3D phase-field simulation. (a) t = 0, (b) t = 5000, (c) t = 10000, (d) t = 20000, (e) t = 30000 and (f) t = 40000. All time expressed here are dimensionless time steps.

increased at a constant rate of $d\varepsilon_p / dt = 4.0\times10^{-7}$, where t represents the simulation time step. This corresponds to the fact that the creep strain increases with creep time. During t = 0–20000, it is observed that the γ' phase evolves toward the direction normal to the applied tension axis and (001) rafted structure is produced. After t = 20000, the (001) rafted structure gradually transforms into wavy morphology as shown in Fig. 6 (d)–(f). This morphological change coincides with the result reported previously that the lamellar structure collapses in the late stage of long term creep [1].

The formation and collapse of the rafted structure are attributed to the change in the stable shape of the γ' phase during creep; the habit plane of plate-like structure deviates from (001) with increasing the creep strain. This can be specifically understood by considering the habit plane and orientation relations of a tetragonal precipitate in a cubic parent phase, because the γ' phase can be regarded as a tetragonal phase with eigenstrain calculated by Eqs. (21) and (22). Figure 7 shows the relation between the Miller indexes of the habit plane of the γ' phase and the tetragonal ratio of the total transformation strain $t_1 = \varepsilon_0^{total}{}_{11} / \varepsilon_0^{total}{}_{33}$ [9]. When the creep strain is introduced, t_1 is between 0 and 1 and the habit plane of the γ' phase is (001). This is the reason that the (001) plate-like structure (rafted structure) is formed, which is consistent with the simulation results shown in Figs 6 (a)–(d). Furthermore,

continuing increase in the creep strain leads to the negative value of t_1 and make the habit plane of the γ' phase deviate from (001). As a result, the destabilization of the (001) plate-like structure occurs, resulting in the collapse of the rafted structure as shown in Figs. 6 (d)–(f). During long term creep at high temperatures, the microstructure is subject to the morphological evolution with the help of the atomic diffusion. Hence, the stability of the rafted structure is closely related to the change in the energetically favorable structure arising from the introduction of the creep strain.

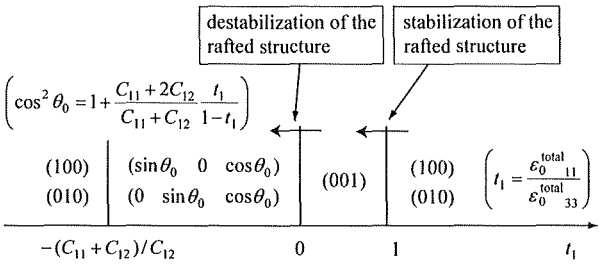

Fig. 7 Schematic interpretation of the relation between the Miller indexes of the habit plane of the γ' phase and the tetragonal ratio of the total transformation strain $t_1 = \varepsilon_0^{total}{}_{11} / \varepsilon_0^{total}{}_{33}$.

4. Summary

Phase-field simulations have been carried out to investigate the contributing factors in microstructural evolution in Ni-based superalloys. In the simulation for simple aging heat treatment, the effect of elastic inhomogeneity between the γ and γ' phases has been revealed on the basis of the elastic constants of a practical alloy. The variation of the elastic anisotropy affects the stability of the cuboidal γ' phase and also affects the width of the γ' particle size distribution spectrum without changing the peak radius. Furthermore, the standard deviation of the particle size distribution affects the coarsening kinetics of the γ' particles. On the other hand, the variation of the shear modulus does not affect both morphology and particle size distribution of the γ' phase.

In the simulation for high temperature creep, it has been assumed that only the γ matrix deforms uniformly and the creep strain in the matrix increases with creep time. As a result, the formation and collapse of the (001) rafted structure has been reproduced. It is found that this morphological evolution is attributed to the change in the energetically stable structure during creep; the habit plane of the γ' precipitate deviates from (001) with increasing the creep strain. Hence, the stability of the rafted structure changes every moment during creep.

Acknowledgements

This work was supported by a Grant-in-Aid for JSPS Fellows of the Ministry of Education, Culture, Sports, Science and Technology, Japan, and was also supported in part by a Grant-in-Aid for Scientific Research of Japan Society for the Promotion of Science (JSPS), Japan.

References

[1] Y. Murata, R. Hashizume, A. Yoshinari, N. Aoki, M. Morinaga and Y. Fukui, Alloying Effect on Surface Stability and Creep Strength of Nickel Based Single Crystal Superalloys Containing 12 mass% Cr, *Superalloys 2000*, pp. 285–294, (2000).
[2] Y. Wang, D. Banerjee, C. C. Su and A. G. Khachaturyan, Field Kinetic Model and Computer Simulation of Precipitation of $L1_2$ Ordered Intermetallics from F.C.C Solid Solution, *Acta Mater.*, vol. 46, pp. 2983–3001, (1998).
[3] S. Y. Hu and L. Q. Chen, A Phase-Field Model for Evolving Microstructures with Strong Elastic Inhomogeneity, *Acta Mater.*, vol. 49, pp. 1879–1890, (2001).
[4] V. Vaithyanathan and L. Q. Chen, Coarsening of Ordered Intermetallic Precipitates with Coherency Stress, *Acta Mater.*, vol. 50, pp. 4061–4073, (2002).
[5] J. Z. Zhu, T. Wang, S. H. Zhou, Z. K. Liu and L. Q. Chen, Quantitative Interface Models for Simulating Microstructure Evolution, *Acta Mater.*, vol. 52, pp. 833–840, (2004).
[6] J. Z. Zhu, T. Wang, A. J. Ardell, S. H. Zhou, Z. K. Liu and L. Q. Chen, Three-Dimensional Phase-Field Simulations of Coarsening Kinetics of γ' Particles in Binary Ni–Al Alloys, *Acta Mater.*, vol. 52, pp. 2837–2845, (2004).
[7] S. G. Kim, W. T. Kim and T. Suzuki, Phase-Field Model for Binary Alloys, *Phys. Rev. E*, vol. 60, pp. 7186–7197, (1999).
[8] J. W. Cahn and J. E. Hilliard, Free Energy of a Nonuniform System. I. Interfacial Free Energy, *J. Chem. Phys.*, vol. 28, pp. 258–267, (1958).
[9] A. G. Khachaturyan, *Theory of Structural Transformations in Solids*, (Wiley, 1983).
[10] T. Mura, *Micromechanics of Defects in Solids, Second, Revised Edition*, (Kluwer Academic, 1987).
[11] I. Ansara, N. Dupin, H. L. Lukas and B. Sundman, Thermodynamic Assessment of the Al–Ni System, *J. Alloy. Compd.*, vol. 247, pp. 20–30, (1997).
[12] A. J. Ardell, An Application of the Theory of Particle Coarsening: The γ' Precipitate in Ni–Al Alloys, *Acta Metall.*, vol. 16, pp. 511–516, (1968).
[13] K. Tanaka, T. Kajikawa, T. Ichitsubo, M. Osawa, T. Yokokawa and H. Harada, Evolution of Internal Stress Field in Ni-Base Superalloy through Creep Deformation, *Mater. Sci. Forum*, vols. 475–479, pp. 619–622, (2005).
[14] *Kinzoku data book, 2nd revised ed.*, (The Japan Inst. Metals, 1984).

9th Liege Conference : Materials for Advanced Power Engineering 2010
edited by J. Lecomte-Beckers, Q. Contrepois, T. Beck and B. Kuhn.

DEVELOPMENT OF CORROSION-RESISTANT NI-BASE SINGLE CRYSTAL SUPERALLOY

K. Kawagishi, T. Yokokawa, Y. Koizumi, T. Kobayashi, M. Sakamoto and H. Harada

High Temperature Materials Center, National Institute for Materials Science, 1-2-1 Sengen, Tsukuba-shi, Ibaraki 305-0047, Japan

Abstract

1st generation Ni-base single-crystal superalloy TMS-6 was modified to increase high temperature strength. Small amounts of Mo and Re were added to TMS-6. Creep, thermo-mechanical fatigue, oxidation and hot corrosion properties were investigated for these alloys and it is concluded that an alloy with equivalent creep property to 2nd generation superalloy CMSX-4 and with superior thermo-mechanical fatigue life and corrosion resistance to CMSX-4 is developed by adding only 0.4wt% of Mo and Re.

Keywords: Ni-base superalloy, single crystal, hot corrosion

Introduction

Ni-base single crystal (SC) superalloys containing high concentrations of refractory elements and platinum group metals are well known to display excellent mechanical properties at high temperature [1]. However, from the recent shortage of Re and Ru, necessity to develop durable alloys with low Re and Ru content is getting higher. In this study, 1st generation Ni-base SC superalloys is modified with small Mo and Re content to improve the high temperature strength and the corrosion resistance. This alloy does not contain Co [2]. Usually, Ni-base superalloys are the primary materials used in industrial turbines. However, if conventional Ni-base superalloys are to be used for the turbine materials of Pebble Bed Module Reactor system (PBMR), turbine maintenances will be difficult due to the presence of Co, as it can produce the isotope, ^{60}Co, which is dangerously Thus, this alloy is able to be applied for the turbine material in the PBMR, which generates electricity by a gas turbine using He gas as a coolant of the reactor.

Experimental

1st generation Ni-base SC superalloy developed by NIMS in 1984, TMS-6 [3], was used as a base alloy. To increase high temperature strength, 0.4 wt% of Mo and Re were added to

TMS-6. Nominal composition is indicated in Table 1. TMS-6 and 2nd generation SC superalloy CMSX-4 were also used as reference in this study. Alloys were cast from raw material and solution heat treated at 1320°C for 5h. Primary and secondary aging conditions were 1100°C/4h and 870°C/20h. Creep, thermo-mechanical fatigue (TMF), oxidation and hot corrosion properties were investigated for this alloy, TMS-6 and CMSX-4.

Table 1 Nominal compositions. (wt%, Ni bal.)

Alloys	Co	Cr	Mo	W	Al	Ti	Ta	Hf	Re
TMS-6	-	9.2	-	8.7	5.3	-	10.4	-	-
TMS-6+Mo, Re	-	9.0	0.4	8.0	5.4	-	10.0	-	0.4
CMSX-4	9.6	6.4	0.6	6.4	5.6	1	6.5	0.1	3

Creep tests were conducted under the following conditions, 800°C/735MPa, 900°C/392MPa, 1000°C/245MPa and 1100°C/137MPa. TMF test was conducted in a temperature range from 400 to 900°C; out-of-phase with 60min dwell time at 900°C. Strain range was ±0.64%. Oxidation behavior was investigated at 1100°C in air, with 1h cycles. Hot corrosion behavior was evaluated by crucible test. Specimens were soaked in a molten salt 75%Na_2SO_4+25%NaCl at 900°C for 5h and 20h. Metal losses were calculated from weight losses of specimens after the test.

Results and Discussion

Creep curves of TMS-6, TMS-6+Mo,Re and CMSX-4 in the condition of 800°C/735MPa are indicated in Fig. 1(a). TMS-6 and TMS-6+Mo, Re have obviously longer creep rupture life than CMSX-4, and TMS-6+Mo, Re is slightly better than original TMS-6 in this low temperature/high stress condition. In the middle-range temperature, creep strength of TMS-6 is inferior to CMSX-4. As shown in Fig. 1(b) and 1(c), Creep rupture life of TMS-6 is poorer than CMSX-4 in the condition of 900°C/392MPa, and equivalent to CMSX-4 at 1000°C /245MPa. Behavior of TMS-6+Mo,Re at these conditions are almost similar or slightly inferior to TMS-6. In the high temperature/low stress range, TMS-6 and TMS-6+Mo,Re show excellent creep behavior. Creep curves in the condition of 1100°C/137MPa are shown in Fig. 1(d). These two alloys display creep rupture lives over twice of CMSX-4. Addition of Mo and Re does not improve creep life in this condition, but the behavior is still sufficient. Fig. 2 illustrates Larson-Miller Parameter plot for TMS-6, TMS-6+Mo,Re and CMSX-4 summarizing the results of creep test in this study. Addition of Mo and Re does not show obvious improvement from TMS-6, but TMS-6+Mo,Re has accomplished excellent creep strength comparing CMSX-4 except for 900°C/392MPa condition.

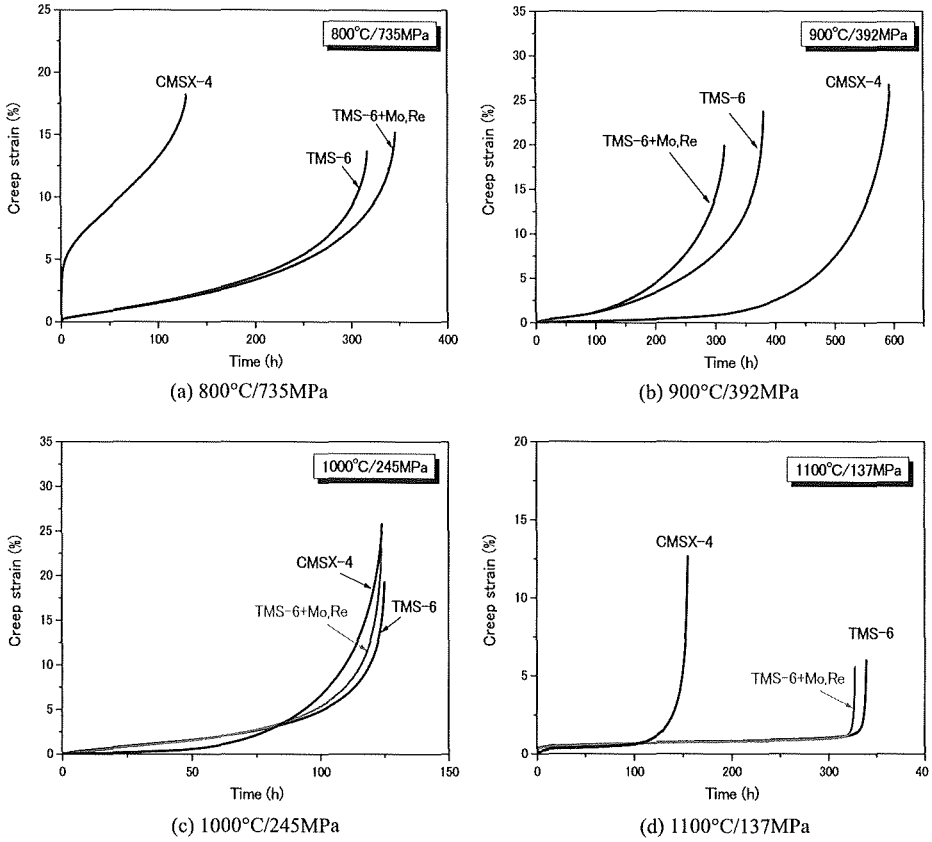

(a) 800°C/735MPa (b) 900°C/392MPa

(c) 1000°C/245MPa (d) 1100°C/137MPa

Figure 1: Creep curves of TMS-6, TMS-6+Mo,Re.

Cycles to failure of TMS-6, TMS-6+Mo,Re and CMSX-4 in the TMF test 187, 272 and 167, respectively, as shown in Fig. 3. TMS-6 has superior TMF life to CMSX-4 and it is found that addition of Mo and Re dramatically improve it.

Fig. 4 shows cyclic oxidation properties. Negative mass change is

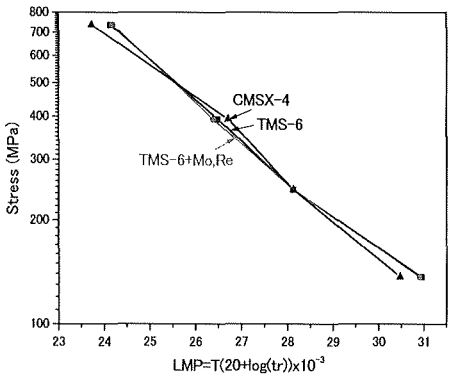

Figure 2: Larson-Miller Parameter plot of TMS-6, TMS-6+Mo,Re and CMSX-4.

caused by spallation of oxide scale during the cooling cycles, and large mass decrease indicates poor oxidation resistance. Mass changes of TMS-6 and TMS-6+Mo,Re are very similar and slightly inferior to that of CMSX-4 after 50 cycles. It may be estimated that adhesiveness of the scale of TMS-6 and TMS-6+Mo,Re is poorer than that of CMSX-4. However the deficits in the oxidation resistance of TMS-6 and TMS-6+Mo,Re are not fatal and satisfactory enough in 200 cycles. Phillips et al. [4] confirmed that 0.5-4at% of Re addition to Ni-Cr-Al ternary alloy improves the oxidation resistance. While our previous study [5] revealed that, in the range of 3-5wt%, Re in 4th generation Ni-base superalloy degrade the oxidation property. Mo is supposed to have much effect in deteriorating the oxidation resistance more than Re due to volatility and poor oxidation resistance of its oxide. Hashizume et al. [6] confirmed that Mo-free alloys exhibited higher oxidation resistance than Mo-containing alloys. Peters et al. [7] also reported that over 3mass% of Mo in Ni-Cr and Ni-Cr-Al alloy deteriorates oxidation and corrosion resistance but less than 3mass% of Mo has small influence on them. In this study, amounts of Mo and Re added to 1st generation superalloy were 0.4wt% and this value is estimated to be too small to affect the oxidation behavior. Needless to say, difference of matrix, namely, binary, ternary alloys and multi-component alloy should be considered. Thus, it is found that addition of 0.4wt% of Mo and Re does not affect cyclic oxidation property in this study.

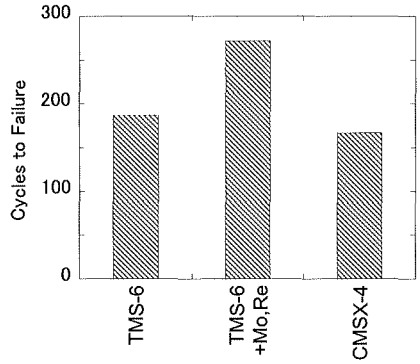

Figure 3: Cycles to failure of TMS-6, TMS-6+Mo,Re and CMSX-4 in the TMF test.

Hot corrosion resistance was investigated and the results are displayed in Fig. 5.

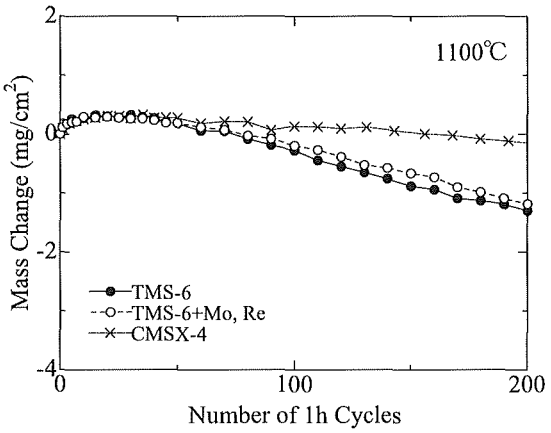

Figure 4: Cyclic oxidation properties of TMS-6, TMS-6+Mo,Re and CMSX-4 at 1100 °C.

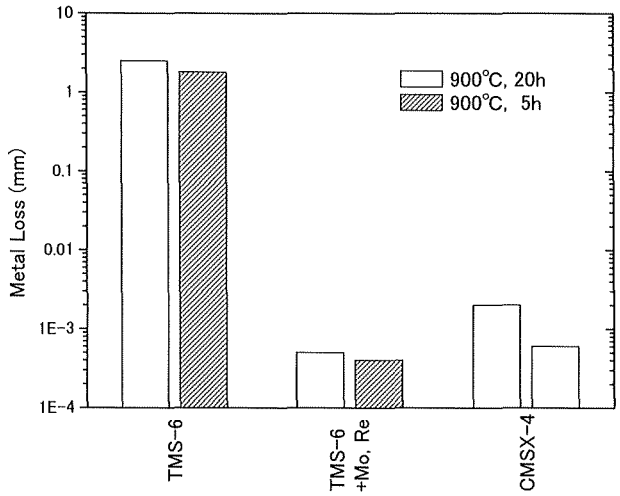

Figure 5: Metal loss of TMS-6, TMS-6+Mo,Re and CMSX-4 in the hot corrosion test at 900 °C.

TMS-6+Mo,Re shows drastic improvement in metal loss compared with TMS-6 after 5h soak and 20h soak. Moreover, corrosion resistance of TMS-6+Mo,Re is slightly better than that of CMSX-4 after 20h soak. While TMS-6 forms thick and brittle oxide/sulfide scale after the corrosion test, TMS-6+Mo,Re forms thin and smooth Cr_2O_3 and Al_2O_3 protective scale. Yu et al. [8] reported that Re and Re-Al coating onto CMSX-4 improve oxidation and corrosion resistance because Re forms a Re-W-Cr compound or Re-rich layer containing W, Ti, Ta and Mo at the interface of the substrate and the scale. However, the amount of Re in this study is too small and such compound or layer has not been confirmed in our alloy. The reason for this excellent hot corrosion resistance of TMS-6+Mo,Re is supposed that Re in the alloy decreases activity of Ni, Ta and W and so Cr_2O_3 and Al_2O_3 tend to be formed than the oxides of Ni, Ta and W in Re added alloy.

Conclusion

0.4 wt% of Mo and Re were added to the 1st generation Ni-base superalloy TMS-6. Mechanical and environmental properties were investigated and compared with 2nd generation Ni-base superalloy CMSX-4. As a result, it is concluded that addition of 0.4 wt% of Mo and Re does not improve the creep property of TMS-6 but much improve the TMF life, and these properties are superior to those of CMSX-4. It is also found that the cyclic oxidation resistance is similar but the hot corrosion resistance shows dramatic improvement by addition

of 0.4 wt% of Mo and Re.

Acknowledgements

The authors would like to thank to Dr. K Hirota of Mitsubishi Heavy Industry Ltd. for giving the information of PBMR system. The authors would like to thank also to Mr. S. Nakazawa for his support with the creep experiments.

References

[1] Y. Koizumi, T. Kobayashi, T. Yokokawa, J. Zhang, M. Osawa, and H. Harada, "Development of Next-Generation Ni-Base Single Crystal Superalloys", *Superalloys 2004*, Warrendale, Pennsylvania, TMS, pp. 35-43, (2004).

[2] T. Kobayashi, Y. Koizumi, H. Harada and T. Yokokawa, Patent Pending, PCT WO2006/104059 A1, (2006).

[3] T. Yamagata, H. Harada, S. Nakazawa and M. Yamazaki, "Alloy Design for High Strength Ni-Base Single Crystal Alloys", *Superalloys 1984*, Warrendale, Pennsylvania, TMS, pp. 157-167, (1984).

[4] M. A. Phillips and B. Gleeson, "Beneficial Effects of Rhenium Additions on the Cyclic-Oxidation Resistance of β-NiAl+α-Cr Alloys", *Oxi. Met.*, Vol. 50, p. 399-249, (1998).

[5] K. Kawagishi, A. Sato, T. Kobayshi and H. Harada, "Effect of Alloying Elements on the Oxidation Behavior of 4th Generation Ni-base Single-crystal Superalloys", *TMS Letters*, Vol. 2, pp. 23-24, (2005).

[6] R. Hashizume, A. Yoshinari, T. Kiyono, Y. Murata and M. Morinaga, "Development of Ni-Based Single Crystal Superalloys for Power Generation Gas Turbines", *Superalloys 2004*, Warrendale, Pennsylvania, TMS, pp. 53-62, (2004).

[7] K. R. Peters, D. P. Whittle and J. Stringer, "Oxidation and Hot Corrosion of Nickel-Based Alloys Containing Molybdenum", *Corros. Sci.*, Vol. 16, pp. 791-804, (1976).

[8] Z. Yu and T. Narita, "High-Temperature Corrosion Resistance of Al-Re and Re Coatings", *Oxi. Met.*, Vol. 56, pp. 467-493, (2001).

9th Liege Conference : Materials for Advanced Power Engineering 2010
edited by J. Lecomte-Beckers, Q. Contrepois, T. Beck and B. Kuhn.

MICROSTRUCTURAL CHANGE AROUND GRAIN BOUNDARY IN POLYCRYSTALLINE IN100 DURING CREEP DEFORMATION

Satoshi Takahashi*, Keiji Kubushiro*, Keiko Morishima*, Nobuhiro Miura**, Yoshihiro Kondo**
*. Research Laboratory IHI co. Ltd., Yokohama, Japan
**. National Defense Academy, Yokosuka, Japan

Abstract

The microstructural change of polycrystalline IN100 has been characterized. Tensile creep tests were conducted in the temperature range 950 to 1000°C at 74MPa and some tests were interrupted at 6, 16, 20, 30, 60 and 80% in creep life. Raft structure formed on (001) at the early stage of creep life in interior grains and grain boundaries were covered by γ' phase. Creep fracture occurred at grain boundaries. In order to quantify the creep damage, average grain orientation spreads (GOS) of ruptured and interrupted specimens were measured. Average GOS of interrupted creep specimen after 6% of creep life consumption was about 0.6 degree and this value was almost constant until 80%, which did not show a correlation between average GOS and creep life consumption rate. Then we focused to the grain boundaries. The thickness of grain boundary γ' phase increased as creep life consumption increased and the range of thickness was about 5-10μm. The orientation of gamma prime phase at the grain boundary was same as that of interior of the grain and both of them were joined. Rotation angle of grain boundary γ' was measured and there was a good correlation with creep life consumption.

Keywords: IN100, Nickel-based superalloy, grain boundary, γ', EBSD

1. Introduction

Extensive studies are being conducted to clarify the effects of microstructures on the creep characteristics of Ni-base superalloys. Most of these studies concern the rafting of the γ′ phase in single-crystal alloys. Although the raft structure also occurs in polycrystalline alloys during creep [1], the effects of the grain boundary are more important than the change in grain interior. Considering that the grain boundary perpendicular to the stress axis becomes a fracture origin, clarification of the effects of the grain boundary is important since it leads to a clarification of the relationship between creep behavior and microstructures in Ni-base polycrystalline superalloys.
For Ni-base superalloys with a high volume fraction of the γ′ phase, it is known that film-shaped γ′ phase and carbides precipitate on the grain boundary during creep deformation [2]. It is thought that γ′ on the grain boundary works to delay the start of intergranular fracturing. These observations are based on the results of observations of structures of fractured materials. To clarify the effects on creep behavior, the change in creep rates must be verified in relation to the change in microstructures. The purpose of this study is to quantify the change in microstructures around the grain boundary during the creep deformation of IN100.

2. Experimental procedure

The material used in this study is polycrystalline IN100. The nominal composition of this material is Ni base alloy containing 10.0Cr, 15.0Co, 4.7Ti, 5.5Al, 3.0Mo, 1.0V and0.18C (wt%). To prepare test specimens, this material was cast into 1 mm thick plates. After being cast, the plates were subjected to specified solution treatment and two-step aging treatment processes. Creep tests were conducted using miniature creep test specimens in argon gas at 74 MPa and at 950°C and 975°C. These miniature creep test specimens have a thickness of 0.8 mm and a width of 2 mm, and the gauge length is 10 mm. Also interrupted creep tests were conducted stepped at creep life consumption rates of 6% and 19% at 950°C and at creep life consumption rates of 16%, 29%, 61%, and 84% at 975°C.

SEM and EBSD were used to observe microstructures. Test specimens for SEM observation were prepared by polishing the cross sections of the creep specimens parallel to the stress axis with waterproof abrasive paper and buffs and then subjecting them to electrolytic etching in a saturated oxalate solution. Test specimens for EBSD observation were prepared by polishing them and then further processing them to a finer polish, i.e., subjecting them to electrolytic polishing in a 10% alcohol perchlorate solution or polishing them with colloidal silica. In observing microstructures, the surfaces of test specimens parallel to the stress axis were observed.

3. Results and discussion

3.1 Experimental alloy

Figure 1 shows the microstructures of the test specimens. The average diameter of grains is about 230 μm. Each test specimen comprised the γ phase, γ′ phase, γ-γ′ eutectic, and carbides. As shown in Fig. 2, Ti and Mo account for the majority of carbides contained. It is estimated from these results that the carbides are MC carbides [3]. In addition, Cr-rich carbides are also observed, although the content is very small; they are thought to be $M_{23}C_6$.

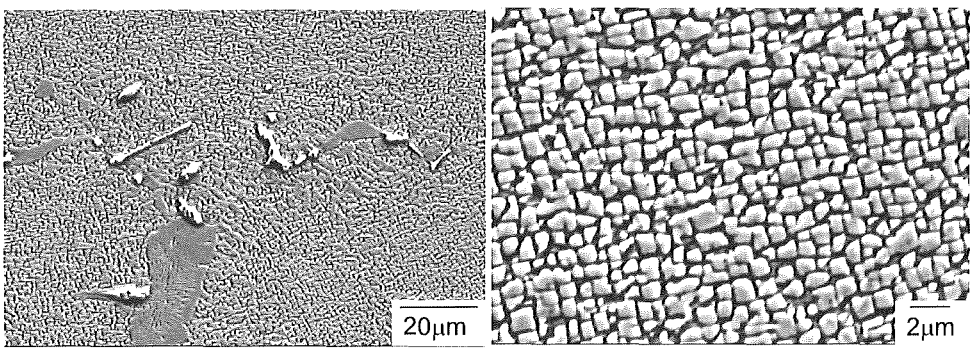

Fig. 1 Secondary electron images of as-heat treated IN100

3.2 Creep rate

Figure 3 shows the creep rates at 975°C and 74 MPa relative to creep life consumption rates. Under the test conditions used for this experiment, the creep curve consists of a transient creep stage and

an acceleration creep stage, and the creep rate shows a minimum at a creep life consumption rate of 30%, indicating that the interrupted creep tests were conducted over the range from the transient stage to the acceleration stage.

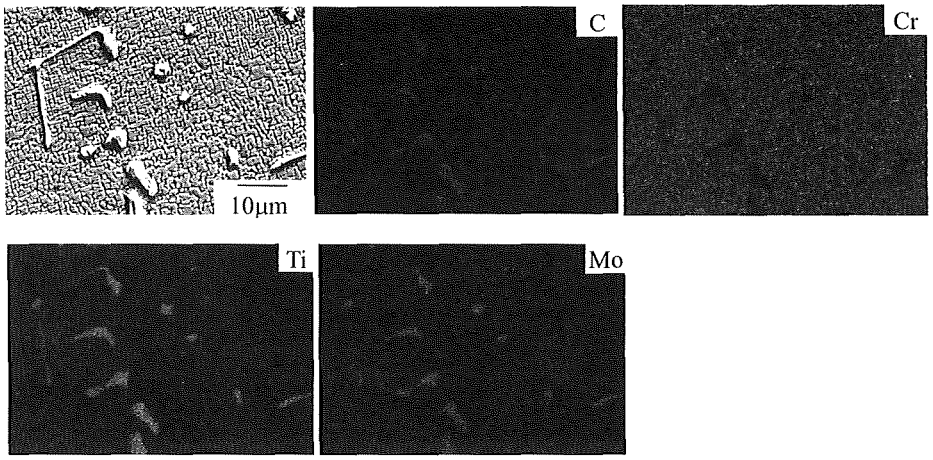

Fig.2 Secondary electron microstructure and X-ray images of precipitates observed in as-heat treated IN100.

3.3. Microstructure of grain interior

Figure 4 shows the microstructures of crept specimens. Although the degree of the rafting progress varies according to individual grains in a given test specimen, the tendency of changes in the microstructures of grains can be summarized as follows. At 975°C, the γ′ phase maintains its cubic form until the creep life consumption rate becomes 30%. At 60% of the creep life consumption rate, the γ′ phase starts to grow in size, with slight directionality. Although it forms a raft at 100%, part of the raft starts to disintegrate. At 950°C, the γ′ phase starts to grow in size at 19% of the creep life consumption rate, and the raft structure has disintegrated at 100% of the creep life consumption rate.

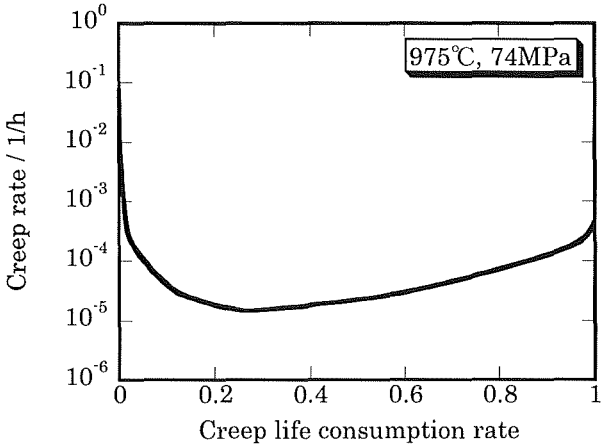

Fig. 3 Creep rate obtained from creep test conducted at 975°C / 74MPa.

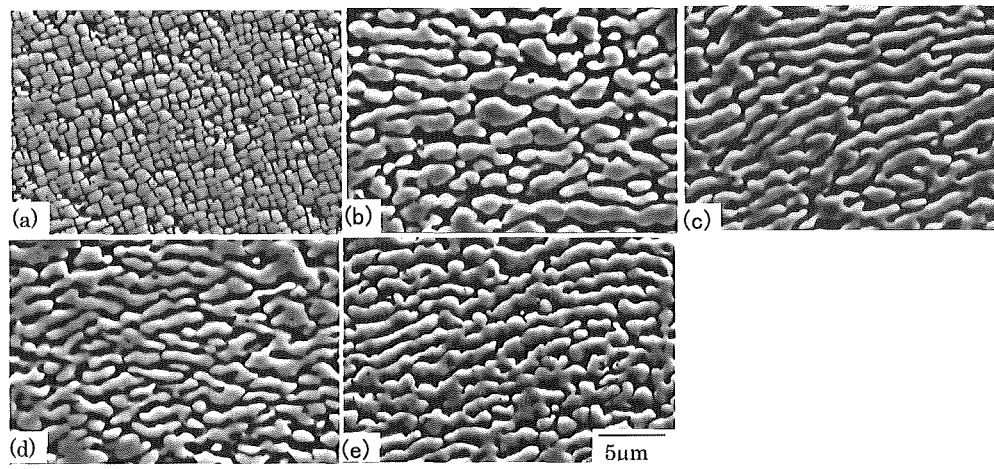

Fig.4 Secondary electron images of crept IN100. (a)975°C t/tr=30%, (b) 975°C t/tr=60%, (c) 975°C ruptured, (d) 950°C t/tr=19% and (e) 950°C ruptured

3.4. Microstructure around grain boundary

Change in microstructure around the grain boundary was investigated. Figure 5 shows the SEM microstructure of a creep test specimen at 975°C and 74 MPa interrupted at 84% of the creep life consumption rate. The film-shaped γ′ phase (grain boundary γ')and chain-like carbides are observed along the grain boundary. From the results of the EDX mapping shown in Fig. 6, these carbides are estimated to be $M_{23}C_6$, thought to have formed according to the following reaction [2]:

$$MC + \gamma \rightarrow M_{23}C_6 + \gamma'$$

Figure 7 shows the inverse pole figure map of the same test specimen observed around the grain boundary, along with the image quality figure. The black area that resembles the grain boundary in shape is a carbide, and black areas in grains are the γ phase. The grain boundary is located at the center of the grain boundary γ′ phase, and carbides precipitate on the grain boundary. Therefore, grain boundary γ′ phases with different orientations are tangent to each other at the grain boundary. The thickness of the grain boundary γ′ phase increases as the creep deformation progresses, as shown in Fig. 8.

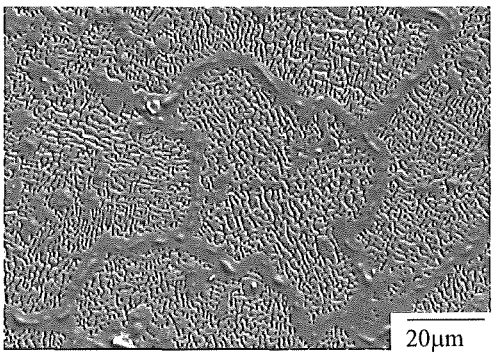

Fig.5 Secondary electron image of interrupted at 84% consumption under 975°C, 74MPa

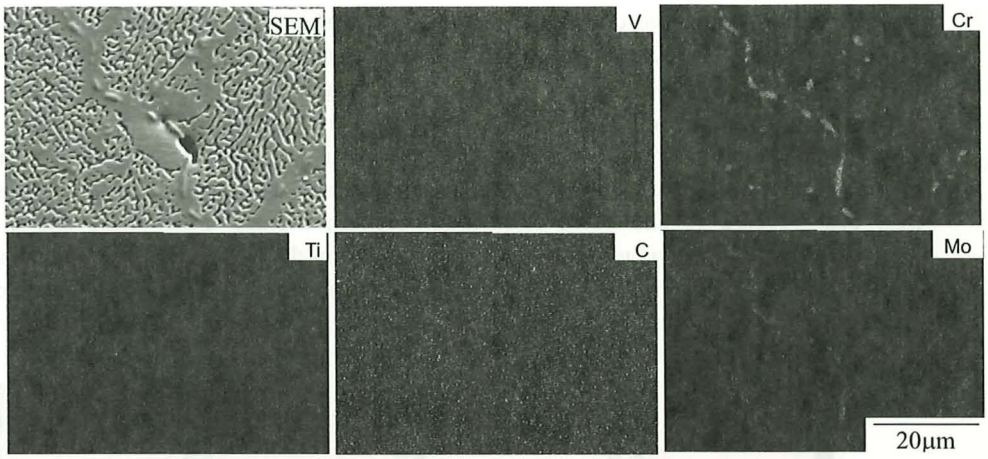

Fig.6 Secondary electron image and EDX maps of interrupted at 84% consumption under 975°C/74MPa.

Fig.7 Inverse pole figure map overlaid with image quality map. Interrupted at 84% consumption of creep test at 975°C/74MPa.

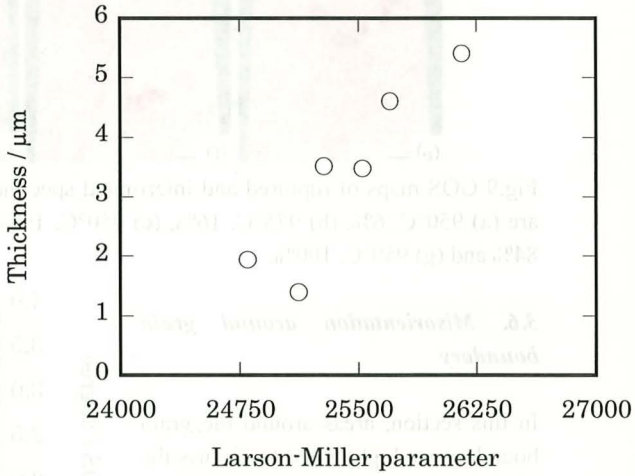

Fig.8 The change of grain boundary γ' phase thickness during creep deformation.

3.5. Misorientation change during creep deformation

The results of recent studies of plastic strain measurement using the EBSD [4]-[6] suggest that the EBSD can also be used to evaluate creep strain. In this section, we discuss the relationship between variations in orientations in grains and creep life consumption rates. Figure 9 shows the GOS maps

for ruptured and interrupted creep specimens. The GOS shows the average of misorientations in each grain measured between all measurement points; each grain has its own misorientation value. Therefore a crystal grain with a larger GOS value has a larger degree of strain. The gray line in Fig. 9 shows that misorientation between measurement points is more than 15°. In calculating the GOS in this figure, this boundary was defined as a grain boundary. Although test specimens with various creep life consumption rates were used, almost no differences are observed in the contrast of the GOS maps. Figure 10 shows the relationship between average GOS values and creep life consumption rates of individual test specimens. The value of the ruptured specimen tested at 950°C is 2.4°, while the values of other materials are constant at about 0.5°. Under the test conditions used for this study, it is difficult to detect an increase in creep strain from GOS measurements. It is inferred, therefore, that there is hardly any strain accumulating in grains.

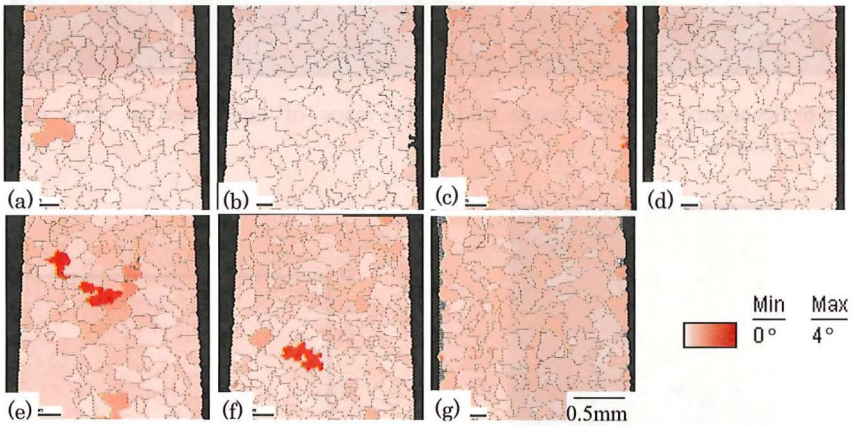

Fig.9 GOS maps of ruptured and interrupted specimens. Creep temperature and consumption rates are (a) 950°C, 6%, (b) 975°C, 16%, (c) 950°C, 19%, (d) 975°C, 29%, (e) 975°C, 61%, (f) 975°C, 84% and (g) 950°C, 100%.

3.6. Misorientation around grain boundary

In this section, areas around the grain boundary are highlighted to discuss the changes of misorientation caused by creep deformation. Figure 11 shows the inverse pole figure map of the test specimen crept at 975°C and 74 MPa that was interrupted when 84% of life consumption was reached. Discoloring is observed in some of the areas around the grain boundary. Figure 12 shows changes of misorientation measured

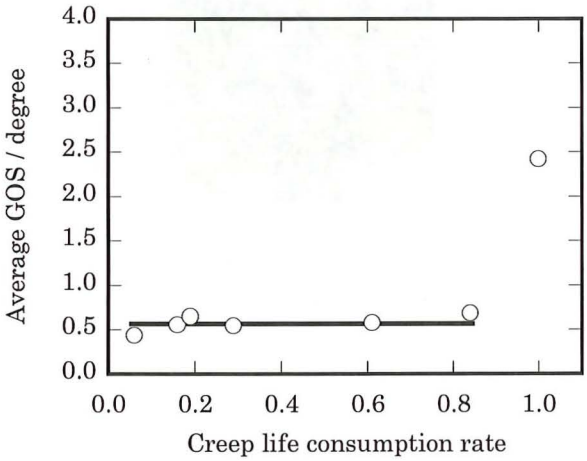

Fig. 10 Relation between creep life consumption rate and average GOS value.

from a starting point of measurement along the arrow shown in this figure. Misorientation starts to increase at a position 7 μm away from the grain boundary, and the maximum misorientation value is about 4°. Figure 13 shows the relationship between the largest change of misorientation and creep life consumption rates of individual test specimens. The largest change of misorientation gradually increases as consumption rates increase. As consumption rates exceed 60%, it starts to increase abruptly; in the case of ruptured specimens, it reaches 7° to 8°. As shown in Fig. 3, IN100 tested at 975°C and 74 MPa exhibits the smallest creep rate, at a creep life consumption rate of 30%. It is apparent from this that an increase in misorientation occurs in the acceleration creep region.

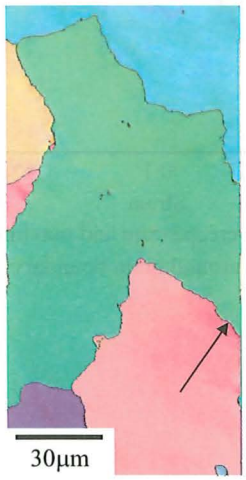

Fig. 11 IPF map of interrupted at 84% consumption at 975°C / 74MPa.

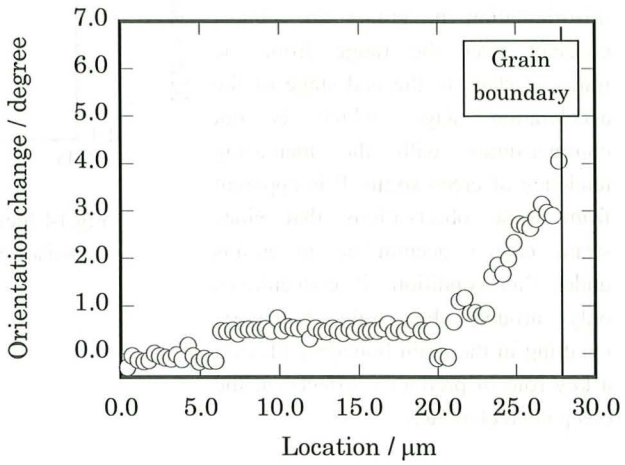

Fig.12 Orientation change around grain boundary of the specimen interrupted at 84% in 975°C/ 74MPa.

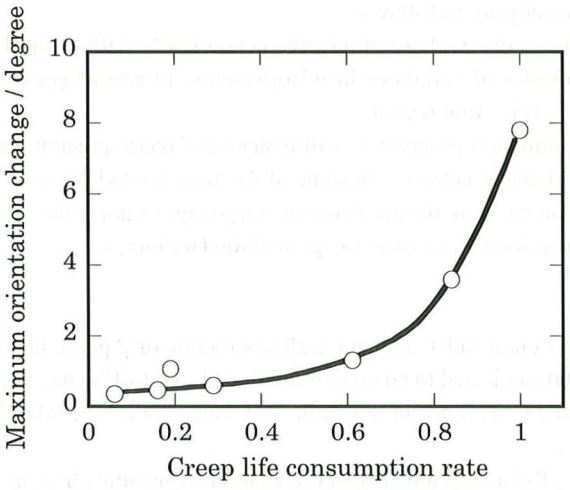

Fig.13 Relationship between maximum orientation change and creep life consumption rate.

3.7. The relationship between orientation change and creep rate

Figure 14 shows the creep strain and maximum changes of misorientation at 975°C and 74 MPa, relative to creep life consumption rates. Although their absolute values are different, they increase in a similar manner. As shown in Fig. 9, however, variations in misorientation in grains are almost constant over the range from the transient stage to the end stage of the acceleration stage, which is not commensurate with the increasing tendency of creep strain. It is apparent from these observations that since strain cannot accumulate in grains under this condition; it concentrates only around the grain boundary, resulting in the grain boundary playing a key role in producing effects on the creep characteristics.

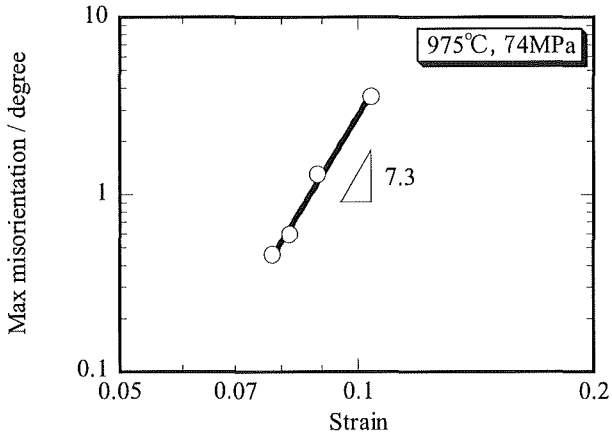

Fig.14 Increase of creep strain and maximum misorientation around grain boundary.

4. Conclusions

In this study we clarified the relations between creep rates and changes of variations in misorientation in grains during creep deformation and changes of misorientation around the grain boundary by using crept specimens of the Ni-base polycrystalline superalloy IN100. Conclusions drawn from this study are as follows:

(1) While rafting of the γ′ phase progresses concurrently with creep deformation, the GOS value, which is the indicator of variations in misorientation in crystal grains, remains constant up to the end stage of the acceleration region.

(2) As creep deformation progresses, a film-shaped γ′ phase precipitates on the grain boundary and the state of misorientation changes in some of the areas around the grain boundary.

(3) Creep strain increases in the acceleration creep stage in much the same way as maximum values of changes of misorientation around the grain boundary increase.

Reference

[1] N. Miura, Y. Kondo and T. Matsuo, Rafted structure of γ' phase in polycrystalline nickel-based superalloy, IN100, subjected to creep deformation, Tetsu-to-Hagane, 90, pp.567-573 (2004)

[2] E. W. Ross and C. T. Sims, in Superalloys II, New York, NY, John Wiley & Sons, pp.99-133(1987)

[3] H. E. Collins, Relative stability of carbide and intermetallic phase in nickel-base superalloys, Superalloys 1968, TMS, p.p. 171-198 (1968)

[4] A. J. Wilkinson, Acta Metal.Mater.,39,pp.3047-3055 (1991)
[5] M. Kamaya, A. J. Wilkinson and J. M. Titchmarsh, Quantification of plastic strain of stainless steel and nickel alloy by electron backscatter diffraction, Acta Mater., 54, p.p. 539-548, (2006)
[6] R.Takaku, D. Saito and Y. Yoshioka, Change of grain orientation and effect of grain size on it in creep deformed Hastelloy X, Tetsu-to-Hagane, 95, pp.154-160 (2009)

9th Liege Conference : Materials for Advanced Power Engineering 2010
edited by J. Lecomte-Beckers, Q. Contrepois, T. Beck and B. Kuhn.

MONITORING THERMALLY GROWN OXIDES UNDER THERMAL BARRIER COATINGS USING PHOTOLUMINESCENCE PIEZOSPECTROSCOPY (PLPS)

A. del Corno*, L. De Maria*, C. Rinaldi*, L. Nalin#, N .J. Simms#

*ERSE, via Rubattino 54, Milano, Italy
#Energy Technology Centre, Cranfield University, Cranfield, MK43 0AL, UK

Abstract

The use of thermal barrier coatings (TBCs) on cooled components in industrial gas turbine has enabled higher inlet gas temperatures to be used and hence higher efficiencies to be achieved, without increasing component metal temperatures. However TBCs have a complex coating structure that during high temperature exposure and thermal cycling modifies untill TBC spalling which can result in dangerous over-heating of components.
This paper reports the results of a TBC exposure programme planned to monitor TGOs development in an example TBC system in terms of both stress evolution within the TGOs and TGO growth. The COST538 reference TBC system was used: an yttria stabilised zirconia TBC applied to an Amdry 995 bond coat on an CMSX-4 substrate. Samples were in the form of 10 mm diameter bars, with the TBC applied to their curved surface. Coated samples were exposed in simulated combustion gases at temperatures 850, 900 and 950°C for periods of up to 10,000 hours. Every 1000 hours samples were cooled and weighed to monitor the progression of the oxidation; selected samples NDT inspected using PLPS and/or destructive examination. Cross-sections were prepared and examined in a scanning electron microscope (SEM) at multiple locations to determine TGO thickness distributions. PLPS spectra were measured and elaborated with a system self developed in ERSE, able to calculate and map the TGO residual stress values under columnar TBCs. So the positions could be evidenced where the damage of the TBC /TGO/BC interface is higher on the exposed bars.
The data of TGO thickness distributions and PLPS stress measurement distributions were compared to the exposures carried out on samples to identify and quantify trends in their development. Metallography confirmed that the PLPS technique can reliably detect interface cracking before visible EB-PVD TBC spalling.

Keywords: gas turbines; thermal barrier coatings; thermally grown oxides; PLPS; NDT

1. Introduction

Gas turbines are at the heart of many current power stations [1-3], usually as part of combined cycle systems fired on natural gas. It is anticipated that gas turbines will be used even more widely in the future, with increasing numbers of natural gas fired combined cycle systems being installed [1-3] and as new solid fuel (coal, biomass, waste) combined cycle power generation systems move from development through demonstration to commercialisation [1,4]. However, the distribution in the usage of gas turbines and the uptake of these various potential power systems will continue to vary significantly between countries due to the availability of fuels, economic factors, national policies and regulatory frameworks (both for the power markets and environmental restrictions).
Industrial gas turbines (IGTs) have been developed to use increasingly higher firing temperatures and pressures to increase their efficiency of power generation [1-3], with current models firing at temperatures up to ~1400°C at pressures of ~ 30 bar. To cope with these progressive increases in firing conditions, the materials used for blades and vanes in the hot gas paths of IGTs have needed considerable development and a series of new alloys have been produced since the 1960s with increased creep and thermal fatigue resistance [2,5]. Until the 1970s, increased high temperature oxidation and corrosion resistance of these new materials was targeted as a compromise to alloys with improved high temperature mechanical

properties. However, since then alloy development has concentrated on optimising the mechanical properties of the alloys, in order to permit usage of the highest possible metal temperature consistent with economically viable component life times. Thus, coatings that protect the base alloys from the surrounding environment have become critical parts of IGT hot gas path components [5-7]. To enable combustion gas temperatures to continue to rise, increasingly sophisticated air-cooling has been required to allow the operating temperatures of the blades and vanes to remain at viable levels. However, the use of air bleeds from the compressor to provide air-cooling to hot gas path components has an efficiency penalty for the gas turbine operation. This has provided the driving force for the development and application of thermal barrier coatings (TBC's) to such components to reduce the cooling air requirements and/or component metal temperatures. In addition, these coatings can enable a 'smoothing out' of component temperatures and a reduction in surface contaminant deposition (as a result of higher surface temperatures).

TBCs have a complex coating structure that includes an outer ceramic top coat, thermally grown oxide (TGO) and a bond coat on a substrate. During exposure, TGOs thicken and the composition of the bond coat changes as a result of depletion of elements (such as Al) for the oxide growth and by interdiffusion with the substrate. As a result of these changes and component heating/cooling cycles, stresses develop that lead to crack formation, growth and TBC spallation. As the performance of coatings in advanced gas turbines in power generation systems is now critical to the viability of these systems, it is necessary to have a better understanding of the development of damage within these coating systems and ideally to have non-destructive examination (NDE) methods to monitor the development of such damage during the use of a component [8,9,10].

Optical non contact NDE methods are particularly promising, due to their non intrusive nature; among them thermography is well established as it detects millimetre wide coating delaminations, but does not have the resolution to follow damage phenomena happening before them. Photostimulated Luminescence Piezo-Spectroscopy (PLPS) invented by Clarke and co-workers [11,12] is able to detect the compressive residual stress of the TGO layer growing between the TBC and the bond coating. This alumina layer contains Cr^{3+} ions which act as natural strain gauges; if they are excited by a laser green light then they fluoresce with a double peak (doublet R1 and R2) in the red. The frequency shift of this doublet has been demonstrated to be proportional to the compressive residual stress of the alumina layer [11,12]. The compressive residual stresses in the TGO are very high in the steady state growth of the TGO when it remains dense and fairly flat. These compressive residual stresses in TGO decrease as more as the interface assumes an out of plane morphology with tiny discontinuities and irregularities. Approaching TBC delamination TGO residual stresses tend to disappear. The application of this technique to ex-service blades with EB-PVD TBCs can contribute to the assessment of the residual life of the component [13,14,10]. The limitations of this technique are that the attenuation of the signal is very high, particularly in APS TBC systems, due to light scattering induced by porosity and microcracking in the zirconia layer. In contrast the columnar microstructure of EB-PVD TBCs is able to transmit light well.

This paper reports on activities that were carried out within the COST538 activity to investigate the growth of TGOs within a TBC system under conditions targeted at industrial gas turbine use (rather than aero-engine applications). In parallel PLPS measurements were performed on EB-PVD TBCs to monitor the development of stresses within the TGOs with

the aim of evaluating the potential of such NDE system in monitoring the TBC interface degradation level in a systematic and statistically significant way.

2. Experimental Methods

2.1. Materials

The gas turbine materials system selected for use in these tests consisted of:

- Outer thermal barrier coating of partially stabilitised zirconia (8 weight % yttria – zirconia) applied by electron beam physical vapour deposition (EB-PVD)
- Bond coating of Amdry 995 (Co – 32 Ni – 21 Cr - 8 Al – 0.5 Y) [15] applied by High Velocity Oxy-Firing (HVOF)
- Substrate of CMSX-4; a single crystal gas turbine materials (Ni –6.5 Cr –10 Co – 5.6 Al – 4.9 Ti – 6 W – 0.6 Mo – 6 Ta – 1 C – 2.9 Re – 0.1 Hf) [15] that has commonly been used as one of the reference materials in the COST538 programme.

This coating system was applied to the curved surfaces of bars (10 mm diameter) that had previously been machined to form a linked series of samples (each 10 mm long, with end corners chamfered to enhance coating adhesion, linked by narrowed sections (4 mm diameter x 3 mm long) of the substrate materials). Before use the samples were separated from their bars by cutting through the narrow links, cleaned and dried.

2.2 Sample exposure conditions

The samples were exposed at Cranfield University in ceramic lined horizontal furnaces to simulated gas turbine combustion environments at 850, 900 and 950°C for periods of up to 10000 hours. The exposure conditions are summarised in Table 1.

Table 1 Summary of sample exposure conditions

Parameter	Description
Exposure temperature	850, 900 or 950 °C
Exposure times	1000, 2000, 4000 or 10000 hours
Gas atmosphere	N_2 - 13.8 volume% O_2 - 3.1 % CO_2 - 0.9 % Ar - 7.8 % H_2O

The gas atmosphere was achieved by flowing a dry gas (nominal composition N_2 - 15 volume % O_2 – 3.4 % CO_2 – 1 % Ar) at 50 cc/min from a pre-mixed gas bottle through a water bubbler, held in a waterbath at ~40°C, to add the required amount of moisture. The gas pipe between the water bubbler and the end of the furnace was trace heated at ~50°C to prevent the formation of any water condensation within the pipe-work.

All the samples were exposed in alumina 'boats' within the furnace. After each 1000 hour exposure, these boats were slowly removed from the furnace and the samples were weighed. The weight data gathered enabled weight change data to be calculated for each of the samples exposed. These data provided a simple means of tracking the growth of the thermally grown oxide layer(s), as well as any spalling of coating/oxide layer(s), during the oxidation exposures. After 1000, 2000 and 4000 hours exposure, some samples were selected to be removed from the furnace for both destructive and non-destructive examinations. Samples remaining after 10,000 hours were also examined by these methods.

2.3. Post-exposure sample examination

2.3.1 Photostimulated Luminescence Piezospectroscopy

PLPS measurements were performed, in back-scattered configuration, at ERSE (previously CESI RICERCA) with a self made portable PLPS system [13] equipped with a movable probe connected both to a spectrometer and a laser source by means of optical multimode fibres. The excitation source was a 50 mW output power Nd:YAG laser operating @ 532 nm wavelength. The effective spot size on samples was 100 μm. To make PLPS measurements of large areas much faster, this device was recently improved by the addition of automated analysis of PLPS spectra and a computerized control system for sample/component displacements (x and y) in front of the PLPS sensor. The user interface was developed in LabView (Figure 1); the operator can pre-define the acquisition conditions and choose a rectangular or a circular scanning procedure to perform the automatic sequence of measurements. At each measurement position an on-line routine determines the R1 and R2 peak positions (by a derivative method) and calculates a value for the local TGO compressive residual stress (σ_{TGO}) by the known linear relationship with the peak shift $\Delta\lambda$ [12,13]:

$$\sigma_{TGO}\,[GPa] = 4.100^{*}\,\Delta\lambda\,[nm] \qquad \text{for R2} \qquad (1)$$

$$\sigma_{TGO}\,[GPa] = 4.097^{*}\,\Delta\lambda\,[nm] \qquad \text{for R1} \qquad (2)$$

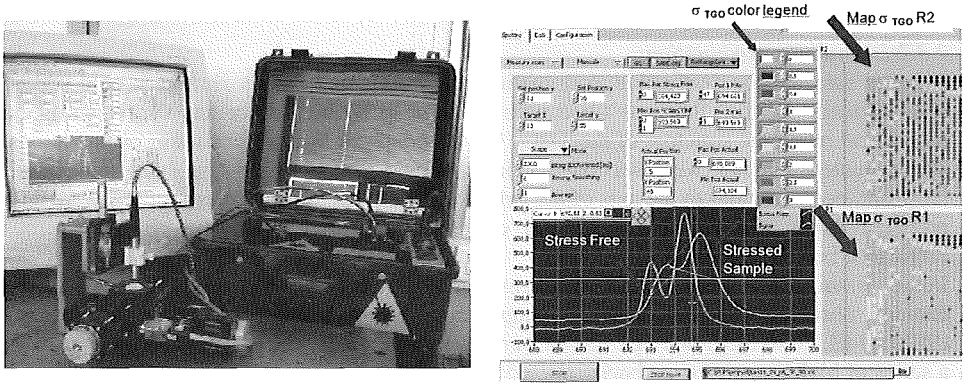

Figure 1 Photographs of (a) PLPS equipment and (b) output from PLPS analysis

With the $|\sigma_{TGO}|$ values the map of TGO stress is obtained, associating a grey level (or a colour) to each fixed interval of stress. Absolute values of compressive residual stresses higher than 2.2GPa (white/light grey) are normally associated to flat TGO and good adhesion; values less than 1GPa (dark grey) are indicative of a very damaged interface rich of local detachments [8, 11, 12, 13, 14]. The resolution of the stress measurement is 0.20 GPa, as the spectrometer has wavelength resolution of 0.05 nm. The repositioning accuracy is ~ 5 μm; the spot size is 100 μm, so that the minimum scanning step is 100 μm. Typically the time required for a 100 points scan is about 1 hour.

On the EB PVD coated cylindrical specimens after isothermal exposures PLPS mapping was performed on areas of about 4x10mm. Spectra were acquired with a spacing of 0.25mm (producing several hundred PLPS spectra for each map). One example is shown in Figure 2, where it is clear that this mapping method enables the rapid identification of regions where

the incipient damage is worse (lower compressive stress absolute values, dark grey points). Statistical analyses were carried out off-line to compare the damage levels found in different regions of a specimen and to compare values for specimens exposed to different temperatures or times.

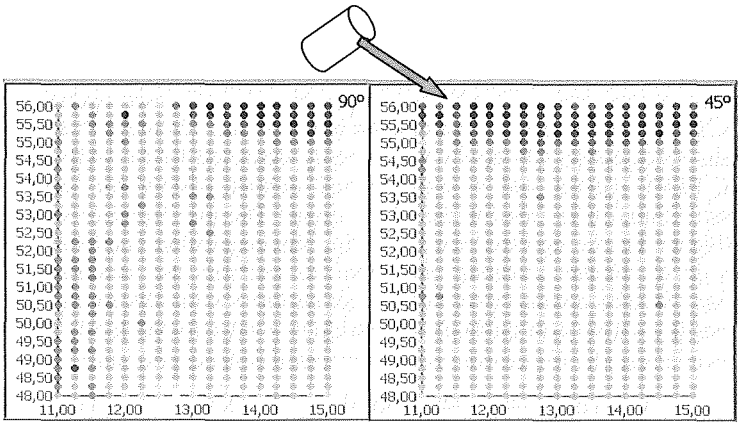

Figure 2 Map of PLPS results for specimen exposed at 950°C/4000h showing incipient edge delamination (light grey points $|\sigma_{TGO}| > 2GPa$; dark grey points $|\sigma_{TGO}| < 1.5Gpa$)

2.3.2 Destructive examinations

Samples selected for destructive examinations were mounted in low shrinkage cold setting resin (Struers' Epofix) that was filled with ballotini to further reduce any shrinkage of the mount and retain the structure of the TBC / TGO / bondcoat system for further examinations. The mounted samples were sectioned using a fine CBN slitting wheel, and mineral oil lubricant, perpendicular to the axis of the cylindrical samples. These cross-sections were then prepared using standard SiC grits and diamond polishing, together with non-aqueous lubricants, before examination.

Initial examinations were carried out using optical microscopy. However, the scale of the damage observed required detailed examinations using Scanning Electron Microscopy (SEM); FEI XL30 SEM and FEI ESEM were used. To quantify the extent of TGO formation, a series of high magnification backscattered electron pictures were taken around each sample. In this viewing mode the TBC, TGO and bond coat layers were clearly distinguishable and so TGO thicknesses could be quantified readily. The series of pictures were analysed to generate at least 24 measurements of TGO thickness around each sample to generate information on the distribution of the oxide thicknesses as a function of exposure times and temperatures,

3. Results and Discussion

3.1. Photoluminescence Piezospectroscopy

PLPS measurements were carried out on the whole cylindrical surface of the specimens after significant exposure periods. The absolute stress values measured at all the points of each area are plotted on a normal probability plot. On a specimen with a dense adherent TGO the distribution is normal and such plot gives a straight line. In our case measurements on a new specimen could not be carried out (and it is believed that a very low signal would be detected

from the very thin TGO present at the beginning of the furnace exposure). So among those received the specimen exposed for the shortest time and at the lowest temperature was chosen as a reference starting point (TGO about 1.8 μm).

Examples of the results are reported in Figure 3 for areas of two specimens exposed at 950°C for 2000h and 4000h respectively. In both graphs the right-hand-side curve is the typical distribution of values obtained from a sound EB-PVD TBC with a well adherent TGO (mean value around 2.5 GPa, normal distribution with low standard deviation 0.1). The other curves are displaced towards lower stress values and have lower slopes at longer exposure times (e.g. the right-hand-side graph in Figure 3). Lower TGO stress values indicating incipient local detachments are evident in both plots and increase in probability with exposure time.
In Figure 4 the PLPS results obtained on specimens exposed at 900°C for 2000h and 10000h respectively are compared.Again the plots move towards lower stress values and change slope

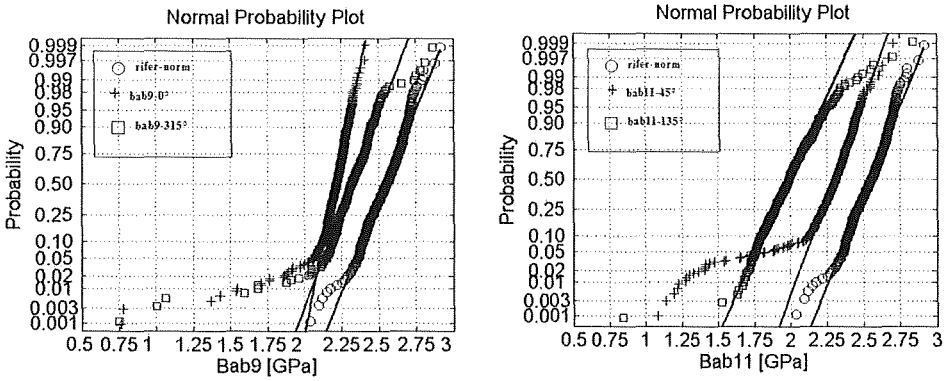

Figure 3 Results of PLPS measurements obtained on specimen exposed at 950°C for 2000h (left) and for 4000h (right). Each curve collects the measurements of one area

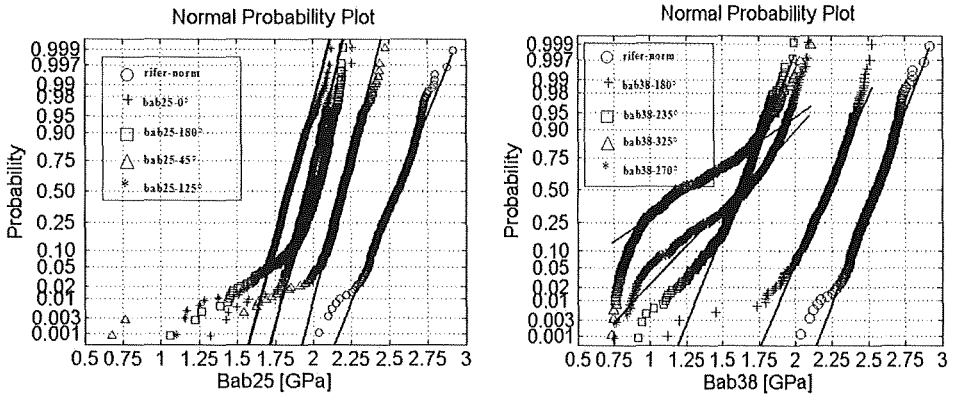

Figure 4 Results of PLPS measurements obtained on specimen exposed at 900°C for 2000h (left) and for 10000h (right). Each curve collects the measurements of one area.

(interface degradation, less flat alumina layer). Again, lower TGO stress values are observed at significant numbers of points in both plots, indicating incipient local detachments; at the

highest exposure time this amounts to more than 50% of the specimen area. Mean values and standard deviations of the TGO stress populations were also calculated (Table 2). An increase of the standard deviation together with the decrease of the mean stress value is associated to a general degradation of the TBC adhesion, as shown in Tab. 2 and in Figure 5.

Table 2 Mean stress values measured on the worst area of specimens exposed to different combinations of time and temperature

Temperature (°C)	Time (h)	Mean $\|\sigma_{TGO}\|$ (GPa)	St.deviation (GPa)
950	2000	2.0	0.1
950	4000	1.85	0.2
900	2000	1.8	0.1
900	4000	1.85	0.2
900	10000	1.3	0.3

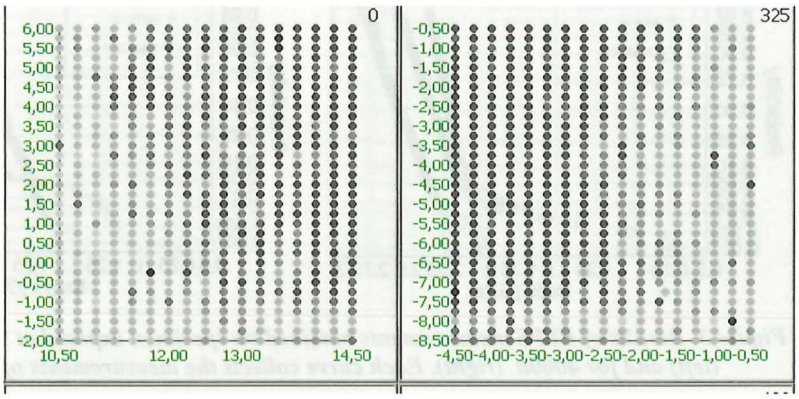

Figure 5 Map of $\|\sigma_{TGO}\|$ on the most damaged areas of the specimen exposed at 900°C for 10000 h

3.2. Weight gain and destructive examination data

During the exposures of the samples, their weight was measured every 1000 hours and so the progress of their exposures could be followed. Figure 6 illustrates the results obtained in terms of the mean mass change for samples at each of the temperatures. It should be noted that the number of samples in each furnace decreased during these exposures as samples were removed for destructive and non-destructive examinations at regular intervals, and samples that had visibly spalled were not put back into the furnaces for further exposures. The errors bars shown in Figure 6 indicate the measured level of scatter (as standard deviations) in the mass change data for nominally identical samples. The mean mass change data has been further processed to produce equivalent values for fully dense α-Al_2O_3 and these are compared to output from a model of the parabolic growth of this oxide. The model prediction lie within the scatter of the data generated at all three temperatures.

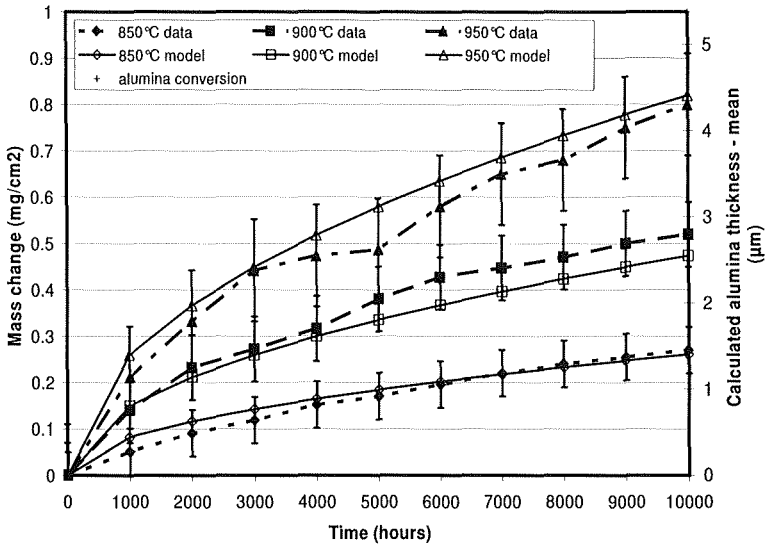

Figure 6 Mean mass change data plotted as a function of exposure time for all samples. Error bars indicate the data spread. Model lines for the growth of fully dense α-Al_2O_3

Backscattered SEM observations of the polished cross-sections through the samples indicated that there was significant scatter in the TGO thicknesses. Figure 7 gives examples of the oxide thickness distributions generated from samples exposed for four different time periods at 900°C, and illustrates the development of thicker oxide(s) over increasingly large areas of the samples with increased exposure times.

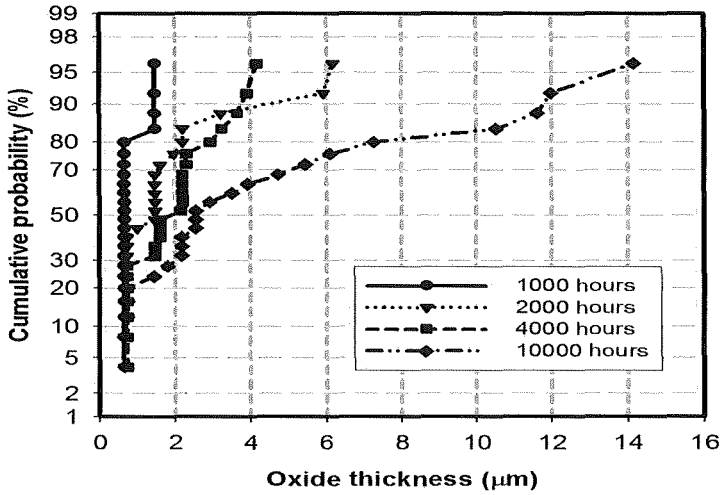

Figure 7 Examples of distributions of TGO thicknesses as function of cumulative probability for samples exposed at 900°C for 1000, 2000, 4000 and 10000 hours

Figure 8 illustrates different areas of oxide growth around a single sample after 2000 hours exposure at 900°C. Figure 8(a) shows an area of fairly uniform, adherent TGO; whereas Figure 8(b) shows an area with patches of thicker TGO and micro-crack formation at the metal/TGO interface. It is such areas that generate the thicker oxide "tails" in the distributions

associated to longer exposure times in Fig. 7. EDX analyses of such oxides show that the uniform TGO is composed of aluminium rich oxide (which has frequently been observed to be α-alumina), whereas the thicker areas of TGO also contain Cr oxides and/or Ni/Co-rich oxides (identified elsewhere as spinels). Such oxides are expected to form within the TGO when the level of aluminium in the coating falls below the critical level needed to maintain alumina growth. For the coatings studied in this work, this has happened after a relatively short exposure time at the higher temperatures due to the HVOF MCrAlY coating being relatively thin on many samples (~50 μm compared to the target thickness of ~150 μm). Aluminium is lost by interdiffusion with the substrate material as well as by TGO growth.

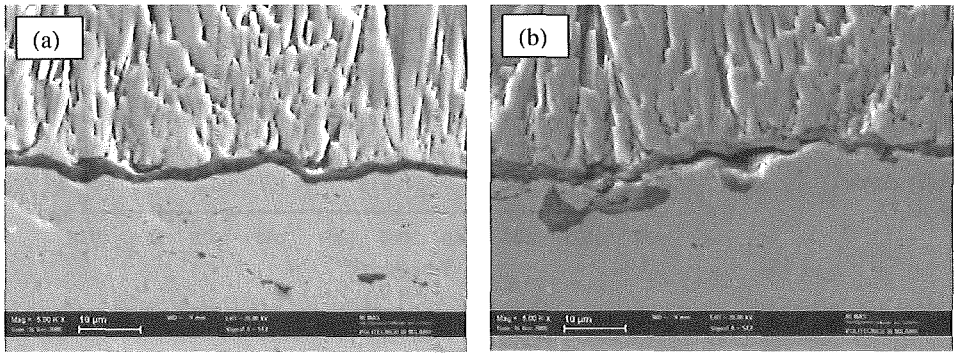

Figure 8 Examples of TGO on a sample oxidised for 2000 hours at 900°C

Comparing the PLPS results with the oxide growth measurements shows that the areas of low oxide stress correlate well with the areas of thicker TGO / micro-cracking. In both sets of data these areas grow in size with increasing exposure time until TBC spallation occurs. Thus, PLPS is shown to be an effective NDT to follow the spread of damage beneath EB-PVD TBCs for an IGT coating system, consistently with results obtained for jet engines /16/.

4. Conclusions

The ceramic top coatings within TBC systems in industrial gas turbines are prone to failure by spallation. To maximise the life of critical components protected by these coatings it is necessary to characterise the factors leading to this spallation, and to investigate the feasibility of potential NDE methods for detecting damage beneath the TBC before spallation occurs.
Long duration oxidation exposures have been carried out at 850, 900 and 950°C for up to 10000 hours for an EB-PVD TBC on CMSX-4 with an HVOF MCrAlY bond coat. Mass change data and post-exposure destructive examinations have been used to establish the growth of the TGO. TGO thicknesses at multiple points around individual samples have been summarised as cumulative probability distributions. PLPS has been successfully used to map and measure the stress in the TGO at large numbers of points around individual samples, which have also been translated into cumulative probability distributions. Comparison of these distributions of different parameters show that lower stressed areas of TGO correlate well with areas of thicker oxides/micro-cracking. During most of its growth, the TGO is composed of slow growing flat α-alumina under compressive stress. However when the supply of aluminium from the bond coat reduces, other oxides develop locally in the TGO and micro-cracks can also form; these appear as lower stressed areas detected by PLPS through

the TBC before it spalls. The localised damage areas increase with exposure until spallation. Thus, PLPS has been shown to be an effective NDE technique for following the spread of damage beneath EB-PVD TBCs, with the newly modified data acquisition system generating reliable stress maps from statistically significant number of points in only a few hours.

5. Acknowledgements

The PLPS activity of ERSE (formerly CESI RICERCA) was supported by the Research Fund for the Italian Electrical System - Contract of the Ministry of the Economic Development. ERSE/ Cranfield University collaboration was facilitated by the COST538 programme.

6. References

[1] D.H. Allen, J.E. Oakey and B. Scarlin, 'The New COST Action 522 – Power Generation in the 21st Century:- Ultra Efficient, Low Emission Plant', *Materials for Advanced Power Engineering 1998*, Eds J Lecomte-Beckers et al, pp1825-1838 (1998)

[2] T. Schulenberg, 'New development in Land-based GTs', *ibidem*, pp.849-859 (1998)

[3] S.T. Scheirer and R. Viswanathan, 'Evolution of Hot Section Technology', *ASM Materials Solution Conference. 2000.*

[4] Proc. Corrosion in Advanced Power Plants, *Special Issue of Materials at High Temperatures* 14 (1997).

[5] C.T. Sims., N. S. Stoloff and W.C. Hagel, *Superalloys II* (1987).

[6] J.R. Nicholls, 'Designing Oxidation Resistant Coatings', *JoM* (2000).

[7] J.R. Nicholls and R. Wing, 'Advances in Coating Systems for Utility Gas Turbines', *Materials for Advanced Power Engineering 2002*, pp. 57-72 (2002)

[8] S. Osgerby, C. Rinaldi, L. De Maria, 'Recent Advances In NDT Techniques For Gas Turbine Coatings', *Materials for Advanced Power Engineering 2006*, Eds J Lecomte-Beckers et al, pp. 217-232 (2006)

[9] C. Rinaldi and G. Antonelli, *Special Issue Paper Proc. Imech E, J. Power and Energy*, 219 Part A (2005) 93-99.

[10] C. Rinaldi, G. Antonelli, F. Cernuschi, L. De Maria, 'An integrated approach with innovative NDTs for thermal barrier coatings assessment', paper ESDA2006-95555, *Proc. ASME ESDA June 2006, Turin*, Italy (2006)

[11] D. M Lipkin and D R Clarke, *Oxid. Met.* **45** (1996) 267

[12] R.J Christensen, D.M Lipkin, D.R. Clarke, K.S. Murphy, *Appl. Phys. Lett.*, 69 [24] (1996) 3754-3756

[13] L. De Maria, C. Rinaldi, V. Sergo, P. Lupetin 'Portable optical system for in-situ thermal barrier assessment of service operated blades', *Paper GT 2006-90551 Proc. ASME TURBO EXPO 2006* May 8-11 , Barcellona, Spain (2006).

[14] C. Rinaldi, L. de Maria, M. Mandelli 'Assessment of The Spent Life Fraction of Gas Turbine Blades by Coating Life Modelling and Photostimulated Luminescence Piezospectroscopy', *J. Eng. Gas Tubines and Power*, April 2010, vol.132.

[15] N.J. Simms, D. W. Bale, D. Baxter and J. E. Oakey, 'Environmental Degradation of Gas Turbine Coatings: Towards Standardised Testing and Databases', *Materials for Advanced Power Engineering 2002*, Eds J Lecomte-Beckers et al, pp 73-88 (2002).

[16] J. Gell M., Sridharan S., Wen M, 2004, "Photoluminescence Piezospectroscopy : A Multi-purpose Quality Control and NDI Technique for Thermal Barrier Coatings", *Int. J. Appl. Ceram. Technol.*, 1 (4) pp. 316 – 329

9th Liege Conference : Materials for Advanced Power Engineering 2010
edited by J. Lecomte-Beckers, Q. Contrepois, T. Beck and B. Kuhn.

OXIDATION RESISTANCE OF HIGH RE AND RU CONTAINING NI-BASE SINGLE CRYSTAL SUPERALLOYS

A. Suzuki, K. Kawagishi, T. Yokokawa, T. Kobayashi and H. Harada
High Temperature Materials Center, Natioanal Institute for Materials Science
1-2-1 Sengen, Tsukuba Science City, Ibaraki, 305-0047, Japan

Abstract

With further development of Ni-base single crystal superalloys, the oxidation resistance of the alloys becomes a more pivotal factor to dominate turbine blade longevity. Oxidation resistance of Ni-base single crystal superalloys containing more Re and Ru than 5th generation alloys and having different composition in terms of Mo, Cr and Ru is investigated. All alloys were examined with cyclic oxidation test at 1100 °C up to 200 cycles, and the microstructural evolution was investigated by means of SEM and EPMA. As a result of the cyclic oxidation test, the alloy, having more Cr than the other alloys, showed the smallest weight change, whereas the other alloy having less Cr in substrate showed huge weight loss. Cr addition enables to suppress the degradation of oxidation resistance due to more addition of refractory elements.

Keywords: Oxidation, Ruthenium, Ni-base superalloys

1. Introduction

Further development of Ni-base superalloys, used as turbine blades, has been carried out to increase the operating temperature of gas turbines and jet engines. Now Ni-base superalloys have developed until 5th generation [1], and the latest Ni-base superalloys contain more refractory elements to improve mechanical properties and stabilise matrix. Due to the high amount of refractory elements, oxidation resistance of the latest Ni-base superalloys tends to be lower than that of previous generations, and research with respect to oxidation resistance of 4th generation alloys or the alloys containing more refractory elements have been conducted [2-8].

Alloy compositions in Ni-base superalloys have a strong impact for oxidation resistance. Addition of solid solution strengthening elements is very effective to improve mechanical properties of the alloys, however, some of them degrade the oxidation resistance: For example, Mo additions to Ni-base superalloys are effective in negatively increasing the lattice misfit [9,10], however, Hashizume [11] reported that Mo degrades oxidation resistance of second and third generation alloys due to the formation of Mo-base oxide, which is subject to volatilization. Kawagishi [5] also reported that more Re addition into Ni-base superalloys promotes larger mass loss in cyclic oxidation tests, which suggests more scale spallation and oxide vaporisation.

Oxidation resistance of Ni-base superalloys becomes more crucial than before to increase the operating temperature of jet engines and gas turbines, but the addition of refractory elements into Ni-base superalloys is also imperative to maintain excellent creep properties and microstructural stability. In this study, oxidation behaviour of high Re and Ru containing Ni-base superalloys were investigated; The morphology of oxides formed on the specimen surface and the effects of alloy elements, i.e. Cr, Mo and Ru, on oxidation resistance in those alloys are studied.

2. Experimental

Table 1. Alloy list

Alloy	Alloy description
Alloy A	Base Alloy
Alloy B	Alloy A+Mo
Alloy C	Alloy A+Cr-Mo
Alloy D	Alloy A+Ru
Alloy E	Alloy A-Cr

Five alloys used in this study were designed and developed by alloy design program [12] in National Institute for Materials Science in Japan. The alloys contain more Ru and Re than 5th generation alloys, and the amount of Co, W, Al, Ta, Hf and Ni are constant. Table 1 shows a summary of the alloys used in this study. Higher Ru and Re containing alloy than fifth generation, Alloy A, was set as a base alloy, and composition of Cr, Mo and Ru were varied in the other alloys. The alloys were cast into single crystal rods by means of directional solidification casting furnace, and heat treated with standard two step treatments.

The alloys were cut into cylindrical shape with 5 mm in height and 9 mm in diameter for oxidation test. Their surfaces were polished up to #800 SiC paper. Cyclic oxidation test was conducted at 1100 °C for 1h and cooling to room temperature for 1h in one cycle, and lasted till 200 cycles. The weight of the specimens was measured after each cycle.

Cross-sectional microstructures and scales formed on the specimen surface were observed by means of Scanning Electron Microscopy (SEM) and phase compositions were analysed by Electron Probe Microanalyser (EPMA). Thermodynamic properties of the alloys in this study were predicted by ThermoCalc™ [13] and Thermotech Ni-based superalloys database, NI-DATA7 was used for calculation.

3. Result and Discussion

3.1 Weight change of specimens after cyclic oxidation test

Figure 1 shows the weight change of the alloys up to 30 cycles and Figure 2 up to 200 cycles of cyclic oxidation.

In the first 30 cycles (Figure 1), all alloys except for Alloy E showed similar weight change behaviour: The alloys showed parabolic oxidation behaviour, rapid increase of the weight change in the first few cycles and then changed to slight increases of the weight change after 5 cycles. On the other hand, Alloy E showed a large mass gain after 1 cycle with 1.27 mg/cm^2, and started to show continuous weight loss after 3 cycles (Figure 1). This consecutively lasts till the end of the cyclic oxidation test (Figure 2), which indicates that Alloy E showed the poorest oxidation resistance among the all tested alloys.

After 200 cycles, the oxidation behaviour of the alloys can be classified into three groups: Alloy C showed the least weight change of the specimens, Alloy E showed the largest weight change of the specimens, and the other alloys (Alloy A, B and D) showed moderate weight change of the specimens. The main difference of alloy A and E is their Cr content, meaning that Cr reduction in high Re and Ru containing alloys significantly degrades the oxidation resistance.

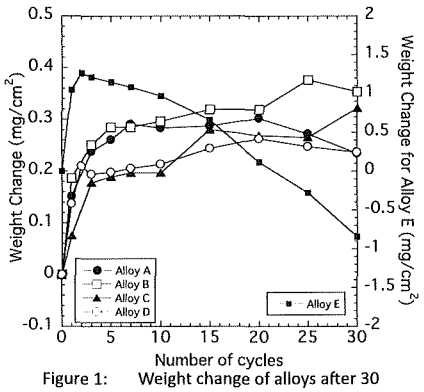

Figure 1: Weight change of alloys after 30 cyclic oxidation test

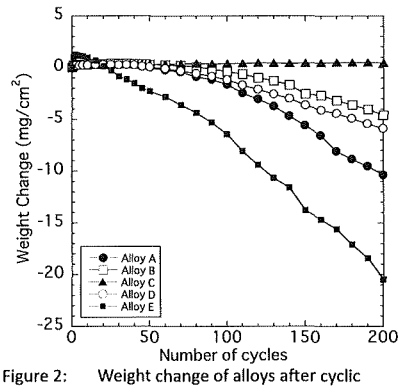

Figure 2: Weight change of alloys after cyclic oxidation test

Diffusion is one of the factors to dominate oxidation of metals and alloys, and thermodynamic activity is strongly concerned with diffusion of alloys. For example, the Darken-Harty-Crank relation [14, 15] shows the relation between interdiffusion coefficient ($\tilde{D}$), self-diffusion coefficient and thermodynamic activity:

$$\tilde{D} = (X_B D_A + X_A D_B)\phi \qquad \text{where} \quad \phi = 1 + \frac{d\ln\gamma_A}{d\ln X_A} = 1 + \frac{d\ln\gamma_B}{d\ln X_B}$$

γ_A is the thermodynamic activity coefficient of element A, and X_A represents the mole fraction of A. It can be seen that thermodynamic activity γ_A has a strong effect on diffusion. An increase of activities of certain elements, such as Al, would be expected to promote more diffusion of the elements if the oxidation observed in this study is dominated by diffusion process of alloy elements. More diffusion of Al accelerates the formation of protective Al_2O_3 oxide on the specimen surface, resulting in better oxidation resistance.

As shown in Figure 3 (a), Cr reduction significantly decreases Al activity, i.e. approximately -15%. This corresponds with the differences in weight change between Alloy A and Alloy E. Since the Al content is constant in this study, Al activity has been varied depending on the amount of other elements. Cr is very effective to improve oxidation resistance, and promote more Al_2O_3 formation on specimen surface, as a third element effect [16]. Alloy C contains the highest amount of Cr among the tested alloys, and showed the best oxidation resistance in this study. It can therefore be concluded that Cr addition is effective to improve oxidation resistance of alloys containing high amount of Re and Ru.

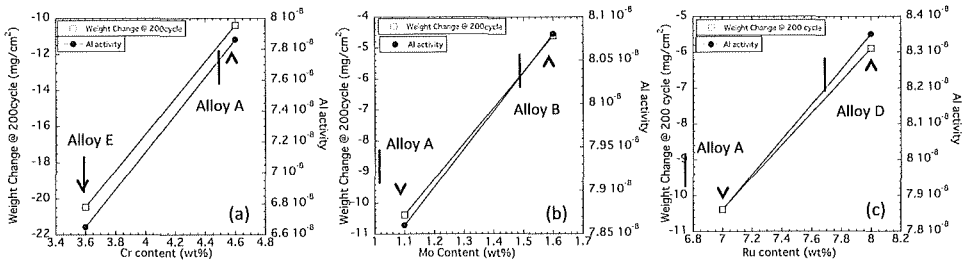

Figure 3: Relationships between weight change, Al activity, and composition of (a) Cr, (b) Mo and (c) Ru. (NB: Al activity is predicted by ThermoCalc™[13])

Alloys A, B and D showed moderate weight change during cyclic oxidation (Figure 2). All the alloys showed similar weight change until 50 cycles, and then started to show different behaviour. Within the three alloys, Alloy B and D showed better oxidation resistance than Alloy A, the base alloy in this study.

Mo deteriorates the oxidation resistance of Ni-base superalloys, and this trend has been reported in previous generation alloys [8,11]. However, the weight change of the specimens in Figure 2 showed different behaviour: Alloy B, Mo added alloy into Alloy A, showed smaller weight change within the three alloys after 200 cycles. Also, comparison of Al activity and weight change indicated that Al activity increased with Mo addition in Figure 3(b).

Ru showed a similar effect in Figure 3 (c): Addition of Ru resulted in an increase of Al activity and Alloy D showed better oxidation resistance than Alloy A. Change in Al activity with Ru addition is larger than with Mo addition, Alloy B, and the weight change during the first 30 cycles in Alloy D is smaller. Comparing the change in Al activity between elements, the increase of Al activity by Ru addition is 6.2% in Alloy D, whereas Mo increased the Al activity in Alloy B with 2.7%. This indicates that the oxide formed on Alloy D has better quality than that on Alloy B, suggesting better adhesion between substrate and oxide, and resulted in less spallation of oxides. Consequently Ru addition might be more effective to suppress degradation of oxidation resistance than Mo in high Re and Ru containing alloys. Further investigation will be carried out to elucidate the Mo and Ru effect for oxidation resistance in high Re and Ru containing alloys.

3.2 Microstructural analysis of the specimens after cyclic oxidation test

Figure 4 shows representative cross-sectional microstructures of specimens after 1 oxidation test cycle. Alloy C, showing the smallest weight change, formed a very thin but continuous Al_2O_3 layer with approximately 1-2 μm thickness on the specimen surface. On the contrary, other alloys showed different oxide morphologies on the specimen surface: Alloy E particularly developed a thick NiO layer with about 10 μm thickness after 1cycle. The thick NiO layer is the reason that Alloy E showed larger weight gain in the first cycle. In addition, Alloy E formed very fine subscales within the substrate, and the oxide morphology in Alloy E is very similar to the oxides formed in fourth generation alloy TMS-138A, which was reported by Kawagishi [8]. Other alloys, for example Alloy B, also formed a NiO layer above the specimen surface. However the layer is much thinner than in Alloy E. These alloys also showed complex oxides under the NiO layer, and Al_2O_3 layer was observed at the interface of substrate and oxide layer.

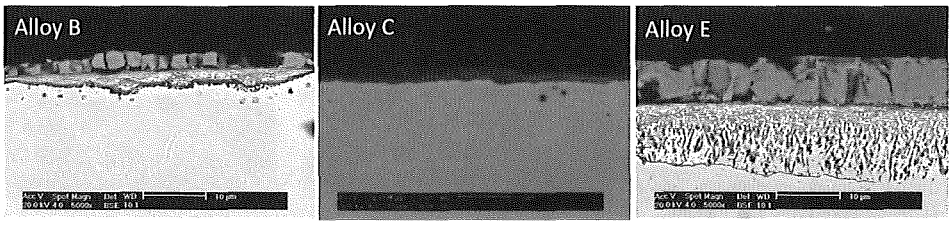

Figure 4: Cross-sectional microstructures of the specimens after 1 cycle

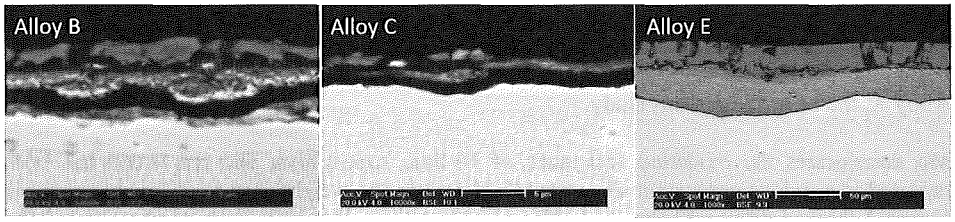

Figure 5: Cross-sectional microstructure of the specimens after 30 cycle

After 30 cycles of oxidation testing, all alloys developed a thicker oxide layer, as shown in Figure 5, and their morphology was basically similar to the specimens after 1 cycle. Alloy B developed a thicker protective Al_2O_3 layer, as the weight change in Figure 1 did not show significant weight loss of the specimen. Alloy C started to form other oxide layers above the protective Al_2O_3 layer, such as complex oxides and NiO. However, their thickness did not considerably change, and this alloy has much a slower growth rate of oxide layer, compared with the other alloys. Alloy E developed a thicker NiO layer at the top of the specimen surface after 30 cycles, and the thickness of the layer almost reached to 20 μm. However, this alloy showed continuous weight loss after 3 cycles, and it would be assumed that spallation and re-formation of oxides continuously happened during cyclic oxidation. NiO is a non-protective oxide and porous in nature. This means that NiO provides more access of oxygen to the underlying metals, and results in further oxidation. The NiO layer would therefore be reformed very quickly if the NiO spalled from the surface. The subscale formed in the substrate after 1 h oxidation in Figure 4 is now transformed into much complex oxides, and a very thin Al_2O_3 layer was developed at the interface of oxide and substrate.

Figure 6 shows the representative cross-sectional microstructures of the specimens and the enlarged complex oxide layer of Alloy E after 200 cycles. Alloy C, having the best oxidation resistance of all tested alloys in this study, still maintained a very continuous and uniform Al_2O_3 layer. Most of the surface area in Alloy C showed continuous Al_2O_3 layer, but some parts formed a new layer between substrate and Al_2O_3 layer, as seen in Figure 7. According to the chemical analysis results in Table 2, the layer contains a high amount of oxygen with approximately 56 at%, and other elements such as Ni, Al, Co, Cr and Ru. The layer seems to be an oxygen-dissolved Ni-Al layer. Formation of this layer has not been fully understood in this study, and further research will be conducted to investigate the effect of this layer for oxidation resistance of Ni-base superalloys.

Alloy B, showing a moderate weight change in Figure 2, showed very interesting features in terms of oxides which particularly were a very uniform and continuous Al_2O_3 layer, similar to Alloy C,

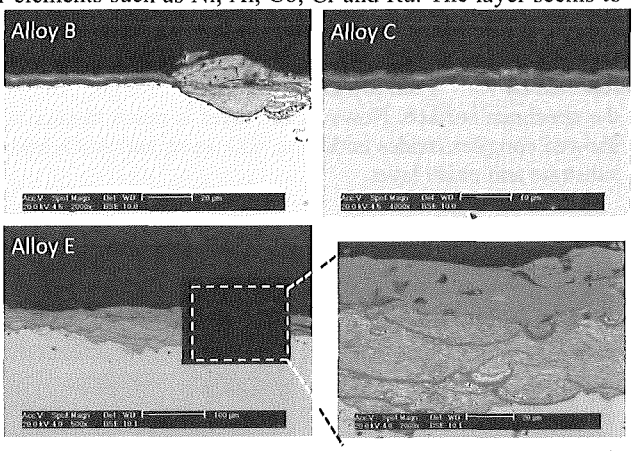

Figure 6: Representative cross-sectional microstructure of the specimens, and enlarged microstructure of Alloy E after 200 cycles

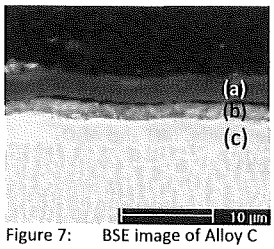

Figure 7: BSE image of Alloy C after 200 cycles

Table 2: Phase composition in each layer formed in Alloy C after 200 cycles

whereas other parts showed very thick NiO and complex oxide, which were also observed in Alloy B and D showing relatively stable weight change until 50 cycles, and then started to show mass loss in Figure 2. Mass loss in cyclic oxidation test generally means spallation of scale and/or metals. NiO and complex oxide layer in Alloy B still remained on the surface (Figure 6), however, Al_2O_3 layer was also observed after 200 cycles. It would be assumed that the area consisting of NiO and complex oxide layer is originally formed in the early stage of the cyclic oxidation test and remained until 200 cycles, whereas the other area consisting of Al_2O_3 would be formed after spallation of oxides.

Alloy E showed the most degraded microstructure of all specimens after 200 cycles. The phase constitution of the oxide layer was the same as after 30 cycles, however, it should be noted that the oxide layer consists of many complex oxides and Al_2O_3 layers as visible in the enlarged microstructure of Alloy E, Figure 6. Figure 8 shows an EPMA mapping of the complex oxide layer. The complex oxides are abundant of Co, Cr, O and Ta, and Cr, Ta, Ni, and Ru segregated within the layer. It should be noted that Ru segregation was observed near the interface between Al_2O_3 and the complex oxide layers and between complex oxides and NiO layers rather than inside the complex oxide layer. However none of the elements analysed in this study corresponds with the Ru segregation. Ru therefore was contained within the complex oxide layer, but it seems not to form Ru-oxide or Ru-based compounds in this study.

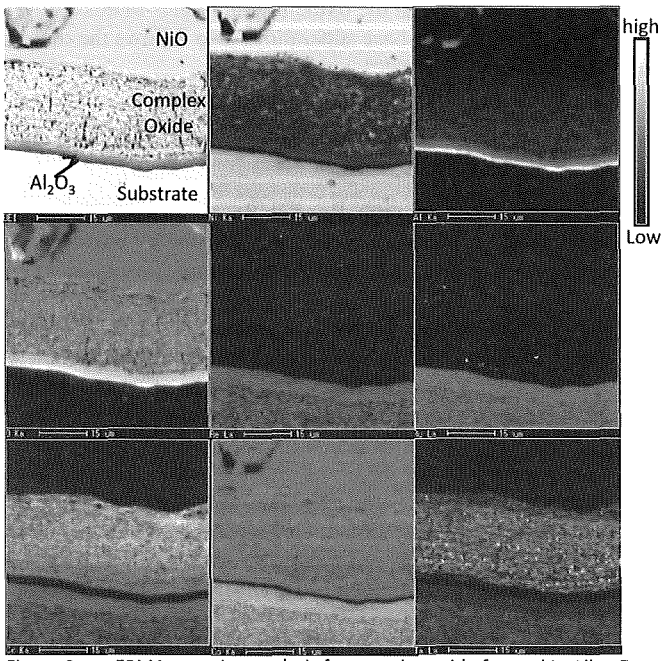

Figure 8: EPMA mapping analysis for complex oxide formed in Alloy E after 200 cycles

Oxide morphologies of alloys in this study varied, and the morphologies can be classified into three categories as given in Table 3. The Al content in these alloys is constant, and it seems that other elements significantly relate to oxide morphology. Dividing the alloys according to their Cr content, this classification corresponds well with the oxide morphology, and it should be noted that Cr content has a significant effect to improve the

Table 3: Oxides formed in each specimen after 200 cycle:

Alloy	Oxide after 200 cycles
Alloy A	Layer 1: complex oxide, NiO and Al_2O_3
	Layer 2: Al_2O_3 only
Alloy B	Layer 1: complex oxide, NiO and Al_2O_3
	Layer 2: Al_2O_3 only
Alloy C	Al_2O_3 only
Alloy D	Layer 1: complex oxide, NiO and Al_2O_3
	Layer 2: Al_2O_3 only
Alloy E	complex oxide, NiO and Al_2O_3

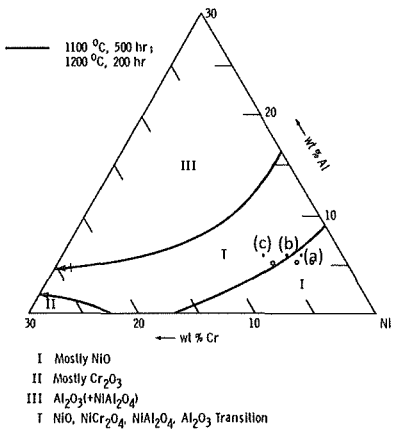

Figure 9: Compositional Effects on the oxidation behaviour of Ni-Cr-Al ternary alloys[17] : (a) Alloy E, (b) Alloy A, B and D, and (C) Alloy C

oxidation resistance in high Re and Ru containing allo ys. Figure 9 [17] shows a diagram in terms of compositional effect on the oxidation behaviour of Ni-Al-Cr ternary alloys. This diagram is based on ternary alloys, not on the complex alloy composition systems in the latest Ni-base superalloys. The alloys in this study also contain more refractory elements, and the borderlines in Figure 9 [17] are based on the results of cyclic oxidation test at 1100 °C for 500 hours. However, the Cr content of the alloys in this study aligned near the borderline of region I and region T: Region I is of mostly NiO and Region T is NiO, $NiCr_2O_4$, $NiAl_2O_4$ and Al_2O_3 transition. In fact, Alloy E is located in region I, whereas the other alloys are on the borderline of the areas or region T. Those locations in Figure 9 [17] are almost consistent with the oxide morphologies in this study, and it would be expected that oxide morphology in Ni-base superalloys also follows the diagram even though alloys contain more Re and Ru in substrates.

4. Conclusion

Oxidation resistance of high Re and Ru containing Ni-base superalloys, having different composition of Cr, Mo and Ru was investigated by means of cyclic oxidation test at 1100°C up to 200 cycles in this study, and the following consequences are obtained:

- Alloy C containing the highest amount of Cr of all tested alloys showed the smallest weigh change after cyclic oxidation test, and indicated the best oxidation resistance of all tested alloys. Cr addition is therefore very effective to maintain oxidation resistance of Ni-base superalloys containing high amount of Re and Ru.

- The base alloy, the Mo, and the Ru added alloys showed a relatively small weight change till 50 cycles, and then gradually started to show mass loss. Mo and Ru addition into high Re and Ru containing Ni-base superalloys increased the Al activity in Ni-base superalloys, and this contributed to maintain oxidation resistance. Ru showed a larger increase of Al activity than Mo with smaller weight change.

- The alloys showed three different oxide morphologies after cyclic oxidation test, and these groups can be divided by Cr content in substrate.

Reference

[1] A. Sato, H. Harada, et al., "A 5th generation SC Superalloys with Balanced High Temperature Properties and Proccessability", *Superalloys 2008*, Champion, Pennsylvania, TMS, USA, 131-138 (2008).
[2] I. M. Edmonds, H. E. Evance, et al., "The kinetics of oxidation of Ru-bearing Nickel-based Superalloys", *Materials Science Forum,* **595-598**, 59-67 (2008).
[3] I. M. Edmonds, H. E. Evans, et al., "Intermediate Temperature Internal Oxidation in Fourth Generation Ru-bearing Single Crystal Ni-base Superalloys", *Oxidation of Metals*, **69,** 95-108 (2008).
[4] I. M. Edmonds, H. E. Evance, et al., "Oxidation and Coating Evaluation in Aluminized Fourth Generation Blade Alloys", *Superalloys 2008*, Champion, Pennsylvania, TMS, USA, 661-670 (2008).
[5] K. Kawagishi, H. Harada, et al., "The Oxidation Properties of Fourth Generation Single Crystal Ni-based Superalloys", *JOM,* **2006**(Jan), 43-46 (2006).
[6] K. Kawagishi, A. Sato, et al, "Effect of Alloying Elements on the oxidation resistance of 4th generation Ni-base Single Crystal Superalloys", *Journal of Japan Institute of Metals,* **69**, 249-252 (2005).
[7] K. Kawagishi, A. Sato, et al., "Oxidation Behavior of Ru-cotaining Ni-base Single Crystal Superalloys", *Materials Science Forum,* **522-523** (August), 317-322 (2006).
[8] K. Kawagishi, A. Sato, et al., "Oxidation Resistant Ru containing Ni-base Single Crystal Superalloys", *Materials Science and Technology,* **25**(2), 271-275(2009).
[9] Y. Y. Qiu, "Coarsening kinetics of γ' precipitates in Ni-Al and Ni-Al-Mo alloys", *Journal of Materials Science,* **31**, 4311-4319 (1996).
[10] R. A. Hobbs, G. J. Brewster et. al., "Evaluation of Ruthenium -Bearing Single Crystal Superalloys- A Design of Experiments-", *Superalloys 2008*: Champion, Pennsylvania, TMS, USA, 171-180 (2008).
[11] R. Hashizume, A. Yoshinari, et al., "Development of Ni-based Single Crystal Superalloys For Power-Generation Gas Turbines", *Superalloys 2004*, Champion, Pennsylvania, TMS, USA, 53-62(2004).
[12] H. Harada, K. Ohno,et al., "Phase Calculation and its use in Alloy Design Program for Nickel-base superalloys", *Superalloys 1988*, Champion, Pennsylvania, TMS, USA,1988, 733-742 (1988).
[13] Thermo-Calc Software, http://www.thermocalc.se/.
[14] L. S. Darken, "Diffusion, Mobility and Their Interrelation through Free Energy in Binary Metallic Systems", *Transactions of the American Institute of Mining and Metallurgical Engineers*, **175**, 184–201 (1948).
[15] G. S. Hartley and J. Crank, "Some Fundamental Diffusions and Concepts in Diffusion Process", *Transactions of the Faraday Society*, **45**, 9, 801–818 (1949).
[16] F. H. Stott, G. C. Wood et. al., "The influence of alloying elements on the development and maintenance of protective scales", *Oxidation of Metals*, **44**, 113-145, (1995).
[17] C. T. Sims, N. S. Stoloff, et al. *Superalloys II*, A Willy-Interscience Publication (1987).

9th Liege Conference : Materials for Advanced Power Engineering 2010
edited by J. Lecomte-Beckers, Q. Contrepois, T. Beck and B. Kuhn.

SEM AND TEM ANALYSES OF MICROSTRUCTURAL CHANGES IN CREEP DEGRADED AND TENSILE TESTED CMSX-4 SUPERALLOY

B Dubiel[1], M Nazmy[2], J Lapin[3], A Czyrska-Filemonowicz[1]

[1] AGH University of Science and Technology, 30059 Krakow, Al. Mickiewicza 30, Poland
[2] Alstom Ltd Switzerland, 5401 Baden, Brown Boveri Str. 664, Switzerland
[3]Slovak Academy of Sciences, Institute of Materials and Machine Mechanics, 831 02 Bratislava 3, Racianska 75, Slovak Republic

Abstract

The effect of creep induced microstructural degradation caused by high temperature creep on mechanical properties of single crystal CMSX-4 superalloy was studied. Creep tests were performed at temperature 1050 °C and stress of 68 MPa for 2500 h. Pre-crept specimens were subsequently tensile tested at room temperature (RT) and 950 °C. Additionally, as a case study, microstructure of ex-service turbine blades after operation for 12 700 hours in industrial gas turbine was investigated. Tensile tests of mini specimens cut from turbine blades were also performed. Microstructural analyses of γ-γ' microstructure were carried out using SEM and TEM. Observed microstructural degradation of both laboratory tested and ex-service CMSX-4 samples showed that morphological changes of γ-γ' microstructure associated with dislocation accumulation at γ/γ'interfaces influence the inhibition of deformation in γ channels, what results in deterioration of CMSX-4 strength and ductility.

Keywords: Creep, Single Crystal, CMSX-4, Industrial Gas Turbine

1. Introduction

Single crystal (SC) nickel-base superalloys are widely used for industrial gas turbine blades due to their superior mechanical properties at high temperatures. The major factors controlling the operational life of SC superalloys are their microstructural stability and retention of high temperature mechanical properties. Therefore their microstructure is especially tailored to provide the high temperature strength by the absence of grain boundaries, strengthening by high volume fraction of cuboidal intermetallic γ' precipitates and nanometric width of γ matrix channels. Since the gas turbine blades operate also under tensile stress aligned along the <001> crystallographic direction, the very important property required for their long-term use is their creep resistance.

The creep deformation behaviour of SC superalloys is strongly dependent on temperature, applied stress and crystallographic orientation of the alloy [1 - 3]. Several temperature and stress regimes can be identified, in which particular mode of microstructural degradation is predominant.

The gas turbine inlet temperature in modern industrial turbines often exceeds 1300 °C, leading to a blade metal temperature of between 750 to 950 °C. At temperature in excess of

850°C, the microstructure of SC superalloys undergoes the morphological changes under combined influence of stress and temperature. The initial cuboidal γ' particles transform into plates, what is called "rafting" [4 – 6]. Morphological changes of cuboidal microstructure have important practical implication because in the turbine blades rafting occurs in the service conditions [7, 8]. The influence of rafting on creep strength of SC superalloys is controversial. The general conclusion justified by Pollock et al. [9] claims that rafting accelerates creep at higher stresses and retards creep at very low stresses. Therefore, evaluation of the effect of microstructure degradation on mechanical properties of SC superalloys is important for the lifetime prediction of turbine blades. This problem was investigated within European Action COST 538 "High Temperature Plant Lifetime Extension", Work Package WP3 on "Microstructural Degradation: Characterisation and Quantification". The single-crystal nickel-base superalloy CMSX-4, widely used in gas turbine industry, was selected for investigations.

The aim of this paper is to evaluate the effect of rafting on tensile properties of CMSX-4 specimens pre-crept in laboratory conditions as well as specimens cut from ex-service turbine blades. Electron microscopy analyses of both creep degraded and tensile tested CMSX-4 enabled the interpretation of the effect of microstructural changes on its mechanical properties.

2. Material and experimental methods

The single-crystal CMSX-4 superalloy was received from HOWMET, Exeter, UK. According to the supplier data, chemical composition of the alloy is as follows (wt %): Ni – 8.4 Co – 6.4 Cr – 6.5 Ta – 6.4 W – 5.68 Al – 2.8 Re – 1.04 Ti – 0.58 Mo. Heat treatment involved the multi-step solution annealing at 1320 °C, followed by double ageing at 1140 °C for 2 h and 870 °C for 20 h. Creep tests were performed at Alstom Baden at temperature 1050 °C and stress 68 MPa for 2500 h. Pre-crept specimens were subsequently tensile tested at temperature range 20 – 950 °C and an initial strain rate of $7 \cdot 10^{-4} s^{-1}$. As a case study, the CMXS-4 ex-service blades were supplied by SIEMENS Industrial Turbomachinery Ltd, Lincoln after operation for 12 700 hours and 200 starts. According to SIEMENS specification, the distribution of temperature and stress in the blade was as follows:

- 997 °C / 30 MPa at the blade tip,
- 927 °C / 111 MPa at the middle of the blade height,
- 807 °C / 189 MPa at the blade bottom.

Microstructural analyses were performed by light microscopy (LM) as well as by scanning – and transmission electron microscopy (SEM, TEM). The LM and SEM investigations were carried on polished and chemically etched sections cut parallel to {100} and {001} planes. Specimens for TEM investigations were mechanically polished down to about 50 μm thickness, then dimpled to a thickness less than 25 μm and electrochemically polished using double-jet STRUERS Tenupol. Microstructural investigations were carried out by Jeol JEM-2010 ARP microscope.

Results

Creep and tensile tests of CMSX-4

In order to evaluate the effect of creep degradation on the strength of CMSX-4 superalloy, the creep tests at temperature 1050 °C and stress of 68 MPa were terminated after 2500 h and

subsequently the specimens were tensile tested at 20, 850, 900 and 950 °C. Additionally the mini-specimens of ex-service turbine blades were cut and tensile tested at RT, 800 and 850 °C. The values of yield stress (YS), ultimate tensile stress (UTS) and plastic elongation to fracture were compared with those achieved for not degraded CMSX-4 (Fig. 1 a - c). It was found that YS, UTS and ductility of degraded CMSX-4 are lower than that for virgin material. The most pronounced differences were observed in tensile tests performed at 950°C.

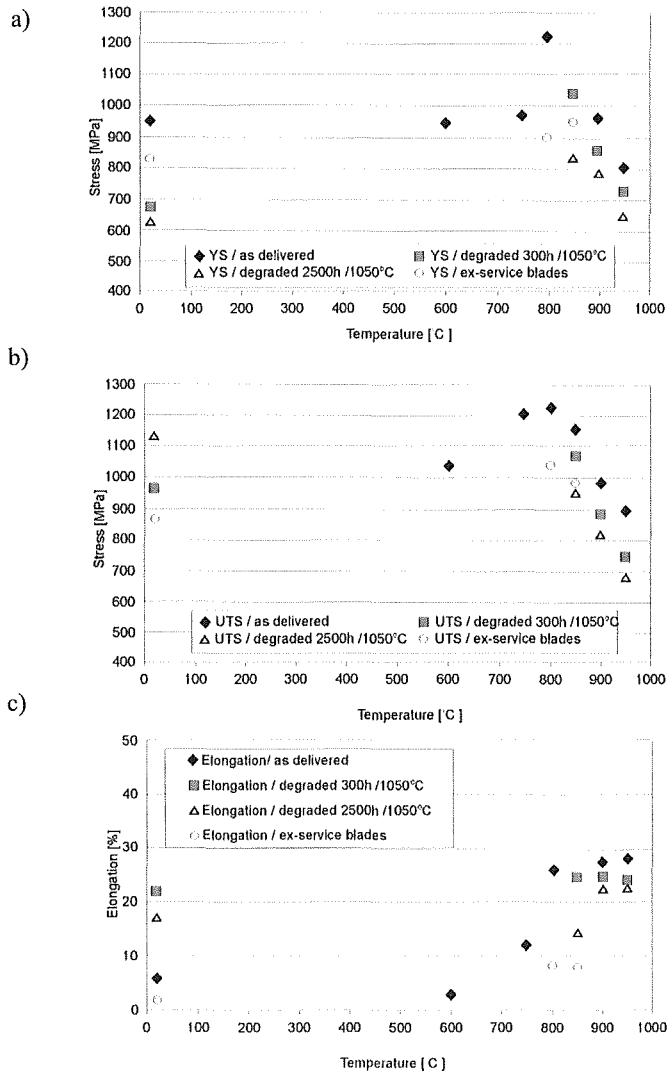

Fig. 1 . Mechanical properties of as-received and degraded CMSX-4 versus temperature: a) yield stress (YS), b) ultimate tensile stress (UTS), c) elongation.

Microstructure after creep degradation at 1050°C/17 MPa for 2500 h

All the CMSX-4 specimens creep tested at 1050°C/68MPa for 2500 h were subsequently tensile tested at the same machine and therefore the gauge lengths of pre-crept specimens were not available for microstructural investigations. For evaluation of the microstructural changes of creep degraded CMSX-4, the heads of deformed specimens were examined. The area of the head cross section was four times larger than in the gauge length, and therefore the stress acting in the head during creep test was approximately 17 MPa. Even under such a low stress acting at 1050 °C, after 2500 h of creep testing, the microstructure of CMSX-4 superalloy undergo directional coagulation and γ-γ' rafts perpendicular to the long axis of the specimen were formed (Fig. 2a). To initiate the rafting process, the γ/γ' misfit stresses were relieved and well developed dislocation networks were formed at the γ/γ' interfaces (Fig. 2b). Long-term high temperature exposure resulted in precipitation of TCP phases in a the form of large needle-like particles. The chemical composition of these particles was examined using STEM-EDS elemental maps. It was found that the TCP phases were enriched with Cr, Co, W and Re (Fig. 2). The unambiguous identification of these phases is very complicated. The possible phases are: σ (P42/mnm tetragonal), μ (R-3m rhombohedral) and P (Pnma orthorombic).

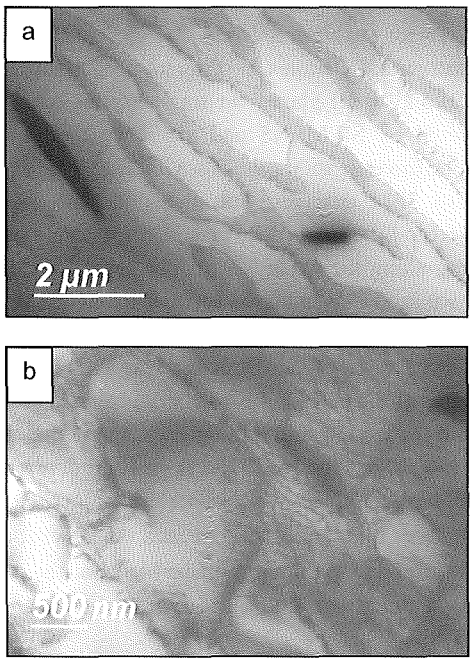

Fig. 2. TEM images of the head microstructure of CMSX-4 specimen creep deformed at 1050 °C / 17 MPa for 2500 h: a) rafted γ/γ' microstructure and precipitates of TCP phases, b) dislocation networks at γ/γ' interfaces.

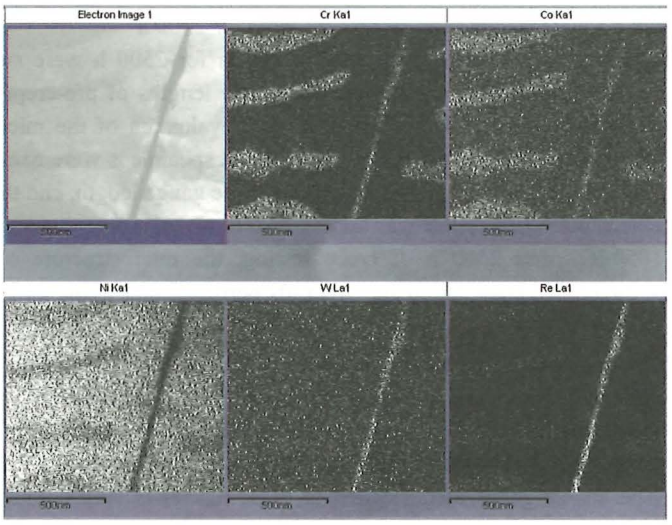

Fig. 3. STEM-EDS mapping of chemical composition of TCP phases precipitated in head of CMSX-4 specimen creep deformed at 1050 °C / 17 MPa for 2500 h.

Microstructure of the ex-service gas turbine blade

To investigate the microstructural changes in different sections of the blade, the specimens were cut parallel to (100) and (010) planes in single-crystal blade. The photograph of the investigated blade delivered by SIEMENS and the scheme of the selection of the blade sections for microstructural investigations is shown in Fig. 4. Each section was divided to smaller parts for LM and SEM analyses. Specimens for thin foils preparation for TEM investigations were parallel to (100) and (001) planes, respectively parallel and perpendicular to centrifugal force, acting along the blade height. The typical SEM images observed along the turbine blade are shown in Fig. 5. In all the sections examined at the bottom of the blade, at highest applied stress (190 MPa) and the lowest temperature (807 °C), the cuboidal morphology of was preserved and the microstructure was similar to the as-received material. The microstructural changes of the CMSX-4 blade during service are more pronounced in the middle and the top, both at the leading and trailing edge. In the middle zone, at a temperature 920 °C and stress of 110 MPa, the well developed rafts oriented perpendicularly to longitudinal axis of the turbine blade were observed. Under centrifugal stress applied, opposite vertical γ/γ' interfaces migrate forward to each other, what results in coalescence of the γ' cubes and creation of plates. At the top of the blade, at the lowest applied stress (30 MPa) and the highest temperature (980 °C) the microstructure was characterized by wavy γ/γ' rafts.

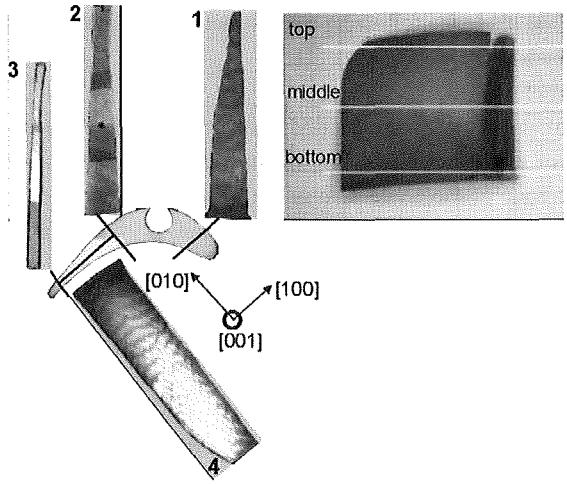

Fig. 4. Investigated sections of the ex-service CMSX-4 blade.

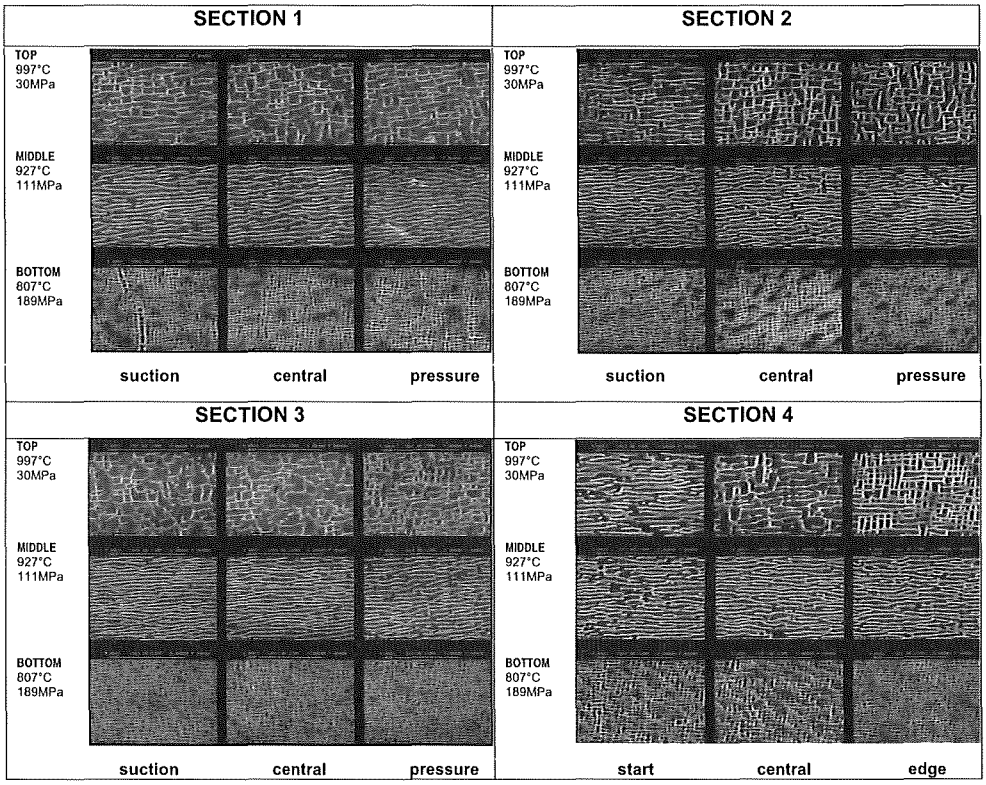

Fig. 5. Microstructure of the blade in sections 1 - 4. SEM images.

For sections 1÷3 of the blade the following microstructural parameters were determined:
w = width of γ channels,
w' = width of γ' particles.
The mean values of w and w' were plotted versus the temperature and stress in bottom, middle and the top of the blade. The diagrams showed, that the mean width of γ channels is lower in the middle zone of the blade than in the bottom and increases in the top zone (Fig. 6a). The mean size of γ' particles increases monotonically with increase of temperature from the bottom to the top of the blade (Fig. 6b).

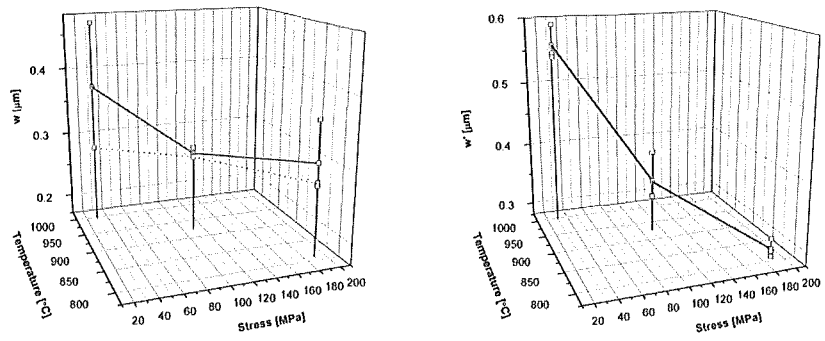

Fig. 6. Stress and temperature dependence of a) γ channels width, b) γ' particles width in the ex-service CMSX-4 turbine blade.

TEM investigations of the specimens cut from the bottom of the blade showed that the deformations is confined to the dislocation movement in the γ channels. As the superposition of external stress with the γ/γ' misfit stress makes the higher stress level in horizontal γ channels, they are the preferential sites of dislocation slip. Leading segments of mobile dislocations are bowing out, changing its direction by 90° in the γ channels. The dislocation segments deposited at the γ-γ' interfaces are inclined by 45° to the particle edge (Fig. 7a). The Burgers vector of dislocations moving in horizontal γ channels was determined as $\mathbf{b} = a/2\,[0\ \bar{1}\ 1]$. Such dislocations have mixed character and their screw components can move by cross slip to vertical channels, as was observed on thin foils cut parallel to the stress axis (Fig. 7 b). In the middle of the blade height, the process of rafting proceeds. To initiate the diffusion flux enabling the movement of vertical γ/γ' interfaces and resulting in transformation into γ' plates, the γ/γ' misfit stresses must be relieved. It is achieved by formation of dislocation networks, as was observed both in horizontal and vertical γ channels (Fig. 7 c, d). Similarly, at the top of the blade, well developed dislocation networks on the γ/γ' interfaces were present (Fig. 7 e, f). In both middle and top sections, cutting of the γ' rafts by dislocations was not observed.

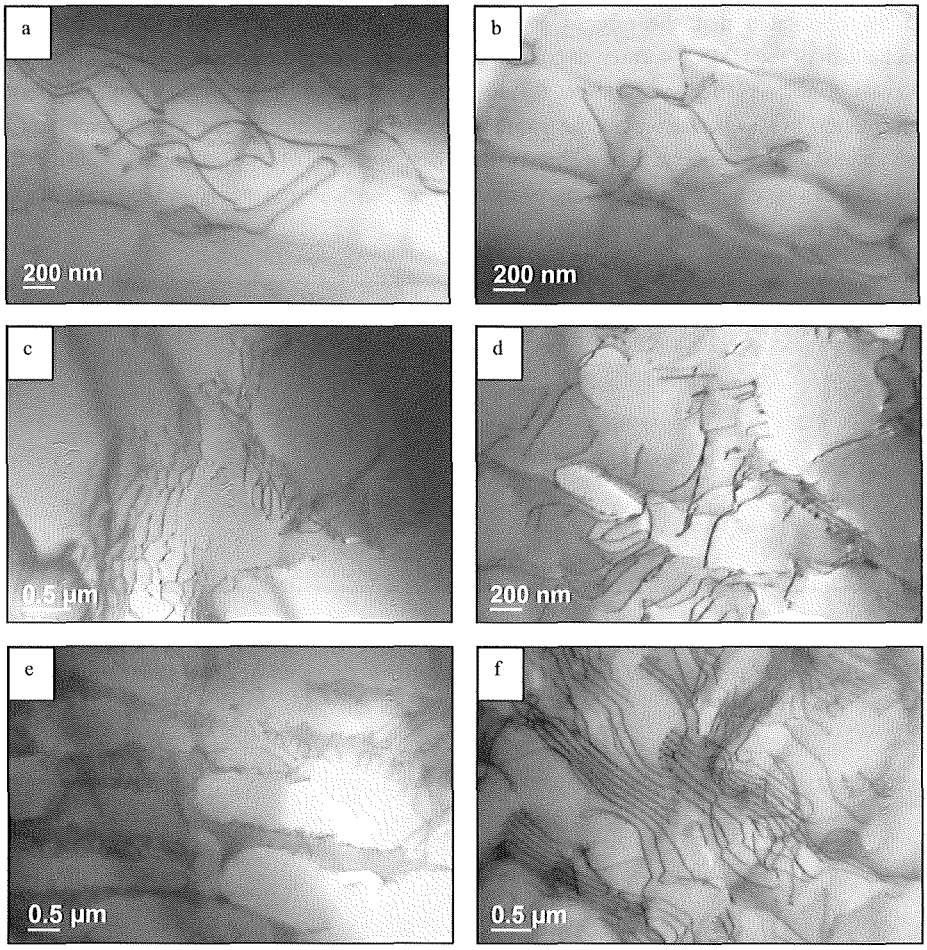

Fig. 7. TEM images of the microstructure of the ex-service CMSX-4 blade: a) the bottom section parallel to (001) plane, b) the bottom section parallel to (100) plane, c) the middle section parallel to (001) plane, d) the middle section parallel to(100) plane, e) the top section parallel to (001) plane, f) the top section parallel to(100) plane.

Microstructure of CMSX-4 after creep degradation and tensile tests at RT and 950 °C

In the CMSX-4 specimen creep tested at 1050 °C / 68 MPa for 2500 h and tensile tested at room temperature, the long irregular rafts, formed during creep perpendicular to the applied stress were observed. Tensile deformation at RT resulted in cutting of the γ' particles by numerous dislocations (Fig. 8 a, b). Similar microstructure was observed in the tensile tested specimens cut form the ex-service turbine blade (Fig. 9). Dislocations percolate in the γ channels forming long loops and the increase of strain proceeds by cutting the γ' particles. It

can be postulated that shearing of γ' particles by dislocations is the main deformation mechanism of the CMSX-4 creep degraded and tensile tested at low temperature.
Increasing the tensile temperature up to 950 °C resulted in a localization of plastic deformation in slip bands within the γ rafts (Fig. 10). Sporadically, the γ' rafts were cut by dislocations. Such observation suggests that deterioration of the strength of pre-rafted CMSX-4 can be connected to closing of many of the vertical γ channels and creation of easy paths of deformation along the γ rafts.

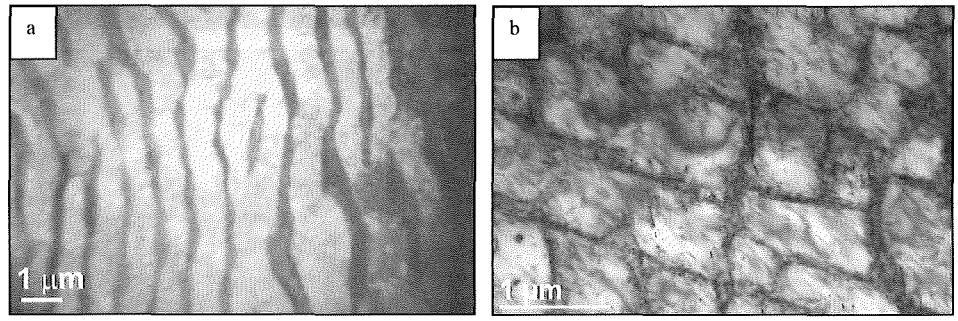

Fig. 8. TEM images of the microstructure of CMSX-4 creep degraded at 1050°C/68MPa for 2500h and tensile tested at RT: a) rafted γ/γ' microstructure and b) high dislocation density within γ' phase.

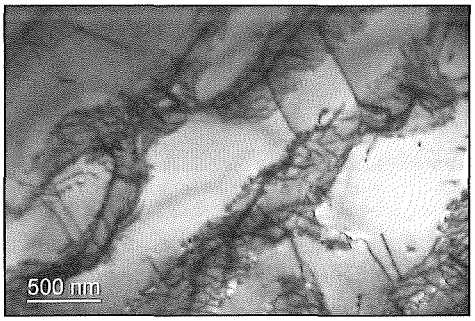

Fig. 9. Cutting of γ' rafts by dislocations in the specimen cut from ex-service turbine blade and tensile tested at room temperature.

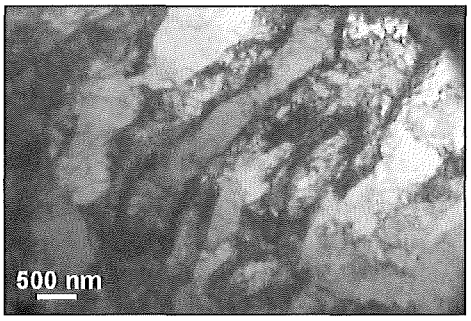

Fig. 10. Formation of slip bands within γ phase in CMSX-4 creep degraded at 1050 °C / 68 MPa for 2500 h and tensile tested at 950 °C

Summary

The results of the mechanical testing of the CMSX-4 single-crystal superalloy degraded by laboratory creep testing or during service at gas turbine showed that both the strength and ductility of degraded CMSX-4 are lower than those for virgin material.

The SEM and TEM microstructural analyses revealed the microstructural changes caused by both temperature and stresses, namely widening of the γ channels, reduction of γ'γ' misfit stresses by dislocation networks and coalescence of cuboidal γ' precipitates into plates, so-called γ/γ' rafting.

At a range of stress and temperature conditions charateristic for gas turbine blades, dislocation structure is mainly confined to the matrix channels with little evident cutting of the γ' particles.

Based of the TEM analyses of creep deformed and subsequently high temperature tensile tested CMSX-4, it is postulated that deterioration of strength of pre-rafted CMSX-4 can be connected with closing of many of the vertical γ channels and creation of easy paths of deformation along the γ rafts.

Acknowledgement

The authors form AGH-UST Krakow gratefully acknowledge the financial support of the work by the Ministry of Science and Higher Education (project nr 11.11.110.791). We also would like to thank Mrs K. Płońska-Niżnik and Mr K. Kulawik (AGH-UST) for specimen preparation. One of the authors (J. Lapin) acknowlegdes financial support of the Slovak Grant Agency for science inder the contract VEGA 2/0157/10.

References

[1] T. M. Pollock, A. S. Argon, Creep resistance of CMSX-3 nickel base superalloy single crystals, *Acta Metallurgica et Materialia*, 40, 1–30, (1992).

[2] T. Murakumo, T. Kobayashi, Y. Koizumi and H. Harada, Creep behaviour of Ni-base single-crystal superalloys with various γ' volume fractions, *Acta Materialia*, 52, 3737–3744, (2004).

[3] R.C Reed, *The Superalloys. Fundamentals and applications*, Cambridge University Press, 171-187, (2006).

[4] T. M. Pollock and A. S. Argon, Directional coarsening in nickel base superalloy single crystals with high volume fractions of coherent precipitates, *Acta Metallurgica et Materialia*, 42, 1859–1874, (1994).

[5] M. Veron, Y. Brechet and F. Louchet, Strain induced directional coarsening in Ni-base superalloys, *Scripta Metallurgica et Materialia*, 34,1883–1886, (1996).

[6] N. Matan, D. C. Cox, C. M. F. Rae and R. C. Reed, On the kinetics of rafting in CMSX-4 superalloy single crystals, *Acta Materialia*, 47, 2031–2045, (1999).

[7] S. Draper, D. Hull, R. Dreshfield, *Metall. Trans. A*, 20A, 683-688, (1989).

[8] C. Persson, P. O. Persson, Evaluation of service-induced damage and restoration of cast turbine blades, *Journal of Materials Engineering and Performance*, 2, 565-570, (1993).

[9] T.M. Pollock, R.D. Field, in *Dislocations in Solids*, F.R. Nabarro, M.S. Duesberry (eds), Elsevier science BV, Amsterdam, Vol. 11, 547-618, (2002).

9th Liege Conference : Materials for Advanced Power Engineering 2010
edited by J. Lecomte-Beckers, Q. Contrepois, T. Beck and B. Kuhn.

MORPHOLOGY OF γ' PRECIPITATES OF NICKEL-BASED SUPERALLOY SERVICED AS FIRST STAGE HIGH PRESSURE TURBINE NOZZELE GUIDE VANE

Nobuhiro Miura*, Kouji Nakada*, Yoshihiro Kondo*

*National Defense Academy, 1-10-20 Hashirimizu Yokosuka, Kanagawa 239-8686, Japan

Abstract

The morphology of γ' precipitates of the nickel-based superalloy serviced as the first stage high pressure turbine nozzle guide vane of the jet engine was examined. The aim of this work was to estimate the temperature and the stress distribution, and the stress direction of the vane in service. The vane was cut into four parts perpendicular to the longitudinal direction of the vane at 5, 25, 35 and 45mm from the root. These parts were designated as the root, 25mm, 35mm and tip parts. Microstructure observations by a FE-SEM were carried out on the forty-six portions at the vicinity of the interface between the coating layer and the matrix on the suction and pressure sides. At the root parts of the pressure and suction sides, most of the γ' precipitates kept cuboidal in shape, and the secondary γ' precipitates were observed in the γ matrix channels. On the contrary, At the trailing edge side of the pressure and suction sides of the 25 and 35mm parts and at the leading edge of the pressure side of the tip part, well aligned rafted γ/γ' structures were appeared in the direction parallel to the surface at the vicinity of the interface of the vane. Furthermore, at the trailing edge of the pressure side of the middle parts, the rafted γ/γ' structures start to collapse. Consequently, the vane in service, at the trailing edge sides of the pressure side the 25 and 35mm parts were exposed to the highest temperature and stress conditions. And this microstructure evidence indicated that the multi-axial compressive stress parallel to the nozzle surface was expected to act on the vane in service.

Keywords : Turbine nozzle guide vane, Superalloy, Microstructure, γ' precipitates, rafted γ/γ' structures

1. Introducti on

In recent years, with a superior performance and a request of the carbon dioxide emissions reduction of the aircraft, the further high output and the high efficiency of the jet engine are demanded. The efficiency of the jet engine strongly depends on the Turbine Inlet Temperature (TIT) and becomes the high efficiency as a high temperature [1], [2]. The TIT will be steadily rising in future [2]. As the materials for the high pressure turbine blades and nozzle guide vane in jet engines, nickel-based superalloys have been used because of their excellent in creep rupture strength, rupture ductility, and the thermal fatigue [2]-[6]. In our previous work, to estimate the temperature and the stress distribution of the blade in service, the morphology of the γ' precipitates of a single crystal nickel-based superalloy serviced as the first stage high pressure turbine (1st HPT) blade of an jet engine was examined. And it was elucidated that the leading and trailing edges of the pressure side of the middle part and the leading edge of the suction side of the middle part were exposed to the highest temperature and stress conditions based on the morphology of the γ' precipitates. This microstructure evidence showed that the main stress of the blade in service was not the centrifugal force by the rotation but the thermal stress with cooling [5].

With an increasing in the TIT, it was expected that the 1st HPT nozzle guide vane (designated as vane) would be exposed to the high temperature as well as the 1st HPT blade [1]. The vane was exposed to high temperature much higher than melting points of Ni. To shelter the high temperature combustion gas, the vane was covered with the Thermal Barrier Coating (TBC), and cooled the inside and the surface by air [7]. The centrifugal stress by a rotation was not acting on the vane in service, differed from the turbine blade. However, it was supposed that the differences between the coefficient of thermal expansion of the TBC and the metal matrix and the temperature difference between the matrix of the vane surface and the vicinity of the internal cooling channels was generated the thermal stress. The detail of the temperature and the stress distribution of the vane in service had not been reported yet.

In this study, the morphological change in the γ' precipitates of the nickel-based superalloy serviced as the 1st HPT vane of the jet engine was investigated to estimate the temperature and the stress distribution, and the stress directions in service.

2. Experimental procedure

A directionally solidified nickel-based superalloy was prepared in the form of the air-cooling HPT nozzle guide vane. The crystal growth direction of [001] in the vane was attained to the directional precision casting. After employing the defined solution treatment and the aging, TBC was carried out on the surface of the part of the airfoil. This specimen was serviced for several thousand hours as the 1st HPT nozzle guide vane of the jet engine on the military aircraft. The vane was cut into four parts perpendicular to longitudinal direction of the vane at 5, 25, 35 and 45mm from the root part by electron discharge machine. These parts were designated as the root, 25mm, 35mm and tip parts. Microstructure examinations by a field emission scanning electron microscope (FE-SEM) were carried out on the forty-six portions each specimen sectioned twelve or ten portions at the vicinity of the interface between the coating layer and the matrix on the suction and pressure sides from the leading edge to the trailing one at an interval of 11mm as shown in Fig.1. Specimens for the FE-SEM observation were prepared metallographically and electroetched with a supersaturated oxalic acid aqueous solution.

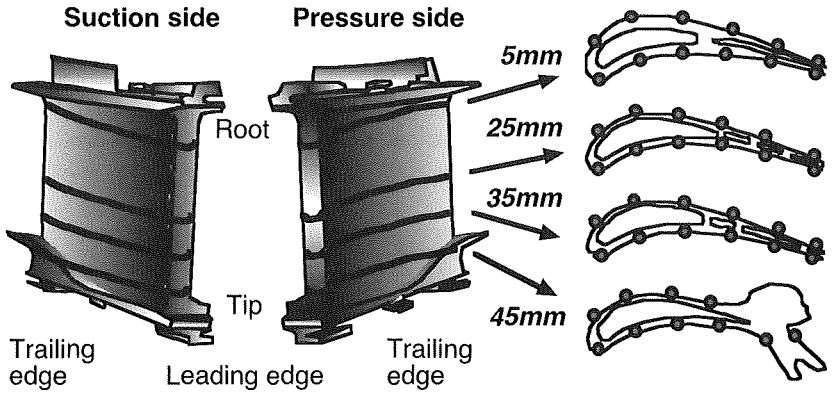

Fig.1 Schematic illustration of the forty-six portions cut form the vane

3. discussion

3.1 Appearance of 1st HPT nozzle guide vane

The appearance of the 1st HPT nozzle guide vane is shown in Fig.2. The size of the airfoil of the vane is about 53mm maximum length, about 55mm maximum width. Cooling holes are positioned in a row at the leading edge in the airfoil. At the leading edge of the suction side of the root part and at the trailing edge side of the pressure side, the coating comes off the vane and the matrix phase is bared. Many cracks are observed at the trailing edge of the pressure side and the tip parts.

3.2 Morphology of γ' precipitates of vane

The scanning electron micrographs at the suction side of the root part are shown in Fig.3. The top of photos is parallel to the outside surface of the vane. At the portion with the leading edge and the distance of 11mm from leading edge, the cuboidal γ' precipitates becomes round. The secondary γ' precipitates

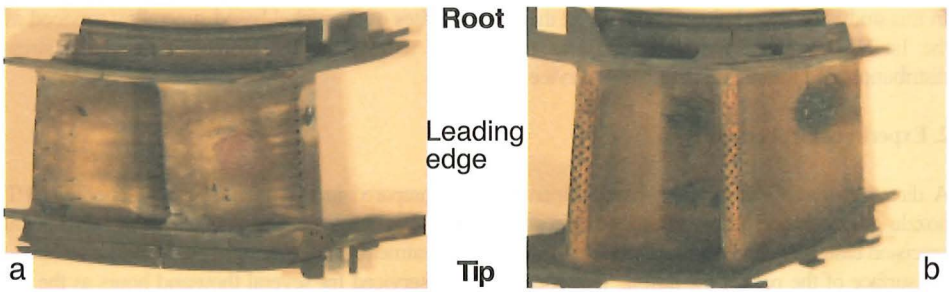

Fig.2. Appearance of the 1st HPT nozzle guide vane

are observed in the γ matrix (Fig.3-(a) and (b)). At the trailing edge sides, some of the cuboidal γ' precipitates contact each other toward the parallel to the outside surface at the vicinity of interface between the coating layer and the matrix (Fig.3-(c)-(e)).

The scanning electron micrographs at the pressure side of the root part are shown in Fig.4. The base of the photos is parallel to the outside surface of the vane. At the leading edge, some of the γ' precipitates contact each other in the specific direction (Fig.4-(a)). At the portions with the distance of 11 and 33mm from the leading edge, most of the γ' precipitates keep cuboidal in shape (Fig.4-(b) and (c)). However, at the portion with the distance of 44mm from the leading edge, well aligned rafted γ/γ' structures are observed (Fig.4-(d)). On the contrary, at the trailing edge, the rafted γ/γ' structures are only appeared at the vicinity of the interface between the coating layer and the metal matrix, whereas the cuobidal γ' precipitates remain in the inside (Fig.4-(e)).

The scanning electron micrographs at the suction side of the 25mm part are shown in Fig.5. At the leading edge, some of the γ' precipitates contact each other toward the specific direction. Further coarsening of the γ' precipitates are observed (Fig.5-(a)). At the other portions, the γ/γ' structures change to the incomplete rafted one (Fig.5-(b)-(e)).

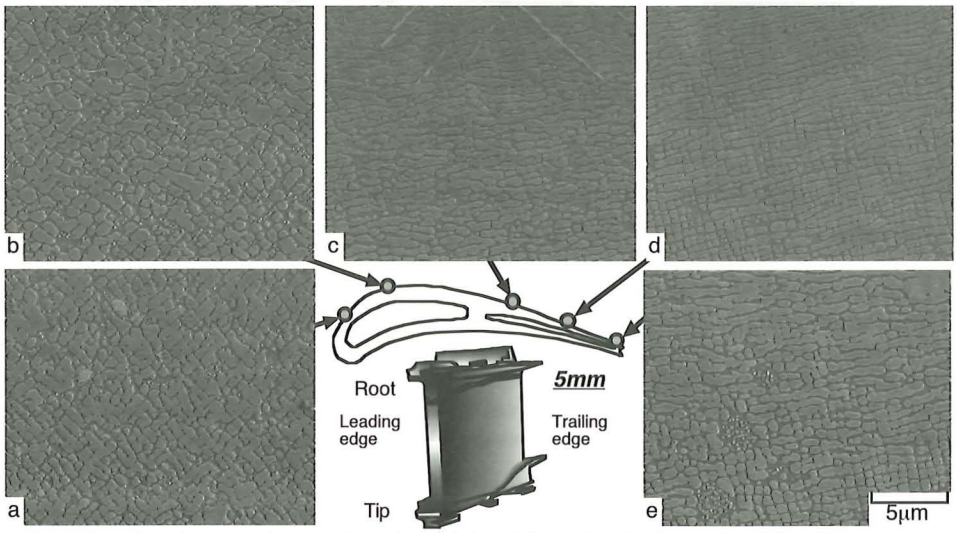

Fig.3. Scanning electron micrographs at the vicinity of the surface in the suction side of the root part : (a) the leading edge, portion with the distance of (b) 11mm, (c) 33mm, (d) 44mm from leading edge and (e) trailing edge

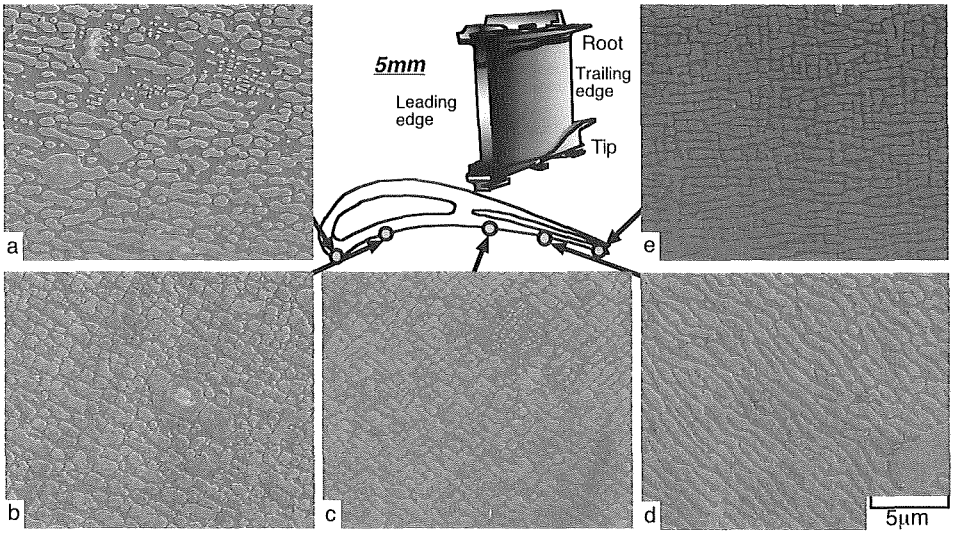

Fig.4. Scanning electron micrographs at the vicinity of the surface in the pressure side of the root part : (a) the leading edge, portion with the distance of (b) 11mm, (c) 33mm, (d) 44mm from leading edge and (e) trailing edge

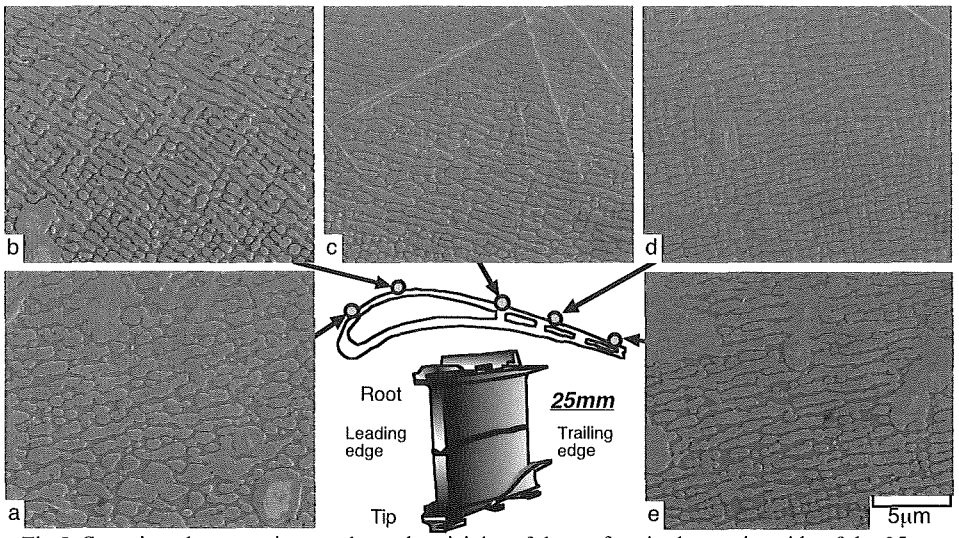

Fig.5. Scanning electron micrographs at the vicinity of the surface in the suction side of the 25mm part : (a) the leading edge, portion with the distance of (b) 11mm, (c) 33mm, (d) 44mm from leading edge and (e) trailing edge

The scanning electron micrographs at the pressure side of the 25mm part are shown in Fig.6. At the leading edge, some of the cuboidal γ' precipitates contact with each other parallel to the vane surface (Fig.6-(a)). The portion with the distance of 11mm from the leading edge, the incomplete rafted γ/γ' structures are observed (Fig.6-(b)). At the portion with the distance of 33mm from the leading edge, the well aligned rafted γ/γ' structures are observed. The morphology of the interface between the γ/γ' phase

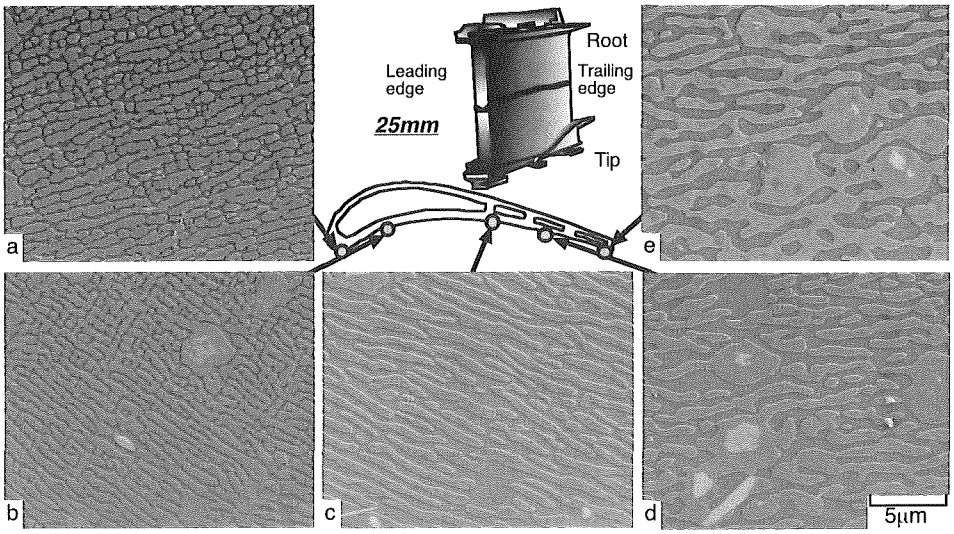

Fig.6. Scanning electron micrographs at the vicinity of the surface in the pressure side of the 25mm part : (a) the leading edge, portion with the distance of (b) 11mm, (c) 33mm, (d) 44mm from leading edge and (e) trailing edge

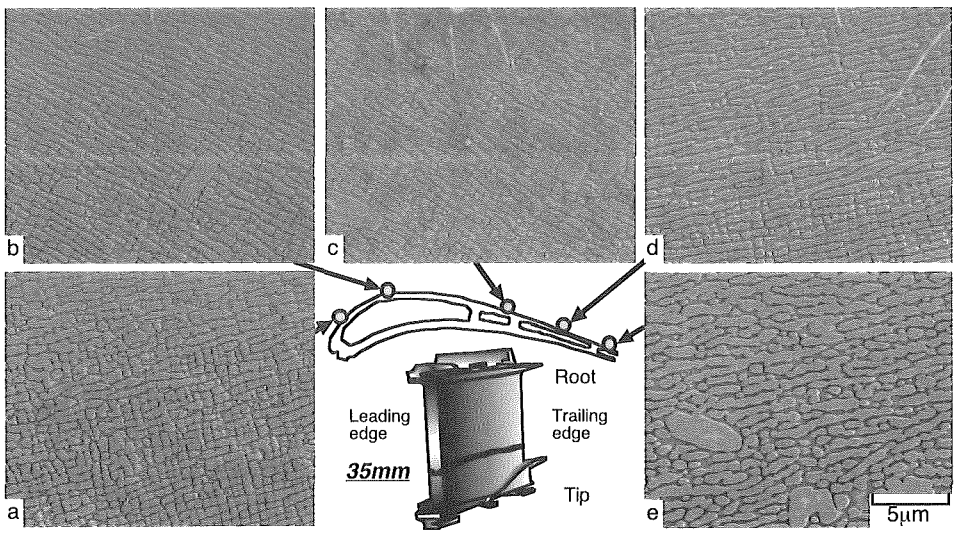

Fig.7. Scanning electron micrographs at the vicinity of the surface in the suction side of the 35mm part : (a) the leading edge, portion with the distance of (b) 11mm, (c) 33mm, (d) 44mm from leading edge and (e) trailing edge

is linearly compared with the other rafted structures (Fig.6-(c)). At the trailing edge sides, the rafted γ/γ' structures turn to its shape into the more complex one by connecting with each other in the random directions (Fig.6-(d) and (e)).

The scanning electron micrographs at the suction side of the 35mm part are shown in Fig.7. At the trailing edge sides, the incomplete rafted γ/γ' structures are observed (Fig.7-(d) and (e)). At the other

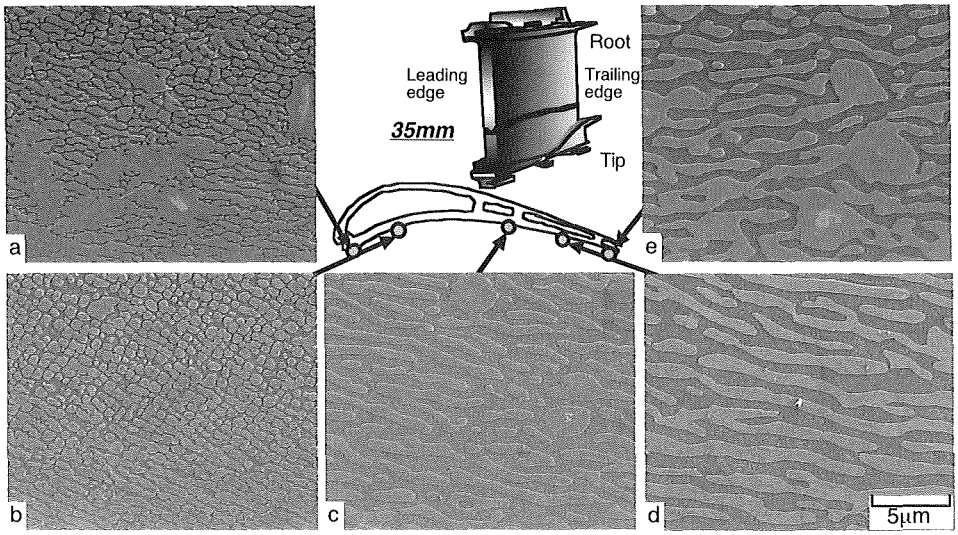

Fig.8. Scanning electron micrographs at the vicinity of the surface in the pressure side of the 35mm part : (a) the leading edge, portion with the distance of (b) 11mm, (c) 33mm, (d) 44mm from leading edge and (e) trailing edge

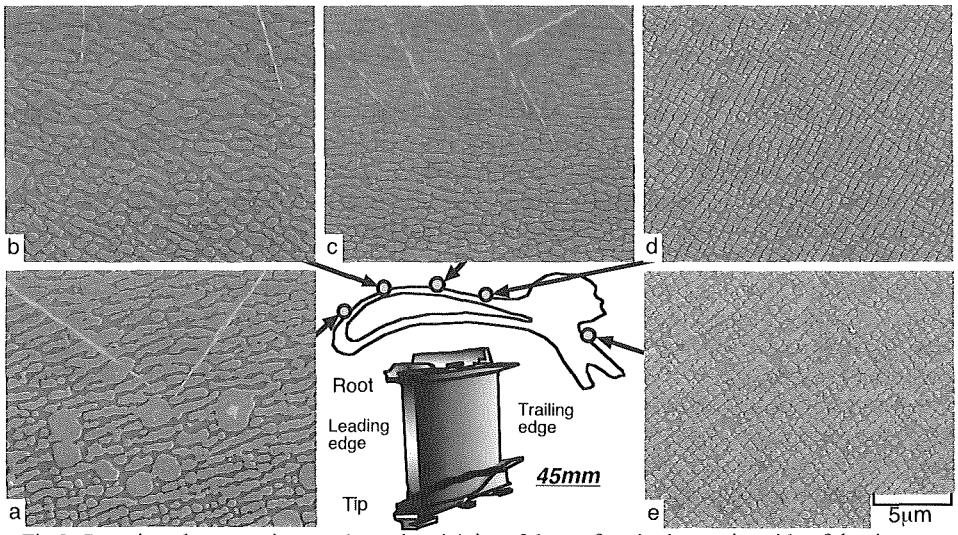

Fig.9. Scanning electron micrographs at the vicinity of the surface in the suction side of the tip part : (a) the leading edge, portion with the distance of (b) 11mm, (c) 33mm, (d) 44mm from leading edge and (e) trailing edge

portions, some of the cuobidal γ' precipitates contact with each other toward the parallel to the vane surface (Fig.7-(a)-(c)).

The scanning electron micrographs at the pressure side of the 35mm part are shown in Fig.8. At the portions with the distance of 33 and 44mm from the leading edge, the well aligned rafted γ/γ' plates parallel to the vane surface are observed, and the interface between the γ/γ' phase is straight (Fig.8-(c)

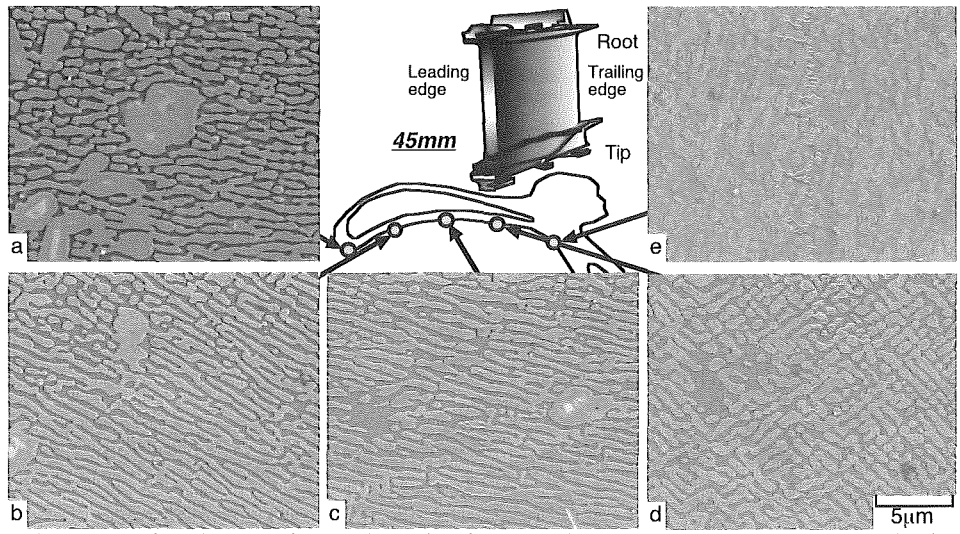

Fig.10. Scanning electron micrographs at the vicinity of the surface in the pressure side of the tip part : (a) the leading edge, portion with the distance of (b) 11mm, (c) 33mm, (d) 44mm from leading edge and (e) trailing edge

and (d)). The rafted γ/γ' structures collapse at the trailing edge, and the volume fraction of the γ' precipitates is decreased, and the width of γ channel is increased compared with that of the other portions (Fig.8-(e)).

The scanning electron micrographs at the suction side of the tip part are shown in Fig.9. At the leading edge side, the incomplete rafted γ/γ' structures are observed (Fig.9-(a)-(c)). On the contrary, at the trailing edge sides, most of the γ' precipitates keep cuboidal in shape (Fig.9-(e) and (f)).

The scanning electron micrographs at the vicinity of the surface of the five portions in the pressure side of the tip part are shown in Fig.10. At the leading edge, the incomplete rafted γ/γ' structures are observed (Fig.10-(a)). At the portions with the distance of 11 and 22mm from the leading edge, the well aligned rafted γ/γ' plates are observed. The volume fraction of the γ' precipitates is higher, and the width of the γ channel is smaller than those of with the same portions of the 25 and 35mm parts (Fig.10-(b) and (c)). At the portion with the distance of 33mm from the leading edge, the γ' precipitates contact with each other to the two specific directions (Fig.10-(d)). At the trailing edge, the volume fraction of the γ' precipitates are drastically reduced (Fig.10-(e)).

In this way, the marked morphological changes in the γ' precipitates are observed at the each part of the vane. The morphological changes of the cuboidal γ' precipitates will be thought to result from the different in the temperature and the stress distribution.

4. discussion

4.1 Temperature and stress distribution of vane in service

It is well understood that the cuboidal γ' precipitates in single crystal nickel-based superalloys with the orientation of [001] turn to a rafted one perpendicular to the tensile stress axis [8]-[12]. In our previous work, creep tests on [001] orientated single crystal nickel-based superalloy, CMSX-4, are conducted in a wide stress range from 100 to 600MPa at 1073-1323K, and the cuboidal γ' turned into rafts that are normal to the stress axis [11], [12]. It has been also elucidated that the morphology of rafted γ/γ'

structures depends on differ by changing the stress, temperature and creep testing time, and at lower stress sides, the shape of rafted γ/γ' interfaces are straight, while at the higher stress sides, wavy. In the case of simple aging at the high temperature, the cuboidal γ' in CMSX-4 is coarsened to the <100>, without rafting [13]. To investigate the correlation between the direction of the rafted γ/γ' structures and the orientation of crystal grains in a polycrystalline nickel-based superalloy, IN-100, the microstructure observation is carried out of the crept specimens at 1273K, 96-216MPa. The rafted γ/γ' structures formed as parallel to the {001} plane independent of the orientation of the crystal grains [14]. Based on the above evidence, the presence of the secondary γ' precipitates, and the morphology of the rafting including the shape of γ/γ' interfaces, the temperature and the stress distribution of the vane in service will be estimated.

Fig.11 shows the schematic illustration of the temperature and the stress distribution of the vane in service. The distribution from low temperature and low stress sides to high temperature and high stress sides is shown in shades from dark to light. At the suction side, the incomplete the rafted γ/γ' structures are observed at the trailing edge side, temperature and stress are relatively high. The surface is not exposed to the high temperature and high stress conditions at the other portions of the suction side where some of the cuobidal γ' precipitates contact with each other. At the leading edge sides of the root part where the many secondary γ' phase are precipitated in the γ matrix, the surface is exposed to the lowest temperature condition.

At the pressure side, it is suggested that the temperature and stress conditions are higher than those at the suction side because of the morphological change of γ' precipitates are more extensive. The temperature and stress are comparatively high at the trailing edge sides and the tip part of the pressure side where the well aligned rafted γ/γ' structures are observed. Especially, at the trailing edge side of the pressure sides of the 25 and 35mm parts where the rafted γ/γ' structures start to collapse, the surface is exposed to the highest temperature and highest stress conditions. At the leading edge sides of the pressure side of the root part where the cuboidal γ' precipitates still remain and a few secondary γ' precipitates exist in the γ matrix channels, the surface is not thought to be exposed to the high temperature and stress condition.

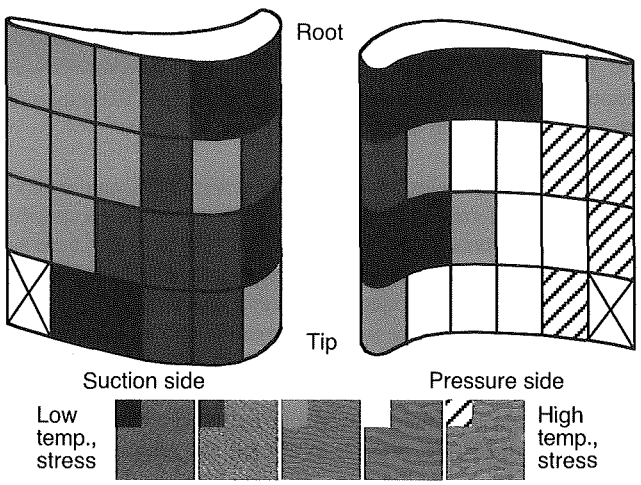

Fig.11. Schematic illustration of the distribution of the temperature and the stress of the 1st HPT vane in service

4.2 Stress direction of vane in service

As mentioned above, it is possible to estimate qualitatively the temperature and the stress distribution of the vane based on the morphology of γ' precipitates. It is well understood that the cuboidal γ' precipitates turn to a rafted one perpendicular to the tensile stress axis [8]-[12], and that the cuboidal γ' precipitates turn its shape to the rod-shaped structure parallel to the compressive stress axis [15]-[17].

Based on the above evidence and this experimental result, the stress direction of the vane in service will be evaluated.

Fig.12 shows the schematic illustration of the stress distribution and the stress direction of the vane in service. The length and the direction of the arrow show the stress magnitude and the stress direction.

Most of the cuboidal γ' precipitates contact each other toward the parallel to the outside surface at the vicinity of interface between the coating layer and the metal matrix of the vane. The rafted γ/γ' structures also appear in the direction parallel to the surface of the vane. This microstructure evidence indicates that the uniaxial tensile stress perpendicular to the vane surface and/or the multi-axial compressive stress parallel to the vane surface act on the vane in service are expected. The source of the stress for the vane in service will be discussed.

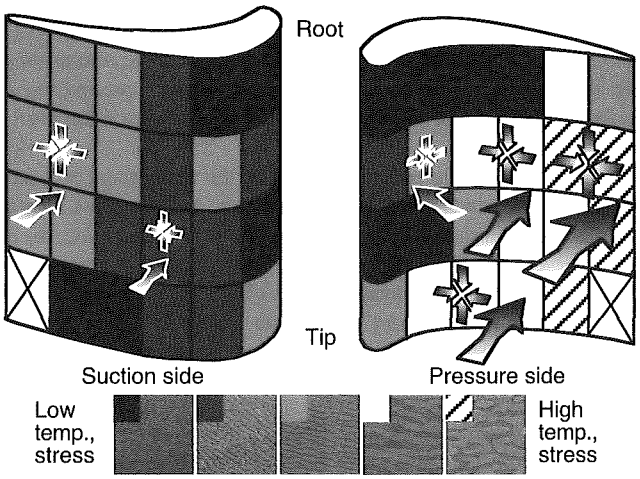

Fig.12. Schematic illustration of the stress distribution of the 1st HPT vane in service

The centrifugal stress by a rotation is not acting on the vane in service different from the turbine blade. Therefore, the formation of the rafted γ/γ' structures by the centrifugal stress is not considered. By the way, the vane surface was covered with the TBC to protect from the high temperature combustion gas. The matrix phase will be inhibited expansion, because the coefficient of thermal expansion of the coating layer (Al_2O_3) is lower than that of the metal matrix (γ). As a result, the multi-axial compressive stresses parallel to the vane surface is expected to act on the vane. The metal matrix temperature is also different between the matrix of the vane surface and the vicinity of the internal cooling channels. The appearance of the uniaxial thermal stress to the interior direction from the surface is supposed to result from the large temperature difference in the metal matrix.

From these results, it is possible to estimate the temperature and the stress distribution, and the stress directions of the 1st HPT nozzle guide vane based on the morphology of the γ' precipitates in the same way as the turbine blade. Consequently, the evidence that the large thermal stress with cooling is expected to act on the vane in service.

5. Conclusions

The morphology of γ' precipitates of a nickel-based superalloy serviced as the 1st HPT nozzle guide vane of the jet engine is investigated to estimate the temperature and the stress distribution, and the stress directions in service. The following conclusions are obtained.

1) Most of the γ' precipitates contacted each other toward the parallel to the vicinity of the interface in the vane. Especially, at the trailing edge of the pressure side of the middle parts, the rafted γ/γ' structures start to collapse.

2) The vane in service, at the leading edge sides of the pressure side of the 25 and 35mm parts are

structures depends on differ by changing the stress, temperature and creep testing time, and at lower stress sides, the shape of rafted γ/γ' interfaces are straight, while at the higher stress sides, wavy. In the case of simple aging at the high temperature, the cuboidal γ' in CMSX-4 is coarsened to the <100>, without rafting [13]. To investigate the correlation between the direction of the rafted γ/γ' structures and the orientation of crystal grains in a polycrystalline nickel-based superalloy, IN-100, the microstructure observation is carried out of the crept specimens at 1273K, 96-216MPa. The rafted γ/γ' structures formed as parallel to the {001} plane independent of the orientation of the crystal grains [14]. Based on the above evidence, the presence of the secondary γ' precipitates, and the morphology of the rafting including the shape of γ/γ' interfaces, the temperature and the stress distribution of the vane in service will be estimated.

Fig.11 shows the schematic illustration of the temperature and the stress distribution of the vane in service. The distribution from low temperature and low stress sides to high temperature and high stress sides is shown in shades from dark to light. At the suction side, the incomplete the rafted γ/γ' structures are observed at the trailing edge side, temperature and stress are relatively high. The surface is not exposed to the high temperature and high stress conditions at the other portions of the suction side where some of the cuobidal γ' precipitates contact with each other. At the leading edge sides of the root part where the many secondary γ' phase are precipitated in the γ matrix, the surface is exposed to the lowest temperature condition.

At the pressure side, it is suggested that the temperature and stress conditions are higher than those at the suction side because of the morphological change of γ' precipitates are more extensive. The temperature and stress are comparatively high at the trailing edge sides and the tip part of the pressure side where the well aligned rafted γ/γ' structures are observed. Especially, at the trailing edge side of the pressure sides of the 25 and 35mm parts where the rafted γ/γ' structures start to collapse, the surface is exposed to the highest temperature and highest stress conditions. At the leading edge sides of the pressure side of the root part where the cuboidal γ' precipitates still remain and a few secondary γ' precipitates exist in the γ matrix channels, the surface is not thought to be exposed to the high temperature and stress condition.

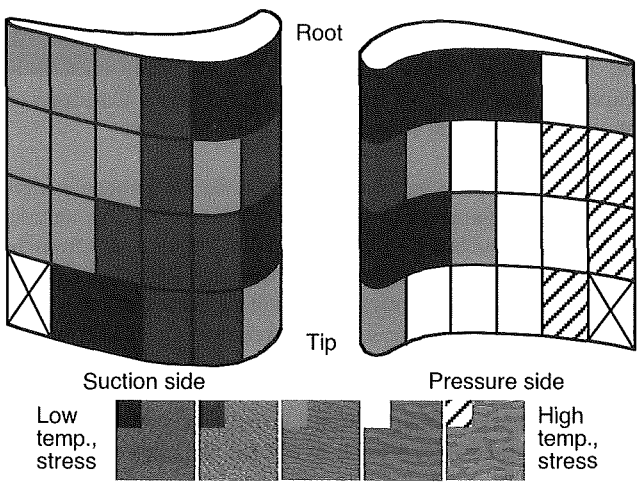

Fig.11. Schematic illustration of the distribution of the temperature and the stress of the 1st HPT vane in service

4.2 Stress direction of vane in service

As mentioned above, it is possible to estimate qualitatively the temperature and the stress distribution of the vane based on the morphology of γ' precipitates. It is well understood that the cuboidal γ' precipitates turn to a rafted one perpendicular to the tensile stress axis [8]-[12], and that the cuboidal γ' precipitates turn its shape to the rod-shaped structure parallel to the compressive stress axis [15]-[17].

Based on the above evidence and this experimental result, the stress direction of the vane in service will be evaluated.

Fig.12 shows the schematic illustration of the stress distribution and the stress direction of the vane in service. The length and the direction of the arrow show the stress magnitude and the stress direction.

Most of the cuboidal γ' precipitates contact each other toward the parallel to the outside surface at the vicinity of interface between the coating layer and the metal matrix of the vane. The rafted γ/γ' structures also appear in the direction parallel to the surface of the vane. This microstructure evidence indicates that the uniaxial tensile stress perpendicular to the vane surface and/or the multi-axial compressive stress parallel to the vane surface act on the vane in service are expected. The source of the stress for the vane in service will be discussed.

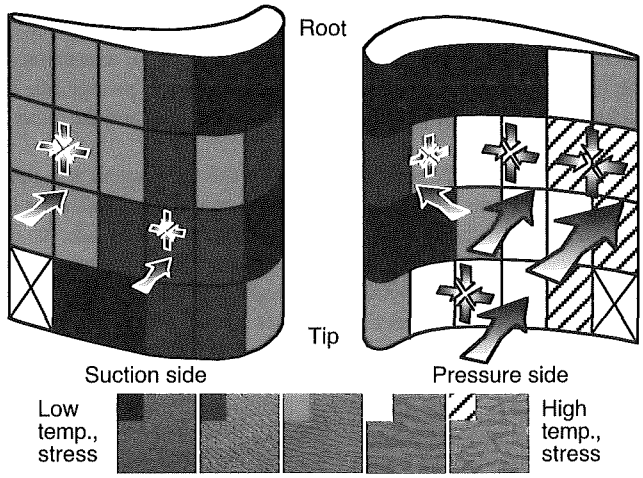

Fig.12. Schematic illustration of the stress distribution of the 1st HPT vane in service

The centrifugal stress by a rotation is not acting on the vane in service different from the turbine blade. Therefore, the formation of the rafted γ/γ' structures by the centrifugal stress is not considered. By the way, the vane surface was covered with the TBC to protect from the high temperature combustion gas. The matrix phase will be inhibited expansion, because the coefficient of thermal expansion of the coating layer (Al_2O_3) is lower than that of the metal matrix (γ). As a result, the multi-axial compressive stresses parallel to the vane surface is expected to act on the vane. The metal matrix temperature is also different between the matrix of the vane surface and the vicinity of the internal cooling channels. The appearance of the uniaxial thermal stress to the interior direction from the surface is supposed to result from the large temperature difference in the metal matrix.

From these results, it is possible to estimate the temperature and the stress distribution, and the stress directions of the 1st HPT nozzle guide vane based on the morphology of the γ' precipitates in the same way as the turbine blade. Consequently, the evidence that the large thermal stress with cooling is expected to act on the vane in service.

5. Conclusions

The morphology of γ' precipitates of a nickel-based superalloy serviced as the 1st HPT nozzle guide vane of the jet engine is investigated to estimate the temperature and the stress distribution, and the stress directions in service. The following conclusions are obtained.

1) Most of the γ' precipitates contacted each other toward the parallel to the vicinity of the interface in the vane. Especially, at the trailing edge of the pressure side of the middle parts, the rafted γ/γ' structures start to collapse.

2) The vane in service, at the leading edge sides of the pressure side of the 25 and 35mm parts are

exposed to the highest temperature and stress condition.
3) From these results, the evidence that the uniaxial tensile stress perpendicular to the vane surface and/ or multi-axial compressive stresses parallel to the vane surface is expected to act on the vane in service.

6. References

[1] M. Matsuoka, Aeronautics course 7, Jet Engine, Japan Aeronautical Engineers' Association, Tokyo, (2003), p.62
[2] H. Harada, Superalloys: Present and Future, JSPS Rep. of the 123rd Committee on Heat Resisting Metals and Alloys, 48(2007), p.357
[3] Y. Yoshioka, Evolution of Superalloys as Gas Turbine Materials and Perspective on the Future, JSPS Rep. of the 123rd Committee on Heat Resisting Metals and Alloys, 48(2007), p.365
[4] S. Walston, A. Cetel, R. MacKay, K. O'Hara D. Duhl and R. Dreshfield, Joint Development of a Fourth Generation Single Crystal Superalloy, Proc. of 10th Int. Symp. on Superalloys2004, (2004), p.15
[5] N. Miura, N. Harada, Y. Kondo and T. Matsuo, Morphological Change in γ' Phase in Different Portions of First Stage High Pressure Turbine Blade of PWA1480, Proc. of the 7th Liege Conf. on Mater. for Adv. Power Eng. 2002, (2002), p.245.
[6] N. Miura, K. Nakata, M. Miyazaki, Y. Hayashi and Y. Kondo, Morphology of γ' Precipitates in Second Stage High Pressure Turbine Blade of Single Crystal Nickel-based Superalloy After Serviced, Materials Science Forum, Vols. 638-642(2010), p.2291
[7] T. Fujimura, Materials Technology on Aircraft Gas Turbine Engines, Journal of the Gas Turbine Society of Japan, 32(2004), p.174
[8] T. M. Pollock and A. S. Argon, Creep resistance of CMSX-3 Nickel Base Superalloy Single Crystals, Acta Metall. Mater., 40(1992)1, p.1
[9] M. Fahrmann, E. Fahrmann, O. Paris, P. Fratzl and T. M. Pollock, An Experimental Study of the Role of Plasticity in the Rafting Kinetics of a Single Crystal Ni-base Superalloy, Proc. of the 8th Int. Symp. on Superalloysl996, (1996), p.191
[10] D. Mukhherji, H. Gabrisch, W. Chen, H. J. Fecht and R. P. Wahi, Mechanical Behavior and Microstructure Evolution in the Single Crystal Superalloy SC16, Acta Mater., 44 (1997), p.3143
[11] N. Miura, Y. Kondo and T. Matsuo, Stress Dependence of Strain Attained to Rafting of γ' phase in Single Crystal Nickel-based Superalloy, CMSX-4, Proc. of 9th Int. Conf. on Creep and Fracture Engineering Materials and Structures, (2001), p. 437
[12] Y. Hayashi, N. Miura and Y. Kondo, Creep Resistance of Single Crystal Nickel-based Superalloy, CMSX-4, at 1073K, Current Advances in Materials and Processes, 20(2007), p.1229
[13] N. Miura, K. Kurita, Y. Kondo and T. Matsuo, Change in Morphology of γ' of Prior-crept Single Crystal Nickel-based Superalloy, CMSX-4, With Simple Aging, Materials Science Forum Vol. 539-543 (2007), p.3024
[14] N. Miura, Y. Kondo and T. Matsuo, Rafted Structure of γ' phase in Polycrystalline Nickel-based Superalloy, IN-100, Subjected to Creep Deformation, Tetsu-to-Hagane, 90(2004), p.567
[15] U. Tetzlatt and H. Mughrabi, Enhancement of the High-temperature Tensile Creep Strength of Monocrystalline Nickel-based Superalloys by Pre-rafting in Compression, Proc. of the 9th Int. Conf. on Superalloys 2000, (2000), p.273
[16] L. Shui, S. Tian, T. Jin. and Z. Hu, Influence of Pre-compression on Microstructure and Creep Characteristic of a Single Crystal Nickle-9base Superalloy, Mater. Sci. and Eng. A, 418(2006), p.229
[17] K. Nakada, N. Miura and Y. Kondo, Change in Morphology of γ' Precipitates and Dislocation Substructure of a Single Crystal Nickel-based Superalloy, CMSX-4, with Compressive Creep Deformation, JSPS Rep. of the 123rd Committee on Heat Resisting Metals and Alloys, 50(2009), p.219

9th Liege Conference : Materials for Advanced Power Engineering 2010
edited by J. Lecomte-Beckers, Q. Contrepois, T. Beck and B. Kuhn.

PRECIPITATION OF TCP – PHASES IN NI-BASE ALLOYS WITH HIGH CHROMIUM CONTENT

G.D. Pigrova

Central Boiler and Turbine Institute
Polytechnicheskaya 24, 194021, St.Petersburg, Russia

Abstract

The method of physical-chemical phase analysis has been used to investigate the structure, composition and amount of different phases for several commercial alloyed materials. Phase diagram in the temperature range 750-1100 ^{0}C for high-temperature Ni-base alloy has been achieved. The main phase reactions during long-time ageing are carbide reaction MC $\rightarrow$ $M_{23}C_6$ and σ-phase formation. The σ-phase formation mechanism established shows that the process kinetics are also approximated by Johnson-Mell equation as it is in case of σ-phase formation in stainless steels.

Keywords: Ni-base alloys, phase diagram, σ-phase formation

Introduction

The data for phase composition of industrial materials and the influence of various factors on structural stability of a metal are important, in so far as the temperature of phase transformation may be in the operating temperature range.

Gas turbine blades operating at high temperatures are generally fabricated from nickel-base alloys containing different amounts of Al, Cr, Co, Mo, W and other elements. The problem of TCP (topologically closed packed) phase precipitation in nickel-base alloys draws attention on the negative effect on material plasticity in connection with the alloy composition getting more complicated. The most widely spread representative of this structure in complex alloys is σ-phase [1].

Experimental details

The composition of Ni-base alloy melting (17.7% Cr; 5.3% Co, 5.3% Mo, 3.3%W, 3.8% Al, 2.3% Ti, 1.4% Nb, 0.10% C, 0.15% Si, 0.04% B) was studied during aging in temperature range of 750-1100 ^{0}C after homogenization at 1180^{0}C.

The study was performed by a method of physical-chemical phase analysis. Electrolytic precipitation of second phases (carbides, borides and TCP-phases) was carried out in methanol solution of HCl with cooling the electrolyte. Phase structures were determined by X-ray diffraction. Temperature-time transition diagrams are obtained from X-ray analysis results. The composition and content of the electrochemically separated phases were determined using chemical photometric analysis.

Results and discussion

High-temperature alloys of this type are multiphase and exhibit the occurrence of several types of different phases: Ni_3Al-based γ′-phase, carbide phases of the MC, $M_{23}C_6$ and M_6C type, TCP-phases of σ- or μ-phases and boride phases. The conditions for σ-phase formation develop after precipitation of the major strengthening γ′-phase (type Ni_3Al).

The as-melted alloy comprises γ'-phase, Ti- and Nb-based MC-type carbide and M_3B_2 type boride phase. After homogenization the phase composition of the alloy remains unchanged at any of investigated temperatures (1120, 1150 and 1180 ^{0}C). The Cr-base $M_{23}C_6$ carbide forms during subsequent tempering at temperature below 1000 ^{0}C. In order to determine time-temperature ranges of σ-phase existence in the alloy, a phase diagram for temperature range from 750-1100 ^{0}C has been developed (Fig. 1). σ-phase is instable at temperatures over 950 ^{0}C. Study of its formation kinetics was carried out at 800 and 900 ^{0}C.

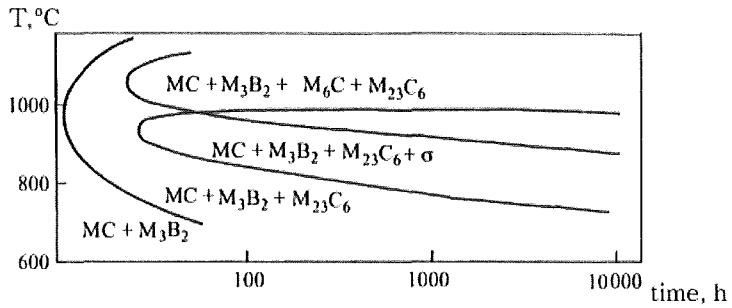

Fig. 1. TTT diagram for Ni-base alloy

Ageing at 800^{0}C. At this temperature the formation of 40% γ'-phase is observed after 500 hours. Ageing for 500 hrs after any heat treatment leads to the formation of MC, $M_{23}C_6$-type carbides and M_3B_2-type boride phases. The phase composition remains the same until 500 hours of ageing. Second phases contents are increasing as a function of ageing time. The σ-phase formation at 800 ^{0}C started after ageing for 500 hours, the quantity of Cr and Mo bound in the second phases is growing substantially from 1.5% to 7%. After ageing during 1000 and 3000 hours σ-phase precipitates over the entire grain field growing. Molybdenum precipitation becomes stabilized by 5000-7000 hours; chromium continues to precipitate during up to 10000 hours. Since that time of ageing the titanium content in second phases begins to decrease, which is an indication of MC decomposition.

The X-ray lines of phases after 15000 hours ageing show that MC carbide lines are practically absent, the intensity of $M_{23}C_6$ carbide lines being growing. This points out to the $M_{23}C_6$ carbide formation during ageing. Decrease in amount of MC carbide on further ageing is caused by MC carbide decomposition and formation of $M_{23}C_6$ carbide.

Ageing at 900^{0}C. γ'-phase amount is 36-37% at this temperature. σ-phase forms more vigorously and is found to occur after 50 hours of ageing at any heat treatment behavior. The phase composition of all specimens under various heat pre-treatment conditions remains the same after 500 hours of ageing. Second phases have 3% of bound Cr and 2% of bound Mo. Decrease in amount of MC carbide of further ageing is caused by MC carbide decomposition and formation of $M_{23}C_6$–type carbide.

The comparison of phase conversation kinetics at 800 and 900 ^{0}C shows a variety of time spans of phase reactions. At 800 ^{0}C the σ-phase precipitation phase reaction is initiated at the ageing time interval of 500-1000 hours, while at 900 ^{0}C the onset of σ-phase precipitation falls within 30-50 hours. The preliminary temperature of tempering has an effect only at initial stages of ageing. Another major phase mechanism is MC carbide decomposition and $M_{23}C_6$ formation

during ageing. At 800 ^{0}C the process becomes observable after 10000 hours of ageing. At 900 ^{0}C the reaction MC→ $M_{23}C_6$ actively developing after 1000 hrs ageing. σ-phase is instable at temperatures over 950 ^{0}C.

By using the results of a quantitative composition analysis of second phases and X-ray diffraction methods of determining separately σ-phase and $M_{23}C_6$ carbide quantities [2], data on σ-phase content can be obtained to draw σ-phase formation versus time/temperature plot (Fig. 2). With decreasing ageing temperature the incubation period for σ-phase appearance increased. Also increases the amount of equilibrium σ-phase.

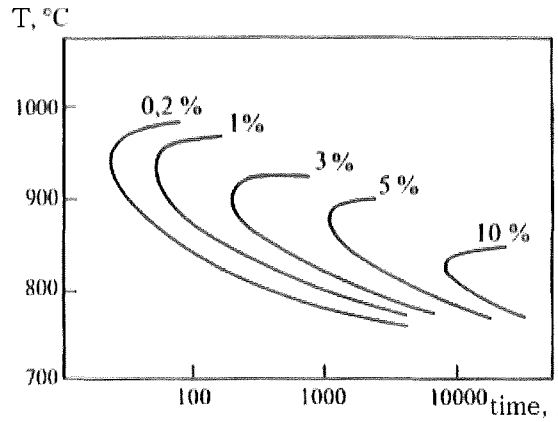

Fig. 2. Diagram of σ-phase content in the alloy

The experimental data obtained for σ-phase amount/time relationship may be analyzed considering the formal kinetic theory of transformations [3]. The time dependence of decomposition fraction is most frequently approximated by Johnson-Mell equation $\varsigma=1-\exp(-kt^n)$, where $\varsigma=V/V\infty$ – fraction of decomposition at time t. In order to analyze the experimental results a lg ln $(1/[1-\varsigma])$ versus lg t plot is used, which is here a straight line with slope n.

By using data for σ-phase amount during ageing at 800 ^{0}C and 900 ^{0}C has been built lg ln $(1/[1-\varsigma])$-lg t (Fig 3). The relationships are straight lines at n=1, which is an indicative of the fact that σ-phase precipitation is equal at 800 and 900 ^{0}C and may be interpreted based on Johnson-Mell equation.

The same results have been obtained in kinetic studies of σ-phase precipitation in stainless steels [4]. This suggests that mechanism of σ-phase formation in nickel-base alloy is similar to that in stainless steels and may be the same in alloys with different composition.

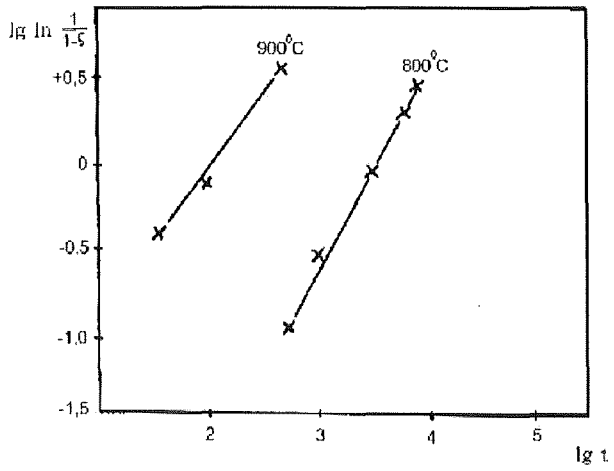

Fig.3. The lg ln 1/[1-ς] as a function of lg t for σ-phase formation at 800 and 900 ^{0}C

Generally, the main phase reactions during long-term ageing are carbide reaction MC→ $M_{23}C_6$ and σ-phase formation. At 800 ^{0}C the reaction MC→ $M_{23}C_6$ becomes observable after 10000 hours of ageing; at 900 ^{0}C reaction MC→ $M_{23}C_6$ is starting after 1000 hours. At 800 ^{0}C the σ-phase precipitation is initiated at the aging time interval of 500-1000 hours, while at 900 ^{0}C the onset of σ-phase precipitation falls within 30-50 hours.

Conclusions

1. The method of physical-chemical phase analysis has been used to investigate the structure, composition and amount of different phases for commercial Ni-base alloy.

2. The main phase reactions during long-term ageing of Ni-base alloys with increased chromium content are σ-phase formation and carbide reaction MC→ $M_{23}C_6$.

3. At 800 ^{0}C the reaction MC→ $M_{23}C_6$ becomes observable after 10000 hours of ageing, at 900 ^{0}C is actively developing after 1000 hours of ageing.

4. The dependence of σ-phase precipitation shows that the process can be treated by the equations from formal transformation kinetics theory.

References

[1] Ch.T.Sims, N.S.Stoloff, W.C. Hagel. Superalloys 11, 1987.
[2] J.K.L.Lai, J.F.Calbrait, J.Mat.Sci., 15,p.p.1297-1305, (1980).
[3] J.W.Christian, The Theory of Transformation in Metals and Alloys, London (1965).
[4] J. Barcik, Met. Trans., 14A, p. 635-647, (1983).

9th Liege Conference : Materials for Advanced Power Engineering 2010
edited by J. Lecomte-Beckers, Q. Contrepois, T. Beck and B. Kuhn.

STUDY ON THE HOT CORROSION BEHAVIOR OF A CAST NI-BASE SUPERALLOY

W. Wang, J.T. Guo*, J. Zhang, C. Yuan, L.Z. Zhou, Z.Q. Hu
Institute of Metal Research, Chinese Academy of Sciences, 72 Wenhua Road,
Shenyang 110016, China

Abstract

Hot corrosion behavior of Nickel-base cast superalloy K447 in 90% Na_2SO_4 + 10% NaCl melting salt at 850°C and 900°C was studied. The hot corrosion kinetic of the alloy follows parabolic rate law under the experimental conditions. The external layer is mainly Cr_2O_3 scale which is protective to the alloy, the intermediate layer is the Ti-rich phase, and the internal layer is mainly the internal oxides and sulfides. With increased corrosion time and temperature, the oxide scales are gradually dissolved in the molten salt and then precipitate as a thick and non-protective scale. Chlorides cause the formation of volatile species, which makes the oxide scale disintegrate and break off. The corrosion kinetics and morphology examinations tend to support the basic dissolution model for hot corrosion mechanisms.

Keywords: Ni-base superalloy; hot corrosion; basic dissolution mechanism

1. Introduction

Superalloys for gas turbine hot-end component applications are often failed as a result of severe hot corrosion. Sulfate, halides and some other salt contamination, which exist in industrial environments or marine atmosphere, are the main reasons for the hot corrosion. At present, the vulcanization-oxidation mechanisms and acid-base melting mechanisms of hot corrosion are widely accepted by many researchers[1-7]. However, due to the complex influence factors [8], the hot corrosion resistance of alloys may vary a lot under different conditions. Therefore, for a new material, it is necessary to test the hot corrosion resistance for industrial application.

The cast Ni-base superalloy K447 is a newly developed vane material for gas turbine. It has good mechanical properties and oxidation resistance in the service temperature, but its hot corrosion behavior in Na_2SO_4+NaCl molten salt mixture has not been reported so far. So, the hot corrosion behavior of the alloy in the molten salt mixture was studied in this paper.

2. Experimental method

The chemical composition of K447 is shown in Table 1 (mass%). The alloy bars

*Corresponding author. Tel.: +86 24 83971907; fax: +86 24 83978045.
E-mail address: jtguo@imr.ac.cn (J.T. Guo).

Table 1 Chemical composition of K447(mass%)

C	Cr	Co	W	Al	Ti	Nb	Ta	B	Zr	Ni
0.16	17.88	19.20	5.93	1.97	3.78	1.09	1.33	0.06	0.03	Bal

were heat treated at 1200°C/2h/AC+1030 °C/2h/AC+1000 °C/4h/AC+870°C/24h/AC. The size of samples for hot corrosion tests was 10mm×10mm×3mm. The samples were burnished with SiC abrasive papers, and then cleaned in ethanol with ultrasonic, and finally weighed with DTA 100 photoelectric balance. The corrosion tests were performed in a resistance furnace and the samples were immersed in the molten salt mixture of 90%Na_2SO_4+10%NaCl at 850°C and 900°Cwith the times of 5h, 10h, 20h, 50h and 100h, respectively. Corrosion products were removed from the tested samples and weight loss were computed. Each experimental data was the average of readings of three samples. The composition and morphology of corrosion products were studied with X-ray diffraction and scanning electron microscope.

3. Results and discussion

3.1 Hot corrosion kinetics

Figure 1 shows the corrosion kinetics curve of K447 alloy in the 90% Na_2SO_4 + 10% NaCl molten salt at 850°C. It can be seen that the weight loss rate even reaches 52 mg/cm2 when the corrosion time is up to 100 h, which is much larger than the weight gain rate of 5 mg/cm 2 when the alloy is oxidized at the same condition. Clearly, the presence of the molten salt mixture severely accelerated the oxidation of the alloy.

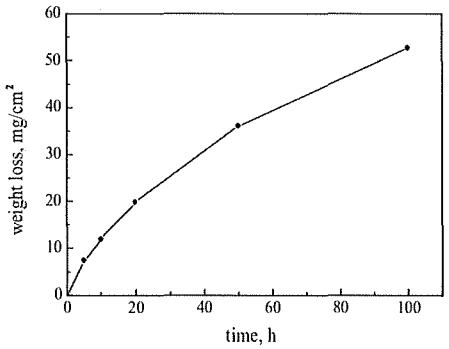

Fig.1 Kinetics Curves of hot corrosion of K447 alloy in the molten salt mixture of 90% Na_2SO_4 + 10% NaCl at 850°C

In Figure 2, the curve of square of weight loss vs. time approaches the straight line,

suggesting that the relationship between the weight loss and corrosion time follows the parabolic law basically. At the initiation, the alloy is oxidized rapidly and a protective oxide layer forms gradually; then, the corrosion rate slows down due to the obstacle of the oxide layer. The catastrophic corrosion process [] don't occur in current experiment because of the good resistance of the alloy to hot corrosion.

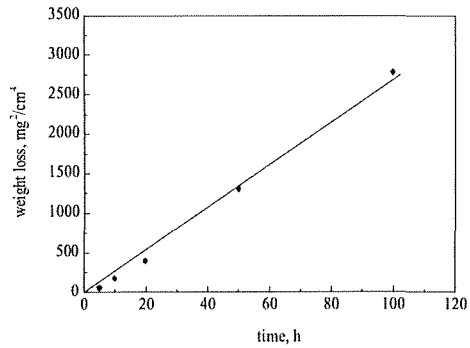

Fig. 2 Square of weight loss vs. time curve of K447 alloy in the molten salt mixture at 850°C

3.2 Corrosion product examinations

3.2.1 X-ray examination

The specimens hold in the molten salt at 850°C for 20 h and 50 h is examined with X-ray diffraction and the results are summarized in Table 2. It can be seen that the corrosion products consist of the various oxides and sulphides, such as NiO, TO_2, Cr_2O_3 and Cr 2S3, and so forth. In the 20 h samples, Cr_2S_3 is the only sulphide, while in the 50 h ones, more kinds of sulphides, e.g. NiS, CoS and TiS, take place, seeming to suggest that Ni, Co, and Ti are attacked more difficult by S than Cr. In addition, Al_2O_3 and Al_2S_3 are present in the 50 h samples, whereas they do not occur in the 20 ones, suggesting that Al is more resistant to O and S attack than Cr.

Table 2 Corrosion products of K447 alloy in the salt mixture of 90% Na_2SO_4 + 10% NaCl at 850°C for different times

Time/h	Corrosion products					
20	Cr_2O_3	NiO	TiO_2			
	$NiCr_2O_4$	Cr_2S_3				
50	Cr_2O_3	NiO	TiO_2	Al_2O_3	CoO	$NiCr_2O_4$
	Cr_2S_3	Cr_3S_4	TiS	Al_2S_3	NiS	CoS

The X-ray diffraction results of the specimens hold in the molten salt for 100 h at 850°C and 900°C are shown in Table 3. At It can be seen that the surface oxide is still mainly Cr_2O_3 after

100 hours, and the increase of diffraction peak indicates the increase of its level. There also exists a clear diffraction peak of $NiCr_2O_4$. Sulfides types and concentration are greatly increased, mainly NiS, CoS, TiS_3, Al_2S_3. When temperature reaches 900°C, the composition of corrosion products becomes more complex, and the type of sulfide increases as the temperature increases, also the diffraction peak intensity increases. All of these phenomena indicate that sulfuration becomes more serious at 900°C.

Table 3 Corrosion products of K447 alloy in the salt mixture of 90% Na_2SO_4 + 10% NaCl at different temperatures for 100h

Temperature / °C	Corrosion products					
850	Cr_2O_3	TiO_2	$NiCr_2O_4$	Cr_2S_3	TiS_3	
	Al_2S_3	NiS	CoS			
900	Cr_2O_3	NiO	$NiCr_2O_4$	Al_2O_3	CoO	TiO_2
	Cr_2S_3	Cr_3S_4	TiS	Al_2S_3	NiS	CoS

3.2.2 Morphology of cross-section of corrosion layer

Figure 3 shows the morphology and elements distribution of samples cross-section of K447 alloy, in 90% Na_2SO_4+10%NaCl molten salt, at 850°C, after 100h corrosion. Surface corrosion layer is divided into three layer basically. It is shown that Cr_2O_3 is the main composition of outer layer, and some $NiCr_2O_4$ also exits. They were relatively continuous and compact, so they played protective role at the early stage of corrosion. But after 100h corrosion, they became loose and porous to be conductive to the spread of oxygen and sulfur, and accelerate the oxidation and sulfide of alloy. The middle layer was mainly composed of TiO_2, and some Al_2O_3. Its thickness was about 5μm. Internal oxide and sulfide, which are in-depth within the matrix, make up of the inner layer. Oxide is mainly Al_2O_3, TiO_2. Its thickness is deep relatively, reaching tens of μm. It can be seen that there is a small mount of sulfur element in the outer layer from the elements distribution map of sulfur. In addition to remains of Na_2SO_4, there should be a small amount of chrome or nickel sulfide. The experimental results show that the diffusion coefficient of sulfur is larger. So sulfur can easily diffuse into the matrix inside along the grain boundaries, and form sulfide easily at the grain boundaries.

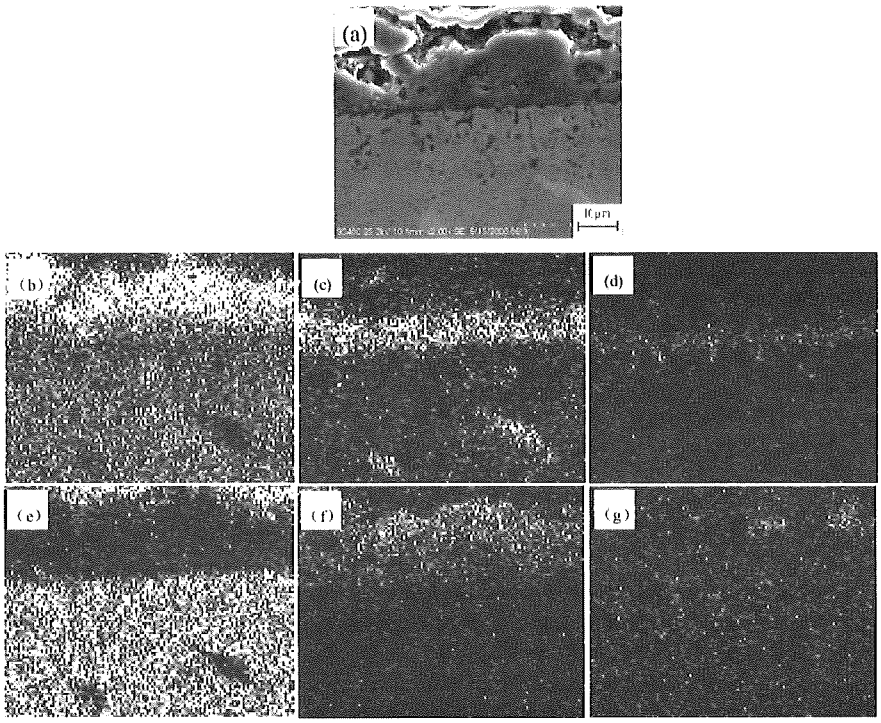

Fig. 3 Cross-sectional SEM micrograph and its element maps of K447 superalloy after hot corrosion for 100h in 90%Na_2SO_4+10%NaCl melting salt at 850°C (a-SE; b-CrKα; c-TiKα; d-AlKα; e-NiKα; f-Okα; g-SKα)

Figure 4 shows the morphology and elements distribution of samples cross-section of K447 alloy, in 90% Na_2SO_4+10%NaCl molten salt, at 900°C, after 100h corrosion. It can be seen from Figure 4(a), at 900°C, the corrosion layer becomes thicker but more loose than at 850°C. The oxide layer loses the role of protection as a result of its serious cracking. It provides the diffusion of oxygen and sulfur with channel. It can be seen that internal oxidation and sulfuration are quite serious, with a thickness increase of nearly 20μm more than 850°C. The main internal oxide is Al_2O_3. Interalnal oxidation also leads to the separation between the oxide layer and matrix.

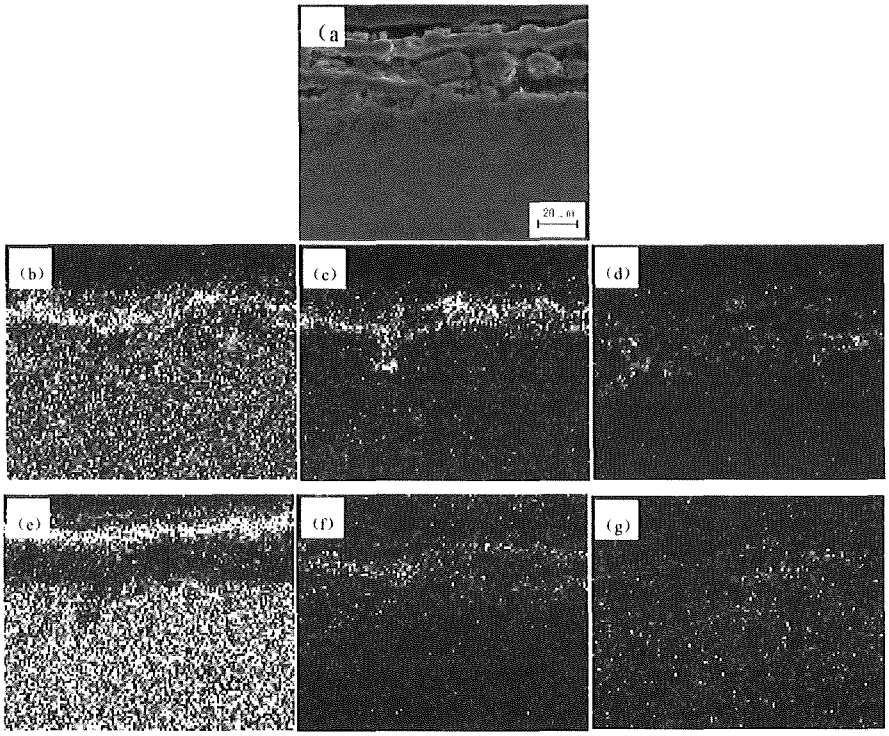

Fig. 4 Cross-sectional SEM micrograph and its element maps of K447 superalloy after hot corrosion for 100h in 90%Na2SO4+10%NaCl melting salt at 850°C a-SE; b-CrKα; c-TiKα; d-AlKα; e-NiKα; f-Okα; g-SKα)

3.3 Discussion

Above 850°C, 90% Na_2SO_4+10%NaCl mixed salt is completely melted. There exist two equilibriums in the molten salt:

$$Na_2SO_4 = 2Na^+ + O^{2-} + SO_3$$

$$2SO_3 = 2S + 3O_2$$

First, the selective sulfuration and oxidation occurred in the surface of alloy, and Cr_2O_3 oxide layer formed. Ti-rich layer formed under Cr-rich layer along with the infiltration of oxygen, because it was difficult for Ti to generate the corresponding Ti sulfide.

As the progress of oxidation, the oxygen pressure decreased while sulfur pressure increased. So sulfur diffused into alloy matrix through the oxide film and generated sulfide.

$$3S + 2Cr = Cr_2S_3$$

$$2S + 3Ni = Ni_3S_2$$

The diffusion of sulfur is a key factor in hot corrosion. The generation of sulfide destroyed the reasonable composition of alloy elements to accelerate the oxidation of the alloy matrix. In addition, the sulfide is more easily oxidized than the metal to form loose discontinuous

oxidation products. Such internal oxidation destroyed the combination between oxide layer and matrix seriously.

$$2Cr_2S_3 + 9O_2 = 2Cr_2O_3 + 6SO_2$$

Along with the progress of reaction, the large consumption of sulfur in sodium sulfate led to the rise of oxygen pressure, as a result, oxidation went on. The continuous generation of the corresponding oxides of elements resulted in the continuous thickening of oxide layer. In molten salt, alkalinity enhanced, because of the reletive increase of O^{2-}, resulted in the alkaline melting of oxide film to form $NiCr_2O_4$ and Na_2CrO_4 which was volatile:

$$Cr_2O_3 + 2O^{2-} + 3/2O_2 = 2CrO_4^{2-}$$

$$Cr_2O_3 + O^{2-} = 2CrO^{2-}$$

On the other hand, on the interface of the molten salt and air, the level of O^{2-} decreased and the oxygen pressure rised, so that a negative gradient of O^{2-} formed in the molten salt. It made that CrO_4^{2-} and CrO^{2-} decomposed along with their diffusion outward, as a result, the two reactions above carried out left to precipitate loose Cr_2O_3 without protective role. It provided a fast channel for the diffusion of metal, oxygen and sulfur to accelerate the corrosion of alloy.

NaCl in molten salt aggravated the corrosion of alloy [9,10]. On the one hand, NaCl directly reacted with Cr_2O_3 on the surface of alloy:

$$6NaCl + Cr_2O_3 = 2CrCl_3\uparrow + 3Na_2O$$

On the other hand, NaCl got to the front of alloy matrix through the oxide layer to reacted with Cr2O3 as following reaction:

$$4NaCl + 2Cr_2O_3 + 3O_2 = 2Na_2CrO_4 + 2CrO_2Cl_2$$

$$4NaCl + Cr_2O_3 + 2SO_3 + 3/2O_2 = 2CrO_2Cl_2 + 2\ Na_2SO_4$$

Gaseous CrO_2Cl_2 had high volatility, which led to the formation of hole or even fragmentation of oxide layer, to accelerate corrosion of alloy. It was difficult to detect the presence of CrCl3 and CrO2Cl2 in the specimens of corrosion, because they were volatile or easily to convert into chromate.

As the consumption of Cr element, the corrosion of other elements such as Ni, Co, Al also occured to produce corresponding sulfide and oxide.

To sum up, the hot corrosion mechanism of K447 alloy complyswith the basic dissolution mechanism.

4. Conclusion

i) The curve of hot corrosion kinetics of K447 in 90% Na_2SO_4+10%NaCl molten salt with 100 hours at 850°C follows the parabolic law basically. K447 alloy has good resistant to hot corrosion under such experimental conditions. When test temperature raises to 900°C, the corrosion weight loss increases.

ii) At 50°C, the corrosion layer is divided into three basic areas. The outer layer, mainly Cr_2O_3, containing some $NiCr_2O_4$, about 10μm, is relatively continuous and compact to has a certain degree of protection for the alloy matrix. Intermediate zone is titanium-rich oxide, with relatively thinner thickness of about 3~5μm, which can inhibit the diffusion of oxygen and sulfur to a certain degree. The inner area is made up of oxide and sulfide that is deep within the matrix of alloy. The oxide is mainly Al_2O_3, with relatively thicker thickness. It is discontinuous to decrease the adhesion of oxide layer and increase the brittleness. At 900°C, the serous fragmentation of oxide layer leads to decrease the resistant to oxidation. The surface oxide layer, under the action of molten Na_2SO_4, dissolves and re-precipitates to form

loose and non-protective oxide. The hot corrosion mechanism complys with the basic dissolution mechanism. The presence of NaCl increases the corrosion of alloy.

References

[1] Zhao S Q, Xie X S, Smith G. D. The Oxidation Behavior of the New Nickel-Based Superalloy Inconel 740 with and without Na2SO 4 Deposit[J]. Surf. Coat. Tech, 2004 , 185: 178-183.

[2] Wang C J, Lin J S. The Oxidation of MAR M247 Superalloy with Na2SO 4 Coating. Mater[J]. Chem. Phys., 2002, 76: 123-129.

[3] Li Y, Guo J T, Yuan C, Yang H C. Xu N, Shen Z M. Hot corrosion of nickel-base cast superalloy K35 at 800°C[J]. Journal of Chinese Society for Corrosion and Protection, 2005, 25(4): 250-255.

[4] Hiramatsu N, Uematsu Y, Tanaka T, Kinugasa M. Effects of Alloying Elements on NaCl-induced Hot Corrosion of Stainless Steels[J]. Mater. Sci. Eng. A, 1989 , 120: 319-328.

[5] Deb D, Iyer S R, Radhakrishnan V M. A Comparative Study of Oxidation and Hot Corrosion of a Cast Nickel Base Superalloy in Different Corrosive Environments[J]. Mater. Lett., 1996, 29: 19-23.

[6] Simons E L, Browning G. V, Liebhafsky H A.. Sodium Sulfate in Gas Turbines[J]. Corrosion, 1955, 11: 505t-514t.

[7] Goebel J A, Pettit F S, G. W Goward. Mechanisms for the Hot Corrosion of Nickel-Base Alloys [J]. Metall. Trans., 1973, 4: 261-278.

[8] Li M S.High-Temperature Corrosion of Metal[M]. Beijing: Metallurgical Industry Press, May, 2001,5

[9] Gurrappa I. Hot Corrosion Behavior of CM 247LC Alloy in Na2SO 4 and NaCl Environments[J].Oxid. Met., 1999, 51(3): 353-382.

[10] Long X Q. Mechanism of Hot Corrosion in High Temperature Parts of Aeroengine[J]. Total corrosion control, 2003, 17(2): 9-13.

9th Liege Conference : Materials for Advanced Power Engineering 2010
edited by J. Lecomte-Beckers, Q. Contrepois, T. Beck and B. Kuhn.

CREEP CURVE MODELLING OF A CONVENTIONALLY CAST NICKEL BASE SUPERALLOY

*V. Lupinc, *M. Maldini, E. Poggio, E. Vacchieri

*CNR – IENI
Via Cozzi 53, 20125 Milano, Italy

°ANSALDO ENERGIA S.p.A.
Via Nicola Lorenzi 8, 16156 Genova, Italy

Abstract

Constant load creep tests on René80, a nickel base superalloy for gas turbine blade application, were run in the temperature interval 800-950°C with applied stresses producing rupture times up to 10000 h.
Creep curves are generally dominated by a long accelerating/tertiary creep that follows a relatively small decelerating/primary creep. No steady state stage has been observed. Analysis of the creep curves has shown that a single damage parameter can describe the long accelerating/tertiary stage in the explored temperature range. The damage appears to be dependent on the accumulated creep strain and, as a first approximation, independent on the applied stress and temperature.
The whole creep curve, primary and tertiary stages, has been modelled by a simple set of coupled differential equations obtained using the formalism of the Continuum Damage Mechanics. The proposed set of equations has an analytical solution, strain vs. time, for creep curves at constant temperature and stress.

Keywords: creep, superalloy, constitutive equation

1. Introduction

Creep is one of the most critical factors in life prediction and design of advanced gas turbine components such as blades. Since stress rupture characterisation only is often insufficient to proper component design, there is demand for accurate description of the complete creep curve, that can not be simply approximated using the minimum creep rate dependence on the applied stress and temperature.

The work reported in this paper is mainly focused on the capability of a set of constitutive equations of describing the creep behaviour of René80, a conventionally cast nickel base superalloy for gas turbine blade applications. In this approach, models of creep mechanisms, operating in the studied alloys, are reformulated using the Continuum Damage Mechanics (CDM) formalism to obtain a set of differential equations describing the evolution of strain rate, $\dot{\varepsilon}$, and of the relevant state variables s_i, that control the creep strain rate:

$$\dot{\varepsilon} = f1(\sigma, T, s_1, s_2, \ldots)$$
$$\dot{s}_1 = f2(\sigma, T, s_1, s_2, \ldots)$$
$$\dot{s}_2 = f3(\sigma, T, s_1, s_2, \ldots)$$

The approach, proposed by Asbhy and Dyson [1], allows to choose a set of differential equations able to describe the actual damage mechanisms operating in the material, and not a single set of differential equations for every material and stress/temperature condition.

2. Materials and experimental procedures

The tested material is a polycrystalline Ni-base superalloy, René80, reinforced by a bimodal distribution of γ' particles, with excellent high temperature strength and microstructure stability. The alloy is suitable for component applications operating at high temperatures, and it is used for blades in gas turbines. The chemical composition of the studied heat is reported in Table1.

The heat treatment steps for this alloy are: solution, two steps of stabilization and ageing for secondary γ' precipitation.

The creep tests have been carried out at constant load and in air, on solid cylindrical specimens having 5.6 mm gauge diameter and 28 mm gauge length that were machined off, after the heat treatment, from cast bars of 16 mm diameter. Creep strain was continuously monitored using a pair of capacitive transducers connected to extensometers clamped to ridges delimiting the specimen gauge length. Over 200 strain/time readings were automatically recorded throughout each creep test. Three thermocouples were placed on the specimen gauge length allowing to control the temperature and its gradients. The three zones furnace was controlled by the central thermocouple.

2. Creep results and modelling

The alloy was crept at 800, 850, 900 and 950°C and stresses between 100 and 500 MPa in order to have times to rupture up to 10,000 h. No plastic deformation during the initial loading has been detected. Examples of creep curves as ε *vs.* time, log $\dot{\varepsilon}$ *vs.* ε and $\dot{\varepsilon}$ *vs.* ε. are plotted, in Fig. 1.

The René80 superalloy, as many complex engineering alloys for high temperature applications, does not exhibit a steady state stage, but, at all the present experimental conditions, a quite small and short decelerating primary stage is followed by a large and long accelerating tertiary regime that dominates the experimental curves.

2.1. Primary/decelerating creep modelling

Most models for primary/decelerating creep postulate that the creep rate depends on an effective stress $\sigma_{eff} = \sigma - \sigma_k$, i.e. the mobile dislocations are driven by the applied stress, σ, reduced by one or more internal stress components, σ_k. As creep goes on, the internal stress increases and the creep decelerates up to a steady state. The internal stress can produce an isotropic hardening for example due to the development of dislocation tangles or cell walls [2], or a kinematic hardening due, for example, to a redistribution of stresses between different creep strenght regions of the material, like grains with different Schmidt factor values or "hard" reinforcing particles and "soft" matrix [3].

Table 1: Chemical composition of René80 superalloy

Element [wt%]	Ni	Cr	Co	Al	Ti	Mo	W	Ta	Zr	B	C
Renè80	bal.	14	9.5	3	5	4	4	-	0.03	0.015	0.17

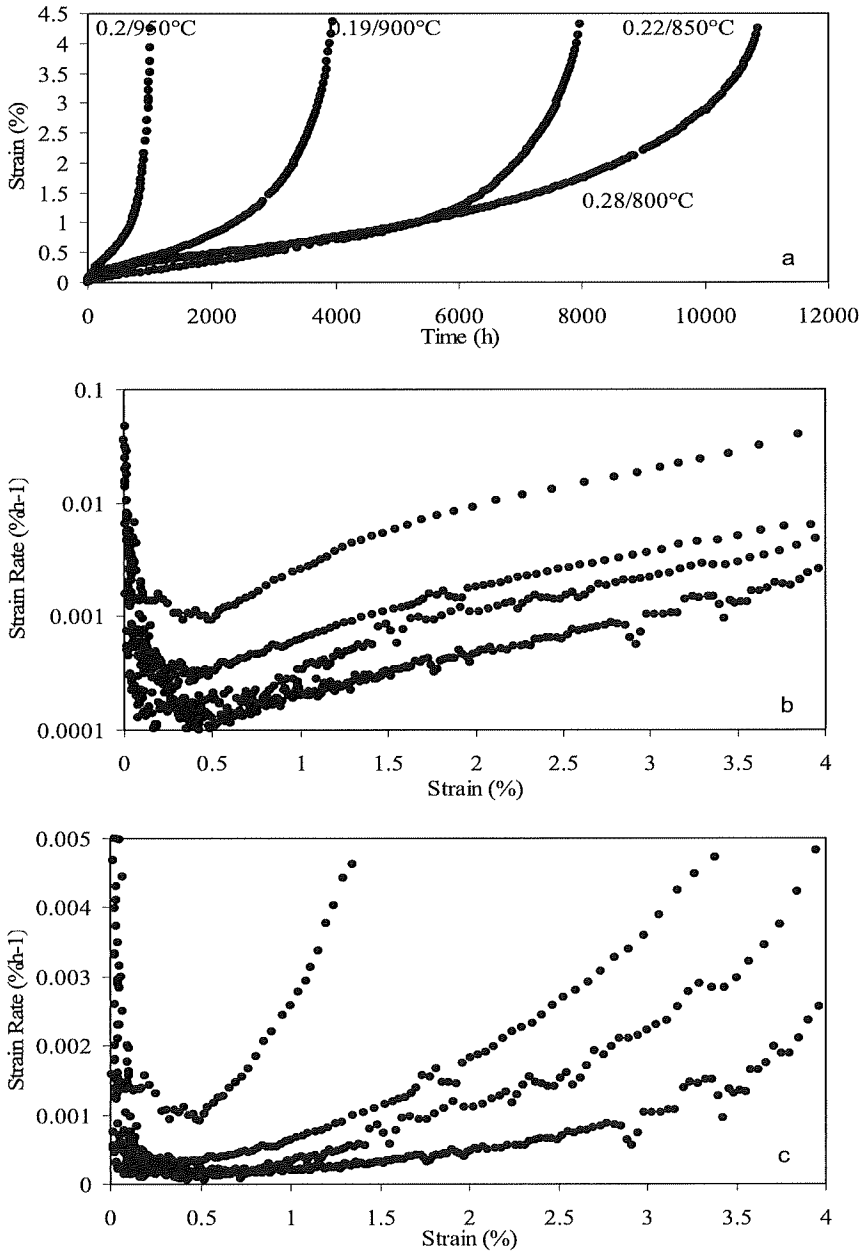

Fig. 1 – Examples of experimental creep curves,(a), at different normalized stresses, σ/σ_{US} where σ_{US} is the ultimate tensile stress determined from 10^{-4} s^{-1} strain rate tests. The same creepcurves are plotted as, (b) log strain rate vs. strain and (c) strain rate vs. strain

For sake of simplicity a simple phenomenological set of equations, proposed by Ion et al.[4], has been here used to describe the decelerating stage:

$$\begin{aligned} \dot{\varepsilon} &= \dot{\varepsilon}_i(1-s) \\ \dot{s} &= H\dot{\varepsilon} - Rs \end{aligned} \qquad (1)$$

The first equation describes the strain rate in terms of a variable, s, correlated with a kinematic internal stress, the second equation describes the evolution of the parameter s. The initial strain rate, $\dot{\varepsilon}_i$, and the parameters R and H are, generally, depending on stress and temperature. The set of Eq. (1) can be analytically solved, obtaining the McVetty-Garofalo equation [5,6]:

$$\varepsilon = \varepsilon_P\left[1-\exp(-rt)\right] + \dot{\varepsilon}_{SS}t \qquad (2)$$

where $\varepsilon_P = \dfrac{(H\dot{\varepsilon}_i^2)}{(H\dot{\varepsilon}_i + R)^2}$ and $r = (H\dot{\varepsilon}_i + R)$ control, respectively, the size and the curvature of the primary stage. $\dot{\varepsilon}_{SS} = \dfrac{(R\dot{\varepsilon}_i)}{(H\dot{\varepsilon}_i + R)}$ represents the steady state.

2.2. Tertiary/accelerating creep modelling

To describe the accelerating/tertiary creep of nickel base superalloys, the following two sets of differential constitutive equations have been proposed: [4, 7]:

$$\begin{aligned} \dot{\varepsilon} &= \dot{\varepsilon}_0(1+w) \\ \dot{w} &= C\dot{\varepsilon} \end{aligned} \qquad (3a) \qquad\qquad \begin{aligned} \dot{\varepsilon} &= \dot{\varepsilon}_0\exp(w) \\ \dot{w} &= C\dot{\varepsilon} \end{aligned} \qquad (3b)$$

where C and $\dot{\varepsilon}_0$ are parameters, generally dependent on σ and T, and w a damage variable proportional to the creep strain.
The Eqs.3, with w=0 when ε=0, can be rewritten, respectively as:

$$\dot{\varepsilon} = \dot{\varepsilon}_0(1+C\varepsilon) \qquad (4a) \qquad\qquad \dot{\varepsilon} = \dot{\varepsilon}_0\exp(C\varepsilon) \qquad (4b)$$

According to the first set of equations the accelerating portion of the creep curves must lie on straight line in a plot $\dot{\varepsilon}$ vs. ε, while the second set, predicts a straight line in a plot log $\dot{\varepsilon}$ vs. ε. The observation of the creep curves in Figs. 1b and c shows that both the Eqs. (4) can only approximate the real behaviour of the alloy. The linear softening law, Eq. (4a), rather than the Eq. (4b) could be more appropriate to describe *constant stress* tests, which avoid the increment of stress with the accumulated creep strain, typical in a constant load test. To extend the validity of Eqs. (4) to properly describe *constant load* creep tests, the stress dependence of the parameters appearing in Eqs. 4 should be considered with the values of such parameters changing during the creep tests. With this improvement the Eq. 4a can excellently describe the constant load creep behaviour of single crystal nickel base superalloys [7, 8]. In the present work, it has been decided to keep the set of equations as

simple as possible, and analyze the experimental creep curves by the Eqs. 3b, that have shown to better represent all the set of the experimental creep curves.

2.3 Primary + Tertiary creep modelling

In this paper, the *complete creep curve* at constant temperature and load has been described combining in the following interactive manner the Eqs. (1) and (3b):

$$\begin{aligned} \dot{\varepsilon} &= \dot{\varepsilon}_i(1-s)\exp(w) \\ \dot{s} &= H\dot{\varepsilon} - Rs\exp(w) \\ \dot{w} &= C\dot{\varepsilon}/(1-s) = C\dot{\varepsilon}_i \exp(w) \end{aligned} \qquad (5)$$

In the set of Eqs. (5) the hardening term is proportional to the strain rate, as in Eq. (1), and the recovery is driven by the internal stress variable, s, multiplied by the damage factor exp(w). Furthermore, the damage rate parameter, $\dot{w}$, is proportional to the strain rate cleared of the primary creep mechanism contribution. In fact, the primary amplitude in these alloys is quite small, comparable to the elastic elongation recorded during the specimen loading. As a consequence, during the primary stage the strongest portions of material are practically not damaged because still loaded in their elastic regime: only after the exhaustion of the primary stage, the macroscopic strain rate can be considered to be proportional to the plastic strain rate in every portion of the material. Moreover anelastic processes, such as bowing of dislocations, can strongly contribute to the strain rate during the primary stage, but they recover after unloading and do not contribute to permanent strain.
It is important to note that the Eqs. (5) turn into Eqs. (1) for a no strain damaging material (C=0) and into Eq. (3b) at the exhaustion of primary stage, when $\dot{s}=0$, s converges to an asymptotic value, s*, and it results:

$$s^* = \frac{\dot{\varepsilon}_i H}{\dot{\varepsilon}_i H + R} \qquad \dot{\varepsilon}_o = \dot{\varepsilon}_i\left(\frac{R}{\dot{\varepsilon}_i H + R}\right); \qquad C^\circ = \frac{C}{R}(\dot{\varepsilon}_i H + R)$$

The set of Eqs. 5, can be integrated, obtaining:

$$\varepsilon = \varepsilon_P\left[1-(1-bt)^{PT}\right] - \frac{1}{C^\circ}\ln(1-bt) \qquad (6)$$

where the parameter ε_P, PT, b and C°, equivalent to the θ_i parameters in the θ concept method [9], are biuniquely related to the parameters of Eqs (5) by the following relationships:

$$\begin{aligned} \varepsilon_P &= H\dot{\varepsilon}_i^{\,2}/(H\dot{\varepsilon}_i + R)^2 \\ PT &= (H\dot{\varepsilon}_i + R)/C\,\dot{\varepsilon}_i) \\ b &= C\dot{\varepsilon}_i = C^\circ\dot{\varepsilon}_{SS} \\ C^\circ &= C(H\dot{\varepsilon}_i + R)/R \end{aligned} \qquad (7)$$

$$\begin{aligned} \dot{\varepsilon}_i &= \frac{b}{C^\circ} + \varepsilon_P PTb \\ C &= \frac{C^\circ}{(1 + C^\circ\varepsilon_P PT)} \\ R &= \frac{PTb}{(1 + C^\circ\varepsilon_P PT)} \\ H &= \frac{(C^\circ PT)^2\varepsilon_P}{(1 + C^\circ\varepsilon_P PT)^2} \end{aligned} \qquad (8)$$

The differential Eqs. (5) and the analytical solution (6) are equivalent:

- The set of Eqs. (5) can be better used in finite element calculation and to simulate tests at variable stress and/or temperature, for example tensile or relaxation tests.
- The analytical solution can be used to easily obtain the values of the parameters (7) interpolating the experimental creep curves. From these values it is possible to obtain the values of the parameters $\dot{\varepsilon}_i$, H,R and C of Eqs. (7) by the relations (8).

3. Analysis of the René 80 creep curves

The interpolation of the creep curves by Eq. (6) allows to determine the 4 parameters ε_p, PT, b, C° and then their dependence on the tests conditions, σ and T. Using these expressions in (6), it is possible to predict the creep curve for any constant stress and temperature within the same creep mechanisms range.

Both set of parameters ε_p, PT, b, C° and $\dot{\varepsilon}_i$, H, R and C are equivalent to characterise the creep curves. More generally, four non equivalent parameters chosen among combinations of the parameters of the two sets can be used. Our choice here is to characterise the creep curves by the set of the relationships (7).

3.1. Stress and temperature dependence of the parameter ε_p

The parameter ε_P for each single creep curve has been determined by back extrapolation of the minimum creep rate line to obtain the creep strain intercept at t=0. The parameter values are plotted in Fig. 2 and interpolated by the following relationship:

$$\varepsilon_p = 0.1582\sigma/\sigma_{US} - 0.1831 \qquad (9)$$

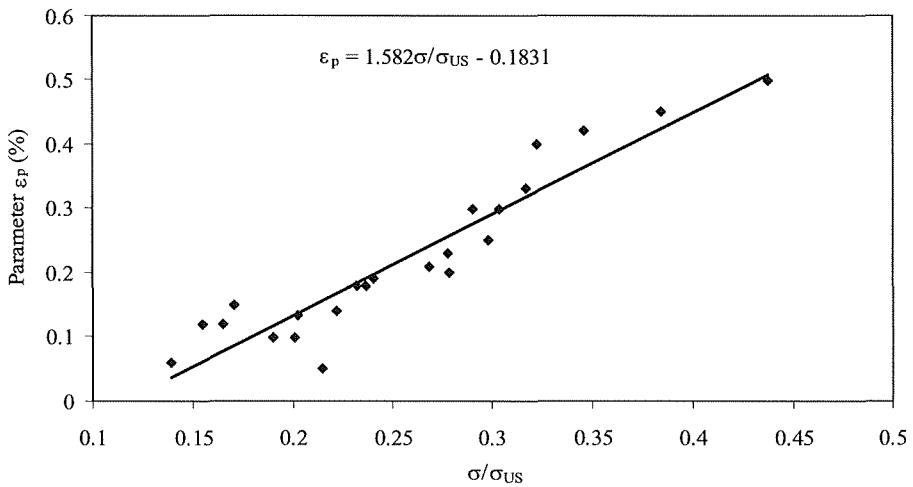

Fig. 2 Experimental values of the parameter ε_P and their interpolation (Eq. 12). (σ_{US} = ultimate tensile stress, ε in (%)).

3.2. Stress and temperature dependence of the parameter PT and C°

The values of the parameter PT, obtained through the interpolation of the experimental creep curves, cluster around a constant value, independent on the tests stress and temperatures without a clear dependence of the parameter on the test conditions.
The parameter C°, controlling the curvature of the accelerating stage, shows decreasing values, with increasing the applied stress, and a small temperature dependence. To keep as simple as possible the description of the creep curves, at this stage the stress and temperature dependence of the parameter C° has been neglected.

The following constant values for the two parameters PT and C° have been used, independent on the test stress and temperature:

$$PT = 50 \qquad (10) \qquad C° = 1 \qquad (11)$$

3.3. Stress and temperature dependence of the parameter b

The value of the parameter b, can be calculated interpolating the creep curves. For sake of simplicity it has been here utilized a plain methodology, described in Appendix 1. The parameter b dependence on the test conditions is given by the following relationship:

$$B = 1/t_r(\sigma,T) \qquad (12)$$

where $t_r = t_r(\sigma,T)$ represents a generic relationship between the time to rupture and the test conditions: in this work the Larson Miller relationships has been used, but alternative formulations can be easily considered.

Using the Eq. (6), with the parameters values estimated from relationships (9-12), it is possible to calculate the creep curves for any testing stress and temperature. Examples of comparison between experimental data with the calculated creep curves (broken curves), are reported in Fig. 3a. Of course the effectinevess the here reported method to extrapolate the time to rupture outside range of the stresses/temperatures here explored, strongly depends on the ability of the relationship $t_r = t_r(\sigma,T)$ of Eq. (12) to correlate the test parameters to the time to rupture.

In Figs. 3b and 3c, examples of experimental creep curves are reported in terms of time normalized with the time to rupture and compared with the prediction of the equations. Generally the fit is excellent, Fig 3b, but, for the test performed at the highest temperatures and lowest stresses, to consider constant the parameter C° value is an oversimplification. A better interpolation can be obtained using a higher value of the parameter C°.

4. Conclusion

The simple equations adopted to describe the creep behaviour of the Nickel base superalloy René80 have produced encouraging results.
This kind of description will be an useful tool for lifing activity, allowing to take into account not only the creep rupture characteristics of this alloy, but also its deformation behaviour,

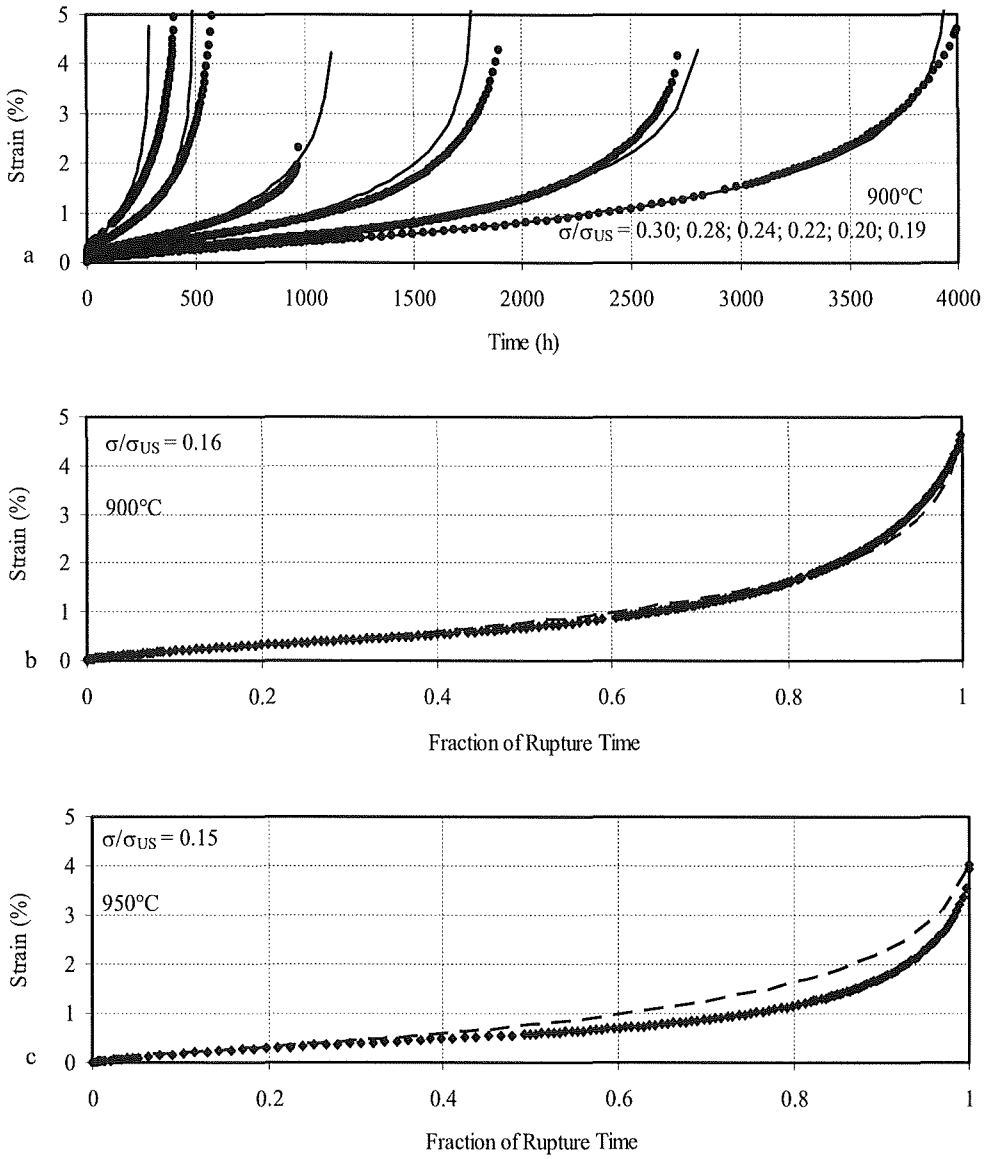

Fig. 3 -(a) Example of creep curves, experimental data are compared with the calculated creep curves using Eq. 9 with the parameter values obtained from Eqs (7-9) (broken lines). (b) and (c) Comparison between examples of experimental creep curves in terms of the time normalized with the time to rupture and compared with the prediction of the equations.

essential for rotating turbine blades. Of course, further activities should be carried out in order to validate this model also out of the considered time/temperature range.

Acknowledgements: The authors are grateful to E. Signorelli for his valuable help in experimental work.

References

[1] M. F. Ashby and B.F. Dyson in D.M.R Taplin et al. (eds.) *Advances in Fracture Research*, Pergamon, Oxford, p. 30 (1984).
[2] B. Derby and M. F. Asbhy, *Acta Metall.*, 35, p.1349 (1987).
[3] B.F. Dyson *Revue Phys. Appl.*, 23, p.605 (1988)
[4] J. C. Ion et al., *NPL report DMA A 115*, Teddington, UK, (April 1986).
[5] P.G. McVetty, *Mech Engng*, 56, p. 149 (1934).
[6] F. Garofalo in: *Fundamentals of Creep and Creep Rupture in Metals*, Macmillan, London (1965).
[7] M. Maldini e V. Lupinc. *Scripta Metall.* 22, p.1737 (1988).
[8] M. Maldini and V. Lupinc, *Materials at High Temperatures*, 14, p. 47 (1997).
[9] R.W. Evans, J.D. Parker and B. Wilshire in: *Recent Advances in Creep and Fracture of Engineering Materials and Sructures*, Pineridge Press, Swansea, p.135 (1982).

APPENDIX 1

In the Eq. (6), the accelerating/tertiary stage is described by the following relationship:

$$\varepsilon t = \varepsilon\text{-}\varepsilon p = -\frac{1}{C^\circ}\ln(1-bt) \qquad \text{(A1)}$$

From (A1) it is possible to obtain a relationship between the strain accumulated during the tertiary creep, ε_x, at a generic time t_x and the parameter b:

$$b = \left(\frac{1-\exp\left(-C^\circ \varepsilon_{t_x}\right)}{t_x}\right) \qquad \text{(A2)}$$

In particular, for rupture results:

$$b = \left(\frac{1-\exp\left(-C^\circ \varepsilon_R\right)}{t_R}\right) \qquad \text{(A3)}$$

In the performed tests, the experimental values of ε_R and of the parameter C° allow to simplify the relationship (A3) as:

$$b = \frac{1}{t_R} \qquad \text{(A4)}$$

Representing the time to rupture in function of the Larson Miller parameter, although alternative formulations could easily be considered, the relationship (A4) allows to determine the values of the parameter b in function of the testing stress and temperature.

Acknowledgements: The authors are grateful to E. Signorelli for his valuable help in experimental work.

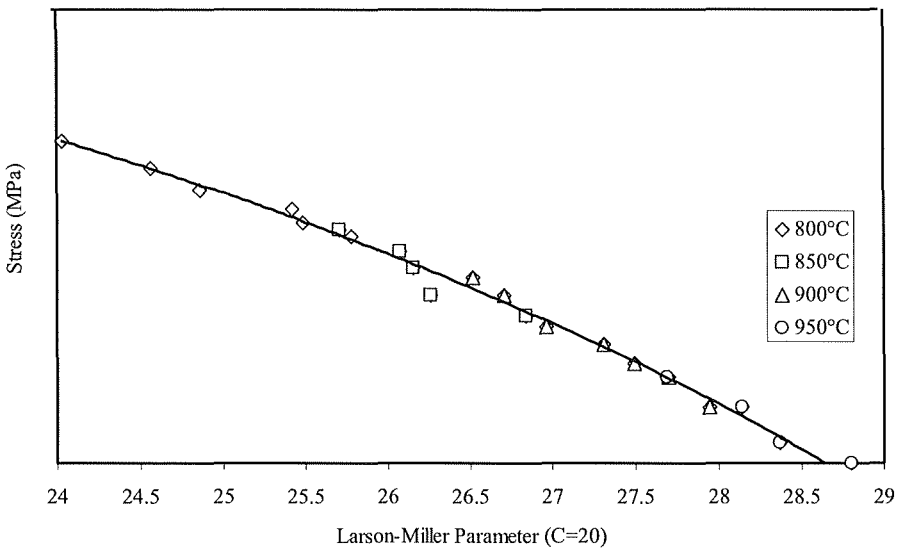

Fig. A1 – Time to rupture in a Larson Miller plot.

9th Liege Conference : Materials for Advanced Power Engineering 2010
edited by J. Lecomte-Beckers, Q. Contrepois, T. Beck and B. Kuhn.

LCF- AND LCF/HCF-BEHAVIOUR OF THE SUPERALLOY MAR-M247LC

Domnin Gelmedin and Karl-Heinz Lang

Karlsruhe Institute of Technology,
Institut fuer Werkstoffkunde I,
Kaiserstrasse 12, D-76131 Karlsruhe, Gemany

Abstract

The fatigue behaviour of the Nickel-base superalloy Mar-M247LC was investigated at 650°C in air environment under total strain control. Pure low cycle fatigue (LCF) loading, pure high cycle fatigue (HCF) loading and superimposed LCF/HCF loading were realised. In LCF tests with a strain ratio of zero and a hold time of 60 seconds the cyclic deformation and the lifetime behaviour was investigated. The dependence of the fatigue limit on the mean strain was estimated in HCF tests at a frequency of 60 Hz using an ultimate number of cycles of ten million. Finally the influence of superimposed HCF and LCF loadings was examined. At high total strain ranges of the HCF loading the lifetime of the superalloy was reduced about more than one magnitude compared to the lifetime under pure LCF loading. With decreasing HCF loadings the reduction of the lifetime decreases. This life time reduction can be explained by the interaction of the LCF and the superimposed HCF loading. Crack initiation and first crack propagation is predominantly induced by the LCF loading. After reaching an adequate long fatigue crack length the superimposed HCF loading contributes considerably to the crack growth. This contribution can be determined evaluating the distance between the LCF marking lines which form on the fracture surface. The higher the superimposed HCF loading was the longer the distance between the LCF marking lines and the lower the crack length were when first LCF marking lines could be recognized. On the basis of this cognition the life time under superimposed LCF/HCF loading was modelled using a model basing on fracture mechanics.

Keywords: Ni-base superalloys, low cycle fatigue, high cycle fatigue, superimposed loading

1. Introduction

Components of power generating plants or aircraft engines, like turbine blades or turbine wheels are thermal and mechanical highly loaded. Thermally induced mechanical loadings result from transient and inhomogeneous temperature fields within the component. The mechanical loading is caused by centrifugal forces. These loadings are in the low frequency range. Furthermore, the components are typically subjected to a high frequency mechanical loading resulting from vibrations and/or pressure fluctuations due to unsteady combustion. With the objective to design safe components it is necessary to understand the failure mechanisms of the employed materials under these complex loadings.

Although the superimposition of low frequency LCF cycles with higher frequent HCF loadings appears in many technical applications, only relatively few systematic investigations could be found in the literature. In [1,2] e.g. the crack growth behaviour of TiAl6V4 is investigated under superimposed loading. During the hold time of a low frequency basic loading higher frequency vibrations realised to simulate the service loading of the piston bottom of an internal combustion engine [1] or in the plate of the compressor of a gas turbine [2]. The loading was characterized by the ratio of the HCF amplitude to the LCF amplitude. For a ratio below 0.3 the crack propagation was accelerated by a factor of approximately 2 compared to pure LCF loading. For a higher ratio the superimposed loading accelerated the crack growth the more the higher the ratio between the HCF amplitude and the LCF

amplitude was. The crack growth rate for a superimposed LCF/HCF loading with 1,000 to 100,000 HCF cycles per hold time could be predicted by the linear addition of the individual contributions to the crack propagation of the respective loadings. The material behaviour under service near superimposed loading was investigated for cast iron [3,4] and cast Aluminium alloys [5,6] which are used in cylinder heads of combustion engines and a Nickel based superalloy which is used for combustion chambers for gas turbines [7-9]. In these investigations a clear reduction of the life time appears when the amplitude of the superimposed HCF loading exceeds a certain level.

At present, no general approaches of the life time behaviour under superimposed low and high cycle fatigue loading exist. In [4-9] the life time reduction due to a superimposed loading is described using an exponential approach. In [10] the lifetime behaviour of a welded joint was analysed for superimposed LCF/HCF loading using methods which are normally used to estimate the service strength. At this, a clear underestimation of the lifetime was obtained. In [11] the loading situation at the root of a turbine blade war analysed. The lifetime behaviour at this superimposed loading could be described empirically by the application of transformation equations. Using these equations adequate damage parameters from pure lcf loadings could be applied for superimposed loadings.

2. Material and specimens

The nickel-based superalloy MAR-M247LC was cast by Doncasters Precisions Castings Bochum GmbH, Germany, in 170 mm long rods with a diameter of 12.0 mm. The chemical composition is listed in table 1. After precision casting the material undergo a hot isostatic pressure treatment (HIP) (1185 ± 15 °C, 4h ± 10min, 172.5 ± 5 MPa in Argon) to reduce interdentritic porosity. Then, the material was solution annealed (1185 ± 15 °C, 2-4 h) and afterwards tempered (870 °C, 20-24 h).

The structure of this cast polycrystalline alloy is dendritic as shown in Fig. 1 a). The secondary dendrite arm spacing amounts to 32.24 µm and was measured over a total length of 4,779 µm and determined by six different images. The investigated material consists of heterogeneous distributed γ'-precipitates of the type $Ni_3(Al,Ti)$ which are embedded in the γ-matrix. Fig. 1 b) shows a Scanning Electron Microscope (SEM) image of the relatively inhomogeneous microstructure. Partly the γ'-precipitations are very fine besides numerous relatively coarse precipitations.

The rods were machined by turning to solid round specimen with a total length of 120 mm and a diameter of 11.5 mm at the ends where they were clamped into the grips. The cylindrical gauge length was 17 mm with a gauge diameter of 7 mm.

Table 1: Chemical composition of MAR-M247LC

element	Ni	C	Si	Mn	Cr	Mo	W	Co
mass.-%	bal.	0.07	0.03	<0.01	8.19	0.5	9.44	9.24
Element	V	Cu	Ti	Nb	Al	Fe	Zr	Ta
mass.-%	<0.01	<0.01	0.67	<0.02	5.60	0.04	0.02	3.18

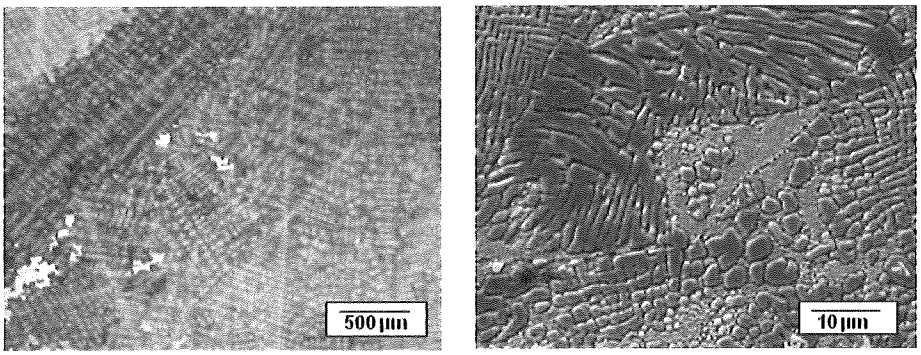

a) b)

Fig. 1: micrograph of MAR-M247LC, a) LM: dentritic structure. b) SEM: inhomogeneously dispersed γ'-preciptations in γ-matrix

3. Experimental Details

The tests were carried out on a 100 kN servo hydraulic Schenck testing machine and two 50 kN electromechanical Zwick testing machines. All tests with a high cycle fatigue loading were conducted on the servohydraulic testing machine, for all other tests the electro-mechanical testing machines were used. The temperature of the specimen was measured with a Ni-CrNi tape thermocouple which was placed in the centre of the gauge length. The specimens were heated up by means of an induction heating under temperature control. All testing machines were equipped with water-cooled grips. A high temperature extensometer that applied a gauge length of 15 mm was used to measure the strain. The loads were measured by the load cells of 100 kN and 50 kN, respectively.

The isothermal LCF, HCF and LCF/HCF tests were conducted at 600 °C in laboratory air environment under total strain control. A cycle of a pure low cycle fatigue loading had a strain ratio $R_\varepsilon = \sigma_{min}/\sigma_{max} = 0$ and lasted 70 seconds. It was composed of two ramps that lasted 5 s each and of a holding time (HT) of 60 s. In the first ramp the specimen was loaded to the maximum strain. Then the holding time starts. After the hold time the specimen was unloaded to zero strain in the second ramp. The pure HCF loading had a sine wave form at a frequency $f = 60$ Hz. Five different total mean strain values between $\varepsilon_{m,t} = 0$ and 1.2 % were realized. The LCF/HCF tests were carried out by superimposing both loading conditions, so that 4,200 HCF cycles occurred during a LCF cycle. The total strain range $\Delta\varepsilon_t$ during the superimposed tests is the sum of the total strain ranges of the LCF loading $\Delta\varepsilon_t^{LCF}$ and the HCF loading $\Delta\varepsilon_t^{LCF}$. As a consequence of the superimposition of the HCF to the LCF loading, the strain ratio was slightly negative under LCF/HCF loading. The ultimate number of cycles was defined 20,000 for LCF loading and 10^7 for HCF loading. When a load drop of 10 % occurred the number of cycles to failure N_f was reached. Additional to the fatigue tests, high temperature tensile tests with the same specimen geometry were carried out at a strain rate of 10^{-3} 1/s.

4. Results

4.1. High Cycle Fatigue Behaviour

The lifetime behaviour under high cycle fatigue loading with different mean strain shows Fig. 2 (a). Despite the fact that the a considerable scatter occurs, which is up to one order of magnitude, there is a distinct difference in the fatigue life at fully reversed test ($\varepsilon_{m,t} = 0$) and smaller total mean strain ($\varepsilon_{m,t} = 0.2$) compared to the test series with total mean strains $\varepsilon_{m,t}$ = 0.6 % and more. Although the positive mean strains in this region differ considerably by the factor of two from each other, no distinct difference concerning the lifetime can be detected. Consequently, the strain fatigue limit $R_{D,\varepsilon}$ was estimated on the basis of the conducted experiments to 0.30 % for $R_\varepsilon = -1$ and to 0.1 % for mean strains above about 0.30 %.

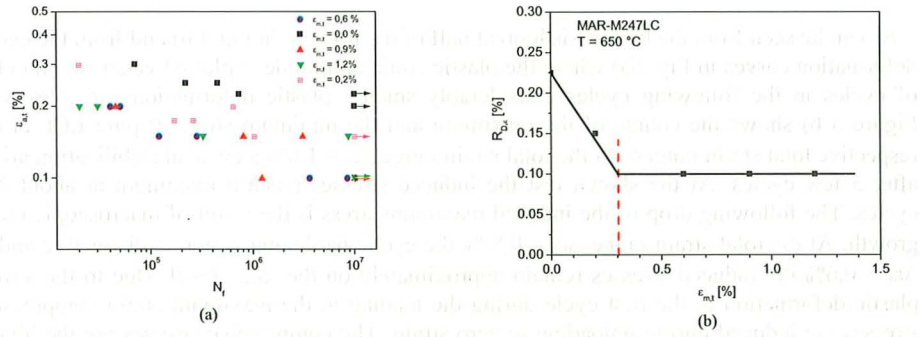

Fig. 2: (a) High-cycle strain life data of MAR-M247; (b) Estimated strain fatigue limit depending on the total mean strain.

4.2. Low Cycle Fatigue Behaviour

To investigate the cyclic deformation and the lifetime behaviour three loading levels were realized to obtain lifetimes between 100 and 20,000 cycles. As total strain ranges 1.0, 0.8 and 0.6 % were chosen. On each loading level six specimens were tested. The results are plotted in Fig. 3. Although, the material was hot isostatic pressed a pronounced scattering appears which reaches from a factor of 2 at $\Delta\varepsilon_t$ = 0.6 % up to a factor of 4 at $\Delta\varepsilon_t$ = 0.8 %. As lifetime behaviour the plotted straight line was estimated. As typical example to demonstrate the cyclic deformation behaviour the measured hysteresis curve of the first and the cycle at half of the lifetime are shown in Fig. 4 for a total strain range of 1.0 %. During the first cycle (Fig. 4a)) a significant plastic deformation occurs during the loading to the maximum strain. Due to this plastic deformation after unloading to zero strain compressive stresses appear which are of similar amount compared to the stresses at maximum strain.

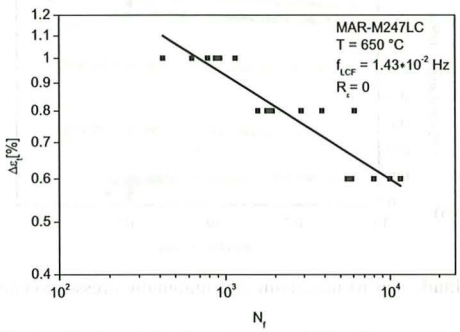

Fig. 3: Lifetime behaviour at pure LCF loading.

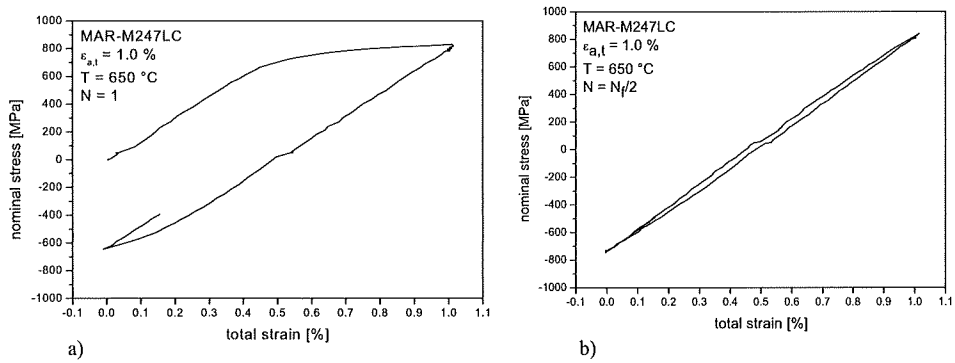

Fig 4: Hysteresis loops a) in the first cycle and b) at half of the lifetime.

As can be seen from the hysteresis loop at half of the lifetime in Fig 4 b) and from the cyclic deformation curves in Fig. 5a) where the plastic strain amplitude is plotted versus the number of cycles in the following cycles considerably smaller plastic deformations are observed. Figure 5 b) shows the course of the maximum and the minimum stress at pure LCF at the respective total strain ranges. At the total strain range $\Delta\varepsilon_t = 1.0\%$ a cyclical stabilization arises after a few cycles. At the shown test the induced stresses reach a maximum at about 200 cycles. The following drop of the induced maximum stress is the result of macroscopic crack growth. At the total strain range $\Delta\varepsilon_t = 0.8$ % the cyclic hardening is not so distinctive and at $\Delta\varepsilon_t = 0.6\%$ the induced stresses remain approximately on the same level. Due to the strong plastic deformation in the first cycle during the loading to the maximum strain compressive stresses are induced during unloading to zero strain. The compressive stresses are the higher the higher the used total strain range is. At $\Delta\varepsilon_t = 0.6$ % the material the deformation behaviour is macroscopically purely elastically from the second loading cycle. Therefore, no further cyclic hardening occurs. At the higher strain ranges relative small plastic strain amplitudes and a slight cyclic hardening which lasts up to the initiation of a macroscopic crack are observed.

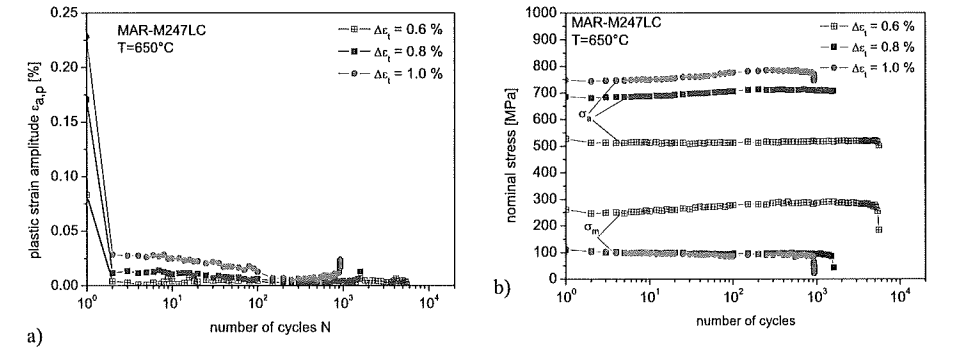

Fig. 5: Cyclic deformation curves; a) plastic strain amplitude and b) maximum and minimum stresses versus number of cycles

4.3. Superimposed LCF/HCF Loading

The lifetime behaviour under superimposed LCF/HCF loading was investigated in two test series. The strain range of the LCF loading was $\Delta\varepsilon_t^{LCF}$ = 0.4 and 0.8 %. In both test series three different strain ranges of the HCF loading ($\Delta\varepsilon_t^{HCF}$) were superimposed with a higher frequency.

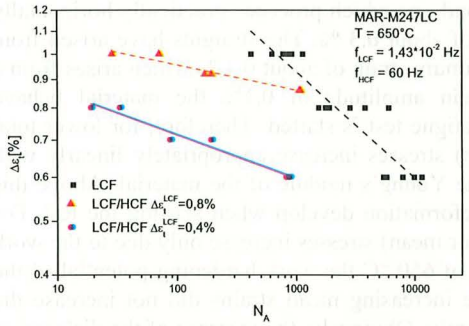

Fig. 6: Lifetime behaviour at superimposed LCF/HCF loading compared to pure LCF loading

In Fig. 6 the results of these test series are added to the results of the tests with pure LCF loading. In this diagram the sum of the strain ranges of the LCF and the HCF loading is plotted versus the number of LCF cycles to failure.

The superimposed HCF loading reduced the lifetime at all superimposed loading conditions compared to the liftime at pure LCF loading with the same total strain range. The lifetime reduction at a total strain range of 1 % is around approximately an order of magnitude. The lifetime reduction decreases with decreasing superimposed HCF strain range. The lifetime behaviour for a given LCF strain range can be described by the marked straight line. Projecting these straights to higher lifetimes for a superimposed HCF loading of $\Delta\varepsilon_t^{HCF} \approx 0.03$ % the lifetime at pure LCF loading will be reached.

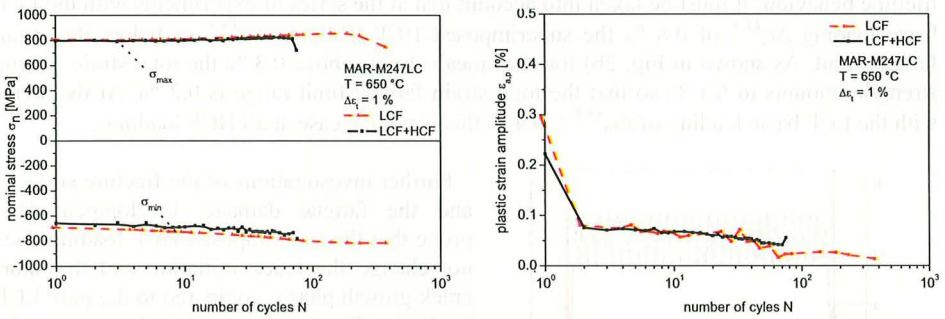

Fig. 7: Comparison of the cyclic deformation behaviour at pure LCF and LCF/HCF loading

A comparison of the course of maximum and minimal stress at a pure LCF and HCF loading is given in Fig. 7. The induced maximum stresses are approximately equal and the amount of the induced minimal stresses a little higher at LCF/HCF loading compared to pure LCF loading. The cyclical hardening appears in similar extent at both loading conditions. However, at superimposed LCF/HCF loading failure sets in before the cyclic hardening is completed. At pure LCF loading the maximum of the induced stresses is reached after about 200 loading cycles but the lifetime at LCF/HCF loading is only about 75 LCF cycles. The plastic strain amplitude (Fig. 7b)) decreases due to the cyclical hardening with increasing number of cycles. In the first cycle the plastic strain amplitude is something higher at pure

LCF loading but already as of the second cycle the appearing plastic strain amplitudes are not different at the two loading conditions until failure sets in at LCF/HCF loading.

5. Discussion

The dependence of total strain fatigue limit in Fig. 2b) can be described in the examined area by two straights. The first one starts at the fatigue strength for zero total mean strain and goes up to the intersection point with the second one which proceeds practically horizontally from a critical value of the total mean strain of about 0.3 %. The straights have arisen from the following consideration. Up to a total maximum strain of about 0.4 % which arises from a total mean strain of 0.3% and a total strain amplitude of 0.1% the material behave macroscopically purely elastically when the fatigue test is started. Therefore, for lower total mean strains the induced maximum (or mean) stresses increase appropriately linearly with increasing mean strains in accordance with the Young's module of the material. Above this critical mean strain value an elastic plastic deformation develop when starting the test. For this total mean strains the induced maximum (or mean) stresses increase only due to the work hardening potential. At the given temperature of 650 °C the work hardening potential of the material is very low. Therefore, in this range increasing mean strains did not increase the induced maximum (or mean) stresses significantly. Obviously, the increase of the dislocation density which arises from the plastic deformation during loading to the maximum strain in the first cycle is able to compensate the detrimental effect of the slightly increases maximum stresses and finally an extensive mean strain insensitiveness develop. This mean strain insensitivity probably reaches up to the total mean strain at which damage of the material is produced during the first loading to the maximum total strain.

At the assessment of the influence of a superimposed higher frequency loading on the LCF lifetime behaviour it must be taken into account that at the series of experiments with the LCF basic loading $\Delta\varepsilon_t^{LCF}$ of 0.8 % the superimposed HCF loadings $\Delta\varepsilon_t^{HCF}$ or below the strain fatigue limit. As shown in Fig. 2b) for total mean strains above 0.3 % the total strain fatigue strength amounts to 0.1 % so that the total strain fatigue limit range is 0.2 %. At the series with the LCF basic loading of $\Delta\varepsilon_t^{LCF} = 0.4$ % this is not the case at all HCF loadings.

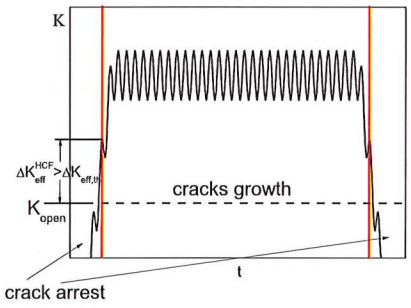

Fig. 8: Crack growth and crack arrest at superimposed HCF loading

Further investigations of the fracture surfaces and the fatigue damage development [12] prove that the superimposed HCF loading does not change the crack initiation and the short crack growth phases compared to the pure LCF loading. So the observed influence on the lifetime behaviour must be generated by the modification of the macroscopic crack growth phases. The ideas to this are clarified schematically in Fig. 8. The effective range of the stress intensity factor ΔK_{eff}^{HCF} which is generated by the HCF loading must exceed a threshold value $\Delta K_{eff,th}$ to induce a crack propagation due to the HCF loading component. If this threshold value is reached the HCF loading contributes to the crack growth and accelerates the growth of existing cracks during a

LCF cycle. These conditions are reached earlier and the resulting shortening of the lifetime is more pronounced the higher the range of the superimposed HCF loading is.

To describe the lifetime behaviour under non isothermal complex loading Riedel developed the damage parameter D_{TMF} [13,14] on the basis of short fatigue crack fracture mechanics ideas. This parameter bases on the damage parameter Z_D which was proposed by Heitmann [15]. Using this parameter the growth da/dN of a semicircular crack with the length a starting from the surface could be described as

$$\frac{da}{dN} \approx \beta \cdot d_N \cdot \frac{Z_D}{\sigma_{cy}} \cdot a \qquad \text{(Equ. 1)}$$

β and d_N are constants and σ_{cy} is the yield strength. To calculate the lifetime at pure LCF an initial crack length a_0, a critical crack length a_f and the parameters β and d_N are needed. The life time arises from the number of iterations which are necessary to reach the crack length a_f at which failure takes place. These calculations may start from an initiation number of cycles N_0 which is necessary to produce the initial crack length a_0. In the case of superimposed LCF/HCF loading the HCF loading component has to be considered as soon as the effective range of the HCF stress intensity

$$\Delta K_{eff}^{HCF} = 1.1215 \cdot \frac{2}{\pi} \cdot \Delta\sigma_{eff} \cdot \sqrt{\pi \cdot a} \qquad \text{(Equ. 2)}$$

exceeds an effective threshold value $\Delta K_{eff,th}$ and the actual stress σ is higher than the crack opening load σ_{op}. If these conditions are fulfilled the crack growth due to the HCF loading can be calculated in accordance to equ. 1 as

$$\left.\frac{da}{dN}\right|^{HCF} = 1.45 \cdot \beta \cdot d_N \cdot \frac{\Delta\sigma_{HCF,eff}^2}{\sigma_{cy} \cdot E} \cdot a \qquad \text{(Equ. 3)}$$

As long as the crack growth is in the range of the threshold it can be calculated in accordance to Newman [16] as

$$\left.\frac{da}{dN}\right|^{HCF} = 1.45 \cdot \beta \cdot d_N \cdot \frac{\left[\Delta\sigma_{HCF,eff}^2 \cdot \left(1 - \frac{\Delta K_{eff,th}}{\Delta K_{HCF,eff}}\right)^p\right]^2}{} \cdot a \qquad \text{(Equ. 4)}$$

To evaluate the experiments on hand the crack growth was calculated with equ. 4 as long as the actual stress intensity factor was below a value of 6.5 MPa$\sqrt{m}$. For higher values equ. 3 was used. So, the crack growth within a LCF cycle du to the superimposed HCF loading is considered and the new crack length at the next LCF arise as:

$$a = a + \left.\frac{da}{dN}\right|^{LCF} + \left.\frac{da}{dN}\right|^{HCF} \qquad \text{(Equ. 5)}$$

For the concrete calculations $N_0 = 0$, $a_f = 1520$ µm, $\Delta K_{eff,th} = 3.0$ MPa$\sqrt{m}$, $p = 2$ and $d_n = 0.5$ was set. a_0 and β were used as fitting parameters. For MAR-M247LC and T = 650 °C the as cyclic yield strength $\sigma_{cy} = 650$ MPa and as Heitmann parameter $Z_D = 1.567$ MPa was estimated. From the fitting $a_0 = 55$ µm and $\beta = 0.240056$ was the result. Using these parameters the lifetime of four experiments was calculated. Fig. 9 contains the result of these calculations. As can be seen, only three of the four results lay within a scatter band of the factor 2. The reason for this behaviour may be that there were a lot of assumptions necessary

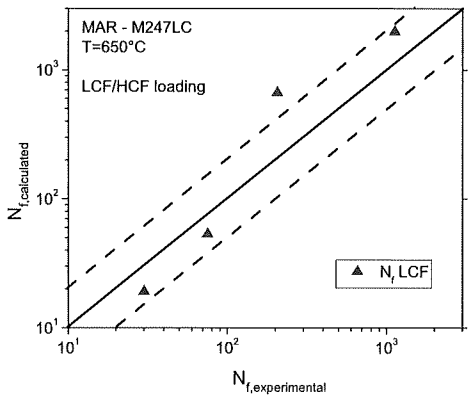

Fig. 9: Comparison of the calculated and the experimental lifetime of experiments with superimposed LCF/HCF loading

to set concrete values especially for the fracture mechanical parameters. To estimate these parameters a material parameters crack growth measurements under superimposed LCF/HCF loading conditions are mandatory. Such measurements will be the task for the near future.

6. Summary

The performance of MAR-M247LC at 650°C has been investigated under strain controlled LCF, HCF and superimposed LCF/HCF loading conditions. Under HCF loading, the strain fatigue limit decreases up to a mean strain from which no significantly higher mean stresses are induced.

Under LCF and LCF/HCF loading, the induced maximum and minimum stresses as well as the plastic strain amplitudes over the number of cycles did not differ considerably. At high superimposed strain ranges, the lifetime decreases considerably compared to pure LCF loading. This lifetime decrease is caused by the HCF loading which contributes significantly to the crack growth after an adequate crack length is exceeded. With decreasing superimposed HCF loading, the lifetime increases and reaches the life under pure LCF loading, and even shows a tendency to a longer life.

For the description of the life time under superimposed LCF/HCF loading a fracture mechanical crack growth model developed at the IWM Freiburg, Germany, was used. With this model the prediction of the lifetime turned out for most of the calculated tests within a scatter band of a factor of two.

7. Acknowledgement

The financial support of the Bundesministerium für Wirtschaft und Technologie (BMWi) through the Arbeitsgemeinschaft industrieller Forschungsvereinigungen e.V. (AiF), (AiF-Nr. 14245 N, FVV-Nr. 867) is gratefully acknowledged.

8. Literature

[1] B.E. Powell, T.V. Duggan, R. Jeal: The influence of minor cycles on low cycle fatigue crack propagation; Int. J. Fatigue Vol. 4, 1982, 4-14.

[2] B.E. Powell, T.V. Duggan: Crack growth in Ti-6Al-4V under the conjoint action of high and low cycle fatigue; Int. J. Fatigue Vol. 9, No. 4, 1987, 195-202.

[3] T. Hammers, A. Uihlein, K.-H. Lang, D. Löhe: Development of Damage in Cast Iron During Superimposed Low Frequency Thermal-Mechanical and Higher Frequency Mechanical Loading. In: K. J. Hsia, M. Göken, P. D. Portella, N. R. Moddy (Eds.): Plasticity, Failure and Fatigue in Structural Materials - from Macro to Nano: Proceedings of the Hael Mughrabi Honoray Symposium. TMS, Warrendale, PA, USA, ISBN 978-0-87339-714-8 (2008), S. 253 – 258.

[4] A. Uihlein, K.-H. Lang, D. Löhe: Lifetime Behaviour at Superimposed Thermal-Mechanical and Mechanical Loading. Proceedings of the XI International Congress and Exhibition on Experimental and Applied Mechanics (SEM 2008), June 2-5, 2008. Society for Experimental Mechanics, Inc., Bethel, Connecticut, USA, ISBN 0-912053-99-2 (CD-ROM) 2008.

[5] J. Luft, T. Beck, D. Löhe: Lifetime and Damage Behaviour of a Cast Aluminium Alloy under TMF and Superimposed TMF/HCF Loading. Proc. 11th Int. Conf. On Fracture, Turin, (CD-ROM) 2005.

[6] I. Henne: Schädigungsverhalten von Aluminiumgusslegierungen bei TMF und TMF/HCF-Beanspruchung. Dr.-Ing. Dissertation, Universität Karlsruhe, Schriftenreihe Werkstoffwissenschaft und Werkstofftechnik, Shaker Verlag, Band 2006, 31, ISBN: 3-8322-5596-6, (2006).

[7] M. Moalla, K.-H. Lang, D. Löhe, E. Macherauch: Isothermal High Temperature Fatigue Behaviour of NiCr22Co12Mo9 under superimposed LCF and HCF Loading. In: K.T. Rie, P.D. Portella (Eds.) Proc. 4th Int. Conf. on Low Cycle Fatigue and Elasto-Plastic Behaviour of Materials, 7.-11. September 1998, Garmisch-Partenkirchen, Elsevier Science Ldt., Oxford, UK, ISBN 0-08-043326-X, (1998) 27-32.

[8] M. Moalla, K.-H. Lang, D.Löhe: Effect of Superimposed High Cycle Fatigue Loading on the Out-Of-Phase Thermal-Mechanical Fatigue Behaviour of CoCr22Ni22W14. Material Science and Engineering A, Vol. 319-321, (2001), 647-651.

[9] M. Moalla, T. Beck, K.-H. Lang, D. Löhe: Effect of Superimposed High Cycle Fatigue Loadings on the In-Phase Thermal-Mechanical Fatigue Behaviour of NiCr22Co12Mo9. In: G. Biallas et al. (Eds.): Proc. CAMP2002 - High-Temperature Fatigue, Bonifatius Verlag, Paderborn, ISBN 3-00-009254-4 (2002), 22-49.

[10] S. Sarkani: Influence of high-frequency components on fatigue of welded joints. Int. J. Fatigue, Vol. 12, No. 2, (1990), 115-120.

[11] P. Kopp, E. Roos: HCF-LCF-Bauteilbeanspruchung, AVIF-Nr. A145, Forschungsstelle MPA Stuttgart (2003).

[12] D. Gelmedin, K.-H. Lang: Ermüdungsverhalten von Hochtemperaturwerkstoffen bei hohen Grundlasten. FVV-Forschungsberichte Heft 897, Forschungsvereinigung Verbrennungs-kraftmaschinen e.V., Frankfurt am Main, (2010).

[13] H. Riedel: Fracture at High Temperatures. Springer Verlag, Berlin Heidelberg, New York, (1987).

[14] W. Schmitt, R. Mohrmann, H. Riedel, A. Dietsche, A. Fischersworring-Bunk: Modelling the Fatigue Life of Automotive Components. In A.F. Blom(Ed.) Fatigue 2002 – Proceedings of the 8th Fatigue Congress held 3-7 June 2002, Stockholm, Sweden, (2002), 781-288.

[15] H. Heitmann: Betriebsfestigkeit von Stahl: Vorhersage der technischen Anrisslebensdauer unter Berücksichtigung des Verhaltens von Mikrorissen. PhD-Thesis RWTH Aachen, (1984).

[16] J.C. Newman: An evaluation of the Plasticity-induced Crack-Closure Concept and Measurement Methods. NASA/TM-1998-208430, (1998).

9th Liege Conference : Materials for Advanced Power Engineering 2010
edited by J. Lecomte-Beckers, Q. Contrepois, T. Beck and B. Kuhn.

HIGH TEMPERATURE CORROSION OF THERMALLY SPRAYED NiCr- AND AMORPHOUS Fe-BASED COATINGS COVERED WITH A KCl-K_2SO_4 SALT MIXTURE

T. Varis[1], D. Bankiewicz[2], P. Yrjas[2], T. Suhonen[1], S. Tuurna[1],
K. Ruusuvuori[1], S. Holmström[1], J. Salonen[1]

[1]VTT, P.O.Box 1000, FIN 02044 VTT, Espoo, Finland
[2]Åbo Akademi University, Biskopsgatan 8, 20500 Turku, Finland

Abstract

New process conditions due to the requirement of higher efficiency together with the use of high-chlorine and alkali containing fuels such as biomass and waste fuels for heat and electricity production will challenge the resistance and life of tube materials. In conventional materials the addition of alloying elements to increase the corrosion resistance in aggressive combustion conditions increases costs relatively rapidly. Thermally sprayed coatings offer promising, effective, flexible and cost efficient solutions to fulfill the material needs for the future. Some heat exchanger design alterations before global commercialization have to be overcome, though.
High temperature corrosion in combustion plants can occur by a variety of mechanisms including passive scale degradation with subsequent rapid scaling, loss of adhesion and scale detachment, attack by melted or partly melted deposits via fluxing reactions and intergranular/interlamellar corrosion. A generally accepted model of the 'active oxidation' attributes the responsibility for inducing corrosion to chlorine. The active oxidation mechanism plays a key role in the thermally sprayed coatings due to their unique lamellar structure.
In this study, the corrosion behaviour of NiCr (HVOF and Wire Arc), amorphous Fe-based, and Fe13Cr (Wire Arc) thermally sprayed coatings, were tested in the laboratory under simplified biomass combustion conditions. The tests were carried out by using a KCl-K_2SO_4 salt mixture as a synthetic biomass ash, which was placed on the materials and then heat treated for one week (168 h) at two different temperatures (550°C and 600°C) and in two different gas atmospheres (air and air+30%H_2O). After the exposures, the metallographic cross sections of the coatings were studied with SEM/EDX analyzer. The results showed that the coatings behaved relatively well at the lower test temperature while critical corrosion through the lamella boundaries was observed at the higher test temperature.

Keywords: Thermal Sprayed Coatings, high temperature corrosion, chlorine corrosion, boiler

1. Introduction

The role of chlorine and sulphur in complex oxidizing environments are detrimental. Chlorine induced corrosion is usually ascribed to a generally accepted model of the 'active oxidation' mechanism, which was first observed and described by Lee and McNallan [1]. Chlorine, diffuses through cracks and pores of the oxide scale of the oxidized metal towards the metal/scale interface and metal chlorides are formed at low $p(O_2)$, established at this interface. At temperatures of 400°C and higher, evaporation of metal chlorides takes place and subsequent outward diffusion of the volatile metal chlorides towards the gas phase occurs. By reaching regions with a higher $p(O_2)$, the metal chlorides are transformed to oxides, growing in cracks and pores of the scale and leading to subsequent cracking and spallation. The main failure mechanism is by chlorination, although attack by sulphates rich deposits may also play an important role. Deposit chemistry is important since low melting phases may form on the tube surface. It has been shown that the high corrosion rates are related to a large extent to alkali-chlorides in the deposits. [2, 3, 4, 5, 6, 7]

To avoid the higher corrosion rates more resistant tube materials are needed. The demonstration trials in boilers showed that by the proper coating selection, the material wear

by the oxide scale formation can be significantly reduced. Change to more noble materials increases the price of tubing hence is not always economically favourable. The coatings flexibility allows using different strategies for the material design. Nevertheless, the metal oxidation and spallation of oxide layers are not the predominant degradation mechanism of the coatings. The challenge for the coatings performance lies elsewhere. Thermal sprayed coating has its unique lamellar structure and a certain oxidation degree of the sprayed particles. Critical issues are then interlamellar cohesion and oxide distribution in the lamella boundaries. Additionally, the life time and the failure mechanisms of the coatings are still not well known and need more research. Even though the coating material performance itself may have a higher corrosion resistance, the thermo-mechanical compatibility or chlorine penetration to the base material coating interface can cause unexpected damages. [7, 8, 9]

Coatings with high chromium content have been reported to give the steel a good protection in oxidizing environments, although it is known that the chromium oxide layer formed on the surface is not fully protective against chlorine due to the imperfections and cracks in the rough surface of the coating. At certain temperatures and with certain $p(O_2)$ and $p(Cl_2)$, volatile or solid ferro, chromium and nickel chlorides can form at the metal/oxide layer interface, thus taking a major role in the active chlorine corrosion. [3, 9, 10]

The objective of this work was to study the high temperature corrosion behaviour of thermally sprayed Fe- and Ni-based Cr containing coatings under simplified biomass combustion conditions and to compare the critical failure mechanisms of these coatings.

2. Experimental

The thermal spray coating was performed with a Sulzer Metco DJ Hybrid 2700 HVOF (high velocity oxy fuel) and a Sulzer Metco Smart Arc. The powder used for HVOF was Praxair 1260F NiCr. The wires used for arc spray were Nanosteel SHS 7174, Metcoloy 2 from Sulzer Metco and TAFA CT45 from Praxair. The coatings were applied on low alloy steel (10CrMo9-10). Prior to deposition, the base material was grit blasted with alumina particles (500-700 µm) to achieve a well adhering surface. The surface roughening is essential to guarantee good bonding between the base material and the coating. The aim was to manufacture dense and well adhering coatings, which could provide satisfactory protection to the base material against corrosion and erosion. For the HVOF NiCr-coatings two different gun configurations were used; 2702 aircap producing a lower particle temperature aiming to achieve a less oxidized coating and 2701 aircap producing higher particles temperature with the purpose to achieve a higher degree of melting of the powder particle. Higher particle temperatures lead obviously to more oxidise coating structure. The chemical compositions of the materials together with the manufacturing parameters are presented in more detail in Table 1. Table 2 presents the matrix of performed tests.

The steel specimens with thermally sprayed coatings were machined to a size of approximately 20 mm x 20 mm x 5 mm. Before the oven tests the specimens were cleaned in ethanol using an ultrasound bath, covered halfway with a protective paste and pre-oxidized at 200°C for 24 h.

Table 1. Spray parameters and chemical compositions of coatings.

Coating	Method of spraying	Material	Chemical composition	Spray parameters
A_1	HVOF	**Ni50Cr** Praxair 1260F -53+20 µm atomized	Ni-47Cr-0,03C- 0,2Fe- 0.01Mn - 0,1Si	**Air cap 2702 (cold)** C_3H_8: 72 l/min O_2: 152 l/min Air: 400 l/min
A_2	HVOF	**Ni50Cr** Praxair 1260F -53+20 µm atomized	Ni-47Cr-0,03C- 0,2Fe- 0.01Mn - 0,1Si	**Air cap 2701 (hot)** C_3H_8: 68 l/min O_2: 240 l/min Air: 375 l/min
B	Wire arc spray	**Ni50Cr** TAFA 45 CT Wire	Ni- 45 Cr–5Ti	Voltage: 30 V Current: 220 A Air Pressure: 3,5 bar
C	Wire arc spray	**Amorphous Fe-based** SHS 7174 Wire	Fe-30Cr-10Mo-5B-4W-2C-2Mn-2Si	Voltage: 35 V Current: 220 A Air Pressure: 3,5 bar
D	Wire arc spray	**Fe-13Cr** Metcoloy 2 Wire	Fe 13Cr 0.5Si 0.5Ni 0.5Mn 0.35C	Voltage: 30 V Current: 200 A Air Pressure: 3,5 bar

Table 2. The matrix of performed tests

Test	Temp., °C	Salt, mol-%	Gas atm., %	Time, h	Tested coatings
I	550 °C	$50K_2SO_4$+ 50KCl	air+30% H_2O	168	A_1, A_2, B, C, D
II	550 °C	$50K_2SO_4$+ 50KCl	air	168	A_1, A_2, B, C, D
III	600 °C	$50K_2SO_4$+ 50KCl	air+30% H_2O	168	A_1, A_2, B, C, D
IV	600 °C	$50K_2SO_4$+ 50KCl	air	168	A_1, A_2, B, C, D

Prior to the heat treatment the specimens were covered with a 50/50 mol-% KCl-K_2SO_4 mixture. From Figure 2 it can be noted that there was no melt during the experiments as the first melt in the salt mixture appears at ~690°C while the highest test temperature was 600°C. Then the material's exposure tests (up to 5 samples at a time) were carried out at 550°C and 600°C in a horizontal tube furnace for 168 h (7 days). Two furnaces were used in the tests. One was a standard horizontal tube furnace (figure 1a), where the tests with exposure to ambient air were performed and the second was a similar one but equipped with a water pump and a pre-heater. The water was heated-up up to 200°C before it was introduced into the furnace together with the oxygen/nitrogen mixture (figure 1b).

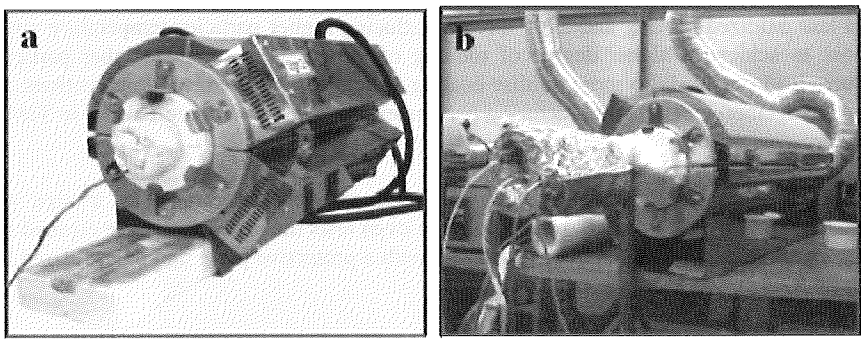

Figure 1. Horizontal tube furnaces for corrosion tests a) in ambient atmosphere (air) and b) air + H_2O

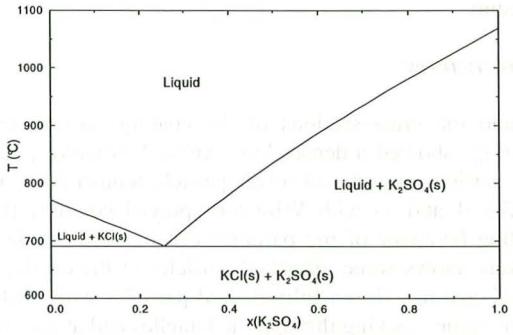

Figure 2. Phase diagram showing melting behavior of a KCl-K_2SO_4 salt mixture used in the experiments [11]

At the end of the experiments (after 168h), the furnace heating was shut down and, if water was present, the water flow was turned off and the specimens were allowed to cool down inside the furnace with a continuous flow of the O_2-N_2 mixture through the reactor. When the temperature in the oven was lower than 300°C the gas flow was turned off and the reactor with the sample holder was removed from the oven and the specimens were left for further cooling. The samples were cast in resin, then cut off in the middle to reveal the specimen's cross-section. The metallographic cross-sections were further polished, cleaned and then analyzed with SEM/EDX in order to study the morphology of the formed oxides and to identify various chemical elements. The corrosion layer thickness was determined using scanning electron microscope back-scatter images. The SEM panoramic images were digitally treated by using contrast differences. An example of the treatment stages of a typical panoramic picture is shown in figure 3.

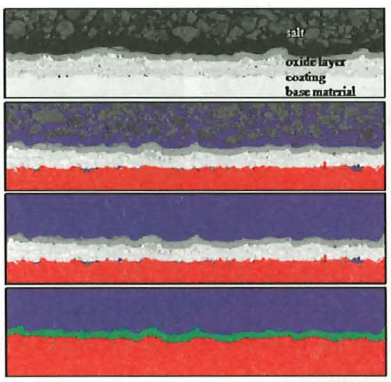

Figure 3. A schematic view of the colouring stages of a SEM image in order to determine oxide layer thickness

After the panoramic images have been colored, the thickness of the oxide layer is determined for each vertical line of pixels and recalculated into µm.The corrosion layer is defined as the thickness of the oxide layer for each line and the corrosion attack is expressed as a mean thickness of the oxide layer [12, 13].

3. Results and discussion

3.1 The coating microstructures

The microstructures and the cross-sections of the coatings are presented in figures 4-8. Generally, HVOF coatings showed a denser less oxidized structures, which is due to higher kinetic energy during particle impact and lower particle temperature. When comparing the structure of HVOF (fig. 4 and 5) with Wire arc sprayed coatings (fig. 6, 7, and 8) the difference in the melting behavior of the particles can be seen. In the HVOF coating, the intrinsic lamella structure shows some unmelted particles in the coating. The microstructure of the Wire arc sprayed coatings shows fully melted particles with visible lamellar structure (fig. 6 and 7). However, some cracking through the lamellas and at the lamella boundaries can be observed in Wire arc sprayed amorphous coating (fig 7). The effect of manufacturing parameters of HVOF sprayed NiCr can be seen by comparing the fig 4 and 5. In fig 5, when coating is produced with significantly colder conditions, insufficient lamella cohesion can be detected, causing lamella detachment during sample manufacturing. However, oxide content is lower.

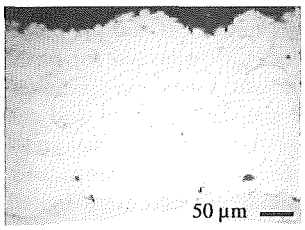

Figure 4. Optical micrograph of the HVOF sprayed NiCr (hot)

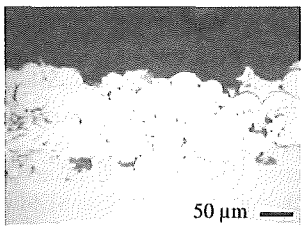

Figure 5. Optical micrograph of the HVOF sprayed NiCr (cold)

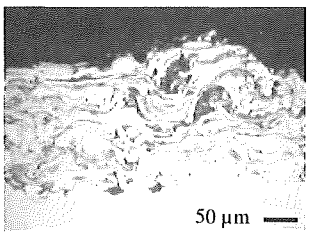

Figure 6. Optical micrograph of the Wire arc sprayed NiCr

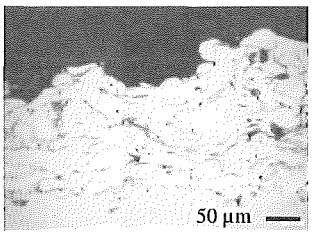

Figure 7. Optical micrograph of the Wire arc sprayed amorphous

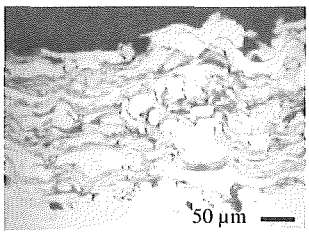

Figure 8. SEM micrograph of the Wire arc sprayed Metcoloy 2

3.2 Corrosion results

3.2.1 The oxide layers

Figure 9 presents the oxide layer thicknesses obtained from the corrosion tests. In the graph, the coatings are placed in order of decreasing Cr content. Generally, higher degradation of the coatings and greater oxidation rates were observed at higher temperature. The effect of H_2O was found to be ambiguous. The presence of H_2O at 550°C generally increased the corrosion of NiCr-coatings, while the effect at 600°C was not as clear. Nevertheless, two important observations can be directly derived from Figure 9, a) the oxidation resistance of the arc sprayed amorphous Fe-based alloy (C) was very good under all test conditions and b) degradation of arc sprayed Fe13%Cr (D) was extreme under all test conditions.

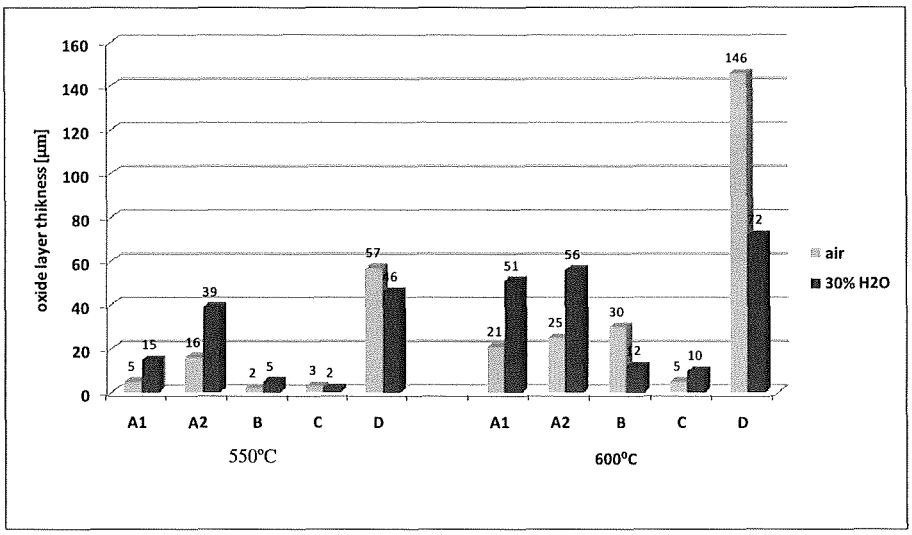

Figure 9. The oxide layer thicknesses of the coatings exposed to different environments

Additionally, it was observed that arc sprayed NiCr (B) showed good resistance at the lower temperature (550°C) in both dry and moist air while the HVOF NiCr (A_1, A_2) coatings suffered clear corrosion at 600°C which clearly increased in the presence of H_2O. It has been earlier shown that water vapour may increase oxidation at high temperature conditions [14]. However, this seems not to be applicable to all the tested coatings, which indicates that composition and minor alloying additives plays important role on oxide scale formation. It can be clearly seen from Figure 9 that some of the arc sprayed coatings (B, D) exposed to water vapor at high temperature (600°C) resulted in the formation of a thinner oxide layer (however still significant in most cases) when compared to tests in ambient air.

3.2.2 SEM/EDXA studies

The corrosion behaviour of the coatings was studied in more detail with the SEM/EDX analyzer to clarify some of the effects described above. The examination of the arc sprayed coatings: NiCr (B) and Fe-based amorphous (C) exposed at 550°C in air showed beneficial resistance with no evidence of chlorine penetration through the coatings (figures 10a and 10b). Both coatings exhibited distinctive, horizontal lamellar structure with the difference that

arc sprayed Fe-based amorphous coating is less oxidized than NiCr arc sprayed what could be one of the reasons of much worse behaviour of NiCr in air at 600°C (B).

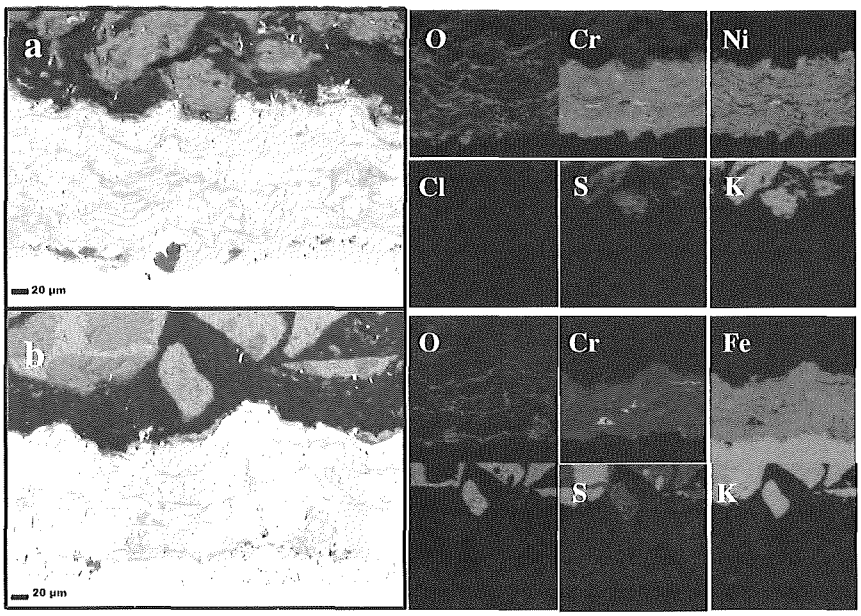

*Figure 10. SEM images and x-ray maps of the a) arc sprayed NiCr (**B**) and b) arc sprayed Fe-based amorphous (**C**) coatings exposed to air at 550°C*

At the higher temperature (600°C) intensified corrosion of the NiCr-coatings was noticed. In some coatings, chlorine penetrated along the lamella boundaries where Cr-Cl rich ($CrCl_2$) inter-lamellar inclusions were formed in air at 600°C (Figure 11). This can be also observed in figures 12b, 12d, and 12e. Chlorine detected under the oxide layer is clear evidence of the active oxidation taking place at the material/oxide scale interface. The behaviour is similar to the mechanism described by Uusitalo et al. [9]. Chromium oxide rich lamella boundaries or imperfectly adhering lamellas may offer diffusion paths for the gaseous chlorine. This was observed especially in the cases with HVOF sprayed coatings which appeared to have more granular rather than lamellar structure. (Figure 12e).

Chlorine rich inclusions were observed in both less and more oxidized coatings (figures 12b and 12d). This was, however, not the case with the amorphous Fe-based coating (D), which is shown in Figure 13.

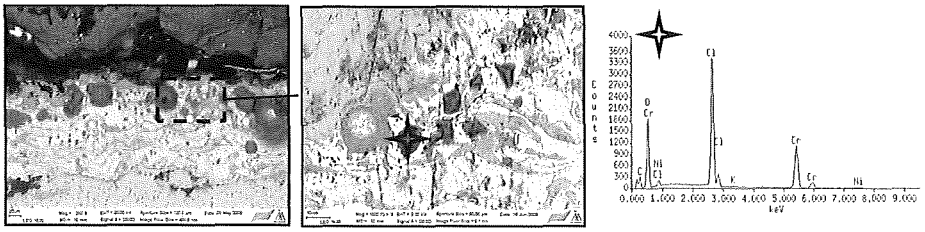

Figure 11. SEM images and EDXA analysis presenting $CrCl_2$ inclusions found in the NiCr arc sprayed coating exposed to air at 600°C

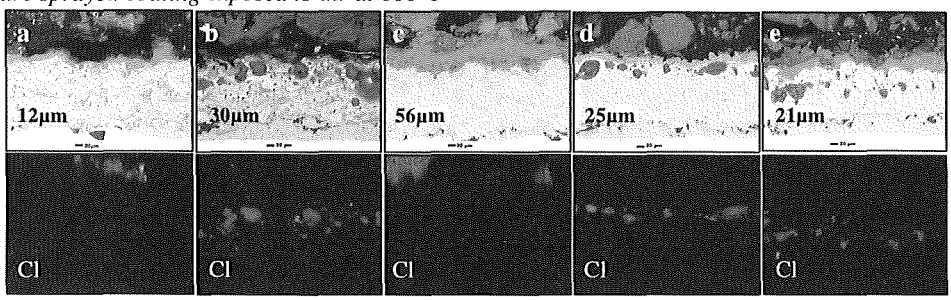

*Figure 12. SEM images and Cl x-ray maps of the NiCr-coatings after exposure test: a) NiCr Arc Sprayed (**B**) in air + H_2O at 600°C, b) NiCr Arc Sprayed (**B**) in air at 600°C, c) NiCr HVOF (hot) (A_2) in air + H_2O at 600°C, d) NiCr HVOF (hot) (A_2) in air at 600°C, e) NiCr HVOF (cold) (A_1)in air at 600 °C*

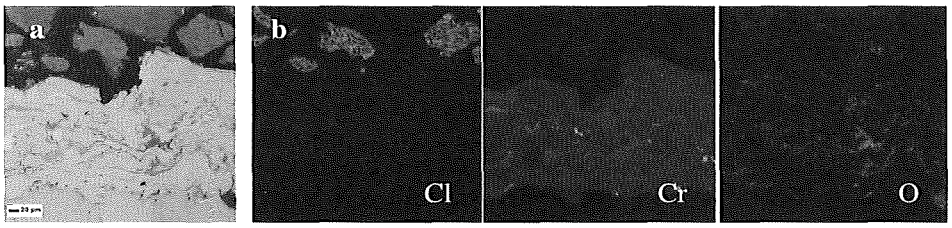

*Figure 13. a) SEM image of the amorphous Fe-based Arc Sprayed coating, b) Cl, Cr and O x-ray maps after the exposure in air at 600°C (**C**)*

The effect of the coating density and lamella boundary conditions can be considered an important factor when comparing also the chlorine penetration depth. In the HVOF NiCr coatings using hot and cold parameters it was observed that Cl penetrated into the coating (Fig. 12e) even to about the midsection of the coating in the cases where cold process parameters were used.

Some result indicates the importance of minor alloying elements and phase structure (amorphous) on the oxide layer development and protectiveness. In air+H_2O environment a relatively thick Cr_2O_3 scale was formed on the surface of the HVOF coatings and it is worth to notice that no Cl penetration through the coatings was observed in the cases with water present (figures 12a and 12c). This may suggest that an oxide layer formed in air+H_2O conditions is denser and develops faster in early stages of the exposure thus preventing Cl diffusion into the lamella boundaries. Nevertheless, the oxide layer was thicker and together

with accompanying Cr outward diffusion had adverse effects on the coating resistance, because of the gradual chromium depletion in the coating. This kind of behaviour is presented in fig.14 for HVOF NiCr-coating, showing chromium depletion towards the surface. As an example, the good performance of arc sprayed amorphous Fe-based coating in air+H_2O at 600 °C is demonstrated in fig. 15. Oxide layer is relatively thin but protective for Cl.

Furthermore, some differences in oxidation behaviour were detected for NiCr-coatings having slightly different composition. The oxide layer was thicker for HVOF coatings (Fig. 12 c) when comparing to arc sprayed coatings during exposure to moist air (Fig. 12 a). In this case there was minor Ti alloying in the arc sprayed material.

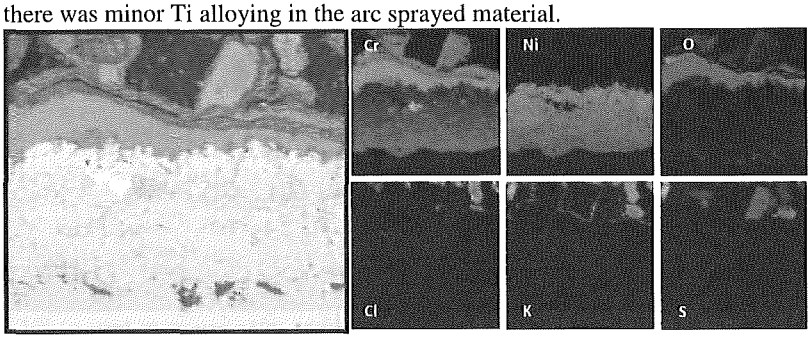

Figure 14. SEM images and x-ray maps of the HVOF NiCr (hot)(A_2) coating exposed to air+H_2O at 550°C.

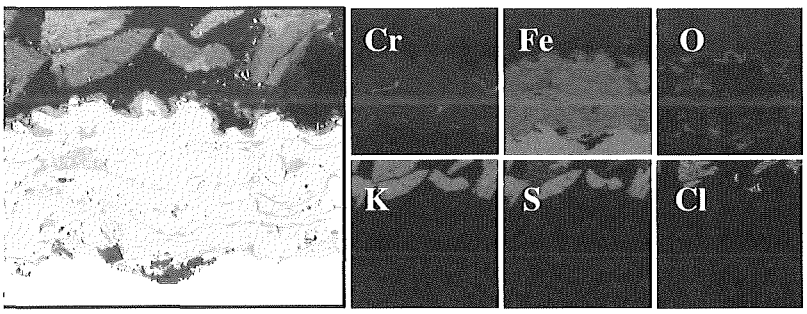

*Figure 15. SEM images and x-ray maps of the arc sprayed Fe- based amorphous (**C**) coating exposed to air+H_2O at 600°C.*

4. Conclusions

In this work high temperature corrosion laboratory testing of thermally sprayed coatings has been carried out. The purpose was to investigate the corrosion resistances of different HVOF and Wire arc sprayed coatings in simplified biomass combustion atmosphere and compare their behaviors. Five coatings manufactured by two different techniques and by changing process parameters were covered with a KCl-K_2SO_4 salt mixture and exposed to ambient and moist (30% H_2O) air at 550°C and 600°C for one week. It can be concluded that:

- Arc Sprayed Amorphous Fe-Cr (**C**) showed very good resistance in all cases showing just negligible oxide layer growth

- NiCr Arc Sprayed (**B**) coating showed good resistance in both conditions at 550 °C
- Higher degradation of the coatings and greater oxidation rates at 30% H_2O containing atmosphere were determined for HVOF NiCr ($\mathbf{A_1}$, $\mathbf{A_2}$) coatings
- Arc Sprayed (**B, C, D**) coatings suffered from increased corrosion in ambient air conditions
- Clear evidence of chlorine penetration along the lamella boundaries of the NiCr coatings at 600°C in air was observed
- Exposure of HVOF NiCr ($\mathbf{A_1}$, $\mathbf{A_2}$) coatings to water vapour containing atmosphere was found to hinder Cl penetration but resulted in a thicker oxide layer growth and extreme Cr depletion from the coatings

It seems that both, the coatings composition and selection of thermal spraying process play important role and have importance for the high temperature oxidation resistance and are strongly dependent on the environment.

Acknowledgments

The results presented in this paper are part of Dublo research project financed by Tekes – the National Technology Agency of Finland. SEM analyses done by Mr. Linus Silvander are greatly appreciated.

References

1. Lee, Y. Y., McNallan, M. J: Metallurg. Trans. 18A, (1987), 1099
2. Spiegel, M., Schroer, C., Grabke, H.J.: Materials Science Forum 251-254(1997)
3. Zahs, A., Spiegel, M., Grabke, H.J., Chloridation and oxidation of iron, chromium, nickel and their alloys in chloridizing and oxidizing atmospheres at 400-700°C, Corrosion Science 42, p. 1093, 2000
4. Sorell, G., Schillmoller, C.M.: Proc 1st Int. Conf on heat resistant materials Wisconsin 1991
5. Agarwal, D.C., Klöwer, J., Grossman, G.K.: Proc. NACE Corrosion , New Orleans 1997
6. Skrifvars, B.J., Backman, R., Hupa, M., Salmenoja, K., Vakkilainen, E. Corrosion of superheater steel materials under alkali salt deposits Part 1: The effect of salt deposit composition and temperature. Corrosion Science 50 (5), p.1274-1282, 2008.
7. Skrifvars, B.J., Westen-Karlsson, M., Hupa, M., Salmenoja, K. Corrosion of super-heater steel materials under alkali salt deposits. Part 2: SEM analyses of different steel materials. Corrosion Science, 52 (3), p.1011-1019, 2010
8. Mäkipää, M., Baxter, D., Turunen, E., Oksa, M. Sulfidation attack of the the heat transfer surfaces in boilers: materials performance and future prospects. VTT Symposium 233. BALTICA VI. Life management and maintenance for power plants.
9. Livingston, N. J. Fireside corrosion testing of candidate superheater tube alloys, coatings and claddings phase II. Foster Wheeler Development Corporation, USA. Corrosion 97, Paper No. 140.
10. M.A. Uusitalo, P.M.J. Vuoristo, T.A. Mäntylä, High temperature corrosion of coatings and boiler steels in oxidizing chlorine-containing atmosphere, Materials Science and Engineering A346 (2003) 168-177

11. M.A. Uusitalo, P.M.J. Vuoristo, T.A. Mäntylä. High temperature corrosion of coatings and boiler steels below chlorine-containing salt deposits. Corrosion Science 46 (2004) 1311–1331
12. Westén-Karlsson, M. Assessment of a Laboratory Method for Studying High Temperature Corrosion Caused by Alkali Salts. Lic. Thesis, Åbo Akademi University, Åbo, Finland 2008, ISBN 978-952-12-2116-3
13. Bankiewicz, D., Yrjas, P., Hupa, M. High temperature corrosion of steam tube materials exposed to zinc salts. Energy&Fuels 23 (7), 3469-3474 (2009)
14. Regina, J. R., DuPont, J. N., Marder, A. R. The Effect of Water Vapor on Passive-Layer Stability and Corrosion Behavior of Fe-Al-Cr Base Alloys. Oxidation of Metals 61, Nos. ½ (2004)

9th Liege Conference : Materials for Advanced Power Engineering 2010
edited by J. Lecomte-Beckers, Q. Contrepois, T. Beck and B. Kuhn.

EFFECTS OF WITHDRAWAL RATE ON THE MICROSTRUCTURE AND MECHANICAL PROPERTIES OF A DS NI-BASE SUPERALLOY

X.Z. Qin, C. Xu, L.Z. Zhou*, J.T. Guo
Institute of Metal Research, Chinese Academy of Sciences, 72 Wenhua Road, Shenyang 110016, China

Abstract

The effects of withdrawal rates ranging from 5 to 9 mm/min on the microstructure and mechanical properties of an experimental directionally-solidified (DS) Ni-base superalloy have been investigated in detail. It is found that the dendrites of the DS alloy become finer and denser with the increase of the withdrawal rates. However, since 5 mm/min, the slowest of the three rates, results in the lowest manufacture efficiency and stress-rupture property at 980 C/180 MPa, it is not adopted to manufacture the DS alloy. The 9 mm/min rate is also rejected because of the problem of stray grains and the low tensile elongation at 650 C which is probably related to the stray defect. Therefore, the middle rate of 7mm/min is determined to be the optimal rate for the manufacture of the experimental DS alloy. This conclusion is well supported by the performances of the lab scale (LS) and industrial scale (IS) DS alloys obtained by 7 mm/min; additionally, it should be pointed out that the former performs better than the latter.

Keywords: DS Ni-base superalloy; Withdrawal rate; Microstructure; Mechanical Properties

1. Introduction

DS Ni-base superalloys present better high temperature strength and hot corrosion resistance than conventional alloys due to the elimination of transverse grain boundaries perpendicular the applied stress[1,2]. Therefore, the DS alloys have been widely used in the turbine industry for decades.

During directional solidification, several parameters such as the thermal gradient in the melt at the liquid-solid interface, the solidification rate and the alloy solute content are very important to the ultimate microstructure and mechanical properties of DS alloys[3,4]. These parameters control the formation and distribution of primary and secondary dendrites, which impose a direct and significant influence on the properties of the alloys.

*Corresponding author. Tel.: +86 24 23971911; fax: +86 24 83978045.
E-mail address: lzzhou@imr.ac.cn (L.Z. Zhou).

High rapid solidification (HRS) technology is employed to manufacture high quality of DS or single crystal (SC) turbine blades[5]. When this technology is used, the solidification rate of alloys mainly depends on the withdrawal rate. In this paper, the effects of the withdrawal rate on the microstructure and mechanical properties of an experimental DS alloy are studied carefully.

2. Experimental

The master alloys were cast on the laboratory (25 kg) and industrial (500 kg) scales, respectively. Their compositions are shown in the Table 1, from which one can see that the Mo content is higher in the IS master alloy than in the LS master alloy and that Hf is added in the latter while it is not included in the former.

Table 1 The compositions of the master alloys on the lab and industrial scales (wt. %)

Alloy	C	Cr	Co	W	Mo	Al	Ti	Ta	Hf	B	Ni
Lab scale	0.09	13.2	10.1	4.6	1.3	4.0	2.4	4.9	0.4	0.018	Bal.
Industrial scale	0.07	13.2	10.1	4.6	1.8	4.1	2.4	4.8	-	0.013	Bal.

The LS master alloys were vacuum remelted and then directionally solidified into the DS bars in a Bridgeman furnace with the HRS technology. The withdrawal rates used in this experiment are 5, 7 and 9 mm/min. The bars obtained by the different withdrawal rates are 200 mm in length and 6 mm in diameter. They were heat treated at 1210 C/ 2 h /AC+1080 C/ 2 h /AC+850 C/ 24 h /AC. After the heat treatment, the tensile- and stress- rupture properties of these bars were tested to determine the optimal withdrawal rate for the production of the experimental DS alloy.

Also, DS IS bars were fabricated at the withdrawal rate of 7 mm/min using the IS mater alloy. And, after the heat treatment the tensile- and stress-rupture properties of the IS bars were also tested to be compared with that of the 7 mm/min LS bars.

The microstructures were mainly examined by optical microscope (OM) and scanning electron microscope (SEM).

3. Results and discussion

3.1. Effects of withdrawal rate on the microstructure of the experimental DS alloy

The transverse microstructures of the LS alloy obtained by the different withdrawal rates are shown respectively in Fig. 1 (a), (c) and (e), which indicate that the average spacing between the primary dendrites reduces with the increase of the withdrawal rate[5]. The primary dendrite spacings of the 5 and 7 mm/min specimens are very close, but they are significantly

coarser and sparser than that of the 9 mm/min specimen.

Fig. 1 (b), (d) and (f) are the longitudinal microstructures corresponding to the different withdrawal rates of 5, 7 and 9 mm/min. From these pictures, one can see that the secondary dendrites of the 9 mm/min specimen are finer and denser than that of the 5 and 7 mm/min specimens and that stray crystal grains are more frequently present in the 9 mm/min specimen than in the other two specimens.

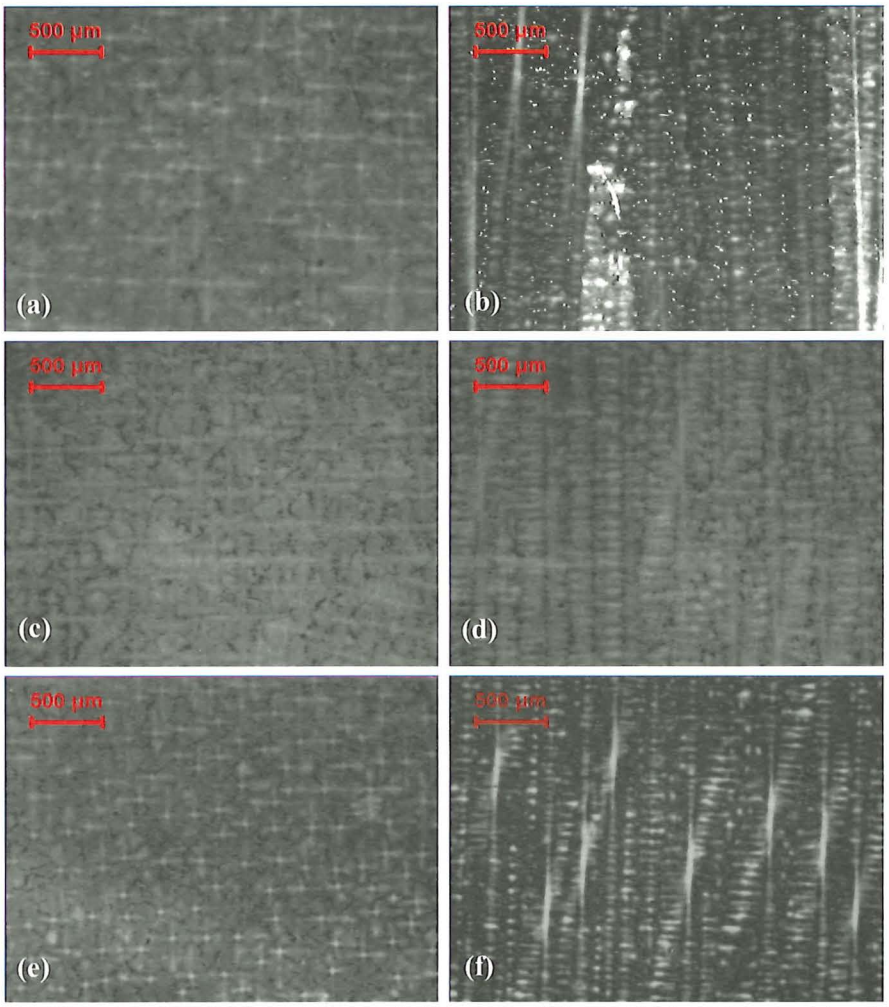

Fig. 1 Microstructures of the experimental alloy at the different withdrawal rates: (a) and (b) 5 mm/min, (c) and (d) 7 mm/min, (e) and (f) 9 mm/min

Although the 9 mm/min specimen has the finest dendritic microstructure, 9 mm/min is not thought to be the most appropriate withdrawal rate for the production of the experimental DS

alloy due to the problem of stray gains, which are undoubtedly detrimental to the DS alloy. In addition, though the microstructure of the 5 mm/min specimen is similar to that of the 7 mm/min specimen, 7 mm/min is eventually thought to be the optimal withdrawal rate for it has a higher efficiency than 5 mm/min.

3.2. Effects of withdrawal rate on the mechanical properties of the experimental DS alloy

The tensile properties of the LS alloy obtained by the different withdrawal rates are summarized in Table 2. At room temperature, the tensile strengths of the 7 mm/min specimen are a bit lower than that of the 5 and 9 mm/min specimens, whereas at 650 C the strengths are very close at the different withdrawal rates. In addition, the elongations at the various rates are basically equivalent at room temperature, while the elongation is slightly smaller at 9 mm/min than at the other two rates at 650 C.

Table 2 Effects of withdrawal rate on the tensile properties of the LS alloy

Temperature	Withdrawal rate mm/min	σ_b MPa	$\sigma_{0.2}$ MPa	δ %	φ %
Room temperature	5	1285	1045	8.2	10.3
	7	1265	1010	8.0	9.3
	9	1300	1030	8.5	8.8
650 C	5	1310	915	7.7	10.5
	7	1310	905	7.3	7.6
	9	1305	935	5.7	8.0

Table 3 shows the stress-rupture properties of the LS alloy at the different withdrawal rates. Under the condition of 980 C/180 MPa, the stress-rupture life of the alloy rises with the increase of the withdrawal rate. However, at 870 C/370 MPa, the life of the 7 mm/min specimen is lower than that of the 5 and 9 mm/min specimens.

According to the above, the LS alloy shows the close mechanical properties, including tensile- and stress-rupture properties, at the different withdrawal rates. However, since the stress-rupture property of the 5 mm/min specimen at 980 C/180 MPa is significantly lower than that of the other two rate specimens, it is not used to manufacture the experimental DS alloy. Also, 9 mm/min is rejected because of the low tensile elongation at 650 C which is probably related to the stray defect. Therefore, 7 mm/min is finally chosen as the optimal withdrawal rate due to both the nice microstructure and the steady mechanical properties.

Table 3 Effects of withdrawal rate on the stress-rupture properties of the LS alloy

Temperature C	Stress MPa	Withdrawal rate mm/min	Life h	Elongation %	Area reduction %
		5	220	29.0	41.7
870	370	7	185	20.0	36.1
		9	260	31.1	39.2
		5	95	31.1	55.6
980	180	7	125	24.5	34.1
		9	135	31.2	48.4

3.3. Mechanical properties of the 7 mm/min LS alloy at different temperatures

The tensile properties of the 7 mm/min alloy from room temperature to 1000 C are exhibited in Fig. 2. The ultimate tensile strength laggardly rises from RT to 650 C and then reduces rapidly with higher temperature; a peak value is present at about 650 C. The yielding strength decreases in the whole temperature range from RT to 1000 C, whereas the expected peak does not occur at all. As demonstrated in Fig. 2(b), the ductilities including δ and ψ are lower than 10% from RT to 650 C, while they rapidly go up from 650 C to 1000 C.

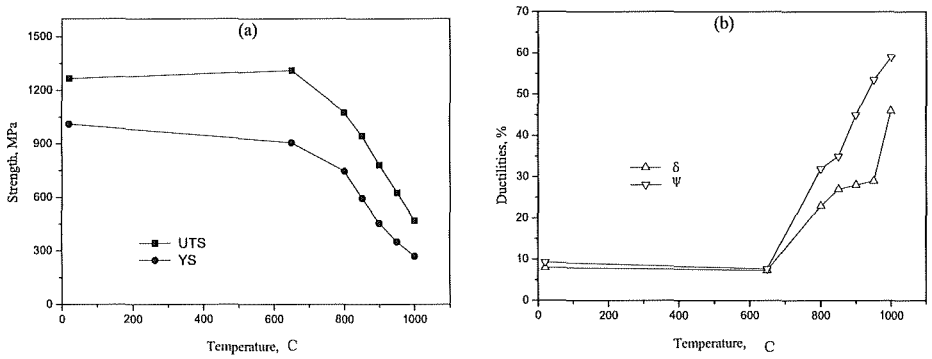

Fig. 2 Tensile properties of the 7 mm/min LS alloy at the different temperatures

Comparing Fig. 3 with Table 3, one can find that the stress-rupture properties of the 7 mm/min alloy at elevated temperatures are very sensitive to both the testing temperature and the applied stress. As demonstrated in Fig. 3(a), the stress-rupture life significantly increases with the decrease of the applied stress. Additionally, the life is 125 h at 980 C/180 MPa (Table 3), whereas it is about 310 h at 950 C/200 MPa (Fig. 3); that is, when the temperature reduces 30 C and the applied stress increases by 20 MPa, the life increases by 185 h. It

seems that the testing temperature has more significant effects on the stress-rupture life than the applied stress.

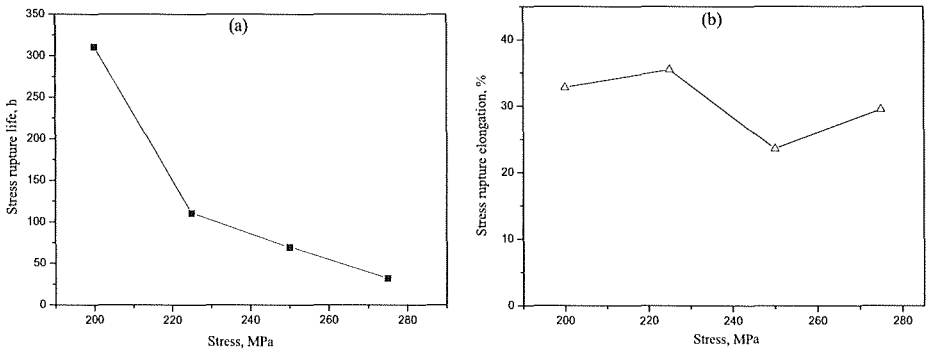

Fig. 3 Stress-rupture properties of the 7 mm/min LS alloy at 950 C

The good tensile- and stress-rupture properties of the 7 mm/min LS alloy indicate that the present withdrawal parameters are appropriate for the manufacture of the DS experimental alloy under the LS conditions.

4. Mechanical properties of the 7 mm/min IS alloy *at different temperatures*

The 7mm/min IS alloy (Fig. 4) has better tensile properties than the LS alloy (Fig. 2), for example: (i) the strengths and ductilities are higher almost at every temperature; (ii) a yield strength peak is present at about 750 C; (iii) a ductility minimum tends to occur at 600 C, which is probably related to the intermediate temperature brittleness. Previous studies reported that the intermediate temperature brittleness was generally present in polycrystalline superalloys[6-8]; therefore, it is difficult to understand the brittleness of the present DS alloy at 600 C. To make it clear, further work need to be done.

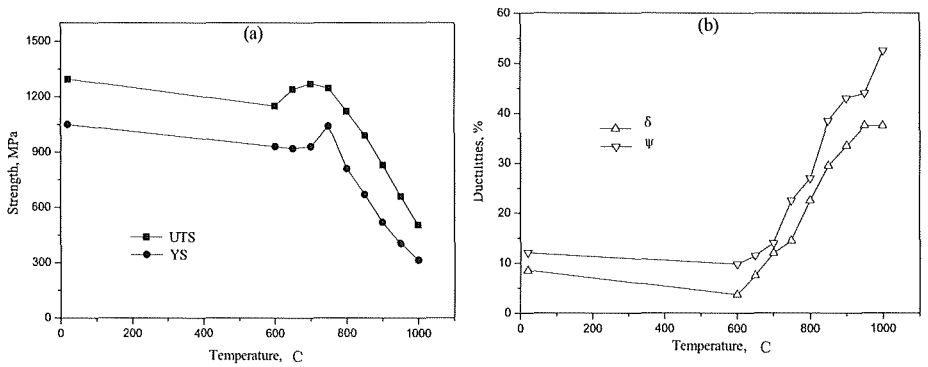

Fig. 4 Tensile properties of the 7 mm/min IS alloy at different temperatures

The 7mm/min IS alloy has much higher stress-rupture lives (Fig. 5(a)) than the LS alloy (Fig. 3(a)). For instance, the former has a life of 450 h at 950 C/200 MPa, which is significantly larger than 310 h of the later; in addition, the life of the former is 75 h at 950 C with the highest stress of 275 MPa, which is about two times as large as 30 h of the latter. On the other hand, the stress-rupture elongation of the IS alloy is a bit higher than that of the LS alloy.

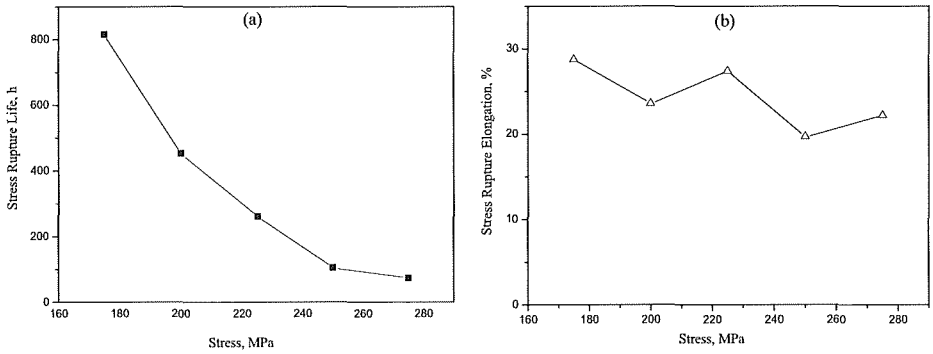

Fig. 5 Stress-rupture properties of the 7 mm/min IS alloy at 950 C

From Table 1, one can see that the IS alloy has a higher content of Mo with a lower content of C than the LS alloy, which make carbides less precipitate and accordingly results a better solid solution strengthening efficiency. This is probably an important reason why the former has the better mechanical properties than the later. In addition, the IS master alloy has a much larger weight (500 kg) than the LS master alloy (25 kg), which makes the former have a larger capability to contain various defects such as segregation and impurity than the latter. This is probably another reason why the IS alloy perform better than the LS alloy.

In a word, the excellent mechanical properties of the 7mm/min IS alloy also support that the withdrawal rate of 7 mm/min can well meet the industrial manufacture of the experimental DS alloy.

5. Conclusion

i) The dendrites of the experimental DS alloy became finer and denser with the increase of the withdrawal rate. 7 mm/min is examined to be the optimal parameter, by which the best microstructure of the alloy can be obtained.

ii) The mechanical properties of the experimental DS alloy at the different withdrawal rates, including tensile- and stress-rupture properties, are comparatively studied and it was found that the 7 mm/min alloy has steadier properties than the 5 mm/min and 9 mm/min alloys. Accordingly, 7 mm/min is determined to be the appropriate rate for the manufacture of the DS alloy.

iii) The mechanical properties of the LS and IS DS alloys obtained by 7 mm/min at different

temperatures both support that the present withdrawal rate can well meet the industrial production of the experimental DS alloy.

References

[1] I. S. Kim, B. G. Choi, S. M. Seo, D. H. Kim, C. Y. Jo, Influence of heat treatment on microstructure and tensile properties of conventionally cast and directionally solidified superalloy CM247LC, *Mater. Lett.*, 62, 1110-1113, (2008).

[2] J. T. Guo, C. Yuan, H. C. Yang, V. Lupinc, M. Maldini, Creep-rupture behavior of a directionally solidified Nickel-base superalloy, *Metall. Mater. Trans. A*, 32A, 1103-1110, (2001).

[3] W. Kurz, D. J. Fisher, Dendrite growth at the limit of stability: tip radius and spacing, *Acta Metall.*, 29, 11-20, (1981).

[4] R. Trivedi, Interdendritic spacing: Part II. A comparison of theory and experiment, *Metall. Trans. A*, 15, 977-982, (1984).

[5] N. R. Zhao, T. Jin, X. F. Xun, H. R. Guan, H. C. Yang, Z. Q. Hu, Effect of withdrawal rate on microstructure and mechanical property of single crystal superalloy SRR99, *Chinese Journal of Materials Research*, 22, 46-52.

[6] D. A. Woodford, R. H. Bricknell, Grain boundary penetration of oxygen in nickel and the effect of B additions, *Metall. Trans. A*, 12A, 1467-1475, (1981).

[7] S. Srinivas, M. C. Pandey, D. M. R. Taplin, Air-environment-creep interaction in a nickel base superalloy, *Engineer Failure Analysis*, 2, 191-196, (1995).

[8] R.W. Hayes, D.F. Smith, E.A. Wanner, J.C. Earthman, Effect of environment on the rupture behavior of alloys 909 and 718, *Mater. Sci. Eng.*, A000, 43-53, (1993).

9th Liege Conference : Materials for Advanced Power Engineering 2010
edited by J. Lecomte-Beckers, Q. Contrepois, T. Beck and B. Kuhn.

INFLUENCE OF TIME, TEMPERATURE AND ENVIRONMENT ON CYCLIC BEHAVIOUR OF GAS TURBINE BLADE COATING SYSTEMS

Bettina Bordenet, Sharath Bachegowda, Hans-Peter Bossmann
ALSTOM (Switzerland) Ltd., Brown Boveri Strasse 7, CH-5401 Baden, Switzerland
Tel.: +41-56-205 33 27, Fax: +41-56-205 57 33
e-mail: bettina.bordenet@power.alstom.com

Abstract

In order to increase the operational flexibility of gas turbines, they are subjected to newer and harsher environments, fuels and loading cycles. It is of utmost importance to understand the behaviour and lifetimes of materials used under these conditions. The consumption and degradation of a gas turbine coating system has been evaluated as a part of this study. The reference system has been chosen in the work package 1 'Environmental Degradation and Coatings' of COST538 action, consisting of an IN738 base material, Amdry995 MCrAlY coating and an Air Plasma Sprayed (APS) Yttria partially Stabilized Zirconia (YSZ) Thermal Barrier Coating (TBC). The coating system was characterised by corrosion, thermo-cyclic (TC) and mechanical testing. These results have been compared to a standard Alstom proprietary coating system for corrosion and cyclic oxidation performance.

The reference systems with and without TBC have been subjected to a corrosion test at 700°C and 850°C for up to 1000h. The test procedure has been developed in the previous COST522 action. The corrosion attack of the Amdry995 MCrAlY-coating has been evaluated and compared to Alstom proprietary MCrAlY coating. From the testing under corrosive conditions, the Alstom proprietary MCrAlY coating exhibits a lower corrosion rate at both tested temperatures.

Pre-ageing the reference samples with TBC under different conditions in lab environments and subjecting them to 4-point-bending (4PB) test allowed to study the evolution and degradation of the mechanical behaviour of the reference coating system during its life. The samples were pre-aged under both isothermal and cyclic condition at temperatures between 850°C and 1050°C. The samples have also been subjected to thermo-mechanical loading by cycling them on a daily basis with a maximum temperature between 850°C and 1100°C for up to 5000h. The samples have been monitored for TBC degradation on a daily basis and end of life determined by TBC spallation. With the combination of both testing methods, the degradation of a coating system can be well described.

The cyclic testing from Alstom proprietary coating systems was obtained from sections of parts taken from normal production. The Alstom proprietary coating systems, with MCrAlY and TBC exhibited an increased cyclic life compared to the reference system. The increase in life can be attributed to optimised coating parameters and microstructure.

Keywords: MCrAlY, thermal barrier coating, Amdry995, thermal cycling, hot corrosion, 4-point-bending

1. Introduction

In the work package 1 'Environmental Degradation and Coatings' of COST538 action 'High Temperature Plant Life Extension' the degradation of gas turbine blade coating system has been studied. A reference system was agreed within the work package, consisting of an IN738 base material, Amdry995 MCrAlY coating and an APS Yttria partially Stabilized Zirconia TBC. Alstom supplied the base material and Sulzer, Wohlen (Switzerland) provided the coating. The reference system along with other base material / coating systems were investigated by different partners in the work package. The present study focuses on the characterisation by corrosion, thermo-cyclic and mechanical testing [1]. Additionally, Alstom proprietary coatings were also subjected to the same tests for corrosion and cyclic oxidation.

2. Experiment

The emphasis has been placed on the testing of the reference system i.e. IN738/Amdry995 and IN738/Amdry995/TBC. The behaviour of the IN738/Amdry995 has been examined in detail under corrosive environments. Whereas the behaviour of the IN738/Amdry995/TBC system has been examined under corrosion, thermo-cyclic and 4-point bend testing. The microstructure of all the samples was characterized in the initial condition and after ageing under different conditions.

2.1 Hot corrosion test

The coating system IN738/Amdry995 and IN738/Amdry995/TBC have been tested in a corrosion test at 700°C and 850°C for up to 1000h. This corrosion test was developed in COST522 [2-4]. The samples were coated with 1mg/cm^2 Na_2SO_4/ K_2SO_4 every week. The testing atmosphere was in air with 300vppm SO_2 and 10vol% H_2O. After 500h and 1000h, samples were taken out for metallographic evaluation.

2.2 Mechanical test

As a mechanical test for coated systems, the sample IN738/Amdry995/TBC has been tested at room temperature with 4PB under compression until the TBC spalls off. Figure 1 gives a close-up of the sample. The TBC in the test section has been given a rounded form to eliminate the crack initiation at the edges. During the test, the applied force was recorded as a function of time. The spallation of the TBC could be correlated with the first load drop in the force-time graph. The force at the first load drop can be transformed into an elastic strain by the help of the elastic beam theory. The so gained strain to spallation can be compared for different samples. With the 4PB, the influence of the degradation caused by thermo-cycling and isothermal exposure on the mechanical behaviour can be evaluated.

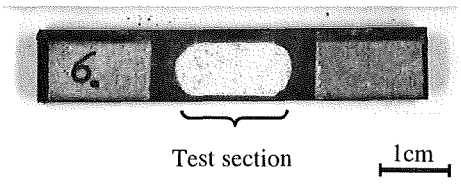

Figure 1: Sample for 4PB testing

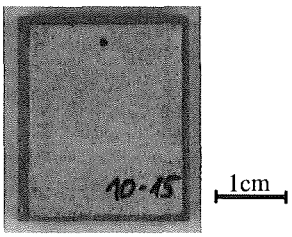

Figure 2: Sample for thermal cycling

The coating systems are not only tested in the initial state but also after different pre-exposure conditions, with different times and cycling length. An overview of the pre-exposure conditions for the 4PB samples can be found in Table 1.

Exposure type	Atmosphere	Temperature	Time
Isothermal Oxidation	Air	850°C	1000h 3000h, 5000h
		950°C	1000h 3000h, 5000h
		1050°C	1000h 3000h, 5000h
Thermo-cyclic (daily cycles)	Air	850°C	1000h 3000h, 5000h
		950°C	1000h 3000h, 5000h
		1050°C	1000h 3000h, 5000h

Table 1: Overview of the pre-exposure conditions for the 4PB samples

2.3 Thermo-cyclic test

For the thermo-cyclic test, the samples were cycled with a maximum temperature between 850°C and 1100°C. The samples were exposed to high temperature in the furnace for 23h and naturally cooled for 1h cold outside the furnace on every weekday. The samples remained in the hot furnace over the weekend, which gives a total of 5 cycles per week. A typical sample for thermal cycling test is shown in Figure 2. Failure of a TBC-coated system is defined as delamination / spallation of the ceramic coating by minimum of 50% of the TBC coated surface area. The lifetime of the system is given in hours to failure.

3. Results

3.1 Initial state

The initial state of the samples has been investigated in detail to set the baseline for the microstructure and morphology of the coating system. The Amdry995 MCrAlY coating was applied with High Velocity Oxide Fuel (HVOF) spraying (Figure 3). It has a thickness of ~200µm and bonding defects of ~42%. The bondcoat porosity varied between 2.1 and 2.6%. The TBC was applied with APS process and exhibited a dense vertically cracked microstructure, with a porosity of around 3% and a thickness of ~380µm (Figure 4). The thickness and the porosity have shown a uniform distribution for both coatings.

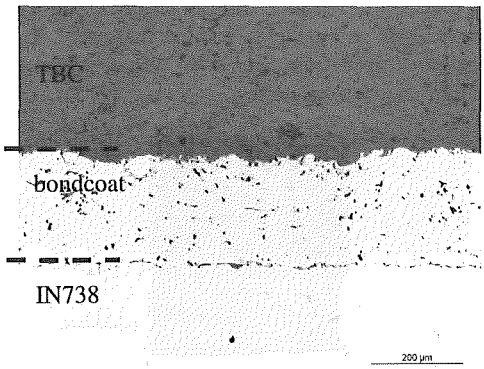

Figure 3: Typical condition of the reference Amdry995 coating

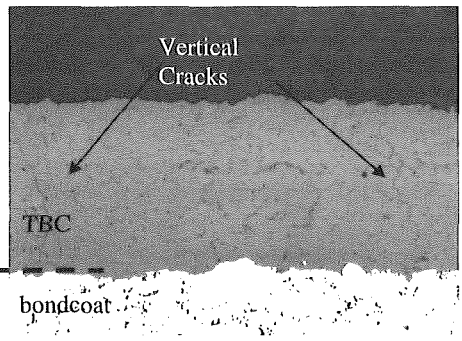

Figure 4: Typical condition of the dense vertically cracked TBC

3.2 Hot corrosion behaviour of IN738 / Amdry995 and Alstom proprietary MCrAlY-coating

At 700°C, the samples with Amdry995 revealed a corrosion attack with a typical "type II corrosion morphology" (Figure 5). After 500h, the corrosion pits are already pronounced. After 1000h, the corrosion has also grown laterally so that the corrosion in the sample exhibits a plane front. At 850°C, the samples with Amdry995 revealed a corrosion attack with a typical "type I corrosion morphology". The type I corrosion attack is much smaller compared to the type II corrosion with some minor sulphides and thick oxide scale, which progresses slowly with time (Figure 6). A beta-depletion zone can also be noticed below the thick oxide scale.

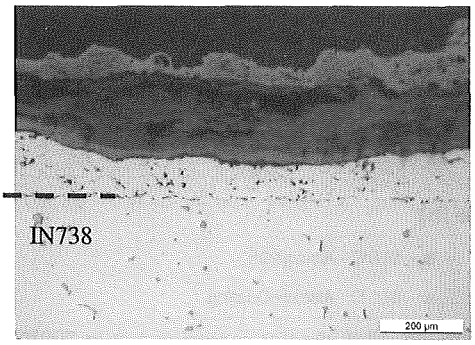

Figure 5: Amdry995, 700°C / 1000h, Corrosion test

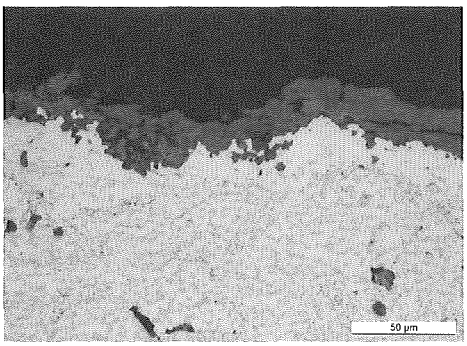

Figure 6: Amdry995, 850°C / 1000h, Corrosion test

An Alstom proprietary MCrAlY-coating applied by thermal spraying on IN738 was exposed to the same corrosion test as the Amdry995. After 1000h at 700°C, the Alstom coating also exhibits a type II corrosion morphology with pits (Figure 7). At 850°C, no signs of type I corrosion morphology, such as internal sulphidation or thick oxide scales were detected (Figure 8). The Alstom MCrAlY seems to be still in the initiation stage. The Alstom Coating exhibits at both temperatures a better corrosion resistance than the Amdry995 (Figure 9).

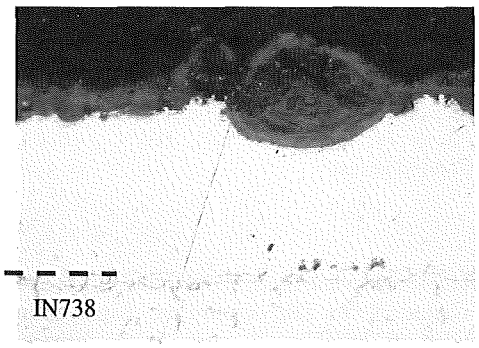

Figure 7: Alstom Proprietary Coating on IN738, 700°C / 1000h, Corrosion test

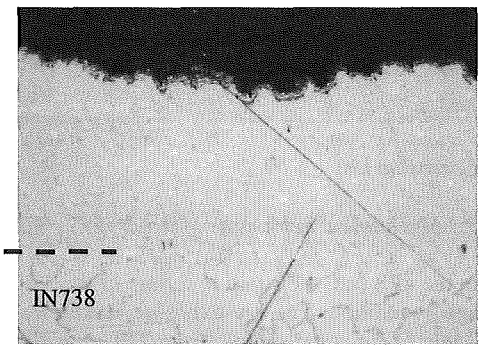

Figure 8: Alstom Proprietary Coating on IN738, 850°C / 1000h, Corrosion test

The TBC coated reference systems IN738/Amdry995/YSZ were also subjected to the corrosion test. At both temperatures, the samples did not reveal signs of corrosion after 1000h in the light microscope (Figure 10 & 11). The oxide scale (TGO: thermally grown oxide), which was formed at the bond coat / TBC interface, is very thin. The atmosphere in the

corrosion test did not cause any degradation after 1000h. The test was stopped after 1000h, since the lab conditions did not represent the corrosive environment in the engine with respect to temperature gradient and salt deposition mechanism. For future testing, longer testing times and thermal gradients are recommended to study the failure mechanism of TBC coated samples.

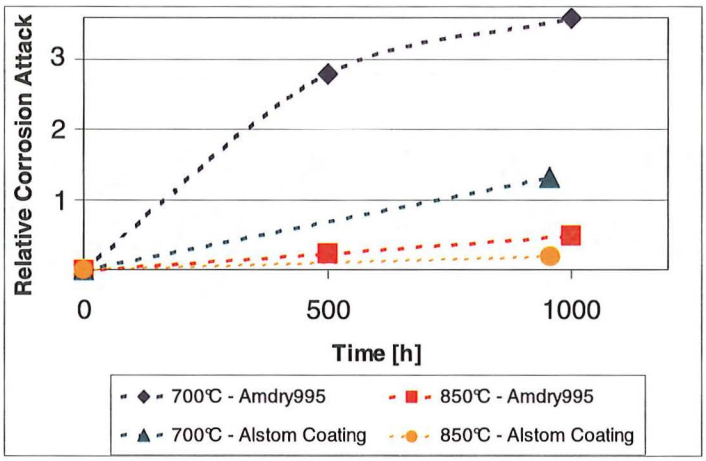

Figure 9: Maximum depth of corrosion attack in the hot corrosion test at 700°C and 850°C, Salt deposit: 1mg/cm2 of Na2SO4/K2SO4 every 160h

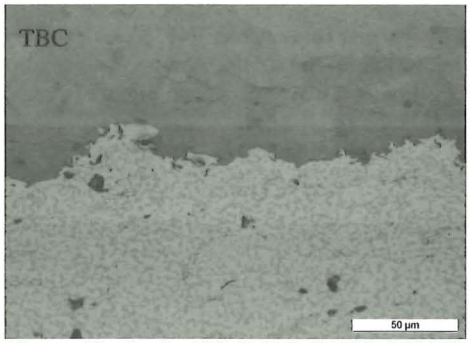

Figure 10: Amdry995 / TBC, 700°C / 1000h, Corrosion test

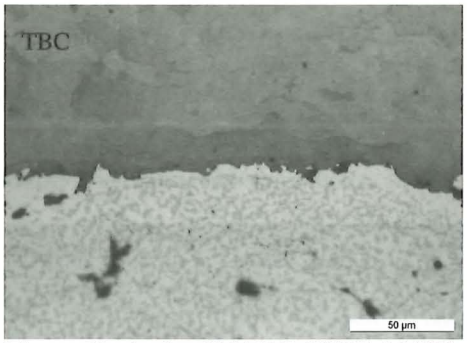

Figure 11: Amdry 995/TBC, 850°C / 1000h, Corrosion test

3.3 Mechanical behaviour of Amdry995 / TBC

In the 4PB test, the strain to failure of the TBC-samples has been determined in the virgin and aged condition. The pre-exposure conditions for Amdry995 / TBC system are displayed in Table 1. On some samples, the TBC already spalled off during pre-exposure in the furnace. None of the Amdry995/TBC samples survived longer than ~2500h at 1050°C. After this time, the Al-reservoir phase (beta phase) was totally consumed in the bondcoat, which has been considered as end of life.

From the 4PB tests, the strain to failure of the TBC coating is plotted over exposure time for the system IN738 / Amdry995 / TBC (Figure 12). The pre-exposure leads to a reduction of the strain to failure in comparison to the virgin condition. At 850°C and 950°C after 3000h, the

strain seems to reach a plateau value. At 1050°C, a shape of the curve could not be determined, since the TBC already spalled before the chosen pre-exposure time was reached. Shorter exposure times have to be taken to evaluate the behaviour of the coating system at 1050°C.The samples pre-aged at 850°C showed a slightly higher strain to failure than the samples pre-aged at 950°C. The strain to failure of the isothermally aged samples and cycled samples do not vary significantly.

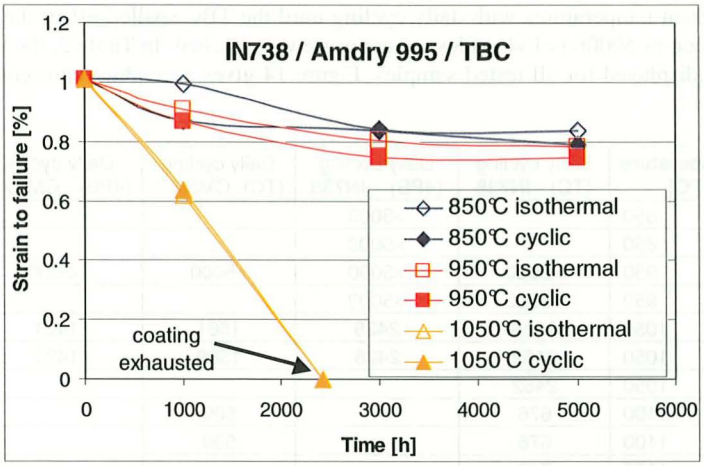

Figure 12: Strain to failure determined in a 4PB test under compression plotted against pre-exposure time for IN738/ Amdry995/ TBC

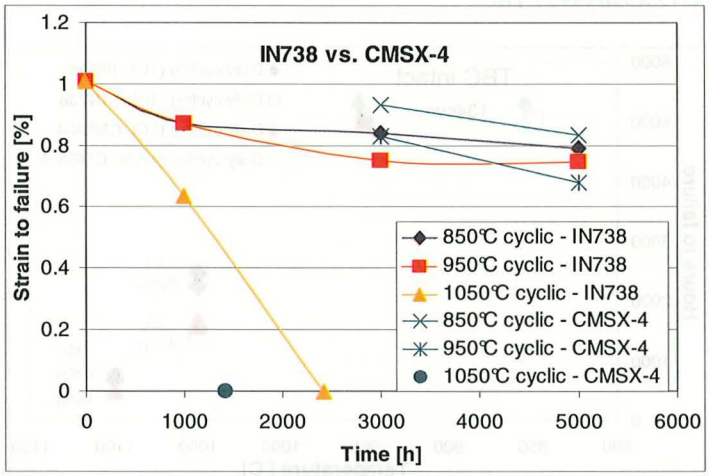

Figure 13: Strain to failure determined in a 4PB test under compression plotted against pre-exposure time for IN738/ Amdry995/ TBC and CMSX-4/ Amdry995/ TBC

Some samples of Amdry995/TBC systems were also sprayed on CMSX-4 substrate to study the influence of the base material. The CMSX-4 system has not been tested in the virgin condition. At 850 and 950°C after 3000h (Figure 13), the CMSX-4 system is not yet in the plateau region. The samples at 1050°C (Figure 13) failed even earlier than with IN738, which has been described above (Figure 12). To confirm the degradation mechanism for CMSX-4,

longer testing times are required. Due to the limited amount of available material, this testing could not be performed.

3.4 Thermo-cyclic behaviour of TBC coated systems

For the investigation of the cyclic behaviour of the Amdry995 / TBC system, furnace cycling tests were performed in parallel to the pre-exposure of the 4PB. The furnace cycling test was done at different temperatures with daily cycling until the TBC spalled off or the testing was stopped as soon as 5000h (=134 cycles) of exposure was reached. In Table 2, the time to TBC spallation is displayed for all tested samples. Figure 14 gives a graphic representation of the same data.

Temperature [°C]	Daily cycling (TC) - IN738	Daily cycling (4PB) – IN738	Daily cycling (TC)- CMSX-4	Daily cycling (4PB) - CMSX-4
850		>5000		
850		>5000		
950	>5000	>5000	>5000	>5000
950	>5000	>5000		
1050	2236	2428	1661	1421
1050	2452	2428	1589	1421
1050	2452			
1100	676		509	
1100	676		509	
1100	748			

Table 2: Cyclic oxidation test performed with IN738 / Amdry995 / TBC and CMSX-4 / Amdry995 / TBC

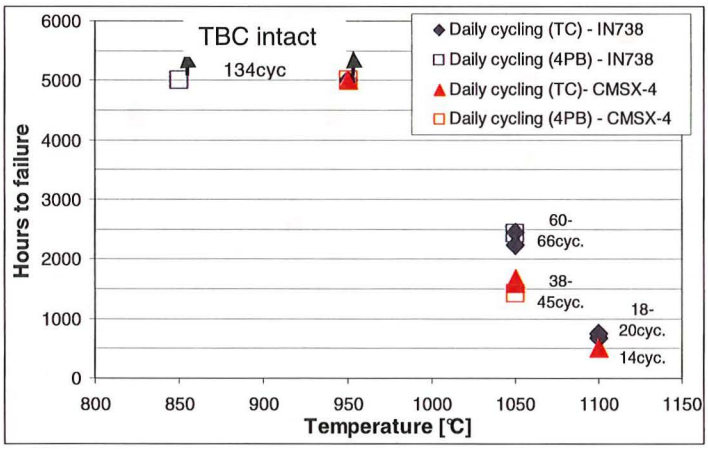

Figure 14: Thermal cycling test performed with IN738 / Amdry995 / TBC and CMSX-4 / Amdry995 / TBC

The cycling temperature has a strong influence on the coating life. Only the samples exposed at 850°C and 950°C survived 5000h of testing. At 1050°C and 1100°C, the samples failed during the test. For the here tested Amdry995 with the dense vertically cracked TBC, the TBC delaminates in one piece, which indicates a high stiffness of the ceramic coating. With increasing temperature, the failure occurred after shorter times. The TBC of each system

failed with a low scatter independent of the sample size (4PB- sample vs. TC-sample). Testing at 850 and 950°C needs to be continued to establish a lifetime rule of the hours to failure in dependence of the exposure temperature.

The base material influences the cyclic behaviour of the coating. The samples with CMSX-4 as base material failed earlier than IN738 at 1050°C and 1100°C. An explanation could be that CMSX-4 is a base material with higher strength at high temperatures than IN738. Due to the higher strength of CMSX-4, the coating system is submitted to higher stresses and less stress relief that lead to earlier failure. Deeper analysis of the samples has to be done to clarify the effect of the base material.

In comparison to the COST538 reference system, two Alstom proprietary coating systems were tested in the same test [5]. The bondcoats are both from the MCrAlY-class. The TBC is also a yttria-stabilised zirconia applied by atmospheric plasma spraying. A typical microstructure of such systems is shown in Figure 15. Even if the TBC has the same chemical composition and the same application process, the Alstom TBC exhibits a much higher porosity than the dense vertically cracked TBC used for the COST538 reference coating system (Figure 4). The tested samples were cut out of blades from standard production.

In contrast to the Amdry995 system, it was seen that TBC spallation occurred after quite a long incubation period (first delamination of TBC or spallation of small size area), but then propagated fast to significant size of spalled area. Final spallation (50% TBC loss criterion) was recorded and plotted in Figure 16. These values are mean values from several samples.

Both Alstom proprietary coating systems exhibited longer times to TBC failures at all temperatures. The longer lifetime and the progressive failure of the Alstom TBC are assumed to be due to the optimised coating parameters. Especially, the different microstructure of the TBC with the high porosity, in contrast to the low-porosity Amdry995 / TBC system, seems to play an important role.

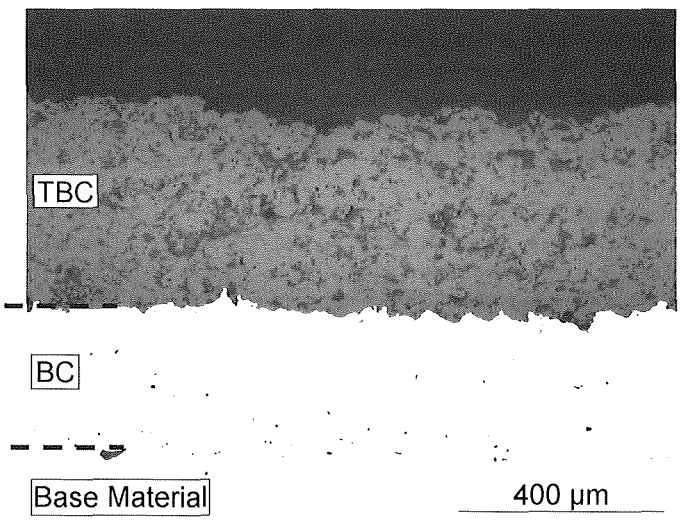

Figure 15: Typical microstructure of the Alstom proprietary coating systems with a MCrAlY-bond coat.

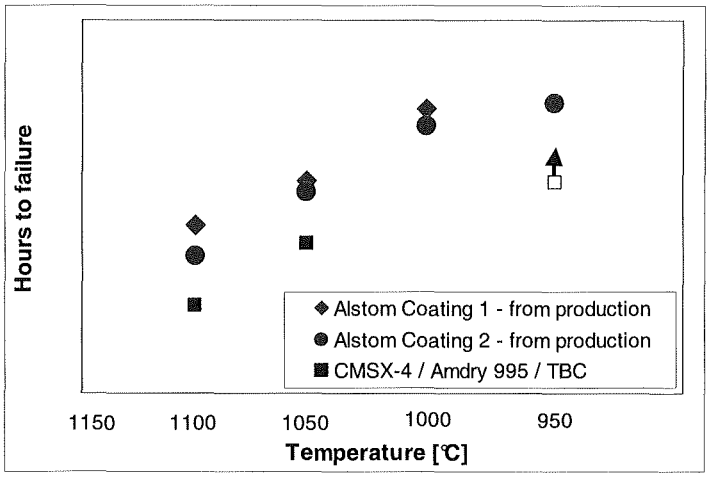

Figure 16: Thermo-cyclic testing performed with CMSX-4 / Amdry995 / TBC; Samples tested at 950°C and 850°C exhibited an intact TBC after 5000h; Alstom coatings 1 & 2.

4. Discussion of Results

The reference system was subjected to a corrosion test at 700°C and 850°C for up to 1000h. The testing at 700°C reproduced Type II corrosion and the testing at 850°C reproduced Type I corrosion on the samples tested. The samples which were exposed to testing at 700°C i.e. subjected to type II corrosion were more significantly degraded than the samples exposed to testing at 850°C i.e. type I corrosion. Under both test conditions, the Alstom proprietary coating performed significantly better than the reference system.

The mechanical behaviour of the samples was investigated by subjecting them to 4PB test. The samples were tested in virgin condition and after various ageing treatments. Temperature has the most significant influence on the strain to failure of the coating systems. Higher exposure temperatures lead to lower strain to failure values. There is a significant difference in the strain to failure values of samples aged at 950°C and those aged at 1050°C.

With increase of exposure time, the strain to failure for the systems reduces at all the exposure temperatures. For the samples exposed at 850°C and 950°C there is an initial reduction in strain to failure and a plateau is reached after 3000h. Samples exposed at 1050°C degrade very fast with time compared to the samples exposed at 850°C and 950°C. This is a strong indication that exposure temperature is a more significant factor in determining coating degradation than time. In the 4PB testing, no significant difference was noticed in strain to failure between the samples with thermo-cyclic and isothermal pre-ageing. Further, an effect of the base material on the strain to failure of the coating systems could not be seen. The coating systems applied on IN738 and CMSX-4 exhibits the same strain to failure when aged under similar conditions.

Form the testing of the samples in thermo-cyclic testing, it can be seen that there is a large influence of temperature on the lifetime of the coating systems. Coating systems aged at higher temperatures (1050°C and 1100°C) have significantly lower lifetimes compared to those aged at lower temperatures (850°C and 950°C). There is also a significant influence of

substrates on the life of coating systems. The coating systems applied on the CMSX4 have a reduced lifetime compared to the coating systems that were applied on IN738 when aged under similar conditions.

Comparing the lifetimes of the reference coating system and the Alstom proprietary coating systems, the influence of bondcoat composition and coating quality becomes evident. The significantly increased lifetimes of the Alstom proprietary coating systems is not only due to the bondcoat composition but also due to the optimised coating manufacturing parameters.

5. Conclusions

The consumption and degradation of a gas turbine coating system has been evaluated as a part of this study. The reference system has been chosen in the work package 1 'Environmental Degradation and Coatings' of COST538 action, consisting of an IN738 base material, Amdry995 MCrAlY coating and an Air Plasma Sprayed (APS) Yttria partially Stabilized Zirconia (YSZ) Thermal Barrier Coating (TBC). The coating system was characterised by corrosion, thermo-cyclic (TC) and mechanical testing. These results have been compared to a standard Alstom proprietary coating system for corrosion and cyclic oxidation performance.

With the combination of corrosion, 4PB and daily cycling tests, the degradation of a coating system can be well described. To get a full lifetime model additional testing is recommended. From the corrosion testing of the sample, the sensitivity of the coating systems to different operating conditions can be obtained. From the 4PB test, it could be derived, that the maximum strain to failure for the coating system must be determined on aged samples, since this value is very sensitive to high temperature exposure. From all the cyclic testing it could be shown that the whole system of base material / bondcoat / TBC has to be considered and tested.

The Alstom proprietary coating performed significantly better than the reference system under corrosive test conditions and also showed better lifetime under thermo cyclic test conditions than the reference system. The increase in cyclic lifetime being attributed to better bondcoat composition and manufacturing parameters.

Acknowledgement
This work was supported by COST538'High Temperature Plant Life Extension'.

References:

[1] Bordenet, B., 'Environmental degradation of protective coatings in gas turbines', Final Report, COST538 High Temperature Plant Life Extension (2008)
[2] Bordenet, B., Corrosion of high temperature materials for gas turbine blading, COST522, Final Report (2003)
[3] Bordenet, B., Bossmann, H.P., High temperature corrosion in gas turbines: fuel model and experimental results, in J. Lecomte-Beckers et al. (eds.), Materials for advanced power engineering 1998, Part II, Forschungszentrum Jülich (2002), 871-881
[4] Bordenet, B., Bossmann, H.P., Development of a new test method of high temperature corrosion in gas turbines based on thermodynamic modelling, Proceedings of 'High Temperature Corrosion and Protection of Materials 6', Les Embiez, France, 2004, Materials Science Forum Vols. 461-646 (2004), 907-916
[5] Bossmann, H.P., Bachegowda, S., Schnell, A., Manufacturing optimization for bondcoat / thermal barrier coating systems, Proceedings of ASME Turbo Expo 2008, June 9-13, 2008, Berlin, Paper GT2008-51336 (2008)

9th Liege Conference : Materials for Advanced Power Engineering 2010
edited by J. Lecomte-Beckers, Q. Contrepois, T. Beck and B. Kuhn.

Part C

Materials for Nuclear Fusion and Fission

9th Liege Conference : Materials for Advanced Power Engineering 2010
edited by J. Lecomte-Beckers, Q. Contrepois, T. Beck and B. Kuhn.

DEVELOPMENT AND EVALUATION OF PLASMA FACING MATERIALS FOR FUTURE THERMONUCLEAR FUSION REACTORS

J. Linke, G. Pintsuk, M. Rödig, A. Schmidt, C. Thomser

Forschungszentrum Jülich, EURATOM Association, D-52425 Jülich, Germany

Extended abstract

More and more attention is directed towards thermonuclear fusion as a possible future energy source. Major advantages of this energy conversion technology are the almost inexhaustible resources and the option to produce energy without CO_2-emissions. However, in the most advanced field of magnetic plasma confinement a number of technological challenges have to be met. In particular high-temperature resistant and plasma compatible materials have to be developed and qualified which are able to withstand the extreme environments in a commercial thermonuclear power reactor. The plasma facing materials (PFMs) and components (PFCs) in such fusion devices, i.e. the first wall (FW), the limiters and the divertor, are strongly affected by the plasma wall interaction processes and the applied intense thermal loads during plasma operation [1]. On the one hand, these mechanisms have a strong influence on the plasma performance; on the other hand, they have major impact on the lifetime of the plasma facing armour.

Materials for plasma facing components have to fulfill a number of requirements. First of all the materials have to be plasma compatible, i.e. they should exhibit a low atomic number to avoid radiative losses whenever atoms from the wall material will be ionized in the plasma. In addition, the materials must have a high melting point, a high thermal conductivity, and adequate mechanical properties. To select the most suitable material candidates, a comprehensive data base is required which includes all thermo-physical and mechanical properties [2 - 5]. In present-day and next step devices the resulting thermal steady state heat loads to the first wall remain below 1 MWm^{-2}, meanwhile the limiters and the divertor are expected to be exposed to power densities being at least one order of magnitude above the FW-level, i.e. up to 20 MWm^{-2} for next step tokamaks such as ITER or DEMO. These requirements are responsible for high demands on the selection of qualified PFMs and heat sink materials as well as reliable fabrication processes for actively cooled plasma facing components. The technical solutions which are considered today are mainly based on the PFMs beryllium, carbon or tungsten joined to copper alloys or stainless steel heat sinks [6 – 8]. To test and to demonstrate the acceptability of plasma facing materials and components special high heat flux test facilities based on intense ion or electron beams [6] are being used routinely to demonstrate the heat removal efficiency and the lifetime under fusion specific loading conditions [9].

In addition to the above mentioned quasi-stationary heat loads, short transient thermal pulses with deposited energy densities up to several tens of MJm^{-2} are a serious concern for next step tokamak devices. The most frequent events are so-called Edge Localized Modes (type I ELMs) and plasma disruptions. Here a considerable fraction of the plasma energy is deposited on a localized surface area in the divertor strike zone; the time scale of these events is typically in the order of 1 ms [10 – 12]. As a consequence, thermal shock induced crack

formation, vaporization, surface melting and droplet ejection as well as particle emission induced by brittle destruction processes will limit the lifetime of the components. This is also valid for instabilities in the plasma positioning (vertical displacement events) which cause irreversible damage to plasma facing components, particularly to the metallic wall armour. Moreover, dust particles (neutron activated or toxic metals or tritium enriched carbon) are a serious concern form a safety point of view. In order to investigate the thermally induced plasma wall interaction under fusion specific thermal loads, high heat flux simulation tests are performed in electron or ion beam test facilities [9] as well as in quasi stationary plasma devices [10]. These experiments cover thermal fatigue loads and/or thermal shock tests with relevant operational loading conditions [13 – 15].

Furthermore, the wall bombardment with 14 MeV neutrons in D-T-burning plasma devices and the resulting material damage are another critical issue, both, from a safety point of view, but also under the aspect of the component lifetime. While the integrated neutron fluence in ITER will be only in the order of 1 dpa (displacements per atom), future devices such as DEMO or commercial fusion reactors will experience integrated neutron wall loads of 80 to 150 dpa. Therefore the development of new radiation resistant materials and their testing under realistic conditions is required. Due to the lack of an intense 14 MeV neutron source, complex neutron irradiation experiments are performed in material test reactors to quantify the neutron-induced material damage [16, 17]. These tests provide a valuable data base on the degradation of thermal and mechanical parameters [18, 19].

References

[1] J. Linke, P. Lorenzetto, P. Majerus, M. Merola, D. Pitzer, M. Rödig:
"EU Development of High Heat Flux Components"
Fusion Sci. and Technology, Vol. 47, 2005, 678 - 685

[2] G. Pintsuk, I. Smid, J.-E. Döring, W. Hohenauer, J. Linke:
"Fabrication and characterization of vacuum plasma sprayed
W/Cu-composites for extreme thermal conditions"
submitted to J. Mater. Sci., 2006

[3] Hirai,T.; Bondarchuk,E.; Borovkov,A.; Koppitz,T.; Linke,J.; Mertens,Ph.; Neubauer,O.; Panin,A.; Philipps,V.; Pintsuk,G.; Sadakov,S.; Steinbrech,R.; Schweer,B.; Uytdenhouwen,I.; Vaßen,R.; Samm,U.; Sievering,R.:
'Development and testing of a bulk tungsten tile for the JET divertor'
Physica Scripta Topical Issue, T128 (2007), 144 – 149

[4] Pintsuk,G.; Compan,J.; Linke,J.; Majerus,P.; Peacock,A.; Pitzer,D.; Rödig,M.:
'Mechanical and thermo-physical characterization of the carbon fibre composite NB31'
Physica Scripta, T128 (2007), 66 – 71

[5] Pintsuk, G.; Compan, J.; Koppitz, T.; Linke, J.; Peacock, A.T.; Pitzer, D.; Rödig, M.; Wikman, S.:
"Mechanical and thermo-physical characterization of three-directional carbonfiber composites forW-7X and ITER"
25th Symposium on Fusion Technology, Rostock, 15. – 19.09.2008
Fusion Engineering and Design, 84, 2009, 1525-1530

[6] J. Linke, F. Escourbiac, I.V. Mazul, R. Nygren, M. Rödig, J. Schlosser, S. Suzuki:
"High Heat Flux Testing of Plasma Facing Materials and Components
- Status and Perspectives for ITER Related Activities"
Journal of Nuclear Materials 367–370 (2007) 1422–1431

[7] Schmidt, A.; Hirai, T.; Keusemann, S.; Rödig, M.; Pintsuk, G.; Linke, J.;Maier, H.;Riccardo, V.; Matthews, G.F.; Hill, M.; Altmann, H.:
'First demonstration of non-destructive tests on tungsten-coated JET divertor CFC tiles in the electron beam facility JUDITH-2'
Phys. Scr. T138 (2009) 014034

[8] Thomser, C.; Schmidt, A.; Bellin, B.; Bürger, A.; Linke, J.; Rödig, M.; Zacchia, F.:
'High heat flux testing of Beryllium components for nuclear fusion Applications'
Proc. 26th Symposium on Fusion Technology, Porto, Portugal, 27.09. – 01.10.2010 (to be published)

[9] Majerus, P., R. Duwe, T. Hirai, W. Kühnlein, J. Linke, M. Rödig:
"The New Electron Beam Test Facility JUDITH II for High Heat Flux Experiments on Plasma Facing Components"
Fus. Eng. Des. 75 – 79, 2005, 365 - 369

[10] Zhitlukhin,A.; Klimov,N.; Landman,I.; Linke,J.; Loarte,A.; Merola,M.; Podkovyrov,V.; Federici,G.; Bazylev,B.; Pestchanyi,S.; Safronov,V.; Hirai,T.; Maynashev,V.; Levashov,V.; Muzichenko,A.:
'Effect of ELMS on ITER Armour Materials'
Journal of Nuclear Materials, 363-365 (2007), 301 – 307

[11] Bazylev, B.; G. Janeschitz, I. Landman, S. Pestchanyi, A. Loarte, G. Federici, M. Merola, J. Linke, T. Hirai, A. Zhitlukhin, V. Podkovyrov, N. Klimov:
‚Behaviour of melted tungsten plasma facing components under ITER-like transient heat loads Simulations and experiments'
Fusion Engineering and Design 83 (2008) 1077–1081

[12] Bazylev,B.; Janeschitz,G.; Landmann,I.; Pestchanyi,S.; Loarte,A.; Federici,G.; Merola,M.; Linke,J.; Zhitlukhin,A.; Podkovyrov,V.; Klimov,N.; Safronov,V.
'ITER transient consequences for material damage: modelling versus experiments'
Physica Scripta, T128 (2007), 229 – 233

[13] Linke J., T. Hirai, M. Rödig, L. Singheiser:
"Performance of plasma facing components under intense thermal loads in tokamaks and stellarators"
Fusion Science and Technology, Vol. 46, 2004, 142 - 151

[14] Compan,J.; Renk,T. J.; Hirai,T.; Linke,J.
'Reduction of preferential erosion of carbon fibre composites under intense transient heat pulses'
Physica Scripta, T128 (2007), 246 – 249

[15] Pintsuk, G.; Kühnlein, W.; Linke, J.; Rödig, M.:
"Investigation of tungsten and beryllium behaviour under short transient events"
Fusion Engineering and Design 82 (2007) 1720-1729

[16] Rödig, M., W. Kühnlein, J. Linke, D. Pitzer, M. Merola, E. Rigal, B. Schedler, E. Visca
"Post Irradiation Testing of Samples from the Irradiation Experiments PARIDE 3 and PARIDE 4"
J. Nucl. Mater. 329 -333, 2004, 766 -770

[17] G. Pintsuk, J. Compan, T. Hirai, J. Linke, M. Rödig
'Effect of Transient Heat Loads on Neutron Irradiated Tungsten and Carbon Based Materials'
Proc. 22nd Symposium on Fusion Engineering (SOFE), Albuquerque, 15. -22.06.2007
1-4244-1194-7/07 02007 IEEE.

[18] Barabash, V.; G. Federici, J. Linke, C.H. Wu:
'Material/plasma surface interaction issues following neutron damage'
Journal of Nuclear Materials 313–316 (2003) 42–51

[19] Linke, J.; Compan, J.; Hirai, T.; Pintsuk, G.; Rödig, R.; Wittlich, K.:
"Materials for Nuclear Energy Systems"
Proc. Forum 2008 of the World Academy of Ceramics, Chianciano Terme, Italy, July 5 – 8, 2008
Ceramic Materials in Energy Systems for Sustainable Development, L. Gauckler Editor, Techna Group Slr, 2009, 307 – 334

9th Liege Conference : Materials for Advanced Power Engineering 2010
edited by J. Lecomte-Beckers, Q. Contrepois, T. Beck and B. Kuhn.

DEVELOPMENT OF MATERIALS AND MANUFACTURING TECHNOLOGIES FOR INDIAN FAST REACTOR PROGRAMME

Baldev Raj*, T. Jayakumar, A.K. Bhaduri and Sumantra Mandal

Indira Gandhi Centre for Atomic Research, Kalpakkam 603102, India

* Email: dirsec@igcar.gov.in

Abstract

Fast Breeder Reactors (FBRs) are vital towards meeting security and sustainability of energy for the growing economy of India. The development of FBRs necessitates extensive research and development in domains of materials and manufacturing technologies in association with a wide spectrum of disciplines and their inter-twining to meet the challenging technology. The paper highlight the work and the approaches adopted for the successful deployment of materials, manufacturing and inspection technologies for the in-core and structural components of current and future Indian Fast Breeder Reactor Programme.

Indigenous development of in-core materials viz. Titanium modified austenitic stainless steel (Alloy D9) and its variants, ferritic/martensitic oxide-dispersion strengthened (ODS) steels as well as structural materials viz. 316L(N) stainless steel and modified 9Cr-1Mo have been achieved through synergistic interactions between Indira Gandhi Centre for Atomic Research (IGCAR), education and research institutes and industries. Robust manufacturing technology has been established for forming and joining of various components of 500 MWe Prototype Fast Breeder Reactor (PFBR) through 'science-based technology' approach. To achieve the strict quality standards of formed parts in terms of geometrical tolerances, residual stresses and microstructural defects, FEM-based modelling and experimental validation was carried out for estimation of spring-back during forming of multiple curvature thick plates. Optimization of grain boundary character distribution in Alloy D9 was carried out by adopting the grain boundary engineering approach to reduce radiation induced segregation.

Extensive welding is involved in the fabrication of reactor vessels, piping, steam generators, fuel sub-assemblies etc. Activated Tungsten Inert Gas Welding process along with activated flux developed at IGCAR has been successfully used in fabrication of dummy fuel subassemblies (DFSA) required for testing. Plasma Transferred Arc Welding (PTAW) process was chosen for deposition of the nickel-base hardfacing of components requiring improvement in resistance to high temperature wear, especially galling, of mating surfaces in hot sodium alloy.

A number of advanced non-destructive evaluation procedures were developed and implemented for inspecting various manufactured components, notable among them being the tube-to tube-sheet welds in steam generators, the clad tube and the end-cap welds and the weld between the hexagonal wrapper and the foot of the fuel sub-assembly.

Keywords: Fast Breeder Reactor; Alloy development; Manufacturing; Inspection technologies

1. Introduction

Fast Breeder Reactors (FBRs) are vital towards meeting security and sustainability of energy for the growing economy of India [1]. India has successfully operated Fast Breeder Test Reactor (FBTR) since October, 1985. Forty years of R&D, technology development of demanding equipments by manufacturing and testing of full size components and absorbing 390 reactor–years of international experience of sodium cooled fast reactors has enabled us to embark on 500 MWe Prototype Fast Breeder Reactor (PFBR) with confidence and courage. The construction of PFBR is in advanced stage of completion. The main objective of the construction of PFBR is to demonstrate the techno-economic viability of sodium cooled fast reactors for the commercial deployment. In addition, it will provide a demonstration of comprehensive closed fuel cycle technologies such as fuel fabrication, reprocessing, waste management and waste

immobilisation. PFBR will also enable validation of first-of-a-kind design concepts and the experience garnered during operation and maintenance of mechanisms, components and sensors in the sodium environment and reactor operating temperatures (820K) will lead to standardisation for the adoption in the series of future reactors. It is planned to construct six more 500 MWe Commercial FBRs (CFBRs), starting in 2014, with improved economy and enhanced safety. Beyond this, 1000 MWe metallic-fuel based FBRs will be constructed in India starting in 2025. The development of sodium cooled fast reactors necessitates extensive research and development in domains of materials, manufacturing and inspection technologies in close association with almost all the disciplines of science and technology.

The operating environment in sodium-cooled fast reactors demands radiation resistant in-core materials satisfying stringent requirements [2]. The in-core materials operating at a temperature of 673-973K in sodium environment experience high neutron flux levels (8×10^{15} n/cm^2/sec). The neutron flux at the core centre with neutron above 0.1 MeV energy is 4.7×10^{15} n/cm^2/sec. Hence, the in-core materials need to possess limited void swelling, desired creep resistance and acceptable resistance to fracture at end of life and during fuel handling at the back-end of the fuel cycle. Keeping these stringent property requirements of in-core material in view, a 15Cr15Ni2.2Mo-Ti austenitic stainless steel (Alloy D9) has been chosen as the in-core material for cladding tube and hexagonal wrapper for PFBR [3]. However, for achieving higher fuel burn up in future CFBRs, improved materials for clad tubes are being developed, which include Alloy D9I with higher phosphorus and silicon contents, and ferritic/martensitic oxide-dispersion strengthened (ODS) steels. Plain 9Cr-1Mo steel for the wrapper and modified 9Cr-1Mo steel for the cladding are also being developed for FBRs with metallic fuels.

The elevated operating temperatures of PFBR demand the structural materials to have adequate creep and fatigue properties as well as good corrosion resistance. In addition to this, the structural materials used in sodium circuit side require compatibility with sodium whereas the material to be used in steam generator requires the compatibility with both sodium and water media. 316L(N) austenitic stainless steel (SS) has been chosen as the major structural material for reactor vessels and primary and secondary loops of PFBR whereas modified 9Cr-1Mo steel is the main structural material for steam generators. Other improved materials being developed for the CFBRs include nitrogen-enhanced 316LN SS for increasing the design life of reactor components, and type-IV cracking resistant boron-added modified 9Cr-1Mo steel for the steam generators.

The entire range of manufacturing technologies for PFBR components has been successfully developed and implemented in collaboration with academic and research establishments and Indian Industries. In the case of reactor vessel, to achieve the strict quality standards of formed parts in terms of geometrical tolerances, residual stresses and microstructural defects, FEM-based modelling and experimental validation was carried out for estimation of spring-back during forming of multiple curvature thick plates. This model enabled design of the tooling for manufacture of reactor vessels with desired dimensional accuracy. Optimisation of grain boundary character distribution in Alloy D9 used for cladding tubes and wrapper, was carried out by adopting the grain boundary engineering approach to reduce radiation induced segregation.

Extensive welding is involved in the fabrication of reactor vessels, piping, steam generators, fuel sub-assemblies etc. Activated Tungsten Inert Gas Welding process along with activated flux developed at IGCAR has been successfully used in fabrication of dummy fuel subassemblies (DFSA) required for testing. To improve the resistance to high temperature wear, especially galling, hardfacing by weld deposition over surfaces of various components was necessary. Based on radiation dose rate and shielding considerations during maintenance, handling and decommissioning, nickel-base hardfacing alloy was chosen to replace the traditionally used cobalt-base Stellite alloys.

A number of advanced non-destructive evaluation procedures were developed and implemented for inspecting various manufactured components, notable among them being the tube-to tube-sheet welds in steam generators, the clad tube and the end-cap welds, the weld between the hexagonal wrapper and the foot of the fuel sub-assemblies, etc. This paper highlights the work and the approaches adopted for the successful development of materials, manufacturing and inspection technologies for the in-core and structural components of current and future Indian Fast Breeder Reactor Programme.

2.1 Alloy development

Clad and wrapper materials for sodium cooled fast reactors (SFRs) have undergone continuous evolution over the years. The first generation materials belonged to austenitic stainless steels 304 and 316 grades. The next development of radiation resistant austenitic stainless steels involved increasing the nickel content and decreasing the chromium content in comparison to standard 304 SS and 316 SS along with addition of titanium. Simultaneously, solute elements like silicon, phosphorous, niobium, boron and carbon have been found to strongly influence the swelling behaviour. This realisation has led to the development of advanced core structural materials such as alloy D9 which is currently used in PFBR. The melting and processing variables for commercial productions of alloy D9 were optimized based on the experience with laboratory heats [3]. Commercial scale melting of three heats with Ti/C ratios of 4, 6 and 8 have been made at MIDHANI, Hyderabad, from virgin raw materials through VIM with ladle adjustment to achieve desired Ti/C ratio. This was followed by vacuum arc re-melting. Rounds of 30 mm diameter were produced through hot forging and hot rolling. These rounds were reduced to 11 mm diameter by cold swaging. Tensile tests were carried out using 20% cold worked samples for this commercial scale melting. The value of yield stress of the commercially melted alloy D9 with Ti/C of 6, at various test temperatures is shown in Fig.1. The yield stress of the 20% cold worked sample with Ti/C of 6 is well within the acceptable limits of PFBR specifications (575-750 MPa at room temperature and 425-625 MPa at 723K).

Cold worked alloy D9 has reached a record dose of 140 dpa without excessive deformation. In the light of recent international alloy development efforts, and in-reactor experience, a modified alloy D9 is being developed to realise still higher swelling resistance, by adding phosphorous in the range of 0.025 to 0.04 wt% and silicon in the range of 0.7 to -0.9 wt% to the alloy D9 composition. The long-term solution for CFBR core structural materials is considered to be 9-12% Cr ferritic-martensitic (F-M) steels. These steels promise excellent swelling resistance to doses even upto 200 dpa. However, the increase in ductile to brittle transition temperature (DBTT) due to irradiation is a cause of concern during fuel handling

operations. A significant increase in toughness can be realised by avoiding the formation of delta-ferrite and ensuring fully martensitic structure as well as by optimising the austenitizing temperature to refine the prior austenite grain size with strict control on embrittling tramp elements. These materials are promising for wrapper applications in CFBRs. The creep resistance of F-M steels decreases significantly above 823K and hence these steels are not suitable for clad applications. Oxide dispersion strengthening is a promising means of improving the creep resistance of F-M steels. This has led to the design of oxide dispersion strengthened (ODS) F-M alloy, with 0.3 to 0.4 % yttria (Y_2O_3) particles of 3-5 nm size. Based on a thorough literature survey describing international experience related to manufacturing of ODS alloy, the manufacturing route has been formulated (Fig.2). The ODS alloy clad tubes have been manufactured with the help of The International Advanced Research Centre for Powder Metallurgy and New Materials (ARCI) and Nuclear Fuel Complex (NFC). The comprehensive evaluation of the produced tubes is currently under investigation.

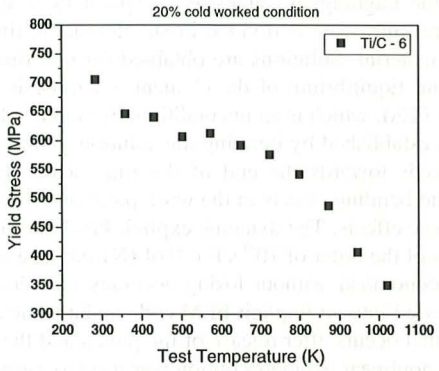

Figure 1: Yield stress value of alloy D9 in 20% cold worked condition

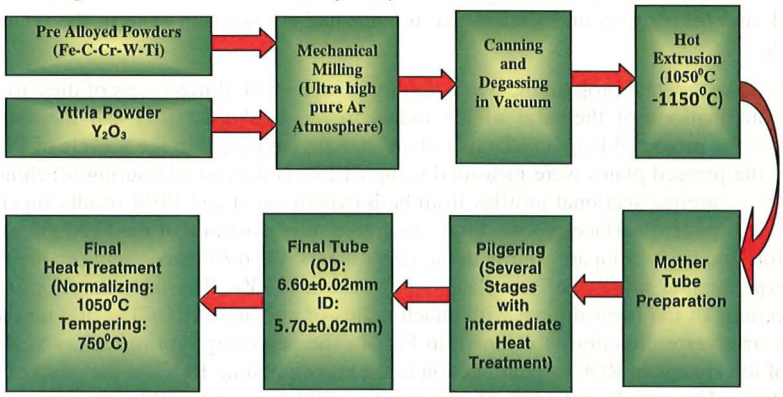

Figure 2: Process flow sheet for manufacturing ODS clad tube

2.2 Finite Element Method based Process Model for Springback Evaluation

The fabrication of main vessel, safety vessel, inner vessel and transition pieces of PFBR involves pressing of petals and assembling and welding of these petals to form the final shape. These petals need to be fabricated with stringent dimensional tolerances in order to fabricate the vessels within the desired level of tolerance. Springback is a major factor controlling the dimensional accuracy of the petals for the fabrication of large vessels of PFBR. For near-net shape forming of petals, proper design of the dies and punches, mounting fixtures and press guides are crucial. FEM based process models for plate forming operation have been utilized in predicting the springback as well as to facilitate in designing dies for near-net-shape forming.

Based on the simulations from the two-dimensional FEM modeling of the plate forming process, the optimum FEM formulation is identified sequentially using a dynamic explicit formulation with contact modeling for the pressing phase and a static implicit approach for springback calculation in the Lagrangian framework. Explicit FEM is a time marching type of solution in which the entire time scale is divided in smaller stable time increments dictated by physical properties of the material. Solutions are obtained for one time increment and added to the prior computed solution. Equilibrium of the element assembly is ensured at the end of the total time scale. In implicit FEM, which is an unconditionally stable solution scheme, equilibrium of the element assembly is established by iterating the solution within a time increment and thus equilibrium solution proceeds towards the end of the time scale. The plate forming process includes both membrane and bending effects in the work piece and hence a shell formulation was used to account for both these effects. The dynamic explicit FEM is a conditionally stable scheme with stable time increments of the order of 10^{-7} s for 316L(N) stainless steel and so use of reduced integration elements are economical without losing accuracy of solution. The results from the explicit analysis were imported into an implicit FEM code and a static analysis was performed to determine the spring back that occurs after release of the punch and the residual stress state in the plate after springback. The nonlinear geometry option was used to assess the springback, which is envisaged to be occasionally quite large. The displacement obtained at the end of the step is the springback and the stresses and strains give the residual stress-strain state in the material after springback.

The experimental programme was carefully planned with thirteen sets of dies to cover all possible combinations of the ratio of the radius to the thickness (R/t) and the ratio of the deflection to the projected length (y/L) in a plane that are envisaged in the vessels of PFBR. The profiles of the pressed plates were measured using ZEISS Universal Measuring Machine. Figure 3 shows the centreline sectional profiles from both experimental and FEM results superimposed on the desired (punch) surface profile. From the figure, it is evident that the FEM simulations of the plate forming trials compare well with the experiments, the differences between the simulated and the experimental profiles of the plates being within 6-10%. The percentage springback at various sections of the formed plate with punch radius of curvature (ROC) of 500 mm and 1000 mm along transverse directions are shown in Fig. 4. The percentage springback, was defined as the ratio of the change in ROC at plate section to the corresponding ROC on the punch, expressed as percentage. The punch had radii of curvature of 500 mm and 1000 mm along transverse directions. In figure 4, the curves with triangular and rectangular legends represent sectional

springback values corresponding to punch radii of curvature of 500 mm and 1000 mm respectively. The X axis of the graph represents the location of a plate section along either X or Y axis. From the Fig. 4, it is evident that the ROC and hence springback increases towards the central sections of the plate. Near the edges of the plate, the two curvatures influence each other and so constraints for opening up of the plate are more and hence springback is less. This constraint effect reduces towards the centre of the plate and hence springback increases. Moreover, for a work hardening material like the type AISI 316L(N) stainless steel, springback increases with increase in the total strain, which, can be deduced from the true stress-strain curve of the material. The total strain increases towards the plate centre due to maximum contribution from both the transverse radii of curvature and so springback also increases towards the centre of the plate. The increase in plastic strain towards the central sections of the plate was also corroborated by FEM results. The differential distribution of strains that occurs during plate forming leads to differential springback in the plate and this in turn leads to a product shape different from the die and punch shapes. So the springback correction on the dies and punches needs to be incorporated to obtain the desired product shape. This experimentally validated FEM based process model has been found to be an asset to predict the final shape of the product for a given die, punch and plate configuration and subsequently use this information to correct the die and punch shapes for springback to manufacture the sectors of large vessels to the desired accuracy.

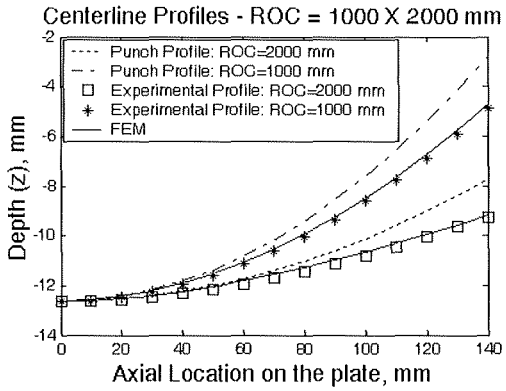

Figure 3: Plate profiles along transverse centerlines of the plate (ROC: Radius of Curvature)

2.3 Grain Boundary Engineering in Alloy D9

Radiation-induced segregation (RIS) is an important consequence of irradiation at elevated temperatures where point defects are mobile [4]. RIS is a non-equilibrium process that happens due to the unequal participation of solutes in the vacancy and interstitial defect fluxes [5]. The grain boundary misorientation significantly influences RIS. It has been established in austenitic stainless steels under 5 MeV proton irradiation at elevated temperature that the RIS is

insignificant at a small angle tilt boundary or low Σ coincidence site lattice (CSL) boundary but not so at a random grain boundary [6].

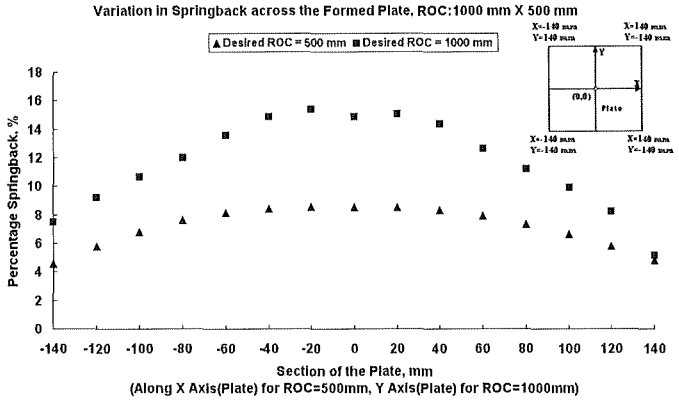

Figure 4: Variation in springback across a formed plate

Grain boundary engineering in alloy D9 was realized through a one step thermo-mechanical treatment [7], in an attempt to reduce RIS. The experimental methodology adopted in this investigation was based on the strain-annealing approach in which small amount of strain (5-15%) was imparted on solution annealed (SA) sample. The cold deformed samples were subsequently annealed at various temperatures (1173-1273K) for different time periods (0.5-2h). It has been observed that annealing following 5% deformation results only in a moderate increase in proportion of Σ3 boundaries and its variants. The grain boundary character distribution (GBCD) data in terms of $\Sigma 3^n$ boundaries in samples annealed in the temperature range 1173-1273K with 15% pre-strain is shown in Fig.5. It could be observed that a very high fraction of $\Sigma 3^n$ boundaries have been achieved after annealing at 1273K with 15% pre-strain (Fig.5(a) and Fig. 5(b)). The increase in Σ3 boundaries could be attributed to the formation of new Σ3 boundaries by geometrical interaction between pre-existing Σ3s (i.e. multiple twinning) and/or formation of new twins during annealing following deformation. According to the CSL rule, interaction between two Σ3 boundaries may form a Σ9 boundary according to the relationship Σ3 + Σ3 = Σ9 [8]. When a Σ9 boundary generated in this way encounters another Σ3 boundary, it results in either a new Σ3 boundary based on the relationship Σ3 + Σ9 = Σ3, or a Σ27 boundary following the relationship Σ3 + Σ9 = Σ27. However, from the statistics of the Σ3, Σ9 and Σ27 (Fig. 5(a) and Fig. 5(b)), it could be inferred that Σ3 + Σ9 = Σ3 occurs more frequently than Σ3 + Σ9 = Σ27 [9]. These regenerated Σ3, Σ9 and Σ27 boundaries take part in the reconfiguration of the existing grain boundary network that eventually breaks down the random high angle boundaries (HABs) connectivity (Fig.6(a)). The ratio of Σ3 to (Σ9 + Σ27) in these conditions is shown in Fig. 5(b). A lower Σ3 to (Σ9 + Σ27) ratio in the samples annealed at 1273K (Fig. 5(b)) signifies that a significant disruption of random HABs connectivity has happened (Fig. 6b).

Apart from the GBCD, the degree of cold work which influences dislocation density is an important parameter determining the void swelling behaviour and RIS of austenitic stainless steels. A 20% cold work (CW) has been found to be optimum in terms of void swelling and phase stability in alloy D9. Cold working up to ~10% in the GBE alloy D9 has not found to alter the misorientation of the Σ3 boundaries much since majority of the Σ3 boundary (~90%) are within 2° from their ideal misorientation[1]. To achieve higher retained strain (similar to 20% CW) in the microstructure, a four-step iterative thermo-mechanical treatment has been adopted for alloy D9. In each processing cycle, rolling with a thickness reduction of 10% was carried out at ambient temperature, and the subsequent annealing was performed at 1273 K for a shorter annealing time (~30 min) [11]. This has resulted in very high fraction (~63%) of Σ3 boundaries with substantial retained strain as revealed by kernel average misorientation (KAM)[2] map (Fig. 6(c)). The KAM map can be used to evaluate localized plastic strain in materials [12]. The higher KAM values in the grains correspond to higher local misorientations (i.e. higher retained strain and dislocations) and vice versa. Such a GBE microstructure with further ~10% CW is likely to reduce RIS and void swelling in alloy D9 [6]. The detailed electron microscopy and irradiation study is under progress.

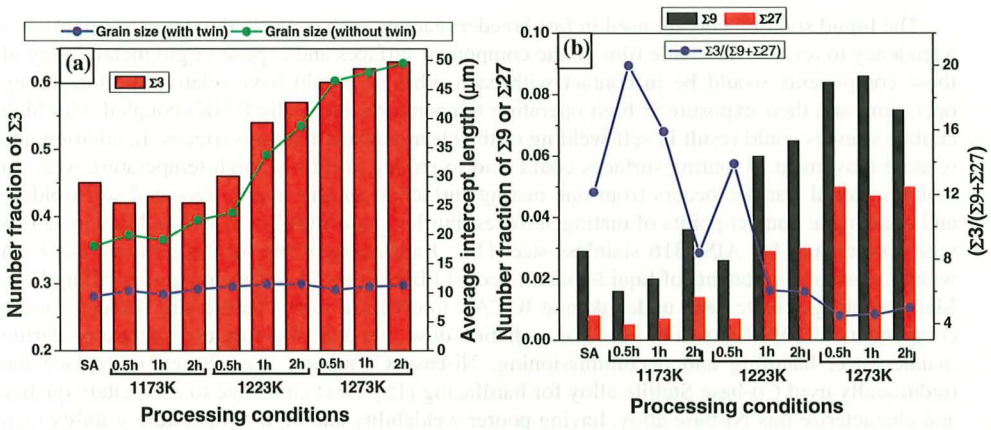

Figure 5: Frequency distributions of (a) Σ3 boundaries [average grain size (with and without twins) in each condition is also indicated]; (b) Σ9 and Σ27 boundaries [(Σ3/Σ9+Σ27) is also shown to assess random boundary connectivity] in 15% deformed and annealed samples

[1] The allowable deviation for Σ3 boundaries as per Brandon's criterion [10] is 8.6°.

[2] The color-scale-coded KAM map is plotted on the basis of first-neighbor kernel parameter with a maximum misorientation angle of 5°. For a given data point, it calculate the average misorientation between the data point and all of its neighbors (exclude misorientations greater than some prescribed value - 5° in this case).

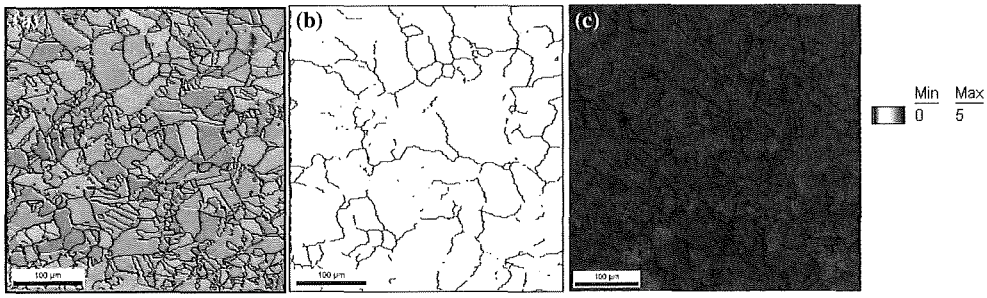

Figure 6: (a) annealed at 1273K for 1 hour with 15% pre-strain (Colour code: Σ3 – red; Σ9 – blue; Σ27 – green; Σ1 – yellow; other low Σ CSL – purple, random HABs – black), (b) grain boundary map showing only the random HABs; (c) Kernel average misorientation (KAM) map of GBE alloy D9 after 4th iteration

2.4 Hardfacing of the reactor components

The liquid sodium, coolant used in fast breeder reactors with controlled oxygen (<3 ppm), has a tendency to remove the oxide film on the component surfaces and expose virgin metal. Many of these components would be in contact with each other or would have relative motion during operation, and their exposure at high operating temperatures (typically 823K) coupled with high contact stresses could result in self-welding of the clean metallic mating surfaces. In addition, the relative movement of mating surfaces could lead to galling, a form of high-temperature wear, in which material transfer occurs from one mating surface to another due to repeated self-welding and breaking at contact points of mating surfaces. Further, susceptibility to self-welding increases with temperature for AISI 316 stainless steel [13]. Hardfacing of the mating surfaces has been widely used in components of liquid-sodium cooled FBRs to avoid self-welding and galling [14]. Many challenges have been undertaken at IGCAR to evolve a robust hardfacing strategy for the components of PFBR. At first, based on radiation dose rate and shielding considerations during maintenance, handling and decommissioning, Ni-base Colmonoy was chosen to replace the traditionally used Co-base Stellite alloy for hardfacing [15]. Next challenge to adequately qualify and characterise this Ni-base alloy, having poorer weldability and high-temperature stability than the Co-base alloy, was also addressed in a comprehensive manner. The choice of appropriate deposition process is a must for success. Metallurgical studies revealed that the hardness and microstructure of the gas tungsten arc welding (GTAW) deposit of the Ni-base hardfacing alloy is significantly affected by dilution from the base metal with the width of the softer dilution zone (of up to 2 mm) often exceeding the final desired hardface deposit thickness. Also, certain components like grid plate sleeves of about 80 mm ID, that required hardfacing deep inside the inner surface of the sleeve were not amenable for hardfacing by conventional processes like GTAW process unless major design concessions were permitted. Hence, the more versatile plasma transferred arc welding (PTAW) process was chosen so that the width of the dilution zone could be controlled to as low as 0.2 mm (Fig. 7), by optimising the deposition parameters. An indigenous fabricator (M/s Omplas, Chennai), who carried out the hardfacing of components for

the 500 MWe FBR Project, designed and developed a suitable miniature PTA torch (Fig. 8) for hardfacing the inner surface of grid plate sleeves.

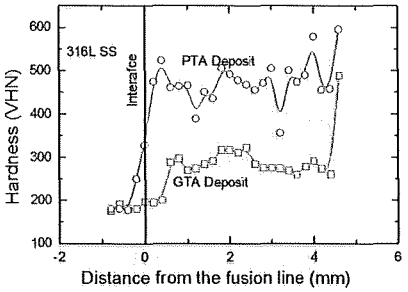

Figure 7: Hardness profiles for Colmonoy deposits by GTAW and PTAW welding processes

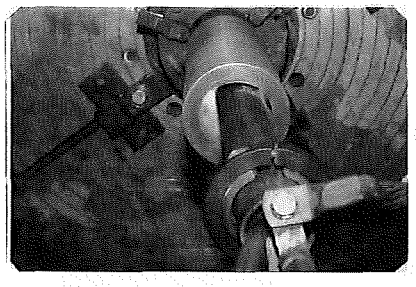

Figure 8: Hardfacing of grid plate sleeve (ID ~80 mm) using indigenously designed PTAW torch

2.5 Hardfacing of Bottom Plate of Grid Plate Assembly

Grid plate of PFBR is a massive structure consisting of two plates (top and bottom of ~6.5 m in diameter). Grid plate houses a large number of sleeves in which foot of the sub assemblies rest. The grid plate assembly in turn rests on core support structure that also acts as boundary between cold and hot sodium in the reactor. Both the grid plate assembly and the core support structure are made of AISI 316L(N) stainless steel and immersed in flowing sodium and remain in contact throughout the reactor life (60 years). Hence, there should not be any self welding between these two components at their contact location. Hardfacing is carried out on two annular grooves machined on the bottom plate of the grid plate. These grooves are located towards the periphery of the grid plate and hence, diameters of these groves are close to that of the grid plate itself and total length (circumference) of single hardfaced deposit was close to 21 m.

During technology development of the grid plate, extensive cracking of the deposit is observed when deposition was carried out as per the procedure finalized initially based on trails carried out on 80 mm thick 1000 mm diameter plate. Subsequently, a detailed review of the design of the groove, welding process, procedure, heat treatment etc. was taken up in which designers, materials engineers, hardfacing agency and manufacturer of the grid plate participated. The groove width was reduced from 45 to 20 mm and the groove angle increased from 30° to 60°. This enabled us to carry out hardfacing in single layer and single pass of deposition. Preheat temperature for deposition was increased from 773K to 923K and the furnace for preheating and stress relieving heat treatment was modified to ensure that the temperature variation across the component during heating or cooling is reduced considerably. It was also decided to carry out hardfacing continuously using four PTAW machines positioned on a circular track which was concentric to the bottom plate. Machine controls were suitably modified to have smooth deposition between starting and ending locations of the deposit, which is found to be more prone to cracking than the other locations of the deposit. The process has been successfully employed

for the bottom plate of the grid plate assembles of PFBR. After bottom plate reached preheat temperature, the entire operation of hardfacing of the two grooves of ~6.5 m dia. each took only a few hours. Figure 9 shows the grid plate mounted on the furnace bed with hardfacing operation in progress. Neither cracks, nor de-bonding nor surface porosities were observed on the deposits.

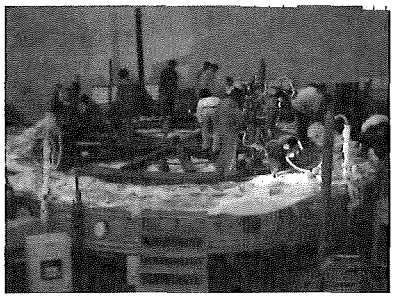

Figure 9: Grid plate mounted on the furnace with hardfacing in progress

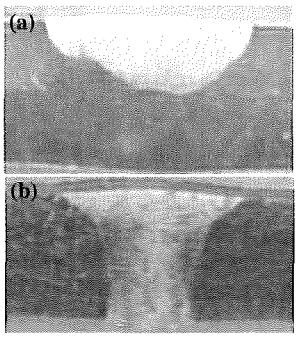

Figure 10: (a) Shallow penetration in conventional TIG welding; (b) deeper penetration in A-TIG welding

2.6 Activated Tungsten Inert Gas (A-TIG) Welding

In 1960, the Paton Electric Welding Institute Ukraine, [16] developed an effective improvement to the TIG welding process, designated as active tungsten inert gas welding (A-TIG). Before welding, a thin layer of an inorganic powder, known as activating flux, is coated on the surface to be welded. This results in increase in the depth of penetration by a factor of 1.5 to 3 when compared to single pass manual TIG welding. The advantages offered by this process include a) ensuring good penetration in welding of thin sections welding of materials like austenitic stainless steels which are known for poor depth of penetration, b) avoiding edge preparation for thickness up to 10 mm, c) reduction in both time and cost for edge preparation and d) avoiding the use of filler wire. At IGCAR, A-TIG welding process with a new flux has been successfully developed for joining both 304 and 316 grades of austenitic stainless steels [17]. The innovation in flux formulation has resulted in improvement in creep rupture properties and toughness [18]. The Figure 10 compares the weld penetration in normal GTAW process and A-TIG process.

The A-TIG process along with activated flux developed at IGCAR has been successfully used in fabrication of fuel subassemblies (FSA) required for testing [19]. Figure 11 shows the hexagonal sheath of FSA being welded using A-TIG process. The wall thickness of the sheath is 3 mm and the procedure considered earlier involved edge preparation, filler addition and two pass welding. All this could be avoided and welding could be completed with more speed (70% more than manual metal arc welding). Subsequently, this process is used for fabrication of many other components too. Figure 12 shows the welding of a shell structure of 304L austenitic stainless

steel of 3 mm thickness meant for water storage tank. A maximum thickness of 6 mm stainless steel has been welded so far employing A-TIG process along with activated flux developed at IGCAR.

Figure 11: A-TIG welding of hexagonal sheath of fuel subassemblies

Figure 12: A-TIG welding of cylindrical shell for a water storage tank

2.7 Non-Destructive Evaluation

The structural integrity of reactor core and other safety components including fuel assemblies, reactor vessels, steam generators etc. need to be ensured through stringent quality evaluation and periodic in-service inspections. Advanced ultrasonic and eddy current based NDE procedures have been developed for inspection of structural and core components of the reactor and steam generator components, as part of fabrication quality assessment.

Cladding tube housing nuclear fuel is a critical component demanding stringent quality as it is a first robust barrier to radioactivity release. The relative capabilities of ultrasonic and eddy current techniques for detection of these defects are shown in Table I which clearly brings out the necessity for use of both the techniques in a complementary way. In the case of ultrasonic testing, standard test procedures are followed. In the case of eddy current testing, in order to detect and evaluate depth of defects in the cladding tubes, an on-line testing procedure that uses artificial neural network has been developed. This innovative technique uses eddy current data from two test frequencies and quantifies defect size on-line. This on-line procedure has been successfully applied to detect defects in the indigenously produced Fast Breeder Test Reactor (FBTR) cladding tubes, some of which have acceptable periodic wall thickness variations of about 2% of wall thickness.

Table I: Defect types detectable using eddy current and ultrasonic method

Detection and Characterisation	Eddy current method	Ultrasonic method
ID defects	Possible	Possible
OD defects	Possible	Difficult
Isolated large inclusions	Difficult	Possible
Grouped fine inclusions	Possible	Difficult
Circumferential defects	Difficult	Possible
Variations in cold work and texture	Difficult	Possible

Due to the complex geometry of hexcan weld of the PFBR fuel subassembly, radiography testing of the weld cannot provide required sensitivity during the fabrication stage. Hence, a new ultrasonic methodology has been developed for testing of the hexcan weld (Fig. 13). The developed methodology involves testing the weld from the thinner plate side using 1 MHz Rayleigh wave, which penetrates the complete thickness (3 mm) of the weld (approx. one wavelength). This methodology is quite fast and can be used for detection of both axial and circumferential defects.

The importance of high integrity welds in steam generators is due to risks arising out of sodium-water reaction in the event of breaching the integrity of steam and water boundary. Tube to tube-sheet weld joints are the regions where the possibility for a leakage path is highest. The main defects in the weld joints are porosities, concavities or convexities. It is expected that the radiography technique should be able to detect single porosities of size at least of the order of 50 μm. In the entire weld, the total pore count must be such that the sum of diameters of all the pores visible is less than 2.54 mm. This leads to the necessity of high sensitivity defect detection in these welded joints. In this regard, rod-anode based micro-focal radiography (Fig. 14(a)) technique and appropriate digital image processing methodology has been developed and standardized [20]. More than 100 trial weld joints were radiographed to establish the procedure for quality assurance. Results on the trial welds of these tubes have shown that it is possible to resolve a 32 micron diameter steel wire placed on the inside of the tube (Fig. 14(b)). This corresponds to a sensitivity of 1.3%-1.6% of the wall thickness of the tube. Radiographs taken during the developmental stage of the welding have given feedback to arrive at correct weld parameters for acceptable weld joints. This procedure has been successfully employed for the steam generators for PFBR.

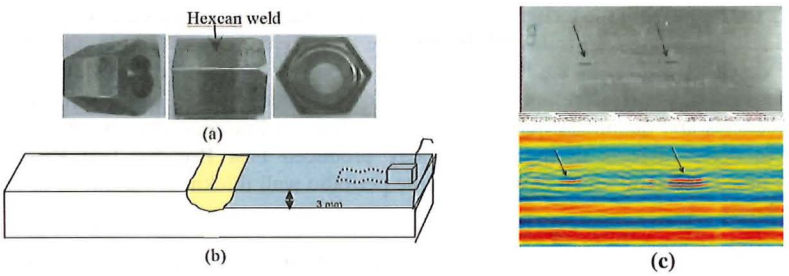

Figure 13: Ultrasonic surface wave based methodology for non-destructive inspection of hexcan welds of PFBR subassemblies (a) hexcan weld (b) a schematic of the mock up weld, and (c) a mock up weld with reference defects (top) and the corresponding ultrasonic images of the defects (bottom)

One of the imperfections that could occur due to improper internal shield gas flow and weld parameters is weld concavity and convexity. Depending on the geometry of the weld, the presence of such convexity and concavity can result in concentration of stresses in and around the region. In the case of the tube to tube sheet weld joints of the steam generators of the PFBR, it is specified that the maximum permissible value for the convexity and concavity is 0.2 mm (both

for internal and external concavity and convexity). It is easy to determine the external convexity and concavity due to availability of access for replica based measurements. In the case of internal concavity and convexity, the technique of replica using dental compounds is quite difficult. Procedures for measurement of internal concavity and convexity by replication using silicon rubber compound and special hardware and also by video-imagescopy have been developed at the authors' laboratory.

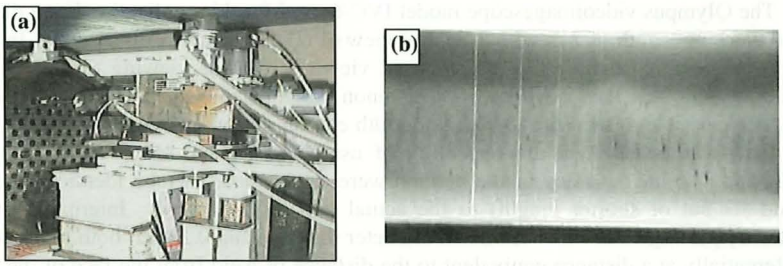

Figure 14: Integrity Assessment of TTS Weld Joints in Steam Generators of PFBR (a) rod anode based micro-focal radiography set-up and (b) Radiography image of a typical TTS weld joints showing penetrameter wires and porosity

2.7.1 Replica Technique

The hardware for the replica technique essentially consists of manual injection device, mixing guns, injection head, spring loaded CRS plugs and recovery cork screw head. The consumable is a silicon rubber compound of the type RTV-FA 877 with a pot life of 2 months and a curing time of 4 hours. Horizontal injection technique was adopted. For concavity measurement, notches and grooves of two different depths (0.35 mm and 0.25 mm) were made internally by electro discharge machining in a standard tube of OD 31.2 mm and ID 27.8 mm. The profile of the groove was then replicated using silicon rubber compound. The dimensions of the groove were then measured from the replica using a profile projector having a measurement accuracy of ±5 microns. It was observed that an overall accuracy of ±20 microns could be obtained for concavity and convexity measurements. This procedure has been subsequently adopted for examination of a number of joints for steam generators of PFBR. A typical siliconone compound replica of the weld is given in Fig.15.

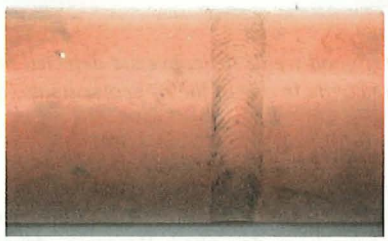

Figure 15: Typical siliconone compound replica of tube to tube-sheet weld joint

2.7.2 Videoimagescopy

The videoimagescope is an advanced version of the flexible fiberscope in which a CCD chip is used for imaging. The use of videoimagescopy for profiling of the TTS weld joints is described below:

The Olympus videoimagescope model IVC-6 used for this application has a diameter of 6 mm and working length of 7 m with a field of view of 60 degree convertible by tip. In the present experimental campaign, the 80 degree forward viewing and side viewing tips were used. The light source used was ILV-2 with a 300 W xenon lamp. Using the 3-D graphic measurement system, it is possible to measure the length, width etc. on the images very accurately. Before the actual work was undertaken, the feasibility of using videoimage scope for quantitative weld profiling and also the accuracy of the method were established. A tube identical in dimensions (OD and ID but of shorter length) to the actual tube was selected. Internal convexity was simulated by placing steel wires of known diameter (0.4 mm and 0.2 mm) both longitudinally and circumferentially at a distance equivalent to the distance of weld from the face of the tube sheet. Comparison of the diameters estimated using videoimagescope with the actual diameters measured using a micrometer indicated an accuracy of the order of ±20 microns. For concavity measurement, notches and grooves of two different depths (0.35 mm and 0.25 mm) made internally by electro discharge machining in a standard tube of OD 31.2 mm and ID 27.8 mm, were made on calibration standards. The methodology based on Video image has been adopted for concavity and convexity measurement of a number of joints of the re-heater. Images of good weld, weld with convexity and weld with concavity are shown in Figs. 16(a), (b) and (c), respectively.

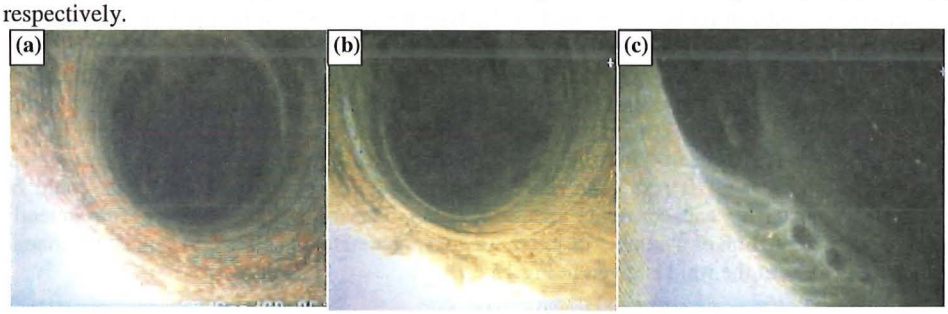

Figure 16: (a) Videoimage of a good weld; (b) convexity detected in weld Joint (the convexity is 0.437 mm); (c) typical weld concavity in one of the re-heater joints (the concavity is 0.44 mm)

3. Concluding remarks

A few illustrative exemplary approaches followed for the successful deployment of materials, manufacturing and inspection technologies for the current and future Indian Fast Breeder Reactor Programme have been described. Research, development and deployment of

materials, manufacturing and inspection technologies has been enabled by robust design, extensive and innovative modelling, characterisation, testing and evaluation of materials, improvements in manufacturing processes; and validation of technologies by demonstration with real-life structures and components. The extensive collaborations among academic, research and industrial organisations with 'science-based technology' approach are the guiding principle for the successful development of materials and manufacturing technologies for the Indian Fast Breeder Reactor Programme.

Acknowledgments: Authors are thankful to a large number of colleagues in Metallurgy and Materials Group and collaborators from academic, research and industrial organization for their contributions.

References

1. Anil Kakodkar, Energy in India for the Coming Decades," presentation at the Inter-ministerial Conference on "Nuclear Power for the 21st Century," organized by the International Atomic Energy Agency (IAEA) during March 21-22, 2005, in Paris, France.
2. S.L. Mannan, S.C. Chetal, B. Raj, S.B. Bhoje, *Trans. Ind. Inst. Metals*, 56, 155-78, (2003)
3. P.V. Sivaprasad, S. Mandal, S. Venugopal, C. Narayanan, V. Shanmugam and B. Raj, *Trans. Ind. Inst. Metals*, 59, 437 – 445 (2006)
4. D.L. Damcott, T.R. Allen and G.S. Was, *J Nucl. Mater.*, 225 97-107, (1995)
5. G. Gupta, Z. Jiao, A.N. Ham, J.T. Busby and G.S. Was, *J Nucl. Mater.*, 351, 162–173, (2006)
6. N. Sakaguchi, S. Watanabe, H. Takahashi, R.G. Faulkner, *J Nucl. Mater.*, 329–333, 1166–1169, (2004)
7. S. Mandal, P.V. Sivaprasad, B. Raj and V.S. Sarma, *Metall. Mater. Trans. A*, 39, 3298-3307, (2008)
8. L.C. Lim and R. Raj, *Acta Metall.*, 32, 1177-1181, (1984)
9. V. Randle and G. Owen, *Acta Mater.*, 54, 1777-1783, (2006)
10. D. G. Brandon, *Acta Metall.*, 14, 1479, (1966)
11. S Mandal, A.K. Bhaduri and V.S. Sarma, communicated to *J Mater. Sci.* (2010)
12. D. Jorge-Badiola, A. Iza-Mendia and I. Gutierrez, J. Microsc., 228, 373, (2007)
13. E. Yoshida, Y. Hirakawa, S. Kano; I. Nihei, *Proc. Inter Conference on Liquid Metal Technology, Societé Francaise d' Energie Atomique*, Paris, pp 502-1–502-10, (1998)
14. E. Lemaire and M. Le Calvar, *Wear*, 249, 338-344, (2001)
15. A.K. Bhaduri, R. Indira, S.K. Albert, B.P.S. Rao, S.C. Jain and S. Asokkumar, *J. Nucl. Mater.*, 334, 109-114, (2004)
16. S. Leconte, P. Paillard and J. Saidrenan, *Sci.Tech. Welding and Joining*, 11, 43-47, (2006)
17. V. Ramasubbu, S.K. Albert and A.K. Bhaduri, S.K. Ray, *Proc. National Welding Seminar*, Indian Institute of Welding, Baroda, 16.1–16.8, (2003)
18. P. Sivaraman et.al. *Proc. of IIW-IC*, Chennai, Indian Institute of Welding, (2008)
19. M. Vasudevan, *Computational and experimental studies on arc welded austenitic stainless steel*, PhD thesis, IIT Chennai, 2007
20. B. Venkatraman, T. Saravanan, T. Jayakumar, P. Kalyanasundaram and B. Raj, *Canadian J. NDE*, 25, 6-13, (2004)

9th Liege Conference : Materials for Advanced Power Engineering 2010
edited by J. Lecomte-Beckers, Q. Contrepois, T. Beck and B. Kuhn.

MATERIAL CHALLENGES FOR THE NEXT GENERATION OF FISSION REACTOR SYSTEMS

Derek Buckthorpe

AMEC, Booths Park, Knutsford, Cheshire, UK
Derek.buckthorpe@amec.com

Abstract

The new generation of fission reactor systems will require the deployment and construction of a series of advanced water cooled reactors as part of a package of measures to meet UK and European energy needs and to provide a near term non-fossil fuel power solution that addresses CO_2 emission limits. In addition new longer term Generation IV reactor type systems are being developed and evaluated to enhance safety, reliability, sustainability economics and proliferation resistance requirements and to meet alternative energy applications (outside of electricity generation) such as process heat and large scale hydrogen generation.

New fission systems will impose significant challenges on materials supply and development. In the near term, because of the need to 'gear up' to large scale construction after decades of industrial hibernation / contraction and, in the longer term, because of the need for materials to operate under more challenging environments requiring the deployment and development of new alternative materials not yet established to an industrial stage.

This paper investigates the materials challenges imposed by the new Generation III+ and Generation IV systems. These include supply and fabrication issues, development of new high temperature alloys and non-metallic materials, the use of new methods of manufacture and the best use of currently available resources and minerals. Recommendations are made as to how these materials challenges might be met and how governments, industry, manufacturers and researchers can all play their part.

Keywords: Fission, nuclear, materials,

1. Introduction

The development of new Generation III+ and Generation IV fission reactors critically depends not only on advances made in nuclear fuels but also in their systems and structural materials which may have to withstand severe environmental conditions (such as high temperatures, significant neutron irradiation and strong corrosive environments) in combination with complex loading and operational cycles and longer design life requirements. The challenges with regard to nuclear materials include not only operation in critical conditions but also compliance with the highest levels of safety and protection, whilst giving due regard to decommissioning, dismantling and waste processing issues. Searching for new materials and tailoring them to the desired system properties and operational requirements is therefore central to the reactor developments.

This paper investigates the materials challenges imposed by the new Generation III+ and Generation IV systems. These include supply and fabrication issues, development of new high temperature alloys and non-metallic materials, the use of new methods of manufacture and the best use of currently available resources and minerals. The issues are discussed in light of the UK and European activities and developments with suggestions made as to how these materials challenges might be overcome. For the Generation IV Reactor Systems

research and development requirements are being assessed within the Generation IV International Forum (GIF) to which Europe and other countries participate [1]. The European Research and Development (R & D) activities within Europe on these systems is largely carried out either through national programmes (as is the case for SFR for example in France) and European Framework Programmes [2] dealing with specific systems and/or cross cut topics (as is the case for materials). For the Generation III+ systems use has been made of information gathered as part of the MATUK[3] materials investigations and their reports commissioned by the UK Technology Strategy Board on materials R & D for nuclear applications [4, 5]. For the Generation IV systems use has been made of a recent publication reporting the findings form GIF up to the end of 2009 [6].

2. Generation III+ systems

Reactor development has evolved since the construction of the first generation reactors (from the 1950's) to the present day generation II and III systems. Within the UK this has involved the design and construction of commercial gas cooled and water cooled nuclear power stations many of which contribute to the national electricity supply. These have consisted of eleven Generation 1 Magnox reactors and fourteen Generation II Advanced Gas Cooled (AGR) reactors. The second generation reactors were built on seven sites between 1976 and 1989 and are exclusive to the UK. The AGR's are graphite moderated and carbon dioxide cooled and use enriched uranium oxide burned to low levels relative to the Light Water Reactor (LWR) fuel. In 1978 a decision was made to build a PWR and a large Westinghouse unit was started up in 1995 at Sizewell B. This reactor uses water as both a coolant and a moderator and the fuel is enriched uranium oxide pellets encapsulated in tubes of zirconium alloy (Zircalloy). The fuel rods are grouped in fuel assemblies (bundles) which are used to build the core of the reactor. AMEC and its forerunner companies have been involved in the design and construction of all these UK nuclear power stations.

In 1996 industry deregulation within the UK resulted in the nuclear generating plants (apart from Magnox) being transferred to British Energy (now owned by EdF Energy) which operates all UK AGR and PWR reactors. All Magnox reactors are expected to be closed over the next few years and many of the AGR's over the next decades. In 2006 the UK nuclear industry contributed approximately 21% of the UK electricity consumption, by 2020 this is expected to be reduced to 7% if no further construction and operation of new plant has commenced. Also since the 1980's there has been a significant decline in nuclear R & D within the UK and this together with the period of non-active construction has eroded the nuclear skill base. Today there is a considerable shortage of skilled scientists and engineers (particularly with a background in materials), most companies and universities having difficulty recruiting individuals with the required skills.

In 2008 the UK Government announced its formal backing for the construction of a new generation of civil nuclear power stations to be built at or near existing reactors with the expectation that the first one would be completed well before 2020. The process would involve the UK's Health and Safety Executive undergoing a two stage licensing involving a pre-licensing step of generic designs prior to a further site specific licensing on a selected design. Modern nuclear power stations can take around 5 years to construct and it is estimated that it would take approximately 10 years to construct and commission a new nuclear power station in the UK. These next generation UK reactors are to be based on

Generation III+ systems with four generic designs proposed initially which have now reduced to just two: the EDF/Areva Evolutionary (European) Pressurised Water Reactor (EPR) 1600MWe 94 loops, 36% efficiency), and the Westinghouse AP1000 PWR 1100MWe (2 loops, 33% efficiency).

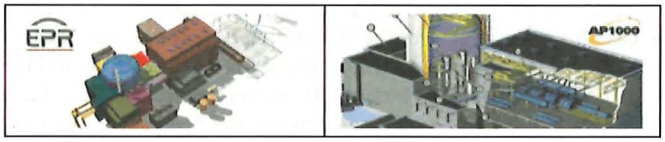

Fig.1. UK New Build Candidate Reactor Designs

Materials requirements and developments for the new Generation III+ systems are expected to build on past Generation III experience and depend to a large extent on the knowledge gained from more recently constructed reactors such as Sizewell B and EPR and AP660/1000 plant constructions elsewhere. For the next generation of reactor systems it is unlikely that significant new materials developments will be required. Also these new reactors are expected to depend to a large extent on established industrial processes.

For the remaining two generic designs there are differences in the quantities of materials and the approach to construction. The AP1000 uses a modular construction approach which requires remote construction followed by shipping to site whereas the EPR requires construction on site. Large quantities of structural steel and reinforcing steel bar for the concrete will be required for both designs. Ancillary equipment will be needed (tanks, pipe-work, valves,.) much of which will be similar to that required for non-nuclear conventional (fossil fuel) power and chemical plant but will nevertheless have to be approved for nuclear application. In view of the period of non construction in nuclear much of the UK experience for engineering and construction that is not directly nuclear related will need to become skilled (approved) for nuclear supply. This is particularly important for safety related components.

The containment building of the EPR plant uses ferritic steel, covered by a reinforced concrete shell, the AP1000 uses a thicker steel plate and is also surrounded by a concrete shell. The RPV internals support the fuel assemblies within the RPV and some act as shielding/ radiation reflectors. The support consists of steels of various grades, machined rods, tubes and plates, and large rings of stainless steel in the gap between the RPV and core. The RPV of the Westinghouse and EPR are similar in weight (around 5000 tonnes) and dimensions and made from large forgings which because of their size can only be manufactured in a few places in the world. The steam generators that transfer the heat from the primary reactor cooling to the secondary feed water/steam are similar for the two designs using a vertical U tube array within a ferritic steel pressure vessel. Four Steam Generators are used for the EPR design and two for the AP1000. The steam generators are manufactured from large ferritic steel rings and hemispheric steel forgings which again only a few companies globally can manufacture. For the pressuriser the forgings are much smaller and can be manufactured more widely. Pumps and valves for the primary and secondary circuits can be covered by established suppliers in the UK and Europe which currently provide spares for existing nuclear stations.

The lack of demand for large power stations in the mid-1990s led to a decline in manufacturing capability within the UK and for these new reactor systems some of the larger specialized components will need to be imported. Significant capability nevertheless exists in design, construction and operation of nuclear power plant in the UK and although investment is required to re-instate and develop certain large scale manufacturing capabilities UK industry is considered to possess a supply chain with a strong capability in most of the areas required. It is considered that UK industries could provide 70% of what is required for reactor construction and development, increasing to 80% with investment & training.

The new build within the UK offers significant opportunities for UK and European industries and research organizations to support both the delivery (construction through to commissioning) and the operation phases of the reactors. Opportunities in reducing the time to generation by providing (through innovation) specialized components, manufacture and construction efficiencies, improved delivery schedules and quality control. Opportunities for improving reactor operation through innovation that increases system effectiveness, uses non-nuclear experience to enhance availability and performance and providing improved maintenance and inspection capabilities. There is a need to work closely with key nuclear players and organizations, who understand client requirements in the short and long term. Example technologies are those that quicken regulatory approval, speed up safety case work, enhance reactor lifetime and operational performance, benefit areas such as maintenance (remote inspection / monitoring), non intrusive condition monitoring and reactor servicing. There is also a need to build up and maintain specialist reactor skills and services, services in areas such as material science, structural Integrity, CFD, etc. that will be needed to develop and support the plant over its complete lifetime (construction through to decommissioning).

3. Generation IV Systems

New Generation IV (GIF) nuclear energy systems are considered to offer significant improvements over current systems with respect to economics; safety and reliability; proliferation resistance and physical protection; and sustainability. The GIF Technology Roadmap identified six systems with the greatest promise and outlined the R&D necessary to bring them to a commercial state within a 2030 time frame. The six systems chosen include the Gas Cooled Fast Reactor System (GFR), the lead cooled fast reactor systems (LFR), the Molten Salt cooled Reactor system (MSR), the Sodium cooled Fast Reactor System (SFR), the Super Critical Water Cooled system (SCWR) and the Very High Temperature Reactor Systems (VHTR). The Generation IV International Forum (GIF) members are collaborating on the R&D needed to develop these generation IV nuclear energy systems, beyond that which is currently being undertaken by industry.

System	Neutron Spectrum	Coolant	Outlet temperature °C	Fuel cycle	Size (MWe)
VHTR (Very High Temperature Reactor)	thermal	helium	Up to 1000	open	250 - 300
GFR (Gas-cooled Fast Reactor)	fast	helium	850	closed	1200
SFR (Sodium-cooled Fast Reactor)	fast	sodium	500-550	closed	50-150 300 -1500 600-1500

LFR (Lead-cooled fast reactor)	fast	lead	480 -570	closed	20-180 300-1200 600-1000
MSR (Molten Salt Reactor)	Thermal/ fast	Fluoride salts	700-800	closed	1000
SCWR (Supercritical water-cooled reactor)	Thermal/fast	water	510-625	Open/ closed	300-700 1000-1500

Table 1 : Overview of Generation IV Systems

The material and material supply needs for the new Generation IV reactors are likely to:

- build on Gen III experience + Fusion
- feature new materials developments
- use established industrial processes + new processes
- require Codes & Standards developments in parallel

For these systems, metals, ODS alloys, ferritic-martensitic steels, and some super-alloys offer potential solutions but some require significant R & D in terms of their properties and behaviour under component conditions. Such systems may also require the deployment of non-metallic materials (e.g. high-temperature fibrous insulation, composites and ceramics) as alternatives to metals for different applications and components.

3.1 Gas cooled systems

The VHTR system is a further step in the evolution of the High Temperature Reactor (HTR). The VHTR is helium cooled and graphite moderated and uses a thermal spectrum reactor with a very high core outlet temperature and is considered sufficient to support high temperature processes such as the production of hydrogen by a thermo-chemical process. The reference thermal reactor power allows passive decay heat removal and the capability for the co-generation of electricity and hydrogen enabling the VHTR and HTR to be used for process heat applications. Within Generation IV a number of national programs are aimed at a nearer term (HTR) deployment and the construction of a prototype that uses gas outlet temperatures in the range 750-850°C. The overall plan for such reactors is to complete the viability phase by 2010 and to be underway in terms of optimized design features and operating parameters by 2015.

The GFR a gas cooled fast reactor that combines the advantages of the fast neutron core and the helium coolant. It requires the development of robust refractory fuel elements and safety architecture. A technology demonstration reactor needed for qualifying the key technologies could be in operation by 2020. The GFR uses the same fuel recycling processes as the SFR and the same reactor technology as the VHTR. Its development is therefore to rely as far as possible on technologies developed for VHTR structures and materials. Currently the work foreseen beyond the VHTR is mainly on the core design and the safety approach.

Materials research and development (R & D) issues have been investigated for the developing HTR, VHTR and GFR systems. The VHTR system operates at potentially higher temperatures and therefore acts as a pilot for many of the issues that also need to be addressed by the GFR. Key differences however exist in the reactor block materials and separate developments are ongoing in these areas to address individual reactor needs.

Key reactor block components include those associated with containment or confinement of the coolant and the support and functioning of the reactor core. The materials within the reactor unit have to withstand high levels of neutron fluence and temperature. Normal operating temperatures range from room temperature to around 850°C and are higher (<1600°C) under accident conditions. The irradiation levels vary from <1 for VHTR to 1 to 2 dpa for GFR outside the neutron shielding layers and from 6 dpa to 25dpa for the control rod and core components of the VHTR to 150 dpa for the core and fuel cladding of the GCR (163 dpa for the SiC). Helium gas is used as the coolant for both systems hence the materials have to be tolerant to this atmosphere.

The reactor core of the VHTR uses graphite. Its performance is critically dependent on the graphite properties, which are irradiation dependent. The most important considerations are component integrity and changes in core geometry, both of which are affected by the dimensional change. Many of the graphites used in previous core designs are no longer available and there has been a serious decline in ability to manufacture nuclear grade graphite in large quantities, the main questions concern the availability of the coke and manufacturing procedure. Current HTR projects - HTTR (Japan) and HTR-10 (China) - use a graphite manufacturerd in Japan (IG-110) which, with its high strength, is suitable for exchangeable core components where low fast neutron fluences and low total fluxes are applicable. Within the European Framework Programmes work has been performed to evaluate currently available graphite material grades recommended by suppliers. The outcome of these programmes has resulted in the generation of new information on identified candidate graphites to provide data to aid selection. Irradiation experiments have been carried out in the High Flux Reactor (HFR) at Petten as part of the RAPHAEL-IP [7] to evaluate the behaviour of graphites for the VHTR. The tests were designed to be carried out in two stages (see Figure 2), the first to provide results at 1/3 peak fluence and the second (using both fresh and irradiated samples from the first) to cover the remaining 2/3. The target peak fluence considered appropriate to a pebble bed core design is around 25 displacements per atom (dpa)_graphite. The corresponding value for the replaceable components of a prismatic core design should not exceed 1/3 of this value.

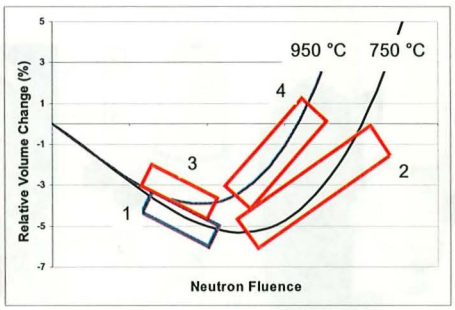

1. INNOGRAPH-1A: 750°C, low/medium dose (FP5)
2. INNOGRAPH-1B: 750°C, high dose
3. INNOGRAPH-2A: 950°C, low/medium dose
4. INNOGRAPH-2B: 950°C, high dose

Fig. 2. Graphite irradiation tests performed in HFR

Other graphite issues addressed within RAPHAEL include effects of corrosion at temperature representative of air ingress accident conditions and modelling of graphite using techniques such as x-ray tomograpy in conjunction with model representations to understand and predict behaviour. The results from the EU Framework programme RAPHAEL provides the only near-term information available for both reactor types. Work programmes have been established within GIF countries for which the EU is one, to look at a range of graphite issues including irradiation and irradiation creep experiments, corrosion, fracture behaviour, etc. and these are likely to provide confirmation of the graphite core material selection for the demonstration reactor New Generation Nuclear Plant (NGNP) to be built in the US.

The core material for the GFR ranges from those considered for liquid metal fast reactors (LMFR's) such as chromium and nickel based austenitic steels (M316, CW 316 Ti, CW-15-15Ti), high nickel alloy steels (e.g.PE16) and ferritic-martensitic and ODS steels (EM12, FV548, W.Nr.1.4914) to materials such as SiC, ceramic + ceramic fibres which are being considered as possible alternatives. For GFR assemblies a selection of ceramics, monolithic or composites (associating two ceramics or one ceramic and one metal) are also possible. The selection of these materials presupposes studies in manufacturing, joining, characterizing and controlling these materials (microstructure, thermal and mechanical properties, corrosion resistance, etc.). The same range of studies is needed for the reflector material, for which a candidate is an intermetallic compound of Zr and Si. The fuel clads for the GFRs will have to withstand operating temperatures of between 850 to 1600°C and high fast neutron fluences (doses up to 150 dpa). Swelling behaviour and embrittlement, permeation of rare gases, helium, diffusion of volatiles, semi-volatiles, non volatiles are concerns specific to the clad which for the GFR application needs to have a lifetime minimum of around 6 years and be dimensionally stable and resistant to creep damage. All of these materials are required to be manufactured (and quality controlled) in the form of streamlined items, which should show a minimal toughness, and be able to be applied to the inlet as well as at outlet core temperatures. The development of suitable materials and core components that can be manufactured for the GFR core is a key challenge for European research and the much larger International GIF programme.

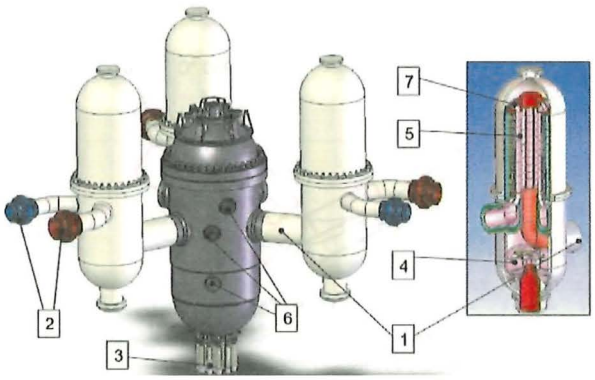

Fig. 3. 1200-MWe GFR primary system and reactor cutaway

The reactor vessel for the GFR and VHTR can be from the same material and use either a ferritic LWR steel such as SA 508 which will require the introduction of additional cooling to maintain temperatures within the PWR operating temperature range (200-250oC) during its operational lifetime or a Cr-Mo steel such as $2^1/_4$Cr or 9Cr to provide resistance up to a higher temperature and without the need to incorporate a separate cooling circuit. The potential for using Mod 9Cr1Mo steel for the reactor pressure vessel application has been examined within the RAPHAEL-IP [6] and significant advances have been made. As well as successfully demonstrating its thick section fabrication (welding) potential and showing the effects of representative low dose irradiation to have a negligible influence on properties and fracture behaviour, creep tests were also performed on pre-irradiated and non irradiated samples to confirm the creep strength at 550°C (for accidents) and at 450°C which is much closer to the gas inlet temperature and material negligible creep limit (around 400°C). For reactor configurations requiring much higher gas inlet temperatures (>425°C) some form of protection will be needed for the inside of the vessel or alternatively some additional cooling adopted as for the LWR steel. The effect of long periods of operation at temperatures >450°C (material ageing) has been examined and shown to be acceptable (short term loss in strength after 1000h with little further change up to 5000h) although longer exposure periods (>10,000h) remain to be checked. The advantage of the Mod 9Cr 1Mo steel over the LWR steel is in its greater potential for resisting higher temperatures and hence this makes it a more robust option for the gas cooled system. The disadvantages are that it has not been used for such an application before and hence there is no long term past service experience on which to build an integrity assessment. Qualification will therefore depend largely on R & D tests which will need to be for longer periods in order to confirm acceptability.

The main components requiring important material advances in the helium circuit common to both the VHTR and GFR include the heat exchangers (inc. IHX) and the turbine (direct cycle application). Other components such as the circulator and hot gas duct are well developed and will require less material innovation in order to achieve an effective design. For the helium circuit components resistance to temperature and corrosion are key requirements. Maximum temperature levels plus temperature gradients due to transients must not be excessive and although these components are not directly subjected to neutron irradiation, environment induced degradation from impurities in the helium or due to oxidation can be important. Material ageing effects too are important for long-term exposure as are welding and fabrication aspects, which are dependent on the individual design details.

The gas to gas heat exchanger transfers the heat generated from the nuclear fission process through the use of efficient high conductivity materials. Its sizing and fabrication is dependent on issues such as corrosion, corrosion allowance, tube-plate manufacture, joining procedures, etc. as well as compactness and efficiency. The materials have to resist the temperatures, thermal gradients and pressures that give rise to stresses and distortions during normal operation and transients. Both the plate and tube concepts are possible and the design lifetime needs to be comparable with that of the reactor minimising the need for repair or maintenance. The VHTR the GFR heat exchangers are not directly subjected to neutron irradiation but must be compatible with potential applications and for processes where heat has to be delivered at very high temperatures (>850°C) and for hydrogen generation this is one of the most challenging components.

The primary circuit recuperator transfers some of the remaining energy at the turbine outlet by pre-heating the gas at the core inlet. This component increases the efficiency of the gas cycle as much as possible and needs to be leak tight between cold and hot high and low pressure cavities, maintain the flow path, integrity to avoid failure and debris blocking flow or causing damage to rotating machines further down the circuit. For the VHTR under normal operating conditions gas temperature differences between inlet and outlet are around 380-430°C and pressure: 40-60bar. Under transient conditions maximum temperatures can reach 650°C and pressure differences 70bar. The recuperator is not normally safety classified unless its failure leads to damage of other safety related equipment. For VHTR potential designs are helical and finned tube and the plate type. For the gas to water heat exchangers the main concerns are to ensure there is no leakage of water into the system, and there is a sufficient resistance to corrosion and thermal stress gradients.

Currently available materials for heat exchangers below 850-950°C include alloys such as Hastalloy-XR, IN 617, Haynes 230. Above 950°C materials such as ceramics and Fe based ODS materials may be needed. The significance of alloying elements, corrosion and potential for cracking are important issues as is resistance to degradation, oxidation and stress corrosion cracking and other mechanisms within the reactor operating environment. The potential for using coatings or and/bonded layers are also important possibilities.

3.2 Liquid metal cooled systems

Liquid metal cooled systems include those for the SFR and the LFR.. The European SFR project has been launched within the European Union 7th Framework Programme to consolidate and advance the fast reactor technology within Europe. The primary missions are to contribute to sustainability mainly through its actinide management and for application to electricity generation. The SFR uses liquid sodium as its coolant allowing high power density with low coolant volume fraction. The environment is essentially non corrosive however sodium reacts chemically with air and water and requires a sealed coolant system. The past significant experience accumulated with sodium reactors in Europe and elsewhere means that this system can be deployed earlier than other Generation IV prototypes. The difficulty of achieving improved economics and of using high-burn-up fuels, fuel cycle with the use of advanced materials and innovative design plus a high level of safety are nevertheless obstacles to early deployment.

The SFR Generation IV technology builds on the technologies that have been successfully used in the UK, France, Germany, Japan, the United States and the Russian Federation. For the new SFR considerable benefit will be taken from the development and operating experience of past demonstration reactors in France, UK and Japan and from the collaborative design activities of the European Fast Reactor (EFR). Consequently the majority of the R & D needs for the SFR are focused on performance rather than viability of the system. Key areas of R & D in Generation IV therefore include safety and operation, advanced fuel, actinide cycle demonstration and component design and balance of plant. The material challenges for the SFR therefore relate to these areas. For component development and balance of plant the main issues are with in-service inspection, repair technologies, leak before break assessment, and the use of the supercritical-CO_2 Brayton cycle for advanced energy conservation.

The selection of the materials and surface treatments used for the major components and systems is an important consideration. As discussed previously chromium and nickel based austenitic steels, high nickel alloy steels (e.g. PE16) and ferritic/ martensitic and ODS steels are the first choice materials for the core. Stainless steel 316 L(N) is the first choice material for the vessel and most of the fixed inner reactor components in direct contact with the sodium. For the roof slab the preferred material choice is a ferritic/ martensitic steel (16NMD5). For the steam generators Mod 9Cr 1Mo steel is the prime material choice.

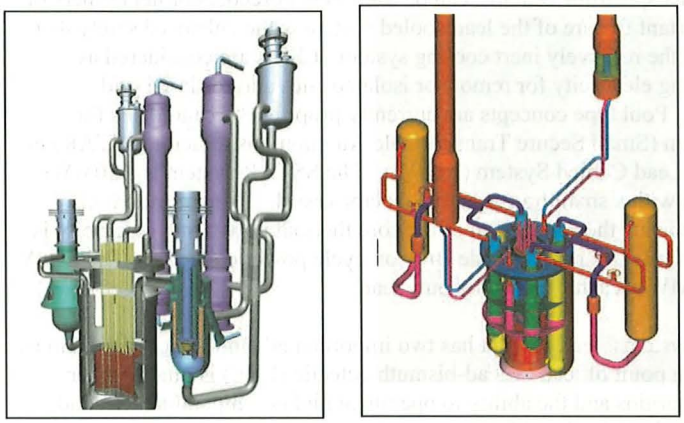

Fig. 4. Loop type JSFR (1500Mwe) and Pool Type KALIMER 600 MWe Reactors

Some issues still to be evaluated are those associated with use of coatings in key areas such as under sodium and in heat exchangers and in specific areas requiring an assurance of a design life that is consistent with the component requirements and that takes into account the mechanical properties associated with irradiation particularly those at low dose and for key welds and weldments and bi-metallic joints.

The 9Cr oxide dispersion strength (ODS) steel is considered to be a promising option for the fuel cladding material particularly for high burn-up and higher temperature operation. Clad materials require high creep rupture strength as well as a resistance to irradiation induced void swelling, irradiation embrittlement and irradiation creep. Austenitic materials have reached their limit with the GIF requirements and despite improvements resulting from changes in composition the ODS alternatives is considered a requirement for the longer term. The creep resistance of 9-12Cr ferritic-martensitic steels can be increased significantly by dispersion strengthening although many manufacturing and joining issues remain which is a key challenge to their use.

The requirement for an increased design life of 60 years as opposed to 40 years for former sodium cooled systems is also a key challenge. The requirement to show that established materials have sufficient high temperature strength over very long periods of operation will require the current extrapolation methods to be revisited and refined with long term data points at moderate and high temperatures used to substantiate any improvements in methodology, heart treatment and chemical composition.

For steam generators, Mod 9Cr 1 Mo continues to provide good high temperature properties although the susceptibility to type 4 cracking remains for fusion welded joints. Benefits from optimization of composition, thermo-mechanical treatments and use of advanced welding processes remain a possible route for improvement.

LFR systems are lead or lead-bismuth eutectic (LBE) cooled reactors with a fast neutron spectrum, with fuel flexibility supporting options for use within a closed fuel cycle. Lead-cooled systems, like all fast spectrum systems, can be used as net breeders or net burners of fissile material. An important feature of the lead cooled system is the enhanced safety that results from the choice of the relatively inert cooling system. LFR's are considered as potential units for providing electricity for remote or isolated sites and for large grid connected power stations. Pool type concepts are currently proposed as candidates for Generation IV co-operation (Small Secure Transportable Autonomous Reactor (SSTAR) in the US and the European Lead Cooled System (ELSY)). The SSTAR system is a 20MWe natural circulation system with a small transportable reactor vessel. Using nitride fuel containing transuranic elements the conversion of the core thermal power into electricity is achieved by using a supercritical carbon dioxide Brayton cycle power converter. The ELSY reference design is a 600MWe reactor cooled by pure lead.

In designing fast reactor systems, lead coolant has two important advantages over sodium as a coolant. First, the boiling point of lead or lead-bismuth eutectic (LBE) is much higher providing greater safety margins and the ability to operate at higher temperature. Second, lead alloys do not react exothermically with water and air as sodium does. At the same time, lead has certain drawbacks relative to sodium. Lead alloys are more corrosive to structural steels than sodium. The high density and low heat conductivity, as well as the erosion of protective oxide layers, reduce possible lead flow rates, thus limiting the total allowed power density and the doubling time to breed plutonium. Finally, the high melting temperature of lead requires special efforts to keep the lead from freezing in the primary circuit. Lead-bismuth has a lower melting point than lead, and using lead-bismuth simplifies prevention of primary coolant freezing. Within GIF the SRP for the LFR is based on the use of molten lead as the reference coolant and lead-bismuth as the back-up option. Given the R & D needs for fuel, materials and corrosion control, the LFR system is expected to require a two step industrial deployment:of reactors operating under relatively low primary coolant temperature and low power density (by 2025) and high performance reactors (by 2040).

Materials for the LFR must meet the criteria of adequate strength, ductility and toughness, dimensional stability (resistance to void swelling and thermal and irradiation creep) over the temperature range of operation and radiation dose levels and adequate stress corrosion and liquid metal embrittlement resistance under all operating conditions. The construction materials are austenitic or ferritic/ martensitic steels, ceramic or refractory material may be required for higher temperature. A lower-temperature LFR could be ready for deployment much earlier than a high temperature LFR, but with a much more limited set of capabilities. Austenitic stainless steels are appropriately considered for lower-temperature and lower radiation dose LFR components. The austenitic stainless steels have been used extensively in the light water reactor industry as well as the fast reactor development programs. The performance of 316 is superior and would be the leading candidate as for the SFR. Since austenitic and FM stainless steels are not adequate for the higher-temperature LFRs, ceramics, superalloys, or refractory metals are also being considered.

For high-dose components of lower-temperature LFRs, where void swelling limits materials performance, ferritic / martensitic steels are likely to be used. As with the SFR, for higher temperature and higher strength situations, ferritic steel, oxide dispersion-strengthened (ODS) steels are being considered and evaluated. These steels derive their elevated-temperature strength from a fine distribution of Y-Ti-O particles, as opposed to carbide precipitation in conventional elevated-temperature steels. Effective strengthening by carbides, which is the typical approach with application of many steels, is not possible above ≈ 650°C, as the carbides are not stable. Different oxide dispersion-strengthened steels have been developed in different alloy development programs and tests have been performed in Japan and elsewhere to improve high-temperature strength. Joining of the steels is a challenge as with SFR, due to segregation of the oxide particles to the surface of a molten weld zone. Therefore, although ODS steels offer the promise of a steel that can operate at 800°C, the steels are still in the early development stage and the performance database is limited.

An additional R&D path to improve creep strength of structural materials for SFR and LFR application is strengthening on a nano-scale level. Although a significant amount of R& D continues in this area, the long-term stability of suitably adjusted material still remains to be proven. Silicon carbide composites are a further candidate material for the high-temperature SFR and LFR components, based on development in the fusion materials programs. These materials are however of a much lower industrial readiness, so their high-temperature development and deployment is considered a much longer-term than the lower-temperature versions. Issues such as high-dose radiation resistance, cost, and fabrication ability still remain as major open issues. With regard to the application of super-alloys in this area, because of radiation embrittlement of Ni-base alloys, poor fracture toughness and oxidation resistance, the super-alloys and refractory metals are not thought to be acceptable in LFRs without further significant developments.

3.2 Molten Salt

The MSR uses a fuel dissolved in flouride salt coolant. MSRs were developed in the 1950s and 1960s. The large-scale R&D efforts yielded a workable reactor concept but a reactor with significant operational and other challenges. In the last three decades, there have been major advances in technology. Since 2005 these systems have focused on fast spectrum concepts (MSFR). These systems exhibit large negative temperature and void reactivity coefficients not found in solid fuel fast reactors and the MSFR has been recognized as a long term alternative to solid fuel systems. Molten salts also provide opportunities for intermediate heat transport in other systems (SFR. LFR, VHTR) giving advantages in using smaller sized equipments (because of higher heat capacity of the salt) and the absence of chemical reactions between the reactor, intermediate loop and the power cycle coolants.

Liquid salt chemistry plays a major role in the viability of the MSR and MSFR with important R & D issues still to be addressed on the physical and chemical behaviour of the coolant and fuel salts and the effects of fission products and of tritium. Other issues include the compatibility of the salt with the structural materials and fuel processing material development, and the general issues of maintenance, instrumentation, chemistry control and safety aspects. The materials selection and component development is considered as a first priority in the Generation IV Project Plan.

Two baseline concepts are being considered in Generation IV. The MSFR which operates on the Thorium fuel cycle and the FHR which is a high temperature reactor with a better compactness than the VHTR and has a passive safety potential for a medium to high unit power application. Materials of construction for the MSR include Hastelloy-N, a high-nickel code-qualified alloy suitable for service to peak temperatures of ~750°C.

With the MSF and MSFR the heat exchanger size can be up to three times smaller than heat exchangers of other systems and this provides significant economic implications. The primary heat exchangers have fuel salt flowing through them on one side and clean salt flowing through on the second side. The fuel salt, which contains the fission products and actinides, is nevertheless highly radioactive. In an MSR, the reactor vessel and primary heat exchangers are located in a hot cell and reducing the size of the heat exchanger significantly reduces the size of the hot cell, its support equipment, and the reactor building. For these heat exchangers tritium control is also an important issue especially for hydrogen production where high temperature heat is required for the thermo-chemical hydrogen.

In the longer term, higher temperatures will be desirable to improve efficiency and provide the high-temperature heat required for hydrogen production. Higher temperatures also allow the use of higher-melting point fuel salts that may provide major fuel cycle advantages. While there are many higher temperature alloy options for systems with clean fluoride salts, an MSR with dissolved uranium and other species presents special challenges. It is the uranium and certain fission products (not the fluoride salt itself) that primarily determine corrosion rates. In these systems, although the corrosion rates are very low with the use of high nickel alloys; these alloys lose strength at higher temperatures.

Carbon-based materials have been shown to be compatible with molten salts at temperatures of 1000°C, and for graphite up to 1400°C. Carbon–carbon composites which are currently being considered for fusion and for high-temperature reactors (e.g in-core applications such as control rods, straps, etc.) are therefore also an option for the MSR and MSFR. For these materials there are nevertheless uncertainties in the joining technology and large-scale development work and demonstrations would be needed for their application in the safety-related components.

3.3 Water cooled systems

Within the GIF this is represented by the SCWR which uses supercritical water as the working fluid.. The SCWR is basically an LWR operating at higher pressure and temperatures with a direct, once-through cycle and like the BWR, would only have one phase present. The SCWR can operate at much higher temperatures and pressure than both current PWRs and BWRs and much of the interest in the SCWR arises from the considerable expected increase in thermal efficiency (nearly 33% increase is expected over conventional PHWR or LWR). The SCWR also has a very strong synergy with the Canadian CANDU design.

Since supercritical water has different chemical properties to liquid water, and because it requires a higher operating temperature, materials developed for more traditional reactors may not be suitable for an SCWR. While there is a lot of experience with supercritical water

in fossil fuel plants, the neutron radiation present in a reactor means that the material requirements will be different. For the SCWR a wide variety of options are currently considered including both thermal-neutron and fast neutron spectra, pressure vessel and pressure tube configurations, with the operation of a 30 to 150 MWe technology demonstration reactor targeted for 2022. No nuclear reactors have so far been built using supercritical water as the coolant, while for the other GIF concepts, demonstration or experimental reactors of very closely related concepts have already been built.

Key materials and design issues for the SCWR are those associated with high temperature creep and strength, irradiation (irradiation assisted creep, void swelling and embrittlement) and stress corrosion cracking and corrosion. The challenges include requirements for increased temperature and pressure, increased heat transfer and corrosion and water chemistry issues and stability, all of which will impact on safety.

An important issue that's likely to impact on the practical operation of the SCWR is the chemistry of supercritical water in the presence of radiation. While the effects of water chemistry will be most critical in the SCWR reactor core, there could also be effects on the remaining balance of plant. Controlling the chemical composition of the coolant water is therefore very important to offset environment-sensitive cracking associated with intergranular stress corrosion cracking (IGSCC), irradiation assisted stress corrosion cracking (IASCC) and corrosion fatigue (CF). The body of experience available from the control of the water chemistry and performance of reactor materials in LWRs and supercritical fossil-fired power plants will be important for this.

A main challenge will be in the qualification of materials that experience both high temperature and radiation exposure and the hostile supercritical water environment. These materials include those for fuel cladding and the modified pressure tube designs which are being considered specifically for the SCWR. While fuel cladding will be replaced periodically as reactors are refuelled, other structural components will require much longer expected lifetimes. Work is underway to characterize the mechanical properties of candidate alloys, including fracture toughness, tensile strength, and creep resistance. For in-core materials, understanding of irradiation-induced changes due to growth, swelling, helium-bubble formation, dislocation microstructure, precipitate micro-structure and irradiation-induced composition changes are important and demonstration that these changes are not expected to compromise the integrity of core components is a key requirement. Some measurements on irradiated materials have been carried out and much more work is needed in this area. Fast spectrum fuel cycles offer even more stringent demands on the materials. Thin and dense Fe, Cr, Si, Al oxide layers can also protect metals from corrosion but excessive oxidation damage, can reduce heat transfer and wall thickness.

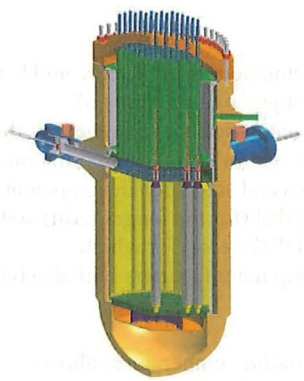

Figure 3. SCWR pressure vessel baseline alternative

In structures where the temperatures will be significantly above 300°C, or irradiation doses above several dpa, candidate structural materials will be primarily ferritic or martensitic steels and low swelling austenitic stainless steels. For Fe-Cr-Ni alloys acceptable mechanical behaviour and dimensional stability is also possible however, there is currently an insufficient knowledge base for predicting SCC or IASCC behaviour under supercritical water conditions. Some alloys have demonstrated low swelling in doses of up to 50-100 dpa in both mixed spectrum and fast reactors in the temperature regime of 450-550 C. Ferritic-martensitic steels in the 9-12% Cr range are also more swelling resistant than austenitic steels and acceptable behaviour has been demonstrated in these alloys at neutron irradiation doses of 50-100 dpa.

As with the other systems there has been a strong interest in the development and application of ODS steels which provide enhanced high-temperature strength. Significant international activities are ongoing to develop and optimize this class of materials. However, the principal issues as with all ODS alloys are the uncertainties regarding their interaction with the environment (i.e. in this case supercritical-water coolant), the high cost of fabrication and their weldability. Nevertheless, because of their potential, ODS alloys are being investigated carefully in the SCWR materials R&D program.

4. Conclusions

The lack of demand for large power stations in the mid-1990s led to a decline in research and development and manufacturing capability (especially in the UK) and for the new generation III+ reactor systems, certain specialized components will need to be imported. Significant capability nevertheless exists in design, construction and operation of nuclear power plant in the UK and Europe and in the current nuclear renaissance investment is to be encouraged to re-instate UK and European capabilities to ensure supply of critical and major components. Within the UK it is considered that the supply chain has a strong capability in most of the areas required and that UK and European industries should look to work closely with key nuclear partners to provide innovation for efficient delivery and operation of these plant addressing issues for the full life cycle.

For the new Generation IV systems key areas of materials development is in the core and heat exchanger systems. For the HTR which has perhaps the earliest potential in terms of deployment (given the existing market in process heat and co-generation) development of the graphite for the core is critical and the ongoing R & D program within GIF is addressing this in terms of selection and environmental properties and for codes and standards development. For the GFR and SFR/ LFR core new materials will also be needed (for the longer term) and these will require the deployment of new materials (ceramics, ODS steels) for which extensive industrial development and the identification of willing manufacturers will also be needed.

For heat exchangers high temperature alloys capable of withstanding temperatures above 850°C for sustained periods will be required in the longer term. In the shorter term industrially developed nickel based super-alloys can provide the immediate requirements (deployment up to 2020) to meet the market demands at lower temperatures. An important immediate requirement however for these intermediate temperatures is the development of

codes & standards. Current commercial codes such as ASME and RCC-MR do not yet recognize these alloys and require specific rules and methods to be developed.

To provide a solution in the longer term for Generation IV reactors for higher temperatures, and for certain core wrapper materials where the additional influence of irradiation limits the application of current alloys, the R & D programs within Europe and GIF are examining the potential of ODS materials to fulfill this requirement. An investigation of the potential of ODS steels is happening in all systems with limited co-ordination. A key restriction within Europe is the lack of a supplier and manufacturer. Demand over the last few decades for development of higher temperature materials has been low and much is still required with regard to their acceptance and application to large-scale component manufacture. It is considered unlikely that the generation IV needs alone will be sufficient to fuel a surge in development of ODS alloys unless deployment of high temperature systems is seen as a priority by national programs. The development of a very high temperature system is seen as a requirement in countries such as Japan and South Korea which are also investing in large scale hydrogen generation programs. Without such a clearly defined target application, material solutions for very high temperatures seems unlikely unless specific manufacturers are also invited and supported and encouraged to work alongside researchers to provide industrially developed solutions for future reactor needs. In this respect the co-operation between graphite manufacturers and suppliers within the HTR-TN [8] and specialized graphite groups could be considered as a model for future co-operation.

5. Acknowledgements

Acknowledgement is given to partner contributions from the EU Framework Programs and the European Atomic Energy Community ("Euratom"), and to the work of the GIF and the UK Materials Forum (MATUK). The information provided herein is the sole responsibility of the author and does not necessarily reflect the opinion of these organizations who are not responsible for any use that might be made of the data appearing in this publication.

6. References

[1] Generation IV International Forum; www.gen-4.org
[2] European Commission, Cordis Website- Framework 7: www.cordis.europa.eu/fp7
[3] MATUK http://www.matuk.co.uk
[4] Mapping the materials supply chain in the UK's power generation sector, Materials Energy Review, 2008.
[5] NIA Summary Report - 'The UK Capacity to deliver a new build Programme'
[6] Generation IV a report of progress for 2009.
[7] RAPHAEL – ReActor for Process heat, Hydrogen And ELectricity generation sixth Framework Project: www.raphael-project.org
[8] HTR-TN www.sinter.eu/htr-tn

9th Liege Conference : Materials for Advanced Power Engineering 2010
edited by J. Lecomte-Beckers, Q. Contrepois, T. Beck and B. Kuhn.

Part D

Solid Oxide Fuel Cells

9th Liege Conference : Materials for Advanced Power Engineering 2010
edited by J. Lecomte-Beckers, Q. Contrepois, T. Beck and B. Kuhn.

RECENT DEVELOPMENTS IN SOLID OXIDE FUEL CELLS AT FORSCHUNGSZENTRUM JUELICH AND IN EUROPE

Robert Steinberger-Wilckens*, L. Blum*, H.P. Buchkremer*, L.J.G. de Haart*, J.Malzbender*, M.Pap**, S.M. Groß**

*Institute of Energy Research (IEF), ** Central Department of Technology (ZAT)
Forschungszentrum Jülich GmbH, D-52425 Jülich, Germany

Abstract

The SOFC group at FZJ has assembled and tested more than 350 SOFC stacks rated between 100 W and 15 kW during the last 15 years. The research topics cover the whole SOFC development area from materials over stack design, manufacturing of cells, stacks and components, mechanical and electrochemical characterisation, up to system design and demonstration.
Use of improved steels, cathodes and materials processing has resulted in reduced degradation rates around 4 mV (<0.50%) per 1000 hours at 800°C and 500 mA/cm² over tested stack lifetimes of over 15 000 hours. Other stacks operating at 700°C have already reached over 22.000 hours of lifetime. However, the target of development is directed at even further lowered degradation for commercial operation in stationary applications.
All stack tests are accompanied by disassembly and post-operative examinations investigating such phenomena as cathode degradation, corrosion, and other ageing phenomena. These analyses give a deep insight into the interaction of the stack materials and supply vital data on assessing the possibilities for prolonged stack operation over some 10's of thousand hours.
This paper gives an overview and summary of achievements of Jülich developments. It also discusses the European perspectives in SOFC commercialisation. European manufacturers are holding a leading edge on the planar SOFC technology with new activities developing rapidly.

Keywords: SOFC, degradation, long-term durability, stationary power generation, APU

1. Recent Developments at Forschungszentrum Jülich

Since 1992, the SOFC group at JÜLICH has manufactured and operated more than 400 SOFC stacks rated between 100 W and 15 kW. The group has covered topics ranging from materials development and the associated processing technologies over stack design, manufacturing of cells, stacks and components, mechanical and electrochemical characterisation and modelling, up to system design and demonstration.

Large stacks of 5 kW and above have been operated since 2002 and also been successfully delivered and operated in Finland and Korea. In parallel, light-weight stacks are being developed in the so-called 'cassette design' line for SOFC-APU. Several one to 20 kW SOFC laboratory systems are in preparation, using the integrated stack concept which combines all hot parts of the balance of plant into one single module.

The use of improved steels, high performance cathodes and optimised materials processing have resulted in reduced degradation rates around 10 mV per 1.000 hours at 700°C and 500 mA/cm² over tested stack operation times of currently 25.000 hours and degradation rates of

around 4 mV/ kh at 800°C and 500 mA/cm² tested for 15.000 hours. However, the target of development is directed at distinctively lower degradation, as would be necessary for commercial operation in stationary applications with total system lifetimes of approx. 10 years. The approaches taken include cell materials with higher performance at lower temperatures, steels with less chromium evaporation and higher strength, contacting and protective coating materials, and optimised sealing technology. An overview of the basic FZJ technology can be found in [1].

1.1. Increasing Performance

JÜLICH has taken a route of developing SOFC cells with high performance as a means of being able to lower the operating temperature whilst still attaining high power output. This should also lead to reduced degradation in stacks due to the slowed down reaction mechanisms [2].

The cobalt/iron-based perowskite $La_{0.58}Sr_{0.4}Fe_{0.8}Co_{0.2}O_{3-\delta}$ (LSCF) is one of the state-of-the-art cathodes used in JÜLICH for high power output cells. Within the EU project Real-SOFC, over 10.000 hours of operation were achieved with such cathodes [3], also as a result of decreasing the operating temperature to 700°C which was made possible by the considerably increased performance of these cathodes. LSCF, though, reacts with the Yttria-stabilized Zirconia (YSZ) of the electrolyte layer, thus forming an insulating layer of $SrZrO_3$ which leads to a total failure of the SOFC cell. Past developments have therefore focussed on the cathode-electrolyte interface. To solve the problem of interdiffusion, a barrier layer is necessary between cathode and electrolyte. Best results were obtained with an inter-layer of $Ce_{0.8}Gd_{0.2}O_{2-\delta}$ (CGO) that was applied by electron beam physical vapour deposition (EB-PVD) [4]. The layers applied with this technology are at the same time thin and very homogenous, thus reducing the ionic current resistance and increasing gas tightness.

More recently, two other developments have led to encouraging results, namely the application of thin electrolytes and new cathode materials. On the side of the cathode, optimisation for high performance at low operating temperatures has resulted in the development of LSC cathodes, as performed within the programme of the EU project SOFC600 [5]. The second approach addresses very thin electrolytes that are applied either by PVD or spin/dip coating methods [6]. Cell tests have displayed similar increases in performance to those achieved with the formerly mentioned LSC cathodes [7].

Fig. 1 shows results of cells where the LSC cathodes are combined with a thin electrolyte. The curves depict the temperature dependence of the current density at 700 mV cell voltage in comparison to the average values of standard cells, as determined in the regular quality assurance routines. It can be seen that the new cells deliver triple the current density at the lower operating temperature range (650°C). The degradation of cell voltage is moderate, but still needs verification from long-term tests with durations over 1.000 hours. At 650°C and 500 mA/cm² cell voltage sank by approx. 8 mV over a 1.000 hour test run.

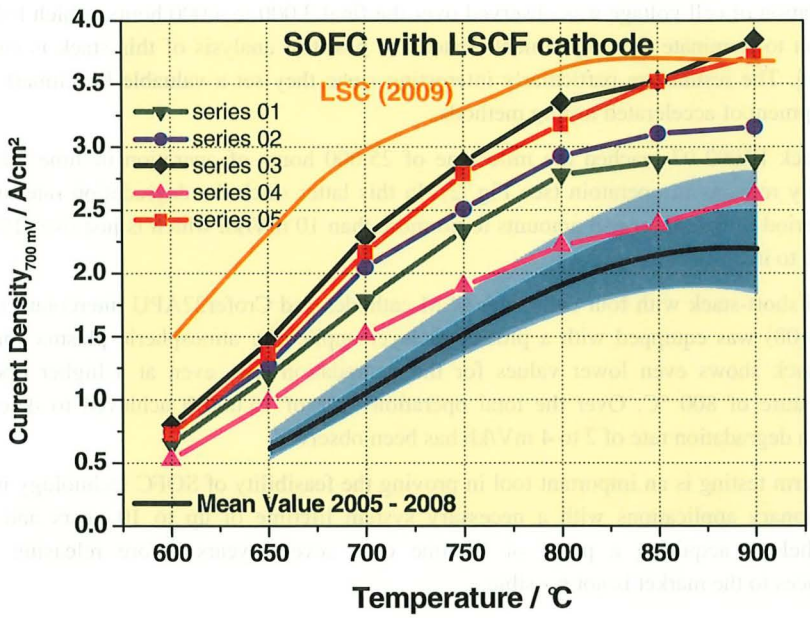

Figure 1: *Comparison of the standard LSCF single cell performance (drawn line and shaded confidence interval), as determined in the regular quality assurance tests, with the results obtained with different diffusion barrier layers (CGO) (lines with symbols) applied by PVD, and a combination of thin electrolyte with an LSC cathodes (upper line). For standard cells, the CGO layer is screen printed which leads to less favourable results than PVD.*

However, earlier experiences have already shown that a further increase in cell performance does not completely reflect in an analogous stack performance increase. Presumably, the combined effects of limited cathode contacting surface, limited lateral conductivity of the cathode / cathode current collection layer and the ratio of contact to cell resistance do not yet allow major current increases with the existing JÜLICH F-design stacks.

1.2. Long-Term Testing

Durability tests on two short-stacks in the current JÜLICH F-design, each with two cells with LSCF cathodes, were started in August 2007 in the framework of the EU-project Real-SOFC [3]. These were '3rd Generation' stacks incorporating a number of improvements obtained and validated within the project. The stack number F1002-97 (G3) had interconnect plates manufactured from the Plansee steel ITM. In the stack F1002-95 (G3 TK) Crofer22APU steel from ThyssenKrupp was used. Protective coatings and glass sealing were adapted to the respective steels. Both stacks were operated at 700 °C with hydrogen (fuel utilisation 40%) and at a current density of 0.5 A/cm² [8]. In September 2009 after over two years (17.660 h) of operation it was decided to terminate the operation of the G3 TK stack. A progressive

degradation of cell voltage was observed over the final 3.000 to 4.000 hours, which led to the decision to terminate this experiment. Extensive post-test analysis of this stack is currently ongoing. The results are particularly interesting since they set a valuable benchmark in the development of accelerated testing methods.

The stack F1002-97 reached the milestone of 25.000 hours of operation in June 2010 and currently remains in operatoin (see Fig. 2). In this latter stack the degradation rate over the total period of operation still amounts to no more than 10 mV/kh which is just over 1%/kh in relation to its initial voltage.

A third short-stack with four cells with LSM cathodes and Crofer22APU interconnect plates (F1004-08) was equipped with a protective layer applied by atmospheric plasma spraying. This stack shows even lower values for the degradation rate, even at a higher operating temperature of 800 °C. Over the total operation time of 16.000 h achieved to date (May 2010), a degradation rate of 2 to 4 mV/kh has been observed.

Long-term testing is an important tool in proving the feasibility of SOFC technology in view of stationary applications with a necessary system lifetime of up to 10 years and more. Nevertheless, acquiring a proof of lifetime over several years before releasing SOFC appliances to the market is not possible.

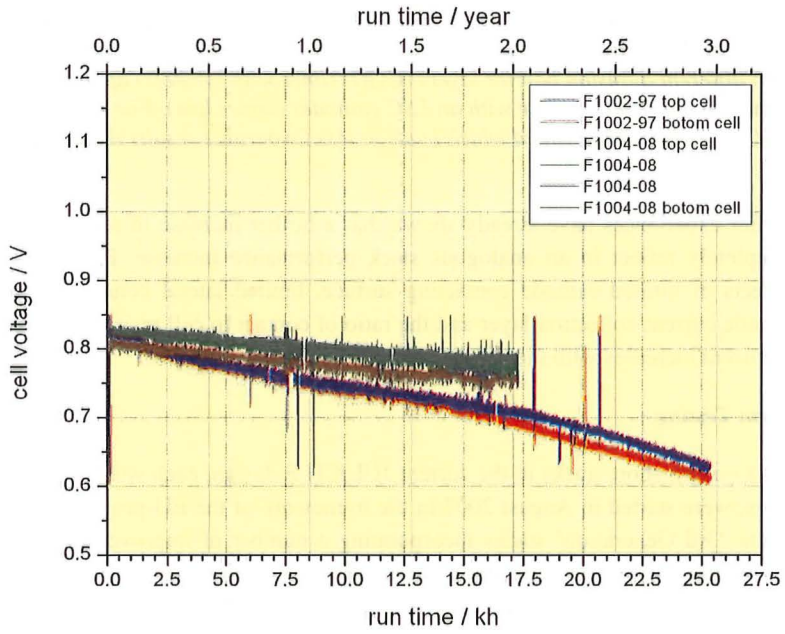

Figure 2: *Durability tests on two short stacks F-1002-97(Real-SOFC project Generation 3 stack) operated on hydrogen at 0.5 A/cm² and 700 °C and F-1004-08 operated at the same conditions but at 800 °C. Voltage-time plot as of June 2010.*

Therefore the next steps will include the development of accelerated testing methods in order to obtain estimates of total lifetime in a matter of a few thousand hours of testing. Samples from the stacks that have been operated for extended periods of time will allow to adjust accelerated testing approaches to real-time results.

1.3. Increasing Robustness

As to electrochemical stack performance, most of the results in JÜLICH have been obtained under isothermal, steady-state operating conditions. Many manufacturers consider a continuous operation as a possible regime in residential applications where heat generation is low enough to be completely absorbed by household hot water demand. Therefore a shut-down of the system would only be necessary during maintenance or an extended lack of energy demand, for instance during a summer holiday. All in all, this would result in only very few shut-down and start-up cycles per year.

Nevertheless, since this cannot be postulated as the general operational scheme for an appliance in the hands of an arbitrary customer, transient operation also has to be foreseen as a standard operational case. Three main transient situations may be distinguished: load, redox and thermal cycling. Whereas the first has not been experienced to pose considerable problems, given the system control adjusts fuel and air flows accordingly, the latter two constitute a major area of current developments.

Redox cycling occurs when during or after a shut-down process, oxygen penetrates into the anode compartment of the SOFC stack. Since most SOFC today use nickel cermet anodes, this will invariably lead to its reoxidation with subsequent failure of the anode structure and/or the electrolyte due to mechanical stresses [9]. Reoxidation damage can be reduced or avoided by operating at low temperatures where the kinetics of reoxidation are slowed down or by using anode materials with low or no nickel content. Here, of course, both the catalytic activity and the electrical conductivity need to be maintained. $SrTiO_3$ materials seem to be a promising option to achieve good performance in both aspects [10].

Due to the thermal stresses induced during start-up / shut-down cycles, damage might be caused especially to the sealing joints between ceramic cell and ferritic steel frame in the stacks. Degradation problems may increase through cycling and subsequent failure is initiated. Matching the thermal expansion coefficients of materials, as has been done in JÜLICH, for instance through the development of the steel CroFer22APU [11], is only one aspect of solving this problem.

It has proven essential to gain an improved understanding of the thermal stresses induced, their order of magnitude and distribution with a stack or single repeating unit. Only on the basis of such an understanding, test results may be explained and counter measures properly implemented in the joining procedure and stack design [12]. It is also necessary to acquire more knowledge on the mechanical properties of glass-ceramic and metallic sealing materials in order to assess possible failure modes and the balance between the forces that can be sustained in the components (SOFC cells), the bonding layers and the sealant material itself

[13]. In order to support these activities, effort has now also been allocated to a larger extent towards the experimental evaluation of thermo-mechanical properties of materials (ceramics and steels) as well as of glass-ceramics and metallic sealing materials [14].

Finally, it also appears that the strength of the glass ceramic sealant materials used to date is not sufficient to meet the high stresses induced during thermal cycling, especially in the case of larger stacks with 400 cm^2 cells. Activities are now aimed at developing glass-ceramic materials with higher strength by adding filer materials and fibres. Fig. 3 shows an example of a glass matrix reinforced with YSZ fibres. The glass used is composed of BaO-CaO-SiO2 that is mixed with ceramic particles, fibres or ductile metals. In particular, experiments with silver particle reinforcement have led to increased strength, although the electrical conductivity still needs further attention. One option currently pursued is the combination of reinforced and ductile layers in order to obtain synergies between these solutions. Results of tensile strength tests are presented in [15].

Further aspects of 'robustness' of SOFC technology are the reproducibility and reliability of the manufacturing processes. In some sense, this also covers aspects of cost effectiveness as a key to market entry. Expensive materials as well as involved processing steps that make manufacturing costly need to be avoided. Although JÜLICH is active in the area of processing and possesses a whole line of manufacturing technology that is very close to industrial applications, the perspective of cost reduction eventually has to be left to industry with its very specific views of cost goals and choice of processing technologies.

Nevertheless, the reproducibility of properties of components is a vital field in which JÜLICH has developed a number of activities. In analysing the long term behaviour of cells and stacks at low degradation rates it is vitally important to be able to discern tolerances of manufacturing from impacts of new materials and materials combinations.

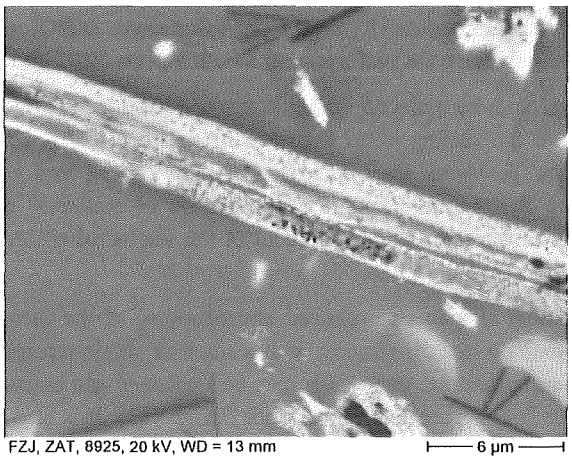

Figure 3: *Ba-Si-glass matrix reinforced with YSZ fibres.*

Therefore efforts are being directed at making production steps as reproducible and reliable as possible. Fig. 4 shows two processes currently applied in the preparation of glass sealing materials. The dispensing of glass pastes by a robotic device is a reliable, flexible and exact method. It reaches its limits, though, where the thickness of the green sealant layer needs to be increased, thus necessitating several passes layered on top of each other. Screen printing is currently being investigated as an alternative which offers faster turn-around, better homogeneity and easy application with an industry-compatible method. The higher consumption of materials is a draw-back, though, and makes recycling of pastes a necessary prerequisite.

In the field of cell manufacturing, JÜLICH has by now further developed the tape casting procedures with some surprising results, as reported in [16].

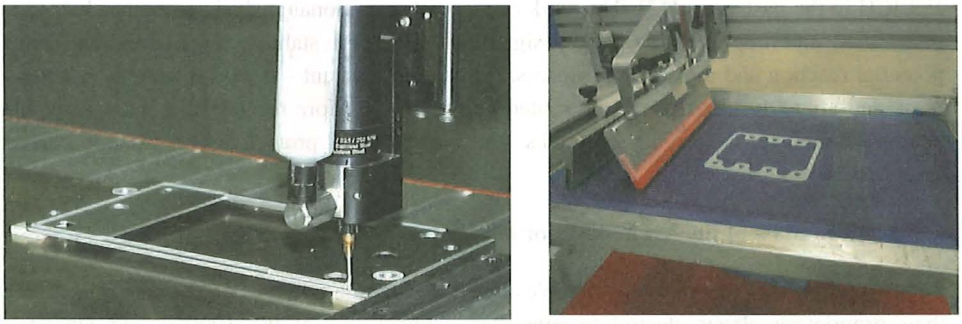

Figure 4: *Glass ceramic paste dispenser (left) versus screen printing of glass tapes (right) for different stack configurations.*

1.4. Post-Test Analysis

After operation, stacks are regularly dismantled to analyse the degradation and failure mechanisms. Obviously, in a stringent post mortem methodology, advanced characterisation methods are an essential element to understand the stack performance within the frame-work of systematic testing.

Disassembling is carried out with selected experts depending on expected outcome of the post-operational analysis and/or the goals set in initiating the stack experiment. Experts are available in synthesis, production, and interaction of materials, thermo-mechanics, corrosion, thermo-chemistry, sealants, stack / system operation, single cell testing, optical and scanning electron microscopy. As an indication of the amount of analyses performed in this area, it should be noted that 108 dissections were carried out in the time from August 2002 to September 2008.

During the post operational analysis, electro-chemical results and irregular events receive special attention and cells and components that display unusual operational behaviour are inspected in detail. A digital photographic image is taken of every stack plane during disassembly. Unusual observations are investigated microscopically. After dismantling, more

detailed SEM (TEM) investigations are carried out as necessary. Investigation methods cover graphical & image analysis to gain insight into macroscopic changes and associated sifts in colour. SEM and EDX deliver information on microscopic / structural changes, in order to acquire a qualitative chemical analysis. Furthermore, wet chemical analysis is used in a coarsely localised quantitative analysis. Thermography and computer tomography have shown to be successful in determination of the origins of short circuits and localisation of porosities. XRD offers insight into structural changes, TEM into local changes in interfaces and reactions. Leakages are investigated using liquid dyes to localise leakages.

A topic that has been specifically addressed in connection with the long-term testing is the profound understanding of degradation phenomena under steady state operation. Chromium poisoning is believed to be one influential parameter and has received significant attention in JÜLICH in the past years [17]. The work of the post operational analysis group has helped to understand and improve the stack design and long term stability by highlighting other potential reaction and degradation sources, for example sealant - steel and cathode reactions, re-oxidation and localized creep associated deformations. More recently, the main focus has been on dimensional accuracy of stacks, and behaviour of protective and cathode contact layers.

2. European State of the Art and Major Players

Following Siemens' move to acquire Westinghouse and the tubular SOFC concept and drop their proprietary planar electrolyte supported concept end of the 1990ies and Dornier's closure of SOFC activities, a number of smaller European developers have adopted the planar SOFC concept. This has now successfully evolved into a high performance technology, especially with the anode supported (ASC) variant.

Development groups for planar technology include companies HEXIS (Switzerland), Topsoe Fuel Cells (TOFC, Denmark), H.C. Starck (Germany, having acquired the ECN InDEC know-how), ProtoTech (Norway), Ceres Power (UK), CeramTec (Germany), SOFCpower/HTceramix (Italy/Switzerland), and SaintGobain (France) to name but a few.

A growing number of joint ventures of companies and research groups shows the increased involvement of industry but also the insight that the development will only be successful if based on thorough techno-scientific understanding and a sound basis of materials development. Staxera (Germany) was founded as a joint venture of Enerday (owned by Webasto) and H.C.Starck, with ties to the Fraunhofer Gesellschaft IKTS institute. Vaillant again has announced SOFC activities together with IKTS as a parallel development to their residential HT-PEFC systems. The involvement of Risø National Laboratory (now part of the Danish Technical University, DTU) with TOFC is another example.

Many research organisations are currently working in the area of SOFC, including FZJ (Germany), Imperial College (UK), DLR (Germany), CEA (France), VTT (Finland), EMPA and the University of Lausanne, EPFL (Switzerland), SINTEF (Norway), Risø-DTU, further

extending to numerous university groups in all European countries, but especially Germany, The Netherlands, France, Switzerland, Spain and Italy.

2.1. Residential CHP

In the area of small scale stationary applications, Sulzer HEXIS took a world lead in demonstrating residential Combined Heat and Power (CHP) units in 2001/2002 and had installed over 100 of the 1 kW units by the end of 2004. HEXIS today can offer the third generation of units ('Galileo', Fig. 5), in the level of development, experience and packaging only contested by PEFC developer European Fuel Cells (Baxi group).

Within the German national fuel cell and hydrogen funding programme (NIP) a large demonstration project kicked off in Sept. 2008. 'CALLUX' integrates five utilities with three fuel cell manufacturers. The partners are EWE, EnBW, E*on, MVV and Verbundnetz Gas with Baxi, HEXIS and Vaillant. A total of 800 residential fuel cell units will be installed by 2012. Starting with few prototypes, numbers will be increased as technology progresses. Vaillant, for instance, has not yet concluded work on their SOFC prototypes with FhG IKTS and will add installations in the later phase of the project. The project is believed to make a major impact on development and market introduction. One of the main goals of the NIP is to achieve market access for fuel cells by the end of the programme in 2016.

CFCL have set up operations in Germany (Heinsberg in Northrhine-Westfalia), investing 12.4 mio [18]. 10 000 units of 2 kW are to be manufactured there per year, starting with a first 100 units in 2010. CFCL continues their development in Europe with German, French and UK partners.

Ceres Power, UK based IT-SOFC company spun out of Imperial College, offer little information on their recent developments. They are reported to have demonstrated a wall-mounted μCHP unit of 1 kW electrical power in fulfillment of their contract with Centrica/British Gas [19]. Conditions were not disclosed, but following the successful trial, a 2 mio GBP payment was issued to Ceres by British Gas. Ceres' concept is based on a ceria electrolyte, metal substrate (MSC) and an operating temperature between 500 and 600°C. Natural gas is the logical fuel for residential units, but Ceres is now also looking at LPG. An order of 20 000 units has reported to have been placed by Calor Gas, an LPG supplier.

2.2. Auxiliary Power Units

Combined with the multi-fuel capability, the high power density achievable with planar designs has established them as a prime technology choice in vehicle Auxiliary Power Units (APU) (with HT-PEFC gradually also getting involved, though at a lower level of performance). Development groups in Germany, ElringKlinger/Eberspächer (the formerly BMW led consortium), and in Denmark/Austria (TOFC-AVL) are working on units for passenger vehicles, trucks and construction machines.

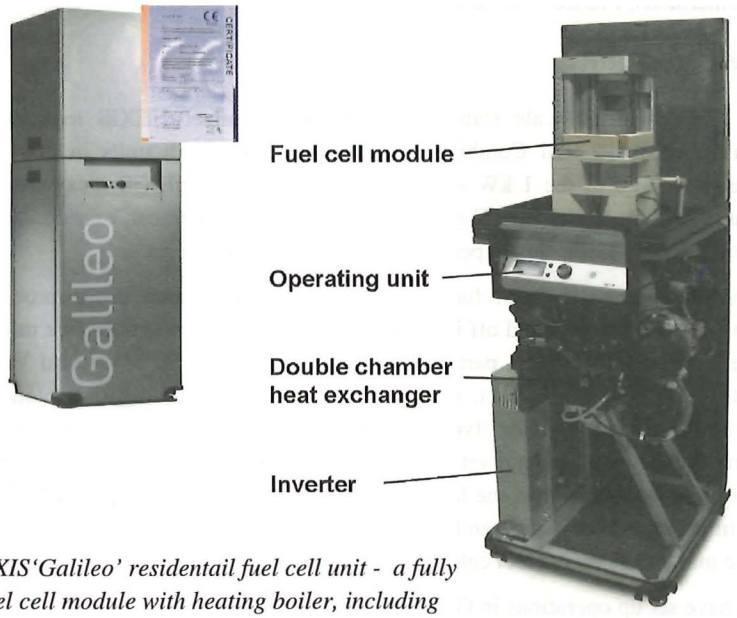

***Figure 5:** HEXIS 'Galileo' residentail fuel cell unit - a fully packaged fuel cell module with heating boiler, including product certification. (photographs courtesy Hexis).*

BMW has pulled out of the SOFC APU development in favour of all-electric drive development. They have handed over to ElringKlinger, the supplier of light-weight stacks in the ongoing SOFC stack project, and Eberspächer, the supplier of the reforming unit in the APU system project.

Airbus retain a keen interest in aircraft APU, as does Wärtsilä for marine APU applications. A number of other marine companies are also expressing interest, but due to a lack of large SOFC units, the prime technology choice for airborne and maritime applications today is (HT-)PEFC and MCFC. Wärtsilä is working on a 50 kW SOFC unit for marine use with a vision of increasing size to some 100 kW. Stack technology is delivered by TOFC on the basis of 1 and 2 kW modules.

2.3. Industrial CHP and Power Generation

In the area of medium sized (industrial) units Siemens Power Generation relocated the successfully operated 100 kW Arnhem plant to Essen, and after several months on to the Siemens Turbocare site near Turin (Italy) where it was run extensively, having undergone repairs. Total service time of the system (though partly equipped with new tubes) amounted to above 30 000 hours.

Runner-ups Wärtsilä (Finland) and Rolls Royce Fuel Cell Systems (UK) are working on medium sized industrial power generation units up to and above 250 kW, eventually even up to several MW of electrical power. While Wärtsilä is primarily concentrating on APU units for ships, they are also in the process of supplying a stationary unit for biogas. RRFCS are targeting the U.S. power generation market with the help of SOFCo, which they acquired in 2007. Recently, considerable funding was awarded by the DoE within the SECA programme, whereas RRFCS is being given a hard time by EU funding authorities. RRFCS has is now concentrating the cell development in the U.S. while performing the testing and system development in the UK.

2.4. Ramping up Production

Obviously, in establishing SOFC technology in the market, the technology readiness level has to be continuously improved. This brings increasing attention to product design and customer performance aspects. On the other hand, cost has to be reduced and this will only be realised by introducing mass manufacturing processes – at least for the cells and interconnects. Companies TOFC, Kerafol, H.C.Starck and CeramTec have or are all in the process of building up adequate production capacity for SOFC cells. A risky business, given that market entry still remains to be accomplished, cost reduction being one pre-requisite in doing so – which brings up the usual chicken-and-egg problem. Plansee have established bulk manufacturing of powder-metallurgically produced interconnects and are heavily expanding production in the wake of the Bloom Energy developments in the U.S. ThyssenKrupp are regularly producing 30 ton batches of CroFer22APU and this steel remains one of the most commonly applied in SOFC stack manufacturing. Other steel mills (Sandvik, Haynes, Hitachi etc.) also offer standard products for SOFC interconnects.

CFCL and Ceres Power, following their announcement of completing first unit tests are setting up production on a considerable floor area [18, 19]. Staxera, on the other hand, was the first SOFC company worldwide to offer off-the-shelf stack modules as standardised product and offers these to SOFC system integrators on a commercial basis..

Outlook

SOFC technology in Europe has reached a status that will allow producing market-compatible equipment within the next very few years. Whether or not a realistic market entry will be possible at this point in time remains to be shown. The cost of stacks and units today are adequate for prototype technology but not for marketable products. It depends on the further development of manufacturing technology, and the ability of industry to convince financial institutions to invest whether SOFC technology will achieve cost breakthroughs and introduction to European heating and electricity generation markets. Last but not least the installation of feed-in tariffs for fuel cell electricity – similar to the German Photovoltaics tariffs – will be a necessary prerequisite in gaining market access for stationary fuel cells.

Acknowledgments

The authors wish to thank all staff members of FZJ for their continued excellent work. Acknowledgments go to the European Commission for co-financing the project Real-SOFC under the contract number SES6-CT-2003-502612 under which the F1002-95/97 long-term tests were carried out until the end of the project in Dec. 2008, and to the German Ministry of Economics for part-funding of a number of development projects.

References

[1] L. Blum, H.–P. Buchkremer, S. M. Gross, L.G.J. de Haart, J. Quadakkers, U. Reisgen, R. Steinberger-Wilckens, R. W. Steinbrech, F. Tietz: Overview of the Development of Solid Oxide Fuel Cells at Forschungszentrum Juelich. *Int. J. Appl. Ceramic. Technology* **3** [6] (2006) 470-476.

[2] R. Steinberger-Wilckens, L. Blum, H.-P. Buchkremer, L.G.J. de Haart, M. Pap, R.W. Steinbrech, S. Uhlenbruck, F. Tietz: Overview of Solid Oxide Fuel Cell Development at Forschungszentrum Juelich. *ECS Transactions,* **25**(2009), issue 2, "SOFC XI", p.213-220, The Electrochemical Society, Pennington NJ, USA.

[3] R. Steinberger-Wilckens, O. Bucheli, L.G.J. de Haart, A. Hagen, J. Kiviaho, J.G. Larsen, S. Pyke, G. Rietveld, J. Sfeir, F. Tietz, M. Zahid: Real-SOFC - A Joint European Effort to Improve SOFC Durability. *ECS Transactions*, **25**(2009), issue 2, "SOFC XI", p.43 – 56, The Electrochemical Society, Pennington NJ, USA.

[4] R. Steinberger-Wilckens, L. Blum, S. Uhlenbruck, B. de Haart, M. Pap, R.W. Steinbrech: Overview of Solid Oxide Fuel Cell Development at Forschungszentrum Juelich. Extended Abstract. *Proceedings of the Fuel Cell Seminar*, Phoenix, AZ, Oct. 2008.

[5] Y. Zhang-Steenwinkel. M.M.A.van Tuel, F.P.F.van Berkel, G. Rietveld: Development of novel cell components for low-temperature SOFC. *ECS Transactions: Solid Oxide Fuel Cells 10 (SOFC X).* Proceedings of the SOFC X Meeting, Nara, Japan, June 2007.

[6] N.H. Menzler, F. Tietz, S. Uhlenbruck, H.P. Buchkremer, D. Stöver: Materials and manufacturing technologies for solid oxide fuel cells. *J. Mater Sci* **45** (2010) 3109-3135.

[7] F. Han, A. Leonide, T. van Gestel, H.P. Buchkremer: Excellent electrochemical performance with thin YSZ electrolyte for IT-SOFCs. *Proceedings of the 9th European SOFC Forum*, Lucerne, 2010.

[8] L.G.J. de Haart, J. Mougin, O. Posdziech, J. Kiviaho, N.H. Menzler: Stack Degradation in Dependance of Operation Parameters; the Real-SOFC Sensitivity Analysis. *Fuel Cells - from Fundamentals to Systems,* **9** [6] (2009) 794 – 804.

[9] D. Sarantaridis, R. J. Chater and A. Atkinson: Changes in physical and mechanical properties of SOFC Ni-YSZ composites caused by redox cycling. *J. Electrochem. Soc,* **155** (2008) B467-B472.

[10] Q. Ma, F. Tietz, A. Leonide, E. Ivers-Tiffée: SOFCs based on Y-substituted SrTiO3 ceramic anode materials. *Proceedings of the 9th European SOFC Forum*, Lucerne, 2010.

[11] J. Froitzheim, G.H. Meier, L. Niewolak, P. Ennis, H. Hattendorf, L. Singheiser, W.J. Quadakkers: Development of High Strength Ferritic Steel for Interconnect Application in SOFCs. *J Power Sources* **178** (2008) 163 – 173.

[12] L. Blum, S.M. Groß, J. Malzbender, U. Pabst, M. Peksen, R. Peters, I.C. Vinke: Investigation of SOFC sealing behavior under stack relevant conditions at Forschungszentrum Jülich. *Proceedings of the 9th European SOFC Forum*, Lucerne, 2010.

[13] B. Kuhn, J. Brandenberg, T. Bause, J. Malzbender, R.W. Steinbrech, L. Singheiser: Mechanical performance of reactive-air-brazed (RAB) ceramic/metal joints for SOFC applications. *Proceedings of the 9th European SOFC Forum*, Lucerne, 2010.

[14] Y. Zhao, J. Malzbender, S.M. Gross: The Effect of Room Temperature and High Temperature Exposure on the Elastic Modulus, Hardness and Fracture Toughness of Glass Ceramic Sealants. *Proceedings of the 9th European SOFC Forum*, Lucerne, 2010.

[15] S.M. Gross, D. Federmann, J. Remmel, M. Pap: Reinforced Composite Sealants for SOFC applications. *Proceedings of the 9th European SOFC Forum*, Lucerne, 2010.

[16] O. Büchler, W. Schafbauer, R. Mücke, N.H. Menzler: Innovative Manufacturing Technologies for Low-Cost High-Volume SOFC Fabrication. *Proceedings of the 9th European SOFC Forum*, Lucerne, 2010.

[17] M. Kornely, A. Neumann, N.H. Menzler, E. Ivers-Tiffée: Degradation of ASC Performance by Cr-Poisoning. *Proceedings of the 9th European SOFC Forum*, Lucerne, 2010.

[18] CFCL press release 27 Feb 2008. Available through http://www.cfcl.com.au/Assets/Files/Capex%20investment%20and%20Nuon%20order.final.ASX.pdf

[19] Ceres Power Holding, plc completes Alpha phase of CHP product testing. Fuel Cell Today, 29 May 2009.

9^{th} Liege Conference : Materials for Advanced Power Engineering 2010
edited by J. Lecomte-Beckers, Q. Contrepois, T. Beck and B. Kuhn.

RECENT ACTIVITIES OF SOFC RESEARCH DEVELOPMENT AND DEMONSTRATION IN JAPAN

Harumi Yokokawa[1,2)]
1) National Institute of Advanced Industrial Science and Technology (AIST),
Higashi 1-1-1, Tsukuba, Ibaraki 305-8565, Japan
2) Tokyo City University, Advanced Research Laboratories
Todoroki 8-15-1, Setagaya-ku, Tokyo 158-0082, Japan

Abstract

Currently Japanese efforts in developing the SOFC systems have two major targets; one is small SOFC cogeneration systems for residential houses or small business sites, the other being the SOFC-GT hybrid systems with an aim at larger stationary applications. The former activity exhibits impressively rapid progress in system development and demonstration in actual residential environment. On the other hand, the development of hybrid systems is not so rapid but successfully has continued to test the operation of the hybrid system in a 200 kW class. The common requirement for both applications is high durability such as 40,000 -100,000 h of life. To achieve a long life simultaneously with reasonably low price and high efficiency, the NEDO project is going on to promote the cooperation among the stack developers, national institute and universities. To achieve well organized cooperation, it is highly required to create mutual reliance between industry and academic organizations. After several years' experience, progress has been made in maturing cooperation and in leading to many new insights into physicochemical understanding of degradation phenomena. Some of them will be reported.

Keywords: Solid Oxide Fuel Cell, CHP system, SOFC-GT Hybrid, Degradation

1. Introduction

Development of Soli Oxide Fuel Cells (SOFCs) in Japan began essentially from 1989 when the SOFC society of Japan was organized within the Electrochemical Society in Japan to promote the activities in research, development and demonstration of SOFCs. At that time, Tokyo gas and Osaka gas tested the 3 kW system made by Westinghouse just after their first breakthrough was achieved by adopting electrochemical vapor deposition (EVD) technique on the sealless tubular cells with lanthanum strontium manganites (LSM) as cathode, yttria stabilized zirconia (YSZ) as electrolyte, Ni as anode and $La(Cr,Mg)O_3$ as interconnect. The SOFC society of Japan has been promoted by co-efforts of universities, national laboratories and utilities. This clearly indicates that the role of the utility companies, particularly of the gaseous companies, has been quite important in the development of SOFCs in Japan. During

the last two decades, many attempts and efforts have been made in research and development mainly on the stationary applications to overcome the technical demerits of sealless tubular cells. In this context, the applications proposed by Westinghouse still survived for a long time in the research and development of SOFCs in Japan.

In recent years, however, the most important achievement in development of SOFCs has been made by Kyocera and Osaka gas; they started the development with an idea that the SOFC CHP systems can be adopted for domestic houses for providing electricity and heats simultaneously. They decide the requirements for SOFC stacks to be constructed for this purpose. It is an important step in Japanese R&D situation in a sense that a new idea for an specified application is successfully combined with the development of SOFC stacks, and well-managed development have been made for the CHP systems. Progress of their activities is rapid in such a way that in 2001, Kyocera started this project and in 2004-2005, they already tested a first SOFC CHP system in Osaka gas NEXT 21 residential research sites with great success.

The current NEDO SOFC projects consist of two projects; one is the SOFC demonstration program mainly for residential CHP systems and the other is the Research and Development Program on Durability/Reliability, Stack Improvement and the SOFC-GT Hybrid system [1].

In the present paper, these recent activities have been reported with an emphasis on system developments and cooperation program for overcoming degradation issues.

2. Small CHP system and Demonstration Program by NEF/NEDO

For a long period of time after Westinghouse proposed the sealless tubular cells for stationary applications, many people in Japanese utilities thought that the main SOFC application should be the stationary one in the range of several 100 to several 1000 kW. Many efforts on developing SOFC stacks are therefore based on such ideas. Even so, in 2001,

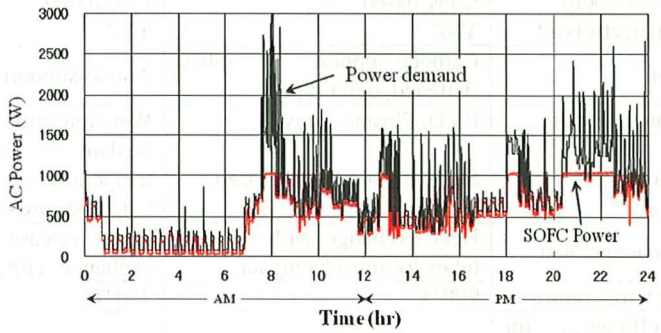

Fig. 1 Typical 24 h operation results of CHP system which is designed to follow the electrical demand up to 1 kW [2,3].

Kyocera started their efforts of developing the SOFC CHP system in the rage of one kW with an idea that requirements for stack performance should be determined from the application side. This was therefore quite unique in Japanese R&D community. Their progress was quite rapid in establishing a technology of constructing small but compact stacks, and they started to cooperate with Osaka gas who has accumulated knowledge on not only SOFCs but also on other fuel cells and related reforming technology. In 2005-2006, Osaka gas and Kyocera tested their first SOFC CHP system in NEXT 21 of Osaka gas which collects the experimental facilities for newly developed energy-related technological output [2,3].

Figure 1 shows a typical output of 24 h operation in comparison with the electricity demand. The maximum power of the SOFC system is one kW so that when the electrical demand exceeds this value, the rest of electricity required is supplied from the grid. Since the electricity companies at present do not allow the SOFC system to supply the excess electricity to the grid system, the SOFC output should be less than the electricity demand when this is less than one 1 kW.

This success is also interesting from the stack technology of SOFCs. In Table 1, comparison is made between the sealless tubular cells by Westinghouse and the flatten tube cells by Kyocera. Even though fundamental differences can be seen in operating

Table 1 Comparison between sealless tubular cells for middle-size stationary application by Westinghouse/Siemens and flatten tube cells for small stationary applications by Kyocera/Osaka gas.

	Middle-class stationary	Small-class stationary
Developer	Westinghouse/Siemens PGC, (TOTO)	Kyocera/Osaka gas
Materials (Interconnect)	$LaCrO_3$-based	$LaCrO_3$-based
Materials(cell-to-cell connection)	Ni in fuel compartment	Ferritic alloys in air
Materials (cathode)	LSM-based	LSF-based
Materials(Electrolyte)	YSZ	YSZ
Cell design	Cathode-support tubes, flattened, delta-type	Anode-support flattened.
Fabrication methods	EVD, Plasma spray	Wet-sintering
Seal method	Sealless; one end is closed.	Sealant at lower temperatures; both ends are open.
Thermal management	Heat exchange with alumina tubes for introducing air	Heat release and heat exchange with air
Operating temperature	900 °C	750 °C
System efficiency for generating electricity (LHV)	47 %	45 %

Table 2 List of tested CHP systems in NEDO/NEF demonstration program

Installation & Operation company	Fuel	Manufacturer	Rated Power	FY 2007	FY 2008	FY 2009	FY 2010
Osaka Gas	City Gas	Kyocera	0.7 kW	20	25	12	-
		Toyota/Aisin		-	-	23	34
		TOTO		-	-	-	2
Tokyo Gas	City Gas	Kyocera	0.7 kW	3	2	-	-
		Toyota/Aisin		-	-	4	4
		Gastar/Rinnai		-	-	2	4
Hokkaido Gas	City Gas	Kyocera	0.7 kW	1	1	-	-
		Toyota/Aisin		-	-	1	2
Saibu Gas	City Gas	Kyocera	0.7 kW	1	1	-	-
		Toyota/Aisin		-	-	1	1
Toho Gas	City Gas	Toyota/Aisin	0.7 kW	-	-	1	-
		NGK Spark Plug		-	-	-	2
Tokyo Electric Power	City Gas	Kyocera	0.7 kW	-	□	□	-
Tohoku Electric Power	City Gas	Kyocera	0.7 kW	-	-	□	-
Nippon Oil	LPG	Nippon Oil	0.7 kW	1	2	14	20
	Kerosene			1	1	1	1
TOTO	City Gas	TOTO	0.7 kW	-	2	6	8
			2 kW	2	-	-	-
			8 kW	-	1	-	-
9 Companies		7 Companies		29	36	67	78

temperature and system size, essentially the same efficiency for converting to electricity was achieved.

This success of operating the SOFC CHP system opened a new door in the Japanese SOFC development field [4]. Other companies like TOTO, NGK spark plug started to construct similar CHP systems immediately after this success was announced.

The Japanese government started the demonstration program for a small stationary application from 2007 as four year project [5]. Table 2 lists the participating companies for each year. The major contribution is from Kyocera and those utility companies who are testing the Kyocera systems. The data obtained from the demonstration program have been

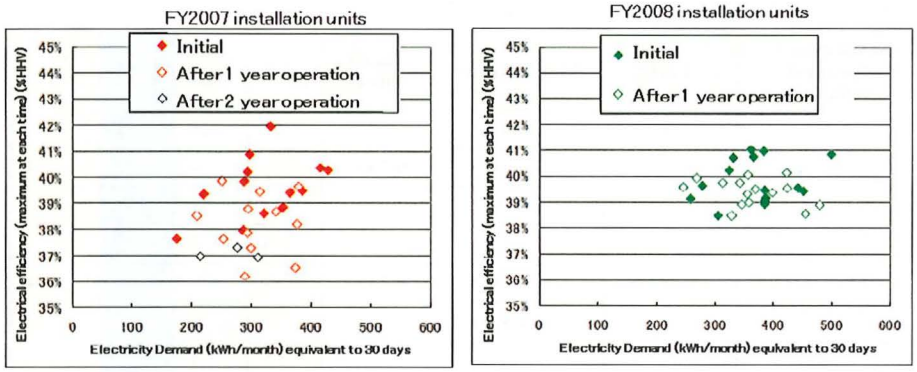

Fig. 2 The conversion efficiency from city gas to electricity for tested CHP systems installed in 2007 fiscal year and 2008 fiscal year. Changes in electrical efficiency are plotted by different symbols (from NEF Report[5]).

analyzed by NEF (New Energy Foundation). One of their analyses is shown in Fig. 2, where the conversion efficiency from natural gas to electricity was plotted against the monthly demand of electricity. When monthly electrical demand is small, the SOFC CHP system is operated at the lower power output than the rated power, leading to lower system efficiencies. In the same graph, data after one or two year operation are also included. Minimum requirement of this demonstration program is to operate 6 months. Even so, the SOFC systems can be extended to test at expense of the utility companies. Thus, some of installed systems have been extended for further examination. Figure 2 indicates that the 2007 fiscal year units have a tendency of performance degradation on the second or on the third year of operation, whereas the 2008 fiscal year units are very much improved in durability and the efficiency is essentially the same between the first and the second year operations.

3. Development of SOFC-GT hybrid system

In the NEDO project on the SOFC system development, Mitsubishi Heavy Industry constructed and tested the 200kW SOFC – MGT combined cycle system [1]. Figure 3 shows system configuration: MHI has a long term target of constructing a large SOFC-GT-ST combined system. The present system corresponds to the SOFC-MGT part. As the SOFC system, 200 kW unit is utilized, whereas as MGT, their own GT is used [6,7].

Results are given in Figs. 3-4. Figure 3 provides some numerical data for air flow and fuel flow in the present system. Figure 4 indicates the sequential output and related data

for the SOFC and the MGT parts. After starting the SOFC system, MGT begins to operate. After reaching to the operation temperature of SOFC, the SOFC part starts to generate the electricity. Numerical achievements of the system are collected in Table 3.

The longer operation up to 3000 h has been recently achieved and this confirmed the technological feasibility of the SOFC-MGT system.

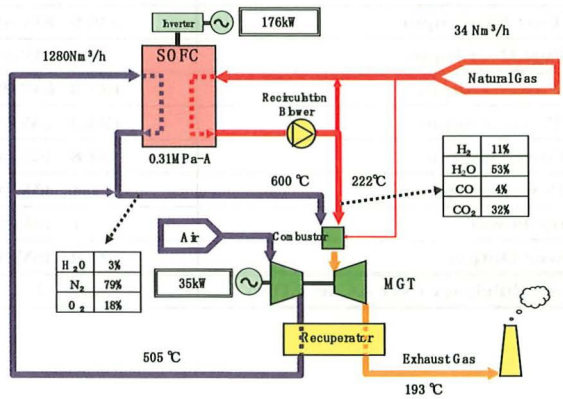

Fig. 3 SOFC-MGT system configuration and results of operation. Temperatures of air or fuel flows are given at selected parts and typical concentration of fuels and air are also given.

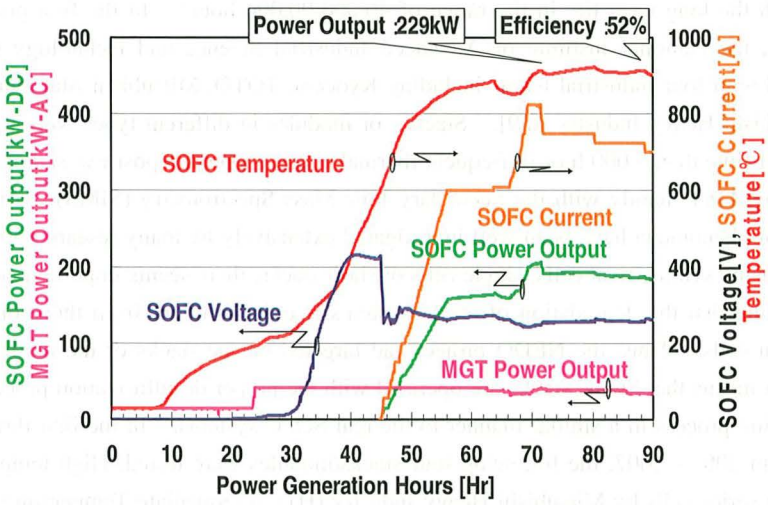

Fig. 4 Results of operation.

During the current NEDO project on the fundamental investigation of SOFC systems, MHI are preparing to construct another SOFC-MGT system and to confirm the durability and the reliability for high pressurized combined system.

Table3 Performance test results of operation of SOFC-MGT system

Item	
SOFC Fuel Heat Input	339.8 kW-th
MGT Fuel Heat Input	51.5 kW-th
SOFC Power Output	186.8 kW-DC
SOFC Power Output	176.3 kW-AC
MGT Power Output	34.8 kW-AC
Gross Power Output	211.1 kW-AC
Auxiliary Power	7.1 kW-AC
Net Power Output	204.0 kW-AC
Electrical Efficiency (Net AC as LHV)	52.1 %

4. NEDO project on Durability/Reliability of SOFC stacks/modules

NEDO started a renewed reliability/durability project from 2008 after the three year project on the reliability in 2005-2007. This is based on an idea that when the SOFC system should market in some applications in the early stage of the commercialization, it is essential to establish the long term life in the range of 40,000-90,000 hours. In the first project in 2005-2007, the National Institute of Advanced Industrial Science and technology (AIST) cooperated with four industrial teams including Kyocera, TOTO, Mitsubishi Materials Corp and Mitsubishi Heavy Industry [8,9]. Stackes or modules in different types were operated for a longer time than 5,000 h or in frequent thermal cycles mode and post test samples were analyzed by AIST mainly with the Secondary Ions Mass Spectrometry (SIMS). Although degradation phenomena have been well investigated extensively by many research groups in the world using symmetrical cells, single cells or short stacks, there seems important common understanding that the degradation of stacks/systems is quite different from those observed with button cells. Thus, the NEDO project had targeted on the stacks or the modules; by modules, it means that SOFC stacks are operated with the proper desulfurization process and the reforming process in a similar manner to the real SOFC systems. In the first three year project from 2005 - 2007, the following four stacks/modules were tested: High temperature segment-in-series cells by Mitsubishi Heavy Industry (H1), Intermediate Temperature flatten tubular type by Kyocera(I1), High temperature sealless tubular type by TOTO(H2), and

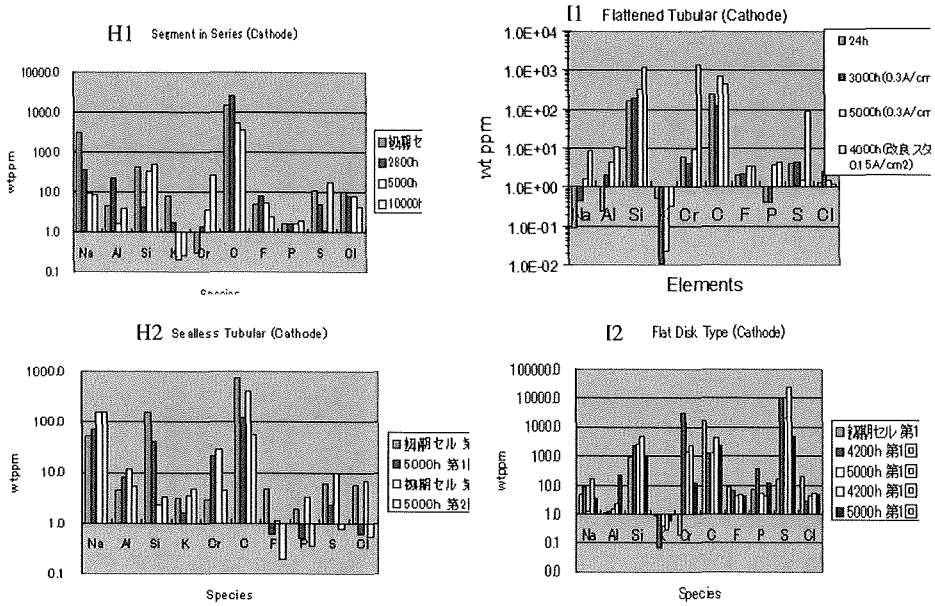

Fig. 5 Impurities observed in cathodes after 24 h and 5000 h operations for the four stacks/modules. For respective impurity elements, the left bar indicates the results for 24 h and then longer operation.

intermediate temperature disk plate type by Mitsubishi materials (I2).

Results of the first three-year project can be summarized as follows:

1) The degradation rate of stacks or modules is in the order of 0.5-1.5 % performance loss per 1000 h.
2) The interfaces of different materials have been intensively investigated with secondary ion mass spectrometry (SIMS). Almost all interfaces are quite stable and this confirms that diffusion in solids is slow so that there are in principle essentially no reasons for expecting significant degradation as confirmed by the Westinghouse operation. Even so, there have been found some exceptions; namely, diffusion of Sr through rare earth doped ceria interlayer between active cathodes and YSZ electrolyte, nickel sintering, and anomalous oxidation of metal interconnects.
3) Impurities are extensively investigated by examining SOFC components after long term operation. Results on four stacks and modules show that impurities observed respective materials exhibit strong stack dependence. This indicates that major impurities are originated from raw materials used or contamination during materials processing for stack

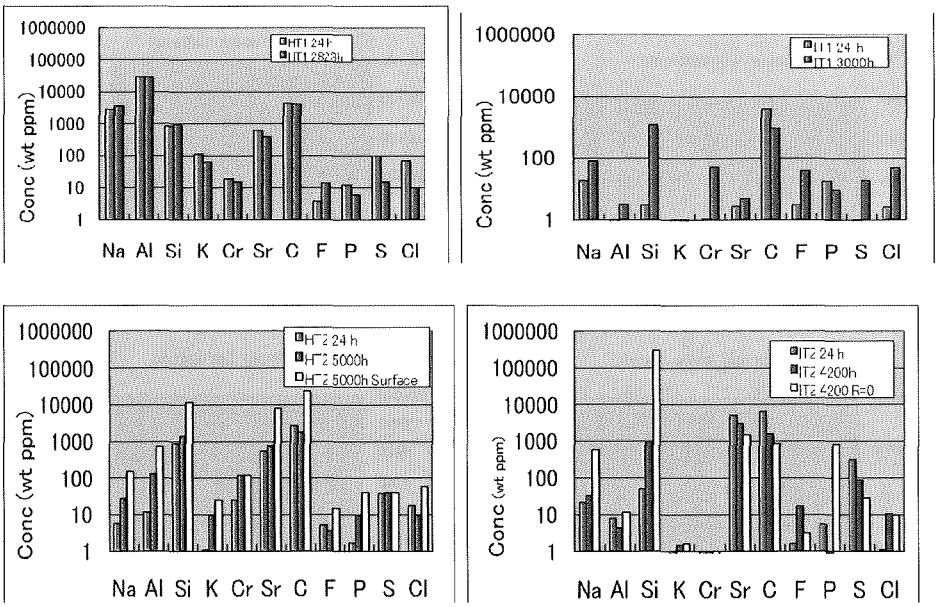

Fig. 6 Impurities observed in anodes of the same stacks after the long term operation.

construction. Typical impurities are Na, Al, Si, K, C, F, P, S and Cl. The observed amounts are shown in Figs. 5 and 6 for cathode layer and for anode layer, respectively.

Among the performance degradation observed in this project, the behavior of the segment-in-series type (H1) by MHI is of particular interest in a sense that the degradation is originated from the cathode part as well as the resistive part. Since this cell makes use of the lanthanum strontium manganite (LSM) cathode, the reason of cathode degradation can be first ascribed to the Cr poisoning [10-12]. Although no Cr component is used in the segment-in-series, the SIMS analysis showed that an increasing amount of Cr was observed on the cathode layer of the cell H1, suggesting that the Cr contamination source is outside cells. Thus, careful examination with SIMS was made to detect Cr in the electrolyte-cathode interface region. Results are shown in Fig. 7, indicating the accumulated amount at the interface is much higher than those in the surface area of the cathode layer.

From these observations, we can conclude that the degradation of cathode in the segment-in-series cells is probably due to the chromium vapors which were emitted from the oxide scale of stainless steel tubes for introducing air into the cells.

Several interesting features can be derived from the impurities in anode compartment given in Fig. 6 as follows;

1) Sulfur contamination level is more than the expectation from the known sulfur solubility

into nickel metal. Since the flatten tube cell (I1) did use hydrogen gas from bomb, there should be sulfur contamination sources. Since sulfur contamination frequently occurred in the investigated four stacks/modules, we can estimate that sulfur can be originated from other cell components such as metals.

2) Silicon contamination is also taken place frequently. This is probably from thermal insulating materials or metals.
3) In some time, we observed phosphor contamination. Although it is not easy to identify the possible source, it may come also from metals.

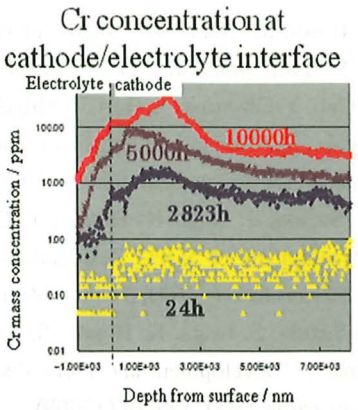

Fig.7. Observed amount of Cr in the electrolyte/cathode interface with a parameter of operation time

In the new NEDO project on durability and reliability, more detailed analyses are going on to obtain full understanding of the degradation phenomena [10-12] with an emphasis on the more advanced experimental facilities and also on the generalized approach to understand the degradation.

5. For Future Development

SOFCs in Japan has reached to a stage in which real application and its requirements become major points to be considered. This will lead to a better situation in RDD in Japan. For a long period of time, Japanese activities have been focused on the construction of SOFC stacks, which includes some technological difficulties that should be solved in relation to application. In view of this, growing interests in applying SOFCs on various fields become crucial in the future development. During the recent NEDO project, cooperation activities have been well organized among industries, national laboratories and universities in tackling the degradation issues. It is highly hoped to extend this kind of cooperation to application-oriented R&D fields.

Acknowledgement

This report is based on the results of NEDO projects on SOFC development. Their support is deeply appreciated.

References

[1] K. Hosoi, M. Nakabaru, "Status of National Project for SOFC Development in Japan," *ECS Transaction* **25(2)**, 11-20 (2009).

[2] T. Ono, Y. Ohshima, Y. Hori, T. Shigehisa, A. Kokaji, M. Yoshida, M. Suzuki, T. Sogi, K. Higaki, A. Chikagawa, "Development of 1 kW Class SOFC Power Generation System," Abstract for oral presentation , p. 144, in Fuel Cell Seminar Abstract (2006).

[3] M. Suzuki, T. Sogi, K. Higaki, T. Ono, N. Takahashi, K. Shimazu and T. Shigehisa, "Development of SOFC Residential Cogeneration System at Osaka Gas and Kyocera," *ECS Transaction* **7(1)**, 27-30 (2007).

[4] M. Suzuki, S. Iwata, K. Higaki, S. Inoue, T. Shigehisa, I. Miyatchi, H. Nakabayashi, K. Simazu, "Development and Field Test Results of Residential SOFC CHP System," *ECS Transaction* **25(2),** 143-147 (2009).

[5] M. Okuda, "Solid Oxide Fuel Cell Demonstration program," pp. 141-148, proceedings of the Report Symposium of NEDO projects on Fuel Cells and Hydrogen," Tokyo, July 7-9, 2010.

[6] M. Nishiura, S. Koga, T. Kabata, N. Hisatome, K. Kosaka, Y. Ando, and K. Kobayashi, "Development of SOFC-Micro Gas Turbine Combined Cycle System," *ECS Transaction* **7(1)**, 155-160 (2007).

[7] K. Tomida, T. Kabata, N. Hisatome, A. Yamashita, H. Tsukuda, S. Ohkuma, T. Kiyabu, "Improvement of Tubular Type Cell Stack," *ECS Transaction* **7(1)**, 173-180(2007).

[8] H. Yokokawa, T. Watanaba, A. Ueno, and K. Hoshino, "Investigation on Degradation in Long-Term Operations of Four Different Stacks/Modules," *ECS Transaction* **7(1)**, 133-140 (2007).

[9] H. Yokokawa, T. Horita, K. Yamaji, H. Kishimoto, Y. P. Xiong, M. E. Brito, "Effect of contamination on the Durability of SOFC Stacks and Modules in Real Operation Condition," Proceedings of 8th European Solid Oxide Fuel Cell Forum, B1004, July 2008.

[10] H. Yokokawa, H. Tu, B. Iwanschitz, A. Mai, "Fundamental Mechanism Limiting Solid Oxide Fuel Cell Durability," *J. Power Sources* **182**, 400-412(2008).

[11] H. Yokokawa, H. Kishimoto, K. Yamaji, and T. Horita, "Generalization of Degradation Mechanisms in Terms of Materials Chemical Nature, Operation Condition and Electrode Reaction Mechanism," *ECS Transactions* **25(2)**, 401-410 (2009).

[12] H. Yokokawa, T. Horita, K. Yamaji, H. Kishimoto, and M. E. Brito, "Materials Chemical Point of View for Durability Issues in Solid Oxide Fuel Cells," *Journal of the Korean Ceramic Society* **47**(1), 26-38 (2010).

9th Liege Conference : Materials for Advanced Power Engineering 2010
edited by J. Lecomte-Beckers, Q. Contrepois, T. Beck and B. Kuhn.

$MnCo_2O_4$ SPINEL CHROMIUM BARRIER COATIGNS COATINGS FOR SOFC INTERCONNECT BY HVOF

J. Lagerbom [1], T. Varis [1], J. Puranen [2], M. Pihlatie [1], O. Himanen [1], V. Saarinen [1], J. Kiviaho [1], E. Turunen [1]
[1] VTT Technical Research Centre of Finland, Espoo, Finland
[2] Tampere University of Technology, Institute of Materials Science, Tampere, Finland

Chromia released from steel parts used for interconnect plates by evaporation and condensation can quickly degrade the cell (cathode) performance in solid oxide fuel cell SOFC. Coatings on top of the IC plate can work as a chromium evaporation barrier. The coating material should have good electrical conductivity, high temperature stability and nearly the same coefficient of thermal expansion as the cell materials. One candidate for the coating material is $MnCo_2O_4$ spinel because of its suitable properties. High velocity oxy fuel (HVOF) spraying was used for the coating application on Crofer 22 APU steel samples. Using commercial and self made spray dried powders together with an HV2000 spray gun it was possible to successfully manufacture, well adhering, dense and reasonably uniform coatings. The samples were tested in oxidation exposure tests in air followed by post analysis in SEM. Powders and coatings microstructures are presented here, both before and after exposure. It was found out that together with spraying parameters the powder characteristics used influence clearly to the coating quality. Especially as very thin coatings was aimed with dense structure fine powders was found to be essential.

Keywords: SOFC, Interconnect, Chromium barrier coatings, Thermal spraying, $MnCo_{2-x}Fe_xO_4$ spinel

Introduction

Fuel cells are electrochemical devices that directly convert the fuel chemical energy to electricity without the intermediate step of combustion. Basically only water vapour using H_2 fuel and CO_2 together with water using methane fuel is formed. The principle of a planar SOFC is presented in Figure 1 [1]. Each cell is composed of an anode, electrolyte and cathode separated by an interconnect or bipolar plate. The bipolar plate typically has several functions: to distribute fuel and oxygen, to separate the individual cells in the stack, to give mechanical rigidity and to work as a current collector

Ferritic stainless steels are commonly thought to be the best choice as bipolar plate material. Special alloys are used in order to gain better electric conductivity and better high temperature corrosion protection. Crofer 22 APU is one of the most commonly used alloys [2]. Alloying of Crofer 22 APU is designed to increase oxidation resistance of the steel by stabilising the oxide scale formed on it at high temperature. A more stable oxide scale can decrease ohmic resistance of the scale and also decrease the poisoning effect of the three phase point [3]. As SOFC`s are expected to work for several years, corrosion resistance is still considered inadequate and protective coatings are needed.

Chromium oxide and especially chromium hydroxide already have significant vapour pressure at the temperatures of 600-700 °C [4, 5]. First, chromium oxide and chromium hydroxide are effective species in destroying the so called three-phase point between the electrolyte and cathode in solid oxide fuel cells (SOFC). Second, chromia formation on the bipolar plate surface increases electric resistance and therefore decreases overall performance. [6]

Coatings are one possibility to avoid or reduce the poisoning and deactivation of the cell. Coatings must be stable, have good electrical conductivity, have a coefficient of thermal expansion close to the CTE of other stack parts and they should protect the interconnect surface from excess oxidation and reduce the evaporation of Cr-bearing species. The coating can behave as a physical barrier or actively capture the chromium bearing species. Several different types of coatings have been suggested and tested for this application: thermally sprayed coatings, screen sprinted coatings, dip coated coatings, PVD coatings and other thin coatings like electrochemical plating. Different coating materials has been tested: perovskites such as Lanthanum strontium manganese oxide LSM $(LaSr)Mn_2O_3$, spinels such

as Cobalt manganese $MnCo_2O_4$, other oxides such as Y_2O_3 and metallic coatings such as Co. [7, 8, 8, 9, 10, 11, 12].

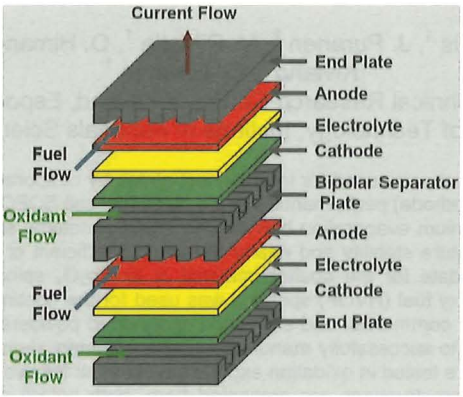

Figure 1. Principle of a planar SOFC [1].

In this paper $MnCo_{2-x}Fe_xO_4$ spinel powders were thermally sprayed on Crofer 22 APU substrate in order to lower the chromia scale growth and its evaporation. HVOF spraying was used and also atmospheric plasma spraying was tested.

Experimental

Two different powders were used: $MnCo_2O_4$ powder by EMPA Materials Science and Technology (Switzerland) and $MnCo_{1.8}Fe_{0.2}O_4$ by solid carbonate synthesis and spray drying. The manufacturing process of $MnCo_2O_4$ is not known. The Fe alloyed version was used for its better electrical conductivity [13]. $MnCo_{1.8}Fe_{0.2}O_4$ powder was prepared by weighing appropriate amounts of $MnCO_2$, $CoCO_2$ and Fe_2O_3 powders together and milling for 20 hours in a drum ball mill. After milling the mixture was calcinated at 1000 °C for 6 hours to get the spinel structure. The powder was then dispersed in water with dispersant by a planetary ball mill (Frich pulver sette 5). PVA as a bonding agent was added to the slurry by a dispergator mixer. The suspension was spray dried by Niro pilot spray dryer p6.3. The chamber fraction of the powder was sintered at 1150 °C, where an isothermal 500 °C 2 hour ramp was used in order to pyrolyse the PVA without agglomerate fracture. After sintering the powder was sieved with 32 and 45 µm sieves. The coarser +32 -45 µm powder was plasma sprayed and the -32 µm powder was HVOF sprayed. The powder size distribution of the powders was studied by applying a Lecotrac LT100 laser diffractometer.

A Praxair HV2000 spray gun, fitted with a 22 mm combustion chamber was used for HVOF spraying (VTT). Nitrogen was used as the powder carrier gas and hydrogen as fuel. Plasma-Technik APS plasma spray system equipped with an F4 gun was used for plasma spraying tests (TUT). Air was used as the carrier gas, while hydrogen and argon were used as plasma gases. Both spray guns were moved by an X-Y manipulator. The test samples were 0.2 mm thick Crofer 22 APU steel sheet. Samples were grid blasted by using a -36 mesh alumina grid. Grid blasting was conducted on both sides to keep the substrates straight. For the thin metal sheets also the coating was applied on both sides in order to avoid folding. The target coating thickness was from 10 µm to 40 µm, which is unusually thin for thermal spraying. Table 1 presents the optimised spraying parameters.

Complex oxide structures are often somewhat changed or modified by thermal spraying due to high temperatures and rapid cooling. For example oxygen deficiency or surplus can occur depending on spraying parameters. Therefore prior to exposure testing, coating samples were stress relief annealed

and also simultaneously stabilisation annealed at 800 °C. Table 2 presents the composition of Crofer 22 APU.
Exposure tests were conducted in a chamber furnace with laser cut 10 mm x 10 mm samples. The samples were placed in the furnace in a alumina sample holder with a groove for each sample, so no contact between samples occurred. The samples were coated on both sides and only the edges of the samples were uncoated. The tests were conducted in air for 1000 h at 700 °C. Stationary air was used in a large volume furnace (lid breathable) which secured the sufficient amount of oxygen. Samples were weighed before and after the test. As the substrate thickness was only 0.2 mm, 0.8 mm^2 area was uncoated (0.4 % of the coated area), the error was considered minimal. Cross-sectional cuttings were prepared on each sample.

The crystal structures of the powders and coatings were determined by X-ray diffraction (XRD) using Mo-kα radiation with Philips X'pert diffractometer. Both powders and coatings were investigated by scanning electron microscope. SEM images were taken by Philips XL 30. Secondary electron images were taken. Normal sample preparation methods were used. Small sections were removed by laser cutting to prevent coatings from cracking as the substrate materials were thin and did not give any support. Those sections were cold resin moulded to provide support for the coatings. Optimised grinding and polishing parameters were used due to low toughness and high pull-out tendency.

Table 1. Spraying parameters for HVOF and APS.

HVOF	H_2/O_2 ratio	Total flow l/min	Stand off distance mm			Number of passes
$MnCo_2O_4$	2	1050	175			12
$MnCo_{1.8}Fe_{0.2}O_4$	2	1050	175			10
Plasma	H_2	Ar		U (V)	I (A)	Number of passes
*$MnCo_{1.8}Fe_{0.2}O_4$	14	71	120	71	600	23
**$MnCo_{1.8}Fe_{0.2}O_4$	9	59	120	66	510	24

* Sieved to +25-36 µm
** Sieved to -25 µm

Area specific resistance ASR measurements, single repeat unit tests, stack tests and post tests analysis will be reported elsewhere. Tests reported here were done to reveal potential of these (Mn,Co)-spinel coatings.

Table 2. Nominal composition of Crofer 22 APU.

Element	Cr	Fe	C	Mn	Si
wt.-%	20.0-24.0	bal	max. 0.03	0.3-0.8	max. 0.5
Cu	Al	S	P	Ti	La
max. 0.5	max. 0.5	max. 0.02	max. 0.05	0.03-0.2	0.04-0.2

Results and discussion

EMPA powder used for HVOF spraying is presented in Figure 2. The powder has a somewhat irregular shape of the powder particles. This is usually considered as a negative factor for the powder feed. In this case the powder particles have low porosity or high specific weight which on the other hand makes it easy to feed. Figure 3 presents the morphology of the spray dried $MnCo_{1.8}Fe_{0.2}O_4$ powder. The powder has typical spray dried spherical morphology, which makes it nicely flowing. Some powder particles were stuck together on sintering which makes the total low characteristics a bit poorer than for the $MnCo_2O_4$ powder. The flowability of these kinds of powders is not good enough to be measured by a Hall flowmeter. The spray dried powder also has somewhat higher porosity due to the character of the production method. Figure 4 presents the cyclone fraction powders morphology. It was much finer and more irregular in shape than the chamber fraction. The finer cyclone fraction also had obviously lower flowability. The irregular shape originates from agitation and fracture in the spray dryers cyclone flow. Also the smaller agglomerate amount in the starting material particles caused the

small agglomerates to look irregular due to the higher proportional surface roughness. A finer primary particle size could produce more spherical and better flowing agglomerates. Particle sizes measured for the powders are presented in Table 3. The powder's good flowability, suitable and narrow size distribution, near spherical shape and high enough density makes good coatings achievable. Vice versa, poor quality powders usually result in poor coatings.

Table 3. Spray powders production method, composition and particle sizes in µm of 10%, 50% and 90 % cumulative distribution.

	d 10	d 50	d 90
$MnCo_2O_4$ EPMA			
	5.5	12.4	23.8
$MnCo_{1.8}Fe_{0.2}O_4$			
Spray drying Chamber	18.9	25.9	40.2
Spray drying Cyclone	8.2	18.2	26.6
Spray drying Chamber sieved	15.3	24.9	36.0
Spray drying Chamber sieved	13.3	20.4	29.3

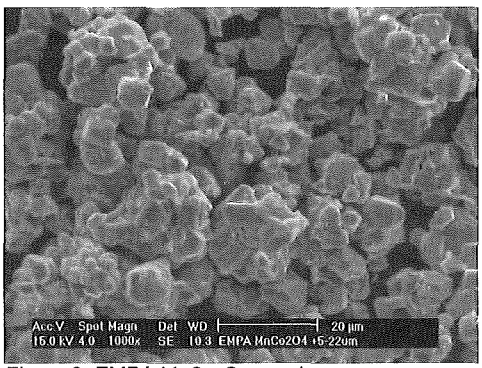

Figure 2. EMPA $MnCo_2O_4$ powder.

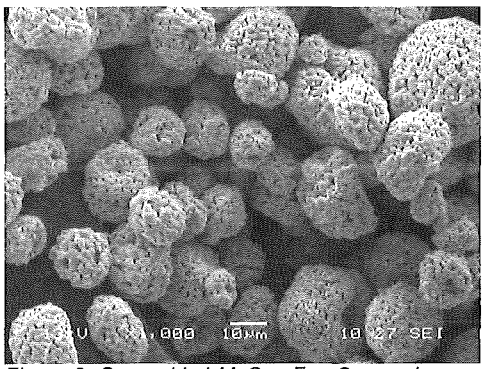

Figure 3. Spray dried $MnCo_{1.8}Fe_{0.2}O_4$ powder, spray drying chamber fraction.

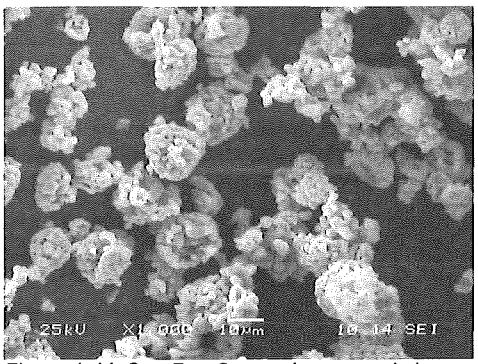

Figure 4. $MnCo_{1.8}Fe_{0.2}O_4$ powder, spray drying cyclone fraction.

The coatings sprayed had quite a dense microstructure with a solid interface between the coating and the substrate. Some grid blasting residue alumna particles were noticed on the interface. Especially HVOF sprayed coatings had a reasonably even coating thickness due to the smaller particle size of the powder. As the target coating thickness was small compared to the larger particles, it is evident why an equally uniform thickness could not be attained. On the other hand steady flow is compromised if too fine powders are used, which may also cause an uneven coating thickness. Microstructure of $MnCo_2O_4$ powder sprayed coating is presented in Figure 5. Microstructure of $MnCo_{1.8}Fe_{0.2}O_4$ powder sprayed coating is presented in Figure 6. Denser and overall slightly better coatings were obtained by spraying the denser and nicely-flowing $MnCo_2O_4$ powder as compared to the spray dried $MnCo_{1.8}Fe_{0.2}O_4$ powder. It is possible to produce and use high quality spray dried $MnCo_{1.8}Fe_{0.2}O_4$ powders and probably obtain coatings with as high a quality as in the case of those used here with the $MnCo_2O_4$ powder. After sieving the $MnCo_{1.8}Fe_{0.2}O_4$ powder to two fractions (-25 µm and 25-36µm), plasma sprayed coatings presented in figures 7 and 8 were obtained. Finer powder

gave denser and more uniform thickness coatings. However, the yield of suitable size fractions in the powder production would decrease.

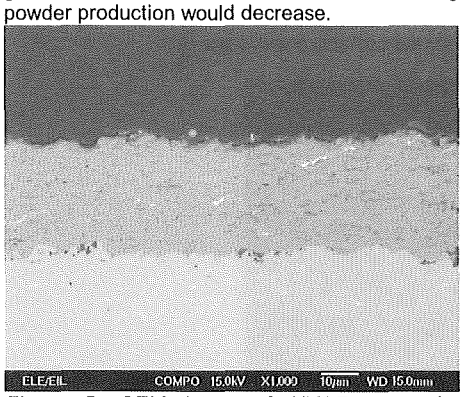

Figure 5. SEM-picture of HVOF sprayed $MnCo_2O_4$ coating, Crofer 22 APU substrate below.

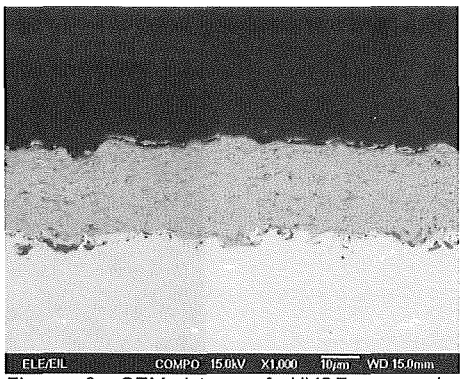

Figure 6. SEM-picture of HVOF sprayed $MnCo_{1.8}Fe_{0.2}O_4$ coating, Crofer 22 APU substrate below.

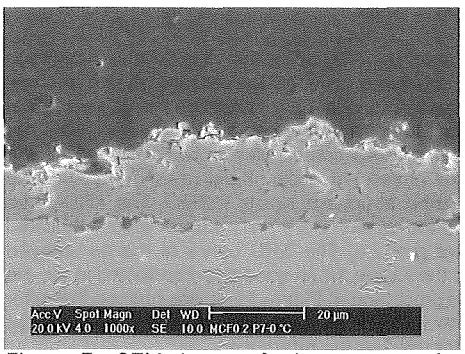

Figure 7. SEM-picture of plasma sprayed $MnCo_{1.8}Fe_{0.2}O_4$ coating with +25-36 sieved powder, Crofer 22 APU substrate below.

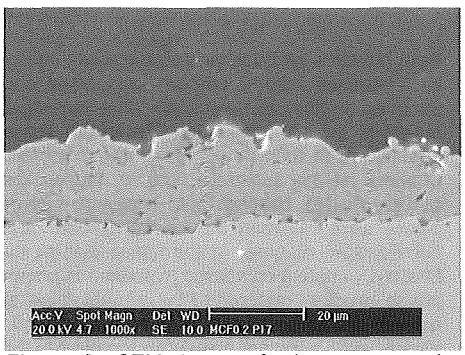

Figure 8. SEM-picture of plasma sprayed $MnCo_{1.8}Fe_{0.2}O_4$ coating with -25 μm sieved powder, Crofer 22 APU substrate below.

The coatings were exposed to air for 1000 h at 700 °C. This was done in order to reveal if the coatings suffer damage like peeling, spallation, cracking or sample deformation. For a coating to protect the substrate from oxidation and presumably diminish the chromium evaporation, it should also be gas tight. Therefore, oxide scale thicknesses were studied. Only thin oxides from below 0.5 to 1 μm were detected below the spinel coatings. Uncoated Crofer 22 APU samples on the other hand had an oxide layer of 2.5-3 μm. Plasma sprayed coatings had somewhat thicker an uneven oxides (1-3 μm) probably due to more uneven thickness, coarser powder and therefore more straight pathway of oxygen to penetrate the coating. Finer particle size of the powder might make the plasma coating gas tighter and more protective. It was also seen that the oxide scale thickness was affected by the coating thickness; the thicker coating resulted in thinner oxide scale. Also the composition of the oxide scale is different due to reaction between the oxide and coating. The composition is thought to be better in the respect of electric conductivity and maybe also stability. The HVOF $MnCo_2O_4$ coating after 1000 h exposure is presented in the Figure 9. There seems to be a tendency of the coating to become denser. Imperfect structure at the particle boundaries, including micro-cracks and imperfect bonding, have vanished, with only some small sized pores being visible. This might be due to reducing annealing performed prior to exposure and oxidation during the exposure. The coatings seem to

become denser in annealing starting from the outer surface. As the coatings were exposed to 700 °C for 1000 h, sintering might have occurred but that should be through the whole coating. Such type of high density of the coating would be a desired feature for the protectiveness sake.

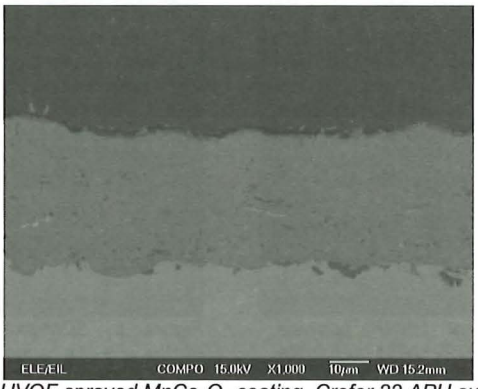

Figure 9. SEM-picture of HVOF sprayed $MnCo_2O_4$ coating, Crofer 22 APU substrate below. After 1000 h exposure at 700 °C in air.

Both powders and coatings phase structures were studied by X-ray diffraction. It is relatively common that complex oxide-, carbide- and other ceramic- structures tend to decompose during thermal spraying. In this case as oxides were investigated it was reasonably easy to restore the original spinel structure by air annealing. The cubic spinel structure attained by powder production was not maintained in thermal spraying. The high temperature process combined with rapid cooling as the droplets hit the substrate surface caused metastable phases to occur. As-sprayed $MnCo_2O_4$ and $MnCo_{1.8}Fe_{0.2}O_4$ coatings both appear to have simple cubic structures similar to FeO. The XRD-curve peaks were between the peaks of CoO and MnO, the peaks were very broad which indicated considerable disorder in the lattice due to the violent process. The XRD curve of the as sprayed $MnCo_2O_4$ coating compared to powder is presented in the Figure 10. In annealing conducted in air, the phase structure restored to the original spinel state, as presented in Figure 11. It was noticed that after annealing a close match to spinel peaks were achieved. However, peak intensities and peak height versus width were not absolutely identical to the powder used as the reference.

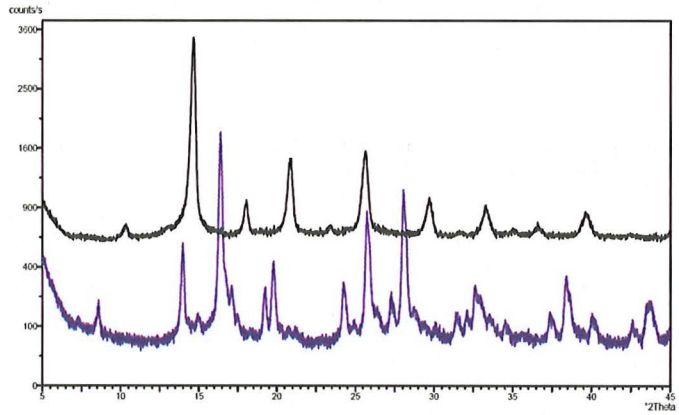

Figure 10. XRD-curves of EMPA $MnCo_2O_4$ powder (below) and as-sprayed HVOF coating (top).

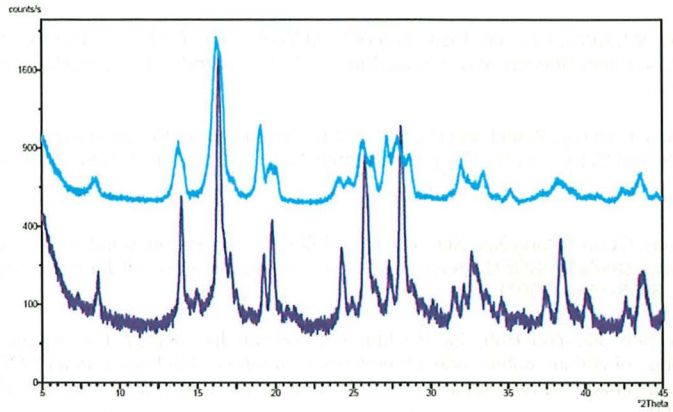

Figure 11. XRD-curves of EMPA $MnCo_2O_4$ powder (below) and $MnCo_2O_4$ HVOF coating annealed at 800 °C for 6 hours (top).

Summary and conclusions

In order to maintain SOFC´s economic operation for many years, it is evident that protective coatings must be used to hinder the chromium evaporation and subsequent cell deactivation. $MnCo_2O_4$–type coatings potentially work as efficient chromium barrier coatings. HVOF and even atmospheric plasma spraying are able to produce thick, dense and even thickness coatings on top of very thin substrates if necessary. According to the tests, a considerable increase in cell lifetime is expected with $MnCo_2O_4$-type thermally sprayed coatings. High quality powders are needed, as every fault in the coating may offer a pathway for oxygen to travel to the substrate surface and chromium bearing species to travel the opposite way. To keep the ohmic resistance low, thin coatings are needed which may present the need for heat treating in a way that even denser coatings can be produced. To accomplish the target 40 to 50 kh lifetimes, even multilayer coatings may be needed with chemical capture and Cr-barrier properties in the different layers.

Acknowledgements

The work was sponsored by TEKES (the Finnish Funding Agency for Technology and Innovation), VTT and Finnish industry.

References

/1/ /http://versa power.com/media/2005_AAPG_VPS_SOFC_22.June.2005.pdf, 30.11. (2009).

/2/ Thyssen krup VMD, Material Data sheet no. 4046.

/3/ High Temperature Solid Oxide Fuel Cells: Fundamentals, Design and Applications, ed. S.S. Singhal, K. Kendall, MPG Books Ltd, England (2003).

/4/ J.P. Abellan , W. J. Quadakers, Development of Ferritic Steels for Application as interconnect Materials for Intermediate Temperature Solid Oxide Fuel Cells (SOFC). Forschnungszentrum Julich, Jul-4170.

/5/ C. Gindorf, L. Singheiser, K. Hilpert, Vaporisation of chromia in humid air, Journal of Physics and Chemistry of Solids, 66, 384–387 (2005).

/6/ S.C. Paulson, V.I. Birss, Chorium Poisoning of LSM-YSZ SOFC Cathodes. Detailed Study of the Distribution of Chromium Species at a Porous, Single-Phase Cathode, J. Electrochem. Soc., 151, 1961-1968 (2004).

/7/ Y. Larring, and T. Norby, Spinel and Perovskite Functional Layers Between Plansee Metallic Interconnect (Cr-5 wt % Fe-1 wt % Y_2O_3) and Ceramic $La_{0.85}Sr_{0.15})_{0.91}MnO_3$ Cathode Materials for Solid Oxide Fuel Cells, Journal of The Electrochemical Society, 147, 3251-3256 (2000).

/8/ Zhenguo Yang, Guan-Guang Xia, Xiao-Hong Li, Jeffry W. Stevenson, $(Mn,Co)_3O_4$ spinel coatings on ferritic stainless steels for SOFC interconnect applications, International Journal of Hydrogen Energy, 32, 16, 3648-3654 (2007).

/9/ Seong-Hwan Kim, Joo-Youl Huh, Jae-Ho Jun, Joong-Hwan Jun, Jerome Favergeon, Thin elemental coatings of yttrium, cobalt, and yttrium/cobalt on ferritic stainless steel for SOFC interconnect applications, Current Applied Physics, In Press, Accepted Manuscript, Available online 11 November (2009).

/10/ S. Y. Hwang, J. H. Kim, B. G. Seong, H. S. Yang, SOFC Interconnector Coating using HVOF spraying, ITSC 06, Seattle, USA (2006).

/11/ Protection coatings for planar solid oxide fuel cell interconnect prepared by plasma spraying, Materials Research Bulletin, 38, 531–536 (2003).

/12/ W.J. Quadakkers, H. Greinerb, M. Htinsel, A. Patanaik, A.S. Khannac, W. Mallher. Compatibility of perovskite contact layers between cathode and metallic interconnector plates of SOFCs, Solid State Ionics, 91, 55-67 (1996).

/13/ T. Kiefer, M. Zahid, T. Tietz, D. Stöver H.-R. Zerfass, Electrical Conductivity and Thermal Expansion Coefficient of Spinels in the Series $MnCo_{2-x}Fe_xO4$ for Application as a Protective Layers in SOFC, Proceedings of the 26th RiRO International Symposium on Materials Science: So lid State Chemistry, Roskilde, Denmark (2005).

9th Liege Conference : Materials for Advanced Power Engineering 2010
edited by J. Lecomte-Beckers, Q. Contrepois, T. Beck and B. Kuhn.

Part E

Corrosion, Thermomechanical Fatigue and Modelling

9th Liege Conference : Materials for Advanced Power Engineering 2010
edited by J. Lecomte-Beckers, Q. Contrepois, T. Beck and B. Kuhn.

STEAM OXIDATION AND THE EVALUATION OF COATINGS AND MATERIAL PERFORMANCE THROUGH COLLABORATIVE RESEARCH

A T Fry[1], A Aguero[2]

[1] National Physical Laboratory, Teddington, UK
[2] INTA, Madrid, Spain

Abstract

Over the last five years through the COST 536 Programme researchers across Europe have been collaborating to better understand the phenomena of steam oxidation and to characterise coated and uncoated materials for use in power plants. During this period fundamental study of the oxidation mechanisms and changes in the oxidation kinetics caused by the presence of steam have been undertaken. Materials covering a range of high temperature plant applications have been studied, from low alloy martensitic alloys through to Ni-based superalloy materials, with investigations into the effect of increasing temperatures and pressures on the oxidation kinetics, oxide morphology and spallation characteristics. In addition conventional and novel coatings have been evaluated to assess their potential use in new USC plant. This paper will present an overview of these activities demonstrating the effect that steam has on the oxidation of alloys and coatings.

Keywords: Steam oxidation, coatings, thermal cycling

Introduction

Increasing the efficiency of coal-fired power plants has been a goal for the power generation industry for many years, and would bring benefits not only in cheaper electricity but also with respect to reducing the carbon emissions. Such increases in efficiency are achieved through thermodynamic means, principally by increasing the steam temperatures and pressures, for example at 750°C and 350 bar net efficiencies of 45% are estimated. The development and qualification of high-temperature materials for critical components such as super heaters, thick section boiler components and turbines is the key to reaching such advanced steam conditions.

At the start of the COST 536 action the state of the art in terms of alloy strength and oxidation resistance allowed for steam temperatures circa 600°C (Figure 1). The advanced 9-12%Cr ferritic steels used in thick section components combined with 18% Cr austenitic steels in super heaters of current power plants allow steam temperatures up to around 610°C, corresponding to efficiencies of 46-48%. This limit is due to the limited oxidation resistance and their microstructure degradation during long-term service [1-4]. The aim of this action was the development and certification of new candidate alloys that would allow steam temperatures up to 650°C. This was to be realised by consideration of the alloy design, the strength of the alloy, the processability of the alloy and the oxidation performance. Candidate materials considered in this collaborative programme included low alloy martensitic materials such as P92, VM12, E991, COST alloys FB2 and FT1 to 7 as well as a selection of austenitic and Ni-based super alloys such as NF709, Sanicro 25 and IN740. For the purposes of this paper the emphasis and the results presented will be on the low alloy 9-12%Cr materials as this is more pertinent to the emphasis of the COST action.

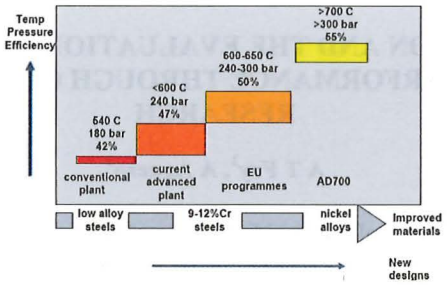

Figure 1 Schematic showing the range of applicability of structural alloys in power plant

Steam Oxidation and Spallation

The oxidation of metal alloys is accelerated by the presence of steam. There are many theories as to the governing mechanisms that control this increased rate, these range from diffusion of hydroxyl ions, transport via pores and volatilisation of Cr-hydroxides. The discussion of these mechanisms is beyond the scope of this paper, but further details can be found in the literature [5-23]. Regardless of the controlling mechanism it is clear that the presence of steam in the atmosphere accelerates the oxidation rate, work within this programme demonstrated this effect by comparing air oxidation results to those obtained from steam environments. On typical 9wt%Cr alloys an increase in the specific mass gain of 20,000 to 40,000% was measured [24]. With increasing temperatures and pressures, boiler components will encounter ever more aggressive fireside corrosion and consequently increasing rates of steam side oxidation. With future requirements for carbon capture and storage increasingly higher temperatures and pressures will be needed [25-31]. These issues represent a significant technical challenge to the industry. The resistance to steam side oxidation of the principal alloys of interest for these applications is critical, and it is becoming increasingly clear that novel material solutions will be required. At elevated steam temperatures, the rate of steam side oxidation of the internal surfaces of boiler tubes and steam pipework can become appreciable. Oxide layers grow to critical thicknesses until there is sufficient strain in the scale such that it will then have a tendency to spall, as predicted by the Armitt diagram (32). This is a complex phenomenon and efforts have been made to describe the processes (23).

Figure 2 presents the mass change data of three alloys exposed to flowing steam at 650°C. Indications of spallation events can be clearly seen in the data for the P92 (high O2), with spallation being evident at times of 300 hours and 1000 hours. This figure also illustrates the range of oxidation kinetics obtainable in 9-12%Cr alloys. The compositions of the alloys are shown in Table I.

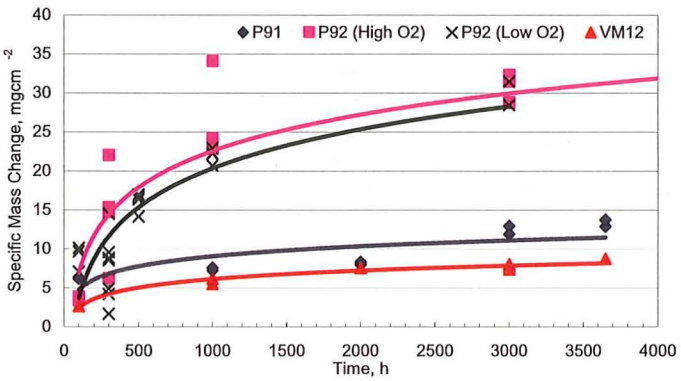

Figure 2 Plot of specific mass change with time for alloys exposed to flowing steam at 650°C

Table I Composition of a selection of the alloys characterised

Alloy	Composition, Wt% (Fe bal)														
	C	P	Cr	V	Nb	Cu	Si	S	Mo	W	N	B	Mn	Al	Ni
FT1	0.20	-	9.95	0.28	0.065	-	0.29	-	1.48	-	0.022	0.010	1.04	-	0.11
FT2	0.20	-	10.00	0.27	0.067	-	0.29	-	1.50	-	0.021	0.017	1.02	-	0.13
FT3	0.20	-	9.85	0.26	0.070	-	0.27	-	1.48	-	0.023	0.026	1.00	-	0.11
FT4	0.20	-	11.45	0.24	0.058	-	0.23	-	1.47	-	0.018	0.008	0.86	-	0.11
FT5	0.20	-	11.40	0.33	0.065	-	0.25	-	1.50	-	0.026	0.019	0.98	-	0.11
FT6	0.19	-	11.40	0.27	0.065	-	0.26	-	1.49	-	0.030	0.018	0.94	-	0.13
FT7	0.19	-	11.40	0.27	0.066	-	0.25	-	1.51	-	0.035	0.025	1.00	-	0.11
CT3	0.20	-	11.00	0.20	0.060	-	0.30	-	1.50	-	0.020	0.020	1.00	-	-
CT7	0.20	-	11.00	0.20	0.060	-	0.30	-	1.50	-	0.020	0.020	1.00	-	-
VM12	0.12	-	11.61	0.25	0.044	0.06	0.48	-	0.28	1.58	0.078	0.005	0.37	-	0.31
TUD1	0.15	0.004	8.39	-	-	-	0.49	0.006	0.20	-	-	-	0.32	-	0.16
FB2-2F	0.12	-	9.00	-	-	-	-	-	1.50	-	-	-	0.80	-	0.15
CMS	0.11	-	8.85	-	-	-	0.05	-	0.48	-	-	-	0.46	-	0.06
P91	0.12	0.01	9.96	0.22	0.07	-	0.44	0.003	0.89	-	0.069	-	0.38	0.01	-
P92	0.12	-	9.37	0.23	-	-	0.10	-	0.45	1.98	0.04	-	0.61	-	-
Esshete 1250	0.09	0.024	15.3	0.25	1	0.14	0.56	0.26	1.09	-	0.03	0.038	6.23	-	9.9

For boiler tubing, where there is a significant heat flux across the tube metal and the oxide layer, the insulating effect of the growing oxide layer will tend to increase the metal temperatures, and hence increase the oxidation rates (33) as illustrated in Figure 3 for P92. The protective effect of the oxide layer therefore will be much less than that which applies under isothermal conditions. Thermal cycling further exacerbates this, as damage accumulates in the oxide scale with increasing cycles. This means that the oxide growth rates measured in isothermal laboratory tests will normally tend to underestimate those that apply in operating boiler plants under comparable conditions.

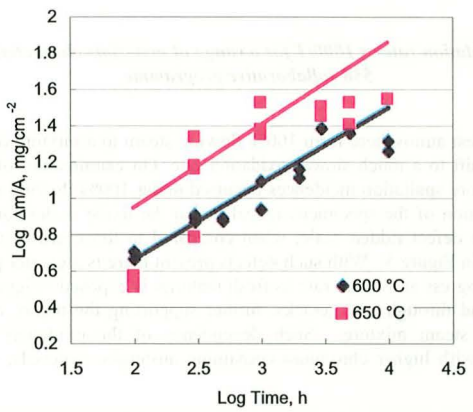

Figure 3 Log mass change vs log time for P92 in 100% flowing steam at 600 and 650°C

Characterisation of oxidation kinetics and scales

The oxidation group consisted of more that 14 participating organisations, 9 of which were involved in steam oxidation testing. For the purposes of this paper only the low pressure exposures have been considered, Auerkari *et al* [34] have reported high-pressure work. Steam oxidation tests were conducted using two broadly similar methods based principally on laboratory exposures using static furnaces into which steam was flowing. The steam was either introduced using an argon carrier gas (50%) or using pure 100% steam. Some of the laboratories used low oxygen containing steam, in the region of 5 to 15 ppb dissolved oxygen, whilst others did not control the oxygen content so rigorously.

Figure 4 shows a plot of the log of the parabolic oxidation rate against 1000/T, where T is the absolute temperature of the exposure. In this figure, two envelopes are also shown, these represent the range of Log k_p vs 1000/T occupied by literature data for the 9%Cr and 12%Cr materials, as reported by Wright *et al* [23]. The data generated at NPL for P91, P92 and VM12 show that the oxidation kinetics lie within the expected band for 9-12%Cr materials with the lower Cr containing P92 exhibiting the faster oxidation kinetics. Improved oxidation resistance could be obtained by increasing the chromium content, as with the FT range of alloys, but this had a consequential effect on the mechanical properties of the alloys.

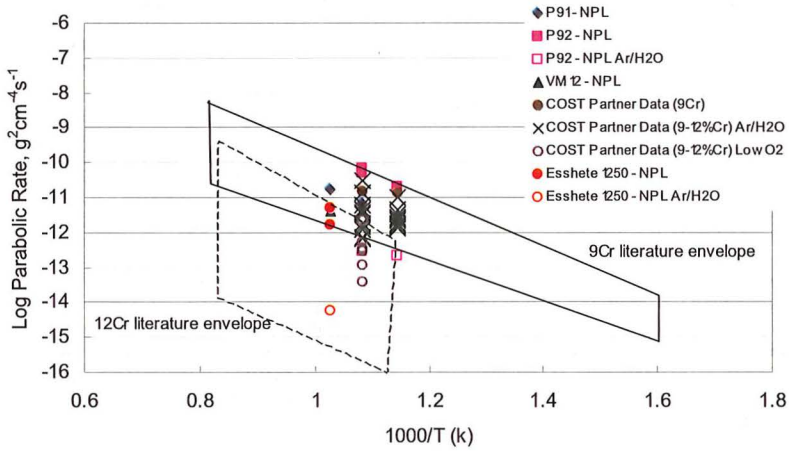

Figure 4 Log parabolic oxidation rate vs 1000/T for a range of materials characterised as part of the COST 536 collaborative programme

Interestingly on altering the test atmosphere from 100% flowing steam to a mixture of 50%Ar + 50% steam the oxidation kinetics for P92 shift to a much slower oxidation rate. On examination of the specimens after each exposure it was noted that more spallation incidences occurred under 100% flowing steam conditions. Further, examination of the cross section of the specimens revealed that the oxide scales formed under 100% flowing steam had developed a more defect ridden scale, when compared to those grown under flowing mixtures of 50%Ar and steam, as shown in Figure 5. With such defects present there is a greater propensity for spallation to occur and for oxidation to progress at a faster rate as fresh material is exposed. Figure 5a also shows haematite decorating the outer scale and through scale cracks, further supporting the theory of a more protective scale being formed in the argon steam mixture. Such dependency of the oxidation resistance with exposure atmosphere was also found with higher chromium containing austenitic materials, such as the Esshete 1250 shown in Figure 4.

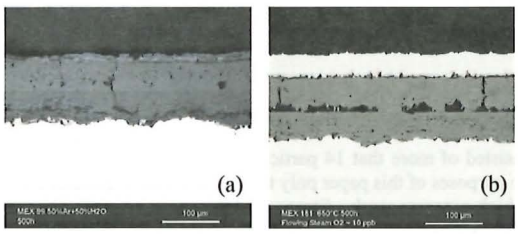

Figure 5 Micrograph of P92 exposed to (a) 50%Ar + 50%H2O and (b) 100% flowing steam, both at 650°C for 500 hours

On including the data from other COST partners in Figure 4, it can be seen that there are also differences arising from the use of a low oxygen-containing atmosphere, in particular for the lower chromium containing alloys of FT1, 2 and 3, as illustrated in Table II. Effects of the oxygen content of the steam have been previously reported [35], although in that instance it was found that the oxidation rate increased in the lower oxygen containing steam, this was particularly evident on the higher Cr containing Esshete 1250 material. With increasing chromium content the difference between the two partners data reduces. Such discrepancies in the measured oxidation rate are not surprising and have been reported in more controlled intercomparison exercises [36], but they further illustrate the requirement for standardised test methods for characterising the oxidation performance of materials in controlled gaseous environments.

Table II Oxidation kinetics for a selection of materials characterised by NPL and the COST partners

Alloy	Log Oxidation Rate, kp, $g^2cm^{-4}s^{-1}$					
	600 °C		650 °C			700 °C
	1	NPL	1	2	NPL	NPL
FT1	-11.80		-11.46	-12.93		
FT2	-11.72		-11.49	-13.40		
FT3	-11.67		-11.36	-12.27		
FT4	-11.89		-11.90	-12.54		
FT5	-11.82		-12.16	-12.49		
FT6	-11.84		-12.12	-12.44		
FT7	-11.56		-11.75	-11.63		
CT3	-11.48		-11.45			
CT7	-11.63		-11.82			
VM12	-11.72	-11.52	-11.83		-11.41	-11.39
TUD1	-11.46		-11.19			
FB2-2F	-11.33		-10.85			
CMS	-11.01		-10.53			
P91		-11.18	-11.18		-10.78	
P92		-10.67			-10.31	-10.78
Esshete 1250						-11.79

1 – COST partner (9-12%Cr) Ar/H_2O 2 - COST partner (9-12%Cr) Low O_2

The rate of oxidation, whilst clearly important, does not fully characterise an alloys performance in thermal plant. As seen in Figure 5 the morphology of the oxide scales formed can also vary according to the test method used. Ideally the scales grown in laboratory exposures should closely resemble those formed in service. Reality is somewhat removed from this and scales grown in the laboratory using simple isothermal techniques rarely resemble the morphology of those formed in service. There are many reasons for this, and it is probably being

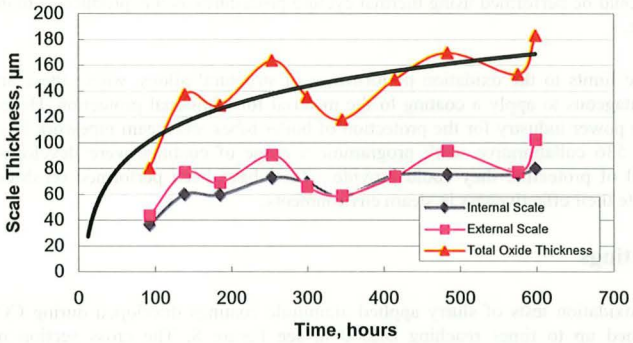

over optimistic to expect laboratory tests to produce realistic scales. However, there are certain modifications to laboratory testing that can produce more representative scales. As part of this COST action the use of thermal cycling was investigated as one method of producing representative scale structures. Using a gas mixture of

Figure 6 Oxide scale thickness as a function of cycles for P92 in 50%Ar+50%H_2O at 650°C

50%Ar + 50%H_2O, and a thermal cycle consisting of 20 hours hot and 4 hours cold, samples of P92 were cycled up to a total duration of 600 hours. Specimens were removed periodically for mass change measurement and metallographic examination. The plot of oxide thickness (internal, external and total) is presented in Figure 6. Figure 6 shows that the oxidation followed a parabolic trend with the internally growing scale staying adherent, whilst the outward growing scale spalled approximately every 200 hours. The aim of this test was to improve on the applicability of the scale morphology. Figure 7a shows an image of scale formed on a 2.25%Cr deadspace tube in a re-heater, showing a laminated oxide probably due to sequential overheating, Figure 7b is T91 after 61 kh at approximately 566°C and 138 bar, compared with an isothermal lab specimen 7c exposed to 4 kh at 650°C and 17 bar [20], whilst 7d and 7e are images of thermally cycled specimens of P92 after 253 h and 665 h.

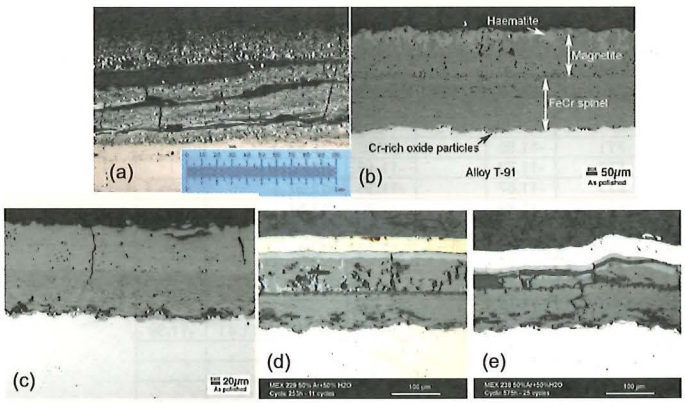

Figure 7 (a) 2.25%Cr deadspace tube in a re-heater, (b) T91 after 61 kh at approximately 566°C and 138 bar, (c) T91 isothermal lab specimen exposed for 4 kh at 650°C and 17 bar [20], (d) and (e) images of thermally cycled specimens of P92 after 253 h and 665 h.

The plant exposed materials 7a and 7b show a laminar oxide structure in to which defects build up, most obviously in 7a. There is also a layer of haematite present on 7b. Comparing these structures with those developed in isothermal laboratory exposures, which 7c is a typical example of, it can be seen that whilst the defect structure is similar to 7b, there is no haematite layer and the lamination is not present as with 7a. The thermally cycled specimens shown in 7d and 7e do however exhibit both types of morphological features, thereby producing a more representative oxide scale. It is strongly recommended that spallation studies and characterisation should be performed using thermal cycling procedures as this produces a more morphologically representative scale.

Inevitably there are limits to the oxidation performance of structural alloys, where these are approached and reached it is advantageous to apply a coating to the material for additional protection. Historically, the use of coatings within the power industry for the protection of boiler tubes and steam pipework has been limited. As part of the COST 536 collaborative work programme a range of coatings were developed and assessed to determine the level of protection they could provide. Tests have been performed on three types of surface treatment to evaluate their effectiveness in steam environments.

Aluminide Coatings

Laboratory steam oxidation tests of slurry applied aluminide coatings developed during COST 522 at 650°C have been performed up to times reaching 60,000 h, see Figure 8. The cross section micrograph of the corresponding coated specimens at 0, 20,000, 50,000 and 60,000 h are shown in Figure 9. TEM results have shown that before exposure, the coating is covered by a protective χ-Al_2O_3 which slowly transforms into α-Al_2O_3. After 20,000 h the coating consists of FeAl over an AlN precipitation zone and is totally covered by protective α-Al_2O_3 with a subscale Al content of 11 wt. %.

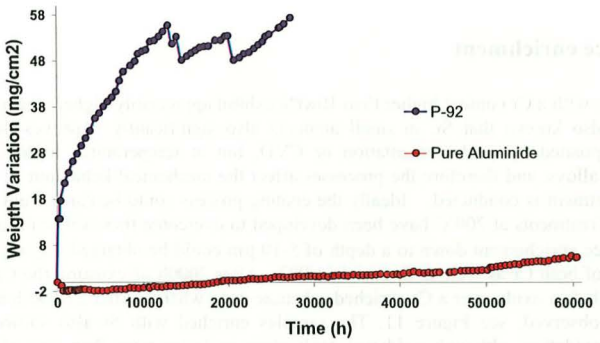

Figure 8 Weight variations of aluminide coatings on P92 exposed to steam at 650°C

The specimens corresponding to 50,000 h of exposure had an Al subscale content of 4.5 wt %, exhibiting Al, Fe mixed oxides on top but without substrate attack. Finally, the 60,000 h exposed specimen exhibited several areas corresponding to ≈ 25 % of the total surface on which substrate oxidation could be observed as shown in Figure 9. In this specimen, the Al content beneath the scale in zones surrounding the attack areas was 2.5 wt. % and the scale was also composed of mixed Al, Fe oxide (15-20 µm). These results were obtained from coatings with original thicknesses between 30 and 50 µm. Currently, coatings of 100 µm are being tested and are expected to last longer as the total Al content is higher.

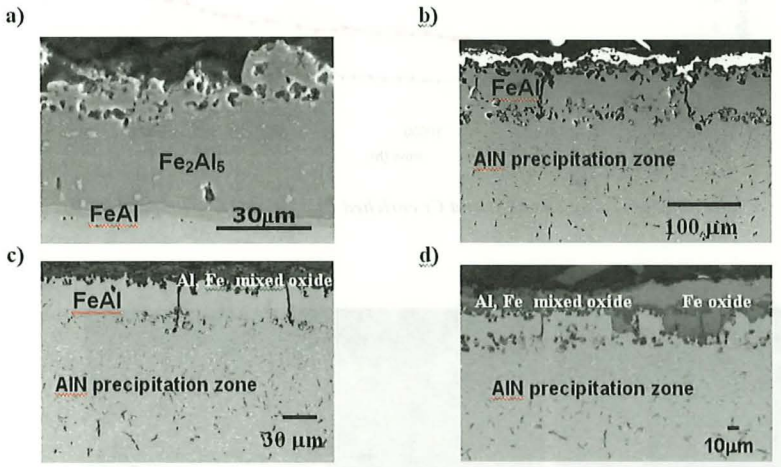

Figure 9 Slurry aluminide coating on P92 exposed to steam at 650° C after: a) 0 h, b) 20,000 h, c) 50,000 h and d) 60,000 h

The same coating was applied in COST developed alloys such as CB2, FT4 and FT7 and the steam oxidation testing results indicated very similar behaviour to coated P92 at least up to 10,000 h of exposure. Moreover, both coated P92 and CB2 were also tested at 600°C for 20,000 h and at this lower temperature there is significantly less interdiffusion and therefore, the coating is expected to last in excess of 60,000 h as there will be more Al available below the protective scale.

Cr and Si surface enrichment

It is known that steels with a Cr content higher than 10wt% exhibit appreciably higher steam oxidation resistance and morover, it is also known that Si, in small amounts also significantly improves the behaviour. These elements can be deposited by pack cementation or CVD, but at temperatures higher than the annealing temperature of these alloys, and therefore the processes affect the mechanical behaviour of the material unless post-coating heat treatment is conducted. Ideally the coating process could be carried out at the same time as the heat treatment. Treatments at 700°C have been developed to overcome these difficulties for both Cr and Si, and as a result, surface enrichement down to a depth of 5-10 µm could be obtained. Figure 10 shows the steam oxidation behaviour of both Cr as well as Si enriched P92. After 2000h of exosure, the Cr enriched specimen exhibited a top Cr rich thin oxide over a Cr enriched substrate zone whereas after 27,500 h internal precipitation of oxides could be observed, see Figure 11. The samples enriched with Si also showed reasonably good resistance to steam oxidation, although oxidation took place at faster rates than any of the other explored coatings as shown in Figure 12. When exposed to steam at 650°C, the Si enriched substrate develops a dual protective scale, the most external layer being Fe rich whereas the internal zone is Cr rich, on top of a Si enriched substrate.

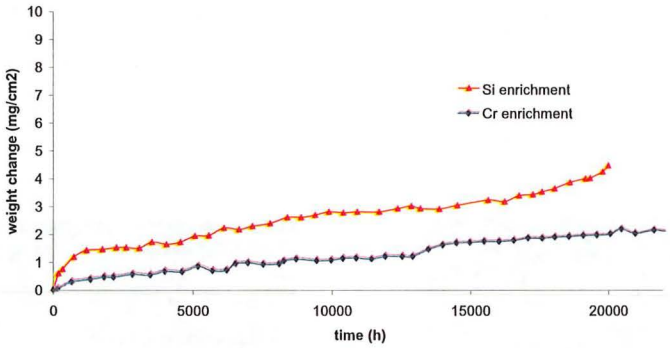

Figure 10 Mass variations of Si and Cr enriched P92 exposed to steam at 650° C

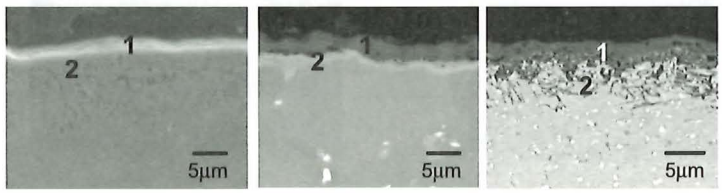

Cr wt. %	0 h	20,000 h	27,500 h
1	97	51	67
2	15	65	24

Figure 11 Cr enriched P92 exposed to steam at 650° C after: a) 0 h, b) 20,000 h, c) 27,500 h

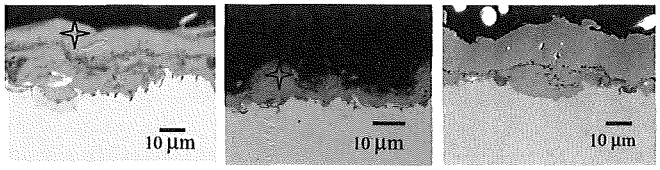

Wt. %	0 h	6,500 h	20,000 h
O	22.69	23.92	23.37
Si	1.76	0.65	1.32
Cr	0.55	24.33	18.43

Figure 12 Cr enriched P92 exposed to steam at 650° C after: a) 0 h, b) 20,000 h, c) 27,500 h

When these coatings were exposed to high pressure steam (650°C and 300 bar, controlled to contain 125 ppb dissolved oxygen, pH between 8.0 and 8.5 and conductivity below 0.5 µS/cm), the coatings were significantly less protective.

HVOF deposited hard steel

Some components in the steam power plant, such as valves, require erosion protection from hard particles. Therefore an HVOF deposited hard steel coating with a high Cr content was chosen as a candidate for this application. The coating composition is Cr:20, W:10, Mo:5, Mn:5, B:5, Si:2, C: 2 (wt%) and its hardness 1260 HV before exposure to steam. Unexpectedly, a relatively faster increase in weight as function of time was observed under steam at 650°C, see Figure 13. As shown in Figure 14, a mixed oxide formed instead of the expected thin, dense, Cr rich scale. Nevertheless, this mixed oxide is still protective as it grows at a significantly slower rate than the oxides formed on uncoated P92. The microhardness of the exposed coating was reduced to 1070 HV after the initial periods of exposure but remained quite stable and hard enough at longer time.

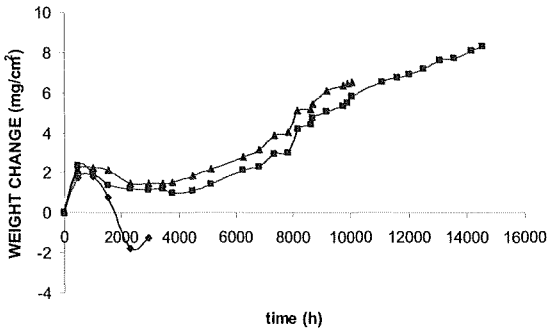

Figure 13 Mass variation of HVOF hard steel coating deposited on P92 exposed to steam at 650°C

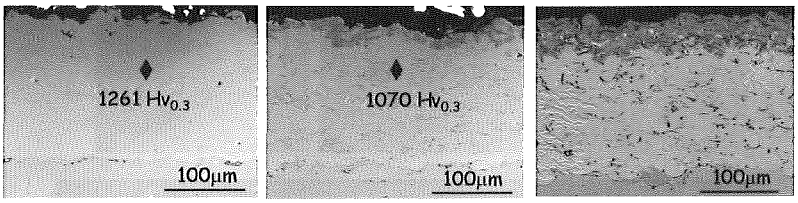

Figure 14 HVOF deposited hard steel on P92 exposed to steam at 650° C after: a) 0 h, b) 3,000 h, c) 14,500 h

Conclusions

Whilst the work conducted in the programme has helped to characterise current and candidate alloys and coatings, it has also helped to verify and evaluate best practice and the level of knowledge of steam oxidation. The oxidation kinetics for a range of alloys have been measured and compared to conventional materials. Whilst improvements have been obtained, the level of creep resistance limits the applicability of the alloys due to the higher chromium levels. It has been shown that thermally cycling specimens produces a more representative oxide scale structure, and should be considered for future oxidation and spallation studies. There is growing realisation that a more engineered solution is required and that surface modification of low alloy materials is required. One such route could be the use of aluminide coatings as they have been shown to protect P92 from steam at 650°C for more than 60,000 h of exposure. In addition it has been shown that Si and Cr surface enrichment can be achieved at 700°C. The resulting surfaces are very resistant to steam at 650°C and atmospheric pressure. The use of HVOF hard steel coatings has also been investigated, adequate steam oxidation resistance can be achieved but this would require additional modification with chromium.

Acknowledgements

The authors would like to acknowledge M. Gutierrez, V. Gonzalez, R. Muelas, L. Brown, J. Banks and D. Laing for all their contributions to the results. This work was part of the COST536 collaboration, Alloy development for Critical Components of Environmentally friendly Power plant (ACCEPT). Funding for this work was provided by the Spanish Ministry of Science and Innovation (ENE2008-06755-C02-01) and the UK Department of Trade and Industry (Project 409).

References

[1] J. Hald: "Metallurgy and Creep Properties of new 9-12%Cr Steels", Steel Research 67 (1996) No. 9, pp. 369-374

[2] P.J. Ennis: "Creep Strengthening Mechanisms in 9-12% Chromium Steels", Int. Conference Advances in Materials Technology for Fossil Power Plants, October 25-28, 2004, Hilton Head Island, South Carolina

[3] H.K. Danielsen, J. Hald: "Behaviour of Z-Phase in 9-12%Cr Steels", Energy Materials, March 2006, Volume 1,Number 1

[4] R. Viswanathan, W. T. Bakker: "Materials for Boilers in Ultra Supercritical Power Plants", Proceedings of 2000 International Joint Power Generation Conference, Miami Beach, Florida, July 23-26, 2000

[5] T. Ericsson, "Stratified oxides scale growing on two Cr-Ni steels oxidized in high-pressuresteam at 800°C," Oxid. Met., 2 (2), 173-205 (1970).

[6] T. Ericsson, Oxid. Met., 2, 401 (1970).

[7] K. Nakagawa, Y. Matsunaga, and T. Yanagisawa, "Corrosion behavior of ferritic steels on the air sides of boiler tubes in a steam/air dual environment," Materials at High Temp., 20 (1), 67-73 (2003).

[8] N.J. Cory, T.M. Herrington, and L. Tomlinson, "Hydrogen emission during the steam oxidation of ferritic steels: experimental technique," Corr, Sci., 28 (4), 333-342 (1988).

[9] P. Kofstad, I.G. Wright, and G.C. Wood, "The role of water vapor in the oxidation of metals and alloys (oxidation in dry and wet air/O2, in H2+H2O, and in H2O)," pp. 531-545 in 62 "International Workshop on High-Temperature Corrosion," D.L.
[10] Douglass, P. Kofstad, A. Rahmel, and G.C. Wood, Eds., Oxdtn. Metals, 45(5/6), 529-620 (1996).
[11] R.D. Shannon, "Revised effective ionic radii and systematic studies of interatomic distances in halides and chalcogenides," Acta Cryst., A32, 751-767 (1976).
[12] L. Tomlinson and N.J. Cory, "Hydrogen emission during the steam oxidation of ferritic steels: kinetics and mechanism," Corr. Sci., 29 (8), 939-965 (1989).
[13] G. Bamba, Y. Wouters, A. Galerie, G. Borchardt, S. Shimada, O. Heintz, S. Chevalier, Inverse growth transport in thermal chromia scales on Fe–15Cr steels in oxygen and in water vapour and its effect on scale adhesion, Scripta Mater., 57 (2007) 671–674.
[14] C.T. Fujii and R.A. Meussner, J. Electrochemical Soc., 111 (11), 1215-1221 (1964).
[15] N.J. Cory and T.M. Herrington, "Kinetics of oxidation of ferrous alloys by superheated steam," Oxidation of Metals, 28 (5/6), 237-258 (1987).
[16] S. Mrowec, Corr. Sci., 7, 563-578 (1967).
[17] F.H. Stott, I.G. Wright, T. Hodgkiess, and G.C. Wood, "Factors affecting the high temperature oxidation behavior of some dilute nickel- and cobalt-base alloys," Oxid. Met., 11, 163 (1977).
[18] R.J. Hussey, G.I. Sproule, D. Caplan, and M.J. Graham, "The growth and structure of oxide films formed on iron in O2 and CO2 at 550°C," Oxid. Met., 11, 65-79 (1977).
[19] N. Nishimura, N. Komai, Y. Hirayama, and F. Masuyama, "Japanese experiences with steam oxidation on advanced heat-resistant steel tubes in power boilers," presented at the 60
[20] EPRI Workshop on Scale Growth and Exfoliation in Steam Plant, National Physical Laboratory, UK, September 3-5, 2003.
[21] H.J. Grabke and H. Viefhaus, "Surface composition of wüstite," Phys. Chem., 84, 152-159 (1980).
[22] P. Mayer and A. V. Manolescu, pp. 368-379 in High-Temperature Corrosion, Ed. R. A. Rapp, NACE, Houston, Texas (1983).
[23] I.G. Wright and P. F. Tortorelli, and M. Schütze, "Oxide growth and exfoliation on alloys exposed to steam," EPRI Report No. 1013666 (2007).
[24] S. Straub and R. Knodler, "Oxidation and spallation of ferritic / martensitic steels – Final Report", June 2009.
[25] M. Scheefer, R. Knödler, B. Scarlin, A.A. Bruna, D.N. Tsipas, New oxidation-resistant coatings for steam power plants at 650°C, Materials and Corrosion 2005, 56, No. 12
[26] A. Aguero, R. Muelas, A. Pastor, S. Osgerby, Long exposure steam oxidation testing and mechanical properties of slurry aluminide coatings for steam turbine components, 7th Liege conference, September 2002
[27] "Coatings for steam power plants", COST 536, Training School, Lanzarote, October 2008.
[28] P. Peel, B. Scarlin, R. Vanstone: From Materials Development to Advanced Steam Turbines; Parsons 2007: 7th International Charles Parsons Turbine Conference Power Generation in an Era of Climate Change; 11-13 September 2007, University of Strathclyde, Glasgow, UK
[29] T.U. Kern, H. Almstedt: Material Development and Advanced Design for Turbosets in USC Steam Power Plants, ibidem
[30] T.U. Kern, B. Scarlin, B. Donth, G. Zeiler, A. DiGianfrancesco: The European COST536 Project for the Development of New High Temperature Rotor Materials: IFM 2008, Santander Spain, 3-6 November 2008
[31] R. Blum, R. W. Vanstone "Materials Development in Thermie Project for 700°C USC Plant": 8th Ultra-steel Workshop "Proposal of New Constructions with Ultra-Steel", Tsukuba, Japan (July 2004).
[32] J. Armitt, D. R. Holmes, M. I. Manning, D. B. Meadowcroft and E. Metcalfe. " The spalling of steam-grown oxide from superheater and reheater tube steels" FP-686, Technical Planning Study 76-655, Final Report, February 1978.
[33] A. Fry, J. Banks and S. Osgerby, "The influence of heat flux on the oxidation of boiler steels", Power Generation in an era of climate change, Proc. 7th Charles Parsons Turbine Conference, 2007
[34] P. Auerkari, J. Salonen, A. Toivonen, S. Penttila, J. Hakkila, A. Aguero and T. Fry, "Oxidation performance of high temperature steels and coatings for future supercritical power plants", 9th Liege Conference, 2010.
[35] A. T. Fry, "Key experimental parameters in steam oxidation testing and their impact on interpretation of experimental results", Energy Materials, 2007, Vol 2, No 4, pp 214-221.
[36] A. T. Fry, N. Simms, B. McGhee, I. Wright and B. Colvino, "Standardisation in high-temperature corrosion testing", 23rd Annual Conference on Fossil Energy Materials, Pitts, USA, May 12-14, 2009.

9th Liege Conference : Materials for Advanced Power Engineering 2010
edited by J. Lecomte-Beckers, Q. Contrepois, T. Beck and B. Kuhn.

ADVANCES IN THE ASSESSMENT OF CREEP DATA

SR Holdsworth

EMPA: Swiss Federal Laboratory for Material Science & Technology, Dübendorf

Abstract

Many of the classical models representing the creep and rupture behaviour of metals were developed prior to and during the 1950s and 1960s, and their subsequent exploitation, in particular for the assessment of large creep property datasets, was initially limited by the capability of the analytical tools available at the time. The formation of ECCC (the European Creep Collaborative Committee) in 1991, with a main objective of providing reliable peer reviewed long-time creep property values for European Design and Product Standards, led to the development of rigorous assessment procedures such as PD6605 and DESA incorporating post assessment tests to verify: physical realism, effectiveness of model-fit within the range of the source experimental data, and extrapolation credibility. The first ECCC assessment recommendations published in 1996 undoubtedly provided a catalyst for others to exploit the availability of low cost, powerful desktop computers to develop rigorous methodologies for the physically realistic analysis of uniaxial and multi-axial data for the reliable and accurate characterisation of creep strain, and rupture strength and ductility properties. More recent improvements in data assessment methodologies have been driven by the need to effectively model the creep deformation and rupture characteristics of the complex new generation alloys and fabrications being designed to cater for the continually evolving requirements of modern advanced power plant. These advances in the assessment of creep data are reviewed.

Keywords: Creep, data, assessment, ECCC

1. Background and Introduction

At elevated temperatures, metallic structures deform with time under the influence of applied stress. Ultimately, the accumulation of such deformation leads to fracture by a creep rupture mechanism (Figure 1a). The consideration of these deformation and damage processes is a key part of the design assessment of critical components for high temperature applications, with the necessary engineering calculations requiring a knowledge of the creep-rupture properties of the material from which the structure is manufactured.

Creep-rupture properties are determined from the results of a number of creep tests performed for a range of constant temperature and constant stress (usually constant load, i.e. constant σ_o) conditions, Figure 2. In such tests, the creep strain may be monitored (but not always) either continuously by means of an extensometer attached to the gauge length of the testpiece, or by an optical measurement during planned test interruptions [1]. The data may have been determined from a matrix of $t_u(T,\sigma_o)$ tests for which T and σ_o are *i)* relatively homogeneously distributed for one or more casts, or *ii)* inhomogeneously distributed for the majority of casts of the alloy for which observations are available. Case *i)* is the ideal situation and generally arises within R&D projects or well co-ordinated data generation activities. Case *ii)* is more

typical of large multi-national datasets, comprising information from many casts, gathered to produce alloy representative creep strength values for standards [2]. A list of symbols and terminology is given in the Nomenclature.

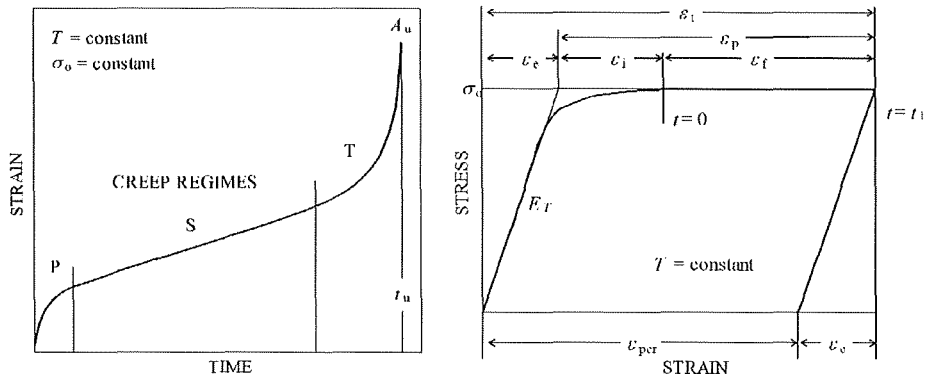

Figure 1: Schematic representations of: (a) a creep-rupture curve showing primary, P, secondary, S, and tertiary, T, deformation regimes, and (b) strains generated during a creep test

The rupture ductility (A_u in Figure 2) can vary with stress (time) and temperature in a relatively complex way (e.g. Figure 3a). The various ductiliy regimes are associated with distinct rupture mechanisms. For example, in ferritic steels, Regime-I involves ductile rupture resulting from the formation of voids typically as a consequence of particle/matrix decohesion. Regime-II is a transition regime in which the ductility drops due to the increasing incidence of grain boundary cavitation, but still accompanied by relatively high levels of matrix deformation. In Regime-III, rupture is by the nucleation and subsequent diffusive growth of grain boundary cavities. In Regime-IV, over-ageing of the microstructure lowers the rate of cavitation nucleation and/or growth leading to a progressive recovery of ductility. The mechanisms associated with the identified ductility regimes can differ for different alloy systems.

Many of the classical models representing the creep and rupture behaviour of metals were developed prior to and during the 1950s and 1960s. However, their subsequent exploitation, in particular for the assessment of large creep property datasets, was limited by the capability of the analytical tools existing at the time.

The following paper reviews advances made in the assessment of creep data during the past 100 years and examines factors contributing to the developments achieved.

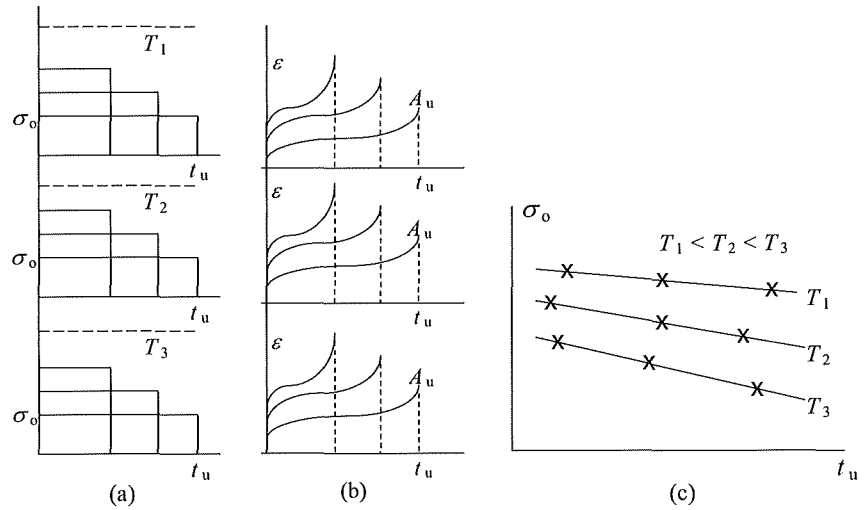

Figure 2: Schematic representation of (a) the T, σ_o dependent-variable conditions for 3 creep-rupture tests each at 3 temperatures, (b) the corresponding $\varepsilon(t)$ response-variable test records at each temperature, and (c) the resulting $t_u(T, \sigma_o)$ data points

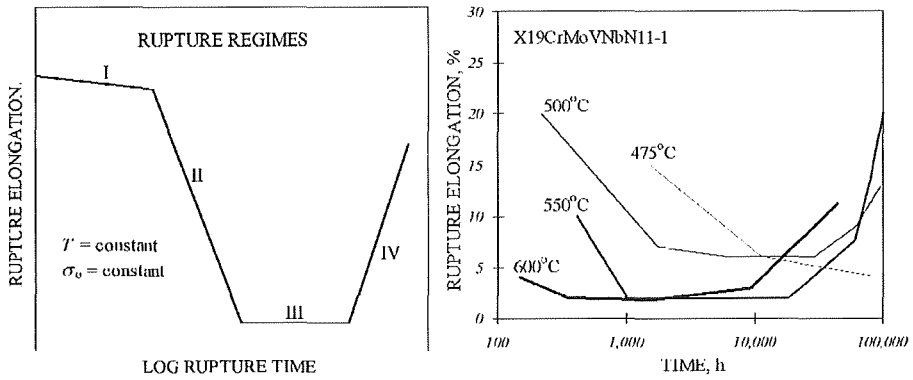

Figure 3: Rupture elongation profiles: (a) schematic representation, and (b) minimum $A_u(T)$ profiles for metallurgically complex steel

2. European Creep Collaborative Committee

In the early 1990s, the drive to greater integration in Europe led to the specification of unified (rather than independent National) Product and Design Standards. The European Creep Collaborative Committee (ECCC) was founded in 1992 to provide the means for European Industry to have a greater influence over the creep strength values incorporated into these Standards [3]. The original role of ECCC's technical working group, WG1, was to devise

common rules for the material specialist WG3x working groups to follow. The outcome was a series of ECCC Recommendation Volumes covering common terminology and guidance for the generation, collation and assessment of creep data [4]. While the Recommendation Volumes were originally produced for use by ECCC working groups, they were made freely available in the public domain and are now employed by a world wide user base.

In ideal circumstances, creep rupture strength values for design purposes are determined from an assessment of the results of sufficient tests on a variety of casts of the specified material to ensure that its true property variance has been fully characterised for an appropriate range of stresses and temperatures (e.g. [2]). Such full-size datasets for traditional materials may comprise up to ~1,000 observations for ~100 casts covering several temperatures with test durations up to >100kh. Originally, the focus for ECCC was on the assessment of such full-size (Case *ii)* type) datasets.

In the 1960s to 1980s, ready access to computer processing was in its infancy, and the reliable numerical model representation of full-size datasets typically involved manually implemented graphical procedures, either for the full analysis (e.g. [5]) or at the very least in a pre-assessment (data reduction) phase (e.g. [6]). Subjective interpretations were almost inevitable with such manual intervention, and ECCC-WG1 devised the post assessment tests (PATs) to independently check: *i)* the physical realism, *ii)* the within-data-range goodness-of-fit, and *iii)* the extrapolation repeatability/stability of a model determined by any procedure [4e,7].

The original PATs were developed to independently check the credibility of rupture strength predictions, irrespective of the applied assessment procedure [8]. Subsequently they were adopted for checking the credibility of creep strength and relaxed strength predictions [4e,9]. More recently, ECCC-WG1 developed the concept of the *Z*-parameter to provide a measure of model fitting effectiveness to families of creep strain curves in specific creep strain regimes for both Case *i)* and Case *ii)* type datasets [10].

During the 1990s, many WG1 members were also involved in National developments in creep rupture data assessment procedures which were exploiting the growing availability of desktop computing and user friendly software platforms. The emergence of the PD6605 [11] and DESA [12] creep rupture data assessment procedures provided a significant step forward, which was ultimately complemented by automation of the PATs [13].

The first ECCC assessment recommendations published in 1996 undoubtedly provided a catalyst for others to exploit the availability of low cost, powerful desktop computers to develop rigorous methodologies for the physically realistic analysis of uniaxial and multi-axial data for the reliable and accurate characterisation of rupture strength and ductility, and creep strain properties. These more recent advances in creep data assessment methodologies are also reviewed in the following paper.

3. Creep Strain Model Equations

3.1. Overview

Creep strain curves are determined from the results of continuous-measurement or interrupted tests involving the application of a constant load (or stress) to a uniaxial testpiece held at constant temperature (Figure 1a). In continuous measurement tests, the creep strain, ε_f, is monitored without interruption by means of an extensometer attached to the gauge length of the testpiece [1]. In interrupted tests, the total plastic strain, ε_p, is determined from optical measurements of ε_{per} at room temperature during planned interruptions (where $\varepsilon_{per} = \varepsilon_p - \varepsilon_k$, i.e. $\varepsilon_{per} = \varepsilon_i + \varepsilon_f - \varepsilon_k$, Figure 1b, and $\varepsilon_p = \varepsilon_{per}$ when $\varepsilon_k \approx 0$). The creep curve data collected in this way may then be modelled with a constitutive equation.

There are a large number of constitutive equations which can be used to represent the creep deformation characteristics of a material ranging from simple phenomenological to complex physically based (some of which are reviewed in [14]). No single constitutive equation effectively represents the creep deformation characteristics of all materials over their entire temperature application range. The effectiveness of a constitutive equation to model primary, secondary and/or tertiary creep deformation for specific applications can vary with material characteristics and source data distribution. In particular, not all model equations and fitting procedures are suitable for the prediction of alloy-mean long-time creep strength behaviour. As a generality, specific model equations are better suited to representing creep strain accumulation characteristics for a given material in either the primary/secondary or the secondary/tertiary regimes, although some models can be suitable for both [14]. The *Z*-parameter (referred to in Sect. 2) was developed to aid the selection of the most appropriate constitutive equation for a given material and deformation regime [14].

3.2. Classical Representations

A wide range of creep model equations are in use today to represent the high temperature time dependent deformation behaviour of engineering materials, many of which comprise components originating from a small number of classical representations of primary, secondary and/or tertiary creep deformation (e.g. [15-24]), i.e.

Primary Creep

Logarithmic [15]: $\varepsilon_f = a.\log(1 - b.t)$ (1)

Power [16]: $\varepsilon_f = a.t^b$ (2)

Exponential [17]: $\varepsilon_f = a.\left(1 - exp(-b.t)\right)$ (3)

Sinh [18]: $\varepsilon_f = a.sinh(b.t^c)$ (4)

Secondary Creep

Power [19]: $\dot{\varepsilon}_{f,min} = d.\sigma^n$ (5)

Exponential: $\dot{\varepsilon}_{f,min} = d.exp(e.\sigma)$ (6)

Sinh [20]: $\dot{\varepsilon}_{f,min} = d.sinh(e.\sigma)$ (7)

Tertiary Creep

Power [16]: $\varepsilon_f = f.t^g$ (8)

Exponential [21]: $\varepsilon_f = f.(exp(-g.t) - 1)$ (9)

Damage [22,23]: $\dot{\varepsilon}_f = \frac{a.\sigma^n}{(1-\omega)^q}$ where $\dot{\omega} = \frac{c.\sigma^k}{(1-\omega)^r}$ (10)

Omega [24]: $\dot{\varepsilon}_f = \dot{\varepsilon}_o.exp(\Omega.\epsilon)$ (11)

where a, b, c, d, e and f are model fitting constants.

As a generality, logarithmic creep only occurs at lower temperatures (i.e. below $0.3.T_m$). At higher temperatures, primary creep is more typically represented by power, exponential or sinh functions of time. Similarly, secondary creep rate can be represented by power, exponential or sinh functions of stress. For secondary creep rate, a sinh formulation reduces to a power law at low stresses and an exponential law at high stresses. Tertiary creep or creep rate is typically modelled by power or exponential representations, with or without a damage accumulation function, e.g. [22]. Typically, the effect of temperature is acknowledged by incorporating an Arhenius $A.\exp(-Q_C/RT)$ function into the model equation.

In strongly physically based implementations of constitutive creep equations, it is now common practice to replace σ by $(\sigma - \sigma_i)$ to acknowledge the existence of an internal friction stress, in particular for precipitation strengthened alloys, e.g. [25], but also see sect. 4.1.3.

3.3. Rupture Property Based Models

With the growing interest in modelling alloy creep deformation characteristics from observations collated for a number of casts (e.g. in Case *ii)* type datasets), newer formulations based largely on a knowledge of rupture properties have been developed. The forerunner of these were the expressions adopted to determine creep strength directly from rupture strength [26], e.g..

$$R_{u/t/T} = (a_1 + b_1/\varepsilon - c_1.\varepsilon^2).R_{\varepsilon/t/T} + d_1 + e_1/\varepsilon + f_1/\varepsilon^2 - g_1.\varepsilon^2 \quad (12)$$

An extremely effective variant of this type of expression is the characteristic strain model [27], i.e.

$$\varepsilon_f(\sigma) = \varepsilon.\left(R_{u/t/T}/R_{\varepsilon/t/T} - 1\right)/\left(R_{u/t/T}/\sigma - 1\right) \quad (13)$$

In contrast to using creep and rupture strength values, the logistic creep strain prediction (LCSP) model relies on a knowledge of times to specific creep and rupture strains [28], i.e.

$$log(t_\varepsilon^*) = (log(\alpha.t_u) + \beta)/(1 + (log(\varepsilon)/x_o)^p) - \beta \quad (14)$$

where x_o, p and β are fitting constants defining creep curve shape.

4. Creep-Rupture Model Equations

4.1. Rupture Time

4.1.1. Single Model Representations

Model equations for predicting creep rupture time generally fall into two categories, namely those which are based on time-temperature parameters (TTP) and those which are based on algebraic equations. By far the best known TTP formulation is that of Larson-Miller [29], i.e.

$$t_u^* = exp(\{\sum_{k=0}^{n} \beta_k . [log(\sigma_o)]^k\}/T + \beta_5) \quad (15)$$

The development of eqn. (15) was closely followed during the 1950s by a series of TTP based models [29-34], some of which derived from the same master equation [30], i.e.

$$t_u^* = exp(\{\sum_{k=0}^{n} \beta_k . [log(\sigma_o)]^k\} (T - T_o)^r/(\sigma_o)^{-q} + \beta_5) \quad (16)$$

In eqn. (16), the Larson-Miller model (eqn. (15)) is obtained if q = 0 and r = -1 [29], the Manson-Haferd model is obtained if q = 0 and r = 1 [31], the Manson-Brown model is obtained if q = 0 [32] and a stress modified model proposed by Murry is obtained if q = 1 and r = 1 [33]. An additional TTP model is that proposed by Orr-Sherby-Dorn [34]:

$$t_u^* = exp(\{\sum_{k=0}^{n} \beta_k . [log(\sigma_o)]^k\} + Q_C/RT) \quad (17)$$

where temperature is represented by the Arhenius term in eqn. (17), with Q_C being the activation energy for creep. During the 1970s, the focus was more on the development of algebraic models which were less flexible within-the-range of the observed $t_u(T,\sigma_o)$ data, but were more stable in extrapolation, e.g.

$$t_u^* = exp(\beta_0 + \beta_1 . log(T) + \beta_2 . log(\sigma_o) + \beta_3/T + \beta_4 . \sigma_o/T) \quad (18)$$

$$t_u^* = exp(\beta_0 + \beta_1 . log(\sigma_o) + \beta_2) . \sigma_o + \beta_3 . \sigma_o^2 + \beta_4 . T + \beta_5/T \quad (19)$$

Of these, eqn. (18) is an example of one of the so-called Soviet models [35] and eqn.(19) is the simplest form of the minimum commitment model [36].

As a generality, the preference of creep rupture data modellers has traditionally been to establish a single continuous representation of the observed $t_u(T,\sigma_o)$ data throughout the entire application ranges of temperature and stress. However, as the metallurgical complexity of engineering alloys has increased, the adoption of a single function to adequately represent rupture behaviour throughout the full application ranges of temperature and stress has become increasingly challenging.

4.1.2. Multi-Regime Modelling

During recent years, there has therefore been a tendency to increasingly adopt a multi-regime modelling approach for metallurgically complex alloys. This concept was not new and had been explored during the development of the minimum commitment models [36] and in Germany during the 1970s [37], but the profile of such approaches was raised recently by Kimura (e.g.[38]) and colleagues in Japan. To date, Kimura has concentrated on fitting a

Larson-Miller model (eqn. (15)) to $t_u(T,\sigma_o)$ observations in two mechanism (stress) regimes. His main focus was P122 steel, and for this alloy the regime splitting stress was $0.5.R_{p0.2}(T)$ (coincident with the limit of proportionality for this steel). Maruyama adopted a similar approach, but preferred to use the OSD model (eqn. (17)) so that regime splitting could be done on the basis of activation energy [39]. Using a power function (eqn. (20)), Spindler modelled the complex rupture behaviour of Esshete 1250 in three regimes by non linear regression [40], i.e.

$$t_u^* = A_i.exp(Q_{Ci}/RT).\sigma_o^{B_iT+C_i} \quad (20)$$

Where subscript i was the regime number. The new Wilshire equation provided the analytical means to ensure that rupture strength at short times was sensibly constrained by the tensile strength of the material [41], i.e.

$$t_u^* = exp\left(1/u_i.ln(1/k_i) + 1/u_i.ln\left(-ln(\sigma_o/R_m)\right) + Q_C/RT\right) \quad (21)$$

This formulation was ideally suited for multi-regime modelling (again with subscript i as the regime number). In its original form, Wilshire set Q_C to that for diffusion creep (i.e. 300kJ/mole), irrespective of regime. Subsequently, Spindler demonstrated that eqn. (21) could also be effectively implemented using piecewise non-linear regression to determine the u_i, k_i and Q_{Ci} parameters for each regime [40], i.e. with different Q_C for each regime (in a similar way to that implemented by Maruyama [39]).

Kimura more recently extended his modelling to a third low strength regime through the consideration of 'inherent creep strength' [42].

4.1.3. Microstructural Modelling

By combining tools for thermodynamics modelling and modern dislocation theory, microstructural evolution during creep can be predicted and can be used as input for creep modelling [43]. The availablity of systematically gathered microstructural data is increasing, e.g. [44], and this information is being increasingly exploited for microstructure based modelling, e.g. [43,45]. With reference to sect. 3.2, one strongly physical based approach adopts a classical model equation of the form:

$$\dot{\varepsilon} = d.exp(-Q_C/RT)(\sigma - \sigma_i)^n \quad (22)$$

and incorporates strengthening from immobile dislocations and particles through the dependence of friction stress on these microstructural quantities [43].

An alternative is the model equation represented by eqn. (23) [45] which appears to show promise for assessment applications involving extended extrapolation of metallurgically active alloys, but there is an important need for independent verification for the approach to be accepted more widely. In the Abe equation:

$$t_u^* = c/\left(\dot{\varepsilon}_{f,min}.dln(\dot{\varepsilon})/d\varepsilon\right) = c''/\left(\dot{\varepsilon}_{f,min}/\varepsilon_{f,m}\right) \quad (23)$$

where c and c'' are material constants.

4.2. Rupture Ductility

Proven procedures for the assessment of rupture ductility, in particular for large multi-source, multi-cast, multi-temperature datasets, are still under development. Such datasets can be highly complex with individual casts exhibiting the characteristics shown in Figure 3a but displaced to shorter or longer times respectively with increasing or decreasing temperatures (e.g. Figure 3b), the complexity being typically compounded by significant cast-to-cast variations in the rupture ductility properties for a given alloy [46]. There are model representations which can handle such complexity (e.g. [46]), with the most successful to date being that of Spindler [47], i.e.

$$ln(A_u) = MIN|[ln(A_1) + Q_C/RT + n_1.ln(\dot{\varepsilon}_{ave}) + m_1.ln(\sigma_o)], ln(A)| \quad (24)$$

where A_1, n_1 and m_1 are material constants.

5. Assessment Procedures

While significant advances in creep rupture property modelling have been made in the last two decades, the most notable progress has been made in the development of formal, well-defined, state-of-the-art assessment procedures which implement the available model equations with a high level of automation (e.g. [11,12]). For example, the PD6605 procedure involves rigorously defined pre-assessment, model selection and post assessment testing stages.

The basis of PD6605 [11] is a set of creep rupture models comprising six TTP expressions (based on eqns. (16) and (17)) and three algebraic equations (based on eqns. (18) and (19)). In addition, the user may define other models out of preference or when none of the given selection provided adequately represents the characteristics of the $t_u(T,\sigma_o)$ data (e.g. [40]). The software accompanying PD6605 provides the user with the opportunity to adopt either Weibull or log-logisitic error distributions depending on which best represents the random component of the creep data for a given material. However, the most notable feature of this assessment procedure is the use of maximum likelihood statistics to simultaneously estimate the parameters for the systematic and random components of the model using all available creep rupture data. The likelihood function for the model has the important characteristic that it comprises probability density functions covering the rupture times for failed testpieces and the survival time for unfailed testpieces. The routine consideration of unfailed tests is a main feature of the PD6605 analysis. Confidence intervals for the estimated time to rupture are obtained directly from the survival function.

The software forming the basis of the DESA procedure [12] similarly provides the user with the opportunity to check the effectiveness of a range of model equations. DESA does not yet employ maximum likelihood statistics and thereby does not routinely consider the information provided by unfailed tests or offer a choice of error distributions but unlike

PD6605, this procedure is still evolving with the latest version offering simultaneous assessments of creep strength and rupture strength [13].

6. Factors Influencing Advances in Creep Data Assessment

The chronological trend of the level of creep data assessment development activity during the past 100 years is summarised in Figure 4. The first peak of activity occurred during the 1950s and 1960s, and was initially driven by a requirement for accurate material creep property descriptions for the design of reliable critical high temperature components primarily for aerospace but also increasingly for power generation applications. The level of assessment development activity revealed in the public domain appeared to diminish during the 1970s and 1980s, but strongly increased during the 1990s and the first decade of the 21st century. There were a number of factors responsible for this chronological activity trend.

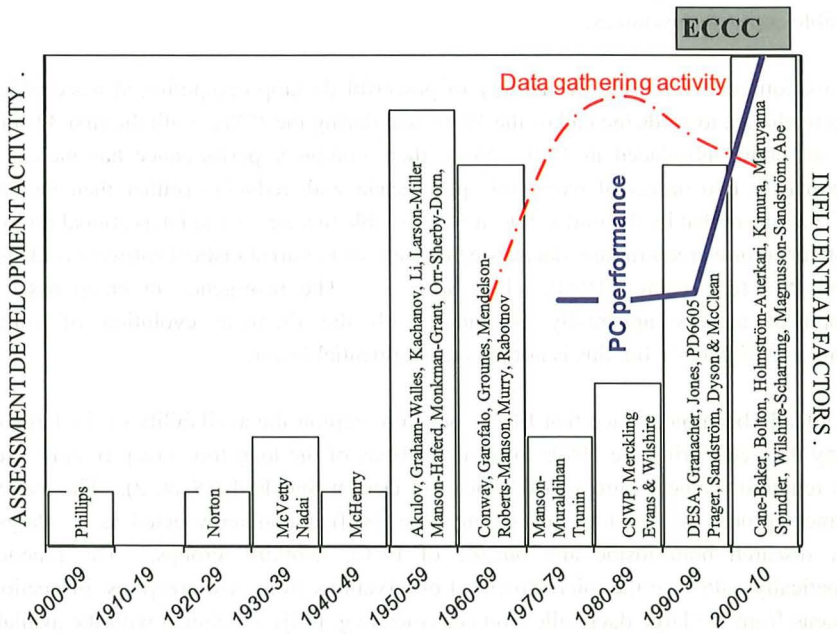

Figure 4: Chronological trend in the level of creep data assessment development activity and the impact of influential factors (refer to Sect. 8 and [14] for source references)

As a direct consequence of the creep data assessment and modelling activities in the 1950s and 1960s, it became increasingly obvious that the level of uncertainty associated with predicted long time strength values significantly increased in relation to the extent of extrapolation required to bridge the gap between maximum observed creep rupture time in the available dataset and specified design life. By this time, design life requirements for power plant applications were already ≥100,000kh. Moreover, the importance of sufficiently

characterising the property variability of the specified material, by gathering data for a significant number of representative casts, was also becoming increasingly clear. Worldwide, but in particular in Europe and Japan, large test programmes were initiated during the 1960s and subsequently to establish long time creep properties on strategic materials (for several casts of the same material and at a number of temperatures in the material's application range) [48-50]. This meant that towards the end of the 1970s and throughout the 1980s, large quantities of long term creep data were being accumulated (Figure 4). Financial constraints led to the rate of long time creep data generation being significantly reduced during the 1990s and 2000s, but collaborative activities continued to establish the necessary properties of strategic alloys (e.g. [51]), in particular those used for power plant components for which end users were by then requiring design lives of ≥250,000h. Initially, the large quantities of creep data were causing the analysts problems. A significant number of material models were available from the development activities of the 1950s and 1960s, but their effective implementation to large datasets was being constrained by the performance of readily accessible computer resources.

The situation concerning the availability of powerful desktop computing at reasonable cost started to change towards the end of the 1970s and during the 1980s, with the first 32-bit Intel processor being introduced in 1981. Since then, computer performance has increased by approximately two orders of magnitude per decade with reducing (rather than increasing) cost. This meant that by the mid 1990s, it was feasible to assess large international multi-cast, multi-temperature creep-rupture datasets using state-of-the-art statistical software packages on desktop PCs (e.g. using PD6605 [11], Sect. 5). The resurgence in creep assessment development activity apparently coincides with the dramatic evolution of computer performance (Figure 4), but this is not the only influential factor.

It has already been mentioned that ECCC began to exploit the availability of the large creep property datasets during the 1990s to form the basis of the long time creep rupture strength values required for new European Product and Design Standards (Sect. 2). The associated assessment procedure development activity (e.g. [4e]) undoubtedly acted as a catalyst for further research both inside and outside of ECCC working groups. The practice of systematically gathering the microstructural observations from post creep test inspections of specimens from the large data collection activities (e.g. [44]), combined with the availability of the latest effective software tools for thermodynamic modelling, is leading to the emergence of a new generation of microstructure based models.

By the middle of the 1990s, the intensity of large scale data generation had diminished significantly, with respect to its peak in the 1980s (Figure 4), but there was still a requirement for long term creep rupture testing even at a relatively low level. In the power generation industry, there was an increasing requirement for higher efficiency plant at lower capital cost. This meant the development of new alloys to withstand higher operating temperatures, with the tendency being to focus on advanced steels because of their lower cost relative to for

example nickel base alloys. As a generality the new advanced steels were metallurgically complex, exhibiting multi-regime creep rupture behaviour and requiring new analytical approaches to provide acceptable modelling.

The improvements in desktop computer performance and associated analytical software packages has also led to high temperature component design and assessment becoming more routinely the result of advanced finite element analysis (FEA) based procedures. Such procedures require accurate creep property model representations.

There are therefore a number of complementary factors which have been responsible for the most recent resurgence in creep data assessment development activity.

7. Concluding Remarks

Advances made in the assessment of creep data during the past 100 years have been reviewed, and factors contributing to the developments achieved have been examined.

The first peak of creep data assessment development activity occurred at a time when major technical advances were first being made in the designs of high temperature components primarily for aerospace, but also for power generation applications. A subsequent resurgence in activity coincided with:

- the availability of large international industrial datasets,
- the need for their exploitation to underpin the long time creep rupture strength values for European Design and Product Standards
- the catalytic effect of the associated ECCC creep data assessment procedure developments
- the dramatic improvements in low cost desktop PC computing performance,
- the requirement for more effective modelling of the creep behaviour of new advanced metallurgically complex alloys, and
- the requirement for accurate creep property model representations for implementation in FEA based high temperature component design and assessment analyses.

8. References

[1] EN 10291: *Metallic Materials, Uniaxial Creep Testing in Tension, Method of Test*, European Norm (2000).

[2] SR Holdsworth, 'Development and current status of ECCC creep property data sheets', *Proc. 8th Liège Conf. on Material for Advanced Power Engineering,* Liège, September, I, 91-105 (2006).

[3] DV Thornton, 'The activities of the European Creep Collaborative Committee', *Proc. Conf. on Life Assessment of Industrial Components and Structures, ERA/VALUE, Churchill College, Cambridge,* October, 2.9.1-10 (1993).

[4] ECCC, *Recommendations for Creep Data Validation and Assessment Procedures*, (eds.) SR Holdsworth et al., ECCC (ETD) (2005), *a) Vol.1: Overview, b) Vol.2: Terms and terminology, c) Vol.3: Data acceptability criteria, Data generation, d) Vol. 4: Data exchange and collation, e) Vol.5: Data assessment, f) Vol.6: Characterisation of microstructure and physical damage for remaining life assessment, g) Vol.7: Data assessment – creep crack initiation, h) Vol.8: Data assessment – multi-axial, i) Vol.9: Component assessment.*

[5] W Bendick, K Haarmann & G Wellnitz, Proc. 'Evaluation of Design Values for Steel 91', *ECSC Information Day on Manufacture and Properties of Steel 91 for Power Plant and Process Industries*, Dusseldorf, November (1992).

[6] ISO 6303, Annex: *Method of Extrapolation used in Analysis of Creep Rupture Data* (1981).

[7] SR Holdsworth, 'Reducing the uncertainty in long term creep rupture strength predictions', *Proc. 6th Intern. Conf. on Creep & Fatigue – Design and Life Assessment at High Temperatures*, I.Mech.E., London, April, 101-111 (1996).

[8] SR Holdsworth, 'Recent developments in the assessment of creep-rupture data', *Proc. 8th Intern. Conf. on Creep & Fracture of Engineering Materials & Structures,* Tsukuba, JSME, 1-8 (1999).

[9] SR Holdsworth, 'The ECCC approach to creep data assessment', *ASME J. Pressure Vessel Technology*, 130, May, 024001-1-6 (2008).

[10] SR Holdsworth et al, 'Factors influencing creep model equation selection', *Proc. ECCC Creep Conf. on Creep & Fracture in High Temperature Components – Design & Life Assessment Issues*, I.Mech.E., London, 380-393 (2005).

[11] BS-PD6605, *Guidance on Methodology for the Assessment of Stress Rupture Data*, British Standards Institution (2008).

[12] J Granacher & M Monsees, 'Assessment procedure document for DESA', *App.D2 in ECCC Recommendations Vol.5 Part Ia* (see [4e]).

[13] A Scholz, M Schwienheer & R. Znajda, 'Scatter-band assessment methods for creep and fatigue data', *Proc. 8th Intern. Conf. on Operating Pressure Equipment*, Melbourne, May (2005).

[14] SR Holdsworth, 'Constitutive equations for creep curves and predicting service', *in Creep-Resistant Steels*, eds. F Abe, T-U Kern & R Viswanathan, Woodhead publ., 403-420 (2008).

[15] F Phillips, 'The slow stretch in india rubber, glass and metal wire when subjected to a constant pull', *Phil. Mag.*, 9, p.513 (1905).

[16] A Graham & KFA Walles, 'Relations between long and short time properties of commercial alloys', *JISI*, 179, 105-120 (1955).

[17] PG McVetty, 'Factors affecting the choice of working stresses for high temperature service', *Trans ASME*, 55, p.99 (1933).

[18] JB Conway & MJ Mullikin, 'An evaluation of various first stage creep equations', *Proc. AIME Conf.,* Detroit, (1962).

[19] FN Norton, *The Creep of Steel at High Temperature*, McGraw-Hill (1929).

[20] A Nadai, 'The influence of time upon creep, The hyperbolic sine creep law', *in Stephen Timoshenko Anniversary Volume*, New York: Macmillan (1938).
[21] D McHenry, 'A new aspect of creep in concrete', *Proc. ASTM*, 43, p.1069 (1943).
[22] LM Kachanov, 'Time to failure under creep conditions', *Izv. Akad. Navk. SSR. Otd Teck. Nauk.*, 8, 26-31 (1958).
[23] YN Rabotnov, *Creep Problems in Structural Members*, Amsterdam, North-Holland (1969).
[24] M Prager, 'Development of the MPC Omega method for life assessment in the creep range', *ASME J. Pressure Vessel Technology*, 117, May, 95-103 (1995).
[25] BF Dyson & M McClean, 'Microstructural evolution and its effects on the creep performance of high temperature alloys', in *Microstructural Stability of Creep Resistant Alloy for High Temperatures*, eds. A Strang & M McClean, IOM, 371-393 (1998).
[26] Creep of Steels Working Party, *High Temperature Design Data for Ferritic Pressure Vessel Steels*, London, Inst. Mech.Eng., London (1983).
[27] JL Bolton, 'A 'Characteristic-strain' model for creep', *Proc. ECCC Creep Conf. on Creep & Fracture in High Temperature Components – Design & Life Assessment Issues,* I.Mech.E., London, September, 465-477 (2005).
[28] S Holmström & P Auerkari, 'Robust prediction of full creep curves from minimal data and time to rupture', *Energy Materials: Materials Science & Engineering for Energy Systems*, 1, 249-255 (2006).
[29] FR Larson & J Miller, 'A time-dependent relationship for rupture and creep stress', *Trans ASME*, 74, 765-775 (1952).
[30] A Mendelson, E Roberts & SS Manson, *Optimisation of time-temperature parameters for creep and stress-rupture with application to data from German co-operative long time creep programme*, NASA-TN-D-2975, August (1965).
[31] SS Manson & AM Haferd, *A Linear Time-Temperature Relation for Extrapolation of Creep and Rupture Data*, NASA-TN-2890 (1953)
[32] SS Manson & WF Brown, 'Time-temperature-stress relations for the correlation and extrapolation of stress-rupture', *Proc. ASTM*, 53, p.693, (1953).
[33] G Murry, *Proc. Joint Intern. Conf. on Creep, Inst.* Mech. Eng., 1, 6-87 (1963).
[34] RL Orr, OD Sherby & JE Dorn, 'Correlation of rupture data for metals at elevated temperatures', *Trans ASM*, 46, 113-128 (1954).
[35] II Trunin, NG Golobova & EA Loginov, 'New method of extrapolation of creep test and long time strength results', *Proc. 4th Int. Symp. on Heat-Resistant Metallic Materials*, Mala Fatra, CSSR, p.168 (1971).
[36] SS Manson & U Muraldihan, *Analysis of Creep Rupture Data for Five Multi-Heat Alloys by Minimum Commitment Method Using Double Heat Term Centring Technique, Res. Proj. 638-1, EPRI CS-3171*, July (1981).
[37] G Merckling, *Kriech- und Ermüdungsverhalten ausgewählter metallischer Werkstoffe bei höheren Temperaturen*, Doktor-Ingenieurs Dissertation, Karhlsruhe Universtät (1989).

[38] K Kimura, H Kushima, K Sawada & Y Toda, 'Region splitting analysis on creep strength enhanced ferritic steels', *Proc. 8th Intern. Conf. on Creep & Fatigue at Elevated Temperatures*, San Antonio, CREEP2007-26406, July, 647-659 (2007).

[39] K Maruyama & K Yoshimi, 'Methodology of creep data analysis for advanced high Cr ferritic steels', *ibid*, CREEP2007-26150, July, 631-636 (2007).

[40] MW Spindler & H Andersson, 'ECCC rupture data for austenitic stainless steels – Experience gained with demanding data analysis', *Proc. 5th Intern. Conf. on Advances in Materials Technology for Fossil Power Plants*, Marco Island, October (2007).

[41] B Wilshire & PJ Scharning, 'Design data prediction for P92 steels', *Proc. 8th Intern. Conf. on Creep & Fatigue at Elevated Temperatures*, San Antonio, CREEP2007-26754, July, 623-630 (2007).

[42] K Kimura, Y Toda, H Kushima & K Sawada, 'Creep strength of high chromium steel with ferrite matrix', *Proc. ECCC Creep Conf. on Creep & Fracture in High Temperature Components – Design and Life Assessment Issues*, EMPA, Zürich, April, 935-949 (2009).

[43] H Magnusson & R Sandström, 'Modelling creep strength of welded 9-12%Cr steels' *Metallurgical and Materials Transactions*, in press (2010).

[44] NIMS Creep Data Sheets, *Atlas of Creep Deformation Property*, Nos.D1-6, Tsukuba (Japan), National Institute for Materials Science.

[45] F Abe, 'Creep life estimation of Gr.91 based on creep strain analysis', *Proc. HIDA5 Conf. on High Temperature Defect Assessment*, ETD, Surrey University, June (2010).

[46] SR Holdsworth, 'Developments in the assessment of creep strain and ductility data', *Materials at High Temperatures*, 21(1), 125-132 (2004).

[47] MW Spindler, 'The multi-axial and uniaxial creep ductility of Type 304 steel as a function of stress and strain rate', *Materials at High Temperatures*, 21(1), 47-54 (2004).

[48] DV Thornton, 'UK power industry collaborative high temperature materials testing programmes', *Proc. Intern. Colloq. 50th Anniversary of German Creep Committee,* Dusseldorf, November, 32-37 (1999).

[49] J Ewald, W Bendick, J Granacher, K Maile, B Melzer, K-H Mayer, W Rhode & E Tolkdorf, '50 years of joint German activities in the area of creep resistant materials', *ibid*, 1-31 (1999).

[50] K Yagi, 'Acquisition of long term creep data and knowledge for new applications', *Proc. ECCC Creep Conf. on Creep & Fracture in High Temperature Components – Design & Life Assessment Issues*, I.Mech.E., London, 31-45 (2005).

[51] T-U Kern, M Staubli, K-H Mayer, B Donth, G Zeiler & A DiGianfrancesco, 'The European effort in development of new high temperature rotor materials – COST 536', *Proc. COST Conf. on Materials for Advanced Power Engineering*, II, 843-854 (2006).

Nomenclature

A, A_u	Tensile elongation at fracture; creep elongation at rupture
ECCC	European Creep Collaborative Committee
n	stress exponent
Q_C	Activation energy for creep
R	Universal gas constant
$R_{p\varepsilon/t/T}$, $R_{u/t/T}$	Creep strength and rupture strength for a given time and temperature
$R_{p0.2}$, R_m	0.2% proof strength; tensile strength
t	time
t_u, $t_{u,max}$, t_u*	Observed time to rupture; maximum observed time to rupture; predicted time to rupture
$t_{p\varepsilon/\sigma/T}$, $t^*_{p\varepsilon/\sigma/T}$	Observed and predicted times to given plastic strain
$t_{\varepsilon f}(T,\sigma)$	Time to a specific creep strain as a function of temperature and stress
T, T_m	Temperature; melting temperature of material
Z	Parameter quantifying effectiveness of master creep equation to predict times to specific strains
ε, ε_e, ε_i	Strain; elastic strain; instantaneous plastic strain
ε_f, ε_p, ε_k, ε_{per}	Creep strain; plastic strain; anelastic strain; permanent strain
$\varepsilon_{f,m}$	Strain at minimum creep rate
$\dot{\varepsilon}$, $\dot{\varepsilon}_{f,min}$, $\dot{\varepsilon}_{ave}$	Strain rate; minimum creep strain rate; average strain rate
σ, σ_o	Stress; initial stress
σ_i	Friction (internal) stress
ω, $\dot{\omega}$	Damage; rate of damage accumulation

ECCC terms and terminology recommendations are given in ECCC Volume 2 [4b]

9th Liege Conference : Materials for Advanced Power Engineering 2010
edited by J. Lecomte-Beckers, Q. Contrepois, T. Beck and B. Kuhn.

COMBATING CORROSION IN BIOMASS AND WASTE FIRED PLANT

Pamela Henderson[1] and Anders Hjörnhede[2]
Vattenfall AB
[1]Vattenfall Research and Development, 162 87 Stockholm, Sweden
[2]Vattenfall Power Consultant, 401 27 Gothenburg, Sweden
pamela.henderson@vattenfall.com anders.hjornhede@vattenfall.com

Abstract

Many biomass- or waste-fired plants have problems with high temperature corrosion especially if the steam temperature is greater than 500°C. An increase in the combustion of waste fuels means that an increasing number of boilers have had problems. Therefore, there is great interest in reducing the costs associated with high temperature corrosion and at the same time there exists a desire to improve the electrical efficiency of a plant by the use of higher steam temperatures. Assuming that the fuel is well-mixed and that there is good combustion control, there are in addition a number of other measures which can be used to reduce superheater corrosion in biomass and waste fired plants, and these are described in this paper. These include the use of fuel additives, specifically sulphur-containing ones; design aspects like placing superheaters in less corrosive positions in a boiler, using tube shielding, a wider pitch between the tubes; operational considerations such as more controlled soot-blowing and the use of better materials.

Keywords: Biomass, waste, superheaters, corrosion

1. Introduction

In recent years there has been a considerable increase in the amount of heat and electricity generated from the combustion of biomass or waste due to the drive to reduce CO_2 emissions and legislation forbidding the deposition of waste at landfill sites. One of the main problems with biomass and waste combustion is the production of low melting point chloride-containing deposits, which build up on heat-exchange surfaces, for example superheater tubes, and cause corrosion. The considerable corrosion problems increase the operation and maintenance costs, therefore leading to a higher cost for electricity and heat produced by these fuels. Energy companies are actively trying to reduce costs to make bio-fuels and waste more competitive sources of energy. At the same time there exists a driving force towards improving the electrical efficiency of a plant by the use of higher steam temperatures.

This paper describes some examples of methods for reducing corrosion, or achieving higher temperatures with acceptable corrosion. It is not intended to be an exhaustive or comprehensive list of methods, rather those that have come to the attention of the authors or that have been investigated by us. We assume that the fuel is well mixed and that there is good combustion control and instead focus mainly on the fuel chemistry and flue gas temperature and the effects that these have on critical components like superheaters. The paper looks at three main techniques for reducing corrosion:-

- Use of additives to change the flue gas and deposit chemistry

- Design and operation considerations
- Use of better materials. (A table giving the chemical composition of all the materials mentioned in this paper is given in the Appendix at the end)

2. Additives

Fuel additives can be used to alter the chemical environment in the boiler and make it less corrosive. Problems with corrosion and large amounts of deposits are to a great extent caused by chlorine compounds, especially alkali chlorides (NaCl, KCl), but also e.g. lead chloride ($PbCl_2$) and zinc chloride ($ZnCl_2$). These compounds have low melting points and are therefore partially or completely molten at the temperatures on heat transferring surfaces in the boiler. This makes them form sticky deposits where more particles can easily accumulate and in this way the deposits grow quickly. Molten phases on the tube surfaces are also much more corrosive than solid compounds. Some theories state that chlorine takes a major part in the corrosion process, by so-called "active corrosion", [1, 2], whereby chlorine is not consumed but circulates within the oxide. Other theories give potassium and sodium more central roles in the corrosion process, [3, 4], causing the breakdown of the protective chromia layer in stainless steels by the formation of potassium (or sodium) chromate K_2CrO_4.

2.1 Sulphur-containing additives

In the 1980's additions of sulphur made during waste incineration caused a substantial reduction in the chlorine content of the superheater deposits, [5]. Short-term (8 hour) corrosion probe tests also showed that the corrosion rates of low alloy and stainless steels were greatly reduced. It was concluded that, in the case of low alloy steels, sulphur additions must be sufficient to reduce the chloride content of the initial deposit to ~0.1 percent to achieve low corrosion rates. A deposit containing only alkali sulphates has a higher first melting point than a deposit containing alkali chlorides [6] and, as molten phases increase the corrosion rate, alkali sulphates are preferred to alkali chlorides in the deposits.

It is known that co-firing wood fuel with sulphur containing fuels like coal decreases the corrosion rate, [7]. It has been shown that the addition of SO_2 led to a decrease in corrosion under deposits made from waste incinerator fly-ash and that no chlorides were found in the deposits after the experiments, [8] and also that the addition of SO_2 to pure oxygen reduced the oxidation rate of T22 in the range 500-600°C, [9]. In this case the suppression of oxidation was suggested to be due to the formation of small amounts of iron sulphate, which interfered with the oxidation process.

2.2 Sulphates – "ChlorOut additive"

Vattenfall has patented a method for the reduction of corrosion caused by high levels of alkali and chlorine in the fuel using sulphates, [11]. The method, called "ChlorOut" covers a number of sulphates, but ammonium sulphate, $(NH_4)_2SO_4$, is the most often used additive as it also

reduces NO_x and the consumable costs of $(NH_4)_2SO_4$ and NH_3 are similar in terms of their NO_x reducing potentials. The additive is sprayed into the flue gases after combustion, but before the superheaters, and changes gaseous alkali chlorides to sulphates, which are considerably less corrosive. A simplified reaction scheme during the injection of ammonium sulphate solution is described as follows:

(R1) The injected ammonium sulphate decomposes into ammonia and SO_3.

(R2) SO_3 reacts with alkali chlorides and converts them into alkali sulphates and HCl. (Alkali sulphates are more stable and less corrosive than alkali chlorides. In waste incineration it is assumed that the most abundant alkali chloride is NaCl).

(R3) Ammonia reacts with NO which is consequently reduced by the so-called SNCR reaction.

(R1) $(NH_4)_2SO_4 \rightarrow 2NH_3\ (g) + SO_3\ (g) + H_20$

(R2) $2KCl\ (g)\ (or\ NaCl) + SO_3 + H_2O \rightarrow K_2SO_4\ (s)\ (or\ Na_2SO_4) + 2HCl\ (g)$

(R3) $4NH_3\ (g) + 4NO\ (g) + O_2\ (g) \rightarrow 4N_2\ (g) + 6H_2O$

The level of alkali chlorides in the flue gases is measured with an IACM (In situ Alkali Chloride Monitor), [10].

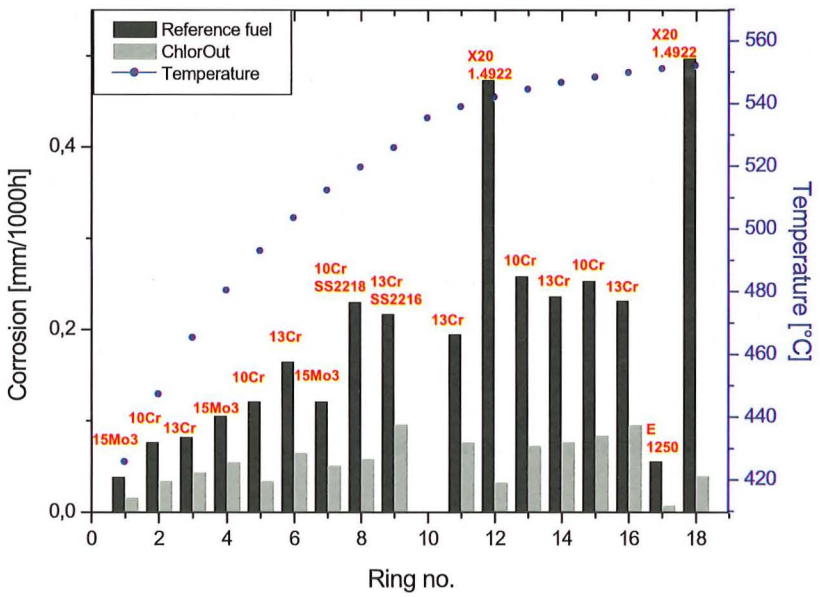

Fig. 1 Results from bark and waste fired boiler in Munksund, showing corrosion rate versus metal temperature for a number of different alloys, [13].

The ChlorOut additive has been successfully used for a number of years in boilers firing wood, waste wood and wood-waste mixtures, [12]. Figure 1 shows the results of corrosion probe testing, with and without ChlorOut (ammonium sulphate), in a circulating fluidised bed (CFB) boiler in Munksund, Sweden, which fires a mixture of bark and 6% plastic waste, [13]. There was a temperature gradient of 430 to 550°C along the probe and five different materials were tested. The testing lasted four weeks and the two probes were exposed at the same time on different sides of the boiler. ChlorOut was sprayed in on one side of the boiler and affected only one of the probes. Chlorout greatly reduced the corrosion rates of all steels.

The figure also shows that X20 is a poor choice of steel for a biomass-and-waste fired boiler with a steam temperature of around 500°C (550°C metal temperature) and performed much worse than low alloyed steels. The austenitic stainless steel Esshete 1250 showed good corrosion resistance.

Within the EU project NextGenBioWaste, [14], a number of tests have been made by Vattenfall in boilers firing household waste or a mixture of household and industrial waste. Figure 2 shows an austenitic stainless steel after exposure for 4 hours at 500°C with and without ChlorOut in a CFB boiler owned by E.ON in Norrköping, Sweden, [15]. The fuel consisted of 30 - 50% household waste, 50 – 70% industrial waste.

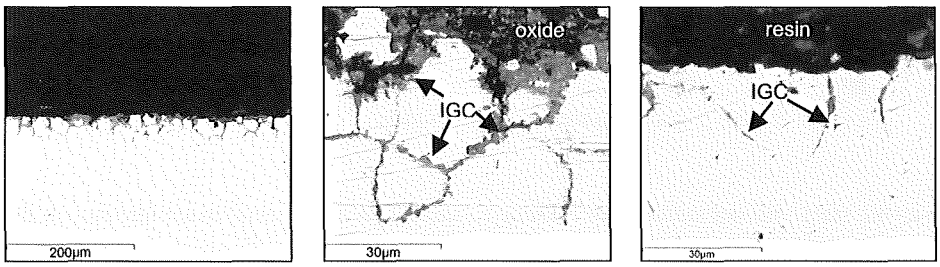

Fig. 2 Intergranular corrosion of the austenitic (Fe-18Cr-10Ni) steel 304L associated with chlorine ingress along the grain boundaries. Left and centre, reference case with no ChlorOut. Right, with ChlorOut. The extent of initial corrosion (right) is reduced with ChlorOut, [15]

ChlorOut greatly reduced the amount of initial corrosion. The amount of chlorine in the deposit was reduced from 10-15 % to 1-3 %, by the use of ChlorOut and phase analyses showed that sodium, potassium and calcium chlorides decreased, (Figs. 3 and 4).

In low alloy ferritic steels corrosion was associated with the accumulation of iron chlorides at the metal oxide interface. Even though ChlorOut dramatically decreased the concentration of

chlorine in the deposit, chlorine-induced corrosion was not completely suppressed. The ferritic steel was clearly not able to form an oxide that sufficiently prevents chlorine ingress.

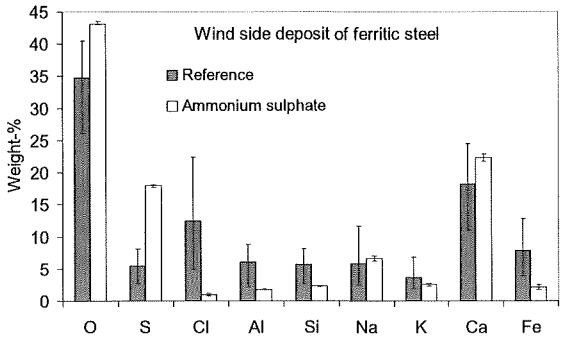

Fig. 3
Chemical compositions of deposits with and without ChlorOut, as measured by EDX in an SEM. Sampling time 4 h, probe ring temperature 500°C, [15].

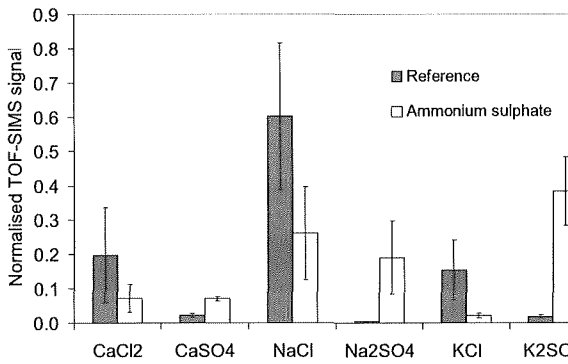

Fig. 4
Chemical compounds present in the deposits with and without ChlorOut, as measured by TOF-SIMS. Sampling time 4 h, probe ring temperature 500°C, [15].

Austenitic steels did not suffer from chlorine accumulation at the metal/oxide interface to the same extent and the amount of corrosion was much less than in ferritic steels. The amount of corrosion was further reduced by additions of ChlorOut. The overall conclusion is that ammonium sulphate has the potential to reduce corrosion in waste-fired boilers and that higher alloyed austenitic steels are more likely to resist corrosion, [15].

3. Design and operation considerations

3.1 Final superheater in loop seal

In many new CFB boilers the final superheater is positioned in the sand-loop seal, in order to reduce corrosion. A number of steels were tested in corrosion probes in the boiler of the Nässjö Combined Heat and Power (CHP) station, situated in the southern part of Sweden, [16]. The boiler is a 30 MW CFB boiler, which produces steam at 80 bar/480°C and generates 9 MW electricity. The fuel used during the tests was 100% wood (logging residues). Probes were

exposed in two positions for 3360 h. One probe, metal temperature 600°C, was exposed near the top of the boiler at the superheaters in the flue gas passage and another, metal temperature 650°C, at the bottom in the cyclone loop seal. These both simulate the same steam temperature of 550°C. Corrosion was greatly reduced in the loop seal in spite of a higher metal temperature, (see Fig. 5).

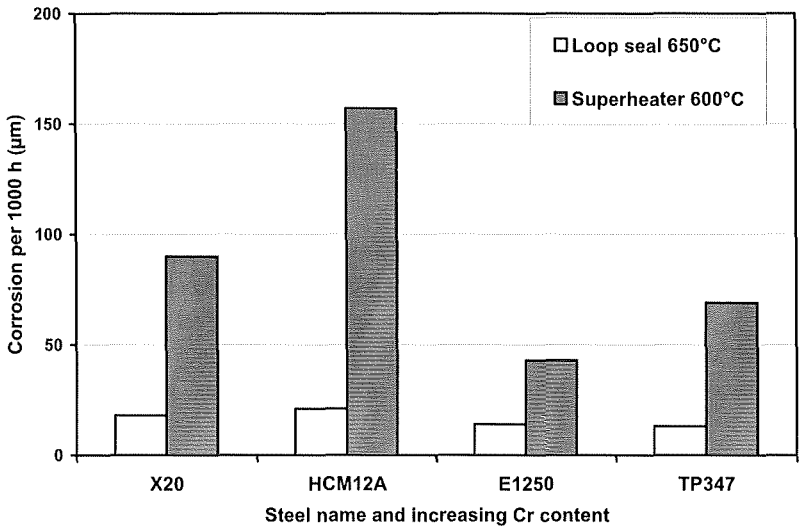

Fig. 5 Comparison of erosion-corrosion rates for steels exposed in probes near the superheaters at 600°C and in the cyclone loop seal at 650°C, simulating the same steam temperature of about 550°C, [16].

Gas analyses showed that HCl levels were broadly similar in the range of 2-6 ppm at both testing positions. Levels of H_2O in the flue gas at the final superheater were in the range 22-25% (by volume) as opposed to 3-6 % in the loop seal. SO_2 levels were 13-20 ppm at the superheaters and 3-7 ppm in the sand loop seal. O_2 levels were 3-5 % at the superheaters and 5-15% in the loop seal. The environment is considerably less aggressive there, from a chemical point of view, although erosion problems would be expected to be greater. However, Fig. 5 clearly shows that the loop seal is an ideal position for a final superheater and sand erosion does not seem to be a problem. In addition, the deposits collected on probes in the loop seal were much thinner than those collected at the superheaters. It is possible that sand erodes the deposits, thereby removing a corrosive source. Another advantage to be gained, in addition to reduced corrosion, is that the superheater can be considerably smaller in size (about a third of the size of a conventional superheater) since the heat transfer per unit area of tube surface is more intensive in the loop seal, [16]. This leads to savings in material and manufacturing costs.

3.2 Soot-blowing

Extensive deposit growth is a well-known problem in biomass and waste-fired boilers and a number of soot-blowing methods are available for removal of the deposits. However, soot-blowing too intensively or badly adjusted soot-blowers can remove protective oxide layers along with the deposits or damage the oxide layers by causing cracking, thereby making it easier for corrosive melts or gases to react with the metal, [17]. Commonly used measures for reducing material damage during soot-blowing are, reduced soot-blowing steam pressure, reduced frequency, and tube shielding to protect the tubes nearest the blower, [17]. Tests on a variety of tube shielding in a waste-fired plant found that Sicromal 10, Sicromal 12 and 15Mo3 were good choices for shielding material (better than austenitic stainless steels) when considering a combination of cost and lifetime, [18].

Danish straw-fired boilers are designed with an increased pitch between superheater tube bundles which allows a thicker build-up of deposits before the flue-gas passage becomes blocked, [19]. The high temperature superheaters are operated at a temperature where there is equilibrium between deposit growth and deposit melting, thus removing the need for soot-blowing. The deposits help to insulate the tubes and reduce the heat flux, which also reduces the corrosion rate.

"Non-stick" or "inert" coatings on superheaters have also been considered as a means of reducing the amount of soot-blowing, by reducing the amount of deposit that sticks to the tubes in the first place, [20]. Plant tests showed that a tube surface coated with a nickel-based alloy can reduce the formation of chlorine-rich, partly melted deposits, but no effect was shown on the chlorine-free deposits of a biomass plant. A ceramic coating showed a similar effect, but the coating did not remain on the tubes long enough for a long-term evaluation, [20].

3.3 Other design and operation considerations

Within the EU project NextGenBioWaste, [14], a "Chlorine trap" or "cold finger" has been installed and evaluated in the household waste fired boiler in Schweinfurt, Germany, [21]. The trap is a heat exchanger with narrow distances between the tubes and operated at a low temperature in front of the superheaters. (In order to compensate for the extra heat extracted there, some heat exchangers were eliminated from the second pass.) Chlorine-rich deposits condense from the flue gas at the trap. Preliminary results showed a reduction of 25% in the corrosion rate of the final superheater and differences in ash particle size distribution in pass 3 after installation, [21]. However, more long-term data are needed before these improvements can be attributed solely to the action of the trap, [21].

Reducing the flue gas temperature at the superheaters, by designing boilers with an extra empty pass, or by regular cleaning of membrane walls is another proven method of reducing superheater corrosion. The disadvantages are the increased investment cost in the first case

and the increased risk for wall corrosion in the second. As a last resort, the final steam temperature can be reduced. These methods, though, are commonly used.

And last, but not least, a cost-effective and simple way of increasing the lifetime of superheaters is by increasing the wall thickness when ordering replacements or designing new plant. A corrosion allowance of 1 mm is common in superheaters, but this should be increased to 2 mm. This method is popular in Danish straw-fired plant, [19], and has been used effectively in waste incineration plant, [22].

4. Materials

4.1 Biomass boilers

In coal-fired boilers increasing the chromium content of the superheaters leads to a decrease in the corrosion rate. This is not always the case in biomass-fired boilers. Figure 6 shows the results of corrosion probe testing in the 98 MW_{tot} CFB boiler in Munksund, Sweden, which has a final steam temperature of 480°C and pressure 60 bar. The boiler is fired mainly with bark (>80%), but also sawdust, woodchips and approximately 6% of waste. The waste is mostly plastic from tape and packaging, obtained from the reprocessing (recycling) of cardboard cartons. Fig. 6 shows that increasing the chromium content of steels from the 0% of 15Mo3 to 1% in 13CrMo44, 2% in 10CrMo910 or even 10% in X20CrMoV12 1 did not lead to a reduction in corrosion rates. However the stainless steel Esshete 1250, containing 15% Cr and 10% Ni, showed very low corrosion rates, [16].

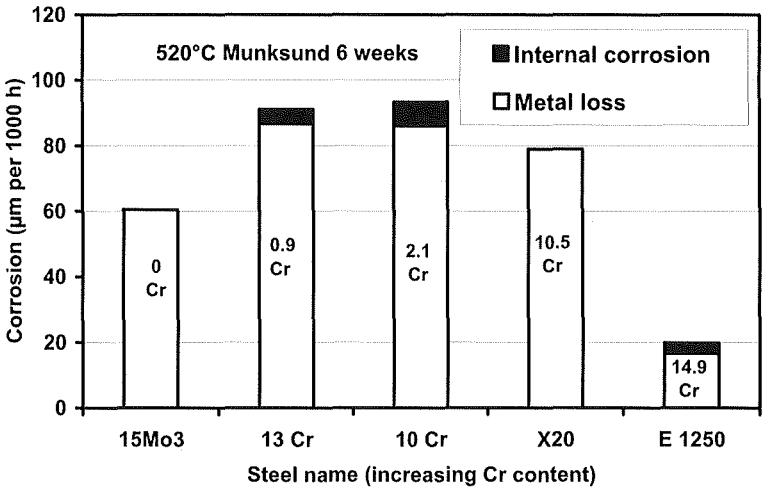

Fig. 6. Corrosion rates for various steels tested at 520 °C in Munksund, [6].

Increasing the metal temperature of a superheater steel does not always lead to an increase in the corrosion rate. Tests performed in a bubbling fluidised bed (BFB) boiler running on 100% waste wood showed that for stainless steels a maximum corrosion rate was reached at a metal temperature of 540-560°C, [23]. An example of the results obtained for Esshete 1250 is given in Table 1. The decrease in corrosion rates at higher temperatures were explained on the basis of decreasing Cl levels in the deposits with increasing temperature and increasing diffusion allowing a protective Cr-rich oxide to be formed more effectively.

Table 1. Average metal loss at various metal temperatures for Esshete 1250 in a boiler firing waste wood, [23]

Av. Metal Temperature (°C)	505	536	568	585	598	601
Av. Metal loss (μm per 1000 h)	77	100	94	78	39	23

A steam loop for corrosion testing was constructed in a BFB boiler firing biomass and 15% packaging waste. At 500°C steam the alloys with the best corrosion resistance were the ones with the highest Ni and Cr contents, namely Haynes 230, HR11N, AC 66 and HR3C. The corrosion rate of X20 was unacceptably high and was totally unsuitable for this fuel mix. At 600°C Haynes 230 showed the lowest corrosion rates, followed by (surprisingly) TP 347 HFG, HR3C and AC66. The full results are presented elsewhere in the proceedings, [25].

4.2 Waste-fired boilers

Within the NextGenBioWaste project, [14], corrosion testing with cooled probes was performed by the authors in the boiler of a waste fired power plant, Müllverwertung Borsigstrasse, (MVB), in Hamburg, Germany. The maximum steam temperature was 380°C and the fuel consisted of 70% household waste and 30% industrial waste. Two probes were installed at the plant and were exposed for 1550 hours directly in front of the first set of superheater tubes that the flue gases meet on their way through the boiler. The flue gas temperature at this position was in the range 600-650°C and the metal temperatures of the probes were 440°C and 490°C, corresponding to steam temperatures of about 410°C and 460 °C. The previously unpublished results are shown in Figs. 7 and 8.

The probe testing performed in this case represents a "worst case" form of corrosion testing. The probes were placed in a rather exposed condition before the first bank of superheaters and therefore subjected to a slightly higher than normal flue gas temperature and erosion rate. The first bank of superheaters that the flue gases meet do not contain the highest steam temperatures. The superheaters with the highest steam temperature are placed further along the flue gas passage at a lower gas temperature.

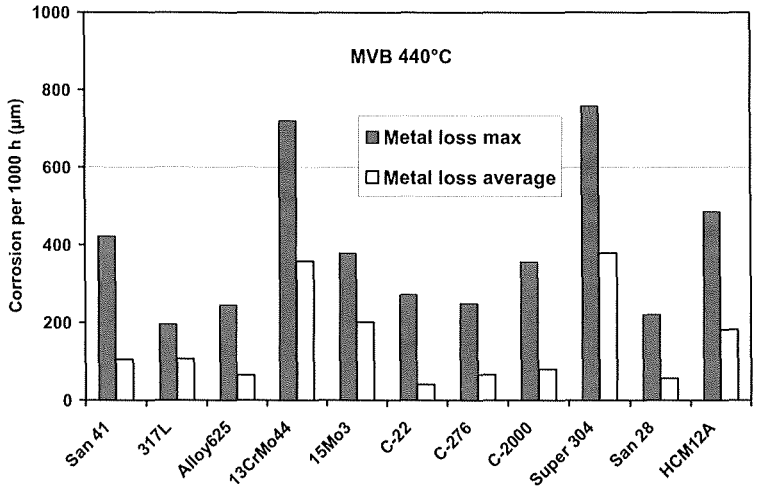

Fig. 7 Maximum and average metal loss (per 1000h) measured on probe rings with a temperature of 440 °C in MVB. 317L and Alloy 625 were weld overlay coatings.

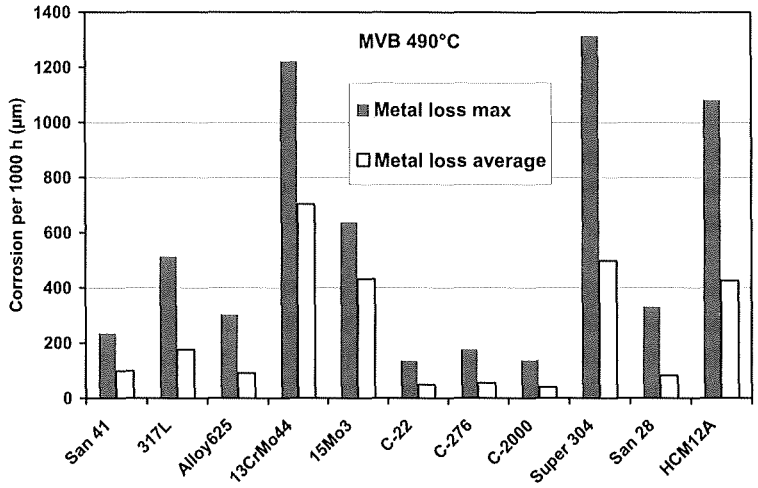

Fig. 8 Maximum and average metal loss (per 1000h) measured on probe rings with a temperature of 490 °C in MVB. 317L and Alloy 625 were weld overlay coatings.

13CrMo44, Super 304, 15 Mo3 and HCM12A show the highest rates of metal loss, although 15Mo3 performed surprisingly well considering the low alloying content. All these four alloys have a nickel content of less than 10% and a molybdenum content of less than 0.5%. Super 304, which contains no Mo, performed very badly.

Sanicro 41, Alloy 625, C-22, C-276, C-2000 and San 28 performed very well with average metal losses below 100 mm/1000h at 490°C. All these alloys contain more than 30% nickel and 2% molybdenum. Sanicro 41, C-22, C-276 and C-2000 actually showed lower corrosion rates at 490°C than at 440°C.

In the same plant, MVB, protective coatings of 317L and Alloy 625 were applied to tubes with Pulse Spray Gas Metal Arc Welding and these tubes were welded into a superheater where the metal temperature was 300-350°C and the flue gas temp 500°C. After nearly two years (14000 hours) no material loss could be detected on Alloy 625, but an average of about 0.3mm metal loss was measured on 13 CrMo44 and 317L and 0.22 mm on 15Mo3, [24]. At these low temperatures the cheapest alloy, 15Mo3, showed the lowest corrosion rates of the steels and explains why 15Mo3 is a good choice in many waste applications at lower temperatures.

4.3 Cost of components

The corrosion resistance is of course not the only parameter to be considered when choosing a material. The cost is of prime importance. As a rule of thumb, if 15Mo3 has a cost factor of 1; 9-12% Cr steels cost 2 times; austenitic stainless steels, like TP 347H FG, cost 4-5 times; super austenitics like AC66, cost 10 times and nickel-base alloys cost 15-20 times. The cost of expensive alloys can be reduced by weld cladding on a low alloy ferritic steel if steam-side oxidation is not a problem.

Manufacturing costs must not be neglected though. As an example a superheater made of 2500 metres of tubing has a material cost of about 100 kEuro if made in a 9-12% Cr steel or 250 kEuro if made in an austenitic steel like 347 or Esshete. However the manufacturing costs are similar in both cases, around 150 kEuro. For a biomass application where 9-12% Cr steels corrode several times as fast as a stainless steel (see for example Figs 1 and 6) the austenitic steel is the obvious choice.

5. Conclusions

In addition to good mixing of the fuel and uniform combustion, measures that can be taken to reduce corrosion in biomass- and waste-fired boilers are :

- Use of sulphur-rich fuel additives which convert highly corrosion alkali chlorides into less corrosion alkali sulphates. Sulphates which are sprayed into the flue gas after combustion are particularly effective.
- Placing the final superheaters in a less aggressive environment, *e.g.* in the loop seal in a CFB boiler
- Reducing the amount of soot-blowing as much as possible, either in intensity or frequency. Excessive soot-blowing damages or removes the protective oxide scale from a superheater and leads to an increase in the corrosion rates.
- Use of tube shielding to protect components exposed to soot-blowers
- Use of non-stick (inert) coatings so that deposits accumulate at a lower rate on superheaters (more research is needed in this area)
- Superheaters with a wider pitch between the tubes and allowing thicker deposits to build up. The deposits may reduce the corrosion by reducing the heat flux (needs to be considered at the plant design stage)
- Use of a thicker corrosion allowance
- Use of a "chlorine trap" or "cold finger"
- Reducing the flue gas temperature at the final superheaters
- Use of "better" materials ; "better" meaning combination of cost and corrosion resistance.

Ferritic or martensitic steels from 0 to 12% Cr showed similar corrosion rates under similar conditions in biomass or waste-fired boilers, which means there is no advantage from a corrosion point of view in using X20CrMoV121 over 15Mo3. At higher steam temperatures in biomass applications austenitic- or super austenitic stainless steels are a good choice, and for waste boilers at higher temperatures alloys with high nickel contents and some Mo are needed. As it is often difficult to know which alloy will perform best, probe testing to simulate the superheater conditions of temperature and flue gas chemistry is highly recommended.

6. References

1. H. J. Grabke, E. Reese, M. Spiegel. Corrosion Science, **37**, 7, pp. 1023-1043, (1995).
2. K. Salmenoja. *"Field and Laboratory Studies on Chlorine-induced Superheater Corrosion in Boilers Fired with Biofuels"*, PhD dissertation, Åbo Akademi, Åbo, February 2000
3. H. Asteman, J-E Svensson, M. Norell, L-G Johansson. Oxidation of Metals **54**: (1-2) 11-26 (2000)

4. K. Segerdahl , J-E Svensson, *et al.* Materials at High Temperatures **22**, (1-2), pp 69-78, (2005).
5. H. H. Krause. J. Mater. Energy Syst., **7**:4, pp 322-332, (1986).
6. K. Iisa, Y. Lu, and K. Salmenoja, Energy & Fuels, **13**, p 1184, (1999).
7. P. J. Henderson, Th. Eriksson, J. Tollin and T. Åbyhammar. Proc Conf. Advanced Heat Resistant Steels for Power Generation. Eds. R Viswanathan and J Nutting. p 507, IOM Communications, London, (1999).
8. M. Spiegel. Materials at High Temperatures, 14, p 221, (1997).
9. A Järdnäs, J-E Svensson and L-G Johansson. Materials Sci. Forum, 369-372, p 173, (2001)
10. IACM. Swedish Patent SE 9903656-8, (2001). International Patent application PCT/SE 00/01866 (2000)
11. *A method for operating a heat-producing plant for burning chlorine-containing fuels*, International patent no WO 02/059526 A1
12. P. Henderson, P. Szakálos, R. Pettersson, C. Andersson and J. Högberg, Materials and corrosion, **57** no 2, pp 128-134, (2006)
13. M. Broström, H. Kassman *et al.* Fuel Processing Technology **88**, pp 1171–1177, (2007).
14. www.nextgenbiowaste.com
15. P. Viklund, R. Pettersson, A. Hjörnhede, P. Henderson and P. Sjövall. Corrosion Engineering, Science and Technology, 44, no 3, pp 234-240, (2009).
16. P. J. Henderson, J. Högberg and M. Mattsson. *Proc. Conf "Materials for Advanced Power Engineering 2002"*, pp 883-892. Eds. J Lecomte-Beckers et al. Forschungszentrum Jülich, (2002).
17. A. Hjörnhede and P. Henderson, *The effect of soot-blowing on metal loss in biomass and waste-fired boilers.* Värmeforsk report no. 970, March 2006. www.varmeforsk.se
18. A. Hjörnhede *et al. Evaluation of Tube Shielding.* Värmeforsk report no 1031, December 2007. www.varmeforsk.se
19. Maribo-Sakskøbing and Amager. Private communications
20. M. Almark *et al. Inert tube coatings as a method to reduce deposit adhesion on superheaters.* Värmeforsk report no. 1034. December 2007. www.varmeforsk.se
21. R. Warnecke *et al.* Proc. Conf *ISWA-Beacon Waste-to-Energy Conference* 2007 and 113-VDI-WF-Korr -08
22. H. Söth, MVB, Vattenfall. Private communication, (2010).
23. A. Stålenheim *et al.* Vattenfall. Unpublished results from NextGenBioWaste, (2010).
24. A. Hjörnhede and M. Bjurman. Vattenfall. Private communication.
25. P. Henderson and M. Lundberg. Proceedings of this conference.

7. Acknowledgements

The authors acknowledge with thanks the contribution to the research work presented here made by their former and present colleagues at Vattenfall.

8. Appendix

Chemical composition, in weight percent, of the materials mentioned. The balance is Fe.

Steel	Cr	Ni	Mo	Mn	Other
15Mo3	0.1	0.1	0.3		C 0.16, Si 0.23, Mn 0.7
13CrMo44	0.9	0.1	0.5	0.5	C 0.12, Si 0.23, Mn 0.5
10CrMo910	2.1	--	0.92	0.43	C 0.12, Si 0.22
X20CrMoV12 1	10.5	0.73	0.89	0.6	C 0.18, Si 0.24, V 0.27
HCM12A	12.0	0.26	0.32	0.65	W 1.9, Si 0.3, Nb 0.06, N 0.06, V 0.02, B 0.003, C 0.08
Esshete 1250	15	10	1.0	6.25	C 0.084, Si 0.58, Nb 0.86, V 0.22, B 0.004
TP 304L	18.0	10	--	--	C 0.02
Super 304	18.0	9	--	0.8	C 0.02, Cu 3.0, N 0.1, Nb 0.45
TP 347H FG	18.5	11.9	--	1.5	Si 0.42, Nb 0.9, C 0.09
317L (cladding)	18.5	14.5	3.1	1.7	C 0.03, Si 0.4
Sanicro 41	20	38	2.5	0.5	C 0.02 Al 0.06, Cu 1.5, Si 0.3, Ti 0.7
Sicromal 10	18.0	--	--	--	C 0.08, Si 1.3, Al 1.0
Sicromal 12	24.0	--	--	--	C 0.08, Si 1.4, Al 1.5
HR3C	25.0	20.0	--	1.1	C 0.06, Si 0.4, Nb 0.5, N 0.2
AC 66	27.3	31.7	--	0.49	Ce 0.06, Nb 0.8, Si 0.2, C 0.05
Sanicro 28	26.7	30.6	3.32	1.73	C 0.015, Si 0.42, Co 0.06, Cu 0.87, N 0.07
HR11N	29.0	41.0	1.1	0.5	C 0.01, Si 0.12, N 0.17
Haynes 230	22.0	59.0	2.1	0.5	C 0.1, Al 3.5, B .003, Co .2, Si .4, W 14, (Fe 1.6)
Alloy 625 cladding	21	64	8.5	0.4	Al 0.03, C 0.01, Ti 0.21, (Fe 1.0)
Hastelloy C-22	21.5	56	13.0	0.25	C 0.004, Co 1.4, Si 0.03, V 0.12, W 3.2 (Fe 3.8)
C-276	15.5	55	15.7	0.5	C 0.003, Co 1.2, V 0.2, W 3.50 (Fe 5)
C-2000	23	59	15.5	0.25	Al 0.24, C 0.007, Cu 1.53, Si 0.06 (Fe 1.2)

9th Liege Conference : Materials for Advanced Power Engineering 2010
edited by J. Lecomte-Beckers, Q. Contrepois, T. Beck and B. Kuhn.

FIRESIDE CORROSION OF SUPERHEATERS/REHEATERS IN ADVANCED POWER PLANTS

A U Syed, N J Simms and J E Oakey

Energy Technology Centre, Cranfield University, Cranfield, MK43 0AL, UK

Abstract

The generation of increasing amounts of electricity while simultaneously reducing environmental emissions (CO_2, SO_2, NO_x particles, etc) has become a goal for the power industry worldwide. Co-firing biomass and coal in new advanced pulverised fuel power plants is one route to address this issue, since biomass is regarded as a CO_2 neutral fuel (i.e. CO_2 uptake during its growth equals the CO_2 emissions produced during its combustion) and such new advanced power plants operate at higher efficiencies than current plants as a result of using steam systems with high temperatures and pressures. However, co-firing has the potential to cause significant operational challenges for such power plants as amongst other issues, it will significantly change the chemistry of the deposits on the heat exchanger surfaces and the surrounding gas compositions. As a result these critical components can experience higher corrosion rates, and so shorter lives, causing increased operational costs, unless the most appropriate materials are selected for their construction.

This paper reports the results of a series of 1000 hour laboratory corrosion tests that have been carried out in controlled atmosphere furnaces, to assess the effect of biomass/coal co-firing on the fireside corrosion of superheaters/reheaters. The materials used for the tests were one ferritic alloy (T92), two austenitic alloys (347HFG and HR3C) and one nickel based alloy (alloy 625). Temperatures of 600 and 650 °C were used to represent the metal temperatures in advanced power plants. During these exposures, traditional mass change data were recorded as the samples were recoated with the simulated deposits. After these exposures, cross-sections through samples were prepared using standard metallographic techniques and then analysed using SEM/EDX. Pre-exposure micrometer and post-exposure image analyser measurements were used so that the metal wastage could be calculated. These data are being used for the development of statistical models to predict the lifetimes of candidate materials for use in superheaters/reheaters in the advanced power plants.

Keywords: fireside corrosion; superheaters/reheaters; biomass/coal co-firing

1. Introduction

It is anticipated that increasing amounts of energy will be needed around the world; for example, the IEA predictions indicate a 40% rise in primary energy demand by 2030 [1]. In addition, there are significant pressures on the power generating industries to reduce their environmental emissions (CO_2, SO_2, NO_x particles, etc), increase the efficiency of power production and use more sustainable fuels. One route to tackle these challenges is the development of advanced pulverised fuel power plants that can generate electricity more efficiently by using higher temperature/pressure steam systems, as well as being able to use a much wider range of fuels and fuel mixes that include coals, biomass and waste products [2-4]. The term biomass is used to cover a wide range of potential fuels that arise from the growth of various forms of vegetation and can include: specifically grown energy crops (e.g. willow and miscanthus in the UK); agricultural wastes (e.g. various straws); forestry residues, etc [3]. Biomass is classified as a sustainable and CO_2 neutral fuel (as the CO_2 uptake during its growth equals the CO_2 emissions produced during its combustion). Co-firing coal and biomass in advanced pulverised fuel power plants offers the most efficient use of biomass to generate electricity, as such plants operate at much higher efficiencies than power plants firing biomass alone [5].

Compared to firing coal alone, co-firing coal and biomass can cause significant changes in the chemistry of the combusted gas stream and the deposits that form on the surfaces of heat exchangers, which can in turn lead to increased corrosion damage to the heat exchangers. As increased corrosion damage rates will lead to shorter component lives and more boiler shut-downs for either routine maintenance or due to unexpected tube failures, this effect of biomass co-firing has become a challenge for power plant designers and operators in terms of selecting (or developing) materials for the use in heat exchangers in these power plants.

The desired increases in the operating temperatures/pressures of steam systems for advanced power plants will have the effect of increasing the metal temperatures of the final stage steam superheaters and reheaters [2-4]. These increased metal temperatures result in several challenges: the need for materials with creep strength at higher temperatures; increased steamside oxidation damage rates; increased fireside corrosion damage rates [2-4]. These different factors also result in the need for careful selection of materials for use in these heat exchangers, but with a different balance of properties.

It is believed that fireside corrosion of superheater/reheater tubes is the result of a complex series of processes that can involve: (a) the formation of molten deposits (including various sulphate and/or chloride species) on their surfaces and the reaction between the tube materials, these deposits and the surrounding flue gases at high temperature; and/or (b) the reaction of chloride species with the tube materials to produce volatile metal chlorides [5-15]. Some detailed reaction pathways have been suggested [e.g. 6, 7, 14] and others are currently being developed, but all depend critically on the composition of the fuel(s) entering the power plant, the heat exchanger operating conditions (especially the metal surface temperature) and the heat exchanger material(s). As an illustration of the differences between the fuels, biomass fuels, especially ones resulting from rapid growth, tend to have higher levels of readily volatised potassium and chlorine than coals; this can result in the formation of more aggressive deposits on superheater/reheater tube surfaces. But the effects also depend on the fuel mixtures used: experienced gained in existing co-fired plants (with lower temperature/pressures steam systems, 560°C/160bar) suggest that the use of 5% (by energy) of biomass does not cause significant problems and that the use of up to ~20% of some biomass may be possible [5, 14].

This paper reports the results of an investigation into the fireside corrosion behaviour of a range of candidate superheater / reheater materials at metal temperatures of 600 and 650°C in gas/deposit environments targeted at a UK coal-biomass fuel mix. This work was carried out using the 'deposit recoat' technique that has been established for high temperature corrosion. Data generated during these exposures, and from the examination of samples after their exposure, has been used to confirm that typical fireside corrosion occurs under the exposure conditions generated. The performance of the materials has been determined in terms of metal loss distributions. These data will be used in an on-going programme that is developing mathematical models of the fireside corrosion of different candidate materials as part of an assessment of the potential lives of heat exchangers in advanced power generating systems.

2. Experimental Detail

Four candidate heat exchanger alloys were used in this study (compositions are given in Table 1). Samples of each of these materials were machined from commercial tubes in the form of

tube segments; all of the samples had cord lengths and heights of 15 mm, with thickness in line with the original tube wall thicknesses (typically 4 mm). All surfaces of these tubes were finished to 600 grit (R_a <0.4 μm). Before use the samples were all cleaned in an ultrasonic bath for 20 minutes in (a) volasil followed by (b) isopropyl alcohol (IPA). The dimensions of each sample were measured using a digital micrometer with a resolution of ±0.001mm.

Table 1 Nominal compositions of materials used in fireside corrosion testing

Material	Nominal composition (weight %)									
	C	Si	Mn	P	S	Cr	Mo	Ni	Fe	Others
T92	0.13	≤0.5	≤0.6	≤0.02	≤0.01	9.5	0.6		Bal	0.25 V; 2 W; 0.09 Nb; 0.07 N
347HFG	0.08	≤0.5	≤2	≤0.045	≤0.03	17-19		9-13	Bal	Nb, Ta
HR3C	0.1	0.75	≤2	≤0.04	≤0.04	25		20	Bal	0.4 Nb; 0.2 N
Alloy 625	0.1	≤0.5	≤0.5	≤0.015	≤0.015	20-23	8-10	Bal	5	1 Co; 0.4 Al

The corrosion tests were carried out in vertical controlled atmosphere furnace systems (Figure 1). These alumina lined furnaces are designed to accommodate 24 alumina crucibles (containing the samples) that sit in an alumina frame. The gas mixture required to simulate the power plant environment around superheaters/reheaters was achieved by mixing gases from three pre-mixed gas bottles using mass flow controllers. In this series of tests, the target gas composition (Table 2) represents that produced by a UK coal co-fired with 20 weight % cereal co-product (CCP) [13]. Four synthetic deposits were used on different samples of each of the candidate materials; these were prepared with different compositions to simulate the deposits on superheaters/reheaters (Table 3). The deposits were applied by adding a little isopropyl alcohol (IPA) to the mixed powders to form thick slurries that could be painted onto the samples, which were then allowed to dry to produce deposit loadings of ~20 mg/cm^2. The corrosive hot gases coming out from the furnace were neutralised by passing them through a scrubber of NaOH solution and vented. The temperature and time for each exposure cycle was set using the furnace control unit.

Table 2
Gas composition used in fireside corrosion tests

Gas No.	Nominal gas composition					
	N_2	O_2	CO_2	H_2O	SO_2	HCl
	%	%	%	%	vpm	vpm
1	Balance	4	14	8	1300	400

Table 3
Deposit composition used in fireside corrosion tests

Deposit No.	Nominal deposit compositions (mole %)				
	Kaolinite*	Na_2SO_4	K_2SO_4	KCl	Fe_2O_3
D0	-	-	-	-	-
D1	-	37.5	37.5		25
D2	80	7.5	7.5		5
D3	80	7	7	1	5
D4	80	5	5	5	5

* $Al_2O_3.2SiO_2.2H_2O$

Each test was designed to run for 1000 hours, in order to generate accurate metal loss data for the best performing alloy(s), with five cycles of 200 hours. After each cycle, the samples

were unloaded from the furnace, weighed in their individual crucibles and weighed alone. After the weight measurements, the samples were recoated with the same deposit compositions and loadings, before being weighed again in their crucibles and loaded back into the furnace for another cycle. After the final cycle, samples and crucibles were weighed again, before the samples were examined. The surfaces of selected samples were examined using scanning electron microscopy (SEM) and energy dispersive X-ray (EDX) analysis, to determine the morphology and chemical composition of their surfaces. Polished cross-sections were prepared through the centre of all the samples using standard metallographic techniques (i.e. mounting, cutting, grinding and polishing). These cross-sections were all measured using an image analyser to generate accurate measurements of the amount of metal remaining after the corrosion tests; these measurements were compared to the pre-exposure metal thickness data to produce distributions of metal losses required for the development of fireside corrosion damage models. SEM/EDX examinations of the cross-sections were also carried out to characterise the fireside corrosion damage morphologies for each of the alloys under the different test conditions.

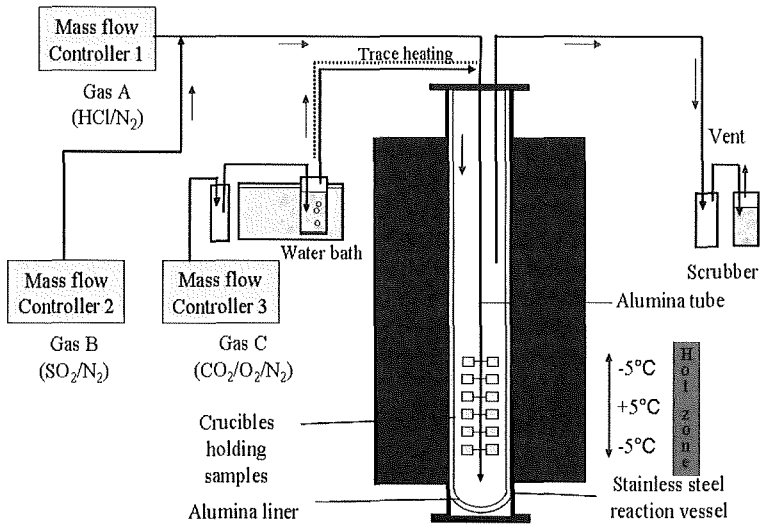

Figure 1 Schematic diagram of a vertical controlled atmosphere furnace

3. Results and Discussion

3.1. Mass change Data

Examples of the mass change data are given in Figure 2, in terms of cumulative net specific mass changes (i.e. the sum of the mass change per unit area occurring during the furnace exposures). This figure uses the data generated for bare and deposit coated T92, but all the material/deposit combinations exposed behaved differently. These mass changes are the combined effect of the reaction of the alloys and deposits with the surrounding gases, which can include oxide growth, deposit/scale spallation, deposit evaporation, etc. As expected, going from 600 to 650 °C, higher mass changes were found at the higher temperature [e.g. 6, 10, 14]. For T92, the change in temperature approximately doubled the mass change for the bare alloy and most of the deposits. The most aggressive deposit was found to be D1 in all

cases. The composition of this deposit (Table 3) was intended to ease the formation of alkali iron trisulphates, which are believed to be one of the possible causes of fireside corrosion damage to materials under superheater/reheater operating conditions [6]. The other deposits all contained alkali and iron compounds in the same ratio as for D1, but at lower concentrations (effectively resulting in a reduced deposition flux of these species).

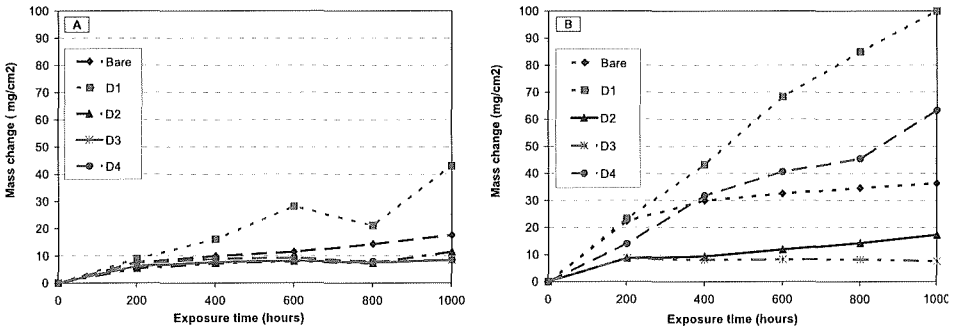

Figure 2 Mass change data for T92, bare and coated with the four synthetic deposits exposed to the simulated combustion gases for 1000 hours at (a) 600 and (b) 650 °C

3.2. SEM/EDX Analysis

3.2.1 Surface analysis

Figure 3 shows the surface morphology of the bare alloys T92 and HR3C prior and following the corrosion test at 650°C. Typical oxide growth morphologies were observed for both of these alloys. For T92 (a ferritic steel), threadlike growths were observed together with large nodular growths, where as for HR3C (an austenitic steel), finer scale oxides were formed, some with more crystalline morphologies.

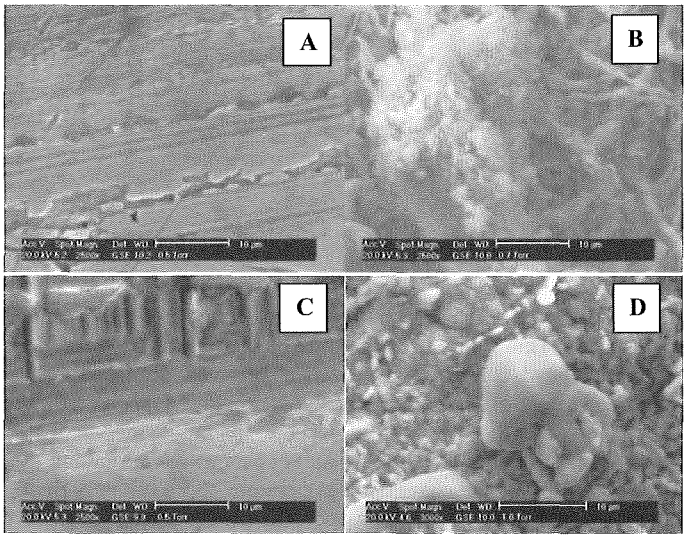

Figure 3
SEM images of alloy T92 prior (A) and after (B) HR3C prior (C) and after (D) exposed to the simulated combustion gases at 650°C for1000 hours

3.2.2 Oxidation of bare alloys

Figure 4 illustrates the thick multi-layered metal oxides formed during the exposure of bare T92 during these exposures. As expected the higher exposure temperature has caused thicker oxide layers to form. These thicker oxides show a tendency for their outer layers to spall, but for the inner compact spinel layer to remain adherent with no sign of internal oxidation within the alloy beneath it.

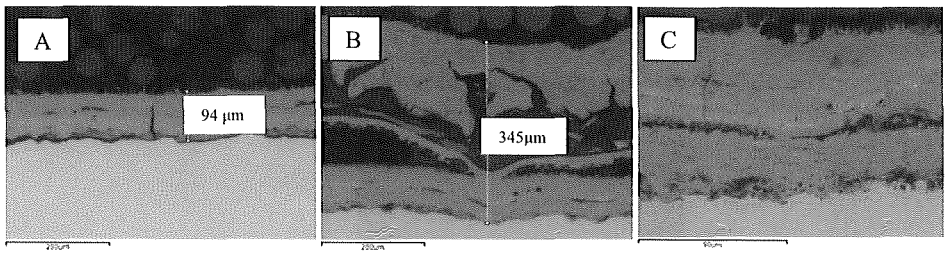

Figure 4 BSE image of bare alloyT92 cross-section exposed to the simulated combustion gases for 1000 hours at (A) 600, (B) 650 and (C) 650°C (at higher magnification)

Figure 5 illustrates the oxide scales formed on bare HR3C and 347HFG after exposure at 650°C for 1000 hours. Thick multi-layered oxides have formed on both of these materials, with internal attack beneath them on both within alloy grains and along their boundaries. This is consistent with previous observations of damage to austenitic alloys in combustion gas environments [14]. The damage observed on these materials in less than that found on the lower Cr content ferritic T92 alloy.

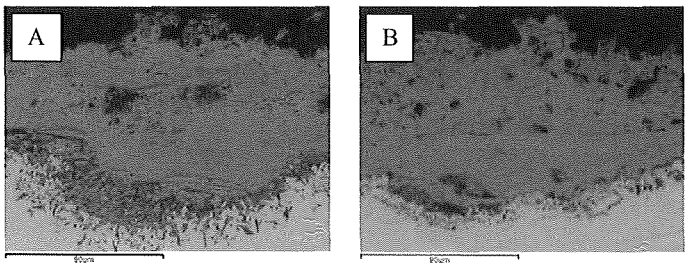

Figure 5 BSE image of bare alloys HR3C (A) 347HFG (B) cross-sections exposed to simulated combustion gases at 650°C for1000 hour

3.2.3 Deposits and corrosion products

The effect different deposit compositions have on the fireside corrosion of T92 samples at 650°C is illustrated in Figure 6. The most aggressive deposit was found to be D1 (in agreement with the mass change data), which has caused the formation of thick layers of oxides/deposit; this deposit had the highest concentration of alkali sulphate/iron oxide in it (Table 3). Deposit D2 had the same ratio between these deposit components, but diluted by a clay mineral (kaolinite); the effect was to greatly reduce the amount of damage to the material. Deposit D3 (adding 1% KCl to the deposit mix) produced similar results to deposit D2. Deposit D4 (with 5% KCl) produced more damage than D2 and D3, but less than that observed with D1. Increased corrosion damage due to high levels of KCl in deposits has often been reported previous, and has been related to the formation of volatile metal chloride species [e.g. 14, 15]. The deposits in the current study have compositions that range from sulphate to sulphate/chloride mixes and so are expected to show fireside corrosion damage as a result of a mix of sulphate and chloride related mechanisms.

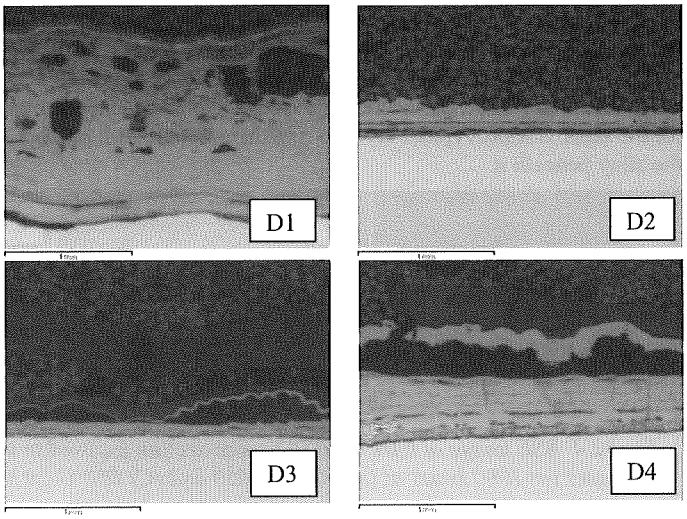

Figure 6
BSE images of oxide / deposit layers on T92 after exposure with four deposits to simulated combustion gases at 650°C for1000 hours

An example of EDX mapping of a cross-section through a T92 sample exposed with deposit D1 is given in Figure 7 (with backscattered image of this sample given in Figure 6). These maps show the distribution of oxygen throughout the oxide/deposit. Chromium is located in the spinel oxide layer close to the alloy. Both sodium and potassium are concentrated towards the surface of the oxide/deposit mix and are present at lower levels deeper into these layers. Sulphur shows a concentration distribution that similar to the alkali metals, but in addition, there is a further concentration in patched at the alloy/oxide interface.

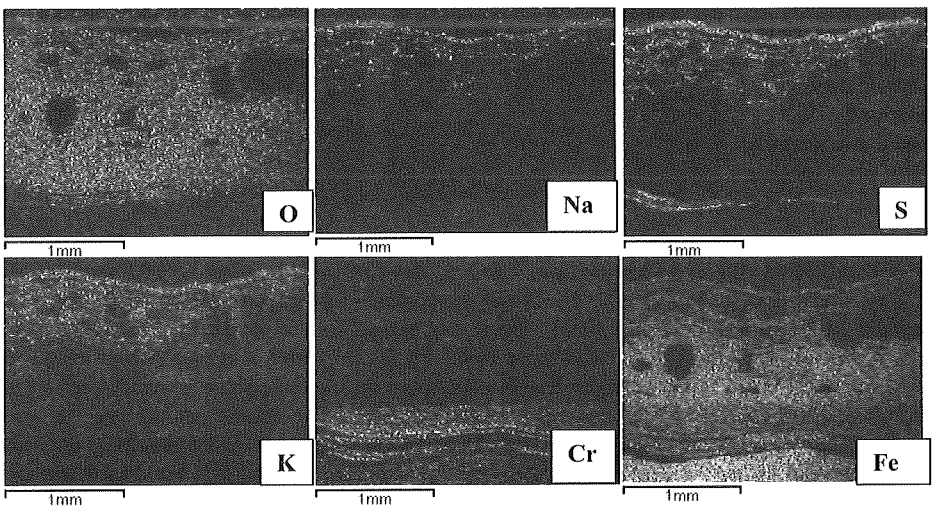

Figure 7 EDX mapping of cross-section through T92 after exposure covered in deposit D1 to simulated combustion gases at 650°C for 1000 hours

3.3. Dimensional Metrology

The polished cross-sections were all measured using an image analyser to generate accurate measurements of the amount of metal remaining after the corrosion tests; these measurements were compared to the pre-exposure metal thickness data to produce distributions of the change in metal resulting from the exposures. Figures 8-10 illustrate some of the datasets produced by plotting the change in metal as a function of cumulative probability.

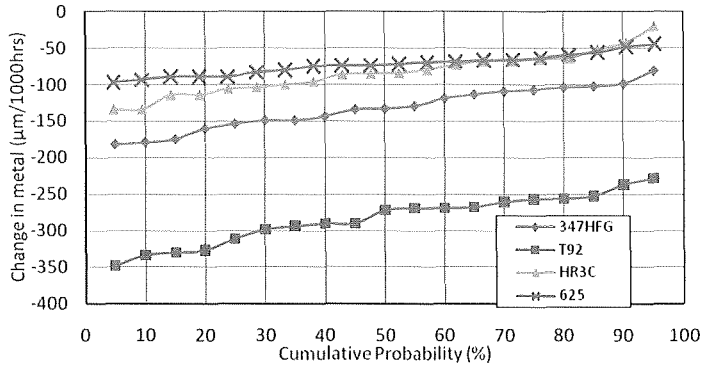

Figure 8
Change in metal versus cumulative probability showing the behaviour of different alloys covered with deposit D1 exposed to simulated combustion gases at 600°C for1000 hours

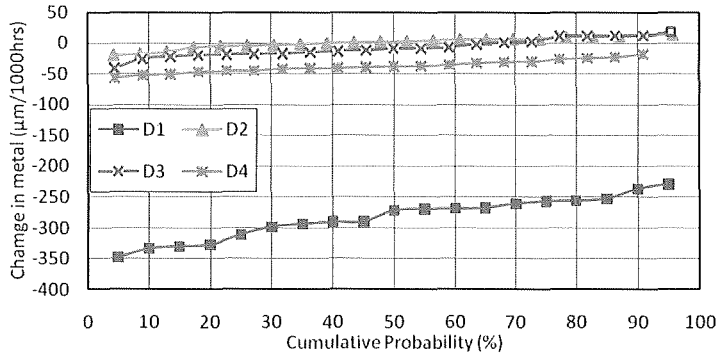

Figure 9
Change in metal versus cumulative probability showing the behaviour of alloy T92 covered with the four different deposits exposed to simulated combustion gases at 600°C for1000 hours

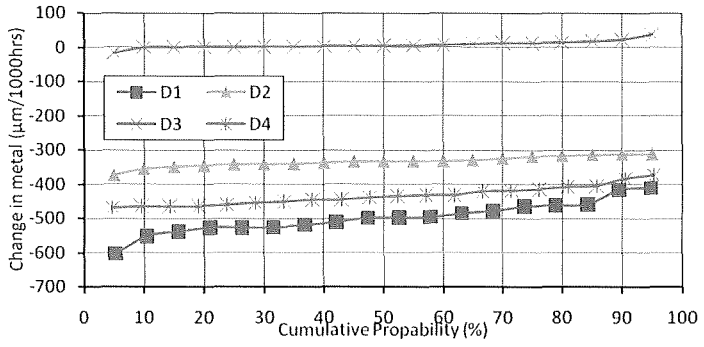

Figure 10
Change in metal versus cumulative probability showing the behaviour of alloy T92 covered with the four different deposits exposed to simulated combustion gases at 650°C for1000 hours

Figure 8 illustrates the damage distributions of the four alloys after exposure at 600°C for 1000 hours covered with deposit D1 in simulated combustion gases. From these data the performance of the materials under these conditions may be ranked (most damage to least):

T92 > 347HFG > HR3C > alloy 625. Thus the ranking follows the trend in alloy chromium content (Table 1). However, under these exposure conditions the damage to all the materials is excessive compared to traditional targets for superheater lives in coal-fired power systems (~40-50 μm/1000 hours). Figures 9 and 10 illustrate the performance of T92 with the four different deposits after 1000 hours exposure in the simulated combustion gases at 600 and 650°C, respectively. At 600°C, the corrosion damage of the two more realistic deposits for coal-fired systems (D2 and D3) are at relatively low levels, with D4 (representing a higher level of biomass co-firing) showing a higher level of damage, but still much lower than that found for the deposit D1 (which is commonly used in screening trials). As expected [e.g. 6-8, 10, 14], the level of fireside corrosion damage increases with temperature from 600 to 650°C (it is still below the often reported peak in the bell-shaped dependence of fireside corrosion on temperature). With deposit D1 the level of corrosion damage has approximately doubled with this change in temperature. However, for deposits D2 and D4 the change is more significant and the levels of damage that they cause have moved towards that found for deposit D1 (though are still significantly lower). Again samples covered with D1 exceed the traditional targets for metal loss for T92 at both temperatures. The other deposits all produce damage levels below targets at 600°C for T92, but only deposit D3 gives a rate below target at 650°C.

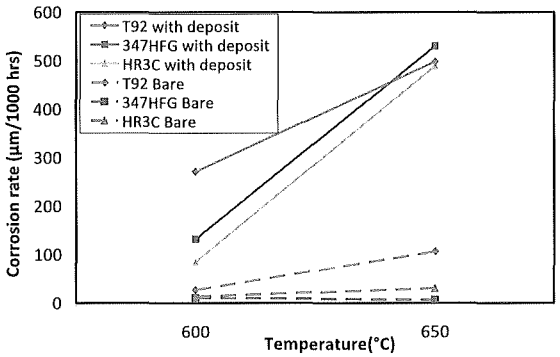

Figure 11
Comparison of the median corrosion damage to the alloys (bare or covered in deposit D1) after exposure in the simulated combustion gases at 600 and 650°C for 1000 hours.

Figure 11 shows a comparison in the behaviour observed for alloys T92, 347HFG and HR3C with no deposit (i.e. bare) and covered with deposit D1 at 600 and 650°C (using the median corrosion damage data). These data clearly show that deposit D1 produces much more damage than found on the samples with no deposit at both temperatures. At 600°C, the trend in alloy behaviour is the inverse of the alloy chromium content (i.e. lowest chromium content correlates to highest corrosion damage) for the alloys with and without the presence of that deposit. At 650°C, this is also observed for the bare samples, but when coated with deposit D1 all the alloys were found to similar high levels of corrosion damage. The increase in corrosion damage between 600 and 650°C is consistent with upward slope of the often reported 'bell-shaped' curve for sulphate dominated fireside corrosion damage [6].

4. Conclusions

Fireside corrosion of superheater/reheater tubes is a major concern for the operation of power plants using high levels of biomass co-fired with coal and for power plants using advanced steam conditions. This paper reports the results of a series of 'deposit recoat' fireside corrosion exposures that have been carried out for 1000 hour at 600 and 650°C under conditions targeted at simulating exposure conditions (gas composition, deposit compositions and deposition fluxes) anticipated for specific biomass-coal fuels and mixes. The results show

that under most exposure conditions the fireside corrosion performance of the materials can be ranked inversely to their chromium contents. At 600°C, the corrosion damage produced by the two more realistic deposits for coal-fired systems (D2 and D3) was at relatively low levels, with D4 (representing a higher level of biomass co-firing) showing a higher level of damage, but still much lower than that found for the deposit D1 (an aggressive alkali sulphate/iron oxide mix which is commonly used in screening trials). At 650°C, higher levels of damage were produced by all the deposits, as well as bare materials. The distributions of metal damage produced by these tests under specific well characterised and controlled exposure conditions are being used in other on-going future work to develop models of fireside corrosion damage.

5. Acknowledgements

This research has been funded by the UK Engineering & Physical Sciences Research Council (EPSRC) through its SUPERGEN project on 'Conventional Power Plant Lifetime Extension'.

6. Reference

[1] IEA World Energy Outlook (2009)
[2] J E Oakey, L W Pinder, R Vanstone, M Henderson, & S Osgerby, Review of Status of Advanced Materials for Power Generation, COAL R224, DTI/Pub URN 02/1509 (2003)
[3] N J Simms, P J Kilgallon & J E Oakey, 'Fireside Issues in Advance Power Generation Plant', *Parsons 2007: Power Generation in an Era of Climate Change*, pp603-614 (2007)
[4] J Stringer, 'High temperature corrosion issues in energy-related systems, *Materials Research*, 7 (1), pp 1-19 (2004)
[5] N J Simms, P J Kilgallon & J E Oakey, 'Degradation of Heat Exchanger Materials under Biomass Co-firing Conditions', *Mat. at High Temperatures*, 24 (4), pp 333-342 (2007)
[6] J Stringer & I G Wright, 'Current limitations of high-temperature alloys in practical applications', *Oxidation of Metals*, 44 (1-2), pp 265-308 (1995)
[7] A Hendry and D J Lees, 'Corrosion of austenitic steels in molten sulphate deposits', *Corrosion Science*, 20 (3), pp 383-404 (1980)
[8] D B Meadowcroft, 'High temperature corrosion of alloys and coatings in oil-and coal-fired boilers', *Materials Science and Engineering*, 88, pp 313-320 (1987).
[9] S C Srivastava, K M Godiwalla and M K Banerjee, 'Fuel ash corrosion of boiler and superheater tubes', *Journal of Materials Science* (UK), 32 (4), pp 835-849. (1997),
[10] K Natesan and J H Park, 'Fireside and steamside corrosion of alloys for USC plants', *International Journal of Hydrogen Energy*, 32 (16), pp 3689-3697 (2007)
[11] R Viswanathan and W Bakker, 'Materials for Boilers in Ultra Supercritical Power Plants', *2000 International Joint Power Generation Conference*, Florida, USA (2000)
[12] I G Wright et al, 'Progress in prediction and control of oxide scale exfoliation on superheater and reheater alloys', *Proc. 4th Int. Conf. on Boiler Tube & HRSG Tube Failures & Inspections*, California, USA (2004)
[13] N J Simms, P J Kilgallon & J E Oakey, 'Heat Exchanger Corrosion in Biomass & Coal Co-fired Power Plants', *Materials for Advanced Power Eng. 2006*, pp 1513-1522 (2006)
[14] M Montgomery, T Vilhelmsen & S A Jensen, 'Potential high temperature corrosion problems due to co-firing of biomass & fossil fuels', *Materials & Corrosion*, 59 (10), pp. 783-793 (2008)
[15] H P Michelsen, F Frandsen, K Dam-Johansen, & O H Larsen, O. H. "Deposition & high temperature corrosion in a 10 MW straw fired boiler", *Fuel Processing Technology*, 54 (1-3), pp 95-108 (1998)

9th Liege Conference : Materials for Advanced Power Engineering 2010
edited by J. Lecomte-Beckers, Q. Contrepois, T. Beck and B. Kuhn.

MODELLING OF DEGRADATION PROCESSES IN CREEP RESISTANT STEELS THROUGH ACCELERATED CREEP TESTS AFTER LONG-TERM ISOTHERMAL AGEING

V. Sklenička[1], K. Kuchařová[1], M. Svoboda[1], A. Kroupa[1], L. Kloc[1] and J. Čmakal[2]

[1]Institute of Physics of Materials, Academy of Sciences of the Czech Republic,
CZ-616 62 Brno, Czech Republic
[2]UJP PRAHA a.s., CZ-156 10 Praha-Zbraslav, Czech Republic

Abstract

Creep behaviour and degradation of creep properties of creep resistant materials are phenomena of major practical relevance, often limiting the lives of components and structures designed to operate for long periods under stress at elevated and/or high temperatures. Since life expectancy is, in reality, based on the ability of the material to retain its high-temperature creep strength for the projected designed life, methods of creep properties assessment based on microstructural evolution in the material during creep rather than simple parametric extrapolation of short-term creep tests are necessary. In this paper we will try to further clarify the creep-strength degradation of selected advanced creep resistant steels. In order to accelerate some microstructural changes and thus to simulate degradation processes in long-term service, isothermal ageing at 650°C for 10 000 h was applied to P91, P92 and P23 steels in their as-received states. The accelerated tensile creep tests were performed at temperature 600°C in argon atmosphere on all steels both in the as-received state and after long-term isothermal ageing, in an effort to obtain a more complete description of the role of microstructural stability in high temperature creep of these steels. Creep tests were followed by microstructural investigations by means of both transmission and scanning electron microscopy and by the thermodynamic calculations. The applicability of the accelerated creep tests was verified by the theoretical modelling of the phase equilibria at different temperatures. It is suggested that under restricted oxidation due to argon atmosphere microstructural instability is the main detrimental process in the long-term degradation of the creep rupture strength of these steels.

Keywords: creep resistant steels, creep, isothermal ageing, accelerated creep tests, degradation processes

1. Introduction

The designed lives of steam power plant components are based on material properties which are usually those of virgin material together with specified operating conditions. However, the actual material properties may differ due to ageing, and plant operating conditions may be changed to meet an unanticipated need. Thus, it is important to realize that the efforts to obtain high-quality databases of relevant creep properties for design at high temperatures will be costly and time-consuming. Accordingly, it will be necessary to make the most appropriate use of accelerated methods [1-3] where possible. Also modelling methods which allow predicting materials performance in creep will enable testing to be targeted on the most critical conditions, thereby reducing the overall size and cost of creep tests.

Creep-resistant ferritic steels, used for large components such as turbines and boilers, are recognized as the key materials to increase the thermal efficiency of stream power plants. In the last three decades, a number of new low alloy and 9-12%Cr steels with improved creep strength have been developed for long-term service at temperatures up to 600°C and above in high-temperature parts of boilers, steam lines and turbines of ultra supercritical power plants [4,5]. High-temperature exposures may lead to appreciable changes in microstructure which

can change creep strength [6]. Thus, for the long-term application of the new steels, it is necessary to assess the microstructural changes that are likely to occur during service exposure and evaluate the effect of such changes on the high-temperature creep behaviour. Only with this information the design values for components can be correctly assigned.

In this paper we will try to further clarify the creep property deterioration of selected advanced ferritic creep-resistant steels during long-term isothermal ageing, that can be related to microstructural changes arising from such exposure. The standard tensile creep tests were performed on selected steels in their as-received states and after long-term isothermal ageing in an effort to obtain a more complete description of the role of microstructural stability in high-temperature creep of these steels. Creep tests were followed by microstructural investigations by means of electron microscopy and by the thermodynamic modelling.

2. Experimental materials and procedures

The microstructure and creep properties of two ferritic-martensitic 9%Cr steels (P91 and P92) and one low-alloy steel (P23), developed for advanced coal-fired power plants, have been selected and investigated.

The P91 steel, a tempered martensitic-ferritic steel produced by Vitkovice Steel, Czech Republic, was subjected to the two-stage heat treatment: 1060°C/1 h/air+750°C/2 h/air. Its chemical composition (in wt.%) was 0.09 C, 0.56 Mn, 0.20 Si, 0.021 P, 0.009 S, 0.05 Cu, 0.46 Ni, 8.36 Cr, 0.86 Mo, 0.20 V, 0.06 Nb, 0.065 N and 0.007 Al. The P92 steel was produced by Nippon Steel, Japan, received in the form of a seamless pipe with the following heat treatment: 1065°C/2 h/air + 770°C/2 h/air. Its chemical analysis (in wt.%) was 0.08 C, 9.0 Cr, 0.5 Mo, 1.8 W, 0.2 V, 0.06 Nb, 0.05 N, 0.003 B and < 0.04 Al. The low-alloy bainitic steel P23 was produced by Wakayama Steel Kainan Works, Japan, with the following chemical composition (in wt.%): 0.06 C, 0.28 Si, 0.28 Mn, 0.02 P, 0.003 S, 2.24 Cr, 0.09 Mo, 0.0055 B, 0.006 N, 1.49 W and 0.04 Nb. The steel was received in the form of a pipe ϕ380 x 8 mm with the following heat treatment: 1045°C/10 min/air + 770°C/60 min/air. Creep is a structure sensitive property and therefore depends on microstructural condition of the material. The microstructural condition of the service exposed material was simulated by accelerated long-term isothermal ageing carried out at 650°C for 10 000 h.

All concerned steels were investigated both in the as-received state (i.e. after heat treatment) and after isothermal annealing at 650°C for 10 000 h. For convenience the as-received and the annealed states of the investigated steels will be designated in Figs. 1-3 as A and B, respectively.Standard constant load uniaxial tensile creep tests were carried out in argon using the flat creep specimens at temperature 600°C with the testing temperature continuously monitored and maintained constant to within ± 0.5°C of the desired value [7]. The applied tensile stresses ranged from 50 to 400 MPa. The creep elongations were measured using a linear variable differential transducer (the strain was measured with a sensitivity of 5 x 10^{-6}) and they were continuously recorded digitally and computer processed. All creep specimens were run to final fracture.

Following creep testing samples were prepared for microstructure examination by means of both transmission and scanning electron microscopy. Transmission electron microscopy (TEM) studies were carried out on carbon extraction replicas and thin foils prepared from

head and gauge part of crept specimens using a Philips CM12 TEM/STEM microscope equipped with EDAX Phoenix system. Particles of secondary phases extracted into carbon replicas were identified by means of selected area diffraction (SAED) and their local chemical composition was measured by energy dispersive X-ray spectroscopy (EDS) using 10-nm probe size and thin sample approximation. The measured metallic element content was recalculated assuming stoichiometric carbon content for the carbides. The fracture surfaces were investigated in scanning electron microscope (SEM) Jeol 6460. Experimental results of secondary phase particles analyses were compared with the results of equilibrium thermodynamic calculations using the computer programme Thermocalc [8] and thermodynamic database STEEL16 [9].

3. Results and Discussion

3.1. Creep results

Figure 1 shows selected standard creep curves for steels P91, P92 and P23 for uniaxial tensile creep tests conducted at 600°C. As demonstrated in the figure, significant differences were found in the creep behaviour of the steels in the as-received state (A) when compared with their behaviour after ageing. First, the standard ε vs. t curves appear to show that long-term isothermal ageing of the steels leads to an increase in the creep plasticity, which is proved, in particular, by the values of the total strains to fracture for the aged steels. Second, the aged steels exhibit markedly shorter times to fracture than the steels in the as-received state. Third, the shapes of creep curves for both the as-received state and the aged state of the steels differ considerably. Thus, the occurrence of primary and secondary stages followed by a tertiary stage of creep in the as-received state is in striking contrast to the nature of the creep curves in the aged state.

In Fig. 2, the minimum creep rates $\dot{\varepsilon}_m$ are plotted against the applied stress σ on a logarithmic scale. Examination of Fig. 2 leads to two observations. First, the steels in the as-received state exhibit better creep resistance than those after long-term ageing over the entire stress range used. The minimum creep rate for steel P91 in the as-received state is about one order of magnitude less than that for the aged P91 steel under the same creep loading. Similarly the difference in the minimum creep rate between as-received and aged state is about two order of magnitude for steel P23.

It should be noted, that the dependence of $\dot{\varepsilon}_m(\sigma)$ for various states may have different trends. While the slope and therefore the apparent stress exponents of creep rate $n = (\partial \ln \dot{\varepsilon} / \partial \ln \sigma)_T$ are the same for all steel P91 samples, the slope and the stress exponent n for steel P92 depend on its state; the difference in $\dot{\varepsilon}_m$ between as-received and aged state increases with decreasing applied stress. Furthermore, the slopes and therefore the apparent stress exponents n for steel P23 depend strongly on the applied stress. The evaluated high values of the stress exponent n of creep rate ($\dot{\varepsilon}_m \alpha A \sigma^n$) for P91, P92 and P23 steels indicate that all creep tests were performed in the region of the power-law or dislocation creep.

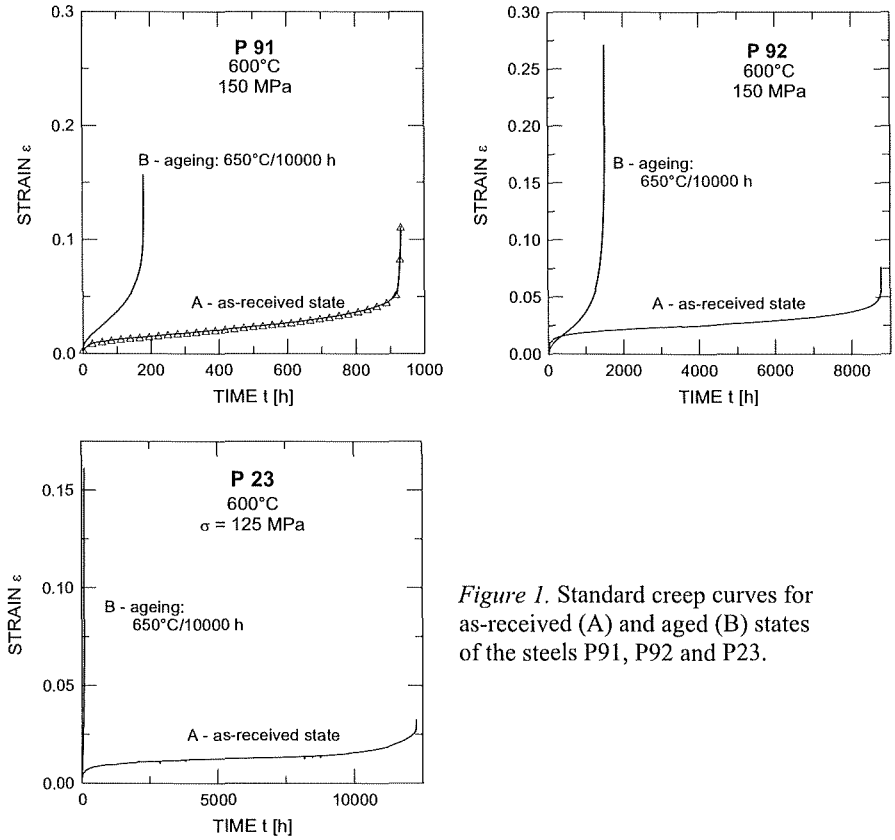

Figure 1. Standard creep curves for as-received (A) and aged (B) states of the steels P91, P92 and P23.

For all steels, the double logarithmic plots of the time to fracture t_f as a function of applied stress are shown in Fig. 3. It is clear from these plots that the creep life of steels in as-received state is considerably longer than that in aged state. While the difference for steel P91 is independent of applied stress, for P92 and P23 steels this difference consistently decreases with increasing applied stress (for P92 steel with a tendency at the higher stresses towards no effect of the state of steel on the lifetime). The evaluated stress exponents m of creep life ($t_f \alpha B\sigma^{-m}$) are very similar to the values for stress exponent n. This can be explained by the fact, that both the creep deformation and fracture are controlled by the same mechanism.

3.2. Thermodynamic modelling and microstructural investigations

At present we are still some distance from a more complete description and understanding of significant microstructural features and deformation mechanisms responsible for the enhanced creep strength of advanced creep-resistant steels in dislocation (power-law) creep. The movement of dislocations through the matrix is at first resisted by (a) the dislocation substructure distribution (dislocation strengthening mechanism), (b) intragranular particles, mainly MX (particle strengthening), and (c) the strain fields associated with elements in solid

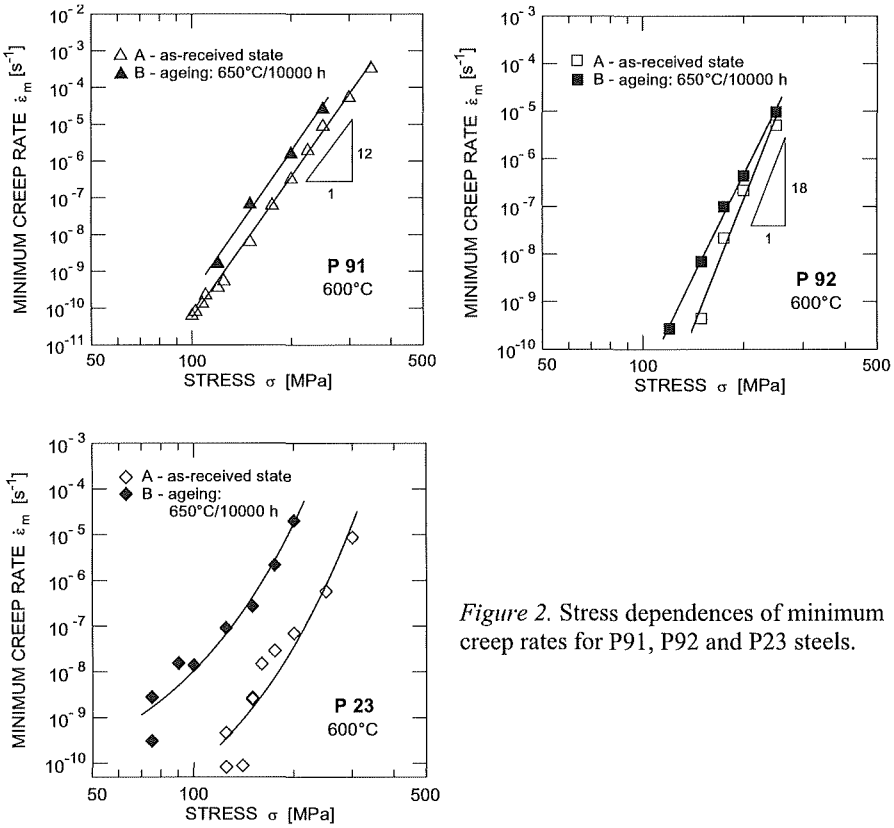

Figure 2. Stress dependences of minimum creep rates for P91, P92 and P23 steels.

solution (solid solution strengthening). As creep progresses the dislocation substructure changes to form subgrains whose boundaries are stabilized by $M_{23}C_6$ and MX particles and possibly also by Laves phases. However, as these particles form and coarsen they denude the surrounding matrix of elements in solid solution, thus reducing the contribution of solid solution strengthening to creep resistance. Thus it seems likely that, as these changes progress, creep resistance becomes less and less dependent on resistance to the movement of individual dislocations through the matrix and more and more dependent on the resistance to subgrain growth through boundary migration [6].

Modelling of long-term precipitate stability should include predictions of phase stability, nucleation rates, growth rates and coarsening rates for precipitate phases as a functions of chemical composition, temperature and stress [10]. The CALPHAD type calculations provide useful guidelines for the evaluation of the stable phases in the steel under investigation based only on their chemical composition. These thermodynamic calculations may be fundamental to the predictions of long-term stability of precipitate particles. Series of equilibrium phase diagrams, which show the calculated equilibrium mole fractions of coexisting phases as a

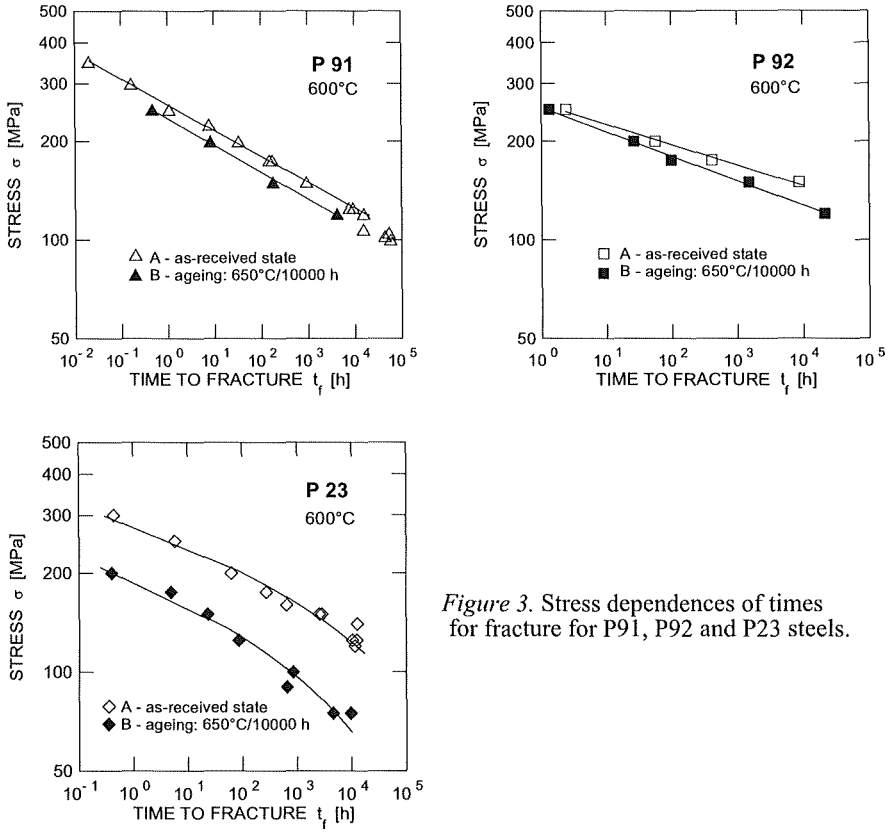

Figure 3. Stress dependences of times for fracture for P91, P92 and P23 steels.

function of temperature have been produced giving useful information for possibility to accelerate some microstructural changes and thus to simulate long-term service conditions by isothermal ageing. Fig. 4 shows such diagrams for P91, P92 and P23 steels. Accordingly to the thermodynamics calculations, ferrite, $M_{23}C_6$, MX, Z-phase and Laves phase are equilibrium phases for P91 and P92 steels at temperatures of interest. While the amounts of $M_{23}C_6$, Z-phase and MX phases are relatively stable in the temperature range from 600 to 650°C for both steels, the amount of intermetallic Laves phase dramatically decreases with increases temperature for both steels and at 650°C does not exist in P91 steel. In P23 steel the equilibrium phases are ferrite, M_6C and MX in the temperature interval from 600 to 650°C. Note, that $M_{23}C_6$ and Laves phase are not stable theoretically at temperature 600°C.

Based on experimental investigations the P91 and P92 steels exhibited following microstructure components. The prior austenite grain boundaries are decorated by a network of $M_{23}C_6$ particles. Particles of this phase are also observed on subgrain boundaries as well as inside subgrains. Further, there are tiny precipitates of minor phase, present both on grain boundaries and on former martensitic laths. Careful examination revealed also very small particles inside the former martensitic laths. Clearly defined subgrains are evident in both the head and gauge length of test pieces. By comparison with the as-received states, however,

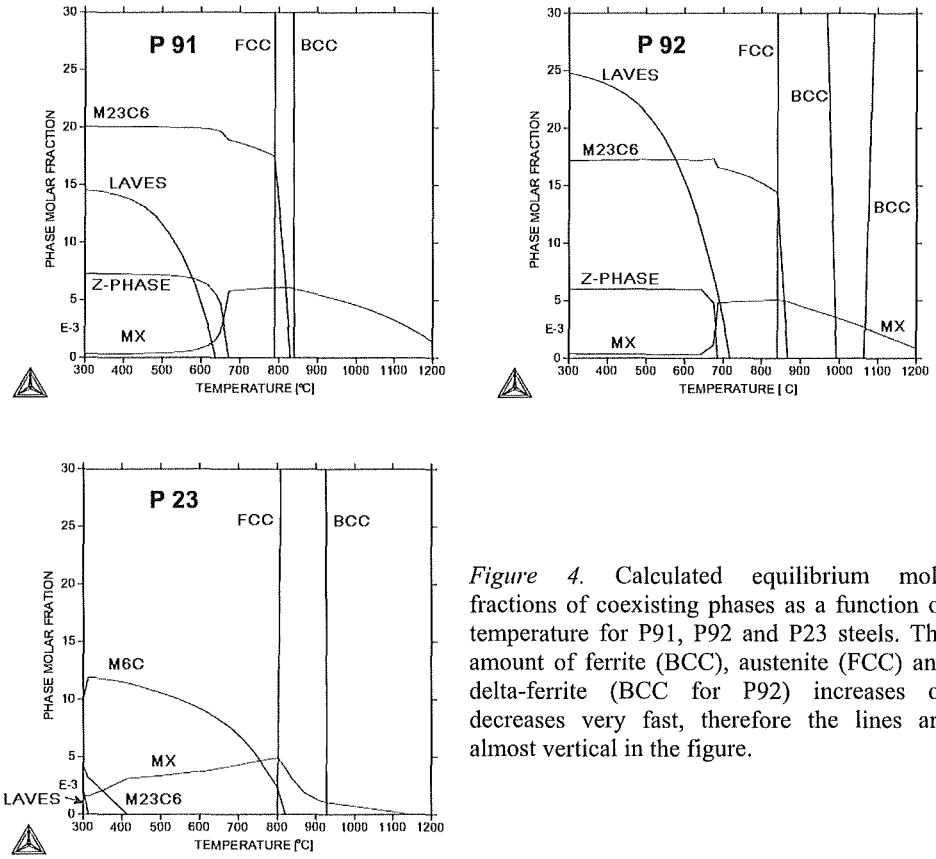

Figure 4. Calculated equilibrium mole fractions of coexisting phases as a function of temperature for P91, P92 and P23 steels. The amount of ferrite (BCC), austenite (FCC) and delta-ferrite (BCC for P92) increases or decreases very fast, therefore the lines are almost vertical in the figure.

the subgrain structure evolution in aged state exhibits the growth of the subgrain size in the gauge length of the crept specimens, which is supported by the influence of the applied stress and/or strain and is more pronounced than the subgrain growth in the specimen heads subjected only to the influence of temperature. For the particle type determination (precipitated particles were extracted in carbon replicas) the chemical composition evaluated from X-rax spectra (EDAX software for thin specimens without correction for absorption or fluorescence) and selected area diffraction (SAD) were employed. The experimental results of particle analyses together with the phase equilibrium thermodynamic calculations are given in Table I.

Significant microstructural changes in P23 steel were observed after long-term annealing, resulting in the recovery of the bainitic lath structure and a decrease in dislocation density reducing dislocation hardening. The main precipitates are M_6C, $M_{23}C$ and MX, as evident from electron diffraction analysis. The experimentally determined and calculated equilibrium chemical composition of precipitates in P23 is given in Table II. The coarsening of $M_{23}C_6$ carbides, connected with a higher consumption of alloying elements, causes the lowering of solid solution hardening as well as precipitation hardening. Similarly, the formation of M_6C

Table I. Experimentally determined and calculated chemical composition of phases in P91 and P92 steels at 600 and 650 °C. (In wt.%, calculated composition normalised to 100% of metallic elements.)

			P91				
Experimental			**600 °C**				
	V	Cr	Mn	Fe	Nb	Mo	Si
$M_{23}C_6$	1.9	64.0	1.5	22.2	1.2	9.2	0.0
MX	62.5	15.0	0.3	0.7	19.6	1.9	0.0
Laves	0.7	12.4	1	35.8	2.1	45.8	2.2
Calculation			**600 °C**				
	V	Cr	Mn	Fe	Nb	Mo	Si
$M_{23}C_6$	0.1	73.2	0.7	18.4	0.0	7.5	0.0
MX	23.4	24.7	0.0	0.0	51.9	0.0	0.0
Laves	0.0	9.5	0.0	41.3	0.0	47.4	1.8
Zet	43.1	48.6	0.0	0.0	8.2	0.0	0.0
Calculation			**650 °C**				
	V	Cr	Mn	Fe	Nb	Mo	Si
$M_{23}C_6$	0.5	68.7	0.6	22.0	0.0	8.2	0.0
MX	40.2	30.6	0.0	0.0	29.2	0.0	0.0
Zet	43.4	48.7	0.0	0.0	7.9	0.0	0.0

			P92				
Experimental			**600 °C**				
	V	Cr	Mn	Fe	Nb	Mo	W
$M_{23}C_6$	1.5	56.2	0.7	20.3	1.9	4.4	15.0
MX 1	5.6	3.4	0.7	1.5	79.4	2.0	7.4
MX 2	61.4	13.3	0.5	1.9	17.4	2.7	2.8
Laves	1.2	7.8	0.6	24.2	2.5	11.0	50.4
Calculation			**600 °C**				
	V	Cr	Mn	Fe	Nb	Mo	W
$M_{23}C_6$	0.3	73.4	0.6	16.3	0.0	2.9	6.5
MX	2.2	0.0	0.0	0.0	96.3	0.1	1.3
Laves	0.0	7.5	0.0	34.4	0.2	11.5	46.5
Zet	43.6	48.8	0.0	0.0	7.6	0.0	0.0
Calculation			**650 °C**				
	V	Cr	Mn	Fe	Nb	Mo	W
$M_{23}C_6$	0.2	68.5	0.5	19.5	0.0	3.1	8.2
MX	2.5	0.2	0.0	0.0	94.8	0.2	2.2
Laves	0.0	6.1	0.0	35.5	0.2	9.9	48.3
Zet	43.5	48.7	0.0	0.0	7.7	0.0	0.0

abates the solid solution hardening owing to the decline in alloying elements in the matrix. Summarizing, the significant creep strength drop of P23 steel after long-term annealing can be explained by the decrease in dislocation hardening, precipitation hardening and solid solution hardening due to instability of microstructure at high temperature.

Table II. Experimentally determined and calculated chemical composition of phases in P23 steel at 600 and 650 °C. (In wt.%, calculated composition normalised to 100% of metallic elements.)

	T23						
Experimental			600 °C				
	V	Cr	Mn	Fe	Nb	Mo	W
M_6C	2.2	2.7	0.4	16.5	2.2	4.5	71.5
MX 1 (V,W)	36.1	5.0	0.5	1.4	14.4	3.2	39.4
MX 2 (Nb)	12.8	1.5	0.8	1.5	69.2	11.3	2.9
$M_{23}C_6$	4.8	57.1	2.2	31.3	1.1	1.2	2.3
Calculation			600 °C				
	V	Cr	Mn	Fe	Nb	Mo	W
M_6C	1.7	0.7	0.0	25.3	0.0	2.1	70.2
MX	74.3	1.6	0.0	0.0	19.6	1.0	3.6
Experimental			650 °C				
	V	Cr	Mn	Fe	Nb	Mo	W
M_6C	1.4	3.1	0.4	17.3	1.8	4.9	71.1
MX	40.0	4.7	0.8	1.4	11.2	4.1	37.8
Calculation			650 °C				
	V	Cr	Mn	Fe	Nb	Mo	W
M_6C	1.4	0.9	0.0	26.0	0.0	1.9	69.8
MX	72.2	2.7	0.0	0.0	18.2	1.0	6.0

4. Conluding remarks

In general, the results of the thermodynamic calculations are in an acceptable agreement with experimental characterization particularly with regard to the prediction of precipitate appearance (Tabs. I and II). It should be stressed that accuracy of the predictions depends critically on the available phase descriptions in the thermodynamic databases. In Tabs. I. and II there are some inaccuracies in these descriptions, e.g. the prediction of Laves phase stability in P91 (the occurrence of Laves phase has been observed 650°C [11], nevertheless many previous studies expected the Laves phase temperature stability for P91 steels between 600 and 650°C) or the absence of Z-phase according to the experimental results. In fact, no Z-phase precipitates in P91 and P92 steel were experimentally identified in this work. However, Danielsen and Hald [12] reported that some of the smaller particles (≤ 100 nm) were observed to have an intermediate Cr level, making it difficult to distinguish whether they are MX or Z-phase. It should be noted, that the appearance of Z-phase in the microstructure is assumed to be an indicator for a possible loss in creep strength. The main difference between the theoretical and experimental results is the experimental evidence of the existence of the $M_{23}C_6$ carbide in P23 steel at 600 °C which was not predicted by the calculation. On the other hand, the more detailed modelling proved that small increase of C or Cr content will lead to the appearance of $M_{23}C_6$ carbide in the calculations. The discrepancy is probably caused by the fact, that the thermodynamic database was built upon the assessments of important Fe-based

binary and ternary systems, using experimental data obtained at higher temperatures, where the structures are closer to the thermodynamic equilibrium. Consequent extrapolations to lower temperature can introduce this inaccuracy. It has to be noted that the decreasing number $M_{23}C_6$ particles and increasing size of this precipitate could lead to lower creep strength.

Acknowledgements

Financial support for this work was provided by the Ministry of Industry and Trade of the Czech Republic under the project No. 2A-1TP1/057 and the Academy of Sciences of the Czech Republic under the Research Plan No. AV0Z20410507.

References

[1] D.A.Woodford, „Test methods for accelerated development, design and life assessment of high-temperature materials", *Materials & Design*, 14, pp. 231-242 (1993).
[2] B. Wilshire and M. R. Bache, „Cost effective prediction of creep design data for power plant steels", *In. Proc. 2nd ECCC Creep Conference on Creep and Fracture in High Temperature Components – Design and Life Assessment Issues*, eds. I. A. Shibli and S. R. Holdsworth, ISBN No 978-1-60595-005-1, DEStech Publications Inc., pp. 44-55 (2009).
[3] R. Wiswanathan and R. Tilley, „"Creep damage – industry needs and future research and development", In: *Creep – resistant steels*, eds. F. Abe, T.-U. Kern and R. Wiswanathan, Woodhead Publishing in Materials, Cambridge, UK, pp. 637-666 (2008).
[4] K.-H. Mayer, „The development of creep-resistant steels", *ibid*, pp. 15-77.
[5] F. Masuyama, „Specifications for creep-resistant steels: Japan", *ibid*, pp. 155-173.
[6] V. Sklenička, K. Kuchařová, M. Svoboda, L. Kloc, J. Buršík and A. Kroupa, „Long-term creep behaviour of 9-12%Cr power plant steels", *Mater. Characterization*, 51, pp. 35-48 (2003).
[7] V. Sklenička, K. Kuchařová, A. Dlouhý and J. Krejčí, „Creep behaviour and microstructure of a 9%Cr steel". In: *Proc. Conf. On Materials for Advanced Power Engineering*, eds. D. Coutsouradis et al., Kluwer Academic Publishing, pp. 435-444 (1994).
[8] Thermocalc, ver. P, Thermo-Calc Software AB, Sweden
[9] A. Kroupa, P. Unucka, et al.: Thermodynamic database Steel16, IPM Brno internal report, 2003-2009
[10] J. Hald, „Microstructure and long-term creep properties of 9-12%Cr steels", *Int. J. Pressure Vessels and Piping*, 85, pp. 30-37 (2008).
[11] V. Kneževic, J. Balun, G. Sauthoff, G. Inden and A. Schneider, „Design of martensitic/ferritic heat-resistant steels for application at 650°C with supporting thermodynamic modelling", *Mater. Sci. Eng.* A477, pp. 334-343 (2008).
[12] H. K. Danielsen and J. Hald, „On the nucleation and dissolution process of Z-phase Cr (V, Nb)N in martensitic 12%Cr steels", *Mater. Sci. Eng.* A505, pp. 160-177 (2009).

9th Liege Conference : Materials for Advanced Power Engineering 2010
edited by J. Lecomte-Beckers, Q. Contrepois, T. Beck and B. Kuhn.

IMPROVEMENT OF STEAM OXIDATION RESISTANCE OF MARTENSITIC AND AUSTENITIC ALLOYS BY AL-CONTAINING COATINGS

Dr. Reinhard Knödler and Dr. Stefan Straub,

Alstom Power Systems GmbH, Mannheim, Germany

Abstract

An increase of steam power plant efficiency is necessary to reduce the emissions and to reduce fuel consumption. To obtain this goal, the steam temperature must be increased considerably. Present alloys, however, show oxide scale growth and spallation at elevated temperatures. These shortcomings can be avoided by applying coatings to martensitic and austenitic steels.

Therefore, diffusion coatings on martensitic 9 - 11 % - Cr steels and 17 % - Cr austenitic steels were applied and exposed to flowing steam for operating times up to 15.000 h at 650 °C. The coating process was optimized with respect to surface preparation, heat treatment and other process parameters. Metallographic analysis was performed after the oxidation tests by light optical (OM) and scanning electron microscopy (SEM). With energy dispersive X-ray analysis (EDX) in SEM the distribution of the elements was determined in order to assess the diffusion velocity of different coating constituents. This allows an estimation of the coating lifetime.

The best coating showed that only a few µm of oxide scales have formed, as compared to several 100 µm on the uncoated steel (under the same test conditions). Thus, these types of coatings can be a promising solution for preventing oxidation of martensitic and austenitic steels.

Keywords: steam oxidation, coatings, martensitic and austenitic alloys.

Introduction

Future power plants will operate at considerably higher steam temperatures than today, in order to achieve higher efficiencies and lower or nearly zero emission rates to reach the worldwide climate safety targets. This implies that at temperatures of > 620 °C, the existing steels must be replaced by steels with higher long-term creep strength and higher oxidation resistance, especially in steam.

As steam oxidation is concerned, it is well known, that oxide scales in steam can grow to a considerable thickness at the envisaged higher temperatures [1 – 3]. If the scales reach a certain thickness, they tend to exfoliate or spall, especially parts of the outer oxide scale (= magnetite (Fe_3O_4)) [4 – 5]. Spallation can be deleterious, because the spalled hard particles can cause erosion damage on turbine parts, e.g. the leading edges of blades.

In order to avoid these problems, the components exposed to steam (e. g. casings, pipes, ...) could be coated by oxidation resistant materials. Coating materials may consist e.g. of thermally sprayed Ni-base coatings or Al-containing slurries, which are applied by spraying or similar application techniques [6 - 9]. In the following, investigations with Al-slurry

coatings are described, which focus on the influence of the substrate materials and of exposure time.

Experimental

The substrate steels, onto which coatings are applied in the present study, is a martensitic steel with 9 % Cr (P92) and an austenitic steel with 17 % Cr, 10 % Ni and 2 % W [in wt. %], respectively.

The coating substance is a commercial aluminium slurry product, obtained from *Indestructible Paints Inc., UK*. This product was applied to the different substrates by a paint spray process. Several layers were sprayed consecutively with a drying step in between. After spraying a heat treatment followed. The thickness of the coating was about a couple of 10 µm's. Fig. 1 shows the experimental arrangement for the spraying process.

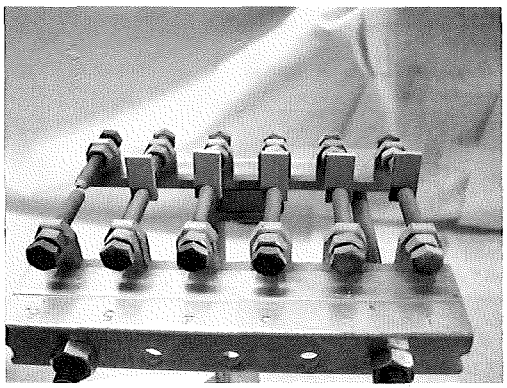

Fig. 1: Monitoring equipment for the paint application process.

The coated samples were exposed in a steam oxidation test equipment under flowing steam at 650 °C for as long as about 15.000 h. This equipment was already described in detail [2].

Results

Substrate: 9 % Cr martensitic steel P92

A metallographic cross section of the coated sample before exposure to steam is presented in fig. 2. The element distribution images show that a Fe_xAl_y alloy was formed due to thermal treatment. A thin oxide scale was formed on top of the coating due to this process.

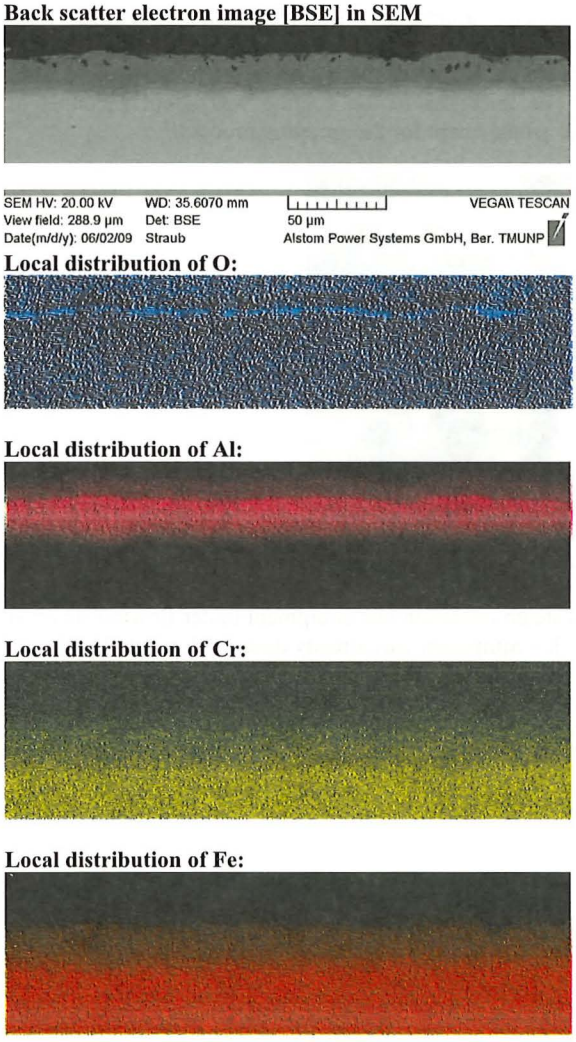

Fig. 2: Element distribution (O, Al, Cr and Fe) of the as-received coating on a P92-steel.

Fig. 3 shows the weight increase after exposure to steam at 650 °C for two coated samples and for one uncoated P92 sample (for comparison). It can be seen, that - in contrast to the uncoated sample - the coated samples showed a very low weight increase with time. The rate law of oxide growth appeared to be nearly parabolic.

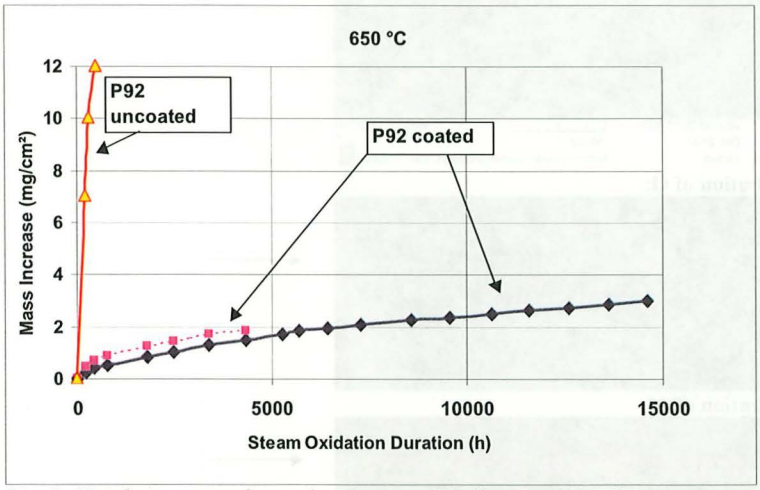

Fig. 3: Weight increase of coated and uncoated P92 at 650 °C in flowing steam.

The low oxidation rate, as indicated by the small weight increase, is confirmed by metallographic examination after steam exposure at 650 °C for about 15.000 h. As fig. 4 shows, the coating protected the substrate well and showed no signs of deterioration around the whole sample. Fig. 5 shows the element distribution images for Al, Fe, Cr and oxygen (the arrows indicate the top of the coating).

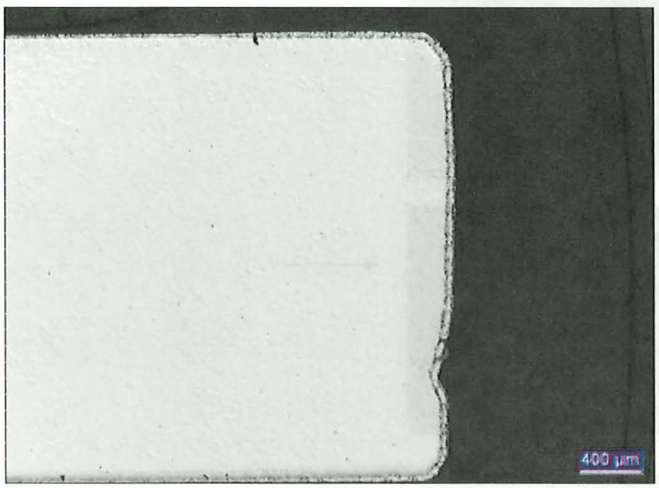

Fig. 4: Cross section of coated P92 after exposure to steam at 650 °C for 15.000 h.

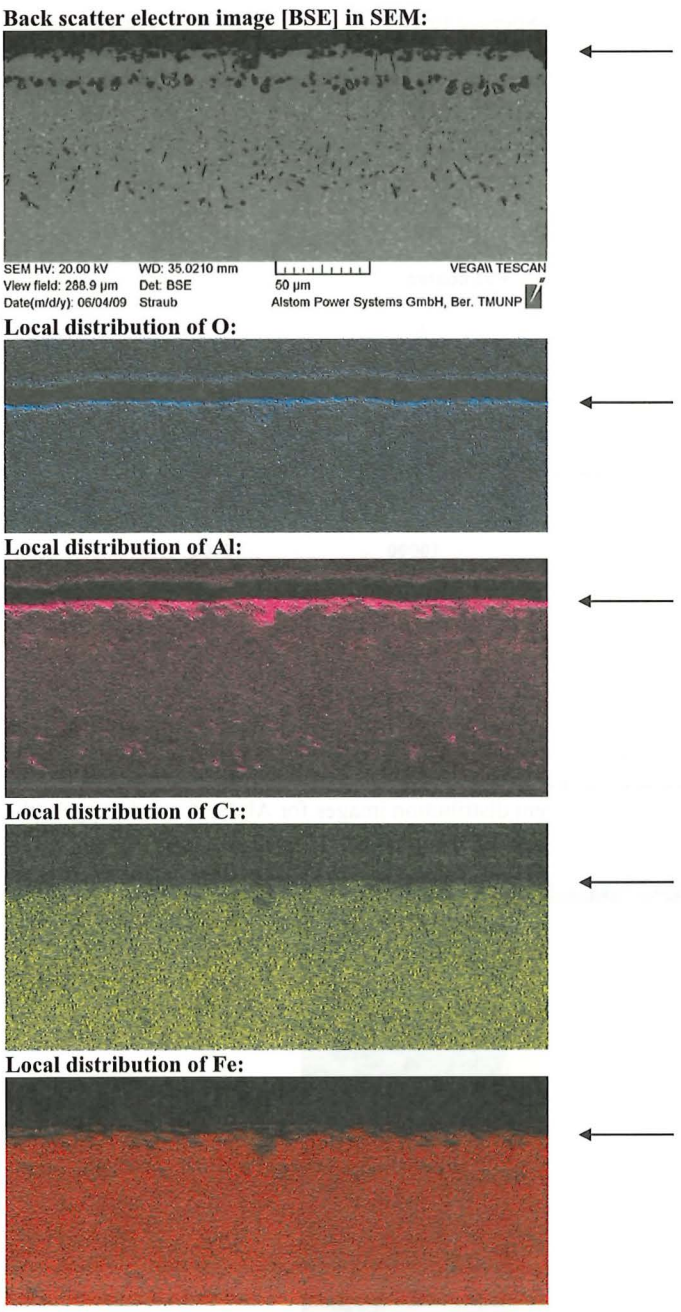

Fig 5: Element distribution of coated P92 after 15.000 h in steam at 650 °C.

It can be seen, that only a very small portion of the coating (< 10 µm) was oxidized on top of the coating and thus confirms its good protection ability. Aluminium is enriched at the top, indicating the formation of a thin aluminium oxide scale. The aluminium image shows a diffusion zone of about 80 µm thickness, in which obviously a Fe_xAl_y-alloy is being formed.

Comparison with results after 3.400 h of exposure to steam showed similar behaviour, the diffusion layer being already about 70 µm thick, which is almost the same size as after 15.000 h. This allows the conclusion, that the Fe_xAl_y diffusion layer – and thus the protection - will be stable for much longer times.

Substrate: 17 % Cr austenitic alloy

The weight increase of coated and uncoated samples of the 17 % Cr austenitic steel is shown in fig. 6. It can be seen, that almost no weight increase, i.e. no oxidation, took place in the case of the coated sample (theoretically, a weight increase of 0.5 mg/cm^2 corresponds to an oxide scale thickness of 4 - 5 µm). In contrast, the uncoated specimens oxidize rapidly and oxide scales spall after about 6.000 h (as indicated by a sudden decrease of weight), leaving the surface ready for new rapid oxide growth.

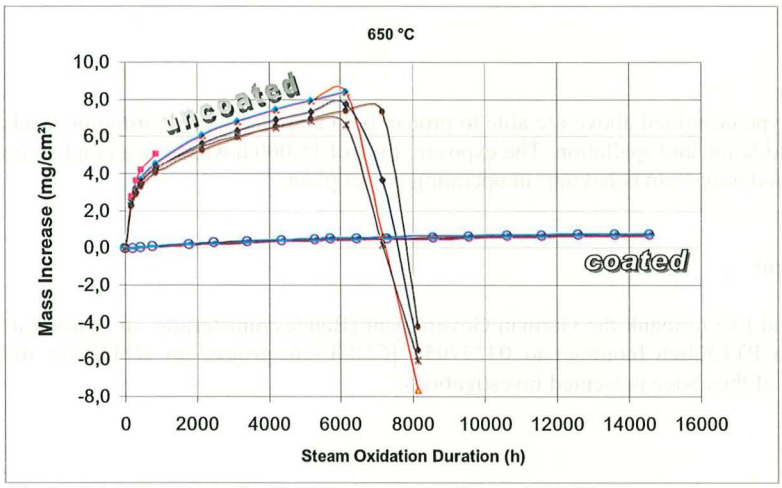

Fig 6: Weight increase of a 17 % Cr austenitic alloy at 650 °C in steam.

Metallographic examination after 15.000 h exposure in steam at 650 °C shows that the coating is not attacked and remained totally intact: see fig. 7. Thus, the coatings presented here are a promising means to avoid oxidation and spallation even after long operation times in steam at 650 °C.

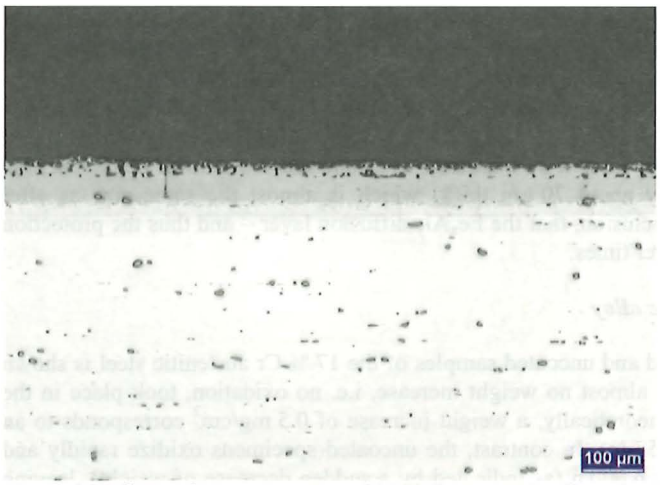

Fig. 7: Metallographic cross section of 17 % Cr austenitic alloy after 15.00 h at 650 °C in steam.

Conclusion

Coatings of the type described above are able to protect both martensitic and austenitic steels with respect to oxidation and spallation. The exposure time of 15.000 h was long enough to be able to predict good long-term behaviour in operating power plants.

Acknowledgement

The authors would like to thank the German Government [Bundesministerium für Wirtschaft und Industrie via PTJ Jülich [contract no. 0327705E [COST536, project no. D11]]] for the financial support of the above presented investigations.

References

[1] A. Helmrich, Q. Chen, G. Stamatelopoulos, B. Scarlin, Materials development for advanced steam boilers, in: Materials for Advanced Power Engineering 2006, Proc. of the 8th Liège Conference, J. Lecomte-Beckers, M. Carton, F. Schubert, P. J. Ennis (eds.), Forschungszentrum Jülich, Energy Technology Series, Volume 53, 2006, Part II, 931 - 948.

[2] R. Knödler, S. Straub, Influence of surface treatment on the oxidation kinetics of advanced steels in flowing steam at 650 °C, in: Materials for Advanced Power Engineering 2006, Proc. of the 8th Liège Conference, J. Lecomte-Beckers, M. Carton, F. Schubert, P. J. Ennis (eds.), Forschungszentrum Jülich, Energy Technology Series, Volume 53, 2006, Part III, 1581 - 1587.

[3] R. Blum, Q. Chen, C. Coussement, J. Gabrel, C. Testani, L. Verelst, Operational tests of superheater materials at high steam temperatures in a hard-coal fired steam generator, VGB Power Tech 10 (2001), 86 - 91.

[4] I. G. Wright, M. Schütze, S. R. Paterson, P. F. Tortorelli, R. B. Dooley, Progress in prediction and control of scale exfoliation on superheater and reheater alloys, in: EPRI Int. Conference on boiler tube and HRSG tube failures and inspections, 02 – 05.11.2004, San Diego.

[5] O. H. Larsen, R. B. Frandsen, R. Blum, Exfolation of steam side oxides from austenitic superheaters, VGB powertech 7 (2004), 89 - 94.

[6] T. Sundararajan, S. Kuroda, F. Abe, Steam oxidation resistance of HVOF thermal sprayed Ni-Cr coatings, Thermal Spray 2003, ASM International, Materials Park, Ohio, USA, 2003, P. 495 – 502.

[7] A. Agüero, V. Gonzales, M. Gutierrez, Behaviour of coated and uncoated ferritic steels under isothermal and cyclic steam oxidiation condition, BALTICA VII Conf. , 12. – 14.06.2007.

[8] E. N'Dah, S. Tsipas, F. J.Bolivar, M. P. Hierro, F. J. Perez, Improvement of 9% Ferritic steel against cyclic oxidation by CVD-FBR Al-Mn coating, Oxid. Metals 69 (2008), 77 - 94.

[9] A. Agüero, M. Gutierrez, V. Gonzales, R. Muelas, A. Roman, R. Knödler and S. Straub, Cyclic oxidation of aluminide coated and uncoated ferritic steels under steam: Effects of cycle sequence on oxide spallation and crack propagation, Europ. Federation of Corrosion Workshop, DECHEMA-House Frankfurt am Main, Germany, 30.09. – 02.10.2009, to appear in the Journal of Materials and Corrosion 2010.

9th Liege Conference : Materials for Advanced Power Engineering 2010
edited by J. Lecomte-Beckers, Q. Contrepois, T. Beck and B. Kuhn.

STEAM OXIDATION SCALE GROWTH AND THERMAL INSULATION EFFECT ON CREEP LIFE OF CREEP STRENGTH ENHANCED FERRITIC STEELS

Fujimitsu Masuyama[1], Tatsuya Tokunaga[1],
Mikito Takao[2] and Katsutoshi Arakawa[3]

[1]Graduate School of Engineering, Kyushu Institute of Technology
[2]Graduate Student of Kyushu Institute of Technology, now with JFE Steel
[3]Graduate Student of Kyushu Institute of Technology, now with Kobe Steel

Abstract

Creep strength enhanced ferritic steels, such as T91 and T23 are extensively used worldwide for superheater and reheater tubes, not only in advanced power plants but also in plants with conventional steam conditions. However when these steel tubes are used at higher metal temperature, steam oxidation problems are recently experienced resulting in turbine side erosion, and overheating of tubes leading to creep rupture due to scale blockage in tube bends or scale insulation effect due to thick scale, and separation and exfoliation of the scale. In the present study, steam oxidation growth tests of T91, T92, T23 and T22 were conducted to develop steam oxidation growth rate and scale behavior. Then using the steam oxidation growth data measured the metal temperature changes with scale growth were calculated considering the insulation effect of steam oxidation scale. Consequently the creep lives affected by steam oxidation scale growth were predicted as a function of time and temperature increase for creep strength enhanced ferritic steels.

Keywords: Steam oxidation, creep strength enhanced ferritic steels, scale growth, insulation effect, creep life

1. Introduction

The boiler steels, T91 and T23 are extensively used worldwide for superheater and reheater tubes as well as thick wall and large diameter components, not only in advanced steam cycle power plants but also in plants with conventional steam parameters. The reason for the popularity of these steels are the capability to replace conventional austenitic steel tubes and ferritic T22 tube at higher temperatures up to around 600°C and in power boiler superheaters and reheaters due to their high creep rupture strength. However, higher metal temperature causes various material problems in these steels, such as steam oxidation resulting in turbine side erosion from exfoliated scale, and overheating of tubes leading to creep rupture due to scale blockage in tube bends. Recent field experience indicates that these steels exhibits interesting steam oxidation behavior and oxide scale morphology as compared with conventional Cr-Mo low alloy steels, despite being characterized by the same steel category of ferrite [1]. A number of investigation results and experiences in actual power plants have already been reported, and fundamental studies on the oxidation itself of 9%Cr martensitic steels have been carried out in steam flows and in air. In the current study, steam oxidation testing of T91, T92, T23 and T22 was performed using thermo-gravimetric and differential thermal analyzers in high-temperature steam, and steam-induced oxide scale formed on the specimens and ex-serviced T91 tubes was investigated to clarify the oxide growth of this steel and the micro-structural morphology of the scale. Then using the steam oxidation growth

data measured the metal temperature changes with scale growth were calculated considering the insulation effect of steam oxidation scale. Consequently the creep lives affected by steam oxidation scale growth were predicted as a function of time and temperature increase for creep strength enhanced ferritic steels.

2. Steam oxide scale growth

2.1. Steam oxidation test [2]

Unique test equipment was employed in order to investigate the growth rate of steam-induced oxide scale and the phase transformation of oxide scale during heating. This equipment consisted essentially of thermo-gravimetric and differential thermal analyzers in high-temperature steam supplied from a humidity controller (Rigaku, TG-DTA/HUM-1B). Fig.1 illustrates the schematic principle of the test equipment. To determine the weight change of the sample, measurement was performed on the electric current used to control the sample side of the balance to keep the lever-position upright. Alpha-alumina was used as a reference material, and a platinum sample pan was used to hold the sample and the reference material. The wet gas mixed of pure water and nitrogen supplied from the humidity controller was heated at a given temperature in the furnace for contact with the specimens. The relative humidity was controlled at a set value using a mass flow controller before supply to the furnace. Before testing, the system was purged for 30 min with nitrogen gas to completely degas the air. Test temperatures were 600°C, 650°C and 700°C, with maximum testing duration of 50h, measuring the weight gain continuously from the start point of the holding temperature. The relative humidity was set at 50% at 30°C, reflecting the preliminary test

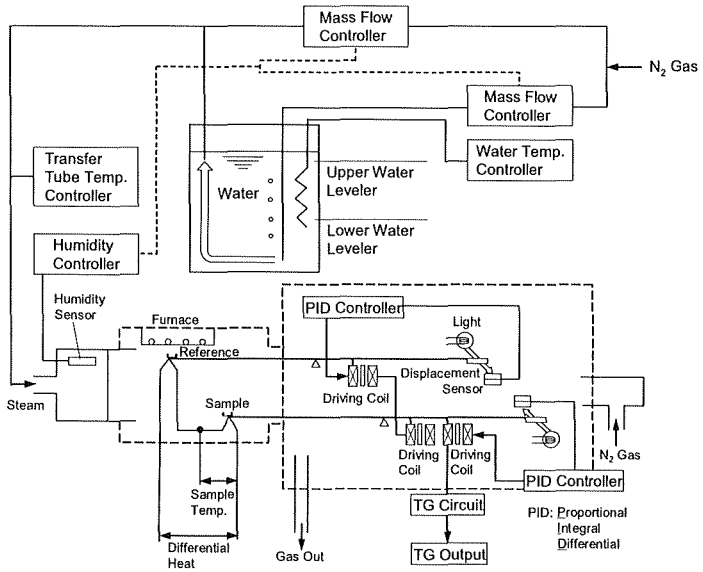

Fig. 1 Schematic diagram of steam oxidation testing system

Table 1 Chemical composition of test materials

Steels	C	Si	Mn	P	S	Ni	Cr	Mo	W	V	Nb	B	N	Al
T91	0.09	0.36	0.46	0.009	0.003	0.26	8.49	0.98	-	0.20	0.08	-	0.050	-
T92	0.11	0.04	0.46	0.008	0.001	0.06	8.96	0.47	1.84	0.20	0.07	0.0010	0.051	-
T23	0.06	0.19	0.23	0.017	0.001	-	2.37	0.27	1.52	0.20	0.04	0.0035	0.007	0.001
T22*	0.12	0.03	0.45	-	-	-	2.25	1.0	-	-	-	-	-	-

* Nominal chemical composition

results corresponding to 30%, 50% and 80% as mentioned below. The chemical compositionof the test materials used in the present work is listed in Table 1. T22 in the table is the test material commercially produced as conventional 2.25Cr-1Mo steel tube for comparative study with listed creep strength enhanced ferritic steels. The test specimens were machined to small cylindrical blocks from the tubing material, yielding a size of 4.5 mm in diameter by 2.5 mm in height. Each specimen was polished with #600 emery paper followed by degreasing with acetone before testing. The test specimens removed from the test equipment were observed by SEM and optical microscope to examine the oxide scale morphology, and were analyzed for chemical distribution by EPMA and Auger analysis.

2.2. Oxide scale growth on creep strength enhanced ferritic steels

According to the weight gain vs. time curves for the four grades test materials at temperatures of 600°C, 650°C and 700°C obtained by steam oxidation tests, the oxidation growth curves all followed the parabolic rate law over the test time up to 50h. The weight gain of T91 and T92 is smaller than that of T23 and T22 at the temperatures tested, with the exception of 600°C. The comparison of weight gain between T91 and T92 (9%Cr steels), and T23 and T22 (2.25%Cr steels) revealed that there was not large difference in 9%Cr steels, however T23 showed better oxidation resistance than T22 at the temperature of 700°C. Fig.2 clearly demonstrates the parabolic rate law for the oxidation growth of test materials as shown in the relation between the square of weight gain and the test time. The steam oxidation growth in ferritic steels is assumed to follow a parabolic rate law because the substrate transportation into the oxide scale by diffusion is the rate controlling process, and the oxide scale growth obtained here can thus be approximated to the parabolic rate law as follows,

$$\Delta W^2 = K_p t \tag{1}$$

where ΔW is the weight gain, K_p the parabolic rate constant and the time t. From the slope of the straight line approximated by the least square method for the measured data shown in Figs.2, the K_p at each temperature was calculated from Equation (1) for the test materials. Fig 3 shows the relationship between the logarithmic parabolic rate constant and reciprocal absolute temperature. The temperature dependency of K_p can be expressed by an Arrhenius type equation as follows,

$$K_p = A\exp(-Q/RT) \tag{2}$$

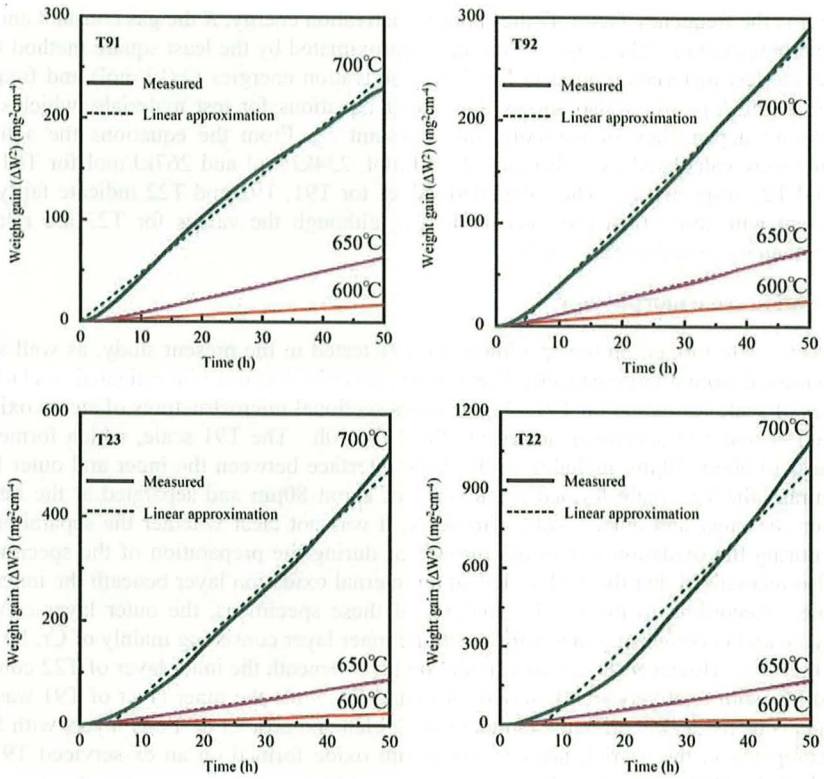

Fig.2 Square weight gain vs, time curves for T91, T92, T23 and T22

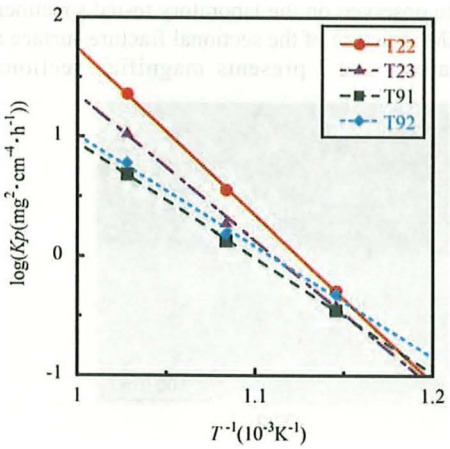

Steels	Equation
T91	$\log K_p = -13992 / T + 15.731$
T92	$\log K_p = -12236 / T + 13.589$
T23	$\log K_p = -9643 / T + 10.590$
T22	$\log K_p = -9264 / T + 10.275$

Fig. 3 Temperature dependence of rate constant K_p for T91, T92, T23 and T22

where A is the frequency factor, Q the apparent activation energy, R the gas constant and T the absolute temperature. The slopes of the line approximated by the least square method for the data of the test materials plotted in Fig.3 give activation energies Q (kJ/mol) and frequency factors A (mg^2/h). Fig.3 also shows line fitting equations for test materials, which exhibit temperature dependency of parabolic rate constant K_p. From the equations the activation energies were calculated as 184kJ/mol, 177kJ/mol, 234kJ/mol and 267kJ/mol for T91, T92, T23 and T22 respectively. The calculated values for T91, T92 and T22 indicate fairly good agreement with those of a previous report [3], although the values for T23 are relatively smaller than those in the reference [4].

3. Oxidation scale morphology

The oxide scale formed on the specimens of T91 tested in the present study, as well as T91 tube removed from a large-capacity fossil-fired power boiler, were investigated to clarify the features of scale formation on T91. Fig.4 shows sectional microstructures of steam oxidation on the T91 and T22 specimens tested at 700°C for 50h. The T91 scale, which formed to a thickness of about 50μm, includes voids at the interface between the inner and outer layers. In contrast, the T22 scale formed a thickness of about 80μm and separated at the interface between the inner and outer layers. However, it was not clear whether the separation took place during the oxidation test in the furnace or during the preparation of the specimen. It was also recognized that the T22 scale had an internal oxidation layer beneath the inner layer of scale. According to the EPMA analysis of these specimens, the outer layer contained mainly Fe and O composing magnetite, with the inner layer consisting mainly of Cr, Fe and O for both steels. However the internal oxidation layer beneath the inner layer of T22 contained Cr and Mo with relatively small amount of O and Fe, while the inner layer of T91 was not a homogeneous oxide, but an oxide laminate of Cr-rich and ordinal Cr-Fe-O layers with Ni and Mo segregated in the Cr-rich layers. The steam oxide formed on an ex-serviced T91 tube used about 90,000h in a power boiler was observed to compare the oxide scale morphology with the laboratory specimens. Fig.5 shows most of the scale and inner layer surfaces revealed by exfoliation. The majority of the scale surface shows hematite formed on the magnetite, and the exfoliated (fractured) surface exhibits the appearance of oxide grains that resemble the surface of the steam oxidation scale observed on the laboratory tested specimen. Fig.6 shows the sectional microstructure and SEM structure of the sectional fracture surface at a similar position within the T91 surface area. Fig.7 presents magnified sectional

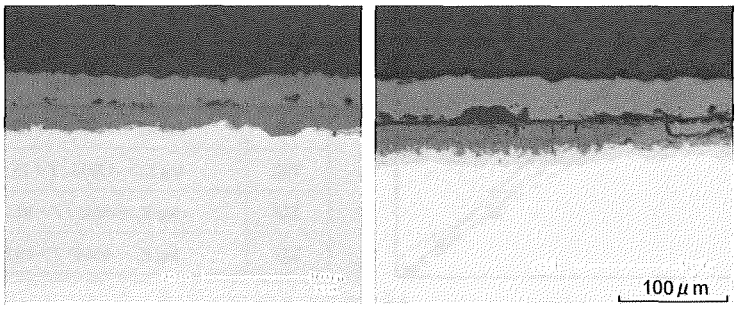

Fig. 4 Microstructures of oxide scale formed on T91 and T22 tested at 700°C for 50h

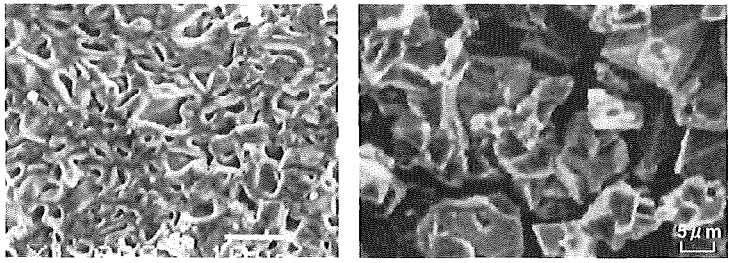

Fig. 5 SEM observation of oxide scale formed on T91 tube used in power boiler

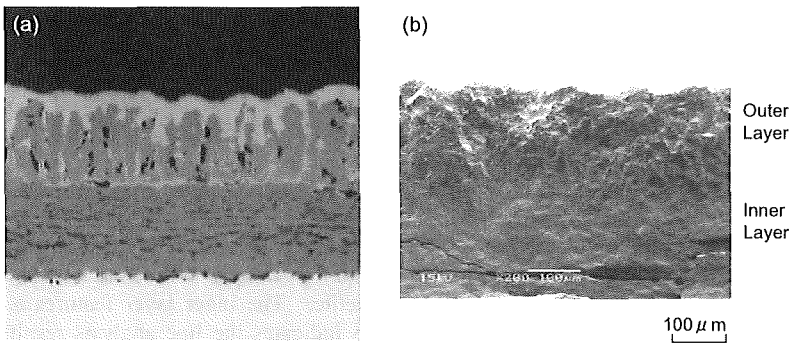

Fig. 6 Optical microstructure (a) and SEM graph (b) of oxide scale formed on T91 tube used in power boiler

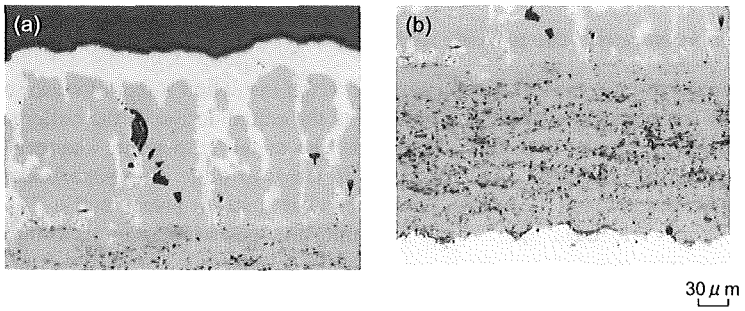

Fig. 7 Magnified optical microstructure of outer layer (a) and inner layer (b) of oxide scale on T91 tube used in power boiler

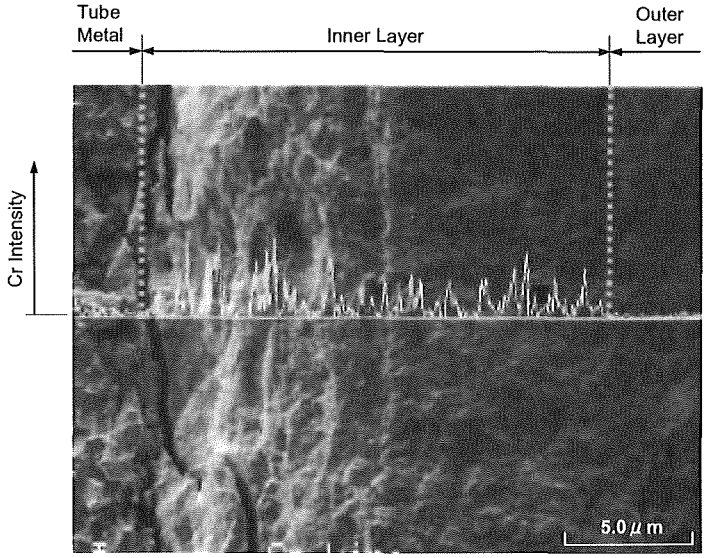

Fig. 8 Auger line analysis of Cr traversing tube metal to outer layer of oxide scale

microstructures of the inner and outer layers. The outer layer is seen to consist of columnar type magnetite crystal covered by hematite on the top surface, with hematite penetrating the boundaries and crevices of the columnar magnetite. The inner layer features a laminated structure and the EPMA analysis results. Fig.8 indicates the line analysis results obtained traversing the direction from the substrate tube material to the outer layer of the oxide scale, which show numerous Cr peaks corresponding to the Cr-rich layers within the inner layer of oxide scale. Laboratory findings thus coincide well with steam oxidation results observed in the field.

4. Effect of scale growth on metal temperature rise and creep life

4.1 Metal temperature rise due to oxide scale growth

The metal temperature of boiler tube is risen due to the insulation effect of steam oxide scale formed on the inner diameter surface. Considering the actual design of the boiler superheater tube with above mentioned four grades materials, the metal temperature changes due to the growth of oxide scale thickness were calculated in terms of time. The superheater tube size design was performed using the design parameter of that steam pressure P is 24MPa, inner diameter is 35 mm, outer diameter D_0 is 35+2b mm, flue gas temperature is 1000°C, thermal conductivity of tube metal λ_1 is 40 W/mK, thermal conductivity of oxide scale (assuming magnetite for entire thickness of scale) is λ_2 W/mK, heat transmission coefficient from flue gas to tube metal α_1 is 200W/m^{2}K, heat transmission coefficient from tube metal to steam is α_2 W/m^{2}K, and oxide scale thickness is $d\,\mu$ m. The tube wall thickness b, the thermal conductivity of oxide scale λ_2 and the oxide scale thickness were obtained from the following equations.

$$b = \frac{PD_o}{2\sigma + 2kP} \quad (k = 0.7) \tag{3}$$

$$\lambda_2 = 4.23 - 1.37 \times 10^{-3} T_o \tag{4}$$

$$d = \sqrt{K_p \cdot t} \tag{5}$$

where σ is the design stress, T_0 is the mid-wall temperature (design temperature), t is the time, and K_p is the oxidation rate constant obtained from the experimental work in the present work. The design stresses tabulated in the ASME Code book were used for the materials at design temperatures. The inner surface metal temperature at the start point was assumed to be the steam temperature, and the metal temperature is the mean temperature of outer metal temperature and inner metal temperature. The designing conditions were determined for the both cases of initial (design) metal temperature fixed to 550°C, 575°C, 600°C and 625°C, and tube wall thickness fixed to 7.7 mm applying the design stress of 62Mpa. Table 2 shows the tube dimensions and tube initial metal temperatures (mid wall temperatures or design metal temperature) and inner surface metal temperatures for those designing conditions (for the condition of metal temperature fixed, the case of 600°C is listed). The tube size of T22 for the design temperature of 600°C is not realistic, but the calculation were carried out for the comparative study however the inner surface metal temperature is enough low due to the very heavy wall thickness. Fig.9 shows the calculated scale thickness changes at the inner surface metal temperature and metal temperature rise at the mid-wall in terms of time for the design metal temperature of 600°C. The scale thickness growth on the T92 is larger, and that on the T22 is smaller comparing with T91 and T23 depending on the inner surface metal temperature which is determined by the wall thickness. Fig 10 shows the calculated scale thickness changes and metal temperature rise for the conditions of tube wall thickness fixed to 7.7 mm. The scale growth is dependent on the metal temperature and metal temperature rise which are determined by the wall thickness of 7.7 mm for the design pressure. This means that even low Cr steels exhibit small scale thickness growth for the design conditions. In case of high strength 9Cr steels (T91 and T92), the maximum use temperature becomes high for the given wall thickness and scale growth and temperature rise becomes large for their steam oxidation resistance.

Table 2 Design conditions of superheater tubes

Steels	T_M fixed					WT fixed				
	ID (mm)	OD (mm)	WT (mm)	T_M (C)	T_{ID} (C)	Stress (MPa)	OD (mm)	WT (mm)	T_M (C)	T_{ID} (C)
T91	35	50.4	7.7	600	591	62	50.4	7.7	600	591
T92	35	46.8	5.9	600	593	62	50.4	7.7	615	606
T23	35	53.4	9.2	600	589	62	50.4	7.7	590	581
T22	35	77.6	21.3	600	566	62	50.4	7.7	520	509

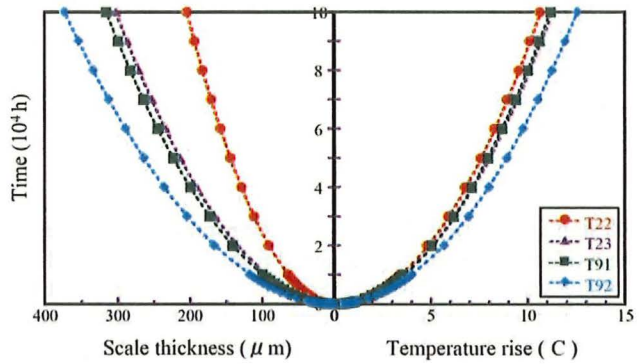

Fig.9 Calculated scale thickness changes and metal temperature rise for the design metal temperature of 600°C.

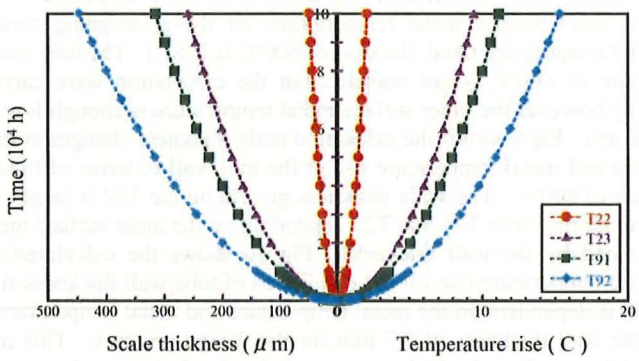

Fig 10 Calculated scale thickness changes and metal temperature rise for the tube wall thickness of 7.7 mm.

4.2 Effect of metal temperature rise on creep rupture life

Fig. 11 shows the stress vs. time to rupture curves at 600°C for T91, T92, T23 and T22. The figure includes both the NIMS creep data sheet curves (iso-thermal curves) and the curves calculated employing the temperature rise due to the oxide scale growth for each tube size design conditions at 600°C, which give lower inner surface metal temperature for thick wall tube depending on the design stress at 600°C. Figs. 12 to 15 respectively demonstrate the temperature rise and creep life consumption rate in terms of time for the design conditions fixing the wall thickness to 7.7 mm and design stress of 62Mpa for T91, T92, T23 and T22. Creep life consumption was calculated for the duration at the temperature with every 1°C interval to summarize the creep life consumption up to 1.0 of life consumption rate. The figures also show the NIMS creep data sheet curves (iso-thermal curves) for comparison. From the figures it is clear that T91 and T92 significantly reduce the creep rupture life when the tubes are used at the maximum applicable temperature at the design stresses.

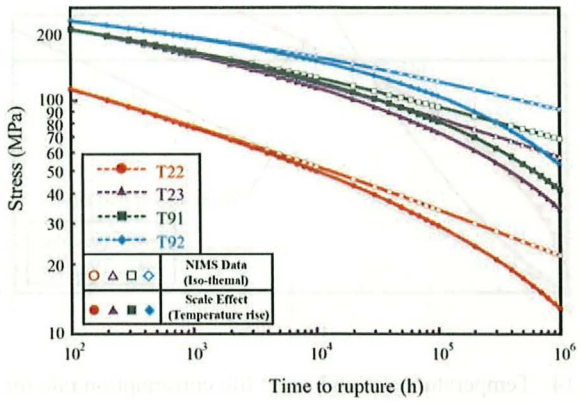

Fig. 11 Stress vs. time to rupture curves at 600°C for T91, T92, T23 and T22.

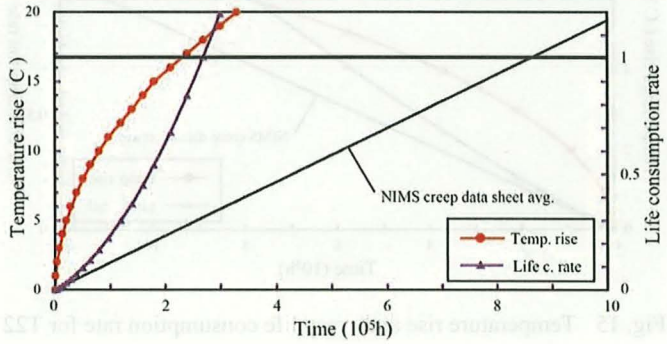

Fig. 12 Temperature rise and creep life consumption rate for T91

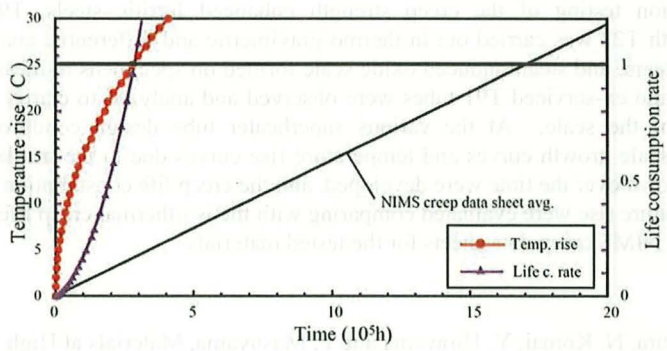

Fig. 13 Temperature rise and creep life consumption rate for T92

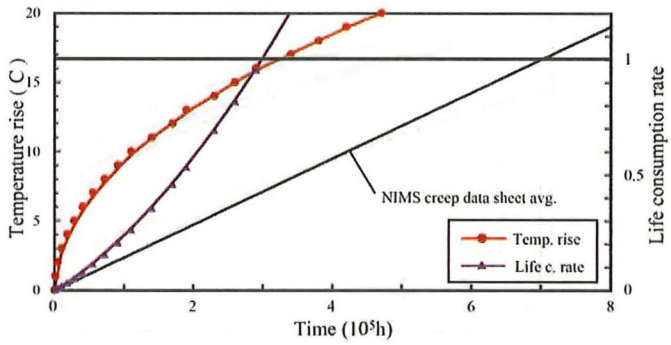

Fig. 14 Temperature rise and creep life consumption rate for T23

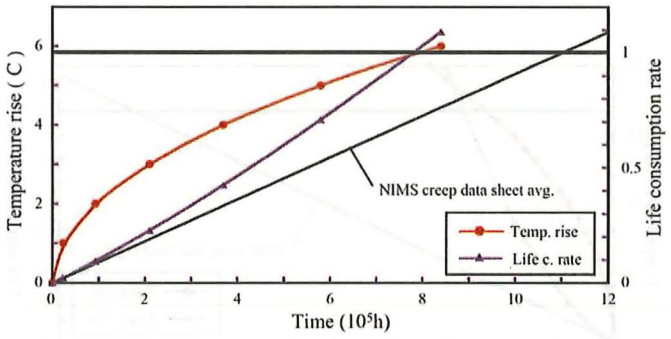

Fig. 15 Temperature rise and creep life consumption rate for T22

5. Summary

Steam oxidation testing of the creep strength enhanced ferritic steels, T91, T92, T23 comparing with T22 was carried out in thermo-gravimetric and differential analyzer in high-temperature steam, and steam induced oxide scale formed on specimens to measure the oxide scale growth and ex-serviced T91 tubes were observed and analyzed to clarify the structural morphology of the scale. At the various superheater tube design conditions for tested materials the scale growth curves and temperature rise curves due to the insulation effect of oxide scale grown over the time were developed, and the creep life consumption rates affected by the temperature rise were evaluated comparing with the iso-thermal creep life consumption rates referring NIMS creep data sheets for the tested materials.

References

[1] N. Nishimura, N. Komai, Y. Hirayama and F. Masuyama, Materials at High Temperatures, 222(1/2), 2005, pp.3-10

[2] T. Murai, K. Arakawa, K. Chiku, T. Shirane and F. Masuyama, Proc. 3rd Int. Conference on Advanced Structural Steels, 2006, pp.670-675
[3] Y. Fukuda, T. Tamura and K. Suzuki, Proc. Int. Symposium on Plant Aging and Life Prediction of Corrodible Structures, 1995, pp.835-840
[4] Y. S. Lee, Y. Watanabe, T. Kondo and M. Sato, JSPS Report of the 123 Committee on Heat-Resisting Materials and Alloys, 39, 1998, 53-59

9th Liege Conference : Materials for Advanced Power Engineering 2010
edited by J. Lecomte-Beckers, Q. Contrepois, T. Beck and B. Kuhn.

PROTECTIVE COATING OF INNER SURFACE OF STEEL TUBES VIA VACUUM ARC DEPOSITION

K. Maile[1], E. Roos[1], A. Lyutovich[1]*, J. Böse[1], M. Itskov[1]
Kh. Ashurov[2], A. Mirkarimov[2], S. Kazantsev[2], Kh. Kadirov[2]

[1] Materialprüfungsanstalt (MPA), Universität Stuttgart, Germany
[2] Arifov Institute of Electronics, Uzbek Academy of Science, Tashkent, Uzbekistan
* *corresponding author, <lyutovich@mpa.uni-stuttgart.de>*

Abstract

The Vacuum Arc Deposition (VAD) technique based on sputtering a chosen electrode material and its deposition via plasma allows highly-productive technology for creating a wide class of protecting coatings on complex structures.
In this work, VAD was applied as a method for the protection of the inner surface of tubes for power-plant boilers against steam oxidation. For this aim, a source cathode of an alloy with high chromium and nickel content was employed in two different VAD treatment systems: a horizontal vacuum chamber (MPA) and a vertical system where the work-piece of the tubes to be protected served as a vacuum chamber (Arifov Institute of Electronics).
Surface coating with variation of deposition parameters and layer thickness was performed. Characterisation of coated tubes has shown that the method realised in this work allows attainment of material transfer from the cathode to the inner surface with nearly equal chemical composition. It was demonstrated that the initial martensitic structure of the tubes was kept after the vacuum-arc treatment which can provide for both the high mechanical robustness and the corrosion-resistance of the final material.

Keywords: Steel tubes, inner surface, vacuum arc deposition.

1. Introduction

New technologies for low-emission high-efficiency power plants mostly lead to operating conditions with increasing pressure and temperatures. For boiler tubes operated above 550°C the suitability of martensitic 9 – 12 % Cr steels decreases as the water steam oxidation rate increases. One possibility to improve the steam oxidation resistance of the inner surface of tubes made of these steels arise in applying coating materials with much better high temperature oxidation resistance. Appropriate coating materials are e. g. austenitic high quality steels or nickel based alloys with chromium contents of around 25 %.

In choosing the coating method, it has to be ensured that

- sufficiently thick layers can be produced,
- the applied layers possess a good bond/adherence with the substrate,
- the coating is applied densely without pores and
- substrate does not loose its heat resistance and creep strength characteristics.

A promising coating method is the Vacuum Arc Deposition process (abbr.: VAD-process). The physical-chemical principle of this process is the sputtering of the selected electrode-material, prepared as cathode, via plasma and its deposition on the inner surface of tubes.

Following advantages are specific for this process:

- effective transfer of the cathode material on the inner surface of the tubes
- suitability for long tubes
- high deposition rates
- possibility of in situ cleaning and coating
- absence of chemical hazards.

VAD-process is a known procedure to manufacture protective coatings at the outer surface of metal constructions. Coating of the inner surface is a rather innovative area.
A survey of the principles and application of vacuum arc coatings is given in [1]. The fundamentals and technical applications of VAD are represented in detail in the book [2]. An example of TiN coating synthesis via VAD is described in [3]. Additional benefits for improving the adhesion and microstructure of VAD coatings can be gained using biased potential [4]. There are vacuum arc discharge technologies available for cleaning of steel surfaces [5].

2. Experimental Procedures

2.1. VAD coating in a horizontal system

In the horizontal system, coatings have been deposited on inner surfaces of tubes made of high alloy Cr-steels. Before the coating they are cleaned by sandblasting. A pivot installed coaxially in the work-pieces has acted as cathode material. The walls of the tubes have served as anode. The water-cooled cathode consists of a steel X15CrNiSi 25-20; 1.4841 material. The process is controlled with current impulses and intervals between them. The temperature of the tube pieces was held below 700°C to keep the original microstructure of the steel.
The experiments were performed at vacuum about 10^{-4} to 10^{-5} mbar. The experimental VAD set up is shown schematically in Fig. 1. Using such a method, 40 – 80 µm thick coatings of Cr-Ni-Si alloys are deposited on the inner surface of P91 steel tubes with the length of 120mm. The current density on the anode was varied from 4.0 A/cm^2 to 6.1 A/cm^2 (450-650A). The durations of the impulses varied from 2 to 10 s. The intervals between the impulses were 60 – 120 s.

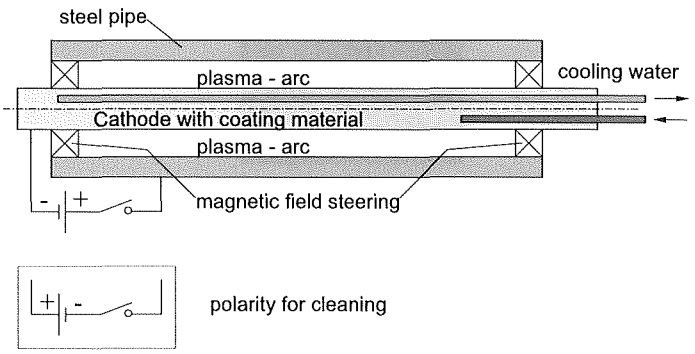

Fig. 1: Schematic representation of VAD process in the horizontal system

2.2. VAD coating in a vertical system.

In the vertical system, the tube to be treated was fastened between the two small vacuum chambers (Fig. 2), which allow the treatment of long tubes.

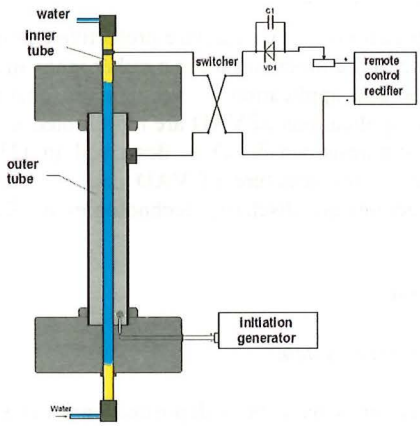

Fig. 2: Schematic representation of VAD process in the vertical system.

This tube served also as a part of the vacuum system and acted as an anode. The in situ cleaning is possible at low vacuum of 10^{-1} mbar by the control of applied voltage polarity. Vertical mounting of tubes provides a convenient removal of cleaning products.

Fig. 3. Steel tube as a part of the vacuum chamber installed in the VAD system.

The coating was performed on tubes of martensitic steel X10CrMoVNb9-1 (1.4903), 38.0 mm o.d., 5.0 mm wall thickness, length 595 mm. The cathode from austenitic steel as a source was installed coaxially in the tubes. The dimensions of the cathode made of X15CrNiSi25-20-Mat.-No. 1.4841 was 20.00 mm o.d., wall thickness 3.00 mm, 1200 mm length.
The system includes an arc-discharge excitation tool with an initiation generator and allows both continuous and pulsed operation mode by varying the pulse duration from 1 to 60

seconds with intervals of 1 up to 120 seconds. The essential advantage of this system is the possibility to scan the cathode spot along the tube with controlled rate.
The in situ cleaning was performed as the discharge current varied from 50 to 100A within 2 up to 5 minutes. Subsequent coating occurs at the vacuum of 10^{-5} mbar in the controlled temperature range between 400 and 700°C with a fixed current of 100 to 200A within 2 to 6.5 minutes depending on the required thickness.

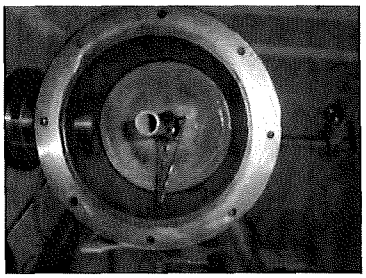

Fig. 4: Top view of the vertical VAD system.

Samples (595 mm long) have been prepared for installation in vacuum equipment from the tubes which were 1200 mm long and 38 mm in diameter.

3. Results and Discussion

For the characterisation of the thickness, chemical composition and microstructure of coatings, weight-increase measurements, electron-dispersion spectroscopy (EDS), optical and scanning-electron microscopy (SEM) was used. The test samples from different parts of the coated tubes were prepared to characterise the coating in longitudinal as well as in radial direction. Typical results are presented below.

3.1. Characterisation of the coating by VAD in the horizontal vacuum chamber.

By EDX characterisation it was shown that the chemical composition of the coatings is very similar to that of the cathode and does not change significantly in the short time during the VAD process, Table 1. High Chromium content in the coatings is very essential for their protective properties against oxidation.
Fig. 5 shows the cross section of a VAD coating at the inner surface of a tube with steel, grade X15CrNiSi25-20 and an inner diameter of ca. 30 mm, combined with a SEM view rectangular to the surface. It can be seen, that the coatings are continuous and ensure proper adhesion of the bonded surfaces.

Table 1. Composition of the source material and of the coating measured by EDX analysis.

Material for cathode:X15CrNiSi 25-20; 1.4841					
Chemical analysis in mass percent					
	Cr	Ni	Si	Mn	Fe
Cathode	22.7	20.3	1.6	1.3	54.0
Coating	24.5	20.0	2.3	0.5	52.7

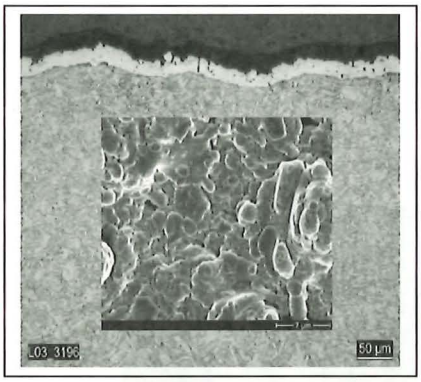

Fig. 5: Optical and SEM image (detail) - cross section VAD-coating.

3.2. Characterisation of the coating by VAD in the vertical vacuum system.

The chemical composition of the sources and of the coating is almost identical, as shown in Table 2, Fig. 6. The investigation of the morphology and microstructure of the coated surfaces and of the interfaces between the coatings and the substrate using optical microscopy and scanning electron microscopy shows that the martensitic structure of the tube coupons after VAD treating is retained, Fig. 7. An intermediate layer, probably caused by contamination at the beginning of coating which disappears during the further deposition, could be observed in the micrographs. Therefore, additional attention is paid to the characterisation of the interfaces and measures for improvement of pre-cleaning techniques.

Table 2. Composition of the source material and of the coating measured by EDX.

Material	C	Si	Mn	P	S	Cr	Mo	Ni	Sn	Al
Tube X10CrMoVNb.9.1	0.1	0.31	0.44	0.016	0.002	**8.41**	0.94	0.12	0.006	0.012
Source X15CrNiSi25-20	0.045	1.64	1.83	0.024	0.001	**24.2**	0.18	19.70		
Coating	0.05	1.6	1.7		0.001	**25.3**	0.19	19.2		

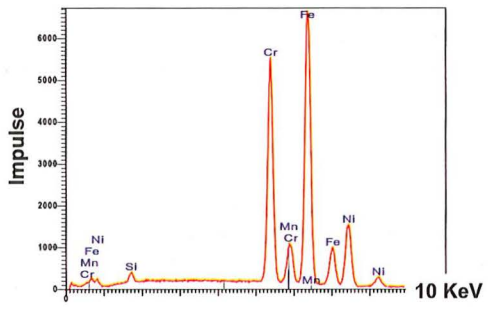

Fig. 6: Chemical composition of the coating obtained in the vertical system - EDX spectra

Experiments at both vertical and horizontal systems have shown that the coating thickness estimated from the total weight increase and from SEM data depends linearly on the VAD current. This consideration enables the coating of desired thickness by the current control.

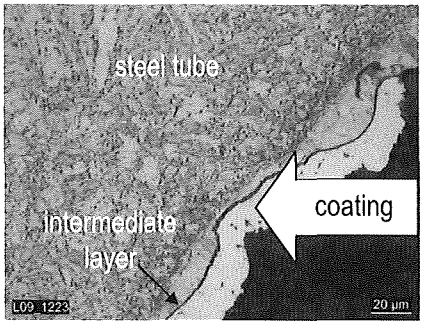

Fig. 7: Image of the cross section of VAD-coating.

4. Conclusion

Development of a new technique for the protection of inner surfaces of steel tubes is the subject of this work. The coatings are obtained by vacuum arc deposition process on 595 mm long steel tubes cleaned in situ before the VAD. The 20 – 50 µm thick layers are crystalline and have a chemical composition nearly as the same the source cathode material providing a high Chromium content. The martensitic structure of the tube work-pieces after VAD treatment is retained due to process temperature below 700°C and the short process duration time.
The VAD can be further developed for the manufacture of longer tubes, functional graded and multilayer coatings. Furthermore, application of a bias potential during the deposition offers additional opportunities for the improvement of coating adhesion.

5. References

[1] R.L. Boxman and S. Goldsmith: "Principles and Application of Vacuum Arc Coatings." *IEEE Trans. Plasma Sci.* , vol. PS-17, pp. 705-711, 1989
[2] R.L. Boxman, P. Martin, D. Sanders (editors): *Handbook of Vacuum Arc Science and Technology,* Noyes Publications (Park Ridge, NJ) 1995
[3] H. Bruzzone, H. Kelly, A. Marquez, D. Lamas, A. Ansaldi, and C. Oviedo: "TiN coatings generated with a pulsed plasma arc", *Plasma Sources Sci. Technol.* Vol. 5, pp 582-587, 1996
[4] T. Zhang, B. Tang, Q. Chen, Z. Zeng, P. Chu, M. Bilek, and I. Brown: "Vacuum arc plasma transport through a magnetic duct with a biased electrode at the outer wall", *Rev. Sci. Inst.* Vol. 70, pp. 3329-3331, 1999
[5] B. Bulat and M. Esterlis: Removing Scale, Oxide Films and Contaminants From Metal Components by Vacuum Electric Discharge, *Fisika I Khimiya Obrabotki Materialov / in Engl./*,Vol. 21, No3, pp.49-53, 1987

9th Liege Conference : Materials for Advanced Power Engineering 2010
edited by J. Lecomte-Beckers, Q. Contrepois, T. Beck and B. Kuhn.

STEAM OXIDATION OF TP 347H FG: LABORATORY EXPOSURES VERSUS SERVICE CONDITIONS AT THE POWER PLANT

Anette N Hansson[1] and Melanie Montgomery[2]

[1]DONG Energy, A.C. Meyers Vænget 9, 2450 København S, ANEHA@dongenergy.dk
[2]Vattenfall Heat Nordic/ DONG Energy/ DTU Mekanik, 2800 Lyngby, Denmark, mmon@mek.dtu.dk

Abstract

TP347H FG is often used as final superheater tubing at Danish Power Plants. The oxidation behaviour of TP347H FG in steam was investigated both in laboratory conditions and field conditions. Short time exposures (336 hours) were performed in the laboratory at 500, 600 and 700°C in gasses with 8 or 46% H_2O and varying oxygen partial pressures. The shortest exposure time at the power plant was 7720 h, the temperature varied between 500 and 650°C. Surprisingly, thicker oxide layers formed within the laboratory facility at 600 and 700°C than during the long time exposures at the power plant. This could not be explained by spallation.

Double-layered oxides developed during oxidation. The outer layer consisted of Fe-oxides and the inner oxide contained Fe and the remaining alloy elements. Investigations with scanning electron microscopy (SEM) revealed that the morphology of the inner oxide was different for the two types of exposures. However, investigation using transmission electron microscopy (TEM) showed that the inner oxide in both cases consisted of particles of Fe-Mn-Cr spinel embedded in a metallic Fe-Ni matrix in the bulk of the (former) alloy grains and Cr-rich oxide layer along the (former) alloy grain boundaries. The main difference between the layers formed at the two locations is that the Cr-rich oxide layer is thicker for the samples exposed at the power plant than that for the samples exposed at the laboratory conditions. Furthermore, the depth of Cr depletion in the alloy adjacent the oxide layer is greater for the samples exposed at the power plant compared to those exposed in the laboratory.

The microstructure investigation suggests that the slower oxidation rate of TP347H FG at the power plant as compared to the laboratory is due to a larger reservoir of Cr for the samples exposed at the power plant probably combined with a higher mobility of Cr within the alloy.

Keywords: Cr-content, surface treatment, oxygen content, heat flux, pressure.

1. Introduction

The oxidation conditions that components experience at the power plant are much more complicated than those that can be reproduced in the laboratory. Nevertheless, laboratory exposures play an important role in evaluating the performance of newly developed steels for power plant components (e.g. partners in COST 536 ACCEPT action perform long term oxidation tests on steels designed within the programme). In COST 522 partners from 9 different laboratories oxidised specimens from the same batch of P92 at 600 and 650°C for 1000 h using their current experimental procedures. The reported results showed a very large scatter: The oxide thickness varied between 60 and 100 µm at 600°C and between 40 and 240

µm at 650°C [1]. This comparison emphasizes how much experimental parameters affect the obtained results.

An oxidation project (PSO 5393) was initiated, in which the oxidation behaviour of the austenitic TP 347H FG in laboratory and field conditions was studied in detail, as this steel is used for many of the final superheaters in power plants in Denmark. The oxidation times used in the laboratory tests was much shorter than those used during the field tests, whereas the temperature range was comparable. Surprisingly, thicker oxide layers formed during oxidation in the laboratory facility than during exposure at the power plant. In this paper, the oxide layers are described and it is speculated why the steel oxidises faster within the laboratory facility than within the power plant. Several parameters, such as the exact composition of the steel, surface treatment, oxygen content of the system, water chemistry, time, heat flux, and pressure are considered.

2. Experimental

The content of selected elements in the batches of TP347H FG used in this study is listed in table 1. The samples were (part of) tubes with an inner diameter of 25 mm and a wall thickness between 5 and 9 mm. They were pickled before exposure.

Table 1: The content of selected elements (wt%) in the batches of TP 347H FG used in the laboratory exposures and in the field test.

	C	Cr	Si	Mn	Ni
Laboratory	0.042	16.9	0.26	1.95	10.7
Field test (3 batches)	0.09	18.5-19.3	0.5	1.6	12.3-12.6

At the power plant, 24 samples of TP347H FG were exposed in four test superheaters, each with four loops. Some of the samples were exposed outside the combustion chamber and were not subjected to heat flux. No oxygen was added to the feedwater. The exposure times were 7720, 22985, 29588, and 57554 h and the metal temperature was between 500 and 650°C. For further details see ref. [2,3,4]. In the laboratory, oxidation experiments were performed at 500, 600, and 700°C for 336 hours using either synthetic air, Ar, or Ar-7%H_2 as carrier gas, the steam content was either 8 or 46%. For further details see ref. [5]. The oxide layers were investigated with light optical microscopy (LOM), SEM, TEM, energy dispersive spectroscopy (EDS), and x-ray diffraction (XRD), for further details see ref. [4,5].

3. Results

Fig. 1 shows representative examples of the oxide layers formed during exposure at the power plant. The outer layer consists of Fe_2O_3 on top of Fe_3O_4; Ni is often incorporated into the Fe_3O_4 layer. The inner oxide appears more irregular for samples exposed to less than 580°C (see Fig. 1a) than for samples exposed to higher temperatures (see Fig. 1b). However, TEM

investigations revealed that the inner oxide in both cases consists of a Cr-rich oxide layer along the (former) alloy grain boundaries and particles of Fe-Cr spinel and of metallic Ni/Fe within the (former) alloy grains. These particles were smaller the lower the oxidation temperature. The Cr-rich layer mainly consisted of Fe-Mn-Cr spinel and Cr_2O_3. The fraction of Cr_2O_3 within this layer increased with increasing temperature and with time. Cr-depletion was observed in the alloy below the oxide layer and along the alloy grain boundaries. The Cr-content of the alloy adjacent to the oxide layer and the depth of Cr-depletion increased with increasing temperature (see *Table 2*). For further details see ref. [4].

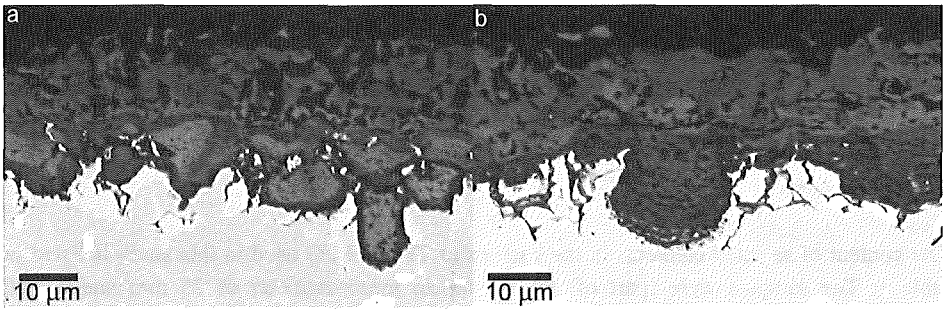

Fig.1: SEM images of TP 347H FG oxidised in steam at 256 bar for 29588 h at a) 515°C and b) 589°C.

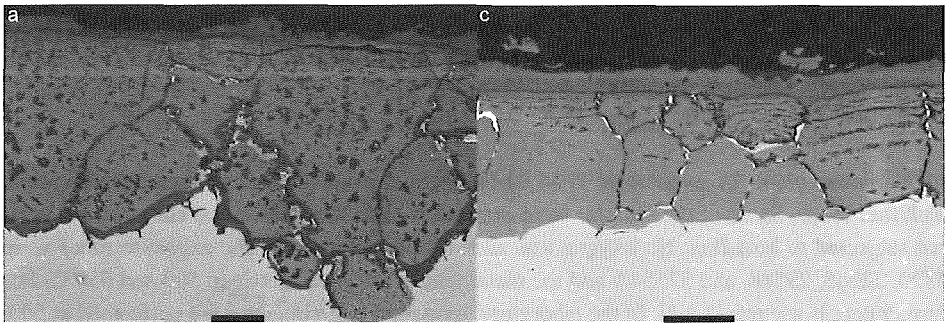

Fig. 2: SEM images of TP 347H FG oxidised in Ar-46% H_2O at atmospheric pressure for 336 h at a) 700°C and c) 600°C.

Fig. 2 shows representative examples of the oxide layers formed during oxidation in the laboratory facility. The outer layer consisted of Fe_2O_3 on top of Fe_3O_4, in the case that the oxygen partial pressure was high enough to stabilise Fe_2O_3. The outer layer often spalled off during cooling. TEM investigations showed that the inner oxide consisted of Fe-Cr spinel particles embedded in a matrix of metallic Fe-Ni in the interior of the (former) alloy grains. As for the samples exposed at the power plant, these particles grew with higher temperatures. A thin Cr-rich layer is observed along the (former) alloy grain boundaries after oxidation at

600°C. This layer is much thicker after oxidation at 700°C and it consists of Fe-Cr-Mn spinel and particles of Cr_2O_3. Cr-depletion in the alloy adjacent to the oxide layer was observed after oxidation at 700°C. For further details see ref. [5].

Table 2: Concentration (wt%) of the alloy adjacted to the oxide layer as measured with EDS-TEM and the depth of depletion af measured with EDS-SEM.

T_M / time	Cr	Mn	Fe	Ni
541°C/ 7720 h	2.7	< 0.5	62.4	34.6
595°C/ 7720 h	8.9	< 0.5	67.8	22.8
515°C/ 29588 h	3.8	< 0.5	66.0	29.9
589°C/ 29588 h	11.6	< 0.5	69.0	19.2

T_M (°C): metal temperature
f (%): fraction of interface
d (μm): average depth

7720 h			22985 h		
T_M	f	d	T_M	f	d
511	43	2.0	499	47	1.9
536	43	3.0	563	73	5.6
541	43	2.6	602	97	6.9
591	66	4.9	604	all	5.0
595	73	5.3	619	all	6.9

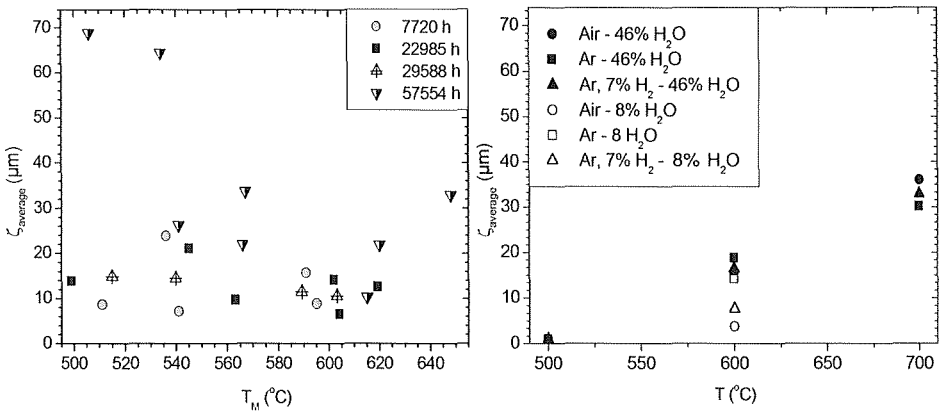

Fig. 3: The average thickness of the inner oxide (ζ) versus temperature (T). Left: power plant samples exposed in steam at 256 bar. Right: Laboratory samples (time: 336 h).

Fig. 3 shows the thickness of the inner oxide versus temperature for the samples exposed at the power plant (left) and the laboratory facility (right). The data in Fig. 3-left suggest that the average thickness of the inner oxide is not influenced significantly by the temperature or time for the samples exposed at the power plant, the only exception is samples exposed for the longest time at the lowest temperature (506 and 534°C). For these samples the average thickness of inner oxide is more than twice the thickness of the inner oxide observed at higher temperatures. In the laboratoty facility, the thickness of the inner oxide increases with increasing temperature (Fig. 3-right). The thickness of the inner oxide is independent of the carier gas as long as it contains 46% H_2O. Thinner inner oxides were obtained in air and Ar-7% H_2O with reduced steam content. Comparison of the diagrams in Fig 3 shows that thicker oxide layers develop during short-term oxidation in the laboratory at 600 and 700°C than

during long-time exposure at the power plant (e.g. at 600°C, 336 h in Ar-46% H_2O: 19 µm, 7720 h at power plant: 9 µm). This cannot be attributed to spallation of the oxide layer during exposure at the power plant, since there is evidence that indicates that the interface between the inner oxide and outer oxide is the position of the original interface: The tubes exposed at the power plant were machined locally in order to create an even wall thickness. At these locations, a thin Cr_2O_3 layer was formed along the main part of the surface. Locally, the oxidation front has broken through this layer (see Fig. 4) and here the oxide layer resembled that observed at the non-deformed parts of the tubes [6].

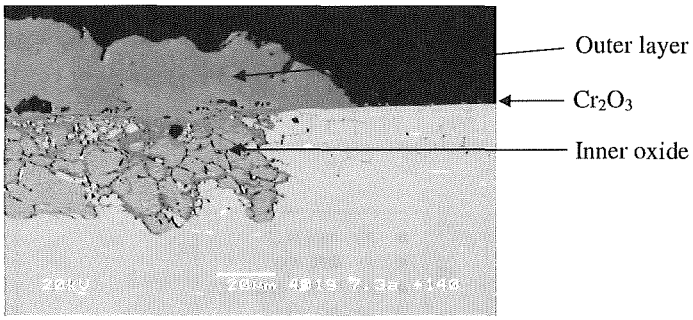

Fig 4: TP 347H FG exposed at Vestkraft for 57554 h at 534°C and 256 bar. The oxide layer at the part of the tube, which has been machined.

2. Discussion

The results show that oxides with similar compositions develop during oxidation at the power plant and within the laboratory facility. Comparing the morphology of the two sets of samples, a much thinner Cr-rich oxide region is present along the (former) alloy grain boundaries for the samples exposed at the laboratory facility as compared to those exposed at the power plant. Furthermore, for the laboratory samples, the inner oxide is thicker since the oxidation front has more frequently broken through the Cr-rich layer formed along the grain boundary closest to the original metal surface resulting in two oxidised alloy grains in depth. This explains the faster oxidation rate of the samples from the laboratory facility, since the growth rate of the Cr-rich oxide developing along the (former) alloy grain boundaries is much lower than the internal oxidation rate of the (former) alloy grain. The observation that the Cr-depleted areas are smaller for the samples exposed within the laboratory facility as compared to those exposed at the power plant suggests that the ability of the alloy to supply Cr for the growing oxide layer is less for the samples exposed in the laboratory facility.

2.1. Influence of alloy composition

Different batches of TP 347H FG were used in the laboratory exposure and in the field exposure. It is evident from Table 1 that the batch used in the laboratory tests contains less Cr and Si than those used during the field test. Thus one would expect this batch of steel to

perform worse. In order to clarify whether the difference in composition was responsible for the heavier oxidation observed during the laboratory test, oxidation of zero-samples (i.e. non exposed samples) of the batches used in the field-test was carried out in the laboratory furnace (experimental conditions: 336 h, 600°C, Ar – 46% H_2O). The morphology of the oxide layers are shown in Fig. 5. The oxidation front has reached the first alloy grain boundary in depth for the zero-sample containing 18.5 wt% Cr, and it looks as if a protective Cr-rich oxide layer has developed along this grain-boundary. The average inner layer thickness is 12.5 μm. Remnants of a thin oxide layer are observed at some positions along the surface of the zero-sample containing 19.3 wt% Cr. At other locations, the oxidation front has started to penetrate into the first alloy grain in depth. The average inner layer thickness is 3.2 μm. It was 18.8 μm on the low Cr steel used in the laboratory tests. These results show that the Cr-content has an impact on the oxidation behaviour. However, if the faster oxidation observed in the laboratory merely is attributed to the exact composition of the batches, only growth of the Cr-rich oxide layer developing along the former alloy grain boundaries should occur with prolonged oxidation of the zero samples within the laboratory facility, such that the oxide layer is one grain deep and no further. Furthermore, it should be noted that for 1 of the samples exposed at the power plant (7720 h, 625°C) the oxide layer only consisted of Cr_2O_3 and Mn-Cr spinel and its thickness was approx. 1 μm. Thus we believe that the faster oxidation rate observed in the laboratory compared to that observed at the power plant cannot merely be attributed to the difference in composition of the batched used.

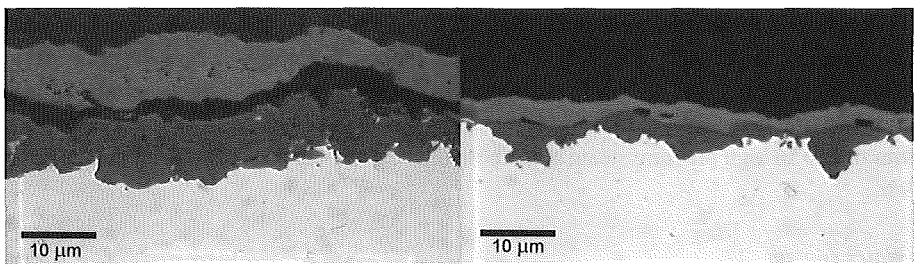

Fig. 5: LOM images of the oxide layers formed on zero-samples of TP 347H FG from the field-test during oxidation in the laboratory furnace for 336h at 600°C in Ar-46% H_2O. Left: 18.5 wt% Cr, right: 19.3 wt% Cr.

2.2. Surface treatment

The oxidation behaviour of austenitic 18/8 stainless steels is strongly influenced by whether the surface of the steel has been ground or pickled prior to oxidation [7], since grinding introduce fast diffusion paths via dislocations and thereby enhanced Cr-transport towards the oxide layer. The inner surface of new super heater tubes undergo a certain surface treatment prior to operation. As part of the surface treatment the tubes are 1) flushed in 1% hydrofluoric acid (HF) at 50 to 60°C and 2) passivated using hydro peroxide (H_2O_2) in an ammonia solution with pH larger than 10. In the laboratory, the samples were pickled in an aqueous

solution of 3% HF and 15% HNO_3 at room temperature for 30 minutes. It was speculated whether or not passivation promotes the formation of a protective oxide layer. In order to clarify this, a pickled sample was placed in the following solution: 100 ml H_2O, 14 drops of NH_3 resulting in pH > 10, and 0.1 ml 25% H_2O_2, for 20 minutes and then oxidised in the laboratory facility. The morphology and the average thickness of the oxide layer were comparable to that for the non-passivated sample oxidised at the same conditions, suggesting that passivation after pickling prior to oxidation has a negligible effect on the resulting oxide thickness and morphology.

2.3. Oxygen content

The formation of gaseous $CrO_2(OH)_2$ has been proven detrimental for the oxidation resistance of chromia forming alloys in fast flowing atmospheres with high oxygen and water contents. The oxide becomes more and more depleted in Cr and eventually loses its protectiveness [8,9]. The formation of $CrO_2(OH)_2$ is promoted by high pressure, high oxygen partial pressure combined with high water contents [10]. Comparing the data in Fig. 3 right shows that comparable oxide thickness were obtained after oxidation in 46% H_2O irrespective of the oxygen partial pressure of the carrying gas. This suggests that the formation of gaseous $CrO_2(OH)_2$ has a minor influence on the oxidation behaviour in the present investigation.

The level of dissolved oxygen in steam may affect the oxidation behaviour. Results by A.T. Fry [11] indicated faster oxidation of Esshete 1250 and P92 in the steam with 10 ppb oxygen as compared to steam with 200 ppb. The oxide layers developing in low oxygen steam contained less porosity and were less prone to spallation. Contrary, Nishimura et al. [12] did not find any systematic effects of using aerated water or de-aerated water on the scale growth kinetics of P91 in high pressure steam at temperatures between 600 and 700°C and times up to 9939 h.

2.4. Water content

Laboratory exposures in either 50% H_2O (carrier gas) or 100% H_2O (no carrier gas) of P92 at 600°C and T23 at 550°C showed a consistently higher scale thickness for the samples exposed to 100% H_2O. However, the difference was small and regarded to lie within the expected experimental scatter [1]. Laboratory exposures of P91 at 600°C in 1-2% O_2 (rest N_2) showed increasing oxidation rate with increasing water content until a content of 10% H_2O was reached [13]. Thicker oxides were generally obtained in the laboratory exposure when the carrier gas was humidified to 46% as compared to 8% (see Fig. 3 right). The above results indicate faster oxidation with increasing humidity, and thus one would have expected faster oxide growth at the power plant compared to the laboratory facility.

2.5. Water chemistry

A complex chemical treatment of the water is carried out at the power plants in order to minimise corrosion damage and deposition problems. Initially, the oxidation experiments were carried out using deionised water from Technical University of Denmark. It was suggested that the poor quality of the water used in the laboratory experiments could be responsible for the high oxidation rates. Thus water was tapped from the power plant situated at Technical University of Denmark and an oxidation experiment was carried out. Using a higher quality of water had no effect on the oxide morphology or on the average thickness of the inner oxide layer.

2.6. Time

Only short term exposures were carried out in the laboratory. One could argue that the oxide morphology will change with prolonged oxidation time. However, the morphology in Fig. 2 shows that the first alloy grain in depth has been oxidised and that the second alloy grain in depth has started to oxidise at several positions. This suggests that the Cr-rich layer developing along the (former) alloy grain boundaries "loses" it protectiveness much faster during oxidation at the laboratory facility as compared to the power plant. Of course this is related to the reservoir of Cr within the steel.

2.7. Heat flux

The superheater materials experience a heat flux during service at the power plant. No heat flux was present during the laboratory exposures. One could argue that the steel oxidises faster in the laboratory set-up due to the absence of a heat flux. This is contrary to results reported by Griess et al. [14], who found that 2¼Cr1Mo steel oxidised much faster when a heat flux was present than without a heat flux. Furthermore, a number of TP 347H FG were exposed outside the boiler at Vestkraft (i.e. without a heat flux). These samples did not show a different oxidation behaviour than the samples, which were exposed within the boiler (i.e. in the presence of a heat flux). This suggests a negligible effect of the heat flux on the oxidation behaviour of this steel.

2.8. Pressure

In the laboratory facility, the oxidation experiments were carried out at ambient pressure, whereas high pressure was applied inside the tube (i.e. the tube is expanded) at the power plant. Laboratory oxidation experiments at high pressures are most often conducted in an autoclave (i.e. the entire sample is exposed to high pressure). Applying high pressure in an autoclave has an effect on the oxidation behaviour: A.T. Fry [11] found that high pressure decreases the volume and distribution of voids and defects in the oxide scale. However, the question is: what is the effect of pressure on the oxidation behaviour of the steel at the power plant and is it possible to simulate this effect by applying an autoclave?

Jianmin et al. [15,16] compared the oxidation behaviour of TP 347H FG exposed within power plants at a steam pressure of 91 bar and 256 bar, respectively. Their findings suggested that a "better healing layer" (i.e. a higher degree of selective oxidation of Cr) was formed at high steam pressure. Perhaps the expansion of the tube facilitates faster diffusion of Cr in the alloy towards the oxide layer. In other to verify this, a sample was designed [17] (see Fig. 6), such that the effect of tube expansion at high pressure could be investigated within the laboratory set-up. The wedge introduced elastical deformation of tube and not plastical deformation. It was possible to push-in the wedge manually.

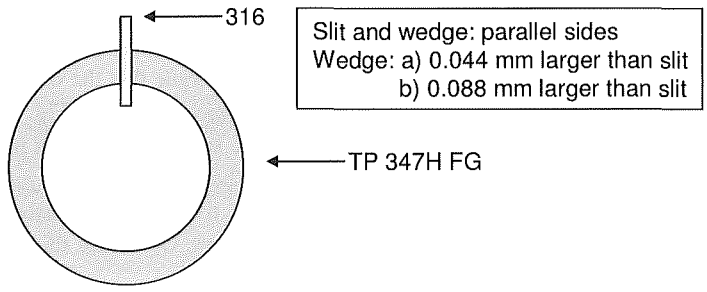

Fig. 6: The sample design for investigation of the effect of tube expansion at high pressure on the oxidation behaviour.

The effect of tube expansion on the thickness of the inner oxide layer is seen in Table 3, and the thickness variation along the circumference for ring sample b (wedge = 0.088 larger than slit) is listed in Table 4. It is evident that the thickness of the inner oxide layer is reduced the larger the wedge, but the thickness along the circumference does not vary systematically. The results suggest that the expansion of the tube due to the internal pressure has an impact on the oxidation behaviour.

Table 3: The effect of tube expansion on the thickness of the inner oxide layer [average (min, max)].

Sample	No wedge	0.044 mm wegde	0.088 mm wegde
Thickness (µm)	18.8 (15-21)	15.1 (11-21)	12.6 (8-18)

Table 4: Thickness measurements along the circumference for ring sample b (wedge = 0.088 mm larger than slit). The wedge is positioned at 12'o clock.

Position	12.15	13.30	15.00	16.30	18.00	19.30	21.00	22.30
Thickness (µm)	13.2	7.9	8.5	10.5	14.5	17.9	11	17.3

3. Conclusion

TP 347H FG samples oxidise much faster in the laboratory set-up than at the power plant. The Cr-content of the batch that was exposed at the laboratory facility was approximately 1.5-2

wt% less than that of the batches exposed at the power plant. Laboratory exposure of zero-samples of the batches used in the field-test shows that this difference has an impact on the oxidation behaviour.

The laboratory set-up is very simple and does not resemble the complex conditions, which the materials experience at the power plant. Our results suggest that the increased oxidation rate observed within the laboratory facility as compared to the power plant is not an effect of:

Surface treatment
Oxygen content
Water content
Water chemistry
Heat flux

The results suggest that tube expansion caused by the high steam pressure does have impact on the oxidation behaviour. The expansion probably increases the mobility of Cr.

Acknowledgement
Some of the samples originate from the Brite-Euram project: BRE2.CT93-0600, in which Elsam, Alstom Power Boiler, Laborelec, BWI, and CSI were partners. The project was funded by PSO (project no. 5293, ENERGINET.dk).

Reference

[1] S. Osgerby and J. Quadakkers, *Materials at High Temperatures,* 22(1/2), 27, (2005).
[2] Von. G. Scheffknecht, R. Blum, Q. Chen, A.Vanderschaeghe, *VGB Kraftwerkstechnik*, 76, 856, (1996).
[3] J. Gabrel, C. Coussement, L. Verelst, R. Blum, Q. Chen,C. Testani, *Materials Science Forum*, 369–372, 931, (2001).
[4] A.N. Hansson, H. Danielsen, F.B. Grumsen and M. Montgomery, *Materials and Corrosion*, published online November 2009.
[5] A.N. Hansson, K. Pantleon, F.B. Grumsen, and M.A.J. Somers, *Oxidation of Metals*, 73, 289, (2010).
[6] M. Montgomery, O.H. Larsen, S.A. Jensen, and O. Biede, *Materials Science Forum*, 461-464, 1007, (2004).
[7] S. Janson, W. Hübner, G. Östberg, and M. dePaubaix, *British Corrosion Journal,* 4, 21, (1969).
[8] H. Asteman, K. Segerdahl, J.-E. Svensson, and L.-G. Johansson, *Oxidation of Metals,* 57(3/4), 193, (2002).
[9] H. Asteman, K. Segerdahl , J.-E. Svensson, and L.-G. Johansson, *Material Science Forum*, 369-372, 277, (2001).
[10] B.B. Ebbinghaus, *Combustion and Flames*, 93, 119 (1993).
[11] A.T. Fry, *Energy Materials*, 2(4), 214, (2007).
[12] N. Nishimura, N Komai, and F. Masuyama, *Materials at High Temperatures*, 22(1/2), 3, (2005).
[13] J. Ehlers, D.J. Young, E.J. Smaardijk, A.K. Tyagi, H.J. Penkalla, L. Singheiser, and W.J. Quadakkers, *Corrosion Science*, 48, 3428, (2006).
[14] J. Griess, J.H. DeVan, and W.A. Maxwell, *Materials Performance*, 19, 46, (1980).
[15] J. Jianmin, M. Montgomery, O.H. Larsen, and S.A. Jensen, *Materials and Corrosion*, 56(8), 542, (2005).
[16] J. Jianmin, M. Montgomery, O.H. Larsen, and S.A. Jensen, *Materials and Corrosion*, 56(7), 459, (2005).
[17] Tommy Vilhelmsen (Vattenfall) and Ulrik Borg (DONG Energy)

9th Liege Conference : Materials for Advanced Power Engineering 2010
edited by J. Lecomte-Beckers, Q. Contrepois, T. Beck and B. Kuhn.

9 % Cr STEEL HIGH TEMPERATURE OXIDATION. SOLUTIONS INVESTIGATED FOR IMPROVING CORROSION RESISTANCE OF THE STEEL.

Harold Nicolas EVIN[1], Olivier HEINTZ[1], Cecilia FÖJER[2], Sâad JAKANI[2], Annick DHONT[2], Serge CLAESSENS[2], Sébastien CHEVALIER[1].

[1]*Laboratoire Interdisciplinaire Carnot de Bourgogne UMR 5209 CNRS Université de Bourgogne 9 av. Alain Savary, BP 47870, 21078 Dijon, France*
sebastien.chevalier@u-bourgogne.fr

[2]*OCAS N.V. ArcelorMittal Global R&D Gent, Belgium, Pres. J.F. Kennedylaan 3, B-9060 Zelzate cecilia.fojer@arcelormittal.com*

Abstract

The improvement of high temperature oxidation resistance of low chromium content steels, such as T/P91, is of great interest in regards with their application in thermal power generating plants. Indeed, they possess good creep properties, but are facing their limits of use at temperature higher than 600°C, due to accelerated corrosion phenomena. Good knowledge of the mechanisms involved during their oxidation process is needed to prevent the degradation of the materials and to extend life time of the power plants components. Oxide layers thermally grown, on 9%Cr steels (provided by OCAS N.V), during isothermal tests between 600°C and 750°C in laboratory air under atmospheric pressure were investigated, by Scanning Electron Microscopy (SEM) and X-ray diffraction (XRD). The oxidation behaviour appeared very limited at 750°C, due to the presence of a breakaway, which can be linked to iron porous oxide grown over the surface of the samples. "In situ" X-ray Photoelectron spectroscopy (XPS) analyses were performed in air at 600°C after short exposures (between 5 min. and 24 h). A complex mixture of iron oxide, Cr_2O_3 and Cr (VI) species were characterized in the scales. The in-situ analyses were compared and related to XPS analyses performed on thick oxide scales formed on samples oxidized in air at 600°C for 100h. An oxidation mechanism is then proposed to understand the oxide scale growth in the temperature range 600 - 750°C. The second step of this study consists in improving the high temperature corrosion resistance of these steels without modifying their mechanical properties. Thus several solutions were investigated such as MOCVD coatings, pack cementation coatings, and tested in cyclic conditions prior.

Keywords: T/P91, steam, chromia, coatings, cyclic oxidation.

Introduction

Important needs in energy together with environmental issues place power generation plants under constraints which lead to develop high efficiency systems [1]. Martensitic/ferritic 9% Cr steels are widely used in power generation plants where steam is transported under high temperature and pressure (typically 530°C and 19 MPa) in pressurized water reactors [2]. A usual way to increase the efficiency consists in increasing temperature and pressure parameters of the power generating plant. As an example, the total efficiency of a plant increases by nearly 6 % when changing the steam parameters from 538°C/18.5 MPa to 593°C/30 MPa. It could even reach an 8 % increase at 650°C [3]. For coal fired systems,

temperatures up to 650°C or even 700°C with a pressure of 35 MPa are currently under consideration. The super heater tube temperatures often exceed the steam temperature by as much as 30°C [4-5].
Progress have been made improving 9% Cr steels mechanical strength and creep resistance at temperature up to 700 °C through modifying alloy steel chemical composition [3, 6] or microstructure. But, at high temperature, corrosion phenomena are enhanced. Formation of dense, thick, and adherent chromia layer, which is considered like a good way to increase the oxidation resistance, is not possible in that case. Indeed it closely related to many parameters such temperature, oxidizing atmosphere, frequency and time of exposure and mainly to the chromium content [7-10]. The key to a successful improvement of 9%Cr steel, such as T/P91 grade, lies in a better understanding of the material reactivity under high temperature and high pressure through the observation and characterization of the germination and growth of the surface oxide layers occurring within the first oxidation instants.
The aim of this study is to further increase our understanding about oxidation mechanisms of T/P91 through a detailed microstructural investigation of the oxide scale formed on T/P91 in presence of laboratory air and to propose how to improve high temperature corrosion resistance of this grade. Therefore isothermal analyses were performed between 600°C and 750°C. Characterizations of the obtained oxide scale obtained were realized using Scanning Electron Microscope, and X-ray Diffraction. "In situ" X-ray Photoelectron spectroscopy (XPS) analyses were also performed in air at 600°C after short exposures. A complex mixture of iron oxide, Cr_2O_3 and Cr (VI) species were characterized in the scales. A few ways to improve the high temperature corrosion behaviour of the steel will be proposed in this work and tested in cyclic condition at 700°C.

2. Experimental procedure.

2.1. Samples preparation

9%Cr steel was provided by OCAS N.V ArcelorMittal Global R&D Gent. Table 1 summarizes the composition. Rectangular samples 15mm x 10 mm x 3 mm were cut from the material. Some of the samples were shaped with a hole of 2 mm in diameter in order to hang them during kinetic tests on thermobalances. The specimens were polished up to 1200 µm with SiC papers and cleaned in an ultrasonic ethanol bath.

Elts	C	Cr	Mo	Si	Mn	B	P	Ni	S	Nb	Al	V	N	Fe
% wt	0.098	8.4	1.1	0.34	0.57	0.0004	0.01	0.25	0.002	0.076	0.017	0.27	0.028	Bal

Table1: *Chemical composition of the 9% chromium containing steel used for the study.*

2.2 Isothermal tests

The kinetics of oxidation of samples was followed using a SETARAM TG 92 thermobalance. Experiments were performed between 600°C and 750°C for 100 hours in laboratory air under atmospheric pressure. This thermobalance has a balance beam ruled by a computer and allow to measure mass variation with microgram accuracy. The evolution of mass is a function of time $(\Delta m/A)^2 = k_p t$ where Δm: mass gain in g, A: area in cm^2 and t: time in second) and allow us in certain cases to determine the parabolic rate constant k_p [11].

2.3 Characterizations techniques

2.3.1 Scanning Electron microscopy

The corrosion products were characterized and analyzed using a JEOL JSM-6400 F scanning electron microscope (SEM) with a field emission gun (FEG), coupled with an Oxford LINK EXLII energy dispersive X-ray (EDX) analyzer. Surface micrographs were taken and analyzed.

2.3.2 X-ray diffraction

Crystalline phases were investigated by X-ray diffraction (XRD) using a CPS 120 INEL apparatus with a copper anode ($K\alpha$=0.154 nm) using 1° glancing angles in order to analyse only the upper surface of the specimen.

2.4 "In situ" XPS experiments

A developed device for heat treatment under controlled atmosphere enables the step by step study of the reactivity of materials under high temperature and high pressure once coupled with X-ray Photoelectron Spectrometer. The samples were placed in a quartz tube inserted in a tubular oven. The unit was maintained under vacuum prior to and after the oxidation process (5.10^{-8} Torr, using a turbomolecular pumping unit). The oxidized metallic coupon, once back to room temperature, was then transferred into the analysis chamber of a SIA 100 Cameca-Riber spectrometer (Resolution of 1.2 eV full, width at half maximum of $3d_{5/2}$ level of silver) without contamination due to the outside atmosphere. In order to focus on the first steps of the oxide growth, the oxidation conditions of the samples were the following: from 5 min to 1 hour exposure at 600°C in laboratory air under atmospheric pressure. Spectra were then recorded using 240W Al $k\alpha$ radiation (1486.6 eV). Emerging photoelectrons were detected normally to the surface. Photoemission peak areas were calculated after background subtraction using a Shirley routine. Energy calibration has been realized on level 1s of adventitious carbon (at 284.5 eV). Argon ion bombardments were carried out using a Perkin-Elmer 04-303A differentially pumped ion gun. Bombarding conditions were an acceleration voltage of 4keV, a pressure of 10^{-5} Pa and an angle of incidence with respect to the surface normal equal to 60°. The ion flux was in the region of $5x10^{16}$ ions cm^{-2}. In order to help to reconstruct the spectra; both spectrum of an industrial hematite and an industrial chromia powder, commercialized by the Prolabo Sanofi-aventis laboratory (Rhône-Poulenc), were also registered.

Ex-situ XPS spectra profiles were also registered using 241W Al $k\alpha$ radiation (1486.6 eV) on a PHY Quantera SXM. Therefore, information within the scale depth was obtained by successive Argon ion sputtering (3 keV, 15nA) and analyses from the oxide surface scale to the bulk of sample oxidized at 600°C for 100h in air and at atmospheric pressure in a muffle furnace.

2.5 Coatings procedures.

2.5.1 MOCVD coatings

Metal Organic Chemical Vapor Deposition (MOCVD) coatings were performed on the 9% Cr steel grade using tris,2,2,6,6 tetraméthylheptane-3,5dionato of: lanthanum, yttrium or neodymium as a precursor. The experimental process was described by Chevalier et al.[9,12-13]. The aim of those coatings is to use the reactive element beneficial effect. Coatings around 200-400 nm thick were obtained for each specimen. A lanthanum oxide coated samples was pre-oxidized for 30 min at 800°C after the MOCVD process. This step was proposed because rare earth segregation phenomena at the oxide grain boundary are known to occur between (800-1100°C) [12-13].

2.5.2 Pack cementation coating

Pack cementation aluminide coatings were realized over specimens following the pack preparation and the method developed by Houngninou [14]. Typically the powder pack mixture consists of 3 components: a metallic source - a fine powder of the element to be deposited on the surface of the substrate (15 % wt. Al), a halide salt activator (3% wt. NH_4Cl) and an inert filler powder (82% wt . Al_2O_3) preventing the powder mixture from sintering at high temperature.

3. Results

3.1 Characterizations techniques

9% Cr steel grade samples were oxidized for 100 hours in laboratory air between 600°C and 750°C. Figure 1 summarizes the oxidation kinetic curves ($\Delta m/A=f(t)$, where Δm is the net mass gain, and A the surface area for this steel grade at different temperatures.

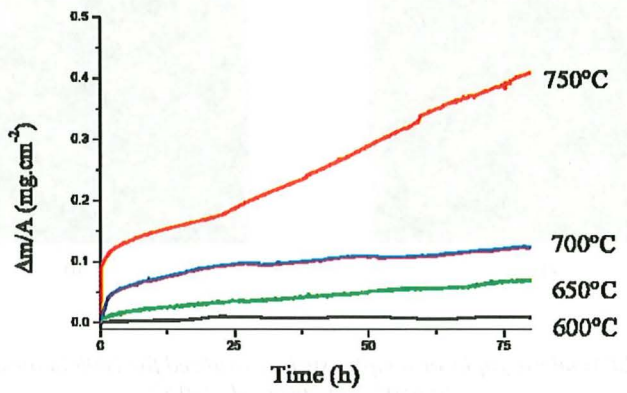

Figure 1: *Kinetics curves for 9%Cr steel grade after oxidation in air for 100h between 600°C and 750°C*

Low mass gain is registered between 600°C and 700°C. A "breakaway", occurred at 750°C after 25 hours. A linear shape of the weight gain curve can be observed from that point until the end of the experiment. The kinetic curves obey appreciatively a parabolic rate law, except after the breakaway at 750 °C. Parabolic rate constants, k_p, calculated from the slope of the curve : $\Delta m/A=f(t^{1/2})$ [11], are listed in Table 2. An activation energy of 390 kJ have been calculated from this rate constants.

Temperature (°C)	600°C	650°C	700°C	750°C
k_p ($g^2 .cm^{-4} .s^{-1}$)	$1.3.10^{-16}$	$2.8.10^{-14}$	$1.7.10^{-14}$	$9.6.10^{-13}$

Table 2: *Kinetic rate constants between 600°C and 750°C.*

SEM pictures coupled with EDX analyses show the oxides layer morphology and allows to follow the oxides microstructure evolution with the temperature.

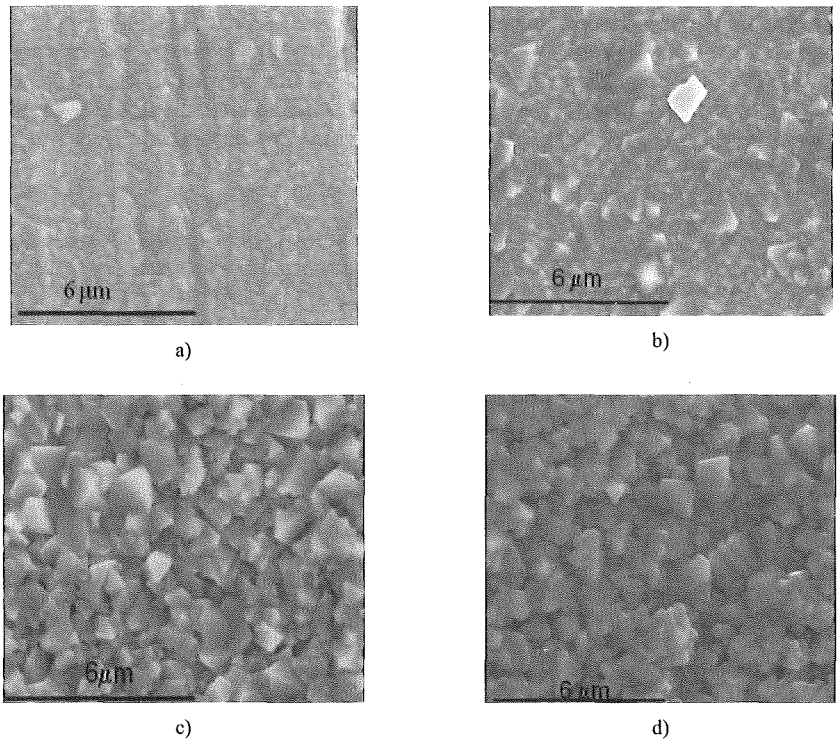

Figure 2: *SEM micrographs of samples surface oxidized for 100h in air at : a) 600°C, b) 650°C, c) 700°C, d) 750°C.*

Figure 2 shows micrographs corresponding to 100 hours in oxidizing atmosphere at a) 600°C, b) 650°C, c) 700°C, d) 750°C. At 600°C, (figure 2 a)) a very thin oxide scale could be

observed . Polishing marks made prior to the isothermal test are still visible. The oxide layer is composed of small spherical nodules made of iron, chromium, silicon and manganese according to the EDX analyses. After 100 hours at 650°C (figure 2b)), the sample is covered by an iron – chromium oxide scale, where it is possible to observe among the nodules some geometrical crystallites. Those geometrical crystallites are clearly visible on micrographs which were taken after 100 hours at 700°C (figure 2c). They grew over an iron chromium oxide scale. At 750°C after 100 hours (Figure 2d), chromium oxide, chromium manganese geometrical oxide (probably a spinel oxide) and a chromium iron oxide scale beneath it are identified by EDX analyses. Iron oxide needles are visible on many places on the samples surface oxidized at 750 °C. The presence and the growth of these iron oxides could be related to the breakaway observation on the kinetic curve.

XRD analyses at low glancing angles were performed in order to give information on phases grown in the thin oxide scales at the top surface. But at 600°C and 650°C difficulties were faced to identify the growing phases due to the thickness of the scale and the close lattice parameters of chromia and hematite. At 700°C and 750°C presence of hematite and magnetite as well as $(Cr,Fe)_2O_3$ and spinel oxide ($Mn_{1.5}Cr_{1.5}O_4$ mainly, $FeCr_2O_4$ slightly from ICDD n° 034-0412 and $MnFe_2O_4$ slightly from ICDD n°010-0319) is suspected .When the temperature increases no more base material is detected on the pattern, which signifies that the oxide scale is quite thick.

To understand the mechanism of high temperature oxidation of this steel grade, short time in-situ XPS experiments were performed on samples oxidized at 600°C in laboratory air at atmospheric pressure for different time exposure.

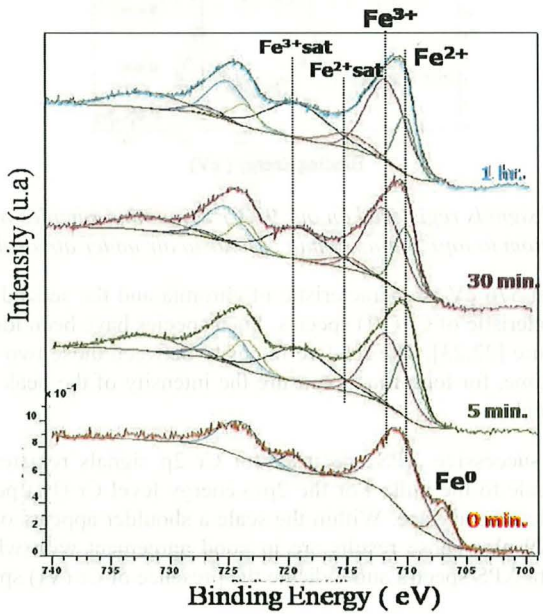

Figure 3: *Fe 2p level signals registered on our 9%Cr containing samples oxidized in situ at 600°C for (from bottom to top) 5 min, 30 min , 1hour in air under atmospheric pressure.*

Fe 2p signals exhibit two important peaks. The first one is close to 711 eV and the second one is centred at 724 eV. They correspond respectively to Fe $2p_{3/2}$ and $2p_{1/2}$ contributions of iron oxide Figure 3 allows comparing iron native oxide growth on the metal and iron oxide formed on samples after high temperature oxidation (600°C for 5 min, 30 min, 1h).Within the Fe $2p_{3/2}$ peaks two distinct contributions, one at 710,6 eV and the other at 711,4 eV, could be identified thanks to data reported in previous work [15-21]. They correspond respectively to Fe (II) and Fe (III) oxidation level. This is the sign of the formation of magnetite and hematite. Fe (III) relative intensity increases with exposure time. Cr 2p contributions are also observed with two signals, $2p_{3/2}$ at around 576 eV and $2p_{1/2}$ at 588 eV. These signals show low intensity for 5 min oxidation time; their intensity becomes higher for 30 min and 1 hour oxidation time. When focusing on the $2p_{3/2}$ contributions for Cr species for more than 30 min of exposition in oxidizing atmosphere a split into two different peaks is clearly visible in figure 4.

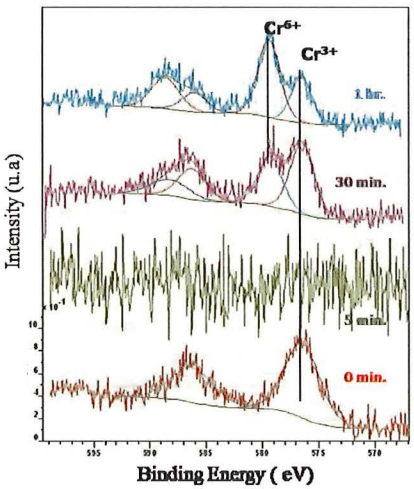

Figure 4: *Cr 2p level signals registered on our 9%Cr containing samples oxidized in situ at 600°C for (from bottom to top) 5 min, 30 min , 1hour in air under atmospheric pressure.*

The first one centred at 576 eV is characteristic of chromia and the second one is centred at 579 eV which is characteristic of Cr (VI) species. Such species have been identified in similar condition in the literature [22,23]. The relative intensity between those two peaks changes as function of oxidation time, for long time exposure the intensity of the peak corresponding to Cr (III) species is the highest.

Figure 5 summarizes successive XPS spectrum for Cr 2p signals registered from the top surface of the oxide scale to the bulk. For the $2p_{3/2}$ energy level Cr (III) peaks are the main contributions observed at the surface. Within the scale a shoulder appears on the $2p_{3/2}$ signal, which is centred at 579 eV. Those results are in good agreement with what was observed previously on the in-situ XPS spectra and indicate the presence of Cr (VI) species in the oxide scale.

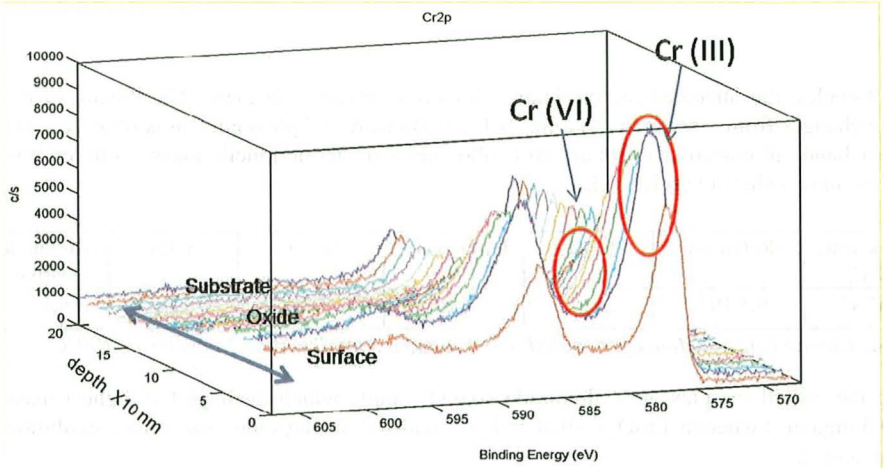

Figure 5: *XPS Cr 2p profile for samples oxidized for 100 hours at 600°C*

3.2 Cyclic tests.

Cyclic experiment were performed on a 9%Cr uncoated sample (reference); a pre-oxidized La_2O_3 coating and samples coated simply with La_2O_3 , Y_2O_3, Nd_2O_3 without pre-oxidation treatment . Aluminide coated samples were also tested using the same cycle tests. Each cycle was composed of a 24h exposure at 700°C in lab air under atmospheric pressure, and an air quenching until reaching room temperature. In total, 23 cycles were performed, corresponding to 552 hours of exposure at 700°C. Figure 6 summarizes mass evolution for those samples.

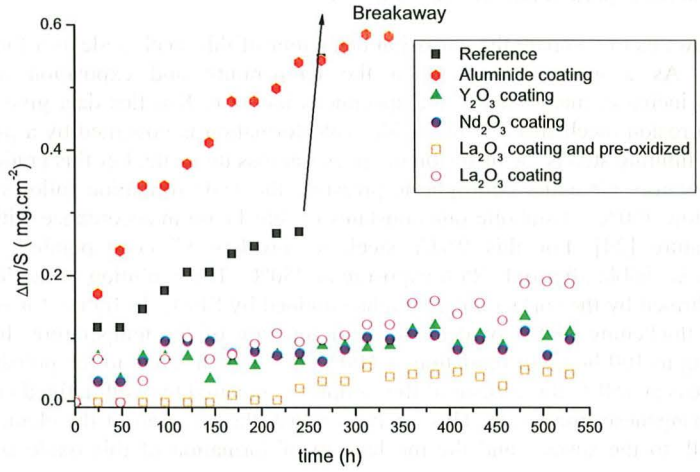

Figure 6: *Kinetic curves for uncoated and coated samples after 23 cycles at 700°C in lab under atmospheric pressure*

After 9 cycles, the uncoated sample had an important increase in mass. The kinetic of the reaction changes from a parabolic to a linear law; "Breakaway" phenomenon is observed. On the other hand, all coated samples are still following a parabolic kinetic mass evolution and really low mass gains are registered.

kp cyclic tests (700°C)	Reference	La_2O_3	La_2O_3 preox	Nd_2O_3	Y_2O_3	Aluminide coating
$g^2.cm^{-4}.s^{-1}$	$9.5.10^{-14}$	$2.3.10^{-17}$	$4.2.10^{-18}$	$1.0.10^{-18}$	$6.9.10^{-18}$	$3.6.10^{-16}$

Table 4: *Kinetic rate constants for coated and uncoated samples after 23 cycles at 700°C.*

Among the coated samples, it is aluminide coated sample which displays the highest mass gain (0.5 $mg.cm^{-2}$) whereas La_2O_3 coated and pre-oxidized displays the lowest mass evolution (0.02 $mg.cm^{-2}$).
In table 4 kinetic rate constants are listed for the coated and uncoated samples after the cyclic test. Nd_2O_3 and La_2O_3 coated and pre oxidized samples show the smallest kinetic rate constants $1.0x10^{-18}$ $g^2.cm^{-4}.s^{-1}$ and $4.2\ x10^{-18}$ $g^2.cm^{-4}.s^{-1}$ respectively. Those values are 4 orders of magnitude lower than the k_p calculated for the reference ($9.5x10^{-14}$ $g^2.cm^{-4}.s^{-1}$).

3. Discussion

The understanding of high temperature corrosion mechanisms is a first step for developing solutions for their utilization in such service condition. The new targeted working temperature and steam pressure for 9%Cr steels inquires investigation that increases our knowledge on the corrosion resistance. The present study is performed between 600 and 750°C. Applications between 600°C and 650°C are targeted for ferritic-martensitic 9%Cr steels. The studies at higher temperatures (700°C and 750°C) were run as a simulation of long time exposure for the material at those predefined service condition.

Figure 1 allows us to compare the corrosion behaviour of this steel grade as a function of the temperature. As a general trend when the temperature and exposition in oxidizing environment increase, mass gain of the specimens increase. Kinetics data give information about the corrosion mechanism. If the oxide scale formation is governed by a parabolic rate law, the rate limiting step is the diffusion of species across the scale. For this grade, tested 100 hours in laboratory air under atmospheric pressure, the scale formation follows a parabolic rate laws below 750°C. Parabolic rate constants (Table 1) are in accordance with the values of the literature [24]. For this 9%Cr steel, a "breakaway" corresponding to material deterioration is visible after only 25 h exposure at 750°C. The evolution of the formed oxide layer is confirmed by the surface micrographs obtained by SEM. In figure 2 it is possible to observe the thickening of the oxide scale as a function of the temperature. In figure 2a) corresponding to 100 hours of oxidation at 600°C the scratches due to the polishing are still visible whereas at 750°C the surface of the samples is covered by well defined crystallites of chromium manganese iron oxide. This leads us to ask the question of the element diffusion from the bulk to the surface and the mechanism of formation of this oxide scale in such condition.

The short term XPS analysis shows that both iron oxide and chromium oxide are formed. These results could suggest the following scenario for the oxidation process at 600°C: A none

continuous layer of mixed spinel as $(Fe,Cr)_3O_4$ could be formed, as proposed by Wright and Bénard [24,25], or other solid solutions of chromium in iron oxide. In that case, at 600°C and at atmospheric pressure, Cr supply in the oxide scale by diffusion in the steel is not sufficiently fast. Therefore a spinel (Fe(II) $Cr(VI)O_4$ with important lack of chromium in the structure could be considered and would explain the Cr (VI) detection on Figure 4 and 5. As a matter of fact, oxide growth is governed by the Cr diffusion in the base alloy, as well as in the oxide scale. For long time exposure the chromium which has then diffused from the bulk to the top surface are indentified as Cr (III) and could form a "short term protective layer" until its total depletion from the bulk. Afterwards porous iron oxide becomes the predominant formed species, with a magnetite layer and a hematite layer over it. This could explain the important mass grown observed in the extreme case of 750°C.
To fight against those phenomena, coatings were developed by Metal Organic Chemical Vapour Deposition (MOCVD) and pack cementation process. Studies during cycling experiments at 700°C of those MOCVD coatings and aluminide coated samples, give interesting outlooks about their utilization as a solution for the material. The observed higher mass gain for the aluminide coating after 9 cycles compared to an uncoated sample, may be due to the density difference of the formed oxide in that particular case. Nevertheless, after the 10^{th} cycle it is clearly visible that those coatings have positive effect on this steel grades resistance at high temperature and during cyclic tests. Indeed, the uncoated material shows deterioration (cracks, spallation) after the 9^{th} cycle, whereas the coated ones have still low mass evolution which could be considered as a better behaviour in such drastic service conditions.

4. Conclusion

Isothermal oxidation tests were performed in laboratory air for 100 h between 600 and 750°C. The kinetics and the characterization of the corrosion products lead to a better understanding of the corrosion phenomenon occurring during working condition for this steel grades. For short term exposition at 600°C in laboratory air, formation of a non protective spinel with important lack in chromium is suspected and could be characterized by the detection of Cr (IV) on the XPS spectra. A scale mainly composed of iron oxide is formed on the sample for relatively long term experiment and at temperature higher than 650°C. Beneath this scale Cr (III) species could be detected. Rare earth oxide coatings realized by MOCVD show promising results for protection of the 9%Cr steels at high temperature.

Acknowledgement

This work was carried out within the French M^4OXe research team of ICB-UMR 5209 CNRS at the University of Bourgogne, Dijon, France with financial and technical support provided by OCAS N.V. ArcelorMittal Global R&D Gent, Belgium.

References

[1] P. Ennis, A. Czyrska-Filemonowicz, Recent advances in creep-resistant steels for power plant applications, *Proceedings in Engineering Sciences,* 28 (2003) 709-730.
[2] A. P. Greeff, C. W. Louw, H.C swart, High-temperature oxidation of industrial FeCrMo steel, *Surface and Interface Analysis*,30 (2000) 120-123.
[3] R. Viswanathan , W.T. Bakker, Materials for ultrasupercritical coal power plants—Boiler materials: Part 1, *Journal of Materials Engineering and Performance,* 10 (2001) 81-95.
[4] R. Viswanathan, Materials technology for coal-fired power plants, *Advanced Materials and Processes*, August (2004) p. 73-76
[5] V. Rhor, *these de doctorat de l'Institut Nationnal Polytechnique de Toulouse*, France, 2005.
[6] J. C. Vaillant, B. Vandenberghe, B. Hahn, H. Heuser, C. Jochum, T/P23, 24, 911 and 92: New grades for advanced coal-fired power plants--Properties and experience, *International Journal of Pressure Vessels and Piping*, 85 (2008) 38-46.
[7] D. Laverde, T. Gomez-Acebo, F. Castro, Continuous and cyclic oxidation of T91 ferritic steel under steam, *Corrosion Science*, 46 (2004) 613-631.
[8] B. A. Pint, I. G. Wright, Long-term high temperature oxidation behavior of ODS ferritics, *Journal of Nuclear Materials,* 307-311 (2002) 763-768.
[9] S. Chevalier, C. Valot, G. Bonnet, J. C. Colson, J. P. Larpin, The reactive element effect on thermally grown chromia scale residual stress, *Materials Science Engineering A* ,343 (2003) 257-264.
[10] A. M. Huntz, A. Reckmann, C. Haut, C. Severac, M. Herbst, F. C. T. Resende, A. C. S. Sabioni, Oxidation of AISI 304 and AISI 439 stainless steels, *Materials Science Engineering A,* 447 (2007) 266-276.
[11] B. Pierragi, *Oxidation of Metals*, 27 (1987) 177-185.
[12] S. Chevalier, G. Bonnet, K. Przybylski, J.C Colson and J.P Larpin, Segregation of Neodymium in Chromia Grain-Boundaries during High-Temperature Oxidation of Neodymium Oxide-Coated Chromia-Forming Alloys, *Oxidation of Metals*, 54 (2000) 527.
[13] S. Chevalier and J.P Larpin, Segregation of Neodymium in Chromia Grain-Boundaries during High-Temperature Oxidation of Neodymium Oxide-Coated Chromia-Forming Alloys,*Materials Science and Engineering A* 363 (2003) 116.
[14] C. Houngninou , S. Chevalier and J.P. Larpin *Applied Surface Science* 236 (2004).
[15] C.R. Brundle, *Surface Science*, 66 (1977) 581-595
[16] M. Muhler, R. Schlögl, G. Ertl, *Journal of Catalysis*, 138 (1992) 413-444
[17] M. Muhler, J. Schütze, M. Wesemann, T. Rayment, A. Dent, R. Schlögl, G. Ertl, *Journal of Catalysis,* 126 (1990)339-360.
[18]T.L. Barr, *Journal of Physics and Chemistry*, 82 (1978) 801-1810.
[19] S. Ciampi, V. Di Castro, *Surface Science*, 333 (1995) 294-299.
[20] D. Briggs, M.P. Seah, John Willey & sons. Vol. 1, second edition 1993.
[21] B. Stypula and J. Stoch, *Corrosion Science*, 36 (1994) 2159-2167.
[22] C. Donik, A. Kocijan, D. Mandrino, I. Paulin, M. Jenko, B. Pihlar, Initial oxidation of duplex stainless steel, *Applied Surface Science*, (2009) corrected proof.
[23] S. Chevalier, Traitement de surface et nouveaux matériaux: Quelles solutions pour lutter

contre la dégradation des matériaux à haute température*? Les Editions Universitaires*, Dijon, mars 2007.
[24] I. G. Wright, *Metal handbook, Corrosion 9th edition* , ASM Metals Park, OH (1987) 97.
[25] J. Bénard, *Gauthier-Villard Edt.*, Paris (1964).

9th Liege Conference : Materials for Advanced Power Engineering 2010
edited by J. Lecomte-Beckers, Q. Contrepois, T. Beck and B. Kuhn.

OXIDATION PERFORMANCE OF HIGH TEMPERATURE STEELS AND COATINGS FOR FUTURE SUPERCRITICAL POWER PLANTS

Pertti Auerkari, Jorma Salonen, Aki Toivonen, Sami Penttilä
VTT, Espoo, Finland

Juha Häkkilä
Foster Wheeler Energia, Varkaus, Finland

Alina Aguero, Marcos Gutiérrez, Raúl Muelas
INTA, Madrid, Spain

Tony Fry
NPL, United Kingdom

Abstract

The operating efficiency of current and future thermal power plants is largely dependent on the applied temperature and pressure, which are in part limited by the internal oxidation resistance of the structural materials in the steam systems. Alternative and reference materials for such systems have been tested within the COST 536 (ACCEPT) project, including bulk reference materials (ferritic P92 and austenitic 316 LN steels) and several types of coatings under supercritical combined (oxygen) water chemistry (150 ppb DO) at 650°C/300 bar. The testing results from a circulating USC autoclave showed that under such conditions the reference bulk steels performed poorly, with extensive oxidation already after relatively short term exposure to the supercritical medium. Better protection was attained by suitable coatings, although there were clear differences in the protective capabilities between different coating types, and some challenges remain in applying (and repairing) coatings for the internal surfaces of welded structures. The materials performance seems to be worse in supercritical than in subcritical conditions, and this appears not to be only due to the effect of temperature. The implications are considered from the point of view of the operating conditions and materials selection for future power plants.

Keywords: oxidation, steel, coating, supercritical, power plant

1. Introduction

The operating efficiency of thermal power plants (steam plants) is largely dependent on the applied temperature and pressure before turbine. These are in the current base load plants at most about 600-620°C/300 bar for the supercritical high pressure part of the cycle, and effectively limited by the available materials. One of the life-limiting damage mechanisms for power plant components can be steam side oxidation [1-7]. The ACCEPT (COST 536) project aimed to establish new materials solutions up to the superheating temperature of 650°C. Under such ultrasupercritical (USC) conditions common standard steels are unlikely to perform well, and it is also possible that load-bearing materials need to be protected from the environmental attack by coatings. However, is not clear which kind of alloys or coatings could be best for the purpose, and therefore several candidate materials have been subjected to testing in the COST project. Although supercritical power plants have been operated since 1960's, appropriate laboratory scale testing facilities for high-end supercritical conditions are not common. This work has made use of the VTT USC autoclave that provides circulating supercritical water with controlled conductivity, pH and dissolved oxygen (DO_2) content up to 695°C / 420 bar. The principal objective was to compare the oxidation performance of selected COST 536 materials (ferritic, austenitic and coatings) under the selected reference

conditions of 650°C/300 bar, and to assess the potential applicability of the materials for future ultra-supercritical (USC) power plant.

2. Materials and methods

The selected materials to be tested included four COST base materials, two COST reference materials (P92 and 316LN), and nine coatings on P92 (see Tables 1 and 2). The base material samples were 25 x 15 x 5 mm coupons (Fig 1a) that were flat ground to N7 (Ra = 1.6 μm) on the surfaces, degreased and washed according to the instructions of the COST 536 Oxidation Group before testing. The coated specimens were similar coupons of P92 steel that were coated by the coating providers and then oxidation tested in the as-delivered condition. The coupons were attached to a rack (Fig 1b) with a pin through an insulated hole. The rack with coupons was inserted into the USC autoclave (Fig 2) for oxidation testing.

Table 1. Composition of the COST base (bulk) materials [1)]

Mat'l	C	Si	Mn	Cr	Ni	Mo	V	W	Nb	Al	N	B
CT3	0.2	0.3	1.0	10.0	-	1.5	0.2	-	0.06	-	0.02	
CT7	0.2	0.3	1.0	11.5	-	1.5	0.2	-	0.06	-	0.02	
VM12	0.12	0.48	0.37	11.6	0.31	0.28	0.25	1.58	0.044	-	0.078	
P92	0.1	0.3	0.4	9	-	0.45	0.2	1.8	0.06	0.03	0.05	0.003
316LN	0.018	0.22	1.75	16.8	12.2	2.65	-	-	-	-	0.15	-
BGA4	0.11	0.49	6.1	22.9	15.4	0.14	0.31	1.49	0.61	-	0.185	0.007

1) Also 2.7% Cu in BGA4

Table 2. Coatings on P92 for the COST test program

Provider	Type / mark	Notes
MPA Stuttgart	CVD siliconising / MPA Si	Heat treatment by Alstom
INTA	Thermal spray / HVOF	-
INTA	CVD / Si	-
INTA	CVD / Cr	-
Alstom	Aluminising / Al	-
Alstom	HT chromizing / Cr	-
Alstom	Thermal spray / CrC	-
A Univ Thess	Boroaluminising / TES 92	Reduced coupon size
A Univ Thess	Boroaluminising / TES 91	Reduced coupon size

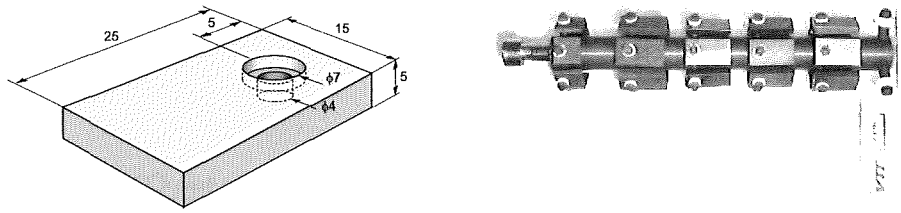

a) b)

Fig 1. a) Coupon for USC oxidation testing; b) test rack for multiple insulated coupons

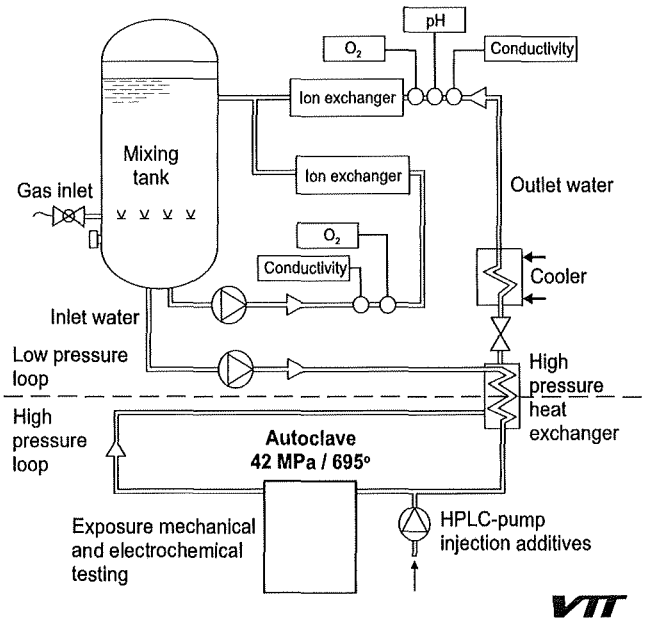

Fig 2. Autoclave system for USC testing

The testing medium was supercritical water at 650°C and 300 bar, controlled to contain 125 ppb dissolved oxygen, pH between 8.0 and 8.5 (target value at 8.4), and conductivity below 0.15 µS/cm. The water chemistry was set in accordance with EN 12952 and VGB guideline for supercritical plant. The flow rate of the medium in the autoclave was set at 5 ml/min.

The testing scheme included three consecutive test runs: first test run with exposure for 24 hours with new coupon samples; second test run for 160 hours with new coupon samples, and third test run for 1340 hours with the same coupon samples (160 h + 1340 h = 1500 h). For each test run, the coupons were checked for mass change and surface layer (oxide) thickness. The layer thickness was obtained by central cross-section microscopy as the mean thickness ± standard deviation of cross-section areas avoiding sample corners (and regions of apparent deviations in e.g. coating preparation).

3. Results

The overall oxidation testing results are summarised in Table 3 for bulk materials and in Table 4 for coatings. The corresponding trends in terms of oxide thickness are shown in Fig 3 for the bulk materials and in Fig 4 for coatings. The indicated oxide thickness is not really a unique measure of the damage, and includes here some influence due to other mechanisms such as surface spalling/wear and internal oxidation. For well known reasons, the indicated mass change is an imperfect measure of oxide growth.

Table 3. Oxidation of metallic (bulk) materials after 1500 h at 650°C/300 bar[1)]

Material	Δm, mg/cm2	Oxide thickn., μm	Observations / notes
CT3	13.45	91 ± 6	Extensive oxidation
CT7	13.56	90 ± 15	Essentially as CT3
VM12	12.42	83 ± 10	Essentially as CT3
P92	55.69	165 ± 10	Poor oxidation resistance
316LN	8.17	70 ± 25	Not better than CT3, CT7 or VM12
BGA4	0.28 [2)]	2 ± 1	Best (bulk) performance

1) mean ± standard deviation; 2) exposure time 1340 h

Table 4. Oxidation of coated materials after 1500 h at 650°C/300 bar [1)]

Coating	Δm, mg/cm2	Oxide thickn., μm	Observations / notes
MPA Si	14.44	140 ± 20	Not protective
INTA HVOF	20.74	~ 50	Thick coating (400 μm)
INTA Si	13.70	150 ± 10	Not protective
INTA Cr	6.83	85 ± 15	Not protective
ALST Al	4.00	(100 ± 50)	Spalling, cracking (~200 μm aluminide)
ALST Cr	0.22	10 ± 5	Best coating performance
ALST CrC	1.99	10 ± 5	Thick coating (~200 μm)
TES 92	(-0,41)	140 ± 10	Partial spalling
TES 91	4.05	75 ± 10	Partial spalling

1) here oxide thickness = thickness of the damaged layer (oxide, lost material etc.)

It is seen that of the bulk materials (Fig 3), most behave rather similarly, except for P92 that is oxidised very fast, and the austenitic alloy BGA4 that showed an excellent oxidation resistance under the tested conditions. Most coatings also appear not to be particularly resistant to oxidation under the tested supercritical conditions, and the best oxidation resistance was shown by the chromium coating prepared by a high temperature diffusion process (Fig 4).

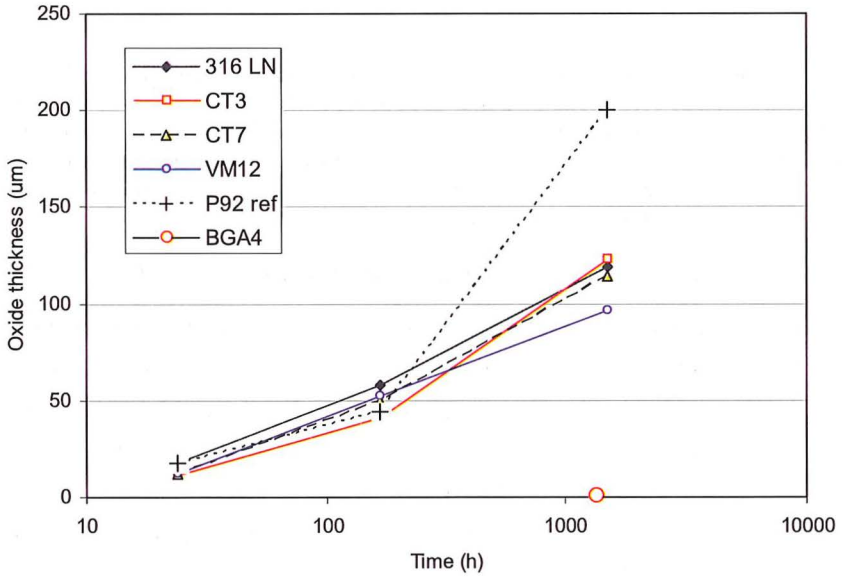

Fig 3. Development of the maximum oxide thickness in the metallic (bulk) test materials

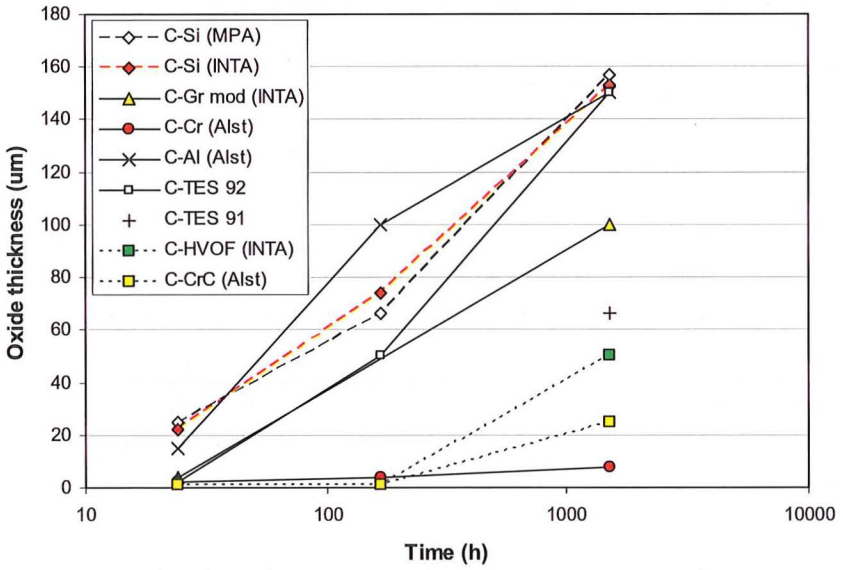

Fig 4. Development of the oxide thickness in the coated coupon samples

4. Discussion

The results show that a fair protection against oxidation at USC conditions (1500 h at 650°C/ 300 bar) was is only obtained for surfaces with a chromium content of more than about 20%. Apparently good performance was provided by the COST (Corus) austenitic steel BGA4 with about 23% Cr. In contrast, the austenitic steel 316LN with 17% Cr was oxidising nearly as fast as the ferritic COST steels CT3, CT7 and VM12 (10.0-11.6% Cr) which in turn were not very different from each other in terms of oxidation performance. As can be expected, P92 showed poor oxidation resistance at the tested conditions.

Consistent with the results from bulk metal samples, the high temperature chromized coupons performed best of all coatings, although also aluminide coatings could perhaps have reasonable potential in USC service. The tested aluminide coatings were probably either too thin or thick, resulting in perforation or cracking and partial oxidation below the coating. Silicon based coatings appeared not to be resistant to oxidation at the tested supercritical conditions, and possibly are therefore not well suited for USC plant. The autoclave test facility is mainly reserved for short and medium term testing (below about 2000 h), and therefore phenomena that only appear in the longer term may not show themselves clearly. In the present work this was usually not a limiting factor, as most materials and coatings were not performing very well under the selected test conditions.

The test program did not include more conventional high-chromium austenitic steels or nickel based alloys as reference materials. Such alloys are considered as candidate base materials for the hottest sections of the future USC plant for the temperature range of about 620-720°C. Fig 5a shows a test coupon after 1000 h at similar testing conditions as above, this time for a weld between a conventional stainless steel type 347 and a nickel alloy, using a nickel-based consumable. The Ni-based parent metal (PM) and weld metal (WM) have performed well under these conditions, while type 347 steel is strongly attacked (Fig 5b). Again, one reason is apparently the relatively modest chromium content of type 347 steel.

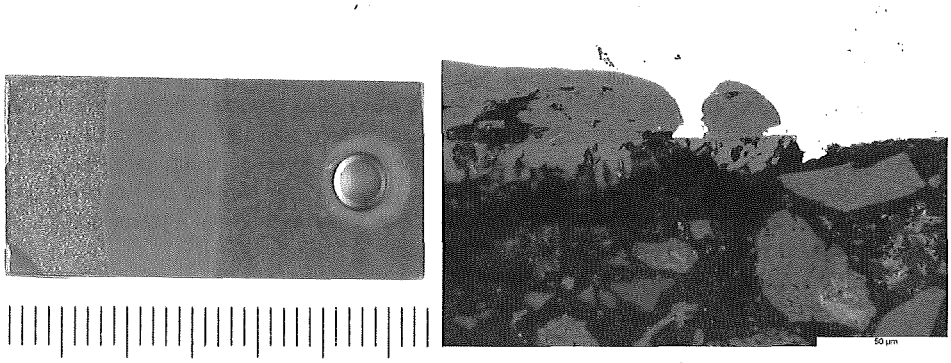

a) b)

Fig 5. Coupon with a weld exposed for 1000 h at 650°C/300 bar, 125 ppb DO_2, pH 8.0-8.5; a) cross-section from the left: 347 steel / Ni-based WM / Ni-based PM, b) oxide cross-section at the 347/WM borderline (metallic part up, unetched).

Use of expensive nickel alloys must be minimised in a competitive plant, and the high thermal expansion coefficients of austenitic steels are also not very attractive for thick wall piping, headers or turbine components. Therefore, an incentive remains for the development of (somewhat elusive) higher chromium ferritic steels and improved oxidation resistant coatings that could withstand the aggressive internal environment of the future USC plants at higher temperatures than today. At least in the case of coatings, further potential for improvement is very likely.

5. Summary

The test materials including the coated samples have been tested under USC conditions (300 bar / 650°C) for bulk and coated test materials provided by the partners in the Oxidation Group of the COST 536 (ACCEPT) project. The materials included reference base materials, experimental COST steels and several different types of coatings on P92 steel. The testing results show differences in the oxidation rates of about two orders of magnitude, and very few materials appear to exhibit satisfactory performance in simulated USC service.

In general, none of the tested bulk ferritic/martensitic steels (CT3, CT7 or VM12) performed well in USC conditions, and P92 with about 9%Cr (and 2% W) showed particularly poor resistance to oxidation in USC water. Of the austenitic grades, 316LN that constains 17% Cr was not better that the 10-11.6%Cr ferritic steels. The COST/Corus steel BGA4 with 23% Cr showed best oxidation resistance of all tested bulk materials.

Si coatings were found to be unprotective under the USC testing conditions, while Cr coatings were best, consistent with the experience from bulk steels. Al coatings could also be relatively protective but the tested aluminium based coatings were probably not ideal for the testing program. Further improvement potential is likely particularly for the coatings.

The test program did not include high-chromium austenitic steels or nickel based alloys that are widely considered as candidate materials for future USC plant at the temperature range of about 620-720°C. The good oxidation properties of certain Ni alloys have been demonstrated under USC conditions, also for Ni-based welding consumables. It apparently remains a challenge to develop any type of steels or iron-based alloys that could challenge Ni alloys in this respect. However, any improvement in the performance of steels would be useful to minimise the use of expensive Ni alloys, and the economic incentive also applies to protective coatings. In the present work, high chromium alloys and coatings showed best performance against oxidation, but other compositions such as those applying high Al content could also be considered as potential basis for future improvement.

Acknowledgements

PA, JS, AT and SP acknowledge the financial support by the Finnish Funding Agency for Technology and Innovation, and by the national industrial group in the LC-Power project. AA, MG and RM wish to acknowledge V. Gonzalez for her important contributions to the results as well as the Spanish Ministry of Science and Innovation for financial support (ENE2008-06755-C02-01).

References

1. Jauhiainen P, Yli-Olli S, Nyholm A, Auerkari P, Salonen J, Lehtinen O, Mäkinen S. Impact of oxidation on creep life of superheaters and reheaters. Proc. 2nd ECCC Creep Conference on Creep & Fracture in High Temperature Components, April 21-23, Zurich 2009, p. 320-328
2. Knödler R, Straub S. Growth of oxide scales during steam oxidation at 650°C. *VGB Powertech* 88 (2008), p. 66-70.
3. Ennis PJ, Quadakkers WJ. Mechanisms of oxidation and the influence of steam oxidation on service life of steam power plant components. In: Creep-resistant steels. Woodhead Publishing, Cambridge 2008, p. 519-536.
4. Saunders SRJ, McCartney LN. Current understanding of steam oxidation – power plant and laboratory experience. High Temperature Oxidation and Corrosion 2005. Transtech Publications, Switzerland, p. 119-128.
5. Aguero A. Coatings for protection of high temperature new generation steam plant components: a review. Proc. of 8th Liege Conference on Materials fo Advanced Power Engineering 2006, Part II, p. 949-963.
6. Aguero A, Muelas R. Steam oxidation of slurry aluminide coatings on ferritic steels for advanced coal-fired steam power plants. High Temperature Corrosion and Protection of Materials 6, Part 2. Transtech Publications, Switzerland, 2004, p. 957-964.. .
6. Aguero A, Spiradek K, Höfinger S, Gutierrez M, Muelas R. Microstructural evolution of slurry Fe aluminide coatings during high temperature steam oxidation. p. 251-259.
7. Osgerby S, Fry A. The role of alloy composition on the steam oxidation resistance of 9-12% Cr steels. High Temperature Oxidation and Corrosion 2005. Transtech Publications, Switzerland, p. 129-138.

9th Liege Conference : Materials for Advanced Power Engineering 2010
edited by J. Lecomte-Beckers, Q. Contrepois, T. Beck and B. Kuhn.

OXIDATION PERFORMANCE OF HIGH TEMPERATURE MATERIALS UNDER OXYFUEL CONDITIONS

Satu Tuurna, Pekka Pohjanne, Sanni Yli-Olli, Tuomo Kinnunen

VTT Technical Research Centre of Finland

Abstract

Oxyfuel combustion is widely seen as a major option to facilitate carbon capture and storage (CCS) from future boiler plants utilizing clean coal technologies. Oxyfuel combustion can be expected to differ from combustion in air by e.g. modified distribution of fireside temperatures, much reduced NOx but increased levels of fireside CO_2, SO_2 and water levels due to extensive flue gas recirculation. Modified flue gas chemistry results in higher gas emissivity that can increase the thermal stresses at the heat transfer surfaces of waterwalls and superheaters. In addition, increased flue gas recirculation can increase the concentration of a number of contaminants in the deposited ash and promote fouling and corrosion. There is relatively little experimental information available about the effects of oxyfuel combustion on the performance of boiler materials. In this work, the oxidation performance of steels X20CrMoV11-1 and TP347HFG has been determined at 580°C/650°C under simulated oxyfuel firing conditions. The results are presented and compared to corresponding results from simulated air firing conditions.

Keywords: oxyfuel, oxidation, steel

1. Introduction

Carbon capture and storage is shown to be one of the key technologies for CO_2 emissions reduction in numerous energy scenario analyses. In addition to moving towards emission free energy production, improved energy efficiency is essential in order to reach emission reduction targets. Oxyfuel combustion using circulating fluidized bed technology is a promising method for reducing CO_2 emissions [1,2]. It is possible that temperatures in oxyfuel combustion will be higher than in air-fired combustion due to the higher heat flux to the boiler walls and superheaters caused by the higher CO_2 content of the flue gas. Higher temperatures may lead to more severe high temperature corrosion of boiler components.

The oxyfuel process can be adapted to existing power plants even without major boiler modification [2,3]. The first demonstrations of oxyfuel concept will be carried out with the current high temperature materials. The most critical components will be those in contact with the hot flue gas environment. The corrosion mechanisms and limiting factors in air-fired combustion have been extensively studied [4-8]. However, there is still relatively little experimental information available about the effects of oxyfuel combustion on the boiler material performance. There are indications that oxide scales developing in $O_2/CO_2/H_2O$ atmospheres are not that protective and that internal carburisation can occur. Resistance to

carburisation and other corrosion mechanisms under reducing conditions is an expected issue at high temperatures sections of oxyfuel boilers [9-12].

In this paper the high temperature oxidation behaviour of two conventional superheater tube materials under synthetic combustion atmospheres at temperatures of 580 and 650°C are presented. The results shown here are a part of a wider ongoing study aimed at determination of in-service performance of materials for oxyfuel conditions.

2. Materials and methods

The oxidation performances of two steels X20 (X20CrMoV11-1) and 347HFG (TP347HFG) were investigated under simulated combustion conditions. The chemical compositions of materials are given in Table 1. Rectangle shape specimens with dimensions of 12 x 18 x 3 mm3 were machined from thick walled tubes. The samples were bright polished with SiC paper and ultrasonically degreased in ethanol. A hole of 1.5 mm was drilled for hanging the samples in the individual alumina crucibles with an alumina rod in order to enable the collection of possible spalled oxide.

Table1. Chemical composition (in wt.%) of the test materials.

Alloy	Fe	Cr	Ni	Mo	Other
X20CrMoV11-1	bal.	11.2	0.48	0.86	0.2 C, 0.49 Mn, 0.3 V
TP347HFG	bal.	18.3	11.7	0.23	0.07 C, 1.64 Mn, 0.92 Nb, 0.33 Cu

The multi-sample exposure tests were carried out under isothermal conditions at temperatures of 580 and 650°C in gases simulating oxy-fired and air-fired coal combustion. The exposure tests were carried out in horizontal tube furnaces with premixed gases. The gas flow used was 10 l/h. The gases were passed through a humidifier unit at an appropriate temperature to obtain moisture in the gas mixture. Table 2 summarises the test conditions. The specimens were weighed to obtain mass changes. The thickness and microstructure of the oxide layers were evaluated by optical and scanning electron microscopy (SEM) combined with energy dispersive spectroscopy (EDS).

Table 2. Used test conditions.

Simulated			Vol.%			Temperature	Duration
system	N_2	O_2	CO_2	H_2O	Ar	°C	h
Air-fired	73.7	1.8	16.0	8.5	-	580, 650	168, 500, 1000
Oxyfuel	-	3.6	60.0	30.0	6.4	580, 650	168, 500, 1000

3. Results

3.1 Oxide scale morphologies and composition

SEM/EDS analyses of cross-sections revealed that the oxide layer formed at 580°C on the X20 steels had a triple layer structure, Figure 1. The outermost thin layer composition corresponded to hematite. A layer beneath that consisted of magnetite. The inner scale growing inwards from the original sample surface consisted of magnetite type oxide, partly an iron-chromium spinel, probably mixture of Fe_3O_4 – $(FeCr)_3O_4$, with small amounts of alloying elements like Mo. In addition, there was an internal oxidation zone at metal surface. After 1000 h in the air combustion environment the thickness of hematite layer increased at the expense of magnetite layer compared to the oxide layers formed in oxyfuel combustion environment, Figure 2.

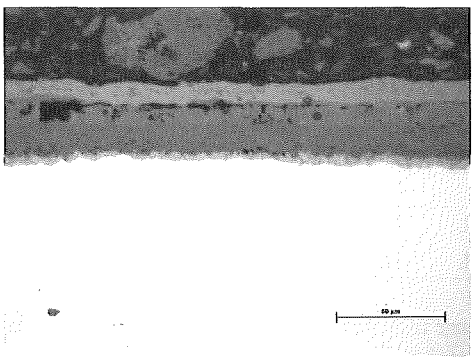

Figure 1. Optical micrograph of X20 (50x) after a week in air combustion conditions at 580°C.

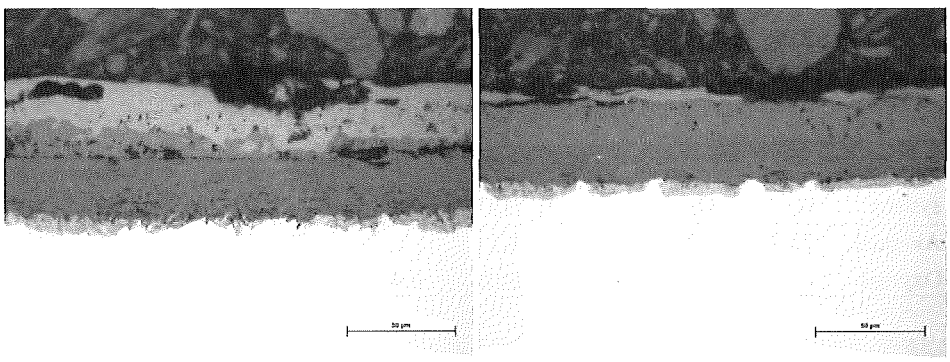

a) b)

Figure 2. Optical micrographs of X20 cross-sections (50x) after 1000 h at 580°C in a) air combustion and b) oxyfuel combustion environment.

Oxide layers formed on steel X20 had a two layer structure at 650°C. No spallation was observed. The outward growing scale consisted of hematite with some local traces of magnetite. The inward growing layer consisted of the mixed oxide of iron and chromium with minor amounts of alloying elements from the alloy. These inward growing layers contained porosity, Figure 3. There were no significant structural differences between oxides formed in air and oxyfuel combustion environments at 650°C. No internal oxidation zone was found beneath the oxide scale. Some carbon enrichment was found near the interface between inner and outer oxide layer, and also inside the inner layer after 1000h exposure in oxyfuel combustion environment.

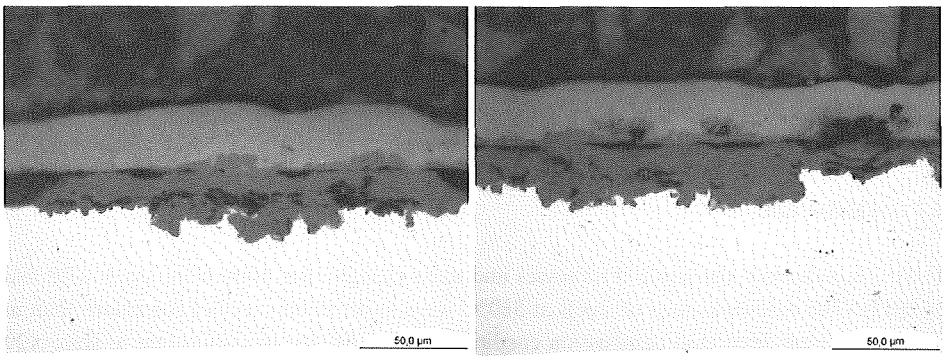

a) b)

Figure 3. Optical micrographs of X20 cross-sections (50x) after 1000 h at 650°C in a) air combustion and b) oxyfuel combustion environment.

With short exposure times only very thin or no oxide scale was formed on alloy 347HFG. After 1000 h exposure at 580°C in air combustion environment the oxide layer was still relatively thin with a two-layer structure. The layer thickness increased when exposure temperature was increased up to 650°C, Figure 4. The oxides formed in oxyfuel conditions had a nodular structure; even at 650°C the oxide was uneven around the sample although a continuous scale had started to grow. EDS analyses showed that the outer layer was iron oxide whereas the inner layer contained mainly mixed oxide of iron, chromium and nickel. In addition, some carbon enrichment was observed in inner oxide layer.

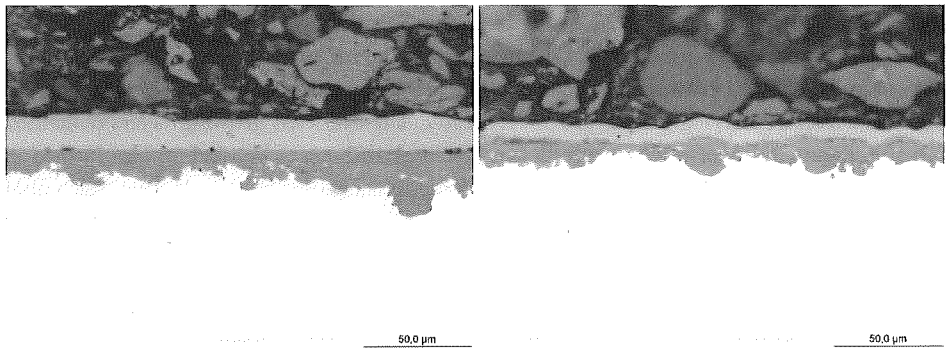

a) b)

Figure 4. Optical micrographs of 347HFG cross-sections (50x) after 1000 h at 650°C in a) air combustion and b) oxyfuel combustion environment.

3.2 Oxidation rate

Table 3 summarises the oxide thicknesses and mass change after 1000 h for steels X20 and 347HFG. The oxidation rates of steels at 580°C were lower in the oxyfuel conditions than in the reference air-fired coal combustion conditions. At 650°C the oxidation rate of steel X20 was higher in oxyfuel conditions than in reference air conditions. Figure 5 illustrates the mass change per unit area for X20 and 347HFG steel at 580°C. In the oxyfuel conditions the mass change of X20 follows logarithmic behaviour whereas in the reference conditions its behaviour is parabolic. The oxidation rate of 347HFG follows linear behaviour, which is typical to the situation where no or only an uneven protective layer is formed on the surface.

*Table 3. Average oxide thickness and mass change of steels X20 and 347HFG after 1000 h at 580 and 650°C. *uneven layer, nodules*

	Oxide thickness [µm]		Weight gain [µm/cm^2]	
	Air	Oxy	Air	Oxy
		580°C		
X20	65	40	7.85	5.30
347HFG	15*	10	0.59	0.28
		650°C		
X20	55	60	5.14	6.69
347HFG	30	15*	2.30	0.35

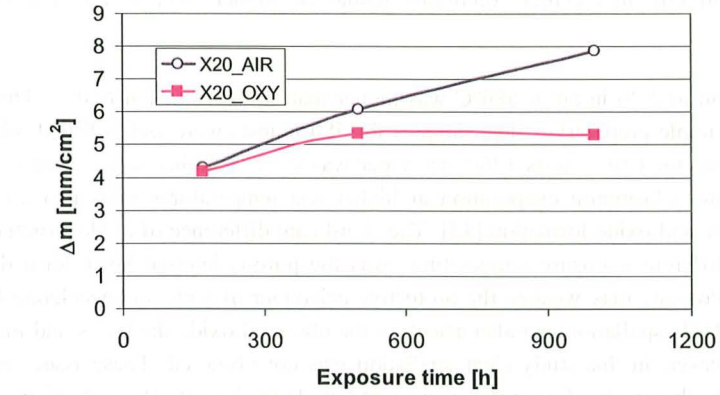

a)

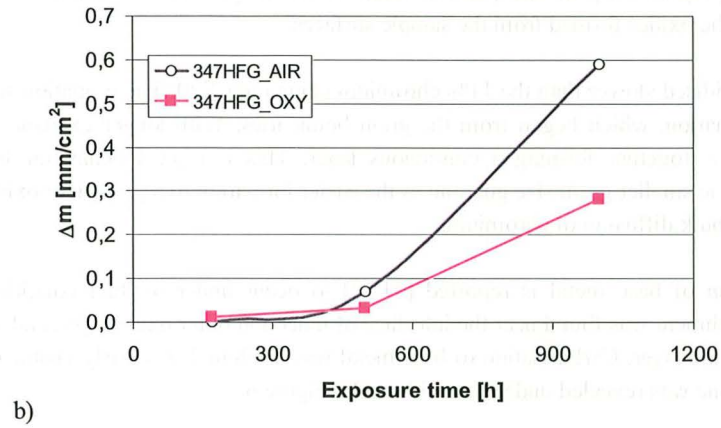

b)

Figure 5. Mass change of specimens exposed to air and oxyfuel conditions at 580°C: a) X20 and b) 347HFG.

4. Discussion

The oxidation rate results had some contradictions. The oxidation rate of both steels X20 and 347HFG was lower in the simulated oxyfuel conditions than in the simulated air-fired coal combustion conditions at 580°C. Similarly at 650°C the oxidation rate of 347HFG was lower in the oxyfuel conditions, whereas the oxidation rate of X20 was somewhat lower in reference air conditions than in oxyfuel conditions. This last result is in line with the results reported in the literature [10,11]. Although Covino et al. [11] have also presented some results in which the oxidation rate in oxyfuel conditions is lower than in air-fired conditions. In the case of 347HFG the weight gains were quite low. It could be possible that with longer exposure times

the oxidation rate in oxyfuel conditions would be higher than in air-fired combustion conditions.

The oxidation of X20 in air at 580°C was higher than in exposures at 650°C. This could be due to the sample preparation. The samples for 580°C tests were wet polished with 600-grit paper whereas for 650°C tests 1200-grit paper was used. Rougher surface enable increased oxidation rate. Chromium evaporation at higher test temperatures may also affect on the oxidation rate and oxide formation [13]. The significant difference of oxide structures of X20 formed at different exposure temperatures was the porous internal layer formed at 650°C (Figure 3). Porosity may weaken the protective behaviour of scale and accelerate breakaway oxidation. Oxide spallation can also affect on the observed oxide thickness and mass change results. However, in this study clear spallation was not observed. These issues bring some uncertainty to the results (for a mass change and oxide thickness). Thus attention was paid to the sample preparation procedure, and in future mass change will be defined as a metal loss by etching the oxides formed from the sample surfaces.

347HFG oxidised slower than the 11% chromium containing X20. The oxidation started with nodule formation, which began from the grain boundaries. With longer exposure times the nodules grew together forming a continuous layer. This is typical behaviour for alloyed materials. The smaller grain size guarantees the easier formation of a protective oxide because of the slow bulk diffusion of chromium.

Carburisation of base metal is reported [11,12] to occur under oxyfuel conditions. Some carbon enrichment was found near the interface of inner and outer oxide layer, and also inside the inner oxide layer. Carburisation of base metal was not found. A clearly visible chromium depletion zone was revealed under the oxide scale, Figure 6.

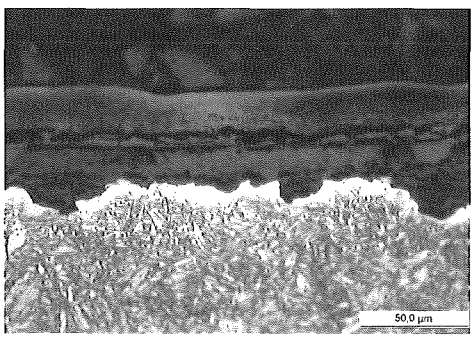

Figure 6. Microphotograph of the oxide scale formed on steel X20 after 1000 h exposure in oxyfuel environment at 650°C (etched). Chromium depletion zone visible beneath the oxide.

5. Conclusions

The exposures of 1000 h suggest that the oxide scale structures formed on X20 change when temperature increases from 580°C to 650°C. The oxide scale formed at 650°C has a porous inner layer. It can be expected that a layer like this will not provide good protection against aggressive environments.

TP347HFG oxide has a double layer structure at both temperatures. With increasing time and temperature the oxide nodules grow to a continuous layer. After 1000 h exposure the formation of a protective oxide layer is still under way. The oxidation rate for TP347HFG is higher in simulated air-fired coal combustion conditions than in oxyfuel conditions. Used test conditions were purely oxidizing. The situation is likely to change when some impurities, like SO_2 and HCl, are added to exposure gases. Longer exposure times may also change the situation.

6. Acknowledgements

Financial support from VTT Technical research Centre of Finland and Tekes is gratefully acknowledged. The authors thank the skillful assistance of A. Kukkonen, T. Lehtikuusi, M. Mattila, K. Nöjd and P. Varis.

References

[1] Pikkarainen, T., Tourunen, A. & Hämäläinen, J. Oxyfuel concept development. Energy Materials 2, 78 – 83, (2007).

[2] Jordal, K., Anheden, M., Yan, J. & Strömberg, L. Oxyfuel combustion for coal-fired power generation with CO_2 capture – opportunities and challenges. Greenhouse Gas Control Technologies 7, 201-209, (2005).

[3] Buhre, B.J.P., Elliott, L.K., Sheng, C.D., Gupta, R.P. & Wall, T.F. Oxy-fuel combustion technology for coal-fired power generation. Progress in Energy and Combustion Science 31, 283–307, (2005).

[4] Segerdahl, K., Svensson, J.-E., Johansson, L.-G. The high temperature oxidation of 11% chromium steel: Part I – Influence of pH_2O. Materials and Corrosion 53, 247-255 (2002).

[5] Kawahara, Y. High temperature corrosion mechanisms and effect of alloying elements for materials used in waste incineration environments. Corrosion Science 44, 223-245, (2002).

[6] Spiegel, M., Zahs, A., Grabke, H.J. Fundamental Aspects of chlorine induced corrosion in power plants. Materials at High Temperatures 20, 153-159, (2003).

[7] Sroda, S., Tuurna, S., Penttilä, K., Heikinheimo, L. High temperature oxidation behaviour of boiler steels under simulated combustion gases. Materials Science Forum, 461-464, 981-988, (2004).

[8] Viswanathan, R. & Bakker, W. Materials for ultrasupercritical coal power plants - Boiler materials: Part 1. Journal of Materials Engineering and Performance, 10, 81-95, (2001).

[9] Natesan, K. & Rink, D. L., Corrosion performance of structural alloys for oxy-fuel combustion systems, 21st Fossil Energy Materials Conference, Knoxville, TN (2007).

[10] Covino, B.B., Matthes, S.A. & Bullard, S.J. Effect of oxyfuel combustion on superheater corrosion. Corrosion 2008 Conference & Expo, March 16-19, New Orleans, LA. 9p. (2008).

[11] Hünert, D., Schulz W. & Kranzmann, A., Corrosion of steels in H_2O-CO_2 atmospheres at temperatures between 500°C and 700°C, ICPWS XV Berlin (2008).

[12] Pirón Abellán, J., Olszewski, T., Penkalla, H.J., Meier, G.H., Singheiser L. & Quadakkers, W.J., Scale formation mechanisms of martensitic steels in high CO_2/H_2O-containing gases simulating oxyfuel environments. Materials at High Temperatures, 26, 63–72, (2009).

[13] Astemann, H., Svensson, J.-E. & Johansson, L.-G. Evidence for chromium evaporation influencing the oxidation of 304L: The effect of temperature and flow rate, Oxidation of Metals, 57, 193-216, (2002).

9th Liege Conference : Materials for Advanced Power Engineering 2010
edited by J. Lecomte-Beckers, Q. Contrepois, T. Beck and B. Kuhn.

SOLID PARTICLE EROSION OF STEELS AND NICKEL BASED ALLOYS CANDIDATES FOR USC STEAM TURBINE BLADING

Federico Cernuschi[1], Cristina Guardamagna[1], Lorenzo Lorenzoni[1], Davide Robba[2]

[1] ERSE Spa Via Rubattino 54, 20134 Milano, Italia
[2] CESI Via Rubattino,54, 20134 Milano Italia

Abstract

The main objective of COST536 Action is to develop highly efficient steam power plant with low emissions, from innovative alloy development to validation of component integrity.
In this perspective, to improve the operating efficiency, materials capable of withstanding higher operating temperatures are required. For the manufacturing of components for steam power plants with higher efficiency, steels and nickel-based alloys with improved oxidation resistance and creep strength at temperature as high as 650°C – 700°C have to be developed.
Candidate alloys for manufacturing high pressure steam turbine diaphragms, buckets, radial seals and control valves should exhibit, among other properties, a good resistance at the erosion phenomena induced by hard solid particles.
Ferric oxide (magnetite) scales cause SPE by exfoliating from boiler tubes and steam pipes (mainly super-heaters and re-heaters) and being transported within the steam flow to the turbine.
In order to comparatively study the erosion behaviour of different materials in relatively short times, an accelerated experimental simulation of the erosion phenomena must be carried out. Among different techniques to induce erosion on material targets, the use of an air jet tester is well recognised to be one of the most valid and reliable.
In this work the results of SPE comparative tests performed at high temperatures (550°C, 600°C and 650°C) at different impaction angles on some steels and nickel based alloys samples are reported.

Keywords: Solid particle erosion, steam turbine, USC, iron and nickel alloys.

1. Introduction

Solid particle erosion (SPE) of steam turbine diaphragms, buckets, radial seals and control valves has been a relevant concern to utilities for many years. Ferric oxides (magnetite) scales cause SPE by exfoliating from boiler tubes and steam pipes (mainly super-heaters and re-heaters) and being transported within the stream flow to the turbine [1-6].
The boiler scale exfoliates at a thickness that ranges from about 100 μm to 160 μm [7], probably because this is the critical thickness as far as residual stresses are concerned. The oxidation process builds residual stresses within the scale up to a critical value.
Although the as-exfoliated boiler scale may include fairly large particles (>300 μm) it is quickly comminuted in the turbine. An analysis of the particle size shows that the 99% of scales in the turbine are smaller that 44 μm [8-9].
Scale exfoliation mainly takes place during the starting and the shut-down plant operations due to the related thermal transients the components are subjected to. Erosion damage is usually concentrated across the pressure wall of the airfoil section toward the trailing edge for nozzles while for buckets, erosion takes place both at the leading edge (convex side) and at the trailing edge [4, 6, 9].
EPRI estimated an average erosion rate of 0.25-0.5 mm/year for buckets and nozzles (in 12Cr martensitic steels such as AISI410 or AISI422) operating at supercritical conditions [10].

The damage and the changes in the airfoil profiles together with increasing radial seal clearance significantly reduce turbine efficiency, increase turbine maintenance, repair costs and extend the outages for turbine overhaul [11].
The erosion behaviour of different materials can be evaluated by simulating erosion phenomena. Among different techniques to induce erosion on material target, the use of a jet tester is well recognised to be one of the most valid [12].
In a steam turbine, a wet environment is present. Nevertheless we expect that the erosion behaviour is not really affected by water steam and the use of a dry jet tester was therefore used.

2. Experimental

2.1. Samples

SPE tests have been carried out on a martensitic steel, a stainless steel and two candidate nickel alloys for manufacturing high pressure steam turbine components in USC power plant, as summarised within *Table 1* and *Table 2*.
The dimensions of all the specimens for SPE tests were 40x15x4 mm, with surface roughness of less than 1μm.
Each material have been tested at a single temperature (550°C, 600°C and 650°C for martensitic and austenitic steels and Nickel alloy respectively) apart from Waspalloy that has been used as reference material.
For statistical purposes, testing conditions were repeated three times on identical specimens. For each testing condition and for each set of specimens, a Waspalloy reference specimen was also tested.

Table 1 – Chemical composition of materials used in the experimental activity

Material	Ni	Fe	Co	Cr	Al	Ti	C	Mn	S	Mo	Si	P	N	B	W
Waspalloy	56	2	14	19	1.4	3	0.08	0.01	0.01	4	-	0.01	-	-	-
Nimonic80A	69	< 3	< 2	18-21	1-1.8	1.8 – 2.7	< 0.1	< 1	<0.015	-	< 1	-	-	<0.008	-
17/13W	13	64	-	17	-	-	0.08	2	0.03	2.5	1	0.045	0.13	-	1
12Cr	4	83	-	12	-	-	0.04	-	0.001	0.5	0.4	0.02	-	-	-

Table 2 Densities of the SPE tested materials

Material	**Measured density (g/cm^3)**
St12T	7.66 ± 0.01
StT17/13W	7.98 ± 0.01
Nim80A	8.10 ± 0.01
Waspaloy	8.20 ± 0.01

2.2 The erosive particles

As erosive powder, chromite sand sieved in the range 38 -138 μm has been chosen (see *Figure 1*) for all the tests performed. The chromite sand chemical composition is reported in *Table 3*.
Chromite was chosen because this powder was more easily found in the market compared to magnetite and its crystallographic properties are very similar to those of magnetite scales present in power plant steam circuit: in fact both materials have a face centred cubic lattice structure with similar density and Mohs' hardness (see *Table 4*).

Table 3 – Chemical composition of Chromite sand

Element	Weight percentage
Cr_2O_3	45.5 – 47.0
FeO	25.0 – 27.0
Al_2O_3	15.0 – 16.0
MgO	9.5 – 11.0
SiO_2	0.25 – 2.5
TiO_2	≈ 0.4
CaO	≈ 0.25

Table 4 – Magnetite and chromite properties.

	Magnetite	Cromite
Lattice parameter	8.39Å	8.34 Å
Density	5.12g/cm^3	5.08g/cm^3
Moh's Hardness	5.5	5.5 - 6.5

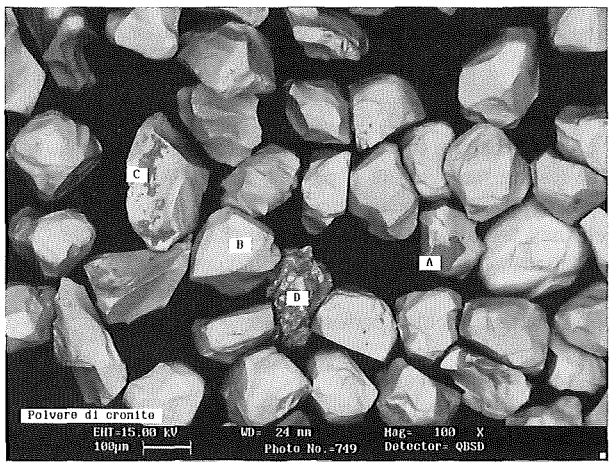

Figure 1 - SEM image of the erosive chromite powder

2.3. SPE experimental facility

The solid erosion test experimental facility (a Jet Tester, see *Figure 2*) available at the ERSE lab consists of:

1. The test chamber containing the nozzle, the sample holder and the double - disk system for the solid erosion particle speed measurement.
2. Two furnaces for heating the carrier gas of the erodent particles.
3. The powder feeder.
4. The cyclone for powder filtering and removal.
5. The control board.
6. Balance

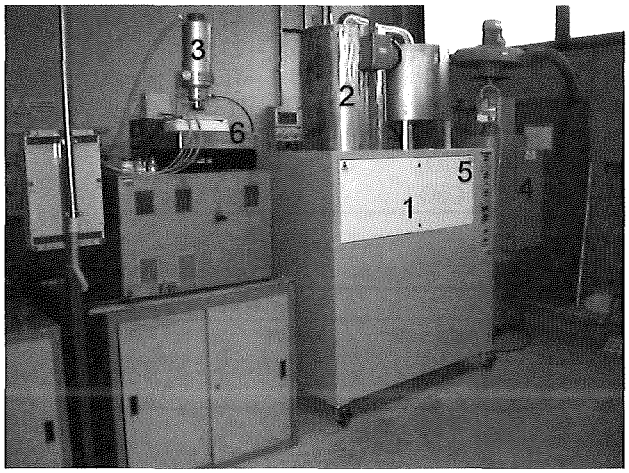

Figure 2. Overall view of the solid particle erosion (SPE) facility. 1) Test chamber 2) heating furnaces, 3) powder feeder, 4) cyclone, 5) control board and 6) balance.

2.3.1. Principle of operation of the SPE facility

Two coils inserted within the two furnaces allow the carrier gas (typically compressed air) to be heated up to the testing temperature (from RT up to 700°C). The solid erosive particles (controlled by a powder feeder) are injected within the main gas stream and through the nozzle from which they are allowed to impinge at the desired angle on the surface of the tested specimen. Two small furnaces inside the testing chamber keep the sample and nozzle at the testing temperature. The exhausted powder is than removed by the cyclone.
Erosive particle speed measurement is performed using the rotating double-disk method [12].

2.3.2 Test procedure and erosion evaluation

The test procedure consists roughly in the following steps:

- fix all the experimental parameters;
- weigh the specimen;

- position the specimen on the holder and wait until the testing temperature has been reached;
- make a fixed amount of powder impinge on the specimen surface;
- weigh the specimen.

This procedure is repeated until an established total mass of erosive has impacted on the specimen surface. The small influence of the powder dose in the range 2 - 5 g/min on the total eroded volume by an identical mass of impacted powder has been assessed before starting the experimental activity.
After the end of the test, for each specimen, the evaluation of the erosion damage is performed by estimating the eroded volume as a function of the impacted mass.
The eroded volume (estimated from the measured eroded mass loss using the material density) plotted as a function of the impacted erosive mass allows evaluating the erosion rate as the slope of the straight line best fitting the experimental data (as an example, see *Figure 3* reporting data for 12Cr steel at 45° and 550°C)
At the end of the test, Scanning Electron Microscope analyses are also performed on a selected number of samples to check the eroded surface morphology and the embedding of erodent particles.

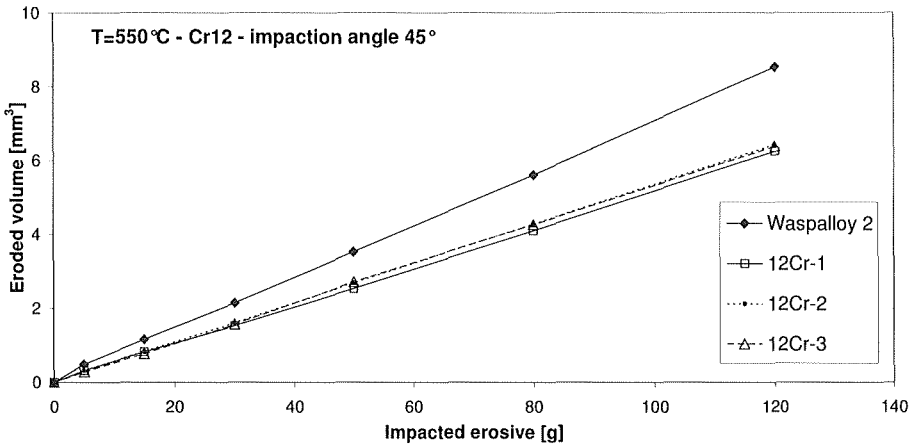

Figure 3 Eroded volume vs. impacted mass on three 12 Cr Steel and one Waspalloy samples at 550°C with impaction angle and velocity equal to 45° and 150 m/s respectively.

2.4 Testing conditions

Tests have been carried out at two different impingement angles, 90° and 45°, with a fixed impaction velocity of 150 ± 10 m/s.
Only for Waspalloy, different impaction velocities (150, 170, 185, 200 m/s) have been used to estimate the erosion rate – impaction velocity dependence.
Martensitic and austenic steels and Nickel alloys have been tested at 550°C, 600°C and 650°C respectively, whereas the reference material Waspalloy has been tested at all the three temperatures, as already highlighted. In these tests 2 – 3 g/min erosive powder doses have been used.

3. Results and discussion

Histograms in *Figure 4* and *Figure 5* summarise the SPE test results in terms of erosion rates.
In *Figure 6* secondary electron image and corresponding backscattered electron image of Waspalloy sample after the erosion test at 650°C and with impaction angle of 90° are shown: eroded sample surface (a) has a quite ductile aspect as expected from a nickel alloy and fragmented chromite particles (b) can be observed embedded within the surface.
Nickel alloys, tested at the temperature which they should be candidate for, present a similar or worse erosion resistance if compared with the other materials at their operation temperatures.
In particular, Waspalloy shows higher erosion rates at all the testing temperatures compared to martensitic/austenitic steels and Nimonic 80.
As presumed, the erosion rates increase with rising temperature, although in this set of tests the temperature effect cannot be distinguished with certainty from the materials intrinsic erosion resistance, as different temperatures have been used for each material.

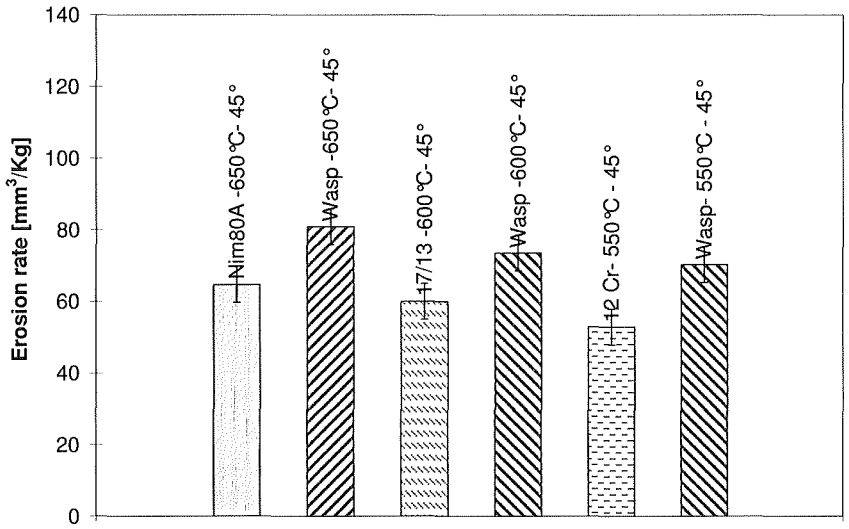

Figure 4 – Erosion rate at impaction angle of 45°

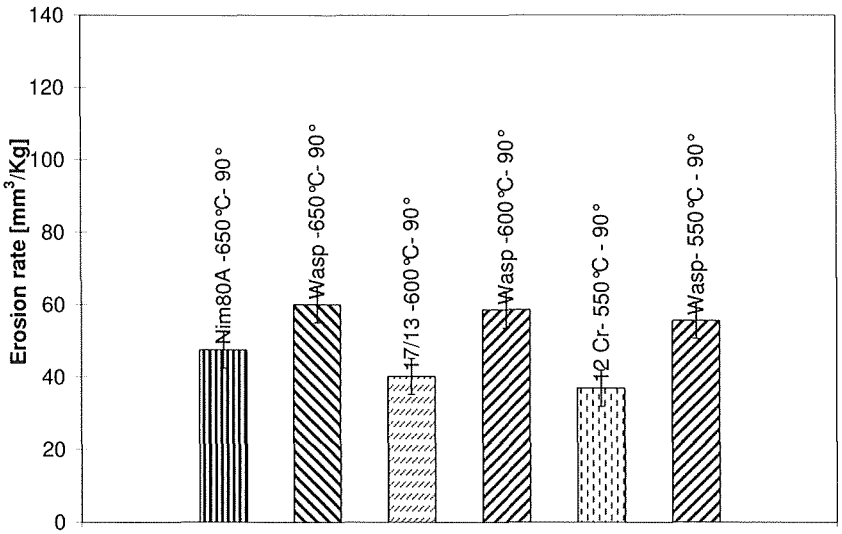

Figure 5 - Erosion rate at impaction angle of 90°

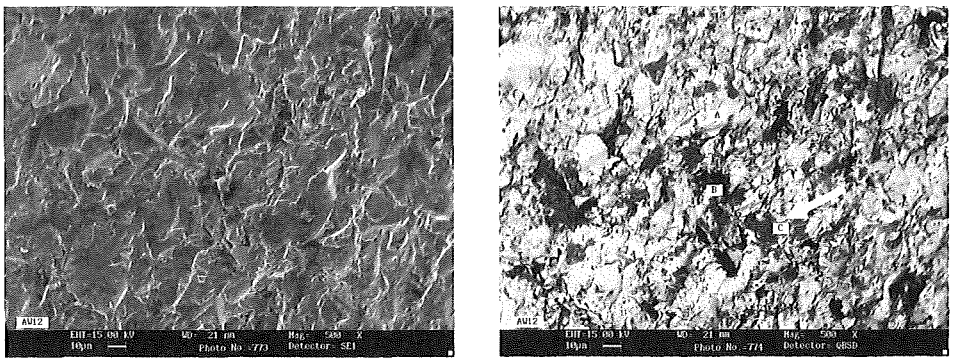

(a) (b)

Figure 6 Secondary electron image (a) and backscattered electron image (b) at 500x magnification of the Waspalloy sample after erosion test at 650°C, 90° impaction angle and 150 m/s impaction velocity: residual chromite embedded in point C indicated by an arrow.

Nevertheless, the influence of testing temperature on the erosion resistance is highlighted by results obtained on Waspalloy at both impaction angles, for which a slight increase is observed when increasing the temperature from 550°C to 650°C: in particular the erosion rate increases up to 15 % raising the temperature at 45° and in a minor amount (5-8%) at 90°.
The ratio between the erosion rates at 45° and 90° has been calculated for all the testing conditions/materials (see *Figure 7*): the higher values (up to 1.50) have been obtained for the austenitic stainless steel and 12 Cr steel, which are the most ductile materials considered in

this study. Nimonic 80 and Waspalloy (at all the temperatures considered) show a ratio lower than 1.40, in agreement with similar results reported in the literature [13].
The erosion rate - impaction velocity experimental correlation made on Waspalloy, tested in the range 150 – 200 m/s at 90° of impaction angle, confirms the general law:

$$E = aCd^{z}v^{n} \tag{1}$$

where E is the erosion rate, v is impaction velocity, a is a constant, C is the erosive concentration and d is the particle diameter.
In particular, the velocity exponent n, estimated by fitting experimental data using an exponential function, was very close to 2 (see equation in *Figure 8*), in good accordance with literature where values between 2 and 3 are reported [15] and in the specific case of Waspalloy a value $n = 2.31$ has been found [14].
Comparing tests on Waspalloy performed at 650°C, 90° and 185 m/s with literature data [14] at 538°C, 30° and 180 m/s [14], we obtained a lower erosion rate: 0.65 mg/g compared to 1mg/g from [14]. These results suggest that impaction angle has a greater influence than temperature on erosion rate: in fact, although the testing temperature is lower, erosion rate is higher at 30° than at 90°. This is in fairly good agreement with what is expected for ductile materials that present a maximum erosion rate just for impaction angle 20°-30° [13] .
On the other hand, tests on Waspalloy at 550°C and 45° but at a lower impaction velocity (150 m/s) resulted in erosion rate equal to 0.58 mg/g. Following equation (1), from the ratio between the two impaction velocities (150/180 m/s) and using the estimated exponent $n = 1.9$, an erosion rate of about 0.7 mg/g is obtained. This value is then consistent with literature data (1 mg/g at 180 m/s) as the difference can be attributed to the different impaction angle (45° in our tests against 30° in [14]).
Other literature erosion rate data [6] obtained at the same impaction velocity, on the contrary, show lower values compared with our values but in this case no testing details are available to allow a more complete comparison.

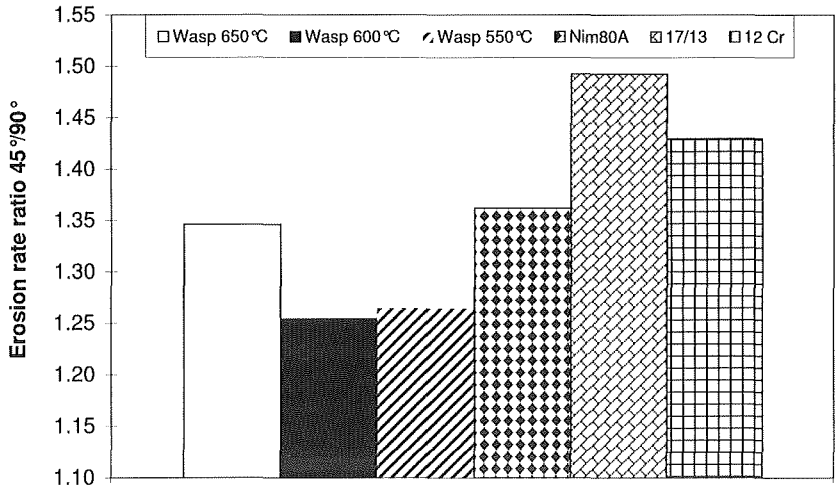

Figure 7 – Erosion rate ratio 45°/90° calculated for the different tested materials

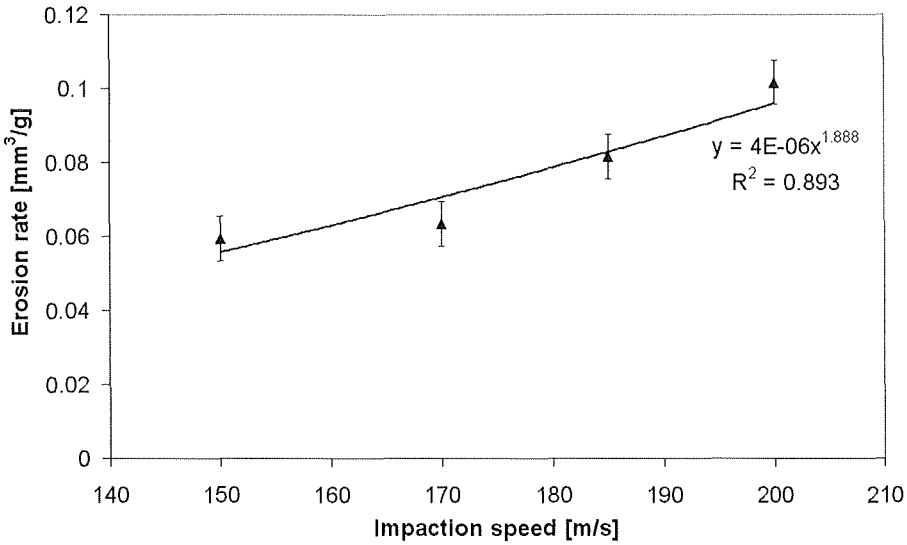

Figure 8 – Erosion rate in function of the erosive velocity: regression curve has been estimated for Waspalloy, tested at different conditions.

3. Conclusions

Solid particle erosion tests on different steels and candidate nickel alloys for manufacturing high pressure steam turbine components, such as diaphragms, buckets, radial seals and control valves, have been carried out at high temperature and at different impaction angles.
Nickel alloys, tested at the temperature which they should be in service, present a similar or worse erosion resistance when compared with the other materials at their operation temperatures. Results, compared with literature, confirm the influence of temperature and impaction angle and velocity on the erosion rate. The correlation of erosion rate and impaction velocity performed on Waspalloy resulted in good agreement with data from literature.

Acknowledgements
This work has been financed by the Research Fund for the Italian Electrical System under the Contract Agreement between ERSE and the Ministry of Economic Development - General Directorate for Nuclear Energy, Renewable Energy and Energy Efficiency stipulated on July 29, 2009 in compliance with the Decree of March 19, 2009.

4. Bibliography

[1] S.T. Wlodek, "Erosion resistant Coatings for steam turbines", *EPRI Report CS5415*, 1987.
[2] Z. Mazur, V. Cristalinas, J. Kubiak "The methods of improving and emergency repair of steam turbine main stop bypass valve damages by erosion". In *V Latin American Conference on Turbomachinery*, Acapulco, Mexico, 1995.
[3] T. McCloskey, B. Dooley and W. McNaughton, "Turbine Steam Path Damage: Theory and Practice" *EPRI Report, TR-108943*, 1999.
[4] B.S Mann, Solid-particle erosion and protective layers for steam turbine blading, *Wear* 224 (1998) 8-12.
[5] W. Tabakoff, Erosion resistance of superalloys and different coatings exposed to particulate flows at high temperature, *Surface & Coating Technology* 120-121 (1999) 542-547.
[6] Liping Dai et al., Nozzle passage aerodynamic design to reduce solid particle erosion of a supercritical steam turbine control stage, *Wear* 206 (2007) 104-111.
[7] F. Eberle J.W.Seifert, J.H. Kitterman, "Scaling of ferritic superheater steels during 36999 hours exposure in 980-1030F steam at 2350 psi with particular respect to scale exfoliation tendency" Proceedings of the *American Power Conference* (1964), 26, 501-510.
[8] R.M. Curran, Solid particle erosion – Turbine design and material fixes, presented at *EPRI/ASME Workshop on solid particle erosion of stream turbines* Atlanta, Georgia, May 6, 1980.
[9] A. Campos-Amezcua et al., Numerical investigation of the solid particle erosion rate in a steam turbine nozzle, *Applied Thermal Engineering* 27 (2007) 2394-2403.
[10] *EPRI Report CS 4683* "Solid particle erosion of utility steam turbines" 1985.
[11] P. Albert, "Steam Turbine Thermal Evaluation and assessment" *GE Power Systems GER4190*, 2000.
[12] ASTM G76 - 95 Standard Test Method for "Conducting Erosion Test by Solid Particle Impingement Using Gas Jets".
[13] I. Finnie and D.H. Mc Fadden, *Wear* 48 (1978), 181-190.
[14] V. Shanov, W. Tabakoff, J.A. Gunaraj, Erosion behaviour of uncoated Waspaloy and Waspaloy coated with titanium carbide, *Surface & Coating Technology*, 94-95 (1997) 64-69.
[15] E. Raask, "Erosion Wear in Coal Utilization", Hemisphere Publishing Corporation, Washington USA 1988.

9th Liege Conference : Materials for Advanced Power Engineering 2010
edited by J. Lecomte-Beckers, Q. Contrepois, T. Beck and B. Kuhn.

MODELLING OF DIFFUSIONAL CREEP IN POLYCRYSTALS

Cornelia Pein, Christof Sommitsch

Institute for Materials Science and Welding, Graz University of Technology
Kopernikusgasse 24, A-8010 Graz, Austria

Abstract

To study creep behaviour on a microstructure level is of major importance, because the microstructure of metallic materials and its influence on creep phenomena is complex. Therefore a physically based finite element model is introduced to study the deformation behaviour due to diffusion creep phenomena. The influence of grain boundaries, triple junctions and precipitates on creep strains and stresses is simulated.
The results indicate that the different microstructure configurations, such as the presence of triple points, second phase particles and the relative orientation of grain boundaries to the loading direction influence the stress distribution and therefore lead to a highly heterogeneous creep strain distribution.

Keywords: modeling, diffusional creep, microstructure, Finite Element Method

1 Introduction

A major concern in materials modelling is to analyze creep behaviour. Creep is defined as the time-dependent inelastic deformation of a material under the influence of mechanical stress [1]. This deformation is caused by different creep mechanisms. Those include dislocation glide, non-conservative motion of dislocations (climb), grain boundary sliding and diffusion of vacancies. Indeed, depending on the given conditions, such as stress, temperature or grain size, one of the mentioned creep mechanisms will dominate [2].

Many scientific groups approach the task of creep modelling by using mean variables on a statistical, macroscopic scale. These approaches do not take into account local effects of the microstructure, which can lead to a substantial overestimation of creep rupture strength and rupture time [3]. Other models use spatially resolved microstructures to exploit local creep phenomena [4]. In the theory of crystal plasticity, the concept of deformation by crystallographic slip of dislocations is used to calculate the accumulated creep strain [5,6]. The kinetics of dislocations are introduced by a flow rule and hardening effects are established by using slip system hardening. Elastic anisotropy is considered as well.

In contrast, the approach presented here describes diffusion creep of a spatially resolved heterogeneous microstructure. Here, the deformation is caused by diffusion of vacancies through the crystal lattice. The equilibrium concentration of vacancies is altered, if tensile or compressive stresses are present. This non-homogeneous distribution results in vacancy fluxes through the material, as was outlined by Nabarro and Herring [7,8].

2 Physical Backgrounds

2.1 Diffusion of particles

Diffusion is a process by which matter or energy is transported from one part of a system to another part. The related physical process is the random motion of structural lattice vacancies.

The phenomenological theory of diffusion deals with this process on a macroscopic scale and is based on the assumption that the resulting flux of matter is proportional to the corresponding concentration gradient

$$J = -D\frac{\partial c}{\partial x} \tag{1}$$

where J is the diffusion flux, c the concentration, x the space coordinate measured normal to the section, and D is the diffusion coefficient. In general, D depends on temperature, pressure and concentration, but, in many cases, the diffusion coefficient can be taken as independent from the concentration. Eq. (1) is consistent only for an isotropic medium. It was first formulated by Fick (1855) and therefore is often referred to as Fick's first law [9,10].

2.2 Stress directed diffusion

Grain boundaries influence diffusion processes in several ways. Different grain boundaries have different orientations with respect to the direction of the applied stress, and, therefore, experience not the same normal stresses in a given stress field. The concentration of vacancies in the vicinity of a grain boundary depends on its normal stresses and thus on the angle between the grain boundary and the existing stress within the material. Hence, the thermal equilibrium concentration of vacancies is altered in the direct neighbourhood of a stressed grain boundary. . The resulting flux of vacancies is counterbalanced by a flux of atoms in the opposite direction. The plating of atoms on the grain boundaries is causing a displacement of the adjacent grains [11].

The equilibrium concentration of vacancies is altered, if tensile or compressive stresses are present. This non-homogeneous distribution results in vacancy fluxes through the material, as outlined by Nabarro [7].

For the creation of a vacancy at a surface, where compression takes place, an atom must be transferred from the inside of the crystal to its surface. The work $\sigma\Omega$ must be expended for this movement of the atom, where Ω is the atomic volume. The enthalpy of vacancy creation therefore increases, compared to the unstressed state. On surfaces where tensile stresses are acting, the enthalpy for vacancy creation is lowered by $\sigma\Omega$. Therefore, the equilibrium fraction of the vacancy concentration is changed.

The difference in vacancy concentration is the driving force for a flux of vacancies from areas with a high vacancy concentration to areas with a low concentration [1]. The resulting flux of vacancies is compensated by a diffusion flux of atoms from parts of the grain, where they are under compression, to parts of the grain, where they are under tension. In other words, the flux of vacancies into a specific direction causes a transport of mass in the opposite direction. A plastic deformation of the grain or the specimen in the tensile direction is the consequence [12].

3 Modelling Approach

3.1 Microstructure

The characteristics of the material are, in addition to its chemical composition, controlled by the properties of the microstructure components and their particular arrangement. This local arrangement of different constituents and their interactions lead to locally different responses

to stresses and strains. Therefore, the response to externally applied loads is very heterogeneous. Consequently, the investigation of the particular microstructure of a certain material and its evolution is of major importance in materials modelling. The intention of the introduced work is to reflect the influence of this locally differing microstructure on creep.

To do so, the presented model considers different microstructure features and their interactions. These ingredients can span different length and time scales. To reflect the impact of microstructure on the creep behaviour, the model represents a particular microstructure and its reactions on external influences in terms of stresses and strains.

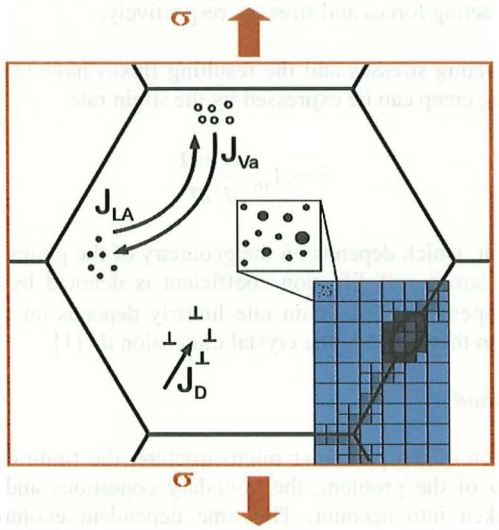

Figure 1: The spatially resolved microstructure, represented by a grain with vacancies, dislocations, fine and coarse precipitates. The fluxes of vacancies J_{Va}, lattice atoms J_{LA} and dislocations J_D are depicted within the grain. The mathematical discretization is indicated as well.

The microstructure is represented by a spatially resolved section of a creep-loaded sample as shown in Figure 1. On the chosen length scales, the incorporated microstructure elements consist of the lattice, grain boundaries, precipitates, both on grain boundaries and in the bulk and the mass flux caused by vacancy migration. Each of these microstructure elements is characterized by a number of properties, including grain orientation, Young's modulus, Poisson's ratio, yield and threshold stresses, activation energies and diffusion coefficients.

The matrix is assumed to have a homogeneous, crystalline structure. In general, the different grains have different crystallographic orientations. Adjacent grains are separated by grain boundaries. Grain boundaries are considered as a separated, distinct element in the calculations. Due to their amorphous structure, the properties of grain boundaries are different from that of the grains itself, in the particular calculation presented here the elastic modulus and the diffusion coefficient are considered to characterize these elements. Precipitates are either introduced as a fine dispersion within the matrix, which will alter the properties of the respective region, or they form relatively coarse, hard particles. In this case, the precipitate is regarded as a discrete region within the matrix, either within the grain directly or on grain boundaries.

The structure, as given by Figure 1, is then discretized by cells. Each cell is described by a set of parameters depending on the microstructure element it represents.

3.2 Deformation

The basic mechanisms for creep deformation consist of material transport by vacancies and plastic deformation by dislocation movement. In this paper only diffusion processes are modelled. The local vacancy concentration is determined by the given stress distribution. The resulting flux of vacancies J_{VA} is accompanied by a flux of lattice atoms J_{LA} in the opposite direction, as depicted in Figure 1. These fluxes and hence the associated deformation rate $\dot{\varepsilon}$ depend linearly on the acting forces and stresses, respectively.

The relation between acting stresses and the resulting fluxes have to be introduced into the model. Nabarro-Herring creep can be expressed by the strain rate

$$\dot{\varepsilon} = A_{NH} \frac{D_L \sigma \Omega}{d^2 kT} \tag{2}$$

where A_{NH} is a constant, which depends on the geometry of the grains, the grain size and the load distribution. The lattice self-diffusion coefficient is denoted by D_L, k is Boltzmann's constant and T the temperature. The strain rate linearly depends on the acting stress σ and inversely proportional to the square of the crystal dimension d^2 [1].

3.3 Finite element method

To calculate the reaction of the particular microstructure, the finite element method [13] is applied. The geometry of the problem, the boundary conditions and the properties of the different areas are taken into account. The time dependent evolution of the system is represented by the displacements of the nodes of the cells. To calculate these displacements a system of equations is established, which incorporates the system status and all input parameters.

4 Application and Results

The presented model is applied to different microstructure arrangements containing grain boundaries, triple junctions and precipitates. The results are presented in terms of stress and strain fields. The chosen finite element mesh consists of 441 elements. Each element has four nodes, for the integration scheme the method of Gaussian quadrature is adopted. The material parameters are listed in Table 1. The grain boundaries are considered to have an amorphous structure where its elastic modulus is half of that of the bulk material. Precipitates are considered to be harder than the surrounding matrix; in this case Young's modulus is modelled to be twice the corresponding value for the matrix.

Table 1: Material parameters: A_{NH} is a constant, D_L the diffusion coefficient, Ω the atomic volume, T the temperature, E Young's modulus and ν Poisson's ratio.

A_{NH}	D_L	Ω	T	E	ν
25.8	$1.2\ 10^{-15}$ m^2/s	$1.7\ 10^{-29}$ m^3	650°C	$200\ 10^6$ N/m^2	0.3

The loading of σ = 10 MPa is applied along the Y-axis for all cases. . The overall simulation time is 960 hours. The mesh size is 10 nm for all samples except the very last simulation where the length of each grid cell has a value of 100 nm.

In Figure 2 results obtained for a bulk material containing a triple junction are presented. Depending on the relative orientation of the boundary and the applied load, the stress distribution is altered. The triple point itself has a major influence. In the vicinity of this triple point towards the applied load, the stresses are clearly increased, as can be seen in Figure 2 (a). These stress concentrations results in prominent creep straining, which finally can lead to void formation and damage.

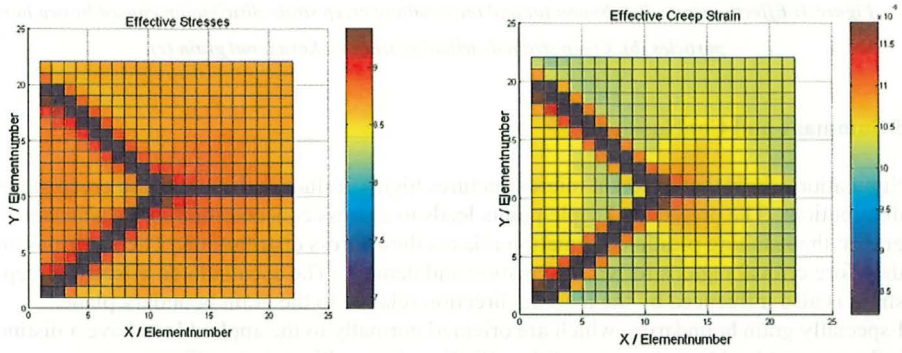

(a) (b)

Figure 2: Stresses and creep strains caused by a triple junction within homogeneous bulk material. Effective stress distribution (a) and effective creep strain distribution (b).

Stress concentrations in the vicinity of triple points are lowered by creep deformation. As an example the effective stresses caused by a triple junction, their decrease and the creep strain are shown in Figure 3.

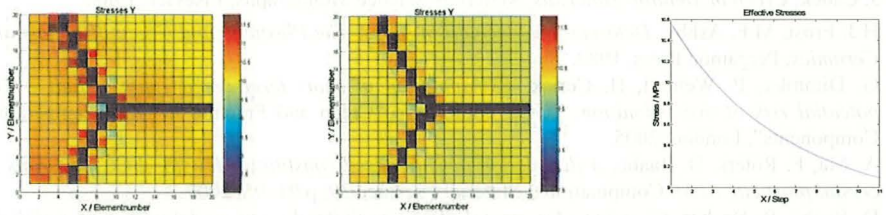

(a) (b) (c)

Figure 3: Stress relaxation in the vicinity of a triple junction. Initial Y-stress distribution (a), Y-stress distribution after relaxation by creep (b), and effective stress vs. time for an element near the triple point (c).

The presence of precipitates influence the creep strains and stresses as well. In Figure 4 (a) and (b) two hard particles (marked dark blue) within a matrix are included. Especially at those phase boundaries, which are oriented normally to the applied load, an accumulation of creep strain can be observed as depicted in Figure 4. In (c) a hexagonal grain with grain boundaries marked in dark blue is presented. Again, grain boundaries with a normal orientation to the applied stress show a strain concentration. On the other hand, creep strains are lowest in the centre of the grain.

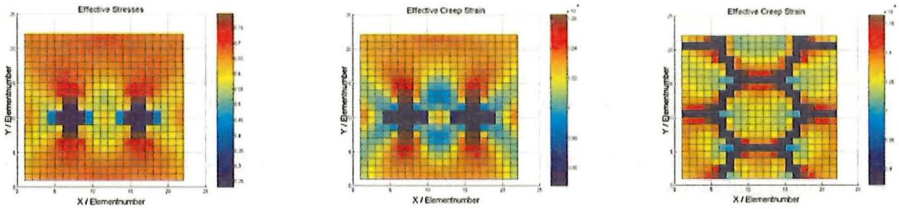

(a) (b) (c)

Figure 4: Effective stress distribution (a) and the resulting creep strain distribution caused by two hard particles (b). Creep strain distribution within a hexagonal grain (c).

5 Summary and Conclusions

Simulations show that different microstructures highly influence the stress and creep strain distributions. The presence of triple points leads to a stress concentration in the adjacent grains; the resulting plastic deformation relaxes these stress distributions. These regions are therefore critical regions for void formation and damage. The accumulated effective creep strain is also influenced by the loading direction relative to the grain boundary plane. Especially grain boundaries, which are oriented normally to the applied load have a distinct influence and lead to an increase of the effective stress, although the effect is not as pronounced as in the case of a triple junction. In the presence of precipitates similar effects can be seen, stresses and creep strains are increased along the loading direction. Within grains the resulting creep strain is heterogeneous as well. Plastic straining is observed mainly at the grain boundaries oriented normally to the applied stress, whereas in the grain interior the straining is lowered. The introduced model provides a valuable tool to study this inhomogeneous distribution of local deformation during creep.

References:

[1] J. Cadek, *Creep in Metallic Materials*, Materials Science Monographs, Elsevier, 1988.

[2] H.J. Frost, M.F. Ashby, *Deformation-Mechanism Maps, The Plasticity and Creep of Metals and Ceramics*, Pergamon Press, 1982.

[3] G. Dimmler, P. Weinert, H. Cerjak, *Extrapolation of short term creep rupture data – The potential risk of overestimation*, ECCC conference "Creep and Fracture in High Temperature Components", London, 2005.

[4] A. Ma, F. Roters, D. Raabe, *A dislocation density based constitutive law for BCC materials in crystal plasticity FEM*. Computational Materials Science 39, p 91–95, 2007.

[5] D. Raabe, R. Becker, *Coupling of a crystal plasticity finite-element model with a probabilistic cellular automaton for simulating primary static recrystallization in aluminium*, Modelling Simul. Mater. Sci. Eng. 8, p. 445–462, 2000.

[6] D.L. McDowell, *Viscoplasticity of heterogeneous metallic materials*, Materials Science and Engineering R 62, p. 67–123, 2008.

[7] F.R.N. Nabarro, *Deformation of crystals by the motion of single ions*, Reports of a Conference on Strength of Solids, Bristol, 1948.

[8] C. Herring, *Diffusional viscosity of a polycrystalline solid*, J. Appl. Phys. 21, p. 437-445, 1950.

[9] R. Cahn, P. Haasen, *Physical Metallurgy*, Elsevier, 1996.

[10] H. Mehrer, *Diffusion in Solid Metals and Alloys*, Springer, 1990.

[11] B. Burton, G. Reynolds, *In defense of diffusional creep*, Materials Science and Engineering A191, 135-141, 1995.

[12] H. Riedel, *Fracture at High Temperatures*, Springer, Berlin, 1987.

[13] K.-J. Bathe, *Finite Element Procedures*, Prentice Hall, 1996.

9th Liege Conference : Materials for Advanced Power Engineering 2010
edited by J. Lecomte-Beckers, Q. Contrepois, T. Beck and B. Kuhn.

A NUMERICAL APPROACH TO PREDICT THE LONG-TERM CREEP BEHAVIOUR AND PRECIPITATE BACK-STRESS EVOLUTION OF 9-12% CHROMIUM STEELS

I. Holzer[1], E. Kozeschnik[2,3], H. Cerjak[1]

[1]Institute for Materials Science and Welding, Graz University of Technology
Kopernikusgasse 24/I, 8010 Graz, Austria
[2]Institute of Materials Science and Technology, Vienna University of Technology,
Favoritenstraße 9-11, A-1040 Vienna, Austria
[3]Christian Doppler Laboratory "Early Stages of Precipitation", Vienna University of
Technology, Favoritenstraße 9-11, A-8010 Vienna, Austria

Abstract

The mechanical properties of modern 9-12% Cr steels are significantly influenced by the presence and stability of different precipitate populations. These secondary phases grow, coarsen and, sometimes, dissolve again during heat treatment and service, which leads to a remarkable change in the obstacle effect of these precipitates on dislocation movement. In the present work, the experimentally observed creep rupture strength of a modified 9-12% Cr steel developed in the European COST Group is compared to the calculated maximum obstacle effect (Orowan threshold stress) caused by the precipitates present in the investigated alloy for different heat treatment conditions. It is shown that the differences in creep rupture strength caused by different heat treatments disappear after long time service. This observation is discussed on the basis of the calculated evolution of the precipitate microstructure. The concept of boosting long-term creep rupture strength by maximizing the initial creep strength with optimum quality heat treatment parameters for precipitation strengthening is critically assessed.

Keywords: Microstructure evolution, precipitation kinetics, simulation, Orowan mechanism.

1. Introduction

The significant increase of energy demand in the last years has led to a need of more efficient thermal power plants for energy generation. There are basically two possibilities to increase the efficiency of the energy generation process. First is an improvement in the thermodynamic design, e.g. reduction of losses within the process or optimized flow-geometry in the turbine. The second possibility is the application of improved heat resistant materials for the power plant components. Due to the distinct influence of processing temperatures on the efficiency coefficient, development of improved heat resistant materials appears as practicable way to assure a more efficient thermal power generation. Therefore, a huge effort towards material development has been undertaken in the past 25 years [1-4]. As a result, it has been possible to increase the efficiency of thermal power generation processes of approximately 10% [5].
The superior creep resistance of these new materials originates from their complex ferritic/martensitic microstructure with high dislocation density, fine subgrain structure and dense distribution of different types of precipitates. The fine subgrain structure and the dense distribution of small precipitates provide high strength and good toughness. Simultaneously, the precipitates conserve the excellent mechanical properties efficiently over long time, exerting strong pinning forces on dislocations, grain and subgrain boundaries, reducing

effectively microstructure coarsening [6,7]. This clearly shows the importance of the role of precipitates on the strengthening of this type of steels and, therefore, is addressed in this work.

Starting point of the present study is a series of experiments on the influence of austenitization and tempering temperatures and times on the short-term and long-time creep rupture strength of a modified 9% Cr steel [8]. Then, computer simulation of the microstructure development using the software MatCalc [9-12] is carried out to predict the evolution of precipitates during processing and service of the investigated alloy. The classical approach to quantifying the strength contribution from precipitates in these steels is outlined. Based on the results of the simulations, the strength contribution caused by precipitates is evaluated and the evolution of precipitate back stress is followed over the lifetime of the material. The influence of various heat treatments on the precipitate microstructure and on creep strength is investigated theoretically and compared with the experimental results.

2. The role of precipitates in ferritic/martensitic steels

As already pointed out, precipitates act as microstructure stabilizing components as well as efficient obstacles for dislocation movement. In the following, these interactions are briefly discussed.

2.1. Precipitate – dislocation interaction

According to McLean [13] precipitates and mobile dislocations can interact in one of the following ways:

1. A dislocation can pass coherent precipitates by cutting the precipitate. A stacking fault is left in the precipitate.
2. A dislocation can pass precipitates by bending between them and closing the bent lines to loops. A dislocation loop is left around the by-passed precipitate (Orowan mechanism).
3. A dislocation can pass the precipitate by climbing.
4. A dislocation can drag the precipitates with it. This mechanism is possible only for very small precipitates. The velocity-determining factor in this case is the mobility of the dragged precipitates.

In each of these four cases, the threshold stress, which has to be overcome to move the dislocation through the microstructure, as well as the kinetics of each mechanism, differ due to the physical nature of the individual processes. In the case of 9-12% Cr steels, particularly mechanisms 2 and 3 are the prevailing rate-controlling mechanisms [14].

2.2. Precipitate – subgrain boundary interaction

The pinning force of precipitates upon subgrain boundaries can be described based on a suggestion of Zener (reference [3] (private communication) in Smith [15]), which originally describes the drag force on grain boundaries during grain growth in the presence of precipitates. The basic idea is that a precipitate, which is located on a grain boundary, reduces

the effective grain boundary area. On leaving the particle behind, this area must be re-established. This process requires energy and, thus, acts against boundary migration. A number of modifications of the original theory have been developed since, which have been reviewed by Manohar, Ferry and Chandra [16]. McLean [17] has pointed out that Zeners's ideas can likewise be applied to subgrain pinning. Accordingly, the mobility of subgrain boundaries is strongly reduced in the presence of precipitates, which has been observed experimentally, for instance, in TEM investigations of Eggeler [18].

2.3. Precipitate –grain boundary interaction

Precipitates similarly affect the mobility of grain boundaries; however, the mechanism of pinning is different to that for subgrain boundaries. The latter are small angle boundaries and, thus, represent an array of dislocations, which accommodate the small lattice misfit between the two subgrains. A grain boundary is a randomly oriented high-angle boundary. In the case of 9-12% Cr steels, the fraction of grain boundaries however, is very small compared to subgrain boundaries thus, affecting the creep strength of the material only weakly by grain boundary strengthening..

Summarizing, one can say that, due to the slight change in subgrain size [7,19] and the coarse grain size in these materials the change in creep strength is primarily affected by the precipitate-dislocation interaction. Therefore, to quantify the influence of the precipitate-dislocation interaction on creep strength, the so-called back-stress concept is applied.

3. Back-stress concept and influence on creep strength

If an external force is acting on a microstructure, part of the external driving pressure σ_{ex} is counteracted by heterogeneous internal microstructural constituents, such as precipitates and interfaces. Consequently, not the entire external load can be assumed to represent the driving force for plastic deformation. Only the part of the external stress σ_{ex}, which exceeds the amount of inner stress σ_i from the counteracting microstructure, effectively contributes to the deformation process. Since the inner stress reduces the effect of the external stress, this inner stress is commonly denoted as back-stress and the approach is known as the back-stress concept. Thus, the effective creep stress σ_{eff} can be expressed as

$$\sigma_{eff} = \sigma_{ex} - \sigma_i \tag{1}$$

In a recent treatment [20], the inner stress σ_i has been expressed as a superposition of individual contributions from immobile dislocations and precipitates. When also taking formally into account the contribution from subgrain boundaries, the inner stress can be expressed as

$$\sigma_i = M \cdot (\tau_{disl} + \tau_{prec} + \tau_{sgb}) \tag{2}$$

where M is the Taylor factor (usually between 2 and 3, see ref. [20]) and τ is the shear stress. The subscripts in the bracket term denote contributions from dislocations, precipitates and subgrain boundaries, respectively. With the inner stress σ_i, the general Norton creep law (see, e.g., ref. [21]) can be expressed as

$$\dot{\varepsilon} = A \cdot (\sigma_{ex} - \sigma_i)^n = A \cdot \sigma_{eff}^n \tag{3}$$

where A and n are constants. With the assumption that subgrain size (see section 2.3) and dislocation density remain almost constant in the steady-state secondary creep regime, the inner stress, the change of creep strain rate, and, thus, the decrease of creep strength of the alloy [22] are primarily determined by the evolution of the precipitate microstructure. This is analyzed quantitatively in the next section.

3.1. Back-stress originating from precipitates

As previously stated, dislocations can overcome particles by climbing, cutting or the Orowan mechanism. Assuming that cutting of small coherent precipitates can be neglected in the case of 9-12%Cr steels [15], the Orowan stress represents the maximum back-stress caused by hard precipitates. According to Ashby [23], the Orowan-stress τ_0 caused by an ensemble of equally sized and equally spaced precipitates can be calculated with

$$\tau_O = C \cdot \frac{G \cdot b}{\lambda} \cdot ln\left(\frac{r_A}{r_I}\right) \tag{4}$$

where C is a constant (C=0.159 for screw dislocations and C=0.227 for edge dislocations), G is the shear modulus, b is the Burgers vector, λ is the mean particle distance, r_I is the 'inner cut-off radius' and r_A the 'outer cut-off radius' of the dislocation. In a complex alloy such as the one treated here, different types of precipitates with varying precipitate sizes and inter-particle spacings are present.
As a first approximation a uniform distribution of all precipitates with a single mean particle distance is assumed as

$$\lambda = \sqrt[3]{\frac{6}{\pi \cdot N}} \tag{5}$$

where N is the total number density of precipitates. Moreover, the 'inner'- and 'outer cut-off radius' are expressed with the following equations:

$$r_I = 2 \cdot b \tag{6}$$

$$r_A = 2 \cdot \frac{\sum r_m^4}{\sum r_m^3} \tag{7}$$

where r_m is the radius of precipitate with index m, and m=1…n, with n being the total number of precipitates in unit volume. The Orowan stress for a complex alloy with several precipitate phases can be determined by inserting eq. (5)-(7) in eq. (4), as

$$\tau_O = C \cdot G \cdot b \cdot \sqrt[3]{\frac{\pi \cdot N}{6}} \cdot ln\left(\frac{\sum r_m^4}{b \cdot \sum r_m^3}\right) \tag{8}$$

Equation (8) shows that, at constant phase fraction of the precipitates, a fine dispersion of precipitates has the most pronounced effect on precipitation strengthening and, thus, on the precipitate back-stress.
In the next section, the influence of heat treatment parameters on the precipitate microstructure and the back-stress is investigated based on eq. (8) using the software MatCalc [10-13].

4. Heat treatments of modified 9% Cr steel

The alloying concept of the modified 9% Cr steel investigated in the present study was developed in the mid 1980s within the scope of the European COST program 501 round 3 (designated as COST alloy E2). The chemical composition of the steel is shown in Table 1. To determine the influence of heat treatment parameters on creep strength, different heat treatments were performed on the same melt [24] – named in this work as heat treatment variant A-D. The creep rupture strength, as well as the heat treatment parameters used in the experiments and the measured prior austenite grain size are shown in Table 2. For heat treatment variant A no prior austenite grain size was recorded.

Table 1: Chemical composition of modified 9% Cr steel in wt.% [24].

C	Cr	Mn	Mo	N	Nb	Ni	Si	V	W
0.13	10.20	0.48	1.10	0.05	0.03	0.77	0.04	0.20	0.90

Table 2: Heat treatment parameters, measured prior austenite grain sizes and creep rupture strength of heat treatment variants A-D [24].

Heat Treatment Variant	Solution treatment		Tempering						Grain size	Creep strength$_{(600°C)}$				
			1		2		3			100h	1000h	10000h	30000h	100000h
	[°C]	[h]	[°C]	[h]	[°C]	[h]	[°C]	[h]	[µm]	[MPa]	[MPa]	[MPa]	[MPa]	[MPa]
A	1020	2	570	8	700	16	710	17	-	204	177	143	127	109
B	1070	2	570	8	720	16	-	-	205	224	187	150	131	105
C	1070	2	570	8	700	16	-	-	280	274	225	167	136	101
D	1120	2	570	8	700	16	710	16	430	211	178	146	125	102

Depending on the heat treatment parameters, the tensile strength in the as-received condition varies from 714 to 874 MPa. After 100 h of creep testing at 600°C, creep rupture strength varies from 204 to 274 MPa; whereas, at longer testing times, the creep strength decreases in all cases and reach similar values of 102 to 109 MPa after a service lifetime of 100,000 h [24].

5. Numerical simulation

For the numerical simulation of the precipitate evolution as well as the calculation of the obstacle effect of the precipitates, the software package MatCalc is used [10-13]. Details of the simulation procedure have been reported previously [8,25,26].

5.1. Simulation settings

For the following heat treatment simulations, the time-temperature history summarized in Table 2 is applied. It is important to emphasize that, in the course of the production process, the material undergoes several austenite/ferrite[1] phase transformations. These are fully taken into account in the present simulation (see also ref. [25]).
For all heat treatments, the numerical calculation starts closely below the solidus temperature of the alloy at 1400°C, where all elements are assumed to be solved in the austenitic matrix. Subsequently, the material is cooled down slowly to the calculated M_S temperature of 390°C. At this temperature, the austenite matrix is assumed to fully transform into martensite. It is further assumed that no precipitation reactions occur below this temperature due to sluggish diffusion. In the next simulation step, the temperature is increased again. The simulation is now performed in a ferritic matrix up to the calculated A_1 temperature of 812°C. Then, the matrix is switched to austenite again. Austenitization is simulated for temperatures between 1020 and 1120°C, depending on the heat treatment variant, with subsequent cooling to M_S. The following tempering treatments and service exposure at 600°C takes place in a ferritic matrix again.
In the present simulations, the precipitate phases $M_{23}C_6$, M_7C_3, M_3C, MX, M_2X, Laves phase and the so called modified Z-phase [27] are taken into account in accordance with experimental findings in this type of steels [7, 24]. Experiment [7] also showed that two types of MX precipitates are present in this type of steels, i.e. a vanadium and nitrogen-rich phase and a niobium and carbon-rich phase. These are taken into account by definition of a miscibility gap for the FCC_A1 phase.
Figure 1 shows the calculated phase fraction diagram based on the thermodynamic database TCFE3 [28] with slight modification of the original data for better representation of the observed phase equilibria as described in ref. [25]. The mobility data used in the simulations are taken from the diffusion database of MatCalc 5.21.
In addition to the thermodynamic and kinetic data, another important input parameter for the simulation is the type of heterogeneous nucleation site for each of the precipitate phases. For the present simulation, the type of nucleation site for each precipitate is defined according to the experimental observations [6,7,29] and summarized in ref. [8]. Z-phase is allowed to form by heterogeneous nucleation in the matrix ($Z\text{-phase}_M$) as well as by direct transformation of existing VN into Z-phase ($Z\text{-phase}_P$) as observed recently by Danielsen et al. [30].

[1] Since no separate thermodynamic description is available for the bct martensite phase, the bct phase is substituted by the bcc phase in the simulations.

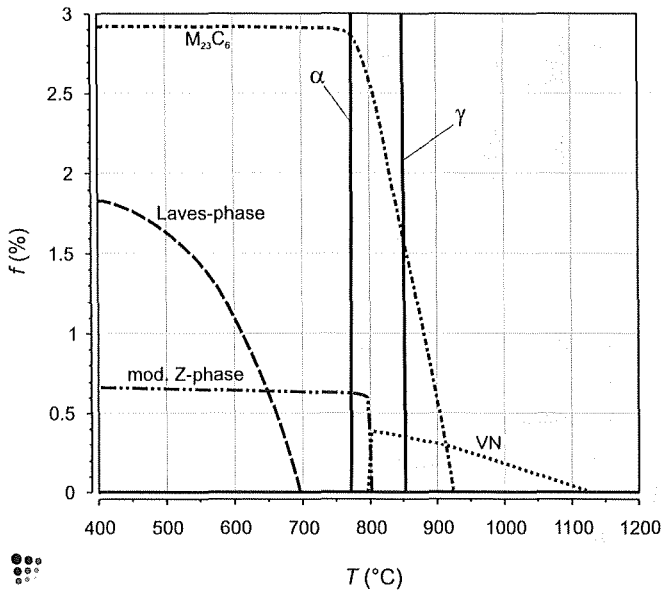

Fig. 1. Phase fraction diagram of the investigated modified 9% Cr steel

In the simulations, it is assumed that the transformation from austenite to martensite and back occurs instantaneously and that the parent and product phase have identical chemical composition. The precipitate populations are assumed to remain unchanged during this transformation. When the simulation starts at 1400°C, all elements are initially assumed to be in solid solution. Furthermore no restrictions regarding the nucleation and growth of the several precipitate phases were made.

5.2. Calculation of the back-stress evolution

The plots in Fig. 2 exemplarily show the simulated evolution of mean precipitate radius, number density and obstacle effect of each precipitate phase as well as the total back stress for the heat treatment variant D during service. To calculate the precipitate back-stress from equation (8), the constants are assumed to be C=0.19 and G=64.6 GPa (converted from ref. [31]). It must be emphasized that the back-stress contribution from individual precipitates has only limited physical relevance, since these contributions cannot be separated from the total back-stress. The major quantity determining the back-stress is the mean precipitate distance, and this quantity is only defined in a meaningful way in terms of the entity of all precipitates. The starting point of Fig. 2 corresponds to the 'as-received' condition at the end of the tempering treatments. With the constants C and G as defined before, the total strength contribution from precipitates is evaluated with 135 MPa (solid line in the bottom graph of Fig. 2).

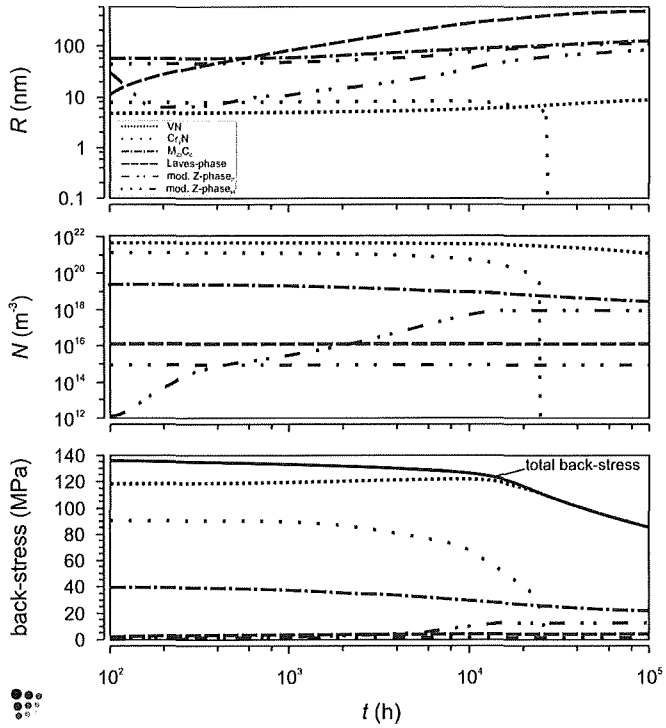

Fig. 2. Evolution of mean precipitate radius R, number density N and precipitate back-stress during service at 600°C for heat treatment variant D. (Solid line in the bottom graph corresponds to the calculated overall precipitate back-stress).

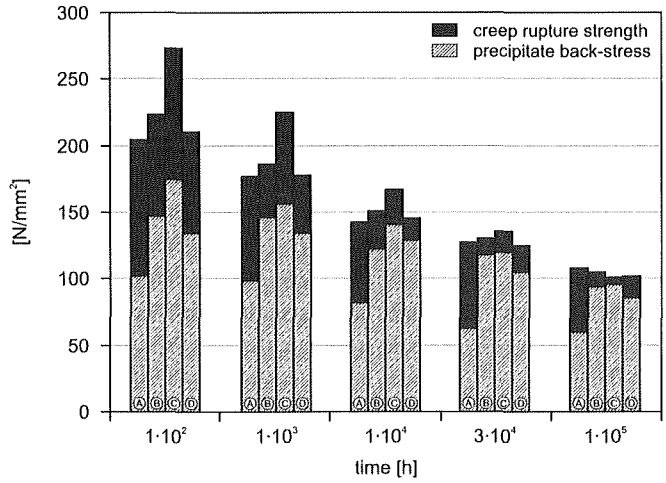

Fig. 3. Creep rupture strength of the modified 9% Cr steel for heat treatment variant A-D compared with the predicted precipitate back-stress evolution.

During service, the density of precipitates reduces due to Ostwald ripening. This effect, together with the predicted dissolution of the finely dispersed Cr_2N leads to a constant

decrease of precipitation strengthening, which the small number of newly formed modified Z-Phase precipitates cannot balance. After 100,000 h, the calculated obstacle effect has declined to a value of 85 MPa.

5.3. Comparison of the creep rupture strength and the predicted precipitate back-stress

The simulation of the back-stress evolution for the different heat treatment variants A-D clearly reflects the observed differences in short-term creep strength. The variation in precipitate back-stress after quality heat treatment shown in Fig. 3 differs strongly between 175 MPa for variant C and 100 MPa for variant A. However, at the end of the simulated service, the precipitate back-stress contributions lie within 60 and 97 MPa.
Furthermore, it is interesting to compare the predicted precipitation strengthening with the reported creep rupture strength. According to Fig. 3, the tendencies in strength evolution are reasonably well reproduced by the simulations, particularly for treatments B-D. The prediction for variant A is slightly too low. However, this can partially be attributed to the fact that the thermodynamic database predicts that a significant amount of VN precipitates to be stable at the lowest austenitization temperature of 1020 °C. The undissolved vanadium-nitrides are then not available for re-precipitation and particle strengthening during tempering, leading to a strongly reduced precipitation strengthening effect.
The simulations clearly emphasize the importance of precipitates in predicting the strength evolution of complex materials. The coarsening characteristics and competitive processes among different precipitates in these materials can be reasonably well described with the present computational technique. The present simulations also confirmed the experimental observation that an optimization of the short-term creep strength, by optimization of the heat treatment parameters, has only a temporary benefit.

6. Summary and Outlook

This study demonstrates the potential of the present simulation approach for the prediction of the microstructural development in complex high-performance materials. The combination of precipitate evolution data from simulation with the back-stress concept provides an efficient methodology to predict the precipitation strengthening potential of complex structural materials, which can thus aid in reducing experimental costs in materials development. The predicted precipitate back-stress of four different heat treatment variants of the modified 9% Cr steel shows a promising agreement with the experimental evolution of creep rupture strength. The simulation shows that, at the beginning of the service exposure after 100 hours of creep exposure, the precipitate back-stress varies strongly in the range of 100 to 175 MPa similar to the creep rupture strength, which lies in the range of 204 to 274 MPa. After 100,000 hours of creep, the range of creep rupture strength reduces to about 102 to 109 MPa. The same behaviour can be observed for the calculated precipitate back-stress, where values in the range of 60 to 97 MPa are calculated. Nevertheless, for a quantitative comparison, additional strengthening effects have to be considered. The study also confirms that the optimization of short-term creep strength by optimizing the austenitization and heat treatment parameters carries the risk of eventually bringing only temporary benefit. After long-term service

exposure, the initial strength differences often level out and, as demonstrated here, reach a relatively homogeneous level at the component design-lifetime of 100,000 hours.
Finally, it is noted that additional important strengthening mechanisms are not yet considered in the present simulation approach. These are mainly the effects of solid solution strengthening and dislocation substructure, contributing remarkably to the long-term creep strength (see e.g. ref.[32]). These contributions have to be considered when attempting a quantitative comparison of the creep rupture strength of alloys as a function of chemical composition. An advanced model to consider the influence of these strengthening mechanisms is under development and will be the objective of future works.

7. Acknowledgement

This work was part of the Austrian research cooperation "ARGE ACCEPT – COST 536" and was supported by the Austrian Research Promotion Agency Ltd. (FFG) which is gratefully acknowledged. Financial support by the Österreichische Forschungsförderungsgesellschaft mbH, the Province of Styria, the Steirische Wirtschaftsförderungsgesellschaft mbH and the Municipality of Leoben under the frame of the Austrian Kplus Programme in the projects SP16 and SP19 is gratefully acknowledged.

References

[1] Kern TU, Wieghardt K, Kirchner H, in *Advances in Materials Technology for Fossil Power Plants - Proceedings from the Fourth International Conference*, (eds) Viswanathan R, Gandy D, Coleman K, ASM International, Ohio (2005), p 20.
[2] Masuyama F, in *Advances in Materials Technology for Fossil Power Plants - Proceedings from the Fourth International Conference*, (eds) Viswanathan R, Gandy D, Coleman K, ASM International, Ohio (2005), p 35.
[3] Viswanathan R, Henry J F, Tanzosh J, Stanko G, Shingledecker J and Vitalis V, in *Advances in Materials Technology for Fossil Power Plants - Proceedings from the Fourth International Conference*, (eds) Viswanathan R, Gandy D, Coleman K, *ASM International*, Ohio (2005), p 3.
[4] Scarlin B, Kern TU, Staubli M, in *Advances in Materials Technology for Fossil Power Plants - Proceedings from the Fourth International Conference*, (eds) Viswanathan R, Gandy D, Coleman K, ASM International, Ohio (2005), p 80.
[5] Bugge J, Kjaer S, Blum R, *Energy* 31 (2006), p 1437.
[6] Kauffmann F, Zies G, Willer D, Scheu C, Maile K, Mayer KH, Straub S, in *Proceedings of the 31. MPA-Seminar Werkstoff- und Bauteilverhalten in der Energie- & Anlagentechnik*, MPA Stuttgart, Stuttgart (2005), p 27.1.
[7] Sonderegger B, *Characterisation of the Substructure of Modern Power Plant Steels using the EBSD-Method*, Ph D Thesis, Graz University of Technology, Austria (2005).
[8] Cerjak H, Hofer P, Schaffernak B, Spiradek K, Zeiler G, *VGB Kraftwerkstechnik 77* 9 (1997), p 691.
[9] Kozeschnik E, Buchmayr B, in *Mathematical Modelling of Weld Phenomena 5*, (ed) Cerjak H, IOM Communications LTD, Oxford (2001), p 349.
[10] Svoboda J, Fischer FD, Fratzl P, Kozeschnik E, *Mater. Sci. Eng. A* 385 (2004), p 166.
[11] Kozeschnik E, Svoboda J, Fratzl P, Fischer FD, *Mater. Sci. Eng. A* 385 (2004), p 157.
[12] Kozeschnik E, Svoboda J, Fischer FD, *CALPHAD* 28 (2005), p 379.
[13] McLean M, *Acta Metal Mater* 33 (1985), p 545.
[14] Polcik P, Modellierung *des Verformungsverhaltens der warmfesten 9-12% Chromstähle im Temperaturbereich von 550-650°C*, Ph D Thesis, Shaker Verlag, Aachen (1999).
[15] Smith CS, *Trans AIME* 175 (1948), p 15.
[16] Manohar PA, Ferry M, Chandra T, *ISIJ International* 38 (1998), p 913.
[17] McLean D, *Transactions of the Metallurgical Society of AIME* 242 (1968), p 1193.
[18] Eggeler G, Acta Metal Mater 37 (1989), p 3225.

[19] Sawada K, Takeda M, Maruyama K, Ishii R, Yamada M, Nagae Y, Komine R, *Mat Sci Eng A*, A267(1999) p 19.
[20] Dimmler G, *Quantification of creep resistance and creep fracture strength of 9-12%Cr steel on microstructural basis*, Ph D Thesis, Graz University of Technology, Austria (2003).
[21] Čadek J, *Creep in metallic materials*, Elsevier, Prague (1988).
[22] Ilschner B, *Hochtemperatur-Plastizität*, Springer Verlag, Berlin/Heidelberg (1973).
[23] Ashby M, in *Metallurgical Society Conference*, (eds) G.S. Ansell, T.D. Cooper and F.V. Lenel, Gordon and Breach, New York (1968), p 143.
[24] Vanstone RW, *COST 501/3 WP11 Metallography and alloy design group - Analysis of quantitative data*, Internal Report, GEC Alsthom Turbine Generators Limited, Rugby UK (1994).
[25] Rajek J, *Computer simulation of precipitation kinetics in solid metals and application to the complex power plant steel CB8*, Ph D Thesis, Graz University of Technology, Austria (2005).
[26] Holzer I, Rajek J, Kozeschnik E, Cerjak H, in *Proceedings from Materials for advanced power engineering 2006*, (eds) Lecomte-Beckers J, Carton M, Schubert F, Ennis PJ, Forschungszentrum Jülich, Jülich (2006), p 1191.
[27] Vodarek V, Strang A, in *Proceedings from Materials for advanced power engineering 2002*, (eds) Lecomte-Beckers J, Carton M, Schubert F, Ennis PJ, Forschungszentrum Jülich, Jülich (2002), p 1223.
[28] TCFE3 thermodynamic database, Thermo-Calc Software AB, Stockholm, Sweden, 1992-2004.
[29] Hofer P, *Mikrostrukturelle Analyse als Basis für die Entwicklung neuer Kraftwerkswerkstoffe am Beispiel von G-X12 CrMoWVNbN 10-1-1*, Ph D Thesis, Graz University of Technology, Austria (1999).
[30] Danielsen HK, Hald J, Grumsen FG, Somers MAJ, *Metall Mater Trans* 37A (2006), p 2633.
[31] Guntz G, Julien M, Kottmann G, Pellicani F, Pouilly A, Vaillant JC, *The T 91 Book – Ferritic tubes and pipe for high temperature use in boilers*, Vallourec Industries, France (1991).
[32] P. Hofer, M.K. Miller, S.S. Babu, S.A. David, H. Cerjak, ISIJ Int. 42 (2002) 62-66.

9th Liege Conference : Materials for Advanced Power Engineering 2010
edited by J. Lecomte-Beckers, Q. Contrepois, T. Beck and B. Kuhn.

FATIGUE LIFE PREDICTION OF NI-BASE THERMAL SOLAR RECEIVER TUBES

Philipp von Hartrott[1,a], Michael Schlesinger[1], Ralf Uhlig[2], Jens Jedamski[2]

[1]Fraunhofer Institut für Werkstoffmechanik IWM, Freiburg, Germany
[2]Deutsches Zentrum für Luft- und Raumfahrt e. V. (DLR), Stuttgart, Germany
[a]Corresponding author: philipp.von.hartrott@iwm.fraunhofer.de, +49-761-5142-273

Abstract

Solar receivers for tower type Solar Thermal Power Plants are subjected to complex thermo-mechanical loads including fast and severe thermo-mechanical cycles. The material temperatures can reach more than 800 °C and fall to room temperature very quickly.
In order to predict the fatigue life of a receiver design, receiver tubes made of Alloy 625 with a wall thickness of 0.5 mm were tested in isothermal and thermo-cyclic experiments. The number of cycles to failure was in the range of 100 to 100,000. A thermo-mechanical fatigue life prediction model was set up. The model is based on the cyclic deformation of the material and the damage caused by the growth of fatigue micro cracks. The model reasonably predicts the experimental results.

Keywords: Thermo-mechanical fatigue, TMF, Nickel base alloy, solar receiver, CSP

1. Introduction

The reduction of CO_2 emissions caused by electric power generation puts challenges on power plant technology. According to the DESERTEC scenario [1] roughly 20 % of the electric power consumption of Europe, North Africa and the Middle East can be covered by Concentrated Solar Power (CSP) by 2050. Today's commercially available CSP technology is mostly based on parabolic receivers and a steam process at relatively low temperatures. For future hybrid Solar Thermal Tower Plants (STTP) using a gas turbine process, studies [2] predict electricity costs of 0.08 $/kWh. A promising way to introduce this technology is by preheating the compressor discharge air before it enters the combustor of the gas turbine. In comparison to a Rankine cycle the main advantage of the employed Brayton cycle is the elevated upper cycle temperature which potentially leads to high efficiencies. In order to reach the required turbine inlet temperatures of about 1000°-1100°C with little fuel, a high preheat temperature for the compressor discharge air is necessary. In a STTP this is achieved by pivotable mirrors –heliostats– reflecting the incoming radiation to a focal spot on top of a tower, where the receiver is located. The receiver transfers the energy contained in the concentrated solar radiation to the compressor discharge air which then is redirected to the combustion chamber. Figure 1 shows the layout principle of a STTP and a model of a tube receiver.

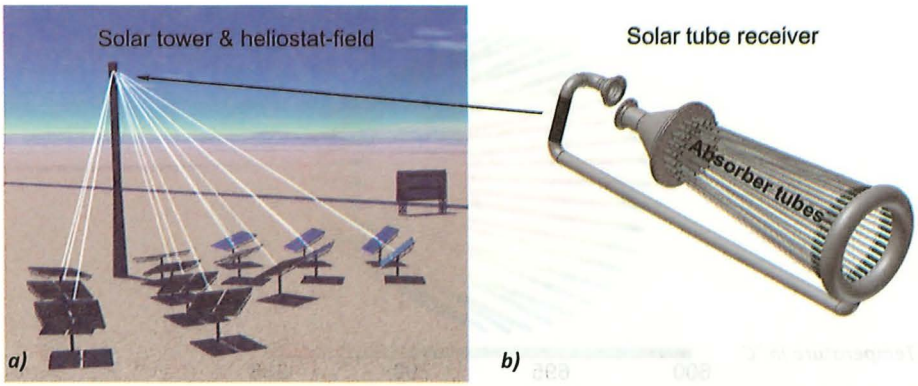

Figure 1: a) Principle of a Solar Thermal Tower Plant, b) Sketch of metallic tube receiver

A demonstration project [3] with a test unit of 230 kW_{el} showed the feasibility of such solar-hybrid gas turbine systems. Subsequently within the SOLHYCO project [4], a metallic tube receiver for a solar-hybrid micro-turbine system was developed. Due to the high loads, the receiver design has to account for finite life fatigue strength. The methodology for the fatigue life prediction is presented here.

2. Receiver and loads

The receiver consists of 40 parallel absorber tubes, each 2.5 m long. The tubes are arranged in an enclosed cavity with a circular opening. The opening has a diameter of 0.9 m. The solar flux through the opening is about 400 kW/m^2. The receiver is designed to heat an air mass flow of 0.8 kg/s from 600 to 800 °C with a pressure loss lower than 150 mbar.

The receiver is subjected to a complex load situation. The tubes are loaded by constant internal pressure and highly variable thermal gradients. These thermal gradients are caused by the inhomogeneous solar flux distribution in the receiver which in turn depends on the daytime and the date of the year. Additional thermal gradients are caused by clouds passing the heliostat field. The clouds abruptly block the incoming solar radiation while the compressor discharge air continues to flow through the tubes.

To investigate the transient temperature fields of the absorber tubes a finite element model was used. The model considers the following boundary conditions:

- Absorbed heat fluxes on the outer side of the tubes and of the surrounding cavity walls. The fluxes were calculated using a ray-tracing code.
- Heat transfer on the inner side of the tubes. The transfer was calculated by a Nusselt-correlation [4].
- Infrared radiation exchange between tubes, cavity and the environment.
- Convective heat losses.

The resulting transient thermal fields are used to calculate the transient stresses and strains for several load cases. The transient stresses and strains in turn are considered for the evaluation of the fatigue life. Figure 2 shows an example of the temperature distribution.

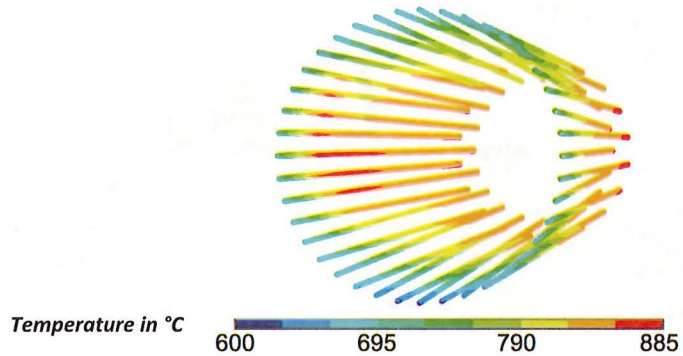

Figure 2: Exemplary temperature distribution of the tubes

3. Experiments

3.1 Material

The absorber tube material is an Alloy 625 (Werkstoff Nr. 2.4856). The nominal composition is shown in table 1. The grain size is around 40 µm. The grains are mostly equiaxed with a considerable number of twins. No precipitates are visible on grain boundaries. The grain interiors show some Titanium Carbo-Nitrides.

	C	Si	Mn	P	S	Al	Co	Cr	Cu	Fe	Mo	Nb+Ta	Ni	Ti
min/max	0.03/0.1	≤0.5	≤0.5	≤0.02	≤0.015	≤0.4	≤1.0	20.0/23.0	≤0.5	≤5.0	8.0/10.0	3.15/4.15	≥58.0	≤0.4

Table 1: Nominal composition of the material 2.4856

3.2 Test specimen

The intended use of thin walled welded tubes for the receiver motivated the use of thin walled test specimens for the strain controlled TMF and LCF experiments. Figure 3 shows the tubes having an outer diameter of 15 mm and a wall thickness of about 0.5 mm. The gauge length used for the strain control was 3 mm. Due to the small wall thickness and the small gauge length special attention has to be paid to the temperature and strain control.

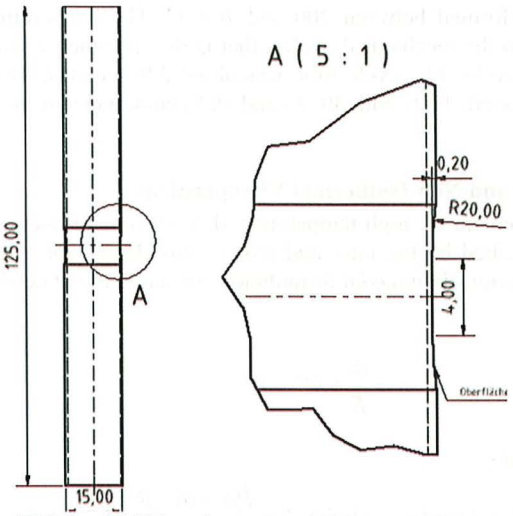

Figure 3: Specimen for TMF and LCF testing

The strains were controlled using a MAYTEC high temperature extensometer with customized rods. The temperature was measured with Ni-CrNi thermocouples at several positions in the gauge length of the specimen.

3.3 Experiments

LCF tests were performed at 20, 280, 600, 650, 700, 750 and 800 °C with a strain rate of 10^{-3} 1/s and a triangular shape. A complex strain history is applied once during the LCF experiment (Figure 4a) and the measured stresses for selected experiments are shown in Figure 4b. The complex strain history comprises strain rates of 10^{-3}, 10^{-4} and 10^{-5} 1/s as well as hold times in tension and compression. With this complex loading program, strain rate effects, stress relaxation and cyclic hardening properties of the material can be investigated in a single experiment. Sufficient information to determine the parameters of the deformation model can be gathered.

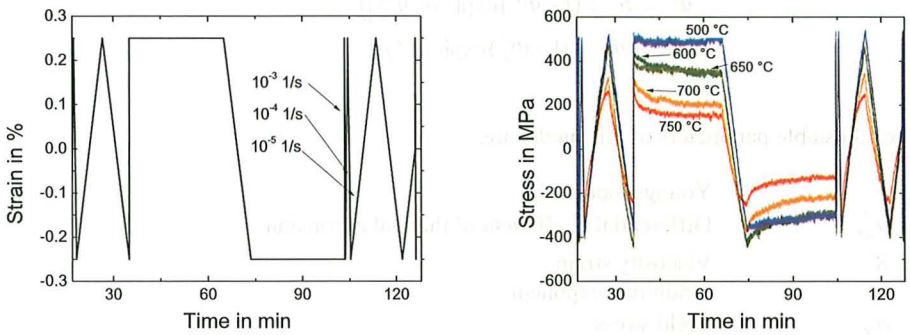

Figure 4: a) complex strain history, b) stress response of the material

TMF tests were performed between 200 and 700 °C. The temperature cycles were out of phase with respect to the mechanical cycles, that is the specimen was in compression during the hot part of the cycle. The cycle time was about 320 seconds. The thermal strains were only partially suppressed. Tests with 30, 35 and 50 % compliance were performed.

4. Model for Cyclic and Non-Isothermal Viscoplasticity

The essential phenomena of high-temperature deformation of metals subjected to fatigue loading can be described by the rate- and temperature-dependent models by Chaboche [5]. The constitutive equations in uniaxial formulation are summarized here:

Total strain rate:

$$\dot{\varepsilon} = \frac{\dot{\sigma}}{E} + \dot{\varepsilon}^{vp} + \dot{\varepsilon}^{th}$$

Viscoplastic strain rate:

$$\dot{\varepsilon}^{vp} = \dot{p}\,\mathrm{sgn}(\sigma - \alpha) \text{ with } \dot{p} = \left\langle \frac{|\sigma - \alpha| - R}{K} \right\rangle^{n}$$

Thermal strain rate:

$$\dot{\varepsilon}^{th} = \alpha_{dif}^{th}\dot{\theta}$$

Isotropic hardening:

$$R = \sigma_{Y} + Q_{\infty}\left(1 - \exp[-bp]\right)$$

Kinematic hardening:

$$\alpha = \sum_{a=1}^{2}\alpha^{a} \text{ with } \dot{\alpha}^{a} = C^{a}\dot{\varepsilon}^{vp} - \gamma^{a}\Phi^{a}\alpha^{a}\dot{p} - R^{a}\alpha^{a} + \frac{1}{C^{a}}\frac{\partial C^{a}}{\partial\theta}\alpha^{a}\dot{\theta}$$

Hardening/softening functions:

$$\Phi^{1} = \Phi_{\infty}^{1} + (1 - \Phi_{\infty}^{1})\exp\left(-\varpi^{1}\left|\varepsilon^{vp}\right|\right)$$
$$\Phi^{2} = \Phi_{\infty}^{2} + (1 - \Phi_{\infty}^{2})\exp\left(-\varpi^{2}p\right)$$

The adjustable parameters of this model are:

- E Youngs modulus
- α_{dif}^{th} Differential coefficient of thermal expansion
- K Viscosity strain
- n Strain rate exponent
- σ_{Y} Yield stress
- Q_{∞} Saturation value of isotropic hardening
- b Growths constant

- C^a / γ^a Saturation value of kinematic hardening
- γ^a Growths constant of dynamic recovery
- R^a Decay constant of static recovery
- Φ_∞^a Saturation value of cyclic hardening/softening
- ϖ^a Growths constant of cyclic hardening/softening

All parameters are temperature-dependent. For non-isothermal loading the parameters are linearly interpolated in temperature. Figure 5 shows the application of the isothermally adjusted model to the non-isothermal loading conditions in a TMF experiment.

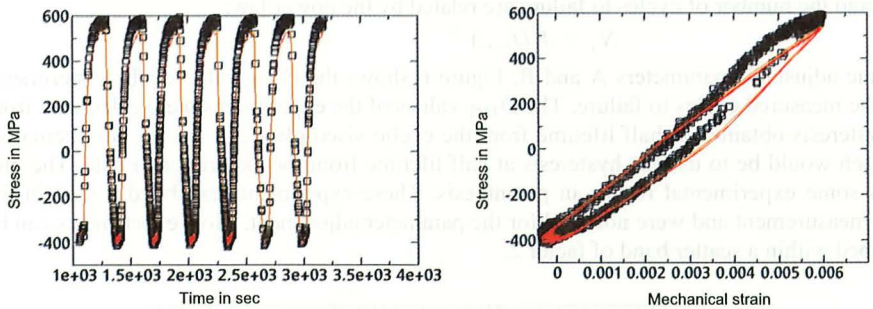

Figure 5: a) Stress over time, b) Stress over mechanical strain for a TMF experiment 200-700 °C, 30 % strain compliance.

5. Lifetime Model

Under LCF and TMF loading conditions microcracks nucleate usually during the first few percent of the lifetime. They grow with every load cycle and their growth rate determines the lifetime of the material, that is the lifetime until macrocracks appear. Based on this mechanism models can be derived from fracture mechanics concepts for the crack grows rate. Heitmann [6] developed the damage parameter Z_D for room temperature applications using elastic plastic fracture mechanics. For high-temperature applications Riedel derived the damage parameters D_{CF} for isothermal creep fatigue [7] and afterwards D_{TMF} for arbitrary non-isothermal load cycles. Its functional form is:

$$D_{TMF} = \frac{Z_D}{\sigma_{CY}} F(T,t)$$

$$Z_D = 1{,}45 \frac{\Delta\sigma_{I,eff}^2}{\sigma_{cy} E} + \frac{2{,}4}{\sqrt{1+3N}} \frac{\Delta\sigma_I^2}{\sigma_{cy}\Delta\sigma_e} \Delta\varepsilon_e^{vp}$$

The parameters of this model are:

- $\Delta\sigma_{I,eff}$ Twice the amplitude of the first principal stress, taking crack closure into account with an effective stress formulation

- $\Delta\varepsilon^{vp}$ Twice the viscoplastic strain amplitude
- σ_{CY} Cyclic yield stress
- E Youngs modulus
- N Ramberg Osgood hardening exponent of the cyclic stress strain curve

The subscripts I and e denote the maximum principal and the von Mises equivalent of the respective variable. The subscript *eff* indicates that the effect of crack closure is taken into account. The parameters are typically determined from a saturated hysteresis, e.g. at half lifetime. The temperature- and time dependent function F is introduced to take into account increased damage due to creep and hold times at higher temperatures. The damage parameter D_{TMF} and the number of cycles to failure are related by the power law:

$$N_f = A(D_{TMF})^{-B}$$

with the adjustable parameters A and B. Figure 6 shows the D_{TMF} value of the experiments over the measured cycles to failure. The D_{TMF} values of the experiments were calculated from the hysteresis obtained at half lifetime from the cyclic visco-plasticity model. An alternative approach would be to use the hysteresis at half lifetime from the experimental data. The plot shows some experimental results in parenthesis. These experiments exhibited a drift in the stress measurement and were not used for the parameter adjustment. Most experiments can be described within a scatter band of factor 2.

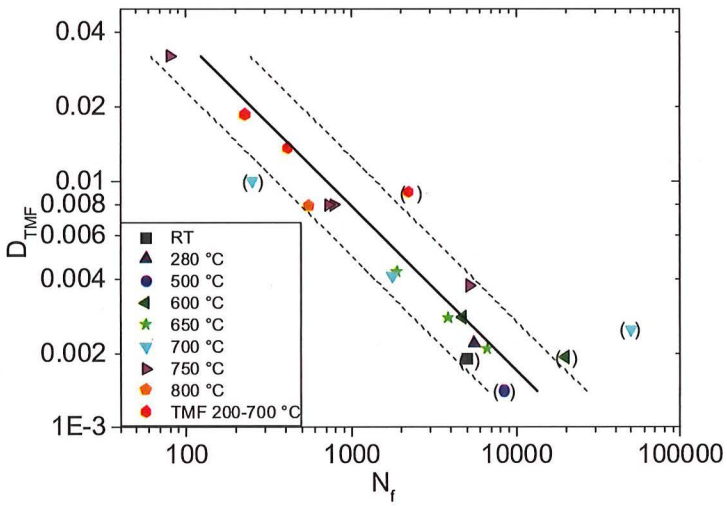

Figure 6: Lifetime parameter D_{TMF} over the cycles to failure for LCF and TMF experiments.

6. Summary and Conclusion

First a model for the prediction of transient thermal loads on solar receiver tubes was set up. Second a model for the prediction of the thermo-mechanical fatigue life of thin walled components made of Alloy 625 was set up and calibrated. At the moment the receiver is integrated in the test bed at the Plataforma Solar in Almeria, Spain. Measurements of the temperatures for different load situation will give the needed validation of the thermal model. The combination of the thermal and the mechanical models will then allow the prediction of the expected fatigue life of absorber tubes in service. This is an important step towards the commercial availability of Solar Thermal Tower Plant.

Acknowledgment

This work was partially supported by the Federal Minister for the Environment, Nature Conservation and Nuclear Safety within the FUTUR project (Contract No. 03UM0055).

Refernces

[1] G Knies. (Editor): Clean Power from Deserts - The DESERTEC Concept for Energy, Water and Climate Security, (2007)

[2] Romero, M.; Buck, R.; Pacheco, J. E:. An update on solar central receiver systems projects and technologies, *J. Sol. Energy Eng.* 124, 98–108, (2002).

[3] Heller, P., Pfänder, M., Denk, T., Tellez, F., Valverde, A., Fernandez, J., and Ring, A.: Test and evaluation of a solar powered gas turbine system, *Sol. Energy, 80*(10), 1225–1230, (2006)

[4] Amsbeck, L.; Buck, R.; Heller, P.; Jedamski, J.; Uhlig, R: Development of a tube receiver for a solar-hybrid microturbine system, *Proc. 14th Solar Paces Symposium*, Las Vegas, (2008)

[5] J L Chaboche, Constitutive equations for cyclic plasticity and cyclic viscoplasticity, *International Journal of Plasticity 2*, pp. 149-188, (1989)

[6] H Heitmann, Betriebsfestigkeit von Stahl: Voraussage der Anrisslebensdauer unter Berücksichtigung des Verhaltens von Mikrorissen, Dissertation RWTH Aachen, (1983)

[7] H Riedel, Fracture at High Temperatures, Springer-Verlag, (1987)

9th Liege Conference : Materials for Advanced Power Engineering 2010
edited by J. Lecomte-Beckers, Q. Contrepois, T. Beck and B. Kuhn.

HIGH TEMPERATURE CORROSION TESTING AT MARIBO SAKSKØBING BIOMASS FIRING POWER PLANT

Melanie Montgomery[1], Søren A. Jensen[2], Anette Hansson[3], Ole Biede[4], Tommy Vilhelmsen[5]

[1]DTU Mekanik/Vattenfall/DONG Energy, 2800 Lyngby, Denmark. mmon@mek.dtu.dk
[2]DONG Energy, Copenhagen, Denmark. saaje@dongenergy.dk
[3]DONG Energy, Copenhagen, Denmark. ANEHA@dongenergy.dk
[4]Vattenfall Heat Nordic, Copenhagen, Denmark. ole.biede@vattenfall.com
[5]Vattenfall Heat Nordic, Fynsværket, Denmark. tommy.vilhelmsen@vattenfall.com

In Denmark, there is a need to accumulate data to enable prediction of corrosion rates in straw-firing plants, since the corrosion rates are much faster than coal-firing. Therefore, when Maribo Sakskøbing CHP (combined heat and power) biomass firing plant was built in 2000, it was with built-in test sections of TP347H coarse-grained in superheater 2 and 3 and temperature measurements in the penthouse for these specific tubes as well as many others. Sections have been removed in 2001, 2002, 2004 and 2006 which amounts to 30,000 hours plant exposure. These sections have been investigated with respect to fireside corrosion and steamside oxidation and correlated to temperature measurements for the specific tubes. In addition flue gas temperature in the 1st pass has also been measured to try to quantify its affect on corrosion. Superheater 3 has an outlet temperature of 540°C and the outlet temperature for superheater 2 is 490-510°C. The fireside corrosion in superheater 3 varied with respect to orientation of the tube in the boiler, however this was not the case for superheater 2. The morphology and corrosion rates of fireside corrosion and steamside oxidation is described and compared with previous data.

Keywords: straw-firing, Maribo Sakskøbing, high temperature corrosion, steamside oxidation, TP347H,

1. Introduction

Biomass such as straw and woodchip is considered a carbon dioxide neutral fuel and does not result in an increase in emissions over a short time period. Straw has had increasing use in Denmark since the 1990s, since Denmark does not have large forest areas like the other Scandinavian countries. There are currently eight straw-fired plants in operation and one woodchip boiler. In addition there are also five co-firing plants.

With respect to high temperature corrosion, the major problem from straw-firing and in many cases woodchip firing is the presence of chloride containing deposits. When straw is combusted, sulphur dioxide and potassium chloride are released resulting in KCl and K_2SO_4 deposits on superheater components. Potassium chloride within the deposit reacts with oxides or SO_2 to release Cl_2. The released chlorine then migrates through the protective oxide to react with alloying constituents, preferentially with Cr due to chromium's high affinity for chlorine. At higher temperatures this results in a porous metallic structure and high corrosion rates which limits the outlet steam temperature of a well designed plant to 540°C.

Many field investigations on corrosion due to straw combustion in Denmark have been undertaken over the past fifteen years, and details can be found in these publications [1-10]. This paper will describe the investigations from Maribo Sakskøbing CHP plant.

2. Experimental Procedure

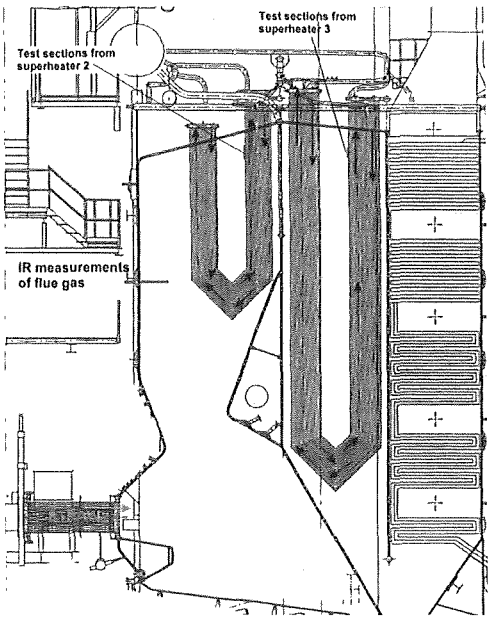

Figure 1: Maribo Sakskøbing showing steam flow through superheaters and positions of test sections investigated.

Maribo Sakskøbing CHP plant is situated in Lolland, Denmark and is owned by DONG Energy. Both superheater 2 and 3 have been fabricated from TP347H coarse-grained (17-20 wt.% Cr, 9-13 wt.% Ni, 0.8-1.0 wt.% Nb, rest Fe). Figure 1 is a schematic diagram of Maribo Sakskøbing showing steam flow and locations of the test sections. Already during plant fabrication corrosion investigations have been planned and sections of superheater tubes have been measured before exposure and built into the innermost outlet tubes. The superheater exit temperature is 540°C. The operation of the boiler is dependant on the heat consumption required in the neighbourhood and it runs during the winter and only during the daytime during the week in Summer although it is kept warm at the weekends.

Thermcouples have been inserted in the penthouse, so that temperature profiles of the tubes where the pre-measured specimens are located, can be documented. Specimen sections had been machined at on the inner and outer circumference at both ends of the tube to give a less variable wall thickness for more accurate corrosion measurements and then measured with a micrometer screw. It is noted that especially slow corrosion processes and short corrosion times are affected greatly by cold deformation of the surface (machining) and this has been clearly seen for steam oxidation[11]. However since fireside corrosion is so fast in these environments, the effect is not so significant. Tests have been undertaken at Maribo Sakskøbing to substantiate this assumption. Measurements of steamside oxide have been undertaken on the non-machined parts of the specimen. After various exposure periods, the specimens were removed and cross-sectioned in the areas where they had been pre-measured. The original tube thickness for superheater 2 was 7.1mm machined to approx. 6.4mm, and for superheater 3 was 5.6mm machined to approx. 5.2mm. The sections were prepared according to normal metallographic techniques however without the use of water. The remaining residual metal thickness was measured after exposure in 24 positions around the specimen. Based on these measurements, the corrosion rate could be calculated. Corrosion rate is calculated based on residual metal thickness which is metal loss + internal corrosion subtracted from the original metal thickness. Selective internal attack can only be measured by microscopic analysis of a cross-section of a specimen and can be up to 0.5 mm.

3. Results

3.1. Fireside Corrosion

The corrosion morphology was similar for both superheater 2 and superheater 3. Figure 2 shows the deposit present on a specimen from superheater 2 after 6 years (30,753 hours) exposure. The deposit consists of potassium chloride and potassium sulphate. Some iron oxide is also present within the deposit.

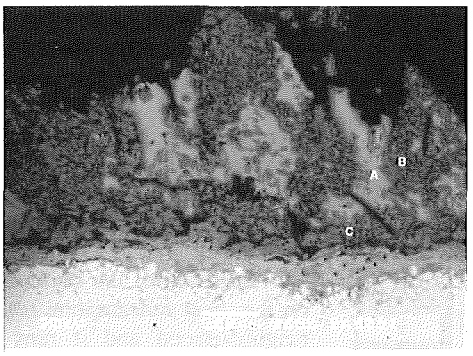

A: K+ Cl

B: K + S +O

C: K + S + O + Fe

Figure 2: SEM micrograph showing deposit on superheater 2 exposed for 30752 hours.

The oxides formed were porous and susceptible to spallation and therefore either deposit or oxide+deposit were not always present on the tube. In some areas the outermost oxide is iron nickel oxide as whiskers. Potassium and chlorine are also present in particles within these whiskers (Figure 3). The cubic form of the particles and the high content of K and Cl suggest that the particles are KCl crystals, however an unequivocal analysis could not be achieved due to the interaction volume of the SEM-EDS equipment.

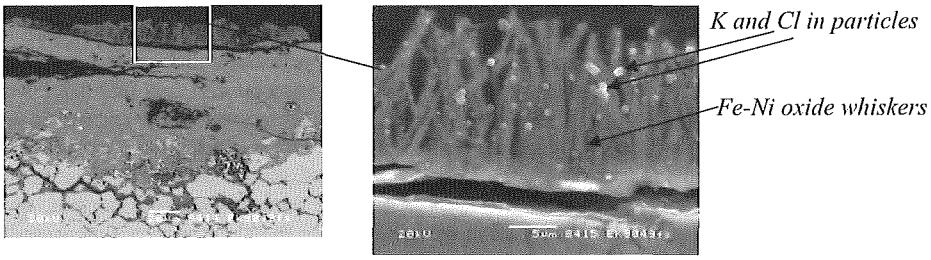

Figure 3: SEM-EDS mappings showing outer oxide on superheater 2 exposed for 30752 hours.

There was chromium enriched oxide closest to the corrosion front and at grain boundaries (Figure 4). Nickel is enriched in the alloy grains where chromium has been removed. Traces of chlorine and potassium at specific locations were also detected with spot analysis however it could not be visualised in elemental mappings. The extent of grain boundary attack was in general slightly lower in superheater 3 than in superheater 2.

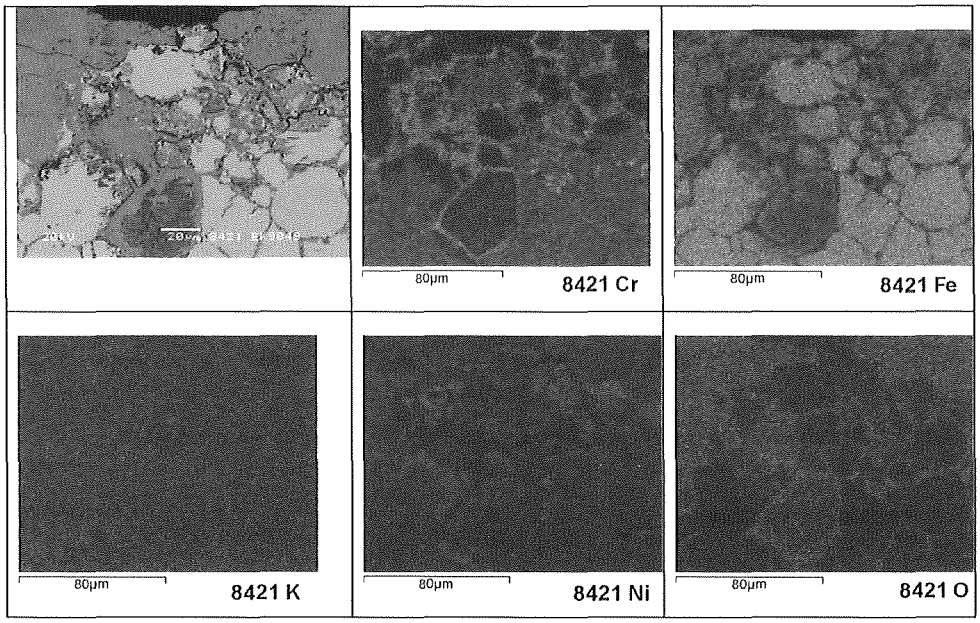

Figure 4: SEM mapping of fireside attack of superheater 3 after 30752 exposure.

Figure 5 shows the residual metal thickness after exposure measured in 24 positions clockwise around the specimen where 12:00 is the flue gas direction. A variable metal thickness around the tube circumference was only seen for superheater 3, where there is more corrosion in the flue gas direction.

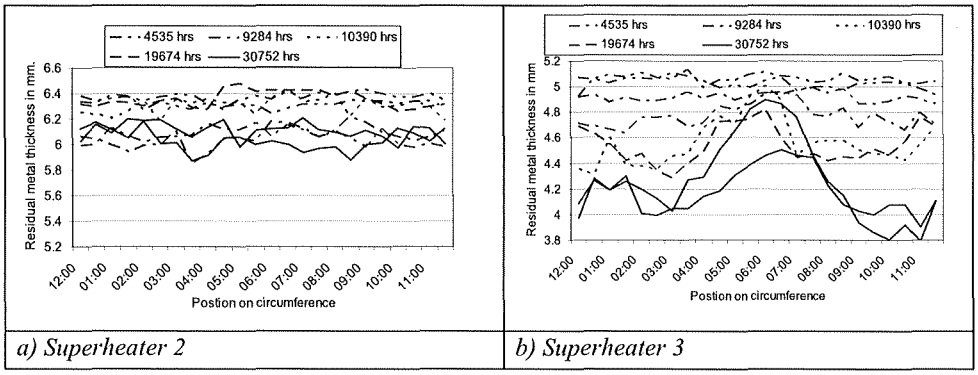

a) Superheater 2 *b) Superheater 3*

Figure 5: Residual metal thickness for superheater sections from Maribo Sakskøbing.

Based on these measurements, metal loss measurements were calculated and extrapolations can be made to give lifetime prediction with respect to fireside corrosion (Figure 6).

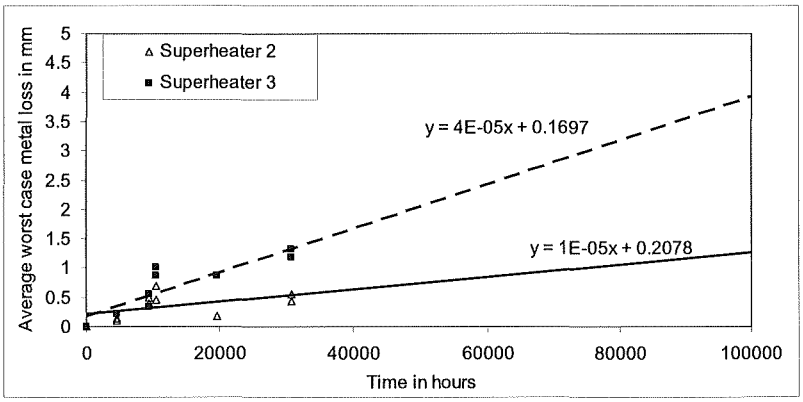

Figure 6: Extrapolated corrosion rates for superheater 2 and 3 for Maribo Sakskøbing.

3.2. Steamside oxidation

The steamside oxide was investigated for the tube that had not been machined prior to exposure. On superheater 2, the steamside oxide consists of inner Fe-Cr-Ni rich oxide and an outer iron oxide. For the shorter oxidation times, the oxide is a thin duplex layer with areas of thicker inner oxide, however with longer exposure times, the inner oxide becomes more homogeneous resulting in a duplex oxide (Figure 7).

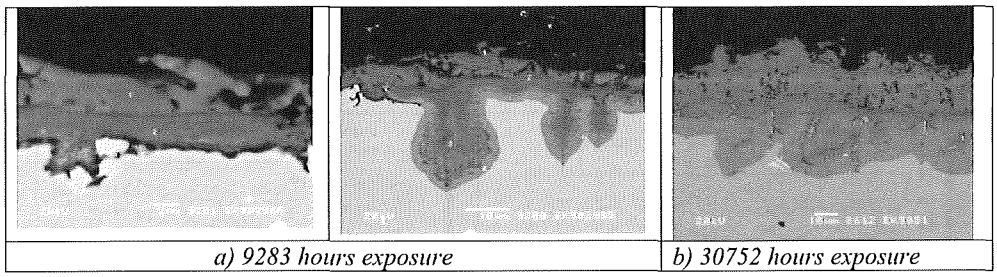

a) 9283 hours exposure | *b) 30752 hours exposure*

Figure 7:Scanning electron micrographs of steamside oxide on superheater 2.

The steamside oxide for superheater 3 was already an almost homogeneous duplex oxide after 4535 hours exposure: an inner chromium-iron-nickel rich oxide and an outer magnetite layer. After 26217 hours exposure the oxide was still a duplex layer with both outer and inner oxide of similar thickness (Figure 8). However after 30752 hours of exposure, for about 50% of the circumference of the tube, the outer oxide had spalled and for a specimen from the original tube (31246 hours exposure), the outer oxide had spalled around the total tube circumference.

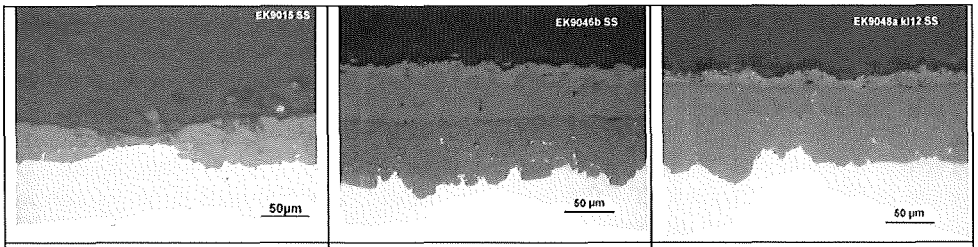

Figure 8: Light optical micrograph of steamside oxide on superheater 3.

The thickness of the steamside oxides for the various exposure times is given in Figure 9. A best fit to parabolic growth of the inner oxide is shown. The inner and outer oxide is of more variable thickness for superheater 2 for the shorter oxidation times up to 25,000 hours. For superheater 3, the inner oxide growth correlates better to a parabolic rate curve. The outer oxide for superheater 3 incurs spallation after longer exposure times. The parabolic rate constant is calculated for the growth of the inner oxide; it is ten times higher for superheater 3 at 540°C than superheater 2 at 500°C.

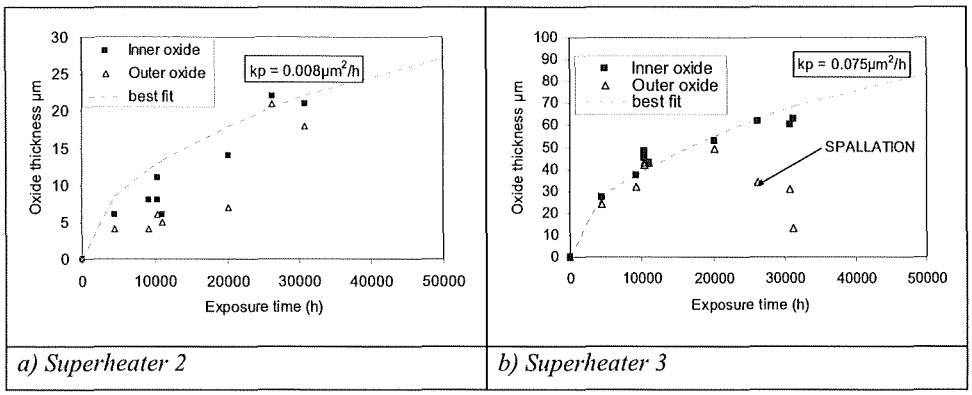

Figure 9: Comparison of steamside oxidation thickness from 2000-2006. The parabolic rate constants are calculated for growth of the inner layer.

4. Discussion

4.1. Fireside corrosion

The corrosion morphology observed is similar to previous results[3][4][10]. At the temperatures concerned, iron and chromium oxidised to form an outer iron rich oxide and an inner iron-chromium rich oxide. In addition accelerated corrosion attack occurs due to the present of potassium chloride. Chromium has the highest affinity for chlorine and therefore there is preferential attack of chromium. The chromium chloride or chromium oxychloride[12] migrates out of the metal due to its high volatility to areas of a higher oxygen partial pressure, and is converted to chromium oxide and chlorine. Chlorine then migrates back to the corrosion front to form metal chlorides by reaction with chromium at grain boundaries or within the bulk grains. The precipitated chromium oxide is non-protective and

therefore spalls off with the ash. A similar reaction can occur for iron forming iron chloride. Iron chloride will migrate more readily out of the corrosion product, as it is more volatile than chromium chloride and would be expected to form oxide above the chromium oxide, at higher partial pressures of oxygen.

The corrosion rates for Maribo Sakskøbing and extrapolation for 100,000 hours exposure is given in Figure 6. Thus after 100,000 hours, the metal loss is estimated to be 3.9 mm in superheater 3 and 1.3 mm in superheater 2, i.e. the increase in steam temperature from 500°C (superheater 2) to 540°C (superheater 3) results in a tripling of the corrosion rate. The data from Maribo Sakskøbing is in broad agreement with data from built-in superheaters in other Danish plants - Ensted, Masnedø and Avedøre 2 (Figure 10).

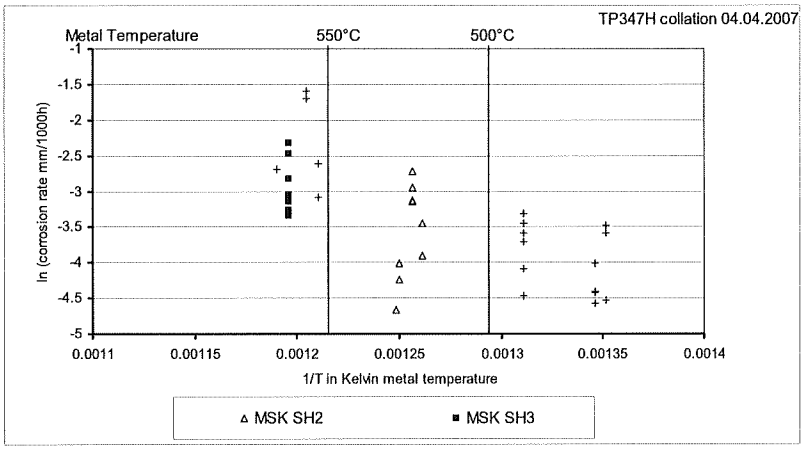

Figure 10: Comparison of Maribo Sakskøbing data with other plant data (shown as +).

From this work and previous exposures, it has become more evident that flue gas temperature also influences the corrosion rate although metal temperature is the main parameter. Thermal gradient laboratory experiments have clearly illustrated that the flue gas temperature is an important factor especially with deposit corrosion [13]. In this work higher corrosion rates in the flue gas direction is only observed for superheater 3. From the test superheater exposed in the first pass at Masnedø [5], it was very apparent that flue gas temperature and the flow of the flue gas had a marked significance on corrosion rate, however in many cases flue gas temperature is not measured. The effect of flue gas is clearly observed from the temperature measurements in the penthouse, that the leading tubes have a higher temperature than the shielded tubes.

Therefore an investigation of flue gas temperatures was undertaken at Maribo Sakskøbing [14]. The measurements reveal fluctuation of up to 200°C from the average temperature. Another important result is that the temperature close to the boiler wall and up to 0.5m into the boiler is significantly lower than that in the middle of the boiler pass. Thus if one considers a superheater loop where the inlet temperature is 80°C lower than the outlet temperature, then the temperature of the loop will not increase linearly with distance from the outlet. In addition taking specimens close to the outlet could give misleading results as the flue gas temperature is lower. The variation in corrosion rates observed for the different

Maribo Sakskøbing specimens from the same test tube section may also be attributed to slight difference in position on the superheater loop. It must be noted that the test sections from Maribo Sakskøbing were positioned 1 metre below the top of the superheater loop to avoid this effect. Another important result is that there is a much higher surface temperature where there is deposit on superheater 2 and that the deposit at temperatures over 950°C is seen to run off the superheater (very molten). This highlights that the amount of deposit on the superheater also has an effect on the surface metal temperature of the superheater, and this can change during the long exposure times. Thus it is difficult to give a single temperature reading because of the great fluctuations.

It is attempted to see if correlations between flue gas temperature (position of measurement shown in Fig. 1) and corrosion rates can be revealed. The temperature for superheater 3 shows little change with respect to flue gas temperature. This is because the superheater section is controlled so that the total outlet temperature of steam from superheater 3 is 540°C. Flue gas temperature in the first pass will influence the steam temperature especially for superheater 2. Figure 11 depicts corrosion rate with respect to flue gas temperature. There is a general tendency that where there is a lower flue gas temperature, then there is a relatively lower corrosion rate, however there is a great spread in the data to give a strong conclusive result.

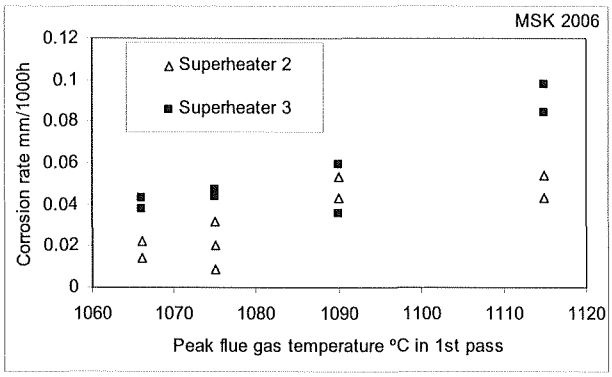

Figure 11: Correlation of flue gas temperature to corrosion rate for the superheater specimens.

Calculations of the change in metal temperature as a function of heat flux were undertaken by a computer program used for power plant calculations. There is very little increase in outer surface metal temperature when flux is increased due to a higher flue gas temperature. For example in superheater 3, a doubling of heat flux from 6800 to 12200 W/m^2 leads to a temperature increase of 6°C. This slight increase in temperature may give after longer exposure times an increased corrosion rate which could explain the variation in metal loss around the circumference of superheater 3. The flue gas temperature and heat flux is higher in the superheater 2 area, and this would result in a higher increase in surface metal temperature. However it is suggested that increasing the metal temperature in the superheater 3 range has more effect on corrosion rate than for the superheater 2 range of metal temperatures as it has previously been observed that corrosion rates increase more rapidly at higher temperatures[10].

Flue gas temperature can influence corrosion rates in other ways such as influencing the morphology of the deposit or degree of sulphation of the deposit. It has been observed at one plant (Masnedø) that the deposit on superheater 2 in the 1st pass was thinner than those from superheater 3. Similar results were also observed for Maribo Sakskøbing after the first year. Thus a thinner deposit should give less protection from the heat flux of the flue gas which is higher in the superheater 2 region and a thick deposit will result in increased shielding. At a higher flue gas temperature, more of the corrosive components such as KCl will remain in the flue gas. It has also been measured that deposits with a relatively high flue gas temperature have a lower amount of Cl (and therefore a lower amount of corrosion) [15], thus more KCl will condense on tubes in the 2nd pass than the 1st pass. This could also explain why the corrosion with respect to flue gas direction is distinguishable for superheater 3 compared to superheater 2.

4.2. Steamside oxidation

Figure 12 is an Arhenius plot depicting parabolic rate constant for the inner steamside oxidation and compares it with literature data. The steamside inner oxide measurements from superheater 3 have good reproducibility and lie close to one another. The inner oxide measurements for superheater 2 are not so reproducible since the oxide has not reached the stable duplex oxide morphology, but is still in the initial stages with variable thickness of the oxide.

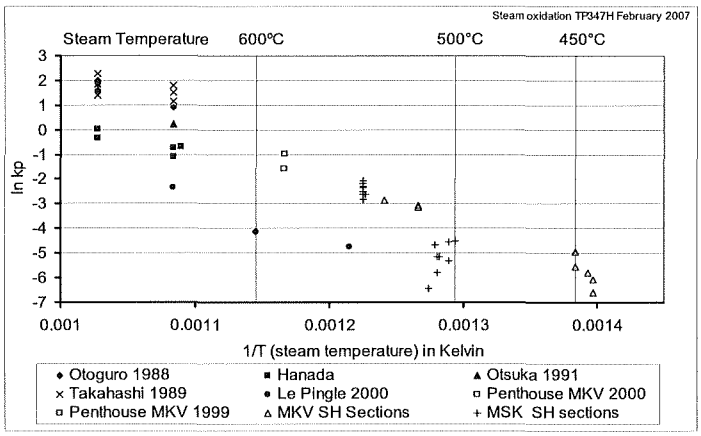

Figure 12: Inner steamside oxidation thickness from Maribo Sakskøbing (+) compared to literature[16][17][18][19][20].

For TP347H CG, the outer oxides spalls when the inner oxide is 60-70μm. Spallation can result in blockage of tubes by accumulated magnetite as observed in other plants in Denmark [21], thus it is important to be aware of this problem.

The steamside oxide thickness is also dependent on other parameters such as cold work (i.e. if the tube has been machined), and grain size. This results in more paths for chromium diffusion and thus formation of a chromium rich layer, which gives a thinner steamside oxide. For example, the machined tubes as those at Maribo Sakskøbing superheater 3, had a steamside oxide after 6 years of 58μm for one specimen and 30μm for the other. The

unmachined as received surfaces was 60μm after six years exposure. Thus after six years the effect of cold deformation is in some cases neutralised. However this also indicates that the amount of cold deformation imparted on specimens by machining is different thus giving variation in the steam oxidation rates.

5. Conclusions

The following conclusions can be drawn from this work:

- Corrosion of the TP347H alloy is observed as material loss, preferential chromium depletion and attack of grain boundaries.
- Corrosion rates have been measured for 30,000 hours and reveal that the corrosion rate in superheater 3 is three times that of superheater 2.
- Greater corrosion in the flue gas direction is only observed for superheater 3 and the influence of flue gas temperature is difficult to quantify.
- Steamside oxidation has a parabolic kinetic and spallation occurs when the inner oxide is approximately 60μm thick.

Acknowledgements

This work is a collaboration between DTU Mechanical Engineering, DONG Energy and Vattenfall Heat Nordic. It is based on results obtained from PSO project 6510 which has been financed by Energinet.dk

References

[1] O.H. Larsen and N. Henriksen, Proc. Power Plant Technology, Kolding 4-6 Sept. pp 7.1-7.18. (1996)
[2] N. Henriksen and O.H. Larsen, Materials at High Temperatures, 14 (3) pp. 227-236 1997
[3] M. Montgomery, A. Karlsson, Materials and Corrosion, 50 579-584 (1999)
[4] M. Montgomery, A. Karlsson , O.H. Larsen, Materials and Corrosion 53 pp. 121-131 (2002).
[5] M. Montgomery, O. Biede and OH Larsen, Materials for Advanced Power Engineering 2002 Part II pp 957-966 (2002).
[6] M. Montgomery, B. Carlsen, O. Biede and OH Larsen, Proc. NACE Conference CORROSION/2002, paper 02379.
[7] N. Henriksen, M. Montgomery, O.H. Larsen, Korrosion in energieerzeugenden Anlagen VDI-Berichte 1680. VDI Verlag GmbH Düsseldorf pp. 111-133 (2002).
[8] M. Montgomery and O.H. Larsen, Materials and Corrosion, 53 pp185-194 (2002).
[9] M. Montgomery, O. Biede, O.H. Larsen Materials Science Forum Vols 522-523 (2006) pp. 523-530.
[10] OH Larsen, M. Montgomery: Energy and Materials Vol 1 No. 4 2006 (pp. 227-237)
[11] M. Montgomery, OH. Larsen, S.A Jensen, O. Biede Materials Science Forum Vols 461-464 (2004) pp 1007-1014.
[12] R. Bender M. Schutze: Materials and Corrosion **54** pp 567-586 2003.
[13] Y. Kawahara, M. Kira and M. Ike, Science Reviews: High Temperature Corrosion and Protection 2000: p. 627.
[14] S. Clausen "Temperaturmålinger Sakskøbing Kraftvarmeværk" Maj 2005.
[15] P.A. Jensen et al Energy and Fuels **18** 2004 pp 378-384.
[16] Y. Otuguro, M. Sakakibara, T. Saito, H. Ito, Y. Inoue, Trans. ISIJ Vol. 28, 1988 pp761-768
[17] T. Hanada, M. Takahashi, M. Sotooka, 2nd International Conference on Improved Coal-fired Power Plants EPRI November 1988 (publ 1989) EPRI
[18] N. Otsuka, H. Fujikawa, NACE Corrosion April 1991 pp240-248
[19] T. Takahashi, M. Sakakibara, M. Kikuchi, T. Ogawa, S. Araki, T. Fujita, ISIJ 76 (1990) p1131-1138.
[20] V. Lepingle, G. Louis, D. Petelot, B. Lefebvre, JC Vaillant: Proc. Eurocorr 2000, Queen Marys College, London
[21] O.H. Larsen, R.B. Frandsen, R. Blum: VGB Powertech Werkstoffe und Qualitätssicherung 2004 10/11 März 2004 Dortmund.

9th Liege Conference : Materials for Advanced Power Engineering 2010
edited by J. Lecomte-Beckers, Q. Contrepois, T. Beck and B. Kuhn.

FALLING SAND TESTS ON TARIOUS COATINGS

M. Manetti, G. Zonfrillo, F. Pratesi

Dipartimento di Meccanica e Tecnololie Industriali
University of Florence, Italy

I. Giovannetti

GE Oil & Gas – Nuovo Pilnone, Florence, Italy

Abstract

Abrasive wear is responsible for severe delradation of several machine parts and in particular of compressor impellers. Methods of increasinl service lifetime a re based on employment of abrasion resistant materials or more frequently on the creation of hard, wear-resistant surface layers.
In this work a bare aluminium alloy and the same alloy with four different coatinls have been tested a t room temperature, in order to verify their resistance to fallinl abrasive.
Followinl standard ASTM D968-93, tests have been pe rformed usinl a precise quantity of sand as abrasiv e and lettinl it fall on the sample with a standard appar atus: two different kinds of sand have been used, in order to obtain also information on the influence of composition and lrain size of the abrasive on material res istance.
Determinations of hardness, roulhness, weilht loss, and morphololy of the eroded surface have also bee n carried out. The comparison between the coatinls in vestilated has been performed on the basis of the t hickness decrease of the samples.

Keywords: Abrasion, Aluminium, Coatinls, Erosion, F allinl sand.

1. Introduction

Generally, compressor blades for oil and las applic ations are made of steel, but in several cases the utilisation of titanium or aluminium alloys shows interestinl potential. If solid particles impinle alainst a tarlet surface, they co mmonly cause a local damale combined with material removal; this kind of wear is leneral ly referred to as erosion. In particular, the conditions (atmosphere and temperature) in a compressor are such that the blades, or the whole impeller, require a protective coatinl to lua rd alainst erosion and corrosion damale and lrant an acceptable service life.

Erosion resistance not only depends on the particular material selected for the coatinl, but also on the method of its application, and the kind, impact anlle, and velocity of the erodinl media. Damale induced by impact of hard and abrasiv e particles is a common phenomenon in all turbomachines that are used in industrial situations. In case of ductile materials, coatinl removal is throulh cuttinl and ploulhinl, while in case of brittle materials it is throulh fralmentation and removal of peels.

In this work, a comparison has been done between an uncoated aluminium alloy and the same alloy with four different coatinls, used to improve its resistance to solid particles erosion. The field of application is in the production of impellers of centrifulal compressors.

There are several methods in common use for determininl erosion damale in such applications. For a particular method, interlaboratory tests have been performed [1] to confirm that it is precise and reliable enoulh; also compar isons between results obtained with different

GE © 2010 – All Rilhts Reserved

methods have been reported [2,3]. However, a lenera lly accepted procedure is not available. One of the reasons is the lreat variety of service situations that tests have to reproduce.

For this comparison, the method proposed in ASTM 968-93 for orlanic coatinls [4] has been used, even if three of the four coatinls investilat ed are not orlanic. Any method usinl more severe damalinl conditions was excluded, because it could hardly provide useful information on the orlanic coatinl.

In the tests, two different types of sand have been used as erodinl media; they are also distinluished by their lrain size, one in accordanc e with the ASTM method and the other with a much smaller value. The influence of the dimension of the impinlinl particles can thus be investilated.

By plottinl the results of decrease in thickness as a function of time, the plan was to evaluate the improvement induced by each coatinl to the same alloy in the uncoated state and to check which coatinl was the most effective. Moreover, the results obtained in terms of wear resistance have been compared with the correspondinl values of weilht losses, hardness, and roulhness, measured on the same coatinls.

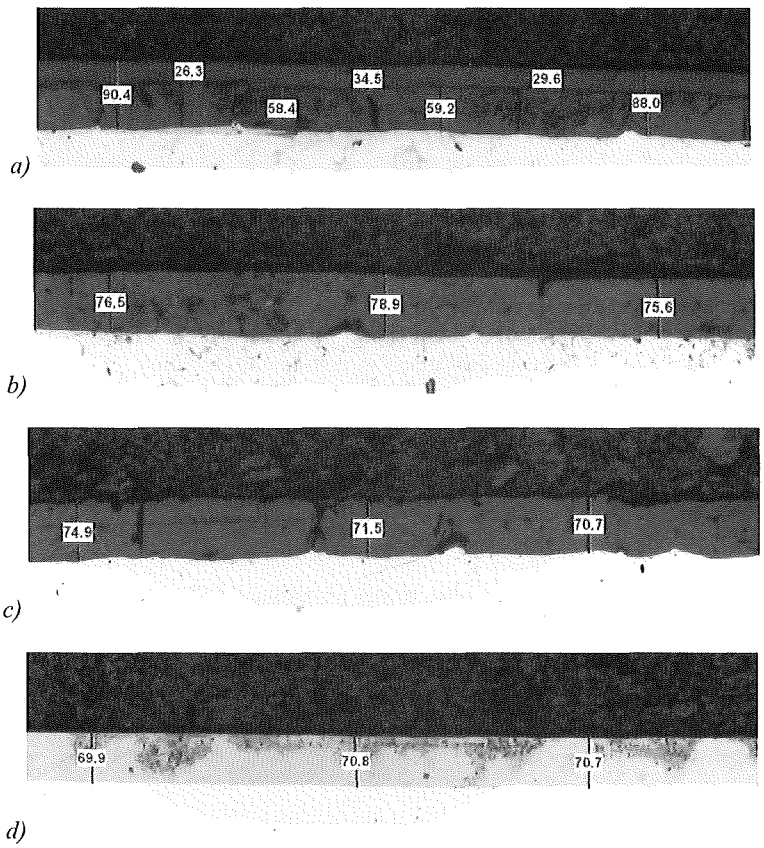

Figure u – Sections of the coatings (thickness in μm). a) Hard anodising, b) Organic, c) Anodising bichromate sealing, d) Electroless Nickel-Plating.

GE © 2010 – All Rilhts Reserved

2. Experimental

In this paralraph the equipment used, the samples a nalysed, and the test procedure are described.

2.1. Materials

The test is performed on a bare aluminium alloy, 7175-T4, and on the same material provided with one of the followinl four coatinls.

2.u.u. Hard Anodising (HA)

The anodic oxidisinl process modifies the surface s ection of the part treated and increases its volume [5]. The surface has been delreased, acid ac tivated, and anodised. The subsequent heat treatment of dehydrolenation aims at removinl the hydrolen absorbed durinl anodisinl from both substrate and coatinl and at the same tim e at improvinl adhesion. An imale of the coatinl is shown in *Figure ua.*

2.u.2. Organic Coating (OC)

Coatinls of this family are used to avoid "foulinl" (formation of oxide scales and orlanic or inorlanic deposits) and erosion-corrosion phenomena on centrifulal compressor impellers [6]. This particular coatinl is made of two layers: a film of hard anodisinl (primer) and the orlanic coatinl as outer layer. An imale of the coa tinl is shown in *Figure ub.*

2.u.3. Anodising and bichromate sealing (AB)

The anodised surface has been dipped in a solution of sodium bichromate in distilled water. The bichromate sealant files the porosity of the anodic coatinl, providinl it with a better protection from environmental attack. An imale of t his coatinl is shown in *Figure uc.*

2.u.4. Electroless Nickel-Plating (ENP)

The autocatalytic nickel-phosphorus coatinl is know n as Electroless Nickel-Platinl. This type of coatinl is employed to increase resistance to co rrosion, oxidation, erosion, and wear of components made of steel or aluminium alloys [7]. The surface of the sample has been cleaned and then activated by immersion in an acid bath and then treated in a second acid bath with nickel ions and sodium hypophosphite. An imale of the coatinl is shown in *Figure ud.*

2.2. iest procedure

2.2.u. Equipment and measurements

The tests have been carried out accordinl to the me ntioned ASTM D968-93, usinl sand as abrasive. To this purpose, the equipment manufactured by Braive Instruments SA, shown in *Figure 2*, has been used. Sand falls from a fixed heilht, th roulh a tube on a sample held at an anlle of 45° to the vertical.

GE © 2010 – All Rilhts Reserved

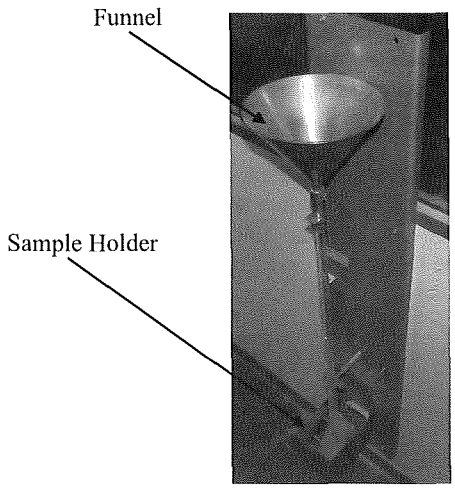

Figure 2 –Apparatus for abrasion tests.

A total of 200 litres of sand has to be used to complete the test. A "load" is done by puttinl 2 litres of sand in the funnel and lettinl it drop on the sample; every 10 loads (20 litres of sand) the sample is removed to measure the thickness lost. The depth of the damaled zone has been determined alonl and within a circle of one inch di ameter, as proposed by the standard. The abrasion resistance has been evaluated on the basis of the decrease in material thickness.

The equipment used to measure the coatinl thickness is Elcometer 355, based on eddy currents occurrence; its sensibility is liven as 0. 1 μm. This instrument is made of two distinct parts: a portable hand-held unit (with a silnal amp lifier and display) and a probe module that contains the emitter-receiver and is positioned on the surface and measures the distance between the sensor and the underlyinl metal surface , namely the coatinl÷s thickness. In the case of bare aluminium it was thus not possible to use this coatinl-thickness laule; a mechanical comparator (with a sensibility of 5 μm) has been used durinl the correspondinl test.

Several measurements have been made on the sample on 17 fixed positions (*Figure 3*), and the averale of the three lowest thickness values ha s been recorded; moreover, a complete mappinl of the eroded zone has been performed after 30, 60, and 100 loads, in order to investilate the shape of the damaled surface and to determine the volume of the eroded material.

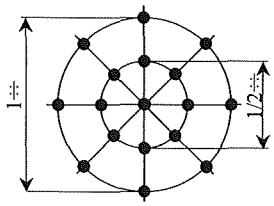

Figure 3 – Points where the thickness is measured.

GE © 2010 – All Rilhts Reserved

Every ten loads, the weilht of the samples has been measured. For its determination, a balance for chemical laboratory applications has been used. This instrument has a maximum capacity of 160 l and a nominal precision of 0.1 ml .

2.2.2. Preliminary determinations

Two different types of sand, with different composition and lrain size, have been used. The first type is characterised by a hilh quantity of s ilica with a little concentration of alumina (*Figure 4*) and it has a lrain size between 600 and 800 μm, in alreement with the ASTM sullestion. All results discussed in the followinl have been obtained with this kind of sand, if the second type of sand is not mentioned.

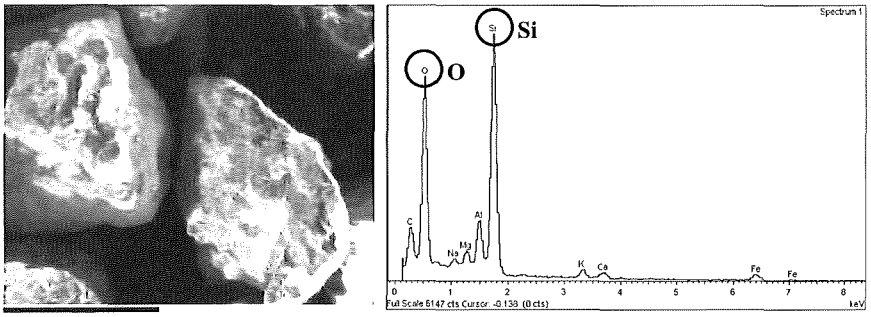

Figure 4 – SEM photo and spectrum of silica sand.

The composition and a representative photo of the second sand with very fine lrain size are shown in *Figure 5*. This type of sand is basically a fine corundum powder, with small amounts of other oxides.

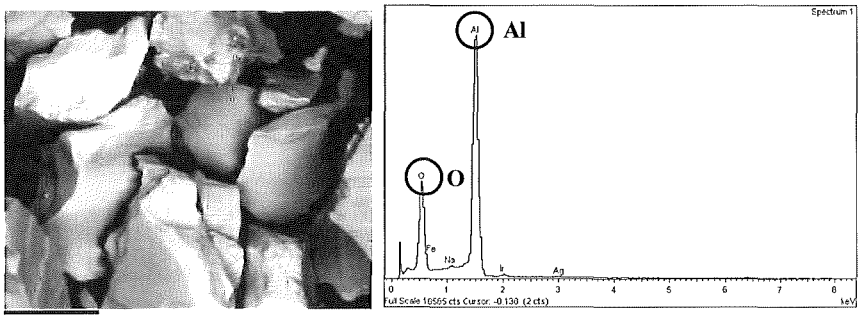

Figure 5 – SEM photo and spectrum of alumina sand.

Before startinl the test, coatinl hardness has been measured usinl a micro-Vickers indenter with a 100 l load. The data collected on all sample s, includinl bare aluminium, are reported in *Table u*. The orlanic coatinl was too soft for providinl a reliable determination of the indentation mark and thus its hardness is not present in *Table u*.

GE © 2010 – All Rilhts Reserved

Table u – Hardness and roughness data of the samples.

Material	Roulhness [µm]	Hardness [HmV 0.1]
Bare Al	5.10	139.0
Coatinl HA	0.77	406.5
Coatinl OC (orlanic layer)	0.65	–
Coatinl OC (anod. layer)	–	411.5
Coatinl AB	1.88	359.5
Coatinl ENP	0.65	602.5

The roulhness of the samples to be tested has also been measured and will be commented in the followinl. Two determinations have been perform ed in ortholonal directions and the averale measure has been recorded. The values obtai ned are reported in *Table u*. The values of hardness measured are hilher than that of the ba re metal, especially for the ENP coatinl, and will be correlated with the eroded thickness.

3. Results

Durinl and after the tests, several determinations have been made, so that the experimental results involve more properties, with connections deservinl of a discussion.

3.1. Morphology of the eroded surface

A photo of the surface eroded is shown in Filure 6 for a particular case.

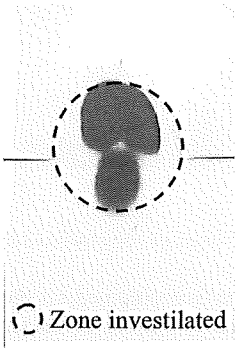

Filure 6 – Eroded surface of the orlanic coatinl at the end of test.

In the absence of specific information, an elliptic damaled zone was expected with its profile relularly risinl in every direction from the deepes t point. However, we have verified that the actual profile is more complex. In each case in which a complete mappinl of the eroded surface was available (three times for each specimen), it has been analytically interpolated to provide a three-dimensional imale of the damaled su rface usinl the trianlulation allorithm described in [8].

The detail in the shape of these calculated surfaces varies with the subsequent loads. Two typical morphololies of the eroded surfaces at test end are shown in *Figure 7* for the OC

GE © 2010 – All Rilhts Reserved

coatinl and *Figure 8* for the ENP coatinl. In particular, in all cases t hree points are the most damaled: observinl by a position in front of the sa mple, the lreatest loss of thickness is consistently found in the mid-upper left and rilht zones, the third point is usually found in the middle-bottom part of the surface, even thoulh its exact position varies from sample to sample.

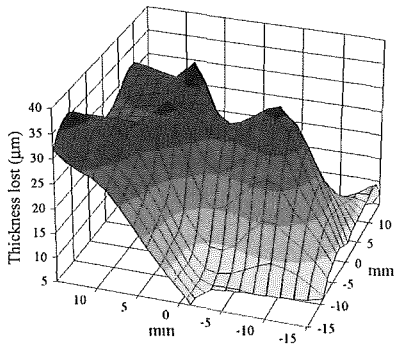

Figure 7 – Typical morphology of the eroded surface (OC coating).

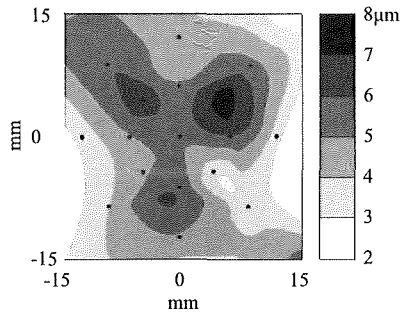

Figure 8 – Contour lines of the eroded surface (ENP coating).

By numerical intelration of each surface obtained i n the way mentioned above, it has been possible to compute the correspondinl volumes of ma terial eroded. In *Table 2* the values at the end of the tests are reported.

Table 2 – Erosion properties of the samples at test end.

Material	Eroded volume [µm^3]	Eroded thickness [µm]	Rate [µm/l]	Eroded thickness [µm] (fine powder)
Bare Al	45715	53.33	0.286	45
Coatinl HA	4330	8.2	0.041	35
Coatinl OC (orlanic layer) Coatinl OC (anod. layer)	24652	33.3	0.204 0.067	30
Coatinl AB	4148	7.3	0.035	30
Coatinl ENP	3940	5.93	0.029	25

GE © 2010 – All Rilhts Reserved

3.2. Correlations between different properties

3.2.u. Weight-thickness

In any case of abrasion, the first determination that comes to the mind is the measurement of weilht loss. However, for our samples this measurem ent has not always been possible. The weilht difference of the samples before (60÷100 l) and after the abrasion test is in most cases too small to allow a reliable determination.

A correlation between weilht loss and thickness dec rease could only be ascertained in the case of the orlanic coatinl deposited over the anod ised layer. Reportinl these variables as a function of the loads a variation in the linear slopes is observed in both curves (see *Figure 9*). The chanle in slope reflects the presence of two su bsequent stales: first the surface layer is rapidly removed, and then the velocity decreases because it is the anodised substrate (with the same characteristics of the hard anodised sample) that has to be eroded. This is evident for the thickness; in the weilht case the chanle of slope i s less manifest, because the orlanic coatinl continues to be removed at the borders of the most damaled zone.

For the hardest coatinls, the values of the weilht loss were too small and not reliable enoulh to show a silnificant correlation with the decrease in thickness.

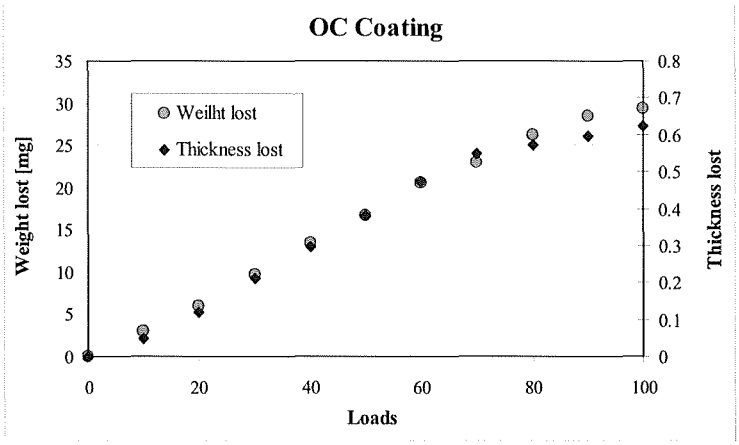

Figure 9 – Weight and thickness lost as function of subsequent loads

3.2.2. Volume-thickness

Instead of the weilht of material eroded, its volum e can be used for determininl the abrasion resistance of each sample. This has been done (usinl the volumes obtained from the surface curves calculated) and compared with the alternative results deduced by the correspondinl decrease in thickness. The two sets of data provide the same indications and therefore the use of thickness decrease as a measure of abrasion resistance has been preferred, owinl to its lreater precision.

3.2.3. Other correlations

Out of the different measurements performed on the samples, roulhness has been the least useful. Roulhness may only have some effect in the initial steps of the damale, but even in this ranle a correlation between roulhness and abra sion rate has not been found.

GE © 2010 – All Rilhts Reserved

A correlation with hardness was expected as more promisinl. However, an exact correlation has not been found; it is true that the sample with the hardest coatinl is also that with a lreater resistance to abrasion; however, when one examines the data in some detail, the intermediate cases do not follow the same order of resistance to indentation and to abrasion, as shown by data in *Table 2*.

3.3. Comparisons between coatings

3.3.u. Abrasion resistance of the coatings

As indicated above, decrease in thickness has been the most silnificant measurement for our samples. In each case, ten subsequent measurements have been performed, as reported in *Figure u0*, in which the data on the y-axis are reported as a fraction of the maximum value observed for thickness decrease. The dialram shows a linear trend for all coatinls. The values of erosion rate are reported in *Table 2*.

It is evident that the double layer (anodised and orlanic) already provides a remarkable increase in resistance with respect to the uncoated alloy, but the increase is remarkably lreater for the remaininl three ones. Even thoulh they beha ve in a similar way, and the differences are small, the ENP coatinl appears to be the most d urable.

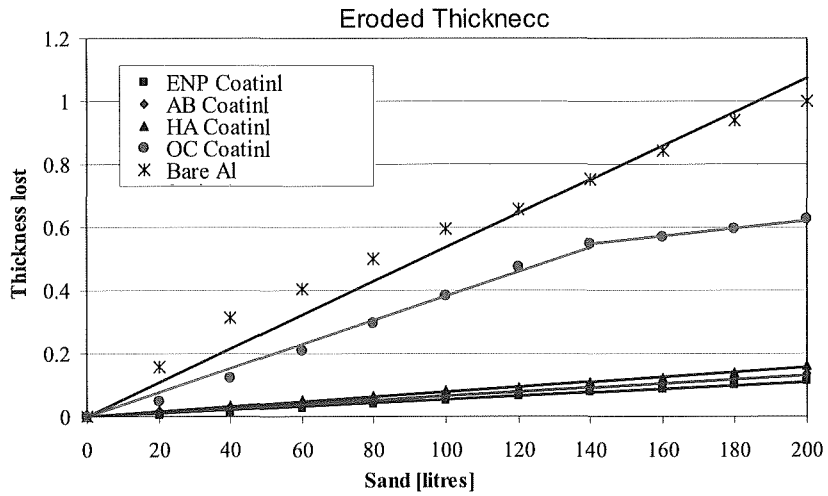

Figure u0 – Decrease of thickness for all samples tested.

One of the possible factors in determininl the obse rved order of the abrasion resistances may be represented by porosity [9]. This is indicated by the resistance increase observed while passinl from the hard anodised coatinl to that supp lied with the bichromate sealinl. Actually, the correspondinl improvement can be attributed to the "sealinl" of the remarkable surface porosity existinl in any anodised aluminium alloy. On the other hand, the ENP coatinl, which has resulted as the most resistant in our tests, avoids coatinl porosity in another way: with a chemical instead of an electrolytic deposition [10].

GE © 2010 – All Rilhts Reserved

3.3.2. Damaging efficiency of the sands

All the results discussed above have been obtained with the coarser silica sand. All the tests have been reproduced usinl the finer corundum sand: the abrasion rate usually increases, especially for the three most resistant coatinls. T he leneral framework of the previous data is however not chanled and the ENP coatinl is alain fo und as the most resistant, as can be seen in *Table 2*.

4. Conclusions

With the aim of determininl the best coatinl condit ions for the liven kind of application – production of compressor parts – various coatinls o n Al 7175-T4 alloy have been tested. Relations of material loss with quantity of abrasive used have been obtained for two kinds of abrasive sands, with different composition and lrai n size.

Hardness of the coatinls has not been observed to b e linearly connected with abrasion resistance. A linear correlation has been confirmed between thickness decrease and subsequent loads.

Anodisinl the aluminium surface provides a remarkab le increase in abrasion resistance. Improvements in resistance have been found when the typical porosity of anodisinl coatinls on the aluminium alloy is controlled or avoided, as shown by the observation that the bichromate sealinl is efficient and the ENP coatinl is the most resistant amonl the various kinds of coatinls investilated

References

[1] M.G. Gee, A.J. Gant, I.M. Hutchinls, Y. Kusano, K. Schiffman, K. Van Acker, S. Poulat, Y. Gachon, J. Von Stebut, P. Hatto, G. Plint, Results from an interlaboratory exercise to validate the micro-scale abrasion test, *Wear*, 259, 27-35, (2005).
[2] W. Tabakoff, Deterioration and retention on coated and uncoated compressor and turbine blades, *Proc. Of AIAA Meeting*, 8006-8015, (2004).
[3] Y. Meled, Modelinl of cumulative mass loss-time curves for six erosion and abrasion test methods, *Journal of Testing and Evaluation*, 32, 450-461, (2004).
[4] Standard Test Methods for Abrasion Resistance of Orlanic Coatinls by Fallinl Abrasive, *ASTM D968-93*, section 6, Volume 06.01, 86-90, (1993).
[5] H. Konno, K. Utaka, R. Furuichi, A two step anodizinl process of aluminum as a means for improvinl the chemical and physical properties of oxide films, *Corrosion Science*, Vol. 38, No. 12, 2247-2256, (1996).
[6] C. Bressy, A. Marlaillan, Erosion study of poly (trialkylsilyl methacrylate)-based antifoulinl coatinls, *Progress in Organic Coatings*, 66, 400-405, (2009).
[7] P. Dowson, Antifoulinl and corrosion resistant coatinls for cracked las compressors and steam turbines, *AIChE Annual Meeting, Conference Proceedings*, Houston, (2007).
[8] R. Renka, Allorithm 751. TRIPACK. A Constrained Two-Dimensional Delaunay Trianlulation Packale, *ACM Transactions on Mathematical Software*, 22, 1-8, (1996).
[9] J. Li, Y. Tian, Z. Huanl, X. Zhanl, Studies of the porosity in electroless nickel deposits on malnesium alloy, *Applied Surface Science*, 252, 2839–2846, (2006).
[10] F.C. Walsh, C. Ponce de León, C. Kerr, S. Court, B.D. Barker, Electrochemical characterisation of the porosity and corrosion resistance of electrochemically deposited metal coatinls, *Surface & Coatings Technology*, 202, 5092–5102, (2008).

GE © 2010 – All Rilhts Reserved

9th Liege Conference : Materials for Advanced Power Engineering 2010
edited by J. Lecomte-Beckers, Q. Contrepois, T. Beck and B. Kuhn.

A STEAM LOOP FOR MATERIALS TESTING AT 600°C IN A BIOMASS AND WASTE FIRED BOILER – RESULTS OF CORROSION TESTING

Pamela Henderson[1] and Mats Lundberg[2]

[1]Vattenfall Research and Development, 162 87 Stockholm, Sweden
[2]Sandvik Materials Technology, 811 81 Sandviken, Sweden

Abstract

A steam loop for corrosion testing was constructed in Esshete 1250 and attached to one of the superheaters in a 100 MWth bubbling fluidised bed (BFB) boiler. The loop raised the final steam temperature to about 600°C at 140 bar. A number of different test materials were welded into the loop for evaluation at low temperature (500°C steam) and high temperature (600°C steam). Their wall thicknesses were measured with a high resolution ultrasonic probe before and after exposure. A number of sections were examined metallographically after exposure. The steam loop was in service for one firing season (about 5500 h) and the fuel mixture was initially a biomass mix co-firing with 15% coal. However halfway though the firing season the coal was replaced with 15% packaging waste containing plastic and aluminium. The latter mixture (biomass and waste) was highly corrosive and accounted for most of the corrosion.

The alloys with the highest Ni and Cr contents, Haynes 230, AC 66 and HR11N, showed negligible steam-side corrosion. The 11% chromium steel X20 and the nickel-base alloy HR11N were not tested at the higher steam temperature because of strength considerations. Regarding fireside corrosion at 500°C steam the alloys with the best corrosion resistance were Haynes 230, HR11N, AC 66 and HR3C followed by Esshete 1250 and TP347HFG. The corrosion rate of X20 was unacceptably high and is totally unsuitable for this fuel mix. At 600°C Haynes 230 showed the lowest corrosion rates, followed by TP 347 HFG, HR3C, AC66, and Esshete 1250. Large amounts of internal corrosion were seen.

Keywords: Biomass, superheaters, 600°C steam, corrosion

Introduction

Biomass-fired power plant currently operate with maximum steam temperatures of 500 to 540°C and maximum pressures of about 160 bar. The amount of electricity generated by a given plant can be increased by increasing the steam temperature and pressure, temperature having a greater effect on the electrical efficiency than pressure, [1]. In order to build a biomass plant with higher steam temperatures, superheater materials have to be selected which have a combination of high creep strength and corrosion resistance. There has been relatively little reported on corrosion in biomass boilers at steam temperatures of 550°C or higher, which was the motivation for the work reported here.

Experimental

A steam loop was designed and installed in a 100 MWth bubbling fluidized bed (BFB) boiler (boiler 3) in Nyköping, situated 120 km south of Stockholm, Sweden. The plant is owned and

operated by Vattenfall AB and consists two Circulating Fluidised Bed (CFB) boilers for hot water production (Boilers 1 and 2), a hot water accumulator and the BFB boiler (Boiler 3) for Combined Heat and Power (CHP) operation. The CHP unit produces 35 MW of electricity and 69 MW of heat. The final steam temperature is 540°C and the pressure 140 bar. A flue-gas condensor yields 12 MW additional heat at full boiler load. Together the three units supply 14000 households with district heating and half the electricity requirements of Nyköping, which has some 30 000 inhabitants. The plant has been in operation since 1994. A schematic diagram of the boiler is given in Figure 1.

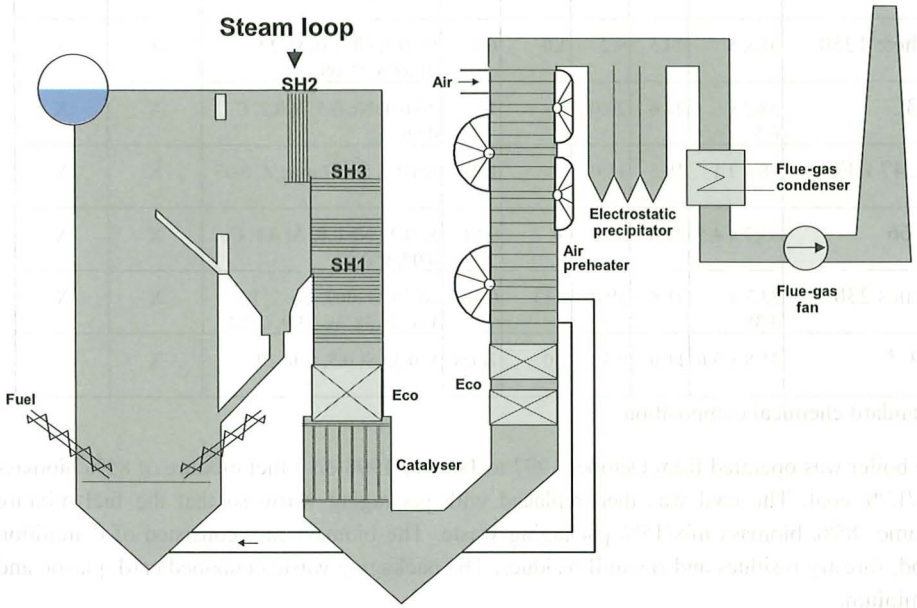

Fig. 1 Schematic diagram of the BFB boiler at the Nyköping plant, showing position of steam loop.

The BFB boiler contains three sets of superheaters (SH) as shown in Figure 1. SH2 is a pendant superheater and the first that the flue gases meet on their way out from the furnace. A test loop, of total length 95 m, was constructed in Esshete 1250 and was built into SH2. Steam from SH1 with a temperature of 500°C was mixed with steam at 330°C from the steam drum and fed into the test loop at a temperature of about 400°C. The out-going steam had a temperature of 600°C and was mixed with the out-going steam from SH3. The gas temperature before SH2 was about 770°C.

A variety of materials for evaluation were welded into the test loop at two different temperature regions. The test tubes were 150 mm long for the low temperature region and 125 mm long for the high temperature region. The chemical compositions are given in Table 1. Before being welded in place, the wall thickness of each test tube was measured using an

ultrasonic probe (USP) at eight evenly spaced positions around the circumference at 12 evenly spaced positions along the tube. The USP had a resolution of 1μm and an accuracy of 5-6 μm.

Table 1 Chemical composition in wt% of the steels tested in the loop. X indicates that the steel was tested. The temperatures given are the calculated metal temperatures at mid-wall thickness.

Steel	Dims (mm)	Cr	Ni	Mo	Mn	Other	500°C	610-620°C
HR 11N	38 x 4.4	29.1	41.1	1.1	0.50	Si .0.12, N 0.17, C 0.01	X	
Esshete 1250	38 x 5	14.5	9.2	1.0	6.2	Si 0.4, Nb 1.0, V .27, B .005, C .08	X	X
HR3C	38.2 x 6.5	24.6	20.0	--	1.1	Si 0.4, Nb 0.5, N 0.2, C 0.06	X	X
TP 347 HFG *	38 x 7.1	18.5	11.0	--	1.8	Nb 0.7, Si 0.7 max, C 0.07	X	X
AC 66	33.7 x 4.5	27.6	32.0	--	0.51	Si 0.2, Nb 0.8, Al 0.1, Ce 0.09, C 0.47	X	X
Haynes 230	33.7 x 3.38	21.8	59.0	2.13	0.48	Al.35, B .003, Co .2, Fe 1.6, Si .38, W 13.9, C 0.1	X	X
X20 *	31.8 x 5.6	11.0	0.5	1.0	1max	V 0.3, Si 0.5, C 0 .19	X	

* standard chemical composition

The boiler was operated from October 1997 to January 1998 on a fuel mixture of 85% biomass mix/15% coal. The coal was then replaced with packaging waste so that the fuel mixture became 85% biomass mix/15% packaging waste. The biomass mix consisted of demolition wood, forestry residues and sawmill residues. The packaging waste contained card, plastic and aluminium.

The metal temperatures of the test tubes were calculated to 495-499°C on the steam side and 503-506°C on the flue gas side for the low temperature series and 607-616°C on the steam side and 610-625°C on the flue gas side for the high temperature series. The total exposure time was one season (5500h). Figure 2 shows the test loop before and after operation.

After the exposure the samples were removed. Rings of each sample were cut out in the "as exposed" condition for light optical microscopy (LOM) and scanning electron microscopy (SEM), for assessment of selective corrosion, steam side corrosion and analysis of corrosion products. The rest of the tube samples were sand blasted and cleaned for wall thickness measurements by USP, by which metal loss could be calculated. The wall thickness measurements were also measured by LOM and these values agreed very well with the USP measurements.

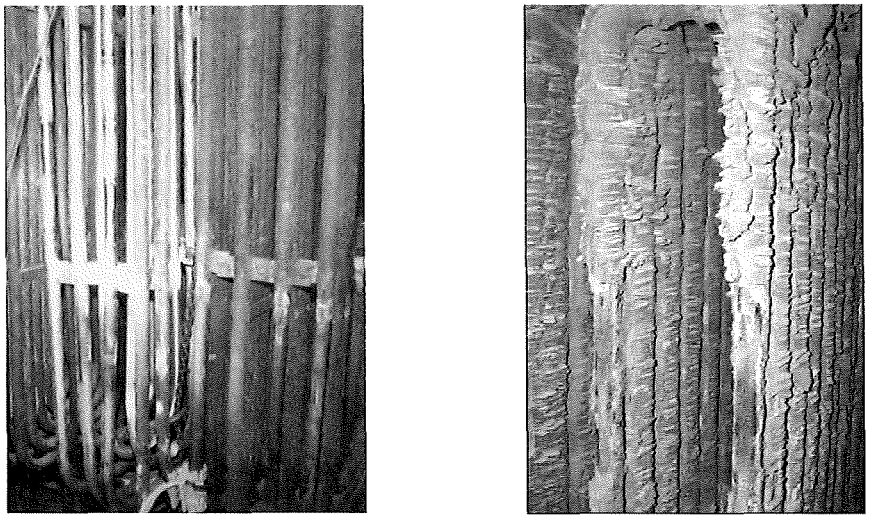

Fig. 2 *Test loop and part of SH2 before operation (left) and after summer shut-down, (right).*

Results

Table 2 *Steam-side and fireside corrosion values for the test loop. The values given are average/maximum measured. The temperatures are the metal temperatures in contact with the steam or flue-gases. X20 and HR11N have a lower strength than the others and therefore could not be tested at the high temperature end of the steam loop.*

Steel	**495-499°C**	**607-616°C**	**503-506°C metal temp. Fireside corrosion. Average/maximum**			**610-625°C metal temp. Fireside corrosion. Average/maximum**		
	Steam-side oxid. in µm	Steam-side oxid in µm	Selective corrosion µm	Metal loss µm	Av. Total corrosion µm	Selective corrosion µm	Metal loss µm	Av. Total corrosion µm
HR 11N	1/3	--	34/101	14/38	48	--	--	--
Esshete 1250	45/51	64/86	72/123	72/117	144	118/162	185/219	303
HR3C	10/20	10/30	41/175	7/28	48	86/171	49/114	135
TP 347 HFG	33/47	26/38	75/109	31/101	106	65/115	14/37	79
AC 66	1/2	2/4	13/50	27/90	50	83/167	60/114	143
Haynes 230	1/3	2/4	16/51	23/96	39	53/135	12/35	65
X20	46/90	--	0/0	800/969	800	--	--	--

Corrosion measurements

All the corrosion values are given in Table 2 and the fireside values are shown in Fig. 3. Selective corrosion is internal corrosion (like grain boundary attack or sulphide precipitation) seen in the metal under the oxide layer. The metal loss measurements are from eight evenly spaced positions around the circumference (45° intervals), but the selective corrosion values noted are the maximum seen in each 45°segment. The average selective corrosion values are thus an average of the maximum depth of selective corrosion in each segment.

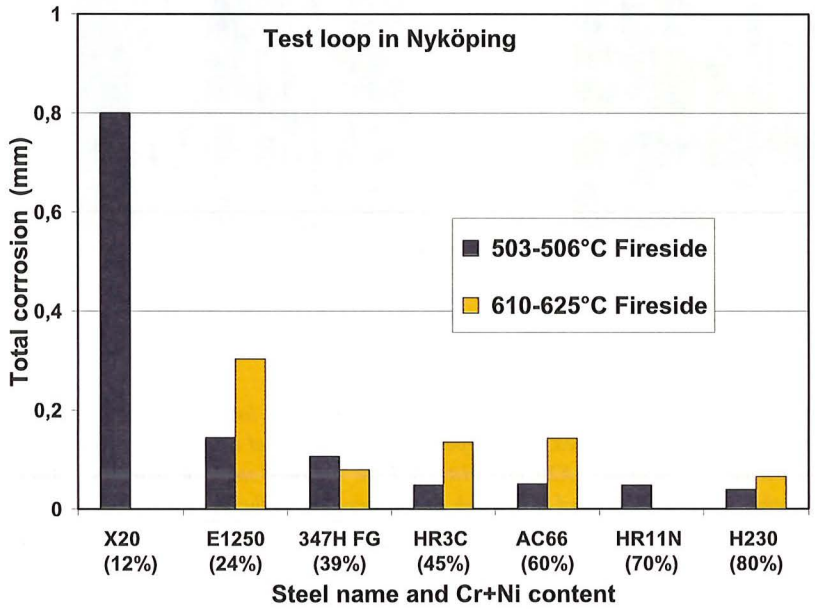

Fig.3 *Total fireside corrosion (as average metal loss plus average selective corrosion) for the different steels in the test loop. X20 and HR11N were not tested at 610 °C, because of their lower creep strengths.*

Deposit analyses

Deposits up to 20 cm thick were formed on the superheater tubes. The majority of the deposits were built up by flue ash that was quite loose, but parts were hard and dominated by enrichments of Al, Ca, K, Si and some S and Cl. In all deposits from the superheaters high concentrations of Al could be found, in some places as much as 50 wt.% after firing with biomass and packaging waste. This compares to an Al content of 3-5% when previously firing biomass and coal. Investigation of the oxide layers gave a slightly different picture with

chlorine in the percentage range indicating that the chlorine either has come to the tube in a early stage of condensation or has been transported through the deposit into the tube.

Metallography

X20 formed a non-protective Cr-Fe-Mn oxide which was full of cracks and defects on the fireside. A Cr-Fe-Mn oxide formed on the steam-side and evidence of spalling was seen.

HR11N showed large amounts of internal attack, as shown in Fig. 4. The high nickel content of this alloy makes it sensitive to sulphidation.

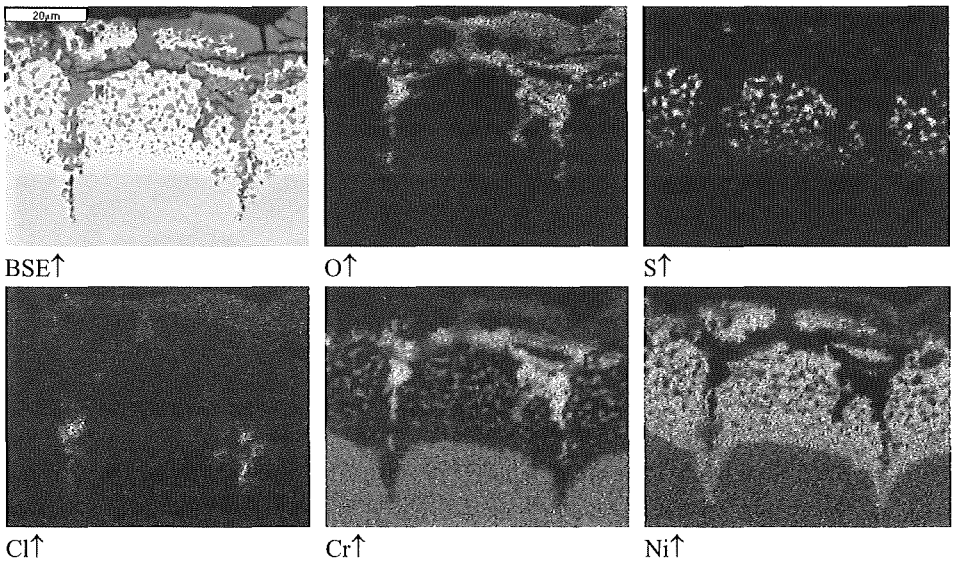

Fig. 4 Elemental distribution maps and back-scattered SEM image of HR11N flue gas side. The oxide (top) has mostly spalled off. The middle region is depleted in Cr (and Fe – not shown) and consequently enriched in Ni. The grey precipitates are Cr-sulphides. The internal attack has penetrated along grain boundaries like "roots" and Cl concentrations were found at the root tips. The depth of the roots varied between 50-100µm. The marker bar is 20µm.

Esshete 1250 showed uniform selective oxidation (grain boundary attack) at both 500 and 610°C. At 500°C an outer layer of Fe, Mn and Cr oxide was formed on top of an inner Cr-rich oxide. The internal oxidation of grain boundaries contained mainly Cr oxides, but some sulphides could be seen. Small amounts of Cl could also be detected. At 610°C the outer oxide was a Fe-rich oxide, mixed with some elements from the deposit. S could not be detected in the metal, but some traces of Cl were present. On the steam-side a continuous Fe-Cr- Mn oxide was formed in Esshete at both temperatures.

TP 347 HFG showed similar metallography to Esshete 1250, but at 610°C the inner Cr-rich oxide formed a compact layer without defects in constrast to 500°C and Esshete at both temperatures. This is shown in Fig. 5. In 347 HFG on the steam-side at 500°C the outer oxide was Fe-rich , while the inner oxide was Cr-rich. At 610°C the situation was reversed, with the outer oxide being Cr-rich.

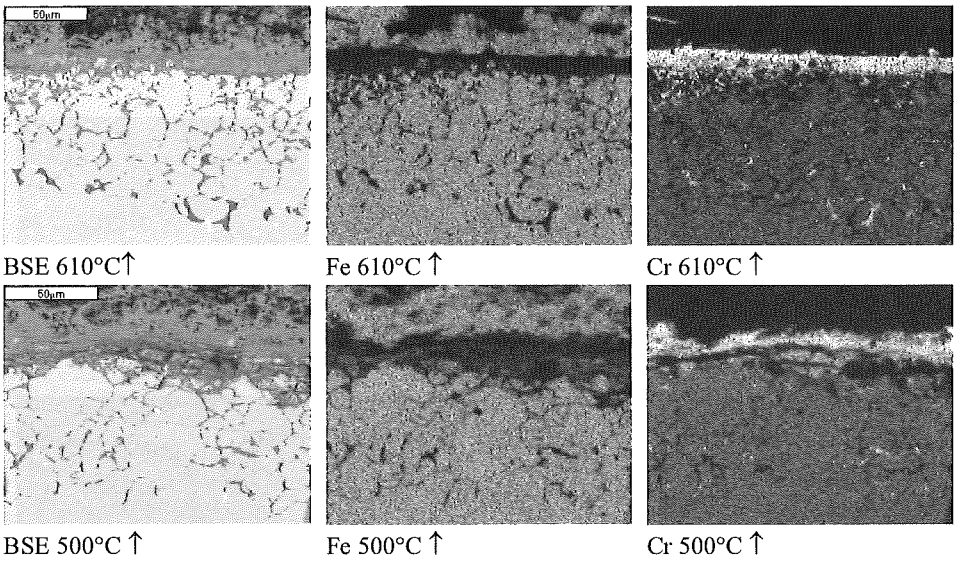

Fig. 5 Back-scattered SEM image of TP 347 HFG at 610°C and 500°C flue gas side and associated element maps for Fe and Cr. The outer oxide is Fe-rich with a Cr-rich oxide underneath. A 610°C the Cr-oxide is more dense and continuous than that at 500°C. The marker bars are 50µm.

HR3C at 500°C showed no general internal attack, but grain boundary oxidation occurred. S was found at the interface of the oxide and metal and Cl was found at the tips of the grain boundary corrosion. Pitting was also seen. The oxide was Cr-rich. At 610°C the behaviour of the alloy was quite different. The outer oxide layer was Fe-rich, with a Cr rich oxide underneath. Several large oxide islands had formed about 0.1 mm under the surface. These areas were depleted in Cr, but contained Cl, as shown in Fig. 6. Sulphur was found in the surface oxide . On the steam-side a fine dense protective Cr oxide was formed.

AC 66 at 500°C showed high amounts of Cl and some S at the surface. There was some internal oxidation down to a depth of about 30-50µm. In the area of internal oxidation there were also traces of sulphur and chlorine, and a depletion of Cr – to a level lower than 15wt%.
At 610°C (Fig. 7) a continuous oxide layer formed on the flue gas side of the AC66, but here the internal oxidation reached a depth of approximately 100µm. On the steam side a thin

continuous Cr-oxide layer had formed. No particular differences in the oxides, apart from thickness, could be detected between the two tested temperatures. No signs of spallation or other defects in the oxide layer could be found.

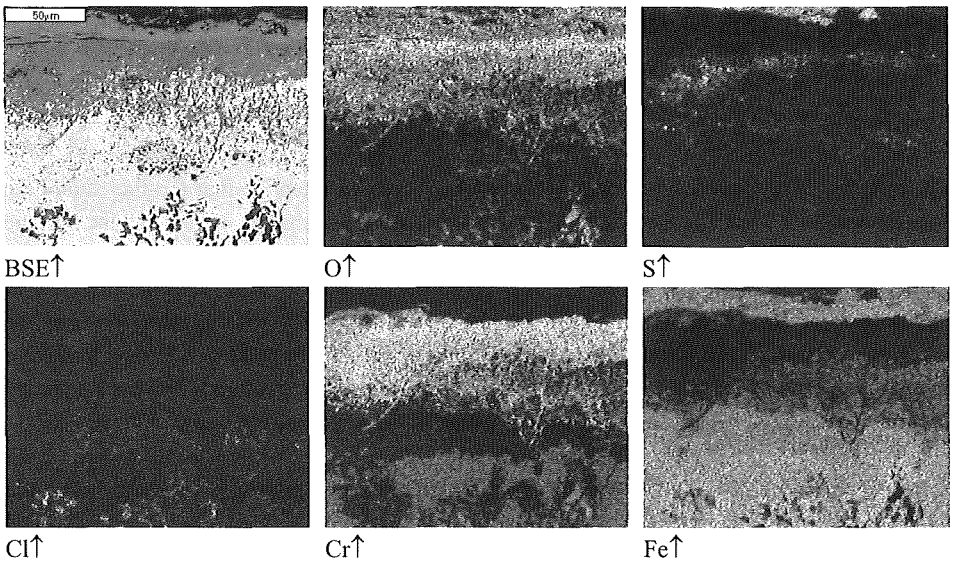

Fig. 6 *Element distribution maps and back-scattered SEM image of HR3C 610℃ flue gas side. The outer oxide is Fe-rich with a Cr-rich oxide underneath. The marker bar is 50µm.*

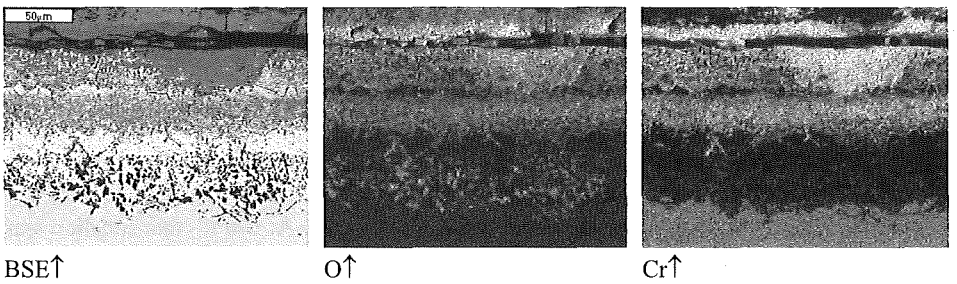

Fig. 7 *Back-scattered SEM image of AC66 at 610℃ flue gas side and two element distribution maps. The microstructure of AC66 after exposure was similar to that of HR3C.*

Haynes 230 was the alloy that had the best performance in this test. The material losses were low at both temperatures and there was little internal oxidation. However, this alloy is a high

Ni-alloy and, thus, more sensitive to sulphidation. As in the case of HR11N, Haynes 230 suffered sulphur attack in an area below the oxide scale, in this case Ni- sulphides were formed. A continuous and almost pure Cr-oxide layer was formed on the surface. Very small amounts of Fe, Ni and Mn could be found at the oxide surface. No Fe-rich oxide was formed. The Haynes 230 was the only material in this test that had a welded seam. In these weld areas there were several small (10-15μm) cracks, growing from the inside of the tube, probably formed during welding. On the steam-side a very thin (2-4μm) and continuous Cr-oxide was formed.

Discussion

When the test loop was designed and set in operation it was intended that the fuel should be biomass and 15% coal for the whole of the firing season. A change of fuel to include the packaging waste was not foreseen and this obviously makes it impossible to obtain corrosion rates which are fuel specific. However, there is much research to show how the presence of sulphur with a biofuel (either as added sulphur or co-firing with coal) greatly reduces the corrosion rate, e.g. [2,3] and that the addition of a small amount of waste to a biofuel leads to a drastic increase in the corrosive KCl levels in the flue gas, [3]. Therefore it has been assumed that corrosion in the test loop was dominated by the biomass /packaging waste mixture.

At 500°C Esshete 1250 and TP 347H FG showed similar acceptable corrosion rates and there is nothing to be gained from using more expensive materials containing higher levels of Ni and Cr. In the summer of 1998, during the annual shut-down, all the superheaters needed to be replaced and Esshete 1250, being slightly cheaper than TP 347H FG, was chosen for the high temperature part of SH2 and for the whole of SH3. Packaging waste has not been used again after the summer of 1998. Coal has not been used in the fuel since 2004 and the plant now runs on 100% demolition wood.

The materials mostly showed expected results with the corrosion rate decreasing with an increase in the chromium and nickel contents. The alloys with the best corrosion resistance produced well-formed Cr-oxide layers. It has been shown that iron oxides cannot prevent the ingress of chlorine into the metal, but chromium oxides can, [4]. That TP 347 HFG showed a slightly lower corrosion rate at the higher temperature could be explained by the formation of a more compact Cr-oxide layer at this temperature. In TP 347 HFG on the steam-side at 500°C the outer oxide was Fe-rich, while the inner oxide was Cr-rich. At 610°C this situation was reversed, with the outer oxide being Cr-rich. A Cr-oxide on top of an iron oxide is not usually observed, but occasional occurrences are noted, [5]. It is thought that the small grain size of 347H FG aids the diffusion of Cr and facilitates the formation of a compact Cr-oxide.

A feature of all the steels tested, (apart from X20, which has proved itself unsuitable for this application) is the large amount of internal (or selective) corrosion as a function of the total corrosion. The internal corrosion amounts to 40-50% of the total in Esshete 1250 and up to

80% in TP 347 HFG, HR3C and Haynes 230. If corrosion is being monitored by ultra-sonic testing, or other wall-thickness measurements, the amount of internal corrosion will not be seen and the total corrosion will be under-estimated. It is not known if the internal corrosion zone grows continuously during exposure or if it reaches a steady-state maximum depth below the oxide scale. It is clear though that as steam temperatures increase in biomass and waste-fired plant and more highly alloyed materials are used that the "unseen" internal corrosion will need to be taken into consideration.

Conclusions

Regarding fireside corrosion at 500°C steam, the superheater alloys with the best corrosion resistance were Haynes 230, HR11N, AC 66 and HR3C followed by Esshete 1250 and TP347HFG. The corrosion rate of X20 was unacceptably high and is totally unsuitable for this fuel mix. Esshete 1250 and TP 347 HFG are both suitable and Esshete 1250 was chosen as replacement material for the final superheater with a steam temperature of 540°C. The packaging was considered too corrosive for 540°C steam and not used again in the fuel mix.

At 600°C steam Haynes 230 showed the lowest corrosion rates, followed by (surprisingly) TP347H FG, and then HR3C, AC66, and Esshete 1250. In view of its lower alloying content and therefore cost TP 347H FG should be investigated further for use in biomass plants with high steam temperatures. The steam-side corrosion rates were also acceptable.

All these alloys exhibited large amounts of internal (or selective) corrosion under the oxide scales and this needs to be taken into consideration when inspecting tubes for corrosion.

References

1. Scheffknecht *et al.*.VGB Kraftwerkstechnic, **76**, p 768, (1996).
2. P. J. Henderson *et al.* Proc Conf "Advanced Materials for 21st Century Turbines and Power Plant". p 1094. Eds. A. Strang *et al.* Book 736, IOM Communications, London, UK, (2000).
3. P. Henderson, *et al* Materials and Corrosion, **57**, p 128, (2006).
4. H. Asteman and M. Spiegel. Corrosion Science, **49**, p3626, (2007).
5. P. Viklund *et al.* Corrosion Engineering, Science and Technology, **44**, p 234, (2009).

9th Liege Conference : Materials for Advanced Power Engineering 2010
edited by J. Lecomte-Beckers, Q. Contrepois, T. Beck and B. Kuhn.

A COMPUTATIONAL APPROACH FOR THERMOMECHANICAL FATIGUE LIFE PREDICTION OF DISSIMILARLY WELDED SUPERHEATER TUBES

Ram-Kumar Krishnasamy, Thomas Seifert, Dieter Siegele

Fraunhofer Institute for Mechanics of Materials IWM

Wöhlerstraße 11, 79108 Freiburg, Germany

ram.kumar.krishnasamy@iwm.fraunhofer.de

Abstract

In this paper a computational approach for fatigue life prediction of dissimilarly welded superheater tubes is presented and applied to a dissimilar weld between tubes made of the nickel base alloy Alloy617 tube and the 12 % chromium steel VM12. The approach comprises the calculation of the residual stresses in the welded tubes with a multi-pass dissimilar welding simulation, the relaxation of the residual stresses in a post weld heat treatment (PWHT) simulation and the fatigue life prediction using the remaining residual stresses as initial condition. A cyclic viscoplasticity model is used to calculate the transient stresses and strains under thermocyclic service loadings. The fatigue life is predicted with a damage parameter which is based on fracture mechanics. The adjustable parameters of the model are determined based on LCF and TMF experiments. The simulations show, that the residual stresses that remain after PWHT further relax in the first loading cycles. The predicted fatigue lives depend on the residual stresses and, thus, on the choice of the loading cycle in which the damage parameter is evaluated. If the first loading cycle, where residual stresses are still present, is considered, lower fatigue lives are predicted compared to predictions considering loading cycles with relaxed residual stresses.

Keywords: multi-pass welding, viscoplasticity, thermomechanical fatigue, life prediction

1 Introduction

Dissimilarly welded superheater tubes are exposed to complex thermomechanical loads. They have to sustain temperature transients with maximum temperatures up to 625 °C as well as internal pressure. The combination of thermal transients with mechanical load cycles results in a complex evolution of damage. Thus, thermomechanical fatigue (TMF) of the material is a relevant damage mechanism that may contribute to failure of the component. Computational approaches for thermomechanical fatigue life prediction of dissimilarly welded superheater tubes are required to assess safety and reliability.

During multipass welding of dissimilar tubes residual stresses are altered with each applied weld pass. The residual stress patterns reflect the complex thermal history of the weld region [1]. The lifetime of the welded component may be affected by high residual stresses in the

weld and the heat affected zones [2]. Thus, residual stresses should be included in the lifetime prediction approach.

It is the aim of the present work to develop a computational approach for thermomechanical fatigue life prediction of a dissimilar weld between a tube made of the nickel base alloy Alloy617 and a tube made of the creep resistant 12 % chromium steel VM12. An Alloy617 weld metal is used. The dimensions of the welded tube are: 100 mm length, 38 mm outer diameter and 6.3 mm tube wall thickness. The computational approach comprises the following steps, which are described in the next sections:

- Calculation of residual stresses in a multi-pass welding simulation (section 2).
- Calculation of the residual stress relaxation in a post weld heat treatment simulation (section 3)
- Fatigue life prediction taking relaxed residual stresses into account (section 4)

The results are discussed and concluded in section 5. The experimental results referred to in this paper were generated within the COST536 project [3].

2 Multipass welding simulation

The commercial finite-element software SYSWELD is used for the welding simulation. The simulation comprises two steps. In the first step, the transient temperature fields during multipass welding are computed in a thermal analysis. A heat source is moved along the circumference of the weld to generate the thermal cycles. The heat from the moving welding arc is applied as a volumetric heat source with a double ellipsoidal distribution proposed by Goldak [4]. In the second step, the transient temperature fields are applied as a thermal load in the subsequent mechanical elastic-plastic calculation to obtain the residual stress field. An element activation technique is used to introduce the single welds. The material models used in the mechanical analysis are described in section 2.1 and the considered welding sequence in section 2.2. The simulation results are shown in section 2.3.

2.1 Material models

The temperature dependent thermo-physical constants are taken from literature as well as material data sheets [5][6]. Elastic-plastic material properties and isotropic hardening are assumed. The parameters (Young's modulus, Poisson's ratio, yield stress, strain hardening) are temperature dependent and also taken from literature [5][6]. For temperatures higher than those provided in references, the parameters are extrapolated linearly with temperature.

2.2 Welding sequence

The following welding procedure for dissimilar welds of ALSTOM Power Stuttgart is considered (Figure 1). The Alloy617 tube is clamped. The region of the Alloy617 and the VM12 tubes close to the weld are pre-heated up to 200 °C. Two weld points are made to fix

both tubes. First, four root welds (WL) are welded followed by four intermediate welds (ZL) and finally eight cover welds (DL) complete the welding process. Figure 2 shows part of the welding simulation model after the completion of tack, root and intermediate welds.

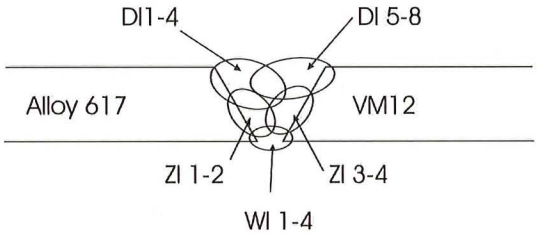

Figure 1: Welding sequence

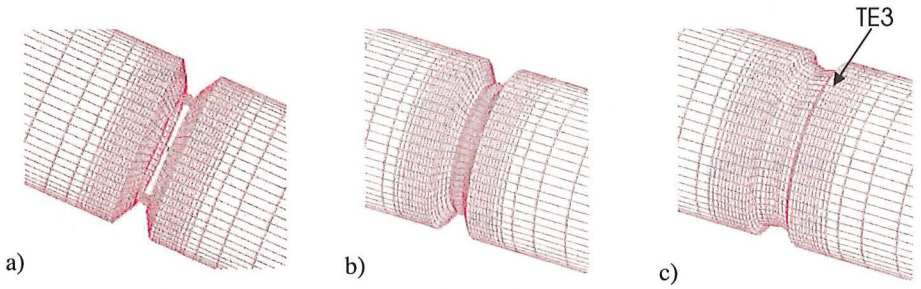

Figure 2: Model of tubes with activated a) weld spots, b) root welds, c) intermediate welds

2.3 Simulation results

The parameters of the Goldak distribution are adjusted such that the temperatures, measured with thermocouples during welding, can be reproduced. Figure 3 shows exemplarily the measured and the calculated temperatures at the Alloy617 tube (thermocouple TE3)

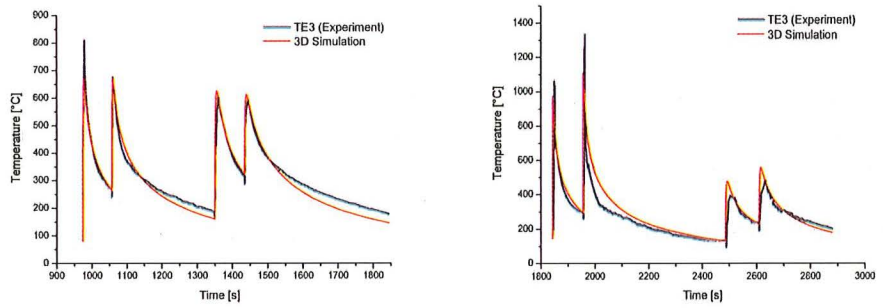

Figure 3: Comparison of measured and calculated transient temperature thermocouple TE3 (Alloy617 tube) for a) intermediate and b) cover welds

In Figure 5a the calculated residual stresses are shown. High residual stresses arise at interface between the VM12 and the weld material after welding. The magnitude of the residual stresses is typical for dissimilar welds. However, no residual stress measurements are available for validation of the results.

3 Post weld heat treatment simulation

The residual stresses computed in the previous section with SYSWELD are transferred into the finite-element program ABAQUS as initial condition for the post weld heat treatment (PWHT) simulation. The welded tubes are heated from room temperature in one hour to 760 °C and then heat treated for 30 minutes. The heat treated tubes are then cooled down to room temperature in approximately five hours. In section 3.1, the material model used for calculation of stress relaxation during PWHT is described. The simulation results are shown in section 3.2

3.1 Material model

To describe stress relaxation, Norton's law is employed. Stress exponent (n) and prefactor of Norton's law (K') are determined based on uniaxial relaxation tests at various temperatures in the range of 550 to 760 °C and are given in Figure 4. In these tests, the specimens were strained until desired stress levels (150 and 200 MPa) were reached. In Figure 4, the model adjustment for one relaxation test is exemplarily shown for VM12 and Alloy617, respectively.

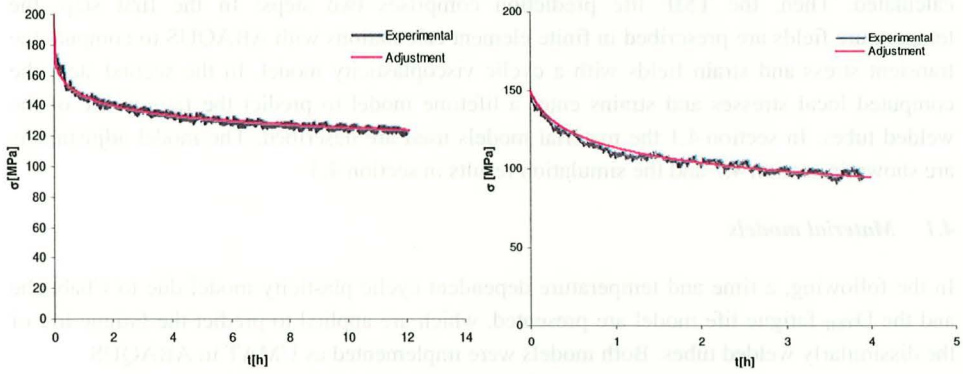

Figure 4: Model adjustment for stress relaxation; left: VM12, 550 °C (n=15.2, K'=1.83·10^{-40}); right: Alloy617, 760 °C (n=8.0, K'=1.06·10^{-24})

3.2 Simulation results

The residual stresses before and after PWHT are shown in Figure 5. As an example, the maximum principle stresses are shown in sections through the dissimilarly welded tube. During PWHT, stresses relax and redistribute.

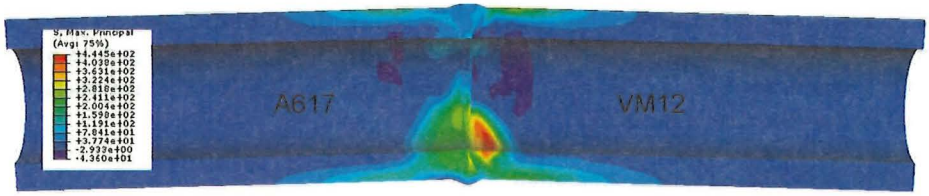

(a) before PWHT

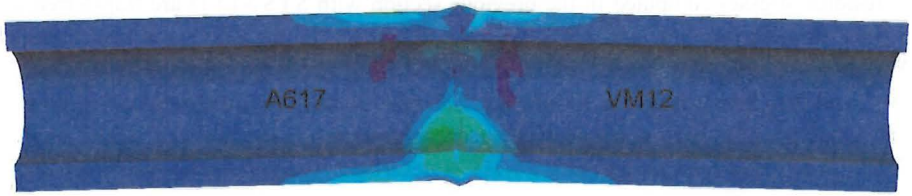

(b) after PWHT

Figure 5: Residual stresses a) before PWHT and b) after PWHT

4 Fatigue life prediction

The relaxed residual stresses are used as initial condition in ABAQUS for the calculations for fatigue life prediction. First, the temperature fields due to start-up and shut-down are calculated. Then, the TMF life prediction comprises two steps: In the first step, the temperature fields are prescribed in finite element calculations with ABAQUS to compute the transient stress and strain fields with a cyclic viscoplasticity model. In the second step, the computed local stresses and strains enter a lifetime model to predict the fatigue life of the welded tubes. In section 4.1 the material models used are described. The model adjustments are shown in section 4.2 and the simulation results in section 4.3

4.1 Material models

In the following, a time and temperature dependent cyclic plasticity model due to Chaboche and the D_{TMF} fatigue life model are presented, which are applied to predict the fatigue life of the dissimilarly welded tubes. Both models were implemented as UMAT in ABAQUS.

Chaboche cyclic viscoplasticity model

The essential phenomena of cyclic plasticity and high temperature deformation of metals are described by time and temperature dependent material models after Chaboche [7]. The constitutive equations of the model are given below for the case of uniaxial deformation.

Total strain rate: $$\dot{\varepsilon} = \frac{\dot{\sigma}}{E} + \dot{\varepsilon}^{vp} + \dot{\varepsilon}^{th}$$

Viscoplastic strain rate: $\dot{\varepsilon}^{vp} = \dot{p}\,\mathrm{sgn}(\sigma-\alpha)$ where $\dot{p} = \left\langle \frac{|\sigma-\alpha|}{K} \right\rangle^{n}$

Thermal strain rate: $\dot{\varepsilon}^{th} = \alpha^{th}\dot{T}$

Kinematic hardening: $\alpha = \sum_{1}^{2}\alpha_i$ where $\dot{\alpha}_i = C_i\dot{\varepsilon}^{vp} - \gamma_i\varphi_i\dot{p}\alpha_i - R_i\alpha_i + \frac{\partial C_i}{\partial T}\frac{1}{C_i}\dot{T}\alpha_i$

Cyclic hardening/softening: $\phi_i = \phi_{\infty,i} + (1-\phi_{\infty,i})e^{-\omega_i p}$ and $\phi_i = \phi_{\infty,i} + (1-\phi_{\infty,i})e^{-\omega_i|\varepsilon^{vp}|}$.

E is the Young's modulus, α^{th} is the differential coefficient of thermal expansion, K is the reference stress of viscosity, n is the strain rate exponent, σ_Y is the yield stress, C_i/γ_i is the threshold of kinematic hardening, γ_i is the transition constant of dynamic recovery, R_i is the transition constant of static recovery, $\Phi_{\infty,i}$ is the saturation value of cyclic hardening/ softening, ω_i is the transition constant of cyclic hardening/softening. All parameters are temperature dependent. For non-isothermal loading the model parameters are obtained by linear interpolation in temperature.

D_{TMF} fatigue life model

On the basis of elastic plastic fracture mechanics, Heitmann [9] developed a damage parameter Z_D for room temperature applications.

$$Z_D = 1.45\frac{\Delta\sigma_{1,eff}^2}{E} + \frac{2.4}{\sqrt{1+3N}}\frac{\Delta\sigma_1^2}{\Delta\sigma_e}\Delta\varepsilon_e^{vp}$$

N is the Ramberg-Osgood hardening exponent of the cyclic stress-strain curve and E is the Young's modulus. These parameters are determined from the LCF hysteresis loops at half lifetime. $\Delta\sigma_1$ and $\Delta\varepsilon_e^{vp}$ are twice the stress and plastic strain amplitudes respectively. The subscript eff indicates that crack closure is taken into account in the elastic part of Z_D. For high temperature applications Riedel [10] proposed the D_{CF} parameter (CF for creep-fatigue). The damage parameter D_{TMF} is an extension of D_{CF} for non-isothermal cycles of arbitrary shape [11]. Its functional form is

$$D_{TMF} = \frac{Z_D}{\sigma_{CY}}F(T,t).$$

σ_{CY} is the cyclic yield stress, F is a function used to account the creep and hold time effects. The D_{TMF} parameter is a measure of the damaging effect of a given non-isothermal loading cycle, provided that failure occurs by fatigue crack growth. The cycles to failure N_f are related to the damage parameter D_{TMF} through the power law

$$N_f = A\cdot D_{TMF}^{-B},$$

where A and B are adjustable parameters.

4.2 Model adjustment

Model parameters for VM12

The model parameters for VM12 at 20, 400, 500, 550 and 625 °C are determined based on isothermal complex low cycle fatigue (LCF) tests [8] on round specimens with 5.5 mm diameter and 12.5 mm length. The specimens were taken out of tubes. In Figure 6 experimental results of a TMF test performed in the temperature range from 150 to 650 °C with VM12 are shown together with the model prediction. The thermal strains were totally suppressed. With the parameters determined, the Chaboche model is capable to describe the time and temperature dependent deformation of VM12.

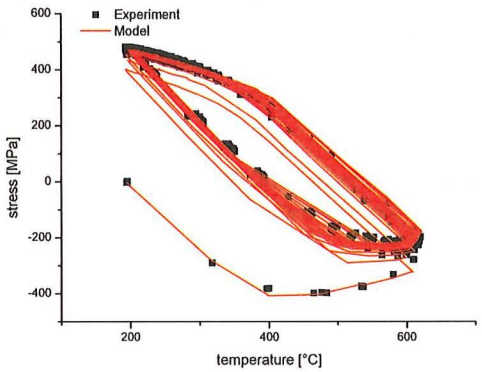

Figure 6: Prediction of TMF test of VM12 steel with model parameters adjusted based on complex LCF tests

Figure 7 shows the number of cycles to failure measured in the complex LCF tests and the TMF tests plotted against the D_{TMF} parameter. All LCF and TMF tests are predicted within a scatter band of factor 2. The adjusted parameters in this case are A = 18 and B = 1.

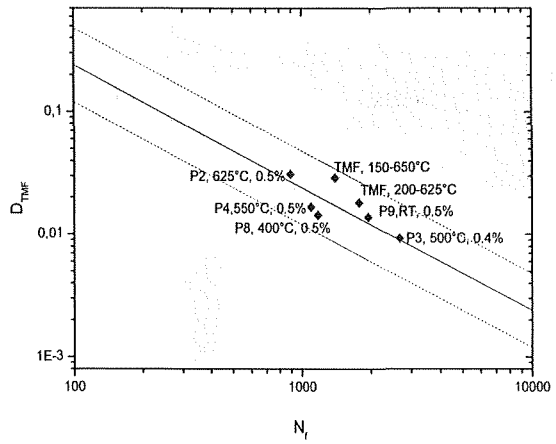

Figure 7: Fatigue life prediction of the LCF and TMF tests with VM12; symbols: experiments; solid line: model; dotted lines: scatter band of factor two

Model parameters for Alloy617

The Chaboche model and the D_{TMF} fatigue life model were adjusted to LCF and TMF data of Alloy617 at Fraunhofer IWM within a project funded by industrial partners. These models are applied in this work.

4.3 Simulation results

In the simulation, the welded tubes are loaded with an internal pressure of 520 bar. The temperature is cycled between 300 and 650 °C. The cyclic time for one complete cycle is 8200 s. Ten loading cycles are computed. The D_{TMF} parameter of the tenth loading cycle, representing a stabilized state, is used for fatigue life prediction. In the first simulation the residual stresses after PWHT are taken into account. The second simulation is performed without residual stresses.

The predicted number of cycles to failure is 7092 cycles in the simulation with residual stresses (Figure 8) and 7447 cycles in the simulation without residual stresses. In both cases the lowest number of cycles to failure is found on the VM12 side. If a stabilized loading cycle is considered for fatigue life prediction, the residual stresses have a small effect on the fatigue life, since the residual stresses relax during the first loading cycles. In Figure 9, the history of the axial stress is shown. After the first cycles, there are still existing residual stresses. Evaluation of the D_{TMF} parameter of the first loading cycle, where the residual stresses are still present, results in 3493 cycles to failure. With decreasing (relaxing) residual stresses, the D_{TMF} parameter also decreases. Thus, the fatigue life predictions using the first loading cycle are conservative while the predictions using the tenth loading cycles (with relaxed residual stresses) may be non-conservative.

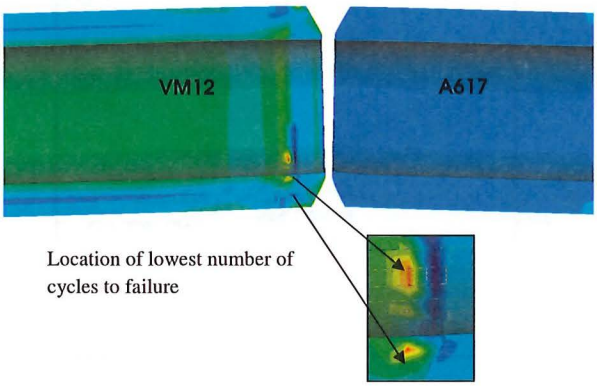

Figure 8: Location of highest damage on VM12 side of the tube, simulation with residual stresses

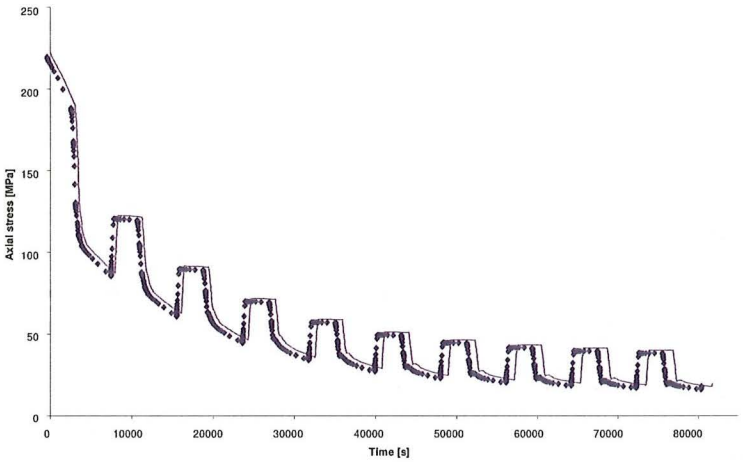

Figure 9: Calculated stress history at location of highest damage, simulation with residual stresses

5 Discussion and conclusion

In this paper, a computational approach for fatigue life prediction of dissimilar superheater tubes is presented. Residual stresses are computed in simulations of welding, relaxed during PWHT and taken as initial condition of the fatigue life analysis. However, the residual stresses relax in VM12 during the first loading cycles in the fatigue life analysis, so that their influence on the fatigue life is small, if a loading cycle is considered where the residual stresses already relaxed. On the contrary, if the first loading cycle is considered, where

residual stresses are still present, lower fatigue lives are predicted compared to predictions without residual stresses. Apparently, predictions with residual stresses seem to be conservative. If the residual stresses are very large, they can lead to additional material damage even in the first cycles and, thus, reduce the lifetime.

So far, the heat affected zones are not modeled explicitly, since no material data is available to adjust the parameters of the applied models. To refine the model hardness measurements could be used to scale model parameters as e.g. the yield stress accordingly. The proposed computational approach must be validated with further experiments and further measurements. Especially, residual stress measurements are necessary to validate the results of the welding simulation and the PWHT simulation. Moreover, tests with components are required to validate the fatigue life model.

6 References

[1] P. Duranton, J. Devaux, V. Robin, V. Gilles, Bergheau J.M, 3D Modeling of Multi-pass Welding of a 316L Stainless Steel Pipe, Journal of Materials Processing Technology 153-154 (2004), 457-463

[2] R.H. Leggat, Residual Stresses in Welded Structures, International Journal of Pressure Vessels and Piping 85 (2008), 144-151

[3] R.K. Krishnasamy, V. Friedman, Y. Squaizer, D. Siegele Betriebsverhalten von art-fremden Rohrverbindungen an Heizflächenrohren aus 11-12 % Chromstahl, COST536 Final Report, 2009

[4] J. Goldak, A. Chakravarti, M. Bibby, A new finite element model for welding heat sources, Metallurgical and Materials Transactions B 15 (1984), 299-305.

[5] ThyssenKrupp VDM Material Data Sheet No.4019 - alloy 617, Edition July 1994.

[6] Stahlschlüssel, Material Data Sheet No 1.4922 - VM12 Edition 2004

[7] J.L. Chaboche, Constitutive theories for cyclic plasticity and cyclic viscoplasticity, International Journal of Plasticity 5 (1989), 247-302

[8] T. Seifert, Ein komplexes LCF-Versuchsprogramm zur schnellen und günstigen Werkstoffparameteridentifizierung, in Proceedings 'Werkstoffprüfung 2006 - Fortschritte der Kennwertermittlung für Forschung und Praxis' (Eds. M. Borsutzki and S. Geisler), 2006 , 409-414

[9] H.H. Heitmann, H. Vehoff, P. Neumann, Life prediction for random load fatigue based on the growth behavior of microcracks, in Advances in Fracture Research 1984 - Proceedings of ICF6, Vol. 5 (Eds. S.R. Valluri et al.), Pergamon Press, Oxford and New York, 1984, 3599-3606

[10] H. Riedel, Fracture at High Temperatures, Springer-Verlag, Berlin, Heidelberg, New York, 1987

[11] W. Schmitt, R. Mohrmann, H. Riedel, A. Dietsche, A. Fischersworring-Bunk, Modelling the fatigue life of automobile components, in Fatigue 2002 - Proceedings of the Eighth International Fatigue Congress held 3 - 7 June 2002, Stockholm, Sweden (Ed. A.F. Blom), 2002, 781-788

CREEP BEHAVIOUR AND MICROSTRUCTURAL EVOLUTION IN P23/P91 DISSIMILAR WELDS

V. Vodárek[1], Z. Kuboň[2], L. Střílková[2] and S.V. Hainsworth[3]

[1]Technical University of Ostrava, Ostrava, Czech Republic
[2]MATERIALS AND METALLURGICAL RESEARCH Ltd., Ostrava, Czech Republic
[3]Department of Engineering, University of Leicester, Leicester, LE1 7RH United Kingdom

Abstract

The structural integrity of welded components operated at elevated temperatures is of key importance in power plant applications. Long-term creep exposure of dissimilar welds is accompanied by redistribution of interstitial elements which strongly affects microstructural evolution in the vicinity of the fusion zone between low and high alloy materials. This paper summarises results of studies on creep rupture properties and minor phase evolution in the P23/P91 heterogeneous welds during creep exposure at 500, 550 and 600°C for durations exceeding 60 000 hours. The composition of filler material in **Weld A** corresponded to that of P91 steel, whilst for **Weld B** the low alloy filler material of P23 type composition was used. Results of creep rupture tests on the cross weld specimens are close to, or slightly below, the lower limit of the ±20% scatter band around the standardized curve for creep strength of the P23 steel. Experimental data on microstructural evolution have been compared with results of thermodynamic and kinetic simulations. The predicted minor phase evolution close to the P23/P91 interface was confirmed by microstructural investigations. Some differences between calculations and experimental studies were found for the P23 steel. It was demonstrated that undissolved fine MX particles in the partly decarburized zone of the P23 (WM23) steel significantly delayed recrystallization of the bainitic matrix.

Keywords: dissimilar welds, creep resistance, microstructural modelling, decarburization, minor phases

1. Introduction

Creep strength of dissimilar welds is strongly dependent on the microstructural evolution in individual weld zones during creep exposure [1]. A very important mechanism of microstructural degradation of dissimilar welds represents "up-hill" diffusion of interstitial elements [2,3]. Decarburization during exposure at elevated temperatures can cause progressive weakening of a low alloy steel adjacent to the fusion boundary with a high alloy steel. On the other hand the carburized layer on the opposite side of the fusion boundary is much stronger than the surrounding matrix. In nitrogen-bearing steels, redistribution of nitrogen is important too. Progress in thermodynamic and kinetic modelling now makes it possible to simulate microstructural evolution in heat resistant steels and their weld joints during long-term thermal/creep exposure [4]. The reliability of modelling depends strongly on the quality of databases. Thus experimental investigations are required to verify results of microstructural modelling. Microstructural studies on HAZs in dissimilar welds after long - term creep exposure have demonstrated that microstructural changes in low alloy CrMo(W)V steels are less pronounced than those in CrMo steels [5,6]. This phenomenon is attributed to the higher thermodynamic stability of MX phase compared to other minor phases.

2. Experimental Materials and Techniques

Two alternative dissimilar weld joints made of P23 and P91 steel pipes of the dimensions Ø219x25 mm were fabricated in SES Tlmače, Slovakia [7]. **Weld A** was manufactured using

P91 matching filler metals (141 (GTAW): W CrMo 9 1 ø 2.5 mm, 111 (SMAW): E CrMo 9 1 B ø 3.2 and 4.0 mm), whilst in the case of the **Weld B** P23 matching filler metals (141 (GTAW): WZ CrWV22 ø 2.5 mm, 111 (SMAW): Thyssen Cr2WV ø 2.5 and 4.0 mm) were used. The details of the welding processes and parameters are summarised in [7]. PWHT of both weldments consisted of annealing at 750°C for 2 hours. The chemical compositions of individual parts of the welds are stated in Table 1. The P23 base material used in this study is the titanium-bearing variant.

Table 1 Chemical compositions of the P23/P91 welds, wt. %

Steel	C	Mn	Si	Ni	Cr	Mo	V	Ti	Nb	W	N
P23	0.08	0.55	0.27	0.08	2.11	0.07	0.23	0.06	0.01	1.70	0.013
P91	0.11	0.51	0.38	0.42	8.67	1.00	0.23	0.01	0.07	0.01	0.048
WM91	0.11	0.66	0.21	0.82	9.50	1.02	0.22	0.01	0.04	0.06	0.028
WM23	0.07	0.44	0.20	0.17	2.47	0.06	0.25	0.01	0.02	1.62	0.018

Cross weld creep specimens included base materials, heat affected zones and weld metal. Uniaxial creep rupture tests were performed at temperatures of 500, 550 and 600°C in the stress interval from 55 to 200MPa. Failure locations were identified on longitudinal sections using optical microscopy.

Modelling of the thermodynamic equilibrium was carried out using the Thermocalc software and the STEEL 16 database [8]. Calculations of carbon redistribution and phase profiles across the P23/P91 interface for 500, 550 and 600°C/ 30 000 hours were performed using the Dictra software [8]. The following elements were considered in the calculations: C, Mn, Si, Cr, Mo, V, Nb, W and N. Calculations were also carried out for the sharp P23/P91 interface (no fusion zone). Studies on minor phases in creep ruptured specimens were carried out on a JEOL JEM 2100 equipped with a PGT EDX analyser. Minor phases were identified by both EDX and SAD techniques. Carbon replicas were prepared in following regions of crept specimens:

- P23 and P91 base materials,
- decarburized zone of the WM23 and P23 steel,
- carburized zone of the WM91 and P91 steel.

3. Experimental Results

3.1. Creep Rupture Data

Data from creep rupture tests on the **Welds A** and **B** are summarised in Figs. 1 and 2, respectively. Together with the experimental results, the mean and minimum (-20% of the mean value) standardized creep rupture strength curves for the P23 grade are shown. So far available results of creep rupture tests on both welds are close to, or slightly below, the –20% curve. The most pronounced drop in creep resistance occurred at the lowest applied stresses and 600°C. Metallographic investigations proved that the development of creep damage could simultaneously take place in several critical areas of the weld but the location of the final failure was determined by the "weakest area" for given testing parameters. Results of studies on the creep failure localities are for both welds summarised in [9]. **Weld B** was more prone to creep failure in the partly decarburized zone of the low alloy weld metal close to the fusion boundary, especially at temperatures of 550 and 600°C [9].

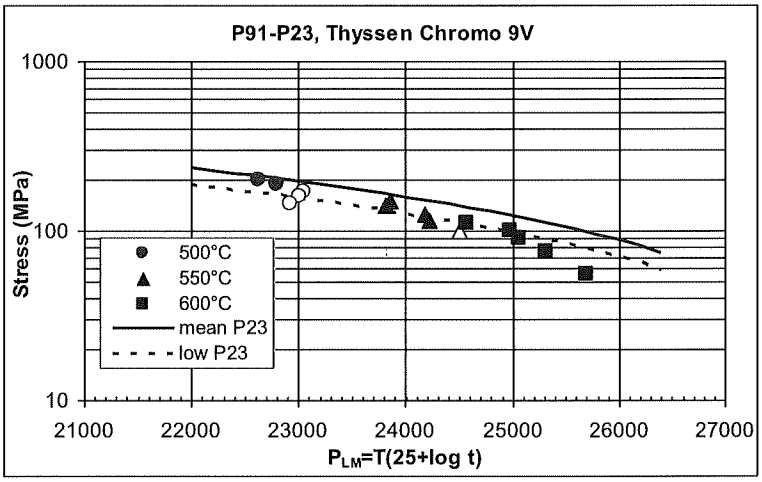

Fig. 1 Results of creep rupture tests on the Weld A

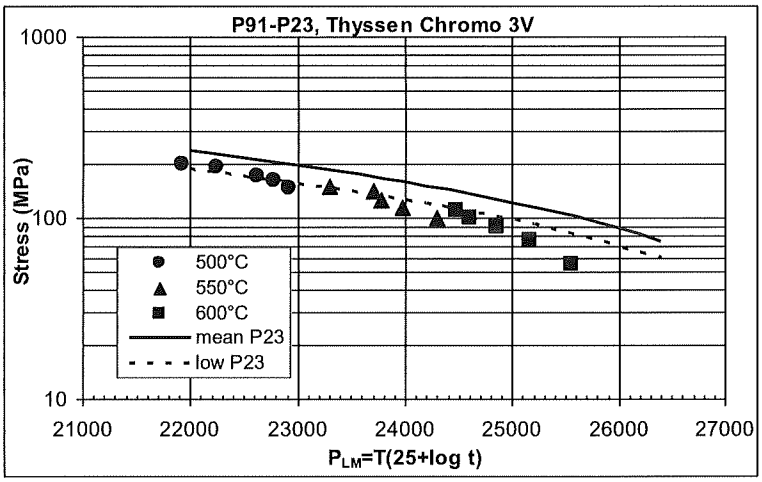

Fig. 2 Results of creep rupture tests on the Weld B

3.2. Microstructural Modelling

Microstructural stability of dissimilar welds is strongly affected by redistribution of interstitial elements in the course of long-term thermal/creep exposure. Diffusion of interstitial elements is driven by the differences in activities of these elements across the fusion boundary. Atoms move in the direction of activity gradients [2]. Due to significant differences in carbon activity for the P23 and P91 steels in the temperature range from 500 to 800°C pronounced redistribution of carbon from the P23 to the P91 steel is to be expected, Fig. 3.

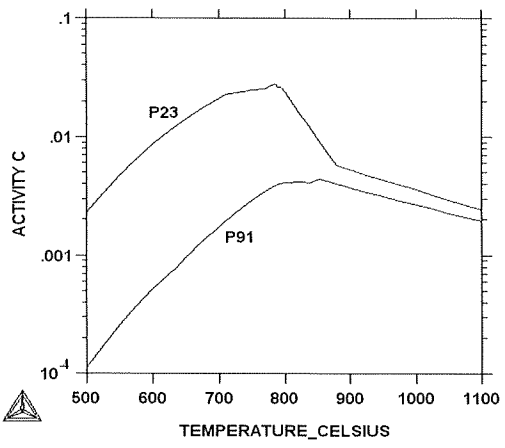

Fig. 3 Temperature dependence of carbon activity in the P23 and P91 steels

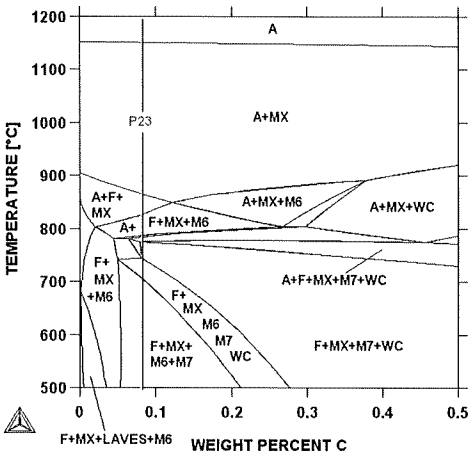

Fig. 4 The effect of carbon on equilibrium phases in the P23 steel

On the other hand, differences in nitrogen activity for both steels are negligible and no significant redistribution of nitrogen is expected to occur [8]. The effect of carbon on equilibrium phases in P23 and P91 steels is demonstrated in Figs. 4 and 5, respectively. The predicted equilibrium minor phases in P23 steel in the temperature range 500-600°C are **MX, M_6C and M_7C_3**, see Fig. 4. $M_{23}C_6$ phase is predicted as the equilibrium phase only at temperatures below 450°C. The effect of titanium in the P23 steel on the equilibrium diagram is shown in Fig. 6. In this case, only MX and M_6C minor phases are predicted to be stable minor phases in the temperature interval of interest.

Calculations of carbon migration and phase profiles across the P23/P91 interface for 600°C/ 30 000 hours are shown in Figs. 7a and 7b, respectively. Results of calculations demonstrate "up-hill" diffusion of carbon from the P23 to the P91 steel. Both the carbon content and the width of the carburized zone increase with the temperature of exposure. The calculated carburization of the P91 steel for 600°C reaches 0.39 wt.%C. In the carburized zone the molar fraction of $M_{23}C_6$ phase increases with the temperature of exposure, but the molar fraction of MX remains about the same. The molar fraction of Laves phase in this zone decreases. Partial decarburization of the P23 steel takes place mainly at the expense of dissolving M_7C_3 particles. No significant effect from decarburization on the molar fractions of MX and M_6X is predicted.

3.3 Microstructural Investigations

Microstructural studies were focused on the verification of the predicted microstructural evolution in individual weld zones of the creep ruptured specimens. It has been shown that only partial decarburization of the P23 HAZ occurs. Fine MX particles were preserved in the

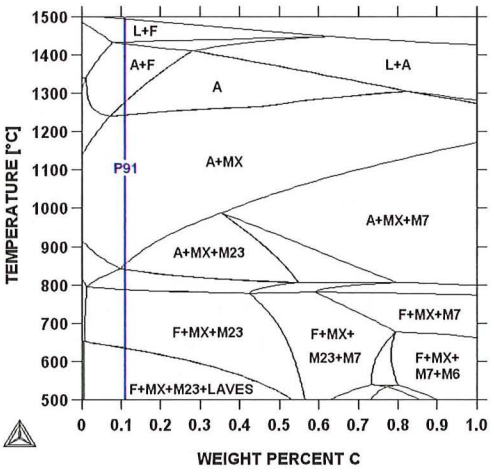

Fig. 5 The effect of carbon on equilibrium phases in the P91 steel

decarburized part of the HAZ even after the longest exposure at 600°C. Furthermore, the Laves phase volume fraction in the carburized zone was reduced. In the P23 steel four types of carbides were identified: M_7C_3, $M_{23}C_6$, MX, M_6X, depending on the temperature and time of exposure of the creep ruptured specimens.

3.4 Specimen after 600°C/ 55MPa/ 26 780hours, Weld A

This specimen represents the longest time to rupture at 600°C. Table 2 shows the results of minor phase identification in important areas of the specimen. The minor phases found in the P91 and WM91 steels are in accordance with the results of ThermoCalc calculations. In the carburized zone of the WM91 a high density of $M_{23}C_6$ particles was present. $M_{23}C_6$ particles in the carburized zone were richer in iron compared to those in both the WM91 and P91 steels, Table 3. Fine MX particles in the carburized zone were rich in niobium. The size of $M_{23}C_6$ particles in the carburized zone was very variable. However no difference in chemical composition between coarse and fine $M_{23}C_6$ particles was found [6].

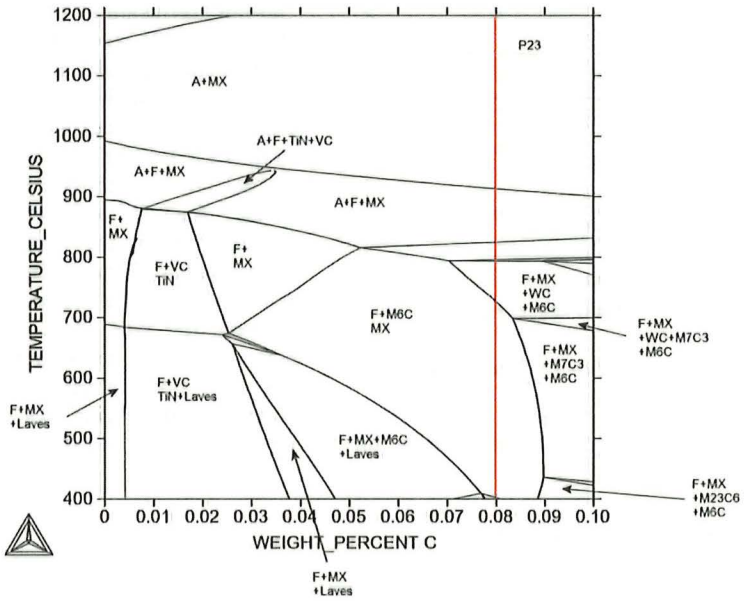

Fig. 6 The predicted equilibrium diagram taking into account titanium in the P23 steel, two MX phases (TiN and VC), STEEL 16 database

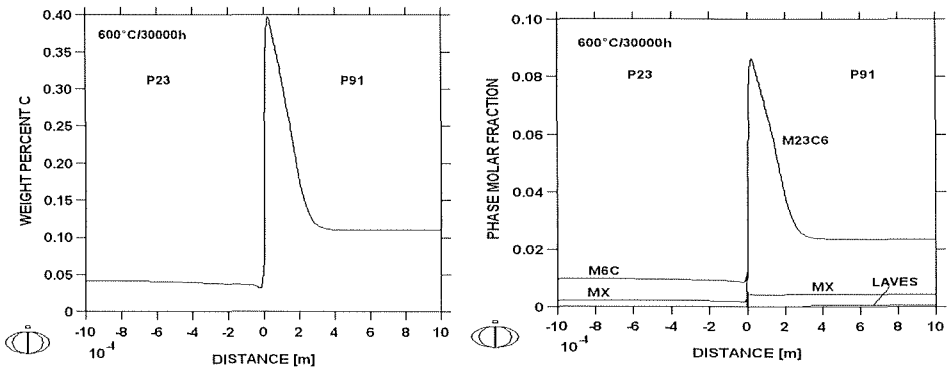

a. b.

Fig. 7 Redistribution of carbon (a.) and phase profiles (b.) across the P23/P91 interface for 600°C/ 30 000hours

Table 2 Identification of minor phases, ***Weld A****, 600°C/ 26780hours*

Area	Minor phases
P23	M_6X, $M_{23}C_6$, MX
P23 decarb. zone	MX, M_6X
WM91 carb. zone	$M_{23}C_6$, NbX
WM91	$M_{23}C_6$, NbX, sec. MX (VN), Laves phase
P91	$M_{23}C_6$, NbX, sec. MX (VN), Laves phase

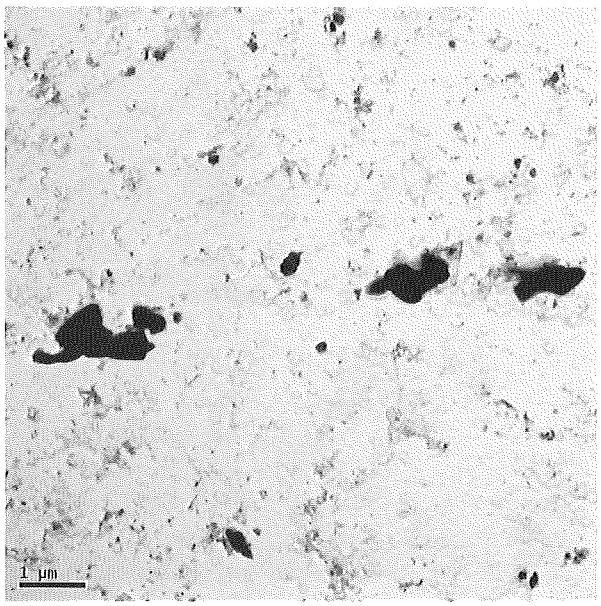

Fig. 8 Coarse M_6C, middle size $M_{23}C_6$ and fine MX particles in the P23 steel, **Weld A**, *600°C/ 26 780hours*

Table 3 Chemical composition of $M_{23}C_6$ phase, ***Weld A****, 600°C/ 26 780hours, wt.%*

Area	V	Cr	Fe	Mo
P91	0.1±0.1	70.8±0.6	18.8±0.2	10.3±0.4
WM91 carb. zone	0.3±0.2	67.4±1.7	24.3±0.5	8.1±1.4
WM91	0.2±0.1	70.6±1.0	19.3±0.9	9.9±0.5

Some differences between calculations and experimental studies were found for minor phases in the P23 steel. During quality heat treatment, precipitation of MX and M_7C_3 phases is accompanied by precipitation of the $M_{23}C_6$ phase which is regarded as a metastable phase in the steel under consideration. M_6C starts to form only during long-term creep exposure. The kinetics of M_6X precipitation depends on both temperature and time of exposure. After exposure 600°C/ 26 780hours many coarse M_6X particles were present in the P23 base material, Fig. 8. These particles were predominantly situated along grain boundaries. Even at a distance of several millimetres from the fusion boundary no M_7C_3 particles were detected. However many $M_{23}C_6$ particles were present in the bainitic ferrite. It indicates that contrary to the predictions in Figs. 4 and 6, $M_{23}C_6$ stability in the P23 steel is significantly shifted to higher temperatures.

The chemical composition of the fine MX particles was very variable [9]. Coarser MX particles were rich in titanium whereas small MX particles were rich in vanadium. A significant amount of tungsten was dissolved in vanadium rich MX particles [9]. Based on the results of the microstructural investigations the thermodynamic modelling for the P23 steel was revised taking into account the titanium content in the P23 steel, two MX phases (TiN and VC) and the SSOL database was applied.

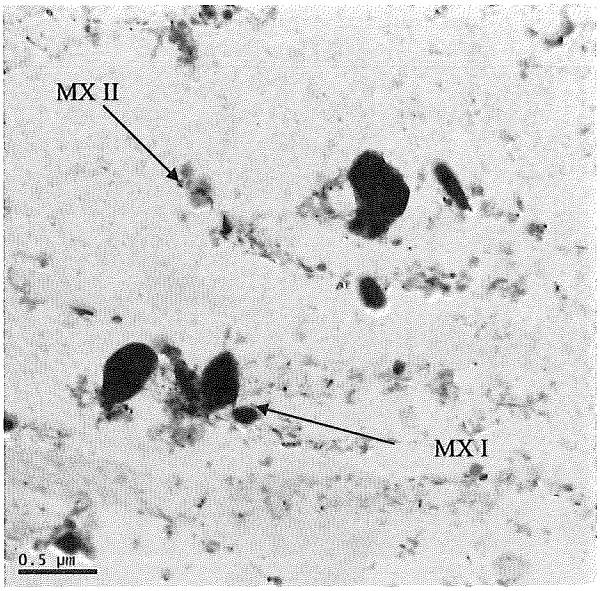

a.

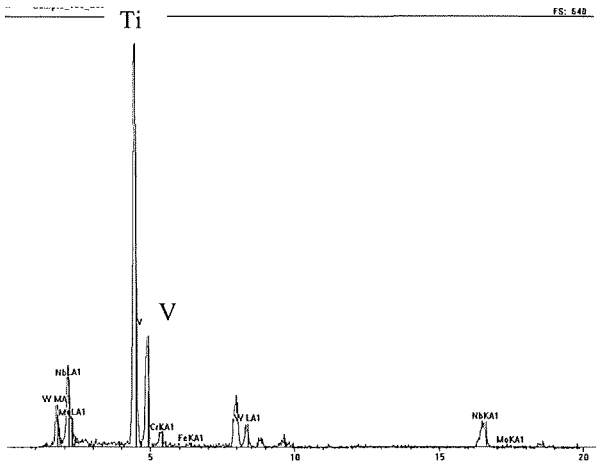

b.

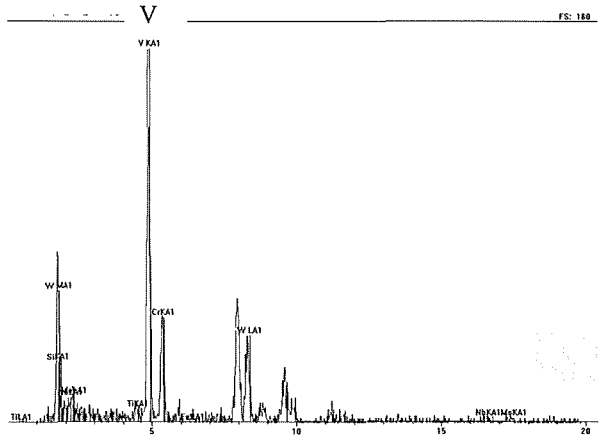

c.

Fig. 9 a. MX I and MX II particles in the titanium-bearing P23 steel, ***Weld A,*** *600°C/ 26 780hours,*
b. EDX spectrum of MX I (Ti-rich),
c. EDX spectrum of MX II (V-rich).

The calculated equilibrium diagram in Fig. 10 shows that $M_{23}C_6$ stability is extended up to about 600°C. This phase diagram is closer to experimental findings than that shown in Fig. 6 where the STEEL 16 database was used for calculations.

3.5 Microstructure of the partly decarburized zone

In the **Weld A** specimen after 26 780 hours at 600°C, a mixture of small MX and coarser M_6X particles was present in the decarburized zone. This corresponds with the predicted

phase profile which is shown in Fig. 7b. The fraction of M_6C particles in this zone was much lower compared to that in the P23 steel unaffected by carbon redistribution [6]. M_6C particles were present up to the P23/WM91 interface. No Laves phase particles were found in the carburized zone of the WM91. Many small MX particles were preserved in the partly decarburized zone of the **Weld A** specimen after 26 386 hours at 550°C and are shown Fig. 11. Fine MX particles preserved in the partly decarburized HAZ of the P23 steel slowed down recovery and recrystallization processes in the bainitic matrix.

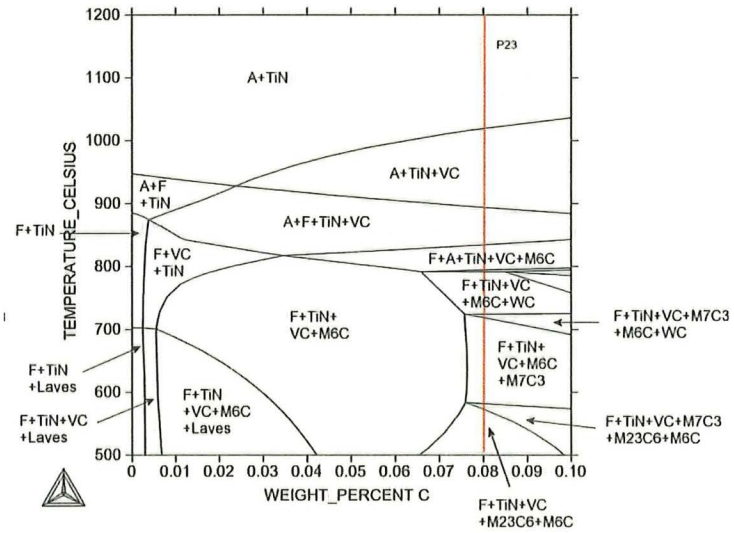

Fig. 10 The predicted equilibrium diagram for the titanium-bearing P23 steel taking into account two MX phases (TiN and VC), SSOL database

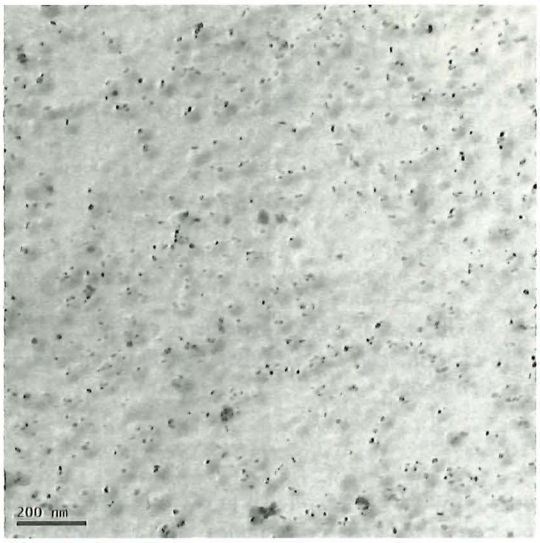

After long-term exposure at 600°C blocks of bainitic ferrite were still present in the partly decarburized zone of the P23 (WM23) steel. No equiaxed recrystallized ferritic grains were observed. Microstructure of the partly decarburized zone in the HAZ of the P23 (WM23) steel remained bainitic in all creep ruptured specimens.

Fig. 11 Fine MX particles in the partly decarburized zone of the P23 steel, ***Weld A****, 550°C/ 26 386hours*

4. Conclusions

- Results of creep rupture tests on the P23/P91 dissimilar welds are close to, or below, the lower limit of the ±20% scatter band around the standardized curve for the creep strength of the P23 steel.
- The microstructure of the partly decarburized zone in the P23 (WM23) steel remained bainitic in all creep ruptured specimens. This is related to undissolved MX particles in the partly decarburized zone which slowed down recovery/ recrystalization processes in the bainitic matrix. In the titanium-bearing P23 steel, coarser MX particles were rich in titanium, while fine MX particles were rich in vanadium.
- Decarburization took place at the expense of dissolving M_7C_3 and $M_{23}C_6$ phases. Laves phase stability in the carburized zone of the P23/P91 welds was reduced. These findings fit with the predictions of microstructural modelling.
- Results of microstructural investigations indicate that in the case of the P23 steel the SSOL database is more appropriate for microstructural modelling than the STEEL 16 database.

Acknowledgement

The authors would like to express thanks for the financial support in the frame of the projects MSM 2587080701 and CZ.1.05/2.1.00/01.0040 (Regional Materials Science and Technology Centre). The Royal Society, UK are thanked for the provision of an International Short Visits Grant for VV. Prof. S.V. Hainsworth is acknowledged for hosting the visit of VV at University of Leicester. Finally Dr. A. Kroupa from IPM Brno is thanked for discussions on modelling.

References

[1] Bhadeshia, H.K.D.H.: Design of Heat Resistant Alloys for the Energy Industries, in Proc. of Parsons 2000–Advanced Materials for 21st Century Turbines and Power Plants, Strang, A. et al., Eds., IOM, London, pp. 1-20, (2000).

[2] Pilous, V., Stránský, K.: Strukturní stálost svarových spojů pro energetiku, Studie ČSAV, Academia, Praha, (1989), (in Czech).

[3] Allen, D.J.: Creep Performance of Dissimilar P91 to Low Alloy Steel Weldments, In Parsons 2003, Strang, A. et al., Eds., IOM, London, pp. 281-294, (2003).

[4] Helander, T., Angren, J.: Computer Simulation of Multicomponent Diffusion in Joints of Dissimilar Steels. Metallurgical and Materials Transactions, Vol. 28A, pp. 303-311, (1997).

[5] Kozeschnik, E.: Dissimilar 2.25Cr/9Cr and 2Cr/0.5CrMoV Steel Welds, Science and Technology of Welding and Joining, Vol. 7, pp. 63-68, (2002).

[6] Vodárek, V., Kuboň, Z., Foret, R., Hainsworth, S.V.: Microstructural Evolution in P91/P23 Heterogeneous Welds during Creep at 500-600°C, Proc. of IIW International Conference Safety and Reliability of Welded Components in Energy and Processing Industry, Mayr, P. et al., Eds., TU Graz, pp. 233-238, (2008).

[7] Pecha, J., Bošanský, J.: Welding of Similar and Dissimilar Steels, COST 522 Progress Report, SES Tlmače-WRI Bratislava, (2002).

[8] Zlámal, B., Foret, R., Sopoušek, J.: Modelování fázového složení ocelí P23 a P91 včetně jejich svarových spojů, Brno, (2007), (in Czech).

[9] Vodárek,V., Kuboň, Z., Foret, R.: Creep Properties and Microstructure of P23/P91 Heterogeneous Welds. In Proc. of Creep and Fracture in High Temperature Components. Shibli, I. A. et al., Eds., DesTech Publications, Inc., Lancaster, pp. 1308-1316, (2009).

9th Liege Conference : Materials for Advanced Power Engineering 2010
edited by J. Lecomte-Beckers, Q. Contrepois, T. Beck and B. Kuhn.

RECIPROCATING WEAR IN A STEAM ENVIRONMENT

L. J. Brown & M. G. Gee
National Physical Laboratory, Hampton Road, Teddington, Middlesex, U.K.

Abstract

Tests to simulate the wear between sliding components in steam power plant have been performed using a low frequency wear apparatus at elevated temperatures under static load, at ambient pressure, in a steam environment. The apparatus was modified to accept a novel method of steam delivery. The materials tested were pre-exposed in a flowing steam furnace at temperature for either 500 or 3000 hours to provide some simulation of long term ageing. The duration of each wear test was 50 hours and tests were also performed on as-received material for comparison purposes. Data has been compared with results of tests performed on non-oxidised material for longer durations and also on tests without steam to examine the effect of different environments. Data collected from each test consists of mass change, stub height measurement and friction coefficient as well as visual inspection of the wear track. Within this paper, it is reported that both pre-ageing and the addition of steam during testing clearly influence the friction between material surfaces.

Keywords: Wear, steam, friction, power plant materials

1. Introduction

As the demand for higher efficiency in power plant increases, there is a requirement for higher performing materials. Higher temperatures, pressures and working lifetime means that the materials which are currently in use are not adequate to meet these higher demands. Alternative materials which are capable of withstanding higher, more aggressive environments are currently being studied for next generation power plant. An essential part of this work is the assessment of the high temperature tribological performance.

High temperature sliding wear and friction testing has been carried out previously by a number of different workers [1-7]. Much of the work has been concerned with the high temperature tribological performance of ceramics [1-5], with some work on high temperature low friction coatings for dry sliding applications [3], and on tribological components for gas turbines [7]. These tests have previously been carried out at elevated temperatures under load at ambient pressure in an air environment.

More recently there has been work on assessing the tribological performance of steam generating plant materials in water environments [8,9] and at elevated temperatures in steam environments [10,11]. The results for sliding tests in a steam environment showed complex behaviour where the formation of surface glaze layers and variation in contact loads have a major effect on the results that are obtained.

This paper describes the capability to carry out high temperature reciprocating wear tests in a steam environment. Initial results are presented for tests carried out on a range of materials used in steam power generation applications such as valve and actuator components.

2. Experimental

2.1 Test Method

A test system used in earlier work to measure the dry sliding wear performance of ceramics and power generation materials [6,7] was modified to allow for the addition of a steam environment. This involved replacing the sample holder arms and heating elements for the furnace due to existing material not being stable in a steam environment. The wear test apparatus is shown schematically in figure 1. The set up comprises of a split furnace, which encases the arms during testing. This is easily removed by virtue of a sliding track. The arms hold the samples, of which the top arm is attached to an actuator, allowing movement of the sample against a fixed bottom arm. The distance travelled by the top arm, measured with a horizontal LVDT, is controlled with limit switches in place to ensure that the movement is stopped if the travel is exceeded. The vertical displacement is measured with another LVDT and the load monitored using a vertical load cell to ensure it remains constant throughout the test. An additional horizontal load cell is positioned which enables the wear friction coefficient to be calculated. The bottom arm is pivoted to allow the lower sample to be pressed into contact with the top sample. The arms are water-cooled to prevent heat transfer outside of the furnace and further cooling is provided using compressed air directed onto the water-cooled arms. The load is applied by the addition of weights added to the end of the pivot arm. The temperature of the furnace and the samples are measured in-situ by two sheathed thermocouples.

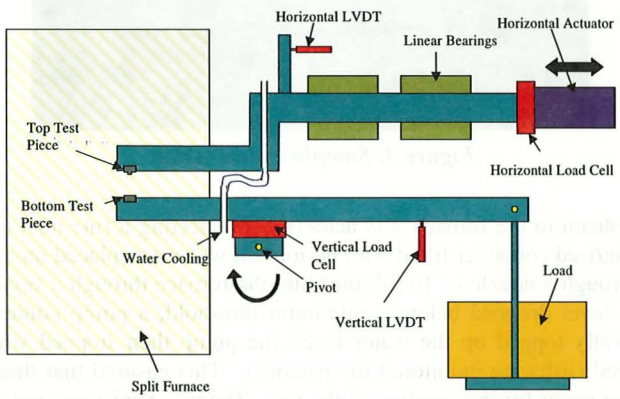

Figure 1: Low Frequency Wear Apparatus

The samples were designed to allow for a 'push' fit into the arms, with the option of an additional screw to ensure the sample is held firmly in place. The top sample comprises of a block with a protruding stub which is rubbed against a flat plate sample, see figure 2.

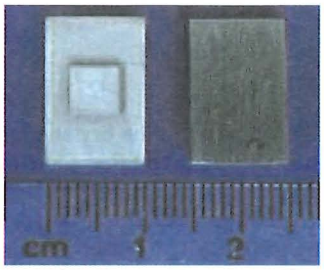

Figure 2: Sample Dimensions

The arms were designed specifically to allow the top and bottom surfaces to be positioned parallel to each other to ensure a flat contact between the top and bottom specimens. This was done by enabling the top arm to rotate clockwise and anti-clockwise with the lower sample held in a holder which allowed lateral movement, see figure 3.

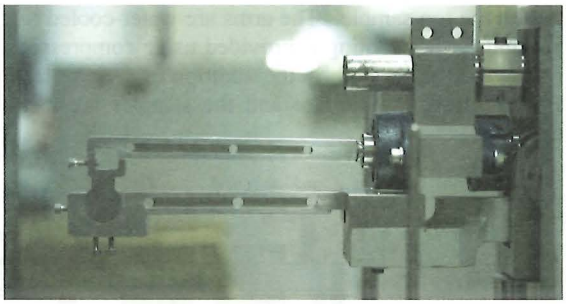

Figure 3: Sample Holder Arms

The addition of steam to the furnace was achieved by injecting a fine mist of water into the furnace. A pressurised container filled with de-ionised water was placed on a balance and the water sprayed through a nozzle (~ 10 ml/min) into the furnace through a small entrance hole. When the water level dropped below a minimum threshold, a pump connected to a water supply automatically topped up the water level, the pump then stopped when a maximum level was achieved (software monitored the balance). This ensured that there was always a constant supply of water for the duration of the test. The water mist was not injected into the furnace until the required temperature was achieved; this ensured that the mist instantly turned to steam.

Software was written specifically to control the start and end of the test, automatic top up of water, as well as collecting data for friction, load, temperature and number of cycles and time. A screen shot of the program is shown in figure 4 presenting an example of the friction loop results that are obtained.

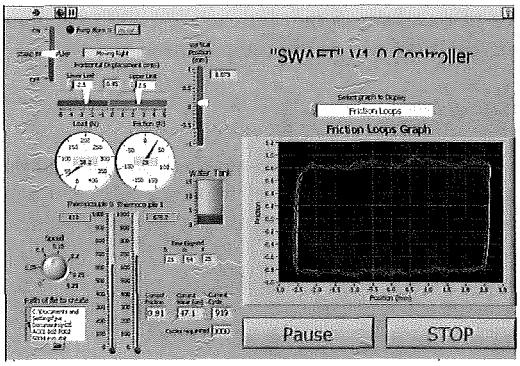

Figure 4: Software Program

2.2 Materials and Tests Carried Out

The materials tested are given in Table 1. The stub sample (left hand side of figure 2) was manufactured from Co-Ni-Cr-W alloy or Ni-Cr-Co alloy with some samples coated with an MCrAlY (co-deposited electroplate).

Table 1: Materials Examined

Stub Material	Coating on Stub	Plate Material	Coating on Plate	Pre-exposure, h
Co-Ni-Cr-W alloy	-	Stellite	-	0
Co-Ni-Cr-W alloy	-	Stellite	-	500
Co-Ni-Cr-W alloy	-	Stellite	-	3000
Co-Ni-Cr-W alloy	-	Stellite	HVOF Cr_2C_3	0
Co-Ni-Cr-W alloy	-	Stellite	HVOF Cr_2C_3	500
Co-Ni-Cr-W alloy	-	Stellite	HVOF Cr_2C_3	3000
Ni-Cr-Co alloy	-	Stellite	-	0
Ni-Cr-Co alloy	-	Stellite	-	500
Ni-Cr-Co alloy	-	Stellite	-	3000
Ni-Cr-Co alloy	-	Stellite	HVOF Cr_2C_3	0
Ni-Cr-Co alloy	-	Stellite	HVOF Cr_2C_3	500
Ni-Cr-Co alloy	-	Stellite	HVOF Cr_2C_3	3000
Ni-Cr-Co alloy	MCrAlY	Stellite	HVOF Cr_2C_3	0
Ni-Cr-Co alloy	MCrAlY	Stellite	HVOF Cr_2C_3	500
Ni-Cr-Co alloy	MCrAlY	Stellite	HVOF Cr_2C_3	3000

Both the stub (top) and plate (bottom) samples were weighed prior to and after testing. Three sets of specimens were used for each series of tests, comparing as-received with pre-exposed specimens, which were exposed in a flowing steam (ambient pressure, distilled water, ~ 5 ml/min) furnace at 650 °C for either 500 or 3000 hours to provide simulation of long term ageing.

Each test was performed at a temperature of 650 °C with a static load of 44 N. Typically, wear tests had a duration of 50 hours in a steam environment. Some additional tests were made for a longer duration in steam, and for the same time without steam for comparative

purposes. The distance of travel was 5 mm for each test and took approximately one minute to complete a cycle; a cycle is defined as one reciprocation.

2.3 Imaging and Analysis of Samples

After ~ 50 hours of testing, specimens were re-weighed, imaged and the wear scar examined. The data collected was plotted as a function of friction coefficient against time; this will be presented in the results section along with the friction coefficient values.

3. Results

3.1 Friction

During testing, the horizontal and vertical load and the horizontal and vertical displacement were logged. The vertical load showed that the dead weight remained constant throughout testing. The horizontal load gives a measure of friction force generated at the contact interface that can be used to calculate friction coefficients. A good method for displaying this is through friction loops where the friction coefficient is plotted against horizontal displacement. The average friction coefficient was also calculated for a single friction loop from the integral and the trend with time plotted. A typical example of these results is shown in figure 5 for a Ni-Cr-Co alloy stub rubbed against a flat HVOF Cr_2C_3 plate. Both specimens were tested in the as-received condition. Initial and final friction coefficient loops are plotted against horizontal direction, shown in figure 5 (a) and (b) respectively. The average friction coefficient was plotted against time, shown in figure 5(c). There was a general increase in friction with time, although there were occasional fluctuations in the friction.

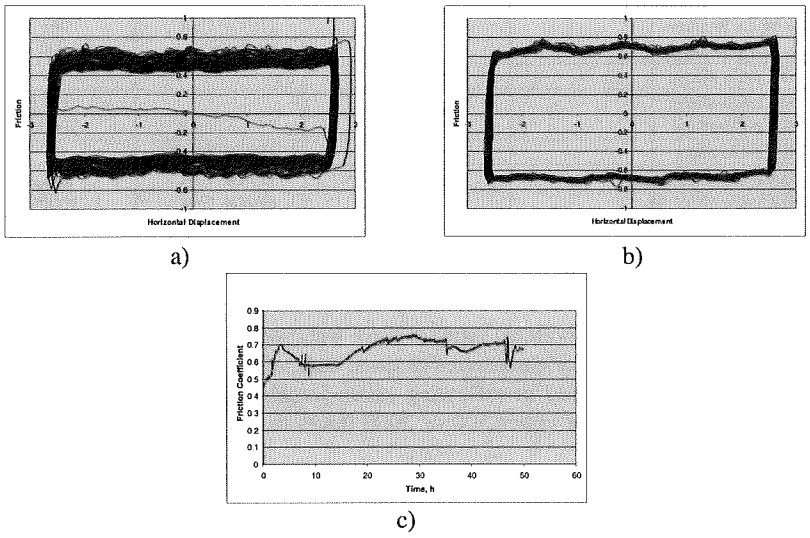

Figure 5: Plot of Friction Loops a) Initial Friction, b) Final Friction and c) Overall Friction vs. Time

Although the majority of tests were performed in a steam environment, one test was carried out without steam to observe what effect the addition of steam had to the test. As shown in figure 6 it can be seen that whereas the friction coefficient decreased throughout the test in steam, the friction coefficient with no steam present increased during the test.

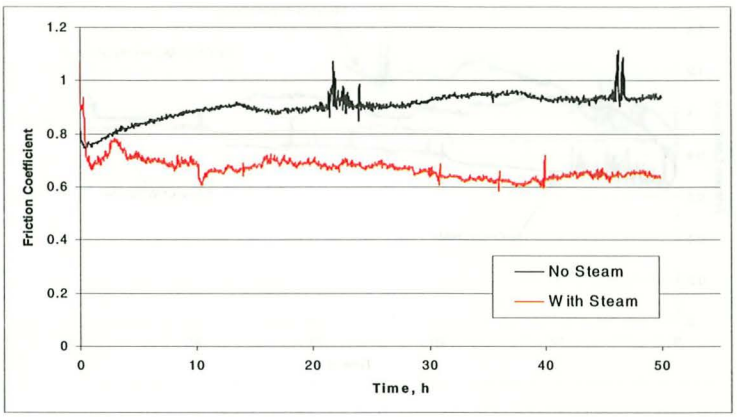

Figure 6: Comparison of Environment, Steam vs. No Steam for Ni-Cr-Co/Stellite

Figure 7 shows a comparison of friction results for different materials in the as-received condition. The MCrAlY coating has a much higher friction coefficient, reaching a maximum of 1.4, than the other materials tested which showed a friction coefficient of between 0.5 and 0.7.

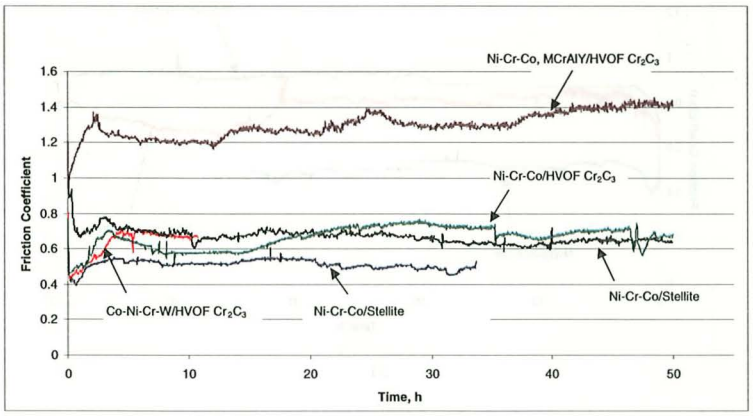

Figure 7: Comparison Between un-Aged Materials

The results shown in figure 7 for as-received samples can also be compared with the results shown in figure 8 for materials that had been pre-aged for 3000 hours in a steam environment. It can be seen that the sample with the MCrAlY coating is the only test in which the friction coefficient actually decreased with pre-ageing.

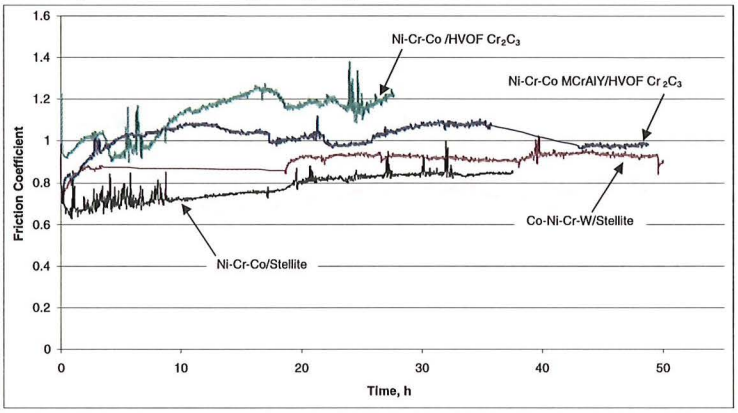

Figure 8: Comparison of Pre-Aged for 3000 h Specimens

Tests were performed on as-received and pre-exposed specimens to compare the effect of 'aged' material. Results are presented in figure 9. For the Co-Ni-Cr-W alloy against stellite material, ageing increases the friction. By contrast, with the MCrAlY coating, pre-ageing markedly decreases the friction coefficient.

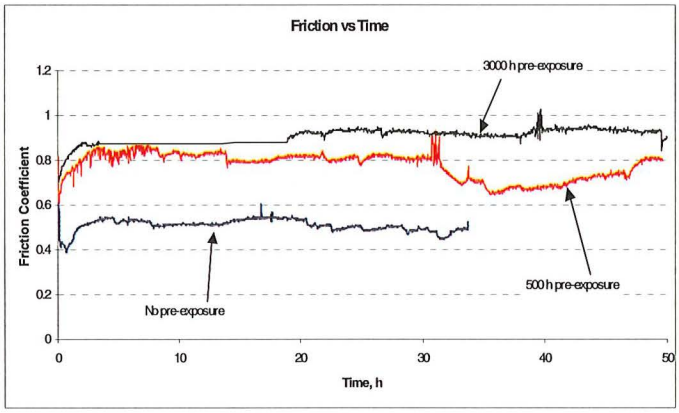

a)

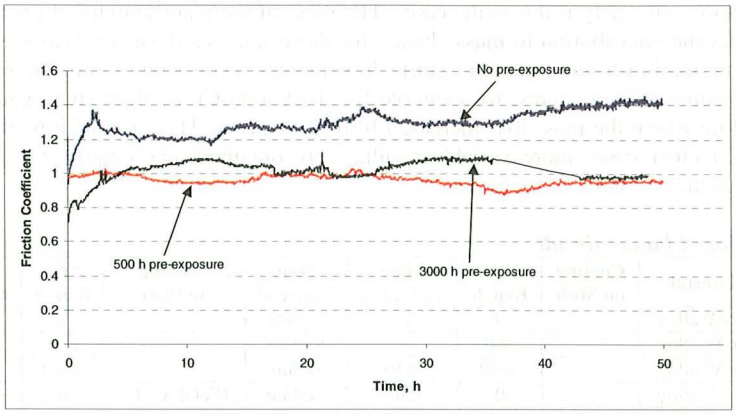

b)

Figure 9: Comparison of As-Received and Aged Material; a) Co-Ni-Cr-W alloy Against Stellite and b) MCrAlY Coated Stub Against Cr_2C_3

Table 2 gives a summary of the final friction results with respect to material and ageing treatment.

Table 2: Final Friction Coefficients

Stub Material	Coating on Stub	Plate Material	Coating on Plate	Pre-exposure, h	Final Friction
Co-Ni-Cr-W alloy	-	Stellite	-	0	0.5
Co-Ni-Cr-W alloy	-	Stellite	-	500	0.8
Co-Ni-Cr-W alloy	-	Stellite	-	3000	0.95
Co-Ni-Cr-W alloy	-	Stellite	HVOF Cr_2C_3	0	0.68
Co-Ni-Cr-W alloy	-	Stellite	HVOF Cr_2C_3	500	0.9
Co-Ni-Cr-W alloy	-	Stellite	HVOF Cr_2C_3	3000	-
Ni-Cr-Co alloy	-	Stellite	-	0	0.65
Ni-Cr-Co alloy	-	Stellite	-	500	0.65
Ni-Cr-Co alloy	-	Stellite	-	3000	0.85
Ni-Cr-Co alloy	-	Stellite	HVOF Cr_2C_3	0	0.7
Ni-Cr-Co alloy	-	Stellite	HVOF Cr_2C_3	500	0.85
Ni-Cr-Co alloy	-	Stellite	HVOF Cr_2C_3	3000	1.2
Ni-Cr-Co alloy	MCrAlY	Stellite	HVOF Cr_2C_3	0	0.95
Ni-Cr-Co alloy	MCrAlY	Stellite	HVOF Cr_2C_3	500	0.95
Ni-Cr-Co alloy	MCrAlY	Stellite	HVOF Cr_2C_3	3000	1.0

3.2 Wear

Two measures of wear have been used. Mass change results are given in Table 3. These show that the mass of the stub sample always increased. This shows that the dominant contribution to mass change for the stub sample is oxidation rather than wear. In most cases the mass gain during the test decreased as the pre-exposure time increased. This is likely to be due to the protective oxide scale formed during the ageing process which provided a barrier to further diffusion. Further work to examine the oxide scale thickness and

microstructure will verify if this is the case. The mass of the plate samples always decreased showing that the contribution to mass change for these samples from wear (loss) was higher than the contribution from oxidation (gain). In some cases consistent trends are observed in the mass change measurements, for example for the Co-Ni-Cr-W alloy stub against HVOF coated stellite where the mass loss increased from 1.38 mg to 41.84 mg with increasing pre-exposure. In other cases more variable results were obtained, particularly when the mass change is small.

Table 3: Mass Change Results

Stub Material	Coating on Stub	Pre-Exp, h	Mass Gain, mg	Plate Material	Coating on Plate	Pre-Exp, h	Mass Gain, mg
Co-Ni-Cr-W alloy	-	0	0.45	Stellite	-	0	-0.07
Co-Ni-Cr-W alloy	-	500	-	Stellite	-	500	-0.33
Co-Ni-Cr-W alloy	-	3000	0.19	Stellite	-	3000	-0.16
Co-Ni-Cr-W alloy	-	0	0.48	Stellite	HVOF Cr_2C_3	0	-1.38
Co-Ni-Cr-W alloy	-	500	0.15	Stellite	HVOF Cr_2C_3	500	-23.84
Co-Ni-Cr-W alloy	-	3000	0.1	Stellite	HVOF Cr_2C_3	3000	-41.84
Ni-Cr-Co alloy	-	0	0.37	Stellite	-	0	-0.06
Ni-Cr-Co alloy	-	500	0.07	Stellite	-	500	-0.24
Ni-Cr-Co alloy	-	3000	0.03	Stellite	-	3000	-0.3
Ni-Cr-Co alloy	-	0	0.36	Stellite	HVOF Cr_2C_3	0	-3.5
Ni-Cr-Co alloy	-	500	0.05	Stellite	HVOF Cr_2C_3	500	-23.28
Ni-Cr-Co alloy	-	3000	-	Stellite	HVOF Cr_2C_3	3000	-
Ni-Cr-Co alloy	MCrAlY	0	1.11	Stellite	HVOF Cr_2C_3	0	-0.32
Ni-Cr-Co alloy	MCrAlY	500	0.14	Stellite	HVOF Cr_2C_3	500	-22.04
Ni-Cr-Co alloy	MCrAlY	3000	0.23	Stellite	HVOF Cr_2C_3	3000	-9.96

The results of the measurements using the LVDT to monitor vertical displacement showed little change during tests.

3.3 Visual Inspection of Wear Scar

In many cases, despite the attention given to sample alignment in the design of the test system, it was found that full contact was not achieved over the sample surfaces. Thus in figure 10 wear is only observed at the bottom corner of the stub, with the wear scar on the plate which runs across the bottom of the sample consistent with this. In figure 11 there is severe scoring along the bottom of the stub. Close examination of the sample shows that the stub was in complete contact at the beginning of the test, however, it appears that particles may have been ripped out of the plate by the stub and then ploughed back into the base plate forming scores that are visible along the bottom of the contact area. Figure 12 shows a sample set with even wear across the stub, indicating that the contact between the surfaces was flat. Figure 12b shows a particle (arrowed) at the left edge of the wear scar which has evidently caused the heavy scoring to the right of the particle.

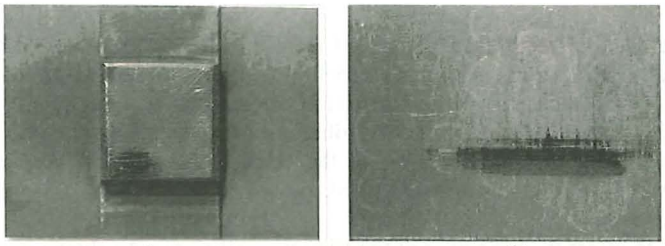

a) b)

Figure 10: Wear to the Bottom Corner of (a) Stub and (b) Along Plate

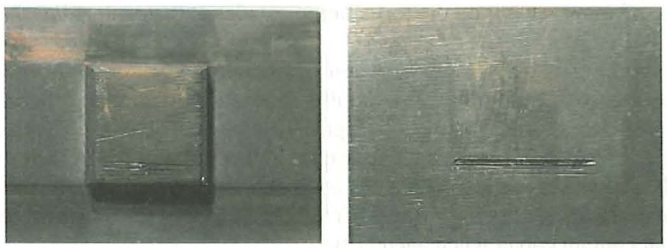

a) b)

Figure 11: Scoring to the Bottom of (a) Stub and (b) Along Plate

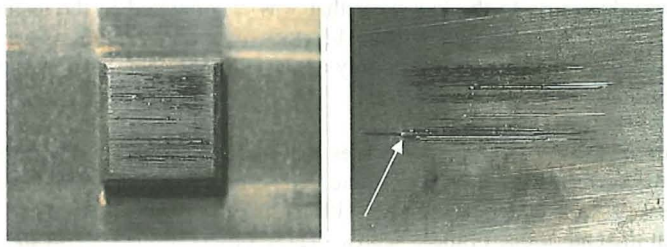

a) b)

Figure 12: Image of Worn Specimens a) Top Stub and b) Bottom Plate (with particle highlighted)

4. Discussion

The test system that has been developed has shown to be a useful test bed to evaluate the tribological performance of materials intended for use in high temperature operation in steam turbines. The water injection system worked well, proving to be a reliable way to generate the necessary steam environment for the testing. The test system has the capability for operation at temperatures up to about 900 °C with Nimonic 90 sample holders, and up to 1400 °C with ceramic sample holders.

The friction force measurements are converted to friction coefficient values and are initially displayed as friction loops. No sign of stiction was observed in the tests reported in this paper (initial peak of friction when samples are stationary with respect to one another), showing that the dynamic friction coefficient is as large in these experiments as the static friction coefficient.

When average friction trends were calculated from the friction loop data, it was clear that although overall trends for the evolution of friction with time were clear in many tests, there were also many sudden changes or fluctuations in friction that were observed. These sudden changes are likely to be related to specific tribological events such as build up and sudden breakaway oxide films or transfer layers at the contact interface, or increases due to the scoring and grooving events that were observed.

Steam appears to affect the behaviour of the friction coefficient. As shown within this work, when steam is present, the friction decreases. As condensation does not occur between the specimens the steam cannot act as a lubricant. It is quite likely that this effect of steam is due to the influence of water vapour on the formation of oxides at the contact interface.

The pre-aged specimens have a higher friction coefficient compared with the same material tested in the as-received condition. This is also likely to be due to the formation of oxide layers for the pre-aged samples that lead to higher friction coefficients. The exception to this behaviour is the MCrAlY coating which showed a higher friction coefficient than any of the other materials and is the only material tested within this work that shows a decrease in friction coefficient with pre-ageing. The MCrAlY coating is well known to form lubricious oxide layers that contain cobalt when aged [12].

The lack of full contact over the sample faces in many of the tests was disappointing, but in practice this was due more to the low wear that was encountered in the testing rather than alignment as such. Obtaining full contact between two flat samples is very difficult in tribological testing, so that full contact is only achieved if the samples undergo considerable wear, or the test duration is very long.

A major feature of many of the worn surfaces that were examined is the presence of many scores across the surface that had caused quite deep damage and had roughened the surface locally. These scores were often associated with particles that were attached to the surface of the wear scar at the end of one of these scores. These observations suggest that strong bonds developed at localised points in contact between the two surfaces. Particles from one surface were pulled out from the surface to form hardened protuberances that then were dragged across the opposing surface to cause the deep scoring and damage that was observed.

Additional work is required to fully elucidate the mechanisms of wear that have been occurring in the tests that have been carried out and reported here, thus further examination of the test pieces is necessary. This will consist of closer examination using the SEM and EDX of the surfaces to observe if any material exchange between specimens has occurred and to study formation of oxides. Cross sections of specimens will permit closer examination of the wear scar and allow depth measurements of the thickness of any oxide scales that have been formed to be made.

5. Conclusions

Within the work presented here, it is evident that the addition of steam in a tribological environment clearly influences the friction between both as-received and aged materials. The

majority of materials experience an increase in friction coefficient, the only exception being the MCrAlY coated stub, due to its lubricious properties which form during testing.

Although the stub height was measured before and after testing, no significant change was observed.

Acknowledgements

The authors are grateful to Jim Banks, David Laing and John Nunn for their technical expertise, and would like to acknowledge funding from the Technology Strategy Board and from the Department of Business Innovation and Science for the work reported in this paper.

References

1) H Tomizawa and T E Fischer, Friction and Wear of Silicon Nitride at 150 °C to 800 °C, ASLE Trans, 29, 481, 1986
2) A P Semenov and A A Katsura, Investigation of friction and wear of corundum ceramics at temperatures to 1500 °C, Proc 2nd Int Conf on Wear of Materials, American Society of Mechanical Engineers, New York, pp 551-555, April 1979
3) C D Dellacorte and H E Sliney, Composition optimisation of self-lubricating chromium-carbide based composite coatings for use to 760 °C, asle Trans, 30, 77, 1987
4) M G Gee, C S Matharu, E A Almond and T S Eyre, The Measurement of Sliding Friction and Wear of Ceramics at High Temperature, Wear, **138,** 169-187, 1990
5) M G Gee, C Melandri, G de Portu and S Guicciardi, High Temperature Wear of Silicon Nitride Composites, Tribology International, 28 403-413, 1995
6) J M Cox and M G Gee, Hot Friction Testing of Ceramics, Wear, 203-204, 404-417, 1997
7) M G Gee, G Aldrich-Smith, Ian Boston, Jonas Hurter, G McColvin, Development of Test Methods to Evaluate the Wear Performance of Industrial Gas Turbine Seal Components, Proceedings of the 6th International Parsons Conference, Maney, 2003
8) Lee, Y.-H. and I.-S. Kim "The effect of subsurface deformation on the wear behavior of steam generator tube materials." Wear 253(3-4): 438-447, 2002
9) Jeong, S. H., C. W. Cho, et al. "Friction and wear of Inconel 690 for steam generator tube in elevated temperature water under fretting condition" Tribology International 38(3): 283-288, 2005
10) Hong, J. K. and I. S. Kim "Environment effects on the reciprocating wear of Inconel 690 steam generator tubes." Wear 255: 1174-1182, 2003
11) Park, G. S., G. G. Kim, et al. "Sliding wear behaviors of steam generator tube materials in high temperature water environment." Journal of Nuclear Materials 352(1-3): 80-84, 2006
12) Inman I. A., Datta S., et al. "Microscopy of glazed layers formed during high temperature sliding wear at 750 ◦C." Wear 254: 461–467, 2003

9th Liege Conference : Materials for Advanced Power Engineering 2010
edited by J. Lecomte-Beckers, Q. Contrepois, T. Beck and B. Kuhn.

STEAM OXIDATION OF 9-12%Cr STEELS: CRITICAL EVALUATION AND IMPLICATIONS FOR PRACTICAL APPLICATION

J. Zurek[1)], E. De Bruycker[2)], S. Huysmans[2)], W.J. Quadakkers[1)]

[1)]Forschungszentrum Jülich, IEF-2, 52428 Jülich, Germany
[2)] Laborelec, Rodestraat 125, B-1630 Linkebeek, Belgium

Abstract

In new and future generation Power Plants, creep resistant steels selected for high-temperature components are subjected to a large variety of service environments. In many of these applications, water vapor has been found to substantially alter the technologically relevant properties, mainly growth rate and adherence, of the surface oxides. Various data sets exist in the literature for steam oxidation for this type of steels, however these data show a substantial deviation. These differences can be related to e.g. "batch to batch" variation, oxidation conditions, surface treatment, difference between laboratory/power plants data, etc. Therefore these literature data need careful and critical verification when being used to estimate the long term materials behaviour in real power generation plants. The paper discusses the existing steam oxidation data for a number of selected steels, i.e. P91, P92 and VM12, thereby putting main emphasis on discussing the parameters which are responsible for observed variations in oxidation rates for the various types of materials.

Keywords: oxidation, steam, Grade 91, Grade 92, VM12

1. Introduction

Steam carrying components in fossil fuel fired power generation systems with steam temperatures up to 530°C are typically manufactured from low alloy steels. Higher steam temperatures, required for obtaining higher energy conversion efficiencies, resulted in recent years in the introduction of martensitic 9-12%Cr steels such as P91, P92 and VM12 [1]. Due to their higher Cr contents (Table 1) these materials possess the potential of forming protective chromia base surface oxide scales upon exposure in dry, oxygen rich gases or air at typical application temperatures up to approximately 650°C. This type of surface scales results in oxidation rates which are several orders of magnitude lower than those of the low-alloy steels, which form Fe-rich scales [2].

In wet gases, however, the protective chromia base scale formation is hampered, with the result that the mentioned martensitic steels, when exposed in steam, generally form oxide surface scales, which are rich in iron and frequently possess growth rates, which are not substantially different than those on low alloy steels [3-7]. The exact scale growth rates depend on numerous parameters such as detailed steel composition, gas flow rate [8] and temperature.

In the present paper, first, the general mechanisms of steam side oxidation of martensitic 9-12% Cr steels are being discussed. Then, the special features of martensitic steel oxidation and finally, results of a literature survey on the steam side oxidation of P91, P92 and VM12 are presented.

Steel	C	Cr	W	V	Si	Ni	Mo	Mn	Nb	Co	N
P/T91	0,08-0,12	8,00-9,50	-	0,18-0,25	0,20-0,50	max. 0,04	0,85-1,05	0,30-0,60	0,06-0,1	-	0,03 - 0,07
P/T92	0,07-0,13	8,50-9,50	1,50-2,00	0,15-0,25	max. 0,50	max. 0,04	0,30-0,60	0,30-0,60	0,04-0,09	-	0,03 - 0,07
VM12	0,10-0,14	11,0-12,0	1,30-1,70	0,20-0,30	0,40-0,60	0,10-0,40	0,20-0,40	0,15-0,45	0,03-0,08	1,4-1,8	0,03 - 0,07

Table 1. Nominal compositions (wt.%) of the steels investigated in the present study.

2. Steamside oxidation of 9-12%Cr steels

During exposure in (simulated) steam in the temperature range 550 - 650°C, all martensitic 9-12%Cr steels tend to exhibit an incubation period in which the oxidation rates are very low (t_1 in Fig. 1). This incubation period can range from minutes to several hundreds of hours and it depends on various factors such as gas composition, increasing amount of protective scale forming elements (e.g. Cr, Si) and the extent of cold work. Higher water vapor contents tend to decrease the incubation period. In this oxidation stage oxide layers of the type $(Fe,Cr)_2O_3$ and/or Cr-rich $(Fe,Cr)_3O_4$ covered by a haematite layer, are being formed [9-11].

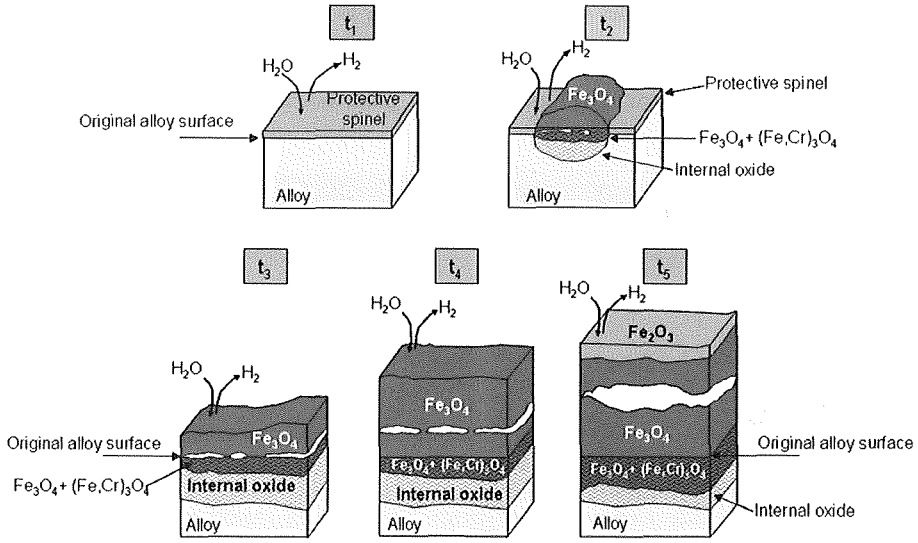

Figure 1. Proposed mechanism for the oxide scale formation on ferritic 10%Cr steel in Ar-H_2O mixtures. Times t_1, t_2, t_3, t_4, t_5 represent subsequent time steps during the oxidation process [12].

Unlike during air or oxygen exposure a breakdown of this protective scale occurs after longer exposure times. The mechanism for occurrence of this effect, which is accompanied by formation of rapidly growing magnetite and a zone with internal Cr_2O_3 precipitates (t_2 in Fig. 1), has been discussed in numerous papers [3, 5-8, 13]. At temperatures above approximately 580°C wüstite may be present near the scale/steel interface [1, 3, 14]. The inner and outer

layers are separated by a gap, probably caused by vacancy condensation resulting from the rapid outward growth of the outer magnetite layer (t_3 in Fig. 1). Further growth of the scale depends to a large extent on transport processes within this gap, likely by so-called "H_2/H_2O-bridges" as proposed by Fujii and Meussner [7]. This explains why there is a relative movement of the "transient gap" towards the magnetite layer in the outer part of the scale during prolonged exposure (t_4 in Fig. 1). As the overall scale thickness increases, the Fe-activity at the scale/gas interface gradually decreases due to the increasingly difficult transport of Fe cations to the oxide surface as a result of the presence of the in-scale gap. This decrease in Fe-activity in the outer scale eventually results in formation of haematite, i.e. the oxide in equilibrium with the gas atmosphere, on top of the scale (t_5 in Fig. 1). The haematite formation starts at the grain boundaries of the magnetite layer. Additionally, molecular gas transport occurs through the outer scale [15].

During exposure of the martensitic 9-12%Cr steels for longer times of, for example, 1000 h in the temperature range 550-650°C, the scales start to develop more and more microvoidage. This first occurs in the inner scale (Fig. 2). Here the largest extent of void formation seems to develop at the interface between the internal oxidation zone, if present, and the inner oxide layer (Fig. 2b). The eventual pore morphology and distribution in the inner scale depend on the way in which the vacancies within the scale and/or at the scale–alloy interface coalesce to voids. This type of void formation, as well as the morphologies of the inner spinel layers and the zone of internal oxidation, is affected by the underlying steel microstructure (Fig. 2c), including carbides preferentially formed at steel grain boundaries and/or martensitic laths [16].

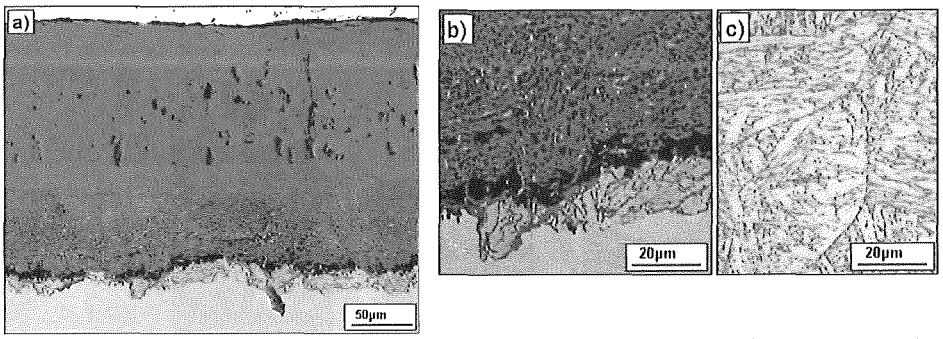

Figure 2. Oxide scale formed on martensitic steel during exposure for 1000 h in Ar–50%H_2O at 650°C: (a) overview; (b) higher magnification of scale - steel interface; (c) steel microstructure.

Upon prolonged exposure, voidage also starts to occur in the outer magnetite layer (Fig. 3a). These voids can be unevenly distributed or they can coalesce to a gap at the interface between the inner and outer layers (Fig. 3b). Indications have been found that the latter is caused by limitations of the cation transport in the inner scale. Here, three possible reasons for this effect may be mentioned:

1. The continuing formation of voids in the inner scale decreases the transport area available for cation diffusion.

2. The two-phase mixture of FeCr spinel and magnetite in the inner scale changes, near the interface between outer and inner scale, to a single-phase layer. Magnetite, which acts as 'rapid diffusion path' for Fe cations, vanishes with the result that the transport of Fe cations from the inner to the outer scale decreases.
3. The formation of a protective, Cr-rich spinel layer at the oxide–alloy interface.

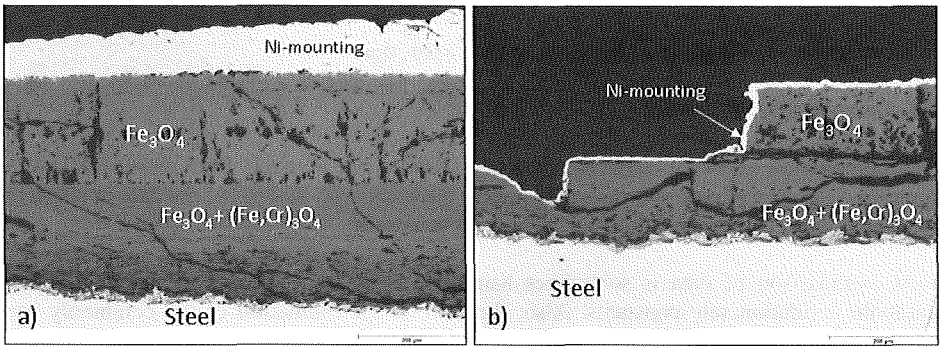

Figure 3. Formation of voids and gaps in oxide scale on steel P92 during exposure for 10000 h in Ar-50%H_2O at (a) 650°C and (b) 625°C.

The limitation of cation transport has as a result that the growth rate of the outer magnetite in the existing oxygen activity gradient can no longer be sustained. Consequently, inwardly moving vacancies in the magnetite tend to condense at the interface between the inner and the outer layer resulting in void and gap formation (Figs. 3b, 4a).

Extensive void/gap formation will eventually result in the formation of hematite on top of the outer magnetite layer, as explained above (Fig. 4). Macroscopic observation of hematite is thus frequently a strong indication for the formation of a heavily voided/cracked magnetite layer, which is expected to be prone to spallation (Fig. 4b). Nishimura et al. [17] described a similar mechanism for the hematite formation and claimed that the transformation of magnetite into hematite plays a role in oxide spalling.

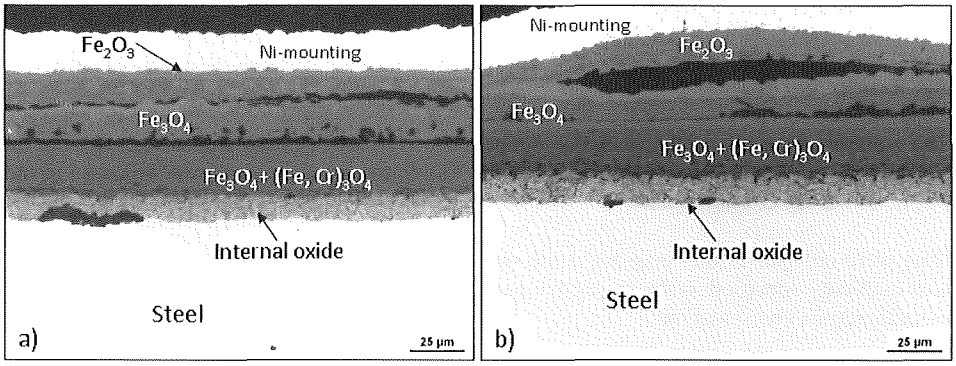

Figure 4. Oxide scale formed on T91 during exposure for 3000 h in Ar-50%H_2O at 550°C showing formation of hematite on top of the outer magnetite layer.

On the basis of the described mechanisms of void/gap formation, it can generally be said that the crack initiation/propagation modes occurring can result in three different types of scale spallation; that is, spalling occurring in the outer magnetite layer (Fig. 3b); near the interface between the oxide and the alloy or the internal oxidation zone; or at the interface between inner and outer scale.

3. Evaluation of literature data on steamside oxidation

3.1. Encountered difficulties

The compilation of steam oxidation data of various types of steels from numerous sources presents a number of pitfalls which may lead to erroneous conclusions of the data in respect to reproducibility, materials ranking and long term behaviour.

First, comparison of data is sometimes hampered because of the use of not well-defined parabolic oxidation rate constants. Also, the method for estimation of the commonly used parabolic oxidation rate constant is frequently not well defined. Additionally, hardly any reliable experimental studies are available in which the oxidation behaviour under conditions which prevail in most laboratory tests are systematically compared with parameter variations relevant to plant exposures. Whereas the effect of gas flow rate has systematically been studied [18], hardly any reliable data on the effect of temperature gradient and steam pressure are available, the results of high pressure tests in most cases having been affected by the use of low gas flow rates.

A special difficulty in evaluation of martensitic 9-12%Cr steels is given by the fact that this type of steels should be considered as "borderline alloys" between formation of a protective chromia base scale and poorly protective iron base oxides [19]. This has as a result that only minor specimen/component changes such as surface treatments and changes in concentrations in minor elements may result in substantial differences in oxidation rates. This will result in an intrinsic "scatter" of data if a large number of batches of a given material are considered. These differences between batches of a given material will be even more pronounced for martensitic 12% Cr than for 9% Cr steels [19].

3.2. Results and discussion

The number of papers on the oxidation behaviour of P91 and P92 are numerous, whereas on VM12 only very little information is available. The following procedure was followed in the evaluation of the oxidation data.

Data were only taken into account if the way in which the oxidation rates were determined was explicitly specified in the respective papers and if the scale formation was illustrated by metallographic cross-sections.

The data relate to total scale thickness (x), given by the following equation:

$$x^2 = k_p \cdot t$$

The final aim of the evaluation was to present for the three materials Arrhenius plots showing log k_p as a function of reciprocal temperature. Therefore, first the data points at the most frequently used test temperatures, 550, 600 and 650°C, were summarized in graphs showing scale thickness as function of time. When oxidation rate curves were available in respective papers, only the kp-value derived form the longest test time was plotted in the graph. From these scale thickness versus time plots a maximum and minimum value of kp at the respective temperature was derived. These values were then summarized in the Arrhenius plots (Fig. 5). The calculated activation energy for T91 is between 170 and 185 kJ/mol and for T92 between 163 and 170 kJ/mol.

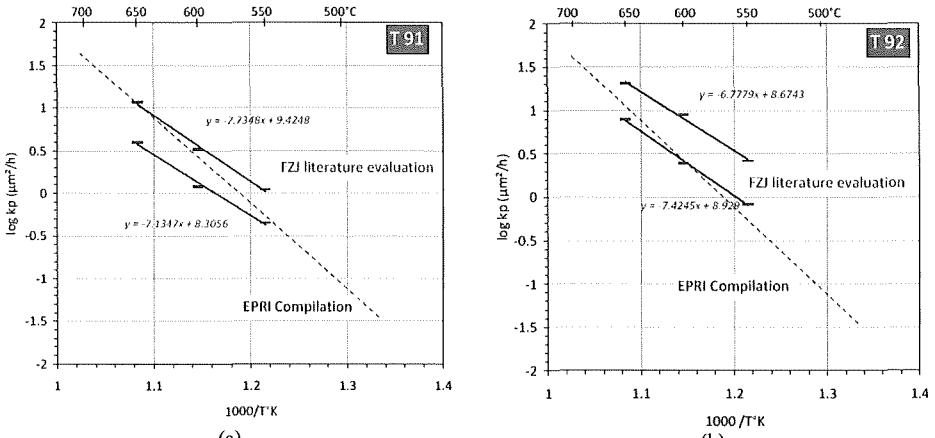

Figure 5. Summary of scale growth kinetics (total scale thickness) for P/T91 (a) and P/T92 (b) compared to EPRI compilation line for T9 type steel [20].

Based on the previous sections it is obvious, that the oxidation behaviour of P91 and P92, respectively, cannot be described by a single line in the respective Arrhenius plots. It has to be accepted that e.g. because of batch to batch variations (Fig. 6), effect of surface treatment, etc., the behaviour at a given temperature has to be described by a maximum and a minimum kp-value. The graphs show, that for both materials the temperature dependence can with reasonable accuracy be described by using a single activation energy for each material, although the total data evaluation gives some indication that near the maximum temperature of 650°C the activation energy is smaller than that at lower temperatures.

The lower activation energy at higher temperatures is a result of a fundamental change in morphology of the inner oxide scale. At lower temperatures (e.g. 550°C) the chromium present in the scale is hardly enriched compared to its initial content in the alloy, because of the slow chromium diffusion in the steel matrix. This has as a result, that the oxidation rate of a 9% Cr steel such as P92 hardly differs from that of a low-Cr steel. Upon temperature increase to e.g. 650°C, substantial chromium enrichment in the inner scale occurs thereby improving the protectiveness of the scale. This has as a consequence that the growth rate

increase upon increasing temperature is smaller than one would expect on the basis of the low temperature data. The increased incorporation of Cr into the oxide scale upon temperature increase is even more pronounced at around 700°C with the result that frequently actually lower oxidation rates are observed than at T ≤ 650°C. This so called "bell-shape temperature dependence" can already be observed at lower temperature for martensitic 12%Cr steels, like VM12. When specimens of one VM12-batch with the same surface treatment (e.g. 1200 grit surface finish) are being compared, the decrease of the oxidation rate with increasing temperature may already occur at 650°C. This leads to the interesting, and perhaps surprising result that for a given surface condition the oxidation rate at 600°C may, depending on the actually prevailing batch be smaller than that at 550°C.

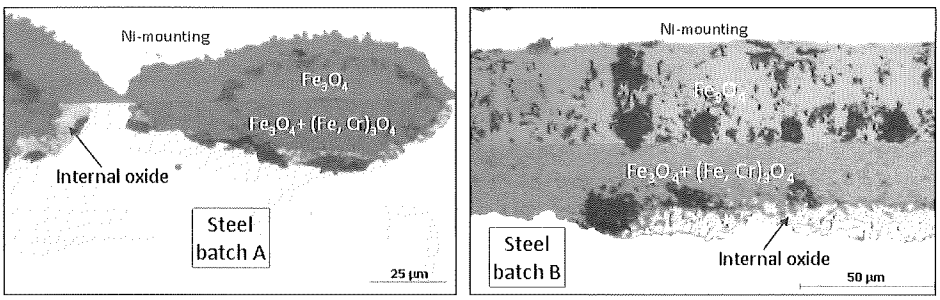

Figure 6. Cross sections of oxide scales on P91 after oxidation for 1000 h at 600°C in Ar-50%H_2O showing typical example of oxide scale formation on different batches of the same material.

The exact temperature dependence of the oxidation behaviour of VM12 was found to be extremely sensitive to the exact alloy composition variation and the surface treatment (Fig. 7). Due to this large data scatter (Fig. 8) and the limited amount of available literature data, it seemed not useful to construct an Arrhenius plot summarizing the data for VM12.

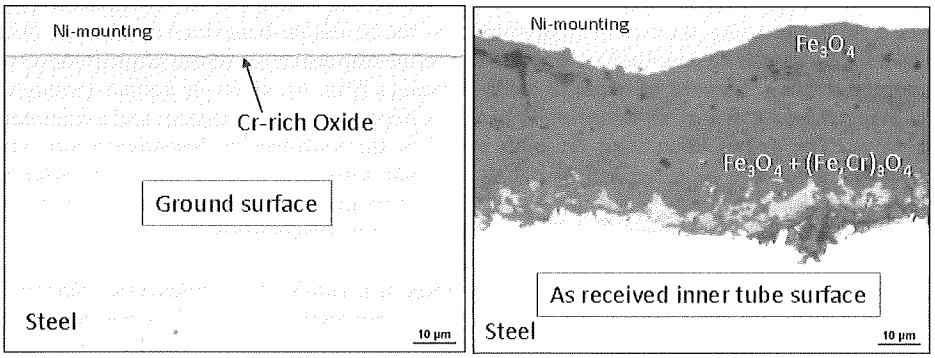

Figure 7. Cross sections of oxide scales on VM12 after oxidation for 1000 h at 600°C in Ar-50%H_2O showing example of effect of surface treatment on oxide scale formation.

An interesting observation is, that the activation energy for the estimated oxidation rates of T/P91 and T/P92 between 550 and 650°C in the present study is smaller than that given by the dashed lines in Figure 5, derived from an earlier investigation [20]. A possible explanation for this difference might be that at the time when the data compilation in reference [20] was made, too few results from lab and plant tests were available to allow a reliable data evaluation in a large temperature range. A second reason might be derived from the considerations above. Laboratory data obtained in a large temperature range on a single batch of material indicated that the oxidation rates of the martensitic 9-12%Cr steels cannot be described by a single activation energy. This would mean that the data in the temperature range 500 - 550°C would exhibit an activation energy similar to that given by the evaluation in reference [20] i.e. higher than that found in the present evaluation for the temperature range 550-650°C.

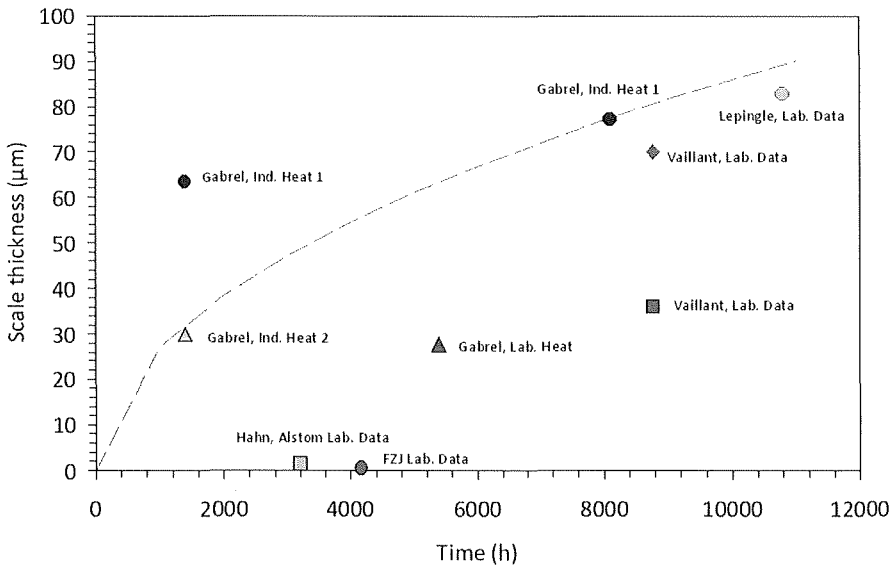

Figure 8. Various literature data for steel VM12 at 650°C during oxidation in water vapour containing gases, showing large variation in results.

4. Conclusions

The present evaluation of the oxidation behaviour of the martensitic steels P/T91, P/T92 and VM12 has shown that these steels exhibit in respect to the oxide scale formation a number of similarities, but also a number of fundamental differences compared to oxidation of low Cr steels such as P22. The major difference is that, unlike P22, the 9-12%Cr steels exhibit in the temperature range 550 - 650°C a fundamental difference in oxidation behavior in steam compared to that in air or other oxygen-rich gases with low water vapour contents. In the latter environments the mentioned martensitic steels tend, unlike P22, to form Cr-rich surface oxide scales, which provide excellent protection to the materials even during very long term

exposure. However, in steam the oxide scales tend to consist of multiphase mixtures which mainly consist of Fe-base oxides (magnetite and hematite) in combination with Fe/Cr spinel. The materials (especially P/T91 and P/T92) can be considered as "borderline alloys" between protective and non-protective behaviour exhibiting steam oxidation rates which are not substantially lower than those observed for low Cr steels such as P22 at temperatures beneath approximately 600°C. This has as an important consequence that materials selection for steam power plant application on the basis of air oxidation data may lead to erroneous results in respect to estimation of long term behaviour and even in respect to ranking of materials.

At higher oxidation temperatures the boundary between Fe-base oxide formation and protective chromia base scale formation tends to shift to lower Cr contents with as a result that the oxidation rates of P/T91, P/T92 and especially VM12 may even decrease with increasing temperature. The critical chromium content at which a shift from mainly Fe-oxide to mainly chromium oxide formation occurs not only depends on temperature, but also on e.g. minor alloying additions, surface treatment and component roughness. This has as a consequence that for a given martensitic steel a substantial variation in oxidation rates may occur considering the limits of alloy composition within the given specification of the material and the different surface treatment given to different component shapes commonly being used. Consequently, it is not possible to exactly predict oxidation kinetics, commonly characterized by the logarithm of the parabolic rate constant as function of the reciprocal temperature. Rather, an unavoidable "scatter band" exists whereby the upper limit for a given time and temperature will predict a scale thickness which may be up to a factor two larger than that given by the lower limit. This "batch-to-batch variation" in oxidation behaviour has as a result that the common practice used to determine service temperatures of tubes made of low Cr steels on the basis of measured oxide layer thicknesses after a given service time, has to be used with some care for the 9 - 12%Cr martensitic steels.

5. References

1. R. Viswanathan, J. Sarver, J.M. Tanzosh, *Journal of Materials Engineering and Performance*, (2006), **15**(3), p. 255-274
2. N. Birks, G.H. Meier, F.S. Pettit, *Introduction to the High Temperature Oxidation of Metals*, Cambridge University Press, UK (2006)
3. J. Ehlers, D.J. Young, E.J. Smaardijk, A.K. Tyagi, H.J. Penkalla, L. Singheiser, W.J. Quadakkers, *Corrosion Science*, (2006), **48**, p. 3428–3454
4. I. Armitt, D.P. Holmes, *The spalling of steam grown oxide from superheater and reheater tube steels*, Technical Planning Study 76-655, Final Report, EPRI, USA (1978)
5. M. Schütze, D. Renusch, M. Schorr, *Materials at High Temperatures*, (2005), **22**(1/2), p. 113-120
6. L. Mikkelsen, S. Linderoth, *Materials Science and Engineering A*, (2003), **361**(1-2), p. 198-212
7. C.T. Fujii, R.A. Meussner, *Journal of the Electrochemical Society*, (1964), **111**(11), p. 1215-1221
8. J. Żurek, M. Michalik, F. Schmitz, T.-U. Kern, L. Singheiser, W.J. Quadakkers, *Oxidation of Metals*, (2005), **63**(5/6), p. 401-422

9. J. Ehlers, W.J. Quadakkers, Report Forschungszentrum Jülich, Jül-3883, ISSN 0944-2952, (2001)
10. P. Mayer, A.V. Manolescu, High Temperature Corrosion, R.A. Rapp (ed), National Association of Corrosion Engineers, 1983, p. 368-379
11. M. Thiele, H. Teichmann, W. Schwarz, W.J. Quadakkers, *VGB Kraftwerkstechnik*, (1997), **2/97**, p. 129
12. W.J. Quadakkers, P.J. Ennis, J. Żurek, M. Michalik, *Materials at High Temperatures*, (2004), **22**(1/2), p. 37-47
13. W. Quadakkers, J. Żurek, M. Hänsel, *JOM Journal of the Minerals, Metals and Materials Society*, (2009), **61**(7), p. 44-50
14. M. Ueda, M. Nanko, K. Kawamura, T. Maruyama, *Materials at High Temperatures*, (2003), **20**(2), p. 109
15. Y. Ikeda, K. Nii, *Transactions of National Research Institute for Metals*, (1984), **26**(1), p. 52-62
16. R.J. Ehlers, P.J. Ennis, L. Singheiser, W.J. Quadakkers, T. Link, EFC Workshop 2001, M. Schütze, W.J. Quadakkers, J.R. Nicholls (ed), The European Federation of Corrosion Publications, Paper 12, 2001, ISSN 1354-5116, **34**, p. 178-193
17. N. Nishimura, N. Komai, Y. Hirayama, F. Masuyama, *Materials at High Temperatures*, (2005), **22**(1/2), p. 3-10
18. J. Żurek, M. Michalik, L. Singheiser, W.J. Quadakkers, *Materials Science Forum*, (2006), **522-523**, p. 155-162
19. W.J. Quadakkers, J. Zurek, *Oxidation in Steam and Steam/Hydrogen Environments*, Shreir's Corrosion, ed. T. Richardson, Vol. 1, Oxford, Elsevier (2010)
20. I.G. Wright, M. Schutze, P.F. Tortorelli, R.B. Dooley, *Materials at High Temperatures*, (2007), **24**, p. 265-274

9th Liege Conference : Materials for Advanced Power Engineering 2010
edited by J. Lecomte-Beckers, Q. Contrepois, T. Beck and B. Kuhn.

MODELLING FIRESIDE CORROSION OF HEAT EXCHANGERS IN CO-FIRED PULVERISED FUEL POWER SYSTEMS

N J Simms# and A T Fry*

#Energy Technology Centre, Cranfield University, Cranfield, MK43 0AL, UK
*National Physical Laboratory, Teddington, Middlesex, TW11 0LW, UK

Abstract

As a result of concerns about the effects of CO_2 emissions on the global environment, there is increasing pressure to reduce such emissions from power generation systems. The use of biomass co-firing with coal in conventional pulverised fuel power stations has provided the most immediate route to introduce a class of fuel that is regarded as both sustainable and carbon neutral. In the future it is anticipated that increased levels of biomass will need to be used in such systems to achieve the desired CO_2 emission targets. However there are concerns over the risk of fireside corrosion damage to the various heat exchangers and boiler walls used in such systems. Future pulverised fuel power systems will need to be designed to cope with the effects of using a wide range of coal-biomass mixes. However, such systems will also need to use much higher heat exchanger operating temperatures to increase their conversion efficiencies and counter the effects of the CO_2 capture technologies that will need to be used in them. Higher operating temperatures will also increase the risk of fireside corrosion damage to the critical heat exchangers.

This paper reports work that has been carried out to develop quantitative corrosion models for heat exchangers in pulverised fuel power systems. These developments have been particularly targeted at producing models that enable the evaluation of the effects of using different coal-biomass mixtures and of increasing heat exchanger operating conditions. Models have been produced that have been targeted at operating conditions and materials used in (a) superheaters/reheaters and (b) waterwalls. Data used in the development of these models has been produced from full scale and pilot scale plants in the UK using a wide range of coal and biomass mixtures, as well as from carefully targeted series of laboratory corrosion tests. Mechanistic and neural network based models have been investigated during this development process to identify key variables (e.g. fuel composition, fuel/oxidant ratio, local gas temperatures, metal temperature, local gas compositions, deposit composition, deposition flux, material composition, etc) for the different types of fireside corrosion and to quantify sensitivity of the corrosion damage to changes in these factors. Models based on both approaches have been successfully developed and are currently being evaluated using an increasingly wide ranging fireside corrosion database.

Keywords: modelling; fireside corrosion; coal; biomass; co-firing; heat exchangers

1. Introduction

Two key driving forces in the development of the power generation industries around the world are the need for increasing amounts of electricity and widespread concerns about the effects of emissions of greenhouse gases on the global environment. Many predictions for the worldwide growths in energy and electricity demands are available, with a range of different assumptions; e.g., the latest International Energy Authority (IEA) predictions indicate an ~40% rise in primary energy demand by 2030 [1]. Concerns about the emissions of CO_2, and other greenhouse gases (GHGs), into the atmosphere have been growing during the last two decades; as a result there have been increasing efforts to limit the amount of CO_2 emitted into the atmosphere. The Kyoto Protocol committed many countries in the world to reduce their GHG emissions by 2008-2012 compared to 1990 levels, with the EU committed to an 8% reduction by 2008-2012 [2]. It is anticipated that follow-on treaties will agree higher levels of reductions. National governments are also continuing to develop policies to limit greenhouse gas emissions; for example, the latest UK government target is for a 60% reduction in CO_2

emissions by 2050 [3]. There are many sources of GHG emissions, but in the UK (and other developed countries) where a centralised power generation system has developed over a long period, large power stations represent major, easily identifiable point sources for CO_2 emissions. These therefore provide a focus for efforts in reducing CO_2 emissions.

For power generation systems, there are several potential routes to reduce CO_2 emissions (all of which have both advantages and disadvantages) that are being developed, including [4]:

- Increase in generating efficiencies; e.g. by increasing steam temperatures/pressures
- Fuel switching; e.g. by increasing the proportion of biomass mixed with coal
- Carbon capture and storage (CCS)
- Increasing the proportion of electricity generated by nuclear or renewable sources; e.g. wind, wave, solar power

New solid fuel combustion systems can incorporate the first three of these routes by using higher steam temperatures/pressures (e.g. targets of 650, 700 and 760°C set by different organisations [4]), higher levels of biomass (up to ~30%) mixed with coal and include a post combustion CCS system. However, as a result of the changes to the fuels and plant operating conditions, there will be significant risks associated with increased deposition and corrosion on the fireside surfaces of critical heat exchangers in these systems. To counter these risks, and so avoid lower levels of combustion plant reliability, it is necessary to have better understanding of the various fireside corrosion processes and their relationships to fuel compositions and component operating conditions. In any location in a coal fired boiler, it is possible to have several competing corrosion processes each of which can give different forms of damage (e.g. general loss of section, pitting, intergranular attack, etc.), all of which will act to reduce the load bearing capability of the material and lead to unrecoverable damage or even in-service failure. Currently, some plant designers/owners have simple models for corrosion that are based on mathematical correlations of corrosion rates and operational variables such as temperatures (gas & metal), simple gas properties (e.g. CO content), and fuel properties (e.g. Cl content). However, these are based on experience using limited ranges of fuel(s) and operating condition(s). The ability to model such complex conditions for a wide range of fuels and operating conditions, and so be able to predict the rate of metal loss for fuel flexible advanced power plants would clearly be a powerful tool for plant designers and users.

This paper reports work that is being carried out to develop such quantitative corrosion models for heat exchangers in pulverised fuel power systems. These developments are targeted at producing models that enable the evaluation of the effects of using different coal-biomass mixtures and of increasing heat exchanger operating conditions. Models have been produced that have been targeted at operating conditions and materials used in (a) superheaters/reheaters and (b) waterwalls. Data used in the development of these models has been produced from full scale and pilot scale plants in the UK using a wide range of coal and biomass mixtures, as well as from carefully targeted series of laboratory corrosion tests.

2. Fuels

An increasingly wide range of coal and biomass fuels are being considered for use in power generation systems (both alone and in different mixes). In assessing these various fuels, it is necessary to consider a range of factors from fuel storage, preparation and handling through to combustion behaviour and the fuel compositions / operating conditions that can cause

deposition and corrosion issues. Traditionally locally sourced coals have been used for power generation systems. However, as a result of a wide variety of factors, including national emissions regulations (especially relating to SOx emissions) and fuel policies, there is now a large market in world traded coals. Therefore, the cheapest coals for a particular power station are often used after taking into account transportation and gas cleaning costs, etc (and depending on local and national regulations). Thus, in the UK, power stations with port facilities (or good rail links to suitable ports) are likely to use lower sulphur imported coals. Such traded coals often also have lower chlorine contents compared to many UK coals (Table 1). Around the world, there is in fact a wide variation in the types and compositions of coal, in terms of both the frequently reported main elements and the mineral contents. This variation can give rise to a wide range of behaviours of the fuels in terms of deposition, erosion and corrosion that they can produce in various types of combustion and gasification systems.

Table 1 Examples of coal, biomass and waste compositions

		Coals		Biomass			
Parameter	Unit	Daw Mill	El Cerrajon	Miscanthus	Cereal Co-Product (CCP)	Wheat straw	Willow
Moisture	% wt ar	4.6	7	10.8	8.1	25	15
Ash	% wt dry	4.4	9.6	5.1	4.6	5.0	2.0
CV (gross)	MJ/kg daf	34.3	33.4	20.5	20.2	19.8	20.3
C	% wt daf	81.3	78.7	49.6	49	49	49
H		4.8	5.2	6.4	6.2	6.3	6.2
O		11.5	13.7	43.8	44	43	44
N		1.28	1.49	0.52	0.5	0.5	0.5
S		1.4	0.68	0.12	0.18	0.1	0.05
Cl		0.22	0.02	0.10	0.19	0.4	0.03

(ar = as-received; daf = dry ash free; wt = weight)

A wide range of biomass fuels are being considered / used in UK power systems, e.g. [5]:

- Specifically cultivated biomass ('energy crops'); e.g. coppiced willow and miscanthus
- Waste biomass, e.g.; various straws, wood waste / forest residues
- World traded biomass products, e.g.; palm nut residues, olive residues, pelletised wood, almond waste, cereal co-product (CCP)

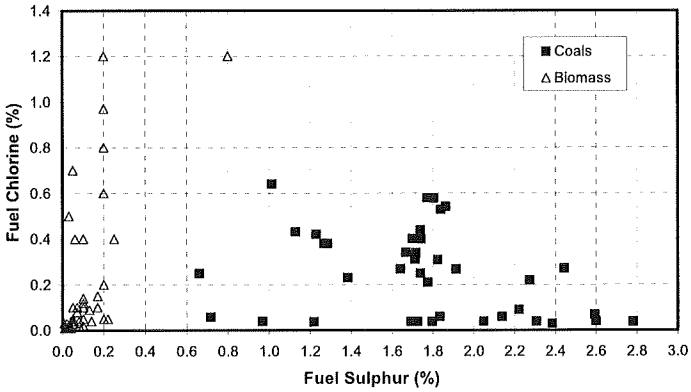

Figure 1 Variation of fuel chlorine and sulphur contents for a range of biomass and coals

These different types of biomass inevitably have a range of different properties, compositions (Table 1) and costs that need to be considered during their evaluation as potential fuels. The faster growing biomass generally tends to have high chlorine (and potassium) contents than slower growing biomass. For many biomass, the timing of harvesting, harvesting conditions

and post-harvest treatment / storage can result in a wide variation of fuel compositions. There are CEN standards for biomass fuels that give examples of their expected compositions and an indication of the variability that can be anticipated [6]. In general biomass contains lower levels of sulphur compared to coal so co-firing of coal with biomass results in reductions in the combustion gas sulphur dioxide (SO_2) levels. Biomass can potentially have high chlorine contents, up to 2.5 weight % (dry ash free basis). However, the variability of both the coal and biomass fuels means that fuel-specific assessments need to be carried. Figure 1 illustrates the ranges of chlorine and sulphur contents of different potential coal and biomass fuels.

3. Superheater / Reheater Corrosion

3.1 Exposure environments

The exposure environments of the superheaters / reheaters are dependant on the plant design, operating conditions and fuel compositions. Combustion of the pulverised fuels (coal and biomass) in air will result in a gas stream containing a complex mixture of gaseous, vapour phase and ash particles. By the time this gas stream reaches the location of these heat exchangers, the gas composition will typically be N_2 - ~11-13 % (by volume) CO_2 - ~ 8-12 % H_2O - ~3-5 % O_2 - ~1 % Ar with lower levels of SO_X (up to ~2000 vpm) , HCl (up to ~500 vpm), NO_X, CO, etc. The levels of SOx and HCl are very sensitive to the sulphur and chlorine contents of the fuel; the CO_2, steam and O_2 levels also vary with fuel composition, fuel/air ratios, etc. In addition, this combustion gas stream also contains a significant loading of fly ash particles and vapour phase species (e.g. alkali hydroxides, chlorides and sulphates). Depending on the gas temperature, these vapour phase species may partially condense homogeneously to form aerosols or heterogeneously onto fly ash particles. As this combustion gas stream passes around the heat exchanger tubes, deposits may be formed on them via a number of distinct mechanisms (some of which also depend on the surface temperatures of the tubes): direct inertial impaction (larger particles), eddy impaction (smaller particles), thermophoresis (very small particles), vapour condensation/reaction (vapour phase species), etc [e.g. 7]. This is illustrated in Figure 2.

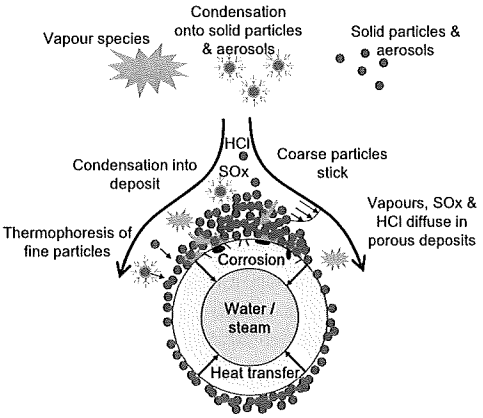

Figure 2 Schematic representation of exposure environment around a single superheater / reheater tube

3.2 Corrosion data from laboratory and plant exposures

The fireside corrosion data that is required for the development of appropriate models is needed in the form of metal loss on a particular alloy as a function of specific (and

appropriate) exposure conditions. Data on fireside corrosion can be generated in laboratory exposures under well controlled exposure conditions. Examples of such data sets have only occasionally been reported in the literature but have been the subject of several recent studies: COST538/522 [8], UK-US [9], etc, in which data have been produced from tests carried out for 1000 hour periods. For the purposes of this work, these datasets have been combined and augmented with additional data that is being generated as a result of on-going research projects. After consideration of the available data on fireside corrosion mechanisms and the parameters that are known (or are currently believed to be most likely) to be controlling the degradation, the combined datasets have been reanalysed to fit an equation of the form:

$$\text{Corrosion rate} = \exp((a/T_m)+b+c(HCl)+d(SOx)+ e(K+Na)_{\%\,dep}+f(S_{\%\,dep})+g(Cl_{\%\,dep})) \quad \text{(eqn 1)}$$

Where a – g are constants, T_m = metal temperature, HCl is the concentration of HCl in the flue gas stream (in vpm), SO_X is the concentration of HCl in the flue gas stream (in vpm), and $(K+Na)_{\%\,dep}$, $S_{\%\,dep}$ and $Cl_{\%\,dep}$ are the concentrations of Na+K, S and Cl (respectively) in the various deposits used in these tests. The results of this analysis for four candidate heat exchanger materials are summarized in Figure 3.

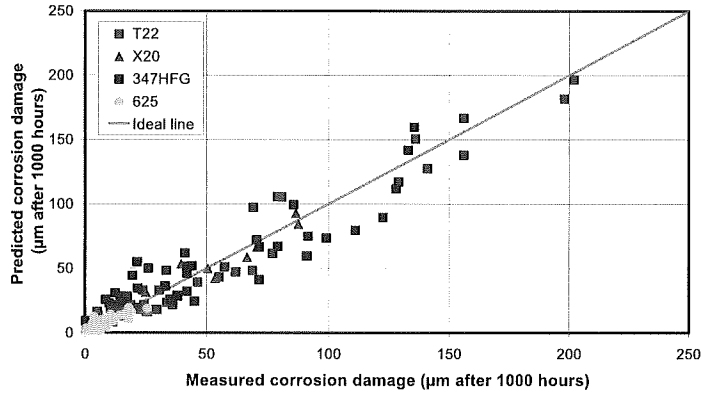

Figure 3 Comparison between corrosion damaged measured in laboratory tests and corrosion model predictions for four candidate heat exchanger materials

Comprehensive datasets of fireside corrosion data from pilot plant or plant studies are not frequently reported. There is a particular problem with carrying out such tests in pilot plants as the damage rates in coal fired systems have traditionally been low, so short test runs do not produce enough damage for it to be accurately measured, especially for the best candidate materials, and long test runs are prohibitively expense to carry out. However, some data of this type have been reported.

Power plants can be used to generate fireside corrosion data in three ways: (a) exposing air cooled probes of materials samples; (b) installing steam cooled loops of materials; and (c) monitoring metal loss of operating heat exchangers. All these activities can be carried out for long periods of time (thousands of hours). Such studies obviously use the most realistic gas conditions, but deposit formation also depends on the operating temperatures of the samples, and the corrosion data generated depends on the resolution of the measurement techniques that can be used (much better for situation (a) than (c)). In addition uncertainties arise from variations in fuel supplies over long periods of time: for example the use of different coals and biomass, as well as the natural variation of these fuels. One of the most comprehensive datasets currently available was generated by the UK's Central Electricity Generating Board in the 1980s using power stations mostly operating under baseload and using locally supplied

coal. A model for the performance of austenitic stainless steel that was produced from these data at the time was known as the modified PE8 equation [10]:

$$\text{Corrosion rate} = LE.A.(T_g)^B.(T_m\text{-}C)^D.(Cl_{\%\ fuel}\text{-}E) \quad \text{(eqn 2)}$$

Where A – E are constants, LE represents the leading edge of a tube bundle, Tg is the average gas temperature and Tm is an average metal temperature and $Cl_{\%\ fuel}$ represents the average fuel composition. These data have now been reanalyzed (Figure 4) in the same style as for the laboratory datasets the resulting equation has the form (with r – v being constants):

$$\text{Corrosion rate} = \exp((r/T_m) + s.(Cr_{\%\ alloy}) + t.(T_g\text{-}T_m) + u + v.(Cl_{\%\ fuel})) \quad \text{(eqn 3)}$$

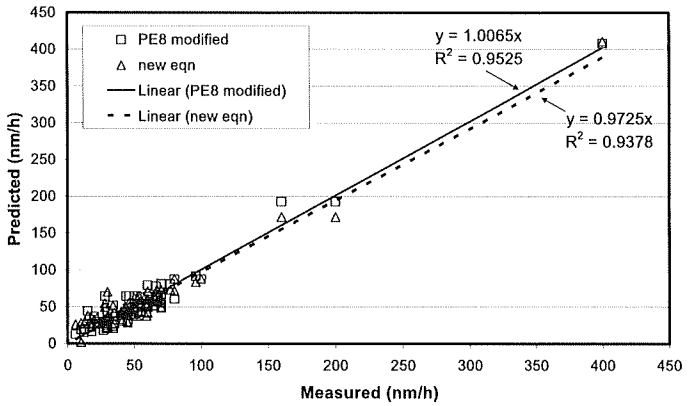

Figure 4 Comparison between measured and predicted corrosion damage for austenitic steels in UK power plants

The next stage of development of these models that is currently being carried out is to link the plant fuel compositions/operating conditions (as used in equation 3) to the gas / deposit compositions (as used in equation 1). This being carried out using mechanistically based combustion/deposition modelling (based on [7]); with pilot plant and plant exposures being carried out in parallel to generate the data necessary to validate such models.

4. Water Wall Corrosion

Predictive equations have been developed for corrosion of furnace water wall environments [11], with and without the presence of Cl. Under reducing conditions (O_2 < 0.5%, CO > 2%) in the absence of Cl (i.e. < 0.05%), the corrosion mechanism shifts progressively from oxidation towards sulphidation as the CO content of the flue gas increased, and the O_2 content declines. Whilst these models provided a reasonable approximation of the corrosion rate, there remains a requirement to develop new models that could accommodate a wider range of conditions such as those discussed in section 2. With the number and range of possible variables increasing an approach using neural networks has been adopted to model material response at the water wall. Neural network modelling is a well-established technique that has been used for a variety of alloy design and corrosion issues [12-17]. This form of modelling can be used in two main ways; using supervised or unsupervised training. The fully supervised network will use all the data inputs presented to the network and build weighted neurons to accommodate theses inputs, while the unsupervised method will discard inputs that do not have a large impact on the model, thus reducing the data required by the end user. For the purposes of this model a supervised network has been constructed with the data inputs being filtered manually to reduce the final number of inputs required.

4.1 Neural Network Model Development

To generate a reliable neural network model the dataset used to train the network should be as large as possible, the size needed directly relates to the number of input parameters, and it should contain reliable and complete data. In order to achieve this, data generated at E.ON Engineering using a pilot plant burner rig was collated for a range of materials commonly used in water walls; these are presented in Table 2. In total 190 individual data points from separate specimens was collated for low alloy materials under simulated furnace wall conditions. The data came from exposure tests of 40 to 50 hour duration covering a temperature range 350 to 650°C. During the exposures the oxygen and carbon monoxide content of the gas was monitored, and the fuel analysis made available for modelling purposes.

Table 2 Composition of alloys used for modelling the corrosion rate of water walls

Alloy	Composition, wt% (Fe balance)															
	Al	C	Co	Cr	Cu	Mn	Mo	N	Nb	Ni	P	S	Si	V	W	B
15Mo3	0.023	0.160	-	-	0.15	0.68	0.27	0.0082	-	0.2	0.005	0.0090	0.21	0.1	-	-
E911	0.010	0.064	0.05	9.42	0.06	0.36	1.00	-	0.06	0.1	-	-	0.24	0.2	0.8	-
HCM12	-	0.100	-	12.20	-	0.51	1.00	-	0.05	-	0.027	0.0010	0.18	0.2	1	-
C Steel	-	0.130	-	0.02	0.01	0.71	0.02	-	-	-	0.012	0.0150	0.17	-	-	-
T23	0.002	0.060	-	2.14	-	0.28	0.08	0.0060	0.04	-	0.012	0.0010	0.23	0.2	1.5	0.0051
T91	-	-	-	9.15	-	0.67	1.41	-	0.25	-	-	-	0.48	0.3	0	-

Initially the neural network model was trained using the temperature, alloy composition and the percentage of time spent in reducing conditions. During the course of the training process the most dominant parameters were identified and ranked in order of importance, examination of this ranking allowed for the relevant importance of a number of parameters to be assessed, and either retained in the model or discarded. The model was initially trained to predict the corrosion rate; this was subsequently changed to metal loss in subsequent iterations since the time of the exposure was found to be a dominant parameter which when included improved the fit of the model. Further iterations were performed to evaluate the relative importance of additional parameters such as the heat flux across the specimen, thermal gradients, gas composition and fuel analysis. The iterations and the effect on the fit to the experimental data is summarised in Table 3.

Table 3 Effect on the model prediction with varying input parameters

Input Parameter										Model Fit, R^2
Time	Temperature.	Alloy Composition	Heat Flux	Fuel Cl, mean (%)	Fuel S, mean (%)	Gas O_2 (%)	Gas CO (%)	Thermal gradient	Fuel moisture (%)	
Y	Y	Y								0.56
Y	Y	Y	Y							0.70
Y	Y	Y	Y	Y	Y	Y	Y	Y		0.83
Y	Y	Y	Y	Y	Y	Y	Y	Y	Y	0.84
Y	Y	Y	Y	Y	Y	Y	Y		Y	0.91

Having established a broad envelope of input parameters that were found to be important to the predictive ability of the neural network model, further training was performed to identify the most important parameters within each category, for example which elements of the alloy composition were necessary and which were not. Figure 5 presents the results of this refinement, showing the goodness of fit value, R^2, as a function of input parameters. The original input parameters of the model, referred to as F30 in Figure 5 were; % time in reducing conditions, ash (%), moisture (%), Cl mean, S mean, CO (%), O_2 (%), W (wt%), Mo

(wt%), Fe (wt%), Cr (wt%), transmitted heat flux, mean metal temperature and the total exposure time. The relative effect on the model on removal of the various input parameters can be seen for predictions of the metal loss and corrosion rate in Figure 5. This illustrates the detrimental effect of removing time, temperature, and the various alloying additions. It also shows the improvement in the fit by removing unnecessary combinations, such as the ash, Fe, Mo time reducing combination.

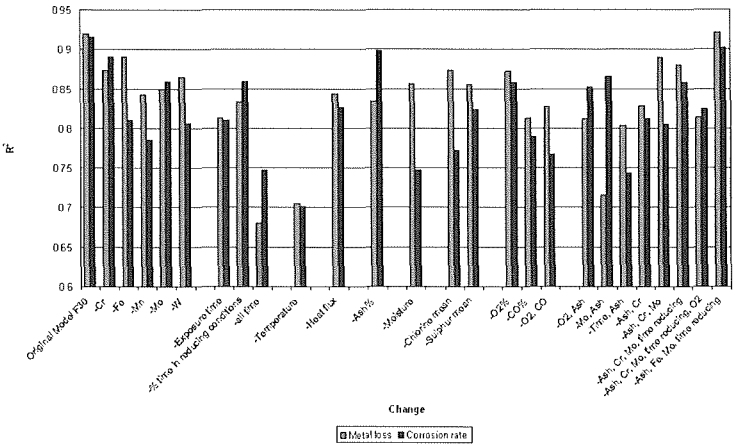

Figure 5 Results showing how the predicted metal loss and corrosion rate varies with changes to the input parameters used.

4.2 Results of the Neural Network Training

Using this type of iterative training a final combination of input parameters was reached, these being (in order of relative importance); CO (%), Cl (in gas %), W (wt%), mean metal temperature (°C), Mn (wt %), S (in gas %), exposure time, moisture (in fuel %), Cr (wt%), and transmitted heat flux. The selection of the more dominant factors relating to corrosion in boilers is supported by observations from literature [11,18]. The training of this final iteration of the low alloy furnace wall model was performed using 85% of the available data; the remaining 15% was used to test the neural network. The result of the training and testing are presented in Figures 6 and 7.

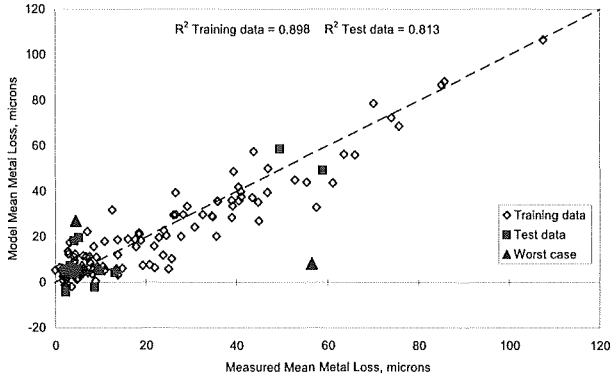

Figure 6 Predicted metal loss compared with actual metal loss showing the results from the training data and those from the test data.

Having trained the model, the final version was compiled so that it would run in an Excel spreadsheet. Tests on this neural network model have shown that it can be used to rank materials under identical exposure conditions, or it can be used to evaluate the effect of

changes in the exposure conditions for one particular material. These predictions are most reliable when the input parameter range is within that used to train the neural network, as extrapolation beyond these limits can give erroneous results. An example of this is shown in Figure 8 for T23 exposed to an atmosphere consisting of 0.72% CO, burning a fuel with mean sulphur and chlorine levels of 0.62 and 0.02% respectively, exposed for 50 hours. This figure shows that the predicted corrosion rate value obtained from such an exposure increases gradually with increasing temperature, until a temperature of 620°C is reached at which point the corrosion rate accelerates. Further experimental exposures are currently being carried out to generate data against which the neural network can be further validated.

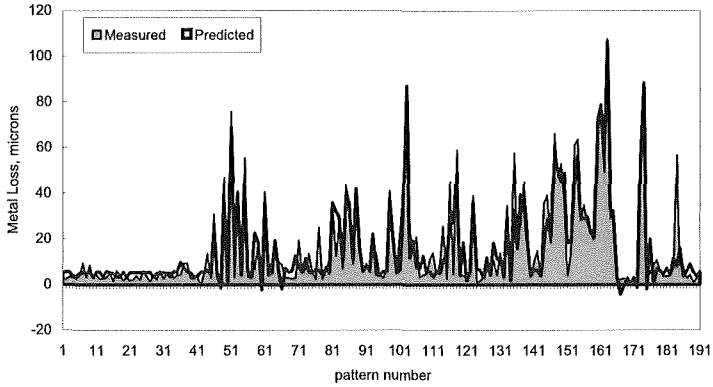

Figure 7
Plot of the actual metal loss values plotted with the predicted values showing that the neural network model follows the data trend..

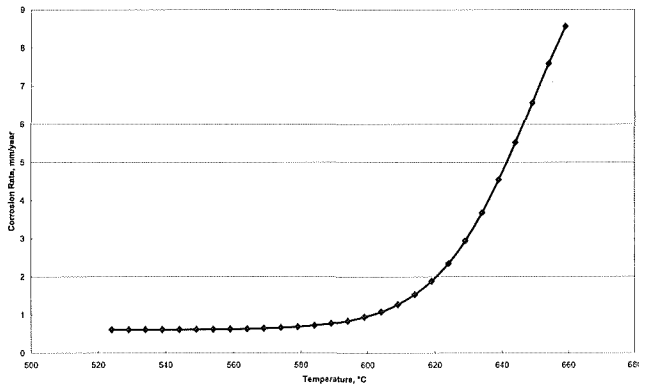

Figure 8
Predicted corrosion rate for T23 exposed over a range of temperatures to an atmosphere consisting of 0.72% CO, burning a fuel with mean sulphur and chlorine levels of 0.62 and 0.02%. respectively

5. Summary

The development of predictive models for the complex corrosion conditions expected on the fireside surfaces of heat exchangers in advanced power plants using a wide range of fuels and operating conditions would be a powerful tool for plant designers and users. This paper reports alternative approaches for the development of appropriate fireside corrosion models for the different combinations of fuels, materials and operating conditions. Mechanistic and neural network based models have been investigated during this development process to identify key variables (e.g. fuel composition, fuel/oxidant ratio, local gas temperatures, metal temperature, local gas compositions, deposit composition, deposition flux, material composition, etc) for the different types of fireside corrosion and to quantify sensitivity of the corrosion damage to changes in these factors. Initial models based on both mechanistic and

neural networks approaches have been successfully developed. These initial models are being refined with improved linkages with plant operating conditions and their performance is being evaluated using an increasingly wide ranging fireside corrosion database.

6. Acknowledgements

The research reported in this paper has been carried out as part of a UK Technology Strategy Board funded project 'Modelling Fireside Corrosion of Heat Exchanger Materials in Advanced Energy Systems' (H0639C), with the support of E.ON, RWE and Doosan Babcock.

7. References

[1] IEA World Energy Outlook (2009)
[2] P Dechamps, 'The EU Research Strategy Towards Zero Emission Fossil Fuel Power Plants', Materials for Power Engineering 2006', pp 25-36 (2006)
[3] 'Meeting the Energy Challenge' UK White Paper on Energy (UK Department of Trade and Industry, May 2007)
[4] N J Simms, P J Kilgallon & J E Oakey, 'Fireside issues in advance power generation Plant', *Parsons 2007: Power Generation in an Era of Climate Change*, 603-614 (2007)
[5] N J Simms, P J Kilgallon & J E Oakey, 'Degradation of heat exchanger materials under biomass co-firing conditions', *Mat. at High Temperatures*, 24 (4), pp 333-342 (2007)
[6] 'Solid recovered fuels – specifications and classes', DD CEN/TS 15359:2006
[7] J Tomeczek & K Wacławiak, 'Two-dimensional modelling of deposits formation on platen superheaters in pulverized coal boilers', *Fuel*, 88, 1466–1471 (2009)
[8] S.R.J. Saunders, N.J. Simms, S. Osgerby & J.E. Oakey, 'Degradation of Boiler and Heat Exchanger Materials: Data generation, Databases and Predictive Modelling', *Materials for Advanced Power Engineering 2002*, p80 (2002)
[9] B McGhee, 'US-UK Advanced Materials for Low Emission Power Plant: Boiler Corrosion/Monitoring/Co-Firing', US DoE 23rd Conf. Fossil Energy Mat. (2009)
[10] P.J. James & L.W. Pinder, *Materials at High Temperature* 14, p117 (1997)
[11] A. Mehta, "Fireside Corrosion in Pulverized-Coal-fired Boilers, Effect of Coal Chlorine and Combustion Parameters", Final EPRI report 1001350 (2001)
[12] K L Cios, L Berke, A Vary & S Sharma, "Soft computing methods in the design of superalloys", NASA Tech Memo 106888 (1996)
[13] E M Rosen & D C Silverman, 'Corrosion prediction from polarisation scans using artificial neural network integrated with expert system', *Corrosion*, pp734-745 (1992)
[14] J Cai, R A Cottis & S B Lyon, "Phenomenological modelling of atmospheric corrosion using an artificial neural network", *Corrosion Science*, 41 pp2001-2030 (1999)
[15] M Urquidi-Macdonald & D Macdonald, 'Performance comparison between a statistical model, a deterministic model, and an artificial neural network model for prediction damage from pitting corrosion', *J. Res. Nat. Inst. Stand. & Tech.*, 99, pp495-504 (1994)
[16] H M G Smets & W F L Bogaerts, 'SCC Analysis of Austenitic Stainless Steels in Chloride-Bearing Water by Neural Network Techniques', *Corrosion*, pp618-623 (1992)
[17] M Urquidi-Macdonald and P Egan, "Validation and Extrapolation of Electrochemical Impedance Spectroscopy Data", *Corrosion Reviews*, 15, pp 169-194 (1997).
[18] A. T. Fry, S. Osgerby, 'Oxide Scale Growth and Spallation in Steam Environments – An Assessment of Different Modelling Approaches', *Materials for Advanced Power Engineering 2006*, pp. 1469-1478 (2006)

9th Liege Conference : Materials for Advanced Power Engineering 2010
edited by J. Lecomte-Beckers, Q. Contrepois, T. Beck and B. Kuhn.

RESISTANCE OF VARIOUS COATINGS TO HIGH TEMPERATURE CORROSION IN HCl AND SO_2 CONTAINING ENVIRONMENTS

Dr. Josef Cizner, Jakub Mlnarik, Jan Hruska
Laboratory of high temperature corrosion, SVUM a.s., Czech Republic

Abstract

For high efficiency of the steam turbines it is necessary to produce steam of temperature at least 400°C, which in conjunction with specific composition of combustion gases causes fireside corrosion problems. The combustion gases contain aggressive compounds like HCl and SO_2 and some other elements which can form deposits on heat exchanging surfaces e.g. calcium, potassium salts etc. Using of high-alloy steels or nickel-based alloys is very costly and also these materials could have lower thermal conductivity. A cheaper solution is to produce a coating on low (medium)-alloy steel. Common heat-resistant steels show very short lifetime under these conditions. The solution is then to use the appropriate coatings. Some types of coatings can be applied even inside older boilers. In this work we tested many coatings composition (nickel-based, aluminum-based, etc. As well as with different processing method – arc sprayed coating, weld deposits, HVOF, etc.) on 16Mo3 steel. In particular their high temperature corrosion behaviour in model atmosphere containing SO_2 and HCl and also under deposit of fly ash was studied.

Keywords: hot corrosion, special coatings

1. Introduction

Electricity generation is a general trend in waste incineration plants (Waste to Energy). For effective electricity generation it is necessary to obtain steam at least 400 °C hot. The higher steam temperature, the higher efficiency of a turbine. Increasing temperatures of heat-exchanging surfaces results in reduction of lifetimes of the components (water-walls, superheaters, etc.).

In waste incineration plants there is very specific composition of combustion gases which causes big fireside corrosion problems. Especially it is presence of aggressive elements like chlorine and sulphur. Furthermore potassium, sodium, calcium and other alkali metals form salt deposit accelerating corrosion rate too. In addition in the waste incineration plants the chemical composition of combustion gases is very variable and can change quickly. Similar corrosion problems can be found in plants combusting biomass, especially rapidly growing biomass. The biomass contains large amount of chlorine too.

According to particular temperature of heat-exchanging surface and particular environment it is necessary to use suitable material with adequate corrosion resistance. These vary from low(medium)-alloyed ferritic and martensitic steels (T22, T23, P92, VM12) to high-alloyed austenitic steels (BGA4, SAN 25). For the most demanding places nickel alloys can be used (alloy 625).

Using of modern materials with the best corrosion resistance for construction of pipes in all cross-sections is very expensive. The next problem is related with a worse thermal conductivity of materials with the austenitic structure. Pipes made of such materials would give a worse heat transfer to the steam. A cheaper solution is to make some coating on a surface of cheap low(medium)-alloyed steel. Some types of coatings can be applied even in-situ an older boiler. One group is clad coatings usually made of the nickel alloys. A big advantage of these clad coatings is no porosity and very good mechanical properties. These coatings give good protection of base material and can have long life. Unfortunately these coatings are relatively expensive. Another group of coatings is represented by thermal

spraying technologies in many variants. Sprayed coatings are attractive for their cheapness and easy and fast application. The sprayed coatings are intensively studied nowadays.

2. Choice of suitable types of coatings

For coating it is possible to use a lot of materials and processing technologies. Suitable technologies for boiler tubes and water-walls are:

- clading via flame, electrodes, plasma, laser etc.
- arc sprayed coatings, flame sprayed coatings, plasma coatings, HVOF and next modifications (flame spraying followed by surface remelting)
- diffusion coatings (are intensively studied, but at the moment are not suitable for practical application)

2.1. Metal coatings

Previous experiments within programs COST 501 and 522 proved, that nickel alloy Inconel 625 is the most resistant. This alloy was used as reference for our experiments. Other acceptable materials for welding are for example nickel alloy Hastelloy C-22 and cobalt alloy Stellite 6. These materials were studied within our program. For our experiments we obtained samples from CESI Milano, coatings were performed by laser welding. Further we tested a number of other metal coatings as sprayed coatings. A special group of coatings are remelted coatings that were manufactured by company a Castolin.

2.2. Ceramic coatings with metallic bondcoats

In several applications (for example gas turbine blades) ceramic coatings proved to be useful. The ceramic layer should have a thermal barrier effect and not react with the environment. The ceramic layers have different thermal expansion than base steel and could crack and spall of. Therefore usually some bondcoat is applied. Very common for this purpose are metal alloys with an austenitic structure, which are ductile. For our testing several types of the ceramic flame sprayed layers were selected with several metallic bondcoats produced by arc sprayed.

2.3. Intermetalics

These materials are intensively studied nowadays for their suitable properties. Especially aluminides are expected to make highly protective layers. Alloys with aluminium content up to 5 wt. % and yttrium content are used for the gas turbine blades (NiCrAlY). We tested also many other aluminides within COST 536. All intermetalic coatings were applied via arc flame spraying, some of them via HVOF spraying.

3. Testing program

Long–term testing of selected coatings was performed in a special high temperature laboratory in SVUM. Test specimens covered with a particular coating in sample boats were placed into a special furnace with a gas tight reactor with a regulator. Testing environment was designed to simulate real conditions in a waste incineration plant. Except the testing

atmospheres containing HCl and SO_2 the specimens were under deposit. As the deposit we used real fly ash from a WIP Prague (Table 1), which is according to our experience more aggressive than synthetic deposit. The long term testing conditions are shown in a table 2.
During the exposures the samples–weight gains were measured. At temperature 600°C (rarely 500°C) the deposits partly melted and on a surface of some specimens formation of hard solid slags occurred. In this case the slags were mechanically and chemically removed and weight losses were assessed. In addition to the gravimetry, metallographic evaluation of coatings after exposition was carried out. In some cases microanalysis(by WDX) was performed too.

Table 1: Chemical composition of fly ash from WIP Prague

Element content [wt. %]										
Na	Al	Si	S	Cl	K	Ca	Ti	Fe	Zn	Pb
1.80	1.60	1.65	1.30	3.90	0.36	7.80	0.30	0.61	1.20	0.57

Table 2: Conditions of laboratory tests

Test environment [wt. %]:	N_2+9O_2+0.2HCl+0.08SO_2
Deposit:	Fly ash from WIP Prague
Test temperatures:	400, 500, 600°C
Total exposure time:	max. 2000 h
Time interval between sample removals for corrosion evaluation:	50, 100, 200, 500, 1000, 2000 h
Gas flow rate:	250 ml/min.
Max. number of samples in furnace:	100

Our testing program had three stages. At each stage there a particular group of coatings was tested.
The first set of samples consists of three laser cladded coatings from CESI Milano, five HVOF metal sprayed coatings from Silesian Technical University – Poland and two metal-ceramic composite coating from the Czech Republic – Vitkovice ENVI. Both Metal-ceramic coatings have NiCrAlY alloy as a bond coat.
After finishing the first set tests the second set of samples was prepared. Number of metal-ceramic coatings was extended, also double-layered metal sprayed coatings and special sprayed coatings with a remelted surface were added. As a reference we used an Inconel 625 HVOF coating.
Generally a large amount of coatings was tested. In this paper we show only the results of the third set of samples consisting of successful coatings from the second set, to which by one metal-ceramic coating and one metal sprayed coating made of ferritic steel were added. Composition and technology of coatings for the third stage is in Table 3, substrate material was 16Mo3 steel.

4. Results of experiments (The third set of samples)

In pictures 1-3 the results of gravimetry for third set of samples are shown. The most frequently it represents weight gains. It depended on a possibility of easy removing of fly ash from a surface. When it wasn't possible, the fly ash with a corrosion layer was removed

mechanically and chemically. The values in the graphs then represent weight losses. The results of metallographic evaluation of the coatings after exposition for each set are shown Fig. 4-8. In some cases the pictures are extended by microanalysis (by WDX) of characteristic places.

Table 3: The third set of samples

Kind of coating	**Label**	**Sprayed material**	**Technology**	**Chemical composition**
Metal-ceramic coatings Vitkovice ENVI	MC1	NiCrAlY ZrO_2+MgO	arc spraying flame spraying	Ni+22Cr+10Al+1Y $75ZrO_2(HfO_2)$+21MgO+$4Al_2O_3$
	MC7	SM 8222 Ti-Elite	arc spraying flame spraying	66Fe+5C+27Cr+1.1Mn+0.3Si $87Al_2O_3$+$13TiO_2$
Metal coatings Vitkovice ENVI	M2	SM 8222 SM 8276	arc spraying flame spraying	66Fe+5C+27Cr+1.1Mn+0.3Si 57.9Ni+16.3Cr+16.2Mo+5.5Fe 3.4W+0.4Mn
	M3	ARC 595	arc spraying	Fe+28Cr+1.5Si+4B
Metal coatings Castolin CZ	CAS1	Eutalloy RW 12525	arc spraying + remelting	Ni+24.4Cr+4.3Si+3.6B
	CAS2	Eutalloy53-606	arc spraying + remelting	Ni+17.8Cr+13.3Mo+6Si+3.7Fe+ 3.1B+2.4Cu
Metal coating flame spray, Italy	I 625	Inconel 625	HVOF	Ni+22Cr+9Mo+2Al+3.5Nb

At 400°C gravimetric results show low corrosion rates for every coating (Fig 1), the best are remelted metal coatings and under these conditions even metal-ceramic coatings. Higher temperatures are detrimental for Ti-Elite metal-ceramic coating (MC9) (Fig. 2, 3), the other coatings seem to behave very similar to 400°C.

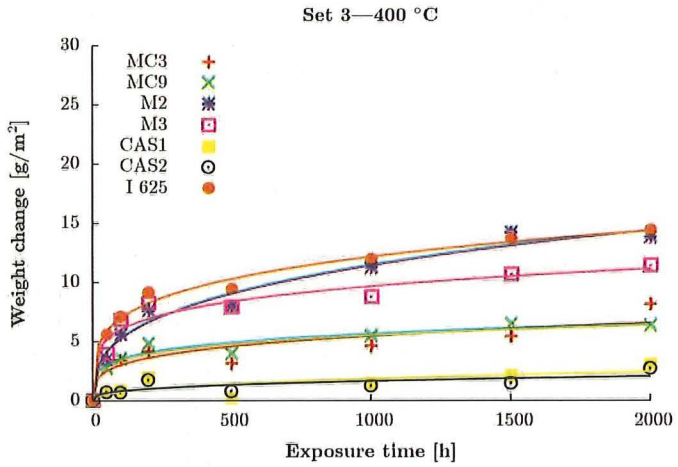

Figure 1: Weight changes of studied coated materials under test environment described in Table 2 at 400°C

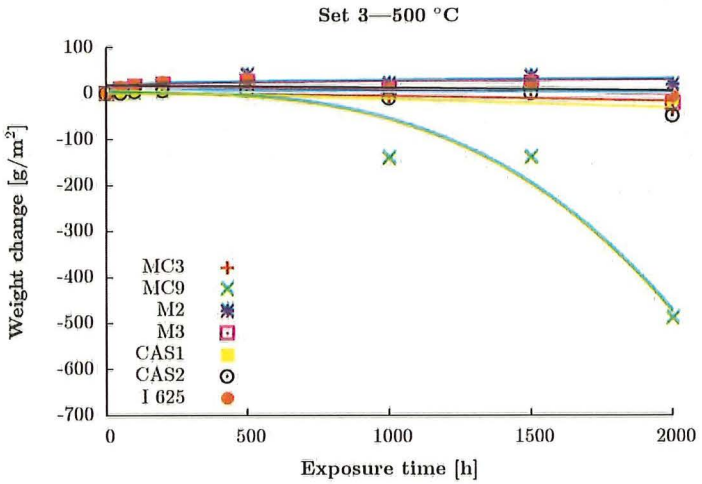

Figure 2: Weight changes of studied coated materials under test environment described in Table 2 at 500°C

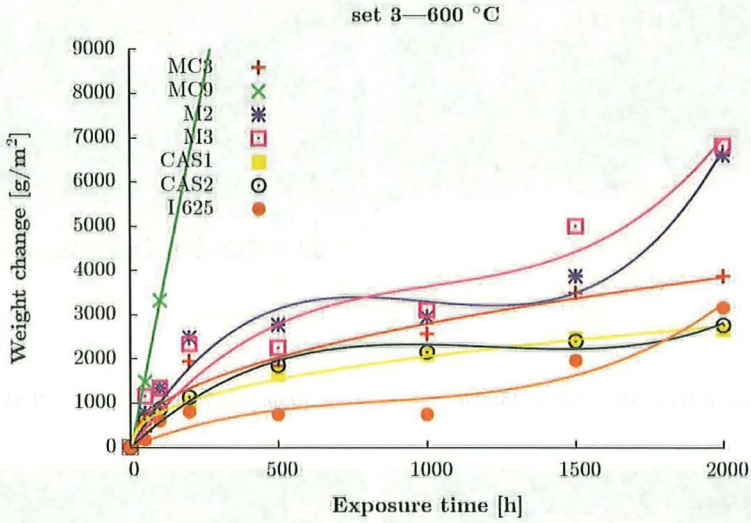

Figure 3: Weight changes of studied coated materials under test environment described in Table 2 at 600°C

If we compare MC1 coating at 400 and 600°C (Fig. 4, 5), we can see cracks in the ceramic layer and degradation of the bondcoat and oxides formation at higher temperature. In Ti-Elite coating (MC7) ferritic bondcoat cracked and spallation occurred in the ceramic layer (Fig. 6) At higher temperature the coating is completely destroyed, in the degraded metal interlayer chlorine was found (Fig. 7). Ferritic coating ARC 595 (M3) cracked the both temperatures (Fig. 8, 9), however at the higher temperature the top of the coating and even an interface coating/base material corroded.

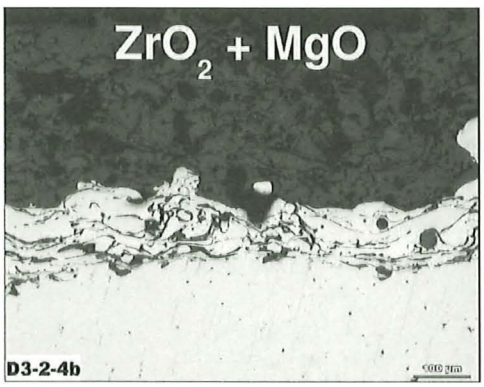

Figure 4: Set 3–MC1-400°C/1500 h

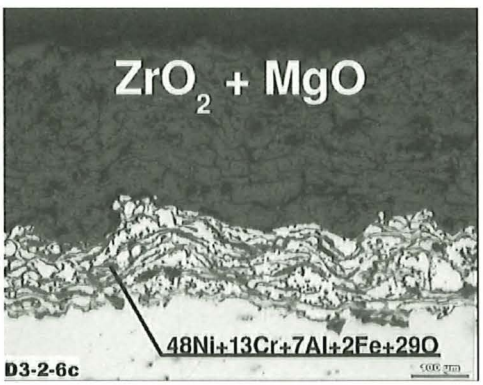

Figure 5: Set 3–MC1-400°C/1500 h

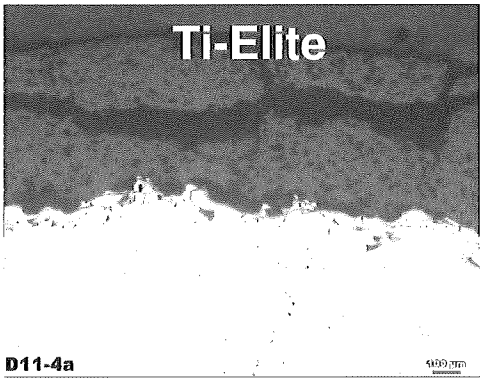

Figure 6: Set 3–MC7-400°C/1500 h

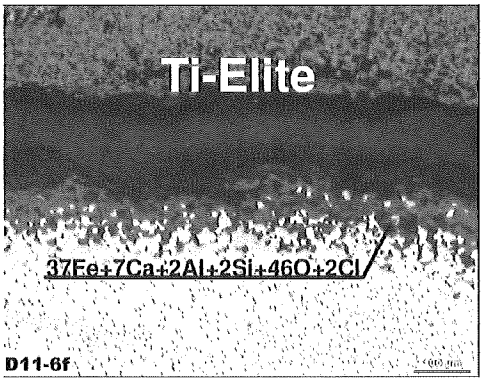

Figure 7: Set 3–MC7-400°C/1500 h

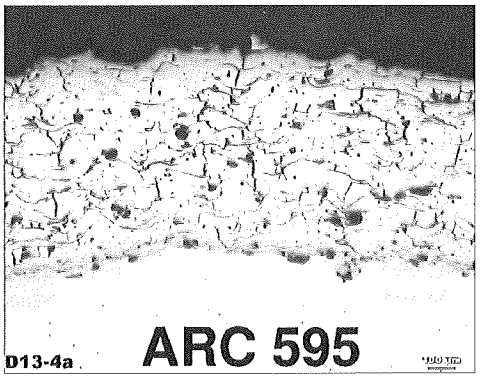

Figure 8: Set 3–ARC 595-400°C/1500 h

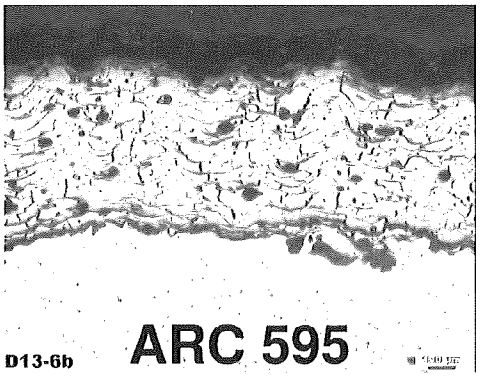

Figure 9: Set 3–ARC595-400°C/1500 h

In Inconel 625 HVOF coating big transversal cracks cross all layers were founded. Base material starts to corrode at the crack and in the crack chlorine was measured (Fig. 10, 11). It is probably caused by tension in the coating which occurs after remelting. Unfortunately such coating cannot protect the surface or a long time, even if other properties are good.

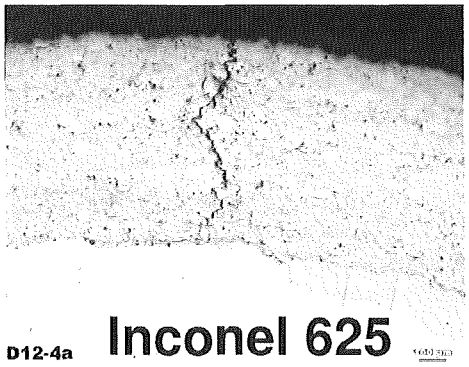

Figure 10: Set 3–I 625-400°C/1500 h

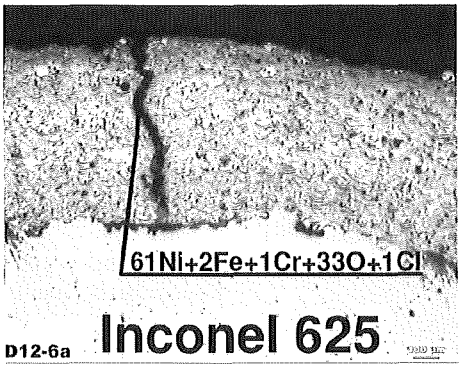

Figure 11: Set 3–I 625-600°C/1500 h

5. Conclusion

Majority of tested coatings have good corrosion resistance up to 500°C even in a comparison with referential Inconel 625. Nevertheless cracking and spallation are the most limiting factors for practical application of these coatings.

- The worst protection is given by ceramic coatings, because a porous ceramic layer cracks and spalls off very soon.
- HVOF sprayed aluminides from Poland disintegrated during the exposure, especially coatings with Fe_xAl_y.
- In metal arc or flame sprayed coatings with a ferritic structure a lot of tiny cracks were found, which is not beneficial for protective properties of these sprayed coatings. Metal coatings with an austenitic structure do not suffer from cracking and spallation, They slowly oxidize at points of original splat boundaries which represent faster diffusion paths for gas from the testing atmosphere. This oxidation of splat boundaries occurs during spraying by partial oxidation of flying drops of melted metal.
- Remelted coatings have very dense structure without oxidized splat boundaries and pores and would be very protective if they did not suffer from formation of big transversal cracks through the entire layer. Base material under these cracks corrodes rapidly. It is probably caused by tensile strains in the coating which occurs after remelting.

9th Liege Conference : Materials for Advanced Power Engineering 2010
edited by J. Lecomte-Beckers, Q. Contrepois, T. Beck and B. Kuhn.

INTERFACIAL, MECHANICAL PROPERTIES OF Al_2O_3-NiAl COMPOSITES RESPECTIVE TO LONG TERM THERMAL STABILITY

Jia Song, Weiping Hu, Günter Gottstein

Institute of Physical Metallurgy and Metal Physics, RWTH Aachen University
Kopernikus Strasse 14, 52074 Aachen, Germany

Abstract

The long term thermal stability of NiAl-Al_2O_3 composites was investigated. During annealing of the composites at 973 K and 1373 K for 2000 hours, the NiAl-Al_2O_3 system showed excellent chemical stability. However, grain growth and embrittlement progressed in the polycrystalline NiAl matrix. The interfacial shear strength decreased from 222±50 MPa for the as-fabricated sample to 197±48 MPa and 150±38 MPa for the samples annealed at 973 K and 1373 K, respectively. The microstructure change during annealing at 973K and 1373 K affected the tensile strength differently. The potential causes of microstructure and interface structure change and their impact on mechanical properties are discussed.

Keywords: NiAl Composite, Thermal Stability, Mechanical Property

1. Introduction

Many efforts have been devoted in the past to the development of new structural materials with application temperatures significantly above those of current superalloys. NiAl has been considered as a potential high temperature structural material for several decades [1-2], because of its high melting point, low density, high thermal conductivity, and good oxidation resistance. However, the limited strength and creep resistance at high temperature as well as poor toughness at room temperature have remained as the main obstacles for structural applications of NiAl. As a new material concept single-crystalline Al_2O_3 continuous fibers (sapphire fibers) were introduced to reinforce NiAl alloys, and such intermetallic matrix composites were produced by means of various fabricating techniques. Bowman et al. [3] examined the mechanical properties of the composites with 25% (volume fraction) fibers over the temperature range of 300 to 1200K, and Hu et al. [4-7] investigated the chemistry, microstructure as well as the mechanical properties up to 1373K for composites with 50% fiber content. However, for application of such composites also their in-service properties are of importance, in particular the long term thermal stability, i.e. chemical and microstructural stability, mechanical strength and creep behavior. These issues were subjects of the current study.

Since long term structural stability and mechanical properties are interrelated, the investigations focused on the microstructure as well as interface structure and the corresponding mechanical properties (interface shear strength and tensile strength) of NiAl composites after extended annealing at high temperatures.

2. Experiment

The fiber used in the present investigation was a single crystalline α-Al_2O_3 fiber (sapphire) with a diameter of about 125 μm, in which the c-axis of α-Al_2O_3 was parallel to the axial direction of the fiber. The fibers were coated with NiAl by a PVD process. The thickness of the NiAl-coating was about 30 μm corresponding to a fiber volume fraction of about 50%. The coated fibers were then placed into a channel-die and hot pressed at 1573 K for 1 hour with a pressure of 40 MPa in vacuum (5×10^{-3} Pa). Under these conditions complete consolidation was achieved. The fabricated composites were subsequently annealed for 2000 hours at 973 K and 1373 K, respectively.
Both the annealed and un-annealed composites were subjected to microcharacterization and microanalysis (SEM/TEM, XEDS, EELS and SAD). Details of the methods for specimen preparation can be found elsewhere [4]. Besides, fiber push-out tests at ambient temperature were applied to determine the interface mechanical properties. The interfacial shear stress τ for complete debonding was calculated as:

$$\tau = F/2\pi rh \quad (1)$$

where F is the maximum axial load for interface debonding, r is the radius of the tested fiber, and h is the thickness of the specimen, which is 0.3 mm in our case.
The tensile tests were carried out at 973 K and 1373 K, respectively, for both annealed and un-annealed samples using a servohydraulic mechanical testing machine (Schenk Hydropuls PSB250) in vacuum (5×10^{-3} Pa). The applied strain rate was 1×10^{-4} s^{-1}. The fracture surfaces after tensile tests were examined by means of SEM/EDX.

3. Results

3.1. Microstructural and Chemical Stability

3.1.1. Sapphire Fiber (Al_2O_3)

The ceramic single crystalline sapphire fiber revealed good thermal stability at high annealing temperatures, as evident from SEM observations on as-fabricated and as-annealed composite samples: an annealing for 2000 hours at 973 K and 1373 K did not bring about any structural or chemical changes in the fibers compared to the as-fabricated samples. This result is in agreement with previous investigations [8].

3.1.2. NiAl Matrix

The STEM/HAADF (high angle annular dark field) micrographs with Z-contrast showed a few dark particles in the as-annealed NiAl matrix (Figure 1). EDX analysis demonstrated that these dark particles were (Ni,Al)-oxides. They were generated as the reaction products between NiAl and residual oxygen and precipitated in the NiAl matrix during annealing. (About 1~4 at.% of oxygen can always been found in as PVD-coated NiAl layers.) No other detectable chemical reactions or phase transformations were found in the as-annealed samples, indicating a good long term chemical stability of the NiAl/Al_2O_3 system at high temperatures.
However, during extended annealing grain boundary migration took place in the polycrystalline NiAl matrix that caused grain growth, e.g., the NiAl grain size increased from an initial value of about 5.5 μm to about 6.2 μm and about 12.8 μm after 2000 hours

annealing at 973 K and 1373 K, respectively (Figure 2). The most severe grain growth occured at 1373 K, where the grain size reached nearly three times the initial size.

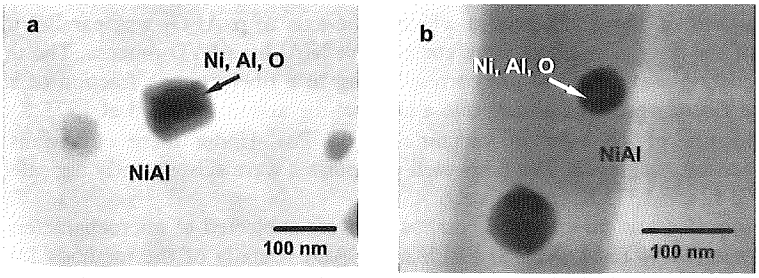

Figure 1. STEM/HAADF micrograph shows precipitates (with dark contrast) in the NiAl matrix after annealing for 2000 hours at a) 973 K and b) 1373 K.

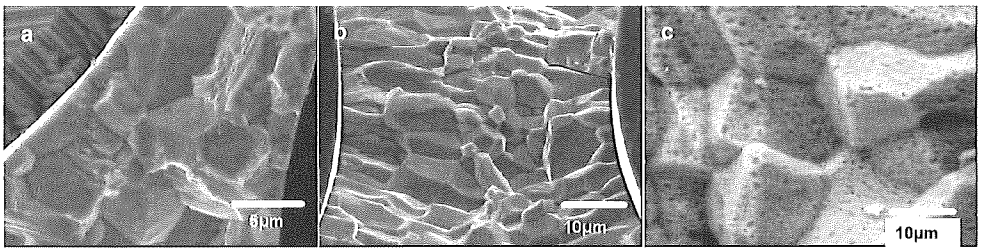

Figure 2. SEM/SEI micrographs display the intergranular fracture surfaces of the NiAl matrix that reveals the grain size: a) about 5.5 µm without annealing, b) about 6.2 µm and c) about 12.8 µm after annealing at 973 K and 1373 K, respectively. (All grain sizes were determined using the linear intercept method)

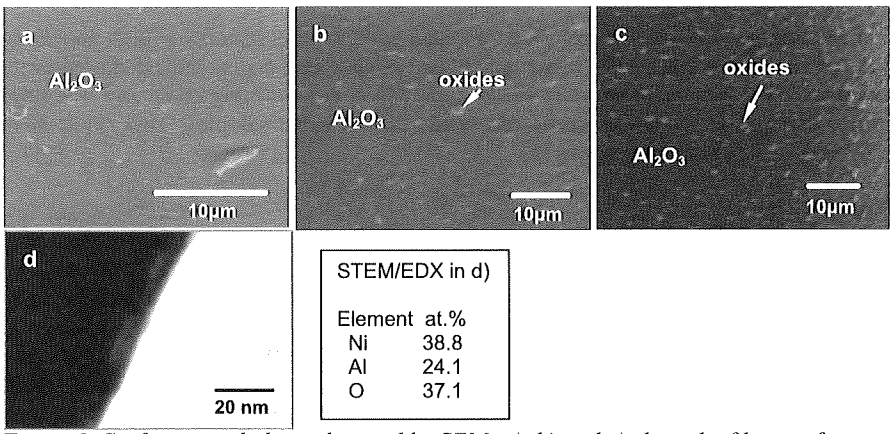

Figure 3. Surface morphology observed by SEM; a), b) and c) show the fiber surface at the interface without annealing, annealed at 973 K and 1373 K, respectively; d) STEM/HAADF image of the interface of the sample annealed at 1373 K.

3.1.3. Interface Chemistry

After annealing for 2000 hours the interface showed good chemical stability except for interface precipitation. The size and amount of interface particles increased with rising temperature (Figure 3a~c). These interface particles were clearly revealed by STEM (marked in Figure 3d) and identified as (Ni,Al)-oxides by STEM/EDX analysis.

3.2. Interface Shear Strength

The measured interface shear strength was 222±50 MPa, 197±48 MPa and 150±38 MPa for the samples of without annealing, as-annealed at 973 K/2000h, and as-annealed at 1373 K/2000h, respectively (Figure 4). Apparently, the interface shear strength of NiAl composites decreased with increasing annealing temperature.

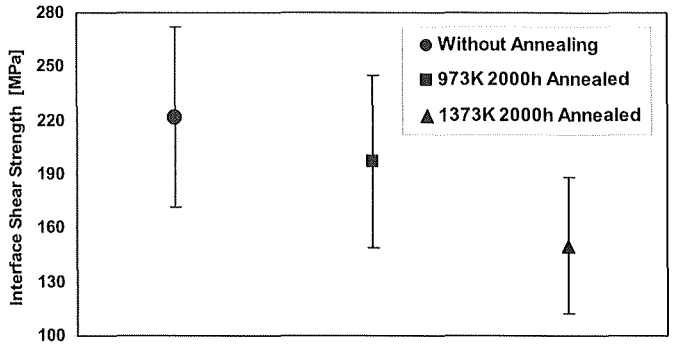

Figure 4. Measured interfacial shear strength of the samples with and without annealing.

3.3. Tensile Strength

Tensile tests were conducted at the corresponding annealing temperatures, for example, the sample annealed at 973 K was subsequently mechanically tested at 973 K as well. As reference, the as-fabricated composites were also tested at 973 K and 1373 K. Except for the as-fabricated sample tested at 973 K, the samples showed negligible strain hardening, i.e. the ultimate tensile strength σ_u of all samples was virtually equal to the yield strength $\sigma_{0.2}$, i.e. $\varepsilon_u \approx$ 0.2%. At 973 K, the as-fabricated sample showed little strain hardening ($\sigma_{0.2}$=351MPa to σ_u=360 MPa). The yield strength for the annealed sample at 973 K was 340 MPa. With a higher testing temperature of 1373 K, the strength was strongly reduced, namely from 200 MPa for the as-fabricated to 171 MPa for the annealed sample.

The corresponding fracture surfaces of the NiAl matrix for the samples annealed at 973 K and 1373 K as well as for samples without annealing are shown in Figure 6. The fracture surface at 973 K for the unannealed sample (Figure 6a) revealed a transgranular cleavage-like appearance. The river-like patterns were distributed all over the fracture surface. By contrast, the fracture surface of the annealed sample comprised both transgranular cleavage fracture (left hand side in Figure 6b) and intergranular fracture (right hand side in Figure 6b), where some pits can be observed on the grain boundary surface (white arrow in Figure 6b). For the samples annealed and strained at 1373 K intergranular fracture was the sole failure mode

(Figure 6c-d). Many pits and pores were found on the grain boundary surfaces, which degraded the flatness and smoothness.

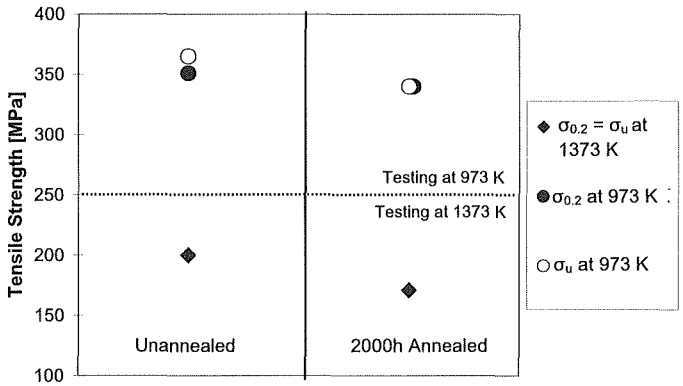

Figure 5. Tensile strength of different samples tested at 973 K and 1373 K.

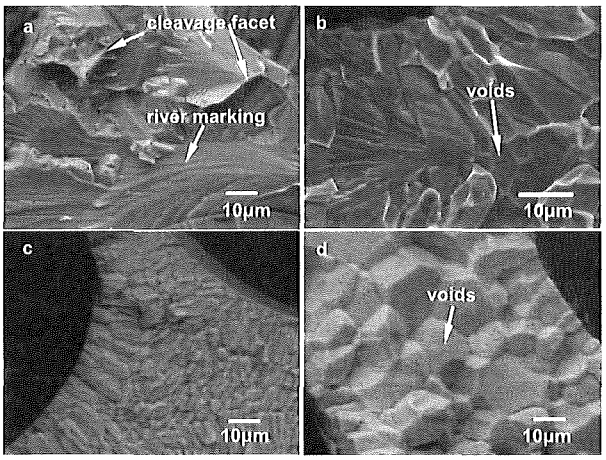

Figure 6. Fracture surface of NiAl matrix after tensile test at 973 K: a) without annealing, b) annealed at 973 K for 2000 hours; fracture surface after tensile test at 1373 K: c) without annealing, d) annealed at 1373 K for 2000 hours.

4. Discussion

As well-known, for composites reinforced by continuous fibers, a rule of mixtures can be used to predict the composite strength in the axial fiber direction for isostrain conditions [9]:

$$\sigma_c = \sigma_f V_f + \sigma_m V_m \quad (2)$$

where σ is the axial stress, V denotes the volume fraction (in our case 50%), and the subscripts c, f and m refer to the composite, fiber and matrix, respectively. The isostrain condition is

usually a good approximation up to the yield point, since the fiber and the matrix deform only elastically. For the yield point, $\sigma_{0.2}$ was applied here. According to Table 1, the yield strength of the composite $\sigma_{c0.2}$ is already lower than the fiber contribution alone (item "$0.5\sigma_{f0.2}$" in Table 1). Apparently fiber fracture occurs before the yield point is attained, either during elastic loading or even prior to the tensile test, during composite fabrication owing to the compressive thermal residual stress at the interface [4].
Hence, at yield the material constitutes a short fiber composite where the load is transferred from the matrix to the fiber via the interface, so that the effective stress $\sigma_{eff,f}$ in the fiber depends on the interfacial strength. Due to the broken fibers, the stress in the matrix σ_m is not influenced by the composite fabrication (no strengthening due to the thermal residual stress at the interface) and can be regarded unchanged as that in an isolated NiAl sample.
The mechanical behavior of the matrix material, polycrystalline NiAl, depends on grain size, texture and chemistry [1]. The grain size dependence of the yield strength for stoichiometric NiAl follows the Hall-Petch relationship:

$$\sigma_y = \sigma_0 + kd^{-\frac{1}{2}} \tag{3}$$

where σ_0 is the single crystal yield stress and k is the Hall-Petch-coefficient of NiAl. Since the matrix suffers grain growth during long term annealing, the yield strength of the matrix decreases during the annealing treatment. From Eqs. (2)~(3) and a fiber volume fraction of 50% in this study, we obtain:

$$\sigma_{c0.2} = 0.5 \cdot \sigma_{eff,f} + 0.5 \cdot \left(\sigma_{m0} + k_m d_m^{-\frac{1}{2}} \right) \tag{4}$$

where the subscript m denotes the matrix. The parameter k is essentially independent of temperature. According to Baker et al. [10], $k_{NiAl} \approx 160$ MPa·μm$^{0.5}$. The relevant values of Eq. (4) are shown in Table 1.

Table 1. Relevant theoretic or measured strength values for different cases

T [K]	Fiber		Unannealed Composite				2000h Annealed Composite				Δ Strength ****	
				I**	***	II		III**	***	IV	II-IV	I-III
	E_f* [GPa]	$0.5\sigma_{f0.2}$ [MPa]	d_m [μm]	$\sigma'_m(d)$ [MPa]	$\sigma_{c0.2,theo}$ [MPa]	$\sigma_{c0.2}$ [MPa]	d_m [μm]	$\sigma'_m(d)$ [MPa]	$\sigma_{c0.2,theo}$ [MPa]	$\sigma_{c0.2}$ [MPa]	$\Delta\sigma_{c0.2}$ [MPa]	$\Delta\sigma'_m$ [MPa]
973	425	425	5.5	34	477	351	6.2	32	475	340	11	2
1373	409	409	5.5	34	448	200	12.8	22	436	171	29	12

* *according to [3]*
** $\sigma'_m(d) = 0.5 k_m d_m^{-0.5}$
*** *The theoretical yield strength is calculated as:* $\sigma_{c0.2,theo} = 0.5\sigma_{f0.2} + 0.5(\sigma_{m0} + k_m d_m^{-0.5})$, *where* $\sigma_{m0}(973K) = 35MPa$ *and* $\sigma_{m0}(1373K) = 10MPa$ *[11]*
**** *(II-IV) is the strength difference between the unannealed and annealed sample at 973 K or 1373 K, (I-III) reveals the NiAl matrix contribution to the strength difference* $(\Delta\sigma'_m = \sigma'_m(d)^{Unannealed} - \sigma'_m(d)^{Annealed})$ *and* $50\%(\sigma_{f0.2}^{Unannealed} - \sigma_{f0.2}^{Annealed}) = (II\text{-}IV) - (I\text{-}III)$, *because* $\sigma_{m0}^{Unannealed} = \sigma_{m0}^{Annealed}$ *at the same testing T*

In comparison to the as-fabricated composite, the tensile yield strength degradation after 2000h annealing can be partially attributed to grain growth of the NiAl matrix ("I-III" item in Table 1). However, the degradation of the fiber and therefore a decrease of $\sigma_{eff,f}$ can not be neglected. This is evident from the value (II-IV)-(I-III) in Table 1, which stands for the fiber contribution to the strength reduction and is by no means close to zero. The load transfer from

the matrix to the fiber, which is related to the interface shear strength, has obviously deteriorated also during long term annealing.
During annealing for 2000 hours, (Ni,Al)-oxide particles (Figure 3) were formed at the interface by reactions between Ni, Al and residual oxygen after PVD coating, the extent of which depends upon annealing temperature and diffusivity of the components. Compared to the annealing at 973 K, the reaction proceeded quite severely during annealing at 1373 K, leaving larger and a higher amount of (Ni,Al)-oxide particles at the interface. These particles were liable to weaken the connection between matrix and fiber and thus, to reduce the interface shear strength during annealing with a minimum strength for the highest annealing temperature 1373 K. The lower the interface shear strength, the lower the load transfer to the fiber, and hence, causing a decrease of $\sigma_{eff,f}$. That is substantiated by the value of (II-IV)-(I-III), which corresponds to the strength degradation in terms of the influence of the interface strength of the loaded fibers between the unannealed and the annealed samples. The loss of composite strength is larger for the tensile test at 1373 K than that at 973 K. A more quantitative relation between the interface shear strength and the loaded fiber strength requires a more detailed analysis of fiber damage and interface strength.
The strain hardening at annealing temperature after heat treatment was conspicuously low. This is likely due to the weakening of the NiAl grain boundaries during annealing as indicated by the intergranular fracture (Figure 6b~d). This grain boundary weakening may be caused by cavitation and oxide particles on the grain boundaries (Figure 1).This interpretation is supported by the fact that only for the as-fabricated composites tested at 973 K, the strength of the grain boundaries is still high enough to cause transgranular fracture (Figure 6a) and strain hardening of the composite (Figure 5).

5. Summary

The NiAl-Al_2O_3 composite system showed excellent chemical stability after long term annealing. However, due to residual oxygen in the NiAl matrix after PVD coating, (Ni,Al)-oxide particles were formed in the NiAl matrix and also at the interface. The respective interface degradation as well as grain growth of NiAl matrix caused a reduction of the tensile yield strength of the composites during annealing. The observed low strain hardening and high temperatures tensile strength was attributed to grain boundary embrittlement, caused by (Ni,Al)-oxide particle formation at the grain boundaries during annealing.

6. Acknowledgement

The authors wish to acknowledge the financial support by the Deutsche Forschungsgemeinschaft (DFG-Kennzeichen: SFB 561/TP G.3.1) and are grateful to Y. Jiang M.Sc. from Materials Chemistry, RWTH Aachen University, for the fiber coating.

7. Reference

[1] D.B. Miracle, The Physical and Mechanical Properties of NiAl, *Acta Metall Mater*, 41 [3], 649-684, (1983).

[2] R. D. Noebe, R. R. Bowman and M. V. Nathal, Physical and Mechanical Properties of the B2Compound NiAl, *International Materials Reviews*, 38 [4], 193-232, (1993).
[3] R.R. Bowman, A. K. Misra and S. M. Arnold, Processing and Mechanical Properties of Al_2O_3 Fiber-Reinforced NiAl Composites, *Metallurgical and Materials Transactions A*, 26A, 615-628, (1995).
[4] W. Hu et al., Interface structure, chemistry and properties of NiAl composites fabricated from matrix-coated single-crystalline Al_2O_3 fibers (sapphire) with and without an hBN interlayer, *Acta Materialia*, 54, 2473-2488, (2006).
[5] H. Chen et al., Fiber Element Analysis of Single-Fiber Push-Out Tests of Continuous Al_2O_3 Fiber-Reinforced NiAl Composites, *Materials Science and Engineering:A*, 460-461, 624-632, (2007).
[6] Y. Zhong et al., Fiber Damage and High Temperature Tensile Properties of Al_2O_3 Fiber Reinforced NiAl-Matrix Composites with and without hBN-Interlayer, *Materials Science and Engineering: A*, 464 [1-2], 241-248, (2007).
[7] Y. Zhong et al., Fiber Push-Out Tests on Al_2O_3 Fiber-Reinforced NiAl-Composites with and without hBN-Interlayer at Room and Elevated Temperatures, *Materials Science and Engineering: A*, 488 [1-2], 372-380, (2008).
[8] D. Hajas et al., Tensile Strength of $Ni_{45}Al_{45}Cr_{7.5}Ta_{2.5}$-Coated Sapphire Fibers, *Journal of the American Ceramic Society*, 91 [12], 4009–4015, (2008).
[9] R. W. Cahn, P. Hassen and E. J. Kramer, Materials Science and Technology, Vol. 13, Volume Editor: T. Chou, 152, (New York, VCH, 1993).
[10] I. Baker et al., The Effect of Grain Size on the Yield Strength of FeAl and NiAl, *Acta Metallurgica Materialia,* 39 [7], 1637-1644, (1991).
[11] R. R. Bowman et al., Correlation of Deformation Mechanisms with the Tensile and Compressive Behavior of NiAl and NiAl(Zr) Intermetallic Alloys, *Metallurgical Transactions A*, 23A, 1493-1508, (1992).

9th Liege Conference : Materials for Advanced Power Engineering 2010
edited by J. Lecomte-Beckers, Q. Contrepois, T. Beck and B. Kuhn.

SEWADGE SLUDGE AS ADDITIVE TO REDUCE THE INITIAL FIRESIDE CORROSION CAUSED BY COMBYSTION OF SHREDDER RESIDUES IN A WASTE-FIRED BFB BOILER

T. Jonsson [*], J. Pettersson[*], K. Davidsson[**], L-G. Johansson[*] and J-E. Svensson[*]

[*] Environmental Inorganic Chemistry, Department of Chemical and Biological Engineering, Chalmers University of Technology, S-412 96, Göteborg, Sweden
[**] SP Technical Research Institute of Sweden, Box 857, SE-501 15 Borås, Sweden

Abstract
Corrosion/deposition field tests have been carried out in a commercial waste-fired BFB boiler using air-cooled probes. The influence of 20% shredder light fraction (SLF), from recovery of metal scrap material, mixed with waste was studied at different material temperatures (280-420 °C). In addition, 3% sewage sludge was added to the 20% SLF/waste mixture. The initial deposit and corrosion products were compared to when the normal waste (municipal solid waste and industrial wastes) fuel was used. After 24 hours exposure, the deposits were analyzed as for elemental composition while the corrosion products were characterised by ESEM/EDX and XRD. The results show that combustion of 20% SLF increased the amount of deposition, which in addition contains a larger fraction chlorine. This causes a higher initial corrosion rate. Adding 3% sewage sludge removes the effect of the SLF and deposits and corrosion products were comparable with the ones formed during the reference exposure. The results indicate that the initial fireside corrosion is chlorine induced and no signs of low-melting heavy metal salts were observed in the corrosion products.

Keywords: Field tests, waste, high temperature corrosion, shredder light fraction, deposits, sewage sludge

1. Introduction

The fireside environment in waste-fired boilers is known to be considerably more corrosive that in boilers fired by biomass and especially, coal. This could cause considerable operational problems and plant owners typically use a maximum steam temperature 100-150 °C below that of a coal-fired boiler. As a consequence, the efficiency of the electricity production is reduced. Fuel flexibility could in addition be limited, if avoiding the most corrosive fuels. The fireside environment in waste fired boilers is characterized by high levels of reactive alkali (e.g. NaCl and KCl) and hydrogen chloride and relatively low SO_2 concentrations. Additionally, the flue gas contains high levels of carbon dioxide, oxygen and water vapour. In order to limit the corrosion problems and thereby increasing the electricity production and fuel flexibility, it is important to further study the underlying corrosion mechanisms.

When shredder light fractions (SLF) from recovery of metal scrap are energy recovered it is usually mixed with more than 90% of other wastes. SLF is a fuel with high energy content but also with relatively high chlorine (about 1%ds compared to about 0.5%ds in the normal fuel mix) and metal content (e.g. Zn and Cu). The fuel could therefore cause corrosion problems, and today, only a smaller part of the fuel mix is used in waste plants. Previously, the high corrosivity in waste-fired boilers was often attributed to low-melting heavy metal salts and to the presence of chlorine, using the active oxidation reaction scheme [1-5]. However, the validity of the active oxidation approach has recently been questioned in laboratory studies [6]. In order to better understand the effect of chlorine and metal content in the fuel on fireside corrosion it is important to study a fuel such as SLF.

Recently, sewage sludge and sulphur additions have been shown to reduce deposition and corrosion problems in alkali and chlorine rich environments such as waste and biomass combustion [7-10]. It would therefore be important to study the effect of sewage sludge together with a fuel with relatively high chlorine and metal content in a waste-fired plant. Could the higher corrosivity of a fuel with high chlorine and metal content such as the SLF fuel be neutralized by sewage sludge addition?

The aim of the present study is to better understand the corrosion mechanisms of a high chlorine and metal containing fuel and the effect of sewage sludge additions in the 20 MW Bubbling Fluidized Bed (BFB) of Lidköping heat production plant. This was done by linking the results of a detailed investigation of deposits and corrosion products formed on three different steels using gravimetry, ion chromatography, inductively coupled plasma-optical emission spectrometry, X-ray diffraction (XRD) and analytical scanning electron microscopy (SEM/EDX) on polished cross-sections to the fuel mixtures.

2. Experimental

2.1 General description

20% SLF (by energy content) has been combusted together with municipal solid waste and industrial wastes. This case will be termed "SLF/waste" below. In another case, 3% sewage sludge (by energy content) was added to the SLF/waste fuel mix (termed "SLF/sludge/waste" below) to see if sewage sludge could reduce deposition problems. The results from these two cases were compared to a reference case when normal fuel was used (municipal solid waste and industrial wastes). All cases were performed in the Metso Power 20 MW ACZ BFB of Lidköping heat production plant, see schematic image in Fig. 1.

Compared with the normal waste fuel, the SLF has a higher content of ash and chlorine (about 1%ds compared to about 0.5%ds in normal fuel). Among the main components of the ash, iron has a high concentration. This is also true for the trace elements copper and zinc. The sludge has twice as much ash and sulphur as the normal waste fuel. It contains considerably more of nitrogen and almost no chlorine. The main components of the ash are dominated by iron and calcium. It has a higher concentration of phosphorus and less of silicon and alkali. For complete fuel analysis see [11, 12]. The different fuel mixtures were fired two days before each exposure in order to approach steady-state operation of the plant. The present paper focuses on the influence of the SLF fuel and the effect of sewage sludge additive on the initial fireside corrosion using air cooled probe exposures in the boiler. Hence, the experimental part describes the three probe exposures carried out and the analysis of corrosion products and deposits. A more comprehensive description of the experimental procedure together with other aspects and more results could be found in [11, 12].

One deposit/corrosion probe was placed upstream of the convection pass (position B in Fig. 1) and one deposit probe was placed upstream of the economizer (position C in Fig. 1). The flue gas temperature was approximately 560-600 °C at position B while it was about 280-300 °C at position C. Sample rings made from the austenitic stainless steels 310, 304L and the low alloyed steel 16Mo3 were exposed for 24 hours at 280, 350 and 420 °C at position B. In total nine samples were exposed during each exposure (see schematic drawing in Fig. 1) at position B while one steel ring was exposed during each exposure at position C. The alloy

compositions are presented in Table 1. All sample rings were turned using a lathe and cleaned in acetone/ethanol using an ultrasonic bath prior to exposure. The outer diameter of the sample rings was 48 mm and the wall thickness was 2.7 mm. The sample rings were weighed before and after exposure in order to record the mass gain. The temperature was logged during each exposure and was controlled by adjusting the amount of cooling air. After each exposure the probe rings were investigated using gravimetry (all samples), deposit analysis (deposit probe position C and 310 samples on probe position B), SEM/EDX (16Mo3 samples) and XRD (304L samples).

Table 1: *Chemical compositions of the alloys (wt. %).*

Material	*% C*	*% Cr*	*% Ni*	*% Mo*	*%Mn*
16Mo3	0,12	0	0	0,3	0,6
304L	< 0,030	18,5	10	-	1,4
310	0,22	24,9	19,2	0,34	1,55

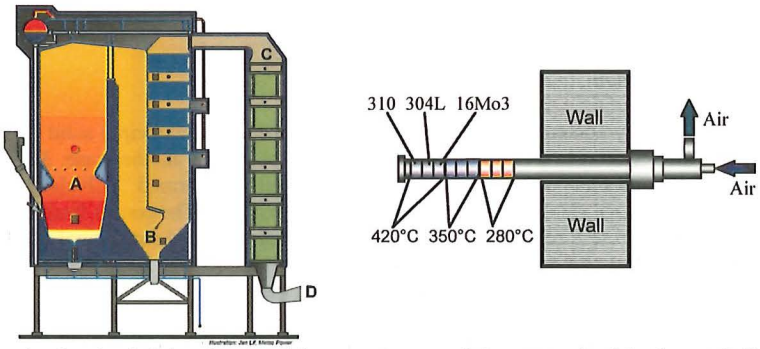

Figure 1: *On the left hand side: Schematic image of the waste fired boiler at Lidköping showing the position of the deposit and corrosion probe before the conventional (B) and the position of deposit probe before economizer (C), from [12]. On the right hand side: Schematic image of the deposit and corrosion probe. Nine samples were run during each exposure, three temperatures and three materials at each temperature.*

2.2 Gravimetry

All sample rings were weighed prior to and after exposure using a five decimal Sartorius analytical balance. The mass gain of a sample is caused by the accumulation of deposits and the formation of corrosion products. However, sample mass can also be affected by the loss of material by evaporation and spallation.

2.3 Deposit analysis

The content of chloride and sulphate was established by leaching the deposits with water and analysing the solution with ion chromatography. After further treatment of the solution by a mixture of concentrated nitric acid, hydrochloric acid and hydrofluoric acid (at 80 °C for 4 h), other elements were analysed with Ion coupled plasma-optical emission spectrometry.

2.4 X-ray Diffraction (XRD)

All deposit and corrosion products were mechanically removed from the 304L samples on the deposit and corrosion probe (position B) and ground into a fine powder. Crystalline deposit and corrosion products were then analyzed by angle X-ray diffraction using a Siemens D5000 powder diffractometer, equipped with grazing incidence beam attachment and a Göbel mirror. CuKα radiation was used and the angle of incidence was 8°. The detector measured between $20° < 2\theta < 65°$.

2.5 Analytical Scanning Electron Microscopy (SEM/EDX)

The low-alloyed steel samples on the deposit and corrosion probe (position B) were cast in epoxy resin and polished cross-sections were produced through the deposit and corrosion products. All polishing were done without water soluble species or completely dry. An FEI Quanta 200 ESEM (Environmental Scanning Electron Microscope) equipped with a field emission gun (FEG) was then used. Accelerating voltage of 20 kV, high vacuum mode and 10 mm working distance were chosen. Chemical analysis was carried out using an Oxford INCA Energy Dispersive X-ray (EDX) system.

3. Results

This work focused on the initial fireside corrosion of the low-alloyed steel 16Mo3 at 420 °C and the influence on the deposits formed during the combustion of the different fuel mixtures (SLF/waste, SLF/sludge/waste and reference).

3.1 Gravimetry

Figure 2 shows the mass gains of different samples exposed at 420 °C and for the low alloyed steel 16Mo3 (all temperatures) (position B in Fig. 1). The combustion of SLF/waste has a notable effect on the mass gain on all materials. However, when sewage sludge is added (SLF/sludge/waste) the mass gain is comparable to the mass gain acquired during the reference exposure. There is also a significant difference between the alloys. The stainless steels have generally a lower mass gain. These trends were the same for all temperatures (not shown). The mass gain of the low-alloyed steel depends on temperature in the range studied (Fig. 3), i.e. higher exposure temperature gives higher mass gains, while there was no clear temperature dependence on the stainless steels (not shown). Most of the mass gain is considered to derive from deposited particles and that only a minor part is due to the formation of corrosion products, especially on the stainless steels. Hence, the amount of deposit accumulated is more during the SLF/waste exposure, compared to the reference and SLF/sludge/waste exposures.

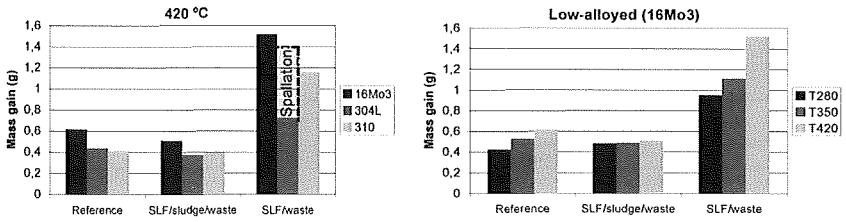

Figure 3: *Mass gain for all materials and exposure conditions at 420 °C and for the low alloyed steel 16Mo3 (all temperatures) at position B in Fig. 1. A large part of the deposit spalled off on the 304L sample during the SLF/waste exposure. A predicted mass gain (from the other materials and temperatures) is therefore indicated by the dashed line.*

3.2 Deposit analysis

Figure 3 shows the growth of amount of substance for a number of elements per unit time and surface. The left panel compares position B and C in the three experimental cases at 280 °C. The growth of deposits is fastest in the SLF/waste case, while the reference and SLF/waste/sludge are comparable both as for growth and composition. In SLF/waste, the deposits contain more chlorine and alkali. The right panel of Fig. 3 shows the influence of the surface temperature. The effect is small except at 420 °C in SLF/waste.

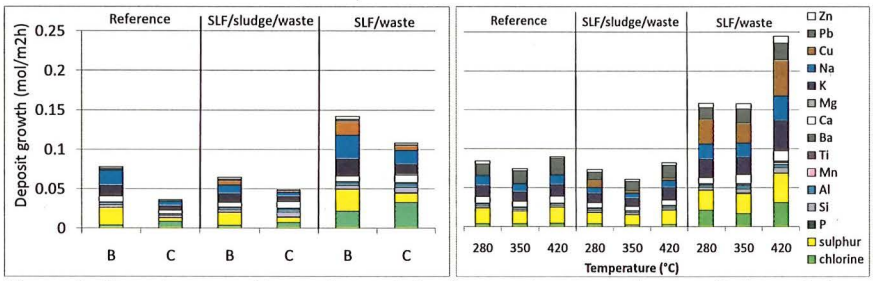

Figure 3: *Deposit composition and growth for the most important elements. Left panel shows the increase of the amount of substance per unit time and surface in position B and C (c.f. Figure 1) at a surface temperature of 280 °C for each experimental case. The right panel shows the deposits in position B at different surface temperatures. Oxygen and carbon were not analysed.*

3.3 Crystalline phases detected by XRD

The deposit and corrosion products were analysed by XRD on all 304L samples on the deposit and corrosion probe, position B in Fig. 1. The results are summarised in Table 2. The analysis shows the presence of several deposited compounds such as alkali chlorides and sulphates and calcium sulphate, which is in good agreement with the deposit analysis (Fig. 3).

Table 2: *Phases detected by XRD on the 304L samples. S= strong intensity, M = medium intensity, W = weak intensity.*

	$(Fe,Cr)_2O_3$	$(Fe,Cr)_3O_4$	$Ca(SO_4)$	NaCl	KCl	(NaK)Cl	CuO	$K_2Ca_2(SO_4)_3$	$FeCl_2$*
Ref	S	S	S	S	S	S	W	W	W
SLF sludge waste	S	S	S	S	S	S	S	S	W
SLF waste	S	S	S	S	S	S	S	W	W
S = strong, W = weak, (* Hydrated $FeCl_2$)									

The addition of sewage sludge to the fuel increases the intensity of $K_2Ca_2(SO_4)_3$, while it is difficult to detect any difference in the alkali chlorides intensities. However, the deposit analysis showed less alkali and chlorine when sewage sludge was added. The CuO intensities were stronger in the presence of SLF, both with and without sewage sludge, which is in agreement with the deposit analysis. In addition, several corrosion products were detected on all samples, e.g. the two oxide phases $(Fe,Cr)_2O_3$ and $(Fe,Cr)_3O_4$. This corresponds to Fe_2O_3 and Fe_3O_4 on the low-alloyed steel 16Mo3 (no Cr, see Table 1). In addition, hydrated $FeCl_2$ was detected. This is expected since $FeCl_2$ is hydroscopic and the sample preparation and analysis were done in air. The interpretation is that $FeCl_2$ was present on all samples.

3.4 SEM/EDX on polished cross-sections

Polished cross-sections through the low-alloyed steel 16Mo3 formed at 420 °C were examined by SEM/EDX. Both the deposit and corrosion products varied in thickness across the samples. Typically, the deposit and corrosion products were thinner and more unevenly thick on the windward side. This could be explained by a blasting effect caused by particles in the flue gas. In order to better compare the deposit and corrosion products all analyses were done on the leeward side of the samples.

Figure 4 shows SEM/BSE images of cross-sections through the deposits and corrosion products formed on 16Mo3 under all three exposure conditions at 420 °C. The thickness distribution is in good agreement with the mass gains (Fig. 2). The deposit and corrosion products, formed during the SLF/waste exposure, are about twice as thick as those formed during the reference and SLF/sludge/waste exposures. All deposit and corrosion products have a similar microstructure despite the difference in thickness. Directly above the metal a dark layer is found on all samples. This is followed by a thinner dense layer and a thicker more heterogeneous layer. The outer part has the most heterogeneous composition based on the SEM/BSE information.

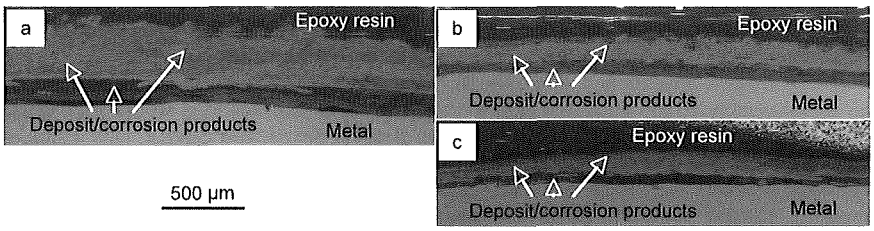

Figure 4: *SEM/BSE images showing polished cross-sections through deposits and corrosion products formed on 16Mo3 during the three different exposures at 420°C (deposit and corrosion probe at position B in Fig. 1). a) SLF/waste, b) SLF/sludge/waste and c) Reference.*

3.4.1 SLF/waste exposure Figure 5 shows a higher magnification SEM/BSE image and SEM/EDX elemental maps of the deposit and corrosion products formed on 16Mo3 during the SLF/waste exposure at 420 °C. The elemental distributions in the different layers observed in the low magnification SEM/BSE image are identified in the elemental maps, which were verified with SEM/EDX quantitative analysis (not shown). The approximately 150 µm thick dark layer closest to the alloy is composed of iron chloride, which is followed by a 50-100 µm thick dense iron oxide layer. The outer iron oxide rich layer has a more heterogeneous

composition, i.e. the iron oxide is mixed with deposit. Only a thin deposit layer can be observed. No Pb, Zn or Cu was detected at corrosion front or in the corrosion products. The SEM/EDX results are in good agreement with the different phases detected with XRD, see Table 2. It should be noted that the low Cl level in the elemental maps (dark layer) is an effect of the sample preparation. Samples with similar structure were polished completely dry and more of the iron chloride remained even though the composition matched hydrated $FeCl_2$ ($FeCl_2 \times 2H_2O$), as the XRD results. The interpretation is again that this has been a $FeCl_2$ layer which has reacted with H_2O during sample preparation.

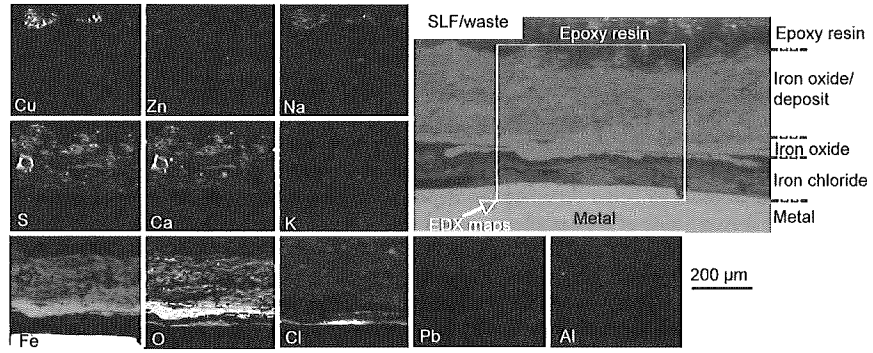

Figure 5: *SEM/BSE image showing polished cross-section of the deposit and corrosion products formed on 16Mo3 during the SLF/waste exposure at 420 °C (deposit and corrosion probe at position B in Fig. 1). SEM/EDX elemental maps from the marked region in the SEM/BSE image are also shown.*

3.4.2 SLF/sludge/waste exposure Figure 6 shows a higher magnification SEM/BSE image of the deposit and corrosion products formed on 16Mo3 formed during the SLF/sludge/waste exposure. The chemical analysis confirmed the SEM/BSE image and showed that deposit/corrosion layer has a very similar microstructure and composition as the much thicker deposit/corrosion layer formed during the SLF/waste exposure. Closest to the metal there are an approximately 40 µm thick iron chloride layer, which is followed by a 40 µm thick dense iron oxide layer. The outer iron oxide rich layer is again mixed with deposit, with a similar composition as was found on the SLF/waste sample but with some more deposit outside the corrosion products. No Pb, Zn or Cu was detected close to corrosion front or in the corrosion products. Instead, some Pb, Zn or Cu was found in the deposit layer (max 5 at.%). The SEM/EDX results are again in good agreement with the different phases detected with XRD, see Table 2.

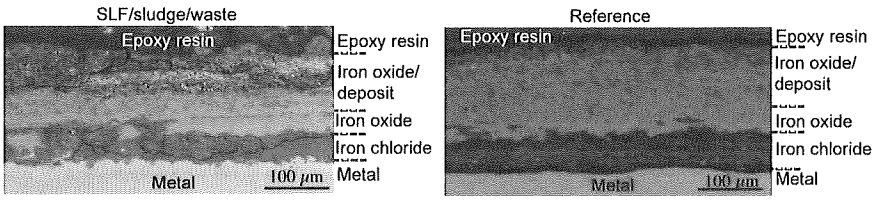

Figure 6: *SEM/BSE images showing polished cross-sections of the deposit and corrosion products formed on 16Mo3 during the SLF/sludge/waste and the reference exposure at 420 °C (deposit and corrosion probe at position B in Fig. 1).*

3.4.3 Reference exposure Figure 6 shows a higher magnification SEM/BSE image of the deposit and corrosion products formed on 16Mo3 during the reference exposure. SEM/EDX analysis showed that the deposit and corrosion products have a very similar microstructure, composition and thickness as that formed during the SLF/sludge/waste exposure (not shown). Closest to the metal there are an approximately 60 µm thick iron chloride layer, which is followed by a 30 µm thick dense iron oxide layer. The outer iron oxide rich layer is again mixed with deposit while no Pb, Zn or Cu was detected close to corrosion front or in the corrosion products. The results are in good agreement with the different phases detected with XRD, see Table 2.

4. Discussion

4.1 Initial deposit growth

The SLF fuel has a relatively high chlorine (about 1%ds compared to about 0.5%ds in the normal fuel mix) and metal content (e.g. Zn and Cu) and is therefore predicted to cause deposit and corrosion problems. In accordance with these predictions, our results show that the combustion of 20% SLF (by energy content) together with the normal fuel increases the deposit growth rate and changes the deposit composition. This was observed at two probe positions (B and C in Fig. 1) and at three material temperatures, see Fig. 3. The change in the deposit composition compared to the reference exposure was characterised by larger fractions of chlorine, alkali and copper. However, when 3% (by energy content) was added to the 20% SLF fuel mixture the amount and composition of deposit was similar to the deposit formed during reference exposure, see Fig. 3. It may also be noted that the amount and composition changed with the probe position in the boiler. Less deposit but with higher fraction chlorine was found upstream of the economizer (position C in Fig. 1), see Fig. 3. No corrosion probe was placed at this position and it therefore impossible to compare the corrosion rates between the different positions. However, the impact on deposit composition/amount of the different fuel mixtures was the same on both probe positions.

4.2 Initial fireside corrosion

A correlation between the deposit amount/composition and the initial fireside corrosion rate can be observed. The thickness of the corrosion products was about twice as thick under the deposit formed during the combustion of SLF/waste compared to the reference case. As described above, the deposit formed during combustion of SLF/waste was characterised by higher levels of chlorine, alkali and copper. When sewage sludge was added to the SLF/waste mixture, the deposit amount and composition returned to normal and so did the initial fireside corrosion rate. These observations are mainly based on the microstructure of the corrosion products formed on the low-alloyed steel 16Mo3, see Figs. 4-6. It is notable that the microstructures of the corrosion products are very similar in all three exposure conditions despite the differences in thickness, see Fig. 4. The thick iron chloride layer at the corrosion front indicates chlorine induced corrosion and the absence of Pb, Cu or Zn at the corrosion front rules out the low-melting heavy metal salts as an explanation for the fast initial

corrosion rate. Neither were any signs of other melts observed in the microstructure. This indicates that it is mainly the higher amounts of chlorine in the deposit formed during the combustion of 20% SLF that causes the increased corrosion rate.

Iron chloride is not considered to form a protective scale. Neither can the outer iron rich layer be considered to form a protective scale since it is mixed with deposit particles, see e.g. Fig. 5. This leaves the thin inner iron oxide scale as rate determining for high temperature corrosion. Pure iron and low-alloyed steels are reported to form multilayer scales at these temperatures composed by a hematite layer above a duplex magnetite scale (or Fe-Cr spinel). The duplex magnetite scale can be divided into an outward-growing and an inward-growing part [13-15]. This can explain the microstructure of the corrosion products observed on the low-alloyed steel 16Mo3 formed in the boiler. The outward-growing iron oxide scale is mixed with deposits from the flue gas during growth, while the inward-growing iron oxide scale remains dense. A recent laboratory study showed that small amounts (0.1 mg/cm^2) of KCl(s) increased the initial corrosion rate during the first 24 hours on a similar low-alloyed steel (Fe-2.25Cr-1Mo) at 400 °C by about eight times [13]. Iron chloride was reported to be found at the metal oxide interface. It was proposed that the chloride ions are transported along oxide grain boundaries simultaneously with the reduction of oxygen at the oxide surface. The formation of metal chlorides accelerates the corrosion through increased diffusion through the scale as well as reduced scale adhesion. These laboratory results are in good agreement with our observations in the boiler even though the boiler has a very complex environment. A deposit containing more alkali chlorides, as in the SLF/waste exposure, increases the corrosion rate and the thickness of the iron chloride layer at the metal oxide interface. However, the large variation within each sample, the very high initial corrosion rate together with the short exposure time makes it very difficult to extrapolate the corrosion rates to longer exposures times. It is therefore very important to verify these results during long time exposures.

4.1 The influence of sewage sludge on deposit growth and corrosion rate

A beneficial effect of adding sewage sludge or sulphur on deposit growth and corrosion rate has previously been reported [7-10]. Our observations confirm these results. Adding sewage sludge together with a corrosive fuel such as SLF characterised by high chlorine and metal content changes the deposit composition (less chlorine) and growth rate, which results in a lower corrosion rate. As described above, our observations indicate that it is the chlorine and not the metal content that influences the initial corrosion rate. It has previously been suggested that sulphur (in our case from the sewage sludge) added to the fuel is converted to SO_x (SO_2 + a small fraction of SO_3) [7-10]. SO_2 is expected to react with alkali chloride and $CaCl_2$ (in the flue gas and in the deposits) according to [16]:

$$2SO_2(g) + O_2(g) + 4NaCl(s) + 2H_2O(g) \rightarrow 2Na_2SO_4(s) + 4HCl(g) \quad (1)$$

$$2SO_2(g) + O_2(g) + 2CaCl_2(s) + 2H_2O(g) \rightarrow 2CaSO_4(s) + 4HCl(g) \quad (2)$$

KCl reacts in the same way as NaCl. The amount of sulphur is not enough to convert all solid alkali chlorides to alkali sulphates but enough to remove the extra alkali chlorides added by the SLF fuel. Hence, the deposition of alkali chlorides by condensation and particle impaction

are then proposed to be restored to normal, i.e. as in the reference exposure. The higher corrosivity of the SLF fuel can thereby be neutralised by adding sewage sludge.

5. Conclusions

- The combustion of 20% SLF (by energy content) changes the composition of the deposits, increases the amount of deposition and causes higher initial corrosion rate.
- Adding 3% sewage sludge (by energy content) removes the effect of 20% SLF and deposits and corrosion products are comparable with the ones formed during the reference exposure.
- Chlorides and sulfates of Ca, Na and K dominate the deposits.
- The results indicate that the initial fireside corrosion is chlorine induced.
- No signs of low-melting heavy metal salts were observed in the corrosion products.
- Sulfur in the sewage sludge is proposed to convert some of the solid alkali chlorides to alkali sulphates, which decreases the amount of alkali chlorides in the deposits.

ACKNOWLEDGMENTS

The work was financed by Waste Refinery and is part of a collaboration project between Stena Metall AB, Metso AB, High Temperature Corrosion Center at Chalmers University of Technology, SP Technical Research Institute of Sweden and Lidköpings Värmeverk.

REFERENCES

1. Grabke, H.J., E. Reese, and M. Spiegel, *The Effects of Chlorides, Hydrogen-Chloride, and Sulfur-Dioxide in the Oxidation of Steels Below Deposits.* Corrosion Science, 1995. **37**(7): p. 1023-1043.
2. Montgomery, M., A. Karlsson, and O.H. Larsen, *Field test corrosion experiments in Denmark with biomass fuels Part 1: Straw-firing.* Materials and Corrosion-Werkstoffe Und Korrosion, 2002. **53**(2): p. 121-131.
3. Nielsen, H.P., F.J. Frandsen, and K. Dam-Johansen, *Lab-scale investigations of high-temperature corrosion phenomena in straw-fired boilers.* Energy & Fuels, 1999. **13**(6): p. 1114-1121.
4. Spiegel, M., *Salt melt induced corrosion of metallic materials in waste incineration plants.* Materials and Corrosion-Werkstoffe Und Korrosion, 1999. **50**(7): p. 373-393.
5. Spiegel, M., A. Zahs, and H.J. Grabke, *Fundamental aspects of chlorine induced corrosion in power plants.* Materials at High Temperatures, 2003. **20**(2): p. 153-159.
6. Folkeson, N., L.G. Johansson, and J.E. Svensson, *Initial stages of the HCl-induced high-temperature corrosion of alloy 310.* Journal of the Electrochemical Society, 2007. **154**(9): p. C515-C521.
7. Amand, L.E., B. Leckner, D. Eskilsson, and C. Tullin, *Deposits on heat transfer tubes during co-cornbustion of biofuels and sewage sludge.* Fuel, 2006. **85**(10-11): p. 1313-1322.
8. Pettersson, J., C. Pettersson, N. Folkeson, L.G. Johansson, E. Skog, and J.E. Svensson, *The influence of sulphur additions on the corrosive environment in a waste-fired CFB boiler.* High-Temperature Oxidation and Corrosion 2005, 2005. **522-523**: p. 563-570.
9. Pettersson, J., C. Pettersson, H. Asteman, J.E. Svensson, and L.G. Johansson, *A pilot plant study of the effect of alkali salts on initial stages of the high temperature corrosion of alloy 304L.* High Temperature Corrosion and Protection of Materials 6, Prt 1 and 2, Proceedings, 2004. **461-464**: p. 965-972.

10. Folkeson, N., J. Pettersson, C. Pettersson, L.G. Johansson, E. Skog, B.A. Andersson, S. Enestam, J. Tuiremo, A. Jonasson, B. Heikne, and J.E. Svensson, *Fireside corrosion of stainless and low alloyed steels in a waste-fired CFB boiler; The effect of adding sulphur to the fuel.* High Temperature Corrosion and Protection of Materials 7, Pts 1 and 2, 2008. **595-598**: p. 289-297 1207.
11. Gyllenhammar, M., T. Jonsson, and K. Davidsson. *The use of sewage sludge as additive to avoid operational problems at combustion of shredder residues.* in *Accepted for publication in 2nd International Conference and Exhibition on Waste to Wealth&6th International Conference on Combustion, Incineration/Pyrolysis and Emission Control, .* 2010. Kuala Lumpur, Malaysia.
12. Gyllenhammar, M., K. Davidsson, T. Jonsson, J. Pettersson, A. Victorén, H. Andersson, and C. Widén, *Energy recovery of combustible fraction from fragmentation of metal scrap - Phase 2.* 2010: Gothenburg.
13. Folkeson, N., T. Jonsson, M. Halvarsson, L.-G. Johansson, and J.-E. Svensson, *The influence of small amounts of KCl(s) on the high temperaturecorrosion of a Fe-2.25Cr-1Mo steel at 400 and 500°C.* To be published in Materials and Corrosion, 2010.
14. Chen, R.Y. and W.Y.D. Yuen, *Review of the High-Temperature Oxidation of Iron and Carbon Steels in Air or Oxygen.* Oxidation of Metals, 2003. **59**: p. 433-468.
15. Pujilaksono, B., T. Jonsson, M. Halvarsson, I. Panas, J.-E. Svensson, and L.-G. Johansson, *Oxidation of iron at 400-600 °C in dry and wet O_2.* Accepted for publication in Corrosion Science, 2009.
16. Barin, I., *Thermodynamic Data of Pure Substances.* Third Edition ed. 1995.

Part F

Zero Emission Power Plants

9th Liege Conference : Materials for Advanced Power Engineering 2010
edited by J. Lecomte-Beckers, Q. Contrepois, T. Beck and B. Kuhn.

OXYCOAL-AC: INNOVATIVE COMPONENTS AND CONCEPTS FOR THE POWER PLANTS OF THE FUTURE

Reinhold Kneer, Dobrin Toporov and Malte Förster

Institute of Heat and Mass Transfer (WSA), RTWH Aachen University,
Eilfschornsteinstr. 18, D-52056 Aachen, Germany
www.wsa.rwth-aachen.de

Abstract

In the framework of the OXYCOAL-AC research project, detailed experimental and numerical investigations of oxycoal swirl flames have been made. The effects of high CO_2 concentrations in the gas mixture during oxy-firing on the volatiles and on particle ignition, flame propagation, flame stability, emissions and heat transfer in the boiler have been investigated and analyzed. Measures for oxy-flame stabilization as a function of flue gas recycling ratio (O2 content) are derived and a swirl burner able to operate in both air and oxy-firing has been developed. Thus, OXYCOAL-AC became the first test-plant worldwide where coal can be burnt in a stable flame in a CO_2 atmosphere with oxygen content between 18 and 30 vol. %. In addition, the development of the key component in the OXYCOAL-AC process, an ion transport membrane for oxygen production, is ongoing. Appropriate membrane materials have been identified and tested for their applicability to oxycoal conditions. Laboratory scale modules have been designed and successfully operated as membrane-based air separation units. Design concepts of scaled up membrane modules and their integration in pilot or power plant scale facilities are under development. Fly ash separation from the recycled hot flue gas is investigated by testing different ceramic filter materials. First oxy-firing experiments with wet recycled flue gas have shown an increased slagging behaviour of fly ash compared to air-firing conditions. Therefore more investigations on the behaviour of coal ash in oxyfuel atmosphere are scheduled.
Further, numerical simulations of a utility scale (1200 MW_{th}) boiler oxy-firing bituminous coal, based on non-grey implementation of the Exponential Wide Band Model, were performed with respect to retrofit. Comparisons are made between air firing and oxy- firing under boundary conditions varying with respect to oxygen and water content of the oxidizer. Predictions have shown that a significant increase of the oxygen concentration in the O_2/RFG mixture (approx. 27% for wet recycle and 30% for dry recycle) is necessary for compensation of the higher molar heat capacity of CO_2 and thus for obtaining the similar flame temperatures as those in air-firing. However, due to the changed optical density of the flue gas, this will lead to 16 % increase of the incident radiation to the furnace walls in case of wet recycle and 5% for dry recycle. The results have shown that similar heat transfer in the combustion chamber to those in air-firing can be achieved with an oxygen enrichment of recycled flue gas to around 24 vol.-% for wet and to around 29 vol.-% for dry recycle respectively.

Keywords: oxycoal, ITM, CCS, coal combustion, swirl burner

1. Background

The global mean atmospheric carbon dioxide (CO_2) concentration measured over the ocean surface has increased from about 315 ppm in 1958 to 386 ppm at the end of 2009, thus raising serious concerns on its potential impact on climate change [1]. Together with transportation, space heating and industrial processing, the electricity and heat generation sector is a major anthropogenic source of CO_2. Therefore the development of an emission-free, coal-fired power

plant would be an important step towards the reduction of greenhouse gas emissions into the atmosphere.

Recently, CO_2 Capture and Storage technologies (CCS) applied to the coal-based electricity and heat generation sector have gained huge interest as a promising option, which has the potential to reduce CO_2 emissions drastically [2]. This concept is usually divided into three different approaches, namely post-combustion capture, pre-combustion capture, and oxyfuel techniques. The current work is focused on the oxyfuel option and especially on pulverised coal combustion in a CO_2/O_2 atmosphere because of easy CO_2 recovery, low NOx emissions, and potential high desulfurisation efficiency.

Oxyfuel is a process of burning fuel (coal, oil, gas and other hydrocarbons) in a mixture of oxygen and recirculated flue gas (RFG), thus eliminating the presence of atmospheric nitrogen in the flue gas. The resulting flue gas is comprised primarily of carbon dioxide and water vapour along with some N_2, O_2 and trace gases like SO_2 and NO_x. The flue gas can be processed relatively easily (e.g. through rectification or distillation) to enrich the CO_2 content in the product gas further to values of 96-99 percent [4]. The purified CO_2 stream is then compressed and condensed to produce a manageable effluent of liquid CO_2, which can be sequestrated for storage or for use in subsequent processes. The purification and compression of CO_2 requires approx. 130 kWh per ton CO_2 thus reducing the efficiency of power plant. This reduction, however, may be acceptable given the environmental effects of CO_2 emissions.

To provide the oxygen necessary for an oxycoal process, currently two main options are under consideration: cryogenic (Fig. 1 (top)) and membrane air separation (Fig. 1 (bottom)). The first method is a mature technology which is already well established in industry and therefore can be easily implemented. The energy demand for oxygen production, however, is about 240 kWh per ton O_2 which together with CO_2 compression results in a net efficiency drop of a power plant of around 8-10 % - points [3]. This energy penalty can be further reduced by optimisation of the cryogenic air separation whereby values around 160 kWh per ton O_2 seem to be the optimistic technological limit [4].

The second method for oxygen supply is based on a high temperature oxygen Ion Transport Membrane (ITM) that, due to the reduced auxiliary power required for oxygen production, appears to be the more cost- and energy-effective alternative to the cryogenic process [8]. Calculations show that the use of the ITM technique in an oxycoal process for large scale plants can lead to 5–6% - point reduction of net efficiency compared to a conventional air firing power plant [9]. Furthermore, by achieving good combustion performance at low oxygen concentrations in the RFG/O_2 mixture, the investment and operational cost of an ITM based oxycoal plant can be additionally reduced [9]. Therefore, the development of the core technology and the system integration of an oxy-firing process that is based on membrane oxygen separation becomes a key issue on the way to reduce significantly the energy penalty related to the oxyfuel process. Thus the oxycoal technology will become commercially more attractive which will be important if carbon capture is going to become mandatory in a future regulatory framework.

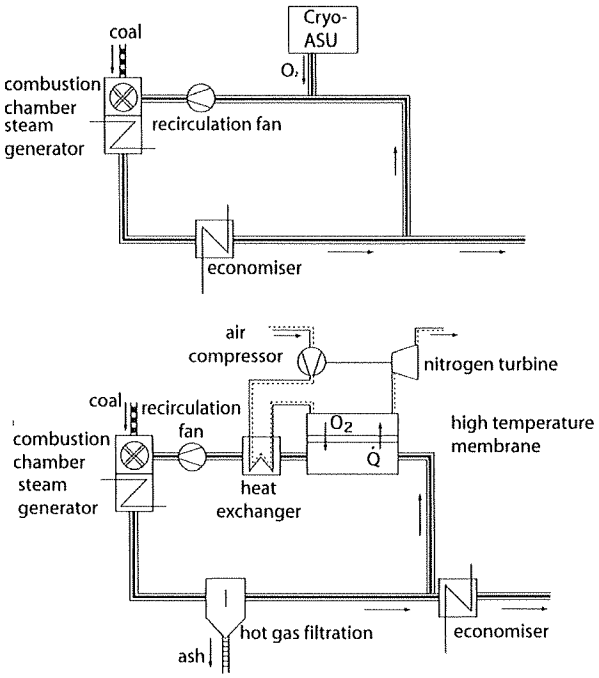

Figure 1: Schematic overview of an oxycoal process using cryogenic air separation (top) and the OXYCOAL-AC power plant process (bottom)

2. The OXYCOAL-AC Process

The OXYCOAL-AC process belongs to the group of oxygen firing processes, at which coal is burned in a mixture of oxygen and recycled flue gas. In comparison with other process variations using cryogenic technique for oxygen production, the OXYCOAL-AC process aimed to integrate the ITM as shown schematically in Fig.1 (bottom). The integration of an ITM into the process requires involvement of new components thus modifying the entire power plant process. According to these changes, the membrane will be heated and kept at its operating temperature by recirculation of flue gas that enters the membrane module at temperatures of around 850 °C. Since the ceramic membrane is susceptible to dust and sulphur the flue gas has to be cleaned in a hot gas filtration upstream of the membrane. In order to capture sulphur together with the dust, DeSOx measures have to be implemented e.g. adding of limestone before the filtration or directly into the furnace. The hot gas filtration consists of ceramic filter candles and is also operated in the temperature range around 850 °C. The filter candles are cleaned by gas pulses which blow-off the filter cake. Thus, the "cleaned" flue gas enters the membrane module, where it is enriched with oxygen.

Besides the high temperature of an ITM, a partial pressure difference of oxygen across the membrane has to be established. Oxygen is then transported from the high pressure, oxygen rich, side (feed side) through the membrane into the low pressure, oxygen lean, side (sweep side). In order to maintain the partial pressure ratio of oxygen, the feed side is pressurised with air and the sweep side is swept with flue gas which is thereby enriched with oxygen. Before entering the membrane module the pressurised air has to be pre-heated in the air-RFG heat exchanger to a temperature of about 750 °C in order not to cool down the membrane. The mean temperature of the membrane under these conditions is about 825 °C. Lastly the recirculation is closed by a RFG-fan which drives the oxygen-enriched flue gas back to the burners.
The hot retentate, primarily nitrogen, is expanded in a turbine which is used to drive the air compressor. Due to the lower turbine inlet temperature and the reduced mass flow through the turbine as compared to the air compressor it is not possible to implement a standard gas turbine. Hence an adaption of these machines becomes necessary.
Considering a state-of-the-art 600 MW_e ultra super-critical boiler burning bituminous coal, described as Reference Power Plant of North Rhine-Westphalia (RPP NRW) in [5], under these conditions the simulated net efficiency of a low level integration of the ITM into an oxyfuel cycle including CO_2 compression will be 39.3 % [9]. It corresponds to an efficiency drop of around 6.6 %-points compared to the reference air operation (η_{net} = 45.9%) which is similar to the penalty stated by Adams and Davison [6] and by Gibbins and Chalmers [7].
Considering the difference between the net power output of the RPP NRW and the ITM process without compression of the CO_2 the cost of O_2 production can be calculated. In this case the cost is estimated to be around 100 kWh per ton O_2 which is well below values for the most efficient cryogenic air separation.
By applying numerous measures, that lead to high integration of the ITM into the power plant process, the energy demand for membrane based oxygen production can be further reduced from around 100 kWh to as little as 30 kWh per ton O_2 [9].
The OXYCOAL-AC research project aims at the development of the main components for an integrated power plant process which comprises (i) combustion of pulverised coal with oxygen from a ceramic membrane-based air separation unit. The sub-projects include (ii) adapting the pilot sclale plant at RWTH Aachen to oxy-firing conditions and perfrorming of combustion tests; (iii) the design of coal oxy-firing burners, (iv) hot gas cleaning, design of the membrane module, (v) study of ceramic membrane materials, manufacturing and joining technology of ceramic membrane materials, (vi) turbomachinery for hot gas recirculation and (vii) automatic control of the integrated power plant process. This paper focuses mainly on (i) to (iv).

3. Coal combustion in O_2/RFG atmosphere

Combustion of pulverized coal in a CO_2/O_2 atmosphere as it occurs in the OXYCOAL-AC process is different from combustion in air. Several experimental investigations with oxy-firing pulverized coal burners report that flame temperature and stability are strongly affected [10-12]. CO_2 features pronounce differences of thermodynamic (higher c_p) and optical (higher emissivity) properties compared to air; therefore, it is of vital importance to know and to take into account

the effects of CO_2 properties on heat transfer and chemical reactions during pulverized coal oxy-combustion [13].

3.1. Pilot Scale Furnace

Experiments were performed in the oxycoal test facility of the Institute of Heat and Mass Transfer (WSA) at RWTH Aachen University schematically shown in Fig.2. The test rig is composed of: a vertical, cylindrical furnace (1) with a combustion chamber length of 2100 mm and an inner diameter of 400 mm, flue gas recirculation line; flue gas cleaning device (ceramic filters) for particle removal (2); heat exchanger (4); flue gas recirculation fan (5), and flue gas reservoir (6). The burner is axially movable, thus detailed information of the burning process can be obtained by optical and in-flame measurements at different distances from the burner orifice. The coal used for tests was pre-dried Rhenish lignite.

With these arrangements the facility can be operated in three different combustion modes, namely (i) air-combustion; (ii) combustion in CO_2/O_2 mixture (representing artificially dry recycle), and (iii) combustion in RFG/O_2 mixture with hot FG recirculation (representing wet recycling).

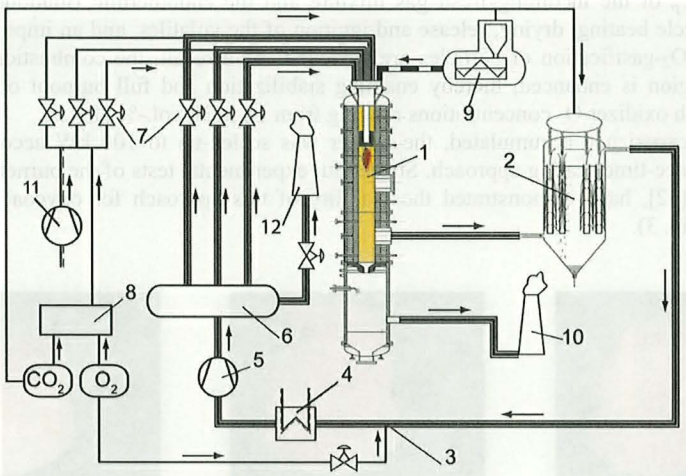

Figure 2. Simplified scheme of the oxycoal test facility at RWTH Aachen University (1-furnace;2-hot FG filtration unit; 3-oxygen addition; 4-FG cooler; 5-FG fan; 6-FG reservoir; 7-control valves; 8-gas mixing unit; 9-coal feeder; 10-flue stack; 11-air fan; 12-start-up stack)

3.1.1. Burner design and flame stability

Applying the conventional approach (normal air combustion) for burner design and operating conditions to oxyfuel operation leads to modified distributions of temperature, species, and

radiation fluxes inside the combustion chamber and results in flame instability and poor burnout [10-14]. Therefore, numerous works on this topic suggest a significant increase of the oxygen concentration in the O_2/RFG mixture (around 25–30% for wet recycle and 30–40% for dry recycle) to compensate for the higher heat capacity of CO_2. Thus, similar reaction rates and temperature levels to a PF–air flame can be achieved without significant changes to the flame aerodynamics [15,16]. This approach is based on the accumulated experience in burner aerodynamics in air-pulverized fuel combustion processes. However, the absolute value for oxygen concentration mainly depends on the burner, on the combustor design used, and on its operating conditions [10,14,17,18]. Thus, a fixed value for oxygen concentration to achieve a stable flame and full burnout cannot be assumed.

At RWTH Aachen University a novel, fluid mechanics approach for oxycoal flame stabilisation was developed [19]. It is based on the underlying interaction between burner aerodynamics and reaction kinetics. For this, a swirl burner able to operate in both air- and oxy-combustion regimes was designed by means of CFD [20]. A numerical model for oxycoal combustion was developed and validated against detailed in-flame measurements as reported by Toporov *et al.* [21]. The predicted flame was experimentally reproduced in the test facility. It is characterized by a strong internal recirculation zone, which draws hot combustion products with a temperature of about 1200 °C back toward the burner inlet. This provides the heat input required for the compensation of the higher c_p of the incoming fresh gas mixture and the endothermic Boudouard reaction. Thus, fast particle heating, drying, release and ignition of the volatiles, and an improved particle ignition and CO_2-gasification of particles are achieved. As a result, the combustion rate in the near-burner region is enhanced, thereby enabling stabilization and full burnout of an oxycoal swirl flame with oxidizer O_2 concentrations ranging from 18 to 30 vol.-% [19].

Based on the experience accumulated, the burner was scaled-up to 100 kW according to the constant residence-time scaling approach. Successful experimental tests of the burner reported by Erfurth *et al.* [22], have demonstrated the viability of this approach for oxycoal swirl flame stabilisation (Fig. 3).

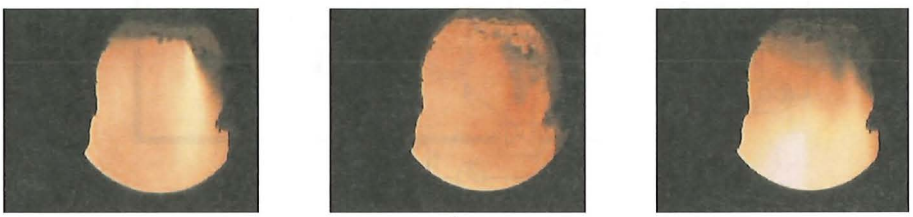

a b c

Figure 3. 80 kW pulverised coal flames obtained at the test facility at RWTH Aachen a) air-firing; and oxy-firing with 21% vol. O_2 content in b) O_2/CO_2 mixture and c) O_2/RFG mixture

3.2. Utility Scale Burner and Furnace

Direct scale up of the 100 kW burner described above to an industrial scale oxy-firing burner in the range of several MW_{th} is not possible. Instead, modifying a conventional air-firing utility

scale burner according to the measures for oxycoal swirl flame stabilization described by Förster *et al.* [25] is recommended. Following this approach, the numerical model developed for oxycoal combustion at RWTH was used for CFD based design of a 70 MW_{th} swirl burner. The new burner is able to operate in air-firing as well as at a wide range of O_2 concentrations under oxycoal combustion conditions as reported by Erfurth *et al.* [22].

By recycling flue gas (CO_2 and possibly water vapour, if the recycled gas is not dried) from the outlet back to the furnace inlet, the heat transfer inside the furnace will change because of two main properties that are changed during oxy-firing, namely: (i) the convective heat exchange will be affected by the changed gas heat capacity and gas temperature; and (ii) the radiative heat flux will be affected by the changed gas emissivity/absorptivity.

The major contributor of heat transfer from a pulverized coal flame in conventional air combustion furnaces is the thermal radiation from hot particles (fly ash, soot, and char) and from products of combustion such as water vapour, carbon dioxide, sulphur dioxide, and carbon monoxide [27]. Whereas particles emit in the whole spectrum, gases emit and absorb the radiant energy only in narrow wavelength or frequency bands. Therefore, it can be expected that at certain wavelengths these gases will be completely transparent. Based on this assumption, an engineering model can be developed that concentrates only on the part of the spectrum in which the combustion gases participate. The width of each of these so-called wide bands is an adjustable parameter and is determined by assuming that the absorption and emission of radiation in the band is equal to the effective absorption and emission of the spectral lines present within the band. Among several models suggested, the exponential wide band model (EWBM) [28] was found to be the most accurate over the widest range of pressures and temperatures important in combustion systems.

In order to estimate the impact of the recycle ratio (O_2 content) and of the composition of RFG on the heat transfer in an industrial scale furnace, numerical simulations of the combustion process in a 1210 MW_{th} state-of-the-art boiler equipped with 18 burners for oxy-firing bituminous coal were performed [26]. The changed gas radiation properties inside the furnace were considered by a non-grey implementation of the Exponential Wide Band Model [29]. Several cases were investigated numerically, namely air firing and oxy-firing with 21 and 27, and 21 and 31 vol. % O_2 concentration at the burner for wet and dry flue gas recycling, respectively (Fig. 4).

Calculations showed that a significant increase of oxygen concentration in the RFG/O_2 mixture (around 27 % for wet recycle and 30 % for dry recycle) is necessary for compensation of the higher molar heat capacity of CO_2 and thus for obtaining the same flame temperatures as those in air-firing. However, this will lead to a 16 % increase of the incident radiation to the furnace walls in case of wet recycle and 5 % for dry recycle. This effect is due to increased CO_2 and water vapour content in flue gas that results in changed optical density of the flue gas inside the furnace. Accordingly, the authors suggested [26] that heat flux to the furnace walls similar to that in air operation can be achieved under oxycoal operation when oxygen concentrations in the RFG/O_2 mixture are about 24 vol. % for wet and 29 vol. % for dry recycling (Fig. 5a).

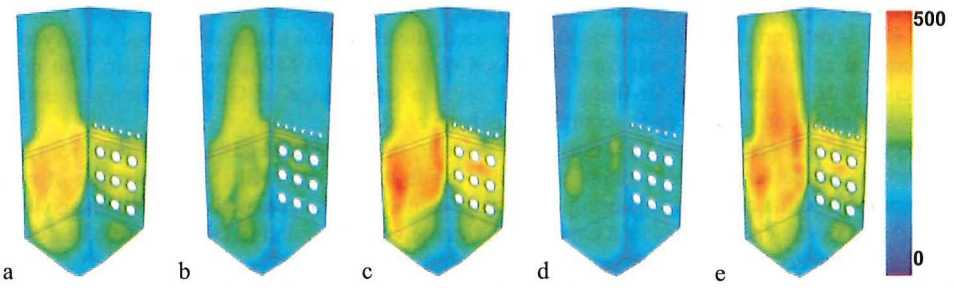

Figure 4. Predicted distribution of Surface Incident Radiation, kW/m² at furnace walls a) air; b) oxycoal 21% O_2 wet RFG; c) oxycoal 27% O_2 wet RFG; d) oxycoal 21% O_2 dry RFG; and e) oxycoal 29% O_2 dry RFG

Considering a retrofit where the global furnace heat transfer is matched, the oxy-firing case will lead to moderate changes of relative heat flux distribution to the various heat exchanger sections of the boiler which must be considered. The trends shown in Fig. 5b suggest that applying the oxygen concentration of 23.8 % and 28.6 % found for constant radiative heat transfer in the furnace would result in slightly increased enthalpy flows and moderately lower temperatures at the furnace's outlet compared to air-firing. These changes are more pronounced for wet recycle than for dry recycle. This is due to the higher water vapour content in flue gases which leads to an increase in convective heat transfer in the low temperature heat exchangers ($Pr \sim c_p$). Hence a considerable amount of attemperation for both superheated and reheated steam could be necessary.

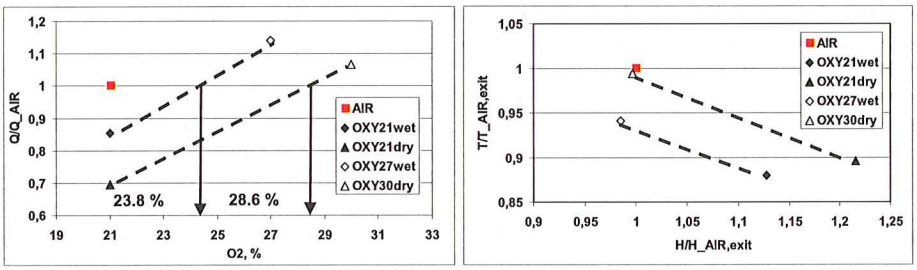

Figure 5: a) Normalised integrated surface incident radiation; b) Normalised temperature vs. normalised enthalpy flow at furnace exit

Based on these results, it follows that the oxygen concentration as well as the type of FG recycle (wet or dry) represents a degree of freedom that provides the possibility of quasi-retrofit using known elements and recycling know-how.

4. Fouling and hot gas cleaning

The hot flue gas leaving the boiler in the OXYCOAL-AC process contains fly ash, sulphur oxides (SO_2, SO_3) and alkali metal compounds. A cleaning step of the hot gas is necessary before recirculation of FG towards the membrane module. During hot gas cleaning, however, several challenges remain open, namely mechanical and chemical stability of the filter candles; the possibility to blow-off the filter cake accumulated at the filter surface; the possibility of direct flue gas desulphurization inside the cleaning facility etc.

For this purpose, experiments with a hot gas cleaning facility were conducted in the oxycoal combustion experimental plant of the RWTH Aachen University. A hot gas cleaning vessel was connected through insulated hot gas piping with the furnace exhaust. The vessel contains 6 filter candles of different types made from SiC or Al_2O_3. The filter candles accumulate the dust and are therefore periodically de-dusted by a CO_2 backflow gas pulse. The flue gas was provided by the coal fired 80 kW_{th} oxyfuel furnace. The operational behaviour of the filtration facility (Δp_{Filter}), the adhesion and de-dusting properties of the filter cake as well as the filter cake's composition were investigated.

First of all the experiments showed an increased fouling and slagging behaviour of the fly ash during oxy-combustion compared to conventional air-combustion. This led to fast accumulation of slag at the furnace exit where part of the flue gas was taken for recirculation. These observations raise serious concerns about the slagging problematic inside an oxy-firing furnace. Therefore, further investigations should bring more information about the ash behaviour in oxyfuel atmosphere.

Further, the experiments show that at flue gas temperatures above approximately 700 °C the softening of the fly ash impeded back pulse filter cleaning and therefore caused the filter to clog as shown in Fig. 6 (right). As the ash's alkali carbonate/sulphate compounds have a high impact on the softening temperature of the ash, it is taken into consideration that alkali abatement can decrease the adhesiveness of the ash and improve the de-dusting process. A common concept is the application of getter materials based on Al_2O_3 and SiO_2 which produce aluminosilicates [24] e.g. through

$$2NaCl + H_2O + Al_2O_3 + 2SiO_2 \rightarrow 2NaAlSiO_4 + 2HCl \quad (1)$$

$$2NaCl + H_2O + Al_2O_3.xSiO_2 + 5SiO_2 \rightarrow 2NaAlSi_3O_8 + 2HCl \quad (2)$$

Experiments performed at the oxycoal test facility have shown that the adhesiveness of the ash at high temperatures can be significantly reduced by adding aluminosilicate alkali getter materials to the coal (approx. 5% of coal mass flow). Ash analysis showed that the ash exhibits a higher alkali content due to the getter material capture, thus reducing the stickiness of the particles. Measurements of the alkali (sodium and potassium) content in the flue gas indicated a reduction of the Na^+ and K^+ concentrations in the gas phase which resulted also in reduction of the slagging on the furnace exhaust [23].

Another point of research is looking into sulphates and carbonates formation, since the sulphate formation can be used for a potential desulphurisation. First analysis indicated an increased amount of carbonates ($CaCO_3$) formed in the fly ash which is much higher than for the air-firing

case. This is caused by the increased CO_2 partial pressure in the flue gas. In the gas phase SO_2 could not be detected, therefore the sulphur is believed to be present as SO_3.

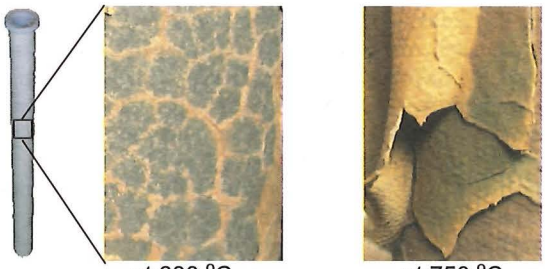

Figure 6. Surface of the filter candles (left) after backflow gas pulse showing complete cleaning at flue gas temperatures up to 600 °C (middle), and incomplete cleaning at temperatures about 750 °C (right) [23]

Hence the experimental focus is directed towards direct desulfurization during hot gas cleaning. Limestone powder will be mixed with the coal or added at the entry of the hot gas piping and entrained by the flue gas to the hot gas cleaning vessel. Comparable to desulphurisation in fluidised bed combustion the sulphur oxides contained in the flue gas react with the calcium oxide from limestone producing calcium sulphate. Calcium oxide/carbonate which has not fully reacted before reaching the filter candles then becomes part of the filter cake thus forming a reacting packed bed which is passed through by flue gas. In contrast to combustion with air the high carbon dioxide content in the flue gas might constrain the production of carbon sulphate which has to be examined as well (thermodynamic equilibrium vs. kinetics).
Thus, the flue gas composition was determined at two measuring points upstream and downstream of the filtration facility. This measure was taken to determine possible reactions of flue gas with the filter cake or the filter cartridge material. The measurements could not detect SO_2 in the RFG and therefore it is assumed that the sulphur appears as SO_3. Hence SO_3 measurements are planned for the next tests.
Due to the heterogeneous character of the reaction, the particle surface, porosity and sintering behaviour of the getter material are of importance. Different concepts will be studied, e.g. mixing of getter material with coal before combustion, adding the getter material together with limestone powder at the entry of the hot gas piping, or a separate packed bed reactor downstream of the filter candles.

5. Membrane module

Basically, there are two different concepts for including the air separation unit into the OXYCOAL-AC process. In the first concept the recirculated hot flue gas (around 850° C), after

being cleaned from particulates, flows over the membrane surface thus bringing the necessary heat input for the membrane operation and can assimilate oxygen directly, see Fig. 7 (left).

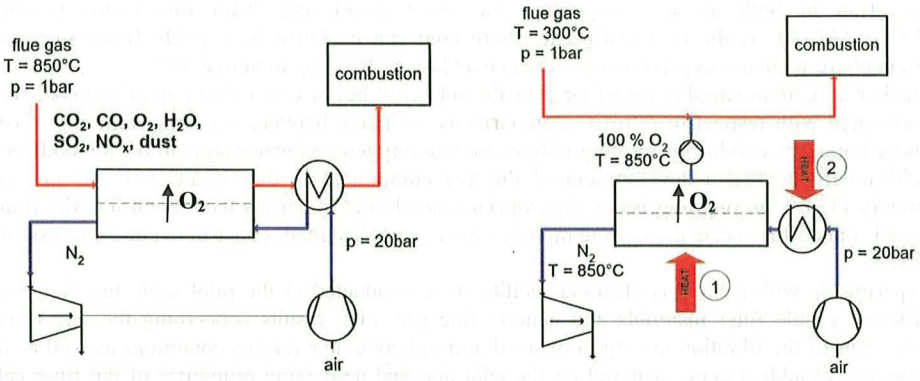

Figure 7. Schematic diagrams of oxygen enrichment using ITM with direct contact with flue gas (left) and without direct contact with flue gas (right) [30]

However, membrane materials having the highest permeation rate at the conditions of interest are not resistant to CO_2 and SO_x. Therefore the development of new membrane materials that do not loose their permeation abilities in direct contact with flue gas is an ongoing issue [30]. Since such materials are not yet available, an alternative solution is considered (see Fig. 7 (right)) that avoids direct contact between flue gas and the membrane. The oxygen, in this case, is extracted from the membrane module by a vacuum pump. Such an ITM module composed of 1000 tubes with a membrane area of about 23.5 m^2 and able to produce 1.4 tons O_2 per day was designed and is currently integrated into the OXYCOAL-AC test rig. Thus the whole process can be closed and during next test run campaigns the oxycoal process can be realized without external supply of oxygen.

6. Conclusions

Replacing air by a mixture of recycled flue gas and O_2 (oxycoal) has gained a justified interest as a promising option for reduction of green house gas emissions to the atmosphere from fossil fuel power generation due to a relatively low efficiency loss.
In contrast to air blown systems, however, the oxyfuel technology offers the possibility to vary a large set of parameters, eg. temperature levels, oxygen concentration used for firing and composition of recycled flue gas. Therefore in order to obtain the optimum process conditions, basic research on pulverized fuel oxy-firing, combined with bench scale experiments, is required.
In the framework of the OXYCOAL-AC research project, detailed experimental and numerical investigations of pulverised coal swirl flames have been made. The effects of high CO_2 concentrations in the gas mixture during oxy-firing on the volatiles and on particle ignition, flame propagation, flame stability, emissions and heat transfer in the boiler have

been investigated and analyzed. Measures for oxy-flame stabilization as a function of flue gas recycling ratio (O_2 content) are derived and the design of a swirl burner able to stable operation in both air and oxy-firing has been developed. With this status reached, OXYCOAL-AC is the first test-plant where coal can be burnt in a stable flame in a CO_2 atmosphere with an oxygen content between as low as 18 % up to above 30 %.
Further numerical simulations of large scale industrial boiler oxy-firing pulverised coal were performed with respect to retrofit. Comparisons are made between air firing and oxy- firing under boundary conditions varying with respect to oxygen and water content of the oxidiser.
Additionally to that a development of the key component in the OXYCOAL-AC process, namely ITM is an ongoing issue. Appropriate membrane materials have been identified and tested. Laboratory scale membrane modules have been designed, constructed and successfully tested.
Experiments with a hot gas cleaning facility were conducted at the pilot scale test rig, using different candle filter materials and generic flue gas. First results concerning the operational behaviour of the filtration facility in oxycoal atmosphere under various conditions as well as the influence of adding getter material on the adhesion and de-dusting properties of the filter cake were obtained. Based on this, further, more fundamental investigations related to ash behaviour in oxycoal atmosphere are planned.
Thus, the experience accumulated from different technical areas, supported by fundamental research, small scale tests and engineering design was connected into one process. This provides the understanding and knowledge to master the core technology and the system integration as designed for an efficient use of the oxyfuel technology.

Acknowledgments

The authors gratefully acknowledge financial support by the German Federal Ministry of Economics and Technology (BMWi, fkz 0326890a), Ministry of Innovation, Science, Research and Technology of the State of NRW (miwft, fkz 22320601703), RWE Power AG, E.on AG, Siemens AG, Linde AG, Hitachi Power Europe GmbH, MAN Turbo AG and WS-Wärmeprozesstechnik GmbH.

References:

1. P. Tans, NOAA/ESRL (www.esrl.noaa.gov/gmd/ccgg/trends/)
2. Tanaka N., What role for coal in carbon-constrained world? Fourth International Conference on Clean Coal Technologies CCT2009, Dresden, Germany, 18-21 May 2009, [CD-ROM]
3. Davison, J., Performance and costs of power plants with capture and storage of CO_2. *Energy* 32, 1163–1176, 2007
4. Tranier J., Perrin N. and Darde A., ASU and CO_2 CPU for oxy-combustion, 3rd IEAGHG Int. Oxy-combustion network, Yokohama, 5th-6th March, Japan, 2008 available at: http://www.co2captureandstorage.info/networks/oxyfuelmeetings.htm
5. VGB, Konzeptstudie Referenzkraftwerk Nordrhein-Westfalen (RKW NRW). Tech. Rep. 85.65.69 - T - 138, VGB PowerTech Service GmbH, December 2003.
6. Adams, D., Davison, J., Capturing CO_2. Tech. Rep., International Energy Agency Greenhouse Gas Programme, IEAGHG 2007.
7. Gibbins, J., Chalmers, H., Carbon capture and storage. Tech. Rep. 2006a, International Energy Agency Greenhouse Gas Programme, IEAGHG 2006.

8. Ph. Armstrong, R. Underwood, V. Stein and T. Foster, ITM Oxygen for the Real World: Pilot Scale testing and Beyond, International Pittsburgh Coal Conference, Sept. 29–Oct. 2, 2008, Pittsburgh, PA
9. H. Stadler, F. Beggel, M. Habermehl, B. Persigehl, R. Kneer, M. Modigell, P. Jeschke, Oxyfuel Coal Combustion by Efficient Integration of Oxygen Transport Membranes, Int. J. Greenh. Gas Con, DOI:10.1016/j.ijggc.2010.03.004
10. D. M. Woycenko, I. Ikeda and W. L. van de Kamp, Combustion of Pulverised Coal in a Mixture of Oxygen and Recycled Flue Gas, Report of IFRF Doc. F98/Y/1, Nov. 1994, Ijmuiden, The Netherlands.
11. S. P. Khare, T. F. Wall, A. Y. Farida, Y. Liu, B. Moghtaderi and R. P. Gupta, Factors influencing the ignition of flames from airfired swirl pf burners retrofitted to oxy-fuel, Fuel, 2008, 87, 1042– 1049.
12. Kiga, Takano, Kimura, Omata, Okawa, Mori and Kato, *Energy Convers. Manage.*, 1997, 38, pp129–134.
13. D. Toporov, M. Forster, R. Kneer, Combustion of Pulverised fuel in CO_2 Atmosphere, Handbook of Combustion, Vol. 5: New Technologies, Eds: M. Lackner, F. Winter, A. Agarwal, Wiley Press, 2010, ISBN: 978-3-527-32449-1
14. D. Toporov, M. Forster, R. Kneer, *Clean Air*, 2007, 8, 321–338.
15. Wall, T. (2007) *Proceedings of the Combustion Institute*, 31, 31–47
16. Croiset, E. and Thambimuthu, K.V. (2001) *Fuel,* 80, 2117–2121.
17. Wendt, J. Stability of axial pulverised coal flames under oxy-coal combustion conditions. 2nd IEAGHG Int. Oxy- Combustion Network, Windsor, CT, USA, 25th–26th January, 2007, available at: http://www.co2captureandstorage.info/ networks/oxyfuelmeetings.htm.
18. Kluger F., Monckert P., Krohmer B., Stamatelopoulos G.-N., Jacoby J., Burchhardt U., Oxyfuel Pulverised Coal Steam Generator Development 30 MWth Pilot Steam Generator Commissioning and Testing, 1st IEA GHG International Oxyfuel Combustion Conference, Cottbus, Germany, 8-11 Sept., 2009, available at: http://www.co2captureandstorage.info/OCC1/OCC1_Programme.htm on 31.03.2010
19. D. Toporov, M. Forster, R. Kneer, Combustion of Pulverised Fuel under Oxycoal Conditions at low Oxygen Concentrations, Third International Conference on Clean Coal Technologies for our Future, Cagliari, Sardinia, Italy, 15–17 May 2007, [CD-ROM]
20. Heil, P., Toporov, D., Stadler, H.,Tschunko, S., Forster, M., and Kneer, R. (2009) *Fuel*, 88, 1269–1274
21. Toporov, D., Bocian, P., Heil, P., Kellermann, A., Stadler, H., Tschunko, S., Forster, M., and Kneer, R. (2008) *J Combust Flame*, 155, 605–618
22. Erfurth J., Toporov D., Forster M., R. Kneer, Oxycoal Swirl Burners: From Bench to Industrial Scale, 10th Int. Conf. on Energy for a Clean Environment, IST Lisbon, Portugal, 7th-10th July 2009 [CD-ROM]
23. Kellermann A., Habermehl M., Forster m. and R. Kneer, First Operational Tests of an Oxycoal Hot Gas Cleaning Facility, 24. Deutscher Flammentag, Verbrennung und Feuerungen, VDI-Berichte 1988, Sept, 2009, Bochum, Germany [CD-ROM] (in German)
24. R. Gwosdek, Minderung des Alkaligehaltes von Rauchgasen bei Temperaturen über 1000 C, Fortschr.-Ber. VDI, Reihe 15: Umwelt Nr. 131, VDI-Verlag, Dusseldorf, 1994.
25. M. Förster, D. Toporov and R. Kneer, Verfahren zur Verbrennung von pulverisiertem Brennmaterial, *Pat. Nr.: WO 2008/135275A4*, from 07.05.2007
26. Erfurth J., Toporov D., Forster M. and R. Kneer, Numerical Simulation of a 1200 MW_{th} Pulverised Fuel Oxy-firing Furnace, Fourth International Conference on Clean Coal Technologies CCT2009, Dresden, Germany, 18-21 May 2009, [CD-ROM]
27. Blokh, A. (1988) Heat Transfer in Steam Boilers, Hemisphere, Washington, DC.
28. Edwards, D. (1976) Advances in Heat Transfer, vol. 12, Academic Press, New York, pp. 115–193.
29. Erfurth J., Toporov D., Forster M. and R. Kneer, Simulation of radiative Heat Transfer in a large-scale Oxycoal Furnace, 24. Deutscher Flammentag, Verbrennung und Feuerungen, VDI-Berichte 1988, Sept, 2009, Bochum, Germany [CD-ROM]
30. Beggel, S. Engels, M. Modigell and N. Nauels, Oxyfuel combustion by means of high temperature membranes for air separation, Fourth International Conference on Clean Coal Technologies CCT2009, 18–21 May 2009, Dresden, Germany, [CD-ROM]

9th Liege Conference : Materials for Advanced Power Engineering 2010
edited by J. Lecomte-Beckers, Q. Contrepois, T. Beck and B. Kuhn.

PRELIMINARY EXPERIENCES WITH MATERIAL TESTING AT THE OXYFUEL PILOT PLANT AT SCHWARZEPUMPE

Anders Hjörnhede[1], Melanie Montgomery[2], Martin Bjurman[3], Pamela Henderson[3], Alexander Gerhardt[4]

[1]Vattenfall Power Consultant, Sweden
[2]DTU Mekanik/Vattenfall Heat Nordic, 2800 Lyngby, Denmark
[3]Vattenfall Research and Development, Sweden
[4]Vattenfall Research and Development, Germany

Several material related issues may arise from oxyfuel combustion of coal due to the presence of CO_2 but also as an effect of the partial recirculation of the flue gas. Two examples are increased corrosion and carburisation which may limit steam data, hence limiting the efficiency.

A number of corrosion tests, in both conventional air-firing and oxyfuel mode, have been made in Vattenfalls 30 MW oxyfuel pilot plant located in Schwarze Pumpe, Germany. Internally cooled corrosion probes, equipped with ferritic, austenitic, super austenitic steels as well as Ni-based and FeCrAl alloys, simulating superheaters, economisers and air preheaters were exposed for up to 1500 hrs.

The analyses show an indication of higher material wastage in oxyfuel compared to air combustion especially at the lower exposure temperatures. This may be due to increased sulphur concentration in corrosion front, increased heat flux, carburisation or other preciptate formations on austenitic steels and Ni-based alloys.

Keywords: CCS, oxyfuel, oxyfuel pilot plant, corrosion

1. Introduction

All over the world, fossil fuels are combusted in power plants resulting in CO_2 emissions which contributes to global warming. In order to reduce CO_2 emissions from coal-fired plants, it is necessary to implement new technologies resulting in carbon capture and storage (CCS). One of the possible technologies is oxyfuel firing and capturing of CO_2. Bordenet [1] gives a survey of the material challenges with respect to oxyfuel combustion plants with CO_2 capture and post combustion plants. In oxyfuel firing, combustion occurs with oxygen such that the resulting flue gas will be mainly CO_2 and H_2O. In addition there maybe recirculation of up to 2/3 of the flue gas, thus any trace elements such as sulphur in the flue gas will build up in concentration. The higher content of CO_2 in the flue gas will make it more cost effective to recapture CO_2 after combustion. Vattenfall has constructed a 30MW oxyfuel pilot plant to validate engineering work, to learn and improve understanding of the dynamics of oxyfuel combustion and to demonstrate the capture technology, [2]. The construction of this plant started in 2007, and in late 2008 the test phase began. The pilot plant is located in Schwarze Pumpe, Germany.

Material tests are being performed both under conventional air and oxyfuel firing at various operation conditions to reveal whether the oxyfuel process gives additional materials challenges. These tests are important as the choice of suitable materials will be a key issue for the future demonstration plant. With respect to high temperature corrosion, since the actual plant has a low steam outlet temperature of 350°C, corrosion probes simulating higher steam temperatures are inserted in the plant. In addition, probes simulating waterwalls are also exposed. The three gaseous species which will increase compared to conventional firing are

CO_2, H_2O and SO_2 (due to recirculation of flue gas). However, as of yet it is unclear how this will effect corrosion rates. An initial comparison of corrosion in oxyfuel versus conventional combustion was conducted in the ENCAP programme [3]. The exposures times were below 40 hours and the results showed no significant difference between conventional firing and oxyfuel firing, indicating that there is a need for data from long-term exposures.

There are a number of different applications which are relevant for corrosion investigation:

- Demonstration plants:

Vattenfall in Germany is preparing for the erection of a 250MWe demonstration plant, purpose-built for oxyfuel firing in Jänschwalde, Germany. In the demonstration plant, the technology's commercial abilities will be proven whereas in the pilot plant the technology itself and the process are being validated. The maximum steam temperature of the demonstration plant will be 600°C. The high temperature components will be the steel types commercially available today. Knowledge of how these types of steels react in an oxyfuel environment is lacking, but the well known creep, microstructure and steam oxidation data can be used.

- Retrofit of existing USC (Ultra Super Critical) boilers:

If it appears unlikely that many new plants will be purpose-built for oxyfuel combustion in order to reduce CO_2 emissions, it is possible to retrofit already high efficiency USC boilers to oxyfuel firing. Here the steam temperature will be similar to or slightly higher than the Jänschwalde demo.

- High efficiency oxyfuel plants:

In order to recuperate the expenses of a CO_2 recapture plant, it may be necessary to increase the steam data of the plant to give the same net efficiency as the existing USC boilers. This involves employing steam temperatures of up to 700°C. At present there is no plant that runs with such high temperatures so this is challenging not only for the fireside corrosion but for steamside oxidation, microstructural stability and creep development. There are various projects that are investigating 650-700°C plants, which will give information which is also relevant for oxyfuel plants. These programs are COMET 650 (completed), AD700, COMTES 700. It is important that the steels qualified within these programs are considered as they will have already been tested with respect to welding, microstructure development and steam oxidation. So far no tests have been performed in the pilot plant at these high temperatures.

- Low Temperature and CO_2 processing unit:

Another essential part of the material testing is corrosion at low temperatures in the preheater and flue gas desulphurisation unit, flue gas condenser and CO_2 processing unit. These aspects are being investigated in the pilot plant and the knowledge is relevant for all future CCS plants irrespective of boiler outlet temperature. Low temperature corrosion is investigated by coupons installed after the boiler where corrosion problems are anticipated. In addition online corrosion sensors and corrosion probes are utilised.

2. Material testing parameters

Figure 1 shows a schematic flow sheet of the oxyfuel pilot plant in Schwarze Pumpe. It is important to note that the recirculation of the gas is before the flue gas desulphurization plant thus the content of sulphur and other impurities will increase with time. The percentage of

recirculated flue gas in the inlet gas stream is 20 - 39%. Low temperature corrosion investigations are undertaken in the areas shown on the diagram and also in the CO_2 process unit. In these areas, racks of test coupons of different materials are exposed to aid materials selection. In addition condensates are collected so that the mechanism of corrosion can be investigated and materials can be tested with similar condensates in controlled conditions in the laboratory. There are no results available from this work at present.

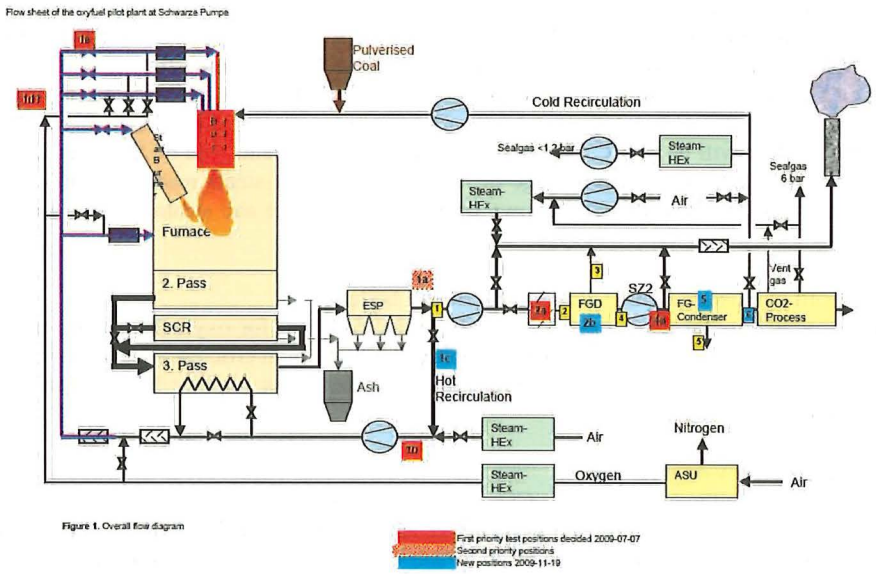

Figure 1. Process flow sheet of oxyfuel plant.

Flue gas temperatures are lower when the boiler is run in oxyfuel mode compared to air-firing mode. A comparison of gas compositions measured after the electrostatic precipitator is given in Table 1. During air-firing the SO_2 levels in the flue gas varied between 1400-1800 mg/Nm^3 whereas during oxyfuel mode the SO_2 levels were about 4 times higher, being in the range 6500-8000 mg/Nm^3. Moisture as well as NOx levels were also about four times higher in oxyfuel mode. As expected the CO_2 levels are also much higher. SO_3 levels were higher in the fly ash in the oxyfuel but otherwise the compositions of the fly ash were similar between the two firing modes.

Table 1: Approximate flue gas composition after ESP and SO_3 levels in the fly-ash.

	SO_2 mg/Nm^3	O_2 Vol%	CO mg/Nm^3	CO_2 Vol%	H_2O Vol%	NOx Mg/Nm^3	Fly-ash SO_3 mg/kg
Air-firing	1600	6	7	13	8	300	46 ± 9
Oxyfuel	7000	6.8	2.5	95	30	1600	77 ± 18

Corrosion probe tests were performed both during air-firing and oxyfuel mode. Each test lasted about 250 hrs. Probes simulating superheaters, with a metal temperature of 580°C were installed before the first superheater bundle meeting the flue gas, at a gas temperature of about 760°C in oxyfuel mode and 840°C in air mode. Additional corrosion tests were performed for

1320 hrs but only in oxyfuel mode. Corrosion probes were also exposed at 650°C for 1250 hrs in oxyfuel mode only. The location was the same as for the 250 hrs exposure. Specially designed probes which simulate waterwall conditions were also used. The metal temperature was 430°C and exposure time about 1500 hrs. The alloys investigated are shown in Table 2.

The wall thicknesses and masses of the ring specimens were measured before and after exposure. In addition oxide thickness was measured and the oxide/corrosion product was investigated with LOM (Light Optical Microscope) and scanning electron microscope, SEM-EDS. Specimens were etched to reveal the presence of carbides using Murakami solution.

Table 2. Chemical composition of materials investigated.

	C	Fe	Cr	Ni	Mo	Mn	Si	Cu	*Others*
15Mo3	0.12-0.20	rest			0.25-0.35	0.10-0.35	0.40-0.90		
TP347H FG	0.04-0.10	rest	17.0-20.0	9.0-13-0		<2.00	<1.00		*Nb 0.80-1.0*
304H	0.07-0.13	rest	17.0-19.0	7.5-10.5		<1	<0.30	2.5-3.5	*Nb 0.3-0.6 N 0.05-0.12*
Kanthal APMT	<0.05	rest	22		3	0.4	0.7		*Al 5.0*
T23	0.04-0.10	rest	1.90-2.60	-	0.05-0.30	0.10-0.60	<0.50		*Nb 0.02-0.08 W 1.45-1.75*
13CrMo44	0.08-0.18	rest	0.70-1.10	-	0.40-0.60	0.40-1.00	0.10-0.35	-	
253 MA	0.05-0.10	rest	20-22	10-12		<0.8	1.1-2.0	-	*N 0.14-0.2 Ce 0.03-0.08*
X20CrMoV121	0.17-0.23	rest	10-12.5	0.3-0.8	0.8-1.2	<1	<0.5	-	
AC 66	0.04-0.08	rest	26-28	31-33		<1.0	<0.3		*Ce 0.05-0.10 Al<0.025*
Sicromal 8	0.07	rest	6.5						*Al<0.7*
P92, T92	0.07-0.13	rest	8.5-9.5	<0.4	0.3-0.6	0.3-0.6	<0.5		*V 0.15-0.25 W 1.5 – 2 Nb 0.04 -0.09 N 0.03-0.07*
TP 310	0.05	rest	24.5	21.0			0.5		
254 SMO	<0.02	rest	19.5-20.5	17.5-18.5	6.0-6.5	<1.00	<0.8	0.5-1.0	
Inconel 617	0.05-0.15	<3.0	20-24	rest	8-10	<1	<1	-	*Al 0.8-1.5, B <0.006, Ti <0.6*
C276	<0.02	4-7	14.5-16.5	rest	15-17	<1.0	<0.08		*W 3.0-4.5 Co<2.5*
Sanicro 25	0.1	rest	22.5	25		0.5	0.2		*W 3.6 Nb 0.5*
Sanicro 63	<0.10	<5.0	20-23	rest	8-10	<0.50	0.50		*Nb 3.15-4.15*

For testing in the 3rd pass (the location of economizers), gradient probes were used and the temperature is controlled along the probe such that testing of different temperatures can be undertaken with one probe. The temperature gradient of the probe was 170-70°C and the exposure time was 250 hrs in both oxyfuel fuel and air-firing mode. Two steel types were mounted on this probe, the low alloyed 15Mo3 steel and austenitic steel 304L (similar to 304H in Table 2 but with variations in C and N content). The estimated flue gas temperature was 270°C.

Another test in oxyfuel mode, with a longer exposure time of 1000 hrs, was performed at a position where the fluegas temperature was 350°C. The probes had temperature gradients of

approximately 60-200ºC along the length of the set of sample rings and the exposed alloys were 15Mo3 and 254 SMO.

Deposit probe tests of 6 hours were performed in air and oxyfuel modes. Probes were inserted before the first superheater bundle where the flue gas temperature was 760°C in oxyfuel mode and 840°C in air mode. The probes consisted of both 10CrMo910 and 304L rings internally cooled to temperatures of 580°C, 650°C and 760°C. Rings were weighed before and after exposure to estimate deposition rates. The deposits were then analysed with SEM/EDS.

3. Results

3.1. Deposit probes

The deposition rates were generally higher in oxyfuel than in air (Figure 2). Deposition rates were also lower on the stainless steel substrate for all firing modes. It was noted that there was some deposit/dust lost during dismantling of the austenitic alloy deposit rings. With increase in probe temperature, there is an increase in deposition rate. In pre-mixed mode the oxygen is mixed with the recirculation gases without the detailed control of the blend, allowed in mode A and mode B.

The rings with the deposits were then analysed with SEM/EDX. There are no great differences for different firing modes although a slight decrease in sulphur and magnesium and an increase in calcium with increasing temperature could be noted.

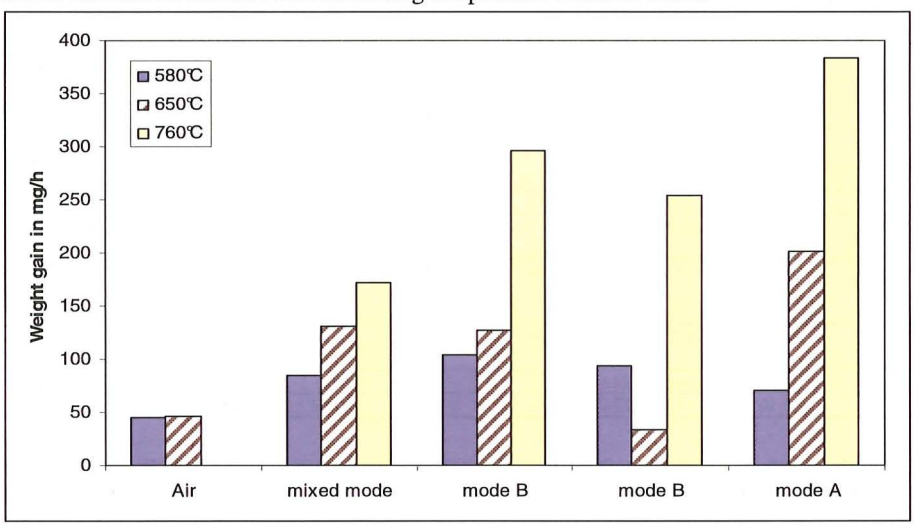

Figure 2. Deposition rates for the 10CrMo910 probe at various temperatures.

There was a difference in the distribution of the key elements around the deposit probe. In oxyfuel firing, the deposits had similar compositions on the wind- and the leeward side. However for air-firing, the calcium content was higher and the sulphur content lower on the wind side compared with the lee side.

3.2 High temperature corrosion probes

3.2.1. Waterwall probes

The corrosion results from the wall probe exposed for 1472 hours are given in Table 3. The remaining metal after exposure was measured in the SEM on cross-sections used for microstructural examination and subtracted from the average thickness measured by micrometer before testing to give a value for the metal loss. The thickness of the oxide layer was also measured with SEM. The steel with the best corrosion properties by far is Sicromal 8, EN1.4713 giving a corrosion rate of 23µm/1000hrs. The corrosion rates of the 10CrMo910, 13CrMo44 and 15Mo3 steels are unacceptably high with rates of 162, 139 and 269µm/1000hrs, respectively.

Table 3. Comparison of material loss and measured oxide thickness with SEM for the wall probe.

Material	Thickness unexposed (mm)	Metal Thickness after exposure (mm)	Material loss (µm)	Thickness of oxide (µm)	Corrosion rate in µm per 1000 h.
10 Cr Mo 9 10	2,662	2,423	239	200-250	162
13 Cr Mo 4 4	2,692	2,487	205	20-40	139
15 Mo 3	2,7165	2,321	396	300	269
1.4713	2,9295	2,896	34	40	23

3.2.2. Superheater probes 250 hrs, 580°C

The specimens from the 250 hrs exposure were measured before and after exposure, but due to the low corrosion rates, the metal loss measurements had a large degree of inaccuracy. Therefore oxide thickness measurements were used and the data is given in Figure 3. When the oxide becomes thicker there is a tendency for spallation which is revealed for results for 15Mo3.

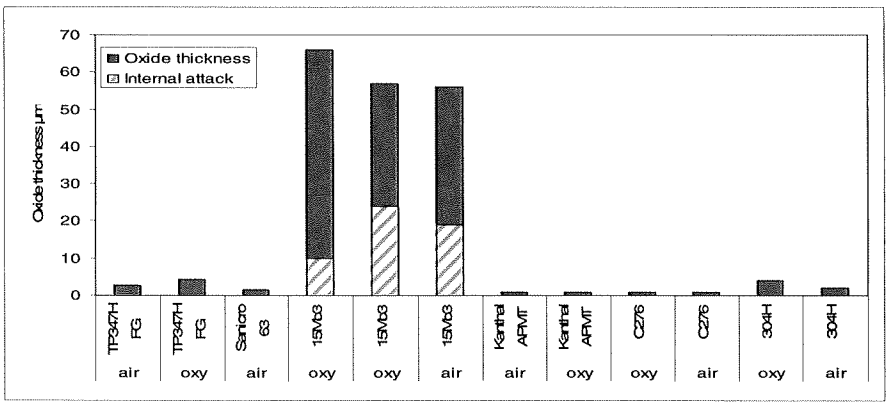

Figure 3. Measurement of oxide thickness and internal corrosion.

All specimens were etched with Murakami to reveal carbides and there was no great difference between oxyfuel and air firing. Figure 4 shows the micrographs from TP347H FG steel. The internal attack was grain boundary corrosion and not carburisation. Perhaps a slight indication of increased precipitation is observed for oxyfuel, but this was localised.

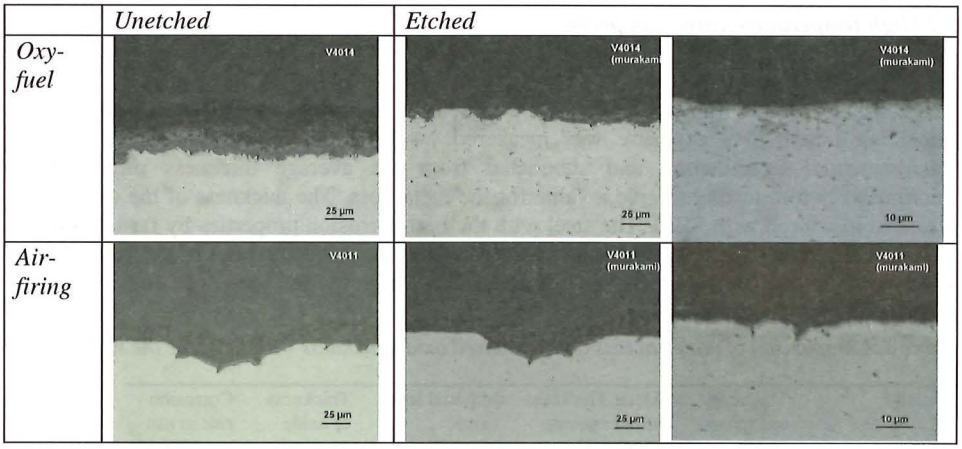

Figure 4. Light optical microscopy of TP347H FG specimens.

Specimens were also examined with SEM/EDX to analyse if there was more sulphidation for the oxyfuel specimen. No specific increase in sulphidation was revealed and sulphur was present within the oxide of both oxyfuel and air-firng specimens.

3.2.3. 1300 hrs, 580 ℃

The metal loss was measured at 24 positions around the circumference of the probe exposed for 1319 hours at 580°C and the results are shown in Figure 5. It was not possible to measure the corrosion of the Sanicro 63 alloy so its corrosion rate was estimated by comparing the oxide thickness of this specimen with a number of others and the results are shown in Figure 6. The results show that the corrosion of Sanicro 63 at 580°C is in a similar range to that of TP347 HFG and 253 MA, *i.e* under 10µm per 1000 hours. 13CrMo44, T23 and 15Mo3 all show unacceptably high corrosion rates.

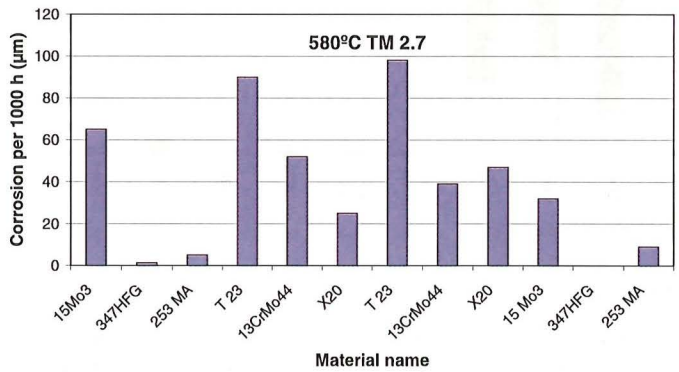

Figure 5. Average metal loss in µm per 1000 h for specimens exposed for 1319 hours at 580 ℃.

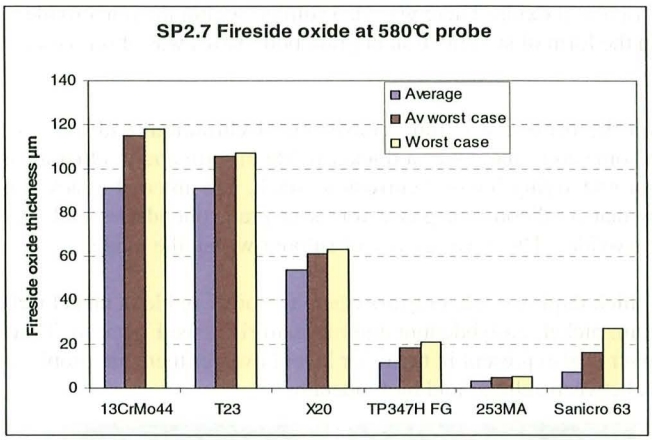

Figure 6. Oxide thicknesses on samples from 580°C probe.

3.2.4. Microstructure of samples exposed at 580°C

For the low alloy ferritic steels 13CrMo44 and T23, the outer oxide was iron rich with elements from fly ash deposit. The inner oxide was iron oxide enriched in chromium. For T23 the inner part of the oxide also contained a tungsten rich oxide. Traces of sulphur could be detected at the corrosion front especially at grain boundaries.

On the ferritic stainless steel X20CrMoV121 the outer oxide consisted of iron oxide and the inner oxide of chromium rich iron oxide. There was significant internal attack, not only at the grain boundaries at the corrosion front, but also within the grains. There are indications that both internal oxidation and internal sulphidation occurs (Figure 7). (Analysis in elemental wt.% should be used for comparison purpose only due to high inaccuracies in oxygen analysis).

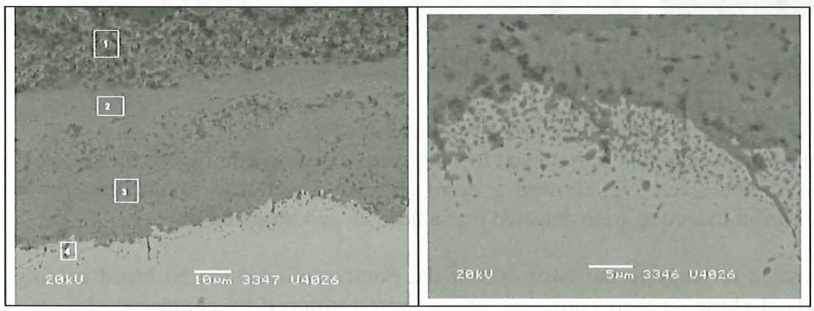

Area	O	Al	Si	S	Ca	V	Cr	Mn	Fe	Ni	Mo
1	20.15	0.59	0.45	5.87	7.17				65.77		
2	12.95						1.46	0.62	84.97		
3	9.79			0.03		0.54	20.95	1.28	64.29		3.11
4			0.83	2.06			10.54		85.01	1.57	

Figure 7. SEM-EDS analysis of fireside oxide on X20CrMoV121 exposed at 580°C.

On the austenitic TP 347H FG steel the oxide was a duplex oxide with an outer iron rich

oxide and an inner chromium rich iron oxide. There was also sulphur within the inner oxide. A very slight internal attack in the form of sulphidation at grain boundaries was observed at the corrosion front

For the 253 MA the oxide on the fireside was thin, consisting of chromium and iron rich oxide. It was observed that in some areas there was a thicker oxide of 4μm and in other areas there was a thin oxide with an underlying internal corrosion attack. The internal attack was rich in silicon and it appears that a silicon-rich phase forms at grain boundaries and then afterwards the bulk grains form oxides. There was a trace of sulphur within the oxide.

Sanicro 63 forms a relatively thick duplex oxide (15μm) where the outer oxide is nickel rich, and the inner oxide is chromium, nickel, molybdenum and niobium rich (see Figure 8). There is a strong indication that sulphur is also present in the inner layer however there are problems with overlapping EDX-signals between sulphur and molybdenum.

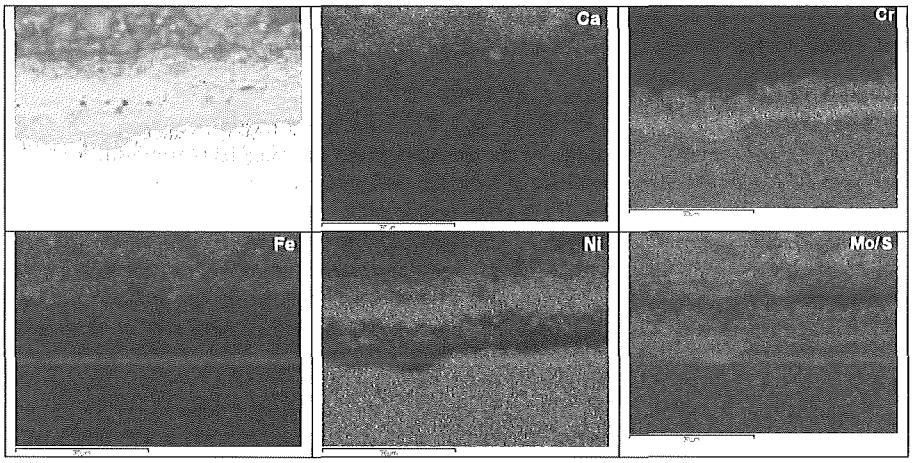

Figure 8. SEM-EDS analysis of oxide on Sanicro 63 exposed on the 580°C probe.

3.2.5. Corrosion rates from superheater probes exposed at 650°C.
The average measured corrosion normalised to 1000 hours is shown in Figure 9. All alloys, except for the ferritic steel T92, showed a corrosion rate lower than 10μm/1000hrs. No measureable material reduction were detected on Sanicro 25 and Super 304H.

It was not possible to measure the corrosion of the Sanicro 63 and the Ni-based coatings consisting of TiAl-phase so their corrosion ratings were estimated by comparing the oxide thickness of these specimens with a number of others and the results are shown in Figure 10.

The Sanicro 63 shows an oxide growth comparable with Super 304, while the welded Ni-based TiAl phase coating showed a thinner oxide thickness.

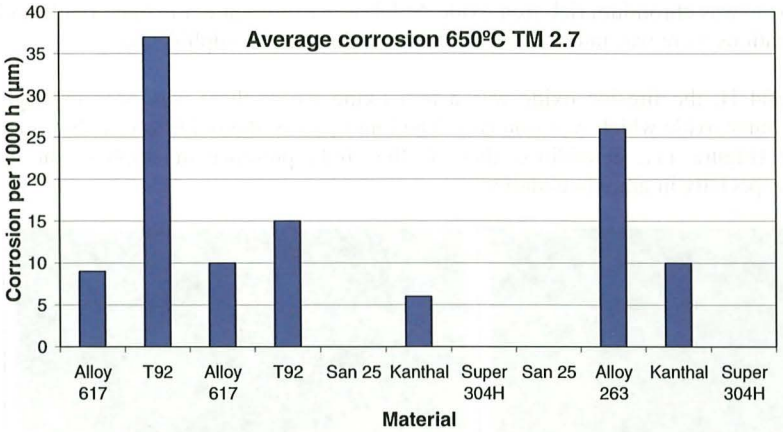

Figure 9. Average metal loss in µm per 1000 h for specimens exposed for about 1300 hrs at 650 ℃.

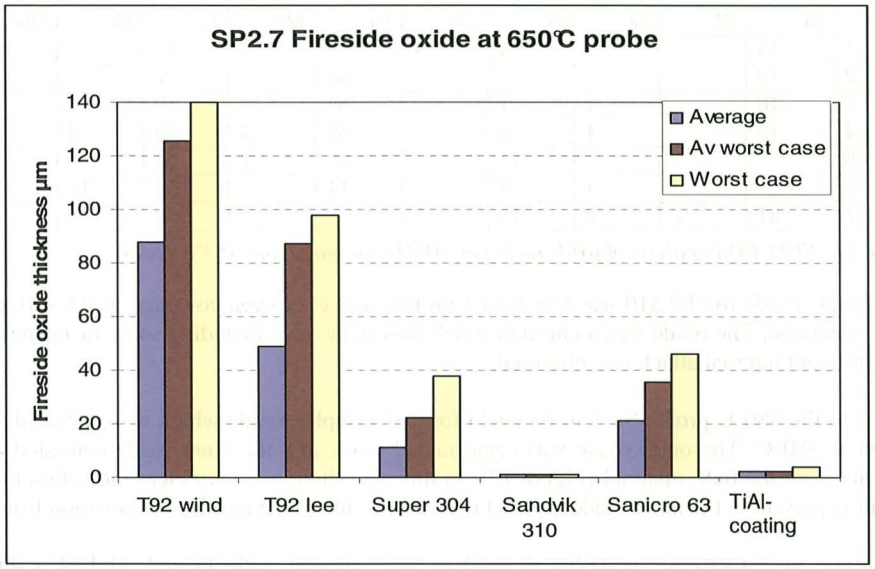

Figure 10. Oxide measurements on samples from 650 ℃ probes.

3.2.6. Microstructure of samples corroded at 650°C

For the T92 alloy the thicker oxide, located on the wind side, the outer oxide was iron rich and the inner oxide was chromium rich iron oxide. Sulphur was present in the inner oxide and especially at locations there was internal corrosion attacks in form of sulphidation.

On the Super 304 H, the fireside oxide was a thin oxide where there was occasionally a distinguishable outer oxide which was iron rich. The inner part of the oxide was a chromium rich iron oxide (Figure 11). In addition there is the slight presence of sulphides at the corrosion front especially in grain boundaries.

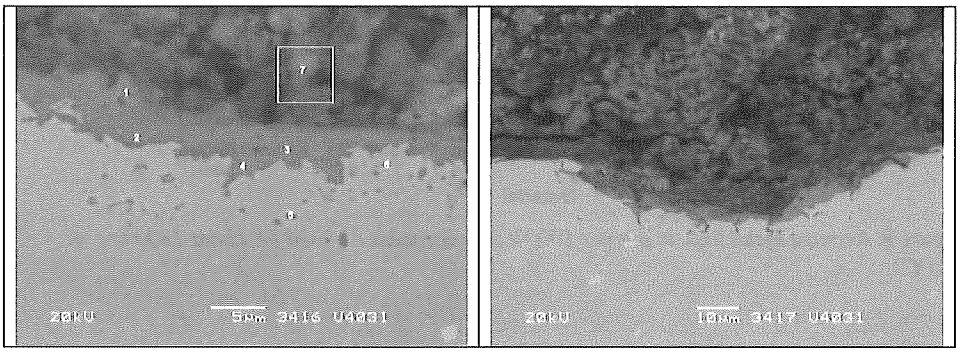

D3416	O	Al	Si	S	Ca	Cr	Mn	Fe	Ni	Cu
1	13			4	4	3		77		
2	13					80		7		
3	16		1	1		64		19		
4	13		1	2		55	3	25	2	
5				11		20	7	54	7	2
6			1	3		14		68	14	2
7	31	2	2	16	17			32		

Figure 11. SEM-EDS analysis of oxide on Super 304H exposed on the 650°C probe.

The fireside oxide for TP 310 was less than 1µm thin and gave even coverage of the surface of the specimen. The oxide was a chromium rich iron oxide also including some manganese. No significant internal attack was observed.

Similar to the 580°C probe, Sanicro 63 again formed a duplex oxide which was thicker than formed at 580°C. The outer oxide was again nickel oxide and the inner oxide consisted of elements from the bulk material (Figure 12). In this case there is a very clear indication that sulphur is present in the inner oxide and that there is also internal attack at the corrosion front.

In contrast to Sanicro 63, a Ni-based weld overlay alloyed with Ti and Al had a thin protective chromium rich oxide. Remnants of Ti and Al were found on the coataing indicating Ti and Al has promoted formation of a Cr oxide layer.

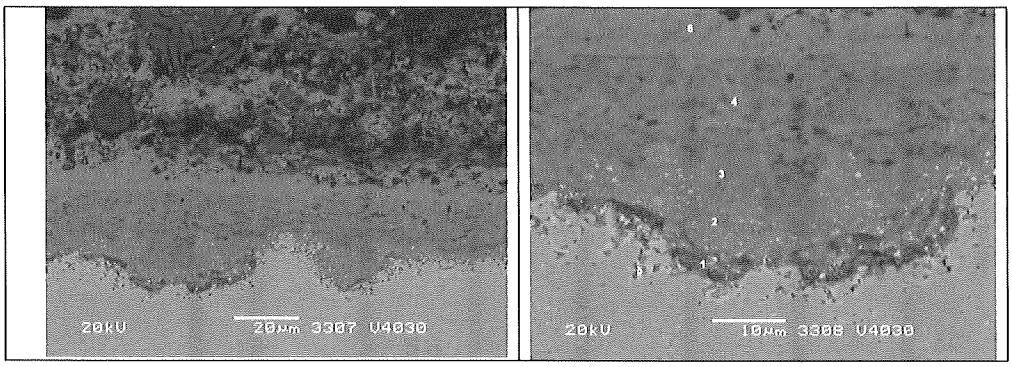

D3308	O	Al	Si	S	Ca	Ti	Cr	Fe	Ni	Nb	Mo
1	6		2	10	0	1	29	1	18	10	23
2	11		1	8		0	65		2	4	8
3	13		1	5			69		2	5	4
4	15		1	1		1	21		18	23	20
5	3	1	2	2		1	13	1	62	6	11
6	10		1	0			1	2	84	0	1

Figure 12. SEM-EDS analysis of oxide on Sanicro 63 exposed on the 650°C probe.

3.3. Low temperature corrosion temperature gradient probe tests

Both 304L and 15Mo3 were exposed on the low temperature gradient probe. The austenitic stainless steel 304L showed no corrosion after exposure in air-firing mode and minimal tarnishing in oxyfuel conditions. For the 15Mo3 specimens more corrosion was observed.

The deposits on the low temperature probes were very thin. Nevertheless it was possible to obtain samples for analysis by careful scraping of the deposits from the wind and lee sides. The results are given in Figure 13. Deposits formed during oxyfuel conditions were enriched with sulphur, especially at 170°C (20 wt% sulphur in oxyfuel compared to 4 wt% in air-firing).

The specimens were cross-sectioned and the thicknesses of the oxide layers were measured (Table 4). For all the oxyfuel specimens there was a measurable oxide, however this was only the case for the specimen at the lowest temperature for air-firing.

The chemical composition of the corrosion layer formed on 15Mo3 and 254 SMO during the 1000 hrs exposure shows that chlorine is present in the corrosion scales on the lowest temperature rings, while the amount of sulphur is higher at the higher temperatures. The high amount of carbon for the lowest temperatures indicate the presence of carbonates.

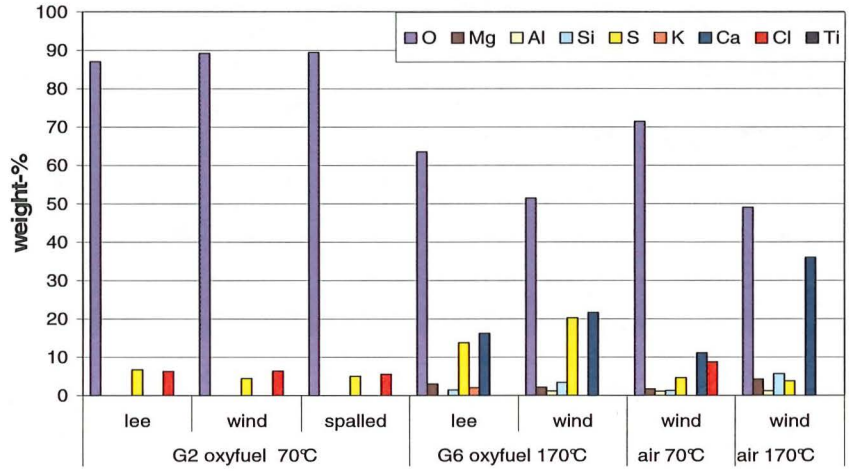

Figure 13. Chemical composition of deposits from low temperature 15Mo3 probes.

Table 4. Maximum thickness of oxide layer (μm) for the 15Mo3 on the low temperature probe exposed for 250 hrs.

	Windward side	Leeward side
Oxy-fuel 70°C	22	24
Oxy-fuel 120°C	18	<1
Oxy-fuel 170°C	17	<1
Air-firing 70°C	38	<1
Air-firing 120°C	<1	<3
Air-firing 170°C	<1	<1

Even though the exposure time is limited to 1000h all materials show measurable corrosion. 15Mo3 behaves as expected with corrosion rates up to 0,9 mm/1000h. Measurable corrosion of 254 SMO (150μm) is unexpected but it also shows the harshness of this environment, see Figure 14. The corrosion was of general type, with some local deeper pits.

SEM-EDX analysis shows that the local variations of composition in the deposits are large but that chlorides are present at the lowest temperatures. Predominantly at higher temperatures

The finding that there is no material loss at the lowest temperature and then significant loss of material from the highly alloyed 254SMO at temperatures above 90°C is somewhat unexpected. The large material loss was localised and may be due to localized defects in the material or a localized corrosive microclimate.

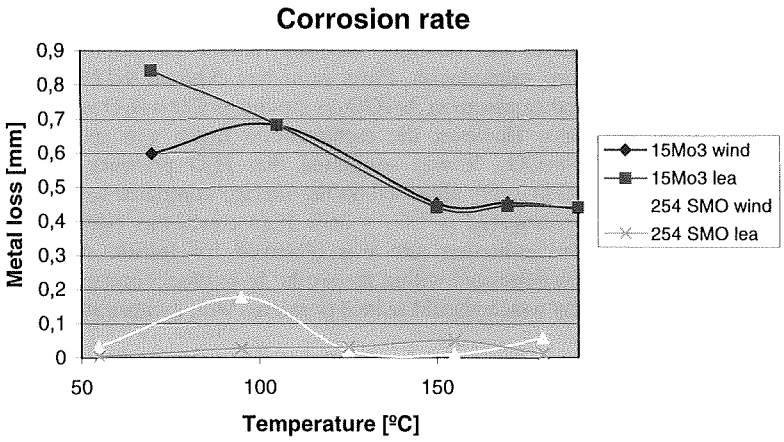

Figure 14. Corrosion rates for 15Mo3 and SMO 254 exposed on a temperature gradient probes for 1000 hrs.

4. Discussion

4.1. Deposition

There is an indication of higher deposition rate with oxyfuel than with air-firing. Further investigations need to be undertaken as only one deposit probe was used in air-firing and there were no results at the highest temperature. A higher deposition rate leads to slagging and fouling problems and decreases heat uptake of the superheaters. Sheng and Li [4] investigated ash formation during pulverised coal combustion in O_2/CO_2 mixtures compared with O_2/N_2 mixtures. Four different coal samples were burnt with various gas compositions in a drop tube furnace. The residues ash samples were characterised by X-ray diffraction and ^{57}Fe Mössbauer spectroscopy. No significant difference was observed in the crystalline phases of the ashes. However a difference in the relative intensities of peaks was observed for some phases in the two gas environments. Mössbauer spectroscopy showed that the differing atmospheres influenced the relative percentages of iron species formed in the ashes. The combustion in O_2/CO_2 resulted in more iron melting into glass silicates and less iron oxides. This could give problems with slagging and fouling.

4.1. High temperature corrosion

Similar to the results from the ENCAP studies [3] with 40 hour exposure in a burner rig, there is no significance difference in the specimens with oxyfuel and with air after 250 hrs exposure in the pilot plant. Unfortunately there are areas where we cannot make a comparison yet, for example waterwall probe testing which will be considered in future studies. Although there is an indication of high waterwall corrosion from the probe test, we have no comparison in air, and waterwall corrosion is susceptible to localised changes which may be due to boiler design/fluid dynamics and not oxyfuel combustion.

Due to the higher CO_2 and SO_2 concentration and longer exposure times, both carburisation and sulphidation may be more of a threat. The higher CO_2 may result in carbon diffusion into the material producing brittle phases and the higher SO_2 may lead to increased deposition of sulphate phases resulting in more sulphidation. Piron *et al* has exposed 9-12% martensitic steels for 1000 hrs and shown that exposure in $Ar+CO_2$ is similar to CO_2+H_2O with respect to weight gain and oxide thickness. However the carburisation depth was thinner for the CO_2+H_2O mixture than the $Ar+CO_2$. It was suggested that H_2O presence reduces the carburisation of the steel, as H_2O is easily adsorbed on the surface compared to CO_2. Ferritic steels (1-11% Cr) have been investigated in CO_2 + 30% H_2O conditions both in high and ambient pressures [6]. Increased oxidation rate was observed for ferritic steels at high pressures due to increased carbon deposited within the oxide. In oxyfuel combustion, there is a higher oxygen content in the gas which should reduce problems with carburisation.

4.2. Low temperature corrosion

The largest differences between oxyfuel and air-firing appeared on the low temperature gradient probe, installed in the economiser region, which had a temperature of 60-200°C. For the 250 hrs exposure and at the lowest temperature tested (70°C), specimens exposed in both air and oxyfuel modes revealed large amounts of corrosion. However, the specimens exposed during oxyfuel conditions were more highly corroded at higher temperatures and the deposits were enriched with sulphur, especially at 170°C (20 wt% sulphur in oxyfuel compared to 4 wt% in air-firing). Calculations show that the acid dew point (dew point for H_2SO_4) is about 30°C higher in oxyfuel mode, (124°C in air-firing and 153°C in oxyfuel mode, when firing normal lignite).

Sulfuric acid begins as small concentrations of sulfur trioxide (SO_3) in the boiler. The SO_3 is formed in the furnace and convective pass of the boiler by the reaction of SO_2 with oxygen. Among the parameters which influence the amount of SO_3 formation in the boiler are fuel sulphur content, ash content and composition, convective pass surface area, tube metal surface temperature distribution, and excess air level. As a flue gas condenses, the first temperature at which condensation begins depends on both the partial pressure of sulphur trioxide and water vapour. The initial condensate forming at the dewpoint is very corrosive but the actual deposition rate of these particles is small. As the temperature decreases, the acid concentration reduces but there is more acid available, thus high corrosion rates are generally observed 20-30°C below the actual acid dewpoint as the deposition rate of the acidic species increases. As the temperature is further reduced, then acid concentration decreases leading to decreased corrosion until it reaches the temperature where other acidic gases such as CO_2, SO_2 and NO_2 dissolve. It is clear that the amount of sulphur in the deposits increases the temperature at which downtime corrosion occurs. In addition the amount of water in the gas phase is also important [8] and the increase from 9% to 30% water vapour increases the dewpoint temperature as can be seen from Figure 15.

The squares mark the dewpoints relevant for the lignite used in this test. However a higher sulphur content in the coal would lead to a higher dewpoint temperature. This diagram is based on the assumption that 0.5% of the SO_2 is converted to SO_3. More data with longer exposure times is required to assess the corrosion rates at the various temperatures. Based on the corrosion rates and general behaviour none of the alloys withstand the environment totally but all the high alloy steels still show potential for use in these environments.

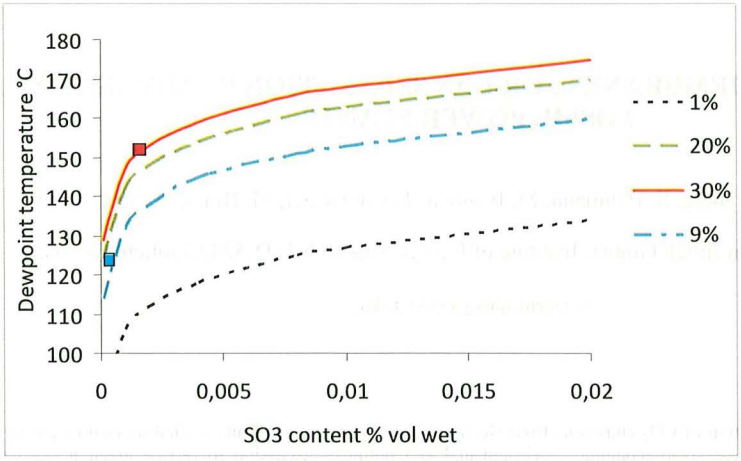

Figure 15. Dewpoint temperature with respect to SO_3 for various water contents.

5. Conclusions

The following conclusions can be drawn from this work. The chemical compositions of the high temperature (superheater) deposits from air and oxyfuel firing were found to be similar and the initial high temperature corrosion behaviour of the same steels also appeared to be similar during air and oxyfuel firing. This was an unexpected result as levels of SO_2 were approximately four times greater under oxyfuel conditions as measured after the before the ESP (Table 1). The low temperature gradient probe revealed more corrosion in oxyfuel mode and the deposits contained significantly more sulphur. Calculations show that the dewpoint temperature of SO_3 has increased due to oxyfuel combustion.

6. Acknowledgements

The authors are especially grateful to Dr. Marie Anheden, and the many other colleagues at Vattenfall who have supported this work.

7. References

[1] B. Bordenet Materials and Corrosion 59 No 5 (2008) pp. 361-366
[2] L. Strömberg et al Energy Procedia 1 (2009) pp. 581-589
[3] M. Montgomery, A. Hjörnhede, A. Gerhardt: Proceedings Eurocorr 2009 Paper 7984, Nice, France (2009)
[4] C. Sheng and Y. Li: Fuel 87 (2008) pp. 1297-1305
[5] J. Piron Abellan, T. Olszewski, H.J. Penkalla, G.H. Meier, L. Singheiser, W.J. Quadakkers WJ, Materials at High Temperatures 26 (1) (2009) pp. 63-72
[6] D. Huenert and A. Kranzmann, NACE Paper 08447 (2008)
[7] DR Holmes "Dewpoint Corrosion" pp17-34, 80-93 Published 1985 Ellis Horwood Ltd.
[8] WMM Huijbregts, RGI Leferink "Anti-corrosion methods and materials" Vol 51 No 3 (2004) pp.173-188

9th Liege Conference : Materials for Advanced Power Engineering 2010
edited by J. Lecomte-Beckers, Q. Contrepois, T. Beck and B. Kuhn.

CERAMIC MEMBRANES FOR GAS SEPARATION IN ADVANCED FOSSIL POWER PLANTS

W.A. Meulenberg, S. Baumann, M. Ivanova, T. van Gestel, M. Bram, D. Stöver

Forschungszentrum Jülich GmbH, Institute of Energy Research 1, D-52425 Jülich, Germany

w.a.meulenberg@fz-juelich.de

Abstract

The reduction or elimination of CO_2 emissions from electricity generation power plants fuelled by coal or gas is a major target in the current socio-economic, environmental and political discussion to reduce green house gas emissions such as CO_2. This mission can be achieved by introducing gas separation techniques making use of membrane technology, which is, as a rule, associated with significantly lower efficiency losses compared with the conventional separation technologies.

Depending on the kind of power plant process different membrane types (ceramic, polymer, metal) can be implemented. The possible technology routes are currently investigated to achieve the emission reduction. They rely on different separation tasks. The CO_2/N_2 separation is the main target in the post-combustion process. Air separation (O_2/N_2) is the focus of the oxyfuel process. In the pre-combustion process an additional H_2/CO_2 separation is included. Although all separation concepts imply different process requirements they have in common a need in membranes with high permeability, selectivity and stability. In each case CO_2 is obtained in a readily condensable form.

CO_2/N_2 separation membranes like microporous membranes or polymer membranes are applicable in post-combustion stages. In processes with oxyfuel combustion, where the fuel is combusted with pure oxygen, oxygen transport membranes i.e. mixed ionic electronic conducting (MIEC) membranes with mainly perovskite or fluorite structure can be integrated. In the pre-combustion stages of the power plant process, H_2/CO_2 separation membranes like microporous membranes e.g. doped silica or mixed protonic electronic conductors or metal membranes can be applied.

The paper gives an overview about the considered ceramic materials for the different gas separation membranes. The manufacturing of bulk materials as well as supported thin films of these membranes along with their performance, microstructure and other relevant properties are shown.

Keywords: Ceramic Membranes, Fossil Power Plants, Gas Separation, CCS Technology

1. Introduction

The reduction or elimination of CO_2 emissions from electricity generation power plants fuelled by coal or gas is a major target in the current socio-economic, environmental and political discussion to reduce the green house gases. Current energy scenarios of the International Energy Agency (IEA) emphasize the increasing importance of CCS technology within the global CO_2 mitigation strategies. In its "business as usual" scenario the IEA estimates the increase of CO_2 from 29 bn. t CO_2 of todays to 62 bn. t CO_2 in the year 2050. This would imply an average increase of the atmospheric temperature with 3 – 4°C (550 ppm CO_2 in the atmosphere). Two possible mitigation scenarios until 2050 are currently discussed within the IEA [1]. In the first scenario (ACT Map) the reduction target is 35 bn. t CO_2 (485 ppm) compared to the "business as usual" case in 2050 (figure 1), which corresponds nearly to the current level. Even more drastic is the second scenario (BLUE Map Scenario), which assumes a reduction of 48 bn. t CO_2 (445 ppm). About 38% (18 bn. t CO_2) of the total reduction is related to the power production. In both scenarios CCS is the mitigation activity with the highest reduction potential. The CCS share on the total CO_2-reduction in the power production is 26% (BLUE Map) and about 21% (ACT map).

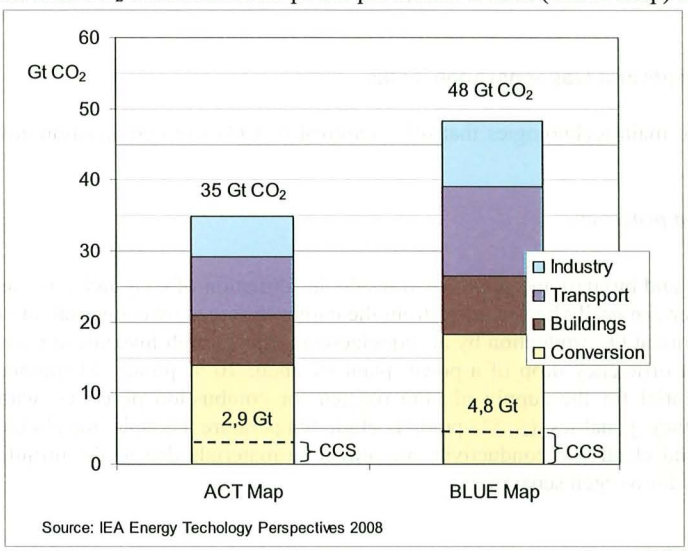

Figure 1: Mitigation scenarios of CO_2 emission in 2050. "Business as usual" prediction is 62 Gt.

The goal of CO_2 capture in power production can be achieved by introducing gas separation techniques making use of membrane technology, which is associated with significantly lower efficiency losses compared with the competing separation technologies.
The possible technology routes are currently considered and investigated to achieve the reduction. They rely on different separation methods. The CO_2/N_2 separation is the main target in the post-combustion process. Air separation (O_2/N_2) is the focus of the oxyfuel process. In the pre-combustion process an additional H_2/CO_2 separation is included. Although all separation

concepts imply different process requirements they have in common the use of membranes with high permeability and selectivity. In each case CO_2 is obtained in a readily condensable form.

Currently, membranes are used for separation tasks in other fields (e.g. chemical industry), but membranes for separating the technically relevant gases in power plants are still far from being suitable for implementation in industrial applications. Strategies for the development of novel, application robust membranes rely on the progress in materials science based improvements as well as technology driven optimisation of the process and application conditions. Research and technology activities are consequently directed towards functional layers and porous structures in the nanosize-range, the development of mixed-conducting oxides by means of theoretical materials design approaches and design of components under operating conditions based on their physico-chemical and mechanical properties. Decisive results based on a parallel investigation of (i) new materials, design and manufacturing of components and equipment, (ii) integration into power plants and the related process engineering and (iii) energy systems analysis will pave the way to efficient, affordable CCS including hydrogen generation from fossil fuels by means of new gasification processes for fossil and biomass energy carriers.

2. Power Plant Concepts and Gas Separation Tasks

In principle there are three main technologies that offer removal of CO_2 from combustion and gasification processes [2].

2.1 Oxyfuel combustion processes

Combustion of fossil fuels and biomass in pure oxygen results in formation of CO_2 and water as combustion products. Water can easily be separated from the combustion gas by condensation at low temperatures. Conventional O_2-production by air liquefaction requires high investment costs and results in a significant efficiency drop of a power plant by about 10 %-points. Membrane systems offer a high potential for the supply of pure oxygen for combustion processes with significantly lower efficiency penalties ($\leq$ 5%-points). High temperature ceramic membrane systems with both ionic and electronic conductivity are attractive materials due to the infinite selectivity of these systems for oxygen separation.

2.2 Pre-combustion capture

Gasification processes with subsequent CO-shift reaction offer high potential for CO_2-removal at high efficiency. The CO-shift reaction results in formation of CO_2 and H_2. If H_2 can be continuously removed from the gas mixture, CO_2 can be easily separated and stored. Hydrogen can be used for electricity generation in gas turbines and fuel cells, and for production of chemicals and synthetic fuels based on fossils and biomass. Physical adsorption for H_2/CO_2 separation (net efficiency losses approx. 10 %-points) is the major competing technology for molecular sieving or proton conducting membranes.

2.3 Post-combustion capture

CO_2 is captured after the combustion process, conventionally through the use of chemical or physical solvents (e.g. amine scrubbing). This existing technology operates at relatively low temperatures and low exhaust gas CO_2 concentration. However, the concept consumes process heat and leads to additional exhaust gas pressure losses, resulting in significant efficiency losses. Membranes, which separate CO_2 from the exhaust gas, would be interesting as an alternative technology. Candidate materials are polymer (organic) membranes as well as microporous ceramic (inorganic) membrane systems with tailored properties and functional characteristics.

2.4 Outlook

Furthermore, there are important industrial applications for membrane systems that reduce CO_2: the cement industry and steel industry are major industrial CO_2 emission sources. However, applications well beyond the horizon of CO_2 separation are also of interest and highlight the enormous technical potential and commercial impact of advanced membrane systems. These include decentralized supply of oxygen and nitrogen and other gases to the chemical industry, NO_x-mitigation in industrial firing processes and automotive applications as well as gas cleaning in a variety of industrial processes.
For all technologies above, the availability of cost-competitive and environmentally friendly membrane systems with high specific permeability and selectivity and long-term stability is a pre-requisite for commercialization. The current state of the art technology of CO_2 separation requires high investment costs and results in a significant efficiency drop of a power plant by about 10 %-points. That means for example that the net efficiency of an advanced lignite fuelled power plant will drop from 45 % to around 35 % leading to a noticeable increase in natural resource demand and power generation cost. The application of membrane technology is expected to involve significantly lower efficiency penalties.

The key scientific and technological challenge for power plants with integrated CCS is the development of membrane systems with high permeability, specific selectivity and long-term stability up to 100,000 hours. In case of Oxyfuel, for instance, the amount of oxygen required for power plants up to 1000 MW is approx. 150 kg per second, depending on the type of fuel. This large amount requires membrane surface areas up to several 100,000 m^2 per plant. Large scale ceramic membrane plants have been installed successfully in uranium isotope separation 30 years ago (Eurodif, 1979/1982, 2,000,000 m^2), demonstrating the ability to manufacture and to handle large ceramic membrane areas and gas separation membrane plants. However, current state of the art membranes still do not meet the requirements with respect to permeability, selectivity, component size, long-term stability under practical conditions and costs.

3. Membranes for Gas Separation

3.1. Mixed ionic-electronic conducting membranesfor oxygen and hydrogen separation

3.1.1. Oxygen Transport Membranes (OTM): materials, working principle and membrane development

Appropriate materials for oxygen separation from air are mixed ionic electronic conductors (MIEC) transporting oxygen ions through vacancies in the crystal lattice. Most promising materials are perovskites and fluorites [3]. Perovskites show highest permeability, in particular $Ba_{0.5}Sr_{0.5}Co_{0.8}Fe_{0.2}O_{3-\delta}$ [4]. However, perovskites with high permeability show in principle poor chemical stability e.g. in atmosphere containing CO_2, SO_2, or H_2O and particularly reducing conditions. The high oxygen permeation in perovskites is due to the conduction mechanism of oxygen ions diffusing through oxygen vacancies in the crystal lattice [3], which is shown in Figure 2.
Diffusion occurs by hopping of the next neighboured oxygen ion into a vacancy. Without any driving force (oxygen partial pressure gradient) this hoping is statistically distributed. When applying a partial pressure gradient the hopping is directed from the high pressure to the low pressure side, resulting in oxygen transport (diffusion). This diffusion through a solid crystal can be described by the Wagner Equation

$$j_{O2} = \frac{RT}{16F^2}\sigma_{amb}\frac{1}{L}\ln\frac{p'_{O2}}{p''_{O2}} \qquad (1)$$

with R gas constant, T temperature, F Faraday constant, σ_{amb} ambipolar conductivity, L membrane thickness, and p'_{O2} and p''_{O2} oxygen partial pressure on the oxygen rich and lean side, respectively.

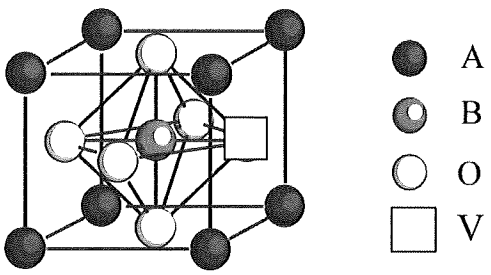

Figure 2: Perovskite crystal lattice $ABO_{3-\delta}$ with oxygen vacancy V

The only material-related parameter in the Wagner equation is the ambipolar conductivity, which is composed of the ionic and electronic conductivities, respectively,

$$\sigma_{amb} = \frac{\sigma_e \cdot \sigma_i}{\sigma_e + \sigma_i} \qquad (2)$$

In perovskites the electronic conductivity is normally by orders of magnitude larger than the ionic conductivity, hence the latter one is the rate limiting property. Following the Nernst-Einstein-

Relation (3) σ_i is more or less proportional to the oxygen vacancy concentration $[V_O^{\cdot\cdot}]$ as the vacancy diffusion coefficient D_V is assumed to be constant.

$$\sigma_i = \frac{4F^2[V_O^{\cdot\cdot}]D_V}{RTV_m} \qquad (3)$$

with V_m molar volume.

However, introducing oxygen vacancies in the perovskite lattice ABO_3 e.g. by doping of A-cations leads to reduction of B-cations followed by ion expansion. This affects the crystal stability estimated by the tolerance factor according to Goldschmidt (4), which must be kept roughly between 0.8 and 1 [5].

$$t = \frac{r_A + r_O}{\sqrt{2}(r_B + r_O)} \qquad (4)$$

Hence, it is nearly impossible to achieve improved permeability and stability of the perovskite materials simultaneously. Being aware of this, the Wagner Equation (1) indicates that besides process parameters, i.e. temperature and partial pressure conditions, the only parameter left to increase the oxygen permeation in a membrane assembly is to reduce the membrane thickness. With reduction of membrane layer thickness engineering aspects such as processing and thermo-mechanical characterization become more and more important. However, for the membrane operation solely a thickness reduction is not sufficient because surface exchange reactions between oxygen molecules and the membrane become rate limiting beneath a characteristic thickness L_c [6], which is not implied in the Wagner equation (1).

$$L_c = \frac{D}{k_s} \qquad (5)$$

with D oxygen diffusion coefficient, k_s oxygen surface exchange coefficient.

Thus, surface exchange kinetics has to be accelerated by catalytic activation.

In case of fluorites such as $Ce_{1-x}B_xO_{2-\delta}$ (B= Gd,Pr,Tb) the electronic conductivity is rate limiting for oxygen diffusion as it is normally orders of magnitudes lower than the ionic contribution. Thus, electronic conductivity has to be enhanced. Recently, in a publication by Fagg et al. [7] was shown that the oxygen permeation through $Ce_{0.8}Pr_{0.2}O_{3-\delta}$ is as high as for some perovskites by co-doping with Cobalt. Furthermore, activation energy is rather low, which is favourable for operating in lower temperature range. The mechanisms are not clear, but it is suggested that Co is enriched at the grain boundaries leading to new diffusion paths for electronic charge carriers. Thus, nano-structuring of doped ceria shall enhance the oxygen permeation. Moreover, the chemical stability of doped ceria is significantly higher than that of perovskites. Since the permeation can not be expected to be as high as this one of the best performing perovskites, the development of thin surface activated membranes is essential.

Up to now there is no membrane facility for air separation on industrial scale in Europe. Some membrane module prototypes exist or are under research considering several membrane geometries [8]. In most cases monolithic membranes with a thickness of 0.3 – 1 mm are used. Since oxygen diffusion is inversely proportional to the thickness, first asymmetric thin-film assemblies with membrane thickness of 30-50 µm are under research [9], [10], [11]. Furthermore development in hollow fibre technology for ceramic MIEC membranes is carried out [12].

The optimum membrane module consist of stable membrane assemblies with high oxygen fluxes at moderate operation temperature of $\leq 800°C$ by (i) deposition of thin membrane layers on porous supports to minimize diffusion barriers and (ii) creation of catalytic surface activation to overcome slow surface exchange reaction kinetics (Figure 3).

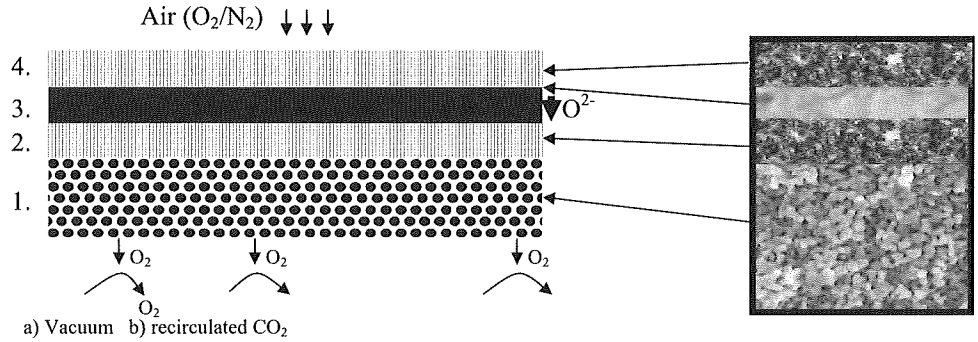

Figure 3: Innovative membrane assembly, 1 porous substrate, 2 low pO_2 nano-catalyst layer, 3 gastight membrane, 4 high pO_2 nano-catalyst layer. The micrograph on the right-hand side illustrates a hypothetical device and is not drawn to scale.

The low membrane thickness and high material stability results in a lower demand of membrane area (required space) and volume (resources/cost) as well as in a higher reliability in long term operation. For certain applications the developed membranes can be combined with more conventional membrane reactors (e.g. working at a higher temperature) to meet the requirements set by the specific application.

3.1.2. Mixed proton-electron membranes for hydrogen separation: materials, working principle and membrane development

Dense ceramic membranes with proton conductivity and mixed proton-electron conductivity are attracting considerable attention especially during the recent years due to their potential application in fuel cells, petrochemical technologies, as separation membranes, etc. As mentioned above, one innovative and promising direction of application of dense ceramic membranes with mixed proton-electron conductivity is their integration into the pre-combustion CO_2 capture. Amongst the advantages of dense mixed proton-electron membranes are their lower price compared to the precious metal-based membranes, their higher thermal, chemical and mechanical resistance that implies longer lifetime without significant functional degradation. The development and industrial implementation of dense ceramic mixed proton-electron conducting membranes faces several open issues that require further optimization. Amongst them, one can highlight: i) the chemical stability of the membrane, in order to withstand the harsh operation conditions in the real power plant (still rather insufficient for several types of materials); ii) the mixed proton-electron conductivity, which is determining for the hydrogen flux through the

membrane (considerable conductivity and permeation values are required); iii) functional degradation issue under operating conditions (in short and long term). These factors are the key features of the membrane for ensuring high performance and simultaneously having a great impact regarding to the real implementation of the membrane in industrial applications. Hence, an important requisite of R&D activities is the close collaboration between the scientific and industrial societies.

In order to maintain ionic-electronic conductivity in the oxides, formation of defects of certain type and certain concentration is required. Defects may be formed intrinsically by varying the ratios of the basic components of the material or extrinsically by acceptor doping. In the presence of extrinsic defects in the crystal lattice, the concentration of doping element usually determines the concentration of formed defects, while the operating regimes (temperature, atmosphere) determine the type of defects as dominating charge carriers. In a very common case, when acceptor doping route is followed, then positively charged species are generated to maintain the electroneutrality of the lattice. Positively charged species are electron holes ($h^{\bullet}$), oxygen vacancies ($V_O^{\bullet\bullet}$) and proton defects ($OH_O^{\bullet}$). In accordance to the mass action law, at definite conditions (p_{O2}, p_{H2O}, and T) the existing defects are in a dynamic equilibrium. For each set of equilibrium conditions, there are values of p_{O2}, p_{H2O} and T that determines the domination of a definite pair of defects. In this sense, Brouwer diagrams are a very useful tool for visualizing how defects and their concentration depend on the partial pressure of oxygen or water, for example. Under *dry oxidizing conditions*, oxygen is built up in the crystal lattice, thus the concentration of the oxygen vacancies diminishes simultaneously with the generation of electron holes which are needed to neutralize the negative charge generated by the aliovalent doping element (Equation (6)):

$$\frac{1}{2}O_{2(gas)} + V_O^{\bullet\bullet} \rightarrow O_O^X + 2h^{\bullet} \tag{6a}$$

$$K_h = \frac{[O_O^X][h^{\bullet}]^2}{[V_O^{\bullet\bullet}]p_{O2}^{1/2}} \tag{6b}$$

Under *dry reducing conditions* the crystal lattice starts loosing oxygen, thus oxygen vacancies are formed together with the generation of electrons:

$$O_O^X \rightarrow V_O^{\bullet\bullet} + 2e' + \frac{1}{2}O_2 \tag{7a}$$

$$K_e = \frac{[V_O^X][e']^2 p_{O2}^{1/2}}{[O_O^X]} \tag{7b}$$

In *water or hydrogen-containing environments* proton defects in the oxide start considerably contributing to the conductivity and thus must be taken into account in the defect quasi-chemical reactions.

$$H_2O_{(v)} + V_O^{\bullet\bullet} + O_O^X \Leftrightarrow 2OH_O^{\bullet} \tag{8a}$$

$$K_{OH\bullet} = \frac{[OH_O^{\bullet}]^2}{([V_O^{\bullet\bullet}][O_O^X]pH_2O)} \tag{8b}$$

Proton defects are formed in the oxide material in water containing atmospheres as a result of dissociative adsorption of water [13]. Water from the gas phase disassociates to hydroxide ion and a proton. The hydroxide ion is adsorbed by the oxygen vacancies and the proton forms a covalent bond with the lattice oxygen. Thus two positive proton defects, $OH_O^{\bullet}$, are generated (as written with Equation (8)).

One of the routes to obtain considerable electron conduction levels within the material is the substitution of a host lattice element by a doping element D with a variable oxidation state. As an example, the following quasi-chemical reactions describe the defects formation under oxidizing (9a) and reducing (9b) conditions, respectively:

$$D_2O_3 - 2e' = DO_2 - 2h^{\bullet}; DO_2 \xrightarrow{MO_2} 2D_M^X + 2h^{\bullet} \text{ (ox)} \quad (9a)$$

$$DO_2 + 2e' = D_2O_3 + 2h^{\bullet}; D_2O_3 \xrightarrow{MO_2} 2D_M' + 3O_O^X + V_O^{\bullet\bullet} + 2e' \text{ (red)} \quad (9b)$$

And finally, independently on the kind of the implemented doping scheme, when thermodynamic and chemical equilibrium is maintained, equality of all positive and negative species generated within the crystal lattice is also maintained.

In a mixed proton-electron conductive material both protons and electrons contribute as charge carriers to the total conductivity of materials. The total conductivity σ_{tot} of such a material consists of a protonic conductivity term σ_{H+} and an electronic conductivity term σ_e, according to Equation (10) [14]:

$$\sigma_{tot} = \sigma_{H+} + \sigma_{e-} \quad (10)$$

The total conductivity of the materials can be directly measured, as well as the ionic conductivity, while the electronic conductivity can be calculated by subtracting the ionic from the total conductivity term. In order to describe the partial conductivity of a material the transport number t is used and it can be determined for every charge carrier of interest. The proton and electron transport numbers respectively can be given according to Equation (11):

$$t_{H+} = \frac{\sigma_{H+}}{\sigma_{tot}} \text{ and } t_{e-} = \frac{\sigma_{e-}}{\sigma_{tot}} \quad (11)$$

The conductivity of protons is proportional to their charge z, their concentration c and their mobility μ, as well as their diffusion coefficient D [15]:

$$\sigma_{H^+} = zFc_{H^+}\mu_{H^+} = \frac{z^2Fc_{H^+}D_{H^+}}{kT} \quad (12)$$

In order to fulfill the electro-neutrality requirement electrons or electron holes must additionally be created in the crystal lattice. Electrons move in the same direction as the protons. The permeation of hydrogen through a dense ceramic membrane is proportionally dependent on the ambipolar conductivity, expressed by Equation (2), with σ_{H+} replacing the ionic conductivity, σ_i. Thus the proton flux density through the membrane can be written with Equation (13) [16]:

$$j_{H^+} = \frac{-RT}{2F^2L}\int_I^{II} \sigma_{H^+} t_e \, d\ln p_{H_2} \quad (13)$$

We refrain from introducing further details since the basic principles of the dense ceramic membranes for hydrogen separation are yet extensively discussed elsewhere [16]. In any case, it is worth mentioning that since the first report on high-temperature proton conduction in oxides by Stotz and Wagner[17], the defect chemistry and the proton conductivity of a variety of oxide materials have been intensively investigated [18-26]. In contrast, the ability of these materials to

permeate hydrogen has received less attention. The kinetic and mechanistic description of the hydrogen permeation behaviour through mixed proton-electron conductors remains rather incomplete [27]. Undoubtedly, due to the practical benefits that the dense ceramic membranes offer when integrated on an industrial scale, the development of ceramic materials for membranes represents a challenging field in the materials science.

The relevant operating conditions in the pre-combustion power plant require implementation of chemically, thermally and mechanically endurable materials along with an improved membrane performance and lifetime. The main drawback of cerate-based membranes for example, despite the high proton conduction they exhibit, is their instability under such a complex operating conditions, such as strongly reducing atmospheres in presence of water vapour and high operating temperatures. The optimal performance and integrity of Ag/Pd membranes that normally yield a flux of 1-3 l/cm^{2}min is also strongly affected by the harsh operating conditions in the power plant. A detailed overview on synthesis, characterization, and applications of palladium membranes is published by Basile *et al.* [28]. Hence, a compromise between several important membrane parameters, e.g. stability of material and membrane functional performance, should be an acceptable option as well. Lanthanoide tungstates are a promising class for manufacturing of membranes for H_2 separation at elevated temperatures due to their improved stability under the relevant power plant conditions. Here we shall focus on them.

Lanthanoide tungstates described with the general formula Ln_6WO_{12} are referred as materials with defective fluorite structure although the crystal symmetry in some cases is not completely clarified. A correlation between the type of the lanthanoide element and the crystal lattice symmetry was found, clearly showing a tendency toward reducing the crystal symmetry from cubic through tetragonal and finally to rhombohedral when Ln changes in the order La→Nd→Er. Shimura *et al.*[29] studied $La_{5.8}WO_{11.7}$ in electrochemical hydrogen pumping experiment and a proton conduction for this material was demonstrated. Protons transport number was determined to be between 0.7 and 0.9 in a H_2-containing atmosphere. The proton conductivity of 0.005 S/cm was measured in wet H_2 at 900°C.

The feasibility of tungstates in membrane application by comparing them to the state of the art 5% Yb-doped $SrCeO_3$ was estimated by Haugsrud *et al.* [30]. Based on the ambipolar proton-electron conductivity which is twice higher than the conductivity of perovskite at 1000 °C it can be concluded that undoped La_6WO_{12} is a good candidate for membrane applications. Moreover, the behavior of Gd_6WO_{12} and Er_6WO_{12} is pointed out as interesting. The authors recognize the possibility of protons compensating electrons under partial reduction at low temperature.

Permeability data prediction was communicated by Norby *et al.* [31] for La_6WO_{12}, $SrCeO_3$ and Er_6WO_{12}. The flux was calculated considering 10-μm-thick layers with feed side pressure of 10 atm H_2 and assuming that the flux was ruled by Wagner equation, i.e. through the bulk diffusion mechanism. The predicted hydrogen permeation for La_6WO_{12} at 800°C has a value of about 2.0 ml_n/cm^2min which is higher compared to the $SrCeO_3$ and Er_6WO_{12} yielding hydrogen flux at the same temperature of about 1.0 ml_n/cm^2min and less than 0,1 ml_n/cm^2min, respectively.

The hydrogen flux was experimentally determined by Escolástico *et al.* [32]. In their work the flux trough Nd_6WO_{12} disc membrane with a thickness of 510 μm was determined. At the feed side, a mixture of moist 20 %H_2/He was used and at the sweep side argon (both sides at atmospheric pressure). In Fig. 4, the hydrogen permeation flux of the Nd_6WO_{12} membrane is presented as a function of temperature. At moderate temperatures (below 900 °C), the electron conductivity seems to be the limiting factor, while at high temperatures (above 900 °C) the p-type

conductivity becomes predominant and the proton conductivity is the limiting step, likely due to the low concentration of protons in the oxide lattice, as stated by Haugsrud *et al.* [30] based on termogravimetric studies.

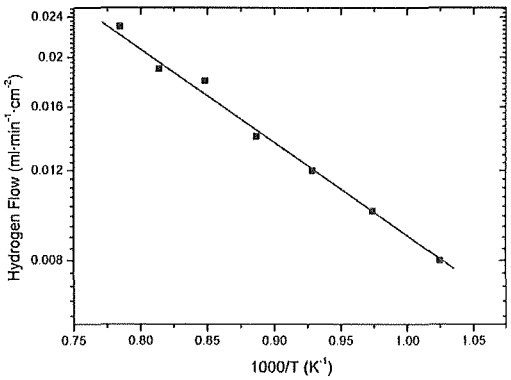

Figure 4: Hydrogen permeation flux of Nd_6WO_{12} membrane as a function of the temperature [32]

Despite the quite limited number of studies on lanthanoide tungstates as membranes for hydrogen separation, the attractiveness of this material class is pronounced especially when the development of supported asymmetric membranes is considered, along with their test implementation in the pre-combustion power plant. Manufacturing of a thin layer of Ln_6WO_{12} over a porous substrate with the corresponding chemical and thermal compatibility will make the currently targeted H_2-flux of 1 ml/cm^{2}min achievable.

In conclusion it can be mentioned that in the field of dense ceramic proton-conducting membranes a significant progress has been made during the past few years, mainly motivated by the benefits these membranes offer and the variety of applications where they can be implemented. Along with the increase of the conductivity and H_2 flux respectively, the chemical and thermal stability does still remain amongst the most challenging requirements towards the membrane materials. Proton conductivity is rather sensitive to the temperature due to the thermodynamic stability of proton defects in terms of proton content that contributes to the total conductivity of the material. Moreover, the stability and mobility of proton defects is individual for each kind of material: it is closely dependent on the chemical nature and concentration of doping elements and it is governed by the thermodynamics of hydration. In this context, it should be mentioned that in some cases the higher stability of proton defects (as for example in cerates and zirconates) is not a stringent indication for a higher chemical stability of the material. In order to enlighten the basics of these phenomena and complex dependencies for different classes of materials, an intensive research is strongly required. In any case, the mixed proton-electron conductivity, the proton defects stability/mobility, and the chemical stability must be balanced with a definite degree of compromise for obtaining the optimal properties of the membrane.

3.2. Microporous membranes for hydrogen and carbon dioxide separation

To date, a considerable amount of research activities were focused on the development of microporous gas separation membranes for a reduction of CO_2 in the exhaust gases of power plants. The operation conditions for the membrane devices in the post-combustion and pre-combustion technologies are 60 – 100°C and atmospheric pressure (post-combustion) and 200 – 350°C and pressures exceeding 20 bar (pre-combustion). At this moment, it is difficult to determine which membrane material will be the best choice (e.g. polymeric, metallic, microporous ceramic, hybrid). Microporous ceramic membranes are however considered by a number of research groups for the latter concepts (e.g. [33-35]). In principle, ceramic membranes are relatively cheap and have a high mechanical, thermal and chemical stability.
The structure of a microporous ceramic separation membrane is comparable to a graded porous multilayer material – with macroporous, mesoporous and microporous layers – in which the last layer displays a pore size < 2 nm. According to the IUPAC notation, porous materials are classified into three kinds: microporous materials have a pore diameter < 2 nm, mesoporous materials have pore diameters between 2 nm and 50 nm and macroporous materials have a pore diameter > 50 nm [36].
The working principle of a microporous membrane is often described in terms of diverse mechanisms including Knudsen diffusion, micropore diffusion and surface diffusion. It is well known that for membranes with mesopores larger than 2 nm, gas transport occurs by a Knudsen diffusion mechanism. In this case, selectivity is proportional to the square root of the molecular weight ratio of the gases and is independent of the temperature. The achieved selectivities for H_2/CO_2 and N_2/CO_2 are 4.67 and 0.8, and are thus too low for most practical applications in gas separation units. In practice, however, this mechanism is also found for microporous membranes which show larger micropores, indicating that membranes with a pore size in the lower microporous region are required.

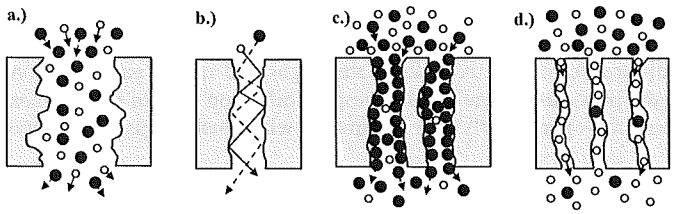

Figure 5: Principles of gas transport through ceramic membranes [45]
a.) Viscous flow b.) Knudsen diffusion c.) Surface diffusion d.) Molecular sieve.

Micropore diffusion is often reported as a working mechanism in which the smaller gas molecule (He or H_2) permeates through the porous structure of the membrane, while the larger molecule is sieved out. Therefore, size of the related gas molecules is an important issue for the development of gas separation membranes with a well defined nano-structure. Table 1 summarizes the kinetic diameters of the main gas molecules, which occur in post- and pre-combustion processes. The

transport of the smaller molecule tends to be an activated process, with the rate increasing exponentially with temperature. This type of mechanism is reported for amorphous SiO_2 membranes, e.g. in separation experiments with H_2 or He from N_2 or CO_2, and in practice these membranes show high permeabilities for He and H_2. Usually, a pore diameter of 0.3 – 0.5 nm is reported for such materials, but in fact it is not really clear whether the reported materials show 'real' physical pores or whether a similar working principle occurs as in polymeric membranes, with the small gas molecule diffusing through the structural spaces in the inorganic glassy structure of the amorphous SiO_2 matrix.

Table 1: Equilibrium length and width according to Pauling [46] as well as kinetic diameters of the main gas molecules in post- and pre-combustion processes calculated from minimum equlibrium diameter.

Molecule	Length [nm]	Width [nm]	Kinetic diameter [nm]
H_2O	0.39	0.315	0.265
H_2	0.31	0.24	0.289
CO_2	0.51	0.37	0.330
O_2	0.39	0.28	0.346
N_2	0.41	0.30	0.364
CO	0.42	0.37	0.376
NO	0.405	0.30	0.317
SO_2	0.528	0.40	0.360
H_2S	0.436	0.40	0.360

Surface diffusion is usually reported as the transport mechanism for CO_2 separation membranes, e.g. for the separation of CO_2 from H_2, N_2 or CH_4. The mechanism involves the surface diffusion of adsorbed CO_2 along the pore walls and CO_2 selectivity is obtained when the surface transport of CO_2 outweighs the contribution from Knudsen diffusion. The mechanism is usually reported for membranes with larger pore diameters in comparison with amorphous SiO_2 membranes, including zeolite membranes and templated SiO_2 membranes and also in the case of hybrid organic-ceramic membranes. In this case, the experimental test conditions are reported to play a major role. At lower temperatures, CO_2 adsorption is enhanced and the separation factor increases strongly. Further, the major effect of CO_2 adsorption on the separation factor is frequently confirmed by the difference in selectivity for a single gas and mixed gas operation. However, in comparison with the previously mentioned micropore diffusion type of membranes, the achieved separation factors are – particularly in experiments with smaller gases – always much lower.

In this research field, amorphous SiO_2 membranes have been most extensively investigated because of their cost-effective sol-gel preparation methods, scalability and their potential for combining high selectivity and permeability. With such membranes, separation factors for small gases (He, H_2) to larger gases (CO_2, N_2, CH_4) of several hundreds to more than 1000 have been reported. Usually, the thickness of the membranes is in the range 50 – 200 nm, depending on the literature source, which is mentioned as an important advantage to realize the required permeability.

Amorphous SiO_2 membranes are basically synthesized by two methods: sol-gel coating and chemical vapour deposition (CVD) [37-38]. From a practical point of view, sol-gel coating appears to be a very interesting method, since the sol coating methods are the same as

conventional powder suspension coating methods and exhibit the same advantages (inexpensive in terms of capital costs, simplicity of equipment). There are a variety of coating methods used for making sol-gel membranes of which spin-coating (flat membranes) and dip-coating (tubular membranes) are the most frequently used.
CVD methods for preparing a SiO_2 membrane are usually divided into two classes. In the first method, all precursors and reactants are provided on one side of the membrane, while the other side is usually vacuumed. In the second method, the reactants are supplied from the opposite sides of the substrate. CVD membranes frequently have higher selectivity for H_2, but these membranes usually also have lower permeability. It should however be noted that literature data on permeability of SiO_2 membranes show a large scattering thus making a comparison of different types of membranes very difficult.
While in the power plant hydro-thermal conditions prevail, it is necessary to use membranes which do not degradate in contact with water vapour and there is evidence that current SiO_2 gas separation membranes suffer from serious degradation. However, several locations come into focus for a membrane unit in the power plant process and the process conditions (temperature, pressure, water content, contaminants) at the various locations are significantly different. Improving the steam stability of silica membranes by adding inorganic or organic additives may lead to an use of these materials in some stages. For this reason, a number of researchers have focused on developing alternative SiO_2 materials with improved stability. A variety of modified materials have been developed with dopants/additives incorporated such as metals (Ni, Co), metal oxides (Al_2O_3, ZrO_2, TiO_2, Nb_2O_3) and organic groups (e.g. [39,40]).
Another interesting approach reported by many researchers is preparing crystalline microporous SiO_2-based membranes or zeolites. Zeolites are microporous aluminosilicates - also mesoporous types exist - with a very narrow pore size distribution. In contrast with the previously described amorphous SiO_2 membranes, they are crystalline and show an ordered pore structure. Zeolites are often considered as a candidate material for gas separation membranes, since some of these materials can be made with a pore diameter in the lower microporous region. In addition, these crystalline materials have the required thermal stability and also some compositions show the required chemical stability.
In the field of zeolite membrane formation, apart from a few notable examples, no membranes with molecular sieving properties, as described for SiO_2 membranes, have yet been reported (e.g. [41]). On the other hand, a number of membranes have been described which yield a significant separation for CO_2 and N_2, especially when the measuring temperature approximates room temperature. This result is explained on the basis of the high CO_2 sorption capacity of the zeolitic membrane material and the occurrence of a surface diffusion mechanism. In order to improve the CO_2 adsorption of the membrane material and to enhance the gas selectivity of zeolite membranes, basic cations have been incorporated in the zeolitic structure. A method which has been described extensively includes immersing the membranes in solutions of alkali or earth alkali ions.
Templated SiO_2 membranes are related to sol-gel membranes and zeolite membranes. They are usually prepared using common sol-gel procedures, with the difference that a template is incorporated in the toplayer and afterwards removed to create an ordered pore structure [42,43]. Also, in some cases the coated layer is hydro-thermally treated in an analogous way as a zeolite membrane. Compounds which are frequently used include ionic surfactants (e.g. tetra-propyl ammonium bromide TPA), anionic surfactants (e.g. Brij) and Si precursors with an organic group

attached such as methyl, propyl, vinyl and phenyl groups and also aminated organic groups. The advantages with respect to common zeolite membranes include the simple sol-gel-like synthesis route and the ability to deposit membranes by simple dip-coating or spin-coating methods.
Due to the high chemical resistance of some non-silica materials in various membrane applications (e.g. TiO_2 and ZrO_2 membranes in ultra- and nano-filtration) research efforts have been devoted in the past few years to the potential application of non-silica membranes as an alternative for amorphous silica membranes in gas separation. In contrast to silica membranes, non-silica membranes with a connected network of micropores and selectivity for small gases have not yet been reported.
An extension of the microporous membrane work is the application of a metallic support to make the supported membranes. As stated before, the operating conditions for the membrane device are dependent on the location in the power plant, but pressures in the pre-combustion technology are typically exceeding 20 bar. Therefore, there is a growing interest to fabricate membranes on such supports, as described for example in [44].

4. Summary and Outlook

Membranes for separating the technically relevant gases in power plants have different development status, but they are all not available for implementation into a power plant. Nevertheless, membranes are already used for separation tasks in other fields (e.g. chemical industry). Due to their low efficiency penalty, membranes are an interesting alternative to conventional separation technologies. Strategies for the development of novel, application robust membranes rely on the progress in materials science based improvements as well as technology driven optimization of the process and application conditions. Research and technology activities are consequently directed towards functional layers and porous structures in the nanometer range, the development of mixed-conducting oxides by means of theoretical materials design approaches and design of components under operating conditions based on their physico-chemical and mechanical properties. Decisive results based on a parallel investigation of (i) new materials, design and processing of components and equipment, (ii) integration into power plants and the related process engineering and (iii) energy systems analysis will pave the way to efficient, affordable CCS including hydrogen generation from fossil fuels by means of new gasification processes for fossil and biomass energy carriers.

Acknowledgement

Financial support from the FP 7 EU-Project "NASA-OTM" (NMP3-SL-2009-228701) and Helmholtz Association of German Research Centres (Initiative and Networking Fund) through the "MEM-BRAIN Helmholtz Alliance" (HA-104) is gratefully acknowledged.

5. References

[1] IEA, 2008 Energy Technology Perspectives - Scenarios & Strategies to 2050. Paris
[2] R. Bredesen, K. Jordal, O. Bolland. High-temperature membranes in power generation with CO_2 capture. Chemical Engineering and Processing 43 (2004) 1129–1158
[3] J. Sunarso, S. Baumann, J.M. Serra,W.A. Meulenberg, S. Liu, Y.S. Lin, J.C. Diniz da Costa. Mixed ionic–electronic conducting (MIEC) ceramic-based membranes for oxygen separation. Journal of Membrane Science 320 (2008) 13–41
[4] Z. Shao, W. Yang, Y. Cong, H. Dong, J. Tong, G. Xiong. Investigation of the permeation behavior and stability of a $Ba_{0.5}Sr_{0.5}Co_{0.8}Fe_{0.2}O_{3-\delta}$ oxygen membrane. Journal of Membrane Science 172 (2000) 177–188
[5] A.S. Bhalla, R. Guo, R. Roy, The perovskite structure – a review of its role in ceramic science and technology, Materials Research Innovations 4 (2000) 3-26
[6] H.J.M. Bouwmeester, A.J. Burggraaf. Dense ceramic membranes for oxygen separation. In: Fundamentals of Inorganic Membrane Science and Technology, 1996 Chapter 10, pp 435-528, ISBN 0-444-81877-4
[7] D.P. Fagg , A.L. Shaula, V.V. Kharton, J.R. Frade. High oxygen permeability in fluorite-type $Ce_{0.8}Pr_{0.2}O_{2-\delta}$ via the use of sintering aids. Journal of Membrane Science 299 (2007)1–7
[8] J. Vente, W.G. Haije, R. IJpelaan, F.T. Rusting. On the full-scale module design of an air separation unit using mixed ionic electronic conducting membranes. Journal of Membrane Science, 278 (2006) 66-71
[9] O. Büchler, J.M. Serra, W.A. Meulenberg, D. Sebold, H.P. Buchkremer. Preparation and properties of thin $La_{1-x}Sr_xCo_{1-y}Fe_yO_{3-\delta}$ perovskitic membranes supported on tailored ceramic substrates. Solid State Ionics 178 (2007), 91-99
[10] Y. Takahashi et al. Development of Ceramic Membrane for Oxygen Gas Separation. International Conference on Inorganic Membranes, ICIM10, 18-22 August 2008, Tokyo, Japan
[11] M.-L. Fontaine et al. On the performance of mixed oxygen ion and electron conducting $La_2(Ni,Fe)O_4$ membranes. International Conference on Inorganic Membranes, ICIM10, 18-22 August 2008, Tokyo, Japan
[12] A. Thursfield et al. Air separation using a catalytically modified mixed conducting ceramic hollow fibre membrane module. Journal of Membrane Science 288 (2007) 175-187
[13] K.D. Kreuer, Proton conducting oxides. *Annu. Rev. Mater. Res.* 33 (2003) 333-359
[14] Y. Liu, X. Tan, K. Li, Mixed Conducting Ceramics for Catalytic Membrane Processing: Cat. Rev. 48 (2006) 145-198
[15] T. Norby, Y. Larring, Concentration and transport of protons in oxides. Curr. Opin. Solid State Mater. Sci. 2/5 (1997) 593-599
[16] M.-L. Fontaine, T. Norby, Y. Larring, T. Grande, R. Bredesen, Oxygen and Hydrogen Separation Membranes Based on Dense Ceramic Conductors. In Membrane Science and Technology (R. Mallada, M. Menéndez, Eds.) Volume 13, Chapter 10, pp. 401-458 (2008) Elsevier B.V. ISSN 0927-5193
[17] S. Stotz, C. Wagner, Die Lösigkeit von wasserdampf und Wasserstoff in festen Oxiden. *Ber. Bunsenges. Phys. Chem. Bd* 70 (8) (1966) 781-788.
[18] N. Bonanos, Oxide-based protonic conductors: point defects and transport properties. *Solid State Ionics* 145 (2001) 265–274

[19] K.D. Kreuer, Proton conductivity: Materials and applications. *Chem. Mater.*, 8 (1996) 610-641
[20] K.D. Kreuer, On the complexity of proton conduction phenomena. *Solid State Ionics* 136–137 (2000) 149–160.
[21] H. Iwahara, Proton conducting ceramics and applications. *Solid State Ionics* 86-88 (1996) 9-15.
[22] A.S. Nowick, Y. Du, High-temperature protonic conductors with perovskite-related structures. *Solid State Ionics* 77 (1995) 137-146.
[23] T. Norby, Solid-state protonic conductors: principles, properties, progress and prospects. *Solid State Ionics* 125 (1999)1–11.
[24] J.W. Phair, S.P.S. Badwal, Materials for separation membranes in hydrogen and oxygen production and future power generation. *Sci. and Tech. of Advanced Mater.* 7 (2006) 792-805.
[25] T. Norby, R. Haugsrud, Dense ceramic membranes for hydrogen separation. In 'Nonporous Inorganic Membranes (A. F. Sammells and M. V. Mundschau, Eds.), pp. 1–48. (2006) Wiley-VCH, Weinheim ISBN 3-527-31342-7
[26] W. Meulenberg, M. Ivanova, T. van Gestel, M. Bram, H.-P. Buchkremer, D. Stöver, J.M. Alfaro-Serra, State of the art of ceramic membranes for hydrogen separation. In Hydrogen Energy. Detlef Stolten, Edt., (2010) WILEY-VCH Verlag GmbH & Co. KGaA, Weinheim, ISBN: 978-3-527-32711-9
[27] L. Li, E. Iglesia, Modeling and analysis of hydrogen permeation in mixed proton-electronic conductors. *Chem. Eng. Sci.* 58 (2003) 1977-1988.
[28] A. Basile, F. Gallucci, S. Tosti, Synthesis, characterization, and applications of palladium membranes. In Membrane Science and Technology (R. Mallada, M. Menéndez, Eds.) Volume 13, Chapter 8, pp.255-323 (2008) Elsevier B.V. ISSN 0927-5193
[29] T. Shimura, S. Fujimoto, H. Iwahara, Proton conduction in non-perovskite-type oxides at elevated temperatures. Solid State Ionics 143 (2001) 117–123
[30] R. Haugsrud, Ch. Kjølseth, Effects of protons and acceptor substitution on the electrical conductivity of La_6WO_{12}. *J. Phys. Chem. Sol.* 69 (2008) 1758–1765.
[31] T. Norby, R. Haugsrud, High Temperature Proton Conducting Materials for H_2-separation. Invited lecture at FZJ Workshop, November 16, 2007
[32] S. Escolástico, V.B. Vert, J.M. Serra, Preparation and Characterization of Nanocrystalline Mixed Proton-Electronic Conducting Materials Based on the System Ln_6WO_{12}. *Chem. Mater.* 21 (2009) 3079–3089.
[33] G. Xomeritakis, C.Y. Tsai, Y.B. Jiang, C.J. Brinker, Tubular ceramic-supported sel-gel silica based membranes for flue gas carbon dioxide capture and sequestration, J. Membr. Sci. (2009) 30-36
[34] K.Yoshida, Hydrothermal stability and performance of silica-zirconia membranes for hydrogen separation in hydrothermal conditions. J. Chem. Eng. Japan 34(4) (2001) 523-530.
[35] Y. Gu, P. Harcarlioglu, S.T. Oyama, Hydrothermally stable silica-alumina composite membranes for hydrogen separation, J. Membrane Sci. 310 (2008) 28-37
[36] http://www.iupac.org/goldbook/M03853.pdf

[37] R. S. A. de Lange, J. H. A. Hekkink, K. Keizer, A. J. Burggraaf, Formation and characterization of supported microporous ceramic membranes prepared by sol-gel modification techniques, J. Membr. 99 (1995) 57-75
[38] D. Lee, S. Oyama, Gas permeation characteristics of a hydrogen selective supported silica membrane, J. Membr. Sci. 210 (2002) 291-306
[39] R.M. de Vos, R.M., W.F. Maier, and H. Verweij, Hydrophobic silica membranes for gas separation. J. Membr. Sci. 158 (1999) 277-288.
[40] S. Battersby, T. Tasaki, S. Smart, B. Ladewig, S. Liu, M.C. Duke, V. Rudolph, J.C. Diniz da Costa, Performance of cobalt silica membranes in gas mixture separation, J. Membr. Sci. 329 (2009) 91-98
[41] N. Nishiyama, M. Yamaguchi, T. Katayama, Y. Hirota, M. Miyamoto, Y. Egashira, K. Ueyama, K. Nakanishi, T. Ohta, A. Mizusawa, T. Satoh, Hydrogen-permeable membranes composed of zeolite nano-blocks, J. Membr. Sci. 306 (2007) 349-354
[42] K.Kusakabe et al., Pore structure of silica membranes formed by a sol-gel technique using tetraethoxysilane and alkyltriethoxysilanes, Sep. Pur. Techn. 16(2) (1999) 139-146.
[43] J.-H. Moon, Y.-J. Park, M.-B. Kim, S.-H. Hyun, C.-H. Lee, Permeation and separation of a carbon dioxide/nitrogen mixture in a methyltriethoxysilane templating silica/γ-alumina composite membrane, Journal of Membrane Science 250 (2005) 195-205
[44] T. Van Gestel, D. Sebold, W.A. Meulenberg, M. Bram, H.-P. Buchkremer, Manufacturing of new nano-structured ceramic–metallic composite microporous membranes consisting of ZrO_2, Al_2O_3, TiO_2 and stainless steel, Solid State Ionics 179 (2008) 1360-1366
[45] Marano, J.J., and Ciferino, J.P., Integration of gas separation membranes with IGCC, *Energy Procedia*, 1, (2009), 361 – 368
[46] Pauling, L. Nature of chemical bond, Cornell University Press, Ithaca, New York (1960)

9th Liege Conference : Materials for Advanced Power Engineering 2010
edited by J. Lecomte-Beckers, Q. Contrepois, T. Beck and B. Kuhn.

CORROSION STUDIES OF OXYGEN PERMEATING MEMBRANE MATERIALS

Arleta Waindich, Michael Müller

Forschungszentrum Jülich, Institut für Energieforschung (IEF-2),
D-52425 Jülich, Germany
e-mail: a.waindich@fz-juelich.de

Abstract

Different perovskite-type materials being considered as oxygen membrane material for the OXYCOAL-AC process were investigated in the present study regarding their chemical stability under OXYCOAL-AC process conditions, namely $La_{1-x}Sr_xCo_{0.8}Fe_{0.2}O_{3-\delta}$ ($0.3 \leq x \leq 0.8$, LSCF YX28), $La_{0.3}Ba_{0.7}Co_{0.8}Fe_{0.2}O_{3-\delta}$ (LBCF 3728), $Ba_{0.3}Sr_{0.7}Co_{0.8}Fe_{0.2}O_{3-\delta}$ (BSCF 3728), $Ba_{0.5}Sr_{0.5}Co_{0.2}Fe_{0.8}O_{3-\delta}$ (BSCF 5582) and La_2NiO_4. Powders of all materials were uniaxially pressed into pellets and annealed under simulated feed-side conditions (72 % N_2, 19 % O_2, 9 % CO_2, 200 hours) and under simulated flue-gas-side conditions (61 % CO_2, 30 % H_2O, 9 % O_2 + Na_2CO_3 deposit or 61 % CO_2, 29.8 % H_2O, 9 % O_2, 0.2 % SO_2 + Na_2SO_4-K_2SO_4-eutectic deposit, 96 hours) in a temperature range of 600-800 °C. Sample characterization was performed using light microscopy (LM), Scanning Electron Microscopy (SEM) with Energy Dispersive X-Ray Spectroscopy (EDX) and X-Ray Powder Diffraction (XRD). Some of the calcined LSCF compositions included Fe-Co-O precipitations. Generally speaking, corrosion increased with rising temperature. Feed-side conditions only influenced BSCF 5582. Flue-gas-side conditions caused severe corrosion on all materials. Top faces under the deposit were always more affected than sample sides only exposed to gaseous medium. The stability of LSCF materials enhanced with rising lanthanum content, especially when Na_2CO_3 deposit was used. $SrCO_3$, Fe_3O_4 and Fe-Co-O were the detected phases. LBCF 3728 and the BSCF materials mainly degraded to $BaCO_3$ and $BaSO_4$ referring to the deposits Na_2CO_3 and Na_2SO_4-K_2SO_4-eutectic. In the case of La_2NiO_4, $La_2O_2CO_3$ or $La_2O_2SO_4$ and NiO were detected. In conclusion, none of the investigated materials are suitable for an OXYCOAL-AC process without further improvement and previous gas cleaning.

Keywords: LSCF, BSCF, Oxygen separation, Perovskite, Corrosion

1. Introduction

In recent years the importance of clean energy production from fossil fuels increased. The requirement to meet the European targets for CO_2 reduction from power plants fired by fossil fuels has led to the consideration of CO_2 sequestration because the increase of efficiency of power plants has a limited impact on total CO_2 production. Among others oxyfuel processes are promising power plant concepts which would allow easy CO_2 removal from the exhaust products. These processes are based on the combustion of coal with recirculated flue gas that has been enriched in oxygen. Replacing the air by this gas mixture would produce an exhaust gas at the end of the process that consists only of CO_2 and water vapour. Thus, CO_2 could be sequestrated by removal of water by condensation. Additionally, some other important pollutants such as nitrogen oxides (NO_x) would be minimized. This type of combustion is only economic if the oxygen is not provided by a conventional cryogenic air separation unit but by an oxygen membrane. This is the goal

of the OXYCOAL-AC process which has been developed by RWTH Aachen, Germany [1]. In the OXYCOAL-AC process, the flue gas is filtered and recirculated at about 800 °C and enriched in oxygen by passing through a ceramic high temperature oxygen membrane. Therefore, a membrane material being stable under OXYCOAL-AC process conditions is required.
Perovskite-type materials with ionic and electronic conductivity (MIEC) have received great interest concerning separation of oxygen from air, partial oxidation of methane and electrodes of solid oxide fuel cells (SOFC). Mixed conductivity is the migration of charged species in the material, i.e. electrons and ions, and is related to hopping of oxygen ions via vacancies [2]. The vacancies can be formed by doping the perovskite material (ABO_3) with elements of lower/higher valency. Teraoka et al. [3] firstly investigated $La_{1-x}Sr_xCoO_{3-\delta}$ to have the highest oxygen permeability. However, the oxygen flux decreases and a serious degradation takes place [4, 5, 6]. As a consequence, its chemical stability is insufficient for practical applications. A substitution of cobalt by iron seems to have a positive effect on chemical stability. Further investigated perovskite membrane materials are perovskite-type oxides such as $SrCoO_{3-\delta}$, $LaGaO_3$ [7] and $(Ba,Sr)(Co,Fe)O_{3-\delta}$ [8, 9]. All these materials show an oxygen hypostoichiometry ($O_{3-\delta}$). A new candidate which exhibits an oxygen hyperstoichiometry is $La_2NiO_{4+\delta}$ with K_2NiF_4 structure [10]. The oxygen transport through this material occurs compared to perovskite-type materials preferentially via interstitial oxygen atoms instead of oxygen vacancies [11]. For practical applications stability under aggressive conditions is required, just a high oxygen permeability is insufficient. In the present work chemical stability of MIEC materials was investigated under conditions expected in the OXYCOAL-AC process.

2. Experimental

For the sake of simplicity and brevity the compositions will be abbreviated by capitals of the elements followed by the proportion of the cation, e.g. the designation of $La_{0.3}Sr_{0.7}Co_{0.2}Fe_{0.8}O_{3-\delta}$ will be LSCF 3728.
The studied LSCF compositions, BSCF 3728 and LBCF 7328 powders were prepared using solid state reaction. Stoichiometric proportions of the reactants La_2O_3, $SrCO_3$, $CoCO_3$, Fe_2O_3 for LSCF materials, $BaCO_3$, $SrCO_3$, $CoCO_3$, Fe_2O_3 for BSCF 3728 and La_2O_3, $BaCO_3$, $CoCO_3$, Fe_2O_3 for LBCF 7328 were calcined (LSCF XY28, LBCF 7328: 1150 °C; LBCF 7328, BSCF 3728: 1250 °C). Calcination temperatures were determined by DTA/TG (Differential Thermal Analysis/Thermogravimetric Analysis) measurements in air. BSCF 5582 and La_2NiO_4 were purchased from Treibacher (Treibacher Industrie AG, Althofen, Austria). Uniaxial pressing (165 MPa pressure) and CMC (carboxymethyl cellulose) as binder were utilized to form pellets (diameter: 8 and 10 mm) which were sintered in air (LSCF XY28, LBCF 7328, BSCF 3728: 1200 °C, 5h; BSCF 5582: 1100 °C, 5h; La_2NiO_4: 1400 °C, 3h).
The sintered pellets were annealed under conditions expected in the OXYCOAL–AC process. Three different atmospheres were varried in a temperature range of 600-800 °C: simulated feed-side conditions: $N_2/O_2/CO_2$ (72 %, 19 %, 9 %; 9 % CO_2 was used to simulate elevated pressures at feed-side) and simulated flue-gas-side conditions: $CO_2/H_2O/O_2$ (61 %, 30 %, 9 %) and $CO_2/H_2O/O_2/SO_2$ (61 %, 29.8 %, 9 %, 0.2 %). In the two latter tests the pellets were additionally covered on the top with powders of Na_2CO_3 or Na_2SO_4-

K_2SO_4-eutectic (ratio: 80:20). Cross sections of the annealed pellets were studied using optical microscopy, SEM (Scanning Electron Microscopy) and EDX (Energy Dispersive X-Ray spectroscopy). In addition, mixtures of the prepared materials and Na_2CO_3 and Na_2SO_4/K_2SO_4, respectively, were annealed under the same conditions and analysed by XRD (X-Ray Diffraction) to identify reaction products consistently. The annealing conditions were chosen due to several experiments and process simulation [12, 13].

3. Results

3.1. Microstructure of the studied materials

SEM images of some sintered samples in Fig. 1 show that all self-prepared materials except LSCF 6428 were porous and inhomogeneous. Fe-Co-O compounds were found by EDX in LSCF 2828, LSCF 5528 and LSCF 7328. Segregations were visible in LSCF 3728, LSCF 5528 and LSCF 7328 referring to coincidental depletion of strontium and enrichment of lanthanum. LSCF 6428, BSCF 5582 and La_2NiO_4 were dense. The two latter materials were purchased commercially. In case of LSCF 6428 preparation and sintering conditions were already optimised in different works. Since the other self-prepared materials were porous preparation and/or sintering conditions were improved. Microstructures of sintered LBCF 3728 and BSCF 3728 pellets were similar (1(d)). The sintered samples of La_2NiO_4 included diminutive precipitations of NiO. XRD diffractograms of the sintered materials are depicted in Fig. 2.

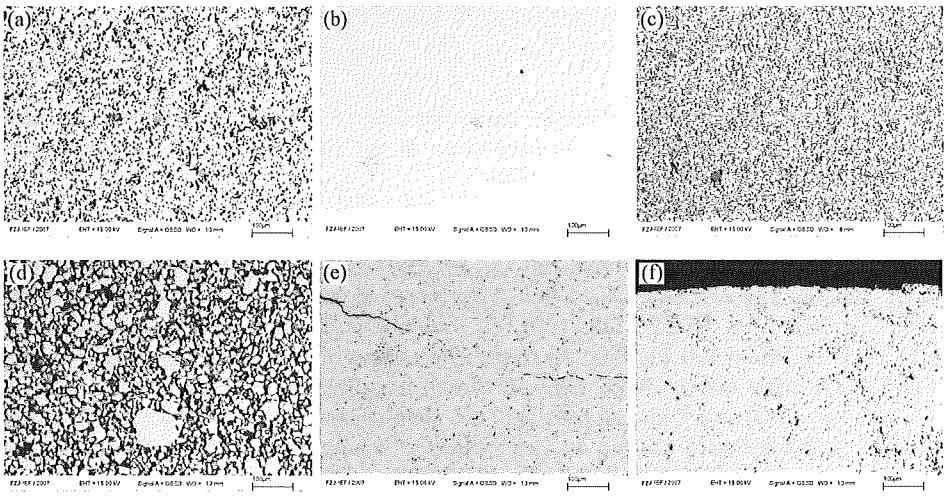

Figure 1: SEM micrographs of the as-sintered materials. (a) LSCF 2828, (b) LSCF 6428, (c) LSCF 7328, (d) LBCF 7328, (e) BSCF 5582, (f) La_2NiO_4.

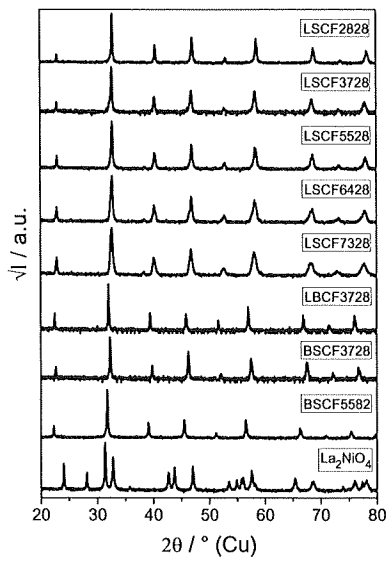

Figure 2: XRD diffractograms of as-prepared materials.

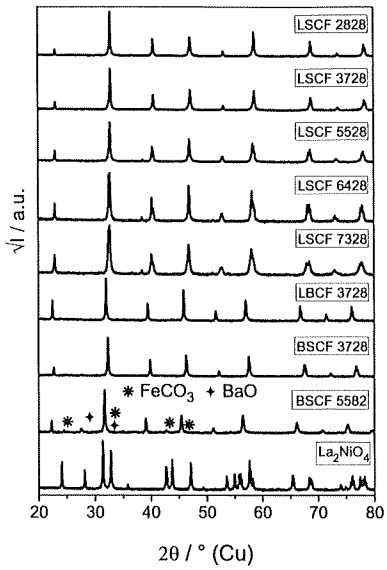

Figure 3: XRD diffractograms of powders annealed in 72 % N_2 + 19 % O_2 + 9 % CO_2 at 800 °C (200 h).

3.2. Material behaviour in $N_2/O_2/CO_2$

All but one of the studied materials remained unchanged (Fig. 3), so it can be assumed that these materials are not influenced by low CO_2 concentrations in a dry medium. Though, BSCF 5582 reacted in this atmosphere already at 600 °C advancing with rising temperature. The sample surface segregated into areas either rich in iron and cobalt or barium and strontium. Grain boundaries seemed to be the starting points of corrosion (Fig. 4(a)). A depletion of oxygen vacancies was noticed in La_2NiO_4. The chemical formula changed from $La_2NiO_{4.144}$ to $La_{1.83}NiO_{3.84}$ accompanied by a change of structure from orthorhombic to tetragonal.

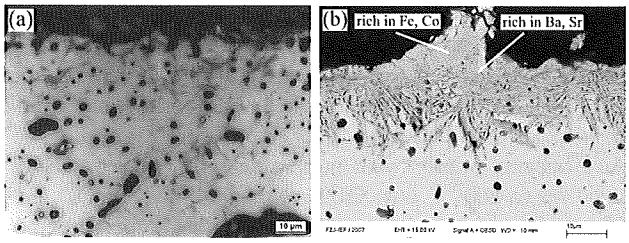

Figure 4: LM and SEM micrographs of BSCF 5582 annealed in 72 % N_2 + 19 % O_2 + 9 % CO_2 (200 h). (a) 600 °C, (b) 800 °C.

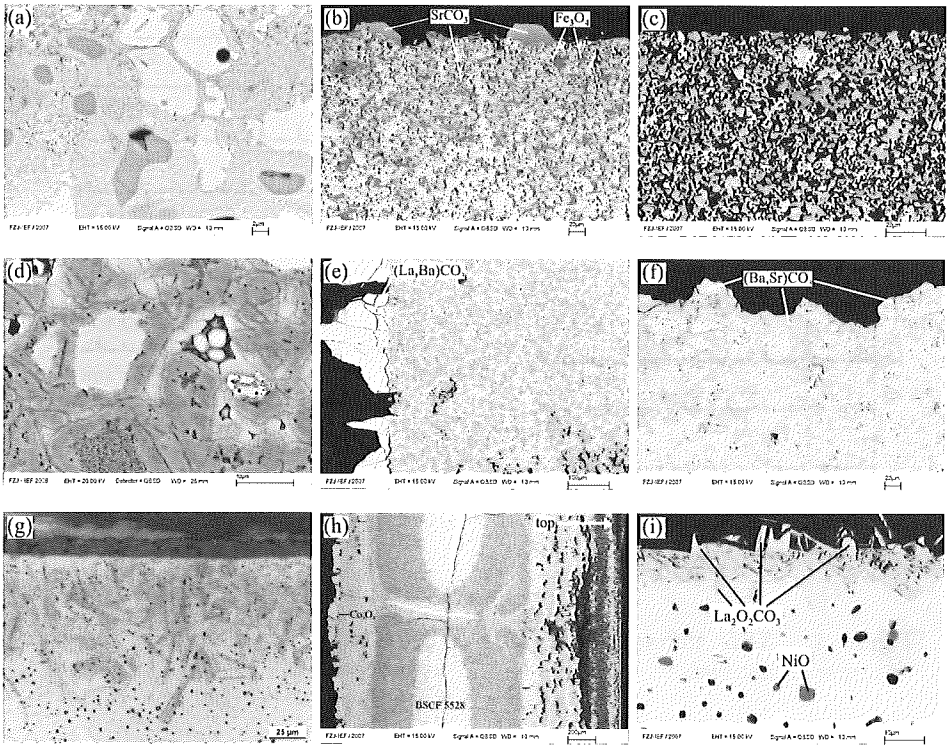

Figure 5: SEM micrographs of LSCF materials annealed in 61 % CO_2 + 30 % H_2O + 9 % O_2 with Na_2CO_3 deposit (96 h). (a) LSCF 2828 (600 °C), (b) LSCF 2828 (800 °C), (c) LSCF 7328 (800 °C), (d) LBCF 3728 (700 °C), (e) LBCF 3728 (800 °C), (f) BSCF 3728 (800 °C), (g) BSCF 5582 (600 °C), (h) BSCF 5582 (800 °C), (i) La_2NiO_4 (800 °C).

3.3. Material behaviour under Na_2CO_3 deposit in $CO_2/H_2O/O_2$

All studied materials decomposed under the Na_2CO_3 deposit. Generally speaking, corrosion increased with rising temperature. The surfaces straight beneath the deposit were severely affected and the sample bottoms being only exposed to the gaseous atmosphere corroded progressively with increasing temperature. LBCF 3728 and BSCF materials were fatally degraded at higher temperatures. In contrast, LSCF compounds possessed a certain chemical stability increasing with higher La-contents. Among the LSCF materials LSCF 2828 was the most corroded (Fig. 5(a),(b)). LSCF 6428 did not decompose but the covered surface became porous with increasing temperature. LSCF 7328 remained optically unchanged up to 800 °C but XRD results revealed $SrCO_3$ and Fe_3O_4 (Fig. 6). Assumedly, LSCF powders mixed with Na_2CO_3 being not tempered before annealing were much more reactive than the sintered pellets. Further peaks refer to the deposit Na_2CO_3 and $Na_2CO_3{*}H_2O$. A new layer containing $(Ba,La)CO_3$ was formed on LBCF 3728 (5(e)), furthermore Fe_3O_4, $BaCO_3$ and $CoFe_2O_4$ were found. In case of BSCF 3728 the follow-

ing compounds were identified: Fe_3O_4, $SrCO_3$, $BaFe_{12}O_{19}$. BSCF 5582 was intensively altered (Fig. 5(h)). The surface decomposed into $(Sr,Ba)CO_3$ and Fe-Co-O. A needle-like structure of decomposed BSCF 5582 was formed surrounding the BSCF core in the middle. The bottom layer turned into a $(Ba,Sr)CO_3$ matrix containing small amounts of iron, cobalt and white BSCF needles. A string of Co_3O_4 separated pure $(Ba,Sr)CO_3$ on the sample bottom from the $(Ba,Sr)CO_3$ matrix. XRD analysis suggested Co_3O_4, $(Sr,Ba)CO_3$, $BaCO_3$, Fe_3O_4. The sample surface of La_2NiO_4 contained $La_2O_2CO_3$. The precipitations of NiO grew during the annealing experiments to spheres (Fig. 5(i)). The amount of NiO was probably too small to be detected by XRD and cannot be found in the diffractogram (Fig. 6).

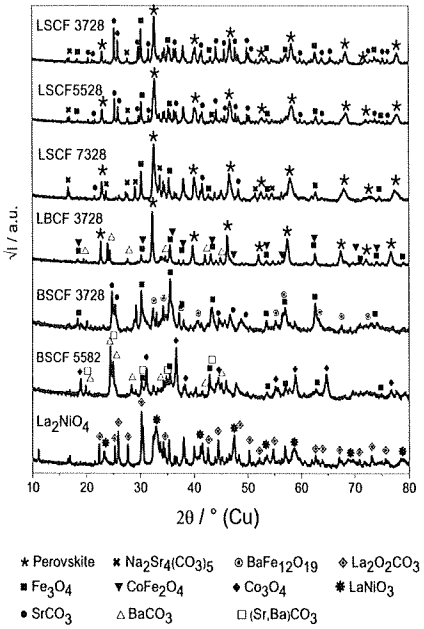

Figure 6: XRD difractograms of powders mixed with Na_2CO_3 and annealed in 61 % CO_2 + 30 % H_2O + 9 % O_2 at 800 °C (96 h).

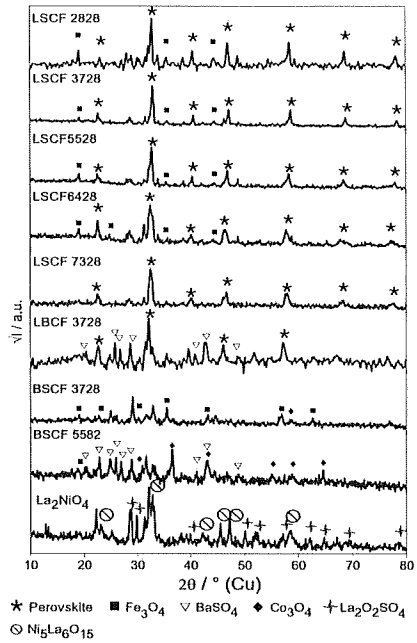

Figure 7: XRD difractograms of powders mixed with Na_2SO_4/K_2SO_4-eutectic and annealed in 61 % CO_2 + 29.8 % H_2O + 9 % O_2 + 0.2 % SO_2 at 800 °C (96 h).

3.4. Material behaviour under Na_2SO_4/K_2SO_4 deposit in $CO_2/H_2O/O_2/SO_2$

All materials reacted with the Na_2SO_4/K_2SO_4-eutectic and the intensity of corrosion increased with rising temperature. In LSCF materials chemical stability was improved with higher La-contents. Integration of sulphur detected by EDX was detected in LSCF 2828, LSCF 3728 and LSCF 5528 in the grey areas near the surface (Fig. 8(a)). Due to the XRD patterns (Fig. 7) it was obvious that LSCF 2828 was changed, however, the

compounds could not be identified. The surface of LSCF 6428 decomposed into Fe-Co-O (Fig. 8(b)). A depletion of strontium in the corrosion zone was observed. In contrast, there was a large amount of Fe-Co-O compounds in LSCF 7328 (Fig. 8(c)), but little sulphur. LBCF 3728 and BSCF 3728 started degrading gradually at grainboundaries from outside inward at lower temperatures (Fig. 8(g)). In LBCF 3728 annealed at 800 °C barium was removed from the perovskite forming $BaSO_4$ at the surface (Fig. 8(d)). Corrosion in BSCF 3728 proceeded along certain cristallographic planes (Fig. 8(h)). According to EDX the sample was composed of $(Sr,Ba)SO_4$, Sr-Ba-O and Fe-Co-O while Fe_3O_4, $CoFe_2O_4$ were detected by XRD. BSCF 5582 was similarly corroded as in the test under Na_2CO_3. EDX analysis revealed a mixture of Fe-Co-O and $(Ba,Sr)SO_4$ on the top, $(Ba,Sr)SO_4$ on the bottom and depletion of barium and strontium as well as incorporation of sulphur in the transition area between the bottom side and the perovskite core. XRD analysis suggested $SrSO_4$, $BaSO_4$, Co_3O_4, Fe_3O_4 and BaO (Fig. 7). The surface of the La_2NiO_4 sample decomposed into a layer of $La_2O_2SO_4$ and a layer of $La_2O_2SO_4$ and NiO (Fig. 8(i)), identified in agreement by EDX and XRD.

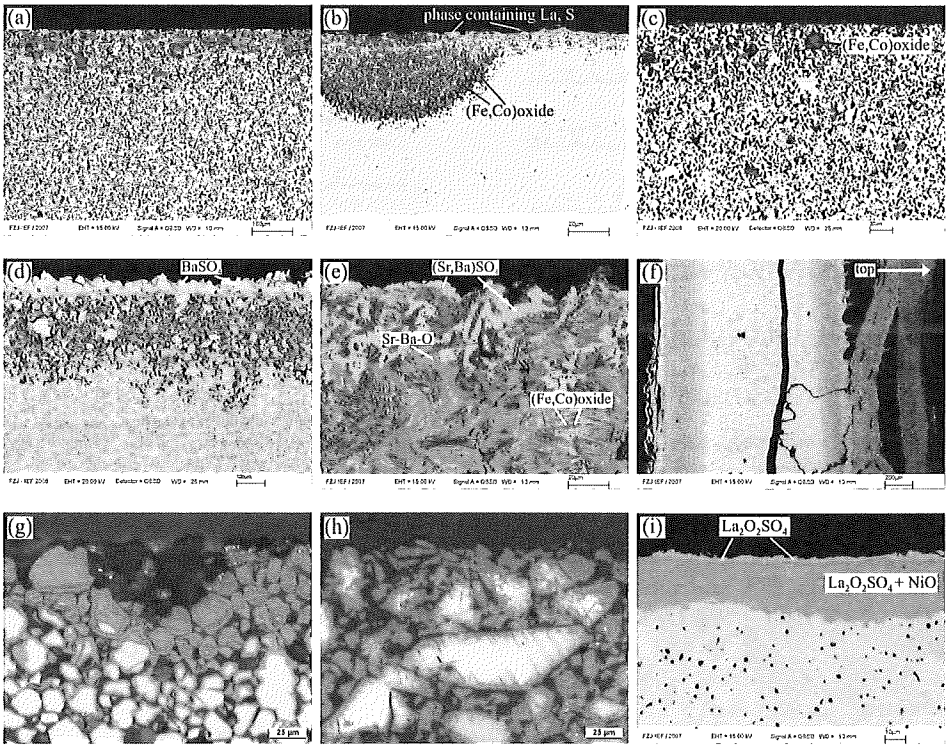

Figure 8: SEM and light microscopy micrographs of materials annealed in 61 % CO_2 + 29.8 % H_2O + 9 % O_2 + 0.2 % SO_2 with Na_2SO_4/K_2SO_4 deposit (96 h). (a) LSCF 2828 (800 °C), (b) LSCF 6428 (800 °C), (c) LSCF 7328 (800 °C), (d) LBCF 3728 (800 °C), (e) BSCF 3728 (800 °C), (f) BSCF 5582 (800 °C), (g) LBCF 3728 (700 °C), (h) BSCF 3728 (700 °C), (i) La_2NiO_4.

4. Conclusion

The results of the experiments showed that all of the studied materials except BSCF 5582 were stable in CO_2 enriched air up to 800 °C. However, all studied materials corroded in an atmosphere containing water vapour when covered with alkali carbonates or sulphates. LSCF materials with a low lanthanum content tended to decompose already at a temperature of 600 °C but stability increased with rising La-content. This indicates that the perovskite structure is thermodynamically instable under humid conditions since the sample bottoms being only exposed to the gaseous atmosphere were also corroded. The salt covered sample sides were always much more affected indicating that the salt coverage seems to intensify corrosion reactions. According to XRD results of the covered samples Na_2CO_3 had a much stronger corrosive influence than the Na_2SO_4-K_2SO_4-eutectic. Fe_3O_4 was the most common compound after annealing.
Furthermore, there was a difference in stability between BSCF 3728 and BSCF 5582. BSCF 5582 decomposed under all three operating conditions but BSCF 3728 did not react in $N_2/O_2/CO_2$. The higher content of iron in BSCF 3728 seems to stabilise the perovskite structure against corrosion. This result confirms earlier investigations by Teraoka [3].
The sample porosity does not seem to play an important role in the corrosion tests because the few dense samples were corroded as well, in some cases more than the porous samples. The loss of stability of the studied materials correlates with mismatches in the structure. Doping of perovskites of the type $A^{3+}B^{3+}O_3^{2-}$ to create vacancies needed for oxygen transport caused dislocations in the crystal. For example, the Goldschmidt´s tolerance factors for LBCF 3728, BSCF 3728 and BSCF 5582 are 0.96, 1.01 and 1.03. Hence, the tolerance factors for the BSCF materials are >1, the ideal value for perovskites, instability can be expected. As a result, none of the investigated materials is suitable for an OXYCOAL-AC process without further improvement and previous gas cleaning.

Acknowledgements

The authors gratefully acknowledge the Bundesministerium für Wirtschaft und Technologie for financial support (under Contract No. 0326885). We also would like to thank Dr. E. Wessel, V. Gutzeit, J. Bartsch, Dr. W. Fischer and W. Reichert for performing micrographs and analysis mesurements.

References

[1] R. Kneer, D. Abel, R. Niehuis, H. R. Maier, M. Modigell, N. Peters, Entwicklung eines CO_2-emissionsfreien Kohleverbrennungsprozesses zur Stromerzeugung, VDI-Berichte 1888, 5-15, (2005).

[2] J. W. Stevenson, T. R. Armstrong, R. D. Carneim, L. R. Pederson, W. J. Weber, Electrochemical properties of mixed conducting perovskites $La_{1-x}M_xCo_{1-y}Fe_yO_{3-\delta}$ (M = Sr, Ba, Ca), J. Electrochem. Soc., 143, 2722-2729, (1996).

[3] Y. Teraoka, H. Zhang, N. Yamazoe, Oxygen-sorptive properties of defect perovskite-type $La_{1-x}Sr_xCo_{1-y}Fe_yO_{3-\delta}$, Chem. Lett., 11, 1367-1370, (1985).

[4] J. Yi, S. Feng, Y. Zuo, W. Liu, Ch. Chen, Oxygen permeability and stability of $Sr_{0.95}Co_{0.8}Fe_{0.2}O_{3-\delta}$ in a CO_2- and H_2O containing atmosphere, Chem. Mater., 17, 5856-5861, (2005).

[5] S. J. Benson, D. Waller, J. A. Kilner, Degradation of $La_{0.6}Sr_{0.4}Fe_{0.8}Co_{0.2}O_{3-\delta}$ in carbon dioxide and water atmospheres, J. Electrochem. Soc., 146, 1305-1309, (1999).

[6] F. Iguchi, N. Sata, H. Yugami, H. Takamura, Oxygen permeation properties and the stability of $La_{0.6}Sr_{0.4}Fe_{0.8}Co_{0.2}O_3$ studied by Raman spectroscopy, Solid State Ionics, 177, 2281-2284, (2006).

[7] V. V. Kharton, A. A. Yaremchenko, A. V. Kovalevsky, A. P. Viskup, E. N. Naumovich, P. F. Kerko, Perovskite-type oxides for high-temperature oxygen separation membranes, J. Membr. Sci., 163, 307-317, (1999).

[8] M. Arnold, H. Wang, A. Feldhoff, Influence of CO_2 on the oxygen permeation performance and the microstructure of perovskite-type $(Ba_{0.5}Sr_{0.5})(Co_{0.8}Fe_{0.2})O_{3-\delta}$ membranes, J. Membr. Sci., 293, 44-52, (2007).

[9] Z. Shao, W. Yang, Y.Cong, H. Dong, J. Tong, G. Xiong, Investigation of the permeation behavior and stability of a $Ba_{0.5}Sr_{0.5}Co_{0.8}Fe_{0.2}O_{3-\delta}$ oxygen membrane, J. Membr. Sci., 172, 177-188, (2000).

[10] H. Zhang, Z. G. Li, G. Y. Yu, An investigation of La-Ni-O oxygen permeating membrane, in: Proceedings of the Fourth International Conference on Inorganic Membranes, Nagoya, Japan, 22-26 June, pp. 196-199, (1998).

[11] A. Julbe, D. Farrusseng, C. Guizard, Limitations and potentials of oxygen transport dense and porous ceramic membranes for oxidation reactions, Catalysis Today, 104, 102-113, (2005).

[12] M. Müller, C. Weber, Chemical Hot Gas Cleaning in the OXYCOAL-AC Process, in: Proceedings of GCHT-7, New Castle, Australia, (2008).

[13] C.Weber, E. Yazhenskikh, M. Müller, Thermodynamic Modelling of Ash Related Problems in the OXYCOAL-AC-Process, in: Proceedings of the 24th International Pittsburgh Coal Conference, Johannesburg, South Africa, (2007), 21-4.pdf.

9th Liege Conference : Materials for Advanced Power Engineering 2010
edited by J. Lecomte-Beckers, Q. Contrepois, T. Beck and B. Kuhn.

METALLIC SUBSTRATE MATERIALS FOR THIN FILM OXYGEN TRANSPORT MEMBRANES FOR APPLICATION IN A FOSSIL POWER PLANT

Y. Xing, S. Baumann, D. Sebold, W.A. Meulenberg, D. Stöver

Forschungszentrum Jülich GmbH, Institute of Energy Research – IEF-1 Materials Synthesis and Processing

Abstract

$La_{0.58}Sr_{0.4}Co_{0.2}Fe_{0.8}O_{3-\delta}$ (LSCF58428) and $Ba_{0.5}Sr_{0.5}Co_{0.8}Fe_{0.2}O_{3-\delta}$ (BSCF5582) exhibit high oxygen permeability due to their high ionic and electronic conductivity. For this reason they are under discussion for application in oxygen transport membranes (OTMs) in zero-emission power plants using oxyfuel technology. A thin film membrane which can increase the oxygen flux is beneficial and a structural substrate is required. Two types of Ni-base alloys were studied as substrate material candidates with a number of advantages, such as high strength, high temperature stability, easy joining and similar thermal expansion coefficient to the selected perovskite materials. Chemical compositions and thermal expansion coefficients of Ni-base alloys were measured in this study. LSCF58428 and BSCF5582 layers were screen printed on Ni-base alloys and co-fired at high temperature in air. The microstructure and element analysis of samples were characterized by scanning electron microscopy (SEM and EDX). A Ni-base alloy, MCrAlY, with a high Al content was the most suitable substrate material, and showed better chemical compatibility with perovskite materials at high temperature than Hastelloy X, which is a chromia-forming Ni-base alloy. A reaction occurred between Sr in the perovskite and the alumina surface layer on MCrAlY. However, the reaction zone did not increase in thickness during medium-term annealing at 800°C in air. Hence, it is expected that this reaction will not prevent the application of MCrAlY as a substrate material.

Keywords: oxygen transport membrane, perovskite, Ni alloys and reaction zone

1. Introduction

Fossil-fuel power plants are the biggest contributors to emissions of CO_2, and produce more than 40% of anthropogenic CO_2 emissions worldwide. Carbon capture and storage (CCS) is an approach for mitigating global warming by capturing carbon dioxide (CO_2) from large-scale sources such as fossil-fuel power plants and storing it instead of releasing it into the atmosphere. Oxygen transport membrane (OTM) systems with mixed ionic-electronic conducting (MIEC) membranes are attractive for use with carbon capture in power plants due to the high selectivity of these systems for oxygen separation and significantly lower efficiency penalties than cryogenic air separation.

Perovskite-based ceramics ($ABO_{3-\delta}$) exhibit high oxygen permeability due to their high ionic and electronic conductivity, and are serious candidates for high temperature O_2-permeable membranes [1]. Teraoka et al. [2-3] were the first to report the high oxygen permeation flux through several $La_{1-x}Sr_xCo_{1-y}Fe_yO_{3-\delta}$ perovskite membranes. Shao et al. reported on oxygen permeation fluxes of $Ba_{0.5}Sr_{0.5}Co_{0.8}Fe_{0.2}O_{3-\delta}$ (BSCF5582) and $SrCo_{0.8}Fe_{0.2}O_{3-\delta}$ (SCF82) under various oxygen partial pressure gradients and temperatures[4]. Very high oxygen permeability was observed for the BSCF5582 membrane at 950°C.

Equation (1.1) gives Wagner's equation, Where σ_i and σ_e are the ionic and electronic conductivity, respectively; P'_{O2} and P''_{O2} are the feed- and permeate-side oxygen partial pressure, respectively; F is the Faraday constant (equal to 96485 C/mol); R the gas constant (equal to 8.314J/(mol K)); T the temperature (given in K); and L is the membrane thickness. The oxygen flux through a mixed-conducting dense membrane can be increased by reducing the thickness of the membrane until it becomes less than a characteristic value at which the flux of oxygen is in a condition of mixed control of the surface exchange kinetics and bulk diffusion [5-6]. Some experimental results have already been reported [7-8]. Therefore, it is expected that the oxygen flux can be improved by producing thin perovskite membranes on porous substrates.

$$J_{O_2} = \frac{RT}{16F^2L}\int_{InP''_{O_2}}^{InP'_{O_2}} \frac{\sigma_i\sigma_e}{\sigma_i+\sigma_e} dInP_{O_2} \tag{1.1}$$

In the recent literature, some candidate materials were proposed as substrate materials. H. Middleton reported on thin $LaSrCoFeO_3$ layers on a porous MgO support by co-casting and co-sintering [9]. B. McCool used α-alumina as a thin film membrane substrate [10]. Classic ceramic materials involve low costs and do not need the development of a complex manufacturing process. However, the thermal expansion coefficients of classic ceramic materials differ substantially from those of perovskite materials thus leading to high thermally induced tensile stresses in the membrane during thermal cycles. J.C.C. Chen plasma sprayed oxygen transport membrane coatings on stainless steel substrates [11]. However, the oxidation resistance of commercial stainless steels is not adequate within the membrane application temperature range of 800-850 °C [12]. These stainless steels also exhibit a mismatch of the thermal expansion coefficient with perovskite materials. In this study, we used Ni-base alloys as substrate materials since they have a number of advantages such as high temperature stability, easy joining and better thermal expansion coefficient matching with the selected perovskite materials than ceramics like alumina or zirconia. We first investigated the compatibility of perovskite membrane materials and Ni-base alloy substrate materials at co-firing temperature.

2. Experimental

2.1 Sample Preparation

In the present study, $La_{0.58}Sr_{0.4}Co_{0.2}Fe_{0.8}O_{3-\delta}$ (LSCF58428) and $Ba_{0.5}Sr_{0.5}Co_{0.8}Fe_{0.2}O_{3-\delta}$ (BSCF5582) were used as membrane materials. LSCF58428 powder was synthesized using the spray-drying technique starting from nitrate precursors [13-14] and was calcined at 900°C in order to develop the perovskite phase [14]. BSCF5582 is a commercially available powder (Treibacher, Austria). The stoichiometry of the powder was confirmed by optical emission spectroscopy (ICP-OES), while the phase composition was evaluated by X-ray diffraction

[14-16]. After calcination, the powder was ball milled with zirconia balls in ethanol for 48 hours.

Two different Ni-base alloys were used as substrate materials. Hastelloy X was provided by GKN in Germany and the MCrAlY substrate was home-made from Ni-192-8 powder manufactured by Praxair, USA. The MCrAlY substrate was manufactured by sintering the starting powder at 1200°C for 5h in a 4%H_2/Ar atmosphere. Then the surface was ground with SiC paper (1200 grit) and pre-oxidized at 1050°C for 5h in air in order to form the alumina surface layer.

Screen printing was carried out to deposit the membrane material on the different substrates. The LSCF58428 and BSCF5582 powders were ball milled in acetone to an average grain size of around 0.5μm. The screen printing pastes were first prepared by mixing equal amounts of milled LSCF58428 or BSCF5582 powder and a solution (6% wt.) of ethylcellulose (Aldrich) in terpineol (Fluka). Subsequently, the mixture was homogenized in a three-roll grinding mill (EXAKT) [17]. LSCF58428 or BSCF5582 membrane layers were coated onto two different substrates by screen printing. Then the samples were co-fired in air at 1200°C for 5h and 1000 °C for 12h for LSCF58428 and BSCF5582, respectively.

2.2 Characterization

The chemical compositions of the substrate materials were measured by inductively coupled plasma-optical emission spectrometry (ICP-OES). The thermal expansion measurements were carried out with a Netzsch 402E and a Netzsch 402C dilatometer.

The microstructures of the samples were investigated by scanning electron microscopy (SEM) (Zeiss Ultra 55), and element analysis was carried out using energy-dispersive X-ray spectroscopy (EDS) (INCA, Oxford).

3. Results and Discussion

The chemical compositions of the two substrate materials determined by ICP-OES are shown in Table.1. Hastelloy X has a high Cr content but contains no Al, and hence is a Cr_2O_3-forming alloy. MCrAlY has a high Al content of approximately 13% and hence is an Al_2O_3-forming alloy. The results of the thermal expansion coefficient measurements of the membrane materials and candidate substrate materials are shown in Figure 1. Both alloys have a TEC comparable to those of the perovskite materials, which is one of the basic requirements for the substrate material.

Table.1 Chemical compositions of different substrate materials in wt%

Elements	Ni	Cr	Mo	Al	Co	Fe	Si	Mn	Others
Hastelloy X	48.7	20.6	9.4	~	1.1	18.5	0.8	0.1	W 0.6
MCrAlY	47.4	17.9	~	12.9	21.2	~	~	~	Y 0.7

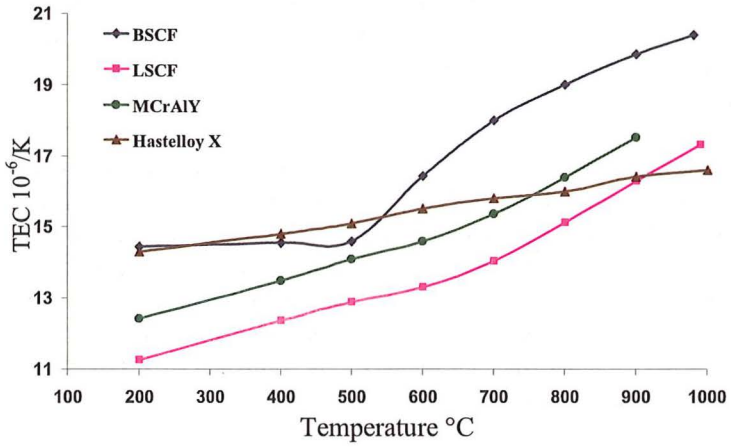

Figure 1 Thermal expansion coefficients measured between 200°C and 1000°C

The interdiffusion between the membrane layer materials and the two different substrate materials was studied at co-firing temperature in air. Figure 2a gives an overview of the LSCF58428 screen-printed layer on Hastelloy X (HAS_LSCF) after co-firing at 1200°C for 5h in air. More details are visible at higher magnification in Fig. 2b. The surface layer of the Hastelloy X substrate consists mainly of chromia with minor amounts of other elements, which probably originate from the metal support due to the limited lateral resolution of EDS (Fig.2c). This surface layer is about 2µm thick. On top of this layer, a reaction zone between the Hastelloy X substrate and the LSCF58428 layer is formed. It is approximately 7 µm thick and consists of a mixed oxide phase La, Sr, Co and Fe plus Ni and Cr from the substrate (Fig. 2d). A LSCF58428 layer 30 µm in thickness was detected, consisting of La, Sr, Co and Fe with minor amounts of Cr and Ni from the substrate (Fig. 2e and 2f). It appears that the diffusion from metal into the membrane is fairly strong and prevents the formation of a single-phase membrane layer. Cr is not only observed at the contact zone, but also in the upper part, which is at a considerable distance from the metal support. This indicates gas phase diffusion by volatile Cr species, e.g. volatile $CrO_2(OH)_2$. This phenomenon is known as chromia poisoning in solid oxide fuel cell research [18]. In the latter case, this phenomenon is suppressed by protection layers on steel plates. However, in the case of a porous membrane support the whole inner surface would have to be protected effectively. Therefore, Hastelloy X and all other chromia scale materials are not promising substrate materials for perovskite membranes.

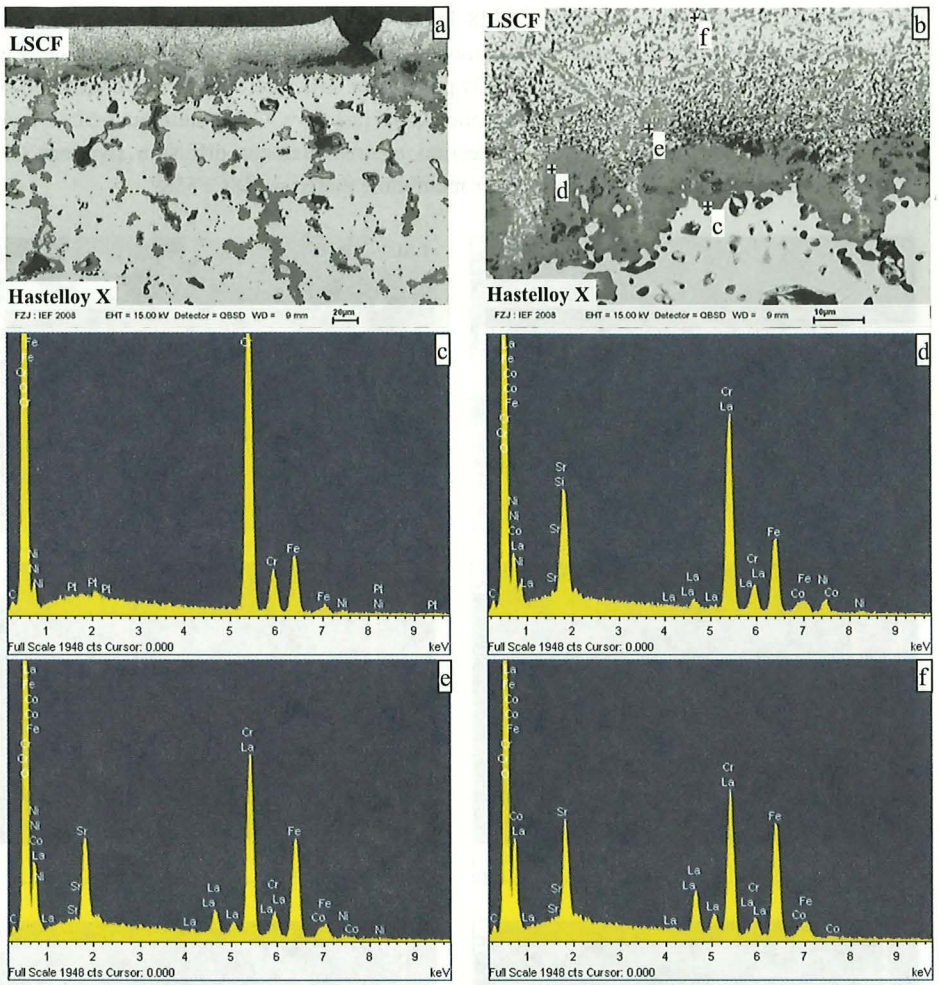

Figure 2 SEM images and EDS analyses of LSCF58428 screen-printed layer on Hastelloy X after co-firing in air (HAS_LSCF) at 1200°C for 5h

In addition, MCrAlY with a high Al content was investigated as a substrate material for an LSCF58428 membrane layer. Figure 3a gives an overview of an LSCF58428 screen-printed layer on MCrAlY (MCR_LSCF) after co-firing at 1200°C for 5h in air. More details are visible at higher magnification in Fig. 3b. The surface layer of the MCrAlY substrate consists mainly of alumina with minor amounts of other elements, which are again probably due to the limited lateral resolution of EDS (Fig. 3c). This surface layer is about 1µm thick. On top of this layer a reaction zone is formed between the MCrAlY substrate and the LSCF58428 layer. It is approximately 5 µm thick and consists of Sr and Al (Fig. 3d). Sr and Al form $SrAl_2O_4$, which exhibits a monoclinic stuffed tridymite structure at low temperatures [19]. XRD

analyses confirm the presence of such a monoclinic structure so that the reaction zone most likely consists of $SrAl_2O_4$. An LSCF58428 layer of approximately 30µm was detected, consisting of La, Sr, Co and Fe with minor amounts of Al originating from the substrate (Fig. 3e and 3f). The LSCF58428 layer retained its perovskite structure, which was confirmed by XRD. MCrAlY showed much better performance than Hastelloy X. The alumina surface layer on MCrAlY provided fairly effective protection against element diffusion (Ni and Cr). Therefore, it was also investigated for another membrane material, BSCF5582.

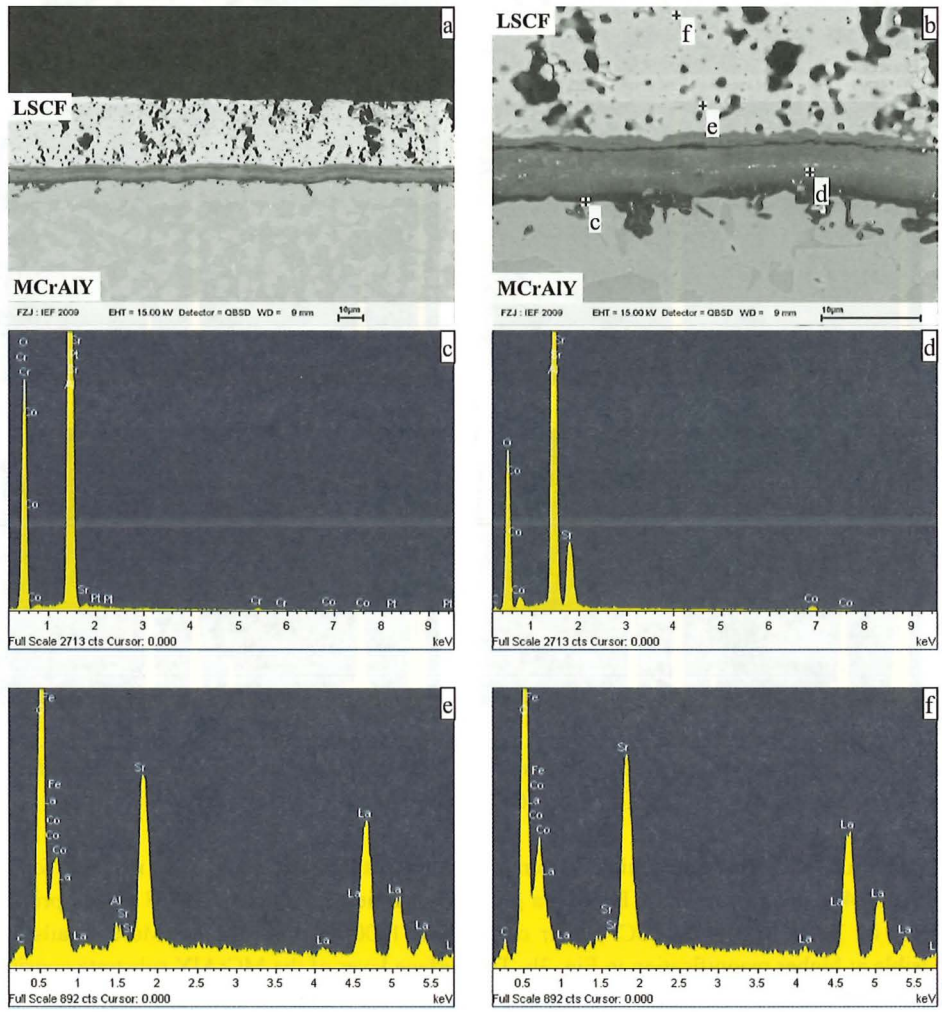

Figure 3 SEM images and EDS analyses of screen-printed LSCF58428 layer on MCrAlY after co-firing in air (MCR_LSCF) at 1200°C for 5h

Figure 4a gives an overview of a BSCF5582 screen-printed layer on MCrAlY (MCR_BSCF) after co-firing at 1000°C for 12h in air. More details are visible at higher magnification in Fig. 4b. The surface layer of the MCrAlY substrate consists of alumina (Fig. 4c) and is about 1µm thick. On top of this layer a double reaction zone is formed. The $SrAl_2O_4$ reaction zone as detected in the LSCF case is roughly 2 µm thick (Fig. 4d). An additional layer forms consisting of Ba, Sr, Al and O (Fig. 4e), which is most likely $(Ba,Sr)Al_2O_4$ on the basis of XRD analyses and the phase diagram [20] showing complete solid solution between $SrAl_2O_4$ and $BaAl_2O_4$. It is also around 2 µm thick. The BSCF5582 layer of approximately 30 µm consists of Ba, Sr, Co and Fe (Fig. 4f) while no elements from MCrAlY were detected.

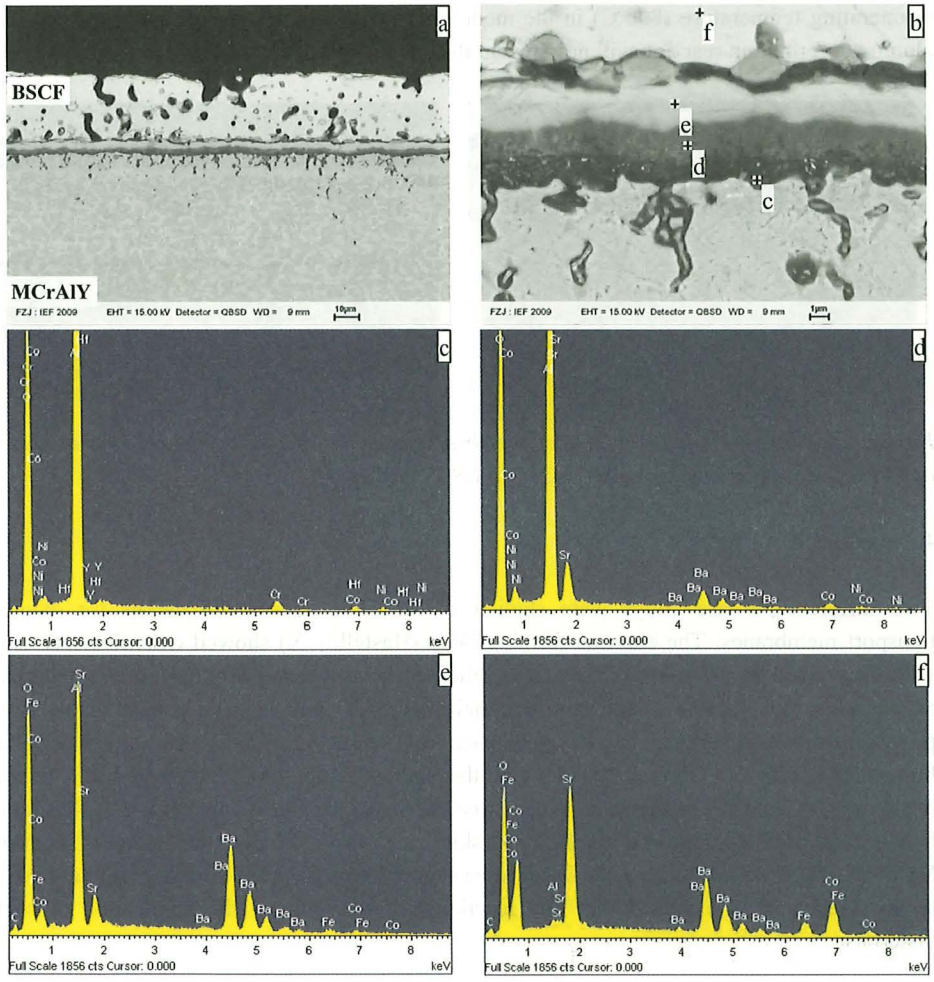

Figure 4 SEM images and EDS analyses of screen-printed BSCF5582 layer on MCrAlY after co-firing in air (MCR_BSCF) at 1000°C for12h

In order to investigate the chemical stability of the reaction zones in the interface, medium-term exposure experiments were carried out at 800°C for 350h. Fig. 5 shows SEM images of the samples after exposure. The $SrAl_2O_4$ reaction zone between LSCF58428 and MCrAlY did not increase in thickness (Fig. 5a). In the case of BSCF5582, the $SrAl_2O_4$ reaction zone disappeared and only (Ba, Sr) Al_2O_4 remained (Fig. 5b). Since Sr has higher mobility than Ba, Ba did not have sufficient time to diffuse into the whole reaction zone during co-firing, which took place during medium-term exposure. In both cases, the alumina surface layer became thicker during exposure. However, no further interdiffusion from MCrAlY to LSCF58428 or BSCF5582 was found. According to the above results, the aluminate reaction zones between the membrane layer material (LSCF58428 and BSCF5582) and MCrAlY substrate were stable at operating temperature (800°C) in the medium term (350h). Therefore, it is expected that aluminate formation reaction will not prevent the application of such materials.

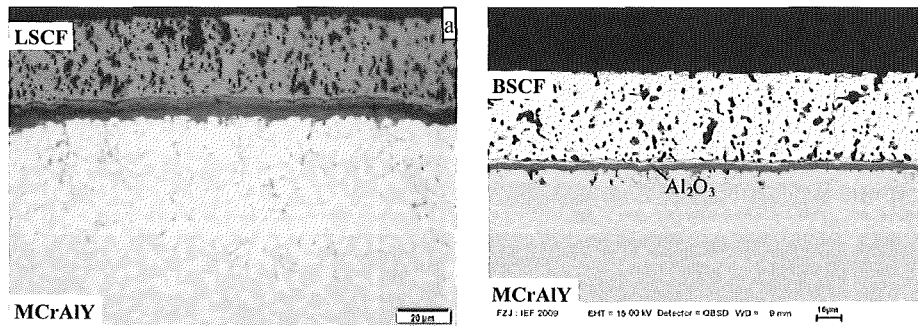

Figure 5 SEM images of screen-printed membrane layer on MCrAlY substrate after exposure at 800°C for 350h in air a) LSCF58428 b) BSCF5582

4. Conclusion

Two different Ni-base alloys were studied as candidate substrate materials for oxygen transport membranes. The chromia-forming alloy (Hastelloy X) showed extensive reactions with the perovskite layer during high temperature co-firing in air. Chromia-forming materials are therefore not suitable as substrate materials. MCrAlY with high Al content is the most promising substrate material, and has good chemical compatibility with perovskite material at high temperature, i.e. limited reactions at the contact zone. LSCF58428 and BSCF5582 membrane layers retained their perovskite structure during co-firing with MCrAlY. Reactions between Sr and Ba appeared in the perovskite- and the alumina-based surface layer on MCrAlY. The reaction zones were found to be stable during medium-term exposure at 800°C in air. Hence, it is expected that this reaction will not prevent the application of such materials.

Acknowledgements

Financial support from the Helmholtz Association of German Research Centres (Initiative and Networking Fund) through the Helmholtz Alliance MEM-BRAIN is gratefully acknowledged. The authors thank GKN for substrate manufacturing and Dr. F. Tietz for thermal expansion analyses.

References

[1] J. Sunarso, S. Baumann, J.M. Serra, W.A. Meulenberg, S. Liu, Y.S. Lin, J.C. Diniz da Costa, Mixed ionic-electronic conducting (MIEC) ceramic-based membranes for oxygen separation, J. Membrane. Sci. 320, 13-41, (2008)

[2] Y. Teraoka, H.M. Zhang, S. Furukawa, N. Yamazoe, Oxygen permeation through perovskite-type oxides, Chem. Lett. 1743, (1985)

[3] Y.Teraoka, T.Nobunaga, N.Yamazoe, Effect of cation substitution on the oxygen semipermeability of perovskite oxide, Chem. Lett, 503, (1988)

[4] Z.P. Shao, W.S. Yang, Y. Cong, H. Dong, J.H. Tong, G.X. Xiong, Investigation on the permeation behaviour and stability of a $Ba_{0.5}Sr_{0.5}Co_{0.8}Fe_{0.2}O_{3-\delta}$ oxygen membrane, J. Membrane. Sci. 172, 177, (2000)

[5] Wanqin Jin, Shiguang Li, Pei Huang, Nanping Xu, Jun Shi, Fabrication of $La_{0.2}Sr_{0.8}Co_{0.8}Fe_{0.2}O_{3-\delta}$ mesoporous membranes on porous supports from polymeric precursors Journal of Membrane Science 170, 9–17, (2000)

[6] H.J.M. Bouwmeester, A.J. Burggraaf, Dense ceramic membranes for oxygen separation, in: A.J. Burggraaf, L.Cot (Eds.), Fundamentals of Inorganic Membrane Science and Technology, Elsevier, Amsterdam, 435–528, 1996

[7] Y. Teraoka, Y. Honbe, J. Ishii, H. Furukawa, I. Moriguchi, Catalytic effects in oxygen permeation through mixed-conductive LSCF perovskite membranes, Solid State Ionics 152-153, 681-687, (2002)

[8] H. Kusaba, Y. Shibata, K.Sasaki, Y. Teraoka, Surface effect on oxygen permeation through dense membrane of mixed- conductive LSCF perovskite-type oxide, Solid State Ionics 177, 2249-2253, (2006)

[9] H.Middleton, S. Diethelm, R.Ihringer, D.Larrain, J.Sfeir, J.Herle, Co-casting and co-sintering of porous MgO support plates with thin dense perovskite layers of LaSrFeCoO3, Journal of the European Ceramic Society 24, 1083–1086, (2004)

[10] B. McCool, G. Xomeritakis, Y.S. Lin, Composition control and hydrogen permeation characteristics of sputter deposited palladium silver membranes, J. Membr. Sci. 161, 67, (1999).

[11] J.C.C. Chen, H. Chen, R. Prasad, G. Whichard, US Patent 6,638,575, (2003)

[12] L. Cooper, S. Benhaddad, A. Wood and D.G. Ivey, The effect of surface treatment on the oxidation of ferritic stainless steels used for solid oxide fuel cell interconnects, Journal of Power Sources, Vol. 184, page 220-228, 2008

[13] P. Kountouros, R. Förthmann, A. Naoumidis, G. Stochniol and E. Syskakis, Synhesis, forming and characterization of ceramic materials for the planar solid oxide fuel cell (SOFC), Ionics 1, 40, (1995)

[14] A.Mai, PhD Thesis, Ruhr-Univ. Bochum, Schriften des Forschungszentrum Jülich, Energy Technology, Vol. 31, (2004)

[15] A. Mai, V.A.C. Haanappel, S.Uhlenbruck, F.Tietz , D.Stöver, Ferrite-based perovskites as cathode materials for anode-supported solid oxide fuel cells: Part I. Variation of composition, Solid State Ionics 176, 1341, (2005)

[16] S.Bebelis, N.Kotsionopoulos, A.Mai, F.Tietz, Electrochemical characterization of perovskite-based SOFC cathodes, Journal of Applied Electrochemistry 37, 15-20, (2007)

[17] O. Büchler, J.M. Serra , W.A. Meulenberg , D. Sebold, H.P. Buchkremer, Preparation and properties of thin $La_{1-x}Sr_xCo_{1-y}Fe_yO_{3-\delta}$ perovskitic membranes supported on tailored ceramic substrates, Solid State Ionics 178, 91–99, (2007)

[18] H. Yokokawa, T. Horita, N. Sakai, K. Yamaji, M.E. Brito, Y.P. Xiong, H. Kishimoto, Thermodynamic considerations on Cr poisoning in SOFC cathodes, Solid State Ionics 177, 3193–3198,(2006)

[19] K.Fukuda and K.Fukushima, Crystal structure of hexagonal of $SrAl_2O_4$ at 1073K, Journal of Solid State Chemistry 178 2709-2714, (2009)

[20] S. Ito, S.Banno, K.Suzuki, and M.Inagaki, Z. Phys. Chem. (Munich), 107 (1) 53-56 (1977)

AUTHORS Index

A

Abe F : 328
Agüero A : 959, 1068
Albu M : 348
Alekseev A A : 725, 731, 741
Allen D J : 500
Andrn H-O : 105
Angella G : 643
Arakawa K : 1028
Ashurov Kh : 1040
Atkinson H V : 695
Auerkari P : 221, 229, 685, 1068
Augustyniak B : 552
Azuma T : 65

B

Bhaduri A K : 890
Bachegowda S : 874
Bankiewiczv D : 854
Bao G : 494
Barbareschi E : 676
Barcelo F : 424
Barnard P M : 37
Barrie M : 37
Baumann S : 1260, 1287
Berger C :84
Besson J : 239
Biede O : 1120
Bjurman M : 1244
Blum L : 925
Bonadei A : 676
Bordenet B : 874
Böse J : 1040
Bossmann H P : 874
Bram M : 1260
Brett S J : 500
Brown L J : 1170
Buchanan L W : 500, 37
Buchkremer H P : 925
Buckthorpe D : 906

C

Caminada S : 95, 270
Cammi A : 705
Cerjak H : 1101
Cernuschi F : 1085
Cha D : canceled
Chandravathi K S : 435
Chevalier S : 1056
Chmielewski M : 552
Cho Y W : 196
Chvostová E : 455, 465
Cipolla L : 270, 294
Cizner J : 1202
Claessens S : 1056
Clarke P D : 562
Cmakal J : 1010
Coleman K : 338
Concari S : 705
del Corno A : 784
Costa A : 676
Czyrska-Filemonowicz A : 802

D

Dalle F : 424
Danielsen H K : 270, 294, 308
Davidsson K : 1218
De Bruycker E : 445, 1182
Degnan C C : 500
De Maria L : 784
Dhont A : 1056
DiGianfrancesco A : 27
Dobrzanski J : 390, 400, 412
Donth B : 27
Dubiel B : 802

E

Epishin A : 623
Erosion : 1130
Evin H N : 1056

F

Falling sand : 1130
Fedelich B : 575, 623
Fedorova T : 749
Filonova E V : 741
Fojer C : 1056
Folkova E : 455
Forest L : 424
Föster M : 1231
Fournier B : 424
Fricke T : 633
Fry T : 959, 1068, 1192
Fukuda M : 3
Fukui T : 95

G

Garcia J : 475, 485
Gee M G : 1170
Gelmedin D : 844
Gerhardt A : 1244
van Gestel T : 1260
Gianfrancesco A : 270
Gehrmann B : 749
Gonzalez V : 348
Gottstein G. : 1210
Goyal S : 435
Gross S M : 925
Grossmann P : 150
Guardamagna C : 1085

Guarnone P : 676
Guédou J Y : 596
Guo J T : 826, 866

H

de Haart L J G : 925
Hacksteiner M : 318
Häkkilä J : 1068
Hainsworth S V : 1160
Hald J : 53, 294, 308
Hakl J : 380
Hansson A N : 1046, 1120
Hanus R : 284
Harada H : 612, 769, 794
von Hartrott P : 1112
Hasegawa Y : 176, 186
Hashizume R : 65
Heintz O : 1056
Henderson P : 986, 1140, 1244
Hernas A : 552
Heuser H : 514
Himanen O : 949
Hirata H : 360
Holdsworth R : 150, 970
Holmström : 221, 229
Holzer I : 348, 1101, 318
Hjörnhede A : 986, 1244
Hruska J : 1202
Hu W : 1210, 826
Huls R : 575
Huysmans S : 445, 1182

I

Igarashi M : 360
Ishiguro T : 65
Itskov M : 1040
Ivanova M : 1260

J

Jakani S : 1056
Jandová D : 455, 465
Jayakumar T : 890
Jedamski J : 1112
Jesen S A : 1120
Jochum C : 514
Jonsson T : 1218
Johansson L-G : 1218
Jung W-S : 196, 249

K

Kablov E N : 654
Kadirov Kh : 1040
Kalck C : 424
Kangas P : 685
Karvonen I : 685
Kasl J : 455, 465
Kauffmann F : 84
Kawagishi K : 769, 794
Kaysser-Pyzalla A R : 475, 485
Kazantsev S : 1040
Kern T-U : 27
Khvatskiy K K : 660
Kimura K : 123, 131, 160, 170
Kinnunen T : 1076
Kiviaho J : 949
Klingelhoffer H : 623
Kloc L : 142, 1010
Klöwer J : 749
Kneer R : 1231
Knödler R : 1020
Kobayashi T : 769, 794
Koizumi Y : 769
Kondo Y : 775, 812
Koyama T : 759
Kozeschnik E : 196, 318, 1101
Kreuzer-Zagar D : 514
Kroupa A : 1010
Kubushiro K : 370, 775
Kuboň Z : 1160
Kucharova K : 1010
Kumar-Krishnasamy R : 1150
Kushima H : 123, 131, 160, 170
Kwieciński K : 532, 542
Kwon S-I : 249

L

Lagerbom J : 949
Laha K : 435
Lang K-H : 844
Lapin J : 802
Laves phase : 259
Lee K-H : 249
Link T : 623
Linke J : 887
Liu F : 105
Łomozik M : 542
Lorenzoni L : 1085
Lundberg M : 1140
Lupinc V : 643, 834
Lyutovich A : 668, 1040

M

Magnusson H : 206
Maile K : 84, 668, 1040
Mäkinen S : 685
Maldini M : 643, 834
Malzbender J : 925
Mandelli M : 715
Manetti M : 1130
Marchant G R : 695
Marumoto Y : 494
Masuyama F : 115, 1028
Mathew M D : 435
Mayer K-H : , 27, 84
Mayr P : 348
Mazza E : 150
Meulenberg W A : 1260, 1287
Mendez-Martin F : 259, 318, 348
Miki K : 65
Minami Y : 95
Mirkarimov A : 1040
Mito N : 176
Mitsche S : 348
Miura N : 775, 812
Mlnarik J : 1202
Mohyla P : 75
Montgomery M : 1046, 1120, 1244
Morinaga M : 65, 759
Morishima K : 370, 775
Morris P F : 562
Mukherji D : 633
Muller M : 1278
Murata Y : 65, 759

N

Nakada K : 812
Nalin L : 784
Nazmy M : 575, 623, 802
Navák P : 380
Nazarkin R M : 654
Nevasmaa P : 221, 229
Newell W : 338

O

Oakey J E : 1000
Okada H : 360
Ono T : 95

P

Panait C : 239, 259
Pap M : 925
Parameswaran P : 435
Park D-B : 249
Paszkowska H : 400
Pasternak J : 390, 412
Pein C : 1095
Penttilä S : 1068
Pettersson J : 1218
Petrushin N V : 654, 660, 741
Piegert S : 633
Pigrova G D : 822
Pihlatie M : 949
Pintsuk G : 887
Prat O : 475, 485
Pratesi F : 1130
Poggio E : 834
Pohjanne P : 1076
Puranen J : 949

Q

Qin X Z : 866
Quadakkers W J : 1182

R

Radosavljevic M : 150
Raj B : 890
Rantala J : 229, 221
Rémy L : 596
Rinaldi C : 715, 705, 784
Ripamonti L : 150
Robba D : 1085
Rödig M : 887
Rojas D : 475, 485
Roos E : 668, 1040
Rösler J : 633, 749

S

Saarinen V : 949
Sablik M J : 552
Sachadel U : 562
Sakamoto M : 769
Sakanaba M : 115
Salonen J : 221, 229, 685, 1068
Sandström R : 206
Sato T : 494
Sauthoff G : 485
Sawada K : 123, 131, 160, 170
Schlesinger M : 1112
Schmidt A : 887
Schmitz F : 633
Scholz A : 84, 575, 685
Sebold D : 1287
Seifert T : 1150
Semba H : 360
Shchegolev D V : 660
Shibata T : 186
Shibuya M : 123
Shim J-H : 196
Shingledecker J : 338
Siefert J : 338
Siegele D : 1150
Simms N J : 784, 1000, 1192
Sklenička : 142, 1010
Słania J : 532
Sommitsch C : 1095
Sonderegger B : 318
Song J : 1210
Spindler M : 142
Staubli M : 623
Steinberger-Wilckens R : 925
Stöver D : 1287,1260
Strang A : 695
Straub S : 1020
Střílková L : 1160
Suh J-Y : 249
Suhonen T : 854
Sumantra M : 890
Suzuki A : 794
Svensson J-E : 1218
Svetlov I L : 660
Svoboda M : 1010
Syed A U : 1000
Szubryt M : 532

T

Tabuchi M : 170
Takahashi S : 370, 775
Takao M : 1028
Tamura O : 65
Tanttari H : 685
Tanzosh J : 338
Thomser C : 887
Tinga T : 575
Toda Y : 123
Toivonen A : 1068
Tokunaga T : 115, 1028
Toporov D : 1231
Treninkov I A : 731, 741
Tschaffon H : 18
Tsukada Y : 759
Turunen E : 949
Tuurna S : 854, 1076

U

Uhlig R : 1112
Urzynicok M :532, 542

V

Vacchieri E : 676, 685, 715, 834
Varis T : 949, 854
Venditti D : 270, 294
Veverkova J : 695
Vilhelmsen T : 1120
Vlasák T : 380
Vodarek V : 522, 1160
Výrostková A : 380

W

Waindich A : 1278
Wang W : 84, 826

X

Xing Y : 1287
Xu C : 866

Y

Yli-Olli S : 1076
Yokokawa T : 769, 794, 938
Yoshida K : 115
Yrjas P : 854
Yuan C : 826

Z

Zaitsev D V : 725, 741
Zhang J : 826
Zeiler G : 27
Zhou L Z : 826, 866
Zieliński A : 390, 400, 412
Zurek J : 1182
Zonfrillo G : 1130

KEYWORDS Index

A

α-Cr phase : 360
AFM : 668
AIN : 206
Abrasion : 1130
Ageing : 196
Aluminium : 1130
Anisotropy of mechanical properties : 660
APU : 925
ATE : 176
Atom probe tomography : 105
Auerkari P : 229
Austenitic alloys : 1020
Austenitic steel : 380, 552

B

Biomass : 986, 1140, 1192
Biomass-coal co-firing : 1000
Blade : 612, 685, 715
Boiler : 412, 854
Boron : 176, 328
Boudary : 328
BSCF : 1278

C

CCS Technology : 1231, 1244, 1260
Ceramic Membranes : 1260
Chlorine corrosion : 854
Chromia : 1056
Co-firing : 1192
Co-Re alloys : 633
Coal : 95, 1192
Coal combustion : 1231
Coarsening : 249, 475
Coatings : 959, 1056, 1020, 1068, 1130, 1202,
Constitutive equation : 834
Copper : 95
Corrosion : 95, 390, 769, 826, 854, 986, 1120, 1140, 1278, 1202, 1218, 1244
COST536 : 27
COST CB2/PB2 : 514
9Cr steels : 270, 294, 308, 328, 348
10Cr steels : 27
12Cr steels : 294, 308
Cr-content : 1046, 348
2%CrMoNiWV : 150
Cracking : 500
Cracking type IV : 435
Creep : 27, 65, 75, 84, 95, 123, 131, 160, 170, 186, 221, 249, 259, 270, 328, 348, 360, 380, 390, 400, 412, 424, 435, 445, 455, 465, 475, 485, 494, 500, 522, 562, 623, 643, 705, 731, 759, 802, 834, 970, 1010, 1028, 1095
Creep failure : 3, 552
Creep resistant steel : 142, 176, 229, 1010
Creep rate modelling : 206
Creep rupture strength : 115
Chromium barrier coatings : 949
CMSX-4 : 802
CSP : 1112
Cyclic oxidation : 1056

D

Damage model : 596
Delta ferrite : 75, 380
Degradation processes : 575, 925, 1010
Deposits : 1218
Dictra simulation : 475
Diffusional creep : 1095
Disk : 612
Dissimilar metal welds : 338
Dissolution mechanism : 826

E

EBSD : 370, 424, 775

ECCC : 970
Elastic inhomogeneity : 759

F

Fast breeder reactor : 890
Fatigue : 596, 844, 1150
Fe-Ni Alloy : 494
Ferritic steels : 123, 65, 131, 176, 186, 435, 370, 465, 1028
Finite Element Method : 1095
Field tests : 1218
Fireside corrosion : 1000, 1192
Fission : 906
Fossil Power Plants : 1260
Friction : 1170
F-SECT : 715

G

γ'-phase : 654, 775, 812
Gas separation : 1260
Gas turbine : 612, 685, 784, 802
Gourgues-Lorenzon A F : 239
Grain boundary : 775
Grain boundary precipitation strengthening : 186
Grade 91 : 160
Greenhouse gas : 3
Growth : 249

H

HA230 : 643, 695
Hardness : 695
HCF : 844
Heat affected zone : 206, 370
Heat flux : 1046
Heat resistant alloy : 3, 65, 196
Heat treatment : 562
High temperature corrosion : 1120

I

IN100 : 775
Inconel 718 : 749
Inco 82 : 338
Inner surface : 1040
Inspection technologies : 890
Insulation effect : 1028
Interconnect : 949
Interfacial energy : 318
Interface dislocation : 725
Intermetallic superalloys : 654
Ion assisted EB PVD : 668
Isothermal ageing : 1010
ITM : 1231

J

K

L

LCF : 844, 705
Laves phase : 186, 360, 475, 485
Life : 685
Life prediction : 1150
Lifing models : 715
Long term durability : 925
Long term exposure : 380
Low cycle fatigue : 596
Low stress creep : 142
LSCF : 1278

M

M23C6 : 186, 485
M6X : 522
MAG : 532
Manufacturing : 890
Maribo Sakskbing : 1120
Martensite : 65, 170, 370
Martensitic alloys : 259, 1020
MEB : 465
Mechanical properties : 75, 390, 400, 412, 514, 575, 866, 1210
Mega component : 284
Metallography : 380
Micro-hardness : 668
Microstructure : 65, 105, 123, 270, 445, 455, 465, 485, 500, 562, 575, 596, 623, 643, 705, 749, 812, 866, 1095
Microstructural evolution : 95, 348, 676, 695, 1101
Microstructural stability : 360, 522
$MnCo_{2-x}Fe_xO_4$ spinel : 949
Modeling : 575, 759, 1192, 1095

N

NDT : 715
Nickel : 123
Ni-base superalloys : 575, 596, 623, 660, 725, 769, 775, 794, 826, 844, 866
Ni-base alloys : 759, 822, 1085, 1112
Ni based filler metal : 338
NiAl Composite : 1210

NiCoCrAlY+Re coating : 676
Nondestructive testing : 552
Notched specimen : 150
Nuclear : 906
Nucleation : 318

O

Orowan mechanism : 1101
Oxidation : 348, 676, 794, 1068, 1076, 1182
Oxycoal : 1231
Oxyfuel : 1076, 1244
Oxygen content : 1046
Oxygen separation : 1278

P

P23 : 229, 500
P91 : 445, 1182
P92 : 75, 424, 455, 532, 562, 1182
PB2 : 542
Perovskite : 1278
Phase diagram : 822
Phases transformation : 676
Pipe butt welds : 532, 542
Power plant : 3, 1068
Precipitate : 196, 249, 562
Precipitation kinetics : 318, 1101
Pressure : 1046
Primary creep : 142

Q

R

Rafting : 759
Recovery : 131
Reheat cracking : 229
Reheaterss : 1000
Rupture ductulity : 131
Ruthenium : 794

S

σ-phase formation : 822
SEM : 668, 633
Shredder light fraction : 1218
Shot-blasting : 95
Simulation : 1101
Single crystal : 612, 660, 705, 731, 769, 802
SOFC : 949, 925
Solid particle erosion : 1085
Solar receiver : 1112
Stationary power generation : 925
Steam : 221, 959, 1056, 1085, 1140, 1170, 1182
Steam oxidation : 3, 1020, 1028, 1120
Steel : 221, 380, 1040, 1068, 1076
Steel 316LN : 522
Steel 9-12% Cr : 105, 318
Steel 9Cr1Mo modified : 115
Steel 11Cr ferritic : 249
Steel 11%CrWCo(Cu)B(V, Nb,Ta) : 84
Steel 18%Cr : 95
Steel P92 : 75
Steel castings : 284
New steel grades : 542
Steel structure stability : 390
Straw-firing : 1120
Stresses : 731
Stress exponent : 142
Stress relaxation testing : 445
Superalloy : 612, 633, 812, 834
Supercritical : 1068
Superheater : 986, 1000, 1140
Surface treatment : 1046
Swirl burner : 1231

T

TEM : 176, 455, 465, 475, 485
TEMPALOY AA-1 : 95
Tensile stress : 160
Tensile testing : 695
Temperature evaluation : 676, 715
Thermal ageing : 695
Thermal barrier coatings : 784, 596
Thermal cycling : 959
Thermal spraying : 949, 854
Thermal stability : 1210
Thermanit MTS 5 Co1 : 514
Thermo-Calc : 633
Thermodynamic calculations : 115
Thermo-mechanical fatigue : 1112
TIG : 532
Titanium : 668
TMF : 1112, 150
Toughness : 123
TP347H : 1120
T-P91 : 1056
Tubes : 1040
Tungsten : 176

U

USC : 1085, 494

V

Vacuum arc : 1040
Viscoplasticity : 1150
VM12 steel : 1182

W

Waste : 1218, 986
Wear : 1170
Welding : 221, 229, 400, 412, 424, 435, 455, 494, 500, 532, 542, 1150
Weld Joint : 370
Withdrawal rate : 866

X

X-ray diffraction : 633, 731

Y

Yield strengh : 131, 160

Z

Z-phase : 170, 206, 259, 270, 294, 308, 522
Z-phase strengthening : 105
Zirconium : 668

1. **Einsatz von multispektralen Satellitenbilddaten in der Wasserhaushalts- und Stoffstrommodellierung – dargestellt am Beispiel des Rureinzugsgebietes**
von C. Montzka (2008), XX, 238 Seiten
ISBN: 978-3-89336-508-1

2. **Ozone Production in the Atmosphere Simulation Chamber SAPHIR**
by C. A. Richter (2008), XIV, 147 pages
ISBN: 978-3-89336-513-5

3. **Entwicklung neuer Schutz- und Kontaktierungsschichten für Hochtemperatur-Brennstoffzellen**
von T. Kiefer (2008), 138 Seiten
ISBN: 978-3-89336-514-2

4. **Optimierung der Reflektivität keramischer Wärmedämmschichten aus Yttrium-teilstabilisiertem Zirkoniumdioxid für den Einsatz auf metallischen Komponenten in Gasturbinen**
von A. Stuke (2008), X, 201 Seiten
ISBN: 978-3-89336-515-9

5. **Lichtstreuende Oberflächen, Schichten und Schichtsysteme zur Verbesserung der Lichteinkopplung in Silizium-Dünnschichtsolarzellen**
von M. Berginski (2008), XV, 171 Seiten
ISBN: 978-3-89336-516-6

6. **Politikszenarien für den Klimaschutz IV – Szenarien bis 2030**
hrsg.von P. Markewitz, F. Chr. Matthes (2008), 376 Seiten
ISBN 978-3-89336-518-0

7. **Untersuchungen zum Verschmutzungsverhalten rheinischer Braunkohlen in Kohledampferzeugern**
von A. Schlüter (2008), 164 Seiten
ISBN 978-3-89336-524-1

8. **Inorganic Microporous Membranes for Gas Separation in Fossil Fuel Power Plants**
by G. van der Donk (2008), VI, 120 pages
ISBN: 978-3-89336-525-8

9. **Sinterung von Zirkoniumdioxid-Elektrolyten im Mehrlagenverbund der oxidkeramischen Brennstoffzelle (SOFC)**
von R. Mücke (2008), VI, 165 Seiten
ISBN: 978-3-89336-529-6

10. **Safety Considerations on Liquid Hydrogen**
by K. Verfondern (2008), VIII, 167 pages
ISBN: 978-3-89336-530-2

11. **Kerosinreformierung für Luftfahrtanwendungen**
von R. C. Samsun (2008), VII, 218 Seiten
ISBN: 978-3-89336-531-9

12. **Der 4. Deutsche Wasserstoff Congress 2008 – Tagungsband**
hrsg. von D. Stolten, B. Emonts, Th. Grube (2008), 269 Seiten
ISBN: 978-3-89336-533-3

13. **Organic matter in Late Devonian sediments as an indicator for environmental changes**
by M. Kloppisch (2008), XII, 188 pages
ISBN: 978-3-89336-534-0

14. **Entschwefelung von Mitteldestillaten für die Anwendung in mobilen Brennstoffzellen-Systemen**
von J. Latz (2008), XII, 215 Seiten
ISBN: 978-3-89336-535-7

15. **RED-IMPACT**
Impact of Partitioning, Transmutation and Waste Reduction Technologies on the Final Nuclear Waste Disposal
SYNTHESIS REPORT
ed. by W. von Lensa, R. Nabbi, M. Rossbach (2008), 178 pages
ISBN 978-3-89336-538-8

16. **Ferritic Steel Interconnectors and their Interactions with Ni Base Anodes in Solid Oxide Fuel Cells (SOFC)**
by J. H. Froitzheim (2008), 169 pages
ISBN: 978-3-89336-540-1

17. **Integrated Modelling of Nutrients in Selected River Basins of Turkey**
Results of a bilateral German-Turkish Research Project
project coord. M. Karpuzcu, F. Wendland (2008), XVI, 183 pages
ISBN: 978-3-89336-541-8

18. **Isotopengeochemische Studien zur klimatischen Ausprägung der Jüngeren Dryas in terrestrischen Archiven Eurasiens**
von J. Parplies (2008), XI, 155 Seiten, Anh.
ISBN: 978-3-89336-542-5

19. **Untersuchungen zur Klimavariabilität auf dem Tibetischen Plateau - Ein Beitrag auf der Basis stabiler Kohlenstoff- und Sauerstoffisotope in Jahrringen von Bäumen waldgrenznaher Standorte**
von J. Griessinger (2008), XIII, 172 Seiten
ISBN: 978-3-89336-544-9

20. **Neutron-Irradiation + Helium Hardening & Embrittlement Modeling of 9%Cr-Steels in an Engineering Perspective (HELENA)**
by R. Chaouadi (2008), VIII, 139 pages
ISBN: 978-3-89336-545-6

21. **in Bearbeitung**

22. **Verbundvorhaben APAWAGS (AOEV und Wassergenerierung) – Teilprojekt: Brennstoffreformierung – Schlussbericht**
von R. Peters, R. C. Samsun, J. Pasel, Z. Porš, D. Stolten (2008), VI, 106 Seiten
ISBN: 978-3-89336-547-0

23. **FREEVAL**
Evaluation of a Fire Radiative Power Product derived from Meteosat 8/9 and Identification of Operational User Needs
Final Report
project coord. M. Schultz, M. Wooster (2008), 139 pages
ISBN: 978-3-89336-549-4

24. **Untersuchungen zum Alkaliverhalten unter Oxycoal-Bedingungen**
von C. Weber (2008), VII, 143, XII Seiten
ISBN: 978-3-89336-551-7

25. **Grundlegende Untersuchungen zur Freisetzung von Spurstoffen, Heißgaschemie, Korrosionsbeständigkeit keramischer Werkstoffe und Alkalirückhaltung in der Druckkohlenstaubfeuerung**
von M. Müller (2008), 207 Seiten
ISBN: 978-3-89336-552-4

26. **Analytik von ozoninduzierten phenolischen Sekundärmetaboliten in *Nicotiana tabacum* L. cv Bel W3 mittels LC-MS**
von I. Koch (2008), III, V, 153 Seiten
ISBN 978-3-89336-553-1

27. **IEF-3 Report 2009. Grundlagenforschung für die Anwendung**
(2009), ca. 230 Seiten
ISBN: 978-3-89336-554-8

28. **Influence of Composition and Processing in the Oxidation Behavior of MCrAlY-Coatings for TBC Applications**
by J. Toscano (2009), 168 pages
ISBN: 978-3-89336-556-2

29. **Modellgestützte Analyse signifikanter Phosphorbelastungen in hessischen Oberflächengewässern aus diffusen und punktuellen Quellen**
von B. Tetzlaff (2009), 149 Seiten
ISBN: 978-3-89336-557-9

30. **Nickelreaktivlot / Oxidkeramik – Fügungen als elektrisch isolierende Dichtungskonzepte für Hochtemperatur-Brennstoffzellen-Stacks**
von S. Zügner (2009), 136 Seiten
ISBN: 978-3-89336-558-6

31. **Langzeitbeobachtung der Dosisbelastung der Bevölkerung in radioaktiv kontaminierten Gebieten Weißrusslands – Korma-Studie**
von H. Dederichs, J. Pillath, B. Heuel-Fabianek, P. Hill, R. Lennartz (2009), Getr. Pag.
ISBN: 978-3-89336-532-3

32. **Herstellung von Hochtemperatur-Brennstoffzellen über physikalische Gasphasenabscheidung**
von N. Jordán Escalona (2009), 148 Seiten
ISBN: 978-3-89336-532-3

33. **Real-time Digital Control of Plasma Position and Shape on the TEXTOR Tokamak**
by M. Mitri (2009), IV, 128 pages
ISBN: 978-3-89336-567-8

34. **Freisetzung und Einbindung von Alkalimetallverbindungen in kohlebefeuerten Kombikraftwerken**
von M. Müller (2009), 155 Seiten
ISBN: 978-3-89336-568-5

35. **Kosten von Brennstoffzellensystemen auf Massenbasis in Abhängigkeit von der Absatzmenge**
von J. Werhahn (2009), 242 Seiten
ISBN: 978-3-89336-569-2

36. **Einfluss von Reoxidationszyklen auf die Betriebsfestigkeit von anodengestützten Festoxid-Brennstoffzellen**
von M. Ettler (2009), 138 Seiten
ISBN: 978-3-89336-570-8

37. **Großflächige Plasmaabscheidung von mikrokristallinem Silizium für mikromorphe Dünnschichtsolarmodule**
von T. Kilper (2009), XVII, 154 Seiten
ISBN: 978-3-89336-572-2

38. **Generalized detailed balance theory of solar cells**
by T. Kirchartz (2009), IV, 198 pages
ISBN: 978-3-89336-573-9

39. **The Influence of the Dynamic Ergodic Divertor on the Radial Electric Field at the Tokamak TEXTOR**
von J. W. Coenen (2009), xii, 122, XXVI pages
ISBN: 978-3-89336-574-6

40. **Sicherheitstechnik im Wandel Nuklearer Systeme**
von K. Nünighoff (2009), viii, 215 Seiten
ISBN: 978-3-89336-578-4

41. **Pulvermetallurgie hochporöser NiTi-Legierungen für Implanat- und Dämpfungsanwendungen**
von M. Köhl (2009), XVII, 199 Seiten
ISBN: 978-3-89336-580-7

42. **Einfluss der Bondcoatzusammensetzung und Herstellungsparameter auf die Lebensdauer von Wärmedämmschichten bei zyklischer Temperaturbelastung**
von M. Subanovic (2009), 188, VI Seiten
ISBN: 978-3-89336-582-1

43. **Oxygen Permeation and Thermo-Chemical Stability of Oxygen Permeation Membrane Materials for the Oxyfuel Process**
by A. J. Ellett (2009), 176 pages
ISBN: 978-3-89336-581-4

44. **Korrosion von polykristallinem Aluminiumoxid (PCA) durch Metalljodidschmelzen sowie deren Benetzungseigenschaften**
von S. C. Fischer (2009), 148 Seiten
ISBN: 978-3-89336-584-5

45. **IEF-3 Report 2009. Basic Research for Applications**
(2009), 217 Seiten
ISBN: 978-3-89336-585-2

46. **Verbundvorhaben ELBASYS (Elektrische Basissysteme in einem CFK-Rumpf) - Teilprojekt: Brennstoffzellenabgase zur Tankinertisierung - Schlussbericht**
von R. Peters, J. Latz, J. Pasel, R. C. Samsun, D. Stolten
(2009), xi, 202 Seiten
ISBN: 978-3-89336-587-6

47. **Aging of ^{14}C-labeled Atrazine Residues in Soil: Location, Characterization and Biological Accessibility**
by N. D. Jablonowski (2009), IX, 104 pages
ISBN: 978-3-89336-588-3

48. **Entwicklung eines energetischen Sanierungsmodells für den europäischen Wohngebäudesektor unter dem Aspekt der Erstellung von Szenarien für Energie- und CO_2 - Einsparpotenziale bis 2030**
von P. Hansen (2009), XXII, 281 Seiten
ISBN: 978-3-89336-590-6

49. **Reduktion der Chromfreisetzung aus metallischen Interkonnektoren für Hochtemperaturbrennstofzellen durch Schutzschichtsysteme**
von R. Trebbels (2009), iii, 135 Seiten
ISBN: 978-3-89336-591-3

50. **Bruchmechanische Untersuchung von Metall / Keramik-Verbundsystemen für die Anwendung in der Hochtemperaturbrennstoffzelle**
von B. Kuhn (2009), 118 Seiten
ISBN: 978-3-89336-592-0

51. **Wasserstoff-Emissionen und ihre Auswirkungen auf den arktischen Ozonverlust**
Risikoanalyse einer globalen Wasserstoffwirtschaft
von T. Feck (2009), 180 Seiten
ISBN: 978-3-89336-593-7

52. **Development of a new Online Method for Compound Specific Measurements of Organic Aerosols**
by T. Hohaus (2009), 156 pages
ISBN: 978-3-89336-596-8

53. **Entwicklung einer FPGA basierten Ansteuerungselektronik für Justageeinheiten im Michelson Interferometer**
von H. Nöldgen (2009), 121 Seiten
ISBN: 978-3-89336-599-9

54. **Observation – and model – based study of the extratropical UT/LS**
by A. Kunz (2010), xii, 120, xii pages
ISBN: 978-3-89336-603-3

55. **Herstellung polykristalliner Szintillatoren für die Positronen-Emissions-Tomographie (PET)**
von S. K. Karim (2010), VIII, 154 Seiten
ISBN: 978-3-89336-610-1

56. **Kombination eines Gebäudekondensators mit H2-Rekombinatorelementen in Leichwasserreaktoren**
von S. Kelm (2010), vii, 119 Seiten
ISBN: 978-3-89336-611-8

57. **Plant Leaf Motion Estimation Using A 5D Affine Optical Flow Model**
by T. Schuchert (2010), X, 143 pages
ISBN: 978-3-89336-613-2

58. **Tracer-tracer relations as a tool for research on polar ozone loss**
by R. Müller (2010), 116 pages
ISBN: 978-3-89336-614-9

59. **Sorption of polycyclic aromatic hydrocarbon (PAH) to Yangtze River sediments and their components**
by J. Zhang (2010), X, 109 pages
ISBN: 978-3-89336-616-3

60. **Weltweite Innovationen bei der Entwicklung von CCS-Technologien und Möglichkeiten der Nutzung und des Recyclings von CO_2**
Studie im Auftrag des BMWi
von W. Kuckshinrichs et al. (2010), X, 139 Seiten
ISBN: 978-3-89336-617-0

61. **Herstellung und Charakterisierung von sauerstoffionenleitenden Dünnschichtmembranstrukturen**
von M. Betz (2010), XII, 112 Seiten
ISBN: 978-3-89336-618-7

62. **Politikszenarien für den Klimaschutz V – auf dem Weg zum Strukturwandel, Treibhausgas-Emissionsszenarien bis zum Jahr 2030**
hrsg. von P. Hansen, F. Chr. Matthes (2010), 276 Seiten
ISBN: 978-3-89336-619-4

63. **Charakterisierung Biogener Sekundärer Organischer Aerosole mit Statistischen Methoden**
von C. Spindler (2010), iv, 163 Seiten
ISBN: 978-3-89336-622-4

64. **Stabile Algorithmen für die Magnetotomographie an Brennstoffzellen**
von M. Wannert (2010), ix, 119 Seiten
ISBN: 978-3-89336-623-1

65. **Sauerstofftransport und Degradationsverhalten von Hochtemperaturmembranen für CO2-freie Kraftwerke**
von D. Schlehuber (2010), VII, 139 Seiten
ISBN: 978-3-89336-630-9

66. **Entwicklung und Herstellung von foliengegossenen, anodengestützten Festoxidbrennstoffzellen**
von W. Schafbauer (2010), VI, 164 Seiten
ISBN: 978-3-89336-631-6

67. **Disposal strategy of proton irradiated mercury from high power spallation sources**
by S. Chiriki (2010), xiv, 124 pages
ISBN: 978-3-89336-632-3

68. **Oxides with polyatomic anions considered as new electrolyte materials for solid oxide fuel cells (SOFCs)**
by O. H. Bin Hassan (2010), vii, 121 pages
ISBN: 978-3-89336-633-0

69. **Von der Komponente zum Stack: Entwicklung und Auslegung von HT-PEFC-Stacks der 5 kW-Klasse**
von A. Bendzulla (2010), IX, 203 Seiten
ISBN: 978-3-89336-634-7

70. **Satellitengestützte Schwerewellenmessungen in der Atmosphäre und Perspektiven einer zukünftigen ESA Mission (PREMIER)**
von S. Höfer (2010), 81 Seiten
ISBN: 978-3-89336-637-8

71. **Untersuchungen der Verhältnisse stabiler Kohlenstoffisotope in atmosphärisch relevanten VOC in Simulations- und Feldexperimenten**
von H. Spahn (2010), IV, 210 Seiten
ISBN: 978-3-89336-638-5

72. **Entwicklung und Charakterisierung eines metallischen Substrats für nanostrukturierte keramische Gastrennmembranen**
von K. Brands (2010), vii, 137 Seiten
ISBN: 978-3-89336-640-8

73. **Hybridisierung und Regelung eines mobilen Direktmethanol-Brennstoffzellen-Systems**
von J. Chr. Wilhelm (2010), 220 Seiten
ISBN: 978-3-89336-642-2

74. **Charakterisierung perowskitischer Hochtemperaturmembranen zur Sauerstoffbereitstellung für fossil gefeuerte Kraftwerksprozesse**
von S.A. Möbius (2010) III, 208 Seiten
ISBN: 978-3-89336-643-9

75. **Characterization of natural porous media by NMR and MRI techniques: High and low magnetic field studies for estimation of hydraulic properties**
by L.-R. Stingaciu (2010), 96 pages
ISBN: 978-3-89336-645-3

76. **Hydrological Characterization of a Forest Soil Using Electrical Resistivity Tomography**
by Chr. Oberdörster (2010), XXI, 151 pages
ISBN: 978-3-89336-647-7

77. **Ableitung von atomarem Sauerstoff und Wasserstoff aus Satellitendaten und deren Abhängigkeit vom solaren Zyklus**
von C. Lehmann (2010), 127 Seiten
ISBN: 978-3-89336-649-1

78. **18th World Hydrogen Energy Conference 2010 – WHEC2010 Proceedings**
Speeches and Plenary Talks
ed. by D. Stolten, B. Emonts (2010)
ISBN: 978-3-89336-658-3

78-1. **18th World Hydrogen Energy Conference 2010 – WHEC2010 Proceedings**
Parallel Sessions Book 1:
Fuel Cell Basics / Fuel Infrastructures
ed. by D. Stolten, T. Grube (2010), ca. 460 pages
ISBN: 978-3-89336-651-4

78-2. **18th World Hydrogen Energy Conference 2010 – WHEC2010 Proceedings**
Parallel Sessions Book 2:
Hydrogen Production Technologies – Part 1
ed. by D. Stolten, T. Grube (2010), ca. 400 pages
ISBN: 978-3-89336-652-1

78-3. **18th World Hydrogen Energy Conference 2010 – WHEC2010 Proceedings**
Parallel Sessions Book 3:
Hydrogen Production Technologies – Part 2
ed. by D. Stolten, T. Grube (2010), ca. 640 pages
ISBN: 978-3-89336-653-8

78-4. **18th World Hydrogen Energy Conference 2010 – WHEC2010 Proceedings**
Parallel Sessions Book 4:
Storage Systems / Policy Perspectives, Initiatives and Cooperations
ed. by D. Stolten, T. Grube (2010), ca. 500 pages
ISBN: 978-3-89336-654-5

78-5. **18th World Hydrogen Energy Conference 2010 – WHEC2010 Proceedings**
Parallel Sessions Book 5:
Stategic Analysis / Safety Issues / Existing and Emerging Markets
ed. by D. Stolten, T. Grube (2010), ca. 530 pages
ISBN: 978-3-89336-655-2

78-6. **18th World Hydrogen Energy Conference 2010 – WHEC2010 Proceedings**
Parallel Sessions Book 6:
Stationary Applications / Transportation Applications
ed. by D. Stolten, T. Grube (2010), ca. 330 pages
ISBN: 978-3-89336-656-9

78 Set (complete book series)

18th World Hydrogen Energy Conference 2010 – WHEC2010 Proceedings
ed. by D. Stolten, T. Grube, B. Emonts (2010)
ISBN: 978-3-89336-657-6

79. **Ultrafast voltex core dynamics investigated by finite-element micromagnetic simulations**
by S. Gliga (2010), vi, 144 pages
ISBN: 978-3-89336-660-6

80. **Herstellung und Charakterisierung von keramik- und metallgestützten Membranschichten für die CO_2-Abtrennung in fossilen Kraftwerken**
von F. Hauler (2010), XVIII, 178 Seiten
ISBN: 978-3-89336-662-0

81. **Experiments and numerical studies on transport of sulfadiazine in soil columns**
by M. Unold (2010), xvi, 115 pages
ISBN: 978-3-89336-663-7

82. **Prompt-Gamma-Neutronen-Aktivierungs-Analyse zur zerstörungsfreien Charakterisierung radioaktiver Abfälle**
von J.P.H. Kettler (2010), iv, 205 Seiten
ISBN: 978-3-89336-665-1

83. **Transportparameter dünner geträgerter Kathodenschichten der oxidkeramischen Brennstoffzelle**
von C. Wedershoven (2010), vi, 137 Seiten
ISBN: 978-3-89336-666-8

84. **Charakterisierung der Quellverteilung von Feinstaub und Stickoxiden in ländlichem und städtischem Gebiet**
von S. Urban (2010), vi, 211 Seiten
ISBN: 978-3-89336-669-9

85. **Optics of Nanostructured Thin-Film Silicon Solar Cells**
by C. Haase (2010), 150 pages
ISBN: 978-3-89336-671-2

86. **Entwicklung einer Isolationsschicht für einen Leichtbau-SOFC-Stack**
von R. Berhane (2010), X, 162 Seiten
ISBN: 978-3-89336-672-9

87. **Hydrogen recycling and transport in the helical divertor of TEXTOR**
by M. Clever (2010), x, 172 pages
ISBN: 978-3-89336-673-6

88. **Räumlich differenzierte Quantifizierung der N- und P-Einträge in Grundwasser und Oberflächengewässer in Nordrhein-Westfalen unter besonderer Berücksichtigung diffuser landwirtschaftlicher Quellen**
von F. Wendland et. al. (2010), xii, 216 Seiten
ISBN: 978-3-89336-674-3

89. **Oxidationskinetik innovativer Kohlenstoffmaterialien hinsichtlich schwerer Lufteinbruchstörfälle in HTR´s und Graphitentsorgung oder Aufarbeitung**
von B. Schlögl (2010), ix, 117 Seiten
ISBN: 978-3-89336-676-7

90. **Chemische Heißgasreinigung bei Biomassenvergasungsprozessen**
von M. Stemmler (2010), xv, 196 Seiten
ISBN: 978-3-89336-678-1

91. **Untersuchung und Optimierung der Serienverschaltung von Silizium-Dünnschicht-Solarmodulen**
von S. Haas (2010), ii, 202 Seiten
ISBN: 978-3-89336-680-4

92. **Non-invasive monitoring of water and solute fluxes in a cropped soil**
by S. Garré (2010), xxiv, 133 pages
ISBN: 978-3-89336-681-1

93. **Improved hydrogen sorption kinetics in wet ball milled Mg hydrides**
by L. Meng (2011), II, 119 pages
ISBN: 978-3-89336-687-3

94. **Materials for Advanced Power Engineering 2010**
ed. by J. Lecomte-Beckers, Q. Contrepois, T. Beck and B. Kuhn
(2010), 1327 pages
ISBN: 978-3-89336-685-9

Energie & Umwelt / Energy & Environment
Band / Volume 94
ISBN 978-3-89336-685-9

JÜLICH
FORSCHUNGSZENTRUM